

Batteries

2017 Annual Progress Report

Vehicle Technologies Office

(This page intentionally left blank)

Disclaimer

This report was prepared as an account of work sponsored by an agency of the United States government. Neither the United States government nor any agency thereof, nor any of their employees, makes any warranty, express or implied, or assumes any legal liability or responsibility for the accuracy, completeness, or usefulness of any information, apparatus, product, or process disclosed or represents that its use would not infringe privately owned rights. Reference herein to any specific commercial product, process, or service by trade name, trademark, manufacturer, or otherwise does not necessarily constitute or imply its endorsement, recommendation, or favoring by the United States government or any agency thereof. The views and opinions of authors expressed herein do not necessarily state or reflect those of the United States government or any agency thereof.

Acknowledgements

The projects reported in this report were supported through various contracts funded by the U.S. Department of Energy, Vehicle Technologies Office. A list of contributing authors appears in the sections for specific projects in this report.

Acronyms

AABC	Advanced Automotive Batteries Conference
ABA	American Bar Association
ABDT	ANSYS Battery Design Tool
ABMR	Advanced Battery Materials Research
ABR	Applied Battery research
ABRT	Applied Battery Research for Transportation
ACB	Acetylene Carbon Black
ACS	American Chemical Society
ADF-STEM	Annular dark-field – scanning transmission electron microscope
AERTC	Advanced Energy Research and Technology Center (at Stony Brook University)
AFM	Atomic force microscopy
AIBN	Azobisisobutyronitrile
AIMD	<i>Ab initio</i> molecular dynamics
AIRSS	<i>Ab initio</i> random structure searching
ALABC	Advanced Lead Acid Battery Consortium
ALD	Atomic layer deposition
ALS	Advanced Light Source (facility)
AMR	Annual Merit Review
ANL	Argonne National Laboratory
APS	Advanced Photon Source (laboratory)
ARC	Accelerated rate calorimetry
ARL	Army Research Laboratory
ASI	Area-specific impedance
ASR	Area-specific resistance
ATR	Attenuated total reflection

ATR-FTIR	Attenuated total reflection-Fourier transform infrared spectroscopy
ATR-IR	Attenuated total reflection- infrared spectroscopy
BCC	Body-centered cubic
BCDI	Bragg Coherent Diffraction Imaging
BEAT	Battery Environmental Assessment Tool
BET	Brunauer, Emmett, and Teller (surface area analysis)
BEV	Battery electric vehicle
BF	Bright field
BLI	Beyond Lithium-ion
BMF	Battery manufacturing facility
BMR	(Advanced) Battery Materials Research (program)
BMS	Battery management system
BNL	Brookhaven National Laboratory
BOL	Beginning of life
BP	Budget period
BSD	Berkeley Software Distribution
BSF	Battery scaling factor
BTC	Battery Technology Center
BTFE	Bis(2,2,2-trifluoroethyl) ether
BYU	Brigham Young University
CABS	Consortium for Advanced Battery Simulation
CAD	Computer-aided Design
CAEBAT	Computer-aided engineering of batteries
CAFE	Corporate Average Fuel Economy
CAMP	Cell analysis, modeling, and prototyping (facility)
CARB	California Air Resource Board

CBA	Carbon/binder additive (geometry)
CCD	Charge-coupled device
CCVD	Catalytic chemical vapor deposition
CDFEM	Conformal decomposition finite element method
CE	Coulombic efficiency
CEI	Cathode electrolyte interfaces
CERC	Clean Energy research Center
CF	Carbon fabric
CFM	Complex framework materials
CFN	Center for Functional Nanomaterials
CID	Current interrupt device
CIF	Crystallographic information file
CIP	Contact ion pair
CLP	Cross-linked polymer
CMC	Carboxymethyl cellulose
CNF	Carbon nanofibers
CNT	Carbon nano-tubes
COTS	Commercial-off-the-shelf
CP	Cross-polarization
CPDB	2-cyano-2-propyl benzodithioate
CPE	Constant phase element
CPI	Compact Power Inc.
CPM	Constant potential method
CPMEA	Cross-linked poly(ethylene glycol) methyl ether acrylate
CPS	Counts per second
CRADA	Cooperative research and development agreement

CS	Charge-sustaining
CSE	Chemical Sciences and Engineering (at ANL)
CSWG	Crash Safety Work Group
CTQ	Critical to quality (criteria)
CV	Cyclic voltammetry
CY	Calendar year
DCB	Dichlorobenzene
DCR	Direct current resistance
DD	Deep-dive
DDSA	Directly doped sulfur architecture
DEC	Diethyl carbonate
DEGDBE	Diethyleneglycol dibutylether
DEGDME	Glycol dimethyl ether
DEIM	Discrete empirical interpolation method
DEMS	Differential electrochemical mass spectrometry
DES	Deep eutectic solvent
DFEC	(4R,5S)-4,5-Difluoro-1,3-dioxolan-2-one
DFT	Density function theory
DFTB	Density functional-based tight binding
DI	De-ionized (water)
DMC	Dimethyl carbonate
DME	Dimethyl ether
DMF	Dimethylformamide
DMSO	Dimethylsulfoxide
DNP	Dynamic nuclear polarization
DOD	Depth-of-discharge

DOE	Department of Energy
DOL	Dioxolane
DOS	Density of state
DOT/NHTSA	Department of Transportation/National Highway Traffic Safety Administration
DP	Dry process
DPA	Destructive physical analysis
DPP	Dynamic particle-packing (model)
DSC	Differential scanning calorimetry
DX	(ANSYS) DesignXplorer
EADL	Electrochemical Analysis and Diagnostic Laboratory (at ANL)
EB	Electron beam
EC	Ethylene carbonate
ECM	Equivalent circuit model
ECS	Electrochemical Society
ED	Electrode domain
EDAX	Energy dispersive x-ray spectroscopy mapping
EDM	Electrode-domain model
EDS	Energy dispersive spectroscopy
EDV	Electric Drive Vehicle
EDX	Energy-dispersive x-ray (spectroscopy)
EDXRD	Energy Dispersive X-ray Diffraction
EELS	Electron energy loss spectroscopy
EERE	Energy Efficiency and Renewable Energy (DOE Office)
EES	Electrochemical energy storage
EGDEG/EGDGE	Ethylene glycol diglycidyl ether
EIS	Electrochemical impedance spectroscopy

EM	Electro-mechanical
EMSL	Environmental Molecular Sciences Laboratory
EOL	End of life
EPA	Environmental Protection agency
EPEAT	Electronic product environmental assessment tool
EPR	Electron paramagnetic resonance
EQCM	Electrochemical quartz crystal microbalance
ETEM	Environmental transmission electron microscope
ETSMC	Ethyl (trimethylsilyl)methyl carbonate
EUCAR	European Council for Automotive Research and Development
EV	Electric vehicle
EVI	Electric vehicle initiative
EVSE	Electric vehicle supply equipment
EXAFS	Extended X-ray absorption fine structure
FCE	First cycle efficiency
FEA	Finite element analysis
FEC	Fluoro ethylene carbonate
FEM	Finite element method
FFT	Fast Fourier-transform
FIB	Focused ion beam
FIR	First cycle irreversible loss
FITR/FTIR	Fourier-transform infrared spectroscopy
FOA	Federal opportunity announcement
FOM	Figure of merit
FOME	Energy figure of merit
FOMP	Power figure of merit

FSI	Bis(fluorosulfonyl)imide (anion)
FSP	Flame spray pyrolysis
FTIR, FT-IR	Fourier-transform infra-red spectroscopy
FWHM	Full width at half maximum
FY	Fiscal year
GAFF	General AMBER Force Field
GB	Grain boundary
GC	Gas chromatography
GGA	Generalized gradient approximation
GHG	Green-house gases
GITT	Galvanostatic intermittent titration
GPC	Gel permeation chromatography
GPE	Gel polymer electrolyte
GREET	Greenhouse gas regulated energy and emissions and transpiration
GSE	Garnet solid electrolyte
HAADF	High-angle annular dark-field
HE/HV	High energy/high voltage
HEHV	High energy high voltage
HEMR	High-energy mechanochemical reduction
HEV	Hybrid electric vehicle
HEXRD	High energy x-ray diffraction
HF	Hydrofluoric acid
HFDEC	Bis (2,2,2 trifluoroethyl) carbonate
HFE	Hydrofluoroether
HFEC	Bis (2,2,2 trifluoroethyl) carbonate
HFIP	Hexafluoroisopropanol

HFP	Hexafluoropropylene
HGN	Hollow graphene nanocages
HMDS	Hexamethyldisilazane
HMPA	Hexamethylphosphoramide
HOMO	Highest occupied molecular orbital
HOPG	Highly oriented pyrolytic graphite
HP	High power
HPC	High performance computing
HPLC	High-performance liquid chromatography
HPLC	High Pressure Liquid Chromatography
HPPC	Hybrid pulse power characterization
HQ	Hydro-Québec
HRTEM	High-resolution transmission electron microscopy
HT	High temperature
HV	High voltage
HXN	Hard x-ray nano-probe
IAPG	Interagency advanced power group
IBA	International battery materials association
ICE	Internal combustion engine
ICEV	Internal combustion engine vehicle
ICL	Initial capacity loss
ICP	Inductively coupled plasma
ICP-AES	Inductively-coupled plasma-atomic emission spectroscopy
ICP-MS	Inductively-coupled plasma-mass spectroscopy
ID	Intensity of the carbon D-band
IEA	International Energy Agency

IEEE	Institute of Electrical and Electronics Engineers
IHTC	International Heat Transfer Conference
ILA	International Lead Association
INL	Idaho National Laboratory
IPA	Isopropyl alcohol
IR	Infra-red
IRCL	Irreversible capacity loss
ISC	Internal short circuit
JACS	Journal of the American Chemical Society
JCI	Johnson Controls, Incorporated
JES	Journal of the Electrochemical Society
JKR	Johnson-Kendall-Roberts (models)
KPFM	Kelvin probe force microscopy
LBNL	Lawrence Berkeley National Laboratory
LCA	Life cycle analysis
LCD	Levelized cost of driving
LCO	Lithium cobalt oxide
LEDC	Lithium ethylene dicarbonate
LEED	Low energy electron diffraction
LEX-RS	Li-excess disordered (rocksalt) transition metal oxide
LFMO	$\text{Li}_2\text{FeMn}_3\text{O}_8$
LFO	Li_5FeO_4
LFP	Li-iron phosphate
LIB	Lithium-ion battery
LIC	Lithium-ion conducting
LIPON	Lithium phosphorous oxy-nitride

LLATO	$\text{Li}_{0.33}\text{La}_{0.56}\text{Al}_{0.005}\text{Ti}_{0.995}\text{O}_3$
LLCZN	$\text{Li}_{6.8}\text{La}_{2.95}\text{Ca}_{0.05}\text{Zr}_{1.75}\text{Nb}_{0.25}\text{O}_{12}$
LLS	Layered-layered spinel
LLTO	$(\text{Li},\text{La})\text{TiO}_3$
LLZ	$\text{Li}_7\text{La}_3\text{Zr}_2\text{O}_{12}$
LLZO	Lithium lanthanum zirconate
LLZT	$\text{Li}_{6.5}\text{La}_3\text{Zr}_{1.5}\text{Ta}_{0.5}\text{O}_{12}$
LMNO	Lithium manganese nickel oxide
LMO	Lithium manganese oxide
LMR	Lithium manganese-rich (layered cathode material)
LNMO	$\text{LiNi}_{0.5}\text{Mn}_{0.5}\text{O}_2$
LNRO	$\text{Li}_{1.2}\text{Ni}_{0.2}\text{Mn}_{0.6}\text{O}_2$
LNTMO	Li-Ni-Ti-Mo oxide
LNTiO	Li-Ni-Ti oxide
LOESS	Locally weighted scatter-plot smoother (regression model)
LPR	Linear polarization resistance
LPS	B- Li_3PS_4
LR	Liquids reflectometer
LS	Low spin
LSB	Lithium sulfur batteries
LSHT/LSTH	$\text{Li}_{1/8}\text{Sr}_{7/16}\text{Hf}_{1/9}\text{Ta}_{1/4}\text{O}_{32}$
LSV	Linear scanning voltammetry
LT	Low temperature
LTO	Lithium titanate, $\text{Li}_4\text{Ti}_5\text{O}_{12}$
LTSR	Low temperature solid-state reduction
LUMO	Lowest unoccupied molecular orbital

MACD	Maximum allowable current density
MAS	Magic angle spinning
MCMB	Mesocarbon micro beads
MD	Molecular dynamics
MERF	Materials Engineering Research Facility
MFCA	Multifunctional cathode additive
MIT	Massachusetts Institute of Technology
MLD	Molecular layer deposition
MPEGA	Methoxy-polyethylene glycol acrylate
MRI	Magnetic resonance imaging
MRL	Manufacturing Readiness Level
MRS	Materials Research Society
MSMD	Multi-scale, multi-domain
MSU	Michigan State University
MTMSMC	Methyl (trimethylsilyl)methyl carbonate
MW	Molecular weight
NASA	National Aeronautics and Space Administration
NCA	$\text{LiNi}_{0.8}\text{Co}_{0.15}\text{Al}_{0.05}\text{O}_2$
NCM	$\text{Li}_{1+w}[\text{Ni}_x\text{Co}_y\text{Mn}_z]_{1-w}\text{O}_2$
NCO	Nickel cobalt oxide
NCSU	North Carolina State University
NDI	Naphthalene diimide
NEB	Nudged elastic band (method)
NETL	National Energy Technology Laboratory
NHTSA	National Highway Transportation Safety Administration
NIST	National Institute of Standards and Technology

NMC	$\text{LiNi}_{1/3}\text{Co}_{1/3}\text{Mn}_{1/3}\text{O}_2$
NMF	Non-negative matrix factorization
NMO	Nickel-manganese-oxide
NMP	N-methylpyrrolidone
NMR	Nuclear magnetic resonance
NP	Nano Particles
NR	Neutron reflectometry
NREL	National Renewable Energy Laboratory
NSLS	National Synchrotron Light Source
NSOM	Near-field scanning optical microscopy
OCV	Open circuit voltage
OEM	Original equipment manufacturer
OPLS	Optimized Potential for Liquid Simulation
ORNL	Oak Ridge National Laboratory
ORR	Oxygen reduction reaction
OS	Organic solvent
PAA	Polyacrylic acid
PAN	Polyacrylonitrile
PARC	Palo Alto Research Center
PAW	Projected augmented wave
PBE	Ethylene glycol ester
PDF	Pair density function
PDI	Polydispersity index
PDMS	Polydimethylsiloxane
PE	Polyethylene

PEFM	Poly(2,7-9,9-dioctylfluorene-co-2,7-9,9-(di(oxy-2,5,8-trioxadecane)) fluorine-co-2,7-fluorenone-co-2,5-1-methylbenzoic ester)
PEG	Polyethylene glycol
PEGDA	Poly(ethylene glycol) diacrylate
PEGDMA	Poly(ethylene glycol) dimethacrylate
PEO	Polyethyleneoxide
PES	Prop-1-ene-1,3-sultone
PET	Polyethylene terephthalate
PEV	Plug-in electric vehicle
PFG-NMR	Pulsed field gradient nuclear magnetic resonance
PFPE	Perfluoropolyether
PHEV	Plug-in hybrid electric vehicle
PI	Principal investigator
PNNL	Pacific Northwest National Laboratory
PPE	Personal protective equipment
PS	Polystyrene
PSD	Pore size distribution
PTA	Polysulfide trapping agent
PTF	Post-test facility
PTFE	Poly(tetrafluoroethylene) (cathode)
PVAE	Poly(vinyl alcohol-co-ethylene)
PVD	Physical vapor deposition
PVDF	Poly(vinylidene fluoride)
R&D	Research and Development
RAFT	Reversible addition–fragmentation chain transfer (polymerization)
RDE	Rotating disk electrode

RE	Reference electrode
RH	Relative humidity
RIXS	Resonant inelastic x-ray scattering
ROM	Reduced-order model
RPT	Reference performance test
RT	Room temperature
RVE	Representative volume element
SAE	Society of Automotive Engineers
SAED	Selected area electrode diffraction
SBIR	Small Business Innovation Research
SBR	Styrene-butadiene rubber (binder)
SBU	Stony Brook University
SCW	Supercritical water
SDS	Safety data sheet
SE	Solid electrolyte
SEET	Structural, electrical, electrochemical and thermal
SEI	Solid electrolyte interphase
SEM	Scanning electron microscopy
SFM	Sulfur infiltrated framework
SHE	Self-healing elastomer
SHP	Self-healing polymer
SIA	Isomorphous alloy
SIB	Sodium ion batteries
SIMS	Secondary ion mass spectrometry
SLAC	Stanford acceleration laboratory
SLD	Scattering length density

SLDV	Scanning laser doppler vibrometer
SLMP	Stabilized lithium metal powder
SLP	Single layer pouch (cells)
SNL	Sandia National Laboratories
SNS	Spallation Neutron Source
SOA	State of the art
SOC	State of charge
SOFC	Solid oxide fuel cell
SOW	Statement of work
SP	Silly Putty
SPH	Smooth particle hydrodynamics
SQS	Special quasi-random structures
SS	Solid-state
SSE	Solid-state electrolyte
SSIP	Solvent-separated ion pair
SSRL	Stanford Synchrotron Radiation Lightsource
SSRM	Solvent-separated ion pair
STDEV	Standard Deviation
STEM	Scanning transmission electron microscopy
STFSI	(4-styrenesulfonyl) (trifluoromethanesulfonyl)imide
STL	StereoLithography
STM	Scanning tunneling microscope
STO	Strontium titanate
STTR	Small Business Technology Transfer Program
STXM	Scanning transmission X-ray microscopy
SUNY	State University of New York

SXAS	Soft x-ray absorption
SXRD	Synchrotron X-ray diffraction
T2M	Technology-to-market
TAC	Technical Advisory Committee
TAMU	Texas A&M University
TBC	Thermal boundary conductance
TBD	To-be-decided
TC	Thermocouple
TCD	Thermal Conductivity Detector
TCL	Tool Command Language
TCP	Technology collaboration program
TD	Transverse direction
TEGDME	Tetraethyleneglycoldimethyl
TEM	Transmission electron microscopy
TERS	Tip-enhanced Raman spectroscopy
TES	Tender-energy x-ray absorption spectroscopy
TEY	Total electron yield
TFSI	Bistriflimide (anion)
TFY	Total fluorescence yield
TGA	Thermal gravimetric analysis
THF	Tetrahydrofuran
TM	Transition metal
TMA	Tri-methyl aluminum
TMS	Trimethylsilyl
TMSF	Trimethylsilyl fluoride
TOF-SIMS	Time-of-flight SIMS

TR-XAS	TR-XRD and absorption
TR-XRD	Time-resolved X-ray diffraction
TTFP	Tris(2,2,2,-trifluoroethyl)phosphite
TVR	Taylor vortex reactor
TXM	Transmission X-ray microscopy
UCL	University College, London
UCSD	University of California, San Diego
UHMW	Ultra-high molecular weight
UHMWPE	Ultra-high molecular weight polyethylene
UHV	Ultra-high vacuum
UI	User interface
UM	University of Michigan
UMD	University of Maryland
UMERC	University of Maryland, Energy Research Center
UPL	Upper potential limit
USABC	United States Advanced Battery Consortium
USCAR	United States Council for Automotive Research
USDRIVE	Driving Research and Innovation for Vehicle efficiency and Energy sustainability
USGS	United States Geological Survey
UTA	University of Texas, Austin
UV	Ultraviolet
UV-VIS	Ultraviolet–visible
UW	University of Washington
VASP	Vienna <i>ab initio</i> Simulation Package
VC	Vinylene carbonate
VGCF	Vapor grown carbon fiber

VIBE	Virtual integrated battery environment
VOC	Volatile organic compounds
VTK	Visualization tool kit
VTO	Vehicle Technologies Office
WP	Wet polishing
WPI	Worcester Polytechnic Institute
WVU	West Virginia University
XANES	X-ray absorption near edge structure
XAS	X-ray absorption spectroscopy
XCH	Excited electron and core hole (approach)
XCT	X-ray computed tomography
XFC	Extreme fast charging
XPD	X-ray powder diffraction
XPS	X-ray photoelectron spectroscopy
XRD	X-ray diffraction
XRF	X-ray fluorescence (microscopy)
XRR	X-ray reflectivity

Executive Summary

Introduction

The Vehicle Technologies Office (VTO) of the Department of Energy (DOE) conducts research and development (R&D) on advanced transportation technologies that would reduce the nation's use of imported oil and reduce harmful emissions. Technologies supported by VTO include electric drive components such as advanced energy storage devices (batteries and ultracapacitors), power electronics and electric drive motors, advanced structural materials, energy efficient mobility systems, advanced combustion engines, and fuels. VTO is focused on funding early stage, high-reward/high-risk research to improve critical components needed for more fuel efficient (and consequently, also cleaner-operating) vehicles.

One of the major VTO objectives is to enable U.S. innovators rapidly develop the next generation of technologies that achieve the cost, range, and charging infrastructure necessary for the widespread adoption of PEVs. An important prerequisite for the electrification of the nation's light duty transportation sector is development of more cost-effective, longer lasting, and more abuse-tolerant plug-in electric vehicle (PEV) batteries. One of the ultimate goals of this research, and currently a strong trend in vehicle electrification, is an EV which can provide the full driving performance, convenience, and price of an internal combustion engine (ICE) vehicle. To achieve this, VTO has established the following overarching goal:

VTO supports early-stage R&D to identify new battery chemistry and cell technology with the potential to reduce the cost of electric vehicle batteries by more than half to less than \$100/kWh and increase the range to 300 miles while decreasing the charge time to less than 15 minutes by 2028.

The cost target supports a levelized cost of driving (LCD) of a 300-mile BEV at \$0.28/mile, which is comparable to that for future ICEs at \$0.27/mile. The ultimate cost goal for a 300-mile BEV battery is \$80/kWh, which achieves an LCD of \$0.26/mile.

During the past year, VTO continued R&D support of PEVs such as plug-in hybrid vehicles, extended range electric vehicles, and all-electric vehicles (EVs), as well as some conventional hybrid vehicle technologies, particularly the 12 volt start/stop hybrid. VTO competitively awards funding through funding opportunity announcement (FOA) selections, and projects are fully funded through the duration of the project in the year that the funding is awarded. Directly-funded work at the national laboratories (also awarded competitively through a lab-call process) is subject to change based on annual appropriations.

Stakeholders for the VTO R&D activities include universities, national laboratories, other government agencies and members of industry including automakers, battery manufacturers, material suppliers, component developers, private research firms, and small businesses. VTO works with key U.S. automakers through the United States Council for Automotive Research (USCAR) – an umbrella organization for collaborative research consisting of the Fiat Chrysler LLC, the Ford Motor Company, and the General Motors Company. Collaboration with automakers through the partnership known as U.S. Driving Research and Innovation for Vehicle Efficiency and Energy Sustainability (US DRIVE) attempts to enhance the relevance and the potential for success of the research portfolio.

This document summarizes the progress of VTO battery R&D projects supported during the fiscal year 2017 (FY 2017). In FY 2017, the DOE VTO battery R&D funding was approximately \$101 million. Its R&D focus was on the development of high-energy batteries for PEVs and very high-power devices for hybrid vehicles. The electrochemical energy storage roadmap (which is found at the EERE Roadmap web page <http://energy.gov/eere/vehicles/downloads/us-drive-electrochemical-energy-storage-technical-team-roadmap>) describes ongoing and planned efforts to develop electrochemical storage technologies for PEVs. To advance battery technology to improve the market penetration of PEVs and hybrid vehicles, the program focuses on overcoming specific technical barriers typically related to the battery's cost, performance, life (both calendar life and cycle life), its tolerance to abusive conditions, and its recyclability/sustainability. Various battery chemistries are being investigated with that aim.

VTO R&D has lowered the cost of EV battery packs to the value of \$219/kWh in 2017, representing an ~80% reduction since 2008, yet even further cost reduction in high-energy batteries is necessary for EVs to achieve head-to-head cost competitiveness (without Federal subsidies). In addition, today's batteries also need improvements in such areas as their ability to accept charging at a high rate – termed extreme fast charging (XFC) where this rate approaches 400 kW; and a better ability to operate at low temperatures – so as to enable EVs an all-weather performance and “refueling” convenience similar to ICE vehicles. Research into “enhanced Li-ion” batteries which would provide such functionalities is one of the R&D focus areas. For even further gains in energy density and reduction in cost, VTO is researching both “next gen” chemistries (which employ an alloy anode and/or a high voltage cathode) and beyond lithium-ion (BLI) chemistries (which can employ a lithium metal anode). Current cycle and calendar lives of next gen and BLI chemistries are well short of the goals set for EVs – most cells employing a significant amount of silicon provide only 500 deep discharge cycles and less than two years of calendar life.

To quantify the improvements needed to accelerate large-scale adoption of PEVs and HEVs, performance and cost targets have been established. Some sample targets for EV batteries are shown in Table ES- 1, both at cell level and at system (pack) level.

Table ES- 1: Subset of EV requirements for batteries and cells.

Energy Storage Goals (by characteristic)	Pack Level	Cell Level
Cost @ 100k units/year (kWh = useable energy)	\$100/kWh*	\$75/kWh*
Peak specific discharge power (30s)	470 W/kg	700 W/kg
Peak specific regen power (10s)	200 W/kg	300 W/kg
Useable specific energy (C/3)	235 Wh/kg*	350 Wh/kg*
Calendar life	15 years	15 years
Deep discharge cycle life	1000 cycles	1000 cycles
Low temperature performance	>70% useable energy @C/3 discharge at -20°C	>70% useable energy @C/3 discharge at -20°C
	*Current commercial cells and packs not meeting the goal	

The batteries R&D effort includes multiple activities, ranging from focused fundamental materials research to prototype battery cell development and testing. It includes, as described above, R&D on BLI and next-gen materials and cell components, as well as that on synthesis and design, and ways to address the high cost. Those activities are organized into several inter-related (and complementary) program elements:

- Advanced Cell and Battery Research and Development
- Advanced Materials Research
- Battery Testing, Analysis, and Design
- Recycling and Sustainability

A short overview of work under each of those program elements is given below.

Advanced Cell and Battery Research and Development

The *Advanced Cell and Battery Research and Development* activity focuses on the development of robust battery cells and modules to significantly reduce battery cost, increase life, and improve performance. This work mainly spans the following general areas:

- United States Advanced Battery Consortium (USABC)-supported battery development & materials R&D (15 projects)
- Advanced processing (nine projects)
- Computer-aided engineering for batteries (CAEBAT) (eight projects)
- High-energy, long-life lithium-ion battery (one project)
- Extreme fast-charging (one project)
- Small business innovative research (SBIR) (multiple Phase I and Phase II projects)

Chapter I of this report describes projects under the *Advanced Cell and Battery Research and Development* activity. A substantial part of this effort occurs in close partnership with the automotive industry, through a cooperative agreement with the USABC. In FY 2017, via the USABC, VTO supported 15 cost-shared contracts with developers to further the development of PEV and HEV batteries and battery components. The estimated DOE share of those USABC contracts (over the life of the contracts) is approximately \$25M. These include lower cost, high energy lithium battery technology being developed by **Envia Systems, Amprius, Inc., LG Chem Power, Inc., Farasis Energy and 24M**. As an example, Figure ES- 1 shows an Envia 11 Ah capacity pouch cell undergoing teardown and failure analysis. The development of lithium-ion battery technology for 12V Start-stop microhybrid batteries is being supported through R&D efforts with **Saft and LG Chem Power**. Additional battery technologies are also supported, including two separator technologies being developed by **Celgard**, and **Entek Membranes**, and high capacity anode materials by **Sinode Systems**. Various battery manufacturing, recycling, benchmarking activities are funded at other industry partners (including those at **Farasis Energy, NOHMs Technologies, PPG, Worcester Polytechnic Institute, and FEV**).



Figure ES- 1. Images of an 11 Ah capacity pouch cell undergoing teardown and failure analysis

In addition to the USABC projects listed above, VTO also supports battery and material supplier R&D projects which are funded/administered by the National Energy Technology Laboratory (NETL). This report contains an account of nine such *advanced processing* projects. Most strategies for increasing the performance and reducing the cost of lithium-ion batteries have focused on novel battery chemistries, material loading modifications, and increasing electrode thickness. Increasing electrode thickness is a known approach for increasing energy density (and in turn, the overall cell capacity). However, practical thicknesses are constrained by ionic transport limitations that occur with the increased thickness, limiting the cell power. The

Palo Alto Research Center's (PARC) co-extrusion (CoEx) technology is aimed at enabling a substantial improvement in the performance of thick electrodes for lithium-ion chemistries. The project aims to demonstrate CoEx printing technology at EV-relevant scales by assembling large (14 Ah) pouch cells. In another project, conducted by **Group14**, the objective is to develop a new low-cost production process capable of mass-producing silicon-based lithium ion battery anode material that can reach 1000 mAh/g after 1000 cycles and with a cell level cost target of < \$125/kWh, validate performance in LIB full cells, and prove the cost basis at pilot scale. Also, a **Miltec** project was recently completed in which a commercial scale system (entitled Miltec CX400) was designed utilizing flexographic printing technology and ultraviolet (UV) curable binder to take advantages of UV technology (which include cost saving, performance improvement, and enhanced safety). The remaining advanced processing projects include another **Miltec** project aimed at UV curing to reduce the manufacturing cost of LIB electrodes; producing low-cost, water-based electrodes via electrodeposition (by **PPG**); a solvent-less processing of thick electron-beam (EB) cured LIB cathodes at **ORNL**; developing novel electrolytes for high-voltage batteries (at **Silatronix**); developing a scalable process to fabricate porous silicon (at **Navitas**) (Figure ES- 2); and electrode processing for lithium-ion batteries (at **ORNL**). The estimated value of those advanced processing projects (over project lifetime) is approximately \$16M.

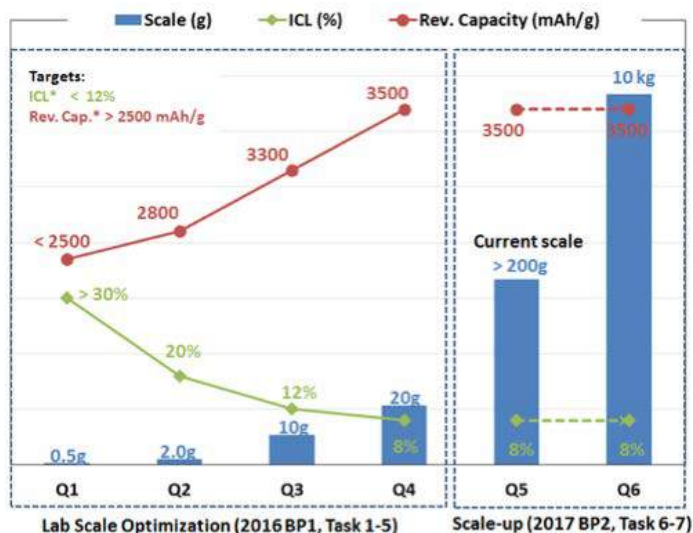


Figure ES- 2. Capacity and ICL both improved during Navitas' material scale up procedures

The advanced cell and battery research activity also includes several projects categorized under the Computer Aided Engineering for Electric-Drive Vehicle Batteries (CAEBAT) Program – which recently evolved into the **Advanced Computer Aided Battery Engineering Consortium** and which seeks to enhance/validate the predictive capability of computationally efficient electrochemical models for thick electrode designs for lower battery cost and increased energy density and mechanical/electrochemical/thermal simulation models of battery physiochemical processes that would take place in the event of a vehicle crash, a possible internal short and thermal runaway – with the objective of providing a better understanding of and enabling safer designs. With the National Renewable Energy Laboratory (NREL) as lead, the Consortium's partner laboratories Argonne National Laboratory (ANL) and Sandia National Laboratories (SNL) perform experimental studies, supported by Purdue University in performing mesoscale modeling. Sample results from the consortium efforts, from a simulation to determine effective electrolyte transport properties in porous electrodes (using geometry from the CT imaging of an actual electrode) are shown in Figure ES- 3.

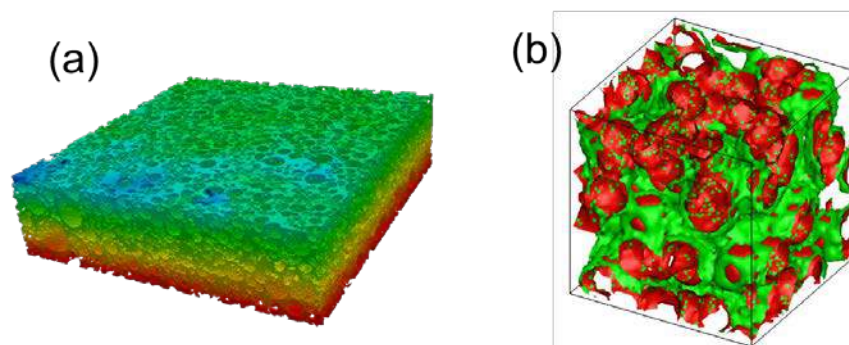


Figure ES- 3. (a) Homogenization simulation to determine effective electrolyte transport properties in porous electrode using geometry from CT imaging of an actual electrode. (b) Stochastic reconstruction of virtual geometry, showing CBA phase (green) on active material matrix (red).

The **consortium for advanced battery simulation** (CABS) is an integrated partnership between Oak Ridge National Laboratory (ORNL), Lawrence Berkeley National Laboratory (LBNL), and SNL. The main cause of battery failure/thermal runaway in crashes involving electric vehicles is believed to be a mechanically induced internal short-circuit. To accurately predict this internal short-circuit, one needs to capture deformed material variations and their influence on transport properties. The associated projects highlight new experiments to develop constitutive relations for mechanical response of constituent materials, effective transport properties for electrochemical behavior of electrodes under deformation, and coupled simulations at layer-resolved scale to predict the behavior of the damaged batteries. The approximate value of the CAEBAT and its follow-on programs is \$14M.

To become truly competitive with the internal combustion engine vehicle (ICEV) refueling experience, EV charging times must also dramatically decrease. A research project to understand/enable extreme fast charging (XFC) in enhanced Li-ion systems began in 2017. XFC, or charging an EV at the power rate of up to 400 kW, would decrease vehicle charging times and increase EV utility. To address this issue, a multi-national laboratory team consisting of ANL, Idaho National Laboratory (INL), and NREL engaged with industry stakeholders to identify barriers and opportunities for technology R&D solutions needed to achieve 400 kW charging power levels and combine the findings into a single document for governments and private industries to reference. Industry perspectives on the direction of fast charging were used to develop a technology gap assessment report, which would inform the team on areas that need an extensive literature review, and would assess the economic feasibility of XFC.

VTO also supports several *Small Business Innovation Research* (SBIR) contracts in addition to the R&D described above. These SBIR projects focus on development of new battery materials/components and serve as the source of new ideas and concepts. At the end of chapter I, a section on SBIR projects includes a short list of recent such projects active in FY 2017.

Advanced Materials R&D

The *Advanced Materials Research & Development* activity addresses fundamental issues of materials and electrochemical interactions associated with rechargeable automotive batteries. It develops new/promising materials and it makes use of advanced material models to discover such materials (and their failure modes), utilizing scientific diagnostic tools and techniques to gain insight into the failure process. The researchers belong to various national labs, universities, and industry partners. The work spans mainly two general areas – “next gen” chemistries (which employ an alloy anode and/or a high voltage cathode) and beyond lithium-ion (BLI) chemistries (which employ a lithium metal anode). The projects are distributed as follows:

- Next generation (Next-gen) lithium-ion battery technologies (48 projects)
 - Advanced Electrodes (four projects)
 - Advanced Anodes (eight projects)

- Advanced Cathodes (13 projects)
- Diagnostics (nine projects)
- Modeling Advanced Electrode Materials (six projects)
- Processing Science (eight projects)
- Beyond lithium-ion battery technologies (29 projects)
 - Metallic Lithium and Solid Electrolytes (11 projects)
 - Lithium sulfur (13 projects)
 - Lithium-Air Batteries (three projects)
 - Sodium-ion batteries (two projects)

The *next generation lithium-ion battery* R&D area's goal is to advance material performances, designs, and processes to significantly improve performance and reduce the cost of Li-ion batteries using an alloy or intermetallic anode and/or high voltage cathode. Specific areas of investigation include high-energy anodes (e.g., those containing silicon or tin), high voltage cathodes, high voltage and non-flammable electrolytes, novel processing technologies, high-energy and low-cost electrode designs, and certain other areas. This work spans a range of US DRIVE activities.

- *Advanced electrode R&D* research includes four projects. **LBNL** is studying inactive components and processing conditions and looking at different binder sources, slurry viscosities, and other parameters to identify physics for a smooth laminate to meet specific performance requirements. **Hydro-Quebec** is developing an electrode architecture-based on nano-Si powders. **MIT** is developing scalable designs and fabrication processes for high density low-tortuosity electrodes.
- *Advanced anodes R&D* includes 8 projects. Four of them, conducted by the five-member National Laboratory Consortium, comprise the **silicon deep-dive program**. Silicon is a viable alternative to graphitic carbon as an electrode in lithium-ion cells and can theoretically store >3,500 mAh/g (i.e., about ten times more than graphite). However, lifetime problems severely limit its use in practical systems – this project is focused on those problems. The consortium tackles the barriers for advanced lithium-ion negative electrodes which would use silicon as the active material. The program performs baseline tests on promising silicon materials in quantities sufficient for electrode preparation within consortium facilities. The other four projects, conducted by various national labs (including NREL, ANL, ORNL, PNNL, and LBNL) and academia/industry partners (including Stanford University and GM) are part of the **silicon electrolyte interface stabilization (SEISta) program** developing a foundational understanding of the formation/evolution of the solid electrolyte interphase on silicon.
- *Advanced cathodes R&D* includes 13 projects. Five of those projects are based at **ANL**, of which three are geared to **enable high-energy/high-voltage cells** via new insights and/or understanding into the failure of present materials/systems. (For example, in one of those projects, an electrolyte based on fluorinated sulfones improved the cycle life of NMC532/Graphite full cells. The performance of the electrolyte additive was evaluated using the high energy high voltage (HEHV) protocol, which predicted the number of cycles that will have 80% capacity retention under the high voltage cycling protocol. The cycle number with 80% capacity retention improved substantially – from 150 cycles with the baseline electrolyte to 400 cycles (Figure ES- 4) in the presence of the new fluorinated electrolyte.) To increase the energy density of lithium-ion batteries, electrochemical cells containing near lithium-stoichiometric, manganese-bearing, nickel-rich layered oxides and graphite-bearing negative electrodes are cycled to higher voltages (>4.35 V) in the Applied Battery Research for Transportation (ABRT) program. However, this reduces the cell life and degrades performance at those high voltages. The cell electrolyte, typically made of carbonate-based solvents, significantly contributes to this performance loss as it tends to oxidize at higher voltages, generating species that degrade the positive electrode. The development of electrolyte systems and of stable interfaces to mitigate performance degradation is a priority. **Daikin America** is working on electrolytes with small fluorinated molecules to achieve stable high voltage (i.e.,

>4.3 V) battery operation. An ANL project on novel cathode materials and processing methods focuses on lithium- and manganese-rich, **'layered-layered' composite materials** and another on exploiting **Co and Ni spinels** in structurally-integrated composite electrodes. Of the remaining eight advanced cathode projects, three are being conducted at LBNL, one each at PNNL, ORNL and BNL, one at Binghamton University, and another at the University of Texas at Austin.

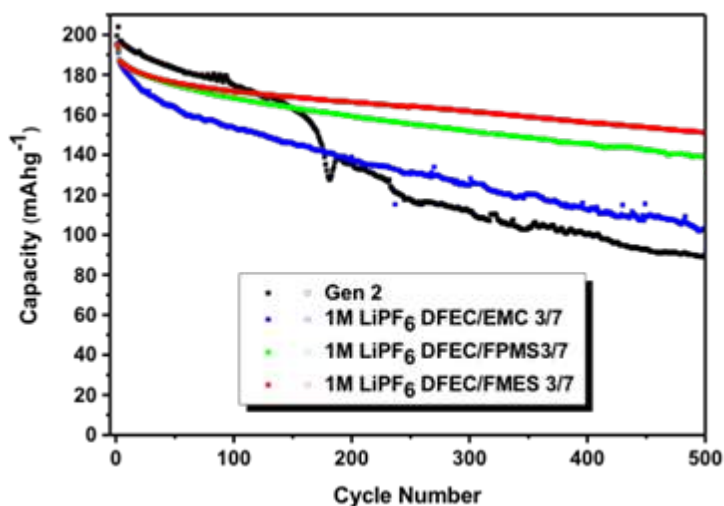


Figure ES- 4. Capacity retention of NMC532/graphite full cells cycled with Gen 2 (non-fluorinated) and various mixtures of fluorinated sulfone-based electrolytes. (C/3 for 100 for cycling between 3.0 and 4.6 V.)

- *Diagnostics* R&D includes nine projects, including two each by teams at ANL and LBNL. The teams at ANL are doing characterization studies of high-capacity composite electrode structures to address interfacial reactivity between electrode and electrolyte while the two LBNL teams are studying interfacial processes and doing *in operando* thermal diagnostics of cells. Also in this area of work, BNL is studying advanced *in situ* diagnostic techniques for battery materials, SLAC is conducting correlative microscopy characterization of oxide electrodes, and PNNL is conducting microscopy investigation on the fading mechanism of electrode materials. The remaining two diagnostics projects are based at universities (namely, the University of Cambridge, and the University of California at San Diego).
- Of the six *modeling* projects being funded, two are based at LBNL, including one on novel electrode materials from first principles and another on large-scale *ab initio* molecular dynamics simulation of liquid and solid electrolytes. A modeling project at ANL focuses on electrode materials design and failure prediction. The three remaining modeling projects are all based at universities (namely, the University of California at Berkeley, Texas A&M University, and the Brigham Young University).
- *Processing Science* R&D includes eight projects. Five of those are based at ANL – one on non-traditional approaches to synthesizing active cathode materials, one on active cathode materials with component concentration gradient structures, one on process R&D and scale-up of critical battery materials, and one on the cell analysis, modeling, and prototyping (CAMP) facility, as well as on materials benchmarking for CAMP. The University of Missouri, Columbia is working on an integrated flame spray process for low-cost production of battery materials, and Vanderbilt University on producing Li-ion battery anodes from electro-spun nanoparticle/conducting polymer nanofibers. A team project on the post-test analysis of lithium-ion battery materials includes three labs (ANL, ORNL, and SNL).

R&D on *beyond Li-ion battery technologies* includes solid-state technology, lithium metal systems, lithium sulfur, lithium air, and sodium-ion. The main areas of focus include new methods to understand/stabilize lithium metal anodes; Li polysulfides to enable the use of sulfur cathodes; and developing electrolytes for

lithium air and lithium sulfur cells. These systems offer further increases in energy and potentially reduced cost compared to the next-gen lithium-ion batteries. However, they also require additional breakthroughs in materials (often at a fundamental level) before commercial use. VTO is investigating the issues and potential solutions associated with cycling metal anodes. The main research topics include: coatings, novel oxide and sulfide-based glassy electrolytes, and *in situ* diagnostics approaches to characterize and understand Li metal behavior during electrochemical cycling.

- *Metallic lithium and solid electrolytes* R&D includes 11 projects, two of which are based at ORNL – one on mechanical properties at the protected lithium interface and another on composite electrolytes to stabilize metallic lithium anodes. A dendrite suppression project is ongoing at PNNL. The remaining eight projects are based at various universities – Stanford University, Texas A&M University (TAMU), University of Pittsburgh, West Virginia University, Pennsylvania State University, University of Michigan, and the University of Maryland. In one project at the University of Maryland, first principles calculations were applied to investigate the interface stability between garnet and formed Li-Al alloys (Figure ES- 5). It was found that the interface between Li-Al alloy and garnet may exhibit good chemical stability, which might facilitate Li ion transport through that interface.

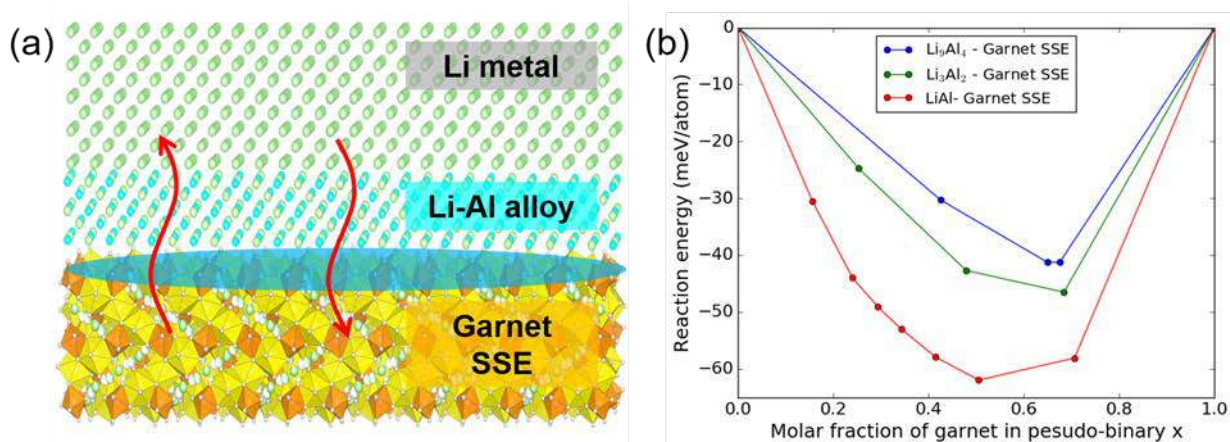


Figure ES- 5. Calculated mutual reaction energy, ΔE_D , of garnet and Li-Al alloy interfaces.

- *Lithium sulfur* R&D includes 13 projects – five of them at national laboratories and the remaining eight at various universities. The lab-based projects include one on lithium-selenium and selenium-sulfur couple (at ANL), advancing solid-solid interfaces (at ANL), multi-functional cathode additives (at BNL), simulations and X-ray spectroscopy of Li-S chemistry (at LBNL) and the development of high energy lithium sulfur batteries (at PNNL). The eight universities with lithium sulfur projects include Stanford University, TAMU, the University of Wisconsin at Madison, the University of Texas at Austin, Stony Brook University, University of Washington, Rutgers University, and the University of Pittsburgh.
- *Lithium-air batteries* R&D includes three projects – one at PNNL, another at ANL and one utilizing stable inorganic molten salt electrolytes at Liox Power.
- There are two *sodium-ion batteries* R&D projects ongoing – one at BNL and the other at SLAC.

The *Battery500 Innovation Center* is a combined effort by a team of four National Labs (PNNL, INEL, BNL and SLAC) and five universities (University of Texas-Austin, Stanford University, Binghamton University, University of Washington, and University of California, San Diego). Its goal is to develop commercially viable Li battery technologies with a cell level specific energy of 500 Wh/kg while simultaneously achieving 1,000 deep-discharge cycles. The consortium keystone projects focus on innovative electrode and cell designs that enable maximizing the capacity from advanced electrode materials. The strategy is to take advantage of electrode materials that are commercially available (or are nearly so) and introduce least perturbation to the

cell configuration and manufacturing process of current technologies. Based on this approach, two battery chemistries, high nickel content lithium nickel-manganese-cobalt oxide (high-Ni NMC, Ni>60%), coupled with Li metal anode, and Li-S chemistry, indicate a potential to achieve an energy density of at least 500 Wh/kg. The Li anode combined with a compatible electrolyte system and two cathodes – one high NMC and another sulfur – is to be studied and developed to reach a high energy density. The consortium will work closely with the R&D community, battery/materials manufacturers and end-users/OEMs to ensure that these technologies align well with industry needs and can be transitioned to production.

Testing and Analysis

The *Battery Testing, Analysis, and Design* activity supports all other battery R&D activities. DOE works in close collaboration with USABC to develop requirements and test procedures. Other projects in this area include conducting testing (for performance, life and abuse) for contract deliverables, laboratory- and university-developed cells, and benchmark systems from industry; thermal analysis, thermal testing and modeling; cost modeling; other battery use and life studies; and the recycling of core materials. Battery technologies are evaluated according to USABC-stipulated battery test procedures. Benchmark testing of an emerging technology is performed to remain abreast of the latest industry developments. The current projects are in the following three areas:

- The *cost assessments and requirements analysis* activity includes an ANL project on developing the performance and cost model BatPaC. This ANL model, developed over time and rigorously peer-reviewed, is used to design automotive Li-ion batteries to meet the specifications for a given vehicle, and estimate the cost of manufacturing it. An analysis using BatPaC compared the estimated costs of cells and packs for different electrode chemistries (Figure ES- 6 shows the pack costs).

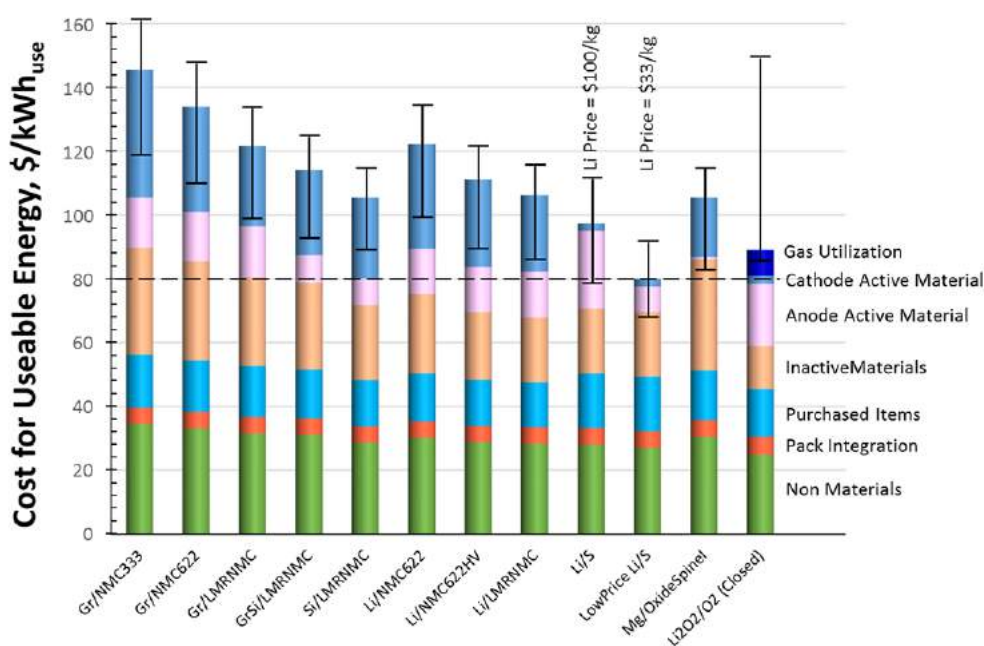


Figure ES- 6. Estimated costs of cells in automotive battery packs with different combination of electrodes. The packs are rated for 100 kWh_{Total} (85 kWh_{Useable}), 300 kW, 315 V, 168 cells, and produced at a plant volume of 100K packs/year.

- The *battery testing* activity includes performance, life and safety testing, and thermal analysis and characterization. It currently includes the following 4 projects:
 - Battery performance and life testing (ANL)
 - Electrochemical performance testing (INL, ANL)

- Battery safety testing (SNL)
- Battery thermal analysis and characterization activities (NREL)
- The *Recycling and Sustainability* activity involves studies of the full life-cycle impacts and costs of Li-ion battery production/use; cost assessments and impacts of various recycling technologies; and the available material and cost impacts of recycling and secondary use. It includes the following three projects:
 - Life cycle assessment of Li ion batteries (ANL)
 - Battery production and recycling materials issues (ANL)
 - Process and cost modeling of recycling activities (ANL)

Collaborative Activities

In addition to the above, VTO has established extensive and comprehensive ongoing coordination efforts in energy storage R&D across all of the DOE complex and with other government agencies. It coordinates efforts on energy storage R&D with both the Office of Science and the Office of Electricity. Coordination and collaboration efforts also include membership and participation in the Chemical Working Group of the Interagency Advanced Power Group (IAPG), in program reviews and technical meetings sponsored by other government agencies, and inviting participation of representatives from other government agencies in the contract and program reviews of DOE-sponsored efforts. DOE coordinates such activities with the Army's Advanced Vehicle Power Technology Alliance, the Department of Transportation/National Highway Traffic Safety Administration (DOT/NHTSA), the Environmental Protection Agency (EPA), and the United Nations Working Group on Battery Shipment Requirements. Additional international collaboration occurs through the International Energy Agency's (IEA's) Hybrid Electric Vehicles Technology Collaboration Program (HEV TCP); the G8 Energy Ministerial's Electric Vehicle Initiative (EVI); and bilateral agreements between the U.S. and China. The *U.S. China Clean Energy Research Center* conducts collaborative research both on rechargeable lithium-ion and beyond lithium-ion battery technologies to help develop the next generation of advanced batteries to help expand electrification of vehicles and enable smart grids internationally and its main objective is to understand and develop advanced battery chemistries based on lithium-ion and beyond lithium ion that meet 300Wh/kg energy density.

Organization of this Report

This report covers all the FY 2017 projects as part of the advanced battery R&D (i.e., energy storage R&D) effort in VTO. We are pleased with the progress made during the year and look forward to continued cooperation with our industrial, government, and scientific partners to overcome the remaining challenges to delivering advanced energy storage systems for vehicle applications.



David Howell

VTO Deputy Director
Vehicle Technologies
Office



Steven Boyd

Manager, Batteries and
Electrification Program
Vehicle Technologies
Office



Tien Q. Duong

Manager, Advanced
Battery Materials
Research and VTO
Battery500 Consortium
Vehicle Technologies
Office



Peter W. Faguy

Manager, Applied Battery
Research and Advanced
Processing R&D
Vehicle Technologies
Office



Brian Cunningham

Manager, Battery
Development; and Battery
Testing, Analysis and
Design; and Small
Business Innovation
Research for Batteries
Vehicle Technologies
Office



Samuel Gillard

Manager, Battery Testing,
Analysis and Design
Vehicle Technologies
Office

Table of Contents

Acknowledgements	iv
Acronyms.....	v
Executive Summary	xxiii
Vehicle Technologies Office Overview	1
Vehicle Technologies Office Organization Chart.....	1
Batteries Program Overview	3
Introduction.....	3
Goals	3
State of the Art.....	4
Battery Technology Barriers.....	6
Program Organization Matrix	6
Battery Highlights from FY 2017	8
I. Advanced Battery and Cell Research and Development	19
I.A USABC Battery Development & Materials R&D.....	19
I.A.1 High Energy Lithium Batteries for Electric Vehicles (Envia Systems)	19
I.A.2 Development of a High Energy Density Cell and Module for EV Applications (LGCPI)	25
I.A.3 High-Performance Semi-Solid Cell for EV Applications (24M Technologies).....	30
I.A.4 Development of High Performance Li-ion Cell Technology for EV Applications (Farasis Energy)	35
I.A.5 Enabling Thicker Cathode Coatings for Lithium Ion EV Batteries (PPG)	40
I.A.6 Advanced High-Performance Batteries for Electric Vehicle Applications (Amprius)	44
I.A.7 Development of Active Materials to be used in Automotive Traction Applications: Rapid Commercialization of High Energy Anode Materials (SiNode Systems)	49
I.A.8 A 12V Start-Stop Li Polymer Battery Pack (LG Chem Power, Inc.).....	55
I.A.9 USABC 12V Start-stop Module Development, Phase II (SAFT).....	60
I.A.10 Advanced Polyolefin Separators for Li-Ion Batteries Used in Vehicle Applications (AMTEK).....	68
I.A.11 Advanced Separators for Vehicle Lithium Battery Applications (Celgard, LLC)	79
I.A.12 Hybrid Electrolytes for PHEV Applications (NOHMs Technologies).....	86
I.A.13 Li-Ion Cell Manufacturing Using Directly Recycled Active Materials (Farasis Energy)..	94
I.A.14 A Closed Loop Recycling Process for End-of-Life Electric Vehicle Li-ion Batteries (Worcester Polytechnic Institute).....	100
I.A.15 Perform USABC/USCAR Benchmarking Activities (FEV North America, Inc.).....	108
I.B Advanced Processing.....	112
I.B.1 Low Cost Manufacturing of Advanced Silicon-Based Anode Materials (Group14 Technologies, Inc.).....	112
I.B.2 Commercially Scalable Process to Fabricate Porous Silicon (Navitas Systems).....	118
I.B.3 New Advanced Stable Electrolytes for High Voltage Electrochemical Energy Storage (Silatronics, Inc.)	123

I.B.4	Improve the Safety Performance of Li-ion Battery Separators and Reduce the Manufacturing Cost using Ultraviolet Curing and High Precision Coating Technologies (Miltec UV International)	130
I.B.5	Co-Extrusion(CoEx) for Cost Reduction of Advanced High-Energy-and-Power Battery Electrode Manufacturing (PARC).....	137
I.B.6	Electrodeposition for Low-Cost, Water-Based Electrode Manufacturing (PPG Industries, ANL, Navitas, ORNL)	145
I.B.7	Development of UV Curable Binder Technology to Reduce Manufacturing Cost and Improve Performance of Lithium Ion Battery Electrodes (Miltec UV International).....	152
I.B.8	Towards Solventless Processing of Thick Electron-Beam (EB) Cured LIB Cathodes (ORNL)	159
I.B.9	Performance Effects of Electrode Processing for High-Energy Lithium-Ion Batteries (ORNL)	166
I.C	Computer-Aided Engineering for Batteries (CAEBAT)	173
I.C.1	Advanced Computer Aided Battery Engineering Consortium (NREL, ANL, SNL, Purdue U)	173
I.C.2	Advanced Tool for Computer Aided Battery Engineering (ANL).....	181
I.C.3	Battery Abuse Testing (SNL).....	186
I.C.4	Consortium for Advanced Battery Simulation (ORNL)	192
I.C.5	Consortium for Advanced Battery Simulation (SNL).....	201
I.C.6	Consortium for Advanced Battery Simulation (ANL, LBNL).....	207
I.C.7	Development and Validation of a Simulation Tool to Predict the Combined Structural, Electrical, Electrochemical and Thermal Responses of Automotive Batteries (Ford Motor Company)	214
I.C.8	High Fidelity Fast Running Multi-scale Multi-physics Battery Pack Software (General Motors, NREL, ANSYS and ESim).....	220
I.D	High Energy, Long Life Lithium-Ion Battery (NREL)	227
I.E	Material and cell studies to enable extreme fast charge (XFC) (INL).....	231
I.F	Small Business Innovation Research (SBIR)	237
II.	Advanced Materials R&D.....	243
II.A	Next-gen Lithium-ion: Advanced Electrodes R&D	243
II.A.1	Higher Energy Density <i>via</i> Inactive Components and Processing Conditions (LBNL) ..	243
II.A.2	Electrode Architecture-Assembly of Battery Materials and Electrodes (Hydro-Quebec)	250
II.A.3	Design and Scalable Assembly of High-Density, Low-Tortuosity Electrodes (MIT)	256
II.A.4	Advanced Lithium Ion Battery Technology – High Voltage Electrolyte (Daikin America, Inc.)	259
II.B	Next Generation Lithium-Ion: Advanced Anodes R&D	267
II.B.1	Next Generation Anodes for Lithium-Ion Batteries: Research Facilities Support.....	267
II.B.2	Next Generation Anodes for Lithium-Ion Batteries: Characterization, Diagnostics, and Analysis (ANL).....	295
II.B.3	Next Generation Anodes for Lithium-Ion Batteries: Materials Advancements (ANL) ...	331
II.B.4	Silicon Electrolyte Interface Stabilization (SEISta) (NREL, ANL, ORNL).....	373
II.B.5	Development of Si-based High-Capacity Anodes (PNNL).....	440
II.B.6	Pre-Lithiation of Silicon Anode for High Energy Li Ion Batteries (SLAC)	448
II.B.7	High Capacity and Long Cycle-Life Silicon Carbon Composite Materials and Electrodes (LBNL)	455

II.B.8	A Combined Experimental and Modeling Approach for the Design of High Current Efficiency Si Electrodes (GM)	462
II.C	Next-Gen Lithium-Ion: Advanced Cathodes R&D	468
II.C.1	Enabling High-Energy/Voltage Li-Ion Cells: Electrochemical Analysis and Evaluation (ANL, LBNL, NREL, ORNL)	468
II.C.2	Enabling High-Energy/Voltage Li-Ion Cells: Materials and Characterization (ANL, LBNL, NREL, ORNL)	477
II.C.3	Enabling High-Energy/Voltage Li-Ion Cells: Theory and Modeling (ANL, LBNL, NREL, ORNL)	485
II.C.4	Studies on High Capacity Cathodes for Advanced Lithium-Ion (ORNL)	493
II.C.5	High Energy Density Lithium Battery (Binghamton University)	502
II.C.6	Development of High-Energy Cathode Materials (PNNL)	509
II.C.7	<i>In situ</i> Solvothermal Synthesis of Novel High-Capacity Cathodes (BNL)	517
II.C.8	Novel Cathode Materials and Processing Methods (ANL)	524
II.C.9	Design of High Performance, High Energy Cathode Materials (LBNL)	531
II.C.10	Lithium Batteries with Higher Capacity and Voltage (UTA)	538
II.C.11	Exploiting Co & Ni Spinel in Structurally-Integrated Composite Electrode (ANL)	545
II.C.12	Discovery of High-Energy Li-Ion Battery Materials (LBNL)	552
II.C.13	Model-System Diagnostics for High-Energy Cathode Development (LBNL)	560
II.D	Next-Gen Lithium-Ion: Diagnostics	568
II.D.1	Interfacial Processes (LBNL)	568
II.D.2	Advanced <i>in situ</i> Diagnostic Techniques for Battery Materials (BNL)	576
II.D.3	NMR and Pulse Field Gradient Studies of SEI and Electrode Structure (University of Cambridge)	583
II.D.4	Advanced Microscopy and Spectroscopy for Probing and Optimizing Electrode-Electrolyte Interphases in High Energy Lithium Batteries (UCSD)	593
II.D.5	Microscopy Investigation on the Fading Mechanism of Electrode Materials (PNNL)	601
II.D.6	Characterization Studies of High Capacity Composite Electrode Structures (ANL)	607
II.D.7	<i>In Operando</i> Thermal Diagnostics of Electrochemical Cells (LBNL)	615
II.D.8	Correlative Microscopy Characterization of Oxide Electrodes (SLAC)	619
II.D.9	Understanding and Mitigating Interfacial Reactivity between Electrode and Electrolyte (ANL)	626
II.E	Next-Gen Lithium-Ion: Modeling Advanced Electrode Materials	632
II.E.1	Electrode Materials Design and Failure Prediction (ANL)	632
II.E.2	Predicting and Understanding Novel Electrode Materials from First Principles (LBNL)	641
II.E.3	First Principles Calculations of Existing and Novel Electrode Material (LBNL)	646
II.E.4	First Principles Modeling of SEI Formation on Bare and Surface/Additive Modified Silicon Anodes (TAMU)	653
II.E.5	Addressing Heterogeneity in Electrode Fabrication Processes (BYU)	658
II.E.6	Large Scale <i>Ab Initio</i> Molecular Dynamics Simulation of Liquid and Solid Electrolytes (LBNL)	664
II.E.7	Dendrite Growth Morphology Modeling in Liquid and Solid Electrolytes (MSU)	669
II.F	Next-Gen Lithium-Ion: Processing Science R&D	676
II.F.1	Advanced Active Battery Materials: Non-traditional Approaches to Synthesizing Active Cathode Materials (ANL)	676

II.F.2	Advanced Active Battery Materials: Active Cathode Materials with Component Concentration Gradient Structures (ANL)	682
II.F.3	Integrated Flame Spray Process for Low Cost Production of Battery Materials for Lithium Ion Batteries and Beyond (University of Missouri)	690
II.F.4	High Performance Li-Ion Battery Anodes from Electrospun Nanoparticle/Conducting Polymer Nanofibers (Vanderbilt University)	695
II.F.5	Process R&D and Scale up of Critical Battery Materials (ANL)	702
II.G	Next-Gen Lithium-Ion: Core and Enabling Support Facilities	710
II.G.1	Cell Analysis, Modeling, and Prototyping (CAMP) Facility Research Activities (ANL)	710
II.G.2	Materials Benchmarking Activities for CAMP Facility (ANL)	732
II.G.3	Post-test Analysis of Lithium-Ion Battery Materials (ANL, ORNL, SNL)	738
II.H	Beyond Li-ion R&D: Metallic Lithium and Solid Electrolytes	744
II.H.1	Mechanical Properties at the Protected Lithium Interface (ORNL)	744
II.H.2	Solid electrolytes for solid-state and lithium-sulfur batteries (University of Michigan, ORNL, ARL, Oxford University)	750
II.H.3	Composite Electrolytes to Stabilize Metallic Lithium Anodes (ORNL)	758
II.H.4	Overcoming Interfacial Impedance in Solid-State Batteries (U of MD)	765
II.H.5	High Conductivity and Flexible Hybrid Solid State Electrolyte (U of MD)	786
II.H.6	Nanoscale Interfacial Engineering for Stable Lithium Metal Anodes (Stanford University)	793
II.H.7	Lithium Dendrite Prevention for Lithium Batteries (PNNL)	802
II.H.8	Understanding Strategies for Controlled Interfacial Phenomena in Li-Ion Batteries and Beyond (TAMU)	809
II.H.9	Engineering Approaches to Dendrite Free Lithium Anodes (U of Pittsburgh)	815
II.H.10	Solid-State Inorganic Nanofiber Network-Polymer Composite Electrolytes for Lithium Batteries (WVU)	821
II.H.11	Electrochemically Responsive Self-Formed Li-ion Conductors for High Performance Li Metal Anodes (Penn State U)	826
II.I	Beyond Li-ion R&D: Lithium Sulfur Batteries	835
II.I.1	New Lamination and Doping Concepts for Enhanced Li-S Battery Performance (U Pittsburgh)	835
II.I.2	Simulations and X-ray Spectroscopy of Li-S Chemistry (LBNL)	843
II.I.3	Novel Chemistry: Lithium-Selenium and Selenium-Sulfur Couple (ANL)	850
II.I.4	Multi-Functional Cathode Additives (BNL)	857
II.I.5	Development of High Energy Lithium-Sulfur Batteries (PNNL)	864
II.I.6	Nanostructured Design of Sulfur Cathodes for High Energy Lithium-Sulfur Batteries (Stanford University)	872
II.I.7	Addressing Internal “Shuttle” Effect: Electrolyte Design and Cathode Morphology Evolution in Li-S Batteries (TAMU)	879
II.I.8	Mechanistic Investigation for the Rechargeable Li-Sulfur Batteries (U Of Wisconsin)	886
II.I.9	Statically and Dynamically Stable Lithium-sulfur Batteries (UTA)	893
II.I.10	Dual Function Solid State Battery with Self-forming Self-healing Electrolyte and Separator (Stony Brook University)	900
II.I.11	Advancing Solid-Solid Interfaces in Li-ion Batteries (ANL)	910
II.I.12	Multifunctional, Self-Healing Polyelectrolyte Gels for Long-Cycle-Life, High-Capacity Sulfur Cathodes in Li-S Batteries (University of Washington)	917

II.I.13	Self-Forming Thin Interphases and Electrodes Enabling 3-D Structures High Energy Density Batteries (Rutgers U).....	925
II.J	Beyond Li-ion R&D: Lithium-Air Batteries	932
II.J.1	Rechargeable Lithium-Air Batteries (PNNL)	932
II.J.2	Efficient Rechargeable Li/O ₂ Batteries Utilizing Stable Inorganic Molten Salt Electrolytes (Liox Power)	940
II.J.3	Lithium-Air Batteries (ANL)	948
II.K	Beyond Li-ion R&D: Sodium-Ion Batteries.....	953
II.K.1	Exploratory Studies of Novel Sodium-Ion Battery Systems (BNL)	953
II.K.2	Advanced Organic Materials for Batteries (Stanford University).....	960
II.L	Beyond Li-ion R&D: Battery500 Innovation Center	967
II.L.1	Innovation Center for Battery500 (PNNL)	967
III.	Testing and Analysis	980
III.A	Cost Assessments and Requirements Analysis.....	980
III.A.1	BatPaC Model Development (Argonne National Laboratory).....	980
III.B	Battery Testing	989
III.B.1	Battery Performance and Life Testing (ANL)	989
III.B.2	Electrochemical Performance Testing (INL)	998
III.B.3	Battery Safety Testing (SNL).....	1002
III.B.4	Battery Thermal Analysis and Characterization Activities (NREL)	1016
III.C	Recycling and Sustainability	1022
III.C.1	Life Cycle Assessment of Li-ion Batteries (ANL).....	1022
III.C.2	Battery Production and Recycling Materials Issues (ANL)	1028
III.C.3	Closed-loop Battery Recycling Model (ANL)	1033
IV.	U.S. China Clean Energy Research Center (CERC)	1036
IV.A	Development of High Energy Battery System with 300Wh/kg (ANL).....	1036

List of Figures

Figure ES- 1. Images of an 11 Ah capacity pouch cell undergoing teardown and failure analysis.....	xxv
Figure ES- 2. Capacity and ICL both improved during Navitas' material scale up procedures.....	xxvi
Figure ES- 3. (a) Homogenization simulation to determine effective electrolyte transport properties in porous electrode using geometry from CT imaging of an actual electrode. (b) Stochastic reconstruction of virtual geometry, showing CBA phase (green) on active material matrix (red).	xxvii
Figure ES- 4. Capacity retention of NMC532/graphite full cells cycled with Gen 2 (non-fluorinated) and various mixtures of fluorinated sulfone-based electrolytes. (C/3 for 100 for cycling between 3.0 and 4.6 V.).....	xxix
Figure ES- 5. Calculated mutual reaction energy, ΔE_D , of garnet and Li-Al alloy interfaces.	xxx
Figure ES- 6. Estimated costs of cells in automotive battery packs with different combination of electrodes. The packs are rated for 100 kWh _{Total} (85 kWh _{Useable}), 300 kW, 315 V, 168 cells, and produced at a plant volume of 100K packs/year.....	xxxix
Figure 1. Chemistry classes, status, and R&D needs.....	5
Figure 2. Potential for Future Battery Technology Cost Reductions.....	5
Figure 3. Battery R&D Program Structure	7
Figure 4. Saft Intensium Stationary Storage Battery	9
Figure 5. Capacity retention of NMC532/graphite full cells cycled with Gen 2 (non-fluorinated) and various mixtures of fluorinated sulfone-based electrolytes. (C/3 for 100 for cycling between 3.0 and 4.6 V.).....	10
Figure 6. Simulated NMC particle shapes obtained under select synthesis conditions. (Bottom) images of NMC particles (LBNL) verifying the modeling results.....	10
Figure 7. Experimental verification of propensity for propagation: the thicker aluminum plates offer higher rates of heat transfer away from the cell and as a result minimize the risk for propagation.....	11
Figure 8. The aqueous processed cracked electrode reaches 70% capacity retention after 620 cycles due to its poor coating quality. With IPA addition to the aqueous binder, cycling performance is comparable to NMP solvent processed electrodes.	12
Figure 9. PSI HA cells cycled from 2.8 to 4.2 and 4.4V deliver ~90% of initial capacity after 1000 cycles.	13
Figure 10. Capacity and ICL both improved during Navitas' material scale up procedures.....	13
Figure 11. Cycling performance of DDSA electrode, PTA coated DDSA electrode, and standard slurry coated electrode.	14
Figure 12. a) Capacity vs cycle number of Li/NMC cells with various electrolytes in EC-EMC solvent. (b-d) Cross-section of Li electrodes after 100 cycles using (b) conventional LiPF ₆ electrolyte, (c) LiTFSO-LiBOB dual-salt electrolyte, and (d) 0.05M LiPF ₆ added dual-salt electrolyte.....	15

Figure 13. Fluorinated protective coating plus high concentration salt electrolyte enables improved Li/Li symmetric cell cycling compared to cells without the coating and in a low concentration salt electrolyte.	15
Figure 14. Evidence that Li metal can effectively bond to a solid ceramic as evidenced by theory (left), and lower wetting angle (right).	16
Figure 15. (a) Cross-sectional elemental mapping of the prepared 811 Core-Gradient cathode. (b) Cross-sectional elemental mapping of the prepared 811 Core-Shell cathode. (c) Comparison of electrochemical performance. (d) Thermal stability comparison.	17
Figure I-1. Current and projected cell development progression throughout the USABC program.	21
Figure I-2. Cell characteristics of the delivered build #2 cells	22
Figure I-3. Normalized capacity versus cycles for 11 Ah and 21 Ah capacity pouch cells.	22
Figure I-4. Images of an 11 Ah capacity pouch cell undergoing teardown and failure analysis	23
Figure I-5. Comparison of the charge/discharge profiles of cells containing 10 and 30% SiO anodes.	27
Figure I-6. Comparison of the cycling performance of cells containing 10 and 30% SiO anodes. Cycling carried out at 1/3°C rate and 25°C.	27
Figure I-7. Comparison of the storability of cells containing 10 and 30% SiO anodes. Storage was at 100% SOC and 60°C.	28
Figure I-8. Comparison of the thickness increase of cells containing 10 and 30% SiO anodes. The cycling was carried out at 1/3 C between 4.2 and 2.5V and 25°C.	28
Figure I-9. Reversible specific discharge capacities measured during USABC screening for high energy density cathode active material candidates for program Phase 2 and Phase 3 development. Screening was performed using full pouch cells containing 24M's proprietary semi-solid electrode format for both the cathode and a control graphite anode.	32
Figure I-10. Voltage vs. discharge capacity plots for pouch full cells using 24M's proprietary semi-solid electrodes measured at a rate of C/3 in a -20°C testing environment for two different electrolytes. The cells using the current baseline electrolyte retained ~15% of their room temperature energy at the test temperature, while the newly developed low temperature electrolyte showed an energy retention of >50% at -20°C.	33
Figure I-11. Capacity for eight of the planned cathode material	36
Figure I-12. Cycle life for the cathode materials	37
Figure I-13. Cycle life comparison of cathode (C1.4) with and without Li source and Si composite as an anode.	38
Figure I-14. Cycle life for the different electrolyte formulations	38
Figure I-15. Cycle life for the different electrolyte formulations	39
Figure I-16. USABC baseline battery performance after 300 cycles. (Data provided by LG Chem Power)	41

Figure I-17. Thicker coatings developed in third quarter. Left, Peel strength and areal capacity are shown and first target and final target regions are highlighted. Right, Coating appearance. (Data provided by PPG).....	42
Figure I-18. Electrolyte formulation was optimized for better Calendar and Cycle Life in Si/NCM (70% Ni) cells.....	46
Figure I-19. CAD drawing and prototype 40 Ah cell with silicon nanowire anode	48
Figure I-20. Si-anode failure mechanisms (left), SiNode graphene-wrapped advanced silicon anode architecture (right)	50
Figure I-21. Evolution of SiNode technology to meet USABC goals and specifications: (from left to right) pure silicon particle -> graphene wrapped silicon alloy (SiO _x , x=0.5) -> C-coated (or MO _x coated) and graphene wrapped silicon alloy (SiO _x , x=0.5).	50
Figure I-22. Improvements in FCE of our anode material seen by optimizing the surface morphology of the carbon coating.	51
Figure I-23. Capacity retention as a function of cycles for 1 and 3 wt% precursor dispersions. The data is in full cell paired with an NCA cathode.	51
Figure I-24. 2017 production forecast and major technical milestones. Project needs and graphene dispersion levels are expected to increase throughout the course of 2017.....	52
Figure I-25. Completed cycle life testing of full SLP cell manufactured with A123 hand coated anode...	53
Figure I-26. Full cell capacity vs. cycle number plot for SiNode 1000 mAh/g anodes vs. NCA cathode with varying degrees of FEC electrolyte additive.....	54
Figure I-27. Example of improvement achieved in the durability of the LTO/LMO cell in this program.	56
Figure I-28. Cycle-life data for LTO/LMO cells at 55oC and 5C charge and discharge rates.	57
Figure I-29. Improvement of cold-cranking power as a function of separator properties.	57
Figure I-30. Improvement in the discharge efficiency of the various generation of cells as a function of cell improvement.	58
Figure I-31. Picture of the 12V Li-ion Start-Stop battery pack delivered to USABC for testing.	58
Figure I-32. (Top) Comparing cold crank performance of cells with Design 2 LTO and carbon free LTO versus the first cell deliverable baseline, (Bottom) Comparing gassing rate of cells with Design 2 LTO and carbon free LTO versus the first cell deliverable baseline.....	63
Figure I-33. (Top) Comparing cold crank performance of cells filled with ester rich electrolyte vs carbonate rich electrolyte, (Bottom) Comparing gassing rate of cells filled with ester rich electrolyte vs carbonate rich electrolyte.....	64
Figure I-34. Front and Side Views of the 46 Ah Pouch Cell (Left side); Photograph Showing Drawn Pouches (Right side). SAFT SDD.....	65
Figure I-35. 3D Model of USABC 12V S/S Prototype Model. SAFT SDD.....	65
Figure I-36. Block Diagram Detailing the Requirements for the Electronic System. SAFT SDD.....	66

Figure I-37. Proof-of-Concept Electrical Control Board. SAFT SDD	66
Figure I-38. SEM images (left) and pore size distribution (right) of inorganic filled separator for increased ionic conductivity.....	69
Figure I-39. Comparison between coat weight requirements for conventional and “nanoparticle” alumina coating onto separator. Conventional formulations require almost twice the coat weight to reach high temperature dimensional stability (<5% at 180°C).	70
Figure I-40. Cycle life of 4.4V cells built with uncoated polyethylene separator (top) and alumina coated separator (bottom).	71
Figure I-41. Open circuit voltage of 4.4V cells stored at 60°C, built with uncoated polyethylene separator (top) and alumina coated separator (bottom). Cells were recharged to 4.4V every 30 days.	72
Figure I-42. Capacity of 4.4V cells stored at 60°C, built with uncoated polyethylene separator (top) and alumina coated separator (bottom). Capacity measurements were made at 30°C every 30 days.	73
Figure I-43. Cycle life of 4.4V cells built with 10 wt% silica filled separator (top) 10 wt% silica filled separator, coated with alumina (bottom).	74
Figure I-44. Open circuit voltage of 4.4V cells stored at 60°C, built with 10 wt% silica filled separator (top) 10 wt% silica filled separator, coated with alumina (bottom). Cells were recharged to 4.4V every 30 days.	75
Figure I-45. Capacity of 4.4V cells stored at 60°C, built with uncoated polyethylene separator (top) and alumina coated separator (bottom). Capacity measurements were made at 30°C every 30 days	76
Figure I-46. Cycle life (top) and storage testing (bottom) for 4.9V HV Spinel cells built with uncoated and ceramic coated separators. Storage testing was performed at 45°C.....	77
Figure I-47. SEM micrographs of the AlOx coated Celgard 2013 by PVD process: surface H2013_15nm AlOx (on left) and cross-section view of H2013_15nm AlOx (on right)	81
Figure I-48. Shut down performance for the PVD coated separators.	82
Figure I-49. Capacity retention of second batch of 18650 cells tested over the voltage ranges 4.0 -4.85 V and 3.5 - 4.9 V. No early failure but cycling is poor due to possible internal impedance increase.	83
Figure I-50. Capacity retention of Farasis pouch cells tested over the voltage ranges 4.0 - 4.85 V and 3.5 - 4.9 V. Significantly improved cycling was observed over 18650 cells.	83
Figure I-51. SEM photographs of Celgard dry process PP (on left) and a commercial wet PE (on right) separator after cycling in 5V cells.....	84
Figure I-52. Program approach from synthesis electrolyte and cell fabrication. The approach encompasses synthesis of novel functional ionic liquids, electrochemical testing, post autopsy analysis, 2 Ah & 10 Ah cell fabrication, and scale-up cost analysis.	87
Figure I-53. Floating voltage profiles of LNMO Li coin cells. The voltages are held for 10hrs at 4.95V & 5.2V. Leak current describes the severity of the oxidative reactions with the cathode surface.....	88

Figure I-54. (A) Floating Voltage in NMC532/Li coin cells at 23°C using 10hr holds at 4.7V and 5.0V. (B) Graphite/Li half-cell galvanostatic cycling at C/10. Baseline electrolyte denoted as (30:70) EC:EMC + 1MLiPF ₆	89
Figure I-55. 45°C vs room temperature comparison of HVE157a electrolyte in 155 mAh NMC442 cells; 3.0V-4.5V; C/2 rate. Cells project an average initial cycling capacity of 145 mAh and 150 mAh for room temperature and 45°C sample groups respectively.....	90
Figure I-56. Cycling Data for 2 Ah NMO cells with NOHMs electrolyte HV242, 1C/2C at 4.8V cutoff. 90	
Figure I-57. Cycling performance of 5 Ah NMC532 cells cycled at 1C and 45°C with a 4.5V cut-off.	91
Figure I-58. Ionic conductivity of base line electrolyte and NOHMs HVE157 electrolyte over a wide temperature range.....	92
Figure I-59. Flow chart for direct recycling process for Li-ion batteries.....	95
Figure I-60. Thermogravimetric analysis of composite positive electrode components at 10°C/minute ...	97
Figure I-61. Specific capacity of positive electrode active material recycled from scrap electrodes.	98
Figure I-62. Voltage curves of NCM111 (vs. Li/Li ⁺ , in 1.2 M LiPF ₆ in EC/EMC 3:7 w/w) which has been chemically delithiated with aqueous Na ₂ S ₂ O ₈ . The comparative specific discharge capacity of pristine reference material is 155 mAh/g.	99
Figure I-63: Detailed precursor and cathode powder information from 4 different experiment for 2 Ah cells. Each 3 kg lot of powder was generated from approximately 30 kg of spent, shredded batteries of the provenance noted above.....	103
Figure I-64: Detailed precursor and cathode powder information from 4 different experiment for 25 Ah cells	105
Figure I-65: The morphology of NMC111 precursor with reaction time at Battery Resourcers	106
Figure I-66: NMC111 cathode powder synthesized by Battery Resourcers.....	107
Figure I-67: 2015 VW e-Golf Battery Pack Physical Overview.....	109
Figure I-68: Capacity Testing Cycles at C/3 Charge, 30min Rest, C/3 Discharge at 30°C	110
Figure I-69: 2016 Toyota Prius Lithium-Ion Battery Pack Specification Summary	111
Figure I-70: Volumetric energy density (Wh/L) for Process Path 2 Si-C composites vs graphite, full cells cycled at C/2 rate with C/10 rate every 20 cycles, 2.5 – 4.2 V, with I/2 hold, 1 M LiPF ₆ in EC:DEC w/10% FEC, LiNiCoAlO cathode, excess anode=2-16%, anode=5% CMC-SBR, 5% Super-P, 59-63% graphite, 27-32% Si-C composite.	113
Figure I-71: SAED analysis of an exemplary Si-C composite corresponding to Process Path #2.	114
Figure I-72: Volumetric energy density (Wh/L) for Process Path 2 Si-C composites vs graphite, anode prelithiated by shorting with Li metal for 1 h prior to assembly, full cells cycled at C/2 rate with C/10 rate every 20 cycles, 2.5 – 4.12 V, with I/2 hold, 1 M LiPF ₆ in EC:DEC w/10% FEC, LiNiCoAlO cathode.	115

Figure I-73: Capacity retention (%) for Process Path 2 Si-C composites vs graphite, anode prelithiated by shorting with Li metal for 1hr prior to assembly, full cells cycled at C/2 rate with C/10 rate every 20 cycles, 2.5 – 4.12 V, with I/2 hold, 1 M LiPF ₆ in EC:DEC w/10% FEC, LiNiCoAlO cathode.	115
Figure I-74: Conventional production of porous silicon uses hazardous hydrofluoric (HF) acid and expensive metal catalyst. Navitas route reduces cost and impact, using SiO ₂ raw material and no HF. .	119
Figure I-75: Nearly theoretical capacity was reached as ICL was reduced to <10% as an indication that residual oxides were successfully removed. Batch size was scaled to multi-kg, adequate to support customer pilot scale electrode coating requests.	120
Figure I-76: Cells prepared using anodes incorporating Si composite anodes at EV battery loadings were able to meet cycle rate requirements and match commercial Si anode materials produced using higher cost materials and processes.	121
Figure I-77: In full cell testing at EV loading, Navitas showed 100% improvement in cycle life and was able to reach >900 cycles. The si anode was 92% active material having 650 mAh/g reversible capacity.	121
Figure I-78: Oxidative stability comparison at high temperature of OS3d vs OS3 [®] vs carbonate control electrolyte.	125
Figure I-79: Parasitic current results for LiPF ₆ -based electrolytes in a 3-electrode cell (Pt: WE, Li/Li ⁺ : CE, RE).	126
Figure I-80: Comparison of LNMO full cell performance with control carbonate electrolyte and 2% OS formulations (all with 1M LiPF ₆). Cells are cycled at C/10 for 2 formation cycles and at C/2 for 10 cycles at 30°C, then continued 50 cycles at C/2 between 3.5 and 4.9 V at 55°C.	127
Figure I-81: (a) SEM images and (b) XPS surface composition data for the de-lithiated LNMO cathode after cycling (50 cycles at C/2 between 3.5 and 4.9 V at 55°C) with control carbonate and 2% OS3 [®] , and 2% OS3c formulations. All electrolytes contain 1M LiPF ₆	127
Figure I-82: Normalized ESI-MS counts as a function of cluster for OS/EC/EMC electrolyte formulations.	128
Figure I-83: Calculated fraction of bulk solvents participating in solvation based upon ESI-MS results in the previous figure.	128
Figure I-84: PE Separator Shrinkage with and without UV Ceramic Coating	131
Figure I-85: In the flexographic process, the anilox meters the coating to the image plate which like a rubber stamp transfers the image to the separator. As shown, the left side is printing a pattern and the right side is printing a continuous coating.	133
Figure I-86: Image of UV ceramic coated separator. The white ridges are the rigid coating that inhibits thermal shrinkage and holes allow more ion flow.	134
Figure I-87: Deeply lithiated graphite anode shows no mirror pattern of patterned coated separator. 10 x 10 Pattern Coated separator (upper left). Lithiated anodes with uncoated separator (upper right), solid coated separator (lower right), and pattern coated separator (lower left).	134
Figure I-88: Commercial Scale Coater, CX 400	135

Figure I-89. (a) Schematic of different CoEx cathode geometries. (b) Summary of CoEx Type 1 and 3 modeling results, plotting gravimetric and volumetric energy densities as a function of discharge rate and CoEx geometry	139
Figure I-90. Confocal profilometry scans of CoEx Type 3 structures, illustrating how electrode thickness varies orthogonal to print direction.	139
Figure I-91. Specific capacity vs (a) discharge rate and (b) discharge current for a variety of CoEx Type 3 structures compared to baseline and thick homogeneous cathode electrodes.....	140
Figure I-92. Comparison of the performance of 6 different slot-die coated graphite anodes in half cells at a loading of (a) 2.6 mAh/cm ² and (b) 6 mAh/cm ²	141
Figure I-93. Cycle life data for 1 Ah and 6 Ah baseline pouch cells. Cells are tested at C/3 charge and discharge with HPPC testing performed every 50 cycles.	143
Figure I-94. (a) Cycle life testing demonstrating improved cycle life of electrocoated films after 500 cycles. (b) DCR measurements performed at 3.0 C. Electrocoated cathode materials demonstrate a lower internal resistance. (c) Rate performance of each electrode with electrocoated electrodes demonstrating an improved capacity retention at high rates. (d) Double-sided areal capacity measurements of five electrocoated films highlighting the reproducibility of targeted film thicknesses with this technique.....	148
Figure I-95. (a) Peel strength measurements of electrocoat binders in cathode films fabricated using both drawdown and electrocoat fabrication processes. (b) Film uniformity measurements of electrocoated cathode films comprised of active materials of varying size and deposition conditions. Non-uniformities present from the use of large particle sizes may be overcome by the electrocoat deposition conditions.	149
Figure I-96. Stable half-cell cycling of UV 94/3/3 power cathode.	154
Figure I-97. Stable half-cell cycling of UV 98/0.5/1.5 power cathode.	154
Figure I-98. Comparison of a NMC cathode utilizing a UV-curable cathode with a single and double layer, each electrode containing approximately the same amount of active material, at approximately the same thickness (~22-24 μm .) The double-layered electrode was made by application, cure, second application, and then a final cure. Each cure was performed with a single UV lamp, and the mass ratio of materials was 90:7:3 NMC: Carbon: UV Binder.	155
Figure I-99. Half-cell cycling data, comparing single and double cathode layers, each applied by slot die coating. The single coated electrode has a thickness of ~12 microns and an active material loading of ~3 mg/cm ² , and the doubly coated electrode has a thickness of ~25 microns and an active material loading of ~6 mg/cm ² . The formulation of each slurry is the same, with a mass loading of 90/5/5 NMC.	156
Figure I-100. Initial cycling tests on an LTO anode using a mass ratio of 93:4:3 LTO/CB/Binder, and electrode mass loading of ~3.0 mg/cm ² of active material. These electrodes were cast by hand using a doctor blade, and cured at 60 fpm.	157
Figure I-101. UV LTO power anode (93/4/3 LTO/C/UV Binder), shows fast stable, high rate cycling. Electrode mass loading was 3.2 mg/cm ² of LTO.	157
Figure I-102. FITR spectra of Ucecoat 7788 and 7689 resins used in runs #2 and #3.	161

Figure I-103. (a) Charge/discharge voltage curves at C/3, (b) rate performance from C/10 to 2C, (c) differential capacity curves at C/3, and (d) cycling performance at C/3 charge/discharge rates for the 1.5 Ah pouch cells.....	162
Figure I-104. SEM images of prepared sample A, B, and D dry powders.	163
Figure I-105. SEM images of Sample A, B and D after calendaring and radiation curing.....	163
Figure I-106. (a) Voltage profiles in Li half cells, (b) rate performance in Li half cells, and (c) selected full-coin-cell cycling performance for samples A and B.	164
Figure I-107. Stability results after exposure of different NMC compositions to water, acid, and base solutions for different time periods. a) Measured filtrate pH values after soaking NMC in aqueous solutions with different pH values. Nitric acid was used to make the pH 2 solution, and ammonium hydroxide was used to make the pH 12 solution. b) % of Lithium leached from NMC (into the filtrate) after soaking in aqueous solutions with different pH values, as measured by ICP-MS.....	168
Figure I-108. Comparison of the capacity retention of single-layer pouch cells made with aqueous- and NMP-processed NMC 811 electrodes after 200 cycles at 0.333C charge/discharge rate. Data is an average of 3 cells, and the error bars represent the standard deviation of each cycle. The small breaks in the data are due to power outages. The active material loadings of the aqueous NMC cathode, NMP-based NMC cathode, and the Superior Graphite SLC 1520T anode were 11.3 mg/cm ² , 11.6 mg/cm ² , and 7.5 mg/cm ² , respectively. The cathode and anode thicknesses were 43 and 53 μ m, respectively, and the porosity of all electrodes was 35%.....	169
Figure I-109. Aqueous processed NMC 532 cathodes with different active material loadings: (a) 15 mg/cm ² , (b) 17.5 mg/cm ² , (c) 20 mg/cm ² and (d) 25 mg/cm ² . (e) Illustration of the drying process. (f) Critical areal loading versus $(1/\gamma)^{1/2}$	170
Figure I-110. SEM images of (a, b) CB electrode, (c, d) CNT-A electrode and (e,f) CNT-B electrode. (g) percentage of capacity (normalized to capacity at C/5) at different discharge C rates. (h) cycling performance at C/3.....	172
Figure I-111. Approach for microstructure characterization and modeling.....	175
Figure I-112. Comparison of model to NMC532 half-cell data for (a) 88 μ m and (b) 129 μ m calendered electrodes.	176
Figure I-113. Compression test results comparing stress- strain curves for fresh cell components against those collected from an aged cell: the anode samples typically show an earlier onset of failure, at lower ultimate strengths; the cathode samples show a very repeatable drop in the modulus – typically characteristic of the current collector. There is no statistical difference in the separator properties for the cell studied under this particular test condition.	177
Figure I-114. Comparison of the electrical and thermal properties of cell components before and after aging.....	178
Figure I-115. (a) Homogenization simulation to determine effective electrolyte transport properties in porous electrode using geometry from CT imaging of an actual electrode. (b) Stochastic reconstruction of virtual geometry, showing CBA phase (green) on active material matrix (red).	179

Figure I-116. FIB-SEM images of (a) calendered baseline, (b) uncalendered, (c) calendered NCM523 electrodes	182
Figure I-117. FIB-SEM of AC015 electrode using an epoxy filler to confine imaging to the image plane.	183
Figure I-118. Full cell electrochemical performance data during 1C discharge after the formation cycles (a) average capacity, and (b) average cell voltage versus electrode coating thickness and porosity (ϵ). The anode (uncalendered graphite, Coating thickness = 173 μm , Porosity = 51.8%) was kept the same for all these measurements.	183
Figure I-119. Performance comparison during 1C discharge in full-cells as a function of (a) electrode coating thickness with porosities fixed at ~47-52% and (b) electrode porosity at fixed thickness of ~107 μm	184
Figure I-120. (a) Chemical diffusion coefficient of lithium-ions in NCM523 oxide particles and (b) c-lattice parameter of the oxide crystal structure NCM523 during charge (delithiation) and discharge (lithiation).	184
Figure I-121. Three point bend testing of fully charged cell. No runaway was observed due to the bending of the cell. Runaway occurred when enough displacement occurred to begin compressing the cell with significant force.	187
Figure I-122. Force vs displacement curve for test performed in the previous figure.	188
Figure I-123. Results of three point bend tests on cells at increasing displacement rates.	189
Figure I-124. Impact of strain rate at cell orientations parallel to cell tabs (top) and diagonal to cell tabs (bottom).	190
Figure I-125. Design drawings of SNL impact tester.	191
Figure I-126. Examples of the results from mechanical testing: a) first principal strain distribution in polymer separator under biaxial loading; (b) tensile cracks in separator lamellae; (c) microstructure of electrode compressed by calendering; (d,e) Young's modulus and yield strength of Celgard separator under different temperatures and strain rates.	193
Figure I-127. Rate performance of NMC(532) electrodes depending on porosity after calendering	194
Figure I-128. X-ray tomography images of an indentation that led to short circuit and XCT images of the copper current collectors showing cracking and mud-cracks	196
Figure I-129. Variation of Young Modulus in 3 different direction as a function of pressure and concentration.....	197
Figure I-130. (a)Reduced extracted capacity of cells damaged under 80% indentation (b) Reduced extracted capacity of electrodes calendered under various pressures	199
Figure I-131. Full cell coupled electrochemical simulation with electrically isolated regions.....	200
Figure I-132. 2D (left) and 3D (right) representations of a small NMC cathode domain illustrating the microtomography-derived particle microstructures combined with the “binder bridge” conductive binder representation.	202

Figure I-133. Computational meshes generated for three calendaring pressures (0 bar, left; 300bar, center; 600 bar, right).....	203
Figure I-134. Effective electrical conductivity and electrolyte-phase tortuosity measured from sampled subdomains with varying porosity. Effective conductivity exhibits linear behavior with a trendline of $k_{\text{eff}} = -0.0334 \varepsilon + 0.021$. Power-law behavior was assumed for tortuosity, with a trendline $\tau = 0.623\varepsilon^{-1.31}$...	204
Figure I-135. Left: Maximum and mean stresses experienced by the NMC particles for all mesostructure representations. Both von Mises stress and maximum shear stress are displayed. Right: Mean von Mises stress for the two binder representations, including cases where particles are separated by a composite binder layer.	205
Figure I-136. LiPF_6 dissociation degree in EC/DEC (1:1 by weight).....	210
Figure I-137. Li^+ transference numbers as functions of concentration, showing correction due to recognition of ion pairing. Published results for other solvents are shown for comparison.	211
Figure I-138. Discharge capacities relative to C/10 capacities for representative cells with cathodes of three thicknesses	212
Figure I-139. Reconstructed slice of pouch cell from micro-tomography trial	213
Figure I-140. Project schematic showing major constituents and progression of Alpha and Beta versions.	215
Figure I-141. Comparison of voltage evolution in two models.	216
Figure I-142. Compare model predictions and measurements of the voltage profile of a type D (left) and type E (right) cell when it is discharged and charged with different initial SOC's.....	217
Figure I-143. Experimental and Simulation setup for Type D Cell	217
Figure I-144. Load displacement curve obtained by experiment and simulation	218
Figure I-145. A diagram of intra- and inter-domain coupling protocols used in NREL's MSMD framework, integrating widely varied scale battery physics in a computationally efficient manner with hierarchical modular architecture.....	221
Figure I-146. Comparison of electrical and thermal response of a battery for mid-size sedan PHEV10 US06 20 minutes driving power profile from the 4 different model combinations	222
Figure I-147. Equivalent circuit model with an SEI formation branch.....	223
Figure I-148. GH-MSMD electrode-domain model (EDM) simulations from Kim, J. Echem. Soc., 2017. (a) Electrolyte salt concentration, (b) electrolyte phase potential, (c) solid surface concentration, and (d) volumetric current density during 5C discharge at 25°C.....	224
Figure I-149. Updated FLUENT MSMD Battery Model panel.....	225
Figure I-150. Illustration for circuit component extraction	226
Figure I-151. Excess Li reservoir used to restore capacity of LMO/graphite pouch cells after ~120 cycles. The graphite/LMO pouch cells were cycled at room temperature with different charge cutoff voltages.	229

Figure I-152. Cycling of 400 mAh ANL silicon-graphite/NMC pouch cells at room temperature without (cells 1-4) and with device inserted but not triggered (cells 5 and 6). These results demonstrate that the device has no unintended negative impact to cycle life when integrated in a cell and left in the idle state.	230
Figure I-153. Cycling of 400 mAh ANL Si pouch cell #3 before and after triggering device showing 8% capacity restored. A.) The measured capacity fade rate before and after triggering the device is relatively constant indicating Li-ions have recovered relatively uniformly. B.) Discharge voltage curve before and after re-lithiation.	230
Figure I- 154. Analysis by California Air Resource Board (CARB) shows increased yearly vehicle miles traveled when using 50 kW fast charging. When compared with a vehicle that never fast charged, nearly a 25% increase in annual miles traveled was realized when 1% to 5% of total charging events were fast charges.	231
Figure I- 155. At high charge rates, a much larger number of lithium ions move to intercalate into graphite as represented by the red dots. However, there is not enough time or space for intercalations; therefore, lithium ions may start plating as metal onto the surface of the graphite electrode, shown as a thick red line).	233
Figure I- 156. XFC station showing different design options such as co-located energy generation and storage which may be used to reduce station operating costs, minimize grid impacts, supplement power provided by the electric grid and accommodate ideal XFC station placement.	235
Figure II-1. SEM of surface of a laminate calendered at 100°C to 30% porosity. Notice flattened and cracked particles.....	244
Figure II-2. Rate performance of a laminate calendered at different temperatures.	245
Figure II-3. Cycling performance of laminates in coin cells calendered at different temperatures.	245
Figure II-4. Resistance for three loadings.....	246
Figure II-5. Cross section of a dry electrode. Note layer on top of the electrode that appears to slightly detach.	246
Figure II-6. 30-sec resistance of four cells: with the surface film, with half the surface film, surface film removed, no film to start with.....	247
Figure II-7. Full cell performance of 1.5 Ah pouch-type cell (a) assembled cell (b) voltage profile during charge-discharge between 2.75 V and 4.4 V at 0.2C rate (c) rate capability at different current rates and (d) cycle life at room temperature.....	251
Figure II-8. SEM images of nano-SiO _x fibers (a) condition A and (b) condition B.	252
Figure II-9. Electrochemical performance of (a) 1st charge/discharge voltage profile with C/24 rate between 1.0 V and 0.005 V and (b) cycle life with C/6 rate at room temperature.	253
Figure II-10. (a) SEM image of nano-Si/C composite made by electrospray process and (b) 1 st cycle discharge/charge voltage profile.	253
Figure II-11. Cell thickness monitoring during cycling with C/24 rate between 1.5 V and 0.005 V at room temperature.	254

Figure II-12. SEM image of (a) version 1 nano-Si/C composite made by electrospray process and (b) version 2.....	254
Figure II-13. Cell performance during cycling at C/6 rate between 1.5 V and 0.005 V at room temperature.	255
Figure II-14. Electrodes of different materials prepared by the non-sintering magnetic alignment method. A, LFP (MTI Corporation). B, OMAC-carbon (Osaka Gas). C, NMC333 (Toda). D, NCA (Toda). E, MCMB (MTI Corporation).	257
Figure II-15: Cycle life (C/3) discharge for a) Hydrocarbon electrolyte charged to 4.5 V (black), 2) fluorocarbon electrolyte charged to 4.5 V (red), and fluorocarbon electrolyte charged to 4.6 volt (blue).....	261
Figure II-16: Gas volume change at 3 weeks (left) and 4 weeks (right) for NMC111 cathodes with graphite anodes when exposed to electrolyte at 60°C.....	261
Figure II-17: TCD chromatogram overlays of 4.6 V LCO and NMC622 cells with 10% FEC concentration in the electrolyte. On the top is the full spectrum, whereas the bottom focuses on 0-10 minutes. H ₂ is seen in the NMC622 cell and PF ₃ in the LCO cell.	262
Figure II-18: Normalized discharge capacity (%) versus cycle number (N) of NMC622 and LCO cells cycled at 4.6 V (top) and 4.2 V (bottom). LCO cells ceased operation after 100 cycles at 4.6 V, whereas NMC622 cells completed the desired 200 charge/discharge cycles. Electrolyte is 1.2 M LiPF ₆ [EC/FEC]/EMC/FE (20:60:20) + 1% PS.	264
Figure II-19: Volume measurements versus time in 4.6 V NMC622 cells during an OCV calendar life test at 45°C as a function of FEC concentration (top). Measured OCV versus time in 4.6 V NMC622 and LCO cells during the same calendar life test also as a function of FEC (bottom)	265
Figure II-20. Battery Performance and Cost (BatPaC) model utilized to establish program relevance ...	268
Figure II-21. Program participants including Laboratories, research facilities, and individual contributors.	269
Figure II-22. Full cell testing protocol.	270
Figure II-23. Full-cell coin-cell results showing average discharge capacity vs. cycle number. The Silicon Deep Dive full cell cycling protocol was used for evaluating the experimental silicon electrodes compared to the original silicon-containing baseline electrode [A-A006A]. The cycling protocol consists of three slow (C/20) formation cycles, an HPPC cycle, and then C/3 aging cycles, followed by a 2nd HPPC cycle, and finally three more slow (C/20) cycles. The capacity values are normalized to the weight of NMC532.	274
Figure II-24. Full-cell coin-cell results showing average discharge capacity vs. cycle number for the Silicon Deep Dive baseline electrodes vs. NMC532 [A-C013A]. Data shows the average values based on 4 coin cells for each electrode pair. The capacity values are normalized to the weight of NMC532.	275
Figure II-25. Image of reactor vessel on roller mill. Note the pressure gauge pointing to the right.....	276
Figure II-26. (Left) Pressure vs time plot showing changes to NMP and water-based Si slurries in sealed pressure vessel. (Right) Mass spectrum of head space collected from water-based Si slurry (blue trace), NMP-based Si slurry (red trace), and ambient air (black trace).....	276

Figure II-27. TGA (Left) and DTGA (Right) of “as received” PAA (dashed red line) and LiPAA (solid blue line). The DTGA of LiPAA was expanded 10X to more easily identify features.	277
Figure II-28. Cycle life of A) LiPAA-based full cells and B) PAA-based full cells. The first 10 cycle Coulombic efficiency of C) LiPAA-based full cells and D) PAA-based full cells. The long term Coulombic efficiency of E) LiPAA-based full cells and F) PAA-based full cells. The secondary drying temperature on the Si-graphite composite anodes are 120°C (red circle), 140°C (gold square), 160°C (green triangle), 180°C (blue diamond), and 200°C (black hour glass). Each point is an average of 3 cells.	279
Figure II-29. Correlation of electrolyte volume and cell cyclability. Discharge capacities during (a) first three cycles at 0.05C/-0.05C, (c) aging cycles at 0.333C/-0.333C, and (e) last three cycles at 0.05C/-0.05C for different electrolyte volume factor groups, F; corresponding irreversible capacity losses (ICLs) during (b) the first three cycles, (d) aging cycles and (f) the last three cycles. Cut-off voltages were 3 and 4.1 V. Voltage for the aging cycle was held at 4.1 V until current reached 0.05C. Error bars correspond to 95% confidence intervals.	281
Figure II-30. SEM images of (a) pristine 15 wt.% Si-graphite anode and (b) F1.5 and (c) F3.5 anode cycled 100 times. Magnification of the images on left and right are 200,000 X and 25,000 X, respectively.	282
Figure II-31. Resistances of 15 wt.% Si-graphite/NMC532 cells from HPPC tests at different voltages during discharge at 4th and 97th cycles for electrolyte volume factor group F1.6 (a), F2.1 (b), F2.6 (c), F3.1 (d), and F3.5 (e).	283
Figure II-32. (a) Impedance spectra of 15 wt.% Si-graphite/NMC532 cells near 3.75 V after 100 cycles with different electrolyte volume factor groups. (b) Total resistances from EIS at different voltages. (Equivalent circuit model for the EIS data fitting is shown in the next figure.)	284
Figure II-33. (a) Equivalent circuit model for EIS data fitting and definitions and four frequency domains of elements. As examples, EIS data of F3.5 at (b) 4.1 V and (c) 3 V after 100 cycles and their data ranges for the fittings.	284
Figure II-34. (Areal specific resistances (ASR) from EIS at different voltages in different electrolyte volume factor groups, (a) ohmic resistance (R_{ohmic}), (b) surface film resistance (R_{sf}), (c) anode charge transfer resistance (R_{ct1}), and (d) cathode charge transfer resistance (R_{ct2}).	285
Figure II-35. Depth profiles of SEI (LiF and carbonates) and active material (Si-Si and Li_xSiO_y) elements. Black dashed and dotted lines are possible ranges of SEI/Si interface and averages of the ranges, respectively. The depth on x-axis was based on the assumption that the film has the same etching rate as SiO_2 . CPS of each element was normalized by its own maximum value.	286
Figure II-36. (a) XPS peaks from depth profiles of F1.6, F2.6, and F3.5 and (b) atomic percentages from the top surface (before sputtering) from XPS survey scans. Depth was calculated based on the sputter rate for SiO_2	287
Figure II-37. Prepared electrodes processed with water (blue) and that will have water present during runaway reactions (red) in comparison to normal non-aqueous systems (right).	289
Figure II-38. (left) Half-cell formation lithiation. (right) DSC results from extracted material.	289

Figure II-39. ARC evaluations for several sample 18650 cells containing undersized electrodes.	290
Figure II-40. Gas sampling results for electrodes containing baseline G8 graphite and 15 wt% silicon using both standard sample vials and cleaned and sealed bottles. Data is shown for analysis completed on organic species (A), hydrocarbons (B), and gases (C).....	291
Figure II-41. Program participants including Laboratories, research facilities, and individual contributors.	296
Figure II-42. Powder X-ray diffraction data collected for the raw and post-processed silicon powders..	297
Figure II-43. (Top) ^{29}Si NMR of Nanoamor (70-130) Si powder processed in NMP (red trace), water with LiPAA binder (green trace), and water (blue trace). All spectra have been normalized to Si-O shift at -120 ppm. (Bottom) - ^1H - ^{29}Si cross polarization NMR and accompanying ^{29}Si NMR of dry milled Si (fuchsia trace and blue trace) and water milled Si (red trace and black trace). Vertical lines designate Si coordinated sites.....	298
Figure II-44. Absorption spectrum from ATR-FTIR of NMP processed Si and water processed Si.	299
Figure II-45. ^{29}Si MAS NMR and deconvolutions (b to d) of pristine and treated commercial HydroQuébec80nm silicon powders. (ANL, Linghong Zhang et al., ACS Applied Materials & Interfaces, 2017, just accepted manuscript).....	301
Figure II-46. (a) ^1H - ^{13}C CP MAS NMR of Paraclete silicon powder batches and corresponding electrochemical performance metrics (b) ^1H - ^{13}C CP MAS NMR of Paraclete powder and NanoAmor 70-130nm powder. (ANL, unpublished work).....	302
Figure II-47. a) Scanning electron microscopy image of silicon nanoparticles b) Mass change of the Si nanoparticles after heat treatment at different temperatures.	303
Figure II-48. FTIR spectra of pristine Si nanoparticles and Si nanoparticles treated at different temperatures.....	304
Figure II-49. a) Specific capacity and b) coulombic efficiency comparison of initial electrochemical performance of Si nanoparticles after different treatments.....	305
Figure II-50. Half cell cycle performance for 500°C -treated and 600°C -treated Si nanoparticles.	306
Figure II-51. a,b): capacity retention and coulombic efficiency of pristine and 400°C -treated Si nanoparticles cycled between 2.5 V and 4.3 V c,d): capacity retention and coulombic efficiency of pristine and 400°C -treated Si nanoparticles cycled between 3.2 V and 4.3 V.	308
Figure II-52. Raman maps of Si-Gr anodes taken before cycling (pristine), after 1 formation cycle, after 2 formation cycles, and after the full cycling protocol (100 cycles). Raman maps were generated by deconvoluting each composite spectrum into the sum of the four components (c-Si, a-Si, graphite, and carbon black).....	309
Figure II-53. Representative normalized Si 2p XPS data collected on 4 different Si-Gr-CB-PAA electrodes produced at ORNL, SNL and ANL.	310
Figure II-54. Capacity versus cycle number plots for full cells containing the SiGr negative electrode with Gen2 electrolyte (black), SiGr negative electrode with Gen2+10 wt% FEC electrolyte (red), and Gr	

negative electrode with Gen2 +10 wt% FEC electrolyte (blue). It is obvious that cells containing the 15 wt% Si show faster capacity decline..... 311

Figure II-55. SEM images of the negative electrode. (a) Pristine Si-Gr electrode showing large graphite flakes (arrow) in contact with Si and carbon nanoparticles in the matrix. (b) The same electrode harvested after 100 cycles from a cell containing Gen2 electrolyte. The graphite particles are completely covered by electrolyte breakdown deposits. In contrast, panel (c) shows a Gr electrode (no Si) harvested from a Gen2 cell after 100 cycles. The graphite flakes and the C45 carbon particles are still clearly observed, as the SEI is relatively thin..... 311

Figure II-56. XPS spectra from pristine SiGr electrode (i) and from negative electrodes harvested from the following full cells: (ii) NCM523/Gr cell, after three formation cycles in Gen2, (iii) NCM523/SiGr cell, after three formation cycles in Gen2, (iv) NCM523/SiGr cell, aged in Gen2, (v) NCM523/SiGr cell, three formation cycles in Gen2 containing FEC, (vi) NCM523/SiGr cell, aged in Gen2 containing FEC. 312

Figure II-57. XPS spectra in (a,c) Li 1s and (b,d) P 2p bands from harvested (a,b) negative electrodes and (c,d) positive electrodes from disassembled cells: (ii) NCM523/Gr cell, after three formation cycles in Gen2, (iii) NCM523/SiGr cell, after three formation cycles in Gen2, (iv) NCM523/SiGr cell, aged in Gen2, (v) NCM523/SiGr cell, three formation cycles in Gen2 containing FEC, (vi) NCM523/SiGr cell, aged in Gen2 containing FEC. 313

Figure II-58. XPS spectra of harvested positive electrodes from cells (i) to (vi) (see inset in panel 'a' for the color table): (i) pristine Si-Gr cell, (ii) Gr cell, after three formation cycles in Gen2, (iii) Si-Gr cell, after three formation cycles in Gen2, (iv) Si-Gr cell, aged in Gen2, (v) Si-Gr cell, three formation cycles in Gen2 containing FEC, (vi) Si-Gr cell, aged in Gen2 containing FEC. The spectral regions are indicated in the panels. 313

Figure II-59. Water loss from hydrated LiPAA binder as observed by thermogravimetry. Note the logarithmic vertical scale. The first section of the plot (indicated with the arrow) corresponds to heating of the sample from 50 to 150°C at 6°C/min, whereas the scattered dots indicate the 150°C isotherm. After the first 3 hours, the mass loss settles into the exponential regime (dashed line)..... 316

Figure II-60. (a) Schematic representation of a Si particle in the advanced stages of aging, with the inner and outer SEI layers formed around the Si core. Mineral compounds derived from Si prevail in the inner SEI while various organic compounds (including alkyl carbonates and inner-carbonate polymers) prevail in the outer SEI, with insoluble salts trapped in the semisolid matrix. Electrolyte and HF molecules can diffuse through the pores and cracks in the outer SEI and react with the particle interior, releasing SiF_4 and water molecules back into the electrolyte. This water joins the hydrolytic cycle for LiPF_6 (shown in panel b). In the latter, water sequentially hydrolyzes PO_xF_y species, consuming five water molecules and releasing five HF molecules in total; the released HF can react with Si particles, continuing the hydrolytic cycle. The two species at the end of this sequence can be observed using NMR spectroscopy in the fluids collected from the aged cells. (c) As the Si particles repeatedly expand and contract during lithiation/delithiation, deep cracks develop allowing access of HF to the core, resulting in its digestion and additional SEI formation..... 317

Figure II-61. Electrochemical reduction of a silicon thin film in a Gen2/FEC electrolyte mixture. 319

Figure II-62. CV comparison of 5% FEC and 20% FEC addition to Gen2 on the cycling of a silicon electrode..... 319

Figure II-63. A comparison of the cycling performance of a silicon thin film electrode versus surface passivation layer thickness.....	320
Figure II-64. ATR FTIR spectra of A) PAA dried at 120°C, B) PAA dried at 120°C, electrochemically reacted with Li metal, C) LiPAA dried at 120°C, D) PAA dried at 220°C, E) PAA dried at 220°C, electrochemically reacted with Li metal, and F) LiPAA dried at 220°C.	321
Figure II-65. FTIR spectra of the pristine Si anode and the Si anode after one formation cycle. FTIR spectra of Li_2SiO_3 , Li_4SiO_4 , NanoAmor silicon, and LiPAA are also shown for comparison.....	322
Figure II-66. FTIR spectra of the Si anode after one formation cycle, after two formation cycles, and after 100 cycles. FTIR spectra of Li_2SiO_3 , Li_4SiO_4 , Li_2CO_3 , LiPAA, and EC are also shown for comparison.	322
Figure II-67. (a) Voltage curve of the cathode/anode cycling at C/3, (b) Voltage curve of the cathode/Li ring cycling at C/50, and (c) Voltage curve of the anode/Li ring cycling at C/50.	323
Figure II-68. Capacity cycling of the three electrode cell with Li replenished from Li ring every 100 cycles.	324
Figure II-69. a) Cathode and (b) anode voltage curve versus reference electrode during capacity fade at C/3 cycling.	324
Figure II-70. Contour mapping of volumetric capacity [Ah/L, black lines] and average delithiation voltage [V, blue lines] of the Si alloy/graphite versus the composition of Si alloy and weight ratio of Si alloy/graphite. Black lines are in 100 Ah/L increment and blue lines are in 0.02 V increment.	325
Figure II-71. Contour mapping of cell stack energy density [Wh/L, red lines] using Si alloy/graphite electrode and volume expansion ratio of the cell stack [black lines]. The increment between adjacent red lines is 10 Wh/L and the increment between adjacent black lines is 1%.....	326
Figure II-72. Contour mapping of cell stack energy density [Wh/L, red lines] and volume expansion ratio [blue lines] of Si alloys. The increment between adjacent red lines is 10 Wh/L and the increment between adjacent blue lines is 20%.....	327
Figure II-73. Program participants including Laboratories, research facilities, and individual contributors.	332
Figure II-74. Synthesis of graft copolymer GC-g-LiPAA via RAFT polymerization.	334
Figure II-75. (A) Cycling performance silicon/graphite electrodes from the polymer binder of PVDF, GC, GC21%-m-LiPAA76 and GC22%-g-LiPAA62 at a current rate of C/10; (B) Coulombic efficiency of the electrodes from different polymer binders, inset is the zoom-in area showing the comparative efficiency of electrodes from GC21%-m-LiPAA76 and GC22%-g-LiPAA62 in the first 30 cycles;.....	335
Figure II-76. Cycling performance of silicon/graphite electrodes from the polymer binder of GC22%-g-LiPAA17, GC22%-g-LiPAA27, GC22%-g-LiPAA62, and GC12%-g-LiPAA71 at a current rate of 0.1 C.	336
Figure II-77. Synthesis scheme of cross-linked catechol groups functionalized chitosan; cycling performance of different polymer binders. (silicon-based anode: 60% SiNPs, 20% polymer binder and 20% carbon black).	337
Figure II-78. Approaches for synthesizing crosslinked PAA binders.....	338

Figure II-79. Specific discharge capacities of half cells of (left) silicon/graphite composite electrodes (15% silicon) and (right) high capacity silicon electrodes (70% silicon) using PAA-based binders during the course of 100 cycles under C/3 rate.	339
Figure II-80. Specific discharge capacities of half cells of (left) silicon/graphite composite electrodes and (right) high capacity silicon electrodes using PAA-based binders during the course of 100 cycles under C/3 rate.	340
Figure II-81. Synthetic route for P4VBA binders.	340
Figure II-82. Specific capacity profiles of cells containing P4VBA and PAA binders.	341
Figure II-83. In situ formation of 3D mesh from polymer and reactive small molecules.	342
Figure II-84. (a) poly(ethylene-alt-maleic anhydride) and (b) poly(methyl vinyl ether-alt-maleic anhydride).	342
Figure II-85. Hydrolysis of poly(anhydride) to poly(acid).	342
Figure II-86. General scheme of in-situ crosslinking of poly(R=H or OCH ₃ -alt-maleic acid) and small molecule, 80:20 (X, Y = OH or NH ₂ , Z = O or NH).	343
Figure II-87. An example of a synthesis of the linear polymer and self-crosslinking product.	344
Figure II-88. Fourier transform infrared (FTIR) spectra of the PPy-based pristine and delithiated electrodes.	344
Figure II-89. Synthesis of anthracene-based polymers. A. anthracenemethyleneoxide methacrylate polymer – P(Ant). B. Copolymer with Triethyleneoxide - P(Ant _{0.7} -co-TEG _{0.3}). Molecular weights and polydispersity (PDI) of the P(Ant) and P(Ant _{0.7} -co-TEG _{0.3}) polymers.	345
Figure II-90. Si nanoparticle cycling with the P(Ant) binder. (Electrode composition is 90% nano Si particles, and 10% binder, 0.4 mg/cm ² of Si materials, cycling rate C/10).	345
Figure II-91. Si nanoparticle and graphite composite electrode cycling with commercial SBR binder. A. Electrode composition and the mass loading of 3 cells made of the same laminate against Li metal electrode. B. Cycling performance of 3 cells at C/3 rate. C. The coulombic efficiencies of the cells.	346
Figure II-92. Mass spectra of one MLD cycle including TMA and glycerol doses. Pulse dosing was used for both precursors to enhance the reactions.	349
Figure II-93. TEM images of the uncoated Si particle (a) and the MLD coated Si particle (b). The particles have the size about 50 nm, were purchased from Alfa.	349
Figure II-94. TEM images of uncoated Si particles (a-c), and MLD coated Si particles (d-f). The Si particles were from NanoAmor, has been used as the new baseline material.	350
Figure II-95. Specific capacity of the uncoated electrode (plotted in black) and the electrode fabricated by using the coated Si particles (plotted in red). The electrode is fabricated by using 73 wt% graphite, 15 wt% Si (NanoAmor, 70-130 nm), 10 wt% poly acrylic acid and 2 wt% Timcal C45. No major difference in electrochemical performance was observed for the coated particles.	350
Figure II-96. (a) Specific capacity of the uncoated electrode (plotted in black) and the electrode fabricated by using the coated Si particles (plotted in red). The electrode is fabricated by using 73 wt% graphite, 15	

wt% Si (Alfa, 50 nm), 10 wt% poly acrylic acid and 2 wt% Timcal C45. Improved electrochemical performance was achieved for the coated particles. (b) Different capacity (dQ/dV) curves of the electrodes made with the graphite, the MLD coated Si and the graphite-coated Si. The inset plot illustrates the capacity contribution from each component.	351
Figure II-97. a) Voltage profile of the graphite-uncoated Si composite electrode cycling between 10 mV and 1 V; (b) Differential capacity (dQ/dV) plots during delithiation at the first cycle; and (c) at the 100th cycle.	352
Figure II-98. (a) Voltage profile of the graphite-coated Si composite electrode cycling between 10 mV and 1 V; (b) Differential capacity (dQ/dV) plots during delithiation at the first cycle; and (c) at the 100th cycle.	352
Figure II-99. Cross-sectional SEM observation of (a) the as-prepared electrode made with the uncoated silicon particles; (b) the uncoated electrode after 100 electrochemical cycles; (c) the electrode made with the coated Si particles, after 100 electrochemical cycles.	353
Figure II-100. SEM images of the surface of (a) and (b) the graphite-uncoated Si electrode after 100 electrochemical cycles; (c) and (d) the graphite-coated Si electrode after 100 electrochemical cycles. ...	354
Figure II-101. (A) Pictures of dispersions of Si NPs in ethanol and (B) FTIR spectra of Si NPs from Nano Amor (black) and Alfar Aesar (red).	355
Figure II-102. FTIR spectra of silicon nano powders. (a) Pristine Si, -Si-OH enriched Si, vinyl-Si-Et-OH and MP-Si-ET-OH, and (b) pristine Si, -Si-OH enriched Si, vinyl-Si-Et-THF and MP-Si-ET-THF.	356
Figure II-103. TGA profiles of (i) pristine Si NPs, (ii) oxidized Si NPs, (iii) vinyl-Si-THF and (iv) MP-Si-THF.	356
Figure II-104. (a) Expanded voltage profile for SEI formation, and (b-d) dQ/dV profiles for the 1 st , 2 nd and 3 rd cycle for the Si-graphite composite anode with Gen2+10% FEC and Gen2 +10% FEC +1% HMDS.	357
Figure II-105. Capacity retention and Coulombic efficiency of Si-graphite/Li half cells with Gen 2 electrolyte, Gen2+10% FEC and Gen2+10% FEC+1% HMDS.	358
Figure II-106. Proposed surface reaction of HMDS with -Si-OH on the surface of Silicon nanoparticles.	358
Figure II-107. SEM images of Si-Sn-C electrodes at (a – d) pristine state, (e - h) the 50 th lithiation, and (i - l) the 50 th delithiation.	359
Figure II-108. (a, b) SEM image, (c) Si, Sn EDS mapping of the selected area (green box in (b)) in Si-Sn sample prepared by high energy mill and (d, e) SEM image, (f) Si, Sn EDS mapping of the selected area (green box in (e)) in Si-Sn sample prepared by Cryomill.	360
Figure II-109. (a, b) SEM image, (c) Si, Sn EDS mapping of the selected area (outlined by green lines in (b)) in Si-Sn sample prepared by high energy mill. (d, e) SEM image, (f) Si, Sn EDS mapping of the selected area (outlined by green lines in (e)) in Si-Sn sample prepared by Cryomill.	361
Figure II-110. (a) XRD patterns and (b) cycling performance of Si-Sn samples produced by chemical reduction method. Cells were cycled between 1.5 and 0.05 V at room temperature.	362

Figure II-111. Voltage profiles of (left) Li/NCM523 and Li/SiO _x cells, and (right) Li/NCM523-LFO and Li/SiO _x cells. The utilization of the NCM electrode is greater as a result of the extra pre-lithiation capacity imparted in the cell from the additive, LFO.	363
Figure II-112. (left) Capacity versus cycle number for SiO _x /NCM523 cells (red filled circles; 2.5 to 4.3 V, C/10), and SiO _x /NCM523-LFO cells (black filled squares; 2.0 to 4.3 V, C/10). (Right) capacity versus cycle number for NCM523-LFO half cells.	363
Figure II-113. (Representative potential profiles for the (a) high capacity LiFePO ₄ reference/counter electrode against Li metal, and (b) 15% Si-graphite electrode against Li metal. In the full/reference cell, as the Si irreversibly consumes Li the LiFePO ₄ electrode has ample Li inventory to continue to supply capacity to the cell.	364
Figure II-114. Representative electrochemical profile versus capacity with cycle number of Si-graphite cycled against a LiFePO ₄ reference electrode at (a) C/10, (b) C/5, and (c) 1C. In (b) and (c) the first and last 3 cycles of each set of 100 cycles were performed at C/10 while the intermediate cycles were performed at C/5 and 1C, respectively.....	365
Figure II-115. Relative capacity fade above and below 3.185 V with respect to cycle number for Si-graphite cycled against a LiFePO ₄ reference electrode at 1C. The first and last 3 cycles of each set of 100 cycles were performed at C/10 while the intermediate cycles were performed at 1C.	366
Figure II-116. Representative differential capacity dQ/dV plots for Si-graphite cycled against a LiFePO ₄ reference electrode at (a) C/10, (b) C/5, and (c) 1C. In (b) and (c) the first and last 3 cycles of each set of 100 cycles were performed at C/10 while the intermediate cycles were performed at C/5 and 1C, respectively. In (a) the * marks (de)lithiation processes attributed to graphite, letters A-C mark lithiation processes of Si, and letters D-E mark delithiation processes of Si.	366
Figure II-117. SEM (a-d) and Raman spectra (e-f) of the pristine Si-graphite electrode (a,b,e) and after 1000 cycles at 1C against a LFP reference electrode (c,d,f). Cross-section images of Si-Gr (c) pristine electrode and (d) cycled and the EDS mapping of C K (cyan), Cu L (red), F K (green), Si K (violet), P K (orange) and O K (yellow) associated to them. Note that the pristine electrode has been extracted from a half cell assembled against metallic lithium and the cycled electrode belongs to the Si-Gr/LFP full cell cycled at C/5 for 100 cycles.....	368
Figure II-118. Raw capacity versus voltage data for cells cycled in the LiPF ₆ electrolyte.....	378
Figure II-119. Capacity versus voltage data for cells cycled in the LiPF ₆ electrolyte shifted to 0.45 V.	378
Figure II-120. Magnified view of capacity versus voltage data for cells cycled in the LiPF ₆ electrolyte above 0.45 V.	379
Figure II-121. Magnified view of capacity versus voltage data for cells cycled in the LiPF ₆ electrolyte below 0.45 V.....	379
Figure II-122. Raw capacity versus voltage data for cells cycled in the LiTFSI electrolyte.	380
Figure II-123. Capacity versus voltage data for cells cycled in the LiTFSI electrolyte shifted to 0.45 V.	380
Figure II-124. Magnified view of capacity versus voltage data for cells cycled in the LiTFSI electrolyte below 0.45 V.....	381

Figure II-125. XPS data collected for an uncycled silicon electrode aged in a glove box and in air for 3 weeks.	381
Figure II-126. TOF-SIMS depth profiles of silicon films on copper foil grown at both NREL (left) and ORNL (right). Only composition profile for the transition-metal impurities and the copper substrate are shown.	382
Figure II-127. TOF-SIMS surface spectra of the ORNL films, showing the changes to the sample surface upon long-term exposure in the ORNL glove box, as well as shorter-term exposure to air.	382
Figure II-128. Optical and negative-polarity TOF-SIMS images from as-received (uncleaned) SEISta round-robin Si(001) wafer sample with native oxide. Mass channel labels are to the lower left of each image. The measurements reveal large amounts of fluorine and chlorine contamination.	383
Figure II-129. Optical and positive-polarity TOF-SIMS images from as-received (uncleaned) SEISta round-robin Si(001) wafer with a native oxide. Mass channel labels are to the lower left of each image. The measurements reveal a large amount of hydrocarbon contamination.	384
Figure II-130. Optical and positive-polarity TOF-SIMS images from RCA-cleaned SEISta round-robin Si(001) wafer with a native oxide. Mass channel labels are to the lower left of each image. Essentially no hydrocarbon contamination is observed.	384
Figure II-131. TOF-SIMS depth profiles of two Si-wafer samples that were also analyzed with SSRM. The red profile is the half-cycle sample, and the green is the full-cycle sample. Consistent with the KPFM data, it appears that the SEI is much thicker for the delithiated sample—an interesting result.	385
Figure II-132. TOF-SIMS 3-D reconstruction of the lithium distribution in the SEI of the full-cycle KPFM specimen (50 μm x 50 μm area, depth currently unknown). The image at left shows the full dataset; image in the middle shows the data from about halfway through the SEI; image at right shows the lithium distribution at transition between the SEI and the silicon.	385
Figure II-133. TOF-SIMS 3-D reconstruction of the C ₂ H ₋ distribution in the SEI of the full-cycle SSRM specimen (50 μm x 50 μm area, depth currently unknown). The image at left shows the full dataset; image in the middle shows the data from about halfway through the SEI; image at right shows the lithium distribution at transition between the SEI and the silicon.	386
Figure II-134. Schematic sketch of the electrochemical cell: 1) the reference electrode and the counter electrode located in the cell cap (top); 2) cell body (middle); and 3) cell base with the working electrode (bottom).	387
Figure II-135. Cross-sectional sketch of the designed electrochemical cell.	387
Figure II-136. The voltage profile during lithiation of silicon wafer samples. Increasing pressure was applied on the stainless-steel current collector to ensure sufficient electrical conductivity.	388
Figure II-137. The voltage profile of the baseline silicon wafer sample, during lithiation and delithiation. The current for both lithiation and delithiation is 10 μA . The reaction duration is limited to 2 hours for both lithiation and delithiation processes.	389
Figure II-138. Summary of binding-energy separations for common inorganic SEI constituents. Reported literature values for specific phases plotted vs. BEs of relevant core levels. Best-fit lines with unity slopes	

were used to determine average BE separations. In each case, values extracted from NREL datasets are shown as a blue square.....	391
Figure II-139. Time-resolved XPS spectra showing <i>in-situ</i> oxygen exposure to form a pristine layer of Li ₂ O on sputter-cleaned Li metal. BE separation for this phase was found to be 476.85 eV, in good agreement with the prior figure.....	392
Figure II-140. Ternary phase diagram of the Li-Si-O system.....	393
Figure II-141. Voltage profile for a) amorphous and crystalline lithium silicides and b) amorphous and crystalline lithium silicates.	394
Figure II-142. Diffusivities in a) lithium silicides are greater than diffusivities in b) lithium silicates. Due to high variability in diffusivities, amplified by a log-scale, error bars are not shown.....	394
Figure II-143. The (a) CIP and (b) SSIP solvation structures.....	395
Figure II-144. Snapshot of a classical MD simulation of a model silicon anode with a crystalline structure (a) and amorphous silicon oxide on top of it (b). A constant electric potential is applied to the model battery cell. Si (yellow), Li (green), C (gray), H (white), O (red), P (blue), and F (cyan).....	395
Figure II-145. Scaled-up plasma reactor, load-lock collection system, and small-diameter (<10-nm) hydrogen-passivated Si NPs.	396
Figure II-146. Example of FTIR data of solid material following reaction of Si NPs and electrolyte.	397
Figure II-147. IR gas cell used for kinetic measurements from two different angles. The path length through the cell is 11 cm, and the KBr windows are 25 mm in diameter by 2 mm thick. The injection port (circled in red) is sealed with a septum, and the outgas port (yellow) can be opened for purging, if necessary.	398
Figure II-148. Plot of change in volume (calculated through buoyancy) of the nanostructured silicon compounds reacting with various electrolytes in pouches. The left plot is of the nanocrystalline and the right is the nanoamorphous.....	399
Figure II-149. Characterization data for the gases produced in the reaction between the silicon nanocrystals prepared by silane and the Gen 2 electrolyte. a) Kinetic IR (black = 14 min, red = 752 min, blue = 1,278 min), insets CO ₂ and CO, and SiF ₄ and PF ₃ . b) Mass spectrum was taken after 480 minutes (sample is red, helium is blue). Boxes around peaks correspond to various compounds (blue = CO, purple = O ₂), SiF ₄ (104 amu, 85 amu, 86 amu, 87 amu), PF ₃ (69 amu), CO ₂ (44 amu), F (19 amu), and H ₂ (2 amu). c) Peak area vs time plot to illustrate any correlation between the evolution of the different gases. Inset is derivative of plot with respect to time. (In both, black = CO ₂ , purple = CO, red = SiF ₄ , and blue = PF ₃).....	400
Figure II-150. Characterization data for the gases produced in the reaction between the nanoamorphous silicon and the Gen 2 electrolyte. a) Kinetic IR (black = 0.936 min, red = 126 min, blue = 559 min, purple = 818 min), insets CO ₂ , and SiF ₄ and PF ₃ . b) Mass spectrum was taken after 14 days (sample is red, helium is blue). Boxes around peaks correspond to various compounds (yellow = H ₂ , black = F, blue = CO, purple = O ₂ , orange = CO ₂ , red = PF ₃ , green = SiF ₄). SiF ₄ (104 amu, 85 amu, 86 amu, 87 amu), PF ₃ (69 amu), CO ₂ (44 amu), F (19 amu), and H ₂ (2 amu). c) Peak area vs time plot to illustrate any	

correlation between the evolution of the different gases. Inset is derivative of plot with respect to time. (In both, black = CO₂, red = SiF₄, and blue = PF₃). 401

Figure II-151. Characterization data for the gases produced in the reaction between the fumed silica and the Gen 2 electrolyte. a) Kinetic IR (black = 0.3 min, red = 184 min, blue = 1,019 min, purple = 1,147 min), insets CO₂, and SiF₄ and PF₃. b) Mass spectrum was taken after 40 days (sample is red, helium is blue). Boxes around peaks correspond to various compounds (yellow = H₂, black = F, blue = CO, purple = O₂, orange = CO₂, red = PF₃, green = SiF₄). SiF₄ (104 amu, 85 amu, 86 amu, 87 amu), PF₃ (69 amu), CO₂ (44 amu), F (19 amu), and H₂ (2 amu). c) Peak area vs time plot to illustrate any correlation between the evolution of the different gases. Inset: derivative of plot with respect to time of peak area vs time plot. (In both, black = CO₂, red = SiF₄, and blue = PF₃). 402

Figure II-152. Characterization data for the gases produced in the reaction between the Stöber silica and the Gen 2 electrolyte. a) In the IR (black = 0.936 min, red = 126 min, blue = 559 min, purple = 818 min), the CO₂, SiF₄, and PF₃ peaks were nonexistent, as identified in the insets. b) The mass spectrum was taken after 48 days, and the reaction gases were present in this spectrum, indicating that the reaction took longer than the IR experiment ran for (sample is red and black, helium is blue). SiF₄ (104 amu, 85 amu, 86 amu, 87 amu), PF₃ (69 amu), CO₂ (44 amu), F (19 amu), and H₂ (2 amu). Boxes around peaks correspond to various compounds (yellow = H₂, black = F, blue = CO, purple = O₂, orange = CO₂, red = PF₃, green = SiF₄). c) From the peak area vs time plot, the three gases produced have inflections in the curves that seem to loosely correlate between the substances, although the derivative plot is difficult to correlate. (In both, black = CO₂, red = SiF₄, and blue = PF₃). 403

Figure II-153. Structures of lithium metasilicate (Li₂SiO₃, left) and lithium orthosilicate (Li₄SiO₄, right) 404

Figure II-154. Characterization data for the gases produced in the reaction between the Li₂SiO₃ and the Gen 2 electrolyte. a) Kinetic IR (black = 0.936 min, red = 126 min, blue = 559 min, purple = 818 min), insets CO₂, and SiF₄ and PF₃. b) Mass spectrum was taken after 27 days (sample is red, helium is blue). Boxes around peaks correspond to various compounds (yellow = H₂, black = F, blue = CO, purple = O₂, orange = CO₂, red = PF₃, green = SiF₄). SiF₄ (104 amu, 85 amu, 86 amu, 87 amu), PF₃ (69 amu), CO₂ (44 amu), F (19 amu), and H₂ (2 amu). c) Peak area vs time plot to illustrate any correlation between the evolution of the different gases. The double y plot allows for a clearer picture of the SiF₄ and PF₃ curves as compared to the CO₂. d) Derivative of plot with respect to time of peak area vs time plot. (In both, black = CO₂, red = SiF₄, and blue = PF₃). The double y plot allows for a clearer picture of the SiF₄ and PF₃ curves as compared to the CO₂. 404

Figure II-155. Characterization data for the gases produced in the reaction between the Li₄SiO₄ and the Gen 2 electrolyte. a) Kinetic IR (black = 0.936 min, red = 126 min, blue = 559 min, purple = 818 min), insets CO₂, and SiF₄ and PF₃. b) Mass spectrum was taken after 19 days (sample is red, helium is blue). Boxes around peaks correspond to various compounds (yellow = H₂, black = F, blue = CO, purple = O₂, orange = CO₂, red = PF₃, green = SiF₄). SiF₄ (104 amu, 85 amu, 86 amu, 87 amu), PF₃ (69 amu), CO₂ (44 amu), F (19 amu), and H₂ (2 amu). c) Peak area vs time plot to illustrate any correlation between the evolution of the different gases. Inset is derivative of plot with respect to time. (In both, black = CO₂, red = SiF₄, and blue = PF₃). 405

Figure II-156. Chart comparing the volume of each gas produced per surface area of material after reacting for 14 hours between the different silicon materials explored in this paper. The PF3 signal was increased by a factor of 100.	406
Figure II-157. Chamber geometry used to deposit Li_xSiO_y thin films.	407
Figure II-158. XPS depth profile analysis of Li_xSiO_y thin film on copper foil. Atomic percentage as a function of sputter depth for a) Si-rich region and b) lithium-rich region.	408
Figure II-159. a) O 1s spectra, b) Si 2p spectra, and c) Li 1s spectra of lithium-rich region and silicon-rich region.	408
Figure II-160. AFM images of a) as-deposited film, b) indented film, and c) imprinted indented film...	409
Figure II-161. Indentation depth plotted against the indentation force for the a) lithium-rich region and b) silicon-rich region. AFM images of indented film at c) lithium-rich region and d) silicon-rich region. ...	410
Figure II-162. AFM height image of a) ductile behavior region, b) brittle behavior region; phase image of c) ductile-behavior region and d) brittle-behavior region; and e) plot of indentation depth at different sites.	410
Figure II-163. Indentation depth profiles of Si, Li_xSi_y , and Li_xSiO_y thin film under indentation force of 5.4 μN	410
Figure II-164. Time evolution of XPS depth profiles on SiO_2 sputtered on Cu foil exposed to electrolyte, from as-deposited (left) to exposed for 72 hours (right). The film evolution and surface is seen to establish rapidly, but affects the SiO_2 depth over time.	411
Figure II-165. Time evolution of XPS depth profiles on $\text{Li}_2\text{Si}_2\text{O}_5$ sputtered on Cu foil exposed to electrolyte, from as-deposited (left) to exposed for 72 hours (right). The time evolution of the film and thickness of the interface layer are markedly different than in the SiO_2 case.	411
Figure II-166. (left) ATR-IR spectra of SiO_2 film sputtered on Cu exposed to electrolyte for various lengths of time. Relatively minor evolution of surface species is noted, and the O-Si-O network is relatively unperturbed. (right) Spectra of $\text{Li}_2\text{Si}_2\text{O}_5$ film subjected to the same conditions. Although the ATR-IR signals start out similarly, the time evolution of the surface products is very different, with more evidence of salt and electrolyte decomposition being noted.....	412
Figure II-167. Charge and discharge profile of a) lithium-rich region and b) silicon-rich region.	413
Figure II-168. Impedance spectra of lithium-rich region and silicon-rich region for the fresh cell and cell sitting for 24 hours.	414
Figure II-169. a) charge and discharge profile of Si and $\text{Li}_x\text{SiO}_y/\text{Si}$. b) Cycle performance and Coulombic efficiency of Si and $\text{Li}_x\text{SiO}_y/\text{Si}$	414
Figure II-170. Phase diagram for the silicon-lithium systems.	416
Figure II-171. Long- (XRD, a and b) and short- (solid state NMR, c and d) range characterization of Li_7Si_3 model compound.	417
Figure II-172. Multinuclear solid-state NMR data of pristine and PVDF-treated Li_7Si_3	417

Figure II-173. Solid-state NMR (a) and XRD data (b) of pristine and LiPAA-treated Li ₇ Si ₃ . ANL, unpublished work.....	418
Figure II-174. Cyclic voltammetry of pristine, melted, and cleaned tin model electrodes swept from OCV to 0.8 V and back to 2 V in 1 M LiPF ₆ /EC:DEC (1:2 wt%) electrolyte.....	419
Figure II-175. <i>Ex-situ</i> FTIR analysis of pristine, melted, and cleaned tin model electrodes cycled up to 0.8 V in 1 M LiPF ₆ /EC:DEC (1:2 wt%) electrolyte at different washing steps.....	419
Figure II-176. Cyclic voltammetry of bare Si (100) wafer and comparison with the modified model electrodes with Li ₂ O, Li ₂ CO ₃ , and LiF thin film deposited within the 0.01–2.0 V potential region. Enlarged potential region of the first reduction process.	420
Figure II-177. Post-mortem SEM images of cycled Si (100) electrode the modified model electrodes with Li ₂ O, Li ₂ CO ₃ , and LiF thin film deposited.	421
Figure II-178. Cyclic voltammetry of Si(100) wafer, 100-nm SiO ₂ /Si(100), and 300-nm SiO ₂ /Si(100) swept from OCV to 0.005 V and back to 2 V in 1.2 M LiPF ₆ /EC:DEC (3:7 wt%) electrolyte.	422
Figure II-179. Si (left) and O (right) K-edge XAS spectra of pristine Si(100) wafer, 100-nm SiO ₂ /Si(100), and 300-nm SiO ₂ /Si(100).	422
Figure II-180. Schematic depiction of SSRM instrumentation and mechanical milling of a sample.....	423
Figure II-181. Contact resistance as a function of applied probe force. Image from Kalanin, S. and Gruverman, A.L., <i>Scanning Probe Microscopy</i> , Springer (2007)	424
Figure II-182. Height (left) and resistance (right) channels showing the lateral and vertical resolution of the instrument. Deeper milling into SEI carried out under higher probe forces reveals SEI layers of significantly lower material resistance. In the resistance channel image at right, higher voltage is indicative of lower resistance.....	424
Figure II-183. Studies of resistance vs. depth for different sample series. The plot at left shows how SEI thickness and vertical homogeneity develops over repeated cycles. The plot at right shows the distinct resistance and thicknesses of the lithiated and delithiated phases of SEI formed in the original cycle. Thickness is calculated by measuring the depth at which Si wafer-substrate equivalent resistance is measured.	425
Figure II-184. NR data (data points) and fits (solid line) for representative data sets collected in this study.	426
Figure II-185. Plot of the refined SLD profile of the film as a function of distance from the thick Si substrate.	426
Figure II-186. Plots of SLD values and layer thicknesses as a function of state of charge for silicon (top) and the SEI (bottom).	427
Figure II-187. F1s XPS data collected for the Si electrodes as a function of cycling.....	428
Figure II-188. C1s XPS data collected for the Si electrodes as a function of cycling.	429
Figure II-189. Plot of C and F atomic concentrations as a function of state of charge and SEI SLD.	431
Figure II-190. Graphical summary of SEI layer chemistry grown on silicon with and without FEC.	432

Figure II-191. Schematic picture of the TERS setup for studying SEI on silicon.	434
Figure II-192. Image of ORNL's TERS setup operated under argon atmosphere.....	434
Figure II-193. Comparison of micro-Raman signal with TERS for the same sample (cycled amorphous Si).....	435
Figure II-194. Shows the TERS results for amorphous silicon cycled 20X. We notice several peaks apart from the silicon coming from the tip centered around 521 cm ⁻¹ . The peak at 1,372 cm ⁻¹ is from CH ₃ symmetric deformation in CH ₃ -COO components. Using the integration of this peak, the CH ₃ -COO components can be mapped in a 500-nm X 500-nm region.....	435
Figure II-195. (a) Schematic illustration of the synthesis of p-Si@C; (b) SEM images showing the morphology and cross section of p-Si@C; (c)-(d) Long-term cycling and rate performance of p-Si (red plot) and p-Si@C (blue plot).	442
Figure II-196. (a) Schematic illustration of the synthesis of p-Si@C; (b) TEM image of the silica nanoparticles; (c) SEM image of the SiO ₂ microspheres by emulsion method; (d) SEM image of the porous Si microsphere; (e) Cycling performance of p-Si/C and nano-Si; (f) rate performance of the p-Si/C.	443
Figure II-197. (a) Schematic illustration of the preparation process of the micro-MWNT-Si composite; (b) TEM image of MWNT/SiO ₂ composite (before emulsion); (c) SEM image of MWNT/SiO ₂ composite (after emulsion); (d) SEM image of MWNT/Si composite after aluminothermic reaction; (e) long-term cycling performance of Si/MWNTC composite; (f) cycling stability of Si/MWNT/C with different mass loadings at the current density of 0.7 mA/cm ²	444
Figure II-198. (a) XRD pattern of LTSR reaction intermediate showing presence of Si, and presence of single-phase elemental Si following HCl treatment. (b) Specific discharge capacity vs. cycle numbers for LTSR-derived Si/CNF nanocomposite. The current rate for the first 3 cycles is 300 mA/g and for the remaining cycles is 1 A/g.....	445
Figure II-199. (a) SEM image and corresponding EDAX mapping of Cu and catalyst layer M of catalyst-coated Cu foil; (b) SEM showing growth of CNT on Cu foil; (c) and (d) low- and high magnification images of electrodeposited Si on CNT/Cu substrates; (e) Specific discharge capacity vs. cycle number for ED-Si/CNT nanostructured binderless electrode tested at 0.3 A/g in Li/Li ⁺ system.	445
Figure II-200. (a), (b) SEM images of Si-based-nanocomposite conducting porous foams with interconnected porosity; (c) Long-term cycling data of nano-Si conducting foam tested at 50 mA/g for the initial 6 cycles followed by 0.5 A/g in a Li/Li ⁺ system.....	446
Figure II-201. Characterization and stability of LiF-Li _x Si NPs. (a) TEM image and (b) XRD pattern of LiF-Li _x Si NPs. (c) The amount of gas released for coated (red) and uncoated (blue) Li _x Si NPs reacted with NMP measured by gas chromatography. (d) First-cycle delithiation capacities of LiF-Li _x Si NPs (solid line) and bare Li _x Si NPs (dashed line) using different solvents to form the slurry. (e) The extraction capacities of LiF-Li _x Si NPs exposed to ambient air (~40% RH) with varying durations. The inset shows the trend of capacity decay of LiF-Li _x Si NPs (red) and Li ₂ O-Li _x Si NPs (black) with varying durations. (f) Cycling performance of LiF-Li _x Si NPs (red), bare Li _x Si NPs (blue) and Si NPs control cell (black) at C/20 for the first several cycles and C/2 for the following cycles (1C=4.2 A/g, and the capacity is based on the	

mass of Si in the electrodes). The Coulombic efficiency is plotted on the secondary y-axis (LiF-Li_xSi NPs: red, and bare Li_xSi NPs: blue)..... 450

Figure II-202. (a, b) SEM images of Ge NPs (a) before and (b) after thermal lithiation. (c) XRD patterns of Ge NPs before (upper) and after thermal lithiation (bottom). (d, e) SEM images of GeO₂ NPs (d) before and (e) after thermal lithiation. (f) First-cycle delithiation capacities of lithiated Ge NPs (blue) and lithiated GeO₂ NPs (red). The capacity is based on the mass of Ge or GeO₂ in the anode. (g) First-cycle delithiation capacities of lithiated Ge NPs (blue) and lithiated GeO₂ NPs (red) before (solid) and after (dash) exposure to ambient-air condition (30%~40% RH) for 6h. 451

Figure II-203. (a, b) SEM images of Sn NPs (a) before and (b) after thermal lithiation. Scale bar, 500 nm. (c) XRD patterns of Sn NPs before (upper) and after thermal lithiation (bottom). (d, e) SEM images of SnO₂ NPs (d) before and (e) after thermal lithiation. Scale bar, 500 nm. (f) First-cycle delithiation capacities of lithiated Sn NPs before (blue) and after (red) exposure to dry-air condition for 5 days. The inset shows the trend of capacity decay of lithiated Si (black), Sn (purple) and Ge (red) NPs. (g) XRD patterns of lithiated Sn NPs exposed to ambient-air condition for 2h (upper) and 6 h (bottom). 452

Figure II-204. Characterizations of the Li_xSi/graphene foil. a, Photograph of large Li_xSi/graphene foil with 8 cm width and 24 cm length. b, Low-magnification TEM image of the overlapped and interconnected graphene sheets. c, TEM image shows a double-layer graphene sheet with the inter-layer distance of 0.334 nm. The inset is the atomic resolution image of the graphene sheet. d, Uniaxial tensile test of the graphene foil (blue), bulky paper (black), Li metal foil (orange), and Li_xSi/graphene foil (red). e, XRD pattern reveals the highly crystalline nature of graphitic carbon and Li₂₂Si₅. f, Top-view and g, cross-sectional view SEM images of the Li_xSi/graphene foil. 453

Figure II-205. Schematic process to make hollow core Si/C composite via spray precipitation and post sintering. 457

Figure II-206. SEM images of the Si/C composite secondary particles. (a-c) the Si/C hollow secondary particles at different magnifications. (d) FIB cross-section of a hollow Si/C particle. (e-f) A single particle and its EDS mapping image of carbon-(f), oxygen-(g) and silicon-(h). The background carbon tape contains carbon and oxygen elements. 458

Figure II-207. (a) The process to coat SiO materials using PPy polymer and sintering to form a carbon coating layer on SiO materials (b) TEM images of the carbon coated SiO materials at different magnification, (c) Raman spectra of the SiO and carbon coated SiO sintered at different temperatures, 400°C (red), 500°C (blue), 600°C (magenta). 459

Figure II-208. (a) The Rate capabilities of pure SiO and SiO-PPy sintering at different temperature. (b) Cycling performance at C/10. (c) Cycling performance at C/3. (d) CE for pure SiO and SiO-PPy samples. 460

Figure II-209. (a) The number of Li atoms reached Si thin film after 150ps MD simulations and the corresponding structure of Si initially coated with (b) SiO₂, (c)SiO₂-LiF, and (c) LiF. 463

Figure II-210. Schematic representation of the SEI Evolution with (d, e, f) and without strain (a, b, c). In practical electrode geometries such as silicon particles, expansion (contraction) of the underlying Si stretches (compresses) the SEI layer and causes in-plane tensile (compressive) stress in the film. 464

Figure II-211. Potential and nominal stress response of composite electrodes with a) 0wt% Si (CB/CMC: 80/20) b) 20 wt% Si (Si/CB/Binder: 20/60/20) and c) 60 wt% Si (Si/CB/Binder: 60/20/20). Si-containing electrodes were prepared with two different binders; Na-Alginate and CMC and their electrochemical and mechanical response are compared in panels b) and c). Specific capacity of silicon and carbon black particles in Si-containing electrodes during 2nd cycle lithiation d).....	465
Figure II-212. Left plot: stress measured over the full potential range and for A through E. Right plot: corresponding potential measurements	466
Figure II-213. Left plots: Full-cell (Si-NMC) discharge capacity and Coulombic (or current) efficiency versus cycle number. Results for two cells are plotted (denoted by 1 and 2). The current density and voltage limits are indicated. Upon reaching a voltage limit, the polarity of the current was immediately changed (i.e., no voltage holds). Right image: Secondary-electron micrograph (upper left) and elemental maps of the electrode cross-section for Si, C, Cu, O, and F after 395 cycles.	466
Figure II-214. (Top) FOME and corresponding FOMP values, in descending order, of tested additive combinations. (Bottom) Plot of FOMP vs. FOME for the additive systems tested.....	470
Figure II-215. Schematic depiction of the electrocatalytic cycle for the baseline electrolyte and the role of TMSPi and TEPI on the formation of oxide surface films and TM dissolution.	471
Figure II-216. a) Capacity and coulombic efficiency of NMC-532//Gr cells containing Gen2 and DFEC/HFDEC electrolytes cycled using a 4.5 V upper cutoff. b) ASI as a function of HPPC cycle for the DFEC/HFDEC cell shown in (a).	472
Figure II-217. a) and c) DFEC/HFDEC compositions (%). b) and d) corresponding dQ/dV profiles for each of the fluorinated compositions in Gr//Li cells on the first-cycle lithiation of graphite.	473
Figure II-218. a) and b) ASI values for various cell configurations as described in the text. c) Oxidation current vs. time at 4.5 V for NMC-532//Gr cells containing DFEC/HFDEC, FEC/HFDEC, and Gen2. .	473
Figure II-219. (left) Cell formation and rate data for duplicate sets of coated NMC-532//Gr. (right) Cycle life plot of Set 1 data between 4.4-3.0 V, C/3 charge and discharge, 30°C.....	474
Figure II-220. Al ₂ O ₃ -coated NMC electrodes vs. graphite (a) NMC-532, (b) 622, and (c) 811. 3.0-4.5 V, 1C charge/discharge.....	475
Figure II-221. NMC-532 powders wet-coated with Al ₂ O ₃ by various wet-chemical methods as a function of (a) wt.% Al ₂ O ₃ , (b) Al salt/solvent system, and (b) 0.5 wt.% Al ₂ O ₃ via a wet impregnation method..	475
Figure II-222. NMC-532 crystal samples with varying particle sizes and morphologies: a) 50 nm, b) 100 nm, c) 1 μm, d) 1 μm, e) 10 μm and f) summary of surface facets and their fraction on NMC-532 crystals.	479
Figure II-223. Half-cell cycling stability comparison of NMC crystal cathodes: a) NMC-333 in 100 nm size, b) NMC-532 in 100 nm size and c) NMC-532 in 10 μm size.	480
Figure II-224. a, b) SEM images of NMC-333 synthesized from a LT-synthesis route. c) TEY Ni L-edge and d) FY Ni L-edge XAS profiles.	481

Figure II-225. a) SEM image of $\sim 0.15\text{Li}_2\text{MnO}_3 \cdot 0.85\text{LiCoO}_2$ particles used for surface and bulk nickel doping. b) HRTEM image showing layered structure of the Ni-doped surface. c) EDS maps showing distribution of surface Al after ALD coating.	482
Figure II-226. Discharge profiles of NMC-442, 532, & 622 thin-film cathodes, 1 μm (left), and 500 nm (right).	482
Figure II-227. a) ^{27}Al NMR spectra of 5 wt.% Al_2O_3 -coated NMC-622 and 811 annealed at 800°C for 8h, compared to Co-rich NCA, Ni-rich NCA and NCMA, and Co-rich NCMA. b) ^7Li NMR for Al_2O_3 -coated NMC-532 with various salt/solvent systems.	483
Figure II-228. a) SEM images of Al_2O_3 -coated NMC-532, NMC-622, and NMC-811 with Al_2O_3 at 1, 2, and 5 wt.% annealed at 800°C for 8 h. b) SEM images of Al_2O_3 -coated NMC-532 with various aluminum sources, solvents, and annealing times.....	483
Figure II-229. Lowest energy configurations of electrolyte molecules on NMC (012) surface. (a) EMC, (b) EC, (c) HFDEC, (d) DFEC, (d) TTFP, (e) TTFP, (f) TTFPa.....	487
Figure II-230. TMSPi interaction with the delithiated NMC (012) surface.....	488
Figure II-231. Ni enriched NMC-111 (012) surface showing a stable arrangement of Ni in a row within the Li layer.	488
Figure II-232. (a) Model slab for the (012) NMC-111 surface coated with 2 layers of $\alpha\text{-LiAlO}_2$. Light blue spheres represent Al, green spheres Li, purple for Mn, blue for Co, silver for Ni and the small red sphere represent O atoms. (b) Transition metal layer configuration for NMC-111, (c) Al swapped with Mn, (d) Al swapped with Ni, and (e) Al swapped with Co. The dashed circles represent the first and second nearest neighbors to Al atoms. The values of energy at the bottom of panels (c) to (e) represent the thermodynamic energy change after swapping Al from the surface layer with different transition metal centers in the bulk of NMC-111.	489
Figure II-233. Change in NMC/ LiAlO_2 interface formation energy with thickness of $\alpha\text{-LiAlO}_2$ and a disordered layer at the surface.	489
Figure II-234. (a) Proposed side reaction mechanism from ref. 11. (b) Electrochemical model for transport and reaction of side reaction components.	490
Figure II-235. (a) Full electrochemical model relaxation of an NMC//Gr cell. (b) Relaxation results with NMC cathode and indicated anode from ref. 11.	491
Figure II-236. CV during 1st and 2nd charge-discharge cycle for $\text{Li}_2\text{Cu}_{0.4}\text{Ni}_{0.6}\text{O}_2$ synthesized using sol-gel method using a chelating agent adipic acid (AA).	495
Figure II-237. (a) X-ray diffraction (XRD) patterns for as received Li_2MoO_4 precursor and the synthesized Li_2MoO_3 . (b) Scanning electron microscopy (SEM) image of the synthesized Li_2MoO_3 particles.	495
Figure II-238. (a) Charge/discharge curves and (b) cycling stability for a Li_2MoO_3 cathode cycled between 2.0-4.8 V vs. Li/Li^+ at 10 mA/g Li_2MoO_3	496
Figure II-239. <i>In-situ</i> mass spectrometry results showing the potential profile and measured O_2 and CO_2 levels evolved from the cell during charge and discharge.	497

Figure II-240. (a) Charge/discharge curve during the first cycle of a Li_2MoO_3 cathode. (b) <i>Ex-situ</i> synchrotron XRD patterns collected at various stages during the first cycle. (c) <i>Ex-situ</i> Raman spectra collected at various stages during the first cycle.....	498
Figure II-241. (a-d) Transmission electron microscopy (TEM) images and (e-h) corresponding selected area electron diffraction (SAED) patterns for a Li_2MoO_3 cathode before cycling and after 1, 2, and 50 cycles.	498
Figure II-242. (a) Cross-sectional SEM image of a sputtered thin film Li_2MoO_3 cathode. (b) XRD pattern of a sputtered Li_2MoO_3 thin film, Li_2MoO_3 powder, and the sputtering substrate (Pt on Al_2O_3). Galvanostatic charge/discharge curves for half-cells containing a (c) thin film Li_2MoO_3 cathode and (d) slurry cast Li_2MoO_3 cathode.	499
Figure II-243. Cycling capacity of the Sn_yFe anode vs Li, in the voltage regimes (a) 0.01 – 1.5 volts and (b) 0.01 – 1.2 volts.	503
Figure II-244. Cycling capacity of the Sn_yFeCu anode vs Li at a C/2 rate.	504
Figure II-245. (a) Cycling curve for LiVOPO_4 before annealing and after annealing for 15 hours, and (b) capacity retention and rate capability of LiVOPO_4 before annealing and after annealing for 15 and 20 hours.....	505
Figure II-246. (a) The first five cycles of Li_xVOPO_4 and (b) the capacity for the first 30 cycles vs a lithium anode.	505
Figure II-247. (a) and (b) Two cells showing reproducibility of electrode components. (c) Cycling data for full cell showing achievement of 4 mAh goal.	506
Figure II-248. Electrode Balancing. Cycling behavior of cells with (a) electrode capacity matched, (b) 20% excess anode, and (c) 50% excess cathode.	506
Figure II-249. Cycling of two Li_xVOPO_4 vs graphite cells with active materials loadings of 8 and 17 mg indicating that loading is not a major factor in capacity fading. 17 mg loading allowed the achievement of the 4 mAh goal. (Right) Comparison of fade behavior of these two cells compared to one with a Sn/Fe anode suggesting that the fade is not due to the anode. a	507
Figure II-250. Comparison of the cycling of Li_xVOPO_4 and LiFePO_4 , showing that two Li cycling in VOPO_4 has a much higher capacity than that of LiFePO_4 . One Li cycling in VOPO_4 has a comparable energy density to LiFePO_4	507
Figure II-251. (a-c) SEM images of (a) pristine, (b) LPO-as-coated, and (c) LPO-infused $\text{LiNi}_{0.76}\text{Mn}_{0.14}\text{Co}_{0.10}\text{O}_2$ cathode materials. (d) High-angle annular dark-field (HAADF) TEM images and EDS maps showing the presence of LPO at the grain boundary inside a secondary particle of $\text{LiNi}_{0.76}\text{Mn}_{0.14}\text{Co}_{0.10}\text{O}_2$. (e) Initial charge/discharge voltage profiles and (f) cycling performance of pristine and LPO-treated $\text{LiNi}_{0.76}\text{Mn}_{0.14}\text{Co}_{0.10}\text{O}_2$ cathode materials at C/3 between ~2.7 and ~4.5 V. Cathode electrode loading is ~4 mg cm^{-2}	511
Figure II-252. Cross-sectional SEM images of (a) pristine and (c) LPO-infused $\text{LiNi}_{0.76}\text{Mn}_{0.14}\text{Co}_{0.10}\text{O}_2$ before and after 200 cycles at C/3 after 3 formation cycles at C/10 between ~2.7 and ~4.5 V. (b) HAADF/bright field (BF) and STEM images of pristine $\text{LiNi}_{0.76}\text{Mn}_{0.14}\text{Co}_{0.10}\text{O}_2$ material after 200 cycles. (d) HAADF and STEM images of LPO-infused $\text{LiNi}_{0.76}\text{Mn}_{0.14}\text{Co}_{0.10}\text{O}_2$ material after 200 cycles.	512

- Figure II-253. (a, d) Cycling performance of Ni-rich $\text{LiNi}_{0.76}\text{Mn}_{0.14}\text{Co}_{0.10}\text{O}_2$ cathode in (a) E-baseline (1 M $\text{LiPF}_6/\text{EC-EMC}$) and (d) E-optimized (0.6 M LiTFSI , 0.4 M LiBOB , and 0.05 M LiPF_6 in EC-EMC) electrolytes during cycling at C/3, 1C, 2C, 5C rates (after 3 formation cycles at C/10) between ~ 2.7 and ~ 4.5 V. (b, c; e, f) HAADF-STEM images of Ni-rich $\text{LiNi}_{0.76}\text{Mn}_{0.14}\text{Co}_{0.10}\text{O}_2$ after 100 cycles at C/3 between ~ 2.7 and ~ 4.5 V in (b, c) E-baseline electrolyte and (e, f) E-optimized electrolyte. 513
- Figure II-254. (a) Initial discharge profiles at C/10, (b) cycling performance and (c) capacity retention of $\text{Li}(\text{Ni}_{0.68}\text{Mn}_{0.22}\text{Co}_{0.10})_{0.99}\text{M}_{0.01}\text{O}_2$ (M = Mg, Al, V, or Y) during cycling at C/3 after 3 formation cycles at C/10 (1C = 200 mA g^{-1}). (d) Initial discharge voltage profiles at C/10, (e) cycling performance and (f) capacity retention of $\text{Li}(\text{Ni}_{0.76}\text{Mn}_{0.14}\text{Co}_{0.10})_{1-x}\text{Al}_x\text{O}_2$ during cycling at C/3 after 3 formation cycles at C/10. Cathode electrode loading: $\sim 4 \text{ mg cm}^{-2}$ 514
- Figure II-255. *In situ* temperature-resolved synchrotron XRD for tracking structural evolution of intermediates in preparing (a) LiNiO_2 , (b) NMC71515 from hydroxides (via solid-state reaction in O_2 flow with a heating rate of 5°C/min). 518
- Figure II-256. (a) Setup for *in situ* neutron and synchrotron diffraction measurements. (b) Contour plot of temperature resolved *in situ* neutron diffraction patterns of intermediates during synthesis of NMC71515. 519
- Figure II-257. (a) Synchrotron X-ray and (b) neutron diffraction patterns of the synthesized NMC71515, in comparison to that from structure refinement. The enlarged spectra in small d-spacing range are shown in the inset. In the plots, open circles are used for the observed data, red lines for the calculated data, pink bars for Bragg positions, blue lines for the difference between the observed and calculated data, and green lines for the refined background. 520
- Figure II-258. (a) Representative time-resolved XRD patterns from NMC71515 during heat treatment (at 850°C). (b) Evolution of the reflections characteristic of layered structure. (c) Illustration of the atomic configuration and reflection planes of (104) and (003) in the layered structure. (d) Evolution of the integrated intensity of the (003) and (104) peaks. 520
- Figure II-259. (a) Evolution of cationic disordering (i.e., Ni ions at 3b sites and (b) Li-slab distance with holding. (Lines: fittings to $y = A \exp(-kx) + y_0$). 521
- Figure II-260. (a) TGA curves of the precursors during holding at constant temperatures (800°C , 850°C , 900°C). (b) Evolution of crystallite size with holding time at the three temperatures (as labeled). 521
- Figure II-261. Structural, chemical and morphological evolution in the intermediates of NMC71515 during heat treatment at 800°C , 850°C , 900°C . (a) Evolution of the cationic disordering (i.e., occupancy of Ni ions at 3b sites). (b) TGA curves of the precursors during holding at constant temperatures. (c) Evolution of crystallite size with holding time. 522
- Figure II-262. a) SEM and b) cycle-life of the LLS baseline material used for all surface treatments. All electrochemical characterization was carried out at 30°C and 15 mA/g . Each material underwent an initial activation cycle between $4.6 - 2.0 \text{ V}$ followed by extended cycling between $4.45 - 2.5 \text{ V}$ vs. Li/Li^+ 525
- Figure II-263. Capacity retention vs. cycle number, as a function of post-treatment annealing temperature, for LLS samples that have undergone surface treatments with a) Li_2WO_4 b) Li_3PO_4 and c) Al_2O_3 . The capacity retention was normalized to the discharge capacity delivered on the 5th cycle for each sample. d) A comparison of the cycle-life vs. cycle number of the baseline LLS with the best performing samples

from each of the surface treatment chemistries presented in a)-c). All samples were cycled between 4.45 – 2.5 V (vs. Li/Li⁺), at 15 mA/g, after an initial activation cycle between 4.6 – 2.0 V. 527

Figure II-264. Normalized capacity vs. cycle number, as a function of post-treatment annealing and discharge rate, for LLS samples that have undergone surface treatments with a) Li₂WO₄ b) Li₃PO₄ and c) Al₂O₃. The capacity of each cycle was normalized to the discharge capacity delivered on the 5th cycle for each sample. d) A comparison of the rate performance of the baseline LLS with the best performing samples from each of the surface treatment chemistries presented in a)-c). All samples were cycled between 4.45 – 2.5 V (vs. Li/Li⁺) after an initial activation cycle (not shown in graph) between 4.6 – 2.0 V. Each charge cycle was carried out at 15 mA/g. The discharge currents were varied as labeled on each graph. 528

Figure II-265. (Left) Normalized capacity vs. cycle number, as a function of x in Li_xCoPO₄ surface treatments with x = 0.25, 0.5, 0.75 and 1.0. The capacity of each cycle was normalized to the discharge capacity delivered on the 5th cycle for each sample. All samples were cycled between 4.45 – 2.5 V (vs. Li/Li⁺) after an initial activation cycle (not shown) between 4.6 – 2.0 V. Each charge cycle was carried out at 15 mA/g. The discharge currents were varied as labeled on the graph. (Right) EDS mapping of labeled elements for Al-treated LLS (left column) and LiCoPO₄ treated LLS (right column)..... 529

Figure II-266. (a) Representative multiple pixels averaged XANES spectra and (b) histogram of Ni K-edge shifts for pristine (black curve), chemically delithiated with NO₂BF₄ (red curve), electrochemically charged (blue curve) and electrochemically discharged (green) samples. 2D mapping of Ni K-edge in the samples (c) pristine NMC; (d) chemically delithiated NMC-622; (e) electrochemically charged NMC-622 electrode and (f) electrochemically discharged NMC-622. 533

Figure II-267. Color mapping of (a) chemically delithiated NMC-622; (b) electrochemically charged NMC-622 electrode and (c) electrochemically discharged NMC-622 electrode. The color mapping was determined using the statistical peak energy as the center, and then -1.5eV (blue) and +1.5eV (red) as the two ends. Arrows point to regions of microcracks, which are less oxidized than surrounding areas..... 534

Figure II-268. Ni L-edge XAS spectra of (a) NMC-622 (b) chemically delithiated NMC-622; (c) electrochemically charged NMC622 electrode and (d) electrochemically discharged NMC-622 electrode collected using TEY (solid black curve) and FY (dashed red curve) modes. 535

Figure II-269. (a) The impedance plots of a Li-S battery, (b) charge and discharge voltage profiles of a Li-S battery (b) with LLZT and LLZT-2LiF as a separator, (c) charge and discharge voltage profiles of a Li-S battery with LLZT-2LiF at different current densities, (d) capacity retention and cycling efficiency of the Li-S battery. 539

Figure II-270. Cycling stability and Coulombic efficiency of the Li-S cell without solid electrolyte nor LiNO₃ additive. 540

Figure II-271. (a) Impedance spectra and (b) Arrhenius plot of LSTH pellet fired by spark plasma sintering. 540

Figure II-272. (a) Charge and discharge voltage profiles of Li/LSHT/LiFePO₄ at 150 and 300 $\mu\text{A cm}^{-2}$. (b) Capacity retention and cycling efficiency of the LiFePO₄/Li cells. (c) Charge and discharge voltage profiles of a Li-S battery with LSHT at different current densities. (d) Capacity retention and cycling efficiency of the Li-S battery..... 541

Figure II-273. Structure of CPMEA.	542
Figure II-274. Charge/discharge voltage curves of all-solid-state Li/CPMEA-LiTFSI/Cu cell at 70°C. .	542
Figure II-275. Cu oxidation time and the corresponding discharge capacity.	543
Figure II-276. Charge/discharge voltage curves of the Cu cathode.....	543
Figure II-277. (a) XRD patterns of $\text{LT-Li}_{1-x}(\text{Co}_{0.9-x}\text{Ni}_{0.1}\text{Mn}_x)\text{O}_2$, (b) high-resolution XRD and (c) electrochemistry of the low-temperature product with the LiMnO_2 composition (LT-LMO phase).....	546
Figure II-278. XRD patterns of sol-gel LiCoO_2 (LCO) and $\text{LiCo}_{0.85}\text{Al}_{0.15}\text{O}_2$ (LCO-Al) samples fired at 400°C (LT) or 600°C (IT). XRD pattern of LCO, synthesized by solid-state reaction, is shown for comparison. Red circles indicate the peaks for Co_3O_4	547
Figure II-279. (a, b) Initial voltage profiles and (c) normalized capacities of the sol-gel prepared samples.	547
Figure II-280. (a) Synchrotron XRD of Li_2MnO_3 , $\text{LiNi}_{0.5}\text{Mn}_{1.5}\text{O}_4$, a 1:1 physical blend of the two, and a $\text{Li}_2\text{MnO}_3 \cdot \text{LiNi}_{0.5}\text{Mn}_{1.5}\text{O}_4$ composite. (b, c) Enlarged regions ranging from 2.5° to 2.8° 2 θ and from 3° to 3.3° 2 θ , respectively.	548
Figure II-281. (a) Initial voltage profiles of spinel $\text{LiNi}_{0.5}\text{Mn}_{1.5}\text{O}_4$, (b) layered Li_2MnO_3 , (c) a $\text{Li}_2\text{MnO}_3 \cdot \text{LiNi}_{0.5}\text{Mn}_{1.5}\text{O}_4$ composite, and (d) a 1:1 physical blend of the two components. (4.8 – 2.0 V at ~C/15 against Li metal).....	549
Figure II-282. (a) Voltage profiles of a Li/LT- $\text{LiCo}_{0.9}\text{Ni}_{0.1}\text{O}_2$ cell showing the points where ex-situ XRD data were collected, (b) corresponding ex-situ XRD patterns, (c) magnified view of the (311) and (400) peaks, (d) simulated XRD patterns of $\{\text{Li}\}_{[\text{tet}]}\text{Co}_2\text{O}_4$ spinel and $\{\text{Li}_2\}_{[\text{oct}]}\text{Co}_2\text{O}_4$ lithiated spinel, and (e) Li (de)intercalation mechanism(s) suggested by DFT calculation.	550
Figure II-283. (a) X-ray diffraction patterns of $\text{Li}_{1.2}\text{Mn}_{0.6}\text{Ni}_{0.2}\text{O}_2$ samples prepared by a solid-state method. Samples are denoted by milling energy followed by milling time_annealing time. (b) The first cycle voltage profiles of $\text{Li}_{1.2}\text{Mn}_{0.6}\text{Ni}_{0.2}\text{O}_2$ samples prepared by a solid-state method. Cells were cycled between 4.8 and 2 V at a current of 25 mA/g.	553
Figure II-284. (a) XRD patterns of $\text{Li}_{2-x-y}\text{Ni}_x\text{TM}_y\text{O}_2$ (TM = Mn, Sn, Ru, Mo), exhibiting layered structure. (b) XRD patterns of $\text{Li}_{2-x-y}\text{Ni}_x\text{TM}_y\text{O}_2$ (TM = Nb, Ti, V), exhibiting non-layered structure.	554
Figure II-285. The first cycle voltage profile of (a) LNMO and (b) LNRO; Differential capacity (dQ/dV) plot of (c) LNMO and (d) LNRO. Cells were cycled between 4.8 and 2.0 V at a current density of 5 mA/g at room temperature.	555
Figure II-286. XRD Rietveld refinement of (a) LNMO, monoclinic $C2/m$, and (b) LNRO, monoclinic $C2/c$; HRTEM image of (c) LNMO, (e) LNRO with FTT of the selected area; ED pattern of (d) LNMO, (f) LNRO.....	556
Figure II-287. sXAS Ni L-edge spectra of (a) LNMO, (b) LNRO electrodes at different states of charge. Solid and dash line indicate FY (~ 50 nm depth) and TEY (2 - 5 nm depth) mode, respectively.	556
Figure II-288. O K-edge RIXS maps of (a) LNMO and (b) LNRO electrodes at various states of charge. The white arrow indicates the specific oxygen redox state that is absent in LNRO.....	557

Figure II-289. In-situ (a) XANES and (b) EXAFS of Ru L-edge; (c) in-situ voltage profiles of LNRO during the first cycle. The in-situ cell was charged at C/10 and discharged at C/7.	558
Figure II-290. a) SEM image, b) and c) Rietveld refinements of synchrotron XRD and neutron patterns of $\text{Li}_{1.3}\text{NMO}$ sample.	561
Figure II-291. a) Voltage profiles of $\text{Li}_{1.3}\text{NMO}$ half-cell cycling and b) DEMS measurement: (top) Voltage profile and (bottom) O_2 and CO_2 gas evolution.	562
Figure II-292. a) Synchrotron XRD and b) neutron patterns of chemically delithiated $\text{Li}_x\text{Nb}_{0.3}\text{Mn}_{0.4}\text{O}_2$ ($0 \leq x \leq 1.3$) crystal samples.	563
Figure II-293. a) and b) Cell volume and phase fraction as a function of x in delithiated Li_xNMO samples, and c) The relationship between the molar ratio of oxidant/oxide and residue Li content in chemically delithiated Li_xNMO samples.	564
Figure II-294. SEM images of chemically delithiated Li_xNMO crystal samples: a) $x=1.3$, b) $x=1.1$, c) $x=0.76$, and d) $x=0.13$	564
Figure II-295. Mn K-edge hard XAS measurements of Li_xNMO crystals: a) hard XAS spectra, b) expanded view of the pre-edge region, c) expanded view of the XANES region and d) relationship between Mn edge position and Li content in the samples.	565
Figure II-296. a) and b) O K-edge soft XAS spectra obtained in TEY and FY modes, c) and d) Intensity ratio between the pre-edge and post-edge absorption peaks and Intensity of the p-band as a function of Li content. In a) and b), black dashed line divides the pre- and post-edge regions and the blue dashed arrow follows the evolution of the p-band intensity.	565
Figure II-297: (a) NMC and NMC/R electrodes capacity retention, and (b-d) charge discharge voltage profiles.	570
Figure II-298: Nyquist plots of coin cells with NMC (a) and NMC/R (b) cathodes. R_s and R_{ct} extracted from the impedance data for NMC (c) and NMC/R (d) electrodes.	571
Figure II-299: XAS-TEY of NMC and NMC/R powders on the range L-edge of (a) Ni, (b) Co and (c) Mn.	572
Figure II-300: (a) XAS-TEY of cycled NMC and NMC/R electrodes on the range L-edge of (a) Ni, (b) Co and (c) Mn.	572
Figure II-301: (a) Raman spectra of NMC powder (blue), PLD-NMC/Al electrode (black) and PLD-NMC/Al electrode after 4.7 V charged (red). (b) Cyclic voltammogram of PLD-NMC/Al electrode at the 3 rd cycle. (c) The voltage-time profile of electrode during in situ AFM experiment. The arrows point at the time when AFM images were acquired. Insert: in situ AFM cell.	573
Figure II-302: 1 x 1 μm AFM images of PLD-NMC/Al electrode after 30 min. polarization at each potential	573
Figure II-303. (a) Illustration of PDF showing that peaks correspond to characteristic bond lengths. (b) Ex situ PDF data of pristine sample and “OCV—1V—3V” sample (c) zoomed in data on the short range region of ex situ PDF data and (d) zoomed in data on the long range region of ex situ PDF data.	578

Figure II-304. (a) Illustration of PDF showing that peaks correspond to characteristic bond lengths. (b) Ex situ PDF data of pristine sample and “OCV—1V—3V” sample (c) zoomed in data on the short range region of ex situ PDF data and (d) zoomed in data on the long range region of ex situ PDF data 579

Figure II-305. (a) ex situ Mn K-edge and Ru K-edge XAS data of pristine $\text{Li}_2\text{Ru}_{0.5}\text{Mn}_{0.5}\text{O}_3$ sample, sample normally cycled 20 times and sample cycled 20 times but first prelithiated, with references of Mn_2O_3 and MnO_2 shown. (b) Ex situ XRD patterns of two cases (with (003), (108) and (110) peaks indexed according to the space group $R3m$): pristine sample, cycled 8 times and cycled 20 times for the normally cycled case (the part below the dash line); pristine sample, cycled 8 times and cycled 20 times for the prelithiated case (the part above the dash line). (c) The ratio between lattice parameter c and lattice parameter a as a function of cycle numbers. The dash line shows the c/a ratio in perfect spinel. 580

Figure II-306. Three-dimensional electron tomography reconstructions of (a) pristine, (b) after 15 charge-discharge cycles of $\text{Li}_{1.2}\text{Ni}_{0.15}\text{Co}_{0.1}\text{Mn}_{0.55}\text{O}_2$ material. The internal pore size distribution weighted by occurrence (upper) and by volume (lower) of (c) the pristine materials and (d) the sample after 15 cycles. 581

Figure II-307. Differential capacity vs. voltage plots of the $\text{Na}_{2/3}\text{Mn}_{1-y}\text{Mg}_y\text{O}_2$ ($y = 0.0, 0.05, 0.1$) compositions. 585

Figure II-308. Ex-situ ^{23}Na MAS ssNMR spectra collected on cells stopped at different points along the first electrochemical charge/discharge cycle of $\text{Na}_{2/3}\text{Mn}_{1-y}\text{Mg}_y\text{O}_2$, where $y = 0.0, 0.05, 0.1$ for (a), (b), and (c), respectively. Spectra are scaled according to the number of scans collected during the experiment, the amount of sample in the rotor, and the NMR signal decay obtained from T_2 relaxation time measurements. Hashes indicate samples for which a lack of experimental data prevent proper scaling of the spectrum. Asterisks indicate spinning sidebands. 585

Figure II-309. (a) ^{23}Na NMR spectra as a function of time during galvanostatic cycling at 2 mA cm^{-2} , showing high surface area Na metal deposits growing in. (b,c) Integral of the normalized ^{23}Na metal resonance for (b) continuous galvanostatic deposition and (c) galvanostatic cycling at three different current densities. (d) Fraction of high surface area (F_{HSA}) Na during galvanostatic cycling at various current densities. A ratio of 1 indicates completely rough deposition and 0 indicates smooth deposition. 586

Figure II-310. (a) Experimental (black) electrochemistry of a Na-Sn cell cycled at C/20 between 2 and 0.001 V compared to theoretical (red/blue) predictions. (b) Operando PDFs and (c) ^{23}Na NMR spectra for Na-Sn cells aligned with the corresponding electrochemistry (d). 587

Figure II-311. Left panel: (a) Structure of NaSn_3 -Pmmm with Na in yellow and Sn in purple (b) operando XRD patterns (c) ex situ ^{23}Na and (d) ^{119}Sn 60 kHz MAS NMR at the end of process 1 and 1'. Right panel: (a) Structure of $\text{Na}_{5-x}\text{Sn}_2$ (b) occupancy vs Na site 3 vs time spent on process 3' (c) fit of the PDF corresponding to the first frame in process 3' 588

Figure II-312. ^1H solution NMR of (a) LP30, (b) LP30 + FEC, and (c) LP30 + 10 vol% $^{13}\text{C}_3$ -FEC before cycling (pristine), and after the 1st and 30th cycles. ^{13}C satellites are marked with an asterisk. 589

Figure II-313. Multiplet pattern of LP30 + $^{13}\text{C}_3$ -FEC in region y of an earlier Figure, (a) experimental pattern; (b) simulated pattern of a four-spin system AA'XX' (cis-H-CR=CR-H). 589

Figure II-314. ^1H - ^{13}C cross-polarization (CP) NMR spectra of SiNWs after 30 cycles in (a) LP30 + 25 vol% $^{13}\text{C}_3$ -EC and (b) LP30 + 10 vol% $^{13}\text{C}_3$ -FEC electrolytes. The room temperature (RT) spectra were measured by conventional ssNMR, whereas the 100 K spectra were measured with DNP NMR. The DCB was used as the radical solvent for DNP.....	590
Figure II-315. (a) Aberration corrected high angle annular dark field (HAADF) STEM image; (b) spatially resolved O K-edge and Mn L-edge EELS spectra; (c) Mn L_3/L_2 ratio fit results from the EELS spectra.	595
Figure II-316. Diffraction data collected for electrode after the (a) 1st cycle and (b) 50th cycle. (c) Experimental schematic of the in situ BCDI setup. Scale bar is $1\text{e-}8\text{ }1/\text{\AA}$	596
Figure II-317. (a) The evolution of the superstructure peak intensity in the pristine state, after 50 cycles, and after the heat treatment. (b) Charge-discharge voltage curves of Li-rich layered oxide cathode with Li-metal as anode.....	597
Figure II-318. ND characterization of cycled electrode after heat treatment. (a) Refined ND patterns of the electrode after the initial cycle. (b-d) Refined ND patterns of the initially cycled electrode after heat treatment under 200, 250 and 300 $^\circ\text{C}$, respectively. (e) Lithium occupancy in transition metal layer and (f) Oxygen occupancy for different samples.....	598
Figure II-319. Morphology changes of the dendritic Li metal as a function of the beam exposure time under: room temperature TEM (a, b, c) and cryo-TEM (d, e, f).....	599
Figure II-320. Cryo-TEM (a) image and (b) its regional zoomed-in image with the bulk and surface FFT results of the EDLi using conventional carbonate electrolyte.	599
Figure II-321. SEM images of (a) pristine agglomerated particles, (b) and (c) TEM specimen prepared by FIB lift-out techniques from cycled electrode. (d-i) STEM-EDS mapping results from the boxed region in panel (c).	602
Figure II-322. Cycle voltage governed intragranular cracking and underlying dislocation-based mechanism. (a) HAADF images overlaid diagram shows the apparent dependence of intragranular cracking on the cycle voltage; when cycled below 4.5 V, intragranular crack can be hardly generated, while above 4.7 V, intragranular density shows a drastic increase; and (b) schematic diagrams to illustrate the dislocation-assisted crack incubation, propagation and multiplication process.....	603
Figure II-323. Experimental set up of the Li-O ₂ nano-battery and the in situ STEM observation of morphological evolution of the reaction products upon discharge-charge cycling of the Li-O ₂ battery. a, Schematic drawing to illustrate the configuration of the Li-O ₂ nano-battery in ETEM chamber. b, The time-resolved HAADF-STEM images depict the morphological evolution of the discharging product (oxygen reduction reaction (ORR)), which is featured by the formation of hollow structure (illustrated by the bottom panel in b. c. The images illustrates the morphological evolution upon charging (oxygen evolution reaction (OER)), which is featured by the collapsing of the hollow structure as illustrated by the bottom panel in c.....	605
Figure II-324. (a) Calculated DFT formation energies of $\text{LiCo}_x\text{M}_{1-x}\text{O}_2$ ($\text{M} = \text{Mn}$ or Ni ; $0 \leq x \leq 1$) in both lithiated spinel (Fd-3m) and layered (R-3m) structures. The mixing energies of (b) $\text{LiCo}_x\text{Mn}_{1-x}\text{O}_2$ and (c) $\text{LiCo}_x\text{Ni}_{1-x}\text{O}_2$. Calculations by S. Kim and C. Wolverton (Northwestern University, IL).	609
Figure II-325. The compositional phase space of a layered(L)-layered(L)-spinel(S) system.....	610

Figure II-326. Rietveld refinement results of (a) synchrotron X-ray and (b) neutron diffraction of the $x = 0.75$ sample. (c) Synchrotron X-ray diffraction of the $x = 1.0$ sample. ND by A. Huq (SNS, ORNL), XRD by Y. Ren (APS, ANL) 611

Figure II-327. a) ^{27}Al MAS-NMR of Al-treated samples annealed at 110°C (red) and 550°C (blue) and an $\text{Al}_2\text{O}_3/\text{Al}(\text{OH})$ reference (green). (b) XPS spectra of LLS followed by Al treatment and annealing at 110°C (red), 400°C (blue), and 550°C (green). (c) Al content (at. %) as a function of annealing temperature, determined by XPS. Red squares represent samples that had previously (before Al treatments) been exposed to air, blue circles are samples not exposed to air (similar results were obtained with both sample sets). XPS by R. Ruther and H. Meyer (ORNL). 612

Figure II-328. (a) Cross-sectional SEM image of Al-treated, LLS particle. (b) TEM image and FFT of surface and bulk regions showing spinel integration at the surface of the particle. (c) STEM-EDX analysis of Al-treated LLS particle showing distribution of Al (top left), Mn (top right), Co (bottom left), and Ni (bottom right). HRTEM by J. Wang (ANL). 613

Figure II-329. Design of 3-omega thermal sensors and how they are incorporated into an electrochemical battery pouch cell for *in-operando* measurements..... 616

Figure II-330. Representative raw data from a measurement on a li-ion cathode half-cell. Left plot is without the presence of electrolyte; right plot is with electrolyte. Red lines show the best fit to the data. The primary property measured is the thermal boundary conductance (TBC) of the interface between the cathode and the separator. Dashed lines demonstrate fit sensitivity by showing best fit lines where the TBC value has been artificially forced to be $\pm 50\%$ as compared to the true best fit value..... 617

Figure II-331. Left, multilayer stack for the measured cathode half-cell, showing a 3-omega sensor launching a thermal wave. Right, a to-scale breakdown of the relative contributions of each layer and interface to the total thermal resistance. Thermal resistance contributions from the Li and Cu are negligible. Thermal waves did not probe deep enough to be affected by the Teflon, which was only included for mechanical support and is not present in the real battery. 618

Figure II-332. First Cycle Average STXM-XAS of LMR-NMC. (a) $dQ\ dV^{-1}$ of the first cycle showing the voltages at which samples were harvested for STXM. The samples are pristine (P), 4.35 V (1), 4.60 V (2), 3.65 V (3), and 2.00 V (4). Regions of the $dQ\ dV^{-1}$ are shaded to show the hysteresis in the O redox relative to the TM–O redox. (b) Schematic and spectra comparing STXM-XAS to various other XAS detection modes (TEY, FY, and fluorescence yield X-ray microscopy, FY-XRM). (c–f) Spatially averaged transmission soft XAS throughout the first cycle at the (c) O K, (d) Ni L_3 , (e) Co L_3 , and (f) Mn L_3 edges. Solid traces indicate electrodes harvested during charge, while dashed traces indicate electrodes harvested during discharge. The red and black traces below each plot indicate the differential spectra between the points indicated. 621

Figure II-333. Spatial Dependence of O and Ni Spectroscopic Response During 4.50 V Plateau. (a) End-member spectra at the Ni L_3 and O K edges throughout the first cycle plateau. (b) Total end-member fractions for each sample used in the NMF analysis as a function of capacity through the plateau. (c) Nanoscale distribution of the end-members in (a) for primary particles at different points in the voltage plateau. Scale bar is 500 nm. Right: spectral line-scans of the magnified particle showing the bulk O oxidation and surface Ni and O reduction. The spectra at the bottom correspond to the near-surface region and those at the top correspond to the bulk..... 622

Figure II-334. Probing the Nature and Stability of Oxygen Redox. (a) RIXS maps at the voltages indicated throughout the first cycle. The unique emission signature at 4.60 V indicated by the white arrow supports an electronic restructuring associated with O redox. Right: XAS obtained in the pristine (brown) and fully charged (tan) state during the first cycle for comparison. (b) RIXS maps acquired before and after the 501st charge on an electrode cycled 500 times at 1C/2C charge/discharge rate, showing that the reversible oxygen redox feature persists for hundreds of cycles. The voltage curves for the second and 501st cycles at C/68 (solid) and 2C (dashed) show that most of the capacity fade over 500 cycles is from increased impedance and overpotential, and that the intrinsic capacity is largely retained. 623

Figure II-335. Plot of the O fractional oxidation state (red) and the migrated TM fraction (green) as a function of capacity, showing the clear link between hysteresis in the TM migration and voltage hysteresis in the O redox. Error bars indicating fitting residual and refinement error for the O oxidation state and TM migration fraction, respectively, are smaller than the data symbols and are therefore not shown. 624

Figure II-336. (a) Picture of a 16-channel high precision leakage current measuring system; (b) schematics showing the connection between the leakage current and the rate of parasitic reactions; (c) evolution of the static parasitic current as a function of the holding potential for the bare aluminum foil. The electrolyte used was 1.2 M LiPF₆ in EC/EMC (3:7 by mass). We have shown that that this reaction is related to the oxidation of ethylene carbonate. 628

Figure II-337. (a) Potential dependence on the static parasitic current for aluminum foil with surface coating of (a) carbon, (b) graphene, and (c) AlPO₄. 629

Figure II-338. (left) In Situ ICP-MS results of Co dissolution upon electro-chemical polarization using the SPRDE system. Working Electrode: LiCoO₂/C/PVDF. Electrolyte: 1.2M LiPF₆ in EC:EMC (3:7 by mass); (right) Total amount of Co dissolution upon electro-chemical polarization using as monitored by the SPRDE-ICP-MS system. 630

Figure II-339. (a-c) According to the *pre-stressed* lithium scenario, tensile stresses act within lithium metal and compressive stresses act inside electrolyte. (d-f) *Relaxed* lithium assumes stress-free condition for lithium metal and electrolyte. When fresh lithium gets deposited, bulk lithium metal, electrolyte and the newly deposited lithium experience compression. 634

Figure II-340. (a-b) Variation in effective exchange current density around the dendritic protrusion. If the current at the peak is greater than that at the valley, dendrites grow. (a) For pre-stressed lithium. (b) For initially relaxed lithium. (c) Ratio of the effective exchange current density at the protrusion peak over that at the valley. For initially relaxed lithium, dendrite growth never occurs at low current operation. 635

Figure II-341. (a) Lithium and polymer electrolyte regions (i) before assembly and (ii) after the regions are fully in contact. Both lithium and polymer have deformed plastically. (b) Stresses within lithium metal and polymer electrolyte regions under the assumption of only elastic deformation. The stresses exceed the elastic limits across much of the domain. 636

Figure II-342. (a) Computational model compared with elastic-plastic stress-strain experimental data. (b) Experimental stress-strain curve for PEO polymer and corresponding numerical model. (c) Ratio of effective exchange current density at the protrusion peak over that at the valley using purely elastic (squares) or elastic-plastic (crosses) models. 637

Figure II-343. Concentration and potential contour within the electrolyte around the dendritic protrusion at high and low rates of current. Potential in lithium metal remains extremely close to zero. (a) Potential contour for $i_{app} = 0.01i_{lim}$. (b) Concentration contour for $i_{app} = 0.01i_{lim}$. (c) Potential contour for $i_{app} = 0.9i_{lim}$. (b) Concentration contour for $i_{app} = 0.9i_{lim}$	637
Figure II-344. (a) Distribution of reaction current from the peak to the valley at two different applied current densities. (b) Reaction current ratio between protrusion peak and valley for different applied current densities. Model predictions are consistent with experiments.....	638
Figure II-345. (a) Impact of stress -factor and current – distribution -factor on the overall reaction current density. Electrolytes with shear modulus 20 times larger than that of lithium may prevent dendrite growth. (b) Phase map demonstrating the correlation between applied current density and electrolyte shear modulus on lithium stabilization.....	638
Figure II-346. (a) Effect of elastic-plastic deformation of both lithium metal and electrolyte on the overall suppression of the dendritic protrusion. (b) Increasing yield strength of the electrolyte may help to prevent dendrite growth even with present day polymer electrolytes.....	639
Figure II-347. Illustration of the initial screening process including the range of considered elements and the preference of surface dopant occupancy to enhance oxygen retention at the surface.....	642
Figure II-348. The defect formation energy of each stable surface facet as compared to the bulk, covering defect transition metal, post-transition metal, and metalloid elements.....	643
Figure II-349. The relative surface oxygen release energy for the top 10 candidate dopants as compared to the pristine systems shown for representative (001) and (010) surface facets. A dark yellow color indicates stronger oxygen retention, while a purple color indicates less protection against oxygen release as compared to the pristine, undoped surface.	644
Figure II-350. Maximal TM site distortion relative to the original bond lengths in ordered LiTMO_2 ground state structures and in cation-disordered LiTMO_2 structures. Contribution of the four symmetry-breaking normal modes, v_2 through v_5 , to the site distortions are shown.....	647
Figure II-351. Energy and relative TM site distortion in $\text{LiNi}_{0.5}\text{Ti}_{0.5}\text{O}_2$ and $\text{LiMn}_{0.5}\text{Ni}_{0.5}\text{O}_2$. Each data point corresponds to a single atomic structure. The error bars indicate the range of distortions for all sites of one TM species within that structure.	648
Figure II-352. Atomic structure of $\text{Li}_{1.25-x}\text{Mn}_{0.5}\text{Nb}_{0.25}\text{O}_2$ and its various oxygen local environments.	648
Figure II-353. Computed O K-edge XAS of $\text{Li}_{1.25-x}\text{Mn}_{0.5}\text{Nb}_{0.25}\text{O}_2$ ($x = 0$ and 0.5).	649
Figure II-354. (a) The first-cycle voltage profiles of LNTMO compounds. (b) Capacity evolution over 20 cycles.	649
Figure II-355. (a) DEMS study of LN20 when charged to 4.8 V and discharged to 1.5 V at 20 mA g^{-1} , along with the DEMS results on O_2 (red circle) and CO_2 (blue triangle). (b) Illustrations of a LNTMO20 particle before and after oxygen loss.	650
Figure II-356. (a) EDS mapping on one area of a LNF15 particle. Scale bars, red: 100 nm, blue: 25 nm. (b) ^{19}F spin echo NMR spectra obtained at 30 kHz MAS for LNF15 and LiF.....	651
Figure II-357. (a) & (b) Cycling performance of LN15 and LNF15. (c) DEMS study of LNF15.	651

Figure II-358. Left: Nucleation of Li_2CO_3 over graphite electrode. Li ions interact with adsorbed O atoms at the graphite edge. Right: Electrostatic potential (eV) of the nucleating phase on the solid electrode. Note the discontinuity at the interface (highlighted).....	654
Figure II-359. Gaussian fit to the “self” part of van Hove function suggests Li_2EDC (left) is crystalline compared to pure EC (right). Correlations are calculated for ps compared to ns in the Li_2EDC case.	655
Figure II-360. Leakage current from the anode to the solvent through the SEI under an external voltage between two nanotips (green).	655
Figure II-361. Interaction energy (E) of one Li-ion with its nearest neighbors within a sphere of 6 Å radius during charging with $E = 1.0 \text{ V}/\text{\AA}$. This is one particular trajectory of a Li-ion from the cathode (1) through the electrolyte (2) to the anode (3). From Ponce et al., JPCC, 121, 12959, (2017).....	656
Figure II-362. Side by side comparison of the rigid μNLP consisting of metal deposited on a glass substrate (left), and the flexible μFLP consisting of metal deposited on a polyimide substrate (right). ..	659
Figure II-363. Cross-section images from models of (a) CPG-A12, (b) Toda 523 (B), and (c) Toda HE5050; carbon-binder domain is red, active material is yellow, and larger pores are blue.....	661
Figure II-364. (a) Power spectral density for various battery films. SLDV results of various battery films with thicknesses of (b) 42 μm (c) 38 μm (d) 26 μm	662
Figure II-365. The C_2N nanosheet (left) and the binding configurations of $\text{C}_2\text{N_Li}_m\text{S}_8$ (right). These binding configurations are searched through genetic algorithms based on DFT calculations.....	665
Figure II-366. The binding energy between the Li_2Sn polysulfur and the C_2N substrate (left), and the formation energy diagram (left) of $\text{C}_2\text{N_Li}_2\text{S}_m$	666
Figure II-367. The formation energy (a), the $\text{Li}_2\text{P}_4\text{O}_2$ configuration (b) and $\text{Li}_4\text{P}_4\text{O}_4$ configuration (c). In (b) and (c), the blue ball is P, red ball is O, and green ball is Li.	667
Figure II-368. Projected band structures of (a) $\text{Li}_1\text{P}_4\text{O}_1$, (b) $\text{Li}_2\text{P}_4\text{O}_2$, (c) $\text{Li}_3\text{P}_4\text{O}_3$ and (d) $\text{Li}_4\text{P}_4\text{O}_4$	668
Figure II-369. Energy landscape for Li^+ transport from electrolyte to Li-metal slab under different potential.	671
Figure II-370. The thermodynamic driving force of the electrochemical reaction at the $\text{Li} \text{Li}_2\text{CO}_3 \text{EC}$ -electrolyte interface, work function shift and Li^+ solvation energy change with Li^+ ion concentration in the EC-electrolyte as a function of excess electron density on Li metal surface. The circle denotes the directly predicated ΔG by DFTB method.	672
Figure II-371. SEI properties-Li dendrite morphology map from phase field simulation.....	673
Figure II-372. <i>in-situ</i> electrochemical optical observation of Li dendrite growth morphology.....	674
Figure II-373. The excess electrons located on La atoms on LLZO surface.	674
Figure II-374. Preliminary phase-field simulation of Li dendrite growth in solid electrolyte results with experimental results as comparison: (a) SEM observation of intergranular Li dendrite growth in LLZO [Cheng E. J., Sharafi A. and Sakamoto J., Electrochimica Acta 223, 85-91 (2017).]; and phase field simulation results: (b) Li-ion concentration distribution in the solid electrolyte battery system; (c) morphology of Li dendrites growth in solid electrolyte.....	675

Figure II-375. Filter Box and glove box style PPE for material collection	677
Figure II-376. Burner Hood with Cabot Inspired Burner	678
Figure II-377. New Hoods and Ventilation	678
Figure II-378. Pilot and Ethanol Spray Flame Operation at the MERF FSP	679
Figure II-379. (1) Hydrothermal Reaction Mechanism, (2) Schematic Diagram of Bench Scale Hydrothermal Synthesis System	680
Figure II-380. Taylor vortex flow enabling micro mixing zones.....	681
Figure II-381. 1L, 10L and 40L TVRs for Process Scalability Evaluation.	681
Figure II-382. Material Synthesis and Optimization Approach: (1) Process Capability Established at MERF and (2) Development of a Customized Synthesis Process for Advanced Cathode Material with Component Concentration Gradient Structure.....	683
Figure II-383. Preliminarily Synthesized 622 Gradient Material with Component Concentration Gradient Structures	684
Figure II-384. X-ray Absorption Spectroscopy on 622 Gradient and Commercial NMC622 Materials (BNL).....	684
Figure II-385. Thermal Stability of Charged 622 Gradient and Commercial NMC622 Materials using Time Resolved XRD (BNL)	685
Figure II-386. Particle Structure Design for 811 Gradient Materials to Achieve Higher Capacity with Stability	685
Figure II-387. SEM with EDS on Synthesized 811 Core-Gradient and Core-Shell Material	686
Figure II-388. Comparison of the Prepared 811 Core-Gradient and Core-Shell Materials with Commercial Products	686
Figure II-389. C/2 Cycling and Rate Performance Comparison at 30°C	687
Figure II-390. C/2 Cycling and Rate Performance Comparison at 55°C	688
Figure II-391. Radar Map Comparison of the Prepared 811 Core-Gradient and Core-Shell Materials with Commercial NMC811.....	688
Figure II-392. Powders produced from the flame spray process, showing average size of 3 microns, much smaller than those obtained from last quarter at 50 microns. The powders also appear to be solid, not porous as before.	691
Figure II-393. Coin cell test of the new powders as compared to the old powders, showing much improved performance.	691
Figure II-394. Carbon coating on a sodium titanate fibrous battery material, showing a uniform, nanoscale carbon coating. The carbon coating is dense without holes.....	692
Figure II-395. (Left) Bare NMC powders as prepared; (Right) after a metal oxide coating.	692
Figure II-396. Charge-discharge profiles on bare and coated NMC electrodes. The coated NMC shows much improved cycling stability (less polarization).	693

Figure II-397. Cycling results of anodes fabricated from electrospun single fiber mats containing 40 wt.% Si and varying content of C and PAA binder.....	696
Figure II-398. XRD pattern of an as-spun Si/C/PAA fiber mat and a reference pattern for Si (PDF No. 27-1402)	697
Figure II-399. (a) SEM image of a Si/C/PAA fiber mat and the corresponding EDX maps showing the (b) carbon and (c) silicon distributions.....	697
Figure II-400. (a) Average Raman spectra for a Si/C/PAA fiber mat containing 35 wt% PAA before and after 50 cycles. (b-c) Raman maps over an area of $\sim 4.5 \times 9.0 \mu\text{m}^2$ showing the Raman shift of the maximum peak for these electrodes (b) before cycling and (c) after 50 cycles at 0.1C.	698
Figure II-401. SEM image of the surface of the electrospun dual fiber mat containing 70 wt.% of Si/PAA (50/50) and 30 wt.% of C/PAN (63/37) fibers.....	699
Figure II-402. Cycling results of an anode fabricated from electrospun dual fiber mat containing 70 wt.% of Si/PAA (50/50) and 30 wt.% of C/PAN (63/37) fibers.	700
Figure II-403. SEM image of the surface of the electrosprayed Si/C/PVAE-PAA 40/25/35 anode annealed at 110°C and supported on Cu foil.....	700
Figure II-404. Cycling results of an anode fabricated from electrosprayed ink containing new PVAE-PAA crosslinkable binder.	701
Figure II-405. Schematic of 3D mesh formation by in-situ cross-linking offunctionalized backbone polymer and small molecules.....	703
Figure II-406. Poly(ethylene-alt-maleic anhydride) and poly(methyl vinyl ether-alt-maleic anhydride)	703
Figure II-407. FT-IR of poly(ethylene-alt-maleic acid) and material cross-linked with 20% molar of triethylene glycol.	704
Figure II-408. Ethyl and propyl trifluoromethyl sulfones.....	705
Figure II-409. Published synthesis of ethyl trifluoromethyl sulfone	705
Figure II-410. Published synthesis of ethyl and propyl trifluoromethyl sulfones.....	705
Figure II-411. Improved synthesis of ethyl and propyl trifluoromethyl sulfones.....	706
Figure II-412. Standard method for synthesis of unsymmetrical carbonates.....	706
Figure II-413. Transesterification method for synthesis of unsymmetrical carbonates.....	706
Figure II-414. Structures of some novel silicon-containing carbonates invented and produced by MERF	707
Figure II-415. 5, 10, 20% w/w ETMSMC in Gen2, graphite//NCM523, 3.0 - 4.4 V cycling (Ch/DCh at C/3), 30°C.	707
Figure II-416. Electrode information for A-A011 containing 30 wt.% 70-130 nm silicon from NanoAmor.	713
Figure II-417. Full-cell coin-cell results showing cycle number vs. average discharge capacity of the new Silicon Deep Dive baseline electrodes (Paraclete Energy silicon) vs. NMC532 [A-C013A]. Data shows	

the average values based on 4 coin cells for each electrode pair. The capacity values are normalized to the weight of NMC532.	714
Figure II-418. Electrode design for Si-Gr//NMC532 and Gr//NMC532 xx3450 pressure study pouch cells. “SS” = single side, “DS” = double side. All electrodes were fabricated at the CAMP Facility and designed for 3.0 to 4.1 V full-cell cycling.....	715
Figure II-419. Representative individual cycle voltage (a,b) and dQ/dV (c,d) profiles of Si-Gr//NMC532 pouch cells at 2 psi per cell (blue), 76 psi per cell (red), and Gr//NMC532 pouch cells at 2 psi per cell (green), 76 psi per cell (black) of the 1 st (a,c) and 3 rd (b,d) cycles during formation. (The green and black curves are often on top of each other, as are the blue and red - indicating little influence of pressure during formation.)	716
Figure II-420. Average rate study performance of Si-Gr//NMC532 pouch cells at 2 psi per cell (blue), 76 psi per cell (red), and Gr//NMC532 pouch cells at 2 psi per cell (green), 76 psi per cell (black) specific discharge capacities as a function of current, mA/g (left) and mA (right). The cells were cycled at 30°C between 3.0 and 4.1 V. The plots show the discharge performance from the 2 nd cycle at C/20 and 3 rd cycle at C/10, C/5, C/2, 1C, and 2C rates. The error bars represent 2σ standard deviation.	717
Figure II-421. Average initial discharge interpolated ASI as a function of open circuit voltage (left) and individual ASI discharge pulse voltages at 10, 50, and 90 % depth of discharge (right) as a function of pulse time for Si-Gr//NMC532 pouch cells at 2 psi per cell (blue), 76 psi per cell (red), and Gr//NMC532 pouch cells at 2 psi per cell (green), 76 psi per cell (black) from initial HPPC testing at 30°C. The error bars represent 2σ standard deviation.....	718
Figure II-422. Average cycle life plots showing discharge capacity (a), specific discharge capacity (b), specific discharge energy (c) and average voltage (d) performance (solid line = discharge, dashed line = charge) for Si-Gr//NMC532 pouch cells at 2 psi per cell (blue), 76 psi per cell (red), and Gr//NMC532 pouch cells at 2 psi per cell (green), 76 psi per cell (black). The error bars represent 2σ standard deviation.	718
Figure II-423. Images of xx3450 and xx6395 partially assembled before pouching (left), and before electrolyte filling (right).....	719
Figure II-424. Electrode design for xx6395 and xx3450 graphite//NMC532 pouch cells. “SS” = single side, “DS” = double side. All electrodes were fabricated at the CAMP Facility.....	720
Figure II-425. Representative individual cycle voltage (a,b) and dQ/dV (c,d) profiles of graphite//NMC532 xx6395 (blue) and xx3450 (red) pouch cells of the 1 st (a,c) and 3 rd (b,d) cycles during formation. Individual formation discharge capacity performance (e). Average discharge specific capacity and coulombic efficiency performance (f). The cells were cycled between 3.0 and 4.1 V at 30°C. The error bars represent 2σ standard deviation.	721
Figure II-426. Average rate study performance of graphite//NMC532 xx6395 (blue) and xx3450 (red) with specific discharge capacities as a function of current, mA/g (left) and mA (right). The cells were cycled at 30°C between 3.0 and 4.1 V. The plots show the discharge performance from the 2 nd cycle at C/20 and 3 rd cycle at C/10, C/5, C/2, 1C, and 2C rates. The error bars represent 2σ standard deviation.	722

Figure II-427. Average interpolated discharge (left) and charge (right) ASI performance for graphite//NMC532 xx6395 (blue) and xx3450 (red) from initial HPPC testing at 30°C. The error bars represent 2σ standard deviation.	722
Figure II-428. Average cycle life plots showing discharge capacity (a), specific discharge capacity (b), specific discharge energy (c) and average voltage (d) performance (solid line = discharge, dashed line = charge) graphite//NMC532 xx6395 (blue) and xx3450 (red) from cycle life testing. The error bars represent 2σ standard deviation.	723
Figure II-429. Effects of moisture exposure on (a) electrochemical performance and (b) oxide structure, imaged by scanning transmission electron microscopy (high angle annular diffraction mode).	725
Figure II-430. Summary of the rate capabilities for the separators in this study in the 3.0-4.3 V and 3.0-4.7 V voltage windows. The data for the Al ₂ O ₃ embedded in PET separator were omitted in this plot.	727
Figure II-431. Cycle life plot of Set 1 full-cell coin-cells – C/3 Charge and C/3 Discharge cycling.	728
Figure II-432. Full cell HPPC ASI (averaged discharge) data for full cells of graphite vs. Pristine, Sample A, Sample B, and Sample C in Set 1 (C/3 C: C/3 D).	729
Figure II-433. SEM images of NMC523 sample 1 (S1) and sample 2 (S2). The right two figures are enlarged views of S1 and S2.	734
Figure II-434. Voltage profiles of NMC532: sample 1 (black) and sample 2 (red)	734
Figure II-435. Specific capacity as a function cycle number: sample 1 (black) and sample 2 (red)	735
Figure II-436. SEM image of pristine NMC532 (left) and coated NMC532 (right). The insets are the EDS for two particle.	735
Figure II-437. Differential capacity plots of pristine (black) and coated (blue) NMC532.	736
Figure II-438. Specific capacity of NMC532 versus cycle number for half cell (left) and full cell (right)	736
Figure II-439. ASI of full cells with pristine (left) and coated (right) NMC532	737
Figure II-440. Images of the anodes from the overcharged cells. The rectangular-shaped voids in some of the images are from sampling for microscopy.	739
Figure II-441. Concentration of metals and phosphorus vs. %SOC for NMP-processed electrodes.	740
Figure II-442. Concentration of metals and phosphorus vs. %SOC for aqueous-processed electrodes. ..	740
Figure II-443. SEM images of the surface of anodes from overcharged cells, NMP processing. The numbers shown in the grey boxes indicate the %SOC that the cell experienced during the overcharge experiment.	741
Figure II-444. SEM images of the surface of anodes from overcharged cells, aqueous processing. The numbers shown in the grey boxes indicate the %SOC that the cell experienced during the overcharge experiment.	741
Figure II-445. XPS results from two anode materials (right) image from the NMP-processed material (left) image from the aqueous processed material.	742

Figure II-446. (a) Concentration vs. binding energy in the O1s energy region from the NMP-processed cathodes. (b) Concentration vs. binding energy in the O1s energy region from the aqueous-processed cathodes.	742
Figure II-447. (a) Concentration vs. binding energy in the F1s energy region from the NMP-processed cathodes. (b) Concentration vs. binding energy in the F1s energy region from the aqueous-processed cathodes.	742
Figure II-448. (a), (c) – (d): Hardness as a function of indentation depth, deposition date, film thickness, location and strain rate. (b) Micrograph of residual hardness impressions in lithium.	746
Figure II-449. Area specific resistance as a function of the adhesion strength of the Li-LLZO interface. Optical microscope images show the fracture surface of the Li and LLZO disks at low and high ASR. The red dashed line indicates the measured tensile strength of Li metal.	748
Figure II-450. XPS analysis of LLZO before and after heat treatment at 400 and 500°C. a) C:(La+Zr) atomic ratio as a function of heat treatment temperature, b) O 1s and c) C 1s core levels, d) percentage of total composition of different oxygen species on the LLZO surface as a function of heat treatment temperature after wet polishing (WP).	752
Figure II-451. Contact angle measurements of molten metallic Li on a) Li_2CO_3 , b) DP-LLZO, c) WP-LLZO, d) WP-LLZO after heat treatment at 500°C.	753
Figure II-452. Calculated work of adhesion (W_{ad}), contact angle (θ), and atomic structure for the a) Li- Li_2CO_3 and b) Li-LLZO interfaces.	754
Figure II-453. a) Schematic of the all solid-state Li-LLZO-Li cell, b) the equivalent circuit used for modeling the EIS data c) representative Nyquist plot of the Li-LLZO-Li cell (for LLZO heat-treated at 500°C), as-assembled (\circ) and after preconditioning at 175°C (\bullet). Markers indicate experimental data and dotted lines are simulated lines extrapolated from the equivalent circuit modeling using the circuit shown in b, d) the Li-LLZO interfacial resistance after preconditioning at 175°C versus the heat-treatment temperature. N=3 for each HT condition. Error bars represent standard deviations.	755
Figure II-454. a) DC cycling of Li-LLZO-Li cells (LLZO HT to 500°C after WP) at room temperature, stepping the current density from 0.01 to 1 $\text{mA}\cdot\text{cm}^{-2}$, b) the critical current density versus Li-LLZO interfacial resistance comparing the result of this study with other studies available in the literature, c) Nyquist plots of Li-LLZO-Li cell after each 20 cycles for cell cycled 100 time, d) Galvanostatic cycling of Li-LLZO-Li at 0.2 $\text{mA}\cdot\text{cm}^{-2}$ for 100 cycles at 0.4 $\text{mAh}\cdot\text{cm}^{-2}$. The blue dotted line shows the times at which EIS was collected and is shown in c.	756
Figure II-455. Normalized volume (to that of PEO) of PEO, polymer electrolyte (with and without TEGDME) and composite electrolyte calculated from experimentally measured density values, compared to the predicted values.	759
Figure II-456. Arrhenius plot of composite formed by spray coating and hot pressing, compared to that formed by dry milling and melt pressing.	760
Figure II-457. DC response of a symmetrical cell of configuration Li/Composite Electrolyte/Li for obtaining Li transference number. Inset, EIS response of the symmetrical cell.	760

- Figure II-458. Left, Arrhenius plot of TEGDME-plasticized composite electrolyte with different salt concentration; Middle, Arrhenius plot of TEGDME-plasticized composite electrolyte with different TEGDME content; Right, Room temperature conductivity of the TEGDME-plasticized composite as a function of the volume fraction of the Ohara ceramic. 761
- Figure II-459. Results for trilayer cell polymer /ceramic/polymer electrolyte. a-c, EIS responses of ceramic plate, polymer electrolytes and trilayer cells. All EIS response are measured at 30C. Inset of c, SEM of trilayer cell. d, Arrhenius plot of interfacial resistance calculated from the trilayer cell data..... 762
- Figure II-460. Comparison of spray coated composite containing DEGDBE (left) and HMPA (right) as plasticizer with results obtained using TEGDME as plasticizer. Conductivity of composite and polymer that does not contain plasticizers is also presented. 762
- Figure II-461. Arrhenius plot of composite containing acid/based treated Ohara powders, compared to that of untreated composite. Left, spray coated samples; Right, dry milled samples. 763
- Figure II-462. (a) EIS of thick and thin LLCZN pellets, (b) thick and thin LFMO pellets, and (c) thick and thin LLCZN/LFMO pellets. 768
- Figure II-463. (a) Photograph of structured garnet surface, bright white spots are garnet columns. (b) EIS of polished smooth garnet surface and structured garnet surface. 769
- Figure II-464 (a) Synthesis procedure of PFPE-DMC. (b) Cyclic voltammetry study of LiTFSI-PFPE electrolyte..... 769
- Figure II-465. (a) Photograph, (b) structure, (c) top and (d) side SEM images of PVDF-HFP gel membrane. (e) Cyclic voltammetry study of Li|PVDF-HPF+IL|Ti. (f) EIS of LLCZN/LFMO interface without (black) and with (red) PVDF-HFP gel electrolyte interface. 770
- Figure II-466. (a) EIS plot of cathode/garnet/cathode symmetric cell without gel electrolyte. (b) EIS of cathode/gel/garnet/gel/cathode symmetric cell and the equivalent circuit. (c) EIS of garnet itself. (d) Schematic of making garnet cell with mixed cathode. (e) EIS of symmetric cell with mixed cathode and gel..... 771
- Figure II-467. (a) Schematic of a cathode/garnet/cathode symmetric cell with aqueous interface. (b) Impedance of this cell with aqueous interface. 771
- Figure II-468. Comparison of cathode/electrolyte interfacial impedance on flat and 3D-structured garnet pellets. (a) EIS plot of garnet without 3D printing and with different 3D printings. (b) Reduction of interfacial resistance with increase in surface area. 772
- Figure II-469. (a) EIS plot of Li/garnet/Li symmetric cell. (b) EIS plot and equivalent circuit of Li/gel/garnet/gel/Li symmetric cell..... 773
- Figure II-470. Schematic illustration showing the structure of symmetric cells with (a) LLZ or (b) Si-coated LLZ SSEs. (c) Electrochemical impedance spectroscopy (EIS) measurements of symmetric cells where the interfacial resistance of the Si-coated garnet cell significantly decreased. Inset of (c) is a digital image of a Li/Si-coated LLZ/Li symmetric cell. (d) Nyquist plots of the Au/LLZ/Au symmetric blocking electrode system at room temperature. The solid black line denotes the experimental data while the red line with hollow spheres represents the fitting data using the equivalent circuit modeling. (e-g) Nyquist

- plots of (e) Li/LLZ/Li and (f) Li/Si-coated LLZ/Li symmetric cells. (g) The equivalent circuit model used in this study. 774
- Figure II-471. Nyquist plots of Li | Garnet SSE | Li (a) and Li | Al-Garnet SSE-Al | Li (b) in the frequency of 1 MHz to 100 mHz at 20°C. 775
- Figure II-472. Characterization of garnet solid state electrolyte/Li metal interface. (a) Schematic of the wetting behavior of garnet surface with molten Li. (b) SEM images of the garnet solid state electrolyte/Li metal interface. Without ALD Al_2O_3 coating, garnet has a poor interfacial contact with Li metal. Inset are photo images of contacts between melted Li-metal and garnet surface. (c) Comparison of EIS profiles of the symmetric Li non-blocking garnet cells. Inset shows the enlarged impedance curve of the ALD treated garnet cell. (d) Comparison of Li tripping/plating behavior of the symmetric garnet SSE/Li cells. Inset is the one cycle of stripping/plating for the ALD treated garnet cell, exhibiting a low overall impedance and stable interfacial property. (e) Voltage profile of the ALD treated garnet symmetric cell at a current density of 0.2 mA/cm². 776
- Figure II-473. (a) Li grand canonical phase diagram of Li-La-Zr-O system. (b) Models for the interfaces between Li metal and garnet surface materials. 777
- Figure II-474. Model for garnet-electrode interfaces, which take inputs from first principles calculations and experimental condition parameters. 777
- Figure II-475. Calculated mutual reaction energy, ΔED , of garnet and Li-Al alloy interfaces. 778
- Figure II-476. Electrochemical window (left) and the decomposition energy $\Delta\text{ED}_{\text{open}}$ (right) of the proposed and previously demonstrated coating layer materials applied between SE and cathode materials. The dashed line in (a) marks the equilibrium voltage to fully delithiate the materials. 779
- Figure II-477. (a) Calculated interphase equilibria and reaction energy between LLZO and Li polysulfides. (b) XPS spectra of garnet interface in Li-S battery. Calculated Li^+ transport pathway (c) and energy barriers (d) of Li_2SO_4 . Calculated Li^+ transport pathway (e) and energy barriers (f) of Li_6ZrO_7 . 780
- Figure II-478. Characterization of bi-layer garnet and performance of Li-NMC battery. (a) Cross sectional SEM image of bi-layer garnet SSE. (b) SEM of garnet SSE with Li metal inside. (c-d) EIS and CV of the Li-NMC battery with garnet SSE. 781
- Figure II-479. Cycling performances of Li-NMC cells with garnet SSE. (a-b) Voltage profiles and cycling performance of Li-NMC cell with 13.5 mg/cm² cathode at 0.1 C rate. Stable capacity at 175 mAh/g was achieved. (c) Cycling performance of Li-NMC cell with 13.5 mg/cm² cathode at various rates. High Coulombic efficiency and capacity retention were achieved over 200 cycles. (d) Voltage profiles of a Li-NMC cell with high NMC loading of 32 mg/cm² at 0.05 C rate. 782
- Figure II-480. Characterization of bi-layer garnet and performances of Li-S battery. (a) Schematic of Li-S battery based on bi-layer garnet. (b) Cross sectional SEM of bi-layer garnet filled with S. (c) EDS of S (green) and La (red) distribution in bi-layer garnet. (d-e) Voltage profile and cycling performance of the solid state Li-S cell with a loading of 7.5 mg/cm² at 0.2 mA/cm². 783
- Figure II-481. Cycling performances of Li-sulfur cell with garnet electrolytes. (a) Voltage profiles of the 1st, 20th and 50th cycle of the solid-state Li-S cell. 1200 mAh/g capacity and low capacity loss were achieved. (b) Cycling results of the solid state Li-S cell. High capacity retention was achieved with near 100% coulombic efficiency. 783

Figure II-482. Photograph of flexible garnet fibrous membranes made from (a) electrospun PAN (3.5 x 3.0 cm) and (b) cellulose textile (4.0 x 4.0 cm) templates.	787
Figure II-483. Characterization of garnet fibrous membrane: (a) Powder XRD patterns of the crushed garnet textile sintered at different temperatures; (b) SEM image of the garnet textile converted from the precursor solution impregnated template.	788
Figure II-484. Impedance spectra of the polymer electrolyte at room temperatures. The Li-ion conductivity is 0.9×10^{-4} S/cm.	788
Figure II-485. Mechanical characterization of garnet fiber: (a) AFM scanning of the nano-indent points on garnet fiber; (b) Load-depth profile of garnet fiber.	789
Figure II-486. Photograph of the flexible hybrid composite polymer electrolyte.	789
Figure II-487. Electrochemical characterization of hybrid composite polymer electrolyte: (a) Ac impedance, Li-ion conductivity is 6.07×10^{-4} S/cm; (b) CV, stable up to 4.5 V	790
Figure II-488. Computer modeling of Li ⁺ transport in garnet nanofibers.	790
Figure II-489. Li diffusion of garnet under strain.	791
Figure II-490. Coulombic efficiency of artificial SEI protected Cu foil and bare Cu foil at a current density of a) 1 mA cm^{-2} (cycling capacity 1 mAh cm^{-2} ; inset, the corresponding voltage profiles at the 20th cycle) and b) 0.25 mA cm^{-2} (cycling capacity 0.5 mAh cm^{-2}).	794
Figure II-491. Top-view SEM images and the corresponding digital photographs of Li deposition after five cycles on a,c) artificial SEI protected Cu and b,d) bare Cu foil. e) Schematic showing the configuration of nanoindentation measurements. f) Elastic modulus versus depth of a representative indentation test.	795
Figure II-492. Schematic showing the design of silly putty (SP) modified Li anode. Top shows the conventional Li dendrite evolution process, while the bottom shows the Li deposition behavior on a SP modified surface.	796
Figure II-493. The rheological study of SP.	796
Figure II-494. CE of Li deposition/stripping (1 mAh cm^{-2}) on SP-modified electrodes and control Cu electrodes at different current densities.	797
Figure II-495. (a) Schematic showing the surface treatment of Li metal with Freon R134a.(b) Proposed major chemical reactions at the early stage of surface treatment.	797
Figure II-496. High-resolution SEM images showing the (a) surface morphology and (b) cross-section of a LiF-coated Li foil.	798
Figure II-497. Time-dependent electrochemical impedance measurement on 3D Li metal symmetric cells with LiF coating.	798
Figure II-498. Schematics illustrating the fabrication process of the 3D Li anode with flowable interphase for solid-state Li battery. (A) 3D Li-rGO composite anode was first fabricated. (B) A flowable interphase for the 3D Li-rGO anode was created via thermal infiltration of liquid-like PEG-LiTFSI at a temperature of 150°C . (C) A CPE layer consisting of PEO, LiTFSI, and fumed silica or an LLZTO ceramic membrane	

was used as the middle layer, and high-mass loading LFP cathode with the CPE as the binder was overlaid to construct the solid-state Li-LFP full cell.	799
Figure II-499. Electrochemical performance of solid-state Li-LFP batteries.	800
Figure II-500. (a) HOMO and LUMO energies of lithium salts (LiPF ₆ , LiTFSI, LiBOB) and solvents (EC, EMC). The vertical lines indicate the electrochemical stability window of related lithium salts and solvents. (b) Schematic illustration demonstrating that LiPF ₆ additive in LiTFSI-LiBOB dual-salt electrolyte improves the stability of the Al current collector and the Li metal anode.	803
Figure II-501. (a) A schematic drawing of the liquid cell device with both anode and cathode integrated into the liquid cell. (b) A photo of the real device.	804
Figure II-502. SEM images (surface and cross-section views) of the deposited Li metal on Cu foils in electrolytes of 1 M LiPF ₆ /PC with different additives (VC, FEC and X) and additive mixtures (VC+X and FEC+X) at 0.1 mA cm ⁻² for 15 hours.	805
Figure II-503. (a) Average Li CE in electrolytes of 1 M LiPF ₆ /PC with different additives (VC, FEC and LiAsF ₆) and additive mixtures (VC+LiAsF ₆ and FEC+LiAsF ₆) tested in Li Cu cells. (b) Cycling stability of these electrolytes in Li NMC111 cells at C/3 rate after two formation cycles at C/10 rate, in the voltage range of 2.7 and 4.3 V.....	805
Figure II-504. (a) Initial charge/discharge voltage profiles at 0.175 mA cm ⁻² and (b) cycling performances of the baseline LiPF ₆ electrolyte and the three different dual-salt electrolytes at a current density of 1.75 mA cm ⁻² after 3 formation cycles at 0.175 mA cm ⁻²	806
Figure II-505. Time evolution of the average Si charge obtained from AIMD simulations. The change of the Si electronic charge is due to electron transfer to the electrolyte, and therefore is proportional to the SEI layer rate of growth. These results were presented at the AMR meeting and published in the Journal of the Electrochemical Society.	811
Figure II-506. Molecular dynamics simulations of surface cracking of a lithiated Si nanoparticle of ~4 nm covered by a LiF model SEI of ~1.5 nm. The expansion of the core leads to cracking which is manifested by bond damaging of the SEI coating initially, then resulting in macroscopically visible fractures.....	811
Figure II-507. Effect of core structure on cracking of ~500 nm nanoparticles. (a) crystalline core; (b) amorphous core. An SEI film covers the particle. There is a larger damage observed in the crystalline than in the amorphous particle.....	812
Figure II-508. SEI of two components with different activation barriers for Li diffusion: purple (A, E _a = 46.1 KJ/mol) and white (B, E _a = 65.3 KJ/mol). SEI morphologies at B volume fractions of 5% in (a) and 33% in (b). (c) Total charging time and SEI thickness for the first charge with varying B volume fraction. (d) Concentration of active Li traveling through the SEI interstitials (c _c) respect to the theoretical maximum (c _M) as a function of SEI thickness for various B volume fractions.	813
Figure II-509. (a) Electrochemically prepared porous metal foam (PMF). (b) Improvement in coulombic efficiency afforded by use of porous metal foam architecture.....	816
Figure II-510. Current-time profiles of cyclic voltammetry of (a) lithium-copper current collector cell (b) lithium-Li-SIA cell; (c) Coulombic efficiency of Li-SIA cell showing stability thereof.	817

Figure II-511. (a) Formation of lithium on stainless steel spacer in coin cell tests (b) Diffusion pathways causing plating of lithium on polymeric coated stainless-steel spacers.	817
Figure II-512. SIA electrodes demonstrate long-term stability though there is a rise in overpotential due to possible phase segregation.	818
Figure II-513. Preparation method for Gen-2 porous metal foams.	818
Figure II-514. (a) SEM image of the high porosity (~85%) Cu foams after sintering and removal of the sacrificial template. (b) Gen-2 Cu Foam electrodes demonstrate stable cycling region of 60 cycles at ~90% coulombic efficiency.	819
Figure II-515. SEM images of the porous Cu foam electrodes after cycling (~200 cycles). (A) Cross-section view, (B) Close up of lithium deposited within the foam structure, and (C) Close up of lithium deposited on top of the foam surface following pore closure by competitive SEI formation in the foam structure.	819
Figure II-516. (a) SEM image of the as-electrospun LLATO nanofiber network. (b) SEM image of the perovskite LLATO nanofibers (the insert is the photograph of the LLATO pellet). (c) Electrochemical impedance spectroscopy (EIS) plot of the LLTO and LLATO pellet.	823
Figure II-517. Pure and Al-decorated $\text{Li}_{0.33}\text{La}_{0.56}\text{TiO}_3$ structures. (a), (b) and (c) are side views of pure, most stable single-Al and double-Al decorated $\text{Li}_{0.33}\text{La}_{0.56}\text{TiO}_3$, respectively. (d) the top view of La-deficient layer of (b). Blue and green color blocks in (d) are used to represent two different regions in Li atom transporting direction. (e) Transporting barriers for Li atoms along transporting direction in pure, single-Al and double-Al decorated $\text{Li}_{0.33}\text{La}_{0.56}\text{TiO}_3$ structure. The transporting trajectory is marked by dash line in the inset.	823
Figure II-518. Synthesis procedure of PE/PEO cross-linked polymer.	824
Figure II-519. (a) Schematic illustration of the fabrication procedure for the lithium-ion-conducting membrane. (b) EIS profiles of the PVDF-HFP/LiTFSI/LLATO and the PVDF-HFP/LiTFSI/LLATO/ Li_3PO_4 electrolyte membranes.	825
Figure II-520. Initial discharge-charge profiles of KB-S70 cathodes in (a) conventional, (b) 0.25 M polysulfide-containing, and (c) 50 vol% DMDS-containing electrolytes with E/S=5 and 10 mL g^{-1} at a current density of 0.2 mA cm^{-2} , and (d) their corresponding cycling performance. (<i>Nano Energy</i> , 2017 , 31, 418.)	827
Figure II-521. (a, c) Discharge-charge profiles and (b, d) cycling performance of prelithiated graphite/sulfur full cells at (a, b) C/10 and (c, d) different C rates in the DOL/BTFE electrolyte. (<i>ACS Appl. Mater. Interfaces</i> , 2017 , 9, 6959.)	828
Figure II-522. Cycling performance of 2 wt% SCPs containing different sulfur contents as additives. (a) PSD containing different sulfur contents. (b) PST containing different sulfur contents. (<i>Nat. Commun.</i> , 2017 , 8, 850.)	829
Figure II-523. Morphologies of lithium metal deposited onto stainless steel substrate. SEM images of lithium metal deposited onto bare stainless steel substrate in the electrolyte with the addition of 8 wt% the SCP-90. (<i>Nat. Commun.</i> , 2017 , 8, 850.)	829

Figure II-524. Cycling performance of cells using electrolytes containing different contents of SCPs. (<i>Nat. Commun.</i> , 2017 , 8, 850.).....	830
Figure II-525. SEM images of the deposited Li after 100 cycles at a current density of 2 mA cm ⁻² and a deposition capacity of 2 mA h cm ⁻² . (<i>Nat. Commun.</i> , 2017 , 8, 850.).....	830
Figure II-526. SEM images of C-SEI layer (a), S-SEI layer (b) and SCP-90-SEI layer (c). (<i>Nat. Commun.</i> , 2017 , 8, 850.).....	830
Figure II-527. AFM images (10 × 10 μm ² scan size) of the C-SEI layer (a), S-SEI layer (b), and SCP-90-SEI layer (c). (<i>Nat. Commun.</i> , 2017 , 8, 850.).....	831
Figure II-528. XPS spectra of C-SEI layer, S-SEI layer and SCP-90-SEI layer. (a) S 2p XPS spectra, (b) C 1s XPS spectra, (c) F 1s XPS spectra. (<i>Nat. Commun.</i> , 2017 , 8, 850.).....	832
Figure II-529. FT-IR of C-SEI, S-SEI and PST-90 SEI layer. (<i>Nat. Commun.</i> , 2017 , 8, 850.).....	832
Figure II-530. Indentation curves of the C-SEI layer (a), S-SEI layer (b), and PST-90-SEI layer (c). (<i>Nat. Commun.</i> , 2017 , 8, 850.).....	833
Figure II-531. Cycling performances of the cells using different Electrolytes at a current density of 2 mA cm ⁻² with a deposition capacity of 1 mA h cm ⁻² . (<i>Nat. Commun.</i> , 2017 , 8, 850.).....	833
Figure II-532. Cycling performance of Li-S pouch cells.....	833
Figure II-533. Cycling performance of Sulfur – infiltrated framework material (SFM).....	837
Figure II-534. (a) FT-IR spectra of CPE after cycling and (b) flammability test result of the CPE.....	838
Figure II-535. Scheme of interaction of PTA with polysulfide.....	839
Figure II-536. Cycling performance of PTA coated DDSA electrode.....	839
Figure II-537. (a) UV – VIS spectroscopy of PTA coated DDSA electrodes showing absence of polysulfide absorbance and (b) Comparison of XPS patterns of commercial sulfur and PTA - DDSA separators after 200 cycles.....	840
Figure II-538. (a) Comparison of experimental and simulated XRD patterns of sulfonic CMS (b) Electrochemical cycling performance of the sulfonic CFM compared with commercial sulfur.....	841
Figure II-539. (a) Simplified X-ray absorption spectroscopy experiment schematic of Li-S cell using a thick cathode where darkened (upper) region of the cathode represents the thickness that was probed by X-rays. (b) Ratio of fluorescence intensity to initial fluorescence intensity measured before discharge indicating the increase in the total amount of sulfur signal detected during discharge.....	844
Figure II-540. (a) Simplified X-ray absorption spectroscopy experiment schematic of Li-S cell using a thin cathode. (b) Ratio of fluorescence intensity to initial fluorescence intensity measured before discharge indicating the total amount of sulfur signal detected during discharge and charge stayed constant (within 20% of error).....	845
Figure II-541. (a) Selected lithium polysulfide dianion spectra simulated using first principles calculations. (b) Ratio of main-edge peak area to pre-edge peak area versus corresponding Li ₂ S _x ‘x’ values, derived from theoretical spectra.....	846

Figure II-542. Discharge of a Li-S cell with a thick cathode and its (a) Sulfur K-edge X-ray absorption spectra probed from the back of cathode, (b) voltage versus capacity (Q), and (c) Average polysulfide chain length for representing the distribution of polysulfide dianions species present in the cathode as a function of capacity.....	846
Figure II-543. Discharge of a Li-S cell with a thin cathode and its (a) Sulfur K-edge X-ray absorption spectra probed from the anode, (b) voltage versus capacity (Q), and (c) Average polysulfide chain length for representing the distribution of polysulfide dianions species present in the cathode as a function of capacity.	847
Figure II-544. (a) voltage versus capacity for Li-S cell with a thin cathode during charge, and (b) Average polysulfide chain length as a function of capacity during charge.	848
Figure II-545. (a) voltage versus capacity for Li-S cell with a thin cathode during charge, and (b) Average polysulfide chain length as a function of capacity during charge.	849
Figure II-546. The first discharge curve of S_5Se_2 /KB cathode in (a) carbonate-based, (b) DME-based and (c) HFE-based electrolyte at C/20. (d) Cycling performance of S_5Se_2 /KB cathode in the three electrolytes. Open symbols indicate discharge; solid symbols mean charge in panel d.....	852
Figure II-547. In-operando 7Li NMR studies of the S_5Se_2 /KB cathode in the HFE-based electrolyte: fit curves to the NMR line shape at (a) open circuit voltage, (b) discharged to 1.0 V, and (c) charged back to 3.0 V. (d) 2D contour plot of NMR signal versus charge/discharge curve at C/30; (e) integrated areas of Li^+ species as a function of charge/discharge process.	852
Figure II-548. (a) contour plot of In-operando Se K-edge XANES and (b) representative Se K-edge XANES spectra on the 4 th cycle of S_5Se_2 /KB cathode at C/10 in HFE-based electrolyte.	853
Figure II-549. Cycling performance at high rates of Se-doped Se-S/KB cathode (50 wt.%) and S/KB cathode with in HFE-based electrolyte.	854
Figure II-550. (a) Pore size distribution of highly porous carbon with pore size of ca. 40 nm (HPC1) and 8 nm (HPC2), (b) cycle performance of $S_{22.2}Se$ /HPC1 (85 wt.%) and $S_{22.2}Se$ /HPC2 (85 wt.%) at C/2 in HFE-based electrolyte.....	855
Figure II-551. Cathode formulation effect on sulfur utilization	858
Figure II-552. Slurry mixing process methods vs. TiS_2 distribution (EDS) within coated cathode.....	859
Figure II-553. Sulfur utilization vs. cathode density, sulfur loading and discharge rate	859
Figure II-554. Sulfur utilization vs. sulfur loading, discharge rate and E/S ratio	860
Figure II-555. 2032 coin cells cycle life	861
Figure II-556. 2032 coin cells discharge temperature effect.....	861
Figure II-557. 2032 coin cells cycling after storage at fully discharge state	862
Figure II-558. 2032 coin cells self- discharge.....	862
Figure II-559. (a) Correlation of electrode porosity and thickness, (b) dependence of volumetric energy density on electrode thickness, (c) minimum electrolyte amounts for electrodes with different porosities, and (d) cycling stability of electrodes compressed to different thicknesses/porosities (Sulfur loading of	

- electrodes: 4 mg cm⁻²; electrolyte 1 M LiTFSI/DOL/DME with 0.2 M LiNO₃ and 0.15 M Li₂S₆ as additives)..... 866
- Figure II-560. SEM images of sulfur cathode (pressed to 60 μm) (A: surface; B: cross section) and corresponding Li metal anode (C: surface; D: cross section) after 200 cycles. (Sulfur loading 4 mg cm⁻² and 250 μm Li)..... 867
- Figure II-561. (a) Cycling stability and coulombic efficiency of thick electrode with sulfur loading 6.5 mg cm⁻² and (b) typical failed charge/discharge profiles (47th cycle), (c) cyclic voltammetry of carbon paper electrodes with electrolytes 1 M LiTFSI/DOL/DME+0.2 M LiNO₃ (black), 1 M LiTFSI/DOL/DME + 0.15 M Li₂S₆ (blue), and stored 1 M LiTFSI/DOL/DME + 0.2 M LiNO₃ + 0.15 M Li₂S₆ (red), and (d) XPS analysis of dried electrolytes 1 M LiTFSI/DOL/DME + 0.15 M Li₂S₆ (blue) and 1 M LiTFSI/DOL/DME + 0.2 M LiNO₃ + 0.15 M Li₂S₆ (red). 868
- Figure II-562. Visual comparison of polysulfide diffusion in H-cell using Celgard 2400 separator with (a) and without (b) C-PAA coating after 1 h rest, (c) SEM image of C-PAA/CNF coated separator, and (d) capacity and coulombic efficiency of Li-S cells using separators with (solid symbols) and without (hollow symbols) C-PAA coating. 869
- Figure II-563. (a) Component weight distribution of Li-S battery with energy density of 300 Wh kg⁻¹, (b) photo of single-layer pouch cell used in present study (Electrode working area 19.4 cm² and sulfur mass loading 5.7 mg cm⁻²), and (c) dependence of first-discharge areal capacity and specific capacity on electrolyte/sulfur ratio (black symbol - pouch cell using pristine separator; red symbol - pouch cell using modified separator). 870
- Figure II-564. (A) First cycle charge voltage profiles of Ni₃S₂-Li₂S, SnS₂-Li₂S, FeS-Li₂S, CoS₂-Li₂S, VS₂-Li₂S, TiS₂-Li₂S and G/CNT-Li₂S electrodes. (B) Energy profiles for the decomposition of Li₂S cluster on Ni₃S₂, SnS₂, FeS, CoS₂, VS₂, TiS₂ and graphene. Top view schematic representations of the corresponding decomposition pathways for (C) Ni₃S₂, (D) SnS₂, (E) FeS, (F) CoS₂, (G) VS₂, (H) TiS₂ and (I) graphene. Here, green, yellow, grey, purple, brown, blue, red, cyan and beige balls symbolize lithium, sulphur, nickel, tin, iron, cobalt, vanadium, titanium and carbon atoms, respectively. S_m represents the sulfur atom in the Li₂S cluster..... 874
- Figure II-565. (A) Galvanostatic charge/discharge voltage profiles of the S-VS₂@G/CNT composite electrodes at different current densities within a potential window of 1.5~2.8 V vs. Li⁺/Li⁰. (B) Comparison of the specific capacity and polarization voltage between the charge and discharge plateaus at 0.2C for different composite electrodes. (C) Cycling performance and Coulombic efficiency of the different composite electrodes at 0.5C for 300 cycles after the rate capability test..... 875
- Figure II-566. Li₂S₆ polysulfide adsorption test: (a) photograph of setup. (b) UV-Vis data of varying concentrations of Li₂S₆ in DOL/DME solution without candidate materials, (c-d) with candidate materials added in 3mM Li₂S₆..... 877
- Figure II-567. First coordination shell of a Li ion (purple) surrounded by DME molecules (top left) at 1M LiFSI concentration, and solvated by salt anions and DME molecules at 4M LiFSI concentration (bottom left). O (red), c (grey), S (yellow), N (blue). Solvation structure of LiS⁸⁻ in DME solution. 880
- Figure II-568. XPS chemical imaging of the Li-electrolyte interfacial region after (a) first charging cycle and (b) first discharging cycle. The Li-F species from F 1s spectra and S₀ polysulfide species from S 2p

spectra are represented as yellow and red regions, respectively. The black region represents the overlapping regions of Li-F and S₀polysulfide species. (c) Schematic representation of various fluorine-based Li-F species predicted from AIMD calculations. (d) Cartoon representation of SEI layer growth mechanism based on the combined XPS and computational results. From Chem. Mater. 29, 4718, (2017).

..... 881

Figure II-569. A new synthesis method was implemented to facilitate a more intimate mixture of S and C via a pressurized autogenic reaction. Schematic figure top left and electrochemical tests bottom left. Top right: Model of the composite material obtained from molecular dynamics simulations (see text). Bottom, right: simulation of discharge reactions in the C/S phase in contact with the electrolyte: Li (purple), S(yellow), C (grey), O (red), H (white). 882

Figure II-570. Identification of different cathode microstructural resistances (a) surface passivation (b) pore blockage and (c) their joint contribution, based on effective property relations for mesoporous carbon structure. Pore blockage resistance is relatively more sensitive to porosity changes and leads to delayed cathode starvation (g). Tuning precipitate morphology (d, f) and pristine porosity (e) lead to different cell performance as expected from microstructural implications (c, g). 884

Figure II-571. The normalized chromatographic peak for each derivatized polysulfide species (R=CH₃) from real-time HPLC results during discharge (A) and charge (B) of Li-S cell. The proposed discharge mechanism (C) and charge mechanism (D) of Li-S cell. (D. Zheng, D. Liu, J. Harris, T. Ding, J. Si, S. Andrew, D. Qu, X.Q. Yang, D. Qu, ACS Appli. Mater. Interfaces 2017,9,4326-4332.) 888

Figure II-572. Chromatograms of derivatized polysulfide mixtures without LiNO₃ (i) and with LiNO₃ (ii). For polysulfide mixture without LiNO₃ and Li metal (i-A), polysulfide mixture (without LiNO₃) with Li metal for 1hour (i-B), polysulfide mixture (without LiNO₃) with Li metal for 4hours (i-C), polysulfide mixture (without LiNO₃) with Li metal for 24hours (i-D), polysulfide mixture (without LiNO₃) with Li metal for 96hours (i-E); For polysulfide mixture with LiNO₃ and without Li metal (ii-A), polysulfide mixture (withLiNO₃) with Li metal for 1hour (ii-B), polysulfide mixture (with LiNO₃) with Li metal for 4hours (ii-C), polysulfide mixture (with LiNO₃) with Li metal for 24hours (ii-D), polysulfide mixture (with LiNO₃) with Li metal for 96hours (ii-E) (D.Zheng, X.Q. Yang, D.Y. Qu, ChemSusChem,2016,9, 2348-2350.)..... 890

Figure II-573. (a) CVs of sulfur electrochemical reduction and oxidation on HOPG-1T (basal plane), HOPG-1L (edge plane), HOPG-2T (edge plane) and HOPG-2L (step plane) at a scan rate of 20 mV/s. (b) The relation between peak potential obtained from (a) and I_D/I_G obtained from Raman analysis. (G.W. Wang, D. Zheng, D. Liu, X.Q. Yang, D.Y. Qu, Carbon, 2017, 119, 460-463.) 891

Figure II-574. Dynamic cycling performance of the cells fabricated with (a) LBL CNF-coated separators, (b) LBL CNT-coated separators, and (c) LBL CNT-coated separators with increasing sulfur loadings of 5.4 mg cm⁻² (black line) and 7.5 mg cm⁻² (red line)..... 895

Figure II-575. Static electrochemical analysis of the Li-S cells fabricated with the LBL CNF-coated separators after resting for 365 days (black, red, and blue lines) and with the polypropylene membrane after resting for 150 days (green line): (a) static electrochemical stability, (b) self-discharge rate, and (c) cyclability..... 896

Figure II-576. Electrochemical analysis of the Li-S batteries fabricated with the cotton-carbon cathodes with a sulfur loading of 30 mg cm⁻², a sulfur content of 80 wt.%, and an electrolyte/sulfur ratio of 6.8: (a)

cycling performance at C/10 and C/5 rates and (b) self-discharge analysis after resting for two months with freshly-made cells and fully-discharged cells. (c) Cycling performance of the cotton-carbon cathode with a higher sulfur loading of 60 mg cm ⁻² at C/10 rate.	897
Figure II-577. Silver-lithium/iodine solid state dual function battery.	901
Figure II-578. EIS for AgI as a function of temperature (A), equivalent circuit model used for quantitative data analysis (Inset)/Source: B.J. Neudecker, W. Weppner, <i>J. Electrochem. Soc.</i> , 1996 , 143(7), 2198-2203. Poulsen, W. Finn, <i>S. S. Ionics</i> , 1981 , 2(1), 53-57, (B) Conductivity plotted as a function of temperature, (Right) Equation used to determine conductivity values from measurement of resistance.	902
Figure II-579. XRD of synthesized Ag ion conductors, KAg ₄ I ₅ (A) and RbAg ₄ I ₅ (B). Conductivity as a function of temperature for LiI + x % MAg ₄ I ₅ (M = K, Rb) (C), and for Li _x % (AgI+20% Al ₂ O ₃).	903
Figure II-580. (A-F) AC impedance of Ag ⁺ /Li ⁺ conductors with varying amount of Al ₂ O ₃ additive, G) Conductivities of AgI with 0, 5, 10, 20, 30% Al ₂ O ₃ additive in temperature range from 30° to 60°C, H) AgI + x Al ₂ O ₃ conductivities at 30°C.....	904
Figure II-581. A) Use of LiI(HPN) ₂ in silver containing LiI electrolyte increases ionic conductivity, B) Various ratios of solid electrolyte and polymer were tested, and conductivity values compared at 30°C.	905
Figure II-582. EIS data: Pristine A) LiI, B) AgI solid electrolyte before and after charging, C) Composition I, a LiI-based electrolyte with AgI and polymer additive before and after charging.	906
Figure II-583. A) I ₂ clearly identified by XRD on positive side, B) Peaks consistent with Li observed on negative side.....	907
Figure II-584. A) EIS data of electrolyte Composition IV before and after (inset) charging with four different interfaces, B) Step-wise charging, C) After charging, all cells maintained stable OCV,.....	908
Figure II-585. Feasibility demonstration of Energy Dispersive X-ray Diffraction of a solid LiI cell in a stainless steel can.	908
Figure II-586. (a) LEED and (b) AFM images of an etched and annealed STO(001) surface. (c) AFM image of the same STO(001) surface after Li deposition. (d-f) XPS core level spectra before (red) and after (blue) Li deposition.	912
Figure II-587. XAS measurements of STO substrates in (a) TEY and (b) TFY modes before (red) and after (blue) Li deposition. (c) Schematic of surface structure after Li deposition (top) and air exposure (bottom).	913
Figure II-588. AFM images of STO(001), (111) and (110) surfaces (a-c) before Li deposition and (d-e) after Li deposition. All images were taken in identical locations. Scale bars on (001) and (110) images are 500 nm, and scale bars on (111) images are 1 μm.	914
Figure II-589. DFT-calculated (a) structures (b) energy changes and (c) electronic densities of states for Li atoms on (100) and (110) surfaces of SrTiO ₃ with different terminations.	914
Figure II-590. XPS core level spectra from Nb:LLZO before (red) and after (blue) Li deposition.	915

Figure II-591. UV-Visible spectra of dbNDI/Py solutions of varying ratios (constant total concentration) in dichloromethane, showing development of peaks in the visible region corresponding to complex formation.....	920
Figure II-592. Our novel polymeric materials form free-standing, self-healing films when mixed together in a 1:1 molar ratio of NDI to Py units. The self-healing temperature of these films can be adjusted over a wide range by doping small molecule NDI or Py compounds into the film, forcing formation of either 1:1 or 2:1 NDI:Py complexes, which have vastly different binding energies. These small molecules can also be used to “passivate” binding sites, adjusting the crosslinking density.	921
Figure II-593. Voltage curves of the 2 nd , 20 th , and 50 th cycle (C/10 rate) of S/C cathodes, in which the mesoporous carbons contain 0-20% wt phenylthiol surface modifier, as well as capacity data over 100 cycles for each cathode. Notably, 10% wt modifier significantly improves capacity and retention while introducing minimal additional overpotential.....	923
Figure II-594. Diagram illustrates the <i>in-situ</i> formation of a metal fluoride positive electrode and a lithium metal negative electrode from the electrolytic decomposition of a Li-based bi-ion glass under polarization	926
Figure II-595. Program approach breakdown	926
Figure II-596. Electrochemical impedance spectroscopy as a function of composition (left) and <i>in-situ</i> direct current conductivity as a function of voltage for several compositions (right)	928
Figure II-597. Voltage profile of an <i>in-situ</i> self-formed battery fabricated using newly implemented maskless scalable patterning technique.....	929
Figure II-598. Energy density in the first discharge at slow rate plotted upon formation at 3.5 and 4.0 V for various architecture combined with new bi-ion conductor chemistry. Labels indicate approach that gained the generation improvement.....	930
Figure II-599. Voltage profile of a cell utilizing hybridization of the transport pathways showing the <i>in-situ</i> formation and first discharge.....	931
Figure II-600. Electrochemical performance of Li-O ₂ batteries with three LiTFSI-DMSO electrolytes cycled under capacity-limited protocol (600 mAh g ⁻¹) in the voltage range of 2.0 to 4.5 V at 0.1 mA cm ⁻² . (a-c) Voltage profiles for LiTFSI-3DMSO electrolyte (a), LiTFSI-4DMSO electrolyte (b), and LiTFSI-12DMSO electrolyte (c). (d) The corresponding cycling stability of the three electrolytes.....	934
Figure II-601. (a) Schematic of the operation principle of prior protection for CNT air electrode and Li metal anode after <i>in-situ</i> electrochemical process. (b) Stable cycling life of Li-O ₂ cells without and with pretreatment cycled at 0.1 mA cm ⁻² . (c-f) SEM surface-view images of the CNT air electrode without pretreatment after 70 cycles (c, d), and the CNT air electrode with 4.3 V/10 min pre-charging treatment after 110 cycles (e, f). (g-j) SEM images of corresponding cycled, untreated Li metal anode (g, h) and pretreated Li metal anode (i, j), where (g, i) are cross-section views and (h, j) top views.	935
Figure II-602. The a.c.-impedance spectra of the Li-O ₂ cells after pre-treatment at 4.3 V/10 min during 110 cycles (a), and pristine Li-O ₂ cells during 70 cycles (b). (c) Evolution of fitted resistance values of the above Li-O ₂ cells after pre-treatment at 4.3 V/10 min and pristine cells. Inset: The equivalent circuit used to fit the impedance spectra.....	936

- Figure II-603. Cycling performances of Li-O₂ cells with optimized in-situ pretreated RuO₂/CNT air electrode (red line) and pristine RuO₂/CNT air electrode (black line), cycled at 0.1 mA cm⁻² in 1 M LiTf-Tetraglyme electrolyte. Blue line is the cycle life of the freshly assembled Li-O₂ cell with the cycled pretreated air-electrode after 190 cycles and new Li metal anode, under the same conditions. 937
- Figure II-604. (a) Discharge curves of Li-O₂ coin cells composed of CNT air electrodes at a current density of 0.1 mA cm⁻² at various temperatures. (b) Temperature dependence of the experimental lifetime of superoxide from NMR and EPR, the calculated electrochemical kinetics, and the discharge capacities at different temperatures. 938
- Figure II-605. a. Galvanostatic discharge curves for Li/O₂ cell containing a LiNO₃-KNO₃ electrolyte and a carbon-based air electrode (T= 150°C, PO₂= 1.4 atm, j= 0.32 mA/cm²). b. Cycling profile of a molten nitrate Li/O₂ cell using a boron carbide-based air electrode (T= 150°C, j= 0.13 mA/cm², B₄C loading ~5 mg/cm²). c. Corresponding in-situ pressure analysis for cell depicted in b. 941
- Figure II-606. a. Li plating/stripping onto Cu (A_{Li}=A_{Cu}=0.502 cm²) at j= 0.5 mA/cm², at 150°C, under Ar, in LiNO₃-KNO₃ melt (Inset: Q vs Cycle number and Li plating/stripping load curve). b. Cycling curve comparison between Li-Li symmetric cell and Li-Cu cell employing LiNO₃-KNO₃ melt, at 0.5 mA/cm², at 150°C. c. EIS data derived from cycled Li-Li symmetric cell (estimated electrolyte thickness: 0.5 mm, A_{Li}= 0.502 cm²). 942
- Figure II-607. a. Li/LLZO/Li symmetric cell cycling at 185°C (with in situ cell pressure analysis) at 0.1 mA/cm² with b. corresponding EIS analysis recorded at OCV (AC signal: 10 mV, from 1 MHz to 1 Hz). 943
- Figure II-608. a. Li/O₂ cell discharge curve using a LLZO-protected Li anode and a molten nitrate catholyte (j= 0.05 mA/cm², 185°C, m_{carbon}= 5 mg/cm², m_{nitrate}= 10 mg/cm²). SEM analysis of Boron Carbide air electrode b. before and c. after discharge under O₂ in LiNO₃-KNO₃ eutectic at 150°C. 944
- Figure II-609. a. SEM of a nickel coated structured electrode. b. CV at 150 °C and a scan rate of 0.01 mV/s for three nickel electrode morphologies performing nitrate reduction (electrolyte: LiNO₃-KNO₃ eutectic). 945
- Figure II-610. a. Li/O₂ cell voltage profile at 175°C using Super P Carbon:PTFE (95:5 wt.%) cathode at 0.05 mA/cm² current density (m_{carbon}= 3 mg, m_{nitrate}= 6.5 mg). b. Molten nitrate Li cell voltage profile at 175°C using nanoporous nickel cathode (Ni:LiNO₃-KNO₃ eutectic 50:50 wt.%) at 0.05 mA/cm² current density (m_{Ni}= m_{nitrate}= 10 mg). 945
- Figure II-611. Molten nitrate Lithium cell voltage profile (3rd cycle) at 150°C using nanoporous nickel/nitrate catholyte and LLZO-protected Li metal anode (Ni to LiNO₃-KNO₃ eutectic 1:1 wt.%, 0.2 mA/cm², m_{Ni}= m_{nitrate}= 10 mg/cm²). 946
- Figure II-612. (a) Discharge/charge profile of a Li-O₂ cell using the “textile” concept for 50 cycles. (b) The termination voltage of charge/discharge for 50 cycles. 951
- Figure II-613. Photograph of cathode discharged to 1000 mAh/g, dried under Ar for 1 hr, and then soaked in 3 mL of TiOSO₄(aq). No apparent color change occurred upon titration indicating no Li₂O₂ is present 952

Figure II-614. (a) *Ex situ* XRD patterns (left) for V_2CT_x upon electrochemical sodiation/desodiation cycling (right), and (b) schematic illustration of the expansion/contraction behavior of V_2CT_x during sodiation/desodiation process: the interlayer distance of V_2CT_x is increased upon Na^+ intercalation during sodiation process, then partially reduced upon Na^+ deintercalation due to the trapped Na^+ between V_2CT_x layers behaves as a pillar during desodiation process..... 955

Figure II-615. (a) *Ex situ* V *K*-edge XANES spectra of V_2CT_x at selected cell voltages during first sodiation/desodiation process (OCV \rightarrow 0.1V \rightarrow 3V), (b) corresponding voltage profile, and (c) variation of V edge energy (at half height of normalized XANES spectra) at selected cell voltage..... 956

Figure II-616. V $L_{2,3}$ -edge sXAS spectra collected on electrodes that are cycled to different voltages. (a) Bulk-sensitive total fluorescence yield (TFY), and (b) surface-sensitive total electron yield (TEY)..... 957

Figure II-617. Charge compensation mechanism upon Na deintercalation/intercalation in β - $NaCu_{0.2}Mn_{0.8}O_2$. (a) in-situ XAS spectra at Mn *K*-edge collected at different charge/discharge states; (b) in-situ XAS spectra at Cu *K*-edge collected at different charge/discharge states (c) The load curve of β - $NaCu_{0.2}Mn_{0.8}O_2$ during the first charge process for in-situ XAS. (d) The enlarged XAS spectra at Cu *K*-edge..... 958

Figure II-618. Ex-situ SEM of the initial nucleation of Li on polymer-coated Cu foil. See top inset for polymer identity. Deposition current density was 1 mA/cm² and a capacity of 0.1 mAh/cm² was deposited in each case. 961

Figure II-619. a) The reaction mechanism of Li_2S oxidation with a redox mediator (RM). b) Voltage profiles of Li_2S electrodes in the first charge/discharge cycle with and without a RM in a DOL/DME electrolyte..... 962

Figure II-620. a) *Ex situ* SEM to monitor morphology evolution of Li_2S particles after 250 cycles with and without RM molecules. b) Capacity retention of a Li_2S electrode in presence of the RM in the electrolyte at 0.5C. 963

Figure II-621. Structural and morphological changes during reversible phase transformation of $Na_2C_6O_6$. a, *In situ* synchrotron XRD patterns of nanoparticle electrodes collected for the every 0.1 Na-stoichiometry change. b, Crystal structure change of $Na_{2+x}C_6O_6$ when charged above 2.9 V. c, *Ex situ* SEM images of nanoparticle electrodes at different states of charge during the first cycle. d-e, Dramatic morphology change and the corresponding voltage profile during the phase transformation. 964

Figure II-622. Electrochemical four-sodium storage of $Na_2C_6O_6$ electrodes in half cells and full cells. a, Rate capability and corresponding cycle performance (inset) of $Na_2C_6O_6$ electrode from 0.5-3.3 V. b, Cycle retention of $Na_2C_6O_6$ electrodes at 500 mA g⁻¹ corresponding voltage profile (inset) for 50 cycles. 965

Figure II-623. (a) Morphology of the in-house synthesized high-Ni NMCs showing spheres with the primary and secondary particles. (b) First cycle voltage profiles and (c) cycle life of Li||NMC cells between 4.4 and 2.8 V. (d) Comparison of the cycling performance of high-Ni $Li_{0.94}Co_{0.06}O_2$ with and without Al doping in cells with Li-metal anode..... 970

Figure II-624. Cycling stability of LiFSI-phosphate electrolytes (E313) in various cell systems, (a) Li||Cu, and (b) Li||NMC622..... 970

Figure II-625. (a, b) Cross-section SEM images of two Maxwell NMC622 thick electrodes: (a) 30 mg cm ⁻² ; (b) 60mg cm ⁻² . (c) Cycling performance at C/3 of three 622/811 cells of different cathode loadings. (d) Specific capacity with cycling for the 30 mg cm ⁻² NMC 622 electrode at C/3 for the first 100 cycles and subsequent resurrection of the cell by replacement of Li anode and electrolyte.	972
Figure II-626. SEM images of the cross section of a porous 3D host for Li metal plating and stripping, demonstrating its macroscopic dimensional stability.	973
Figure II-627. (a) Comparison of calculated and experimental charge/discharge curves for a Li NMC622 cell. (b) Internal profiles for solid phase current density, solid phase potential, electrolyte potential and overpotential (clockwise from top left). The dashed red line and blue lines are for different porosity uniform electrodes while the black line is associated with a graded porosity electrode.....	974
Figure II-628. (a) Picture of the 1 Ah and 300 Wh kg ⁻¹ pouch cell with Li NMC622 system. (b) Cell capacity and capacity retention vs cycle number for a 1.1 Ah, 300 Wh kg ⁻¹ Li NMC 622 pouch cell with a PNNL developed electrolyte. The capacity retention of 78% is obtained at the 50th cycle.	975
Figure II-629. (a) Schematic of modelled system and (b) comparison between model and experimental data for a NMC622 cell.....	976
Figure II-630. One-dimensional intensity vs. q (scattering vector) at the Li (110) peak through one plating and stripping cycle at 1.5 mA cm ⁻²	976
Figure II-631. Representative results from in situ XRD measurements of Li plating onto copper substrate. (a) Integrated intensity of Li (110) XRD peak vs. time passed throughout four Li plating and stripping cycles at 1.0 mA cm ⁻² in 1 M LiPF ₆ in EC/DMC. (b) Corresponding electrochemical (Coulombic) and XRD efficiencies (ratio of amount stripped to plated).....	977
Figure III-1. Estimated costs of cells in automotive battery packs with different combination of electrodes. The packs are rated for 100 kWh _{Total} (85 kWh _{Useable}), 300 kW, 315 V, 168 cells, and produced at a plant volume of 100K packs/year.	983
Figure III-2. Effect of charging time on anode thickness and cell cost. ΔSOC=80%.....	984
Figure III-3. Effect of charging time on charger power requirement. ΔSOC=80%.....	984
Figure III-4. Effect of the maximum allowable current density (MACD) on anode thickness, cell temperature, and cell cost. ΔSOC=80%.....	985
Figure III-5. Solvent content in electrode layer and the drying rate as a function of time. 150 μm layer, 95°C air temperature.	986
Figure III-6. Comparison of drying of electrode layer with NMP and water solvents. 150 μm layer, 95°C air temperature. The electrode was loaded with the same volume of solvent.....	987
Figure III-7. Average relative capacity vs. time for the calendar life cells. The error bars represent ±1σ.	991
Figure III-8. Average relative capacity vs. time for the cycle life cells. The error bars represent ±1σ. ...	991
Figure III-9. Average relative resistance vs. time for the calendar life cells. The error bars represent ±1σ.	992

Figure III-10. Average relative resistance vs. count for the cycle life cells. The error bars represent $\pm 1\sigma$.	993
Figure III-11. (a) Relative power vs. time for the calendar life cells. The error bars represent $\pm 1\sigma$ (b) Relative power vs. cycle count for the cycle life cells. The error bars represent $\pm 1\sigma$.	994
Figure III-12. Average change in relative capacity vs. total capacity throughput for cells tested using the CC-CV protocol.	995
Figure III-13. Average relative capacity vs. total capacity throughput for cells tested using the China protocol.	995
Figure III-14. Optical images of the negative electrodes taken during the post-test analysis of the fast-charge cells from the CC-CV and China test protocols.	996
Figure III-15. Representative cell temperatures and voltages during a thermal ramp test of a multicell 1kWh Li-CoO ₂ pack	1005
Figure III-16. Testing setup for COTS 3Ah 5-cells pack with passive thermal management (copper spacer of 1/8" thickness shown in picture). Failure initiation by nail penetration into cell 1 with the following thermocouple (TC) and copper (C)/or aluminum mapping consistent between tests.	1006
Figure III-17. Temperature and voltage data collected during propagation testing with the additional of thermal management (aluminum spacers). Left plots show limited propagation to the neighboring cell with 1/16" aluminum (cell 2 voltage drop at 3.5 min into test) and right plots show no propagation with 1/8" aluminum between cells.	1007
Figure III-18. Cell temperature data collected both experimentally and simulated by NREL's model during failure propagation testing for AI-1 case showing good agreement	1007
Figure III-19. Schematic for 1S2P setup bridged by constantan wire to measure short circuit current during failure propagation. Improved mechanical robustness achieved through cell holders and additional pressure applied at the failure point to maintain contact during runaway event.	1008
Figure III-20. String current across bridge and voltage measured during the failure propagation test for NMC 18650 in no extra mechanical contact during test (top) and with improved mechanical contact (bottom) in 1S2P configuration	1009
Figure III-21. Left: Still images (pre and posttest) and right: temperature and voltage data as a result of successful thermal runaway initiated by a 20 pulse laser	1011
Figure III-22. External and CT images comparing electrode damage on discharged cells using 20 pulse laser or blunt rod.	1011
Figure III-23. Temperature and voltage data from laser testing in a COTS 3 Ah LiCoO ₂ cylindrical cell and CT analysis of internal damage	1012
Figure III-24. Temperature and voltage data collected during runaway initiated by laser in a COTS 3.1 Ah NCA cylindrical cell	1012
Figure III-25. Voltage and temperature data collected during failure propagation testing initiated by overcharge of cell 1 (left) or nail penetration of cell 1 (right).	1013

Figure III-26. Efficiency of cells tested at 30°C in NREL’s calorimeters during FY15/FY16/FY17.....	1018
Figure III-27. Efficiency of silicon blended cells tested at 30°C in NREL’s calorimeters under charge/discharge currents.....	1019
Figure III-28. Entropic response to graphite, titanate and silicon blended cells test at 30°C.....	1020
Figure III-29. Heat efficiency of an ultracapacitor under test in the calorimeter at 30°C.....	1020
Figure III-30. Total energy breakdown for LIB production. LCO stands for LIB based on LiCoO_2 cathode material, LMO LiMn_2O_4 , NMC $\text{LiNi}_{1/3}\text{Mn}_{1/3}\text{Co}_{1/3}\text{O}_2$, NCA $\text{LiNi}_{0.8}\text{Co}_{0.15}\text{Al}_{0.05}\text{O}_2$, LFP LiFePO_4	1024
Figure III-31. Comparison of lead acid and LIB energy use and emissions on a per-kg, per-Wh, and per-vehicle lifetime basis, dashed line represents LMO results within LIBs. Lifetime basis assumes three lead acid batteries and one LIB per vehicle lifetime. Solid orange LIB is LCO while black dashed line is LMO.	1025
Figure III-32. BEVs and ICEV considering GHG and SO_x emissions on a per kilometer basis. BEVs utilized LMO and LCO cathode chemistries for the two LIB comparisons.	1026
Figure III-33. Framework for BEAT	1027
Figure III-34. Dependence of lithium loss on severity of treatment.....	1030
Figure III-35. Process Flow Diagram for Commercialized Hydrometallurgical Recycling Process for LIB	1031
Figure III-36. Increase in energy savings as more materials are recycled to useful products.....	1032
Figure III-37. Closed-loop flow of the battery recycling model	1034

List of Tables

Table ES- 1: Subset of EV requirements for batteries and cells.	xxiv
Table 1: Subset of EV requirements for batteries and cells. (Cost and low temperature performance are critical requirements).	3
Table 2: Subset of targets for 12V start/stop micro-hybrid batteries (cost and cold cranking are critical requirements)	4
Table 3: Battery500 Seedling Projects.....	18
Table I-1: Characteristics of the annual cell deliverables in the program.....	31
Table I-2: Scale up line trials for USABC baseline failure root cause analysis.....	42
Table I-3: Amprius' 10 Ah Silicon-NCM cells exceeded USABC performance goals.....	47
Table I-4: USABC Cell & Module Performance Targets and SAFT Test Results.....	61
Table I-5: Physical properties of samples optimized for increased ionic conductivity.	69
Table I-6: USABC Project Design Goals and Approaches.....	81
Table I-7: Gurley number of the PVD coated separators.....	82
Table I-8: A summary of the Static Capacity (C/3, 3.5 - 4.9 V, no CV), OCV, AC Impedance at 1 kHz, and Cell Weight of the cells delivered to ANL.....	84
Table I-9: Overview of Program Hardware Deliverables and Build Strategy	96
Table I-10: Comparison between synthesized material and commercial material.....	106
Table I-11: Overview of Data Produced via the PNNL Collaboration.	116
Table I-12: Physical properties of current μpSi powder.....	120
Table I-13: Performance Goals for Ceramic Coating Applied to 16 μm Trilayer, PP and PE	132
Table I-14: Demonstrated Results.....	132
Table I-15: Composition and Processing Parameters for Baseline Anode Pouch Cells	142
Table I-16: Active material screening in electrocoated electrodes. Suitable particles must demonstrate a coverage density of $> 10 \text{ mg/cm}^2$ during electrocoat and battery performance characteristic of the active material used.	150
Table I-17: Summary of the high speed curing trial runs at ebeam Technologies.....	160
Table I-18: EB doses for different sample on the top and bottom of the samples.....	161
Table I-19: Dry powder samples prepared for electrostatic spraying trial runs.....	162
Table I-20: Parameter for component of the cell.	218
Table I-21: Summary of capacity recovered using excess Li reservoir for commercial graphite cells	229
Table I- 22: BatPaC simulation comparing the effects of charging time on the required anode thickness, heat generation in the pack, and the resulting temperature rise, pack cost, and incremental cost of charging	

faster than 1-C (60 minutes) rate. Cell Chemistry: NMC 622-Graphite, Pack Energy: 85 kWh; Rated Power (10-second burst): 300 kW; Maximum Allowable Current Density (MACD): 4 mA/cm ² ; Number of Cells per Pack: 240.....	234
Table II-1: Molecular weights for five commercial binders.....	247
Table II-2: Gas Composition of LCO and NMC622 Cells as a Function of FEC Concentration Determined by GC-MS/TCD.....	263
Table II-4: Half-cell coin-cell formation testing results of experimental silicon samples from Paraclete Energy. The capacity values are normalized to the total weight of the silicon, graphite, and carbon black present in the electrode.	273
Table II-5: Half-cell coin cell formation testing results of new baseline 15wt.% silicon-containing electrodes. The silicon powders used are “Sample D” and “Scaled-up Sample D” from Paraclete Energy. The capacity values are normalized to the total weight of the silicon, graphite, and carbon black present in the electrode.	274
Table II-6: Summary of synthesized cPAAs.....	339
Table II-7: Summary of P4VBA and PAA binders cycled.....	341
Table II-8: Surface treatments investigated on a LLS Li _{1.18} Mn _{0.54} Co _{0.18} Ni _{0.28} O ₂ (~ 6% spinel)	526
Table II-9: Relative L3 high to L3 low peak intensity ratio from nickel L-edge XAS spectra.	535
Table II-10: Experimental conductivity results (with 95% confidence intervals) from using μ NLP and μ FLP on the same electrode sample.	659
Table II-11: Experimental conductive property results (with 95% confidence intervals) from using μ FLP on the three electrode samples.	660
Table II-12: Simulated and experimental effective ionic transport results, following drying and calendaring steps.....	661
Table II-13: Measured and calculated properties of the battery films coated layer.....	662
Table II-14: The lithiation reactions and their corresponding voltages for Li-S battery cathodes based on Li ₂ Sn-C ₂ N and Li _m S ₈ -C ₂ N.....	666
Table II-15: Key Properties not used for DFTB parameterization, but compared with DFT (GGA/PBE) for validation.....	670
Table II-16: MERF FSP System Parameters	679
Table II-16: The cell capacities of high loading electrodes using NCA9152, NCM622 and LCO.	693
Table II-17: Energy densities using NCA9152, NCM622 and LCO, with discharge voltages of 3.81, 3.82, and 3.96 V vs Li/Li ⁺ , respectively.	694
Table II-18: Summary of Electrode Library distributions	724
Table II-19: Commercial separators used in this study.....	726
Table II-20: Electrochemical impedance with fitting data for Li/LLCZN/Li cells with and without ALD coating on both sides of the garnet SSEs.	775

Table II-21: The mutual reaction energy ΔED , min, mutual (in meV/atom) of the coating layer materials with the SE or LCO materials.	779
Table II-22: Performance Requirements for Project Li-S Battery	836
Table II-23: S-TiS ₂ hybrid electrode formulation optimization.....	858
Table II-24: Quarterly milestones and verification for Year 1.	902
Table II-25: Conductivity of LiI composite electrolytes at 30°C.....	905
Table II-26: Initial Solvate Ionogel Formulations and Their Conductivities at 23°C	922
Table III-1: Electrode material costs to estimate the cost of battery packs.....	982
Table III-2: Status of Deliverables for Testing	990
Table III-3: Articles Tested for USABC.....	1000
Table III-4: Articles Tested for Benchmark.....	1000
Table III-5: Articles Tested for Applied Battery Research (ABR).....	1001
Table III-6: Articles Tested for the 2011 FOA: ‘Develop Advanced Cells and Design Technology for Electric Drive Vehicle Batteries’	1001
Table III-7: Passive Thermal Management Testing Matrix and Results	1006
Table III-8: Summary of Results for Short Circuit Current during Failure Propagation.....	1010
Table III-9: Energy Injection Comparisons between Failure Modes.....	1013
Table III-10: Material Demand to 2025 vs. USGS Reserve Estimates.....	1029
Table III-11: Challenges for Li-Ion Battery Recycling.....	1030

(This page intentionally left blank)

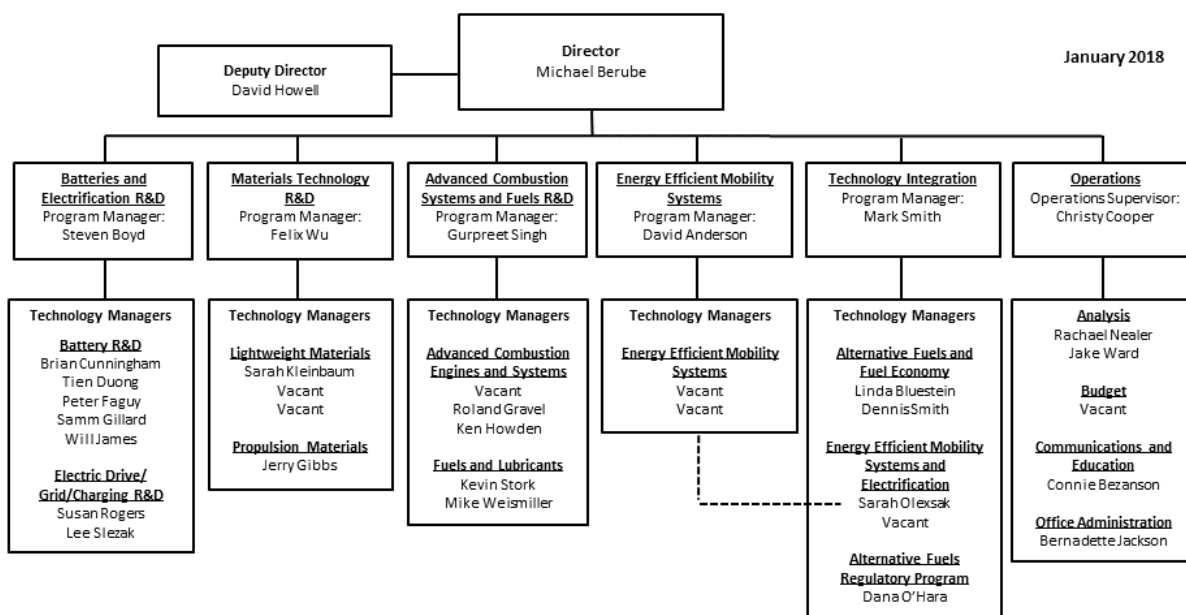
Vehicle Technologies Office Overview

Vehicles move our nation. Vehicles transport more than \$36 billion worth of goods each day¹ and move people more than 3 trillion vehicle-miles each year². Growing our national economy requires transportation and transportation requires energy. The average U.S. household spends nearly one-fifth of its total family expenditures on transportation³, making transportation the most expensive spending category after housing. The transportation sector accounts for 70% of U.S. petroleum use. The United States imports 25% of the petroleum consumed – sending more than \$10 billion per month⁴ overseas for crude oil.

To strengthen national security, enable future economic growth, and increase transportation energy efficiency, the Vehicle Technologies Office (VTO) funds early-stage, high-risk research on innovative vehicle and transportation technologies. VTO leverages the unique capabilities and world-class expertise of the national laboratory system to develop innovations in electrification, advanced combustion engines and fuels, advanced materials, and energy efficient mobility systems.

VTO is uniquely positioned to address early-stage challenges due to strategic public-private research partnerships with industry (e.g., U.S. DRIVE, 21st Century Truck Partnership). These partnerships leverage relevant expertise to prevent duplication of effort, focus DOE research on critical R&D barriers, and accelerate progress. VTO focuses on research that industry does not have the technical capability to undertake on its own, usually due to a high degree of scientific or technical uncertainty, or it is too far from market realization to merit industry resources. VTO's research generates knowledge that industry can advance to deploy innovative energy technologies to support affordable, secure, and efficient transportation systems across America.

Vehicle Technologies Office Organization Chart



¹ <https://ops.fhwa.dot.gov/publications/fhwahop16083/ch1.htm#1>

² <https://www.fhwa.dot.gov/policyinformation/statistics/2015/vml.cfm>

³ <https://www.bls.gov/cex/2015/standard/multiyr.pdf>

⁴ Transportation Energy Data Book Edition 34, ORNL, Table 1.7 and Table 10.3; Overseas includes countries and territories outside the 50 States and the District of Columbia.

(This page intentionally left blank)

Batteries Program Overview

Introduction

During the fiscal year 2017 (FY 2017), the Vehicle Technologies Office (VTO) battery program continued research and development (R&D) support of technologies for plug-in electric vehicles (PEVs), e.g., plug-in hybrids, extended range electric vehicles, all-electric vehicles, and some hybrid electric vehicles (including those with 12 volt start/stop hybrid). One of the objectives of this support is to enable U.S. innovators to rapidly develop the next generation of technologies that achieve the cost, range, and charging infrastructure necessary for the widespread adoption of PEVs. Stakeholders involved in VTO R&D activities include universities, national laboratories, other government agencies and industry partners – including automakers, battery manufacturers, material suppliers, component developers, private research firms, and small businesses. VTO works with key U.S. automakers through the United States Council for Automotive Research (USCAR) – an umbrella organization for collaborative research consisting of Fiat Chrysler LLC, the Ford Motor Company, and the General Motors Company. Collaboration with automakers through the US DRIVE (Driving Research and Innovation for Vehicle Efficiency and Energy Sustainability) partnership enhances the relevance and the success potential of the research platform. An important prerequisite for the electrification of the nation's light duty transportation sector is the development of more cost-effective, longer lasting, and more abuse-tolerant PEV batteries and accordingly, VTO battery R&D is focused on the development of high-energy batteries for PEVs and very high-power devices for hybrid vehicles.

Goals

The goals of this research are to address barriers which hold back EVs from matching the full driving performance, convenience, and price of an internal combustion engine (ICE) vehicle. EVs have the advantage of a very high efficiency compared to other vehicle types, a simplified drive train, and a flexible primary energy source (i.e., the electricity needed to charge an EV can come from coal, natural gas, wind turbines, hydroelectric, solar energy, nuclear, or any other resource). Another current focus is the 12V start/stop (S/S) micro-hybrid architecture, in which the engine is shut down whenever a vehicle stops. Vehicles with the S/S functionality are being deployed worldwide. The 12V battery provides power for auxiliary equipment (e.g., the radio and air conditioning) and then restarts the engine when the vehicle moves. Current 12V S/S batteries, typically lead-acid batteries, have a poor life. Table 1 and Table 2 show a subset of the targets for EV and 12V start/stop micro hybrid batteries that have been set by U.S. DRIVE.

Table 1: Subset of EV requirements for batteries and cells.
(Cost and low temperature performance are critical requirements).

Energy Storage Goals (by characteristic)	System Level	Cell Level
Cost @ 100k units/year (kWh = useable energy)	\$100/kWh*	\$75/kWh*
Peak specific discharge power (30s)	470 W/kg	700 W/kg
Peak specific regen power (10s)	200 W/kg	300 W/kg
Useable specific energy (C/3)	235 Wh/kg*	350 Wh/kg*
Calendar life	15 years	15 years
Deep discharge cycle life	1000 cycles	1000 cycles
Low temperature performance	>70% useable energy @C/3 discharge at -20 °C	>70% useable energy @C/3 discharge at -20 °C
*Current commercial cells do not meet this goal		

**Table 2: Subset of targets for 12V start/stop micro-hybrid batteries
(cost and cold cranking are critical requirements)**

Energy Storage Goals (by characteristic)	Under the hood	Not under the hood
Maximum selling price	\$220*	\$180*
Discharge pulse (1s)	6 kW	
Cold cranking power, (-30 °C)	6 kW for 0.5s followed by three 4 kW/4s pulses*	
Available energy	360 Wh	
Peak recharge rate (10s)	2.2 kW	
Sustained recharge rate	750 W	
Cycle life	450 k	
Calendar life	15 years at 45 °C*	15 years at 30 °C**
Maximum weight	10 kg	
Maximum volume	7 liters	
	*Current commercial cells do not meet this goal **Current cells almost meet this goal	

State of the Art

Battery R&D attempts to advance battery technology to help improve the market penetration of PEVs and hybrid vehicles by overcoming the current barriers. To accomplish this, it focuses on: (1) a significantly reduced battery cost, (2) increased battery performance, e.g., extreme fast charge (XFC) and low temperature performance for enhanced Li-ion, (3) improved life advanced chemistry cells, (4) increased tolerance to abusive conditions; and (5) more cost-effective recycling and sustainability.

The current status of the broad battery chemistry types (current Li-ion, next gen, and BLI) is summarized in Figure 1. Battery R&D spans mainly three areas:

- **Current Technology (enhanced) Li-ion:** Cells with today's materials (i.e., graphite anode/transition metal oxide cathode), but with features like XFC compatibility, low temperature performance and improved abuse tolerance.
- **Next-gen Li-ion:** Cells containing an alloy anode, usually Silicon-based, and/or a high voltage (>4.5 V) cathode.
- **Beyond Li-ion (BLI):** Cells containing Li metal anodes.

Over the past seven years, PEVs have become more commercially viable, with battery costs dropping almost 80% since 2010. Further cost reductions in high-energy batteries for PEVs are always desirable. In addition, although today's batteries approach very attractive cost numbers, they still need the ability to accept extreme fast charging (XFC) and to perform better in low-temperature operations, to favorably match ICEs in all-weather performance and "refueling" convenience. Research into "enhanced Li-ion" batteries (which would providing these functionalities) is one of the R&D focus areas.

For further gains in energy density and cost reduction, research is needed in both "next gen" chemistries (which employ an alloy anode and/or a high voltage cathode) and BLI chemistries. Cycle and calendar lives of next-gen and BLI chemistries are well short of EV goals. Most cells employing a significant amount of silicon provide (at most) 500 deep discharge cycles and less than two years of calendar life; BLI cells typically provide much less (a cycle life of 100 cycles or less). In addition, the requisite low temperature performance and extreme fast charge capability are lacking in all chemistries.

Current Technology Lithium-ion Graphite/NMC	Next Generation Lithium-ion Silicon Composite/High Voltage NMC	Longer Term Battery Technology Lithium Metal																														
Battery Pack Cost <ul style="list-style-type: none">Current: \$235/kWhPotential: \$100-160/kWh	Battery Pack Cost <ul style="list-style-type: none">Current: \$256/kWhPotential: \$90-125/kWh	Battery Pack Cost <ul style="list-style-type: none">Current: ~\$320/KWhPotential: \$70-120/kWh																														
<table><tr><td>Large format EV cells</td><td>20-60 Ah</td></tr><tr><td>Current Cycle life</td><td>1000-5000</td></tr><tr><td>Calendar life</td><td>10-15 yrs</td></tr><tr><td>Mature manufacturing</td><td>Nearing</td></tr><tr><td>Fast Charge</td><td></td></tr></table>	Large format EV cells	20-60 Ah	Current Cycle life	1000-5000	Calendar life	10-15 yrs	Mature manufacturing	Nearing	Fast Charge		<table><tr><td>Large format EV cells</td><td>20-60 Ah</td></tr><tr><td>Current Cycle life</td><td>500-700</td></tr><tr><td>Calendar life</td><td>Low</td></tr><tr><td>Mature manufacturing</td><td></td></tr><tr><td>Fast Charge</td><td></td></tr></table>	Large format EV cells	20-60 Ah	Current Cycle life	500-700	Calendar life	Low	Mature manufacturing		Fast Charge		<table><tr><td>Large format EV cells</td><td></td></tr><tr><td>Current Cycle life</td><td>50-100</td></tr><tr><td>Calendar life</td><td>TBD</td></tr><tr><td>Mature manufacturing</td><td></td></tr><tr><td>Fast Charge</td><td></td></tr></table>	Large format EV cells		Current Cycle life	50-100	Calendar life	TBD	Mature manufacturing		Fast Charge	
Large format EV cells	20-60 Ah																															
Current Cycle life	1000-5000																															
Calendar life	10-15 yrs																															
Mature manufacturing	Nearing																															
Fast Charge																																
Large format EV cells	20-60 Ah																															
Current Cycle life	500-700																															
Calendar life	Low																															
Mature manufacturing																																
Fast Charge																																
Large format EV cells																																
Current Cycle life	50-100																															
Calendar life	TBD																															
Mature manufacturing																																
Fast Charge																																
R&D Needs <ul style="list-style-type: none">High Voltage Cathode/ElectrolyteLower Cost Electrode Processing TechnologyExtreme Fast Charging	R&D Needs <ul style="list-style-type: none">High Voltage Cathode/ElectrolyteLower Cost Electrode ProcessingDurable Silicon Anode with increase silicon content	R&D Needs <ul style="list-style-type: none">High Voltage CathodeLithium ProtectionHigh Conductive Solid Electrolyte																														

Figure 1. Chemistry classes, status, and R&D needs

An overview of the candidate battery technologies and their likely ability to meet the DOE cost goals are shown in Figure 2. Because of the large variation in different battery technologies, battery research also includes multiple activities focused to address remaining high cost areas within the entire battery supply chain.

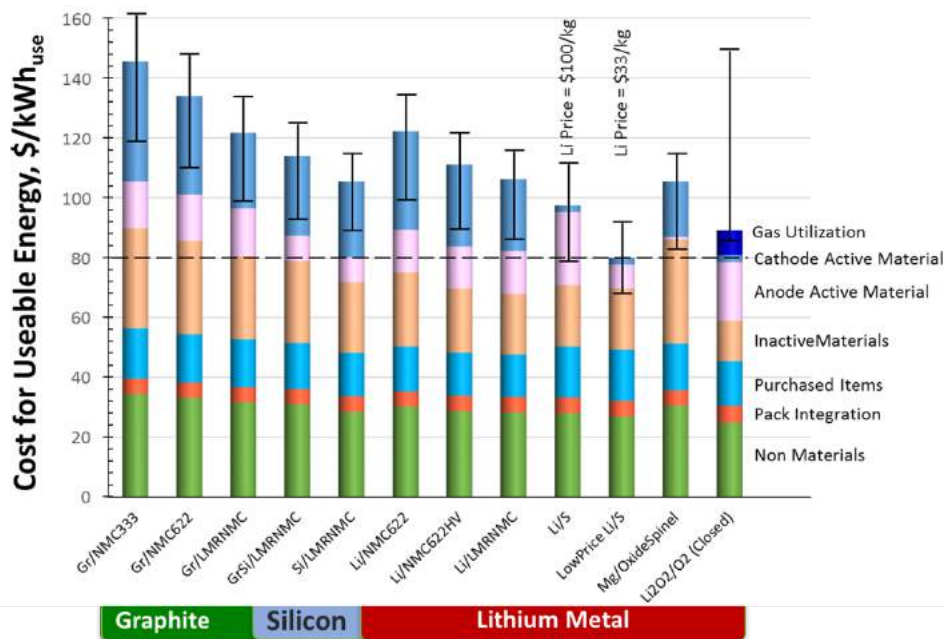


Figure 2. Potential for Future Battery Technology Cost Reductions

Battery Technology Barriers

The major remaining challenges to commercializing batteries for EVs and 12V SS micro-hybrid batteries are as follows:

A. Cost. The current cost of high-energy Li-ion batteries is approximately \$200 - \$300/kWh (on usable energy basis), a factor of two-three times too high from where it needs to be. The cost of Li-ion-based 12V micro-hybrid batteries (which offer significantly better life than conventional lead acid batteries) is approximately 50% too high compared to lead acid. The main cost drivers are the high cost of raw materials, costs associated with materials processing, the cell and module packaging, and manufacturing.

B. Performance. Historically, a higher energy density was needed to reduce the weight and volume of PEV batteries, but those weight and volume issues have been to a large degree been addressed. The use of higher energy materials is still an effective way to reduce costs further, but cell chemistries that provide higher energy have life and performance issues. Also, existing chemistries (e.g., graphite anodes paired with transition metal oxide cathodes) need improvement in XFC and low temperature performance to compete favorably with gas-powered vehicles in the areas of performance and customer convenience. The main performance issue with Li-ion 12V start/stop batteries is a challenging “cold start” requirement at -30°C coupled with high or room temperature life.

C. Life. The life issue for mature Li-ion technologies has mainly been mostly addressed. However, both next-gen and BLI cell technologies still suffer major cycle and calendar life issues. The life of Li-ion-based 12V start/stop micro-hybrid batteries is relatively good, however enhancing cold crank performance often shortens high temperature life.

D. Abuse Tolerance. Current Li-ion automotive batteries are generally used consistent with safe practices. Thus, although Li-ion is not intrinsically tolerant to abusive conditions (as is the case for gasoline as well), it can be engineered in a commercially acceptable product. The characteristics of next-gen and BLI chemistries to abusive conditions are not well understood. However, Li-metal-based batteries have a long history of problematic dendrite growth which can lead to internal shorts and thermal runaway.

E. Recycling and Sustainability. Currently, automotive OEMs pay a relatively large cost (5-15% of the battery cost) to recycle end of life PEV batteries. The various chemistries used in Li-ion cells results in variable backend value. Alternatively, unless they get recycled, Li-ion batteries could lead to a shortage of key materials (lithium, cobalt, and nickel) vital to the technology. Finding ways to decrease the cost of recycling could thus significantly reduce the life cycle cost of PEV batteries, avoid material shortages, lessen the environmental impact of new material production, and potentially provide low-cost active materials for new PEV battery manufacturing.

Program Organization Matrix

VTO's energy storage effort includes multiple activities, ranging from focused fundamental materials research to prototype battery cell development and testing. The R&D activities can involve either shorter-term pre-competitive research by commercial developers or exploratory materials research generally spearheaded by national laboratories and universities. The program elements are organized as shown in Figure 3.

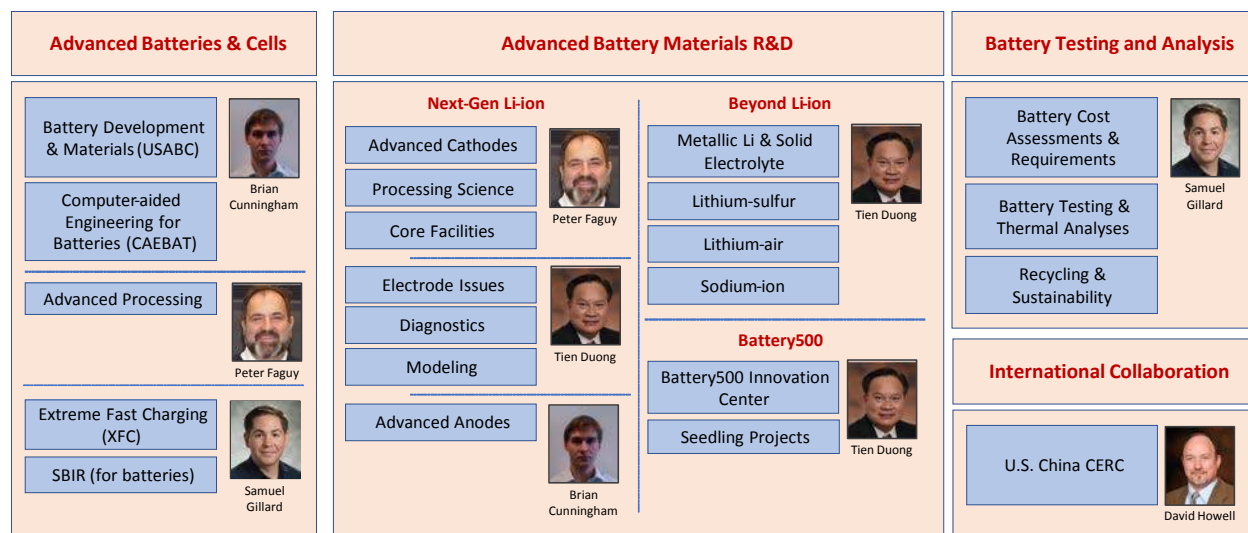


Figure 3. Battery R&D Program Structure

As a further resource, the Electrochemical Energy Storage Roadmap describes ongoing and planned efforts to develop electrochemical storage technologies for PEVs and can be found at the EERE Roadmap page <http://energy.gov/eere/vehicles/downloads/us-drive-electrochemical-energy-storage-technical-team-roadmap>. Battery R&D activities are organized into four program elements which are inter-related and complementary, namely:

- Advanced Batteries and Cells R&D
- Advanced Battery Materials R&D
- Battery Testing and Analysis
- International Collaboration

The *Advanced Cell and Battery Research and Development* activity focuses on the development of robust battery cells and modules to significantly reduce battery cost, increase life, and improve performance. Part of this effort takes place in close partnership with the automotive industry, through a cooperative agreement with the United States Advanced Battery Consortium (USABC). In this report, **Chapter I** focuses on the Advanced Cell and Battery R&D activity, including a short list of the energy storage SBIR project-starts. In FY 2017, the USABC supported thirteen cost-shared contracts with developers to further the development of batteries and battery components for PEVs and HEVs. In addition to the USABC projects, DOE supports battery and material suppliers via contracts administered by the National Energy Technology Laboratory (NETL) and development of tools for the computer aided engineering of batteries. Finally, a research project to understand and enable XFC in enhanced Li-ion systems was begun in 2017 and is described in that chapter of the report as well. Several Small Business Innovation Research (SBIR) projects, also supported by VTO, are focused on the development of new battery materials and components and are the source of new ideas and concepts and are covered in that chapter.

The *Advanced Materials Research* activity addresses fundamental issues of materials and electrochemical interactions associated with rechargeable automotive batteries. It develops new/promising materials and uses advanced material models to discover them and their failure modes, as well as scientific diagnostic tools and techniques to gain insight into why they fail. This work is carried out by researchers at several national labs, universities, and commercial entities. DOE recently focused research into the nature and stability of the solid-electrolyte interphase that forms on silicon anodes (a critical component of next-gen Li-ion cells). In this report, **Chapter II** focuses on the Advanced Materials Research activity. The silicon deep dive and SEISta programs are described in this chapter. Also, there is a high-energy high-voltage (HEHV) deep dive effort focused on understanding and mitigating the failure modes of transition metal oxide cathodes when operated at

high (>4.5V) voltages. This chapter also describes research into BLI technologies, such as solid-state battery technology, lithium metal, lithium sulfur, and lithium air systems. Some of the areas of focus include new methods to understand and stabilize lithium metal anodes; how to contain Li polysulfides to enable the use of sulfur cathodes; and developing electrolytes that support lithium air and lithium sulfur cells. The newly-started VTO Battery500 projects are managed in conjunction with this program element.

The *Battery Testing, Analysis, and Design* activity has a supporting role toward the other battery programs. It works in close collaboration with USABC to develop requirements and test procedures. Other projects in this area include performance, life and abuse testing of contract deliverables, laboratory- and university-developed cells, and benchmark systems from industry; thermal analysis, thermal testing and modeling; cost modeling; secondary usage and life studies; and recycling studies for core materials. It evaluates battery technologies according to USABC-stipulated battery test procedures and performs benchmark testing of emerging technologies to remain abreast of the latest industry developments. In this report, **Chapter III** focuses on the Battery Testing, Analysis, and Design activity. The *Recycling and Sustainability* element of this activity involves studies of full life-cycle impacts and costs of battery production and use; cost assessments and impacts of various battery recycling technologies; and the material availability for recycling and secondary usage and their cost impacts.

VTO has established extensive and comprehensive ongoing *collaboration* efforts in energy storage R&D across the DOE and with other government agencies, and this coordination is a key attribute of battery R&D efforts. It coordinates efforts on energy storage with the Office of Science, and the Office of Electricity. Coordination and collaboration efforts include membership and participation in the Chemical Working Group of the Interagency Advanced Power Group (IAPG), in program reviews and technical meetings by other government agencies, and the participation of representatives from other government agencies in the contract and program reviews of DOE-sponsored efforts. DOE also coordinates with the Department of Army's Advanced Vehicle Power Technology Alliance, the Department of Transportation/National Highway Traffic Safety Administration (DOT/NHTSA), the Environmental Protection Agency (EPA), and the United Nations Working Group on Battery Shipment Requirements. Additional international collaboration occurs through a variety of programs and initiatives. These include: the International Energy Agency's (IEA's) Hybrid Electric Vehicles Technology Collaboration Program (HEV TCP); the G8 Energy Ministerial's Electric Vehicle Initiative (EVI); and bilateral agreements between the U.S. and China. The collaborative activities with China under U.S. China CERC are described in **Chapter IV**.

Battery Highlights from FY 2017

The following are some highlights associated with battery R&D funded by VTO (including highlights related to market developments, R&D breakthroughs, and commercial applications).

- **EV market expanding globally.** The U.S. remains a leading market for EVs. It produces some of the most advanced PEVs available today. Recently, both the European Union and China experienced rapid growth in EV sales (the combined sales in those top three markets reaching almost 2 million in 2016). Consumer interest in PEVs is growing, despite occasional drops in gasoline prices. In 2017, U.S. PEV sales jumped 30% from 2016 levels as worldwide PEVs sales increased almost 50% (through September, for both years). There were 39 PEV models being offered for retail sale in the U.S. and nearly 750,000 PEVs on U.S. roads near the end of 2017.
- **Battery cost reduction.** The 2017 DOE PEV battery cost reduction milestone of \$225/kWh was accomplished. DOE-funded research has helped reduce the current cost projection for an EV battery (for three DOE-funded battery developers) to an average \$213/kWh of useable energy. This cost projection is calculated using ANL's public domain Battery Production and Cost model (BatPaC). It assumes a production volume of at least 100,000 batteries per year, the batteries meeting DOE/USABC system performance targets. DOE's goal is to continue to drive down battery cost to \$100/kWh by 2022.

- **Technical assessment of extreme fast charge functionality.** Extreme fast charging (XFC), or charging an EV at power rates of up to 400 kW, stands to increase the utility of EVs. (For example, it has been found that utilizing 50kW fast charging for 1-5% of all annual charges leads to a nearly 25% increase in annual vehicle miles traveled.) ANL, INL, and NREL have collaborated together and with industry partners to identify the technical challenges for XFC. R&D efforts for XFC could be focused on batteries, vehicles, infrastructure, and economic feasibility. The goal would be to explore technology solutions needed to achieve XFC. The key XFC challenges include:
 - more rapid and powerful charging generates higher temperatures, which can lead to battery degradation and safety issues (including the issue of lithium plating);
 - current power electronics are built for slower overnight charging and may be unable to withstand the stresses of higher-voltage battery systems for XFC; and
 - XFC's high, but intermittent demands for electricity could pose challenges to grid stability.

The XFC research team is exploring solutions to these issues and examining factors related to vehicle technology, new demands on system design, and thermal management requirements.

- **Successful commercial applications.** VTO has a successful track record of planning and executing R&D on critical battery technologies which later move into commercial applications. Hybrid and electric vehicles on the market from all major car manufacturers use lithium-ion technologies developed under prior VTO-funded projects. Some lithium-ion chemistries developed with DOE support have also found their way into stationary applications. For example, the Saft Intensium system, which uses graphite/NCA chemistry developed with VTO support (Figure 4), has been installed at various locations in California, Hawaii, and Finland.



Figure 4. Saft Intensium Stationary Storage Battery

- **Fluorinated electrolyte to improve the performance of high voltage NMC532/graphite cells.** ANL discovered that an electrolyte-based on fluorinated sulfones improved the cycle life of NMC532/Graphite full cells. It evaluated performance of the electrolyte additive using a high energy high voltage (HEHV) protocol, which predicted the cycle number that will have 80% capacity retention under the protocol. This cycle number improved from 150 cycles with baseline electrolyte to 400 cycles in the presence of the new fluorinated electrolyte (Figure 5).

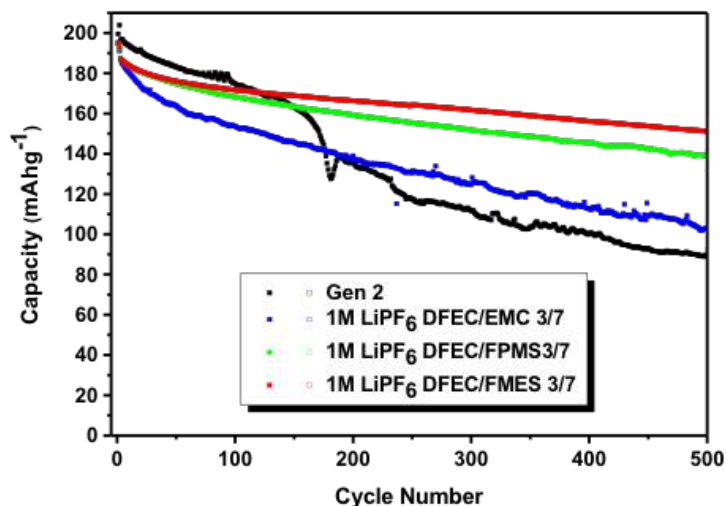


Figure 5. Capacity retention of NMC532/graphite full cells cycled with Gen 2 (non-fluorinated) and various mixtures of fluorinated sulfone-based electrolytes. (C/3 for 100 for cycling between 3.0 and 4.6 V.)

- Morphology and stability of NMC materials.** The instability of NMC-based cathode surfaces is a major impediment to their use in high-energy, high-voltage Li-ion cells. Computational modeling at ANL revealed how NMC particles take shape under different synthesis conditions; and subsequent experimental synthesis at LBNL confirmed the predictions. Results of the study predict that the (012), (104), and (001) surfaces (Figure 6) are the dominant surfaces under normal synthesis conditions. However, only the (012) and (104) surfaces can pass lithium during cycling. In addition, the (104) surface is more stable than the (012). Thus, tailoring synthesis conditions to favor the formation of the (104) surface would enhance both the electrochemical performance and stability of NMC particles.

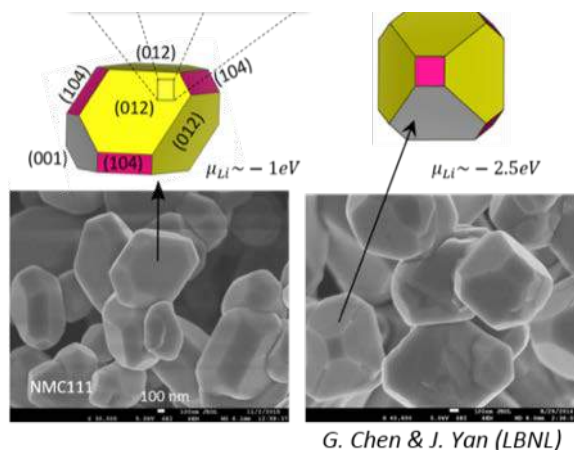


Figure 6. Simulated NMC particle shapes obtained under select synthesis conditions. (Bottom) images of NMC particles (LBNL) verifying the modeling results.

- Understanding oxygen redox processes in high capacity Li-ion cathode materials.** Li- and Mn-rich layered oxides demonstrate an exceptionally high capacity (>250 mAh/g), well beyond the theoretical capacity solely from Ni and Co redox (i.e., 127 mAh/g for Ni redox in $\text{Li}_{1.2}\text{Ni}_{0.2}\text{Mn}_{0.6}\text{O}_2$). Lattice oxygen is typically believed to compensate for additional charge beyond transition metal (TM) redox. LBNL used cutting edge synthesis and characterization techniques, including resonant inelastic x-ray scattering (RIXS) and differential electrochemical mass spectrometry, to probe the activity of lattice oxygen in those cathodes. A striking feature appears at the charged state of $\text{Li}_{1.2}\text{Ni}_{0.2}\text{Mn}_{0.6}\text{O}_2$ which disappears after

2.0 V discharge. However, no such feature was observed for $\text{Li}_{1.2}\text{Ni}_{0.2}\text{Ru}_{0.6}\text{O}_2$. This unique feature, observed for the first time, is evidence of oxygen redox in the electrochemistry of $\text{Li}_{1.2}\text{Ni}_{0.2}\text{Mn}_{0.6}\text{O}_2$ and provides insight into oxygen redox to achieve high capacity cathode materials.

- Surface dopants for oxygen retention in Li-excess cathode materials.** Li-excess materials show promise as high-energy cathodes except for certain barriers (e.g., a significant first-cycle oxygen release). High-throughput computational screening of multiple elements found suitable for surface doping and surface oxygen retention indicated Os, Sb, Ru, Ir, and Ta as best dopants for enhancing surface oxygen retention. LBNL measurement of 2% Ta-doped $\text{Li}_{1.3}\text{Nb}_{0.3}\text{Mn}_{0.4}\text{O}_2$ indicated that despite the low amount of Ta, the Ta-doped Li-excess cathode improved its electrochemical performance and significantly reduced oxygen evolution compared to the un-doped material.
- A tool to map abuse response of Li-ion batteries.** The Energy Storage Team at NREL incorporated component level abuse models into a generic “safety-map” for Li-ion modules. The rate of heat generation from an abuse event is related to the short resistance. Additionally, the higher the thermal conductivity of the packaging material, the greater the rate of heat rejection from the cell to the surroundings. By plotting the rate of heat generation vs. heat rejection, NREL evaluated multiple module design parameters, e.g., the spacing between cells, flow rates for coolants, etc. Researchers from SNL then constructed battery modules consisting of 3 Ah LiCoO_2 COTS pouch cells in a 5-cell configuration. Aluminum and copper plates of 1/8, 1/16, and 1/32” thickness, were placed between cells as a passive thermal management barrier. Reduced propagation is achieved when a slight increase in material thickness from 1/16” to 1/8” was implemented, Figure 7. When plate thickness is decreased to 1/32”, full propagation was observed. Mapping the rate of heat generation versus rejection, one can evaluate a variety of module design parameters.

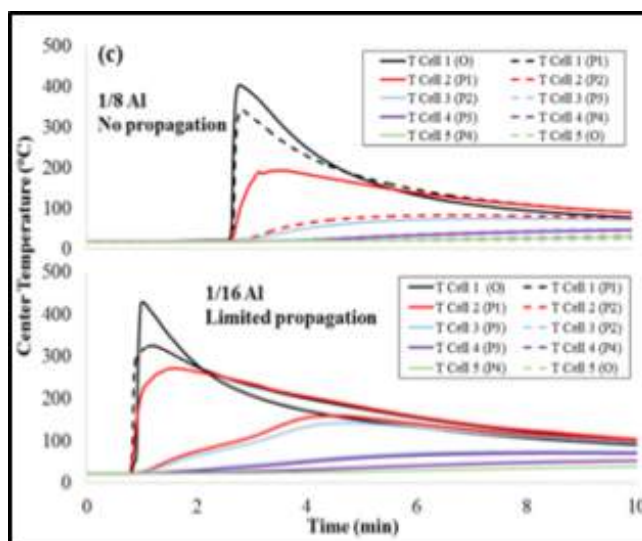


Figure 7. Experimental verification of propensity for propagation: the thicker aluminum plates offer higher rates of heat transfer away from the cell and as a result minimize the risk for propagation.

- Low/Zero VOC processing of thick, crack-free electrodes.** The use of thick electrodes ($>25\text{mg}/\text{cm}^2$, $>4\text{mAh}/\text{cm}^2$) offers the opportunity to produce lower-cost, higher energy Li-ion batteries. In an effort to avoid cracking during electrode drying (often seen with aqueous binders) the influence of solvent surface tension on cracking was investigated. Small amounts of isopropanol (IPA) and/or Methyl Acetate (MeOAc) were tested, mixed in water as novel solvents, for electrode processing. Thick crack-free cathodes were produced with comparable performance to electrodes processed with conventional NMP solvent, Figure 8.

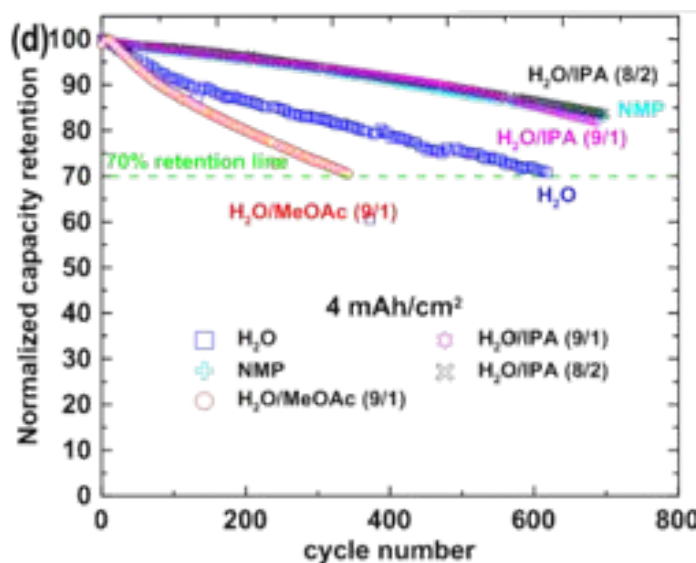


Figure 8. The aqueous processed cracked electrode reaches 70% capacity retention after 620 cycles due to its poor coating quality. With IPA addition to the aqueous binder, cycling performance is comparable to NMP solvent processed electrodes.

- Porous Si electrodes enable long cycle life and controlled swelling.** One challenge to using Si-based anodes is the swelling it undergoes. A PNNL team designed a porous Si/C-graphite electrode to illustrate controlled swelling. Excellent agreement between the theoretical design and experimental data was demonstrated. The practical electrode (3 mAh/cm² loading) with a specific capacity of 650 mAh/g had an approximate 82% capacity retention over 450 cycles. The initial electrode swelling upon full lithiation was less than 20%. The calendered electrodes demonstrated less than 56% end-of-life swelling and approximately 90% capacity retention after 200 cycles. The NMC111 and the pre-lithiated anode full-cell achieved an approximately 84% capacity retention over 300 cycles.
- High active material electrodes.** Physical Sciences Inc. (PSI) developed a technology for higher energy density Li-ion batteries by eliminating or reducing inactive, non-energy storing components, while extending the maximum voltage. PSI developed an active material coating that enables high active (HA) loading, greater than 98% by mass (Li-ion batteries typically have active material contents of 90-95%). It also provides a denser coating thus increasing the energy per unit volume. 3Ah cells constructed with HA electrodes cycled at 4.4V deliver 90% of their initial capacity after 1,000 cycles, see Figure 9.

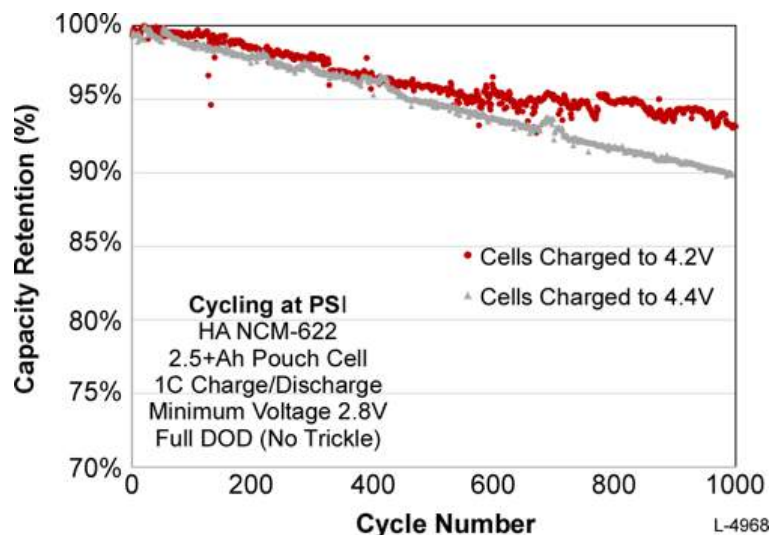


Figure 9. PSI HA cells cycled from 2.8 to 4.2 and 4.4V deliver ~90% of initial capacity after 1000 cycles.

- Microporous silicon (μ Si) anode production.** Navitas Systems, in collaboration with ANL and NexTech Materials, demonstrated a novel, scalable approach to manufacture μ Si for next-gen Li-ion cells. The result is a manufacturing process for battery grade μ Si powder in high volume at a cost suitable for post-processing. The electrode is able to meet the 1300mAh/g and \$25/kg target anode capacity and cost needed to reach DOE cost and performance goals, Figure 10.

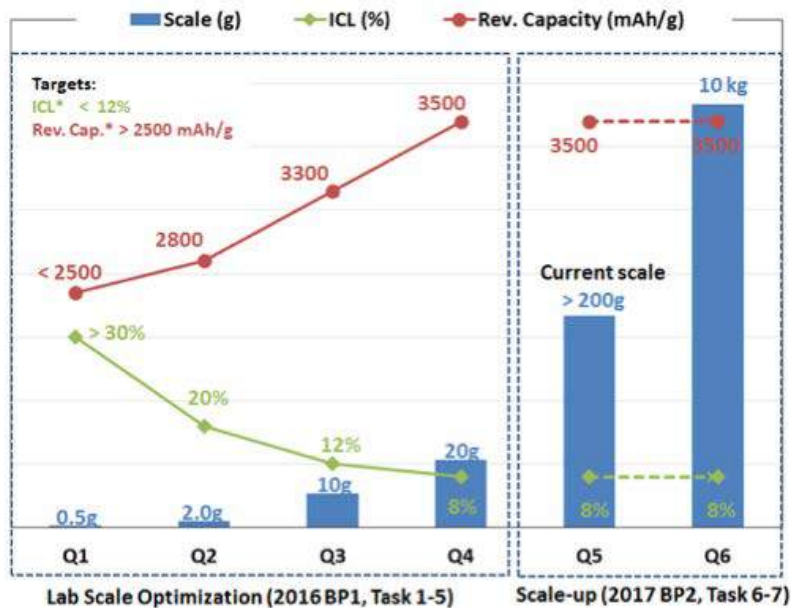


Figure 10. Capacity and ICL both improved during Navitas' material scale up procedures

- Freon-mediated dense and conformal LiF protection layer on Li metal anodes.** Stanford University explored the possibility of gas phase reaction (using Freon R134a, 1,1,1,2-tetrafluoroethane, as the reagent) to produce high-quality, conformal, LiF passivation layers on 3D Li-metal anodes. This gas has several advantages: (1) gaseous Freon exhibits high permeability to coat the 3D surface conformally; (2) Freon 134a is low cost and commercially available; and (3) Freon 134a is non-toxic and environmentally friendly. By exposing lithium metal to Freon R134a gas, assisted with controlled gas

pressure, and reaction temperature, it was able to coat a dense and uniform LiF layer with tunable thickness directly onto metallic lithium. Symmetric-cell cycling corroborated the enhanced stability with LiF coating, with negligible voltage fluctuation observed for over 200 cycles.

- Polysulfide trapping agent for improved Li/S batteries.** The University of Pittsburgh developed a directly-doped sulfur architecture (DDSA) electrode enabling high sulfur loadings of approximately 18 mg/cm² (18 mAh/cm²) (approximately five times higher than typical slurry-coated electrodes). The DDSA electrodes are then coated with polysulfide trapping agent (PTA) that can bind polysulfides, preventing their entry into the electrolyte where they often migrate to the Li metal anode and cause capacity fade. Both the DDSA electrodes and PTA coated DDSA electrodes were tested in coin cells against lithium metal anode (Figure 11).

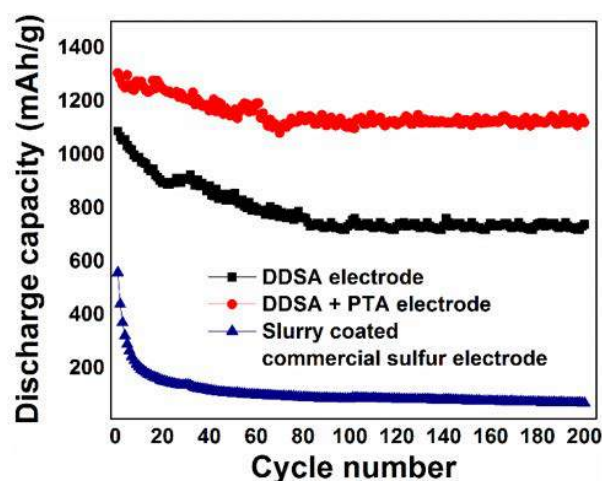


Figure 11. Cycling performance of DDSA electrode, PTA coated DDSA electrode, and standard slurry coated electrode.

- Novel electrolyte enables fast charging and stable cycling of Li metal batteries.** PNNL discovered that an optimal amount (0.05 M) of LiPF₆ additive in LiTFSI–LiBOB dual-salt/carbonate-solvent-based electrolytes enhances the charging capability and cycling stability of Li metal batteries. In a Li metal battery using a 4-V Li-ion cathode at a loading of 1.75mAh/cm², 97.1% capacity retention after 500 cycles is attained (Figure 12) along with very limited increase in electrode overpotential at a current density up to 1.75mA/cm². The fast charging and stable cycling performances are ascribed to the generation of a robust SEI at the Li metal surface and the stabilization of aluminum current collector.

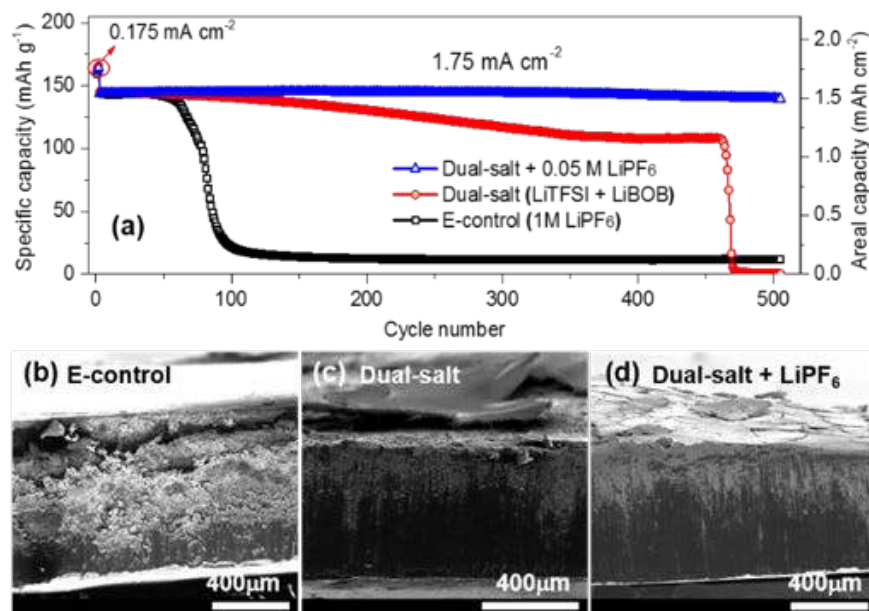


Figure 12. a) Capacity vs cycle number of Li/NMC cells with various electrolytes in EC-EMC solvent. (b-d) Cross-section of Li electrodes after 100 cycles using (b) conventional LiPF₆ electrolyte, (c) LiTFSO-LiBOB dual-salt electrolyte, and (d) 0.05M LiPF₆ added dual-salt electrolyte.

- Self-forming artificial SEI for Li metal electrodes.** General Motors developed a simple physical vapor deposition process to coat Li metal electrodes with fluorinated nanocomposite coatings. The self-forming coating forms an SEI layer, conformal and dense, which effectively isolates Li metal from the electrolyte. The flexibility of the coating makes it easy to accommodate electrode volume changes. The high conductivity of the coating leads to more uniform current distribution to ensure homogenous Li plating and stripping. The protected Li metal electrodes, combining with high concentration salt electrolyte developed at PNNL, show significantly improved cycle stability in symmetrical cells under harsh testing conditions (Figure 13).

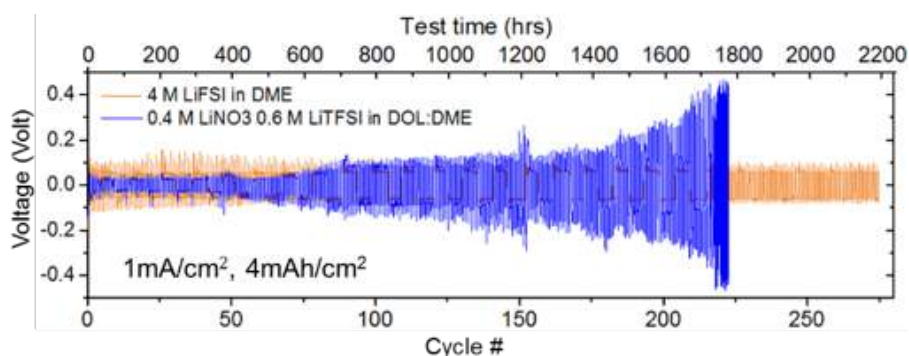


Figure 13. Fluorinated protective coating plus high concentration salt electrolyte enables improved Li/Li symmetric cell cycling compared to cells without the coating and in a low concentration salt electrolyte.

- Improved interfacial contact between solid electrolyte and Li metal electrodes.** Over the last two decades, several solid electrolytes have been discovered. One class of ceramic solid, based on mineral garnet atomic structure, exhibits a good combination of rapid ion transport and stability. For the battery to function effectively, the garnet must bind tightly to the Li metal to reduce interfacial impedance; and metals typically do not bond to ceramics. Ideally, bonding between lithium and garnet electrolyte should be achieved with no coating. Recently, this was demonstrated at the University of Michigan that a simple

heat treatment to clean the surface, allows bonding between metallic lithium and the garnet, Figure 14. Without cleaning, the solid garnet electrolyte surface is passivated by a contamination layer consisting of lithium carbonate due to reaction with air. By removing the lithium carbonate layer through heat treatment, molten lithium bonds or wets the GSE as shown by the contact angle experiment. In addition, the effect of surface treatment is maintained upon cooling to ambient temperature. These findings could accelerate the development of advanced solid-state batteries that double the energy density of conventional Li-ion batteries.

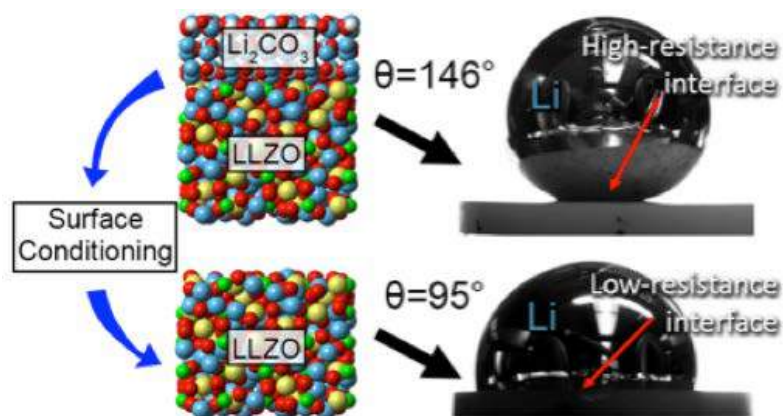


Figure 14. Evidence that Li metal can effectively bond to a solid ceramic as evidenced by theory (left), and lower wetting angle (right).

- MERF– concentration gradient research.** Cathode materials with high energy materials in their cores and more stable materials on their surfaces promise both high energy, improved life, and enhanced abuse tolerance. The ANL MERF facility used scalable manufacturing processes to prepare two types of gradient materials in this class: 811 core-gradient and 811 core-shell, Figure 15a and Figure 15b. Figure 15c compares the electrochemical performance of the 811 core-gradient, core-shell and a commercial NMC811 cathode. The 811 core-gradient and core-shell cells show a 20% improved capacity retention compared to the commercial 811 non-core shell material. In addition, the core shell and concentration gradient cathodes show higher onset temperature and 35% reduced heat generation compared with the commercial NMC811, Figure 15d; thus showing enhanced abuse tolerance. These results demonstrate that the gradient particle structure is a practical and effective approach to stabilize high-energy and highly stable nickel-rich NMC cathode materials.

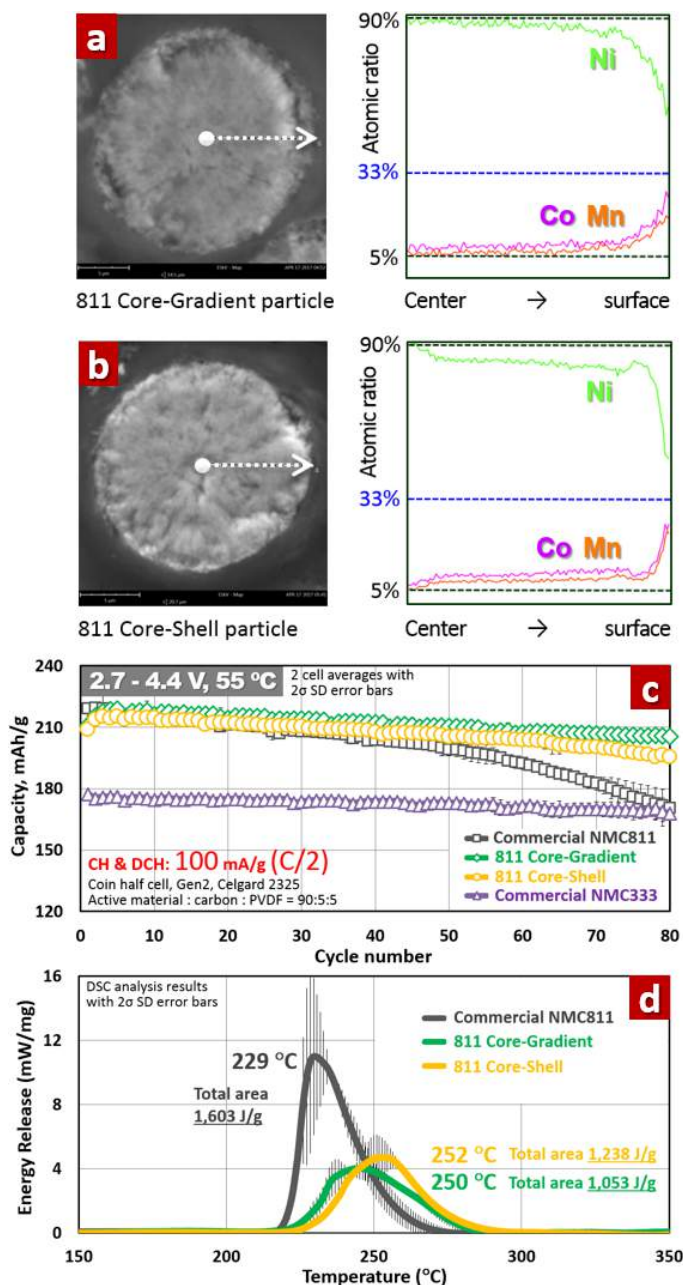


Figure 15. (a) Cross-sectional elemental mapping of the prepared 811 Core-Gradient cathode. (b) Cross-sectional elemental mapping of the prepared 811 Core-Shell cathode. (c) Comparison of electrochemical performance. (d) Thermal stability comparison.

- **BatPaC version 3.1 released.** BatPaC is a spreadsheet tool for the design of automotive Li-ion cells and batteries. Using user-supplied cell and pack design, it calculates the large volume manufacturing cost of cells and battery packs (50K-500K packs per year). New capabilities in the tool in v 3.1 include incorporating the cost of fast-charge and recycling cost recovery at the end of a battery's life.
- **Battery500 seedling projects.** DOE, in collaboration with the Battery500 team, awarded 15 "seedling projects" to supplement work within the Battery500 project. It is hoped that the seedling projects (Table 3) will bring additional ideas for solving difficult technical issues associated with lithium metal-based cells, and possible new ways of achieving the Battery500 goals.

Table 3: Battery500 Seedling Projects

Organization	Description	Funding
University of Maryland: College Park	Research innovative iron-based materials for high energy cathodes for high energy Li-ion battery technologies.	\$400,000
Lawrence Berkeley National Laboratory	Research thick cathodes using freeze casting methods for solid-state lithium batteries.	\$400,000
Penn State University Park	Research multifunctional Li-ion conducting interfacial materials that enable high- performance lithium metal anodes.	\$399,194
Mercedes-Benz Research & Development North America, Inc.	Research a scalable synthesis to enable very thin coatings on solid state electrolyte membranes to enable high performance Li-Sulfur Battery.	\$400,000
University of Maryland: College Park	Using 3D printed, low tortuosity frameworks, develop solid state Li-ion batteries.	\$400,000
General Motors LLC	Design, engineer, develop, and integrate pouch-format cells for lithium-sulfur batteries to achieve high energy density and long cycle life.	\$400,000
University of Pittsburgh	Research sulfur electrodes utilizing Li-ion conductor (LIC) coatings for high energy density advanced lithium-sulfur (Li-S) batteries.	\$400,000
Cornell University	Research highly loaded sulfur cathodes and conductive carbon coated separators that enable high energy batteries.	\$360,000
University of Maryland: College Park	Research advanced electrolytes to limit dendrite growth in lithium-metal cells.	\$400,000
Texas A&M Engineering Experiment Station	Utilize an analytical and experimental approach to examine the interface between solid state electrolytes and lithium-metal anodes and identify potential methods for mitigating dendrite growth.	\$400,000
Navitas Advanced Solutions Group, LLC	Research a solvent-free process to fabricate all-solid Li batteries.	\$400,000
Wayne State University	Research novel full-cell, ultra high-energy Li- metal batteries based on 3-dimensional architectures.	\$225,000
Oregon State University	Research and develop a new process to produce Li ₂ S@graphene composite cathodes to inhibit polysulfides to enhance cycle life.	\$353,500
SUNY University at Stony Brook	Research li-sulfur batteries using a novel sulfur rich nanosheet composite cathode.	\$400,000
University of Houston	Research high-energy solid-state lithium batteries with organic cathode materials.	\$400,000

I. Advanced Battery and Cell Research and Development

I.A USABC Battery Development & Materials R&D

I.A.1 High Energy Lithium Batteries for Electric Vehicles (Envia Systems)

Herman Lopez, Principal Investigator

Envia Systems Inc.
7979 Gateway Boulevard, Suite 101
Newark, CA 94560
Phone: 408-406-3210
E-mail: hlopez@enviasystems.com

Brian Cunningham, Technology Manager

U.S. Department of Energy
Phone: 202-287-5686
E-mail: Brian.Cunningham@ee.doe.gov

Start Date: June 1, 2014

End Date: December 31, 2017

Total Project Cost: \$7,718,493

DOE share: \$3,859,246

Non-DOE share: \$3,859,247

Project Introduction

Electric vehicles (EVs) have received intense attention as a possible solution to reducing our dependence on fossil fuels and decreasing greenhouse gas emissions. One barrier preventing the widespread adoption of EVs relates to the lack of available high energy, low cost and safe energy storage solutions. Lithium-ion batteries (LIBs) are presently among the best energy storage solutions for current EVs. Further improving the performance of LIBs by integrating high capacity active materials, novel passive components and unique cell designs will be critical to the success and mass adoption of EVs.

This project is developing a new battery system based on novel high capacity Ni-Co-Mn (NCM) cathode blends and high capacity silicon-based anode composites that could meet the United States Advanced Battery Consortium (USABC) EV cell performance targets for 2020. In order to enable high Si-content anodes, a manufacturable and cost-effective pre-lithiation process will need to be developed to compensate for the high irreversible capacity loss (IRCL) of the anode. At the conclusion of the program, Envia aims to demonstrate LIBs with usable specific energy greater than 350 Wh/kg and a usable energy density greater than 750 Wh/l while meeting other performance requirements of EV cells (power, calendar life, cycle life, safety and cost). This will be achieved through collaboration among several organizations, each providing expertise on specific components of the material, processing and cell. Ultimately, large format cells meeting the USABC goals will be built and delivered to the national laboratories for testing.

Objectives

- Develop high capacity silicon-based anode composite electrodes capable of supporting long cycle life by controlling electrode pulverization, lithium consumption and conductivity loss.
- Develop high capacity cathode blend composites capable of supporting the energy, cycle life, calendar life, power, safety, and low/high temperature cell requirements.
- Develop a manufacturable cost effective pre-lithiation process that enables fabrication of large-format high-capacity pouch cells.

- Screen and down-select best electrolyte formulation and separator to support meeting USABC performance, cost and safety cell targets.
- Design and optimize active and passive cell materials with cell design meeting USABC EV cell goals.
- Build, test and deliver large format pouch cells integrating high capacity Si-based anode and cathode composites along with optimized electrolyte, separator and pre-lithiation processes that meet the USABC EV cell goals.

Approach

Envia is utilizing a system-level approach to screen, develop and optimize critical cell components (cathode, anode, electrolyte, separator), pre-lithiation processes (process and dose), cell design (N/P ratio, electrode design) and cell formation and testing protocols that will meet the USABC EV cell level goals for the year 2020. This consists of integrating high capacity Ni-Co-Mn cathode blends, pre-lithiated silicon-based high capacity anodes, high voltage electrolyte and coated separator into large capacity (~50 Ah) pouch cells. The developed cells will exhibit high energy density and power, good cycle life and calendar life and acceptable low temperature performance while meeting cell level cost and safety targets. Cells will be delivered and tested by three national laboratories: the Idaho National Laboratory (INL), the Sandia National Laboratories (SNL) and the National Renewable Energy Laboratory (NREL).

Envia is leveraging its material, process and cell development expertise to develop, modify and engineer material and cell-level solutions to meet cell specifications. In this project, Envia partnered with Daikin America (for electrolyte), Asahi Kasei (for separator), Nanoscale Components (for pre-lithiation processing), A123 Venture Technologies (for cell manufacturing), 3M (for Si alloys), and DuPont (for n-Si composites) to develop superior materials, processes and cells.

The program has been structured in a way that as it progresses, the cell targets increase in difficulty in specific energy, energy density, cycle life and cell cost. The program consists of five (5) cell-builds that include an initial baseline and a final program cell-build intended to integrate the lessons from the program and meet the final cell targets. The program has finished the first three cell-builds and is currently working on both cell-build #3 (CB#3) and cell-build #4 (CB#4) which are the final cell-builds and program deliverables. Cell-build #3 is an internal cell-build with the goal of developing 11 Ah capacity cells with specific energy >300 Wh/Kg and a cycle life of 1000 cycles. The internal cell development of cell-build #3 will serve to freeze the final cell design of the program (build #4). Figure I-1 shows the measured and projected specific energy, energy density, cycle life and cell cost for the various program cell-builds. As the figure shows, different cell-builds focused on different format and capacity cells. The baseline cell-build consisted of 21 Ah capacity cells, cell-build #1 consisted of smaller 1.2 Ah capacity cells, cell-build #2 consisted of 11 Ah capacity cells, while the remaining cell-build #3 and #4 will focus on 11 Ah and 50 Ah capacity cells, respectively.

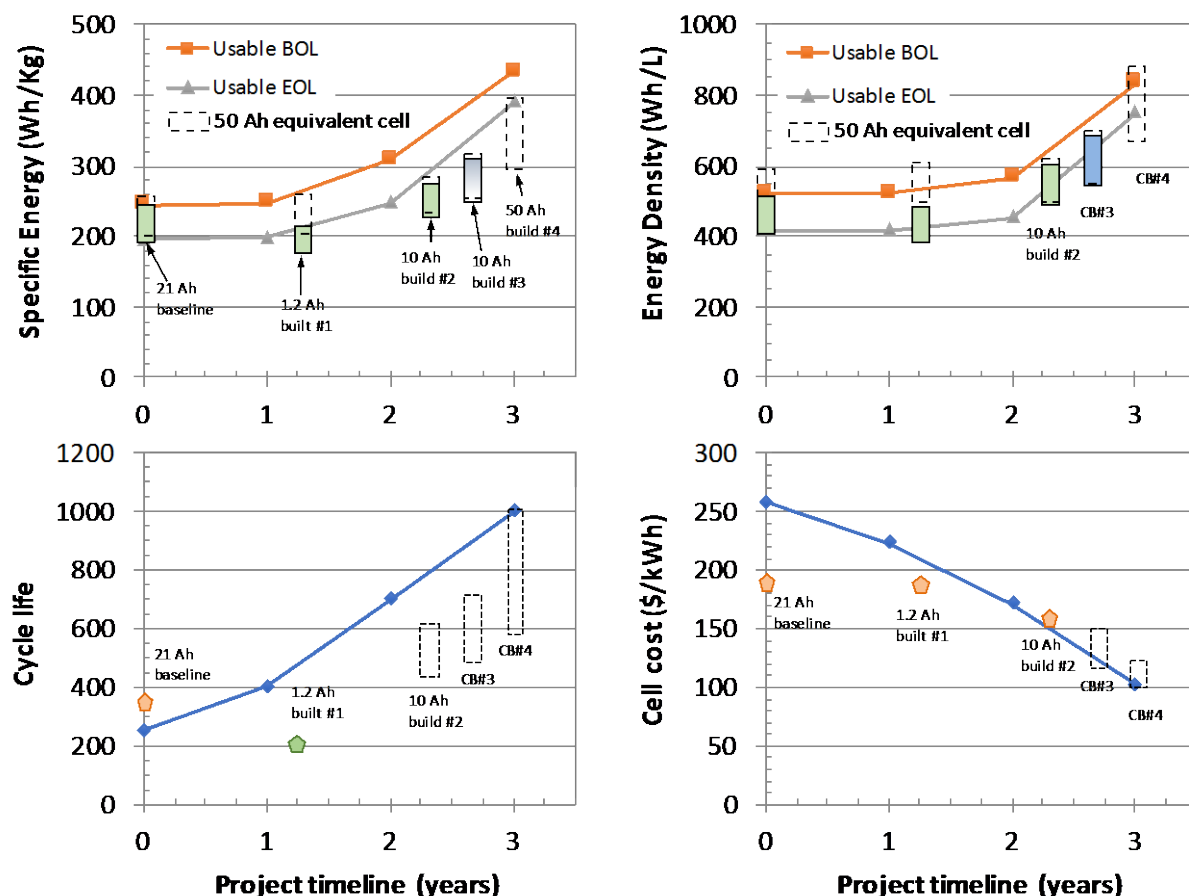


Figure I-1. Current and projected cell development progression throughout the USABC program

Results

Cell Development. Envia completed the assembly and validation of 11 Ah capacity (280 Wh/Kg specific energy) cells as part of the program's cell-build #2 (CB#2) deliverable. Envia delivered 28 pouch cells to the national laboratories (17 cells delivered to INL, 8 cells delivered to SNL & 3 cells delivered to NREL) in late May 2017. Build #2 cells improve upon the baseline by incorporating a higher efficiency 11 Ah cell design, as well as making use of a semi-automatic lithium powder pre-lithiation process enabled by Envia's recently acquired equipment. The pre-lithiation process using the new lithium metal powder equipment will continue to be used and improved for the remaining program cell-builds. Figure I-2 shows the reproducible cell capacity, specific energy, weight and thickness of the 28 cells delivered to the national labs as part of build #2 deliverable.

Cycle life continues to be one of the major challenges of working with silicon-based anodes. Due to the large volume expansion associated with silicon-based anode materials, pulverization and fragmentation are common failure modes that can greatly limit cycle life. Envia continues to optimize the cell design (loading, density, N/P, etc.) and material selection (anode, cathode, electrode additives, electrolyte, and separator) to enable high specific energy cells targeting >300 Wh/Kg and a cycle life of 1,000 cycles. Figure I-3 shows a normalized capacity plot of 21 Ah capacity pouch cells (245 Wh/kg) cycling at a C/3 rate in excess of 700 cycles before reaching 80% capacity retention, as well as 11 Ah capacity pouch-cells from a more weight- and volume-efficient cell form factor showing promising cycle life (> 500 cycles). The design of the 11 Ah capacity cells is similar to build #2 cells delivered to the national laboratories which show a specific energy of 280 Wh/Kg and a cycle life > 500 cycles before reaching 80% capacity retention.

It is encouraging to note that both cell designs integrate similar high SiO_x containing (>50%) anode electrodes and a high capacity cathode incorporating Ni-rich and Mn-rich NMC cathode blends. Cell design and material selection continue to be fine-tuned, as part of cell-build #3 (CB#3) development, to further improve the cycle life to > 1000 cycles and at the same time increase the specific energy > 300 Wh/Kg. Similar, yet higher capacity anode and cathode electrodes are being explored and integrated into new 11 Ah capacity cell designs as part of cell-build #3 development targeting the USABC cell specifications.

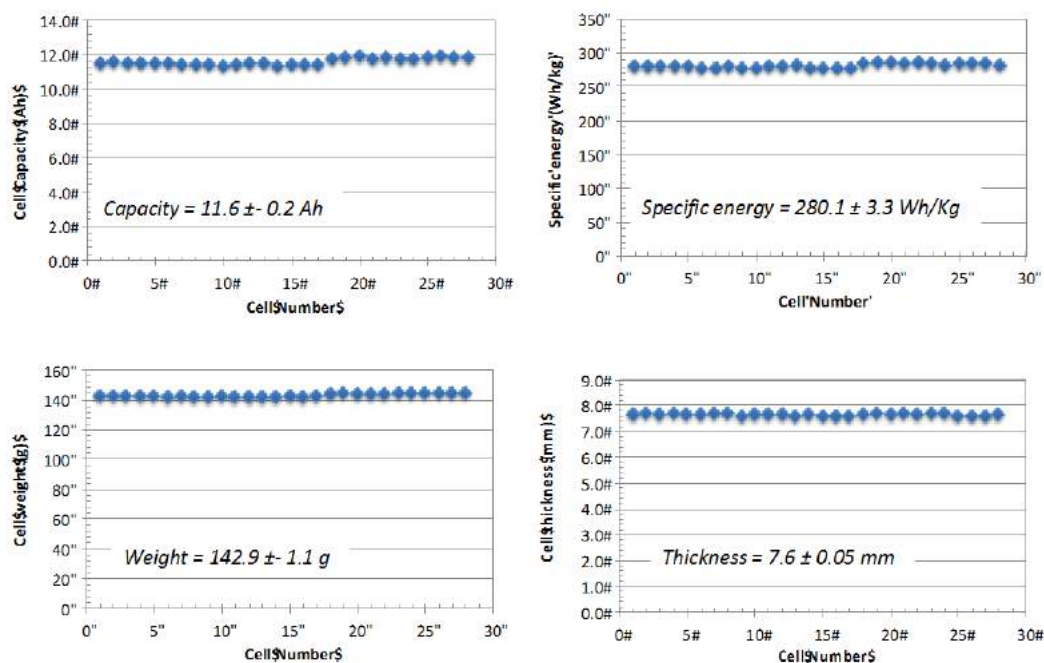


Figure I-2. Cell characteristics of the delivered build #2 cells

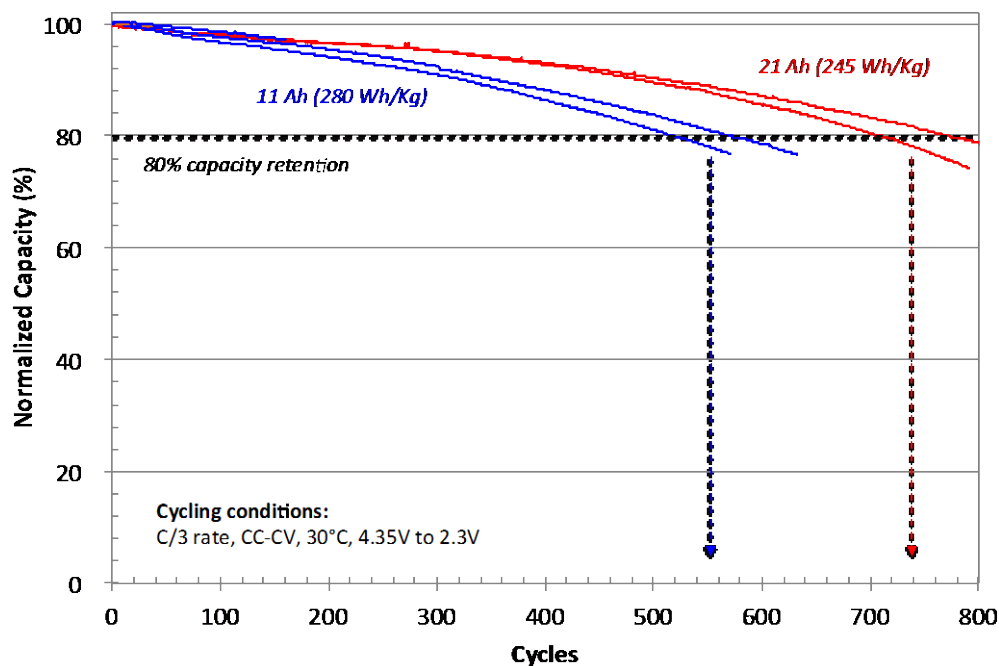


Figure I-3. Normalized capacity versus cycles for 11 Ah and 21 Ah capacity pouch cells

As part of the cell development, Envia continues to focus on failure analysis and cell teardown to understand and mitigate the failure modes of cycled cells. Extensive physical, chemical, structural and electrochemical analysis of cycled cells has shown that the electrochemical integrity of both SiO_x anode composites and NMC cathode blends remain intact even after 700 cycles. This suggests that the typical anode pulverization related failure is under control in our anode electrode systems. Moving forward, similar anode electrode systems are being integrated and optimized in current cell designs to meet USABC cell target specifications. Figure I-4 shows typical images of an open pouch cell undergoing the teardown and failure analysis.

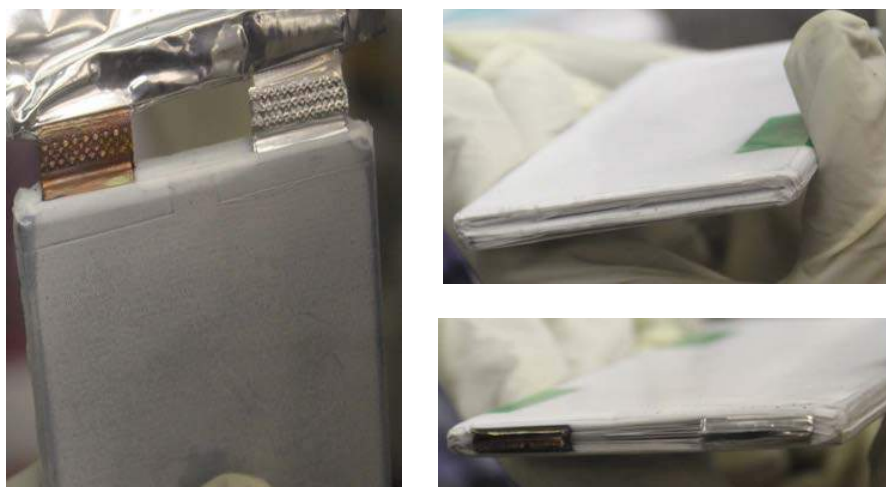


Figure I-4. Images of an 11 Ah capacity pouch cell undergoing teardown and failure analysis

For the final cell deliverable (cell-build #4) of the USABC program, Envia modified the Statement of Work to deliver large capacity cells to:

- Enable a fair comparison to other programs in the USABC portfolio that are also delivering large capacity cells
- Deliver a production representative cell
- Deliver cells which are closer to customer needs
- Gain experience in building and testing large capacity cells

The cell format for final large-capacity pouch cells has been finalized. The USABC technical team provided four options for the larger cell format, consisting of two sizes and two tab orientations. In order to maximize power and energy from the cells, the format with tabs on opposing sides was selected. To choose between the two suggested cell footprint options, the cell capacity as a function of specific energy, cell thickness, cell weight and number of anode layers was modeled. Based on the model results, a 50 Ah capacity pouch cell with a length of 320 mm and width of 102 mm was selected as the cell footprint to be developed and delivered at the conclusion of the USABC program. Envia will deliver 50 Ah capacity cells from the final cell-build #4 to the national laboratories for independent testing of cycle life, calendar life, energy, capacity, power, safety and thermal performance.

Pre-lithiation Development. A consequence of working with high capacity silicon-based anodes, and especially with SiO_x -based materials, is an inherent high irreversible capacity loss. To compensate for this loss, pre-lithiation is a requirement. Envia has partnered with Nanoscale Components, which pre-lithiates anodes via a scalable, manufacturable and cost-effective roll-to-roll electrochemical process. Early in the program, Nanoscale successfully pre-lithiated and delivered silicon-based anode electrode (A#7) to support 1 Ah

capacity build #1 cells. Other anode formulations and compositions were attempted and continue to be optimized during the program to develop a pre-lithiated anode capable of meeting the USABC EV cell targets.

Nanoscale completed its larger pilot scale pre-lithiation line, which can pre-lithiate electrodes up to 300 mm wide for large format pouch cells. Using the new pilot scale line, Nanoscale pre-lithiated Envia's high capacity A#14 anode formulation to the full target dosage. Excellent uniformity of pre-lithiation dosing was also demonstrated; sampled sections showed a standard deviation of dosage of less than 0.5% of anode capacity. Envia assembled 11 Ah capacity pouch cells with the pre-lithiated anode. Cell performance with the resulting cells is not yet optimized due to potential shipping and handling issues. Envia and Nanoscale continue to improve shipping and handling of pre-lithiated anodes so that resulting cells achieve optimal performance. (It should be made clear that, due to a number of technical hurdles, NS prelithiation won't be used in the final deliverable cells.)

Conclusions

Envia has shown >700 cycles before reaching 80% capacity retention from 21 Ah capacity pouch cells integrating a high SiO_x content anode composite, Ni-rich and Mn-rich NCM cathode blend, lithium powder-type pre-lithiation and optimized electrolyte, separator and cell design. Envia completed the assembly and delivery of 11 Ah capacity - 280 Wh/Kg specific energy cells as part of the program's cell-build #2 (CB#2) deliverable. 28 pouch cells were delivered to the national laboratories for independent testing. Envia continues to use a system-level approach to further develop and optimize critical material and cell components (cathode, anode, electrolyte, separator), pre-lithiation, cell design (N/P ratio, electrode design) and cell formation and testing protocols that will enable meeting the USABC EV cell targets. Development will continue as part of cell-build #3 with the goal of down-selecting the best materials, components and processes to integrate as part of cell-build #4 final program deliverable.

Key Publications

1. "High Energy Lithium Batteries for Electric Vehicles", ES247_Lopez_2017_p, US DOE Vehicle Technologies Program Annual Merit Review, AMR, 2017.
2. "High Energy Lithium Batteries for Electric Vehicles", ES247_Lopez_2016_p, US DOE Vehicle Technologies Program Annual Merit Review, AMR, 2016.
3. "High Energy Lithium Batteries for Electric Vehicles", ES247_Lopez_2015_p, US DOE Vehicle Technologies Program Annual Merit Review, AMR, 2015.

I.A.2 Development of a High Energy Density Cell and Module for EV Applications (LGCPI)

Mohamed Alamgir, Principal Investigator

LG Chem Power, Inc.
1875 Technology Drive
Troy, MI 48083
Phone: 248-291-2375
E-mail: alamgir@lgchem.com

Chulheung Bae, Principal Investigator

Ford Motor Company
Dearborn, MI 48121
Phone: 313-410-1398
E-mail: cbae@ford.com

Brian Cunningham, Technology Manager

U.S. Department of Energy
Phone: 202-287-5686
E-mail: Brian.Cunningham@ee.doe.gov

Start Date: February 1, 2015
Total Project Cost: \$3,280,000

End Date: January 31, 2018
DOE share: \$1,640,000

Non-DOE share: \$1,640,000

Project Introduction

The development of a high energy density, low-cost EV battery fulfilling USABC requirements necessitates a very high capacity cathode as well as a high energy density anode. A survey of current cathode and anode materials having potential for meeting the performance, life and cost targets show that high energy density cathodes (such as Li-rich NCM or high Ni-content NCM) and Si-based anodes are the most attractive choices for this purpose. The current program is aimed at utilizing these electrode materials to achieve the objectives.

Objectives

- Development of a high energy density, low-cost cathode material to meet USABC targets for a long-range EV battery.
- Development of a high capacity Si-based anode capable of long cycle-life.
- Understanding/Optimizing high capacity electrode structures that will enable the manufacturing of low-cost, long-life EV batteries.
- Fabrication and testing of modules comprising high capacity cathodes and Si-based anodes using a suitable thermal management system. Since cells using Si anodes are expected to undergo a considerable volume change, the objective will be to develop a mechanical structure that will be effective in retaining the cells as well as thermally managing them to prolong life.

Approach

In order to achieve the program objectives, the following approach was pursued in partnership with LG Chem, South Korea.

- Use high capacity NCM cathodes (both Mn rich as well as high Ni content cathode materials).

- Use high capacity Si-based anode that has the best cycle-life at a high loading level.
- Develop high loading electrode to realize high energy density.

Results

A dual approach has been pursued to develop a high capacity and long-life cathode material: using Mn-rich NCM as well as Ni-rich NCM. Although the Mn-rich NCM has a very high capacity (~250 mAh/g), when charged to 4.6V, it has several well-known drawbacks such as inferior life, gassing, voltage fade as well as high resistance at low SOC. We have pursued multiple avenues such as ALD coating, doping, chemical activation, as well as various electrolyte additives to solve these issues. While this led to improvement in data, it was not large enough to warrant continued studies with this material. For example, Figure I-5 shows the data for a cell built using our most optimum Mn-rich cathode and a high loading Si-based anode (prepared as the first baseline deliverable). The data show considerable impact on the delivered capacity as function of the upper voltage cutoff of 4.4 and 4.6V. The cycle-life of the cell was, however, poor as the capacity faded to less than 80% after 25 cycles at room temperature. A more dramatic fade was observed during storage at 60°C and SOC of 80%. Structural evolution, Mn dissolution and thick SEI formation are attributed to the rapid decay in cell performance. Given these poor life characteristics, studies with this cathode material were discontinued and Ni-rich NMC was selected as our primary path for the cathode chemistry. We selected ALD coating as one of the routes for improving cathode durability. Data showed that the capacity and the rate capability of the cathode are not adversely affected by the coating and even showed a slightly higher capacity and better capacity retention compared to its untreated counterpart.

In order to approach the usable energy density target of 750 Wh/l stipulated by USABC, one needs to significantly increase the loading level of Si-anode material. Since a high Si content adversely affects electrode properties such as adhesion, wettability etc. studies were carried out to optimize binder and conductive agents. Careful attention needs to be given to both the type and content of these components since they can impact various cell properties. For example, data show that the type and ratio of conductive agents within the electrode control the side reactions that can affect the first cycle Coulombic efficiency and discharge capacity.

To assess the impact of Si content on performance and durability, 10% and 30% loading levels were taken as case studies in our program. The cells contained a Ni-rich cathode.

Figure I-5 compares the voltage profiles of the cells using the 10% or 30% SiO-containing anodes. Data reveal that the OCV of the cell is reduced more by a higher SiO content (3.59V vs 3.51V). Further, the discharge resistance increases more in the lower SOC range for the 30% SiO cell.

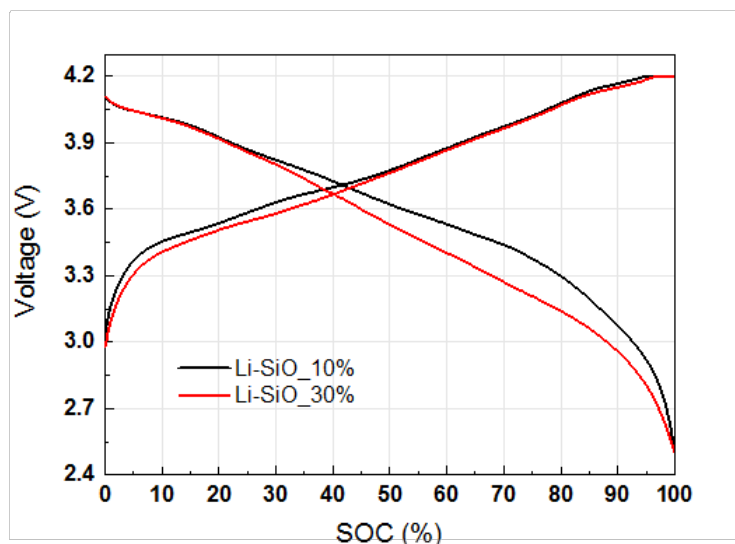


Figure I-5. Comparison of the charge/discharge profiles of cells containing 10 and 30% SiO anodes.

Figure I-6 compares the cycling performance of the 10% and 30% SiO-containing cells. For full depth-of-discharge cycling (100%-0%), there is a clear decrease in cycle-life when the SiO content is raised from 10% to 30%. However, when the cells are cycled within a narrower SOC window of 100%-20%, the cycle-life performances of SiO 10% and SiO 30% are not significantly different from each other in the first 100 cycles.

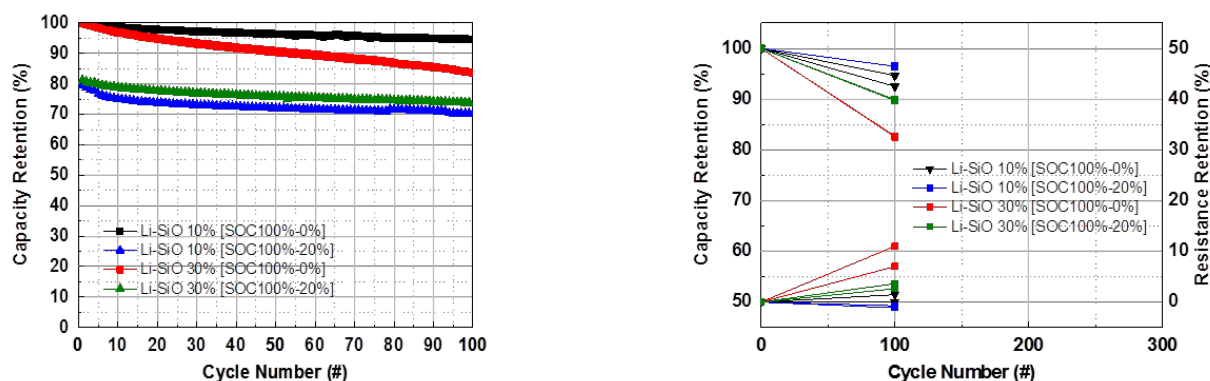


Figure I-6. Comparison of the cycling performance of cells containing 10 and 30% SiO anodes. Cycling carried out at 1/3°C rate and 25°C.

The storability of the two types of cells are shown in Figure I-7 during storage at 60°C and SOC=100%. As the data indicate, there is a considerable decrease in the capacity retention, and a concomitant rise in resistance, for the cell having the higher amount of SiO.

It is well-known that a key challenge in working with Si-based anodes is to manage its swelling during cycling. To better understand this feature, we carried out cell thickness measurement during charge and discharge (Figure I-8). As the data show, increasing the SiO content leads to a significantly larger thickness increase in the first charge/discharge cycle. For example, the 10% cell showed an increase of ~2.4% during charging from 0 to 100%, while the 30% SiO cell showed an increase of 6%. The ratio of thickness increase, however, from 30% to 100% SOC was 1.3 and 4.4 for the 10% and 30% SiO cells, respectively. The change in thickness over life for these two types of cells remains to be evaluated.

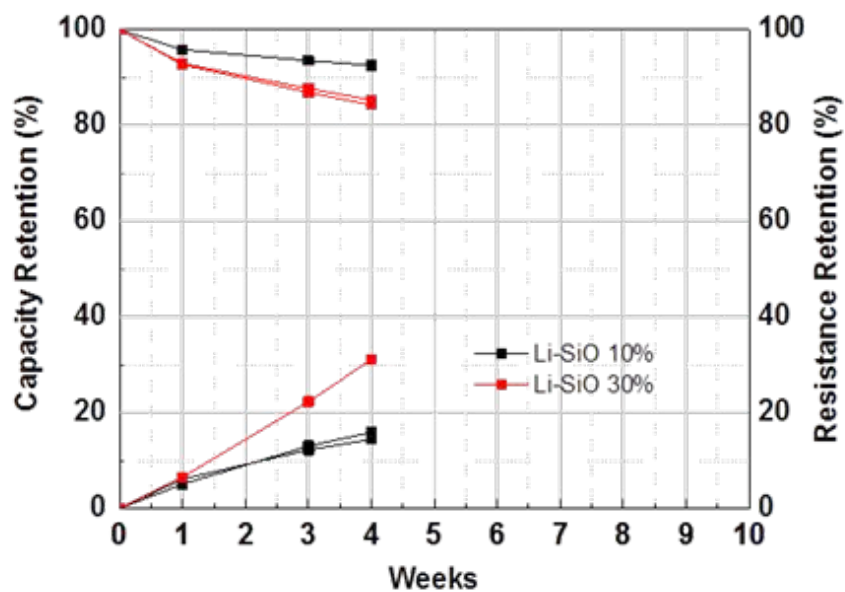


Figure I-7. Comparison of the storability of cells containing 10 and 30% SiO anodes. Storage was at 100% SOC and 60°C.

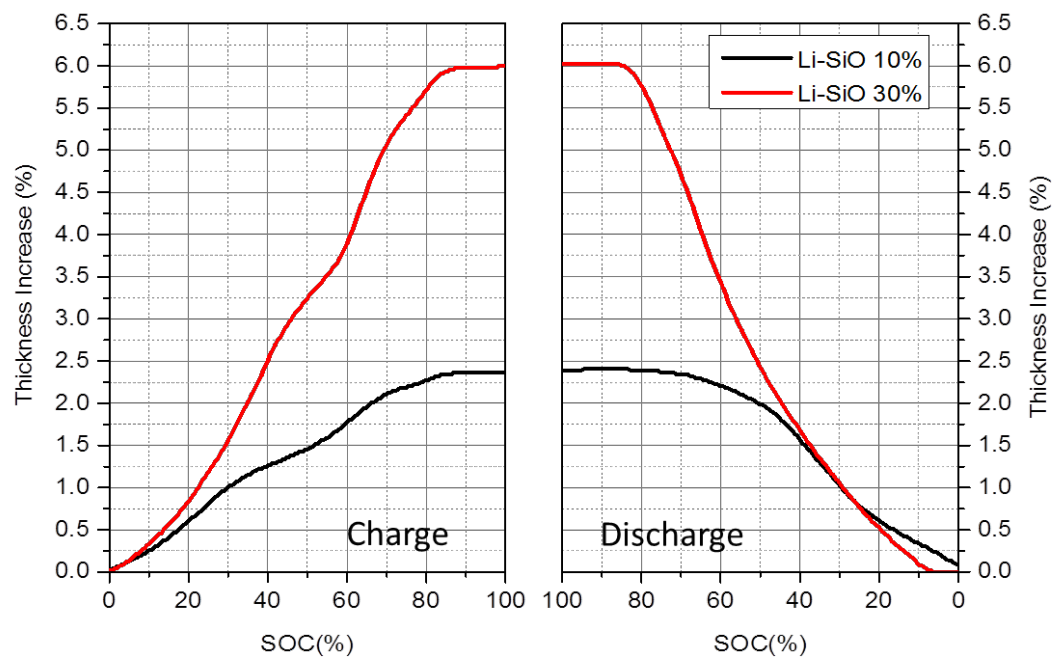


Figure I-8. Comparison of the thickness increase of cells containing 10 and 30% SiO anodes. The cycling was carried out at 1/3 C between 4.2 and 2.5V and 25°C.

Conclusions

Despite comprehensive studies involving doping, surface treatment and electrolyte optimization, among others, we did not find significant improvement in the durability of Mn-rich cathode containing cells; so work with this cathode was abandoned in favor of Ni-rich cathode. We showed that ALD coating improves the durability of the cells. Significant amount of studies were carried out to develop high performance Si-anodes by optimizing binder and conductive agents which are especially critical for high loading electrodes where adhesion issues become very pronounced. Preliminary studies with high loading Si-based anode showed reasonably good cycling at room temperature but the capacity fade and resistance rise at elevated temperature were still quite unsatisfactory.

However, work with Si-based anodes showed that we are unable to meet the USABC program targets and still be able to scale up and deliver large size EV cells (> 50 Ah) that are practical and have reasonable life targets.

I.A.3 High-Performance Semi-Solid Cell for EV Applications (24M Technologies)

Naoki Ota, Principal Investigator

24M Technologies, Inc.
130 Brookline Street
Cambridge, MA 02139
Phone: 617-553-1012 x132
E-mail: nota@24-m.com

Brian Cunningham, Technology Manager

U.S. Department of Energy
Phone: 202-287-5686
E-mail: Brian.Cunningham@ee.doe.gov

Start Date: June 15, 2016

End Date: June 14, 2019

Total Project Cost: \$6,998,594

DOE share: \$3,499,297

Non-DOE share: \$3,499,297

Project Introduction

24M Technologies has developed a breakthrough manufacturing process that leverages proven and emerging chemistries to deliver lithium-ion batteries with a lower cost and containing less inactive materials than any current lithium-ion cell. In this program, 24M will develop large-format, automotive-scale cells leveraging high-energy advanced lithium-ion chemistries. 24M's unique electrode and cell architectures are capable of accommodating large volume-change active materials, and 24M's cells exhibit unprecedented levels of abuse tolerance. The manufacturing process requires less than one-half the number of unit operations of conventional lithium-ion technology; and, has been demonstrated in automated pilot production.

24M's proprietary semi-solid electrode technology enables unique cell architectures with several advantages over conventional Li-ion batteries. For automotive applications, the novel manufacturing method dramatically reduces manufacturing complexity and cost. Also, it is readily scalable per market demand. The small footprint for equipment and comparatively low capital equipment investment further reduce manufacturing risk.

24M's unique electrode and cell architectures significantly lower materials cost in each cell. 24M believes that its cell design has a lower material cost on energy basis (\$/kWh) than any other Li-ion cell of comparable energy and power in the market or under development. Cells based on semi-solid electrodes have a higher active to inactive materials ratio than conventional Li-ion cells, providing an inherently sustainable advantage in the cell bill of materials.

Finally, unlike most other development approaches for advanced batteries, 24M's core technologies are platforms for electrode and cell design and manufacturing not limited to any particular set of active materials. Therefore, 24M's cells can leverage all of the active materials available today and those to be developed in the future. As a platform player, 24M maintains the flexibility to drop-in next generation active material as lithium-ion chemistries evolve and as alternative chemistries (such as Na-ion or Mg-ion) emerge.

Objectives

24M will demonstrate that its novel electrode, cell and manufacturing approach can be applied to high-energy density lithium-ion chemistries to enable mass production of automotive-capable prismatic Li-ion cells with a dramatically lower cost. The approach outlined below has been planned to develop high energy density semi-solid electrode formulations, and to demonstrate manufacturing of prototype cells based on those formulations that meet or exceed the USABC targets outlined in Table I-1 for each phase of the program.

Table I-1: Characteristics of the annual cell deliverables in the program

	Phase 1	Phase 2	Phase 3
Cell Footprint (cm ²)	80	80	80
Capacity (Ah)	6	10	10
Energy Density* (Wh/L)	400	640	800
Specific Energy** (Wh/kg)	200	290	350
Number of Cells	30	30	30

*Assuming 80% volumetric packing efficiency

**Assuming >95% gravimetric packing efficiency

Approach

24M has planned the following activities to achieve the objectives identified in the preceding section.

1. High Energy Materials Evaluation and Selection

Developing new semi-solid electrode formulations utilizing high energy active materials requires evaluation and selection of materials comprising a semi-solid suspension – containing active materials, additives, and electrolyte – as well as developing an appropriate mixing procedure that yields the semi-solid suspension with excellent electrochemical performance. Different combinations of active materials and additives will be formulated into semi-solid suspensions where the physical properties will be evaluated and ranked. The rheology of material suspension will also be tested in order to determine the consistency and repeatability of the electrode forming process. Candidate electrode formulations will then be used in cell fabrication to evaluate the electrochemical performance of the electrode. Ultimately, active materials and electrode formulations will be selected to optimally balance tradeoffs of power performance, safety, processibility, and life (cycle and calendar) in a 24M automotive cell.

2. Processing Methods for Increased Active Solids Loading

Although increases in active solids loading may seem incremental, each time solids loading is increased, an entirely new formulation must be developed and processing method evaluated to ensure that ion and electron transport and rheological properties are optimized for manufacturing and cell performance. In this activity, 24M's current and alternative mixing methods will be evaluated and developed to obtain semi-solid electrodes with active materials loadings necessary for target high energy densities while achieving cycle life and safety performance target. This activity is complementary to, but distinct from, the active material evaluation and selection activity outlined above. New mixing methods and equipment are continually developed at 24M and these will be evaluated, and as necessary, developed to achieve the active materials loading levels required for a cell meeting USABC targets. 24M will create quality control metrics, and measure electrochemical performance to evaluate the performance of the semi-solid suspensions from the various processing methods.

3. Electrode Architecture Development

24M's current electrode forming process is based on automated dispensing and shaping of both anode and cathode semi-solid suspensions, using conventional foil current collectors. This activity will evaluate alternative electrode forming methods and cell architectures, including current collectors and investigations into cell formats with increased volumetric efficiency. As 24M continues to transition from pilot manufacturing to high-volume manufacturing methods, we anticipate continual improvements in the electrode and cell making operations. Additionally, the ideal processing methods for highly-loaded semi-solid suspensions based on high-energy active materials may differ from those developed for earlier electrode formations. Initially, this activity will evaluate current electrode structure and forming methods for compatibility with high energy active materials. Throughout the program, there will be continual evaluations to ensure that the developed cells are capable of meeting or exceeding the automotive power performance requirements. Finally, this area of activity will include a specific focus on safety and abuse testing of the developed 24M automotive cell.

4. Cost Modeling

24M's novel manufacturing approach is different from traditional Li-ion manufacturing methods and conventional cost models such as the USABC cost model cannot be directly applied for cost forecasting. Therefore, an additional activity is planned to develop and commission a cost model for 24M automotive cells to understand the cost at scale and the necessary level of capital investment. In Phase 1, the developed cost model for automotive cells will be developed and commissioned in consultation with USABC. Throughout the duration of the program, it will be applied to scrutinize the viability of the 24M automotive cell.

Results

We have achieved notable progress along numerous development pathways:

Successful screening of high energy density cathode candidate active materials for project Phase 2 and Phase 3 development.

Looking beyond Phase 1 development of NMC111, dozens of high energy cathode active materials from numerous suppliers were examined as candidates for Phase 2 and Phase 3 cell chemistries. Many of these materials were eliminated from consideration due to physical property of the powder and processing constraints. Of the materials tested electrochemically, three stood out as most promising for further development. One sample of engineered NCM 622 and two of NCM 811, each from different suppliers, showed a promising combination of reversible specific capacity (Figure I-9) HPPC performance. Therefore, these three materials were chosen for development in this program. In addition, the team continues to source promising candidate active materials from a network of suppliers, ensuring a strong pipeline of candidate material moving forward. Physical and electrochemical characterization procedures for these incoming materials have been streamlined and progress quickly upon samples being received.

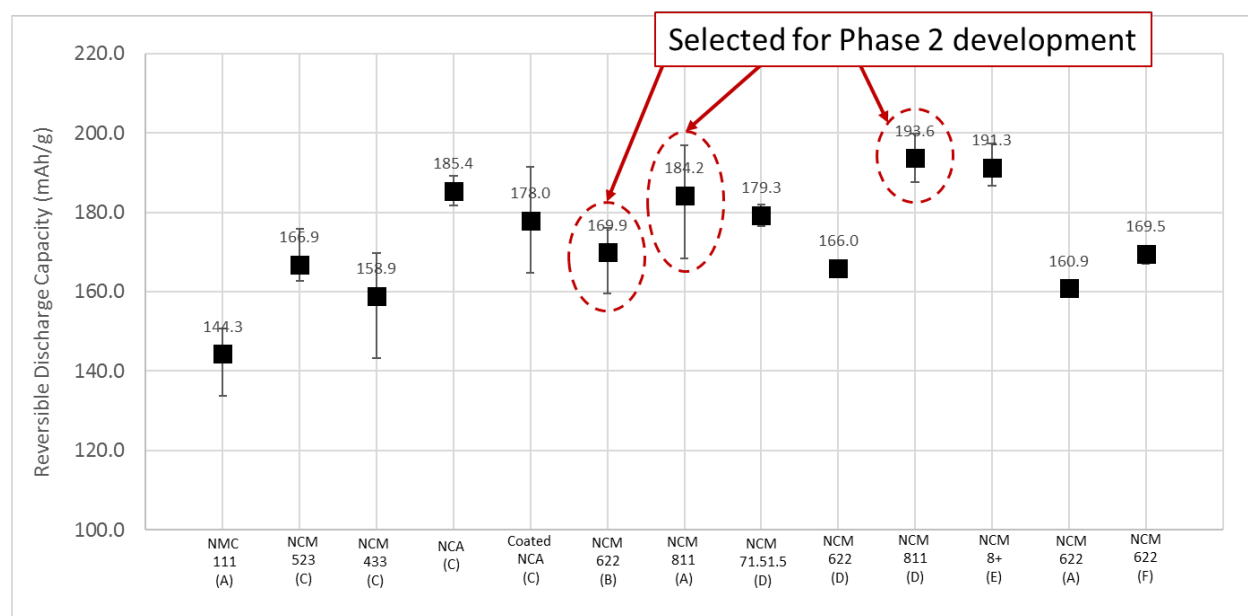


Figure I-9. Reversible specific discharge capacities measured during USABC screening for high energy density cathode active material candidates for program Phase 2 and Phase 3 development. Screening was performed using full pouch cells containing 24M's proprietary semi-solid electrode format for both the cathode and a control graphite anode.

Developed promising electrolyte with high low-temperature performance and a unique chemistry.

During Phase 1 of this project, the low temperature performance of 24M's cells fell below USABC targets. For the baseline electrolyte in use at the time, 80cm² active area pouch cells exhibited a retained energy of ~14% at -20°C compared to room temperature performance, both tested galvanostatically at a rate of C/3. To improve this performance, work was conducted to find electrolytes or electrolyte additives that would help increase retained energy under low temperature testing conditions. Focus was paid to electrolyte components that did not drastically diminish electrolyte ionic conductivity, had a low freezing point, and maintained appropriate viscosities at low temperatures. A new electrolyte formulation was mixed using components fitting these criteria and tested in full pouch cells with NMC111 cathodes and graphite anodes. A voltage vs. discharge capacity curve for these cells during a galvanostatic discharge at a rate of C/3 in a -20°C test chamber is plotted in Figure I-10, which also shows a curve for a cell with an identical architecture but using a baseline electrolyte rather than the low temperature electrolyte. The cell using the low temperature electrolyte retained >50% of the cell's room temperature discharge energy. This result is very promising in that it demonstrates that low temperature performance is not fundamentally limited by ionic transport across the thick, high areal capacity electrodes in 24M's cells.

Delivered Phase 1 deliverable cells of planned quantity and size on schedule.

Stacked cells with 24M's Phase 1 deliverable formulation were built using 24M's automated pilot manufacturing line and delivered on schedule. 30 test units with a median reversible discharge capacity of 6.17 Ah and a median C/3 useable energy of 22.3Wh were shipped to designated USABC testing partners. To satisfy internal development needs and external deliverables, 78 total stacked cells were built towards this milestone. The initial cells were used to validate process scale-up and the remainder for internal testing and/or were yielded out.

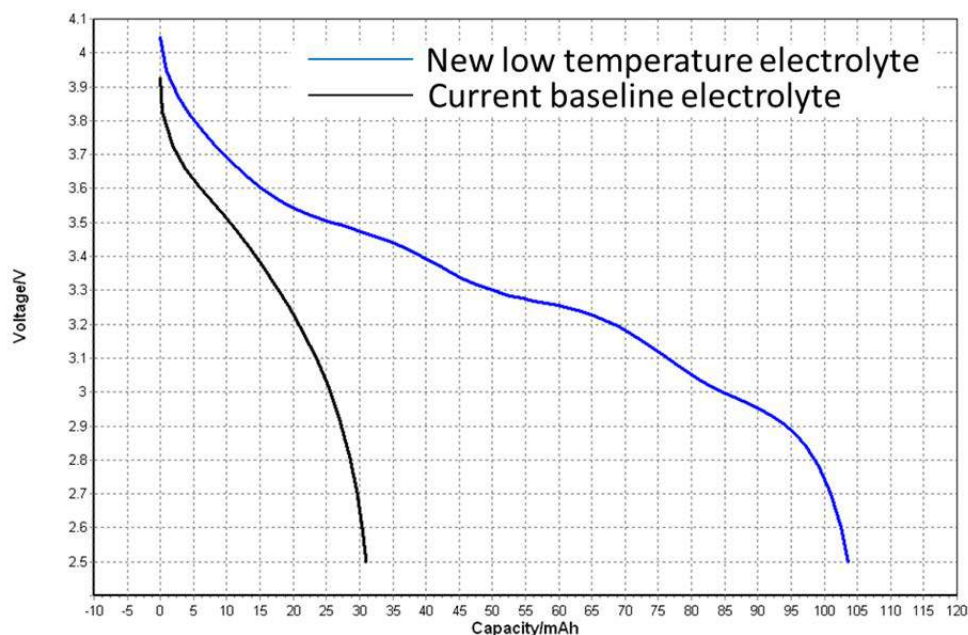


Figure I-10. Voltage vs. discharge capacity plots for pouch full cells using 24M's proprietary semi-solid electrodes measured at a rate of C/3 in a -20°C testing environment for two different electrolytes. The cells using the current baseline electrolyte retained ~15% of their room temperature energy at the test temperature, while the newly developed low temperature electrolyte showed an energy retention of >50% at -20°C.

Transitioned pilot manufacturing and processing procedures to NMC622 cathode active material.

Following completion of the deliverables for Phase 1 of this project in June 2017, the 24M USABC team began the process of transitioning the active material used in its semi-solid cathodes from NMC111 to NMC622 in order to improve cell energy density. The difference in physical properties for the NMC622 chosen for development during active material screening compared to the NMC111 previously employed necessitated process optimization to mix and form semi-solid electrodes of the desired quality and quantity for project Phase 2 development. At the conclusion of this optimization, the 24M build capability for NMC622 exceeds that achieved in Phase 1. Further, the relative ease of transition between NMC111 and NMC622 provides additional evidence that 24M's electrode and cell production method is chemistry agnostic and may be applied to a wide variety of cell chemistries.

Conclusions

In this program to date, 24M has successfully demonstrated a unique manufacturing method and electrode format for lithium-ion battery cells that can be applied to NMC111/graphite cells. Project Phase 1 deliverable cells were produced and delivered on schedule to USABC, and testing of these cells is ongoing. In addition, the 24M team has made significant progress in selecting active materials and improving processing capabilities for Phase 2 and Phase 3 development as cell energy densities requirements increase.

Key Publications

1. "Semi-solid Lithium-ion: A Breakthrough Battery and Manufacturing Platform," Naoki Ota (invited speaker), International Conference on Advanced Lithium Batteries for Automotive Applications, 2017.

I.A.4 Development of High Performance Li-ion Cell Technology for EV Applications (Farasis Energy)

Keith D. Kepler, Principal Investigator

Farasis Energy
21363 Cabot Boulevard
Hayward, CA 94545
Phone: 510-732-6600
E-mail: kkepler@farasis.com

Brian Cunningham, Technology Manager

U.S. Department of Energy
Phone: 202-287-5686
E-mail: Brian.Cunningham@ee.doe.gov

Start Date: February 1, 2017
Total Project Cost: \$5,900,000

End Date: September 30, 2019
DOE share: \$2,950,000

Non-DOE share: \$2,950,000

Introduction

The goal of this project is to develop a high energy density, low-cost Li-ion cell technology that meets USABC goals for advanced batteries for EV's (for 2020 commercialization).

Objectives

- Develop an EV cell technology capable of providing 350 Wh/kg after 1,000 cycles at a cost target of \$0.10/Wh.
- Develop improved cathode materials to meet USABC EV goals through collaborative development efforts with partner organizations.
- Develop Si-based anode electrodes to meet high energy cell design goals.
- Develop pre-lithiation technology.
- Develop and optimize electrolyte and conductive additives to stabilize high voltage cathode, achieve improved cycle life and abuse tolerance of the cells.

Approach

- The key barriers for this project are achieving high energy density with stable chemistry to meet cycle life and calendar life goals as well as the manufacturing processes compatible of the new materials. To meet the USABC target of 350 Wh/kg, Farasis needs to use high-capacity anode (silicon) and cathode materials. To achieve desired energy density and cycle life, Farasis is screening critical cell components such as cathode, anode, electrolyte and separators. In addition, Farasis is pursuing Li source development for pre-lithiation, optimization of Li source, electrode design, cell design as well as the optimization of formation and test protocols. During this initial phase, the project focused on screening of the anode and cathode materials in coin cells. The capacity of the cathode should be higher than 200mAh/g and the anode must deliver between 500-1800mAh/g. The materials will be screened in single layer pouch cells and evaluated for impedance, rate and cycle life. 18650 cells were built using baseline anode and cathode electrodes to be used for electrolyte optimization and for relative safety of materials. Results from this initial screening were used to narrow the electrolyte compositions best suited for this chemistry and will be used for further optimization in the second round of small cell-builds. Farasis is continually working on the synthesis of lithium source materials and incorporating them as a pre-lithiation source. A

combination of device level testing and fundamental electrochemical measurements are used to guide the development of large form-factor cells for the Phase II of the project.

- Phase II of the project lasts approximately 17 months and shifts to manufacturing and testing of larger format pouch cells using a refined subset of cell chemistries. Some ongoing chemistry development will continue in this phase to address specific issues identified in Phase I builds and to pursue further optimization of cell level performance. This will occur in two iterations starting with 10 -30 Ah Gen 1 cells and progressing to the final deliverable cells based on a larger pouch cell form factor, which will be 60 Ah using the optimized high-energy cell chemistry. Phase II will also include testing to guide system development in future applications; these tests will characterize cells in small groups to efficiently evaluate their behavior on a large scale where thermal management, cycling-induced gradients, and failure isolation become important.

Results

Collaborative Material Development

Cathode Active Materials Development.

Farasis has mapped the capacity of eight cathode materials targeting cathode capacity between 187-210 mAh/g and energy density of 297-325 Wh/kg (based on large form factor cells, 10Ah). For Gen1, we are targeting energy density of > 300 Wh/kg. (See Figure I-11.)

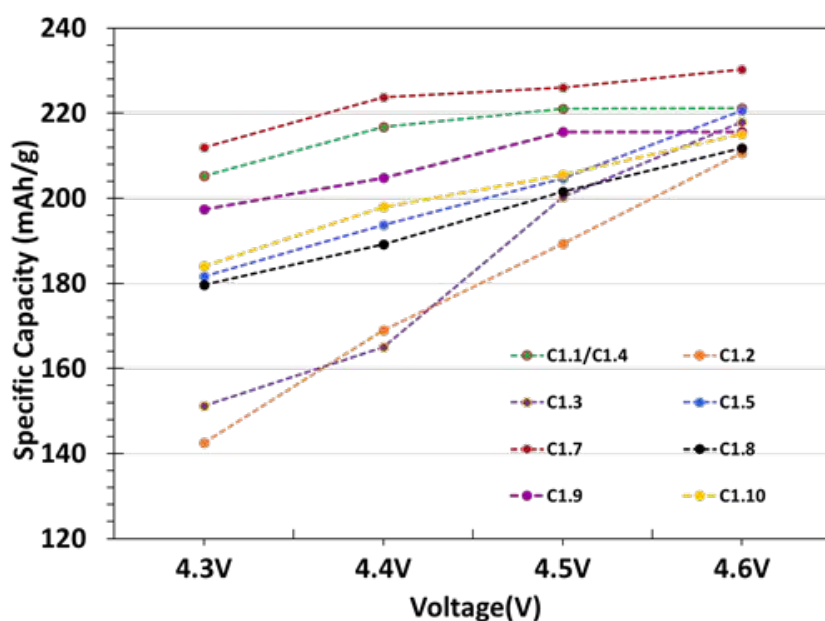


Figure I-11. Capacity for eight of the planned cathode material

Farasis then evaluated 12 cathode materials (high voltage NCM, LMR with NCM and Ni rich NCM) in a single layer pouch cells with a fixed capacity of Si anode with a target energy density of 290-310 Wh/kg in 10 Ah pouch cells. Based on the results for cycle life, DCR and rate capability Farasis down-selected the cathode materials with a target energy density of 300 Wh/kg. The down-selected cathode materials will go on to further optimization for the Gen 1 deliverable cells with a target cycle life of > 400 cycles and an energy density at the beginning of life of 300 Wh/kg. In parallel, Farasis is using the down-selected cathode material for optimization of the lithium source in single layer pouch cells to improve cycle life, and investigate the impact on impedance and safety of the cells. Figure I-12 shows the cycle life for the different cathode material with fixed anode capacity and targeted energy density of 300 Wh/kg in 10-30 Ah form factor cells.

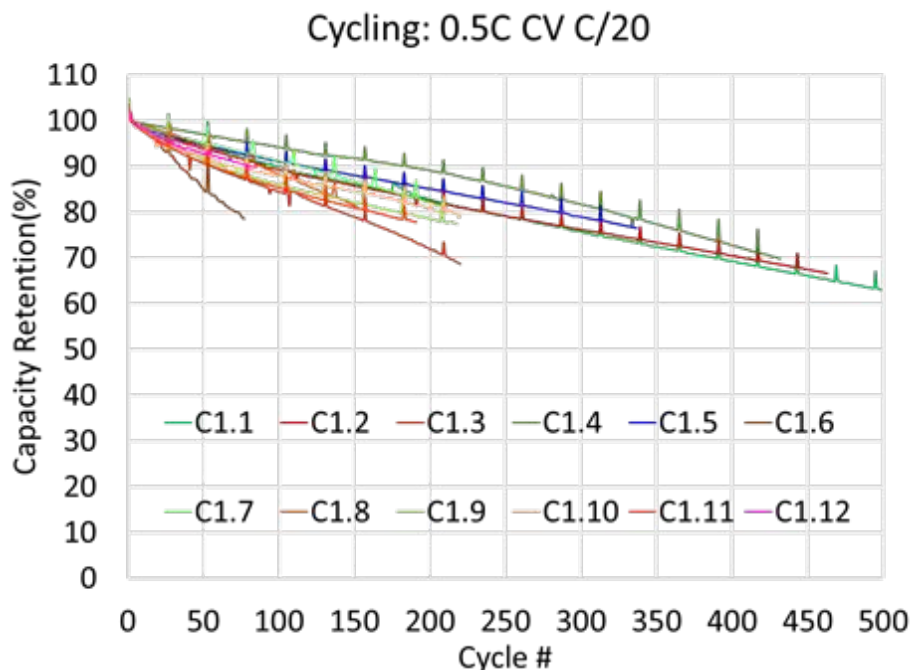


Figure I-12. Cycle life for the cathode materials

Negative Electrode Technology Development

Farasis has evaluated a range of Si materials (Si alloy, SiO, Si nanowires and Si nanoparticles) from suppliers in a single layer pouch cell format with target energy density of 290-310 Wh/kg. Farasis evaluated a range of Si materials with five (5) different cathode materials, and based on the cycle life, impedance and the rate capability of the materials the chemistry for the 300 Wh/kg cells, those materials were down-selected. To meet the USABC final goal of 400 Wh/kg,

Pre-lithiation Development

Farasis synthesized the lithium sources for pre-lithiation. During the 1st year it successfully synthesized large batches of lithium source material (for prelithiation) and tested those materials in full single layer pouch cells containing a Si-based anode. Farasis built small pouch cells incorporating the pre-lithiation source to determine its impact on cycle life. Figure I-13 shows comparisons of cycle life for the Si composite (> 1000mAh/kg) and cathode with and without a Li source.

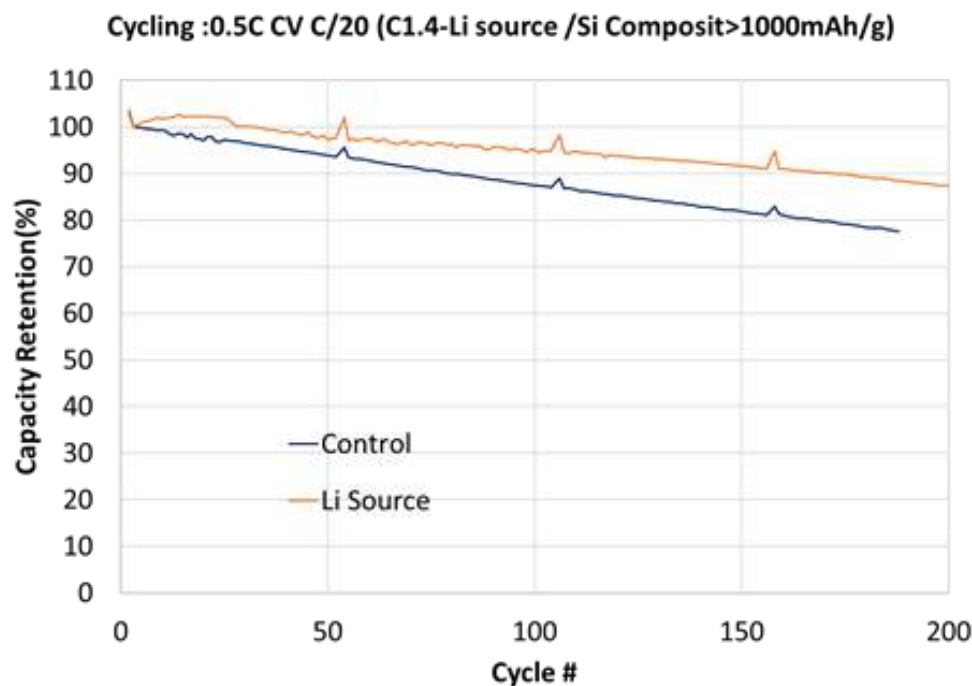


Figure I-13. Cycle life comparison of cathode (C1.4) with and without Li source and Si composite as an anode

Electrolyte Technology Development

Farasis is performing electrolyte exploration, evaluation and optimization in 3 Ah 18650 cells as well as on single layer pouch cells. Figure I-14 shows cycle life results for different electrolyte formulations paired with 300 Wh/kg chemistry without pre-lithiation in 10-30 Ah cells. The results show that the cycle life for EV12 is better (450 cycle @ 80% retention) as compared to other electrolytes. The cells with EV12 also exhibited lower impedance and better rate capability.

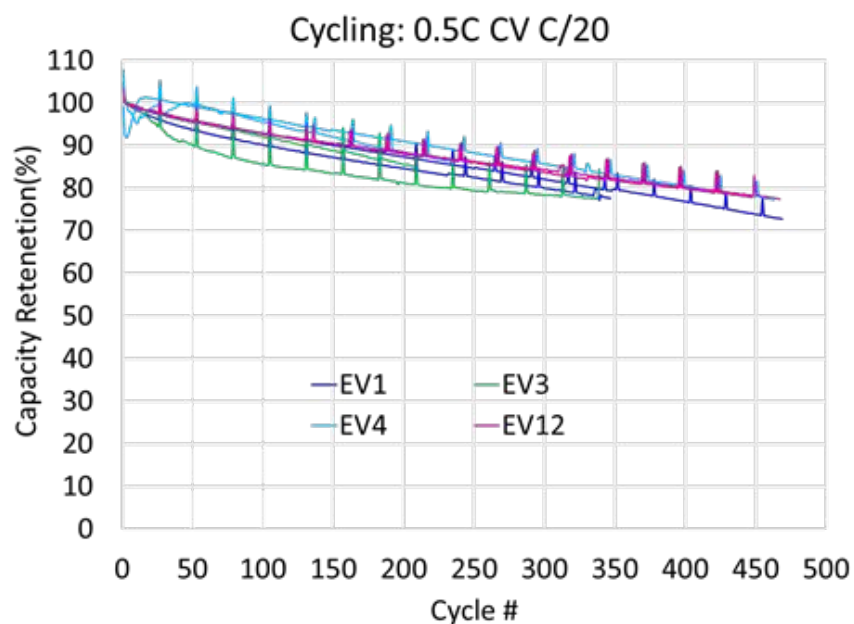


Figure I-14. Cycle life for the different electrolyte formulations

Cell Development

Farasis delivered baseline cells for testing during the first six months of the project. To meet the USABC target for Gen 1 (300 Wh/kg), Farasis built 200 3Ah 18650 cells with promising anode and cathode materials to be used in electrolyte optimization and to understand the relative safety of the materials. Based on the results of 18650 and single layer pouch cells with different anodes and cathodes, Farasis built 100 1.5Ah pouch cells for the down-selected chemistry targeting 300Wh/kg in 10-30 Ah cells design. The Gen1 chemistry during the 4th and 5th quarter will include further development for electrolyte optimization as well as the safety testing. In order to meet the USABC target, Farasis will continue to build multiple high capacity cells by implementing the improved chemistry from small cell results (cycle life, impedance, rate and safety) as well as the optimization of other cell components. Figure I-15 shows the cycle life for 1.5 Ah pouch cells. The predicted cycle life for these cells are in between 350-400 cycles.

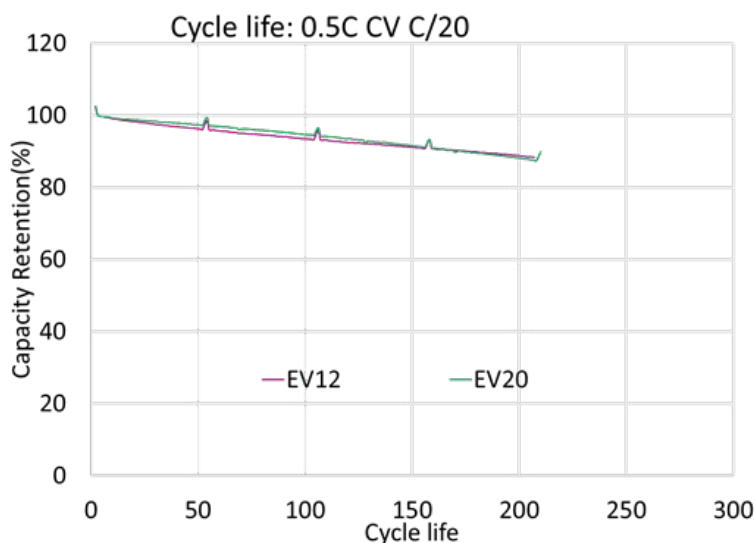


Figure I-15. Cycle life for the different electrolyte formulations

Conclusions

During the first eight months of the program, Farasis evaluated 12 possible high capacity cathode materials and four possible Si anodes. Farasis down-selected the chemistry for Gen1 deliverable (300 Wh/kg) cells with a cycle life of 450 while retaining 80% capacity in single layer pouch cells and without a prelithiation source. This chemistry can provide 300 Wh/kg in 10-30 Ah cells. Farasis had done the relative safety test on the different chemistries. Further optimization in Gen 1 chemistry is continuing for the different conductive additives and electrolytes. To meet the USABC goal, it will start working on high capacity Si (> 1000 mAh/g) with pre-lithiation. Farasis has incorporated a Li source in small layer pouch cells for high capacity anode materials to begin optimizing the impact on the capacity, cycle life, impedance as well as the safety of the cells.

I.A.5 Enabling Thicker Cathode Coatings for Lithium Ion EV Batteries (PPG)

Stuart Hellring, Principal Investigator

PPG Industries Inc.
4325 Rosanna Drive
Allison Park, PA 15101
Phone: 412-492-5526
E-mail: hellring@ppg.com

Brian Cunningham, Technology Manager

U.S. Department of Energy
Phone: 202-287-5686
E-mail: Brian.Cunningham@ee.doe.gov

Start Date: February 1, 2017
Total Project Cost: \$1,200,000

End Date: February 28, 2019
DOE share: \$600,000

Non-DOE share: \$600,000

Project Introduction

To lower the overall cost of the electric vehicle (EV) lithium ion battery, PPG Industries, Inc. and partner LG Chem Power, Inc. will develop and demonstrate NMP-free cathode coatings with higher achievable thickness compared to conventional state-of-the-art coatings. These thicker coatings will permit fabrication of higher energy density batteries without decreasing electrochemical performance. Additional cost savings and reduced environmental impact will be realized through the elimination of NMP-based manufacturing.

Objectives

The objective of this program is to develop solvent-based binder systems for lithium ion cathode coatings that do not require the use of NMP and can be coated at a thickness of 150 micron (μ), and develop water-based binder systems that can be coated at a thickness of 110 μ . Coatings and subsequent lithium ion cells will be manufacturable using existing standard industry equipment and demonstrate cell performance capability equivalent to current state of the art.

Approach

Reconfigure the electrode binder system into a novel formulated product in which polymer binder is dispersed, as opposed to dissolved, as nanoparticles in a solvent. This binder dispersion is stable chemically and possesses excellent shelf life. The unique design of PPG's NMP-free binders along with optimized processing parameters will mitigate film stress and enable the assembly of thicker, more flexible, homogeneous cathode coatings with higher active material loading per unit area. PPG's binders are fluoropolymer-based in combination with customized resins. The binder fluoropolymers and resins together form a composite that is designed to enhance dispersion stability and rheology to aid application, as well as final coating properties such as flexibility, cohesion, adhesion, etc., and electrochemical properties such as low resistance, and cycle and calendar life stability. Cell performance will be demonstrated in 1 Ah pouch cells built in partnership with LG, and tested in accordance with the USABC EV test manual.

Results

A successful binder scale-up enabled an application line trial to be conducted to prepare double-sided cathode foil for the baseline evaluation of current PPG solvent borne NMP-free coatings at an intermediate coating thickness before increasing to the very thick cathode coatings. The cathode formulations contained a Li-ion active material, Lithium Nickel Cobalt Manganese Oxide (NCM or NMC), conductive carbon, and PPG binder. Coating was applied on each side sequentially at a total coating weight per side of 22.7 mg/cm² comprising a weight ratio of 93/3/4 NMC/carbon/binder. This corresponds to an energy density of 3.17 mAh/cm² per side. These coated foils were calendar-pressed at our coating partner, to a porosity of 32% and

tested at PPG for peel strength and flexibility. Peel strength exceeded the 12.6 gf/15 mm target and passed the 25.4 mm mandrel-bend flexibility test. A roll of cathode-coated foil was shipped to LG Chem to be fabricated into 14 each of 1-Amp-hour pouch cells for battery performance evaluation. PPG also tested the binder shelf life stability.

The electrochemical performance testing indicates poor performance of the baseline cathode coating. The battery fails after 50 cycles. As shown in Figure I-16, from 50 cycles to 200 cycles, the resistance increased 4 times and the capacity retention dropped below 20%. After cycling, the pouch cell was disassembled for evaluation, and no electrolyte droplet was observed. Li metal plating was found on the anode and anode-facing side of the separator. This indicates potential electrolyte consumption by electrolyte side reaction.

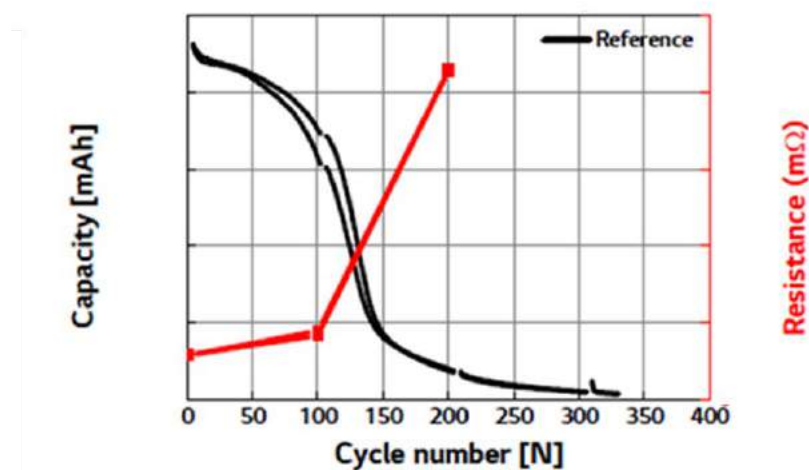


Figure I-16. USABC baseline battery performance after 300 cycles. (Data provided by LG Chem Power)

The project team identified the following possible root causes of the battery failure at LG Chem:

1. Binder side-reaction.
2. Cathode-anode mismatch.
3. Aged active material used for baseline.
4. Electrolyte side-reaction with additives.
5. Bad coatings made during line trials.
6. International shipping in uncontrolled condition.
7. Moisture exposure.

To identify the root cause of the battery failure, the PPG team is currently repeating the baseline cathode formulation with controlled variables. In the original baseline cathode coating sent to LG Chem, NMC 111 of unknown age was used as the active material. In a recent repeat, a fresh batch of NMC 111 from a different supplier is used to eliminate the problems related to aged active material and side-reaction with electrolyte. PPG also identified binder additives that can possibly cause side-reaction with electrolytes, and prepared an additive free binder formulation.

Scale-up line trials were conducted at PPG's coating partner to repeat the USABC baseline, and make an additive-free baseline repeat, and an NMP control. The coatings were assembled into 18650 cells for electrochemical performance testing at the coating partner's facility. The details of line trials coatings are listed in Table I-2. During initial high precision coulometry cycling, the cathode demonstrated good capacity

retention and the Coulombic inefficiency per hour performed better than the NMP control. The suspect additives also did not make a significant difference on cathode performance.

Table I-2: Scale up line trials for USABC baseline failure root cause analysis

Job Description	Active/Carbon/Binder	Active Material	Carbon	Mass Loading	Cell Type
Baseline repeat	93/3/4	Shanshan NMC 111	LITX 200	25.4mg/cm ²	18650
Additive free baseline	93/3/4	Shanshan NMC 111	LITX 200	25.4mg/cm ²	18650
NMP control	93/3/4	Shanshan NMC 111	LITX 200	24.4mg/cm ²	18650

So long as the current testing passes 150 cycles, we will remake the baseline binder to have new baseline cells produced at LG Chem.

The goal of the second milestone is to formulate a thicker coating while maintaining adhesion, flexibility, and electrical conductivity. Toward the end of the third quarter, PPG prepared NMC 111 coatings with areal capacity of 4.5mAh/cm² and thickness of 129μm. The thicker cathode coating demonstrated high flexibility and passed ¼" Mandrel bend test. The 90° peel strength of pressed thicker coating is 106 gf/15mm, passing the requirement of 100 gf/15 mm. Figure I-17 demonstrated all the coatings developed for the first target and the areal capacity and adhesion (peel strength) are shown. Due to the extremely low binder content (3%), it is challenging to prepare a coating of thickness higher than 100μm while maintaining proper adhesion and flexibility.

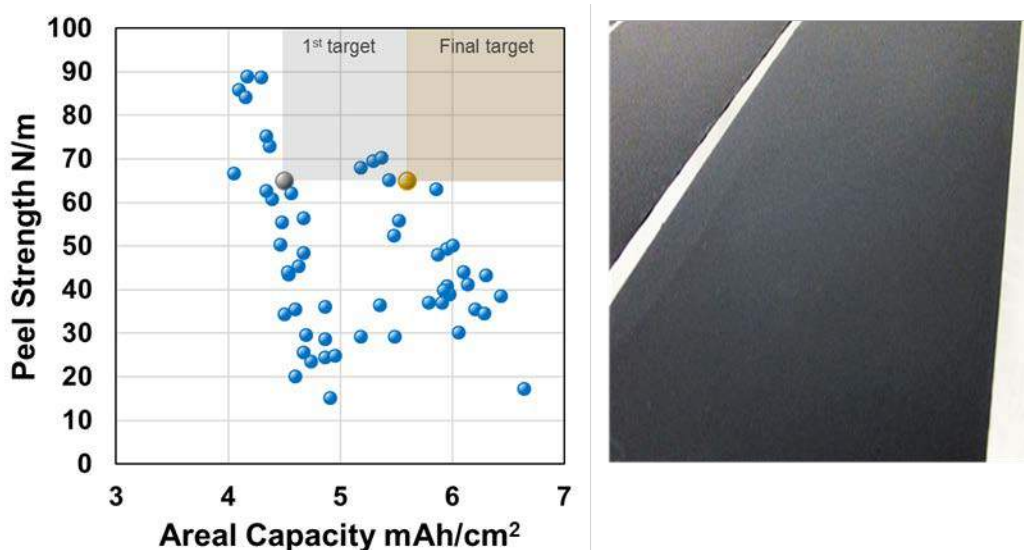


Figure I-17. Thicker coatings developed in third quarter. Left, Peel strength and areal capacity are shown and first target and final target regions are highlighted. Right, Coating appearance. (Data provided by PPG)

To meet the milestone target, PPG's effort focused on resin chemistry, formulation optimization, and process control. In a fully formulated slurry, properly dispersed carbon can form a percolated conductive pathway and decrease the resistivity. Another benefit of investing in carbon dispersion is better rheology control of final slurry, leading to better control on the film build after coating process. PPG improved the out-of-cell coating properties by optimizing carbon dispersions. By controlling the carbon dispersion, we can modify the viscosity of the fully formulated slurry and the final coating thickness. Another challenge is maintaining high adhesion

at high areal capacity. PPG explored the effect of resin chemistry, binder content, and carbon chemistry to optimize the peel strength of the final coating. The pouch cell testing for a thicker coating is on hold due to the baseline failure. A fresh repeat of the baseline coating will be sent to LG Chem in environmentally controlled packaging. A decision will be made once the battery testing results become available from LG Chem.

Conclusions

Problems were encountered with the first baseline cell-build. Another baseline test is underway, and preliminary results are encouraging. Once sufficient test cycles pass, PPG will remake the baseline cells at LG Chem and make the cells to test the coating for the second milestone.

I.A.6 Advanced High-Performance Batteries for Electric Vehicle Applications (Amprius)

Ionel Stefan, Principal Investigator

Amprius, Inc.
225 Humboldt Court
Sunnyvale, CA 94089
Phone: 800-425-8803
E-mail: ionel@amprius.com

Brian Cunningham, Technology Manager

U.S. Department of Energy
Phone: 202-287-5686
E-mail: Brian.Cunningham@ee.doe.gov

Start Date: January 1, 2015
Total Project Cost: \$5,500,000

End Date: October 31, 2018
DOE share: \$2,250,000

Non-DOE share: \$2,250,000

Project Introduction

Silicon has significant potential as a new anode material because it offers nearly 10 times the theoretical energy capacity of graphite. However, when charged with lithium ions, silicon swells up to four times its volume, causing capacity fade and mechanical failure. Because of swelling, conventional approaches to silicon anodes have not produced cells with the long cycle life required for electric vehicle applications. Amprius' rooted silicon nanowire structure mitigates material and mechanical issues, and enables high energy density products with reasonable cycle life.

Objectives

- Amprius is engaged in a three-year, anode-focused USABC project to develop and deliver vehicle-size cells that meet technical requirements specified by USABC. Throughout the project, Amprius will improve its silicon nanowire anode material and cell performance in a baseline cell, and then transfer lessons learnt to larger cells. At the end of the project, Amprius will deliver ~40 Ah cells with end of life specific energies of 350 Wh/kg and energy densities of 750 Wh/L.
 - The project addresses the key performance and production challenges to the commercialization of high-capacity cells and batteries with silicon nanowire anodes. Barriers addressed:
 - Energy: Low Wh/kg & Wh/L
 - Cycle Life: <1,000 Cycles
 - Size: Small Anodes and Cells
 - Cost: High \$/kWh
- Amprius' goal is to deliver cells that meet USABC's EV battery goals. Amprius' will deliver high-capacity pouch cells at the conclusion of the project's first, second and third years. Idaho National Laboratory will independently test the performance and safety of Amprius' cells according to USABC's test protocols.
 - Specific technical targets:
 - Available Energy Density @ C/3 Discharge Rate: 750 Wh/L
 - Available Specific Energy @ C/3 Discharge Rate: 350 Wh/kg

- DST Cycle Life: 1,000 Cycles
- Peak Discharge Power Density, 30 s Pulse: 1500 W/L
- Peak Specific Discharge Power, 30 s Pulse: 700 W/kg
- Peak Specific Regen Power, 10 s Pulse: 300 W/kg
- Calendar Life: 15 Years
- Selling Price @ 100K units: \$100
- Operating Environment: -30°C to +52°C
- Normal Recharge Time: < 7 Hours
- High Rate Charge: 80% ΔSOC in 15 min
- Peak Current, 30 s: 400 A
- Unassisted Operating at Low Temperature: > 70% Useable Energy @ C/3 Discharge Rate at -20°C
- Survival Temperature Range, 24 Hr: -40°C to + 66°C
- Maximum Self-discharge: < 1%/month

Approach

Amprius possesses an innovative silicon technology – an anode made of silicon nanowires attached to the current collector – that mitigates silicon swelling, unlocking silicon’s potential, and can meet USABC’s commercialization criteria.

Amprius’ technology is unique in three respects: material, structure, and results. First, Amprius’ anode material is made of silicon rather than graphite or a graphite-silicon composite. Second, Amprius’ anode structure is composed of nanowires physically attached to the current collector, rather than particles. Third, Amprius has demonstrated both high energy and long cycle life in full cells with silicon nanowire anodes.

Amprius’ unique, patent-protected material and structure – nanowires that are “growth-rooted” (i.e., grown directly on the current collector, without binders) – addresses swelling by enabling silicon to successfully expand and contract internally. Because the nanowires are attached to the current collector, Amprius does not rely on particle-to-particle contact and is able to achieve not only long cycle life, but also high electrical conductivity and power.

Before the USABC project, Amprius achieved >700 Wh/L at start of life and >400 cycles at C/2 rate and 100% depth of discharge (DOD). To meet the USABC goals during the project Amprius will:

- Increase specific energy and energy density by tuning anode structure and using advanced components (e.g., thinner substrates and separators). Amprius will also transition from LCO to NCM.
- Extend cycle life by optimizing anode structure and identifying and/or developing electrolyte formulations that improve Solid Electrolyte Interphase (SEI) stability and cell performance.
- Increase anode and cell size by developing methods for handling larger anodes; improving the uniformity of silicon growth and deposition technologies; reducing defect density; and utilizing manufacturing methods that inherently scale to larger dimensions.

Results

Amprius reduced the main gap in performance, cycle life, by identifying electrolyte additives that improve Solid Electrolyte Interphase (SEI) stability.

In FY2017, Amprius screened over 100 electrolyte formulations that included a variety of additives, solvents and salts. The main focus was on reducing reactions that produce gases at the cathode, especially at a high state-of-charge and high temperature. These reactions are particularly accelerated at high capacity NMC cathodes rich in nickel. The task is complicated by the fact that the electrolyte composition has to include additives that are beneficial to the cycle life of silicon anodes, not necessarily stable at high voltage, high temperature or on catalytically active cathodes. Thus, cathode additives were explored, as well as coatings on the cathode materials.

For screening, Amprius measured the relative capacity retention after either storing cells at full charge at 50°C or after cycling cells at 50°C for a number of cycles. For concentration optimization, it used a design of experiment methodology to reduce the number of combinations. In cycling, Amprius uses a typical test method: CC-CV at C/2 rate with 10% current taper and C/2 discharge rate, over the full voltage range (2.85-4.25V).

A sample set of results are shown in Figure I-18. Formulation ELY280 was developed in Year 1 for 10 Ah cells because it had very good room temperature and low temperature (not shown here) performance. However, a new formulation had to be developed in FY2017 (Year 2) to improve performance at high temperature (both Calendar and Cycle Life). Formulation ELY572 was selected for Year 2 deliverable cells. Electrolyte formulation development was done in Si/NCM cells with a 70% Ni-content cathode.

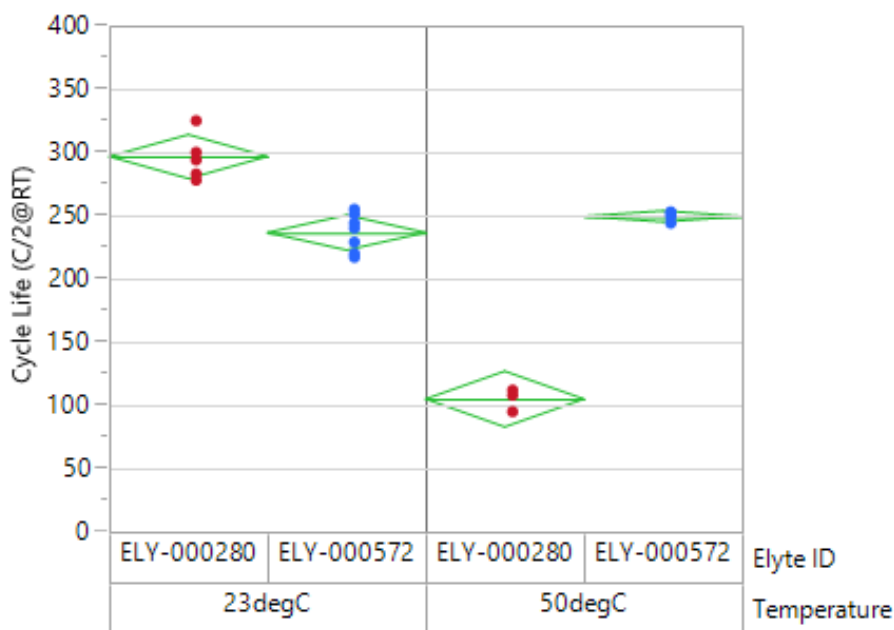


Figure I-18. Electrolyte formulation was optimized for better Calendar and Cycle Life in Si/NCM (70% Ni) cells

Amprius built and delivered to DOE for testing Silicon-NCM cells with average capacities of 10.6 Ah, specific energies of 345 Wh/kg, and energy densities of 860 Wh/L, an increase of 12% compared to previous year.

Amprius continued the cell design and development work started in Year 1 of the project by iterative design optimization of larger form factor. The Year 2 form factor, a 10 Ah cell, required a doubling in length and thickness of the cell tested in Year 1.

In parallel, more energy dense cathode materials were evaluated, including materials with high content of Ni (60 to 80% content). Amprius delivered a larger number of cells compared to that scheduled, to allow a comparison of the effects of Ni-content on cell performance and safety. *Amprius achieved an increase of about 12% in specific energy and energy density in Year 2 cells compared to Year 1 cells.*

The initial performance evaluation of Amprius' ≥ 10 Ah Silicon-NCM cells exceeded USABC's targets for Peak Discharge Power Density, Peak Specific Discharge Power, Peak Specific Regen Power, and Energy Density and is within 5% of the target in specific energy. Cycle Life and Calendar Life, as well as safety performance are under evaluation at Idaho National Laboratory and Sandia National Laboratory. A summary of the initial evaluation is shown in Table I-3.

Table I-3: Amprius' 10 Ah Silicon-NCM cells exceeded USABC performance goals

Characteristics at 30°C and End of Life	Units	USABC 2020 Goals Cell Level	Amprius 10 Ah Cells Si/NCM (70%Ni)
Peak Discharge Power Density, 30 s Pulse	W/L	1500	1900
Peak Specific Discharge Power, 30 s Pulse	W/kg	700	735
Peak Specific Regen Power, 10 s Pulse	W/kg	300	540
Available Energy Density @ C/3 Discharge Rate	Wh/L	750	860
Available Specific Energy @ C/3 Discharge Rate	Wh/kg	350	345

Amprius designed and started the project's final, Year 3 cells, to achieve a target capacity of ≥ 40 Ah.

Amprius selected the VIFB—/99/300 form factor for ≥ 40 Ah cells. This is a pouch cell with tabs on opposite sides (see Figure I-19). Amprius will use cell components (e.g., separator, pouch material and electrolyte) selected and/or optimized in the smaller, Year 1 and Year 2 form factors. The main effort of the task in FY2017 was to scale up the equipment and tooling for the 40 Ah form factor. In particular, Amprius started producing anode foils of larger size both in its batch, laboratory process, as well as in the newly developed roll-to-roll anode pilot line.

With the same components as the 10 Ah cells, Amprius achieved a small increase in specific energy (348 vs. 343 Wh/kg), and a much larger increase in energy density (921 vs. 862 Wh/L), due to a more favorable geometry. One of the first cells made in this form factor is shown in Figure I-19, next to its CAD model.

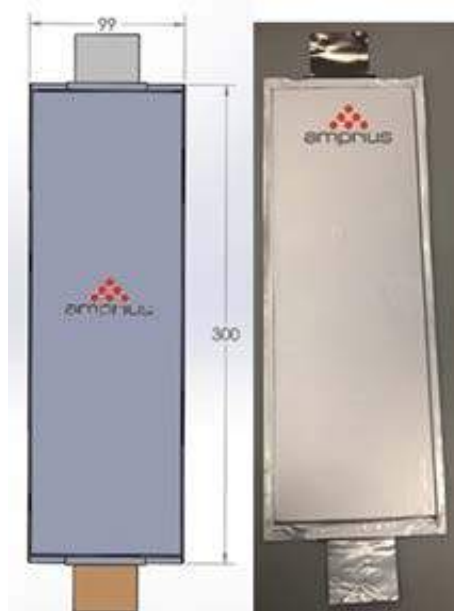


Figure I-19. CAD drawing and prototype 40 Ah cell with silicon nanowire anode

The 40Ah cells achieved the following specifications:

- Rated Capacity: 45.9 Ah at C/3 rate
- $V_{\max 100} = 4.1\text{V}$
- $V_{\min 0} = 2.5\text{V}$
- Cell weight = 450.7g
- Cell size = 6.0 x 96 x 288 mm (body only)
- **348 Wh/kg and 921 Wh/L**

Performance evaluation is ongoing and further design and assembly iterations are planned before delivery of the final cells.

Conclusions

During the project's second year, Amprius continued to make significant progress increasing cell energy, extending cell cycle life, and demonstrating that the silicon nanowire anode-based cells exceed USABC's goals. Amprius built and delivered 30 cells in the interim form factor, with a capacity of 10Ah. The initial evaluation at Idaho National Laboratory confirmed Amprius' results, including achievement of the initial power and energy targets.

Over the remaining year, Amprius will continue to increase cell energy by optimizing anode structure and exploring advanced components, extend cell cycle life by tuning anode structure and testing new electrolyte formulations, and finish the design and assembly of the final cells with capacities ≥ 40 Ah.

Key Publications

1. "Advanced High-Performance Batteries for Electric Vehicle (EV) Applications", ES41_Stefan_2017, US DOE Vehicle Technologies AMR, 2017.

I.A.7 Development of Active Materials to be used in Automotive Traction Applications: Rapid Commercialization of High Energy Anode Materials (SiNode Systems)

Cary Hayner, Principal Investigator

SiNode Systems

3440 S. Dearborn Street, #113N

Chicago, IL 60616

Phone: 612-220-3846

E-mail: caryhayner@sinode-systems.com

Brian Cunningham, Technology Manager

U.S. Department of Energy

Phone: 202-287-5686

E-mail: Brian.Cunningham@ee.doe.gov

Start Date: May 1, 2016

End Date: October 31, 2018

Total Project Cost: \$3,995,245

DOE share: \$1,997,622.50

Non-DOE share: \$1,997,622.50

Project Introduction

As global usage of electric vehicles steadily increases, so does the power/energy requirement to meet mainstream needs. Performance trajectories of traditional lithium-ion technology, despite an annual 3-5% improvement in energy density since inception, suggest that long-term electric vehicle needs will not be met without an evolution beyond traditional energy storage materials (i.e., graphitic anodes). SiNode Systems has developed a novel Si-based, negative-electrode material which can enable a quantum leap in battery energy and power density, and significantly impact battery weight and run-times that burden today's electric vehicles.

Objectives

The project entitled "Rapid Commercialization of High Energy Anode Materials" has been established with the aim of extending, benchmarking and demonstrating the performance of SiNode System's advanced silicon-based anode materials in battery form factors and designs relevant for electric vehicle applications.

Approach

SiNode Systems has demonstrated a novel high energy density (>1,000mAh/g) Si-based negative-electrode materials technology with a long-term potential to replace graphitic-based anodes in lithium-ion batteries. SiNode's technology uses a proprietary silicon alloy-graphene material architecture to achieve: i) category-leading performance and ii) solutions to long-standing Si anode technical hurdles. The proprietary combination of silicon-based alloys and a flexible 3D graphene network helps to stabilize the active material during charge and discharge (see Figure I-20) by providing an interfacial barrier between the active material and the electrolyte which can accommodate large volumetric changes through a laminar graphene sliding mechanism. The 3D graphene-silicon architecture results in a minimization of capacity losses due to electrical disconnection, significantly improved active utilization (mAh/g) and partial stabilization of the SEI interface with a flexible physical barrier between electrolyte and active material.

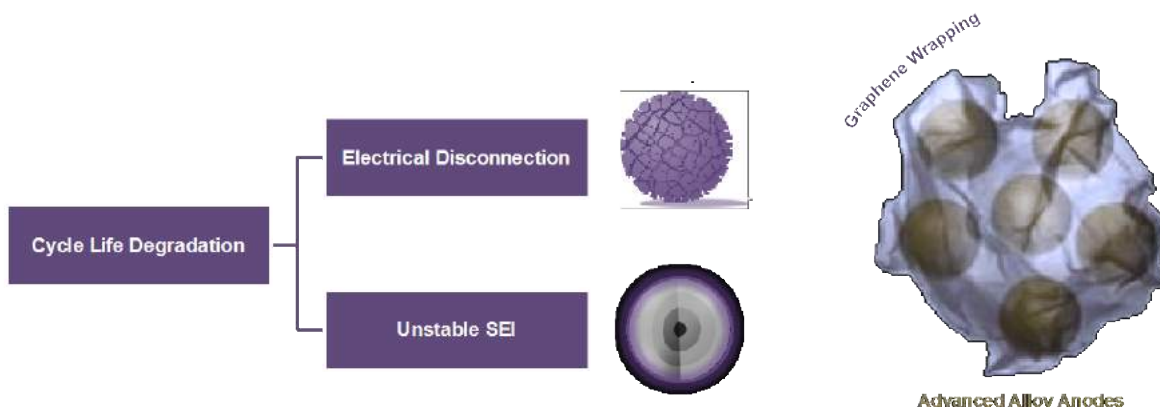


Figure I-20. Si-anode failure mechanisms (left), SiNode graphene-wrapped advanced silicon anode architecture (right)

SiNode has made continuous improvements against key USABC advanced electrode metrics over time, and demonstrated an attractive trajectory towards USABC advanced electrode goals. The goal of the program is the advancement and commercialization of advanced silicon-based active materials for high energy / high power EV batteries. Specifically, the program aims to demonstrate that SiNode technologies can exceed USABC electric vehicle performance targets in USABC-recognized cell form factors, be produced at-scale by commercially viable methods and reach USABC cost targets at scale. To this end, a series of tasks have been developed to address the core technology gaps and their associated barriers: Task 1: Materials Stabilization and Analysis, 2. Manufacturing Scale-Up, 3. System Cost Reduction, 4. Cell Prototype Evaluation, 5. Downstream Cell Process Optimization and 6. Cell Characterization and Performance Evaluation.

SiNode has two strategic partners for this program. A123 systems will work with SiNode on Tasks 4 and 6, the pouch cell deliverables and PPG will work with SiNode on Tasks 2 and 3 to scale up the anode material.

Results

This year SiNode has developed a novel carbon-coating method for stabilizing the surface and SEI of its SiO_x active particles, prior to graphene wrapping. (See Figure I-21.) Recently, this carbon coating process was refined and optimized. Experiments were undertaken with the goal of better understanding the impact of carbon coating amounts on the electrochemical cycling performance of the final composite, as well as improving the coating process to reduce the initial cycle loss and improve the first Coulombic efficiency (FCE).

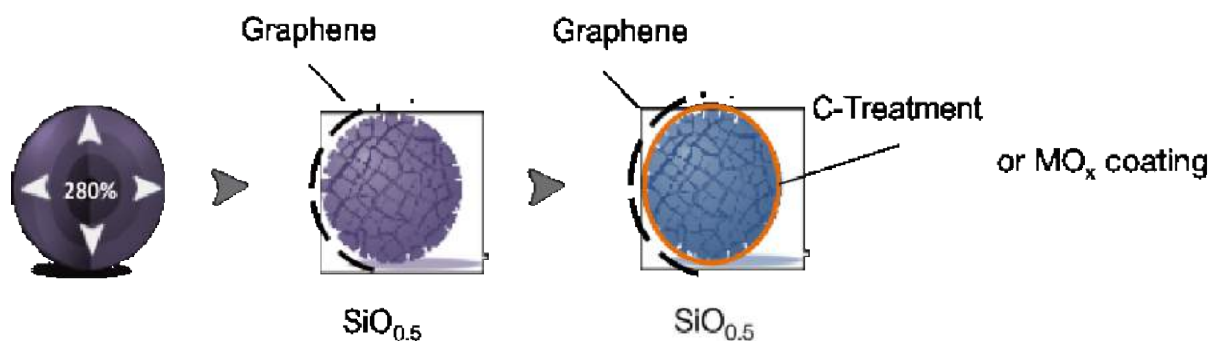


Figure I-21. Evolution of SiNode technology to meet USABC goals and specifications: (from left to right) pure silicon particle - > graphene wrapped silicon alloy (SiO_x, x=0.5) -> C-coated (or MO_x coated) and graphene wrapped silicon alloy (SiO_x, x=0.5).

Through this work, SiNode was able to better understand and optimize our carbon coating procedure. Improvements to the surface morphology of the C-SiO_x particle led to higher first cycle efficiency values (FCE), as shown in Figure I-22, and therefore higher energy. For our standard C-coating level, FCE improvements of 3% were observed by improving the carbon coating procedure, raising the pure material (i.e., >1500 mAh/g) FCE to over 79% - very close to the 80% target value cited by our customers.

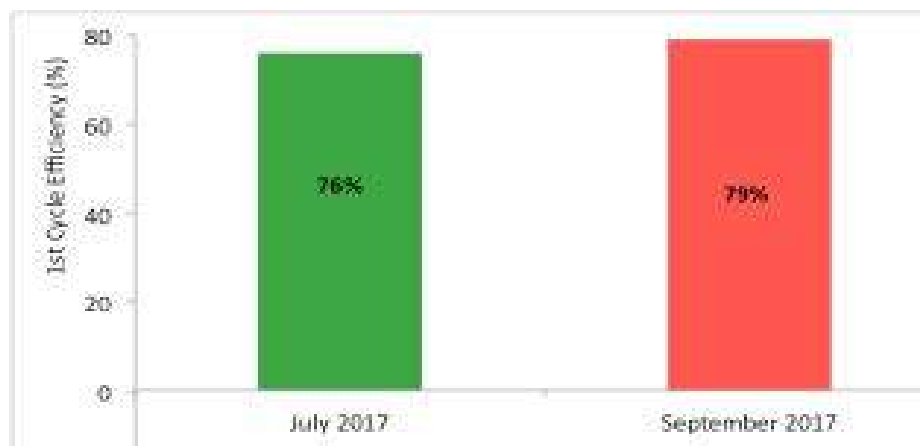


Figure I-22. Improvements in FCE of our anode material seen by optimizing the surface morphology of the carbon coating.

Next, SiNode focused on both the scale-up and process refinement of an optimized C-coated graphene wrapped silicon alloy. A monthly production level of 2 kg has been achieved. In addition to improvements in production efficiency through increased solids-loading of our precursor, SiNode has also introduced process refinements and quality checks to ensure that the larger quantity of material produced remains up to par. The goal over the next quarter is to continuously improve SiNode's internal bandwidth to accommodate the needs of subsequent builds while maintaining consistent material performance.

This increased production has required improvements in the repeatability of the powderization process. By developing process controls, SiNode has been able to produce material that performs the same week-to-week. (See Figure I-23.)

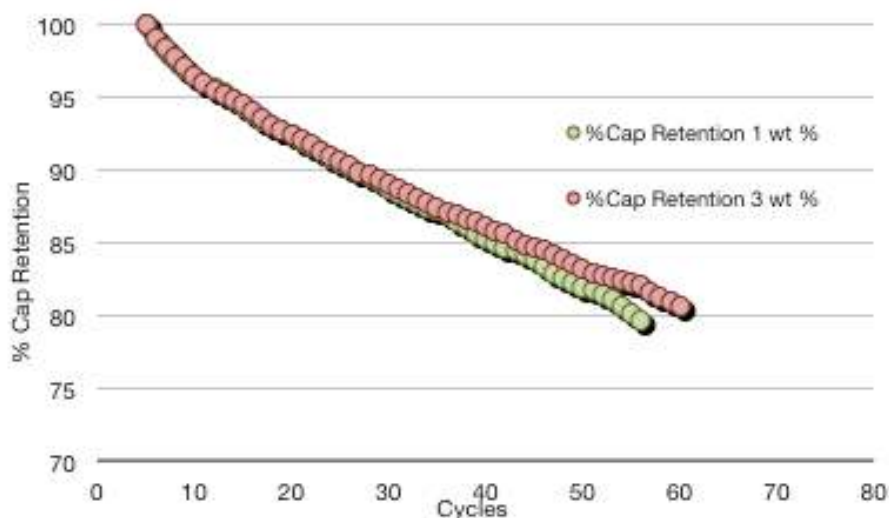


Figure I-23. Capacity retention as a function of cycles for 1 and 3 wt% precursor dispersions. The data is in full cell paired with an NCA cathode.

The production roadmap to the 1 Ah cell deliverables was analyzed in Q6, and is shown in Figure I-24. There has been a gradual migration to higher graphene dispersions over time (from 1-3%), which has enabled additional bandwidth and higher production efficiency. In parallel, SiNode external production collaborations are expected to come online in the November-December timeframe which will provide additional production bandwidth as a result of larger pilot-scale equipment.

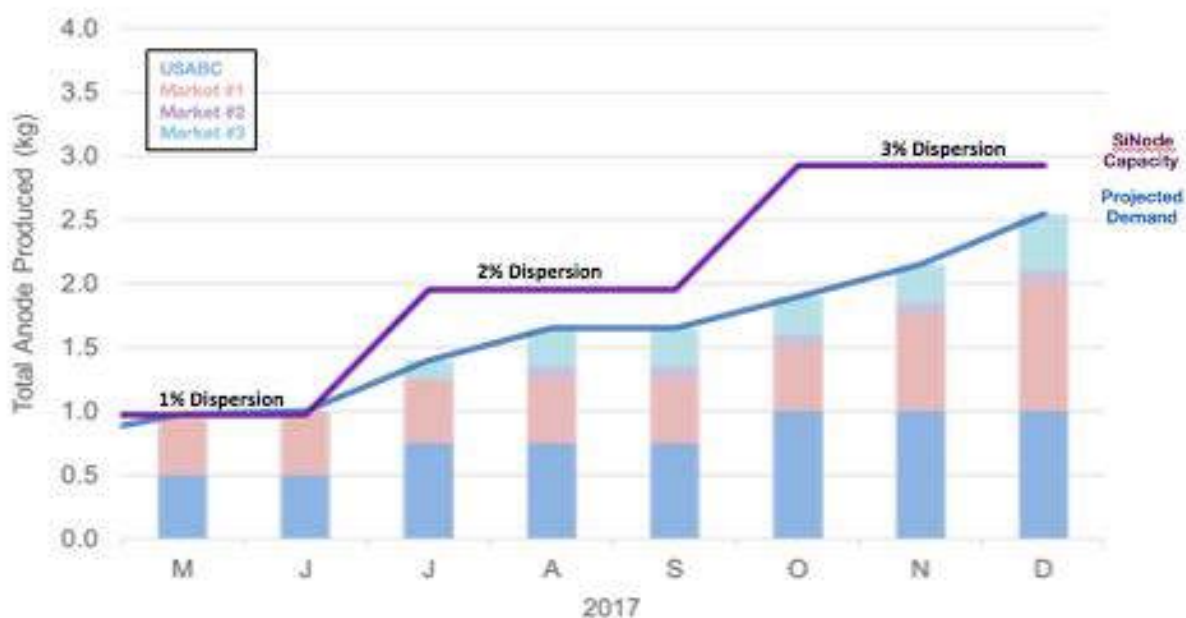


Figure I-24. 2017 production forecast and major technical milestones. Project needs and graphene dispersion levels are expected to increase throughout the course of 2017

For the 1 Ah cell deliverables, A123 was initially able to carry out a successful lab-based coating of the targeted 1000 mAh/g anode on a lab scale. The graph in Figure I-25 demonstrates updated cycling data from this cell, which completed its testing during this quarter.

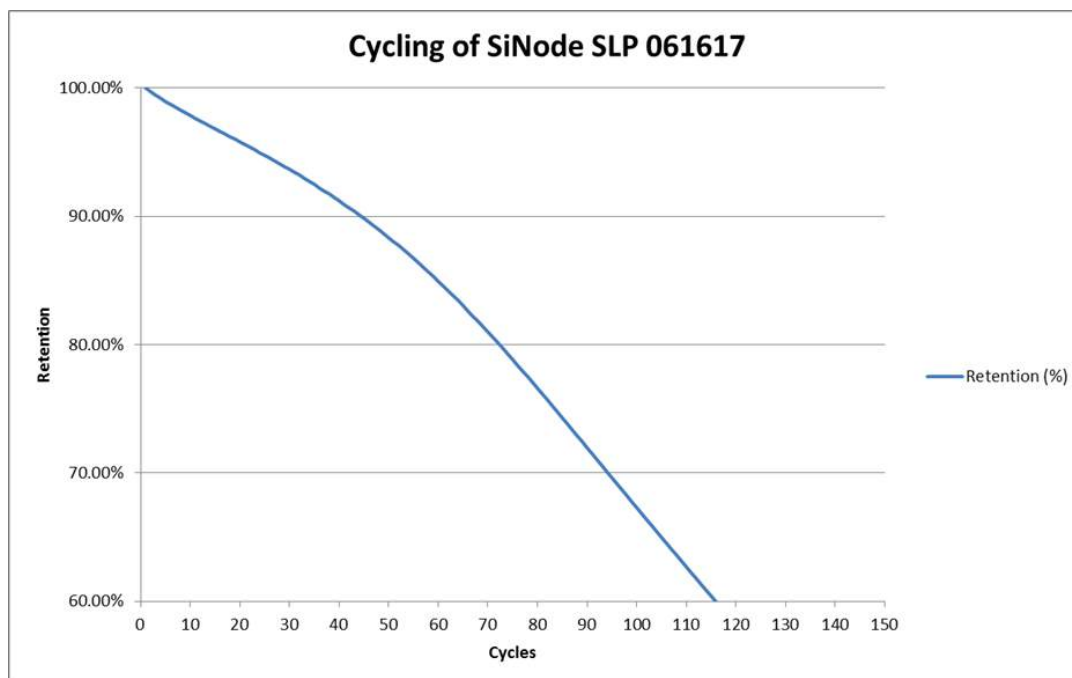


Figure I-25. Completed cycle life testing of full SLP cell manufactured with A123 hand coated anode

A123's goal was ultimately to be able to replicate this result using a large number of higher capacity deliverable cells, with anode successfully coated on full manufacturing equipment at its facility. During the latest quarter, A123 was able to complete the full manufacturing coated material (around 80 meters of double-sided electrode) required for the deliverable cells. The next step in the process is to move forward with the cell manufacturing process, with expected cell delivery during the final quarter of 2017.

Next, experiments were completed in which the amount of FEC used in SiNode's electrolyte formulations was reduced. Due to the addition of carbon coatings which stabilized the SiO_x surface, it is no longer necessary to add high quantities (20%) of FEC to stabilize the active silicon. Electrodes were constructed at the USABC-targeted 1000 mAh/g capacity and tested in a full cell format against an NCA cathode. As shown in Figure I-26, the cells were able to demonstrate the same cycling performance with 10% FEC as with the standard 20% FEC, enabling a decrease in the amount of FEC used by 50%. No other undesirable effects (i.e., low capacity, swelling) were observed when moving to 10% FEC. These improvements help align our cell design with industry practice and will help with cell manufacturing challenges such as gassing and swelling.

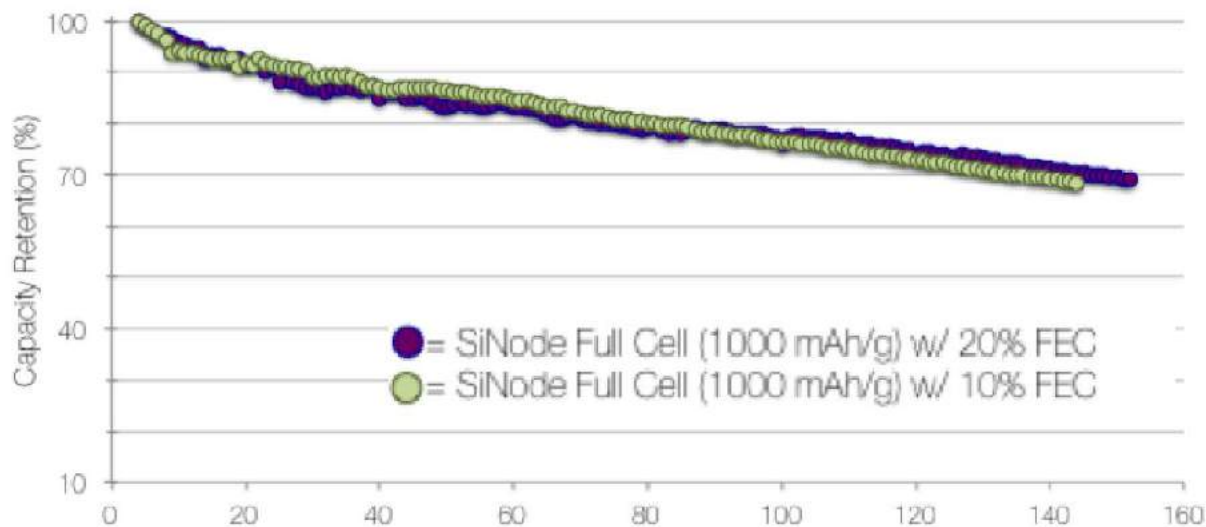


Figure I-26. Full cell capacity vs. cycle number plot for SiNode 1000 mAh/g anodes vs. NCA cathode with varying degrees of FEC electrolyte additive.

Conclusions

SiNode has entered the 18th month of the 30-month-long project. The 1 Ah cell deliverables will be delivered this quarter. A major milestone was achieved in the materials scale up with SiNode successfully completing the materials scale up for the 1 Ah cells.

Several challenges need to be surmounted over the coming year, including consistent improvements of the average coulombic efficiency, cycle life, electrode expansion, multi-kilogram production, successful battery electrode design and line-of-sight on materials cost reductions (i.e., graphene and silicon).

SiNode has demonstrated a cadence of innovation and product development over the past 18 months, and looks optimistically towards demonstration of viable performance in commercially relevant EV cells.

I.A.8 A 12V Start-Stop Li Polymer Battery Pack (LG Chem Power, Inc.)

Mohamed Alamgir (LG Chem Power - PI)

LG Chem Power, Inc.
1857- Technology Drive
Troy, MI 48083
Phone: 248-291-2375
Email: alamgir@lgchem.com

Brian Cunningham, Technology Manager

U.S. Department of Energy
Phone: 202-287-5686
E-mail: Brian.Cunningham@ee.doe.gov

Start Date: January 1, 2015
Total Project Cost: \$1,820,000

End Date: March 29, 2017
DOE share: \$910,000

Non-DOE share: \$910,000

Project Introduction

12V Start-Stop batteries are gaining increasing attention as cost-efficient solution for global reduction of carbon emission. To achieve this goal, Li-ion batteries offer promising alternative to the incumbent lead acid (PbA) batteries because of their much higher specific energy and longer life. Key challenges for realization of this objective are cold-cranking power and cost, which were the focus of this program.

Objectives

The goal of this program was to develop a low-cost, abuse-tolerant 12V Start-Stop Li-ion battery that will be capable of meeting the life, cold-cranking and cost targets of USABC.

Approach

To achieve the above objectives, the following approaches were pursued.

- Develop a long-life, abuse-tolerant cell using LTO/LMO active materials.
- Tailor cathode and anode material properties such as morphologies/surface area to increase power.
- Optimize cathode and anode compositions, their porosities as well as electrolyte compositions, with respect to life and power.
- Develop a low-cost battery pack using a simplified BMS.

LG Chem, Seoul, South Korea, was the partner in this program.

Results

We present below a summary of the work carried out in this program.

Optimization of Cell

We developed three generations of cells in the course of this program. Different types of LMO cathode material were evaluated to develop a high power cell that meets the cold-cranking power goal. The materials varied in their particle sizes, surface areas, doping elements and doping levels as well as surface coatings. We also evaluated cathodes having different compositions by varying the type and amount of conductive agents and binder. These characteristics were optimized to lower electrode resistance to increase cell power. Approaches similar to these were also pursued to develop a high power LTO anode. A number of electrolyte compositions as well as separators of different thickness and porosities were also studied.

We also carried out studies to improve processing conditions such as electrode manufacturing and aging. For example, LTO is a nano-material and has the propensity to adsorb moisture that is deleterious to cell performance such as life and swelling. Thus, appropriate processing conditions needed to be developed to ensure a well-functioning LTO electrode.

Considerable improvement in cell life and power was achieved via the above studies. As an example, we show in Figure I-27 the continuous improvement in storage characteristics of the cells developed in this program. While the initial studies showed poor performance at 60°C and 70% SOC, the A1 sample showed significant improvement in high temperature durability. Excellent cycle-life was also achieved even at the high temperature of 50°C at the charge/discharge rate of 5C/5C (Figure I-28).

As mentioned earlier, a key challenge of Li-ion batteries for Start-Stop applications is to meet the cold-cranking power requirement. While the first generation cell delivered good performance and reasonable durability, its cold-cranking power capability was poor and the USABC target could be met only at 100% SOC. By tailoring the cathode, separator and electrolyte properties, the cell characteristics were improved and the final cell was able to deliver cold-cranking power at SOC = 70%. We do note here that to meet the USABC requirement the cold crank power needed to be met at SOC = 40%. These are Beginning-of-Life (BOL) data and cold-cranking power at End of Life (EOL) need to be verified. In addition, the durability of the cell was also significantly enhanced as evidenced by reduction in gassing at high temperatures. (See Figure I-29.)

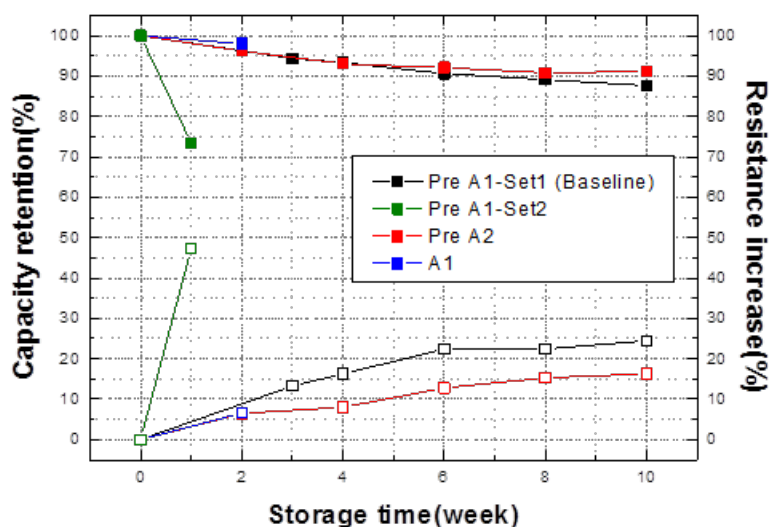


Figure I-27. Example of improvement achieved in the durability of the LTO/LMO cell in this program.

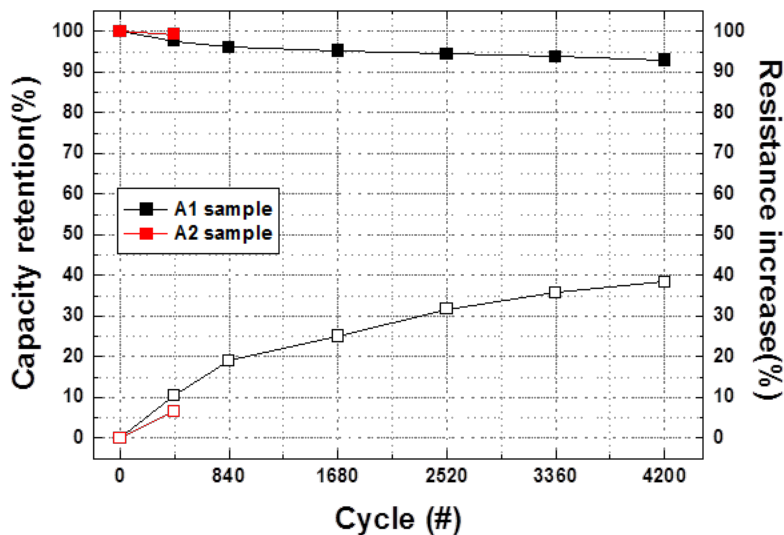


Figure I-28. Cycle-life data for LTO/LMO cells at 55°C and 5C charge and discharge rates.

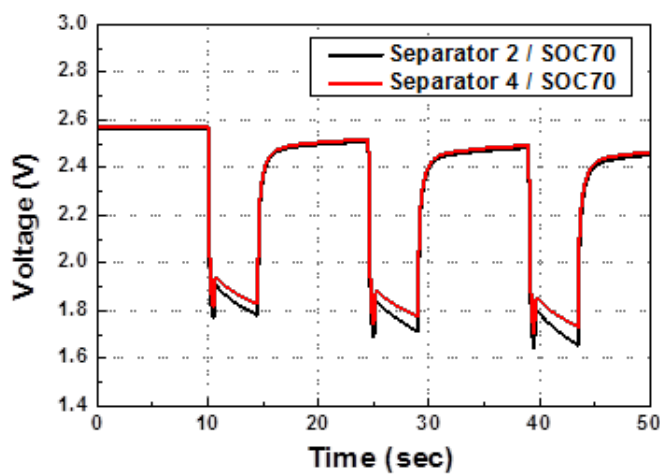


Figure I-29. Improvement of cold-cranking power as a function of separator properties.

Calorimetric studies were also carried out by NREL to thermally characterize the various generations of the cells. This involved heat generation, heat capacity and IR imaging measurements. The data showed that the efficiency of the cells improved through the cell generations (Figure I-30). For example, A1 cell showed a discharge efficiency at 0°C comparable to the preliminary cell version efficiency at 30°C. Additionally, for the A1 cell at a 2C full discharge, the efficiency of the cell dropped from 98.9% at 30°C to 96.9% at 0°C – a very attractive performance with regards to temperature. Under low rate discharges ($< C/1$), the cell chemistries' endothermic response dominates the Joule heating within the cell.

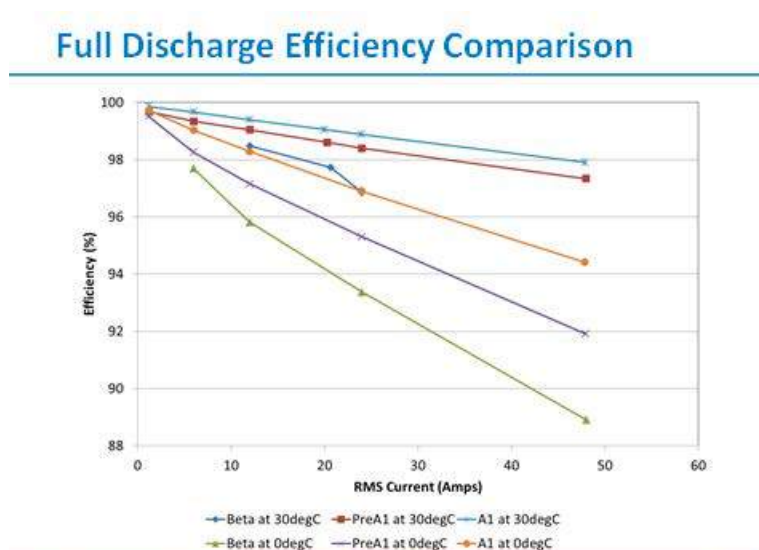


Figure I-30. Improvement in the discharge efficiency of the various generation of cells as a function of cell improvement.

The program cells showed outstanding abuse-tolerance. While the nail penetration and short-circuit tests yielded results with EUCAR ratings of 3 and lower, both the thermal stability and overcharge tests showed a EUCAR rating of 4 (venting with > 50% electrolyte loss).

Development of the 12V Start-Stop Battery Pack

A key objective of our pack development studies was to develop a long-life and low-cost battery pack using a simplified BMS system. A number of options to hold the cells in a mechanically robust manner were evaluated. Since the pack is under hood, a thermal management strategy was adopted to efficiently shield the cells from exterior heat while also allowing for heat rejection by the cells during operation. A low cost insulating foam was chosen which is also used as the cell retention frame. Illustrative simulations and tests demonstrated efficient cooling of the cells during operation and storage. For example, experimental data acquired from the pack at 75°C for four (4) hours agreed quite well with these estimations indicating that the cells remain below 50°C during this storage. A simple and low-cost battery management system was developed that is capable of cell balancing and state-of-charge estimation.

Two versions of packs were developed and delivered to the USABC for testing and evaluation. As the 2nd and final delivery, six battery packs were built and delivered to the National Labs for testing and validation according to USABC protocols. (See Figure I-31.)



Figure I-31. Picture of the 12V Li-ion Start-Stop battery pack delivered to USABC for testing.

Conclusions

Results we have acquired and presented above show that this two-year program was able to achieve significant progress towards the development of an LMO/LTO cell-based 12V Start-Stop battery that is technically and commercially competitive with its PbA counterpart. Considerable advances were made in the critical areas of cold-cranking power, life and abuse-tolerance. We also developed a simple thermal management and cell retention strategy that is low-cost but capable of meeting the thermal and mechanical requirements for automotive use. This approach in combination with a low-cost and potentially simplified BMS makes the LMO/LTO pack technology a next generation alternative to the 12V PbA battery.

To make it more competitive with a PbA battery, we need to further improve the cold-cranking capability. In addition, we need to address the gassing/cell swelling issues especially for higher temperatures application characteristic of under hood deployment. There is also a gap to the USABC cost target. Pack data obtained from the National Labs will aid in further establishing the gap to the USABC requirements and cycling data will enable us to determine whether one can use simplified BMS also.

Key Publications

1. “A 12V Start-Stop Li Polymer Battery Pack”, ES249_Alamgir_2017_p, US DOE Vehicle Technologies AMR, 2017.

I.A.9 USABC 12V Start-stop Module Development, Phase II (SAFT)

Thomas Greszler, Principal Investigator

SAFT SDD

107 Beaver Court

Cockeysville, MD 21030

Phone: 410-568-2590

E-mail: Thomas.Greszler@saftamerica.com

Alla Ohliger, Principal Investigator

SAFT SDD

107 Beaver Court

Cockeysville, MD 21030

Phone: 443-933-4944

E-mail: Alla.Ohliger@saftamerica.com

Brian Cunningham, Technology Manager

U.S. Department of Energy

Phone: 202-287-5686

E-mail: Brian.Cunningham@ee.doe.gov

Start Date: June 1, 2015

End Date: December 31, 2017

Total Project Cost: \$6,100,000

DOE share: \$3,064,700

Non-DOE share: \$3,035,300

Project Introduction

Saft proposed to develop an advanced, high-performance battery module for 12V Start-Stop (12VSS) vehicle applications based on SAFT's proprietary LTO lithium-ion cell technology and continuation of development efforts undertaken in Phase I of the project.

Objectives

- Continue development of the cell electrochemistry based on SAFT's proprietary lithium titanate (LTO) lithium-ion battery technology and meet USABC technical targets listed in Table I-4.
- Design and develop 46 Ah cell and prototype module to meet USABC energy and cost targets.
- Develop module management and electronic controls.
- Deliver 46 Ah cells and 12V prototype modules to USABC.

Table I-4: USABC Cell & Module Performance Targets and SAFT Test Results

End of Life Characteristics	Units	USABC Target	Note 1	Note 2
(Capacity 1.5 Ah, Scaled-up 46 Ah)			1st Batch Cells	2nd Batch Cells
			45 °C Calendar life	45 °C Calendar life
			Under hood	Oct-17
Discharge Pulse, 1s	kW	6	24	Note 3
Max discharge current, 0.5s	A	900	901	Note 3
Cold cranking power at -30 °C (three 4.5-s pulses, 10s rests between pulses at min SOC)	kW	6 kW for 0.5s	6	7.3
	kW	4 kW for 4s	3.98	4.4
Min voltage under cold crank	Vdc	8	8	8
Available energy (750W accessory load power)	Wh	360	501	545.6, Note 3
Peak Recharge Rate, 10s	kW	2.2	2.2	Note 3
Sustained Recharge Rate	W	750	750	750
Cycle life, every 10% life RPT with cold crank at min SOC	Engine starts	450k	276.5K	Note 3
Calendar Life at 30 °C, 45 °C if under hood	Years	15 at 45°C	RPT12	Note 3
			6.7% complete	
Minimum round trip energy efficiency	%	95	99	99.5
Maximum allowable self-discharge rate	Wh/day	2	0.11	0.87
Peak Operating Voltage, 10s	Vdc	15	15	15
Sustained Operating Voltage – Max.	Vdc	14.6	14.5	14.5
Minimum Operating Voltage under Autostart	Vdc	10.5	10.5	10.5
Operating Temperature Range (available energy to allow 6 kW (1s) pulse)	°C	-30 to + 75	-1- to 75 °C	-1- to 75 °C
30 °C – 52 °C	Wh	360 (to 75 °C)	502	Note 3
0 °C	Wh	180	437	Note 3
-10 °C	Wh	108	138.5	Note 3
-20 °C	Wh	54	Fail	Note 3
-30 °C	Wh	36	N/A	Note 3
Survival Temperature Range (24 hours)	°C	-46 to +100	N/A	Note 3

Notes:

1st batch 1.5 Ah pouch cells delivered in April 2016, 2nd batch 1.5 Ah pouch cells delivered in July 2017, Testing in progress

Approach

The cost of a Li-ion battery product is generally the most challenging requirement for deployment in the automotive industry. SAFT focused on optimization of the cell electrochemistry and cost-efficient design for cell and module suitable for mass production. SAFT's approach was to develop a low-cost lithium-ion cell electrochemistry meeting USABC technical performance requirements. SAFT analyzed technical gaps discovered during testing of the 1st batch C-size cells and continued to optimize cell electrochemistry to increase cycle-life/calendar life, limiting the impedance growth over time, and minimizing gassing. For electrode, SAFT focused on rational design of positive and negative electrodes including active materials, carbon network, binders and implementation of surface coatings; all have significant impact on cold crank and gassing. Samples of the LTO powder were delivered to Argonne National Laboratory, ForgeNano and ALD Nanosolutions for surface coating evaluation. For electrolyte, Saft focused on experiments to achieve good electrolyte conductivity at low temperatures.

To meet cost targets SAFT focused on industrialization plan for manufacturing of cells & modules. The approach was to develop cost-effective producible 46 Ah cell and module design (including electronics) and eliminate numerous design features that contribute to the overall cost while retaining performance and lifetime characteristics that are necessary for an automotive application.

Results

SAFT completed testing of the 1st batch C-size pouch cells and started testing 2nd batch cells with improved electrochemistry. The overall performance targets, outlined by USABC, are shown in Table I-4. Table I-4 also presents Saft's test results obtained from the 1st and 2nd batch cells. Batch 1 cells have impedance growth at high temperature 55°C and 65°C leading to decreased cold crank performance after initial control testing. Cells have no significant capacity fade after 1 year testing at 45°C cycle life, 45°C calendar life and 55°C calendar life. After one year of cycling testing at 45°C, batch 1 cells have minimal impedance growth. SAFT started testing cells from batch 2. Significant improvement can be seen in initial cold crank performance between batch 1 and batch 2.

Electrochemistry Development

LMO/LTO system has a higher gassing rate than LFP/LTO or NMC/LTO cells. In order to increase high temperature stability, SAFT reduced the Mn³⁺ content in active material. LCO was selected as an active material to be blended with LMO for its lack of Mn³⁺ content, OCV curve and high specific capacity. The trials concluded that the LMO:LCO (80:20) positive electrode combined with LTO decreased gassing rate, however degraded the cold crank performance. Therefore, LMO was selected as the final positive active material.

For negative electrode, it was found that LTO contributes to 70-80% of the cell total impedance. Therefore, SAFT focused to optimize LTO electrode formulation. Supplier 4 was selected as the final LTO supplier for 46 Ah cells. This LTO material improved cell cold crank performance while reducing gassing rate. Different electrode compositions were tested in order to reduce gassing. Two designs: design 2 with carbon black and graphite as conductive network, and carbon free design were down-selected as offering the best cold crank performance and minimizing cell gassing rate (Figure I-32). LTO carbon free was selected as optimal electrode design since this formulation allows increasing cell capacity while maintaining overall cell performance. Moreover LTO with high loading was selected and will be implemented in 46 Ah cells. This LTO design meets cold crank performance and gassing requirements along with a cell cost reduction.

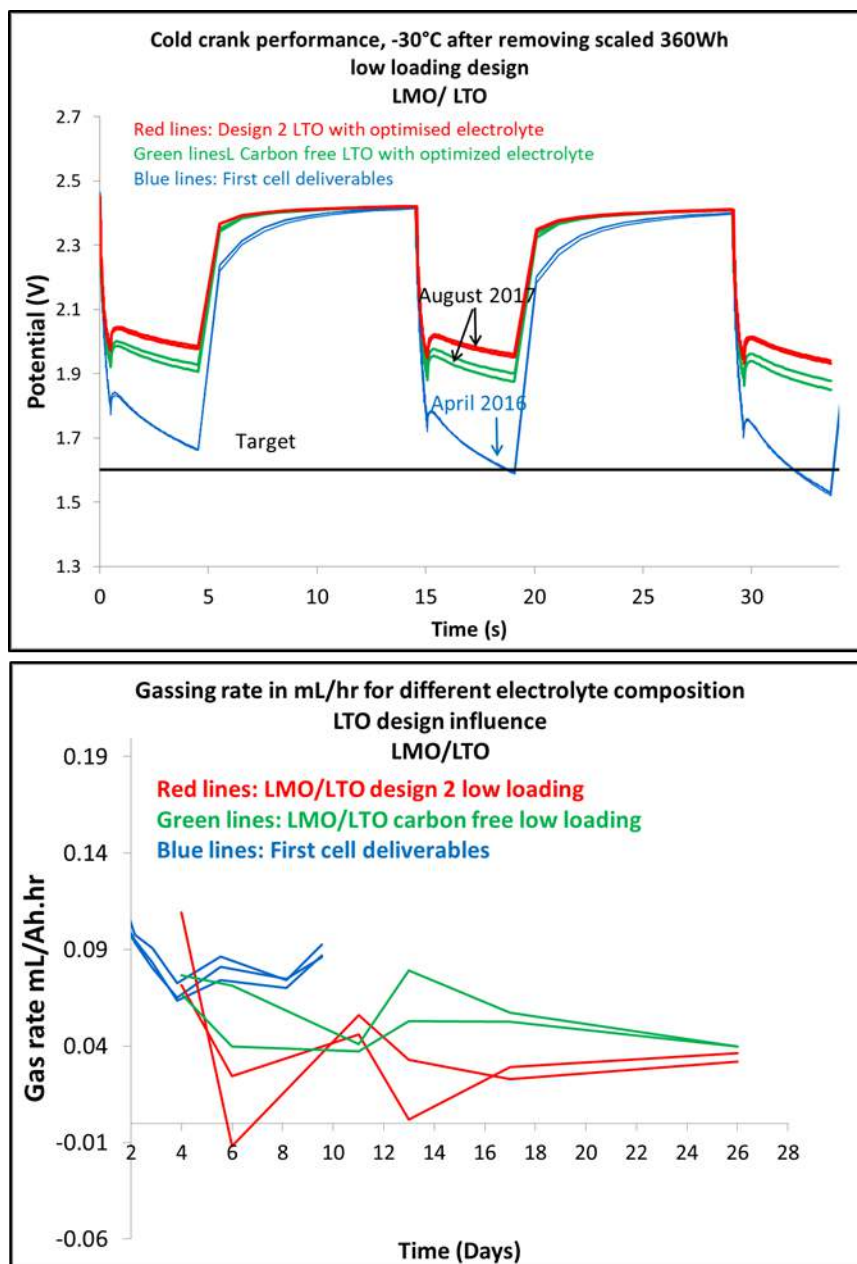


Figure I-32. (Top) Comparing cold crank performance of cells with Design 2 LTO and carbon free LTO versus the first cell deliverable baseline, (Bottom) Comparing gassing rate of cells with Design 2 LTO and carbon free LTO versus the first cell deliverable baseline

SAFT tested alumina coated separator and PP separator with different thicknesses and porosity. The goal was to improve cell wetting and cold crank performance. The separator 12 microns PP was selected as the best option to meet USABC requirements, specifically cold crank performance, and will be used for 46 Ah cells.

In conclusion SAFT selected LMO, LTO and separator suppliers for 46 Ah cells. LMO electrode formulation was finalized, while two LTO formulations are still being considered for 46 Ah cells. SAFT continues testing cold crank performance to finalize LTO formulation.

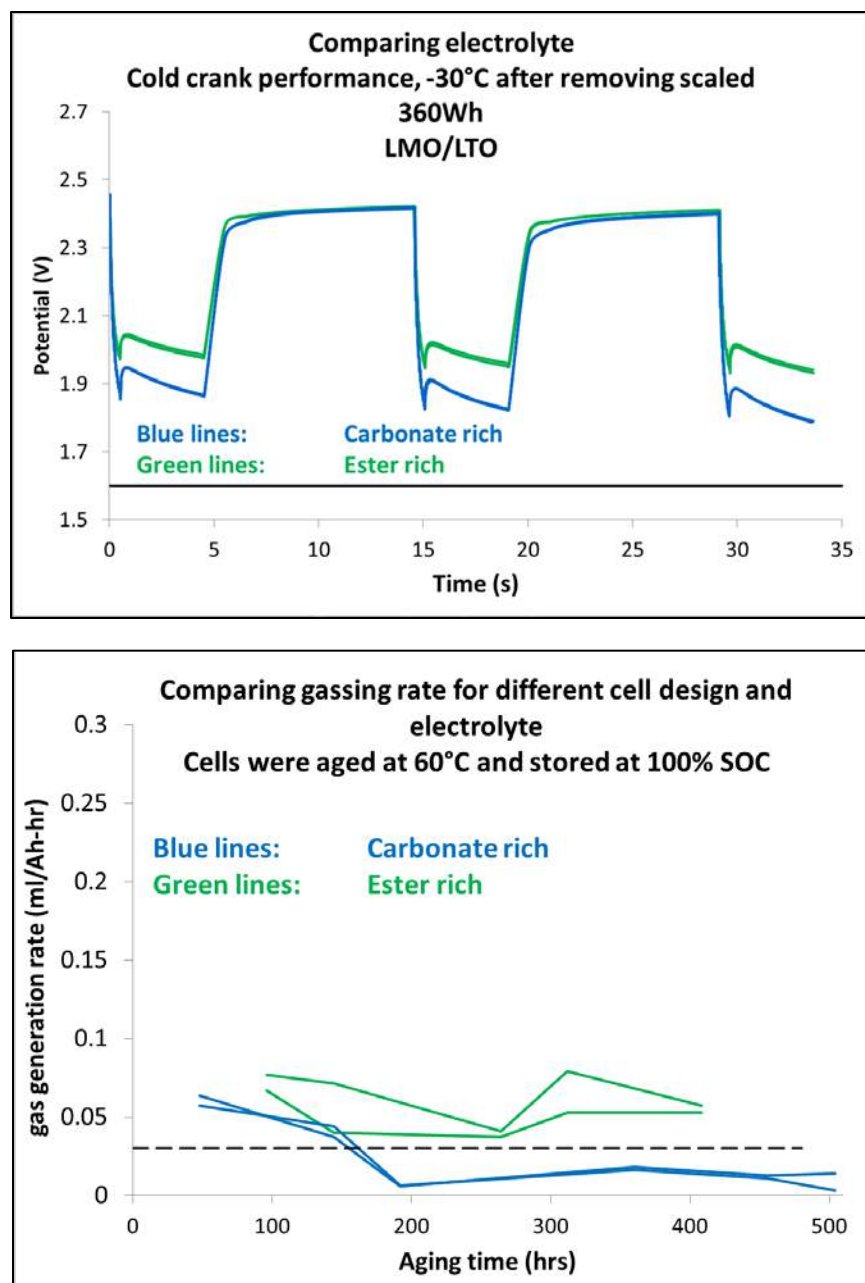


Figure I-33. (Top) Comparing cold crank performance of cells filled with ester rich electrolyte vs carbonate rich electrolyte, (Bottom) Comparing gassing rate of cells filled with ester rich electrolyte vs carbonate rich electrolyte.

To select electrolyte, SAFT tested electrolytes for conductivity at low temperature, boiling point, flash point, cell cold crank performance and cell gassing rate. Two electrolytes were down-selected and are being considered for 46 Ah cells fabrication: carbonate-rich electrolyte and ester-rich electrolyte. Both electrolytes offer good cold crank performance and gassing rate. The LMO/LTO cells with carbonate-rich electrolyte offer longer calendar/cycle life than ester-rich cells. Both cold crank results and gassing behavior for the two electrolytes are illustrated in Figure I-33.

Cell/Module Development

SAFT completed mechanical design of 46 Ah cell. The estimated finished cell size: 250 millimeters (W) x 216 millimeters (L) x 20.1 millimeters (T), and cell weight is ~1.99 kg, shown in Figure I-34.

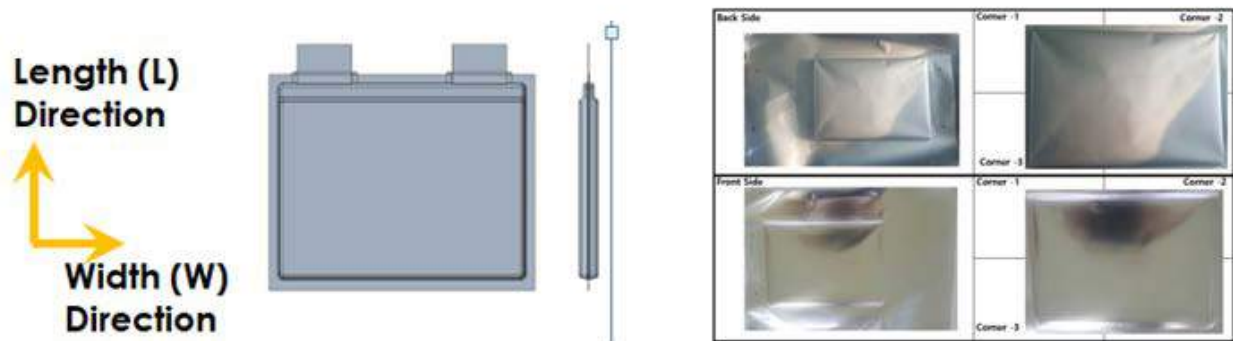


Figure I-34. Front and Side Views of the 46 Ah Pouch Cell (Left side); Photograph Showing Drawn Pouches (Right side).
SAFT SDD

SAFT developed manufacturing process and ordered special tooling for manufacturing of 46 Ah cells. SAFT also completed design of the prototype battery module, shown in Figure I-35.

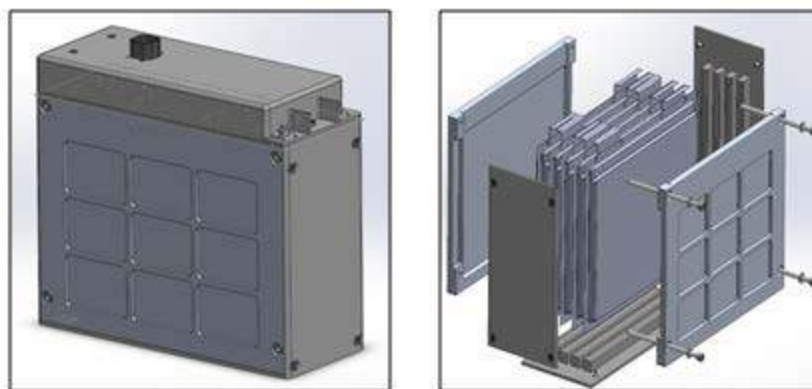


Figure I-35. 3D Model of USABC 12V S/S Prototype Model. SAFT SDD

Preliminary calculations on preliminary prototype module design (including electronics) resulted in overall volume of 9 liters (8 liters is USABC target). For mass production implementation additional design efforts are required to reduce module volume to meet USABC target. Weight of the module with cells and electronics was estimated to be 14.5 kg, meeting the USABC 15kg target.

For module electronics, SAFT has identified the overall structure of the system development and its integration into the module design. Battery module management will include: **cell voltage monitoring** (1.2 mV accuracy), **cell balancing circuitry** (60mA/cell capable), **temperature monitoring** (1 thermistor/cell) and **broadcast status** (state of charge/health, max current in/out and fault status). Figure I-36 shows block diagram detailing requirement for the electronic system.

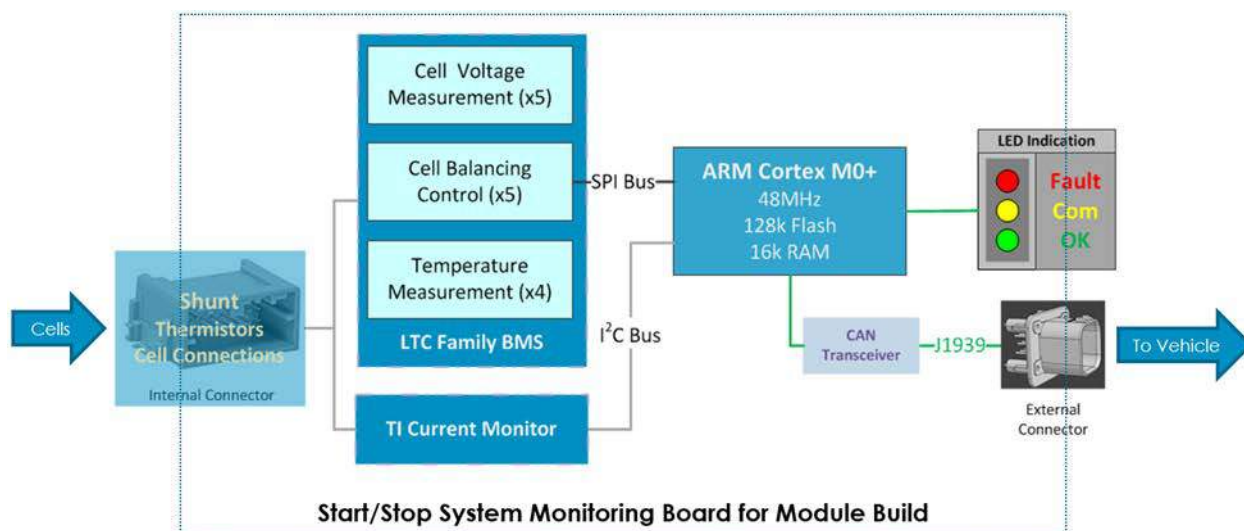


Figure I-36. Block Diagram Detailing the Requirements for the Electronic System. SAFT SDD

SAFT designed electrical control boards and manufactured proof-of-concept boards with test fixture, shown in Figure I-37. The proof-of-concept boards will be tested later this year.

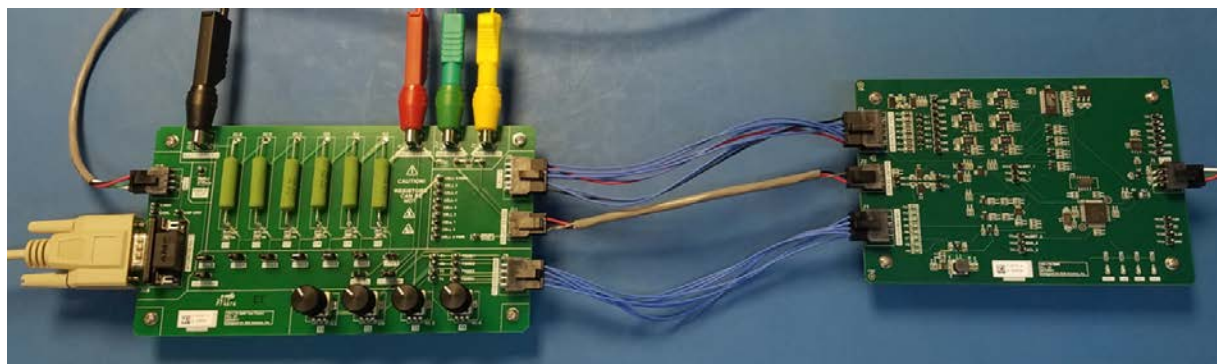


Figure I-37. Proof-of-Concept Electrical Control Board. SAFT SDD

Battery Module Cost Analysis

USABC cost target is \$220 per unit. Preliminary cost analysis for cells, module hardware and electronics-based on 250k modules manufactured per year indicates meeting USABC target.

Deliverables

During reporting period Saft delivered 2nd batch of 1.5 Ah C-size pouch cells and 13 Ah prismatic cells to Idaho National Laboratory for testing.

Conclusions

SAFT delivered 2nd batch of 1.5 Ah C-size pouch cells with optimized electrochemistry to Idaho National Lab for testing. The 2nd batch cells with optimized chemistry were also tested at SAFT and met cold crank requirements. Testing is underway to complete calendar and cycle life for these cells.

SAFT continued to optimize electrochemistry formulations and suppliers to improve cell performance. For 46 Ah cells, SAFT finalized formulations and suppliers for LMO positive electrode, LTO negative electrode, separator and electrolyte.

SAFT completed mechanical design for 46 Ah pouch cell and prototype module, and moving forward with procurement of special tooling and development of manufacturing processes.

Key Publications

1. Thomas Greszler, “Li-Ion Technology for Space, Defense and Industrial Applications”, March 2017.

I.A.10 Advanced Polyolefin Separators for Li-Ion Batteries Used in Vehicle Applications (AMTEK)

Weston Wood, Principal Investigator

AMTEK Research LLC
250 N. Hansard Avenue
Lebanon, OR 97355
Phone: 541-259-3901
Email: wwood@entek.com

Robert Waterhouse, Principal Investigator

AMTEK Research LLC
250 N. Hansard Avenue
Lebanon, OR 97355
Phone: 541-259-3901
Email: rwaterhouse@entek.com

Brian Cunningham, Technology Manager

U.S. Department of Energy
Phone: 202-287-5686
E-mail: Brian.Cunningham@ee.doe.gov

Start Date: June 1, 2015
Total Project Cost: \$2,085,490

End Date: January 31, 2018
DOE share: \$1,042,745

Non-DOE share: \$1,042,745

Introduction

One of the main barriers to mass adoption of electric vehicles is the cost of the battery pack for the given performance requirements (energy density, rate performance, safety, cycle life, calendar life). ENTEK will work towards helping move this technology forward by developing a separator for lithium ion batteries that will assist in enabling low cost, high voltage cells for EV applications. The overall goal of this project is to develop an advanced separator with high voltage oxidation resistance, improved safety features, and reduced cost to meet the electric vehicle requirements given by the USABC Program.

Objectives

The objectives for this work are to develop advanced separators with improved high voltage oxidation resistance, safety features (high temperature dimensional stability, shutdown temperature), and lower cost for lithium ion batteries in electric vehicle applications.

Approach

ENTEK's approach for this work is to incorporate nanoparticle filler into the microporous polyolefin base separator and apply a ceramic coating layer onto the surface of the separator for improved wettability, increased ionic conductivity, reduced thermal shrinkage, and improved oxidation resistance. In order to lower the cost of the separator using lower cost, in-line coating technologies will be evaluated that are compatible with our existing manufacturing process. In-line process capability, as opposed to an off-line secondary process, will be critical for achieving the lowest possible cost structure.

Results

The main tasks for November, 2016 through October, 2017 were 4.4V cell development for inorganic filled and ceramic coated separator. In addition, 4.9V cell development for ceramic coated separator has been initiated, and is currently under way.

Inorganic Filled Separator Development:

Various separators with silica filler loading levels ranging from 2.25 wt% to 20 wt% were previously investigated. The separator processing conditions were maintained constant throughout the trial and for all the filler compositions. Figure I-38 shows SEM images and pore size distribution of the inorganic filled separators compared to the control separator without filler (20 EPH). Despite the filled separator having higher porosity, the pore structure and pore size distribution between the filled and control separators appeared to be very similar. Table I-5 shows physical properties of selected trial samples. Increasing levels of filler resulted in higher porosity, higher air permeability (lower Gurley value) and lower electrical resistance (MacMullin Number). There was also a decrease in puncture strength with increasing filler level that was consistent with the decrease in polymer volume fraction in the separator. Puncture strength was still much higher than the limits set by USABC. The main benefits of such highly porous, filled separators are improved rate performance and wetting.

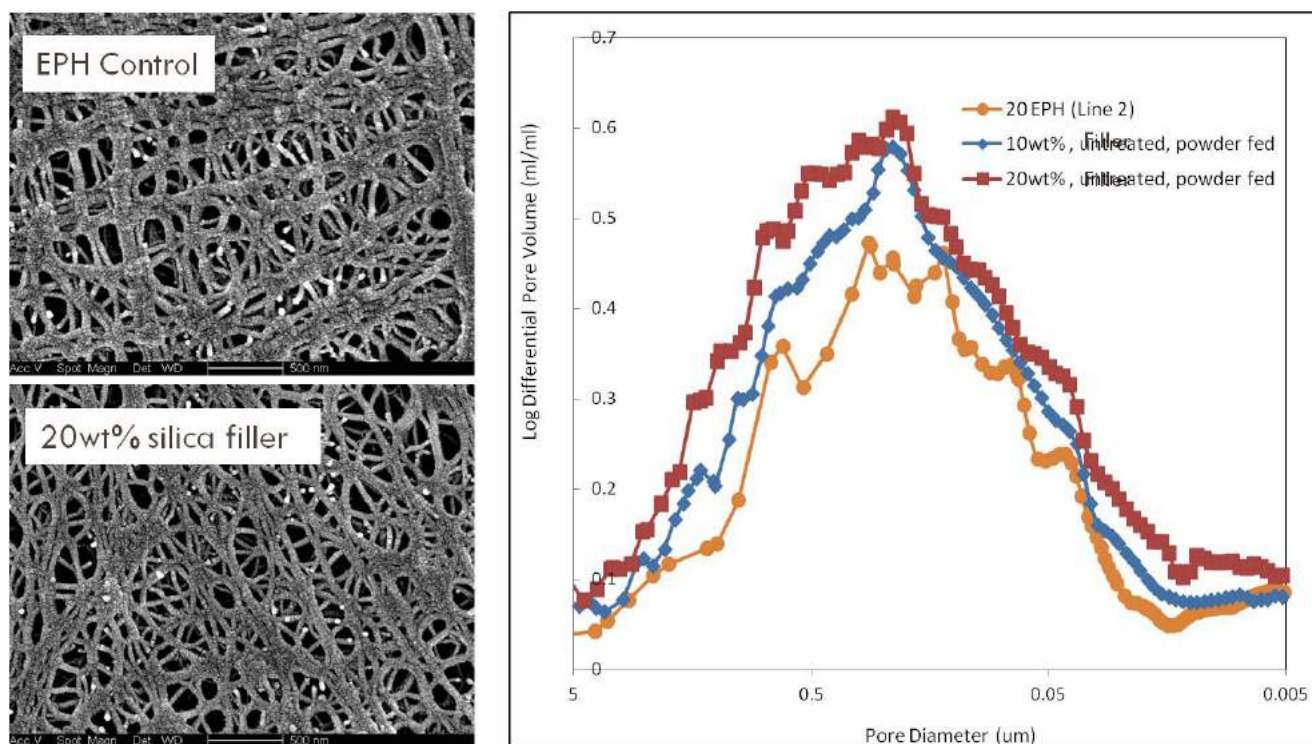


Figure I-38. SEM images (left) and pore size distribution (right) of inorganic filled separator for increased ionic conductivity.

Table I-5: Physical properties of samples optimized for increased ionic conductivity.

Sample Description	Porosity %	Thickness μm	Puncture gF	MacMullin# Dimensionless
20 EPH Control	48	20	463	7.5
Trial #5: 10 wt% Filler	59.0	20	440	4.3
Trial #5: 20 wt% Filler	65.3	20	393	3.3

Ceramic Coated Separator Development:

ENTEK's approach for ceramic coated separator development is to use nanoparticle coating formulations. Figure I-39 (top) shows a comparison between ENTEK's nanoparticle coated separator (primary particle size of about 20nm) and a more conventional coated separator with ceramic particle diameter of about 0.5 μm . SEM images in Figure I-39 (top) show a clear improvement in surface uniformity compared to conventional coated separator. Figure I-39 (bottom) also shows that less than half the coat weights required to reach high temperature dimensional stability when using the nanoparticle formulation compared to conventional coated separator. Reduced coating requirements may translate to reduced coated separator cost through raw materials reduction and faster coating speeds.

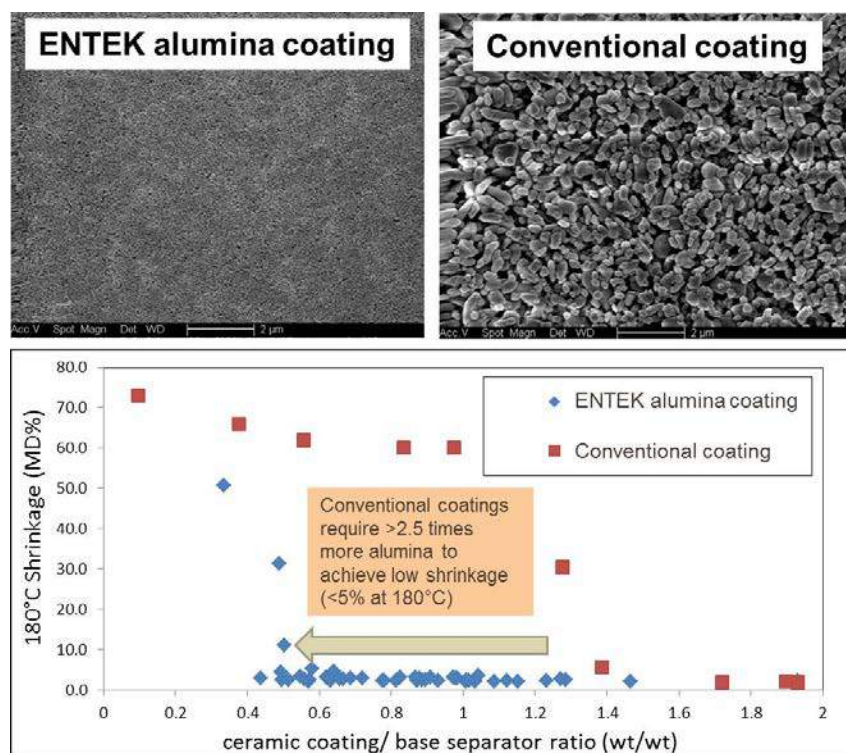


Figure I-39. Comparison between coat weight requirements for conventional and “nanoparticle” alumina coating onto separator. Conventional formulations require almost twice the coat weight to reach high temperature dimensional stability (<5% at 180°C).

4.4V Cell testing; NMC 622 positive electrode; coated separator evaluation.

Multiple sets of 18650 4.4V cells with 622 NMC positive electrodes were built at Farasis with ENTEK control (20 EPH), and ENTEK ceramic coated (HTDS 1604) separators. Cycle testing results (Figure I-40) show a considerable improvement in cycle life for the ceramic coated separator (HTDS) compared to the uncoated control (EPH). Furthermore when storing cells at 60°C, stability of open current voltage was improved (Figure I-41) and capacity fade was minimized (Figure I-42). We attribute these results in part due to an improvement in the voltage oxidation resistance of the ceramic coating on the separator.

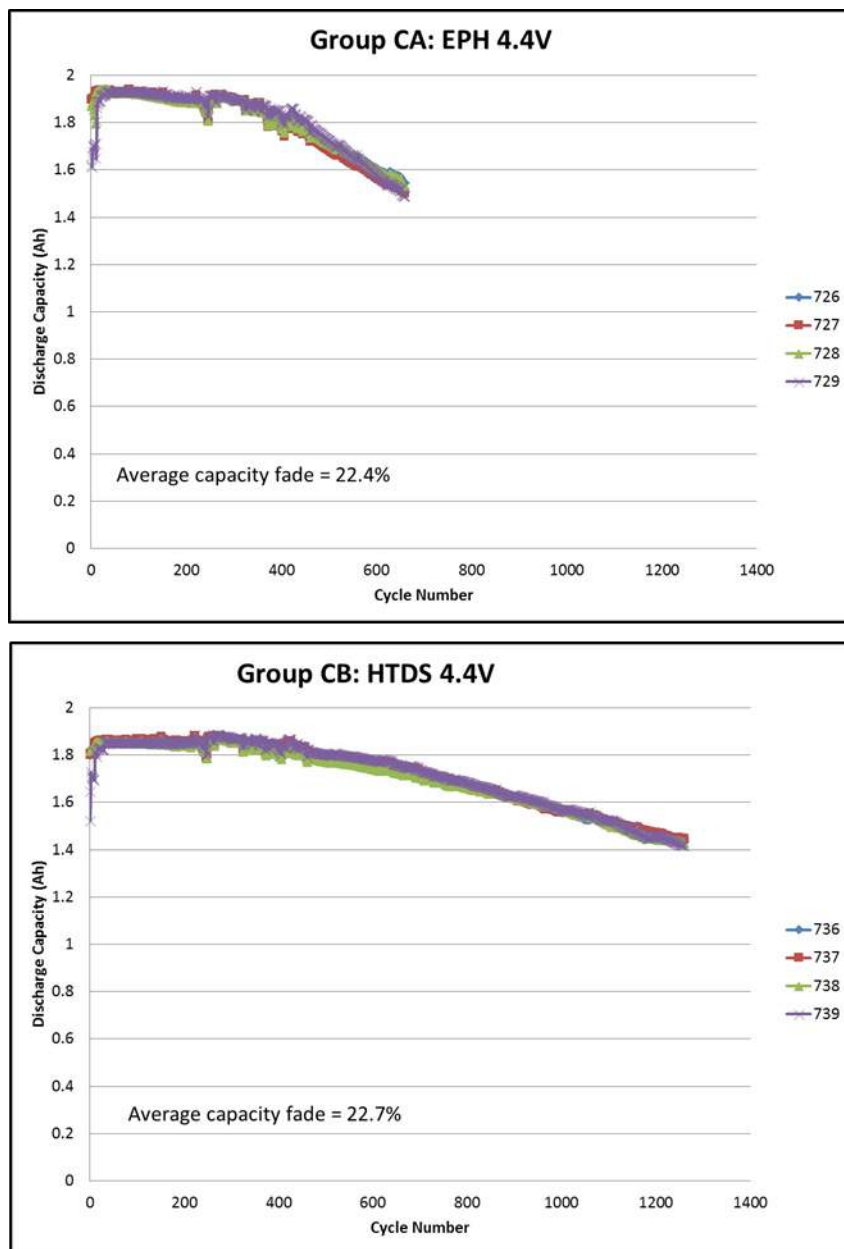


Figure I-40. Cycle life of 4.4V cells built with uncoated polyethylene separator (top) and alumina coated separator (bottom).

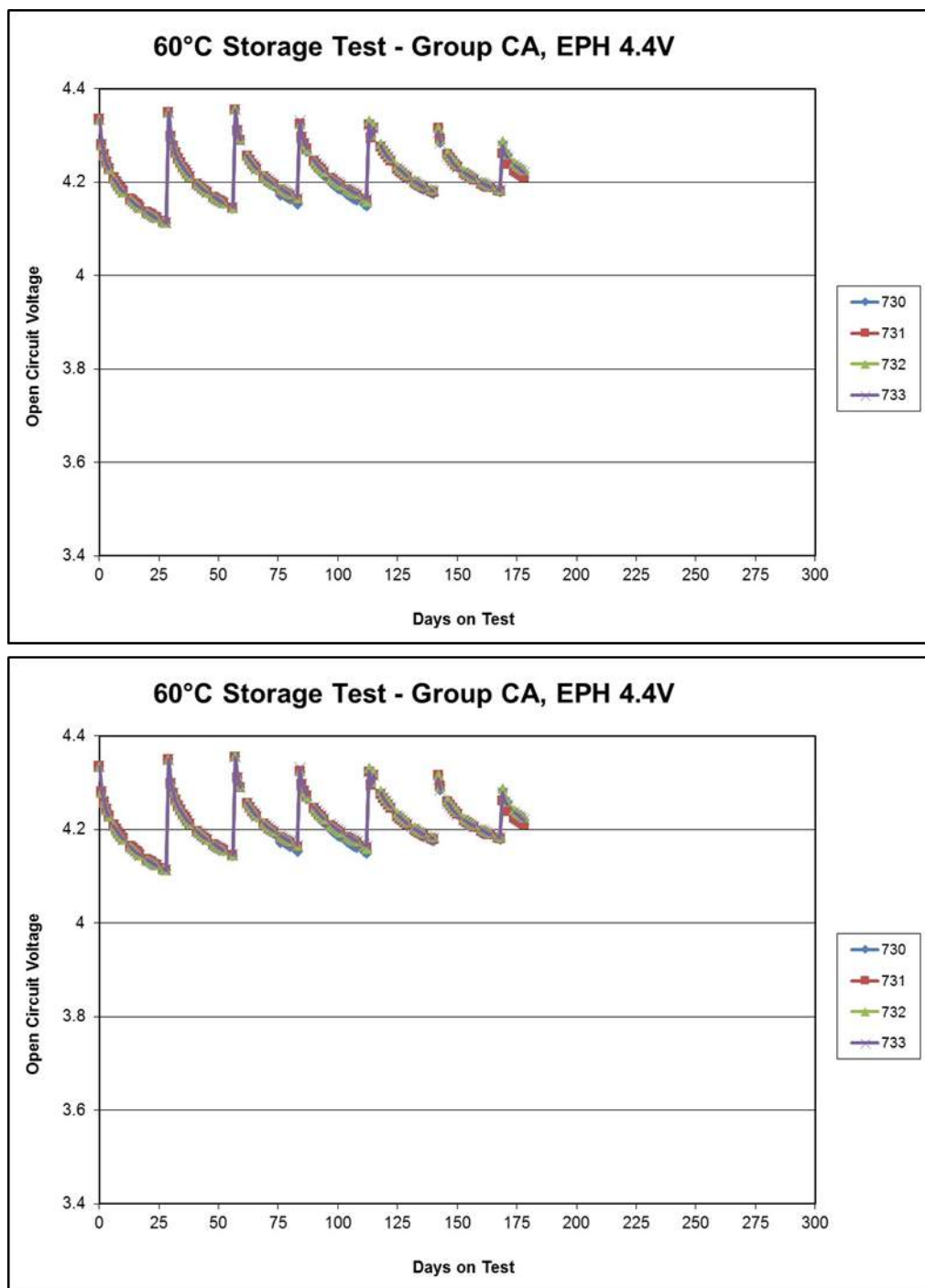


Figure I-41. Open circuit voltage of 4.4V cells stored at 60 °C, built with uncoated polyethylene separator (top) and alumina coated separator (bottom). Cells were recharged to 4.4V every 30 days.

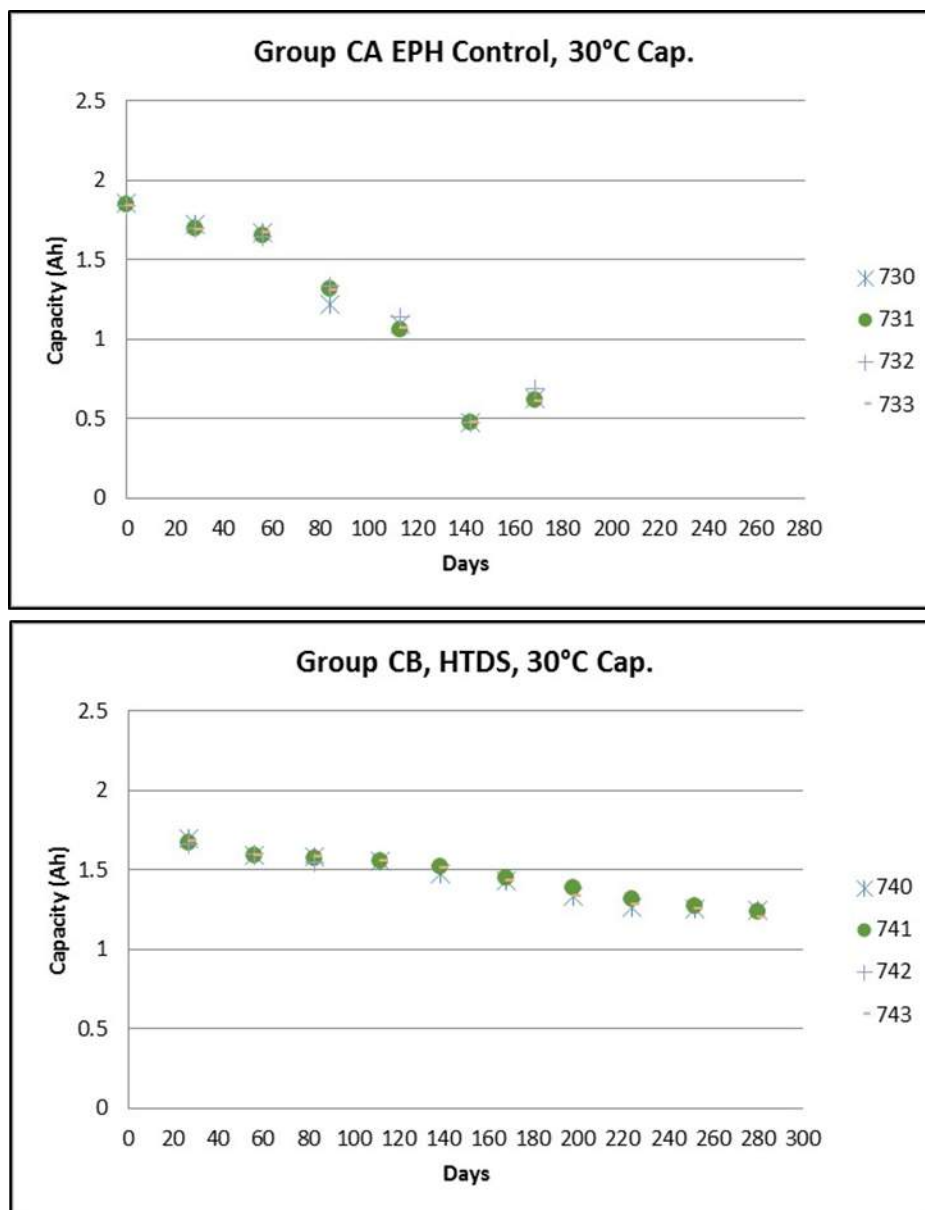


Figure I-42. Capacity of 4.4V cells stored at 60 °C, built with uncoated polyethylene separator (top) and alumina coated separator (bottom). Capacity measurements were made at 30 °C every 30 days.

4.4V Cell testing; NMC 622 positive electrode; inorganic filled separator evaluation.

Multiple sets of 18650 4.4V cells with 622 NMC positive electrodes were built at Farasis with inorganic filled separators having different filler contents. Applying a coating to the separator improved both cycle life (Figure I-43) and dramatically improved open current voltage stability (Figure I-44, Figure I-45).

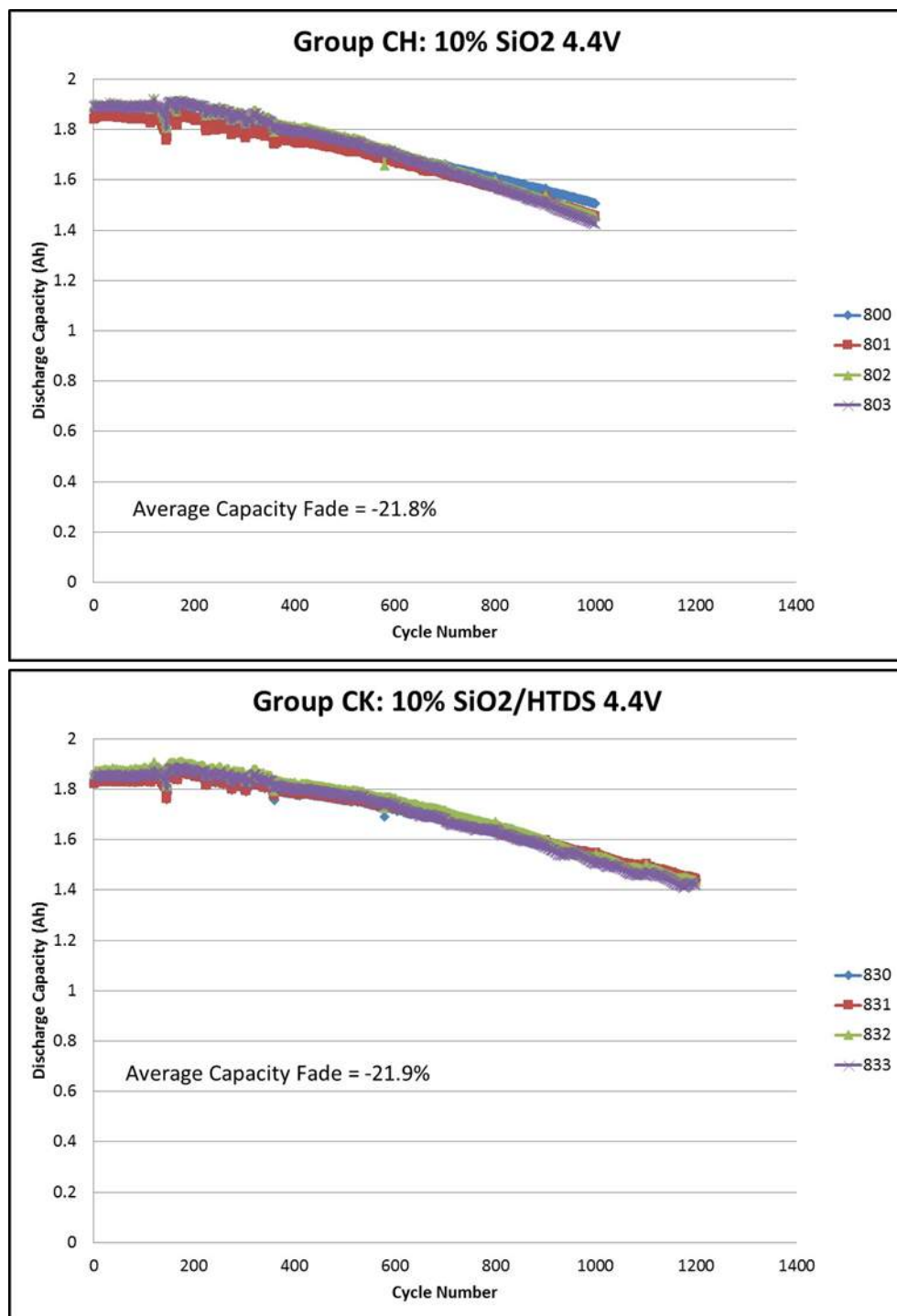


Figure I-43. Cycle life of 4.4V cells built with 10 wt% silica filled separator (top) 10 wt% silica filled separator, coated with alumina (bottom).

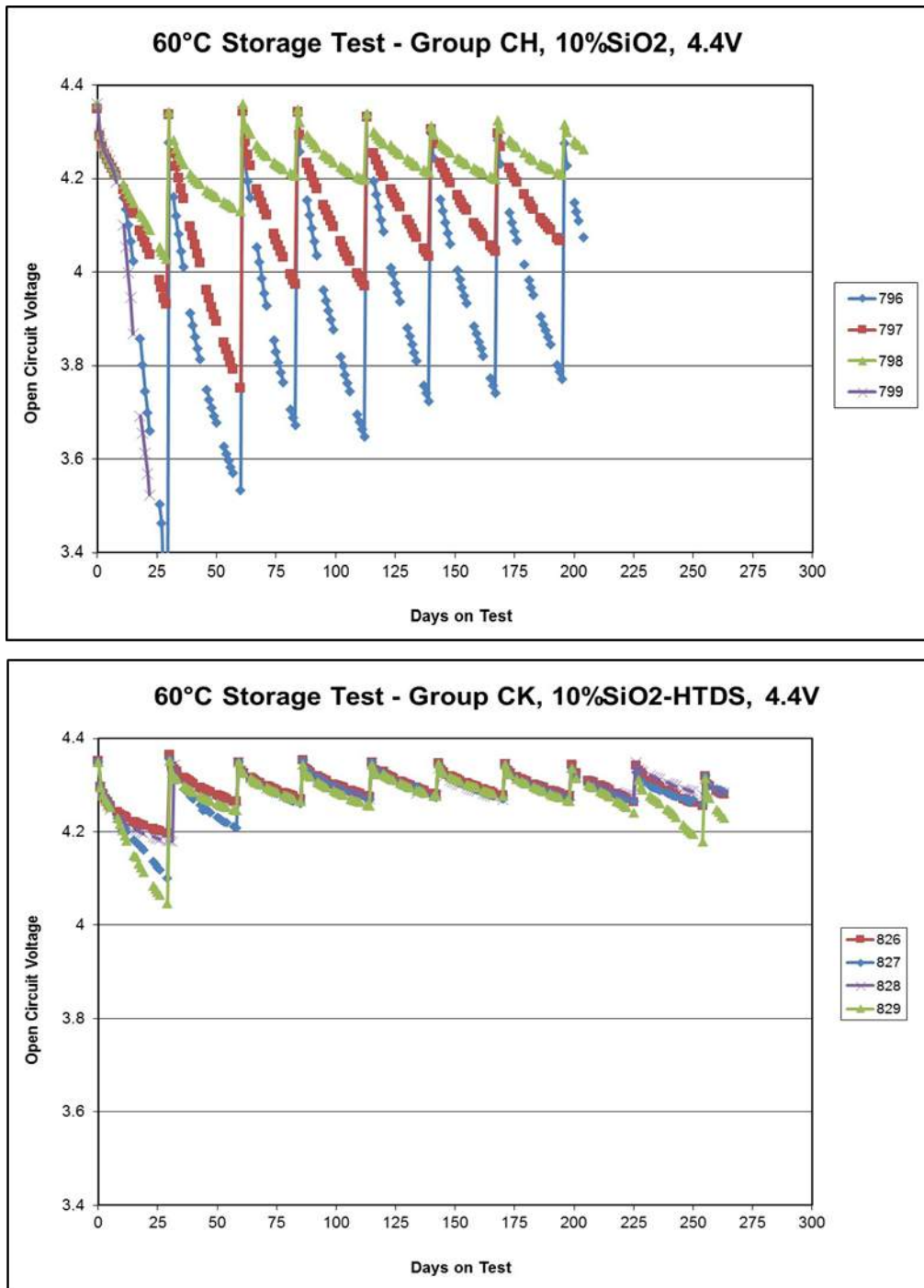


Figure I-44. Open circuit voltage of 4.4V cells stored at 60 °C, built with 10 wt% silica filled separator (top) 10 wt% silica filled separator, coated with alumina (bottom). Cells were recharged to 4.4V every 30 days.

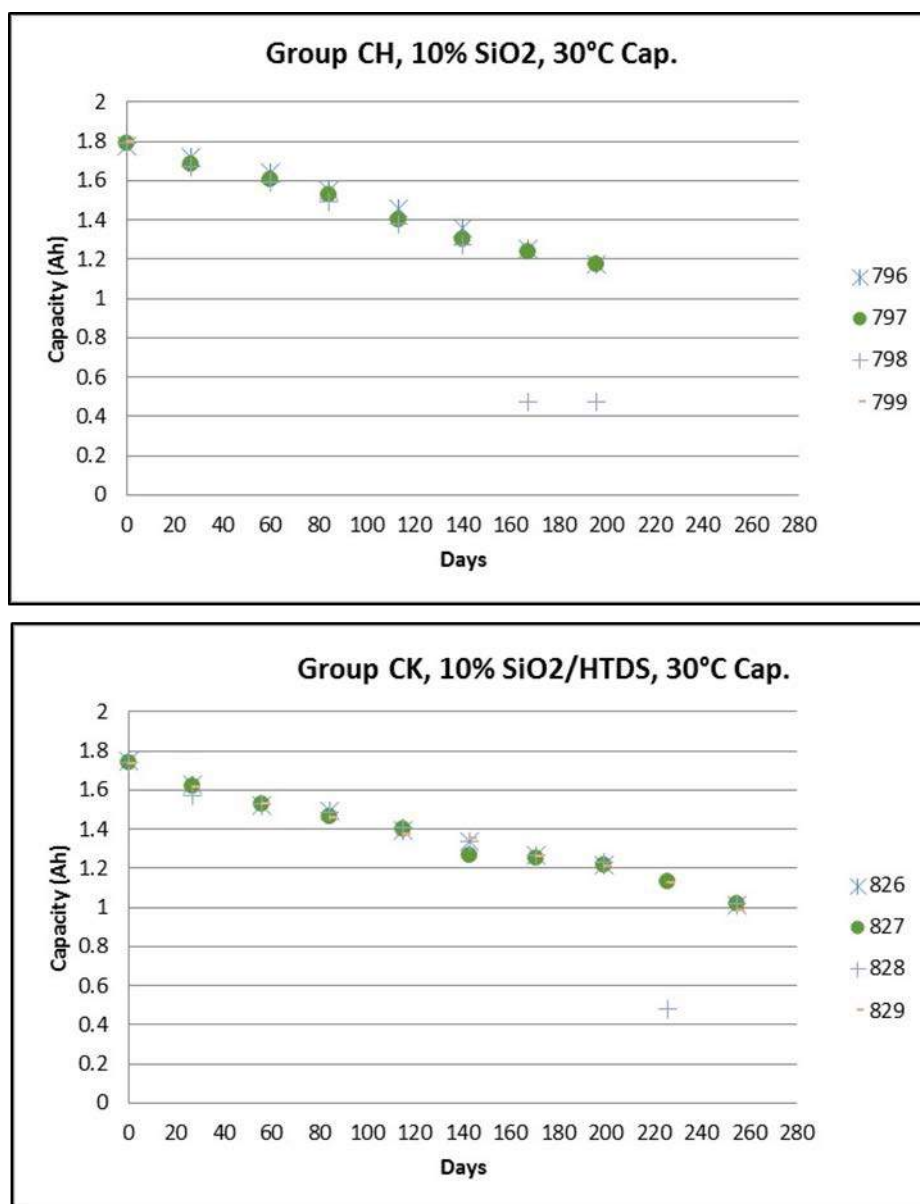


Figure I-45. Capacity of 4.4V cells stored at 60 °C, built with uncoated polyethylene separator (top) and alumina coated separator (bottom). Capacity measurements were made at 30 °C every 30 days

4.9V Cell testing, HV Spinel positive electrode:

Three sets of 4.9V pouch cells with HV Spinel positive were built at Farasis with uncoated control, nanoparticle ceramic coated separator (HTDS) and alumina coated separator with reduced moisture (LM). Figure I-46 shows cycle life (top) and storage testing (bottom) of the three sets of cells tested. Results showed 4.9V HV spinel cells built with ceramic coated separator outperformed uncoated microporous polyethylene control (EPH) with regard to cycle life and storage testing. Gas formation was more severe in cells built with the uncoated control separator. Severe degradation was observed on the uncoated control separator after tear down of the cells (brittle, black on cathode side). In contrast, the integrity and toughness of the ceramic coated separators were maintained. There appeared to be further improvement with the low moisture ceramic coated separator version (LM) though further work is required to verify this result. Further work will include ceramic and binder optimization to further improve cycle life and storage testing of the HV Spinel cells.

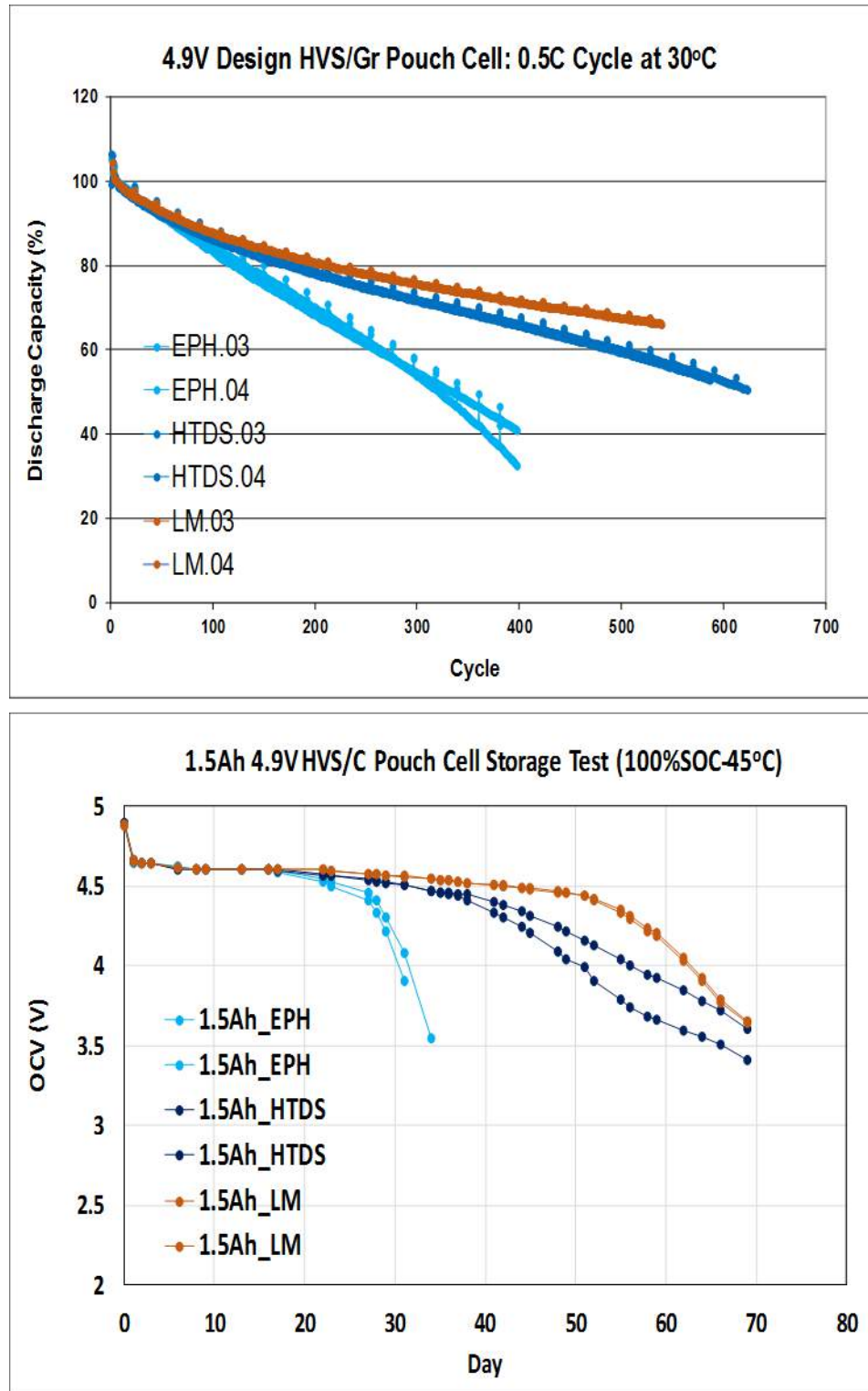


Figure I-46. Cycle life (top) and storage testing (bottom) for 4.9V HV Spinel cells built with uncoated and ceramic coated separators. Storage testing was performed at 45°C.

Conclusions

- The incorporation of moderate amounts of fumed silica into the base sheet yields large improvements in separator porosity and ionic conductivity. Mechanical strength is reduced, but is still acceptable.
- Ceramic coated separator with nanoparticle formulation (primary particles ~20nm) requires less than half the coat weight to reach high temperature dimensional stability (<5% shrinkage at 180°C) compared to conventional coated separator. This may translate to reduced coated separator cost (less raw materials required and thinner coating allows for faster coating speed).
- 4.4V cells built with NMC 622 cathode show considerable improvement in both cycle life and 60°C storage testing when incorporating ceramic coated separator compared to cells built with the uncoated control.
- Additionally, 4.9V HV spinel cells show considerable improvement in both cycle life and 60°C storage testing when incorporating ceramic coated separator. We attribute these results in part due to an improvement in the voltage oxidation resistance of the ceramic coating on the separator.
- Future work will include continuing the development of coatings for the improved voltage oxidation resistance for HV Spinel cells.

I.A.11 Advanced Separators for Vehicle Lithium Battery Applications (Celgard, LLC)

Junqing Ma, Ph.D., Principal Investigator

Celgard, LLC.

13800 South Lakes Drive

Charlotte, NC 28273

Phone: 704-588-5310

E-mail: Junqing.Ma@celgard.com

Brian Cunningham, Technology Manager

U.S. Department of Energy

Phone: 202-287-5686

E-mail: Brian.Cunningham@ee.doe.gov

Start Date: March 3, 2017

End Date: March 15, 2019

Total Project Cost: \$2,500,000

DOE share: \$1,130,000

Non-DOE share: \$1,370,000

Project Introduction

Increasing the cell voltage and electrode capacity may be one of the most effective approaches to increasing the energy density of lithium ion batteries. Increasing cell voltage, however, would accelerate degradation of cell components including electrolyte, separator, and electrode binder to name a few. With recent advancements in electrolytes, the separator becomes a new limiting factor in advancing toward a high voltage (5 V class) battery system. When operated at high voltages, particularly at elevated temperatures, Li-ion cells may undergo degradation that is partially attributed to oxidation of the separator or to a deterioration in separator performance. During extended cycling at high voltages, especially at elevated temperatures, separators can suffer from intensified oxidizing electrochemical attacks on the surface facing the positive electrode, as well as degradation due to the strongly reducing environment on the surface facing the negative electrode.

Objectives

To enable the technical evolution towards 5.0 V lithium batteries, Celgard proposed to develop advanced separators that are cost effective and durable at high voltages, in collaboration with battery manufacturers. Two integrated approaches to the project are proposed in order to maximize success. The first is a unique coating technology capable of creating continuous, nanometer coatings on a base polyolefin separator. The second approach is a novel separator comprised of polymers that are stable in a 5.0 V Li-ion battery. A baseline of the present separator/coating technologies will be produced and compared against these advanced development concepts. Celgard will then work to select the most suitable material. Evaluation of the material will be conducted in conjunction with USABC and Farasis Energy, Inc. of Hayward, CA, USA. The battery maker subcontractor (Farasis) will provide a reproducible 5.0 V battery system to be used for testing during the program.

Approach

The work focuses on moving the current state of the art separator products from polyethylene (PE) or polypropylene (PP) plus binder and solvent-based ceramic coatings to an advanced product and process. Two basic approaches will be taken. The first approach includes a continuation of coatings but with an emphasis on moving to a novel advanced method to deposit continuous, nanometer coatings which will be used to protect the PP and/or PE from high voltage attack. The second approach includes the evaluation of novel polymers that are capable of withstanding the 5.0 V lithium battery environment.

Rationale for Novel Coatings

In this proposed research, Celgard will address such issues by developing several strategies to mitigate chemical and electrochemical attack on separators: (1) High efficiency blocking mechanism. Celgard will develop a nanometer-scale, ultra-dense coating on current polyolefin separators that will be highly efficient in protecting the polyolefin materials (such as PE and/or PP) from chemical attack without sacrificing porosity or the ionic conductivity of the electrolyte filled separator. (2) Chemical/free radical scavenging mechanism. The nanometer-scale coating will serve as a chemical/free radical scavenger that will quickly decrease the local concentration of free radicals before the oxidizing manganese ions and/or free radicals attack the separator material. The migration of side-reaction products from the high voltage spinel cathode to the graphite anode is responsible for much of the parasitic reactions damage at the graphite SEI and the consumption of active Li^+ in the cells. The proposed method for delivering the coating or layer is physical vapor deposition (PVD). This method is commonly used to produce very thin layers on plastic film materials and is proposed to be similarly deployed for the case of Celgard's battery separator films. The resulting coatings are extremely thin (nanometer-scale vs. micron-scale as obtained with the present slurry-based technologies), binder-free and homogeneous.

Rationale Novel Polymers

Besides polyolefin microporous membranes, a variety of new polymers have been used for preparing microporous membranes for lithium ion batteries in the past decade. The three most reported polymers are polyvinylidene fluoride (PVDF), polyacrylonitrile (PAN), and poly(methyl methacrylate) (PMMA). Many of them, such as microporous PVDF membranes, are chemically and electrochemically stable in lithium ion batteries using today's conventional technologies. In this proposed research, Celgard will investigate the application of two new materials to high voltage lithium ion batteries poly(4-methyl-1-pentene) (PMP) and PVDF. Celgard will develop two new separator materials (PMP and PVDF) and evaluate their stability in high voltage lithium ion battery applications.

For these candidate new separator materials, fabrication of novel separator and their performance in 5.0 V batteries will be demonstrated and evaluated in this project. It is challenging for any new polymers to be fabricated into battery separators since the resulting membranes must possess appropriate porosity and mechanical strength. Celgard has demonstrated that both PVDF and PMP can be integrated into Celgard's core separator manufacturing technology, however, the membrane properties need further improvements. An internal R&D effort is ongoing at Celgard to demonstrate PVDF-based separators. Despite their challenges, these new polymer separators have advantages when compared to PP and PE separators. For example, PVDF membranes are mechanically strong and have great wettability due to good affinity of PVDF to liquid electrolyte solutions.

Results

Celgard is working on the program tasks including separator design, cell demo and producing the required separator. The present status on this effort is displayed in Table I-6. Celgard completed a PVD coating trial at Bobst Manchester and successfully fabricated the planned separators. Celgard and Bobst fabricated several types of samples in this trial using the Celgard tri-layer H2013 separator as base material: (1) H2013 + 15 nm AlOx ; (2) H2013 + 30 nm AlOx ; and (3) H2013 + ~50 nm multi-layer coated separators. Samples #1 and #2 will be used to study the effect of coating thickness on cell performance. Sample #3 was prepared to evaluate the effectiveness of coating a combination material vs. AlOx coating alone.

For the new polymer separator approach, Celgard continued to evaluate: (1) PMP-PP composite separators using a solvent coating process and (2) PMP or similar high temperature polymer separators using Celgard dry separator manufacturing process. We are currently in the process of preparing the samples. Further testing in cells will be performed at Celgard and Farasis.

Table I-6: USABC Project Design Goals and Approaches

Design Goal	Current State of the Art	Advanced Product and Process	Collaboration / Partner	Status Update
	High Temperature Melt Integrity	Binder Free Nanometer-Coatings		
Design Approaches	Binder and Solvent Based Ceramic Coatings 2 to 4 μm coating thickness	Novel High Voltage Coatings to Protect PP and PE	Bobst Manchester, Dunmore, etc. PVD trial runs, fee-based	PVD coated separators prepared: H2013 base film with AlOx coatings 15 and 30 nm; ~50 nm multiple layer coatings
		Novel High Voltage Polymers to replace PP and PE as single Layer or Multilayer Constructions	Celgard test run; Specific Polymers, Such as PMP and/or PVDF	PMP/PP composite preparation in progress; PMP/polymer dry process planned;

All the fabricated PVD samples are currently being characterized by scanning electron microscope (SEM), Gurley number measurements, dielectric breakdown, and cycling test in NMC532 pouch cells (for evaluation of coating effectiveness only). All samples will be provided to Farasis for evaluation in LNMO-based 5 V cells. Figure I-47 shows some SEM micrographs of H2013 trilayer separator coated with 15 nm and 30 nm thick AlOx by PVD. The top-view and cross-section photos show that the coating is homogeneous and does not block the pores in the microporous structures. This uniformity of the coating is also confirmed by the Gurley number as summarized in Table I-7 (No significant change was observed.) The coated separators are not expected to decreased ionic conduction or rise the cell impedance, as the Gurley number decreased by only 10% over the original value for the base separator. Figure I-48 shows the shut-down performance of the PVD coated separators. All separators shut down at 127-130°C and a somewhat enhanced thermal stability was observed for the PVD samples at 170°C.

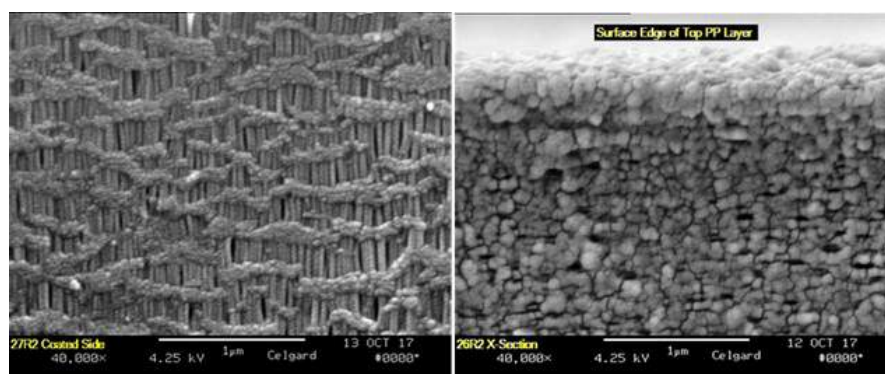


Figure I-47. SEM micrographs of the AlOx coated Celgard 2013 by PVD process: surface H2013_15nm AlOx (on left) and cross-section view of H2013_15nm AlOx (on right)

Table I-7: Gurley number of the PVD coated separators.

Sample	H2103	H2013_15nm AlOx	H2013_15nm AlOx	H2013_50nm Multilayer
AVG	372	328	339	335
STDEV	1.6	2.7	2.3	2.6
MAX	374	335	343	343
MIN	369	323	334	332
COUNT	15	15	15	15

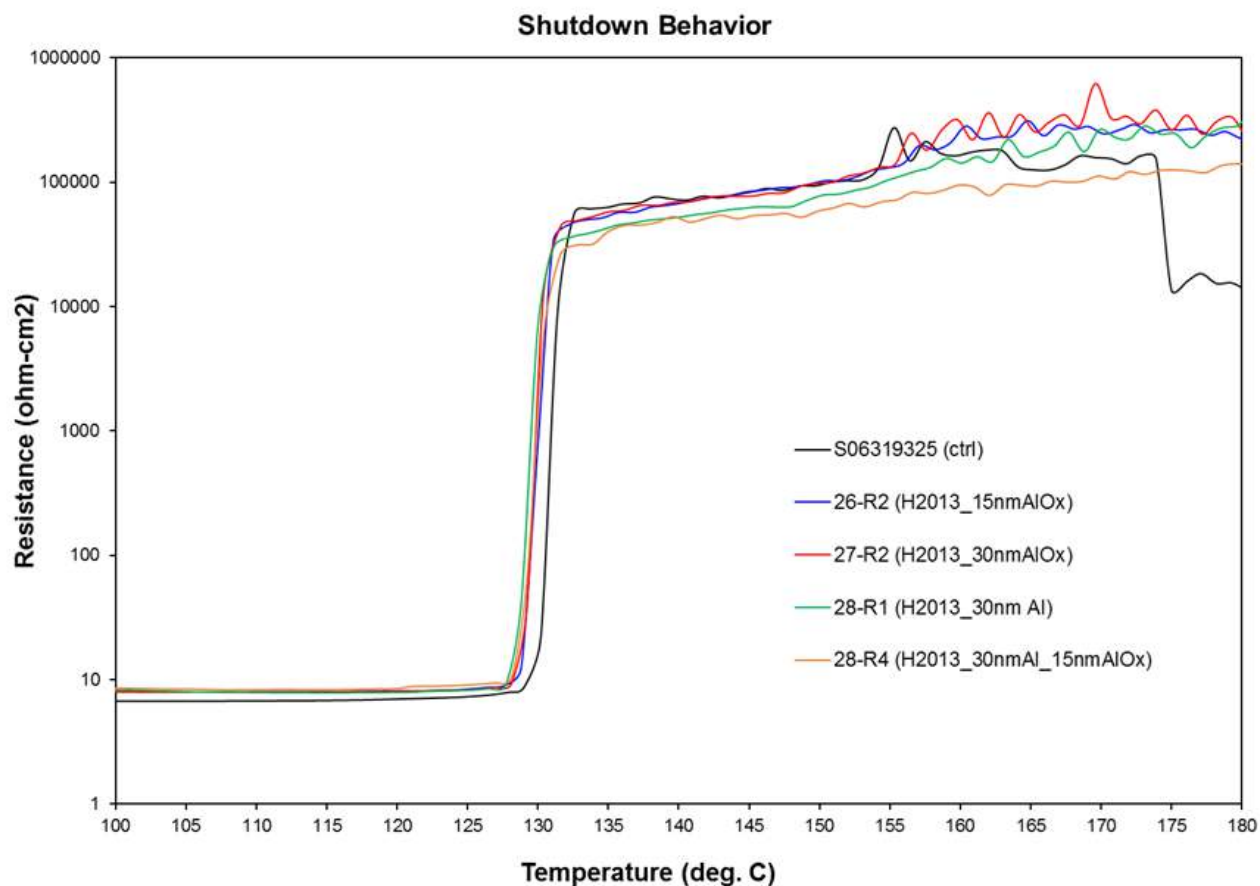


Figure I-48. Shut down performance for the PVD coated separators.

Farasis Energy has successfully fabricated and tested baseline 1.5 Ah LNMO/Graphite cells in the program. Farasis is currently working on improving the cycling performance by optimizing electrode formulations, electrolytes and cell design/configuration. Farasis fabricated the pouch cell by first initial sealing of cells and degassing after formation cycles. For 18650 cells, the cells header with current interrupt device (CID) were crimped after electrolyte was filled. Due to lack of a degassing mechanism, in-cell pressure slowly built up as a result of gassing therefore causing cell impedance to develop over testing and eventually, for some cells, CID was triggered and the cells were stopped. Figure I-49 and Figure I-50 show the cycling performance of H2013 control and ceramic coated baseline cells in 18650 and pouch cells respectively. Farasis continued this initial test and delivered six (6) pouch cells with the baseline separator to USABC in September 2017, according to the program's schedule.

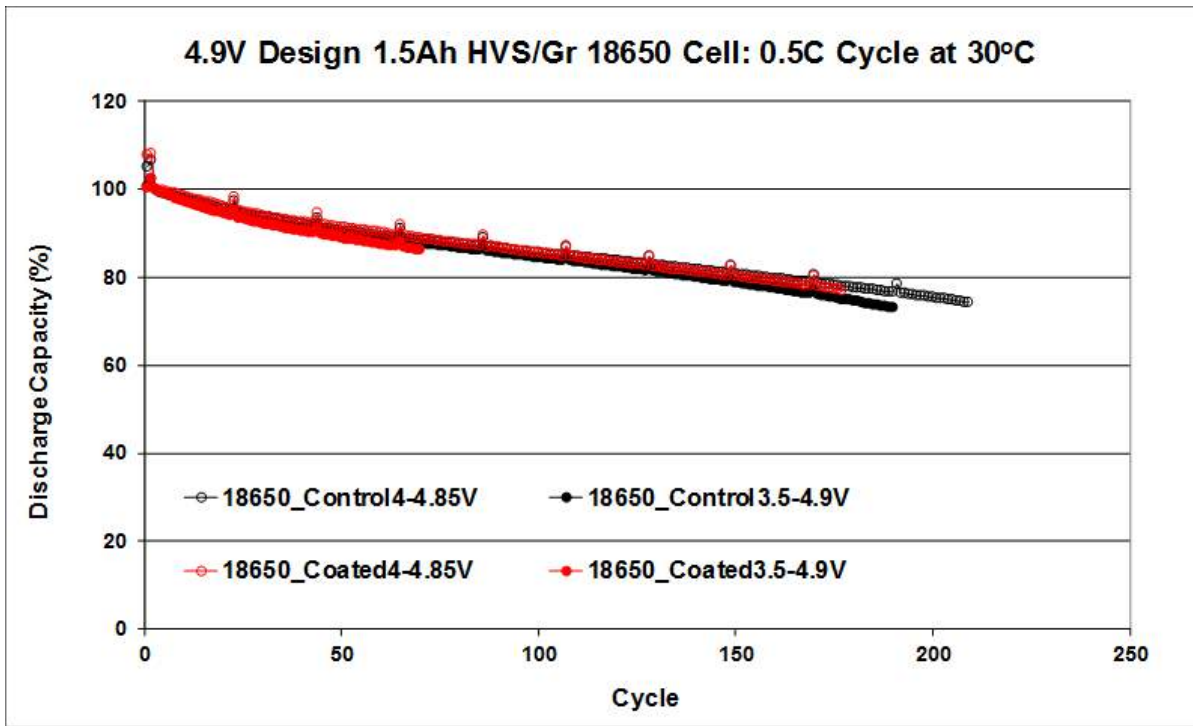


Figure I-49. Capacity retention of second batch of 18650 cells tested over the voltage ranges 4.0 - 4.85 V and 3.5 - 4.9 V. No early failure but cycling is poor due to possible internal impedance increase.

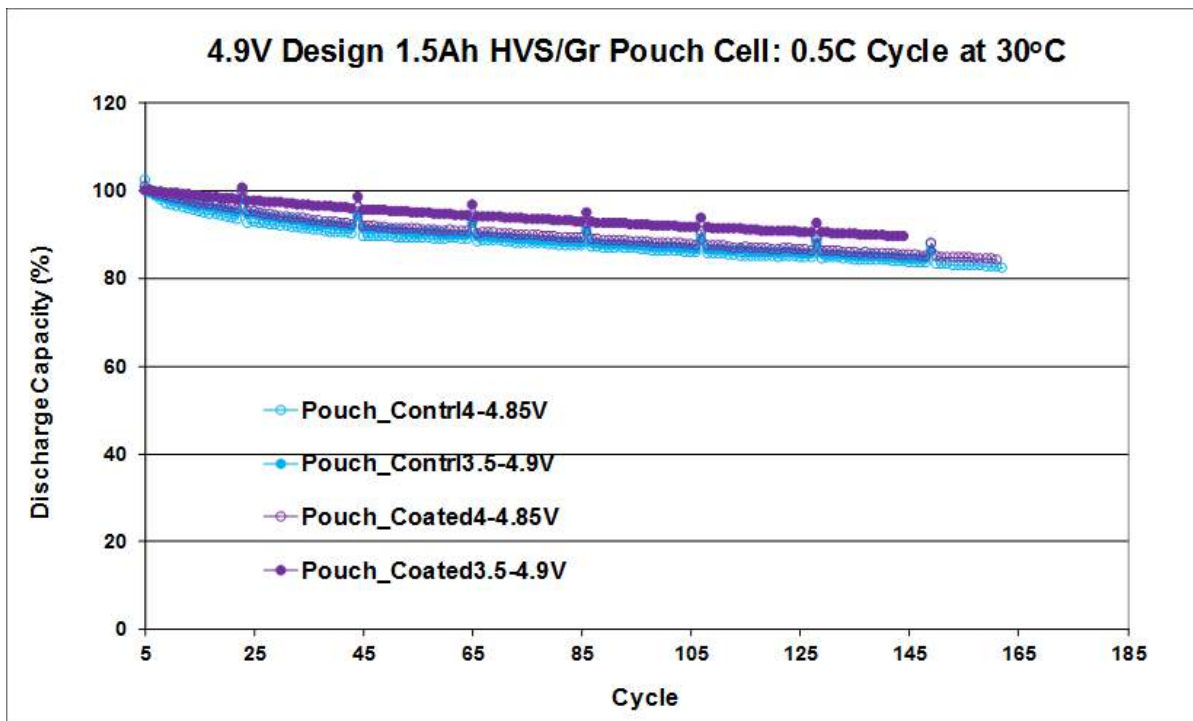


Figure I-50. Capacity retention of Farasis pouch cells tested over the voltage ranges 4.0 - 4.85 V and 3.5 - 4.9 V. Significantly improved cycling was observed over 18650 cells.

Some of the separators after cycling at Celgard and Farasis are currently being examined for damages/ degradation as a part of the failure mechanism study in this program. For the separators cycled in 5V cells, degradation was observed for all control separators. On the surface of Celgard PP film after the cycle test, thick electrolyte decomposition products was observed; however, the pores of the separator were not closed or collapsed. No decomposition products were observed for the PE separators after the cycle test. All PP and PE separators showed a decreased molecular weight after cycling in 5V cells. Wet PE separator in comparison, showed severe carbonization and complete pore collapse was observed (Figure I-51, on right).

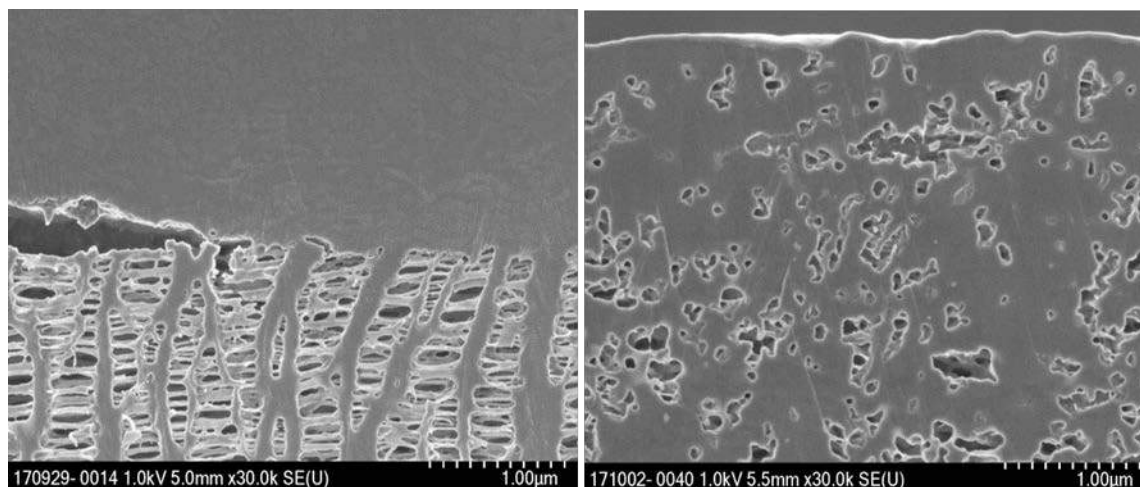


Figure I-51. SEM photographs of Celgard dry process PP (on left) and a commercial wet PE (on right) separator after cycling in 5V cells.

Farasis has delivered a set of six 1.5 Ah pouch cells to ANL as the 6-month deliverables. The six cells are 4.9 V HVS/C pouch cells with Celgard Q20S1HX ceramic coated separators. The electrolyte used is a developmental electrolyte formulation by Farasis. The cell capacity is around 1110 mAh at C/3 discharge (averaged static capacity measured from the six deliverable cells). Cell data shown in Table I-8 summarizes the Static Capacity (C/3, 3.5 - 4.9 V, no CV), open circuit voltage (OCV), AC impedance at 1kHz, and cell weight of the cells delivered.

Table I-8: A summary of the Static Capacity (C/3, 3.5 - 4.9 V, no CV), OCV, AC Impedance at 1 kHz, and Cell Weight of the cells delivered to ANL.

Cell I.D.	Static Capacity/mAh (C/3 to 3.5V @30°C)	AC imp. @1kHz/mΩ and 25°C	OCV/V	Cell Wt/g (w/o Fixture)	Comment
Q20S.01	1076	64.4	4.602	36.17	Data collected prior to shipping
Q20S.02	1137	75.6	4.603	36.32	"
Q20S.03	1133	60.5	4.603	36.36	"
Q20S.04	1071	69.5	4.602	36.46	"
Q20S.05	1108	64.2	4.603	36.59	"
Q20S.06	1140	47.5	4.604	36.27	"

The six cells all went through formation steps at Farasis. The cycling conditions (at 0.5 C rate, between 3.5 – 4.9 V at 30°C) developed by Farasis include the following conditions and specific requirements: Fixtures and static pressure required; regular cycle at 0.5 C; 0.5 C constant current (CC) charge to 4.9 V; Rest for 3min.; no constant voltage (CV) charging; 0.5 C CC discharge to 3.5 V; Rest for 3 min.; repeat for 20 cycles, and insert

one 0.2 C rate cycle for every 20 regular cycles and Repeat the above steps. Alternative voltage window for this test is between 4 and 4.85 V.

Conclusions

- The physical vapor deposition (PVD) process can effectively deposit an ultra-thin aluminum oxide layer on microporous separators, coating all micro-structures without blocking the pore or significantly decreasing the dielectric breakdown or increasing the Gurley Number.
- A 5 V chemistry has been demonstrated by Farasis using a proprietary stabilized electrolyte. Cycle life is decent for prototype cells and ANL will confirm cell performance using USABC testing protocols.
- Current commercially available polyolefin micro-porous separators suffer from structural degradation in high voltage cells, especially at elevated temperatures. An initial failure study suggests that the degradation of polyolefin separators and structural damages dependent on the separator material. The effectiveness of protection provided by the ceramic coating and PVD AlO_x or by Al metal will be further evaluated to provide better understanding of separator degradation mechanism.
- Scalability of PVD coating process is promising. Low cost production appears highly achievable.

I.A.12 Hybrid Electrolytes for PHEV Applications (NOHMs Technologies)

Surya Moganty, Principal Investigator

NOHMs Technologies
1200 Ridgeway Avenue
Rochester, NY 14615
Phone: 607-379-5444
E-mail: surya@nohms.com

Brian Cunningham, Technology Manager

U.S. Department of Energy
Phone: 202-287-5686
E-mail: Brian.Cunningham@ee.doe.gov

Start Date: August 15, 2015
Total Project Cost: \$1,639,044

End Date: October 15, 2017
DOE share: \$819,522

Non-DOE share: \$819,522

Project Introduction

Rechargeable lithium ion batteries (Li-ion) are promising energy storage options for plug-in-hybrid electric vehicles (PHEVs) and all electric vehicles (EVs). However, among other requirements for Li-ion batteries to be viable for transportation applications a high energy density cathode is required. High voltage cathodes have the potential to provide a solution for low cost, longer-range electric vehicles. This new class of electrode material can deliver capacity $>250 \text{ mAh g}^{-1}$, that is $\sim 65\%$ higher than that delivered by current state-of-the-art cathodes. To access this high capacity, one has to operate the cell at a higher potential $>4.5 \text{ V vs Li/Li}^+$. Conventional Li-ion battery electrolytes, however, are not stable above 4.2 Volts. Development of electrolytes that are stable at these higher voltages is critical to make use of this class of high voltage cathodes. An electrolyte innovation that enables temperature-stable 5V cell operation would transform the industry and enable rapid growth of new market segments.

Research and Development at NOHMs has resulted in a family of novel electrolyte formulations, which include ionic liquids to improve high voltage performance, safety, and high temperature durability of Plug in Hybrid Electric Vehicle ("PHEV") lithium ion batteries. NOHMs proprietary functional ionic liquids in-development for lithium ion battery electrolytes have displayed excellent electrochemical and thermal stability compared to state-of-art lithium ion battery electrolytes, and when compared with previously reported ionic liquid electrolytes demonstrate improved stability against graphite-containing anodes and high voltage cathodes, as well as improved rate capability and low temperature performance.

Objectives

The program objective centered on the development of functional ionic liquid-based electrolyte combinations with appropriate co-solvent combinations that exhibit high ionic conductivity, excellent cathodic & anodic stability and high thermal stability for applications in 5V Li-ion batteries. NOHMs objective was to create optimized electrolyte formulations that are stable above 4.5V, non-flammable, and which simultaneously overcome traditional barriers of effective SEI layer formation and cation co-intercalation in graphite associated with ionic liquids. The final project objective was to demonstrate the feasibility of these ionic liquid-based electrolyte systems in 2 Ah and 10 Ah Graphite// $\text{LiMn}_{1.5}\text{Ni}_{0.5}\text{O}_4$ and Graphite// $\text{Li}_{1.2}\text{Mn}_{0.55}\text{Ni}_{0.15}\text{Co}_{0.1}\text{O}_2$ full cells.

Approach

NOHMs has established partnerships with A123 Systems (A123) and Xerox to meet the USABC long term criteria for electrolytes - (1) cost, (2) high-voltage stability, (3) low-temperature performance, and (4) abuse tolerance. The A123 partnership for manufacturing and testing of cells, and a chemical company (Xerox)

partnership to scale a low-cost and high-purity synthesis process for NOHMs ionic liquid electrolytes. (See Figure I-52.) Research and development at NOHMs has resulted in a family of novel electrolyte formulations, containing functional ionic liquids projecting excellent high voltage stability. Effective component combinations were the result of carefully designed experiments, positioned to expose molecules with desirable physical characteristics, electrochemical competency, and thermal stability. Building on these results, NOHMs developed and evaluated novel electrolyte formulations suitable for NMC532 (4.5V) and LNMO (4.8V) cathode materials.

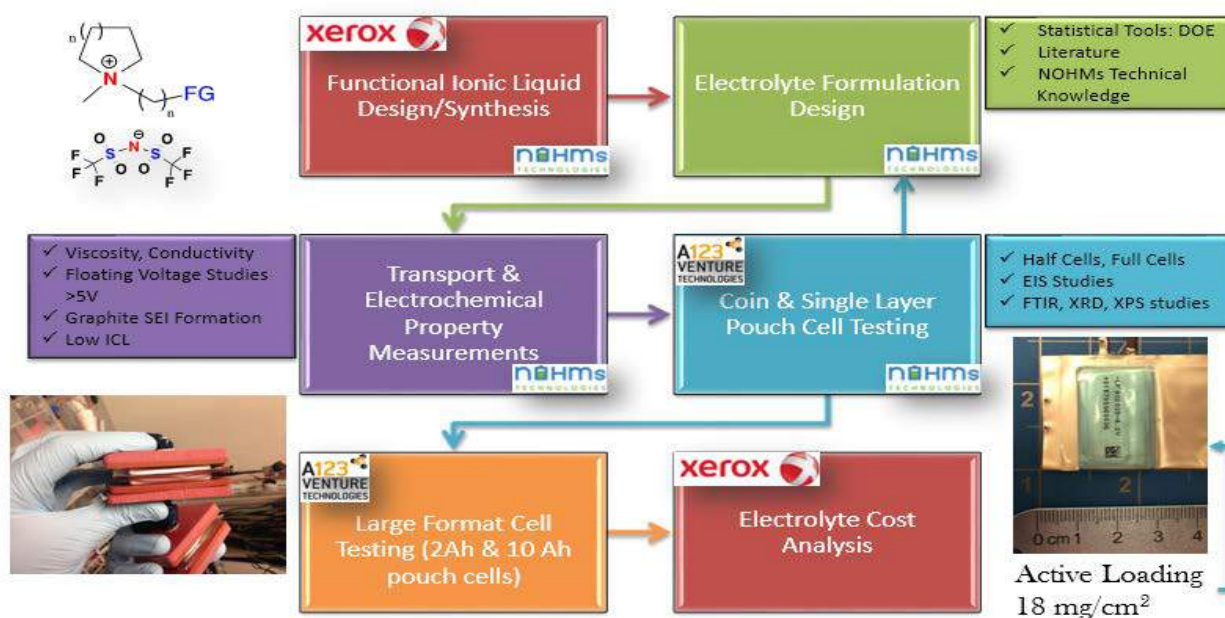


Figure I-52. Program approach from synthesis electrolyte and cell fabrication. The approach encompasses synthesis of novel functional ionic liquids, electrochemical testing, post autopsy analysis, 2 Ah & 10 Ah cell fabrication, and scale-up cost analysis.

Results

High Voltage Stability

Building on electrolyte screening protocols, NOHMs developed electrolytes and evaluated high voltage stability against NMC532 and LNMO using floating voltage measurements. Figure I-53 compares the measured leak current density of LNMO-Li half-cells, containing baseline and NOHMs electrolyte formulations. Two separate groups of cells were evaluated at 25°C and 45°C. Low leak current density is indicative of reduced oxidation at the specified voltage. NOHMs designed formulations showed excellent oxidative stability. NOHMs HVE135 electrolyte formulation showed excellent stability at the LNMO cathode. Even at elevated temperatures (i.e., 45°C) the NOHMs formulation outperformed the baseline.

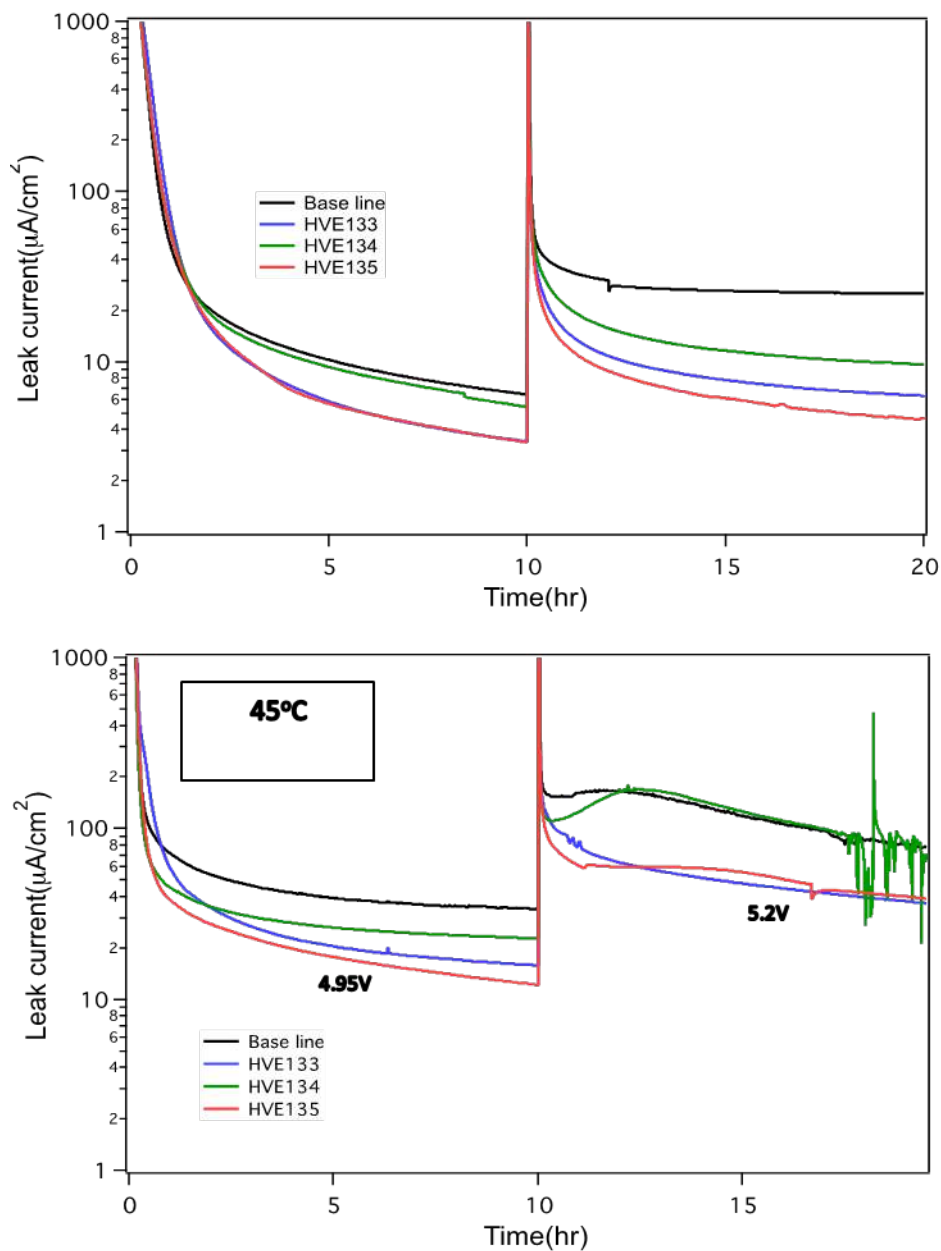


Figure I-53. Floating voltage profiles of LNMO|Li coin cells. The voltages are held for 10hrs at 4.95V & 5.2V. Leak current describes the severity of the oxidative reactions with the cathode surface.

Compounding desirable performance of graphite SEI formation with high voltage stability leads to well-rounded deliverable electrolytes. For instance, Figure I-54(A) reveals the superior voltage stability of the NOHMs 157 deliverable electrolyte when compared to baseline, and Figure I-54(B) portrays greater capacity retention from NOMHs 157 containing graphite/Li cells.

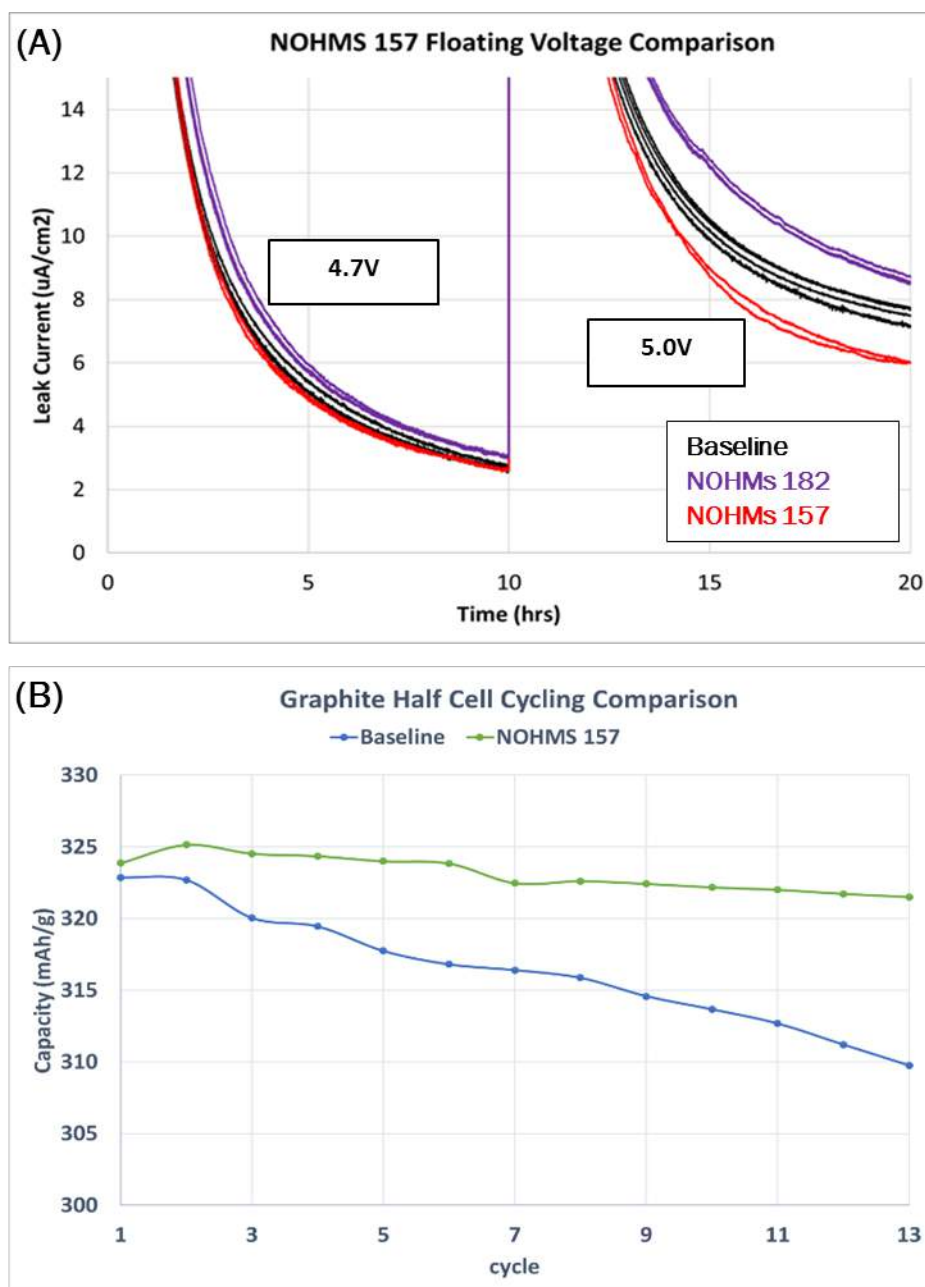


Figure I-54. (A) Floating Voltage in NMC532|Li coin cells at 23°C using 10hr holds at 4.7V and 5.0V. (B) Graphite|Li half-cell galvanostatic cycling at C/10. Baseline electrolyte denoted as (30:70) EC:EMC + 1M LiPF₆

2) Full Cell Formulation Development

Thermal stability has been a focus for the high voltage formulations. Combining elevated temperature and high voltage cycling imposes additional stress on the cell, allowing decomposition reactions to become more severe and the SEI to degrade. Floating voltage and galvanostatic cycling at 45°C has helped in pursuing formulations that remain stable when exposed to both elevated voltage and temperature. Figure I-55 shows that HVE157a, the 10 Ah NMC cell deliverable electrolyte, demonstrates no significant change in cycle-life when tested at room temperature (23°C) and elevated temperature (45°C). Figure I-56 shows the performance of 2 Ah NMO cells cycling at 1C/2C, 4.8V with NOHMs electrolyte HVE242.

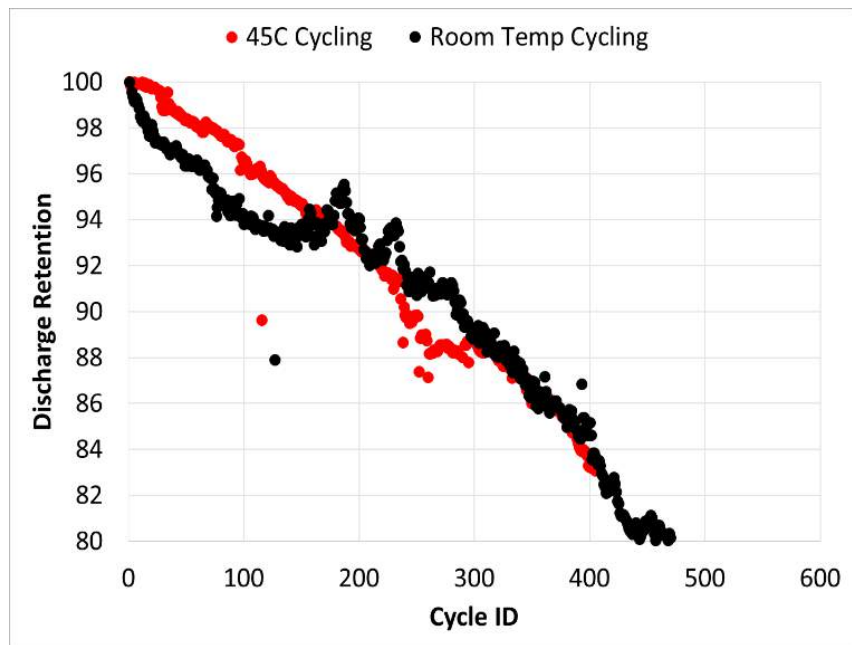


Figure I-55. 45°C vs room temperature comparison of HVE157a electrolyte in 155 mAh NMC442 cells; 3.0V-4.5V; C/2 rate. Cells project an average initial cycling capacity of 145 mAh and 150 mAh for room temperature and 45°C sample groups, respectively.

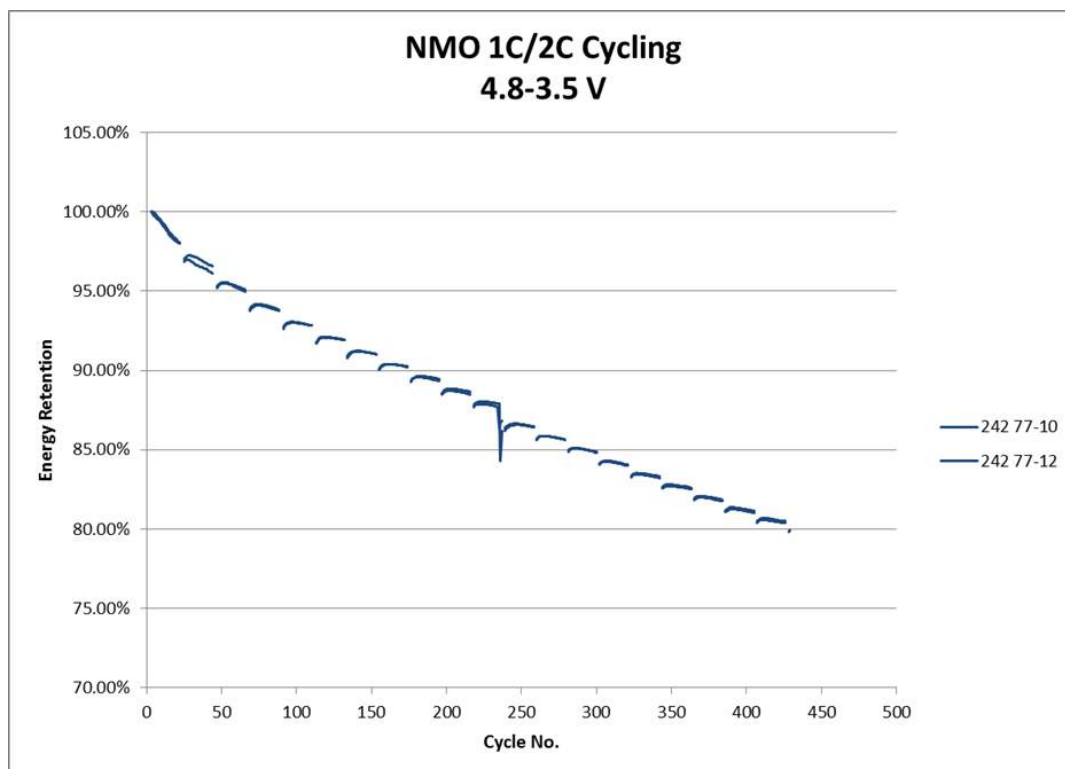


Figure I-56. Cycling Data for 2 Ah NMO cells with NOHMs electrolyte HV242, 1C/2C at 4.8V cutoff.

3) Elevated Temperature Storage and Operation

Elevated temperature storage tests revealed a weakness associated with the high voltage chemistries. Cells charged to 100% SOC and held at 60°C for extended durations resulted in cell gas generation. NOHMs conducted storage tests on 155 mAh NMC442 and 5 Ah NMC532 cells to screen potential gas suppressing formulations. The formulation HVE302 shows great promise in reducing gas generation. The HVE302 formulation also demonstrated desirable performance characteristics, such as low impedance increases, little voltage change, and high capacity retention throughout the storage period. HVE302 having losses close to 15%, less than half the value of the baseline electrolyte (>30%). In addition, the HVE302 demonstrated promise in cycle-life and scalability when tested in 5 Ah cells. Figure I-57 demonstrated a 1.75x increase in cycle-life when compared to the baseline. These cells were cycled at 45°C using 1C, demonstrating favorable thermal stability and rate capability respectively.

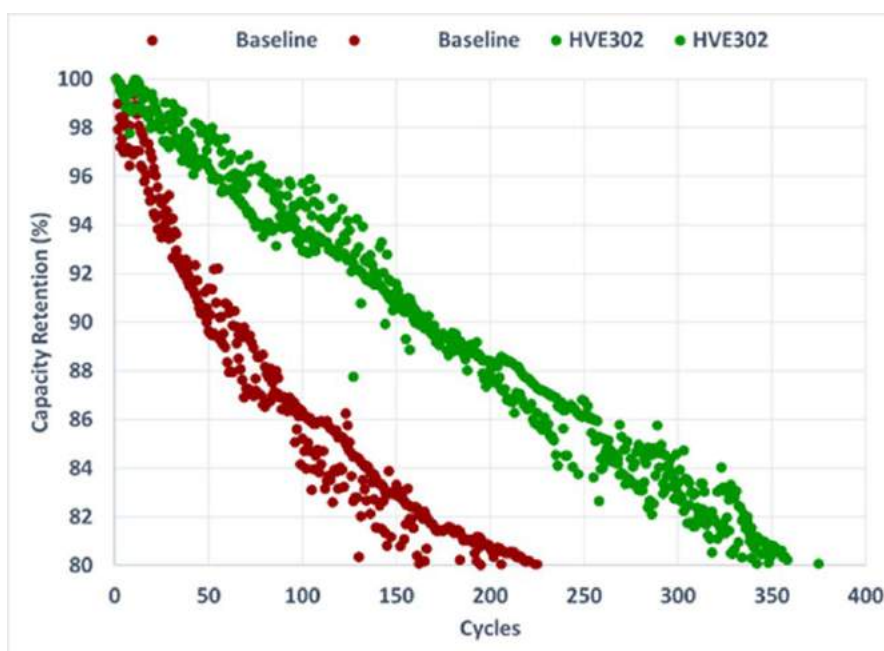


Figure I-57. Cycling performance of 5 Ah NMC532 cells cycled at 1C and 45°C with a 4.5V cut-off.

4) Formulation Transport Characteristics

A significant attribute in ensuring favorable rate and low temperature performance, is the ionic transport properties of the electrolyte. Ionic liquids showing favorable performance have acceptable viscosities and do not require great electrolyte concentrations to perform, thus granting near baseline values in ionic conductivity. Figure I-58 compares the ionic conductivity of NOHMs HVE157 with baseline electrolyte. The conductivity values are comparable over a wide temperature range.

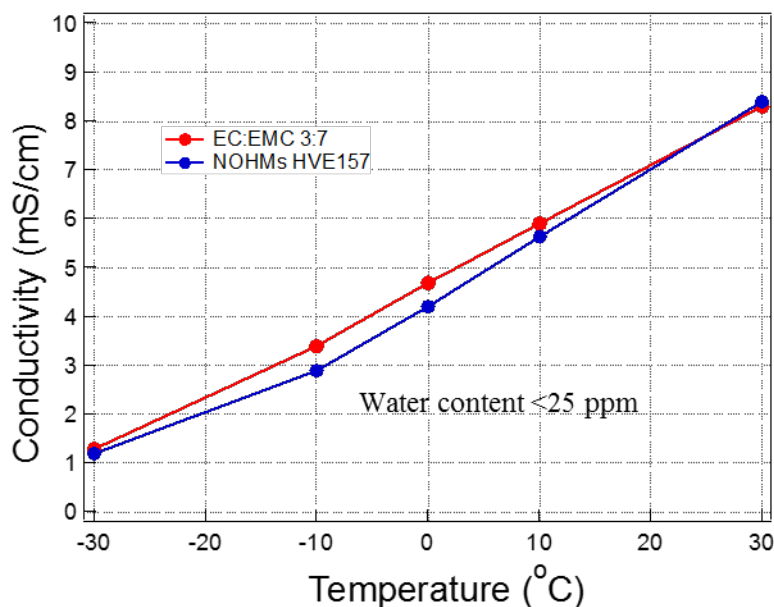


Figure I-58. Ionic conductivity of base line electrolyte and NOHMs HVE157 electrolyte over a wide temperature range.

5) NMC Deliverable Cell Performance

2 Ah NMC Cells tested at Idaho National Laboratory under-went calendar life testing, achieving greater than 4RPT segments. Cells show some decline in usable power at RPT4, but good retention of usable energy. Charge-sustaining (CS) and charge-depleting (CD) modes of operational power and energy were tested, in both modes of operation there is minimal loss in energy. Loss in power is a result of increased cell resistance. Decreasing resistance, increasing thermal stability, and gas reduction has shown promise in post deliverable electrolyte optimization, and is continuously pursued. Beginning of life (BOL) cold crank testing, using the battery size factor (BSF) of 379, revealed great voltage retention at -30°C from all 3 completed cycles. The results were consistent across the two cells tested.

Abuse tolerance testing at Sandia National Laboratories consisted of overcharge, blunt force rod, short-circuit, and thermal ramp testing. The cells performed very well in short-circuit tests, and provided favorable results in the thermal ramp testing. The results from the accelerated rate calorimetry (ARC) further supported the thermal ramp results, demonstrating thermal runaway >210°C. Given challenges with gassing at elevated temperatures and high voltage of the cathode at 100%SOC, it is no surprise the overcharge and blunt force rod test at 55°C + 100% SOC, would be a focus point for future electrolyte optimizations.

Conclusions

A variety of functional ionic liquids were synthesized and screened against graphite anode and high voltage cathodes (NMC532, NMO) for both cathodic and anodic stability. Based on numerous screening tests (at NOHMs and A123 facility), NOHMs developed HVE157a deliverable electrolyte for thirty 10 Ah NMC532 pouch cells and HVE242 deliverable electrolyte for thirty 2 Ah LNMO pouch cells. Deliverable cells were submitted for testing at national labs.

Results from 2 Ah NMC & 10 Ah NMC cells show positive attributes highlighted in RPT4, and the 2 Ah NMO cells revealed great performance benefits, having >425 cycles to 80% capacity retention when cycled using 2C. National lab testing has also exposed areas of improvement, specifically in impedance reduction, thermal stability, and gas suppression. The HVE302 optimized electrolyte formulation has demonstrated great promise in tackling these areas of improvement, and may offer for future enhancements.

Fundamental understanding of the working mechanism of NOHMs designed electrolytes is ongoing to optimize the electrolyte composition.

In collaboration with A123, NOHMs will be delivering thirty 10 Ah LNMO (4.8V) cells for independent testing.

Key Publications

1. Hybrid electrolytes for PHEV applications, Surya Moganty et al., DOE Annual merit review meeting, June 2017.

I.A.13 Li-Ion Cell Manufacturing Using Directly Recycled Active Materials (Farasis Energy)

Michael Slater, PhD, Principal Investigator

Farasis Energy, Inc.
21363 Cabot Boulevard
Hayward, CA 94545
Phone: 510-262-6600
E-mail: m Slater@farasis.com

Brian Cunningham, Technology Manager

U.S. Department of Energy
Phone: 202-287-5686
E-mail: Brian.Cunningham@ee.doe.gov

Start Date: February 1, 2017
Total Project Cost: \$1,761,490

End Date: February 28, 2019
DOE share: \$880,745

Non-DOE share: \$880,745

Project Introduction

Rapid performance gains of Li-ion batteries in the past few decades have led to its adoption at an unprecedented scale. For this growth to be sustainable, the entire life cycle of the batteries must be accounted for, from raw material sourcing to end-of-life disposal and reuse. So far, the cost associated with end-of-life disposition of these batteries has not been included in the product price; coupled with a drive to use less costly materials in the batteries themselves we are arriving at a situation in which there is less intrinsic value in the elemental composition of the battery than it costs to recycle/dispose of them in a responsible manner. Thus there is a need for a recycling method that goes beyond treating the battery as an ore and can harvest some of the additional value that is invested in the product during complex raw material and cell manufacturing processes.

Objectives

There are four main objectives for this project:

1. Optimize direct recovery processes at larger scale (>8 kg cell/module input)
2. Optimize electrode formulations to make best use of refurbished active materials
3. Manufacture full-size LiBs on commercial production line using direct-recycled active materials
4. Quantify cost benefits of recovered material (economic analysis and include cost related metric in Gap Analysis)

Approach

Farasis Energy has been working on recycling technology for Li-ion batteries for a number of years. They have addressed the challenges of closing the loop of the Li-ion product life cycle by developing a method for recovery and reuse of valuable components in the batteries. The “Direct Recycling” approach refers to a technology for battery recycling in which material recovery is performed using physical separation processes and active materials are reused with minimal processing, ideally without the need for intermediate chemical transformation. In this way, some of the value invested in the materials (*e.g.*, synthesis process energy, particle size distribution and shape) can be recovered without the need to resynthesize these materials from their lowest value elemental form. Figure I-59 shows a flow chart for a straightforward direct recycling process used to recover the high value components of the Li-ion battery. In this approach, the entire cell or module is shredded after being fully discharged and deactivated. Safety is a key requirement for this step, and therefore measures

to prevent release of hazardous materials and fires are a primary consideration. The shredded material is subjected to a solvent extraction step, which removes the electrolyte while also stabilizing the cell chemistry by removing a source of hydrofluoric acid, which can damage the valuable active materials upon exposure to air and water during subsequent processing. The shredded mass is then screened/sieved to remove other battery components from the micron-sized active materials. This detritus is sent to the existing metals recycling industry leaving only the “Black Mass,” a mixture of active anode and cathode particles with some binder, carbon, and small amounts of other components as contaminants. In this state, the recovered active materials are not immediately ready for use in new Li-ion cells for a number of reasons. The cathode material recovered is missing some lithium due to the inherent losses during the formation process and extended cycling and the graphite anode material contains some lithium and surface species generated during the formation and cycling processes. Finally, any contaminant species, including cathode material in the anode material, will render the materials unusable in new Li-ion cells.

Consequently, the next unit operations, while technically challenging, are critical to the success of the Direct Recycling approach. They involve the separation of the cathode and anode active materials from each other, the purification of these materials by removing contaminants, restoring the lithium content in the cathode material, and final regeneration in which the structural integrity of the materials is returned to its pristine state. Farasis has developed proprietary approaches to achieve these final steps that are chemistry independent, and have demonstrated the capability to achieve good separation yields, high purity and high performance materials using these methods.

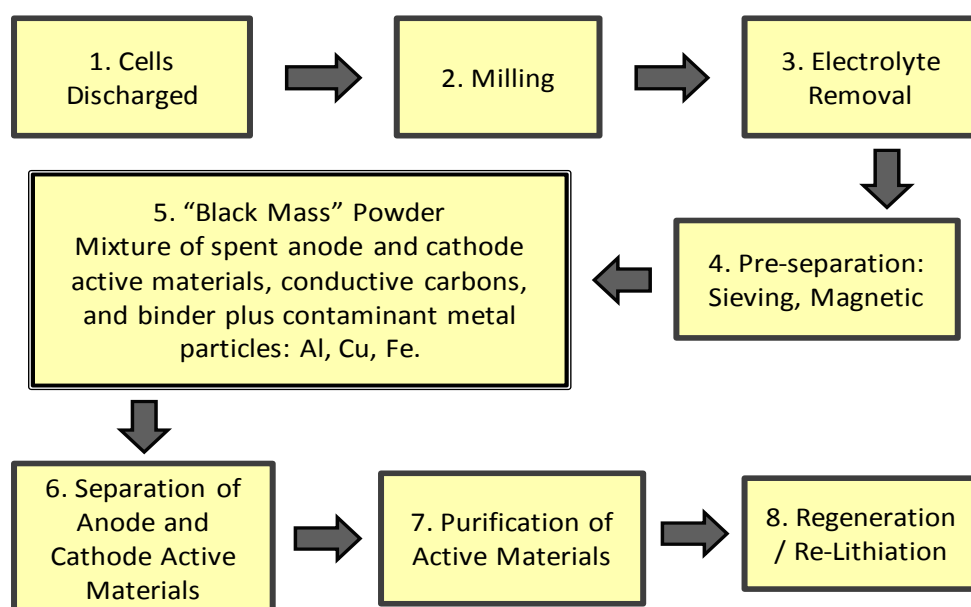


Figure I-59. Flow chart for direct recycling process for Li-ion batteries

Available evidence to-date suggests that modified surface chemistry of the isolated active materials is the primary challenge to address, which also provides an opportunity for improvements on the pristine materials' properties. Detailed structural investigations as to the nature of the changes are being explored in collaboration (via subcontract) with Robert Kostecki at Lawrence Berkeley National Laboratory in recognition of the team's leadership in battery materials characterization and research. The suite of analytical tools that will be used to inform the optimization of the recycling steps include:

- High resolution X-ray instrumentation at DOE's Synchrotron User Facilities, enabling detailed investigation of structural parameters such as microstrain and lattice defect

- SEM will be used for imaging particle morphology and surface chemical analysis by EDAX
- Electrochemical Impedance Spectroscopy will be used to determine intrinsic conductivity of materials and for electrode-level characterization during formulation research with recycled materials
- Particle size distribution measurements and gas adsorption analysis will be used to determine material physical characteristics such as particle size, surface area, and internal microporosity
- Raman spectroscopy will be used to study surface and near surface changes in material structure and chemistry which are difficult to characterize by other methods.
- Neutron diffraction will be employed in conjunction with XRD to more accurately characterize the structure of Li-containing materials. Due to the extremely weak scattering cross section of Li for X-rays, neutron diffraction is required to positively locate Li in the crystal structures (as opposed to inferring its presence from lattice spacing, which is not quantitative).

The direct recycled active materials will be used in iterative cell-builds of increasing feed complexity, through which insight will be gained on how to best incorporate recycling technologies in battery manufacturing resulting in more environmentally friendly, lower cost production of Li-ion batteries. A high-level summary of project deliverables (internal and external) may be found in Table I-9.

Table I-9: Overview of Program Hardware Deliverables and Build Strategy

Hardware Deliverable	Description	Source Material	Quantity ANL/FEI*	Delivery Date
Cell-build 1 (66 x ~ 2 Ah cells)	Control: pristine NMC/pristine Gr	commercial powders	9/12	Month 13
	recycled NMC/recycled Gr	manufacturing scraps	9/12	Month 13
	recycled NMC/pristine Gr	manufacturing scraps	0/12	Month 13
	pristine NMC/recycled Gr	manufacturing scraps	0/12	Month 13
Cell-build 2 (54 x ~2 Ah cells)	Control: pristine NMC/pristine Gr	commercial powders	9/12	Month 17
	100% recycled NMC/100% recycled Gr	BOL cells/QC rejects	9/12	Month 17
	blended: TBD % of recycled/TBD % new	BOL cells/QC rejects	0/12	Month 17
Final Build (54 x 25 Ah cells)	Control: 25 Ah FEI production cells	commercial powders	15/12	Month 22
	25 Ah cells with optimized (maximum) recycled content in each electrode	EOL cells and module parts	15/12	Month 22

* Each build will include cells for external (USABC/ANL) and internal (Farasis Energy) testing and evaluation

The measure of success of the program is being quantified by measuring the gap between recovered material and equivalent control test articles made using commercial grade active materials, which will be included with each build to allow comparative evaluation. While not included in the final deliverables, there will be development work addressing how best to handle mixed chemistry feed streams, which is an inherent challenge for direct recycling processes. Specifically, recovery of feed streams with NMC532 and mixed NMC/spinel compositions will be studied. Another important outcome of the program will be to refine current assumptions of a scaled production process (including milling, separation, purification, and regeneration operations) and evaluate revenue potential against capital and energy requirements and operating costs, thus ensuring that the technology is economically relevant.

Results

The initial phase of this project addressed increasing the scale of Farasis Energy's recycling process, moving to a scale relevant for commercial manufacturing equipment. This included qualification and installation of a 2 HP mill for shredding batteries, solvent extraction apparatus for electrolyte recovery, and vibratory screening gear for size-based separation as well as fume hoods and associated ventilation and power.

There are multiple potential feedstocks to address spanning manufacturing (scrap to end-of-life) systems. The first stage of the project has focused on the least complex feedstock: manufacturing residues, which eliminates some of the required processing steps; scaled-up processing for entire cells and systems will be optimized subsequently. A combination of thermal treatment and mechanical processing are used to isolate active materials (graphite or metal oxides) from current collector foils.

Composite electrodes are complicated metamaterials and complete de-mixing of the various components is not possible. Selective degradation of the minor components allows isolation of the desired active material. One approach to achieve this outcome is thermal decomposition; study of this process has revealed significant interaction between different components as evidenced by the thermogravimetric analysis results in Figure I-60, and these synergies will be strategically leveraged in the upcoming optimization work.

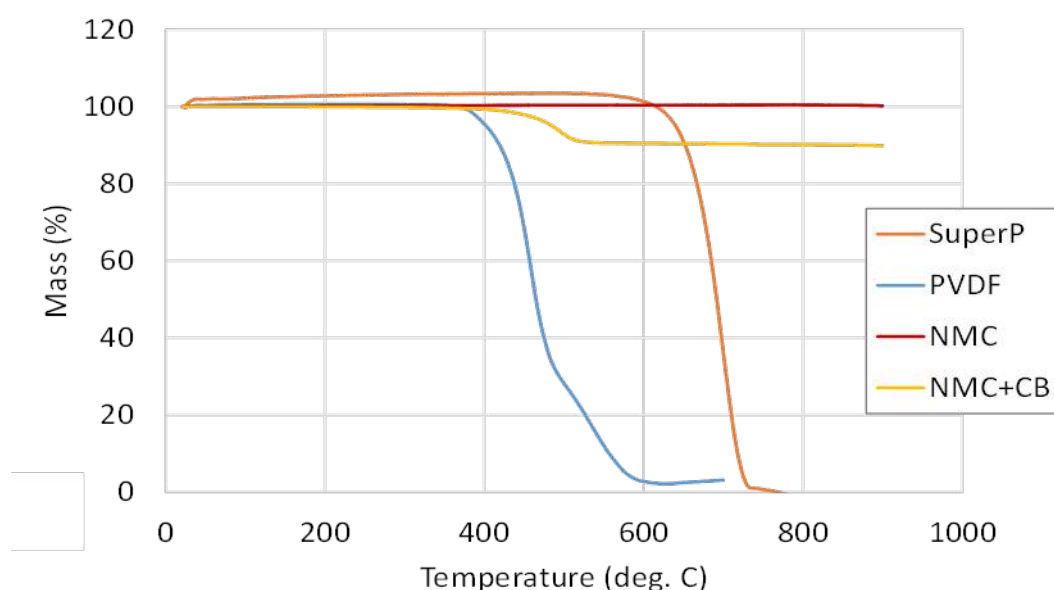


Figure I-60. Thermogravimetric analysis of composite positive electrode components at 10°C/minute

The shredding method and accompanying energy input can be tuned to increase the effectiveness of the process and subsequent processing steps. Tuning process parameters allows recovery of active materials with identical properties as the pristine versions of these materials as illustrated in Figure I-61.

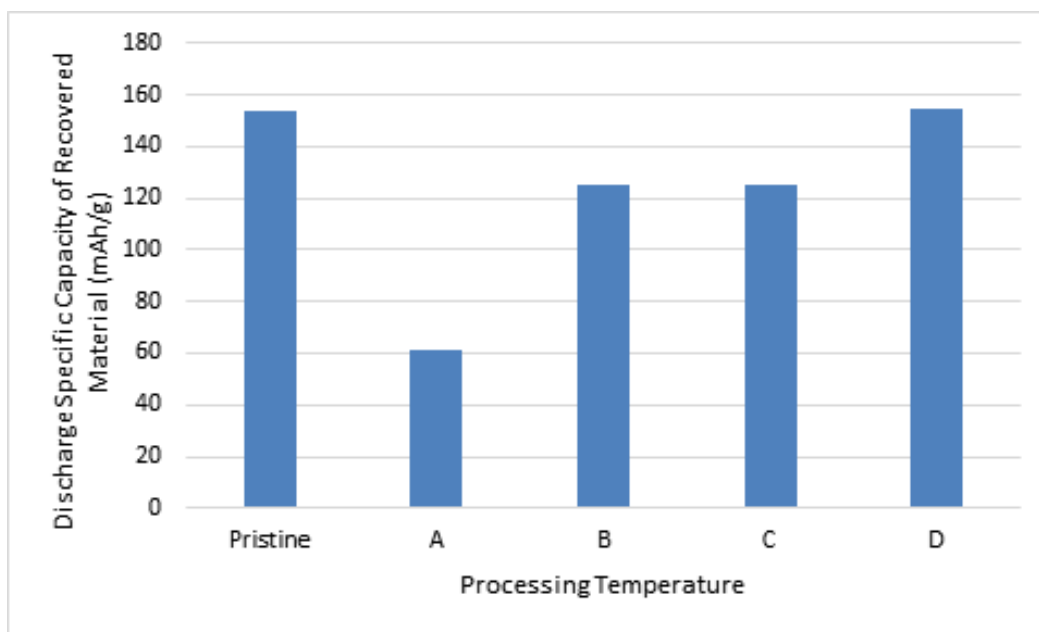


Figure I-61. Specific capacity of positive electrode active material recycled from scrap electrodes.

With feedstocks of cells that have been through the formation process, it is necessary to restore the lithium content of the cathode active material that is lost to the negative electrode for SEI formation. In advance of processing these input streams we have explored working with synthetically aged materials for reconditioning experiments. Multiple experiments into chemical delithiation using aqueous sodium persulfate and nonaqueous nitronium tetrafluoroborate were investigated for this purpose. Delithiation of NCM111 using sodium persulfate produced materials with voltage curves that have the expected shape, which indicates that delithiation has occurred, but the specific capacities were anomalously low as described in Figure I-62. It appears that it is difficult for chemical delithiation to produce materials with properties similar to electrochemically delithiated materials using commonly reported procedures, most likely due to stress gradients induced by rapid delithiation in the absence of electric fields present in a cell that facilitate lithium migration, although it may be possible to modify the reaction conditions to overcome this discrepancy.

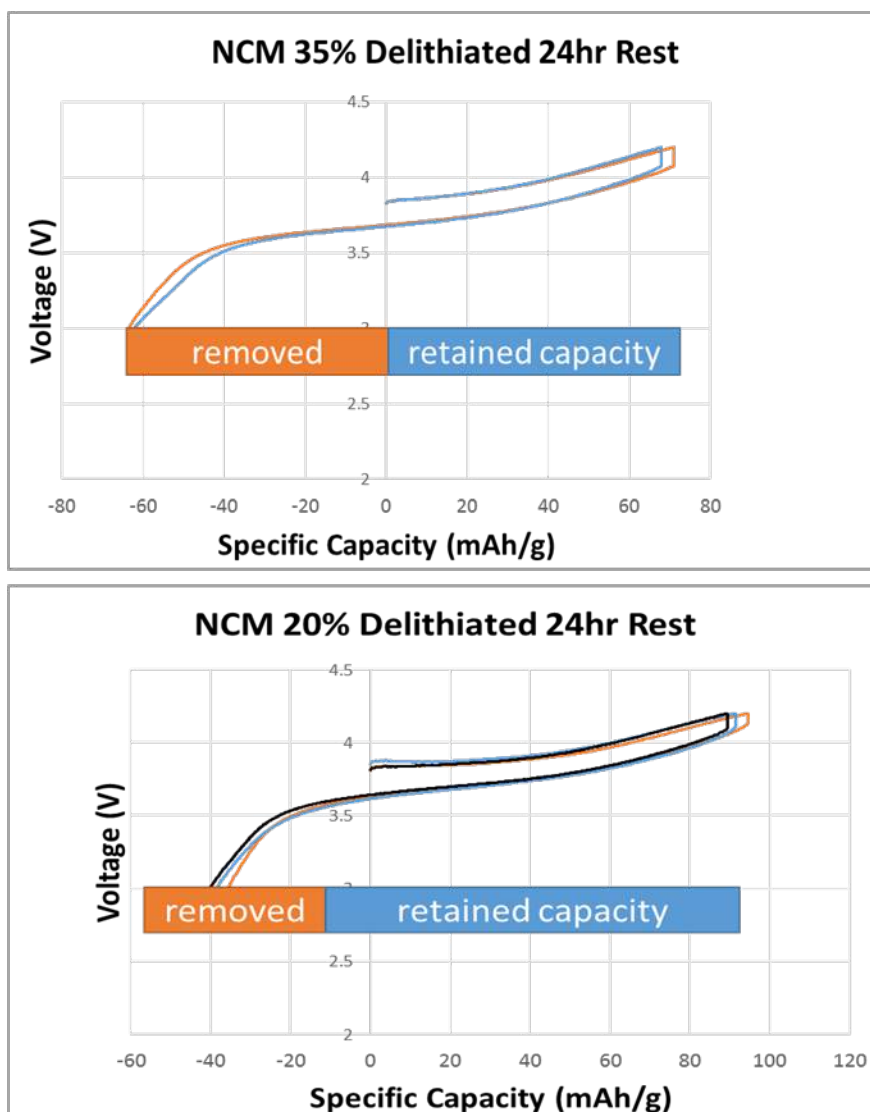


Figure I-62. Voltage curves of NCM111 (vs. Li/Li⁺, in 1.2 M LiPF₆ in EC/EMC 3:7 w/w) which has been chemically delithiated with aqueous Na₂S₂O₈. The comparative specific discharge capacity of pristine reference material is 155 mAh/g.

Conclusions

Scaled up processing equipment for Li-ion battery recycling was evaluated and installed at Farasis Energy in Hayward. Initial processing of manufacturing residues has demonstrated that recovery of active materials with properties nearly identical to pristine materials is practical using commercially relevant Graphite//NMC cell chemistries. The next phase of the project will incorporate these recovered materials in deliverable test articles while process optimizations will begin on the more complex feedstocks comprised by aged cells and complete battery systems.

I.A.14 A Closed Loop Recycling Process for End-of-Life Electric Vehicle Li-ion Batteries (Worcester Polytechnic Institute)

Yan Wang, Principal Investigator

Worcester Polytechnic Institute
100 Institute Road
Worcester, MA 01609-2280
Phone: 508-831-5453
E-mail: yanwang@wpi.edu

Brian Cunningham, Technology Manager

U.S. Department of Energy
Phone: 202-287-5686
E-mail: Brian.Cunningham@ee.doe.gov

Start Date: February 2, 2016
Total Project Cost: \$1,024,740

End Date: January 15, 2018
DOE share: \$512,370

Non-DOE share: \$512,370

Project Introduction

The purpose of this USABC project is to successfully recycle multiple 10 kg size batches of end of life EV batteries consisting of different incoming cathode chemistries via the patent pending recycling process developed at WPI, and produce PHEV format cells of a single chemistry using the recovered NMC111 cathode. Over the course of the two year development program, WPI/A123 systems/Battery Resourcers will improve the performance of the recovered cathode materials so that they exhibit performance equivalent to current commercial materials, as confirmed by A123 and National Lab testing using USABC PHEV test procedures. Other materials including steel, copper, aluminum, etc. will also be recycled.

Objectives

The objective of this program is to scale up and demonstrate the WPI-developed novel and efficient Li-ion battery recycling process, verify its claim of no or minimal sorting, and develop PHEV cell designs with a lower cost structure for improved industry sustainability. The USABC development program will advance the WPI recycling technology through the completion of three major tasks: 1) optimizing the synthesis parameters of the recovered $\text{LiNi}_{0.33}\text{Mn}_{0.33}\text{Co}_{0.33}\text{O}_2$ (NMC111) cathode materials for improved particle density, particle size and electrochemical performance; 2) improving the recycling efficiency of cathode materials and lithium and 3) scaling the process from the existing 1 kg scale to the 10 kg scale or greater, as required.

Approach

In this project, WPI has been collaborating with A123 Systems and Battery Resourcers. Battery Resourcers is a start-up company that was co-founded by Yan Wang, Eric Gratz and Diran Apelian to commercialize WPI's recycling technology. WPI's primary focus is on developing and optimizing the recycling process and recovering NMC111 powder, A123's focus is on powder characterization and cell fabrication, and Battery Resourcers' focus is on scale up and cost analysis. The project goals are achieved through execution of the key tasks detailed below:

Improve the electrochemical performance of NMC111

One of the major tasks of the program is to increase the capacity and expected life of NMC111 that is recovered from a multi-chemistry mixture of PHEV/HEV/EV batteries to be equivalent to commercially available cathode material, or show no more than 5% difference in the metrics being tracked. WPI will further refine the ability to tailor the Ni, Mn and Co stoichiometry to consistently deliver the 1:1:1 product regardless of incoming chemistry variations. The project is structured to advance from beginning of program status involving coin cell testing through an intermediate 2 Ah cell to the final deliverable 25 Ah cells. WPI is

working with industrial partner A123 systems to evaluate and improve the properties and electrochemical performance of the recovered cathode material. By optimizing process parameters such as precipitation time and stirring rate, WPI can increase the particle density and specific capacity, which are key to successful commercialization of the recycling technology. The project is striving to increase the reversible capacity of the recycled cathode from 150 mAh/g to 155 mAh/g. However, project emphasis is ultimately aimed at the relative difference between cells made with recovered material and commercial NMC versus the absolute performance of both, as the latter can be affected by many factors unrelated to the recycling technology itself. For this reason, commercial control cells are generated at every stage for a meaningful benchmark and the difference is tracked using the recycling-adapted 3-tiered gap charts.

Improve the recovery efficiency

There are two facets to recovery efficiency: minimizing losses of desirable components in the various processing steps and minimizing the quantity of virgin materials required to supplement the incoming stream of spent batteries. Both aspects are being addressed in order to deliver the most favorable economics. To maximize the recovery efficiency of Ni, Mn, and Co as $\text{Ni}_{1/3}\text{Mn}_{1/3}\text{Co}_{1/3}(\text{OH})_2$, the pH will be closely monitored and controlled. The most important step is the impurities removal operation in which Al, Cu and Fe impurities are removed as hydroxides. The amount of Ni, Mn and Co lost at this stage depends upon two primary factors: their concentration in solution and the pH. The lowest pH which can be obtained while maintaining impurity levels below targets must be determined, so as to allow for the maximum recovery efficiency. To maximize the recovery efficiency of lithium carbonate, the amount of water that is evaporated must be strategically tuned. By determining the concentration of the impurities ions present in solution (Na^+ , SO_4^{2-}) from measured concentrations of sodium and sulfur, the exact volume point at which sodium sulfate becomes insoluble can be calculated using the K_{sp} of sodium sulfate at the temperature in question. This is be used to optimize the water added and subsequently evaporated, along with other purification and temperature related refinements to minimize unnecessary dilution and maximize yield.

Scale-up

The significant challenge of going from 1kg to 10kg experiments was approached by conducting the scale-up in stages. (The scale indicates the mass of shredded, spent battery feed entering the process). First, the work proceeded from 1kg experiments to 3kg (factor of 3), and then to 10kg (increase factor of 3.3). At each scale (1 kg, 3 kg, 10 kg), recovered material properties were compared against commercial cathode material using both powder and resultant cell attributes in clearly defined, measureable milestones. Ultimately, WPI exceeded the original targets of scaling the process to a 10 kg feed scale, and were able to successfully process multiple lots of 30-40 kg (each) of spent batteries.

Results

In order to generate NMC111 powder for 2 Ah cells, WPI conducted 5 large scale experiments, with each experiment using spent batteries from different and intentionally diverse recycling streams. A number of key process modifications were made as part of the optimization required in order to achieve the desired powder attributes, and the process was ultimately converted from a batch process to a semi-continuous one, and one capable of accommodating an incoming feed of 30 kg. of spent batteries. Each experiment produced over 3kg of NMC111 for evaluation and cell fabrication. The experimental information is the following.

Lot 03272017

Recycling stream: GM Volt batteries and LFP cells from A123

Cathode tap density: 2.30g/cc, D50: 20 μm

Lot 04212017

Recycling stream: FCA batteries

Cathode tap density: 2.51g/cc, D50: 11.6 μm

Lot 05152017

Recycling stream: GM Volt batteries, FCA batteries, electronics batteries and LFP cells from A123

Cathode tap density: 2.52g/cc, D50: 14.1 μm

Lot 06202017

Recycling stream: Ford Focus batteries

Cathode tap density: 2.60g/cc, D50: 10.2 μm

Figure I-63 shows the precursor and cathode material information for the 4 experiments used for the 2 Ah deliverables, and highlights the ability of the process to handle a diverse makeup of feed chemistries (see feed descriptions on the right). The slight variations in tap density and particle size reflect small differences in several process parameters between the lots, as the optimization effort was still underway as powder morphology was refined in approach of the target attributes. The 4 batches of powder represented below have been delivered to A123 for 2 Ah cell fabrication, and fulfillment of one of the project deliverables. Their electrochemical properties are shown in Table I-10 below, as tested by A123 Systems.

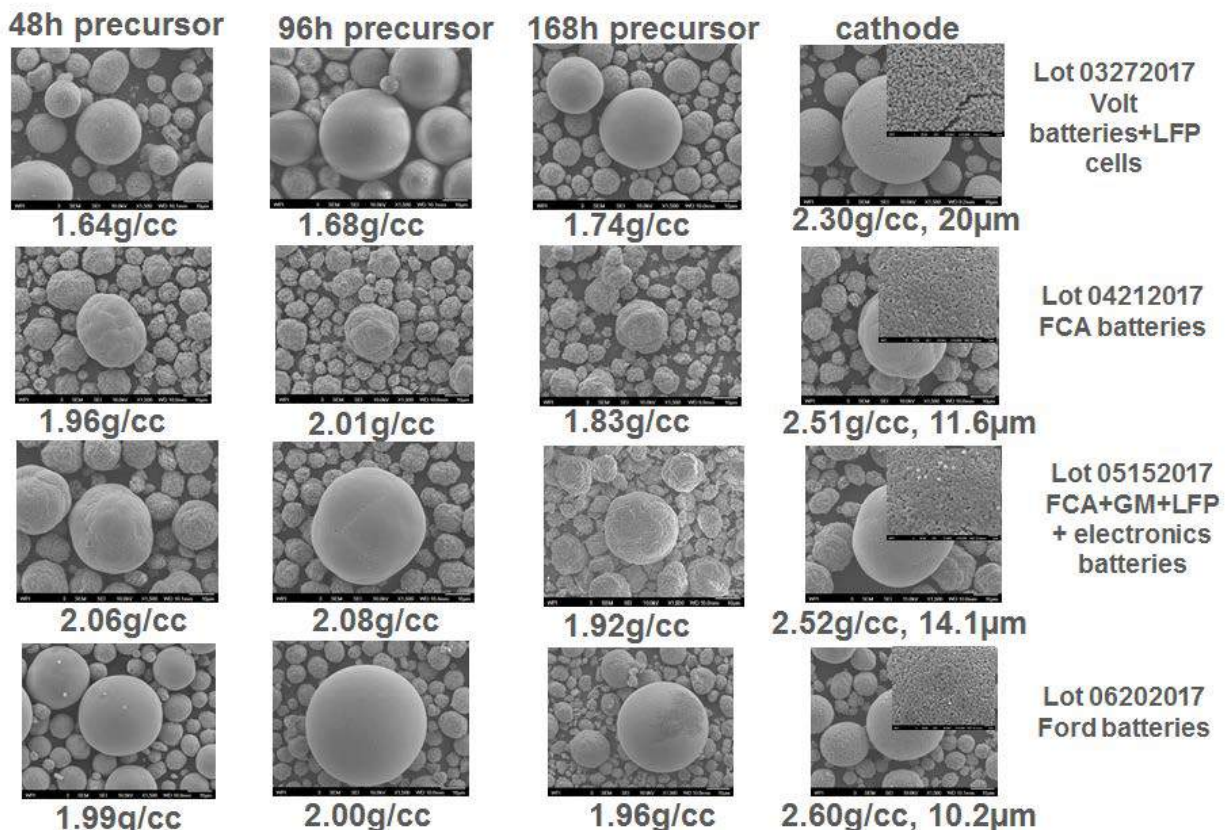


Figure I-63: Detailed precursor and cathode powder information from 4 different experiment for 2 Ah cells. Each 3 kg lot of powder was generated from approximately 30 kg of spent, shredded batteries of the provenance noted above.

In order to generate the required 8kg NMC111 powder for each of the two 25 Ah cells builds, WPI needed to conduct 2 experiments, with each experiment generating ~4kg NMC111 powder (and using a spent battery feed of >30 kg). One recycling stream consisted of Ford Focus batteries and LFP cells and the other recycling stream was comprised of FCA batteries. WPI completed the 4 final experiments and delivered 2 combined batches of 8kg powder to A123 for 25 Ah cell fabrication. Figure I-64 shows the precursor and cathode material information for the 4 experiments, with the details listed below.

Lot 08112017

Recycling stream: Ford Focus batteries and LFP cells

Cathode tap density: 2.56g/cc, D50: 13.9 μm

Lot 08302017

Recycling stream: Ford Focus batteries and LFP cells

Cathode tap density: 2.56g/cc, D50: 10.7 μm

Lot 09192017

Recycling stream: FCA batteries

Cathode tap density: 2.65g/cc, D50: 11.9 μm

Lot 10092017

Recycling stream: FCA batteries

Cathode tap density: 2.50g/cc, D50: 9.81 μm

The powder from the different recycling experiments shows similar morphology, tap density and particle size when compared to the previous 3kg powder lots for the 2 Ah cells. The first 8 kg batch of powder was obtained by mixing lots 08112017 and 08302017. Its tap density is 2.58g/cc and D50 is 11.7 μm . The second 8 kg batch of powder combined lots 09192017 and 10092017. At the time of writing of this report, the second batch was undergoing material characterization by A123 in advance of cell fabrication. Based upon the consistency of results with prior lots, it is expected that the powder will pass quality control evaluation and be used for the final deliverable 25 Ah cell-build. To date, A123 has tested numerous batches of WPI-recovered NMC111 and control powders with coin cells, and the most recent results are shown in Table I-10. A123's test results demonstrate that WPI synthesized material from different recycling streams exhibit similar electrochemical performance as the commercial material, and generally show better rate performance, which is quite unexpected. In addition to the coin cells, A123 has fabricated and tested single layer pouch cells with both control and WPI-recovered powder. The results again show that WPI recovered NMC111 has similar performance with control powder (The single layer pouch cells have been cycled more than 2,000 cycles.). Most of the 2 Ah pouch cells have now been built by A123 and will allow larger format comparative evaluation of WPI material performance versus control powders (commercial NMC111). Finally, the aforementioned 8 kg batches of WPI powder will be used by A123 to produce the 25 Ah final deliverables, which again will be evaluated against equivalent hardware control counterparts. Both 2 Ah and 25 Ah cells will be delivered to Argonne National Laboratory for independent assessment based on USABC PHEV testing protocol.

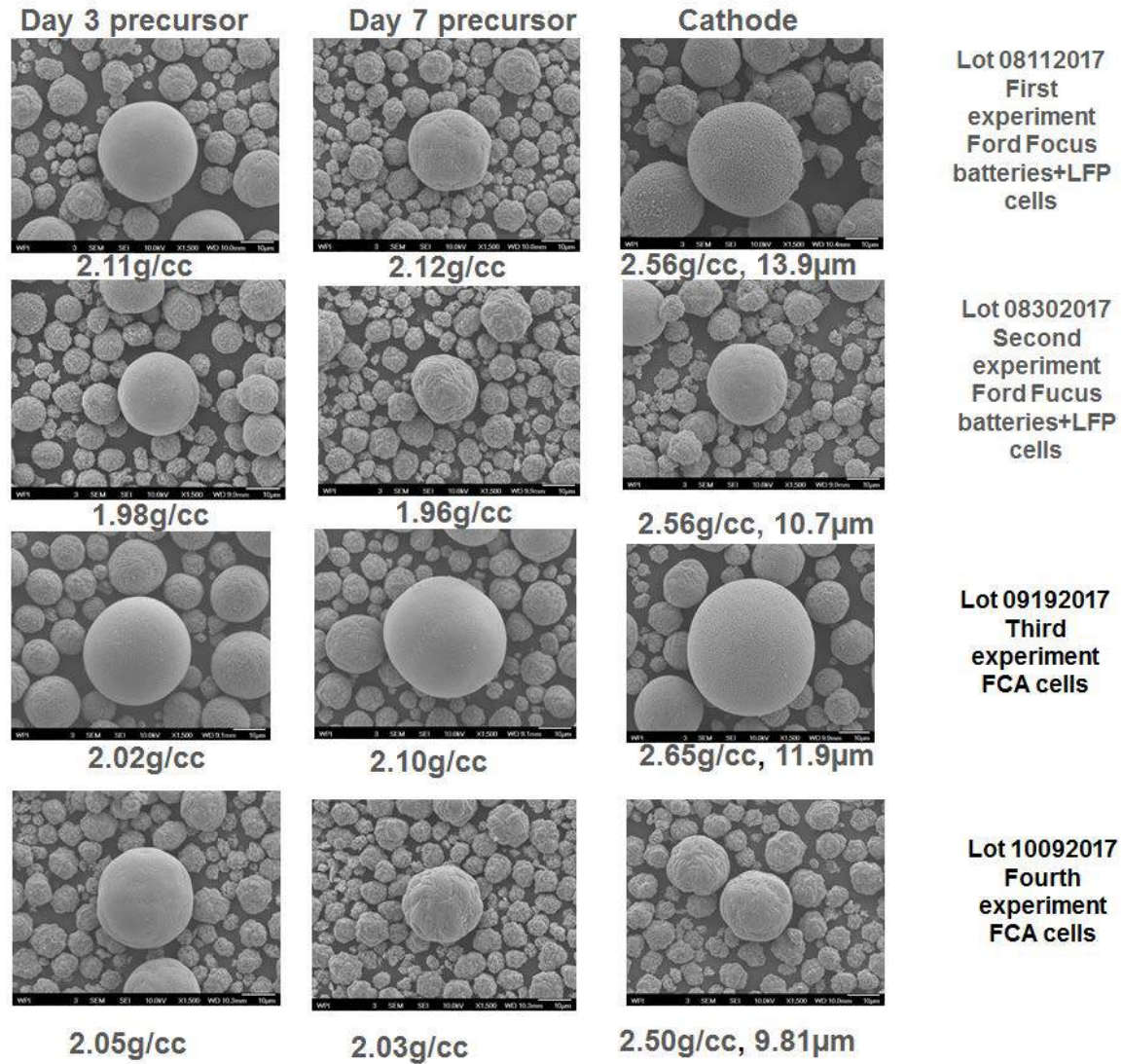
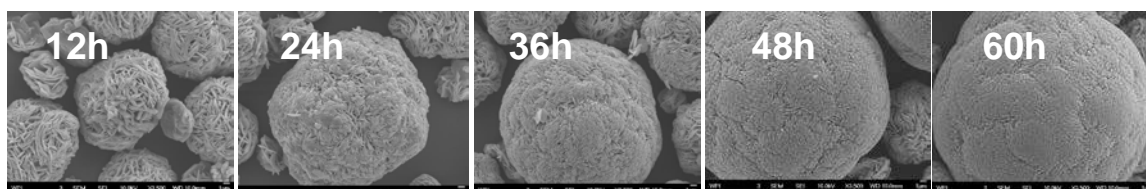


Figure I-64: Detailed precursor and cathode powder information from 4 different experiment for 25 Ah cells

Table I-10: Comparison between synthesized material and commercial material

Test	Metric	Control Powder (B)	03272017 3Kg Powder	04212017 3Kg Powder	05152017 3Kg Powder	06202017 3Kg Powder
Tap Density	g/cc	2.84	2.15	2.31	2.36	2.51
D50 PSD	um	9.2	20	11.6	14.1	10.2
BET	m ² /g	0.28	1.41	0.53	0.36	0.65
FCC/ FDC	mAh/g	174.7/ 157.2	177.3/ 163.5	178.1/ 152.3	170.1/ 149.2	177.3/ 157.0
Efficiency	%	90.0	92.2	85.5	87.7	88.6
1C	mAh/g	130.9	136.3	123.1	137.4	129.2
2C	mAh/g	119.4	128.6	113.0	128.4	120.8
5C	mAh/g	40.4	59.5	75.4	76.2	76.2
Full coating		Complete	Complete	Complete	Complete	Complete

Battery Resources officially joined the USABC project in February 2017 to further scale up the WPI process to a 50 kg (spent feed) scale, with the option of using their material for 25 Ah cells, if it was confirmed comparable or superior to the WPI powder. The validation of the process at the higher scale is expected to further inform commercialization potential of this technology and will allow a more meaningful economic model to be developed. Battery Resources adopted WPI parameters and conducted a few experiments with GM Volt batteries. Figure I-65 shows the precursor morphology progression over the course of the experiment. The particles become more spherical with increasing time, much like the WPI results. The tap density of the precursor is ~1.9g/cc, which is within the expected range. Battery Resources has synthesized cathode powder (tap density: 2.4g/cc) and delivered 200g cathode powder (Figure I-66) to A123 independent evaluation. The electrochemical results are increasingly similar to that of WPI recovered powder.

**Figure I-65: The morphology of NMC111 precursor with reaction time at Battery Resources**

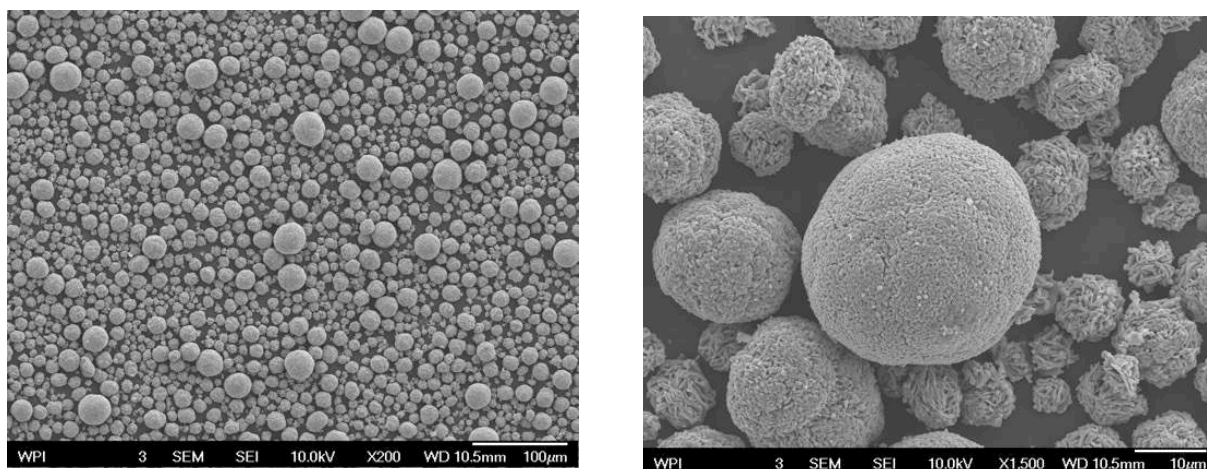


Figure I-66: NMC111 cathode powder synthesized by Battery Resourcers

Conclusions

In order to generate enough powder for 2 Ah and 25 Ah cells, significant process improvements were realized throughout the past year, and have allowed achieving and in some cases exceeding the powder and process targets established in the SOW. Furthermore, the process can now run with minimal supervision due to numerous improvements in system configuration and controls, as opposed to the constant oversight that was required at the beginning of the program. So far, WPI has recycled 1 GM Volt battery pack, 1 Ford Focus battery pack and 1 FCA 500e battery pack, significantly surpassing the quantities specified in the SOW.

During the recycling experiments, WPI has successfully demonstrated its capability of recovering NMC111 powder from different, chemically diverse recycling streams. The recovered powder shows high tap density, and good morphology. WPI has successfully delivered to A123 four 3kg lots of powder for the 2 Ah cells and two 8 kg lots of powder for 25 Ah cells. Based on initial coin cell and single layer pouch cell testing at A123, WPI recovered powder has similar performance with commercial cathode powder, with somewhat higher rate performance. These results clearly demonstrate the scalability and repeatability of WPI recycling technology.

In addition, Battery Resourcers has adopted and further scaled the WPI recycling technology, and has been able to generate promising, in-specification NMC111 powder, as recently confirmed by A123 Systems.

Key Publications

1. Yan Wang, Zhangfeng Zheng, Mengyuan Chen, A Closed Loop Process for the End-of-Life Electric Vehicle Li-ion Batteries, U.S. DOE 2017 Annual Merit Review and Peer Evaluation Meeting, Washington, D.C., June 5-9, 2017.

I.A.15 Perform USABC/USCAR Benchmarking Activities (FEV North America, Inc.)

Thomas D'Anna, Principal Investigator

FEV North America, Inc.

4554 Glenmeade Lane

Auburn Hills, MI 48326

Phone: 248-724-2861

E-mail: DAnna@fev.com

Greg Kolwich, Principal Investigator

FEV North America, Inc.

4554 Glenmeade Lane

Auburn Hills, MI 48326

Phone: 248-724-2924

E-mail: Kolwich@fev.com

Brian Cunningham, Technology Manager

U.S. Department of Energy

Phone: 202-287-5686

E-mail: Brian.Cunningham@ee.doe.gov

Start Date: June 1, 2015

End Date: October 31, 2017

Total Project Cost: \$442,763

DOE share: \$144,900

Non-DOE share: \$297,863

Project Introduction

In the process of developing new powertrains for vehicles, benchmarking data (and subsequent analysis) is beneficial in the identification and characterization of similar products. Through this process, development targets can be established for the new products, relevant design features identified, and their influence on key attributes evaluated. A technical benchmark study is performed on the 2015 Volkswagen e-Golf as well as a detailed cost analysis performed on the 2016 Toyota Prius lithium-ion battery pack.

Objectives

- The 2015 VW e-Golf benchmark study consists of vehicle testing, key component (test stand) testing, and teardown analysis.
- The 2016 Toyota Prius lithium-ion battery pack cost analysis consists of a full battery pack tear-down for general part and manufacturing information gathering, process parameter model and database review, and cost modeling analysis.

Approach

For both programs, hardware tear-down, testing, and applicable analysis are performed at FEV's in-house facilities in Michigan. Technical reviews are collaboratively executed with feedback and guidance from OEM and DOE counterparts.

Results

- In 2017, battery pack tear-down (Figure I-67) and performance tests were completed. The e-Golf's battery pack was tested in an environmental chamber to understand its performance characteristics. The battery pack was connected to an AV-900 battery emulator to run the pack through multiple charge and discharge cycles at varying temperatures. Data including temperature and voltages were recorded while testing (Figure I-68).

- Upon disassembly of the Prius battery pack (Figure I-69) to the sub-component level, all parts were documented generating a manufacturing comparison bill of materials. This information feeds into the creation of process flows for manufacturing assumption-quote summary worksheets detailing rates and cost contributions (i.e., material, labor, manufacturing overhead and mark-up) for each operation involved in producing a component. Approximately 75% of the battery pack components are calculated using detailed cost models and the remaining 25% costed using benchmark/commodity pricing.

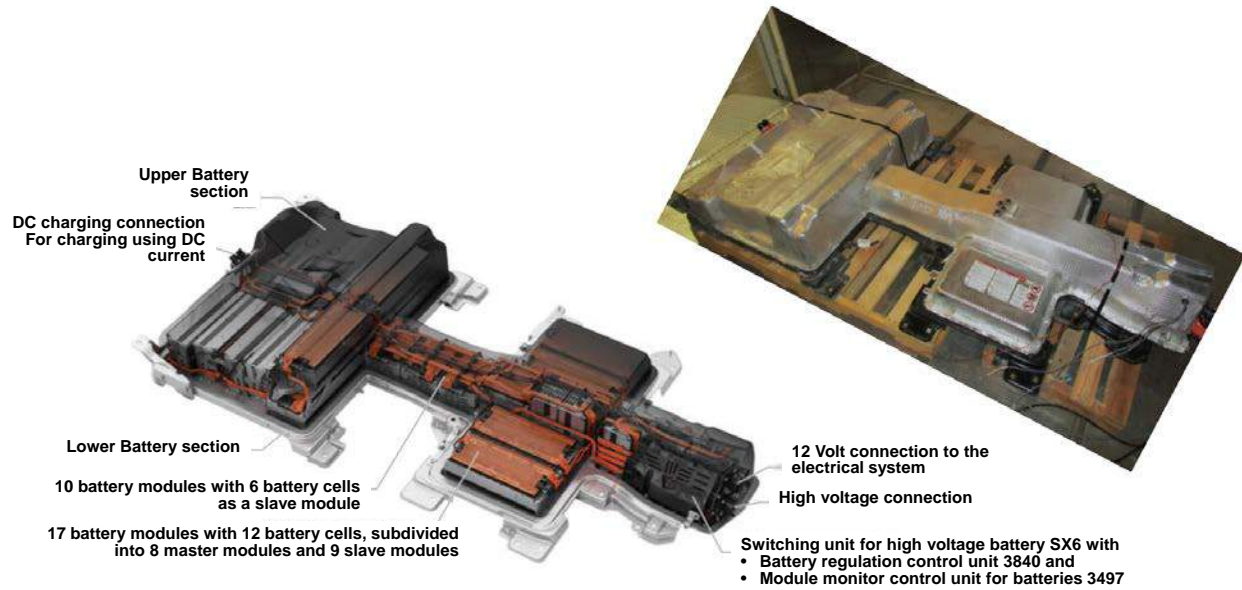


Figure I-67: 2015 VW e-Golf Battery Pack Physical Overview

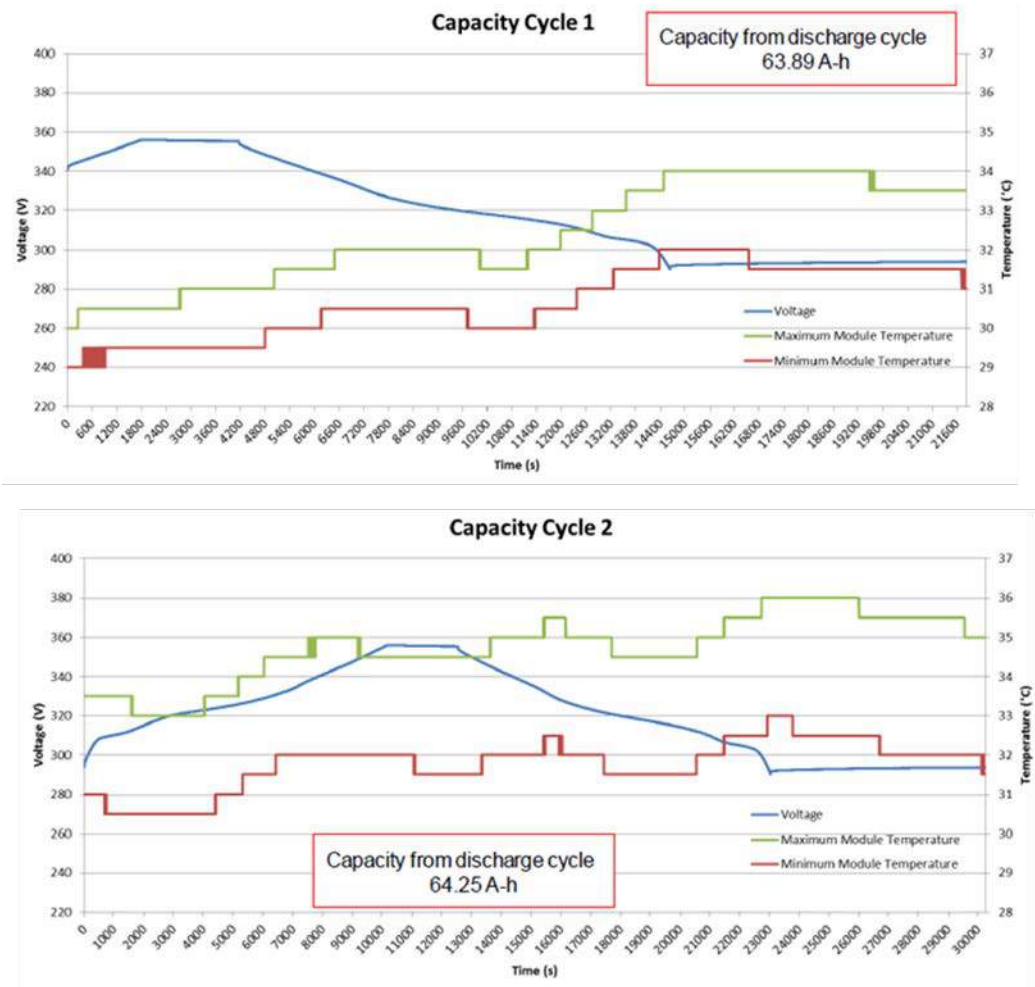


Figure I-68: Capacity Testing Cycles at C/3 Charge, 30min Rest, C/3 Discharge at 30°C

USCAR – 2016 Toyota Prius Benchmarking Features & Specifications



MANUFACTURER'S HIGH VOLTAGE BATTERY TECHNICAL DATA

Nominal Voltage.....	201.6 V
Voltage Per Module.....	7.2 V
System Voltage.....	600 V max
Capacity.....	6.5 Ah
Modules.....	28
Cells.....	168
Volume.....	35.5 L

Lithium-Ion (Li-Ion) Battery – Not available with E-Four

Nominal Voltage.....	207.2 V
Voltage Per Cell.....	3.7 V
System Voltage.....	600 V max
Capacity.....	3.6 Ah
Cells.....	56
Volume.....	30.5 L



Subsystem	Information
Type	Li-ion HV Battery
Cells	56 Cells (26/row)
Nominal Voltage	DC207.2V
Capacity	3.6 ampere hour
Max System Voltage	600V
Cooling Specs	Air Cooled



Figure I-69: 2016 Toyota Prius Lithium-Ion Battery Pack Specification Summary

Conclusions

- The HV battery testing results showed that the battery pack performed nominally with capacity ranging from a low of 50.34 Ah during the -30°C test to a high of 65.03 Ah in the 45°C test. This compared favorably to the rated capacity of 66.1 Ah. The resistance of the battery pack varied from a low of ~0.09Ω during the 45°C test to a high ~0.52Ω during the -30°C test. The Pulse Power Capability of the battery pack varied from a low ~35 kW during the -30°C test to a high of ~180 kW during the 45°C test. Pack hardware and associated components are further detailed in the final report.
- FEV provided in-depth analysis of cost scenarios based on scaled volume (450k, 100k, and 50k units/year) assessments. A collaborative cell manufacturing assumption review with OEM and DOE counterparts motivated update recommendations to the USABC cost model templates.

I.B Advanced Processing

I.B.1 Low Cost Manufacturing of Advanced Silicon-Based Anode Materials (Group14 Technologies, Inc.)

Henry R. Costantino, Ph.D., Principal Investigator

Group14 Technologies, Inc.

100 NE Northlake Way, Suite 300

Seattle, WA 98105

Phone: 206-547-0445; Fax: 206-546-5304

E-mail: rcostantino@group14technologies.com

Peter Faguy, Technology Manager

U.S. Department of Energy

Phone: 202-586-1022

E-mail: Peter.Faguy@ee.doe.gov

Start Date: January 1, 2016

End Date: December 31, 2017

Total Project Cost: \$4,040,000

DOE share: \$2,810,000

Non-DOE share: \$1,230,000

Project Introduction

Despite substantial investment in Lithium-Ion Battery (LIB) technology, most commercial cells still rely on graphite anodes – originally deployed in the ‘90’s, because of their low cost and acceptable lithium capacity. A shift is underway to replace the graphite anode with a silicon containing material, but due to elaborate manufacturing techniques current costs exceed \$100/kg. It is our vision to develop new anode materials that are high performance, and also easily scalable, employing low-cost materials and manufacturing processes. To this end, we have launched Group14 Technologies, spun out of EnerG2 Inc., a leader in carbon materials development, manufacturing, and commercialization. Group14’s strategy is to develop low cost processes for manufacturing silicon-carbon (Si-C) composite materials that will enable a dramatic reduction in the cost structure of silicon-carbon anodes, i.e., by an order of magnitude, while maintaining the high performance that the LIB industry demands of these advanced anodes.

Objectives

The objective of this project is to develop a new low cost production process that is capable of mass-producing silicon-based lithium ion battery (LIB) anode material that can reach 1000 mAh/g after 1000 cycles and with a cell level cost target of < \$125/kWh, validate performance in LIB full cells, and prove the cost basis at pilot scale.

Approach

Group14 is leveraging EnerG2’s carbon technology to develop new approaches for low-cost manufacturing of high-performing Si-C composites. These Si-C composites comprise nano-sized and/or nano-featured silicon. The approach focuses on raw materials that are low cost and readily sourced. Likewise, the approach focuses on manufacturing processes that are low-cost and readily scalable. Specifically, both carbon and silicon components within the Si-C composite are based on low-cost precursors.

Group14 approach is to down-select Si-C composite materials and manufacturing processes at lab-scale, supported by robust characterization, including electrochemical characterization with a focus on electrochemical testing of the Si-C composite anode materials in full cell Li-ion batteries such as coin cells or pouch cells. Our philosophy for the electrochemical characterization is to employ relatively standard procedures and materials, i.e., industry-standard electrolyte, cathode, and battery cycling conditions. While we

are interested in potential synergies with our Si-C composite materials and the next generation of other battery materials (cathodes, electrolyte, etc.) our current intent is that our Si-C composite materials are a “drop-in” replacement for graphite powder as an anode material, compatible with current commercial anode and Li-ion battery manufacturing lines.

Consistent with our project plan, we have down-selected materials and processes, and have ordered manufacturing equipment for pilot scale (e.g., 1-10 kg) production. We are currently gearing up for pilot scale in terms of site readiness in preparation of equipment receipt, installation, and commissioning. Once all equipment has been commissioned, the purpose of the final stage of the project is to prove the cost basis at pilot scale, as well as validate the performance of the scaled-up Si-C composites in Li-ion battery full cells.

Results

The accomplishments during the first quarter of 2017 (Jan-Mar 2017) included further improvement of Si-C cycle stability at lab scale, progress towards scale up, and increased understanding of physicochemical characteristics relevant to electrochemical performance.

Down-selected path #2 (DSS #2) and down-selected path #3 (DSS #3) – collectively, Process Path 2 - represent an internal path with respect to processing the Si-C composite. Regarding this path, the continued improvement in electrochemical performance at lab scale is presented in Figure I-70 (on a volumetric energy basis).

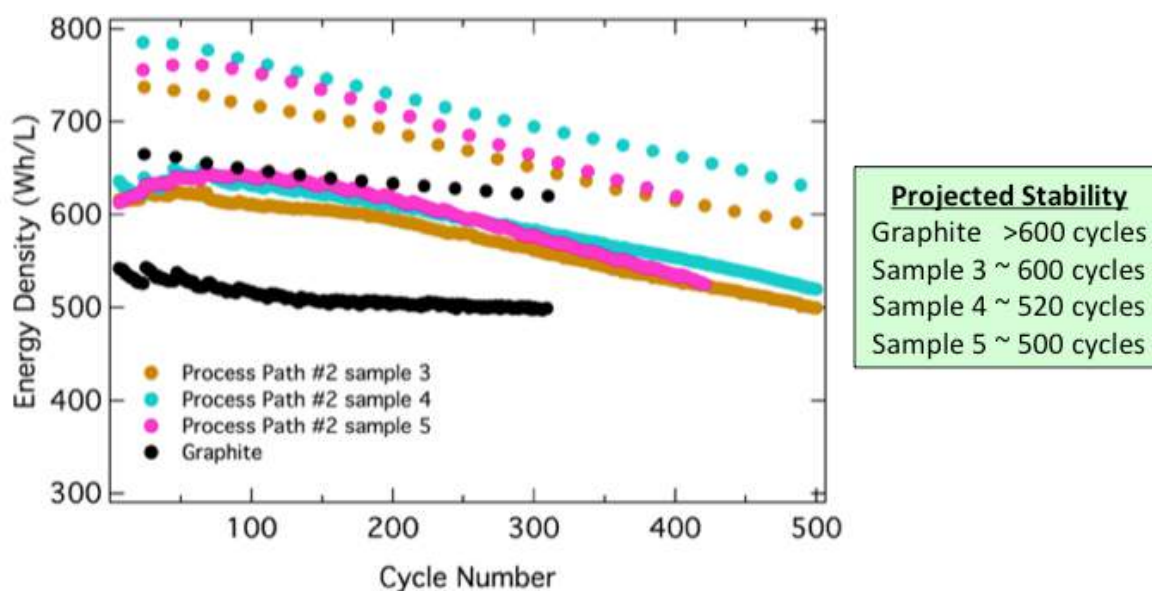


Figure I-70: Volumetric energy density (Wh/L) for Process Path 2 Si-C composites vs graphite, full cells cycled at C/2 rate with C/10 rate every 20 cycles, 2.5 – 4.2 V, with 1/2 hold, 1 M LiPF₆ in EC:DEC w/10% FEC, LiNiCoAlO cathode, excess anode=2-16%, anode=5% CMC-SBR, 5% Super-P, 59-63% graphite, 27-32% Si-C composite.

The data for volumetric energy density were calculated based on total volume (or mass) of anode and cathode materials, i.e., does not include other components of the battery system such as current collector, separator, or electrolyte. The anode comprised a blend of Si-C composite, conductive carbon, and graphite to achieve a capacity in the range of ~ 450 to 650 mAh/g, wherein the anode was paired with LiNiCoAlO (NCA) cathode. Details regarding the electrode and device preparation, as well as full cell testing parameters, are provided below Figure I-70. As can be seen, the performance of the Si-C composite lab scale is over 600 cycles.

Also during the first quarter of 2017, we made progress regarding our collaboration with Dr. Chongmin Wang and Dr. Langi Luo at Pacific Northwest National Laboratory (PNNL). Regarding this collaboration, we

analyzed numerous Si-C composite samples for not only their measured 2-dimensional and calculated 3-dimensional expansion by TEM during lithiation, but also their general structure, homogeneity, phase of silicon and/or carbon, primary particle size (Si-C composite size) and secondary particle size. Herein, we present the selected area electron diffraction (SAED) analysis of an exemplary Si-C composite corresponding to Process Path 2. The data are presented in Figure I-71. According to our collaborator's interpretation, there was no observable phase variation, in other words, the data were consistent with homogeneous distribution of nano silicon (~10 nm secondary particles) through the amorphous carbon matrix (~5 μm primary particles).

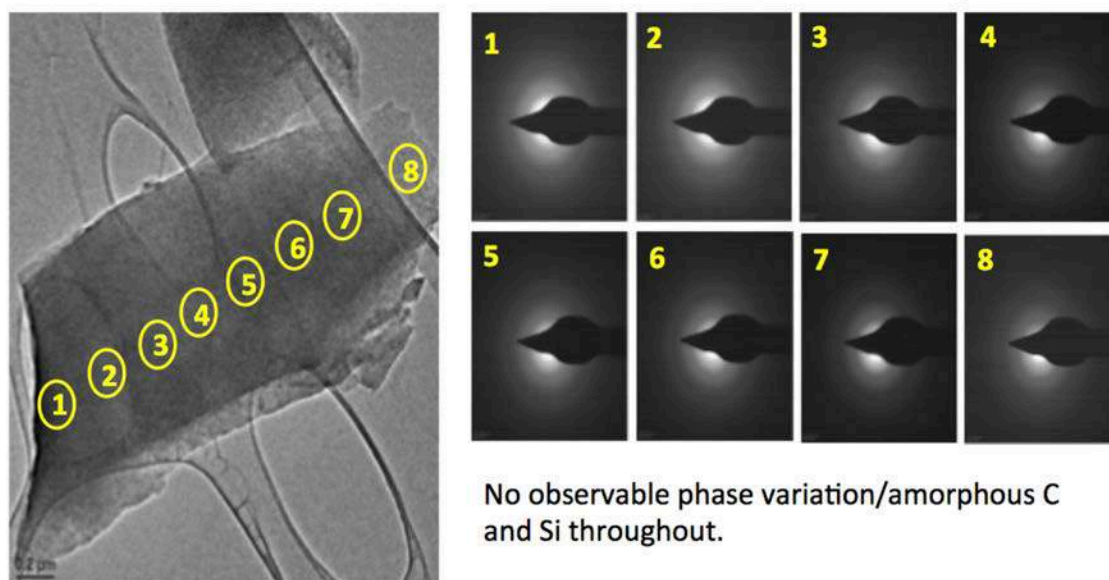


Figure I-71: SAED analysis of an exemplary Si-C composite corresponding to Process Path #2.

The second quarter of 2017 (Apr - Jun 2017) focused on achieving the project milestone to “Synthesize 1x10g Si-C with 1000 mAh/g; predicted 1000 cycles; < \$125/kWh projected cost.” To this end, we have presented to the DOE our achievement of 1000 cycle stability in a full cell coin cell as shown in Figure I-72 (on Wh/L basis) and Figure I-73 (on capacity retention basis), as presented to the DOE during a telecom held June 16, 2017. It was discussed that these data were generated for an electrochemical testing system wherein we employed an anode comprising a blend of Si-C composite (produced with Process Path 2, as discussed in previous reports) wherein said blend comprised typically ~30% Si-C, 60% graphite, 5% CMC-SBR, and 5% Super-P, and the anode excess in the full cell coin cell was typically 5-15%. It is noted that the 100 cycle stability achievement at this time involved cell optimization, specifically, pre-lithiation and voltage window of 2.5 – 4.12 V as noted in the legends to Figure I-72 and Figure I-73.

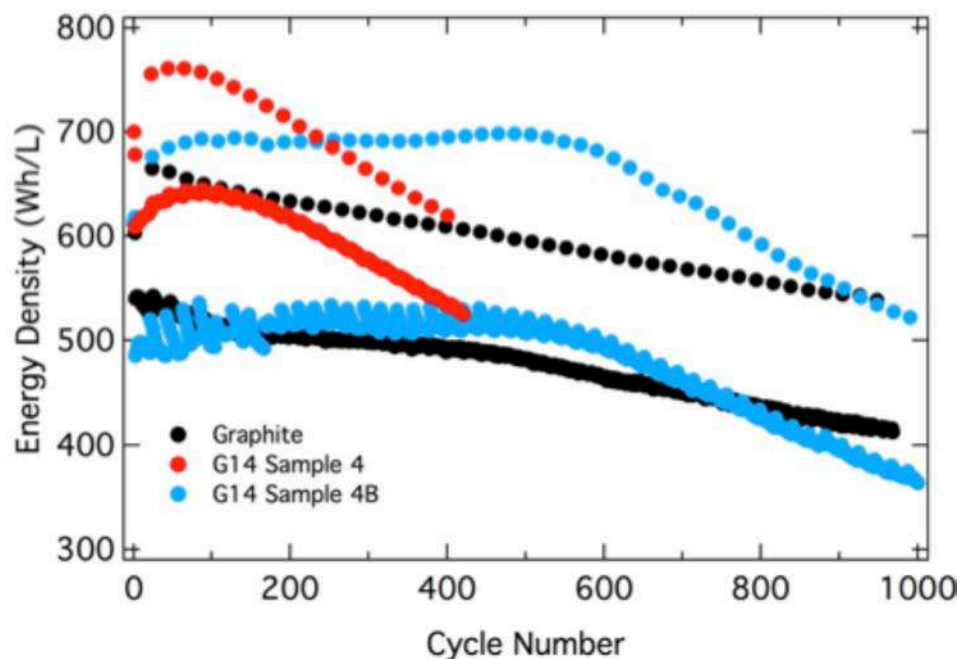


Figure I-72: Volumetric energy density (Wh/L) for Process Path 2 Si-C composites vs graphite, anode prelithiated by shorting with Li metal for 1 h prior to assembly, full cells cycled at C/2 rate with C/10 rate every 20 cycles, 2.5 – 4.12 V, with I/2 hold, 1 M LiPF₆ in EC:DEC w/10% FEC, LiNiCoAlO cathode.

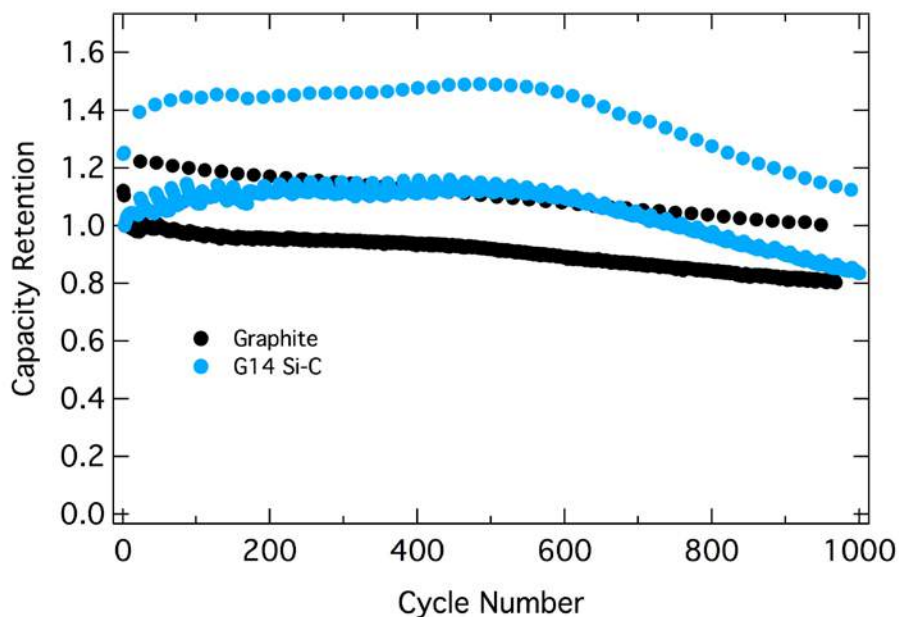


Figure I-73: Capacity retention (%) for Process Path 2 Si-C composites vs graphite, anode prelithiated by shorting with Li metal for 1hr prior to assembly, full cells cycled at C/2 rate with C/10 rate every 20 cycles, 2.5 – 4.12 V, with I/2 hold, 1 M LiPF₆ in EC:DEC w/10% FEC, LiNiCoAlO cathode.

We have made further progress regarding our collaboration with PNNL. Regarding this collaboration, numerous Si-C samples were analyzed for primary and secondary particle size, measured 2D expansion, phase of silicon and carbon, general structure and homogeneity. The data overview is presented in Table I-11.

Table I-11: Overview of Data Produced via the PNNL Collaboration.

#	Si wt %	Primary/Secondary Particle Size	Measured 2D Expansion	Phase of Silicon/Carbon	General Structure	Homogeneity
1	40	5 μ m	20-47%	a-Si&L-Gr-C	Dense porous structure	Good
2	46	5 nm /2-5 μ m	20-36%	Poly-Si&a-C	Fine Si NPs in a-C matrix	Good
3	48	10-20 nm/2-5 μ m	55-76%	a-Si&L-Gr-C	Uniform dense particle of LGC with a-Si	Great
4	42	50-100 nm/2-5 μ m	20-42%	Poly-Si&a-C	c-Si NPs on porous C scaffold	Good
5	34	50-100 nm/2 μ m	19-45%	Poly-Si&Gr-C	c-Si NPs on porous C scaffold with C coating	Good
6	41	30-40 nm/2 μ m	37%	Poly-Si&a-C	c-Si NPs aggregates on a-C	Great
7	39	20-30 nm/2-8 μ m	19-58%	Poly-Si&Gr-C	c-Si NPs aggregates covered with Gr-C	Great

Gr-C: Graphitic Carbon; L-Gr-C: Less Graphitic Carbon; Poly-Si: very fine poly Si NPs which shows on SAED pattern; a-C: amorphous carbon; c-Si: larger Si NPs which show scattered spots on SAED pattern; Homogeneity rate is based on the portion of the major phase.

It is important to note in Table I-11 that the interpretations and wordings are presented as provided by PNNL. As can be seen, the Si-C composites produced by Group14 can achieved 30-50% silicon loading in the carbon, wherein the reported silicon particle size can be as low as 5-100 nm for a primary carbon particle size in the range of 2-8 μ m. Various silicon and carbon phases can be achieved. Importantly, the reported 2-D particle expansion was as low as 19%, and the silicon distribution throughout the carbon particle was reportedly consistent with good or great homogeneity.

The primary focus during the third quarter 2017 (Jul – Sep 2017) – and our ongoing focus - concerns scale up towards pilot production (~1-10 kg). We have completed our down selection and equipment specification process. The deliverable for this activity was the ordering of the Si-C compounding reactor, and well as critical auxiliary equipment. The procurement of the Si-C compounding reactor and critical auxiliary equipment is underway. An important next step is the factory acceptance test, which is scheduled by the equipment vendor in mid-December 2017. Assuming a successful factory acceptance test, the equipment will be shipped and receipt is expected by end of December.

It was important to select a site for suitable and safe operation of the pilot equipment. To this end, we have considered various options, including installation of the equipment within the current EnerG2 facility in Seattle, WA. After careful consideration of the options, we decided to procure a new site for Group14. Specifically, Group14 has signed a lease for a ~4,000sf site in Woodinville, WA. Regarding this site, certain facility upgrades are underway in preparation of pilot plant installation. All such upgrades are planned for completion prior to receiving and installing the pilot equipment.

Conclusions

Group14 Technologies is developing low-cost, high-performing Si-C composite materials suitable as a drop-in for Li-ion battery anodes. We have successfully down-selected samples for scale up, and we have demonstrated ongoing performance improvements. We are also conducting mechanistic investigations into the stability afforded by our Si-C composites; in particular, our collaboration with PNNL has confirmed very low volume expansion for our materials. Regarding performance, we have demonstrated the potential to achieve 1000 cycle stability at lab scale. Our current focus is on the scale up towards pilot scale (1-10 kg), commensurate with the remaining project milestones.

Key Publications

1. US provisional patent application 62/469444, filed 09-Mar-2017.
2. USCAR talk entitled “Low Cost Manufacturing of Advanced Silicon-Based Anode Materials,” presented on May 16, 2017 at Detroit, MI.
3. Poster entitled “Low Cost Manufacturing of Advanced Silicon-Based Anode Materials,” presented on June 8, 2017 at the Annual Merit Review (AMR) meeting in Washington, DC.

I.B.2 Commercially Scalable Process to Fabricate Porous Silicon (Navitas Systems)

Pu Zhang, Principal Investigator

Navitas Systems
4880 Venture Drive
Ann Arbor, MI 48108
Phone: 734-205-1435
E-mail: pzhang@navitassys.com

Peter Faguy, Technology Manager

U.S. Department of Energy
Phone: 202-586-1022
E-mail: Peter.Faguy@ee.doe.gov

Start Date: November 17, 2015

End Date: June 30, 2016

Total Project Cost: \$1,181,766

DOE share: \$1,181,766

Non-DOE share: \$0

Project Introduction

Navitas Advanced Solutions Group developed a novel, commercially scalable approach to supply microporous silicon (μpSi) to lithium ion battery manufacturers (Figure I-74) intended to reduce the cost and environmental impact of high capacity anodes needed to meet the EV battery goals.

Silicon nanocomposite materials have been identified as a viable anode technology for EV batteries. Presently, high capacity silicon-based anodes rely either on materials that are expensive (e. g., silane or nano-silicon powder) or on processes that are limited by low yield methods (e.g., chemical vapor deposition). Microporous silicon potentially avoids these limitations and is attracting increasing attention as a lower cost alternative for the manufacture of high capacity silicon-based anodes. Microporous silicon suitable for EV batteries is not currently available as a commodity material. Microporous silicon can be produced at lab scale through a metal catalyzed hydrofluoric acid etching process. However, this process is expensive and hazardous. Our proposed production route facilitates the availability of μpSi to lithium ion battery producers and developers at a scale and cost able to support EV battery production.

Objectives

The objectives for this program were:

1. Optimize at bench scale each of three process steps used to manufacture microporous silicon (μpSi) powder and identify associated critical to quality (CTQ) criteria
2. Qualify low-cost precursor materials for production of μpSi powder
3. Transfer technology to NexTech (scale-up partner) and establish pilot scale μpSi production (>1.0kg/batch).
4. Validate materials performance in an open-source baseline prototype cell design. (Irreversible capacity loss <25% and 4-week self-discharge < 15% at 60°C)
5. Establish the economic feasibility of μpSi manufacturing process (<25 \$/kg at 1300 mAh/g).

The outcome of this program was a validated novel manufacturing process to provide a source of microporous silicon for EV battery production. The Navitas team transitioned this process from MRL 3 to MRL 6 (Manufacturing Readiness Level), providing the ability to deliver μpSi in adequate quantity to support pilot

scale electrode coating by EV battery OEM's at the scale needed to support cell design validation (typically 500 – 600 cells in the EV battery cell format)

Approach

To accomplish these goals Navitas teamed with Nexceris and Argonne National Lab (ANL) to establish a reliable domestic source of μpSi . Nexceris provided powder manufacturing scale up development and expertise. ANL performed material characterization and gives input to improve material design and process optimization. Navitas advanced this process from MRL 3 to MRL 6, providing the ability to deliver μpSi in adequate quantity to support pilot scale electrode coating by EV battery OEM's at the scale needed to support cell design validation (typically 500 – 600 cells in the EV battery cell format).

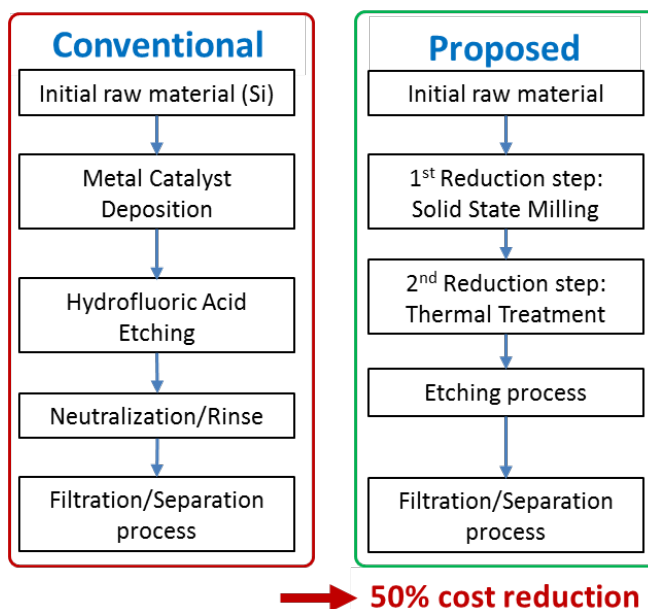


Figure I-74: Conventional production of porous silicon uses hazardous hydrofluoric (HF) acid and expensive metal catalyst. Navitas route reduces cost and impact, using SiO_2 raw material and no HF.

The proposed μpSi production comprises a three-step process involving the usage of inexpensive commodity grade silicon oxide (refer to Figure I-74, Figure I-75, Figure I-76, and Figure I-77). Each step employs scalable industrial processing methods (i.e., mechanical mixing, thermal reduction, and etching). The combination of two steps reduces process temperature and times for the complete reduction silica, reducing operating cost compared to other methods. In addition, by avoiding usage of hydrofluoric acid, the proposed process also has environmental and non-hazardous advantages over the conventional route.

Results

In Budget Period (BP1), Navitas optimized μpSi powder fabrication process at lab scale and transferred thermal treatment and oxide removal process technology to Nexceris for scale-up. Navitas and ANL carried out detailed analytical characterization and electrochemical evaluation in a baseline nanocomposite anode design. The lab-scale μpSi powder met all the targeted properties (refer to Table I-12).

Table I-12: Physical properties of current μpSi powder

Property	Target	Actual
Particle size (μm)	5 - 50	10 - 30
BET surface area (m^2/g)	< 200	28
Tap density (g/cm^3)	> 0.6	0.63
True density (g/cm^3)	2.0 - 2.4	2.2

Navitas and Nexceris developed a cost model for the μpSi manufacturing process. The cost model projected high volume (e.g., 1MT/month) manufacturing cost of μpSi at 50% lower cost than that of the conventional HF etching process. Further, a Si composite anode made with μpSi precursor will meet the EV Everywhere goal of \$125/Wh for EV battery pack at anode cost < \$25/kg (when combined with high Ni NCM cathode)

In Budget Period 2 (BP2), Navitas used Robust Engineering methods to optimize the mechanical milling process at an intermediate scale of 200g. The less influential parameters were relaxed to improve throughput and reduce milling time. Improved milling parameters were applied to large scale runs by an industrial milling partner who demonstrated results consistent with the lab scale powder. Navitas and the milling partner supplied enough milled precursor powder to Nexceris for the final demonstration.

Nexceris designed and built a thermal treatment furnace capable to process up to 10kg/batch. Calcination runs were conducted at 2kg scale. XRD diffraction analysis confirmed material composition and reproducibility. Additionally, Nexceris has designed and built the system for acid washing and powder filtration. The reactor can process > 4kg of calcined powder. Figure I-75 summarizes the progress under the program

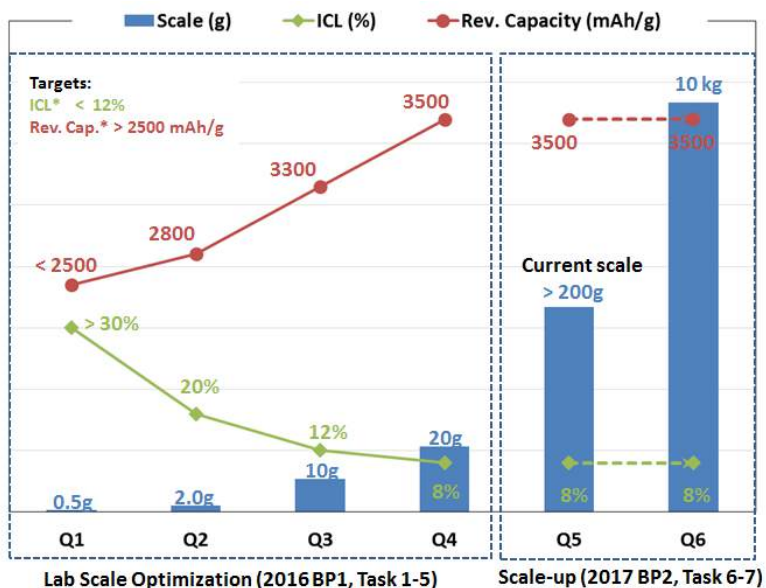


Figure I-75: Nearly theoretical capacity was reached as ICL was reduced to <10% as an indication that residual oxides were successfully removed. Batch size was scaled to multi-kg, adequate to support customer pilot scale electrode coating requests.

Navitas and ANL carried out analytical characterization, in addition to validation by electrochemical performance. The μpSi produced at 1kg/batch has shown a reversible capacity of ~3300mAh/g with an 8% ICL. The pilot scale μpSi powder met all the targeted properties (refer to Table I-12). The cost model

developed in BP1 was updated using data from the scale-up system. The model projects that the new processed μ pSi powder costs 50% lower than the conventional HF etched powder.

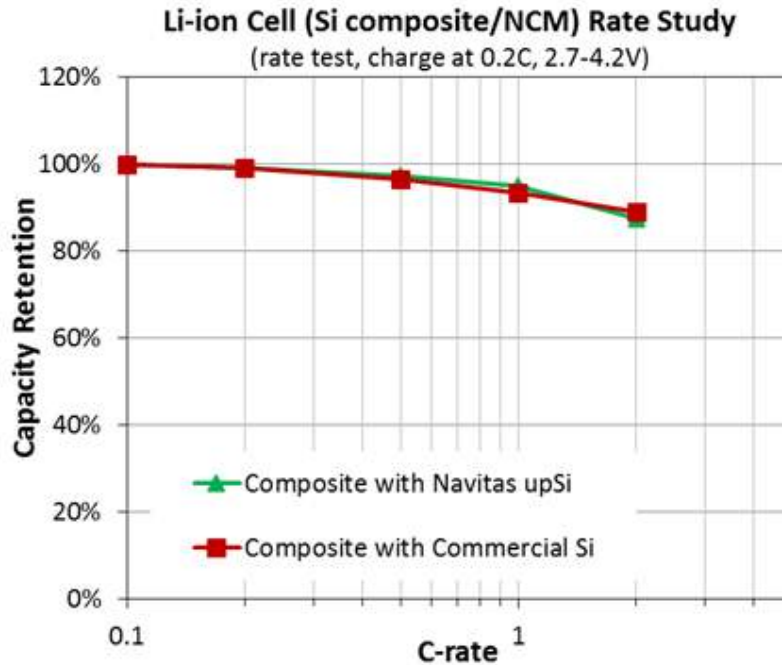


Figure I-76: Cells prepared using anodes incorporating Si composite anodes at EV battery loadings were able to meet cycle rate requirements and match commercial Si anode materials produced using higher cost materials and processes.

Full cells were assembled producing Si composite electrode using Navitas upSi. Rate and cycle life data are plotted in Figure I-76 and Figure I-77:

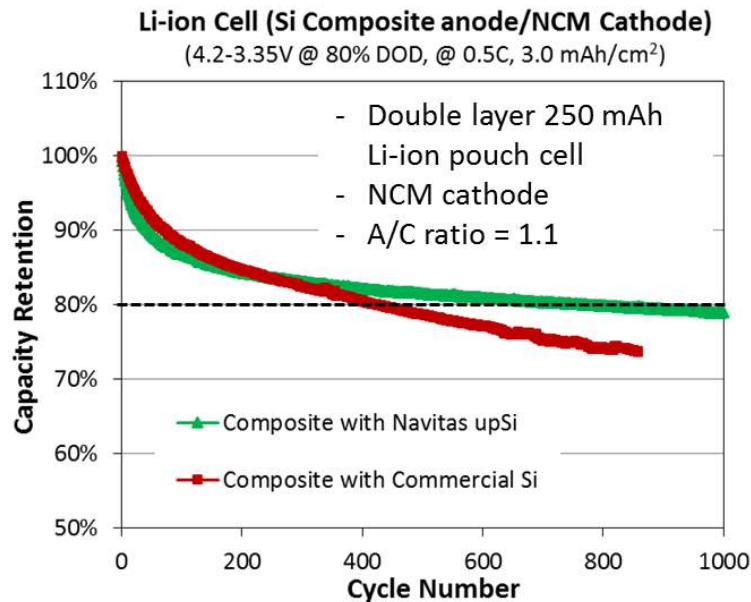


Figure I-77: In full cell testing at EV loading, Navitas showed 100% improvement in cycle life and was able to reach >900 cycles. The Si anode was 92% active material having 650 mAh/g reversible capacity.

Conclusions

The Navitas μpSi fabrication process represents a novel approach to reduce the cost of silicon anode material manufacturing. This program met most of the MRL 6 criteria through a pilot scale demonstration for the manufacturing of porous silicon powder, while minimizing raw material added cost and limiting hazardous and environmental impact and using scalable industrial processing (i.e., mechanical milling, thermal reduction).

This process has been shown to be more efficient (higher yield) and economical on scaling up than conventional metal-assisted etching. The process significantly reduces the cost on \$/mAh basis versus existing anode materials. The μpSi powders can be modified by customers to form nanocomposite structures through blending with graphite or coating with carbon or a metal oxide to decrease initial capacity loss (ICL) and improve cell cycle life, a key barrier to adoption of silicon anodes into EV batteries.

Key Publications

Processes to fabricate porous silicon and its use as feedstock for secondary battery electrodes WO 2017008050 A1

Application number	PCT/US2016/041619
Publication date	Jan 12, 2017
Filing date	Jul 8, 2016
Priority date	Jul 8, 2015
Inventors	Peter Aurora, Pu Zhang, Michael Wixom

I.B.3 New Advanced Stable Electrolytes for High Voltage Electrochemical Energy Storage (Silatronix, Inc.)

Peng Du, Principal Investigator

Silatronix, Inc.
3587 Anderson Street Suite 104
Madison, WI 53704
Phone: 608-661-1964; Fax: 608-661-4630
E-mail: pdu@silatronix.com

Peter Faguy, Technology Manager

U.S. Department of Energy
Phone: 202-586-1022
E-mail: Peter.Faguy@ee.doe.gov

Start Date: October 1, 2015

End Date: February 28, 2018

Total Project Cost: \$1,665,825

DOE share: \$1,332,660

Non-DOE share: \$333,165

Project Introduction

High-voltage mixed oxide cathode materials present several challenges due to their high chemical reactivity and electrochemical driving force at high cathode potentials. Uncontrolled surface reactions lead to significant decreases in capacity, increased cell resistance, and increased leakage current through the formation of SEI layers and leaching of metal ions from the oxides. In addition, carbonate electrolytes release CO₂ under oxidizing conditions, which leads to undesired surface film formation, as well as internal pressurization of the cell that can result in leakage or explosive release of the electrolyte. To date, no solvent system has been identified that meets all the requirements for compatibility with high-voltage cathodes including high electrochemical stability, low viscosity, wide temperature stability, and low cost.

Silatronix® is developing advanced, stable, high-voltage electrolytes to meet the DOE goals for electrochemical energy storage in transportation systems. Early generations of OS solvents have not been on Li-ion Road Maps, but recent Silatronix® innovations have created new OS3® solvents that exhibit exceptional electrochemical stability under the oxidizing conditions associated with high-voltage (HV) cathodes (exceeding 7V vs. Li/Li⁺ before onset of significant parasitic breakdown current at Pt electrodes) and meet fundamental metrics (conductivity, viscosity) necessary for cell performance (i.e., rate capability, low temperature) in transportation applications and should therefore be considered for the roadmap.

Objectives

Silatronix® proposes to synthesize, characterize, and integrate novel solvents and additives into electrolytes to create the conditions necessary for reliable, long-lasting cells which operate at high-voltages (> 5V). This program will investigate the fundamental mechanisms of complex electrolyte behavior building upon advanced research by Silatronix® in new solvents and electrolyte formulations developed with these solvents. OS solvents have been shown to maintain synergy with existing electrolyte components, as well as advanced electrolyte salts and additives under development. Specific component materials developed by US Army Research Laboratory (ARL) for use in advanced electrolyte formulations will be evaluated for synergy with OS advanced solvents and used to demonstrate state-of-the-art voltage stability and commercially viable performance characteristics (e.g., rate). High voltage state-of-the-art electrodes from Argonne National Laboratory (ANL) and US Army Research Laboratory (ARL) will be evaluated with candidate formulations. The work plan includes the following specific targeted metrics to demonstrate electrolyte or electrolyte enabled performance:

- Synthesize, characterize, and integrate novel solvents and additives into electrolytes to create the conditions necessary for reliable, long-lasting cells which operate at high-voltages ($> 5\text{V}$).
 - Specific metric: oxidative stability in reference system (Pt electrode)
 - Prevent oxidative breakdown voltage above 6 V.
 - Provide parasitic current below 0.02 mA/cm^2 after 10 hours above 6 V at 50°C .
- Investigate the fundamental mechanisms of complex behavior of new solvent and additive materials within formulations containing commercial electrolyte components (solvents, salts, additives).
- Demonstrate commercially viable performance characteristics using state-of-the-art high voltage electrodes from Argonne National Laboratory (ANL) and US Army Research Laboratory (ARL).
 - Specific metric: cycling performance in 5V LNMO full cells
 - Full cell initial capacity \geq carbonate control
 - Over 80% initial capacity after 300 cycles at $\geq 55^\circ\text{C}$

Approach

Silatronix® and ARL are synthesizing new materials based upon rational molecular design to achieve the superior oxidative stability required for HV applications. The fundamental electrochemical behavior of these materials is studied in reference cells to determine the oxidative breakdown voltage and mechanism of breakdown to produce a library of materials with superior fundamental oxidative stability for evaluation.

The performance and safety of the new HV solvents and additives in formulated electrolytes are evaluated with the HV cathodes provided by ANL (5V LNMO). Surface analysis is conducted after cycling to identify underlying mechanisms of degradation (i.e., surface film formation, metal dissolution, cathode morphology changes). Differential scanning calorimetry (DSC) is conducted on de-lithiated cathode material to understand the safety impact of the new HV materials. Solvation studies, using ESI-MS and NMR spectroscopy methods, is conducted to understand the Li^+ solvation behavior of the new OS solvents. These studies expand the understanding of the fundamental mechanistic behavior and include the relationship between the structure and properties of individual electrolyte components and the performance of a complete system. Top performing HV formulations identified are tested in 5V LNMO pouch cells (13 layers, 200-300 mAh) at ANL. The pouch cell analysis focuses on cycling stability and pouch swelling.

Results

Evaluation of New Solvents in Pt Reference Cells

In this program, Silatronix® synthesized more than 12 organosilicon (OS) solvents and characterized their physical properties and electrochemical behavior. These solvents include members of the high stability OS3® structural family and advanced OS4 family solvents which contain different functional groups than OS3®. Generally, these OS materials provided superior oxidative stability in Pt reference cells by linear scanning voltammetry (LSV) and constant voltage floating tests at 30°C and 50°C . As described in the 2016 report, four OS3® family solvents (OS3®, OS3a, OS3b and OS3c) with LiPF_6 salt satisfied the Go/No-Go Metric #1 (breakdown potentials $> 6\text{V}$ at 30°C) and are good candidates for HV systems. Furthermore, the parasitic currents of these OS3® family electrolytes showed superior stability and satisfied Go/No-Go Metric #2 (50°C parasitic current $< 0.02\text{ mA/cm}^2$ at 6V). During this year, the oxidative stability of several more OS3® family solvents and two additional OS4 family solvents were evaluated in Pt reference cells using the same methods.

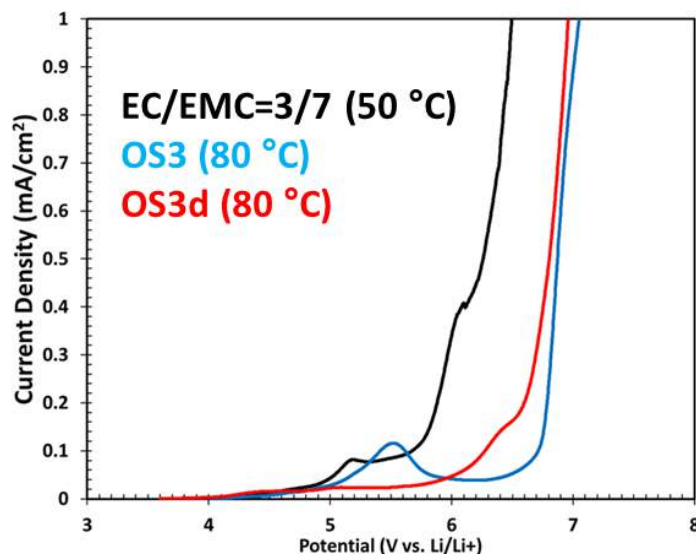


Figure I-78: Oxidative stability comparison at high temperature of OS3d vs OS3[®] vs carbonate control electrolyte.

Figure I-78 summarizes the oxidative stability (vs. Li/Li^+) measured at 80°C for OS3d (new OS3[®] family molecule made this year) and OS3[®], and measured at 50°C for the carbonate control (EC/EMC, 3/7 %v). All electrolytes contain 1M LiPF_6 . OS3d shows excellent oxidative stability between 5 and 6V. The measurement was conducted at elevated temperature as OS3d is a solid and does not dissolve LiPF_6 at room temperature. Figure I-79 shows the parasitic current behavior at 80°C for OS3d and OS3[®] with LiPF_6 in a 3-electrode cell (Pt: WE, Li/Li^+ : CE, RE). Overall, the behavior at 5.0 and 5.5V is similar for OS3[®] and OS3d. Neither shows a significant current increase at these voltage levels. At 6.0V, OS3[®] does not show an increase in parasitic current while OS3d does (< 0.01 vs. 0.04 mA/cm^2). At 6.5V, both OS3[®] and OS3d show higher parasitic currents but OS3d has a significantly lower current density (0.06 vs. 0.16 mA/cm^2). Therefore, OS3d is a good candidate for the $>5 \text{ V}$ HV system.

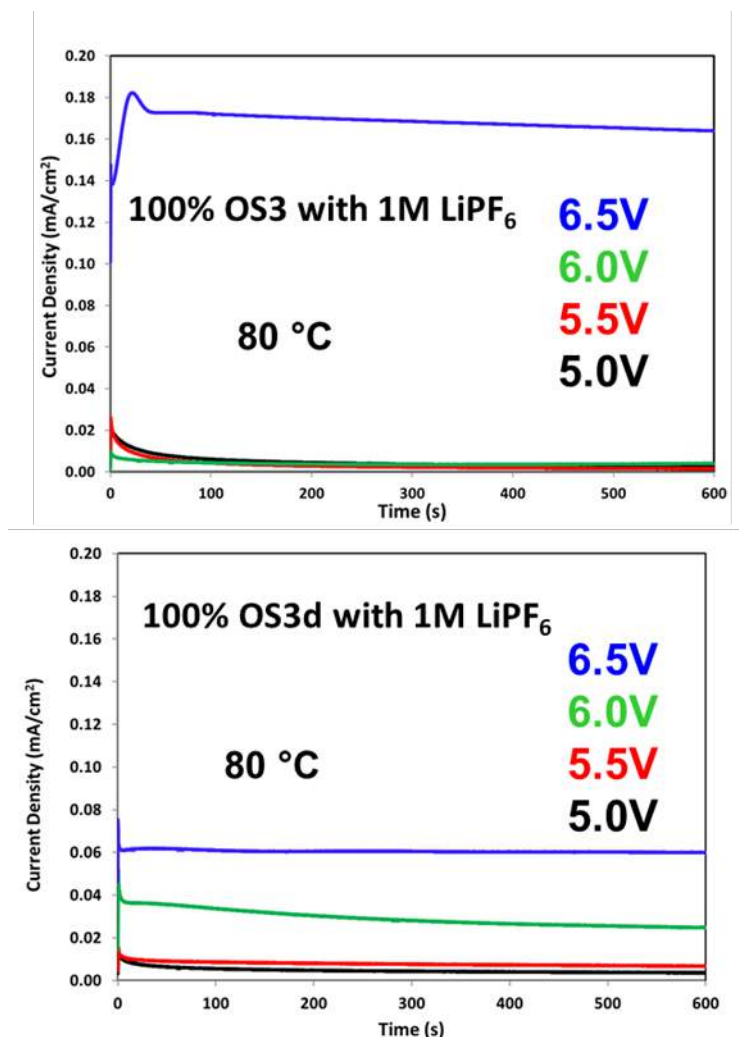


Figure I-79: Parasitic current results for LiPF₆-based electrolytes in a 3-electrode cell (Pt: WE, Li/Li⁺: CE, RE).

In addition, OS4a and OS4b (OS4 family solvents) demonstrate a higher breakdown voltage than the EC/EMC carbonate control and OS3[®], and will be evaluated in 5V LNMO full cell.

Full Cell Cycling and Stability Performance

ANL delivered single side coated 5V LNMO and MCMB electrodes to Silatronix[®] and ARL for the evaluation of advanced HV electrolyte materials. Initial screening of OS electrolytes was completed last year using a refined electrochemical method in both 5V LNMO half cells and full cells. Furthermore, cycling in LNMO half cells and full cells confirmed the importance of additives. The effect of OS3[®] concentration on full cell cycling performance was examined in coin cells previously in this program. Based upon the performance improvement observed for 2% OS3[®] and 5% OS3[®], similar formulations were tested for OS3d, OS4a and OS4b. Figure I-80 summarizes the full cell cycling results for these new OS structures tested at the 2% concentration level. Both OS4 family molecules (OS4a – purple data, OS4b– green data) show improved capacity retention compared to the carbonate control. The enhanced stability OS3d (blue data) shows similar performance to the carbonate control blend. These OS formulations and the carbonate control have been selected for the first round of pouch cell testing at ANL. Each pouch cell undergoes formation (including de-gassing) followed by a rate test, HPPC test, and finally cycle life testing. All testing occurs at 30°C with a 3.5 to 4.9V voltage window.

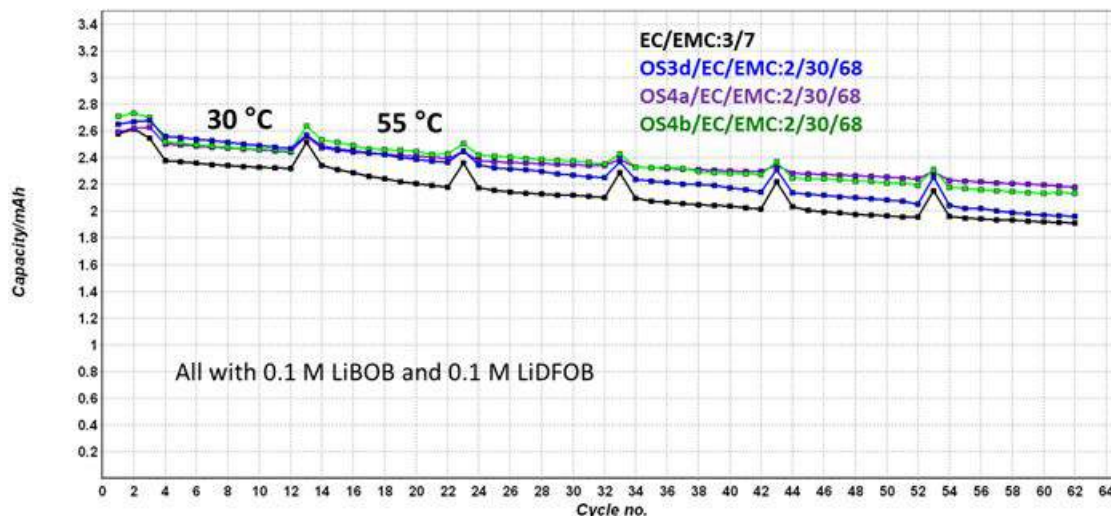


Figure I-80: Comparison of LNMO full cell performance with control carbonate electrolyte and 2% OS formulations (all with 1M LiPF₆). Cells are cycled at C/10 for 2 formation cycles and at C/2 for 10 cycles at 30°C, then continued 50 cycles at C/2 between 3.5 and 4.9 V at 55°C.

During the first round of testing, all pouch cells exhibited a large amount of gassing and the initial rate test could not be completed. After another de-gas step, the cells were transferred to the HPPC and cycle life tests. However, gassing continued and all cells failed quickly. Based on this result, this year Silatronix® continued the screening of HV electrolyte formulations in 5V LNMO cells focused on reducing gassing. In addition, Post-test degradation analysis was conducted, including XANES measurements at Argonne National Laboratory's Advanced Photon Source on beamline BM20 and SEM and XPS measurements at University of Wisconsin–Madison. The post-test degradation analysis serves to identify the composition of and evaluate the stability of the SEI layer and the bulk structure of the cathode active material after cycling.

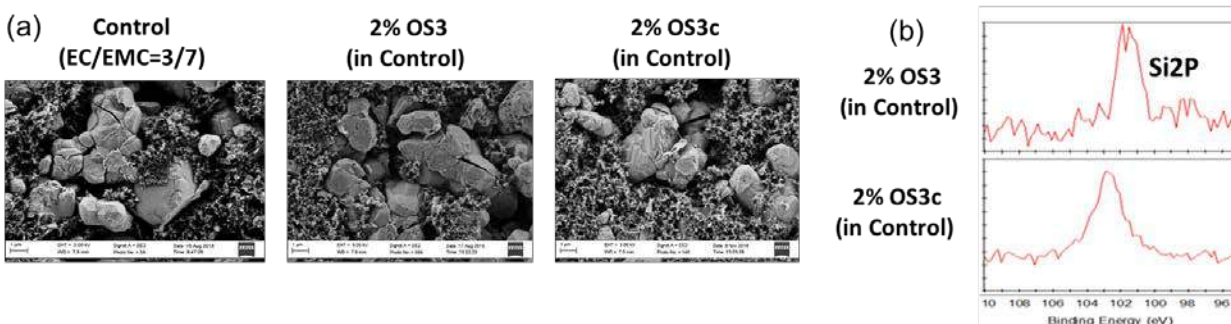


Figure I-81: (a) SEM images and (b) XPS surface composition data for the de-lithiated LNMO cathode after cycling (50 cycles at C/2 between 3.5 and 4.9 V at 55 °C) with control carbonate and 2% OS3®, and 2% OS3c formulations. All electrolytes contain 1M LiPF₆.

Figure I-81 summarizes surface analysis data for 5V LNMO cathodes recovered from cells cycled with 2% OS3®, 2% OS3c and the carbonate control. The morphology of the electrode surfaces at 50% SOC was examined using scanning electron microscopy (SEM) to evaluate the SEI layer morphology and mechanical integrity. In Figure I-81a, the surface morphology of the cathodes is similar regardless of the specific electrolyte formulation. Therefore, the addition of 2% OS3® or 2% OS3c does not significantly affect the thickness and morphology of any surface layers formed on the LNMO cathode. Information regarding the composition of any surface layers formed on the LNMO cathode was obtained using X-ray photoelectron spectroscopy (XPS). Figure I-81b shows data from the Si(2p) regions for the cathode surface layers formed with 2% OS3® and 2% OS3c formulations. XPS surface analysis showed silicon present on cathode samples

after cycling with 2% OS3[®] and OS3c electrolytes, indicating that OS solvents are involved in cathode film formation. Similar results were obtained for anode samples after 50 cycles at 55°C, which means OS solvents also participate in anode SEI formation. Due to the gassing issues observed in the first pouch cell-build, post cell analysis using X-ray absorption spectroscopy (XANES) was performed to identify the stability of the bulk structure of the cathode active material. XANES spectra show more apparent shifts are present in the Ni K-edge data compared with Mn K-edge data, which indicates the oxidation of Ni(III) to Ni(IV) is the major contributor of this LNMO cathode, and the Li lost during cycling is more related to Ni-bonded Li rather than Mn-bonded Li. Among different electrolyte formulations, little to no change in the crystal structure is observed with or without OS molecules. This trend does not agree with the cycling performance differences observed and suggests the cathode/anode SEI layers lay a major role in cycling performance.

ESI-MS experiments were continued this year at ARL to investigate the Li⁺ solvation behavior of OS3[®]/EC/EMC and OS3d/EC/EMC electrolytes. A summary of the results is shown in Figure I-82 and Figure I-83. Both OS3[®] and OS3d consistently coordinate with Li⁺ more strongly than EC or EMC. Clusters of Li⁺ with two solvents were the best represented in ESI-MS data. OS3d has a larger population of OS3d+EMC clusters than OS3d+EC, which is the most common OS3[®]/carbonate cluster. OS3d also shows lower populations of all non-OS3d clusters in general. Figure I-83 shows that OS3d appears to displace carbonate solvents from the Li⁺ solvation sheath more than OS3[®] and is a stronger Li⁺ solvator than OS3[®].

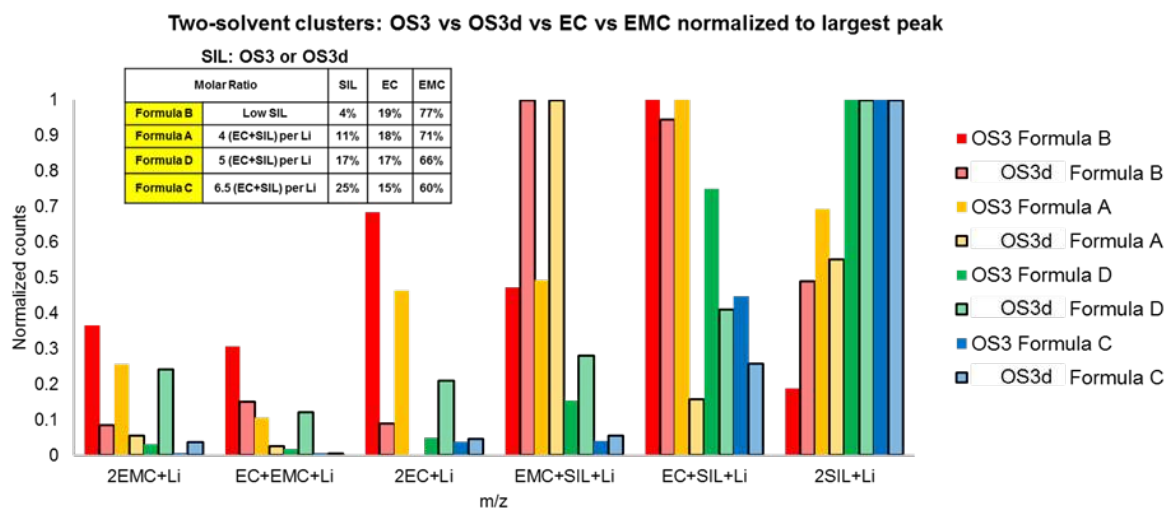


Figure I-82: Normalized ESI-MS counts as a function of cluster for OS/EC/EMC electrolyte formulations.

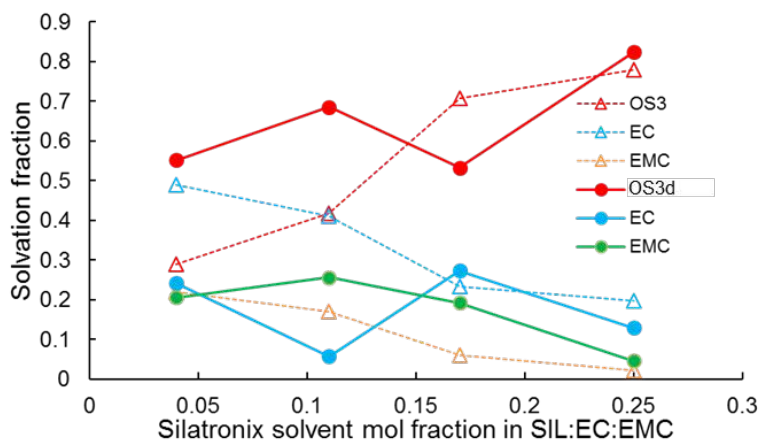


Figure I-83: Calculated fraction of bulk solvents participating in solvation based upon ESI-MS results in the previous figure.

Since the analysis of Li^+ solvation in HV electrolytes using an ESI-MS technique demonstrates that OS3[®] or OS3d compete well with EC for solvation of Li^+ and may contribute to the formation of SEI layers, Silatronix[®] performed Li^+ solvation studies using ^{13}C and ^{15}N NMR spectroscopy to evaluate Li^+ solvation behavior in the bulk solution. The competition between OS3[®] family solvents and commercial carbonate solvents (EMC, EC) was investigated in binary mixtures. Results show that OS molecules participate in Li^+ coordination in all electrolytes tested and certain modification of the functional group on the silicon can enhance or impede competition with EC and EMC.

Finally, due to the gassing issue observed in the 1st pouch cell-build, the 2nd pouch cell-build at ANL has focused on electrolytes with higher EMC content (lower EC content) and newer OS solvents (e.g., OS3d and OS4b). In addition, we revised our pouch cell testing plan to run the same test steps (Formation, Rate Study, HPPC and Cycle Life) with the new voltage window of 3.5-4.7 V to further reduce gassing. ARL also continued the electrolyte optimization in higher EMC content formulation using different HV additive packages. The results demonstrate that despite initial improvement in 30°C cycling capacity by all additives, only the HFIP additive exhibits high temperature stability and reliably improves high temperature cycling performance. Since the FEC containing electrolytes also showed gassing, additive optimization has focused on HFIP or borate additives (e.g., LiBOB, LiDFOB). Based on previous coin cell and pouch cell testing results, 8 high voltage (HV) electrolyte formulations were selected by Silatronix[®] and delivered to ANL for testing. Cells containing three HV electrolytes finished cycle life testing (422 cycles total) with ~70% capacity retention, which is superior to the carbonate control (~50% capacity retention after 222 cycles). Based on pouch cell cycling results from this round, six more electrolytes were optimized at Silatronix[®] and delivered to ANL in Q8. Cycle life testing and gas generation for these formulations are in progress and will be summarized in our final program report.

Conclusions

The focus of this program is the fundamental evaluation of high stability OS solvents and performance of OS-containing high voltage (HV) electrolyte formulations in 5V LNMO full cells. All OS molecules evaluated in this year demonstrate similar properties as previously tested OS molecules, including higher flash points than the carbonate control (EC/EMC, 3/7 %v). Superior oxidative stability (above 6V) is observed for new OS molecules in reference cells (Pt) by linear scanning voltammetry (LSV) and floating current testing. Full cell testing found that the addition of 2% OS3[®], OS3d, OS4a and OS4b improves the 55°C cycling performance by reducing capacity degradation across 50 cycles compared to the EC/EMC control. ARL continued the analysis of Li^+ solvation in HV electrolytes using an ESI-MS technique, which demonstrates that both OS3[®] and OS3d consistently coordinate Li^+ more strongly than EC or EMC. Clusters of Li^+ with two OS are the best represented in ESI-MS data. Silatronix[®] continued the analysis of Li^+ solvation in HV electrolytes and results show all OS solvents participate in Li^+ solvation in EC and EMC binary mixtures at all tested carbonate concentrations. XANES spectra found little or no change in the crystal structure of the LNMO cathode based upon electrolyte formulations (with or without OS). This suggests the cathode and anode SEI layers are a key factor for cell performance. Due to the gassing issue observed in the first pouch cell-build, full cell testing has focused on electrolytes with higher EMC content, lower OS solvent concentration, and a reduced voltage window (4.7 vs 4.9V). To date, several electrolytes completed both the initial cycle life testing (222 cycles) and an additional 200 cycles. These formulations demonstrate much better cycling performance than the carbonate control. A final cycling testing and gas generation study are in progress to examine the behavior of the final six optimized HV electrolytes.

I.B.4 Improve the Safety Performance of Li-ion Battery Separators and Reduce the Manufacturing Cost using Ultraviolet Curing and High Precision Coating Technologies (Miltec UV International)

Dr. John Arnold, Principal Investigator

Miltec UV International

146 Log Canoe Circle

Stevensville, MD 21666

Phone: 410-604-2900; Fax: 410-604-2906

Email: gvoelker@miltec.com; jarnold@miltec.com

Peter Faguy, Technology Manager

U.S. Department of Energy

Phone: 202-586-1022

Email: Peter.Faguy@ee.doe.gov

Start Date: October 1, 2014

End Date: June 30, 2017

Total Project Cost: \$2,354,000

DOE share: \$1,955,000

Non-DOE share: \$399,000

Project Introduction

This project was successfully completed this year. A commercial scale system (Miltec CX400) utilizing flexographic printing technology and UV curable binder was designed, built and operated to demonstrate the cost saving and performance enhancing potential of UV technology for the manufacture of ceramic coated separators. Polyethylene or polypropylene or layered polyolefins PP/PE/PP are the most common separators for Li-ion battery separators. These thermoplastic separators typically melt between 130-160°C. While these temperatures are well above the normal operating temperature of lithium batteries, in the rare event something goes wrong, these temperatures can be reached. At such elevated temperatures, they can easily shrink to 60% of their original size—at that point they are not preventing the anode and cathode from touching, so the battery escalates from being too hot to being on an irreversible thermal runaway path until the battery dies or ignites. To prevent high temperature shrinkage and provide better structural strength and insulation, separator manufacturers are coating separators with a thin ceramic layer. (See Figure I-84.) Ceramic coated separators are considered an essential safety component of any large or high energy density battery, including EV or hybrid car batteries. The objective of this cost shared contract was to develop and demonstrate safer coatings and less expensive processes for ceramic coated separators. It is the intent of this project that the development of this technology will lead to safer vehicle batteries and faster incorporation and acceptance of hybrid and electric vehicles.

Objectives

The project had multiple objectives:

- To further develop and demonstrate the use of Ultraviolet (UV) curing technology to reduce the cost of applying ceramic coatings onto Li-ion battery separators by more than 50% while not decreasing the porosity of the separator by more than 10% and improving the safety attributes by reduced shrinkage and overall reduced risk of thermal runaway. Previously identified UV curable binders and associated curing technology will be shown to reduce the time required to cure separator ceramic coatings from tens of minutes to less than one second. This can result in increases in process speeds and significantly reduced capital cost, operating cost, and energy consumption.

- Develop and exercise a cost model to verify the cost savings.
- Investigate the use of patterns applied with high speed coating technology to improve the safety and performance of ceramic coated separators as well as reduce the cost of separators in a Li-ion battery.

UV Ceramic Coated 16 μ m PE Separator barely shrinks after 0.5 hour @ 180°C.

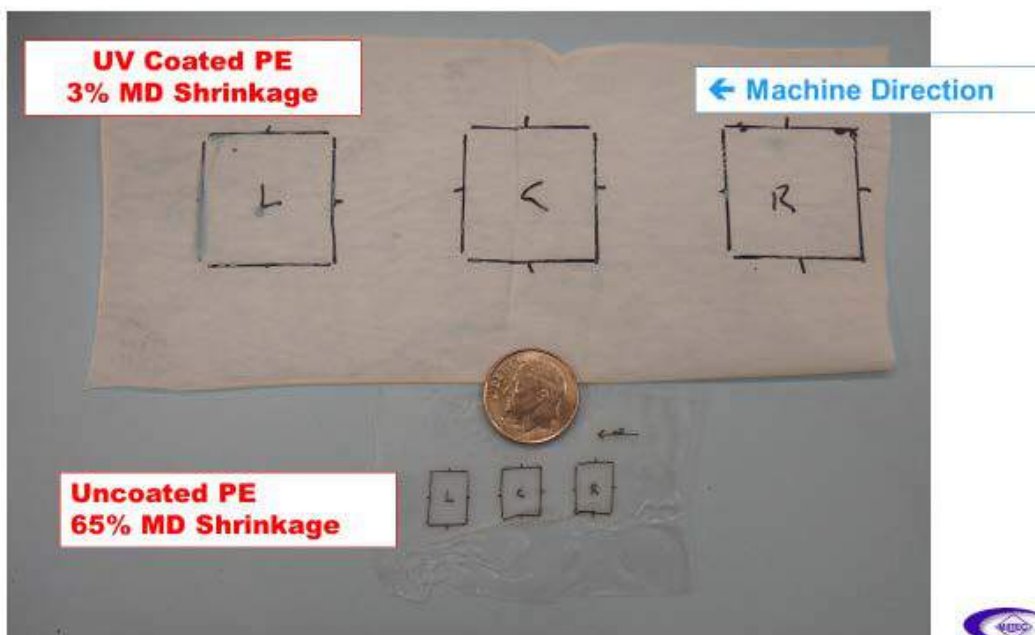


Figure I-84: PE Separator Shrinkage with and without UV Ceramic Coating

Approach

This project employed an iterative process of technology evaluation, implementation, testing, and resulting optimization. Multiple samples of ceramic coated separators were prepared using a combination of various UV curable binder chemistries and printing patterns. Multiple analytical tests were conducted to determine characteristics such as: porosity, tear strength, thermal transfer, puncture strength, thermal shrinkage, and permeability. At the end of this iterative development, printing patterns and optimum UV chemistries and base separator materials were coated using the Miltec UV CX400 and ceramic coated separators were prepared for extensive evaluation. Miltec received separator base material from various vendors; including Celgard, and applied either single or double sided ceramic coatings using the UV CX400 unit. After in-house testing, the coated samples were submitted to the vendors for extensive further evaluation. ANL conducted electrochemical and physical tests on the cells as well as the analytical tests. In addition to a UV curing process, we have developed a flexographic coating process specifically designed for separators to print and change patterns at a fraction of the cost. The ability to print patterns is another innovation of this project. By printing patterns, we should be able to maximize ionic flow through the separator while still providing the protection of a ceramic layer and reinforcing the separator against thermal shrinkage.

Results

The specific performance goals are shown in the tables below.

Table I-13: Performance Goals for Ceramic Coating Applied to 16 μm Trilayer, PP and PE

Parameter	Goal
Ceramic coating thickness and material	4 μm Aluminum Oxide (0.5-1 μm diameter.)
Gurley # (permeability) of coated separator	<10% increase over base uncoated separator
Shrinkage, Trilayer, and PP	MD <5% at 1 h, 150°C TD <3% at 1 h, 150°C
Ceramic coating cost	<\$0.20 /m ²
Reduced thickness base separator	6-10 μm

Table I-14: Demonstrated Results

	Uncoated	Gurley's	Shrinkage			Coated	Gurley's	Shrinkage		
	Thickness, μm		130	150	180	Thickness, μm		130	150	180
PP	16	12	12.50%			6	21	1.10%		
trilayer	20	19	23.10%	29.30%		4	23		0.70%	
PE	14	6.7		40%		3+	9		1.60%	
Cellulose	25	1.4		0%		3+	2.5		0%	
UHMWPE	14	6		55%		4	11	(double sided coating of 2 μm)		4 %
PE	12	8.8	13.80%			1	11.1	2.20%		
PE	5	4.3	24.30%			1	5.9	7.50%		

As shown in Table I-14, the performance goals related to the use of a UV binder for shrinkage and permeability preservation for PP were all met or exceeded, with the exception of Gurley #. The interim goal of the project for PE was designated as 5% at 130°C and that value was obtained with the exception of one PE separator of 5 μm thickness. The 5 μm thick separator with a 1 μm thick costing reduced the shrinkage from 24% to 7.5% at 130C.

As an additional process advancement we incorporated the flexographic process (Figure I-85) with our UV process. UV will work with roll and all forms of gravure, but there are advantages to the flexographic process. The accuracy of the flexographic process far exceeds that of the separator industry. Note the separator film does not go through a bath, when the press starts and stops the plate cylinder engages and disengages the film. This makes film and coating changeovers, cleaning, and many other processes quick and easy.

Besides introducing the concept of flexographic printing to the separator industry, we introduced the concept of printing ceramic patterns instead of the conventional solid coatings. The primary advantage of the patterned ceramic coating is that it allows more ion flow than the solid coating, while providing less shrinkage and more insulation than that of the uncoated separator. Many patterns were printed and tested for shrinkage. The pattern shown in Figure I-86 where the cross hatch is line with the MD and TD directions of the roll was most effective at reducing shrinkage.

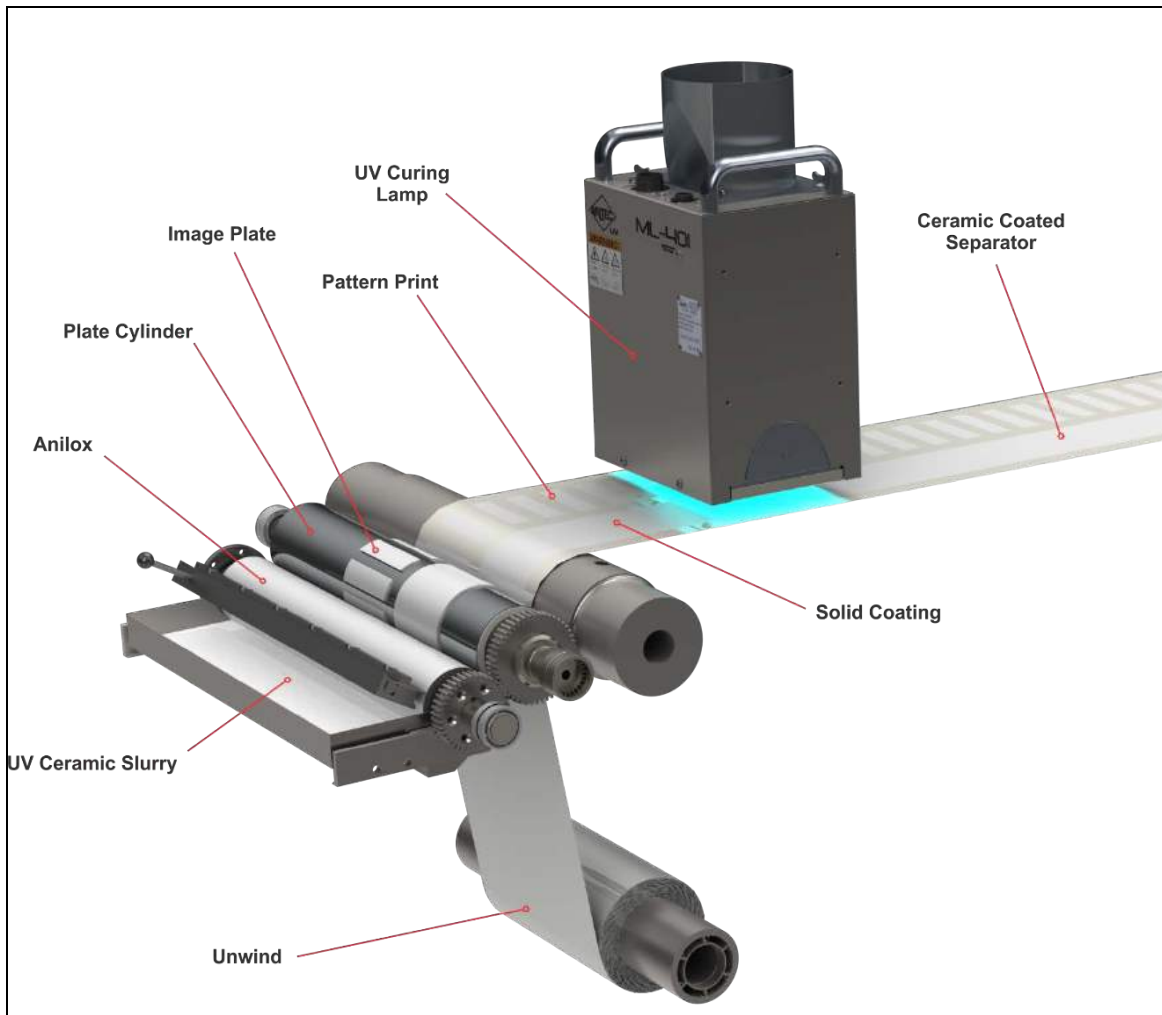


Figure I-85: In the flexographic process, the anilox meters the coating to the image plate which like a rubber stamp transfers the image to the separator. As shown, the left side is printing a pattern and the right side is printing a continuous coating.

Besides the advantage of ion flow and shrinkage reduction, there is 39% reduction in coating weight for the pattern shown in Figure I-86 versus that of a solid coating.

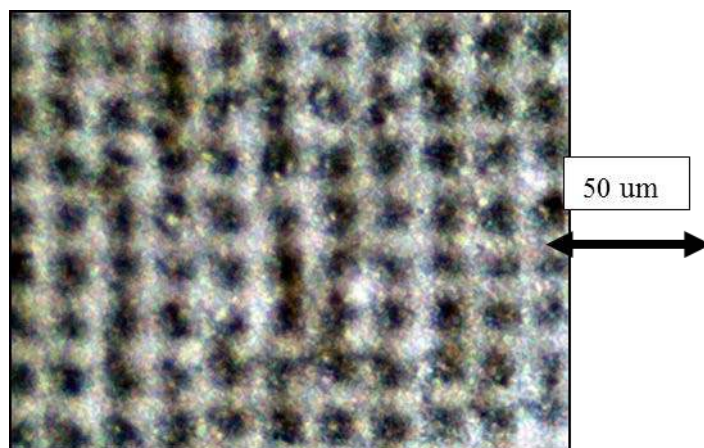


Figure I-86: Image of UV ceramic coated separator. The white ridges are the rigid coating that inhibits thermal shrinkage and holes allow more ion flow.

When we initially proposed the idea of pattern coatings, one objection raised by industry was that the differential ion flux through the separator might lead to dendrite growth.

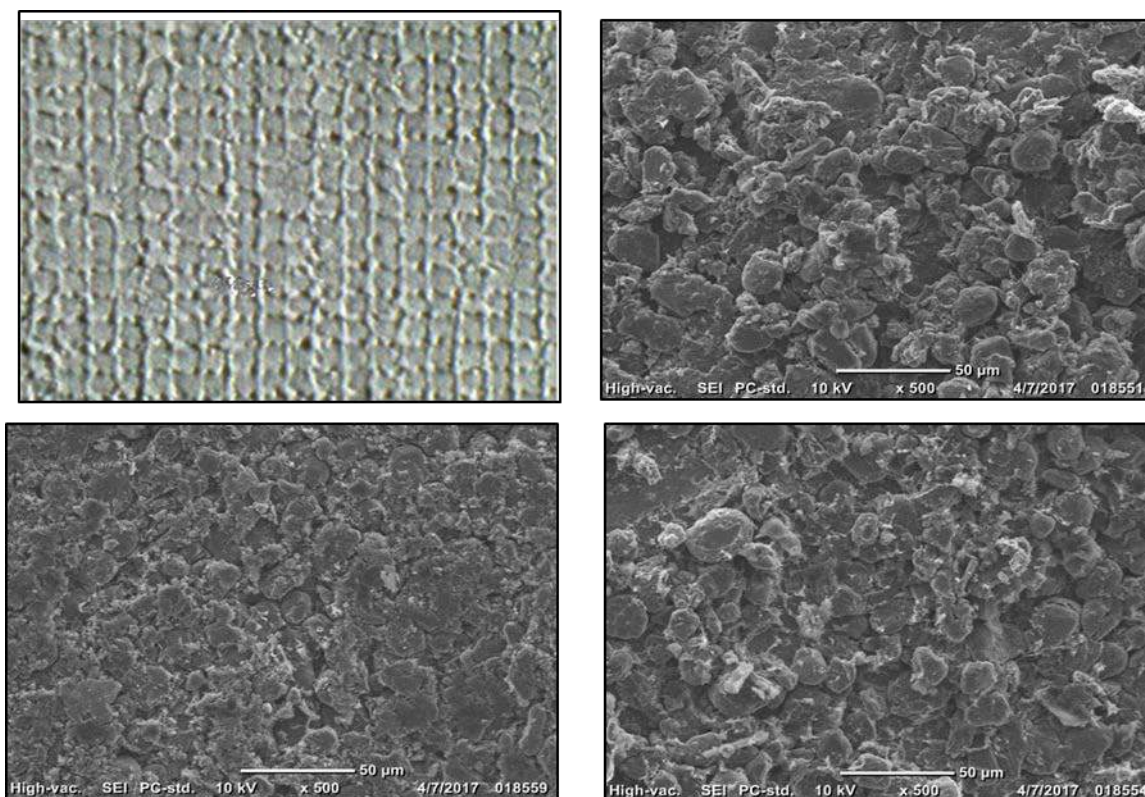


Figure I-87: Deeply lithiated graphite anode shows no mirror pattern of patterned coated separator. 10 x 10 Pattern Coated separator (upper left). Lithiated anodes with uncoated separator (upper right), solid coated separator (lower right), and pattern coated separator (lower left).

To evaluate this concern, we built coin $\frac{1}{2}$ cells using a graphite anode. After 300 cycles, dendrites clearly grew. However, the dendrite growth showed no mirror pattern of the printed separator nor was there difference between the anodes for the uncoated and coated separators (Figure I-87). Therefore, we conclude that pattern

printed ceramic coatings on separators do not lead to significantly more dendrite growth than standard separators.

The initial coating experiments were conducted on a laboratory scale flexo coater and UV curing continuous line. From the successful operation of this unit, we developed design criteria for a commercial scale flexo coating and UV curing system capable of coating continuously up to 400 fpm.

The commercial scale coater/UV curing system called the CX400 (Figure I-88) was designed specifically to handle super thin polyolefin separator material with superior web handling, edge control, tension control and high-speed precision coating. The CX400 was designed to handle 440 mm wide separator material and operate at 400 fpm and 10 μm separator material. Miltec has successfully coated 5 μm thick separator material on the CX400. The CX400 has minimum unsupported web and a chill drum to achieve precise tension and separator temperature control. The separator is fully supported from nip to coating, drying, curing, and rewind to eliminate unsupported stress. It has a very small footprint and precise thickness control of <1 μm .



Figure I-88: Commercial Scale Coater, CX 400

Conclusions

By successfully completing this project Miltec UV has demonstrated:

- Precision single and double sided ceramic coatings (2-4 μm in thickness) on multiple base separator materials using a commercial scale machine (400 mm width and processing speeds to 130 m/min) that result in porosity decreases less than 10% and final shrinkage from 1-5% depending upon base material, temperature and time meeting USABC Li-ion battery separator requirements.
- Demonstrated the application of patterned ceramic coatings resulting in 39% material savings with no reduction in performance and demonstrated no additional dendrite growth as a result of the patterned ceramic coating.

- Developed and exercised a cost model to show a ceramic coating can be applied for less than \$0.20/m² and further reductions to \$0.09/m² are achievable with alternate ceramic materials.

Key Publications

1. Gary Voelker and Dr. John Arnold gave a presentation on the merits of UV binder for ceramic coated separators to the DOE USCAR representatives from Ford, Chrysler, GM and EPRI in Detroit May 17, 2017
2. Miltec UV had an exhibit with visuals and a video presenting the progress on UV binder for ceramic coated separators at the International Battery Conference, Fort Lauderdale, FL in March 2017 and the Battery Show, Novi, MI September 2017.
3. John Arnold presentation titled *UV Coating Processes to Enhance Li-ion Battery Performance and Reduce Costs* to the Electrochemical Society meeting at National Harbor Fall 2017.
4. Miltec UV website presenting details on the performance and potential for ceramic coated separators.
<http://www.miltec.com/technology/battery/uv-ceramic-coated-separators/>

I.B.5 Co-Extrusion(CoEx) for Cost Reduction of Advanced High-Energy-and-Power Battery Electrode Manufacturing (PARC)

Ranjeet Rao, Principal Investigator

Palo Alto Research Center (PARC)

3333 Coyote Hill Road

Palo Alto, CA 94304

Phone: 650-812-4373

E-mail: ranjeet.rao@parc.com

Peter Faguy, Technology Manager

U.S. Department of Energy

Phone: 202-586-1022

E-mail: Peter.Faguy@ee.doe.gov

Start Date: December 1, 2015

End Date: August 31, 2019

Total Project Cost: \$3,790,000

DOE share: \$3,000,000

Non-DOE share: \$790,000

Project Introduction

Most strategies for increasing the performance and reducing the cost of lithium-ion batteries have focused on novel battery chemistries, material loading modifications, and increasing electrode thickness. Increasing electrode thickness is a known approach to increase energy density and in turn overall cell capacity. However, practical thicknesses are constrained by ionic transport limitations that occur with increasing thickness, limiting cell power. We believe PARC's Co-Extrusion (CoEx) technology can overcome this limitation, enabling a substantial improvement in the performance of thick electrodes for most lithium-ion chemistries. CoEx has the potential to disrupt current manufacturing processes and enable the DOE 2022 goal of \$125/kWh by enabling the simultaneous deposition of alternating regions of high ionic transport and high lithium density

Objectives

Our overall project objectives are to demonstrate Co-Extrusion (CoEx) printing technology at electric vehicle (EV) relevant scales by assembling large, 14 Ah pouch cells. These pouch cells will demonstrate an estimated $\geq 30\%$ reduction in \$/kWh costs through thick, structured high energy and high power electrodes, and a gravimetric energy density improvement of $\geq 20\%$ relative to conventional electrodes of the same chemistry.

Approach

Co-Extrusion (CoEx) Cathode

Co-Extrusion (CoEx) is a deposition technology developed at PARC that uses engineered fluidic channels to cause multiple streams of dissimilar fluids to impart shape to one another [1]. The result is a high-speed, continuous deposition process that can create fine structures much smaller than the smallest physical feature within the printhead. By eliminating the small channels necessary for conventional extrusion and injection processes, CoEx is able to deposit highly loaded and viscous pastes at high process speeds under reasonable operating pressures. Depending on particle size, the CoEx process is capable of direct deposition of features as small as 25 μm with aspect ratios of 5 or greater, and print speeds $> 400 \text{ mm/s}$ ($\sim 80 \text{ ft./min}$). A CoEx printhead can serve the same function as the slot die printhead in modern battery manufacturing lines, depositing the electrode slurry onto the current collector web in a continuous roll-to-roll process. The thicknesses, widths, and lengths of the deposited CoEx features are dependent on the internal printhead geometry, slurry rheology, and process conditions. The precise flow paths are constructed out of a stack of replaceable printhead layers that can be easily exchanged, allowing for precise tailoring of the final deposited features within a single printhead design. PARC's scale-up of CoEx batteries for EVs builds on a solid base of experience in applying CoEx to solar cell manufacturing [2]. We have chosen a commercially relevant chemistry, $\text{LiNi}_{0.5}\text{Co}_{0.2}\text{Mn}_{0.3}\text{O}_2$ (NCM

523) and our strategy will be to scale the technology from coin cells (BP1) to 14 Ah pouch cells (BP3) by project completion. Our partner, Ford Motor Company, will provide PARC with baseline cell specifications in addition to EV-relevant cell characterization on the pouch cells developed during the course of the project.

High Capacity Graphite Anode

While PARC will use CoEx to develop thick, high performance cathode electrodes, ORNL will develop the thick, high capacity anode that will match the CoEx cathode. In addition, they will utilize ORNL's Battery Manufacturing Facility (BMF) to fabricate small scale pouch cells in BP2 and assist PARC with technology scale-up on ORNL's roll coater, in addition to running electrochemical rate and cycling tests. As part of the anode development, ORNL will refine graphite-based anode slurries for improved coating adhesion, agglomerate cohesion, and high ionic and electronic conductivity by modifying binder and conductive additive. Anodes will be prepared with an NMP/PVDF solvent/binder system and slot-die coated to a sufficient thickness to balance the CoEx cathodes. Beginning with baseline anode coatings with targets of 50-80 μm in thickness after calendaring, 2.5-30 mAh/cm^2 in loading, and capacity > 350 mAh/g , ORNL will then work to demonstrate anodes that are thick (125 – 200 μm) to match the high capacity CoEx cathodes. These anodes will be shown to maintain their integrity after drying and calendaring to 30-40% porosity.

Results

Co-Ex Cathode Modeling Results

CoEx modeling focused on three different CoEx models, cross-sections of which are outlined in Figure I-89a. Each structure is composed of the two alternating regions which would be created by CoEx inks that are co-deposited. For all of these structures, Region 1 is fixed to be a 90/5/5 composition of NCM/PVDF/Acetylene Carbon Black (ACB) by weight ratio, with volume fractions for the active material, inactives (PVDF and ACB), and electrolyte of 0.512, 0.152, and 0.336, respectively. The main difference between the structures is the nature of Region 2. For CoEx Structure Type 1, Region 2 is modeled as pure electrolyte, *i.e.*, 100% porosity. For CoEx Structure Type 2, Region 2 is modeled as a porous NMC electrode like Region 1, but with a higher porosity. CoEx Structure Type 3 is a hybrid design in which Region 2 is compositionally similar to Region 1, but is much thinner. A standard macrohomogeneous porous electrode model [1,3,4] was implemented in COMSOL [5] and extrapolated to two dimensions to capture the cross-section of the CoEx cathode geometry. The FY2016 report outlined our modeling results for the three types CoEx Types. These results are summarized in Figure I-89b, which shows gravimetric vs volumetric energy density for the highest performing structures (CoEx Type 1 and 3) as well as the baseline case. The thickness indicated in the legend is the thickness of Region 1, and for CoEx Type 3 structures the pad thickness is 50 and 70 μm for Region 1 thicknesses of 120 and 170 μm , respectively. Unless otherwise noted, the ratio of the width of Region 1 and Region 2 is 4. In general, modeling shows that CoEx Type 1 structures show higher gravimetric energy density but minimal gravimetric energy density benefit except for the case of extreme thickness (170 μm) or a high Region 1 / Region 2 ratio of 9. By contrast, the CoEx Type 3 structures are predicted to show an increase in both gravimetric and volumetric energy density even at moderate thicknesses and structure ratios.

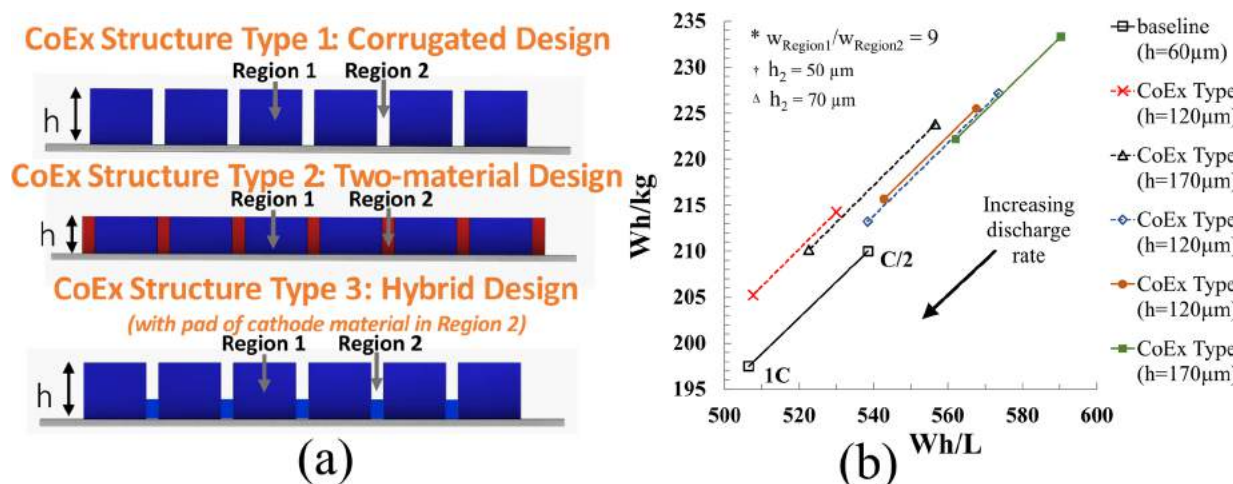


Figure I-89. (a) Schematic of different CoEx cathode geometries. (b) Summary of CoEx Type 1 and 3 modeling results, plotting gravimetric and volumetric energy densities as a function of discharge rate and CoEx geometry

Co-Ex Cathode Print & Electrochemical Results

Based on the modeling work above, cathode electrode structures were printed with the goal of replicating the CoEx Type 3 topology. The CoEx printhead takes two different battery ink formulations as input, which form Regions 1 and 2 when deposited. While the Region 1 formulation has the standard 90/5/5 (NMC / PVDF / Carbon Black) formulation as described in the modeling work in the previous section, the Region 2 ink formulation was modified with a higher solvent content such that upon drying, Region 2 would experience greater shrinkage, resulting in the “corrugated” structure seen in Figure I-90. Figure I-90 shows thickness profile measurements for CoEx cathode prints comparing three different Region 2 formulations. These thickness profile measurements were performed using a Stil chromatic confocal sensor on electrodes in the dried state, and a best effort was taken to overlay scans to align Region 1 and 2 between the different electrodes. The measurements shown are taken after calendaring, showing that the CoEx structure is maintained after this standard electrode processing step. As can be seen, the main difference between these prints is the amount of material present in Region 2, with a minimum thickness ranging from approximately $5\mu m$ (close to the CoEx Type 1 structure) to $80\mu m$. Region 1 thickness is similar for all three prints. Due to slumping during the drying process, the shape of Region 2 is more triangular rather than the rectangular shape that was modeled.

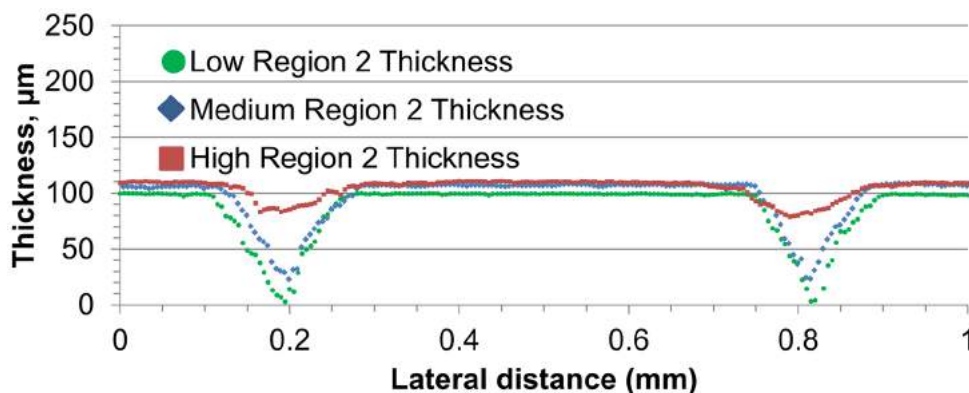


Figure I-90. Confocal profilometry scans of CoEx Type 3 structures, illustrating how electrode thickness varies orthogonal to print direction.

In order to test the effectiveness of CoEx electrode structuring, these cathodes were tested in half-cell configuration, the results of which are shown in Figure I-91 displaying (a) specific capacity vs. discharge rate and (b) specific capacity vs. discharge current. In these plots, we compare the three CoEx cathodes described above to the baseline electrode as well as a thicker, homogenous (unstructured) cathode that more closely matches the active material loading of the CoEx electrodes. Median values of the ~ 12 coin cells in each configuration are plotted, with a quadratic fit included to guide the eye. The legend below indicates the thickness of the electrode in Region 1 as well as the active material loading. A few conclusions can be drawn from these data. For one, all the CoEx cathodes perform similar to the baseline at discharge rates up to D/2, with performance dropping off at higher rates. Secondly, the CoEx cathodes perform much better than the unstructured electrode of similar loading, showing that the CoEx structuring is enabling greater utilization of the electrode. In fact, when plotted with respect to discharge current, which advantages thicker electrodes, the two CoEx electrodes with the thickest Region 2 pads outperform the baseline electrode. Based on this data, we can extrapolate the expected energy density improvement at the pouch cell level. If we consider a theoretical 1 Ah pouch cell, use of thicker CoEx cathodes results in fewer inactive layers (*i.e.*, current collectors and separators) compared to the baseline cathode. Using this simple geometric scaling argument, CoEx cathodes with a thick Region 2 are expected to show an improvement of approximately 10% in gravimetric and volumetric energy density at C/10 compared to the baseline condition. At C/5, the advantage is approximately 5%.

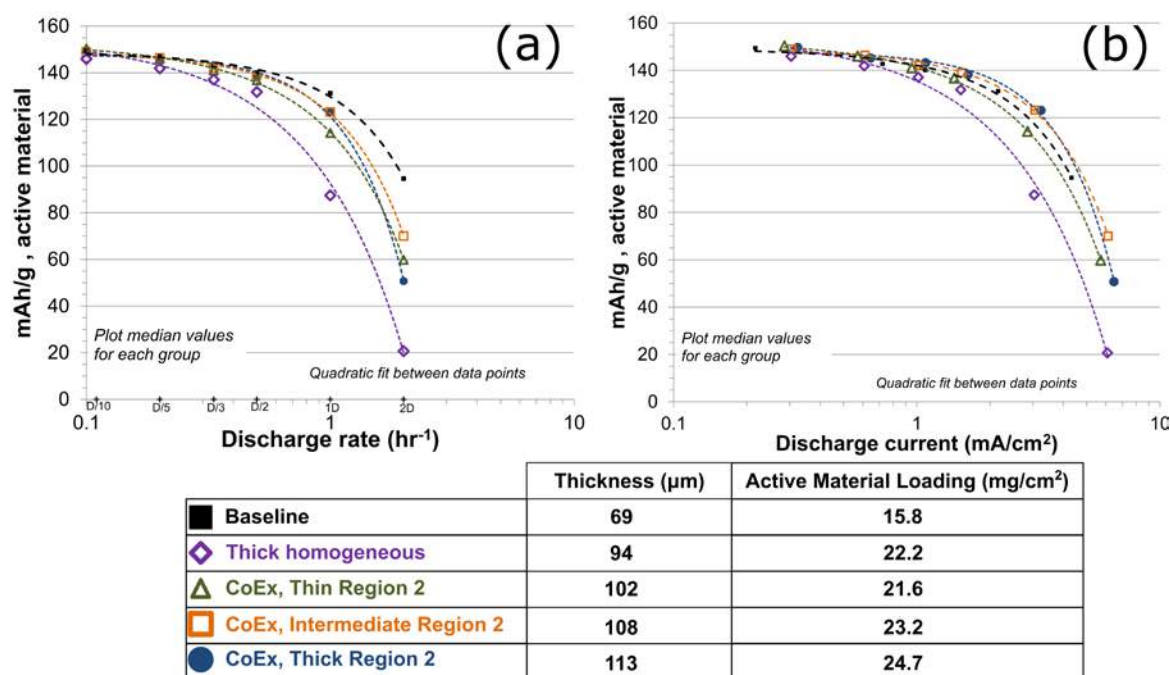


Figure I-91. Specific capacity vs (a) discharge rate and (b) discharge current for a variety of CoEx Type 3 structures compared to baseline and thick homogeneous cathode electrodes.

Slot-Die Coated Anodes

In order to perform a more accurate rate performance comparison between a wider range of graphite materials, we made four additional slot-die coated anodes to compare with the Showa Denko and Hitachi MAGE 3 coatings made previously. These additional graphite materials were chosen based on their excellent electrochemical performance in our previous half coin cell tests carried out with doctor blade coatings. The rate performance of these four additional anodes was evaluated at two different areal capacities ($\sim 2.6 \text{ mAh}/\text{cm}^2$ and $\sim 6 \text{ mAh}/\text{cm}^2$) in half coin cells using 1.2M LiPF_6 in 3:7 wt% EC/EMC electrolyte. Results for all six slot-die coated anodes (including the two coated previously) are plotted in Figure I-92.

While the performance of all six graphites was similar at 2.6 mAh/cm² below 1C discharge rates, Showa Denko and Superior SLC 1520T demonstrated slightly higher capacity retention at discharge rates \geq 1C. While the, ConocoPhillips A12 and GrafTech APS19 showed slightly higher capacity retention at discharge rates \geq 1C, these graphites along with the Hitachi MAGE exhibited significant delamination from the copper current collector after calendaring. This delamination could be seen in many of the electrodes punched for coin cells, and in some cases, the electrodes separated from the copper foil entirely. We confirmed these observations more quantitatively by performing 180° peel tests on each different coating to determine the adhesion of the coating to the underlying copper current collector. Based on the observed delamination during processing and the peel test results, the ConocoPhillips A12, GrafTech APS19, and Hitachi MAGE graphites were eliminated as potential candidates. The three remaining graphite materials (Showa Denko, Hitachi MAGE 3, and Superior SLC 1520T) show similar electrochemical rate performance at 6 mAh/cm² (Figure I-92b). Therefore, we built single-layer pouch cells with each graphite to more reliably determine how they would perform in a full cell configuration and further narrow the graphite selection.

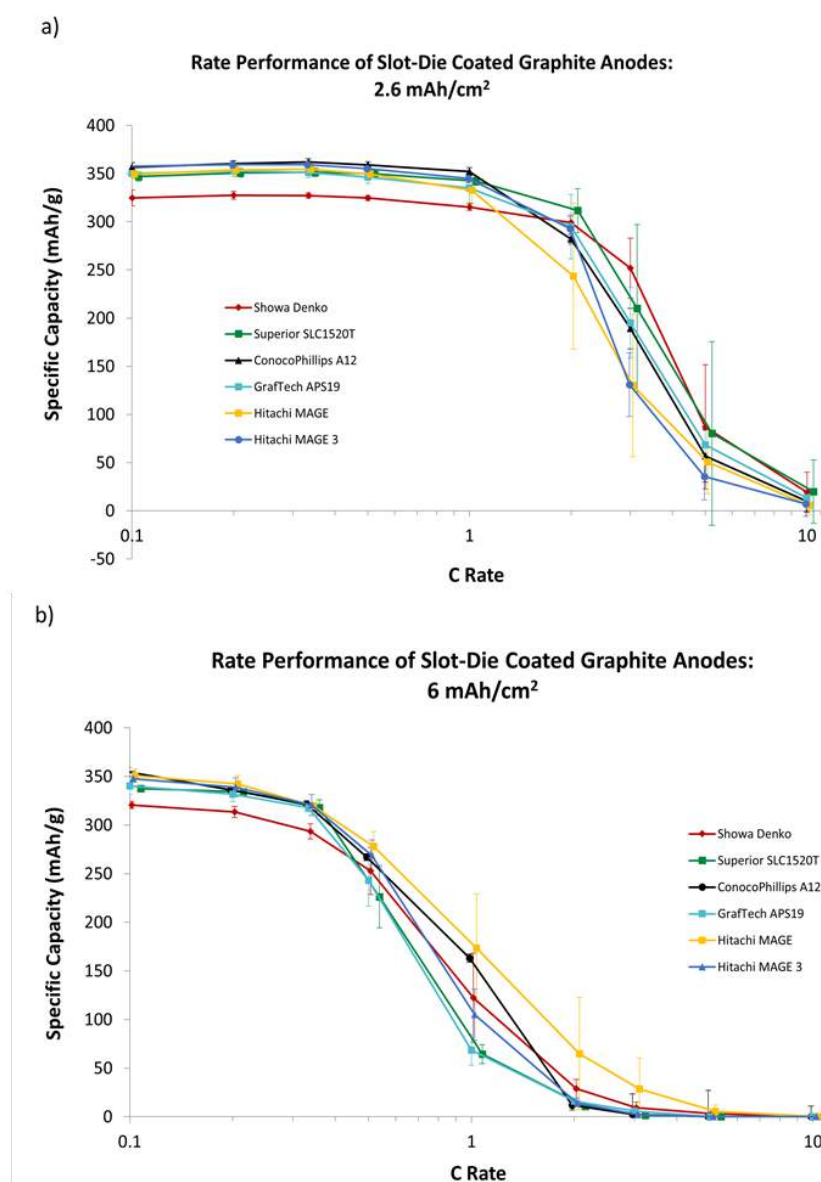


Figure I-92. Comparison of the performance of 6 different slot-die coated graphite anodes in half cells at a loading of (a) 2.6 mAh/cm² and (b) 6 mAh/cm².

Baseline Pouch Cells

Baseline pouch cells were made at two different capacities (1 Ah and 6 Ah) according to the specifications established previously. The recipes, areal loadings, and thicknesses for the anode and cathode coatings are listed below in Table I-15. Six pouch cells were made at each capacity. Half of the cells were used to evaluate the rate performance (C/5 Charge, Discharge at different C rates), while the other half were used to perform long-term cycle life testing (C/3 Charge, C/3 Discharge). Each 6 Ah cell contains two jelly rolls stacked on top of one another, each with its own set of tabs.

Table I-15: Composition and Processing Parameters for Baseline Anode Pouch Cells

	Anode	Cathode
Active Material	92 wt% Superior SLC 1520T Graphite	90 wt% Toda NMC 532
Conductive Additive	2 wt% Imerys C-Nergy Super C65 Carbon Black	5 wt% Denka Carbon Black
Binder	5 wt% Solvay 5130 PVDF	6 wt% Kureha 9300 PVDF
Areal Loading	7.5 mg/cm ²	14.7 mg/cm ²
Electrode Thickness	63 µm	55 µm
Calendering	45% Porosity	35% Porosity

Long-Term Cycle Life

Figure I-93 shows updated cycle life data for the 1 Ah and 6 Ah baseline pouch cells after 512-900 cycles. One of the 6 Ah pouch cells experienced a power outage interruption, so the data shown only includes 512 cycles (even though the other two 6 Ah cells have completed 750 cycles). Although the 6 Ah cells continue to show marginally lower capacity fade than the 1 Ah cells, both sets of cells demonstrate slightly higher capacity fade than anticipated, with the 1 Ah cells decaying to 68% of their original capacity after 900 cycles. This may be a result of calendering the anode to 45% porosity rather than the typical 35%. This porosity value was originally chosen based on the results of our coin cell study with both calendered and uncalendered anodes, which showed that uncalendered anodes (~50-60% porosity) exhibited better rate performance than calendered anodes (~35% porosity). Conversely, calendering generally improves both the adhesion to the current collector and the electrical conductivity, which can influence long-term cycle life calendering. Therefore, 45% porosity was chosen for the baseline anodes in order to take advantage of the rate performance benefits of higher porosity and the adhesion and conductivity benefits of lower porosity. However, it appears that the capacity fade observed in the baseline cells made with higher porosity anodes may outweigh the rate performance benefits. Despite this capacity fade, the very similar performance of the 1 Ah and 6 Ah cells and the low cell-to-cell variation again demonstrate the ability to scale up pouch cell capacity without sacrificing performance.

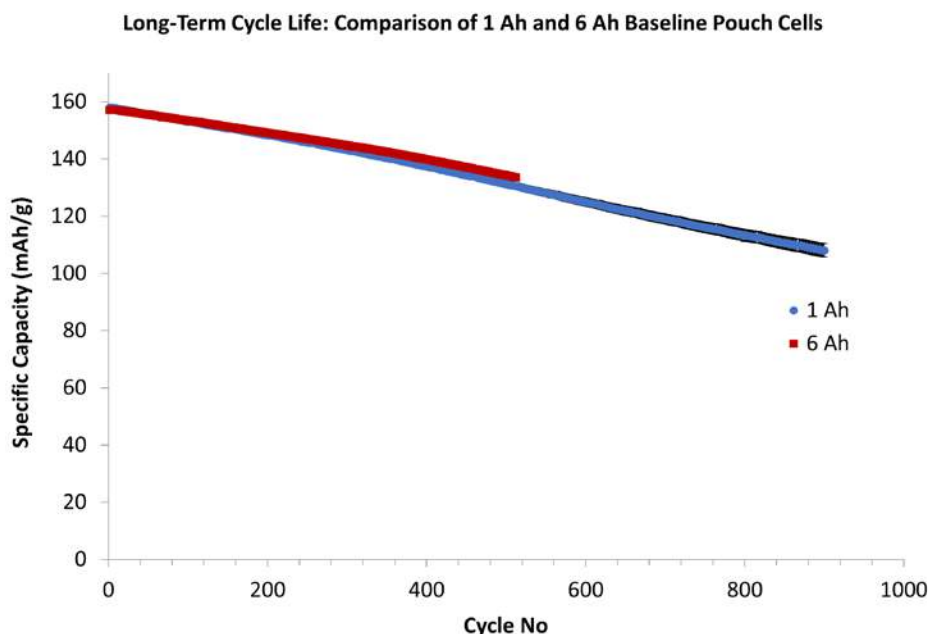


Figure I-93. Cycle life data for 1 Ah and 6 Ah baseline pouch cells. Cells are tested at C/3 charge and discharge with HPPC testing performed every 50 cycles.

Conclusions

PARC, ORNL, and Ford are collaborating to create a pilot scale demonstration of PARC's CoEx battery manufacturing technology for structured high energy and high power cathodes for cost-effective EVs. This year, we have completed the modeling of CoEx cathodes, identifying the most promising CoEx geometries for further study. Based on this modeling results, we have designed CoEx battery formulations that produce heterogeneous cathode structures with a variety of geometries. Our electrochemical testing shows that CoEx electrodes perform better than homogeneous electrodes of similar loading, supporting our hypothesis that interdigitating regions of high porosity within the cathode electrode improves lithium utilization in thick electrodes. We have also identified high performance anode materials and used them to create high capacity pouch cells which have been tested for performance and cycle life.

Key Publications

1. C.L. Cobb and S.E. Solberg, "Analysis of Thick Co-Extruded Cathodes for Higher-Energy-and- Power Lithium-Ion Batteries," *J. Electrochem. Soc.*, **164** (7), A1339-A1341, 2017
2. R.B. Rao, "Co-Extrusion of Electrodes for Both Energy and Power", U.S. Drive Electrochemical Energy Storage Technology Discussion, Southfield, MI, May 16 2017
3. C.L. Cobb, "Co-Extrusion: Advanced Manufacturing for Energy Devices," *2016 AIChE Annual Meeting, Battery and Energy Storage Technologies*, San Francisco, CA, November 14, 2016. (Session Keynote)
4. C.L. Cobb, "Modeling Co-extruded Cathodes for High Energy Lithium-ion Batteries," *229th ECS Meeting*, San Diego, CA, June 1, 2016.

References

1. C.L. Cobb *et al.*, “Modeling Mass and Density Distribution Effects on the Performance of Co-extruded Electrodes for High Energy Density Lithium-ion Batteries,” *J. of Power Sources*, **249**, 357-366, 2014.
2. L.P. Richter *et al.*, “Progress in Fine Line Metallization by Co-extrusion Printing on Cast Mono Silicon PERC Solar Cells,” *Solar Energy Materials and Solar Cells*, Vol. 142, pp. 18-23, 2015.
3. M. Doyle, T.F. Fuller, and J. Newman, “Modeling of Galvanostatic Charge and Discharge of the Lithium/Polymer/Insertion Cell,” *J. Electrochem. Soc.* 140, 1526-1533, 1993.
4. T.F. Fuller, M. Doyle, and J. Newman, “Simulation and Optimization of the Dual Lithium Ion Insertion Cell,” *J. Electrochem. Soc.*, 141, 1-10, 1994.
5. COMSOL v5.1: <https://www.comsol.com/>

I.B.6 Electrodeposition for Low-Cost, Water-Based Electrode Manufacturing (PPG Industries, ANL, Navitas, ORNL)

Stuart Hellring, Principal Investigator

Senior Scientist
PPG Industries
4325 Rosanna Drive
Allison Park, PA 15101
Phone: 412-492-5526
E-mail: hellring@ppg.com

Peter Faguy, Technology Manager

U.S. Department of Energy
Phone: 202-586-1022
E-mail: Peter.Faguy@ee.doe.gov

Start Date: October 1, 2016

End Date: December 31, 2018

Total Project Cost: \$3,999,034

DOE share: \$1,399,275

Non-DOE share: \$999,759

Project Introduction

The state of the art for the manufacture of lithium ion cathodes is slot-die coating of a high-viscosity slurry of active battery materials, conductive additives, and a polymeric binder that is dissolved in N-methyl-2-pyrrolidone (NMP). NMP is an expensive consumable in electrode manufacturing with serious health concerns. It is on the candidate list of Substances of Very High Concern for authorization in the European Union. In the United States, NMP is on the EPA's Toxics Release Inventory and the California Department of Occupational Safety and Health has proposed a Threshold Limit Value of 1 ppm in air, similar to occupational exposure limit values established in Japan (1 ppm) and Germany (20 ppm). Alternative organic solvents have been insufficient to meet the needs of incumbent binder systems and present their own cost and exposure difficulties.

The current cost of high-energy Li-ion batteries (LIBs) is approximately \$500-\$800/kWh, while the EV Everywhere Blueprint 2022 goal is \$125/kWh. Main cost drivers are the high cost of raw materials and materials processing, the cost of cell and module packaging, and manufacturing costs. Our proposed project addresses materials processing and manufacturing costs. To estimate the cost savings achievable by converting to an aqueous, electrocoat-based cathode coating system, PPG consulted with Argonne National Lab. Using BatPac, an estimated 17.1% savings on a per-cell basis was determined. Eliminating NMP from the process reduces cost by 8.9%. Further cost savings can be realized by eliminating the need to calender electrodes, and by an expected reduction in binder costs, for an estimated 17.1% savings over state of the art.

Solvent-based electrodeposition of pre-formed cathode active powders for producing electrodes for secondary lithium ion batteries has been evaluated by several groups. A variety of active materials have been electrodeposited onto various current collectors in solvents such as acetone and ethanol. Cathode active particle sizes used for these studies ranged from an average of 300 nm to 10.3 μm . Cathodes produced by solvent-based electrodeposition showed promising battery performance for metrics which include discharge capacity/rate capability, coulombic efficiency and cycle life retention.

However, the use of volatile organic solvents for manufacturing electrode coatings by electrodeposition has a number of serious drawbacks including VOC emissions, explosion risk, health risks from worker exposure, and cost. Using waterborne coatings significantly mitigates most of the concerns associated with organic solvent-based coating formulations. Benefits include lower voltage/current, better process temperature control and faster deposition rates due to a higher dielectric constant. Binder design, proprietary additives, and

electrochemical processing methods are used to ensure quality during manufacturing, to disperse pigment particles and stabilize the aqueous formulation bath against agglomeration and settling. Since charge-bearing functionality typically is hydrophilic, these functional groups are converted by crosslinking during the coating curing process to render the final film less hydrophilic.

Objectives

The objective of the project is to develop and demonstrate novel binders to enable a low-cost, water-based, electrodeposited lithium ion battery electrode coating system and manufacturing process capable of reducing cell costs by at least 20% while improving battery performance. In addition, the project will demonstrate a battery supply chain model that mirrors traditional automotive OEM supply chain models to reduce the risk of electric vehicles (EVs) and increase adoption. During this year, specific objectives for this project are as follows:

- Electrocoat an electrode with an energy density of 2.5 – 3.0 mAh/cm².
- Complete cell testing on 0.2 – 0.3 Ah pouch cells.
- Design and construct a pilot scale electrocoat roll-to-roll coater.
- Adjust estimate of cost savings using BatPac model.
- Demonstrate the ability to produce or commercially acquire kg quantities of active material suitable for the electrocoat process.

Approach

Electrocoat offers several manufacturing advantages over conventional slot-die or roll-coater application processes. One advantage is a greater coating density. Because electrophoretic deposition moves solid components to the substrate and dewater a coating as it deposits, high density coatings with 90% by weight solids content are produced routinely from dilute formulation baths that have low viscosity. As an example, an aqueous wet film with 90% by weight solid content comprised of active, carbon, and binder will produce a dry cathode coating with less than 30 percent porosity. High density in electrodeposited coatings is achieved by controlling packing through particle size distribution where small particles embed in larger particle matrices through electrophoretic impregnation. Deposition of a dense wet film lowers stress in the dried film, a benefit for adhesion and cohesion. The self-insulating nature of the film build leads to high thickness uniformity. Unlike electroplating, electrocoat formulation are comprised of preformed and prequalified materials such as cathode-active powders, conductive carbon additives and binders that are deposited together to form the cathode coating.

The project will develop a viable electrodeposition process and will design and synthesize electrodeposable binders with flexibility and ionic mobility. The project will tailor and fabricate high-energy density active materials for compatibility and formulate stable water-based cathode coating systems. The project will establish electrodeposition process parameters and validate the performance and economics of the technology at a 1 Ah scale to ensure a path to commercialization. Argonne national labs will provide guidance and assistance developing active materials that are compatible with the waterborne electrocoat process through the synthesis of custom particles and particle coatings. Oak Ridge national lab will develop optimized drying conditions for electrocoat films through residual water analysis and pouch cell testing. Navitas Systems will provide testing of larger format cells.

Budget Period 1 includes development of the materials necessary for a successful e-coated electrode. Work will be split between concurrent active materials modification and e-coat system development. At the end of BP 1, targeted materials will be selected based on their performance characteristics.

Budget Period 2 will refine the coatings system to improve baseline performance. Cell validation scale will begin to increase, enabling refined quantification of the achievable cost reductions. The design and build of a bench scale coater for representative evaluation will support scale up in BP 3.

Budget Period 3 will optimize the coating system components to the point that large format cells will be built and evaluated. The budget period includes obtaining optimized, representative electrodes that will be tested for performance properties both independently and within cells.

Results

Battery performance improvements verified through pouch cell testing

Cathode electrodes for 60 mAh pouch cells were fabricated using electrocoat binders and the electrocoat deposition process. These cells were compared to cathode electrodes fabricated using a commercially available waterborne binder and drawdown application methods. Commercially available NCM 111 active materials were used in a formulation comprised of 92% active material, 4% conductive carbon, and 4% binder material. Double-sided, electrocoated electrodes with an average loading of 1.7 mAh/cm² per side (3.4 mAh/cm² per electrode) were fabricated into a 60 mAh full-cell pouch cell by Navitas Systems. Single-layer electrodes with an average loading of 1.5 mAh/cm² were fabricated into 60 mAh full-cell pouch cells by Navitas Systems using identical active materials and a commercially available waterborne binder. Pouch cells made from electrocoated cathodes demonstrated improved rate capability, cycle life, and internal resistance compared to the cathode electrodes fabricated using the commercially available waterborne binder (Figure I-94).

Additional testing is underway at Navitas Systems for 0.2 Ah pouch cells using commercially available LFP and NCM 111 materials. Pouch cells have been fabricated using double-sided electrocoated cathodes with an average loading of 2.5 mAh/cm² per side using NCM111 materials and an average loading of 1.0 mAh/cm² per side using LFP materials. Initial cycling data demonstrates similar battery performance as 60 mAh cells.

Electrocoat parameters optimized for film uniformity and adhesion

Electrocoat resins and formulations were engineered to produce uniform films with high film adhesion. An optimization of the resin composition and deposition parameters resulted in peel strength values comparable to those obtained using NMP-based application methods. The film adhesion of electrocoated and drawdown electrodes of identical composition and thickness were measured using a 90° peel test. Films were tested at a loading of 1.5 mAh/cm² using a composition of 92% NCM 111, 4% conductive carbon, and 4% binder material. The composition of the electrocoat binder played a significant role in the adhesion of both the drawdown and electrocoated films. The value of 81 N/m obtained using formulation 3 surpassed the value of 79 N/m obtained from the NMP-PVDF control sample at the same thickness (Figure I-95a). However, resin compositions with improved adhesion had reduced battery performance. Work is ongoing to realize high adhesion and energy storage capacity.

Electrocoat deposition parameters were designed to produce uniform films over large areas for a range of active material particle sizes. Active materials with a large particle size settle over time in low-viscosity electrocoat baths. Two approaches were considered to overcome the resulting film non-uniformity: (1) the formulation of a stable bath using small particle size and (2) the modification of deposition parameters to accommodate bath instability with large particle size. The first approach used NCM 111 cathode materials with an average particle size of 7 µm. These were easily stabilized in an electrocoat bath and did not settle overnight. The second approach used deposition conditions that accounted for non-uniformity in the bath solids concentration by locally modifying the deposition rate over the electrode surface. Optimized electrocoat parameters produced uniform films with a particle size of 11 µm enabling the use of commercially available powders (Figure I-95b).

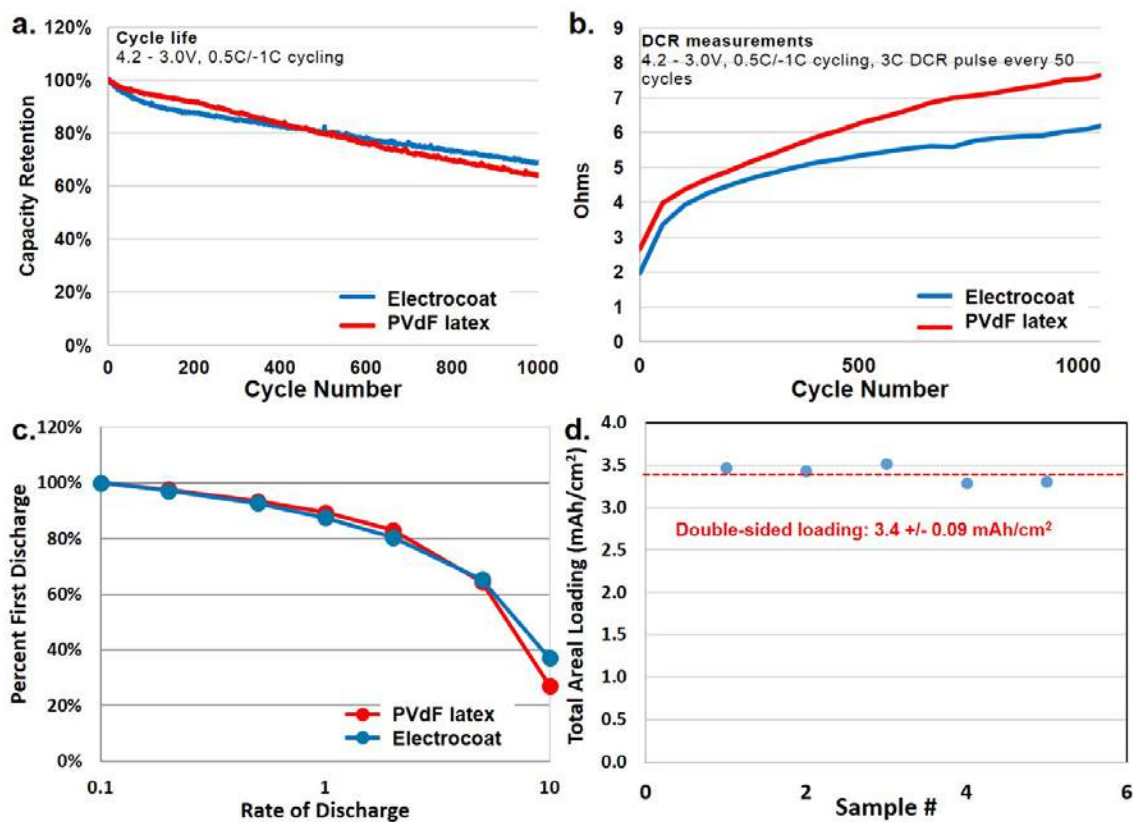


Figure I-94. (a) Cycle life testing demonstrating improved cycle life of electrocoated films after 500 cycles. (b) DCR measurements performed at 3.0 C. Electrocoated cathode materials demonstrate a lower internal resistance. (c) Rate performance of each electrode with electrocoated electrodes demonstrating an improved capacity retention at high rates. (d) Double-sided areal capacity measurements of five electrocoated films highlighting the reproducibility of targeted film thicknesses with this technique.

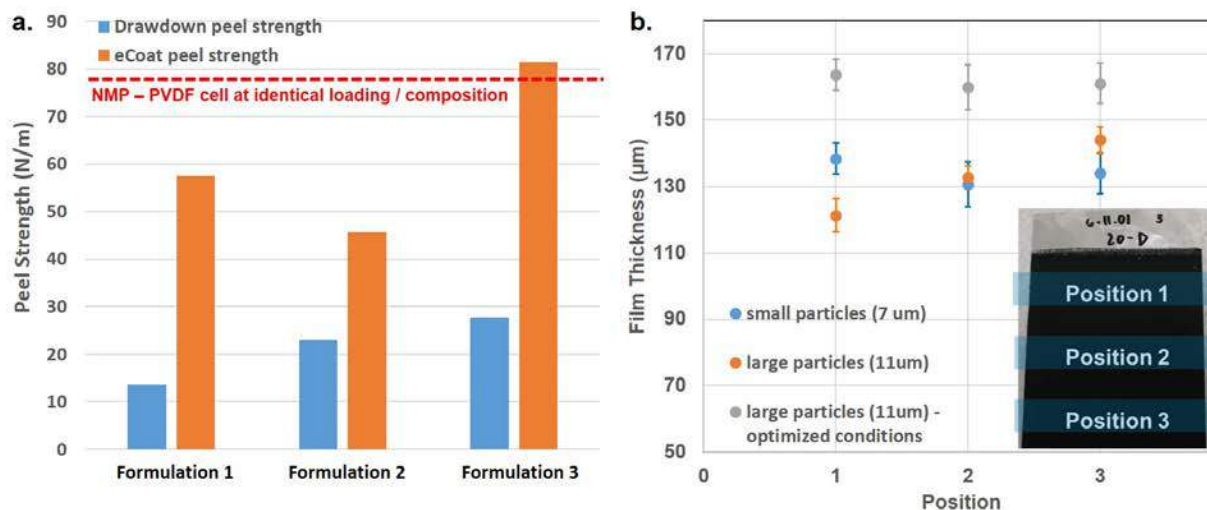


Figure I-95. (a) Peel strength measurements of electrocoat binders in cathode films fabricated using both drawdown and electrocoat fabrication processes. (b) Film uniformity measurements of electrocoated cathode films comprised of active materials of varying size and deposition conditions. Non-uniformities present from the use of large particle sizes may be overcome by the electrocoat deposition conditions.

Suitable active materials for electrodeposition were identified

Active materials that can be produced economically in kg quantities were investigated for compatibility with the electrocoat system. TVR synthesized NCM111 materials from Argonne National Lab and commercially available materials were screened for electrocoat deposition kinetics and battery performance. Two commercially available NCM111 materials, one commercially available LFP material, and one surface-treated commercially available NCM622 material demonstrated both high deposition rates and acceptable reversible capacities in a half-cell coin cell (Table I-16). Cells were cycled between 3.0 – 4.3V.

Table I-16 also shows the results from surface treatments were applied commercial material to increase the stability of a given active particle with the electrocoat system. Surface treatments on NCM622 resulted in significantly improved capacity, however, the electrocoat deposition kinetics suffered. ANL provided CO₂ surface treatments to improve the capacity retention of NCM111 materials with minimal impact on the electrocoat deposition kinetics.

Roll-to-roll coating system under construction

A pilot scale minicoater is under construction by PPG Coating Services (MetoKote) to demonstrate roll-to-roll processing of electrocoated electrodes. Designs are completed for the mini-coater system and constructions has begun. Progress is on track to have a fully functional mini-coater delivered within the current budget period. A 5-inch wide foil will move through the coater at an adjustable speed designed to produce films with an areal capacity of 1.5 mAh/cm².

Table I-16: Active material screening in electrocoated electrodes. Suitable particles must demonstrate a coverage density of $> 10 \text{ mg/cm}^2$ during electrocoat and battery performance characteristic of the active material used.

Material	Electrocoat Mass Deposited (mg/cm^2)	Initial Discharge Capacity at 0.1C (mAh/g)	Capacity at 1.0C Rate (mAh/g)
Preliminary NCM111-ANL material	8.76	81	0
Preliminary NCM111-ANL material	6.45	99	0
Preliminary NCM111-ANL material	12.75	121	0
NCM 111-Supplier 1	23	160	130
NCM 111-Supplier 2	4.83	142	101
NCM 111-Supplier 3	18	0	5
NCM111-Supplier 3 ANL surface treatment	15.09	131	62
NCM 111-Supplier 4, surface treated	15	132	60
NCM 523-Supplier 1	1	0	0
NCM 523-Supplier 2	3	0	0
NCM 523-Supplier 3	14.4	117	2
NCM 523-Supplier 3, ANL surface treatment	11.5	118	5
LFP-Supplier 1	17.1	130	3
LFP-Supplier 2	13.1	170	129
NCA-Supplier 1	13	0	0
NCA-Supplier 1, surface treated	9.03	0	0
NCM622 – Supplier 1	4.6	178	101
NMC622 – Supplier 2	13.4	0	0
NCM622 –Supplier 2, surface treatment A	2.46	163	19
NCM622 –Supplier 2, surface treatment B	5.76	178	49
NCM622 –Supplier 2, surface treatment C	5.22	183	144
NCM622 –Supplier 2, surface treatment D	4.92	165	102
NCM622 –Supplier 2, surface treatment E	4.92	168	102
NCM622 –Supplier 2, surface treatment F	5.99	174	96

Conclusions

Film adhesion and uniformity targets have been met using electrocoat fabrication of cathode electrodes. Sufficient film uniformity and adhesion, on par with solvent-based systems, has been demonstrated. In addition, the process of electrocoat improves film adhesion compared to conventional drawdown application methods.

Energy storage performance that meets the targets for this budget period were reached using materials produced on the kg scale. Commercially available active materials were identified that produce reliable energy storage properties with the chosen electrocoat formulation. Additionally, electrocoated cathode electrodes demonstrated improved battery performance compared to other commercially available waterborne binders in 60 mAh pouch cell testing at Navitas Systems.

A pilot scale roll-to-roll coater is under construction and the final design for the coater and oven system is completed. The operation of this system will demonstrate the commercial feasibility of this electrocoat process and electrodes will be tested on the 1 Ah scale.

Key Publications

1. Presentation at the 2017 U.S. Drive
2. Poster presentation at the 2017 Annual Merit Review

I.B.7 Development of UV Curable Binder Technology to Reduce Manufacturing Cost and Improve Performance of Lithium Ion Battery Electrodes (Miltec UV International)

Dr. John Arnold, Principal Investigator

Miltec UV International

146 Log Canoe Circle

Stevensville, MD 21666

Phone: 410-604-2900; Fax: 410-604-2906

E-mail: gvoelker@miltec.com, jarnold@miltec.com

Peter Faguy, Technology Manager

U.S. Department of Energy

Phone: 202-586-1022

Email: Peter.Faguy@ee.doe.gov

Start Date: December 1, 2015

End Date: September 30, 2018

Total Project Cost: \$2,568,200

DOE share: \$1,742,560

Non-DOE share: \$513,640

Project Introduction

Previously identified UV curable binders and associated curing technology have been shown to significantly reduce the time required to cure electrode coatings. This revolutionary approach can result in dramatic increases in process speeds and significantly reduced capital costs and operating costs, reduced energy requirements and reduced environmental concerns and costs due to the virtual elimination of volatile organic solvents and associated solvent dryers and recovery systems.

The accumulated advantages of higher speed, lower capital cost, lower operating cost, reduced footprint, lack of VOC recovery, and reduced energy cost is a reduction in the manufacturing cost of electrodes. When commercialized, the resulting cost reduction in lithium-ion batteries will allow storage device manufacturers to expand their sales in the market and thereby accrue the energy savings of broader utilization of HEVs, PHEVs and EVs in the U.S., and a broad export market is also envisioned. In addition to equipment required to make and UV cure hand drawn cathode samples on high speed web conveyors with UV lamps; Miltec UV has a continuous coating and UV curing system (using three very high intensity UV lamps) to demonstrate the primary objectives of the project.

Objectives

The primary objective of this project is to provide performance data sufficient for lithium-ion battery manufacturers to commit to the first steps of making their own HEV, PHEV and/or EV lithium-ion electrodes with a UV drying process. This project involves an iterative R&D effort: making coin cells and pouch cells, followed by testing and analyses, then by adjustments in chemistry, mixing, coating, and UV curing to produce layered pouch cells at high processing speeds (200-300 feet per minute (fpm)) with performance equal or greater than that of a conventional cell with electrodes using PVdF and dried in a standard oven. This effort focuses on cathodes made with UV curable binders and is also investigating UV curable binders in the manufacturing of LTO-based anodes.

As a supplemental effort, Miltec and its team will investigate high speed coating techniques to demonstrate consistent thickness and edge control and will also conduct supplemental research on applying a UV cathode layer on top of an existing UV cathode layer to produce a thicker high energy cathode with sufficient porosity.

Approach

A major innovation of the use of UV curable binders in LIB electrode manufacturing is the potential for much higher processing speeds. Miltec UV and its partners have shown that once a condition for complete UV curing is determined (speed, thickness, number of lamps, etc.) then there is a linear correlation between process speed and number of UV lamps. For example, it has been shown that if UV curable coating completely cures at a cathode coating thickness of 20 μm with 1 lamp (600 W/in lamp) at a speed of 100 fpm, then that same 20 μm coating will completely cure at a speed of 300 fpm with 3 lamps.

Based on the difficulty of coating UV curable binder with slot die at higher speeds (>150 fpm), it is believed that coating technology other than slot die will most likely be required to achieve the very high process speeds made possible by UV curable binders (100 meters/minute). Miltec will evaluate and adapt the best from two coating processes used in the printing industry, flexography and letterpress printing.

Another important innovation being demonstrated in this project is the ability to make cathodes with multiple coating layers. This is made possible by the fact that, unlike a solvent-based system, the second and subsequent layers can be applied without the solvent in the second layer dissolving material in the layer below and the time between application and cure is so short that the second layer of liquid coating does not have time to flow into the pores of the first layer. Multilayered coating introduces the ability to make thicker, higher active material loading cathodes for EV applications. It also introduces the ability to change porosities and other characteristics such as material composition (active material and carbon) between layers. Miltec and ORNL will investigate and evaluate multilayered coatings and the potential advantages in this project.

The expected outcome of the project is to generate performance data from multilayer pouch cells (0.5–1.0 Ahr) fabricated using UV curable binder to demonstrate capacity, long term cycling, rate capacity, impedance, and repeatability equal to or better than a pouch cell with cathodes made using PVDF as a binder. Miltec is in contact with battery manufacturers and it is our belief that they will take the next steps once we demonstrate equivalent pouch cell performance. The most likely next step after the completion of this project would be the addition of a UV curing system to an existing cathode manufacturing line as a demonstration project; or possibly a stand-alone demonstration unit because of the relatively low capital and operating cost of a UV curing system.

Results

While the performance of the UV cathodes compares well with commercial batteries, there is always a technical drive to go to higher loadings. In an attempt to get ahead of the trend, we explored higher NMC loadings. Figure I-96 and Figure I-97 show a progression of higher NMC percentages, using different types of NMC and different loadings. By keeping the mass loading of the electrode at ~ 5 mg/cm², we discovered that we could maintain relatively stable cycling.

So, in the realm of power cathodes, cathodes produced with a versatile, high speed, high capacity UV process can offer cost savings and some performance advantages.

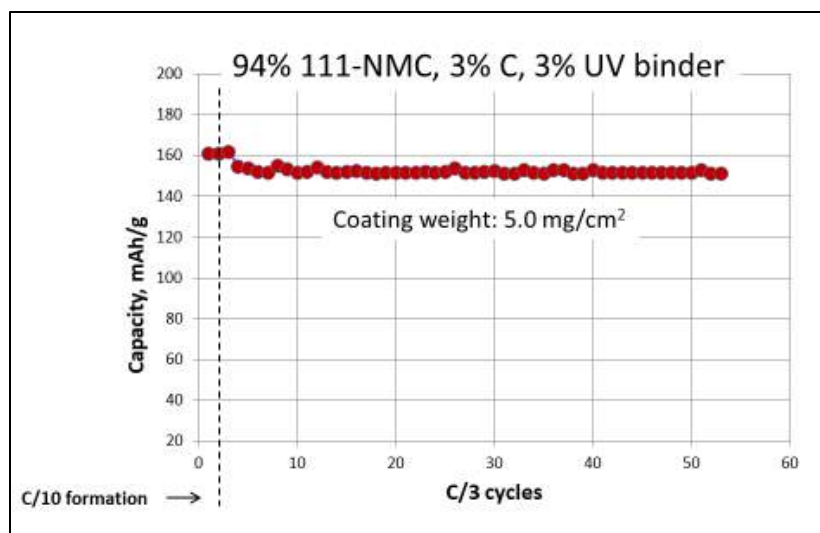


Figure I-96. Stable half-cell cycling of UV 94/3/3 power cathode.

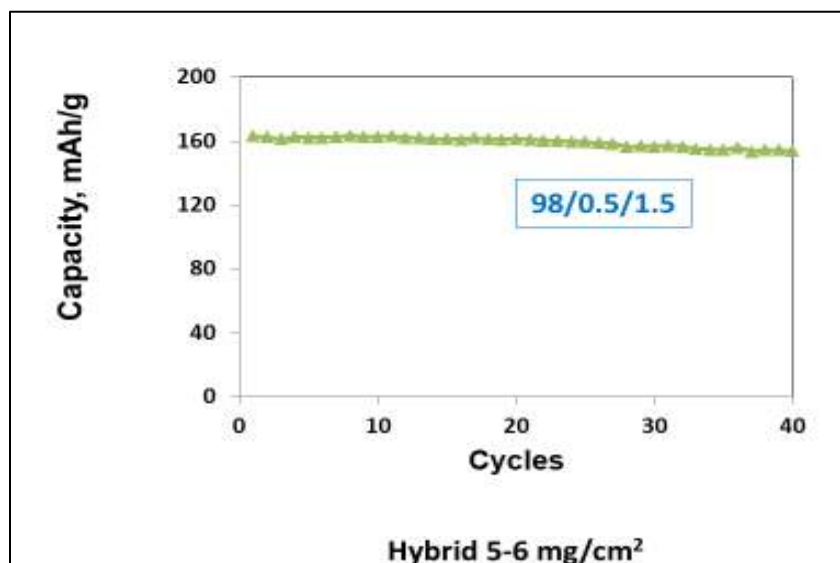


Figure I-97. Stable half-cell cycling of UV 98/0.5/1.5 power cathode.

Layered Cathode Coatings

For UV curing to work, light must penetrate through the coating. With various degrees of success, very thick coatings have been made. However, in real world production, the goal is to manufacture defect free product 100% of the time. Thicker coatings involve more risk. Instead of taking the risk path to make thicker coatings, we chose the path of layered coatings. Layered electrode coatings are an exciting possibility, offering flexible manufacturing and the potential for controlling electrode content at various depths. Many high-speed printing presses use layers of base coats, inks, and top coats to produce durable text and graphics. Multilayer UV printing is common in most print shops.

A major potential issue in manufacturing a LIB electrode is applying and curing a second layer without destroying or significantly altering the first layer. This issue becomes especially severe when using any solvated polymer (like PVdF) in an evaporative process. Because drying does not chemically change the

polymer, applying a second layer allows for solvent in the second layer to flow into the first layer and re-solvate it, thereby eliminating the advantage of a layered coating. In addition to the potential for changing the first layer, there is less reason to be interested in layered coatings when using PVdF and the traditional NMP solvent, as the evaporation speed for two separate layers will not be faster than evaporating a single layer at the same overall thickness. This eliminates a speed advantage for layered oven-dried binders.

UV overcomes both issues. UV irradiation eliminates the acrylate groups and forms a cross linked polymer that is not soluble in its original carrier. So, the wet applied top layer has no ability change the crosslinked first layer. Secondly, the process of application and curing in a UV process is significantly faster than oven-dried binders, meaning that there is not enough time for the second layer to flow into the first layer. To test these assumptions, we began by applying a single and double-layered electrode using a flexographic process. The goal was to produce two electrodes with the nearly the same thickness ($\sim 22\text{-}24\text{ }\mu\text{m}$) and mass loadings ($\sim 5\text{ mg/cm}^2$), yet one would be made in a single layer and the other in 2 layers. The double layered electrode was made by the method of application, cure, application, and a final cure, each using a single microwave UV lamp. Figure I-98 shows cycling results from this initial experiment.

As Figure I-98 demonstrates, the double-coated electrode performed even better than the single-layer electrode. This result shows there is no early signs of a barrier layer between the first and second layer.

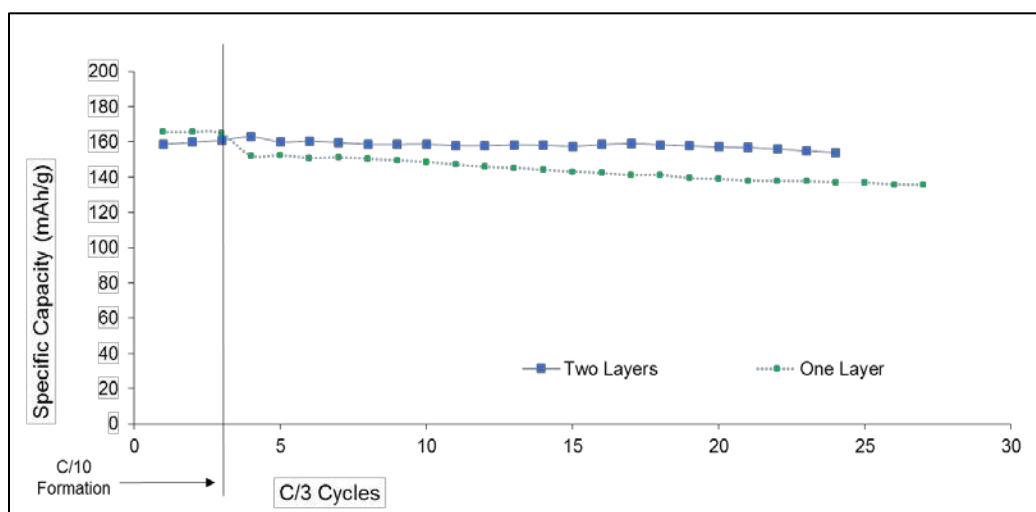


Figure I-98. Comparison of a NMC cathode utilizing a UV-curable cathode with a single and double layer, each electrode containing approximately the same amount of active material, at approximately the same thickness ($\sim 22\text{-}24\text{ }\mu\text{m}$.) The double-layered electrode was made by application, cure, second application, and then a final cure. Each cure was performed with a single UV lamp, and the mass ratio of materials was 90:7:3 NMC: Carbon: UV Binder.

The layered coating in Figure I-98 establishes feasibility but does nothing toward producing a thicker electrode. Next, we used a slot die coater and made thicker electrodes. In this case we made a 90/5/5 NMC/Carbon/UV binder. The single coated electrode has an active material loading of $\sim 3\text{ mg/cm}^2$, and the double coated electrode has an active material loading of $\sim 6\text{ mg/cm}^2$. Cycling results from the half cells taken from this slot die run is shown in Figure I-99. The capacity retention of the double layer, double thick cathode is as good as that of the single layer cathode.

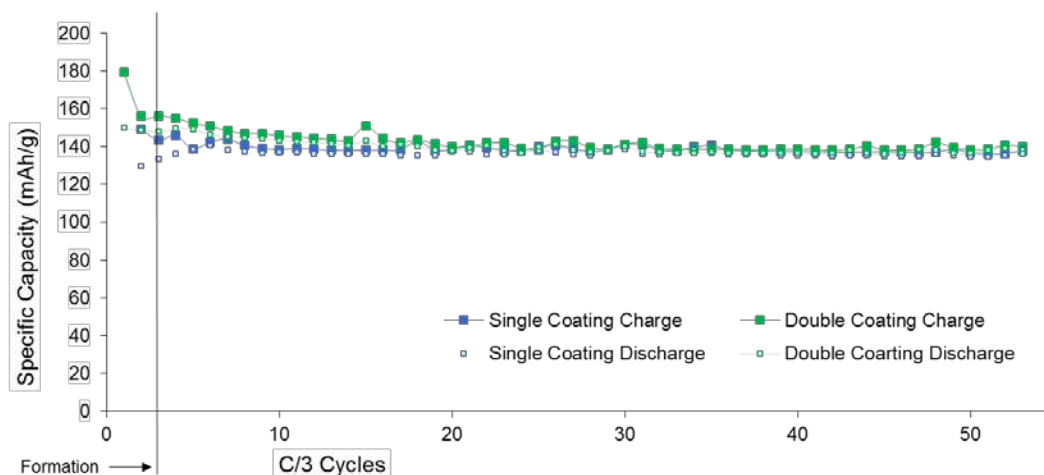


Figure I-99. Half-cell cycling data, comparing single and double cathode layers, each applied by slot die coating. The single coated electrode has a thickness of ~12 microns and an active material loading of ~3 mg/cm², and the doubly coated electrode has a thickness of ~25 microns and an active material loading of ~6 mg/cm². The formulation of each slurry is the same, with a mass loading of 90/5/5 NMC.

Current work is developing thicker layers. At this point we have produced 12 mg/cm² of electrode material with one layer. The next experiment will aim to demonstrate that we can produce production reliable 24 mg/cm² coatings with only two layers.

LTO Anode

Attempts to produce graphite anodes in the past were achieved but complicated by the high monomer absorbency of graphite and carbon and the UV absorbance of the carbon-based materials. Since most commercial graphite processes are water-based and not do not use NMP, the health advantages for UV graphite anodes are less than they would be for an NMP-PVdF process.

Discussions with industry partners led us to pursue the production of Lithium Titanate (LTO)-based anodes. That LTO is a white, light reflective material was serendipitous, and makes it an especially facile material to adapt into a UV process. We began by cycling half cells of a UV-cured LTO anode. Three C/10 cycles were followed by C/3 cycling, using a commercially-relevant active material loading of ~3.0 mg/cm². The results of this initial experiment are shown in Figure I-100.

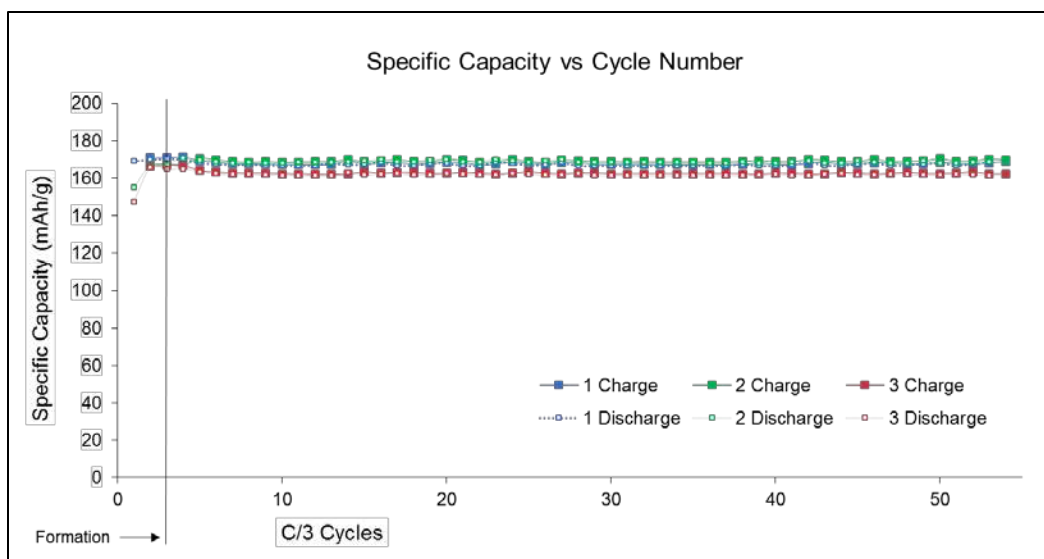


Figure I-100. Initial cycling tests on an LTO anode using a mass ratio of 93:4:3 LTO/CB/Binder, and electrode mass loading of $\sim 3.0 \text{ mg/cm}^2$ of active material. These electrodes were cast by hand using a doctor blade, and cured at 60 fpm.

With stable cycling established, we moved on to test how the rate capability of LTO, which is a distinct advantage listed for this electrode material, would be preserved using our crosslinked UV-curable binders. The result of this experiment is shown in Figure I-101, where we used the same formulation and electrode mass loading, but ramped up the rate every three cycles, starting at C/10, then moving on to C/5, C/2, C, 2C, 5C, and then 10C, and finally returning to C/5. Even at 10C, 60% of capacity was maintained.

With these recent successes with LTO, we intend to work with research and industry partners to produce LTO full cells using a UV-curable binder.

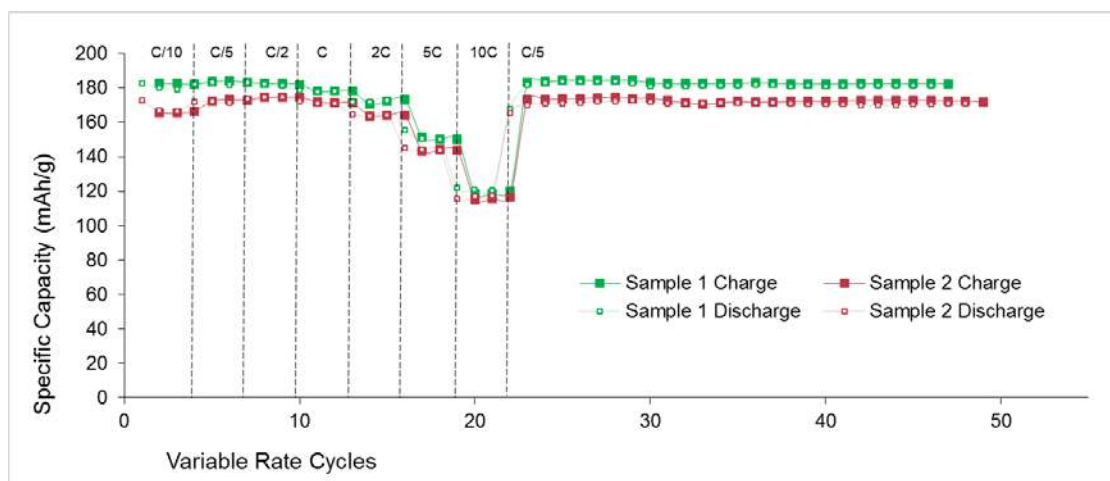


Figure I-101. UV LTO power anode (93/4/3 LTO/C/UV Binder), shows fast stable, high rate cycling. Electrode mass loading was 3.2 mg/cm^2 of LTO.

Conclusions

Miltec UV International and Argonne National Laboratory and Oak Ridge National Laboratory have made significant progress toward meeting the goals of this project. A three lamp UV curing system with a slot die coater and an interchangeable letterpress coater with a reel to reel control system is operational. Cathode coatings of 3%, 2% and 1% UV binder have been prepared, made into pouch cells and cycled with performance equal to PVdF reference cells. Double layered cathode coatings have been made with performance equal or greater than equivalent single-layer electrodes. This shows there is no impact on performance of this second layer, at least during the first 50 cycles. In addition, Miltec has demonstrated the ability to make LTO anodes using UV binder with performance equal to conventional LTO anodes. The coating and UV curing system in place will allow Miltec UV to complete the optimization and demonstrate the full potential of this technology. Miltec UV intends to vigorously pursue full development and commercialization of UV systems as applied to lithium-ion battery electrodes.

Key Publications

Miltec UV made various public releases of project results during the last year. These include:

1. Presentation at the DOE Annual Merit Review sponsored by the Vehicle Technology Office in June of 2017.
2. Gary Voelker and Dr. John Arnold gave a presentation on the merits of UV binder for LIB electrodes to the DOE USCAR representatives from Ford, Chrysler, GM and EPRI in Detroit, MI May 17, 2017.
3. Miltec UV had an exhibit with visuals and a video presenting the progress on UV binder for LIB electrodes at the International Battery Conference, Fort Lauderdale, FL March 2017 and the Battery Show, Novi, MI September, 2017.
4. Dr. John Arnold gave a presentation titled *UV Coating Processes to Enhance Li Ion Battery Performance and Reduce Costs* to the Electrochemical Society meeting at National Harbor Fall 2017.
5. Miltec UV has a fully operating website presenting details on the performance and potential for LIB electrodes made with UV curable binder. <http://www.miltec.com/technology/battery/cathode-binders/>

I.B.8 Towards Solventless Processing of Thick Electron-Beam (EB) Cured LIB Cathodes (ORNL)

David L. Wood, III, Principal Investigator

Oak Ridge National Laboratory
NTRC-2, 2370 Cherahala Boulevard, MS-6479
Knoxville, TN 37932
Phone: 865-574-1157
E-mail: wooddl@ornl.gov

Peter Faguy, Technology Manager

U.S. Department of Energy
Phone: 202-586-1022
E-mail: Peter.Faguy@ee.doe.gov

Start Date: October 1, 2014
Total Project Cost: \$1,425,000

End Date: September 30, 2019
DOE share: \$1,425,000

Non-DOE share: \$0

Project Introduction

There are a variety of technical attributes to electron beam (EB) curing of lithium-ion battery (LIB) binders. EB curing uses solvent-free compositions that have low emissions (VOCs, etc.) and are recognized by federal, state and local governments as being a more desirable technology. Solvent or water-based processing requires high drying energy and results in significant CO₂ emissions. EB curing offers significant process energy savings, is ultra-high speed, and utilizes much more compact equipment than conventional drying ovens (much less plant floor space required). Furthermore, it is a relatively cool process and is compatible with heat-sensitive substrates. Conventional thermal drying of LIB electrodes is typically conducted using multiple temperature stages; however, EB can be conducted in a single step. Solvent-free electrode compositions are rated as non-flammable, which translates into lower insurance costs, less stringent storage requirements and, a reduction in handling hazards.

EB treatment is a fast, robust materials processing technology that commonly delivers low cost and excellent performance for high-volume materials production. Based on decades of development and commercial deployment, self-shielded machines routinely operate with high reliability and low maintenance in industrial roll-to-roll production environments. ORNL is developing, demonstrating, and transitioning technology for high-speed roll-to-roll EB processing of LIB electrodes (i.e., coating formation and binder curing) – in particular high-area-loading (4 mAh/cm²) NMC 532 cathodes for this project. Further specific advantages of this processing route for LIBs are:

- Unmatched throughput – We estimate ≥ 600 m²/min throughput can be achieved based on ≥ 300 m/min line speed for roll widths up to 2 m (\$1.5-2.0M installed with machine footprint ~ 10 m²).
- Thicker electrodes – Up to 150 microns can be achieved at the throughput rate mentioned above. Coatings of several hundred microns could be processed at higher capital cost per unit throughput, modest reduction in energy efficiency, and larger equipment footprint.
- Excellent energy efficiency – Electrical efficiencies $\geq 60\%$ are possible, including voltage transformer losses (i.e., $\geq 60\%$ of electrical line energy is converted to productive EB energy).
- Environmentally friendly – EB processing requires no solvent or initiator and has low emissions.

Objectives

- Significant process energy savings demonstrated with NMC 532 cathodes.
- Ultra-high electrode processing speed.
- Utilization of significantly more compact processing equipment than conventional drying ovens.

Approach

ORNL is working on a multiphase approach to develop, demonstrate, and transition EB processing of roll-to-roll LIB materials:

- Phase 1 – Demonstrate the technology’s key differentiating attributes of high throughput and thick layer processing (FY15-16) with ebeam Technologies.
- Phase 2 – Address the key challenges of EB curing parameters and resulting material performance; develop coating methods requiring little or no solvent. (FY17-18) with ebeam Technologies and Keyland Polymer.
- Phase 3 – Demonstrate an optimized curing system together with a high-speed coating line in partnership with a key equipment manufacturer and LIB producer (FY19).

Results

To successfully EB cure the resins into binders for thick electrodes (25 mg/cm^2) at high speed (500 ft/min), several strategies were used: (1) improvement of formulation to obtain crack-free, thick coatings (Z. Du, et al. J. Power Sources 354 (2017) 200); (2) Calendering before curing to lower the porosity and reduce trapped air in pores; (3) improvement of nitrogen purging in the curing chamber to reduce O_2 level; (4) increasing electron dose to generate more free radicals for offsetting the O_2 inhibition.

Table I-17 shows a summary of the trial runs at ebeam Technologies in Davenport, IA. Cathode coating samples were taped onto a paper leader material using clear packaging tape around the periphery of the sample. Prior to taping down the trailing edge of the packaging film over the coated electrodes, samples were purged several times with nitrogen. Then the film was pressed down to remove the majority of the nitrogen and quickly taped closed to minimize any air intrusion. The two packaging films implemented (biax nylon and Stretch-tite) were each about $15 \text{ }\mu\text{m}$ thick, and the EB curing occurred at 500 ft/min (the upper limit of the ebeam Technologies pilot line) at 60 kGy and 250 kV.

Table I-17: Summary of the high speed curing trial runs at ebeam Technologies.

Run No.	Sample Name	Experimental details	EB conditions
1	1A	No packaging film;	275kV/60kGy
	1B	Covered and N_2 inerted using biax nylon film;	300 ft/min
	1C	Covered and N_2 inerted using Stretch-tite film.	300 ppm O_2
2	2A	No packaging film;	250kV/50kGy
	2B	Covered and N_2 inerted using Stretch-tite film;	500 ft/min
	2resin	Uncovered dry Ucecoat 7788 & 7689 resin.	560 ppm O_2
3	3A	No packaging film	250kV/60kGy
	3B	Covered and N_2 inerted using biax nylon film;	500 ft/min
	3C	Covered and N_2 inerted using Stretch-tite film.	300 ppm O_2
	3resin	Uncovered dry Ucecoat 7788 & 7689 resin	

Figure I-102 shows the FTIR spectrum of pure resins in runs #2 and #3, with the “C=C” peak at $\sim 810 \text{ cm}^{-1}$. The cross-linking at a high speed of 500 ft/min was confirmed by a decrease in the transmittance peak

intensity. A higher voltage used for run #3 yielded a higher extent of cross-linking compared to run #2 due to a higher electron dose for run # 3.

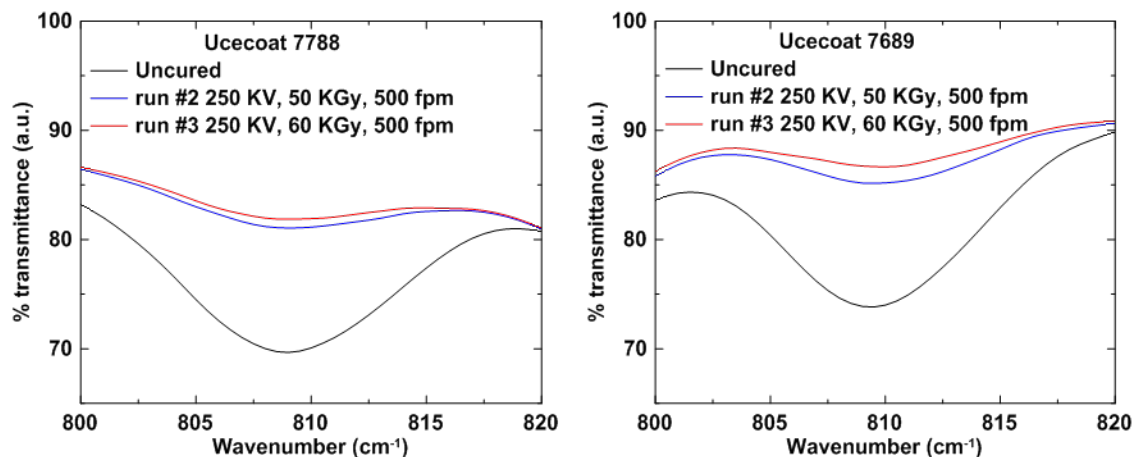


Figure I-102. FTIR spectra of Ucecoat 7788 and 7689 resins used in runs #2 and #3.

Table I-18 shows a summary of the actual electron doses measured using dosimeters. A first dosimeter was placed under the packaging film directly on top of the coating (labeled as “Top”), and a second dosimeter was placed directly underneath the coated aluminum foil (labeled as “Bottom”). The values labeled “w/o Al foil” were calculated by eliminating dose reduction from the 15 μm Al foil. For 60 kGy curing, the samples with a line speed of 300 ft/min had the highest dose reading at the bottom, while a line speed of 500 ft/min slightly decreased the dose penetration into the samples. It was observed that the NMC 532 cathode coatings in the thickness direction received a dose range of 40-68 kGy, indicating the resins were fully cross-linked. Run #2 was carried out at dose of 50 kGy, and the overall coating dose range was within 30-53 kGy.

Table I-18: EB doses for different sample on the top and bottom of the samples.

Trial Number	Sample No	Conditions	Dose (kGy)		
			Top	Bottom	w/o Al foil
#1: 60 kGy, 275 keV, 300 ft/min, 300 ppm O ₂	1A	No Film	61.1	34.7	43
	1B	Stretch-tite	61.4	36.7	46
	1C	Nylon	52.9	39.6	45
#2: 50 kGy, 250 keV, 500 ft/min, 560 ppm O ₂	2A	No Film	50.3	22.9	30
	2B	Stretch-tite	52.3	23.9	31
#3: 60 kGy, 250 keV, 500 ft/min, 300 ppm O ₂	3A	No Film	65.6	29.3	40
	3B	Stretch-tite	67	28.7	40
	3C	Nylon	66.5	29	40

The cured electrodes in Run #3 were assembled into 1.5 Ah pouch cells, and it was demonstrated that all cells had typical NMC 532 charge/discharge curves (Figure I-103a) and differential capacity curves (Figure I-103b). Good rate performance was achieved from C/10 to 2C (Figure I-103c), comparable to NMP processed electrodes with similar areal loadings. The retested cells retained about 91% capacity after 100 cycles, and 80.2% after 300 cycles (Figure I-103d), which achieved the stretch milestone specified for this project. Cell performance of the same coatings without any EB curing treatment were also included in Figure I-103d for comparison. As can be seen from the figure, the capacity drops rapidly for the first several cycles with only 60% capacity retention after 20 cycles.

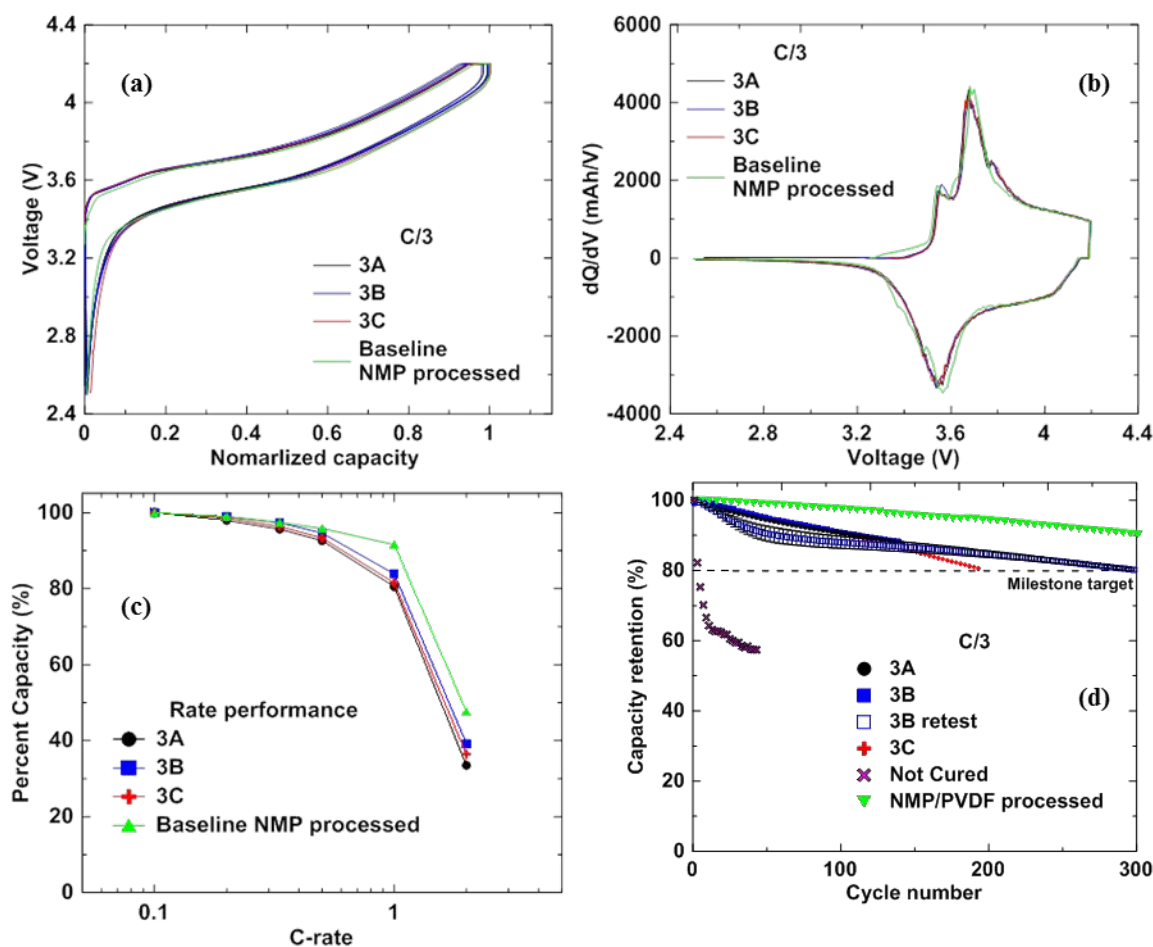


Figure I-103. (a) Charge/discharge voltage curves at C/3, (b) rate performance from C/10 to 2C, (c) differential capacity curves at C/3, and (d) cycling performance at C/3 charge/discharge rates for the 1.5 Ah pouch cells.

To develop an electrode coating method compatible with the ultra-high line speeds associated with EB curing, electrostatic spraying on aluminum foil was conducted at Keyland Polymer Ltd. using dry cathode powder that was composed of 8 wt% resin, 87 wt% NMC 532 and 5 wt% C65 carbon black. Prior to spraying, the dry cathode powder was prepared at ORNL as listed in Table I-19. Sample A was employed to demonstrate minimal water use for binder distribution in dry powder mixing. Samples B and D demonstrated the use of dry powders with the binder well dispersed over the powder surface. Samples C and E were equivalent formulations to samples B and D with the exception that a photoinitiator was added for UV curing.

Table I-19: Dry powder samples prepared for electrostatic spraying trial runs.

Sample	Resin	Photoinitiator (PI)	Solvent	Curing Method
A	Ucecoat 7689	None	No additional water	EB
B	Ucecoat 7689	None	DI water	EB
C	Ucecoat 7689	Omnirad 500	DI water	UV
D	PA50	None	Acetone	EB
E	PA50	Keyland Polymer	Acetone	UV

The morphology of the prepared dry powders is shown in Figure I-104. No difference was observed among samples A, B and D, indicating the binder was well dispersed in the NMC 532 and carbon black mixtures. After electrostatic spraying, samples were calendared (which significantly improved adhesion in all cases) followed by UV or EB curing. SEM images of the final electrode microstructures are shown in Figure I-105, and it was observed that sample A had good dispersion of carbon black among the NMC particles. Samples B and C exhibited typical morphology consistent with our standard aqueous processed NMC 532 cathodes. The carbon-black dispersion in NMC was excellent for samples D and E, which were processed with acetone, but it is not yet clear whether the addition of acetone promotes this improved dispersion.

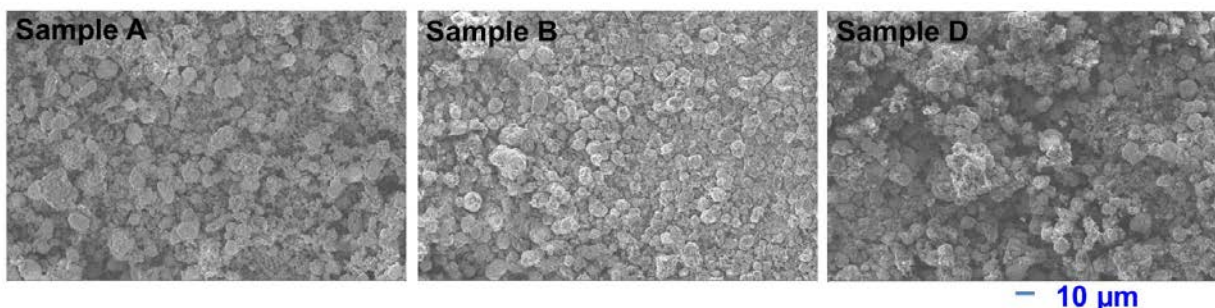


Figure I-104. SEM images of prepared sample A, B, and D dry powders.

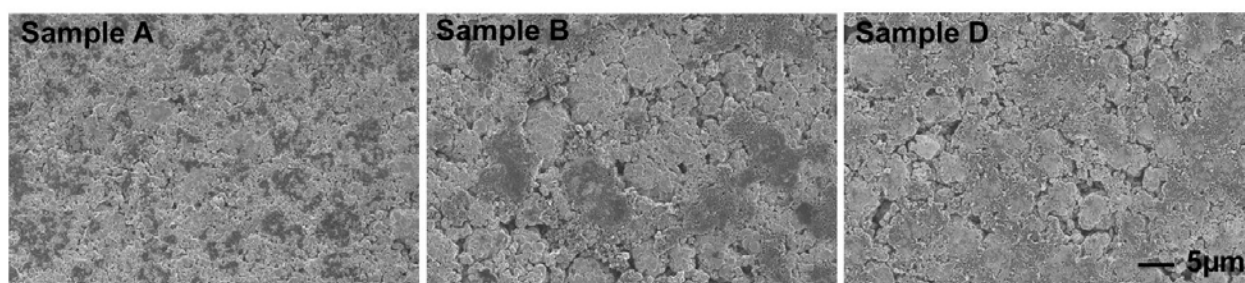


Figure I-105. SEM images of Sample A, B and D after calendaring and radiation curing.

The half-coin-cell charge and discharge profiles and rate performance for these formulations (samples A-E) are shown in Figure I-106, and they were tested using C/20 charging and discharging for the first three formation cycles followed by C/5 to 5C rate test with voltage cut-offs of 2.5 V and 4.2 V. All cells showed the typical charge/discharge features of an NMC cathode, indicating that the resin did not affect the lithiation/delithiation processes. Our baseline PVDF electrode performance is not shown in Figure I-106 since these electrodes had greater thickness, which affects the comparison. Sample E showed superior rate performance up to 3C discharging as compared to sample C, which could be ascribed to the better dispersion of carbon black in the cathode. Full coin cells were made for samples A and B to obtain short-term cycling performance when paired with graphite anodes (see Figure I-106c), and these cells were cycled at C/3 charge/discharge rates. Greater than 90% capacity retention was achieved after 100 cycles for both formulations, demonstrating that there is no benefit from adding additional water to the formulation (sample B vs. A).

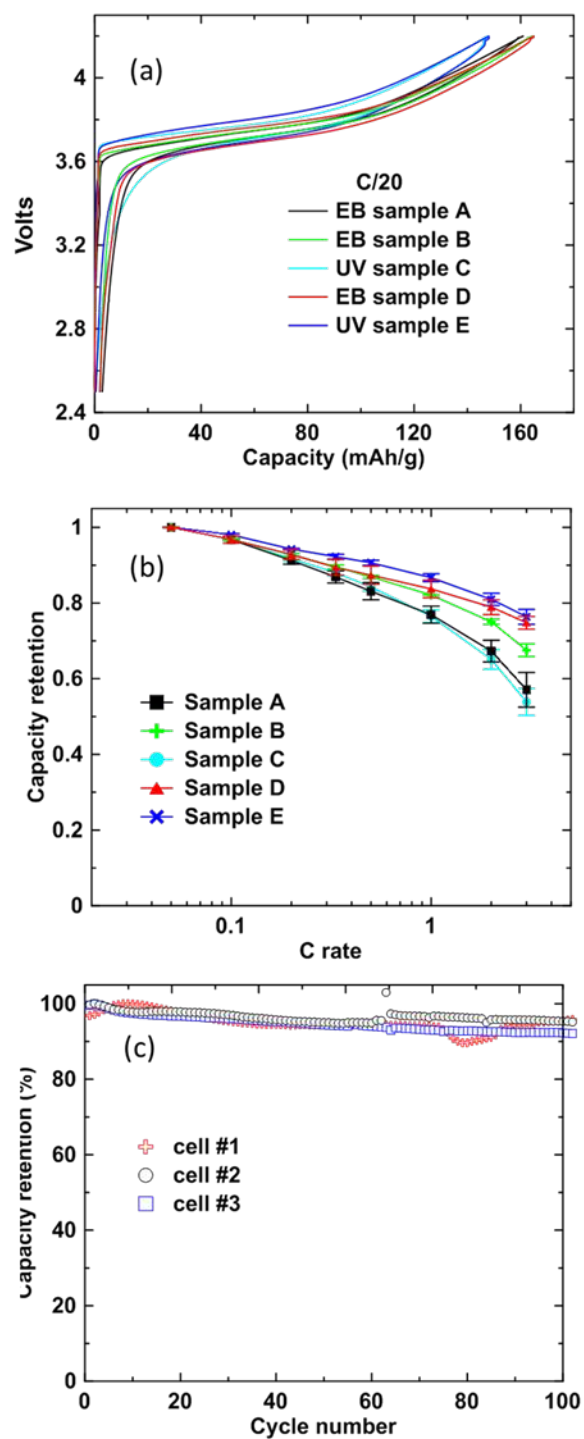


Figure I-106. (a) Voltage profiles in Li half cells, (b) rate performance in Li half cells, and (c) selected full-coin-cell cycling performance for samples A and B.

Conclusions

The project stretch milestone was successfully met by demonstrating no more than 20% capacity fade through 300 cycles at 0.33C/-0.33C in 1.5 Ah pouch cells with optimized cathode EB curing formulation and areal loading of 25 mg/cm² at a curing speed of 150-200 m/min, and completing pouch cell rate performance from C/20 to 1C. A “Go” decision was made by demonstrating 25 mg/cm² NMC 532 cathode coating areal weight with full EB cure and down-selected electrode formulation with selected industrial partner at 150-200 m/min.

Technical achievements include: (1) 150 m/min EB curing pilot line demonstration, (2) 1.5 Ah pouch cell performance evaluation, (3) dry powder mixing evaluation, and (4) electrostatic spraying of powder coating with good electrochemical performance.

Collaborative accomplishments include: (1) high speed curing trials are currently being scaled up at ebeam Technologies pilot line in Davenport, IA. (2) Electrostatic spraying powder coating is evaluated at Keyland Polymer in Cleveland, OH.

Commercial deployment is highly likely for this technology because of strong industrial collaboration, significant electrode production cost reduction, and impact on cell energy density ($\geq 2\times$ thicker cathodes).

Key Publications

1. U.S. Provisional Patent Application No. 62/492,370, “A Method of Solvent-Free Manufacturing of Composite Electrode Incorporating Radiation Curable Binders,” 2017.
2. D. L. Wood, Z. Du, C. J Janke, J. Li, C. Daniel and C. Eberle, “Towards Solventless Processing of Thick Electron-Beam (EB) Cured Lithium-Ion Battery Cathodes,” ES 207, DOE Annual Merit Review, June 8, 2017.
3. Z. Du, C. J Janke, J. Li, C. Daniel, D. L Wood, “Towards Solventless Processing of Thick Electron-Beam (EB) Cured Lithium-Ion Battery Electrodes,” 232nd ECS meeting, National Harbor, MD, Oct 4, 2017.
4. Z. Du, K.M. Rollag, J. Li, S.J. An, M. Wood, Y. Sheng, P.P. Mukherjee, C. Daniel, D.L. Wood III, “Enabling Aqueous Processing for Crack-Free Thick Electrodes,” *J. Power Sources*, **354**, 200 (2017).
5. J. Li, Z. Du, R. E. Ruther, S. J. An, L. A. David, K. Hays, M. Wood, N. D. Phillip, Y. Sheng, C. Mao, S. Kalnaus, C. Daniel, D. L Wood, “Toward Low-Cost, High-Energy Density, and High-Power Density Lithium-Ion Batteries,” *JOM*, **69**, 1484 (2017).
6. Z. Du, D.L. Wood, C. Daniel, S. Kalnaus, and J. Li, “Understanding Limiting Factors in Thick Electrode Performance as Applied to High Energy Density Li-Ion Batteries,” *Journal of Applied Electrochemistry*, **47**, 405 (2017).

I.B.9 Performance Effects of Electrode Processing for High-Energy Lithium-Ion Batteries (ORNL)

David L. Wood, III, Principal Investigator

Oak Ridge National Laboratory
NTRC-2, 2370 Cherahala Boulevard, MS-6479
Knoxville, TN 37932
Phone: 865-574-1157
E-mail: wooddl@ornl.gov

Peter Faguy, Technology Manager

U.S. Department of Energy
Phone: 202-586-1022
E-mail: Peter.Faguy@ee.doe.gov

Start Date: October 1, 2016
Total Project Cost: \$1,015,000

End Date: September 30, 2019
DOE share: \$1,015,000

Non-DOE share: \$0

Project Introduction

This project at the DOE Battery Manufacturing R&D Facility (BMF) at ORNL builds on past research successes on battery electrode process development and optimization, cost reduction, and cell energy density and manufacturability improvements, which support the Vehicle Technologies Office (VTO) and Electrochemical Energy Storage Tech Team ultimate targets of \$80-100/kWh-usable system cost, 500 Wh/kg cell energy density, and 800 W/kg cell power density. Our goal is to perform the science needed to reduce high-risk, high-payoff technologies to lower risk levels, such that U.S. industry will consider their integration in future products. Once a new material, process, or concept has demonstrated feasibility for integration and scaling, the BMF will work to make it a viable processing methodology (preferably with an industry partner) with validated performance in a full pouch cell design. While doing so, the BMF will leverage a large array of complimentary projects and sponsors that will provide additional experience and a fast, efficient methodology for solving problems faced by the domestic lithium-ion battery (LIB) industry.

Objectives

To generate a deep understanding of process-property-performance relationships that lead to lower cost and higher performing lithium-ion cells:

- Optimize electrode formulation chemistry and dispersion mixing and relate colloidal structure to electrode architecture.
- Develop understanding of relationship between coating deposition physics, electrode quality, and electrode performance.
- Optimize drying and calendering protocols for thick electrodes.
- Determine compatibility of Ni-rich cathodes (NMC and NCA) with water-based processing.
- Reduce cell formation and electrode wetting time and elucidate impact on SEI and CEI layer chemistry, morphology, and functionality.
- Develop materials and chemical characterization methods for high-speed electrode processing.

Approach

- Enable thick electrode coatings with next generation cell chemistries (NMC 811, NCA, Si/graphite, etc.) through thorough understanding of colloidal science and formulation chemistry.
- In-depth study of interrelationship of electrode processing steps.
- Generate processing science knowledge that can be used to strengthen U.S. domestic lithium-ion battery supply chain.
- Develop cohesive processing-property-performance database.
- Develop and utilize novel materials and chemical characterization techniques to shed light on active and inactive materials processability.

Results

pH and ICP-MS analysis of NMC cathode active materials after exposure to water

We analyzed the stability of four different NMC compositions in water to evaluate the feasibility of using aqueous processing to prepare Ni-rich NMC electrodes for high energy density LIBs. The experimental procedure was designed to mimic actual electrode processing conditions. Samples of NMC 333, 532, 622, and 811 powders were each exposed to aqueous solutions at three different pH values (pH 2, pH 6.6 (DI Water), and pH 12) for three different time periods (4 h, 1 day, and 1 week). The powder was then filtered out of each solution, and the filtrate was analyzed by ICP-MS to determine the concentrations of Li and transition metal ions that leached out of the NMC material. The pH of the filtrate was also measured to provide additional information on changes occurring during water exposure. This first water exposure step is analogous to slurry preparation, where the active material is mixed with solvent (in addition to carbon black and binder) before being coated and dried.

Two sets of experiments were performed—one at high solids % (~63 wt%) to represent actual slurry conditions, and one at low solids % (~8 wt%) as a worst-case scenario to enhance the effect of water exposure. The pH results for both sets of samples at all three initial pH values are shown in Figure I-107a. Regardless of the starting pH, all of the high-solids samples become quite basic very quickly (> pH 11.5 within the first 4 hours). In general, the higher the nickel content, the higher the final pH, although the differences were small. The pH results for the low-solids samples (exposed to a greater volume of water) were similar, but NMC 333 showed a slightly greater time dependence at pH 2.

Figure I-107b shows the percentage of Li leached from the NMC samples during water exposure at all three initial pH values as measured by ICP-MS. In all cases, the higher the Ni content in the NMC, the higher the Li loss (NMC 811 had the highest leaching). As expected, the low-solids samples exposed to a greater volume of water showed more Li leaching and a greater time dependence than the high-solids samples. For instance, the amount of Li leached from NMC 811 after 1 week in DI water was ~9% for the *low*-solids case, compared to ~3% for the *high*-solids case. This difference was the greatest for NMC 811 and decreased with lower Ni content. In addition, the amount of Li leached from the *low*-solids samples increased over time, whereas it remained almost constant for the *high*-solids samples. Interestingly, the initial pH of the solution had little effect on the amount of Li leaching. However, it is important to note that if different acids or bases had been used to adjust the solution pH, the impact may have been greater. The corresponding ICP-MS transition metal results (not shown) indicate that Ni, Mn, and Co leaching from NMC is minimal (< 0.19%) at all concentrations and initial pH values.

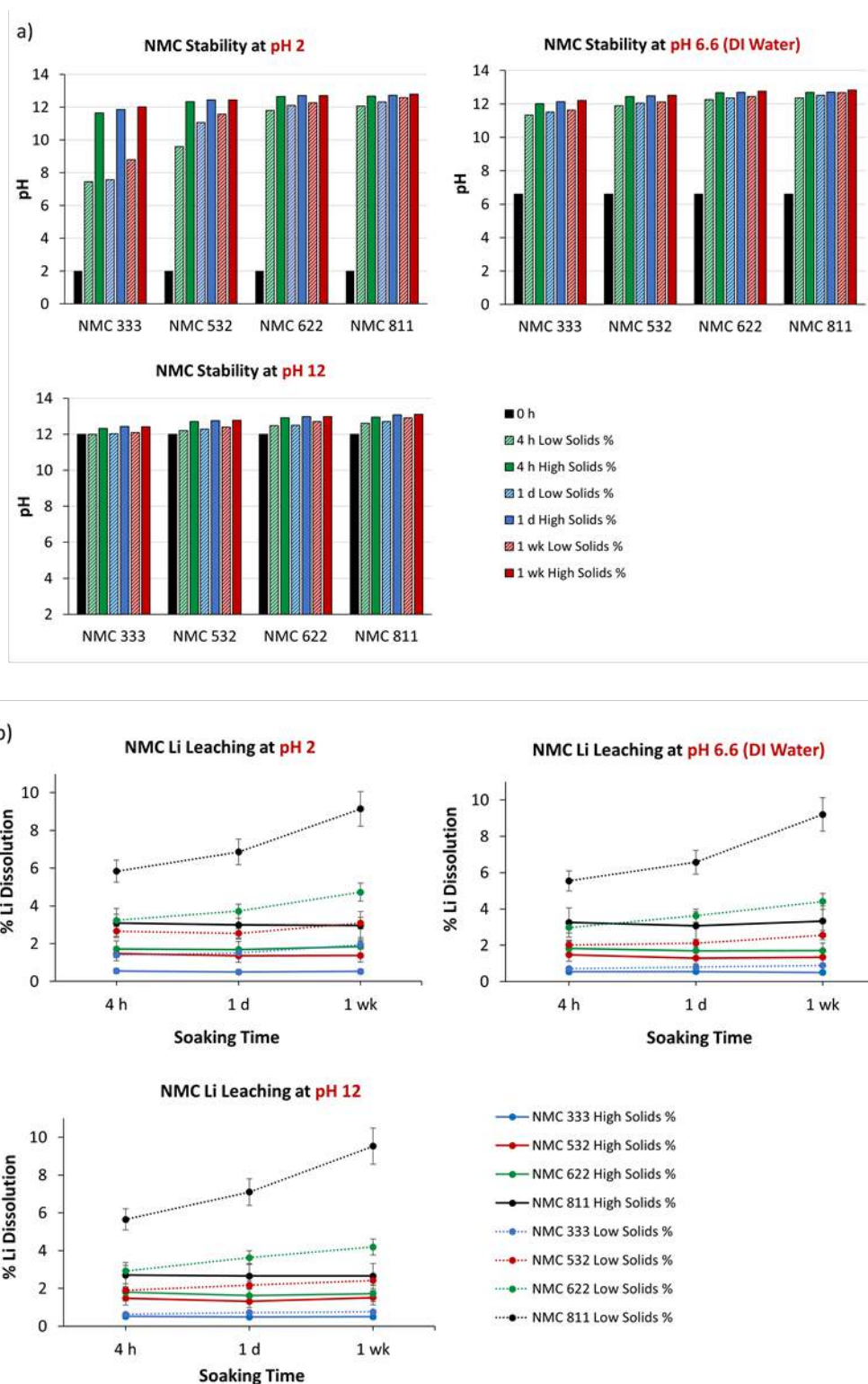


Figure I-107. Stability results after exposure of different NMC compositions to water, acid, and base solutions for different time periods. a) Measured filtrate pH values after soaking NMC in aqueous solutions with different pH values. Nitric acid was used to make the pH 2 solution, and ammonium hydroxide was used to make the pH 12 solution. b) % of Lithium leached from NMC (into the filtrate) after soaking in aqueous solutions with different pH values, as measured by ICP-MS.

A separate set of identical samples was made for characterization. These were prepared as described above, except instead of filtering out the powder particles after water exposure, the water was evaporated from the powder in a vacuum oven to simulate the typical two-step electrode drying process (in which the wet electrode coating is dried immediately, and a secondary drying step is performed in a vacuum oven before cell assembly). The dried powders were characterized by XPS, XRD, and Raman, which confirmed that there were no substantial changes to the NMC structure after water exposure.

Aqueous processing of NMC 811 single-layer pouch cells

Single-layer pouch cells (~100 mAh) were made using NMC 811 cathodes processed with either water or NMP (for comparison) and matching graphite anodes. The composition of the aqueous NMC 811 cathode slurry was 90 wt% Targray NMC 811, 5 wt% Denka carbon black, 1 wt% Ashland carboxymethylcellulose (CMC), and 4 wt% Ashland acrylic emulsion, and the composition of the NMP-based NMC 811 cathode slurry was 90 wt% Targray NMC 811, 5 wt% Denka carbon black, and 5 wt% Solvay 5130 PVDF. Figure I-108 shows the capacity retention of aqueous- and NMP-processed NMC 811 cells after 200 cycles at 0.333C charge/discharge rates (charged to 4.2V). Although cells made with aqueous-processed NMC 811 cathodes show a slightly greater capacity fade (93% of original capacity after 200 cycles vs. 97% of original capacity for NMP-processed), the initial capacities of both sets of cells were the same, and both demonstrated good capacity retention after 200 cycles. Further optimization of the aqueous slurry rheology, by changing the order of addition or incorporating additives/dispersants, could help further improve performance. Binder supply chain delays have postponed our work in this area; nonetheless, these initial cycling results demonstrate that NMC 811 electrodes can be successfully made using aqueous processing, and cells made with these electrodes cycle nearly as well as cells made with the corresponding NMP-processed NMC 811 electrodes.

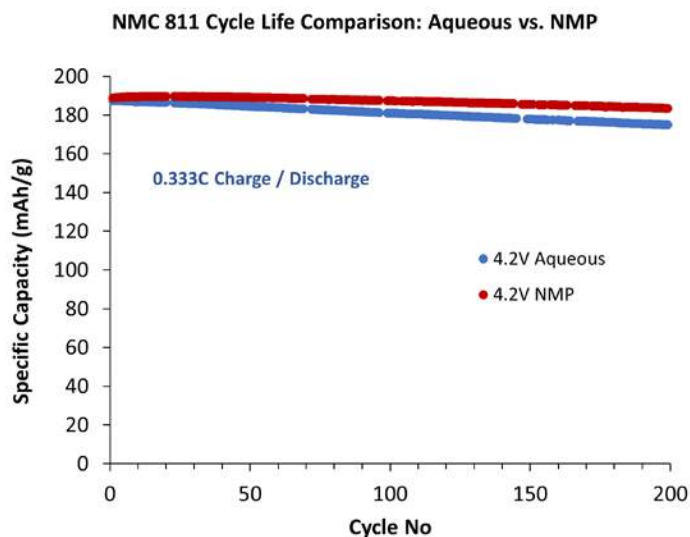


Figure I-108. Comparison of the capacity retention of single-layer pouch cells made with aqueous- and NMP-processed NMC 811 electrodes after 200 cycles at 0.333C charge/discharge rate. Data is an average of 3 cells, and the error bars represent the standard deviation of each cycle. The small breaks in the data are due to power outages. The active material loadings of the aqueous NMC cathode, NMP-based NMC cathode, and the Superior Graphite SLC 1520T anode were 11.3 mg/cm², 11.6 mg/cm², and 7.5 mg/cm², respectively. The cathode and anode thicknesses were 43 and 53 μ m, respectively, and the porosity of all electrodes was 35%.

Aqueous processing of thick electrodes

Thick lithium-ion battery (LIB) electrodes promise to substantially increase energy density due to increased volume fraction of active materials and to reduce cost due to the elimination of the toxic organic N-methylpyrrolidone (NMP) solvent, but cracking of electrode coatings becomes a critical issue with aqueous processing of the cathode as active material loading increases above 20–25 mg/cm² (3.5–4.0 mAh/cm²) as shown in Figure I-109a–d. The NMC 532 cathode with 15 mg/cm² loading was uniform and crack-free, but noticeable cracks with gap width of 50 μm and length of 300 μm were observed in the cathode with 17.5 mg/cm² loading. Further crack propagation is seen in Figure I-109c–d for increased loading in the manner of both crack quantity and crack dimension (width and length).

Figure I-109e is an illustration of cracking due to the build-up of capillary pressure during the drying process. Initially, all particles are suspended in the solvent after the slurry is cast onto Al foil. As the solvent evaporates, the air-solvent interface reaches the sediment surface. Menisci are formed between particles on the surface, and particles are subjected to a compressive force perpendicular to the air-liquid interface resulting from capillary pressure. As particles consolidate further, capillary pressure builds up and local gaps widen due to the increasing in-plane capillary forces. Eventually, the film cracks to release these stresses.

Since the capillary pressure during drying initiates film cracking, the reduction of surface tension is a straightforward method to alleviate or eliminate cracks. Isopropyl alcohol (IPA) is a widely used solvent in industry with a very low surface tension (23.00 mN/m, 20°C), and it is also miscible with water. The critical thickness or loading of the coating without cracking versus the solvent composition is shown in Figure I-109f. The crack-free loading increased gradually when more IPA was used during slurry preparation, which is attributed to reduced surface tension leading to decreased capillary forces during coating drying. A linear relationship was obtained between the critical loading and $(1/\gamma)^{1/2}$ where γ is the solvent mixture surface tension.

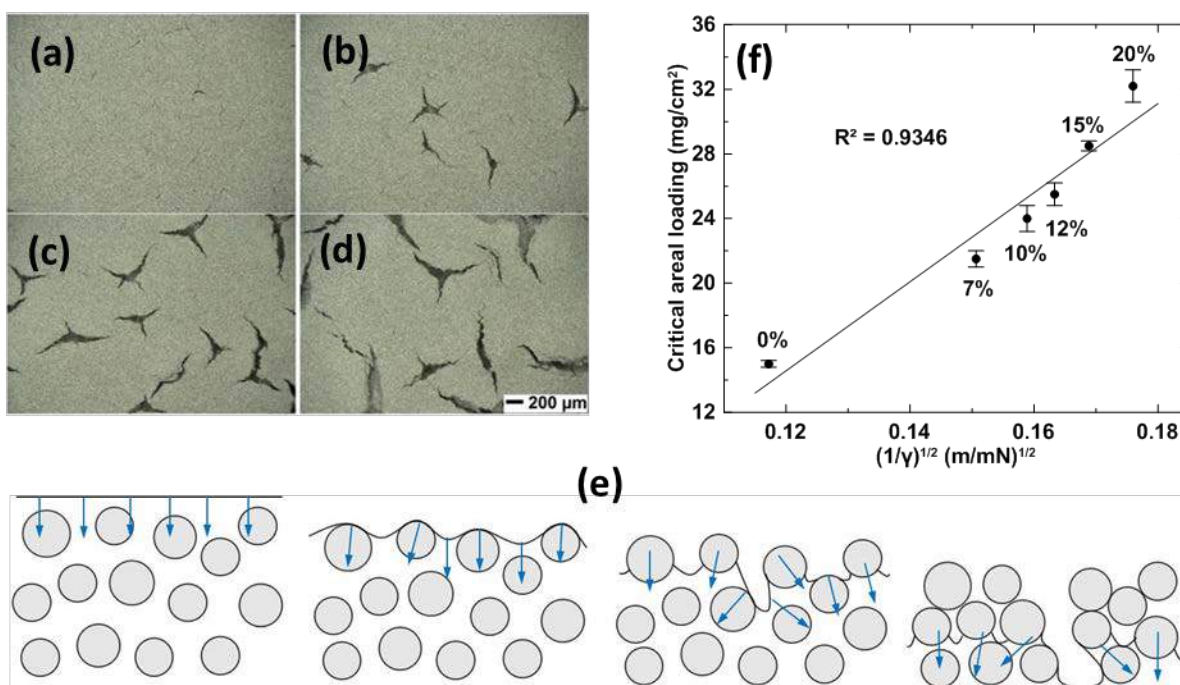


Figure I-109. Aqueous processed NMC 532 cathodes with different active material loadings: (a) 15 mg/cm², (b) 17.5 mg/cm², (c) 20 mg/cm² and (d) 25 mg/cm². (e) Illustration of the drying process. (f) Critical areal loading versus $(1/\gamma)^{1/2}$.

Compared to co-solvent optimized cathodes, the capacity of cracked electrodes deteriorated significantly when the discharge rate in 170-mAh pouch cells was higher than C/2 due to the poor quality of the coating. With the reduction of solvent surface tension during processing, coatings with good quality were formulated; thus, the rate performance capacity was improved with electrodes using IPA/water co-solvent processing. Long-term 170-mAh pouch cell cycling performance using different NMC 532 cathodes was evaluated, and with the addition of IPA during formulation, electrodes with IPA/water co-solvent processing exhibited greatly improved capacity and cycling performance compared to fully aqueous processed electrodes. Cathodes using IPA/water co-solvent processing had long-term cycling performance comparable to NMP processed electrodes, both achieving 83% capacity retention after 700 cycles.

Aqueous processing using carbon nanotubes (CNTs) as conductive additives

Aqueous processing of NMC 532 cathodes was investigated by incorporating CNTs as the conductive additive. Figure I-110a-f shows SEM images of these cathodes, and for the carbon black (CB) electrode (5% carbon black, 5% binder in the electrode), aggregates were formed in the interstitial space between NMC secondary particles. Being 0D in nature, the CB agglomerates do not connect with each other to form continuous and effective electronic paths. Higher resolution SEM in Figure I-110b shows some bare NMC primary particles without any coverage by carbon black. Therefore, the electrons associated with the local charge-transfer reaction have long transport pathways across several NMC primary particles to reach the CB conductive network. For the CNT-A electrodes (2.5% CNT, 5% binder), the CNTs were well dispersed across the electrode, and no obvious aggregates are seen in Figure I-110c. Figure I-110d shows that CNTs are uniformly spread over the entire surface of individual primary NMC particles. This 3D CNT network and intimate contact between CNT and primary NMC particles form a highly efficient electron conducting pathway. The CNT-B electrodes (1.5% CNT, 2.5% binder) in Figure I-110e-f show a similar morphology to CNT-A, even though the ratio of CNTs in the electrode is reduced to 1.5 wt%.

Figure I-110g and Figure I-110e show the normalized percentage capacity versus discharge rate for 85-mAh pouch cells. The cell capacity of the three different NMC 532 cathodes is nearly identical up to C/2 indicating the electrode conductivity is sufficient when discharged at C/2. However, there was significant deviation in performance at $\geq 1C$ between the CB baseline and the CNT substituted cells. The capacity of the CNT-B electrodes was also slightly better than that of the CNT-A electrodes from 1C to 3C, possibly due to better dispersion of CNTs in the electrode from the lower concentration of CNTs in the slurry. Long-term cycling performance of the three electrode types is shown in Figure I-110h for 85-mAh pouch cells. The CB baseline electrode showed relatively good performance with about 94.6% capacity retention after 200 cycles, but the cycling performance of the CNT-A and CNT-B cells was much higher with about 99.4% capacity retention remaining after 200 cycles.

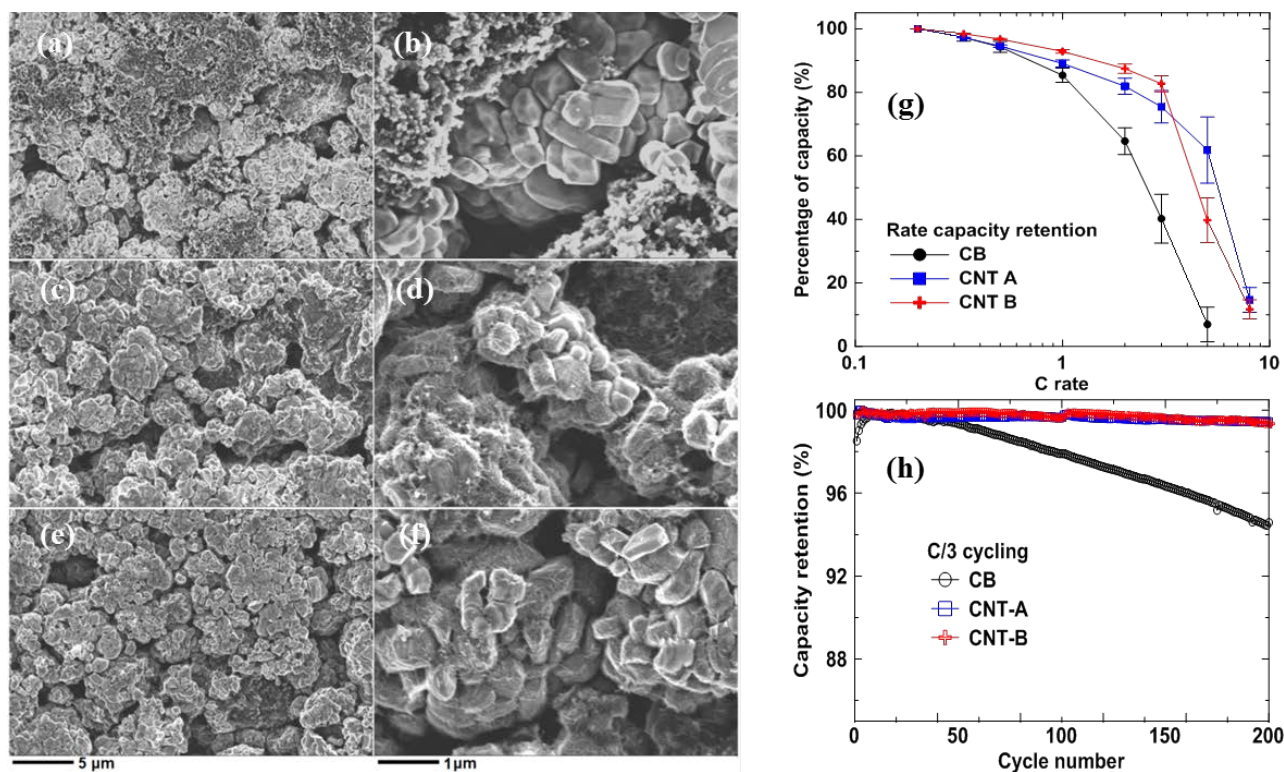


Figure I-110. SEM images of (a, b) CB electrode, (c, d) CNT-A electrode and (e, f) CNT-B electrode. (g) percentage of capacity (normalized to capacity at C/5) at different discharge C rates. (h) cycling performance at C/3.

Conclusions

The measured pH values of the NMC active materials exposed to water were comparable to the pH of an actual aqueous NMC 532 slurry (measured at 12.18), which confirms the relevance of our measurements. Overall, the Li ICP-MS results confirm that while Li leaching during water exposure is higher for Ni-rich NMC, it is minimal at actual slurry concentrations. Cathodes using IPA/water co-solvent processing had long-term cycling performance comparable to NMP processed electrodes, both achieving 83% capacity retention after 700 cycles. This finding was expected from the good morphology and physical integrity of electrodes using IPA/water co-solvent processing, which eliminates the detrimental interfacial resistances from the cracks in electrode. Besides better electrochemical performance of CNT-based cathodes, the total inactive components (binder and conductive additives) were also significantly reduced compared to CB electrode. It was calculated that the energy density of the cathode was increased by 11.7% at C/3 with a corresponding capacity loading and voltage increase of 6.67% and 4.77%, respectively. Therefore, this processing and electrode architecture modification is an extremely effective method for improving the energy and power density of Li-ion batteries.

Key Publications

1. Z. Du, K.M. Rollag, J. Li, S.J. An, M. Wood, Y. Sheng, P.P. Mukherjee, C. Daniel, D.L. Wood III, "Enabling Aqueous Processing for Crack-Free Thick Electrodes," *J. Power Sources*, **354**, 200 (2017).
2. U.S. Provisional Patent Application No. 62/492,475, "Manufacturing of Thick Composite Electrode Using Solvent Mixtures," 2017.
3. Z. Du, D.L. Wood, III, C. Daniel, S. Kalnaus, and J. Li, "Understanding Limiting Factors in Thick Electrode Performance as Applied to High-Energy-Density Li-Ion Batteries," *Journal of Applied Electrochemistry*, **47**, 405–415 (2017).

I.C Computer-Aided Engineering for Batteries (CAEBAT)

I.C.1 Advanced Computer Aided Battery Engineering Consortium (NREL, ANL, SNL, Purdue U)

Dr. Kandler Smith, Principal Investigator

National Renewable Energy Laboratory
15013 Denver West Parkway
Golden, Colorado 80401
Phone: 303-275-4423
E-mail: kandler.smith@nrel.gov

Dr. Daniel Abraham, Principal Investigator

Argonne National Laboratory
9700 Cass Avenue
Lemont, IL 60439
E-mail: abraham@anl.gov

Dr. Joshua Lamb, Principal Investigator

Sandia National Laboratories
1611 Innovation Parkway, SE
Albuquerque, NM 87185
E-mail: jlamb@sandia.gov

Dr. Partha Mukherjee, Principal Investigator

Purdue University
585 Purdue Mall
West Lafayette, IN 47907
E-mail: mukher28@purdue.edu

Brian Cunningham, Technology Manager

U.S. Department of Energy
Phone: 202-287-5686
E-mail: Brian.Cunningham@ee.doe.gov

Start Date: October 1, 2016

End Date: September 30, 2018

Total Project Cost: \$5,150,000

DOE share: \$5,150,000

Non-DOE share: \$0

Project Introduction

Building upon previous work under DOE's Computer Aided Engineering for Electric-Drive Vehicle Batteries (CAEBAT) Program, the current project seeks to (1) enhance and validate the predictive capability of computationally efficient electrochemical models for thick electrode designs as a path to lower battery cost and increase energy density; (2) develop and validate mechanical/electrochemical/thermal simulation models that describe the physiochemical processes encountered by batteries in the event of vehicle crash, possible internal short and thermal runaway, providing better understanding and enabling safer designs; (3) develop 3D models of electrochemical processes on the electrode microstructure length scale, providing better understanding of inhomogeneous electrode utilization that causes performance limitations and premature degradation. With NREL as lead, the Advanced Computer Aided Battery Engineering Consortium includes partner laboratories Argonne National Laboratory (ANL) and Sandia National Laboratories (SNL) conducting complementary experimental studies and Purdue University conducting complementary mesoscale modeling studies. ANL and SNL experimental studies are further described in separate chapters of this report.

Objectives

The Advanced Computer Aided Battery Engineering Consortium is working to develop modeling capabilities that help industry accelerate development of electric-drive vehicle (EDV) batteries, promote deeper and quantitative physical understanding and thereby improve battery performance, energy density, cost, safety and life. The project is divided into three tasks with the following objectives:

1. Computationally Efficient Electrochemical Modeling

Build upon recently published multiscale multidomain (MSMD) 3-D battery electrochemical-thermal simulation models with 100-1000 fold speedup to develop electrochemical parameter libraries for NMC523 and graphite electrodes from ANL Cell Analysis, Modeling and Prototyping (CAMP) facility. Demonstrate the accuracy of those models to capture the electrochemical performance of the CAMP electrode library with electrode loadings ranging from 1.6 to 7.5 mAh/cm². Identify tortuosity and other rate limitations inherent to these thick electrode designs to promote future lower cost, higher energy density batteries.

2. Mechanical/Electrochemical/Thermal Abuse

With SNL, build and experimentally validate simulation tools to predict the thermal-runaway behavior of lithium ion cells after a crash-induced crush. Include rate-dependent mechanical failure of individual cell components coupled with electrical, thermal and electrochemical reactions. Capture changes in cell behavior with aging. Implement battery crash abuse models in LS-DYNA coupling solid mechanics response with electrochemical/ thermal abuse user-defined functions. Partner with the USCAR Crash Safety Work Group (CSWG) to evaluate models, obtain feedback, and ensure they meet the needs of crash safety engineers.

3. Microstructure Modeling

Use microscopy and tomography experiments to characterize the microstructure of Ni_{0.5}Co_{0.3}Mn_{0.2} (NMC523) and graphite porous electrodes with varying thickness, recipe and calendaring condition from the ANL CAMP library. With Purdue and ANL, identify and elucidate critical factors of electrode microstructure influencing rate limitations and inhomogeneous utilization using microstructural analysis, stochastic reconstruction, homogenization and direct numerical simulation of electrochemical physics on the complex 3-D geometry.

Approach

1. Computationally Efficient Electrochemical Modeling

Leveraging commercial materials and electrode designs from other DOE programs, the ANL CAMP facility produced high-quality electrodes of varying thickness and porosity. Negative electrodes using ConocoPhillips CGP-A12 graphite were produced with four different loadings ranging from 2.0 to 7.5mAh/cm² and in uncalendered and calendered variants with porosities of 51% and 37%, respectively. Positive electrodes utilized Toda Li_{1.03}(Ni_{0.5}Co_{0.3}Mn_{0.2})_{0.97}O₂ active material with loadings ranging from 1.6 to 5.8 mAh/cm² and uncalendered/calendered variants of similar porosity. All cells used Gen II electrolyte, 1.2M LiPF₆ in EC:EMC (3:7,w/w). In addition to microstructure imaging experiments described later, all electrodes underwent electrochemical testing that consisted of galvanostatic intermittent titration (GITT) and constant current discharge rate tests. For modeling, the baseline thin electrode GITT and C/100 data were used to extract solid state thermodynamic, transport and reaction kinetic properties. Thick electrode data were used to validate macro-homogeneous electrochemical models and provide an estimate of tortuosity, a difficult to quantify parameter controlling effective electrolyte transport rate capability in the porous electrode.

2. Mechanical/Electrochemical/Thermal Abuse

We recently reported [\[1\]](#) a modeling approach to investigate propagation of mechanical failure across different layers within a cell. This approach enables us to identify the extent of damage across each component, when a lithium ion cell is subjected to mechanical impact and help us identify the limiting factor contributing to subsequent electrical and thermal events that follow a crash event. In FY17, the team gathered validation data by testing cells under a variety of different mechanical loading conditions – including variations to cell orientation, strain rates and ambient temperature. These results are summarized in section II.C.3 of this report.

In this section, we explore how thermal, mechanical and electrical properties of the cell components, which govern the failure response of the cell, evolve as the cell ages. All test samples were obtained from teardown of commercial NMC/graphite pouch cells. The cells were aged at 25°C under 2C charge and 1C discharge rates across a voltage window of 4.1V to 3.0V for over 5000 cycles. All mechanical tests below were conducted using an Instron 5966 Dual Column Testing System. High strain-rate measurements using a modified dynamic tension fixture, are currently underway.

3. Microstructure Modeling

Figure I-111 shows the overall approach for microstructure characterization and modeling. Microstructure geometries are either experimentally or numerically generated. ANL and University College of London (Prof. Paul Shearing) generated FIB-SEM and X-ray computed tomography (CT) images of the ANL CAMP electrodes, resolving different length scales. CT imaging reasonably captures active material geometry (~0.5 to 100 μm) however is not capable of resolving carbon/binder additive (CBA) geometry due to inadequate resolution and phase contrast. To overcome this limitation, Purdue University has developed a set of algorithms to numerically generate the CBA and match its properties to FIB-SEM and electrochemical data. The microstructure geometry is used for several purposes: (1) for 3D electrochemical simulation on NREL's high performance computer (HPC), Peregrine, and (2) for calculation of effective properties that are applied in macro-homogeneous electrochemical models. Macro models are well suited to wide design space searches. The micro models inform the macro models and provide deeper physical understanding how electrode morphology influences performance and degradation. In FY17 the team initiated a study of tortuosity of the ANL CAMP electrodes that also included experimental measurements performed by Brigham Young University (Prof. Dean Wheeler).

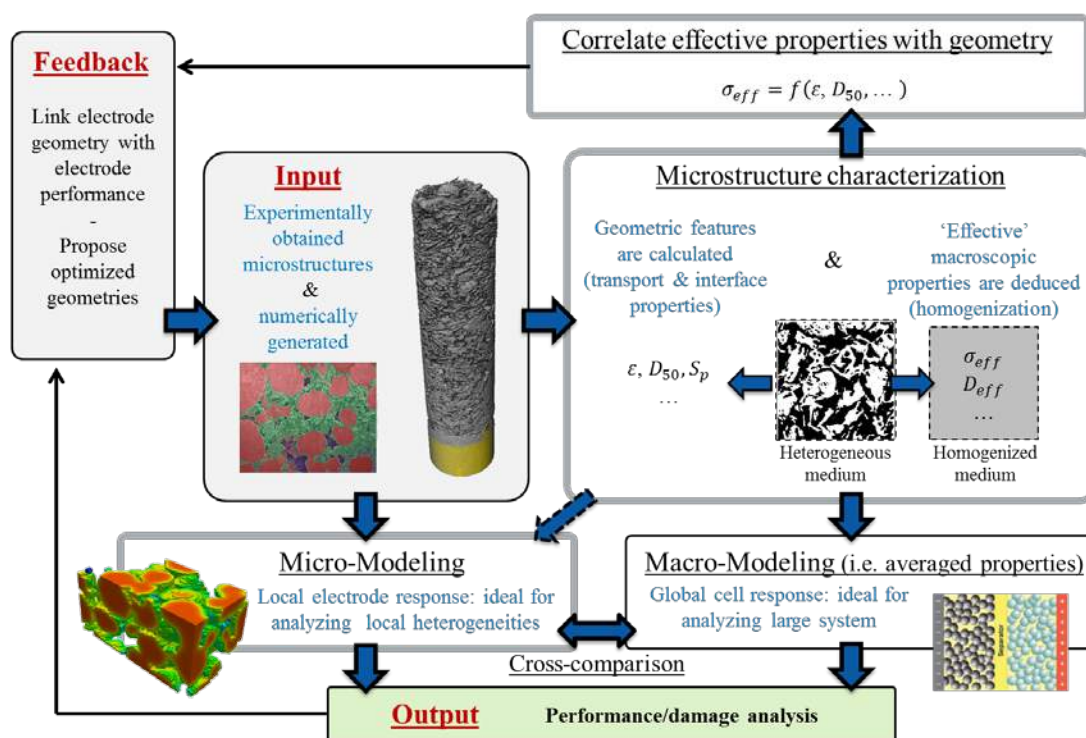


Figure I-111. Approach for microstructure characterization and modeling

Results

1. Computational Efficient Electrochemical Modeling

A parameter library was developed for ANL CAMP graphite and NMC532 electrodes using macro-homogeneous electrochemical models [2]. The team published its analysis of GITT and constant current data

for the ANL CAMP baseline 34 μm NMC532 electrode [3]. A similar article is under preparation for the baseline 44 μm graphite electrode. The kinetic and solid-state transport parameters were then applied in a modeling study of the twelve thicker electrodes from the ANL CAMP library. While most electrochemical model properties are measureable from unique experiments, electrode tortuosity – inhibiting Li^+ ionic transport in the electrolyte phase – was treated as an adjustable parameter in the model. (Direct experimental measurements and microstructure modeling predictions of tortuosity are given in the microstructure section.)

Figure I-112 shows an example model voltage prediction compared to NMC532 half cell data for two different thickness electrodes. Figure I-112(a) shows excellent model agreement for the 88 μm calendared electrode. That electrode achieves 685 mWh/g-NMC energy density at the 1C rate. Figure I-112(b) compares model vs. data for the 129 μm calendared electrode. While thicker electrodes typically have higher energy density than thinner electrodes, the 129 μm electrode has less energy density, 635 mWh/g-NMC at 1C due to high tortuosity inducing electrolyte transport limitations. Tortuosity – the penalty for an ion to conduct and diffuse through a porous media of electrolyte as opposed to an open bath of electrolyte – can be expressed in terms of tortuosity, τ , or as a Bruggeman exponent, p ,

$$D_{eff} = \frac{\varepsilon}{\tau} \times D_{bulk} = \varepsilon^p \times D_{bulk}$$

where ε is the volume fraction of pore space in the electrode, D_{bulk} is the diffusivity of ions in the open bath and D_{eff} is the effective diffusivity in the porous electrode medium. A Bruggeman exponent of 1.5 is typically used in the literature. The present study however found Bruggeman exponents in the range of 2-2.3 for ANL NMC electrodes and 2.7-3.3 for graphite electrodes. These values have implications when optimizing electrodes for high-rate capability and energy density. For the current electrochemical system, the NMC electrode cannot increase beyond 90 μm thickness without experiencing electrolyte transport limitations at the 1C rate, limiting 1C energy density to ≤ 250 Wh/kg.

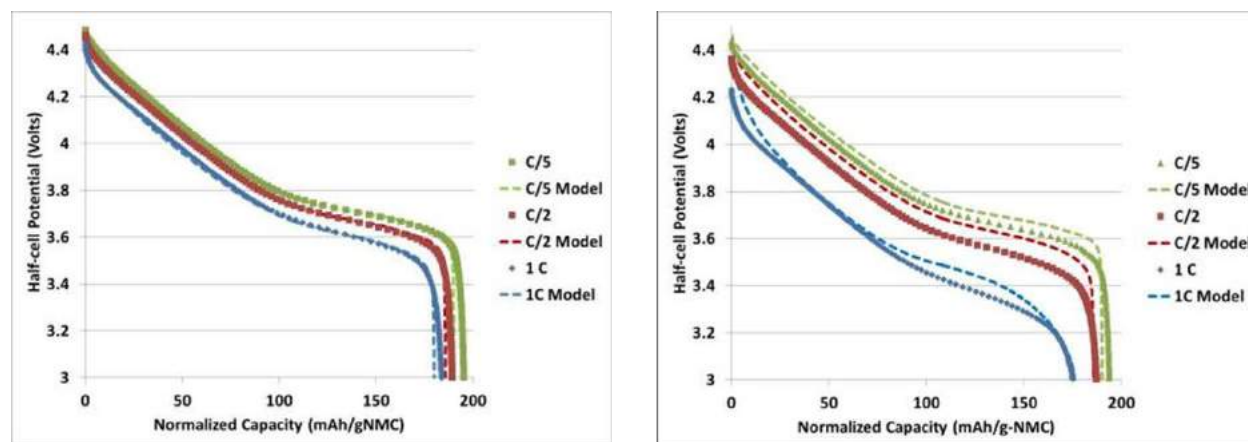


Figure I-112. Comparison of model to NMC532 half-cell data for (a) 88 μm and (b) 129 μm calendared electrodes.

2. Mechanical/Electrochemical/Thermal Abuse

Under the mechanical abuse modeling task, the team focused on characterizing properties of anodes, cathodes and separators from lithium-ion cells that were aged under different conditions and assessing the impact of cell aging on safety. Figure I-113 highlights some findings on the mechanical evaluation of cell components before and after aging. The tensile test results showed much more variability due to the large sample size requirement and non-uniform aging of the electrodes across the cell.

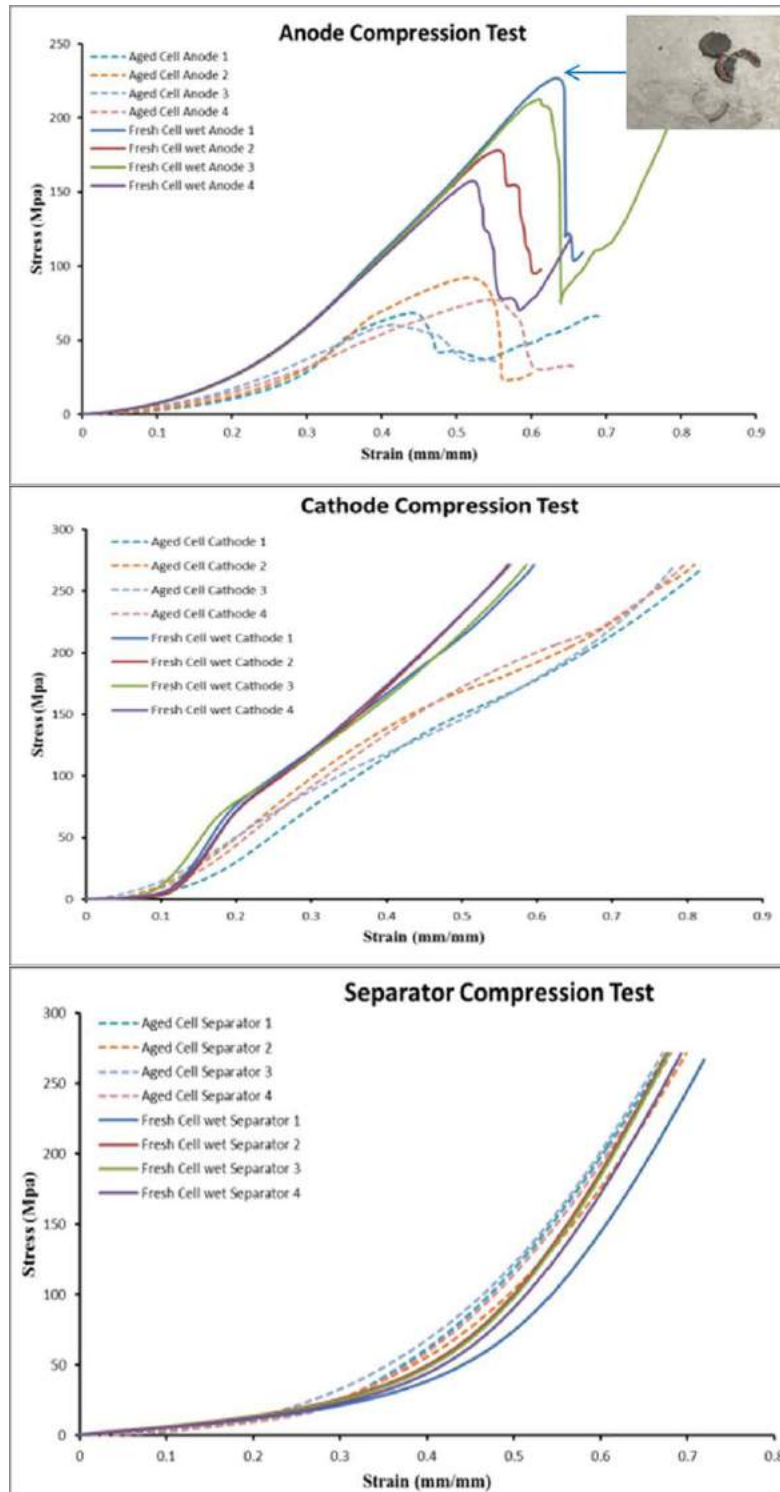


Figure I-113. Compression test results comparing stress- strain curves for fresh cell components against those collected from an aged cell: the anode samples typically show an earlier onset of failure, at lower ultimate strengths; the cathode samples show a very repeatable drop in the modulus – typically characteristic of the current collector. There is no statistical difference in the separator properties for the cell studied under this particular test condition.

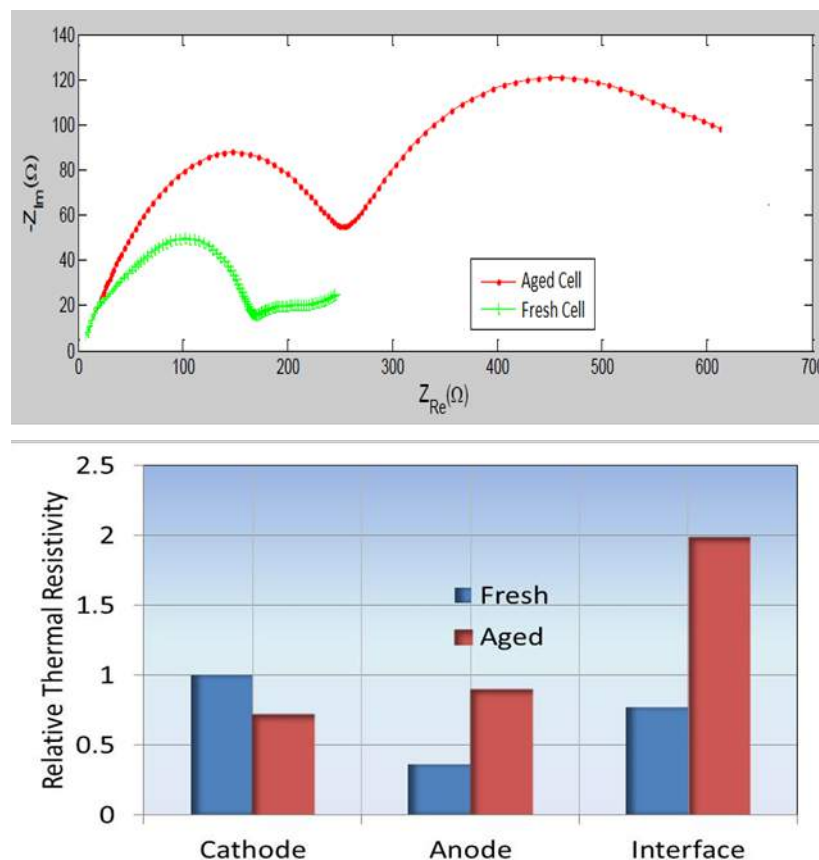


Figure I-114. Comparison of the electrical and thermal properties of cell components before and after aging

Similar analyses were performed to characterize the growth in the electrical resistance using electrochemical impedance spectroscopy (EIS) and thermal impedance using xenon flash reflectometry. Figure I-114 shows sample results. The cathode showed very little degradation compared to the anode in these tests as well. Careful measurement of thermal impedances in fact showed that the bulk thermal impedance of the cathode was no longer the dominant barrier for the heat generated within the cell to be transferred out of the cell. The interfacial contact between the anode and the separator accumulates more and more heat as the cell ages, signaling the onset point for thermal events within the cell.

3. Microstructure Modeling

A 3D electrochemical direct numerical simulation model was created in the FEniCS finite-element open-source environment to provide deeper insight into, for example, inhomogeneous utilization of the electrode not predicted by macro-homogeneous models. Such insight is needed for the community to continue to advance energy density and lifetime. The simulation domain size is chosen based on careful representative volume element (RVE) analysis in which larger and larger domain sizes are considered until results converge. Described in the article [4], electrode microstructure simulations must capture a volume as large as $(60-90\mu\text{m}^3)$ in order to fully represent volume fraction, particle size, connectivity, tortuosity and specific surface area of NMC. Graphite volumes can be slightly smaller. The model is being optimized to solve for several million degrees of freedom necessary to capture electrochemical transport/reaction physics on the full RVE domain using HPC. Initial numerical experiments demonstrate the model scales well to hundreds of parallel processors.

A present gap in predictive capability of electrochemical models is to predict the influence of inert components of carbon and binder – the so-called CBA domain – on electrode performance. CBA geometry is visible from small scale FIB-SEM images but not from the larger, electrode length scale CT imaging experiments. Purdue University developed mesoscale models and stochastic algorithms to virtually grow the CBA phase on active material from either virtual (Figure I-115b) or CT-imaged geometries (Figure I-115a). Described in the article [5], the amount and morphology of CBA has significant effect on electrochemical active surface area and electrode tortuosity. The team initiated a comparative study of tortuosity of the ANL CAMP electrodes as determined from (1) macro-homogeneous model fitting to electrochemical data, (2) microstructure homogenization, and (3) experimental measurement using symmetric cells and intercalation-blocking electrolyte (Dean Wheeler, BYU). Preliminary results show good agreement with the macro-homogeneous model results discussed previously. Additional findings on anisotropy of tortuosity include:

- NMC electrodes (quasi-spherical particles) are nearly isotropic, though small domains can be anisotropic
- Graphite electrodes (non-spherical platelets, sometimes agglomerated into potato-like particles) are highly isotropic. Transport is much slower in through-plane direction than in-plane
- Calendering increases anisotropy, slightly elongates NMC particles and reduces sphericity of both NMC and graphite particles.

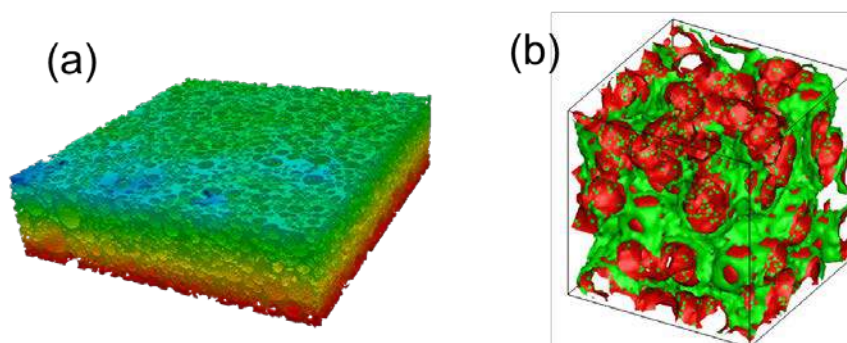


Figure I-115. (a) Homogenization simulation to determine effective electrolyte transport properties in porous electrode using geometry from CT imaging of an actual electrode. (b) Stochastic reconstruction of virtual geometry, showing CBA phase (green) on active material matrix (red).

Conclusions

The Advanced Computer Aided Battery Engineering Consortium – a partnership between NREL, ANL, SNL and Purdue University, with additional collaborators at UCL and BYU – continues to develop and validate simulation models that promote deeper understanding of battery physics and enable acceleration of next generation designs. In this second year of the three year project, mechanical abuse models were enhanced to capture the abuse response of aged cells. In the final year, those models will be validated versus off-axis and high speed crush tests at SNL. This year, the team further published electrochemical properties of ANL CAMP electrodes, validated electrochemical models and carried out a comparative study quantifying electrode tortuosity using different modeling and experimental methods. In the final project year, the 3D electrochemical microstructure model will be applied in validation studies versus ANL CAMP electrodes and the combined model toolset will be applied in studies to promote deeper physical understanding of electrode inhomogeneity and enable higher energy density and higher rate designs.

Key Publications

1. Z. Wu, L. Cao, J. Hartig, S. Santhanagopalan, "Effect of Aging on Mechanical Properties of Lithium-Ion Battery Components," *ECS Trans.*, 77 (11) 199-208 (2017).
2. C. Zhang, S. Santhanagopalan, and A. Pesaran, "Simultaneously Coupled Mechanical-Electrochemical-Thermal Simulation of Lithium-Ion Cells," *ECS Trans.*, 72 (24) 9-19 (2016).
3. S. Santhanagopalan, C. Zhang, M.A. Sprague, and A. Pesaran, "A Representative-Sandwich Model for Simultaneously Coupled Mechanical-Electrical-Thermal Simulation of Lithium-ion Battery Cell under Quasi-Static Indentation Tests." *J. Power Sources*, 298, p. 102-113 (2016).

References

1. C. Zhang, J. Xu, L. Cao, Z. Wu and S. Santhanagopalan, "Constitutive Behavior and Progressive Mechanical Failure of Electrodes in Lithium-ion Batteries," *J. Power Sources*, 2017.
2. G-H. Kim, K. Smith, J. Lawrence-Simon, and C. Yang, "Efficient and Extensible Quasi-Explicit Modular Nonlinear Multiscale Battery Model: GH-MSMD," *J. Electrochem. Soc.*, A1076-1088, 2017.
3. Verma, K. Smith, S. Santhanagopalan, D. Abraham, K.P. Yao, P.P. Mukherjee, "Galvanostatic Intermittent Titration and Performance Based Analysis of $\text{LiNi}_{0.5}\text{Co}_{0.2}\text{Mn}_{0.3}\text{O}_2$ Cathode," *J. Echem. Soc.*, accepted.
4. F. Usseglio-Viretta, K. Smith, "Quantitative Microstructure Characterization of a NMC Electrode," *ECS Transactions*, 77 (11) 1095-1118 (2017).
5. A. Mistry, D. Juarez-Robles, M. Stein IV, K. Smith, P.P. Mukherjee, "Analysis of Long-Range Interaction in Lithium-Ion Battery Electrodes," *J. Echem. Energy Conversion & Storage*, 13 (3) 2016.

I.C.2 Advanced Tool for Computer Aided Battery Engineering (ANL)

Dr. Daniel Abraham, Principal Investigator

Argonne National Laboratory
9700 Cass Avenue
Argonne, IL 60439
Phone: 630-252-4332
E-mail: abraham@anl.gov

Brian Cunningham, Technology Manager

U.S. Department of Energy
Phone: 202-287-5686
E-mail: Brian.Cunningham@ee.doe.gov

Start Date: October 1, 2016
Total Project Cost: \$200,000

End Date: September 30, 2018
DOE share: \$200,000

Non-DOE share: \$0

Project Introduction

The main goals of DOE's Computer Aided Engineering for Electric-Drive Vehicle Batteries (CAEBAT) Program were introduced in a prior section. In this section, we describe the experimental studies conducted at Argonne National Laboratory (ANL) to support the development of 3D models of electrochemical processes on the electrode microstructure length scale and to provide an understanding of factors that limit electrode performance and cause premature degradation. These studies are intended to complement and enhance the experimental and computational work being conducted at the partner national laboratories and universities.

Objectives

The key objectives of our work can be summarized as follows:

1. To provide the positive and negative electrodes needed to accomplish the various tasks listed in an earlier section.
2. To characterize the electrodes using conventional electrochemical techniques, both in half-cell and full-cell configurations, and to provide the data for the development of 3D electrochemistry models.
3. To develop advanced tools, including spectroscopy and diffraction techniques, which can provide deeper insights on the correlations between electrode microstructure and electrochemical performance.

Approach

1. FIB-SEM imaging of positive and negative electrodes.

Positive and negative electrodes, of varying thickness and porosities, were fabricated at the Cell Analysis, Modeling, and Prototyping (CAMP) facility located at ANL. These electrodes were used to generate electrochemistry and microstructure data to support the computational efforts at the National Energy Renewable Laboratory (NREL) and Purdue University (Purdue). Focused Ion Beam (FIB)-Scanning Electron Microscopy (SEM) images of representative electrodes were obtained at the Frederick Seitz Materials Research Laboratory, University of Illinois at Urbana-Champaign. Images of electrode cross-sections were then used to generate 3D images of the electrode microstructure. X-ray tomography data were also obtained at the Advanced Photon Source (APS) located at ANL. These FIB-SEM and X-ray images are used to complement the computed X-ray tomography (CT) data obtained by our partners at University College London. Electrode microstructure information obtained from these various data are used as input for the 3D models that relate electrochemistry to electrode architecture.

2. Electrochemistry data in a Full cell configuration

In the previous year (FY 2016), we reported the *half-cell* performance of positive and negative electrodes of varying thicknesses and porosities. This year we obtained *full-cell* data, using a fixed porous graphite-based negative electrode and NCM523-based positive electrode of various thicknesses and porosities to elucidate the effect of the latter variables. Our cells contained the Gen2 electrolyte, which comprises 1.2 M LiPF_6 salt in ethylene carbonate (EC): ethyl methyl carbonate (EMC) (3:7, w/w) solvent and Celgard 2325 separator. The electrochemistry tests were conducted under galvanostatic conditions, with currents that ranged from 0.1C to 1C. The resulting data were provided to partner laboratories for electrochemistry model development.

3. Lithium-ion diffusion coefficients and their relationships to changes in oxide crystallography

We obtained the lithium-ion diffusion coefficient in the NCM523 layered oxide, using the galvanostatic intermittent titration technique [1]. In order to explain and elucidate the trends obtain in the diffusion coefficient vs. oxide lithium content profile, we conducted in operando X-ray diffraction measurements at beamline 6-BM of the APS. We noted strong correlations between the lithium-ion diffusion coefficients and crystallographic parameters of the NCM523 oxide, which increased our confidence in the lithium-ion diffusion data provided to NREL for battery modeling.

Results

1. FIB-SEM imaging of the positive electrodes (cathodes)

Resolving the carbon-binder distribution around active particles in electrodes is a challenge using X-ray tomography. Therefore, the X-ray data were supplemented by FIB-SEM imaging with nanometer scale resolution. The calendered standard ANL electrode (AC015, porosity = 34%, thickness = 34 μm) and a thick electrode in its uncalendered (LN2487-113-13, porosity = 49%, thickness = 160 μm) and calendered (porosity = 37%, thickness = 129 μm) states were imaged. As shown in Figure I-116, the low porosity calendered electrodes show tighter active particle packing compared to the uncalendered electrode.

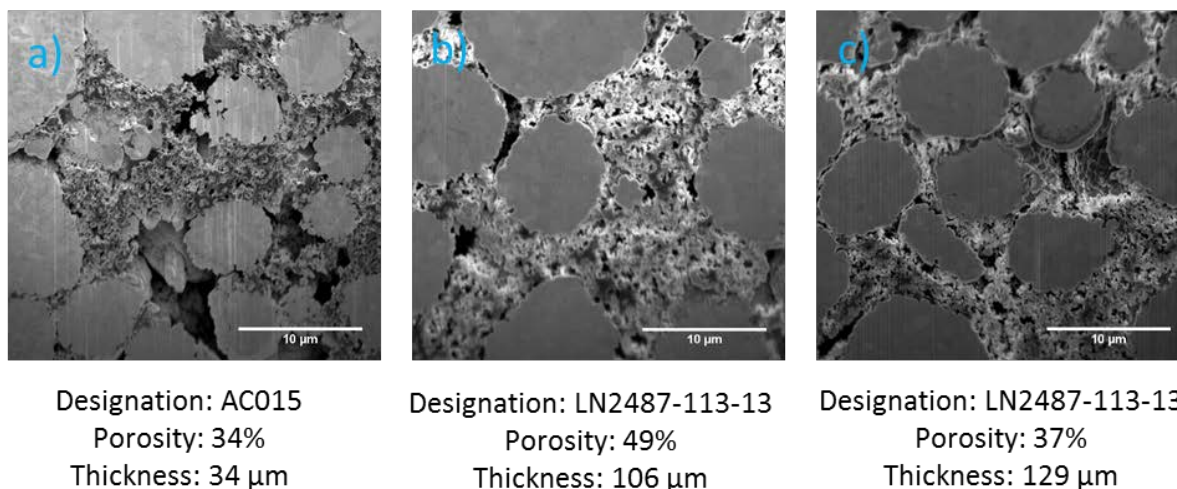


Figure I-116. FIB-SEM images of (a) calendered baseline, (b) uncalendered, (c) calendered NCM523 electrodes

The carbon-binder structure displays both nanometer and micrometer scale pores which are expected to be the channels for electrolyte transport through the electrode. The nanopores are distributed within the carbon structure while micropores are seen around the NCM523 active particles. The micropore openings near the active particles are likely regions of increased lithium insertion/extraction from the electrolyte while area covered with carbon-binder are electron hotspots. As is shown in the CAEBAT report by our partner at NREL, the presence of these additional fillings increase the effective tortuosity from a Bruggeman exponent of 1.5, when modeling the electrode as packed spherical particles, to 2-2.3. It is unclear from these images whether the packing of the nanoporous carbon-binder structure increases after calendering. Interestingly, the sphericity

of active particles appears to decrease upon calendaring (compare Figure I-116b and Figure I-116a, Figure I-116c). Additional FIB-SEM images are being obtained, and image quantification is being performed, to elucidate the contribution of the carbon-binder structure to the increase of the tortuosity and Bruggeman factor.

One specific issue with the FIB-SEM images shown in Figure I-116 is the visibility of structures behind the imaging plane which complicates quantification of the amount of material within the image plane. In an effort to address this issue, epoxy (KwikWeld steel reinforced epoxy glue) was used to fill the micropores so as to confine imaging to the imaging plane. Filling of the macropores was achieved; however, because of contrast similarity between the carbon-binder structure and the epoxy filler in the SEM images we were unable to obtain accurate quantification of the pore volume and the carbon-binder matrix (see Figure I-117). A filler that can provide sufficient contrast difference composite is still being sought for accurate quantification of various features in the electrode microstructure.

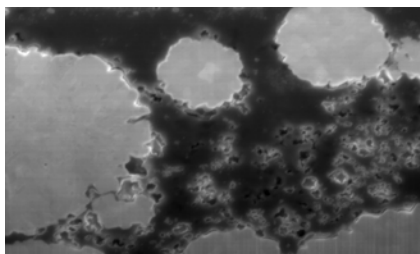


Figure I-117. FIB-SEM of AC015 electrode using an epoxy filler to confine imaging to the image plane.

2. Electrochemistry data in Full cell configuration

The performance of NCM523 cathodes against a fixed graphite anode (LN3024-126-5, uncalendered) was quantified. Results of these electrochemical characterization are presented in Figure I-118 and Figure I-119.

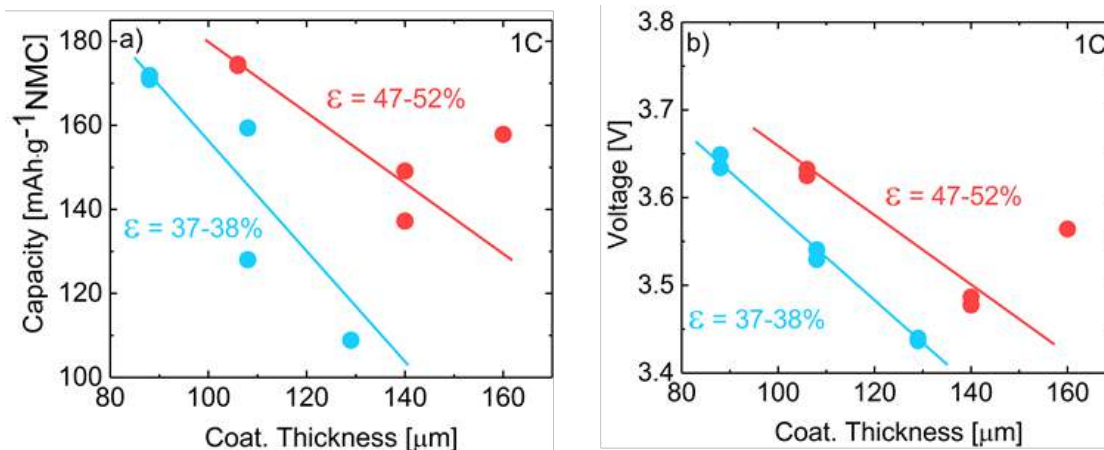


Figure I-118. Full cell electrochemical performance data during 1C discharge after the formation cycles (a) average capacity, and (b) average cell voltage versus electrode coating thickness and porosity (ϵ). The anode (uncalendered graphite, Coating thickness = 173 μm, Porosity = 51.8%) was kept the same for all these measurements.

Generally, as the cathode porosity is decreased via calendaring, capacity output (Figure I-118a) and average cell voltage (Figure I-118b) decreases during cell discharge. Figure I-119 shows details of the influence of cathode thickness and porosity on discharge capacity and voltage at a 1C cell discharge rate. Discharge capacity and average cell voltage increase with decreasing thickness for a given porosity (Figure I-119a); also, capacity and average cell voltage increase with increasing porosity for a given thickness (Figure I-119b). These findings hold for rates ranging from 0.1C to 1C.

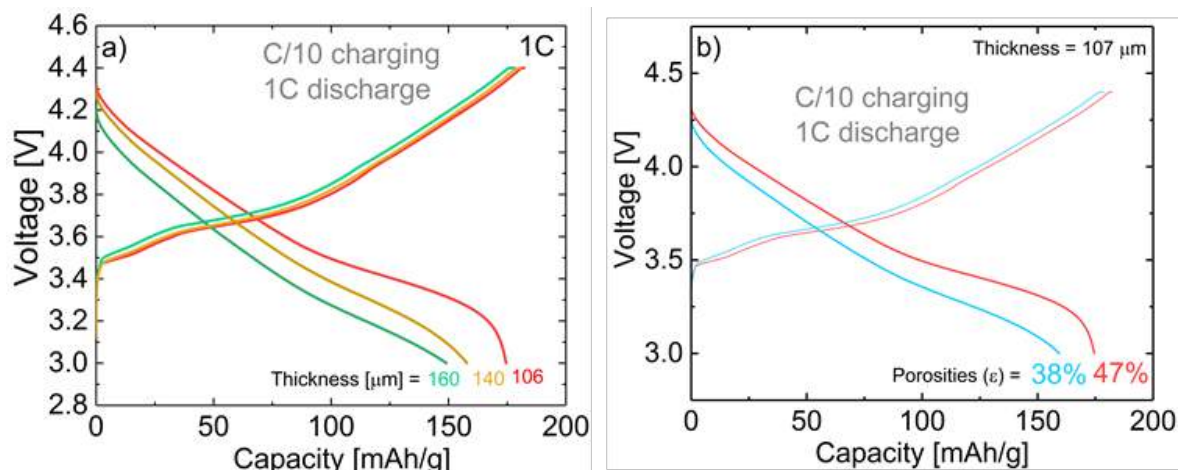


Figure I-119. Performance comparison during 1C discharge in full-cells as a function of (a) electrode coating thickness with porosities fixed at ~47-52% and (b) electrode porosity at fixed thickness of ~107 μm.

3. Lithium-ion diffusion coefficients and their relationships to changes in oxide crystallography

Measurements of lithium-ion diffusion coefficient in the NCM523 oxide electrode by the GITT technique were reported in reference [1]. The validity of the extracted values, and trends versus lithium content of the oxide, was systematically examined in the framework of crystallography. We explain modulations of the diffusion coefficient as a function of charge in Figure I-120.

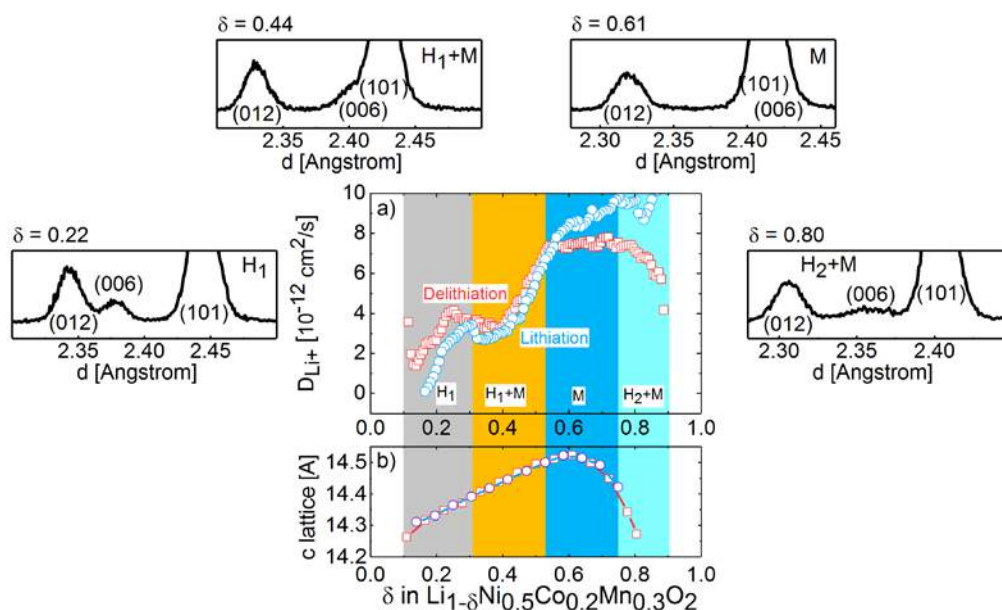


Figure I-120. (a) Chemical diffusion coefficient of lithium-ions in NCM523 oxide particles and (b) c-lattice parameter of the oxide crystal structure NCM523 during charge (delithiation) and discharge (lithiation).

Some noteworthy findings from our study are as follows: (i) mobility of lithium-ions in NCM523 increases fivefold (Figure I-120a) after roughly half the lithium-ions in the oxide are removed because of the large expansion of the crystal lattice along the *c*-direction (Figure I-120b); (ii) four crystal symmetry changes occur in NCM523 during discharge and charge (see sample XRD spectrum provided for each highlighted region in Figure I-120); (iii) these crystal symmetry changes are responsible for major inflections in the mobility of lithium in the active materials and (iv) the diffusion coefficient profile is correlated to overpotentials (voltage increase) during fast charging. This work is complementary to the work reported in reference [1], and a manuscript is currently being prepared for publication [2].

Conclusions

In support of the various tasks listed in section II.C.1 we have conducted electrochemical characterization of twelve different cathodes and anodes fabricated to attain various porosities and thicknesses. These data have been provided to our partner organizations (NREL and Purdue) for the development of 3D computational models of electrochemical behavior.

We have demonstrated through high resolution FIB-SEM imaging that the carbon-binder matrix in the NCM523 electrodes display both micropores and nanopores, which can significantly affect the measured electrode tortuosity and ancillary Bruggeman factor.

Calendering of electrodes results in compaction and deformation of the active NCM523 particles in battery electrodes, which increases tortuosity. The microstructural changes caused by calendaring has been shown to impact the electrochemical performance both in half-cells and full cells; in summary, the performance decreases with increasing electrode thickness and decreasing porosity.

With the goal of increasing confidence in the lithium-ion diffusion coefficient values obtained on the NCM523 oxide using a galvanostatic intermittent titration technique, operando energy dispersive X-ray diffraction data were obtained at the Argonne Advanced Photon Source. We show that the lithium-ion diffusion coefficients increases because of the *c*-lattice parameter increase observed during oxide delithiation. Other changes in the diffusion coefficients were related to the crystal symmetry changes that occur in the oxide lattice. We also showed that the diffusion coefficient values have a strong effect on the lithium-ion transport during high-current charging, and needs to be considered during the design of electrodes for fast-charge scenarios.

References

1. Verma, K. Smith, S. Santhanagopalan, D. Abraham, K.P. Yao, P.P. Mukherjee, “Galvanostatic Intermittent Titration and Performance Based Analysis of $\text{LiNi}_{0.5}\text{Co}_{0.2}\text{Mn}_{0.3}\text{O}_2$ Cathode,” J. Electrochem. Soc., 2017, 164, A3380–A3392.
2. Koffi P.C. Yao, John S. Okasinski, Jonathan D. Almer, Daniel P. Abraham, “Phase Modulation of Lithium-Ion Diffusion in $\text{Li}(\text{Ni}_{0.6}\text{Co}_{0.2}\text{Mn}_{0.2})\text{O}_2$: Implications for Fast Charging”, manuscript in preparation (2017).

I.C.3 Battery Abuse Testing (SNL)

Joshua Lamb, Principal Investigator

Sandia National Laboratories
1515 Eubank SE
Albuquerque, NM 87185
Phone: 505-284-9709
E-mail: jlamb@sandia.gov

Brian Cunningham, Technology Manager

U.S. Department of Energy
Phone: 202-287-5686
E-mail: Brian.Cunningham@ee.doe.gov

Start Date: October 1, 2016
Total Project Cost: \$400,000

End Date: September 30, 2018
DOE share: \$400,000

Non-DOE share: \$0

Project Introduction

This project aims to provide experimental support, including support for validation and parameterization, for mechanical failure modeling work as part of DOE's Computer Aided Engineering for Electric-Drive Vehicle Batteries (CAEBAT) program. This work involves mechanical deformation testing on both charged and discharged cells, including abusive mechanical testing leading to battery failure. The mechanical data generated is provided to the modeling teams to provide empirical parameterization as well as validation for newly developed models. Testing fully charged cells and packs (abusive battery testing) also allows for a better understanding of what conditions are most likely to lead to a potentially hazardous thermal runaway event.

Objectives

Experimental determination of mechanical properties of lithium ion batteries and materials

- Experimentally validating simulation tools used to predict thermal runaway events caused by crash induced crush. This includes rate-dependent mechanical failure and properties of individual cells as well battery packs.
- Provide collected data to the consortium to aid in model development.
- Partner with the USCAR Crash Safety Work Group to obtain feedback on experimental methods as well as develop new tests that may be of relevance to crash safety engineers.

Approach

Sandia's Battery Abuse Test Laboratory was used to perform mechanical testing on full cells and packs for this project. This facility can contain and withstand thermal runaway of lithium ion cells and packs of up to 1 kWh of total energy. Mechanical test capabilities include a 100 klb_f large crush fixture and a 10 klb_f nail penetration and small-scale crush fixture. Recording capabilities include force, displacement, temperature and voltage measurements at rates of up to 1 kHz. Data recording rates varied depending on duration of testing.

Mechanical deformation results collected at Sandia have been provided to NREL and the technical working groups. This has also included collaboration and information sharing with the USCAR Crash Safety Working Group, with the ultimate goal of understanding what hazards lithium ion batteries may pose during extreme mechanical deformation events, such as an auto collision. Quarterly meetings also provide information sharing and collaboration with the broader consortium, including NREL, ANL, SNL and Purdue University, as well as members of the ORNL consortium.

Results

Testing at Sandia in FY17 focused on determining the mechanical behavior of single cells both in charged and discharged states. This builds upon work performed in FY16 looking at the overall mechanical behavior of packs and preliminary work looking at single cells. Three point bend tests were performed on 5 amp hour commercial off the shelf (COTS) lithium ion cells. The first tests performed were on fully charged cells to determine at what point catastrophic failure is likely to occur when subjecting these cells to extreme mechanical deformation. Selected results from testing on fully charged cells are shown in Figure I-121 and Figure I-122.

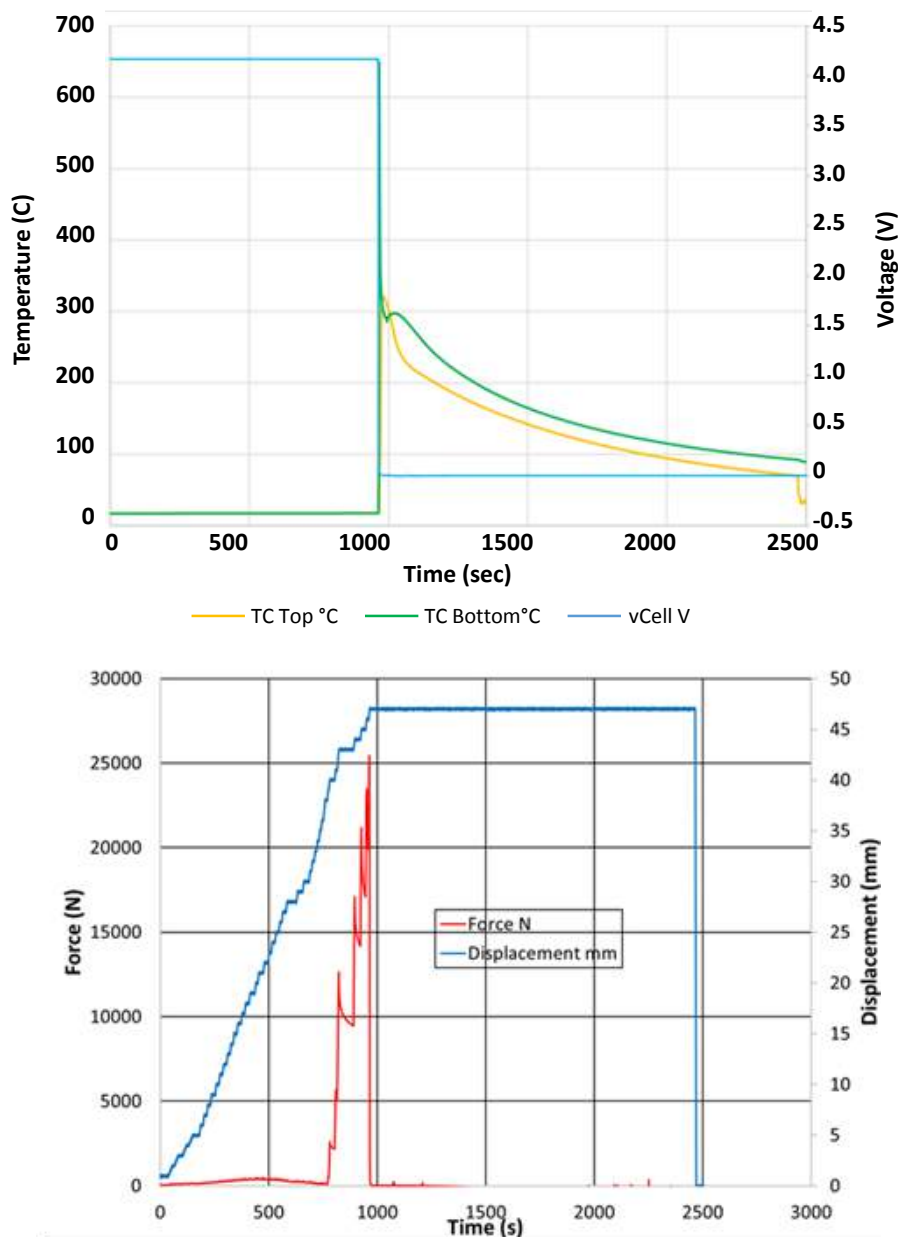


Figure I-121. Three point bend testing of fully charged cell. No runaway was observed due to the bending of the cell. Runaway occurred when enough displacement occurred to begin compressing the cell with significant force.

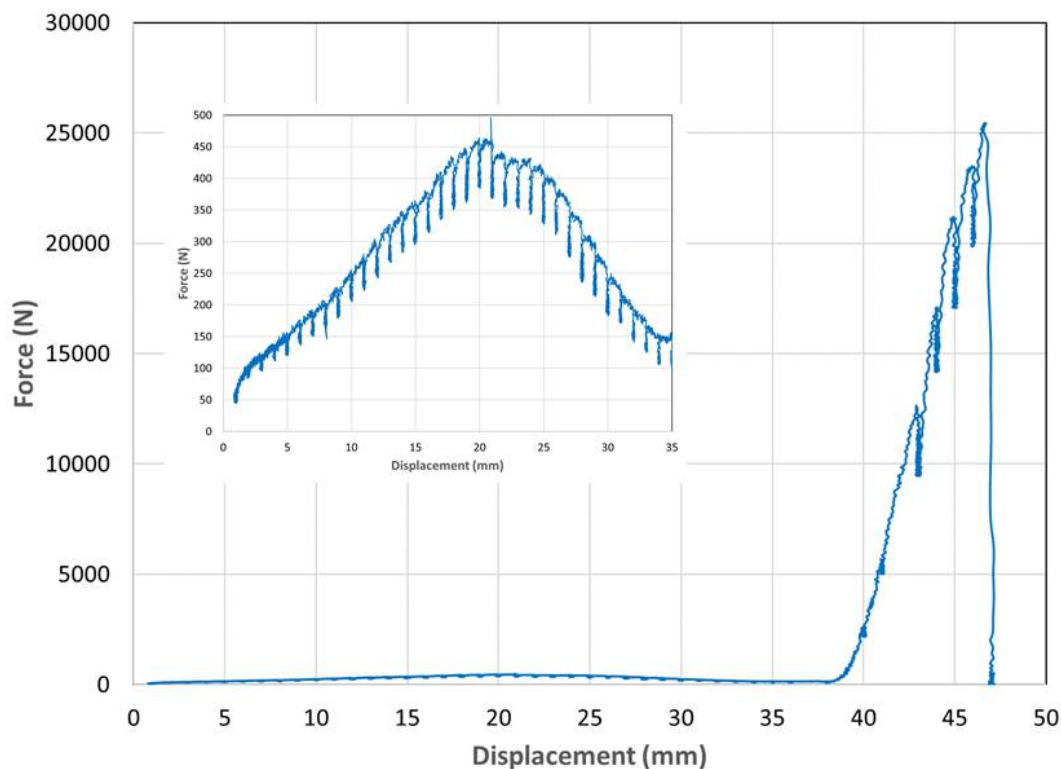


Figure I-122. Force vs displacement curve for test performed in the previous figure.

In Figure I-121 and Figure I-122, deformation was applied in 1 mm increments with voltage and temperature monitoring to determine at what level of displacement thermal runaway occurred. Figure I-121 shows the voltage, temperature, force and displacement results versus time, while Figure I-122 shows the Force vs. Displacement curve for the test. No runaway was observed during the initial bending. The observed thermal runaway occurred when enough deformation occurred to begin compressing the cell against the base of the fixture, with cell failure occurring due to compression of electrode layers rather than breakage from the bending force.

The next step of this work was to determine the mechanical behavior of these cells under these conditions. The bend test was applied at strain rates from 0.01 mm/sec to 10 mm/sec to observe how the deformation was impacted under increasing rates of deformation. This data is shown in Figure I-123. This shows that there is little apparent strain rate impact at low levels of deformation, however some changes were seen in the yield points of the cells where a maximum force was reached and the cells exhibited irreversible plastic deformation. The data shows yield stresses that shift towards lower deformation levels and a higher overall force observed before the yield occurred as the deformation rate was increased.

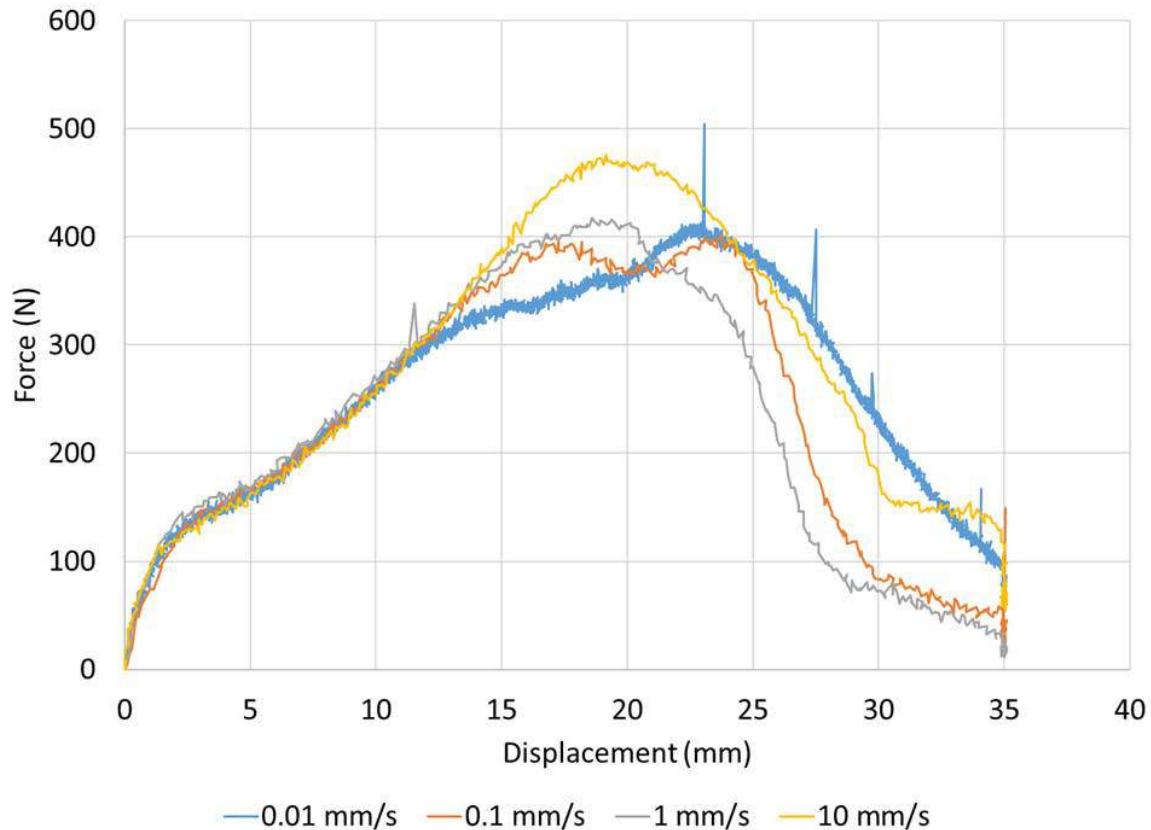


Figure I-123. Results of three point bend tests on cells at increasing displacement rates.

Building on work presented in the previous year, alternate orientations of compressive force were applied to cells. These results are shown in Figure I-124. This shows compression along an axis parallel to the tabs (Figure I-124, top) and diagonally through the cell (Figure I-124, bottom). Both orientations show little effective change at the lowest rates, with little change from 0.01 to 0.1 mm/sec in either orientation. The compression parallel to the tabs saw a more significant shift in the force at higher rates, with the force dropping at equivalent displacements when rates of 1 and 10 mm/sec were applied. Changes were observed in the diagonal orientation as well, however these changes were less systematic than other observed results. The diagonal direction also saw some evidence of fracturing failure within the cell at higher levels of force, with sudden drops in the force as the electrode stack likely fractured.

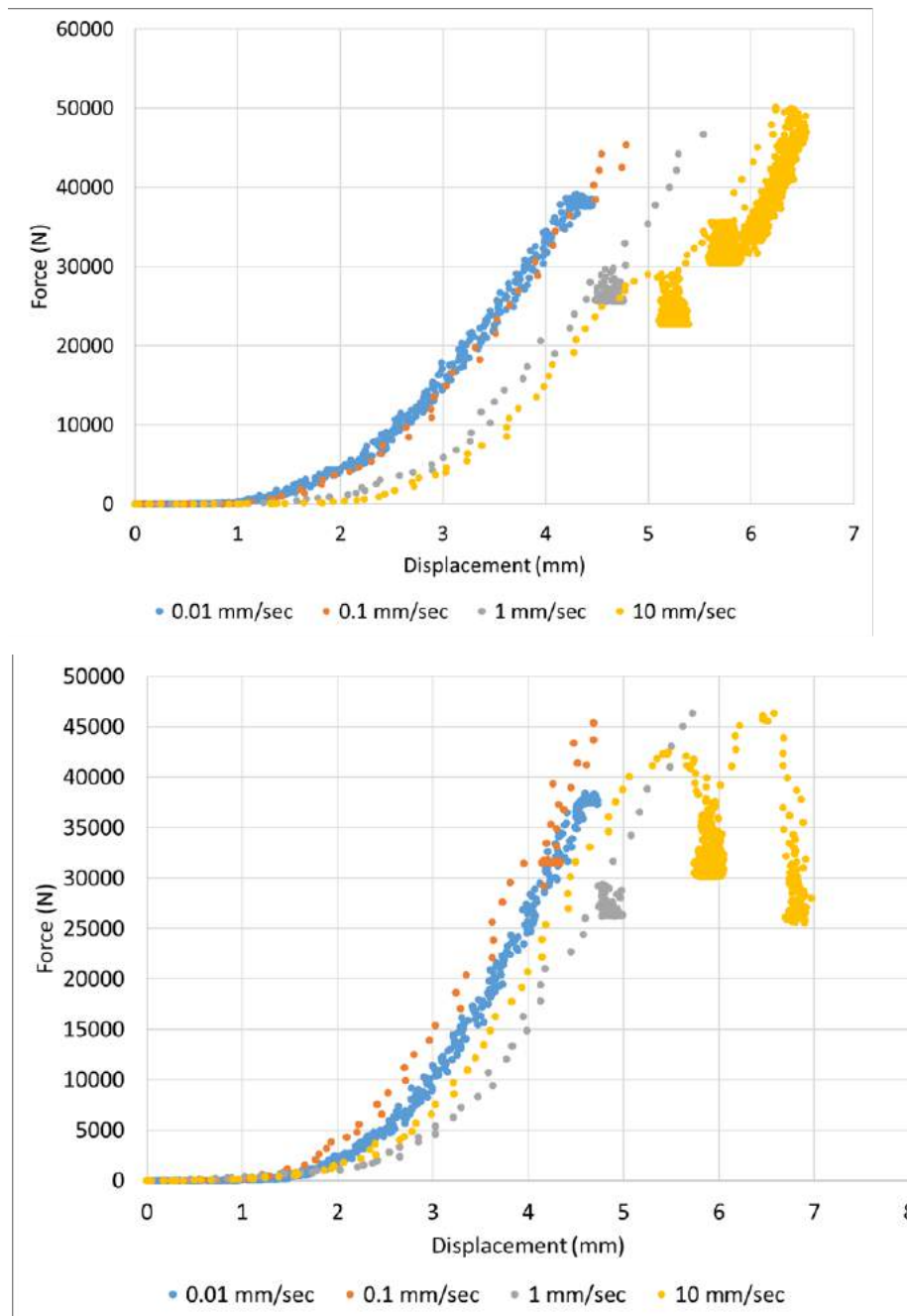


Figure I-124. Impact of strain rate at cell orientations parallel to cell tabs (top) and diagonal to cell tabs (bottom).

Work performed to date has focused on deformation rates that are predominantly quasi-static. These tests are useful for determining materials properties and establishing parameters for fundamental materials modeling. However, understanding how batteries fail during the types of impacts observed during auto collisions requires the use of elevated strain rates. A drop tower apparatus is under construction at SNL. (See Figure I-125.) Final fabrication is underway with initial testing planned for early CY 18.

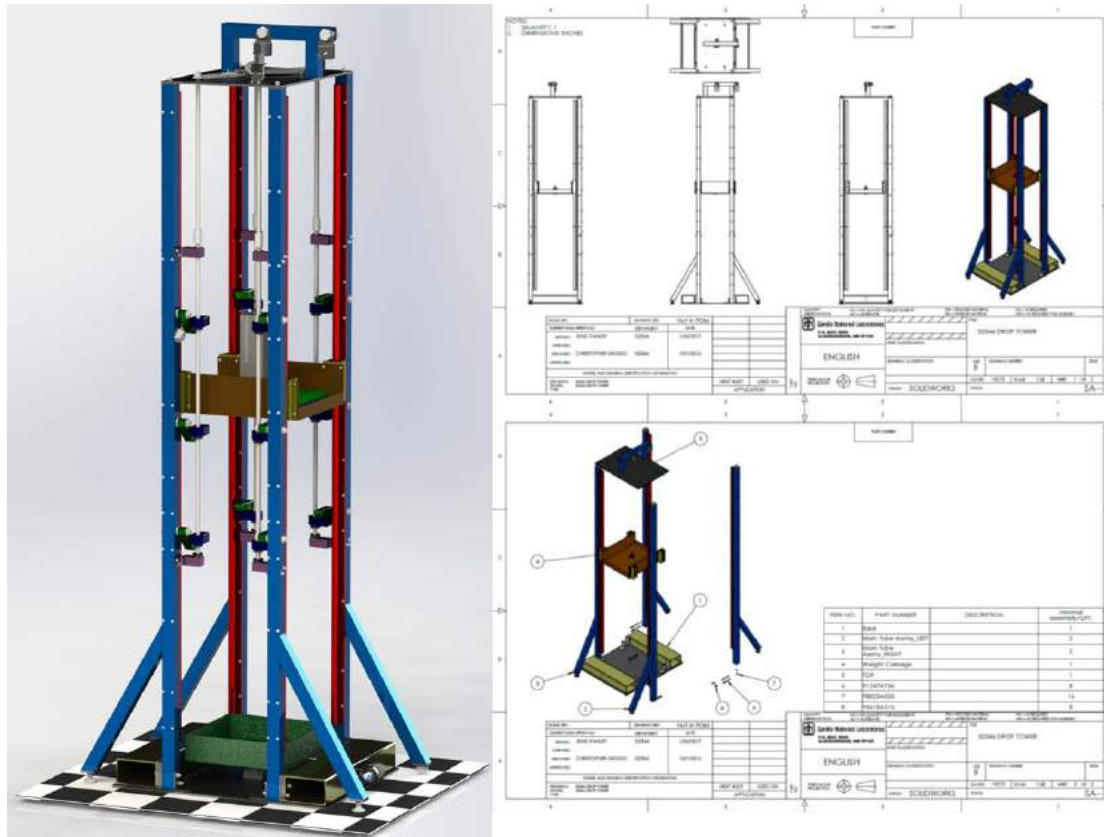


Figure I-125. Design drawings of SNL impact tester.

Conclusions

Sandia continues to provide experimental validation results to the NREL consortium as well as providing a broader understanding of the conditions likely to cause a potentially dangerous thermal runaway event in lithium ion batteries. The current work shows that mechanical compression events continue to be the most likely to cause a thermal runaway event. A single bend introduced to the cell was not able to create a thermal runaway in and of itself. Further testing will be providing experimental support to determine the mechanical failure response of aged cells, as well as the response of cells and packs to high rate mechanical deformation.

I.C.4 Consortium for Advanced Battery Simulation (ORNL)

John Turner, Principal Investigator

Oak Ridge National Laboratory
1 Bethel Valley Road
Oak Ridge, TN 37831-6164
Phone: 505-412-1945
E-mail: turnerja@ornl.gov

Brian Cunningham, Technology Manager

U.S. Department of Energy
Phone: 202-287-5686
E-mail: Brian.Cunningham@ee.doe.gov

Start Date: October 1, 2015
Total Project Cost: \$1,000,000

End Date: September 30, 2018
DOE share: \$1,000,000

Non-DOE share: \$0

Project Introduction

CABS is an integrated partnership between Oak Ridge National Laboratory (ORNL), Lawrence Berkeley National Laboratory (LBNL), and Sandia National Laboratories (SNL). The project report is divided into three sections (I.C.4, I.C.5, and I.C.6) that include contributions from individual Laboratories. Sections I.C.5 and I.C.6 also report updates from industry-led projects. Mechanically induced internal short-circuit is believed to be the main cause of battery failure and thermal runaway in crashes involving electric vehicles. To accurately predict the internal-short we need to capture the deformed material variations and its influence on the transport properties. In this report, we highlight new experiments conducted to develop constitutive relations for mechanical response of constituent materials, effective transport properties for electrochemical behavior of electrodes under deformation, coupled simulations at layer resolved scale to predict the behavior of the damaged batteries.

Objectives

The objective of this project is to characterize failure of the cell components under mechanical crush, develop coupled simulation tools to predict electrochemical behavior, and develop constitutive relations and failure criterion for mechanical response. The progress towards these objectives is achieved by delivering the following milestones for FY17:

1. E4: Data from mechanical deformation tests
2. C2: Validated constitutive models and failure criteria for electrode materials and spirally wound, wound prismatic, and stacked electrodes under indentation
3. I4: Demonstrated ability of VIBE to simulate onset of short-circuit due to mechanical abuse informed by microstructure

Approach

To address some of the critical impediments in understanding the battery failure, we first developed new experimental protocols to measure mechanical properties of electrode materials and cell components. This ensures that we have gathered all the necessary material parameters for the constitutive relations used in the models. Simultaneously we have developed new experimental protocols to study failure leading to internal short circuit. The diagnosis from this experimental evidence is used to develop formulation of new models for mechanical behavior of battery components. Also, we had to understand the influence of mechanical impact on transport properties and how it acts as a precursor to the internal short of the cell. To this end, we have developed electrochemical models at the continuum scale informed from the mesoscale simulations on NMC

microstructures. These various efforts allowed us to investigate some of the challenging internal short simulations under extreme mechanical deformations and predict the behavior of the batteries.

Results

Milestone E4: Data from mechanical deformation tests:

Mechanical properties of battery components have been experimentally measured under different loading conditions in order to aid development of constitutive models for mechanics of battery cell and couple to thermal models. (See Figure I-126.) Significant effort was dedicated to mechanics and failure of battery separators, as these are critical safety components in the cell. Overall the following are the highlights of the results (detailed description can be found in the Milestone E4 “Data from mechanical tests” report submitted to EERE):

- Complete study of temperature and strain rate effect in battery separators
- Data from biaxial tests and critical failure strain
- Coupling between electrode parameters (thickness, porosity) and electro-chemical behavior
- Mechanical behavior of battery electrodes and pouch material

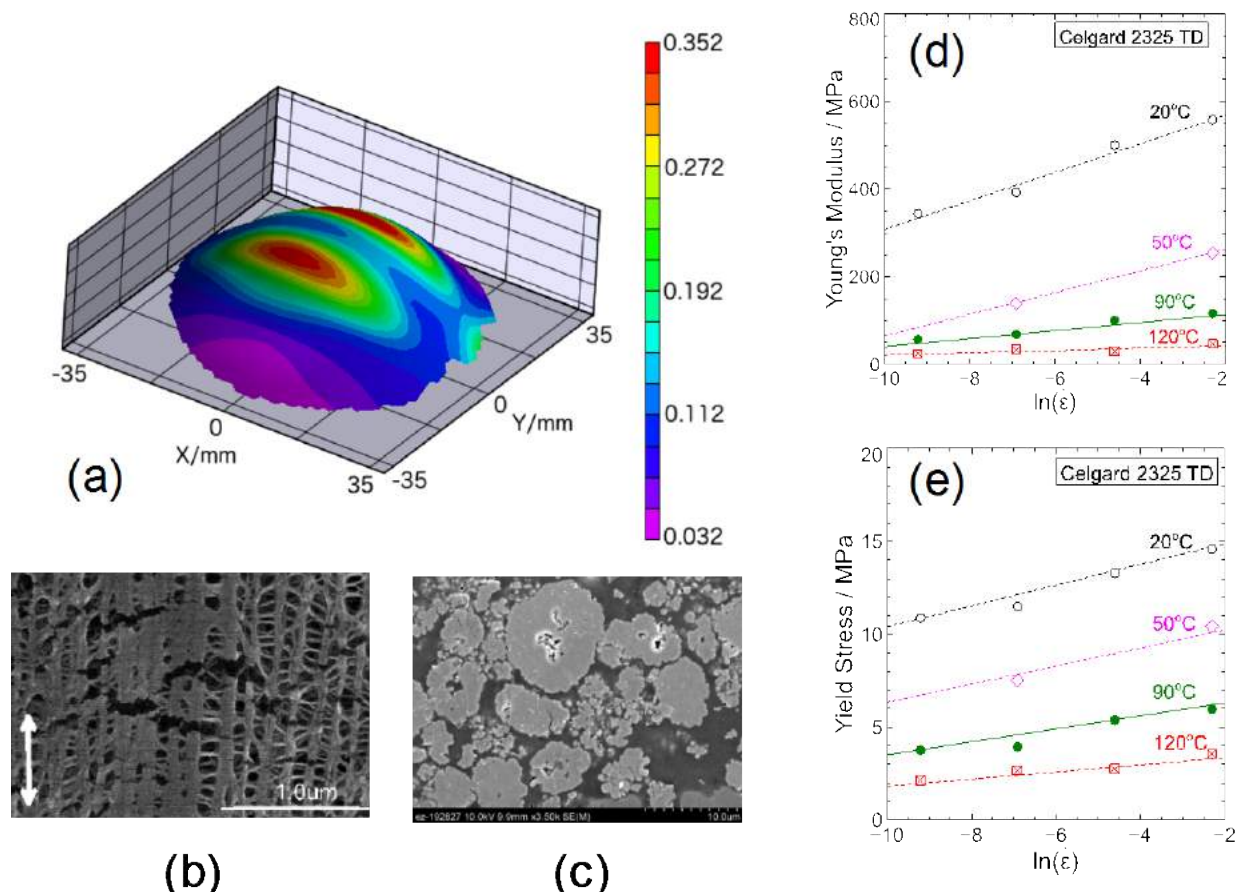


Figure I-126. Examples of the results from mechanical testing: a) first principal strain distribution in polymer separator under biaxial loading; (b) tensile cracks in separator lamellae; (c) microstructure of electrode compressed by calendaring; (d,e) Young's modulus and yield strength of Celgard separator under different temperatures and strain rates.

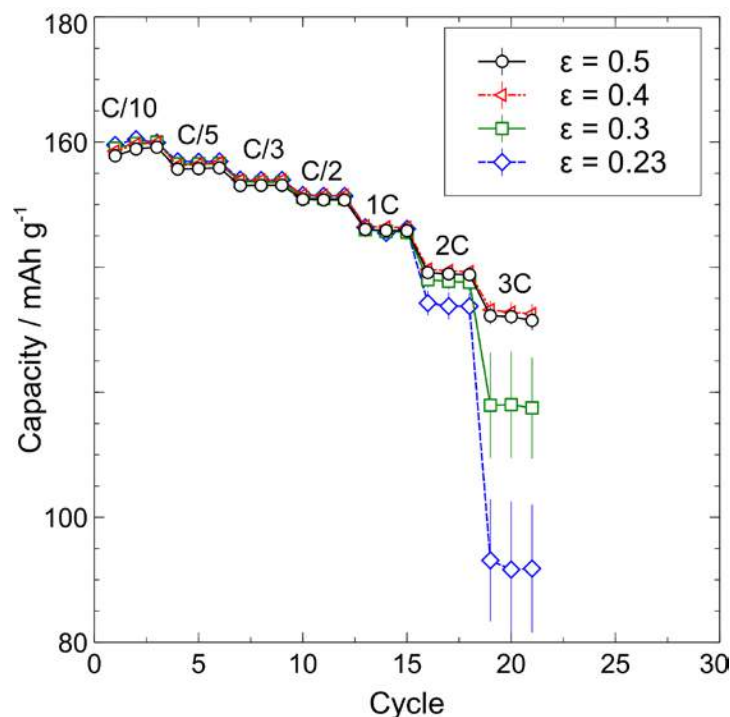


Figure I-127. Rate performance of NMC(532) electrodes depending on porosity after calendaring

In addition to investigation of mechanical behavior of battery components, effect of electrode microstructure on cell performance was studied. (See Figure I-127.) For this purpose, positive (NMC532 (Toda America); wt% NMC/PVdF/carbon black 90/5/5) electrodes were made at the ORNL Battery Manufacturing Facility and calendared to create a set of samples with six different porosities (0.53, 0.5, 0.4, 0.3, 0.23, 0.18). Fracture of electrode particles and fragmentation can be noticed (Figure I-126(c)) as the result of calendaring. The electrodes were tested in coin cell hardware vs Li metal electrodes. The porosity of 30% appears to be a demarcation line after which the performance of positive electrode decreases, especially at high applied current densities.

Milestone C2: Validated constitutive models and failure criteria for electrode materials and spirally wound, wound prismatic, and stacked electrodes under indentation:

Experimental Characterization of Deformation and Failure

In order to understand the response to the materials inside the cells, we carried out incremental indentations of the cells in aluminum cans, established FEA model to simulate the deformation. Post-mortem analysis using cross-section imaging and x-ray computed tomography (XCT) were performed on indented cells. The on-set of internal short-circuit and various failure modes of anode, cathode and separator have been analyzed. An unexpected fragmentation of anode current collectors was first observed by XCT and later confirmed by examination of single components using x-ray radiography and scanning electron microscopy (SEM). The origin of short-circuit under spherical indentation has been attributed to the cathode current collector failure. Finite element analysis model was modified to simulate the spherical indentation and cell response. The simulated load vs. displacement curves were validated by experimental results. The simulation model is also used to validate results obtained from 3-point bending tests.

Li-ion cells in aluminum cans for small electronic appliances were used in the single-side indentation tests with 650-670 mAh in capacity. A half inch diameter indenter was used at a loading speed of 0.05"/min. A series of cells were indented with increments of 0.01" and 0.02" followed by several cells indented until internal short circuit was detected from open circuit voltage drop. The FEA simulation was based on a

previously developed model. One set of the indented cells were cut in half, back filled with epoxy and polished for cross-section imaging. Other cells were scanned with a 3D X-ray computed tomography (XCT) at ORNL before cross-sectioning. 3-point bend tests were also performed.

XCT images, Figure I-128, were taken across the indented area from X and Y directions. The layers were stretched and started to fold symmetrically away from the indenter. At the very last image(s), which were at the center of the indentation, 2-3 cathode layers collapsed and electrode-to-electrode contacts were visible. In XCT we also observed mud-cracks in the current collectors. When the indented cell components were taken out for examinations, there was no visible cracking in the area surrounding the failure point. The anode was scanned by x-ray, which penetrated carbon but not the copper. The radiographs clearly showed extensive cracking of the copper current collector. On the other hand, the anode did not show any cracking under SEM. At a closer look, a crack was observed in the exposed copper layer near the center hole. The remaining area was covered by graphite without any sign of cracking. This was the first experimental proof that hidden fragmentations were induced by the spherical indentation in the anodes. The graphite, in the presence of electrolyte, was able to move and fill the cracked area without showing any cracks on the surface. The fragmented current collectors play important roles in the safety and continuous operation of the cells. It also provided additional details of the cell components behavior under mechanical compression. Out of the three layers in a jellyroll, the separator can be stretched very thin and the anode can also take large deformation due to the fragmentation of the current collectors. The final failure was induced when the aluminum current collector reached its strain limit. When the first Al layer cracks, it propagates to more than one layer creating a shear which can propagate through the bonded active anode material and rip the separator along the same crack lines. The initial contact was created between the anode and cathode. We were able to experimentally confirm the behavior of all the layers and identify which layer is responsible to the failure that leads to short-circuit:

1. Anode with Cu current collectors: Graphite is more compressible and the fragmentation of Cu helps the anode to take more deformation
2. Separator: The separators can be stretched far beyond the thickness of the cell without failure. It is unlikely to be the first failure layer
3. Cathode with Al current collectors: When the other two layers could take more compressive loading, Al layer would eventually crack and trigger internal short-circuit. Therefore, it had been identified as the origin of failure.

We also performed 3-point bending tests on a series of cells, with 3.81 mm to 1.91 mm displacement. The load vs. Time plots of four cells with incremental displacements all followed the same loading curves and showed very repeatable mechanical responses.

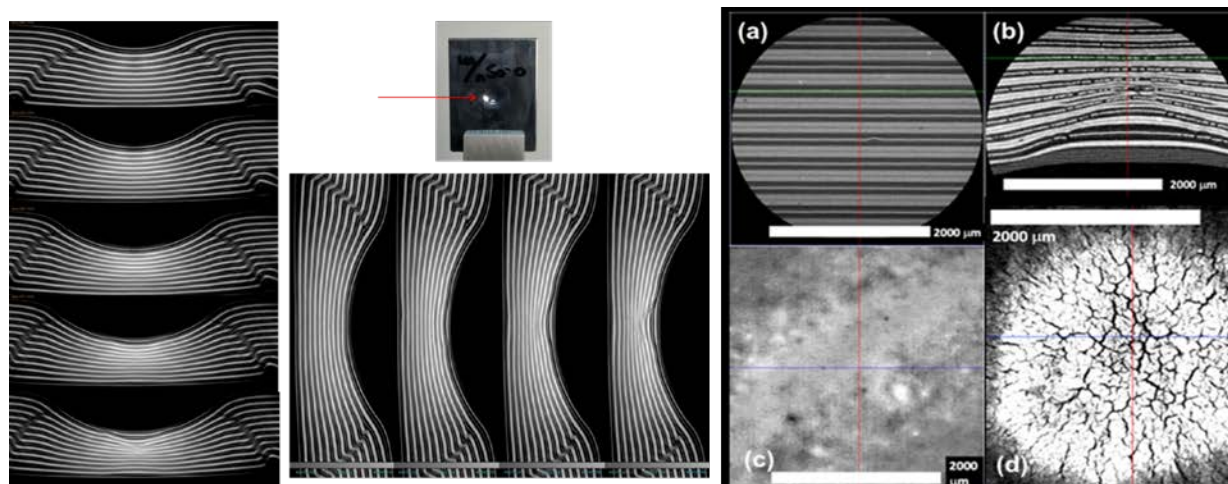
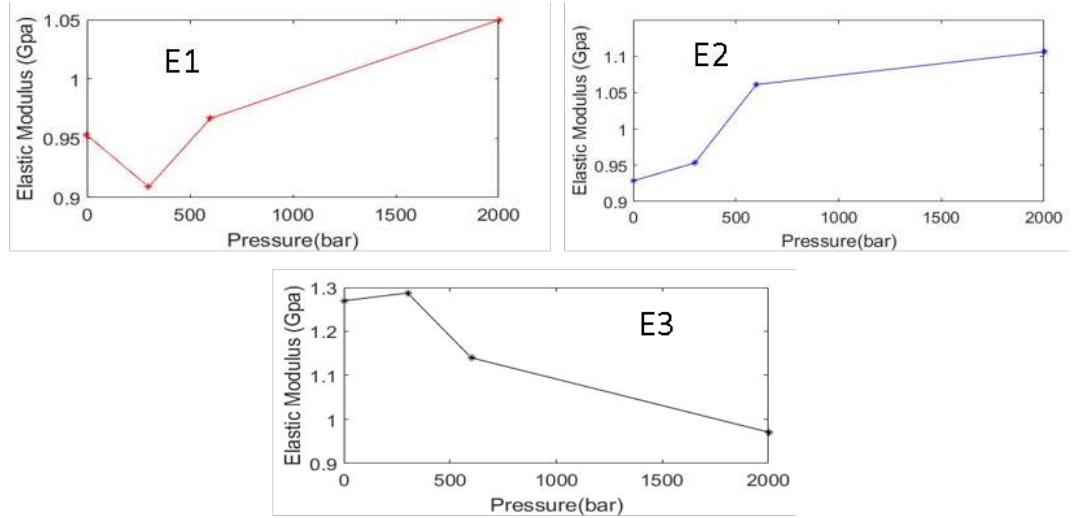


Figure I-128. X-ray tomography images of an indentation that led to short circuit and XCT images of the copper current collectors showing cracking and mud-cracks

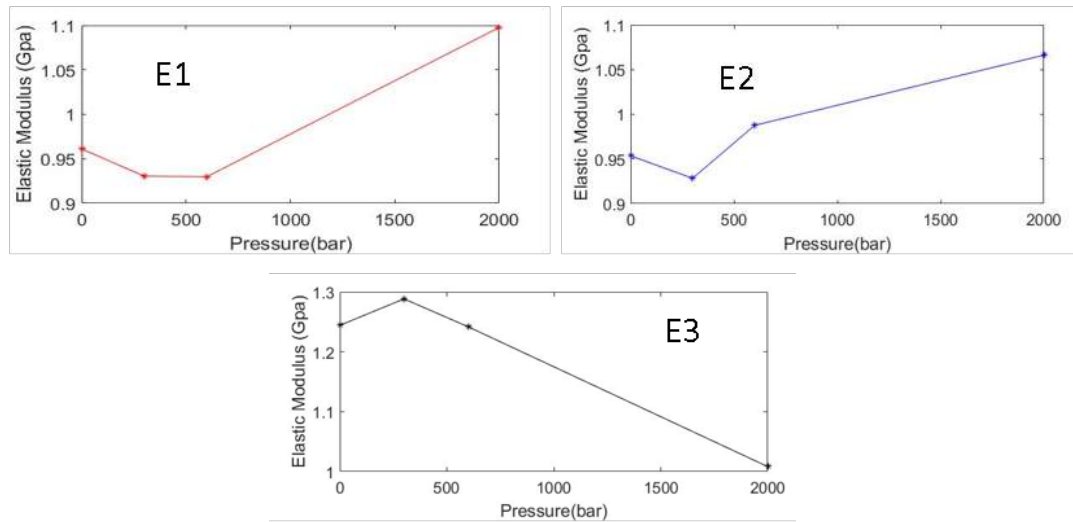
Upscaling of mechanical behavior from geometric features of mesoscale structures

The electrodes can be considered as granular media, where the mechanical connectivity, force networks, and transport could be described using Fabric Tensor formulations. Fabric Tensors are well-established, non-local directional measures of internal connectivity and structure of granular media and solids. They are also extensively used in the field of damage mechanics [1] to describe the deterioration of material due to cracks and the reduction in the connectivity and force transport pathways. Using these tensors descriptions granular and damage mechanics can be constituted with a physical interpretation of microstructure effects and correlate to macroscopic properties such as skeleton stress tensors and stiffness tensors. In our previous work [1] we have explored the use of Fabric Tensor as a method of modeling the inter-particle contacts and connectivity of the active particle network in the battery electrode microstructure. Based on Ebner's experimental data we have calculated the Fabric Tensor for different calendaring pressure and concentration of Lithium ion in the battery. Building on this work, a second order deviatoric Fabric Tensor is used to characterize the fabric anisotropy in electrode material. To describe anisotropic elasticity in a porous medium, we use Cowin's [1] expression of stiffness tensor as a function of second-order fabric tensor, F_{ij} , representing the anisotropic geometry of internal structure in electrode material. Based on spherical approximation, the Fabric Tensor (F) is calculated using model described in [1] for the experimental data at concentration of 90, 92 and 96 percentage and the pressure value of 0, 200, 600 and 2000 bar. The value for bulk modulus (k) and shear modulus (g) is taken as 0.5 and 0.2 GPa respectively. The variation of Young Modulus in 3 different directions for various loading of NMC 90, 92 and 96% is shown in Figure I-129. The ratio of modulus in 3rd direction and 1st direction had decreased with increase in pressure. With this formulation, we have successfully demonstrated that given the mechanical properties in isotropic case we can predict the evolutions of properties due to reorganization of microstructure under deformation.

90%



92%



96%

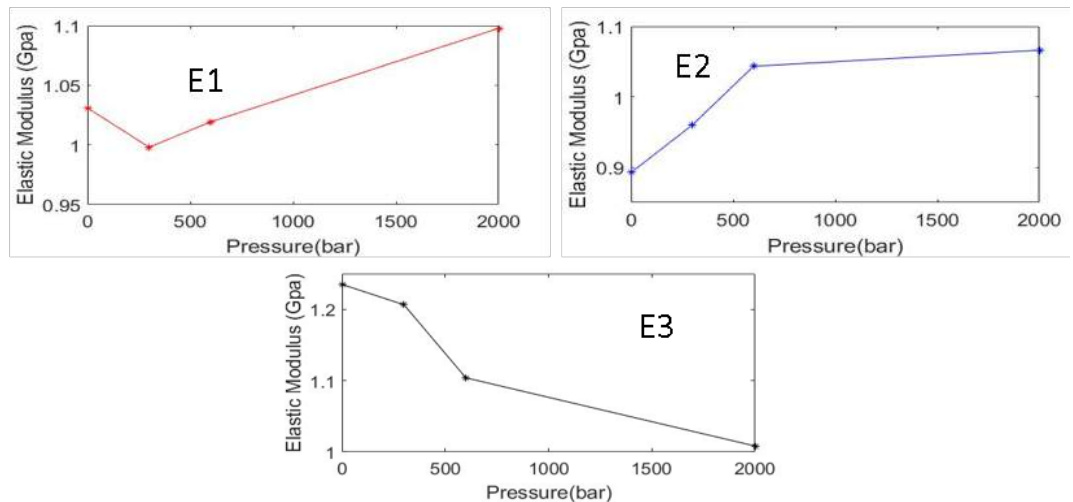


Figure I-129. Variation of Young Modulus in 3 different direction as a function of pressure and concentration

Milestone I4: Demonstration of VIBE/OAS to simulate onset of short-circuit due to mechanical abuse informed by microstructure simulations

For this milestone, we developed a computational framework to investigate the cycling behavior of the damaged cells. Towards this effort a constant loading of electrodes calendared at different pressures are constructed for estimation of total thickness of the NMC reconstructions from the mesoscale imaging data ETH-Zurich. Using these multiple thickness values corresponding to different porosities, homogenized meshes with resolved components for cell sandwich are generated. The effective electronic conductivities are calculated by Sandia team for different porosities with assumed binder distribution from the meso-structure simulations on the NMC cathode described in section I.C.5. Using these properties on the continuum scale meshes we were able to simulate constant current discharge behavior that was able to predict reduced capacity, as seen in Figure I-130(b).

This clearly shows influence of calendared pressures on the material reorganization at the meso-scale and the effect on transport at the electrode scale and the ability of the framework to capture these effects. In the next study, we want to show the coupling of mechanical and electro-chemical simulations to reproduce the capacity loss in the damaged cell due to deformation. Once the cell undergoes permanent damage, the performance evaluation of the cell shows ~5.0% reduction in extracted capacity, as seen in Figure I-130(a). We saw the evidence from X-ray tomography imaging from previous section on the fragmentation of copper current collectors prior to the internal short. Thus, we rezoned the areas where the copper is fragmented as electrically isolated regions. As we go deep into cell thickness away from the point of contact the area of fragmentation is reduced. Then we performed a constant current discharge on the full cell to compare against the un-deformed cell. In the Figure I-131 we show the solid phase potential and concentration on the first three layers starting from the point of contact. The contour plots show gradients developed across the in-plane direction between electrically damaged copper collector and the undamaged regions. The electrically isolated regions do not contribute to the extracted capacity during the discharge of the cell and hence a reduced capacity of the cell.

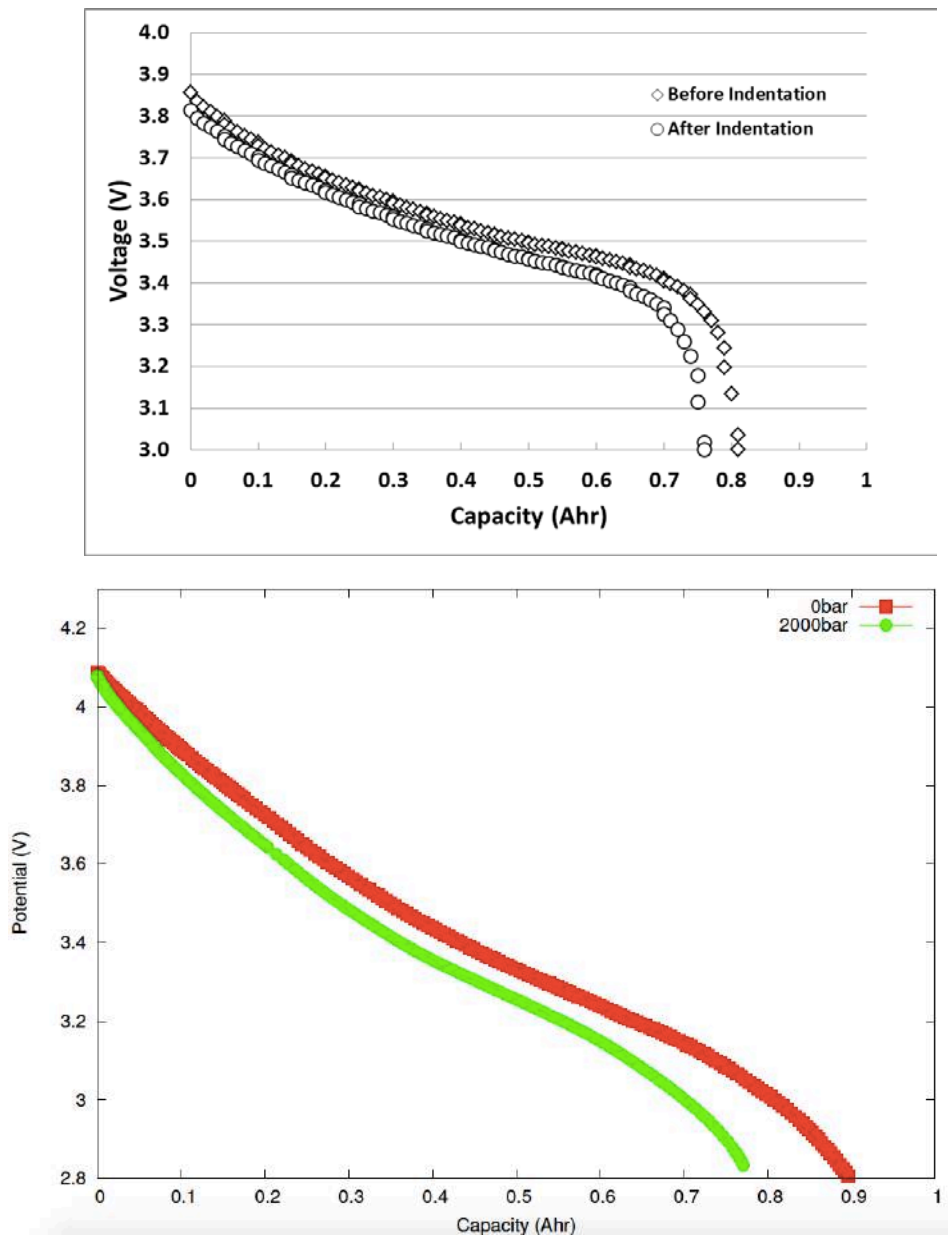


Figure I-130. (a) Reduced extracted capacity of cells damaged under 80% indentation (b) Reduced extracted capacity of electrodes calendered under various pressures

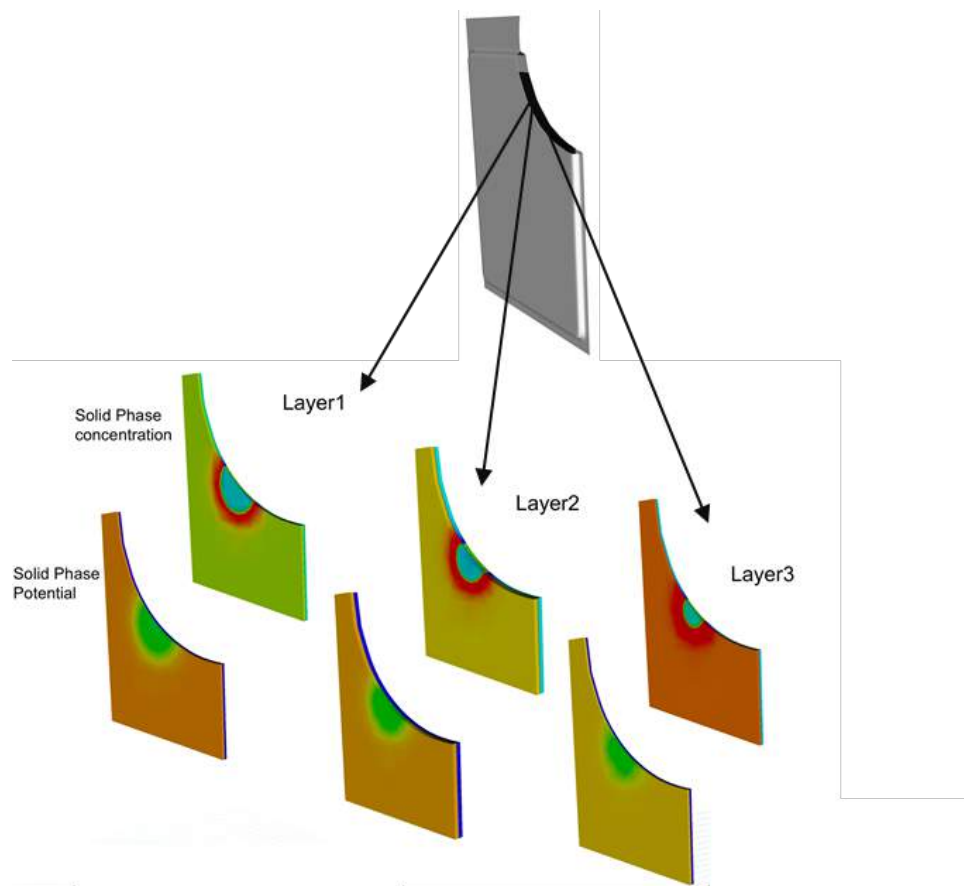


Figure I-131. Full cell coupled electrochemical simulation with electrically isolated regions

Conclusions

Understanding the failure of battery components under extreme mechanical deformations has been the prime motivation for this project. Several experiments have been conducted on individual constituent materials to characterize the mechanical and transport behavior and evaluate parameters for the material models. Using these material models in the VIBE computational framework developed under CAEBAT program, the cumulative response of the battery under crush is simulated. A prior to short, the damage to the copper current collectors caused permanent loss of the cycling capacity of the batteries. Robust numerical algorithms were developed to predict the material failure and capacity loss of the batteries.

Key Publications

1. Kalnaus, S., Wang, Y., Turner, J.A. Mechanical behavior and failure mechanisms of Li-ion battery separators. *Journal of Power Sources* 2017, 348, 255-263
2. Wang, H., Kumar, A., Simunovic, S., Allu, S., Kalnaus, S., Turner, J.A., Helmers, J.C., Rules, E.T., Winchester, C.S., Gorney, P. Progressive mechanical indentation of large-format Li-ion cells. *Journal of Power Sources* 2017, 341, 156-164
3. Wang, H., Watkins, T. R., Simunovic, S., Bingham, P. R., Allu, S., Turner, J. A. Fragmentation of copper current collectors in Li-ion batteries during spherical indentation. *Journal of Power Sources* 2017, 364, 432–436.

References

1. Stershic A.J., Simunovic S. and Nanda J., Modeling the evolution of lithium-ion particle contact distributions using a fabric tensor approach, *Journal of Power Sources* 2015, 297, 540-550.

I.C.5 Consortium for Advanced Battery Simulation (SNL)

Scott A. Roberts, Principal Investigator

Sandia National Laboratories
1515 Eubank SE
Albuquerque, NM 87123-0836
Phone: 505-844-7957
E-mail: sarober@sandia.gov

Brian Cunningham, Technology Manager

U.S. Department of Energy
Phone: 202-287-5686
E-mail: Brian.Cunningham@ee.doe.gov

Start Date: October 1, 2015
Total Project Cost: \$1,350,000

End Date: September 30, 2018
DOE share: \$1,350,000

Non-DOE share: \$0

Project Introduction

Multi-physics simulations of battery performance are typically performed at the macroscale, including entire cells, cells stacks, batteries, packs, and modules. These types of simulations typically model the electrodes using homogenized equations and properties, often utilizing effective medium theory. These electrodes, however, are comprised of packs of active material particles, polymeric binders, and conductive additives. These materials are combined to form a complex mesostructure that is influenced by material choices and processing conditions. This mesostructure strongly influences the macroscopic performance of the electrode and is of particular importance in abuse scenarios, where it is difficult to experimentally determine mesostructure evolution and properties.

Study of the influence of these mesoscale effects on the macroscale behavior of electrodes is the focus of this project. We are utilizing microtomography of NMC cathodes to create detailed simulation domains within Sandia's Sierra/Aria code suite using the Conformal Decomposition Finite Element Method (CDFEM). These imaging-derived particle networks are augmented with a conductive binder morphology that we designed. Physics simulations are then performed on these mesostructures, including the calculation of effective properties (e.g., electrical conductivity, ionic tortuosity, Young's modulus) and fully coupled electrochemical-mechanical (dis)charge simulations. The results of these simulations are upscaled to feed into macroscale models developed by our ORNL teammates.

Objectives

The objective of this project is to improve the fidelity of battery-scale simulations of abuse scenarios through the creation and application of microscale (particle-scale) electrode simulations. Our specific FY2017 objectives are twofold:

1. Accurately represent NMC microstructure, including the active binder phase, within the simulation framework
2. Begin to feed information from the microscale to the battery scale

Successfully accomplishing these objectives will impact the VTO by improving the ability to assess battery response to abuse scenarios (e.g., crush) computationally, enabling many parametric computer tests rather than expensive and dangerous experiments.

These objectives have been formalized into three FY2017 milestones that have been completed and were contributed to by this project:

1. I3: Demonstration of ability to construct 3D meshes of electrodes using reconstructions from micro-tomography
2. I4: Demonstration of VIBE/OAS to simulate onset of short-circuit due to mechanical abuse informed by microstructure simulations (ORNL lead, SNL contributor)
3. CDa/1.8: Investigate the role of polymeric binders for mitigating stress

Approach

Our approach centers around simulations performed using Sandia's Sierra Mechanics suite of codes. In particular, physics simulations are performed using the Sierra/Aria multi-physics code and the mesoscale geometric representation is performed using CDFEM implemented within Sierra/Krino.

Experimentally gathered electrode tomography data forms the foundation of our mesostructure representation. We are in the process of utilizing data gathered within the scope of this project by our CABS teammates and collaborators at Lawrence Berkeley National Laboratory (LBNL) and Argonne National Laboratory (ANL) (Higa, et al., 2017). For the work shown here, however, we have utilized microtomography from Vanessa Wood's group from ETH-Zurich. Specifically, Ebner *et al.* (Ebner, Geldmacher, Marone, Stampanoni, & Wood, 2013), published and made publicly available a high-quality data set of NMC electrodes. Material properties were gathered from a variety of sources detailed in our FY2016 report.

Computational representations of the NMC particle mesostructures are created using the CDFEM algorithm. This workflow has been discussed in detail in two journal publications (Roberts, Brunini, Long, & Grillet, 2014) (Roberts, et al., Insights Into Lithium-Ion Battery Degradation and Safety Mechanisms From Mesoscale Simulations Using Experimentally Reconstructed Mesostructures, 2016), but will be summarized here for completeness. The commercial software Avizo (Thermo Fisher Scientific) is used to binarize images, label individual particles, and create a smooth surface mesh for each particle which can then be exported as a faceted STL file. The faceted STL representation of each particle is then superimposed on top of a regular tetrahedral background mesh. CDFEM is used to decompose the background mesh to be conformal to the particles. A new addition to this workflow/approach this year is the subsequent addition of a conductive binder phase to create a "binder bridge" morphology. The details on this level-set-based algorithm was published by Trembacki et al. (Trembacki, Noble, Brunini, Ferraro, & Roberts, 2017) and will be discussed in more detail in the results section. A visualization of the resulting geometry is shown in Figure I-132.

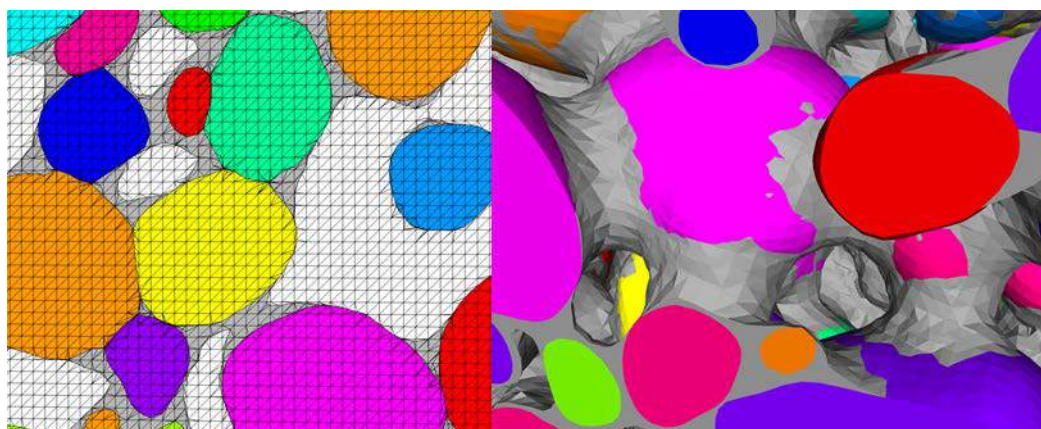


Figure I-132. 2D (left) and 3D (right) representations of a small NMC cathode domain illustrating the microtomography-derived particle microstructures combined with the "binder bridge" conductive binder representation.

Results

The key technical results arising from our three FY2017 milestones are derived in this section.

Milestone I3: Demonstration of ability to construct 3D meshes of electrodes using reconstructions from micro-tomography

One of our overarching goals is to understand how the manufacturing process (primarily calendaring pressure, in this case) affects the cathode microstructure, and therefore battery performance. Additionally, mechanical abuse can change the porosity in similar ways to calendaring pressure, and understanding these changes on the microscale will help to predict cell performance under mechanical insult.

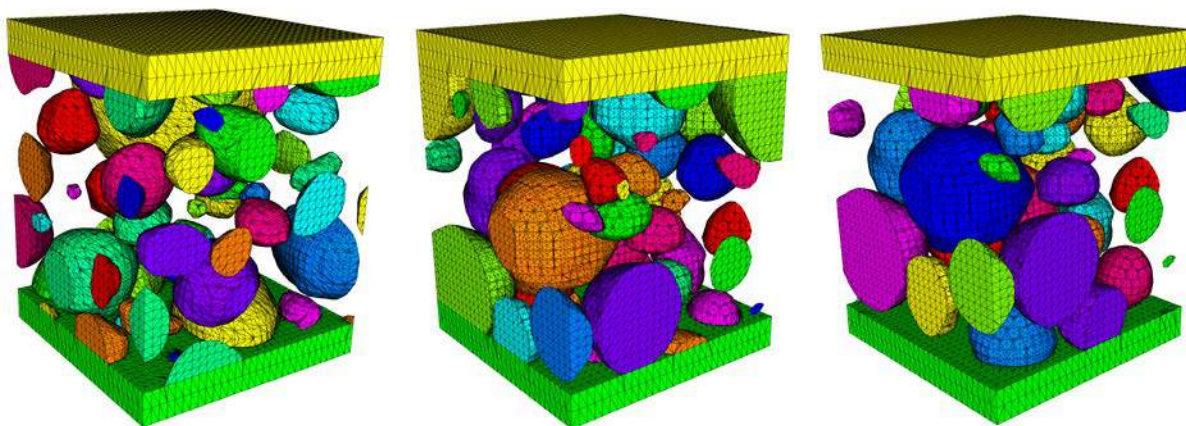


Figure I-133. Computational meshes generated for three calendaring pressures (0 bar, left; 300bar, center; 600 bar, right)

To begin to address these issues, we have created meshes for three calendaring pressures (0, 300, and 600 bar) from the ETH-Zurich data set, and the resulting meshes are found in Figure I-133. These data are for a subset of the domain ($30\ \mu\text{m} \times 30\ \mu\text{m} \times 30\ \mu\text{m}$) for ease of rapid processing and for visualization. These images clearly show that at higher calendaring pressures, the particles are more consolidated (closer together). This should impact performance characteristics such as the effective electrical conductivity, simulations that are currently underway.

It is worth noting that the mesh resolution for this reconstruction is relatively coarse, with just a few (5-10) elements across the width of most particles. Solution verification work is underway that suggests target mesh resolutions for desired solution error levels. This will likely require more refined meshes than are currently used, and the meshes will be appropriately updated upon the conclusion of that work.

Milestone I4: Demonstration of VIBE/OAS to simulate onset of short-circuit due to mechanical abuse informed by microstructure simulations

While this milestone was primarily owned by ORNL partners, we performed a number of mesoscale simulations to support the mechanical abuse simulations. The effective properties of NMC cathodes were computed from the electrodes images using X-ray computed microtomography described in the previous section.

As mentioned in the previous section, requisite data for full 3D mesostructure reconstruction of a crushed cathode is not readily available. Thus, we must utilize alternate sources to visualize the mesostructure evolution over the course of a crush test. Data made publicly available by Ebner et al. (Ebner, Geldmacher, Marone, Stampanoni, & Wood, 2013) provides tomography data at multiple values of binder composition and calendaring pressures. This allows us to approximate the early stages of cathode compression by surveying effective property dependence on the porosities obtained from different calendaring pressures. Primary properties of interest will include effective electrical conductivity of the NMC particle network and the tortuosity of the cathode electrolyte phase.

Effective conductivity and tortuosity values can be obtained by solving charge conservation equations on the full mesostructure reconstructions. For the values presented here, we use data for 92 wt% NMC333 cathodes calendered at 0 bar, 300 bar, 600 bar, and 2000 bar. The full domains in each case spanned a significantly large area, so simulations were performed on smaller subdomains taken at random locations throughout the full sample. These domains measured $100\mu\text{m} \times 100\mu\text{m} \times 60\mu\text{m}$, which was determined to be a significantly large subdomain size by a recent Sandia verification study (Roberts, Mendoza, Brunini, & Noble, A Verified Conformal Decomposition Finite Element Method for Implicit Geometries). Material properties for NMC333 were detailed in a previous report (Ferraro & Roberts, 2016). Effective property results are shown in Figure I-134.

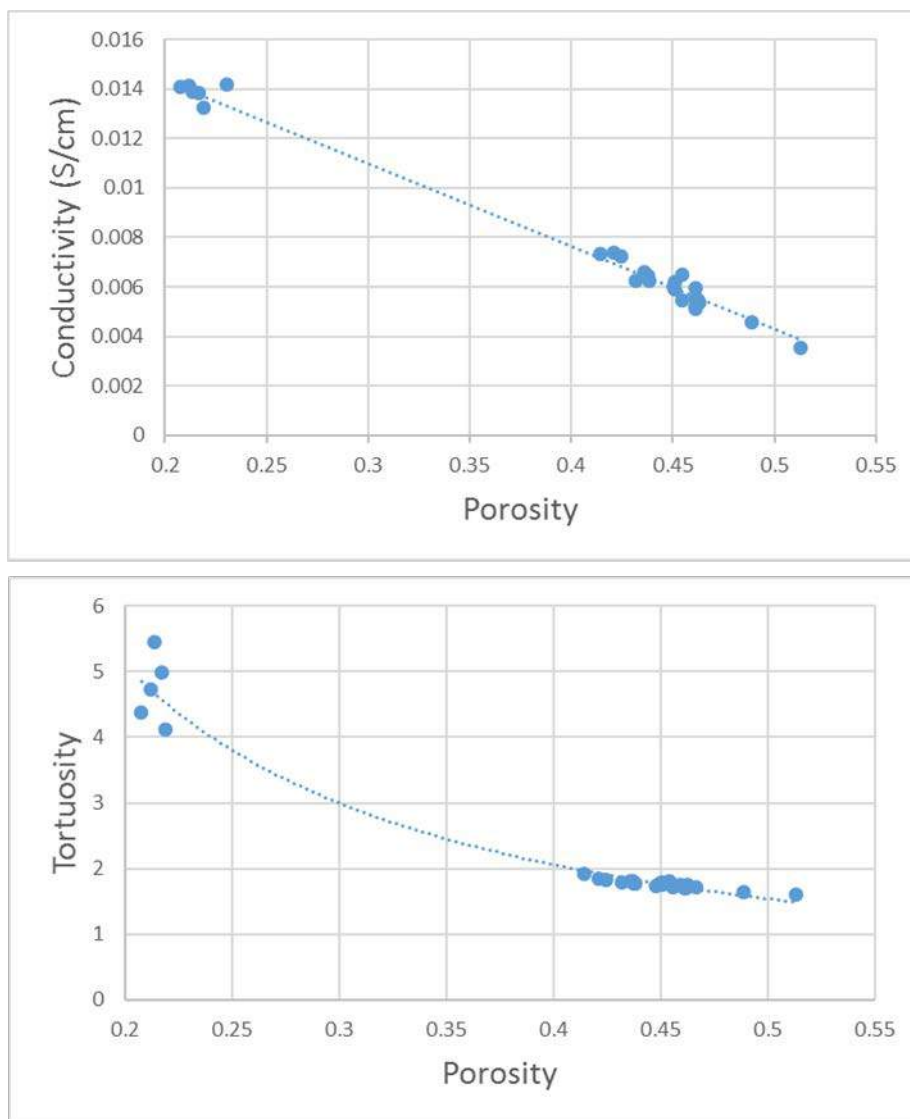


Figure I-134. Effective electrical conductivity and electrolyte-phase tortuosity measured from sampled subdomains with varying porosity. Effective conductivity exhibits linear behavior with a trendline of $k_{\text{eff}} = -0.0334 \varepsilon + 0.021$. Power-law behavior was assumed for tortuosity, with a trendline $\tau = 0.623\varepsilon^{-1.31}$.

Charge conservation over a fixed voltage drop allowed us to calculate both effective conductivity and tortuosity of the NMC cathodes. Results are reported for individual subdomains sampled from the four reported calendering pressures. Subdomain porosities varied slightly throughout each cathode, but remain close to the reported values in each case. Overall, we can obtain a linear trend of effective conductivity vs.

porosity which demonstrates an increase in conductivity as the particles are compressed closer together, thus decreasing porosity. Additionally, we see that tortuosity increases as the cathode becomes compressed. Typically, tortuosity is estimated from a Bruggeman approximation $\tau = \varepsilon^{-0.5}$. However, this approximation is known to underestimate tortuosity for porosities under 0.5. Thus, we have shown a trend demonstrating the same power-law behavior $\tau = a\varepsilon^{-b}$ which is able to represent the higher tortuosity values calculated for these subdomains.

Milestone CDA/1.8: Investigate the role of polymeric binders for mitigating stress

Sandia's FY17 goal as part of the CD-adapco FOA project is to investigate the role of polymeric binder within NMC cathode particle-bed mesostructures. We investigated the binder's role in effective electrode properties and behavior through advanced methods development and accompanying simulations. Our investigation of stresses generated within the mesostructure both with and without considering the presence of binder is of relevance to this milestone. The work was published in the *Mathematical Modeling of Electrochemical Systems at Multiple Scales Focus Issue* of the *Journal of the Electrochemical Society* (Trembacki, Noble, Brunini, Ferraro, & Roberts, 2017).

In this publication, we demonstrated that even a thin layer of binder separating adjacent NMC particles can reduce swelling-induced stress predictions by a factor of 4.5 versus a case where NMC particles are in contact (Figure I-135). This indicates that incorporating sufficient binder when manufacturing electrodes may be necessary to reduce or mitigate swelling-induced stresses experienced by NMC particles and therefore reduce the likelihood of mechanical degradation and fracture.

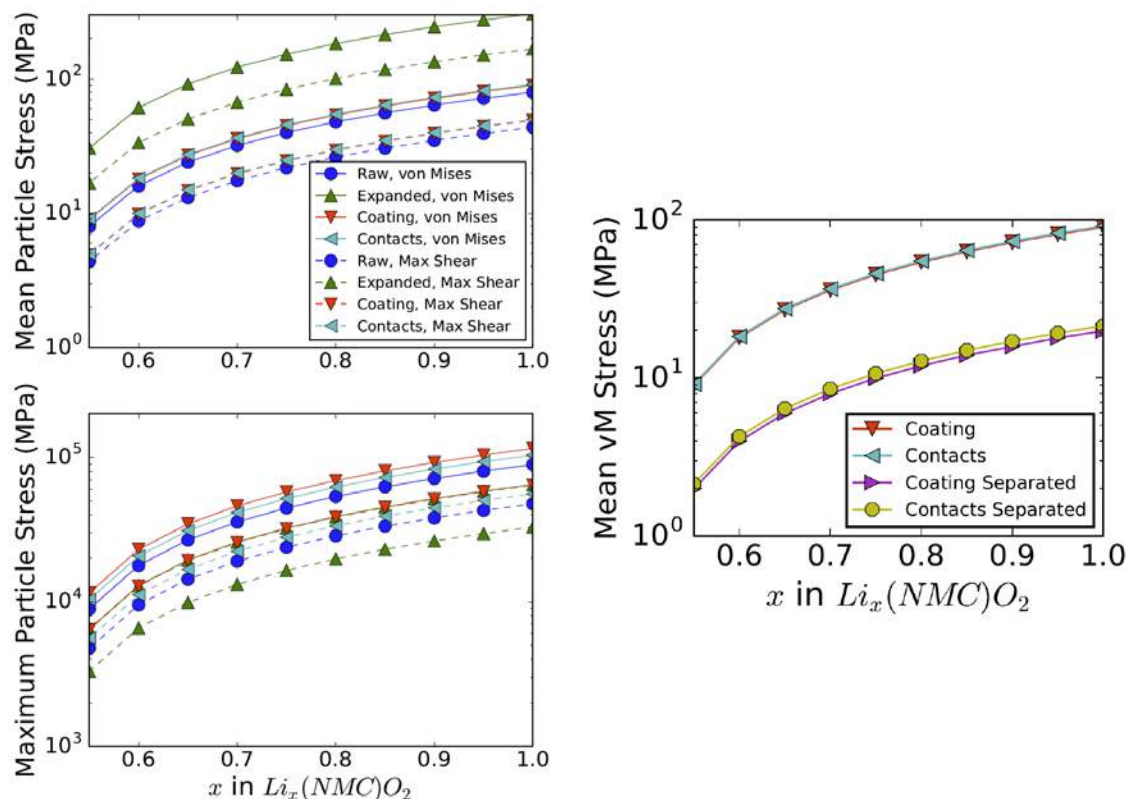


Figure I-135. Left: Maximum and mean stresses experienced by the NMC particles for all mesostructure representations. Both von Mises stress and maximum shear stress are displayed. Right: Mean von Mises stress for the two binder representations, including cases where particles are separated by a composite binder layer.

Conclusions

We have demonstrated an approach for representing experimentally derived battery electrode mesostructures in a computational framework suitable for performing coupled multi-physics battery performance simulations. In pursuit of this we have created a new algorithm for analytically representing the secondary conductive binder phase morphology in these mesoscale representations and demonstrated the importance of accurately capturing this morphology. We have used this model to calculate many effective properties that are relevant for mesoscale modeling efforts. These effective properties have been upscaled and implemented within the VIBE code and used to analyze battery abuse scenarios.

Key Publications

1. Ebner, M., Geldmacher, F., Marone, F., Stampanoni, M., & Wood, V. (2013). X-Ray Tomography of Porous, Transition Metal Oxide Based Lithium Ion Battery Electrodes. *Advanced Energy Materials*, 3, 845--850.
2. Ferraro, M., & Roberts, S. (2016). *Collect Constitutive Models for NMC Materials and Report on Use of Mesoscale Data to Project Lead: CABS Milestone C1.1 Report*.
3. Higa, K., Wu, S.-L., Parkinson, D., Fu, Y., Ferreira, S., Battaglia, V., & Srinivasan, V. (2017). Comparing Macroscale and Microscale Simulations of Porous Battery Electrodes. *Journal of The Electrochemical Society*, 164, E3473-E3488.
4. Roberts, S., Brunini, V., Long, K., & Grillet, A. (2014). A Framework for Three-Dimensional Mesoscale Modeling of Anisotropic Swelling and Mechanical Deformation in Lithium-Ion Electrodes. *Journal of The Electrochemical Society*, 161, F3052-F3059.
5. Roberts, S., Mendoza, H., Brunini, V., & Noble, D. (n.d.). A Verified Conformal Decomposition Finite Element Method for Implicit Geometries. *Journal of Computational Physics*.
6. Roberts, S., Mendoza, H., Brunini, V., Trembacki, B., Noble, D., & Grillet, A. (2016). Insights Into Lithium-Ion Battery Degradation and Safety Mechanisms From Mesoscale Simulations Using Experimentally Reconstructed Mesostructures. *Journal of Electrochemical Energy Conversion and Storage*, 13, 031005--031005.
7. Trembacki, B., Noble, D., Brunini, V., Ferraro, M., & Roberts, S. (2017). Mesoscale Effective Property Simulations Incorporating Conductive Binder. *Journal of The Electrochemical Society*, 164, E3613-E3626.

I.C.6 Consortium for Advanced Battery Simulation (ANL, LBNL)

Venkat Srinivasan, Principal Investigator

Argonne National Laboratory
9700 S. Cass Avenue
Lemont, IL 60439
Phone: 630-252-6003
E-mail: vsrinivasan@anl.gov

Brian Cunningham, Technology Manager

U.S. Department of Energy
Phone: 202-287-5686
E-mail: Brian.Cunningham@ee.doe.gov

Start Date: October 1, 2015
Total Project Cost: \$588,004

End Date: September 20, 2018
DOE share: \$588,004

Non-DOE share: \$0

Project Introduction

Our CABS teammates are developing simulations of battery operation at both the microscale and macroscale. This project focuses on obtaining experimental data required for simulation development. For microscale simulations, electrode microstructure information is needed to construct simulation domains, and information about microstructure evolution is needed to understand electrode degradation. At both the microscale and macroscale, electrolyte solution transport properties for concentrated solution theory are needed to accurately describe battery operation under realistic, high-rate conditions.

Our “CD-adapco” subproject complements the main CABS project by focusing on the development of techniques and tools for obtaining reliable electrochemical cycling data and for rapidly process large quantities of electrode tomography data. This subproject aims to combine these approaches to obtain qualitative insight into electrode performance, allowing rapid screening of candidates for simulation studies.

Objectives

1. Provide microstructural information about battery electrodes by using X-ray microtomography
 - A. For both pristine electrodes and electrodes soaked in electrolyte solution
 - B. For cycled electrodes
2. Provide electrolyte solution transport properties that are compatible with concentrated solution theory
3. Provide tools to analyze tomography data and apply these for the imaged electrodes to construct surface meshes for use in simulation and further analysis to understand connections between electrode structure and performance.
4. Collect cycling data and provide insight into the influence of cell construction on observed performance.

Approach

Pulsed field gradient nuclear magnetic resonance (PFG-NMR) experiments performed by Kee Sung Han of EMSL at PNNL were used to determine concentration dependence of the tracer diffusion coefficients of lithium ions (Li^+), hexafluorophosphate ions (PF_6^-), EC, and DEC. Binary diffusivities were obtained by applying the generalized Darken relation, in which the binary diffusivities are related to the tracer diffusivities and mole fractions of each species. Concentrated solution theory was then applied to calculate the conductivity, transference number and diffusivity of the salt. These were then corrected for the degree of ion

pairing, which was obtained by fitting the conductivity calculated through concentrated solution theory to the experimental conductivity measured by a conductivity meter.

For the “CD-adapco” subproject, composite electrodes containing 4% (by mass) PVDF, 3.2% conductive additive, and 92.8% NMC532 particles obtained from our ORNL teammates were fabricated in an argon-filled glovebox in LBNL’s battery fabrication laboratory (collaboration with Yanbao Fu and Vince Battaglia, LBNL). Three doctor blade heights were used. After the laminates were left to dry overnight in the glovebox, their dry thicknesses were measured by a micrometer as approximately 40 microns, 76 microns, and 122 microns, corresponding to cells designed for higher power density or higher energy density. This fulfilled our Q1 milestone under the “CD-adapco” subproject.

A no-go decision was taken for the Q2 “CD-adapco” milestone, for which it was determined through discussions at both ANL and LBNL that obtaining electrochemical data using pouch cells containing reference electrodes would not be cost-effective, given the time and cost to construct these cells and concerns about proper interpretation of the resulting data. Instead, coin cells were constructed in the LBNL battery fabrication laboratory from the laminates produced for the Q1 milestone, with the help of tools designed and fabricated for this project that ensured precise placement of cell components. Future work will use these tools to probe the effect of variations in cell construction on cell performance. The cells were placed in temperature chambers and attached to galvanostats. They underwent the same formation procedure used by our teammates at ORNL for cells using the same NMC active material (four cycles at C/20 rate), followed by a sequence of charging at C/10 rate and discharging at a range of increasingly fast rates (to the extent that this was possible), ranging from C/10 to 10C (with rates based on capacities estimated from laminate masses).

Small (5/64” diameter) disks were punched from the laminates produced for the Q1 milestone using a hammer-driven punch and interleaved with polyimide disks in custom sample holders designed under the CABS project in FY16. These holders maintain light pressure on the samples, holding the samples relatively flat for imaging, and also allow for optional injection of electrolyte solution for investigating binder swelling due to solution uptake. These samples were assembled at LBNL and transported to ANL for microtomography imaging at APS beamline 2 with the assistance of beamline scientist Xianghui Xiao. These were imaged with a 10x optical lens, and reconstructions were performed with the TomoPy package from ANL, fulfilling our Q3 milestone.

In order to meet the Q4 milestone efficiently, it was necessary to automate the tomography data postprocessing pipeline developed under the “CD-adapco” subproject in FY16. Fully automating this process already required substantial restructuring and rewriting of existing computer programs, so it was determined that only a moderate amount of additional effort would be needed in order to package the software for release as open-source software. The software is designed so that users can adjust our usual pipeline to their needs by modifying the sample processing scripts. The key steps in this processing pipeline are described in the following paragraphs.

Tomography reconstructions produced by both TomoPy and by the ImageJ and Octopus-based ALS reconstruction software come in the form of a sequence of TIFF-format image files representing successive horizontal “slices” of voxels through the cylindrical reconstruction volumes. The sample holders and punch diameter selected for extracting samples from laminates were chosen to be only slightly larger than the reconstructed volumes. This was done to minimize the amount of material through which X-rays are transmitted but which are not inside the reconstructed volume; this excess material reduces the quality of the reconstructed data. As the sample holder diameters are slightly larger than the punch size, samples can shift slightly during assembly, and as multiple samples are stacked into each holder to improve imaging throughput, the samples rarely have perfect vertical alignment, so compromises are made during sample positioning in order to maximize the amount of usable data. Invariably, the edges of some samples, showing some damage from the punch, will appear in some reconstructions. In addition, the reconstruction algorithms frequently show numerical artifacts near the axis of the reconstructed cylinders. At the same time, manual extraction of

usable data tends to be time-consuming and inconsistent, particularly when one wants to examine enough image data in order to ensure good representations of the extracted samples. The first task is to extract a ring of non-overlapping cuboid columns that extend through the length of the reconstructed cylinder and which are located away from both the axis as well as the outer edge. These blocks are then used in further processing.

The postprocessing software then examines each block, computing average voxel intensities across each horizontal slice and making use of statistical clustering in order to distinguish slices that contain electrode regions from the surrounding foil and plastic material. By doing this, the software may be able to distinguish multiple electrode samples stacked into a single sample holder. The success of this clustering approach is dependent on good contrast in the reconstructions and suitable guesses of cluster means.

The individual electrode samples are typically slightly tilted relative to the camera horizontal, which complicates their use in analysis. In order to calculate the degree to which these samples are tilted, several small columns are extracted from each electrode region, and the clustering method is again employed to estimate the height of one of the electrode surfaces in each column. A linear least-squares fit is used to fit a plane to these interface locations, and rotations along the two axes in the horizontal plane are then calculated from the fitting plane. Each electrode block is rotated virtually. To remove directional bias, the corners of the rotated region are tracked so that a final cuboid can be extracted from the rotated region without including any filler voxels that were originally outside of the electrode.

Histograms are then computed for each finished electrode block. A heuristic for detecting unusable samples (such as those with cracks or those that might have been improperly processed) based on histogram shape is then employed, leaving a final set of usable samples. The histograms of these remaining blocks are compared with experimental data to obtain intensity thresholds that can be used to segment the electrode blocks according to expected component volume fractions. Electrode porosity was determined based on wet electrode thicknesses measured from tomography reconstructions, which differ from dry electrode thicknesses as we reported in our first 2017 publication.

It is at this point that one can optionally produce Avizo (FEI) TCL script files that direct Avizo to load the voxel data files, segment voxels by material type, and produce particle surface meshes. This procedure was adopted from one provided by our teammates at SNL and makes use of Avizo's particle separation capabilities, which can create interfaces between neighboring voxelized particles that cannot be clearly distinguished in the X-ray microtomography data due to imaging limitations or artifacts. Separate surface meshes are created to envelop each particle, as required by our teammates at SNL. Our implementation of this procedure has reduced the computer memory requirements for processing, allowing data sets that originally could not be processed within 32 GB of RAM to run on computers with as little as 4 GB of RAM.

While the construction of particle surface meshes was needed to fulfill part of our role within the CABS team, that is, generating surface meshes suitable for use in microscale simulations, the construction of individual particle meshes also has the advantage of providing detailed information about each particle. To fulfill the Q4 "CD-adapco" milestone, computer programs using the VTK library were written to examine the arrangement of surface meshes, providing quantitative information about electrode microstructure.

Finally, in preparation for the FY18 milestone involving tomography imaging of cycled electrodes, a trial pouch cell with a 1 cm² NMC532 cathode was constructed at the CAMP facility by Andrew Jansen (ANL) and again imaged at APS beamline 2 with the help of beamline scientist Xianghui Xiao.

Results

The degree of dissociation as a function of concentration of LiPF₆ in EC/DEC, determined by using concentrated solution theory to analyze both conductivity and self-diffusivity measurements, is shown in Figure I-136. Only 61% of salt molecules are dissociated at 0.1M. This decreases to 37% at 1.25M and then appears to increase to 39% at 1.5M. This limited salt dissociation has implications for solution-phase transport.

It is standard practice to assume complete salt dissociation. Applying concentrated solution theory and instead accounting for the limited degree of dissociation results in corrections to the solution transport properties. The salt diffusivity correction (not shown) is relatively small, but the corrected transference number values show stronger concentration dependence and are generally significantly smaller than the uncorrected values (see Figure I-137).

The microtomography postprocessing pipeline software package was approved for release as open-source software by LBNL and DOE, and was released on August 4, 2017 as the “TomPost” package. This Python 2 package should be compatible with a range of platforms. It requires the installation of the ImageJ image processing package from NIH, and optionally, a license for the Avizo meshing package, along with the “sed” stream editor, which is commonly found on Linux, BSD, and Mac OS X systems, and which is available on Windows systems through Cygwin. More information is available on the TomPost website at <https://sites.google.com/a/lbl.gov/tompost/>, which contains a link to the download site on Bitbucket.org, which tracks download counts for this package as required by DOE rules. This automated approach to postprocessing provides several benefits. The postprocessing script provides a precise record of the lengthy postprocessing procedure used to transform the raw reconstructed data into data suitable for analysis and use in simulation domains. The automated system also saves time and reduces errors by minimizing the need for user involvement. It is now only necessary to provide straightforward configuration and hints to the program (such as sample orientation, which is readily visible from the reconstructed data) before running the pipeline. An examination of records from FY16 suggests that the full automation of this process has reduced postprocessing time from days to hours, enabling the processing of large quantities of tomography data. Finally, automation minimizes human visual bias in analyzing the tomography data; for example, determining the boundary between an electrode sample region and a plastic spacer or current collector can be done visually, but this is time consuming and introduces the possibility of use of inconsistent visual criteria by a single researcher over time or among multiple researchers. In FY18, the TomPost package and electrode data, including tomography reconstructions of electrodes fabricated by our ORNL teammates in FY16, will be made available from a centralized repository alongside other software and data released by the CABS team.

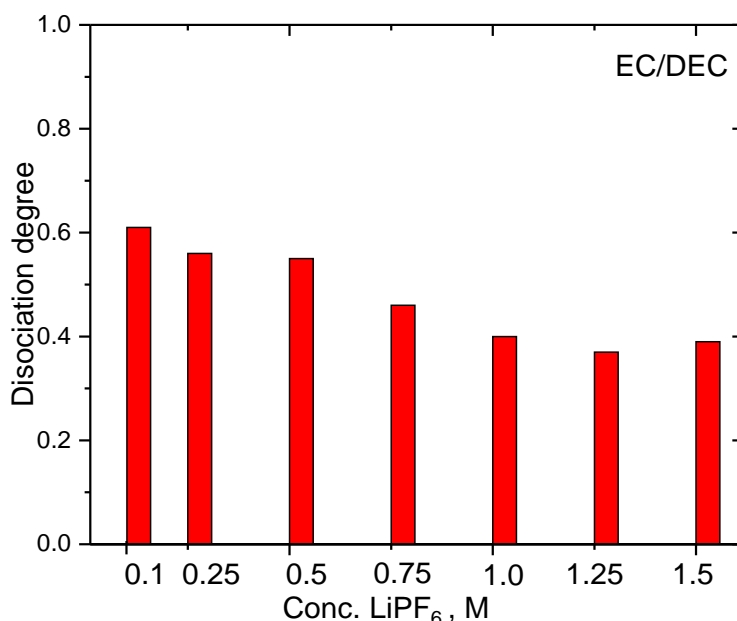


Figure I-136. LiPF_6 dissociation degree in EC/DEC (1:1 by weight).

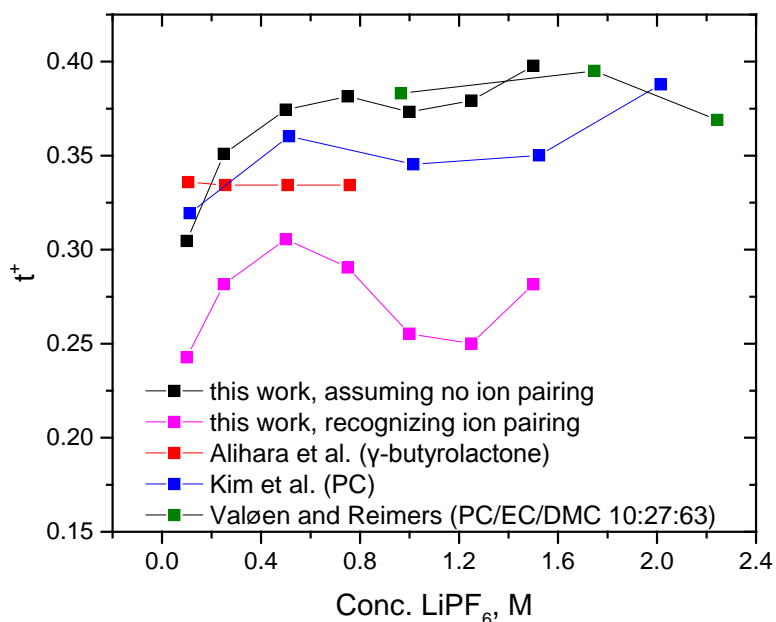


Figure I-137. Li⁺ transference numbers as functions of concentration, showing correction due to recognition of ion pairing. Published results for other solvents are shown for comparison.

Figure I-138 shows capacity data from the cycling experiments with coin cells constructed from the electrodes fabricated with three distinct thicknesses. All discharge capacities have been normalized to capacities at C/10. All three cells show sharply decreased capacity at with increasing C-rate, although at lower C-rates this is consistent among the electrodes of different thickness and so likely to be due to solid-phase transport limitations rather than resulting from electrode structure. At higher C-rates, increasing electrode thickness has a significant effect on relative capacity reductions. Previous modeling work by our group and others has suggested that such decreases result from transport limitations in the solution phase within the electrode pores, with thicker electrodes requiring ions to travel farther, on average.

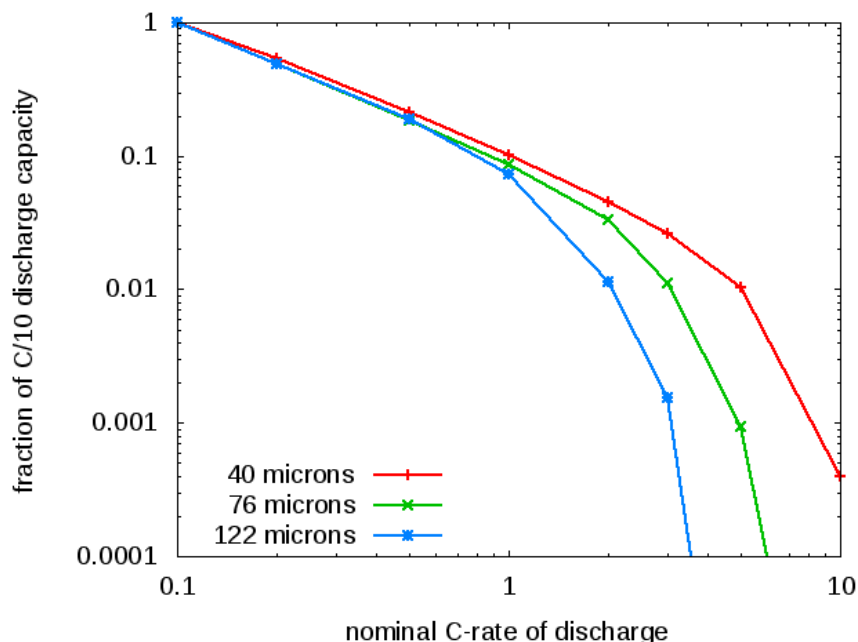


Figure I-138. Discharge capacities relative to C/10 capacities for representative cells with cathodes of three thicknesses

Our postprocessing pipeline generates a separate surface mesh for each particle, allowing a closer look at particle arrangements. Custom VTK-based programs were used to calculate particle location distributions and radial distribution functions from the particle mesh data sets, with approximate particle centroids determined by averaging surface mesh vertices. Particle volume distributions were computed directly from voxel intensities in the fully-processed voxel blocks. However, we were unable to detect any clear correlations between electrode thickness and internal structure. It is therefore likely that varying only doctor blade height has little effect on NMC particle arrangement in the resulting laminates beyond changing electrode thickness.

In preparation for the FY18 cycled electrode microtomography milestone, a trial pouch cell was imaged at APS beamline 2. A reconstructed slice through this cell is shown in Figure I-139. The cathode and surrounding pouch are readily visible, and single particles within the electrode can be seen. Similar reconstructions of these pouch cells, taken before and after cycling, will be used with the TomPost package and custom analysis tools in order to detect subtle changes in electrode structure.

Some of the text in this report, describing the transport property measurements, along with the accompanying figures, was taken from our second publication of 2017. (Reproduced with permission from *J. Electrochem. Soc.*, 164, A2434 (2017). Copyright 2017, The Electrochemical Society)

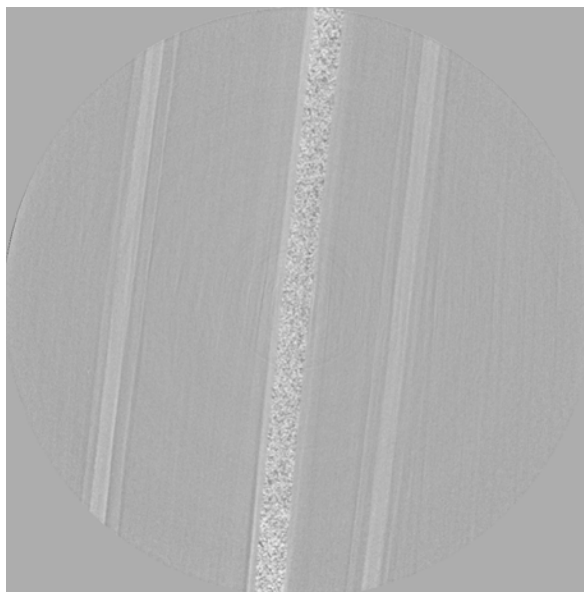


Figure I-139. Reconstructed slice of pouch cell from micro-tomography trial

Conclusions

Pulsed field gradient NMR and conductivity data was used to determine degree of dissociation of LiPF_6 in EC/DEC (1:1 by weight), using on the generalized Darken relation and concentrated solution theory. The degree of dissociation was found to decrease from 0.61 to 0.37 as concentration was increased from 0.1M to 1.25M. Analysis of our previous published data for LiPF_6 in PC, showed that the dissociation degree decreased from 0.675 to 0.51 over a concentration range of 0.5M to 2.0M. This ion pairing information was then used to correct transport property values computed for concentrated solution theory, with the transference number values showing particularly large changes.

Under the “CD-adapco” subproject, we have packaged and released our tomography postprocessing pipeline as open-source software. It performs fully-automated postprocessing of TIFF image stacks into particle surface meshes, reducing processing times from days to hours. This has been used to process microtomography data that we obtained for electrodes fabricated with three different thicknesses. As expected, electrode thickness appears to affect cell capacity at high C-rates. However, detailed analysis of particle surface meshes does not suggest a correlation between electrode thickness and particle arrangement within porous electrodes when electrode thickness is varied only by adjusting doctor blade height.

A trial test of pouch cell imaging for the FY18 cycled electrode tomography milestone showed promising results. Further imaging work is scheduled at APS for December 2017.

Key Publications

1. K. Higa, S.-L. Wu, D. Y. Parkinson, Y. Fu, S. Ferreira, V. Battaglia, and V. Srinivasan, “Comparing Macroscale and Microscale Simulations of Porous Battery Electrodes,” *J. Electrochem. Soc.*, 2017, 164, 11, E3473-E3488, doi: 10.1149/2.0501711jes
2. Z. Feng, K. Higa, K. S. Han, and V. Srinivasan, “Evaluating Transport Properties and Ionic Dissociation of LiPF_6 in Concentrated Electrolyte,” *J. Electrochem. Soc.*, 2017, 164, 12, A2434-A2440, doi: 10.1149/2.0941712jes
3. Open-source software: K. Higa, “Tomography Postprocessor for Battery Electrodes (TomPost)”, <https://sites.google.com/a/lbl.gov/tompost/>, released on August 4, 2017.

I.C.7 Development and Validation of a Simulation Tool to Predict the Combined Structural, Electrical, Electrochemical and Thermal Responses of Automotive Batteries (Ford Motor Company)

Dr. Chulheung Bae, Principal Investigator

Ford Motor Company
Energy Storage Research
2101 Village Road
Dearborn, MI 48121
Phone: 313-410-1398
E-mail: cbae@ford.com

Brian Cunningham, Technology Manager

U.S. Department of Energy
Phone: 202-287-5686
E-mail: Brian.Cunningham@ee.doe.gov

Start Date: January 1, 2016

End Date: December 31, 2018

Total Project Cost: \$4,375,000

DOE share: \$3,500,000

Non-DOE share: \$875,000

Project Introduction

This is the second year of a three-year project to develop a practical simulation tool for predicting battery abuse response. The project plan including major constituents and progression based on case studies is shown in Figure I-140.

The first half of the project is focused on developing an Alpha version of the model. This includes developing new, battery-specific keywords within LS-DYNA, identifying electrical, thermal, and mechanical input parameters, validating the model for performance situations where the cells are cycling in their intended operating mode, demonstrating preliminary abuse simulations for external short and crush, and enhancing the composite element formulations within LS-DYNA to provide accurate representations of battery material mechanics. Importantly, one-way coupling mechanisms linking the structural response to the electrical and thermal response have been implemented, and initial simulation predictions have been compared to test results from previous studies to confirm that the solvers are directionally accurate. Physical testing of full cells has recently begun to for model validation, and additional testing of cell components has been conducted to better determine critical physical parameters for the model.

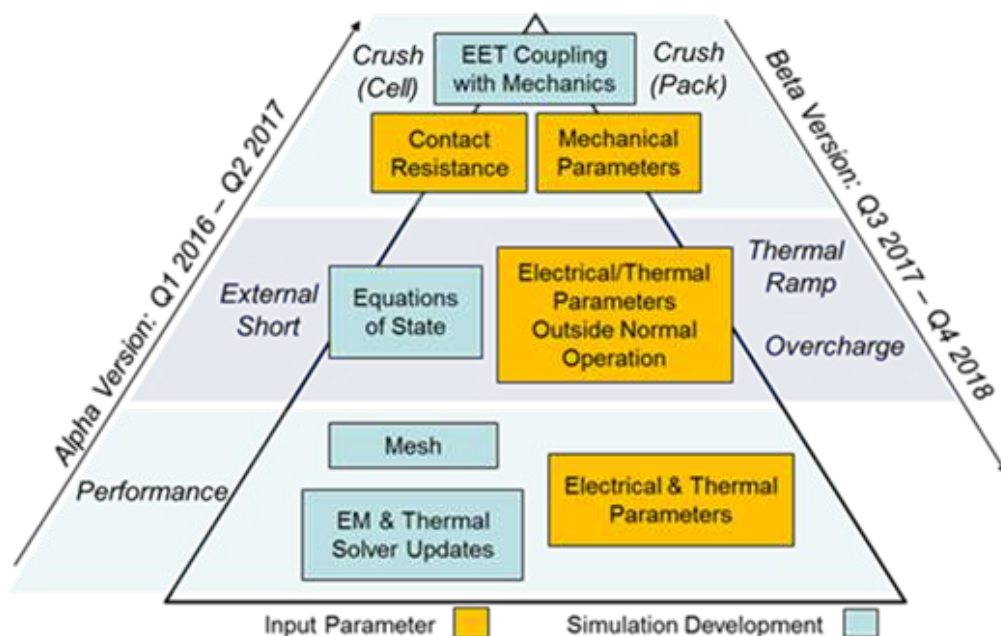


Figure I-140. Project schematic showing major constituents and progression of Alpha and Beta versions.

Objectives

Develop and validate a simulation tool to predict the combined structural, electrical, electrochemical and thermal (SEET) response of automotive batteries to crash-induced crush and short circuit, overcharge, and thermal ramp, and validate it for conditions relevant to automotive crash.

Approach

Develop material constitutive models and finite element method (FEM) element formulations that capture the mechanical response of cell components, including the case material, electrodes, separator, and their interactions with electrolyte.

Clearly identify the required input parameters for the material constitutive models, FEM element formulations, and exothermic, electrochemical reaction state equations governing multiphysics phenomena during crush-induced electrical short, thermal ramp, and overcharge conditions.

Design and execute a test matrix encompassing automotive crash strain rates, at a number of kinetic energy levels and physical orientations likely to occur in vehicle impacts.

Develop integrated modeling tools which demonstrate high-fidelity predictions of the onset of thermal runaway from the experimental test matrix using commercially available cells, module, and packs, spanning multiple chemistries relevant to automotive applications.

Maintain high-fidelity predictions while exploring methods to reduce the computational complexity of the model, and deliver a practical tool that is integrated with ORNL's OAS, for a broad customer base within automotive product development.

Results

The second year saw significant progress in many areas leading to a workable, validated model. Work continued in refining the mechanical, EM and thermal solvers with composite t-shell elements, all of which are now essentially complete and in use. It was shown that using composite t-shell elements in the mechanical solver can save computational time significantly while achieving almost the same result as using standard solid elements. Since in impact events the mechanical solver takes the majority of the simulation time, using composite t-shell elements has a potential to reduce the total simulation time considerably, which is critical in large-scale simulations such as module or pack level simulations. It was also shown that simulation results using composite t-shell elements are almost identical to results using solid elements in the EM and thermal solvers (see Figure I-141). Because of that, composite t-shell elements can currently be applied to all the solvers that are needed in the proposed battery safety model. It allows us to use one mesh for the entire model and saves time in the model development process. (Note that in previous reports and presentations we used both composite t-shell and layered solid elements in reference to the same mesh. In this report, we use only the term composite t-shell.)

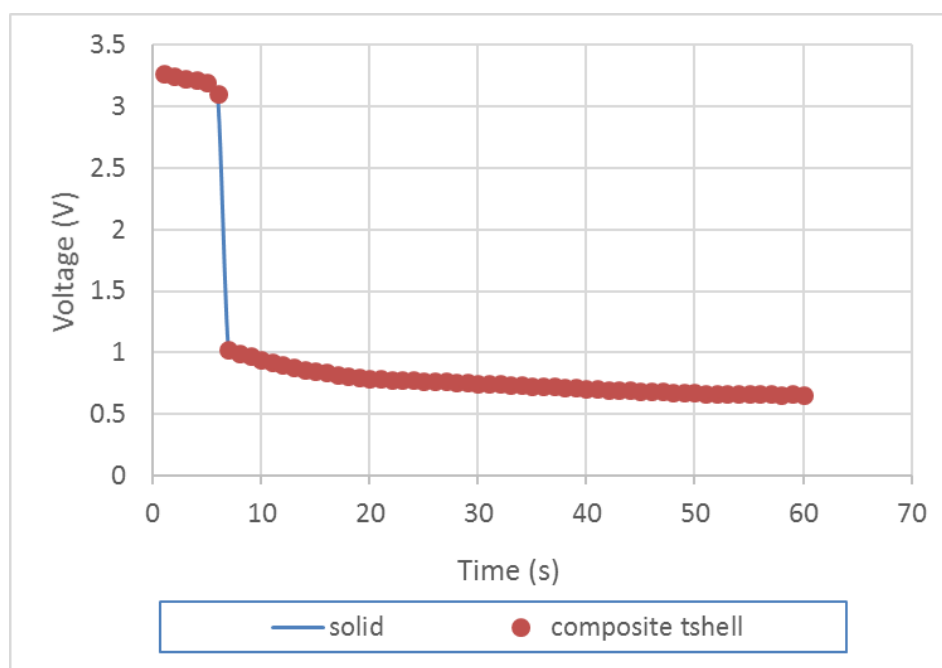


Figure I-141. Comparison of voltage evolution in two models.

The electrochemical properties of type D and E cells have been obtained from the cycling tests data via optimization processes. With these properties, the model prediction of the cell voltage profile during discharging and charging matches measurements very well. We built models for type D and E cells, applying the same boundary conditions as experiments in order to check if experimental results can be captured by simulations. The comparison of cell voltage profile during charge and discharge at different temperatures with different initial SOC is shown in Figure I-142, where it can be seen that the model results match experimental measurements well. This indicates that the parameters used in Randle circuit models for both types of cells may capture the battery behaviors over a wide range of conditions.

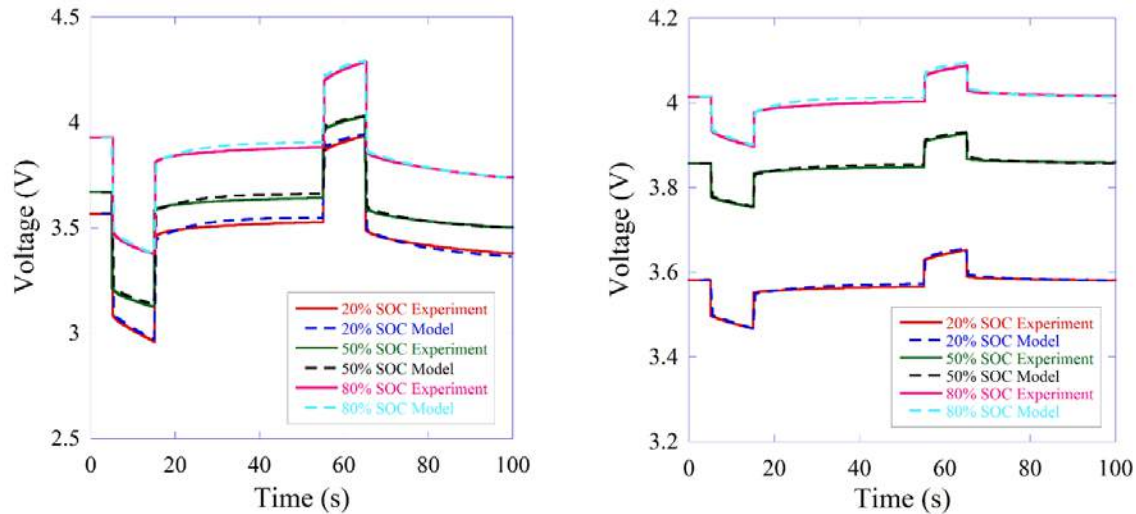


Figure I-142. Compare model predictions and measurements of the voltage profile of a type D (left) and type E (right) cell when it is discharged and charged with different initial SOC's.

Additional simulations for shear and crush were run on Type D cells using composite t-shell elements (Figure I-143) with very good agreement with experimental data for load/displacement (Figure I-144). We have performed the simulation for the shear test using the composite t-shell element as shown in the right hand side of Figure I-143. The dimension for the cell is 164 mm X 220 mm X 5.58 mm. Due to symmetric boundary condition we modelled only the half of the cell in x direction and a portion of the cell (10 mm in length) in y-direction. Nodes on the left hand side is fixed while the right hand has symmetric boundary condition. Top node are moved with a fixed velocity till displacement of 1.5 mm. We have used 9 elements across the thickness and each element has 16 integration points comprising 4 integration points for positive electrode (cathode), negative electrode (anode) and separator, 2 integration points is used to represent current collectors. All the components are modelled using MAT-24 material model, parameters for all the components are given in Table I-20. The number of composite t-shell elements is 1188 and it took 554 second to complete the simulation on 16 processors. These simulations worked better – had better agreement, fewer elements, less computation time – than simulations with standard solid elements.

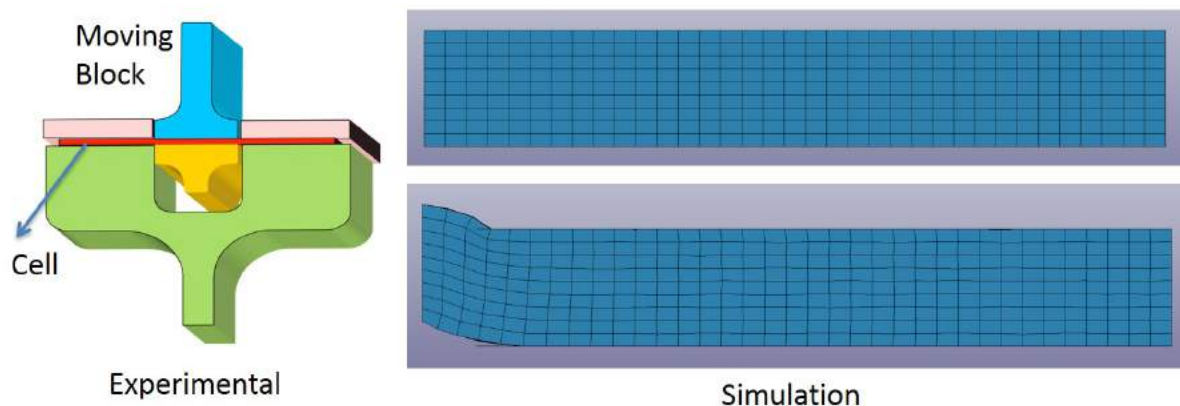


Figure I-143. Experimental and Simulation setup for Type D Cell

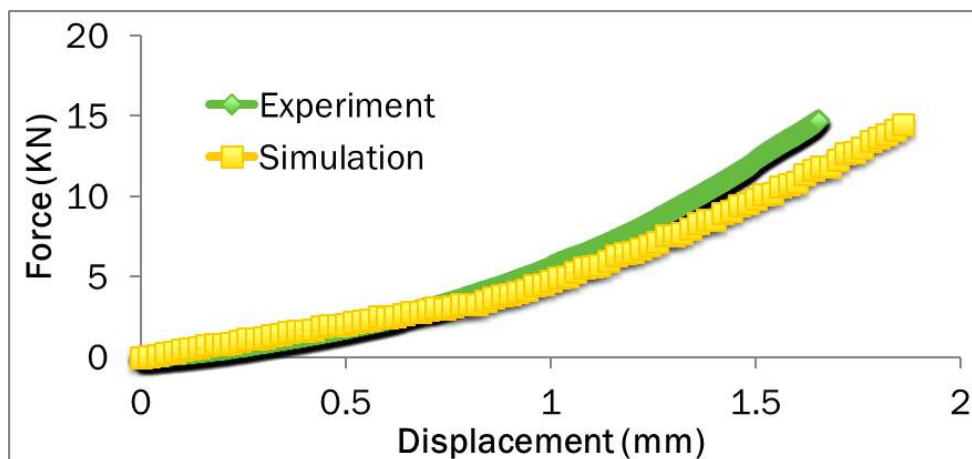


Figure I-144. Load displacement curve obtained by experiment and simulation

Table I-20: Parameter for component of the cell.

Component	Thickness (mm)	Elastic Modulus (Gpa)	Yield Strength (Gpa)	Tangent Modulus (Gpa)
Anode	0.064	0.45	0.04	0.01
Separator	0.023	0.50	0.045	0.01
Cathode	0.053	0.55	0.04	0.01
Aluminum Current Collector	0.015	70	0.24	0.1
Copper Current Collector	0.009	110	0.24	0.1

Both Type D&E cells were tested under shear conditions at Ford, and then shipped to ORNL for x-ray computed tomography analyses. Type D cell analysis results indicated that excessive damage was observed in the shear-stressed area and 2 – 3 step shearing might provide details on the progress of the cell component deformation. Additional shear tests were then run again to detectable short circuit, and also stopped at displacements less than creating a short.

Work continued using microphotographs of cell separators to determine statistics of the void fractions, which were then used to create 3D reconstructions. During this year, new models were created and refined and fibrils were added to better simulate type D & E separators. Simulations based on the new models compared well with experimental results.

Required platens and indenters were constructed at Intertek, and quasi-static crush testing started. Several Type D and E cells were tested but there were no shorts induced at the highest loading with the current equipment. New load cells, platens, and indenters were designed, purchased or constructed, and testing will resume in the fourth quarter. Fabrication of fixtures for the high-speed impact tests should also be completed and testing started in the fourth quarter.

A test matrix was developed for the cells, and a test site is selected. A preliminary version of the software has been developed and demonstrated for external short circuit and crush leading to internal short circuit scenarios. Techniques such as the use of composite t-shell elements and macro scale meshes were developed to reduce simulation complexity, and demonstrated significant reductions in calculation times. In the coming year,

validation experiments will be performed and simulations will be carried out to confirm the model predictions align with physical experiments.

Conclusions

The second year has been successful, with the project essentially on track and nearly all milestones accomplished. Cell characterization experiments were completed, as were the multi-physics solvers. Model integration was completed and the Beta version assumptions developed. Validation testing was started, but is behind schedule. Spending continues to be below estimated. It is expected that the final year will result in a validated, practical simulation tool that can be used to predict battery response to abuse.

Key Publications

1. The PI made a presentation on this project at the Department of Energy Annual Merit Review on Publications June 6, 2017.
2. Jie Deng gave a presentation at *the 232th ECS Meeting* in National Harbor, MD, on October 4, 2017.
3. Modeling of Battery Cells Using New Composite t-shell Element Formulation, in preparation, *Journal of Power Sources*.

I.C.8 High Fidelity Fast Running Multi-scale Multi-physics Battery Pack Software (General Motors, NREL, ANSYS and ESim)

Dr. Shailendra Kaushik, Principal Investigator

General Motors LLC (Prime)

30500 Mound Road

Warren, MI 48092-2031

Phone: 248-807-4156

E-mail: Shailendra.Kaushik@gm.com

Dr. Kandler Smith, Principal Investigator

National Renewable Energy Laboratory (Sub)

15013 Denver West Parkway

Golden, CO 80401

Phone: 303-275-4423

E-mail: Kandler.Smith@nrel.gov

Erik Ferguson, Principal Investigator

ANSYS, Inc. (Sub)

10 Cavendish Court

Lebanon, NH 03766

Phone: 603-727-5631

E-mail: Erik.Ferguson@ansys.com

Dr. Ralph White, Principal Investigator

ESim, LLC (Sub)

5 Brandywine Lane

Columbia, SC 29206

Phone: 803-240-7132

E-mail: White@cec.sc.edu

Brian Cunningham, Technology Manager

U.S. Department of Energy

Phone: 202-287-5686

E-mail: Brian.Cunningham@ee.doe.gov

Start Date: March 22, 2017 End Date: December 31, 2019

Total Project Cost: \$2,477,808 DOE share: \$1,738,968

Non-DOE share: \$738,840

Project Overview

Building upon previous projects under DOE's Computer Aided Engineering for Electric-Drive Vehicle Batteries (CAEBAT) Program, the current project seeks to significantly enhance the computational efficiency and usability of simulation software to optimize and accelerate the design of automotive battery cells and packs. The project consists of the following five tasks: (1) To implement the new computationally efficient multiscale multidomain (GH-MSMD) electrochemical simulation method in ANSYS FLUENT, (2) Extend development of a holistic multiphysics reduced-order model (ROM) builder based on ANSYS FLUENT simulation results and the existing infrastructure of ANSYS DesignXplorer (DX) using deep-learning methods including neural networks, (3) Research the discrete empirical interpolation method (DEIM) as an option for improving the efficiency and accuracy of a nonlinear ROM for the electrode domain or cell domain, (4) Develop and implement an interactive system interface for MSMD and GH-MSMD in ANSYS and (5) Develop and implement physics-based life models of Li-ion batteries in ANSYS.

Objectives

The overarching objective of this project is to develop multiscale multiphysics battery pack engineering software that significantly surpasses the most advanced software in computational speed by a factor of 100 while resolving complex interplays of physics across length scales ranging from materials (~micrometers) to large automotive battery pack systems (~meters). Specific objectives include enhancing computation speed and stability while still resolving nonlinearities of the battery's dynamics and enhancing multiphysics integrity of the pack-level model, and enabling model-based diagnostics and prognostics for battery life and safety. To meet these needs, the project team will perform collaborative research, development, and demonstration in multiple synergistic directions, including cell/module/pack scale-coupling methods, ROM modeling techniques, battery life models, and user interface (UI) enhancements. The project will enhance the ANSYS Battery Design Tool (ABDT) that was originally developed in previous CAEBAT projects. For clarity in what follows, the ABDT is the software layer that provides a battery-specific UI, automates battery-simulation workflow, and calls proprietary ANSYS products as services.

Approach

Physicochemical processes in lithium ion batteries occur in intricate geometries over a wide range of time and length scales. As the size of the battery increases, macroscopic design factors in combination with highly dynamic environmental conditions significantly influence the electrical, thermal, electrochemical, and mechanical responses of a battery system. NREL pioneered the multiscale multidomain (MSMD) model, overcoming challenges in modeling the highly nonlinear multi-scale response of battery systems. The MSMD model as shown in Figure I-145 provides flexibility and multi-physics expandability through its modularized architecture. The project team previously collaborated on combining new and existing battery models into engineering simulation software that provides 3-D battery pack simulation modeling capability. Because of increasing complexities when configuring additional electrical and thermal connections between the cells, the computational cost of simulating a battery pack response is still high: results take weeks, unless low-fidelity sub-models are used to represent the battery's current/voltage response. Therefore, substantial improvement of computational efficiency is needed. Software tools also need improved usability and flexibility to reduce both the computational time and the engineering labor required to keep pace with battery design changes, including geometry and configuration. These improvements would enable the use of models in design and management tradeoff studies of performance/life in large vehicle battery pack systems, which are typically composed of several hundred large-format individual cells.

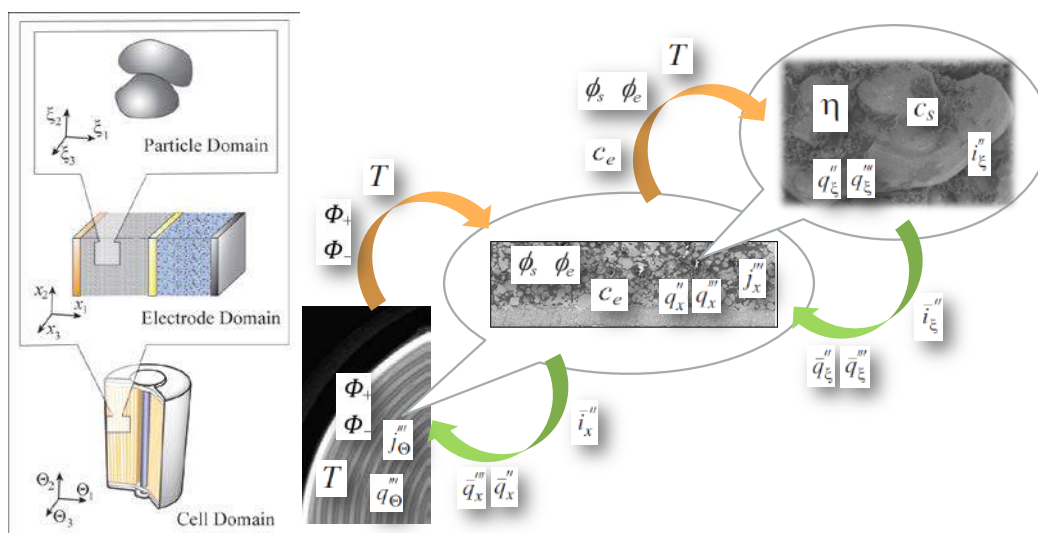


Figure I-145. A diagram of intra- and inter-domain coupling protocols used in NREL's MSMD framework, integrating widely varied scale battery physics in a computationally efficient manner with hierarchical modular architecture

For large automotive battery pack design and development, the current state-of-the-art battery pack engineering software lacks the combination of sufficient computational speed, physics-based predictive capability and solution accuracy. Led by General Motors (GM), the team comprised of GM, ANSYS, NREL and ESim proposed to develop and implement an innovative nonlinear multi-scale battery model framework in the commercial software package, ANSYS FLUENT. The proposed software offers greater computational efficiency while retaining expandability and modularity. In a previous project supported by DOE, NREL developed a new innovative quasi-explicit nonlinear multi-scale multi-physics framework, GH-MSMD. The new framework uses time-scale separation and variable decomposition to eliminate several layers of nested iteration but keeps the modular framework architecture that is critical to battery behavior simulations. Fast electronic charge balance is differentiated from processes related to slow ionic movements. During the preliminary benchmark test carried out at the electrode domain model (EDM) level, the GH-MSMD implementation demonstrates significant computational speed improvement compared to the original MSMD. Figure I-146 presents the comparison of electrical and thermal response predicted by 4 different model combinations, simulating a battery for a mid-size PHEV10 sedan driving a US06 cycle for 20 minutes. The model outputs from different models are nearly identical. The most efficient GH-MSMD model option runs the 1200 second simulation in only 0.74 seconds, while the original MSMD runs the same case in 654 seconds. Based on the encouraging preliminary benchmark result at the EDM level, we propose to improve computational speed of the pack-level simulation by a factor of 100 from the state-of-the-art models.

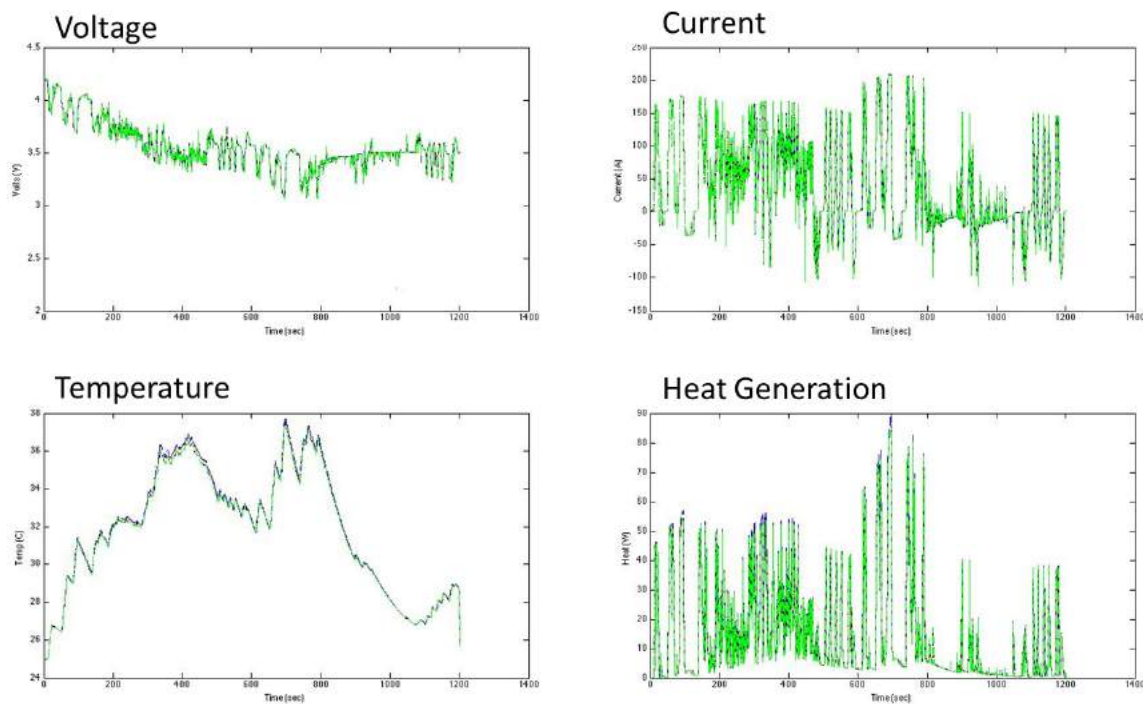


Figure I-146. Comparison of electrical and thermal response of a battery for mid-size sedan PHEV10 US06 20 minutes driving power profile from the 4 different model combinations

Due to the pace of battery design change, the physical complexity of packs, and the number of user application scenarios that need to be studied, system-simulation with ROM remains an essential research need. Addressing ROM limitations will complement the expected progress from GH-MSMD, in a multi-pronged attack on the computational-efficiency challenge. It is increasingly evident that more advanced ROM techniques – available from the general literature – need to be integrated into the CAEBAT software tools to have the maximum impact on battery innovation. One particular area of importance is macro-modeling approaches for designs in

which parameters other than battery state of charge and coolant flow rate vary. The designer needs to approximate the electrical and thermal performance of the pack while varying design parameters such as the geometry and physical properties. Extending the system modeling with parameterized ROM techniques will allow manufacturers to look at many "what-if" scenarios, and perform optimization and sensitivity analysis, after a single ROM-building process. Effective parallelization and intelligent sampling of the parameter space are the key elements that need to be investigated and developed. This ROM can be built from a FLUENT analysis, driven by the ANSYS DesignXplorer software tool with its design of experiments and response surface processes. It will be exposed both as a generator of fast approximate predictions in ANSYS Workbench, and as a reusable model for use in systems-engineering analysis tools, vehicle simulators, or even real-time battery management systems with hardware in the loop. In addition, state-of-the-art ROMs typically lose validity when severe nonlinearities arise in the system. Because vehicle batteries are often used in a regime where nonlinearity becomes significant (e.g., continuous high-rate charge/discharge or low-temperature cycling), a nonlinear ROM, which is fast enough while coupling kinetic, thermodynamic, and transport equations over complex component geometries, has been desired. The team is exploring a new ROM that retains acceptable accuracy under severe nonlinear conditions at a computational cost comparable to existing ROMs. The project team will further investigate partial orthogonal decomposition (POD) and DEIM ROMs where the battery electrochemical behavior is coupled with the thermal behavior. We have implemented DEIM for one- and two-cell batteries. Applying it to larger batteries will require either a method for connecting such small DEIM models together, or obtaining the connectivity information from FLUENT and applying DEIM directly to the full geometry of a multi-cell battery.

Finally, new modeling approaches developed in CAEBAT I are being investigated for application at the electrode domain level to enhance computational efficiency and track changes in battery cell performance during lifetime of the cell. Developed by ESim, a new nonlinear state variable implementation of the Newman P2D electrochemical model will help accelerate studies of non-uniform usage of a battery for temperature gradient or non-optimized electrical design. The merit of this novel application of ROM will be researched and evaluated. During CAEBAT I, ESim further extended an existing equivalent circuit model (ECM) to include capacity fade due to cycling of cells by adding a branch for the capacity loss on charge due to the solid electrolyte interface (SEI) formation reaction at the anode. Figure I-147 presents this ECM, where an SEI formation branch has been added in parallel with the anode branch.

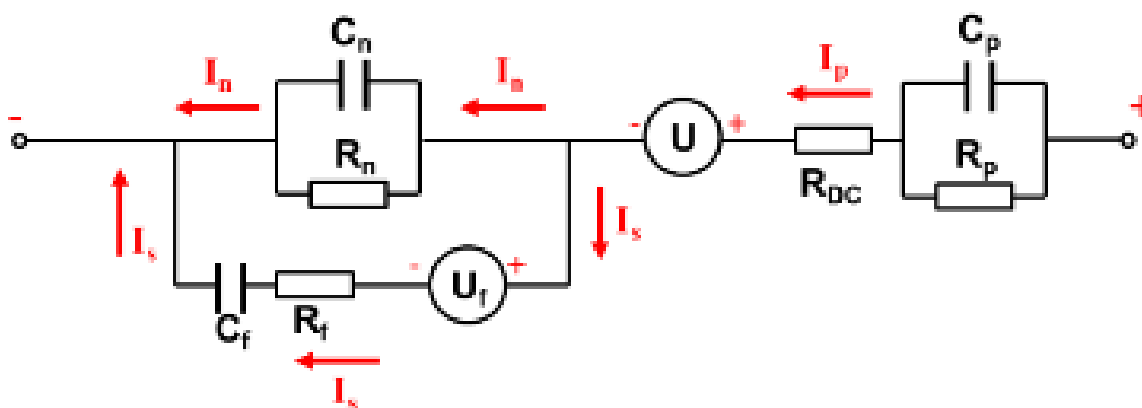


Figure I-147. Equivalent circuit model with an SEI formation branch

Results

Earlier this year, NREL documented and published the GH-MSMD modeling approach in The Journal of the Electrochemical Society [1]. Figure I-148 shows an example EDM simulation. NREL is supporting GH-MSMD implementation in ANSYS FLUENT and has introduced the GH-MSMD method to project team members. NREL has also performed preliminary evaluation of the ANSYS interactive system interface.

MATLAB is selected to run ANSYS FLUENT as a server for interactive simulation demonstration to accomplish a model feasibility study on fast, high-fidelity model-based diagnostics and prognostics of pack-level life and safety.

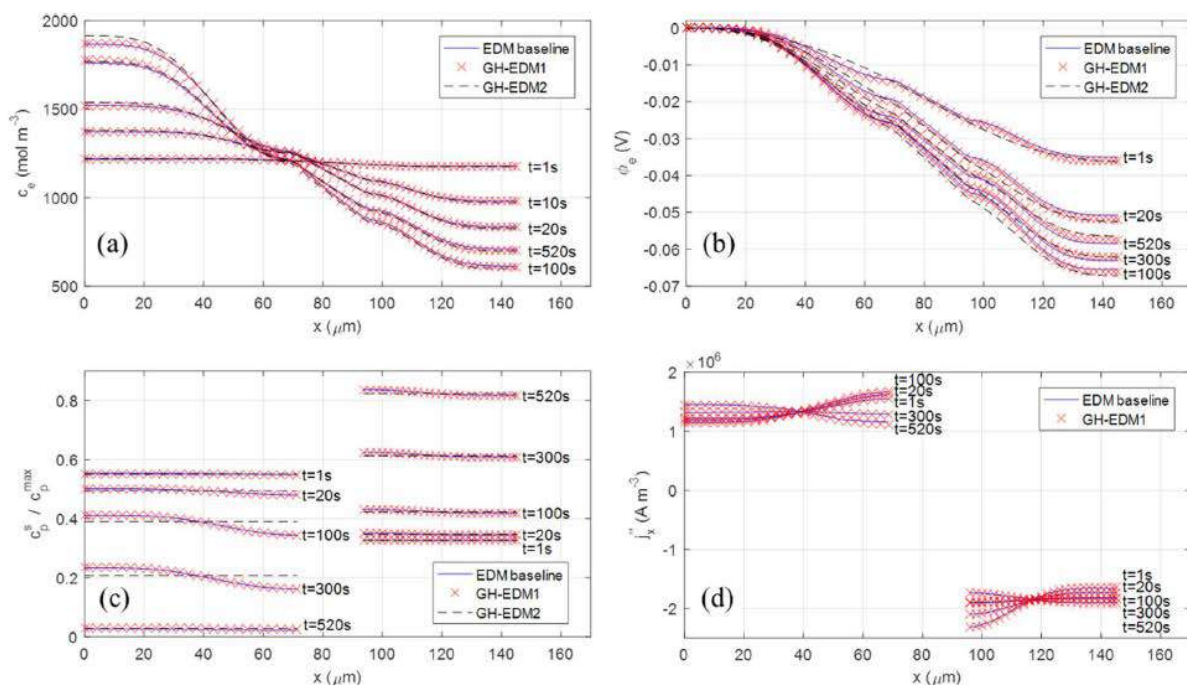


Figure I-148. GH-MSMD electrode-domain model (EDM) simulations from Kim, J. Echem. Soc., 2017. (a) Electrolyte salt concentration, (b) electrolyte phase potential, (c) solid surface concentration, and (d) volumetric current density during 5C discharge at 25°C.

ANSYS has begun implementation of the GH-MSMD method in FLUENT. The essential idea of the GH-MSMD method is similar to the circuit model used in FLUENT. It assumes that at each level (pack domain, electrode domain, cell domain), the potential change can be written as $\Phi = G + Hi$. G and H at the higher level can be constructed from the G and H at the lower level. As a result, a battery pack's electric load condition can be quickly distributed to the lower hierarchical level and avoid the need for inner iterations. In NREL's GH-MSMD paper [1], this method was applied to the Newman P2D model. Focusing on the cell-level during the first year, the team identified several opportunities to implement GH concepts. When solving electrochemical physics at the 3-D cell level, the GH method allows transfer current to be distributed non-uniformly throughout the cell and still maintain good computational efficiency. The need to repeatedly solve cell potential distribution is eliminated. Thanks to algebraic relationships, the Newman P2D electrochemical sub-model is solved only once per time step, instead of once per iteration in the direct method. Figure I-149 shows the updated FLUENT user interface, where the GH-MSMD model will be available by enabling cell clustering as an enhancement to the FLUENT reduced-order method. It is compatible with all the electrochemical sub-models including the NTGK, ECM, Newman's P2D and the user-defined electrochemistry model. These enhancements are planned to be released in FLUENT R19.0 in January 2018.

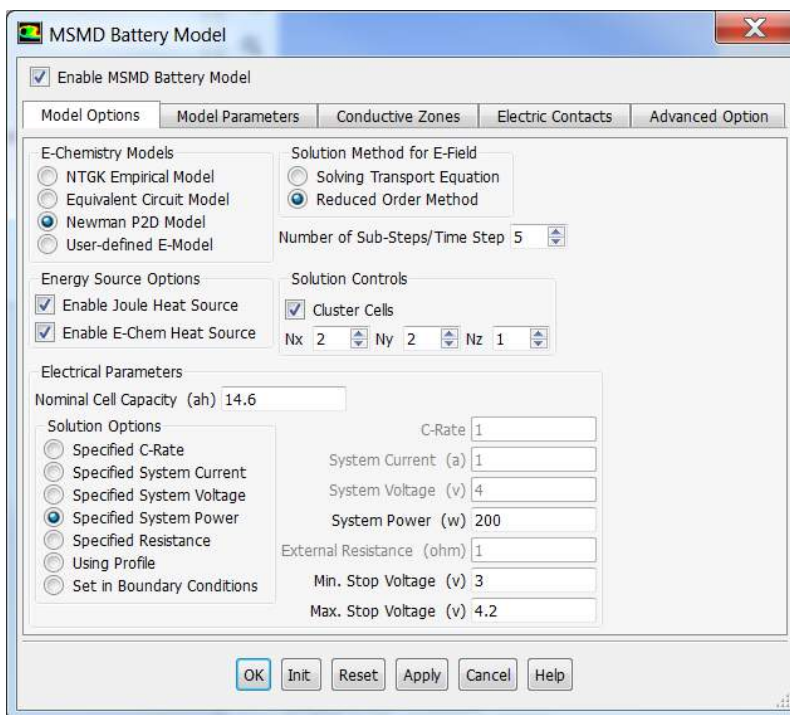
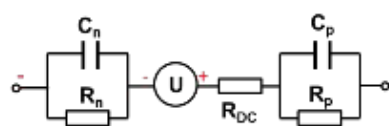


Figure I-149. Updated FLUENT MSMD Battery Model panel

ESim extracted the values for the circuit components (C_p , R_p , C_n , R_n , R_{DC} , and U) from the HPPC data obtained at 25°C and different cycling stages (BOL, 500 cycles, and 1000 cycles). In fitting the model to the HPPC data, the SEI branch is ignored. In the HPPC tests, the transient responses of a cell at different depths-of-discharge (DODs) were measured. During a specific high power pulse, the change in DOD is very small, so all the parameters can be regarded as constants. By fitting the model to the transient response data during a pulse, the parameter values at a specific DOD can be obtained. Through a pulse-to-pulse fitting procedure, the circuit parameters as functions of DOD can be obtained. This procedure is illustrated in Figure I-150.

Conclusions

The project is on track to finish by the end of 2019. GH-MSMD implementation in FLUENT is ongoing. Initial implementation has shown up to 20x computational speedup capturing 3-D electrochemical physics. Non-linear, dynamic ROM for fast simulation of battery packs using deep neural networks has begun and preliminary results show promise for additional computational speedup of 3-D thermal/flow physics. Novel approaches including an additional branch in the equivalent circuit model to represent SEI layer growth show promise to efficiently model battery life and extract relevant model parameters from aging test data.



The side reaction branch is neglected in fitting the HPPC data, and all of circuit parameters are regarded as constants during a specific pulse operation

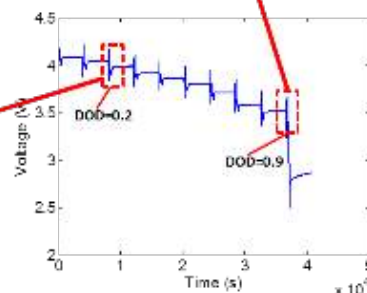
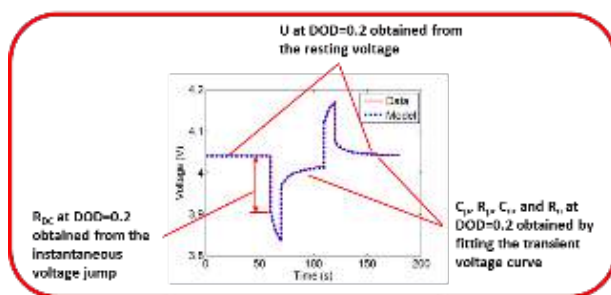
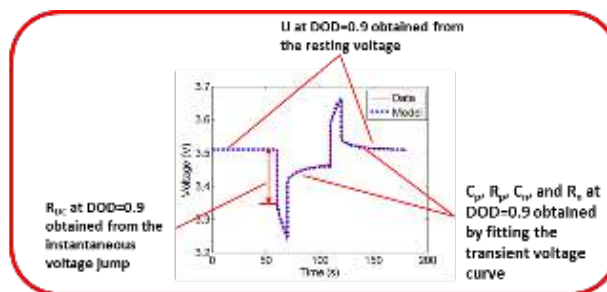


Figure I-150. Illustration for circuit component extraction

Key Publications

1. M Guo, X Jin, and R E White. "Nonlinear State-Variable Method (NSVM) for Li-Ion Batteries: Finite-Element Method and Control Mode." J. Electrochem. Soc. 164.11 (2017): E3200-E3214.
2. M Guo, X Jin, and R E White. "Nonlinear State-Variable Method for Solving Physics-Based Li-Ion Cell Model with High-Frequency Inputs." J. Electrochem. Soc. 164.11 (2017): E3001-E3015.

References

1. G.-H. Kim, K. Smith, J. Lawrence-Simon, C. Yang, "Efficient and Extensible Quasi-Explicit Modular Nonlinear Multiscale Battery Model: GH-MSMD", J. Electrochem.Soc., 164(6), A1076-A1088 (2017)

I.D High Energy, Long Life Lithium-Ion Battery (NREL)

Kandler Smith, Principal Investigator

National Renewable Energy Lab
15013 Denver West Parkway
Golden, CO 80401
Phone: 303-275-4423
E-mail: Kandler.Smith@nrel.gov

Brian Cunningham, Technology Manager

U.S. Department of Energy
Phone: 202-287-5686
E-mail: Brian.Cunningham@ee.doe.gov

Start Date: October 1, 2016
Total Project Cost: \$600,000

End Date: March 31, 2018
DOE share: \$600,000

Non-DOE share: \$0

Project Introduction

Energy-dense, long-life energy storage is needed to improve market readiness and enable higher penetration of electric vehicles. Today's state-of-the-art lithium-ion EV battery lasts around 10 years and provides just 100-250 miles range, both inferior to conventional vehicles. Across virtually all of today's Li-ion chemistries, Li loss capacity fade is the dominant mechanism that limits lifespan. High-energy Li-ion electrode materials presently under research and development (e.g., silicon) suffer even shorter life than today's materials because of large volume change during cycling that fractures electrode surface films and accelerates Li loss. In addition to lifetime challenges, large irreversible Li loss on the first cycle limits the beginning-of-life performance of these high-energy electrodes. To boost initial capacity, these materials presently require pre-lithiation as an extra manufacturing step, adding unwanted cost to the cell. This project seeks to overcome the barrier presented by limited useable Li inventory in order to enable higher energy, longer life batteries.

Objectives

The objective of the project is to increase cycle lifetime of both graphite and silicon (Si)-based Li-ion cells. For cells employing Si, the proposed technology will also increase initial capacity. The device will be low cost, passively controlled, and occupy minimal weight and volume. Specific objectives include:

- Extend calendar and cycle life by 50% for Li-ion graphite/NMC (nickel-manganese-cobalt) and Si-X/NMC systems
- Re-lithiate the Si anode following the formation cycle to increase Si-anode Li-ion system energy density by 20%
- Design the system such that it adds less than 5% to the cost, weight, and volume of Li-ion cells, and is compatible with cell manufacturing and safety
- Pending resources, work with commercialization partner in year 3 to transition the technology to the marketplace

Approach

The proposed objectives will be met by introducing an excess Li reservoir into Li-ion cells that can be released to boost capacity upon demand, increasing initial performance and extending lifetime. Different from previous concepts, the proposed technology is controlled passively and can deliver a slow, continuous release of Li ions throughout the cell lifetime and/or a fast, triggered release of Li ions on demand. The device is projected to add less than 1% to the cost, weight, and volume of today's cells. In addition to extending lifetime, the device is a practical way to pre-lithiate Li-starved systems to boost their initial capacity, addressing a present roadblock hindering commercialization of high-energy anode materials such as silicon. The successful project will design and demonstrate the proposed device on cells using both today's graphite-based and tomorrow's high-energy Si-based negative electrode material presently under investigation by the DOE Applied Battery Research for Transportation (ABRT) program.

The team leverages unique expertise at NREL and ANL. NREL is a recognized expert in the electrochemical characterization and model-based design of electrochemical couples and large-format cells under DOE's CAEBAT program, including diagnosis and modeling of degradation mechanisms in automotive systems and environments. ANL's Cell Analysis, Modeling, and Prototyping (CAMP) laboratory is the leading DOE facility for producing high-quality electrochemical couples in partnership with DOE's Si Deep-Dive project. (See Section IV.B.1 of this report for additional description of the CAMP facility.) ANL's high energy density Si anodes when demonstrated together with NREL's supplemental Li technology may represent the best progress to date amongst labs, universities, and industry to reach DOE's VTO Battery500 Strategic Goal for EV batteries of 500Wh/kg and 1000 cycles.

Results

During FY 2017, NREL demonstrated significant capacity recovery and life extension for three different graphite-based cells. Recently, the excess Li device was used to recover capacity in high energy density silicon anodes cells fabricated by ANL at their CAMP facility. Major accomplishments include:

- 20-33% capacity recovery demonstrated for graphite/lithium manganese oxide (LMO) pouch cells
- 5.5% capacity recovery demonstrated for commercial graphite/lithium iron phosphate (LFP) 18650 cell
- 4% capacity recovery for graphite/NMC commercial 18650 cell after 400 cycles
- 7-8% capacity recovery for ANL Si anode pouch cells after 50 cycles

The excess Li reservoir device was inserted into several low capacity LMO/graphite pouch cells to demonstrated capacity recovery and life extension. LMO is a good demonstration candidate because Mn dissolution catalyzes SEI growth which irreversibly consumes Li at the graphite anode surface resulting in rapid capacity fade. The cells were cycled approximately 120 times with different charge cutoff voltages at room temperature resulting in 34-50% capacity fade (Figure I-151). Next, the cycling was suspended and lithium-ions were inserted into the active cell from the excess Li reservoir. Due to the location of the device the re-lithiation was done at a very rapid rate and only required two days to complete. Figure I-151 shows the resulting capacity restored was between 20-33% for all three cells.

Similar cycle aging and re-lithiation has also done for higher capacity commercial cells with graphite anodes. Results are summarized in Table I-21. Capacity recovery and life extension has been demonstrated for 18650 A123 cells with graphite/LFP chemistry having an initial name plate capacity of 1.1 Ah. A123 cells were cycled at their operational limit of 55° C to accelerate capacity fade from loss of available lithium ions. Commercial graphite/NMC cells with a nameplate capacity of 2.2 Ah were cycled at their operation limit of 45°C. Both cell types were cycled at C/2. For the A123 cell, life was extended by approximately 50% using the excess lithium reservoir once. The device is designed to be able to use multiple times or continuously which would further extend life.

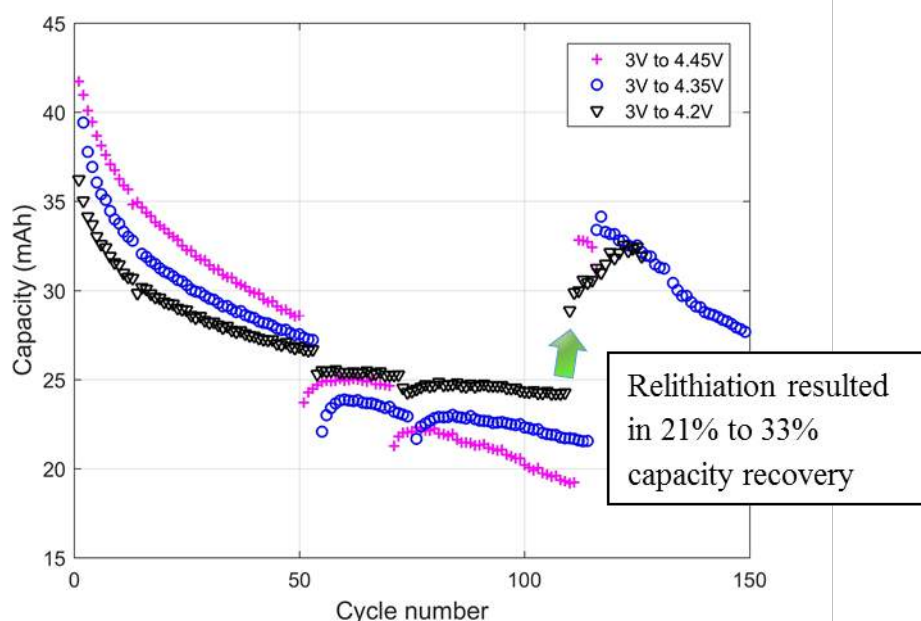


Figure I-151. Excess Li reservoir used to restore capacity of LMO/graphite pouch cells after ~120 cycles. The graphite/LMO pouch cells were cycled at room temperature with different charge cutoff voltages.

Table I-21: Summary of capacity recovered using excess Li reservoir for commercial graphite cells

Cell	Graphite/LFP	Graphite/NMC
Number of Cycles	150 at 55°C	400 at 45°C
Capacity Fade	120 mAh (-11%)	400 mAh (-18%)
Capacity Recovered	60 mAh (+6%)	90 mAh (+4%)

Capacity recovery from the proposed excess lithium reservoir is an ideal technique to restore capacity for next generation Si-based anodes that suffer from high rate of lithium consumption due to rapid SEI growth. To support demonstration of the device, the ANL CAMP facility supplied NREL with 400 mAh Si- graphite/ NMC pouch cells. These cells consist of 14 electrode pairs with each having an active area of 14.1 cm². The anode consists of 15 wt% Si and has an initial capacity of 520-590 mAh/g-electrode and 600-670 mAh/cm² compared to 350 mAh/g and 400 mAh/cm² for a standard graphite-only electrode. Initial cycling of 6 cells at room temperature is shown in Figure I-152. Cycling protocol consists of 8 initial cycles at C/10, then 8 cycles at C/5, and continuous cycling at C/3 all with a voltage range of 3.0V to 4.1V. Cycling shown for cells 1-4 are standard pouch cells, while cells 5 and 6 have the NREL device inserted prior to cycling and sitting in an idle state. These results show the device has been successfully inserted and, as-desired, the non-triggered device has no negative impact to cycle life.

After 50 cycles, the excess Li reservoir device was added to cells 2 and 3 and used to recover capacity. Cycle capacity before and after adding the idle device remained the same. A capacity boost of 27 mAh (8% of C/3 capacity) was achieved for cell 3 after triggering the excess Li reservoir to recover usable Li ions as shown in Figure I-153. The measured capacity fade rate before and after re-lithiation was approximately 1.4 mAh/cycle. The fade rate not accelerating indicates that lithium-ions have been inserted back into the active cell in a uniform fashion. Similar recovery and fade results were also achieved for cell 2.

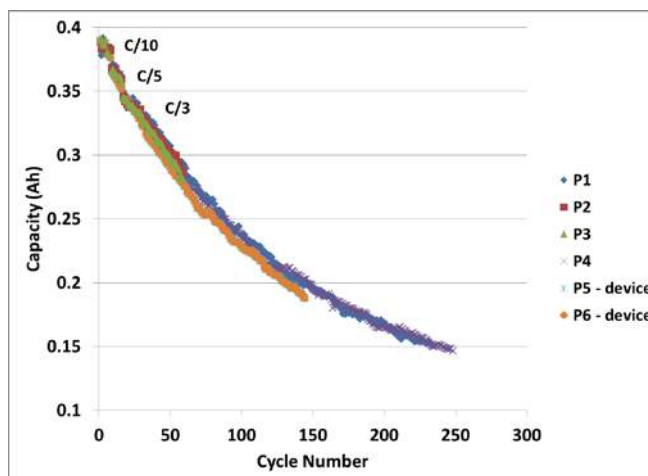


Figure I-152. Cycling of 400 mAh ANL silicon-graphite/NMC pouch cells at room temperature without (cells 1-4) and with device inserted but not triggered (cells 5 and 6). These results demonstrate that the device has no unintended negative impact to cycle life when integrated in a cell and left in the idle state.

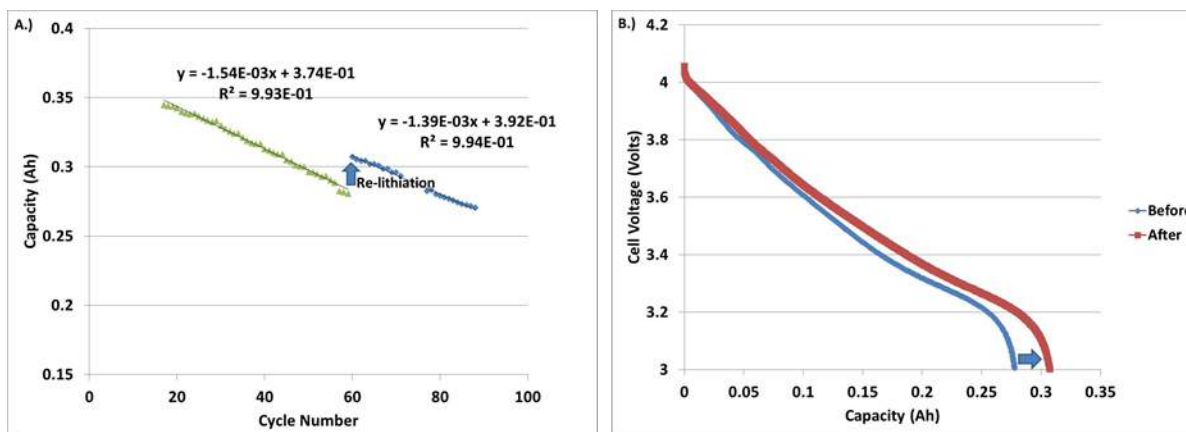


Figure I-153. Cycling of 400 mAh ANL Si pouch cell #3 before and after triggering device showing 8% capacity restored. A.) The measured capacity fade rate before and after triggering the device is relatively constant indicating Li-ions have recovered relatively uniformly. B.) Discharge voltage curve before and after re-lithiation.

Conclusions

NREL has demonstrated that the proposed excess Li reservoir device can be used to recover capacity and extend lifetime for both state of the art graphite and silicon-based cells. Significant capacity recovery of 20% to 33% has been shown for LMO/graphite pouch cells at relatively high re-lithiation rates. A life extension of 50% has also been demonstrated for A123 commercial cells. Further, the device has been shown to also enable capacity recovery and life extension for high energy density silicon-based cells. Next steps include exploring the best location for device, working with commercial vendor(s) to develop device that is manufacturing ready, determining the rate at which the device can be used, and using the device continuously while the cell is cycling.

Key Publications

1. "LONG-LIFE RECHARGEABLE ION BATTERIES" U.S. Patent Application # 15/685,485 filed on 08/24/2017

I.E Material and cell studies to enable extreme fast charge (XFC) (INL)

Christopher J. Michelbacher, Principal Investigator

Idaho National Laboratory

2525 Fremont Avenue

Idaho Falls, ID 83402

Phone: 202-586-3384

E-mail: christopher.michelbacher@inl.gov

Samuel Gillard, Technology Manager

U.S. Department of Energy

Phone: 202-287-5849

E-mail: Samuel.Gillard@ee.doe.gov

Start Date: July 1, 2016

End Date: May 31, 2017

Total Project Cost: \$775,000

DOE share: \$775,000

Non-DOE share: \$0

Project Introduction

Decreasing energy consumption across the U. S. transportation sector, especially in commercial light-duty vehicles, is essential for the United States to gain energy independence. Recently, powertrain electrification with plug-in electric vehicles (PEVs) have gained traction as an alternative due to their inherent efficiency advantages compared to the traditional internal combustion engine vehicle (ICEV). To be truly competitive to the ICEV refueling experience, battery electric vehicle (BEV) charging times must dramatically decrease. Extreme fast charging (XFC), or charging an EV at up to 400-kW stands to decrease vehicle charging time as well as increase the utility of a BEV. As such, Figure I- 154 shows how utilizing fast charging at 50-kW for 1-5% of all annual charges nets the vehicle owner a nearly 25% increase in annual vehicle miles traveled (from [1, 2]). Automotive companies, battery manufacturers, codes and standards bodies, charger manufacturers and

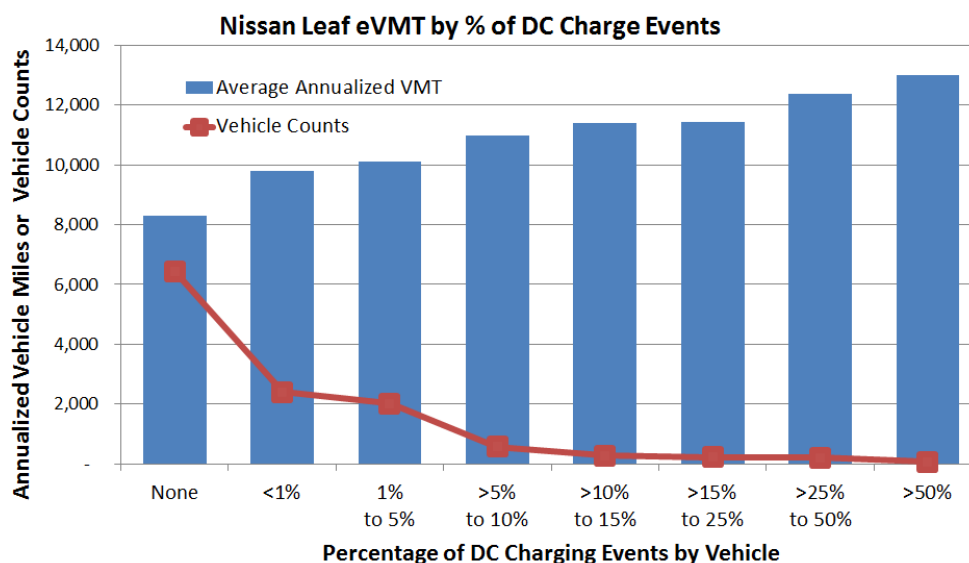


Figure I- 154. Analysis by California Air Resource Board (CARB) shows increased yearly vehicle miles traveled when using 50 kW fast charging. When compared with a vehicle that never fast charged, nearly a 25% increase in annual miles traveled was realized when 1% to 5% of total charging events were fast charges.

network operators, and utility suppliers can all be impacted with the introduction of XFC technologies. For successful XFC implementation, collaborations across technology intersections and overlaps need to be fostered. To accelerate these interactions, the project team engaged with industry to identify technical challenges and develop a report outlining the limiting factors for XFC implementation in BEVs. A combined analysis found in the report includes impacts to and R&D recommendations for battery performance, battery thermal management, vehicle design, and infrastructure with economic considerations.

Objectives

For XFC to be successful, stations should be able to recharge a BEV in less than 10 minutes and provide approximately 200 additional miles of driving. However, this introduces a host of new challenges that need to be addressed. As a result, it is expected that packs designed to meet XFC will initially be significantly more expensive than BEVs optimized for current charging technology. From the battery cell to the power grid these 400-kW chargers are connected to, this research outlined in the report discusses issues that need to be addressed at each level in order to implement a 400-kW charging network. Although the report is U.S.-focused, the findings should be applicable to other countries with mature automotive infrastructures. Technical gaps and challenges posed by XFC are investigated and divided into primary focus areas: batteries, vehicles, and infrastructure with economic considerations. Outcomes from this research could be used to inform the development of technical targets and research and development plans for stakeholders.

Approach

A multi-national laboratory team consisting of Argonne National Laboratory (ANL), Idaho National Laboratory (INL), and National Renewable Energy Laboratory (NREL) engaged with industry stakeholders to identify barriers and opportunities for technology R&D solutions needed to achieve 400 kW charging power levels and combine the findings into a single document for governments and private industries to reference. Industry perspectives on the direction of fast charging were used to guide and bound the technology gap assessment report, inform the team on areas needing an extensive literature review, and develop use-cases to assess the economic feasibility of XFC. The report was broken into three sections: (1) an executive summary, (2) a summary report, and (3) appendices complete with four technical manuscripts. The executive summary is intended to introduce XFC and convey the high-level technical challenges/gaps and introduce potential R&D solutions with minimal technical discussion. In the summary report, these gaps and R&D solutions are addressed with more technical detail. The reader should be able to understand the bulk issues and linking technicalities associated with XFC by reading the summary report; however, the reader does not need to be an expert in the field. The manuscripts contained in the appendices are intended for persons with technical backgrounds or those looking to learn more about XFC technologies through a technical lens. The appendices were written with the intent to be published in technical peer-reviewed journals for which citations are listed in the Key Publications section.

Results

Battery

The U.S. Department of Energy (DOE) has a goal of reducing the production cost of a BEV battery to ultimately \$80/kWh, increase the range of EVs to 300 miles, and decrease charge time to 15 minutes or less. In order to achieve this goal, a major effort within the battery research community has focused on increasing the energy density of the cell, which refers to the amount of energy stored in a specified weight or volume. Increasing electrode thickness is an effective way of improving the energy density of a cell. However, thicker electrodes present several barriers to fast charging. As electrode thickness increases, charge times must also increase in order to avoid lithium plating. Lithium plating occurs when the charge rate exceeds the rate the lithium ions can intercalate into the crystal structure of the anode, which causes metallic lithium to form on the surface as shown in Figure I- 155 (from [3]). Lithium plating can negatively affect performance of the electrode and lead to accelerated degradation of the battery, as well as impact cell safety. Therefore, it is thought that thinner electrodes are better suited for XFC applications, but this occurs with a tradeoff in increased battery cost. Referencing Table I- 22 (from [4]), the analysis indicates that fast charge nearly

doubles cell cost from \$103/kWh to \$196/kWh. The increase in cell cost is largely based on decreasing the anode thickness. Using thinner electrodes requires more cells to achieve the same energy density.

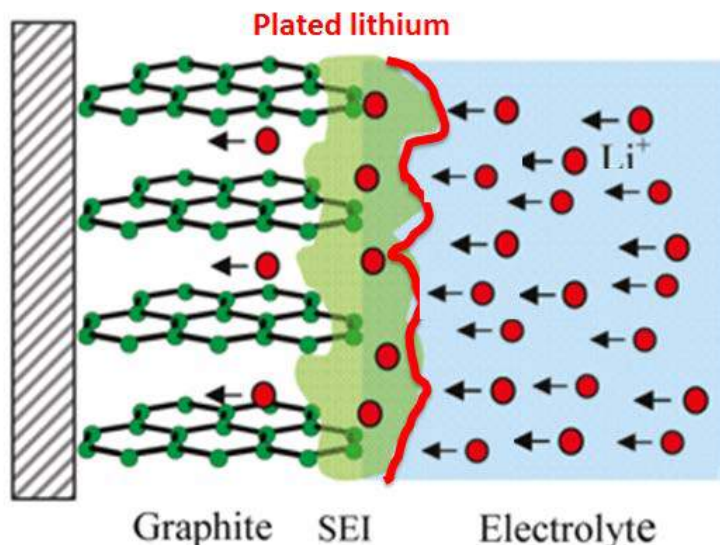


Figure I- 155. At high charge rates, a much larger number of lithium ions move to intercalate into graphite as represented by the red dots. However, there is not enough time or space for intercalations; therefore, lithium ions may start plating as metal onto the surface of the graphite electrode, shown as a thick red line).

Managing the heat generated in the battery during a charging event is also a potential barrier to XFC because temperatures in excess of 45°C will rapidly degrade battery lifetime. Higher temperatures can also introduce safety concerns as materials contained within the battery can begin to chemically and mechanically degrade.

The report cites the need for materials R&D in order to minimize or mitigate localized heating and lithium plating with thicker electrodes. Research in electrode design can help with implementation of advances made through materials' innovations. A study of the impact of XFC on the existing current-state-of-the-art can inform material, electrode, and cell design research. These studies may also reveal differences in the safety of cells subjected to XFC protocols, which is an area also in need of more research to fully understand the impacts and to develop mitigations. Research toward development of new charging protocols that may extend battery life should also be considered.

Development of new technologies for XFC battery pack thermal management is needed in order to preserve battery life. More complex battery management systems may be needed to cope with higher pack voltages, more complex thermal management systems, and cell balancing during charging. Higher voltage packs also bring additional electrical safety concerns that need to be understood.

Table I- 22: BatPaC simulation comparing the effects of charging time on the required anode thickness, heat generation in the pack, and the resulting temperature rise, pack cost, and incremental cost of charging faster than 1-C (60 minutes) rate. Cell Chemistry: NMC 622-Graphite, Pack Energy: 85 kWh; Rated Power (10-second burst): 300 kW; Maximum Allowable Current Density (MACD): 4 mA/cm²; Number of Cells per Pack: 240

Charging Time, ΔSOC=80%, minute	8	10	23	47	53	61
Charging Time, ΔSOC=60%, minute	5	7	15	30	34	39
Charger Power Needed, kW	601	461	199	100	88	77
Anode Thickness, μm	14	19	43	87	98	103
Heat Generated during Charge, kWh per pack	2.35	2.20	1.89	1.77	1.75	1.45
Post-Charge Cell Temperature (ΔSOC=80%), degrees C	22.4	24.4	25.9	26.4	26.4	19.5
Cell Mass, kg	2.75	2.40	1.74	1.49	1.46	1.45
Cell Cost to Original Equipment Manufacturer, \$ per kWh	\$229	\$196	\$132	\$107	\$104	\$103
Cost Difference, \$ per kWh	\$126	\$93	\$30	\$4	\$1	\$0

Vehicles

Similarly as with the battery, the vehicle is constrained by cost, weight, and volume. For XFC-capable vehicles, these parameters are greatly influenced by the current delivered to the vehicle during a 400-kW charge, where all parameters rise with increased current. By increasing the BEV battery pack voltage from the current industry standard of 400 V to more than 800 V, the current needed for XFC drops by at least half. However, increasing the pack voltage impacts components such as the electric drive motor and the power electronics onboard the vehicle, including the power inverters. Higher voltages also bring new challenges associated with interoperability because legacy and XFC-enabled vehicles could interface with the same charging infrastructure. Developing an XFC-capable vehicle may introduce challenges with the high-voltage system architecture, power electronics and electric machines, the charging system, thermal management, cyber and physical security, and BEV/EVSE interoperability. The trade-off between driving range and recharge time has historically been a barrier to BEV adoption. XFC seeks to balance these parameters, along with vehicle cost.

BEV owners require consistent charging experiences; therefore, interoperability of XFC charging systems with vehicles of different models and charging capabilities could be studied. Cybersecurity research of the vehicle and charger communications is needed to ensure BEVs can provide reliable transportation. Furthermore, standardization to ensure interoperability between new and legacy vehicles accessing XFC and existing networks is needed. Testing and evaluation of existing vehicles to XFC charger connectors to determine safe, reliable, and robust operating limits could be considered. Researching the impact higher pack voltage has on the overall volume, weight, and cost for power electronics may be needed for XFC-enabled vehicles. Increased system bus voltages will require reevaluation of semiconductor materials used in vehicle power electronics, in addition to improved insulation materials needed to maintain electrical safety and durability.

Infrastructure

Successful installation of nationwide, 400-kW capable, public infrastructure requires many barriers to be addressed. A key challenge is to coordinate across the many stakeholders such as vehicle manufacturers, utility suppliers, XFC charger manufacturers and network operators, battery developers, codes and standards

bodies, and policy makers. Specific topics such as power requirements for XFC charger installations, utility rate structures, and the connector type for vehicle-to-charger connections can impact the effectiveness of XFC and should be considered by stakeholders as a group. XFC infrastructure should be able to accommodate all vehicle types, even if the vehicle is not XFC capable.

Optimization of XFC charging station location is needed within cities and across highway corridors to account for user convenience and availability of power from the utility. Co-located distributed energy resources as seen in Figure I- 156 (from [5]), may be needed to minimize station operation costs, limit grid impacts, supplement power provided by electric grid, and accommodate ideal XFC station placement.

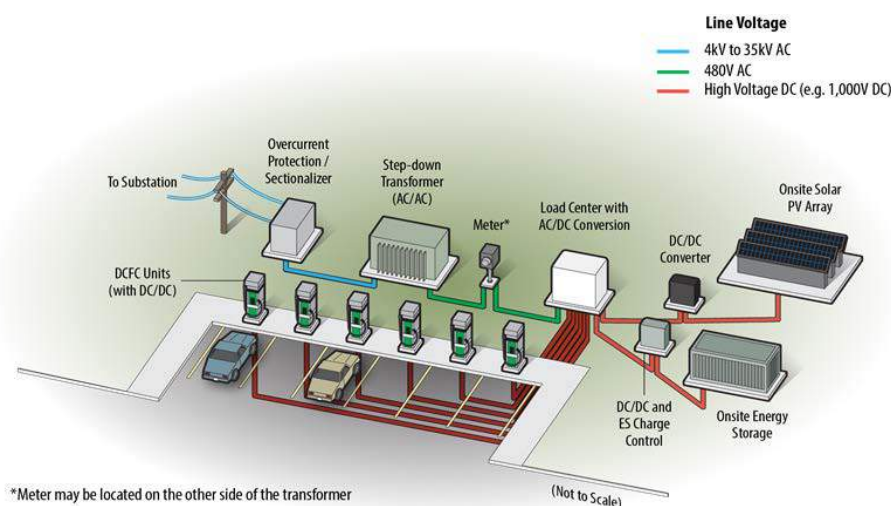


Figure I- 156. XFC station showing different design options such as co-located energy generation and storage which may be used to reduce station operating costs, minimize grid impacts, supplement power provided by the electric grid and accommodate ideal XFC station placement.

Researching advanced materials to reduce and manage thermal loads within the charger and the cable connecting the vehicle-to-charger is needed for XFC applications. Automation for XFC should be considered; however, this may increase overall system cost. Stakeholder engagement to harmonize XFC station permitting and siting requirements, along with codes and standards related to liquid-cooled cables and vehicle-to-charger connector design, should be a focus. Best conducted by industry, understanding where XFC stations need to be sited to serve demand, both commercial and private, and where appropriate grid resources exist to initially serve the greatest number of consumers should be investigated. The tradeoffs and operational benefits realized by using co-located distributed energy resources integrated with utility generation could be considered and studied.

Conclusions

Many technical gaps and challenges for XFC have been identified in this research which impact several key technology sectors such as automotive OEMs, battery manufacturers, codes and standards bodies, EVSE manufacturers and network operators, and utility suppliers. For XFC to be successfully implemented, these technology sectors need to foster new levels of collaboration and communication regarding technology intersections and overlaps.

Battery cost is often cited as a barrier to EV adoption. XFC could increase the cost of a cell by more than 90%, with anode thickness the primary cost driver. Within the battery cells, a bulk of the research identified centers around the anode and mitigating the onset of lithium plating and minimizing heat generation, which can lead to dramatic cell degradation and pose safety concerns. Heat generation in general is a known mechanism for electrochemical and mechanical battery material degradation. As such, thermal management of

batteries when subjected to XFC protocols require R&D. Thermal management research coupled with robust battery management controls and charging protocols R&D will help achieve XFC while prolonging life.

For vehicles, higher voltage battery packs, up to 1000V from conventional EV's 400V systems, can drive much research in the electrical architecture of the vehicle and power electronics which support the electric drive system. Cybersecurity and interoperability of vehicle and EVSE communications is needed to ensure XFC capable vehicles, and legacy vehicles alike, can provide reliable transportation and not be disrupted by cybersecurity events or differences in charging equipment.

In infrastructure, conductive EV charging using a cord and plug require research in thermal management of the charger power electronics and charge cable. For wireless charging technologies, electromagnetic field shaping and shielding have the bulk of the R&D investment. XFC's intermittent demand for electricity could pose challenges to the electric grid's stability which raises concerns from utilities as a potential for cybersecurity vulnerabilities. Infrastructure sees the introduction of the largest and most broad base of stakeholders ranging from EVSE manufacturers and network operators to utility suppliers and regulators. Coordination and cooperation within this group of stakeholders is recommended in order for XFC to make it to market.

The gaps identified within this research could serve as a useful guide for research programs spanning varying degrees of technology maturity across a broad industry landscape. Identification and dissemination of XFC technical issues will help the stakeholder community focus and advance each technology area at a quicker pace than may otherwise be possible if each organization were to undertake a similar effort on its own.

Key Publications

1. Bloom, I. et al. "Enabling Fast Charging – A Battery Technology Gap Assessment." *Journal of Power Sources*, vol. 367, 1 Nov. 2017, pp. 250–262., doi:10.1016/j.jpowsour.2017.06.055.
2. Keyser, M. et al. "Enabling Fast Charging – A Battery Thermal Technology Gap Assessment." *Journal of Power Sources*, vol. 367, 1 Nov. 2017, pp. 228–236., doi:10.1016/j.jpowsour.2017.07.009.
3. Meintz, A. et al. "Enabling Fast Charging – Vehicle Considerations." *Journal of Power Sources*, vol. 367, 1 Nov. 2017, pp. 216–227., doi:10.1016/j.jpowsour.2017.07.093.
4. Dufek, E. et al. "Enabling Fast Charging – Infrastructure and Economic Considerations." *Journal of Power Sources*, vol. 367, 1 Nov. 2017, pp. 237–249., doi:10.1016/j.jpowsour.2017.06.079.

References

1. Lutsey, N., S. Searle, S. Chambliss, and A. Bandivadekar, 2015, "Assessment of Leading Electric Vehicle Promotion activities in United States Cities," *International Council for Clean Transportation*, July 2015.
2. McCarthy, Michael, 2017, "California ZEV Policy Update," *SAE 2017 Government/Industry Meeting*, Society of Automotive Engineers, January 25, 2017, Walter E. Washington Convention Center, Washington, DC, conference presentation.
3. Challenges for Rechargeable Li Batteries, John B. Goodenough and Youngsik Kim, *Chemistry of Materials* 2010 22 (3), 587-603, DOI: 10.1021/cm901452z.
4. Howell, David, et al. "Enabling Extreme Fast Charging: A Technology Gap Assessment." *Department of Energy, Office of Energy Efficiency Renewable Energy*, 23 Oct. 2017, <https://energy.gov/eere/vehicles/downloads/enabling-extreme-fast-charging-technology-gap-assessment>.
5. Francfort, J. et al. "Considerations for Corridor and Community DC Fast Charging Complex System Design." INL/EXT-17-40829, Idaho National Laboratory, May 2017.

I.F Small Business Innovation Research (SBIR)

Samuel Gillard, Technology Manager

U.S. Department of Energy

Phone: 202-287-5849

E-mail: Samuel.Gillard@ee.doe.gov

Objectives

Use the resources available through the Small Business Innovation Research (SBIR) and Small Business Technology Transfer (STTR) programs to conduct research and development of benefit to the advanced batteries effort within the Vehicle Technologies Office.

Introduction and Approach

The advanced batteries effort of the Vehicle Technologies Office supports small businesses through two focused programs: Small Business Innovation Research (SBIR) and Small Business Technology Transfer (STTR). Both programs are established by law and administered by the Small Business Administration. Grants under these programs are funded by set aside resources from all Extramural R&D budgets; 3.0% of these budgets are allocated for SBIR programs while 0.45% for STTR grants. These programs are administered for all of DOE by the SBIR Office within the Office of Science. Grants under these programs are awarded in two phases: a 6-9 month Phase I with a maximum award of \$150K and a 2 year Phase II with a maximum award of \$1M. Both Phase I and Phase II awards are made through a competitive solicitation and review process.

The advanced batteries team participates in this process by writing a topic which is released as part of the general DOE solicitation. Starting in FY12, the advanced batteries team decided to broaden its applicant pool by removing specific subtopics and allowing businesses to apply if their technology could help advance the state of the art by improving specific electric drive vehicle platform goals developed by the DOE with close collaboration with the United States Advanced Battery Consortium.

Phase II Awards Made in FY 2017

Under the SBIR/STTR process, companies with Phase I awards made in FY 2016 are eligible to apply for a Phase II award in FY 2017. The following two Phase II grants were awarded in FY 2017 (from among the four Phase I grants that were conducted in FY 2016):

Coulometrics (Chattanooga, TN 37404-2812)

This project will develop state-of-the-art processes for the conversion of natural flake graphite and other graphitic materials into high quality lithium-ion battery (LIB) grade anode materials. This will enable a \$1B industry to develop and create a supply chain for graphite that does not exist in the United States today. This project will complete 4 years of work by Coulometrics to develop new environmentally friendly and low cost processes for the conversion of graphitic materials into a high quality LIB anode material that exhibits: Lower cost; improved purification through an environmentally friendly process, and; A high quality and consistent material suitable for demanding electric vehicle applications. Currently, all natural graphite for lithium ion batteries originates in China. This represents the most profitable value-added market for graphite with no current beneficiaries in the US. This is true even though vast high-quality flake graphite deposits exist in the US and Canada and the US also boasts some of the highest quality petroleum coke that can be used to produce synthetic graphite. Many junior graphite and petroleum companies are eager to see their materials used for LIB anode material. However, new state-of-the-art process technologies are required that will: spheronize the graphite with higher yield than what is currently used in China; purify the spheronized and synthetic graphite, and; CVD coating of the spheronized graphite to provide high efficiency and long life in LIBs. Coulometrics has increased spheronization yield from 30 to 70%, demonstrated new thermal purification technologies that achieve record graphite purity, and developed a new CVD coating process that has allowed us to achieve

unprecedented LIB life even when compared to world class cells used in Tesla vehicles today. Coulometrics graphite anode materials meet all automotive specifications including high capacity (>355 mAh/g) and high first cycle efficiency (92-95%). Coulometrics is already working with leading US battery manufacturers and has support for this effort from Tesla Motors and K2 Energy. It considers each a beachhead customer for both automotive and military markets that are the focus of our commercialization plan. The goal of the Phase II effort is to continue the development of graphite products that focus on longer life, higher charge rate and resistance lithium plating, and cost reductions through process innovation. Coulometrics is currently able to build and test 2.4 to 3.0 Ah 18650 cylindrical lithium ion batteries and performance state-of-the-art high precision coulometry testing to determine life and charge rate capabilities. This work also involves commercial partners and sending full 18650 cylindrical cells for verification. Full qualification and a current target price of \$4-5/kg could make this material attractive to LIB manufacturers currently paying more than \$14/kg in high volume. Coulometrics has established a new joint venture called PUREgraphite with Graphitecorp funding the commercialization effort with \$10M. Coulometrics owns 50% of PUREgraphite and will continue to develop the material.

Saratoga Energy (Berkeley, CA, 94710-2737)

A breakthrough electrolysis process to manufacture graphite from carbon dioxide has been developed. Graphite is the primary active anode component used in lithium-ion batteries for electric vehicles and constitutes 10-14% of the total cell cost. The graphite produced could offer a 70% cost saving compared to commercial incumbents. In addition, the company's graphite features another very important characteristic: it enables fast-charging of lithium-ion batteries – up to three times faster than standard anodes. Thus, upon success of the project, it will contribute to: reducing the cost of batteries for electric vehicles and dramatically improving charging performance. During Phase I, the company improved the performance of its graphite anode material by optimizing synthesis conditions and demonstrated long-term cycling stability on small full-cells. In Phase II of this SBIR project, three objectives will be met. The first objective is to further refine the graphite production process to maximize material performance. The second objective is to demonstrate fast charging capabilities and long-term cycling stability on larger, 2 Ah lithium-ion full cells. The third objective is to demonstrate the feasibility of this process at a small pilot scale, paving the way for further customer sampling and qualification, as well as providing necessary process data for a demonstration-scale plant design. Lower cost and improved battery charging will contribute to greater customer acceptance of electric vehicles, helping the deployment of clean energy technologies. As an added benefit, this graphite could be made from waste carbon dioxide and, if produced from renewable electricity, would have a negligible carbon footprint.

Phase I Awards Made in FY 2017

Nine Phase I grants were awarded in the Summer of FY 2017.

Amasatan Technologies (Andover, MA)

The fundamental functional components within lithium ion batteries are the anode, cathode, and electrolyte. Currently, cathode material dictates battery performance and is the most expensive of the three, accounting for up to 25% of the battery pack cost. Reducing the cost of the cathode material represents a significant decrease in the cost of the battery. Cathode cost is determined mostly by raw material and production costs. The goal of this project is to reduce (i) the production cost of cathode materials and (ii) the environmental footprint associated with cathode material production while maintaining high- performance. For this, the company will focus on NMC 532, which is the current industry standard for state of the art automotive batteries. The company expects the underlying technology to be developed in this program to be broadly applicable to all transition metal oxide cathodes, and maybe also resulting in more viable pathways to the next generation cathode materials – the so-called ni- rich NMC's. It will use Amastan's UniMelt™ single-step continuous microwave- generated plasma materials processing technology. Unlike conventional incumbent cathode material manufacturing techniques requiring many processing steps and producing environmentally unfriendly chemical byproducts, adding to cost, the proposed process is carried out in a continuous single step without process byproduct. The UniMelt process uses solution precursor mixed at the molecular level as feedstock. The solution precursor is used to produce uniform diameter droplets that are injected into a uniform temperature

electrodeless plasma column of up to 4" in diameter, where they undergo chemical reactions. This offers each precursor droplet the same thermal path and thermal history, leading to tight control of phase purity, size and size distribution of the product. The preliminary technical results of this phase will enable comprehensive cost analysis of the final cathode material production at commercial scale.

Ge Solartech, LLC (Troy, MI)

Ge Solartech, LLC will develop and demonstrate a novel synthesis process that can efficiently produce nickel-rich NMC materials. This proprietary process uses pure metals as precursors, avoiding time and energy consuming steps in the conventional hydroxide co-precipitation process because the cost of pure metals is much lower than that of their corresponding compounds and can directly be used as the starting materials without requiring any further treatment. This process can reduce process cost by 70% compared with that of the current hydroxide co-precipitation process. The success of this synthesis process will help in achieving objectives for novel low-cost materials and improvements in manufacturing processes. In Ni-rich materials, a replacement of a small amount of Li by Ni gives larger reversible capacity because NiO₂ slabs bonded together by the Ni allow much more Li ion de-intercalation. However, Ni atoms in the Li layer can block the passage of Li⁺ transport, leading to poor performance in rate capacity. Therefore, Ni²⁺ cations in lithium layers should be controlled within a certain range in order to obtain higher performance. In order to tailor the degree of cation mixing, there is a need for a new synthetic protocol. The proposed solid-state synthesis method enables the control of the amount of cation mixing by programming reaction conditions. The conditions, such as precursors, duration of ball milling, reaction temperatures and oxygen environments, are crucial in determining crystal structure and cation mixing that influence the electrochemical performance of the NMC electrodes. Working with the Chemical and Materials Engineering Department at the University of Kentucky, Ge Solartech will, during Phase I, develop and test new nickel-rich NMC cathodes and will characterize and optimize material formulations, as well as improve synthesis methods. Based on its PI Dr. Huang's previous experience as a Senior Scientist in the Battery Materials Division of BASF, it expects that materials capable of 250-270 mAh/g could be developed in Phase I. Ge Solartech plans to use high capacity Si and graphite composites as anodes to build full cells. By using thick, high performance nickel-rich cathodes and Si-graphite composite anodes, Ge Solartech expects full cells to reach a capacity close to 200 mAh/g. At the completion of Phase I, Ge Solartech will submit a proposal to the DOE for a Phase II project that will scale up production of nickel-rich NMC materials to a prototype level. In Phase II, a full cell capable of 2 Ah will be built to validate the findings of Phase I.

Giner Inc. (Newton, MA)

Conventional lithium-ion batteries demonstrate great potential for applications in electrical vehicles, but they face some major challenges such as low energy density and high cost. It is worthwhile to pursue alternative strategies to address the barriers of cost and energy density. This company proposes to develop advanced rechargeable lithium-sulfur (Li-S) batteries that have much higher theoretical energy density and lower cost. It will improve the practicality and cycle life of Li-S batteries to make them more commercially viable. In the Phase I project, it will improve the energy density and cycle life of Li-S batteries via two approaches. First, highly conductive lithium-ion exchange membranes will be used as battery separators. Second, concentrated Li electrolytes will be used in electrodes. These efforts will prevent cathode sulfur loss due to the polysulfide shuttle mechanism, thus significantly enhancing the cycle life of Li-S batteries. The proposed lithium-sulfur technology will address two major barriers for electrical vehicles, cost and energy density; therefore directly facilitating the deployment and commercialization of electrical vehicles. It may also be applicable in the consumer market to portable electronics and communication devices.

NextGen Battery Technologies, LLC (Arlington, VA)

Cathode materials with significantly higher specific capacities than what is currently available are critical to meeting the DOE's specific energy and energy density goals of 350 Wh/kg and 750 Wh/L at the cell-level, respectively. New materials capable of accommodating more than one lithium ion per transition metal can have a transformational impact on the energy density. Manganese-based cathode compositions, while low-cost and environmentally friendly, are also capable of multi-electron transfer. The proposed Phase I effort aims to

advance the state the art by demonstrating manganese-based cathode materials with ultrahigh capacity and cycling stability. The objective of the Phase I program is to develop and demonstrate at the pouch cell level, a new high energy density cathode material that is capable of meeting DOE's target of 350 Wh/kg cell-level energy density. Building on previous work, the Phase I feasibility effort will show that novel ionic substitutions in the crystal structure of manganese-based cathode materials can lead to a high capacity cathode material that is stable to long term cycling. Stabilized manganese-based cathode materials will be synthesized in gram quantities and characterized for composition, phase purity, particle size, surface area and thermal stability. Select batches with the desired particle characteristics will then be tested for electrochemical properties (e.g., specific capacity, rate capability and cycle life) in a coin cell format. A large batch of the most promising candidate material will be produced to demonstrate scalability, and the powder will be used to fabricate and test pouch cells with a capacity of at least 200 mAh. The market for lithium ion batteries is growing rapidly driven by the growth in electric vehicles and grid-based storage. The availability of low-cost and high performance battery materials, particularly cathode powder, is key to enabling battery manufacturing infrastructure in our country. The proposed program, when successfully implemented, will lead to rechargeable lithium-ion batteries with significantly higher energy density than what is currently possible today.

CAMX Power (Lexington, MA)

Successful commercialization and market adoption of electric drive vehicles (EVs) requires development of Li-ion storage technologies that can deliver >350Wh/kg, well above what can be achieved with current battery materials. Implementation of next generation cathode and anode materials is needed to further increase specific energy of Li-ion cells. However, without pre-lithiation, some of the most promising anode materials having high capacity (but low efficiency) cannot be used. CAMX Power would develop a safe and scalable pre-lithiation technology that will enable the use of very high capacity, long life, but low first cycle efficiency Si-based anodes to demonstrate lithium-ion cells capable of meeting specific energy, power, and life targets for EV batteries. It will leverage its CAM-7® cathode material and its work on Si-based anodes to demonstrate lithium-ion cells that utilize pre-lithiation and are able to meet the 350Wh/kg target. During the Phase I effort it will explore the impact of active materials on the extent of pre-lithiation achieved and test different pre-lithiation process parameters and environmental stability of pre-lithiated electrodes. It will also demonstrate that optimally pre-lithiated cells with a Si-based anode can meet the scaled energy targets. Moreover, process scalability will be demonstrated in 200+mAh pouch cells. Proposed technology will enable production of batteries with >350Wh/kg specific energy making it extremely attractive for implementation in both portable power and EV batteries. By increasing the energy density of EV batteries, and thus increasing the driving range of vehicles between recharges, it is anticipated that this technology will further lead to increased market adoption of electric vehicles.

CAMX Power (Lexington, MA)

For use in congested traffic, the start-stop vehicle technology (micro-hybrid) offers the promise of significant increases in fuel economy and reduction of pollutant emissions, without a large increase in the vehicle sales price. A key enabling component of the start-stop system is the battery. Present start-stop systems employ lead acid batteries because of their low initial cost and excellent low-temperature performance, but these batteries suffer from life limitations especially when subjected to repeated deep-cycling and high charge rates. Consequently, alternate battery systems with improved life characteristics are the key to enabling widespread adoption of start-stop vehicles. Li-ion technology is the leading candidate to replace lead-acid batteries in start-stop systems and several battery companies have announced Li-ion batteries for start-stop applications. However, most Li-ion battery systems offered today suffer from one or more disadvantages such as poor low-temperature performance, poor high-rate charge acceptance, or high cost relative to lead acid batteries. This is at least in part because the materials in these batteries are not optimized for the specific requirements of start-stop applications. CAMX Power is developing Li-ion technology for start-stop applications that overcomes the limitations of the current Li-ion systems by tailoring its proprietary CAM-7 cathode material for use opposite lithium titanate anode (LTO) anode in pouch cells that provide excellent cold-cranking capability, elevated-temperature stability, cycle life and safety for 12V start-stop batteries. CAMX Power has already shown that CAM-7 cathode/LTO anode pouch cell technology provides excellent (-30°C) cold cranking capability and

elevated-temperature stability (without pouch cell gassing/swelling). In the proposed program, CAMX will optimize the CAM-7 material for the start-stop battery application, and will develop a scheduled maintenance procedure for CAM-7/LTO start-stop vehicle batteries that further extends performance and life. The CAMX POWER start-stop battery technology will facilitate widespread commercialization of start-stop micro-HEVs by enhancing the available energy, dynamic charge acceptance, and life of Li-ion batteries used in micro-HEVs. Rapid, widespread adoption of affordable micro-HEVs in traffic-congested areas of the country can yield benefits including reduced adverse health impacts from pollution in urban and other high traffic areas, and reduced economic impacts of fluctuations in global petroleum supply and price.

Saratoga Energy Research Partners, LLC (Berkeley, CA)

Saratoga Energy, a start-up company located in Berkeley, California, is developing a breakthrough electrolysis process to manufacture low-cost carbon nanotubes (CNTs) from carbon dioxide. CNTs provide an exceptional array of properties that enable the fabrication low-cost, high-energy lithium-ion batteries thus addressing the driving range limitations of electric vehicles. The global market size for CNTs was estimated to be \$2.26 billion in 2015 making this an attractive opportunity. In the work conducted thus far, Saratoga Energy has established that its synthesis process could potentially be 90 times less energy intensive than the state-of-the-art (CCVD) and it has the potential to manufacture CNTs for under \$5/kg - 100X cheaper than the current market price for CNTs. Lithium-ion batteries using Saratoga Energy CNTs have up to 20% higher volumetric and specific energy which translates to extended driving range of electric vehicles, or smaller, less expensive battery packs. Thus, upon the success of the project, it will provide two essential contributions fully aligned with the mission of the DOE Vehicle Technologies Office: reducing the cost of electric vehicles and dramatically improving driving range. In Phase I of this SBIR project, two tasks will be addressed. The first objective is to produce a masterbatch of CNT material and optimize its dispersion properties. The second objective is to fabricate high areal capacity anodes with the aid of the companies CNTs and demonstrate high performance on 250 mAh lithium-ion full cells paired with NMC cathodes. In Phase II, the project will attempt demonstrating the feasibility of the synthesis process at a small pilot scale, paving the way for further customer sampling and qualification, as well as providing necessary process data for a semi-works plant design. In parallel, the long-term cycling stability, cycling efficiency, and abuse resistance of lithium-ion batteries (constructed with Saratoga Energy's CNTs) will be demonstrated on larger 2 Ah cells. The societal and public benefits directly derived from the features of Saratoga Energy CNTs – lower cost, improved energy density, and rate capability will contribute to greater customer acceptance of electric vehicles - helping the deployment of such technologies. As an added benefit, the company's CNTs are made from carbon dioxide, and if produced from renewable electricity, would have a negligible carbon footprint.

Hazen Research, Inc. (Golden, CO)

Development of superior Li-ion batteries (LIBs) is a critical part of the DOE mission to improve the economic, social, and environmental sustainability of electric vehicles (EV). DOE seeks to reduce the cost of the EV batteries from the current more than \$250/kWh to less than \$125/kWh by 2022. To achieve this goal, the materials and manufacturing costs of the battery components must be reduced significantly. This is especially true for the cathode materials and their manufacturing methods, which account for approximately 30% of the total cost of the state-of-the-art LIB. A large percentage of the total cost is due to the high cost of the components of the cathode materials and their complex manufacturing methods. Layered Ni-rich oxides of the type $\text{Li}(\text{Ni}_{1-x-y}\text{Mn}_x\text{Co}_y)\text{O}_2$ with Ni greater than 0.6 (Ni-rich NMC) have recently gained prominence because of their high capacities (200 to 225 mAh/g), high-voltage cyclability (2.0 to 4.5 V), and low cost. Significantly improved performance of hierarchically structured (compositionally gradient) Ni-rich NMC (Ni equals 0.4) cathode powders exhibiting local elemental segregation have been reported through spray pyrolysis. It is believed that both the chemistry (all-nitrate precursors) and the method (horizontal spray pyrolysis) can be further improved and developed into a scalable manufacturing method for the new generation of low-cost, high-capacity, high-voltage Ni-rich NMC cathode materials, such as $\text{Li}(\text{Ni}_{1-x-y}\text{Mn}_x\text{Co}_y)\text{O}_2$ (Ni greater than 0.6). These cathode materials will contain the desired compositional gradient and surface chemistry that will enable superior long-term performance. Hazen Research, Inc., in collaboration with the National Renewable Energy Laboratory (NREL), will develop and demonstrate a high-throughput and scalable manufacturing

method for the production of Ni-rich NMC cathode materials of the type $\text{Li}(\text{Ni}_{1-x-y}\text{Mn}_x\text{Co}_y)\text{O}_2$ (Ni greater than 0.6) by combining a vertically fed spray pyrolysis with a fluidized-bed reaction in a single reactor. This approach will mitigate the possibility of agglomeration, and uniform Ni-rich NMC cathode particles can be produced in a single reactor, making it a continuous production process. The $\text{Li}(\text{Ni}_{1-x-y}\text{Mn}_x\text{Co}_y)\text{O}_2$ (Ni greater than 0.6) particles having a Ni-rich core, but a Mn-rich surface, will be produced through rationally developed precursors for spray pyrolysis. The proposed single solution precursors will use Li, Ni, Mn, and Co starting materials with similar decomposition temperatures (nitrates) along with minor components of Ni and Mn materials with increasing decomposition temperatures (carboxylates and fluorinated carboxylates) maintaining the overall stoichiometry. This novel inorganic–metalorganic composite precursor is expected to form particles with the targeted Ni-poor and Mn-rich surfaces upon spray pyrolysis. Amorphous powders formed during spray pyrolysis can be reacted further and crystallized to uniform particles with increased tap density through fluidized-bed reactor processing. The approach, combining spray pyrolysis and fluidized-bed reaction in a single reactor, using an inorganic–organic precursor, is novel and is expected to lead to a low-cost manufacturing method for the production of these next-generation cathode materials. Along with its high capacity, the Ni-rich NMC cathode particles of $\text{Li}(\text{Ni}_{1-x-y}\text{Mn}_x\text{Co}_y)\text{O}_2$ (Ni greater than 0.6) produced by this combined method are expected to retain the compositional gradient favorable for the high voltage (2.0 to 4.5 V) and stable cycling performance. During this Phase 1 effort, the Hazen–NREL team will perform the following tasks: develop inorganic–metalorganic precursors for the spray pyrolysis to produce compositionally gradient Ni-rich NMC, $\text{Li}(\text{Ni}_{1-x-y}\text{Mn}_x\text{Co}_y)\text{O}_2$ (Ni greater than 0.6) cathode powders; design, build, and demonstrate a combined spray pyrolysis and fluidized-bed reactor for the manufacturing of Ni-rich NMC cathode powders with capacity more than 200 mAh/g and cycling between 2.0 and 4.5 V; validate greater than 200 mAh full cells (with more than 95% capacity retention over 250 cycles) using the cathode powders produced under the recommended USABC testing protocols. The EV market is estimated to be \$12.8 billion in 2017, with an annual growth close to 60% from 2008–2017; the North American portion of the market alone is expected to reach \$5.8 billion in revenue. Through an improved and scalable manufacturing of the low-cost high-performance Ni-rich NMC cathode powders, our approach will directly influence this market and significantly reduce the cost of state-of-the-art EV batteries. The demand for layered LiMO_2 (M=Co/Mn/Ni/Al) type cathode powders was approximately 75,000 t in 2014 and is projected to be approximately 225,000 t in 2025, representing an approximate 200% increase in demand in less than 10 years. The technology developed under this proposal is directly applicable to manufacturing of materials with a huge market demand. The project will further advance EV battery technology and assist in accomplishing the following: improve the competitive position of United States industry in the field of advanced materials and manufacturing to create jobs; enhance energy security by reducing dependence on foreign oil; save money by cutting fuel costs for American families and businesses; and protect health, environment, and safety by mitigating the effect of energy production on climate change.

II. Advanced Materials R&D

II.A Next-gen Lithium-ion: Advanced Electrodes R&D

II.A.1 Higher Energy Density via Inactive Components and Processing Conditions (LBNL)

Vincent Battaglia, Principal Investigator

Lawrence Berkeley National Laboratory
1 Cyclotron Road
Berkeley, CA 94720
Phone: 510-486-7172
E-mail: vsbattaglia@lbl.gov

Peter Faguy, Technology Manager

U.S. Department of Energy
Phone: 202-586-1022
E-mail: Peter.Faguy@ee.doe.gov

Start Date: October 1, 2015

End Date: September 30, 2018

Total Project Cost: \$3,600,000

DOE share: \$3,600,000

Non-DOE share: \$0

Project Introduction

The vast majority of automobiles purchased in the US use internal combustion engines. This is because the alternative, renewable option, the plug-in electric vehicle (PEV), is considered to be too expensive and lacks the accustomed range one gets from filling a vehicle with a petroleum-based fuel. It is generally believed that if a battery could be produced with higher energy density, electric vehicles could meet a 300-mile range and approach a cost payback period of 5 years, making them much more attractive to the average consumer. Many researchers are attempting to increase energy density by extracting more capacity from today's Li-ion battery chemistries or developing new anode and cathode materials altogether. The goal of this project is to increase the energy density by reducing the fraction of inactive components by determining how to produce thicker electrodes.

As it turns out this is not as simple as increasing the gap in the slot-die coater. Thicker electrodes tend to delaminate more easily, especially during the slitting process. Thicker electrodes also require more time to dry which changes the balance of the physics during drying. More drying time allows more time for the denser active materials to settle through the polymer rich slurry resulting in a non-uniform distribution of components. Thicker electrodes also experience greater hoop stress on the outer surface during winding. It is possible that these phenomena can be effectively addressed by changing the molecular weight of the binder and the morphology of the conductive carbon additive. This project seeks to investigate this approach using tools at our disposal at the Lawrence Berkeley National Laboratory.

Objectives

By investigating different binder sources, slurry viscosities, binder molecular weights, binder fractions, conductive additive morphologies, calendaring temperatures, and drying rates, we hope to identify the physics that dictates the conditions for a smooth laminate that adheres well to the current collector has a high loading and is windable to a ½ cm mandrel. A basic understanding of the interplay of these parameters should help electrode manufacturers to specify the properties required of the individual components and for the suppliers of those components to develop the next generation materials sooner.

Approach

Over the last decade our group has developed the techniques and skills necessary to fabricate high quality electrodes with small quantities of materials: by small, we mean as little as 10 grams of active material. These electrodes, when cycled in 12 cm² pouch cells or 1.6 cm² coin cells perform as well as laminates produced on pilot and large production coaters with regard to power density and cycleability. This allows us to do a multitude of experiments in a short amount of time with minimal effort and waste. Two years ago we established a means of cross sectioning electrodes and performing EDS measurements to establish the average composition as one moves from the current collector up to the surface. We have established excellent relationships with Tier 1 battery suppliers that are willing to send us their highest-grade materials and are also willing to send us experimental material and discuss with us some work they have performed in the area.

This combination of resources allows us to produce non-ambiguous results. Thus, through a combination of investigating a host of processing conditions, materials, using relevant diagnostic techniques, we expect to determine the properties of electrodes required for high functionality and to be able to relate those properties to processing conditions and individual materials' characteristics.

Results

What follows is a compilation of results for fiscal year 2017 in roughly chronological order. One of our earliest investigations was the impact of calendering temperature on electrode workability. A single laminate of NCM of approximately 4 mAh/cm² was fabricated and allowed to dry by natural convection in the glovebox. Once dry, the calendering machine was turned on and the temperature of the rollers adjusted and allowed to come to equilibrium at several different temperatures (27, 50, 75, 100, and 125°C). A section of the laminate was calendered to 30% porosity at each of the different temperatures. An SEM was taken of each of the compressed electrodes. The SEM revealed that for all of the electrodes, the secondary particles of NCM were flattened and, for most particles, cracked. An example is provided in Figure II-1 of the laminate calendered at 100°C.

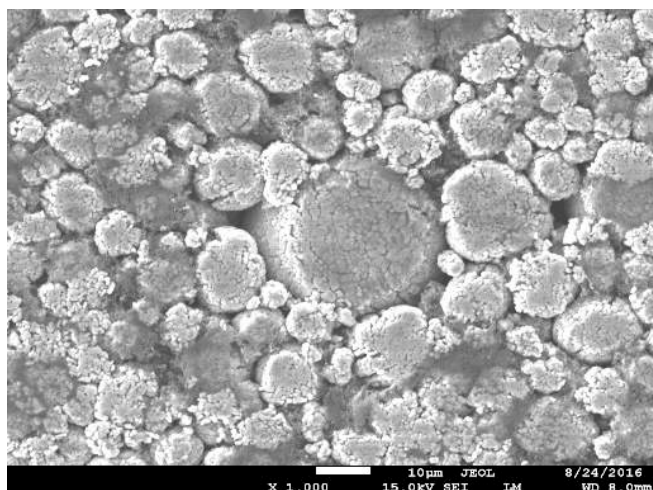


Figure II-1. SEM of surface of a laminate calendered at 100°C to 30% porosity. Notice flattened and cracked particles.

Once the electrodes were calendered, they were assembled in coin cells for electrochemical testing. The electrodes were put through a rate performance test and long-term cycling. The rate tests revealed that all of the laminates performed relatively the same (Figure II-2), indicating that the calendaring temperature had little impact on power performance. Once the rate performance test was completed, the cells were put on full charge and discharge cycle tests at C/3. As it turned out, the electrodes calendered at 100°C cycled the best (Figure II-3). At 350 cycles, these electrodes only displayed a 12.5% capacity fade. The others were very near to or greater than 20% capacity fade, which is considered end-of-life. These results still need to be confirmed with additional cell testing.

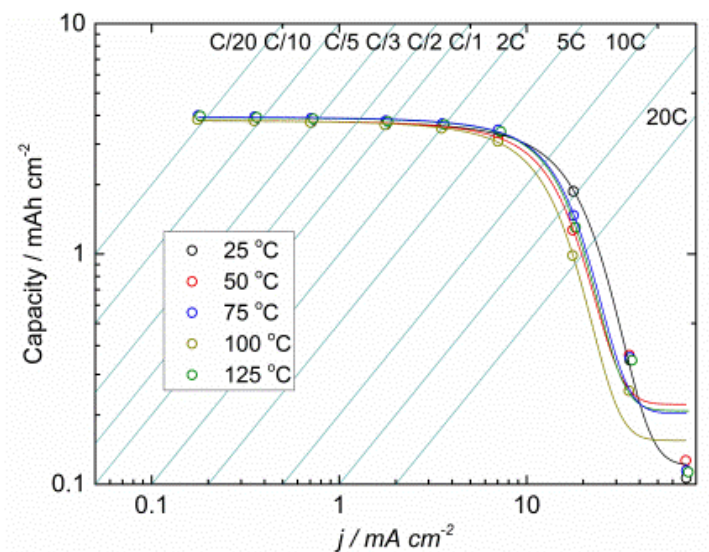


Figure II-2. Rate performance of a laminate calendered at different temperatures.

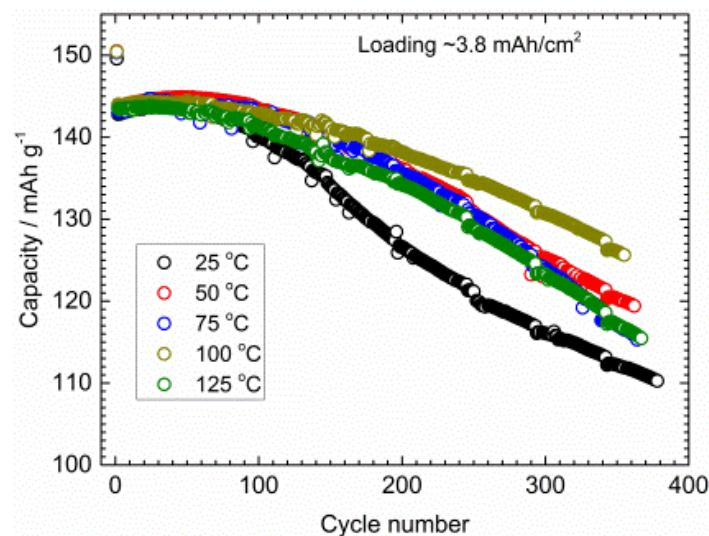


Figure II-3. Cycling performance of laminates in coin cells calendered at different temperatures.

Figure II-4 is a plot of cell resistance of the cathode *versus* depth of discharge for three cells with reference electrodes. The data shows that the area specific resistance drops with electrode thickness. If the resistance is normalized for cathode particle area, the order of resistance reverses but are more closely bunched together. This strongly suggests that the resistance of the electrodes is dominated by the charge transfer resistance of the active material. We intend to use similar cells to quantify cell failure modes of cycled, thick electrodes.

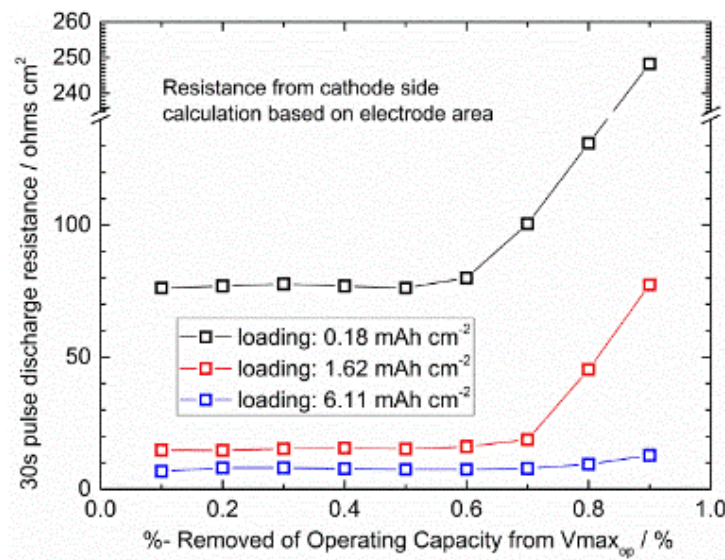


Figure II-4. Resistance for three loadings.

As described in one of our first reports in 2016 on the fabrication of thick electrodes, if we follow our typical procedures for making thick electrodes as we do low- and mid-loading electrodes, which includes drying in a glovebox *via* natural convection, a film of carbon and binder forms on the surface of the electrode. We investigated the impact this film has on cell performance.

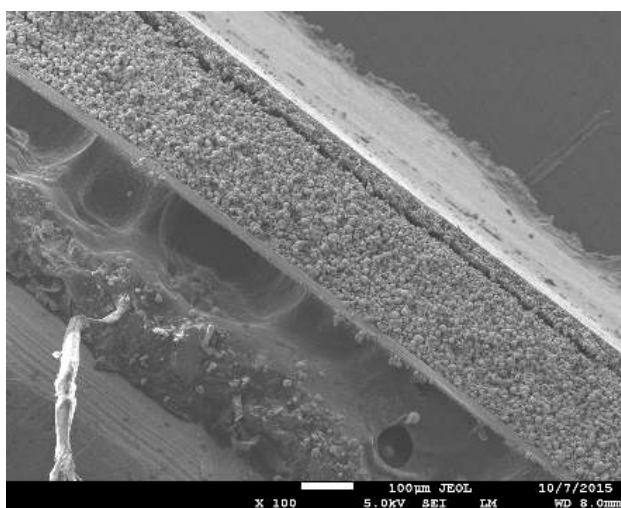


Figure II-5. Cross section of a dry electrode. Note layer on top of the electrode that appears to slightly detach.

Figure II-5 shows an SEM of a cross sectioned electrode made using our typical electrode fabrication procedures. A film can clearly be seen on the electrode surface. EDX indicates that this film consists almost entirely of carbon black and PVDF binder. This laminate was tested in a coin cell in three ways: 1) as is, 2) with the film removed from half of the surface, and 3) with the entire film removed. A fourth electrode of

similar loading was also produced using the same electrode formulation but modifying the processing conditions to prevent film formation. Figure II-6 shows the 30-second pulse discharge resistance for the four different cells *versus* depth of discharge. The electrode with the surface film shows twice as much resistance as the electrode where the film was removed. The electrode with half of the film removed, shows a resistance that is halfway between the two. The electrode prepared to have no surface film to begin with has nearly as low a resistance as the cell with the film removed. It is possible that this film consists of excess binder and carbon black that is not needed to make a high power electrode. We shall attempt to measure the fraction of carbon black and polymer in the surface film and fabricate a laminate without this excess. It will be interesting to see if electrodes can be produced that perform as well without the excess and that this might prove to be a method for determining the minimum amount of binder and conductive carbon one requires for producing a thick electrode with high power performance.

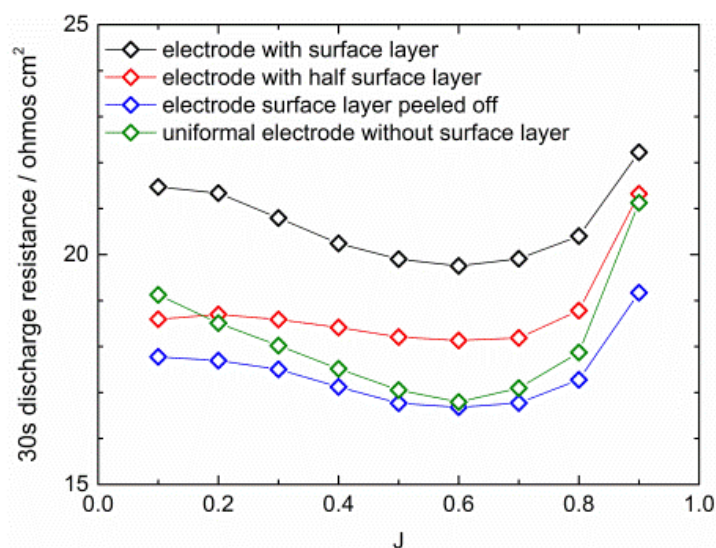


Figure II-6. 30-sec resistance of four cells: with the surface film, with half the surface film, surface film removed, no film to start with.

To date, we have been investigating changes to electrode homogeneity and performance as a result of changes to the inactive components and to the processing conditions. This includes changes to the binder molecular weight, the slurry viscosity, the addition of carbon nanotubes, and impacts of calendaring at different temperatures. Because binder molecular weight appears to have the greatest impact, we dove deeper into the effect of this parameter by assessing five binders of different molecular weights, see Table II-1.

Table II-1: Molecular weights for five commercial binders.

PVDF Commercial Name	KF1100	Kynar 761	HSV500	HSV800	HSV900
Molecular Weight	280 k	400 k	>400 k	<1 M	> 1 M

With our experience over the past few years in fabricating thick laminates, it is clear that the viscosity of the laminate is critical to its final homogeneity, especially when allowed to dry *via* natural convection in a glovebox. As the molecular weight of the binder goes up, the viscosity of the laminate goes up. In order to cast electrodes through a doctor blade, more NMP is required of slurries consisting of higher molecular binders. Once the laminates are cast and allowed to dry, they are cross sectioned and evaluated for their compositional uniformity using techniques developed here at LBNL. Other parts of the laminates are put through a bend test of rollers of ever reducing diameters while still other portions of the laminate are cut into circular electrodes

for coin cell testing. This assessment was not completed in time for this report; there are, however, some preliminary results.

As stated, when electrodes are allowed to dry overnight, the laminate with the lowest molecular weight binder ends up with a thin layer of binder and conductive carbon on the surface of the laminate. We believe that when provided a long time to dry (hours), the dense, large, active material particles can settle down to the current collector and the lighter, conductive agent and binder float to the top. A higher molecular weight binder appears to inhibit this separation.

We also find that laminates with higher molecular weight binders can be bent around smaller mandrels. Thus, higher molecular weight binders are beneficial to making thick electrodes that are to be wound to form cylindrical cells.

Since electrodes in industry are typically dried in approximately three minutes (this is based on a coating speed of 30 m/min and a drying length of *ca.* 100 m), we think it is imperative to perform studies on electrode uniformity and performance based on electrodes dried on the order of minutes, not hours. Efforts to dry laminates freshly cast in a glovebox are now underway. Preliminary results indicate that thick electrodes with low molecular weight binders dry uniformly, but those of high molecular weight display large crevices (mud cracking) where the current collector is clearly visible when looking down at the electrode. Unfortunately, thick laminates of low molecular weight binders do not possess the required properties to prevent delamination or adequate electrode bending. Mud cracking often occurs when a solvent leaves the pores of a slurry resulting in a layer of solvent around a portion of the solids with surface tension that pulls the solids together. If the solids cannot move easily, stress builds in the laminate until a defect occurs and a crack is generated that relieves the stress. These results suggest that an optimization of the binder content and molecular weight may result in both uniform laminates that bind well and do not crack under bend tests. We shall also assess electrodes made from a combination of binders of different molecular weights. Preliminary results in this area were very encouraging.

Conclusions

From the effort in 2017, we have been able to conclude the following.

Calendering

Electrodes of NCM that consist of 10 micron secondary particles and a binder and carbon content of less than 8% should not be calendered below 40% porosity, no matter the temperature, otherwise the risk of breaking the active material particles escalates. Calendered electrodes do not “bounce back” after the addition of electrolyte even after a week of soaking but do expand to their original thickness after cycling. Calendering improves the mechanical properties of the laminates but this may strictly be a geometric factor where thinner electrodes have less hoop stress than thicker electrodes when wound around the same mandrel diameter.

Natural convection drying

Slow drying allows more time for active material particles to settle and separate from the conductive carbon and polymer leading to a film of carbon and binder on the surface of the electrode. This film increases the areal resistance of the electrode when measured in a pouch cell. If the film is gently removed, the resistance of the electrode is decreased to that of an electrode that is prepared in such a way as to avoid forming a film. At this point, we know we can make thick electrodes without a film if we either increase the molecular weight of the binder or reduce the amount of solvent in the slurry – both result in a higher viscosity slurry. Thus, we don’t know if viscosity is solely responsible for the improvement or if chemistry plays a role. Thick electrodes with high molecular weight binder can be wrapped around a smaller mandrel than those with low molecular weight binder. Thick electrodes with high molecular weight binder have a more uniform composition and adhere more strongly to the current collector than electrodes with low molecular weight binder.

Fast drying

When attempting to fabricate thick electrodes at today's industrial rates (*ca.* 3 minutes), we find that electrodes with low-molecular weight binder dry more evenly than those with high molecular weight binder. Those with high-molecular weight binder display “mud cracking.” This phenomena can be attenuated if the drying temperature is sufficiently lowered to extend the time to drying by a factor of three (this would effectively reduce production rates by a factor of three, hence, increasing cost.)

These findings suggest that to produce laminates at a rate of 30 m/min may require a binder of a molecular weight between 300,000 and 1,000,000. Our goal for the rest of the project continues to follow the original proposal trajectory of investigating methods to fabricate thick electrodes at drying rates commensurate with today's manufacturing rates.

Key Publications

1. Manuscript on the effect of binder content on electrode fabrication in preparation.
2. “Nature of the Impedance at Low States of Charge for High-Capacity, Lithium and Manganese-Rich Cathode Material Batteries and Energy Storage,” Wenfeng Mao, Guo Ai, Yiling Dai, Yanbao Fu, Xingyun Song, Herman Lopez, and Vincent Battaglia, *J. Electrochem. Soc.* **163**(14): A3091-A3098, 2016
3. “Improving the over-all performance of Li-S batteries *via* electrolyte optimization with consideration of loading condition,” Guo Ai, Zhihui Wang, Yiling Dai, Wenfeng Mao, Hui Zhao, Yanbao Fu, Yunfei En, Vincent Battaglia, Gao Liu, *Electrochimica Acta*, Volume **218**, 10, Pages 1–7, 2016

II.A.2 Electrode Architecture-Assembly of Battery Materials and Electrodes (Hydro-Quebec)

Karim Zaghib, Principal Investigator

Hydro-Québec (IREQ)
1806 Lionel Boulet
Varennnes, QC J4X 1S1
Phone: 450-652-8019
E-mail: Zaghib.Karim@ireq.ca

Tien Duong, Technology Manager

U.S. Department of Energy
Phone: 202-586-7836
E-mail: Tien.Duong@ee.doe.gov

Start Date: October 1, 2012

End Date: December 31, 2017

Total Project Cost: \$340,666

DOE share: \$170,333

Non-DOE share: \$170,333

Project Introduction

The target of the DOE Program is to identify the next generation of high-energy batteries. Achieving this target will require materials of higher capacity and improved coulombic efficiency or cells with higher voltage. High-capacity anode materials such as Si or Sn alloys have the potential to fulfill the energy density requirements for EV/PHEV applications. However, large volume expansion during the lithiation process of these materials usually leads to fast capacity fade that hinders its practical applications. Real-time SEM observations during charge/discharge of Si-anodes demonstrated that decreasing the particle size to nanometer scale is an effective means of accommodating the volume change, and thus delaying its degradation.

HQ proposed a strategy to design the architecture of the Si-anode material that tolerates the volumetric expansion and provides acceptable cycle life with low capacity fade. The particle size, binder type and electrode composition are the main parameters that define the formulation of the Si-anode. The porosity of the electrode has a direct impact on the performance, and therefore was optimized by investigating various mixing methods.

Objectives

The goal of this project is to develop an electrode architecture based on nano-Si powders. To achieve the objective, this project investigates the structure of nano-Si powders that provide acceptable volume change and long cycle life, while still maintaining the high capacity performance of Si. In our previous work, we successfully produced low-cost metallurgical nano-Si powders that yielded nano-Si/C composites which showed better processability during mixing and coating. However, designing full cells with high energy density and long cycle life is still a big challenge. Anodes with high loading are a prerequisite for high energy density. A long cycle life of > 900 cycles with low loading electrodes was achieved, but it was very difficult to achieve >100 cycles with the appropriate loading level.

The project scope will include the control of the particle size distribution of the Si nano-powder, crystallinity, Si composition and surface chemistry of the nano-particles. At this stage of the project, a significant effort will be allocated to failure mode analysis of nano-Si anodes before and after cycling. We expect that this analysis will help to understand the failure modes of the anode and help guide the effort to improve the particle morphology and electrode architecture.

Approach

1. Explore a variety of synthesis methods to produce low-cost nano-Si materials with controlled purity and particle morphology.
2. Develop an appropriate silicon-anode architecture that tolerates volumetric expansion and provides an acceptable cycle life with low capacity fade.
3. Identify a binder and electrode composition by investigating parameters that define the electrode structure such as porosity, loading and electrode density. The optimized Si-anode will be matched with a high-voltage NMC cathode to fabricate large format Li-ion cells.
4. Use *in-situ* techniques such as SEM and impedance spectroscopy to monitor the particle and electrode environment changes during cycling.
5. Achieve cost reduction by moving from the more costly Si (>\$50/kg) to metallurgical Si which is projected to be \$3~\$5/kg.

Results

1. 1.5Ah Full Cell Test Result

Li-ion pouch laminated cells based on NMC//nano-Si/C composite with a capacity of 1.5Ah were assembled (Figure II-7a). The loadings are 2.2 and 10.3 mg/cm², respectively, for the anode and cathode. The anode/cathode ratio was 1.15 based on the capacities of the half cells with these cathode and anode materials. The electrochemical performance (formation capacity, rate capability and cycle stability) were evaluated. The capacity of the cell at 0.2C rate revealed a discharge capacity around 1400 mAh between 2.75 V and 4.4 V, which is 95% of the designed cell capacity (Figure II-7b).

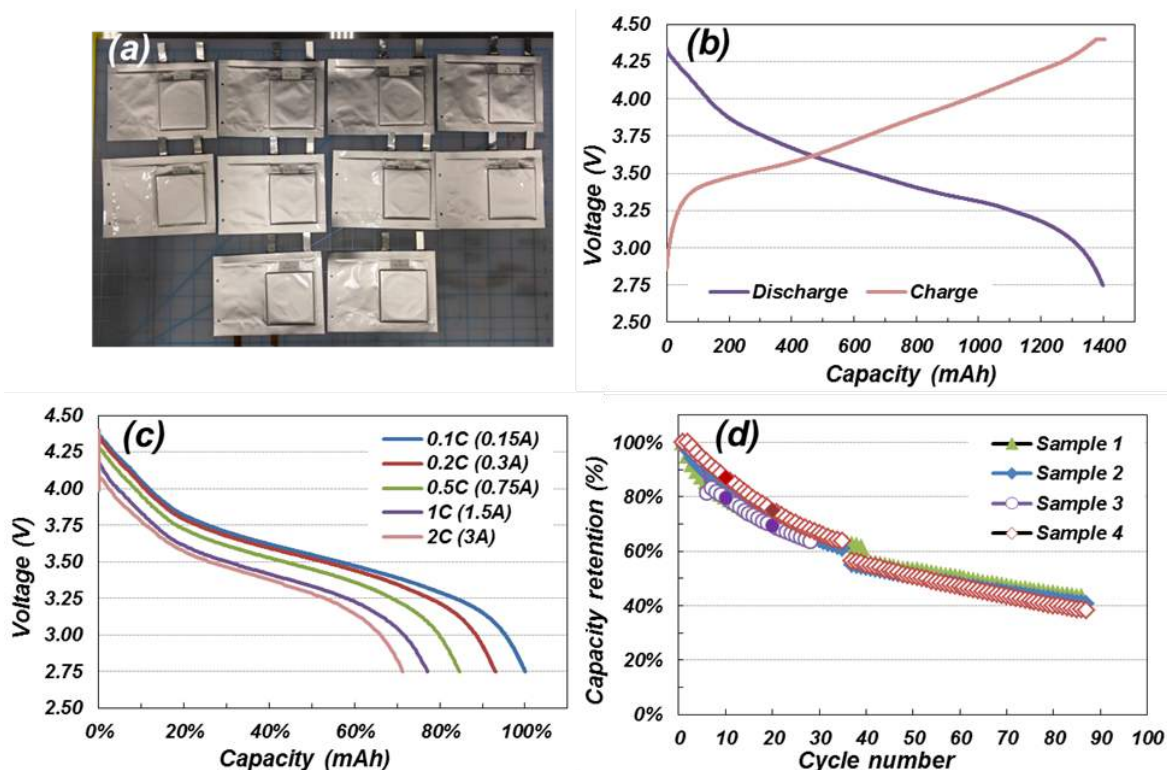


Figure II-7. Full cell performance of 1.5 Ah pouch-type cell (a) assembled cell (b) voltage profile during charge-discharge between 2.75 V and 4.4 V at 0.2C rate (c) rate capability at different current rates and (d) cycle life at room temperature.

The rate capability of the cells was evaluated at different currents (0.1-2C). At 2C rate, the cell delivered 70% of the capacity obtained at 0.1C (Figure II-7c). The voltage profiles showed similar behavior at the different rates, and the cells have low IR drop. However, the cycling stability of these cells shows high capacity fade (Figure II-7d). The capacity decreases continuously with cycles, and the capacity retention was only 40% during the experiment lasting 90 cycles. We attribute this capacity fade to the instability of the anode material. The loss of contact between Si anode particles and the mechanical disintegration of the anode film are the main cause of this capacity fade.

2. nano-SiO_x

As part of an effort to mitigate the volume expansion of Si particles during charge/discharge, Hydro-Quebec synthesized SiO_x with a mixed morphology of nano-fibers and nano-particles. Figure II-8 shows that the material is composed of randomly mixed nano-fibers with a diameter 10-100 nm and nano-particles < 100 nm. The material is synthesized in the one-step plasma process without post treatment. The process parameters, such as precursor feeding rate, gas flow rate, and carrier gas concentration, were controlled to obtain the morphology with different fiber-to-particle ratio. Figure II-8 shows the results obtained by using 2 different process conditions. For condition A, a mixture of Ar and He was used as a plasma sheath gas, while a mixture of Ar and H₂ was used for condition B.

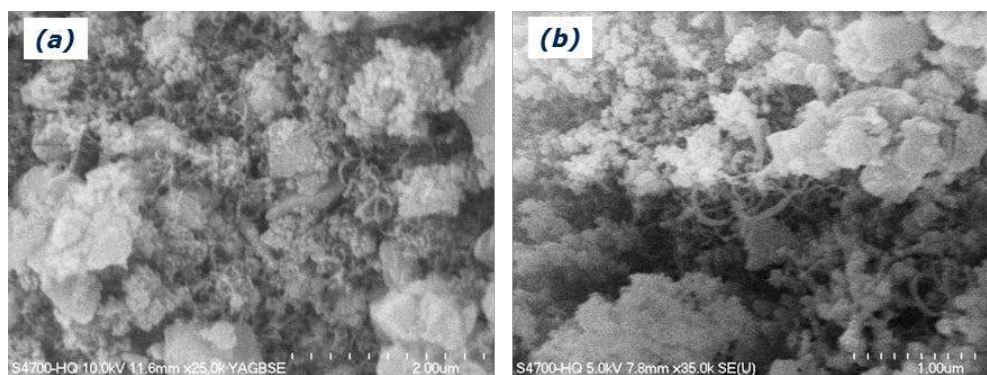


Figure II-8. SEM images of nano-SiO_x fibers (a) condition A and (b) condition B.

The electrochemical performance was tested with a coin-type half-cell containing 1M LiPF₆-EC-DEC-10% FEC, and the result is shown in Figure II-9. The loading of active material (SiO_x) was around 0.5 mg/cm² and the electrode density was 0.7 g/cc. The composition of nano-SiO_x was 50% and a water-based binder was used in the electrode. The capacity was about 1050 mAh/g for condition A and 1150 mAh/g for condition B at C/24. After the first charging reaction, where the irreversible capacity is obtained due to the conversion reaction of SiO_x with Li⁺, the coulombic efficiency was > 95% in the following cycles. The capacity retention was quite stable without capacity loss after 90 cycles at C/6 rate (Figure II-9b).

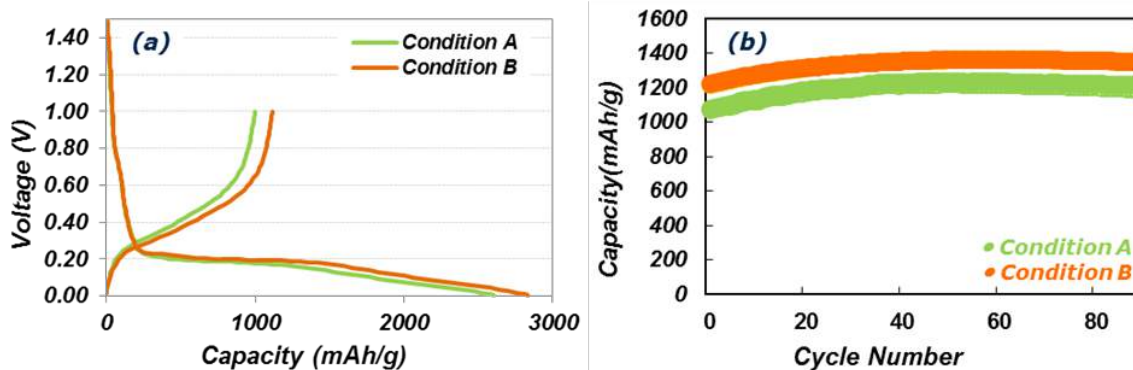


Figure II-9. Electrochemical performance of (a) 1st charge/discharge voltage profile with C/24 rate between 1.0 V and 0.005 V and (b) cycle life with C/6 rate at room temperature.

The results show that SiO_x is a promising material in high-capacity anodes. However, further effort is needed to improve the morphology and enhance the coulombic efficiency in the first cycle.

3. Electrospray Process

During this project year, Hydro-Quebec focused on improving the electrochemical performance with different synthesis routes to produce nano-Si/C composites by exploring the electrospray process. In our previous efforts, the capacity and cyclability was improved with heat treatment of the electrode with polyimide binder. Based on this result, we synthesized nano-Si/C composite secondary powders with polyimide-binder solutions.

The syringe was charged with slurry at a high electric potential of 20kV, and the distance from the ground electrode plate was 10 cm. The powder samples are obtained with a water bath filled to 5 mm with deionized water, and the injection speed was 50 $\mu\text{l}/\text{min}$. The samples are filtered and heat treated at 600°C for 3 hours in a N_2 flow furnace. As it can be seen in Figure II-10a, the powder is composed of two different shapes; small-size flakes (< 100 μm) and large-size spheres (< 400 μm). The electrochemical performance was tested with a coin type half-cell, and the results are shown in Figure II-10b. The anode loading was approximately 1.05 mg/cm^2 , and the electrode density was about 1.0 g/cc . A water-base acrylic resin was used as a binder without any problem with gas generation. The capacity was about 3500 mAh/g at C/24, and the 1st cycle efficiency was 76%.

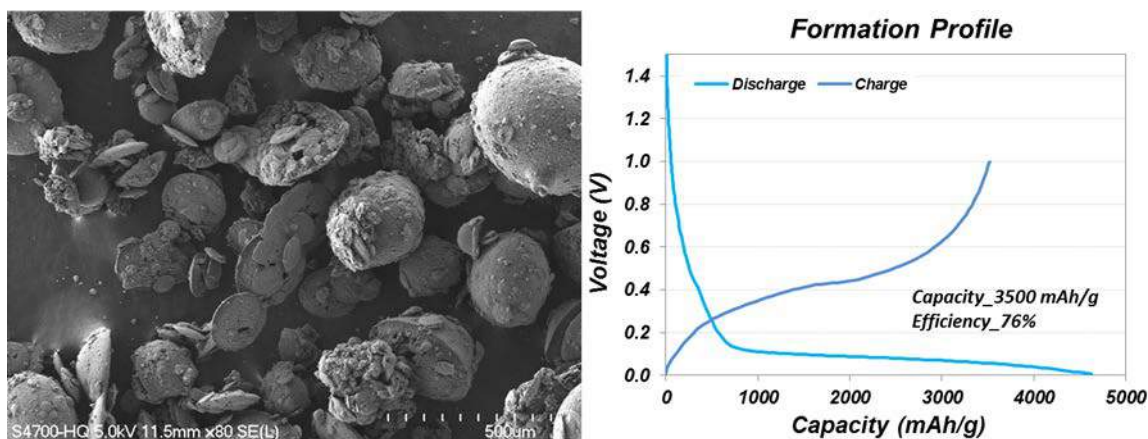


Figure II-10. (a) SEM image of nano-Si/C composite made by electrospray process and (b) 1st cycle discharge/charge voltage profile.

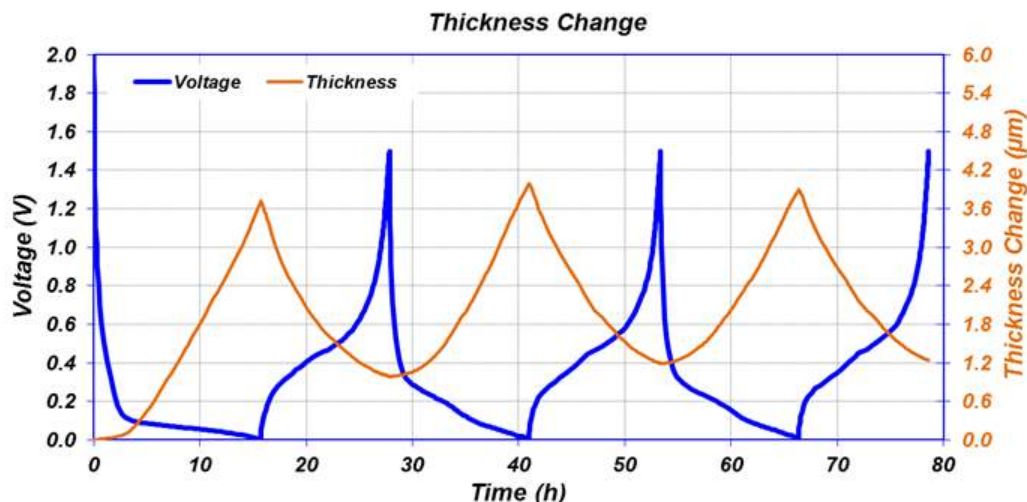


Figure II-11. Cell thickness monitoring during cycling with C/24 rate between 1.5 V and 0.005 V at room temperature.

The anode thickness change was monitored by an electrochemical dilatometer, see in Figure II-11. The thickness increases after SEI formation and reached 3.7 μm at the end of the 1st discharge. The thickness increase is equivalent to 12% of the fresh electrode. In the following charge step, the thickness decreases by about 2.7 μm , and the electrode is 1 μm thicker than that of the fresh electrode due to SEI formation during the first cycle. Further effort will focus on understanding the variation in thickness during cycling by modifying the binder and the electrolyte.

4. Optimization of Electrospray Process

In the previous electrospray trials, a composite of secondary micro-size nano-Si/C with polyimide binder solution was produced. Based on this result, we evaluated different stable nano-Si/C composites with various types of carbons to optimize the electrospray process.

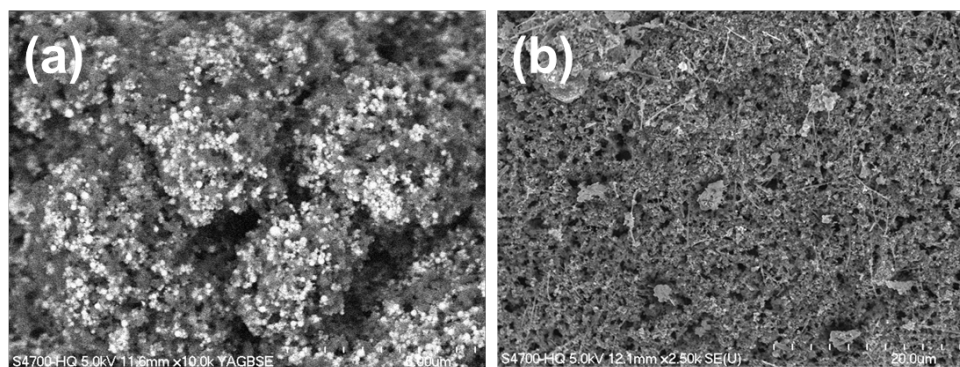


Figure II-12. SEM image of (a) version 1 nano-Si/C composite made by electrospray process and (b) version 2.

The powder was produced by the same procedure in a water bath. The composite version 1 is composed of nano-Si, acetylene black and polyimide binder. In composite version 2, carbon fibers are added in the formulation. Figure II-12a shows an SEM image of composite version 1; the powder is well mixed with carbon but looks less dense. On the other hand, in Figure II-12b with composite version 2, the structure of the composite with carbon fibers appears stronger and textured.

The electrochemical performance was tested with a coin type half-cell, and the results are shown in Figure II-13. The total loading of the anode was around $1\text{mg}/\text{cm}^2$ ($1\text{mAh}/\text{cm}^2$), and the cells were cycled at C/6 rate for charge and discharge. The composite version 2 that contains carbon fiber showed more stable

capacity than that with composite version 1 after more than 100 cycles. In addition, the coulombic efficiency of the cell containing composite version 2 was higher. After ~50 cycles, the cell with composite version 1 showed decreasing efficiency, whereas the efficiency of the cell with composite version 2 continued improving. This behavior is attributed to the presence of the carbon fiber network, which helps to maintain the electronic contact between particles in spite of the volume changes.

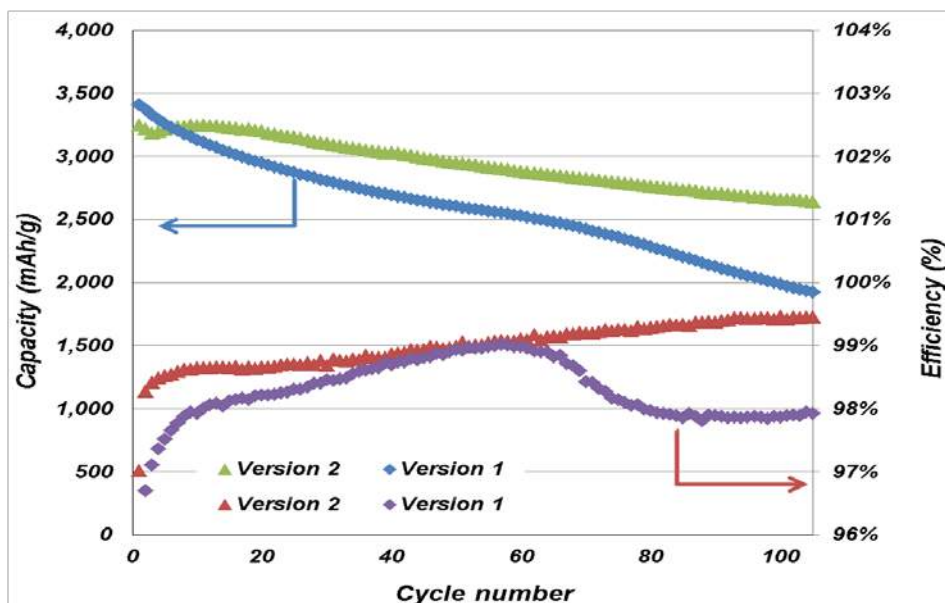


Figure II-13. Cell performance during cycling at C/6 rate between 1.5 V and 0.005 V at room temperature.

Conclusions

During this year, Hydro-Quebec synthesized nano-SiO_x fibers by a plasma process. This material has showed a stable cycle life, but effort is still needed to improve the 1st cycle coulombic efficiency. The electrospray method was explored to produce nano-Si/C composites with polyimide binder. With this method, we obtained mechanically stronger powder than with other binders, PVDF, CMC and Alginic acid. The carbon in the electrospray composition has an effect on performance of the final product. Adding VGCF carbon fiber showed a net improvement in the cycle life and coulombic efficiency by maintaining the electronic contact between particles in spite of the volume changes.

As deliverables of project year 2017, Hydro-Quebec delivered SBR/CMC binder materials and 1.5 m of anode electrode with water-based CMC/SBR binder in the 3rd Quarter, and 20 g nano-Si/C composite powders produced by the electrospray process in the 4th Quarter.

Key Publications

1. BMR 2017 1st Quarterly Report, January, 2017
2. BMR 2016 2nd Quarterly Report, April, 2017
3. BMR 2016 3rd Quarterly Report, July, 2017
4. BMR 2016 4th Quarterly Report, October, 2017

II.A.3 Design and Scalable Assembly of High-Density, Low-Tortuosity Electrodes (MIT)

Yet-Ming Chiang, Principal Investigator

Department of Materials Science and Engineering
 School of Engineering
 Massachusetts Institute of Technology
 77 Massachusetts Avenue
 Cambridge, MA 02139-4307
 Phone: 617-253-6471
 E-mail: ychiang@mit.edu

Tien Duong, Technology Manager

U.S. Department of Energy
 Phone: 202-586-7836
 E-mail: Tien.Duong@ee.doe.gov

Start Date: May 22, 2013

End Date: April 3, 2017

Total Project Cost: \$1,075,344

DOE share: \$1,075,344

Non-DOE share: \$0

Project Introduction

The high cost (\$/kWh) and low energy density of current automotive lithium-ion technology is in part due to the need for thin electrodes and associated high inactive materials content. If successful this project will enable use of electrodes based on known families of cathode and anode actives but with at least 3 times the areal capacity (mAh/cm²) of current technology while satisfying the duty cycles of vehicle applications. This will be accomplished via new electrode architectures fabricated by scalable methods with higher active materials density and reduced inactive content, and will in turn enable higher energy density and lower-cost EV cells and packs.

Objectives

The objective of this project is to develop scalable high density low-tortuosity electrode designs and fabrication processes enabling increased cell-level energy density compared to conventional Li-ion technology and characterize and optimize the electronic and ionic transport properties of controlled porosity and tortuosity cathodes as well as densely-sintered reference samples. Success is measured by the area capacity (mAh/cm²) that is realized at defined C-rates or current densities.

Approach

Two techniques are used to fabricate thick, high density electrodes with low tortuosity porosity oriented normal to the electrode plane: 1) Directional freezing of aqueous suspensions; and 2) Magnetic alignment. Characterization includes measurement of single-phase material electronic and ionic transport using blocking and non-blocking electrodes with ac and dc techniques, electrokinetic measurements, and drive-cycle tests of electrodes using appropriate battery scaling factors for EVs.

Within ABMR, this project collaborates with Antoni P. Tomsia (LBNL) in fabrication of low-tortuosity, high-density electrodes by directional freeze-casting, and with Gao Liu (LBNL) in evaluating Si anodes. Outside of ABMR, the project collaborates with Randall Erb (Northeastern Univ.) on magnetic alignment fabrication methods for low tortuosity electrodes.

Results

This project was completed during the second quarter of FY 2017. The following two milestones were completed:

1. Go/No-Go Milestone: Fabricate and test half-cells and full lithium-ion cell in which both cathode and anode are prepared by magnetic alignment, and in which at least one electrode is prepared by non-sintering process. Go/No-Go Criteria: Measured area capacity of a half-cell is at least 10 mAh/cm² and of a full cell is at least 8 mAh/cm². (12/31/16). (Completed)
2. All milestones have already been completed. For this report, additional results are reported for preparation of low-tortuosity thick electrodes from other materials beyond what were previously demonstrated, using the non-sintering magnetic alignment method. (03/31/17). (Completed)

In the second quarter of FY 2017, additional results were reported for preparation of low-tortuosity thick electrodes from materials beyond LiCoO₂ (Umicore, average particle size 2–4 μm) and MCMB 6-28 (Osaka Gas, average particle size 6 μm), which were reported in the previous quarterly reports for this project. The goal is to investigate whether the non-sintering magnetic alignment method can be generally applied to various electrode materials.

Commercially available electrode materials were chosen for this study: LiFePO₄ (LFP, MTI Corporation, D50 ~3.5 μm), OMAC-carbon (Osaka Gas), LiNi_{1/3}Mn_{1/3}Co_{1/3}O₂ (NMC333, Toda, average particle size ~10 μm), LiNi_{0.8}Co_{0.15}Al_{0.05}O₂ (NCA, Toda, average particle size 2-5 μm), and MCMB (MTI Corporation, D50 ~18 μm). These materials were mixed with acetylene black, polyvinyl alcohol, water, and a small amount of ferrofluid (~5 vol%) and sonicated using an ultrasonic probe to make the emulsion-based slurries, whose formulations are similar to those used for LiCoO₂ (Umicore) and MCMB 6-28 (Osaka Gas) reported in our previous quarter reports. The slurries were then dried in silicone molds on top of magnets to make the electrodes. After initial drying, the electrodes were rinsed thoroughly using kerosene and acetone and further dried at 100°C under vacuum.

The electrodes were cross-sectioned and examined using scanning electron microscopy (Figure II-14). Figure II-14A and Figure II-14B show that vertically aligned pore channels are successfully introduced into LFP and OMAC-carbon electrodes. The result with NMC333 electrode was less satisfactory (Figure II-14C).

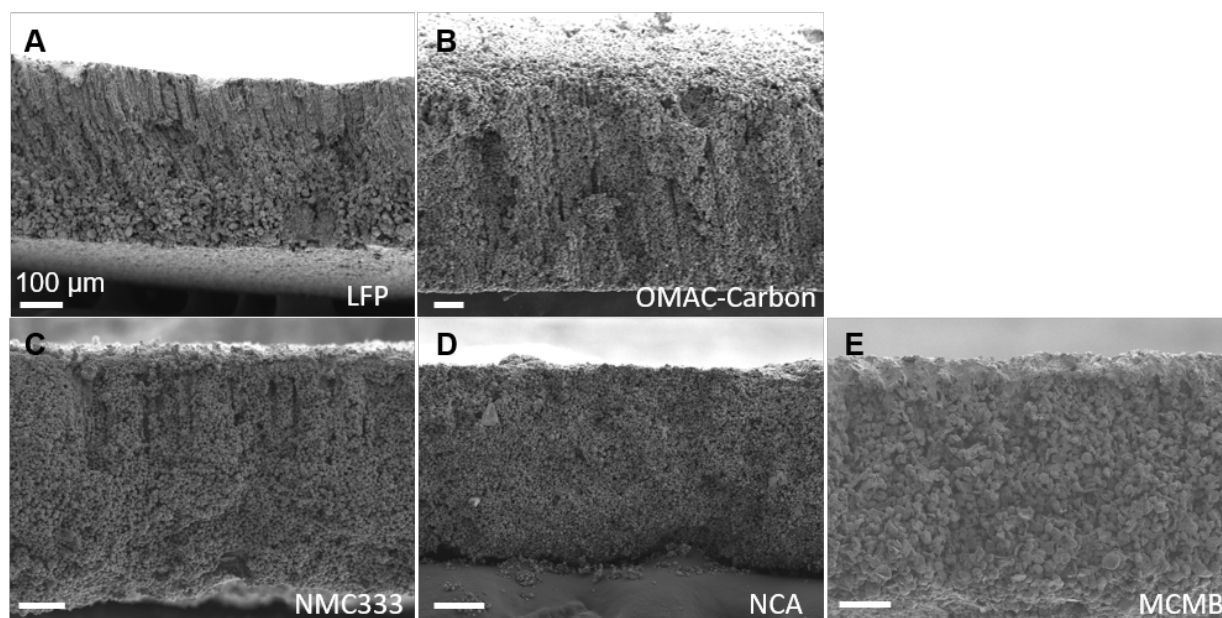


Figure II-14. Electrodes of different materials prepared by the non-sintering magnetic alignment method. A, LFP (MTI Corporation). B, OMAC-carbon (Osaka Gas). C, NMC333 (Toda). D, NCA (Toda). E, MCMB (MTI Corporation).

Conclusions

The results demonstrate that the non-sintering magnetic alignment method can indeed work with electrode materials beyond the previously tested LiCoO_2 (Umicore) and MCMB 6-28 (Osaka Gas). The result with NMC333 electrode was less satisfactory. Vertically aligned pore channels were observed but they did not completely span the thickness of the electrode. For NCA and MCMB (MTI) electrodes, vertically aligned pore channels were not observed. The specific reasons are not yet clear, but particle size and surface chemistry may play important roles; these factors may be further investigated.

II.A.4 Advanced Lithium Ion Battery Technology – High Voltage Electrolyte (Daikin America, Inc.)

Ron Hendershot, Principal Investigator

Daikin America, Inc.
2749 Highway 20 West
Decatur, AL 35601
Phone: 256-260-6302
E-mail: hendershot@daikin-america.com

Joseph Sunstrom, Principal Investigator

Daikin America, Inc.
2749 Highway 20 West
Decatur, AL 35601
Phone: 256-260-6314
E-mail: sunstrom@daikin-america.com

Alec Falzone, Principal Investigator

Daikin America, Inc.
2749 Highway 20 West
Decatur, AL 35601
Phone: 256-260-6342
E-mail: afalzone@daikin-america.com

Tien Duong, Technology Manager

U.S. Department of Energy
Phone: 202-586-7836
E-mail: Tien.Duong@ee.doe.gov

Start Date: October 1, 2016	End Date: December 31, 2019	
Total Project Cost: \$1,826,895	DOE share: \$1,250,000	Non-DOE share: \$576,895

Project Introduction

The use of electrolytes containing small fluorinated molecules to enable stable high voltage (> 4.3 V) battery operation is the focus of this project. Previously, Daikin has shown that it is possible to operate lithium ion batteries utilizing several different cathode chemistries up to 4.5 V. This is accomplished by reducing the gas generation originating from electrolyte decomposition at high voltage. The primary mechanism for this is not completely understood, but the hypothesis is that the fluorinated molecules form a film on the highly oxidizing cathode. It is known that battery cycle performance above 4.5 V drops significantly, however the source of the observed performance loss is not yet understood. The target for this project is to achieve 300 cycles above 80% capacity retention at 4.6 V. A better understanding of gas evolution, which happens above 4.3 V and the failure mode above 4.5 V, is sought in order to propose mitigation strategies which will facilitate better high voltage performance in lithium ion batteries.

The battery industry trend for cathode materials is toward reducing the overall cobalt content (i.e., higher nickel) for a variety of reasons. Some of which include: increasing cost, loss of supply, and human rights issues. The experiments proposed for this project will encompass a range of cathode materials with successfully higher nickel content. This will be performed in order to comprehend how fluorinated electrolyte interacts with various cathode surfaces. This is with the anticipation that the lithium ion battery industry will

move towards nickel-rich cathodes, which can operate at higher voltage in order to achieve more energy-dense batteries.

Objectives

This three-year project can be divided into three main milestone topics, each spanning one fiscal year:

1) understanding of gassing mechanisms and kinetics, 2) examining physical and chemical aspects of film formation, and 3) observation of chemical and structural evolution of electrode surfaces at various operating conditions. The FY 2017 budget period involves the analysis of electrolyte gassing mechanisms as a function of cathode chemistry, voltage, temperature and fluoroethylene carbonate (FEC) concentration. The Daikin formulations often contain at least two fluorinated compounds, one of which is FEC. It has been established in a previous Daikin project that while FEC appears to enhance cycling performance, it gasses at high voltage. Sampling of gas generated during cycling is to be accomplished by gas chromatography/mass spectrometry (GC/MS). It is hoped by identifying individual gases both qualitatively and quantitatively that a better knowledge of the factors which contribute to gas formation can be attained. We then aim to select mitigation strategies to avoid decomposition pathways due to gas generation.

Approach

The baseline of current best-practice fluorinated electrolyte was determined by reviewing already obtained data from high-voltage lithium ion batteries from a previously funded project (DOE EE0006437). In parallel, an up-to-date literature and patent review has also been performed to explore other cutting edge developments in 2017. Three electrolytes were selected as standards for this project: 1.2 M LiPF₆ ethylene carbonate (EC)/ethyl methyl carbonate (EMC) 80:20 (v/v %), 1.2 M LiPF₆ EC/EMC/fluoroether (FE) 20:60:20 (v/v %) and 1.2 M LiPF₆ FEC/EMC/FE 20:60:20 (v/v %). These represent electrolytes with zero, one and two fluorinated solvents added, respectively. All electrolytes also contain propane sultone (PS) (1% w/w) as an additional anti-gassing additive. 200 mAh dry wound cells have been purchased as test vehicles. The cathode chemistries studied (with increasing mole fractions of nickel are: LiCoO₂ (LCO), LiNi_xMn_yCo_zO₂ (NMC xyz = 111, 532, 622) and LiNi_{0.8}Co_{0.15}Al_{0.05}O₂ (NCA) all paired with artificial graphite anodes. Analysis of the gases produced at high voltage (> 4.3 V) will be completed and compared to cells cycled at a baseline voltage of 4.2 V, which is the current battery industry standard. A post mortem analysis of the gas sampled cells will be conducted for qualitative and quantitative gas analysis. In addition, the cathodes and anodes will be removed for surface analysis to observe SEI film formation and changes in material properties. A mass balance approach to the cells will be used in order to propose performance limiting factors and strategies to overcome them.

Results

Setup of Experimental Tools, Review State of the Art and Establish Study Baselines – Milestone 1

Work in the first year (FY 2017) has been divided into two tasks which progress against the first four milestones: 1) establishing a baseline based on knowledge learned from first DOE funding opportunity and 2) initiating setup of instruments and samples for gas analysis.

Final cell test results from Argonne National Laboratory were received at the end of March. The cycle testing results are shown in Figure II-15 for three groups:

- a. Group 1 hydrocarbon electrolyte cycled to 4.5 V, (black trace)
- b. Group 2 fluorocarbon best practice electrolyte cycled to 4.5 V, (red trace)
- c. Group 3 fluorocarbon best practice electrolyte cycled to 4.6 V, (blue trace)

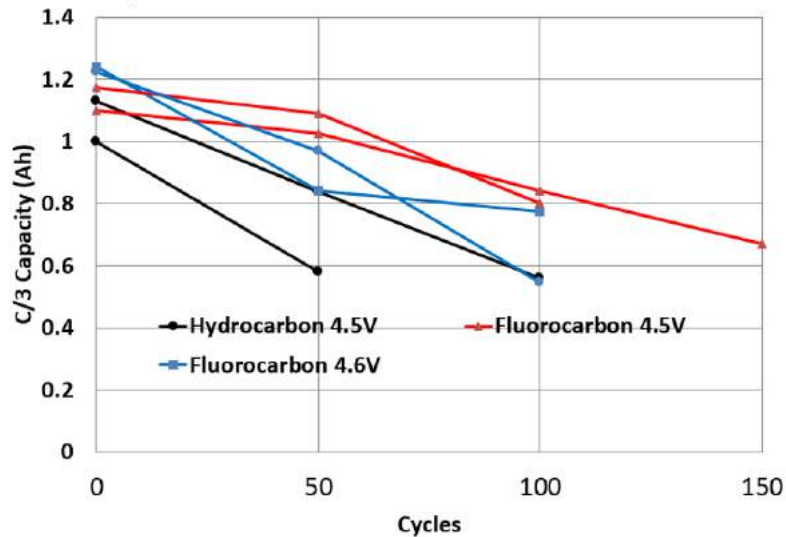


Figure II-15: Cycle life (C/3) discharge for a) Hydrocarbon electrolyte charged to 4.5 V (black), 2) fluorocarbon electrolyte charged to 4.5 V (red), and fluorocarbon electrolyte charged to 4.6 volt (blue)

The results confirm previous Daikin internal results which indicate that fluorocarbon electrolyte performs better than hydrocarbon up to 4.5 V but there is a performance decrease when the upper voltage is extended to 4.6 V. This result fixed the study voltages to 4.2 (both electrolytes work), 4.5 (only fluorinated electrolyte works) and 4.6 V (neither electrolyte works) as initially proposed.

Additional baseline experiments were performed in order to adjust experimental parameters to generate gas in a reasonable timeframe for analysis. Figure II-16 displays the volume change in pouches containing NMC111 charged cathodes with graphite anodes stored with electrolyte at 60°C. The targeted temperature settings were established at 35, 45 and 50°C.

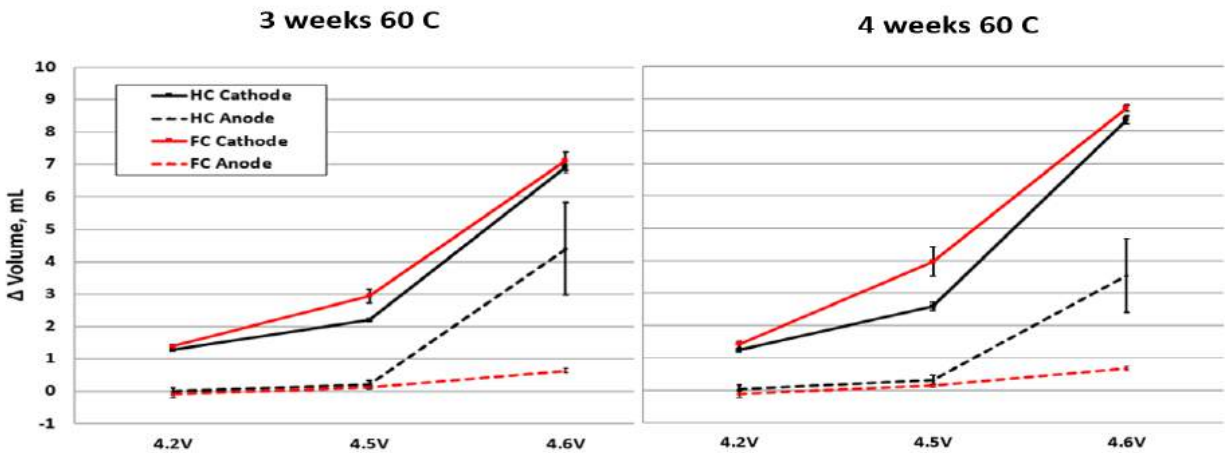


Figure II-16: Gas volume change at 3 weeks (left) and 4 weeks (right) for NMC111 cathodes with graphite anodes when exposed to electrolyte at 60 °C

Gas Composition as a Function of Voltage and Cathode – Milestone 2

In order to determine the gas composition as a function of various operating conditions (FEC, voltage, cathode material, etc.), we constructed ninety (LCO, NMC622) 200 mAh cells for an extended open circuit voltage (OCV) test to be carried out at various temperatures for analysis. These cells underwent initial formation then were charged to constant voltage to the desired voltage (4.2, 4.5, and 4.6 V) and placed into ovens at 35, 45, and 55°C. Following this extended aging period with intermittent volume measurements, the cells were discharged and punctured with a gas tight syringe for headspace analysis.

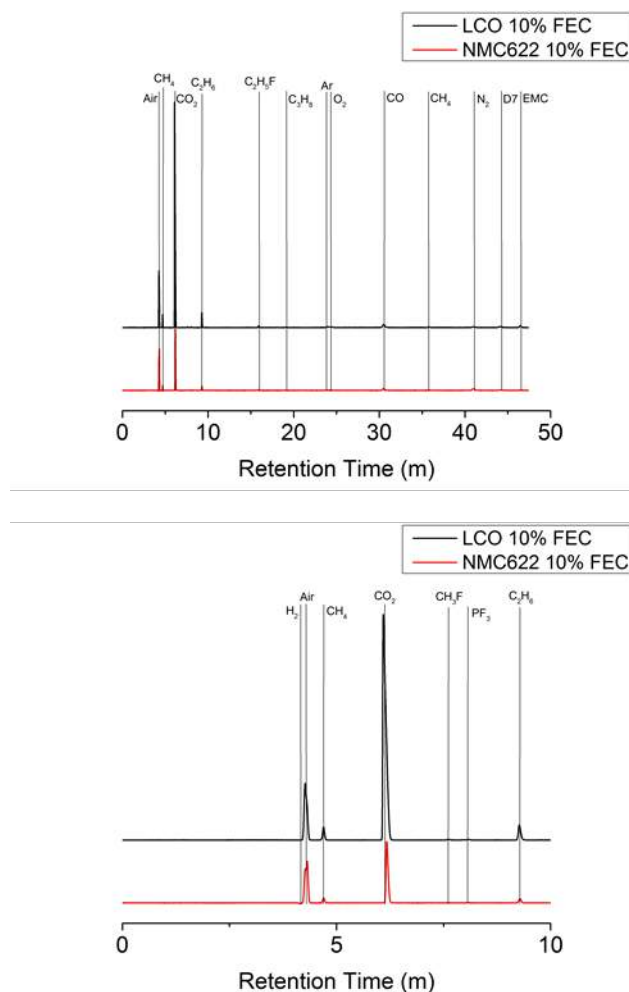


Figure II-17: TCD chromatogram overlays of 4.6 V LCO and NMC622 cells with 10% FEC concentration in the electrolyte. On the top is the full spectrum, whereas the bottom focuses on 0-10 minutes. H₂ is seen in the NMC622 cell and PF₃ in the LCO cell.

Gas analysis and the determination of components was performed using GC-MS/TCD (thermal conductivity) instrument. Figure II-17 depicts the full TCD chromatograms (left) and 0-10 minutes (right) of both LCO and NMC622 cells with 10% FEC. The peaks in the TCD chromatograms were confirmed through integration with mass spectrometric detection (MS). It was necessary to compare the retention times of detected species in different cells in order to confirm their assignment and reproducibility.

Table II-2 summarizes GC-MS/TCD qualitative results from a calendar (4.6 V, 55°C) life test. The cells underwent formation (2 cycles), were charged to constant test voltage of 4.6 V, and then placed in a 55°C oven. The cell volume and OCV were monitored over a period of 3-4 weeks.

Table II-2: Gas Composition of LCO and NMC622 Cells as a Function of FEC Concentration Determined by GC-MS/TCD

[FEC]	CH ₄	C ₂ H ₂	C ₂ H ₄	C ₂ H ₆	C ₃ H ₆	C ₄ H ₁₀	CH ₃ F	C ₂ H ₅ F	CO	CO ₂	O ₂	H ₂	PF ₃
LCO 10%	X		X	X	X	X	X	X	X	X	X		X
LCO 20%	X	X		X		X	X	X	X	X	X		
NMC622 10%	X		X	X			X	X	X	X	X	X	
NMC622 20%	X	X		X			X	X	X	X	X	X	

Two different concentrations of FEC (v/v %) were tested during the extended aging experiment. The LCO cathode cells with 10% FEC exhibited the largest amount of gas produced, in addition to the only battery evolving the larger hydrocarbon gases. In all batteries, CO₂ and CO are the largest components of the analyzed gas. Also present are quantifiable amounts of methane, ethane, and O₂. The additional gases (PF₃, etc.) are present in trace, but measureable quantities. Although the NMC 622 cells produce quantifiable amounts of H₂, we cannot rule out the presence in LCO cells due to detection limits (> 8.5 v/v %) while using helium as the carrier gas in a GC-MS/TCD instrumental setup.

Although the molar quantification of detected gases is ongoing, the integrated TCD intensities can be compared to determine the ratio of gas generation. Of the cells investigated to date, the cells with the highest nickel % (NMC622) generate larger amounts of both fluorinated gases (CH₃F and CH₂F), however did not generate flammable hydrocarbons such as butane, propane, and propene. Further investigation into the origin of higher hydrocarbons in LCO cells is underway.

The presence of PF₃ in the LCO cell at 4.6 V with 10% FEC was an unexpected development, and can be attributed to decomposition of the LiPF₆ salt. The mechanism for the formation of PF₃ is not currently understood.

Gassing Kinetics of FEC – Milestone 3

Cycle life testing with intermittent gas measurement experiments were performed on cells containing either LCO or NMC622 cathodes to understand the effect of FEC on battery cycling and gassing. The baseline electrolyte was 1.2 M LiPF₆ EC/EMC/FE (20:60:20) + 1% PS. A series of test electrolytes were made by replacing EC with FEC in 5% increments with the final end member electrolyte being 1.2 M LiPF₆ FEC/EMC/FE (20:60:20) + 1% PS. Figure II-18 depicts the discharge capacity versus cycle number of both NMC622 and LCO cells at 4.6 V and 4.2 V. As expected, discharge capacity at 4.2 V was retained throughout 200 cycles, with all cells ranging from 93-95% after cycling at 0.7C. In addition, there was no noticeable effect on the capacity of batteries with the addition of FEC for 4.2 V cycling (Figure II-18).

Addition of FEC into the electrolyte resulted in better cycle performance in both chemistries. However, LCO cells cycled at 4.6 V hit the 80% cutoff at < 50 cycles regardless of the FEC content of the electrolyte and ceased operation after 100 cycles (Figure II-18 top). However, the NMC622 cells when cycled at 4.6 V showed remarkable improvement with added FEC. Only three electrolytes (0, 5, 15% FEC) are shown for clarity. The noticeable cycling improvement is first evident with 10% FEC, with marginal improvements up to 20%. The NMC622/graphite cell (blue trace, Figure II-4 top) cycled at 4.6 V is trending toward project target of 300 cycles. This data along with the gassing and OCV data above suggest that the performance drop in the LCO system at high voltage is due to degradation of the cathode but additional experiments to examine the cathode structure/chemistry need to be completed for confirmation.

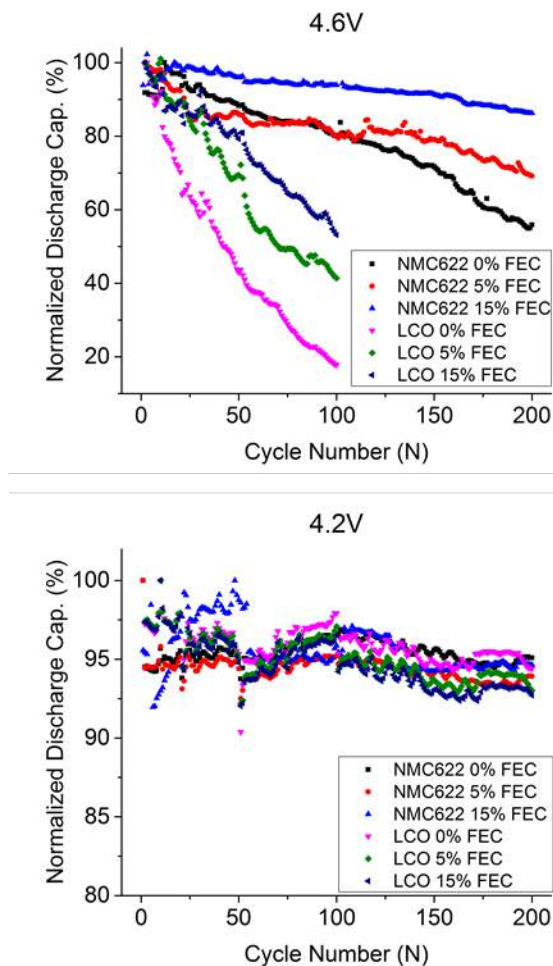


Figure II-18: Normalized discharge capacity (%) versus cycle number (N) of NMC622 and LCO cells cycled at 4.6 V (top) and 4.2 V (bottom). LCO cells ceased operation after 100 cycles at 4.6 V, whereas NMC622 cells completed the desired 200 charge/discharge cycles. Electrolyte is 1.2 M LiPF_6 [EC/FEC]/EMC/FE (20:60:20) + 1% PS.

Gassing Kinetics Based on Cathode Composition – Milestone 4

Gassing kinetics of two cathode chemistries (LCO and NMC622) have been determined through volume change measurements over a period of 3-4 weeks, with cells stored at 45°C after formation and final charge to 4.6 V. The data shown in Figure II-19 (top) shows the volume change versus time (days) of both LCO and NMC622 cells with two different electrolytes: 1.2 M LiPF_6 EC/EMC/FE (20:60:20) + 1% PS and 1.2 M LiPF_6 EC/FEC/EMC/FE (10:10:60:20) + 1% PS. The measured OCV versus time of these cells is also depicted in Figure II-19 (bottom).

As seen in Figure II-19, there is more gas generated in the LCO cells at 4.6 V (left), which is consistent with the OCV drop (right). A decrease in measured OCV indicates that the cathode is being reduced. The cathode can be reduced through multiple mechanisms, one of which includes the oxidation of the graphite anode. One other mechanism includes oxygen defect formation in the cathode material due to crystal structure instability. While additional FEC seems to delay OCV loss, it does not impact gas generation to the same degree.

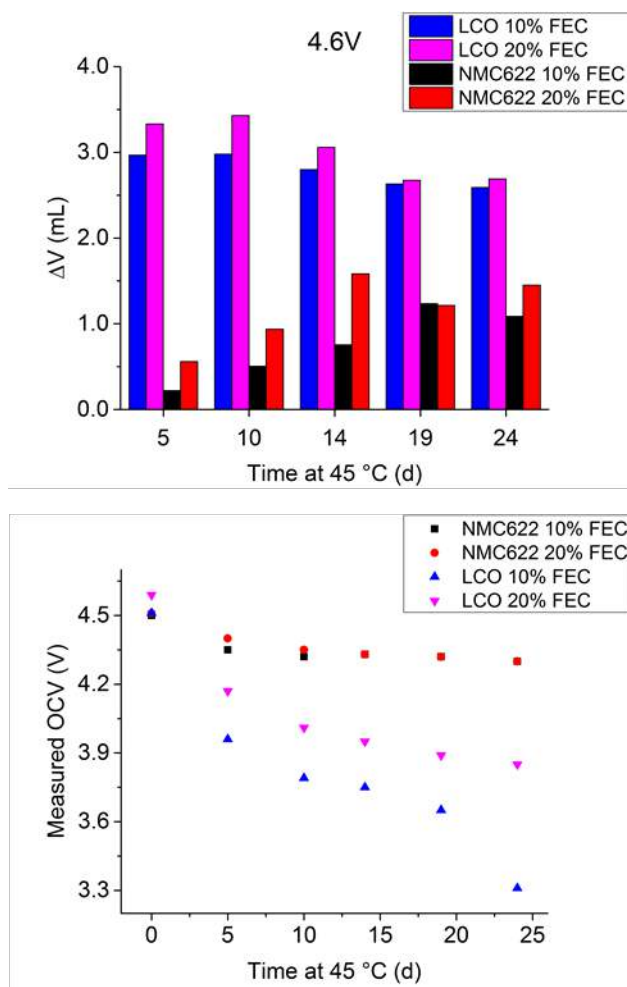


Figure II-19: Volume measurements versus time in 4.6 V NMC622 cells during an OCV calendar life test at 45°C as a function of FEC concentration (top). Measured OCV versus time in 4.6 V NMC622 and LCO cells during the same calendar life test also as a function of FEC (bottom)

Conclusions

Significant work at Daikin in the first year involved setup and validation and training for equipment needed to complete this project. This included expanding our cell cycling capability from 20 to 104 channels and commissioning of several new pieces of equipment (e.g., GC/MS).

An examination of both the existing data and current literature was completed to set baselines for this study. Third party data from final cells of previous Daikin project confirm the there are two battery performance failure points. The first occurs above 4.3 V, which is attributed to electrolyte decomposition resulting in gas generation. It has been shown that the use of fluorinated electrolyte greatly diminishes the decomposition reaction, resulting in enhanced performance. The second failure point occurs above 4.5 V. The baseline experimental voltages for this project have been set at 4.2, 4.5 and 4.6 V in order to study chemical and physical changes which occur when at or near these failure points.

Gas composition has been established for both the LCO and NMC622 cathode materials. Both contain significant amounts of CO, CO₂, CH₄ and O₂ along with select fluorinated hydrocarbons attributed to the decomposition of FEC in the electrolyte.

For both chemistries studied, the addition of FEC to electrolyte results in increased cycle life and capacity retention. However, that benefit for LCO cells is not sufficient to permit viable high voltage operation. The full cycling performance benefit of FEC in the electrolyte is realized at a 10% (v/v %), and can be marginally increased with additional FEC. The data obtained thus far for LCO cells (OCV loss, gas evolution, etc.) suggests that decreased performance is due a non-electrolyte component failure, but rather the result of an inherent property of the cathode material.

II.B Next Generation Lithium-Ion: Advanced Anodes R&D

II.B.1 Next Generation Anodes for Lithium-Ion Batteries: Research Facilities Support

Dennis Dees, Principal Investigator

Argonne National Laboratory
9700 South Cass Avenue
Argonne, IL 60439
Phone: 630-252-7349
E-mail: dees@anl.gov

Peter Faguy, Technology Manager

U.S. Department of Energy
Phone: 202-586-1022
E-mail: Peter.Faguy@ee.doe.gov

Start Date: October 1, 2015

End Date: September 30, 2019

Total FY17 Project Cost: \$3,600,000 DOE FY17 share: \$3,600,000 Non-DOE share: \$0

Project Introduction

Silicon has received significant attention as a viable alternative to graphitic carbon as the negative electrode in lithium-ion batteries due to its high capacity and availability [1]. Elemental silicon can theoretically store >3500 mAh/g, nearly an order of magnitude higher than graphite (372 mAh/g and 818 mAh/mL, respectively). However, several problems have been identified that limit its utility including large crystallographic expansion (~320%) upon lithiation which translates to particle cracking, particle isolation, and electrode delamination issues. Further, there are fundamental and volume change related SEI stability issues, which affect cycling efficiency. The wealth of previous studies in this area is both a testament to its potential and the size of the challenge that must be overcome, requiring a great amount of innovation on multiple fronts.

BatPaC [2], a techno-economic program designed to model lithium-ion battery performance and cost, was utilized to establish program relevance by connecting DOE/USABC pack performance targets to anode targets. Generally, research with silicon containing anodes is focused on improving the specific capacity of graphite. However, this simple metric requires a more detailed analysis with factors such as the impact on average cell voltage, and volumetric capacity. It is notoriously difficult to select appropriate metrics that will enable an accurate calculation of the energy of a single electrode. Most methods estimate the volumetric energy density of active materials with the simplistic assumption that bulk density of the electrode does not undergo change in volume during cycling. While this serves well for most cathodes where the voltage can be fixed against lithium it is inappropriate for electrodes such as silicon.

As shown in Figure II-20 (left frame), BatPaC calculations indicate anode volumetric capacities greater than 1000 mAh/cm³ ($= \rho \cdot \epsilon \cdot Q$ [g/cm³_{act} · cm³_{act}/cm³_{elect} · mAh/g]) generally minimizes battery cost with an advanced NMC cathode. Note that higher capacities result in diminishing savings in cost. The analysis (right frame) also predicts that silicon-graphite electrodes with less than 75 wt% graphite can achieve the target. Finally, alloys of inactive metals (not shown) with silicon (or tin) can meet the volumetric capacity target as long as the metal choice is inexpensive (e.g., iron rather than nickel or cobalt).

Next Generation Anodes for Lithium-Ion Batteries, also referred to as the Silicon Deep Dive Program, is a five National Laboratory consortium assembled to tackle the barriers associated with development of an advanced lithium-ion negative electrode based upon silicon as the active material. This research program baselines

promising silicon materials that can be developed or obtained in quantities sufficient for electrode preparation within the consortium facilities. Composite electrode and full cell development leverages recent investments made by DOE-EERE-VTO in electrode materials and characterization. The primary objective of this program is to understand and eliminate the barriers to implementation of a silicon-based anode in lithium-ion cells. The Labs are focused on a single program with continuous interaction, clear protocols for analysis, and targets for developing both the understanding and cell chemistry associated with advance negative electrodes for lithium-ion cells. First and foremost, this undertaking is a full electrode/full cell chemistry project leveraging baseline electrodes prepared at the consortium facilities. All efforts are directed to understanding and developing the chemistry needed for advancing silicon-based anodes operating in full cells. Materials development efforts include active material development, binder synthesis, coatings, safety, and electrolyte additives. Efforts include diagnostic research from all partners, which span a wide range of electrochemical, chemical and structural characterization of the system across length- and time-scales. Specialized characterization techniques developed with DOE-EERE-VTO funding, include neutrons, NMR, optical, and X-ray techniques being employed to understand operation and failure mechanisms in silicon-based anodes. In addition, several strategies to mitigate lithium loss are being assessed. The project is managed as a single team effort spanning the Labs, with consensus decisions driving research directions and toward development of high-energy density lithium-ion batteries. A detailed list of participants is given in Figure II-21.

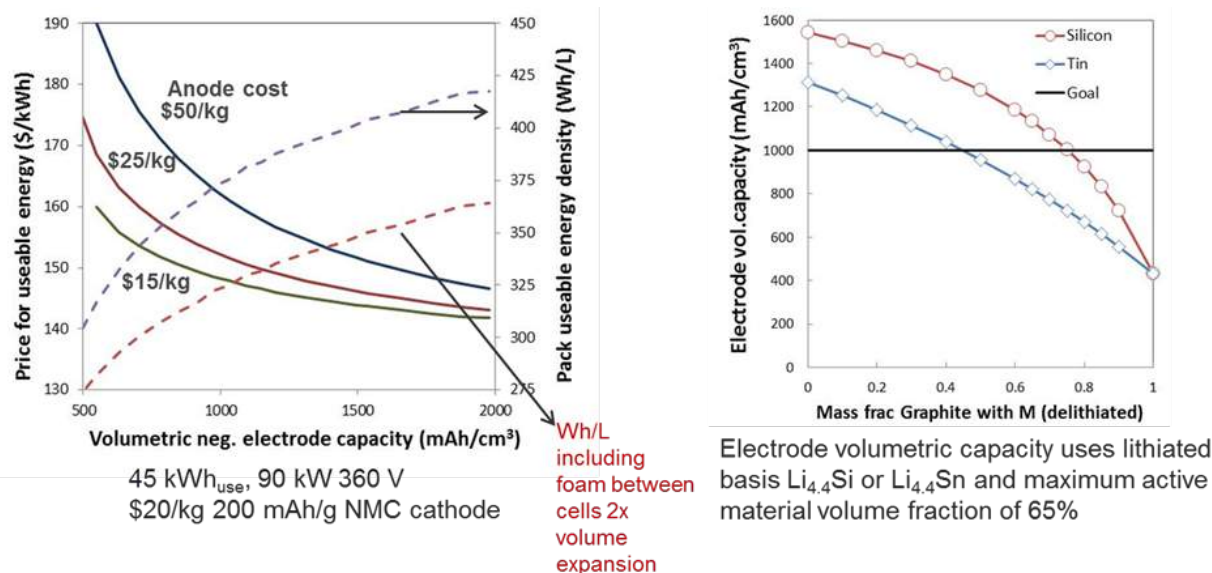


Figure II-20. Battery Performance and Cost (BatPaC) model utilized to establish program relevance



Research Facilities

- Post-Test Facility (PTF)
- Materials Engineering Research Facility (MERF)
- Cell Analysis, Modeling, and Prototyping (CAMP)
- Battery Manufacturing Facility (BMF)
- Battery Abuse Testing Laboratory (BATLab)

Contributors

- | | | |
|-------------------|------------------------------|---------------------------|
| ▪ Daniel Abraham | ▪ Jinghua Guo | ▪ Rose Ruther |
| ▪ Eric Allcorn | ▪ Atetegeb Meazah Haregewoin | ▪ Niya Sa |
| ▪ Seong Jin An | ▪ Kevin Hays | ▪ Tomonori Saito |
| ▪ Chunmei Ban | ▪ Bin Hu | ▪ Yangping Sheng |
| ▪ Javier Barenó | ▪ Andrew Jansen | ▪ Seoung-Bum Son |
| ▪ Ira Bloom | ▪ Christopher Johnson | ▪ Xin Su |
| ▪ Anthony Burrell | ▪ Kaushik Kalaga | ▪ Robert Tenent |
| ▪ Yang-Tse Cheng | ▪ Baris Key | ▪ Lydia Terborg |
| ▪ James Ciszewski | ▪ Robert Kostecki | ▪ Wei Tong |
| ▪ Claus Daniel | ▪ Gregory Krumdick | ▪ Stephen Trask |
| ▪ Dennis Dees | ▪ Jianlin Li | ▪ Jack Vaughey |
| ▪ Fulya Dogan Key | ▪ Min Ling | ▪ Gabriel Veith |
| ▪ Wesley Dose | ▪ Gao Liu | ▪ David Wood |
| ▪ Zhijia Du | ▪ Wenquan Lu | ▪ Koffi Pierre Claver Yao |
| ▪ Alison Dunlop | ▪ Jagjit Nanda | ▪ Liang Zhang |
| ▪ Trevor Dzwiniel | ▪ Kaigi Nie | ▪ Linghong Zhang |
| ▪ Kyle Fenton | ▪ Ganesan Nagasubramanian | ▪ Lu Zhang |
| ▪ Kevin Gallagher | ▪ Christopher Orendorff | ▪ Shuo Zhang |
| ▪ Steve George | ▪ Bryant Polzin | ▪ Zhengcheng Zhang |
| ▪ James Gilbert | ▪ Krzysztof Pupek | ▪ Tianyue Zheng |
| | ▪ Philip Ross | |

Figure II-21. Program participants including Laboratories, research facilities, and individual contributors.

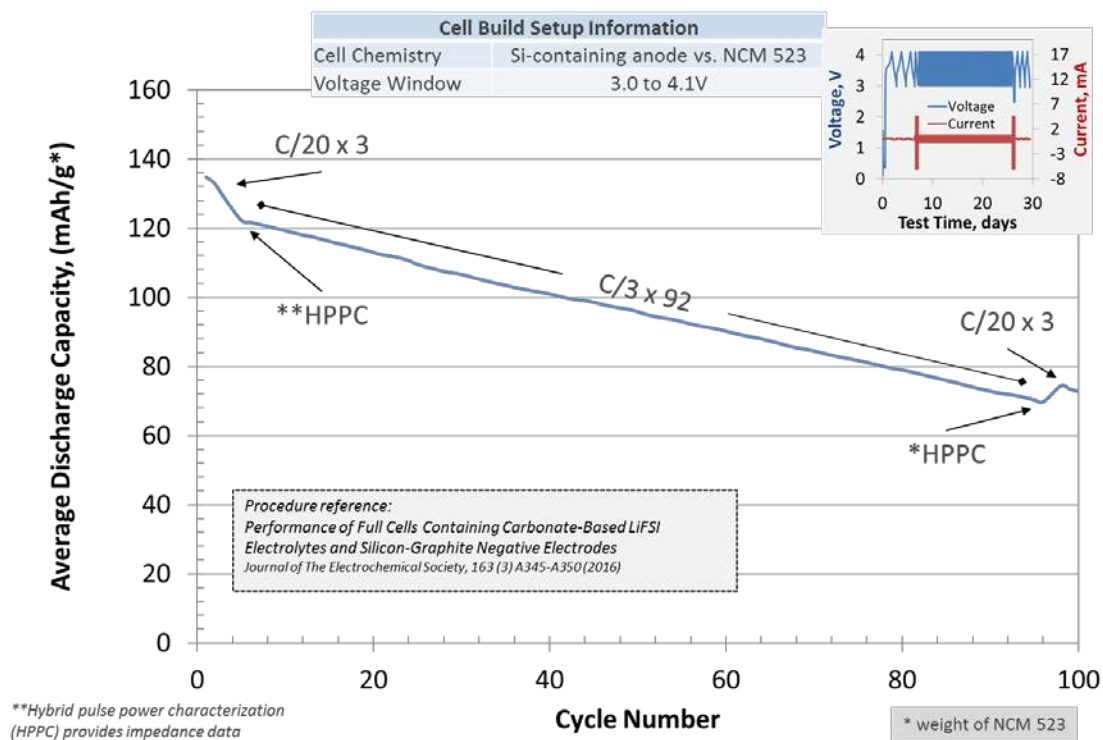
Objectives

- Understand and overcome the science and technology barriers to the use of silicon-based anodes in high-energy density lithium-ion batteries for transportation applications.
 - Stabilize the SEI
 - Stabilize the electrode
- Demonstrate functional prototype lithium-ion cell chemistries which meet the DOE/USABC performance targets.

Approach

Sandia National Laboratories (SNL), Oak Ridge National Laboratory (ORNL), National Renewable Energy laboratory (NREL), Lawrence Berkeley National Laboratory (LBNL), and Argonne National Laboratory (ANL) have teamed together to form an integrated program. Technical targets have been developed and regular communications have been established. Throughout the program, there is a planned focus on understanding, insights into, and advancement of silicon-based materials, electrodes, and cells. All anode advancements will be verified based on life and performance of full cells. Toward that end, baseline silicon-based materials, electrodes, and cells have been adopted, along with full cell testing protocols.

In examining improvements, changes to the baseline cell technology will be minimized. As an example, silicon active material coating improvements will be verified on baseline silicon materials in electrodes fabricated by the battery research facilities. All other components in the prototype cells (i.e., positive electrode, separator, electrolyte, etc.) will be from the baseline technology. There are many testing protocols that can be utilized to benchmark the baseline technology. This program has adopted a testing protocol from the literature [3] that has worked well for lithium-ion cells with silicon containing anodes. Shown pictorially in Figure II-22 the test starts with three slow (C/20) formation cycles, an HPPC cycle, and then the C/3 aging cycles. The test ends with another HPPC cycle and three more slow (C/20) cycles. All constant current cycling is symmetric between charge and discharge rates. The tests are run at 30°C. If there is little or no aging in the first 100 cycles, the protocol can be repeated. This protocol effectively examines capacity, impedance, and aging effects in about a month's worth of testing.



As the program matures, materials developments will be incorporated into baseline silicon-based materials, electrodes, and cells. Scale-up of materials, incorporation of materials advancements into electrodes and prototype cells, and characterization and testing of cells, as well as evaluation of safety and abuse tolerance are part of a wide range of integrated studies supported by battery research facilities at the National Labs working closely with the program. These research facilities include the Battery Abuse Testing Laboratory (BATLab), the Battery Manufacturing Facility (BMF), the Cell Analysis, Modeling, and Prototyping (CAMP), the Materials Engineering Research Facility (MERF), and the Post-Test Facility (PTF).

Communication of programmatic progress to battery community is critical. This will generally be accomplished through publications, presentations, reports, and reviews. Further, the program is open to industrial participation and/or collaboration that does not limit program innovation or the free flow of information. Finally, this program is highly integrated with our sister program on SEI-Stabilization, called SEI-Sta for short. In general, SEI-Sta is focused on the development and characterization of model systems,

thin-film well-defined active area electrodes on which it is easier to extract fundamental information on lithium-silicon phase formation, lithium transport, and interfacial phenomena (e.g., SEI formation and growth).

Results

Development of New Baseline Electrodes (ANL)

Silicon Supplier: Nanostructured and Amorphous Materials

The Silicon Deep Dive program acquired 6 kg of 70-130 nm average particle size (APS) silicon from Nanostructured and Amorphous Materials (NanoAmor, Prod:0143KE) and MagE3 graphite from Hitachi. Early in FY17, these materials were designated to become a new baseline silicon electrode due to data suggesting ~150 nm particle size for silicon being a good target to receive capacity (mAh/g) benefits by having a lower ratio of inactive surface components to active components. In addition, the previous baseline silicon material (50-70 nm APS from NanoAmor) had been discontinued by the supplier.

The 70-130 nm silicon from NanoAmor was put through the same process of slurry preparation and electrode fabrication as the previous baseline material. From these processes we observed several differences including: powder color and handling, particle morphology, range of particle distribution sizes outside of the product spec, slurry gas generation, poor coating quality, and material capacity compared to the 50-70nm from NanoAmor. These differences highlight potential challenges presented in slurry preparation and electrode fabrication for various silicon products even when being provided from the same source.

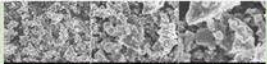


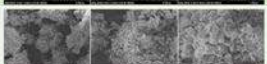
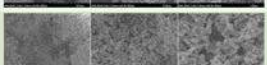

While the NanoAmor materials have served as a valuable source of silicon powders in early developments of slurry design and electrode coating strategies, ultimately, due to the change in product selection, unexpected powder properties, and the difficulty to coat a 15 wt.% 70-130 nm silicon electrode at >3 mAh/cm², the program looked for alternative sources and products to become the next baseline material for the Silicon Deep Dive.

New Silicon Supplier: Paraclete Energy (PE) based in Chelsea, MI

A promising U.S. silicon supplier, Paraclete Energy (PE), provided multiple samples for evaluation. The received powders were described as SiO or Si core with a SiO₂ shell with an average particle size of 150nm. The particle size analysis (MERF at ANL) and SEM images (Linghong Zhang at ANL) were collected and demonstrate Paraclete's improved control of particle size (Table II-3). Initial electrochemical performance evaluations also showed expected capabilities from previous silicon powders and warranted further evaluation. A scaled-up 500 gram (Initial Scale-up) sample of the original (initial 100g) sample was received and evaluated via NMR (Baris Key at ANL). The NMR results of the "Initial Scale-up" showed a large amount of organic carbon with concern over the possible negative impact on the electrochemical performance. Thus, Samples A, B, C, and D were processed with different variables at PE and sent to Argonne for analysis. The collaboration gives ANL the ability to have the product tailored to the Silicon Deep Dive needs.

Multiple experimental electrodes were fabricated using the aqueous slurry processing and coating strategies described earlier in this section by the CAMP Facility. The high quality 15 wt.% silicon electrodes were fabricated using the powders found in Table II-3 at the ~2 mAh/cm² to match to the Electrode Library that the CAMP Facility maintains. Additional electrode optimization was not needed to coat these electrodes and the initial 15 wt.% silicon coatings show promise in coating high quality >3 mAh/cm² electrodes with minimal to no slurry preparation or coating adjustments necessary.

Table II-3: (Top) Experimental silicon samples from Paraclete Energy with particle size and SEM image information. (Bottom) Brief sample descriptions.

Sample	Description	D50 (um)	SEM Images of powder at various level of magnification
K16-013-MC	Initial 100g	0.96	
C17-301-LS	"Initial Scale up"	0.12	
C17-001-LS	Sample A	0.1	
C17-016-LS	Sample B	0.09	
C17-022-LS	Sample C	0.1	
C17-021-LS	Sample D	0.11	

ID	Description
Initial sample	Initial Scoping Sample
Initial Scale-up	Scale-up of initial sample
Sample A	Scale-up of initial sample with improved drying
Sample B	Different silicon feed stock with improved drying
Sample C	Initial sample silicon feed stock manufactured using alternative method
Sample D	Initial sample silicon feed stock, but oxidized in a different manner

Half-cell coin-cell data of 15 wt.% silicon experimental electrodes are shown in Table II-4. The formation data shows the 1st discharge (lithiation) capacity, irreversible capacity loss, reversible charge (delithiation) capacity at a C/10 rate, and 1st cycle coulombic efficiency. Silicon-containing electrodes generally have lower cycling coulombic efficiencies throughout cycling compared to graphite-only electrodes, so determining a true reversible cycle capacity can be arbitrary. All of the testing was performed using 4 coin cells (CR2032) for each electrode using electrolyte with the composition 90 wt.% (1.2 M LiPF₆ in EC:EMC 3:7 by wt.%) + 10 wt.% (FEC) using the cycling window of 0.05 to 1.5 V vs. Li metal. The results suggest comparable initial capacities between the samples.

Table II-4: Half-cell coin-cell formation testing results of experimental silicon samples from Paraclete Energy. The capacity values are normalized to the total weight of the silicon, graphite, and carbon black present in the electrode.

Sample	1 st Cycle Discharge Capacity (mAh/g)	Irreversible Loss (mAh/g)	Reversible Cycle Charge Capacity (mAh/g)	1 st Cycle Efficiency (%)
Original Sample	831	151	679	92.4
Sample A	750	61	684	90.6
Sample B	618	108	592	88.3
Sample C	743	87	656	89.3
Sample D	747	93	653	90.9

Voltage Window: 0.05–1.5 (V)

Full-cell coin-cells were then fabricated using the various ~2 mAh/cm² (0.05 to 1.5 V vs. Li metal) silicon-containing (PE) electrodes versus a standard 90 wt.% NMC532, 5 wt.% Timcal C45 carbon black, and 5 wt.% PVDF made for the Electrode Library at the CAMP Facility [A-C013A]. The approximate n:p capacity ratios for the electrode couples are between 1.1 and 1.3 for a voltage window of 3.0 to 4.1 V in a full cell. The Silicon Deep Dive cycling protocol was used to evaluate these materials and for comparison purposes.

Figure II-23 shows the resulting full cell testing on the Paraclete Energy silicon samples. Samples A and D showed the best performance of the 4 samples provided by PE and are similar to the previous baseline electrode performance (50-70 nm Si NanoAmor, [A-A006A]). Sample D performed slightly better than Sample A in the final 3 cycles, thus “Sample D” was selected to be scaled-up to a 500 g sample “Scale-up of Sample D” for purposes of becoming the new silicon material for the future baseline electrodes. Early indications from initial coatings show improved coating quality and integrity with the “Scale-up Sample D” for both low and high (>3.0 mAh/cm²) coating loadings after calendaring. Henceforth, in this section the “Scale-up Sample D” powder was used as the silicon components of the electrodes fabricated. The initial baseline electrodes [A-A012] using the new silicon source (PE) for this project was coated at a loading of 3.63 mg/cm² with an expected mAh/cm² of ~2 in half-cell testing (Table II-5).

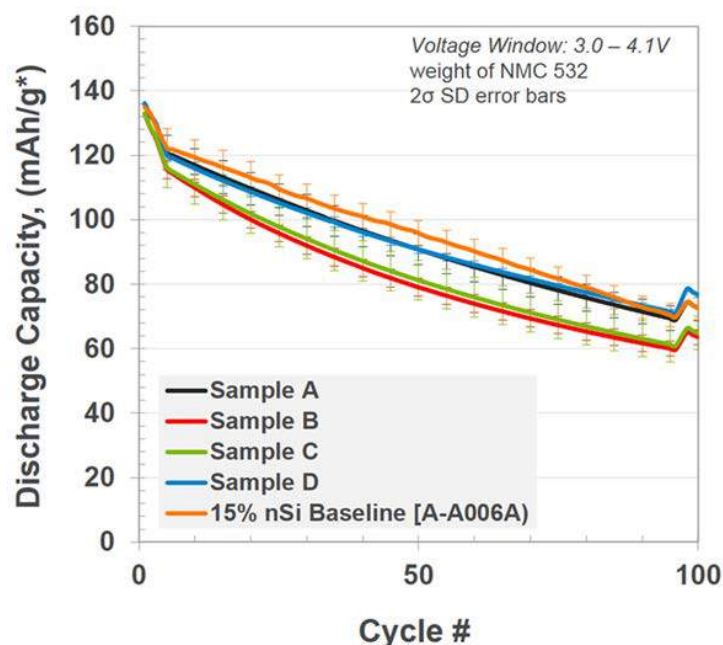


Figure II-23. Full-cell coin-cell results showing average discharge capacity vs. cycle number. The Silicon Deep Dive full cell cycling protocol was used for evaluating the experimental silicon electrodes compared to the original silicon-containing baseline electrode [A-A006A]. The cycling protocol consists of three slow (C/20) formation cycles, an HPPC cycle, and then C/3 aging cycles, followed by a 2nd HPPC cycle, and finally three more slow (C/20) cycles. The capacity values are normalized to the weight of NMC532.

Table II-5: Half-cell coin cell formation testing results of new baseline 15wt.% silicon-containing electrodes. The silicon powders used are “Sample D” and “Scaled-up Sample D” from Paraclete Energy. The capacity values are normalized to the total weight of the silicon, graphite, and carbon black present in the electrode.

Sample	Total Coating Loading (mg/cm ²)	1 st Cycle Discharge Capacity (mAh/g)	1 st Cycle Efficiency (%)	Reversible Cycle Charge Capacity (mAh/g)	Reversible Cycle Charge Areal Capacity (mAh/cm ²)
Sample D	3.88	747	90.9	653	2.39
A-A012	3.63	803	91.0	723	2.56
A-A013	3.00	842	89.3	716	2.07

Voltage Window: 0.05–1.5 (V), 30°C

A 2nd baseline electrode [A-A013] with the same materials and composition but at a lower coating loading of 3.00 mg/cm² was made to lower the n:p ratio closer to 1.1. Full cells were then made using these new baseline materials paired against the same cathode [A-C013A] using the Silicon Deep Dive Protocol to evaluate the cycling performance. Figure II-24 shows the full cell cycling performance comparison of the original baseline material [A-A006A], Sample D, and the new baseline electrodes [A-A012] and [A-A013] being tested under the Silicon Deep Dive full cell cycling protocol. The protocol reveals that similarities of the performance for the 4 electrodes suggesting that the “Scale-up Sample D” powder is adequate to replace the previous baseline electrode and the two n:p ratios chosen retain a similar capacity retention (Figure II-24).

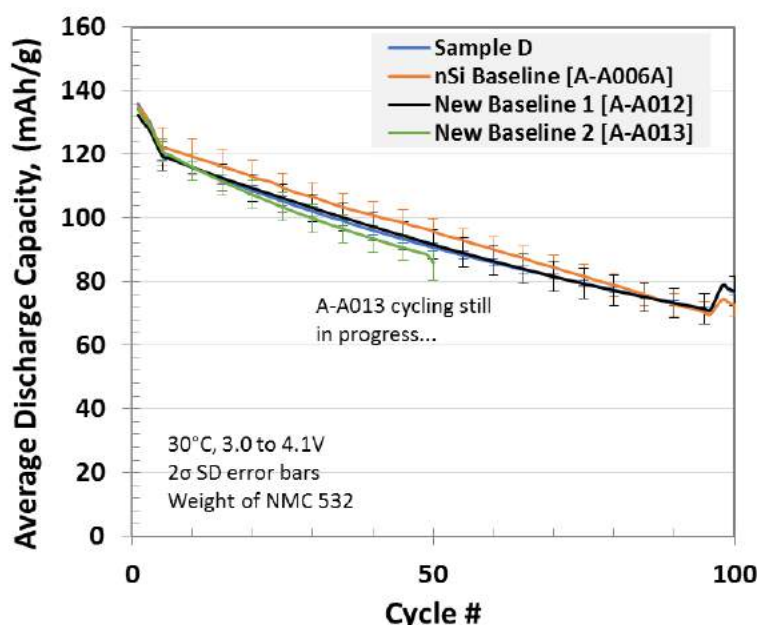


Figure II-24. Full-cell coin-cell results showing average discharge capacity vs. cycle number for the Silicon Deep Dive baseline electrodes vs. NMC532 [A-C013A]. Data shows the average values based on 4 coin cells for each electrode pair. The capacity values are normalized to the weight of NMC532.

Encouraging aspects of working with Paraclete Energy are that they have demonstrated their ability to control particle size and customize processing steps to target surface chemistries. The electrochemical data is also comparable to the previous baseline electrode performance and the silicon source provides a dependable and repeatable silicon powder from batch to batch. Lastly, Paraclete Energy has been eager to engage in collaborations with the CAMP Facility and the Silicon Deep Dive Program to further develop their processing techniques of silicon products for improved lithium-ion battery performance.

Processing Science of Silicon Containing Anodes (ORNL)

The transition from *n*-methyl-2-pyrrolidone (NMP) to aqueous processing has proven important for graphite anodes. These aqueous-based electrodes function as effectively as their NMP counterparts, but without the environmental concerns of NMP. The addition of Si into graphite electrodes has made for a more difficult transition to aqueous-based slurries. Unlike graphite, Si has increased reactivity with water, the consequences of which are not yet fully understood. Furthermore, minimizing the water in Li ion batteries is crucial to avoid unwanted parasitic side reactions that can cause the production of gasses through reduction to H₂ and additional HF build through the hydrolysis of LiPF₆. Here we study both NMP and aqueous systems for Si-graphite electrode fabrication. During this work we identified severe gassing reactions that occur during electrode formulation mixing. The effects of solvent selection were examined by gas analysis of Si-graphite composite slurries. Si powders from these slurries were further examined with FTIR and NMR.

A custom stainless steel sealed vessel was manufactured to measure changes in pressure of Si slurries, Figure II-25. The 0.5 L vessel was designed to replicate the mixing of Si slurries for large scale preparation of Si-graphite electrodes. This vessel mixed the slurry using a roller mill and ZrO₂ media. Though this does not match the energy of a planetary ball mill commonly used in our slurry preparation, it gives a relative indication of any reaction that may occur over a reasonable time scale. Si powder (Nanoamor 70-130 nm), carbon black (Imerys C45), and the slurry solvent were mixed for up to 100 hours, (Figure II-26-Left). Between 0 and 1 hours, both water and NMP-based slurries decreased in pressure, likely due to the consumption of O₂ from the air, after that the water-based slurry slowly increased in pressure for the first 24 hours before rapidly

increasing after additionally mixing. The NMP-based slurry did not change significantly after the initial pressure lost. In addition to the Nanoamor Si, Alfa Aesar 325 mesh Si was tested in water-based slurry and produced a similar pressure build. This shows that the reaction occurs independent of Si particle size. Gas was collected from the head space and tested by mass spectrometry, (Figure II-26-Right). The water-based Si slurry showed a large H₂ signal, which is not present for the NMP-based slurry. This accounts for the large increase in pressure for the water-based slurry, following reaction 1.

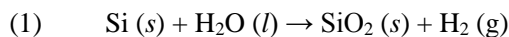


Figure II-25. Image of reactor vessel on roller mill. Note the pressure gauge pointing to the right.

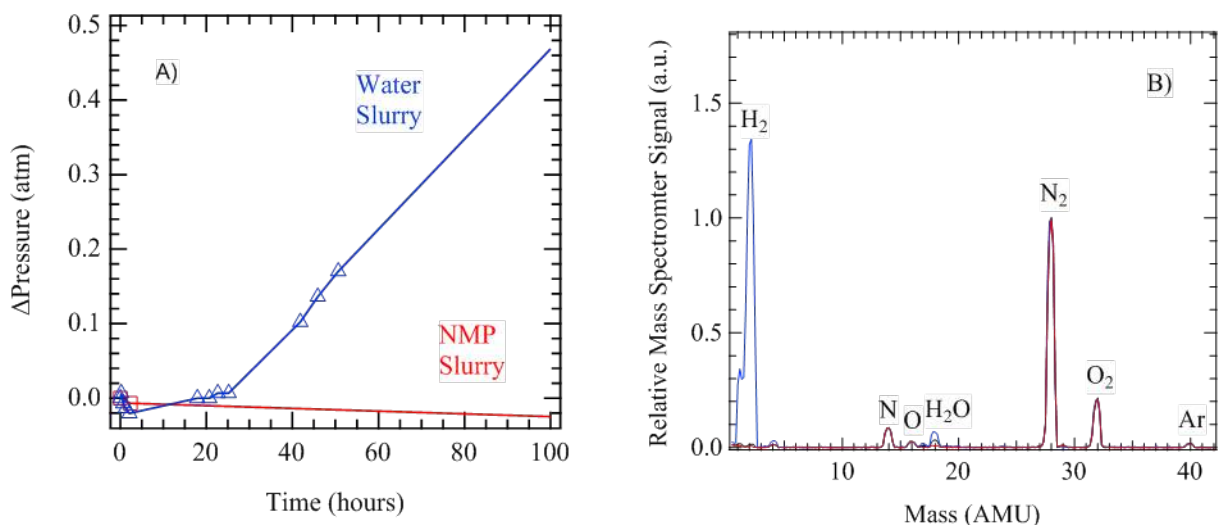
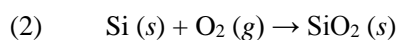


Figure II-26. (Left) Pressure vs time plot showing changes to NMP and water-based Si slurries in sealed pressure vessel. (Right) Mass spectrum of head space collected from water-based Si slurry (blue trace), NMP-based Si slurry (red trace), and ambient air (black trace).

In addition to hydrogen all samples showed various decreases in oxygen content (relative to atmospheric N₂ in the cell) which we attribute to oxidation from O₂ in the air which reacts during milling according to reaction 2. In both cases the oxidation proceeds but the extent of oxidation varies pointing to a role of the solvent in the reactivity of the silicon. Additional studies showed evidence for the formation of CO₂ from the decomposition of binders and/or reactions with graphite and carbon black. Together these results indicate a quite complex reaction environment that is actively changing the electrode chemistry and its resulting cycleability and reproducibility.



Role of Drying Temperature in Reproducible and Reliable Si Anodes (ORNL)

Water is a major impurity in silicon electrodes. [4] In addition to the Si, polyacrylic acid (PAA) is a well-known “superabsorber” of water. [5] To evaluate its effect and ways to mitigate it a drying study was completed. To determine if residual water is problematic in Si-graphite electrodes when utilized in full cells, coatings were tested using LiPAA binder in a water slurry and PAA binder in an NMP-based slurry. Secondary drying of each was completed at temperatures ranging from 100°C to 200°C.

Thermogravimetric analysis (TGA) of PAA and LiPAA binders

Water was analyzed in PAA and LiPAA by Karl-Fisher titration. As received PAA was 1.14% water by weight, compared to LiOH titrated LiPAA (dried at 80°C), which was only 0.03%. TGA was used to investigate optimal temperatures to remove water from these binders (Figure II-27 Left). The TGA of PAA displays four distinct regions of weight loss, which are more easily identified by its first derivative (DTGA), (Figure II-27 Right). Though not immediately recognizable, LiPAA shares these same regions of weight loss, but with a much more gradual sloping profile. The DTGA is expanded 10X for LiPAA to identify the peaks of interest. In both binders, the first two regions of weight loss can be assigned to free water (40°C) and adsorbed water (75°C for LiPAA and 125°C for PAA). In PAA, this is followed by another region of weight loss, beginning at 140°C and reaching a maximum at 208°C. This feature is much broader in DTGA of LiPAA, starting at 85°C and reaching a maximum at 190°C. This weight loss is related to the dehydration of carboxylic acid group. [6] These neighboring carboxylic acid group will react to form an anhydride, subsequently releasing water as a byproduct. This extent of this reaction is considerably less for LiPAA since 80% of the carboxylic acid groups are already substituted for carboxyl groups paired with Li⁺ counter ions. This decomposition continues at 250°C for PAA with breakdown of the anhydride and releasing of CO₂, but this occurs at temperature beyond normal electrode drying conditions. To our knowledge, a detailed study of the thermal degradation of LiPAA has not been completed, but other alkaline earth polyacrylates are known. NaPAA undergoes main chain and side group scission above 400°C, meaning it is stable in normal electrode drying conditions. [7]

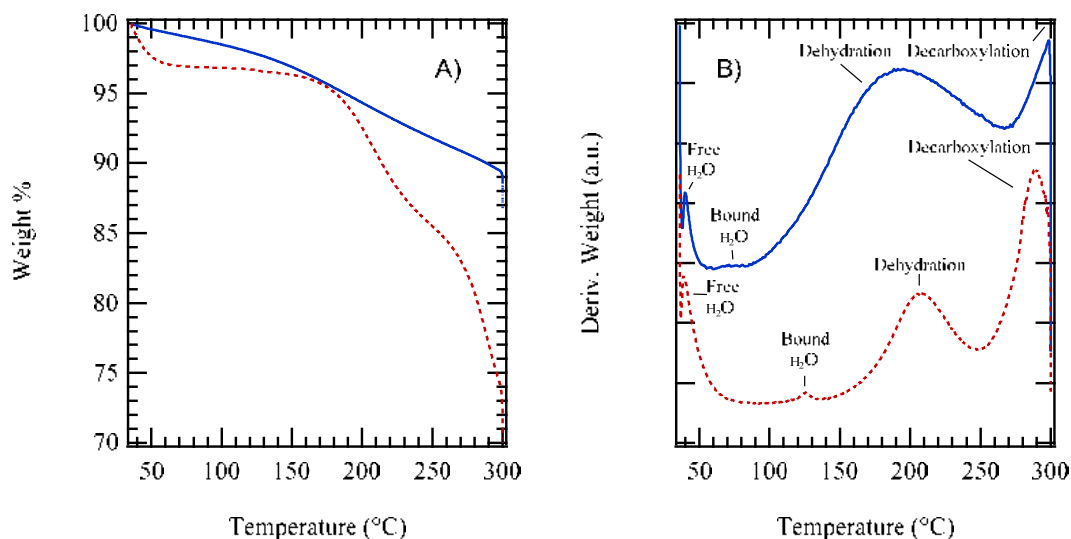


Figure II-27. TGA (Left) and DTGA (Right) of “as received” PAA (dashed red line) and LiPAA (solid blue line). The DTGA of LiPAA was expanded 10X to more easily identify features.

KF titration of electrode materials

Given the cross-linking reaction indirect KF titration of the electrodes in chloroform was used to get an accurate water content without heating the material to drive water off. Each slurry was dried at room temperature, the solid components were ground, and each were dried under vacuum overnight at the designated temperature. Both LiPAA and PAA-based Si-graphite electrodes had a similar water content of ~2100 ppm when dried at 120°C. Upon increasing the drying temperature to 150°C, PAA-based electrodes increased to roughly 4 times (i.e., 7927 ppm) the water content of the LiPAA-based electrode. TGA shows that PAA begins to decompose around this temperature, releasing water as a byproduct. It is well known that Si strongly binds water at temperatures up to 250°C. [4] The water content of PAA-based electrodes increase at this temperature, because any water released during the decomposition of the binder is adsorbed by the Si, which cannot be driven off at this temperature. Though the value of 7927 ppm seems high, it is still below the theoretical value of 12,500 ppm, which is the max amount of water released during the decomposition of PAA, where the binder accounts for 10% of the total mass of the electrode.

Influence of Drying on Full Cell Performance.

The water results presented above were used to direct the investigation of a Si-graphite:532 NMC cathode full cell. The Si-graphite composite electrodes were produced with 15% (by mass) Si nanoparticles (Nanoamor, 70-130 nm), 73% graphite (Hitachi, Mage 3), 2% carbon black (Imerys, C45), and 10% binder (LiPAA or PAA). LiPAA-based electrodes utilized a water-based slurry while PAA-based electrodes used n-methyl-2-pyrrolidone (NMP, Sigma-Aldrich, ≥99%). Slurries were then prepared by first dry mixing dried Si, carbon black, and either NMP or water in a planetary ball mill. This Si/carbon black slurry was added to a graphite/binder slurry and mixed in a planetary mixer. The solid content was ~36% by mass. The slurries were coated on Cu foil by custom slot die (Frontier Industrial Technology) and coated to loadings 3.4 mg cm⁻² and 3.3 mg cm⁻² for PAA and LiPAA-based anodes, respectively.

Electrodes underwent secondary drying in a vacuum oven at a desired temperature for 18 hours under static vacuum at 25 mm Hg. Full cells were matched against 12.9 mg cm⁻² LiNi_{0.5}Mn_{0.3}Co_{0.2}O₂ (NMC-532, Toda) cathodes. Based on initial capacities of each anode, the LiPAA-based Si-graphite composite had an anode to cathode capacity ratio of 1.30, while the PAA composite was 1.13. Pouch cells were filled to 3X the total pore volume of the pouch cells with Gen 2 electrolyte. Cells were cycled following the ANL protocol.

Full cell cycling data for both composites at various secondary drying temperatures is displayed in Figure II-28. LiPAA-based Si-graphite cells had no detectable variation based on secondary drying temperature. The initial discharge capacity of 137 mAh g⁻¹ (per mass cathode) aligns well with first cycle Coulombic losses. There was a slight degradation in capacity upon increasing rate to C/3 127 mAh g⁻¹ and continued to decrease during aging to 91 mAh g⁻¹. Returning to C/20 after 97 cycles saw 8 mAh g⁻¹ increase, comparable to the initial capacity drop in line with the rate change.

PAA-based Si-graphite cells displayed a trend along with secondary drying temperature. 140°C PAA Si-graphite cells and below performed better than those above this drying temperature. First cycle discharge capacity ranged between 130 and 116 mAh g⁻¹, with electrodes dried at 160°C being the highest and 120°C being the lowest, though all within the error bars of each other. 160°C PAA Si-graphite cells and above declined rapidly in capacity to ~75 mAh g⁻¹, before settling at 62 mAh g⁻¹ after 96 cycles, while 140°C PAA Si-graphite cells and below showed a more gradual decline in capacity to 71 mAh g⁻¹. Similar to those constructed with LiPAA Si-graphite cells, all PAA cells increased in capacity by 9 mAh g⁻¹ upon return to C/20.

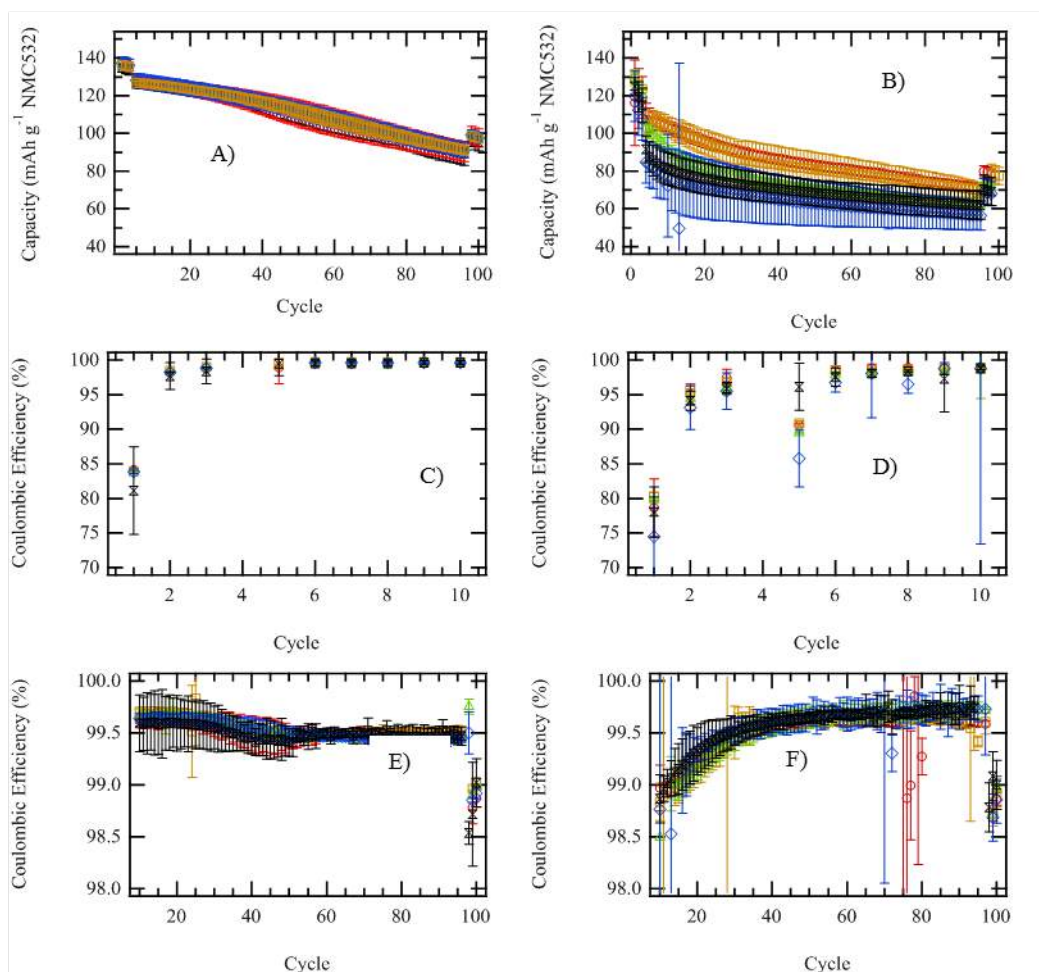


Figure II-28. Cycle life of A) LiPAA-based full cells and B) PAA-based full cells. The first 10 cycle Coulombic efficiency of C) LiPAA-based full cells and D) PAA-based full cells. The long term Coulombic efficiency of E) LiPAA-based full cells and F) PAA-based full cells. The secondary drying temperature on the Si-graphite composite anodes are 120°C (red circle), 140°C (gold square), 160°C (green triangle), 180°C (blue diamond), and 200°C (black hour glass). Each point is an average of 3 cells.

LiPAA Si-graphite cells obtained first cycle Coulombic efficiencies of 84%, except for the 200°C LiPAA Si-graphite cells, which were slightly lower at 82%. These cells rapidly increased to 99.6% within the first 5 cycles and maintained this for 30 cycles for degrading slowly to 99.5%. Upon returning the LiPAA Si-graphite cells to C/20, they dropped to a Coulombic efficiency of 98.9%. PAA Si-graphite cells had a first Coulombic efficiency of 80%, except for 180°C PAA Si-graphite cells, which were 75%. Opposed to the LiPAA Si-graphite cells, the PAA Si-graphite cells slowly increased in Coulombic efficiency over 40 cycles to 99.6%. PAA Si-graphite cells cycled at 140°C and below leveled off at 99.6%, while cells at 160 and above continued to slowly increase to 99.7%. All the cells dropped to a Coulombic efficiency of 98.8 - 99.0% after returning to C/20 which is clearly not ideal for a commercial application

In summary, this data shows that the electrodes cast in water (LiPAA binder) with lower residual water content cycle better than the NMP cast PAA electrodes (with higher water content). Interestingly, the PAA performance is dramatically influenced by drying temperature. This is consistent with the previous TGA data which showed significant water loss above 140°C due to dehydration. At higher temperatures, the decomposition of the PAA produces a far worse binder.

Cell Optimization, Impact of Electrolyte Volume Addition (ORNL)

This study aims to explore the correlations between electrolyte volume, electrochemical performance, and properties of the solid electrolyte interphase in pouch cells with Si-graphite composite anodes and NMC532 cathodes. [8] We conclude that a minimum electrolyte volume factor of 3.1 times the total pore volume of cell components (cathode, anode, and separator) is needed for better cycling stability. Less electrolyte causes increases in ohmic and charge transfer resistances. Lithium dendrites are observed when the electrolyte volume factor is low. The resistances from the anodes become significant as the cells are discharged. Solid electrolyte interphase thickness grows as the electrolyte volume factor increases and is non-uniform after cycling.

For this study the electrolyte was 90 wt.% “Gen 2” and 10 wt.% fluoroethylene carbonate (FEC). Gen 2 is the electrolyte formulation adopted by Argonne National Laboratory (ANL) and Oak Ridge National Laboratory (ORNL) and is 1.2 M LiPF₆ in ethylene carbonate:ethylmethyl carbonate (EC:EMC) (3:7 by weight). FEC was included as an additive in Gen 2 because of improvement in cycle life of Si anode with it. Electrolyte volume factor, *F*, was defined as the supplied electrolyte volume divided by the total cell pore volume (the sum of pore volumes in anode, cathode, and separator). The contribution of electrode separation and edge effects to the total void volume depends on the cell geometry and configuration. Thus, the optimum factor, *F*, would be expected to be different for other cell designs such as 18650’s. The electrolyte volume would also vary with the surface roughness of the electrodes. Five volume factors from 1.6 to 3.5 were investigated at 25°C with four cells in each volume factor group. Each cell had 100 mAh capacity at C/20 with a single-side coated anode and cathode. Details of the processes and conditions for the cell assembly, test equipment, and test set-up are elaborated elsewhere. [8] All cell assembly was completed in the DOE Battery Manufacturing R&D Facility (BMF) dry room (dew point ≤ -55°C) at ORNL. The electrodes were fabricated at, and provided by, the Cell Analysis, Modeling, and Prototyping (CAMP) Facility at ANL. The anode contained 73 wt.% graphite, 15 wt.% 50-70 nm silicon, 10 wt.% lithium polyacrylate (LiPAA), and 2 wt.% carbon. [9] The LiPAA binder was prepared by titration of polyacrylic acid with LiOH to neutral pH.

Testing included 3 formation cycles at C/20 charge and discharge rates, an initial DC resistance test (1 cycle), 92 aging cycles, a final DC resistance test (1 cycle), and 3 final cycles. [9] Cells were cycled with cut-off voltages of 4.1 V and 3.0 V for all tests. The voltages were held at 4.1 V during charging until the current dropped to C/20. AC electrochemical impedance spectroscopy (EIS) tests were included after the final cycles to analyze resistances in detail. The hybrid pulse power characterization (HPPC) test was used to investigate the DC resistance of full cells at different depths of discharge (DOD). Discharge C-rate for the HPPC pulses was 3C (1C rate is based on 130 mAh g⁻¹ of NMC). XPS depth profiles were used to estimate the SEI layer thicknesses and insoluble components. All cells were discharged to 3 V at C/20 before disassembly, and the anodes were harvested in an argon atmosphere glove box. The harvested electrodes were lightly rinsed with EMC solvent, dried in the glove box, and loaded in a vacuum transfer module to avoid air and moisture contact. The transfer module was directly inserted into the XPS chamber with a base pressure 10⁻⁹ Torr. Hence, the electrode samples analyzed by XPS were never exposed to ambient air and moisture. The analysis depth is expected to be 5–10 nm. [10]

Correlation of Electrolyte Volume and Capacity Fade

During the first three cycles, cell-to-cell variations in discharge capacity were large for all factor groups. Figure II-29 shows average discharge capacities and irreversible capacity losses (ICLs) during first three (1st – 3rd cycle) at C/20, aging cycles (4th – 97th cycle) at C/3, and last three cycles (98th – 100th cycle) at C/20 charge and discharge rates with 95% confidence intervals as error bars. During the first three cycles (Figure II-29a - b), F1.6 showed the lowest average discharge capacities (87 - 97 mAh g⁻¹) with the largest error bars (44 - 43 mAh g⁻¹, one-side) while F2.1 showed the smallest error bars (9 - 3 mAh g⁻¹, one-side) and the highest average discharge capacities (134 mAh g⁻¹). ICLs at F1.6 were also the highest (30.4 mAh g⁻¹, 3.6%) while those at F2.6 were the lowest (21.3 mAh g⁻¹, 1.5%). After 100 cycles (Figure II-29e - f), F3.5 group showed the highest discharge capacity (65 mAh g⁻¹) which was slightly higher than F3.1 group (63 mAh g⁻¹) but the difference was insignificant considering the error range. Their ICLs were also the lowest (2.7%). Capacities of F1.6 at C/20 during the final cycles seem closer to those of F3.1 and higher than those of

F2.1 and F2.6. However, the capacities of F1.6 remained far below the other groups during the aging cycles at higher rate (C/3) (Figure II-29c). While the error bars for the F1.6 group were large, clear trends in the capacity and ICL were observed for the other groups after the aging cycles (Figure II-29e and 10f). During the aging cycles, both F3.1 and F3.5 showed the highest capacity retentions (about 52% from the maximum capacity to the final capacity) and the lowest ICLs (Figure II-29c and Figure II-29d). In general, capacity and capacity retention increased with increasing volume factor up to F3.1.

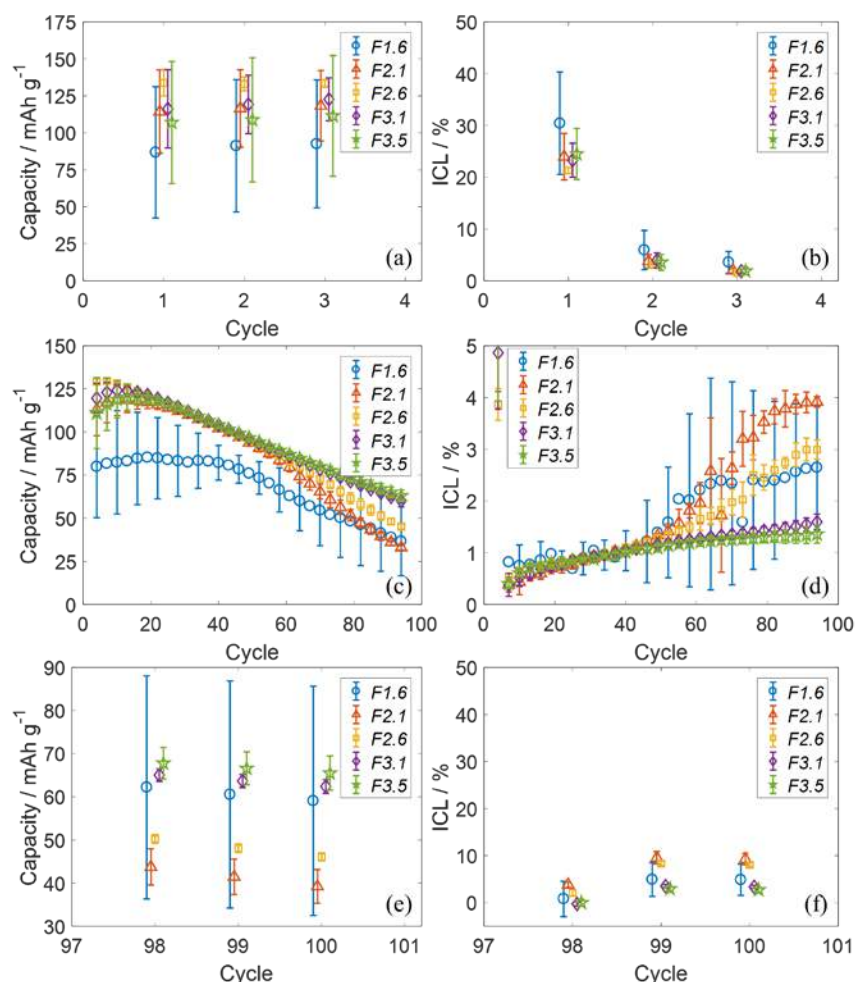


Figure II-29. Correlation of electrolyte volume and cell cyclability. Discharge capacities during (a) first three cycles at 0.05C/-0.05C, (c) aging cycles at 0.333C/-0.333C, and (e) last three cycles at 0.05C/-0.05C for different electrolyte volume factor groups, F; corresponding irreversible capacity losses (ICLs) during (b) the first three cycles, (d) aging cycles and (f) the last three cycles. Cut-off voltages were 3 and 4.1 V. Voltage for the aging cycle was held at 4.1 V until current reached 0.05C. Error bars correspond to 95% confidence intervals.

The Si particles experienced changes not only in volume but also in shape, which further destabilized the SEI layer. Figure II-30 shows top-down SEM images of (a) the pristine Si-graphite anode and (b) F1.6 and (c) F3.5 anodes cycled for 100 times and discharged. Unlike the pristine anode, which showed spherical Si and conductive carbon particles (not distinguishable in the image), the shape of particles covered by SEI became irregular after cycling. The change in particle shape agreed well with an earlier TEM study. [11] SEI covering the particles was bulkier for F3.5 compared to F1.6, which implies that electrolyte decomposed more on Si particles at F3.5 due to the more abundant electrolyte (reactant). SEI thickness analysis also showed thicker SEI at F3.5 than at F1.6 and is elaborated later.

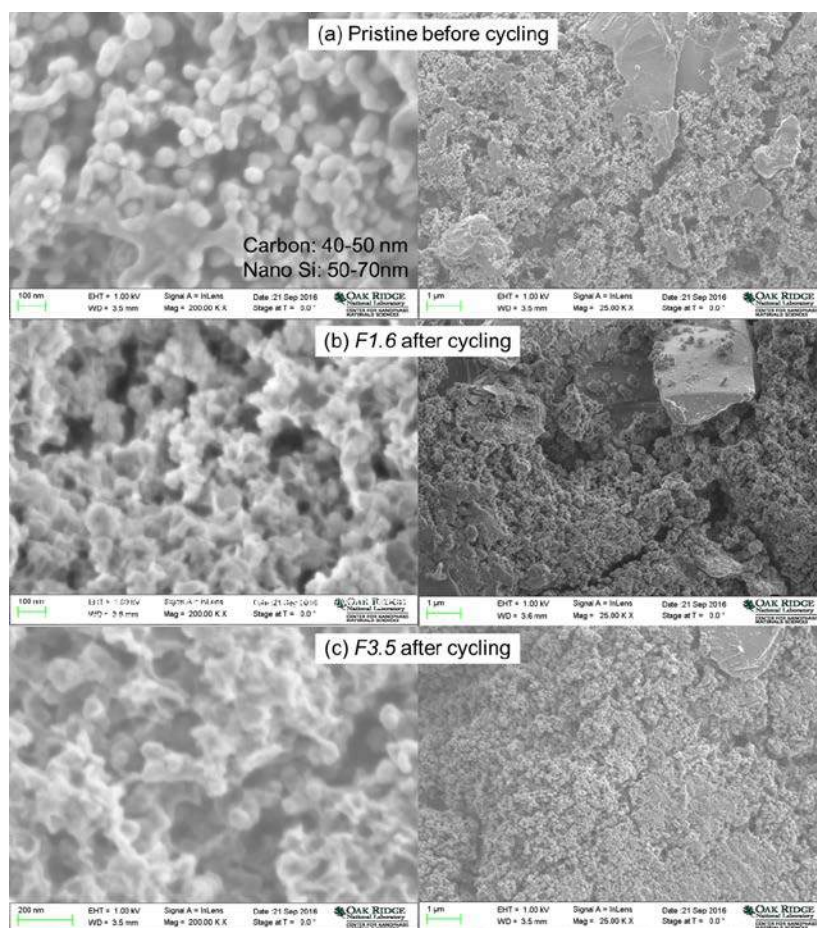


Figure II-30. SEM images of (a) pristine 15 wt.% Si-graphite anode and (b) F1.5 and (c) F3.5 anode cycled 100 times. Magnification of the images on left and right are 200,000 X and 25,000 X, respectively.

The SEM images also show the presence of some relatively bare graphite particles that were not covered with silicon and carbon. This is consistent with the Raman mapping data reported in this report. EDS results from F1.6 and F3.5 showed that the silicon-carbon rich areas had more oxygen and fluorine elements than the graphite-rich areas. This indicates that SEI was formed preferentially on the silicon-carbon areas, since oxygen and fluorine are key elements of SEI components such as lithium carbonate and LiF. EDS analysis showed 3.5-4.8 atomic percentage of Si at the graphite rich zone because effective analysis depth is large at 20 kV (e.g., 1-2 μm in Si). Because of the same reason, silicon atomic percentage was not significantly high at the silicon-carbon rich zone.

Low electrolyte volume, F1.6, led to lithium dendrite formation on an anode. After 100 cycles, the separator for F1.6 was also dry. Visual inspection of the F1.6 anode revealed that some regions of the electrode did not contribute to charge-discharge processes properly due to lack of electrolyte. These areas were relatively bright and light green in color similar to the pristine anode. Darker areas indicated where the electrode did cycle. The color change is due to the conversion of crystalline Si to amorphous Si during lithiation. The dendrites formed on dark areas surrounded or near by the relatively-bright areas due to the locally low negative-to-positive capacity ratio. Unlike F1.6, there was plenty of electrolyte on the separator for F2.6 and F3.5 groups and no lithium dendrites were observed.

Resistance Analysis of Full Cells

Resistances were characterized before and after aging cycles using HPPC. Figure II-31 shows the individual cell resistances during discharge for different factor groups. F1.6 showed the highest resistance on average with large cell-to-cell variations. In general, the resistances of all cells increased as voltage decreased. The initial resistances (4th cycle) of F2.1 and above were almost identical (32 – 35 Ohm-cm² near 3.6 V) while those of F1.6 were much higher (57 – 66 Ohm-cm² near 3.6 V). After the 97th cycle, cells in the F3.1 and F3.5 groups demonstrated the lowest resistance (about 50 Ohm-cm² near 3.6 V), followed by F2.6 (average 73 Ohm-cm²), F2.1 (over 90 Ohm-cm²), and F1.6 (average 127 Ohm-cm²). Hence, F3.1 represented the minimum electrolyte amount to minimize resistance increase during cycling. This was also consistent with the long-term cycling data (Figure II-32), which showed the least capacity fade for the F3.1 and F3.5 groups. The resistances were also measured using EIS at different voltages after 100 cycles. Figure II-32 shows selected impedance data of different factor groups between 3.7 V and 3.8 V and areal resistances at different voltages. The EIS results were in agreement with the HPPC results with the lowest resistance at F3.1 and F3.5 groups (26 – 30 Ohm-cm² near 3.6 V), which was just a few Ohm-cm² lower than the HPPC results. Similar to the HPPC results, there was no significant difference in resistances from F3.1 and above.

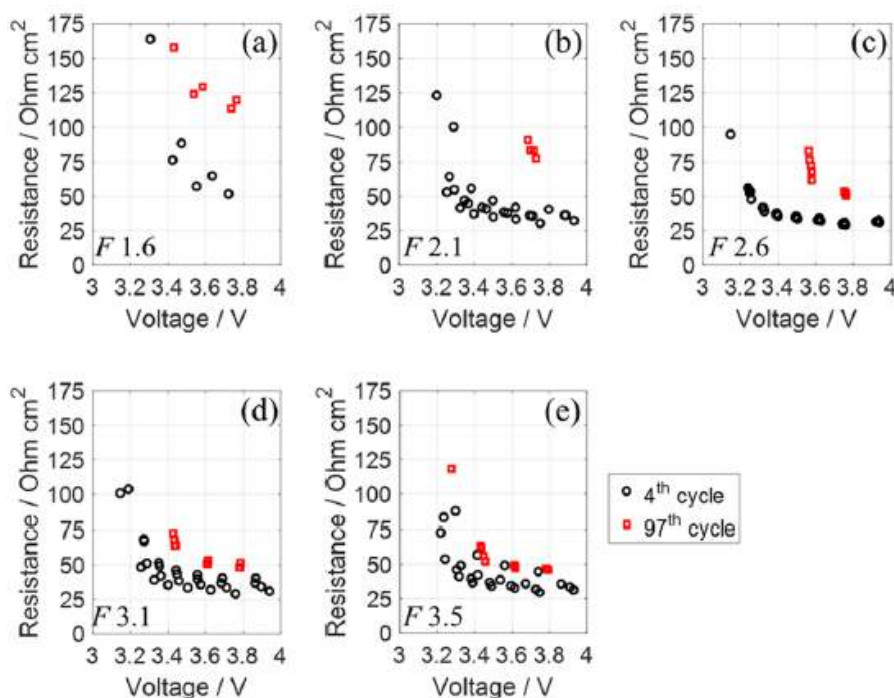


Figure II-31. Resistances of 15 wt.% Si-graphite/NMC532 cells from HPPC tests at different voltages during discharge at 4th and 97th cycles for electrolyte volume factor group F1.6 (a), F2.1 (b), F2.6 (c), F3.1 (d), and F3.5 (e).

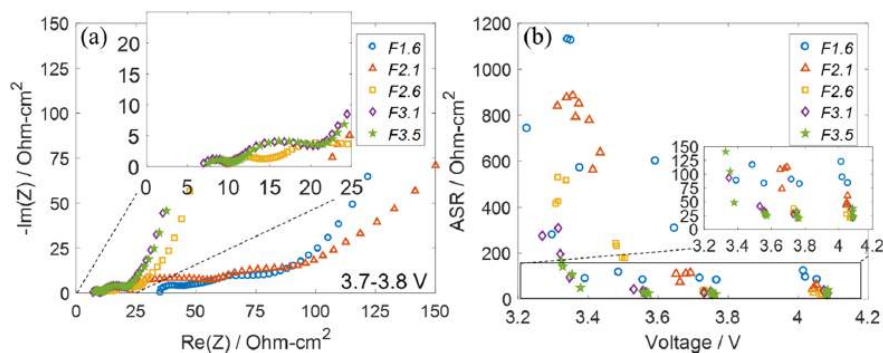


Figure II-32. (a) Impedance spectra of 15 wt.% Si-graphite/NMC532 cells near 3.75 V after 100 cycles with different electrolyte volume factor groups. (b) Total resistances from EIS at different voltages. (Equivalent circuit model for the EIS data fitting is shown in the next figure.)

Figure II-33a shows the equivalent circuit model used to fit the EIS data along with definitions of the circuit elements and their frequency domains. As examples, Figure II-33b and Figure II-33c illustrate EIS data ranges and the corresponding frequency domains of F3.5 for the fits at 4.1 V and 3 V. The resistance elements obtained in this study were ohmic resistance (R_{ohmic}), surface film resistance (R_{sf} , or SEI resistance), charge transfer resistance I (R_{ct1} , or anode charge transfer resistance), and charge transfer resistance II (R_{ct2} , or cathode charge transfer resistance). For full cells with graphite anodes, the frequency domain II that belongs to anode charge transfer resistance, R_{ct1} , does not generally appear as a distinct semi-circle. [12,13] However, the R_{ct1} was a significant component for full cells with Si-containing anodes, especially at low voltages.

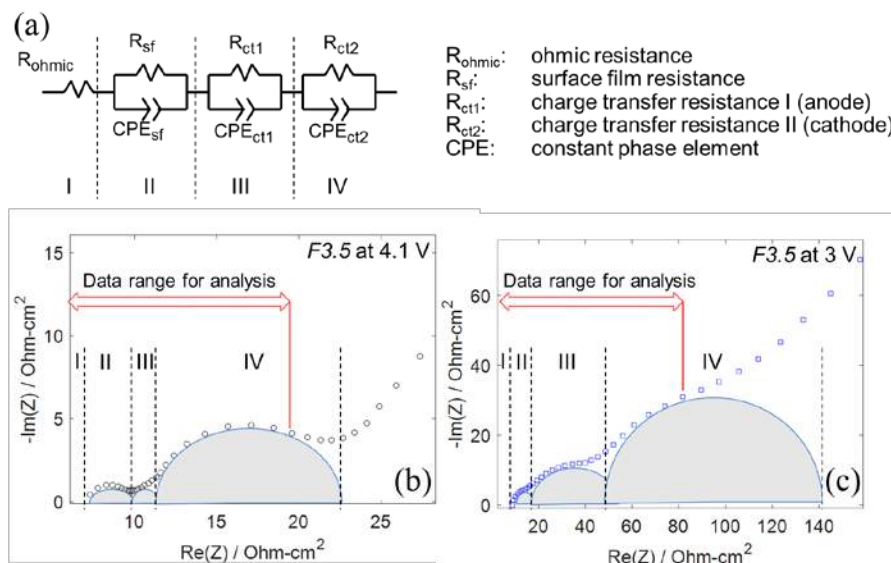


Figure II-33. (a) Equivalent circuit model for EIS data fitting and definitions and four frequency domains of elements. As examples, EIS data of F3.5 at (b) 4.1 V and (c) 3 V after 100 cycles and their data ranges for the fittings.

Each resistance derived from the EIS after 100 cycles is shown in Figure II-34. The electrolyte resistances indicated as R_{ohmic} were affected by low electrolyte volumes. The highest R_{ohmic} was measured for F1.6 (about 35 Ohm-cm^2) followed by F2.1 (about 20 Ohm-cm^2). F2.6 and above showed similar electrolyte resistance (about 10 Ohm-cm^2). R_{ohmic} was independent of voltage, as expected. In contrast, all other resistances increased at lower voltages. Surface film resistance, R_{sf} , is related to the SEI layer and was the lowest at F3.1 and F3.5 (2 - 3 Ohm-cm^2 near 3.6 V). While the SEI layer for the higher factor group (F3.5) was thicker than the lower factor group (F1.6 and F2.6), this SEI layer was likely porous. Anode surface analysis

section explains SEI thicknesses and porosities in detail. F3.1 and F3.5 also showed the lowest anode (R_{ct1} , 2 - 3 $\text{Ohm}\cdot\text{cm}^2$ near 3.6 V) and cathode charge transfer resistance (R_{ct2} , 12 - 13 $\text{Ohm}\cdot\text{cm}^2$ near 3.6 V). The charge transfer resistances for volume factors of F2.6 and below were higher than those of F3.1 and F3.5 especially at voltages below 3.6 V. The charge-transfer resistance also became more voltage-dependent as the electrolyte volume decreased. This is reasonable because energy requirement resulting in voltage loss becomes higher as the electrolyte volume decreases.

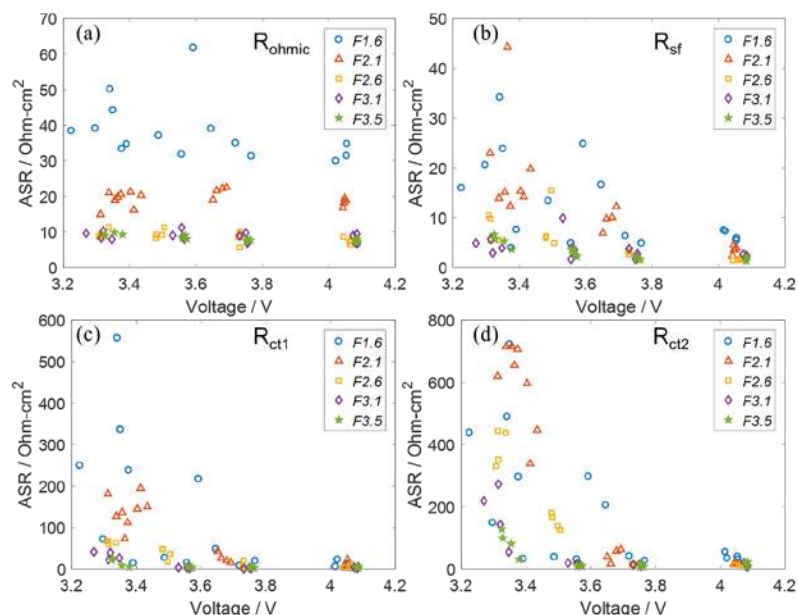


Figure II-34. (Areal specific resistances (ASR) from EIS at different voltages in different electrolyte volume factor groups, (a) ohmic resistance (R_{ohmic}), (b) surface film resistance (R_{sf}), (c) anode charge transfer resistance (R_{ct1}), and (d) cathode charge transfer resistance (R_{ct2}).

Anode Surface Analysis

Three factor groups (F1.6, F2.6, and F3.5) were selected for anode surface analysis since the electrochemical performance of F3.1 is similar to F3.5. The thicknesses of the surface film (SEI) were estimated using XPS depth profiles and were consistent with FTIR data. Figure II-35 shows surface film element profiles of the three groups along the depth direction from the surfaces. All specimens were taken from the same location at each anode to avoid a geometric effect. The depth was calculated based on the assumption that the film has the same etching rate as SiO_2 . The counts per second (CPS) data from element peaks were smoothed using the LOESS model (locally weighted polynomial regression). The thicknesses were estimated based on the CPS of elements corresponding to SEI or silicon active components along the thickness direction. [12] Four elements were chosen for the estimation: Li from LiF (55.6 eV), Si from bulk Si0 (99.6 eV) and Li_xSiO_y (102.8 eV), C from carbonates (292.6 eV), and O from carbonates (532 eV for $\text{C}=\text{O}$ and 533.5 eV for $\text{C}-\text{O}$). LiF and carbonates form SEI components from electrolyte decomposition. Li_xSiO_y forms from the conversion of surface silicon oxides and is one of dominant species on cycled silicon surfaces. [10, 14, 15] In Figure II-35, each CPS of elements was normalized by its own maximum because the CPS varied with different elements.

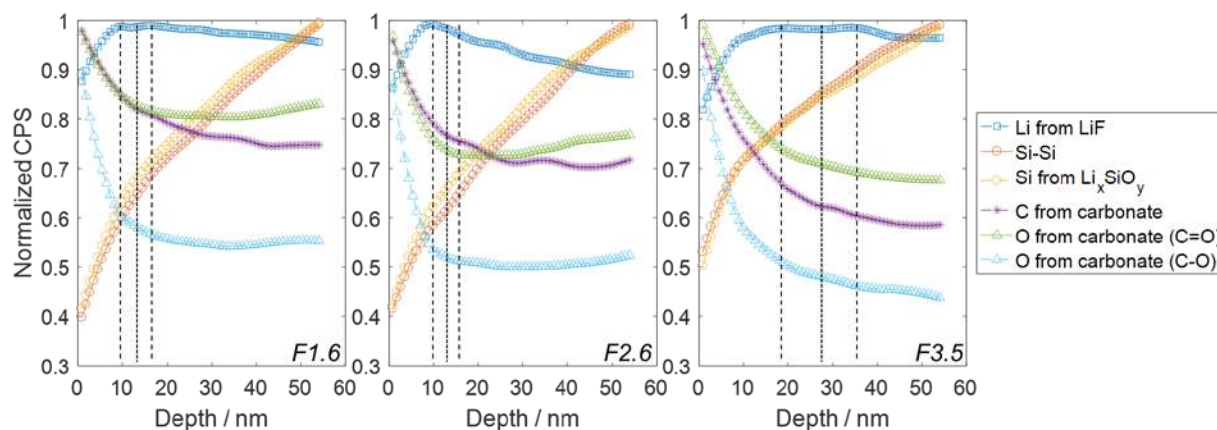


Figure II-35. Depth profiles of SEI (LiF and carbonates) and active material (Si-Si and Li_xSiO_y) elements. Black dashed and dotted lines are possible ranges of SEI/Si interface and averages of the ranges, respectively. The depth on x-axis was based on the assumption that the film has the same etching rate as SiO_2 . CPS of each element was normalized by its own maximum value.

The ranges of estimated SEI thicknesses were 9–16 nm for both F1.6 and F2.6, and 17–34 nm for F3.5. The estimated thickness of SEI at F3.5 is near the radius of the original Si particle (50–70 nm). The thick SEI layer is ascribed to Si because the SEI layers on pure graphite anodes without Si are only about 10 nm thick or less. [12] Since the electrochemical reactions for F1.6 were not uniform, the results from the F1.6 specimen only represent the dark (cycled) areas at which the local current density might have been higher. The SEI thickness increased significantly from F1.6 and F2.6 to F3.5. This increase can happen when an SEI layer on an electrode is not electronically insulating or insufficiently dense to prevent electrolyte diffusion towards the electrode surface. In either case the electrolyte continuously decomposes. This result agreed well with SEM images showing larger SEI precipitations at F3.5 than F1.6. On the other hand, the surface film (SEI) resistance of F1.6 from the EIS analysis was higher than that of F3.5, which seems inconsistent with SEM and XPS results. This apparent contradiction can be explained if the SEI is porous. A porous SEI would appear in EIS as a part of the ohmic resistance rather than the surface film resistance. Considering all of the results from EIS, SEM, and XPS, larger electrolyte volume formed thicker SEI layers with some porosity or channels/cracks. The thickness of the SiO_2 layer on Si was not estimated since Li_xSiO_y continuously increased like Si-Si during the depth analysis, which implies that the SiO_2 /Si interface was not sharply delineated. Instead, it is possible that Li_xSiO_y was present throughout the Si particles because its CPS even increased continuously at the depth of original diameter of the silicon particle (50–70 nm). The spherical shape of silicon particle probably changed to rough shapes, larger surface area, after large volume changes during cycling. The irregularly expanded silicon surfaces after lithiation might partially cover Li_xSiO_y and leave or trap it in the inner surfaces during contraction. If this repeats, Li_xSiO_y can be found in side of the silicon although the silicon may not cover it entirely.

The non-uniform SEI was verified from the $\text{Si}2p$ peaks in Figure II-36a (0 nm depth) and Si atomic percentages in Figure II-36b. Si^0 (99.6 eV for Si 2p) was clearly detected from the top surfaces of the anode, especially at F3.5, implying SEI did not cover the Si particle surfaces uniformly. It should be noted that the electron escape depth is only 5–10 nm beneath the anode surface. Hence, Si^0 was present not only under the SEI but also on top of the SEI or near the top surface. In Figure II-36a, Li 1s, O 1s and P 2p peaks indicated the amount of dense lithium compounds (e.g., LiF, Li_2O , Li_2CO_3) increased as the analysis depth approached the SEI/Si interface. C 1s, O 1s, and P 2p peaks showed polymeric carbonates and phosphorus compounds mostly distributed in the outer surface of the SEI. The graphite peak intensity (284.5 eV) was not clear after 100 cycles, which also happened in another study. [9] According to the results of XPS survey scans from the top surface (before sputtering) (Figure II-36b), F3.5 showed a higher ratio of carbonate compounds

(C 1s and O 1s) and lower ratio of Li compounds (Li 1s) than F1.6 and F2.6. Hence, F3.5 might have a higher ratio of polymeric compounds than the lower electrolyte volume factor groups.

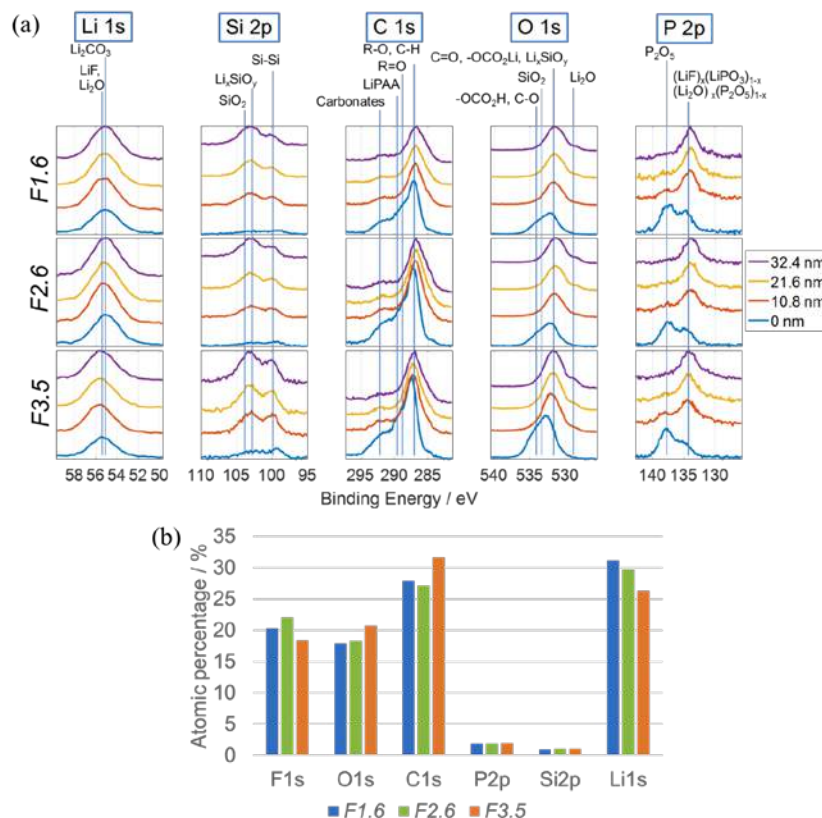


Figure II-36. (a) XPS peaks from depth profiles of F1.6, F2.6, and F3.5 and (b) atomic percentages from the top surface (before sputtering) from XPS survey scans. Depth was calculated based on the sputter rate for SiO₂.

In summary, the electrolyte volume effects were investigated with lithium ion batteries in pouch format with 15 wt.% Si-graphite as the anode and LiNi_{0.5}Mn_{0.3}Co_{0.2}O₂ (NMC532) as the cathode. The electrolyte was 90 wt.% 1.2 M LiPF₆ in EC:EMC with 10 wt.% FEC. This work determined a baseline condition for electrolyte volume when integrating Si into graphite anode, which provided insights on practical cell and pack design. The electrolyte volume to total pore volume needs to be at least 3.1 to achieve the best performance. However, the optimized capacity retention in this study was still lower than that of cells with pure graphite anodes without silicon. Less electrolyte resulted in higher ohmic resistance, larger cell-to-cell capacity variation, and greater capacity fade. HPPC tests demonstrated the lowest resistance for the volume factor 3.1 and 3.5 groups, followed by 2.6, 2.1, and 1.6. For the volume factor 1.6, lithium dendrites were found on the anode surface after cycling. Unlike typical full cells having graphite anodes, significant anode charge transfer resistances were detected in EIS measurements and became more pronounced as the cell voltage decreased. Irreversible capacity loss also continuously increased in all factor groups as cells were cycled. SEM and EDS analysis showed that SEI covering the active particles was bulkier for the volume factor 3.5 compared to 1.6. SEI formed thicker layers on Si-rich areas compared to graphite-rich areas. XPS results also showed SEI thicknesses around 10 to 35 nm after 100 cycles, and the SEI thickness increased as the electrolyte volume factor increased. The XPS elemental analysis along the depth of anode indicated that Li_xSiO_y formed throughout the Si particles rather than just as a surface layer. Considering all of the results from EIS, SEM, and XPS, it was found that the SEI on Si has large pores or channels that are permeable to electrolyte.

Thermodynamic Understanding and Abuse Performance (SNL)

As we develop new materials to increase performance of lithium ion batteries for electric vehicles, the impact of potential safety and reliability issues become increasingly important. In addition to electrochemical performance increases (capacity, energy, cycle life, etc.), there are a variety of materials advancements that can be made to improve lithium-ion battery safety. Issues including energetic thermal runaway, electrolyte decomposition and flammability, anode SEI stability, and cell-level abuse tolerance behavior. Introduction of a next generation materials, such as a silicon-based anode, requires a full understanding of the abuse response and degradation mechanisms for these anodes. This work aims to understand the breakdown of these materials during abuse conditions in order to develop an inherently safe power source for our next generation electric vehicles.

The effect of materials level changes (electrolytes, additives, silicon particle size, silicon loading, etc.) to cell level abuse response and runaway reactions will be determined using several techniques. Experimentation will start with base material evaluations in coin cells and overall runaway energy will be evaluated using techniques such as differential scanning calorimetry (DSC), thermogravimetric analysis (TGA), and accelerating rate calorimetry (ARC). The goal is to understand the effect of materials parameters on the runaway reactions, which can then be correlated to the response seen on larger cells (18650). Experiments conducted showed that there was significant response from these electrodes. Efforts to minimize risk during testing were taken by development of a smaller capacity cylindrical design in order to quantify materials decision and how they manifest during abuse response.

The effect of materials level changes (electrolytes, additives, silicon particle size, silicon loading, etc.) to cell level abuse response and runaway reactions will be determined using several techniques. Experimentation will start with base material evaluations in coin cells and overall runaway energy will be evaluated using techniques such as differential scanning calorimetry (DSC), thermogravimetric analysis (TGA), and accelerating rate calorimetry (ARC). The goal is to understand the effect of materials parameters on the runaway reactions, which can then be correlated to the response seen on larger cells (18650). Experiments conducted showed that there was significant response from these electrodes. Efforts to minimize risk during testing were taken by development of a smaller capacity cylindrical design in order to quantify materials decision and how they manifest during abuse response.

This work continues the efforts from last year, which aimed to evaluate electrochemical and abuse response for electrodes provided from the CAMP facility at Argonne National Laboratory. This included evaluation of anodes containing between 0 and 15 wt% silicon from NanoAmor. Investigations were completed on coin cell and 1.25 Ah 18650 form factors. Several experiments showed a high level of gas generation and overall runaway for cells containing silicon electrodes. To further understand the response of these materials, this work focused on understanding the effect of several factors to runaway response and gas generation including solvent selection, electrode processing, silicon content, and the effect of water. The primary reaction believed to be resulting in significant contribution to runaway reaction is the water reaction. This is particularly interesting in systems using polyacrylic acid (PAA) binders as one of the products during degradation of PAA is water, which could lead to increase runaway energetics. During degradation of PAA, water is evolved at the expected temperature of 100°C as well as a second peak around 250°C, which is presumably from polymer degradation reactions.

In order to investigate the effect of binder during runaway, electrodes were prepared with several processes to identify the contribution to overall runaway enthalpy based upon water content during processing and during high temperature breakdown. Figure II-37 shows the electrodes used to evaluate runaway energetics. Electrodes were made with nanoamor 70-130 nm silicon, Hitachi Mag-E graphite, Timcal C45 carbon, and several different binders in weight percentage ratios of 15/73/2/10 respectively. Electrodes parameters were 45 μm thickness, 45% porosity, and areal capacity of 1.9 mAh/cm².

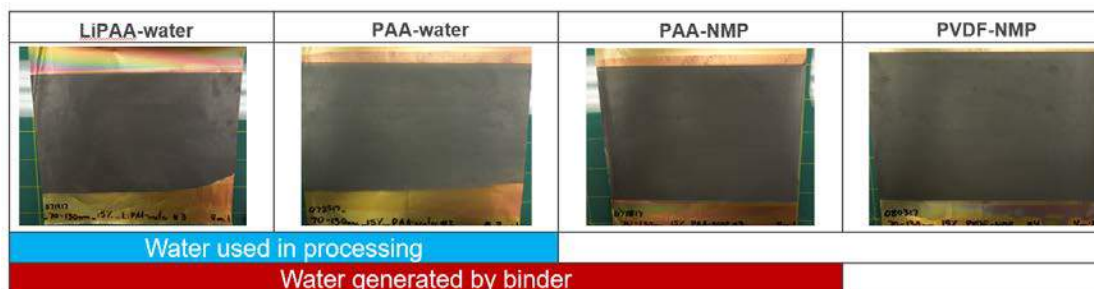


Figure II-37. Prepared electrodes processed with water (blue) and that will have water present during runaway reactions (red) in comparison to normal non-aqueous systems (right).

Coin cells were assembled and formation cycling was conducted on all electrodes. After 5 cycles, each cell was held at 100% state of charge and disassembled for differential scanning calorimetry (DSC) to evaluate the heat generated during thermal abuse conditions. Each sample had an additional amount of electrolyte added to make a 1:1 wt% ratio between active material and electrolyte. All cells performed similarly under formation conditions, as seen in Figure II-38 left, with the exception of the PVDF, which was expected as it is known to be a slightly lower performing binder for the silicon system. DSC results can be seen in Figure II-38 right, which all show similar responses with a slight exotherm around 225°C with full material runaway occurring near 275°C.

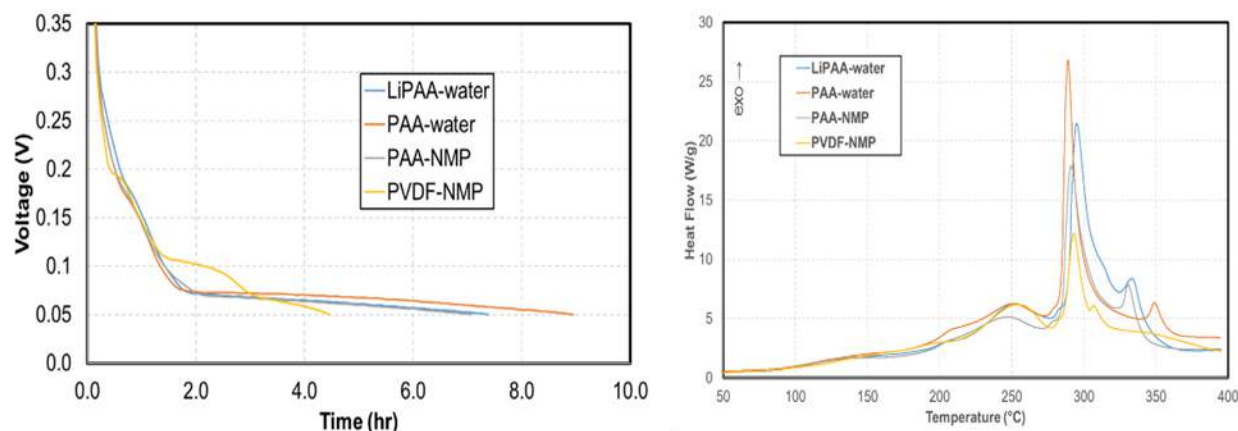


Figure II-38. (left) Half-cell formation lithiation. (right) DSC results from extracted material.

Normalization of heat flow to mass of active material shows fairly consistent results for overall runaway energy of between 40 - 55 W/Ah peak heating rates. While the reaction with water, both residual from processing and produced during runaway, plays a role in runaway it is not the sole contributing factor. Previous work has shown clear correlations to silicon content, silicon particle size, and state of charge.

Full cells were built using the 0, 5, 10, and 15 wt% silicon electrodes and built into 18650 format cells for larger cell evaluation of decomposition and abuse response. To mitigate potential safety issues, electrodes were made to be approximately half the normal length for construction into an 18650 cell. The resulting void volume within the case was taken up by either a tube of copper or a length of current collector foil wrapped to make the right jelly roll diameter. Either case, the extra copper component was then attached to the copper current collector of the anode to ensure proper electrical continuity to the negative case. All cells were formed with five formation cycles, held at 100% SOC, and then evaluated using ARC.

No clear trend was observed for electrodes of half-length using both extra current collector (Figure II-39, yellow and blue) or solid copper tubing inserts (Figure II-39, green and pink). To make sure that the differences seen were not due to residual electrolyte degradation for extended periods of time, inspection of ARC data between 50 and 150°C shows no appreciable difference between the two cells types, as seen in Figure II-39, right panel.

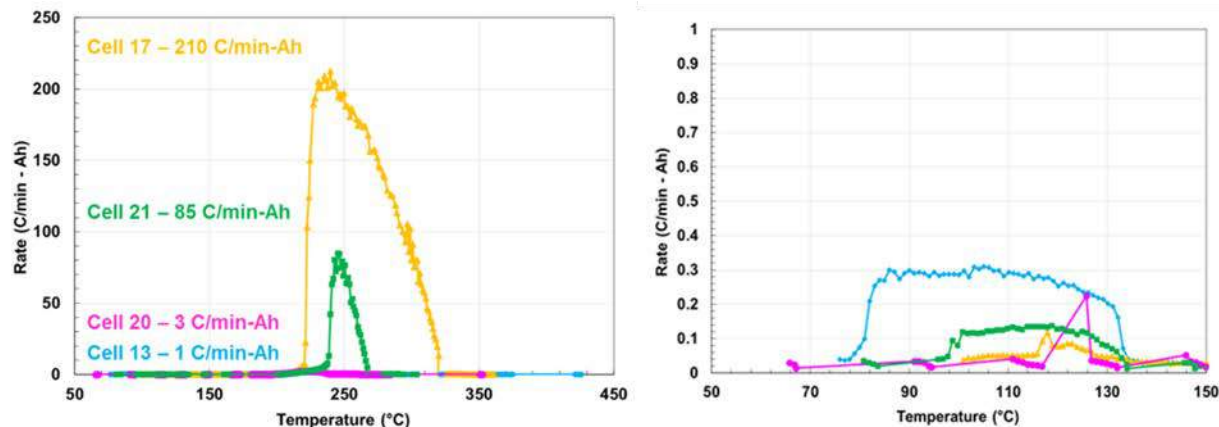


Figure II-39. ARC evaluations for several sample 18650 cells containing undersized electrodes.

During ARC evaluations, a gas samples system was assembled that would actuate a valve at 275°C to open and take a grab sample of vapor. This would then allow for isolation after full runaway of the cell, which was sent for gas sampling evaluation and chemical analysis. This was done for baseline NMC 523 vs Conoco Phillips G8 graphite using a standard sample bottle, 15 wt% Nanoamor silicon using a standard sample bottle, and 15 wt% Nanoamor silicon using a cleaned and sealed sample vial. Figure II-40 shows the results of analysis for organic components (Figure II-40A), hydrocarbons (Figure II-40B), and gases (Figure II-40C).

The primary differences seen in the gas sampling data are that there is a significantly larger amount of ethanol in the baseline samples without silicon but a significantly larger amount of ethane in the samples that do contain silicon. This is particularly interesting in light of the significant gas generation seen previously for larger cells evaluated with ARC. These evaluations were done by an independent lab, which requires transportation time for the samples. Many of the reactive species that could be present during cell runaway are likely to have already reacted in this scenario. Efforts will continue to work towards the ability to analyze gas generation in real time for a more complete understanding of reaction chemistry during runaway for these next generation materials.

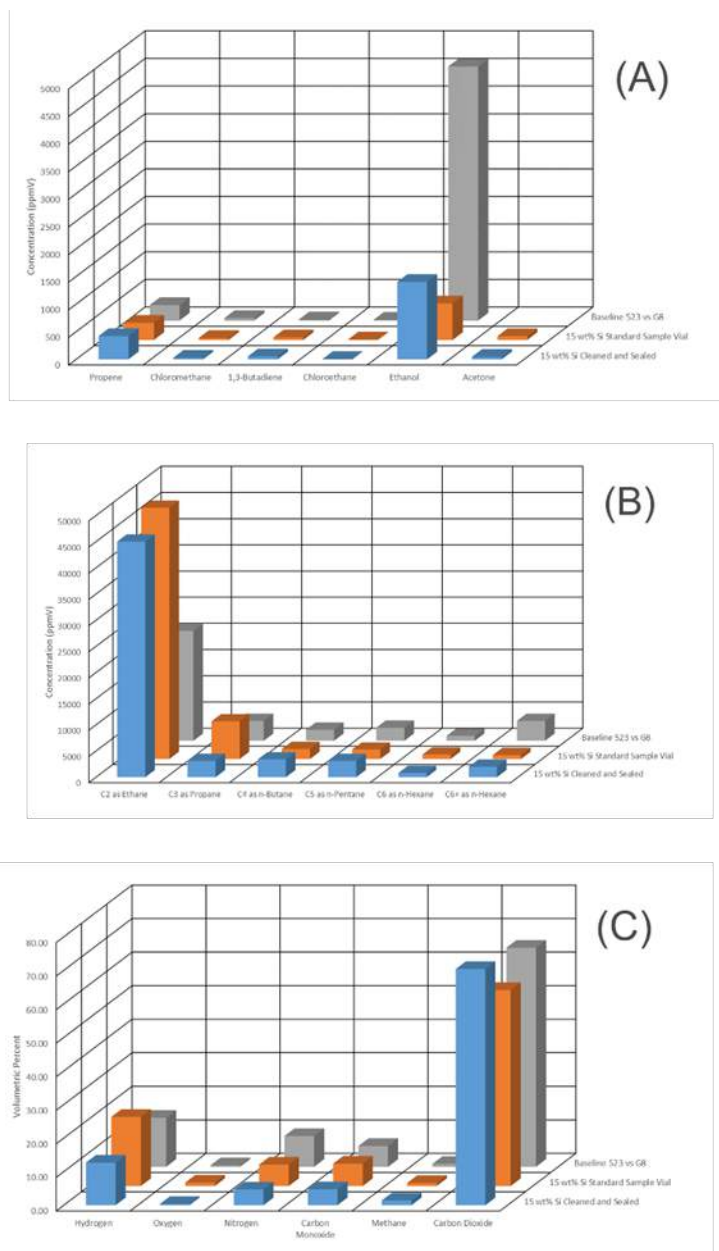


Figure II-40. Gas sampling results for electrodes containing baseline G8 graphite and 15 wt% silicon using both standard sample vials and cleaned and sealed bottles. Data is shown for analysis completed on organic species (A), hydrocarbons (B), and gases (C).

Conclusions

Recent efforts to develop new baseline electrodes have identified a promising U.S. silicon supplier, Paraclete Energy, as a source for silicon materials. Paraclete has provided multiple samples for evaluation and screening. Encouraging aspects of working with Paraclete Energy are that they have demonstrated their ability to control particle size and customize processing steps to target surface chemistries. Electrochemical data is comparable to our best electrode performance and more importantly the silicon source provides a dependable and repeatable silicon powder from batch to batch.

Water-based processing studies of silicon containing anodes have identified the reaction of silicon with water as a degradation mechanism that can lead to processing issues and impact final electrode performance. These include significant hydrogen generation during processing and conversion of silicon to silica on the silicon particle surface. Further, the role of electrode drying temperature on anode performance was examined in detail. Electrodes cast in water (LiPAA binder) with lower residual water content cycle better than the NMP cast PAA electrodes (with higher water content). Interestingly, the PAA performance is dramatically influenced by drying temperature. This is consistent with the previous TGA data which showed significant water loss above 140°C due to dehydration. At higher temperatures, the decomposition of the PAA produces a far worse binder.

The electrolyte volume effects were investigated with lithium ion batteries in pouch format using baseline electrodes. The relationship between electrolyte volume, electrochemical performance, and properties of the solid electrolyte interphase in pouch cells with Si-graphite composite anodes and NMC532 cathodes was examined. We conclude that a minimum electrolyte volume factor of 3.1 times the total pore volume of cell components (cathode, anode, and separator) is needed for better cycling stability. Less electrolyte causes increases in ohmic and charge transfer resistances. Lithium dendrites are observed when the electrolyte volume factor is low. The resistances from the anodes become significant as the cells are discharged. However, solid electrolyte interphase thickness grows as the electrolyte volume factor increases and is non-uniform after cycling.

Thermodynamic understanding and abuse performance studies demonstrate that there is an impact on safety response with nanoscale silicon materials compared to graphite-based anodes. Changes to material and cell level properties can have impact on safety and thermal response characteristics. We have reported thermal runaway properties of cells (coin cells and cylindrical cells) containing nanoscale silicon up to 15 percent by weight. We continue to develop the understanding of abuse response for these anodes to better understand how these next generation negative electrode materials will impact cell and battery-level abuse tolerance.

Key Publications

1. Eric Allcorn, Ganesan Nagasubramanian, Kyle Fenton. "Materials Safety Study of Practical Nano-Silicon + Graphite Anodes for Lithium-Ion Batteries." Prime 2016, Honolulu, HI, Oct. 2 - 7, 2016.
2. Kyle Fenton, Chris Orendorff, Ganesan Nagasubramanian, Josh Lamb, Eric Allcorn. "Impact of next Generation Electrode Materials on Abuse Response." Prime 2016, Honolulu, HI, Oct. 2 - 7, 2016.
3. L. Zhang, Y. Liu, B. Key, S. E. Trask, Z. Yang and W. Lu, "Si nanoparticles: stability in aqueous slurries and the optimization of oxide layer thickness for optimal electrochemical performance", submitted.
4. L. Zhang, Y. Liu, S.E. Trask, Z. Yang and W. Lu, "Silicon and silicon monoxide as the anode for lithium-ion batteries", presentation given at energy storage seminar at Argonne National Laboratory, January 2017.
5. L. Zhang, Y. Liu, S.E. Trask, Z. Yang and W. Lu, "Silicon and silicon monoxide as the anode for lithium-ion batteries", invited talk given at University of Loyola Chicago, January 2017.
6. L. Zhang, Y. Liu, S.E. Trask, Z. Yang and W. Lu, "The effect of oxide layer thickness on the electrochemical performance of silicon anode for lithium-ion batteries", selected talk given at Gordon research seminar, March 2017.
7. L. Zhang, Y. Liu, S.E. Trask, Z. Yang and W. Lu, "The effect of oxide layer thickness on the electrochemical performance of silicon anode for lithium-ion batteries", poster given at Gordon research seminar and Gordon research conference, March 2017.

8. L. Zhang, Y. Liu, S.E. Trask, Z. Yang and W. Lu, "Optimization of oxide layer thickness for silicon as the anode for lithium-ion batteries", CSE postdoc seminar at Argonne National Laboratory, May 2017.
9. "Next Generation Anodes for Lithium-Ion Batteries: Overview," 2017 U.S. Department of Energy Vehicle Technologies Office Annual Merit Review and Peer Evaluation Meeting, June 5-9, 2017, Washington, DC.

References

1. *Alloy Negative Electrodes for Li-Ion Batteries*. M.N. Obrovac and V.L. Chevrier, Chem, Rev. 2014, 114, 11444-11503.
2. *Modeling the Performance and Cost of Lithium-Ion Batteries for Electric-Drive Vehicles*. Second Edition, Argonne National Laboratory Report, ANL-12/55.
3. *Performance of Full Cells Containing Carbonate-Based LiFSI Electrolytes and Silicon-Graphite Negative Electrodes*. S.E. Trask, K.Z. Pupek, J.A. Gilbert, M. Klett, B.J. Polzin, A.N. Jansen, and D.P. Abraham, Journal of The Electrochemical Society, 163 (3) A345-A350 (2016).
4. Yoshida, S.; Masuo, Y.; Shibata, D.; Haruta, M.; Doi, T.; Inaba, M., Adsorbed Water on Nano-Silicon Powder and Its Effects on Charge and Discharge Characteristics as Anode in Lithium-Ion Batteries. *J. Electrochem. Soc.* **2017**, *164*, A6084-A6087.
5. Buchholz, F. L.; Graham, A. T., *Modern Superabsorbent Polymer Technology*. Wiley-VCH: 1997.
6. McNeill, I. C.; Sadeghi, S. M. T., Thermal Stability and Degradation Mechanisms of Poly(Acrylic Acid) and its Salts: Part 1 Poly(Acrylic Acid). *Polym. Degrad. Stabil.* **1990**, *29*, 233-246.
7. McNeill, I. C.; Sadeghi, S. M. T., Thermal Stability and Degradation Mechanisms of Poly(Acrylic Acid) and its Salts,: Part 2 Sodium and Potassium Salts. *Polym. Degrad. Stabil.* **1990**, *30*, 213-230.
8. An, S. J.; Li, J.; Daniel, C.; Meyer, H. M.; Trask, S. E.; Polzin, B. J.; Wood, D. L., Electrolyte Volume Effects on Electrochemical Performance and Solid Electrolyte Interphase in Si-Graphite/NMC Lithium-Ion Pouch Cells. *ACS Applied Materials & Interfaces* **2017**, *9*, 18799-18808.
9. Bareño, J.; Shkrob, I. A.; Gilbert, J. A.; Klett, M.; Abraham, D. P., Causes and Mitigation of Capacity Fade in NCM523/Si-Gr Lithium-ion Cells. *J. Electrochem. Soc.* **2017**, Under review.
10. Philippe, B.; Dedryvère, R.; Allouche, J.; Lindgren, F.; Gorgoi, M.; Rensmo, H.; Gonbeau, D.; Edström, K., Nanosilicon Electrodes for Lithium-Ion Batteries: Interfacial Mechanisms Studied by Hard and Soft X-ray Photoelectron Spectroscopy. *Chem. Mater.* **2012**, *24*, 1107-1115.
11. Nie, M.; Abraham, D. P.; Chen, Y.; Bose, A.; Lucht, B. L., Silicon Solid Electrolyte Interphase (SEI) of Lithium Ion Battery Characterized by Microscopy and Spectroscopy. *J. Phys. Chem. C* **2013**, *117*, 13403-13412.
12. An, S. J.; Li, J.; Sheng, Y.; Daniel, C.; Wood III, D. L., Long-Term Lithium-Ion Battery Performance Improvement via Ultraviolet Light Treatment of the Graphite Anode. *J. Electrochem. Soc.* **2016**, *163*, A2866-A2875.
13. An, S. J.; Li, J.; Mohanty, D.; Daniel, C.; Polzin, B. J.; Croy, J. R.; Trask, S.; Wood, D. L., Correlation of Electrolyte Volume and Electrochemical Performance in Lithium-ion Pouch Cells with Graphite Anodes and NMC532 Cathodes. *J. Electrochem. Soc.* **2017**, *164*, A1195-A1202.

14. Young, B. T.; Heskett, D. R.; Nguyen, C. C.; Nie, M.; Woicik, J. C.; Lucht, B. L., Hard X-ray Photoelectron Spectroscopy (HAXPES) Investigation of the Silicon Solid Electrolyte Interphase (SEI) in Lithium-Ion Batteries. *ACS Appl Mater Interfaces* **2015**, 7, 20004-20011.
15. Philippe, B.; Dedryvère, R.; Gorgoi, M.; Rensmo, H.; Gonbeau, D.; Edström, K., Role of the LiPF₆ Salt for the Long-Term Stability of Silicon Electrodes in Li-Ion Batteries – A Photoelectron Spectroscopy Study. *Chem. Mater.* **2013**, 25, 394-404.

II.B.2 Next Generation Anodes for Lithium-Ion Batteries: Characterization, Diagnostics, and Analysis (ANL)

Dennis Dees, Principal Investigator

Argonne National Laboratory
9700 South Cass Avenue
Argonne, IL 60439
Phone: 630-252-7349
E-mail: dees@anl.gov

Peter Faguy, Technology Manager

U.S. Department of Energy
Phone: 202-586-1022
E-mail: Peter.Faguy@ee.doe.gov

Start Date: October 1, 2015

End Date: September 30, 2019

Total FY17 Project Cost: \$3,600,000 DOE FY17 share: \$3,600,000 Non-DOE share: \$0

Project Introduction

Silicon has received significant attention as a viable alternative to graphitic carbon as the negative electrode in lithium-ion batteries due to its high capacity and availability [1]. Elemental silicon can theoretically store >3500 mAh/g, nearly an order of magnitude higher than graphite (372 mAh/g and 818 mAh/mL, respectively). However, several problems have been identified that limit its utility including large crystallographic expansion (~320%) upon lithiation which translates to particle cracking, particle isolation, and electrode delamination issues. Further, there are fundamental and volume change related SEI stability issues, which affect cycling efficiency. The wealth of previous studies in this area is both a testament to its potential and the size of the challenge that must be overcome, requiring a great amount of innovation on multiple fronts.

Next Generation Anodes for Lithium-Ion Batteries, also referred to as the Silicon Deep Dive Program, is a five National Laboratory consortium assembled to tackle the barriers associated with development of an advanced lithium-ion negative electrode based upon silicon as the active material. This research program baselines promising silicon materials that can be developed or obtained in quantities sufficient for electrode preparation within the consortium facilities. Composite electrode and full cell development leverages recent investments made by DOE-EERE-VTO in electrode materials and characterization. The primary objective of this program is to understand and eliminate the barriers to implementation of a silicon-based anode in lithium-ion cells. The Labs are focused on a single program with continuous interaction, clear protocols for analysis, and targets for developing both the understanding and cell chemistry associated with advanced negative electrodes for lithium-ion cells. First and foremost, this undertaking is a full electrode/full cell chemistry project leveraging baseline electrodes prepared at the consortium facilities. All efforts are directed to understanding and developing the chemistry needed for advancing silicon-based anodes operating in full cells. Materials development efforts include active material development, binder synthesis, coatings, safety, and electrolyte additives. Efforts include diagnostic research from all partners, which span a wide range of electrochemical, chemical and structural characterization of the system across length- and time-scales. Specialized characterization techniques developed with DOE-EERE-VTO funding, include neutrons, NMR, optical, and X-ray techniques being employed to understand operation and failure mechanisms in silicon-based anodes. In addition, several strategies to mitigate lithium loss are being assessed. The project is managed as a single team effort spanning the Labs, with consensus decisions driving research directions and toward development of high-energy density lithium-ion batteries. A detailed list of participants is given in Figure II-41.



Figure II-41. Program participants including Laboratories, research facilities, and individual contributors.

Objectives

- Understand and overcome the science and technology barriers to the use of silicon-based anodes in high-energy density lithium-ion batteries for transportation applications.
 - Stabilize the SEI
 - Stabilize the electrode
- Demonstrate functional prototype lithium-ion cell chemistries which meet the DOE/USABC performance targets.

Approach

Sandia National Laboratories (SNL), Oak Ridge National Laboratory (ORNL), National Renewable Energy laboratory (NREL), Lawrence Berkeley National Laboratory (LBNL), and Argonne National Laboratory (ANL) have teamed together to form an integrated program. Technical targets have been developed and regular communications have been established. Throughout the program, there is a planned focus on understanding, insights into, and advancement of silicon-based materials, electrodes, and cells. All anode advancements will be verified based on life and performance of full cells. Toward that end, baseline silicon-based materials, electrodes, and cells have been adopted, along with full cell testing protocols.

The fundamental understanding of silicon-based electrode active materials is based on extensive electrochemical and analytical diagnostic studies on components, electrodes, and cells conducted within the program. This effort contains in-situ and ex-situ studies on full and specialty cells, including reference electrode cells. Overall, the diagnostic studies are intended to help establish structure-composition-property relationships, including lithium-alloying surface and bulk transport and kinetic phenomena. Further, they

should form the basis for accurately assessing component and electrode failure modes and lay a path for advancements.

Communication of programmatic progress to battery community is critical. This will generally be accomplished through publications, presentations, reports, and reviews. Further, the program is open to industrial participation and/or collaboration that does not limit program innovation or the free flow of information. Finally, this program is highly integrated with our sister program on SEI-Stabilization, called SEI-Sta for short. In general, SEI-Sta is focused on the development and characterization of model systems, thin-film well-defined active area electrodes on which it is easier to extract fundamental information on lithium-silicon phase formation, lithium transport, and interfacial phenomena (e.g., SEI formation and growth).

Results

Characterization of Si from NMP and water-based slurries (ORNL)

Si slurry was collected from the mixing vessels in both water and NMP experiments. The slurries were dried and the powders were collected for X-ray, ATR FTIR and NMR characterization studies. Figure II-42 shows comparison X-ray diffraction data collected for the Si before and after processing. From this data one notices a significant broadening of the Si peak after milling in water due to the decrease in Si particle sizes from 71 nm to 53 nm. Smaller changes are observed in NMP processed electrodes. This means that the observed gassing reaction is actively consuming the silicon in the nanoparticles. This is critical because the loss of silicon, and the resulting formation of an oxide coating reduces the theoretical capacity of the electrode.

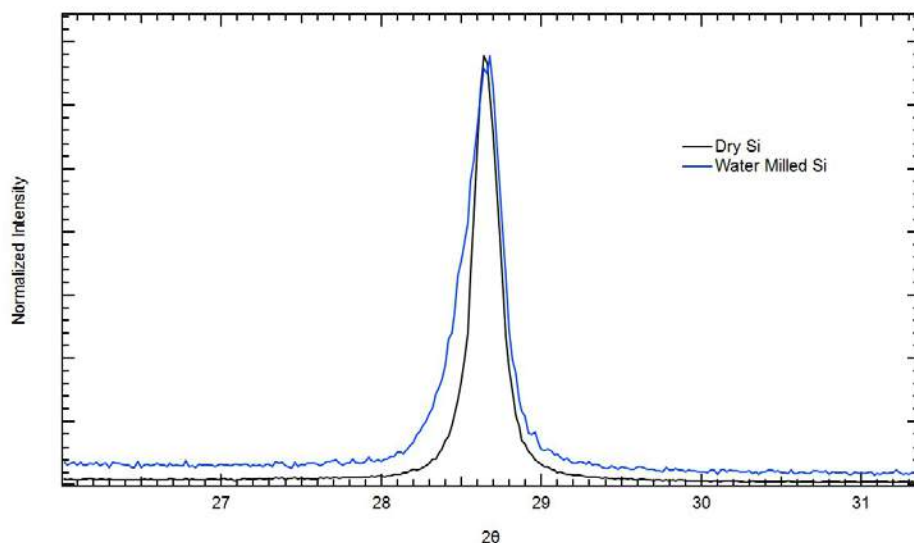


Figure II-42. Powder X-ray diffraction data collected for the raw and post-processed silicon powders.

In collaboration with Baris Key (ANL) the silicon was further with ^{29}Si NMR to determine the difference in the elemental Si to SiO_x ratio (Figure II-43). Figure II-43-Top shows the intensity of the NMR spectra was normalized to a shift at -120 ppm relating to SiO_x . A decrease in the Si peak at -80 ppm indicates more Si was converted to SiO_x during processing. NMP processed Si showed the least SiO_x production, while water processed showed the most consistent with the X-ray data. Interestingly aqueous-based LiPAA proved effective in passivating most of the additional oxidation of the silicon caused by water processing pointing to an interesting processing pathway which may yield more reproducible electrodes. ^1H - ^{29}Si cross polarization NMR was used to observe differences in the surface environment of water processed Si against Si milled free of any solvents (Figure II-43-Bottom). “Dry” Si has an abundance of Si-H and $(\text{SiO})_2 - \text{Si} - (\text{OH})_2$ (labeled Q2) coordinated sites, which disappear in the water processed sample. The Q3 and Q4 sites, which represent $(\text{SiO})_3 - \text{Si} - (\text{OH})$ and $(\text{SiO})_4 - \text{Si}$ respectively remain relatively constant between both milling methods. This

result indicates that the processing changes the Si surface chemistry which will influence SEI formation and binder affinity in ways that have not been explored, but are proposed as future research directions depending on funding.

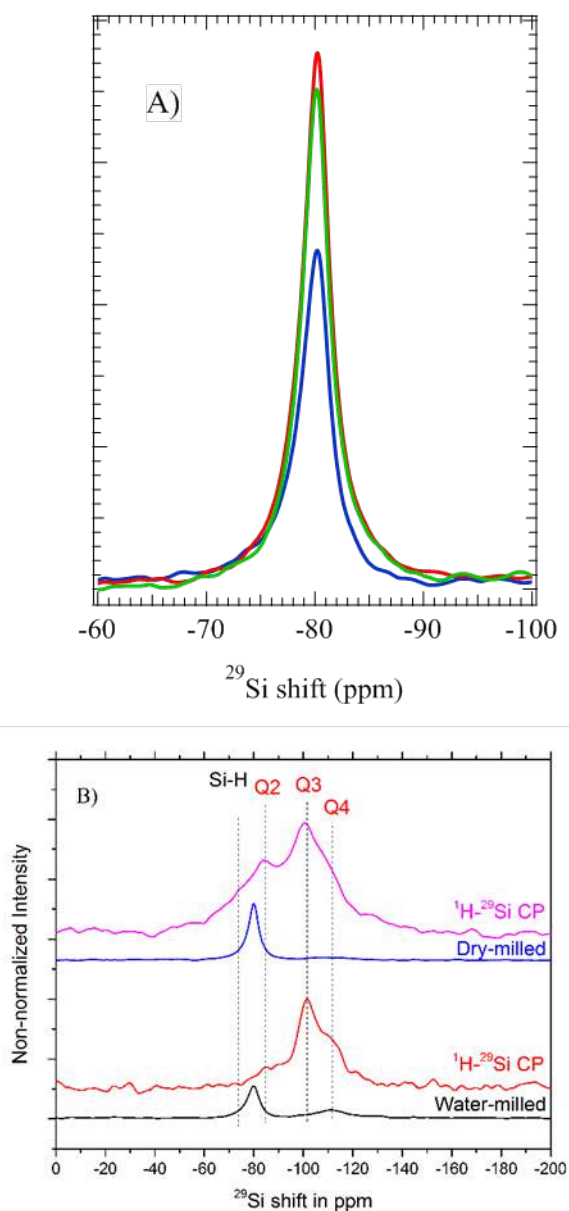


Figure II-43. (Top) ^{29}Si NMR of Nanoamor (70-130) Si powder processed in NMP (red trace), water with LiPAA binder (green trace), and water (blue trace). All spectra have been normalized to Si-O shift at -120 ppm. (Bottom) - ^1H - ^{29}Si cross polarization NMR and accompanying ^{29}Si NMR of dry milled Si (fuchsia trace and blue trace) and water milled Si (red trace and black trace). Vertical lines designate Si coordinated sites.

There are also major differences in the FTIR absorbance spectra of the Si samples, Figure II-44. Each show the broad band of the Si-O-Si stretching in the range of 900 – 1200 cm^{-1} , but the NMP processed Si has additional bands absent in the water processed Si. Bands at 2900 cm^{-1} , 1275 cm^{-1} , and 880 cm^{-1} in the NMP processed Si can be linked to methyl groups on Si surface. Three intense bands in the NMP processed Si at 1670 cm^{-1} , 1580 cm^{-1} , and 1430 cm^{-1} have yet to be identified, but show there is a strong difference in the surface functionalization of these two Si powders. This result indicates that the processing changes the Si surface

chemistry which will influence SEI formation and binder affinity in ways that have not been explored, but are proposed as future research directions depending on funding.

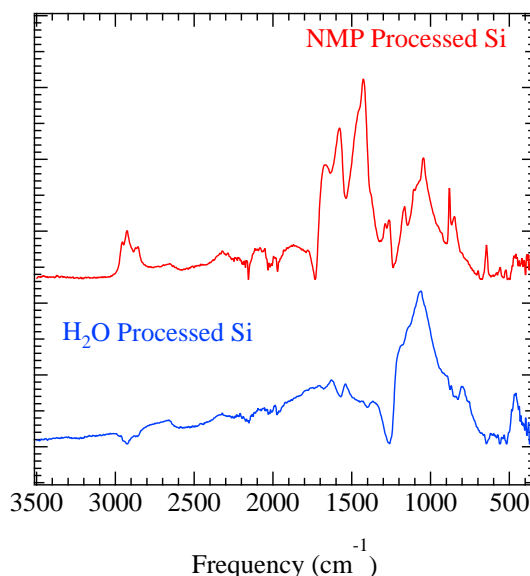


Figure II-44. Absorption spectrum from ATR-FTIR of NMP processed Si and water processed Si.

The selection of slurry solvent plays a major role in the performance of full cell batteries utilizing Si-graphite composite anodes. When completed in water, mixing needed to break up agglomerations of Si can result in additional oxidation. This can be minimized in NMP, but NMP radically changes the surface chemistry of the Si, the consequences of which are not fully understood. Also, the solvent can dictate the choice of binder, as LiPAA is not soluble in NMP. Though LiPAA-based Si-graphite electrodes must be coated using aqueous slurries, their respective full cell batteries still perform better than their NMP counterparts. PAA binder does not perform well because of its low degradation temperature, making it difficult to drive off all absorbed water. Furthermore, it is believed that this PAA is not electrochemical stable, slowly converting to LiPAA and contributing to a poor Coulombic efficiency. A better understanding of how slurry solvents interact with the surface of Si will be needed to further progress Si-based electrodes, as these functionalizations play a key role in binder selection and may change SEI contributions over long term electrochemical cycling.

NMR Studies of Composite Silicon Electrodes (ANL)

Solid state (NMR) have been instrumental in understanding lithiation and delithiation mechanism and SEI composition of silicon electrodes in the last decade [2-6]. The summarized results indicate formation of complex amorphous phase compositions upon lithiation of silicon and local formations of reactive overlithiated phases that lead to significant and complex side reactions in the electrolyte. The extent of these reactions, coupled with large volume changes, is believed to be responsible for poor cyclability of silicon electrodes.

The type of local order determines key electrochemical performance metrics in intermetallic anode systems such as silicon anodes. The study focused on characterization of the baseline commercial materials and their evolution and degradation on extended electrochemical cycling. Correlations between structure and activity relationships are drawn to help the team to optimize powders used in composite electrodes as well as detailed characterization of cycled electrodes to identify key reactions.

A multinuclear solid state NMR method has been used on pristine commercial silicon powders. Local ^{29}Si , ^{13}C , ^1H , ^7Li order is probed to gain comprehensive insights into pristine commercial powder compositions. By optimizing the ^{29}Si NMR signal and quantification of the silicon content in elemental silicon and silicate

phases, average silicate shell thicknesses were estimated from NMR and results were found to corroborate well with complementary methods.

Solid State Magic Angle Spinning (MAS) NMR spectroscopy has also been used to qualitatively and quantitatively probe the silicon ordering in the pristine and treated powder samples. NMR spectroscopy has previously been shown to effectively resolve elemental silicon from silicates regardless of sample crystallinity [7]. Figure II-45 shows ^{29}Si MAS NMR spectra collected for the pristine and treated powders. For each spectrum, the sharp resonance at -80 ppm is due to elemental silicon and the broad resonance at -110 ppm is assigned, according to literature [7], to amorphous SiO_2 on the outer shell (based on TEM and XRD findings) of largely spherical particles. With heat treatment, an increasing trend in the intensity of the -110ppm resonance was observed. Using the fully quantitative relative ratios of areas under the Si vs. SiO_2 resonances, the following average silicon molar contents have been extracted from spectra deconvolutions; 79:21 for pristine sample, 72:28 for 400°C treated sample and 56:44 for 600°C sample, respectively. Based on these ratios, an average of 6.1nm, 8nm and 12nm amorphous SiO_2 shells were estimated for pristine, 400°C and 600°C samples, respectively. The referenced paper also shows favorable electrochemical performance for the 400°C sample over the baseline and 600°C sample with a much thicker shell. It must be noted that NMR is an averaging bulk technique and perfectly spherical particles with 80nm diameters was assumed. Therefore it is possible to have an under or overestimation of the modelled thicknesses depending on the mean particle size distribution.

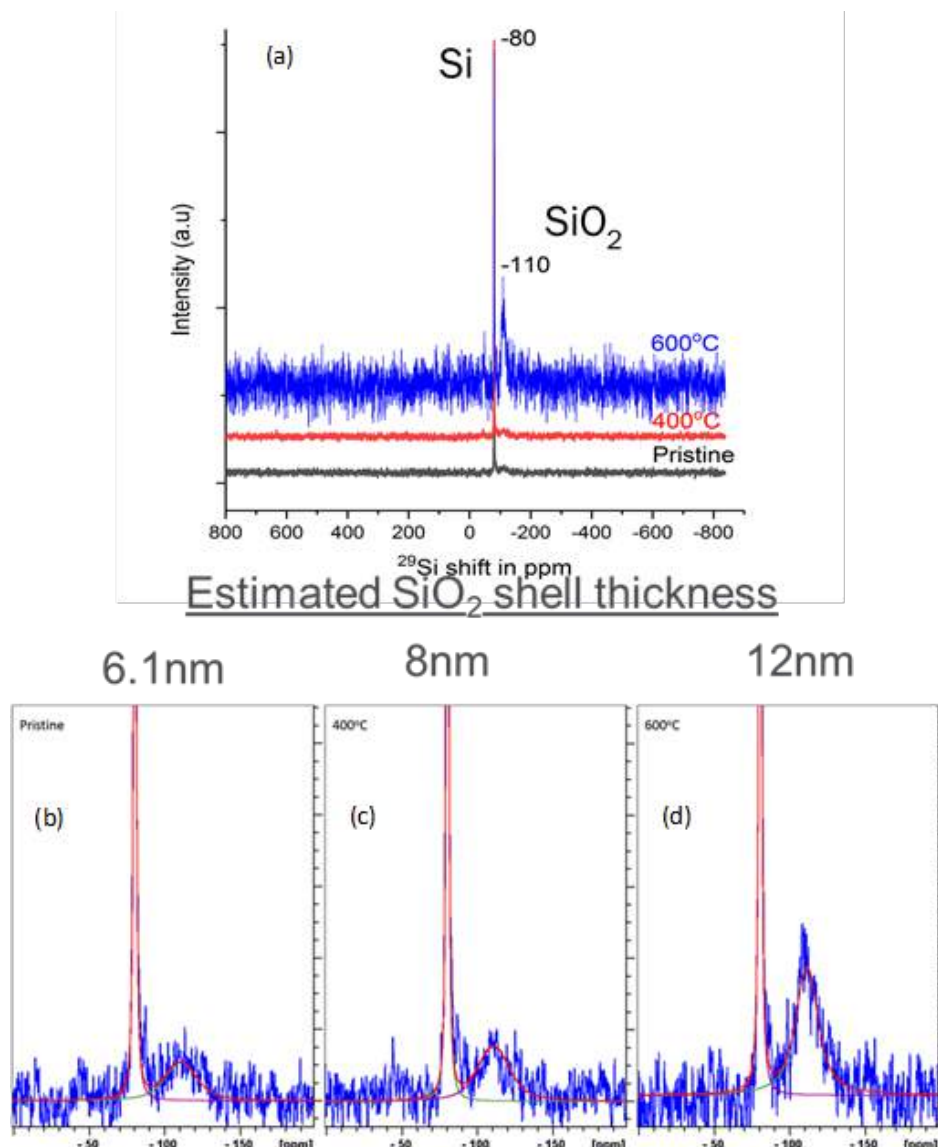


Figure II-45. ^{29}Si MAS NMR and deconvolutions (b to d) of pristine and treated commercial HydroQuébec80nm silicon powders. (ANL, Linghong Zhang et al., ACS Applied Materials & Interfaces, 2017, just accepted manuscript)

When compared to other commercial powders such as NanoAmor 70-130nm or Paraclete silicon powders only slight variations in Si: SiO_2 contents were found, the latter mainly correlated inversely with increasing average particle size. Different commercial batches, due to their production and processing variations vary in particle size distribution and morphology, and marginally in performance. The surface termination of the commercial powders mainly found to vary in -OHs and aliphatic proton content. The aliphatics were further confirmed by ^1H - ^{13}C CP MAS NMR as shown in Figure II-46 for Paraclete and NanoAmor commercial powders. In addition, depending on manufacturer processing the "coating" on the particles contained hydroxyl or ether organic groups, and in the case of NanoAmor powders, carbonyl and or ester groups. The CAMP full cell data on the Paraclete samples with varying "coatings" has been shown to demonstrate slightly different electrochemical performance metrics, with sample D performing marginally better. The stability of this surface treatment on the particles is currently under investigation. Furthermore, typical water treatment of the pristine commercial powders in electrode making, such as slurry making with LiPAA binder, has been shown to increase the thickness of the SiO_2 shell considerably (15-25%) while generating H_2 gas and negatively impacting electrode performance.

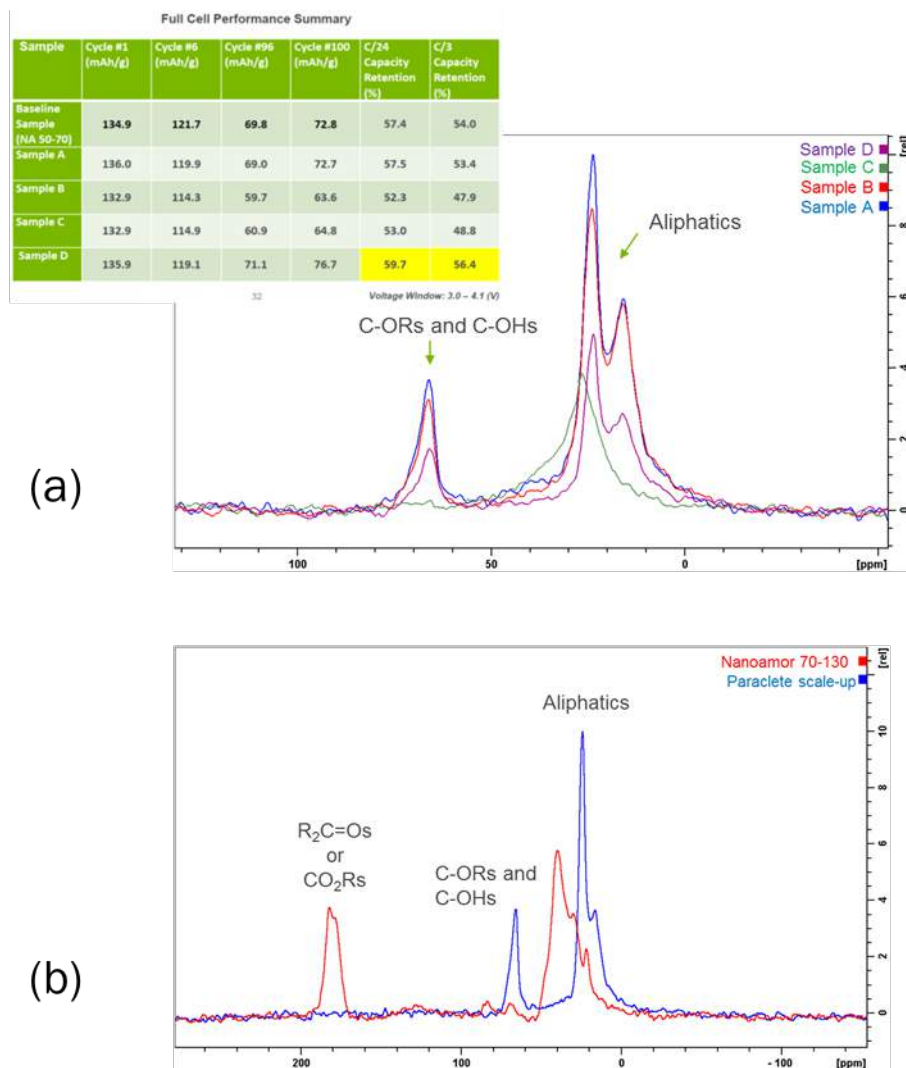


Figure II-46. (a) 1H - ^{13}C CP MAS NMR of Paraclete silicon powder batches and corresponding electrochemical performance metrics (b) 1H - ^{13}C CP MAS NMR of Paraclete powder and NanoAmor 70-130nm powder. (ANL, unpublished work)

Silicon Nanomaterials: Stability in Aqueous Slurries and Optimization of Oxide Layer Thickness for Electrochemical Performance (ANL)

When silicon is in contact with air, a native oxide layer of several nanometers will form. As the size of the silicon particle becomes smaller, this oxide layer takes up a larger volume and weight and thus plays a more and more important role. The actual thickness of the oxide layer may also vary due to the manufacturing processes and storage history. While the use of Si nanoparticles largely mitigates the particle pulverization problem observed in micron-sized Si particles, the impact of oxide layer on the electrochemical performance of Si nanomaterials becomes non-marginal. Xun and coworkers reported that the presence of oxide layer harms the initial performance of the silicon anodes in a non-aqueous system [8, 9]. When the oxide layer was partially etched away by HF, improved initial reversible capacity as well as decreased initial irreversible capacity loss per surface area was observed. Recently, Toudjine and coworkers reported that the native oxide layer around silicon is not thick enough to prevent further reaction of water with the inner silicon core [10]. This wet oxidation reaction forms porous silicon oxide, which is accompanied by the generation of hydrogen gas, and also harms the reversible capacity of the material. With the current trend going towards water-based laminate making processes due to both better electrode performance and economic reasons, the presence of

oxide layer in the silicon electrodes is inevitable. Therefore we need to consider the Si electrode materials (especially Si nanomaterials) used with aqueous binders as Si core materials with a thin SiO₂ shell, and understand its stability and electrochemical performance as a whole. The purpose of this work is to understand how the oxide layer thickness affects the stability of the Si nanoparticles in aqueous slurries, and furthermore to optimize the oxide layer thickness to achieve optimal initial electrochemical performance as well as cycle performance.

In this work, we investigated the effect of oxide layer on the electrochemical performance of silicon anodes by growing the oxide layer of Si nanoparticles in a controlled manner. Si nanoparticles with an average size of 80 nm were used. Lithium polyacrylate (LiPAA) with a pH of ~7 and carbon black (C45) were mixed with the Si material to fabricate the electrodes. Brunauer-Emmett-Teller (BET) surface analysis, transmission electron microscopy (TEM) as well as Fourier-transform infrared spectroscopy (FTIR) were performed to characterize the silicon nanoparticles. Finally, the electrochemical performance of the silicon anodes of different oxide layer thicknesses was analyzed and the oxide thickness is optimized based on the electrochemical performance.

Figure II-47a shows the SEM image of the as-received Si nanoparticles. The particles are spherical shaped with most particles in the ~100 nm range. Some larger particles with diameters of several hundred nanometers can also be observed. Figure II-47b shows the mass change of silicon particles after heat treatment at different temperatures. As the heating temperature increases, the mass change increased from 1.9% at 300°C, to 35% at 700°C, in an exponential manner, showing that the oxidation process is kinetically-controlled.

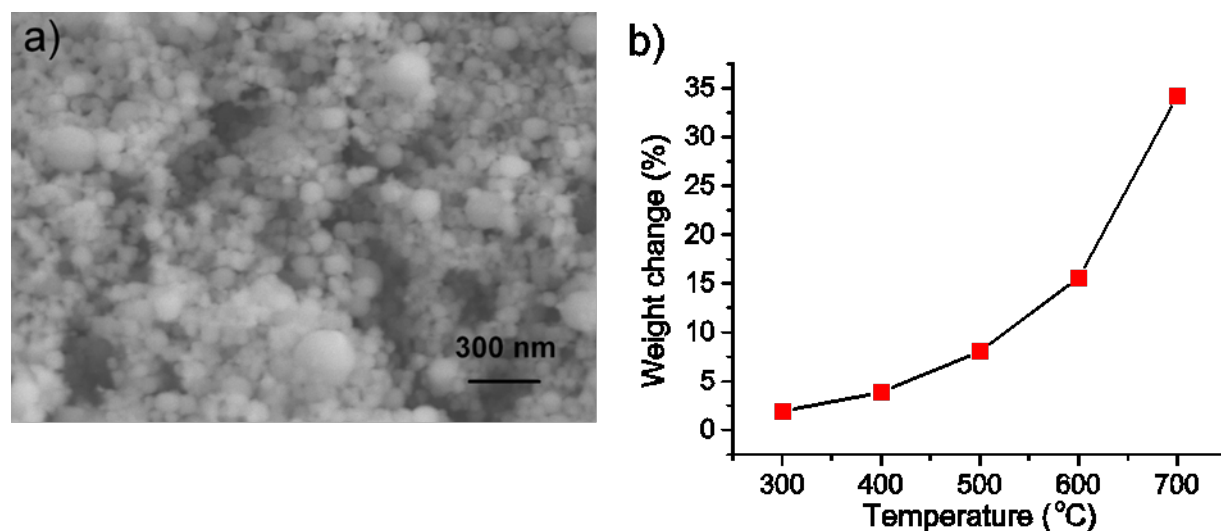


Figure II-47. a) Scanning electron microscopy image of silicon nanoparticles b) Mass change of the Si nanoparticles after heat treatment at different temperatures.

Fourier-transform infrared spectroscopy is a powerful technique to characterize the IR-active species on surface as well as in bulk. Figure II-48 shows the FTIR spectra of the pristine and treated Si nanoparticles measured in the attenuated total reflection mode. The pristine Si nanoparticles showed a broad feature containing peaks from surface Si-O-Si stretching (1250 cm⁻¹ – 850 cm⁻¹) and bending vibrations (850 cm⁻¹ – 750 cm⁻¹) in the 1250 cm⁻¹ – 700 cm⁻¹ region. The peaks are broad due to the random packing of the tetrahedral unit of Si-O in the amorphous SiO₂ layer. As the treatment temperature increases, the peaks become narrower and less convoluted, indicating the packing form of the Si-O tetrahedral unit becomes more ordered. Noticeably for the 600°C and 700°C treated Si nanoparticles, an additional sharp peak around 1120 cm⁻¹ appeared. This peak is assigned to oxide in bulk Si by Mawhinney and co-workers, indicating that at elevated temperatures, oxygen may further diffuse into bulk silicon to form oxide inside bulk silicon [11]. A more-ordered packing structure of the SiO₂ layer as well as existence of oxide in bulk silicon could all affect the

resistivity and lithium ion diffusivity of the SiO₂ layer, and further affect the electrochemical property of the whole particle.

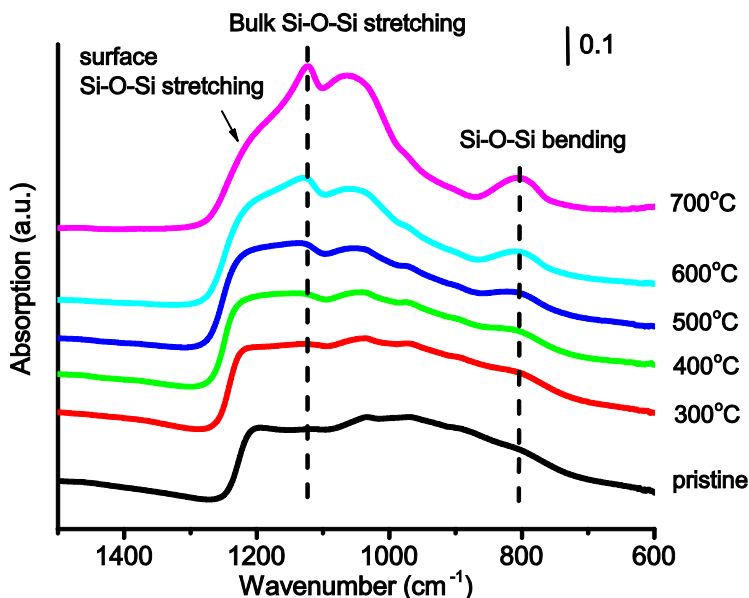


Figure II-48. FTIR spectra of pristine Si nanoparticles and Si nanoparticles treated at different temperatures.

The reaction between Si nanoparticles and water generates H₂ gas. To test the stability of our silicon samples in aqueous slurries, we monitored the gas formation after the Si nanoparticles were mixed into the slurry at both room temperature and elevated temperature of 75°C, at which the laminates are usually dried.

Three samples were chosen for this test: pristine, 400°C-treated and 600°C-treated Si samples, as they represent different oxide layer thicknesses. The Si samples were mixed with LiPAA, C45 and 18 MΩ de-ionized water using a centrifugal mixer (Thinky Mixer) at 2000 rpm to obtain good slurry property. The slurries were then transferred into pouches and the pouches were vacuum-sealed immediately. The whole process took about 20 minutes. The pouches were then placed at room temperature and monitored for 2 weeks for possible swelling behavior that could be caused by gas generation. We did not observe any pouch swelling during the 2 week period. Since previous reports observed significant H₂ formation within the first 2 hours at room temperature, we conclude that in our case we did not observe significant reaction between water and our silicon samples under room temperature. Our laminates are usually dried at 75°C for 4 hours, therefore we further tested the stability of the slurries at elevated temperature of 75°C. We observed significant swelling for the pristine Si sample, slight swelling for the 400°C-treated sample and no swelling for the 600°C-treated sample.

To conclude, all of our silicon samples are fairly stable in room-temperature aqueous slurries. There is no significant wet oxidation and corresponding gas generation when the silicon nanoparticles are subject to lab-scale mixing and sitting at room temperature for 2 weeks. At elevated temperature of 75°C, pristine Si nanoparticles showed significant gas generation corresponding to wet oxidation. However, heat-treated Si samples with even slightly thicker oxide layer showed significant improvement on the stability in aqueous slurries. Our results suggest two scenarios:

- a) For small lab-scale slurry making process, a small slurry of several grams is usually produced at a time and the heat dissipation is relatively good. In this case the temperature rise of the slurries as well as the time the slurries stay at elevated temperatures is usually limited. In this case, there may not be significant amount of wet oxidation to significantly change the overall oxide layer of the silicon nanoparticles.

- b) Large-scale slurry making process usually involves mixing of slurries on the kilogram scale. It usually requires much harsher mixing conditions such as intensive high energy ball milling for an extended amount of time. During this process significant temperature rise may happen to the slurries. The slurries may also stay at higher temperature for much longer time. This can result in significant wet oxidation reaction between silicon and water. In this case, the stability of Si particles at elevated temperatures should be taken into consideration.

To obtain initial electrochemical performance information of heat treated Si nanoparticles, we cycled the assembled half cells between 10 mV and 1.5 V at C/10 rate for 3 cycles. Figure II-49 compares the electrochemical performance of the initial formation cycles for the Si electrodes with Si nanoparticles of different treatments. Si nanoparticles treated at 700°C did not show any reversible capacity from silicon and is therefore not shown in Figure II-49.

Comparing the performance of 500°C and 600°C-treated Si nanoparticles with the pristine Si nanoparticles, we observed decreased specific capacity and coulombic efficiency. The decreased specific capacity is mostly likely caused by the significant decrease of the active Si from the heat treatment processes, and the decreased coulombic efficiency is likely due to the increased parasitic reactions from the irreversible reactions between SiO₂ and lithium ions.

On the other hand, the Si nanoparticles after 300°C and 400°C heat treatment showed comparable specific capacity and coulombic efficiency during the formation cycles. While the pristine Si nanoparticles started with slightly higher reversible capacity, the heat-treated samples retained their capacity better during the 3 formation cycles, which resulted in very comparable reversible capacity at the 3rd formation cycle. This better capacity retention at formation cycles suggests that the mechanical integrity of the Si nanoparticles may be improved after the treatment. In conclusion, the initial electrochemical performance comparison of different Si samples shows that while too thick of an oxide layer may decrease the initial coulombic efficiency and reversible specific capacity of the material, a slight increase of the oxide layer thickness does not harm the initial performance.

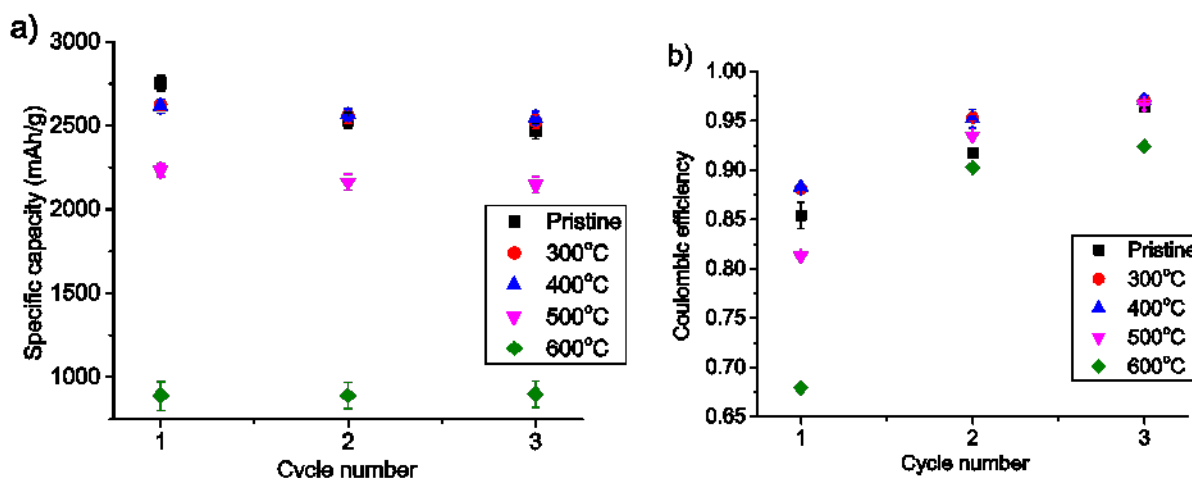


Figure II-49. a) Specific capacity and b) coulombic efficiency comparison of initial electrochemical performance of Si nanoparticles after different treatments.

It was noted by Xun and coworkers that when comparing the initial performance, irreversible capacity loss per surface area should be taken into consideration as treatment may change the surface area significantly and affect the surface area available for parasitic reactions [8]. Here we measured the BET surface area of our silicon samples and calculated irreversible capacity loss per surface area for the 1st cycle. BET surface area measurements show that our oxidation treatment did not result in any significant decrease of the surface area. The calculated irreversible capacity loss per surface area shows that treating the silicon nanoparticles at 300°C and 400°C resulted in slightly decreased irreversible capacity loss per surface area, whereas treating the

nanoparticles at 500°C and 600°C increased irreversible capacity loss per surface area. For 600°C-treated Si, the result from initial formation cycles done at C/100 is shown since we observed an interesting capacity increase over cycles when the electrodes were cycled at C/10, indicating the electrode was not fully activated at the first three cycles at C/10 rate.

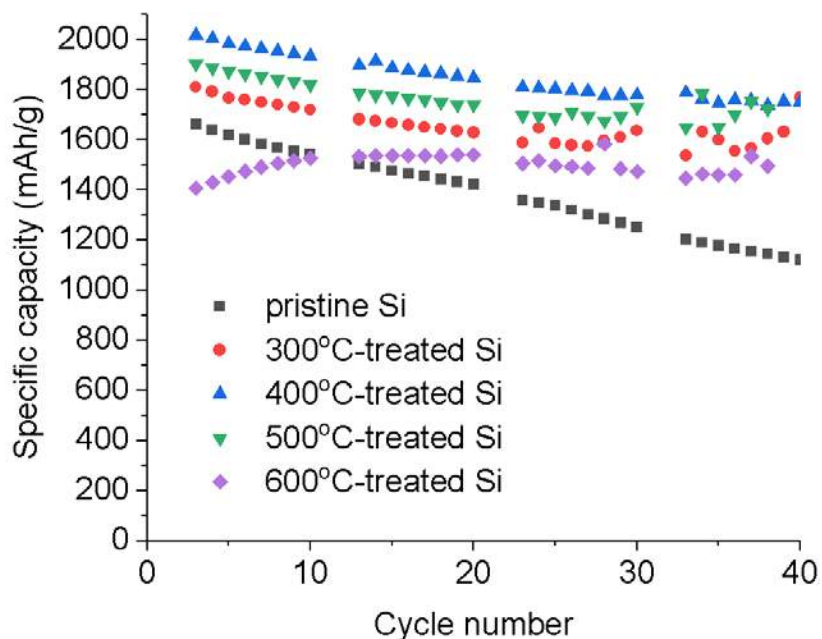


Figure II-50. Half cell cycle performance for 500°C-treated and 600°C-treated Si nanoparticles.

Figure II-50 shows half cell cycle performance for pristine, 300°C-treated, 400°C-treated, 500°C-treated and 600°C-treated Si electrodes for 40 cycles. The cells went through initial formation cycles (C/10 rate between 1.5 V and 10 mV for 3 cycles) and rate cycles (delithiation rate at C/5, C/3, C/2, 1C and 2C for 3 cycles each while lithiation rate set to C/5 for all cycles) before subjecting to cycle tests. For half cell cycle tests, the cells were cycled between 1.5 V and 10 mV at C/3 rate with a HPPC cycle at every 10th cycle. We observed improved capacity retention with all treated samples. The 400°C-treated Si electrode showed the highest specific capacity with improved capacity retention. For 500°C-treated and 600°C-treated Si electrodes, although the reversible capacity is compromised in both cases in the initial formation cycles, both treated samples showed improved capacity retention during the 40 cycles of cycle test. This supports that a thicker oxide layer improves the mechanical stability of the particles during cycling, thus improving the capacity retention.

We further compared the cycle performance of the 400°C-treated Si nanoparticles with the pristine silicon nanoparticles in a full cell configuration with $\text{LiNi}_{0.5}\text{Co}_{0.2}\text{Mn}_{0.3}\text{O}_2$ (NCM523) used as the cathode. To get full cell cycle performance information, we cycled the assembled full cells at C/3 rate for 50 cycles after three formation cycles at C/10 rate. Figure II-51 a-b shows the cycle performance of the 400°C-treated and the pristine silicon nanoparticles between 2.5 V and 4.3 V. The anode capacity is used here since the performance of anodes is compared in this study. The specific anode capacity in full cell tests appears lower than the specific capacity in half cell tests. This is because in full cell tests, an N/P ratio of 1.1-1.2 is utilized so that anode has some extra capacity and lithium plating on the anode can be prevented. The presence of extra silicon in the anode leads to the lower specific anode capacity. Compared to pristine silicon nanoparticles, the 400°C-treated Si nanoparticles showed an improvement of capacity retention from 52.91% (3 cell average) to 59.70% (3 cell average) when cycled under the same voltage window. It should also be noted that a significant improvement in capacity retention was observed for both sets of cells when we raised the lower cutoff voltage from 2.5 V to 3.2 V, as shown in Figure II-51c-d. In this case, about 17% less lithium was cycled compared to the case where the cells were cycled between 2.5 V- 4.3 V due to the smaller cycling voltage window.

Compared to the pristine silicon cells, the 400°C-treated Si full cells showed an improvement of capacity retention from 72.23% (3 cell average) to 78.31% (2 cell average) when cycled under the same voltage window. At the end of the 50 cycles, the specific capacity of the cells cycled with 3.2 V lower-cutoff voltage retains a larger specific capacity than the cells cycled with a 2.5 V lower-cutoff voltage. The much better capacity retention with a 3.2 V lower-cutoff voltage can be explained by the higher coulombic efficiency observed over cycling, as shown in Figure II-51b and Figure II-51d. This higher coulombic efficiency can be caused by the better structural stability when less lithium is cycled. Another likely reason for the higher coulombic efficiency is the better electrochemical stability of the solid electrolyte interphase layer of silicon. When the 2.5 V lower-cutoff voltage is utilized, the solid electrolyte interphase of silicon is more likely to be subject to a more oxidizing potential and therefore is more likely to be oxidized. This oxidation and subsequent re-formation of the SEI layer at each cycle leads to extra irreversible lithium consumption which leads to poor capacity retention.

Note that for pristine and 400°C-treated Si nanoparticles, better capacity retention is observed in half cells compared with full cell testing results. In half cell tests, the lithium inventory is unlimited, therefore the effect of irreversible lithium consumption caused by parasitic reactions (such as new SEI formation) on capacity fading is not properly reflected. Full cell testing results better reflect the capacity retention in practical applications.

The coulombic efficiency comparison in Figure II-51b and Figure II-51d shows that the initial coulombic efficiency of the 400°C treated Si full cells is on average higher than the coulombic efficiency of the pristine Si full cell for both voltage windows. However, when cycled between 2.5 V and 4.3 V, the coulombic efficiency decreased for 400°C-treated Si full cells before it rose again as the cells cycle. This phenomenon was not observed for the 400°C-treated Si full cells cycled between 3.2 V and 4.3 V. This suggests that the lower cutoff voltage may degrade the oxide layer in some way. More study need to be conducted to fully understand this phenomenon.

The improved cycle performance we observed agrees with the previous work conducted by Sim and coworkers, where they studied the impact of SiO₂ coating thickness on the capacity retention of 1.4 μ m Si particles, and found that with a thicker SiO₂ layer, the capacity retention is improved [12]. They attributed the improvement to the suppression of the volume expansion by the SiO₂ coating to the particles. In our case, the capacity retention improvement may also be attributed to the improved mechanical integrity of the particles, as better mechanical property makes particles less likely to crack during the cycling, thus less lithium consumption caused by SEI formation.

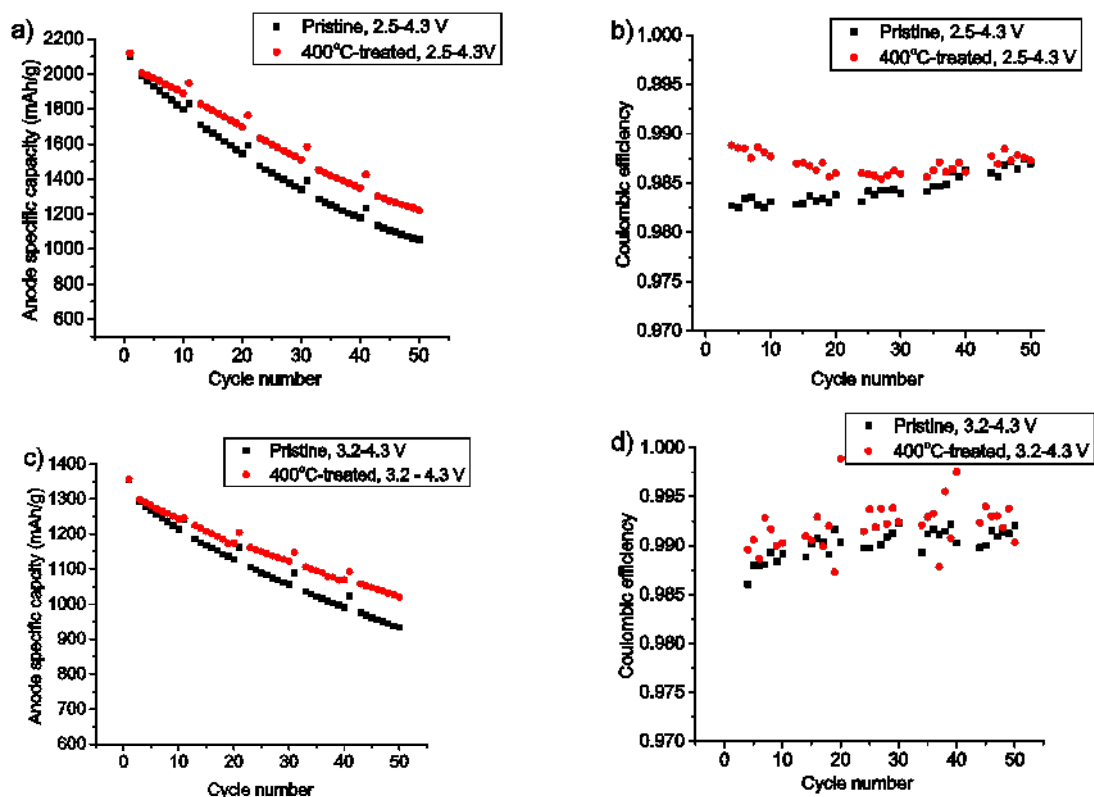


Figure II-51. a,b): capacity retention and coulombic efficiency of pristine and 400°C-treated Si nanoparticles cycled between 2.5 V and 4.3 V c,d): capacity retention and coulombic efficiency of pristine and 400°C-treated Si nanoparticles cycled between 3.2 V and 4.3 V.

Characterizing Electrode Heterogeneity as a Function of Processing (ORNL)

With all of the processes that are occurring chemically during the processing of the silicon electrode another issue is whether or not the electrodes are cast with the best structure. We note that the change in surface chemistry, particle sizes and gas evolution will all impact the electrode and how uniform it is. To investigate these we have been performing extensive characterization studies of the cast electrodes. Electrode homogeneity is also key to improving performance and extending cycle life. Figure II-52 shows Raman maps of the Si-Gr anodes before and after cycling. To visualize anode heterogeneity, Raman maps were analyzed using a combination of cluster and basis analysis. Silicon, graphite, and carbon all have strong Raman-active modes, making Raman microspectrometry and mapping well-suited to characterize the composite anodes. The lithiation of Si can easily be followed across the electrode by monitoring the transition from crystalline silicon (c-Si) to amorphous silicon (a-Si). Raman maps (50 x 50 μm , 2500 spectra) were collected on Si-Gr composite anodes after 1, 2, and 100 cycles (Figure II-52). The maps were analyzed by treating each spectrum in the composite as a linear combination of the individual components (c-Si, a-Si, graphite, and carbon black). In the pristine anode, much of the map is dominated by c-Si as expected. After cycling, a-Si is found across large areas of the electrode, but some c-Si remains even after 100 cycles. The presence of c-Si was further verified with XRD. This indicates that parts of the electrode remain electronically or ionically isolated and unable to participate in the alloy reaction with lithium.

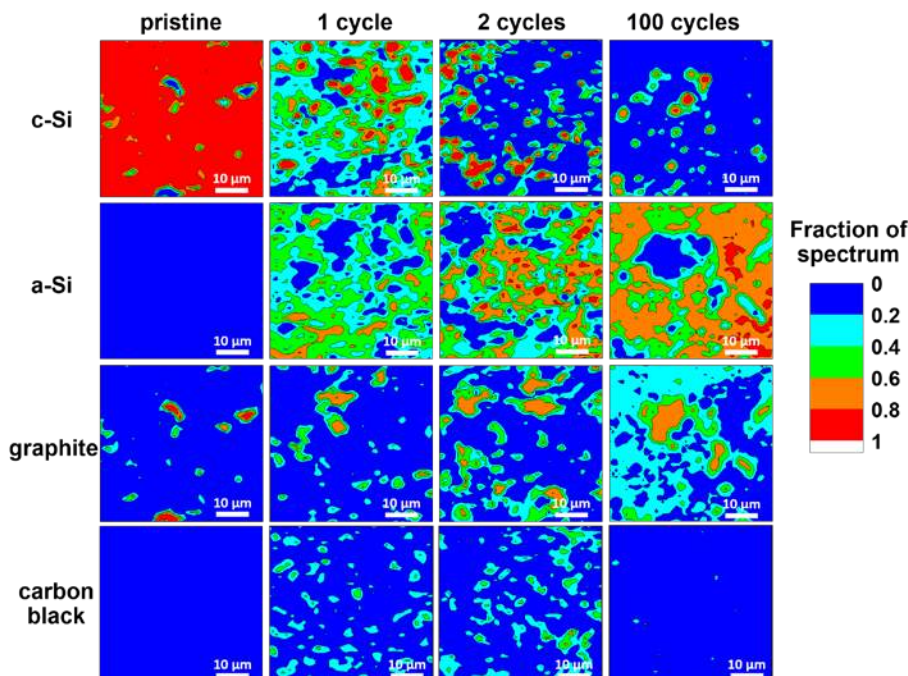


Figure II-52. Raman maps of Si-Gr anodes taken before cycling (pristine), after 1 formation cycle, after 2 formation cycles, and after the full cycling protocol (100 cycles). Raman maps were generated by deconvoluting each composite spectrum into the sum of the four components (c-Si, a-Si, graphite, and carbon black).

Similar to the Raman maps, XPS data was collected on silicon electrodes cast at ORNL, SNL and ANL for comparison. Figure II-53 shows representative Si 2p XPS data collected for several of these samples. The data was all normalized to the Si^0 species to highlight the changes in oxidized silicon. There are several unique features in this data. First, there is clear evidence for the Si in the spectra which is surprising given the predicted thickness of the polymer binder on the electrode surface which is estimated to be at least 15-20 nm thick. A layer of this thickness would totally attenuate the photoelectrons generated from the Si. This means that the binder is not homogeneously coating the Si despite the belief that PAA/LiPAA adheres to the Si surface strongly. This heterogeneity leaves extensive tracks of Si exposed to the electrolyte where it can react or become isolated with cycling. The second thing these XPS results show is that the relative concentration of Si^{4+} is changing significantly depending on the processing consistent with the previous NMR data. These results point to the need to dramatically improve the processing of the electrodes to enable total Si utilization. We proposed to investigate the processing of these electrodes with future funding including evaluating solvent choice, order of reagent addition, and other processing conditions.

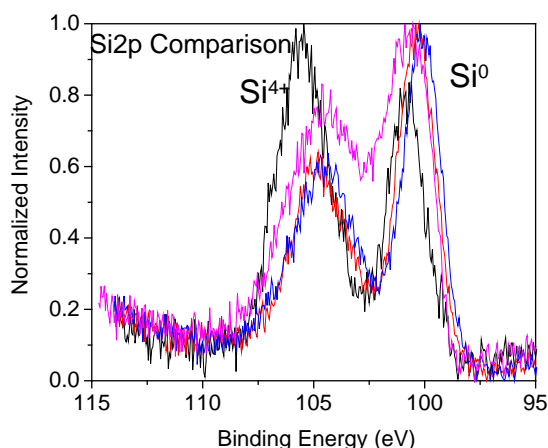


Figure II-53. Representative normalized Si 2p XPS data collected on 4 different Si-Gr-CB-PAA electrodes produced at ORNL, SNL and ANL.

Capacity Fade and Its Mitigation in Li-ion Cells with Silicon-Graphite Electrodes (ANL)

Previous research on Si electrodes implicates erosion of silicon particles by hydrofluoric acid (HF) as one of the leading causes of performance deterioration, as this acid readily reacts with the SiO_2 shell and silicon core of the particles. This acid is generated when the conventional LiPF_6 salt is hydrolyzed by moisture. The latter can have several origins, but the most likely source is the negative electrode itself, as it is often processed from an aqueous slurry. Indeed, the coupling of silicon and graphite is not an easy one, as the Si/ SiO_2 particles are strongly hydrophilic, whereas Gr and carbon particles are strongly hydrophobic. For Gr electrodes, the binder is typically PVdF (polyvinylidene fluoride), a hydrophobic and inert polymer, and the organic solvent is N-methyl-2-pyrrolidone. For Si and Si-Gr electrodes, carboxylated polymers (such as lithiated polyacrylic acid, LiPAA, and carboxymethylcellulose, CMC) have been used as the binder, as they form strong contacts with all of the particles present in the matrix, and the solvent is often water. While residual water from the electrode fabrication process has less effect on the performance of Gr electrodes, it has significant effect on the performance of Si electrodes. The role of this residual water in cell capacity fade is an important consideration in our study.

Our approach was to examine performance and longevity of full cells, prepared using electrodes fabricated (with commercially available materials) by the Cell Analysis, Modeling, and Prototyping (CAMP) facility at Argonne. The positive electrode (NCM523) contained 90 wt% $\text{Li}_{1.03}(\text{Ni}_{0.5}\text{Co}_{0.2}\text{Mn}_{0.3})_{0.97}\text{O}_2$, 5 wt% carbons and 5 wt% PVdF binder. The negative electrode (SiGr) contained 73 wt% graphite, 15 wt% nanosilicon (50-70 nm), 2 wt% carbons, and 10 wt% LiPAA binder (450 kDa); the silicon-free graphite (Gr) negative electrodes contained 88 wt% graphite, 2 wt% carbons, and 10 wt% LiPAA. The baseline (Gen2) electrolyte was 1.2 M LiPF_6 in a 3:7 w/w mixture of ethylene carbonate (EC) and ethyl methyl carbonate (EMC) solvents; cells with this electrolyte are the Gen2 cells. Some cells contained 10 wt% fluoroethylene carbonate (FEC) added to the Gen2 electrolyte; these are referred to as the FEC-cells.

The causal mechanisms for capacity fade in these full cells were inferred from data obtained by electrochemistry, microscopy, spectroscopy and thermogravimetry techniques. The cell cycling protocol consisted of three (formation) cycles at a nominal C/20 rate, 94 (aging) cycles at a C/3 rate, and three (final) cycles at a C/20 rate, for a total of 100 cycles in the 2.5-4.1 V voltage range at 30°C. This protocol was repeated multiple times for cells tested beyond 100 cycles. Scanning electron microscopy (SEM) images were obtained with a Hitachi S-4700-II microscope to observe changes to the bulk morphology of the electrodes before and after cycling. XPS (surface analysis) data were obtained on electrode samples with a PHI 5000 VersaProbe II system from Physical Electronics; the samples were inserted into the XPS analysis chamber through the glovebox, without exposure to ambient air. Thermogravimetry was carried out in helium flow

using a Perkin Elmer Pyris 1 TGA thermogravimetric analyzer coupled to a Perkin Elmer Clarus 680 gas chromatograph – mass spectrometer.

Electrochemical characterization of NCM523/SiGr and NCM523/Gr cells: Figure II-54 shows cell discharge capacities as a function of cycle number. The Gen2 and FEC cell capacities are comparable during the early (to ~10) cycles. Subsequently, the Gen2 cell shows rapid capacity decrease, whereas the FEC cell shows a more gradual (yet significant) capacity decrease. After 100 cycles, the specific capacity and capacity loss for the Gen2 cell are 13 mAh/g and 91.8%, respectively, and the corresponding values for the FEC cell are 72 mAh/g and 53.5%, respectively. These results show that while the addition of FEC slows the capacity fade, it does not prevent it fully. In contrast, NCM523/Gr full cells containing the FEC electrolyte show only ~9% capacity loss after 100 cycles. The only difference between these NCM523/Gr and NCM523/Si-Gr cells is the presence of 15 wt% Si nanoparticles in the negative electrode, which implicates the silicon as the dominant contributor to capacity fade.

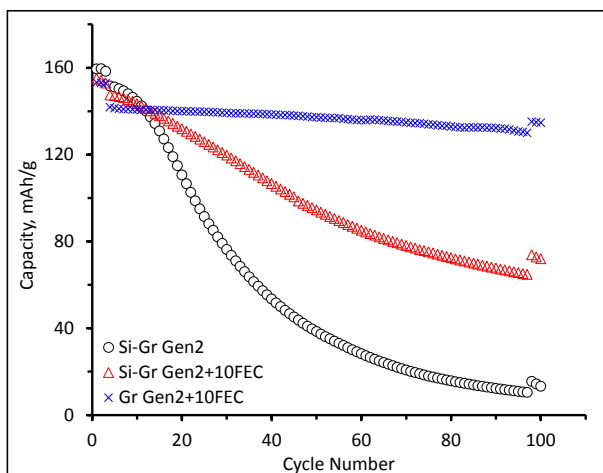


Figure II-54. Capacity versus cycle number plots for full cells containing the SiGr negative electrode with Gen2 electrolyte (black), SiGr negative electrode with Gen2+10 wt% FEC electrolyte (red), and Gr negative electrode with Gen2 +10 wt% FEC electrolyte (blue). It is obvious that cells containing the 15 wt% Si show faster capacity decline.

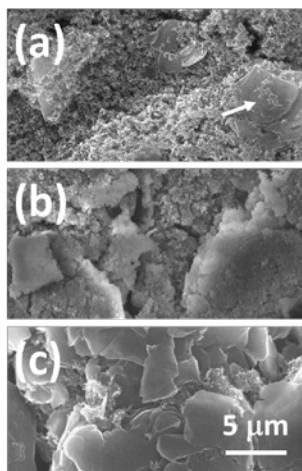


Figure II-55. SEM images of the negative electrode. (a) Pristine Si-Gr electrode showing large graphite flakes (arrow) in contact with Si and carbon nanoparticles in the matrix. (b) The same electrode harvested after 100 cycles from a cell containing Gen2 electrolyte. The graphite particles are completely covered by electrolyte breakdown deposits. In contrast, panel (c) shows a Gr electrode (no Si) harvested from a Gen2 cell after 100 cycles. The graphite flakes and the C45 carbon particles are still clearly observed, as the SEI is relatively thin.

SEM images from Graphite (Gr), and 15wt% Si-Gr (SiGr) electrodes: Figure II-55a and Figure II-55b show SEM images of a SiGr electrode before and after one hundred 2.5-4.1 V cycles in a full cell configuration. The graphite, nanosilicon and C45 (nano)carbons are evident in the pristine electrode (Figure II-55a). In the cycled SiGr electrode, the SEI deposits form a thick covering on both silicon (and carbon) nanoparticles and the micron-size graphite flakes. In contrast, the graphite flakes can be readily distinguished in images of Gr electrodes (Figure II-55c) harvested from NCM523/Gr cells cycled under similar conditions. Figure II-55 is a graphic illustration of the difference between the Gr and SiGr electrodes from cycled cells. For the SiGr electrodes, the SEI deposits becomes so extensive that they fill up the electrode pores, eventually isolating the active material from lithium-ions in the electrolyte and/or electronic contact with the current collector. The Gr electrodes, on the other hand, show much less (and thinner) SEI deposits and function well for hundreds of additional cycles.

X-ray photoelectron spectroscopy (XPS) data on positive and negative electrode samples: Electrodes for XPS analyses were harvested from full cells held at 2.5 V for 24 h before disassembly. Hence, the negative and positive electrodes are expected to be in the delithiated and lithiated states, respectively. Data from electrodes harvested from a 3-cycle NCM523/Gr cell are included for comparison. Figure II-56 to Figure II-58 show XPS plots for C 1s, O 1s, F 1s, Si 2p, Li 1s and P 2p regions for both negative electrodes (anodes) and positive electrodes (cathodes). The scattered open symbols in these plots indicate the background-corrected XPS data, whereas the smooth lines are the least-squares fits of these data. Note that the ejected photoelectrons arise from the top five to ten nanometers of the electrode. As the graphite and silicon particles become covered with decomposed electrolyte, these thick deposits are the main contributors to the overall XPS spectra for the aged electrodes. We begin our discussion with data from the negative electrodes (Figure II-56a-d, Figure II-57a,b).

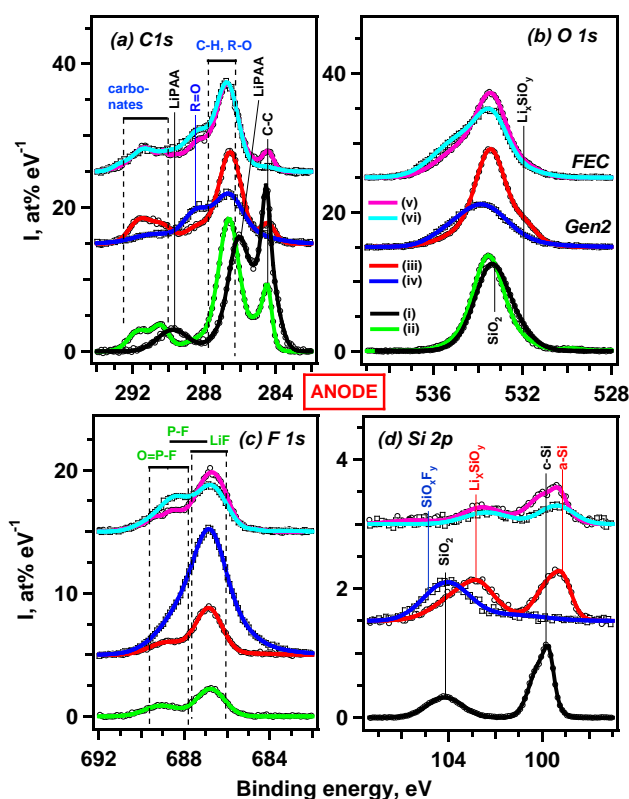


Figure II-56. XPS spectra from pristine SiGr electrode (i) and from negative electrodes harvested from the following full cells: (ii) NCM523/Gr cell, after three formation cycles in Gen2, (iii) NCM523/SiGr cell, after three formation cycles in Gen2, (iv) NCM523/SiGr cell, aged in Gen2, (v) NCM523/SiGr cell, three formation cycles in Gen2 containing FEC, (vi) NCM523/SiGr cell, aged in Gen2 containing FEC.

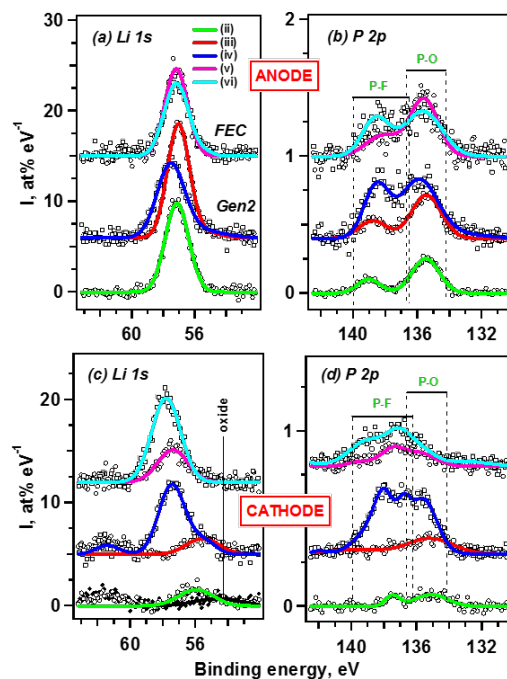


Figure II-57. XPS spectra in (a,c) Li 1s and (b,d) P 2p bands from harvested (a,b) negative electrodes and (c,d) positive electrodes from disassembled cells: (ii) NCM523/Gr cell, after three formation cycles in Gen2, (iii) NCM523/SiGr cell, after three formation cycles in Gen2, (iv) NCM523/SiGr cell, aged in Gen2, (v) NCM523/SiGr cell, three formation cycles in Gen2 containing FEC, (vi) NCM523/SiGr cell, aged in Gen2 containing FEC.

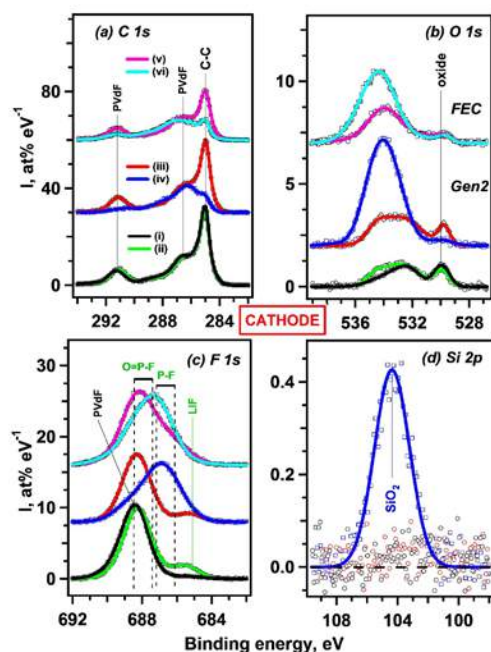


Figure II-58. XPS spectra of harvested positive electrodes from cells (i) to (vi) (see inset in panel 'a' for the color table): (i) pristine Si-Gr cell, (ii) Gr cell, after three formation cycles in Gen2, (iii) Si-Gr cell, after three formation cycles in Gen2, (iv) Si-Gr cell, aged in Gen2, (v) Si-Gr cell, three formation cycles in Gen2 containing FEC, (vi) Si-Gr cell, aged in Gen2 containing FEC. The spectral regions are indicated in the panels.

The C 1s spectrum (Figure II-56a) of the pristine Si-Gr electrode (trace i) show intensities arising from the graphite (284.5 eV) and LiPAA binder (286.0, 289.5 eV). The graphite peak intensity decreases significantly after formation cycling and is not seen after 100 cycles for either cell (traces iv and vi), confirming our SEM observation that graphite in the Si-Gr cells is buried under the overlying SEI deposits. A similar observation can be made about the LiPAA peaks, which are not observed even after formation cycling and indicating that the binder is covered by the SEI. Peak intensities centered around 286.5 eV (R-O), 288.5 eV (R=O), and in the 290-292 eV range (R-OCO₂), where R=C_xH_y, are observed in the cycled electrodes; these signals arise from electrolyte decomposition products that could include alkyl carbonates (such as ethylene dicarbonate from EC reduction) and alkyl fluorophosphates. Overlapping with these R-O peaks are the C-H peaks from the polymeric component. For Gen2 cells, the decrease in 286.5 eV and 290-292 eV intensities and increase in 288.5 eV intensity for the 100 cycle electrode (relative to the 3-cycle electrode) suggests that the alkyl carbonates are being covered by compounds that include fluorophosphates, as cell aging proceeds. The FEC cells (traces v and vi) also show the 288.5 eV intensity increase suggesting an increase in the phosphate content, but without a corresponding decrease in the alkyl carbonate intensities.

The Si 2p spectrum from the pristine electrode (trace i in Figure II-56d) shows two strong peaks near 100 eV (Si) and 104 eV (SiO₂), which reveals that the silicon nanoparticles have a SiO₂ shell. From an examination of the XPS spectrum, and from an analysis of the Si-Gr half cell electrochemistry data, we conclude that the SiO₂ shell thickness is less than 5 nm. After 3 cycles, both the Gen2 and FEC cells show intensities around 99.5 eV, which arises from the delithiated amorphous silicon. For the Gen2 cell (trace iii), strong intensities are also seen in the 102 – 105 eV range, suggesting the presence of Li_xSiO_y (102.8 eV, strong), SiO₂ (104 eV, weak) and SiO_xF_y (105 eV, weaker) phases. The FEC cell (trace v) shows relatively weaker Li_xSiO_y intensities, and negligible SiO₂ and SiO_xF_y intensities. After 100 cycles, the Gen2 cell (trace iv), shows negligible intensity in the 98.5-100.5 eV range indicating complete coverage of the silicon nanoparticles by SEI deposits that include SiO₂ and SiO_xF_y species formed by progressive substitution of the oxide anions by F⁻ anions. In contrast, the FEC spectrum (trace vi) shows weak Si and Li_xSiO_y intensities and negligible SiO_xF_y signals.

Parallel developments are seen in the F 1s spectra (Figure II-56c). The pristine electrode does not show fluorine signals, which is as expected. After 3 cycles both Gen2 and FEC electrodes (traces iii and v) display intensities in the 686-688 eV range (LiF and P-F bonds in Li_xPF_yO_z) and in the 688-690 eV range (O=P-F bonds in Li_xPF_yO_z). Previous studies have shown LiPF₆ exists in equilibrium with LiF and PF₅. Hydrolysis of the PF₅ results in a variety of Li_xPF_yO_z compounds, including POF₃, PO₂F₂⁻ and PO₃F₂⁻ species; the greater extent of hydrolysis leads to the increasing oxygen-rich species content. After 100 cycles the Gen2 sample (trace iv) shows a large increase in both 686-688 and 688-690 eV ranges indicating substantial hydrolysis of the LiPF₆ salt. The FEC electrode (trace vi) shows an increase in the 688-690 eV signals but a small decrease in the 687-688 eV signals, indicating slower generation of the F-rich species, and more conversion to the O-rich Li_xPF_yO_z compounds. This observation suggests that the FEC-generated SEI is more protective than the EC-generated SEI.

Signals consistent with increasing LiPF₆ salt hydrolysis on aging are also seen in the P 2p spectra (Figure II-57b). For the Gen 2 samples (traces iii and iv), both P-F signals (137-139 eV) and P-O signals (around 134-136 eV) increase on aging. Smaller changes are seen for the FEC samples, again indicating a more protective SEI. The Li 1s spectra (Figure II-57a) and O 1s spectra (Figure II-56b) also show changes on aging; these plots are harder to interpret as multiple species contribute to the spectral features. For both Gen2 and FEC samples, changes in the O 1s spectra reflect the decrease in alkyl carbonate content (533.5 eV) as these compounds are increasingly buried under the salt decomposition and hydrolysis products (535.5 eV). The Li 1s spectra indicate changes in Li-speciation for the Gen2 samples, and less so for the FEC samples.

The XPS spectra for the NCM523 positive electrodes are shown in Figure II-57c, d and Figure II-58a-d. The C 1s spectra (Figure II-58a) from the pristine electrode (trace i) shows show intensities arising from the C45 carbon black (285 eV) and PVdF binder (286.3 and 291 eV). On cycling the intensities arising from both graphite and PVdF decrease, indicating coverage by mostly inorganic surface species. Although weak, the

graphite and PVdF intensities are still observed even after 100 cycles (see traces iv and vi) indicating a relatively thin or non-uniform surface coverage.

The reduction in PVdF intensities on aging are also observed in the F 1s spectra (Figure II-58c). The pristine electrode contains a peak at 688.5 eV arising from C-F bonds in PVdF. After 3 cycles (traces iii and v), additional intensities around 685 eV signify the presence of LiF. After 100 cycles (traces iv and vi), strong intensities in the 686-687 eV range indicate the presence of $\text{Li}_x\text{PF}_y\text{O}_z$ compounds, which are the products of LiPF_6 decomposition and hydrolysis. Corresponding intensity increases on aging are also seen in the Li 1s spectra (Figure II-57c) and P 2p spectra (Figure II-57d).

Perhaps the most significant observation is the presence of silicon (~ 3 at%) on the positive electrode of the aged Gen2 cell. Judging from the binding energies, this signal at 104 eV (Figure II-58d, trace iv) stems from silicon dioxide (or lithium silicate). None of the other positive electrodes examined showed noteworthy Si 2p intensities, indicating that (i) the deposition is enhanced by cycling, and (ii) the FEC additive hinders Si loss from the Si-Gr electrode. The presence of SiO_2 could also partially explain the increased intensities on aging in the O 1s spectra (Figure II-58b) for the Gen2 cell (traces iii and iv) compared to those of the FEC cell (traces v and vi). Yet, even after 100 cycles, weak intensities around 529.8 eV, arising from O_2^- anions in NCM523, indicates that the coverage is thin enough ($\lesssim 5$ nm) to allow photoelectrons emitted from the oxide below it to pass through.

Characterization of water loss from LiPAA using thermogravimetry: To quantify water loss from LiPAA, an aqueous solution containing 10 wt% LiPAA was first evaporated to a thick slurry and then water was removed at 120°C over 5 h in a vacuum oven. The material was subsequently equilibrated with water vapor for 40 h under the ambient conditions. The hydrated LiPAA gel initially contained ~ 2.2 water molecules per monomer unit, and one-half of this water was quickly lost as the temperature increased to 150°C (Figure II-59). For the next 3 h, the loss followed $t^{1/2}$ behavior that is typical for diffusion-limited mass loss and then it settled into the exponential mode with $1/e$ time constant of 11 h. As seen from the plot, after 3-4 h at 150°C , ~ 0.1 mol.eq of water was retained in the sample, and 0.02 mol.eq was retained even after 10-15 h. Note that the water loss was quantified for the pure LiPAA binder; water loss from the composite material can be still slower, as water molecules can form H bonds both with silanol groups on the silica surface and the carboxylate anions adhering and interacting with this surface.

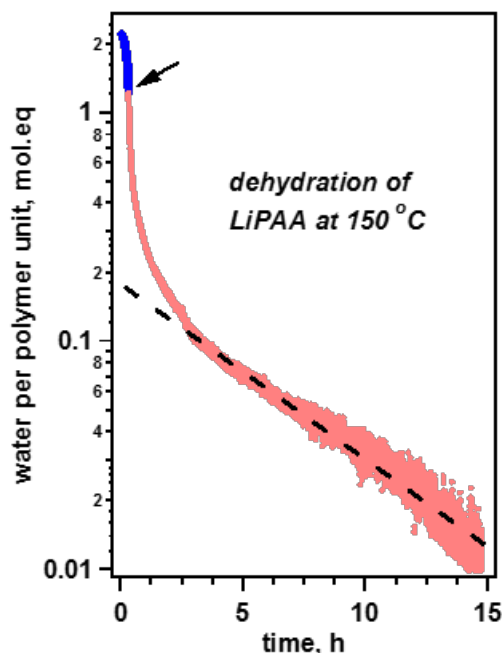


Figure II-59. Water loss from hydrated LiPAA binder as observed by thermogravimetry. Note the logarithmic vertical scale. The first section of the plot (indicated with the arrow) corresponds to heating of the sample from 50 to 150°C at 6 °C/min, whereas the scattered dots indicate the 150°C isotherm. After the first 3 hours, the mass loss settles into the exponential regime (dashed line).

Why residual water in the SiGr electrode matters: The as-received Si nanoparticles have a SiO₂ shell, which is lined with silanol (\equiv Si-OH groups). After cycling we note the gradual disappearance of Si and Li_xSi signals in the Si 2p XPS spectra and the concomitant increase in the SiO_xF_y, SiO₂ and Li_xSiO_y signals; continuous increase in the LiF and LiPO_xF_y signals in the F 1s and P 2p spectra is also seen. The oxide-by-fluoride (O-by-F) substitution, and the gradual conversion of nonfluoride lithium salts to LiF can be rationalized through reactions of hydrolytically generated HF. Specifically, LiPF₆ disproportionates to LiF and PF₅, and the pentafluoride hydrolyses to POF₃ releasing two molecules of HF in the process. Further hydrolysis can yield PO₂F₂⁻ and PO₃F⁻ anions releasing more HF. The latter can react with silica, silicon, lithium salts (such as alkoxides and alkyl carbonates) in the negative electrode, and (lithiated) transition metal oxides and hydroxides on the positive electrode, forming the fluorides. A schematic of these concepts is shown in Figure II-60.

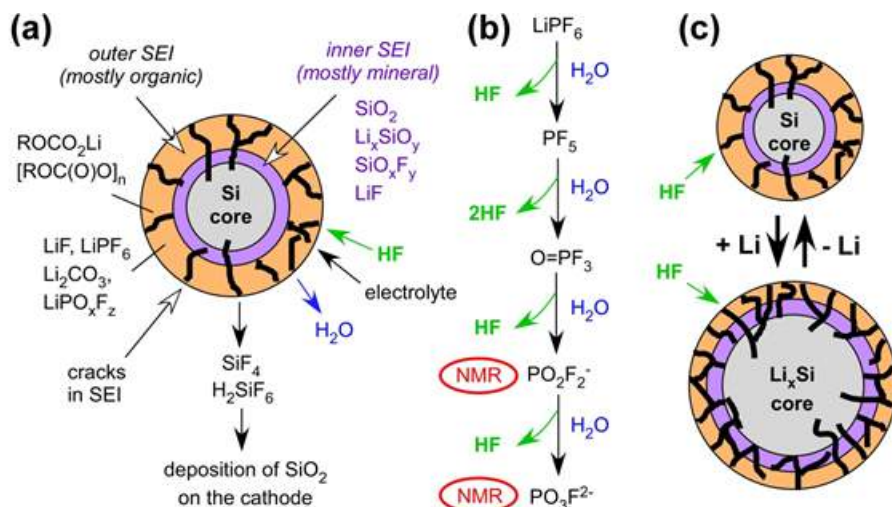
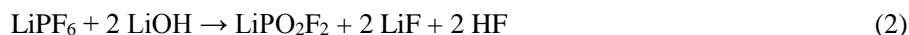


Figure II-60. (a) Schematic representation of a Si particle in the advanced stages of aging, with the inner and outer SEI layers formed around the Si core. Mineral compounds derived from Si prevail in the inner SEI while various organic compounds (including alkyl carbonates and inner-carbonate polymers) prevail in the outer SEI, with insoluble salts trapped in the semisolid matrix. Electrolyte and HF molecules can diffuse through the pores and cracks in the outer SEI and react with the particle interior, releasing SiF_4 and water molecules back into the electrolyte. This water joins the hydrolytic cycle for LiPF_6 (shown in panel b). In the latter, water sequentially hydrolyzes PO_xF_y species, consuming five water molecules and releasing five HF molecules in total; the released HF can react with Si particles, continuing the hydrolytic cycle. The two species at the end of this sequence can be observed using NMR spectroscopy in the fluids collected from the aged cells. (c) As the Si particles repeatedly expand and contract during lithiation/delithiation, deep cracks develop allowing access of HF to the core, resulting in its digestion and additional SEI formation.

For example, reaction 1 illustrates interaction of the surface silanol groups on silica with HF yielding fluorinated species and releasing a water molecule, which can cause further hydrolysis of LiPF_6 .



Another possibility is that the residual bound water in the binder matrix transforms to LiOH during the first cycle. Subsequent hydrolysis (or basic hydrolysis) of LiPF_6 occurs according to the net equation



releasing HF that reacts with the various electrode components forming fluorides and releasing water (e.g., via reaction 1) which enters the hydrolytic cycle.

At the advanced stage of this O-by-F substitution, tetrafluorosilane (SiF_4) and/or hexafluorosilicic acid (H_2SiF_6) can be generated. These are highly soluble compounds that can diffuse out of the negative electrode and into the electrolyte before they hydrolyze there to the silicic acid (H_4SiO_4). The SiF_4 or H_2SiF_6 could also reach the positive electrode and react with the lithiated metal oxides (either directly or via hydrolysis) forming the corresponding fluorides and converting to SiO_2 (such reactions of transition metal oxides are used for ore refinement). In this manner, silicon is transferred from the negative to the positive electrode and becomes deposited at the layered oxide surface where it can be observed in XPS spectra.

EQCM Studies of Silicon Anodes (ANL)

Silicon electrodes for LIB systems are a leading contender for the next generation of anode material. The ten-fold increase capacity seen for silicon-based systems vs graphitic carbons could have a significant impact on overall electrochemical cell storage market if issues related to their cycling stability can be addressed. We have

focused on determining the interfacial properties of a charged silicon electrode, the silicon oxide passivation layer, and explored this interface using simple film forming additives that mediate lithium transport.

The natural passivation layer of silicon is generally related to its handling on formation. The natural passivation layer is usually found to be approximately a 2-3 nm thick layer of silica. A combination of experimental and theoretical work has shown that this passivation silica layer reacts with electrolyte decomposition products around 900 mV to form lithium silicate. Previously we demonstrated that the lithium silicate formed is a kinetic product and on cycling it loses the equivalent of a lithia molecule and reverts to the more stable lithium orthosilicate. In the past year Baris Key extended this work to show that the lithium orthosilicate eventually diffuses away from the interface and gets incorporated into the SEI layer. Last year we re-established our EQCM spectroscopic effort to determine how the passivation layer reactivity is affected by the addition of small amounts of the common electrolyte additive FEC to the Gen2 electrolyte system. Without FEC the system was found to form a relatively porous SEI layer that got thicker as a function of state of charge. Addition of FEC (1-5 wt%) to the electrolyte was found to create a much denser SEI layer than the SEI formed in Gen2 electrolyte. In a continuation of these studies we evaluated the role of higher amounts of FEC on the system and looked at the role of the salt counter-ion, as PF_6 anion has been implicated in some of the decomposition pathways by also evaluating systems using the TFSI anion.

Utilizing thin film model silicon electrodes, the role of surface passivation, electrolyte additives, and electrolyte can be investigated as a function of state of charge. The thin film electrode format is conducive to a variety of spectroscopic studies and utilizing a combination of 29-Si, 7-Li, and 19-F NMR (with Baris Key (ANL)) combined with electrochemical quartz crystal microbalance (EQCM) the interfacial properties can be correlated with the observed electrochemical performance.

The interface between the silicon electrode and electrolyte is a key point of contact in the electrochemical cell. Silicon is well known to have an unstable SEI layer due in part to its reactivity at high states of charge and lack of dimensional stability on cycling, as opposed to graphitic carbon which has exceptional dimensional stability [1, 13]. As part of this effort we have utilized a combination of EQCM spectroscopy and film forming additives to study the role of film thickness and density on the electrochemical properties of a silicon anode. Last year we reported the densification of the SEI on addition of FEC and the role silica passivation played in SEI formation. This is speculated to result from the breakdown of the FEC molecule happening at a higher voltage than the similar molecule EC and utilizing a different pathway that yields a different and denser polymer coating [14]. Building on this study, we evaluated the role of the amount of the film forming additive FEC in the electrolyte and, as seen in Figure II-61, there are several changes that are observed. As the film thickness increases (approximated by %FEC added) the silicon reduction peak sharpens and moves to lower potential, indicative of better lithium diffusion at the particle-electrolyte interface, additionally the samples with highest amount of FEC (20%) have much broader peaks that can be tied to higher viscosity, interfacial resistance, and lower electrolyte conductivity. Since addition of FEC to electrolytes is typically done as an additive rather than a salt/solvent mixture, addition of 20% FEC to Gen2 results in a drop in salt concentration from 1.2M to 0.96M and movement off the peak in electrolyte conductivity.

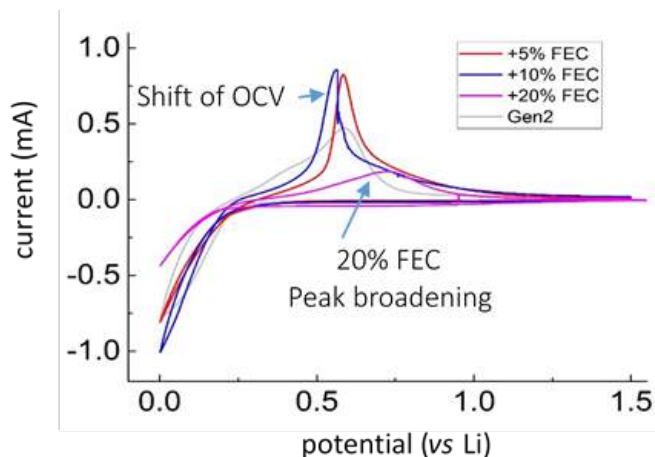


Figure II-61. Electrochemical reduction of a silicon thin film in a Gen2/FEC electrolyte mixture.

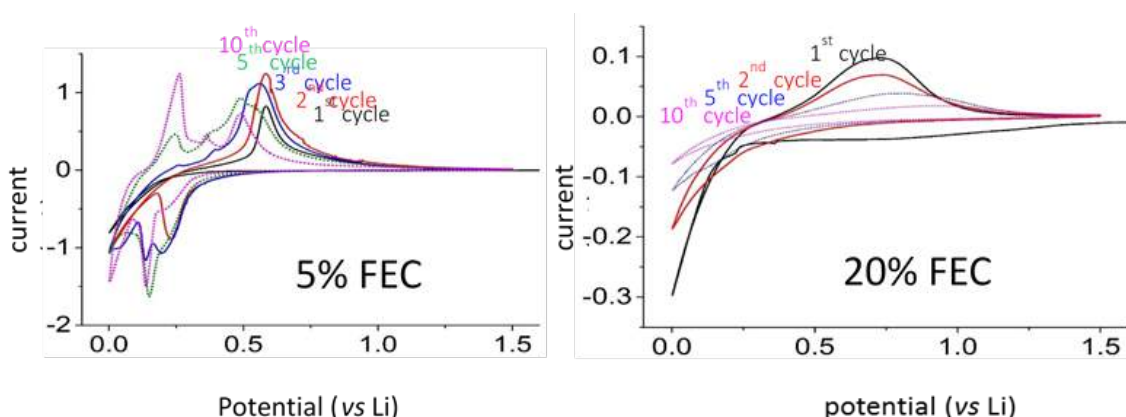


Figure II-62. CV comparison of 5% FEC and 20% FEC addition to Gen2 on the cycling of a silicon electrode.

Additional EQCM studies have shown that the role of film stability and electrochemical properties. Whereas the FEC forms a dense polymeric film on the surface of the electrode, the propensity of the silicon electrode to crack (Si film thickness ≈ 50 nm) on cycling leads to active material isolation and electronic isolation. This can be seen (Figure II-62) in a comparison to an electrode cycled in 5% FEC/Gen2 vs 20% FEC/Gen2. The sample(s) with lower amounts of FEC additive show a new peak growing in around 250 mV (vs Li) [15]. This peak, assigned in the literature to either electrode degradation (Si isolation) or Cu diffusion into the charged electrode (from Cu current collector) grows in rapidly when the FEC film is thinner. This is consistent with either mechanism or a combination as the copper solubility and lattice expansion are both maximized at low voltage (maximum lithiation). Efforts to assess the copper loss from the current collector (e.g., pitting) are planned.

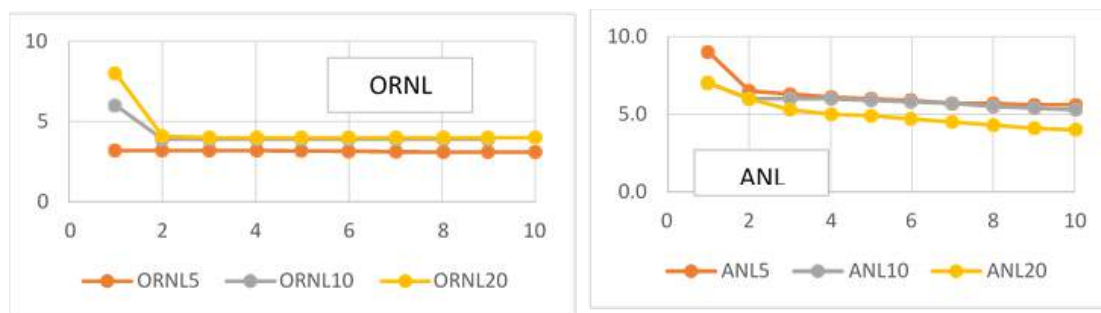


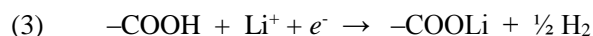
Figure II-63. A comparison of the cycling performance of a silicon thin film electrode versus surface passivation layer thickness.

In addition we also assessed the issues associated with the silica passivation coating in association with Gabe Veith as ORNL. As part of the SEISa Round Robin effort, we were provided with a series of silicon thin film electrodes for evaluation. After several weeks of aging these electrodes had thicker and more uniform silica passivation layers than our 'fresher' films and thus were good choices to assess the role of the interfacial silica on FEC film formation [16]. Electrochemical evaluation of the films was consistent with the earlier work noted. The aged electrodes had a higher silica content (nominally both had the same amount of Si/cm³). From the data shown in Figure II-63, the ORNL samples have much more cycling stability, albeit at a lower capacity. Both of these are consistent with the role proposed for the silica passivation layer as the silica acts to buffer the surface but also consumes silicon to make the buffer. The FEC appears to have a positive impact, notably for the ANL samples, which show better cycling stability than the cells cycled with no FEC additive. Both sets of materials show increasing first cycle irreversibility, consistent with the irreversible electrochemical reduction of FEC, which has been shown to take several cycles depending on concentration.

Understanding Capacity Losses with Silicon Anodes (ORNL)

Analysis of Coulombic Inefficiencies of PAA-based Si-Graphite Half Cells

PAA based full cells also display a first cycle Coulombic efficiency ~5% worse than LiPAA-based cells. The electrochemical reduction of additional water in the cells accounts for some Coulombic losses, but there are continuous losses through the first 40 cycles, summing up to a difference between the two systems of 71 mAh g⁻¹. Lucht et. al., has previously proposed the reduction of the acidic proton on the carboxylic acid of PAA to form LiPAA, following reaction 3. [17]



To verify these observations, PAA was mixed with 17% carbon black and coated on Cu foil. The coatings were dried at 120° C or 220° C, above and below the decomposition temperature of PAA. A modified pouch cell was produced with Li foil as the counter electrode and 1.2 M LiPF₆ in 3:7 (w:w) EC:EMC. The cell was held at 1 V vs Li metal for 1 week and analyzed for gassing by the Archimedes method. [18] The PAA coating was removed, rinsed in DEC, and scraped from the Cu foil for ATR FTIR. The resulting spectra (Figure II-64) show new peaks at 1567 cm⁻¹ and 1416 cm⁻¹ for the 220° C PAA sample, closely matching the carboxyl stretch of LiPAA. The 120° C PAA sample also displays a change in the spectra, but with a broad range of peaks from 1670 cm⁻¹ to 1580 cm⁻¹. While the exact reason for this is still unclear, it is recognized the symmetric and asymmetric carboxyl stretches can vary based on the coordinating environment of the carboxylate ion. [19] For both drying temperatures of PAA, a peak at 1700 cm⁻¹, from the carboxylate stretch of PAA, shows that not all the PAA has been converted to LiPAA, likely due to the poor electrical conductivity of the binder. This observation closely matched the gradual Coulombic efficiency gains of the PAA-based cells through the first 40 cycles compared to the LiPAA-based cells. After the voltage hold, the volume increased within the cell by 130 µl, presumably due to H₂ generation from the reduction of PAA. A more detailed gas analysis is needed to identify the content of the gassing, but the volume produced here is on the right order expected for H₂ generation based on reduction of PAA.

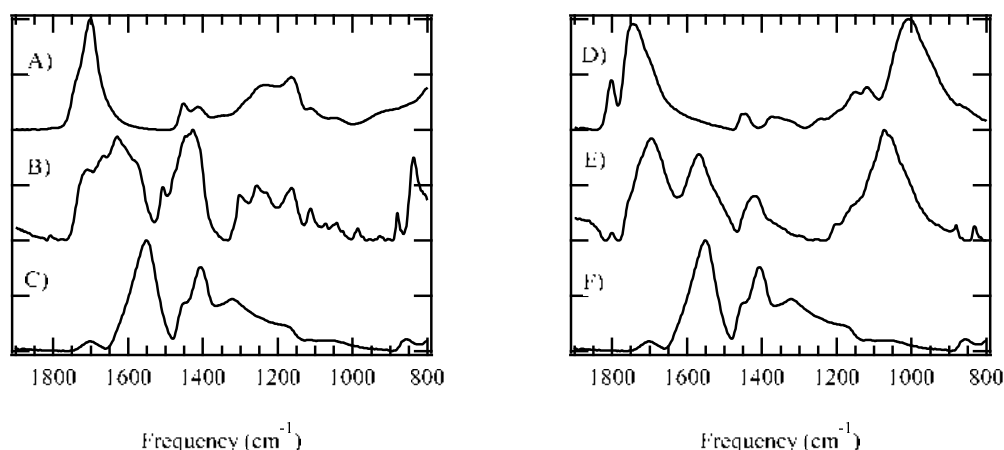


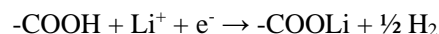
Figure II-64. ATR FTIR spectra of A) PAA dried at 120°C, B) PAA dried at 120°C, electrochemically reacted with Li metal, C) LiPAA dried at 120°C, D) PAA dried at 220°C, E) PAA dried at 220°C, electrochemically reacted with Li metal, and F) LiPAA dried at 220°C.

Analysis of Coulombic Inefficiencies of PAA Based Si-Graphite Full Cells

FTIR and Raman spectroscopy provide highly complementary information about the chemical changes that occur in Si anodes during battery cycling. FTIR is sensitive to changes in the binder and SEI chemistry, while Raman spectroscopy probes structural changes in the active materials. Despite the power of these techniques, Raman and FTIR are generally only applied to electrodes cycled in half cells for a few cycles. The mechanisms that lead to cell failure are often very different in half cells compared to full cells, [20] and some of these processes may not be evident after only a few cycles. Therefore, we carried out detailed vibrational analysis of Si-Gr composite anodes cycled in full cells with NMC532 cathodes. The anodes were analyzed after formation cycling and after long-term cycling when significant capacity fade had occurred.

Single-layer pouch cells were built at the ORNL BMF with silicon-graphite composite anodes (A-A006A) and $\text{LiNi}_{0.5}\text{Mn}_{0.3}\text{Co}_{0.2}\text{O}_2$ cathodes (A-C013A) coated by the CAMP facility at ANL. The electrolyte was 90 wt.% Gen 2 and 10% wt.% FEC and the electrolyte volume factor was 3.5-4.5. Cells were cycled between 3.0 and 4.1 V using the standard ANL protocol for a total of 100 cycles. Anodes were harvested after 1 formation cycle, 2 formation cycles, and the full cycling protocol. Anodes were analyzed by FTIR spectroscopy without air exposure. To gain insights into the SEI composition, FTIR spectra of cycled anodes were compared to a library of reference spectra of common SEI components.

The FTIR spectra of the Si-Gr composite anodes change significantly after one electrochemical cycle (Figure II-65). The broad SiO_2 band from 1000 – 1250 cm^{-1} largely disappears consistent with the electrochemical reduction of the oxide. Broad overlapping bands between 650 and 1100 cm^{-1} emerge that are a good match for lithium silicates ($\text{Li}_x\text{SiO}_{2y}$). The vibrational signatures of the LiPAA binder also change after one cycle. The pristine anode shows a broad shoulder near 1700 cm^{-1} that can be assigned to the carbonyl stretch of the acid (COOH) groups in LiPAA. This mode disappears after cycling indicating that the acidic protons in the binder are reduced according to the following reaction: [17, 21]



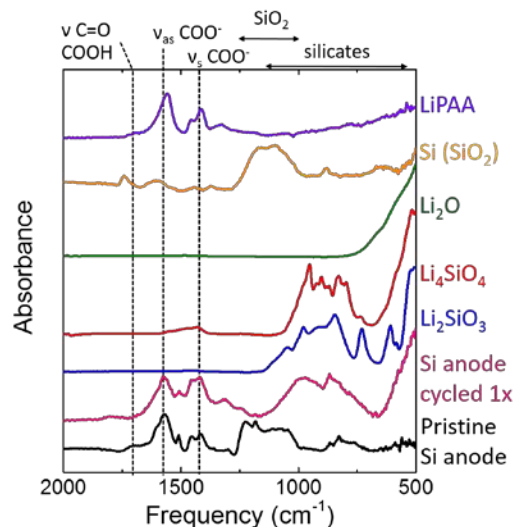


Figure II-65. FTIR spectra of the pristine Si anode and the Si anode after one formation cycle. FTIR spectra of Li_2SiO_3 , Li_4SiO_4 , NanoAmor silicon, and LiPAA are also shown for comparison.

This result is consistent with the half-cell data presented previously. Hydrogen evolution has been observed with silicon anodes using mass spectrometry and is typically attributed to residual water or FEC reduction. [22] The reduction of acid groups in the binder is another important mechanism that has received relatively little attention.

The SEI on the Si-Gr composite anodes continues to evolve with extended cycling (Figure II-66). After 100 cycles, the mode near 1400 cm^{-1} increases in intensity significantly. This is most likely due to the build-up of Li_2CO_3 , which may form as an innate component of the SEI or as a reaction production from residual water. Further evidence for the growth of the SEI layer comes from the EC signal ($\nu(\text{C}=\text{O})$ near 1800 cm^{-1}) that remains after 100 cycles. The EC is likely trapped in a thick SEI and cannot be removed by washing. All the reactions characterized by FTIR (silicate formation, carbonate formation, and binder decomposition) consume lithium ions and contribute to capacity fade. FTIR is therefore an excellent tool to evaluate the stability of the SEI formed on composite anodes and ultimately improve performance.

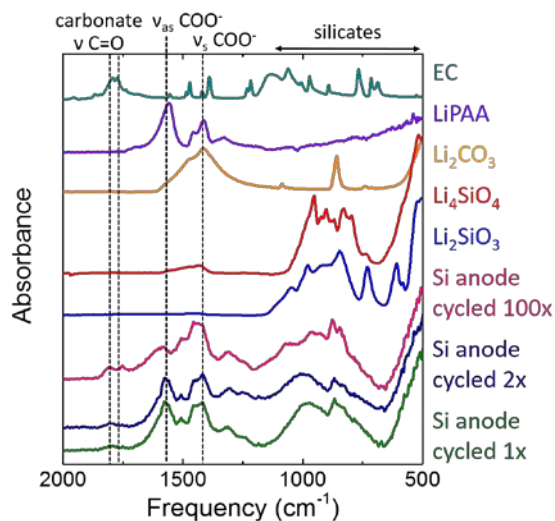


Figure II-66. FTIR spectra of the Si anode after one formation cycle, after two formation cycles, and after 100 cycles. FTIR spectra of Li_2SiO_3 , Li_4SiO_4 , Li_2CO_3 , LiPAA, and EC are also shown for comparison.

In the future, FTIR will be combined with gas analysis to fully characterize the reactivity of binders with carboxylic acid groups. Factors that influence silicon passivation (electrolyte additives, nature of the oxide layer) will be systematically studied by monitoring the changes in SEI chemistry with FTIR. Raman mapping of electrode homogeneity and measurement of inactive silicon will characterize improvements in electrode formulation and processing. Insitu Acoustic Time of Flight (ToF) analysis of Si/Gr-NMC full cells during formation as well as various SOC's combined with EIS and microstructural analysis will be reported in coming quarters. This will provide more fundamental insights on the amorphization and alloying of semi-crystalline silicon during lithiation (delithiation).

Quantification of the Li Losses During Full Cell Cycling

Capacity fade of Si-based electrode in Li-ion cells has been ascribed to (1) electrical disconnection from structural degradation and (2) active lithium loss from SEI destruction/re-construction, and (3) our recently identified PAA titration. To explore the SEI component three-electrode cell analysis was performed to elucidate the SEI destruction/re-construction is the dominant factor leading to capacity fade. The electrodes used in three-electrode cell were received from CAMP facility. Anode is made of 73 wt% Hitach MAGE, 15 wt% NanoAmor silicon (50–70 nm), 2wt% C-45 carbon (Timcal) and 10wt% LiPAA (LiOH titrate) with a loading of 3.28 mg/cm². Cathode is made of 90 wt% LiNi_{0.5}Mn_{0.3}Co_{0.2} (TODA), 5 wt% C-45 carbon (Timcal), 5 wt% PVDF (Solvay 5130) with a loading of 11.32 mg/cm². A Li ring was used as reference electrode.

For the first 100 cycles, constant current cycling at C/3 was applied between cathode and anode in Figure II-67 (left). The cell showed a rapid capacity fade after 100 cycles. Then the constant current cycling was applied between cathode and Li ring (so-called cathode half-cell) in Figure II-67 (middle) at slow rate of C/50 since they are not facing each other. The open circuit potential of NMC cathode is close to 4.0 V, indicating the cathode is lithium deficit at oxidation state. During the first charge, only a small fraction of capacity (0.27 mAh compared to 1.7 of original capacity) can be obtained. This means limited active lithium was left due to the consumption of active lithium during SEI destruction/re-construction at the anode side. During discharge, 1.3 mAh capacity is re-gained, meaning the NMC cathode can be replenished from Li ring. Figure II-67 (right) shows the anode half-cell can be cycled close to its original capacity. This means the capacity fade is not from electric disconnection of the active material, but rather the active lithium loss. That is because the capacity cannot be regained if the fade is from electric disconnection due to structural degradation. Figure II-68 further demonstrates the argument which shows the capacity can always be re-gained close to its original value by Li replenishment from reference Li ring.

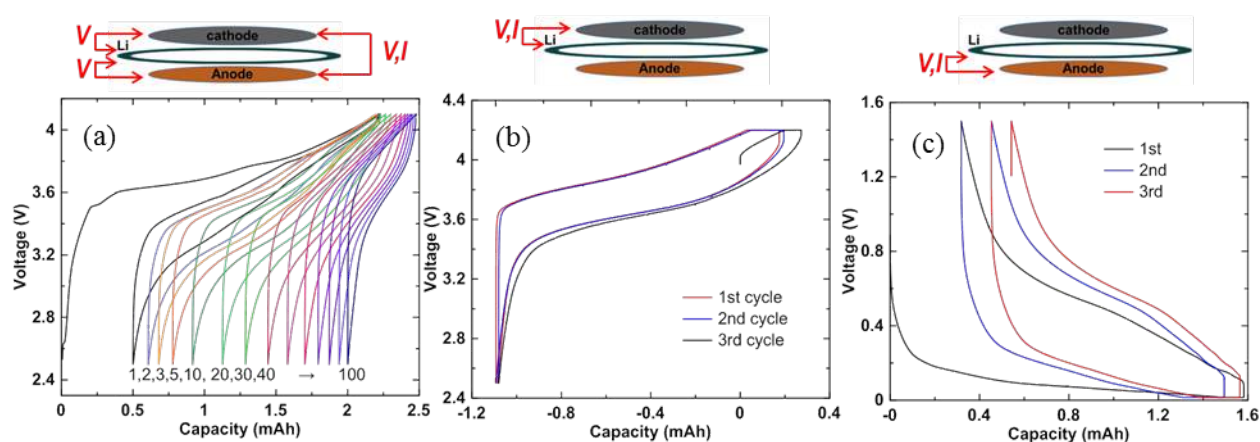


Figure II-67. (a) Voltage curve of the cathode/anode cycling at C/3, (b) Voltage curve of the cathode/Li ring cycling at C/50, and (c) Voltage curve of the anode/Li ring cycling at C/50.

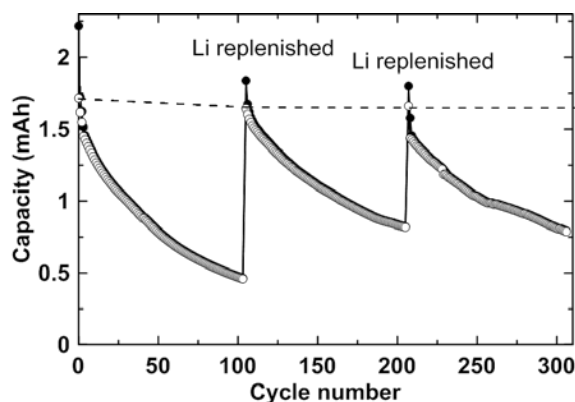


Figure II-68. Capacity cycling of the three electrode cell with Li replenished from Li ring every 100 cycles.

The voltage curves of the cathode and anode versus reference electrode during capacity fade at C/3 cycling are shown in Figure II-69. During discharge, the cathode voltage curve overlaps with each other for the top part. However, the elbow at the end of discharge gradually increases in voltage with less and less lithium can be re-intercalated into the cathode during cycling. Meanwhile, the cathode voltage during charge starts at higher voltage with less capacity available during cycling. This means the cathode is cycling in the top part of the voltage curve due to disappearance of bottom part of the voltage curve from lithium loss at the anode side. For the anode side, the end of charge voltage is also increasing with cycle number due to less active lithium available to further intercalate into graphite and lithiation of silicon.

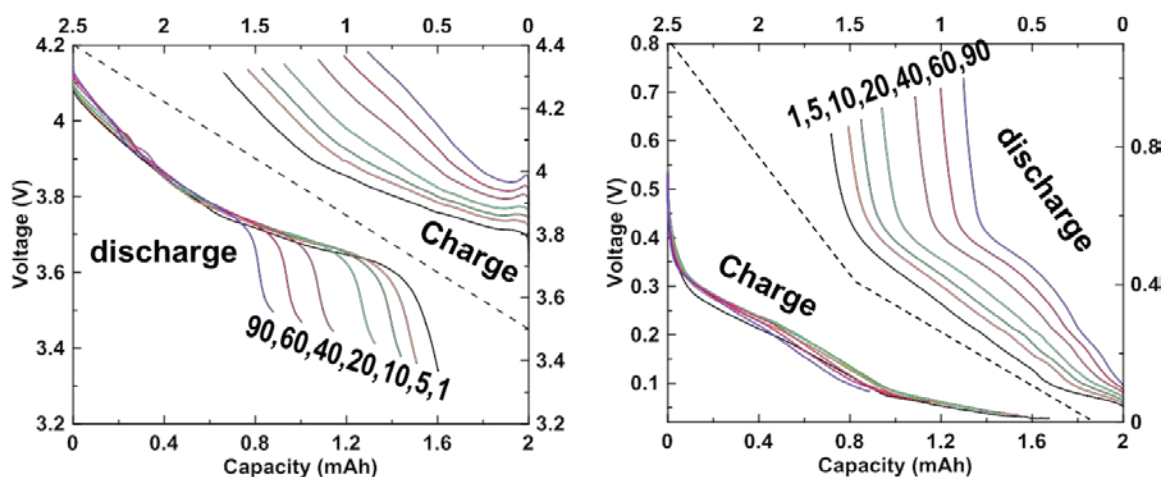


Figure II-69. a) Cathode and (b) anode voltage curve versus reference electrode during capacity fade at C/3 cycling.

Cell Modeling Silicon Alloy Electrodes (ORNL)

Si alloys, where Si is diluted by inactive component, are being investigated. The inactive component buffers the volume expansion and is also beneficial to the electrochemistry of Si, which could suppress the formation of $\text{Li}_{15}\text{Si}_4$. The cycling performance is improved because there is no particle fracture induced by a two-phase reaction front. A typical formula is written as $\text{Si}_x[\text{M}]_{1-x}$, where x is the “atomic ratio of active Si” and M is “inactive phase in the alloy” such as Fe, Ni, Mo, etc. Two questions need to be answered: 1) what is the best way to incorporate Si alloys in anode coatings; and 2) how much energy density improvement in a lithium-ion full cell can be achieved? Such information is not included in the latest version of BatPac.

In the study by Du et al., electrodes with good cycle life, high energy density, and low volume expansion were obtained when alloys were blended with graphite and calendered to high densities [25], which has been shown to be the most beneficial way to implement Si in practical Li-ion cells. [26, 27] This model is based on the well-studied conclusions: (1) lithiation of silicon alloys follows Vegard's law (molar volume of lithium requires 9 mL/mol) [23]; (2) the porosity in the Si alloy/graphite coating remains constant during charge/discharge; and (3) the volumetric capacity and energy density have to be calculated at fully expanded (lithiated) state.

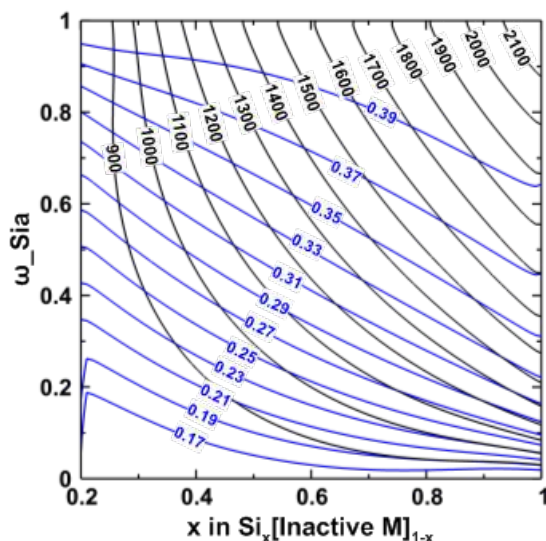


Figure II-70. Contour mapping of volumetric capacity [Ah/L, black lines] and average delithiation voltage [V, blue lines] of the Si alloy/graphite versus the composition of Si alloy and weight ratio of Si alloy/graphite. Black lines are in 100 Ah/L increment and blue lines are in 0.02 V increment.

It has been shown that the most likely way to implement Si alloys in practical Li-ion cells is blending with graphite, [24, 25, 26] which introduces a variation of ω_{Si_a} , which is the weight ratio of Si alloy in the mixture. In Figure II-70, the volumetric capacity is shown to increase with an increase in either ω_{Si_a} (more Si alloy), or x (more active component in Si alloy), or both. Another important factor for anode design is the average delithiation voltage. It has been pointed out by Obrovac and Chevrier that the anode voltage has more effect on volumetric energy density than the anode volume, [26] because active anode materials occupy a rather small portion of the total cell volume, while the cell energy is proportional to the cell voltage. The anode voltage should be as low as possible to get high voltage output when paired with the cathode. Since graphite has much lower voltage compared to Si, the average voltage of the Si alloy/graphite decreases with increasing graphite content as shown in Figure II-70. Therefore, a competing trend exists in the Si alloy/graphite coating design for high energy density cells: increasing active Si content in the coating increases the volumetric capacity while decreasing the anode voltage requires more graphite in the coating.

One of the most important anode metrics for new material implementation is the associated cell volumetric energy density. A contour plot of volumetric energy density is shown in Figure II-71 for cells with Si-alloy/graphite composite anodes and $\text{LiNi}_{0.5}\text{Mn}_{0.3}\text{Co}_{0.2}\text{O}_2$ (NMC532) cathodes. It is seen that the baseline cell with pure graphite (0% Si alloy) has about 740 Wh/L energy density. The energy density gradually increases from the bottom left corner (low ω_{Si_a} , low x) to the upper right corner (high ω_{Si_a} , high x). One macroscopic issue associated with the volume expansion of Si alloy is the dimensional change in Li-ion cells. Conventional Li-ion cells with pure graphite electrode have about 3-4% thickness change during charge/discharge due to inter-plane distance change between graphene layers. It is understood that cell expansion is much greater when Si alloy particles are incorporated into the anode, but, so far, there is no published analysis considering how

the large volume needed for the expansion of these anodes can be accommodated by the cell during initial assembly. This volume change should be kept as small as possible for practical cell and battery pack design.

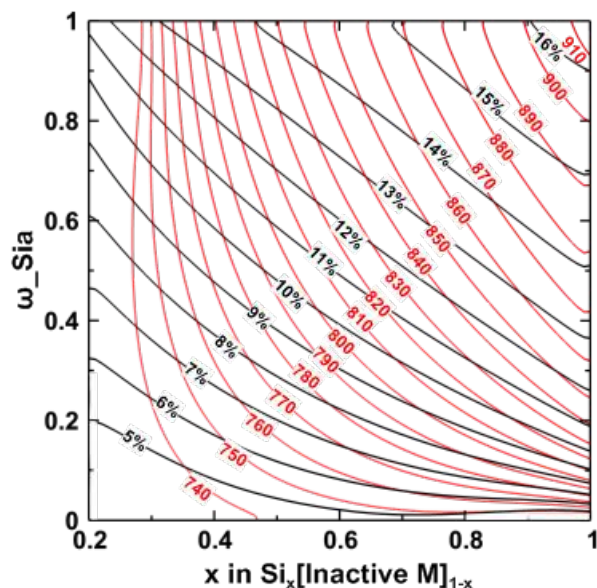


Figure II-71. Contour mapping of cell stack energy density [Wh/L, red lines] using Si alloy/graphite electrode and volume expansion ratio of the cell stack [black lines]. The increment between adjacent red lines is 10 Wh/L and the increment between adjacent black lines is 1%.

The result of the degree of cell stack expansion is shown in Figure II-71, and it is seen that to achieve the same energy density of the cell and minimize the cell stack expansion, the preferred strategy is using a high capacity (greater x) Si alloy. This strategy increases the content of graphite in the coating (lower ω_{Sia}), which contributes to the total energy density but has a low particle expansion rate (10% for graphite particles).

Figure II-72 shows the contour plots volume expansion of the Si alloy particles together with energy density of the cell stack. The volume expansion of Si alloy tends to affect the SEI layer which has little elasticity since the components in SEI are decomposition products of reactions between solvents, salts, lithium ions, and impurities in the electrolyte. [28, 29] The SEI layer on Si alloys is unstable because it can be easily broken by the large Si volume changes during lithiation/delithiation. The fresh Si surface exposed to electrolyte will form new SEI, which further consumes cell lithium inventory, leads to reduced coulombic efficiency (CE) and results in a high rate of capacity fade in full cells. Meanwhile, the ever-thickening SEI layer eventually fills pore volume in the anode, leading to the electrode failure due to blocking of Li^+ diffusion pathways. Therefore, Si alloy particles with smaller volume expansion (smaller x) are preferable in terms of less active lithium loss during new SEI formation. Figure II-71 and Figure II-72 together suggest competing strategies for maximizing the cell energy density with respect to the volume change issue. To achieve the same energy density improvement, Figure II-71 suggests using high capacity (greater x) Si alloy to minimize the expansion of the cell stack. However, Figure II-72 suggests using Si alloy particles with relatively low capacity (smaller x for smaller volume expansion) to alleviate the SEI instability.

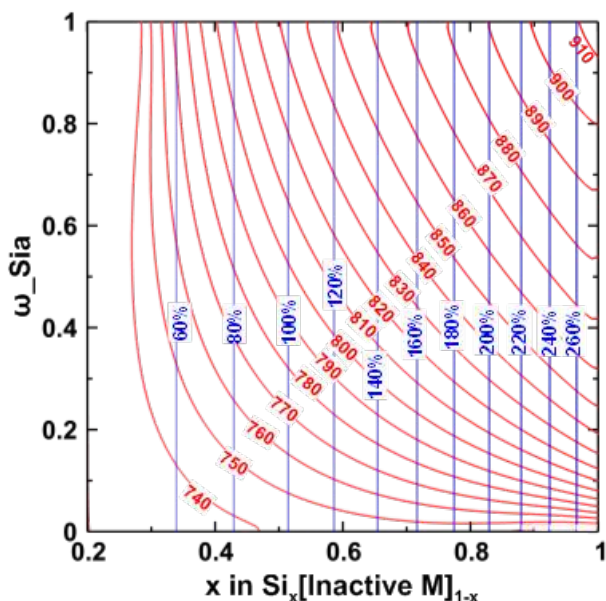


Figure II-72. Contour mapping of cell stack energy density [Wh/L, red lines] and volume expansion ratio [blue lines] of Si alloys. The increment between adjacent red lines is 10 Wh/L and the increment between adjacent blue lines is 20%.

Conclusions

Developing the initial particle size and morphology, as well as surface characteristics, of the silicon that will be compatible to processing and stable during cycling is critical for the program success. To this end, the development of techniques to characterize the silicon materials that allow the dynamics of processing and cycling to be understood is an important first step. Silicon NMR results suggest that very small average particle sizes (<50nm) result in large compositions (up to 40%) of silicon oxide type order that could be significantly detrimental in electrochemical performance. Raman maps and XPS data of cycled electrodes present clear evidence of nonuniformity during cycling associated with processing. NMR and ATR-FTIR studies indicate the selection of slurry solvent in electrode processing plays a major role in the performance of full cell batteries utilizing Si-graphite composite anodes. When completed in water, mixing needed to break up agglomerations of Si can result in additional oxidation. This can be minimized in NMP, but NMP radically changes the surface chemistry of the Si, the consequences of which are not fully understood. A better understanding of how slurry solvents interact with the surface of silicon will be needed to further progress silicon-based electrodes. Partial oxidation of silicon nanoparticles was examined to minimize the interaction of silicon with aqueous slurries. The oxidized silicon nanoparticles demonstrated improved stability in aqueous slurries at elevated temperatures. We also found that with a slightly increased oxide layer thickness to ~3 nm, the initial electrochemical performance was not compromised. Furthermore, an improvement in rate performance and full cell cycle performance can also be achieved.

Electrochemical and analytical studies on baseline cells subjected to 100 cycles and the harvested electrodes indicates extensive SEI formation in the negative electrode (with or without FEC) and Si deposition on the positive electrode (without FEC) were observed. The chemical patterns of these changes were consistent with advanced HF acidolysis of Si/SiO₂ particles. Once water becomes inadvertently introduced into the Si-containing electrode, it continuously cycles through the system, yielding HF acid. This HF acid causes considerable damage to Si particles, while hydrolysis of LiPF₆ keeps on supplying fluoride anions for this cycle. Given that HF plays such pivotal and dramatic roles in this capacity fade, it is noteworthy that a part of the problem is the presence of water in electrodes that are processed from aqueous solutions of polycarboxylate binders. This is especially vexing because it might be impossible to remove all of this matrix-trapped water, as high temperatures are needed to shift the hydration equilibria and release the water from the

hydrates, whereas at such temperatures the residual $-\text{CO}_2\text{H}$ groups in the polycarboxylate binder decompose, releasing more water. If water cannot be removed from the matrix, then using lithium salts that do not hydrolyze and yield HF can be a way to address this problem; however, most of such salts are known to corrode aluminum current collectors; finding alternatives to LiPF_6 , thus, remains a continuing challenge for lithium-ion cells.

The role of interfaces in developing a better understanding of the silicon electrode in a lithium-ion battery configuration by comparing the results of using a polymer coating on the surface and varying the amount of silica. Electrochemical quartz crystal microbalance (EQCM) and CV studies have identified the role of FEC in forming films of varying thickness and the role these films play in impedance and cycling stability. Adding silica as the interfacial phase was found to increase first cycle irreversible capacity as expected and had minimal impact on the samples with denser silica layers. Samples with less dense layers showed a larger benefit from the FEC additive, in terms of increase cycling stability over the first 10 cycles, maximized at 10wt% FEC. Above this amount increased film thickness and lower electrolyte conductivity counteract any benefit of increased amounts.

Electrochemical and analytical studies on materials, electrodes, and cells were utilized to understand capacity losses with silicon anodes. Analysis of coulombic inefficiencies in PAA binder-based Si-graphite full cells identified the importance of using the lithiated binder. FTIR was used to identify SEI reaction products and was shown to be an excellent tool to evaluate the stability of the SEI formed on composite anodes and ultimately improve performance. Three electrode full cells were used to examine electrode shifts with cycling and clearly demonstrated that capacity losses occurred at the anode. Also, the third electrode of lithium was used to replenish the lithium in the full cell, effectively increasing cycle life and suggesting the importance of lithium inventory issues.

An engineering model was developed to study silicon alloy/graphite electrodes. The analysis of silicon containing electrodes indicates that optimum electrode characteristics will be a balance of composition, loading, porosity, and SEI stability. The model should help determine electrode limitations and how best to take advantage of electrode improvements.

Key Publications

1. J. Bareño, I.A. Shkrob, J.A. Gilbert, M. Klett, D.P. Abraham, "Capacity Fade and Its Mitigation in Li-ion Cells with Silicon-Graphite Electrodes", *J. Phys. Chem. C*, Accepted for Publication (2017).
2. M. Klett, J.A. Gilbert, K.Z. Pupek, S.E. Trask, D.P. Abraham, "Layered Oxide, Graphite and Silicon-Graphite Electrodes for Lithium-ion Cells: Effect of Electrolyte Composition and Cycling Windows", *J. Electrochem. Soc.* 164 (2017) A6095.
3. M. Klett, J.A. Gilbert, S.E. Trask, B.J. Polzin, A.N. Jansen, D.W. Dees, D.P. Abraham, "Electrode Behavior RE-Visited: Monitoring Potential Windows, Capacity Loss, and Impedance Changes in $\text{Li}_{1.03}(\text{Ni}_{0.5}\text{Co}_{0.2}\text{Mn}_{0.3})_{0.97}\text{O}_2/\text{Silicon-Graphite Full Cells}$ ", *J. Electrochem. Soc.* 163 (2016) A875.
4. C.D. Malliakas, K. Leung, K.Z. Pupek, I.A. Shkrob, D.P. Abraham, "Spontaneous aggregation of lithium ion coordination polymers in fluorinated electrolytes for high-voltage batteries", *Phys. Chem. Chem. Phys.* 18 (2016) 10846-10849.
5. I.A. Shkrob, J.F. Wishart, D.P. Abraham, "What Makes Fluoroethylene Carbonate Different?", *J. Phys. Chem. C* 119 (2015) 14954.
6. D.P. Abraham, K. Kalaga, S.E. Trask, "Passivation of the Silicon-Graphite negative electrode during Aging of Lithium-ion Full Cells", International Society of Electrochemistry (ISE) Fall meeting, Providence, RI, Aug 28-Sept. 1, 2017.

7. D.P. Abraham, Invited Speaker, "Designing Silicon-containing Lithium-ion Cells", Case Western Reserve University, Cleveland, OH, October 20, 2016.
8. D.P. Abraham, "Electrochemical Diagnostics in the Silicon Deep Dive Program", DOE Program Update, Argonne National Laboratory, October 18, 2016.
9. D.P. Abraham, "A Closer Look at Silicon-Graphite (SiGr) Composite Electrodes During Cycling in NCM523/SiGr Full Cells", Advanced Automotive Battery Conference (AABC 2016), Detroit, MI, June 14-17 2016.
10. D.P. Abraham, "Designing high-energy lithium-ion cells with Si-containing electrodes", Gordon Research Conference on Batteries, Ventura, CA, February 21-26, 2016.
11. "Next Generation Anodes for Lithium-Ion Batteries: Overview," 2017 U.S. Department of Energy Vehicle Technologies Office Annual Merit Review and Peer Evaluation Meeting, June 5-9, 2017, Washington, DC.

References

1. *Alloy Negative Electrodes for Li-Ion Batteries*. M.N. Obrovac and V.L. Chevrier, Chem, Rev. 2014, 114, 11444-11503.
2. B. Key, R. Bhattacharyya, M. Morcrette, V. Seznec, J-M. Tarascon, C. P. Grey, J. Am. Chem. Soc., 2009, 131 (26), pp 9239–9249
3. B. Key, M. Morcrette, J-M. Tarascon, C. P. Grey, J. Am. Chem. Soc., 2011, 133 (3), pp 503–512
4. A. L. Michan, M. Leskes, C. P. Grey, Chem. Mater., 2016, 28 (1), pp 385–398
5. A. L. Michan, D. Divitini, A. J. Pell, M. Leskes, C. Ducati, C. P. Grey, J. Am. Chem. Soc. 2016, 138, 7918–7931
6. A. L. Michan, B. S. Parimalam, M. Leskes, R. N. Kerber, T. Yoon, C. P. Grey, B. L. Lucht, Chem. Mater., 2016
7. *Multinuclear Solid-State Nuclear Magnetic Resonance of Inorganic Materials*, Volume 6, 1st Edition, Authors: Kenneth MacKenzie M.E. Smith
8. S. Xun et al., "The effects of Native Oxide Surface Layer on the Electrochemical Performance of Si Nanoparticle-Based Electrodes", Journal of the Electrochemical Society, 2011, 158(12)
9. S. Xun et al., "Improved Initial Performance of Si Nanoparticles by Surface Oxide Reduction for Lithium-Ion Battery Application", Electrochemical and Solid-State Letters, 2011, 14(5)
10. A. Toudjine et al., "Partially Oxidized Silicon Particles for Stable Aqueous Slurries and Practical Large-Scale Making of Si-Based Electrodes", Journal of the Electrochemical Society, 2015, 162(8)
11. Mawhinney et al., "Ftir Study of the Oxidation of Porous Silicon", Journal of Physical Chemistry B, 1997, 101(5)
12. Sim et al., "Critical Thickness of SiO₂ Coating Layer on Core@Shell Bulk@Nanowire Si Anode Materials for Li-Ion Batteries", Advanced Materials, 2013, 25(6)
13. X. Su, Q. Wu, J. Li, X. Xiao, A. Lott, W. Lu, B. W. Sheldon, Ji Wu Adv. Energy Mater., 4, 1300882 (2014).

14. Roland Jung, Michael Metzger, Dominik Haering, Sophie Solchenbach, Cyril Marino, Nikolaos Tsiouvaras, Christoph Stinner, Hubert A. Gasteiger *Journal of The Electrochemical Society*, 163 (8) A1705-A1716 (2016)
15. Zhijia Du, Hui Liu, S. N. Ellis, R. A. Dunlap, M. Zhu, M. N. Obrovac *Journal of The Electrochemical Society*, 163 (7) A1275-A1279 (2016)
16. Aude A. Hubaud, ZhenZhen Yang, David J. Schroeder, Fulya Dogan, Lynn Trahey, John T. Vaughey *Journal of Power Sources* 282 (2015) 639-644
17. Nguyen, C. C.; Yoon, T.; Seo, D. M.; Guduru, P.; Lucht, B. L., Systematic Investigation of Binders for Silicon Anodes: Interactions of Binder with Silicon Particles and Electrolytes and Effects of Binders on Solid Electrolyte Interphase Formation. *ACS Appl. Mater. Interfaces* **2016**, 8, 12211-12220.
18. Aiken, C. P.; Xia, J.; Wang, D. Y. H.; Stevens, D. A.; Trussler, S.; Dahn, J. R., An Apparatus for the Study of In Situ Gas Evolution in Li-Ion Pouch Cells. *J. Electrochem. Soc.* **2014**, 161, A1548-A1554.
19. Deacon, G. B.; Phillips, R. J., Relationships between the Carbon-Oxygen Stretching Frequencies of Carboxylate Complexes and the Type of Carboxylate Coordination. *Coordin Chem Rev* **1980**, 33, 227-250.
20. Dupre, N.; Moreau, P.; De Vito, E.; Quazuguel, L.; Boniface, M.; Bordes, A.; Rudisch, C.; Bayle-Guillemaud, P.; Guyomard, D., Multiprobe Study of the Solid Electrolyte Interphase on Silicon-Based Electrodes in Full-Cell Configuration. *Chem. Mat.* **2016**, 28, 2557-2572.
21. Bachman, G. B.; Astle, M. J., The Dropping Mercury Electrode in Acetic Acid. I. Discontinuous Current-Voltage Curves. *J. Am. Chem. Soc.* **1942**, 64, 1303-1309.
22. Jung, R.; Metzger, M.; Haering, D.; Solchenbach, S.; Marino, C.; Tsiouvaras, N.; Stinner, C.; Gasteiger, H. A., Consumption of Fluoroethylene Carbonate (FEC) on Si-C Composite Electrodes for Li-Ion Batteries. *J. Electrochem. Soc.* **2016**, 163, A1705-A1716.
23. Obrovac, M. N.; Christensen, L.; Le, D. B.; Dahn, J. R., Alloy Design for Lithium-Ion Battery Anodes. *Journal of The Electrochemical Society* **2007**, 154, A849-A855.
24. Du, Z.; Liu, H.; Ellis, S. N.; Dunlap, R. A.; Zhu, M.; Obrovac, M. N., Electrochemistry of $\text{Cu}_x\text{Si}_{1-x}$ Alloys in Li Cells. *Journal of The Electrochemical Society* **2016**, 163, A1275-A1279.
25. Du, Z.; Dunlap, R. A.; Obrovac, M. N., High Energy Density Calendered Si Alloy/Graphite Anodes. *Journal of The Electrochemical Society* **2014**, 161, A1698-A1705.
26. Obrovac, M. N.; Chevrier, V. L., Alloy Negative Electrodes for Li-Ion Batteries. *Chemical Reviews* **2014**, 114, 11444-11502.
27. Zhao, H.; Yuan, W.; Liu, G., Hierarchical electrode design of high-capacity alloy nanomaterials for lithium-ion batteries. *Nano Today* **2015**, 10, 193-212.
28. Arora, P.; White, R. E.; Doyle, M., Capacity Fade Mechanisms and Side Reactions in Lithium-Ion Batteries. *Journal of The Electrochemical Society* **1998**, 145, 3647-3667.
29. Nie, M.; Abraham, D. P.; Chen, Y.; Bose, A.; Lucht, B. L., Silicon Solid Electrolyte Interphase (SEI) of Lithium Ion Battery Characterized by Microscopy and Spectroscopy. *J. Phys. Chem. C* **2013**, 117, 13403-13412.

II.B.3 Next Generation Anodes for Lithium-Ion Batteries: Materials Advancements (ANL)

Dennis Dees, Principal Investigator

Argonne National Laboratory
9700 South Cass Avenue
Argonne, IL 60439
Phone: 630-252-7349
E-mail: dees@anl.gov

Peter Faguy, Technology Manager

U.S. Department of Energy
Phone: 202-586-1022
E-mail: Peter.Faguy@ee.doe.gov

Start Date: October 1, 2015

End Date: September 30, 2019

Total FY17 Project Cost: \$3,600,000

DOE FY17 share: \$3,600,000

Non-DOE share: \$0

Project Introduction

Silicon has received significant attention as a viable alternative to graphitic carbon as the negative electrode in lithium-ion batteries due to its high capacity and availability [1]. Elemental silicon can theoretically store >3500 mAh/g, nearly an order of magnitude higher than graphite (372 mAh/g and 818 mAh/mL, respectively). However, several problems have been identified that limit its utility including large crystallographic expansion (~320%) upon lithiation which translates to particle cracking, particle isolation, and electrode delamination issues. Further, there are fundamental and volume change related SEI stability issues, which affect cycling efficiency. The wealth of previous studies in this area is both a testament to its potential and the size of the challenge that must be overcome, requiring a great amount of innovation on multiple fronts.

Next Generation Anodes for Lithium-Ion Batteries, also referred to as the Silicon Deep Dive Program, is a five National Laboratory consortium assembled to tackle the barriers associated with development of an advanced lithium-ion negative electrode based upon silicon as the active material. This research program baselines promising silicon materials that can be developed or obtained in quantities sufficient for electrode preparation within the consortium facilities. Composite electrode and full cell development leverages recent investments made by DOE-EERE-VTO in electrode materials and characterization. The primary objective of this program is to understand and eliminate the barriers to implementation of a silicon-based anode in lithium-ion cells. The Labs are focused on a single program with continuous interaction, clear protocols for analysis, and targets for developing both the understanding and cell chemistry associated with advanced negative electrodes for lithium-ion cells. First and foremost, this undertaking is a full electrode/full cell chemistry project leveraging baseline electrodes prepared at the consortium facilities. All efforts are directed to understanding and developing the chemistry needed for advancing silicon-based anodes operating in full cells. Materials development efforts include active material development, binder synthesis, coatings, safety, and electrolyte additives. Efforts include diagnostic research from all partners, which span a wide range of electrochemical, chemical and structural characterization of the system across length- and time-scales. Specialized characterization techniques developed with DOE-EERE-VTO funding, include neutrons, NMR, optical, and X-ray techniques being employed to understand operation and failure mechanisms in silicon-based anodes. In addition, several strategies to mitigate lithium loss are being assessed. The project is managed as a single team effort spanning the Labs, with consensus decisions driving research directions and toward development of high-energy density lithium-ion batteries. A detailed list of participants is given in Figure II-73.



Figure II-73. Program participants including Laboratories, research facilities, and individual contributors.

Objectives

- Understand and overcome the science and technology barriers to the use of silicon-based anodes in high-energy density lithium-ion batteries for transportation applications.
 - Stabilize the SEI
 - Stabilize the electrode
- Demonstrate functional prototype lithium-ion cell chemistries which meet the DOE/USABC performance targets.

Approach

Sandia National Laboratories (SNL), Oak Ridge National Laboratory (ORNL), National Renewable Energy laboratory (NREL), Lawrence Berkeley National Laboratory (LBNL), and Argonne National Laboratory (ANL) have teamed together to form an integrated program. Technical targets have been developed and regular communications have been established. Throughout the program, there is a planned focus on understanding, insights into, and advancement of silicon-based materials, electrodes, and cells. All anode advancements will be verified based on life and performance of full cells. Toward that end, baseline silicon-based materials, electrodes, and cells have been adopted, along with full cell testing protocols.

Supported by the diagnostic studies, materials development on silicon-based materials, electrodes, and cells is being conducted to enhance interfacial stability, accommodate intermetallic volume changes, and improve overall performance and life. Key to this effort is the development and testing of coatings and additives designed to modify and stabilize the dynamic silicon-electrolyte interface. Further, functional polymer binders designed to accommodate volume changes, increase conductivity, and improve adherence are being developed and analyzed. Finally, the program is exploring active material development. Alternative high-energy silicon-alloy/composite materials are being considered. Also, strategies for introducing additional lithium inventory into the cell are being developed.

Communication of programmatic progress to battery community is critical. This will generally be accomplished through publications, presentations, reports, and reviews. Further, the program is open to industrial participation and/or collaboration that does not limit program innovation or the free flow of information. Finally, this program is highly integrated with our sister program on SEI-Stabilization, called SEI-Sta for short. In general, SEI-Sta is focused on the development and characterization of model systems, thin-film well-defined active area electrodes on which it is easier to extract fundamental information on lithium-silicon phase formation, lithium transport, and interfacial phenomena (e.g., SEI formation and growth).

Results

Polymer Binders for Silicon Anodes (ORNL)

A high-performance polymer binder can mitigate the volume expansion stress and maintain the electrical contact with conductive additive and current collector to achieve long-term cycling capacity. Recent progress in the field of polymer binders for silicon-based anode has clearly demonstrated the importance of adhesion strength and mechanical property of the polymeric materials. The graft polymers have been attracting significant attentions due to their efficient control over the structure and the corresponding properties of obtained materials. [2-5] The graft copolymer with chemically distinguished grafted side chains and polymer backbones can retain their desired properties from both polymer components, and enable efficient control of both chemical/physical interaction and mechanical performance, [3, 5] which are extremely important for polymer binder applications. The PAA grafted polyvinylidene fluoride (PVDF) and NaPAA grafted CMC are reported to exhibit improved cycling performance compared with linear analogues, while their architecture effect on polymer binder performance were not investigated due to the limitation of synthetic strategy which do not allow a defined polymer architecture.

To elucidate the architecture effect of synthetic polymers on the polymer binder performance, ORNL team (Saito, Cao) synthesized a novel graft block copolymer with readily tunable architecture parameters such as side chain length and grafting density (Figure II-74) and tested as the polymer binder for the high-mass loading silicon (15wt%)/graphite (73wt%) composite electrode (active materials > 2.5 mg/cm²).

The novel graft copolymer glycol chitosan-g-lithium polyacrylate (GC-g-LiPAA) with GC as backbone and LiPAA as side chains was obtained by amidation reaction and RAFT polymerization (Figure II-74). The (g) signifies grafted. The side chain length and the degree of grafting density were tailored by changing the feed ratio during the reaction. For example, 22.1% of the GC repeating units was functionalized, which corresponds to 88 arms per graft copolymer. RAFT polymerization of acrylic acid from the macro GC22%-RAFT allows the growth of polymer side chains. Followed by neutralization with LiOH, the synthesized GC-g-LiPAA resulted in the GC22%-g-LiPAA62 where 62 represents the chain length and is a measure of the degree of polymerization (DP_n).

The composite electrode with 73% graphite and 15% silicon as the active materials at a loading of active materials > 2.5 mg/cm²; thickness > 30 μm was fabricated. The theoretical specific capacity is calculated to be 875 mAh/g. Moreover, the good water solubility of the obtained graft copolymer GC22%-g-LiPAA62 allows to use water as the solvent. Energy-dispersive X-ray spectroscopy mapping showed the homogenous distribution of silicon and formation of a uniform porous structure.

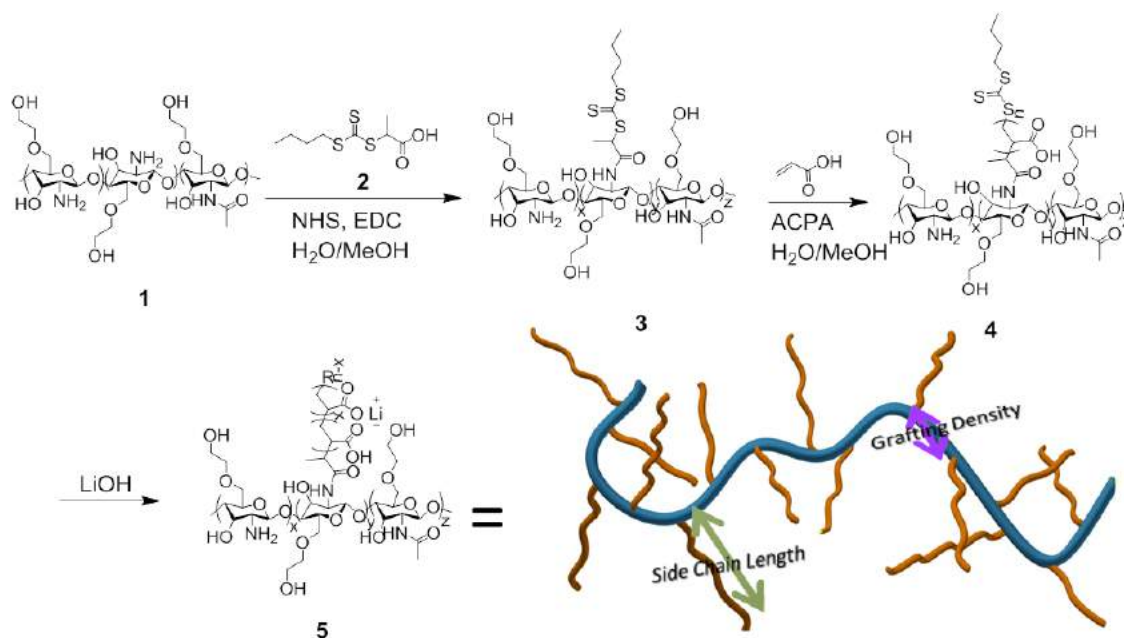


Figure II-74. Synthesis of graft copolymer GC-g-LiPAA via RAFT polymerization.

The architecture effect of synthetic polymer binders on the electrochemical performance of silicon/graphite electrode was investigated by comparing the synthesized graft copolymer with the linear analogues. Pure GC and physical mixture (indicated by “m”) of GC and LiPAA (GC21%-m-LiPAA76) were utilized as the linear analogues for comparison purpose. As illustrated in Figure II-75(A), the electrodes based on PVDF and GC showed acceptable de-lithiation capacities at the first cycle. However, a rapid capacity loss was observed for the subsequent cycles, and only less than 300 mAh/g capacity was retaining, which is mostly contributed by the graphite. Addition of neutralized linear LiPAA to the GC can promote the physical interaction with the silicon materials and provide extra lithium-ion access to mitigate the de-activation of silicon particles. [6-9] As expected, the electrodes with the physical mixture of LiPAA and GC (GC21%-m-LiPAA76) as the binder showed higher initial de-lithiation capacity and better cycling performance (356 mAh/g after 100 cycles) than GC and PVDF. The electrodes with graft copolymer GC22%-g-LiPAA62 showed high initial de-lithiation capacity (745 mAh/g) and significantly improved cycling performance with a de-lithiation capacity of 495 mAh/g after 100 cycles. Moreover, as illustrated in Figure II-75(B), the graft copolymer GC22%-g-LiPAA62 exhibited higher initial coulombic efficiency than its linear analogues (90.3% vs 62.8%, 76.1%, and 88.1%). The interesting phenomenon that worth our attention is the significantly improved cycling performance of GC22%-g-LiPAA62 compared with that of GC21%-m-LiPAA76 in both retaining capacity and coulombic efficiency. With the same chemical composition and functional-group ratio, the significantly improved cycling performance clearly suggests the advantage of a multi-grafted architecture over the physical mixture which may be contributed by the formation of a better interfacial architecture.

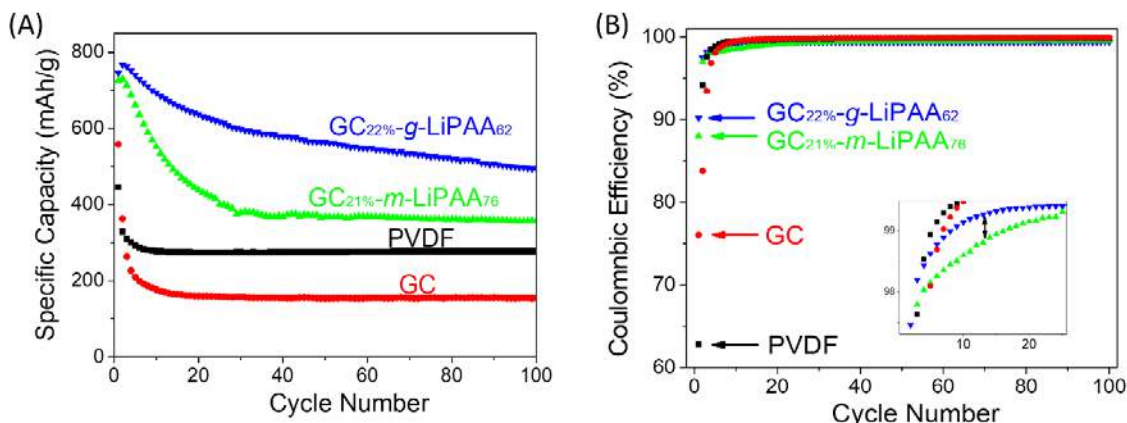


Figure II-75. (A) Cycling performance silicon/graphite electrodes from the polymer binder of PVDF, GC, GC21%-m-LiPAA76 and GC22%-g-LiPAA62 at a current rate of C/10; (B) Coulombic efficiency of the electrodes from different polymer binders, inset is the zoom-in area showing the comparative efficiency of electrodes from GC21%-m-LiPAA76 and GC22%-g-LiPAA62 in the first 30 cycles;

The improved binder performance of graft copolymer GC22%-g-LiPAA62 can be explained as follows. First, the incorporation of numerous LiPAA side chains in the graft copolymer allows more efficient interaction with the SiNPs, which can efficiently prevent the isolation of SiNPs from the surrounding conductive network. The significantly higher peeling force of the electrode made from GC22%-g-LiPAA62 (~ 0.75 N/cm) compared with that from GC22%-m-LiPAA76 (< 0.1 N/cm) confirms improved adhesion strength of GC22%-g-LiPAA62 with the electrode composite. Secondly, the enhanced interaction and extra lithium-ion source should help forming a stable solid electrolyte interphase (SEI) layer on SiNPs. Lastly, the comparative higher solution viscosity of the graft copolymer may also contribute to the formation of a homogenous electrode film due to the reason pointed out above.

The side chain length of grafted copolymer is adjusted by changing the feeding ratio of monomer (acrylic acid) to macro RAFT-CTA (GC22%-RAFT, 4). Significant improvement was observed when the side chain length of GC22%-g-LiPAAx increased from DPn=17 to DPn=27 in terms of both first-cycle de-lithiation capacity and long cycling performance. Comparable initial discharge capacity was obtained when further increasing the side chain length from DPn=27 to DPn=62. In terms of long-term cycling performance, the electrode made of GC22%-g-LiPAA62 showed better performance than that with the GC22%-g-LiPAA27, while this difference is much less significant comparing with that when the DPn of side chain increased from 17 to 27 (See Figure II-76).

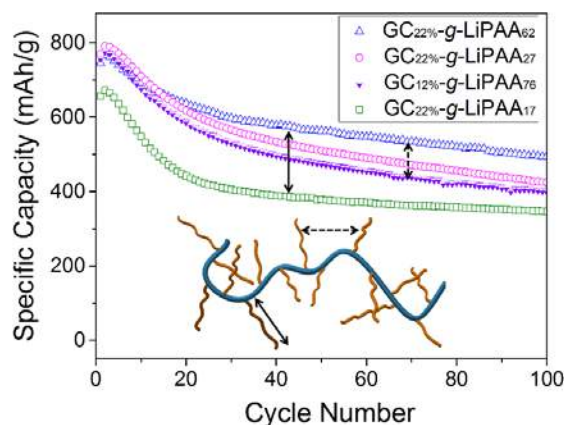


Figure II-76. Cycling performance of silicon/graphite electrodes from the polymer binder of GC22%-g-LiPAA17, GC22%-g-LiPAA27, GC22%-g-LiPAA62, and GC12%-g-LiPAA71 at a current rate of 0.1 C.

The galvanostatic result showed that the electrode with GC12%-g-LiPAA76 exhibited comparable initial delithiation capacity with that from GC22%-g-LiPAA62 (758 mAh/g vs 745 mAh/g) (Figure II-76). However, after 10 cycles, the graft copolymers with higher grafting density start showing the advantage in the long-term cycling performance (67% retaining capacity for GC22%-g-LiPAA62 vs 54% retaining capacity for GC12%-g-LiPAA76 at 100th cycle). The better cycling performance of the graft copolymer with higher grafting density should be mainly attributed to the increased number of anchoring points (88 arms vs 48 arms) that interact with the active material and conduction network. Similar to the explanation above, the higher peeling strength and increased solution viscosity (23.1 mPa.S to 195 mPa.S) suggest that the enhanced interaction of the high grafting-density graft copolymer with electrode composite is responsible for the improved binder performance.

Advanced Polymer Binders

Saito and Cao have designed a cross-linked catechol group functionalized chitosan as the polymer binder for SiNPs-based anode for further improving the adhesion and the mechanical stability. In this project, a nature-derived polymer, chitosan was functionalized by catechol groups (Chitosan-CG) as shown in Figure II-77. Then after mixing the Chitosan-CG with SiNPs and carbon black, different weight percents of glutaraldehyde (GA) was added as the cross-linker. The synthesized polymer binders not only provide strong adhesion to silicon surface by catechol groups, but also resist the deformation of the anode during lithiation/delithiation process by cross-linking.

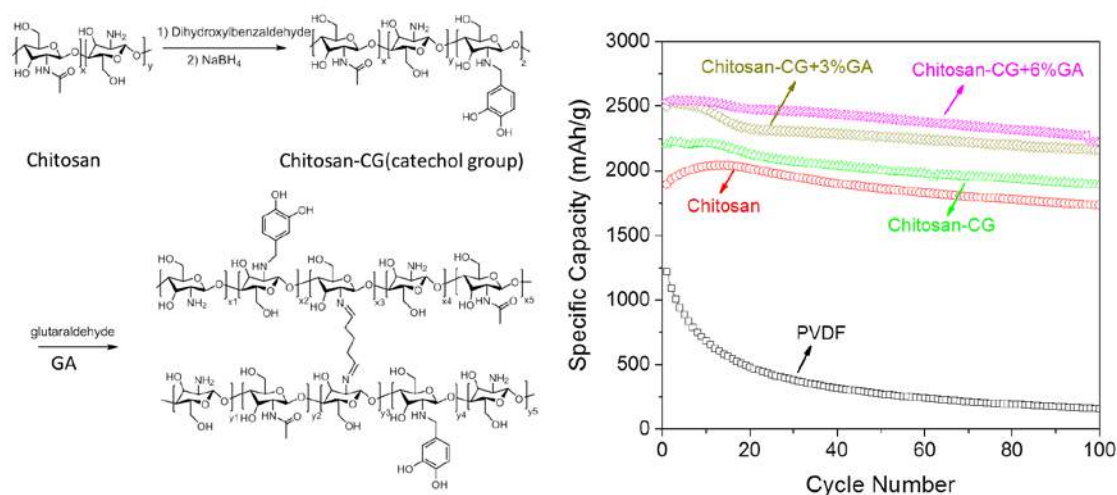


Figure II-77. Synthesis scheme of cross-linked catechol groups functionalized chitosan; cycling performance of different polymer binders. (silicon-based anode: 60% SiNPs, 20% polymer binder and 20% carbon black).

The cycling performance of different polymer binders was shown in Figure II-77. It can be seen that the chitosan showed better cycling performance than typical polymer binder PVDF. After functionalization by catechol groups, the cycling performance of the fabricated anode improved due to the physical interaction of the catechol groups with the SiNPs. In-situ cross-linking will further provide the mechanical robustness of the polymer binders which can resist the deformation of SiNPs during the lithiation and de-lithiation process. Therefore, with 6w% of GA added, the silicon-based anode with Chitosan-CG+6%GC exhibited excellent long-term stability with retaining capacity over 2350 mAh/g after 100 cycles. This is an extremely promising research direction we propose to continue to investigate depending on funding availability in FY18.

Polymer Binder Development for Silicon Anodes (ANL)

A series of new polymeric binders have been developed by utilizing flexible backbones and incorporating hydrophilic groups that could improve the desired properties, and some examples include carboxymethyl cellulose (CMC), alginate, and poly(acrylic acid) (PAA), etc. With some success, many of those binders provided much improved cycling performance for silicon anodes. However, those improvements are still far from enough for practical applications and significant capacity losses were still observed during extended cycling tests. As one of the most important components that directly works with silicon particles, those binders still need significant improvement in terms of physical, electrochemical as well as mechanical properties, including adhesion, cohesion, elasticity, conductivity, electrochemical stability, yield strength, tensile strength, fatigue strength, and crack resistance, etc. There are still many blanks that need to be filled in the binder field. In this project, we are trying to improve the cycling performance of silicon-based anodes by re-engineering the best performing existing binders, such as PAAs.

Crosslinked Poly(acrylic acid) Binders for Silicon Anode

Polymeric materials can be divided into three categories based on their overall structures: linear, branched and crosslinked polymers. And those structures have huge impact on the polymer properties, especially on physical and mechanical properties. Most binders that have been studied are linear polymers, and only a few examples of novel binders have used branched or crosslinked polymers and very little has been done to systematically study the impact of those structural changes on polymer properties and more importantly on cycling performance. [10] Here we proposed and started to develop new polymeric materials by re-design the promising linear polymeric binders into crosslinked structures, hoping to understand the associated property changes and improve the cell cycling performance by pushing those properties to the desired directions. In this report, we used PAAs as the base material and adapted two approaches to crosslink those linear polymers.

To prepare the crosslinked PAA (cPAA) binders, two approaches have been proposed and conducted (See Figure II-78): firstly, commercially available PAA polymers were reacted directly with crosslinkers that have two or more linking groups, such as ethylene glycol diglycidyl ether (EGDGE). The epoxy groups in EGDGE can efficiently react with carboxyl groups at room temperature and form a bridge between two carboxyls. This allows quick screening of the cross-linkers and finding the optimal molar ratios for a better performance. Secondly, acrylic acid (AA) monomers were co-polymerized with the vinyl type cross-linkers, such as poly(ethylene glycol) diacrylate (PEGDA). Reversible Addition-Fragmentation chain Transfer (RAFT) was used to prompt higher molecular weights and low polydispersity index (PDI). This approach has a better control of the crosslinking reaction sites as well as the molecular weights of cPAAs.

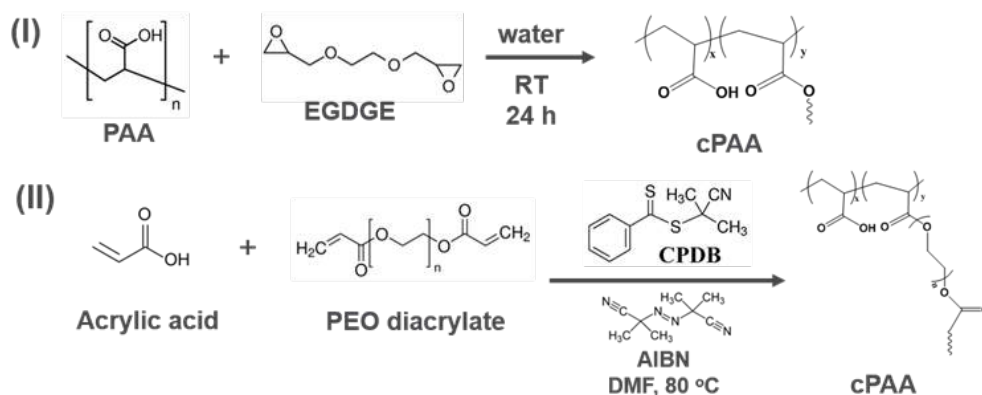


Figure II-78. Approaches for synthesizing crosslinked PAA binders.

For cycling characterization, half cells containing the new developed binders were used. Two types of silicon electrodes were used to evaluate those binders in this report, including silicon/graphite composite electrode, which contains 15% silicon particles, and high capacity silicon electrode, which contains 70% silicon particles.

Five cPAAs have been synthesized and their characterization results are summarized in Table II-6. Two binders, cPAA1 and cPAA2, were synthesized via approach I, and a PAA polymer with number average molecular weight (M_n) around 30 k were used as the precursor to react with EGDEG crosslinkers at different concentrations. By design, if crosslinking happened, a much increased M_n for cPAA1 and cPAA2 should be expected. However, we were surprised to see that cPAA1 and cPAA2 demonstrated very similar M_n values, which is also close to that of the precursor PAA polymer. This unexpected result may indicate that the crosslinking reaction didn't occur as hoped to bridge two PAA chains but rather connect two carboxyl groups from a single PAA chain, leading to no crosslinking but intramolecular bridging. In that case, the more crosslinker added, the more constrained conformation should be expected considering more intramolecular bridges formed. The two cPAAs were evaluated in half cells and the specific capacity profiles are compiled in Figure II-79. As shown in the left, for silicon/graphite composite electrode, cPAA1 seems to work well and affords comparable cycling performance to that of PAA cells but no obvious improvement was observed either. The cell containing cPAA2, on the other hand, delivered much worse initial capacity as well as capacity retention (see Table II-6). The results actually are supporting our speculation on the intramolecular crosslinking reactions. With low content of EGDEG, as those crosslinkers were attached to each individual PAA chain but no crosslinking between different chains occurred, cPAA1 should still behave very much the same as linear PAAs. For cPAA2, the higher content of EGDEG may lead to more constrained conformation by those intramolecular linking, which may account for the much worse performance. However, this conformation change is a good new for high capacity silicon anodes. As shown in the Figure II-79(right), for the high capacity silicon anode test, the cPAA2 binder delivered much better initial capacity and capacity retention compared to those of linear PAA cells. We suspected that the conformation changes may lead to better adhesion of cPAA2 binder to silicon particles, accounting for the improved cycling performance.

Overall, approach I could produce cPAAs in a very efficient way but due to the abundant carboxylic acid groups, there is very little control of the crosslinking sites on PAA polymers and therefore the majority of crosslinkers only attached to each PAA chains by linking adjacent carboxyl groups instead of bridging different chains. A better control of the crosslinking reactions should be needed.

Table II-6: Summary of synthesized cPAAs.

Approach	Polymer	Crosslinker ^a	Crosslinker % ^b	DP ^c	Mn ^d	PDI	Initial capacity (mAh/g)	Capacity retention
I	cPAA1	EGDEG	0.01%	404	34.3 K	2.66	722	39%
	cPAA2	EGDEG	0.1%	404	38.3 K	2.36	474	31%
II	cPAA3	PEGDA1	0.05 %	690	50.3 K	1.50	704	28%
	cPAA4	PEGDA2	0.2 %	631	44.1 K	1.77	751	76%
	cPAA5	PEGDA2	0.1 %	736	64.8 K	1.45		

- The number average molecular weights (Mn) of PEGDA1 and PEGDA2 are 8,000 and 250 Da, respectively.
- This value is the weight percentage of the crosslinkers to the PAA polymers.
- DP (degree of polymerization) is the number of repeating units of the polymer.
- Mn is the number average molecular weight of the methylated crosslinked PAA, characterized by gel permeation chromatography (GPC).

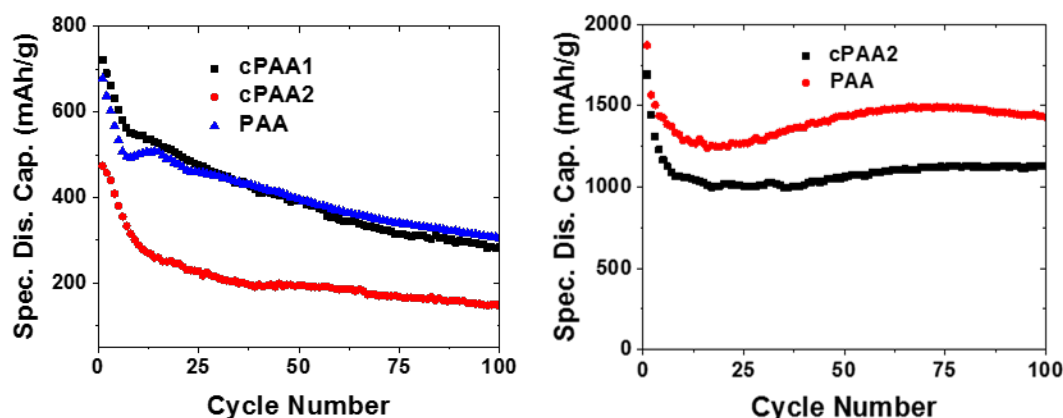


Figure II-79. Specific discharge capacities of half cells of (left) silicon/graphite composite electrodes (15% silicon) and (right) high capacity silicon electrodes (70% silicon) using PAA-based binders during the course of 100 cycles under C/3 rate.

Approach II was proposed to produce cPAAs by co-polymering the monomers and crosslinker molecules. cPAA3, cPAA4, and cPAA5 were synthesized by heating the mixture of acrylic acid (AA), 2-cyano-2-propyl benzodithioate (CPDB, RAFT agent), azobisisobutyronitrile (AIBN, initiator) as well as poly(ethylene glycol) diacrylate (PEGDA, crosslinker). The RAFT agents (CPDB) help to control the molecular weight and polydispersity (PDI) of the produced polymers. Since the crosslinking reactions occurs as the chain grows, there should be a good chance for the crosslinkers to bridge two chains instead of growing on the same chain. Two PEGDA (PEGDA1, 8000 Da and PEGDA2 250 Da) were used in the synthesis. As shown in Table II-6, all three polymers were produced with reasonable PDI values. The different percentage of crosslinker doesn't seem to impact the overall molecular weights very much and all three cPAAs have similar Mn values. Figure II-80 plots the specific capacity as a function of cycle numbers for the half cells containing cPAA3, cPAA4 and liner PAA binders. The cycling test of cPAA5 is ongoing. For silicon/graphite composite electrodes, cPAA3 cell delivered reasonable initial capacity but worst capacity retention, possibly due to the large Mn of the crosslinker used. On the other hand, cPAA4 binder demonstrated a strikingly attractive cycling performance with the highest initial capacity and capacity retention values among the results of this report.

Even though the cycling was not complete and only at 86th cycles, the 76% capacity retention still puts cPAA4 among the most promising binders that have ever been reported for silicon/graphite composite electrodes. Currently, more detailed study regarding further optimizing the crosslinker content as well as electrode loading is ongoing. As shown in Figure II-80(right), cPAA4 also demonstrated improved cycling performance for the high capacity silicon electrode, where better initial capacity and capacity retention were observed.

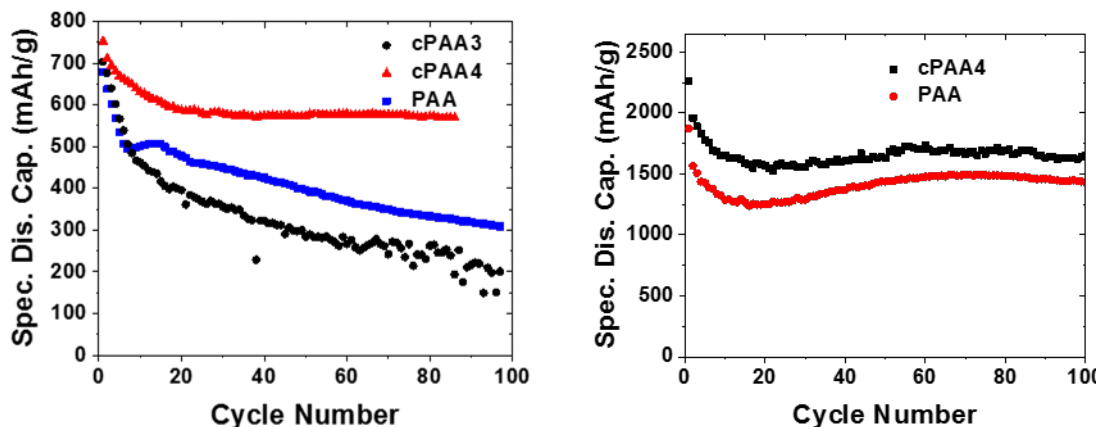


Figure II-80. Specific discharge capacities of half cells of (left) silicon/graphite composite electrodes and (right) high capacity silicon electrodes using PAA-based binders during the course of 100 cycles under C/3 rate.

Engineered Stiff PAA Based Binders for Silicon Anode

As the most promising silicon binder, PAAs offer attractive properties, such as good aqueous and nonaqueous solubility, excellent chemical stability, tunable acidity for improved adhesion, etc. However, as one kind of soft polymers, PAA-based binders often suffer performance degradation possibly due to the related weak mechanical properties. Here we report a new family of PAA-based binders, poly(4-vinylbenzoic acid) (P4VBA) (see Figure II-81), by introducing stiffness enhancing moieties into PAA structures. P4VBA binders have an extra benzene ring in the repeating units compared to those of PAAs, and it is believed that such modification should lead to enhancements of the mechanical properties. [11]

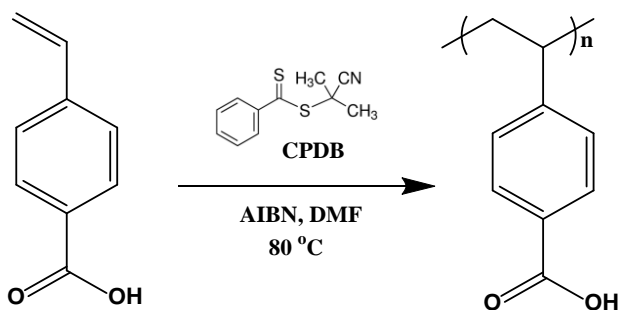


Figure II-81. Synthetic route for P4VBA binders.

P4VBA binders are not commercially available and have been synthesized using reversible addition-fragmentation chain-transfer (RAFT) polymerization method, which can afford good control of the molecular weight of the synthesized polymers.

For cycling characterization, half cells containing silicon/graphite composite electrode were used to evaluate the new developed binders, which contains 73 wt% graphite flakes, 15 wt% silicon particles, 2 wt% C45 and 10 wt% binder. The slurry was processed using water or N-Methyl-2-pyrrolidone (NMP) solvent.

P4VBA binders were synthesized by polymerization of 4-vinylbenzoic acid monomers, which contain not only all the functionality of PAAs, such as flexible poly(ethylene) backbone and pendant carboxyl groups but also have an additional benzene ring in the repeating units, which is believed to prompt the mechanical properties, such as yield strength, tensile strength, fatigue strength, and crack resistance, etc. Two P4VBA binders with different number average molecular weights (M_n) have been synthesized and their characterization results are summarized in Table II-7. By using RAFT method and controlling reaction time, we can control the molecular weight of the synthesized polymers. The M_n of P4VBA1 is controlled at lower range at 7.4 K while P4VBA2 is at 55.4K. To fairly compare the performance, two PAA binders with similar degree of polymerization (DP) were used as control materials. P4VBA binders are soluble in NMP but not in water, therefore NMP was used to prepare the slurry. NMP and water were both used to prepare the slurries of PAA binders.

Table II-7: Summary of P4VBA and PAA binders cycled.

Polymer	DP ^a	M_n^b	PDI	Initial Capacity (mAh/g)	Capacity Retention
P4VBA1	46	7.4 K	1.31	648	40%
P4VBA2	342	55.4 K	2.37	786	36%
PAA1	42	3.6 K	1.89	603	41%
PAA2	338	29.1 K	3.11	676	32%

(a) DP (degree of polymerization) is the number of repeating units of the polymer.

(b) M_n is the number average molecular weight of the methylated crosslinked PAA, characterized by gel permeation chromatography (GPC).

As shown in Figure II-82, specific capacity profiles of cells using P4VBA and PAA binders were compiled. For those low DP binders shown in the left, the cycling performance of the cell containing P4VBA is very similar to that of the cell fabricated using PAA1 water solutions. But for the cell that used PAA1 solution in NMP, the cycling was actually worse. For the high DP materials shown in the right, the P4VBA2 cell showed significant improvement over the cell of PAA2 (water) in terms of initial capacity and capacity retention. On the other hand, the cycling performance of the PAA2 (NMP) cell was much worse.

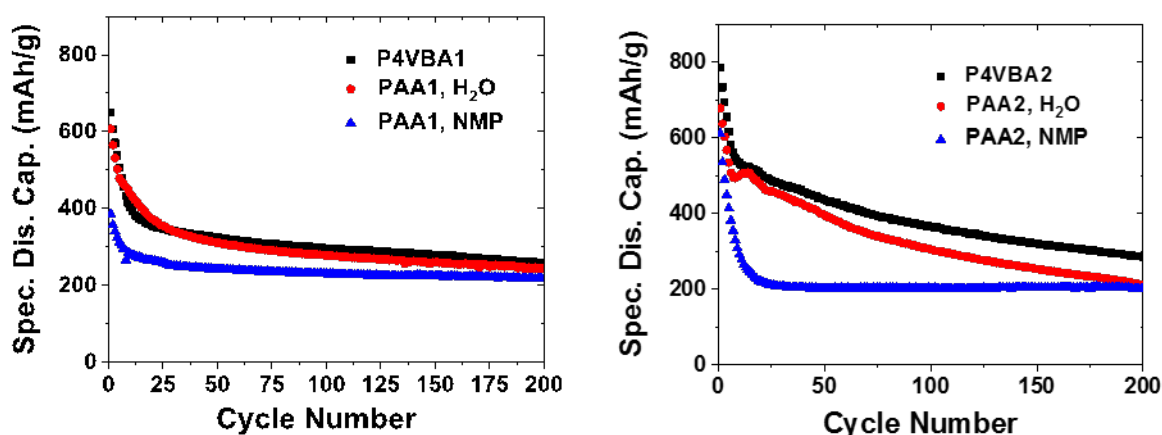


Figure II-82. Specific capacity profiles of cells containing P4VBA and PAA binders.

Development of Binary Polymeric Binder Systems Capable of in-situ Crosslinking

We are working on development of binary polymeric systems able to in-situ crosslinking during the process of electrode laminate manufacturing. The two components of the system need to be stable and non-reactive during aqueous slurry preparation process to allow for casting but should undergo rapid thermally induced crosslinking during laminate drying. The selection of proper components for the binary system needs to take

under consideration several criteria required for binder for LIBs electrode. The components of the binary system need to be soluble or forming stable emulsion in water, the cross-linked polymer needs to be chemically compatible with electrolyte and other electrode materials and electrochemically stable during cycling of the batteries. The polymer needs to be characterized by good adhesion to the current collector and good cohesion between particles of the composite anode.

The intra- and extra-molecular crosslinking will result in a flexible 3D mesh holding silicon and graphite particles together preventing loss of electrical contact and mechanical degradation of the electrode during cycling. Interaction of the backbone polymer with Si surface may further strengthen the structure and improve performance (Figure II-83).

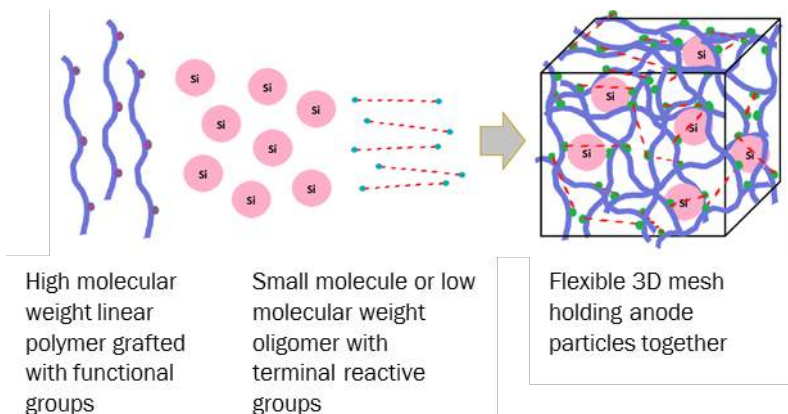


Figure II-83. In situ formation of 3D mesh from polymer and reactive small molecules.

We selected commercially available poly(ethylene-alt-maleic anhydride), $M_w = 100 - 500$ kD and poly(methyl vinyl ether-alt-maleic anhydride), $M_w = 216$ kD as a starting material for synthesis of backbone polymers (Figure II-84). The anhydride moiety in the starting materials were hydrolyzed to the corresponding poly(acid) co-polymer ($R = H, OCH_3$) (Figure II-85). The acids were used in a series of “proof-of-concept” experiments to investigate in-situ cross linking (Figure II-86).

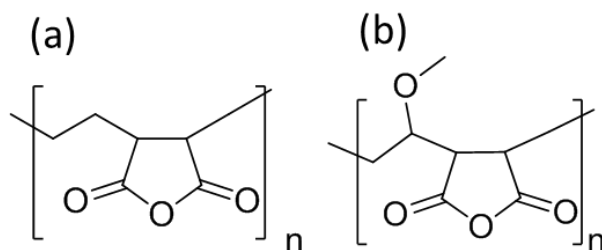


Figure II-84. (a) poly(ethylene-alt-maleic anhydride) and (b) poly(methyl vinyl ether-alt-maleic anhydride).

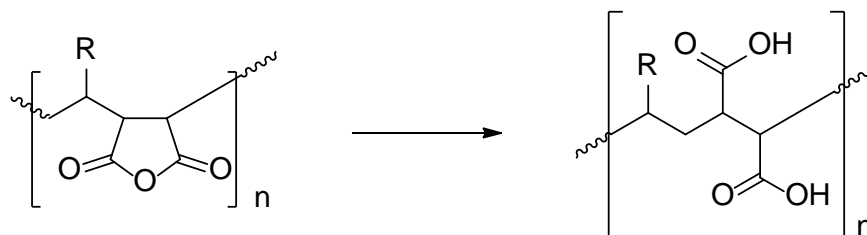


Figure II-85. Hydrolysis of poly(anhydride) to poly(acid).

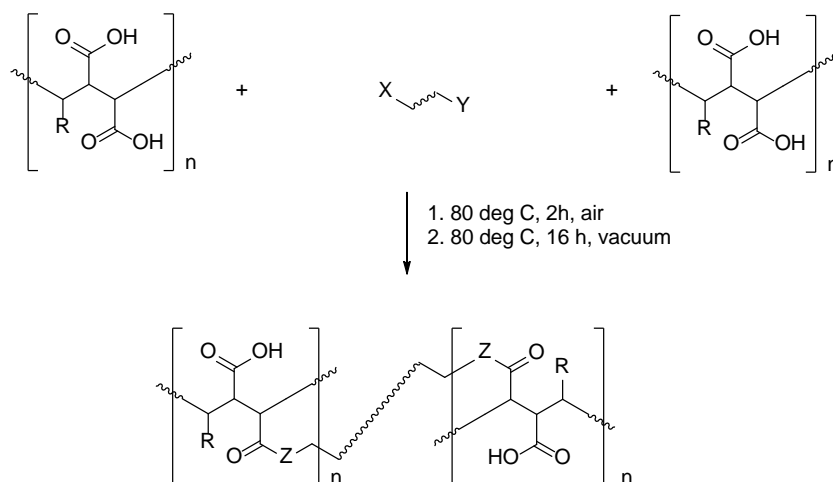


Figure II-86. General scheme of in-situ crosslinking of poly(R=H or OCH₃-alt-maleic acid) and small molecule, 80:20 (X, Y = OH or NH₂, Z = O or NH).

The following small molecule linker were used in the experiments: triethylene glycol, PEG400, PEG1000, 1,4-butanediol, and 4-aminobutan-1-ol. FTIR analyses of the resulting materials revealed, in each case, formation of the expected crosslinks as evident by presence of ester or/and amide bonds. Small amount of anhydride in the product was also observed.

We also synthesized a series of poly(R=H or OCH₃-alt-maleic acid) derivatives that possess capability of intra- and intramolecular crosslinking via condensation reaction. An example of a synthesis of the linear polymer and self-crosslinking product is represented on Figure II-87. The following linear polymer derivatives were synthesized: poly(ethylene-alt-maleic anhydride) with ammonia (1:1 mol/mol), poly(ethylene-alt-maleic anhydride) with 6-aminohexan-1-ol (1:1 mol/mol), poly(ethylene-alt-maleic anhydride) with 6-aminohexan-1-ol and ammonia (1:0.05:0.95 mol/mol), poly(methyl vinyl ether-alt-maleic anhydride) with 4-butan-1-ol and ammonia (1:0.1:0.9 mol/mol).

Investigation and Development of Aqueous Based Polymer Binders (LBNL)

This work is part of the polymer binder group research on understanding and developing new polymer binders for Si-based materials. This is a first year of a multi-year project to develop aqueous-based emulsion binders for Si-based materials. This year work is on investigation of the stability of the conductive polymer binders, synthetically introducing new anthracene-based conductive moiety to the methacrylate backbone, and decipher the formulation of aqueous-based emulsion of Si-based electrode systems.

Characterization of the stability of the Polymethacrylatepyrene (PPy) type of binders in Si composite electrode

PPy type of conductive polymer binder and Si graphite materials are fabricated into composite electrode based on ANL baseline composition. The performance characteristics of the electrode are compared with the ANL baseline performance. At C/10 rate, the cycling of PPY-based electrode is very stable and at theoretical gravimetric capacity. The analysis of the electrode after cycling demonstrate the both chemical and electrochemical stability of the PPY binder. Although the electrode is extensively washed after the cycle test by DMC, the FTIR spectra shows the stable PPY binder on the surface of the composite electrode (Figure II-88). The electrode also has similar adhesion strength before and after the electrochemical test, demonstrating the superb adhesion properties of the PPY binder materials [\[12\]](#).

Synthesis of a group of conductive polymer binder and test its performance.

After confirmed the stability of the PPY binder, a series of conductive polymer binders based on methacrylate polymer backbone is synthesized to demonstrate the versatility of this side chain conducting mechanism, and

its utilization as a binder in the Si-based electrode. We have developed two new polymer binder materials, of anthracene methyloxide side chains homopolymer – P(Ant), and its copolymer with triethyleneoxide methylether P(Ant_{0.7}-co-TEG_{0.3}) (Figure II-89). Anthracene has delocalized pi bonds, similar to the pyrene structure. The polymer molecular weight is around 20K with a PDI of 2.2, which are similar the PPY binder developed previously in our lab. The P(Ant) binder is combined with Si nanoparticle to formulate into electrode, shown in Figure II-90. As demonstrated in the binder testing with the Si materials, the P(Ant) conductive polymer binder works effectively as both binder and conductive agent for the Si electrode.

Si electrode fabrication based on aqueous-based SBR binder, and investigation of its performance.

SBR water emulsion is used as aqueous-based binder for the Si and graphite composite electrode. We are using the commercial SBR and CMC to develop Si and graphite-based electrode, and testing the electrode performance. The goal of this effort is to gain experience of fabrication of the electrode based on the aqueous emulsion system. As demonstrated in Figure II-91, the electrode capacity is consistent across 3 cells, and the cycling is stable at C/3 cycling in the first 30 cycles. The first cycle efficiency is also very consistent among all 3 cells.

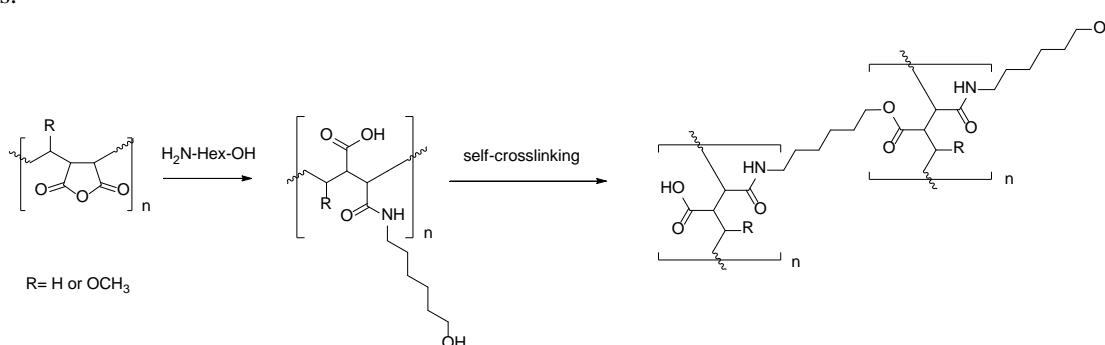


Figure II-87. An example of a synthesis of the linear polymer and self-crosslinking product.

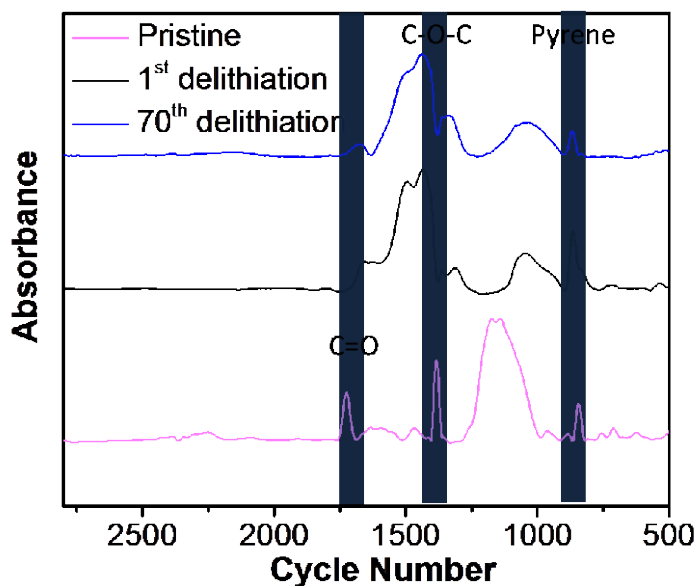


Figure II-88. Fourier transform infrared (FTIR) spectra of the PPY-based pristine and delithiated electrodes.

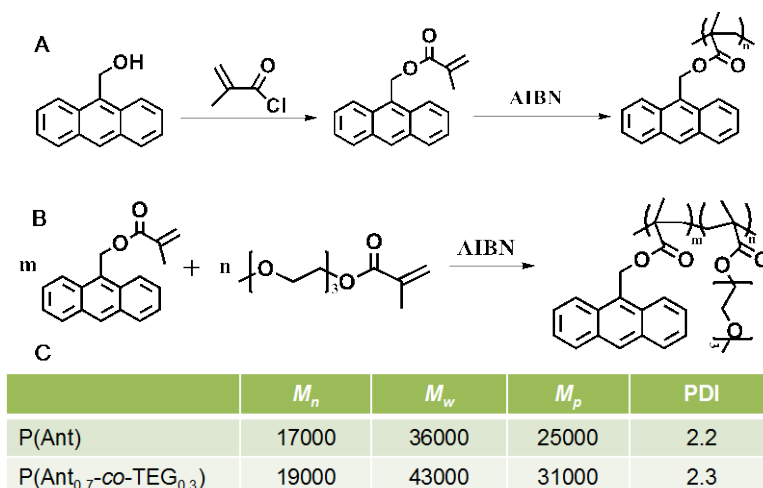


Figure II-89. Synthesis of anthracene-based polymers. A. anthracenemethyleneoxide methacrylate polymer – P(Ant). B. Copolymer with Triethyleneoxide - P(Ant_{0.7}-co-TEG_{0.3}). Molecular weights and polydispersity (PDI) of the P(Ant) and P(Ant_{0.7}-co-TEG_{0.3}) polymers.

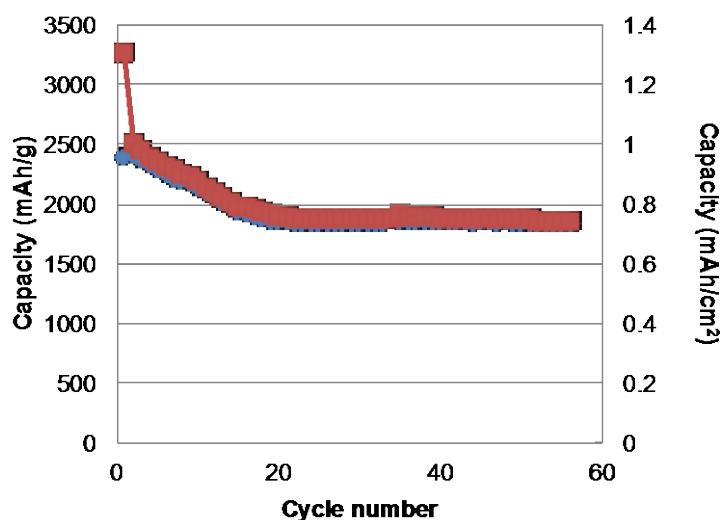
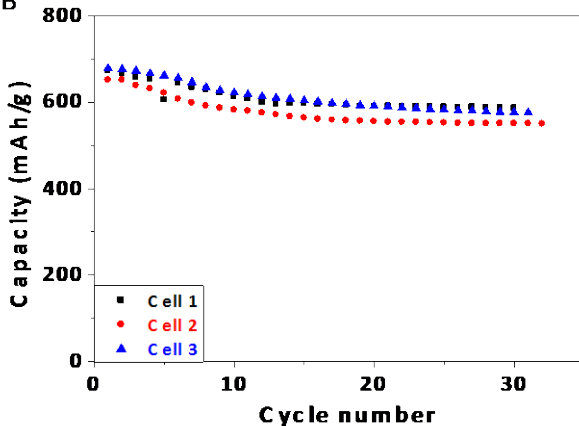


Figure II-90. Si nanoparticle cycling with the P(Ant) binder. (Electrode composition is 90% nano Si particles, and 10% binder, 0.4 mg/cm² of Si materials, cycling rate C/10).

A

Electrode: magE/nanoSi/C45/CMC/SBR = 90/10/2.5/3/2.4	Mass Loading (mg/cm ²)	Thickness (μm)	1 st Cycle Efficiency
Cell 1	2.60	30	0.890
Cell 2	2.85	33	0.894
Cell 3	2.63	27	0.905

B



C

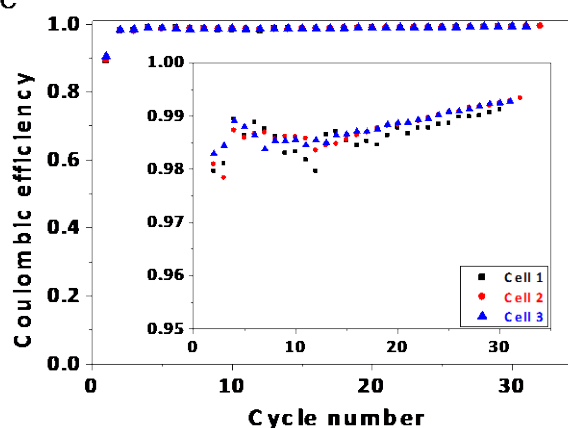


Figure II-91. Si nanoparticle and graphite composite electrode cycling with commercial SBR binder. A. Electrode composition and the mass loading of 3 cells made of the same laminate against Li metal electrode. B. Cycling performance of 3 cells at C/3 rate. C. The coulombic efficiencies of the cells.

All the synthesized polymer are investigated for physicochemical properties required for a binder. Selected materials will be used to manufacture composite silicon (Paraclete Energy, nSiO and SM-Silicon™ powders)/graphite electrode.

Silicon Surface Modification Using Molecular Layer Deposition (NREL)

The overall goal of this project is to develop sustainable high-energy density of Si-based nanocomposite electrodes for use in vehicular applications. In this work, surface modifications, which chemically or physically change the surface of electrode components, has been applied to improve the interphase chemistry, conductivity, and mechanical integration in Si-based electrodes. It is the nanostructured architecture that greatly increases the overall capacity; however, decreasing the particle size also increases both the surface area and electrolyte-reduction reactions resulting in the formation of solid-electrolyte-interphase (SEI) layer and the associated irreversible loss of Li. Surface modifications on both active particles and laminated electrodes have the capability to modify the solid-electrolyte-interphase (SEI) through the control of composition, thickness and mechanical properties.

Unlike other electrode materials, Si particles are covered by an insulating oxide layer, but also suffer from the morphological changes during Li cycling. Therefore, besides the requirement for the chemical stability, a functional coating is required with the control of thickness and mechanical properties. Molecular layer deposition (MLD) will be used to produce a conformal surface coating composed of an elastic aluminum alkoxide polymer with a tunable elastic modulus and chemical reactivity, depending on composition. Based on low-temperature, sequential and self-limiting surface reactions, MLD can also apply to the laminate electrodes (summarized in FY16) and the particles (FY17 focus area), resulting in conformal coatings with atomic-level control of film thickness while maintaining the electrode architecture and inter-particle electronic path.

ALD technique has proven itself to be the *best method to deposit continuous, conformal and pinhole-free films*. Our recent work has proven ALD as an important tool in mitigate the parasitic side reactions between the liquid electrolyte and electrode surface, leading to the improved performance of LIBs electrodes. But the rigid inorganic coatings, such as Al_2O_3 coating, are not robust enough to provide structural support when applied to large-volume-expansion materials such as Si. In order to address the challenge of Si's dramatic volumetric change, NREL have utilized MLD to grow a mechanically robust, flexible coating as a surface modification for high capacity Si nanocomposite anodes. Based on the similar mechanism of ALD, MLD method allows for the integrating the organic fragments into metal oxide matrix, leading to the formation of hybrid organic-inorganic materials. The thin, conformal, and flexible MLD coating is able to penetrate the electrode's porous structure and covalently bind to available surfaces. This creates a strong, flexible network within the electrode that binds the materials and ensures sufficient contact area throughout cycling.

Addition of 15 wt.% of Si into the graphite-based electrode results in the increase of specific capacity from 372 mAh/g to 918 mAh/g, and improved Coulombic efficiency (CE). This is an eclectic approach as the electrode solely made of Si particles rapidly fails due to the enormous volume changes of Si with lithiation. FY17, the research has been focused on demonstration of the composite electrodes, comprised of the graphite and the silicon particles. Both NanoAmor Si particles and Alfa Si particles were used to identify the coating effects on the electrochemical properties. Different from the previous study, poly acrylic acid has been used as the polymer binder additive—instead of polyvinylidene fluoride used in FY16—to enhance the mechanical integrity, increase the mass loading thereby improve the area capacity. This research elucidates the important role of the surface modification in stabilizing the cycling performance, but also shed light on the interaction between the graphite and the Si particles.

Molecular Layer Deposition

Aluminum alkoxide (AIGL) films were grown directly on the particles or the laminated electrodes using trimethylaluminum and glycerol precursors at 180°C for the particles, and at 150 °C for the particles. The typical growth rate for the AIGL chemistry is 2.5 Å per cycle. The typical AIGL reaction sequence was: i) Dose trimethylaluminum for 2 seconds, ii) hold trimethylaluminum pressure static for 90 seconds, iii) flow purge for 180 seconds, iv) 5 cycles of argon static purge, v) dose glycerol for 2 seconds, vi) hold glycerol pressure static for 120 seconds, vii) flow purge for 240 seconds, viii) 7 cycles of argon static purge. Flow purge is performed by pumping out excess precursors and reaction byproducts while flowing argon through the reactor. Argon static purge is performed by dosing argon for 20 seconds, holding argon pressure static for 5 seconds, pumping for 45 seconds, and flow purging for 20 seconds. This sequence constitutes of one AB cycle of AIGL. The electrodes were coated with 10 cycles of AIGL. Pulse dosing was also used to enhance the completion of the reactions, see details in the result section.

Preparation of electrodes and coin cells

Standard types of 2032 half coin cells with Li metal foil as counter electrodes were prepared for these experiments. The anode mixture was composed of Si, graphite, carbon black and poly acrylic acid (PAA) binder with a wt.% ratio of 15%-73%-2%-10%, and mixed with using 1-methyl-2-pyrrolidinone (NMP) solution. The mixture was coated on Cu foil and then dried under air. Before assembling the cells the 1.4 cm punched electrodes were dried overnight (120°C) in a vacuum oven. 1.2 M LiPF_6 in ethylene carbonate, diethyl carbonate (3:7 wt%) and fluoroethylene carbonate (10%) was used as the electrolyte. Cells were assembled in an Ar filled glove box and tested at room temperature. Constant current (CC) is applied during discharge and charge between the voltage range of 0.01 V and 1.0 V.

Development of the MLD alucone coating for silicon particles

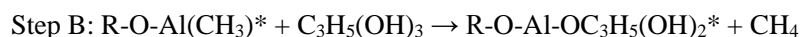
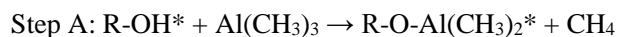
The research in FY16 was directed towards understanding the impact of MLD coating on the various electrodes made of different Si particles and binders. Significantly improvements have been achieved for the Si electrode (made of 60 wt.% 50nm Si from Alfa, 20 wt.% PVDF and 20 wt.% carbon black) coated with MLD aluminum glycerol (AIGL) ultrathin film. Then, the same MLD coating chemistry has been applied to the electrodes made with the functional binders, including lithiated polyacrylic acid (LiPAA) and carboxymethyl

cellulose (CMC). Both binders were believed to have the chemical interaction with the surface of Si particles, resulting in enhanced mechanical integrity, thus improved cycling reversibility. The Si-LiPAA electrode provided by CAMP is consisted of 15 wt.% Si (50-70nm from NanoAmor), 73 wt.% Hitachi Mag-E graphite and the LiPAA binder. The Si-CMC electrode is made here with 60 wt.% Si (50nm from Alfa), 20 wt.% carbon black and 20 wt.% CMC binder. Surprisingly, cycling behavior of MLD coated electrodes shows no difference compared with the uncoated electrodes. Note that both binders have the strong chemical interaction with the surface of silicon particles. Therefore, the surface of silicon particles has been already covered/modified by the functional binders, which blocks the direct contact and prevents the reactions between MLD precursors and the Si particles. It is believed that the interaction between the binders and Si particles negates the coating effects. Therefore, in FY17, we have modified the MLD coating technology to coat both particles and the laminated electrodes. The coated particles can be used to make electrodes with different functional binders.

Si particles (70-130 nm) from NanoAmor AIGL were selected as our new baseline material, because Si particles (30-50nm, NanoAmor) were discontinued. Then, the Si particles from both Alfa (50nm) and NanoAmor (70-130nm) have been coated with MLD AIGL chemistry. The films were grown on nano-Si powder in an ALD fluidized bed reactor. Si particles were heated to 180°C and dried under a low-pressure nitrogen flow. The pressure drop across the powder bed was determined at various nitrogen gas flow rates in order to determine an appropriate gas flow rate for fluidizing the powder. The AIGL reaction sequence was the following: i) dose TMA until the mass spectrometer indicates saturation of the TMA surface reaction; ii) purge with nitrogen; iii) dose glycerol until the mass spectrometer indicates saturation of the TMA surface reaction; iv) purge with nitrogen. This sequence constitutes of one cycle of the AIGL MLD process. The growth rate is $\sim 2.3\text{\AA}$ per cycle. 10 MLD cycles were applied to Si nanoparticles from Alfa, while 5 MLD cycles were performed for NanoAmor Si particles.

Real time residual gas analyzer mass spectrometry has been equipped into the MLD process, in order to measure the composition of the gas flow. The changes in composition of the gas flow can be used to determine the completion of MLD reactions.

TMA ($\text{Al}(\text{CH}_3)_3$) and glycerol ($\text{C}_3\text{H}_5(\text{OH})_3$) were used as precursors to form aluminum glycerol (AIGL)16 coating and the reactions are as follow:



where asterisks indicate surface species and R represents the Si. Mass spectrometer was used to monitor the reaction process and determine the completion of the reaction. Figure II-92 exhibits the intensity of the residue gas as a function of reaction time. The cumulative intensity of the product (hydrocarbon, m/z 15, methane) was observed along the TMA dose and glycerol dose. During either TMA or glycerol doses, the intensity of methane keep increasing linearly with time. After couple TMA/glycerol doses, the intensity of the product starts decreasing, while the excess TMA/glycerol was observed in the gas flow. It indicates the completion of the half-cycle reaction.

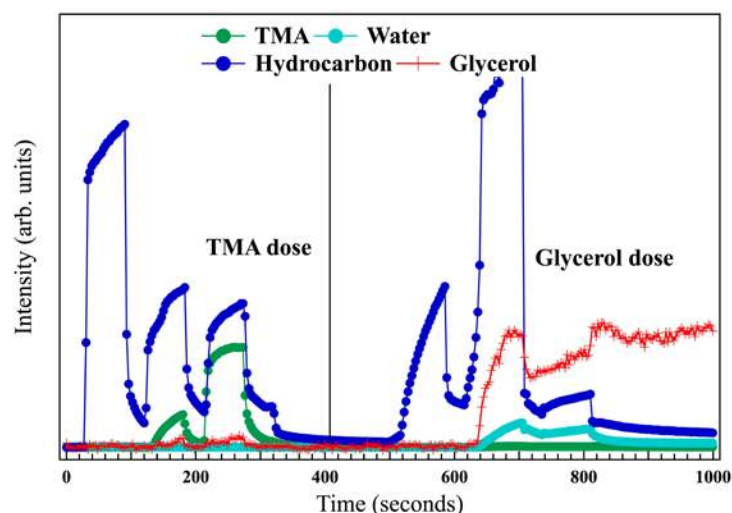


Figure II-92. Mass spectra of one MLD cycle including TMA and glycerol doses. Pulse dosing was used for both precursors to enhance the reactions.

Si particles from NanoAmor show quite different morphology compared with the particles purchased from Alfa. Figure II-93a and Figure II-94 a-c show the morphology of the as-received particles. The particles from Alfa have uniform and spherical morphology, however, the particles from NanoAmor have irregular shaped morphology. After MLD coating, uniform coating with a thickness of ~5nm has been successfully obtained for the Alfa Si particles. In contrary, it is hard to identify the coating layer for the NanoAmor particles. We expect that the ball milling process—used in NanoAmor sample preparation—results in surface amorphization. It causes the difficulty to identify the coating layer after MLD reaction, as displayed in Figure II-94 (d-f). Besides, the high content oxide and organic impurities were expected for the NanoAmor silicon particles—reported by other team members. The impurities can limit the growth of MLD coating materials.

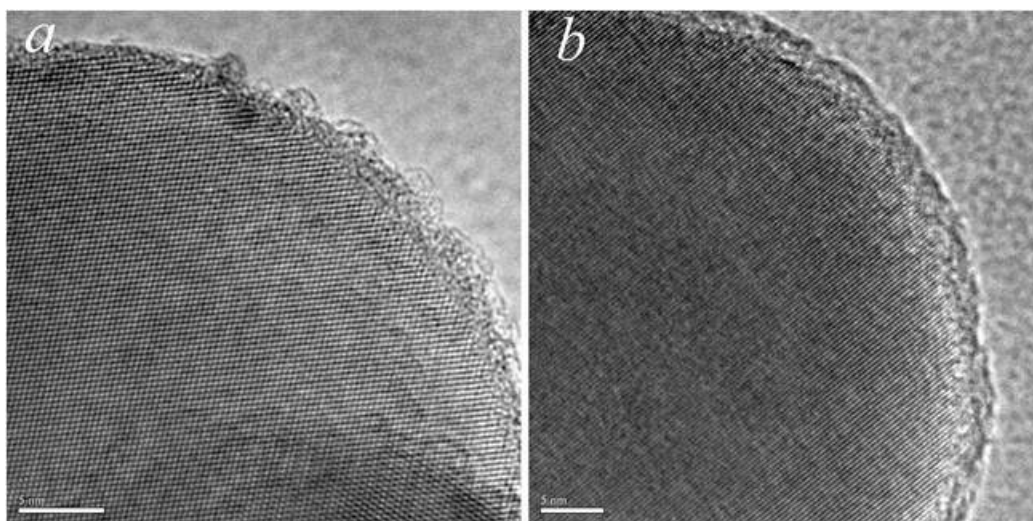


Figure II-93. TEM images of the uncoated Si particle (a) and the MLD coated Si particle (b). The particles have the size about 50 nm, were purchased from Alfa.

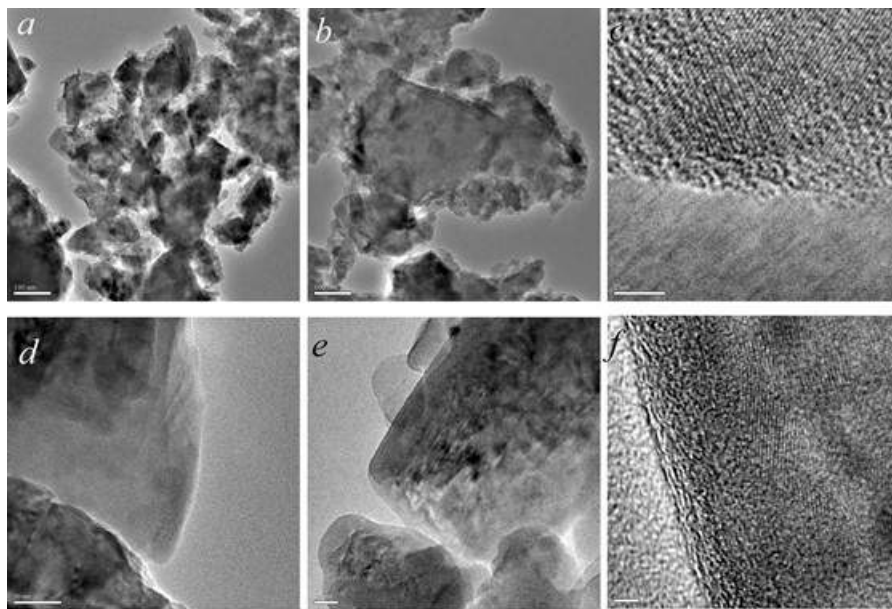


Figure II-94. TEM images of uncoated Si particles (a-c), and MLD coated Si particles (d-f). The Si particles were from NanoAmor, has been used as the new baseline material.

Impact of the coating on the electrochemical performance of the composite electrode

The electrodes were fabricated at NREL, with the 73 wt% graphite, 15 wt% Si (Nano & Amor, 70-130nm), 10 wt% lithiated poly acrylic acid (LiPAA) and 2 wt% Timcal C45. The MLD alucone coating was applied on both particles (purchased from Alfa and NanoAmor). 10 MLD alucone coating was initially applied on the particles from Alfa. However, the thick coating has significantly affected the electronic conductivity, thereby, very low capacities were obtained for the coated particles. Therefore, thin alucone coating obtained by 3 MLD cycle was performed later and the electrochemical performance is shown here. The electrochemical properties of the electrodes made with NanoAmor silicon particles were shown in the Figure II-95. Based on the electrochemical cycling data, there is no major difference between the as-received particles and the coated particles, except for the improved Coulombic efficiency (CE) for the coated particles. Combining the morphologic analysis for the NanoAmor silicon particles, we believe that the alucone coating was not fully covered the particles. The poor coating quality can be attributed to the organic impurities on the surface of silicon particles. And, the shapeless morphology, as shown in Figure II-94 may cause the difficulty to form uniform and conformal coating on the surface of the particles.

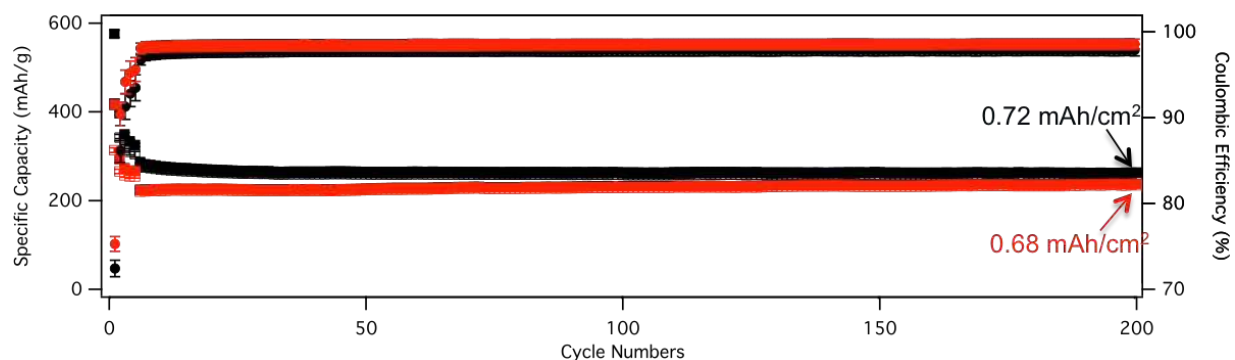


Figure II-95. Specific capacity of the uncoated electrode (plotted in black) and the electrode fabricated by using the coated Si particles (plotted in red). The electrode is fabricated by using 73 wt% graphite, 15 wt% Si (NanoAmor, 70-130 nm), 10 wt% poly acrylic acid and 2 wt% Timcal C45. No major difference in electrochemical performance was observed for the coated particles.

In contrary, significant improvement was observed for the coated Alfa particles. The electrochemical cycling performance of the alucone coated Alfa silicon particles was plotted in Figure II-96a. The alucone-coated particles have shown highly reversible capacity for over hundred cycles, as compared to the fast capacity degradation in the uncoated particles. PAA has been used as polymer binder additive, to enhance the mechanical integrity. Unexpectedly, the decay in electrochemical performance was shown in the uncoated particles after 50 cycles.

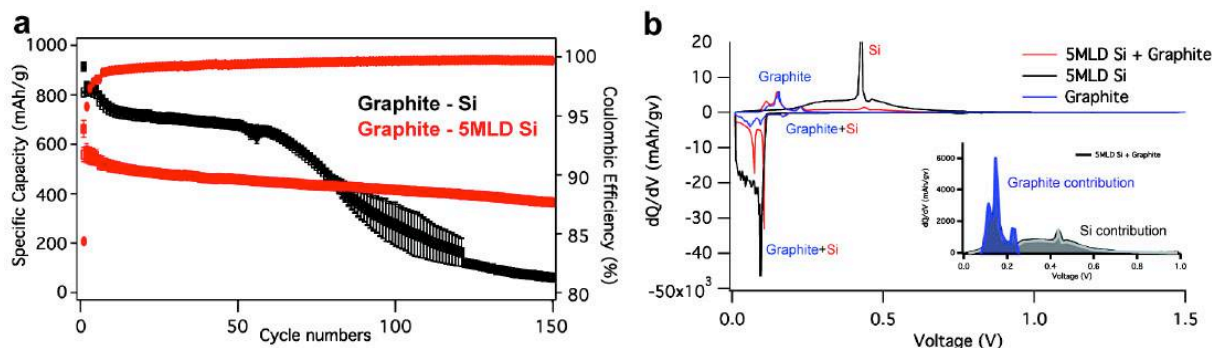


Figure II-96. (a) Specific capacity of the uncoated electrode (plotted in black) and the electrode fabricated by using the coated Si particles (plotted in red). The electrode is fabricated by using 73 wt% graphite, 15 wt% Si (Alfa, 50 nm), 10 wt% poly acrylic acid and 2 wt% Timcal C45. Improved electrochemical performance was achieved for the coated particles. (b) Different capacity (dQ/dV) curves of the electrodes made with the graphite, the MLD coated Si and the graphite-coated Si. The inset plot illustrates the capacity contribution from each component.

Addition of 15 wt.% of Si into the graphite-based electrode results in the increase of specific capacity from 372 mAh/g to 918 mAh/g, and improved Coulombic efficiency (CE). This is an eclectic approach as the electrode solely made of Si particles rapidly fails due to the enormous volume changes of Si with lithiation. Figure II-96a shows the cycling performance of the composite electrode. Fast capacity degradation is observed after 60 cycles and the composite electrode loses the entire reversible storage capability after 150 cycles. This indicates that even small portion of Si materials in the graphite-based electrode can negatively affect the reversible lithiation/delithiation in the composite electrode. Without the addition of Si particles, the graphite anode has shown reversible capacity for hundreds of cycles (not shown here).

In order to understand the failure mechanism in the composite electrodes, we have studied the differential capacity (dQ/dV) plots for the graphite anode (Si not added, Graphite-CB-PAA, 88 wt.% - 2 wt.% - 10 wt.%), the Si anode (graphite not added, Si-CB-PAA, 70 wt.% - 15 wt.% - 15 wt.%), and the composite electrode (Graphite-Si-CB-PAA, 73 wt.% - 15 wt.% - 2 wt.% - 10 wt.%). Note that the anodic potential peaks occurred at 0.25-0.5 are due to the delithiation of Si anode, while the delithiation of graphite usually completes before 0.3 V. However, it is hard to distinguish the cathodic potential peaks of the Si component from the lithiation peaks of the graphite anode. Therefore, we used the delithiation dQ/dV (cathodic) curves to evaluate the reversibility of the Si component, as shown in the Figure II-96b. Inset of Figure II-96b displays the contribution of delithiation capacity from the each component, the graphite and the Si particles respectively. The graphite-coated Si composite electrode has the sustainable cycling performance, although the initial reversible capacity of the graphite-coated Si composite electrode is lower than that of the graphite- uncoated Si composite electrode. Figure II-97 and Figure II-98 present the voltage profile and the dQ/dV curves of the graphite-uncoated Si composite electrode and the graphite-coated Si composite electrodes, respectively. The dQ/dV curves for the 1st and 100th cycle have been plots for these two electrodes. Both electrodes show similar behavior at the 1st cycle, with the equal capacity contribution from both components. In both the graphite-uncoated Si electrode and the graphite-coated Si electrode, the delithiation peaks from the Si component become broadened and the peak currents gradually decrease for both cells. However, at 100th cycle, the peaks from the graphite component disappear in the cell with the graphite-uncoated Si composite electrode. When using coated Si in the composite electrode, the delithiation peaks from the graphite component are well

maintained. For the electrode made with the uncoated Si particles, the capacity fading in both graphite and Si components leads to the performance decay. Interestingly, the electrochemical behavior of Si in the composite electrode affects the cycling performance of the other component (graphite).

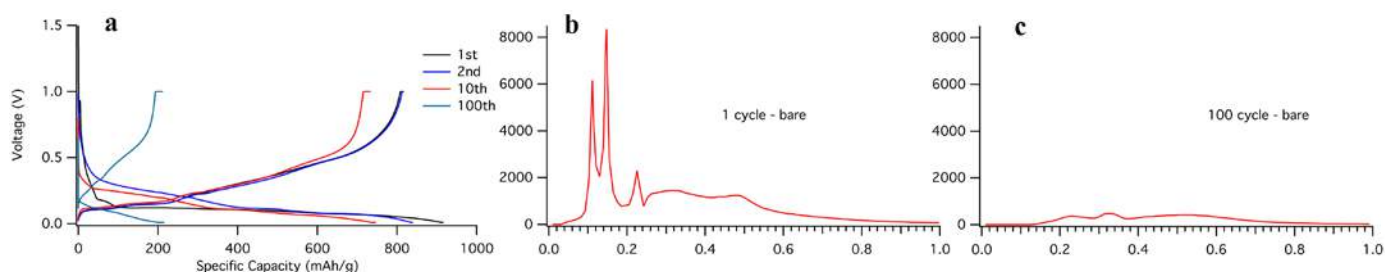


Figure II-97. a) Voltage profile of the graphite-uncoated Si composite electrode cycling between 10 mV and 1 V; (b) Differential capacity (dQ/dV) plots during delithiation at the first cycle; and (c) at the 100th cycle.

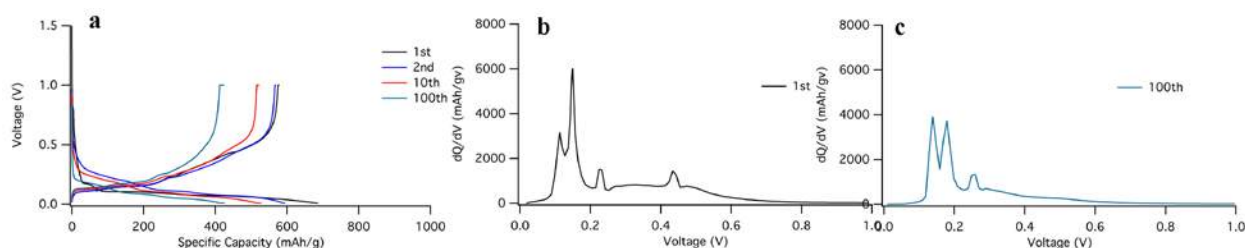


Figure II-98. (a) Voltage profile of the graphite-coated Si composite electrode cycling between 10 mV and 1 V; (b) Differential capacity (dQ/dV) plots during delithiation at the first cycle; and (c) at the 100th cycle.

Impact of the coating on the electrode structure

The cross-sectional SEM images of the composite electrodes—the graphite-uncoated Si electrode and the graphite-coated Si electrode—reveal the similar porous structure of the electrodes, as shown in 27a. The electrode has the average thickness of 30 μm . After one hundred cycles, the electrode made with the uncoated silicon particles experienced dramatic volume expansion at the thickness direction, as indicated in Figure II-99b. It is not surprising that the Si-based electrodes have the volumetric expansion, due to the volumetric fluctuation of Si particles along with the electrochemical reactions. But the large volumetric changes are not expected for the electrode with such a low content of Si particles (only 15%). It is very possible that the original electrical paths have been damaged/blocked after the large volume changes. On the contrary, the electrode made with the coated Si particles shows the original morphology with a limited volumetric expansion, which greatly help maintaining the initial electrical matrix for conducting the electrons.

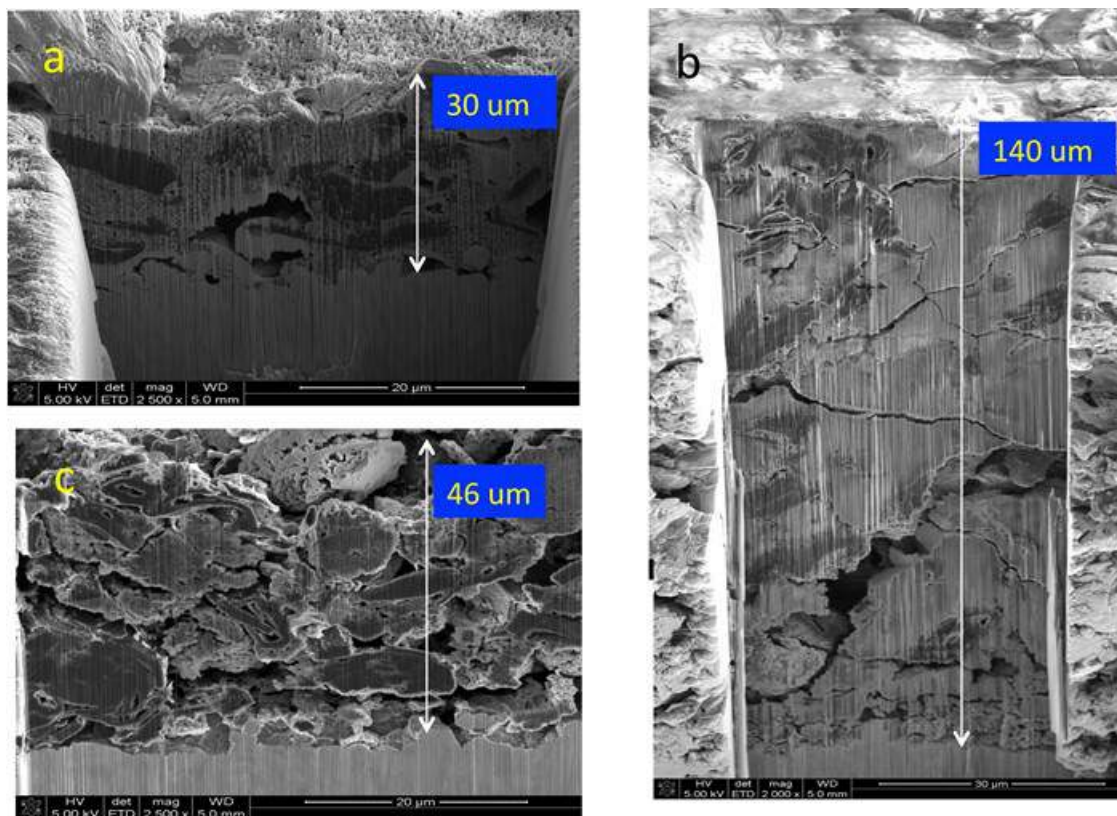


Figure II-99. Cross-sectional SEM observation of (a) the as-prepared electrode made with the uncoated silicon particles; (b) the uncoated electrode after 100 electrochemical cycles; (c) the electrode made with the coated Si particles, after 100 electrochemical cycles.

SEM images are presented in Figure II-100 for the surface morphology of the cycled electrodes, including the graphite-uncoated Si electrodes, and the graphite-coated Si electrodes. After 100 cycles with the uncoated silicon particles, a large number of cracks with different sizes were formed on the electrodes. The surface of the electrodes seems to be heavily covered, mostly likely by the formed solid electrolyte interface (SEI) layer. By coating the silicon particles with 5 MLD alucone (about 1nm), the amount of crack was significantly reduces as shown in Figure II-100 (c) and (d). It is worthy to mention that the 15 wt.% Si particles (50nm) have much higher surface area than those of graphite particles (more than 30 μm), thereby dominates the surface area of the electrode. The formation of the thick SEI for the uncoated silicon particles can cause the high impedance, and exacerbate the volume expansion, finally lead to the loss of the electron conductive paths. As a consequence, the capacity starts fading after 60 cycles for the electrode made with the uncoated Si particles.

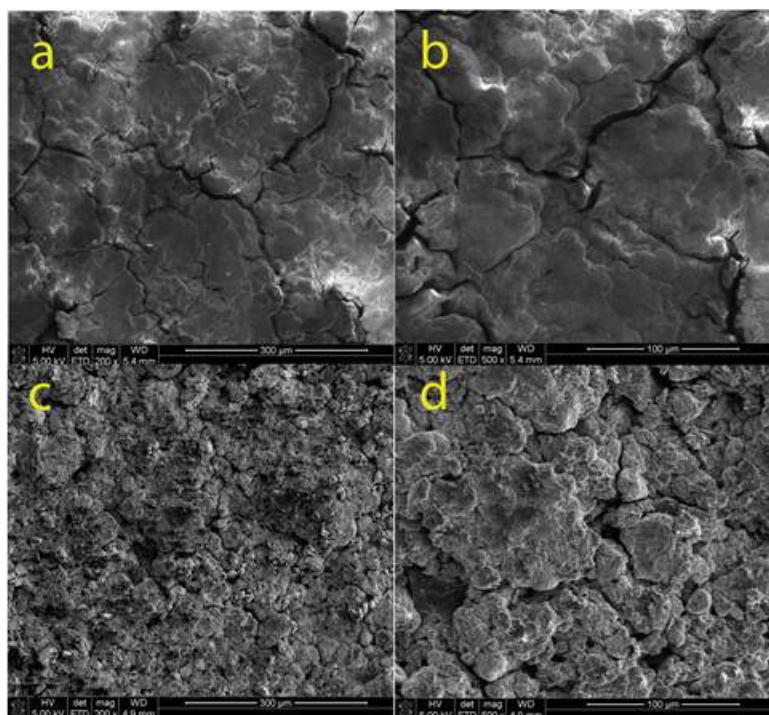


Figure II-100. SEM images of the surface of (a) and (b) the graphite-uncoated Si electrode after 100 electrochemical cycles; (c) and (d) the graphite-coated Si electrode after 100 electrochemical cycles.

Interfacial Modification of Si Anode – Surface Modification (ANL)

The chemical and electrochemical reaction on the surface of the silicon (Si) and lithiated silicon (Li_xSi) with electrolyte solvent/additive plays a significant role in the battery performance of silicon anode. The non-volatile reaction products deposit on the particle and form the so-called solid-electrolyte-interface (SEI). For the traditional graphite-based anode, this exclusively Li^+ -conducting SEI layer passivates the surface of the lithiated graphite and prevents the further reactions with electrolyte thus enables the reversible lithiation/delithiation chemistry of lithium ion battery. However, due to the huge volume expansion/contraction of silicon-based anode, the surface passivation is not established since the SEI cracks and reforms with cycling which consumes considerable amount of active lithium resource from the cathode leading to the rapid capacity decay.

The overall goal of this project is to develop sustainable high-energy density of Si-based nanocomposite electrodes for electric vehicle application. Specifically, in this work, we try to engineer the Si surface chemistry through different approaches with a target to stabilize the interface affording a Si anode with extended cycle life. The first approach is to develop new electrolyte/additive that could chemically/electrochemically decomposes and deposits on the lithiated Si surface forming a resilient SEI layer that stabilizes the interfacial reactivity of Li_xSi and electrolyte. Fundamental understanding of how the reactivity of electrolyte/additive with Si anode and how the chemical composition of SEI affects the cell performance will be systematically performed. The second approach is to functionalize the surface of Si particles through organic silane chemistry with a target to stabilize the interface affording a Si anode with extended cycle life.

Small-Molecule Functionalized Silicon Nano Particles (NP)

When exposed to air, a native oxide layer of up to 5-7 nm will form on the surface of silicon particles and the surface functionalities are vary with storage history and handling process. Figure II-101a shows the pictures of the nano silicon particles from Nano Amor and Alfa Aesar dispersed in ethyl alcohol. The color of the two materials are very different, and the surface functionalities are quite different as well based on the FT-IR

results shown in Figure II-101b. Silanol group -Si-OH is universally present on the surface of Si NPs. To obtain Si particles with homogeneous distribution of surface silanol as a reaction platform, a -Si-OH enrichment reaction was performed on the pristine Nano Amor silicon NPs with an average particle size of 70-130 nm. The -Si-OH enriched Si NPs are further reacted with alkoxy silanes through a hydrolysis/condensation reaction. Ethyl alcohol (Et-OH) and dry tetrahydrofuran (THF) were used as solvents to synthesize silane-functionalized Si nanoparticles.

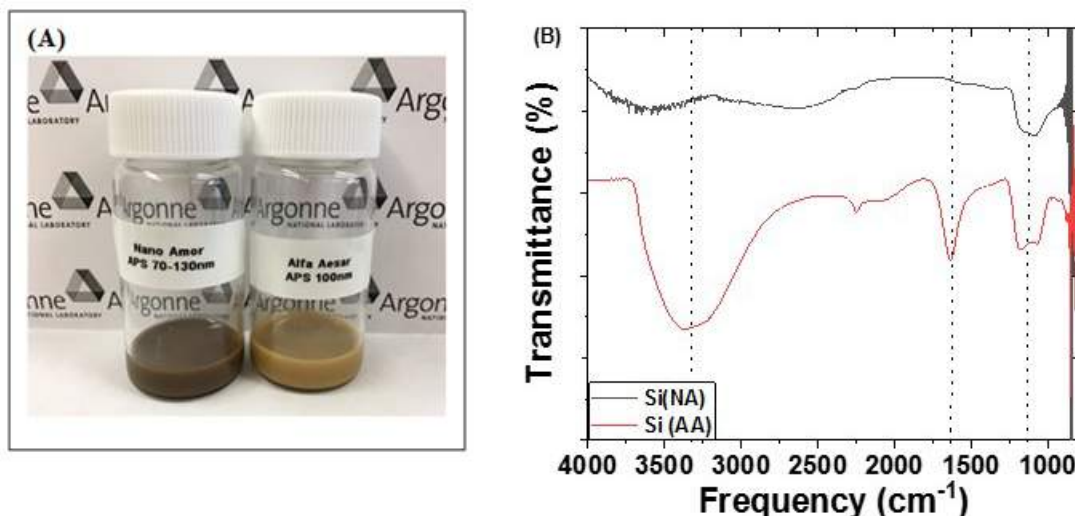


Figure II-101. (A) Pictures of dispersions of Si NPs in ethanol and (B) FTIR spectra of Si NPs from Nano Amor (black) and Alfa Aesar (red).

Figure II-102 shows the FTIR spectra of the synthesized Si NPs with vinyl and methyl methacrylate groups. In Figure II-102, the peaks around 1000-1200 cm^{-1} corresponds to the vibrational Si-O-Si bond, which is evident that the surface of the pristine Si NPs is oxidized to SiO_x to some extent. After the -Si-OH group enrichment, the peaks at 3000-3500 cm^{-1} , an area of typical -OH vibration, becomes larger and broader than that of the pristine Si particles, indicating the increased concentration of Si-OH group on the surface of the treated Si NP. Figure II-102a shows the FTIR spectra of the vinyl-Si-Et-OH (iii) and MP-Si-Et-OH (iv) as well as the pristine (i) and oxidized silicon NPs (ii). Only one new peak at 1650 cm^{-1} (-C=C-) appeared for vinyl-Si-Et-OH (iii) and MP-Si-Et-OH (iv) functionalized silicon. However, the vinyl-Si-THF (iii) and MP-Si-THF (iv) synthesized using THF as a solvent showed a new peak at 2900 cm^{-1} (Figure II-102b) which is the typical of C-H bond vibration on $\text{-CH}_2=\text{CH-}$ group. In addition, the peak at 1750 cm^{-1} confirms the presence of carbonyl (C=O) group for the MP-Si-THF (iv) sample. It is evident that the surface functionalization process is successful when the dry THF is used as a solvent.

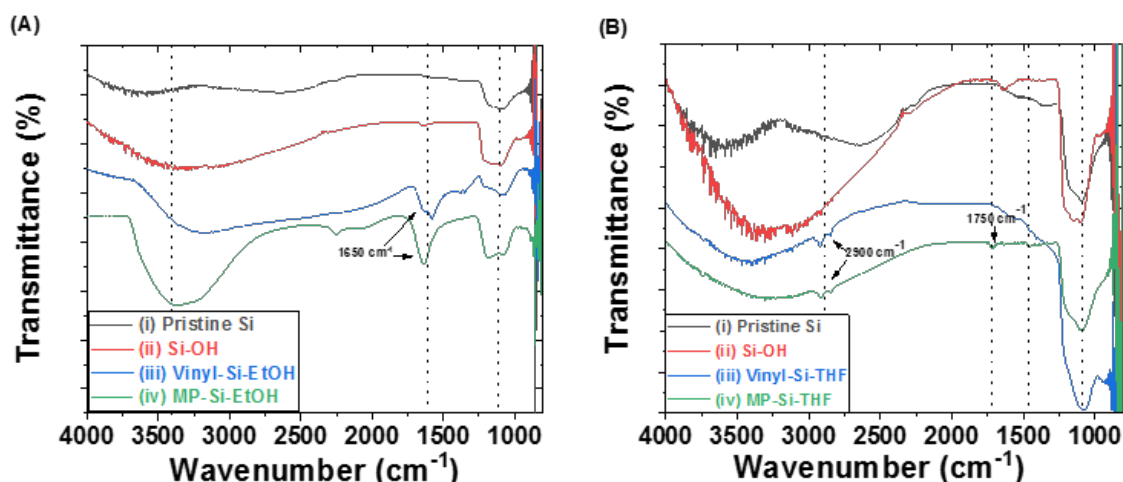


Figure II-102. FTIR spectra of silicon nano powders. (a) Pristine Si, -Si-OH enriched Si, vinyl-Si-Et-OH and MP-Si-Et-OH, and (b) pristine Si, -Si-OH enriched Si, vinyl-Si-Et-THF and MP-Si-Et-THF.

Figure II-103 shows the TGA profiles of the surface enriched Si NPs, vinyl-Si-THF and MP-Si-THF as well as the pristine silicon. For the surface enriched Si NPs, it only showed a 0.5% weight loss at the end of the heating temperature 800°C, while a much higher weight loss was observed for the two functionalized Si NPs with 1.5% loss for vinyl-Si-THF and 3.75% loss for MP-Si-THF, respectively. The weight retention confirmed the attachment of different surface structure on the Si NPs. The electrochemical properties of these functionalized Si NPs will be studied in the near future.

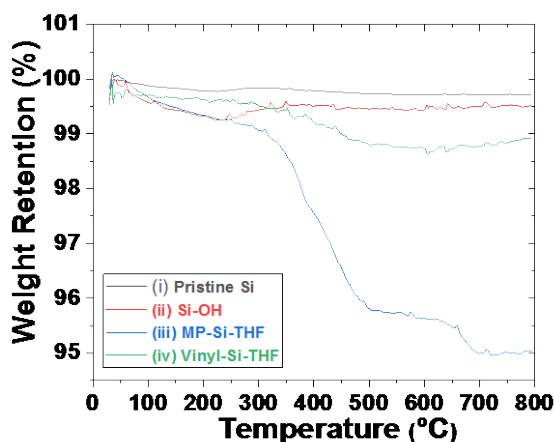


Figure II-103. TGA profiles of (i) pristine Si NPs, (ii) oxidized Si NPs, (iii) vinyl-Si-THF and (iv) MP-Si-THF.

Electrolyte Additive Electrochemistry and Working Mechanism

SEI formation process involving FEC additive and the FEC/hexamethyldisilazane (HMDS) additive is quite different evaluated by the Si-graphite/Li half cells. Figure II-104a shows the expanded voltage profiles where the SEI formation occurs. The addition of silazane additive alters the reduction of the electrolyte and chemical composition of the SEI. Figure II-104b-Figure II-104c shows the differential capacity voltage profiles (dQ/dV) for the first three cycles. In contrast to results reported by other groups, the crystalline Li_{4.4}Si phase exists for each cycle for the FEC/HMDS additive cell, while FEC-additive-only cell did not show this phase. At this stage, it is not fully understood yet whether the appearance of the Li_{4.4}Si phase is correlated with the cell performance. Figure II-105 summarizes the cycling data and the Coulombic efficiency of Si-graphite/Li half cells with Gen 2 electrolyte, Gen2+10% FEC and Gen2+10% FEC+1% HMDS. The capacity retention of the

FEC/HMDS mixture additive cell is significantly improved compared with the baseline electrolyte and the FEC-only-additive cells. The working mechanism of the mixture additive is illustrated in Figure II-106. It is evident that the HMDS is reactive with moisture from the electrolyte and absorbed by the Si particles within the electrode. Further, the reaction of HMDS with silanol group ($-\text{Si}-\text{OH}$) on the Si NPs forms a trimethylsilyl-terminated surface functionality that can act as an artificial SEI that could prevent the side reaction of the lithiated Si with electrolyte.

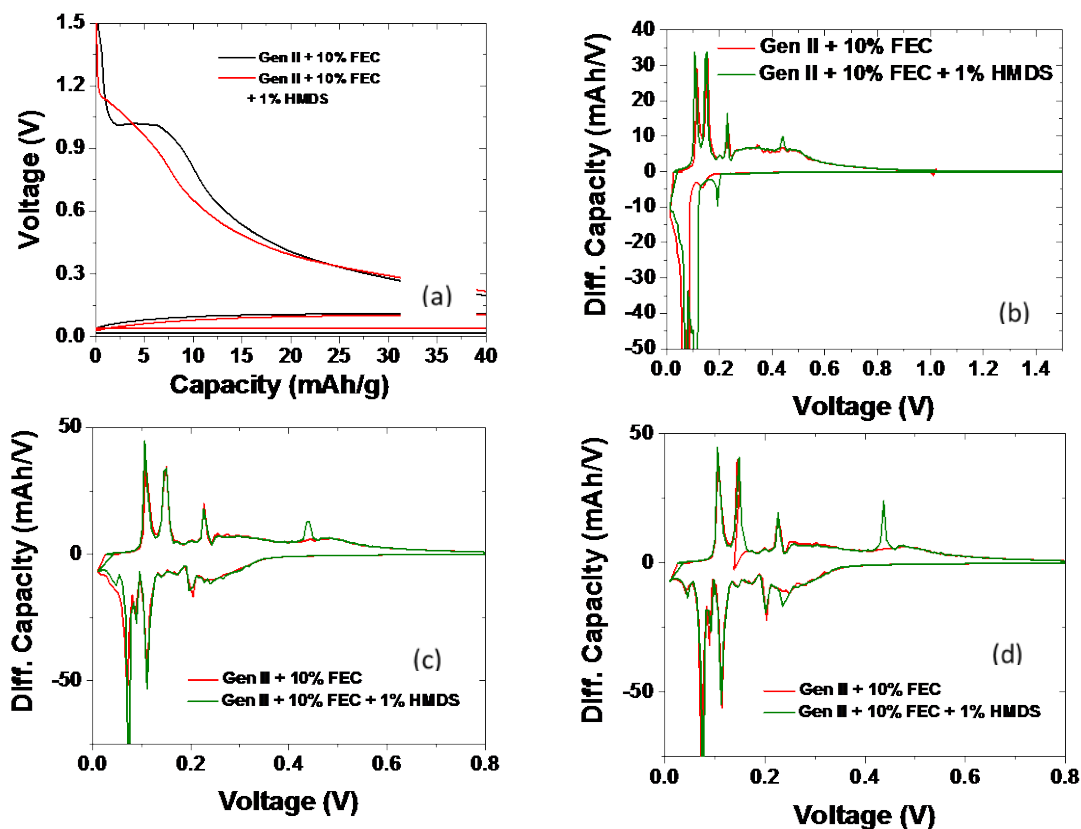


Figure II-104. (a) Expanded voltage profile for SEI formation, and (b-d) dQ/dV profiles for the 1st, 2nd and 3rd cycle for the Si-graphite composite anode with Gen2+10% FEC and Gen2 +10% FEC +1% HMDS.

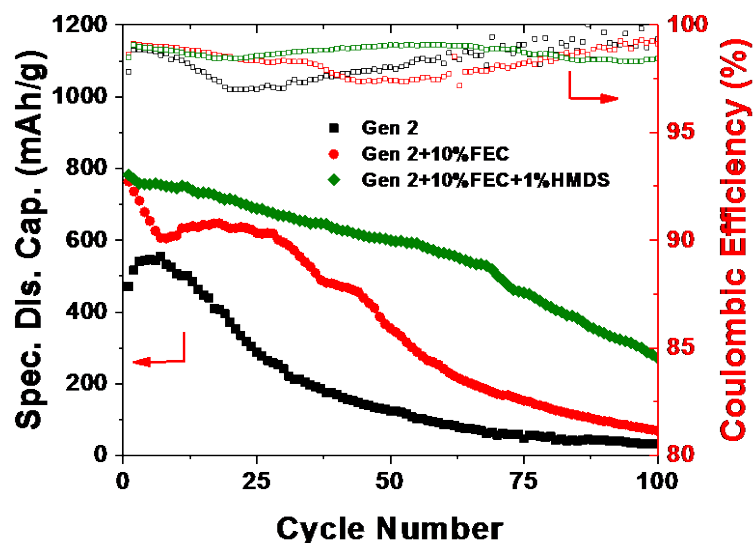


Figure II-105. Capacity retention and Coulombic efficiency of Si-graphite/Li half cells with Gen 2 electrolyte, Gen2+10% FEC and Gen2+10% FEC+1% HMDS.

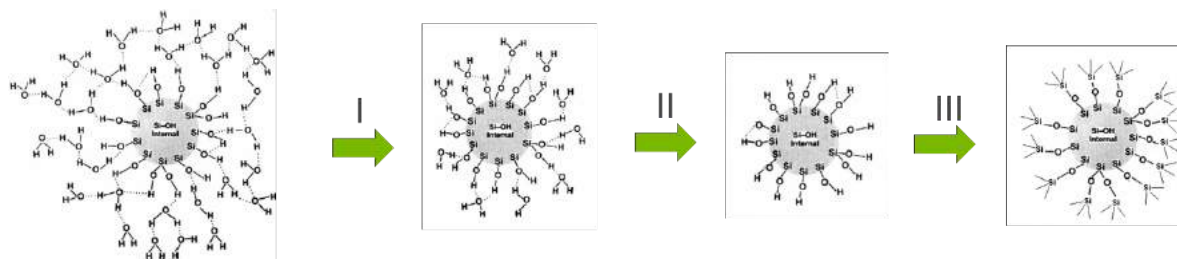


Figure II-106. Proposed surface reaction of HMDS with -Si-OH on the surface of Silicon nanoparticles.

Development of High Energy Metals (LBNL)

Dahn's group identified amorphous Si-Sn films with Sn content lower than 40 mol% as the ideal compositions in thin film batteries, for example, $\text{Si}_{0.64}\text{Sn}_{0.36}$ showed a large reversible capacity of ~ 1900 mAh/g and low irreversible capacity of ~ 100 mAh/g during the 1st cycle. [13] Ahn et al., later confirmed amorphous Si-Sn nanocomposite electrode films produced by magnetron co-sputtering method demonstrated improved cycling performance compared to amorphous Si film at a similar thickness. [14] Sputtered films with phase separated amorphous Si embedded in the Sn matrix also delivered a reversible capacity of 1400 mAh/g with good cycling stability at Si/Sn ratio close to 1. [15] Attempt to prepare nanocomposites of Si/Sn-based nanoparticles enwrapped in porous carbon nanofibers led to an initial specific capacity of 1347 mAh/g and 1073 mAh/g was retained at the 50th cycle. [16] Kwon et al., reported a sophisticated synthesis of carbon-coated $\text{Si}_{70}\text{Sn}_{30}$, the composite electrode exhibiting a high reversible capacity of 2032 mAh/g and excellent capacity retention (97% after 60 cycles). [17] All the previous work showed promising electrochemical performance within Si-Sn system, it would be interesting to apply a facile and scalable method to capitalize on the large theoretical capacity of Si, high electrical conductivity of Sn, as well as potential improvement in structural stability of the host electrode. [1]

We explored the synthesis of Si-Sn nanocomposites via mechanical milling method that is cost-effective, facile, and scalable. Using the base $\text{Si}_{0.66}\text{Sn}_{0.34}$ identified from the previous work [13], we have investigated the effect of milling method on the phase formation and electrochemical properties as well as the introduction of

graphite during the synthesis. In addition, we also explored the synthesis of Sn, Si-Sn nanoparticles by chemical reduction method.

In FY16, the synthesis of Si-Sn nanocomposites was first explored on both Retsch planetary and Spex shaker mill. We explored the effect of milling energy and time as well as the addition of graphite on the phase formation and electrochemistry. The best sample, Si-Sn-C nanocomposites, delivered an initial reversible capacity of about 1000 mAh/g with the 1st cycle coulombic efficiency of 80.2%. The capacity retention of Si-Sn-C nanocomposites was about 80% at Cycle 50. To investigate the origin of the capacity loss, SEM images were collected on the Si-Sn-C electrodes at pristine state, the 50th lithiation, and the 50th delithiation (Figure II-107). Comparing Figure II-107 a, e, i, we noticed the change in morphology on the electrode after 50 cycles, and some cracking occurred at the electrode level after the 50th delithiation. Electrode cracking was mainly due to the fact that both Si and Sn experiences volume changes during lithiation-delithiation process. Such volume change was even more pronounced at higher magnifications. According to Figure II-107 d, h, l, the volumes of the particles significantly increased after lithiation, and the volumes cannot fully resumed back upon delithiation. Instead, the electrode became pulverized and led to additional side reactions between electrode and electrolyte, which largely accounted for the capacity loss over the extended cycles even at a lower electrode loading. This is believed to be a major contributing factor for capacity decay, given the presence of a number of defects generated by high energy milling process.

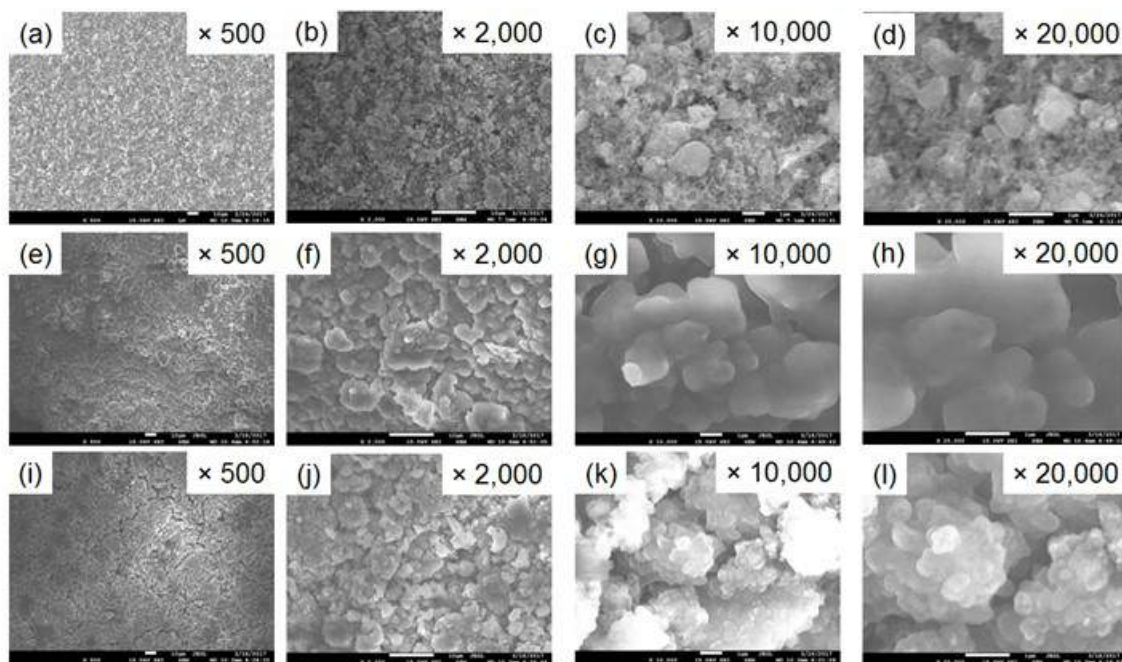


Figure II-107. SEM images of Si-Sn-C electrodes at (a – d) pristine state, (e - h) the 50th lithiation, and (i - l) the 50th delithiation.

According to the previous studies on Si-Sn nanocomposites, a proper control of the morphology, particle size and homogeneity is of critical importance for the electrochemical performance, ideally, mixed Si and Sn at an atomic level. However, inhomogeneous particle size distribution was noticed (Figure II-108 a, b). Moreover, uneven elemental distribution of Si and Sn in the particle was also revealed (Figure II-108 c) with some relatively large Si particles (yellow color) being clustered and embedded in the Sn matrix (blue color). Therefore, we investigated the synthesis by Cryomill, which was tailored for cryogenic grinding by enabling continually cooled grinding jar via liquid nitrogen during milling, thus offering the potential to break down particle size, achieve good mixing, and avoid Sn melting. As shown in Figure II-108 d-f, Si-Sn sample prepared by Cryomill has a more uniform particle size distribution, meanwhile, much more homogeneous Si,

Sn mixing was achieved by Cryomill. However, the as-prepared sample by Cryomill did not exhibit improved cycling performance, likely due to the insufficient mechanical energy input.

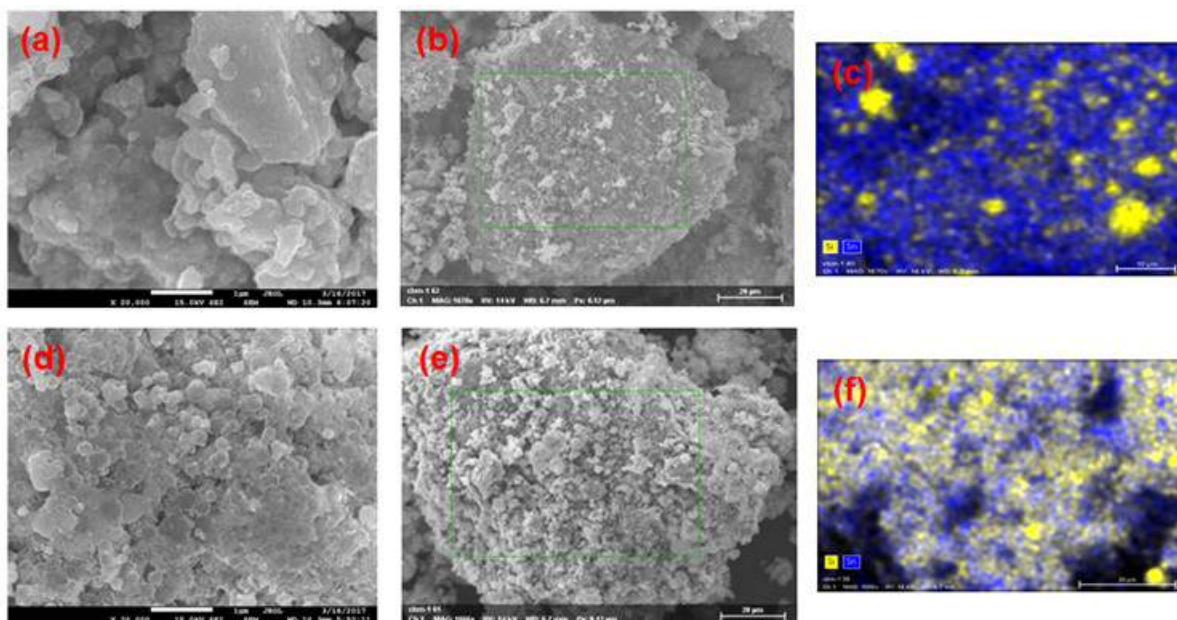


Figure II-108. (a, b) SEM image, (c) Si, Sn EDS mapping of the selected area (green box in (b)) in Si-Sn sample prepared by high energy mill and (d, e) SEM image, (f) Si, Sn EDS mapping of the selected area (green box in (e)) in Si-Sn sample prepared by Cryomill.

Therefore, we explored chemical reduction method, which can enable the design of materials with controlled surface and bulk composition, i.e., core-shell structure, which will allow the in-depth understanding of the reaction mechanism of Si-Sn phases with lithium. This synthesis process typically involves reduction of metal salts (metal chlorides, metal nitrates etc.) using borohydride reducing agent (sodium borohydride, potassium borohydride) to precipitate the homogeneous or heterogeneous mixtures of un-reacted, nanoscale elemental constituents. In our studies, we first prepared Sn nanoparticles by reducing SnCl_2 in NaBH_4 solutions for 5 min and 150 min. As shown in Figure II-109 a-d, both samples demonstrated a similar morphology, with the particle size varying between 100 nm and 1 μm . Effective Sn metal reduction was confirmed by XRD (Figure II-110 a). We also investigated elemental distribution in the Sn sample prepared by 5 min reduction to investigate the completion of reaction. It can be seen in Figure II-109 e-h that Sn, Cl, and O were observed in the final product, the atomic ratio of O and Cl was estimated to be $\sim 15.7\%$ and 7.4% , corresponding to 75 mol% Sn, 20 mol% SnO , and 5 mol% SnCl_2 .

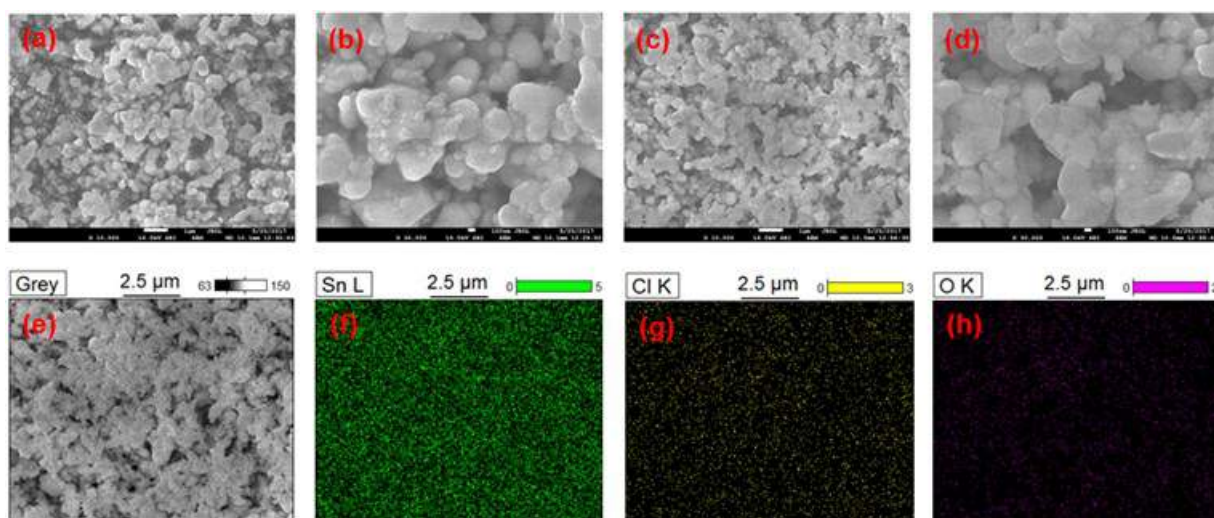


Figure II-109. (a, b) SEM image, (c) Si, Sn EDS mapping of the selected area (outlined by green lines in (b)) in Si-Sn sample prepared by high energy mill. (d, e) SEM image, (f) Si, Sn EDS mapping of the selected area (outlined by green lines in (e)) in Si-Sn sample prepared by Cryomill.

After evaluating the effectiveness of Sn metal reduction, we prepared Si-Sn samples using chemical reduction method. We first added Si nanoparticles into NaBH_4 solution and ultrasonically mixed them to facilitate Si dispersion, followed by adding SnCl_2 solution into the NaBH_4 solution with Si nanoparticles at a speed of 0.2 mL/sec and mixing for two extreme durations, 5 min and 15h. Afterward, we removed the supernatant and centrifuge the insoluble materials, washed and dried the final product under vacuum. Formation of Si-Sn nanocomposites in both samples was revealed by XRD (Figure II-110 a). From the preliminary electrochemical evaluation (Figure II-110 b), the sample prepared by 15h reduction exhibited an initial capacity of 1060 mAh/g at a low electrode loading (0.82 mg), increasing electrode loading to 1.43 mg led to a reduction of the initial capacity to 984 mAh/g. Both samples showed capacity fade when cycled at $C/3$ after the first three formation cycles, with the capacity of ~ 750 and 400 mAh/g remained in the early cycles. As a comparison, the sample prepared by 5 min reduction showed a relatively higher capacity (1327 mAh/g) compared to that reduced for 15h, but followed by a faster capacity decay. These preliminary results demonstrated that the chemical reduction is effective in preparing metals by reducing salts, but a proper control of reacting conditions to drive complete reaction, avoid oxide impurity formation, while remain efficient control of the particle size and morphology of the final product, is critical to produce metal anodes by chemical reduction method.

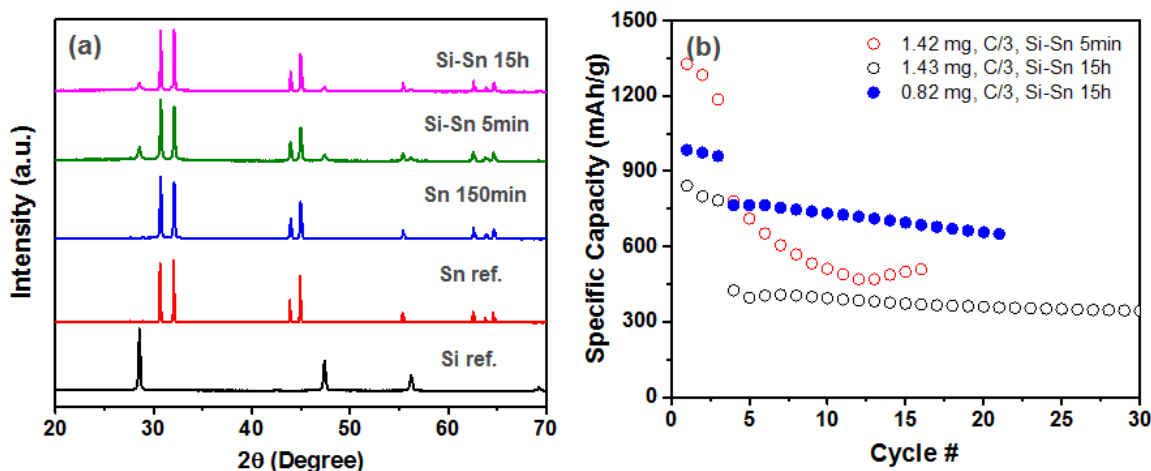


Figure II-110. (a) XRD patterns and (b) cycling performance of Si-Sn samples produced by chemical reduction method. Cells were cycled between 1.5 and 0.05 V at room temperature.

Exploring Li Inventory Strategies (ANL)

Lithium inventory control is an issue that is part of the Si deep dive (DD) project. Si/graphite blended electrodes require careful cell-capacity balancing to begin to enable the technology. Typically this requires much thicker (and heavier) cathodes to account for first cycle irreversible capacity losses (ICL). In addition, due to electrode voltage slippage, the SOC is hard to control, and cell capacity can be compromised. The usable capacity begins to shrink in the cell, and eventually Li-trapping in the Si material wins out, and lifetime is exhausted. The behavior must be understood and then addressed by the lithium inventory team as part of the overall project.

Cycling Si-based electrodes is complicated by destruction and reformation of the SEI on the Si electrode surface. Unfortunately the Li is siphoned from the full cell as a result which causes stresses on the cathode and loss of capacity. Thus an analysis of lithium inventory is needed in order to track the losses in the cell. Certainly, the SEI problems arising from excessive Li_xSi volume changes is problematic, but how the lithium loss as a function of cycle life occurs, and if there is a specific voltage window (or Li_xSi alloy phase) that predominates Li loss is unknown. Furthermore, for a Si-graphite blended cell, does the graphite experience particle electrochemical grinding from Li_xSi volume changes? Such processes need to be determined and once knowledge gained, solutions found.

A combination of specially designed full cells, examination of pre-lithiation additives, cycling results, and SEM, Raman, and Li-NMR are needed to follow Li inventory in Si containing cells. We will pursue these research strategies for analysis of these electrochemical and chemical processes.

SiO_x /NCM-LFO Cell Results

This past year we synthesized new batches of LFO, blended them with NCM523 powder, made electrodes that were balanced with a SiO_x anode and cycled the full cells. The extra lithium delivered from the LFO portion (~40 mAh/g) ensured that the LFO would provide pre-lithiation property to the Si-containing cell. Figure II-111 shows the voltage profiles of SiO_x anode together with individual NCM523 cathode (left) or a NMC:LFO (100:7 w:w) (right) blended electrode (80:10:10 active:PVDF:C45). The voltage profiles are shown between 4.3 to 3 V and the electrolyte was Gen 2 (w/ FEC). The blended electrode enables the NCM523 to access its full capacity without overcharge. The lithium inventory is controlled from a pre-lithiation approach. As a result better utilization of the cathode is realized as is presented in Figure II-112. The left hand side of the Figure II-112 is a graph of the capacity of the cathode as a function of cycle number to 50 cycles. Note that the capacity delivered is higher with LFO (black filled squares) than without (red filled circles). The right hand

side shows that the rate capability of the blended electrode - NMC-LFO, is not limiting. The Li half-cell is cycled at C/3 with HPPC tests done intermittently.

In addition to full cell cycling diagnostic analysis experiments described above, complementary work focused on synthesis scale-up with MERF using iron oxide and iron oxalate precursors at 50 g scale. The scale-up synthesis of the material is then to be used in CAMP facility for electrode making. We are now in the process of testing the material in CAMP electrodes.

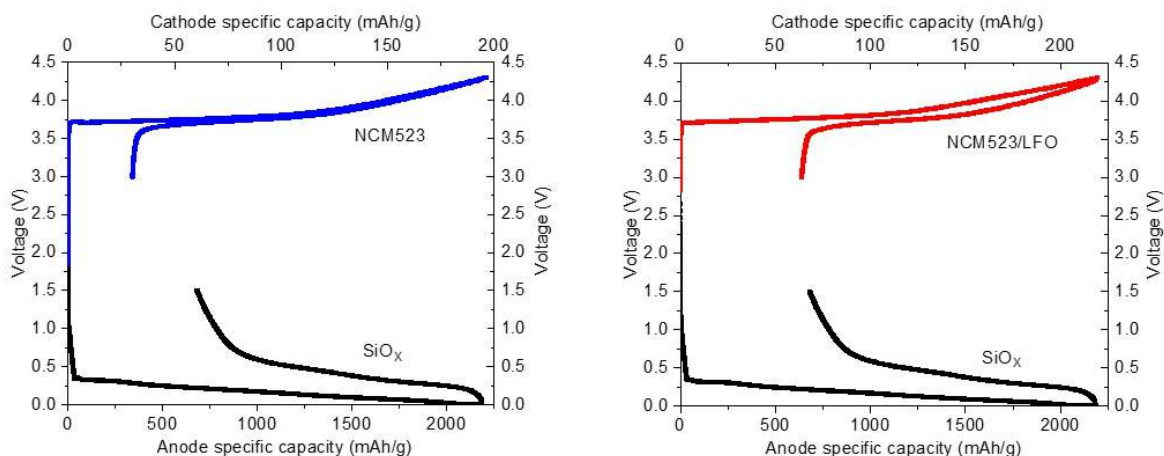


Figure II-111. Voltage profiles of (left) Li/NCM523 and Li/SiO_x cells, and (right) Li/NCM523-LFO and Li/SiO_x cells. The utilization of the NCM electrode is greater as a result of the extra pre-lithiation capacity imparted in the cell from the additive, LFO.

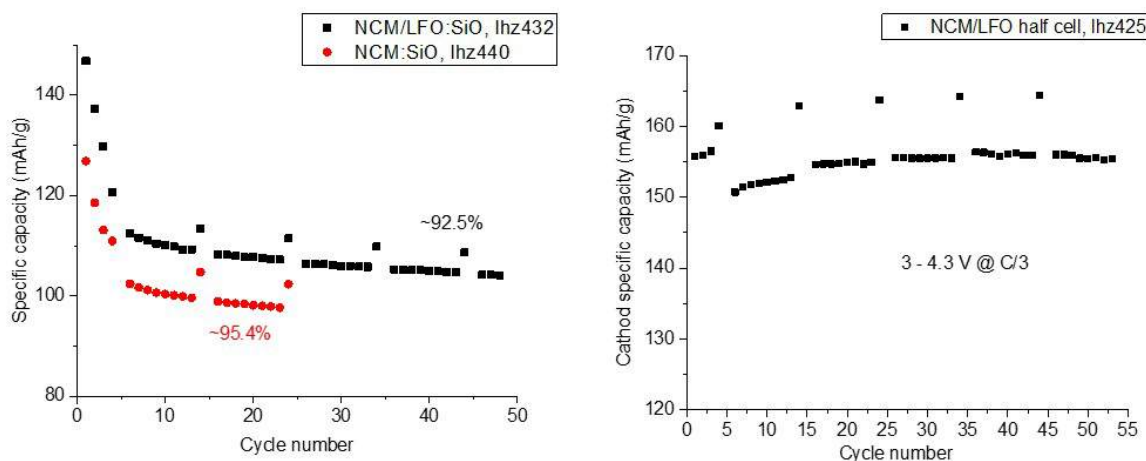


Figure II-112. (left) Capacity versus cycle number for SiO_x/NCM523 cells (red filled circles; 2.5 to 4.3 V, C/10), and SiO_x/NCM523-LFO cells (black filled squares; 2.0 to 4.3 V, C/10). (Right) capacity versus cycle number for NCM523-LFO half cells.

Lithium Inventory and Tracking of 15%Si-Graphite Anode

The CAMP NCM523 cathode (electrode library ID: A-C013A) is known to drop 20% of its capacity (3 to 4.1 V cycling voltage window) over 100 cycles when paired with a 15%Si-graphite CAMP anode (electrode library ID: A-C013A). This was documented in last year's Si DD annual report (page 9). The resultant cathode capacity at 100 cycles is below 80 mAh/g. This deleterious behavior has to be understood and improved. The main failure mechanism is thought to be the poor coulombic efficiency caused by lack of formation of robust SEI layer on the Si material. As a result, cyclable Li is extracted irreversibly from the NCM523 cathode

leading to capacity loss. To probe this behavior, we decided to replace the NCM523 electrode with a high-capacity LiFePO₄ (LFP) cathode, and employ the electrode as a reference/counter electrode in the cell. To this end this strategy allows us to (1) establish a stable dQ/dV plot to track the lithium inventory that occurs at the 15%Si-graphite anode, (2) provide an excess of Li that will replenish Li to the cell, and (3) keep the cathode from being overcharged. By controlling these three parameters, we should be able to track the lithium inventory. Figure II-113 shows the voltage profiles of the (a) Li/LFP half-cell showing over 4 mAh capacity, and (b) the Li/15%Si-graphite half-cell. Notably, the capacity of this cell is a lower 1 mAh.

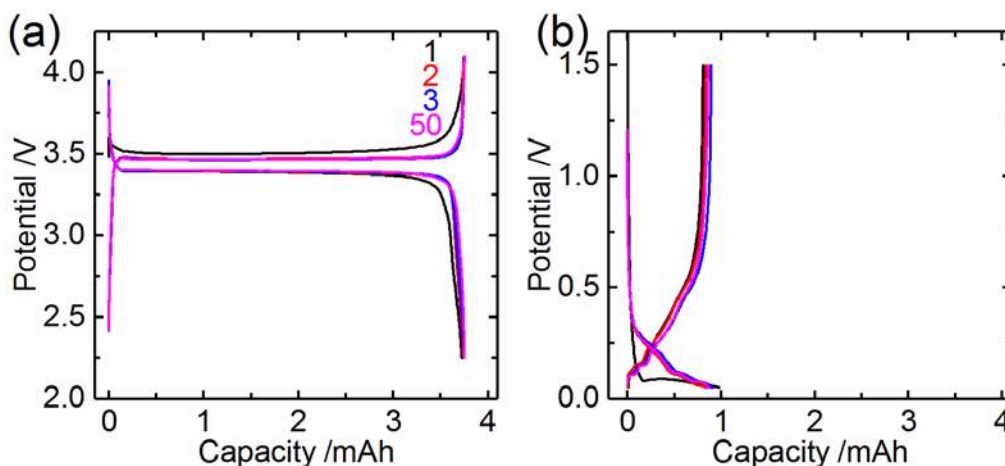


Figure II-113. (Representative potential profiles for the (a) high capacity LiFePO₄ reference/counter electrode against Li metal, and (b) 15%Si-graphite electrode against Li metal. In the full/reference cell, as the Si irreversibly consumes Li the LiFePO₄ electrode has ample Li inventory to continue to supply capacity to the cell.

The full cell voltage profiles of 15%Si-graphite/LFP are provided in Figure II-114. As noted earlier, the use of a high capacity LFP reference electrode makes extended cycling of a Si-containing electrode possible. To this end, the cell tested at a 1C rate was cycled 1000 times. After 100 cycles the cell cycles with efficiencies >99.5%, and therefore consumes little Li each cycle and the LFP Li inventory is not exhausted. On cycle 1000 the cell is cycling between (approx.) 2.79 and 3.29 mAh on the LFP electrode. The capacity retention, measured at C/10 every 100 cycles, decays approximately linearly and is 74% after 100 cycles, 57% after 500 cycles, and 41% after 1000 cycles. The cycle efficiency on the C/10 cycles improves with cycling; 96.8% on cycle 100, 98.5% on cycle 500, and 99.0% on cycle 1000. The improving cycling metrics observed here are consistent with current Si failure models. In later cycling the SEI growth and delamination fill the pores, and mechanical stresses and particle agglomeration densify the electrode structure. This likely impedes Li diffusion and limits it to regions nearest the separator and/or other accessible surface regions, thereby decreasing the lithiation capacity. Consequently, the volume expansion would be less and the SEI cracking and number of freshly exposed surfaces reduced. This would lead to lower capacity fade and higher cycle efficiencies, as observed in this study.

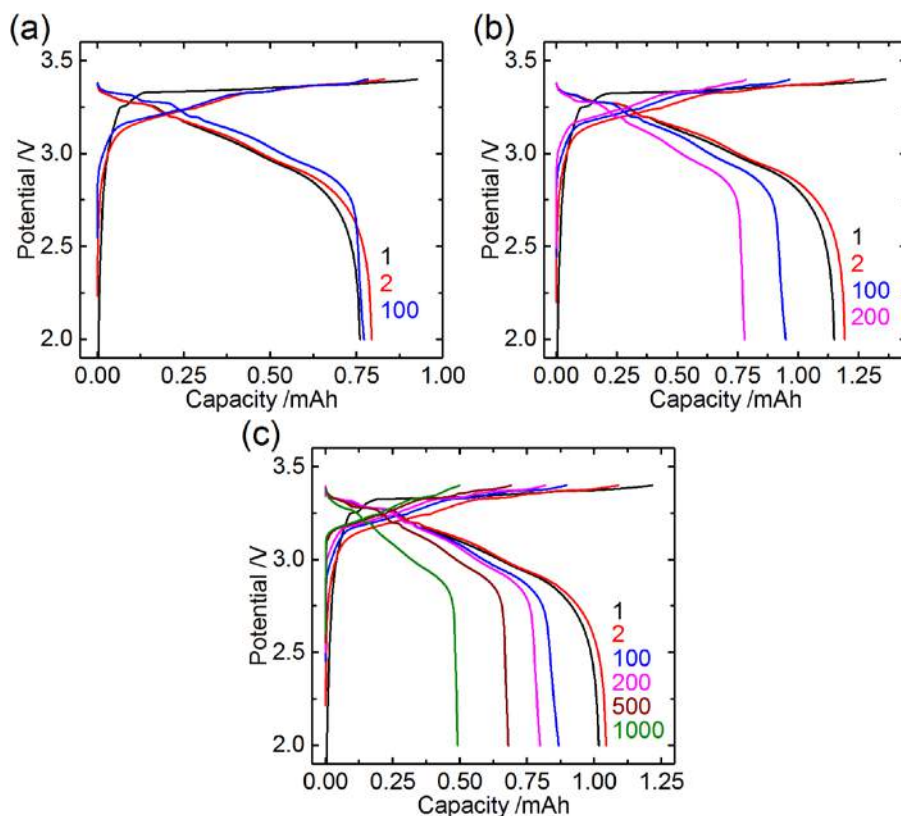


Figure II-114. Representative electrochemical profile versus capacity with cycle number of Si-graphite cycled against a LiFePO₄ reference electrode at (a) C/10, (b) C/5, and (c) 1C. In (b) and (c) the first and last 3 cycles of each set of 100 cycles were performed at C/10 while the intermediate cycles were performed at C/5 and 1C, respectively.

Figure II-115 considers a breakdown of the delithiation capacity delivered above and below 3.185 V. From the dQ/dV (Figure II-116) it is clear that graphite is the main contributor to the capacity at potentials higher than 3.185 V (0.205 V versus Li⁰), although Si may also make a contribution. Below 3.185 V the capacity is solely from Si delithiation. Therefore, Figure II-116 shows an approximation of the relative capacity retention of the Si and graphite components in the blended electrode. Capacity fade of Si is most rapid in the first 400 cycles, dropping to 61 %, and thereafter decreasing steadily to 46% after 1000 cycles. Meanwhile, the capacity above 3.185 V is >80% after 400 cycles, but begins to decrease approximately linearly to be around half its initial value after 1000 cycles. The most severe losses are from the graphite process at 3.372 V.

The potential at which the dQ/dV intensity begins to rise in region A changes gradually between cycle 20 and cycle 100, increasing by ~40 mV. This is likely caused by gradual ionic isolation of Si particles, particularly those closest to the current collector which makes the lithium mobility to these particles kinetically limiting and more difficult (resistance increases). The two minor Si lithiation processes at 3.27 and 3.30 V (B and B', 0.20 and 0.17 V versus Li⁰) and the process at ~3.35 V (C, ~0.12 V versus Li⁰) are related to lithiation of the larger Si clusters, which causes them to be further broken down to smaller clusters. Conspicuously, minimal capacity fade is noted in region C after 100 cycles. Between cycle 20 and 100 the potential at which this process occurs steady increases, however, suggesting the over-potential for this process increases with cycling. The 1C cycling data shows the potential rise is greater at higher cycling rates and the trend continues beyond 100 cycles.

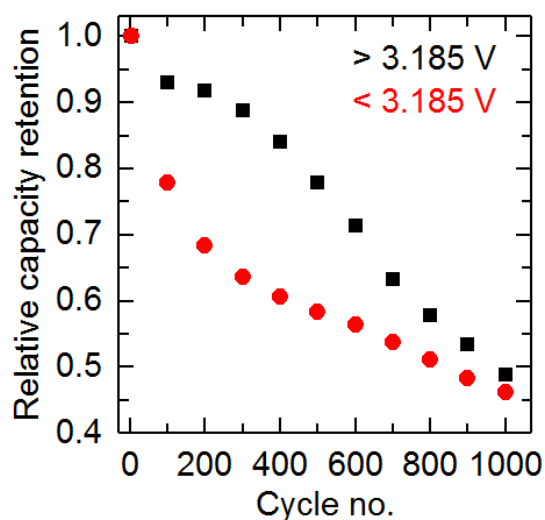


Figure II-115. Relative capacity fade above and below 3.185 V with respect to cycle number for Si-graphite cycled against a LiFePO₄ reference electrode at 1C. The first and last 3 cycles of each set of 100 cycles were performed at C/10 while the intermediate cycles were performed at 1C.

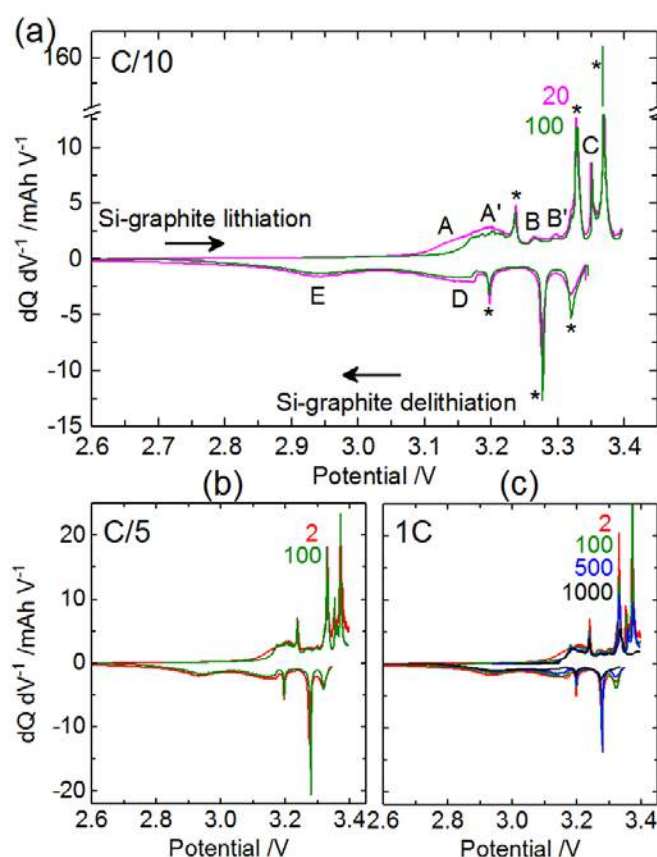


Figure II-116. Representative differential capacity dQ/dV plots for Si-graphite cycled against a LiFePO₄ reference electrode at (a) C/10, (b) C/5, and (c) 1C. In (b) and (c) the first and last 3 cycles of each set of 100 cycles were performed at C/10 while the intermediate cycles were performed at C/5 and 1C, respectively. In (a) the * marks (de)lithiation processes attributed to graphite, letters A-C mark lithiation processes of Si, and letters D-E mark delithiation processes of Si.

To understand the rate of capacity loss in regions A-E, the dQ/dV intensity at 3.14 (A), 3.20 (A'), 3.27 (B) and 3.30 V (B') on lithiation, and 3.16 (D) and 2.94 V (E) on delithiation vs. cycle number for the C/10 cell was analyzed (not shown). Firstly, there is a significantly greater rate of capacity loss in region A (3.14 V, or 0.33 V versus Li^0) compared to other regions. The rate of loss is around three times greater and is highly linear with respect to cycle number. This suggests a continual degradation rather than a catastrophic failure mechanism, consistent with Li trapping at or near the surface of Si grains. It also demonstrates that the greatest losses occur on lithiation as amorphous Si is broken down to form silicon clusters. Losses are less severe and less linear with cycle number during lithiation at other potentials. Rates of loss on delithiation are just slightly higher in region D (3.16 V or 0.23 V versus Li^0) relative to region E (2.94 V or 0.45 V versus Li^0).

SEM images reveal the differences that exist in the topography of pristine Si-graphite blended electrodes and those cycled at C/5 for 100 cycles. As Figure II-117a illustrates, two domains can be clearly distinguished in the uncycled electrode, the darker regions corresponding to graphite particles of micrometer size and the lighter areas due to the mixture of nanosized silicon and conductive carbon. Conversely, in the cycled electrodes (Figure II-117b) such domains disappear in favour of the formation of a homogeneous surface where particle-like aggregates are found. Based on this, it seems likely that the aggregate growth initiates around the graphite domains encountered in the pristine electrode as a result of the volume expansion/contraction suffered by Si during cycling, which contributes to silicon covering the entire surface of the electrode. Conversely, EDS mapping of the cross-section of the pristine (Figure II-117c) and cycled electrodes (Figure II-117d) manifests no divergences between them. The presence of carbon domains (graphite) and Si is observed in both, revealing that in the expansion and contraction of Si the graphite particles are simply buried beneath the electrode surface.

The Raman spectra is shown in Figure II-117f, (as compared to uncycled pristine electrode in Figure II-117e). The results show the expected crystalline Si to amorphous structural change. The large graphite domains are no longer clearly observed. The graphite domains do have a similar Raman spectrum to those in the pristine electrode as previously indicated in the EDS map cross-section. However, the D band (disorder mode) is broader and may imply the graphite particles are broken into smaller pieces, by Si during repeated cycling. Si aggregation is also evident after cycling, as reported in the literature and tends to occur on or near the graphite particles.

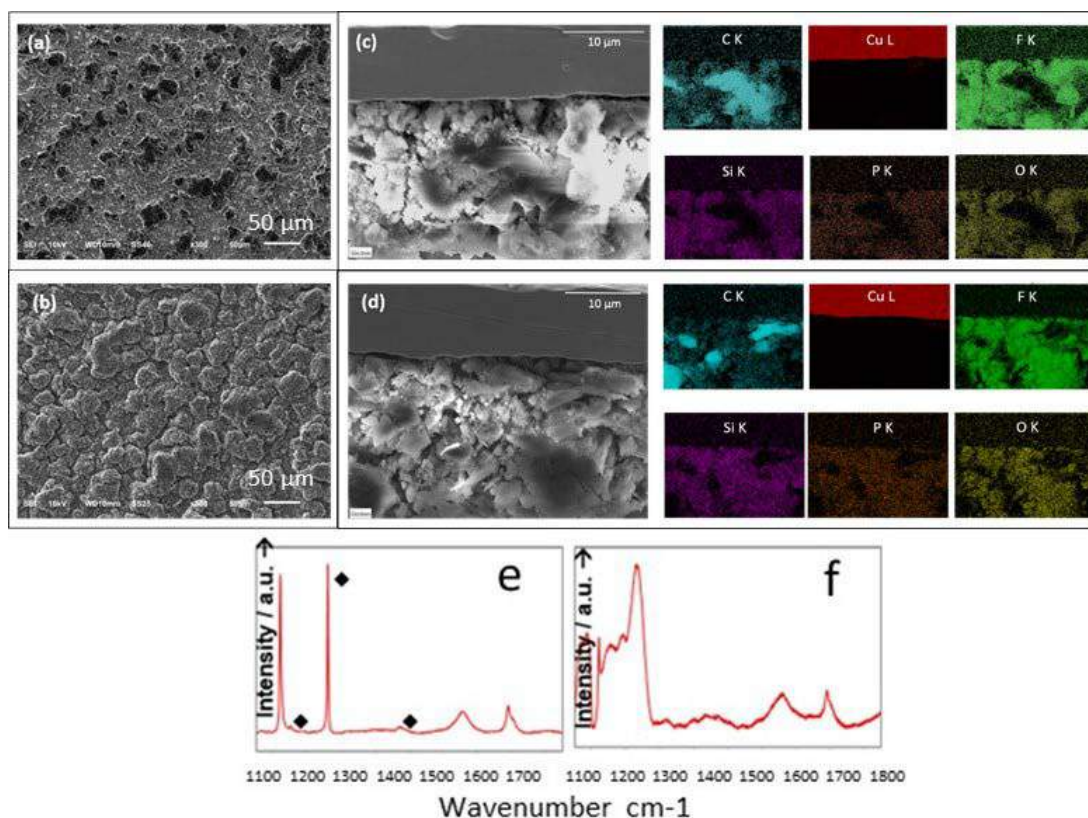


Figure II-117. SEM (a-d) and Raman spectra (e-f) of the pristine Si-graphite electrode (a,b,e) and after 1000 cycles at 1C against a LFP reference electrode (c,d,f). Cross-section images of Si-Gr (c) pristine electrode and (d) cycled and the EDS mapping of C K (cyan), Cu L (red), F K (green), Si K (violet), P K (orange) and O K (yellow) associated to them. Note that the pristine electrode has been extracted from a half cell assembled against metallic lithium and the cycled electrode belongs to the Si-Gr/LFP full cell cycled at C/5 for 100 cycles.

Conclusions

The development of high-performance polymer binders for silicon-based electrodes is being pursued. These binders are designed to mitigate the volume expansion stress and maintain electrical contact with conductive additive and current collector to achieve long-term cycling capacity. Several different approaches are being explored. Graft copolymers (i.e., GC-g-LiPAA via RAFT polymerization) show improved cycling performance over PVDF and GC binders. Improving on these binders, crosslinked catechol group functionalized chitosan was designed and developed as a polymer binder to further improve adhesion and the mechanical stability. Early cycling results with these materials are promising.

A series of cPAA binders has been developed via two approaches. Approach I allows quick and efficient synthesis but with no control of the crosslinking sites and approach II prompts the intermolecular crosslinking by incorporating the crosslinking reaction into the chain growth process. The cPAA1 and cPAA2 binders obtained by approach I demonstrated no improvement on the cycling performance of silicon/graphite anodes possibly due to the intra-molecular crosslinking and the resultant constrained conformations. cPAA3 and cPAA4 were synthesized by copolymerization of AA monomers and crosslinker molecules. cPAA4 demonstrated a much-improved cycling performance in the half cell of the silicon/graphite electrode. The initial capacity and capacity retention are 751 mAh/g and 76% at the 86th cycle, and both are much higher than those of the linear PAA cell. cPAA4 is so far the best performing binder within this class and is worthy of more detailed investigation. Both cPAA2 and cPAA4 delivered surprisingly improved cycling performance of

high capacity silicon anodes (70% silicon). More systematical investigations of those crosslinked PAA binders are currently on going, including optimizing crosslinking reactions, and electrode post-characterizations.

A new family of PAA-based binders was developed. The incorporated arene ring is expected to afford additional stiffness that could benefit the cell performance. P4VBA binders with two different molecular weights were synthesized and characterized. The improved cycling performance of P4VBA2 may indicate that the incorporated benzene ring of the repeating unit of P4VBA2 may contribute to the improved the desired mechanical properties. Detailed characterization regarding the mechanical properties of these binders is ongoing.

Binary polymeric systems able to crosslink in-situ during electrode processing is being explored. Specific components are being identified that allow casting but undergo rapid thermally induced crosslinking during laminate drying.

Finally, development of conductive polymer binders is continuing with work focused on investigation of the stability of the conductive polymer binders, synthetically introducing new anthracene-based conductive moiety to the methacrylate backbone, and decipher the formulation of aqueous-based emulsion of Si-based electrode systems. Analysis of the electrode stability of the Polymethacrylatepyrene (PPy) type of binders after cycling demonstrate both chemical and electrochemical stability of the PPy binder. After confirmation of the stability of the PPy binder, a series of conductive polymer binders based on methacrylate polymer backbone were synthesized that works effectively as both binder and conductive agent for the Si electrode.

The alucone MLD coating has been developed on the Si particles. The TEM images confirmed that the conformal coating was achieved for the Si particles from Alfa, but failed on the Si particles from NanoAmor. For the electrodes made with the NanoAmor Si particles, the coating impact is negligible in terms of the electrochemical cycling performance. It is believed that the oxide and organic impurities on the surface of Si particles negatively affect the growth of the coating materials. The poor coating quality and coverage is not sufficient to affect the electrochemical properties of the silicon particles; thereby, there is no major difference in the electrochemical cycling behavior.

The greatly improved reversibility was obtained for the Alfa Si particles. After the MLD coating (1nm), the electrodes made with the coated Si particles shows highly reversible cycling performance over hundreds cycles, as compared with the electrodes comprised of the uncoated Si particles. PAA was used here to enhance the mechanical integrity for the electrodes, thereby enable the high mass loading for high area capacity. In all of the cells, a high mass loading of ($>3\text{mg/cm}^2$) was used. Due to the low conductivity of the pristine alucone coating, the electrodes made with the coated Si particles always show lower reversible capacity. Although the electrodes made with the uncoated Si particles offer higher reversible capacity, but much low capacity retention after 50 cycles. The study of capacity contribution from each component has revealed that the capacity fading has been observed for the active components, graphite and Si particles. When combining with the coated Si particles, the graphite offers stable cycling performance. The SEM analysis supported the effectiveness of the surface protection strategy. The alucone coating suppressed the growth of the SEI layer, reduced the impedance and help maintaining the original electrode structure. Furthermore, the flexible alucone coating can also accommodate the volume changes, and further secure the stability of the entire electrode and therefore improve the cycling performance.

A fundamental understanding of the reactivity of the electrolyte with silicon-based anodes and how the chemical composition of the SEI affects cell performance is being systematically performed through organic-based interfacial modifications. Specifically, in this work, we engineer the silicon surface chemistry through two approaches targeted at stabilizing the interface affording extended cycle life. The first approach is to develop new electrolyte/additive that chemically/electrochemically decomposes and deposits on the lithiated Si surface forming a resilient SEI layer that stabilizes the interfacial reactivity of Li_xSi and electrolyte. The second approach is to functionalize the surface of Si particles through organic silane chemistry with a target to

stabilize the interface affording a Si anode with extended cycle life. Both approaches have been shown to effectively modify the SEI and early promising cycling results have been observed.

We explored the synthesis of Si-Sn nanocomposites via mechanical milling method that is cost-effective, facile, and scalable. We completed the post-mortem analysis on the spatial distribution of the phases in the pristine and cycled Si-Sn-C electrodes using SEM and EDS. Change in morphology on the electrode along with some cracking at the electrode level was observed after 50 cycles. Meanwhile, we explored Cryomill and chemical reduction methods. Cryomill demonstrated effectiveness in preventing particle agglomeration. Chemical reduction method was effective to produce Sn metal by reducing Sn salts, even by 5 min. From our preliminary studies, Si-Sn samples produced by this method delivered an initial capacity of over 1000 mAh/g without further synthesis optimization. The necessity of optimizing the reaction conditions to achieve complete reduction, avoid oxide impurity, and optimize particle size and morphology was revealed by EDS. In next year, we will focus on the production of Si-Me anode using splat quenching method, which is a commonly used method in metallurgy and well suited for preparation of metal/alloy materials that are near-amorphous, non-crystalline.

Lithium inventory control in Si-graphite/NCM cells is critically important to the success of such advanced cells in EV transportation applications and we are tasked from DOE to understand and solve this problem. In summary, two tasks were completed this past year. First, LFO pre-lithiation additive was shown to improve the cycling and utilization of a full SiOx/NCM523-LFO full cell. Second, a Si-graphite blended electrode has been paired with a high capacity LFP reference electrode. LFP provides a stable reference potential and abundant Li inventory to understanding the irreversibility and capacity fade in Si-based electrodes during extended cycling. The losses in capacity observed in the different potential plot (dQ/dV) have been related to the evolution in the Si local structure, electrode morphology and mechanical properties during (de)lithiation. Extended cycling of the Si-graphite electrode showed slowing capacity fade and increasing cycle efficiencies, particularly after 100 cycles, consistent with current Si-containing electrode failure mechanisms. Further work is required to more fully understand the interactions between Si and graphite components in the blended electrode, and the role graphite plays in Li diffusion to the bulk of the electrode and capacity retention.

Key Publications

1. Hu, B.; Zhang, J.; Jiang, S.; Zhang, Z.; Zhang, L., "Cross-linked Poly(Acrylic Acid) Binder for Silicon Anode of Lithium-Ion Batteries". ABAA-10, poster, Oct 1-4, 2017, Oakbrook, IL.
2. Hu, B.; Zhang, J.; Jiang, S.; Zhang, Z.; Zhang, L., "Cross-linked Poly(Acrylic Acid) Binder for Silicon Anode of Lithium-Ion Batteries". Manuscript in preparation.
3. Hu, B.; Zhang, L.; Zhang, S.; Zhang, J.; Zhang, Z.; Lu, W.; Zhang, L; "Understanding Molecular Weight Effect of Poly(Acrylic Acid) Binders for Silicon Anode of Lithium-Ion Batteries", to be submitted.
4. Hu, B.; Zhang, J.; Shkrob, I. A.; Zhang, Z.; Zhang, L. "Poly(4-vinylbenzoic acid) binders for the silicon lithium-ion batteries", invention report, IN-17-019.
5. Hu, B.; Zhang, J.; Shkrob, I. A.; Zhang, Z.; Zhang, L. Poly(4-vinylbenzoic acid) binders for the silicon anode of lithium-ion batteries. Manuscript in preparation
6. S. Son and C. Ban, "Systematic Investigation of the Alucone-Coating Enhancement on Silicon Anodes with Polyvinylidene Fluoride as Binder", ACS Applied Materials & Interfaces, Accepted.
7. 231st ECS Meeting in New Orleans, LA, 2017, "Nanostructure Silicon-Based Hierarchical Architectures for High-Performance Lithium-Ion Battery Anode".
8. 231st ECS Meeting in New Orleans, LA, 2017, "An in-Depth Investigation of the Alucone Coating Impact on the Performance of the Silicon Anode".

9. C. Ban, C. Jiang, ECS PRIME, 2016, “Examining Electrical Properties of Solid Electrolyte Interface on Silicon Electrodes”.
10. C. Ban, 18th International Meeting on Lithium Batteries 2016, “Surface Modification of Silicon Anodes for Durable and High-Energy Lithium-Ion Batteries”.
11. J. Xu, M. Ling, L. Terborg, H. Zhao, F. Qiu, J. J. Urban, R. Kostecki, G. Liu, W. Tong*, “Facile Synthesis and Electrochemistry of Si-Sn-C Nanocomposites for High-Energy Li-ion Batteries,” *Journal of the Electrochemical Society*, 164, A1378-A1383 (2017).
12. Wesley M. Dose, Premkumar Senguttuvan, James Blauwkamp, Christopher S. Johnson, The Effect of Pre-lithiation Chemistry on Li Inventory in High-Energy Li-ion Cells, 232nd The Electrochemical Society Meeting, National Harbor, MD, Oct. 1-5, 2017
13. W. M. Dose, V. A. Maroni, M. J. Piernas-Muñoz, I. Bloom, C. S. Johnson, Capacity loss in silicon-graphite blended anodes upon extended cycling: a new approach to Li inventory, Advanced Batteries for Automotive Applications (ABAA10), Oak Brook, IL Oct. 22-25, 2017
14. “Next Generation Anodes for Lithium-Ion Batteries: Materials Advancements,” 2017 U.S. Department of Energy Vehicle Technologies Office Annual Merit Review and Peer Evaluation Meeting, June 5-9, 2017, Washington, DC.

References

1. *Alloy Negative Electrodes for Li-Ion Batteries*. M.N. Obrovac and V.L. Chevrier, *Chem. Rev.* 2014, 114, 11444-11503.
2. Shi, H.; Zhao, Y.; Dong, X.; Zhou, Y.; Wang, D., Frustrated crystallisation and hierarchical self-assembly behaviour of comb-like polymers. *Chem. Soc. Rev.* **2013**, 42, 2075-2099.
3. Liang, H.; Cao, Z.; Wang, Z.; Sheiko, S. S.; Dobrynin, A. V., Combs and Bottlebrushes in a Melt. *Macromolecules* **2017**, 50, 3430-3437.
4. Daniel, W. F. M.; Burdyska, J.; Vatankhah-Varnoosfaderani, M.; Matyjaszewski, K.; Paturej, J.; Rubinstein, M.; Dobrynin, A. V.; Sheiko, S. S., Solvent-free, supersoft and superelastic bottlebrush melts and networks. *Nat. Mater.* **2016**, 15, 183-189.
5. Zhang, J.; Schneiderman, D. K.; Li, T.; Hillmyer, M. A.; Bates, F. S., Design of Graft Block Polymer Thermoplastics. *Macromolecules* **2016**, 49, 9108-9118.
6. Song, J.; Zhou, M.; Yi, R.; Xu, T.; Gordin, M. L.; Tang, D.; Yu, Z.; Regula, M.; Wang, D., Interpenetrated Gel Polymer Binder for High-Performance Silicon Anodes in Lithium-ion Batteries. *Adv. Funct. Mater.* **2014**, 24, 5904-5910.
7. Magasinski, A.; Zdyrko, B.; Kovalenko, I.; Hertzberg, B.; Burtovyy, R.; Huebner, C. F.; Fuller, T. F.; Luzinov, I.; Yushin, G., Toward Efficient Binders for Li-Ion Battery Si-Based Anodes: Polyacrylic Acid. *ACS Appl. Mat. Interfaces* **2010**, 2, 3004-3010.
8. Pieczonka, N. P. W.; Borgel, V.; Ziv, B.; Leifer, N.; Dargel, V.; Aurbach, D.; Kim, J.-H.; Liu, Z.; Huang, X.; Krachkovskiy, S. A.; Goward, G. R.; Halalay, I.; Powell, B. R.; Manthiram, A., Lithium Polyacrylate (LiPAA) as an Advanced Binder and a Passivating Agent for High-Voltage Li-Ion Batteries. *Adv. Energy Mater.* **2015**, 5, 1501008-n/a.
9. Li, J.; Le, D.-B.; Ferguson, P. P.; Dahn, J. R., Lithium polyacrylate as a binder for tin-cobalt-carbon negative electrodes in lithium-ion batteries. *Electrochim. Acta* **2010**, 55, 2991-2995.

10. Koo, B.; Kim, H.; Cho, Y.; Lee, K. T.; Choi, N.-S.; Cho, J., A Highly Cross-Linked Polymeric Binder for High-Performance Silicon Negative Electrodes in Lithium Ion Batteries. *Angewandte Chemie International Edition* 2012, 51 (35), 8762-8767.
11. Odian, G., Principles of Polymerization, 4th Edition. Wiley-Interscience, New York: 2004; p 832.
12. Ling, M.; Liu, M.; Zheng, T. Y.; Zhang, T.; Liu, G., Investigating the Doping Mechanism of Pyrene Based Methacrylate Functional Conductive Binder in Silicon Anodes for Lithium-Ion Batteries. *J. Electrochem. Soc.* 2017, 164 (4), A545-A548.
13. T. D. Hatchard and J. R. Dahn, *Journal of The Electrochemical Society*, 2004, **151**, A1628-A1635.
14. H.-J. Ahn, Y.-S. Kim, K.-W. Park and T.-Y. Seong, *Chemical Communications*, 2005, DOI: 10.1039/B407264B, 43-45.
15. X. Xiao, J. S. Wang, P. Liu, A. K. Sachdev, M. W. Verbrugge, D. Haddad and M. P. Balogh, *Journal of Power Sources*, 2012, **214**, 258-265.
16. H. Wang, H. Huang, L. Chen, C. Wang, B. Yan, Y. Yu, Y. Yang and G. Yang, *ACS Sustainable Chemistry & Engineering*, 2014, **2**, 2310-2317.
17. Y. Kwon and J. Cho, *Chemical Communications*, 2008, DOI: 10.1039/B716694J, 1109-1111.

II.B.4 Silicon Electrolyte Interface Stabilization (SEISta) (NREL, ANL, ORNL)

Anthony Burrell, Principal Investigator

National Renewable Energy Laboratory
15013 Denver West Parkway
Golden, CO 80401
Phone: 303-384-6666
E-mail: Anthony.Burrell@nrel.gov

Brian Cunningham, Technology Manager

U.S. Department of Energy
Phone: 202-287-5686
E-mail: Brian.Cunningham@ee.doe.gov

Start Date: July 1, 2016

End Date: September 30, 2019

Total FY17 Project Cost: \$2,650,000 DOE FY17 share: \$2,650,000 Non-DOE share: \$0

Introduction

The SEISta project was developed to specifically tackle the foundational understanding of the formation and evolution of the solid electrolyte interphase on silicon. This project will have as its primary goal an understanding of the reactivity of the silicon and lithiated silicon interface with the electrolyte in lithium-ion systems. It consists of researchers from multiple national laboratories (ANL, SNL, ORNL, LBNL, and NREL) working toward clear unified goals.

Silicon is a viable alternative to graphitic carbon as an electrode in lithium-ion cells and can theoretically store >3,500 mAh/g. However, lifetime problems have been observed that severely limit its use in practical systems. The major issues appear to involve the stability of the electrolyte and the uncertainty associated with the formation of a stable solid electrolyte interphase (SEI) at the electrode. Recently, calendar-life studies have indicated that the SEI may not be stable even under conditions where the cell is supposedly static. Clearly, a more foundational understanding of the nature of the silicon electrolyte interface is required if we are to solve these complex stability issues. A new multi-lab consortium has been formed to address a critical barrier in implementing a new class of materials used in lithium-ion batteries that will allow for smaller, cheaper, and better performing batteries for electric-drive vehicles. This consortium, nicknamed the Silicon Electrolyte Interface Stabilization (SEISta) project, was formed to focus on overcoming the barrier to using such anode materials. Five national laboratories, led by the National Renewable Energy Laboratory (NREL), are involved: NREL, as well as Argonne (ANL), Lawrence Berkeley (LBNL), Oak Ridge (ORNL), and Sandia National Laboratories (SNL).

Objectives

- Overarching Mission: Develop a stable SEI layer for silicon anodes to enable the use of intermetallic anodes for lithium-ion batteries.
 - Critical Questions:
 - What are the properties of the lithiated silicon electrolyte interface?
 - What is the silicon SEI actually made of and what reactions are contributing to it?
 - How fast does the silicon SEI grow?
 - Does it stop growing?
 - Is it soluble?
 - Can it be stabilized?

- After we solve these critical questions, we need to understand how the following variables affect the SEI layer:
 - Voltage
 - Temperature
 - Electrolyte and additives
 - Cathode transition metals
 - % lithiation
- FY17 Objectives
 - Quarter 1 Milestone:
 - Established protocols for sample synthesis, preparation, characterization, and analysis to ensure compatibility of experimental data from all consortium members. Protocols will be posted on the shared cloud drive and provided to the ANL lead silicon electrode deep-dive.
 - Quarter 2 Milestone:
 - Completed round-robin sample analysis to ensure protocols established in Quarter 1 are functional. Results based upon less than 5% variance in electrochemical performance between laboratories to ensure equivalent starting materials and preparations.
 - Quarter 3 Milestone:
 - Define the relationship between the surface of the lithiated silicon and the nature of the SEI by demonstrating that the chemical or physical properties are or are not affected by the nature of the silicon surface treatment—specifically, by contamination, oxide content, dopant level, or degree of crystallinity.
 - Quarter 4 Milestone:
 - Determine if the nature of the silicon (purity level, doping, and/or structure) have an effect on formation and evolution of the SEI. This will be determined by observing measurable chemical and physical changes in the SEI layer between substrates.

Approach

The SEISta team works to ensure that protocols for sample preparation, experimental design and implementation, as well as data reporting are consistent across the whole team. Each laboratory is working toward the same set of quarterly milestones using its own specific talents and capabilities in a concerted effort with the other team members. This joint focus results in multiple researchers interacting to produce and analyze data to ensure that individual experimental variations are not leading to erroneous results. Critical to the success of this effort is the use of standard samples that can be shared by all parties. In the first FY, a round-robin sample test was established to ensure that data could be duplicated at the different laboratories by different researchers. In addition to weekly whole-team video presentations, we have held on-site face-to-face meetings each quarter for all team members, and other interested parties, to brainstorm and sort out issues with existing experiments and jointly develop new experimental plans.

Results

- *In-situ* neutron reflectometry was used to identify and follow the thickness and composition of the SEI layer with fluoroethylene carbonate (FEC) additives.
- Developed tip-enhanced Raman spectroscopy method to characterize the SEI.

- Completed round-robin analysis of vapor-deposited thin films and identified key areas to address.
- Explored the gassing of silicon-based materials and the influence of the surface chemistry of these materials on the reactivity.
- Completed an investigation of the passivating behavior of tin-based model electrodes. The effect of oxygen species and electrolyte formulation has been studied. The reductive decomposition reaction of ethylene carbonate:diethyl carbonate (EC:DEC)-based electrolytes has been revealed, demonstrating that Li_2CO_3 is the primary product of EC decomposition.
- Determined the role of a dense thermal oxide layer on Si. Relative to the native oxide on the Si surface, the thermal oxide reduces side reactions with the electrolyte and inhibits cracking; but it also impedes lithiation of the underlying Si. There was no evidence of a conversion reaction of the oxide or formation of a known bulk silicate during initial stages of cycling. Thermal oxide coatings to Si anodes could be beneficial with optimization of thickness and morphology of the Si.
- Thin films of Li_2O , Li_2CO_3 , and LiF were applied to Si wafer model electrodes as preliminary steps to the development/study of the concept of “artificial SEIs” on the electrochemical properties of Si anodes. The preliminary results were similar to those reported above for the thermal oxide. More work is needed to explore this approach further.
- Conducted comprehensive Fourier transform infrared (FTIR) spectroscopy characterization of solid-phase material to elucidate chemical reactivity of different forms of Si, SiO_2 , and Li_xSiO_y with electrolyte (EC/LiPF₆ and Gen2).
- Determined key process parameter (W/cm³) to tune plasma-synthesized Si nanoparticle phase: a-Si → a-Si:H → c-Si.
- Completed design and testing of scaled-up load-lock collection system for plasma-prepared Si nanoparticles.
- Successfully devised a high-yield synthesis of Li_7Si_3 , an intermediate product in the lithiated silicon system (“ $\text{Li}_{2.3}\text{Si}$ ”). About 4 g of product were characterized and passed onto the team via round-robin or reaction studies.
- Showed that even in 3 ppm or less of air or water, the surface of the material will self-discharge to produce $\text{Li}_{12}\text{Si}_7$ (“ $\text{Li}_{1.7}\text{Si}$ ”, by X-ray diffraction (XRD), ²⁹Si nuclear magnetic resonance (NMR)) and $\text{Li}_2\text{O}/\text{LiOH}$ (via Raman, FTIR).
- Reactivity studies followed by ²⁹Si or ⁷Li NMR showed significant rapid reactivity of lithiated silicon with the conventional binder PVDF, and limited reactivity with ANL CAMP standard-LiPAA.
- Developed a method, using XRD and NMR, to directly probe and study the inherent reactivity of lithium silicides vs. typical Li-ion battery components.
- Purchased, installed, and tested systems for air-free transfer of samples between Ar glove box, focused-ion-beam mill, Fishione Nanomill, and FEI F20 UT FEG STEM.
- Began electron microscopy analysis of selected Si anode samples.
- Developed scanning spreading resistance microscopy (SSRM), an atomic force microscopy (AFM)-based nano-electrical probe, to map in nm resolutions the three-dimensional electronic resistance of SEI. This was done laterally by the sharp probe and vertically by milling away SEI materials layer by layer.

- The electronic resistance of the SEI was found to be large (up to 10^9 Ohm-cm) but finite, and relatively uniform within one order of magnitude in the lateral direction; but it decreases sharply along the vertical direction from the SEI surface toward the Si.
- The electronic resistance and thickness of the SEI was observed to depend on lithiation/delithiation parameters, most sensitively on the electrolyte.
- Established protocol for sample preparation and testing.
 - Completed round robin on Cu samples
 - Initiated round robin on Si samples
- Established deposition conditions for controlled Li:Si ratio silicates.
 - Deposited Li:Si 0 to over 8
 - Deposited test samples
 - Characterized film evolution on model SEIs in lithiated and nonlithiated states
- Test cells built, tested, and distributed to teams.

Summary of Milestones for FY17

Quarter 1 Milestone

Establish protocols for sample synthesis, preparation, characterization, and analysis to ensure compatibility of experimental data from all consortium members. Protocols will be posted on the shared cloud drive and provided to the ANL lead silicon electrode deep-dive.

This milestone was 100% completed. The project required the development of multiple procedures for shipping, testing, and analysis of samples. All materials were purchased from single sources and distributed by the purchasing laboratory, and then packaged and shipped to partner organizations. SNL purchased copper foil, NREL purchased silicon wafers and electrolytes, and ORNL purchased lithium foil.

Quarter 2 Milestone

Complete round-robin sample analysis to ensure protocols established in Quarter 1 are functional. Results based on less than 5% variance in electrochemical performance between laboratories to ensure equivalent starting materials and preparations. As new samples and partners are added, these protocols need to be updated and added to.

This milestone is 100% complete, although it was delayed from the initial Q2 date until Q4 and we did not achieve the 5% threshold, with a 7% spread in the data being achieved. This difference was due to the unanticipated difficulty in selecting samples and getting delivery, as well as the need for unified testing equipment. The analysis of the data, which was based on thin-film samples all prepared at ORNL is described below, but can be summarized in the following points. 1) Sample preparation adds some variability to the data, but storage time has a more significant impact on the data. 2) Storage and treatment of the samples result in variances that need to be addressed in the next year. 3) Potential issues with cell design have to be addressed moving into FY18 because each laboratory used its own cell configuration (punch size and alignment). 4) The potential for damage to the sample needs to be addressed in future work. Use of the standard cell, which is described below, will help address many of these issues.

Quarter 3 Milestone

Define the relationship between the surface of the lithiated silicon and the nature of the SEI by demonstrating that the chemical or physical properties are or are not affected by the nature of the silicon surface treatment—specifically, by contamination, oxide content, dopant level, or degree of crystallinity.

This milestone is 100% complete. The nature of the silicon has a dramatic effect on the chemical reactivity of the interface even before electrochemistry. This is described below in the different chemical reactivity studies.

Quarter 4 Milestone

Determine if the nature of the silicon (purity level, doping, and/or structure) has an effect on formation and evolution of the SEI. This will be determined by observing measurable chemical and physical changes in the SEI layer between substrates.

This milestone is 100% complete. The nature of the silicon has a dramatic effect on the formation of the SEI. Clear differences between the commercially prepared wafer samples are apparent in the electrochemistry, as well as differences between the sputtered samples and the wafers.

Round-robin analysis of vapor-deposited thin films to identified key areas to address in integrated laboratory experimental work.

As part of the SEISta program, we executed a round-robin evaluation of electrode materials with the goal of identifying reproducibility between labs and reproducibility of producing samples. ORNL prepared 18 sets of identical samples that were distributed to the partner labs. These films consisted of amorphous silicon deposited on battery-grade copper foil (SNL). The films were deposited at an applied power of 90 W at a distance of 7.0 cm from substrate to target. Samples were deposited at 7.0 mtorr of argon pressure, which is the same pressure used to deposit the sample used for the Neutron Reflectometry (NR) studies. The thickness of the films was determined to be 55 ± 2 nm based on quartz-crystal microbalance and neutron reflectometry measurements. The density of the films was estimated to be 2.1 g/cc from the NR data. The initial and final samples were kept at ORNL; the remaining samples were distributed to the team members to try to identify changes in materials chemistry or surfaces as a function of target aging.

The films were punched into electrodes with diameters from 10 to 15 mm at the various labs and assembled into half-cell-type coin cells using a standard 18-mm Celgard 2325 separator and 200 μ L electrolyte/cm² of electrode. This procedure was provided on the Box site. The electrolyte was purchased in bulk and distributed to each of the team members. There were two base electrolytes: 1.2 M LiPF₆ and 1.0 M LiTFSI in 3:7 wt% ethylene carbonate: ethyl methyl carbonate. Cells were cycled at a rate of C/10 in a constant current/constant voltage-type measurement. The procedure was provided to all the team members via the Box site. The cycled data were aggregated at ORNL.

Figure II-118 shows the data collected for the LiPF₆-based electrolyte. From these data, several unique features are observed. First, there appears to be a wide discrepancy in the capacity of the cells measured at each laboratory. Second, there is evidence for an electrochemical transition or reaction at 0.5 V (vs. Li/Li⁺), which is likely the reduction of EC on the electrode surface.

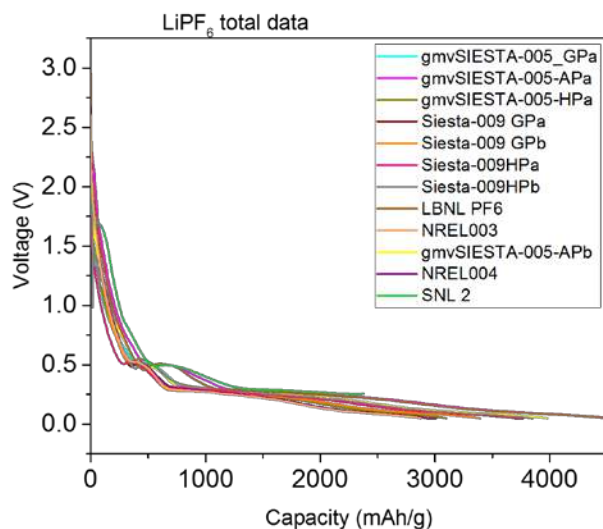


Figure II-118. Raw capacity versus voltage data for cells cycled in the LiPF₆ electrolyte.

This 0.5 V transition appeared constant for all the samples evaluated in this study. Given this consistency, all the data were normalized to a point below this transition (0.45 V vs. Li/Li+). This normalized data are shown in Figure II-119. A magnified view of the data above 0.45 V and below 0.45 V is shown in Figure II-120 and Figure II-121, respectively. The data show that most of the differences observed in capacities (Figure II-118) are due to reactions that are occurring at potentials above 0.5 V. Indeed, the average capacity for the electrodes is within 417 mAh/g after shifting to 0.45 V. This is within 7% of the theoretical capacity of the electrodes and close to the 3.2% error associated with the uncertainty in silicon thickness (± 2 nm). The key issue now is identifying the reactions that are occurring above 0.5 V and why they vary between all the electrodes. Potential variables include aging of the sample, storage conditions (air or argon), and sample-handling procedures.

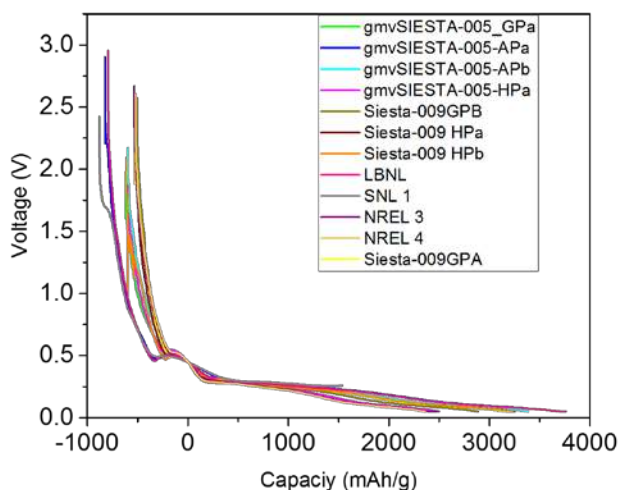


Figure II-119. Capacity versus voltage data for cells cycled in the LiPF₆ electrolyte shifted to 0.45 V.

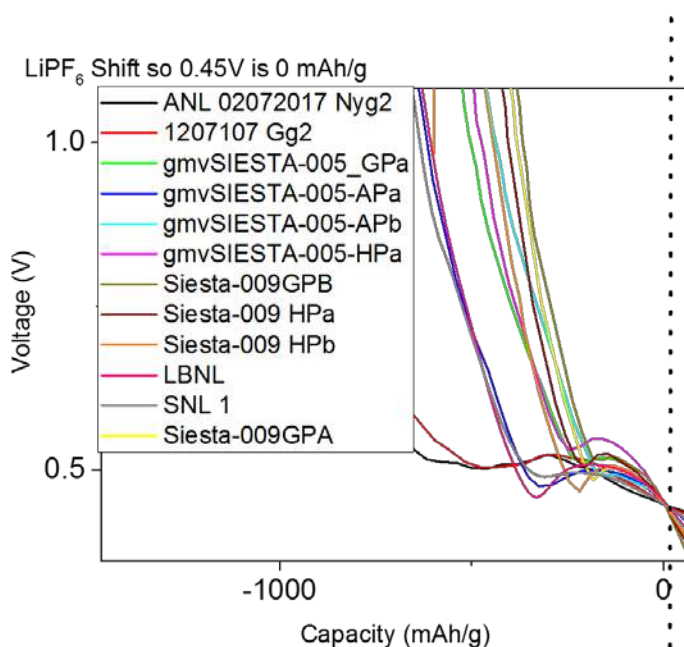


Figure II-120. Magnified view of capacity versus voltage data for cells cycled in the LiPF₆ electrolyte above 0.45 V.

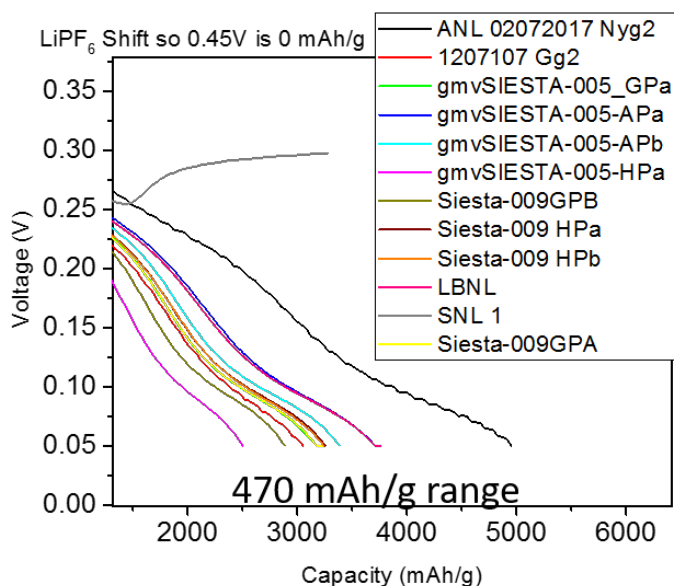


Figure II-121. Magnified view of capacity versus voltage data for cells cycled in the LiPF₆ electrolyte below 0.45 V.

Identical electrodes were cycled in an electrolyte with LiTFSI as a salt. The aggregated data is shown in Figure II-122. Again there were large differences in observed capacities along with a plateau at 0.5 V vs. Li/Li⁺. The consistency of this voltage plateau would confirm the reaction is coming from the reduction of the solvent since it is the same as the LiPF₆ electrolyte. Again the data were shifted so that zero capacity is located at 0.45 V vs. Li/Li⁺. Figure II-123 and Figure II-124 show magnified views of this shifted data above and below 0.45 V respectively. Again the largest variation in capacity is due to the electrochemical reactions that occur above 0.5 V. The capacities below 0.45 V are within 1000 mAh/g, which is a 22% error. This is far

larger than the LiPF₆ data but points to a different reaction mechanism with LiTFSI versus LiPF₆ likely in the SEI formation. Interestingly the samples with the highest capacities above 0.5 V also had the largest capacities below 0.45 V. This points to a reaction mechanism where whatever changes the surface reactions continues to mediate the reactivity during lithiation. Understanding this correlation will enable a more detailed understanding of the SEI formation mechanism and the role of the salt.

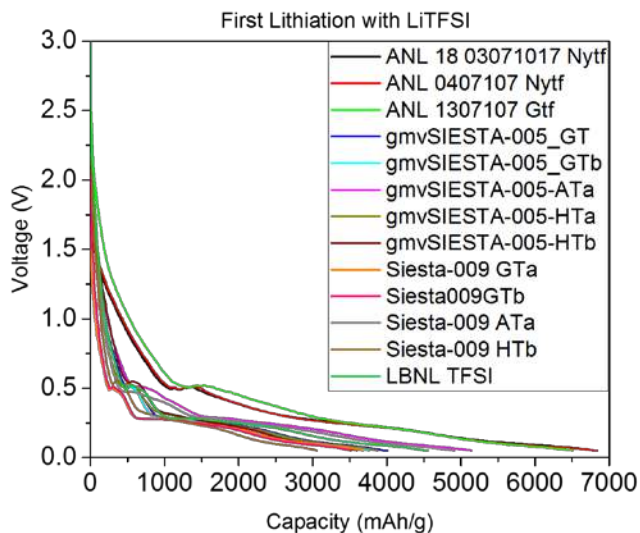


Figure II-122. Raw capacity versus voltage data for cells cycled in the LiTFSI electrolyte.

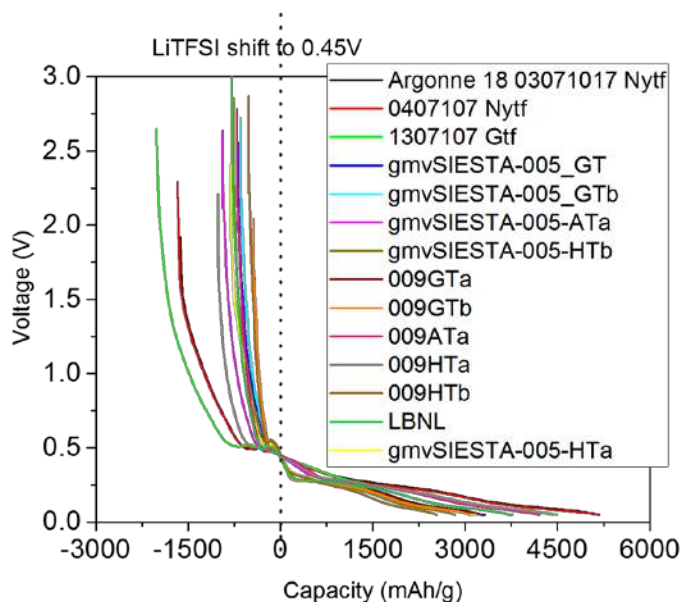


Figure II-123. Capacity versus voltage data for cells cycled in the LiTFSI electrolyte shifted to 0.45 V.

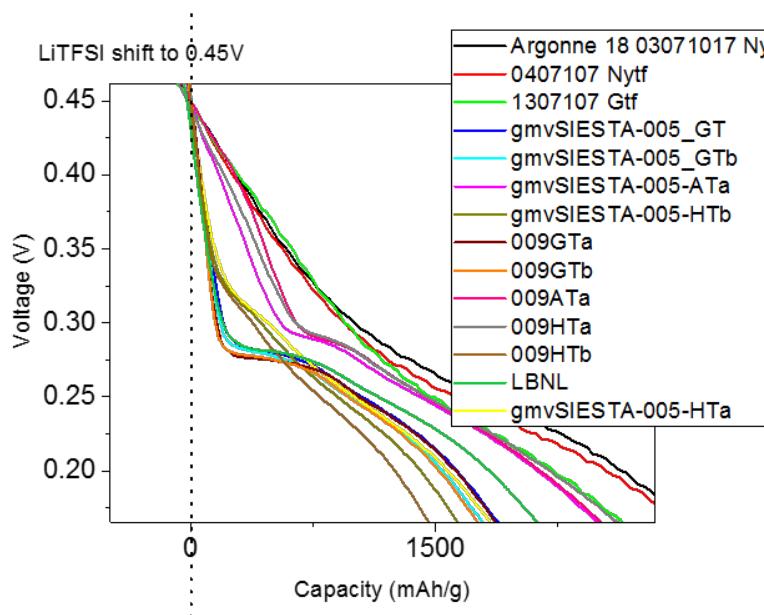


Figure II-124. Magnified view of capacity versus voltage data for cells cycled in the LiTFSI electrolyte below 0.45 V.

To understand the origin of this capacity above 0.5 V, we performed XPS measurements on uncycled Si electrodes stored in air and in an argon-filled glove box. The data from these measurements are presented in Figure II-125, which shows a clear change in the surface Si-O with storage condition. This means that the surface is becoming progressively more oxidized with time in air. This surface oxide may be the cause of the capacity differences. Furthermore, these data indicate that time is a critical variable in the analysis of silicon electrodes. Future studies will include time-dependent data and records to identify these effects.

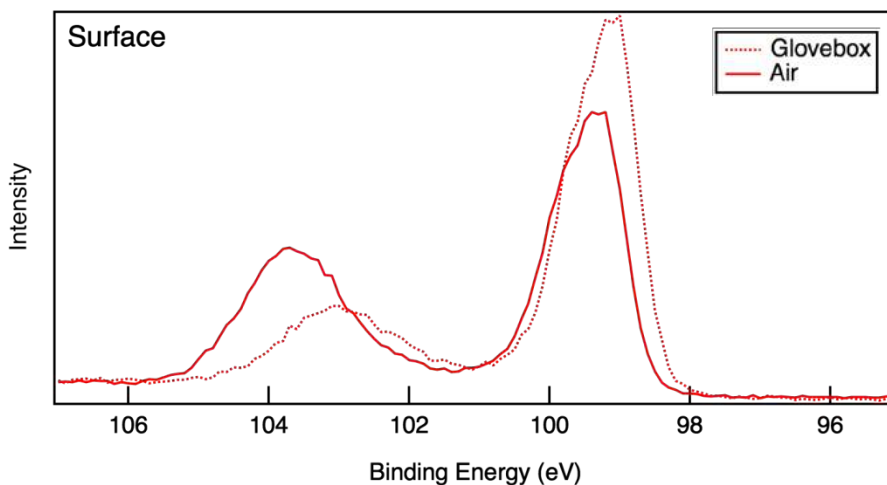


Figure II-125. XPS data collected for an uncycled silicon electrode aged in a glove box and in air for 3 weeks.

Time-of-flight SIMS (TOF-SIMS) depth-profiling measurements were performed on sputter-deposited silicon on copper-foil films prepared at both NREL and ORNL. Some of the profile data sets are shown in Figure II-126. In addition to observed variations in oxygen and fluorine content in the silicon films between the sites (not shown), the figure illustrates that transition-metal impurities were noted in the silicon films deposited at both sites. Because these transition metals are all constituents of stainless steel, it is believed these impurities are coming from the stainless-steel ring that holds the silicon sputter target in place. Although the

SIMS data sets are not quantified, the concentrations of these species likely fall in the 1×10^{16} – 1×10^{19} atoms/cm³ range. It remains unclear whether impurities at those levels affect electrochemical performance to a significant degree.

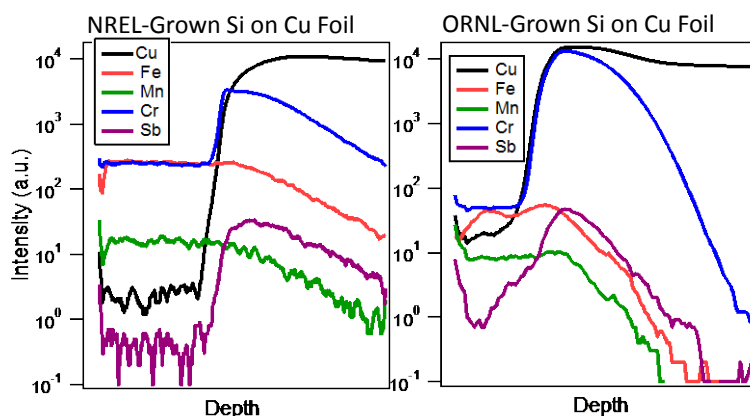


Figure II-126. TOF-SIMS depth profiles of silicon films on copper foil grown at both NREL (left) and ORNL (right). Only composition profile for the transition-metal impurities and the copper substrate are shown.

To assist in understanding the variability in the round-robin tests of sputtered Si films on Cu-foil substrates, in late FY17 we performed initial measurements on samples stored in glove boxes at each site. The aim is to assess whether the variability observed in electrochemical performance is due to surface contamination caused by various glove box ambients, or perhaps due to variability in implementation of the testing protocol.

We have performed TOF-SIMS measurements on samples from two sites so far, NREL and ORNL. Preliminary TOF-SIMS and XPS analyses of the ORNL samples suggest there are some changes to the samples upon long-term storage in the ORNL glove box. We observed lower surface coverages of fluorine and chlorine for the three ORNL samples, as shown in Figure II-127. In addition, we noted the presence of a high-intensity peak at mass 147, which we attribute to pump oil ($C_8H_3O_3$) on the sample that was in the glove box for 3 months. This peak was clearly not present in the sample exposed to air for 2 weeks, or in the sample that was in the glove box for 2 weeks. Thus, we tentatively conclude that introduction of large amounts of surface contamination from the glove box ambient is not a major source of error, at least for samples in the box for short times at the ORNL location. Analysis of samples from other sites is expected in early FY18.

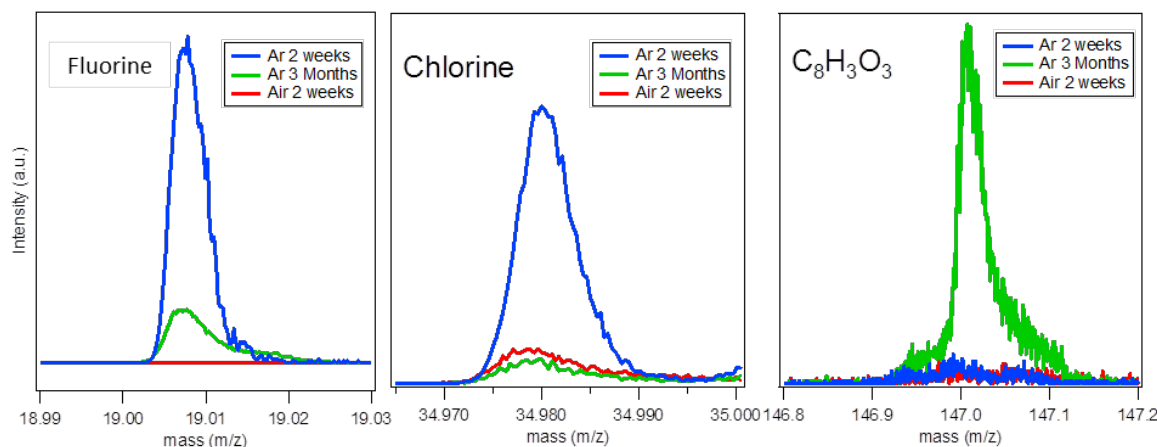


Figure II-127. TOF-SIMS surface spectra of the ORNL films, showing the changes to the sample surface upon long-term exposure in the ORNL glove box, as well as shorter-term exposure to air.

We have concluded that the variation in sample handling and cell assembly may have contributed to the variance in the data; therefore, we implemented a new cell-design project to ensure that this variability was minimized.

In light of the variability of the thin-film samples, a set of wafer samples was selected to duplicate the round robin, and this test is currently beginning for FY18. SEISta initial characterization of the wafer samples was completed in FY17, and the analysis and second round robin for these samples are scheduled for Q1 FY18. In FY17, NREL TOF-SIMS capabilities supported the SEISta Si wafer round-robin study with surface characterization and depth-profiling measurements of the prepared Si wafer surface prior to cycling. The goal of these and other surface-characterization measurements was to document surface cleanliness and correlate with subsequent electrochemical properties and cycling performance. In these studies (summarized in Figure II-128 through Figure II-130), we noted from principal-component statistical analysis of the spectra that samples subjected to RCA cleaning after the native-oxide formation process had much less surface contamination in the form of carbon-containing species, sodium, fluorine, and chlorine.

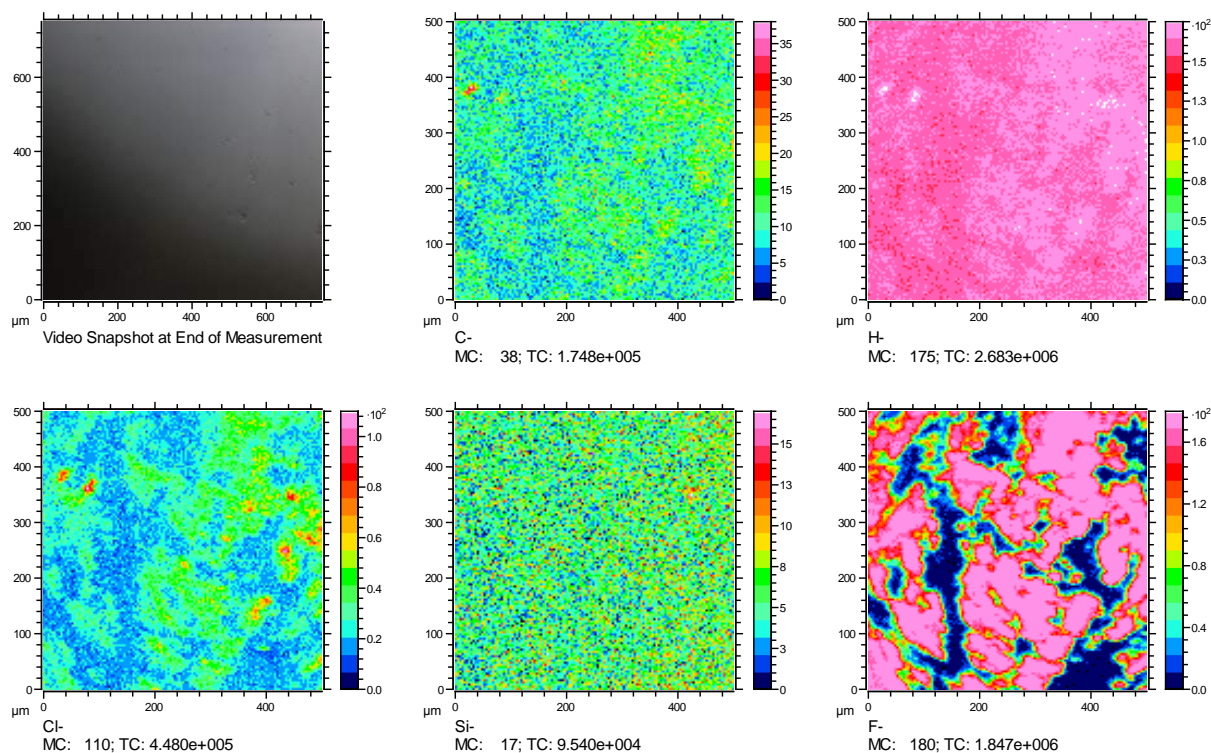


Figure II-128. Optical and negative-polarity TOF-SIMS images from as-received (uncleaned) SEISta round-robin Si(001) wafer sample with native oxide. Mass channel labels are to the lower left of each image. The measurements reveal large amounts of fluorine and chlorine contamination.

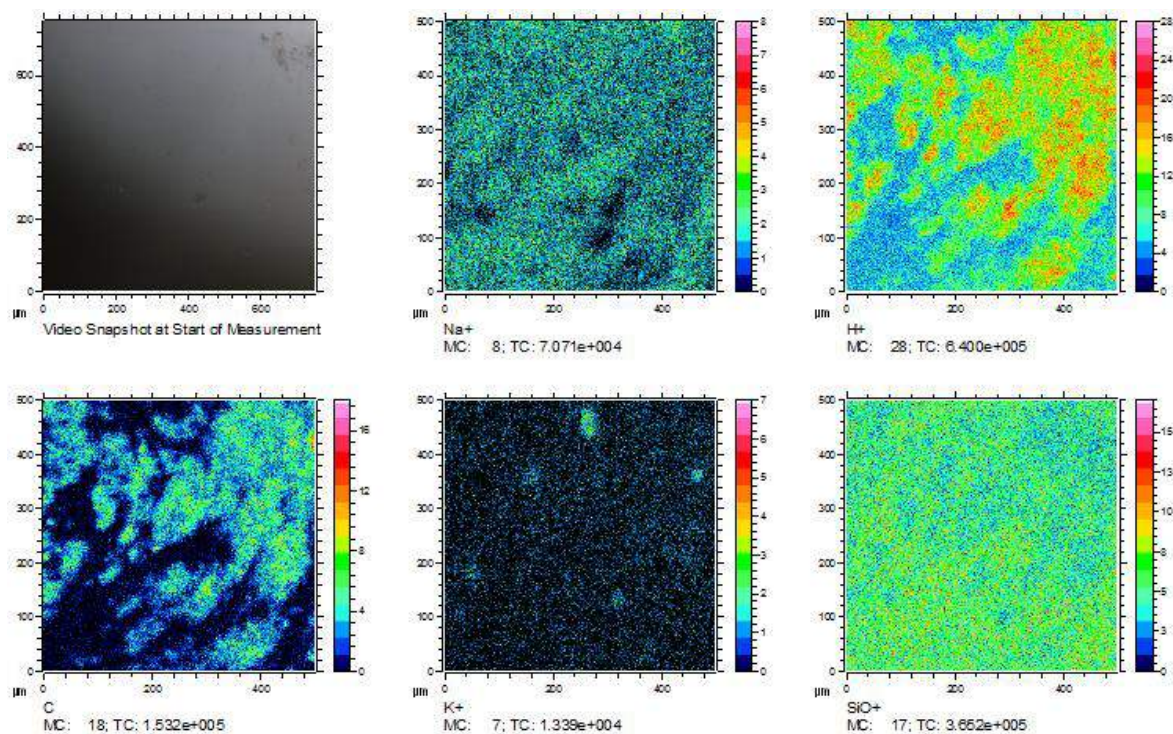


Figure II-129. Optical and positive-polarity TOF-SIMS images from as-received (uncleaned) SEISta round-robin Si(001) wafer with a native oxide. Mass channel labels are to the lower left of each image. The measurements reveal a large amount of hydrocarbon contamination.

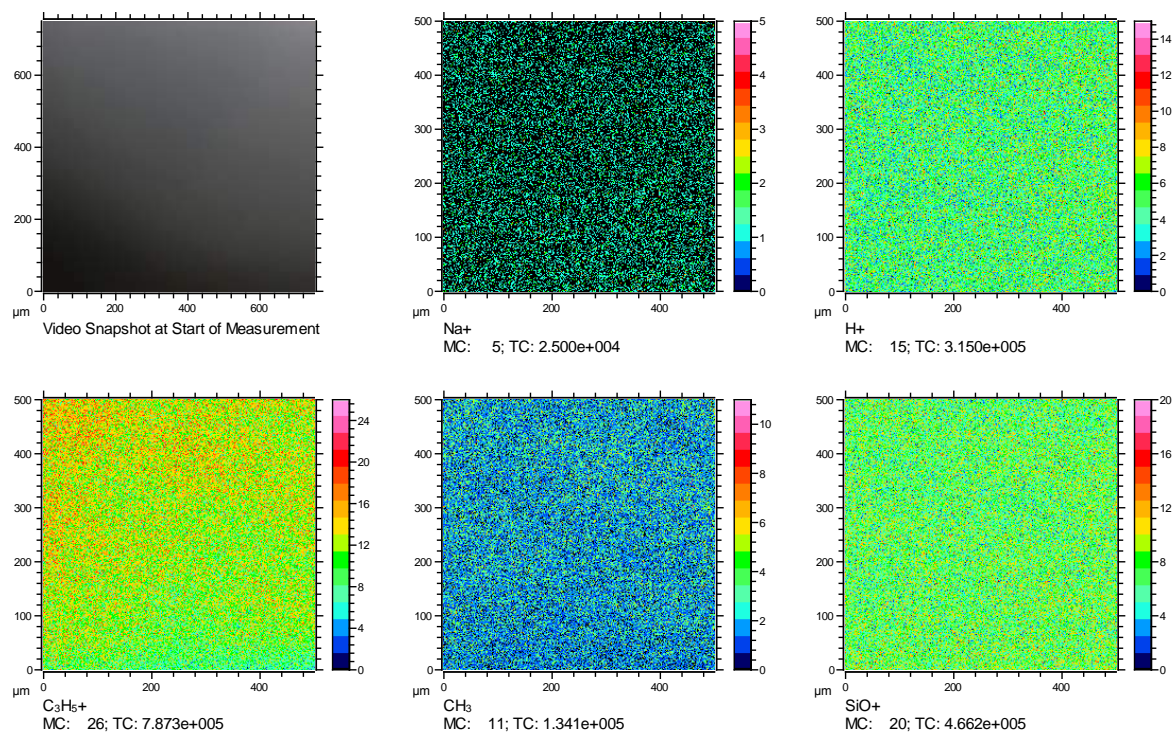


Figure II-130. Optical and positive-polarity TOF-SIMS images from RCA-cleaned SEISta round-robin Si(001) wafer with a native oxide. Mass channel labels are to the lower left of each image. Essentially no hydrocarbon contamination is observed.

TOF-SIMS depth profiling and 3-D tomography measurements were also completed on cycled Si-wafer samples to support the Kelvin probe force microscopy (KPFM) and scanning spreading resistance microscopy (SSRM) experiments also performed at NREL. Surface spectra, standard depth profiling, and 3-D tomography (100-nm lateral resolution) measurements were completed on half-cycle (lithiated) and full-cycle (delithiated) samples. The TOF-SIMS depth profile results support the very interesting observations of SSRM milling experiments that the SEI is substantially thicker for the half-cycle specimen than the full-cycle specimen. The data presented in Figure II-131 show profiles of two species associated with the SEI layer for the two samples taken under identical analysis conditions. The TOF-SIMS sputter-crater depths will be verified by a second set of AFM measurements so that precise determinations can be made for overall SEI thicknesses in the two cases.

TOF-SIMS 3-D tomography at 100-nm lateral resolution can reveal the chemistry and microstructure of the SEI, and representative results for the full-cycle SSRM sample are shown below (Figure II-132 and Figure II-133) for the lithium and hydrocarbon distributions, respectively, within the SEI, which appear to accumulate within the observed cracked areas.

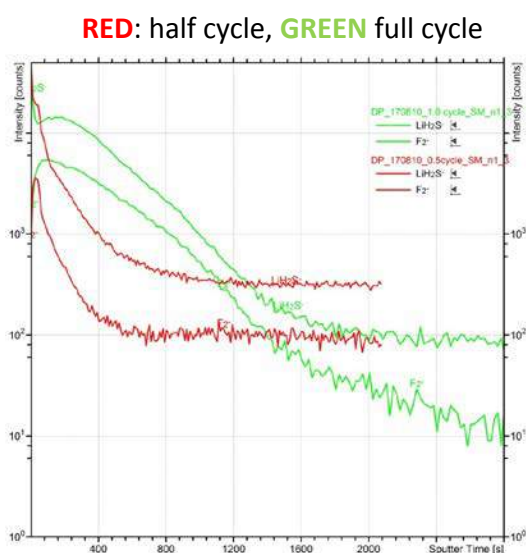


Figure II-131. TOF-SIMS depth profiles of two Si-wafer samples that were also analyzed with SSRM. The red profile is the half-cycle sample, and the green is the full-cycle sample. Consistent with the KPFM data, it appears that the SEI is much thicker for the delithiated sample—an interesting result.

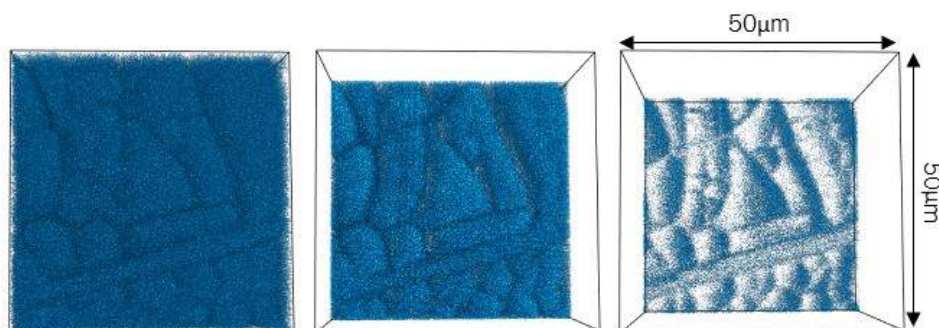


Figure II-132. TOF-SIMS 3-D reconstruction of the lithium distribution in the SEI of the full-cycle KPFM specimen (50 μm x 50 μm area, depth currently unknown). The image at left shows the full dataset; image in the middle shows the data from about halfway through the SEI; image at right shows the lithium distribution at transition between the SEI and the silicon.

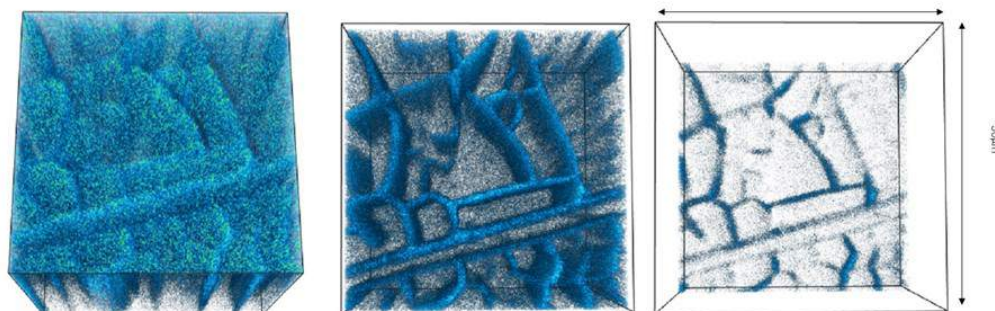


Figure II-133. TOF-SIMS 3-D reconstruction of the C2H⁻ distribution in the SEI of the full-cycle SSRM specimen (50 μm x 50 μm area, depth currently unknown). The image at left shows the full dataset; image in the middle shows the data from about halfway through the SEI; image at right shows the lithium distribution at transition between the SEI and the silicon.

To ensure reliability of data collected with these new wafer samples, the test cell will be used by all partners in future studies. We have begun the implementation of a standardized three-electrode cell that can accommodate the future work in thin films, wafers, and even composite electrodes.

Design of three-electrode electrochemical cell

To diagnose and distinguish the individual electrode performance, it is necessary to use three-electrode cells. The three-electrode cell enables the separate monitoring charge and discharge potentials at the anode and cathode. There are many existing fixtures, including customized and commercially available products that can perform the three-electrode electrochemical characterization. However, there is large cell-to-cell variation in the cells without a good control of the electrode size, distance between electrodes, amount of electrolyte, and position of each electrode. It is extremely important to standardize the cells to obtain reliable and reproducible electrochemical data. More importantly, the SEISTa project is multi-lab research consortium; the research has been performed by more than 20 PIs across five national labs. Reliable and reproducible data are required to conduct the multi-lab research and are requested for achieving an accurate fundamental understanding of electrochemical properties. Therefore, in this study, a three-electrode electrochemical cell was designed, assembled, and used by team members under the SEISTa project.

The electrochemical cell with three electrodes is shown in Figure II-134 and Figure II-135. The counter electrode and the reference electrode were located in the cell cap and locked by a retainer plate against the working electrode located at the bottom. A locate pin was used to help align the electrodes. Stainless steel (316) was used to collect current and was connected to the banana jack for outside wiring. The stainless-steel current collector was pressed to the working electrode, herein, a silicon wafer. A torque screwdriver was used to apply the pressure on the current collector to enhance the sufficient electrical transfer from the current collector to the silicon wafer samples. The three electrodes are connected via electro wiring to a potentiostat that applies voltage between the working electrode and the reference electrode while measuring the current flow between the working electrode and the counter electrode.

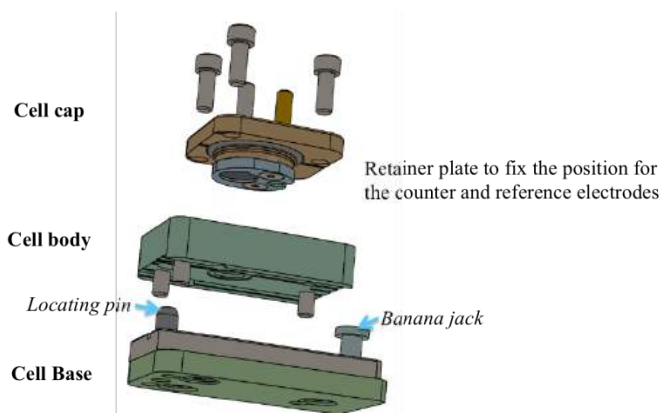


Figure II-134. Schematic sketch of the electrochemical cell: 1) the reference electrode and the counter electrode located in the cell cap (top); 2) cell body (middle); and 3) cell base with the working electrode (bottom).

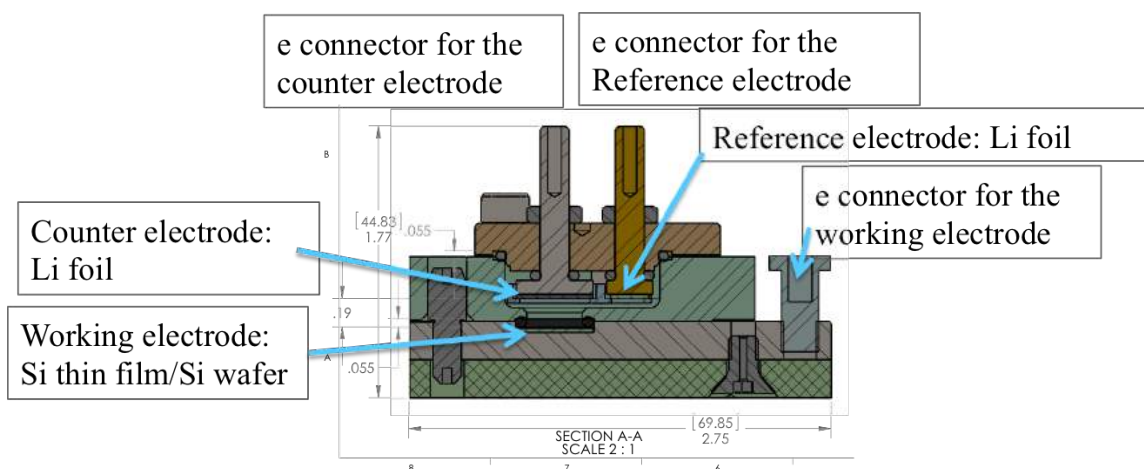


Figure II-135. Cross-sectional sketch of the designed electrochemical cell.

A silicon wafer was selected as the model sample in this project. All of the silicon wafer samples were cut and cleaned by the NREL team, using the standard protocol (described in a previous report). Due to the low conductivity in silicon samples, the pressure between the silicon wafer samples and the stainless-steel current collector is extremely important. As indicated in Figure II-136, the pressure applied on the bottom of the stainless-steel current collector can affect the electrochemical properties. With low pressure (<3 lbs-in), the working electrode experiences a high overpotential, leading to low electrochemical activity with much lower capacity. With high pressure (>5 lbs-in), the brittle silicon wafer samples are easily broken, which generally causes a very noisy electrochemical response, and finally, abnormal electrochemical behavior. When appropriate pressure is applied, reproducible electrochemical behavior can be obtained.

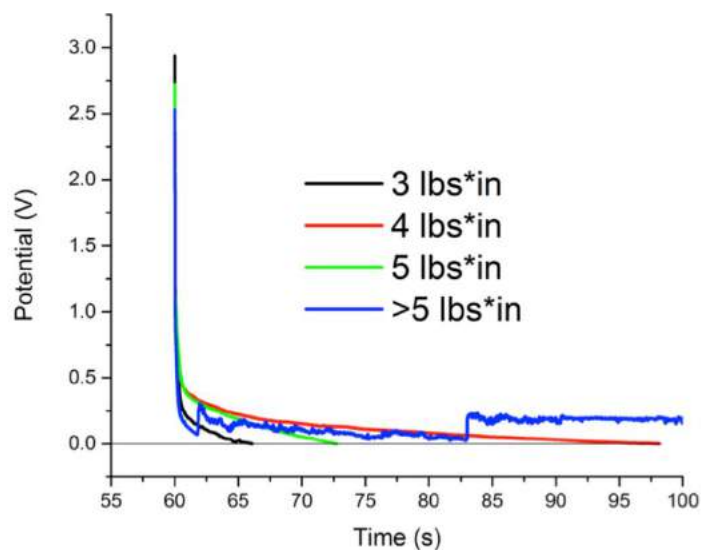


Figure II-136. The voltage profile during lithiation of silicon wafer samples. Increasing pressure was applied on the stainless-steel current collector to ensure sufficient electrical conductivity.

Due to the high reactivity of the organic carbonate electrolyte, any side reactions between the cell components and the electrolyte may cause unexpected electrochemical responses. Therefore, before assembly, it is highly recommended to check all of the components—including the screws, cell body, current collectors, and O-rings—to make sure all components are untouched without color changes, clean and dry, and in their original shape. Here, we have summarized the procedure for cell assembly.

1. Place the stainless-steel spacer directly on the cell base, and put the silicon wafer on the top of the stainless-steel spacer; finally, put the O-ring on the top of the silicon wafer.
2. Put the cell body on the top of the cell base. Use the locate pin to make sure the O-ring is in place, and use the grooves located on the cell body to hold the O-ring.
3. Tighten the screw on the cell body to seal the silicon wafer.
4. Use the torque screwdriver (5716A52, slip-release adjustable torque-limiting screwdriver with bit set) to apply pressure on the screw back of the silicon wafer. Do not apply too much pressure. The torque of 4 lb-in on 18-8SS screw (8/36NF, 3/4" long) can offer good sealing and sufficient contact.
5. Add the electrolyte. Now we add 0.7 mL of electrolyte for the vertical position. We need a little more electrolyte for the other position (testing is going on).
6. Place the lithium metal counter electrode and the lithium reference electrode on the current collectors, which are located on the cell cap. Note that we did not use the retainer plate for now due to the corrosion found on the screws for the retainer plate.
7. Once the cell cap was ready, put the cell cap into the cell body and tighten the screws on the cell cap.
8. Connect the cell with the banana plugs.
9. At this moment, to reduce the inferior effects of the poor wetting/bubbles, we use the vertical position to run the cell.
10. Rest the cell for 4 hours, and use 10 μ A to run the lithiation for 6 hours and delithiation for 6 hours.

The three-electrode cell has been used to demonstrate the electrochemical behavior of our baseline silicon samples, as shown in Figure II-137. The cell resistances, particularly generated from the contact between the backside of silicon wafer samples and the current collector, result in the ohm drop at the beginning of lithiation. In addition to the silicon wafer samples with the native oxide, we plan to investigate the thermal oxide-coated samples. To mitigate the contact resistances, we are currently working with other team members to develop conductive glue and new procedures for enhanced electrical conductivity. In FY18, this cell will continue to be refined and used for both standardization of experiment, but also for spectroscopic measurements.

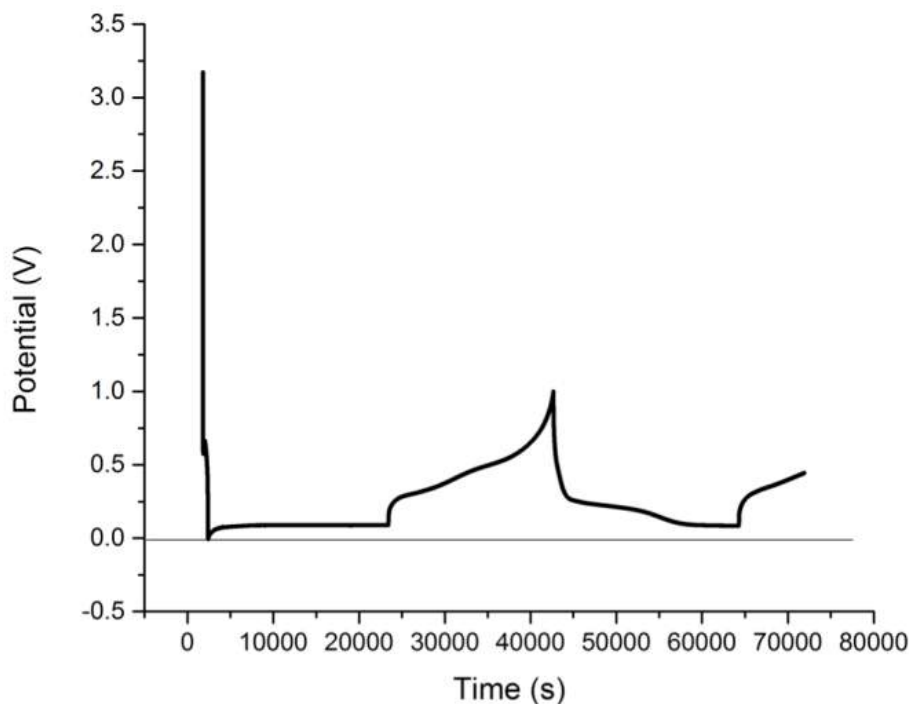


Figure II-137. The voltage profile of the baseline silicon wafer sample, during lithiation and delithiation. The current for both lithiation and delithiation is 10 μ A. The reaction duration is limited to 2 hours for both lithiation and delithiation processes.

Methods to Facilitate Accurate Inter-Lab Comparisons of SEI Chemistry Based on XPS Peak Assignments

One of the key methods employed in the round-robin studies to examine the nature and variation of the silicon thin-film samples was *situ* X-ray photoelectron spectroscopy (XPS). *Ex-situ* XPS analysis is frequently used to help identify chemical states and phases that are present within an SEI. The validity of these analyses depends critically on accurately measuring core-level binding energies (BEs) and correctly assigning peaks to particular chemical states. This task can be quite challenging, in part because the co-existence of multiple overlapping chemical states is a common situation in a complex SEI. For example, more than ten frequently encountered Li functionalities lie within a range of ~ 3 eV in the Li 1s core level. Further complicating accurate XPS chemical-state analysis is the fact that many materials relevant for battery applications are poor electronic conductors, and consequently, they suffer from electrostatic charging effects that artificially shift XPS core levels. To attempt to compensate for these effects, many researchers calibrate XPS BEs by shifting the lowest-observed carbon peak to 284.8 eV (or a similar value, e.g., 284.6 eV), indicative of C-C bonding. This approach often works well, but can lead to inaccuracies in reported core-level BE values if the amount of surface species characterized by C-C bonding is minimal and difficult to detect (a possibility when air-free transfers are employed to minimize effects on highly reactive battery materials), or if another lower-BE functionality is also present in the C 1s region (e.g., carbonate). A result of these complicating factors is that binding energies reported using C-C as a calibration, especially for battery materials, can be highly inaccurate. For example, the literature reported that BEs for a metallic Li vary over a range of nearly 7 eV.

To overcome these issues, we have developed an XPS analysis methodology that can reliably correct for lab-to-lab variability in XPS BE calibration procedures that are exacerbated by charging effects on electronically insulating materials. The approach developed relies on two basic guidelines:

- Each chemical phase should be characterized by a well-defined BE separation between individual elemental core levels associated with that phase. For example, if Li₂O is thought to be a component of the SEI, the BE difference between the O 1s and Li 1s peaks should be constant regardless of charging effects.
- Elemental ratios must be appropriately constrained during peak fitting. This means that if components of a specific spectrum are thought to arise from Li₂O, then a 2:1 Li to O ratio of relative intensities should be observed/fit.

The inability to achieve adequate fits to a subset of XPS spectra while simultaneously applying appropriate elemental-ratio and BE separation constraints described above is generally a strong indication that one or more phases have not been correctly identified. Further, if during peak fitting only one of these two rules is found to be true, then other possibilities should be investigated. For example, possibly both Li₂O₂ and Li₂O are present on the surface rather than just Li₂O and it should be fit accordingly in both core levels. To demonstrate validity of the BE separation rule, a literature survey was completed for available XPS data sets and core-level BEs were plotted (Figure II-138) for inorganic SEI phases. Each of these plots demonstrates a strong linear (unity slope) correlation, as expected if the primary sources of BE errors are simple offsets caused by electrostatic charging. We speculate that outliers in the compiled data sets in Figure II-138 are likely incorrect peak assignments. To confirm some of the BE separation values—and, when possible, identify absolute BEs—specific functional groups were synthesized *in-situ* in the XPS chamber, preventing additional contamination that could cause inaccuracies in the measurements. In these experiments, it was also possible to use the Li 1s and valence-band maximum values from sputter-cleaned metallic Li foils as absolute BE calibrations. Additionally, measurements on thin overlayers (e.g., Li₂O) on metallic Li are much less susceptible to charging phenomena. Data sets obtained in this manner were in good agreement with BE separations calculated from the linear regression of reported literature values (Figure II-139, and blue squares in Figure II-138).

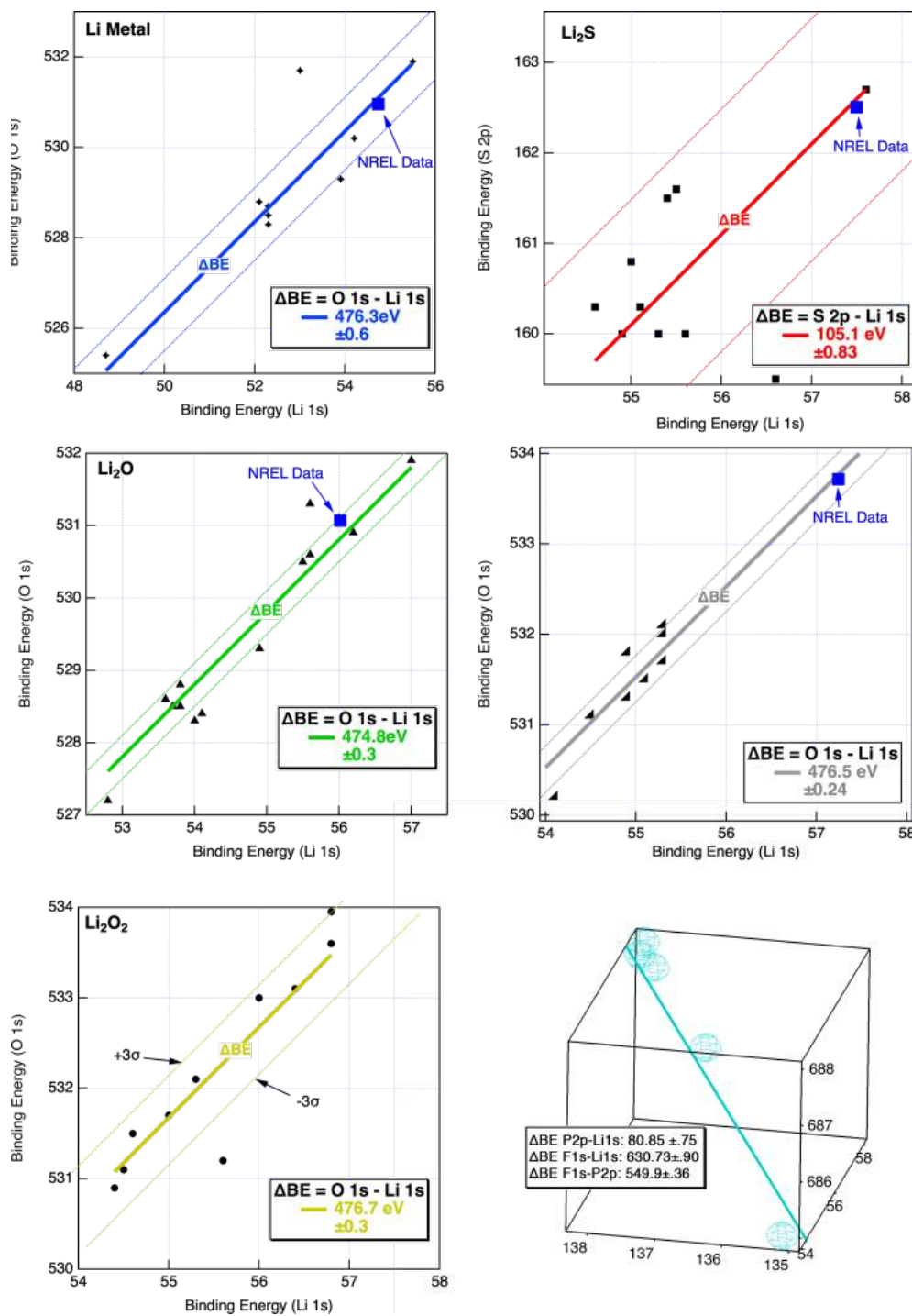


Figure II-138. Summary of binding-energy separations for common inorganic SEI constituents. Reported literature values for specific phases plotted vs. BEs of relevant core levels. Best-fit lines with unity slopes were used to determine average BE separations. In each case, values extracted from NREL datasets are shown as a blue square.

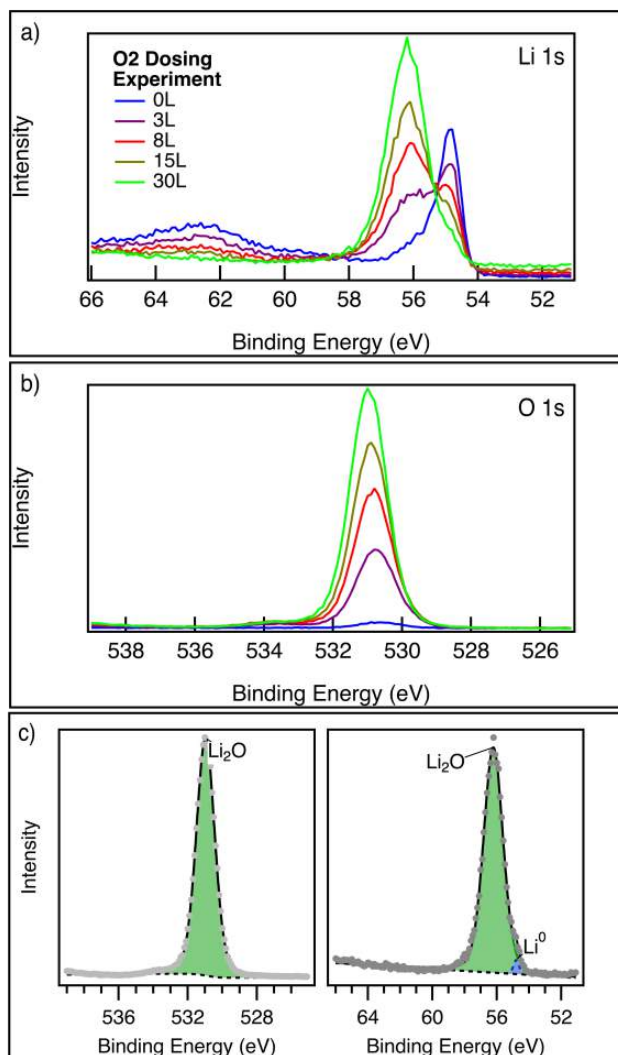


Figure II-139. Time-resolved XPS spectra showing *in-situ* oxygen exposure to form a pristine layer of Li₂O on sputter-cleaned Li metal. BE separation for this phase was found to be 476.85 eV, in good agreement with the prior figure.

Using Computational Methods to Understand the Silicon-Electrolyte Interface

Within the bulk anode, we are interested in dopants or additives to Si that favorably impact its properties. Such properties include a more uniform discharge profile, higher voltage, volumetric expansion, and higher discharge rate. Literature reports show that conversion electrodes lose crystallinity as they charge and become amorphous. The anode will thus be modeled as an amorphous material. As a precursor to additives, amorphous Si with a native oxide layer will be benchmarked to ensure a fundamental understanding of the thermodynamics and kinetics of lithiation of the amorphous electrode.

To generate amorphous configurations, a random liquid configuration of the desired composition is generated using Packmol and the system is brought to equilibrium at high temperature. Snapshots of the resultant melt are then quenched using simulated annealing to generate amorphous phases that preserve the short-range order of the liquid state. Diffusivity calculations are performed in a similar manner using *ab initio* molecular dynamics (AIMD) to simulate elevated temperatures. Equilibrium structures give a glimpse of the thermodynamics of the system, while diffusion captures the kinetics of the system.

We perform classical molecular dynamics simulation (MD) to characterize the solvation structure, self-diffusion coefficient, and other macroscopic properties of the bulk electrolyte (1.2M LiPF₆ in EC, EC/EMC, and EC/FEC). We used two sets of potentials: Optimized Potential for Liquid Simulation (OPLS) and General AMBER Force Field (GAFF). The calculated property results are compared with the experimental results to validate the potentials for MD simulation. With the calculated solvation structure, the 6-31++g* level quantum chemical calculation is conducted to get the IR spectrum result. The calculated and experiment-obtained IR spectra are compared to assign peaks with certain species so that solvation structure information can be deciphered accordingly.

Classical MD is also used to find possible reaction pathways to SEI formation. Si anode at the initial state before charging is modeled with a crystalline structure and an amorphous native silicon oxide layer on top of it. A constant-potential method (CPM) is used with charge fluctuation at the electrode surface to simulate experimental conditions. Harnessing CPM with classical MD, compared to time-consuming AIMD, enables us also to extend the time scale of simulation long enough to explore the dynamics of electrolyte molecules at the charge-fluctuating electrode surface.

Calculated equilibrium phase diagrams (Figure II-140) predict that lithiation of Si will generate lithium silicates (Li_xSi) that discharge to form Si. SiO₂, however, under lithiation is thermodynamically predicted to eventually phase separate into Li_xSi and Li₂O (in deep charge). Upon discharge, the Li_xSi can reform Si, while the Li₂O will stay inactive, contributing to capacity loss. Voltage profiles from the phase diagrams show that the SiO₂ (Figure II-141b) initially discharges at a much higher potential than Si (Figure II-141a); however, the potential drops off rapidly and becomes comparable to the Si potential. This is consistent with the phase diagram, showing that silicides are the discharged species at higher lithium concentration. The high potential of the native oxide provides insight into the formation of the SEI and should be compared to experimental results. The larger potential provides a more favorable potential for electrolyte decomposition and electrolyte formation.

Furthermore, kinetics of the model Si anode were evaluated through Li self-diffusivity using *ab initio* molecular dynamics. Figure II-142 shows the diffusivities of the corresponding Li_xSi and Li_xSiO₂ phases. Most notably in Figure II-142, it is evident that the SiO₂ exhibits significantly slower diffusion for Li from the electrolyte/SEI to the bulk of the Si, and hence, it impedes lithiation of the Si anode.

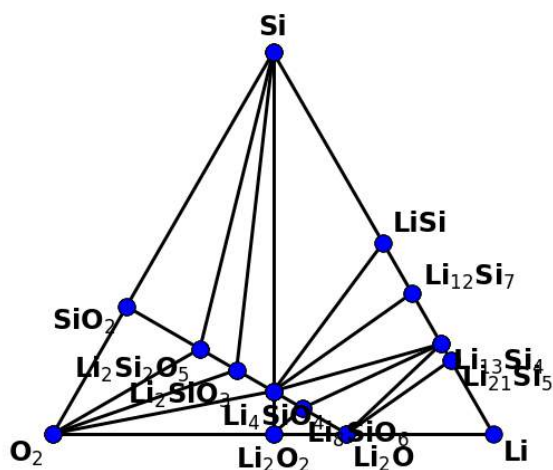


Figure II-140. Ternary phase diagram of the Li-Si-O system.

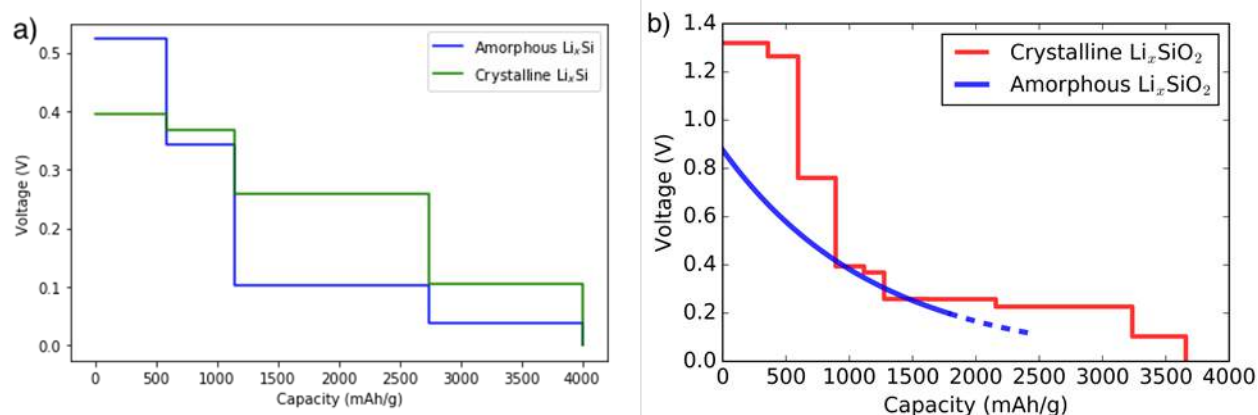


Figure II-141. Voltage profile for a) amorphous and crystalline lithium silicides and b) amorphous and crystalline lithium silicates.

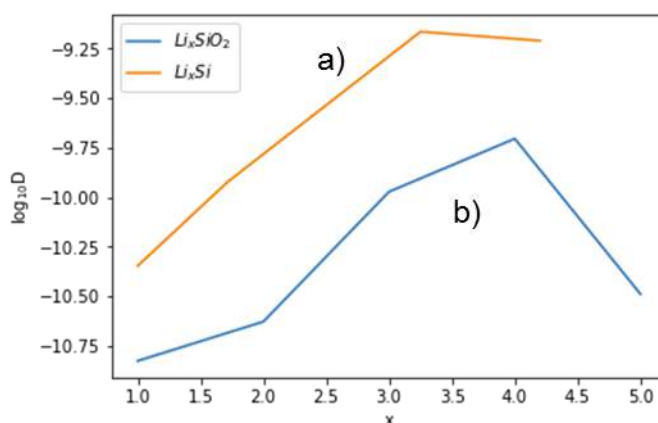


Figure II-142. Diffusivities in a) lithium silicides are greater than diffusivities in b) lithium silicates. Due to high variability in diffusivities, amplified by a log-scale, error bars are not shown.

The bulk properties for pure EC were calculated. For the two sets of potential adopted, OPLS gives better enthalpy and ϵ results, whereas GAFF underestimates the ϵ . However, GAFF gives better viscosity results compared to experimental results. Then, 5 ns of NVT run of MD simulation were conducted for 1.2 M LiPF_6 in EC. According to the radial distribution functions (RDFs), the total coordination number (CN) for Li ion is around 5.69~5.77 for both OPLS and GAFF, which signifies some over-coordination due to the non-polarizable force fields. Two basic solvation structures are observed (Figure II-143): contact ion pair (CIP) and solvent-separated ion pair (SSIP). For both force fields, the SSIP is the dominating species, with about 20% CIPs. Interestingly, there also exists a small portion of aggregate solvates (AGGs). At 1.0 M, the abundance of CIP has dropped to about 10% of the Li solvation structures.

Peaks of the IR spectrum from experimental results were designated as coordinated ones and uncoordinated ones based on calculation and IR database, which gives us information of solvation structure. By comparing the calculated and experimental results, we can conclude that they have similar shifts for CIP and SSIP, respectively, despite small differences in absolute frequency values. Thus, going forward, we can use the computed values to identify majority and minority solvation species from experimental results. We can also get the ratio of CIP and SSIP by comparing the intensity in future studies, which will, in turn, be compared with the MD results.

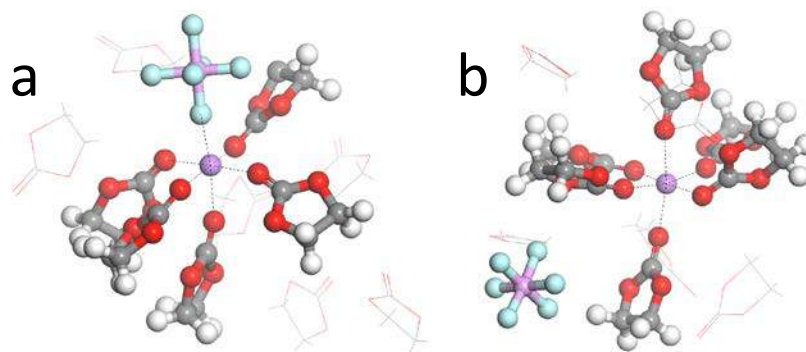


Figure II-143. The (a) CIP and (b) SSIP solvation structures.

Interfacial properties of ions/electrolyte molecules of LiPF₆/EC at the Si anode at the initial charging step is being studied via the constant potential method (CPM) in classical MD. We will first investigate the solvation structure of electrolyte molecules at Si anodes. 1 M LiPF₆ in EC is employed as the electrolyte, and neat crystalline Si with/without native silicon oxide layer as the anode (Figure II-144). The complicated structure at the electrode surface makes the electric field act heterogeneously on each molecule; thus, the electrode is modeled with CPM, where constant electric potential is applied to the battery cell as in typical experimental conditions. This model will allow us to investigate more realistic structural properties as well as more accurate dynamical properties—e.g., diffusion, ion conduction, and lithiation—because the response of the molecules in the electrolyte phase to an external field can be described explicitly.

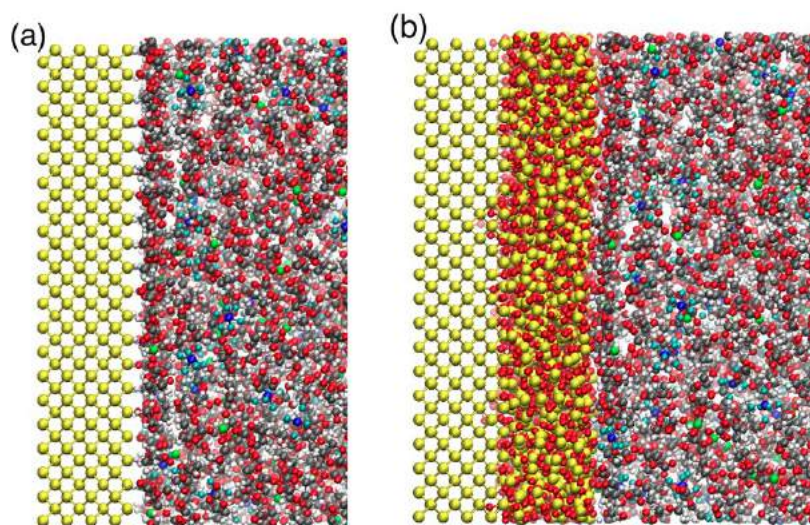


Figure II-144. Snapshot of a classical MD simulation of a model silicon anode with a crystalline structure (a) and amorphous silicon oxide on top of it (b). A constant electric potential is applied to the model battery cell. Si (yellow), Li (green), C (gray), H (white), O (red), P (blue), and F (cyan).

Materials development for baseline materials within SEISta

One key task within SEISta explores plasma-synthesized silicon nanoparticles (Si NPs) as model systems for Li_xSi anodes. Such plasma-prepared Si NPs are valuable because they feature hydrogen-passivated surfaces and a high surface area resulting from their $<10\text{-nm}$ diameter, which makes them well suited for chemical reactivity studies to understand 1) early-stage SEI layer growth, as well as 2) individual SEI component chemical stability. With our existing capabilities, we have determined that the plasma power density can be used to tune the Si NPs from amorphous (a-Si) to hydrogenated (a-Si:H) to crystalline (c-Si), which are each expected to provide different anode characteristics in planned FY18 electrochemical studies. Making larger-diameter (10–200 nm) Si NPs and at a greater scale ($>100\text{ mg}$) additionally required new hardware and plasma-system components. In FY17, we acquired a 12-kg cylinder of 100% silane (SiH_4) gas precursor, installed a higher-flow (500 sccm) SiH_4 mass flow controller, and have designed and completed testing on a new load-lock collection system capable of collecting $\sim 10\text{ g}$ of Si NPs per reactor run (Figure II-145). An alternate insert within this load lock will facilitate up to five different samples per reactor run, greatly increasing our throughput as we explore the conditions necessary to produce larger-diameter particles.



Figure II-145. Scaled-up plasma reactor, load-lock collection system, and small-diameter ($<10\text{-nm}$) hydrogen-passivated Si NPs.

Next, a comprehensive FTIR characterization of solid-phase material elucidated the chemical reactivity of the small-diameter Si NPs with electrolyte (EC/ LiPF_6 and Gen2, Figure II-146). Model systems with alkoxide and silyl ester groups (suspected chemical species following carbonate electrolyte decomposition) that were intentionally bound to the surface of Si NPs revealed that the silica (SiO_x) formed in the presence of surface-bound alkoxides is relatively robust against dissolution, whereas SiO_x on the surface of Si NPs functionalized with silyl esters is susceptible to chemical attack. Similar studies on different forms of commercial SiO_x found that fumed SiO_x and 30–50-nm NanoAmor Si (which is primarily SiO_x) are chemically unstable to EC/ LiPF_6 and Gen2 electrolytes. In contrast, Stöber SiO_x (prepared via a sol-gel process) is virtually unreactive toward these electrolytes. Finally, the reactivity of two types of lithium silicates— Li_2SiO_3 and Li_4SiO_4 , prepared at ORNL—evoked as SEI components were additionally compared. Interestingly, we found that Li_2SiO_3 coordinates carbonates whereas Li_4SiO_4 is relatively unreactive. The attenuated total reflectance (ATR)-FTIR analysis of reacted electrolytes with three different SiO_x forms supports reactivity results of each SiO_x , and additional characterization of reacted electrolytes with Si NPs or lithium silicates will be performed to complement the previous results. This work provides insight into the types of chemical species present in the SEI layer that either afford stability or lead to its dissolution.

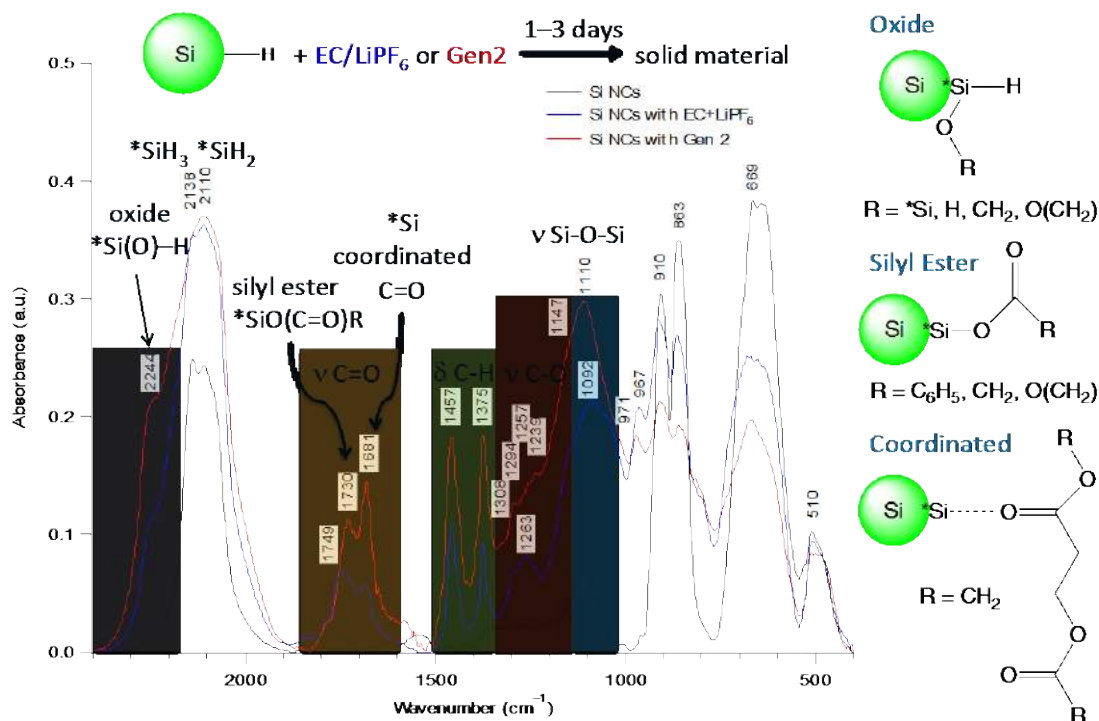


Figure II-146. Example of FTIR data of solid material following reaction of Si NPs and electrolyte.

Complementary studies characterizing the gaseous products from the chemical reactions of Si, SiO_x, and Li_xSiO_y with electrolytes were performed (see below) and correlate well with the above solid-phase results. In addition to this work between NREL and ORNL, SEISta-facilitated assistance has been supplied by University of California Berkeley, where density functional theory (DFT) experiments are under way to confirm many of the new vibrational modes that were assigned from these chemical reactivity studies. A publication detailing the combined experimental and computational results will be extremely valuable to the field because currently no such comprehensive spectroscopic characterization of SEI components exists. Additional work in new capability development is planned in FY18 to explore the molecular nature of species dissolved in the electrolyte that would present a complete accounting of all products during early-stage chemical SEI formation.

Reactivity studies of silicon and lithiated silicon samples

The nature of the silicon electrolyte interface is critical in developing the SEI. This interface is complex, and as such, a significant portion of the SEISta team is focused on the reactivity of the silicon, its surface, and the lithiated versions and variants.

Explored the gassing of silicon-based materials and the influence of the surface chemistry of these materials on the reactivity.

As the primary basis for the silicon work, we wanted to understand if the silicon surface had any fundamental limitation in its compatibility with the silicon electrode. Therefore, we began by examining the chemistry of silicon and silicon oxide particles (high surface area for better resolution) with traditional electrolyte components. It has been observed that extensive gassing occurs upon exposure to the baseline electrolyte (EC:DMC 30:70 1.2M PF₆). To explore these reactions and identify ways to prevent them, we used an assortment of silicon-based materials to explore different surface influences of the reaction chemistry that may influence the surface reactivity of the materials. The silicon-based materials are a nanocrystalline silicon synthesized from silane (nanocryst – NREL), a nano-amorphous silicon commonly used in making silicon electrodes, both fumed and Stöber-prepared silica, lithium metasilicate, and lithium orthosilicate. The silane-based silicon (nanocryst) has a particle size of 7 nm and is terminated with hydrogens, whereas the

nanoamorphous silicon is 70–130 nm in size and has a known native oxide layer. Samples were dried in the evacuation chamber to the Ar glove box prior to use. All materials were handled in the argon glove box. Electrolyte used for the studies includes 3:7 ethylene carbonate:ethyl methyl carbonate that was either 1.2 M in LiPF₆ (Gen 2) or 1.2 M in LiTFSI. All others were made, including the fluoroethylene carbonate, which was simply added to the Gen 2. The LiClO₄ salt was 1 M in 3:7 EC/DMC.

To follow the rates in the gassing reaction, kinetic IR experiments were run on an Agilent Technologies Cary 680 FTIR. These studies could track CO, CO₂, SiF₄, PF₃, HF, and electrolyte, but not H₂ or O₂ gas. In a glove box, a known amount of silicon-based material (~0.2 g) is weighed and transferred onto a boat (40 mm x 13 mm x 2 mm). The boat is inserted into the IR gas cell (Figure II-147)), and the cell is sealed around KBr windows, as well as with a septum (SupleCo GR-2 septum, 6 mm) in the injection port. A small syringe is filled with electrolyte (400 μ L), and brought out of the glove box along with the gas cell. The cell is placed on the holder in the IR spectrometer, and a background scan is taken. The electrolyte is injected through the injection port, first making sure that the boat is situated under the port inside the cell. Once the electrolyte is injected, the kinetic experiment is started.

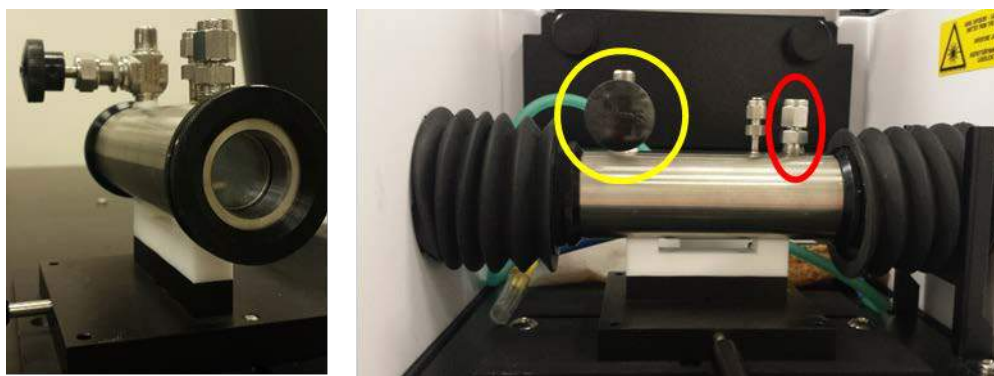


Figure II-147. IR gas cell used for kinetic measurements from two different angles. The path length through the cell is 11 cm, and the KBr windows are 25 mm in diameter by 2 mm thick. The injection port (circled in red) is sealed with a septum, and the outgas port (yellow) can be opened for purging, if necessary.

CO and CO₂ calibration curves were constructed by purging the gas cell with Ar gas, with a needle and hose leading through the injection port and leaving the outgas port open. The outgas port was closed and the needle removed to take the background, and then a known concentration of gas was flowed into the gas cell. Scans were taken with the outgas port closed and the injection needle removed so that there was no interference from the incoming gas or escaping gas in the resulting spectrum.

Silicon/silica particles

The Archimedes' principle was employed to evaluate the amount of gas released by the reactions between the silicon materials and the electrolytes. The gas released was followed by the relating change in the buoyancy to the change in gas volume of pouches over time as shown in Figure II-148. All reactions were duplicated to illustrate the reproducibility. The nanocryst Si immediately produced gas upon contact with Gen2 and produced 0.2 mL of gas in 480 minutes (Figure II-148-left). Interestingly, removing the salt from the electrolyte showed that no gas evolved, suggesting that the salt has a major role in the reaction mechanism. Because PF₆⁻ anion is known to undergo hydrolysis, we replaced the Gen2 anion with TFSI. The TFSI electrolyte showed slight gassing, with the rate being 115 times slower than Gen2. As the TFSI electrolyte evolved only 0.02 mL of gas, we conclude that the identity of the anion does matter in producing gas. The effect of the standard FEC additive on spontaneous gas production was also measured. A 10% solution of FEC in Gen 2 was prepared, and the pouches produced the same amount of gas for the FEC/Gen 2 sample as for the Gen 2, indicating that either the main gassing reaction does not involve the decomposition of the solvent, or the decomposition is not something that the FEC can prevent. In comparison, the nanoamor (Figure II-148 - right) took much longer (days to weeks) to begin degassing. The reaction with Gen2 produced 4 mL of gas

between 3–5 days. This was an order-of-magnitude more gas produced than with nanocryst, although it was much slower, which suggests that the oxide layer influences the kinetics and mechanism. Here, we saw that the FEC doubled the time delay for gas production, but the same amount of gas was produced. Replacing the PF6-anion with ClO₄⁻ prevented the reaction from occurring, again indicating that the LiPF₆ salt is an integral part of the reaction.

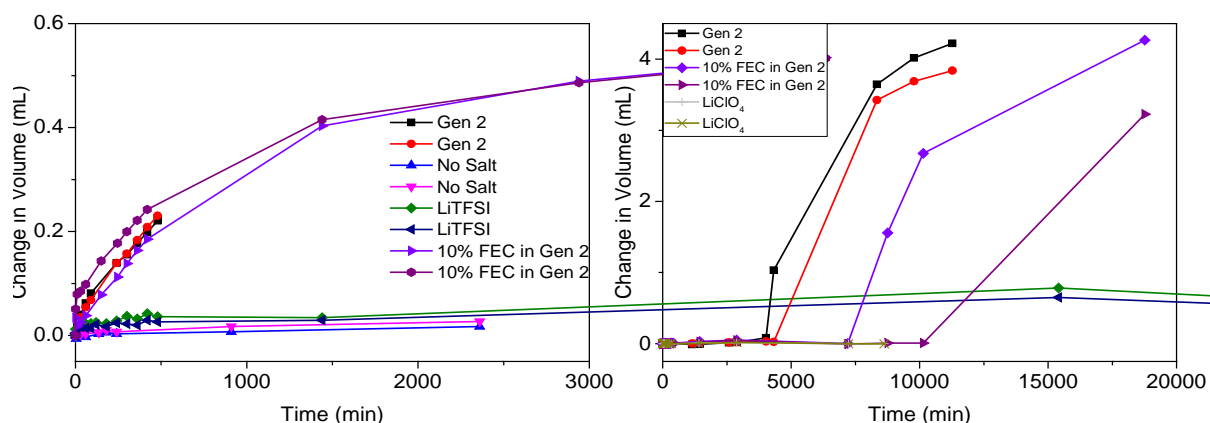


Figure II-148. Plot of change in volume (calculated through buoyancy) of the nanostructured silicon compounds reacting with various electrolytes in pouches. The left plot is of the nanocrystalline and the right is the nanoamorphous.

There are no data on TFSI salt with nanoamor, or on any of the other materials, because the IR experiment of it with nanocryst revealed a large amount of HF gas forming. So the reactions were stopped due to safety concerns.

Mass spectroscopy was conducted on the gases in the pouch cells. Figure II-149-B shows the mass spectroscopy data of the Gen2-nanocryst Si pouch after 480 minutes. The gases evolved in the pouch were found to be O₂ (32 amu) and CO/ethylene (28 amu). *In-situ* IR spectra of the air space's evolution were also recorded in real time. Here, the sealed gas cell volume of 36 mL was fixed (Figure II-147). Representative transient spectra are shown in Figure II-149-A, at selected time points, as many more spectra were taken to accurately follow the evolution over time. Within the data, most peaks are attributed to solvent vapor. Because the solvent is volatile, the referenced background was taken to be the first 10 seconds after solvent addition. Peaks that appeared at later times and grew throughout the reaction were attributed to products of the reaction, such as carbon dioxide (2,350 cm⁻¹), carbon monoxide (2,200 cm⁻¹), silicon tetrafluoride (725 cm⁻¹), and phosphorous trifluoride (475 cm⁻¹). The insets on the IR plot give a representative view of the products over time. The CO, SiF₄, and PF₃ peaks increase in intensity with time, indicating that they are being produced throughout the entire reaction. The CO₂ peak went negative before growing, indicating that initial concentrations of the gas were used in the reaction, or simply dissolved into the solution, as CO₂ is known to be highly soluble in carbonates [1]. Figure II-149-C shows the integrated IR signal over time for the different gas products. For the first 500 minutes, the only product changing is carbon monoxide. At around 500 minutes, the CO starts to increase, as the CO₂ decreases. From 900 minutes, all curves begin to increase, with the CO, SiF₄, and PF₃ peaks flattening slightly at 1,150 minutes. From this, it can be determined that the evolution of the gases is highly correlated. Further proof of their correlation can be found in the derivative plot, which is an inset of Figure II-149-C. All four curves line up from 650 to 950 minutes, and then they begin to rise at varying slopes from there. There is a spike in CO, SiF₄, and PF₃ at 1,190 minutes, corresponding to the bump in the integrated signal vs time plot. This indicates that the reaction mechanism is changing with time and that certain products or species are involved in different reactions.

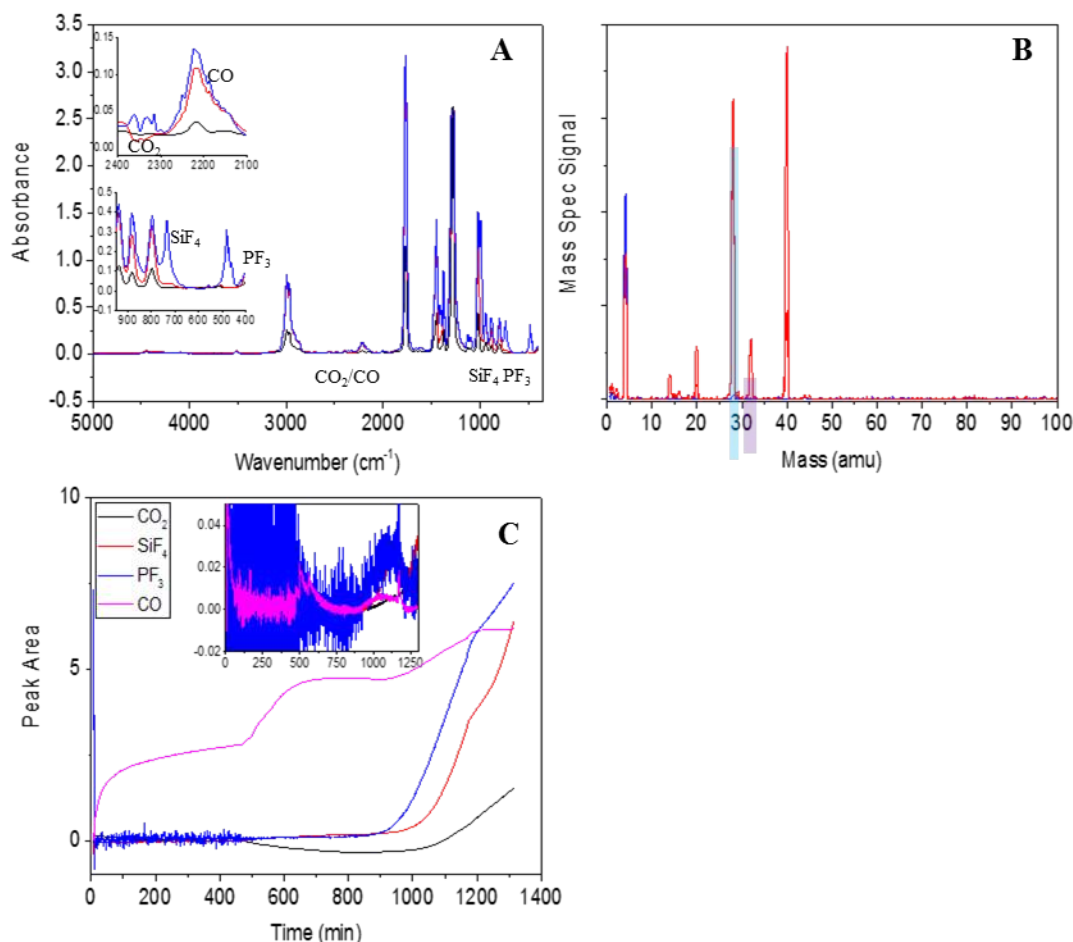


Figure II-149. Characterization data for the gases produced in the reaction between the silicon nanocrystals prepared by silane and the Gen 2 electrolyte. a) Kinetic IR (black = 14 min, red = 752 min, blue = 1,278 min), insets CO₂ and CO, and SiF₄ and PF₃. b) Mass spectrum was taken after 480 minutes (sample is red, helium is blue). Boxes around peaks correspond to various compounds (blue = CO, purple = O₂). SiF₄ (104 amu, 85 amu, 86 amu, 87 amu), PF₃ (69 amu), CO₂ (44 amu), F (19 amu), and H₂ (2 amu). c) Peak area vs time plot to illustrate any correlation between the evolution of the different gases. Inset is derivative of plot with respect to time. (In both, black = CO₂, purple = CO, red = SiF₄, and blue = PF₃).

The nanoamor Si showed drastically different results in the MS and IR. Here, the major reaction products are CO₂, SiF₄, and PF₃, and H₂ forming (Figure II-150-B). H₂ evolution could be attributed to water reacting with silicon ($\text{Si} + 2\text{H}_2\text{O} \rightarrow \text{SiO}_2 + 2\text{H}_2$), or silicon reacting with an H-C-O compound, such as the solvent molecules. The IR spectra show that gases begin evolving immediately upon mixing in the reaction, which is drastically different from the buoyancy experiments.

The PF₃ evolves the fastest, but begins to slow down around 100 minutes when the CO₂ and SiF₄ rate increases. Just after 200 minutes, the CO₂ reaction increases in rate again, and the SiF₄ decreases until equilibrium is presumably reached. The PF₃ gas begins to disappear around 500 min, suggesting its consumption for another reaction. The small amount of PF₃ in the MS may be from the continued consumption of PF₃ gas for the next two weeks before reaching the point that the mass spectrum was taken. Clearly, the mechanism of electrolyte degradation is different between the two Si particles.

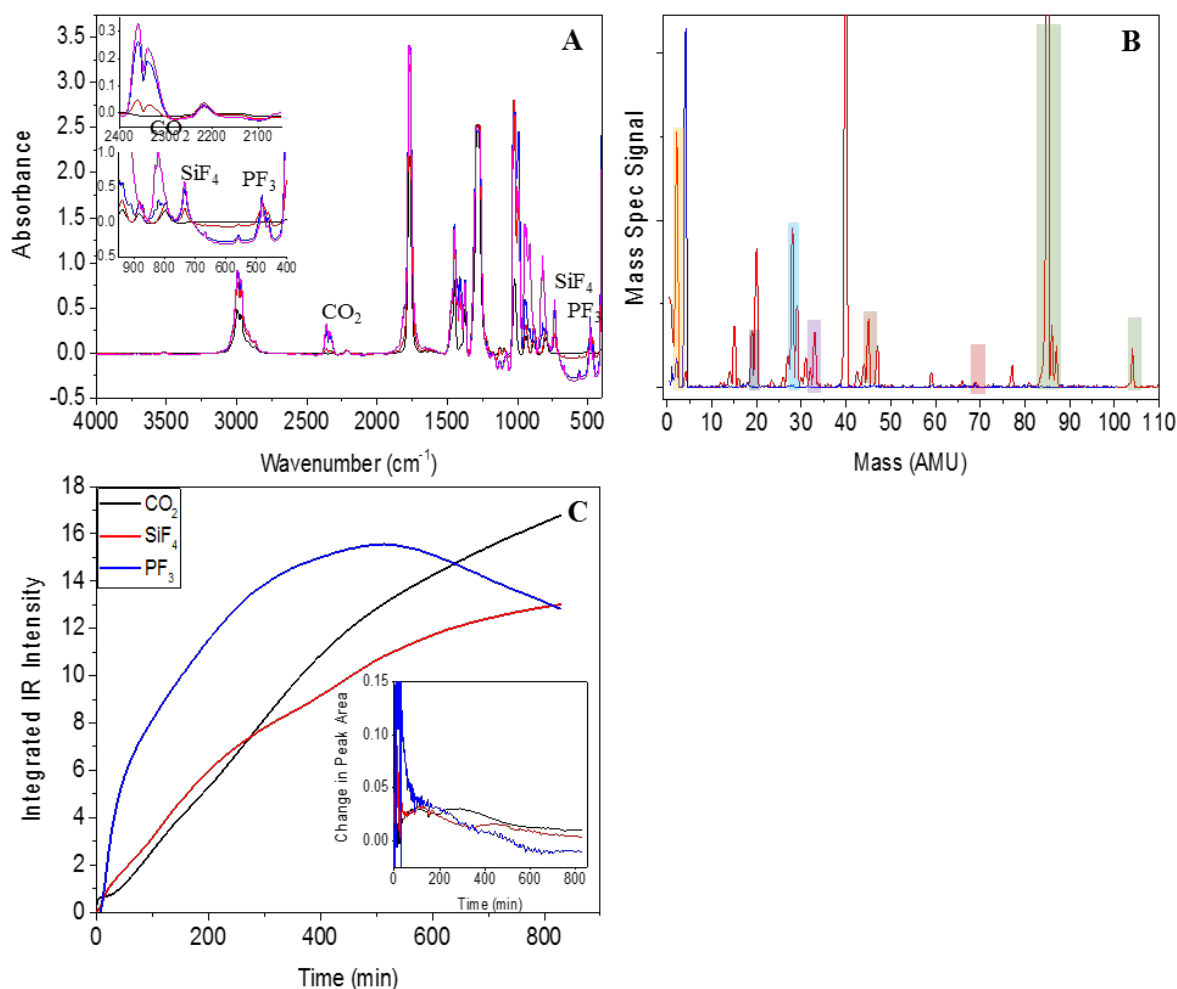


Figure II-150. Characterization data for the gases produced in the reaction between the nanoamorphous silicon and the Gen 2 electrolyte. a) Kinetic IR (black = 0.936 min, red = 126 min, blue = 559 min, purple = 818 min), insets CO₂, and SiF₄ and PF₃. b) Mass spectrum was taken after 14 days (sample is red, helium is blue). Boxes around peaks correspond to various compounds (yellow = H₂, black = F, blue = CO, purple = O₂, orange = CO₂, red = PF₃, green = SiF₄). SiF₄ (104 amu, 85 amu, 86 amu, 87 amu), PF₃ (69 amu), CO₂ (44 amu), F (19 amu), and H₂ (2 amu). c) Peak area vs time plot to illustrate any correlation between the evolution of the different gases. Inset is derivative of plot with respect to time. (In both, black = CO₂, red = SiF₄, and blue = PF₃).

Silica

To test the theory of the importance of the native oxide layer for the production of CO₂, multiple silica compounds were tested in the same fashion. First tested was a fumed silica (S5505, Sigma Aldrich), which was dried in a glove box antechamber before use. Figure II-151-B shows the mass spectrum of the gas evolved in the pouch reaction between the S5505 and the Gen 2 electrolyte after 40 days. The products were found to be CO, CO₂, H₂, PF₃, and SiF₄ (SiF₄ (104 amu, 85 amu, 86 amu, 87 amu), PF₃ (69 amu), CO₂ (44 amu), O₂ (32 amu), CO (28 amu), F (19 amu), and H₂ (2 amu)). These indicate that both the decomposition reaction of the solvent and the salt reaction with the silicon substrate are occurring. From the selected plots from the kinetic IR in Figure II-151-A, the reaction clearly produces the CO₂, SiF₄, PF₃, and CO, as seen in the previous reactions. Therefore, the solvent is still reacting to decompose, and the salt has sufficient access to the silicon to react with it, forming SiF₄. In Figure II-151-C, the plot of the integrated intensity vs time, the CO₂ curve closely resembles that of the silane-sourced silicon. First, the curve is flat, indicating that any CO₂ produced is remaining in the solvent or in equilibrium with surrounding CO₂ gas dissolving in and out of the solvent. At

750 minutes, the CO₂ begins to disappear, again corresponding to the onset of SiF₄ production. As the CO₂ begins to increase again at 850 minutes, the SiF₄ peak has a plateau that jumps again as the CO₂ flattens off at 1,150 minutes. The PF₃ curve follows the same plateau and increase pattern as the SiF₄, indicating that the evolution of all three gases is connected. The carbon monoxide curve behaves the same as in the nanoamor, with the peak growing quickly in the first couple of minutes, and then staying flat around 2.5 intensity units for the rest of the reaction. The derivative plot has peaks around 850 and 1,100 minutes for all three products, corresponding to the increase in the intensity plots. Somehow, the reactions are correlated in this mechanism because they tend to increase alongside each other.

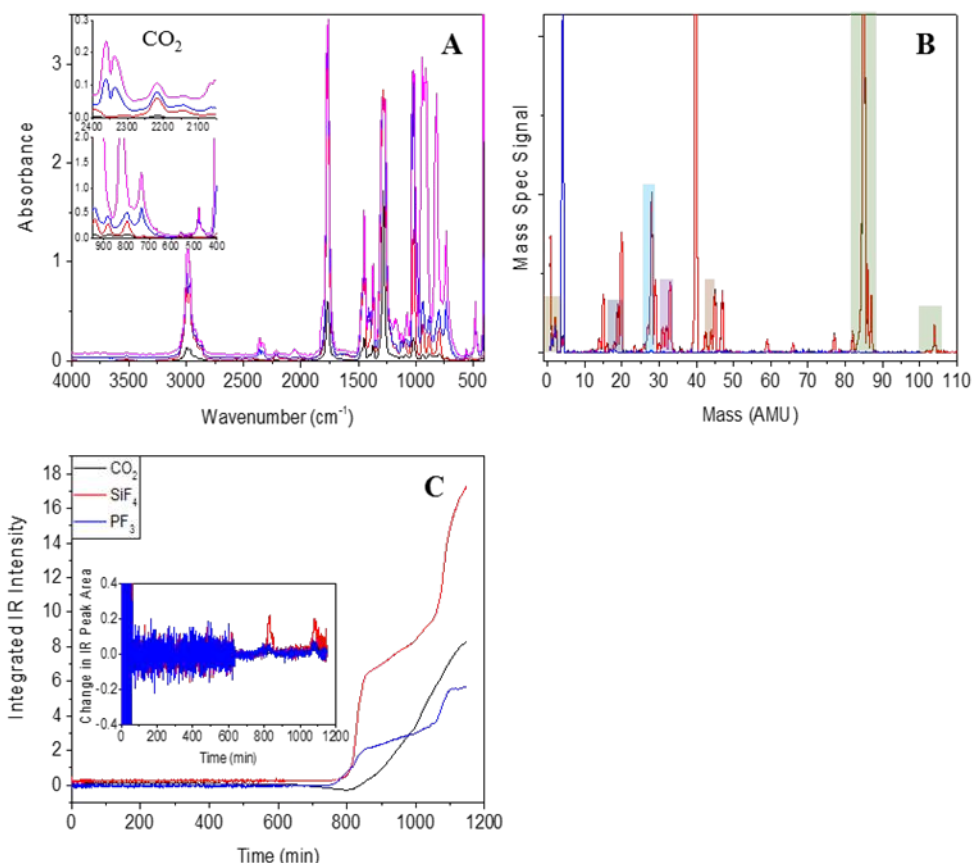


Figure II-151. Characterization data for the gases produced in the reaction between the fumed silica and the Gen 2 electrolyte. a) Kinetic IR (black = 0.3 min, red = 184 min, blue = 1,019 min, purple = 1,147 min), inserts CO₂, and SiF₄ and PF₃. b) Mass spectrum was taken after 40 days (sample is red, helium is blue). Boxes around peaks correspond to various compounds (yellow = H₂, black = F, blue = CO, purple = O₂, orange = CO₂, red = PF₃, green = SiF₄). SiF₄ (104 amu, 85 amu, 86 amu, 87 amu), PF₃ (69 amu), CO₂ (44 amu), F (19 amu), and H₂ (2 amu). c) Peak area vs time plot to illustrate any correlation between the evolution of the different gases. Inset: derivative of plot with respect to time of peak area vs time plot. (In both, black = CO₂, red = SiF₄, and blue = PF₃).

Silica prepared by the Stöber method was used as a comparison to determine if morphology influenced the gassing. Figure II-152-B shows the mass spectrum of the reaction with Gen 2, and was taken after the pouch sat reacting for 48 days. The gases evolved were determined to be CO, O₂, CO₂, SiF₄, F, and H₂. The CO, O₂, CO₂, and H₂ can all be attributed to solvent decomposition or the reaction of the termination layer on the silica. The excess of CO and O₂ compared to the CO₂ may indicate the decomposition of the CO₂, or simply the solvent molecule decomposing, either the EC or the EMC, prefers to form CO than CO₂. The SiF₄ results from the reaction between the LiPF₆ salt and the silicon in the electrode. Interestingly, there is no PF₃ present, a natural product of the reaction generating the SiF₄. It is possible that the PF₃ formed is used in a further

reaction related to passivation of the silica. As usual, a kinetic IR experiment was performed to follow the changes in the individual gases over time. From the inset plots in Figure II-152-A, the CO₂ is decreasing in intensity, indicating that the initial amount present in the background spectrum is either dissolving into the solvent, or reacting to form another product. The CO peak is much stronger next to the decreasing CO₂, and the SiF₄ and PF₃ peaks do not appear to be changing. Figure II-152-C, the IR integrated signal vs time plot, does not indicate there to be any correlation between the gassing of each product relative to the others, which is supported by the derivative plot. The CO₂ peak is decreasing, as observed in the IR spectrum. However, as some CO₂ is observed in the mass spectrum, it must be produced later than the 12 hours of the kinetic IR experiment could track. The SiF₄ peak grows toward the end of the reaction, which would eventually lead to the large amount seen in the mass spectrum. The carbon monoxide trend is consistent with the S5505 and nanoamor peaks—growing to an integrated value of around 2.5 in the first 10 minutes and then staying level for the rest of the experiment. It does not indicate any further correlation between the production of the gases, again indicating that this reaction follows a different mechanism than those prior to it. Another interesting detail from this reaction was that an orange liquid formed in both the pouch and the IR cell. Although it is unclear exactly what this liquid is, some phosphorous compounds such as P₂H₄ are orange, and the ATR spectrum taken of the liquid line up with signals from Li₃F₃ and other combinations thereof [2].

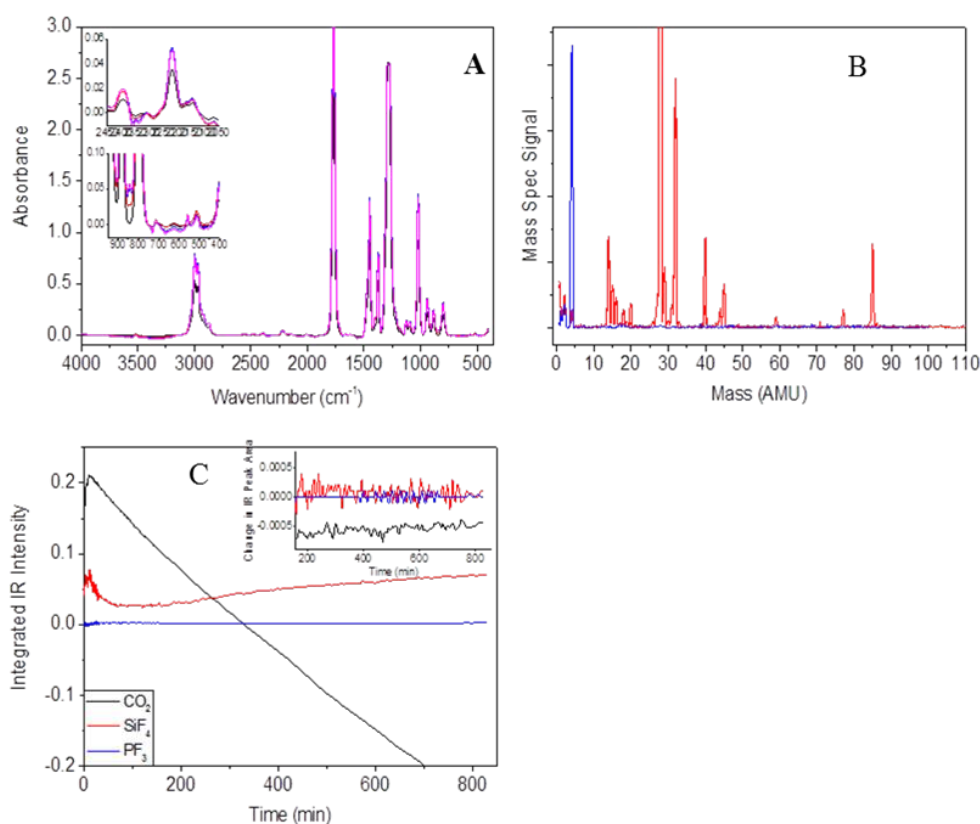


Figure II-152. Characterization data for the gases produced in the reaction between the Stöber silica and the Gen 2 electrolyte. a) In the IR (black = 0.936 min, red = 126 min, blue = 559 min, purple = 818 min), the CO₂, SiF₄, and PF₃ peaks were nonexistent, as identified in the insets. b) The mass spectrum was taken after 48 days, and the reaction gases were present in this spectrum, indicating that the reaction took longer than the IR experiment ran for (sample is red and black, helium is blue). SiF₄ (104 amu, 85 amu, 86 amu, 87 amu), PF₃ (69 amu), CO₂ (44 amu), F (19 amu), and H₂ (2 amu). Boxes around peaks correspond to various compounds (yellow = H₂, black = F, blue = CO, purple = O₂, orange = CO₂, red = PF₃, green = SiF₄). c) From the peak area vs time plot, the three gases produced have inflections in the curves that seem to loosely correlate between the substances, although the derivative plot is difficult to correlate. (In both, black = CO₂, red = SiF₄, and blue = PF₃).

In the pouches, an orange gas is also present that is corrosive and has a negative effect on the mass spectrometer. This would indicate the presence of a fluorinated compound, but it is unclear from the data gathered what the exact composition is.

Lithium silicates

To simulate the gassing reaction with an SEI layer, lithiated silicate compounds were tested. Both lithium metasilicate (Li_2SiO_3) and lithium orthosilicate (Li_4SiO_4) were tested (Figure II-153) to see if the ratio of oxygen to silicon made a significant impact.



Figure II-153. Structures of lithium metasilicate (Li_2SiO_3 , left) and lithium orthosilicate (Li_4SiO_4 , right).

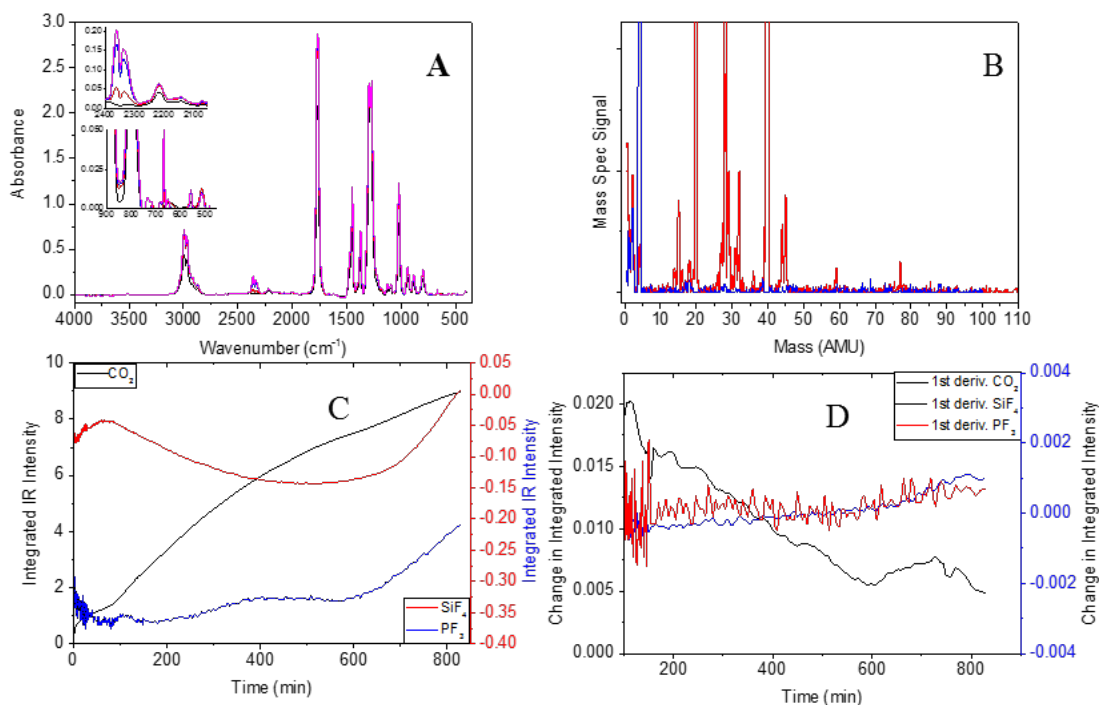


Figure II-154. Characterization data for the gases produced in the reaction between the Li_2SiO_3 and the Gen 2 electrolyte.

- Kinetic IR (black = 0.936 min, red = 126 min, blue = 559 min, purple = 818 min), insets CO_2 , and SiF_4 and PF_3 .
- Mass spectrum was taken after 27 days (sample is red, helium is blue). Boxes around peaks correspond to various compounds (yellow = H_2 , black = F , blue = CO , purple = O_2 , orange = CO_2 , red = PF_3 , green = SiF_4). SiF_4 (104 amu, 85 amu, 86 amu, 87 amu), PF_3 (69 amu), CO_2 (44 amu), F (19 amu), and H_2 (2 amu).
- Peak area vs. time plot to illustrate any correlation between the evolution of the different gases. The double y plot allows for a clearer picture of the SiF_4 and PF_3 curves as compared to the CO_2 .
- Derivative of plot with respect to time of peak area vs. time plot. (In both, black = CO_2 , red = SiF_4 , and blue = PF_3). The double y plot allows for a clearer picture of the SiF_4 and PF_3 curves as compared to the CO_2 .

In the reaction of lithium metasilicate (Li_2SiO_3) with Gen 2 electrolyte in the pouches, the mass spectrum (Figure II-154-B) indicated the formation of CO , CO_2 , H_2 , and O_2 , indicating solvent decomposition. The mass spectrum does not indicate the presence of SiF_4 or PF_3 , even after the 28 days of reacting in the pouch. If any had evolved, it must have reacted further during that time. Figure II-154-A, the kinetic IR spectrum, indicated mainly the presence of CO_2 , with resonance peaks appearing beyond the normal peak at $2,350\text{ cm}^{-1}$. The peak that appears around 650 cm^{-1} in the inset usually depicting the SiF_4 and PF_3 peaks can be attributed to CO_2 . Very little SiF_4 and PF_3 evolved in the reaction, which could also be seen in the integrated IR signal vs time plot (Figure II-154-C). The double-y axes allow for the trends between the materials to be compared, even as the change in the CO_2 is much greater than that of the other two. The carbon dioxide curve shows an increase in CO_2 over time, but the derivative plot shows the rate of evolution to be decreasing throughout the reaction. As with the Stöber, the CO evolution is rapid initially, but remains level at about 2.5 area units for the duration of the reaction. From the low level of gas evolved in the pouch, and the lack of SiF_4 and PF_3 peaks in the mass and IR spectra, it can be determined that the addition of lithium to the silicate compound helps prevent the reaction of the silicon with the LiPF_6 salt.

As with the lithium metasilicate, the lithium orthosilicate mass spectrum, Figure II-155-B, shows the evolution of CO , CO_2 , and O_2 from the reaction with the Gen 2 electrolyte in the pouch after 19 days. There is no

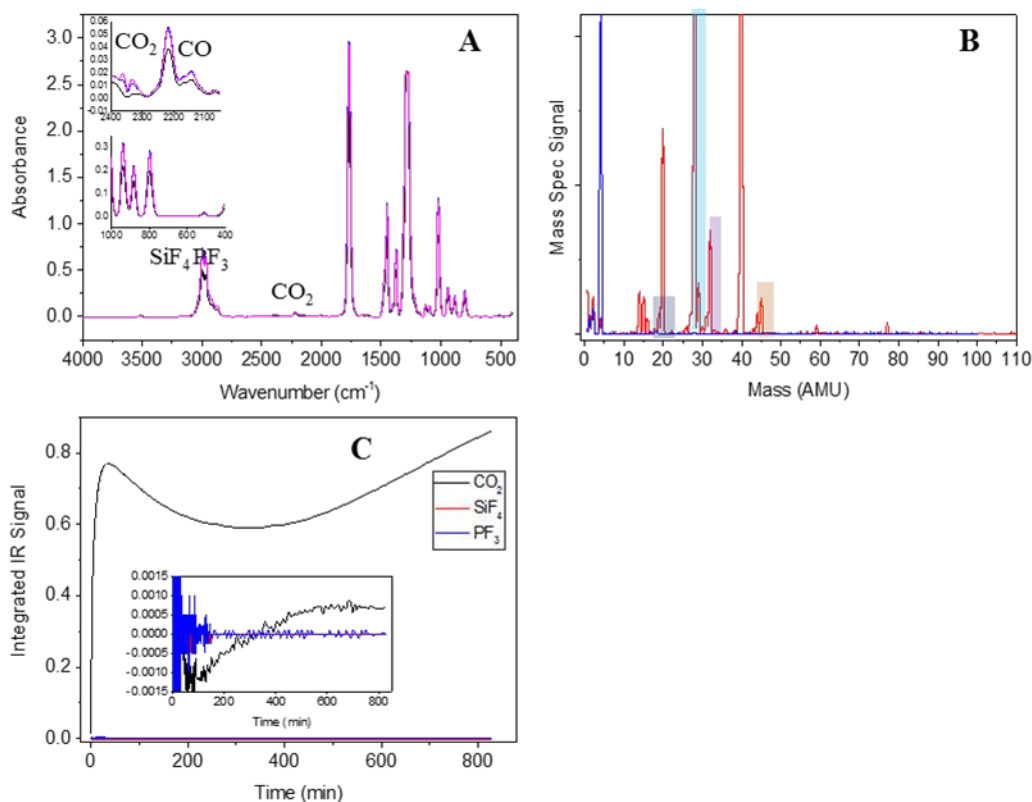


Figure II-155. Characterization data for the gases produced in the reaction between the Li_4SiO_4 and the Gen 2 electrolyte.

- Kinetic IR (black = 0.936 min, red = 126 min, blue = 559 min, purple = 818 min), insets CO_2 , and SiF_4 and PF_3 .
- Mass spectrum was taken after 19 days (sample is red, helium is blue). Boxes around peaks correspond to various compounds (yellow = H_2 , black = F, blue = CO, purple = O_2 , orange = CO_2 , red = PF_3 , green = SiF_4). SiF_4 (104 amu, 85 amu, 86 amu, 87 amu), PF_3 (69 amu), CO_2 (44 amu), F (19 amu), and H_2 (2 amu).
- Peak area vs time plot to illustrate any correlation between the evolution of the different gases. Inset is derivative of plot with respect to time. (In both, black = CO_2 , red = SiF_4 , and blue = PF_3).

evidence of SiF_4 or PF_3 in the mass spectrum, indicating again that only the electrolyte solvent is decomposing. The fluorine peak seen in the mass spectrum is an artifact from the column, as the HF from other pouches started appearing in all spectra. Figure II-155-A shows the spectra from the kinetic IR experiment, where once again the only gases evolving are CO and CO_2 , not SiF_4 or PF_3 . This trend is further visible in Figure II-155-C, the plot of integrated intensity vs time, where the SiF_4 and PF_3 curves are flat lines, and the CO_2 peak increases to 0.8 area units, and stays relatively constant for the remainder of the reaction. This is also the case with the CO curve as it follows the same trend as in the Li_2SiO_3 reaction. From the data, it looks like the Li_4SiO_4 is even better than the Li_2SiO_3 at preventing gassing reactions. The pouch data show almost no growth over time, and the IR plots show very consistent behavior for each product throughout the reaction time, indicating that there was almost no reaction.

Once the moles of each gas were determined, from the calibration plots, they could be compared across samples by normalizing with respect to the surface area of the material. Figure II-156 shows the amount of gas produced by each material, normalized by amount and surface area of the silicon material. As the lithium silicates have surface areas of around 1 m^2/g , the amount of gas produced is the same as if it were calculated per gram of material. This is why the other materials show much less gas evolving per m^2 , even if the pouches showed much more total gas evolving. However, it is possible to see from the diagram which gases are evolved from which materials, and which are not. The silicon nanocrystals from silane, the nanoamor, and the S5505 silica all produce all three gases in the reaction, but in varying ratios. The S5505 produces almost equivalent amounts of CO_2 and SiF_4 per m^2 , while the silicon produced from silane and nanoamor produce a higher amount of SiF_4 . The PF_3 cannot be considered in this ratio, as the value is multiplied by a factor of 100 to make it visible on the plot. The lithium silicates are also interesting to compare, as the Li_2SiO_3 produced only CO_2 , while the Li_4SiO_4 produced much more SiF_4 than CO_2 . The structure of the material must play a significant role in the catalysis of CO_2 formation. Interestingly, none of the materials produced no gas, even though some of the pouch curves were flat. This indicates that electrolyte decomposition is easily catalyzed on silicon-based materials, and that the silicon is highly reactive in that environment itself. The mechanisms of all these reactions are not understood yet. Furthermore, it is clear that the reactions are highly correlated. Understanding these reactions will enable us to identify processes or methods to stop them.

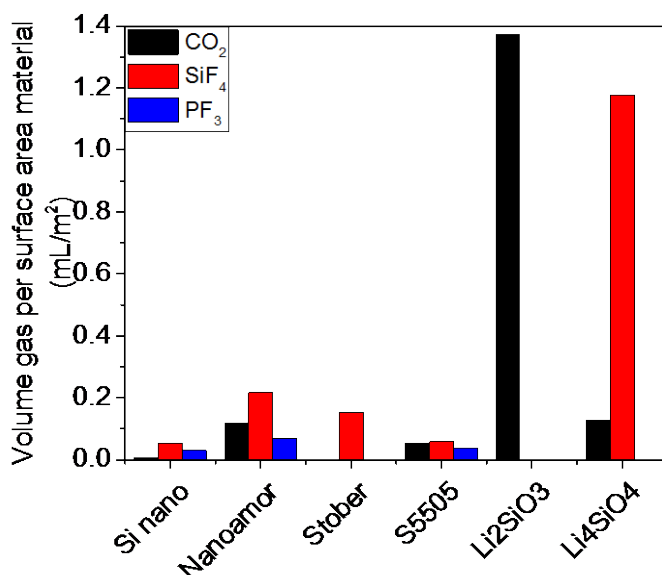


Figure II-156. Chart comparing the volume of each gas produced per surface area of material after reacting for 14 hours between the different silicon materials explored in this paper. The PF_3 signal was increased by a factor of 100.

Reactivity of model silicon lithiated materials

Although there is an unexpected reactivity of standard silicon materials, we expected that lithiated silicon and silicon oxides would show enhanced reactivity toward standard electrolytes. One of the most interesting components of the silicon system is Li_xSiO_y , which comes from the lithiation of the native SiO_x layer. Study of the native SiO_x layer on Si particles has also drawn attention because, on one hand, it confines the volume expansion of Si; on the other hand, it induces interfacial reactions that consume lithium. Lithiation of SiO_x is complicated by dependence on the discharge state. At the initial state, SiO_x is lithiated to a mixture of Li_xSi_y , Si, and Li_xSiO_y for the first few cycles. Si and Li_xSi_y components progressively disappear when SEI gets thicker [3]. Although it is unclear as to the nature of the lithiated surface on silicon on electrodes, most recent studies focus on lithium silicate as the lithiation product of SiO_x [4].

In this work, Li_xSiO_y thin films with different lithium-to-silicon ratios were studied. Li_xSi_y and Si were also studied to provide a baseline for future comparison. Li_xSiO_y can be obtained by simply exposing Li_xSi_y thin film in a low-O ppm glove box. Mechanical and electrical properties are discussed in the following text. A proof-of-concept multilayer thin film was deposited to study the possibility of Li_xSiO_y passivating the Si surface. Although Li_xSiO_y showed ductile behavior, it is still not able to passivate the Si surface because of its high electrical conductivity.

Experimental procedure: The Li_xSiO_y thin film was synthesized by RF magnetron sputtering (13.56 MHz) using a lithium target (Lesker, 99.9%, 2") and silicon target (Lesker, 99.999%, 3" diameter). The chamber geometry is depicted in Figure II-157. The lithium target is 8 cm away from the substrate, and the silicon target is 12 cm from the substrate on axis. Ar (99.999% purity) was introduced to generate a plasma at a constant pressure of 3 mtorr. 30 W RF power was applied on both the lithium and silicon target. The film was deposited at room temperature and turn out to be amorphous, as expected. A combinatorial strategy was applied to screen properties of the lithium silicon compound with different lithium-silicon-oxygen composition. The film will have a higher ratio of Si-Li at the region closer to silicon and vice versa at the region further from silicon.

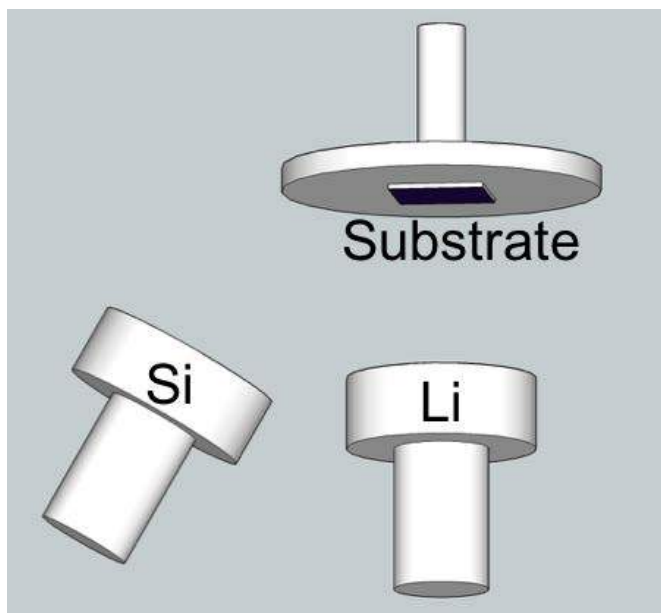


Figure II-157. Chamber geometry used to deposit Li_xSiO_y thin films.

Depth-profile XPS was collected for the lithium-rich region and silicon-rich region. Ar⁺ ions were used to sputter away the film layer by layer until the copper substrate was revealed. Nanoindentation was applied to determine the mechanical properties. Indentation experiments were performed with a DDESP-10 tip in an argon-filled glove box. Controlling deflection set-points (voltage) applied on the tip allows the force to be controlled. Calibrations were done to quantitatively convert the voltage to load force. A diamond SSRM tip was held to the surface with varied magnitudes of force. Four sites with increasing lithium concentration gradient were indented with varied deflection set-points. Each indentation duration was held for 10 seconds. After unloading the indenter, a tapping mode was used to investigate the indentation depth, and images were also taken with tapping mode nondestructively. Electrochemical properties were investigated by making coin cells. Airless transfer through a vacuum vessel was adopted because of the high reactivity of Li_xSiO_y.

XPS data were collected for the Li_xSiO_y thin film. In Figure II-158, depth-profile core-level spectra are shown for Li1s, Si2p, and O1s. However, keep in mind that these profiles can be affected by a knock-on effect by the sputtering of Ar ions. From the depth profile, significant oxidation is noted at the surface. Due to the extreme affinity of lithium to oxygen and carbon, the surface layer can be easily oxidized into a form, during the transfer process from deposition chamber to XPS chamber, that is assumed to be Li₂CO₃ and Li₂O-based on the XPS carbon spectrum as in Figure II-158.

In the bulk, from the O 1s spectrum in Figure II-159a, only the characteristic peak of Li_xSiO_y at 532 eV was observed. Li_xSiO_y is the only species with oxygen in the film. On the other hand, there are two peaks in the Si 2p spectrum in Figure II-159b—one at 102.5 eV for Li_xSiO_y and one at 99 eV for Si. From the peak intensity ratio, we can easily tell that the Si-rich region contains more Si phase than the Li-rich region. Also, notice that there is a shoulder at the Si peak of the Si-rich region at the lower binding energy, which might come from lithium silicide. This is also true for the Li 1s spectrum in Figure II-159c.

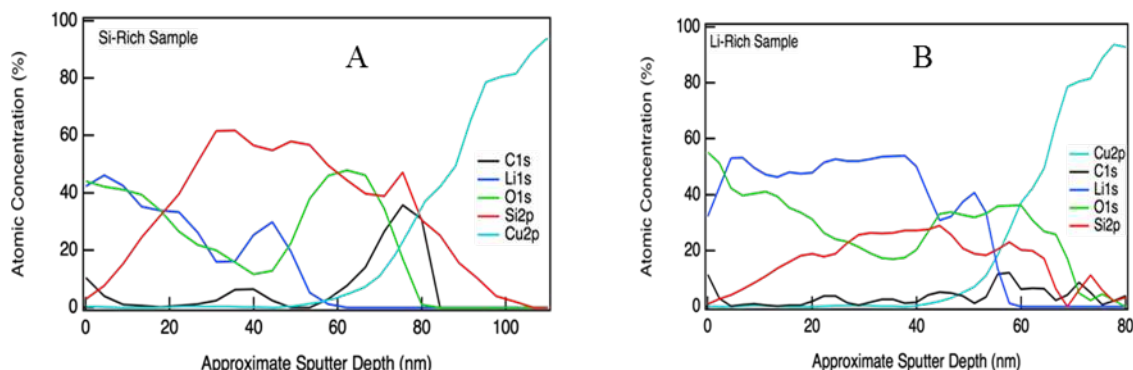


Figure II-158. XPS depth profile analysis of Li_xSiO_y thin film on copper foil. Atomic percentage as a function of sputter depth for a) Si-rich region and b) lithium-rich region.

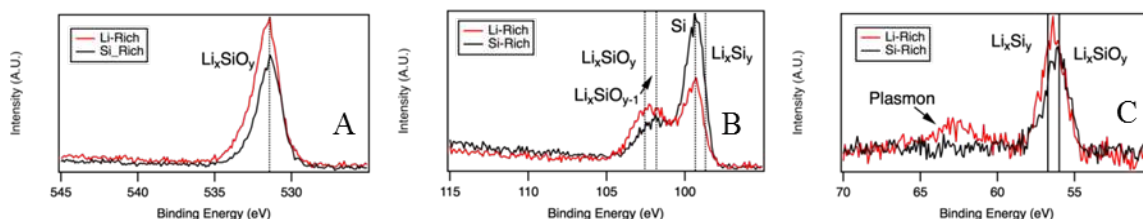


Figure II-159. a) O 1s spectra, b) Si 2p spectra, and c) Li 1s spectra of lithium-rich region and silicon-rich region.

To summarize the XPS results, a mixture of silicon and Li_xSiO_y exists in the bulk with a different ratio with respect to the distance to the lithium target. There is sudden jumps of carbon and oxygen at the surface of copper, and they are suspected to be from the organic species from copper, which was not removed

completely. The lithium-rich region has an approximate formula of Li_2SiO , and the silicon-rich region has a formula of LiSi_3O with O content normalized throughout the film depth. Because the two regions are deposited at the same time, oxygen levels of the two regions are very close. Different lithium-to-silicon ratios can be referred to different degrees of lithiation of SiO_x .

Mechanical behavior measured by AFM nanoindentation

AFM indentation measurements were performed on Si, Li_xSi_y , and $\text{Li}_x\text{Si}_y\text{O}_z$ thin films. The $\text{Li}_x\text{Si}_y\text{O}_z$ thin film is just an aged form of Li_xSi_y , which means that AFM was measured after 48 hours after deposition.

For the AFM nanoindentation experiments, the film was deposited on a hard glass substrate. Surface morphology is depicted in Figure II-160a. Surface roughness is on the order of 20 nm in an area $0.5\ \mu\text{m}$ by $0.5\ \mu\text{m}$. Typical residual indentation imprints were shown in Figure II-160b. An inverted projection image is reflecting the tip geometry imprinted during indentation, as shown in Figure II-160c. As discussed in the XPS atomic profile, there is a lithium concentration gradient throughout the thin film across one direction. A total of four sites with different lithium atomic ratios were measured with various applied loads. It is assumed within each area that the lithium atomic ratio is uniform. Within each region, indentation tests with various applied loads have been performed at small distance intervals from each other, allowing for the visualization of several indentation imprints in the same high-resolution image. Dependence of the indentation depth on the lithium concentration was observed throughout the combinatorial sample.

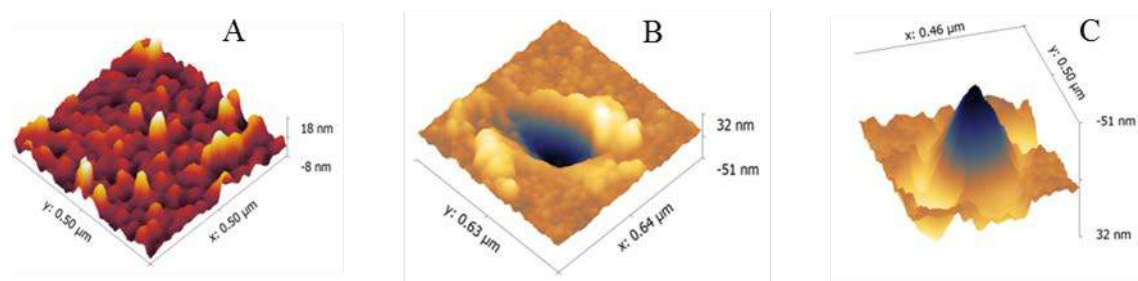


Figure II-160. AFM images of a) as-deposited film, b) indented film, and c) imprinted indented film.

Figure II-161 is a typical residual indentation imprint of film that reflects the film behavior on different force loads. Mechanical response of the lithium-rich area is shown in Figure II-162a, and a linear increase of indentation depth with loads was observed. However, the silicon-rich area shows brittle behavior as exhibited by how the probe easily broke through the film, and the cracks propagate to the substrate. Brittle behavior of the glass substrate also explains why the indentation depth is larger than the film thickness. Another distinct difference between these two behaviors is the following: in the ductile film, the film piles up at the edge of the indentation imprint from the indentation depth curve, whereas in the brittle film, there is no pile-up. The difference between ductile and brittle films are shown in Figure II-162 with AFM height and phase images. Note that we are investigating amorphous film rather than crystalline silicon, which usually cracks along the crystal plane; amorphous film cracks isotopically.

A brief summary on the mechanical response of thin film is shown in Figure II-162e, which plots the indentation depth vs. loads at different sites with increasing lithium atomic ratio. An interesting finding is that $\text{Li}_x\text{Si}_y\text{O}_z$ has changing properties when x in the formula changes. When x is larger, the indentation depth is larger, which means that the hardness of the film is smaller. This is a qualitative characterization of the film hardness that is adopted in many reported results. When x continues decreasing, the film changes from ductile to brittle. This changing behavior suggests that the initial lithiation product of SiO_x is not flexible; it could easily break down upon cycling. When lithium is extracted, it could become less fracture-resistant. As it gradually turns into $\text{Li}_x\text{Si}_y\text{O}_z$, as in the lithium-rich area, it is ductile and more resistant to fracturing.

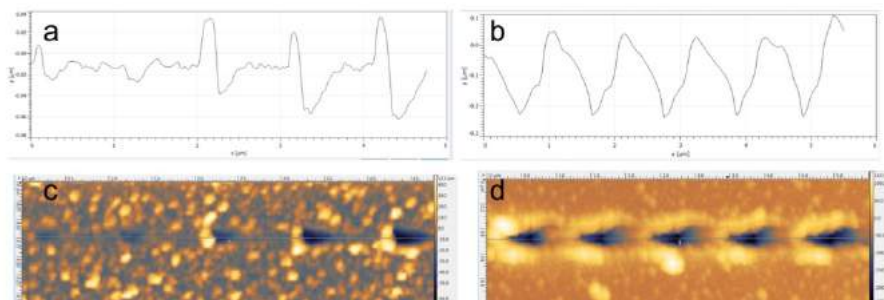


Figure II-161. Indentation depth plotted against the indentation force for the a) lithium-rich region and b) silicon-rich region. AFM images of indented film at c) lithium-rich region and d) silicon-rich region.

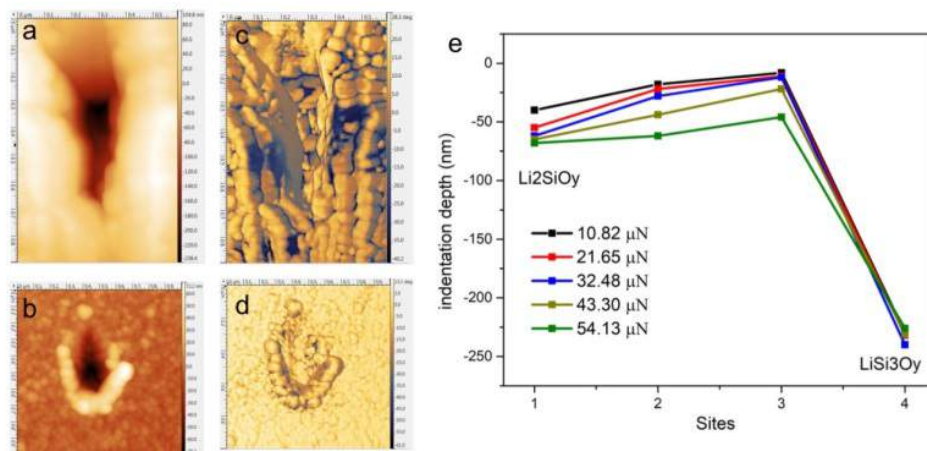


Figure II-162. AFM height image of a) ductile behavior region, b) brittle behavior region; phase image of c) ductile-behavior region and d) brittle-behavior region; and e) plot of indentation depth at different sites.

Figure II-163 is the plot of indentation response from Si, Li_xSi_y , and Li_xSiO_y thin film under the indentation force of 5.4 μN. Li_xSi_y film is fresh film after deposition, whereas Li_xSiO_y film is the oxidized Li_xSiO_y film (48 h after deposition). From the indentation depth, we can easily conclude that hardness of these thin films follows a sequence of $\text{Si} > \text{Li}_x\text{Si}_y > \text{Li}_x\text{SiO}_y$ because the indentation depth follows the sequence of $\text{Si} < \text{Li}_x\text{Si}_y < \text{Li}_x\text{SiO}_y$ before cracks occur.

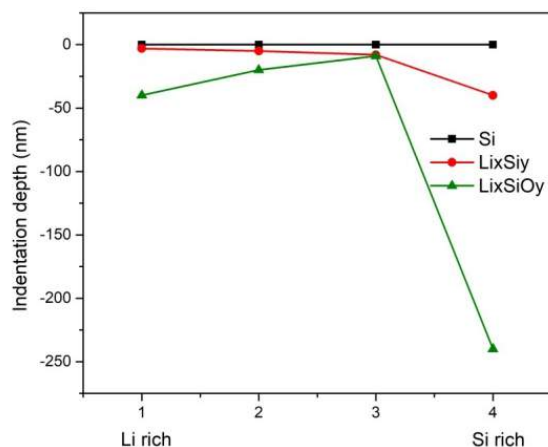


Figure II-163. Indentation depth profiles of Si, Li_xSi_y , and Li_xSiO_y thin film under indentation force of 5.4 μN.

XPS analysis of starting material

In addition to the materials described above, additional samples were prepared and analyzed using depth-profiling XPS to determine the composition and bonding states of the elements as films of varying compositions were exposed to electrolyte for various amounts of times. Samples similar to those used in the round robin were prepared with either a ~50-nm-thick SiO₂, or a 50-nm-thick Li:Si 1:1 ratio film (nominally Li₂Si₂O₅). The depth profiles were taken every ~30 Å along a profile depth (based on the sputter rate of pure SiO₂ as a standard). Composition and bonding states for C, Cu, F, Li, O, Si, and P were collected. The results are shown in Figure II-164 for SiO₂ and Figure II-165 for Li₂Si₂O₅.

Between these two films, it is clear that the time evolution of the structure and composition of the film is markedly different, indicating that surface chemistry of the starting film will affect how the SEI forms and its subsequent structure evolves. For the SiO₂ film, very little evolution of the surface layer is evident in a short time, whereas the surface layer in the lithiated film more clearly indicates film growth over time. In addition, there is some evidence that fluorine in the films evolved at the surface (penetrating into the film over time), even though this electrolyte does not contain FEC; fluorine here must be coming from the penetration of the salt anion into the film structure, although the phosphorus signal does not indicate phosphorus penetration to the same extent. It is worth noting that these samples were deposited on copper foil, which had a relatively high roughness, which will skew some of the thickness measurements.

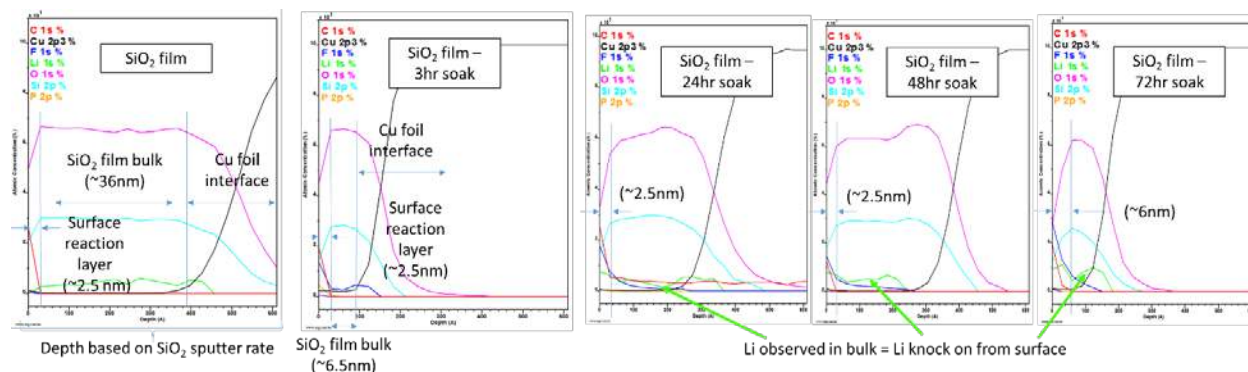


Figure II-164. Time evolution of XPS depth profiles on SiO₂ sputtered on Cu foil exposed to electrolyte, from as-deposited (left) to exposed for 72 hours (right). The film evolution and surface is seen to establish rapidly, but affects the SiO₂ depth over time.

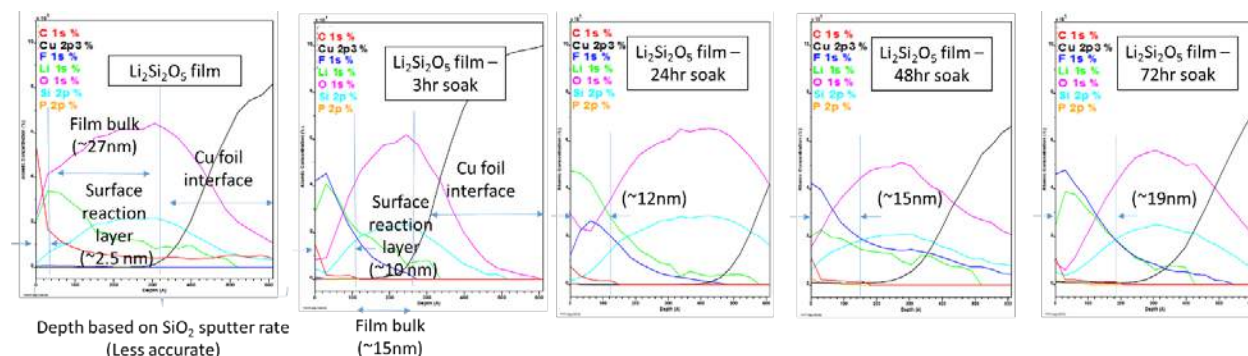


Figure II-165. Time evolution of XPS depth profiles on Li₂Si₂O₅ sputtered on Cu foil exposed to electrolyte, from as-deposited (left) to exposed for 72 hours (right). The time evolution of the film and thickness of the interface layer are markedly different than in the SiO₂ case.

A similar trend toward formation of more complex structures can be seen using ATR-IR. Although the two sample sets (SiO₂ and Li₂Si₂O₅) look similar in the as-deposited state (except for some expected differences

in the region near 800 cm^{-1} attributed to the presence of the lithium in the silicate structure), the time evolution of these films on exposure to electrolyte is markedly different. In Figure II-166A, a sample of SiO_2 grown on Cu is exposed to the electrolyte for increasing amounts of time, and the ATR-IR spectra are collected on the same sample after exposure. Five regions of interest exist, with the region around 550 cm^{-1} being attributed to adsorbed or residual LiPF₆ from the electrolyte that was not removed upon rinsing. The region from 700 to 900 cm^{-1} is associated with a number of phosphate and carbonate groups that contain lithium replacements for hydrogen. The region between 1,000 and 1,250 cm^{-1} is normally associated with O-Si-O stretching of the silicate peak. The region of 1,400 to 1,500 cm^{-1} is associated principally with a lithiated version of carbonic acid, and the region from 1,700 to 1,800 cm^{-1} is associated with alkyl carbonates and ethylene carbonate from the electrolyte. As can be seen in the figure, relatively little evolution of the surface is seen until longer times, and what is seen primarily is evidence of salt decomposition due to the formation of the phosphates and residual LiPF₆ trapped on the surface. Additionally, some minor decomposition of the EC is visible as a retained product on the surface at long times. Note also the broad peak in the O-Si-O region, indicating that the network is relatively unperturbed up to 72 hours.

Contrast this with a starting film of the 1:1 Li:Si lithium silicate (Figure II-166B). Significant decomposition products appeared in as little as 1.5 hours of exposure to the electrolyte, and the region of salt decomposition products shows much higher levels of salt residuals and phosphate byproducts than in the SiO_2 case. The region for stretching of the silicate network has evolved several distinct peaks, which may indicate disruption of the network expected during lithiation. Also note the evolution of the lithiated carbonic acid on the surface, and generation (and possible subsequent extinction) of the alkyl carbonates from the electrolyte decomposition occurring on the surface. Clearly, having lithium in the starting film evokes a much richer time evolution of the SEI formation, even with no active electrochemistry being performed.

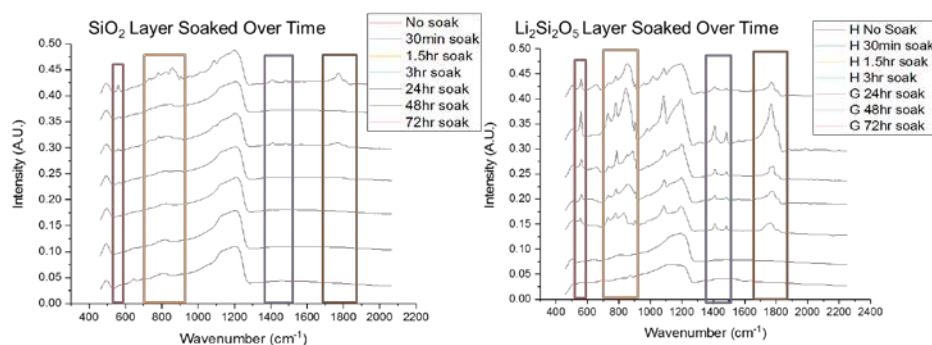


Figure II-166. (left) ATR-IR spectra of SiO_2 film sputtered on Cu exposed to electrolyte for various lengths of time. Relatively minor evolution of surface species is noted, and the O-Si-O network is relatively unperturbed. (right) Spectra of $\text{Li}_2\text{Si}_2\text{O}_5$ film subjected to the same conditions. Although the ATR-IR signals start out similarly, the time evolution of the surface products is very different, with more evidence of salt and electrolyte decomposition being noted.

Scanning spread Resistivity Microscopy

The scanning spread resistivity microscopy technique was applied on Li_xSiO_y thin film. A bias voltage is applied between the STM tip and the sample during contact AFM topography imaging, and the resulting current flowing between the tip and the sample is measured. A surprising result from the SSRM measurements is that Li_xSiO_y has a fairly low resistivity of 10^3 and 10^4 ohms across the whole film with different Li/Si ratios. However, these results were measured at a high bias voltage of -8 V, which might lead to lithium diffusion and cause composition change in the film.

Electrochemical properties

Galvanostatic charge and discharge were performed. 14-mm-diameter thin film was punched out from the silicon-rich region and lithium-rich region. The electrolyte was 1M LiPF₆ in a 1:1 (volume) ethylene carbonate

(EC) and dimethyl carbonate (DMC) mixture. Lithium metal was used as the reference electrode. The cells were first charged to 1.5 V and then discharged to 50 mV. Because it is difficult to estimate the density of Li_xSiO_y , we simply plotted the capacity vs. voltage in Figure II-167. A small amount of lithium can be extracted from the film, even up to 1.5 V. This low charge capacity indicates that little Li_xSi_y exists in the film. It also proves that the majority of lithium exists in a form of Li_xSiO_y as detected in XPS.

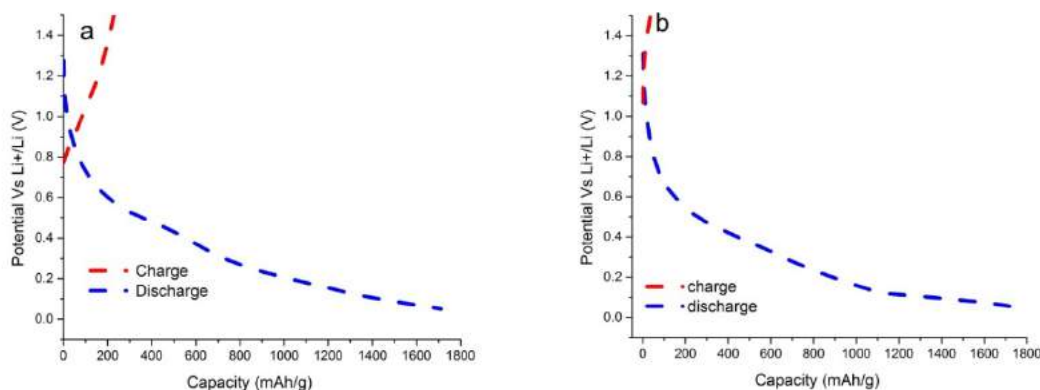


Figure II-167. Charge and discharge profile of a) lithium-rich region and b) silicon-rich region.

Whether a component is beneficial or not as SEI also depends on the chemical reactivity of the material with electrolyte. Here, we did a preliminary measurement of the reaction of Li_xSiO_y with electrolyte by AC impedance at the open-circuit voltage. The electrolyte adopted in the coin cell is a mixture of EC and DMC. As Li_xSiO_y soaked in electrolyte, the surface continuously reacts with electrolyte and the charge transfer resistance is time dependent. The silicon electrode did not show much activity, because the impedance is not time dependent at open-circuit voltage. The reactivity depends on the degree of lithiation. Several papers have discussed [5] possible reduction mechanisms of EC ethylene carbonate on the surface, with different degrees of lithiation due to different mechanisms. A higher degree of lithiated Si was found to be more reactive compared to a low degree of lithiated Si. The difference of reactivity originated from the ability of EC molecules to interact with Li^+ ions on the surface. During the lithiation, SiO_x becomes increasingly reactive to electrolyte as it takes increasingly more lithium.

Surface reactivity of both silicon-rich and lithium-rich regions were studied by impedance measurement. Impedance evolution was investigated by collecting spectra of a fresh cell and 24 hours later. AC impedance data were collected in a frequency range of 100 KHz to 100 MHz. In Figure II-168, the charge transfer resistance for the fresh cell is much higher than for the bare silicon sample. The higher resistance is suspected to come from the reaction that occurs at the surface of the Li_xSiO_y with the electrolyte. The higher the lithium concentration in the compound, the lower the potential it has versus lithium; thus, the easier it reduces the electrolyte. This would cause a problem when the SiO_x is lithiated to Li_xSiO_y ; if this layer is not fully covered with the other chemically stable electrolyte decomposition product, it will induce more reduction of electrolyte and eventually it will cause more consumption.

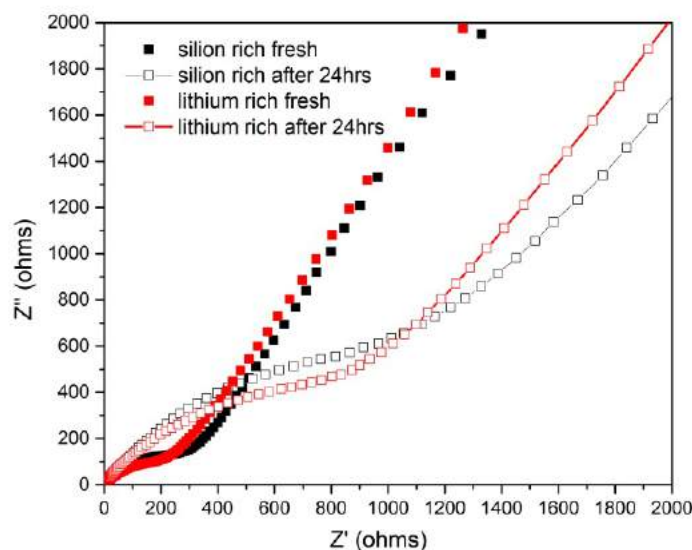


Figure II-168. Impedance spectra of lithium-rich region and silicon-rich region for the fresh cell and cell sitting for 24 hours.

Proof-of-concept of using Li_xSiO_y as SEI

A proof-of-concept multilayer thin film was deposited with LiSiO_y on top of a silicon thin film. The thickness of Li_xSiO_y was controlled to 10 nm and the silicon thin film is 50 nm thick. Both silicon and Li_xSiO_y -covered silicon ($\text{Li}_x\text{SiO}_y/\text{Si}$) were then punched to 14 mm diameter and assembled into a coin cell for the cycling test. From the first cycle-discharge profile, Li_xSiO_y -covered silicon had a lower OCV of only 1.5 V, and it began to reduce electrolyte at a higher potential range as seen in Figure II-169. The lower potential range behaviors for both films are very similar because the same thickness of silicon film was deposited. Galvanocharge and discharge cycling was performed for both the silicon film and $\text{Li}_x\text{SiO}_y/\text{Si}$ film with a current of 5 μA . What was observed in the cycling is $\text{Li}_x\text{SiO}_y/\text{Si}$ showed lower Coulombic efficiency and less stable performance compared to silicon. The lower Coulombic efficiency is consistent with the impedance measurement that Li_xSiO_y continues to react with electrolyte and consumes the electrolyte. Another explanation for this behavior is the low electrical resistivity of Li_xSiO_y and that it does not passivate the reduction of electrolyte.

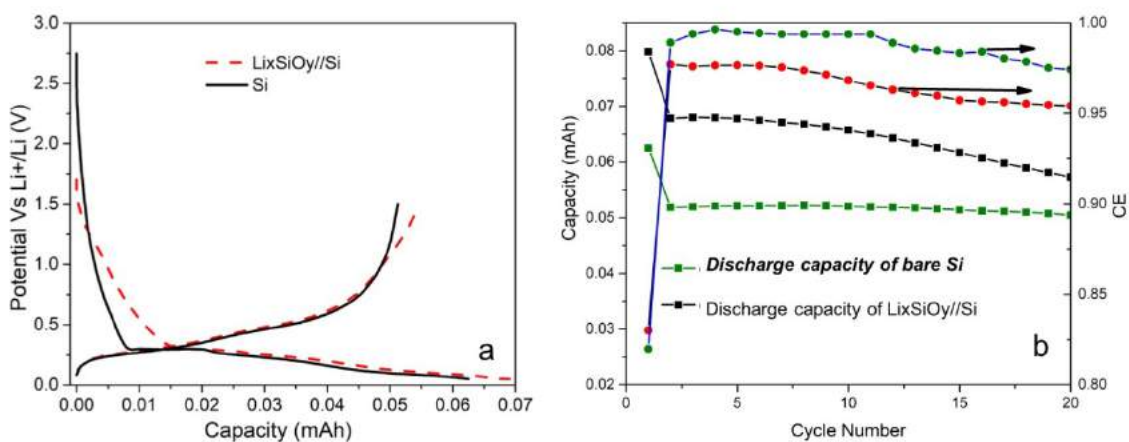


Figure II-169. a) charge and discharge profile of Si and $\text{Li}_x\text{SiO}_y/\text{Si}$. b) Cycle performance and Coulombic efficiency of Si and $\text{Li}_x\text{SiO}_y/\text{Si}$.

The mechanical and electrical properties and chemical reactivity of Li_xSiO_y thin film were thoroughly investigated. Highly lithiated Li_xSiO_y film is ductile and more resistant to fracture, but this still does not make

Li_xSiO_y able to passivate the Si surface. Low electrical resistivity explains why Li_xSiO_y is incapable of passivating the Si surface. Mechanical property is not a single criterion to judge whether SEI is stable; low chemical reactivity and low electrical conductivity are also important for SEI stability.

Chemical stability and reactivity of lithiated silicon Li_xSi_y

The natural passivation layer of silicon is generally related to its history, environment, and handling on formation. The natural passivation layer is usually found to be about a 10-Å -thick layer of silica. More aggressive passivation regimes—for example, ozone treatment—can yield denser layers up to 30–50 Å thick. Previous theoretical work has indicated that this passivation silica layer reacts with electrolyte decomposition products around 900 mV to form Li_4SiO_4 , which generally condenses and, over time, diffuses into the SEI layer [6]. Within the SEI layer exist the various breakdown products of the reactivity of the (lithiated) silicon surface with its environment. Besides silicates and siloxanes, various salt, binder, and solvent-based species have been identified. However, the lithiated silicon electrode is relatively nonhomogenous, on charge or discharge, and correlating the formation of specific species in the SEI with specific species in the silicon Zintl anode (or even local potential) is difficult because many species may have seen one or more reducing events or reacted with salt breakdown products (e.g., PF5). The structure/property relationships can be more easily determined by testing the reactivity under more-controlled conditions using lithiated silicon samples.

Using lithiated silicon materials as model silicon electrodes, the role of surface passivation, electrolyte additives, and electrolyte can be investigated as a function of state of charge. New insights into how the SEI layer is built and ages can be determined and used to better understand its limitations by the following: testing the reactivity of these model compounds against various cell components, then following the reaction product distribution—using MAS-NMR (^{29}Si , ^7Li , ^{31}P) and other spectroscopic techniques—to correlate with state of charge, composition, and the various materials available to react.

The interface between the silicon electrode and electrolyte is a key point of contact in the electrochemical cell.

Silicon is well known to have an unstable SEI layer due, in part, to its reactivity at medium to high states of charge with many of the key components of the laminate and the electrochemical cell altogether. A synthetic effort was undertaken to make key model compounds based on stoichiometries in the Li-Si phase diagram (Figure II-170). We studied the inherent reactivity of the lithium silicides with battery components such as binders, electrolytes, and additives to directly isolate and elucidate some of the reactivity problems associated with Li-Si materials in a Li-ion battery. Synthetically, the materials are unstable to most oxide-based containers at elevated temperature and tantalum was found to be the most stable for use. Single-phase Li_7Si_3 could be isolated between 650°–760°C in a closed container to limit lithium loss via evaporation with limited time in the liquid region ($> 750^\circ\text{C}$). Based on previous work, lithium and silicon phase identification and common impurities can be assigned effectively [7–9]. Powder X-ray diffraction showed that the samples, isolated from the correct range of temperature, were mainly Li_7Si_3 , with small amounts of $\text{Li}_{12}\text{Si}_7$ and SiO_2 depending on time at temperature, box atmosphere, length of time after cooling to analysis, and purity of silicon (a source of SiO_2). Samples were noted by several research teams to self-discharge against small amounts of impurities due, in part, to active lithium availability. Raman and ^{29}Si NMR were able to detect various amounts of amorphous SiO_2 that seemed to track sample age and starting materials.

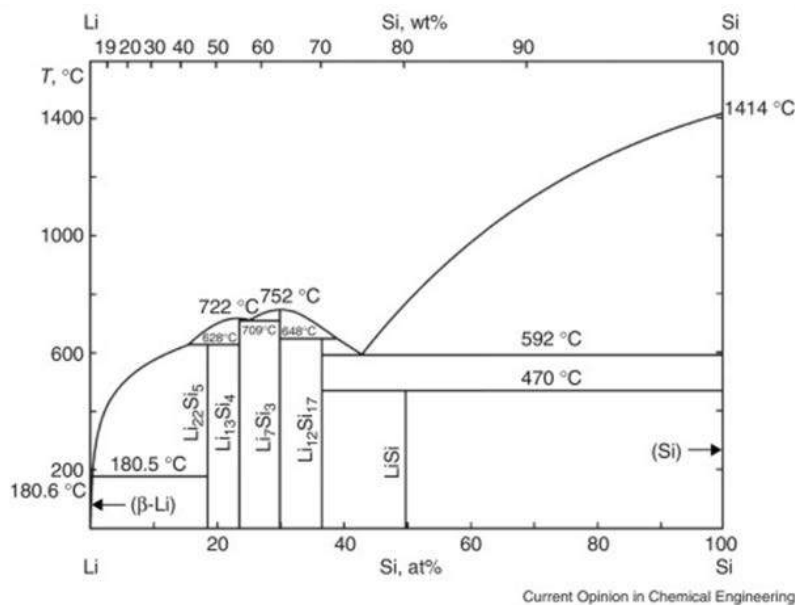


Figure II-170. Phase diagram for the silicon-lithium systems.

To date, X-ray diffraction and solid-state magic angle spinning (MAS) NMR spectroscopy have been used to qualitatively and quantitatively probe reactivity of the model compounds with typical binders used in Li-ion cells. NMR spectroscopy has previously been used [7,8] to effectively study the Li and Si phases in amorphous and crystalline phases of lithium silicides. Using this, the trends in ^7Li and ^{29}Si NMR can be used to follow the Li and Si inventory quantitatively pre- and post-treatment. The Li_7Si_3 model compound was treated with 10 wt.% PVDF (polyvinylidene fluoride) binder in an Ar glove box. Any reaction on the bulk material and the binder was followed by solid-state NMR in Figure II-171. A clear shift was observed for Li in ^7Li to less Li per Si consistent with loss from Li_7Si_3 while affecting mainly the aliphatic carbon and protons of the PVDF binder without affecting the fluorine groups. The Li loss was also found to be consistent in Si NMR. Similarly, Li_7Si_3 model compound was also treated with 10 wt.% lithiated PAA (polyacrylic acid) binder. Only minor changes were observed in Si NMR and XRD (and Li NMR, data not shown), with a slight shift in the main peak to lower lithium content per Si, as well as a minor formation of Si-rich $\text{Li}_{12}\text{Si}_7$ phase in Figure II-172. The specific reaction sites on the binder molecules are currently under investigation. Overall, the results for the binder treatments were found to be consistent with the superior electrochemical performance of LiPAA binder over PVDF for silicon anodes, as noted by ANL's Cell Analysis, Modeling, and Prototyping (CAMP) team in their electrochemical evaluation studies.

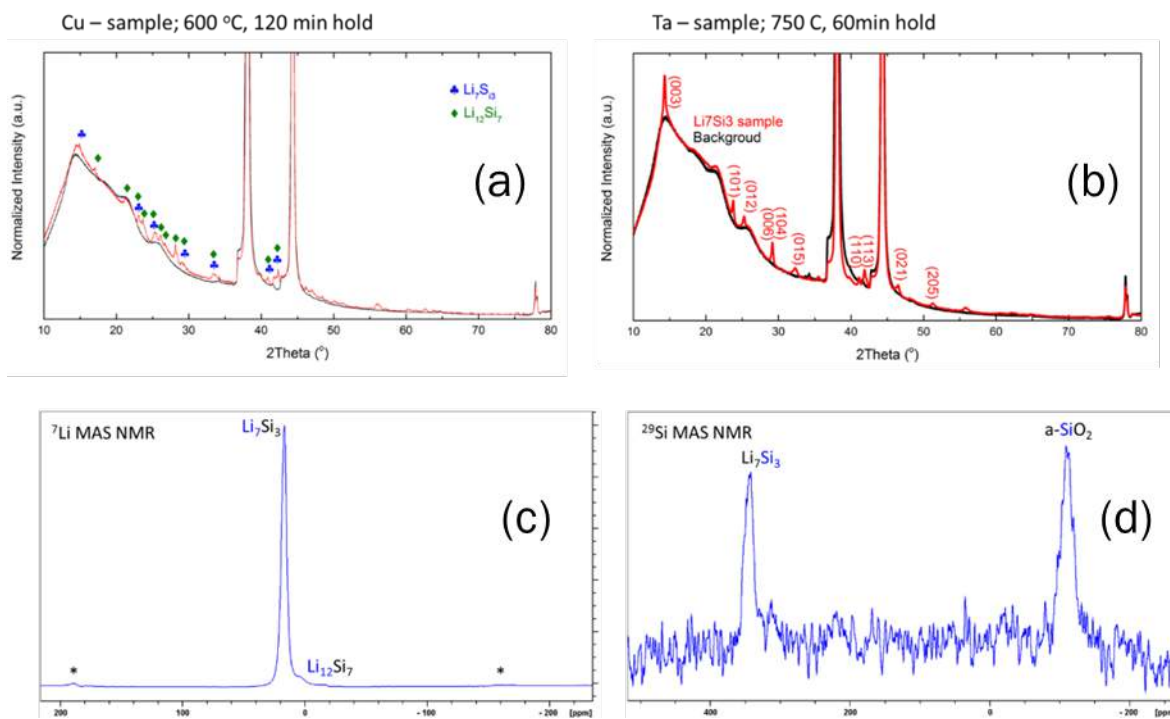


Figure II-171. Long- (XRD, a) and b) and short- (solid state NMR, c) and d) range characterization of Li_7Si_3 model compound.

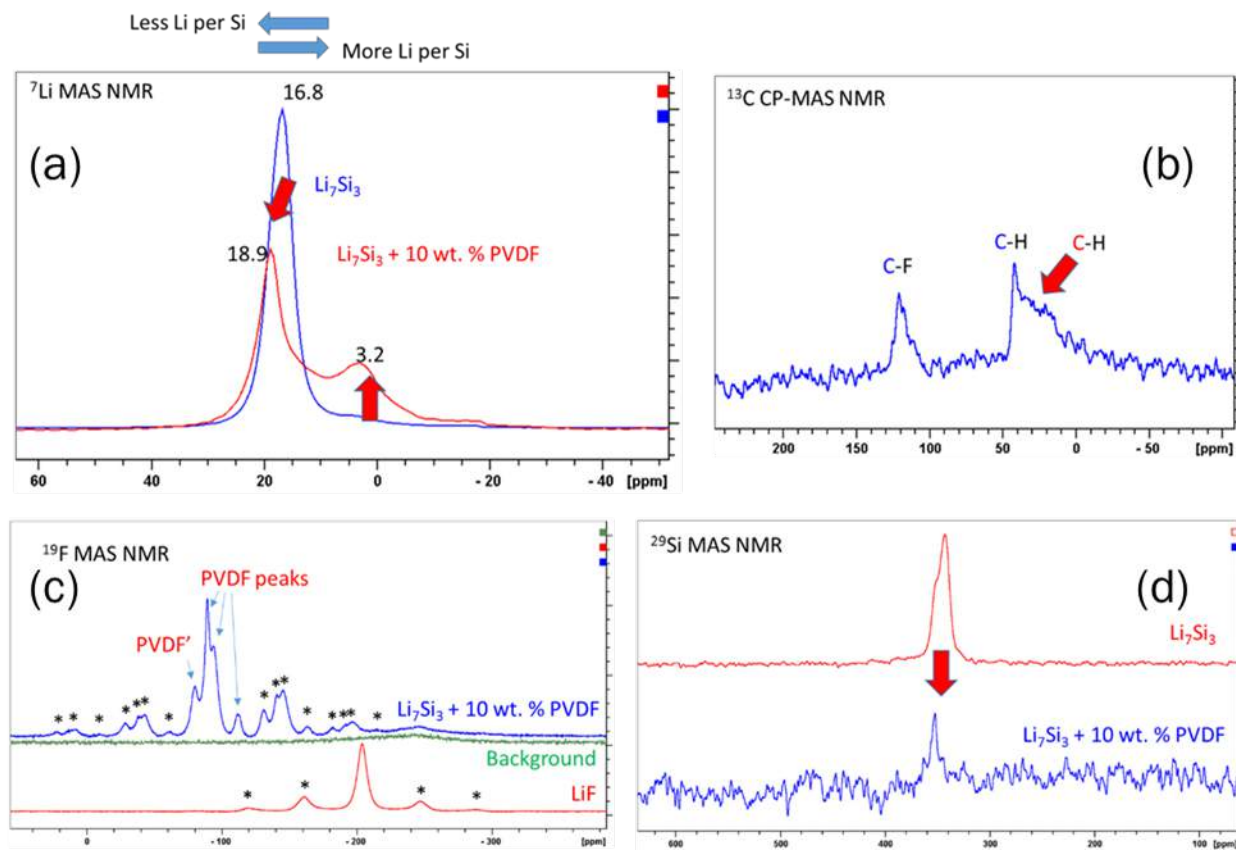


Figure II-172. Multinuclear solid-state NMR data of pristine and PVDF-treated Li_7Si_3 .

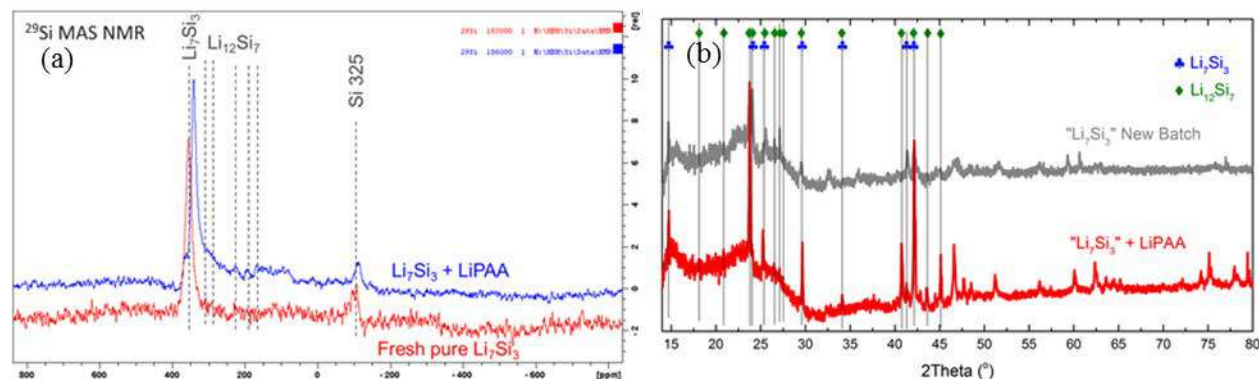


Figure II-173. Solid-state NMR (a) and XRD data (b) of pristine and LiPAA-treated Li_7Si_3 . ANL, unpublished work.

Silicon-rich Li-Si model compounds have been successfully synthesized within bulk and powder forms for investigation of inherent reactivity of lithiated silicon at a single well-defined state of charge. The initial material chosen was Li_7Si_3 , a composition associated with the plateau between 280–300 mV (vs Li). Synthesis and scale-up were carried out in Ta tubes under inert atmosphere using bulk silicon. NMR and XRD results suggest significant reactivity of the compound Li_7Si_3 vs. PVDF binder and only minor reactivity vs. lithiated PAA binder (Figure II-173). The former reaction is proposed to progress via the aliphatic protons of the binder, as opposed to the fluorine groups, whereas the latter results in minor lithium loss and surprisingly the associated formation of the crystalline $\text{Li}_{12}\text{Si}_7$ phase, the product of the slight oxidation of the electrode material, but not disproportionation or surface degradation.

Investigating the formation of SEI on model systems

Tin model electrodes

Tin presents a strong catalytic activity toward the organic-based electrolyte being responsible of a poor electrode passivation leading to continuous electrolyte reduction upon cycling [10,11]. A fundamental understanding of the kinetic processes occurring at the Sn/electrolyte interface will begin with a rational and basic study on the SEI components properties. We have undertaken this by designing three types of model electrodes, each differing in the content of oxygen at both bulk and surface level [12]. A schematic representation of the developed systems to be investigated is reported in Figure II-174. The "pristine" electrode consists of a commercially available high-purity tin metal foil, whereas the "melted" version has been obtained by melting the pristine tin foil in inert atmosphere (i.e., glove box environment), thus obtaining a model electrode with a lower content of oxygen dissolved in the bulk and a higher amount of SnO on the electrode surface. The "cleaned" version corresponds to an oxygen-free tin electrode, obtained by removing the SnO layer from the melted electrode by polishing. Chemical composition and structural properties have been confirmed by XRD, XPS, and soft X-ray absorption spectroscopy (sXAS) analysis.

The electrochemical analysis performed in 1M LiPF_6 EC:DEC (1:2 wt.%) revealed surprisingly different passivating behavior most likely attributable to the presence of oxygenated species dissolved in the bulk of the model electrodes (see Figure II-174). It appears that a lower content of dissolved oxygen strongly improves the passivating behavior of the electrode, limiting the electrocatalytic activity of tin toward the reductive electrolyte decomposition. These results confirm our earlier observations that the surface film on the pristine Sn cannot prevent continuous electrolyte reduction and that a large fraction of the reaction products dissolves in the electrolyte.

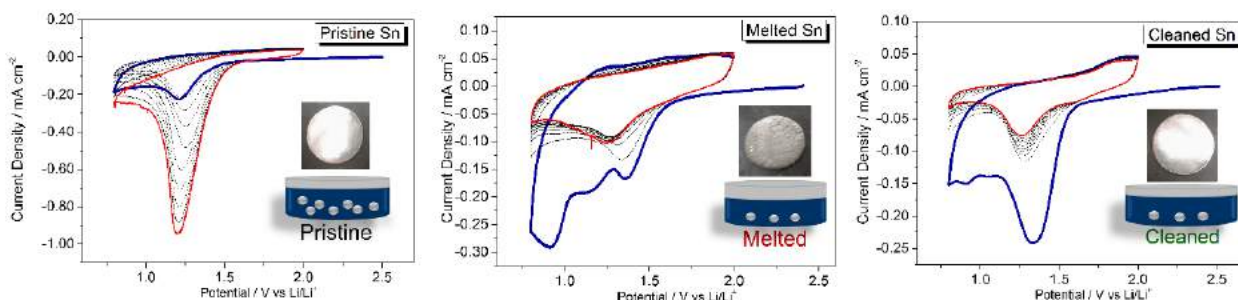


Figure II-174. Cyclic voltammetry of pristine, melted, and cleaned tin model electrodes swept from OCV to 0.8 V and back to 2 V in 1 M LiPF₆/EC:DEC (1:2 wt%) electrolyte.

To gain insights into the mechanism of the electrolyte decomposition and SEI layer (re-)formation upon cycling, we investigated the surface layer film by FTIR.

The results, shown in Figure II-175, evidence a different film composition that is most likely responsible of the observed differences in the passivating behavior. Li₂CO₃ has been identified to be the main component in the surface layer. To investigate the role of Li₂CO₃ and the corresponding reaction mechanism of the electrolyte decomposition, electrochemical tests have been performed, employing single solvent-based electrolyte, such as 1M LiPF₆, DEC. *Ex-situ* FTIR and XAS analysis clearly revealed that the formation of Li₂CO₃ is the result of the selective decomposition of EC. We observed that the passivating behavior of the tin electrodes can be strongly improved by avoiding the use of EC. In fact, all the three model electrodes cycled in DEC exhibit satisfactory passivating properties. However, despite the deleterious effect of EC, its decomposition and subsequent formation of Li₂CO₃ is not the ultimate cause leading to the poor passivating properties of the tin electrodes. The improved passivation properties observed for the melted and cleaned electrodes in EC:DEC-based electrodes relies on the presence of other compounds in the SEI as demonstrated in the FTIR spectra. In addition, we demonstrate that the use of additives in the electrolyte and the employment of engineered electrolyte formulations may also be an effective strategy for improving the surface layer stability during cycling. The role of LiF and Li₂CO₃ used as additives in the electrolyte has been investigated through cyclic voltammetry and *ex-situ* FTIR measurements. These preliminary results show improved passivating behavior of the tin electrodes in the presence of LiF and Li₂CO₃.

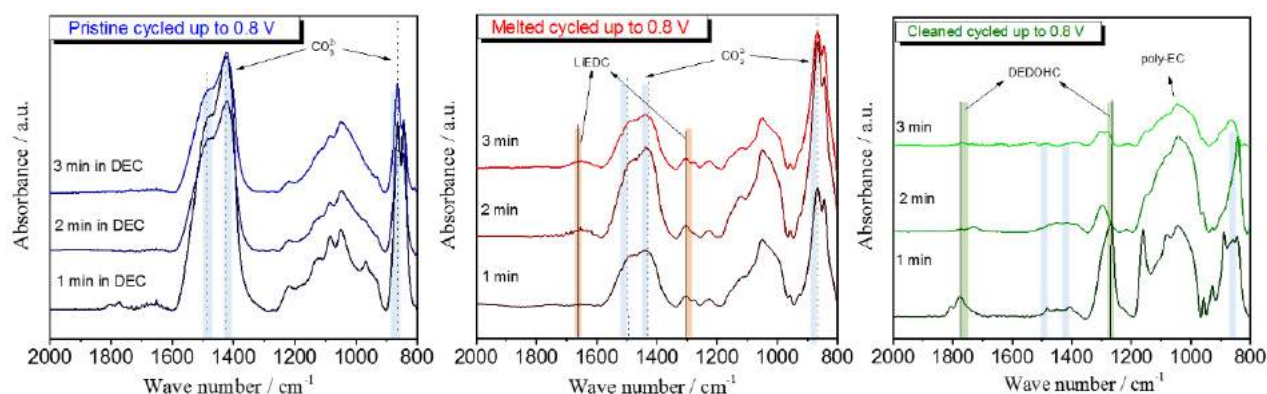


Figure II-175. *Ex-situ* FTIR analysis of pristine, melted, and cleaned tin model electrodes cycled up to 0.8 V in 1 M LiPF₆/EC:DEC (1:2 wt%) electrolyte at different washing steps.

The interfacial properties occurring at the electrode/electrolyte interface of Sn, Si, and SiO₂ have been analyzed by combining electrochemical investigation and surface chemistry analysis. Our results suggest that the poor passivating behavior of Sn electrodes can be mitigated by reducing oxide species dissolved in the bulk of the electrode and by formulating unique electrolyte compositions.

Artificial SEI Modified Silicon Model Electrodes

We believe that the stabilization of the SEI and the mitigation of the electrolyte reduction upon cycling may be mitigated by designing tailored artificial SEI with a proper thickness and chemical composition. The presence of an artificial SEI layer on model silicon electrodes not only can help improve interfacial properties of Si, but can also lead to a better basic understanding of the interfacial processes occurring at the Si/electrolyte interface. It has been reported that the main components of the silicon SEI are Li_2O , Li_2CO_3 , and LiF and contribute to the stability of the passivating film and the lithium-ion transport mechanism through the film [13,14]. To evaluate the effect of Li_2O , Li_2CO_3 , and LiF on the reactivity toward the electrolyte, thin films were deposited on p-type-doped Si (100) wafer model electrodes via the pulsed laser deposition (PLD) technique [15]. The main advantages of PLD can be summarized as follows: 1) conceptually simple—a laser beam vaporizes a target surface, producing a film with the same target's composition; 2) versatile—many materials can be deposited in a wide variety of gases over a broad range of gas pressures; and 3) fast—high-quality samples can be grown reliably in 10 or 15 minutes.

LiF , Li_2O , and Li_2CO_3 thin films have a thickness ranging from 40 to 50 nm. Unfortunately, none of the thin films was smooth and perfectly planar. The film surface shows large drop-like features (micrometric dimension). The cyclic voltammetry (CV) measurements are within the 0.01–2.0 V potential range at a scan rate of 0.1 mV sec⁻¹. Figure II-176 exhibits the first CV cycle. The enlarged potential region corresponds to the electrolyte decomposition region.

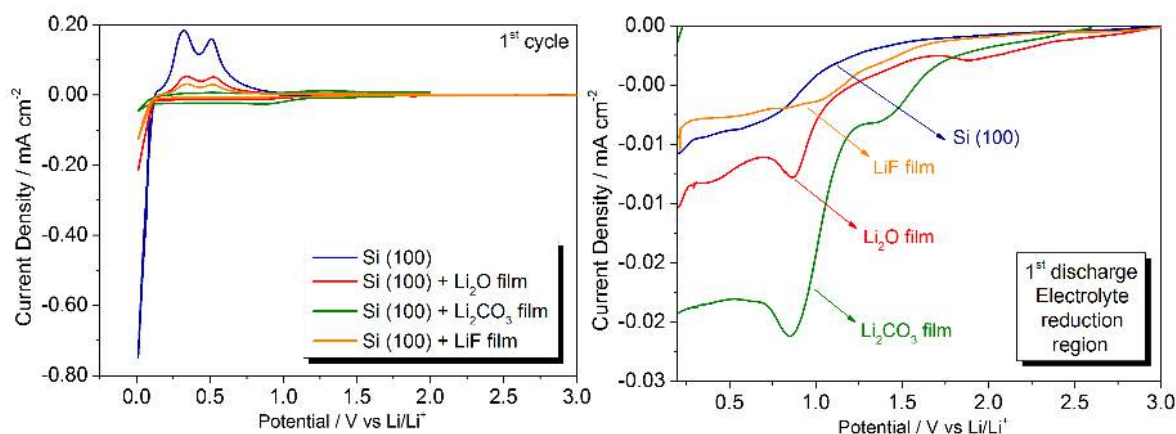


Figure II-176. Cyclic voltammetry of bare Si (100) wafer and comparison with the modified model electrodes with Li_2O , Li_2CO_3 , and LiF thin film deposited within the 0.01–2.0 V potential region. Enlarged potential region of the first reduction process.

Clearly, all the Si samples with the LiF , Li_2O , and Li_2CO_3 thin film deposited on the surface inhibit the lithiation process, which is reflected by low lithiation and delithiation currents.

Interestingly, as shown in the enlarged potential region between OCV and 0.2 V, the presence of Li_2CO_3 and Li_2O induces a higher cathodic current and total amount of cathodic charge with respect to the LiF -coated and pristine silicon wafer, most likely attributable to the altered reactivity of silicon toward the carbonate-based electrolyte.

Post-mortem SEM images clearly confirm that the presence of the thin solid films inhibits the (de-)lithiation as documented by fewer cracks in the Si electrodes when compared to the bare silicon wafer (see Figure II-177).

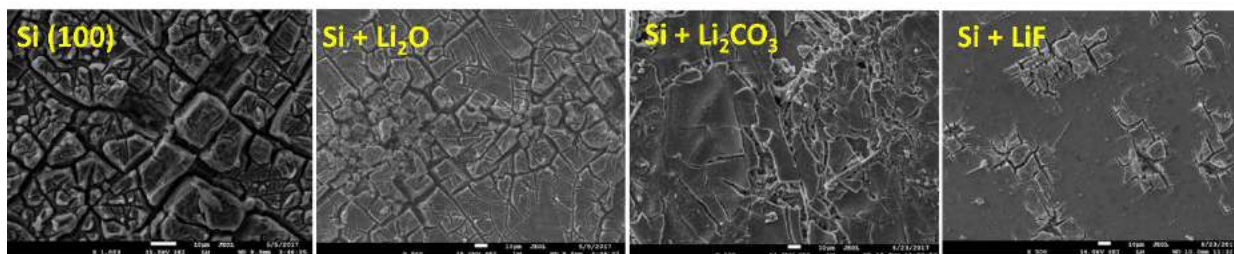
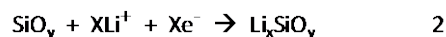
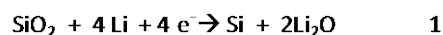


Figure II-177. Post-mortem SEM images of cycled Si (100) electrode the modified model electrodes with Li₂O, Li₂CO₃, and LiF thin film deposited.

This study represents the preliminary step necessary for understanding the single components effect on the Si/electrolyte interfacial processes. Future work is needed to better understand the effect of the thickness on the surface-layer behavior [16].

Silicon oxide-coated model electrodes

The role of a native and artificially grown SiO₂ layer on the surface chemistry of a Si electrode has been investigated. For this purpose, we used a Si(100) wafer with different oxide thicknesses (native oxide, 100-nm and 300-nm thermal oxides) as a model electrode. Electrochemical analysis and various spectroscopic and microscopic techniques have been applied to study the effect of the oxide layer on the interfacial processes occurring at the Si/electrolyte, oxide/electrolyte, and Si/oxide/electrolyte interface. The investigation is based on the assumption that the lithiation of the oxide layer may lead to the conversion of the surface oxide to Li₂O and Si (Equation 1) or formation of silicate (Equation 2). On the other hand, SiO₂ could also act as a barrier for the lithiation of the Si electrode because it is not a good Li⁺ conductor.



To evaluate the feasibility of these assumptions, we studied the lithiation mechanism and the composition and structure at the interface during cycling.

Figure II-178 shows the cyclic voltammetry of Si(100), 100-nm SiO₂/Si(100), and 300-nm SiO₂/Si(100) electrodes using 1.2 M LiPF₆/EC:DEC (3:7 wt%) electrolyte. The results reveal that the cathodic current around 1 V increases and becomes broader as the oxide thickness increases. This may be attributable to both the conversion reaction as shown in Equation 1 and to the interfacial properties of the oxide layers leading to changes of the electrolyte reduction mechanism, similarly to what we observed in the presence of Li₂CO₃ and Li₂O. As the potential is swept in the anodic direction, lower reversible capacity is observed as the oxide thickness increases.

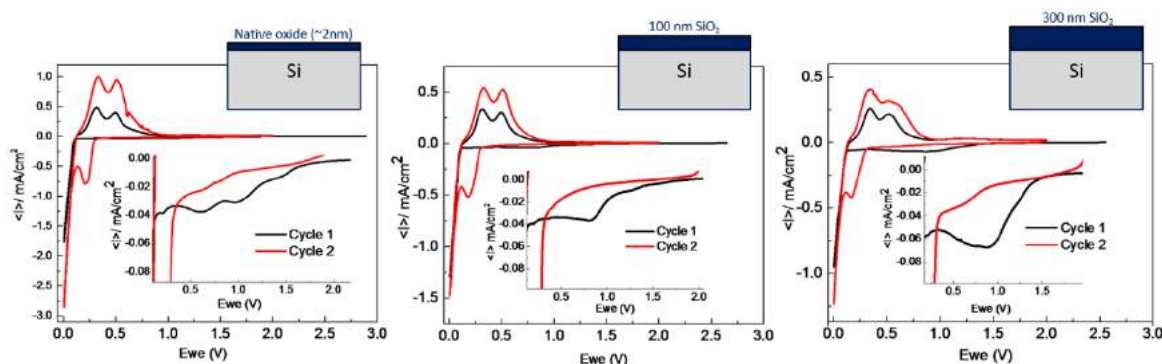


Figure II-178. Cyclic voltammetry of Si(100) wafer, 100-nm SiO₂/Si(100), and 300-nm SiO₂/Si(100) swept from OCV to 0.005 V and back to 2 V in 1.2 M LiPF₆/EC:DEC (3:7 wt%) electrolyte.

Using spectroscopic and microscopic techniques such as attenuated total reflectance-mode Fourier Transform Infrared (ATR-FTIR) spectroscopy, XAS at ALS, XPS, *in-situ* X-ray reflectivity (XRR) at SLAC, and scanning electron microscopy-energy-dispersive X-ray spectroscopy (SEM-EDX), we studied the effect of the oxide layer on the interfacial properties and linked with the electrochemical results. The O K-edge XAS results reported in Figure II-179 shows that there is no formation of Li₂O due to the conversion reaction. Although red shift is observed due to the lithiation process, both the Si and O K-edge features are different from the features of Li₂SiO₃ and Li₄SiO₄.

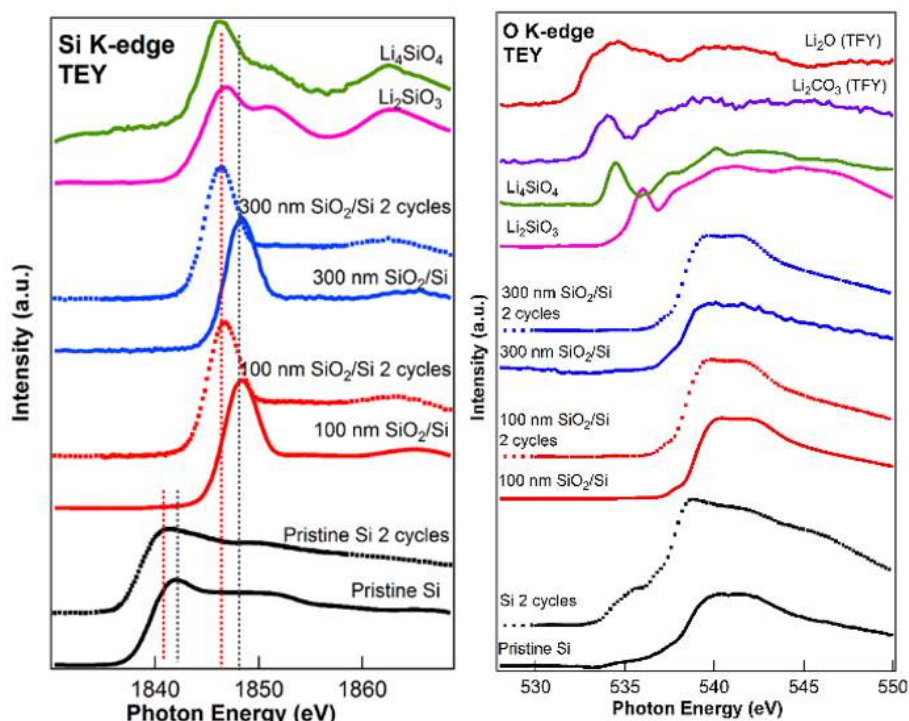


Figure II-179. Si (left) and O (right) K-edge XAS spectra of pristine Si(100) wafer, 100-nm SiO₂/Si(100), and 300-nm SiO₂/Si(100).

Our result suggests that the thermal oxide acts as a barrier for bulk lithiation and avoids the complete lithiation of the silicon electrode, which leads to the decrease in specific capacity. Hence, thinner oxides (5–20 nm) should be considered for model studies of the effect of the oxide on the interfacial properties.

The initial cycling of a lithium-ion battery results in the formation of a SEI layer between the electrolyte and the anode. This passivating layer, consisting of decomposition products from the electrolyte solution, is critical to the reliability and performance of the battery. The SEI must be both electronically insulating and ionically conductive—permeable to lithium ions yet resistant to electron flow. The mechanisms of SEI formation, stabilization, and evolution are still poorly understood. Moreover, reactivity and diffusivity of lithium present difficulties in SEI characterization, because many sputtering and milling techniques may significantly change chemical composition.

Artificially created simplified interfaces have enabled observation of the effect of SEI single components on the overall behavior of model Si electrodes. The Li_2O , Li_2CO_3 , and LiF thin films deposited on $\text{Si}(100)$ wafers inhibited the lithiation and delithiation process. The electrolyte decomposition mechanism was also altered by the presence of the thin film and its effect on the Si surface reactivity. We believe that the artificial thin films may affect the charge and mass transfer processes.

In the same way, we demonstrated that the SiO_2 film on the surface of silicon model electrodes presents a barrier for lithiation. No signs of conversion reaction could be detected. More work is needed to better understand the effect and role of surface layers on Si electrodes. Thinner oxide layers (5–20 nm) should be considered instead of thick films (100–300 nm) and such an effort is currently ongoing. Accordingly, thinner layers on LiF , Li_2O , and Li_2CO_3 are also being investigated for an improved understanding of the kinetic processes occurring at tailored Si/electrolyte interfaces.

In the past months, we have adapted scanning-spreading resistance microscopy (SSRM) to characterize SEI (Figure II-180). Originally, SSRM was developed as a characterization technique to measure electron-carrier distribution in semiconductor materials. SSRM measures current when applying a bias voltage between the probe tip and sample. When operating the probe at forces that are orders of magnitude greater than other scanning probe techniques, the contribution of the contact resistance between tip and sample becomes minor and the resistance indicates the spreading resistance (Figure II-181), a material property related by the Maxwell equation, $R = \rho/4a$, where R is the resistance measured, ρ is the material-dependent spreading resistance, and a is the electrical radius of the probe. Using SSRM instrumentation on soft materials allows for SEI to be mechanically milled away laterally, giving resistivity measurements for the material located at that depth. Thus, the technique demonstrates high lateral and vertical resolution when characterizing SEI.

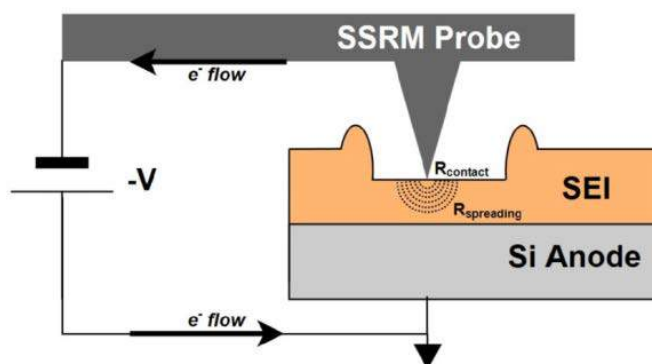


Figure II-180. Schematic depiction of SSRM instrumentation and mechanical milling of a sample.

To date, our characterization of SEI has focused on cycled silicon wafers prepared under varied cycling conditions. Preliminary results show that the SSRM profiling of SEI can quantitatively measure SEI thickness and semi-quantitatively assess lateral and vertical inhomogeneity of SEIs. Recent work depth-profiling SEIs with TOF-SIMS and XPS has shown agreement with conclusions from SSRM studies, and future work will begin to associate resistivity data with known SEI chemical compositions.

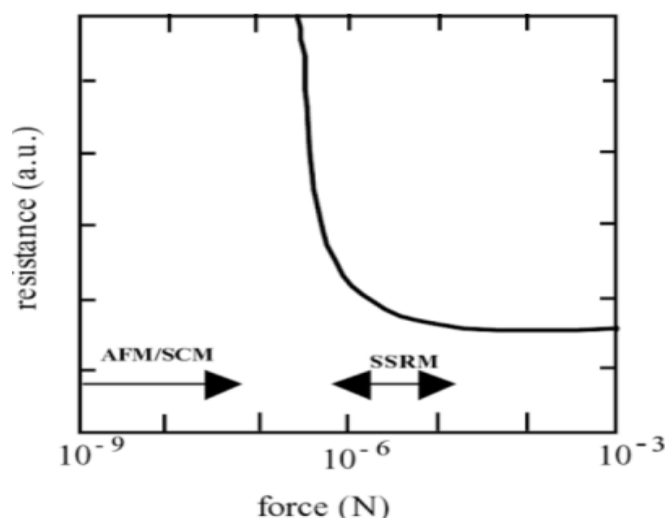


Figure II-181. Contact resistance as a function of applied probe force. Image from Kalanin, S. and Gruverman, A.L., *Scanning Probe Microscopy*, Springer (2007)

Figure II-182 shows an example of the SEI milling and resistance measurement. As milling depth (left panel) increases throughout the SEI layer to the underlying Si, the resistance decreases to the value of Si (higher SSRM signal converts to lower resistance). Figure II-183 shows two series of the SSRM resistance and SEI thickness measurements. The two SEI series show significant differences in both resistance and thicknesses, illustrating that the SEI electronic resistance depends sensitively on electrochemical cycling conditions and electrolyte compositions. Further understanding of SEI resistivity is expected with detailed chemical composition information.

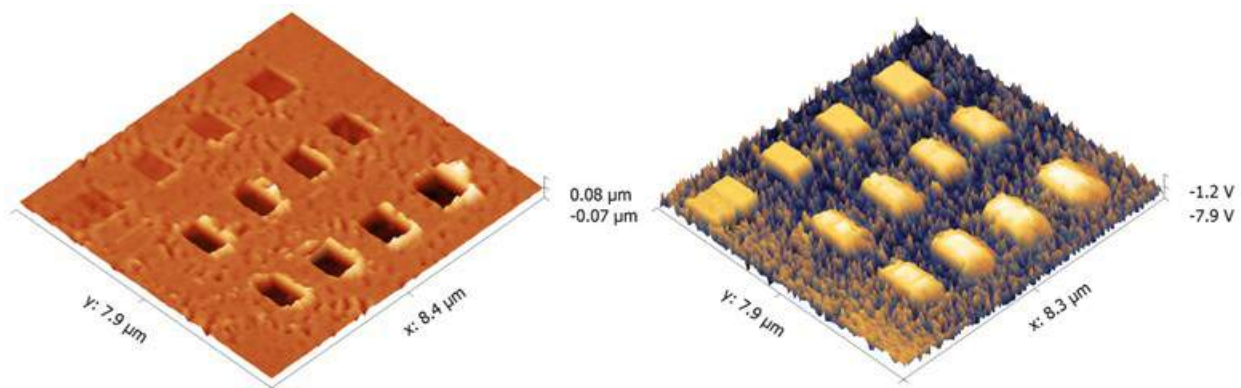


Figure II-182. Height (left) and resistance (right) channels showing the lateral and vertical resolution of the instrument. Deeper milling into SEI carried out under higher probe forces reveals SEI layers of significantly lower material resistance. In the resistance channel image at right, higher voltage is indicative of lower resistance.

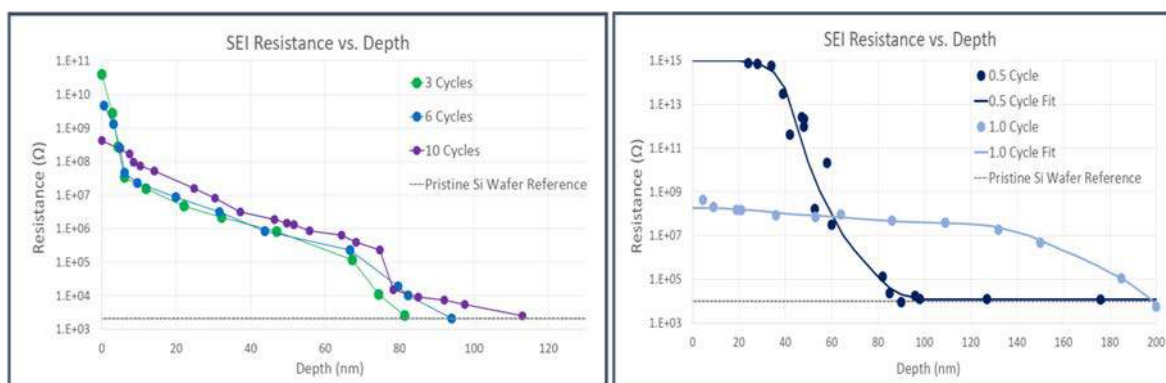


Figure II-183. Studies of resistance vs. depth for different sample series. The plot at left shows how SEI thickness and vertical homogeneity develops over repeated cycles. The plot at right shows the distinct resistance and thicknesses of the lithiated and delithiated phases of SEI formed in the original cycle. Thickness is calculated by measuring the depth at which Si wafer-substrate equivalent resistance is measured.

In-situ neutron reflectometry

In this work, we sought to provide insight into the role of FEC in SEI formation by characterizing the SEI growth *in situ* using neutron reflectometry (NR) and *ex situ* using infrared and X-ray photoelectron spectroscopies. In NR, the specular reflection of neutrons from an interface is measured as a function of the wave vector transfer, $Q = 4\pi\sin(\theta)/\lambda$, perpendicular to the sample surface. The angle of incidence θ is between the incoming neutron beam and the sample surface, and λ is the wavelength of the neutron. Analyzing the neutron reflectivity gives us information about the thickness and composition of the film layers. This ability to follow chemistry and composition has been used to follow the swelling of silicon anodes during alloying/dealloying with Li [17-19]. However, the real power of NR comes from the sensitivity of neutrons to low z components (i.e., H, Li, C, O, F), which makes it a good complementary method to X-rays.

The samples consisted of a 5-mm-thick, 2"-diameter silicon wafer coated with 20 nm of copper, which acts as a contrast layer, diffusion barrier, and current collector, with 50 nm of amorphous silicon deposited on top. These layers were grown following the SEISa protocols and were demonstrated to cycle with the expected profile of amorphous silicon (see round-robin results). Li-coated TiZr was used as the counter electrode (half-cell-type configuration). TiZr (Ti_{0.47}Zr_{0.53}) was selected as the Li current collector for several reasons. First, TiZr is a null scatterer of neutrons and would not contribute to the NR spectrum. Second, TiZr is stable in contact with metallic Li and does not react electrochemically with Li. Long wires were bound to the Si and TiZr plates using silver epoxy (Illinois Tool Works), which was allowed to dry overnight. The silver epoxy was placed on the edge of the Si wafer to contact the Cu, which was spilled around the wafer during deposition. The epoxy was never in contact with the electrolyte. The components were assembled in a He-filled glove box located at the beamline (H₂O < 1 ppm; O₂ < 7 ppm). The electrodes were separated by a Teflon-coated Viton O-ring with a 0.8-mm cross-sectional diameter. The total cell volume is about 2.5–2.8 mL depending on the amount of Li on the TiZr. NR measurements were carried out on the liquids reflectometer (LR) at the Spallation Neutron Source (SNS) at Oak Ridge National Laboratory.

Figure II-184 shows representative NR data, along with the fits to the data. From the data in Figure II-184, it is clear that there are significant changes in the reflectivity profile as a function of cycling, as evident by the changes in peak position, corresponding to changes in layer thicknesses and compositions. From the fits, we can estimate layer thickness (based on the separation between the peaks) and layer composition (based on the intensity) and is reported as scattering length density, which is a measure of the nuclear cross-section of the layer. Figure II-185 shows a representation of the refined scattering length density (SLD) profile of the film at different states of charge versus layer thickness. These data show clear changes in layer thickness and composition. Figure II-186 summarizes the electrochemical data (black line) with the resulting Si and SEI

thicknesses and SLD values. The Si thicknesses were estimated from the electrochemical data and were used to confirm the modeling of the NR data. Extensive XPS characterization and IR characterization were performed to provide chemical specificity, and they support the interpretation of the refined SLD data.

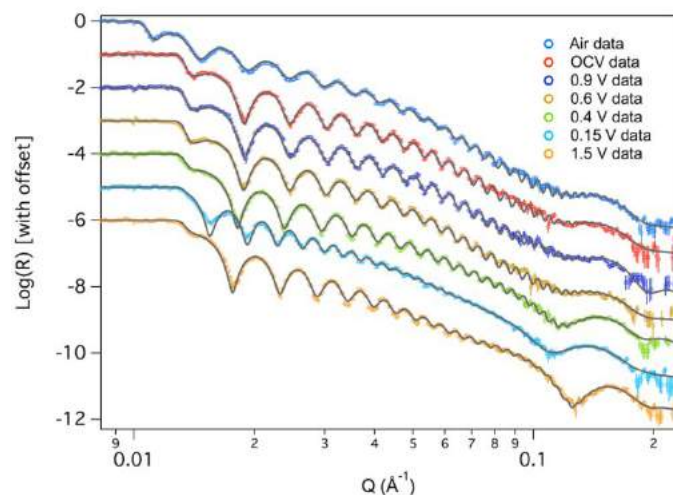


Figure II-184. NR data (data points) and fits (solid line) for representative data sets collected in this study.

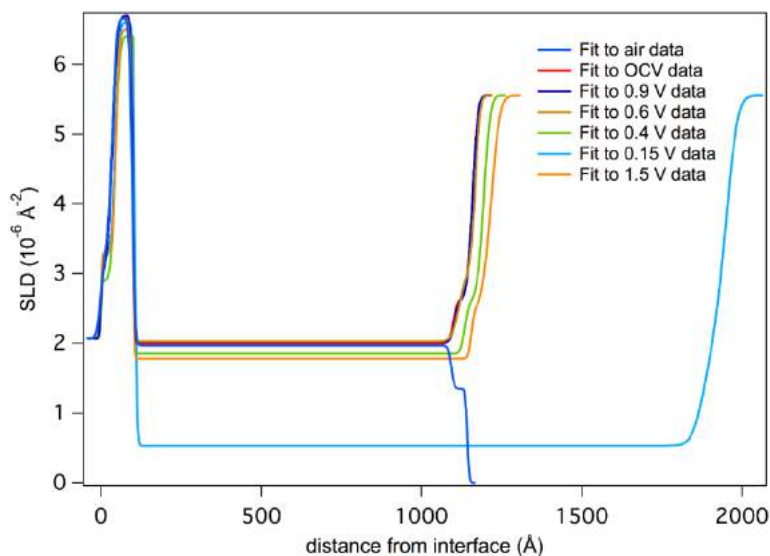


Figure II-185. Plot of the refined SLD profile of the film as a function of distance from the thick Si substrate.

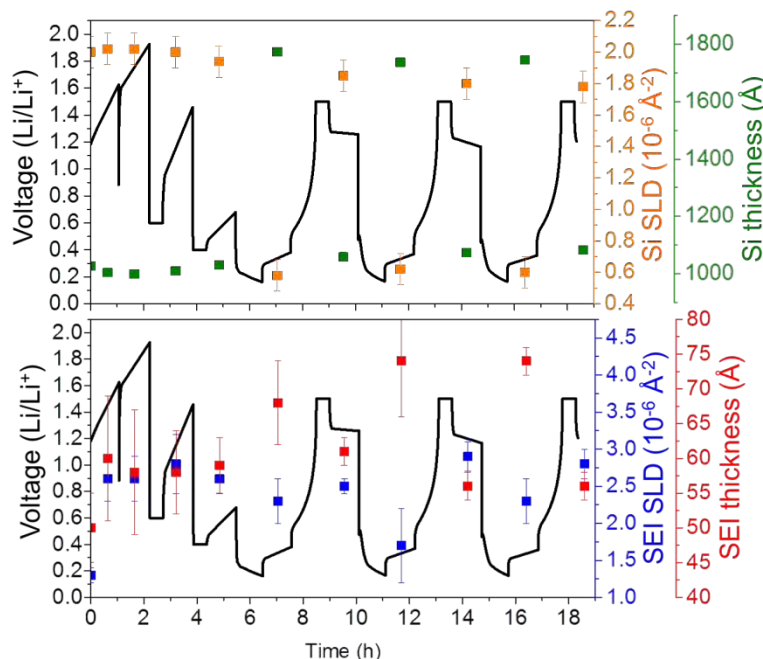


Figure II-186. Plots of SLD values and layer thicknesses as a function of state of charge for silicon (top) and the SEI (bottom).

After cell assembly, the electrode was in contact with the electrolyte for 90 minutes during the setup and alignment procedure. During this time, there is clear evidence for the modification of the silicon surface from the reaction with the electrolyte. Indeed, the SLD of the interface layer increased from 1.3 ± 0.1 to 2.6 ± 0.3 along with a small increase in the layer thickness (50 ± 5 to 60 ± 9 Å). Given that the SLD values of almost all of the components of the electrolyte (D, C, O, P, or F) have high bound coherent scattering lengths (6.6, 6.6, 5.8, 5.1, 5.6 fm, respectively), this layer has to have a high concentration of Li or H (from the FEC) that have negative scattering lengths that would account for the relatively low SLD of the layer.

This change in the surface chemistry is consistent with the measured XPS data where there is a decrease in the concentration of the Si-O bonds at higher binding energies (~ 104 eV) and C on the surface. In addition, there is an increase in F (Figure II-186), P, and Li, which has to originate from the LiPF₆ or FEC (in the case of F) given the lack of binder in these cells. Analysis of the F1s spectra is consistent with the presence of Li-PF₆ (690 eV, 6% F species) and Li-P-O-F (687.6 eV, 94% of F species) due to this salt decomposition. In addition there is a change in the C1s spectra (Figure II-187, Figure II-188), from the sample exposed to air, where there is the growth of C=O-type species (287.1 eV) from the decomposition of the solvent or FEC along with the loss of C-O species. Together, these data indicate that the Si-O is being chemically reacted away, likely by the HF originating from the well-documented LiPF₆ reaction with water [20]. But this reaction layer is not simply dissolving, it is being replaced with a new reaction layer formed by the decomposition of salt and solvent species. Such a reaction layer has been observed before for Si electrodes in aprotic solvents and likely represents the initial stages of SEI formation [21-24].

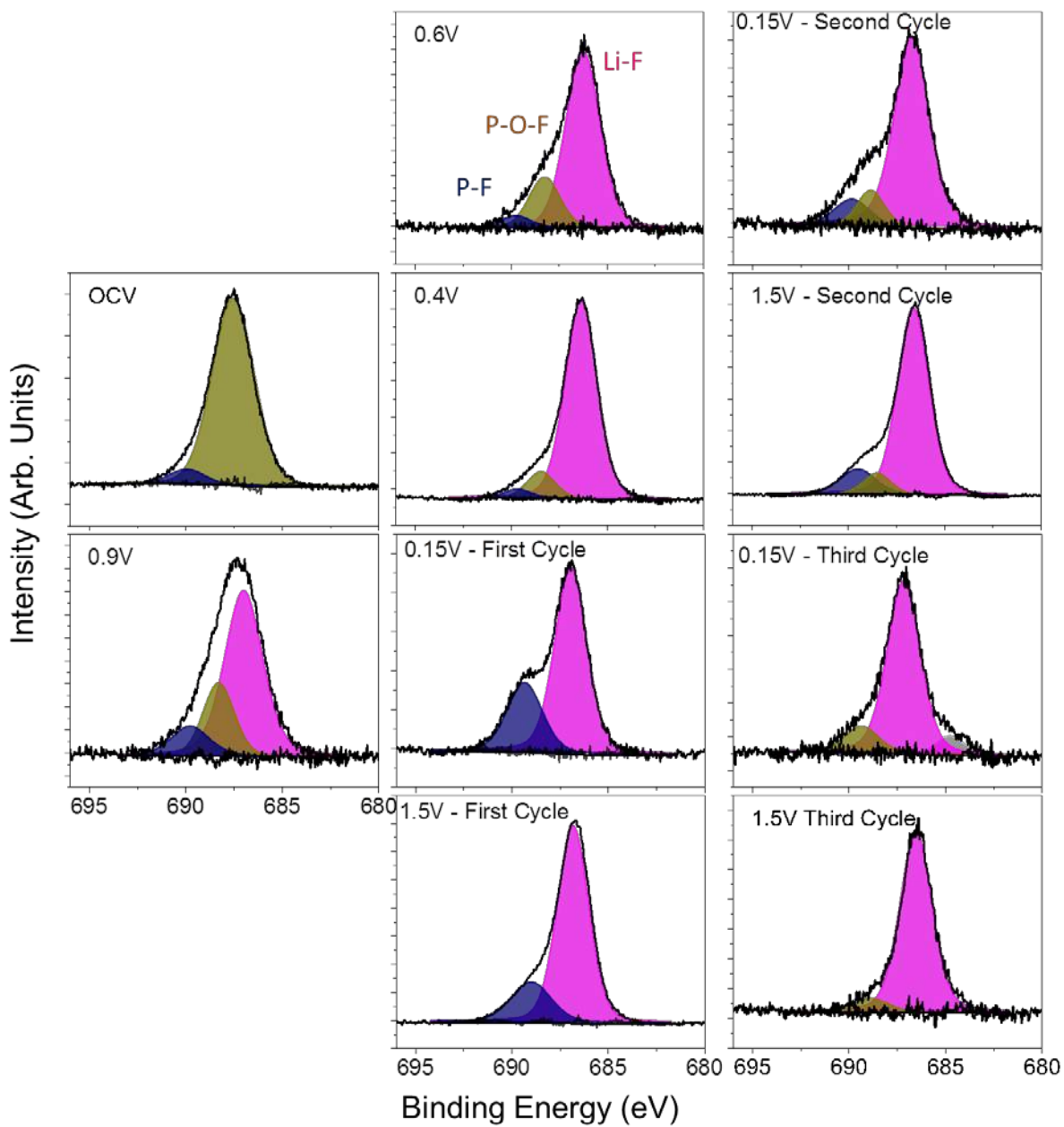


Figure II-187. F1s XPS data collected for the Si electrodes as a function of cycling.

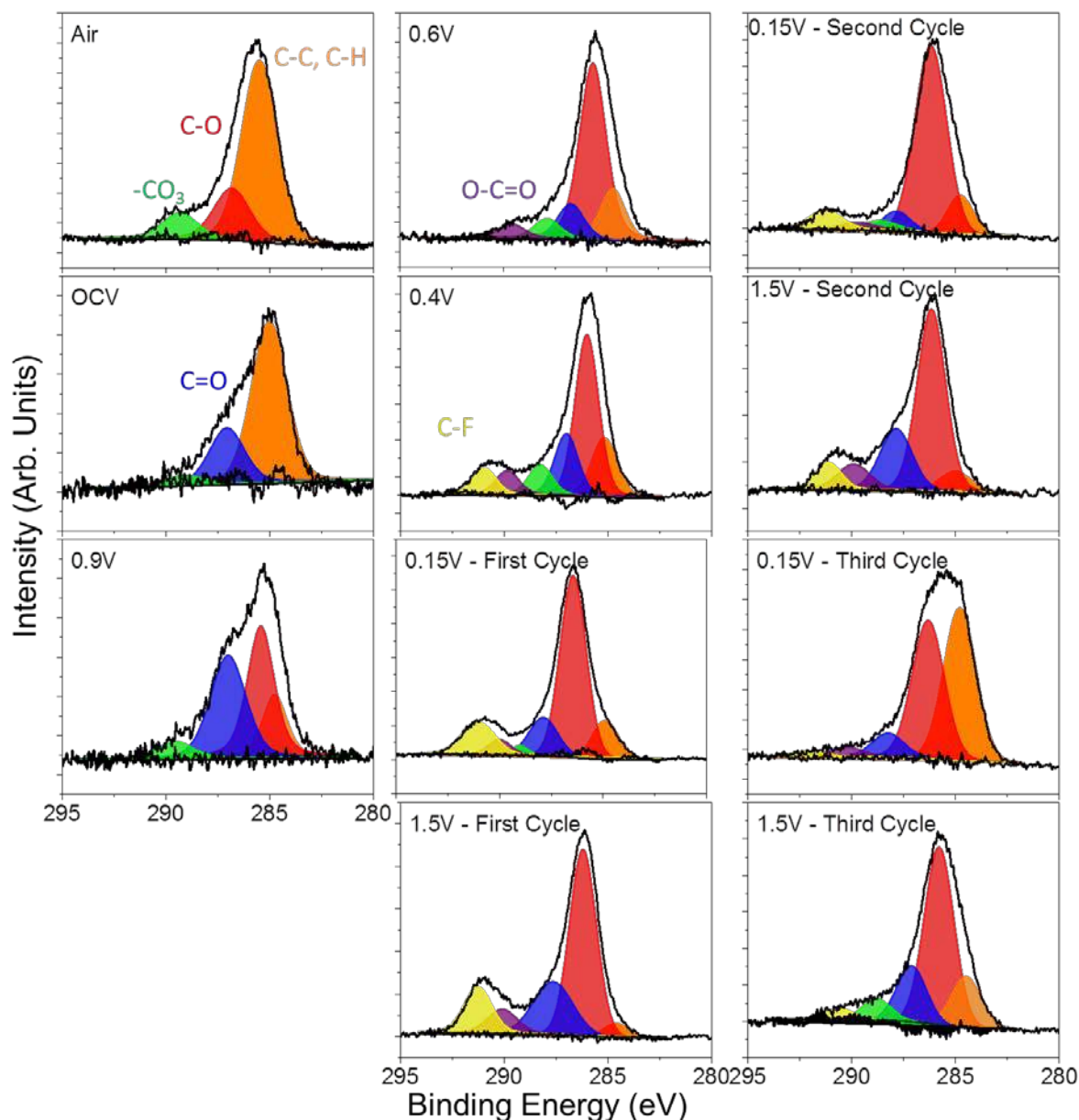


Figure II-188. C1s XPS data collected for the Si electrodes as a function of cycling.

With further lithiation, we start to see evidence of changes in the Si electrode chemistry at potentials less than 0.6 V vs. Li/Li⁺. Indeed, at 0.6 V, there is a small 8 Å increase in Si thickness (versus as-prepared Si) and a corresponding decrease in the Si layer SLD from 2.0 ± 0.1 to a calculated SLD of 1.93, consistent with Li entering the Si electrode and causing the layer to swell and a decrease in SLD due to the negative SLD of Li (-0.87). At 0.4 V, the thickness increased by 24 Å and the SLD decreased further to 1.85, again consistent with the extent of lithiation and the expected swelling of Li:Si alloys reported by Chevrier [25].

At these stages of lithiation, there is no apparent change in the SEI SLD or thickness based on the NR data. However, there are clear changes in the XPS data, again due to the formation of more C-O species (~285.5 eV) and O=C-O moieties (~288 eV), from the breaking of C=O bonds in the solvent or polymerization of the cyclic carbonates, and additional LiF at the expense of residual Li-P-F and Li-P-O-F species. In addition, we see

evidence for a higher binding-energy C1s species (290 eV) attributed to C-F species due to the reduction of FEC. Interestingly, there is a low-energy Li1s peak (56.2 eV) evident in the XPS data measured for the 0.4-V sample in addition to the main LiF peak at 56.7 eV. This new feature corresponds to Li-Si bonding in the anode that is detectable due to its concentration and the thin SEI (59 ± 4 Å), which does not attenuate the excited photoelectrons. These data support the validity of the SEI thickness derived from the analysis of the NR data, i.e., the SEI is less than 10 nm thick. If the SEI were more than 10 nm thick, it would attenuate and block the XPS signal from the Si. Finally, these data differ from previous XPS reports [26] of FEC-based electrolytes over Si(100) electrodes, which were dominated by C-C/C-H species, not C-O bonds, indicating a different reaction mechanism over crystalline Si versus the amorphous Si here.

Cycling of Li-Si anodes (0.15–1.5 V)

NR data collected for the silicon anode with extensive Li cycling revealed significant and dynamic changes in the SEI thicknesses and composition. The electrodes were repeatedly cycled from a Li-Si stoichiometry close to LiSi to a Li_{0.1}Si. Upon lithiation, the electrode swelled to about 1778 ± 8 Å (from 995 ± 6 Å), causing a significant decrease in the Si SLD; during delithiation, the Si returned to a thickness of 1056 ± 4 Å due to slight irreversibility of the cell. The fitted SLD values and thicknesses determined for the silicon layer were in good agreement with the predicted values based on the electrochemical measurements. Furthermore, the XPS data collected on these electrodes revealed that the Si2p spectra still contained information demonstrating the presence of reduced Si from the electrode. Together, these data confirm that the SEI is less than 10 nm thick and again supports the validity of our NR model.

The more interesting data were obtained for the SEI layer. As demonstrated in Figure II-186, the SEI layer increased in thickness by about 12–13 Å with lithiation, and its SLD decreased to about 2.3 ± 0.3 (from 2.6 ± 0.3). Upon delithiation, the SEI shrunk to its prelithiation thickness and the SLD increased to 2.5 ± 0.1 . This swelling and contracting of the SEI layer thickness is consistent with the “breathing” reported for silicon anodes measured by previous NR studies, as well as XPS, TOF-SIMS, and atomic force microscopy studies [21, 22, 27–30]. We should note that in the case of the FEC, the thickness of the SEI “breathes” in the opposite direction of the non-FEC case. The expansion upon lithiation with FEC would indicate that the electrolyte continues to decompose as the layer expands. Given the apparent increase in organic signal and the higher SLD, this would indicate solvent decomposition.

XPS analysis of the Si electrodes at various states of charge reveals significant changes in the SEI chemistry with cycling that follow the changes in SEI SLD that occur with the electrode “breathing.” Figure II-189 shows a graphical representation of the atomic concentrations of C and F as a function of state of charge and SLD measured for the SEI. The C concentration data are a surrogate for the organic portion of the SEI, while the F signal (originating primarily from LiF) represents the inorganic portion of the SEI. From these data, it is clear that at states of high lithiation (0.15 V), the organic fraction of the SEI increases while the inorganic fraction decreases. Upon delithiation, the concentration of the species reverses and the inorganic fraction of the SEI dominates the SEI layer while the organic content is reduced. These data indicate that the growth in the SEI thickness with lithiation originates from the further decomposition of organic solvent molecules, resulting in a more organic layer as the Si swells. Upon delithiation, this deposited organic layer is decomposed off or dissolves into the electrolyte. The addition of Li and H (from the FEC) drives the SLD of the SEI down during lithiation, while the removal of these species leads to the increase in SLD during delithiation.

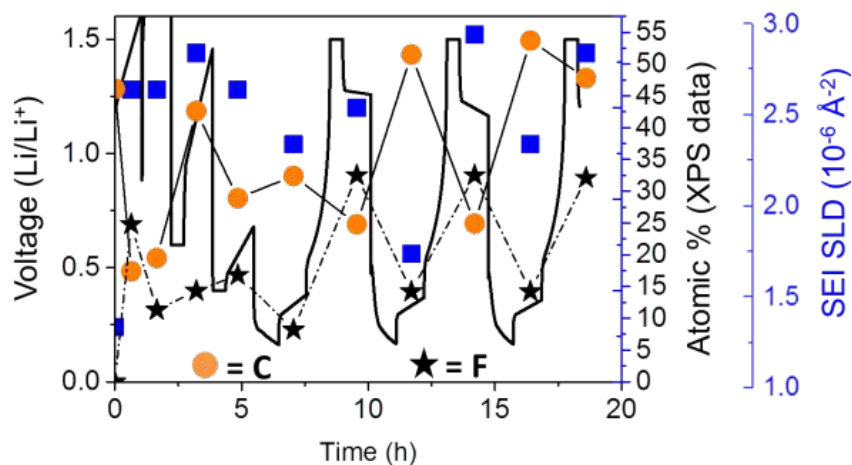


Figure II-189. Plot of C and F atomic concentrations as a function of state of charge and SEI SLD.

Fitting the individual spectra collected for each sample reveals additional changes to the SEI chemistry of both the organic and inorganic components. The C1s data, originating from the organic component (Figure II-188), show that the resulting SEI is still dominated by C-O bonding (~ 286 eV), from the polymerization of the cyclic carbonates or polymerization of the C=O bonds from the solvent, along with small concentrations of C-F (~ 291 eV) from the decomposition of the FEC, C=O, O-C=O, $-\text{CO}_3$, and C-C/C-D from the decomposition of the solvent. The presence of the carbon-oxygen moieties is supported/confirmed by the O1s data. The spectral contribution from each of these species stays relatively constant with cycling—only the absolute concentration changes. These data confirm the dissolution of the organic species upon delithiation. In addition, the O1s data show for the 0.15 V data the growth of a new species with a binding energy around 530.2 eV attributed to the formation of inorganic Li-O. This Li-O has been reported previously [31]. Interestingly, this Li-O disappears during charging, indicating the possible formation of a reactive oxygen species that is known to decompose organic electrolytes [32, 33].

The F1s data, originating from the inorganic components, show a more dynamic chemistry than the C-containing components. For all the samples, the F1s spectra are dominated by Li-F-type species. However, with lithiation, there appears to be an increase in P-F components due to decomposition and trapping of the LiPF_6 salt (evident in the high binding-energy F1s species (~ 689.5 eV)). This is confirmed with the P2p data, which show more P-F species (~ 137.6 eV) at 0.15 V. Upon charging, the P-F revert to more P-O-F (688.3 eV for F1s and ~ 135 eV for P2p data). Together, this indicates a continuous decomposition of the Li salt in addition to the solvent molecules described above.

The above data demonstrate the structure and composition of the SEI formed over a silicon anode with lithium cycling in an electrolyte that contains FEC as an additive. At this point, we will compare these data with previously reported NR data collected for electrolytes without FEC in the same electrochemical experiment. The SEI thickness and SLD values for these two samples are summarized graphically in Figure II-190. The OCV for both sets of data show a similar condensed layer with a thickness of about 50 Å, indicating a similar starting point to SEI formation. However, with cycling, the previous non-FEC-containing electrolyte data showed the immediate formation of SEI layer with a thickness between 180 and 250 Å. This SEI layer shows a similar “breathing” as observed for data in this publication; however, the magnitude of the breathing (60 Å) is significantly larger than the 13 Å measured for the FEC-containing electrolyte. The thickness of the SEI measured with NR is less than what was observed for a composite electrode reported by Xu et al., (> 15 nm) during lithiation. However, the SEI was observed to thin upon delithiation [27], similar to what we report here. This may indicate additional reactions promoted by binders and carbon additives influencing SEI chemistry. Reported TOF-SIMS data indicate that the SEI grown over a silicon thin film with FEC when delithiated was about 6.6 nm thick, in good agreement with these results [28]. The TOF-SIMS data for the same electrode

lithiated show an SEI that is 35.1 nm thick [28]. This is consistent with our results, although we note the actual SEI thickness in this report [28] is probably quite a bit thinner than the 35.1 nm. This is evident by exemplifying the Si2p signal from Si(0) present in their XPS data and is most likely due to an artifact, in there sample, caused by using a different sputter rate for the two SEI layers, resulting in changes in the SEI chemistry organic/inorganic composition.

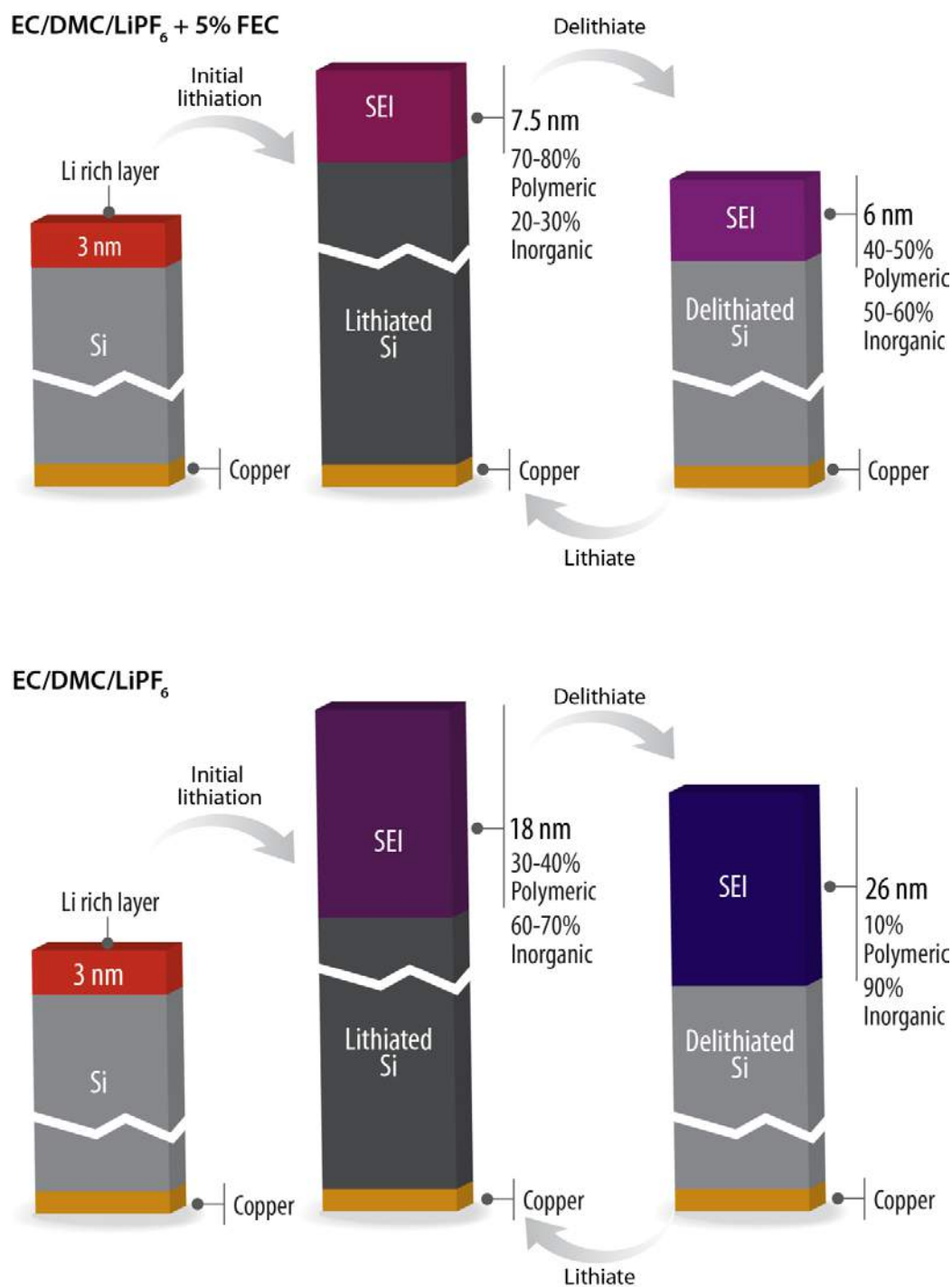


Figure II-190. Graphical summary of SEI layer chemistry grown on silicon with and without FEC.

Comparing the SEI compositions of the two NR studies reveals that the non-FEC-containing electrolyte SEI (at 0.12 V vs. Li/Li+) comprised similar functionality (i.e., C-C/C-H, C-O, C=O, O-C=O, -CO₃, LiF, POF, etc.), but the organic content comprised about 4 at% carbon. There was a correspondingly larger increase in inorganic F-containing species (~ 80% LiF) in non-FEC electrolyte. This is significantly fewer organic components than the SEI produced from FEC-containing electrolyte. These results are in good agreement with previous XPS studies that show a more organic SEI with FEC [26-28, 34-38] and NMR studies showing more LiF without FEC [39,40].

Together, these data provide insights into how FEC aids in the cycling of Si anodes for use in Li-ion batteries. The preferential reduction of FEC at potentials greater than 0.9 V (vs. Li/Li+) forms a more organic C=O-containing polymeric surface layer. This layer is not the SEI, but the SEI precursor, which further reacts at 0.6 V to form a layer with more C-O species from the polymerization of cyclic carbonates (likely from FEC) [30, 39-41]. The SEI layer formed during charging from the electrolyte without FEC comprises more inorganic LiF-like components. The polymeric FEC electrolyte effectively keeps the SEI from growing to the ~200 Å level measured for cells without FEC.

Despite this clear improvement in SEI chemistry, problems are still evident with the FEC. In both cases, the “breathing” measured for the SEI originates from the consumption of electrolyte. This consumption lowers the cycle life of the electrode by consuming the electrolyte needed to move Li ions. The thinner FEC SEI and the much reduced “breathing” of the FEC SEI results in less electrolyte consumption, resulting in the reported increase in cycle life of Si-based electrodes. However, even these batteries fail with time as the FEC gets consumed. These data would indicate that a more flexible SEI built from polymeric-like C-O functionality that forms at much higher potentials (vs Li/Li+) may provide a pathway to improve the cycleability of Si anodes.

In summary, following the SEI formation using *in-situ* neutron reflectometry revealed detailed insights to the role that FEC plays in forming a stable SEI over silicon anodes. The FEC selectively binds and reacts to the silicon surface at potentials around 0.9 V, forming a polymer-rich condensed layer on the silicon surface. In contrast, without FEC, the layer becomes more LiF-like. Upon further lithiation, the chemistry evolves from a clear polymerization of the C=O functionality to more Li-O-C-D polymeric species with a low concentration of LiF (~14 at% vs 80% without FEC). Furthermore, the FEC-based SEI is only ~70 Å thick versus ~200 Å without FEC. Together, this indicates that the FEC-based electrolytes are thinner and built from likely more-flexible polymeric components. This thin polymeric layer likely has the flexibility to bend and readjust that LiF-based SEI layers would not. This flexibility ensures a more stable SEI that would more effectively passivate the surface against further reactions. However, the FEC-based SEI is still not perfect because it changes in thickness and composition with cycling (0.15–1.5 V). Specifically, the layer becomes more organic at high states of lithiation and more inorganic at low states of lithiation due to dissolution of the polymer. This points to a potential path to make a more stable SEI through the formation of a more cross-linked, less-soluble polymer SEI, possibly through the design of more elaborate, large-molecule, fluorinated carbonates. It would be interesting to explore this chemistry as a function of oxide surface termination and polymer binders, which likely also participate in the SEI passivation reaction and change the reaction mechanism(s).

Probing the nanoscale heterogeneity of SEI on cycled amorphous silicon using tip-enhanced Raman spectroscopy

SEI on silicon typically is reported to be in the range of tens of nanometers and can be compositionally heterogeneous. Normal vibrational spectroscopy techniques such as micro-Raman and FTIR are widely used, but they only provide chemical information at a relatively bulk scale, typically much greater than 100 nm from the sample surface. This makes it harder for getting information from the real SEI, which can be on the order of tens of nanometers. Tip-enhanced Raman spectroscopy (TERS) is based on the field enhancement of the Raman active signal locally at regions close to the tip. The configuration of the sample and its relative position to the Raman laser and tip is illustrated in Figure II-191. The Raman cross-section is enhanced at least several orders of magnitude due to resonance coupling between surface plasmon modes (of the tip) and the electromagnetic field of the excitation laser. In this report, we provide preliminary results on characterization

of SEI on cycled amorphous silicon using TERS. This method is highly complementary to the IR data collected at LBNL.

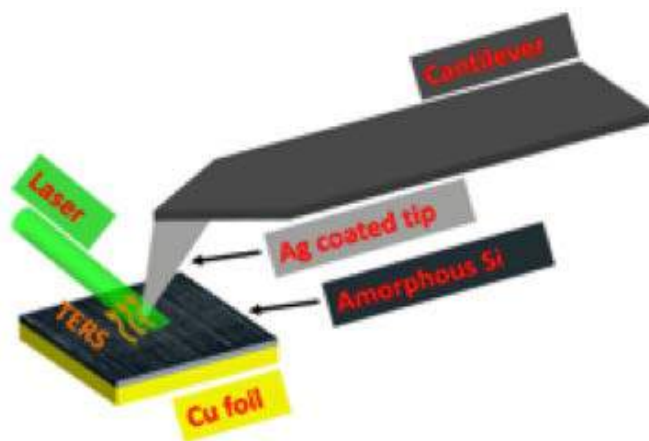


Figure II-191. Schematic picture of the TERS setup for studying SEI on silicon.

An amorphous silicon sample of 80 nm thick on a copper current collector was cycled 5X and 20X times using Gen-2 electrolyte (Sample # Gabe-1609 SiC CHYS, GY-0206 Cell-D-20cyc, 1.5V–0.05V EC/DMC in 1.2M LiPF₆). Amorphous Si samples were sputter-deposited at ORNL and cycled as per the procedure finalized by the SEIsta round-robin team. TERS experiments were conducted using a HORIBA Nano Raman Platform integrated with AIST-NT's SPM system, as shown in Figure II-192. The laser wavelength was 532 nm and the objective was 1.5/100X. The setup was modified to work under argon atmosphere for studying SEI on samples under inert condition. A special Ar-compatible antechamber was designed (not shown) for preparing and transferring the sample for TERS experiments. The silicon tip used for TERS is 7 nm in diameter and sputter-coated with 2 nm of chromium as an adhesion layer, followed by a 40-nm Ag layer and 1.5-nm aluminum protection layer.

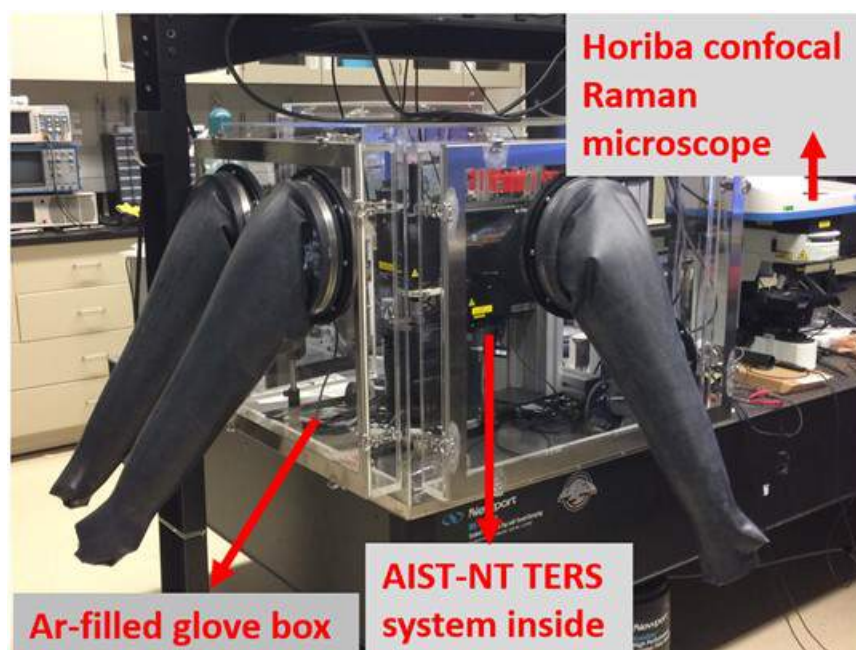


Figure II-192. Image of ORNL's TERS setup operated under argon atmosphere.

As a proof-of-principle example of the usefulness of TERS, we compare below in Figure II-193 a normal micro-Raman signal with TERS for the same sample (cycled amorphous silicon). The standard micro-Raman spectrum (red) shows only the normal silicon Raman bands at 521 nm, whereas the TERS (black) shows several additional peaks coming exclusively from the Raman active SEI on Si. For example, the band at 1,052 cm^{-1} is assigned to siloxane (Si-O-Si) stretch. Peaks between 1,100 cm^{-1} and 1,600 cm^{-1} are most likely from the R-OCOO-M or R-Si (R is methyl group and M is Li⁺ or Si) [41,42]. The TERS signal shown above has an enhancement factor of around 103. However, under optimized conditions, the enhancement factor would be on the order of 105. Figure II-194 shows the TERS signal from 20X cycled amorphous silicon collected under argon atmosphere. The maximum peak intensity occurs at 1,372 cm^{-1} , which could be assigned to symmetric CH₃ stretch. The two peaks at 1,436 and 1,458 cm^{-1} are due to asymmetric stretch of CH₃. The band at 1,552 cm^{-1} is attributed to -COO asymmetric stretch. The 1,697 cm^{-1} peak is an overtone of -COO deformation at ~650 cm^{-1} and CH₃ rocking mode (at ~1,050 cm^{-1}). The existence of those bands clearly indicates that these spectral information originate from the SEI on silicon that are otherwise not visible under normal Raman or FTIR. We are currently analyzing the detailed peak positions with their relative enhancement factor, which will be reported shortly as a journal paper.

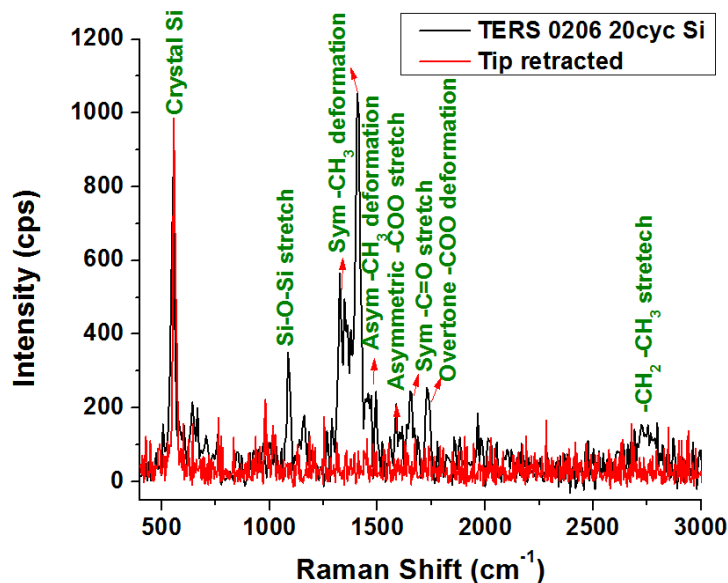


Figure II-193. Comparison of micro-Raman signal with TERS for the same sample (cycled amorphous Si).

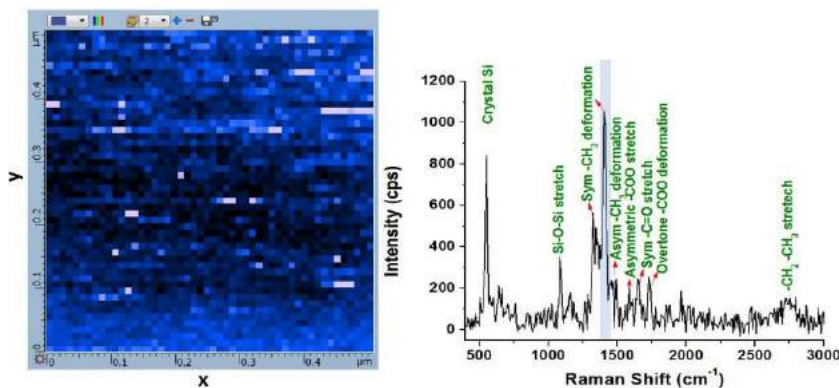


Figure II-194. Shows the TERS results for amorphous silicon cycled 20X. We notice several peaks apart from the silicon coming from the tip centered around 521 cm^{-1} . The peak at 1,372 cm^{-1} is from CH₃ symmetric deformation in CH₃-COO components. Using the integration of this peak, the CH₃-COO components can be mapped in a 500-nm X 500-nm region.

In the future, TERS analysis will be combined with FTIR, micro-Raman, TOF-SIMS, and XPS analysis to provide a more comprehensive picture of the SEI morphology and its spatial heterogeneity and distribution. This will help to resolve the issue of various chemical phases that preferentially form in the surface region of the SEI versus bulk and their relative abundancies. TERS measurements are being planned on chemically passivated and electrochemically lithiated SiO₂/Si wafers in collaboration with LBL and NREL to provide insights into the subsurface chemical structure the SEI and its spatial variability across the thickness.

Conclusions

The first year of the SEISta project has shown that there is a critical need for standardization of research samples and procedures if the understanding of the SEI on silicon is to progress. Even with all team members using the same electrolytes, current collectors, and counter electrodes, getting comparable data is very difficult because of the way the silicon sample is treated, its life history, and minor variations in cell assembly. SEISta will continue to focus on the need for standardization and consistent and repeatable experimental data. In FY18, a standardized cell confirmation will be employed to ensure that some of the variation observed in the FY17 round robin is eliminated. Also, close attention to the experimental timing needs to be a focus for any experiments. The samples that are transported from laboratory to laboratory need to be examined and experiments carried out in timely fashion. The delays caused by minor equipment issues, across the partners, resulted in up to 6 months difference in data collection and contributed to the delay of Milestone 2 and probably added to the variation between samples seen in the round robin. This clearly had an impact on data spread and on the surface chemistry of the sputtered silicon samples.

The unexpected complexity of the basic reactivity of the silicon and silicon oxides with simple organic materials and the salts in the electrolyte has added to the silicon SEI story. All of the silicon samples examined show some form of reactivity with Gen 2 electrolytes. Exploring and understanding the limits of this will be a focus for FY18, specifically understanding what the surface-electrolyte interface looks like before electrochemistry begins so that SEI formation can be better understood.

The nature of the silicon, oxide coatings, and density, for example, clearly have an impact on both the fundamental chemistry of the electrolyte reaction and the ongoing electrochemical behavior of the SEI. In the next year, we will focus on exploring this interaction and the ways it affects the formation and growth/stabilization and solubility of the SEI components in well-characterized systems.

The SEISta team will also be more interactive with the Silicon Deep Dive project using their "top-down" approach and the understanding gained to help tailor both our choice of samples and experiments moving forward.

Key Publications

1. "Fundamental Studies of Silicon-based Electrodes for Li-Ion Batteries – SEISta Program" DOE Hydrogen Program and Vehicle Technologies Program Annual Merit Review, Washington, DC, June, 2017.
2. I. Hasa, T. Otani, T. Homma, P. N. Ross, R. Kostecki, "Surface Reactivity of a Tin Electrode in Organic Carbonate Electrolytes", 2017/9/1, ECS Meeting Abstracts
3. A. M. Haregewoin, L. Terborg, L. Zhang, J. Guo, P. N. Ross, and R. Kostecki, "Fundamental Understanding of the Effect of Polymer Binder on the Interfacial Properties of Si-Electrode Model Systems. 2017/9/1, ECS Meeting Abstract 143
4. Atetegeb Meazah Haregewoin, Lydia Terborg, Liang Zhang, Sunhyung Jurng, Brett L. Lucht, Jinghua Guo, Philip. N. Ross and Robert Kostecki, "The Electrochemical Behavior of Poly 1-Pyrenemethyl Methacrylate (PPy) Binder and its Effect on the Interfacial Chemistry of a Silicon Electrode", Journal of Power Sources, submitted

5. Coyle, J., Apblett, C. A., Stoldt, C., "Composition and Structure of Lithium Silicate Thin Film Electrolytes Deposited by Radio Frequency Magnetron Sputtering", 229th ECS, San Diego, CA, May 29-June 2nd, 2016
6. Coyle, J., Stoldt, C., Apblett, C., "Initial Irreversible Capacity Loss Mitigation Through Engineered SEI Layer on Silicon Electrode", 231st ECS, New Orleans, LA, May 28-June 1st, 2017
7. Coyle, J., Apblett, C., Brumbach, M., Ohlausen, A., Stoldt, C., "Structural and Compositional Characterization of RF Magnetron Co-Sputtered Lithium Silicate Films: From $\text{Li}_2\text{Si}_2\text{O}_5$ to Lithium-Rich Li_8SiO_6 ", JVST A, JVSTA-A-17-242, accepted.
8. Burrell, AK. "Silicon Where to Now?" Plenary Talk Advance Automotive Battery Conference June 19-2017
9. Burrell, AK. "Silicon Where to Now?" Plenary Talk Power Our Future The 3rd International Forum on Progress and Trends in Battery and Capacitor Technologies, Vitoria, Spain July 2017

References

1. Abramowitz, S.; Acquista, N.; W. Levin, I., Infrared matrix spectra of lithium fluoride. J. Res. National Bur. Stand. 1968, 72A, 487–493.
2. Burtsev, A. P.; Bocharov, V. N.; Ignatov, S. K.; Kolomiitsova, T. D.; Sennikov, P. G.; Tokhadze, K. G.; Chuprov, L. A.; Shchepkin, D. N.; Schrems, O., Integral intensities of absorption bands of silicon tetrafluoride in the gas phase and cryogenic solutions: Experiment and calculation. Opt. Spectrosc. 2005, 98, 227–234.
3. Dupré, N.; Moreau, P.; De Vito, E.; Quazuguel, L.; Boniface, M.; Bordes, A.; Rudisch, C.; Bayle-Guillemaud, P.; Guyomard, D., Chemistry of Materials 28 (8), 2557–2572 (2016).
4. Radvanyi, E.; De Vito, E.; Porcher, W.; Jouanneau Si Larbi, S., Journal of Analytical Atomic Spectrometry 2014, 29 (6), 1120–1131.
5. Martinez de la Hoz, J. M.; Leung, K.; Balbuena, P. B., ACS Applied Materials & Interfaces 2013, 5 (24), 13457–13465.
6. Hubaud, A. A.; Yang, Z. Z.; Schroeder, D. J.; Dogan, F.; Trahey, L.; Vaughey, J., J. Power Sources 2015, 282, 639.
7. Key, B.; Bhattacharyya, R.; Morcrette, M.; Seznec, V.; Tarascon, J.-M.; Grey, C. P., J. Am. Chem. Soc. 2009, 131 (26), 9239–9249.
8. Key, B.; Morcrette, M.; Tarascon, J.-M.; Grey, C. P., J. Am. Chem. Soc. 2011, 133 (3), 503–512.
9. MacKenzie, K.; Smith, M. E., Multinuclear Solid-State Nuclear Magnetic Resonance of Inorganic Materials, Volume 6, 1st Edition.
10. Lucas, I. T.; Syzdek, J.; Kostecki, R., Electrochem. Commun. 2011, 13, 1271–1275.
11. Ayache, M.; Lux, S. F.; Kostecki, R., J. Phys. Chem. Lett. 2015, 6, 1126–1129.
12. Qiao, R.; Lucas, I. T.; Karim, A.; Syzdek, J.; Liu, X.; Chen, W., Adv. Mater. Interfaces 2014, 1, 1–6.
13. Schroder, K. W.; Celio, H.; Webb, L. J.; Stevenson, K. J., J. Phys. Chem. C. 2012, 116, 19737–19747.
14. Sina, M.; Alvarado, J.; Shobukawa, H.; Alexander, C.; Manichev, V.; Feldman, L., Adv. Mater. Interfaces 2016, 3, 1–10.

15. Perea, A.; Gonzalo, J.; Afonso, C. N.; Martelli, S.; Montereali, R. M., *Appl. Surf. Sci.* 1999, 138–139, 533–537.
16. Li, C.; Gu, L.; Maier, J., *Adv. Funct. Mater.* 2012, 22, 1145–1149.
17. Wang, H.; Downing, R. G.; Dura, J. A.; Hussey, D. S., Chapter 6: In situ Neutron Techniques for Studying Lithium Ion Batteries. In *Polymers for Energy Storage and Delivery: Polyelectrolytes for Batteries and Fuel Cells*; ACS Symposium Series, American Chemical Society: 2011; Vol. 1096, pp 91–106.
18. Jerliu, B.; Hüger, E.; Dörrer, L.; Seidlhofer, B. K.; Steitz, R.; Oberst, V.; Geckle, U.; Bruns, M.; Schmidt, H., Volume Expansion during lithiation of amorphous silicon thin film electrodes studied by in-operando neutron reflectometry. *J. Phys. Chem. C* 2014, 118, 9395–9399.
19. Seidlhofer, B.-K.; Jerliu, B.; Trapp, M.; Hüger, E.; Risse, S.; Cubitt, R.; Schmidt, H.; Steitz, R.; Ballauff, M., Lithiation of crystalline silicon as analyzed by operando neutron reflectivity. *ACS Nano* 2016.
20. Lux, S. F.; Chevalier, J.; Lucas, I. T.; Kostecki, R., HF formation in LiPF₆-based organic carbonate electrolytes. *ECS Electrochem. Let.* 2013, 2, A121–A123.
21. Fears, T. M.; Doucet, M.; Browning, J. F.; Baldwin, J. K. S.; Winiarz, J. G.; Kaiser, H.; Taub, H.; Sacci, R. L.; Veith, G. M., Evaluating the solid electrolyte interphase formed on silicon electrodes: A comparison of ex situ X-ray photoelectron spectroscopy and in situ neutron reflectometry. *Phys. Chem. Chem. Phys.* 2016, 18, 13927–13940.
22. Veith, G. M.; Doucet, M.; Baldwin, J. K.; Sacci, R. L.; Fears, T. M.; Wang, Y.; Browning, J. F., Direct determination of solid-electrolyte interphase thickness and composition as a function of state of charge on a silicon anode. *J. Phys. Chem. C* 2015, 119, 20339–20349.
23. Veith, G. M.; Baggetto, L.; Sacci, R. L.; Unocic, R. R.; Tenhaeff, W. E.; Browning, J. F., Direct measurement of the chemical reactivity of silicon electrodes with LiPF₆-based battery electrolytes. *Chem. Comm.* 2014, 50, 3081–3084.
24. Browning, J. F.; Baggetto, L.; Jungjohann, K. L.; Wang, Y.; Tenhaeff, W. E.; Keum, J. K.; Wood, D. L.; Veith, G. M., In situ determination of the liquid/solid interface thickness and composition for the Li ion cathode LiMn_{1.5}Ni_{0.5}O₄. *ACS Appl. Mater. Interfaces* 2014, 6, 18569–18576.
25. Chevrier, V. L.; Dahn, J. R., First principles model of amorphous silicon lithiation. *J. Electrochem. Soc.* 2009, 156, A454–A458.
26. Vogl, U. S.; Lux, S. F.; Crumlin, E. J.; Liu, Z.; Terborg, L.; Winter, M.; Kostecki, R., The mechanism of SEI formation on a single crystal Si(100) electrode. *J. Electrochem. Soc.* 2015, 162, A603–A607.
27. Xu, C.; Lindgren, F.; Philippe, B.; Gorgoi, M.; Björefors, F.; Edström, K.; Gustafsson, T., Improved performance of the silicon anode for Li-ion batteries: Understanding the surface modification mechanism of fluoroethylene carbonate as an effective electrolyte additive. *Chem. Mater.* 2015, 27, 2591–2599.
28. Schroder, K.; Alvarado, J.; Yersak, T. A.; Li, J.; Dudney, N.; Webb, L. J.; Meng, Y. S.; Stevenson, K. J., The effect of fluoroethylene carbonate as an additive on the solid electrolyte interphase on silicon lithium-ion electrodes. *Chem. Mater.* 2015, 27, 5531–5542.
29. Shen, C.; Wang, S.; Jin, Y.; Han, W.-Q., In situ AFM imaging of solid electrolyte interfaces on HOPG with ethylene carbonate and fluoroethylene carbonate-based electrolytes. *ACS Appl. Mater. Interfaces* 2015, 7, 25441–25447.

30. Breitung, B.; Baumann, P.; Sommer, H.; Janek, J.; Brezesinski, T., In situ and operando atomic force microscopy of high-capacity nano-silicon based electrodes for lithium-ion batteries. *Nanoscale* 2016, 8, 14048–14056.
31. Xu, K., Electrolytes and interphases in Li-ion batteries and beyond. *Chem. Rev.* 2014, 114, 11503–11618.
32. Younesi, R.; Veith, G. M.; Johansson, P.; Edstrom, K.; Vegge, T., Lithium salts for advanced lithium batteries: Li-metal, Li-O₂, and Li-S. *Energy & Environmental Science* 2015, 8, 1905–1922.
33. Veith, G. M.; Dudney, N. J.; Howe, J.; Nanda, J., Spectroscopic characterization of solid discharge products in Li-air cells with aprotic carbonate electrolytes. *J. Phys. Chem. C* 2011, 115, 14325–14333.
34. Dalavi, S.; Guduru, P.; Lucht, B. L., Performance enhancing electrolyte additives for lithium ion batteries with silicon anodes. *J. Electrochem. Soc.* 2012, 159, A642–A646.
35. Bordes, A.; Eom, K.; Fuller, T. F., The effect of fluoroethylene carbonate additive content on the formation of the solid-electrolyte interphase and capacity fade of Li-ion full-cell employing nano Si-graphene composite anodes. *J. Power Sources* 2014, 257, 163–169.
36. Etacheri, V.; Haik, O.; Goffer, Y.; Roberts, G. A.; Stefan, I. C.; Fasching, R.; Aurbach, D., Effect of fluoroethylene carbonate (FEC) on the performance and surface chemistry of Si-nanowire Li-ion battery anodes. *Langmuir* 2012, 28, 965–976.
37. Nguyen, C. C.; Lucht, B. L., Comparative study of fluoroethylene carbonate and vinylene carbonate for silicon anodes in lithium ion batteries. *J. Electrochem. Soc.* 2014, 161, A1933–A1938.
38. Young, B. T.; Heskett, D. R.; Nguyen, C. C.; Nie, M.; Woicik, J. C.; Lucht, B. L., Hard X-ray photoelectron spectroscopy (HAXPES) investigation of the silicon solid electrolyte interphase (SEI) in lithium-ion batteries. *ACS Appl. Mater. Interfaces* 2015, 7, 20004–20011.
39. Michan, A. L.; Divitini, G.; Pell, A. J.; Leskes, M.; Ducati, C.; Grey, C. P., Solid electrolyte interphase growth and capacity loss in silicon electrodes. *J. Am. Chem. Soc.* 2016, 138, 7918–7931.
40. Michan, A. L.; Leskes, M.; Grey, C. P., Voltage dependent solid electrolyte interphase formation in silicon electrodes: Monitoring the formation of organic decomposition products. *Chem. Mater.* 2016, 28, 385–398.
41. Arreaga-Salas, D. E.; Sra, A. K.; Roodenko, K.; Chabal, Y. J.; Hinkle, C. L., Progression of solid electrolyte interphase formation on hydrogenated amorphous silicon anodes for lithium-ion batteries. *J. Phys. Chem. C* 2012, 116, 9072–9077.
42. Socrates, G., *Infrared and Raman Characteristic Group Frequencies: Tables and Charts*. John Wiley & Sons: 2004.

II.B.5 Development of Si-based High-Capacity Anodes (PNNL)

Ji-Guang Zhang, Principal Investigator

Pacific Northwest National Laboratory
902 Battelle Blvd, Mail Stop K2-44
Richland, WA 99352
Phone: 509-372-6515
E-mail: Jiguang.Zhang@pnnl.gov

Jun Liu, Co-Principal Investigator

Pacific Northwest National Laboratory
902 Battelle Blvd, Mail Stop K2-44
Richland, WA 99352
Phone: 509-375-4443
E-mail: Jun.Liu@pnnl.gov

Prashant N. Kumta, Co-Principal Investigator

University of Pittsburgh
815C Benedum Hall
3700 O'Hara Street
Pittsburgh, PA 15261
Phone: 412-648-0223
E-mail: pkumta@pitt.edu

Tien Duong, Technology Manager

U.S. Department of Energy
Phone: 202-586-7836
E-mail: Tien.Duong@ee.doe.gov

Start Date: October 1, 2015

End Date: September 30, 2017

Total Project Cost: \$1,190,000

DOE share: \$1,190,000

Non-DOE share: \$0

Project Introduction

Silicon has been extensively studied as a high-capacity anode for next-generation high-energy Li-ion batteries. However, fast capacity fade still greatly limits its practical application. A large volume change during lithiation and delithiation causes pulverization and subsequent loss of electrical contact, repeated breaking/formation of the solid electrolyte interphase (SEI) and continuous consumption of electrolyte.

In this project, we combined micron-sized Si with nanoporosity (mSi-np) generated by a low-cost process with a conformal high quality carbon coating on the surface of porous Si to enable stable operation of a Si-based anode. The mSi-np provides nanoporosity to allow intrinsic volume expansion and still retain a low surface area. Carbon coating enables high first-cycle efficiency (FCE) and high coulombic efficiency (CE). The target capacity is 1000 mAh/g for the Si-based anode (including Si, carbon additive, and binder) in the high loading condition (>3 mAh/cm²) required for electric vehicle (EV) applications. We take advantage of PNNL's state-of-the-art material synthesis and characterization capabilities to optimize the structure of Si at both the particle level and electrode level. The stability of the SEI layer was systematically investigated by in situ microscopic analysis. Our partner, University of Pittsburgh (UPitt), applied their extensive experience in this field to synthesize Si-based nanocomposites using high-energy mechanical milling and other low-cost methods. The

best Si anode developed in this work was combined with the optimized binder/electrolyte and matched with a high-capacity cathode in a full-cell configuration.

Objectives

The objectives of this project are to advance the fundamental understanding of the degradation mechanism of Si-based anodes, including the mechanical and electrochemical stability, and develop high-energy, long life silicon (Si)-containing anode materials using low-cost synthesis approaches to enable their practical application in Li-ion batteries for plug-in hybrid electric vehicles and EVs.

Approach

- Develop micron-sized Si nanoparticles with nano pores and high quality carbon coating by three approaches:
 - Develop a low temperature (210°C) aluminothermic reduction of SiO₂ using an eutectic salt mixture of AlCl₃ and ZnCl₂.
 - Synthesize micron-sized porous silica as the precursor of thermic reduction using microemulsion self-assembly to improve the tap density as well as the electrochemical performance of Si anodes.
 - Synthesize a hierarchically structured Si/multi-walled carbon nanotube (MWNT) composite as the precursor of thermic reduction to accommodate the swelling of silicon particles and stabilize its structural and electrolyte integrity.
- Use high-energy mechanical milling of silicon oxides with different reducing agents and electrodeposition to generate Si – lithium conducting nanocomposite material.

Results

1.1 Micron-sized porous Si (p-Si) anodes synthesized by low temperature aluminothermic reduction

A low temperature (210°C) aluminothermic reduction process has been developed to synthesize p-Si with addition of a eutectic salt mixture of AlCl₃ and ZnCl₂, which not only serves as the mediator to reduce the reaction temperature, but also as reactant that enables reduction through a unique reaction route. The development has two main advantages. First, it greatly reduces the thermite reaction cost by lowering the process temperature. Second, with carbon pre-coating on the porous SiO₂ precursor, the final product of carbon coated porous Si (p-Si@C) can have the desired morphology and porous structure and has good electrochemical performance. Figure II-195 shows the synthesis process, structural characterization, and electrochemical performance of p-Si@C. Pure Si was obtained after the aluminothermic reaction and acid washing. The porous structure of the SiO₂ precursor was maintained in the final product. Scanning electron microscopy (SEM) showed highly porous Si spheres with a pore size of ~30–50 nm. p-Si@C electrodes delivered a high specific capacity of ~2100 mAh/g (based on the active material of Si) after the formation cycles. After 250 cycles, the p-Si@C was able to retain ~86% of its initial capacity at the current density 1.2 A/g and a high specific capacity ~1290 mAh/g at the current density of 8 A/g.

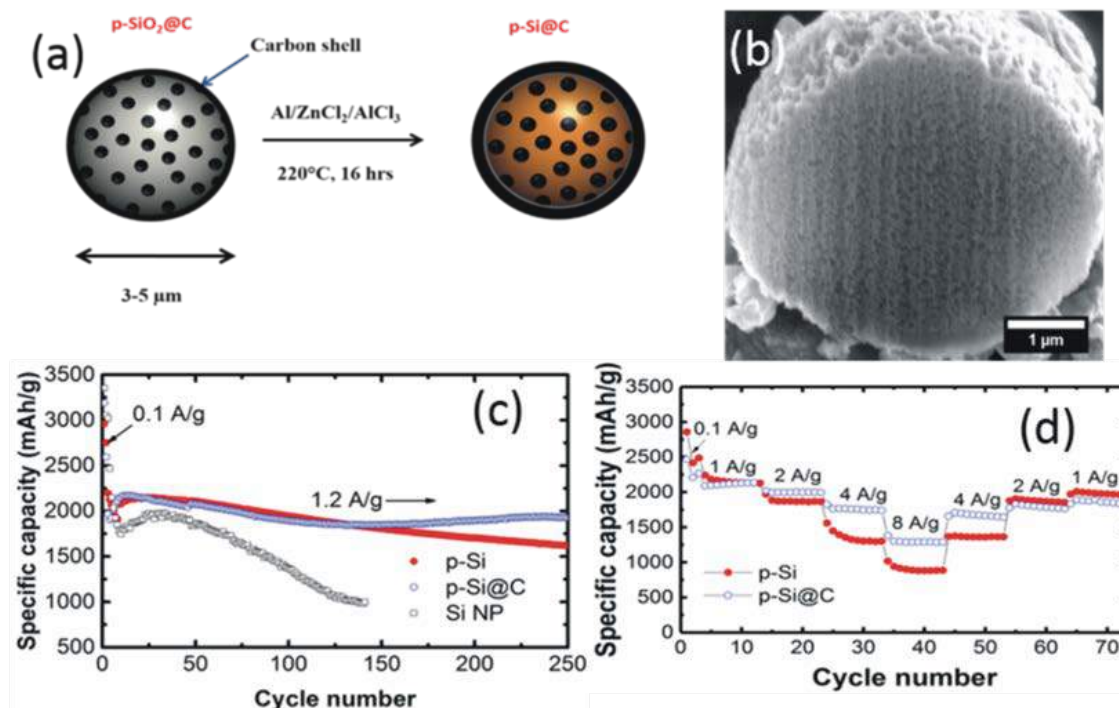


Figure II-195. (a) Schematic illustration of the synthesis of p-Si@C; (b) SEM images showing the morphology and cross section of p-Si@C; (c)-(d) Long-term cycling and rate performance of p-Si (red plot) and p-Si@C (blue plot).

1.2 Porous silicon synthesized using micron-sized silica prepared from microemulsion of silica nanoparticles

In another effort, micrometer-sized porous silicon was synthesized by magnesiothermic reduction using micrometer-sized porous silica as the precursor, which was prepared from nanosized silica using microemulsion. Figure II-196a illustrates the synthesis process of the porous Si microspheres. The step-by-step synthesis products, from SiO₂ nanoparticles to SiO₂ microspheres, to porous Si spheres, are shown in the SEM images in Figure II-196b-Figure II-196d. The preserved void space and subsequent carbon coating enable good mechanical and electrical stability of the porous Si and enhance its cycle life and rate capability compared to nano-Si. The obtained porous Si (p-Si/C) delivers a high reversible capacity of 1467 mAh/g at 1C with 90% capacity retention over 200 cycles (Figure II-196e). The p-Si/C electrode also shows good rate performance, as shown in Figure II-196f.

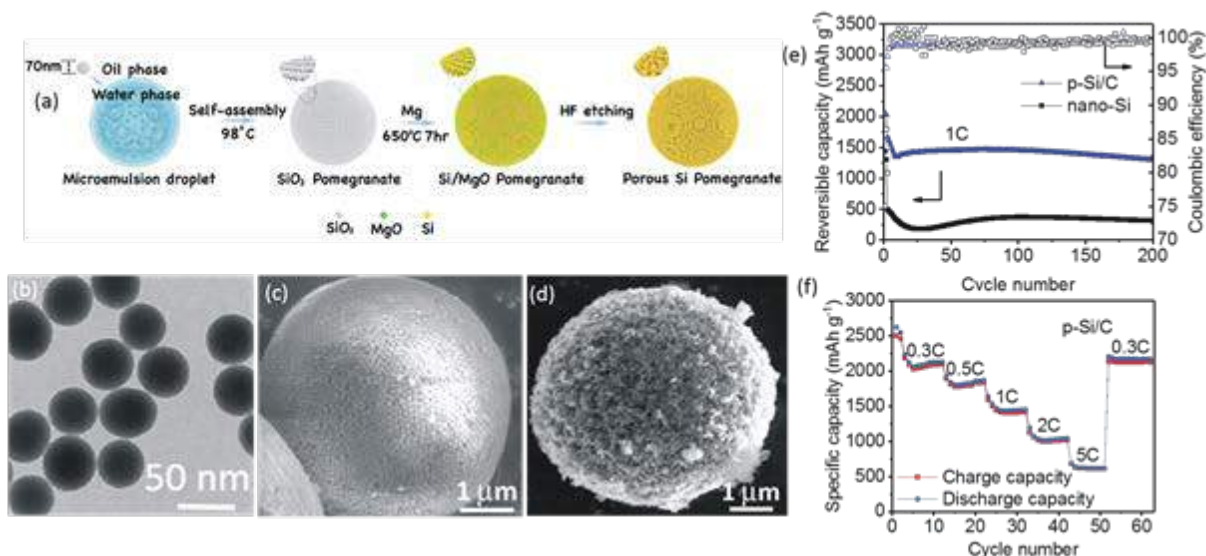


Figure II-196. (a) Schematic illustration of the synthesis of p-Si/C; (b) TEM image of the silica nanoparticles; (c) SEM image of the SiO₂ microspheres by emulsion method; (d) SEM image of the porous Si microspheres; (e) Cycling performance of p-Si/C and nano-Si; (f) rate performance of the p-Si/C.

1.3 Hierarchically structured Si/MWNT composite

Hierarchically structured micron-sized Si/MWNT particles were synthesized by aluminothermic reduction of the microspheres of SiO₂/MWNT, which was prepared by the hydrolysis of tetraethyl orthosilicate on an MWNT surface. The unique structure of Si/MWNT composite provides (1) enough void space to accommodate the volume change so that the swelling of the composite can be reduced; (2) good mechanical structure and electronic conductivity from the MWNT matrix. The in situ transmission electron microscope (TEM) study reveals limited volume changes of this hierarchically structured Si/MWNT composite. With well-controlled porosity, the composite only shows ~30% apparent volume change at full lithiation, 1/10th of the expansion of bulk Si or Si nanoparticles. Figure II-197a shows the schematic illustration of the preparation process of the Si/MWNT microspheres. Figure II-197b-d are the step-by-step characterization of the structure of MWNT@SiO₂ coaxial cables, MWNT/SiO₂ microspheres, and the final product of Si/MWNT, which maintained the spherical morphology of the precursor. After Si/MWNT composite was coated with a thin layer of conductive carbon using chemical vapor deposition, the Si/MWNT/C composite demonstrated good electrochemical performance with a theoretical specific capacity of 2200 mAh/g (1C) calculated on the basis of the total composite weight. Figure II-197e shows that the Si/MWNT/C electrode delivers an initial reversible capacity of 1884 mAh/g, very close to the theoretical value. After 300 cycles, the electrode is able to retain ~87% of its highest initial capacity achieved at 1C. Although the Si/MWNT/C has a low FCE of 75%, the CE quickly reaches >99% after 5 cycles and remains stable. The Si/MWNT/C also exhibits good cycling stability for high loading electrodes. Figure II-197f shows the cycling performance of electrodes at different loadings. It is believed that good porosity control is a key reason for the good cycling stability.

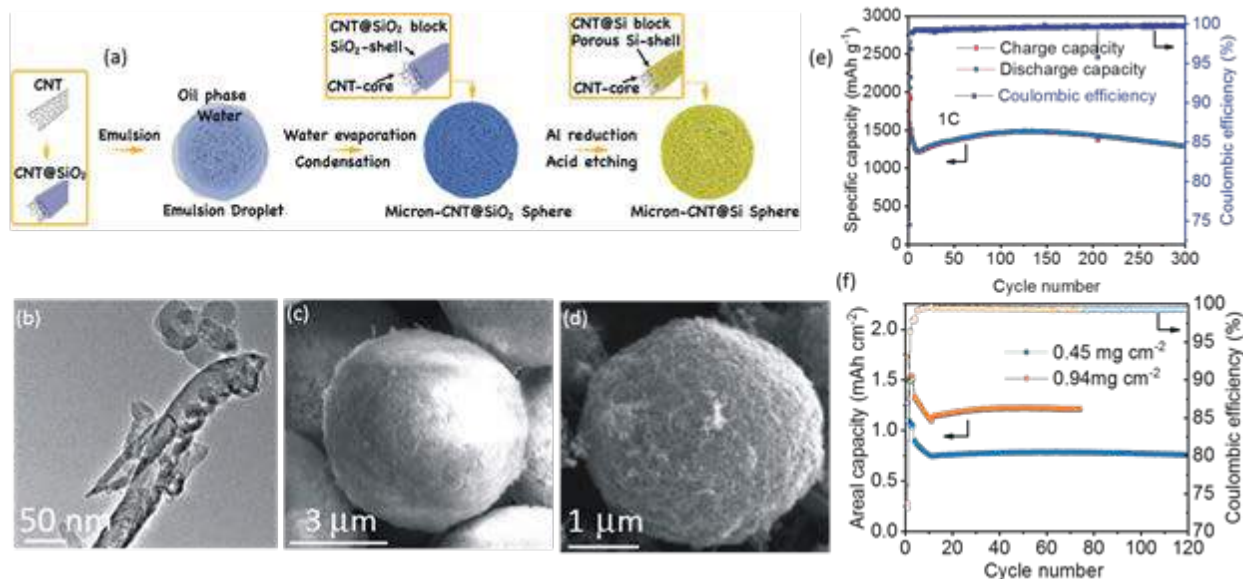


Figure II-197. (a) Schematic illustration of the preparation process of the micro-MWNT-Si composite; (b) TEM image of MWNT/SiO₂ composite (before emulsion); (c) SEM image of MWNT/SiO₂ composite (after emulsion); (d) SEM image of MWNT/Si composite after aluminothermic reaction; (e) long-term cycling performance of Si/MWNTC composite; (f) cycling stability of Si/MWNT/C with different mass loadings at the current density of 0.7 mA/cm².

2. Use high-energy mechanical milling of silicon oxides with different reducing agents and electrodeposition to generate Si-Li conducting nanocomposite material

Electrochemically active silicon was obtained by the reduction of silicon precursor (SiX) using inorganic reductants (IR) through low temperature solid-state reduction (LTSR). Figure II-198a shows x-ray diffraction (XRD) patterns of the heat-treated mixture indicating the formation of Si along with different intermediate phases, but more importantly, showing no peaks corresponding to IR after the reduction of SiX at 200°C for 6 h. The undesired intermediate phases were dissolved in 1 M HCl to obtain Si. The LTSR-derived Si was then embedded in carbon nanofibers (CNF), followed by thermally induced carbonization at 700°C for 1 h and subsequent testing as an anode for Li-ion application. The Si/CNF material showed first-cycle discharge and charge capacities of ~2870 mAh/g and ~2067 mAh/g, respectively, at a current rate of ~50 mA/g, with a first-cycle irreversible (FIR) loss of ~25–30%. During the initial cycles of prolonged testing (Figure II-198b), Si/CNF showed capacities of ~2161 mAh/g and ~1210 mAh/g at current rates of 0.3 A/g and 1 A/g, respectively.

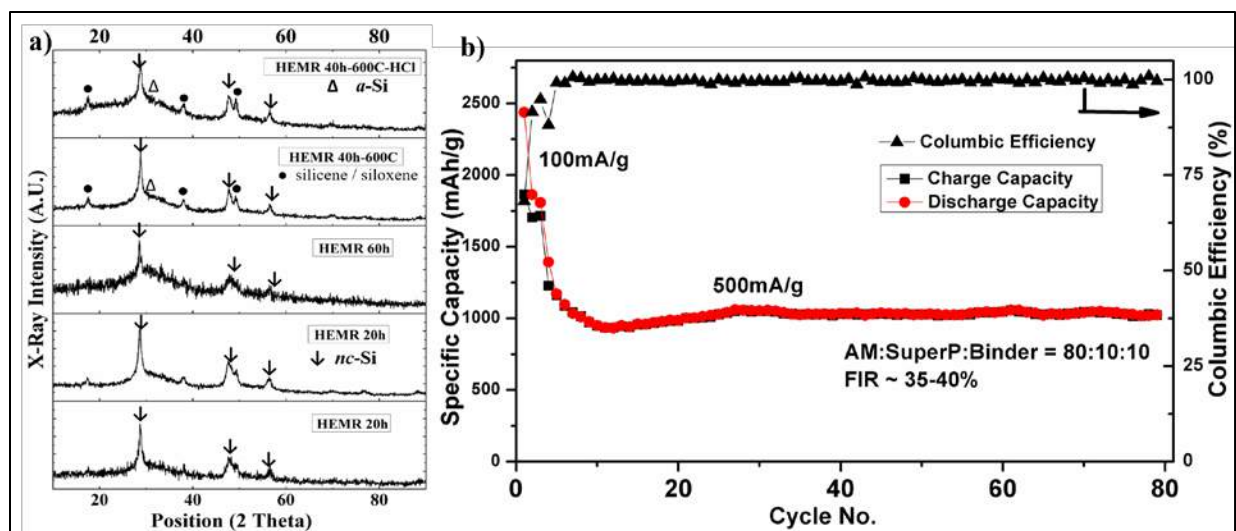


Figure II-198. (a) XRD pattern of LTSR reaction intermediate showing presence of Si, and presence of single-phase elemental Si following HCl treatment. (b) Specific discharge capacity vs. cycle numbers for LTSR-derived Si/CNF nanocomposite. The current rate for the first 3 cycles is 300 mA/g and for the remaining cycles is 1 A/g.

In another effort, a promising anode consisting of amorphous Si deposited on carbon nanotubes (CNTs) was synthesized by a commercially viable facile electrodeposition (ED) process. The SEM image and energy dispersive x-ray spectroscopy (EDAX) mapping (Figure II-199a) of M-Cu (M represents a catalyst) confirmed that a distinct layer ($<1 \mu$) of catalyst M is coated on the Cu foil. The SEM image of CNT/M-Cu (Figure II-199b) shows the formation of CNTs well adhered to the M/Cu substrate. Amorphous Si was deposited on the CNT/M-Cu by a commercially viable electrodeposition process using a nonaqueous ionic electrolyte consisting of silicon-containing precursors. The SEM analysis of Si-deposited CNT/M-Cu (Figure II-199c and Figure II-199d) shows a uniform deposition of Si on the CNTs, and the size of the silicon particles is < 100 nm. The loading density of ED-Si is ~ 0.25 mg/cm² to 0.31 mg/cm². The ED-Si/CNT electrodes show first-cycle discharge and charge capacities of ~ 3435 mAh/g and ~ 2050 mAh/g, respectively, with an FIR loss of ~ 35 – 45% (Figure II-199e) at a charge/discharge current rate of ~ 300 mA/g. The ED-Si/CNT also shows excellent capacity retention with a stable capacity of ~ 1870 mAh/g up to 70 cycles (Figure II-199e).

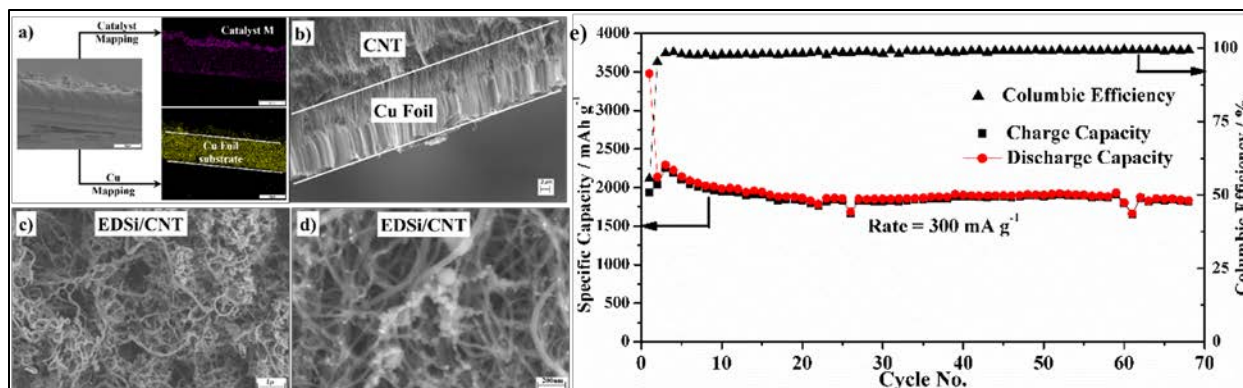


Figure II-199. (a) SEM image and corresponding EDAX mapping of Cu and catalyst layer M of catalyst-coated Cu foil; (b) SEM showing growth of CNT on Cu foil; (c) and (d) low- and high magnification images of electrodeposited Si on CNT/Cu substrates; (e) Specific discharge capacity vs. cycle number for ED-Si/CNT nanostructured binderless electrode tested at 0.3 A/g in Li/Li+ system.

High-energy mechanical reduction (HEMR) of silicon monoxide (SiO) was carried out for 20 h, 40 h, and 60 h using a stoichiometric amount of inorganic reducing agent. The formation of Si from SiO after 20 h and 60 h of HEMR was confirmed by XRD analysis. Additionally, peaks of silicene/siloxene are also observed that result from partial oxidation of the products during HEMR. The composite material obtained after 40 h of HEMR was heat treated ($\sim 600^\circ\text{C}$) for 6 h to achieve complete reduction of SiO, and the undesired oxide matrix was dissolved in HCl to obtain pure nano-Si. The loading density of nano-Si in the electrodes was $\sim 3.5\text{--}4.0\text{ mg/cm}^2$. The electrodes made from the nano-Si showed first-cycle discharge and charge capacities of $\sim 2430\text{ mAh/g}$ and $\sim 1870\text{ mAh/g}$, respectively, with an FIR loss of $\sim 30\text{--}40\%$ at a charge/discharge current rate of $\sim 100\text{ mA/g}$. The obtained nano-Si also shows an excellent capacity retention with a stable capacity of $\sim 1050\text{ mAh/g}$ at the end of 80 cycles at a charge/discharge rate of 500 mA/g . Difficulty in achieving higher loading density and expansion of the slurry-cast Si electrode itself still persisted in slurry-cast electrodes. To address this issue, a commercial water soluble template-based approach was developed to incorporate Si nanoparticles in a porous, electrochemically inactive but electrically conducting metallic foam to maintain the electrical continuity and achieve high loading densities ($5\text{--}10\text{ mg/cm}^2$) within the pores, providing free space to counter the volume expansion of the Si electrode. SEM images of the cross section of the nanocomposite foam (Figure II-200a, b) show completely interconnected porosity with pores replacing the sacrificial template upon dissolution of the pre-foamed compact. The electrodes show first-cycle discharge and charge capacities of $\sim 2970\text{ mAh/g}$ and $\sim 1940\text{ mAh/g}$, respectively, with an FIR loss of $\sim 30\text{--}45\%$ (Figure II-200c) at a charge/discharge current rate of $\sim 50\text{ mA/g}$. The obtained porous nano-Si/conducting foam shows good capacity retention with a stable capacity of $\sim 1025\text{ mAh/g}$ ($\sim 4\text{ mAh/cm}^2$) at the end of 55 cycles at 500 mA/g (Figure II-200c).

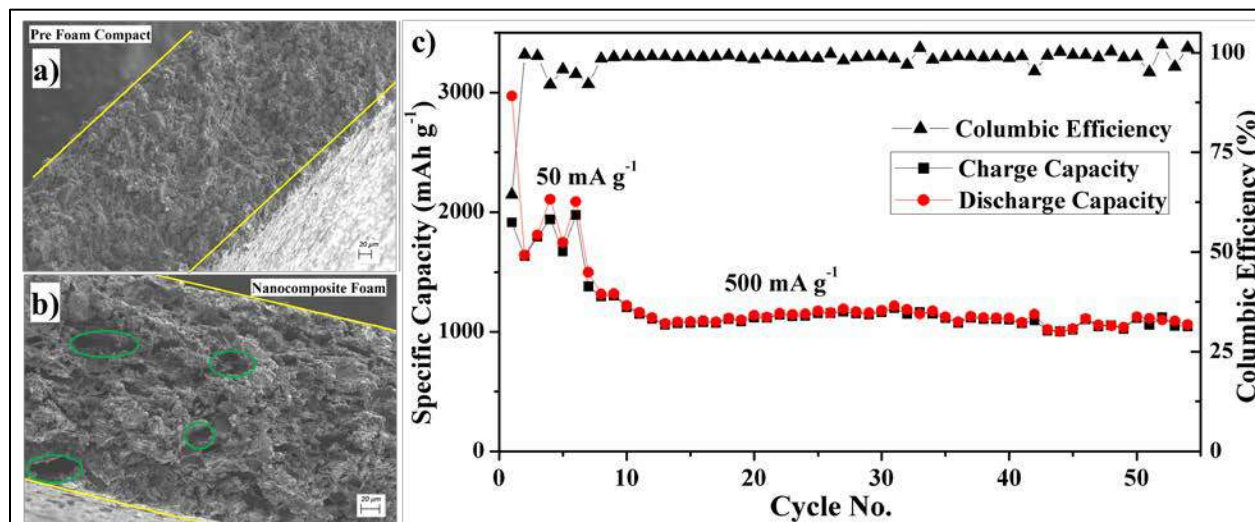


Figure II-200. (a), (b) SEM images of Si-based-nanocomposite conducting porous foams with interconnected porosity; (c) Long-term cycling data of nano-Si conducting foam tested at 50 mA/g for the initial 6 cycles followed by 0.5 A/g in a Li/Li⁺ system.

Conclusions

We have developed several approaches to synthesize micrometer-sized silicon with nano-porosity and demonstrated their good electrochemical performance. The low temperature thermic reaction (210°C) developed in this work can greatly reduce the production cost. The porous Si (p-Si@C) can have desired morphology and porous structure and has good electrochemical performance. Micrometer-sized porous silicon synthesized from nanosized silica using microemulsion delivers a high reversible capacity of 1467 mAh/g at 1C with 90% capacity retention over 200 cycles. Si/MWNT composite prepared via scalable hierarchical assembly and aluminum reduction demonstrates good electrochemical performance with a reversible capacity of 1290 mAh/g at 1C and a capacity retention of 87% after 300 cycles. In another effort, several scalable

methods were explored to generate nano-Si and Si-based nanostructures by commercially viable low-cost synthesis routes and technologies. The LTSR-derived Si embedded in CNF show a stable discharge capacity of 1210 mAh/g at a current rate of 1 A/g with an FIR loss of ~25–30%. Nano-Si obtained from HEMR was embedded in CNF, and showed a stable discharge capacity of ~1050 mAh/g at a current rate of 0.5 A/g and an FIR loss of ~30–40%. Electrodeposited Si on CNT-Cu foils also showed highly stable performance with a discharge capacity of ~1870 mAh/g, FIR loss of 35–45% at a current rate of 0.3 A/g, and high CE of ~99.95%. Opportunities exist for conducting further optimization studies.

Key Publications/Patents

1. Xiaolin Li, Pengfei Yan, Xingcheng Xiao, Jae Ha Woo, Chongmin Wang, Jun Liu, and Ji-Guang Zhang, Design of porous Si/C–graphite electrodes with long cycle stability and controlled swelling, *Energy Environ. Sci.*, 2017, 10, 1427-1434.
2. Kuber Mishra, Jianming Zheng, Rajankumar Patel, Luis Estevez, Haiping Jia, Langli Luo, Patrick El Khoury, Xiaolin Li, Xiao-Dong Zhou, and Ji-Guang Zhang, High Performance Porous Si@C Core-Shell Structured Anodes Enabled by the Low Temperature Aluminothermic Reduction Reaction, U.S. Patent application filed in March, 2017.
3. Bharat Gattu, Rigved Epur, Prashanth H. Jampani, Ramalinga Kuruba, Moni K. Datta and Prashant N. Kumta, “Silicon-Carbon Core-Shell (C@Si@C) Hollow Nanotubular Configuration - High Performance Lithium-Ion Anodes”, *Journal of Physical Chemistry - C*, 2017, 121 (18), pp 9662–9671.
4. Bharat Gattu, Prashanth H. Jampani, Moni K. Datta and Prashant N. Kumta, “Water-soluble template derived nanoscale silicon nano-flakes and nano-rods morphologies: stable architectures for lithium ion anodes”, *Nanoresearch*, 2017, <https://doi.org/10.1007/s12274-017-1707-z>.
5. Bharat Gattu, Rigved Epur, Pavithra M. Shanti, Prashanth H. Jampani, Ramalinga Kuruba, Moni K. Datta, Ayyakkannu Manivannan, and Prashant N. Kumta, “Pulsed current electrodeposition of silicon thin film anodes for lithium-ion battery applications”, *Inorganics*, 2017, 5(2), 27.

II.B.6 Pre-Lithiation of Silicon Anode for High Energy Li Ion Batteries (SLAC)

Yi Cui, Principal Investigator

Department of Materials Science and Engineering
Stanford University
McCullough 343, 476 Lomita Mall, Stanford University
Stanford, CA 94305
Phone: 650-723-4613
E-mail: yicui@stanford.edu

Tien Duong, Technology Manager

U.S. Department of Energy
Phone: 202-586-7836
E-mail: Tien.Duong@ee.doe.gov

Start Date: October 1, 2015

End Date: December 31, 2017

Total Project Cost: \$300,000

DOE share: \$300,000

Non-DOE share: \$0

Project Introduction

Rechargeable lithium-ion batteries (LIBs) are widely used for consumer electronics and exhibit great potential for electrical vehicle and grid-scale energy storage. In existing lithium-ion technology, Li is provided by Li-intercalated cathode materials. Graphite is the most commonly used anode material. Various alternative high-capacity anode materials such as silicon, with a theoretical capacity more than ten times of graphite, have been well studied and have already shown promise in potential applications. The formation of a solid electrolyte interphase (SEI) layer on the anode surfaces is a critical process that occurs prior to regular battery operations and consumes a significant amount of Li. Graphite anodes exhibit an irreversible capacity loss of 5–10% from the initial battery charging process, while for high-capacity anode materials, the first-cycle Li loss is even higher (e.g., 15–35% for Si). Low first-cycle Coulombic efficiency leads to the consumption of an excess amount of cathode material solely for the first cycle and thereby, significantly reduces the energy density. It is also challenging to effectively compensate for the Li loss through loading excessive cathode materials as a result of kinetic limitations on the cathode thickness. Accordingly, there is a strong motivation to develop high-capacity materials to prestore a large amount of Li in either cathode or anode to compensate for the initial loss.

Objectives

This study aims to develop high-capacity prelithiation additives that can work as a secondary Li source and compensate the initial Li loss in LIBs. This study pursues two main directions: 1) developing different anode prelithiation additives to increase first-cycle Coulombic efficiency of LIBs, and 2) increase the stability of prelithiation additives in the electrode fabrication environments.

Approach

Usually, prelithiation of cathode materials was previously achieved by treating spinel cathode materials or metal oxides with chemical reagents, like n-butyllithium, LiI, or molten Li. However, the prestored capacity is still relatively low (100–800 mAh/g). Anode materials are more attractive Li reservoirs because of the high specific capacities. In previous studies, there have been three main approaches to realize anodes with prestored Li. One approach is electrochemical prelithiation by shorting electrolyte-wetted anodes with Li foil. Another approach is to incorporate microscale stabilized lithium metal powder (SLMP; FMC Lithium Corp.) into anodes. However, synthesis of SLMP in the research laboratory is difficult. In our previous report, we showed chemically synthesized $\text{Li}_x\text{Si}/\text{Li}_2\text{O}$ core shell nanoparticles (NPs) as an effective prelithiation reagent. The NPs maintained their capacities only in the dry air but that their capacities were reduced drastically after exposure to ambient air. In the follow-up study, we showed that using 1-fluorodecane to modify the surface gives rise to an artificial SEI coating consisting of LiF and Li alkyl carbonate. However, these particles maintain their

capacity only in air with low humidity levels (<10% relative humidity (RH)) and their stability in NMP is not possible. The LiF formed at room temperature with this method is amorphous, and the coating consists of side products resulting in a less dense coating which is unable to prevent the penetration of water and NMP.

Therefore, we develop a high temperature and gas phase surface fluorination reaction to synthesize LiF-Li_xSi NPs. The dense and crystalline LiF coating improves the stability of Li_xSi NPs in both humid air and regular slurry solvent (NMP), indicating that LiF-Li_xSi NPs are compatible with industrial electrode fabrication processes.

Group IV elements such as Ge and Sn also have relatively high specific capacities (1640 mAh/g for Ge, and 993 mAh/g for Sn) and similar volumetric capacities to Si (2574 mAh/cm³ for Si, 2275 mAh/cm³ for Ge, and 2111 mAh/cm³ for Sn), making them also suitable for pre-storing Li. Therefore, we developed a one-pot metallurgical process to synthesize Li₂₂Z₅ alloys (Z = Ge and Sn) and Li₂₂Z₅-Li₂O composites by using Z and ZO₂ as the source materials, respectively. Both Li₂₂Z₅ alloys and Li₂₂Z₅-Li₂O composites are reactive enough to prelithiate various anode materials such as graphite and Sn, thereby achieving high 1st cycle CEs of >100%.

Alloy anodes with much higher capacity have been recognized as promising alternatives to graphites. Without prestored Li in anodes, the energy density is limited by the low capacity of Li metal oxide cathodes. Recently, Li metal has been revived as a high-capacity anode, but faces many challenges resulting from its high reactivity and uncontrolled dendrite growth. Therefore, we develop an air-stable and free-standing Li_xSi/graphene foil as an alternative to Li metal, inheriting the desirable properties of alloy anodes and pure metal anodes.

Results

LiF-coated Li_xSi NPs stable in NMP and humid air

With low solubility in both water and organic solvents, LiF coating could be applicable to Li_xSi NPs to improve the compatibility with industrial electrode fabrication processes. We find the fluoropolymer, CYTOP, gradually decomposes and releases pure F₂ gas upon heating, which reacts with Li_xSi NPs to form a uniform and compact LiF coating. The TEM image in Figure II-201a indicates a uniform and continuous coating with a thickness of 20 nm. After coating, a new XRD peak at 38.7 degree is indexed as LiF (PDF# 00-004-0857), confirming the crystalline nature of the coating (Figure II-201b). The reaction between Li_xSi and NMP as well as the improved stability after LiF coating was studied by gas chromatography (GC, Figure II-201c). After soaking in NMP for 6 h, 20 mg Li_xSi NPs reacted with NMP vigorously to release 18145 ppm H₂ and 938 ppm CH₄. With LiF coating, the reaction with NMP is considerably suppressed. The GC signal of H₂ decreases to only 15% of that of uncoated Li_xSi, and no signal of CH₄ is detected. To confirm the stability of LiF-Li_xSi NPs in the slurry, LiF-Li_xSi NPs were mixed with Super P and PVDF (65:20:15 by weight) in 1,3-dioxolane (DOL) or NMP to form a slurry which was then drop cast on copper foil. Previously, we found that bare Li_xSi is stable in DOL but reacts vigorously with NMP to leave almost no extraction capacity (dashed lines, Figure II-201d). Consistently, LiF-Li_xSi NPs shows a high capacity of 2879 mAh/g using DOL as the slurry solvent, based on the mass of Si in the cell. Replacing DOL with NMP, only a small fraction of capacity (~13%) is sacrificed (Figure II-201d). In contrast to our previous work, Li_xSi directly reacts with F₂ gas at high temperature, forming a dense and crystalline LiF coating which imparts improved stability in NMP. Because of the limited solubility of LiF in water, LiF further improves the stability of Li_xSi NPs in humid air. After being stored in humid air (~40% RH) for 1 day, the capacity is 2328.9 mAh/g, showing a high capacity retention of 85.9% (Figure II-201e). The capacity decay is slow, compared with Li₂O-Li_xSi NPs as shown in the inset of Figure II-201e. The crystalline and dense LiF coating eliminates the side reactions in both NMP and humid air, increasing the feasibility of incorporating LiF-Li_xSi NPs in the commercial electrodes fabrication process. Compared with Si NPs and bare Li_xSi NPs, LiF-Li_xSi NPs exhibit improved cycling performance with 13% capacity decay after 650 cycles (Figure II-201f). Li_xSi NPs are already in their fully-expanded state, which contributes to the excellent cyclability. Void space is created during the delithiation process, which accommodates further volume expansion of subsequent lithiation process. Therefore, each particle does not squeeze against each other to damage the structure of the whole electrode during cycling. The average CE of bare Li_xSi NPs (from the fourth cycle to the 400th cycle) is 99.79%, lower than the value of the LiF-coated Li_xSi NPs (99.92%, from the third cycle to the 650th cycle). With exceptional chemical stability, the LiF coating

effectively minimizes electrolyte decomposition and side reactions on the electrolyte/electrode interface during cycling, which contributes to the high CE.

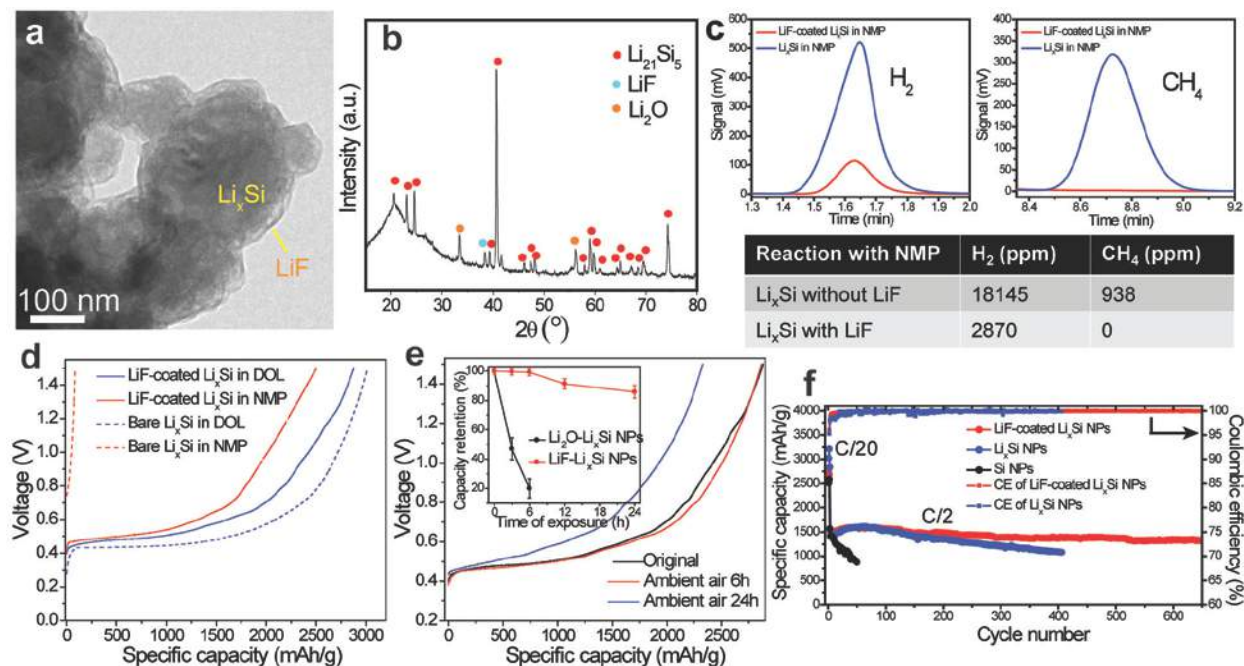


Figure II-201. Characterization and stability of LiF-Li_xSi NPs. (a) TEM image and (b) XRD pattern of LiF-Li_xSi NPs. (c) The amount of gas released for coated (red) and uncoated (blue) Li_xSi NPs reacted with NMP measured by gas chromatography. (d) First-cycle delithiation capacities of LiF-Li_xSi NPs (solid line) and bare Li_xSi NPs (dashed line) using different solvents to form the slurry. (e) The extraction capacities of LiF-Li_xSi NPs exposed to ambient air (~40% RH) with varying durations. The inset shows the trend of capacity decay of LiF-Li_xSi NPs (red) and Li₂O-Li_xSi NPs (black) with varying durations. (f) Cycling performance of LiF-Li_xSi NPs (red), bare Li_xSi NPs (blue) and Si NPs control cell (black) at C/20 for the first several cycles and C/2 for the following cycles (1C=4.2 A/g, and the capacity is based on the mass of Si in the electrodes). The Coulombic efficiency is plotted on the secondary y-axis (LiF-Li_xSi NPs: red, and bare Li_xSi NPs: blue).

Li₂₂Ge₅ alloys and Li₂₂Ge₅-Li₂O composites as stable prelithiation reagents

Ball-milled Ge NPs and GeO₂ NPs were used as the starting materials to form the Li_xGe alloy and Li_xGe-Li₂O composite, respectively. SEM was utilized to characterize the morphology of the Ge and GeO₂ NPs before and after lithiation. After ball milling, the size of Ge NPs is in the range of 100~300 nm, while that of GeO₂ NPs is in the range of 150~350 nm as shown in Figure II-202a,d. The sizes of the derived Li_xGe alloy and Li_xGe-Li₂O composite were larger than those of the starting materials because of the volume expansion and some degree of particle aggregation during the metallurgical process (Figure II-202b,e). XRD confirms the crystalline nature of ball-milled Ge powder (PDF# 00-004-0545) and a small portion of GeO₂ (PDF# 00-036-1463) resulting from the high-energy ball-milling process in air (Figure II-202c, upper). XRD confirms the complete transformation of Ge in both Ge powder and the intrinsic oxide GeO₂ to crystalline Li₂₂Ge₅ (PDF# 01-081-6059) during the thermal alloying process (Figure II-202c, bottom). The small peaks of Li₂O (PDF# 00-012-0254) come from the conversion of the small amount of intrinsic oxide GeO₂. XRD analysis also shows the complete formation of crystalline Li₂₂Ge₅ and Li₂O during the thermal alloying process of GeO₂ powder and molten Li. The only difference is the much higher percentage of Li₂O in the final product. To measure the prelithiation capacities of the Li_xGe alloy and Li_xGe-Li₂O composite, the electrodes were charged to 1.5 V directly at a slow rate of C/20 (1C = 1640 mA/g for Ge and 1126 mA/g for GeO₂). The prelithiation capacities were 1335 mAh/g and 892 mAh/g based on the masses of Ge and GeO₂ in the electrode, respectively (Figure II-202f). To test the air stability of Li_xGe, Li_xGe NPs was exposed to ambient air (30%~40% RH) for 6 h, exhibiting a high extraction capacity of 947 mAh/g (30% capacity loss, Figure II-202g). Although the specific

capacity is relatively lower, $\text{Li}_x\text{Ge-Li}_2\text{O}$ NPs exhibit superior ambient-air stability with a higher capacity retention of 85% (15% capacity loss) compared to bare Li_xGe NPs.

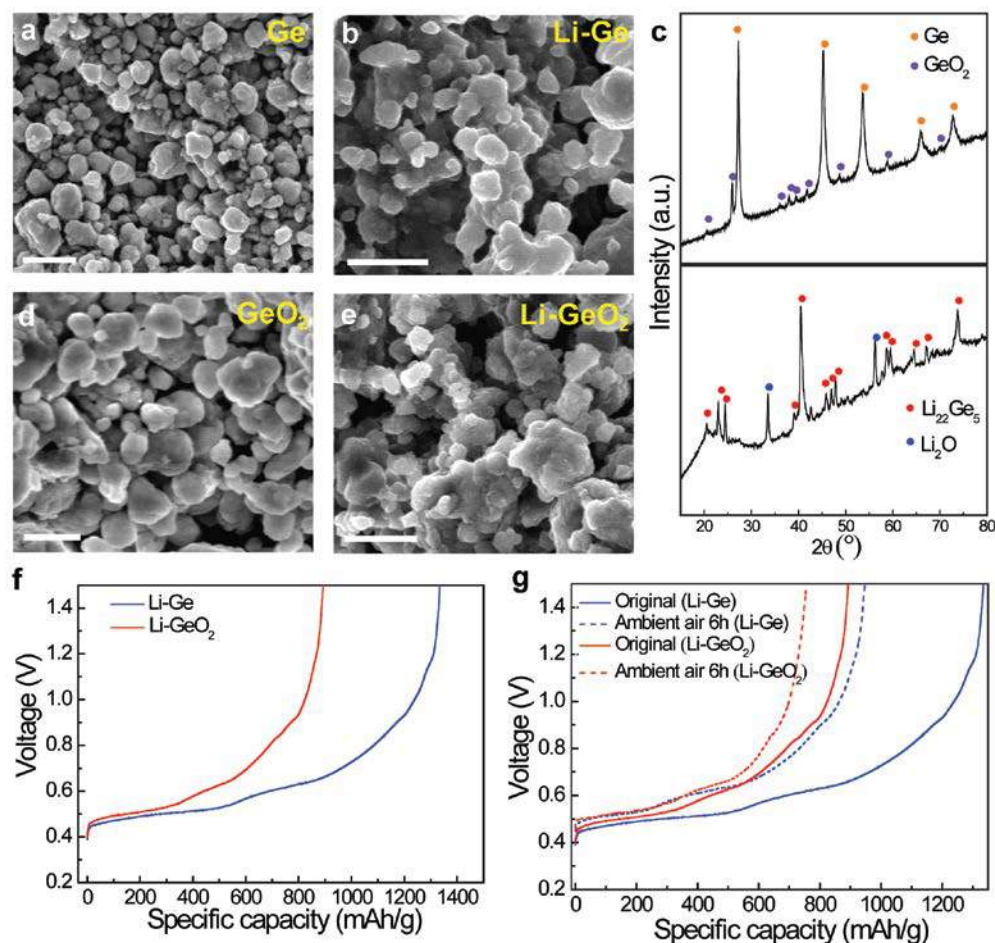


Figure II-202. (a, b) SEM images of Ge NPs (a) before and (b) after thermal lithiation. (c) XRD patterns of Ge NPs before (upper) and after thermal lithiation (bottom). (d, e) SEM images of GeO_2 NPs (d) before and (e) after thermal lithiation. (f) First-cycle delithiation capacities of lithiated Ge NPs (blue) and lithiated GeO_2 NPs (red). The capacity is based on the mass of Ge or GeO_2 in the anode. (g) First-cycle delithiation capacities of lithiated Ge NPs (blue) and lithiated GeO_2 NPs (red) before (solid) and after (dash) exposure to ambient-air condition (30%~40% RH) for 6h.

$\text{Li}_{22}\text{Sn}_5$ alloys and $\text{Li}_{22}\text{Sn}_5\text{-Li}_2\text{O}$ composites as stable prelithiation reagents

Sn NPs and SnO_2 nanoclusters were used as the starting materials to form the Li_xSn alloy and $\text{Li}_x\text{Sn-Li}_2\text{O}$ composite, respectively. The alloying temperature should be maintained between the melting points of Li metal and Sn NPs to ensure the preservation of the morphology of Sn NPs. SEM was utilized to characterize the morphology of the Sn NPs and SnO_2 nanoclusters before and after lithiation. SEM image confirms that the Sn NPs have sizes less than 200 nm (Figure II-203a). After metallurgical lithiation, the shape of the NPs is retained, whereas the particle sizes are larger due to volume expansion and some aggregation (Figure II-203b). XRD confirms the transformation from Sn (PDF# 00-004-0673) to $\text{Li}_{22}\text{Sn}_5$ (PDF# 01-081-6569) after thermal alloying with molten Li (Figure II-203c). The small amount of Li_2O arises from the intrinsic oxide SnO (PDF# 04-005-4541) in Sn NPs. The hydrothermal-synthesized SnO_2 nanoclusters are uniform both in size (~50 nm) and shape as confirmed by SEM (Figure II-203d). The monodisperse SnO_2 nanoclusters were utilized as the precursor for the $\text{Li}_x\text{Sn-Li}_2\text{O}$ composite. After thermal lithiation, the morphology of SnO_2 nanoclusters was preserved, whereas the size of the clusters slightly increased to 75 nm because of volume expansion (Figure II-203e). XRD of lithiated SnO_2 shows the same final products as lithiated Sn NPs with a higher

percentage of the Li_2O phase. To compare their dry-air stability, different Li_xZ ($\text{Z} = \text{Si}, \text{Ge}$ and Sn) alloys were stored in a dry room (dew point = -50°C) for 5 days. The remaining capacity of Li_xSn NPs exposed to dry air over many days were studied by charging the Li_xSn NPs electrodes to 2 V at a low rate of C/20 (Figure II-203f). After 5 days' exposure, Li_xSn NPs exhibit a high capacity of 845 mAh/g, corresponding to a capacity retention of 93%. The capacity decay for Li_xSn alloy and Li_xGe alloy is much slower compared with Li_xSi alloy. Among the Li_xZ alloys, Li_xGe shows the best dry-air stability with negligible (6.5%) capacity decay after 5 days of exposure. No new peaks are present in the XRD pattern of Li_xSn NPs exposed to ambient air ($\sim 40\%$ RH) for 2 h (Figure II-203g, upper). The XRD pattern reveals small peaks belonging to $\text{Li}(\text{OH})\cdot\text{H}_2\text{O}$ (PDF# 04-010-4336), and $\text{Li}_{22}\text{Sn}_5$ remains the major component after being exposed to ambient air for 6 h (Figure II-203g, bottom). Because of the excellent air stability, the Li_xSn alloy and $\text{Li}_x\text{Sn}-\text{Li}_2\text{O}$ composites are potentially compatible to the industry battery fabrication process.

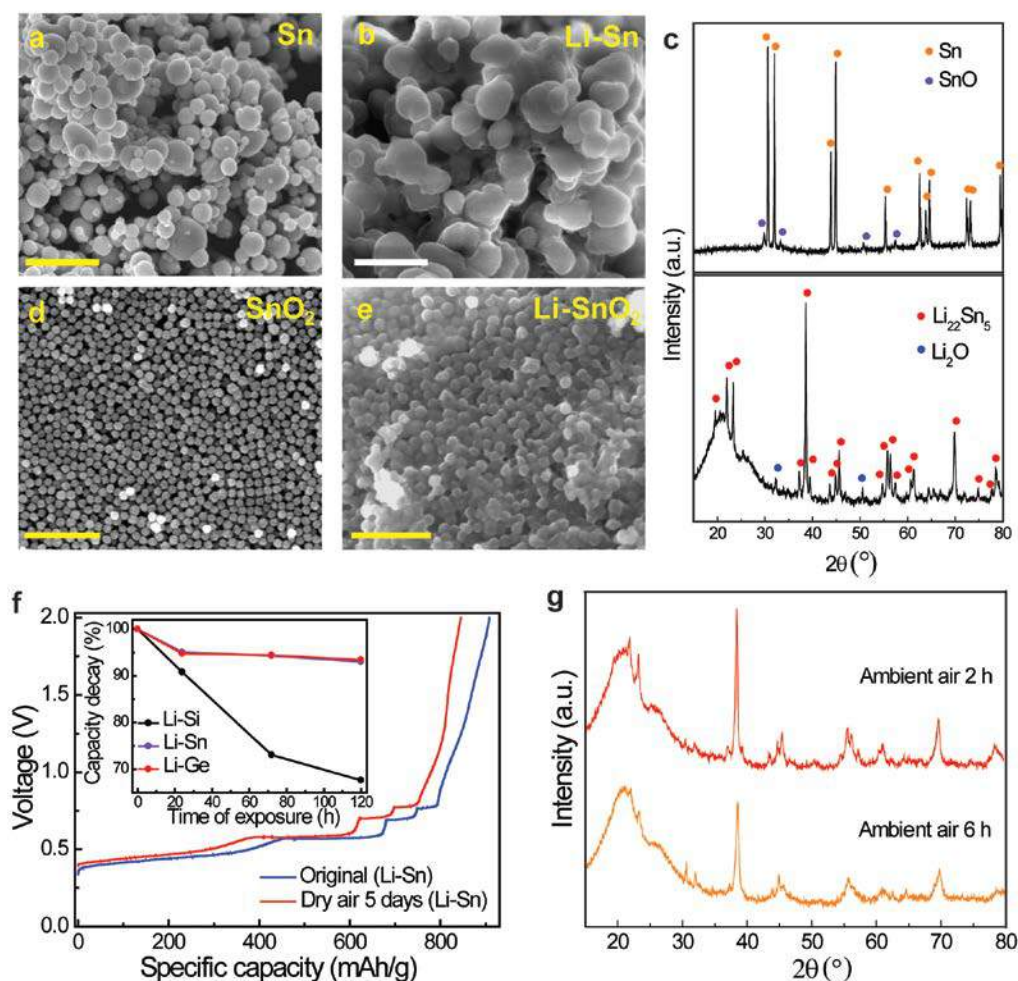


Figure II-203. (a, b) SEM images of Sn NPs (a) before and (b) after thermal lithiation. Scale bar, 500 nm. (c) XRD patterns of Sn NPs before (upper) and after thermal lithiation (bottom). (d, e) SEM images of SnO_2 NPs (d) before and (e) after thermal lithiation. Scale bar, 500 nm. (f) First-cycle delithiation capacities of lithiated Sn NPs before (blue) and after (red) exposure to dry-air condition for 5 days. The inset shows the trend of capacity decay of lithiated Si (black), Sn (purple) and Ge (red) NPs. (g) XRD patterns of lithiated Sn NPs exposed to ambient-air condition for 2h (upper) and 6 h (bottom).

Air-stable and free-standing Li_xSi /graphene foil as an alternative to Li metal

This large-scale freestanding Li_xSi /graphene foil consists of fine nanostructures of densely-packed Li_xSi NPs encapsulated by large graphene sheets. Li_xSi NPs were mixed with graphene sheets and SBS rubber (80:10:10

by weight) in toluene to form a slurry, which was then casted on a PET release film. After drying, it can be easily peeled off. The photograph (Figure II-204a) shows a large Li_xSi /graphene foil with 8 cm width and 24 cm length. The right side of the foil is rolled around a thin tube to illustrate the good flexibility. The superior mechanical property of the Li_xSi /graphene foil is further demonstrated by the uniaxial tensile test, which shows a similar trend to a Li metal foil with much higher stress (Figure II-204d). TEM image with low magnification (Figure II-204b) shows overlapped and interconnected graphene sheets with size up to several microns. A double-layer graphene sheet is clearly observed in Figure II-204c, with the average inter-layer distance of 0.334 nm. XRD pattern (Figure II-204e) of the Li_xSi /graphene foil contains peaks of $\text{Li}_{22}\text{Si}_5$ (PDF# 01-077-2882), graphitic carbon (PDF# 00-056-0159), and Li_2O (PDF# 04-008-3420). Li_xSi NPs are identifiable underneath the thin graphene sheet (Figure II-204f). After calendared at large stress 40 MPa, Li_xSi NPs are in a densely-packed state as shown in the cross-sectional view of the SEM image (Figure II-204g). With fully-expanded Li_xSi confined in the highly-conductive and chemically-stable graphene matrix, this foil maintains a stable structure and cyclability in half cells. The Li_xSi /graphene foil is successfully paired with high-capacity Li-free cathodes, such as V_2O_5 and Sulphur, to achieve stable full-cell cycling. The Li_xSi /graphene foil is stable in ambient air, owing to the unique structure as well as the hydrophobicity and gas impermeability of graphene sheets.

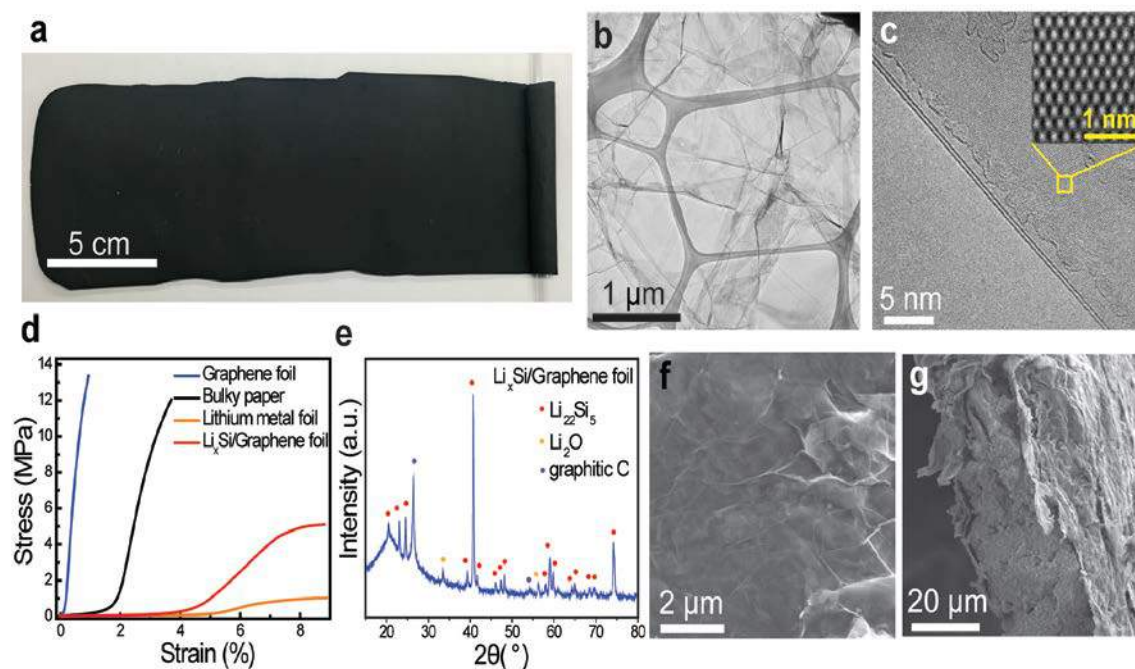


Figure II-204. Characterizations of the Li_xSi /graphene foil. a, Photograph of large Li_xSi /graphene foil with 8 cm width and 24 cm length. b, Low-magnification TEM image of the overlapped and interconnected graphene sheets. c, TEM image shows a double-layer graphene sheet with the inter-layer distance of 0.334 nm. The inset is the atomic resolution image of the graphene sheet. d, Uniaxial tensile test of the graphene foil (blue), bulky paper (black), Li metal foil (orange), and Li_xSi /graphene foil (red). e, XRD pattern reveals the highly crystalline nature of graphitic carbon and $\text{Li}_{22}\text{Si}_5$. f, Top-view and g, cross-sectional view SEM images of the Li_xSi /graphene foil.

Conclusions

In the past year, we developed a surface fluorination process to form a homogeneous and dense LiF coating on Li_xSi NPs. With this coating, Li_xSi NPs are stable in both humid air and regular slurry solvent (NMP), indicating that LiF- Li_xSi NPs are compatible with industrial electrode fabrication processes. Aside from Si-based prelithiation reagents, we developed Li_{22}Z_5 alloys ($\text{Z} = \text{Ge}$ and Sn) and $\text{Li}_{22}\text{Z}_5\text{-Li}_2\text{O}$ composites with better air-stability by using Z and ZO_2 as the source materials, respectively. Li-containing anodes afford remarkable battery performance either as anode additive or anode material by itself. The synthesized air-stable and free-standing Li_xSi /graphene foil serves as an alternative to Li metal, inheriting the desirable properties of alloy anodes and pure metal anodes.

Key Publications

1. J. Zhao, L. Liao, F. Shi, T. Lei, G. Chen, A. Pei, J. Sun, K. Yan, G. Zhou, J. Xie, C. Liu, Y. Li, Z. Liang, Z. Bao, and Y. Cui, "Surface fluorination of reactive battery anode materials for enhanced stability", *JACS* **139**, 11550 (2017).
2. J. Zhao, J. Sun, A. Pei, G. Zhou, K. Yan, Y. Liu, D. Lin, and Y. Cui, "A general prelithiation approach for group IV elements and corresponding oxides", *Energy Storage Materials*, in press.
3. J. Zhao, G. Zhou, K. Yan, J. Xie, Y. Li, L. Liao, Y. Jin, K. Liu, P-C Hsu, J. Wang, H-M Cheng, and Yi Cui, "Air-stable and freestanding lithium alloy/graphene foil as an alternative to lithium metal anodes", *Nat. Nanotech.* **12**, 993 (2017).

II.B.7 High Capacity and Long Cycle-Life Silicon Carbon Composite Materials and Electrodes (LBNL)

Gao Liu, Principal Investigator

Lawrence Berkeley National Laboratory
1 Cyclotron Road
Berkeley, CA 94720
Phone: 510-486-7207
E-mail: gliu@lbl.gov

Brian Cunningham, Technical Manager

Phone: 202-287-5686
E-mail: Brian.Cunningham@ee.doe.gov

Start Date: October 1, 2016
Total Project Cost: \$565,000

End Date: September 30, 2017
DOE share: \$565,000

Non-DOE share: \$0

Project Introduction

The low energy density and limited lifetime are two of major drawbacks of the automobile Li-ion batteries for electric vehicle (EV)/plug-in hybrid EV (PHEV) applications. State-of-the-art Li-ion technology is based on a graphite negative electrode and a layered metal oxide, spinel, or olivine phosphate positive electrode system. The theoretical specific capacity of graphite is 372 mAh/g, which is far less than some of the suggested alternative Li-ion storage materials such as tin (Sn) (994 mAh/g) or silicon (Si) (4,200 mAh/g). However, the graphite material has unique advantages in the established Li-ion system: it is structurally stable and incurs only ~10% of volume change during the Li-ion insertion and removal process. This structural stability helps to maintain both electrode integrity and overall cell volume stability. The structural stability is also important to maintain a stable solid electrolyte interface (SEI) layer on graphite to prevent further electrolyte reactions on the surface. The Li-ion electrolyte and additive combinations, which has been developed over the past two and half decades, ensures the formation of electrochemically stable SEI on the graphite surface at very low voltage potential. In order to advance anode chemistry for EV/PHEV applications, any new anode materials need to have a higher capacity than those of graphite, at least the same surface stability of a graphite anode (for long term cycling and storage), and an overall electrode design that is suitable for high-capacity materials.

Si is a naturally abundant material. It possesses the highest capacity of any Li-ion anode material. Si and Li alloys also have a low potential plateau at around 0.45 V (Li/Li⁺) during the de-lithiation process. Si anodes, combined with cathode materials at 4 V and above, can offer higher energy density storage for EV/PHEV.

However, despite its remarkable high storage capacity and the intensive research done in this field, applications of Si in Li-ion cells are limited. One reason is that the cycle life of a battery containing Si does not generally exceed 500 cycles. The primary issue is the high-volume change associated with Li-ion insertion into Si. Almost 280% volume expansion occurs as the material transitions from the pure Si phase to the Li₁₅Si₄ phase. This high-volume change tends to disrupt the electronic integrity of the composite electrode and induce high and continuous surface side reactions leading to drastic capacity fade.

Si volume expansion, along with the excessive side reactions on the Si surface due to lithiation and delithiation cycling, poses significant challenges to utilizing Si to its highest potential. This project aims to develop high-capacity and long-life Si/C composite anodes to prolong battery cycling and storage lifetime, and to provide an in-depth understanding of Si electrode design strategies to stabilize Si material volume change and to prevent surface side reactions. This work combines novel materials design and innovative synthesis process to synthesize mechanically robust and dimensionally stable Si/C composite materials.

Objectives

This project addresses the low energy density and limited lifetime of the lithium-ion (Li-ion) battery for EV and PHEV applications. This research aims to stabilize Si material volume change to achieve high capacity, stable electrode design and to prevent surface side reactions to prolonged battery cycling and storage lifetime. This project developed synthetic processes to make silicon carbon anode composite materials to reduce volume expansion during charge and discharge process, and applied surface coating to reduce surface side reactions.

Approach

Materials synthesis approach to address the volume expansion and surface reactions is inspired by recent progresses in this field by the LBNL team and other groups, which have shed light on the potential directions for further optimization of the Si materials. First, it was shown that large, secondary-particle-based Si materials allow longer cycle life, higher loading, and improved rate performance. A second key area of recent progress in the field is the development of dimension-stable Si nanotube, which tends to stabilize cycling and reduce side reactions. Si nanotubes with SiO₂ protection layers allow the Si cycling for more than 6,000 cycles with minimum decomposition deposits on the nanotube surface. In this case, the SiO₂ layer is a dense layer, preventing the electrolyte from contacting the Si reactive surface. The Si tubes expand inward during lithiation, so that the surface of the SiO₂ in contact with electrolyte does not change with cycling. Therefore, a physically stable SEI can be formed on the surface of the nanotube. We propose to combine both approaches (large particle size and stable surfaces) to develop both dimension- and surface-stable Si composite materials.

1) Use spray precipitation to synthesize micron size Si/carbon (Si/C) composite particles.

The design approach is a hollow shell-structured Si/C composite particle. The outer diameter of the composite particle has a mean size of 20 μm. The inner diameter of the hollow core is approximately 10 μm. The silicon nanoparticles are distributed in the shell of the carbon matrix. The Si nanoparticle size is approximately 10 nm. Sonication spray is a method to generate controlled particle size droplet in the range of 20 μm and above. A sonication spray-precipitation method is used to generate spherical secondary composite particles. Controlled strength of ultrasound dispersion is used during the spray of Si/polymer slurry in solvent A into a solvent B to produce a spherical precipitate. In this case, the polymer binder dissolved in solvent A but precipitated in solvent B. Solvent A and B are miscible. When the slurry droplet is falling into solvent B, the polymer will solidify at the surface of the droplet to form micron-size particles. Solvent A and the polymer will continue transport from the center to the surface of the particles, and precipitate towards the surface where solvent B has a higher concentration. The polymer and solvent A will drag the silicon particles to the outer surface. The net effect of the particle morphology is a hollow core spherical Si and polymer composite particles. By controlling the slurry solvent content and sonication strength, the outer diameter of the particles and the size of hollow core can be controlled. Further sintering these particles around 500-800°C will lead to hollow core spherical Si/C materials. The hollow core of the Si/C secondary particles will accommodate volume expansion of primary Si particles, so the outer surface expansion of the secondary particles is reduced.

2) Secondary particle surface coating to reduce electrolyte side reactions with Si/C composite particles.

Additional coating will be applied to the secondary particle surface either before or after the sintering processing. After the coating, the materials will go through another sintering process to solidify the coatings to form a lithium-ion conducting but electrolyte expelling thin layer in the range of 10-100 nm. Since the existence of the internal void space, the overall volume expansion of the secondary particles will tend to be much lower. The purposes of this coating are two folds. First, it will provide a robust layer to further reduce the outer expansion of the secondary particles. Second, it will isolate the electrolyte interaction with the reactive Si surfaces. The choice of coating materials will be carbon precursors or Li-ion conducting glass ceramics.

This comprehensive design will solve the volume change issues in the secondary particle level. The large particle size will ensure small gravimetric specific surface area for low side reactions. Large pore formation in the electrode will allow for rapid electrolyte ion transport. Since the Si/C composite only expands inwardly, the electrode made by these particles is dimensionally stable. Therefore, the overall cell volume change is very

small. Due to the surface coating layer and the stable secondary particles size, the electrolyte will not contact the Si nanoparticles. Because of the internal void space and carbon clamping, the expansion and contraction will only happen inwardly. This design can solve the most critical issues of continued surface reaction between the high capacity Si and electrolyte.

Results

A sonication spray-precipitation method is developed to generate spherical hollow core composite secondary particles. The process is detailed in Figure II-205. Controlled strength of ultrasound dispersion was used during the spray of Si/polymer composite secondary slurry (in solvent A) into a non-solvent (solvent B) of the polymer to produce a spherical precipitate. By controlling the slurry solvent content and sonication strength, the average size and hollow core of the composite secondary particle precipitated can be controlled. The collected particles will be sintered around 500°C to form Si/C hollow core particles.

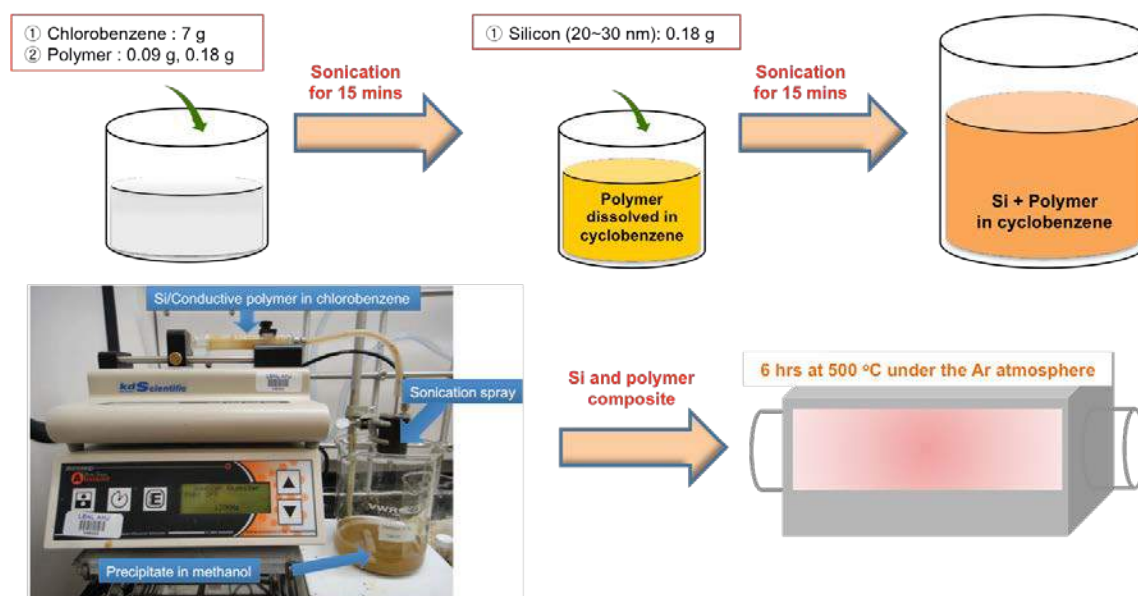


Figure II-205. Schematic process to make hollow core Si/C composite via spray precipitation and post sintering.

Hollow spherical composite secondary particles were fabricated, as shown in Figure II-206. An average particle size of 10 μm in diameter was achieved, as seen in the scanning electron microscope (SEM) image of the particles collected. The initial droplet size from the spray nozzle is controlled by the ultrasonic power at the nozzle. The smallest droplet diameter can be achieved is around 20 μm based on the manufacturer's configuration. Further reduction of composite secondary particle size was achieved by increasing the chlorobenzene (solvent A) content of the slurry. The dried composite secondary particles, ranging from 2 μm diameter to 20 μm diameter, were made when controlled at the smallest spray droplet of 20 μm diameter. The higher the solvent content in the slurry, the further size reduction there is after the droplets precipitate into the non-solvent. When the slurry droplets are sprayed into the non-solvent (solvent B), the migration of slurry solvent (A) from the droplets to the non-solvent (B) starts from the surface of the droplets. The surface polymer solidifies first. Due to the particle size is fixed before the center slurry solvent all migrates out of the spheres, a hollow core forms in the end of the precipitation. These materials have large void space with a diameter of around 10 μm . The void space is expected to accommodate the large volume change of Si during the charging/discharging process. The wall thickness of Si and polymer sample is around 5 μm . The cross-section SEM images of the hollow particles obtained using Focused-Ion-Beam (FIB) milling are shown in Figure II-206d. The cross-section SEM images show large void space in the Si/C composite. Thus, the integrity of the Si/C secondary particles can be maintained during cycling. The distribution of the carbon and

Si is very uniform within the composite, as shown in the EDS mapping image of the elemental Si, carbon (C), and oxygen (O).

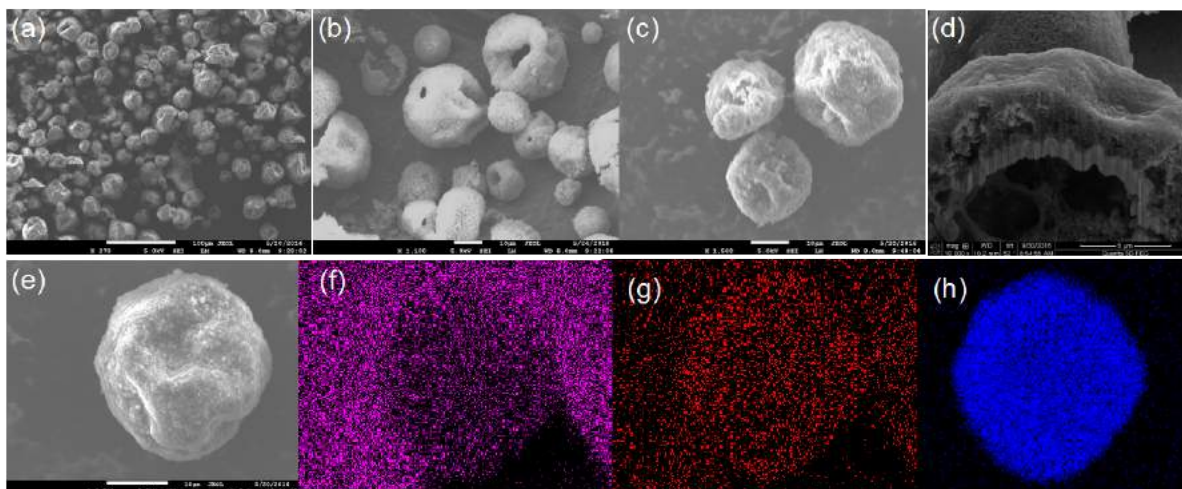


Figure II-206. SEM images of the Si/C composite secondary particles. (a-c) the Si/C hollow secondary particles at different magnifications. (d) FIB cross-section of a hollow Si/C particle. (e-f) A single particle and its EDS mapping image of carbon- (f), oxygen-(g) and silicon-(h). The background carbon tape contains carbon and oxygen elements.

As for the carbon coating to stabilized Si surface, SiO is chosen as active materials. The pyrene-based homopolymer poly(1-pyrenemethyl methacrylate) (PPy) is used as a polymer precursor to generate carbon coating after sintering process. The PPy polymer has layer structure due to the π - π stacking of the pyrene moiety, and forms a graphite-like structure at low sintering temperature. PPy polymer is soluble in organic solvent, and can be coated on the SiO surface easily. A schematic illustration of the process for fabricating the SiO/PPy composite materials is shown in Figure II-207. Typically, SiO micrometer size particles are dispersed in PPy THF solution and sonication for 0.5 h. Then, the solvent were evaporated by rotary evaporator to collect the SiO/PPy precursors. Finally, the sample was sintered at 400, 500, 600°C in an inert gas (sample name: SiO-PPy-T). The obtained final products were uniformly coated with a carbon layer. This carbon coating can effectively prevent the direct contact of SiO with electrolyte and improve the electronic conductivity. Raman spectroscopy is used to obtain the structural information about the SiO-PPy-T composites. A broad peak at 480 cm^{-1} extending asymmetrically down to approximately 430 - 515 cm^{-1} corresponds to the amorphous SiO is observed in all samples. For the SiO-PPy-T composites, the two prominent peaks at 1340 cm^{-1} and 1605 cm^{-1} which correspond to the D band and G band respectively. The intensities of D and G band decrease with the temperature increase. The I_D/I_G ratios are 0.645, 0.580 and 0.561 for SiO-PPy-400, 500 and 600 samples, respectively, indicating the carbon coating graphitic degree increase with increasing the sintering temperature.

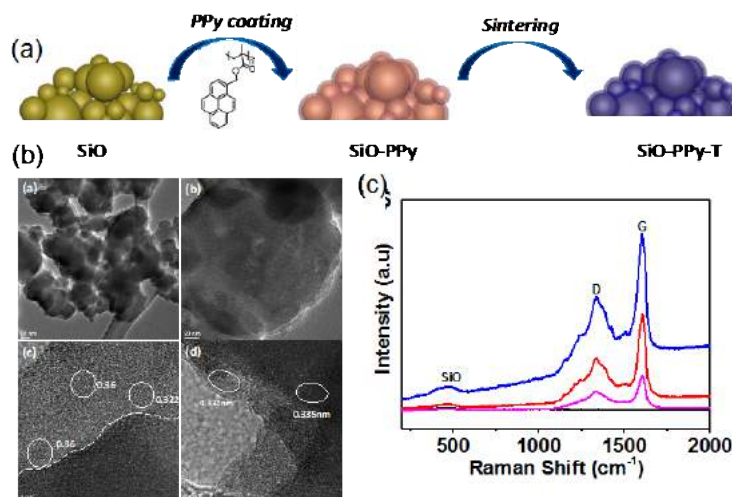


Figure II-207. (a) The process to coat SiO materials using PPy polymer and sintering to form a carbon coating layer on SiO materials (b) TEM images of the carbon coated SiO materials at different magnification, (c) Raman spectra of the SiO and carbon coated SiO sintered at different temperatures, 400 °C (red), 500 °C (blue), 600 °C (magenta).

Galvanostatic charge - discharge curves of pure SiO, and SiO-PPy-400, 500, 600 electrodes cycled ranging from 0.1C to 2C. The SiO-PPy-500 delivers a capacity of 1127.5 mAh/g at the rate of 0.1C, and then gradually decreases to 649.9 mAh/g at the rate of 0.5 C, to 487.0 mAh/g at the rate of 1 C. (See Figure II-208.) Even at high rate of 2C, a reversible capacity of 317.6 mAh g⁻¹ can be still achieved. Notably, when the rate restored to 0.1C, SiO-PPy-500 composite electrode return of higher capacity of 1145.7 mAh/g, completely recovers its initial capacity. The results are remarkably superior to those of pure SiO, SiO-400 and 600, which show a continuous capacity decrease at each current density in the same range. The results show that the SiO-PPy-500 displays the excellent rate performance with a stable cycling behavior at different current densities. After the first two cycles at 0.05C rate for the formation step, the cells were then cycled at 0.1C over 50 cycles between 0.01-1.0 V. The SiO-PPy-500 electrodes show much higher reversible a specific capacity with 1090.2 mAh/g after 50 cycles than that of the other samples, which is 299.2 mAh/g for SiO-PPy-400 and 846.1 mAh/g for SiO-PPy-600 and 771.6 mAh/g for uncoated SiO electrode, respectively. The initial coulombic efficiency (CE) of SiO-PPy-500 is 62.2%. In comparison, the SiO-PPy-400, SiO-PPy-600, and uncoated SiO electrodes are only able to demonstrate an initial CE of 30.5%, 55.6%, and 54.8%, respectively. At C/3 rate, the specific capacity of the uncoated SiO electrode after 200 charge/discharge cycles is 534.8 mAh g⁻¹ with capacity retention of 65.8%. The SiO/PPy composite sintering at 500 °C exhibit improved specific capacity and cycling stability, a higher specific capacity of 793 mAh/g after 200 charge/discharge cycles is achieved. The corresponding capacity retention is as high as 74.5%. When the sintering temperature of the SiO/PPy composite are 400 and 600 °C, the reverse specific capacity of the electrode are 264.6 and 396.3 mAh/g at the 200th cycle respectively. These results clearly show that SiO-PPy-500 has the best electrochemical performance and the sintering temperature plays an important role in affecting the structure of the coating layers, obtained from sintering of PPy. The SiO-PPy-500 demonstrates a rapid increase of stabilized efficiency greater than 99.5% after only 5 cycles including the first formation cycle, and very stable in the rest cycles. This high cycling efficiency is quite promising for commercialization of alloy anodes into full-cell systems.

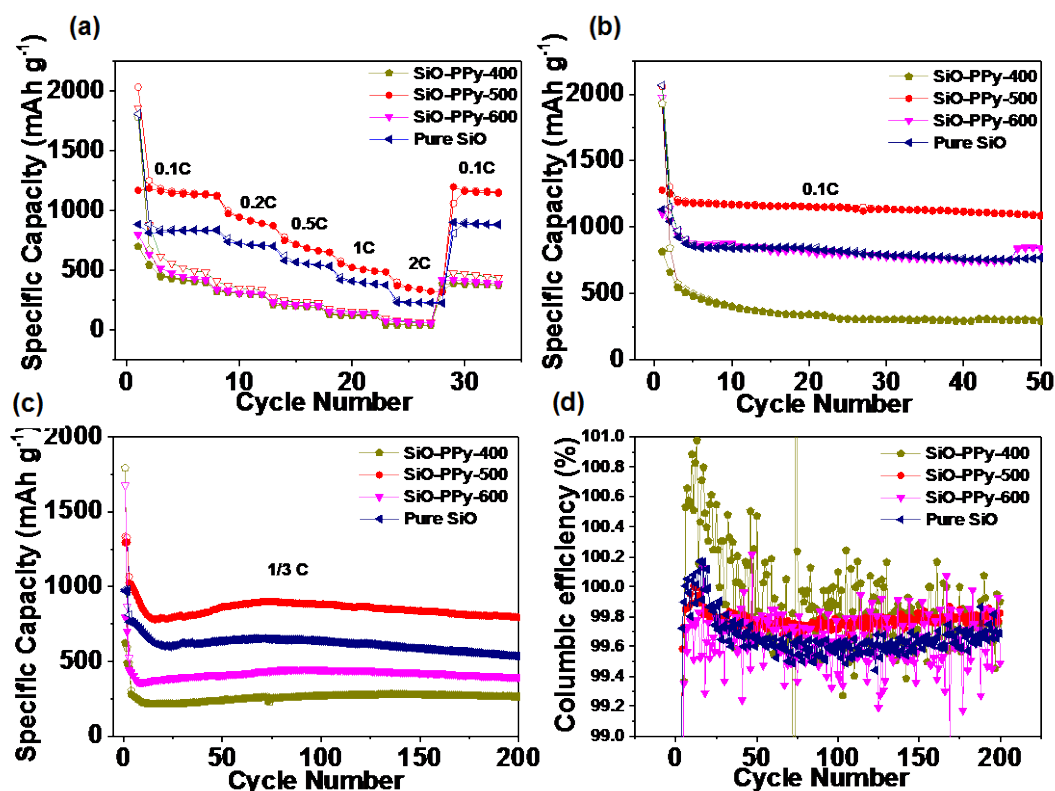


Figure II-208. (a) The Rate capabilities of pure SiO and SiO-PPy sintering at different temperature. (b) Cycling performance at C/10. (c) Cycling performance at C/3. (d) CE for pure SiO and SiO-PPy samples.

Conclusions

The Si/C hollow composite particles are synthesized using sonication spray-precipitation followed by pyrolysis method. The sonication spray of Si and polymer slurry successfully generated Si polymer composite hollow secondary particles. The sintering of the Si polymer composite particles retains the original morphology to yield the Si/C hollow particles. The distribution of carbon and Si is uniform across the secondary particles. An effective and scalable carbon coating process is also developed for SiO materials. The PPy is a very good polymer precursor to form highly graphitic carbon coating on the surface of SiO at a low sintering temperature of 500°C. The carbon coated SiO materials based on PPy precursor demonstrates superb cycling performance and rate capability.

Key Publications

1. Zheng, H. Y.; Qu, Q. T.; Zhu, G. B.; Liu, G.; Battaglia, V. S.; Zheng, H. H. *Acs Applied Materials & Interfaces* **2017**, 9 (14), 12445-12452.
2. Xu, J.; Ling, M.; Terborg, L.; Zhao, H.; Qiu, F.; Urban, J. J.; Kostecki, R.; Liu, G.; Tong, W., *J. Electrochem. Soc.* **2017**, 164 (7), A1378-A1383.
3. Shi, Q.; Liu, W. J.; Qu, Q. T.; Gao, T.; Wang, Y.; Liu, G.; Battaglia, V. S.; Zheng, H. H., *Carbon* **2017**, 111, 291-298.
4. Self, E. C.; Naguib, M.; Ruther, R. E.; McRen, E. C.; Wycisk, R.; Liu, G.; Nanda, J.; Pintauro, P. N. *ChemSusChem* **2017**, 10 (8), 1823-1831.
5. Ling, M.; Zhang, L.; Zheng, T. Y.; Feng, J.; Guo, J. H.; Mai, L. Q.; Liu, G. *Nano Energy* **2017**, 38, 82-90.

6. Ling, M.; Liu, M.; Zheng, T. Y.; Zhang, T.; Liu, G. *J. Electrochem. Soc.* **2017**, *164* (4), A545-A548.
7. Higa, K.; Zhao, H.; Parkinson, D. Y.; Barnard, H.; Ling, M.; Liu, G.; Srinivasan, V., *J. Electrochem. Soc.* **2017**, *164* (2), A380-A388.
8. Fang, S.; Tong, Z. K.; Nie, P.; Liu, G.; Zhang, X. G., *Acs Applied Materials & Interfaces* **2017**, *9* (22), 18766-18773.
9. Caihong Feng, Xianpu Meng, Xiaolu Song, Xueting Feng, Yun Zhao and Gao Liu *RSC Advance* **2016**, *6*, 110266-110273.
10. Guo Ai, Yiling Dai, Wenfeng Mao, Hui Zhao, Yanbao Fu, Xiangyun Song, Yunfei En, Vincent S. Battaglia, Venkat Srinivasan, and Gao Liu *Nano Letters* **2016**, *16* 5365-5372.
11. Jing Mao, Mengze Ma, Panpan Liu, Junhua Hu, Guosheng Shao, Vince Battaglia, Kehua Dai, Gao Liu, *Solid State Ionics*, **2016**, *292*, 70–74.
12. Yan Feng, Yuzhen Wei, Zhe Jia, Yuliang Zhang, Vince Battaglia, Gao Liu *Chemistry Select*, **2016**, *1* (2) 309-317.

II.B.8 A Combined Experimental and Modeling Approach for the Design of High Current Efficiency Si Electrodes (GM)

Xingcheng Xiao, Principal Investigator

GM Global Research and Development
30500 Mound Road
Warren, MI 48090
Phone: 248-912-8132
E-mail: Xingcheng.xiao@gm.com

Yue Qi, Co-Principal Investigator

Michigan State University
3509 Engineering Building
East Lansing, MI 48824
Phone: 517-432-1243; Fax: 517-432-1105
E-mail: yueqi@egr.msu.edu

Tien Duong, Technology Manager

U.S. Department of Energy
Phone: 202-586-7836
E-mail: Tien.Duong@ee.doe.gov

Start Date: June 1, 2013

End Date: March 31, 2017

Total Project Cost: \$1,318,947

DOE share: \$1,318,947

Non-DOE share: \$0

Project Introduction

The use of high capacity Si-based electrode has been hampered by its mechanical degradation due to the large volume expansion/contraction during cycling. Nanostructured Si can effectively avoid Si cracking/fracture. Unfortunately, the high surface to volume ratio in nanostructures leads to unacceptable amount of solid-electrolyte interphase (SEI) formation and growth, thereby low current/coulombic efficiency and short life. Based on mechanics models we demonstrate that the artificial SEI coating can be mechanically stable despite the volume change in Si, if the material properties, thickness of the SEI, and the size/shape of Si are optimized.

The real challenges to developing a model that allows us to design high current efficiency Si electrodes with electrochemically and mechanically stable artificial SEI layer are: a) poor understanding of SEI failure mechanisms; b) lack of accurate mechanical properties of the SEI; and c) difficulty in validation of the model. All of these are due to the extreme challenges associated with characterizing the properties of nano-meter thin SEI layer on lithiated Si in real battery systems. Therefore, we will first address these questions based on simpler thin film electrodes

Objectives

The use of high capacity Si-based electrode has been hampered by its mechanical degradation due to the large volume expansion/contraction during cycling. Nanostructured Si can effectively avoid Si cracking/fracture. Unfortunately, the high surface to volume ratio in nanostructures leads to unacceptable amount of solid-electrolyte interphase (SEI) formation and growth, thereby low current/coulombic efficiency and short life. Based on mechanics models we demonstrate that the artificial SEI coating can be mechanically stable despite the volume change in Si, if the material properties, thickness of the SEI, and the size/shape of Si are optimized. Therefore, the objective of this project is to develop an integrated modeling and experimental approach to understand, design, and make coated Si anode structures with high current efficiency and stability.

Approach

- Combine simulation with experiments to obtain critical material properties of SEI layer and lithiated Si, with in-situ electrochemical characterization capabilities developed at GM R&D Center.
- Develop a multi-scale model to establish correlation between coulombic efficiency and mechanical degradation of SEI on Si;
- Use the validated model to guide synergetic design of surface coating with Si size/geometry/architecture.

Results

Further explored Li diffusion through the SEI layer/intrinsic passivation layer (SiO_2) on Si

The mixed LiF/ SiO_2 Reactive MD simulations were performed to investigate the effect of composite coating on LiF. Previously, we have shown that Li diffuses very fast through the SiO_2 coating by lithiating it first (Figure II-209b) and LiF acts as a barrier for Li diffusion (Figure II-209d). For a SiO_2 -LiF mixed coating (50 Volume % for each phase), we noticed that Li diffusion through the composite coating is almost as slow as that in LiF coating. Lithiation of SiO_2 was observed, but few Li atoms were able to diffuse through. One possible reason is that lithiated SiO_2 in the composite coating was under large compressive stress, as the LiF phase prevented its volume expansion. Therefore lithium diffusion through the SiO_2 is hindered dramatically.

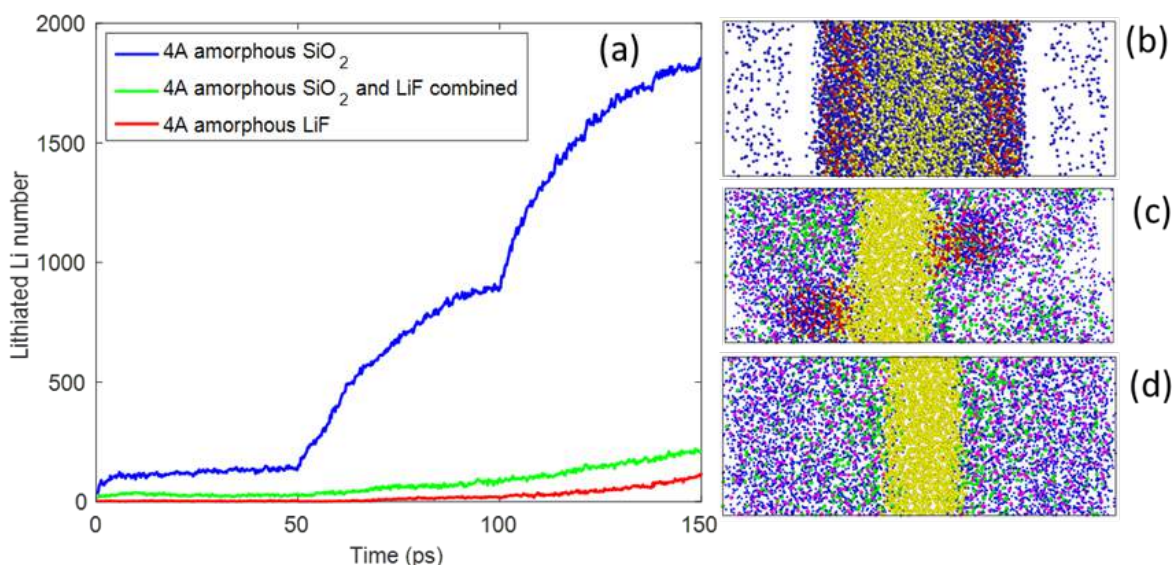


Figure II-209. (a) The number of Li atoms reached Si thin film after 150ps MD simulations and the corresponding structure of Si initially coated with (b) SiO_2 , (c) SiO_2 -LiF, and (d) LiF.

Further elaborated the failure mechanism of SEI layer on Si electrode

The comparisons between continuous Si thin films and patterned Si islands made it possible to measure the excess Li consumption due to the strain in the SEI. Figure II-210 schematically shows how SEI evolved with mechanical strain caused by Si volume changes during lithiation and delithiation process. The key direct observation from this study is that large in-plane strains in the SEI layer lead to substantial increases in the formation of inorganic Li-containing constituents, without significantly altering the overall SEI thickness. By combining in situ AFM observations with electrochemical lithium loss measurements, an irreversible capacity vs. strain map was obtained to correlate the extra capacity losses resulting from SEI break/repair effect at different SOC. More generally, the experimental approach in our work provides a useful tool for evaluating the relationships between capacity loss and mechanical deformation of the SEI. The correlation between irreversible capacity and strain will depend on several different properties in the SEI. Improved understanding

of these phenomena can provide important insight into designing improved SEI films that can minimize capacity losses.

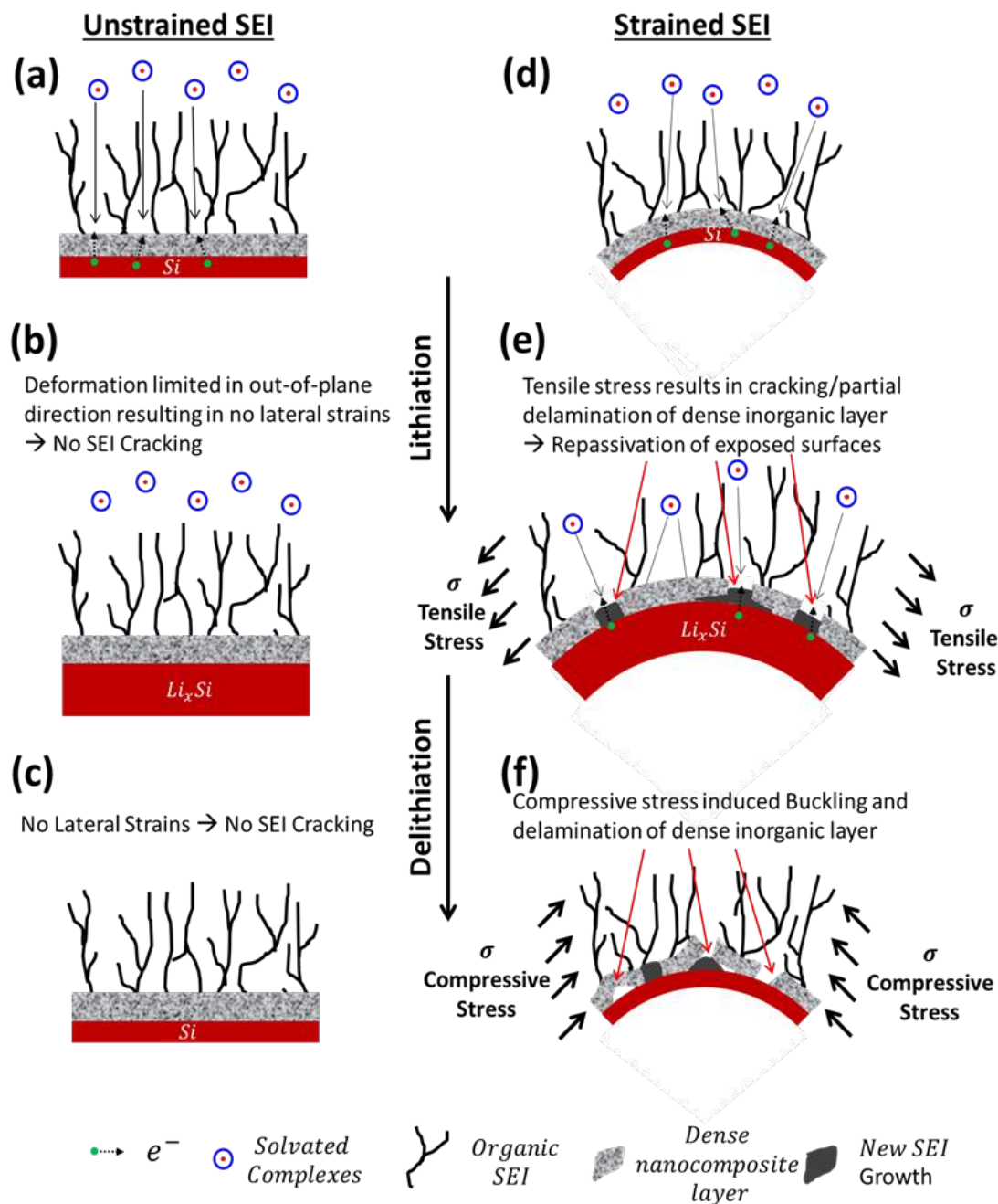


Figure II-210. Schematic representation of the SEI Evolution with (d, e, f) and without strain (a, b, c). In practical electrode geometries such as silicon particles, expansion (contraction) of the underlying Si stretches (compresses) the SEI layer and causes in-plane tensile (compressive) stress in the film.

Explored the mechanical integrity using in situ measurements of lithium-induced stresses in silicon nanoparticle-based composite electrodes

The effects of silicon nanoparticle loading and two different binders on the stress buildup in porous composite electrodes were investigated, as shown in Figure II-211. The in-situ stress evolutions in these electrodes were

measured by monitoring the changes in the curvature of an elastic substrate. The stress measurements of reference carbon black electrodes (CB/CMC: 80/20 wt%) show an approximately linear and reversible stress change which is consistent with an elastic response. However, the stress response of Si electrodes exhibit several stages during both lithiation and delithiation. For the 20 wt% Si-NP electrodes, compressive stress develops during lithiation which increases rapidly with capacity up to ~200 mAh/gSi, and then exhibits a clear transition (softening) after which it continuously increases at a slower rate. The maximum average composite stress at the full-lithiation reaches -35 to -50 MPa in these electrodes. In comparison, the 60wt% Si electrodes exhibit an additional hardening behavior towards later stages of lithiation which reflects the complex ways in which the particles interact with each other and the binder. At full lithiation, average in-plane nominal stresses in these electrodes range from -100 to -150 MPa. The stress measurements also indicate that the Na-Alginate leads to higher stresses than the CMC binder. This implies that the deformation of the entire composite electrode is directly impacted by the binder mechanical properties. The thickness changes measured using FIB cross-sections suggest that part of the volume expansions in these electrodes is accommodated by decreasing the porosity. Therefore, porosity plays a key role in suppressing the volume expansion and need to be optimized to get long-term performance. Simple cell models with periodic arrays of spherical core-shell particles (core: active particle, shell: binder) were constructed to visualize the structural changes in these electrodes. In absence of rigorous microstructural models, they provide an initial basis for understanding particle interactions and internal changes.

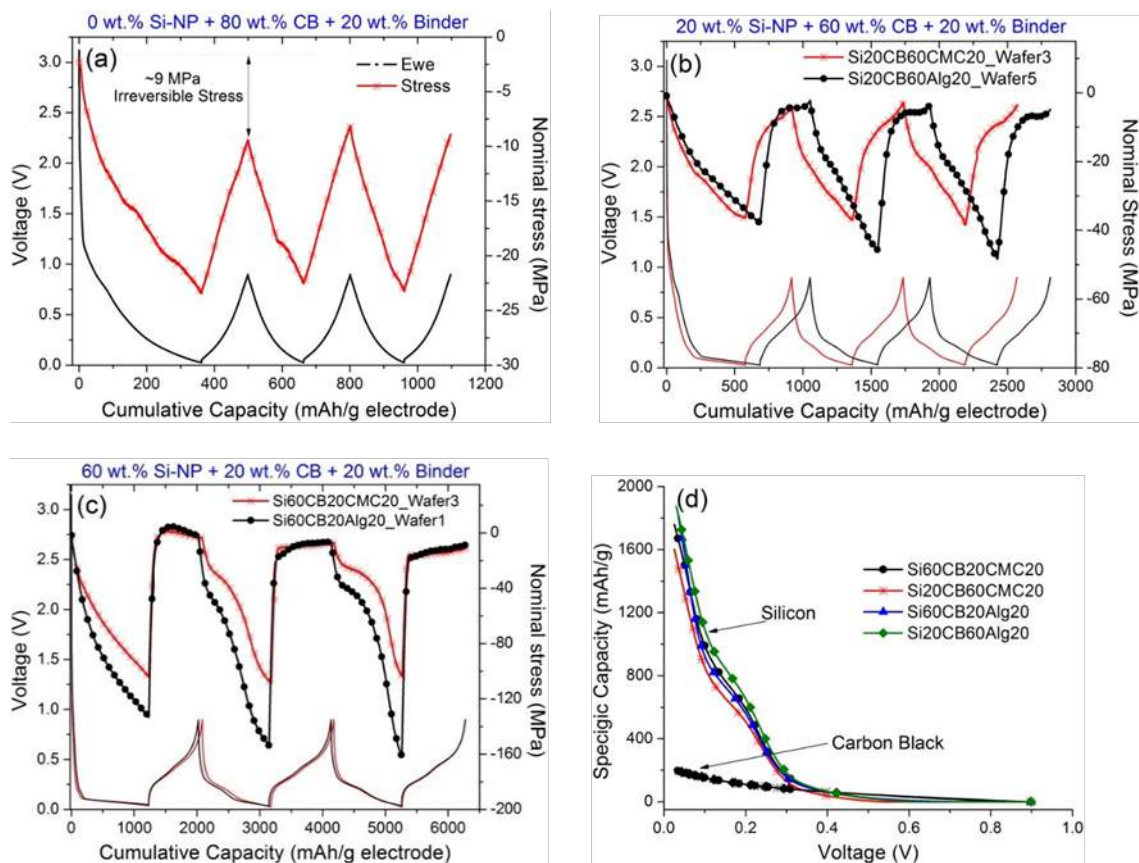


Figure II-211. Potential and nominal stress response of composite electrodes with a) 0wt% Si (CB/CMC: 80/20) b) 20 wt% Si (Si/CB/Binder: 20/60/20) and c) 60 wt% Si (Si/CB/Binder: 60/20/20). Si-containing electrodes were prepared with two different binders; Na-Alginate and CMC and their electrochemical and mechanical response are compared in panels b) and c). Specific capacity of silicon and carbon black particles in Si-containing electrodes during 2nd cycle lithiation d).

A new strategy has been developed to stabilize the SEI and Si-based electrode

By controlling the cycle potential window, we have demonstrated the excellent cycle performance of columnar Si film electrode paired with Li Ni_{0.6}Mn_{0.2}Co_{0.2}O₂ counter electrode. It has been demonstrated that the controlled potential window leads to half of the mechanical stress and it was retained at compressive state, when the Li-Si electrode is operated between 0.13 and 0.55 V versus a Li reference. The deformation of Si electrode is maintained at elastic region and no plastic flow is observed during cycling. (Figure II-212) The combining effects can mitigate the mechanical degradation therefore leading to significantly improved cycle life. The full cells have 90% capacity retention of the initial cell capacity even after 400 cycles, as shown in Figure II-213 left plot. Figure II-213 also shows the cross-section of Si film electrode after different cycles. Although the thickness has increased to 10 microns from 3 microns, the film still retains the mechanical integrity and good adhesion to current collectors. The constraint from the current collector leads to Si expansion along the thickness direction. The SEI has been observed along the boundary of the columnar structure, indicating Si has become porous which can effectively accommodate the volume expansion and reduce the stress. In addition, the thickness of Si film electrode does not show significant changes after first 10 cycles, which provides the very useful information for battery cell design.

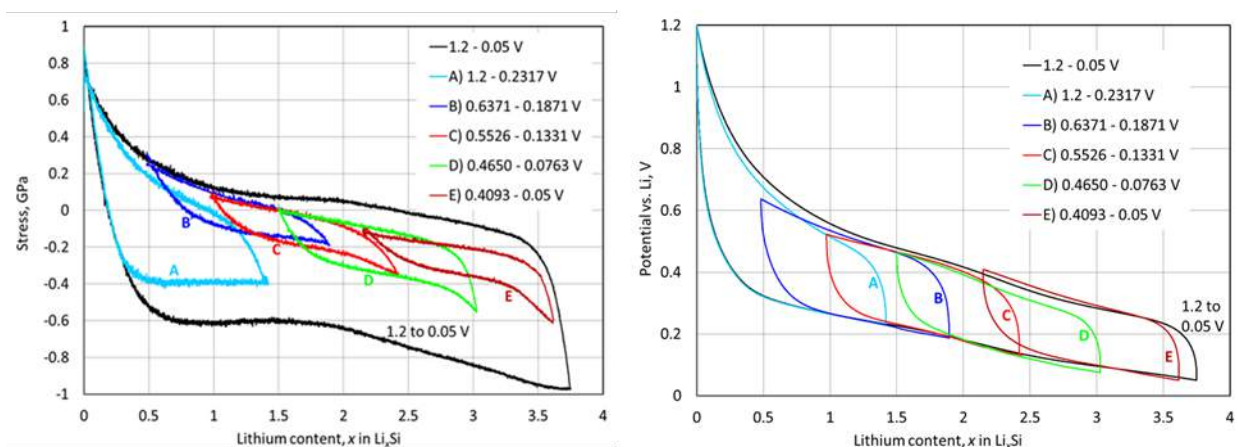


Figure II-212. Left plot: stress measured over the full potential range and for A through E.

Right plot: corresponding potential measurements

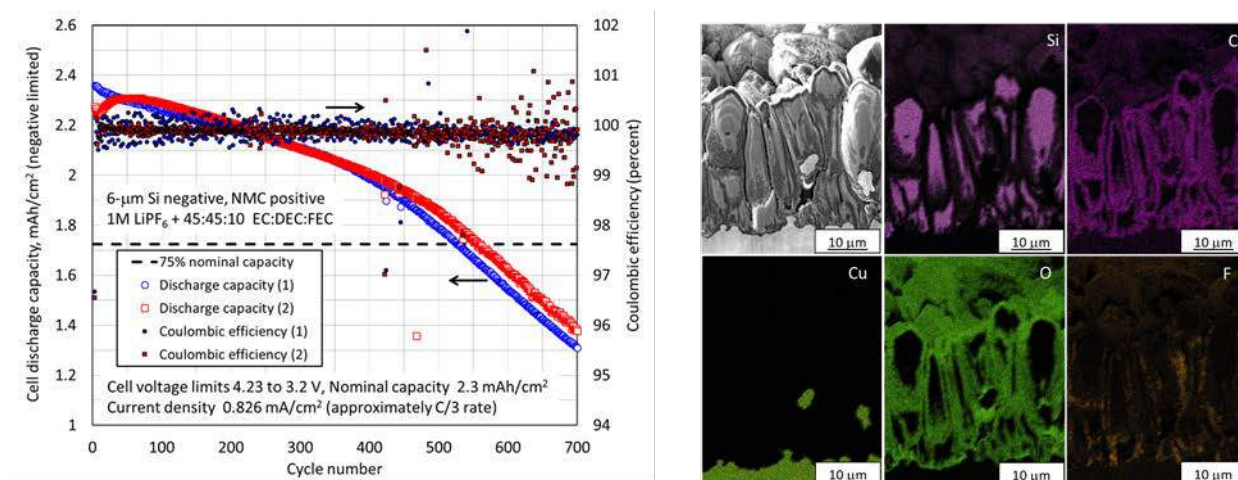


Figure II-213. Left plots: Full-cell (Si-NMC) discharge capacity and Coulombic (or current) efficiency versus cycle number. Results for two cells are plotted (denoted by 1 and 2). The current density and voltage limits are indicated. Upon reaching a voltage limit, the polarity of the current was immediately changed (i.e., no voltage holds). Right image: Secondary-electron micrograph (upper left) and elemental maps of the electrode cross-section for Si, C, Cu, O, and F after 395 cycles.

Conclusions

By using combined in-situ electrochemical experiments and modeling techniques, we were able to identify SEI failure modes. The in-plane strains in the SEI layer lead to substantial increases in the amount of inorganic phase formation, without significantly affecting the overall SEI thickness. Better understanding of these phenomena can provide important insight into designing desirable SEI films that can minimize capacity losses.

Tailoring the nanostructure and architecture to control stress/strain distribution in Si base active materials can sufficiently mitigate the mechanical degradation and stabilize SEI layer. With the optimized SEI formation protocols and electrolyte additives (FEC), high cycle efficiency was achieved (>99.8% with first cycle CE>94%)]

Key Publications

1. R Kumar, A Tokranov, BW Sheldon, X Xiao, Z Huang, C Li, T Mueller, In situ and operando investigations of failure mechanisms of the solid electrolyte interphase on silicon electrodes, *ACS Energy Letters* 1 (4), 2016, 689-697
2. M. Verbrugge, X. Xiao, Q. Zhang, M. Balogh, K. Raghunathan, D. Baker, Fabrication and Characterization of Lithium-Silicon Thick-Film Electrodes for High-Energy-Density Batteries *Journal of The Electrochemical Society* 164 (2), 2017, A156-A167
3. Q. Zhang, L. Han, J. Pan, Z. Chen, and Y. Cheng, Chemically stable artificial SEI for Li-ion battery electrodes, *Appl. Phys. Lett.* 110, 133901 (2017).
4. X. Su, K. Guo, T. Ma, P.A. Tamirisa, H. Ye, H. Gao, and B. W. Sheldon. Deformation and Chemomechanical Degradation at Solid Electrolyte–Electrode Interfaces. *ACS Energy Letters* 2 (2017): 1729–1733
5. K.J. Kim, J. Wortman, S. Y. Kim, Y. Qi, Atomistic Simulation Derived Insight on the Irreversible Structural Changes of Si Electrode during Fast and Slow Delithiation, *Nano Letters*. 2017, 17, 4330-4338
6. Y. Wang, Q. Zhang, D. Li, J. Hu, D. Dang, X. Xiao, and Y. Cheng, “Mechanical Property Evolution of Silicon Composite Electrodes Studied by Environmental Nanoindentation.” *Advanced Energy Materials*, DOI: 10.1002/aenm.201702578 (2017)
7. R. Kumar, J. Woo, X. Xiao, B.W. Sheldon, Internal Microstructural Changes and Stress Evolution in Silicon Nanoparticle Based Composite Electrodes Batteries and Energy Storage, *J. Electrochem. Soc.* 2017 164(14): A3750-A3765
8. F. M. Hassan, Q. Hu, J. Fu, R. Batmaz, J. Li, A. Yu, X. Xiao, and Z. Chen, Hot-Chemistry Structural Phase Transformation in Single-Crystal Chalcogenides for Long-Life Lithium Ion Batteries, *ACS Appl. Mater. Interfaces*, 2017, 9 (24), pp 20603–20612
9. X Li, P Yan, X Xiao, JH Woo, C Wang, J Liu, JG Zhang, Design of Porous Si/C-Graphite Electrodes with Long Cycle Stability and Controlled Swelling, *Energy & Environmental Science*, 2017, 10.1039/C7EE00838D

II.C Next-Gen Lithium-Ion: Advanced Cathodes R&D

II.C.1 Enabling High-Energy/Voltage Li-Ion Cells: Electrochemical Analysis and Evaluation (ANL, LBNL, NREL, ORNL)

Daniel P. Abraham, Principal Investigator

Argonne National Laboratory
9700 S. Cass Avenue
Lemont, IL 46039
Phone: 630-252-4332
E-mail: abraham@anl.gov

Peter Faguy, Technology Manager

U.S. Department of Energy
Phone: 202-586-1022
E-mail: Peter.Faguy@ee.doe.gov

Start Date: October 1, 2014
Total Project Cost: \$4,000,000

End Date: September 30, 2018
DOE share: \$4,000,000

Non-DOE share: \$0

Project Introduction

High energy density lithium-ion batteries are needed for transportation applications in order to increase the driving range of vehicles on a single charge. Towards this end, electrochemical cells containing near lithium-stoichiometric, manganese-bearing, nickel-rich layered oxides ($\text{Li}_{1+x}\text{Ni}_a\text{Mn}_b\text{Co}_c\text{O}_2$, x typically <0.05) and graphite-bearing negative electrodes are being cycled to higher voltages (> 4.35 V) as part of the Applied Battery Research (ABR) for Transportation program. Cell lifetimes are, however, affected by these voltages with performance degradation being greater at the higher voltages. The cell electrolyte, typically containing carbonate-based solvents, is a major contributor to this performance loss as it tends to oxidize at the higher voltages leading to the generation of deleterious species that degrade the positive electrode. Hence, the development of electrolyte systems and stable interfaces that mitigate this performance degradation is a priority. This project is intended to "enable" high-energy/high-voltage (HE/HV) cells via new insights and/or understanding, not currently available, of why present materials/systems fail. This chapter deals with electrochemical investigations focused on gaining such insights and understanding; more specifically, studies relating to electrolyte and surface stability including solvents, additives, and surface coatings are presented.

Objectives

The goals of this project are related to acquiring a deeper, fundamental understanding of the processes that influence the stability of NMC surfaces and the subsequent strategies, such as electrolyte formulations and surface coatings, which are aimed at stabilizing these surfaces under high-voltage operation, and are as follows:

- Identify additives, which when incorporated into the baseline electrolyte consisting of 1.2M LiPF₆ in EC:EMC (3:7 w/w), denoted as Gen2, reduces cell degradation
- Provide an understanding of electrolyte-additive mechanisms through experimental and computational techniques
- Investigate fluorinated electrolyte systems with decreased activity at charged cathode surfaces
- Investigate the efficacy of coated surfaces, using various coating methods, under long-term electrochemical cycling

- Report and publish the knowledge gained so as to accelerate the development of high-energy/high-voltage cells that are suitable for vehicular applications

Approach

The goals listed above will be pursued through the following experimental thrusts:

- Systematic study and evaluation of various *additive systems* to include:
 - Previously identified and new additive combinations
 - Electrochemical evaluation under standard project protocols
 - Development of Figure of merit (FOM) metrics for reliable evaluation of systems
 - Mechanistic determination of additive performance
- Investigation of *fluorinated electrolytes* and their electrochemical stability including:
 - Various electrolyte formulations
 - Measurements of oxidative stability
 - Characterization of cathode surface stability
- Electrochemical evaluation of *coated cathode surfaces* including:
 - NMC cathodes, modified with Al₂O₃-based coatings, using various wet-chemical processes
 - Al₂O₃-coated, NMC particles and electrodes using atomic layer deposition (ALD)

Results

Additive Systems

In this work, all experiments were conducted using electrodes from ANL's cell fabrication facility (CAMP) with cell assembly and testing following the standard HE/HV protocols (Long et al., JES **163**, A2999, 2017) in a voltage window of 3.0-4.4 V vs. graphite. The additives in this study were chosen to mitigate the known effects of Li⁺ trapping at graphite SEI layers or impedance growth arising at the cathode. Additives include 2,4,6-trivinylcyclotriboroxane (tVCBO), Prop-1-ene-1,3-sultone (PES), Phenyl boronic acid ethylene glycol ester (PBE), Li-bis(oxalato)borate (LiBOB), Vinylene carbonate (VC), Li-difluoro(oxalato)borate (LiDFOB), Tris(trimethylsilyl) phosphite (TMSPi) and Triethyl phosphite (TEPi). Additives are listed in Figure II-214b (right) according to their reported efficacy at either the anode or cathode.

To compare performance of the various additive compounds Figure of Merit (FOM) values were defined for cell Energy (relates to capacity) and Power (relates to impedance). These FOM values were based on cells containing the baseline (Gen2) electrolyte – for these cells the energy density decreases to 80% of its initial value (713 to 570 Wh/kg_{oxide}) after 170 cycles, and the power density decreases to 80% of its initial value (135 to 108 mW/cm²) after 23 cycles. For the additive-bearing cells, the Energy FOM (FOME) is the extrapolated cycle number at which the energy density decreases to 570 Wh/kg_{oxide} and the Power FOM (FOMP) is the extrapolated cycle number at which the power density decreases to 108 mW/cm²; note that the FOM values do not depend on the initial energy and power density values of the additive-bearing cells.

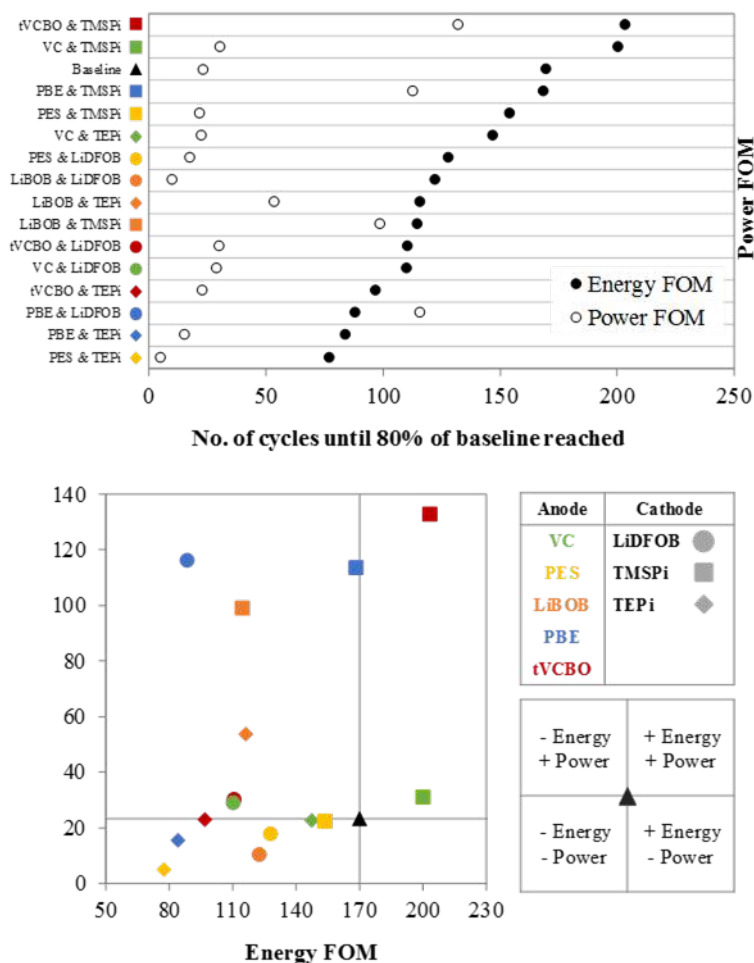


Figure II-214. (Top) FOME and corresponding FOMP values, in descending order, of tested additive combinations. (Bottom) Plot of FOMP vs. FOME for the additive systems tested.

Figure II-214 (left) shows the electrolytes in descending order of FOME and the corresponding FOMP. The plot indicates no obvious correlation and suggests that the mechanisms governing long-term energy performance are relatively independent from those that govern the long-term power performance of the cells.

Figure II-214 (right) shows a plot of FOMP vs. FOME. Here a direct comparison between the baseline system (located at the intersecting lines) and the additive systems can be made, where points in the top-right would indicate improved performance and point in the bottom-left degraded performance. An examination of the data shows that only cells with the 0.25% tVCBO + 1% TMSPi combination would have significantly better long-term energy *and* power retention than the baseline. The data in Figure II-214 represents a large amount of information and it is clear that the approach of combining standardized protocols and FOM values is a powerful approach. This methodology can be used to evaluate new electrolyte systems, optimize electrolyte formulations, and gain insights into the mechanisms of electrolyte behavior. Furthermore it has now been adopted to the study of cathode coatings.

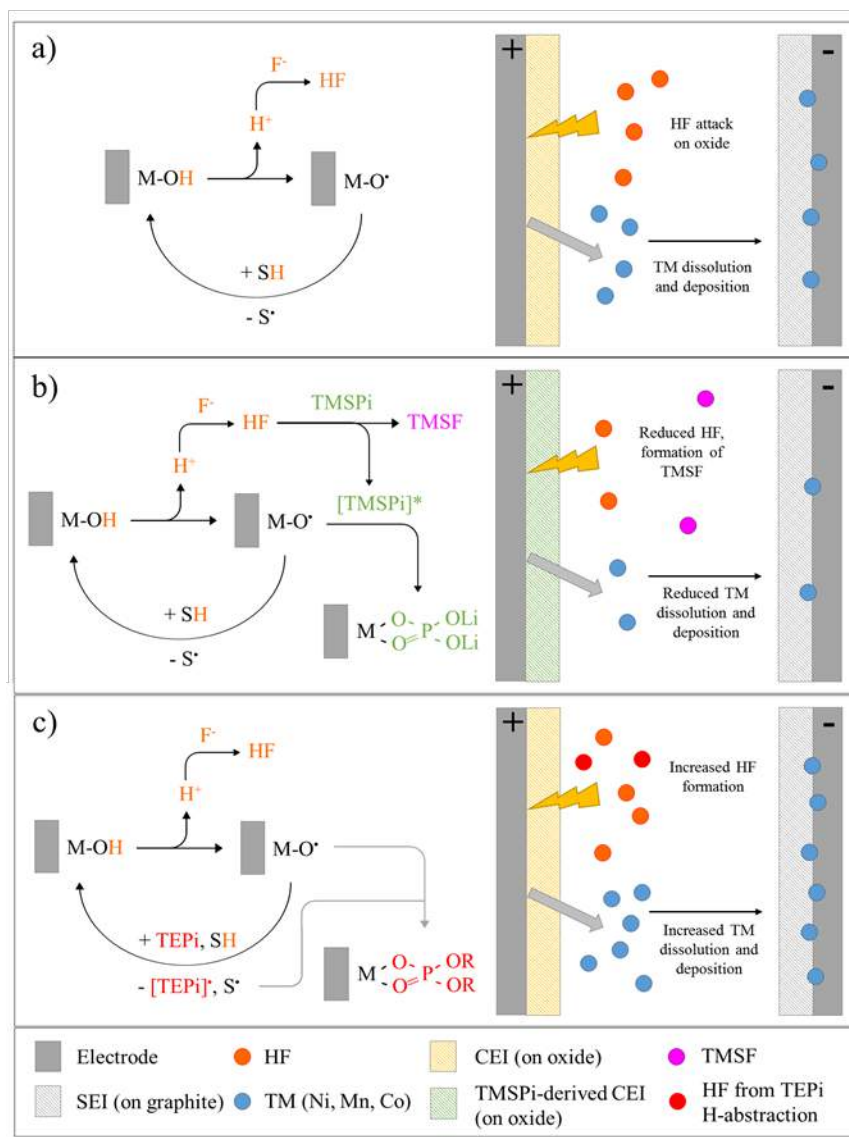


Figure II-215. Schematic depiction of the electrocatalytic cycle for the baseline electrolyte and the role of TMSPi and TEPI on the formation of oxide surface films and TM dissolution.

TMSPi has emerged as a useful electrolyte additive and the data in the FOM plots above indicate that this is an additive of interest. Therefore, TMSPi and the structurally analogous TEPI were further examined. Cycling data revealed lower capacity fade, lower impedance rise, and lower TM deposition on anodes for cells utilizing TMSPi compared to cells with TEPI. Furthermore, X-ray photoelectron spectroscopy (XPS) showed P- and O-rich surface films on the positive electrodes of TMSPi cells. These observations suggest that removal of TMS groups from the central P-O core of the TMSPi additive enables formation of a protective oxide surface film. In contrast, oxidation of the structurally analogous TEPI does not yield a protective positive electrode film, which results in inferior performance.

For baseline cells, the following degradation mechanism is proposed, shown in Figure II-215a. At higher voltages, reactive M-O• radicals abstract hydrogen atoms from solvent molecules generating solvent radicals and transient M-OH species. The abstracted hydrogen can react with fluorine species in the electrolyte to form corrosive acids (e.g., HF) that enhance TM dissolution from the oxide. These dissolved TMs can migrate and

deposit at the negative electrode and accelerate electrolyte reduction and Li^+ trapping in the SEI and, therefore, capacity fade.

For TMSPi, it is proposed that the reaction of the TMS groups with HF leads to the formation of trimethylsilyl fluoride (TMSF) and a phosphorus intermediate, [TMSPi*], Figure II-215b. In close proximity to the oxide surface the reactive M-O^* species form bonds with the central P atoms of the [TMSPi*], leading to a P- and O-rich surface film, as detected by XPS. For these bonds to form, the scission of at least one TMS group must occur; however, the removal of two or all of the TMS groups from the central P-O moiety, prior to surface film formation, is possible. Quenching of reactive M-O^* sites by the phosphorus-bearing film reduces hydrogen abstraction and in turn reduces formation of corrosive species. For TEPI, it is proposed that oxidation of TEPI occurs via hydrogen abstraction from the TEPI alkyl groups, initially generating more HF species compared to the baseline cell (Figure II-215c). Unlike TMSPi, TEPI does not initially form a surface film on the oxide electrode, allowing the M-O^* catalytic centers to continue oxidizing solvent molecules and generating corrosive acids. Thus, increasing TM deposition at the negative electrode and accelerating capacity fade.

Fluorinated Electrolytes

The use of conventional organic carbonate electrolytes results in instabilities at the cathode/electrolyte interface that contribute to a loss of capacity and a rise in interfacial impedance. One strategy to address these instabilities is through new solvent designs that are more intrinsically stable at charged cathode surfaces. This project has developed a fluorinated, carbonate-based electrolyte and evaluated its electrochemical performance at high voltages in NMC-532//graphite cells (Gr). Preliminary results indicated potential benefits, especially at the cathode/electrolyte interface, relative to the baseline electrolyte (Gen2). However, details of the observed electrochemical properties are not well understood. This work aims to gain insights into the working mechanisms of fluorinated electrolytes when used in NMC//Gr systems cycled to high voltages (≥ 4.4 V).

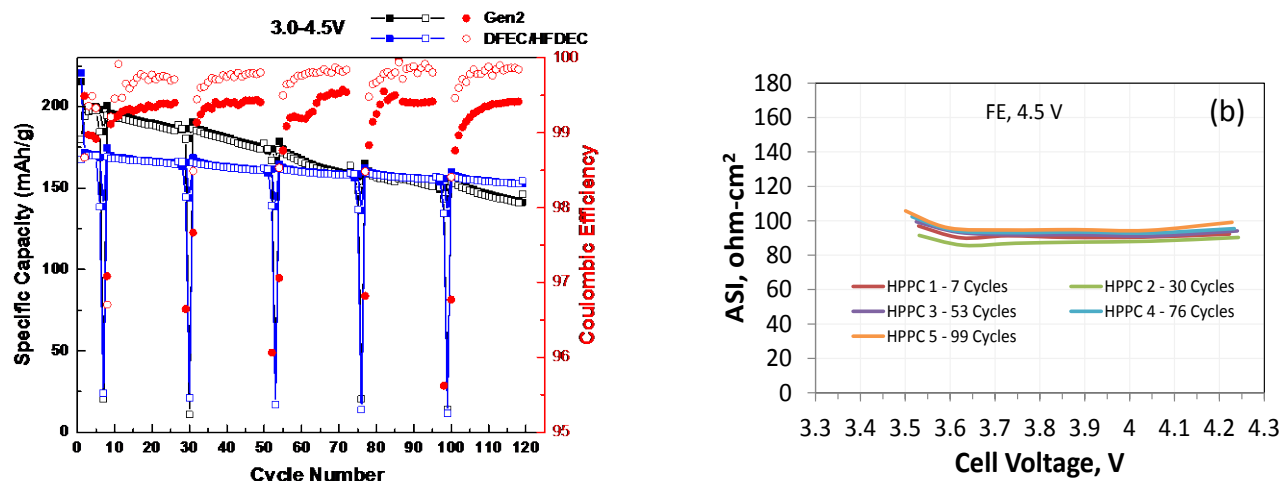


Figure II-216. a) Capacity and coulombic efficiency of NMC-532//Gr cells containing Gen2 and DFEC/HFDEC electrolytes cycled using a 4.5 V upper cutoff. b) ASI as a function of HPPC cycle for the DFEC/HFDEC cell shown in (a).

The fluorinated electrolyte developed in this project maintains the same 3:7 solvent ratio of cyclic carbonate to linear carbonate as the Gen2 formulation. However, EC is substituted with a difluoro cyclic carbonate, 4,5-difluoro ethylene carbonate (DFEC) and the EMC with a hexafluorinated diethyl carbonate, bis (2,2,2-trifluoroethyl) carbonate (HFDEC). The fluorinated formulation has a LiPF_6 concentration of 1.0 M and is abbreviated herein as DFEC/HFDEC. Figure II-216a shows capacity vs. cycle number and coulombic efficiency (right axis) for NMC-532//Gr cells containing the Gen2 electrolyte and DFEC/HFDEC electrolyte. The area specific impedance (ASI), as a function of hybrid pulse power characterization (HPPC) cycles, shown as low points in the cycling data of Figure II-216a, is presented in Figure II-216b. Three points of interest are observed. 1) DFEC/HFDEC results in the same first-cycle charge capacity as Gen2 but with lower first-cycle

efficiency, leading to lower initial cycling capacity; 2) the coulombic efficiency for the DFEC/HFDEC cell is significantly higher than the baseline Gen2 cell; 3) the ASI for the DFEC/HFDEC cell is initially higher than the Gen2 cell ($\sim 25 \Omega \cdot \text{cm}^2$ for Gen2, not shown) but does not increase with cycling. Interestingly, Gen2 cells eventually (~ 75 cycles) show ASI values higher than those of the DFEC/HFDEC cell shown in Figure II-216b.

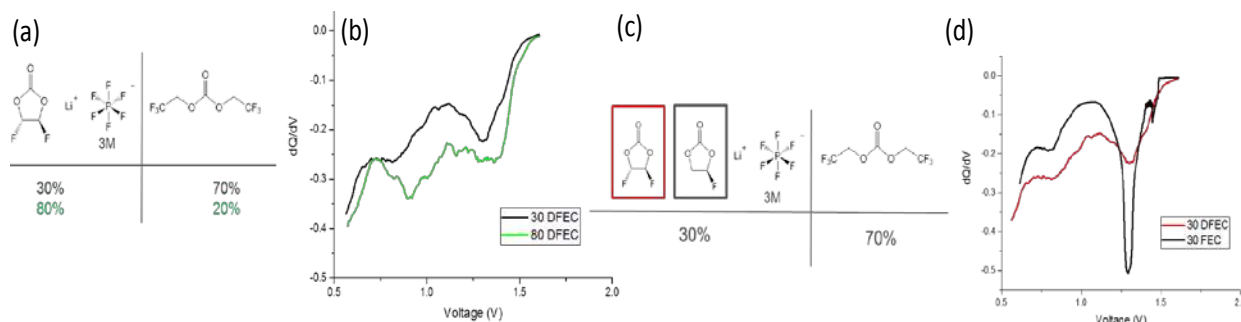


Figure II-217. a) and c) DFEC/HFDEC compositions (%). b) and d) corresponding dQ/dV profiles for each of the fluorinated compositions in Gr//Li cells on the first-cycle lithiation of graphite.

Figure II-217a and Figure II-217b show electrolyte compositions and dQ/dV profiles, respectively, for the first lithiation process of Gr//Li cells. Cells with 80% DFEC (20% HFDEC) showed significantly larger dQ/dV peaks at nearly all potentials relative to cells with 30% DFEC (70% HFDEC). These peaks are all at higher potentials than the dominant electrochemical activity of graphite, and thus are attributed to electrolyte reduction. Figure II-217c and Figure II-217d show that when 30% FEC is substituted for DFEC, there is substantially less reduction occurring below ~ 1.3 V. These data reveal that reduction of the DFEC component in the DFEC/HFDEC electrolyte is a major contributor to the initial capacity loss and poor first-cycle efficiency observed in Figure II-216a. Several tests were also conducted to understand the origin of the high ASI values observed in Figure II-216b.

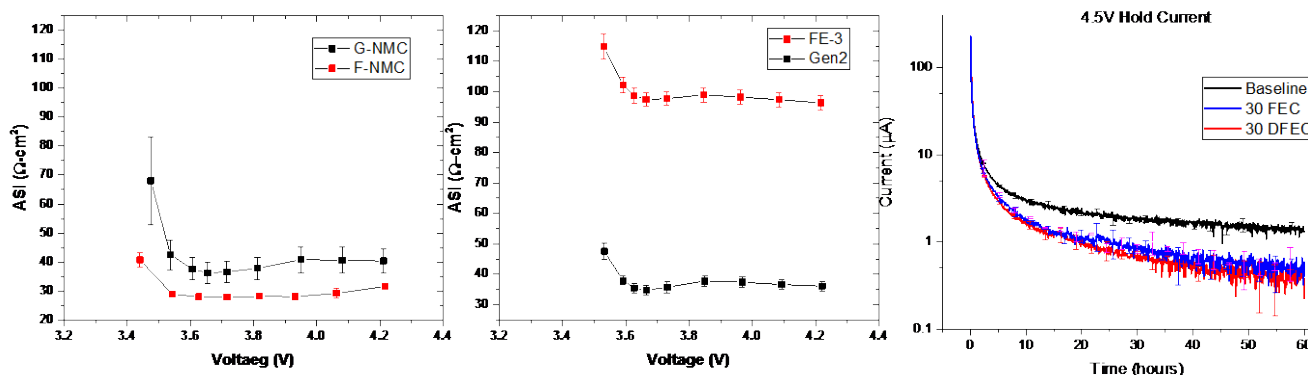


Figure II-218. a) and b) ASI values for various cell configurations as described in the text. c) Oxidation current vs. time at 4.5 V for NMC-532//Gr cells containing DFEC/HFDEC, FEC/HFDEC, and Gen2.

Figure II-218a shows ASI values for two cells containing Gen2 electrolyte as well as graphite anodes that had been previously formed using Gen2. However, the cathodes (NMC-532) of these cells were previously formed with either Gen2 (black curve) or DFEC/HFEC (red curve) electrolytes. The small impedance difference between these two conditions indicates that forming the cathode with the fluorinated electrolyte is not the source of the high impedance observed in Figure II-216b. Figure II-218b shows the ASI for two cells that both contain graphite anodes previously formed with DFEC/HFDEC electrolyte, and paired with pristine NMC-532 cathodes in cells containing either Gen2 (black curve) or DFEC/HFDEC (red curve) electrolytes. The large impedance change between these two cells, along with the data in 5a, shows that the formation environment of the graphite anode (or NMC cathode) is not the dominant contributor to high impedance. Clearly, the identity of the electrolyte itself is a major factor in determining the ASI observed in Figure II-216b. Finally,

Figure II-218c shows a plot of oxidation current vs. time (at 4.5 V) for NMC-532//Gr cells containing DFEC/HFDEC, FEC/HFDEC, and Gen2. Clearly, the fluorinated compositions lead to less oxidation current and thus greater stability at high voltages than the Gen2 baseline. These data taken together show that fluorinated electrolytes, and particularly the FEC/HFDEC composition, are of interest for high-voltage applications. Work is ongoing to better understand the nature of SEIs formed on graphite anodes using these, and other, fluorinated compositions.

Coated NMC Cathodes

Cathode coatings, particularly Al_2O_3 , are often reported as beneficial to high-voltage operation. However, a wide variety of results can be obtained from the literature. This project is aimed at systematic studies of coatings in order to gauge their efficacy in enabling high-voltage performance. The systems tested included various NMCs coated by ALD (particles and electrodes) as well as wet-chemical methods (discussed elsewhere). Figure II-219 (top) and Figure II-219 (bottom) show summary data from a detailed study, conducted by Argonne's Cell Analysis, Modeling and Prototyping (CAMP) facility in collaboration with Forge Nano (Louisville, Co). Forge Nano delivered three coating levels of Al_2O_3 on NMC-532 powders to CAMP for electrode fabrication and testing. Sample A being the thinnest (2 ALD cycles) coating followed by samples B (4 cycles) and C (8 cycles). The table in Figure II-219 (top) shows cell formation and rate data of duplicate sets of full cell coin-cells.

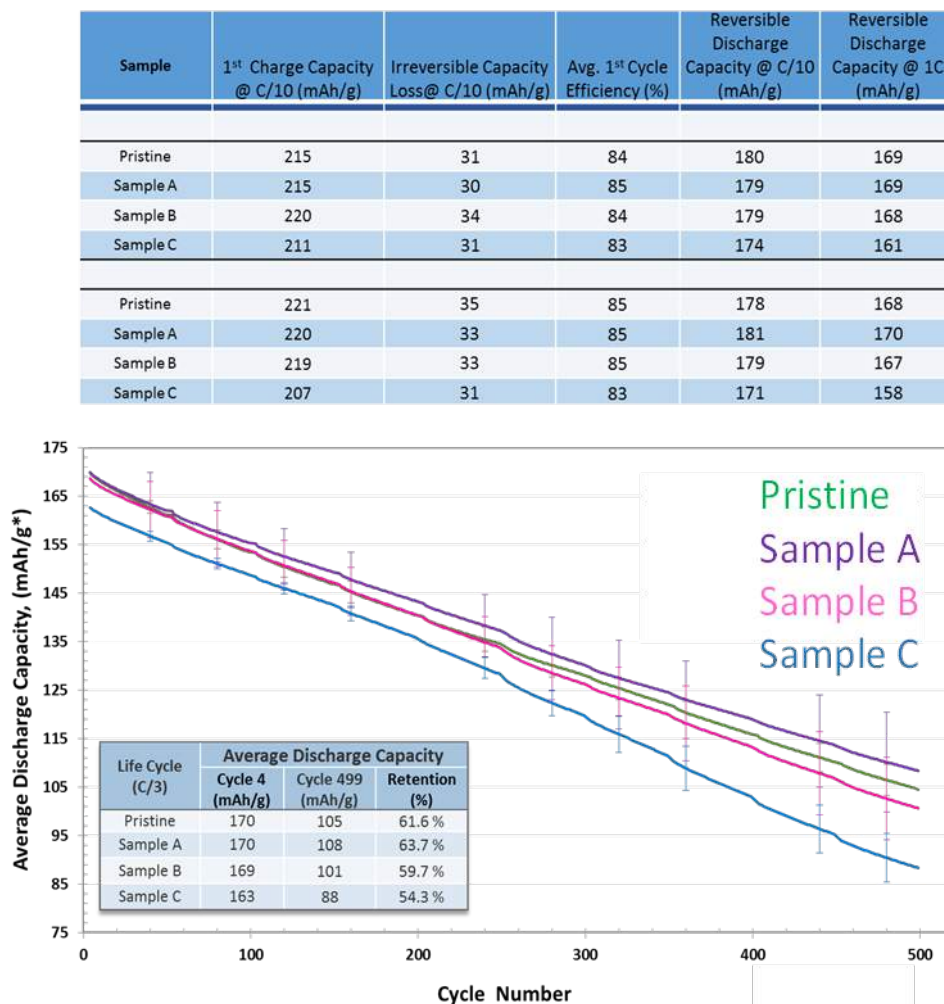


Figure II-219. (top) Cell formation and rate data for duplicate sets of coated NMC-532//Gr. (bottom) Cycle life plot of Set 1 data between 4.4-3.0 V, C/3 charge and discharge, 30 °C.

Cells consisted of the coated cathodes, graphite anodes, and Gen2 electrolytes. All cells underwent formation, rate studies, HPPC, and cycle life testing. Figure II-219b shows cycle life testing of samples A, B, and C between 4.4-3.0 V at a C/3 charge and discharge rate. The main conclusions of this more detailed study can be arrived at from the data in Figure II-219. Specifically, ALD- Al_2O_3 coatings on NMC-532 did not significantly improve performance over the uncoated baseline under any of the conditions tested. A negative trend in performance was found with increasing ALD cycles (coating thickness). Preliminary data of ALD- Al_2O_3 coatings on electrode laminates, conducted at NREL, present similar conclusions with a possible NMC composition dependence for these coatings. For example, Figure II-220 shows NMC-532, 622, and 811 electrodes coated via ALD with Al_2O_3 . No clear trend is observed for NMC-532 or 811, however, the NMC-622 data may indicate a net positive benefit. Future studies will focus on the effects of cathode composition on ALD coatings.

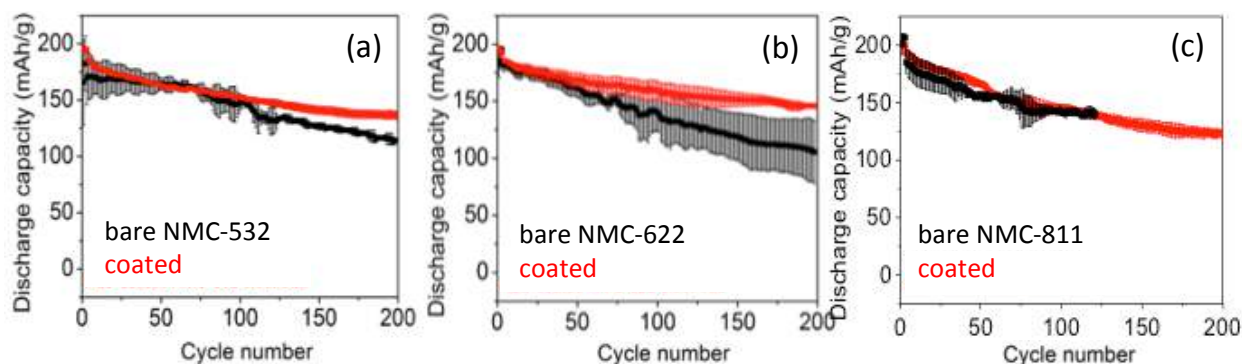


Figure II-220. Al_2O_3 -coated NMC electrodes vs. graphite (a) NMC-532, (b) 622, and (c) 811. 3.0-4.5 V, 1C charge/discharge.

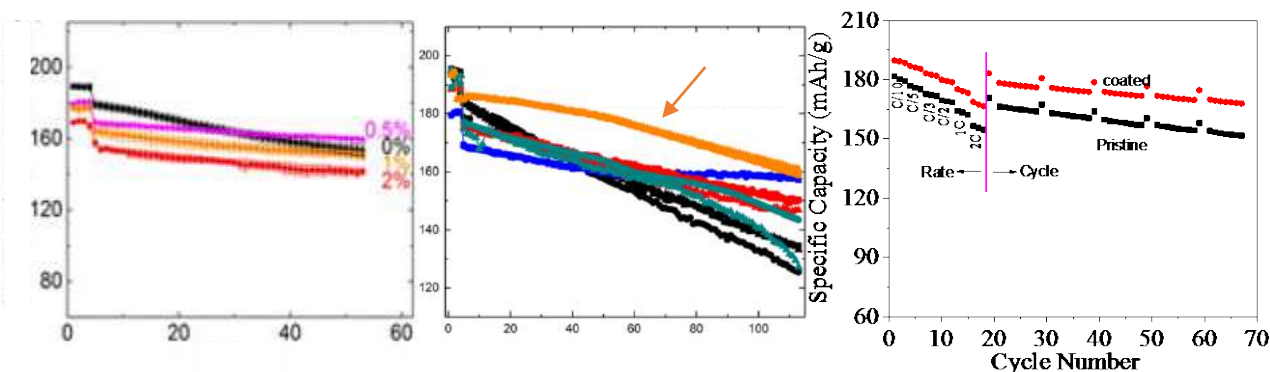


Figure II-221. NMC-532 powders wet-coated with Al_2O_3 by various wet-chemical methods as a function of (a) wt.% Al_2O_3 , (b) Al salt/solvent system, and (c) 0.5 wt.% Al_2O_3 via a wet impregnation method.

Figure II-221a-c show wet-chemical coatings of Al_2O_3 on NMC-532 cathodes. In general, it can be observed that 1) thinner coatings lead to better performance; 2) the precursor/solvent system plays a role where Figure II-221b shows that 0.2 wt. % Al_2O_3 , coated on NMC-532 by way of Al-isopropoxide in methanol, outperforms the uncoated material; 3) The wet impregnation method leads to greatly reduced initial impedance (not shown) and, subsequently, higher cycling capacities as a function of rate.

Conclusions

- Protocols and Figure of merit values have been developed that allow for reliable comparisons of electrolyte formulations and insights into the mechanisms of their success or failure
- Fluorinated electrolytes have been developed that show increased stability at charged cathode surfaces and unique SEI films with enabling properties at graphite anodes
- Al_2O_3 coatings on NMC cathodes have been studied in great detail and, while findings thus far do not substantially support the idea that this particular material can enable long-term, high-voltage stability in NMC//Gr systems, certain synthesis conditions/methodologies show more promise than others
- Future studies will focus on select methodologies and their ability to promote stable surfaces in NMC//Gr systems at higher voltages.

Chapter Acknowledgments Daniel P. Abraham, John Zhang, Adam Tornheim, Meinan He, James A. Gilbert, Cameron Peebles, Ira Bloom, Ritu Sahore, Juan Garcia, Javier Bareño, Hakim Iddir, Chen Liao, Katherine Hurst, Robert Tenent, Chunmei Ban, Xuemin Li, Yongan Yang, Iyla A. Shkrob, Kaushik Kalaga, Stephen E. Trask, Bryant J. Polzin, Andrew N. Jansen, Alison Dunlop, Jack Vaughey, Binghong Han, Fulya Dogan, Wenquan Lu, Xin Su, Xiaoping Wang

Key Publications

1. J.A. Gilbert, J. Bareño, T. Spila, S.E. Trask, D.J. Miller, B.J. Polzin, A.N. Jansen, D.P. Abraham, *J. Electrochem. Soc.* **164**, A6054 (2017).
2. A. Tornheim, C. Peebles, J.A. Gilbert, R. Sahore, J.C. Garcia, J. Bareño, H. Iddir, C. Liao, D.P. Abraham, *Journal of Power Sources* **365**, 201 (2017).
3. R. Sahore, C. Peebles, D.P. Abraham, J. Gilbert, I. Bloom, *Additive Effects in High-Voltage Layered-Oxide Cells: A Statistics of Mixtures Approach*, *Journal of Power Sources*, *accepted* (2017).
4. C. Peebles, R. Sahore, J.A. Gilbert, J.C. Garcia, A. Tornheim, J. Bareño, H. Iddir, C. Liao, D.P. Abraham, *J. Electrochem. Soc.* **164**, A1579 (2017).
5. I.A. Shkrob and D.P. Abraham, *J. Phys. Chem. C* **120**, 15119 (2016).
6. R. Sahore, A. Tornheim, C. Peebles, J. Garcia, F. Dogan, D. C. O'Hanlon, C. Liao, H. Iddir, Z. Zhang, J. Bareño, I. Bloom, *Methodology for understanding interactions between electrolyte additives and cathodes: a case of tris(2,2,2-trifluoroethyl) phosphite additive*, (*submitted*, *J. Mat. Chem. A*, 2017).

II.C.2 Enabling High-Energy/Voltage Li-Ion Cells: Materials and Characterization (ANL, LBNL, NREL, ORNL)

John Vaughey, Principal Investigator

Argonne National Laboratory
9700 S. Cass Avenue
Lemont, IL 46039
Phone: 630-252-8885
E-mail: vaughey@anl.gov

Guoying Chen, Principal Investigator

Lawrence Berkeley National Laboratory
1 Cyclotron Road
Berkeley, CA 94720
Phone: 510-486-5843
E-mail: gchen@lbl.gov

Peter Faguy, Technology Manager

U.S. Department of Energy
Phone: 202-586-1022
E-mail: Peter.Faguy@ee.doe.gov

Start Date: October 1, 2014
Total Project Cost: \$4,000,000

End Date: September 30, 2018
DOE share: \$4,000,000

Non-DOE share: \$0

Project Introduction

The inability to charge commercially available $\text{Li}_{1+x}\text{Ni}_a\text{Mn}_b\text{Co}_c\text{O}_2$ (NMC-abc, where x is typically <0.05), cathode materials beyond ~4.3 V (vs. graphite) without incurring excessive surface damage, electrolyte decomposition, structural instabilities, gassing, and loss of lithium inventory is a significant challenge in meeting next-generation energy storage targets. This project aims to understand the underlying failure mechanisms associated with these issues that prevent state-of-the-art Li-ion battery systems from achieving higher practical energy densities than are currently obtainable. To do so, several research thrusts have been established across the overall project including cathodes, electrolytes and additives, surfaces and interfaces, testing and analysis, modeling, and cell fabrication. In addition to these areas of focus, cross-cutting collaborations are targeted at obtaining information on the failure mechanisms of NMC/graphite (Gr) cells that affect systems-level performance when cycled at high voltages. This project is intended to "enable" high-energy cells via new insights and/or understanding, not currently available, of why present materials/systems fail. This chapter deals with the materials and characterization component of the project; more specifically, detailed studies of the structure and behavior of NMC surfaces, and their interactions with materials applied as surface stabilizers, as a function of synthesis are presented.

Objectives

The goals of this project are related to acquiring a deeper, fundamental understanding of the processes that influence the stability of NMC surfaces and identify strategies, such as coatings, aimed at stabilizing these surfaces under high-voltage operation, and are as follows:

- Understand the complex relationships between NMC particle morphology and the associated, facet-dependent electrochemical properties

- Design, synthesis, and characterization of model systems that are directly compatible with experimental and theoretical approaches to allow for unique, atomic-scale insights into the reactivity of NMC surfaces
- Develop surface-sensitive, structural characterization tools that allow better correlations to be made between the morphology and composition of pristine and coated, Ni-rich cathodes, and their associated electrochemical properties
- Understand the effects of surface coatings on cathode interfaces and bulk structures as a function coating methodology (technique, annealing temperature, and coating content) and cathode composition
- Understand the effects of cathode composition on surface segregation, coating efficiency, and electrochemical performance of Ni-rich cathodes

Approach

The goals listed above will be pursued through the following experimental thrusts:

- Synthesis of *model systems* that allow for detailed experimental and theoretical characterization of NMC surfaces including:
 - Single-crystal, NMC particles with well-defined compositions, sizes, and morphologies
 - Surface-modified particles
 - Thin-film, NMC cathodes
- Systematic studies of *coated NMC particles* using Al_2O_3 as a baseline, to include:
 - NMC composition (442, 532, 622, 811, NCA, and LCO)
 - Characterization and effect of initial surface-Li content and Li leaching
 - Aqueous vs. non-aqueous solvents coupled with various Al precursors with oxidizing and non-oxidizing associated anions
 - Post-synthesis annealing temperature and diffusion/solubility of Al, LiAl_2O_3 , and Al_2O_3
 - Structure and morphology of coatings as a function of the above variables
 - Wet-chemical methods compared to atomic layer deposition (ALD)
 - Physical and electrochemical characterization

Results

Synthesis of Model Systems

In this work, a modified molten-salt synthesis approach is used to fabricate layered, NMC single-crystal samples with well-defined particle morphologies, sizes, and compositions. In a typical synthesis procedure, stoichiometric amounts of transition-metal (TM) precursors, $\text{Mn}(\text{NO}_3)_2 \cdot 4\text{H}_2\text{O}$, $\text{Co}(\text{NO}_3)_2 \cdot 6\text{H}_2\text{O}$ and $\text{Ni}(\text{NO}_3)_2 \cdot 6\text{H}_2\text{O}$, are dissolved in a small amount of de-ionized water. A lithium source, LiNO_3 , Li_2CO_3 , or $\text{LiOH} \cdot \text{H}_2\text{O}$ is added to the solution followed by the addition of a flux, typically KCl (m.p. = 771°C) or CsCl (m.p. = 645°C). The mixture is then transferred into an alumina crucible, covered with a lid, and trace amount of residual water is removed by gentle heating at 200°C . The resulting dry powder is further heated at a controlled rate to an elevated temperature, typically 850°C or 900°C , and then soaked at the high temperature for 8-12 hours before cooling to room temperature. The final product is thoroughly washed with de-ionized water to remove the flux and dried in a vacuum oven overnight. Choice of precursors, flux, ratio between precursor and

flux, soaking time, and temperature can be adjusted to influence the uniformity and physical characteristics of the synthesized crystals.

Previously, crystal samples with varying TM ratios, including NMC-333, NMC-532, NMC-622, and NMC-811, were synthesized using the above procedures as shown in the SEM of Figure II-222. Importantly, these data were used to corroborate density functional theory (DFT) calculation carried out by Iddir et al., showing that, energetically, (012) surfaces dominate under highly oxidizing synthesis environments (see also II.A.3.iv). The (001) surface appears in all samples in a nearly constant fraction, while the coverage of (104) planes increases as the degree of crystal truncation increases, Figure II-222f. Furthermore, as shown in Figure II-223, these crystals can be fabricated into composite electrodes and cycled in electrochemical cells. These results support and verify the strategy of using “practical”, model systems that can be directly understood by experiment, advanced characterization, and theory.

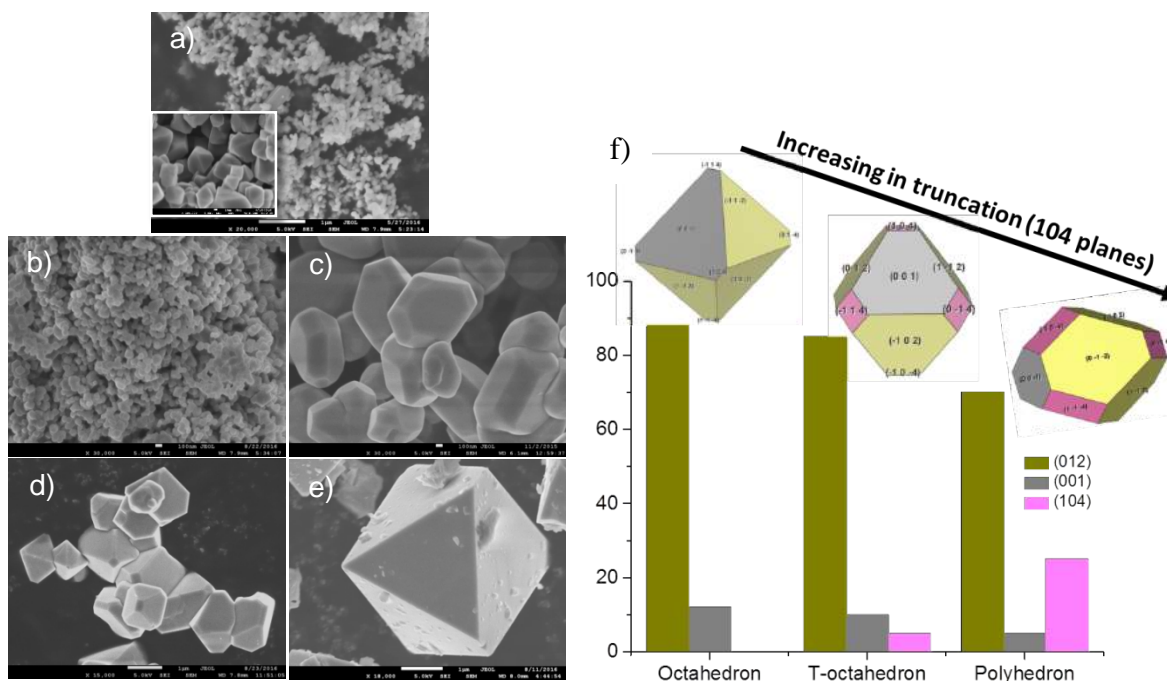


Figure II-222. NMC-532 crystal samples with varying particle sizes and morphologies: a) 50 nm, b) 100 nm, c) 1 μm, d) 1 μm, e) 10 μm and f) summary of surface facets and their fraction on NMC-532 crystals.

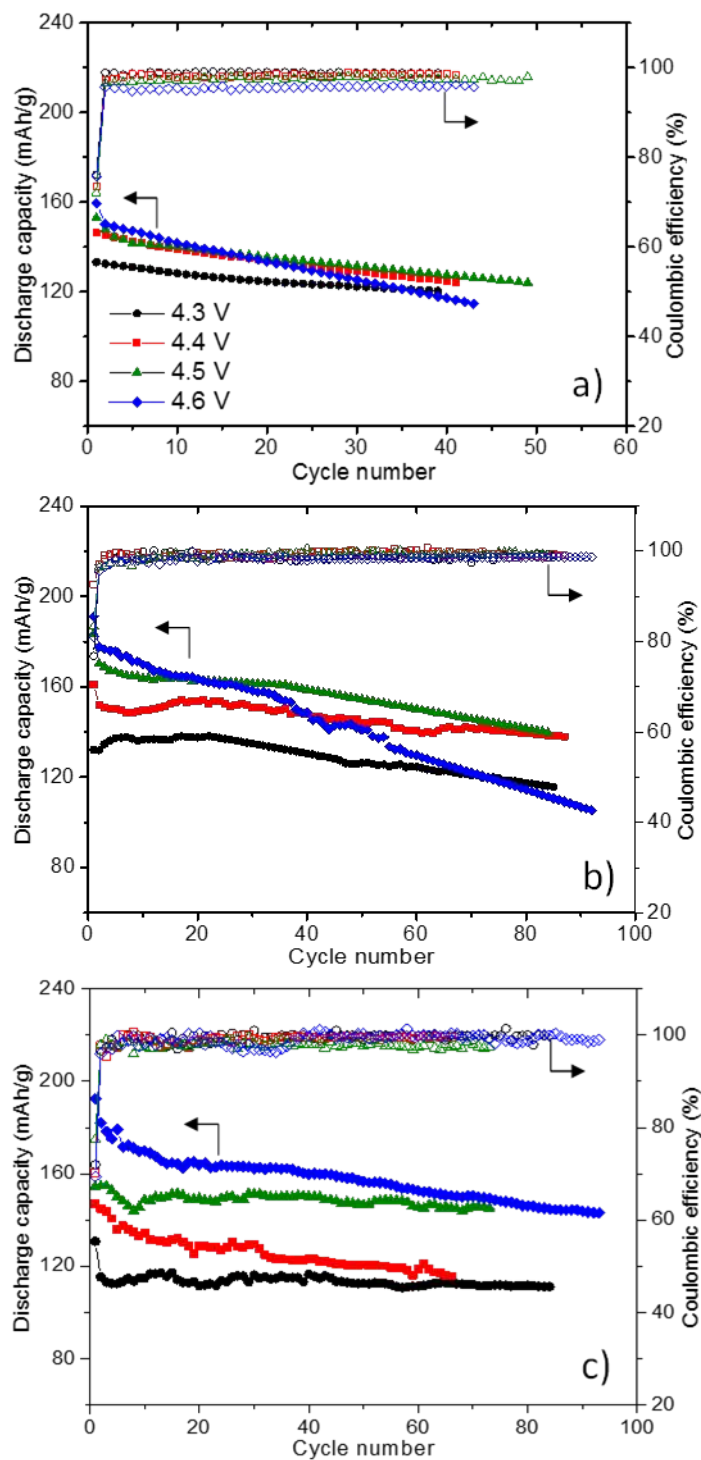


Figure II-223. Half-cell cycling stability comparison of NMC crystal cathodes: a) NMC-333 in 100 nm size, b) NMC-532 in 100 nm size and c) NMC-532 in 10 μm size.

Low-temperature (LT) synthesis routes ($\sim 500^\circ\text{C}$) were also explored, as part of a Go/No-Go milestone, in order to obtain other particle morphologies. Figure II-224a and Figure II-224b show SEM images of NMC-333 crystals synthesized through a LT route. Hexagonal nano-platelets, with an average particle size of 200-300 nm and a thickness of ~ 70 -80 nm, were obtained and this particle morphology was found to be insensitive to NMC

composition. XRD data shows that the crystals adopted a phase-pure, layered structure. As such, a Go decision was made on pursuing these LT synthesis routes. High-resolution TEM (HRTEM) studies are underway to better understand the atomic-scale properties of these particles.

Spectroscopic characterization was performed on various NMC crystals to investigate the effect of Ni content on pristine surface properties. Figure II-224c and Figure II-224d show the soft X-ray absorption (XAS) data collected on NMC crystals with compositions of NMC-333, 532, 622, 811. All crystals had the same particle size of 1 μm and the same particle shape of truncated-octahedron (Figure II-222d), which is predominately enclosed by the (012) family of surface facets. The spectra were collected in either total electron yield (TEY) mode, which probes a depth of ~ 5 nm (e.g., surface), or fluorescent yield (FY) mode, which has a probing depth of ~ 50 nm (e.g., bulk). No obvious differences were observed in the oxidation states of Mn or Co (not shown), suggesting minimal impact of Ni concentration on similar surface planes. Ni oxidation state was found to increase along with the increase of Ni content, evidenced by the increasing intensity ratio of Ni L_3 high/low peaks between 852-858 eV (Figure II-224c). A comparison with the bulk Ni oxidation state, collected in FY mode (Figure II-224d), shows that surface Ni is more reduced than the bulk in all NMC crystal samples. The particles presented above, and variations thereof, will be used to investigate the atomic-scale, facet-dependent, electrochemical properties of NMC surfaces and inform further theoretical studies.

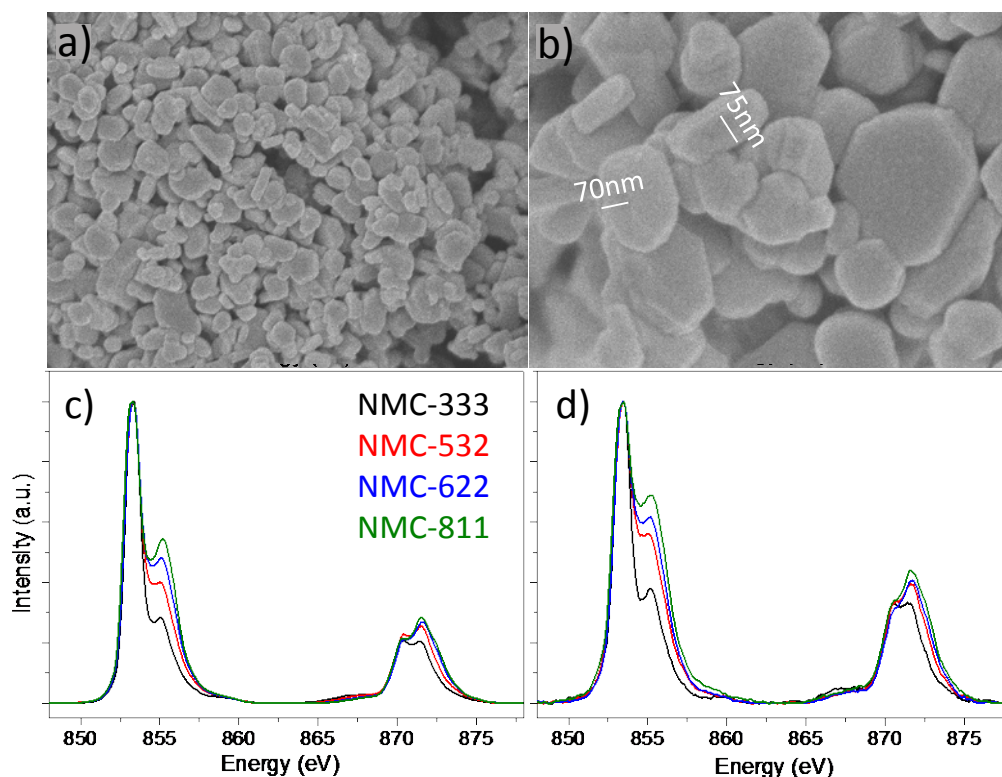


Figure II-224. a, b) SEM images of NMC-333 synthesized from a LT-synthesis route. c) TEY Ni L -edge and d) FY Ni L -edge XAS profiles.

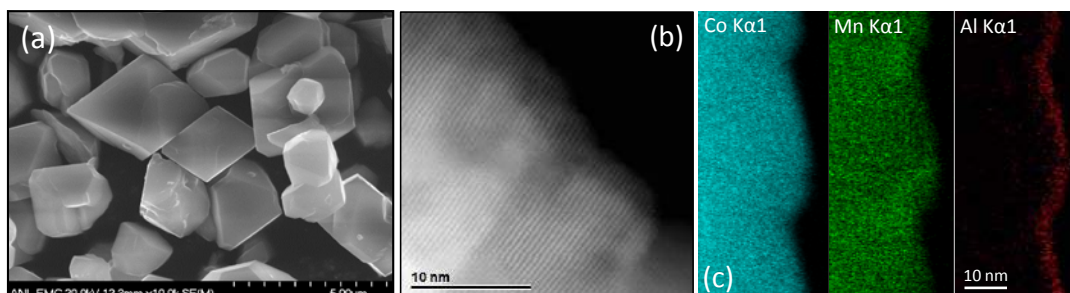


Figure II-225. a) SEM image of $\sim 0.15\text{Li}_2\text{MnO}_3 \cdot 0.85\text{LiCoO}_2$ particles used for surface and bulk nickel doping. b) HRTEM image showing layered structure of the Ni-doped surface. c) EDS maps showing distribution of surface Al after ALD coating.

Figure II-225a shows single-crystal particles synthesized via a salt-flux method having a composition of $\sim 0.15\text{Li}_2\text{MnO}_3 \cdot 0.85\text{LiCoO}_2$. The composite nature of the material gives LiMn_6 -type ordering and Li sites within the TM layers. Treatment of these particles, in an acidic solution containing Ni^{2+} cations, and subsequent annealing leads to the incorporation of Ni^{2+} into the Li sites of the TM layers in an exchange process, thereby creating a Ni-doped, layered, R3-m-type of oxide. Depending on post annealing time/temperature, Ni can be doped primarily within the surface regions or distributed more deeply into the bulk. HRTEM data (b) and spectroscopy (not shown) reveals regions of Ni incorporated into a well-layered structure to a depth of ~ 20 nm for samples annealed at $\sim 600^\circ\text{C}$. Preliminary XAS results show that the electrochemical behavior of Ni is different for samples annealed at 900°C (e.g., bulk incorporation of Ni) compared to 600°C (e.g., surface-doped Ni); even when protected by coatings such as Al_2O_3 , Figure II-225c. Further analyses, as well as spectroscopic studies using various coatings and additives, are ongoing to better understand these systems and the role of surface vs. bulk nickel in nickel-rich cathodes.

Thin film cathodes have been produced by magnetron sputtering from NMC-442, 532, 622, 811, and NCA targets. XRD, ICP, and electrochemical profiles have been used to determine the sputtered phases and lithium contents of films produced under different processing conditions. Thin-film NMC-442, 532, and 622, heat-treated in air to 700°C , demonstrated proper phase content and voltage profiles but with low initial capacities for two, different film thicknesses (Figure II-226). NMC-811 and NCA sputtered films demonstrated voltage plateaus that did not agree with the established profiles for these materials, where ICP results indicated lithium-rich compositions for these films. Process optimization is ongoing.

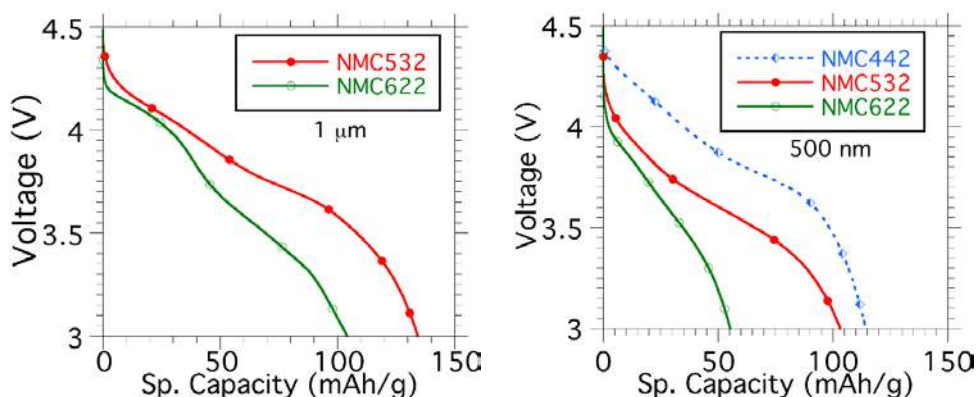


Figure II-226. Discharge profiles of NMC-442, 532, & 622 thin-film cathodes, 1 μm (left), and 500 nm (right).

Coating Mechanisms and NMC Cathode Particles

The effect of NMC metal ratios on surface and bulk composition, morphology, and electrochemical performance for Al_2O_3 -coated samples was studied with NMC-532, 622, and 811 prepared with aqueous coatings, varying Al_2O_3 content, and annealing temperatures. Surface elemental distributions, local chemical

and atomic structures, surface species and bulk changes were examined by SEM, TEM, XRD, and solid-state nuclear magnetic resonance spectroscopy (NMR). Results show that with compositional change from 532 to 811, the Al_2O_3 coatings begin to diffuse into the bulk on high-temperature annealing due to Al compatibility with Ni-rich materials, Figure II-227a. Because diffusion of surface Al_2O_3 into the bulk of 811 is easier, and more evenly distributed when compared to 532 and 622, morphology differences can be observed, SEM Figure II-228a. ^{27}Al NMR data showed formation of a surface LiAlO_2 phase for all compositions when annealing temperatures increased to 800°C . The diffusion of Al into the lattice was found to negatively affect electrochemical performance, indicating the importance of compatibility between surface coatings and bulk oxides.

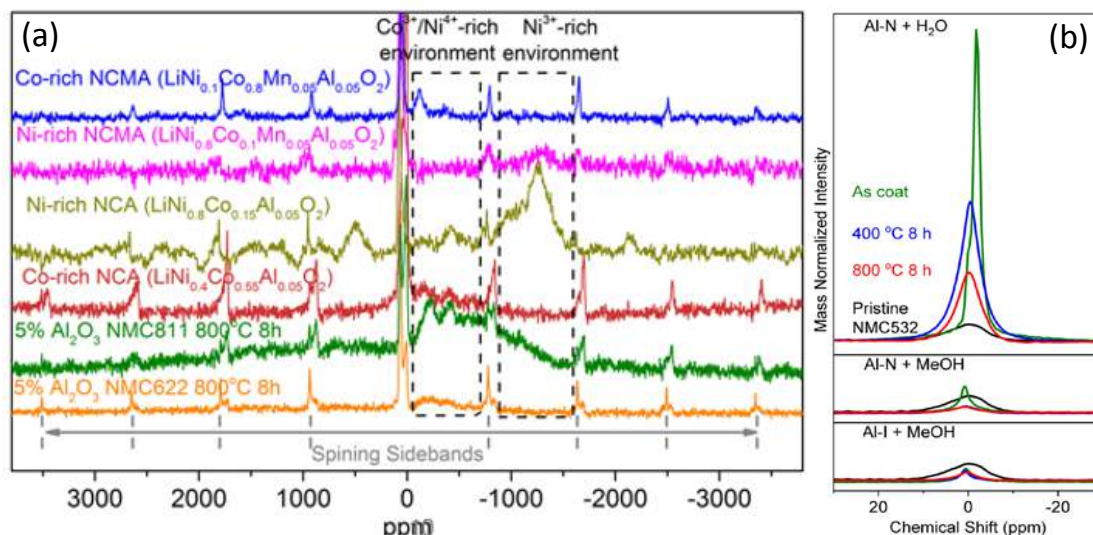


Figure II-227. a) ^{27}Al NMR spectra of 5 wt.% Al_2O_3 -coated NMC-622 and 811 annealed at 800°C for 8h, compared to Co-rich NCA, Ni-rich NCA and NCMA, and Co-rich NCMA. b) ^7Li NMR for Al_2O_3 -coated NMC-532 with various salt/solvent systems.

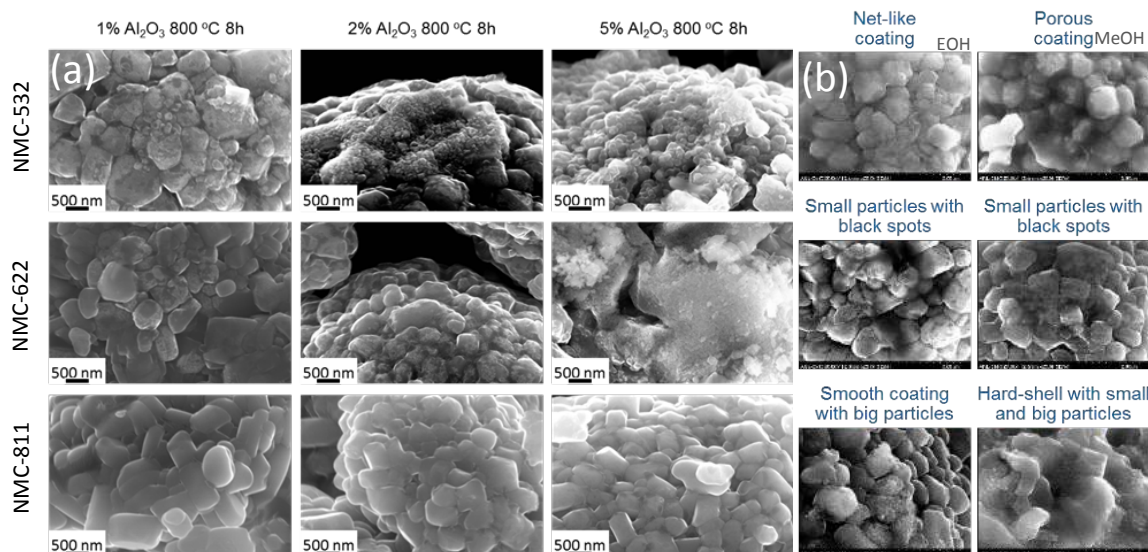


Figure II-228. a) SEM images of Al_2O_3 -coated NMC-532, NMC-622, and NMC-811 with Al_2O_3 at 1, 2, and 5 wt.% annealed at 800°C for 8 h. b) SEM images of Al_2O_3 -coated NMC-532 with various aluminum sources, solvents, and annealing times.

NMR has also shown the presence of surface proton and lithium species, Figure II-227b. In addition, lower initial capacities in comparison to pristine samples were observed with aqueous solvents, suggesting possible

lithium loss or displacement from the bulk of cathode oxides during coating. In order to mitigate these challenges, alternative Al precursors and solvent systems were studied. Experiments were performed on NMC-532 with 2 wt.% Al-nitrate and isopropoxide as aluminum sources, and ethanol, methanol, and xylene as solvents. Coated samples were annealed at 400°C and 800°C to study the temperature effect on coating composition and electrochemical performance. Results show that surface-lithium contents after annealing are indeed influenced by choice of solvent (Figure II-227b), and particle morphologies are altered when changing both solvent and aluminum precursor, Figure II-228b. Furthermore, electrochemical performance was improved with the use of Al-isopropoxide/methanol in comparison to the Al-nitrate/water pair (II.C.1). Theoretical calculations have also been carried out on Al₂O₃-coated NMC surfaces and important insights gained on the interface structures of coated NMC materials (II.C.3).

Conclusions

A major goal of the overall project is an atomic-scale understanding of the physiochemical properties of NMC surfaces and interfaces. In order to obtain unique insights into these materials, model systems were pursued that will allow for combined experimental and theoretical studies that can be correlated by practical experiments and tractable calculations. FY17 efforts have shown that well-defined, single-crystal particles can be synthesized and facet-dependent properties probed. In addition, model cathode particles and thin-film cathodes have been fabricated for combined spectroscopic and electrochemical characterization. Furthermore, a detailed study on the effects of NMC composition, precursors, solvents, and annealing conditions has been carried out to elucidate the mechanisms of protecting NMC surfaces by means of coating methods. It has been shown that all parameters act in concert to arrive at the final product and profoundly influence electrochemical performance. In particular, the propensity for lithium leaching in aqueous solvents, coating thicknesses, and the driving force for Al segregation and diffusion, both strong functions of TM content, play a particularly important role in realizing efficient particle coatings. The electrochemical properties of these and other coatings is presented in II.C.1.

Chapter Acknowledgments Guoying Chen, Jian Zhu, Jason R. Croy, Mahalingam Balasubramanian, Dan O'Hanlon, Hakim Iddir, Jack Vaughey, Binghong Han, Fulya Dogan, S. Sharifi-Asl, R. Shahbazian-Yassar, Gabriel M. Veith, Rose E. Ruther, Andrew Kercher, David Wood III, Lamuel David, Jagjit Nanda

Key Publications

1. J. Garcia, J. Bareño, J. Yan, G. Chen, A. Hauser, J.R. Croy, and H. Iddir, *Phys. Chem. C* **121**, 8290 (2017).
2. B. Han, T. Paulauskas, B. Key, C. Peebles, J.S. Park, R.F. Klie, J.T. Vaughey, and F. Dogan, *ACS Appl. Mater. Interfaces* **9**, 14769 (2016).
3. F. Dogan, J.T. Vaughey, H. Iddir, and B. Key, *Appl. Mater. Interfaces* **8**, 16708 (2016).
4. B. Han, C. Peebles, T. Paulauskas, J.T. Vaughey, F. Dogan, *Effects of Sintering Temperature and Cathode Composition on Al₂O₃ Coatings of Li-ion Cathodes*, 231st ECS Meeting, New Orleans, May 28th (2017).
5. B. Han, C. Peebles, T. Paulauskas, J.T. Vaughey, F. Dogan, *Characterization of Al₂O₃ Coatings on Li-ion Cathodes: Effects of Annealing Temperature and Composition*, 2017 MRS, Phoenix, April 17th (2017).
6. Binghong Han, Baris Key, Saul H. Lapidus, Juan C. Garcia, Hakim Iddir, John T. Vaughey, Fulya Dogan, *ACS Appl. Mater. Interfaces*, DOI: 10.1021/acsami.7b13597 (2017).

II.C.3 Enabling High-Energy/Voltage Li-Ion Cells: Theory and Modeling (ANL, LBNL, NREL, ORNL)

Hakim Iddir, Principal Investigator

Argonne National Laboratory
9700 S. Cass Avenue
Lemont, IL 46039
Phone: 630-252-4505
E-mail: iddir@anl.gov

Dennis Dees, Principal Investigator

Organization: Argonne National Laboratory
Address: 9700 S. Cass Avenue
Lemont, IL 46039
Phone: 630-252-7349
E-mail: dees@anl.gov

Peter Faguy, Technology Manager

U.S. Department of Energy
Phone: 202-586-1022
E-mail: Peter.Faguy@ee.doe.gov

Start Date: October 1, 2014
Total Project Cost: \$4,000,000

End Date: September 30, 2018
DOE share: \$4,000,000

Non-DOE share: \$0

Project Introduction

The inability to charge commercially available $\text{Li}_{1+x}\text{Ni}_a\text{Mn}_b\text{Co}_c\text{O}_2$ (NMC-abc, where x is typically <0.05), cathode materials beyond ~4.3 V (vs. graphite) without incurring excessive surface damage, electrolyte decomposition, structural instabilities, gassing, and loss of lithium inventory is a significant challenge in meeting next-generation energy storage targets. This project aims to understand the underlying failure mechanisms associated with these issues that prevent state-of-the-art Li-ion battery systems from achieving higher practical energy densities than are currently obtainable. To do so, a more complete description of the atomic-level structure and reactivity of NMC surfaces is needed. This chapter deals with atomistic and electrochemical modeling studies focused on understanding material surfaces and interfacial reactions as well as relating electrochemical performance measurements to diagnostic studies on lithium-ion cells.

Objectives

The goals of this project are related to acquiring a deeper understanding of the atomic-scale processes that influence the structure and stability of NMC surfaces under various electrochemical environments by:

- Determination of surface structures and the driving forces for surface elemental segregation
- Theoretical predictions of electrolyte- and additive-NMC surface interactions
- Theoretical predictions of electrolyte decomposition and dissolution products and related effects
- Effect of NMC, transition metal (TM) composition on the synthesis of Al_2O_3 -based NMC coatings
- Understanding the effects of side reactions and electrode crosstalk through electrochemical modeling

Approach

The goals of the project will be accomplished through *atomistic modeling* using density functional theory (DFT) and *electrochemical modeling* using continuum-based transport equations combined with kinetic and thermodynamic expressions. All atomistic calculations were carried out by spin-polarized DFT as implemented in the Vienna Ab Initio Simulation Package (VASP). The exchange-correlation potentials are treated by the generalized gradient approximation (GGA) parametrized by Perdew, Burke, and Ernzerhof (PBE). The interaction between valence electrons and ion cores is described by the projected augmented wave (PAW) method. Furthermore, the GGA+U scheme is used for applying the on-site correlation effects among 3d electrons of the TMs, where the parameter of (U-J) is set to 5.96 eV, 5.00 eV, and 4.84 eV for Ni, Co, and Mn, respectively. The wave functions were expanded in the plane wave basis up to a kinetic energy of 500 eV. All surface calculations were performed using a periodically repeating slab separated by vacuum layers along the surface normal. A vacuum thickness of 10 Å was adopted to remove interactions between the slab layers. The lattice parameter of the supercell was fixed at its bulk value. All ions were allowed to relax until the total energy differences were no more than 0.003 eV. After geometry optimization within the DFT+U framework, electronic relaxation was performed using a single point calculation with the hybrid functional HSE06 to determine the surface energy at that level of theory.

NMC-111 is used as a model material because the TM-layer, ionic configuration is known. In order to establish the ion ordering in the TM layers, it is necessary to use a supercell that is at least three times bigger in the a and b directions than for a single-metal, layered material such as LiCoO₂. A k-point mesh of 3x3x3 was found sufficient to get accurate electronic energies for bulk calculations on this unit cell. Each ion has six neighbors consisting of groups of the other TMs arranged in a triangular shape. This ordering was found to be the most favorable using solid state NMR. This structure was also confirmed by DFT calculations of an initial set of 30 lowest-energy configurations determined based on electrostatic interactions only. The ordering can be explained based on the local charge balance. The sum of the electrovalencies of the nearest-neighbor cations should be equal to the charge of the anion in ordered rock-salt structures. Adsorption and reaction energies (ΔE) were calculated using the following expression:

$$\Delta E = E_{\text{surf+adsorbate}} - E_{\text{surf}} - E_{\text{adsorbate}} \quad (1)$$

Where $E_{\text{adsorbate}}$ is the energy of the isolated molecule in the vacuum, E_{surf} is the energy of the bare slab, and $E_{\text{surf+adsorbate}}$ is the total energy of the molecule adsorbed on the slab. Bulk solvent effects were accounted for by using an implicit solvation model as implemented in the DFT code VASP. Additionally, calculations of reactions in solution were performed with the Gaussian 09 implementation of DFT at the B3LYP/6-31+G(d,p) level of theory. Frequency calculations were performed for all structures in order to determine the nature of the stationary points. The ultrafine integration grid was employed in all calculations.

Results

Atomistic Modeling

Oxidation mechanism of electrolyte molecules on pristine and delithiated NMC surfaces

DFT calculations were used to estimate the interaction of electrolyte solvent molecules with the surfaces of NMC particles. Solvent molecules included ethyl methyl carbonate (EMC), ethylene carbonate (EC), hexafluorinated diethyl carbonate (HFDEC), and difluoro ethylene carbonate (DFEC), see II.A.3.iii. It was shown in an earlier report that the most reactive NMC facet is the (012) surface [1]. This facet was used as the prototype surface to determine cathode electrolyte interactions. Ab initio Molecular Dynamics (AIMD) was also used to explore the configuration space of the molecules over the surfaces. Several adsorption configurations were evaluated in order to find atomic positions that minimized the adsorption energy on the fully lithiated and delithiated NMC surfaces. The lowest energy configuration for EMC is shown in Figure II-229a. In this configuration the EMC molecule is chemically oxidized via hydrogen abstraction. The negative reaction energy denotes an exothermic reaction. The reaction produces a radical that is stable under the simulation conditions. However, this radical intermediate is highly reactive so its reactivity was tested by adding an alkene molecule to the simulation box. In the presence of an alkene the intermediate polymerizes

until a termination step is provided. Note that the hydrogen abstraction process transfers one electron to the lattice reducing a TM at the surface. EC interaction with the NMC (012) surface (Figure II-229b) takes place in an equivalent process. However, according to the calculated reaction energies, EC oxidation is more thermodynamically favorable than EMC oxidation. This indicates that EC would decompose preferentially in a Gen2 electrolyte. Contrary to EC and EMC, the fluorinated molecules HFDEC and DFEC do not react with the lithiated surface. The adsorption configurations of the fluorinated electrolyte molecules are shown in Figure II-229c and Figure II-229d. The interaction of HFEC and DFEC with the surface is weak, leading to an adsorption energy of -0.11 eV and -0.03 eV respectively. There is no charge transfer during this interaction. Hence, no TM reduction is expected. The molecules interact in an analogous manner on the delithiated slab. On the other hand, the interaction of the additive Tris(2,2,2-trifluoroethyl) phosphite (TTFP) with the surface differs from the electrolyte molecules mentioned above. On the lithiated surfaces the interaction of TTFP is weak ($\Delta E = -0.04$ eV). This matches the interaction of the fluorinated electrolytes molecules. In contrast, on the delithiated surface TTFP prefers to form a phosphorous-oxygen bond (Figure II-229e). The hydrogen abstraction is not favorable in this case, probably due to steric effects. Furthermore, the produced phosphate TTFPa molecule readily detaches from the surface without any energy barrier. Indeed, the reaction energy ($\Delta E = -3.1$ eV) of taking an oxygen from the surface at this level of lithiation is very similar to the computed energy of oxidation of TTFP to TTFPa in solution ($\Delta E = -3.5$ eV) [2, 3]. Oxidation of TTFP to TTFPa, creates an oxygen vacancy at the surface and leaves two electrons in the lattice that reduce the TMs. The reduction of the TMs and the creation of oxygen vacancies at the surface is likely the trigger of a surface phase change (e.g., layered to spinel).

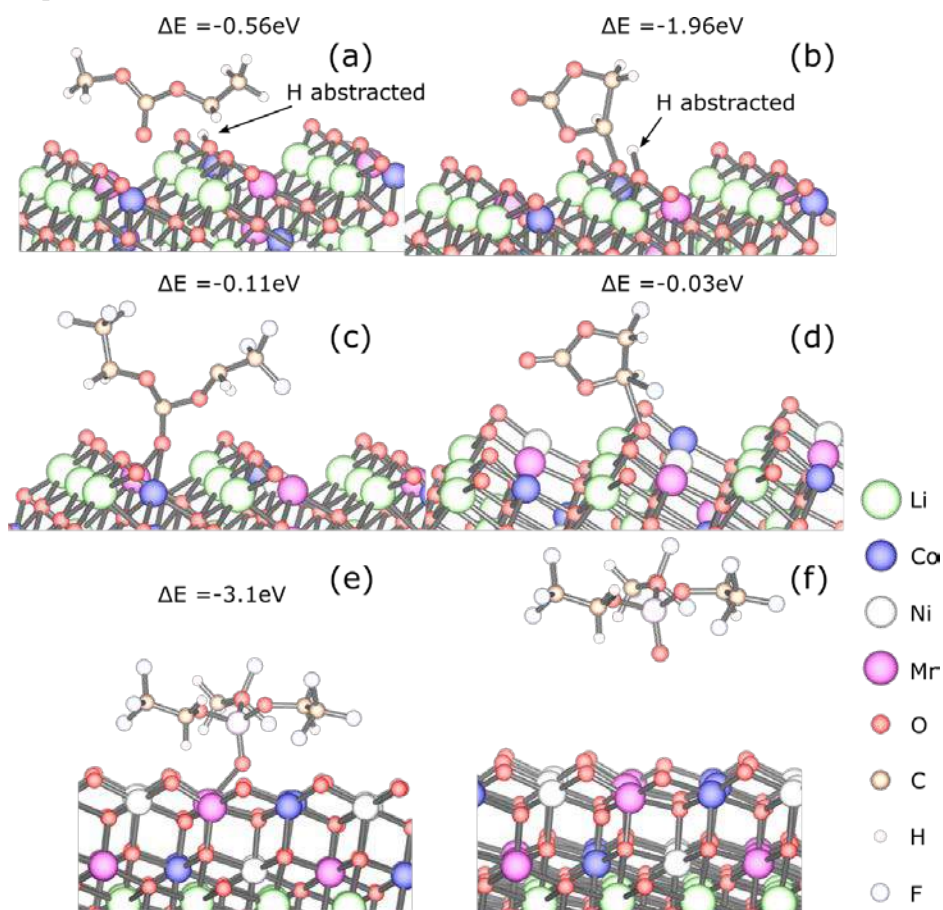


Figure II-229. Lowest energy configurations of electrolyte molecules on NMC (012) surface. (a) EMC, (b) EC, (c) HFDEC, (d) DFEC, (d) TTFP, (e) TTFP, (f) TTFPa

Interaction of select additive decomposition products with NMC surfaces

The interaction of the additive Tris(trimethylsilyl) phosphite (TMSPi) with the NMC (012) surface was also investigated. It was found that the decomposition products of TMSPi are stable on the surface in an oxidized state as phosphates. Figure II-230 shows the interaction of TMSPi with the delithiated (012) surface. The interaction of the additive is weak due to the steric effect of the bulky TMS groups. However, TMSPi can lose a TMS group (reaction with PF_5 and HF) and form a phosphate at the surface. The phosphate adsorbs favorably at the surface. The adsorbed species could produce a passivation effect at the cathode, in agreement with experimental findings that show a low impedance rise and much reduced TM dissolution (II.C.2). TMSPi was also compared with Triethyl phosphite (TEPi). Although the two additives are both phosphites, contrary to TMSPi, the TEPi leads to higher metal dissolution, higher impedance, and lower capacity retention [4, 5]. A more detailed mechanistic study is underway.

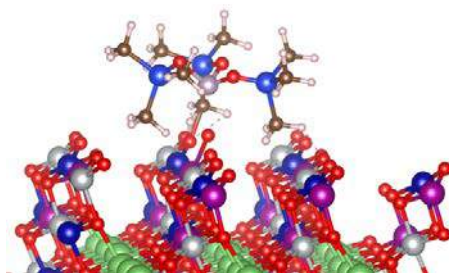


Figure II-230. TMSPi interaction with the delithiated NMC (012) surface.

Transition metal segregation to specific NMC surfaces

Calculations show that a thermodynamic driving force for Co segregation to the (104) facet of NMC surfaces exists [1]. However, no driving force was found for preferential segregation, via the TM layer, to the (012) surface. On the other hand, Ni segregation to (012) facets is related to surface-phase transformation. Previous work has found the (012) surface to be Ni rich. (See Figure II-231.) In order to gain some insights into these processes, a bulk Li/Ni anti-site defect formation energy of $E_f \approx 0.3$ eV was computed, which leads to an equilibrium concentration:

$$C = N_{conf} e^{\frac{-E_f}{RT}} \rightarrow 1.3\%$$

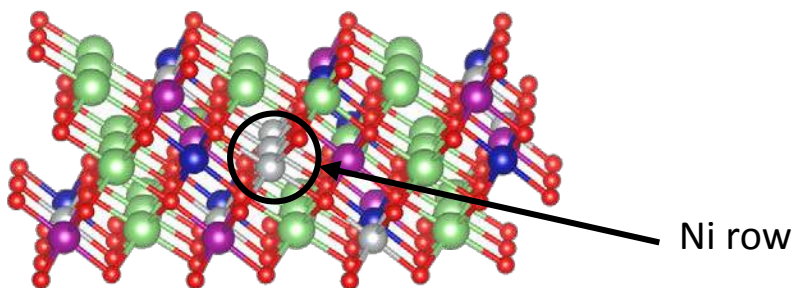


Figure II-231. Ni enriched NMC-111 (012) surface showing a stable arrangement of Ni in a row within the Li layer.

The energy of formation of a second anti-site defect in the same TM layer is ~ 1.8 eV. A third anti-site defect in the same TM layer produces a spinel-like region. The energy of formation of this defect is 0.4 eV. This indicates that the formation of rows of Ni in the Li layer near the surface is more favorable than randomly localized defects. This mechanism is likely at the origin of the observed formation of Ni-rich facets. However, in order to explore such surface-phase transformations (e.g., layered to spinel), thicker slab models need to be considered. Such systems are computationally expensive. Furthermore, to accurately describe key electronic structure features, hybrid functionals are required, adding to computational costs of DFT calculations. The convergence of the self-consistent loop is very hard to achieve at this level of theory and model sizes. However, good progress has been made and results are in preparation for publication.

Theoretical Insights on how Transition Metal Composition Affects Alumina Coatings on Ni-Rich Cathodes

A model slab for the (012) surface (Figure II-232) was used that was found to contribute the most to the overall surfaces of NMCs and was in agreement with the experimental results. Five layers of NMC-111 and two layers of α -LiAlO₂ on each side of the slab (symmetric configuration) were constructed. This configuration was chosen because α -LiAlO₂ is isomorphic with NMC. The matching unit cells produced a model with negligible strain. The likelihood of forming a different phase on top of the α -LiAlO₂ was investigated. In order to model this system, a disordered α -LiAlO₂ phase, which could be considered as a precursor to a phase transformation to γ -LiAlO₂, was constructed. The interface energy (E_i) between the LiAlO₂ layer and the NMC part of the material was computed as:

$$E_i = E_{\text{LiAlO}_2\text{-surface}} + E_{\text{NMC-bulk}} - E_{\text{NMC-LiAlO}_2}$$

Where $E_{\text{LiAlO}_2\text{-surface}}$ is the energy of a LiAlO₂ slab, $E_{\text{NMC-bulk}}$ is the energy of a bulk NMC-111 model with the same number of unit cells as the slab model, and $E_{\text{NMC-LiAlO}_2}$ is the energy of the NMC slab surface with a LiAlO₂ coating film. Figure II-233 shows the change in the interface energy with the thickness of the α -LiAlO₂ region. The energy decreases when the α -LiAlO₂ region increases. This result indicates that the α -LiAlO₂ phase could stabilize a different phase if the thickness of the film is larger than four atomic layers. Also, this is evidence of a possible presence of an interfacial α -LiAlO₂ between NMC and a different phase, such as γ -LiAlO₂.

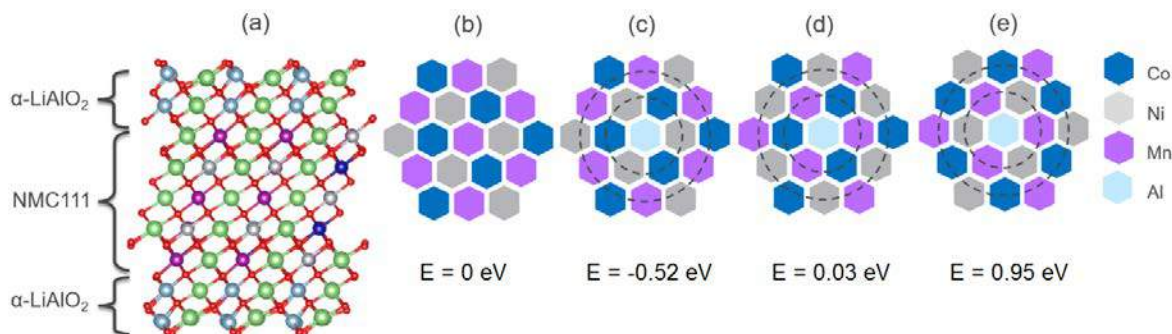


Figure II-232. (a) Model slab for the (012) NMC-111 surface coated with 2 layers of α -LiAlO₂. Light blue spheres represent Al, green spheres Li, purple for Mn, blue for Co, silver for Ni and the small red sphere represent O atoms. (b) Transition metal layer configuration for NMC-111, (c) Al swapped with Mn, (d) Al swapped with Ni, and (e) Al swapped with Co. The dashed circles represent the first and second nearest neighbors to Al atoms. The values of energy at the bottom of panels (c) to (e) represent the thermodynamic energy change after swapping Al from the surface layer with different transition metal centers in the bulk of NMC-111.

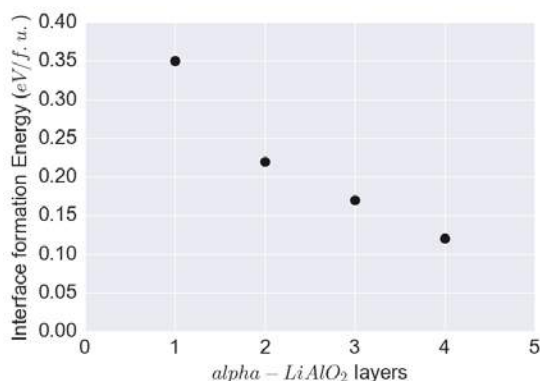


Figure II-233. Change in NMC/LiAlO₂ interface formation energy with thickness of α -LiAlO₂ and a disordered layer at the surface.

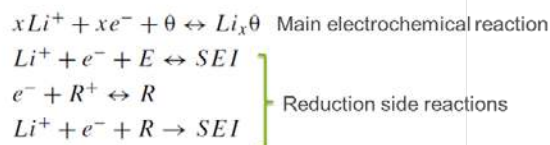
The ion ordering within the TM layer of NMC-111 is shown in Figure II-232b. This configuration allows the simulation of different environments for Al if different TM cations (from NMC) are swapped with Al from the surface LiAlO_2 layers. The only thermodynamically favorable configuration is the interchange of Al with Mn as shown in Figure II-232c. In this configuration the Al atom is exclusively surrounded by Ni and Co while the second nearest neighbors within the TM layer maintains the NMC-111 configuration. The negative number for the energy means that it is 0.52 eV more stable than the original configuration shown in Figure II-232b. All the configurations with Mn as a first neighbor (to Al) produce a positive change in energy with respect to the reference configuration (Figure II-232d and Figure II-232e). This result shows that Al prefers to be surrounded by Co and Ni cations (not Mn) in the TM layers of NMC. The existence of Mn in the TM layer can, therefore, greatly block the diffusion of Al from the surface to the bulk of the NMC particles. Previous work has also shown that there is a driving force for Co-Al clustering in Ni-rich environments.

Electrochemical Modeling

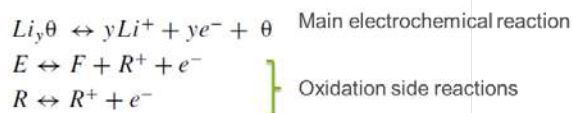
The focus of electrochemical modeling studies this year has been on side reactions and crosstalk in lithium-ion cells. An interesting study conducted within this program is utilized to establish and help calibrate a proposed model [6]. In that study, constant voltage relaxation currents for NMC/graphite (Gr), Li, or LTO, in standard and special coin and pouch cells, were measured over a wide range of voltages and conditions. Most noteworthy are the long relaxation time constant of 10s of hours and the final $\mu\text{A}/\text{cm}^2$ level currents observed. The study also proposes a series of side reactions on both electrodes (Figure II-234a).

(a)

Negative electrode:



Positive electrode:



(b)

Electrochemical Side Reaction Kinetics at Solid SEI Interface

$$i_n = i_0 \left\{ \exp \left[\frac{\alpha_d F}{RT} (\Phi_1 - \Phi_2 - U - \eta_c) \right] - \exp \left[-\frac{\alpha_c F}{RT} (\Phi_1 - \Phi_2 - U - \eta_c) \right] \right\}$$

Steady-State Diffusion of Side Reactants through SEI

$$\frac{\sum i_n}{z_i F} = -D_i \frac{c_{R,SEI} - c_{R,S}}{\delta_{SEI}} \quad \eta_c = \frac{RT}{nF} \sum_i s_i \ln \frac{c_{R,S}}{c_{R,SEI}} \quad \sum_i s_i M_i^z \leftrightarrow ne^-$$

Growth of SEI

$$\frac{d\delta_{SEI}}{dt} = \frac{\sum i_n}{F} V_{SEI}$$

Transport of Side Reactants through Electrolyte

$$\frac{\partial \varepsilon c_i}{\partial t} = \nabla \cdot \left(\frac{\varepsilon D_i}{\tau} \nabla c_i \right) + a \sum j_n$$

Figure II-234. (a) Proposed side reaction mechanism from ref. 11. (b) Electrochemical model for transport and reaction of side reaction components.

An earlier study on oversized negative electrodes indicated that long cell time constants can arise from edge effects [7]. Applying the electrochemical model to the present study, a long relaxation time constant was observed for the lithium concentration in the negative, however, the cell current relaxed relatively quickly. Ignoring the edge effects, the standard electrochemical model was modified to account for SEI growth, reactant species electrolyte transport, and side reaction kinetics and thermodynamics as given in Figure II-234b. Initial studies with the electrochemical model indicated that, when one electrode has a flat open circuit voltage (OCV) curve (e.g., graphite electrode) and one has a sloping OCV (e.g., NMC), the constant voltage relaxation current at long times is controlled by side reactions occurring at the electrode with the sloping OCV. A previous cell aging study was utilized in order to estimate the level of side reactions on the graphite negative [7]. As shown in Figure II-235, the slow relaxation can be modeled with a combination of SEI growth and reactant stabilization. This was accomplished with a relatively high initial side reactant concentration in the electrolyte and a slow SEI growth rate. While the current level and the long time constant can be matched, a close comparison of the relaxation indicates further improvement in the fitting is needed.

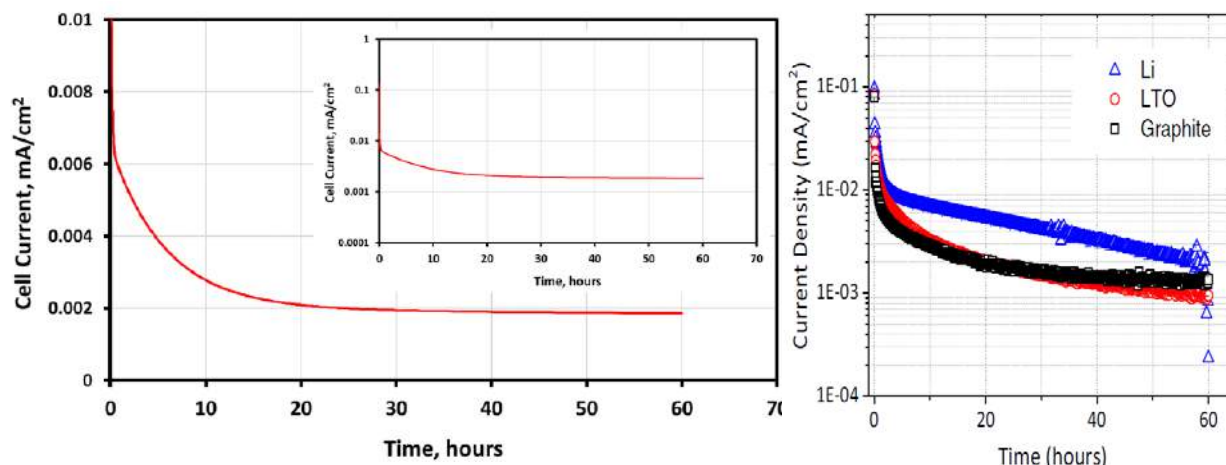


Figure II-235. (a) Full electrochemical model relaxation of an NMC//Gr cell. (b) Relaxation results with NMC cathode and indicated anode from ref. 11.

Conclusions

DFT calculations have been used to understand the pristine structure of NMC cathode surfaces where the (012) facet of NMCs has been shown to be one of the most prevalent and reactive surfaces. The (012) structure was further utilized in calculations to understand the interaction of electrolyte solvent and additive molecules on pristine and charged cathodes. It was found that, in Gen2, EC preferentially oxidized relative to EMC via hydrogen abstraction and subsequent reduction of surface TMs. Conversely, select fluorinated solvents (HFDEC and DFEC) were found to interact only weakly with the cathode surface. Oxidation of the phosphite additive molecule, TTFP, was found as a possible trigger to surface oxygen loss and phase transformation, whereas the phosphite additive molecule, TMSPI, was found to decompose on the (012) surface and create a passivating phosphate-based film. Interestingly, the use of a different phosphite molecule, TEPi, led to higher TM dissolution and impedance rise.

Studies on TM segregation have revealed a driving force for Co segregation to the (104) facet and the observed tendency for Ni segregation to the (012) facet of some NMCs was found to be related to the formation tendency of Li/Ni ant-site defects.

Detailed calculations of Al₂O₃-based coatings on NMCs suggest that an interfacial phase of α -LiAlO₂, between NMC surfaces and the bulk, coating phase, could stabilize surface structures such as γ -LiAlO₂. In addition, substitution of Al into the surfaces of NMCs favors Al surrounded by Co and Ni (e.g., Mn/Al exchange).

Initial electrochemical modeling results show that experimental data, related to side reactions and crosstalk in lithium-ion cells, can be understood in terms of a modified electrochemical model. Electrolyte transport of reactive species, SEI growth, and side reaction kinetics and thermodynamics were incorporated and qualitative agreement with experimental data was achieved. These results bode well for continuing studies aimed at understanding crosstalk in NMC//Gr systems.

Chapter Acknowledgments Hakim Iddir, Juan Garcia, Guoying Chen, Jian Zhu, Dennis Dees, Daniel P. Abraham, John Zhang, Adam Tornheim, Meinan He, James A. Gilbert, Cameron Peebles, Ritu Sahore, Juan Garcia, Javier Bareño, Chen Liao, Iyla A. Shkrob, Baris Key, Jack Vaughey, Binghong Han, Fulya Dogan

Key Publications

1. Binghong Han, Baris Key, Saul H. Lapidus, Juan C. Garcia, Hakim Iddir, John T. Vaughey, Fulya Dogan, ACS Appl. Mater. Interfaces, DOI: 10.1021/acsami.7b13597 (2017).

2. Han, T. Paulauskas, B. Key, C. Peebles, J.S. Park, R.F. Klie, J.T. Vaughey, and F. Dogan, ACS Appl. Mater. Interfaces **9**, 14769 (2016).
3. F. Dogan, J.T. Vaughey, H. Iddir, and B. Key, Appl. Mater. Interfaces **8**, 16708 (2016).
4. B. Han, C. Peebles, T. Paulauskas, J.T. Vaughey, F. Dogan, *Effects of Sintering Temperature and Cathode Composition on Al₂O₃ Coatings of Li-ion Cathodes*, 231st ECS Meeting, New Orleans, May 28th (2017).
5. B. Han, C. Peebles, T. Paulauskas, J.T. Vaughey, F. Dogan, *Characterization of Al₂O₃ Coatings on Li-ion Cathodes: Effects of Annealing Temperature and Composition*, 2017 MRS, Phoenix, April 17th (2017).

References

1. J. Garcia, J. Bareño, J. Yan, G. Chen, A. Hauser, J.R. Croy, and H. Iddir, Phys. Chem. C **121**, 8290 (2017).
2. R. Sahore, A. Tornheim, C. Peebles, J. Garcia, F. Dogan, B. Key, D. O'Hanlon, C. Liao, H. Iddir, Z. Zhang, J. Bareño, I. Bloom, *Insights into the reactions of tris(2,2,2-trifluoroethyl) phosphite additive in high-voltage, lithium-ion cells (submitted, J. Mat. Chem. A, 2017)*.
3. A. Tornheim, S. Sharifi-Asl, J. Garcia, H. Iddir, R. Shahbazian-Yassar, Z. Zhang, *Effect of electrolyte composition on rock-salt surface degradation in NMC cathodes during high voltage potentiostatic holds (in preparation)*.
4. C. Peebles, R. Sahore, J.A. Gilbert, J.C. Garcia, A. Tornheim, J. Bareño, H. Iddir, C. Liao, and D.P. Abraham, D. P., J. Electrochem. Soc. **164**, A1579 (2017).
5. A. Tornheim, C. Peebles, J.A. Gilbert, R. Sahore, J.C. Garcia, J. Bareño, H. Iddir, C. Liao, and D.P. Abraham, D. P., Journal of Power Sources **365**, 201 (2017).
6. N. Vadivel, S. Ha, M. He, D. Dees, S. Trask, B. Polzin, and K. Gallagher, J. Electrochem. Soc. **164**, A508 (2017).
7. B. Long, S. Rinaldo, K. Gallagher, D. Dees, S. Trask, B. Polzin, A. Jansen, D. Abraham, I. Bloom, J. Bareno, and J. Croy, J. Electrochem. Soc. **163**, A2999 (2016).

II.C.4 Studies on High Capacity Cathodes for Advanced Lithium-Ion (ORNL)

Jagjit Nanda, Principal Investigator

Oak Ridge National Laboratory
1 Bethel Valley Road
Oak Ridge, TN 37831-6124
Phone: 865-241-8361; Fax: 865-574-4357
E-mail: nandaj@ornl.gov

Tien Duong, Technology Manager

U.S. Department of Energy
Phone: 202-586-7836
E-mail: Tien.Duong@ee.doe.gov

Start Date: October 1, 2015
Total Project Cost: \$400,000

End Date: September 30, 2018
DOE share: \$400,000

Non-DOE share: \$0

Project Introduction

Development of high energy density, low-cost, and safe electrode materials is one of the key enablers for advanced batteries for transportation. Currently, one major technical barrier towards development of high energy density lithium-ion batteries is the lack of robust, high-capacity cathodes. Traditional layered LiMO_2 ($M = \text{Mn, Co, Ni, etc.}$) cathodes cannot reversibly cycle their entire Li supply (e.g., $x \leq 0.5$ in $\text{Li}_{1-x}\text{CoO}_2$). When charged beyond ~ 4.3 V vs. Li/Li^+ , many lithium-transition metal oxide cathodes undergo irreversible structural changes with concomitant oxygen gas evolution, resulting in irreversible capacity loss and voltage fade during cycling.[1-3] Understanding and addressing these structural instabilities is of vital importance to design next-generation cathode materials which can better utilize their Li supply without sacrificing cycle life.

In FY16, we developed $\text{Li}_2\text{Cu}_{0.5}\text{Ni}_{0.5}\text{O}_2$ cathodes which have a very high theoretical capacity of 250 mAh/g (assuming complete Li extraction).¹ Nearly 400 mAh/g of capacity was obtained during the first charge, but only ~ 125 mAh/g was reversible. The large first-cycle irreversible loss is attributed to oxygen evolution and irreversible structural transformations. To address these issues, Q1 of FY17 focused on developing a new sol-gel synthesis route to produce carbon-coated Ni-rich $\text{Li}_2\text{Cu}_x\text{Ni}_{1-x}\text{O}_2$ cathodes ($x = 0.6$).

We also developed Li_2MoO_3 cathodes which may be used as a structural stabilizing unit in layered-layered composite cathodes. [4, 5] Li_2MoO_3 has $R\bar{3}m$ symmetry and thus is expected to coherently blend with traditional layered LiMO_2 materials. Furthermore, Mo can access multiple oxidation states (e.g., Mo^{4+} - Mo^{6+}), allowing for reversible Li storage in both the Li_2MoO_3 and LiMO_2 moieties. Finally, Li_2MoO_3 is expected to have improved oxidative stability compared to Li_2MnO_3 due to reversible anionic charge compensation.[4] To aid the development of composite $x \text{ Li}_2\text{MoO}_3 \cdot (1-x) \text{ LiMO}_2$ cathodes, detailed structural analysis of the Li_2MoO_3 component was performed in FY17. The oxidative stability and structural evolution of these cathodes were evaluated using a suite of advanced characterization methods including in-situ mass spectrometry, Raman spectroscopy, synchrotron X-ray diffraction (XRD), and transmission electron microscopy (TEM). Combining the information gained from these experiments, new insights are made on the possible use of Li_2MoO_3 in layered-layered composite cathodes to be developed in FY18.

Objectives

- Synthesize Ni-rich $\text{Li}_2\text{Cu}_x\text{Ni}_{1-x}\text{O}_2$ cathodes with $x = 0.2$ and 0.3 and evaluate their high voltage capacity and oxidative stability [goal of > 225 mAh/g, 25 cycles].
- Complete *in-situ* and *ex-situ* x-ray, neutron, and spectroscopic studies of Ni-rich $\text{Li}_2\text{Cu}_x\text{Ni}_{1-x}\text{O}_2$ and related high voltage cathode compositions.

- Synthesis of one particular class and composition of disordered cathodes- Li_2MoO_3 and/or Cr substituted Li_2MoO_3 .
- Complete structural and electrochemical performance analysis of disordered cathodes- Li_2MoO_3 and/or Cr substituted Li_2MoO_3 .

Approach

We employ a number of synthesis routes including solid state, hydrothermal, solvothermal, and sol-gel reactions to produce cathode materials. The cathode compositions and phases are selected based on: (i) phase diagram analysis and modeling from work by Ceder and others, (ii) thermal safety, and (iii) materials availability and cost. When appropriate, we utilize ORNL's expertise to produce thin film electrodes with these new chemistries. Thin film electrodes do not require polymer binders or conductive carbon additives, and can therefore facilitate our understanding of the intrinsic properties of the cathode material. We also have an active interest in developing coatings that can improve cathode properties such as conductivity or interfacial stability. For optimizing our cathode synthesis process and improving cell level performance, we correlate electrochemical properties with information obtained from advanced characterization methods including micro-Raman spectroscopy, mass spectrometry, microscopy, and X-ray and neutron diffraction.

Results

Accomplishments

- A sol-gel synthesis route was developed to produce carbon-coated Ni-rich $\text{Li}_2\text{Cu}_x\text{Ni}_{1-x}\text{O}_2$ ($x = 0.6$). During the 1st charge cycle, the material undergoes an irreversible structural transition from orthorhombic to trigonal phase accompanied by oxygen loss.
- Synthesis conditions to produce phase-pure Li_2MoO_3 powders and sputtered thin films with the desired structure were identified.
- *In-situ* mass spectrometry studies demonstrate that Li_2MoO_3 cathodes have very stable lattice oxygen and do not evolve O_2 or CO_2 gases even when charged to very positive potentials (e.g., 4.8 V vs. Li/Li^+). This unique property makes Li_2MoO_3 a promising candidate for stabilizing the structure of layered-layered composite cathodes.
- Investigate solid-state and sol-gel synthesis routes to produce composite layered-layered cathodes with the general formula $x\text{Li}_2\text{MoO}_3 \cdot (1-x)\text{LiMO}_2$. Identify stable phases with the compositional space with $x = 0.2 - 0.4$ and $M = \text{Mn}, \text{Ni}, \text{and/or Co}$. The initial goal is to achieve capacities in the range of 225 mAh/g with low or minimal lattice oxygen evolution at potentials > 4.4 V vs. Li/Li^+ .
- Explore fluorine substitution in Mo-based cathodes as a strategy to increase their operating potential and/or oxidative stability.
- Perform additional studies with the sputtered thin film Li_2MoO_3 cathodes. Unlike conventional slurry cast cathodes, the thin films have a dense structure which is absent of conductive carbon and polymer binder. These properties will facilitate interpretation of XPS and EIS experiments to better understand the fundamental characteristics (e.g., charge compensation mechanism, charge transfer kinetics, and Li transport rates) of Li_2MoO_3 cathodes.

Redox Activity of Ni-Rich $\text{Li}_2\text{Cu}_x\text{Ni}_{1-x}\text{O}_2$ Cathodes

In FY16 we successfully synthesized Li_2CuO_2 and $\text{Li}_2\text{Cu}_{0.5}\text{Ni}_{0.5}\text{O}_2$ compositions and studied their capacity retention, oxidative stability, and structural transformation during cycling. Substituting 50% Ni at Cu sites improved the redox voltage and stability. In Q1 of FY17 we focused on stabilizing Ni-rich $\text{Li}_2\text{Cu}_x\text{Ni}_{1-x}\text{O}_2$ with $x = 0.60$. This was necessary before trying to achieve a higher Ni-content of around 75%. Additionally, we aimed to improve the electrochemical kinetics by using adipic acid (AA) as a chelating agent which formed an amorphous carbon coating and reduced the primary particle size (determined from EDX and SEM, results

not shown). Figure II-236 shows cyclic voltammograms (CV) of $\text{Li}_2\text{Cu}_{0.4}\text{Ni}_{0.6}\text{O}_2$ synthesized with molar ratios of AA ranging from 0 to 0.75 relative to the overall metal-ion content. During the 1st charge cycle the material underwent an irreversible structural transition from orthorhombic to trigonal phase accompanied by oxygen loss as reported earlier. The 2nd cycle CV represents the signature of $\text{Li}_2\text{Cu}_x\text{Ni}_{1-x}\text{O}_2$ redox activity with two broad oxidation peaks at 3.9 and 3 V. The corresponding reduction peaks were shifted by 300 mV towards lower voltage implying significant kinetic barrier. These electrochemical test data also show lower capacity compared to $\text{Li}_2\text{Cu}_{0.5}\text{Ni}_{0.5}\text{O}_2$, and as such, the focus during the remainder of FY17 was shifted to the development of disordered Mo-based cathodes.

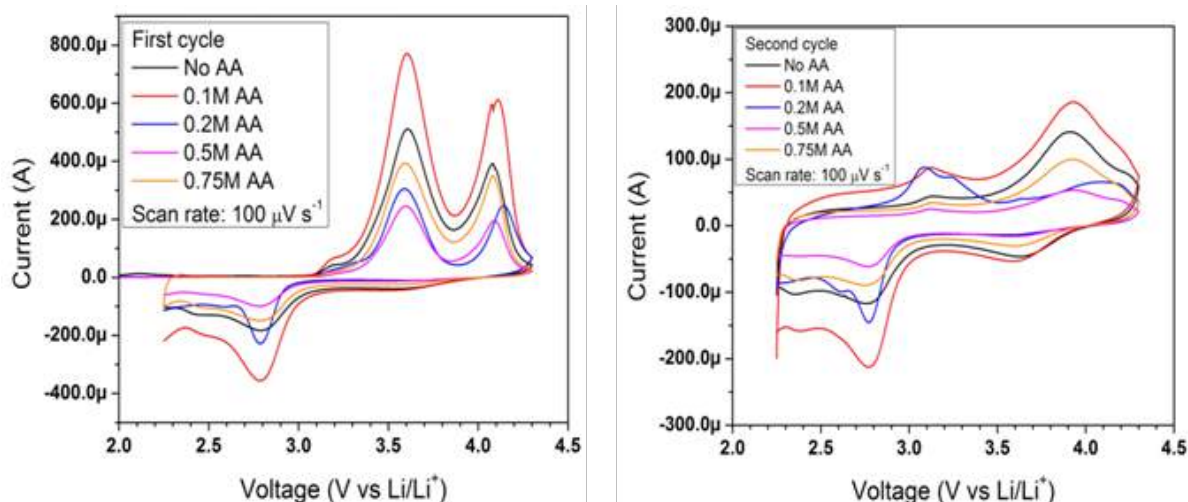


Figure II-236. CV during 1st and 2nd charge-discharge cycle for $\text{Li}_2\text{Cu}_{0.4}\text{Ni}_{0.6}\text{O}_2$ synthesized using sol-gel method using a chelating agent adipic acid (AA).

Synthesis and Redox Properties of Li_2MoO_3 Cathodes

We investigated the stability and oxygen activity of a new multi-lithium cathode composition, Li_2MoO_3 . The goal of this study was not to use this material as a high voltage cathode candidate, but rather to consider this as one of the structural units for composite cathodes with the general formula $x\text{Li}_2\text{MoO}_3 \cdot (1-x)\text{LiMO}_2$. Li_2MoO_3 was synthesized through the reduction of Li_2MoO_4 powder at 675°C for 12 or 48 h under flowing Ar/ H_2 . As shown in Figure II-237a, the shorter reaction time resulted in mixed phases of LiMoO_4 and Li_2MoO_3 , whereas the product obtained after 48 h contained phase-pure Li_2MoO_3 (used for all subsequent experiments) with $R\bar{3}m$ symmetry. The scanning electron microscopy (SEM) image in Figure II-237b shows the Li_2MoO_3 powder consisted of irregularly shaped particles which were on the order of 1 – 10 μm in size.

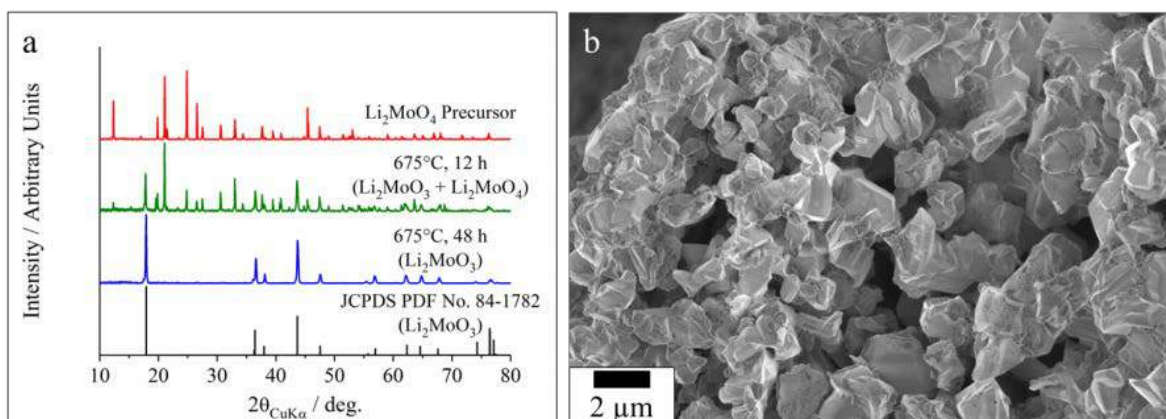


Figure II-237. (a) X-ray diffraction (XRD) patterns for as received Li_2MoO_4 precursor and the synthesized Li_2MoO_3 . (b) Scanning electron microscopy (SEM) image of the synthesized Li_2MoO_3 particles.

The electrochemical properties of slurry cast Li_2MoO_3 cathodes were characterized through galvanostatic charge/discharge experiments in half cells. During the first charge cycle, a sloping potential profile over 3.6 – 4.8 V vs. Li/Li^+ was observed with a corresponding delithiation capacity of 223 $\text{mAh}/\text{g}_{\text{Li}_2\text{MoO}_3}$ (see Figure II-238a). The theoretical capacity of Li_2MoO_3 assuming complete Li extraction is 340 mAh/g , indicating 34% of the Li remained in the cathode structure after charging to 4.8 V. Upon the first lithiation cycle, a dramatically different profile was observed with a reversible capacity of 147 $\text{mAh}/\text{g}_{\text{Li}_2\text{MoO}_3}$ (corresponding to 0.86 Li cycled per Mo) and an average operating potential ~ 2.5 V vs. Li/Li^+ . The large hysteresis between the charge and discharge steps suggests that an irreversible phase transformation occurred during the first cycle. During subsequent cycles, the cathode showed gradual changes to the voltage profile in which most of the redox activity occurred at potentials < 3.5 V vs. Li/Li^+ due to the oxidation/reduction of the Mo reaction center. The sloping nature of these profiles suggests that the lithiation/delithiation proceeded through a single, disordered phase rather than a two-phase intercalation reaction. After 50 cycles, the electrode exhibited moderate voltage fade with a reversible capacity of 119 mAh/g (see Figure II-238b). Note that the spurious data point at cycle 31 was due to a temporary power outage of the battery testing equipment.

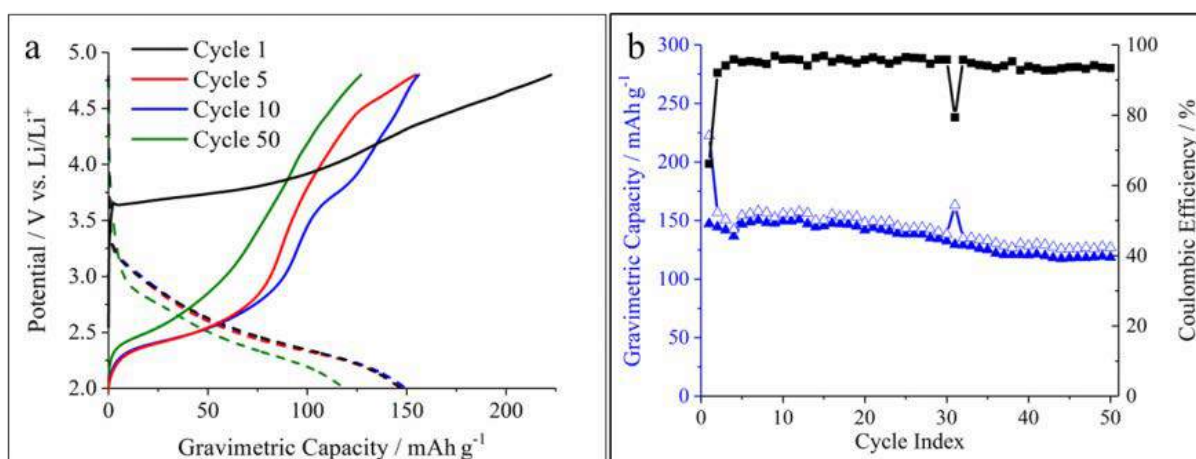


Figure II-238. (a) Charge/discharge curves and (b) cycling stability for a Li_2MoO_3 cathode cycled between 2.0–4.8 V vs. Li/Li^+ at 10 $\text{mA}/\text{g}_{\text{Li}_2\text{MoO}_3}$.

Stability of Lattice Oxygen in Li_2MoO_3 Cathodes

Under the aggressive cycling tests used in Figure II-238 (i.e., charging up to 4.8 V vs. Li/Li^+), the oxygen lattice in most conventional cathodes (e.g., LiMO_2) becomes unstable, resulting in evolution of O_2 or CO_2 gas and poor cycling stability caused by this irreversible structural change. To evaluate the oxidative stability of Li_2MoO_3 , *in-situ* mass spectrometry was used to measure gas evolution which occurred during electrochemical delithiation/lithiation. The measured potential and gas profiles are shown in Figure II-239. After a 1 h rest at open-circuit, the background O_2 and CO_2 levels (due to evaporation of the electrolyte) were 0.23 and 0.16%, respectively. Upon galvanostatically charging/discharging the cell, the O_2/CO_2 gas levels remained at or below their baseline values, demonstrating that the lattice oxygen in Li_2MoO_3 is stable up to 4.8 V vs. Li/Li^+ . Interestingly, the liquid carbonate-based electrolyte may be expected to decompose to O_2/CO_2 gases beyond its anodic stability limit (approximately 4.5 V vs. Li/Li^+), but this was not observed here. One possible explanation is that the electrolyte decomposed to form solid species which were not detectable with the mass spectrometry setup.

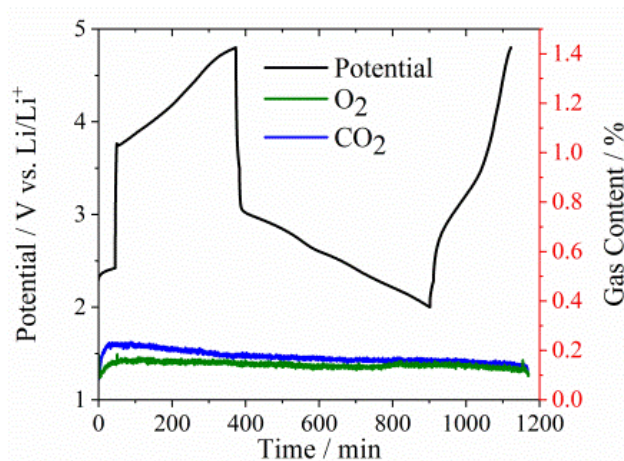


Figure II-239. *In-situ* mass spectrometry results showing the potential profile and measured O₂ and CO₂ levels evolved from the cell during charge and discharge.

Structural Evolution of Li₂MoO₃ Cathodes

A series of *ex-situ* X-ray diffraction (XRD) were performed to assess how the Li₂MoO₃ structure evolved during the first cycle. In these studies, the cathodes were cycled galvanostatically to predetermined voltage followed by a 5 h potential hold. The harvested cathodes were then thoroughly rinsed with dimethyl carbonate and dried prior to characterization. Figure II-240b shows synchrotron XRD patterns collected for the cathodes at various stages during initial lithiation/delithiation. For the pristine powder, the integrated intensity of the (003)/(104) diffraction peaks was 1.3, indicating the presence of a well-ordered R3m structure with little cation mixing (i.e., Mo was located primarily in the 3b sites).^[6] The (003)/(104) ratio remained fairly constant (ranging from 1.3 to 1.5) during charging but decreased to 1.04 and 0.73 for electrodes discharged to 2.00 and 2.50 V vs. Li/Li⁺, respectively. This result indicates that upon discharge, the Li₂MoO₃ became more disordered (i.e., some Mo migrated to the 3a sites) compared to the pristine sample.

In addition to changes in the (003)/(104) ratio, the Li₂MoO₃ diffraction peaks became broader with attenuated intensity during the first cycle, indicating a decrease in crystallinity. To qualitatively determine the extent of amorphization, the integrated intensity of the Li₂MoO₃ (003) diffraction peak was divided by that of the Al current collector's (111) peak. Since all samples had approximately the same loading (2.77 ± 0.80 mg_{Li₂MoO₃}/cm²), decreases in the (003)_{Li₂MoO₃}/(111)_{Al} ratio correspond to lower crystallinity of the Li_{2-x}MoO₃ phase. The pristine electrode had a (003)_{Li₂MoO₃}/(111)_{Al} ratio of 0.67 which rapidly decreased to 0.12 at the end of charge. Upon lithiation, this ratio remained relatively unchanged, indicating the Li₂MoO₃ irreversibly lost much of its crystallinity during the first charging cycle.

The irreversible structural transformation which occurred during the first cycle was also explored using *ex-situ* Raman spectroscopy. Figure II-240c shows Raman spectra for Li₂MoO₃ cathodes harvested at various stages during the first cycle. The pristine Li₂MoO₃ powder and slurry cast cathode exhibited several distinct Raman bands which agree well with previous reports.^[5,7] The Raman signature was unchanged when charging to 3.75 V vs. Li/Li⁺. However, when charging to 4.0 V (corresponding to a capacity of 113 mAh/g and a cathode stoichiometry of Li_{1.33}MoO₃), dramatically different spectra were recorded. Specifically, two broad bands appeared which were centered around 300 and 880 cm⁻¹ and contained multiple convoluted peaks. These features changed subtly throughout the lithiation/delithiation process, but the electrode clearly did not return to the original structure when re-lithiated to 2.0 V vs. Li/Li⁺. These Raman results substantiate the conclusions drawn from the XRD analysis and indicate a disordered amorphous phase formed during the first cycle.

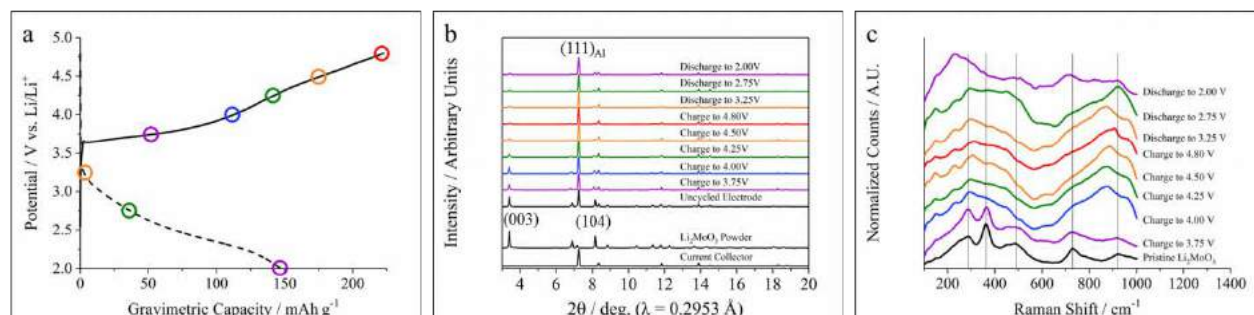


Figure II-240. (a) Charge/discharge curve during the first cycle of a Li_2MoO_3 cathode. (b) *Ex-situ* synchrotron XRD patterns collected at various stages during the first cycle. (c) *Ex-situ* Raman spectra collected at various stages during the first cycle.

To understand how the structure evolved beyond the first cycle, additional XRD data (using $\text{Cu K}\alpha$ radiation, $\lambda = 1.540562 \text{ \AA}$) and Raman spectra were collected on cathodes in either the charged or discharged states after 10 cycles (results not shown here). The diffraction peaks of the electrodes after 10 cycles were extremely weak, and the Raman spectra contained broad bands similar to those observed during the first charge/discharge cycle (Figure II-240c). Overall, the results demonstrate the lithiation/delithiation of Li_2MoO_3 proceeded through an amorphous phase rather than the crystalline solid solution mechanism proposed by Ma et al. [4]

The amorphous $\text{Li}_{2-x}\text{MoO}_3$ phase which formed during cycling was also characterized using *ex-situ* transmission electron microscopy (TEM). Figure II-241 shows the morphology (a-d) and selected area electron diffraction (SAED) patterns (e-h) for electrodes cycled 0, 1, 2, and 50 times. The pristine sample showed the presence of a highly crystalline Li_2MoO_3 phase as indicated by the periodic spacing of the diffraction spots (collected from the [100] zone axis). After 1 and 2 cycles, the SAED patterns contained a few, low intensity spots corresponding to a crystalline phase with $R\bar{3}m$ symmetry. However, these samples show predominantly diffuse patterns indicating the formation of amorphous phases nucleated randomly throughout the material. After 50 cycles (Figure II-241h), the SAED pattern was very diffuse, indicating the cathode became completely amorphous after extended cycling.

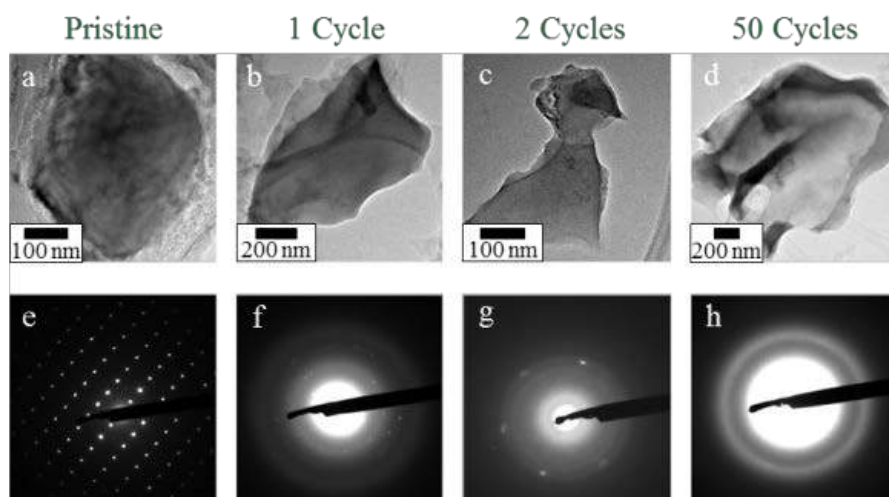


Figure II-241. (a-d) Transmission electron microscopy (TEM) images and (e-h) corresponding selected area electron diffraction (SAED) patterns for a Li_2MoO_3 cathode before cycling and after 1, 2, and 50 cycles.

Investigation of Sputtered Thin Film Li_2MoO_3 Cathodes

Interpreting *in-situ* and *ex-situ* data collected with traditional slurry cast electrodes is oftentimes complicated by the presence of conductive carbon and polymer binder which may produce signals that overlap with or dominate the desired signal from the active material. For example, the Raman scattering intensity from the conductive additive is generally much stronger than that of Li metal oxide cathode materials. Sputtered thin film cathodes composed entirely of active material can potentially resolve these issues, and thus experiments during Q4 focused on preparing and characterizing Li_2MoO_3 thin film cathodes for comparison with previous results obtained with traditional slurry cast electrodes.

Li_2MoO_3 films with thicknesses ranging from 1.0 – 1.2 μm were sputtered onto a Pt-coated Al_2O_3 substrate followed by heating at 675°C for 2 h under flowing Ar/H_2 (96/4). Figure II-242a shows a cross-sectional scanning electron microscopy (SEM) image of the resulting film which was uniform and dense in appearance. The X-ray diffraction (XRD) patterns in Figure II-242b demonstrate a phase-pure Li_2MoO_3 film with $R\bar{3}m$ symmetry was produced, and all diffraction peaks of this film could be assigned to either Li_2MoO_3 or the Pt-coated Al_2O_3 substrate.

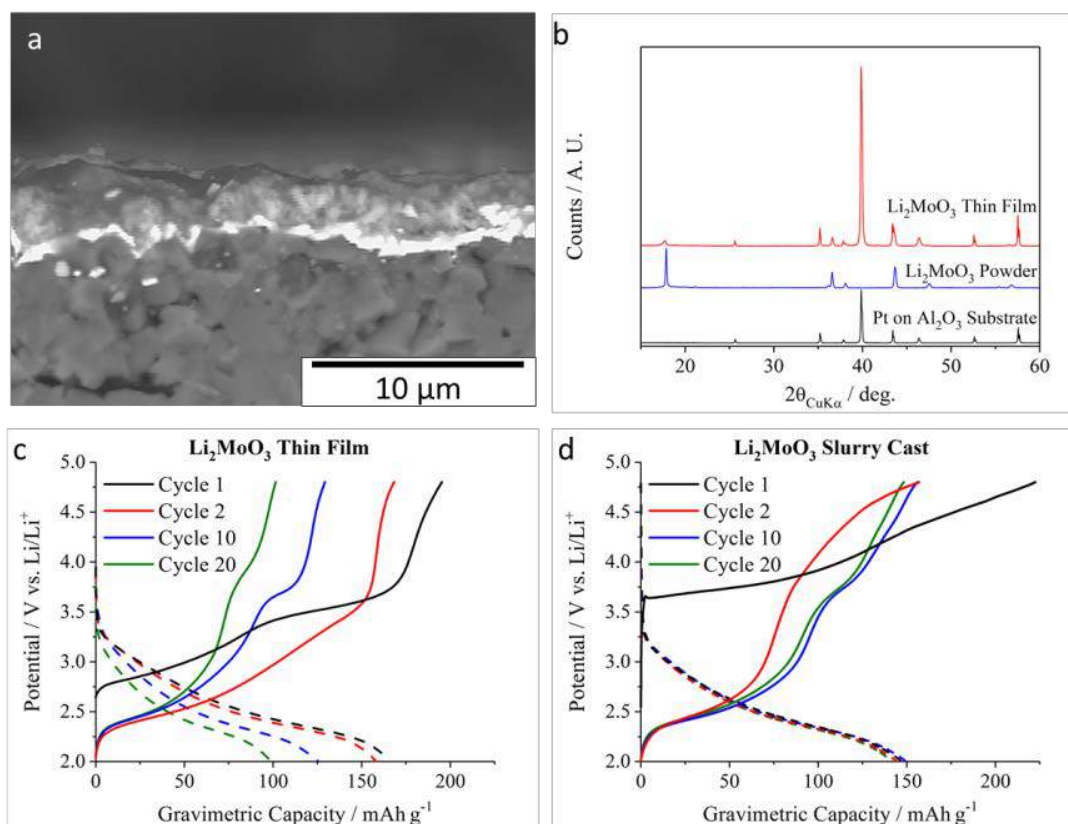


Figure II-242. (a) Cross-sectional SEM image of a sputtered thin film Li_2MoO_3 cathode. (b) XRD pattern of a sputtered Li_2MoO_3 thin film, Li_2MoO_3 powder, and the sputtering substrate (Pt on Al_2O_3). Galvanostatic charge/discharge curves for half-cells containing a (c) thin film Li_2MoO_3 cathode and (d) slurry cast Li_2MoO_3 cathode.

Galvanostatic charge/discharge experiments were conducted between 2.0 – 4.8 V for coin cells containing a Li_2MoO_3 thin film cathode and a Li metal anode. As shown in Figure II-242c, the cathodes exhibited an initial charge capacity of 190 mAh/g and reversible capacity of 166 mAh/g . The voltage profile and initial capacities of the thin films are in reasonable agreement with our previous studies on slurry cast Li_2MoO_3 cathodes (223 and 147 mAh/g , respectively, see Figure II-242d). However, while these slurry cast electrodes demonstrated excellent cycling stability, the thin film cathodes showed moderate capacity fade over 20 cycles. Future work

on the thin film Li_2MoO_3 cathodes will include additional synthesis and electrochemical characterization to understand the cause of this capacity fade. Despite this discrepancy, *ex-situ* Raman spectroscopy and XRD studies indicated that cycling the thin films induced a crystalline to amorphous transformation similar to that shown in Figure II-240 (results for thin films not shown). Unlike conventional slurry cast electrodes which contain complex pore structures, the planar structure of the sputtered thin films is ideal for studying the charge transfer kinetics and Li^+ transport rates in Li_2MoO_3 using electrochemical impedance spectroscopy (EIS). These experiments will be initiated in FY18 to provide complementary information to that obtained with conventional electrode architectures.

Conclusions

A sol-gel synthesis route was developed to produce Ni-rich $\text{Li}_2\text{Cu}_{0.4}\text{Ni}_{0.6}\text{O}_2$ cathodes, but these materials exhibited lower capacity compared to $\text{Li}_2\text{Cu}_{0.5}\text{Ni}_{0.5}\text{O}_2$ developed in FY16. As such, the focus during the remainder of FY17 was shifted to the development of disordered Mo-based cathodes. For Li_2MoO_3 cathodes, an irreversible crystalline to amorphous transformation was initiated when charging to potentials ≥ 4.0 V vs. Li/Li^+ . This amorphization reaction proceeded with further cycling, and there was no apparent crystallinity remaining in the cathode after 50 cycles. These conclusions are supported by complementary information obtained from X-ray diffraction (XRD), Raman spectroscopy, and transmission electron microscopy (TEM). Interestingly, the amorphization of Li_2MoO_3 did not prevent reversible Li storage from occurring. Li_2MoO_3 cathodes exhibited an initial reversible capacity of 147 mAh/g $_{\text{Li}_2\text{MoO}_3}$ with an average operating potential ~ 2.5 V vs. Li/Li^+ . The cathodes retained 81% of their initial capacity after 50 cycles.

In-situ mass spectrometry studies demonstrated the amorphization of Li_2MoO_3 did not involve the release of lattice oxygen even when charged to very oxidative environments (i.e., 4.8 V vs. Li/Li^+). This observation makes Li_2MoO_3 quite unique compared to traditional LiMO_2 compounds which evolve significant amounts of O_2 and/or CO_2 at potentials $> \sim 4.5$ V vs. Li/Li^+ . The excellent oxidative stability of Li_2MoO_3 may be a useful property to exploit in the preparation of layered-layered composites cathodes (i.e., $x\text{Li}_2\text{MoO}_3 \cdot (1-x)\text{LiMO}_2$). Various synthesis strategies will be explored in FY18 to produce such materials.

These studies broadly demonstrate the challenges associated with multi-lithium transition metal oxides, where there is close interplay between structure, transport, and oxygen loss that limits their use as high capacity cathodes for advanced lithium-ion systems.

Key Publications

1. Probing Multiscale Transport and Inhomogeneity in a Lithium-ion Pouch Cell Using In-situ Neutron Methods, H. Zhou, K. Ann, S. Allu, S. Pannala, J. Li, H. Z. Bilheux, S. K. Martha, J. Nanda, *ACS Energy Letters* 1, 981-86 (2016)
2. High Capacity Cathodes for Advanced Lithium-ion: Challenges and Opportunities 11th Lithium Battery Power & Safety Conference, Nov 1st- 4th, 2016 Baltimore, MD [Invited]
3. Electrochemical Energy Storage Materials: From Transportation to Grid Storage, J. Nanda International Society on Advances in Electrochemical Science & Technology (ISAEST-11), Chennai, India December 7-9th (2016) [Invited]
4. Structural Transformations in High-Capacity $\text{Li}_2\text{Cu}_{0.5}\text{Ni}_{0.5}\text{O}_2$ Cathodes, R. E. Ruther, A. S. Pandian, P. Yan, J. N. Weker, C. Wang, J. Nanda, *Chem. Mater.* 29, 2997-3005 (2017)
5. Meso and micron scale chemical and morphological heterogeneities in high capacity battery materials, MRS Spring Meeting. April 17-21, 2017, Phoenix, Arizona [Invited]
6. Structural Transformations in High Capacity $\text{Li}_2\text{Ni}_{0.5}\text{Cu}_{0.5}\text{O}_2$ Cathodes, R. Ruther, J. Nanda et al., ECS Spring Meeting May 28th - June 1st 2017, New Orleans, USA

7. High Capacity Multi-lithium Cathodes for Advance Lithium-ion, J. Nanda and R. E. Ruther, *US Drive Highlights (Energy Storage)*, DOE (2016)
8. High Capacity Multi-Lithium Oxide Cathodes and Oxygen Stability, R. E. Ruther, E. C. Self, and J. Nanda, *2017 AMR Meeting in Washington, DC* (2017)
9. Oxygen Stability of Disordered, Multi-Lithium Oxide Cathodes for Li-ion Batteries, E. C. Self, R. E. Ruther, G. M. Veith, and J. Nanda, *232nd Meeting of the Electrochemical Society in National Harbor, MD* (2017)

References

1. R. E. Ruther, H. Zhou, C. Dhital, K. Saravanan, A. K. Kercher, G. Chen, A. Huq, F. M. Delnick, J. Nanda, Synthesis, Structure, and Electrochemical Performance of High Capacity $\text{Li}_2\text{Cu}_{0.5}\text{Ni}_{0.5}\text{O}_2$ Cathodes, *Chem. Mater.* **27**, 6746-6754 (2015).
2. M. Sathiya, G. Rousse, K. Ramesha, C. P. Laisa, H. Vezin, M. T. Sougrati, M. L. Doublet, D. Foix, D. Gonbeau, W. Walker, A. S. Prakash, M. Ben Hassine, L. Dupont, J. M. Tarascon, Reversible anionic redox chemistry in high-capacity layered-oxide electrodes, *Nat. Mater* **12**, 827-835 (2013).
3. R. E. Ruther, A. S. Pandian, P. Yan, J. N. Weker, C. Wang, J. Nanda, Structural Transformations in High-Capacity $\text{Li}_2\text{Cu}_{0.5}\text{Ni}_{0.5}\text{O}_2$ Cathodes, *Chem. Mater.* **29**, 2997-3005 (2017).
4. J. Ma, Y.-N. Zhou, Y. Gao, X. Yu, Q. Kong, L. Gu, Z. Wang, X.-Q. Yang, L. Chen, Feasibility of Using Li_2MoO_3 in Constructing Li-Rich High Energy Density Cathode Materials, *Chem. Mater.* **26**, 3256-3262 (2014).
5. J. Ma, Y. Gao, Z. Wang, L. Chen, Structural and electrochemical stability of Li-rich layer structured Li_2MoO_3 in air, *J. Power Sources* **258**, 314-320 (2014).
6. C. Julien, A. Mauger, K. Zaghib, H. Groult, Optimization of Layered Cathode Materials for Lithium-Ion Batteries, *Materials* **9**, 595 (2016).
7. D. Li, H. He, X. Wu, M. Li, Electrochemical behavior of submicron Li_2MoO_3 as anodes in lithium-ion batteries, *J. Alloys Compd.* **682**, 759-765 (2016).

II.C.5 High Energy Density Lithium Battery (Binghamton University)

M. Stanley Whittingham, Principal Investigator

Binghamton University (SUNY)
85 Murray Hill Road
Vestal, NY, 13850
Phone: 607-777-4673
E-mail: Stanwhit@binghamton.edu

Tien Duong, Technology Manager

U.S. Department of Energy
Phone: 202-586-7836
E-mail: Tien.Duong@ee.doe.gov

Start Date: October 1, 2014
Total Project Cost: \$1,265,773

End Date: June 30, 2018
DOE share: \$1,265,773

Non-DOE share: \$0

Project Introduction

The project objectives are to develop the anode and cathode materials for high-energy density cells for use in plug-in hybrid electric vehicles (PHEVs) and in electric vehicles (EV) that offer substantially enhanced performance over current batteries used in PHEVs and with reduced cost. Specifically, the goal of this project is to enable cells with an energy density exceeding 1 kWh/liter. The carbon anode in today's Lithium-ion cells will be replaced with a tin-based anode with double the volumetric capacity of carbon. Similarly, the present intercalation cathodes will be replaced by materials, which are capable of reacting with up to two lithium ions per redox ion. Moreover, these cell reactions will occur within the stability limit of today's electrolytes, leading to longer-lived batteries.

Objectives

We propose to develop the anode and cathode materials for high-energy density cells for use in plug-in hybrid electric vehicles (PHEVs) and in electric vehicles (EV) that offer substantially enhanced performance over current batteries used in PHEVs and with reduced cost. Specifically the primary objectives are to:

- Increase the volumetric capacity of the anode by a factor of 1.5 over today's carbons by using a SnFeC composite conversion reaction anode
- Increase the capacity of the cathode by using a high capacity conversion reaction cathode, CuF_2 , and/or using a high capacity 2 Li intercalation cathodes, VOPO_4 .
- Enable cells with an energy density exceeding 1 kWh/liter.

Approach

Innovative Approach

The approach of this "beyond Li-ion" battery concept is (a) to remove the volume intensive intercalation-based carbon anode in today's Li-Ion batteries, and replace it with a conversion reaction-based material, and (b) to replace the present cathodes that mostly react with less than one Li ion per transition metal ion with cathode materials that can react with more than one Li ion. This latter is similar to the concept of using the divalent magnesium with its two-electron transfer. However, we believe that moving two of the much more mobile singly charged lithium ions is more viable, and moreover today's electrolytes, SEI additives and cell technology can be used. Attainment of the goals proposed here will lead to a 50-100% increase in the volumetric and gravimetric energy storage capability of both the anode and the cathode, which will allow for the realistic attainment of the next generation batteries for PHEV vehicles. At the same time, the science

generated will be applicable to other energy storage systems, such as anodes for Li/S. The anode and cathode components in this approach are:

1. A SnFeC composite for the anode which reacts by a conversion mechanism giving Li_xSn and Fe.
2. A CuF_2 containing material for the cathode which reacts with 2 Li ions by a conversion mechanism giving Cu and LiF.
3. A VOPO_4 containing cathode which reacts with up to 2 Li ions by an intercalation mechanism giving Li_2VOPO_4 .

The optimized anode and cathode from the above will then be combined in a full cell.

Results

We have achieved the following progress:

The Fe/Sn/C anode

Last year we reported the excellent cycling of the Fe/Sn/C composite anode formed by a mechanochemical process. This year we have developed an alternative approach, that is more scalable, to produce a $\text{Sn}_2\text{Fe}/\text{Sn}_5\text{Fe}$ mixture. The first 550 cycles of this material are shown in Figure II-243 for two voltage regimes. Although charging to 1.5 volts leads to a larger capacity, much of the added capacity is at too large a potential to be useful in a full cell. The capacity can be increased slightly by replacing a part of the iron by copper as shown in Figure II-244. After 200 cycles the capacities were 465 mAh/g and 1.26 Ah/cc at the C/2, significantly higher than that of graphite.

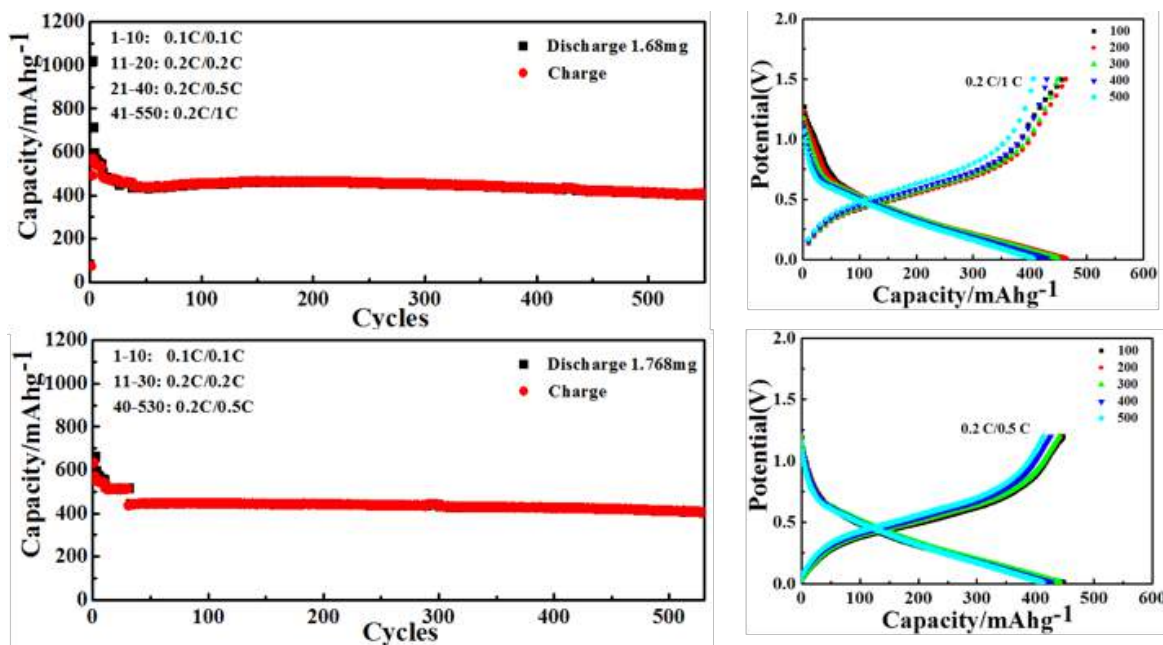


Figure II-243. Cycling capacity of the Sn_7Fe anode vs Li, in the voltage regimes (a) 0.01 – 1.5 volts and (b) 0.01 – 1.2 volts.

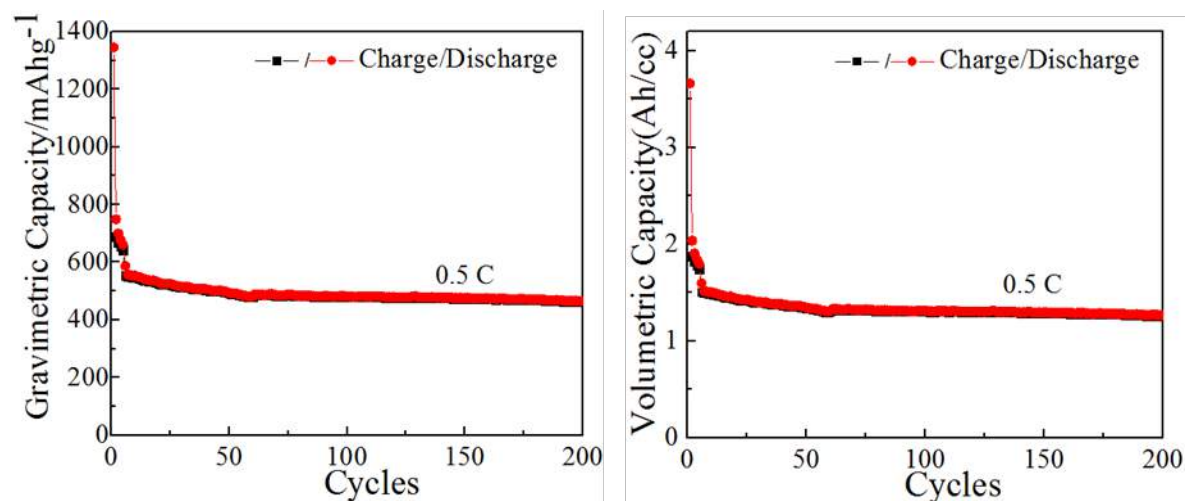


Figure II-244. Cycling capacity of the Sn_yFeCu anode vs Li at a C/2 rate.

The Cathode CuF_2

We now better understand the challenges facing the CuF_2 cathode. It can be fully discharged to LiF and Cu metal achieving a capacity of over 500 mAh/g, but on recharge there is a competition between transport of Li^+ and Cu^+ ions to the anode in all the electrolytes we have studied including organic and ionic liquids, and organic and inorganic solid electrolytes. As a result, significant amounts of copper metal are plated out on the anode particularly at potentials above 3.5 volts, and the capacity rapidly decays on each cycle. The mixed $\text{Cu}_{0.5}\text{Fe}_{0.5}\text{F}_2$ cathode cycles much better, but a spectroscopic study indicates that this is a result of the Fe cycling from metallic iron to FeF_3 .

The Cathode Li_xVOPO_4

The large particle size of LiVOPO_4 synthesized at elevated temperatures required that it be ball-milled to reduce the particle size to achieve high capacities. However, such ball-milling significantly degrades the crystallinity of the material. Ball-milling followed by a moderate temperature anneal, 450°C , was found to improve the crystallinity but not to that of the original crystalline LiVOPO_4 . However, the smaller particle size is retained, and the electrochemical capacity is increased from 225 mAh/g to over 300 mAh/g as shown in Figure II-245(a). The rate capability is also increased achieving around 250 Ah/g at the C/2 rate. Increasing the annealing time to 20 hours reduces the capacity at all rates, as shown in Figure II-245(b).

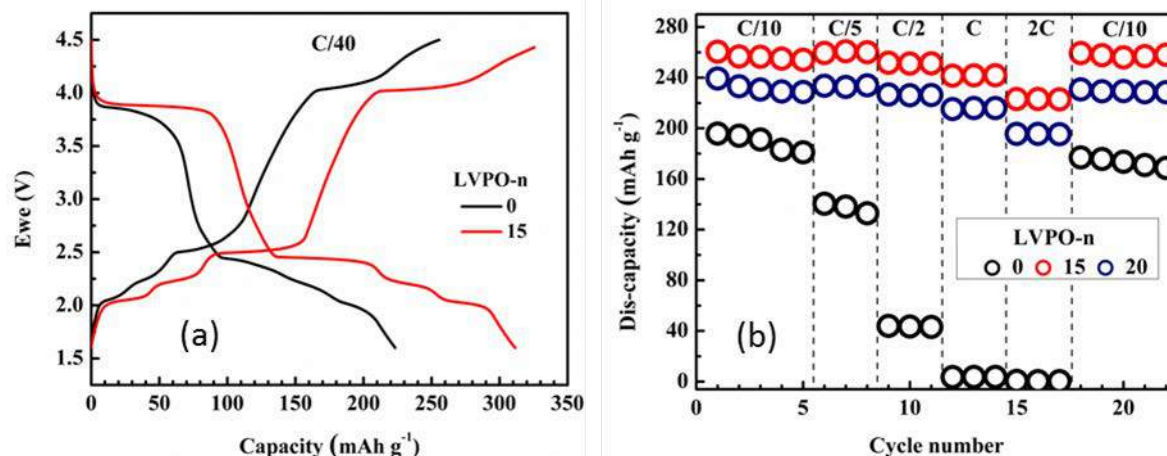


Figure II-245. (a) Cycling curve for LiVOPO_4 before annealing and after annealing for 15 hours, and (b) capacity retention and rate capability of LiVOPO_4 before annealing and after annealing for 15 and 20 hours.

Subsequent to the above finding, we developed a totally new synthesis approach that formed smaller particles in the initial step so that no ball-milling or annealing was required. The first five cycles vs a lithium anode of this material are shown in Figure II-246(a), and the excellent capacity retention is shown in Figure II-246(b). This material was used for the full cell tests described in the next section.

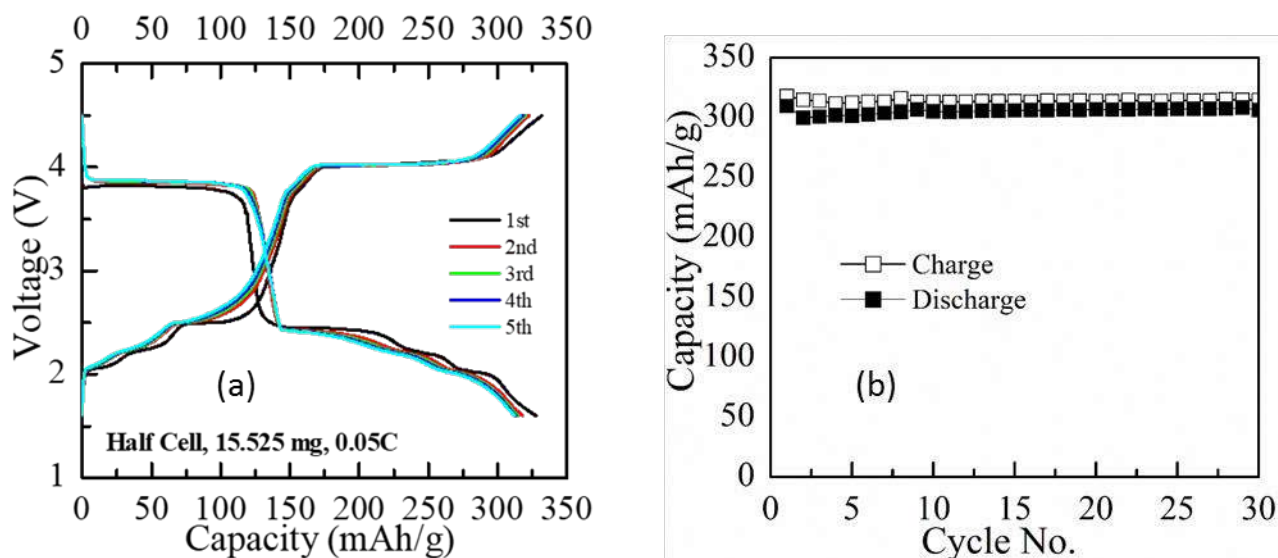


Figure II-246. (a) The first five cycles of LiVOPO_4 and (b) the capacity for the first 30 cycles vs a lithium anode.

The Full Cell: $\text{Sn/Fe/C} // \text{LiVOPO}_4$

The cell components were evaluated separately vs lithium metal to determine cell reproducibility. They were quite reproducible as shown in Figure II-247. A full cell was then constructed with a loading of the cathode exceeding 20 mg to ensure that a capacity exceeding the 4 mAh/g goal. This accomplishment is also shown in Figure II-247(c).

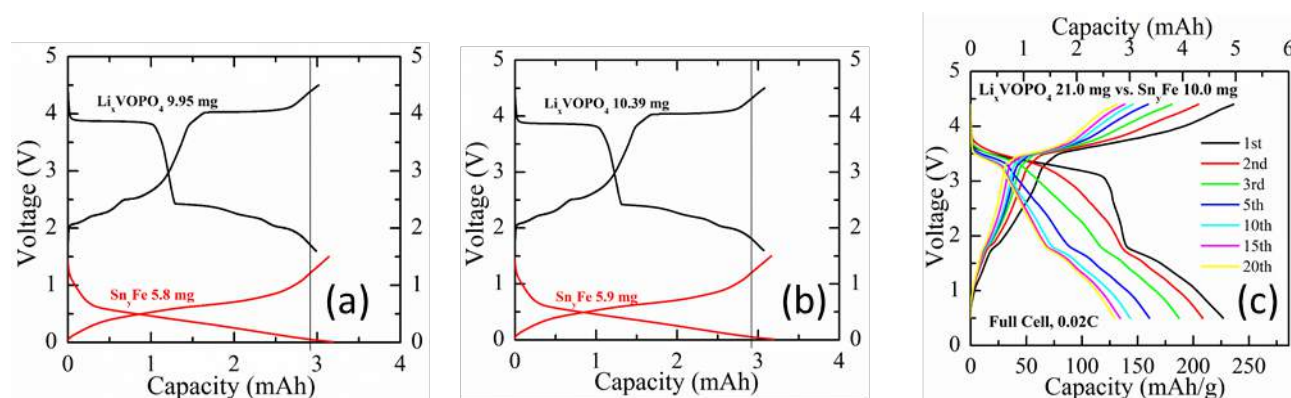


Figure II-247. (a) and (b) Two cells showing reproducibility of electrode components. (c) Cycling data for full cell showing achievement of 4 mAh goal.

To ameliorate the rapid capacity fading observed in Figure II-247, a study was made of the appropriate relative loadings of the two electrodes. The results are shown in Figure II-248. As can be observed an excess of the anode results in the highest capacity and capacity retention. Between 15 and 20 cycles were obtained in excess of the 4 mAh cell goal. However, there is still an unacceptably high capacity fade rate.

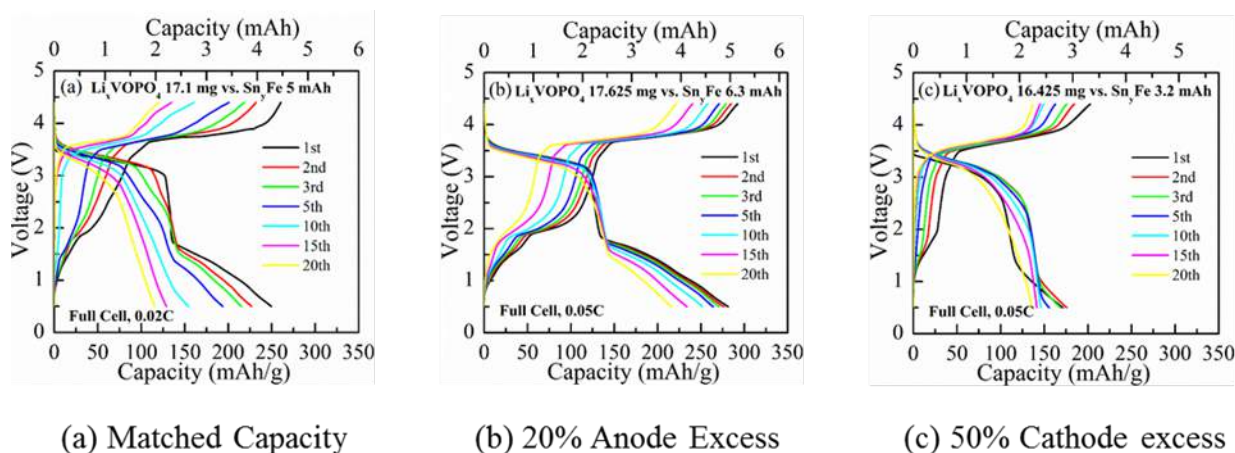


Figure II-248. Electrode Balancing. Cycling behavior of cells with (a) electrode capacity matched, (b) 20% excess anode, and (c) 50% excess cathode.

To ascertain the cause of this capacity fade, the impact of active material loading and of the anode material was determined. Figure II-249(a) and (b) show the impact of doubling the electrode loadings. Doubling the electrode loading has no negative impact, and in fact leads to better capacity retention. However, as shown in Figure II-249(c), the capacity fade is the same for the graphite anode as for the Sn_7Fe anode suggesting the cause of the capacity fade is not related to the anode, but rather to the Li_xVOPO_4 cathode.

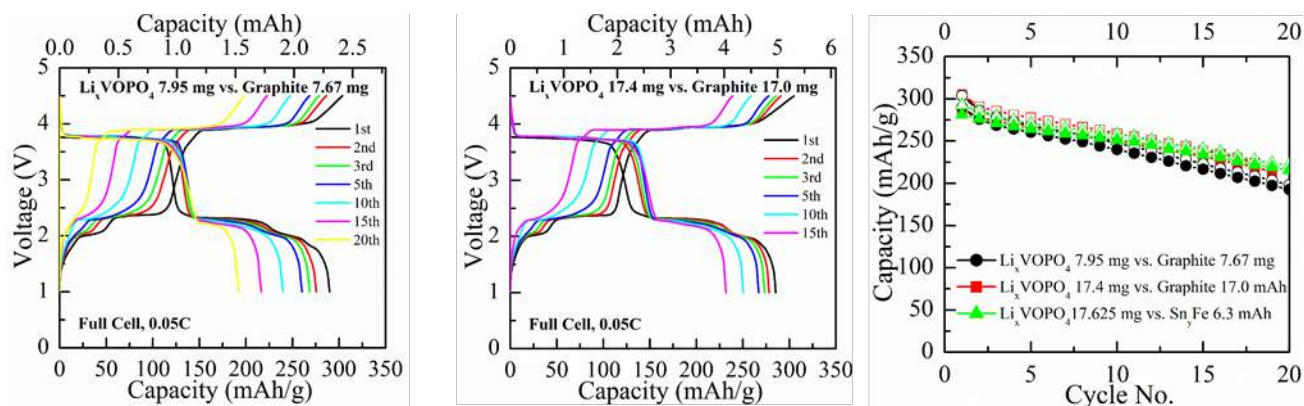


Figure II-249. Cycling of two Li_xVOPO_4 vs graphite cells with active materials loadings of 8 and 17 mg (left and center) indicating that loading is not a major factor in capacity fading. 17 mg loading allowed the achievement of the 4 mAh goal. (Right) Comparison of fade behavior of these two cells compared to one with a Sn/Fe anode suggesting that the fade is not due to the anode. a

The baseline couple for this study is the graphite/ LiFePO_4 cell. A comparison with $\text{Sn/Fe/Li}_x\text{VOPO}_4$ shows that the latter has 70% more capacity when two lithium ions are intercalated than one lithium in LiFePO_4 . Even when only one lithium ion is intercalated in VOPO_4 in the 4 volt plateau, the energy stored is comparable to that of LiFePO_4 as shown in Figure II-250. The energy stored in this two electron lithium couple is much higher than that stored by the alternative, the two-electron one- magnesium ion intercalation couple.

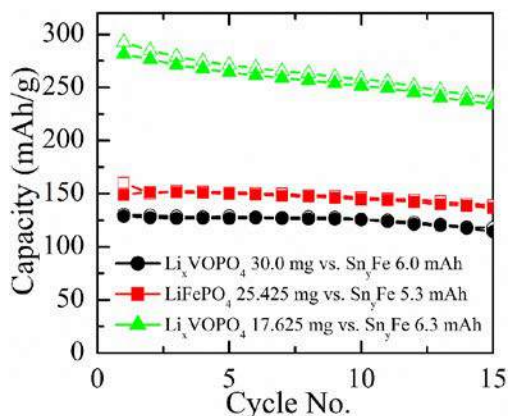


Figure II-250. Comparison of the cycling of Li_xVOPO_4 and LiFePO_4 , showing that two Li cycling in VOPO_4 has a much higher capacity than that of LiFePO_4 . One Li cycling in VOPO_4 has a comparable energy density to LiFePO_4 .

Conclusions

We have made significant progress in both the cathode and anode conversion materials. The $\text{Sn}_2\text{Fe/C}$ composite has achieved well over 1.5 times the volumetric capacity of the graphitic anode based on the lithiated product. This has been achieved for over 500 full cycles and over a range of C rates. A second synthesis approach has been successfully developed, and copper

We have shown that copper fluoride electrodes have capacities around 500 Ah/kg on the first discharge at low rates, and that even at rates as high as C/5 the capacity remains above 400 Ah/kg. We have shown that on charging the Cu/LiF product of the discharge reaction, cuprous ions are transported through the electrolyte, whether liquid or solid, leading to plating of copper metal at the anode. In the mixed CuFe fluoride, the capacity after the first few cycles almost totally is due to the Fe redox.

We have shown that the two-electron redox cathode, lithium vanadyl phosphate, LiVOPO_4 , can be readily cycled at rates up to 2C. It shows a substantially higher energy density than the alternative approach using magnesium.

Full cells comprising a SnFe anode and a LiVOPO_4 cathode have achieved over 4 mAh for 15 cycles, when there is a slight excess of the anode. The cycle life appears to be limited by the LiVOPO_4 cathode and not the anode. The capacity and energy density of this cell is much higher than the baseline cell, graphite// LiFePO_4 .

Key Publications

1. “ ϵ - and β - LiVOPO_4 : Phase Transformation and Electrochemistry”, ACS Appl. Mater. & Interfaces, 9, 28537–28541 (2017). Hui Zhou, Yong Shi, Fengxia Xin, Fredrick Omenya, and M. Stanley Whittingham. DOI: 10.1021/acsami.7b07895.

II.C.6 Development of High-Energy Cathode Materials (PNNL)

Ji-Guang Zhang, Principal Investigator

Pacific Northwest National Laboratory
902 Battelle Boulevard
Richland, WA 99354
Phone: 509-372-6515
E-mail: Jiguang.Zhang@pnnl.gov

Jianming Zheng, Co-Principal Investigator

Pacific Northwest National Laboratory
902 Battelle Boulevard
Richland, WA 99354
Phone: 509-372-4762
E-mail: Jianming.Zheng@pnnl.gov

Tien Duong, Technology Manager

U.S. Department of Energy
Phone: 202-586-7836
E-mail: Tien.Duong@ee.doe.gov

Start Date: October 1, 2015

End Date: September 30, 2018

Total Project Cost: \$1,200,000

DOE share: \$1,200,000

Non-DOE share: \$0

Project Introduction

The lithium ion battery (LIB) is the most promising energy storage system for electric vehicles (EVs) and plug-in hybrid electric vehicles (PHEVs) that can help reduce environmental pollution and promote energy security in the United States. However, the large-scale market penetration of EVs has been hindered by several barriers, including limited energy density, high cost, and safety concern with cathodes in LIBs. Conventional layered oxide LiCoO_2 (LCO) has been widely used in LIBs developed for consumer electronics, but the high cost of cobalt and low lithium utilization (~ 0.5 Li) has limited its application for EVs. To enable the EVs to drive over 300 miles on a single charge and promote the market penetration of EVs, low-cost electrode materials with high tap density, high energy density, good rate capability, and long-term cycle life must be developed. Ternary layered oxides $\text{LiNi}_x\text{Mn}_y\text{Co}_z\text{O}_2$ (NMCs) are promising cathode materials, because they combine the advantages of Ni, Co, and Mn in the structure. Replacement of Co with high Mn/Ni content also reduces production cost significantly. NMC cathode materials that have been successfully adopted in commercial LIBs, including $\text{LiNi}_{1/3}\text{Mn}_{1/3}\text{Co}_{1/3}\text{O}_2$ (NMC333) and $\text{LiNi}_{0.4}\text{Mn}_{0.4}\text{Co}_{0.2}\text{O}_2$ (NMC442), can deliver a reversible capacity of about 160 mAh g^{-1} with very decent long-term cycling if they are charged to a voltage of 4.3 V vs. Li^+/Li . However, this capacity and energy density are still not sufficient to support high-energy Li-ion batteries for EVs.

We proposed to develop high-energy cathodes based on modified NMC, which can be charged to a high voltage with long-term stability. Extending the charge cutoff voltage is one simple method to increase the utilization of lithium ions in the NMC materials, but this is at the expense of shortened cycle life. Another efficient strategy to improve the energy density of NMC is to develop NMC materials with higher Ni content, which involves both the $\text{Ni}^{2+/3+}$ and $\text{Ni}^{3+/4+}$ couples and offers a high discharge capacity of more than 200 mAh g^{-1} . The energy density of Ni-rich NMC cathodes can reach $\sim 800 \text{ Wh kg}^{-1}$ (calculated based on cathode only), which is 30% higher than that of conventional LiCoO_2 cathodes (570 Wh kg^{-1}). However, several technical challenges still exist with these Ni-rich NMCs due to their structural/interfacial instability and poor thermal stability. In FY17, we took several effective approaches, including grain boundary engineering, use of novel

electrolytes, and lattice doping, to enhance the structural/interfacial stability of Ni-rich NMC cathodes, which significantly improves their long-term cycle life.

Objectives

- Develop high-energy cathode materials with improved safety for PHEV and EV applications
- Develop low-cost synthesis routes for environmentally benign cathode materials with long cycle life

Approach

1. Engineer the grain boundary to enhance the structural integrity and interfacial stability of Ni-rich NMC materials.
2. Identify an optimized electrolyte that could efficiently stabilize the electrode/electrolyte interface of Ni-rich NMC cathodes.
3. Identify metal elements (Mg, Al, V, and Y) for lattice doping to enhance the cycling stability of Ni-rich NMC cathodes at high charge cutoff voltages. Electrochemical results demonstrated that Al doping helped improve the cycle life of Ni-rich NMCs.

Results

(1) Tailoring the grain boundary to improve the cycle life of Ni-rich NMC cathodes

Lithium phosphate (LPO) solid electrolyte coating and thermal infusion technology was adopted to improve the structural integrity/stability of Ni-rich NMC cathodes, e.g., $\text{LiNi}_{0.76}\text{Mn}_{0.14}\text{Co}_{0.10}\text{O}_2$, and hence enhance their electrochemical performance.

The pristine Ni-rich $\text{LiNi}_{0.76}\text{Mn}_{0.14}\text{Co}_{0.10}\text{O}_2$ sample was composed of secondary particles of 10~15 μm that was constructed with primary particles of 100~300 nm (Figure II-251a). After atomic layer deposition (ALD), a thin layer of LPO was coated on the surface of secondary particles (Figure II-251b). Thermal treatment at 600°C infused the thin-film LPO into the interior grain boundaries of secondary particles (Figure II-251c), as confirmed by transmission electron microscope (TEM) energy dispersive spectroscopy (EDS) mapping (Figure II-251d). Electrochemical data (Figure II-251e, f) demonstrated that the as-coated cathode material delivered lower discharge capacity, because the coating layer blocked the fast lithium-ion diffusion pathways. With thermal treatment, the LPO-infused $\text{LiNi}_{0.76}\text{Mn}_{0.14}\text{Co}_{0.10}\text{O}_2$ secondary particles exhibited similar initial discharge capacity to that of the pristine material, but the long-term cycling stability of Ni-rich $\text{LiNi}_{0.76}\text{Mn}_{0.14}\text{Co}_{0.10}\text{O}_2$ was significantly improved. The LPO-infused material achieved 91.6% capacity retention after 200 cycles, which is much higher than the 79.0% retained by pristine material.

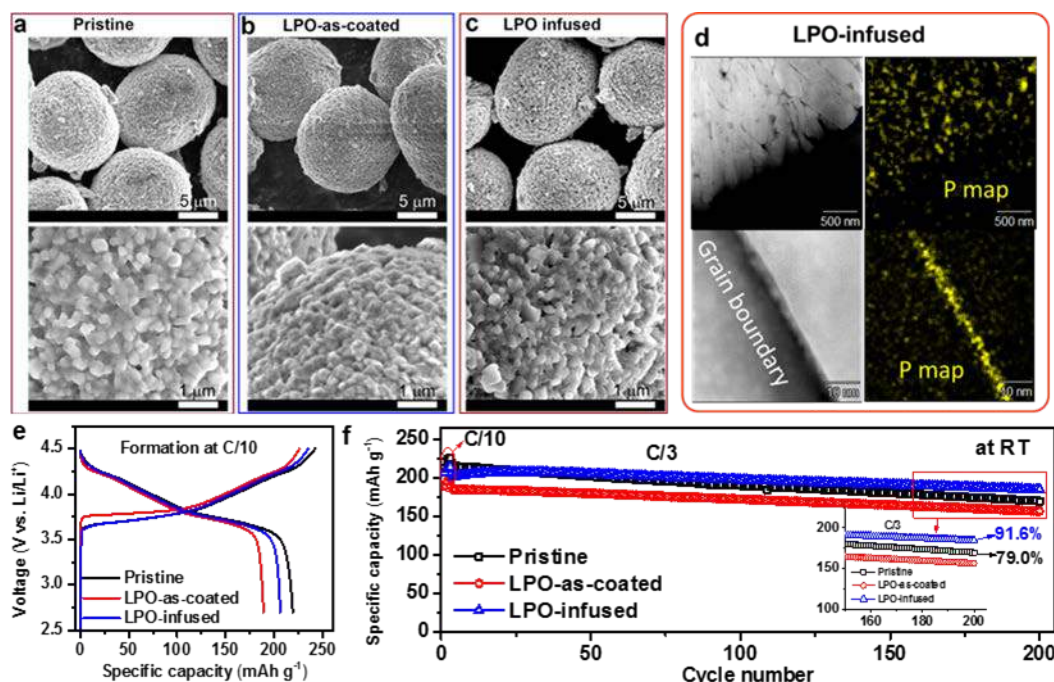


Figure II-251. (a-c) SEM images of (a) pristine, (b) LPO-as-coated, and (c) LPO-infused $\text{LiNi}_{0.76}\text{Mn}_{0.14}\text{Co}_{0.10}\text{O}_2$ cathode materials. (d) High-angle annular dark-field (HAADF) TEM images and EDS maps showing the presence of LPO at the grain boundary inside a secondary particle of $\text{LiNi}_{0.76}\text{Mn}_{0.14}\text{Co}_{0.10}\text{O}_2$. (e) Initial charge/discharge voltage profiles and (f) cycling performance of pristine and LPO-treated $\text{LiNi}_{0.76}\text{Mn}_{0.14}\text{Co}_{0.10}\text{O}_2$ cathode materials at C/3 between ~2.7 and ~4.5 V. Cathode electrode loading is $\sim 4 \text{ mg cm}^{-2}$.

The functioning mechanism of LPO solid electrolyte coating was systematically investigated using focused ion beam (FIB) scanning electron microscopy (SEM), scanning TEM (STEM), and electrochemical impedance spectroscopy (EIS) analysis. The pristine material showed substantial crack formation after cycling (Figure II-252a), indicating a poor capability to accommodate the micro-strain generated during deep Li-ion extraction processes. Accompanying the crack formation, the electrolyte then penetrated into the interior of secondary particles along the crack network, leading to the formation of a resistive solid electrolyte interface (SEI) layer at the grain boundaries. This increased cell resistance, especially the charge transfer resistance. Therefore, the pristine material showed faster capacity fading. In contrast, the LPO-infused material exhibited greatly improved structural integrity upon cycling (Figure II-252c), with no obvious cracks being observed. This indicates that the LPO solid electrolyte network could effectively buffer the detrimental micro-strain generated during deep delithiation, contributing to superior long-term cycle life.

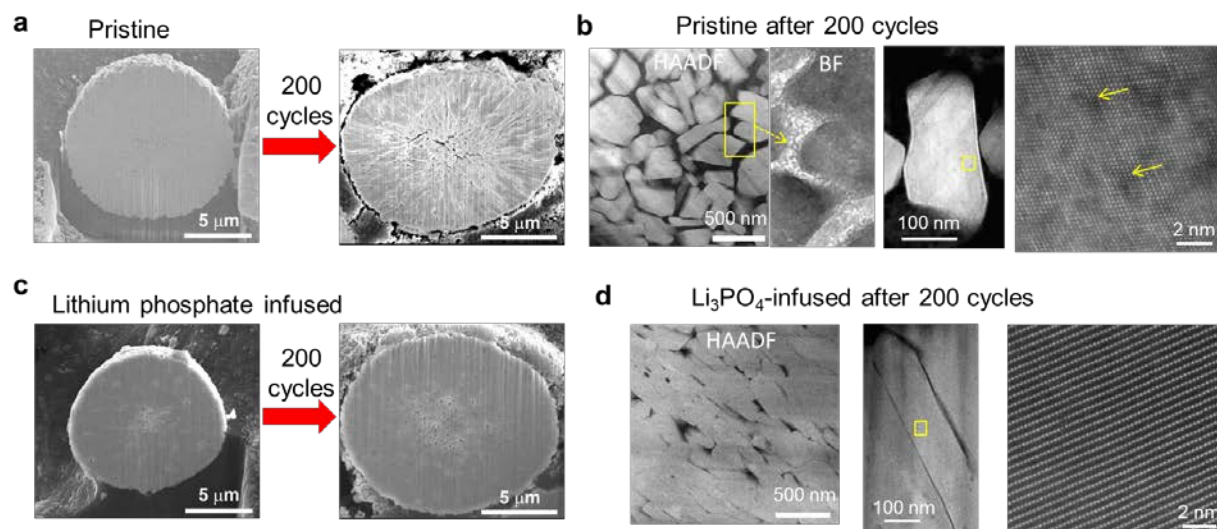


Figure II-252. Cross-sectional SEM images of (a) pristine and (c) LPO-infused $\text{LiNi}_{0.76}\text{Mn}_{0.14}\text{Co}_{0.10}\text{O}_2$ before and after 200 cycles at C/3 after 3 formation cycles at C/10 between ~ 2.7 and ~ 4.5 V. (b) HAADF/bright field (BF) and STEM images of pristine $\text{LiNi}_{0.76}\text{Mn}_{0.14}\text{Co}_{0.10}\text{O}_2$ material after 200 cycles. (d) HAADF and STEM images of LPO-infused $\text{LiNi}_{0.76}\text{Mn}_{0.14}\text{Co}_{0.10}\text{O}_2$ material after 200 cycles.

High resolution STEM was further employed to study the microstructural changes of pristine and LPO-infused $\text{LiNi}_{0.76}\text{Mn}_{0.14}\text{Co}_{0.10}\text{O}_2$ after electrochemical cycling. The pristine material before cycling showed a dense packing of the layered primary particles within the secondary particles. However, the unmodified material exhibited severe structural changes after 200 cycles at C/3 between ~ 2.7 and ~ 4.5 V (Figure II-252b). The grain boundaries between primary particles separated from each other and the gap between primary particles was filled with by-products of the parasitic side reactions between active material and the electrolyte. Also, the layered structure of Ni-rich NMC was transformed to disordered rock-salt structure. The degradation of the electrode crystal structure and the electrode/electrolyte interface was considered the main reason for the fast capacity decay of pristine Ni-rich $\text{LiNi}_{0.76}\text{Mn}_{0.14}\text{Co}_{0.10}\text{O}_2$. In contrast, the LPO-infused material showed well-maintained dense packing of the primary particles and well-preserved layered structure without serious phase transformation in the cycled particles (Figure II-252d). The enhanced structural and interfacial stability led to the greatly improved cycle life of Ni-rich $\text{LiNi}_{0.76}\text{Mn}_{0.14}\text{Co}_{0.10}\text{O}_2$. These fundamental findings validate the artificial solid electrolyte coating in conjunction with thermal infusion as a promising technology for developing stabilized Ni-rich cathode materials for high-energy-density Li-ion batteries.

(2) Tailoring the electrode/electrolyte interface to improve the cycle life of Ni-rich NMC cathodes

The electrode/electrolyte interfacial stability of the Ni-rich NMC cathode, i.e., $\text{LiNi}_{0.76}\text{Mn}_{0.14}\text{Co}_{0.10}\text{O}_2$ was enhanced by using an optimized electrolyte (E-optimized) composed of 0.6 M lithium bis(trifluoromethanesulfonyl)imide (LiTFSI), 0.4 M lithium bis(oxalate)borate (LiBOB), and 0.05 M LiPF_6 in ethylene carbonate (EC)-ethyl methyl carbonate (EMC) (4:6 by wt.), leading to significantly enhanced electrochemical performance.

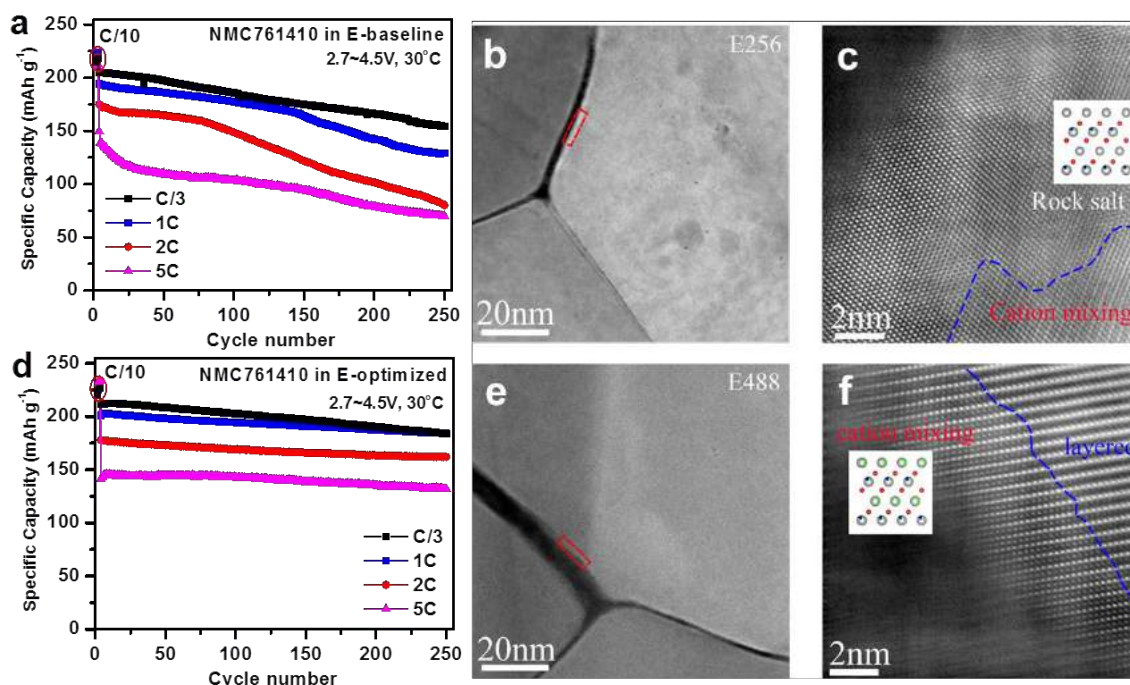


Figure II-253. (a, d) Cycling performance of Ni-rich $\text{LiNi}_{0.76}\text{Mn}_{0.14}\text{Co}_{0.10}\text{O}_2$ cathode in (a) E-baseline (1 M $\text{LiPF}_6/\text{EC-EMC}$) and (d) E-optimized (0.6 M LiTFSI , 0.4 M LiBOB , and 0.05 M LiPF_6 in EC-EMC) electrolytes during cycling at C/3, 1C, 2C, 5C rates (after 3 formation cycles at C/10) between ~ 2.7 and ~ 4.5 V. (b, c; e, f) HAADF-STEM images of Ni-rich $\text{LiNi}_{0.76}\text{Mn}_{0.14}\text{Co}_{0.10}\text{O}_2$ after 100 cycles at C/3 between ~ 2.7 and ~ 4.5 V in (b, c) E-baseline electrolyte and (e, f) E-optimized electrolyte.

The electrochemical performance data showed that, using optimized electrolyte, the Ni-rich $\text{LiNi}_{0.76}\text{Mn}_{0.14}\text{Co}_{0.10}\text{O}_2$ was able to deliver an initial discharge capacity of 220 mAh g^{-1} and achieve 86.9% capacity retention after 250 cycles, far superior to those (215 mAh g^{-1} , 75.2% retention after 250 cycles) obtained in baseline electrolyte (1 M $\text{LiPF}_6/\text{EC-EMC}$) (Figure II-253a,d). Meanwhile, the advantage of using E-optimized for Ni-rich NMC is further evidenced by the much improved stability in long-term cycling at higher charge/discharge C rates of 1C, 2C, and 5C, as compared to those using E-baseline (Figure II-253a, d).

The mechanism of improved cyclability of the NMC cathode using E-optimized electrolyte was systematically investigated using SEM, TEM, x-ray photoelectron spectroscopy (XPS), and EIS. E-optimized has been previously proven to be much more stable with the Li metal anode, thereby suppressing the polarization increase occurring on the anode side. In addition, the E-optimized electrolyte greatly enhanced the surface structural stability of $\text{LiNi}_{0.76}\text{Mn}_{0.14}\text{Co}_{0.10}\text{O}_2$. Although similar particle cracking was observed in the two electrolytes, less corrosion and much less structural transformation (from R-3m layered to Fm-3m disordered rock salt) were detected at the particle surface of Ni-rich NMC cycled in E-optimized (Figure II-253e,f), as compared to those observed in E-baseline (Figure II-253b,c). This improvement can be ascribed to the absence of HF acidic species that could etch the cathode particle surface, resulting in the phase transformation from layered to disordered rock-salt phase. The enhanced surface structural/interfacial stability is regarded as the primary reason for the improved capacity retention and mitigated voltage decay of Ni-rich $\text{LiNi}_{0.76}\text{Mn}_{0.14}\text{Co}_{0.10}\text{O}_2$. The results highlight the importance of maintaining the particle surface structural/interfacial stability to enable the sustainable operation of Ni-rich cathode materials for high-energy-density Li-ion batteries.

(3) Doping the lattice to enhance the cycling stability of Ni-rich NMCs

Surface lattice doping has been adopted to enhance the cycling stability of Ni-rich NMC cathode materials at a high charge cutoff voltage of 4.5 V. Using the spherical $\text{Ni}_{0.68}\text{Mn}_{0.22}\text{Co}_{0.10}(\text{OH})_2$ precursor, the effects of dopants on the electrochemical performance of $\text{Li}(\text{Ni}_{0.68}\text{Mn}_{0.22}\text{Co}_{0.10})_{0.99}\text{M}_{0.01}\text{O}_2$ ($\text{M} = \text{Mg}, \text{Al}, \text{V}, \text{or Y}$) were systematically investigated. The lattice-doped materials were prepared by mixing the $\text{Ni}_{0.68}\text{Mn}_{0.22}\text{Co}_{0.10}(\text{OH})_2$ precursor (with a secondary particle size of $\sim 10 \mu\text{m}$) with the dopant precursors; the mixture was then blended with lithium hydroxides and annealed at the optimum calcination temperature of 775°C for 24 h. The cycling performance of the obtained 1%-metal-doped cathode materials was evaluated in lithium half-cells using baseline electrolyte (1 M $\text{LiPF}_6/\text{EC-EMC}$ (4:6 by wt.)). Electrochemical performance results showed that the additional lattice doping slightly reduced the discharge capacity, due to electrochemical inactivity of the dopants (Figure II-254a). During long-term cycling, only the Al doping improved the capacity retention, while the other dopants (Mg, V, and Y) deteriorated the cyclability of the Ni-rich NMC cathodes (Figure II-254b, c).

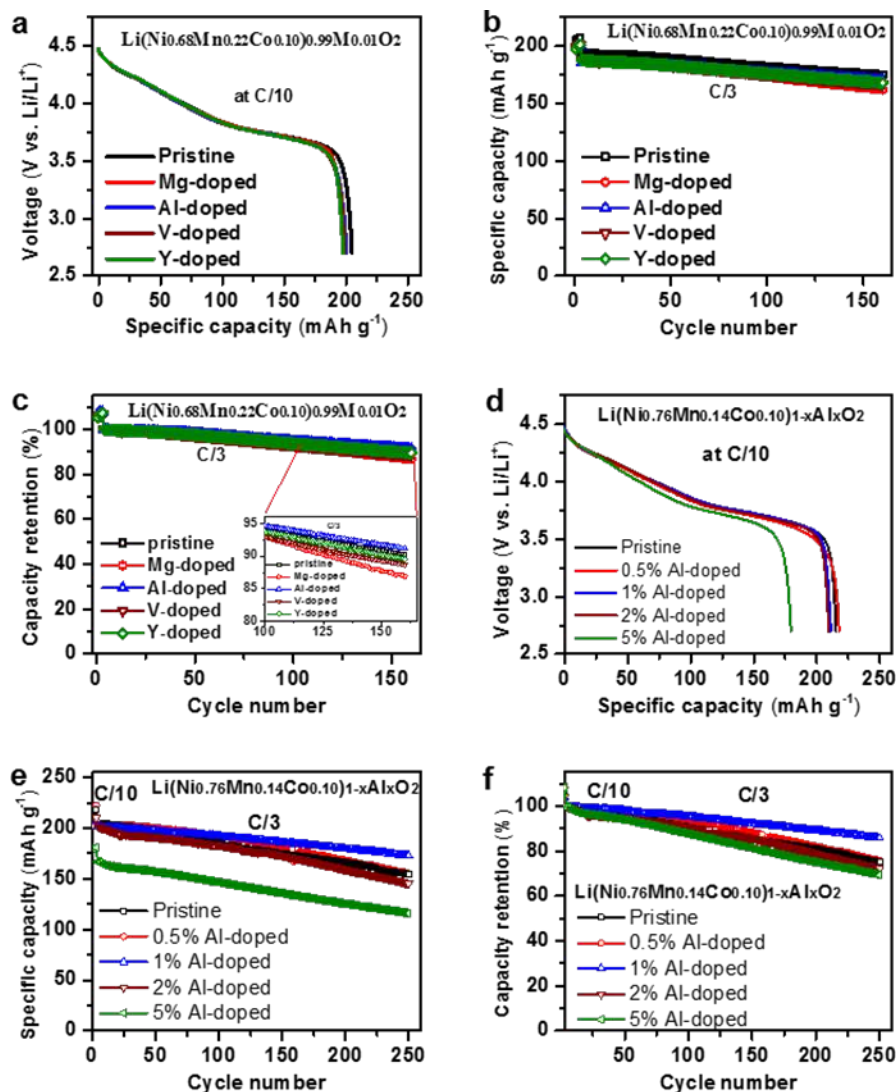


Figure II-254. (a) Initial discharge profiles at C/10, (b) cycling performance and (c) capacity retention of $\text{Li}(\text{Ni}_{0.68}\text{Mn}_{0.22}\text{Co}_{0.10})_{0.99}\text{M}_{0.01}\text{O}_2$ ($\text{M} = \text{Mg}, \text{Al}, \text{V}, \text{or Y}$) during cycling at C/3 after 3 formation cycles at C/10 ($1\text{C} = 200 \text{ mA g}^{-1}$). (d) Initial discharge voltage profiles at C/10, (e) cycling performance and (f) capacity retention of $\text{Li}(\text{Ni}_{0.76}\text{Mn}_{0.14}\text{Co}_{0.10})_{1-x}\text{Al}_x\text{O}_2$ during cycling at C/3 after 3 formation cycles at C/10. Cathode electrode loading: $\sim 4 \text{ mg cm}^{-2}$.

The effect of Al doping content on the electrochemical performance of another Ni-rich NMC $\text{Li}(\text{Ni}_{0.76}\text{Mn}_{0.14}\text{Co}_{0.10})_{1-x}\text{Al}_x\text{O}_2$ (synthesized at 750°C) was also investigated. The doping amount had significant effect on the long-term cycling performance of the Ni-rich NMC $\text{Li}(\text{Ni}_{0.76}\text{Mn}_{0.14}\text{Co}_{0.10})_{1-x}\text{Al}_x\text{O}_2$ (Figure II-254e, f). Increasing the doping amount to above 1% leads to decreased discharge capacity, owing to the electrochemical inactivity of Al (Figure II-254d). The pristine $\text{LiNi}_{0.76}\text{Mn}_{0.14}\text{Co}_{0.10}\text{O}_2$ showed relatively fast capacity fading during cycling, exhibiting a capacity retention of 75.2% after 250 cycles. With 0.5 mol% and 1 mol% Al doping, the capacity retention after 250 cycles was improved to 75.8% and 85.8%, respectively. Further increasing the Al doping amount to above 1 mol% led to fast capacity degradation. The materials with 2 mol% and 5 mol% Al doping showed inferior cycling stability, maintaining only 72.1% and 69.4% of their initial capacity, respectively, after 250 cycles. This could be because excess Al precursor could not be successfully doped into the layered structure lattice, but formed a thick coating on the surface, which dramatically increased the kinetic barrier for lithium ion transportation and the reversible lithium ion de/intercalation processes. The results suggest that both the doping elements and the doping amount must be carefully optimized in Ni-rich NMC cathodes to maximize their electrochemical performance.

Conclusions

Three approaches were pursued to improve the structural and interfacial stability of high-energy-density Ni-rich NMC cathode materials for LIBs.

In the first approach, a thin Li_3PO_4 solid electrolyte layer was infused along the grain boundaries of Ni-rich $\text{LiNi}_{0.76}\text{Mn}_{0.14}\text{Co}_{0.10}\text{O}_2$ secondary particles via ALD coating and thermal infusion. The infused LPO solid electrolyte network could block the diffusion of electrolyte during cycling and act as an efficient buffer to minimize the detrimental influence of the micro-strain generated during deep delithiation. Therefore, the LPO-infused material showed well-maintained dense packing of the primary particles along with well-preserved layered structure without serious phase transformation even after long-term cycling. The homogeneous solid electrolyte coated material demonstrated significantly enhanced cycling stability, achieving the improved capacity retention of 91.6% after 200 cycles. These fundamental findings prove that artificial solid electrolyte infusion is a promising technology for prolonging the cycle life of high-energy-density Ni-rich cathode materials.

In the second approach, an optimized electrolyte (0.6 M LiTFSI, 0.4 M LiBOB, and 0.05 M LiPF_6 in EC-EMC) was shown to improve the electrode/electrolyte interface of Ni-rich $\text{LiNi}_{0.76}\text{Mn}_{0.14}\text{Co}_{0.10}\text{O}_2$. The optimized electrolyte significantly improved the long-term cycling stability of $\text{LiNi}_{0.76}\text{Mn}_{0.14}\text{Co}_{0.10}\text{O}_2$ at different C rates ranging from C/3 to 5C. In particular, when cycled at C/3, the capacity retention with E-optimized was increased to 86.9% after 250 cycles, far superior to the 75.2% retention obtained with E-baseline. In addition to improving the stability of the Li metal anode, another important reason for the improved cycling performance is formation of an enhanced CEI layer that can better protect the Ni-rich $\text{LiNi}_{0.76}\text{Mn}_{0.14}\text{Co}_{0.10}\text{O}_2$ cathode against electrolyte corrosion and suppress the structural transformation from layered to disordered NiO type rock-salt phase.

The third approach used in this work is lattice doping, which can effectively enhance the surface structural stability of Ni-rich NMCs. Several lattice dopants (Mg, Al, V, and Y) were investigated. Al dopant showed improved long-term cycling stability of Ni-rich materials including $\text{LiNi}_{0.68}\text{Mn}_{0.22}\text{Co}_{0.10}\text{O}_2$ and $\text{LiNi}_{0.76}\text{Mn}_{0.14}\text{Co}_{0.10}\text{O}_2$. With 1 mol% Al doping, the capacity retention after 250 cycles of a Ni-rich $\text{LiNi}_{0.76}\text{Mn}_{0.14}\text{Co}_{0.10}\text{O}_2$ cathode was improved to 85.8%, which is much better than that obtained for pristine material (75.2% after 250 cycles). Further increasing the Al doping amount above 1 mol% led to faster capacity degradation. This could be explained by an increased kinetic barrier for lithium ion transportation caused by excess Al precursor that could not be successfully doped into the material structure, but only existed as a thick coating layer. The results suggest that doping elements and doping amount should be carefully optimized to maximize the performance of Ni-rich NMC cathodes.

Based on the above achievements and fundamental understanding, future work will be focused on lattice modification, effective grain boundary engineering, and identification of effective electrolyte additives (or a combination of these) to maximize the long-term cycle life of Ni-rich NMC cathode materials. Any improvement identified in lithium half-cells will be further evaluated in full-cell configurations using graphite or a higher capacity Si/C composite as anode materials.

Key Publications

1. The roles of oxygen non-stoichiometry on the electrochemical properties of oxide-based cathode materials, Jianming Zheng, Jie Xiao, and Ji-Guang Zhang, *Nano Today*, 11(5), 678-694 (2016).
2. Intragranular cracking as a critical barrier for high-voltage usage of layer-structured cathode for lithium-ion batteries, Pengfei Yan, Jianming Zheng, Meng Gu, Jie Xiao, Ji-Guang Zhang, Chongmin Wang, *Nature Communications*, 8, 14101 (2017).
3. Li- and Mn-Rich Cathode Materials: Challenges to Commercialization, Jianming Zheng, Seung Myeong, Woongrae Cho, Pengfei Yan, Jie Xiao, Chongmin Wang, Jaephil Cho, and Ji-Guang Zhang, *Advanced Energy Materials*, 7(6), 1601284 (2017).
4. Suppressed oxygen extraction and degradation of $\text{LiNi}_x\text{Mn}_y\text{Co}_z\text{O}_2$ cathodes at high charge cut-off voltages, Jianming Zheng, Pengfei Yan, Jiandong Zhang, Mark Engelhard, Zihua Zhu, Bryant Polzin, Steve Trask, Jie Xiao, Chongmin Wang, Ji-Guang Zhang, *Nano Research*, <https://doi.org/10.1007/s12274-017-1761-6>.
5. High capacity and stable cathode materials, Jianming Zheng, Ji-Guang Zhang, Pengfei Yan, Chongmin Wang, Wengao Zhao, Shuru Chen, Wu Xu, U.S. Patent Application No. 15/597,025.

II.C.7 *In situ* Solvothermal Synthesis of Novel High-Capacity Cathodes (BNL)

Feng Wang, Principal Investigator

Brookhaven National Laboratory
Sustainable Energy Technologies Department
Upton, NY 11973
Phone: 631-344-4388
E-mail: fwang@bnl.gov

Jianming Bai, Co-Principal Investigator

Brookhaven National Laboratory
National Synchrotron Light Source II
Upton, NY 11973
Phone: 631-344-2583
E-mail: jmbai@bnl.gov

Tien Duong, Technology Manager

U.S. Department of Energy
Phone: 202-586-7836
E-mail: Tien.Duong@ee.doe.gov

Start Date: October 1, 2015
Total Project Cost: \$1,050,000

End Date: September 30, 2018
DOE share: \$1,050,000

Non-DOE share: \$0

Project Introduction

Despite considerable interest in developing new battery electrodes, only a small number of known materials show real promise for achieving significant improvement in capacity and/or a reduction in cost. The preparation of new compounds or materials with unique properties often relies on trial and error as there are a variety of synthesis parameters (precursor concentration, temperature, pressure, *pH* value, cation type and reaction time, etc.) that can have a strong influence on the material properties (crystal structure, morphology, particle size) and electrochemical performance. Most synthesis reactions are carried out in a sealed autoclave and therefore the reactor is a black box – the inputs and outputs are known, but little is known about intermediate phases and overall reaction pathways. *In situ*, *real-time* probing of synthesis reactions can provide the details of reactions, elucidating intermediate phases and how temperature, pressure, time and the precursor concentrations affect the reaction pathways. The results of such studies enable strategies to optimize synthesis reactions, particularly the formation of materials of desired phases and properties. With a better understanding of the correlation between synthesis conditions, crystallization processes, and material properties, a rational design of advanced battery materials should emerge.

Objectives

The goal is to develop novel high-capacity cathodes through synthetic control of the phase, stoichiometry and morphology.

Approach

One unique approach taken in this project is to develop *in situ* techniques/capabilities for diagnostics and synthetic design of new battery materials using the world-best facilities at Brookhaven and other national laboratories. More specifically, synchrotron X-ray, neutron-based *in situ* techniques are developed and applied to studies of synthesis reactions during preparation of high-capacity cathode materials, allowing access to the structural chemistry involving intermediate and short-lived phases. Insights obtained from *in situ* studies will provide knowledge on how the synthesis conditions (temperature, pressure, *pH*, precursor concentration, etc.)

affect the kinetics and pathways of synthesis reactions. *Ex-situ* characterization conducted using synchrotron X-ray, neutron scattering, transmission electron microscopy (TEM), electron energy-loss spectroscopy (EELS) and various electrochemical techniques helps us to gain understanding of how structure, composition, and synthesis affect electrochemical performance. Together, *in situ* studies of synthesis process coupled with *ex situ* structural/electrochemical characterization of the synthesized materials provide a basis for synthetic design of phase-pure cathodes of desired stoichiometry and morphology.

Results

In situ studies of synthesis reactions in preparing layered oxides

In the last fiscal year, *in situ* studies were made on synthesis reactions in preparing LiNiO_2 and the Co-substituted variants ($\text{LiNiCo}_x\text{O}_2$), and with the insights gained from the studies, synthesis procedures were developed for making Ni-rich layered oxides with synthetic control of structural and electrochemical properties. The developed *in situ* approaches were further applied to studies of synthesis reactions in making LiCoO_2 , LiNiO_2 , and a series of solid solutions $\text{LiNi}_{1-x}(\text{CoMn})_x\text{O}_2$ from hydroxide precursors. Synchrotron X-ray was employed for fast acquisition of high-resolution diffraction patterns with wide Q range, allowing access to intermediates and short-lived phases under real synthesis conditions.

Precursors were made from mixtures of Li source (LiOH) with transition metal hydroxides, $\text{TM}(\text{OH})_2$ ($\text{TM} = \text{Ni, Co, Mn}$ of varying molar ratios). Time-resolved synchrotron x-ray diffraction (XRD) patterns were recorded from the hydroxide mixtures upon heating from low to high temperatures. Figure II-255 shows representative contour plots of the XRD patterns recorded from intermediates at low temperatures ($\leq 500^\circ\text{C}$) in preparing LiNiO_2 and $\text{LiNi}_{0.7}\text{Co}_{0.15}\text{Mn}_{0.15}\text{O}_2$ (NMC71515). The phase transformation process is overall similar in these two cases, both from initial hydroxides (space group: $p\text{-}3m1$) to the layered phase ($R\text{-}3m$). But more complex reaction occurred in the precursors containing 2 and 3 elements, along a much different pathway than that in those precursors containing only Ni or Co. For example, heat treatment led to decomposition of $\text{Ni}(\text{OH})_2$ at $\sim 230^\circ\text{C}$, giving rise to rock-salt (NiO), and no layered phase was observed at temperatures up to 500°C (Figure II-255a). In contrast, $\text{Ni}_{0.7}\text{Co}_{0.15}\text{Mn}_{0.15}(\text{OH})_2$ transformed into structurally similar intermediates at temperatures between $218\text{--}313^\circ\text{C}$, and layered phase thereafter, through complex anionic exchange and cationic migration/re-ordering processes (Figure II-255b). Results from *ex situ* XRD measurements showed that, with elongated sintering time, the transformation from $\text{Ni}_{0.7}\text{Co}_{0.15}\text{Mn}_{0.15}(\text{OH})_2$ to the intermediates occurred at a much lower temperature ($\sim 120^\circ\text{C}$), and then to the layered at temperature as low as 200°C . Quantitative structure analysis is now under way for better understanding of the synthesis process and dependence of kinetic pathway on transition element species in the precursors.

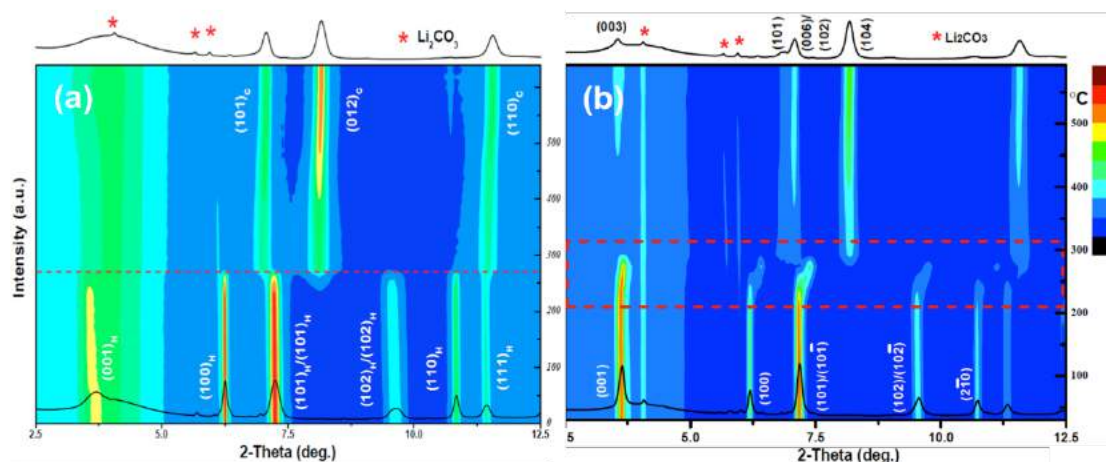


Figure II-255. *In situ* temperature-resolved synchrotron XRD for tracking structural evolution of intermediates in preparing (a) LiNiO_2 , (b) NMC71515 from hydroxides (via solid-state reaction in O_2 flow with a heating rate of $5^\circ\text{C}/\text{min}$).

Technique development for *in situ* probing cation ordering

In addition to various *in situ* reactors built for X-ray experiments, a new design of *in situ* reactor, with configuration suited for neutron diffraction (ND) measurements was recently developed, with a gas-flow system integrated allowing for probing solid-state reaction under controlled atmosphere (Figure II-256a). The reactor has been used for *in situ* ND studies of synthesis reactions in preparing NMC71515. Figure II-256b shows one representative contour plot of temperature-resolved ND patterns from the measurements, revealing the entire reaction process, from the precursors (a mixture of Li/transition metal hydroxides) to intermediates, and then to the final layered NMC71515. The results are consistent with the *in situ* XRD observation (Figure II-255b), but more details were obtained from *in situ* ND measurements (particularly on cation ordering), owing to the unique capabilities of neutron scattering in detecting light elements (*e.g.*, Li) and differentiation of the involved transition metals (Ni, Mn, Co).

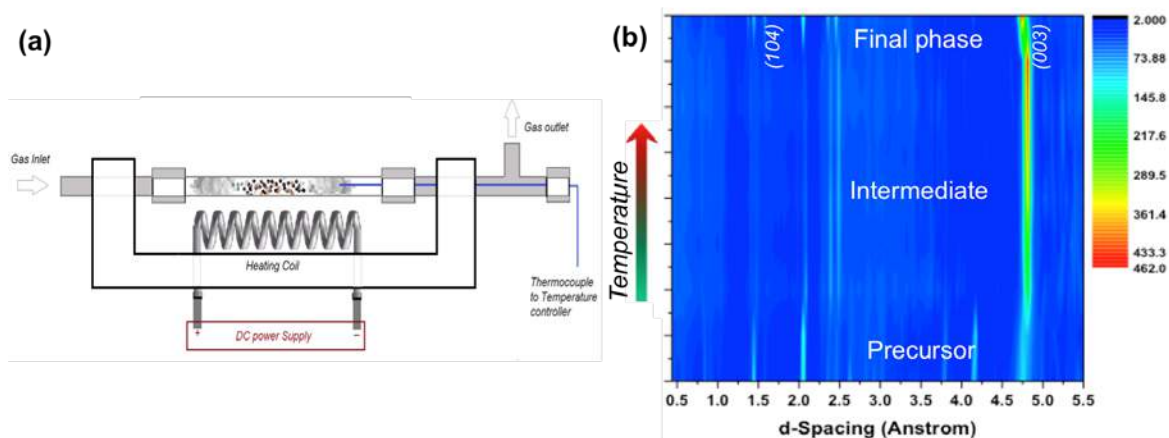


Figure II-256. (a) Setup for *in situ* neutron and synchrotron diffraction measurements. (b) Contour plot of temperature resolved *in situ* neutron diffraction patterns of intermediates during synthesis of NMC71515.

Details of the synthesis reactions can now be obtained through joint refinement of *in situ* XRD and ND data acquired from the same system (as demonstrated in Figure II-257), not only on the overall structural evolution, but potentially on the ordering of all the involved cations, thereby offering new insights into kinetic and thermodynamic parameters governing synthesis process in preparing Ni-rich layered oxides.

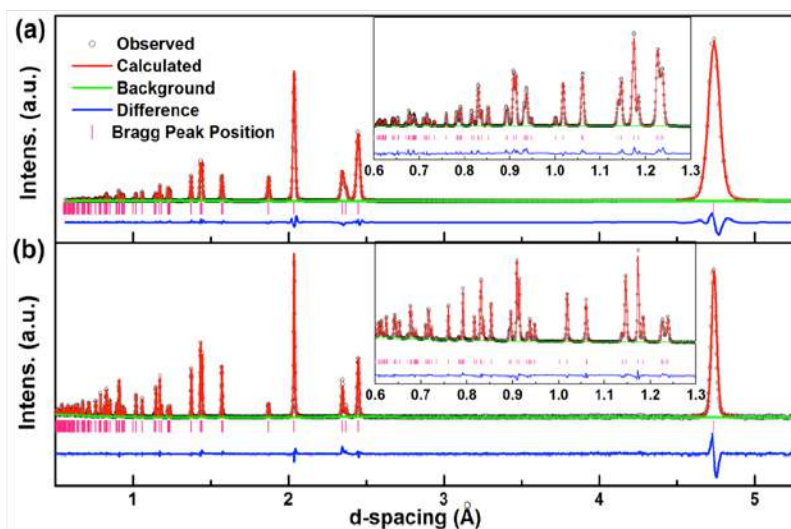


Figure II-257. (a) Synchrotron X-ray and (b) neutron diffraction patterns of the synthesized NMC71515, in comparison to that from structure refinement. The enlarged spectra in small d-spacing range are shown in the inset. In the plots, open circles are used for the observed data, red lines for the calculated data, pink bars for Bragg positions, blue lines for the difference between the observed and calculated data, and green lines for the refined background.

Kinetic control of the cation ordering in NMC71515

In addition to studies on the reaction pathway of the whole synthesis process (as given above), synchrotron and neutron-based *in situ* techniques were also applied to probing and synthetic control of the cation ordering in Ni-rich layered oxides subjected to heat treatment at high temperatures. Representative time-resolved synchrotron XRD patterns from NMC71515 are shown in Figure II-258a. The evolution of diffraction peaks, such as fast rise of (003) peak, indicates rapid improvement of cation ordering during the heat treatment and strong dependence on temperature (Figure II-258b-d).

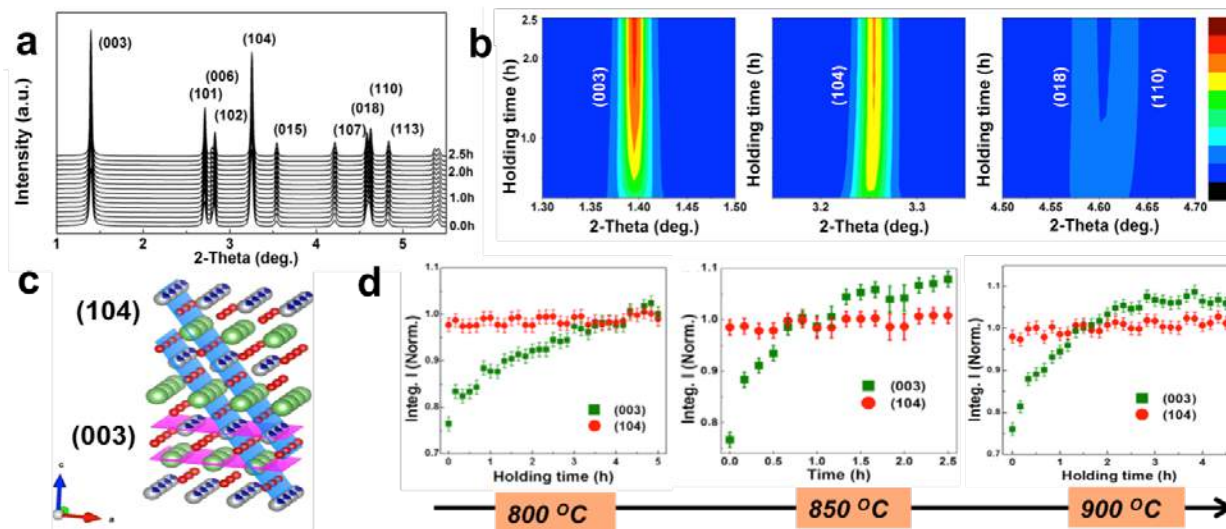


Figure II-258. (a) Representative time-resolved XRD patterns from NMC71515 during heat treatment (at 850°C). (b) Evolution of the reflections characteristic of layered structure. (c) Illustration of the atomic configuration and reflection planes of (104) and (003) in the layered structure. (d) Evolution of the integrated intensity of the (003) and (104) peaks.

Details on structural ordering processes, such as the evolution of Li-slab distance and Li/Ni disordering with holding time, were obtained through quantitative analysis of XRD data (Figure II-259a, b). The results from this study revealed a complex synthesis process, involving competition between cationic ordering and disordering processes (largely due to Li/O loss) that concomitantly occur during heat treatment. Treatment at elevated temperature would always facilitate the ordering process, but the ordering kinetics did not increase monotonically with temperature -- being compromised by the accelerated disordering with an increase of temperature. Kinetic control of the cationic ordering, *via* finely tuning heating temperature and time, was found to be crucial to optimizing structural ordering of the final products.

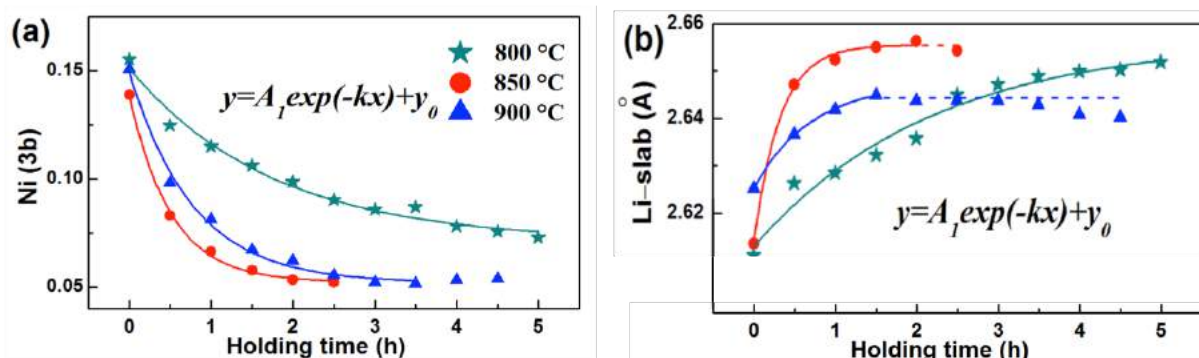


Figure II-259. (a) Evolution of cationic disordering (i.e., Ni ions at 3b sites) and (b) Li-slab distance with holding. (Lines: fittings to $y = A_1 \exp(-kx) + y_0$).

The impact of synthesis conditions on the kinetic pathway and structural ordering of the final products was evaluated through *in situ* XRD, X-ray absorption spectroscopy (XAS), thermogravimetric analysis (TGA), and *ex situ* structural characterizations. The combined studies revealed a strong temperature dependence of the kinetics of cationic ordering in NMC71515 as a result of thermal-driven oxidation of transition metals and Li/O loss (Figure II-260a) that concomitantly occurred during heat treatment. In addition, particles grew quickly upon high-temperature treatment (Figure II-260b). Kinetic control of the cationic ordering and morphology, *via* finely tuning heating temperature and holding time, was found to be crucial to optimizing the electrochemical performance of the final products.

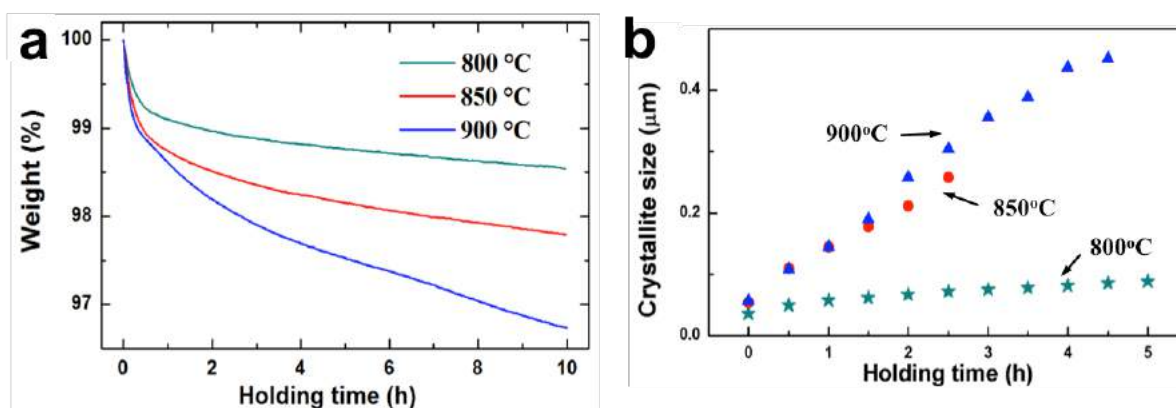


Figure II-260. (a) TGA curves of the precursors during holding at constant temperatures (800 °C, 850 °C, 900 °C). (b) Evolution of crystallite size with holding time at the three temperatures (as labeled).

Evaluation of synthesis conditions on the electrochemical performance of the final products

The findings from this study enabled us to identify optimal conditions for synthesizing NMC71515 with low cationic disordering and high electrochemical activity. Figure II-261a displays the representative charge/discharge voltage profiles of synthesized materials, indicating much higher discharge capacity in the sample synthesized at 850 °C, 197 mAh g⁻¹, compared to that obtained at 800 and 900 °C, 162 and 174 mAh g⁻¹, respectively. In addition, a lower overpotential was obtained in the sample heated at 850 °C. The measured electrochemical performance is in good agreement with structural analysis, that is, the sample heated at 850 °C has low Li/Ni mixing at 3b sites, large Li slab, and moderate crystallite size. Excellent capacity retention was obtained in the three samples obtained at 800, 850, and 900 °C, of 93.5%, 84.1%, and 84.5% after 50 cycles (Figure II-261b). The extension of electrochemical windows to 4.5, 4.7 V led to greatly increased capacity, but at the cost of capacity retention. The findings from this study provide new insights into synthetic design of high-Ni layered oxide cathodes.

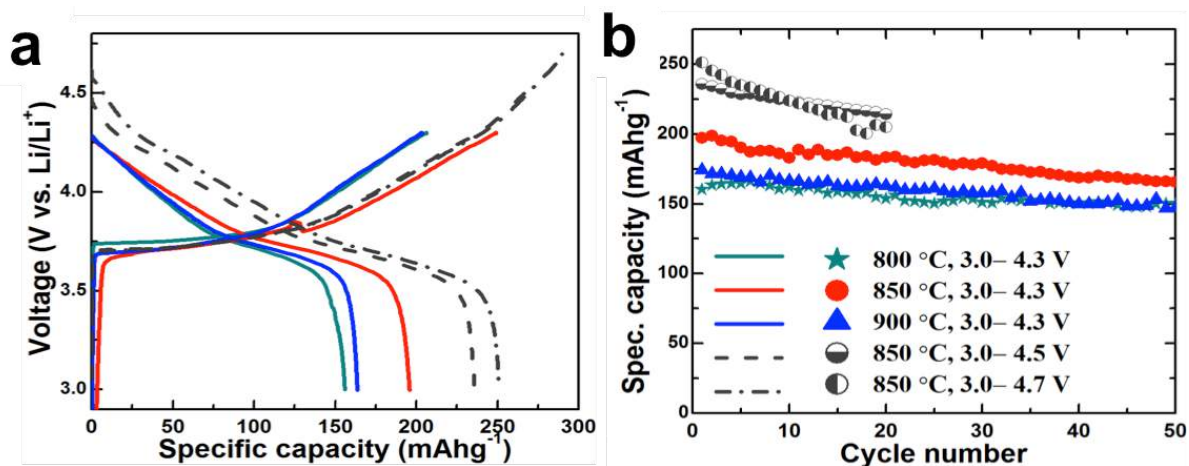


Figure II-261. Structural, chemical and morphological evolution in the intermediates of NMC71515 during heat treatment at 800 °C, 850 °C, 900 °C. (a) Evolution of the cationic disordering (i.e., occupancy of Ni ions at 3b sites). (b) TGA curves of the precursors during holding at constant temperatures. (c) Evolution of crystallite size with holding time.

Conclusions

New capabilities were developed under this project, enabling *real time* probing of cation ordering in Ni-rich layered oxides during synthesis under controlled atmosphere. Details of the synthesis reactions can now be obtained through joint refinement of *in situ* XRD and ND data acquired from the same system, not only on the overall structural evolution, but the ordering of all the involved cations, thereby offering new insights into kinetic/thermodynamic parameters governing synthesis process in preparing Ni-rich layered oxides.

Following the previous studies on synthesis of LiNiO₂, LiNi_{0.8}Co_{0.2}O₂, *in situ* studies were further conducted on synthesis reactions in preparing high-Ni layered oxides, with focus on the specific composition of NMC71515, for getting deep insights into synthetic control of structural ordering in this type of materials. Time-resolved *in situ* HEXRD, XAS, ND were employed, coupled with quantitative data analysis, to track the kinetic reaction pathway and cationic ordering in the intermediates towards forming NMC71515 when subjected to high-temperatures heat treatment. The *real-time* observation revealed a dynamically competing cationic ordering/disordering process, arising from thermal-driven cationic oxidation and Li/O loss that concomitantly occurs during heat treatment. Through synthetic control of kinetic reaction pathway, the structural ordering of the final products was tuned for obtaining highly ordered NMC71515 with excellent electrochemical performance. The findings shed light on designing high-performance Ni-rich layered oxides through synthetic control of the kinetic reaction pathway and structural ordering in the materials.

In the future, *in situ* studies will be carried out for developing different types of cathodes, but with a focus on compositionally heterogeneous NMC layered oxides, wherein both high capacity and long cycling stability are expected to be achieved *via* synthetic control of local oxidation and ordering of cations in the materials.

Key Publications

1. D. Wang, R. Kou, Y. Ren, C-J. Sun, H. Zhao, M-J. Zhang, Y. Li, A. Huq, J.Y.P. Ko, F. Pan, Y-K. Sun, Y. Yang, K. Amine, J. Bai, Z. Chen and F. Wang, “*Synthetic Control of Kinetic Reaction Pathway and Cationic Ordering in High-Nich Layered $\text{LiNi}_{0.7}\text{Co}_{0.15}\text{Mn}_{0.15}\text{O}_2$ Cathodes*”, **Adv. Mater.** 29 (2017) 1606715.
2. Y-U. Park, J. Bai, L. Wang, G. Yoon, W. Zhang, H. Kim, S. Lee, S-W. Kim, J.P. Looney, K. Kang and F. Wang, “In situ Tracking Kinetic Pathways of Li^+/Na^+ Substitution during Ion-exchange Synthesis of $\text{Li}_x\text{Na}_{1.5-x}\text{VOPO}_4\text{F}_{0.5}$ ”, **J. Am. Chem. Soc.** 139 (2017) 12504.
3. J. Zhao, W. Zhang, A. Huq, S.T. Misture, B. Zhang, S. Guo, L. Wu, Y. Zhu, Z. Chen, K. Amine, F. Pan, J. Bai, F. Wang, “*In-situ Probing and Synthetic Control of Cationic Ordering in Ni-rich Layered Oxide Cathodes*”, **Adv. Energy Mater.** 7 (2017) 1601266.
4. F. Wang, X. Wang, J. Graetz, P. Khalifah, “*Nanostructured Copper Vanadium Oxides as High-Capacity Cathodes for Lithium-ion Batteries*”, **US non-provisional patent** (filed in Sept. 2017).
5. ACS Spring Meeting, April 17-21, 2017, “*In-situ Structure-tracking Aided Design in Synthesis of Energy-Storage Materials*”, F. Wang and J. Bai.
6. ACS Spring Meeting, April 17-21, 2017, “*Synthetic Control of Structural and Electrochemical Properties of High-Ni Layered Oxide Cathodes for Next-generation Li-ion Batteries*”, D. Wang, M-J. Zhang, J. Bai and F. Wang.
7. MRS 2017 Spring Meeting, April. 17-21, 2017, “*In Situ Tracking of the Structural Chemistry during Synthesis of Ni-Rich Layered Oxides as High-Energy Cathodes for Li-Ion Batteries*”, J. Bai, J. Zhao, D. Wang, J.Y. P. Ko, A. Huq and F. Wang.
8. Annual Merit Review, DOE, Washington, D.C. (June 5 – 9, 2017): “*In-situ Solvothermal Synthesis of Novel High- Capacity Cathodes*”, F. Wang and J. Bai.
9. MRS 2016 Fall Meeting, *Developing High-Capacity Ni-rich Layered Oxide Cathodes for Li-ion Batteries via in-situ Synthetic Control of the Structure and Material Properties*, Nov. 27--Dec. 2, 2016, in Boston, Massachusetts, D. Wang, J. Bai, J. Zhao, W. Zhang, and F. Wang.

II.C.8 Novel Cathode Materials and Processing Methods (ANL)

Michael M. Thackeray, Principal Investigator

Argonne National Laboratory
9700 South Cass Avenue
Lemont, IL 60439
Phone: 630-252-9184
E-mail: thackeray@anl.gov

Jason R. Croy, Principal Investigator

Argonne National Laboratory
9700 South Cass Avenue
Lemont, IL 60439
Phone: 630-252-9184
E-mail: croy@anl.gov

Peter Faguy, Technology Manager

U.S. Department of Energy
Phone: 202-586-1022
E-mail: Peter.Faguy@ee.doe.gov

Start Date: October 1, 2015
Total Project Cost: \$500,000

End Date: September 30, 2018
DOE share: \$500,000

Non-DOE share: \$0

Introduction

Research in lithium-ion batteries (LIB) is intensely focused on the development of next-generation systems capable of meeting ever-increasing demands placed on energy and power densities, while maintaining acceptable levels of cost and safety. Lithium- and manganese-rich, ‘layered-layered’ (LL), composite materials, $x\text{Li}_2\text{MnO}_3 \cdot (1-x)\text{LiMO}_2$ ($M = \text{Mn, Ni and Co}$; $0 < x < 0.5$), have received considerable attention owing to their high reversible capacities (~ 250 mAh/g) when compared to competing LIB cathodes that deliver capacities of < 180 mAh/g (i.e., LiCoO_2 , LiMn_2O_4 , $\text{Li}_{1+x}\text{Ni}_{1-a}\text{Mn}_b\text{Co}_c\text{O}_2$ (NMC) and LiFePO_4). In addition, Mn-rich materials are attractive due to their favorable cost and safety characteristics with respect to Co- and Ni-rich systems. However, key challenges to the wide scale adoption of LL composite cathodes remain. Notably, irreversible structural changes occur on the extraction of lithium from Li- and Mn-rich domains within the composite structure during first-cycle charge and “activation” above ~ 4.4 V (vs. Li/Li^+). These changes lead to subsequent voltage fade and hysteresis in the charge/discharge curves and slowly decrease the energy output of cells. Furthermore, the activation process leads to surface degradation that contributes to the material’s poor rate performance, especially at low states of charge.

A promising approach to stabilizing LL structures has been to integrate a structurally compatible spinel component to form a complex, ‘layered-layered-spinel’ (LLS) composite. Previous work done under this project has shown that by controlling the amount of spinel integration, while limiting excess lithium contents, several metrics can be simultaneously improved. Specifically, voltage fade, rate capability, and first-cycle efficiencies are all enhanced for LLS cathodes with respect to their spinel-free, LL counterparts. In terms of surfaces, oxygen loss, surface reconstruction, and Mn dissolution are all surface issues that can contribute to poor cycle-life and rate performance of Li- and Mn-rich cathode materials and countless treatments/coatings have been tried in attempts to mitigate the adverse effects of unstable surfaces. Treatments have included carbons, phosphates, oxides, polymer coatings, and more. This chapter deals with efforts aimed at further stabilizing Mn-rich cathode materials. Specifically, a previously developed LLS composition is used to

systematically explore the effects of various surface chemistries and synthesis processes on rate and cycle-life of lithium-ion cells containing LLS cathodes.

Objectives

- To develop low-cost, high-energy and high-power Mn-oxide-based cathodes for lithium-ion batteries that will meet the performance requirements of PHEV and EV vehicles
- Improve the design, composition and performance of advanced electrodes with stable architectures and surfaces, facilitated by an atomic-scale understanding of electrochemical degradation processes

Approach

Exploit the concept and optimize the performance of structurally-integrated “composite” electrode structures with a prime focus on LLS materials. Alternative processing routes, in collaboration with Argonne’s Materials Engineering Research Facility (MERF), will be investigated; Argonne National Laboratory’s comprehensive synthesis and characterization facilities will be used to explore novel surface and bulk structures in the pursuit of advancing the properties of state-of-the-art cathode materials.

Results

Several surface treatments and processing routes were investigated with respect to their efficacy in improving the cycle life and/or rate capability of a baseline LLS cathode. Preliminary studies aimed at optimizing the synthesis of a baseline LLS material were conducted using co-precipitation reactors at MERF, and within ANL’s Chemical Sciences and Engineering (CSE) division. This effort resulted in high-quality LLS particles that were subsequently scaled to the ~1 kg level and used in surface-treatment studies.

The baseline LLS has a composition of $\sim\text{Li}_{1.18}\text{Mn}_{0.54}\text{Co}_{0.18}\text{Ni}_{0.28}\text{O}_2$ with an integrated ~ 6% spinel component. Figure II-262a shows a scanning electron microscopy (SEM) image of the final, lithiated product. Particle analysis revealed a D50 (μm) = 20.7 and a reasonably high tap density of 2.0 g/cc. The material exhibited a reversible capacity of ~200 mAh/g when cycled between 4.45 – 2.5 V, after an initial activation cycle between 4.6 – 2.0 V, as shown in Figure II-262b. All electrochemical testing was carried out at 30°C using 15 mA/g charge and discharge currents in cells containing lithium-metal anodes.

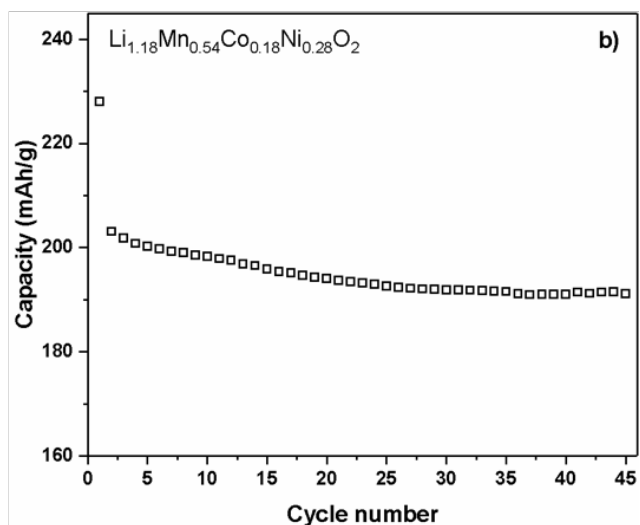
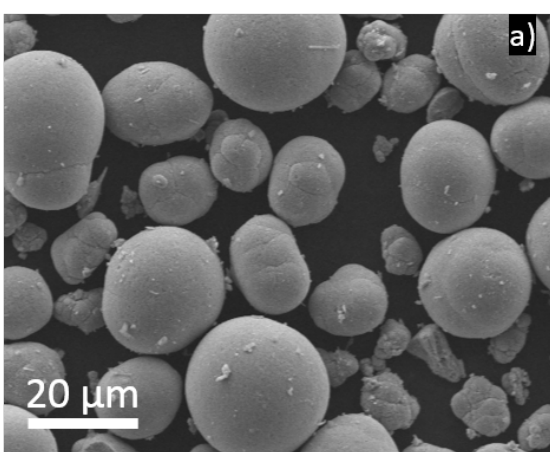


Figure II-262. a) SEM and b) cycle-life of the LLS baseline material used for all surface treatments. All electrochemical characterization was carried out at 30°C and 15 mA/g. Each material underwent an initial activation cycle between 4.6 – 2.0 V followed by extended cycling between 4.45 – 2.5 V vs. Li/Li⁺.

The surface treatments consisted of three chemistries (Li_2WO_4 , Li_3PO_4 , and Al_2O_3) and their respective processing conditions. A summary of the processing conditions for each treatment is found in Table II-8. In short, each treatment was carried out via a wet-chemical method (aqueous) followed by several different post-synthesis annealing temperatures. The weight percent (wt.%) of each surface-treatment chemistry was previously optimized. In general, the capacity of the treated samples increased as the wt.% of the surface treatment decreased. The wt.% shown in Table II-8 for each surface-treatment chemistry exhibited improved cycle life while still maintaining an initial capacity similar to that of the baseline material (~ 200 mAh/g). SEM/energy dispersive spectroscopy (SEM/EDS) measurements on surface-treated samples suggest that homogenous coverage of the baseline material was achieved and that the morphology was unaffected during the surface treatments. Representative images are shown later in Figure II-265 (right).

Table II-8: Surface treatments investigated on a LLS $\text{Li}_{1.18}\text{Mn}_{0.54}\text{Co}_{0.18}\text{Ni}_{0.28}\text{O}_2$ (~ 6% spinel)

Chemistry	Wt. %	Temp 1	Temp 2	Temp 3	Temp 4	Precursors
Li_2WO_4	2	500 °C	650 °C	850 °C	-----	Li_2WO_4 Sigma Aldrich
Li_3PO_4	1	100 °C	200 °C	550 °C	750 °C	Lithium hydroxide and ammonium dihydrogen phosphate
Al_2O_3	0.5	100 °C	200 °C	400 °C	550 °C	Aluminum nitrate nanohydrate

The effect of post-treatment annealing temperature on the capacity retention for each of the surface-treatment chemistries is shown in Figure II-263(a-c). The untreated, baseline, LLS is shown as black squares in all figures. No clear trend was observed for samples treated with Li_2WO_4 with respect to the annealing temperature, Figure II-263a. However, a decrease in performance on going from 650°C to 850°C suggests that a volcano-type plot may result with more data points and that the optimum temperature is close to 650°C. Nonetheless, each of the samples treated with Li_2WO_4 exhibited superior cycle-life with respect to the baseline LLS. Surprisingly, the cycle-life improved as the annealing temperature was decreased for the samples treated with Li_3PO_4 (Figure II-263b) and Al_2O_3 (Figure II-263c). Interestingly, the samples treated at the lowest temperature of 100°C for both the Li_3PO_4 and Al_2O_3 (Figure II-263c) exhibited the best capacity retentions after 50 cycles. Overall, most of the surface-treated samples demonstrated improved capacity retention, irrespective of the chemistry. In fact, Figure II-263d reveals that the “best” sample for each of the surface chemistries produces similar capacity retention.

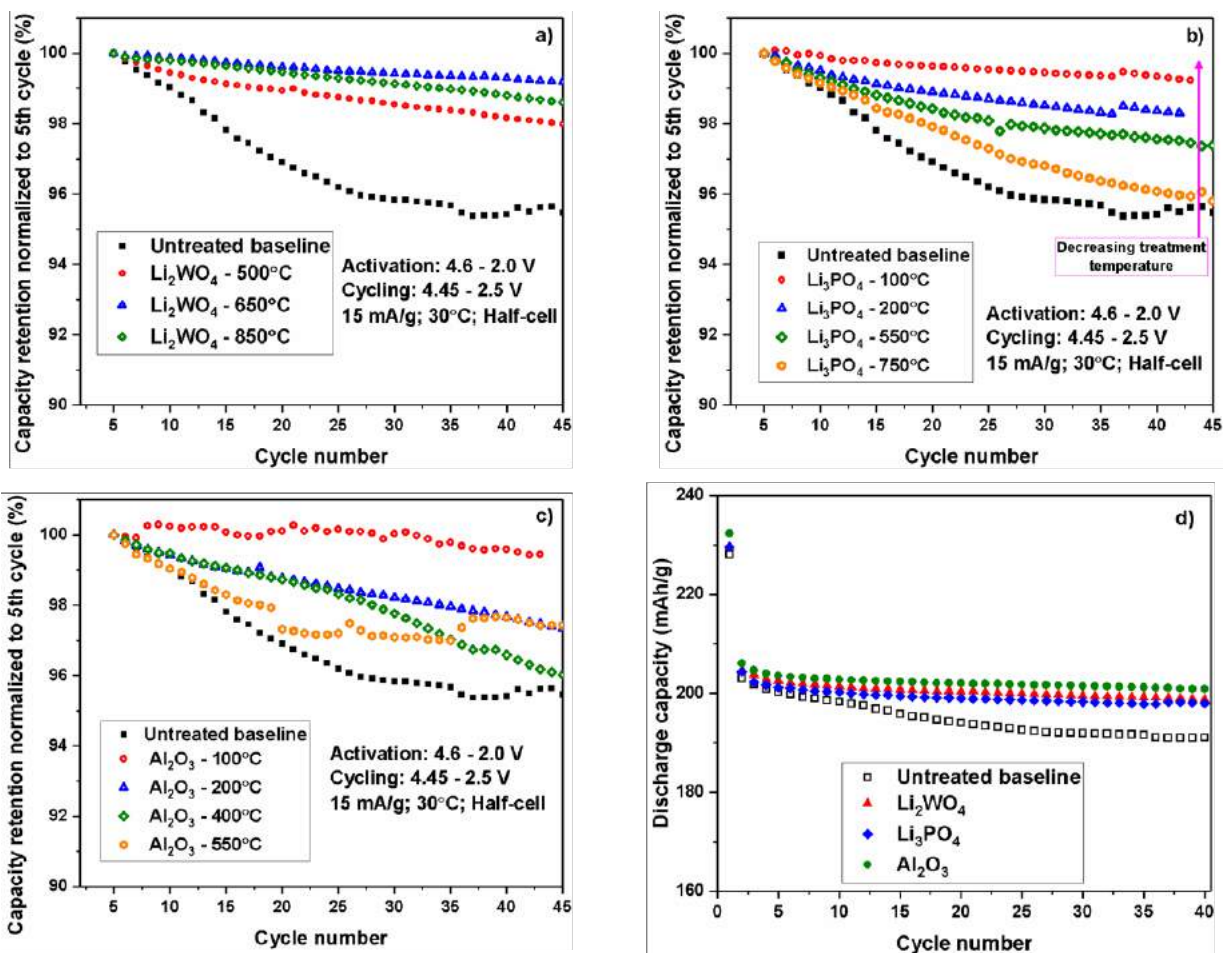


Figure II-263. Capacity retention vs. cycle number, as a function of post-treatment annealing temperature, for LLS samples that have undergone surface treatments with a) Li_2WO_4 b) Li_3PO_4 and c) Al_2O_3 . The capacity retention was normalized to the discharge capacity delivered on the 5th cycle for each sample. d) A comparison of the cycle-life vs. cycle number of the baseline LLS with the best performing samples from each of the surface treatment chemistries presented in a)-c). All samples were cycled between 4.45 – 2.5 V (vs. Li/Li^+), at 15 mA/g, after an initial activation cycle between 4.6 – 2.0 V.

The rate performance of each of the samples was also tested at 30°C. An initial activation cycle was carried out between 4.6 – 2.0 V at 15 mA/g. All rate cycles were conducted between 4.45 – 2.5 V with a constant charge rate of 15 mA/g while the discharge rates were varied as shown in Figure II-264. As shown in Figure II-264(a-c), the post-treatment annealing temperatures did not affect the rate performances at low-to-intermediate currents (15 – 300 mA/g) for any of the surface chemistries investigated. However, at high currents (750 – 1500 mA/g) the rate performance of the surface treated samples revealed a direct correlation with the annealing temperature. The high rate performance of each surface chemistry improved as the annealing temperature decreased. In the case of the surface chemistries that contain lithium (Li_2WO_4 and Li_3PO_4 , see Figure II-264(a-b), the sample treated with the highest annealing temperature performed similarly to the baseline LLS. While in the case of the surface chemistry that did not contain lithium (Al_2O_3 , see Figure II-264c) the two samples treated at the highest annealing temperatures performed even worse than the baseline LLS. Similar to what was observed in the cycle life testing, a majority of the surface treatments improved the high rate performance of the underlying baseline material. The best performing samples for each of the chemistries are plotted against the baseline in Figure II-264d. The results suggest that similar improvements to the performance can be achieved with the appropriate annealing temperature after the surface treatment has been applied.

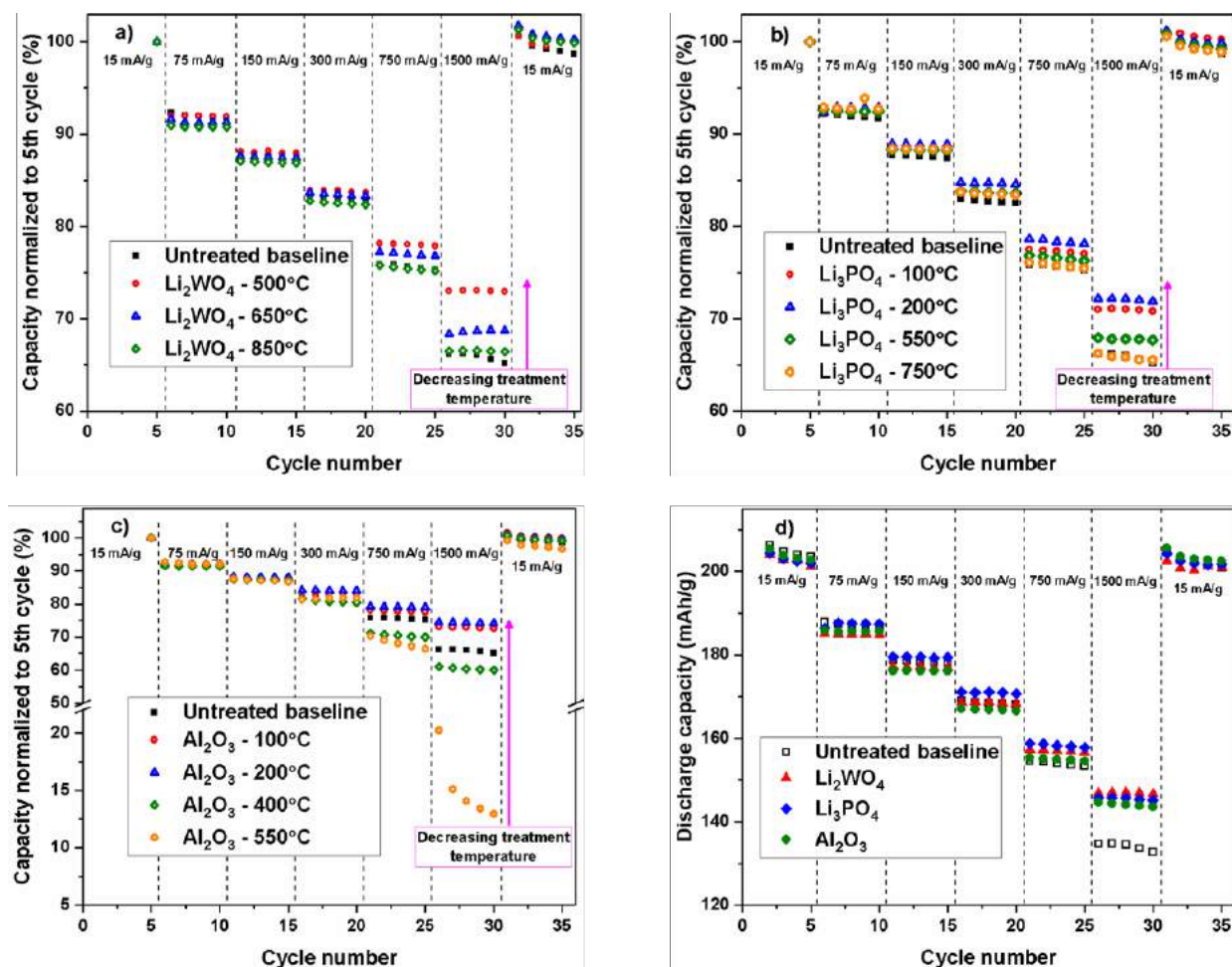


Figure II-264. Normalized capacity vs. cycle number, as a function of post-treatment annealing and discharge rate, for LLS samples that have undergone surface treatments with a) Li₂WO₄ b) Li₃PO₄ and c) Al₂O₃. The capacity of each cycle was normalized to the discharge capacity delivered on the 5th cycle for each sample. d) A comparison of the rate performance of the baseline LLS with the best performing samples from each of the surface treatment chemistries presented in a-c). All samples were cycled between 4.45 – 2.5 V (vs. Li/Li⁺) after an initial activation cycle (not shown in graph) between 4.6 – 2.0 V. Each charge cycle was carried out at 15 mA/g. The discharge currents were varied as labeled on each graph.

To gain a better understanding of the possible role lithium may be playing in the chemistry of the surface treatments, a series of samples was treated with 1 wt.% Li_xCoPO₄ with $x = 0.25, 0.5, 0.75$ and 1.0. The same LLS baseline material (~Li_{1.18}Mn_{0.54}Co_{0.18}Ni_{0.28}O₂ with ~ 6% spinel present) was used. In order to isolate the effect of the lithium content, the annealing temperature was kept constant (700°C). Each of the samples then underwent rate performance testing. The same protocol was used as before: initial activation cycle between 4.6 – 2.0 V followed by cycling between 4.45 – 2.5 V with a constant charge capacity of 15 mA/g. Each of the samples delivered a capacity of ~200 mAh/g when discharged at 15 mA/g, similar to the untreated baseline. The capacities delivered at subsequent discharge currents were normalized to respective, 5th cycle capacities. The results are shown in Figure II-265. Unlike the previous chemistries that were tested, samples treated with LiCoPO₄ all demonstrated superior rate performance, at all currents, when compared to the baseline LLS. Little to no difference was observed in samples with varied lithium contents in the surface treatments at discharge currents between 15 – 750 mA/g. Upon increasing the current to 1500 mA/g it was observed that, in general, the rate performance improved as the lithium content decreased in Li_xCoPO₄. Based on previous experiments with similar systems, it is hypothesized that phosphate-based (and other) treatments may leach lithium from cathode surfaces during processing. Subsequently, achieving optimized lithium contents and

structures, of both surface phases (e.g., LiCoPO_4) and the underlying cathode surfaces themselves, is not straightforward. The end product is dependent on processing parameters such as initial solution composition, pH, and post-annealing treatments. The strategy implied by the above results suggests an alternative route to incorporating integrated spinel phases at cathode particle surfaces via surface-treatment processing.

Characterization efforts are ongoing to understand the phases present at the surfaces of these treated cathodes.

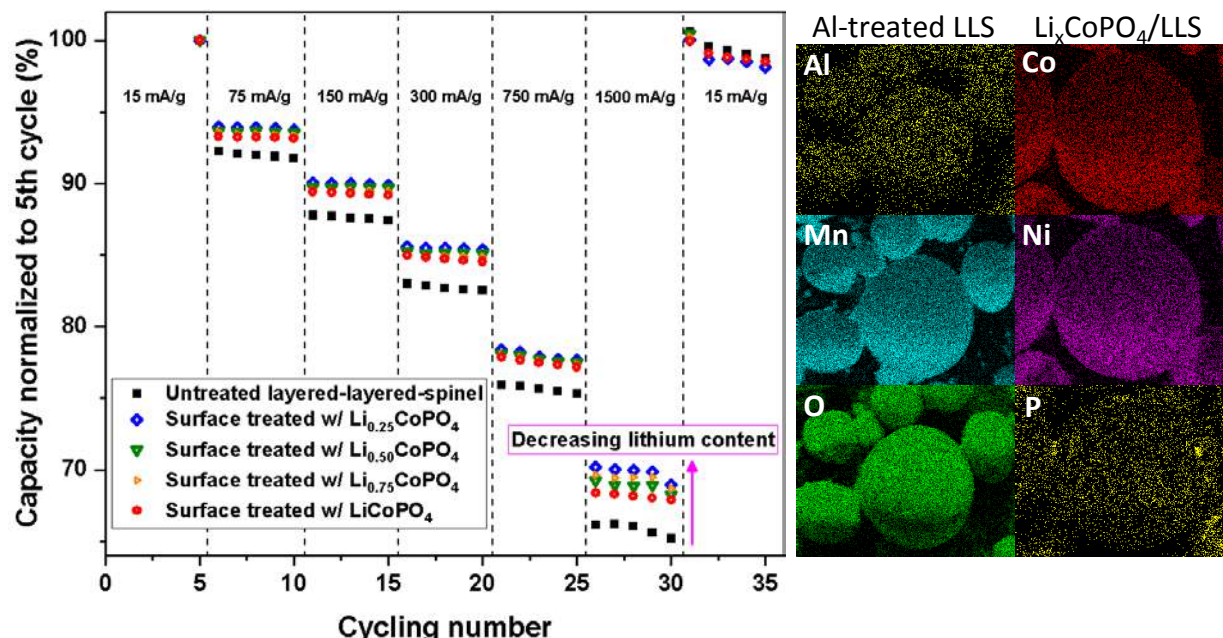


Figure II-265. (Left) Normalized capacity vs. cycle number, as a function of x in Li_xCoPO_4 surface treatments with $x = 0.25, 0.5, 0.75$ and 1.0 . The capacity of each cycle was normalized to the discharge capacity delivered on the 5th cycle for each sample. All samples were cycled between $4.45 - 2.5$ V (vs. Li/Li^+) after an initial activation cycle (not shown) between $4.6 - 2.0$ V. Each charge cycle was carried out at 15 mA/g. The discharge currents were varied as labeled on the graph. (Right) EDS mapping of labeled elements for Al-treated LLS (left column) and LiCoPO_4 treated LLS (right column)

Conclusions

The stabilization of Li- and Mn-rich, LLS, cathode particle surfaces was explored herein. From previous work done by this project, a baseline LLS composition of $\sim\text{Li}_{1.18}\text{Mn}_{0.54}\text{Co}_{0.18}\text{Ni}_{0.28}\text{O}_2$, with $\sim 6\%$ integrated spinel, was scaled to the ~ 1 kg level and used for all surface treatments investigated. Among the parameters explored were surface-treatment chemistry and post-treatment annealing temperatures. Surface chemistries included both lithium- and non-lithium-containing oxides and phosphates. Interestingly, it was found that similar improvements to cycle-life and rate performance, with respect to the untreated baseline material, could be achieved by the appropriate choice of processing conditions for any of the given treatments, regardless of surface chemistry. In addition, lower-temperature, post-annealing conditions consistently led to better high-rate performance. Furthermore, the study revealed the complex interactions between particles surfaces and the solution chemistry. These interactions (e.g., Li leaching) were found to play an important role in determining the final electrochemical properties of surface-treated materials.

The results of this project show that surface treatments can indeed lead to improved performance of Mn-rich, LLS materials and that such treatments will be a critical and necessary aspect of future developments. However, due to the ambiguity of the observed improvements, where no surface chemistry resulted in a clear advantage over others, an important hypothesis might be formed to direct future research; as long as particle surface-treatments result in good uniformity of coverage with surface phases that do not obstruct Li-ion diffusion (e.g., thin or low-level treatments), enhancements over non-treated materials can be observed. It is

important to note that this hypothesis is not necessarily positive and may be particularly relevant to cells that do not utilize graphite anodes; where effects such as metal deposition at graphite surfaces leads to enhanced capacity fade. In this respect, ongoing experiments are looking at the efficiency of different treatments in mitigating metal dissolution from cathode surfaces. Finally, due to the unique surface properties and electrochemical mechanisms of Li- and Mn-rich materials, unique surface treatments and processing methods need to be developed in order to better address the novel challenges presented by these materials. Such materials and processes will be the focus of future work.

Key Publications

1. Arturo Gutierrez, *The Next Generation of Li-ion Batteries for Transportation Applications: Perception, Promises and Problems*, University of Illinois Chicago, Chicago, IL, 08 November 2016. **Invited**
2. Jason R. Croy, Mahalingam Balasubramanian, Daniel C. O'Hanlon, Kevin G. Gallagher, Arturo Gutierrez, Eungje Lee, and Michael M. Thackeray, *The Pursuit of High-Capacity Cathodes for High-Energy Lithium-Ion Cells*, IBA 2017, Nara, Japan, 07 March 2017. **Invited**
3. A. Gutierrez, B. Yonemoto, M. He, E. Lee, R. Benedek, Y. Ren, H.M. Meyer II, J.R. Croy, and M.M. Thackeray, *Advancement of Li- and Mn-Rich High Energy Cathodes for Lithium-Ion Batteries*, Advanced Photon Source User Meeting (Lemont, IL), 9, May 2017.
4. M.M. Thackeray and J.R. Croy, *Tailoring Integrated Layered and Spinel Electrode Structures for High Capacity Lithium-Ion Cells*, ES049, DOE Vehicle Technologies Program Annual Merit Review (Arlington, VA), 5-9, June 2017.
5. J.R. Croy, *Development of Cathode Materials for Lithium-Ion Applications at Argonne National Laboratory*, ANL Battery Industry Day (Lemont, IL), 14, June 2017. **Invited**
6. Jason R. Croy, Michael M. Thackeray, Arturo Gutierrez, *Surface Treatment for Lithium Battery Electrode Materials*, U.S. Application filed 62/466,070.

II.C.9 Design of High Performance, High Energy Cathode Materials (LBNL)

Marca M. Doeff, Principal Investigator

Lawrence Berkeley National Laboratory
1 Cyclotron Road, M/S 62R0100
Berkeley, CA 94720
Phone: 510-486-5821
E-mail: mmdoeff@lbl.gov

Peter Faguy, Technology Manager

U.S. Department of Energy
Phone: 202-586-1022
E-mail: Peter.Faguy@ee.doe.gov

Start Date: October 1, 2015
Total Project Cost: \$1,800,000

End Date: September 30, 2018
DOE share: \$1,800,000

Non-DOE share: \$0

Project Introduction

Ni-rich NMC ($\text{LiNi}_x\text{Mn}_y\text{Co}_z\text{O}_2$; $x+y+z \approx 1$, $x \geq y+z$) cathodes have strong potential to increase energy density in lithium ion batteries in the near term, due to their high practical capacities (up to 200 mAh/g depending on Ni content and voltage limits used). As Ni content is increased, however, cycle life is diminished and safety is adversely impacted [1]. The aim of this project is to understand the surface, interfacial, and bulk properties of Ni-rich NMCs (in FY 2017, particular emphasis was placed on NMC-622), and how they affect the thermal and electrochemical properties.

Our previous work showed that NMC cathodes suffer from surface reconstruction to a rock salt-like phase under a variety of conditions including storage in electrolytic solution, normal cycling, and high voltage cycling [2]. The surface reconstruction is probably responsible for the first cycle coulombic inefficiencies that are commonly observed, even when using conservative voltage limits. In addition, high voltage cycling results in the formation of an unfavorable cathode/electrolyte interface (CEI) layer that increases cell impedance [3]. It is this rise in cell impedance, rather than deterioration of the bulk material, that results in capacity fading during cycling to high potentials. Driving forces in both of these phenomena are the high reactivity of surface Ni ions, and the strong tendency for Ni-containing oxides to lose surface oxygen, particularly at high states-of-charge. Soft X-ray absorption studies reveal that charge compensation occurs mainly on the transition metal ions in the bulk (primarily Ni in Ni-rich NMCs) but at the surface, oxygen has a greater tendency to undergo redox processes [4]. It is the high reactivity of surface oxygen that is responsible for surface reconstruction and formation of resistive reaction layers on particle surfaces via reactions with components in the electrolytic solution. One strategy to ameliorate these phenomena includes partial Ti substitution for Co. In NMC-442, the presence of Ti delays loss of oxygen to higher levels of delithiation [5]. Improved cycling behavior is observed for Ti-substituted NMC materials when delithiated to the same level as unsubstituted NMC during high voltage cycling [6]. Synthetic methods can also be used to make materials with reduced Ni contents on particle surfaces. NMC-442 made by a simple and scalable spray pyrolysis method, exhibited a graded composition such that the Ni content was naturally lower on both the primary and secondary particle surfaces than in the bulk [7]. Materials made by this method exhibited better cycling behavior to high potentials and decreased amounts of surface reconstruction. During FY17, we focused on NMC-622, with the goal of understanding the role of heterogeneity on the electrochemical properties by studying both chemically and electrochemically delithiated samples and comparing them. The results of this study showed that the electrolytic solution plays a critical role in the surface reconstruction and cathode/electrolyte interface formation. A number of experiments were also carried out to understand the thermal properties of NMC-622 by studying partially and fully delithiated materials by various synchrotron techniques to understand surface and bulk processes. Much of this work is still being analyzed and will be reported during the next fiscal year.

Objectives

Our objectives are to understand what limits the cycling behavior of Ni-rich NMCs and to gain a deeper understanding of their thermal properties. Once this is done, methods to improve the robustness of the materials can be developed, ranging from partial substitution with Ti (for example), coatings, and synthetic strategies to reduce surface Ni content.

Approach

We use a highly collaborative approach to understand electrochemical and thermal characteristics of Ni-rich NMC materials. In some cases, commercially provided materials are studied, but we also synthesize our own, either by classic co-precipitation methods or by spray pyrolysis. Chemically delithiated samples are compared to those prepared electrochemically. Electrochemical characterization is carried out in lithium half-cell configurations. A combination of synchrotron radiation and electron microscopy techniques (in collaboration with A. Mehta, D. Nordlund, T.-C. Weng, and Y. Liu at SSRL and H. L. Xin at BNL) are used to understand the surface and bulk characteristics of the NMCs (commercial materials, synthesized materials, chemically and electrochemically delithiated samples, etc.). Several physical techniques (XRD, SEM, OES-ICP, etc.) are used to characterize materials before and after electrochemical cycling under a variety of conditions.

Nanotomographic imaging (Transmission x-ray microscopy, TXM) at SSRL is used to determine chemical gradients in particles and correlate this with electrochemical behavior. Soft x-ray absorption spectroscopy (XAS) experiments carried out at SSRL are used to probe oxidation states of transition metals at particle surfaces and in the bulk as a function of their electrochemical history. These results are correlated with scanning transmission electron microscopy (STEM) and electron energy loss spectroscopy (EELS) experiments at Brookhaven National Laboratory to obtain a full understanding of what governs the behavior of NMCs as a function of composition, temperature and cycling history. For a full overview of the behavior of NMCs, the PI works closely with other PIs in the Advanced Battery Materials Research program, including R. Kostecki (interfacial characteristics using spectroscopy), W. Tong (novel materials), B. McCloskey (differential electrochemical mass spectroscopy to measure gas evolution), and C. Ban (NREL, atomic and molecular layer deposition for protective layers on cathode materials).

Results

A comprehensive study to detail inhomogeneity in NMC-622 cathode materials was carried out in FY 2017. One goal of the study was to determine what differences there are between chemically and electrochemically delithiated samples. This is important because chemically delithiated samples are commonly used to model electrochemical processes in NMCs and other electrode materials. For this study, we subjected a commercial NMC-622 to partial chemical delithiation with either NO_2BF_4 or Br_2 . NO_2BF_4 is a stronger oxidizing agent than Br_2 ; it is possible to completely delithiate NMCs with the former (although it is complicated by proton exchange), but not with the latter. We also partially charged a sample in an electrochemical cell and subjected another sample to full charge and then partial discharge. All samples were approximately in the halfway lithiated state, with some variation in the exact degree of delithiation.

Examination by scanning electron microscopy indicated that the chemically delithiated samples were damaged by the oxidation process, whereas the electrochemically prepared samples remained intact and particles resembled that of the pristine sample. Specifically, there was loss of contact between primary particles in the large secondary particles for the chemically delithiated samples. This is attributable to mechanical damage from stirring, and possibly to evolution of NO_x gases from the sample treated with NO_2BF_4 . Ni K-edge X-ray absorption spectroscopy was used to determine the oxidation state of Ni, which is closely related to the degree of lithiation (Co is also electroactive, but most charge compensation occurs at Ni). Shifts in the Ni K-edge were consistent with the coulometry in the case of the electrochemically prepared samples, or with the elemental analysis of the chemically delithiated material.

Representative multi-pixel averaged XANES spectra, histograms of the distribution of the Ni oxidation states (positions of the Ni K-edge) and 2 dimensional mapping of the Ni K-edge from the TXM experiments are shown in Figure II-266. These results reveal considerable heterogeneity in the Ni oxidation state in the pristine

commercial sample. Both chemically and electrochemically delithiated samples are more homogeneous, as the narrowing of the histogram peaks show. However, by carrying out the 2D mapping using a finer scale, heterogeneities in all of the partially delithiated samples can be observed (Figure II-267). In particular, Ni oxidation states are lower at the cracks in the chemically delithiated sample because these cracks, induced by mechanical damage, are exposed to the oxidant for a shorter period of time. Similar heterogeneities are seen in the samples treated with bromine (not shown). The source of the heterogeneity of the electrochemically oxidized samples are more likely due to disconnection of primary particles as they undergo redox-related volume changes.

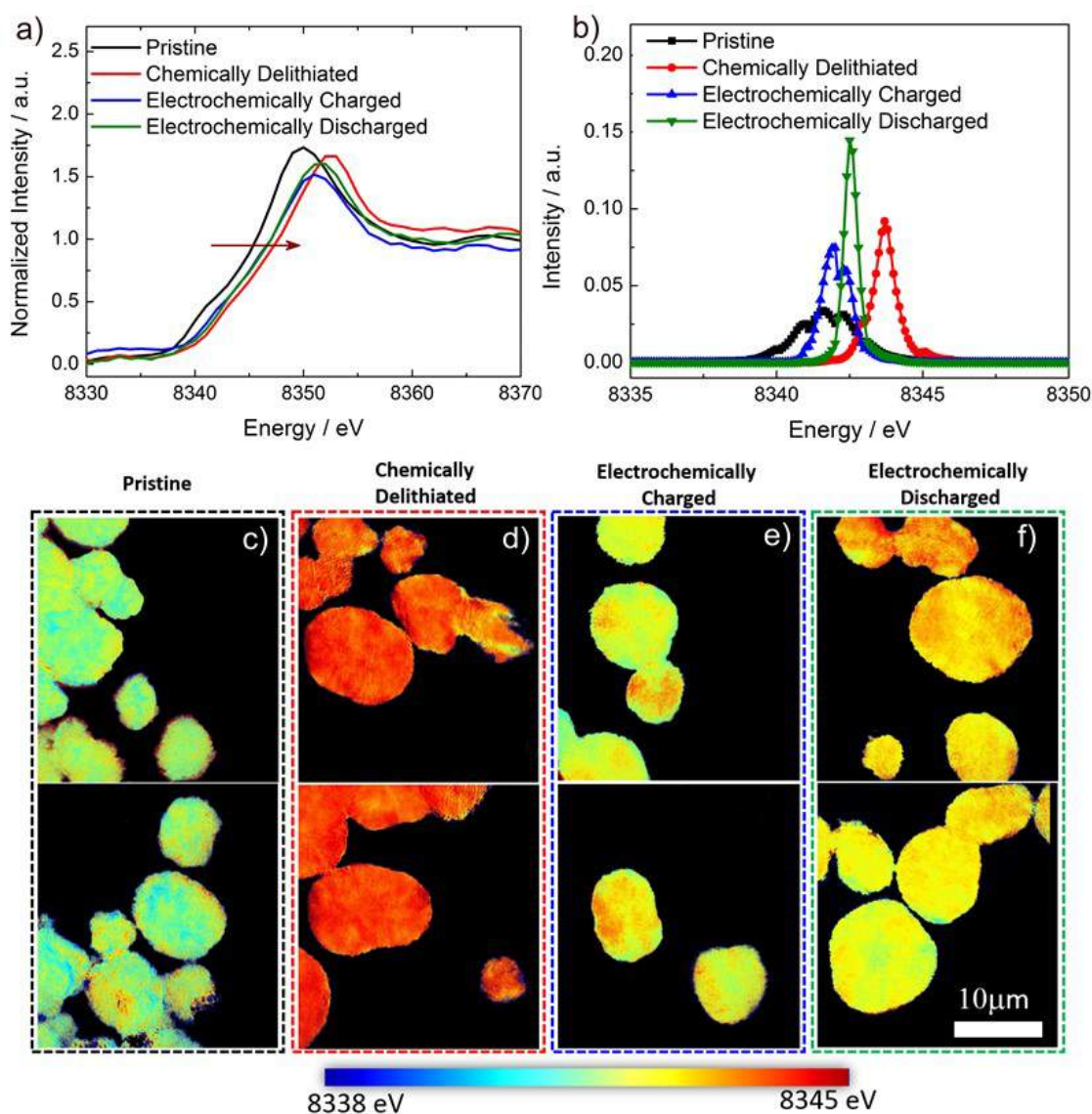


Figure II-266. (a) Representative multiple pixels averaged XANES spectra and (b) histogram of Ni K-edge shifts for pristine (black curve), chemically delithiated with NO_2BF_4 (red curve), electrochemically charged (blue curve) and electrochemically discharged (green) samples. 2D mapping of Ni K-edge in the samples (c) pristine NMC; (d) chemically delithiated NMC-622; (e) electrochemically charged NMC-622 electrode and (f) electrochemically discharged NMC-622.

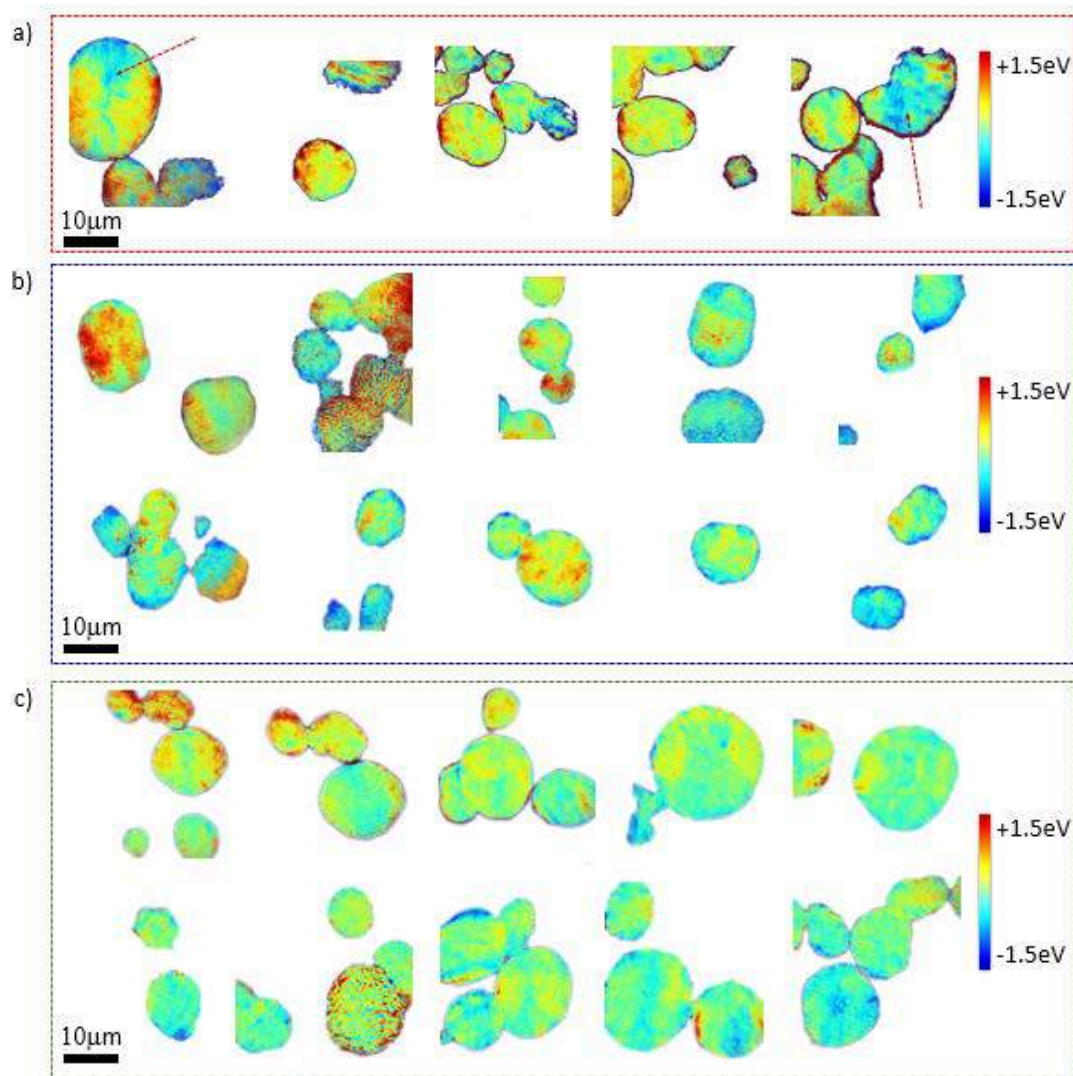


Figure II-267. Color mapping of (a) chemically delithiated NMC-622; (b) electrochemically charged NMC-622 electrode and (c) electrochemically discharged NMC-622 electrode. The color mapping was determined using the statistical peak energy as the center, and then -1.5eV (blue) and +1.5eV (red) as the two ends. Arrows point to regions of microcracks, which are less oxidized than surrounding areas.

Here dramatic differences can be observed among the different samples. In particular, the chemically delithiated sample shows almost no difference between the surface and the bulk. In contrast, a good deal of surface reconstruction is seen in the pristine sample already, and in the electrochemically delithiated sample. These differences can be quantified (Table II-9) and suggest strongly that exposure to the electrolytic solution drives the surface reconstruction. For the rock salt to form, metal ions must be reduced, but this requires something else to be oxidized. Components in the electrolytic solution serve this purpose during electrochemical oxidation, showing that surface reconstruction and CEI formation are intimately related. In the case of the chemical oxidation, there is no available material that can reduce the surface of the NMC particles and in turn be oxidized.

Table II-9: Relative L3 high to L3 low peak intensity ratio from nickel L-edge XAS spectra.

L ₃ high/L ₃ low Intensity (γ)	Pristine	Electrochemically charged 50%	Electrochemically discharged 50%	Chemical delithiation 50%
γ_{TEY}	0.56	0.87	0.57	1.64
γ_{FY}	0.83	1.28	1.04	1.78
$\Delta = \gamma_{TEY} - \gamma_{FY}$	0.27	0.41	0.47	0.14

Figure II-268 shows Ni L-edge XAS results on the samples in two different modes. Total electron yield (TEY) probes about 5 nm into the particle surfaces, whereas fluorescence yield (FY) mode probes about 50 nm in, or into the bulk. Differences between the ratios of the two L₃ edges in the two different modes are diagnostic of surface reconstruction, as the rock salt surface layer contains metal ions in a reduced state compared to that in the bulk layered structure.

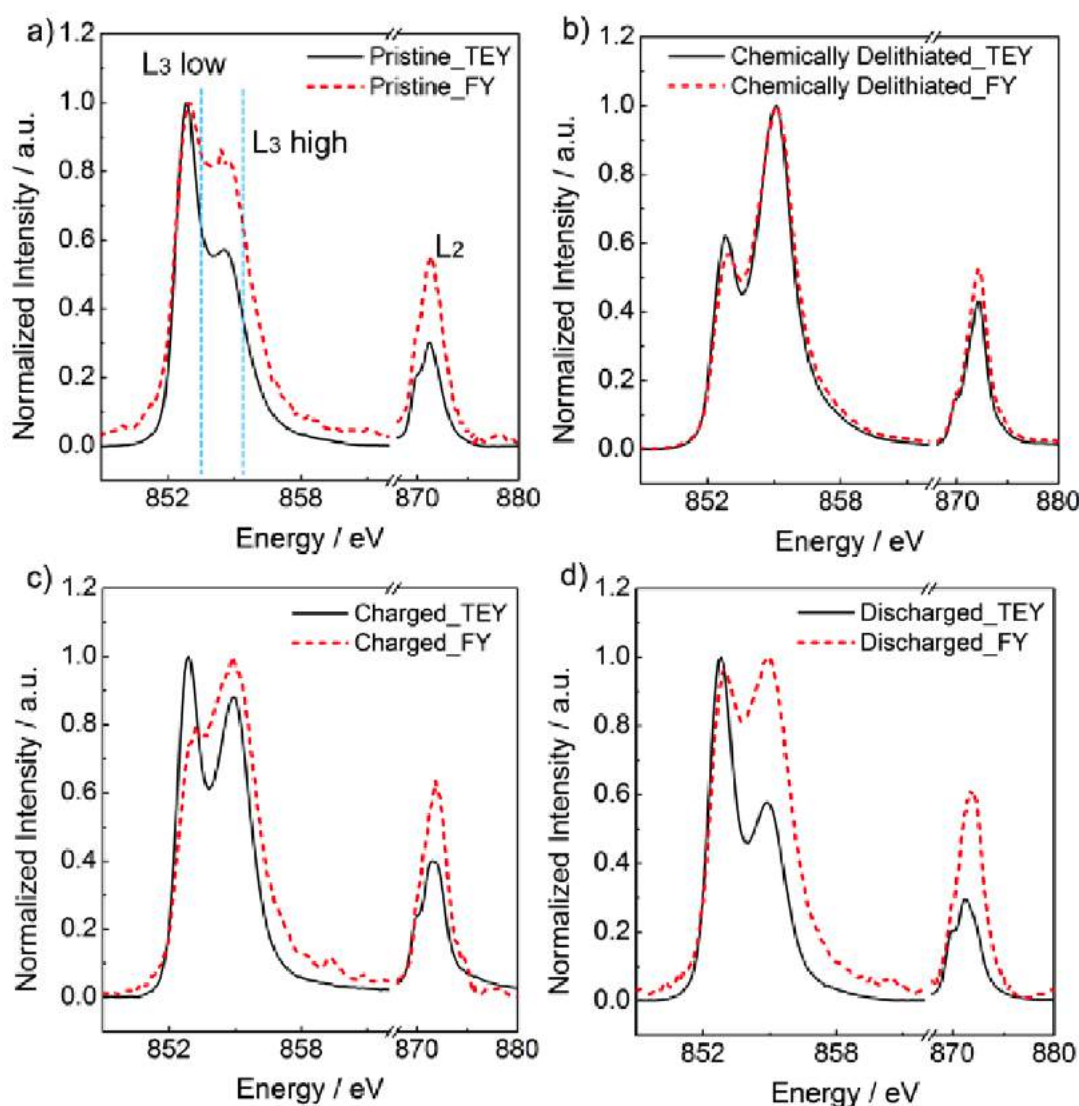


Figure II-268. Ni L-edge XAS spectra of (a) NMC-622 (b) chemically delithiated NMC-622; (c) electrochemically charged NMC622 electrode and (d) electrochemically discharged NMC-622 electrode collected using TEY (solid black curve) and FY (dashed red curve) modes.

Conclusions

Commercial NMC-622 samples show considerable heterogeneity even in the pristine state. While chemical or electrochemical delithiation results in some homogenization, variations in oxidation states exist. These can be attributed to mechanical damage from the chemical oxidation process or disconnection of primary particles during electrochemical cycling. A significant finding is the fact that chemically delithiated samples show much less surface reconstruction than the electrochemically delithiated ones. This strongly suggests that contact with the electrolytic solution plays an important role in this phenomenon.

References

1. H.-J. Noh, S. Youn, C.S. Yoon, and Y.-K. Sun, *J. Power Sources*, **233**, 121 (2013).
2. Feng Lin, Isaac Markus, Dennis Nordlund, Tsu-Chien Weng, Mark Asta, Huolin L. Xin, and Marca M. Doeff, *Nature Commun.* **5**:3529, DOI: 10.1038/ncomms4529 (2014).
3. Feng Lin, Isaac M. Markus, Dennis Nordlund, Tsu-Chien Weng, Huolin L. Xin, and Marca M. Doeff, *Energy & Environ. Sci.* **7**, 3077 (2014).
4. C. Tian, D. Nordlund, H. Xin, Y. Xu, Y. Liu, D. Sokara, F. Lin, and M. Doeff, *J. Phys. Chem. A* submitted (2017).
5. Isaac Markus, Feng Lin, Kinson Kam, Mark Asta, and Marca Doeff, *J. Phys. Chem. Lett.* **5**, 3649 (2014).
6. S. Wolff-Goodrich, F. Lin, I. Markus, D. Nordlund, H. Xin, M. Asta, and M. M. Doeff, *Phys. Chem. Chem. Phys.* **17**, 21778 (2015).
7. F. Lin, D. Nordlund, Y. Li, M. K. Quan, L. Cheng, T.-C. Weng, Y. Liu, H.L. Xin and M. M. Doeff, *Nature Energy* **1**, 1 (2016).

Key Publications

1. “Synchrotron X-ray Techniques for Studying Materials Electrochemistry in Rechargeable Batteries”, Feng Lin, Yijin Liu, Xiqian Yu, Lei Cheng, Andrej Singer, Oleg G. Shpryko, Huolin Xin, Nobumichi Tamura, Chixia Tian, Tsu-Chien Weng, Xiao-Qing Yang, Ying Shirley Meng, Dennis Nordlund, Wanli Yang, and Marca Doeff, **Chem. Rev.** 10.1021/acs.chemrev.7b00007 (2017).
2. “Crystal Chemistry and Electrochemistry of $\text{LiMn}_{1.5}\text{Ni}_{0.5}\text{O}_4$ Solid Solution Cathode Materials”, Wang Kan, Saravanan Kuppan, Lei Cheng, Marca Doeff, Jagjit Nanda, Ashfia Huq, and Guoying Chen **Chem. Mater.** DOI: 10.1021/acs.chemmater.7b01898 (2017).
3. “ $\text{Co}_{11}\text{Li}[(\text{OH})_5\text{O}][\text{PO}_3\text{OH}](\text{PO}_4)_5$], a Lithium-Stabilized, Mixed-Valent Cobalt (II, II) Hydroxide Phosphate Framework” J. Ludwig, S. Geprägs, D. Nordlund, M. Doeff, and T. Nilges, **Inorg. Chem.** DOI:10.1021/acs.inorgchem.7b01152 (2017).
4. “Direct Synthesis and Characterization of mixed-valent $\text{Li}_{0.5-\delta}\text{CoPO}_4$, a Li-deficient Derivative of the *Cmc* Polymorph of LiCoPO_4 ”, J. Ludwig, C. Alarcón-Suesca, S. Geprägs, D. Nordlund, M.M. Doeff, I. Puente Orench, and T. Nilges, **RSC Advances** **7**, 28069 (2017).
5. “Enhanced Lithium Ion Transport in Garnet-type Solid State Electrolytes” Lei Cheng, Huaming Hou, Simon Lux, Robert Kostecki, Ryan Davis, Vassilia Zorba, Apurva Mehta, and Marca Doeff, **J. Electroceramics** DOI: 10.1007/s10832-017-0080-3 (2017).
6. “Synthesis and Characterization of Metastable, 20 nm-sized $\text{Pna}21\text{-LiCoPO}_4$ Nanospheres” Jennifer Ludwig, Dennis Nordlund, Marca M. Doeff and Thomas Nilges, **J. Solid State Chem.** **248**, 9 (2017).

7. “Particle Size-controllable, Microwave-assisted Solvothermal Synthesis of the High-Voltage Cathode Material LiCoPO_4 using Water/Ethylene Glycol Solvent Blends” Jennifer Ludwig, Dominik Haering, Marca M. Doeff, and Tom Nilges, **Solid State Sciences**, 65, 100 (2017).
8. “Investigating the Intercalation Chemistry of Alkali Ions in Fluoride Perovskites”, Tanghong Yi, Wei Chen, Lei Cheng, Ryan D. Bayliss, Feng Lin, Michael R. Plews, Dennis Nordlund, Marca M. Doeff, Kristin A. Persson, and Jordi Cabana, **Chem. Mater.**, 29, 1561 (2017).
9. “The Road to Solid State Batteries for Vehicle Applications” The 12th Pacific Rim Conference on Ceramic and Glass Technology, Waikoloa, HI, May 21-26, 2017. (invited)
10. “The Future of Energy Storage for Vehicle Applications” Marca M. Doeff, SVC TechCon 2017, 60th Annual Society of Vacuum Coaters Technical Conference, Providence RI, April 29-May 4, 2017. (invited)
11. “Studies on NMC and LLZO Materials for Lithium Batteries” Marca M. Doeff, Bosch Research and Technology Center, North America, Palo Alto CA, April 13, 2017. (invited)
12. “Materials for Next Generation Electric Vehicle Batteries” Materials Sciences and Engineering Colloquium, Fu Foundation School of Engineering and Applied Science, Columbia University, New York, NY March 24, 2017. (invited)
13. “Recent Progress on Battery Materials”, Marca M. Doeff, The 2nd International Symposium on Renewable Energy Technologies”, Sydney, Australia, Nov. 30-Dec. 4, 2016. (invited)
14. “Illuminating Performance Characteristics of Battery Materials Using Synchrotron Techniques: Advanced NMCs, Sodium-Ion Batteries, and Solid Garnet-Type Electrolytes” Marca M. Doeff, Energy Harvesting USA, Santa Clara CA, November 16-17, 2016. (invited)
15. “The Future of Solid State Batteries for Electric Vehicles” Marca M. Doeff, The Northern California Chapter of The American Vacuum Society, San Jose, CA November 16, 2016.
16. Design of High Performance, High Energy Cathode Materials” Marca M. Doeff 2017 DOE Annual Peer Review Meeting Presentation.
17. “Editorial for the JECR Special Issue on All Solid-State Batteries” J. L. M. Rupp, D. Rettenwander, J. Kilner, and Marca M. Doeff, **J. Electroceramics**, DOI 10.1007/s10832-017-0102-1 (2017).
18. “The Mechanism of Impedance Increase in Nickel-Rich NMC Cathodes” R.C. Lee, C. Tian, M. Doeff, and R. Kostecki, 232nd Meeting of the Electrochemical Society, National Harbor, MD, Oct. 1-6, 2017.
19. “Ionic Liquid Enabled High Energy-Density Lithium-Ion Batteries” T. Evans, D. Molina Piper, S.C. Kim, S. Han, M. Doeff, C. Ban, S.J. Cho, K.H. Oh, and S. Lee, 231st Meeting of the Electrochemical Society, New Orleans, LA, May 28-June 2, 2017.
20. “Controlling the Surface Chemistry of Cathode Materials for High Energy Rechargeable Batteries” F. Lin and M. M. Doeff, 231st Meeting of the Electrochemical Society, New Orleans, LA, May 28-June 2, 2017.
21. “Structural Stability of Nickel-Rich Layered Cathode Materials” Chixia Tian, Yahong Xu, Dennis Nordlund, Huolin Xin, Yijin Liu, and Marca Doeff. PRIME 2016, Honolulu, HI, October 2-7, 2016.

II.C.10 Lithium Batteries with Higher Capacity and Voltage (UTA)

John B. Goodenough, Principal Investigator

The University of Texas at Austin
 204 E. Dean Keeton St.
 Austin, TX 78712
 Phone: 512-471-1646
 E-mail: jgoodenough@mail.utexas.edu

Tien Duong, Technology Manager

U.S. Department of Energy
 Phone: 202-586-7836
 E-mail: Tien.Duong@ee.doe.gov

Start Date: April 16, 2015
 Total Project Cost: \$398,000

End Date: June 30, 2018
 DOE share: \$398,000

Non-DOE share: \$0

Project Introduction

The dependence of modern society on the energy stored in a fossil fuel is not sustainable. A fossil fuel, once burned, is not recyclable; the gases from fossil-fuel combustion are already choking large population in major cities such as Beijing in China and Delhi in India. The introduction of an all-electric road vehicle powered by a rechargeable battery that is competitive in cost, safety, and convenience with today's road vehicles powered by the internal combustion engine would reduce, if not remove, the distributed air pollution generated on the highways of the world. Such a battery would also allow storage of electric power harvested from the sun's energy that arrives daily.

The flammable liquid electrolyte of the Li-ion battery of the wireless revolution has prevented the development with today's technology of a safe, cost-competitive battery that can compete with the internal combustion engine.

Objectives

Replacement of the flammable liquid electrolyte with a solid electrolyte from which an alkali-metal anode can be plated/stripped reversibly and dendrite-free as the anode would provide a safe, rechargeable battery of higher volumetric energy density than the Li-ion battery, but the low cation conductivity of known solids and the problems of a solid/solid electrode/electrolyte interface with changing volumes of the electrodes have suppressed investigation of high-energy-density all-solid-state rechargeable batteries with a long charge/discharge cycle life. The objective of this project was to explore whether these problems can be overcome.

Approach

Characterize several Li^+ solid electrolytes stable on contact with metallic lithium that provide dendrite free plating of a metallic-lithium anode. Investigate whether this solid electrolyte is stable with an aqueous and/or an organic liquid electrolyte. Develop a test cell with a lithium anode and a Cu cathode.

Results

The project was conducted in collaboration with others in my group supported for parallel work. We have reported previously only results obtained with regard to milestones specified by this project. Here, our previously supported results are placed in the broader context of our collaboration effort.

We began with the choice of a ceramic solid Li^+ electrolyte that would not be reduced on contact with metallic lithium. The $\text{Li}_7\text{La}_3\text{Zr}_2\text{O}_{12}$ (LLZO) with the garnet structure had been reported to have a room temperature Li^+

conductivity $\sigma_{\text{Li}} \approx 10^{-4} \text{ S cm}^{-1}$, and we had improved the bulk conductivity to $\sigma_{\text{Li}} \approx 10^{-3} \text{ S cm}^{-1}$ by substituting Ta for Zr in $\text{Li}_{6.5}\text{La}_3\text{Zr}_{1.5}\text{Ta}_{0.5}\text{O}_{12}$ (LLZT), but we found the materials to be highly hygroscopic; Li_2CO_3 and LiOH formed at the surface of the grains reduce performance. Both LiOH and Li_2CO_3 are Li-ion insulators, which leads to a large grain-boundary resistance of the garnet electrolyte and the lithium/garnet interface also has a large plating/stripping impedance. We used LiF to increase the stability of the garnet electrolyte LLZT against moisture and carbon dioxide in air; the grain-boundary and interfacial resistances were reduced significantly, which makes LLZT a possible solid electrolyte in Li-S batteries.

To demonstrate the advantages of the LiF modification that decreases the interfacial resistance, Li-S cells with a LLZT and a LLZT-2LiF solid electrolyte were assembled. The solid electrolyte can efficiently block the polysulfide shuttle, which is a severe problem in Li-S batteries. The total resistance of the cells with LLZT and LLZT-2LiF in Figure II-269(a) were 1000 and $2620 \Omega \text{ cm}^{-2}$, respectively. The cells with LLZT and LLZT-LiF display well-defined discharge/charge plateaus and low overpotentials. The cell with LLZT-2LiF exhibited a much lower gap (0.34 V) between charge and discharge voltages than that with LLZT (0.59 V) at the current density of $200 \mu\text{A cm}^{-2}$. The much reduced interfacial resistance allows the cells to be cycled at high current densities. As shown in Figure II-269(c), discharge capacities of 1137, 1074, and 1042 mAh g^{-1} can be obtained at the rates of 100, 200 and $300 \mu\text{A cm}^{-2}$, respectively. Notably, since the polysulfide shuttle can be completely blocked by the solid electrolyte, the hybrid cells assembled also exhibit a stable cyclability at $200 \mu\text{A cm}^{-2}$. The reversible capacity stabilized at 988 mAh g^{-1} after 100 cycles with the retention of 93% of the stabilized capacity in the second cycle (Figure II-269(d)). Furthermore, the Coulombic efficiency maintains almost 100% over the subsequent 100 cycles, which is much higher than the Li-S cell without garnet in Figure II-270, indicating that the solid electrolyte can successfully block the polysulfide shuttle during the whole cycling processes.

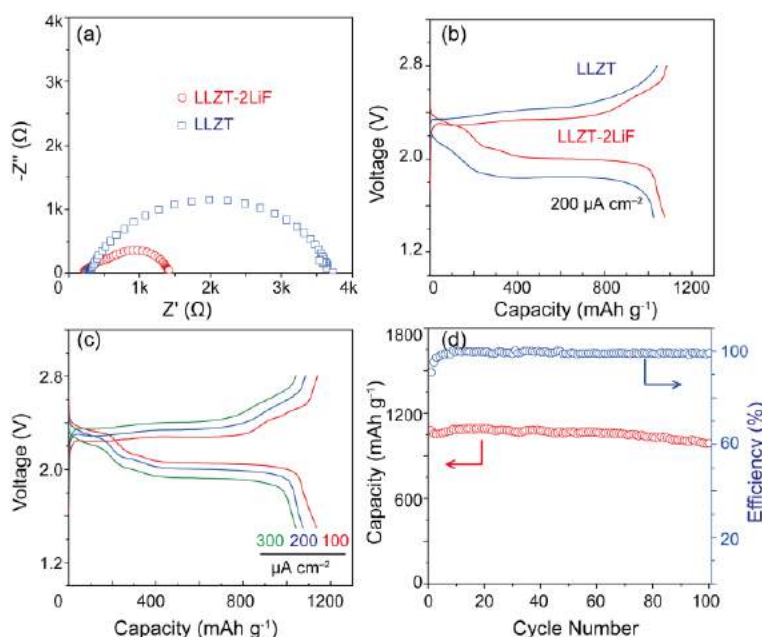


Figure II-269. (a) The impedance plots of a Li-S battery, (b) charge and discharge voltage profiles of a Li-S battery (b) with LLZT and LLZT-2LiF as a separator, (c) charge and discharge voltage profiles of a Li-S battery with LLZT-2LiF at different current densities, (d) capacity retention and cycling efficiency of the Li-S battery.

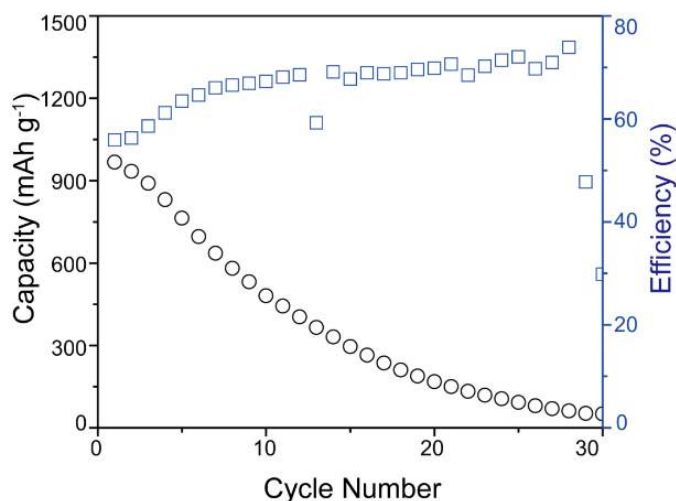


Figure II-270. Cycling stability and Coulombic efficiency of the Li-S cell without solid electrolyte nor LiNO_3 additive.

Although we were able to reduce the Li_2CO_3 contamination by introducing LiF at the grain surfaces, removal of Li_2CO_3 was not complete, so we turned to investigate a ceramic with the perovskite structure. (In subsequent work, we have developed a preparative procedure that removes all the Li_2CO_3 and shown that the garnet is then wet by a Li-metal anode to give dendrite-free plating/stripping of a lithium anode with little interface impedance; the cells operate well at 60°C .)

In the second quarter, we investigated a perovskite Li^+ solid electrolyte, $\text{Li}_{1/8}\text{Sr}_{7/16}\text{Hf}_{1/9}\text{Ta}_{1/4}\text{O}_{32}$ (LSHT) that we could make 99.9% dense by spark plasma sintering. LSHT has a room-temperature Li-ion conductivity $\sigma = 4.4 \times 10^{-4} \text{ S cm}^{-1}$ and a small activation energy of 0.33 eV from 298 to 420 K (Figure II-271). Another advantage of LSHT is its good stability in air; unlike the garnet electrolyte which reacts with moist air to form Li_2CO_3 , there is no Li_2CO_3 detectable with a Raman shift at 1080 cm^{-1} on the surface of a perovskite LSHT pellet after exposure to air for 3 months.

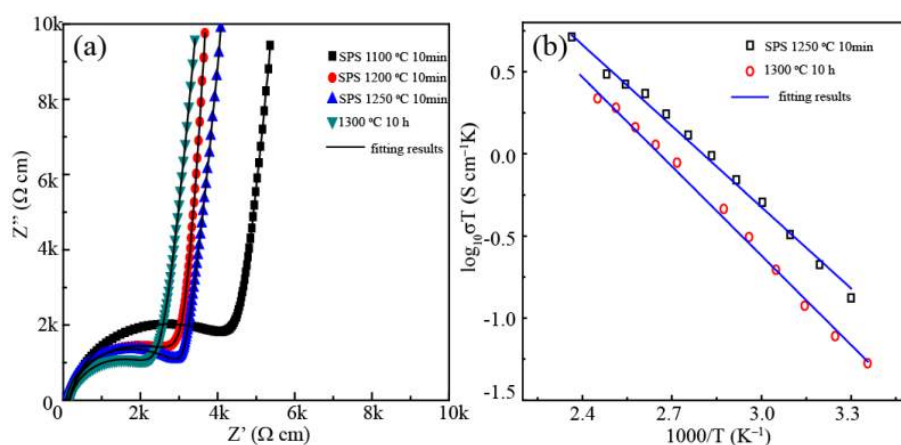


Figure II-271. (a) Impedance spectra and (b) Arrhenius plot of LSHT pellet fired by spark plasma sintering.

Because of its stability, LSHT shows a small interfacial resistance with a solid polymer electrolyte and commercial organic electrolyte; moreover, it is chemically and electrochemically stable with a polysulfide catholyte. An all-solid-state $\text{Li}/\text{LiFePO}_4$ battery with LSHT as electrolyte had a small resistance, high coulombic efficiency of 99.5~100 %, and long cycling life (Figure II-272). A Li-S battery with dense LSHT as

a separator that blocks the polysulfide transport towards the Li-metal delivered an initial discharge capacity of 1100 mAh g^{-1} , had a high coulombic efficiency of 99.5 %, and kept 93 % capacity after 400 cycles.

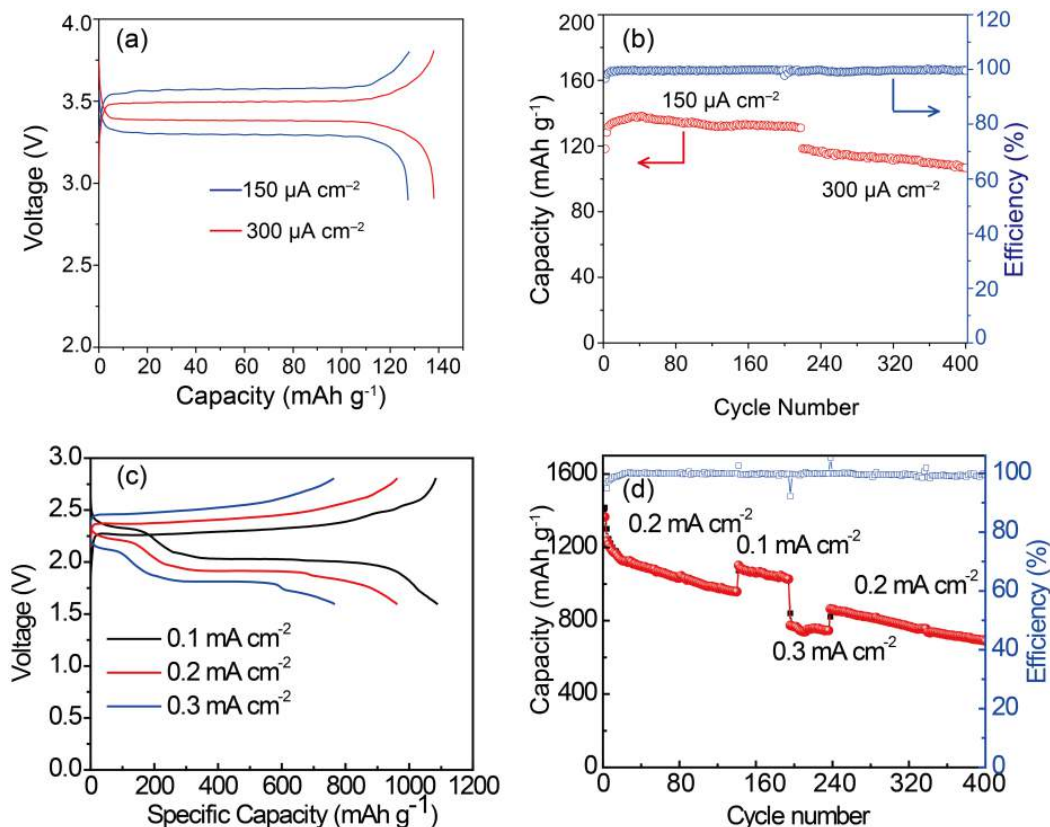


Figure II-272. (a) Charge and discharge voltage profiles of Li/LSHT/LiFePO₄ at 150 and 300 $\mu\text{A cm}^{-2}$. (b) Capacity retention and cycling efficiency of the LiFePO₄/Li cells. (c) Charge and discharge voltage profiles of a Li-S battery with LSHT at different current densities. (d) Capacity retention and cycling efficiency of the Li-S battery.

In the third quarter, we studied a new battery concept with the Cu^+/Cu^0 redox couple in the cathode of an all-solid-state lithium battery. In this concept, the Cu^+/Cu^0 redox couple determines the cell voltage and a solid Li^+ electrolyte provides Li^+ ions. We have used a cross-linked poly(ethylene glycol) methyl ether acrylate (CPMEA; Figure II-273) membrane with LiTFSI salt as the solid electrolyte. The membrane was shown to be electrochemically stable up to 4.8 V vs. Li at 65°C. A battery-grade Cu foil was used as a cathode current collector and a Cu^+/Cu^0 redox source. The Cu foil was directly placed on one-side of the CPMEA membrane, and a lithium metal foil was placed on the other side.

Figure II-274 shows an initial charge/discharge voltage curve of the solid-state Li cell at 70°C. During charging, a constant voltage plateau at $\sim 3.5 \text{ V}$ vs. Li was observed, which corresponds to the electrochemical Cu dissolution via the Cu^+/Cu^0 redox reaction. Li plating occurs at the anode while the dissolved Cu^+ ions keep the charge neutrality of the polymer electrolyte. During the following discharge, two voltage regions were noticed, one at $\sim 3.3 \text{ V}$ and the other at $\sim 2.1 \text{ V}$. The upper voltage region should be responsible for the Cu^+/Cu^0 redox couple. However, the corresponding capacity is only about a half of the charging capacity. It is partly because the initially dissolved Cu^+ ions diffuse away from the Cu foil owing to the concentration gradient, and therefore, the diffusional overpotential increases as the electrochemical Cu^+ reduction proceeds at the Cu surface during discharge. The results suggest that higher Li^+ and Cu^+ concentrations are necessary to increase cell capacity and reaction kinetics. For the lower voltage reaction at $\sim 2.1 \text{ V}$, the discharge mechanism is not understood yet, and further study is needed.

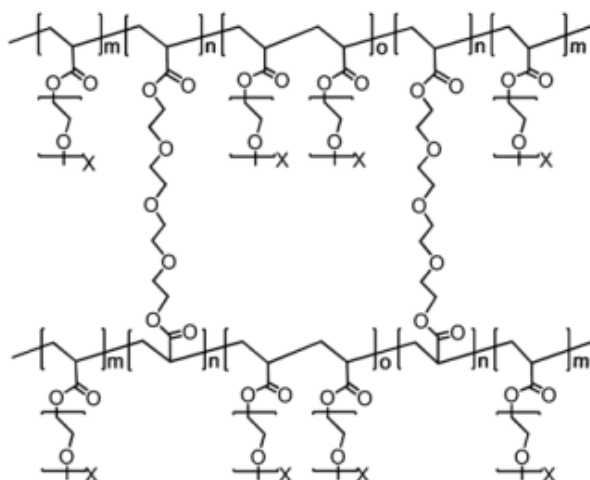


Figure II-273. Structure of CPMEA.

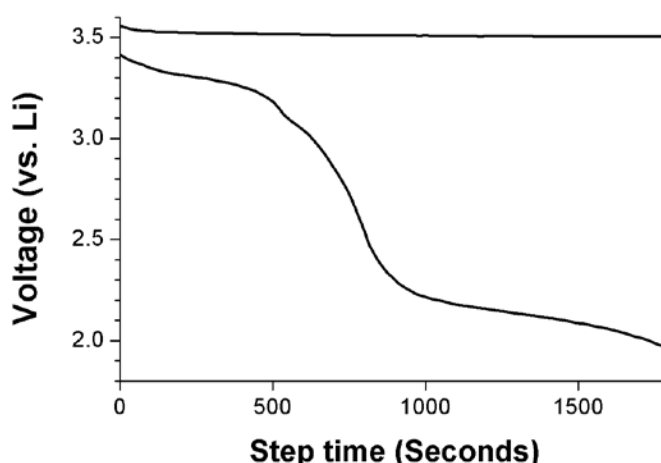


Figure II-274. Charge/discharge voltage curves of all-solid-state Li/CPMEA-LiTFSI/Cu cell at 70°C.

In the fourth quarter, the Cu^+/Cu^0 redox couple in the cathode was tested in a quasi-solid-state lithium battery cell. To collect more reproducible cell data, we have fabricated a gel polymer electrolyte membrane based on PVDF-HFP instead of the crosslinked polymer membrane, CPMEA. LiTFSI and poly(ethylene glycol) methyl ether acrylate were added to the PVDF-HFP solution in acetone; the clear solution was then cast on a Teflon dish. After vacuum drying at 50°C overnight, the membrane was used as a separator in a quasi-solid-state cell. We investigated several experimental parameters that affect the electrochemical performance of the Cu^+/Cu^0 redox couple.

Electrochemical feed of Cu^+ ions into the separator membrane and its effect on the discharge capacity

First, we have made coin half-cells with Cu foil as the cathode and Li metal as the anode. During the first charge, Cu dissolves into the polymer membrane and exhibits a voltage plateau at around 3.4 V. The electrochemical oxidation time was changed (10, 20, and 40h at 20 μA and 60°C) to control the Cu^+ concentration in the membrane and to check its effect on the discharge capacity (Figure II-275). The results suggest that (i) a higher Cu^+ concentration in the membrane is needed to promote Cu^+ conduction and deliver a higher reversible capacity, (ii) Cu^+ diffusion away from the cathode interface must be solved to enhance the Coulombic efficiencies, and (iii) Cu plating at the Li surface should be prohibited.

Chemical feed of Cu^{2+} ions into the separator membrane and its effect on the discharge capacity

Second, to enhance electrochemical performance, vacuum-dried Cu^{2+} perchlorate was chemically incorporated into the polymer composite during the membrane fabrication. Cu^{2+} concentration was set to be 1:1 ratio to the Li^+ concentration. The Cu-incorporated membrane couldn't be solely used as a separator owing to the spontaneous Cu^{2+} reduction reaction at the Li surface: a bare gel polymer membrane was introduced between the Li anode and the Cu-incorporated membrane. Figure II-276 shows the charge/discharge voltage curves of the coin cell with Cu foil as the cathode. The cell was charged first and then discharged at $20\ \mu\text{A}$ and 60°C . Compared to Figure II-275, the discharge capacity was greatly improved. It is clear that having sufficient Cu ion concentration in the membrane is critical to deliver a higher cell capacity and a higher Coulombic efficiency.

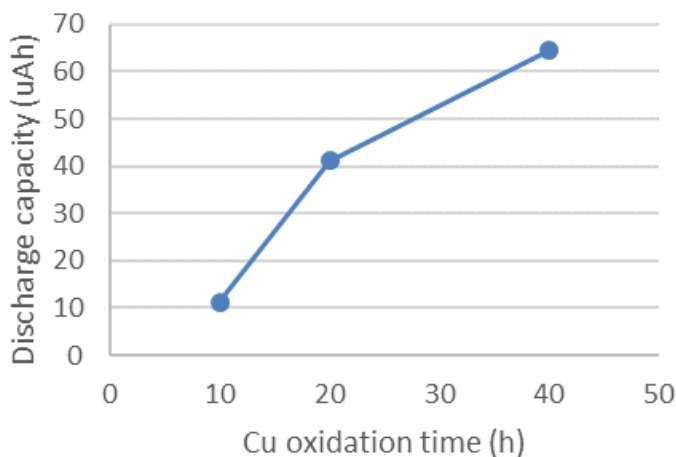


Figure II-275. Cu oxidation time and the corresponding discharge capacity.

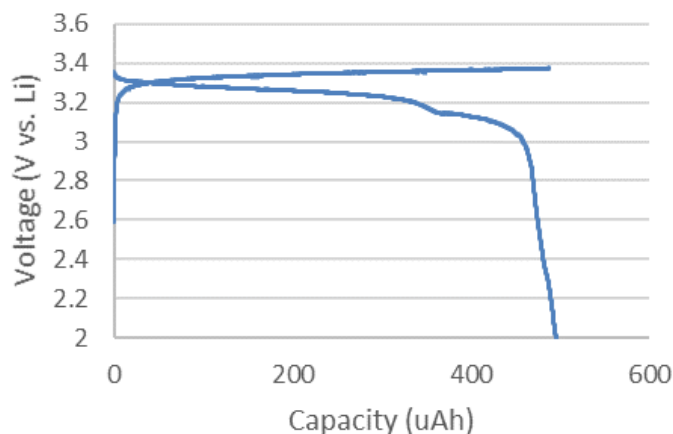


Figure II-276. Charge/discharge voltage curves of the Cu cathode.

Conclusions

The data have shown that dendrite-free alkali-metal anodes can be plated reversibly with low plating/stripping impedance if the alkali-metal wets the solid electrolyte, i.e., if the anode-electrolyte bonding is stronger than bonding of the alkali metal with itself, and if the solid electrolyte is not reduced on contact with metallic lithium. Moreover, the solid electrolyte can block soluble species from the cathode as in a Li-S cell. Investigation of a new concept was initiated in the last half of the years; it consists of plating/stripping of metallic lithium on the anode and of metallic copper on a copper cathode with a dual-electrolyte system, the ceramic solid electrolyte contacting the anode.

Key Publications

1. K. Park, J. B. Goodenough, “Dendrite-suppressed lithium plating from a liquid electrolyte via wetting of Li_3N ”, Adv. Energy Mater. DOI: 10.1002/aenm.201700732.

II.C.11 Exploiting Co & Ni Spinel in Structurally-Integrated Composite Electrode (ANL)

Michael M. Thackeray, Principal Investigator

Argonne National Laboratory
9700 S. Cass Aveue
Lemont, IL 60439
Phone: 630-252-9184
E-mail: thackeray@anl.gov

Jason R. Croy, Principal Investigator

Argonne National Laboratory
9700 S. Cass Aveue
Lemont, IL 60439
Phone: 630-252-9184
E-mail: croy@anl.gov

Peter Faguy, Technology Manager

U.S. Department of Energy
Phone: 202-586-1022
E-mail: Peter.Faguy@ee.doe.gov

Start Date: October 1, 2015
Total Project Cost: \$500,000

End Date: September 30, 2018
DOE share: \$500,000

Non-DOE share: \$0

Project Introduction

The structural instability of lithium- and manganese-rich, $x\text{Li}_2\text{MnO}_3 \cdot (1-x)\text{LiMO}_2$ ($M=\text{Mn}, \text{Ni}, \text{Co}$), ‘layered-layered’ (LL) materials, at high states of charge, is a critical barrier to their implementation in commercial battery systems [1]. One promising strategy to enhance structural stability has been to incorporate a spinel component to form complex, structurally-integrated, ‘layered-layered-spinel’ (LLS) electrodes [2-5]. LLS spinel, and even layered-spinel (LS), composites have been explored with positive results utilizing the incorporation of stoichiometric, manganese-based spinels such as $\text{Li}_{1+y}\text{Mn}_{2-y}\text{O}_4$ or $\text{LiNi}_{0.5}\text{Mn}_{1.5}\text{O}_4$. However, several interesting options for integrated spinel components have yet to be studied. For example, lithiated cobalt-rich spinels, $\text{LiCo}_{1-x}\text{M}_x\text{O}_2$ ($M=\text{metal cations}$), may be attractive as alternative spinel components for several reasons: (1) $\text{LiCo}_{1-x}\text{M}_x\text{O}_2$ (alternatively, $\text{Li}_2[\text{Co}_{2-2y}\text{M}_{2y}]\text{O}_4$) spinels have close-packed structures with a rock-salt stoichiometry, making them compositionally and structurally compatible with layered structures such as LiMO_2 and Li_2MnO_3 ; (2) Relative to that of manganese and nickel, cobalt has a lower propensity to migrate during electrochemical redox reactions ($\text{Co}^{3+/4+}$) at high potentials [6], thereby, possibly helping to mitigate voltage fade with cycling; and (3) Lithium extraction from a lithiated cobalt-rich spinel component, $\text{Li}_{2-x}\text{Co}_{2-2y}\text{M}_{2y}\text{O}_4$ ($0 \leq x \leq 1$), occurs at a potential (~ 3.6 V) [7, 8] significantly higher than that of its lithiated manganese-oxide spinel analogue, $\text{Li}_2\text{Mn}_2\text{O}_4$ (~ 2.9 V) [9, 10]. This chapter deals with efforts within this project to develop stable, Co-based spinels as possible end-member compounds for integration into more complex LLS systems in order to realize stable, high-energy, Mn-rich cathode materials capable of meeting the cost and safety requirements of EV and PHEV vehicle applications.

Objectives

The objective of this project is to stabilize high-capacity, structurally-integrated (LL), Mn-rich cathodes by introducing a stabilizing spinel component into the parent electrode with a particular emphasis on lithium-cobalt-oxide and lithium-nickel-oxide spinel components that accommodate lithium at ~ 3.5 V vs. metallic lithium.

Approach

The approach is to design, synthesize and characterize new spinel-related materials, compositions and structures that operate between 3 to 4 V and to determine their structural/electrochemical property relationships. This information will be used to identify the most promising spinel components that can be used, in low concentration, to stabilize high capacity $x\text{Li}_2\text{MnO}_3 \cdot (1-x)\text{LiMO}_2$ ($M=\text{Ni, Mn, Co}$) electrode structures.

Results

Synthesis of Co-based, lithiated-spinel materials with cation substitutions

Impurities

$\text{LiCo}_{1-x}\text{M}_x\text{O}_2$ ($M = \text{Ni}$ and Mn) materials, synthesized at low temperature (LT), have lithiated spinel structures that could be used as stabilizing components in high capacity, lithium- and manganese-rich composite cathodes. After exploring a large portion of the $\text{LT-Li}(\text{Co}_{1-x-y}\text{Ni}_x\text{Mn}_y)\text{O}_2$ compositional phase space, it was found that Ni and Mn substitution improves the phase purity and electrochemistry of lithiated-spinel cathodes. However, impurity phases are easily formed during LT synthesis, and thus the range of Ni and Mn substitution has to be limited to a small degree in order to obtain monophasic materials. The formation of impurity phases is related to the relative stability of possible oxide phases in a given overall composition. For example, in lithiated-spinel $\text{Li}(\text{Co}_{1-x}\text{Mn}_x)\text{O}_2$ compounds, the transition metal (TM) cations should maintain an overall oxidation state of +3 to satisfy the charge neutrality condition. However, Mn cations having a preference for the +4 oxidation state will drive the stabilization of a Li-Mn(IV)-O impurity phase, as shown in previously reported examples of $\text{LT-Li}(\text{Co}_{1-x-y}\text{Ni}_x\text{Mn}_y)\text{O}_2$ materials with high Mn contents.

Different from the stoichiometric $\text{LT-LiCo}_{1-x}\text{M}_x\text{O}_2$ compounds, that have a Li:TM ratio of 1, the $\text{LT-Li}_{1-x}(\text{Co}_{0.9-x-y}\text{Ni}_y\text{Mn}_x)\text{O}_2$ composition is designed to maintain the Mn(IV) oxidation state by decreasing Li content with Mn substitution. In Figure II-277a, $\text{LT-Li}_{1-x}(\text{Co}_{0.9-x-y}\text{Ni}_y\text{Mn}_x)\text{O}_2$, with $x = 0.1$ and 0.2 , do not show an impurity phase related to Mn(IV) cations, however, the peaks for Co_3O_4 are clearly detected; the decreased Li content in $\text{Li}_{0.9}(\text{Co}_{0.8}\text{Ni}_{0.1}\text{Mn}_{0.1})\text{O}_2$ and $\text{Li}_{0.8}(\text{Co}_{0.7}\text{Ni}_{0.1}\text{Mn}_{0.2})\text{O}_2$, devised to maintain the Mn(IV) oxidation state, actually induces the formation of a Co_3O_4 impurity phase. For the $x = 0.4$ sample, a third phase, denoted as LT-LMO, is observed in addition to the LT-spinel and Co_3O_4 phases. From the analysis of the LT-LiMnO_2 , the LT-LMO phase is identified as a $\text{Li}_2\text{MnO}_3 \cdot \text{Li}_4\text{Mn}_5\text{O}_{12}$ composite phase. The high-resolution x-ray diffraction (XRD) pattern of LT-LiMnO_2 (Figure II-277b) shows the presence of a spinel structure while the additional peak marked with an asterisk suggests superstructure ordering of Li/Mn as in Li_2MnO_3 . The electrochemical behavior of LT-LiMnO_2 further confirms the composite structure by clearly exhibiting characteristics of both Li_2MnO_3 and $\text{Li}_4\text{Mn}_5\text{O}_{12}$ in the voltage curves of Figure II-277c. These results, combined with previous data, point to Co_3O_4 spinel, $\text{Li}_x\text{Ni}_{1-x}\text{O}$ rocksalt, and a $\text{Li}_2\text{MnO}_3 \cdot \text{Li}_4\text{Mn}_5\text{O}_{12}$ composite as the main impurity phases during the low-temperature synthesis of ‘NMC spinel’ materials. Therefore, alternative synthesis routes that can deter the formation of those stable impurity phases, such as soft chemistry methods, need to be explored.

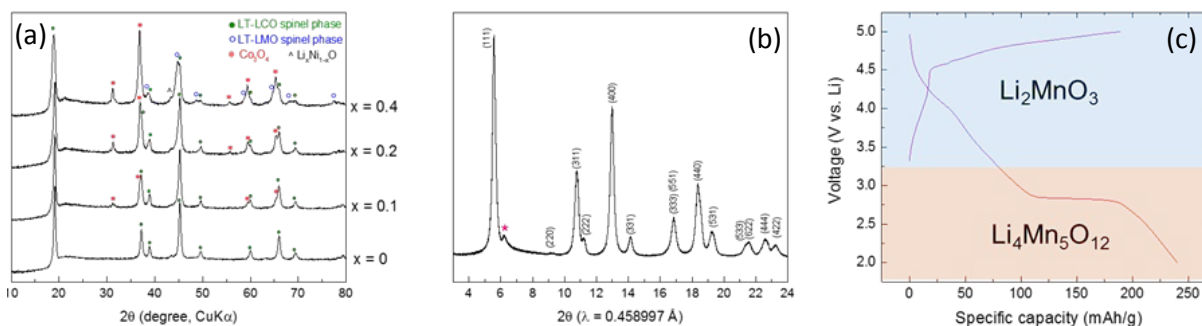


Figure II-277. (a) XRD patterns of $\text{LT-Li}_{1-x}(\text{Co}_{0.9-x}\text{Ni}_{0.1}\text{Mn}_x)\text{O}_2$, (b) high-resolution XRD and (c) electrochemistry of the low-temperature product with the LiMnO_2 composition (LT-LMO phase).

Al-substitution

The effect of Al substitution on the structure and electrochemical properties of LT-LCO was also explored. This approach was adopted because of the important role that Al substitution plays in fortifying the structures of several well-known, lithium-TM-oxides, such as layered $\text{LiNi}_{0.8}\text{Co}_{0.15}\text{Al}_{0.05}\text{O}_2$ (NCA) and lithium-manganese-oxide spinel materials. A series of Al-substituted $\text{LiCo}_{1-x}\text{Al}_x\text{O}_2$ (LCO-Al) samples was synthesized by sol-gel reactions of metal acetates and glycolic acid; the resulting sol-gel precursors were subsequently fired in air at 400°C (LT) or at an intermediate temperature of 600°C (IT).

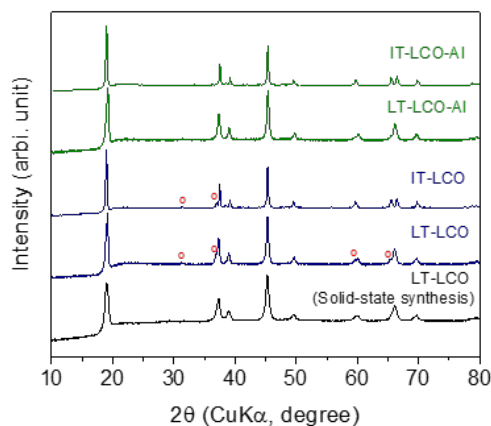


Figure II-278. XRD patterns of sol-gel LiCoO_2 (LCO) and $\text{LiCo}_{0.85}\text{Al}_{0.15}\text{O}_2$ (LCO-Al) samples fired at 400°C (LT) or 600°C (IT). XRD pattern of LCO, synthesized by solid-state reaction, is shown for comparison. Red circles indicate the peaks for Co_3O_4 .

In Figure II-278, the LT-LCO sample is indexed to a cubic spinel structure, consistent with products made by solid-state synthesis at 400°C. LT-LCO particles prepared by the sol-gel method were observed to have a larger crystalline size (smaller FWHM) relative to solid-state LT-LCO, and to contain a Co_3O_4 impurity phase that was also apparent in IT-LCO samples, but in lower concentration (reduced peak intensities). The IT-LCO product prepared at 600°C had a well-defined layered structure, indicated by the split of the (018) and (110) peaks at $\sim 66^\circ 2\theta$, unlike the materials prepared by solid state reaction that required a higher synthesis temperature ($\geq 700^\circ\text{C}$) to produce well-ordered layered structures.¹ LCO-Al samples had a similar structure to their LCO analogues but did not contain a Co_3O_4 impurity phase. The lower firing temperature required to order the lithium and TM ions and the growth of larger crystallites in the final products suggest that, relative to solid state reactions, the sol-gel method lowers the kinetic barriers to the formation of well-defined LCO structures. Voltage profiles of lithium cells with LT-LCO and LT-LCO-Al cathodes showed two voltage plateaus corresponding to layered (3.9 V) and spinel (3.6 V) components, whereas cells with IT-LCO and IT-LCO-Al electrodes exhibited only the 3.9 V plateau, corroborating the XRD data (Figure II-279a and Figure II-279b). Al-substitution improves the cycling stability of both LT and IT electrodes (Figure II-279c).

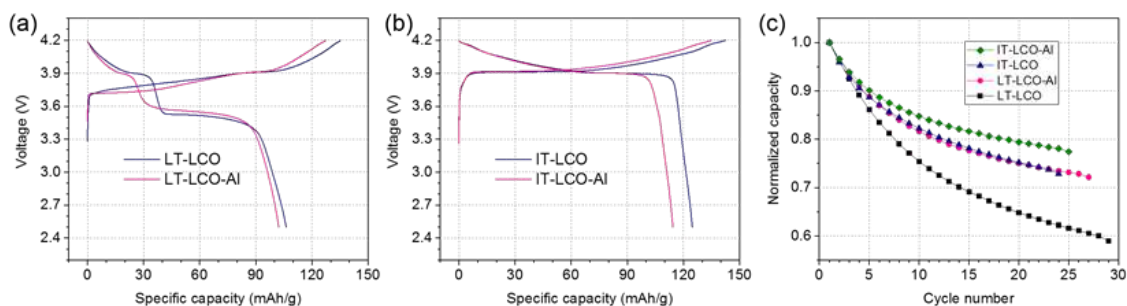


Figure II-279. (a, b) Initial voltage profiles and (c) normalized capacities of the sol-gel prepared samples.

Modified sol-gel synthesis method for layered-spinel composite cathodes

Encouraged by the improved performance of the Al-substituted, Li-Co-O spinel materials, prepared by the sol-gel route, synthesis efforts were expanded to prepared LS composite materials via a modified sol-gel method. Previous reports have discussed the structure and electrochemistry of LS $\text{Li}_2\text{MnO}_3 \bullet \text{LiMn}_2\text{O}_4$ cathodes. For these lithium-manganese-oxide materials, with relatively simple elemental components, the formation of structurally-integrated, layered and spinel domains is readily achieved by high-temperature firing of homogeneously-mixed precursors. However, such simple synthesis routes rely on thermodynamic phase segregation into composite structures and, therefore, have limitations in preparing multi-element samples. As such, alternative synthesis routes that enable more precise control over compositional and structural arrangements at the nano-scale are desired and hence a modified sol-gel process was explored to synthesize a LS $\text{Li}_2\text{MnO}_3 \bullet \text{LiNi}_{0.5}\text{Mn}_{1.5}\text{O}_4$ composite structure in which a heterogeneous distribution of Ni and Mn in the component phases is required.

Single-phase powder samples of layered Li_2MnO_3 and spinel $\text{LiNi}_{0.5}\text{Mn}_{1.5}\text{O}_4$ were prepared by a sol-gel method. An aqueous solution of metal acetates (Mn or Mn/Ni) was added to a glycolic acid or citric acid solution at 70°C and ammonium hydroxide was used to adjust the pH values to between 7-9. The final solutions were dried under stirring until a gel was formed. The gel products were fired at 400°C to remove the

polymer precursors and subsequently heat-treated at 800°C, for 12 hours, to produce well-crystallized powder samples of Li_2MnO_3 and $\text{LiNi}_{0.5}\text{Mn}_{1.5}\text{O}_4$. To produce a LS $\text{Li}_2\text{MnO}_3 \bullet \text{LiNi}_{0.5}\text{Mn}_{1.5}\text{O}_4$ composite structure, the Li_2MnO_3 and $\text{LiNi}_{0.5}\text{Mn}_{1.5}\text{O}_4$ sols were mixed together prior to gel formation. With continued stirring and heating, the mixed sol quickly formed a gel. The gel product was then decomposed at 400°C and heat-treated under the same conditions as those used for the single-phase powder samples (800°C, 12 hours).

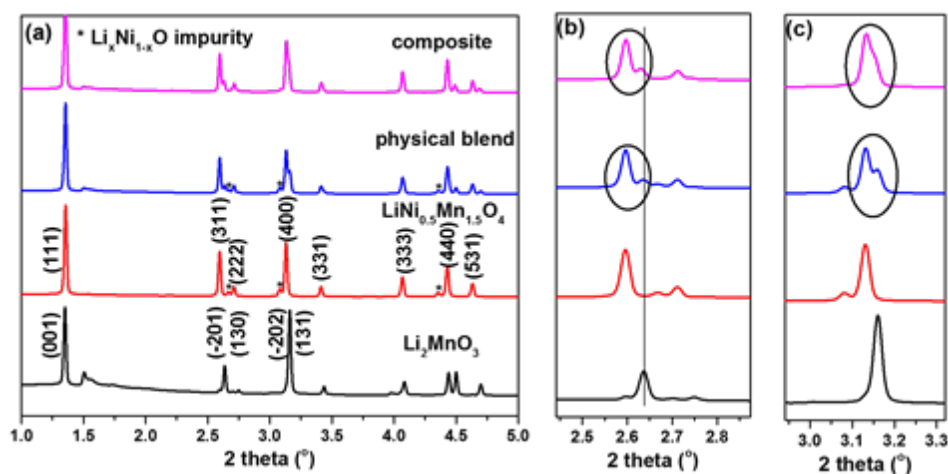


Figure II-280. (a) Synchrotron XRD of Li_2MnO_3 , $\text{LiNi}_{0.5}\text{Mn}_{1.5}\text{O}_4$, a 1:1 physical blend of the two, and a $\text{Li}_2\text{MnO}_3 \bullet \text{LiNi}_{0.5}\text{Mn}_{1.5}\text{O}_4$ composite. (b, c) Enlarged regions ranging from 2.5° to 2.8° 2θ and from 3.0° to 3.3° 2θ , respectively.

For comparison, a physical blend of the Li_2MnO_3 and $\text{LiNi}_{0.5}\text{Mn}_{1.5}\text{O}_4$ powders, in a 1:1 molar ratio, was also prepared. The synchrotron XRD patterns for the composite material in Figure II-280(a-c) show a merging of the peaks for each single-phase component together with some peak broadening. This merging effect is noticeably different in the corresponding XRD patterns of the physical blend, indicating a more complex structure than the simple mixture. In Figure II-281(c), the electrochemical profiles for the composite material display the characteristics of both Li_2MnO_3 (Figure II-281b) and $\text{LiNi}_{0.5}\text{Mn}_{1.5}\text{O}_4$ (Figure II-281a), but with much improved electrochemical performance relative to the physical blend of the individual components (Figure II-281d). These X-ray and electrochemical data indicate that the modified sol-gel method provides an effective route to produce structurally-integrated electrode materials.

Lithium intercalation mechanism of lithiated spinel LiCoO_2

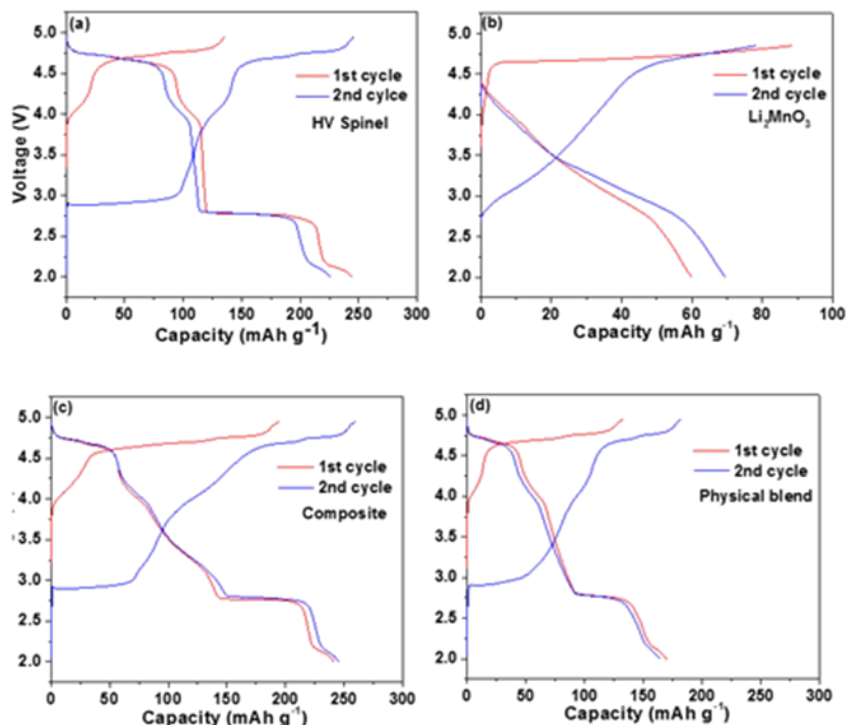


Figure II-281. (a) Initial voltage profiles of spinel $\text{LiNi}_{0.5}\text{Mn}_{1.5}\text{O}_4$, (b) layered Li_2MnO_3 , (c) a $\text{Li}_2\text{MnO}_3 \bullet \text{LiNi}_{0.5}\text{Mn}_{1.5}\text{O}_4$ composite, and (d) a 1:1 physical blend of the two components. (4.8 – 2.0 V at $\sim C/15$ against Li metal).

An interesting electrochemical behavior observed in the lithiated spinel $\text{LiCo}_{1-x}\text{M}_x\text{O}_2$ materials is a unique voltage hysteresis between the charge (~ 3.7 V) and discharge (~ 3.5 V) processes, which is more prominent than that in layered LiCoO_2 or spinel LiMn_2O_4 . In order to understand the lithium deintercalation mechanism that is responsible for such a prominent voltage hysteresis, ex-situ XRD analyses and DFT calculations were conducted. Figure II-282a shows the initial voltage curve of a Li/LT- $\text{LiCo}_{0.9}\text{Ni}_{0.1}\text{O}_2$ cell. The points where the cycled electrodes were extracted for ex-situ XRD measurement are marked on the curve. In Figure II-282b, the corresponding ex-situ XRD data indicates no significant structural changes. Detailed examination of the (311) and (400) peaks, however, reveals a reversible change in their relative intensities ($I_{(311)}/I_{(411)}$) during the charge-discharge cycle: $I_{(311)}/I_{(411)}$ increases during charging and decreases during discharging (Figure II-282c; $I_{(311)}/I_{(411)} = 0.44, 0.64$, and 0.45 for the patterns (1), (4), and (6), respectively). The $I_{(311)}/I_{(400)}$ value is dependent on the relative Li^+ occupancies of tetrahedral (T_d) vs. octahedral (O_h) sites in the spinel structure. For example, $I_{(311)}/I_{(400)}$ is greater for the $\{\text{Li}\}_{\text{tet}}\text{Co}_2\text{O}_4$ spinel structure than for the $\{\text{Li}_2\}_{\text{oct}}\text{Co}_2\text{O}_4$ lithiated spinel structure as compared in the simulated XRD patterns in Figure II-282d. Therefore, the ex-situ XRD result suggests Li^+ migration from O_h to T_d sites during charging and from T_d to O_h sites during discharging.

Kinetic mechanisms for the Li (de)intercalation process(s) from the LiCoO_2 , lithiated-spinel structure were investigated by DFT simulations wherein the energetically most favorable lithium vacancies were created in every lowest-energy, model structure of $\text{Li}_{16-x}\text{Co}_{16}\text{O}_{32}$. The DFT calculations found that (1) Li^+ migration from O_h to T_d sites is favorable during charging; (2) meta-stable structures such as $\{\text{Li}\}_{\text{tet}}\{\text{Li}_{10}\}_{\text{oct}}\text{Co}_{16}\text{O}_{32}$ form during charging until the $\{\text{Li}_{0.5}\}_{\text{tet}}\text{CoO}_2$ structure is stabilized at the end of charge; (3) the discharge process follows the equilibrium reaction pathway between the $\{\text{Li}_{0.5}\}_{\text{tet}}\text{CoO}_2$ and $\{\text{Li}\}_{\text{oct}}\text{CoO}_2$ structures; (4) the voltage for the meta-stable path is ~ 0.2 V higher than that for the equilibrium path. These experimental and theoretical data corroborate each other and provide a deeper understanding of the electrochemical and structural behavior of cobalt-based, lithiated-spinel cathodes.

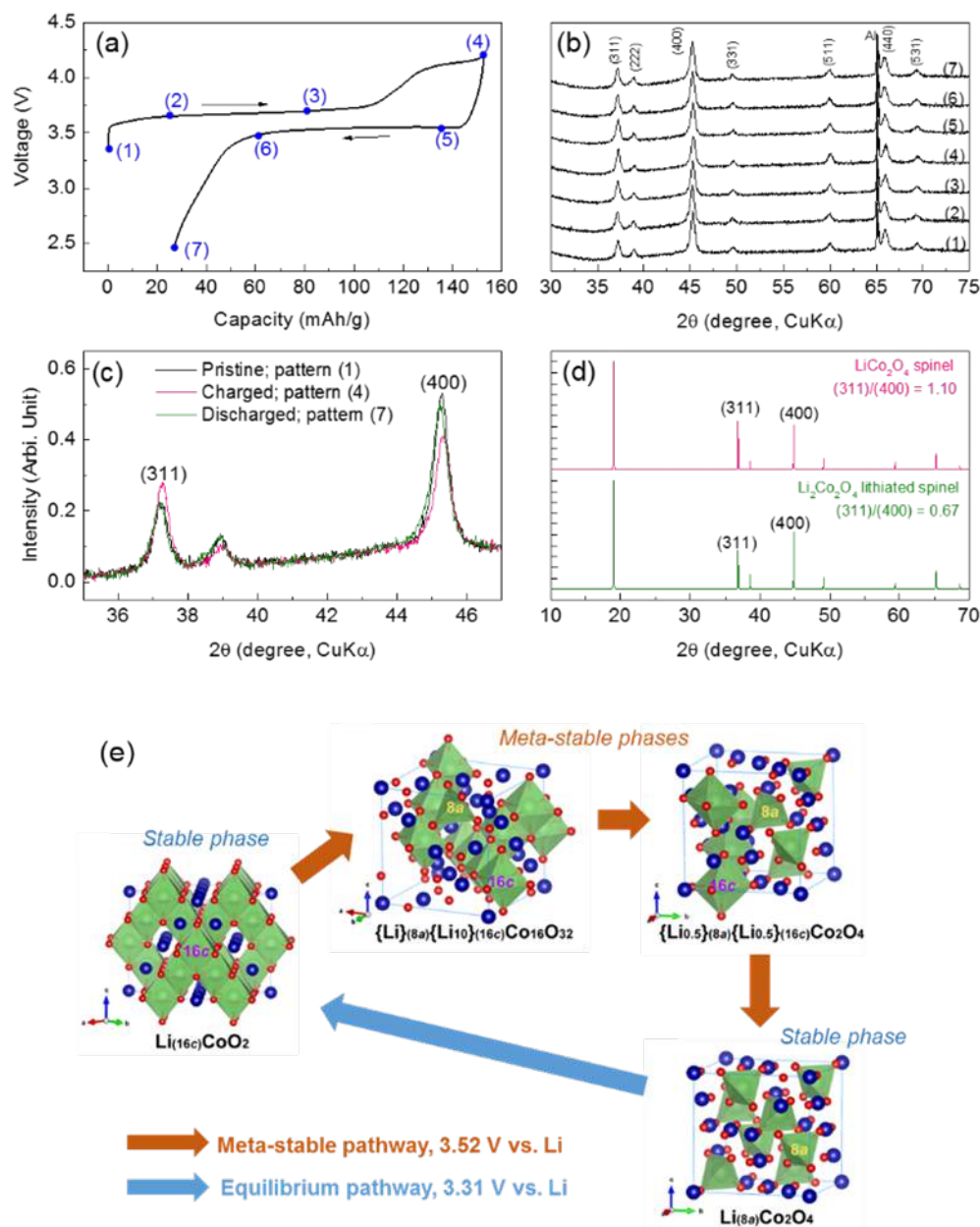


Figure II-282. (a) Voltage profiles of a Li/LT-LiCo_{0.9}Ni_{0.1}O₂ cell showing the points where ex-situ XRD data were collected, (b) corresponding ex-situ XRD patterns, (c) magnified view of the (311) and (400) peaks, (d) simulated XRD patterns of {Li}_[tet]Co₂O₄ spinel and {Li₂}[_{oct}]Co₂O₄ lithiated spinel, and (e) Li (de)intercalation mechanism(s) suggested by DFT calculation.

Conclusions

- A better understanding of the complex relationships that exist between synthesis, composition, structure, and electrochemical performance of lithiated-spinel, Li-Co-Ni-Mn-O materials has been acquired via systematic synthesis, characterization, and computational efforts
- Layered Li₂MnO₃, spinel Li₄Mn₅O₁₂, spinel Co₃O₄, and rock salt Li_xNi_{1-x}O are identified as common impurity phases that could be generated depending on compositions and synthesis conditions

- Inactive Al substitution is proven to be a promising strategy to stabilize Co-based, lithiated-spinel structures and improve cycling performance
- The synergistic advantage of atomic incorporation between layered and spinel structures has been confirmed in $\text{Li}_2\text{MnO}_3 \cdot \text{LiNi}_{0.5}\text{Mn}_{1.5}\text{O}_4$ composite materials prepared by a modified sol-gel synthesis route
- DFT calculations and ex situ XRD data suggest that lithiated-spinel, LiCoO_2 follows asymmetric reaction pathways during charge (meta-stable pathway) and discharge (equilibrium pathway) processes, that are responsible for its large, voltage hysteresis.

Key Publications

1. M.M. Thackeray and J.R. Croy, *Tailoring Integrated Layered and Spinel Electrode Structures for High Capacity Lithium-Ion Cells*, ES049, DOE Vehicle Technologies Program Annual Merit Review (Arlington, VA), 5-9, June 2017.
2. E. Lee, J. S. Park, H. Kim, Q. Li, F. C. Castro, J. Wu, V. P. Dravid, S. Kim, C. Wolverton, P. Yan, C. Wang, R. Benedek, J. R. Croy, and M. M. Thackeray, *Coherently Integrated Layered-Spinel Cathodes for Lithium-Ion Batteries*, 68th Annual Meeting of the International Society of Electrochemistry (Providence, RI), August 27 - September 1, 2017.

References

1. J. R. Croy, M. Balasubramanian, K. G. Gallagher, A. K. Burrell, *Acc. Chem. Res.* **48**, 2813 (2015).
2. S.-H. Park, S.-H. Kang, C. S. Johnson, K. Amine and M. M. Thackeray, *Electrochem. Comm.* **9**, 262 (2007).
3. D. Kim, G. Sandi, J. R. Croy, K. G. Gallagher, S.-H. Kang, E. Lee, M. D. Slater, C. S. Johnson and M. Thackeray, *J. Electrochem. Soc.* **160**, A31-A38 (2013).
4. B. R. Long, J. R. Croy, J. S. Park, J. Wen, D. J. Miller, and M. M. Thackeray, *J. Electrochem. Soc.*, **161** (14) A2160-A2167 (2014).
5. E. Lee, J. Blauwkamp, F. C. Castro, J. Wu, V. P. Dravid, P. Yan, C. Wang, S. Kim, C. Wolverton, R. Benedek, F. Dogan, J. S. Park, J. R. Croy, and M. M. Thackeray, *ACS Appl. Mater. & Interfaces*, **8**, 27720 (2016).
6. J. Reed and G. Ceder, *Chem. Rev.* **104**, 4513 (2004).
7. R. J. Gummow, M. M. Thackeray, W. I. F. David and S. Hull, *Mater. Res. Bull.* **27**, 327 (1992).
8. R. J. Gummow and M. M. Thackeray, *J. Electrochem. Soc.* **140**, 3365 (1993).
9. M. M. Thackeray, W. I. F. David, P. G. Bruce and J. B. Goodenough, *Mater. Res. Bull.* **18**, 461 (1983).
10. J. M. Tarascon and D. Guyomard, *J. Electrochem. Soc.* **138**, 2864 (1991).

II.C.12 Discovery of High-Energy Li-Ion Battery Materials (LBNL)

Wei Tong, Principal Investigator

Lawrence Berkeley National Laboratory
1 Cyclotron Road, MS62R0203
Berkeley, CA 94720
Phone: 510-486-7084
E-mail: weitong@lbl.gov

Peter Faguy, Technology Manager

U.S. Department of Energy
Phone: 202-586-1022
E-mail: Peter.Faguy@ee.doe.gov

Start Date: October 1, 2015
Total Project Cost: \$450,000

End Date: September 30, 2018
DOE share: \$450,000

Non-DOE share: \$0

Project Introduction

Currently, the commercial Li-ion batteries adopt a wide use of intercalation cathodes such as layered lithium metal oxide, spinel-type lithium manganese oxide, and olivine-type lithium iron phosphate. However, these cathodes can only deliver a reversible capacity of 140 - 170 mAh/g based on the cationic redox. Attempt to charge layered oxides to higher potentials (> 4.7 V) results in a higher initial capacity (> 200 mAh/g), but leads to an irreversible phase transformation and ultimately a capacity decay. Recently, Li-, Mn-rich layered oxides have demonstrated a high reversible capacity of > 250 mAh/g, which outperforms most of the commercially available Li-ion cathodes. However, this family of compounds experience a series of structural rearrangement and gas evolution, demonstrating continuous voltage/energy decay over the extended cycles. In this project, we propose to develop new Li-rich metal oxides that utilize $\text{Ni}^{2+}/\text{Ni}^{4+}$ redox, meanwhile, incorporate a second transition metal (TM) that is located on the first and second row in the periodic table, which is designed to stabilize the crystal structure and/or contribute electrochemical redox. The presence of Li excess in the structure is expected to increase the number of Li diffusion paths, therefore, enable more accessible Li.

Objectives

- Develop a cathode that can cycle > 200 mAh/g while exhibiting minimal capacity and voltage fade
 - Target at Li-rich compositions in Li-Ni-O chemical space that utilizes $\text{Ni}^{2+}/\text{Ni}^{4+}$ redox to potentially overcome capacity limitation per TM
 - Integrate a second TM on the first and second row to improve structural stability and/or contribute electrochemical redox
- Gain in-depth understanding on the correlation between composition and electrochemistry in Li-rich metal oxides
 - Understand the participation/contribution of cationic and anionic redox in electrochemistry
 - Investigate the potential impact of TMs on oxygen reactivity

Approach

This project integrates material design, synthesis, physical and electrochemical evaluation to search for new high capacity cathodes within Li-Ni-O chemical space. We initiated our material synthesis efforts with Li, Mn-rich layered oxide to identify the optimal synthetic condition via a facile solid-state reaction that is ultimately employed for the synthesis of Li-rich Ni-based metal oxides. Integration of a second TM is expected to

stabilize structure and/or contribute electrochemical redox. The materials are subjected to a variety of synchrotron-based radiation and spectroscopy techniques to characterize the crystal structure and electronic structure of both TMs and oxygen.

Results

We first studied the correlation between the synthesis and electrochemical performance to identify the key variables that govern the electrochemical properties. $\text{Li}_{1.2}\text{Mn}_{0.6}\text{Ni}_{0.2}\text{O}_2$ (LNMO) samples were synthesized *via* solid-state method using Li_2CO_3 , $\text{Ni}(\text{OH})_2$, and MnCO_3 precursors. Raw materials were mixed by either High Energy (HE) or medium Energy (ME) mechanical milling process, and then annealed at 950°C . The effect of the synthetic condition, include milling energy, milling time, and annealing time on the electrochemical performance was studied. Figure II-283a and Figure II-283b shows the XRD patterns and the first cycle voltage profiles of four LNMO samples synthesized with various conditions. Overall, all the samples demonstrated similar XRD patterns that are consistent with those reported in the literature, and no significant effect of the synthetic condition on the crystal structure of LNMO was detected by XRD. In contrast, we clearly observed the effect of synthetic conditions on the electrochemical performance. Despite of the similar voltage profiles, consisting of an electrochemical activation plateau around 4.5 V as well as a sloping voltage profile during the discharge, it can be clearly seen that LNMO sample prepared at a high energy for 3 h and annealing for 15 h delivered the highest discharge capacity (259 mAh/g), corresponding to 0.82 Li per formula. In comparison, the discharge capacity of the sample prepared at a medium energy was only 215 mAh/g. This capacity was about 17% lower compared to the best sample (HE3h_15h), although the XRD patterns of these two samples were similar. This clearly translates into the difference in LNMO active materials rather than process variables (*i.e.*, slurry formulation, electrode fabrication, and cell assembly). Simply comparing these two samples led to a combined effect of milling method and annealing time. The optimal synthetic condition for LNMO will be used to prepare other Li-rich metal oxide cathodes.

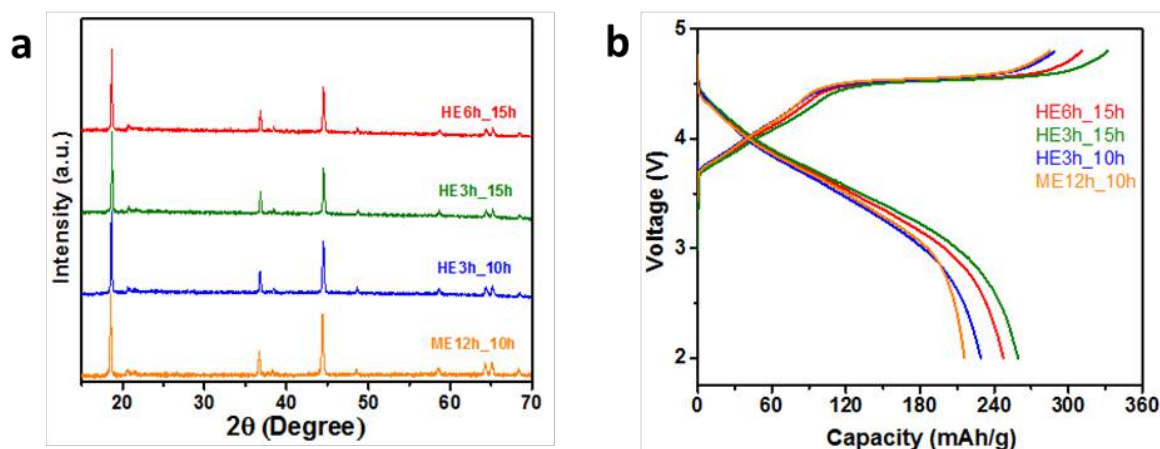


Figure II-283. (a) X-ray diffraction patterns of $\text{Li}_{1.2}\text{Mn}_{0.6}\text{Ni}_{0.2}\text{O}_2$ samples prepared by a solid-state method. Samples are denoted by milling energy followed by milling time_annealing time. (b) The first cycle voltage profiles of $\text{Li}_{1.2}\text{Mn}_{0.6}\text{Ni}_{0.2}\text{O}_2$ samples prepared by a solid-state method. Cells were cycled between 4.8 and 2 V at a current of 25 mA/g.

In the second quarter, different transition metals (TM = Mn, Ru, Sn, Mo, Nb, Ti, V) with a general formula of $\text{Li}_{2-x-y}\text{Ni}_x\text{TM}_y\text{O}_2$ ($0 < x, y < 1$) were synthesized *via* a solid-state reaction using the optimal synthetic condition identified above for LNMO. Selection of the second TM was mainly based on the theoretical capacity. The XRD patterns of the as-produced samples are presented in Figure II-284. Samples that incorporate Ru, and Sn showed very similar XRD patterns to that of LNMO. A shift in XRD peaks was observed due to the difference in ionic radius of these three TM cations. For TM = Mo, more X-ray diffraction peaks were observed, however, it can be seen that the major characteristic peaks of LNMO were reserved along with more diffraction peaks in the two-theta region of $20 - 35^\circ$. The crystal structure seemed consistent with those of the samples

with TM = Mn, Ru, Sn. Careful search and match of TM = Mo pattern in the ICDD database showed a consistency with Li_4MgWO_6 , which belongs to the monoclinic crystal system. For the other TMs we tested, the crystal structure of the final products was very different, as shown in Figure II-284b. For both Ti and Nb, the XRD patterns can be easily assigned to the disordered rock salt phase. Although NiO possesses a rock salt structure, the complete absence of any XRD peak that is related to lithium and another TM precursors or byproducts suggests incorporating Ti and Nb very likely led to the formation of a disordered rock salt phase in the final products. As for TM = V, Li_3VO_4 was a thermodynamically favorable phase in our synthesis and observed as the major phase along with NiO. The electrochemical properties of the as-produced samples were tested, the Ru compound, which showed good electrochemical performance, was used for detailed characterization.

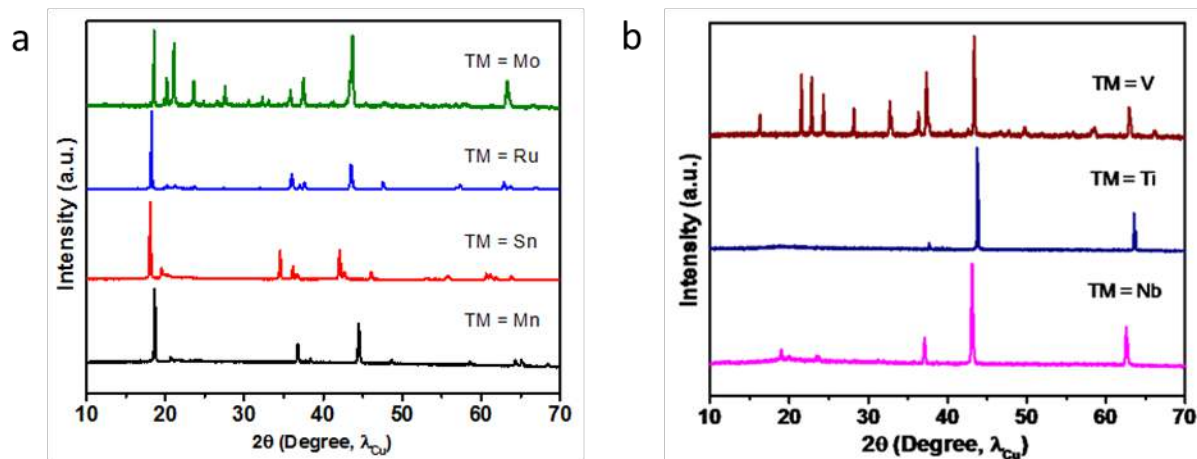


Figure II-284. (a) XRD patterns of $\text{Li}_{2-x}\text{Ni}_x\text{TM}_y\text{O}_2$ (TM = Mn, Sn, Ru, Mo), exhibiting layered structure. (b) XRD patterns of $\text{Li}_{2-x-y}\text{Ni}_x\text{TM}_y\text{O}_2$ (TM = Nb, Ti, V), exhibiting non-layered structure.

The first cycle voltage profiles and differential capacity (dQ/dV) plots of $\text{Li}_{1.2}\text{Ni}_{0.2}\text{Ru}_{0.6}\text{O}_2$ and $\text{Li}_{1.2}\text{Ni}_{0.2}\text{Mn}_{0.6}\text{O}_2$, denoted as LNRO and LNMO, are shown in Figure II-285. The LNRO sample demonstrated a charge capacity of 239 mAh/g and a discharge capacity of 213 mAh/g, leading to a coulombic efficiency of 88.9%. In comparison, LNMO sample exhibited a coulombic efficiency of 75.0%. Both samples revealed a common feature of about 1 Li^+ removal during the charge process, but noticeably different charge profiles. Instead of exhibiting a long plateau at 4.55 V in LNMO, a sloping curve with most of the capacity extracted below 4.5 V was observed for LNRO. This difference was also pronounced in the dQ/dV curves (Figure II-285 c, d). The charge profile of LNMO was characterized by a strong anodic peak at 4.55 V, corresponding to the extended voltage plateau, as well as two weak anodic peaks around 3.8 and 4.1 V associated with $\text{Ni}^{2+}/\text{Ni}^{4+}$ oxidation. This strong anodic peak in the high voltage region was absent during the charge of LNRO, instead, a relatively strong peak at 3.65 V was observed to superimpose with some minor peaks at 3.75 and 4.1 V. The corresponding cathodic peaks, which were clearly visible in the LNRO, unlike the LNMO, were located around 3.7 and 3.4 V.

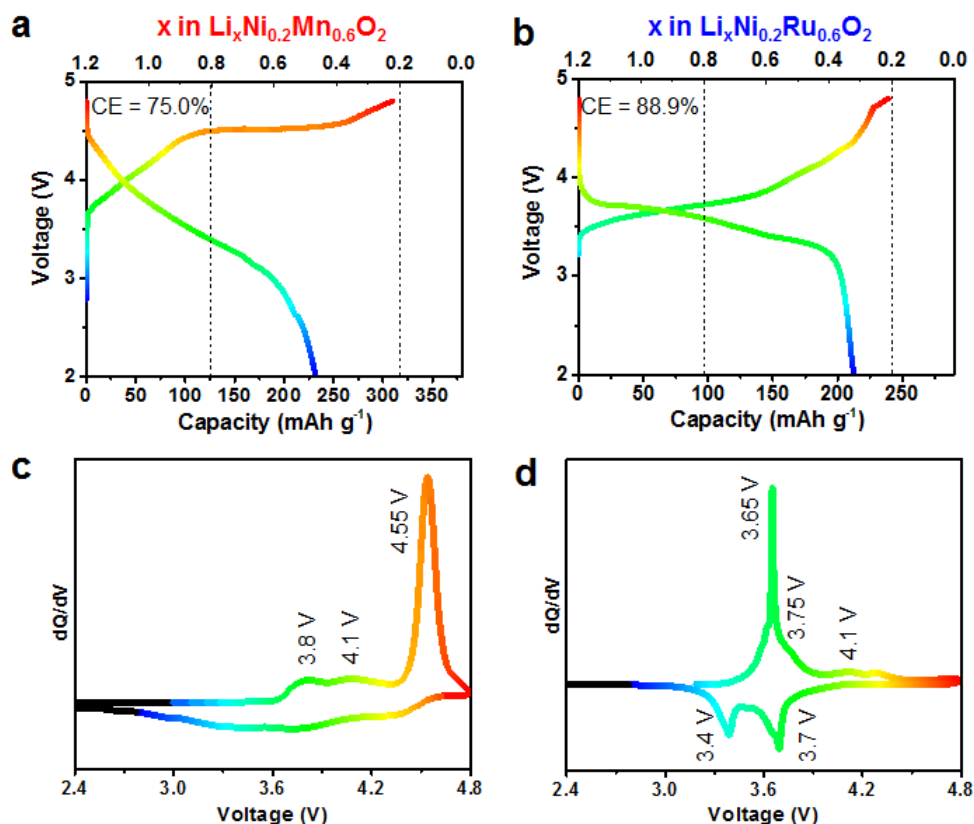


Figure II-285. The first cycle voltage profile of (a) LNMO and (b) LNRO; Differential capacity (dQ/dV) plot of (c) LNMO and (d) LNRO. Cells were cycled between 4.8 and 2.0 V at a current density of 5 mA/g at room temperature.

LNMO and LNRO showed a similar crystal structure, which was confirmed by Rietveld refinement and HRTEM analysis (Figure II-286). Both LNMO and LNRO samples fit the structural model of monoclinic solid solution, and electron diffraction (ED) patterns and fast Fourier transformation (FFT) results along the [001] and $[30\bar{1}]$ zone axis of $C2/m$ and $C2/c$ from LNMO and LNRO particle showed high structural consistency.

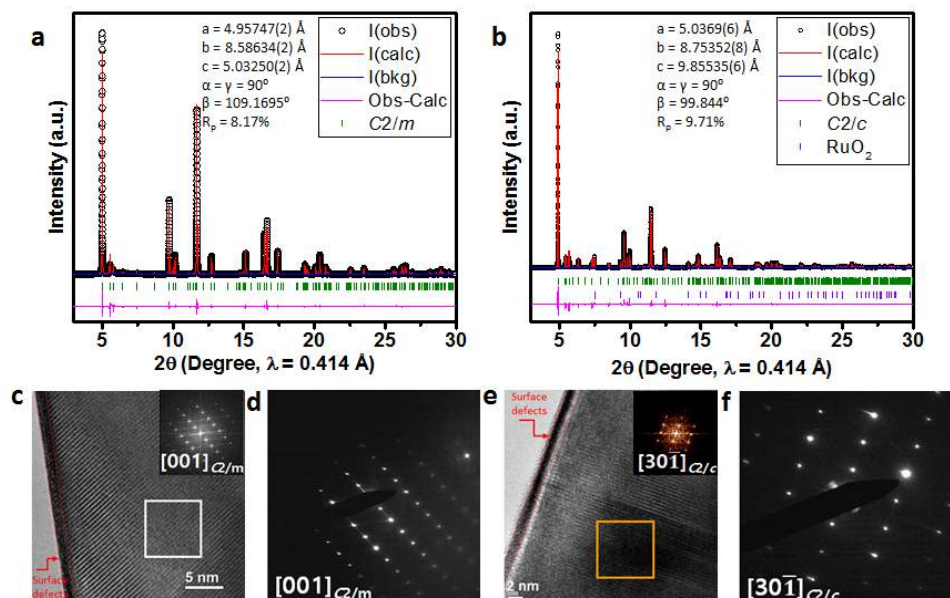


Figure II-286. XRD Rietveld refinement of (a) LNMO, monoclinic $C2/m$, and (b) LNRO, monoclinic $C2/c$; HRTEM image of (c) LNMO, (e) LNRO with FFT of the selected area; ED pattern of (d) LNMO, (f) LNRO.

To understand the different electrochemical behaviors in LMNO and LNRO of similar structure, the cationic redox of Ni and Ru were examined by X-ray absorption spectroscopy (XAS). The Soft XAS Ni L₃-edge spectra of LNRO and LNMO is shown in Figure II-287. Ni L₃-edge exhibits splitting features at high and low energy, the ratio between which is in accordance with Ni valence state. In comparison with reference compounds, Ni was determined to be 2+ in both pristine LNMO and LNRO. Upon charging, an increase in Ni L₃-edge peak at the high energy suggests the oxidation of Ni. Further increasing charge voltage to 4.8 V did not lead to an obvious change in Ni oxidation state, suggesting the completion of Ni redox by 4.5 V and 4.3 V for LNMO and LNRO, respectively. The Ni valence state reverts back to its divalent state after the first discharge, as the discharged material spectra are similar to those of the pristine material. Comparison between FY and TEY mode for both compounds revealed a slight Ni reduction at the surface of the charged electrodes, as evidenced by a slight decrease in the relative intensity of the TEY Ni L₃-edge feature compared to the analogous FY spectra at high energy. Meanwhile, the Ni oxidation state during charging process was lower in LNRO compared to that in LNMO.

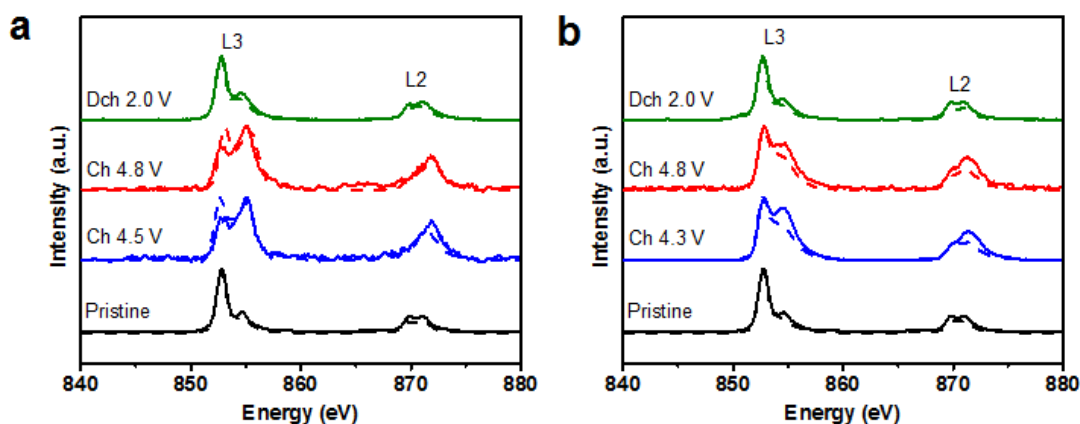


Figure II-287. sXAS Ni L-edge spectra of (a) LNMO, (b) LNRO electrodes at different states of charge. Solid and dash line indicate FY (~ 50 nm depth) and TEY (2 - 5 nm depth) mode, respectively.

We further investigated the anionic oxygen redox in both compounds by resonant inelastic X-ray scattering (RIXS). In O K-edge RIXS maps (Figure II-288), the RIXS intensity was plotted against the excitation energy (y axis) and emission energy (x axis). For LNMO electrodes (Figure II-288a), one relatively large fluorescence feature was observed at an excitation of ~ 529.2 eV (t_{2g} orbitals) along with a relatively small feature at ~ 531.5 eV (e_g orbitals) in the pristine state. Upon charging, the 529.2 eV feature tended to grow due to its more covalent nature (corresponding to Ni oxidation). The most striking phenomenon was the appearance of an additional feature (marked by arrow) at an excitation energy, 530.9 eV, between the pre-edge peaks, but at a slightly lower emission energy (~ 1 eV) in LNMO at 4.8 V charge. More importantly, this additional feature disappeared and the other two pre-edge features reverted to their original states at 2 V discharge. In contrast, the main features of the LNRO spectra (Figure II-288b) were similar to those of LNMO, except at slightly different excitation energies, 528.5 and 531.1 eV. However, at 4.8 V charge, the new feature at 530.9 eV excitation observed in LNMO was absent in LNRO. We hypothesize this additional feature that appears at 530.9 eV excitation and 523.2 eV emission energy is a direct evidence of the participation of electrons from anionic oxygen in the electrochemistry of LNMO. Therefore, we infer minimal electrons from anionic oxygen participate in the electrochemistry of LNRO, instead, Ni and Ru are electrochemically active.

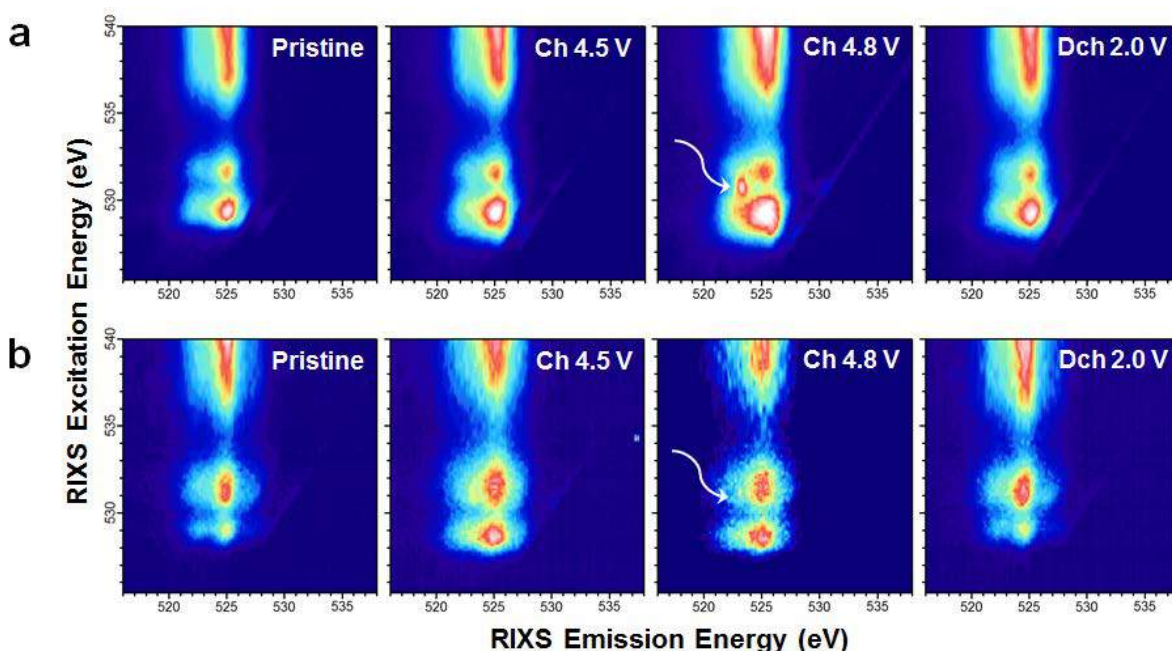


Figure II-288. O K-edge RIXS maps of (a) LNMO and (b) LNRO electrodes at various states of charge. The white arrow indicates the specific oxygen redox state that is absent in LNRO.

As discussed above, Ni is electrochemically active in both LNMO and LNRO, the additional capacity was contributed by the participation of electrons from O in LNMO. For LNRO, the reversible Ru redox is anticipated because the RIXS maps of O K-edge imply that lattice oxygen is not contributing to charge compensation. To verify our hypothesis, in-situ hard XAS (Figure II-289) were collected on Ru K-edge during the first cycle of LNRO. Compared to the X-ray absorption near edge spectra (XANES) of the reference compounds the oxidation state of Ru was determined to be 4+ in pristine LNRO (Figure II-289a). Upon charging, the Ru edge gradually shifted from its pristine state to higher energies, indicating Ru was oxidized. Meanwhile, the Ru edge moved back to the lower energy and almost to its original valence state upon discharge. On the other hand, extended X-ray absorption fine structure (EXAFS) shown in Figure II-289b exhibits two distinct shells around 1.4 and 2.3 Å, corresponding to Ru-O and Ru-TM interactions, respectively. The two shells shifted slightly to smaller distances as a result of Ru oxidation during the charge process, then reverted back to their pristine distances after discharge, indicating the reversible nature of the Ru redox process.

during LNRO cycling. In further support of the Ru redox reversibility, no obvious change in amplitude of the Ru-O and Ru-TM shells was observed, revealing no change in Ru coordination during the electrochemical process. In-situ XAS results clearly demonstrated the electrochemical activity of Ru and its good reversibility during electrochemical cycling, lending support to our earlier hypothesis that lattice oxygen redox did not participate in charge compensation during Li insertion/extraction.

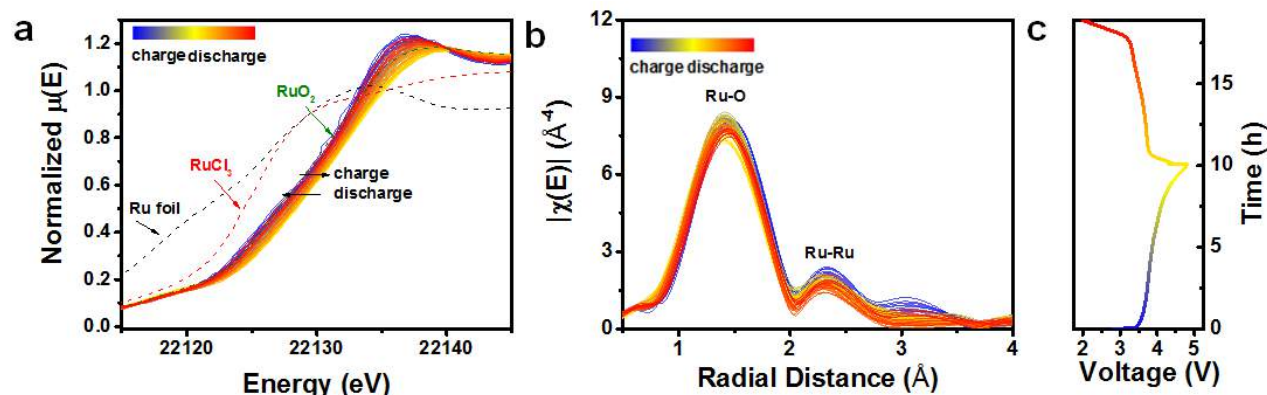


Figure II-289. In-situ (a) XANES and (b) EXAFS of Ru L-edge; (c) in-situ voltage profiles of LNRO during the first cycle. The in-situ cell was charged at C/10 and discharged at C/7.

Conclusions

In conclusion, optimal solid-state synthesis of Li-, Mn-rich layered oxides was identified and employed to synthesize a series of Li-rich metal oxides through the combination of Ni and a second TM beyond Mn (*i.e.*, Ru, Sn, Mo, Nb, Ti, V). The initial synthetic efforts led to the formation of two types of phases, layered oxides and disordered rock salts. In FY17, we focused on Li_{1.2}Ni_{0.2}TM_{0.6}O₂ (TM = Mn, Ru) and performed detailed characterization on crystal structure and charge compensation mechanism in both compounds. We observed three interesting phenomena from these two compounds: (1) they exhibited a similar crystal structure, (2) they enabled a similar amount of Li⁺/e⁻ (de)insertion during the charge-discharge process, but (3) they demonstrated distinctly different charge voltage profiles, as evidenced by 4.55 V plateau in LNMO *vs.* none in LNRO. Using combined X-ray spectroscopy techniques, we illustrated the charge compensation mechanism and verified the electrochemical activity of Ni and O in LNMO and Ni and Ru in LNRO. In particular, a signature of anionic oxygen redox was directly observed using RIXS to map the O K-edge in cycled LNMO, whereas the absence of this signature in charged LNRO indicated no such oxygen redox in LNRO. The sharp contrast between LNMO and LNRO clearly demonstrates the critical role that TM plays in the anionic oxygen activity in Li-rich metal oxides. Moreover, these two compounds of similar crystal structure, but distinct contrast in oxygen activity, offer us a platform to elucidate the correlations between structural evolution and oxygen redox. We will study the structural evolution of these two compounds upon cycling to understand its impacts on subsequent electrochemical behaviors for Li-rich metal oxides. Meanwhile, the structural and electrochemical properties of the as-produced Li-rich metal oxides by incorporating other TMs will be evaluated as well.

Key Publications

1. J. Xu, S. Renfrew, M. A. Marcus, M. Sun, B. D. McCloskey, W. Tong*, "Investigating Li₂NiO₂-Li₂CuO₂ Solid Solutions as High-Capacity Cathode Materials for Li-Ion Batteries," *Journal of Physical Chemistry C*, 121, 11100-11107 (2017).
2. J. Xu, F. Lin, M. M. Doeff, and W. Tong*, "A Review of Ni-based Layered Oxides for Rechargeable Li-Ion Batteries," *Journal of Materials Chemistry A*, 5, 874-901 (2017).

3. J. Xu, E.-Y. Hu, D. Nordlund, A. Mehta, S. N. Ehrlich, X.-Q. Yang, and W. Tong*, “Understanding the Degradation Mechanism of Lithium Nickel Oxide Cathode for Li-ion Batteries,” *ACS Applied Materials & Interfaces*, 8, 31677-31683 (2016).
4. C. Ma, J. Alvarado, J. Xu; R. Clément, M. Kodur, W. Tong, C. Grey, Y. S. Meng, “Exploring Oxygen Activity in the High Energy P2-Type $\text{Na}_{0.78}\text{Ni}_{0.23}\text{Mn}_{0.69}\text{O}_2$ Cathode Material for Na-ion Batteries,” *Journal of the American Chemical Society*, 139, 4835-4845 (2017).
5. W. Tong*, G. G. Amatucci, “Silver Copper Fluoride: a Novel Perovskite Cathode for Lithium Batteries,” *Journal of Power Sources*, 362, 86-91 (2017).
6. Z. Xing, Y. Qi, Z. Tian, J. Xu, Y. Yuan, C. Bommier, J. Lu, W. Tong*, D. Jiang, and X. Ji, “Identify the Removable Substructure in Carbon Activation,” *Chemistry of Materials*, 29, 7288-7295 (2017).

II.C.13 Model-System Diagnostics for High-Energy Cathode Development (LBNL)

Guoying Chen, Principal Investigator

Lawrence Berkeley National Laboratory
1 Cyclotron Road
Berkeley, CA 94720
Phone: 510-486-5843
E-mail: GChen@lbl.gov

Peter Faguy, Technology Manager

U.S. Department of Energy
Phone: 202-586-1022
E-mail: Peter.Faguy@ee.doe.gov

Start Date: October 1, 2016
Total Project Cost: \$550,000

End Date: September 30, 2019
DOE share: \$550,000

Non-DOE share: \$0

Project Introduction

To meet DOE targets for Li-ion batteries intended for vehicular applications, electrode materials with high-energy density and high stability are needed. Critical performance issues associated with electrode structural and morphological instabilities, side reactions with the electrolyte, and transport limitations are sensitive to material's properties such as chemical compositions, crystal structures, surface facets, and particle sizes. Advances in materials development, therefore, require a better understanding of these relationships between properties and functions, yet this has been difficult to achieve on conventional aggregated secondary particles. This project addresses these challenges in a systematic way, by synthesizing single-crystal version of the commercially promising yet complex electrode materials, obtaining new insights into the materials utilizing state-of-the-art analytical techniques that are mostly inapplicable or ineffective on conventional secondary particles, and subsequently establishing the relationships between structure and function. The goal is to use these findings to rationally design and synthesize advanced electrode materials with improved performance.

Objectives

This project will use a rational, non-empirical approach to design and synthesize next-generation high-energy, high-voltage cathode materials. Combining a suite of advanced diagnostic techniques with model cathode materials and model electrode/electrolyte interfaces, the project will perform systematic studies to achieve the following goals: 1) obtain new insights into solid-state chemistry, particularly cationic and/or anionic redox activities during charge and discharge of lithium transition-metal oxides, 2) gain fundamental understanding on cathode/electrolyte interfacial chemistry and charge transfer process as well as the impact of operating voltage window, 3) reveal performance- and stability-limiting properties and processes in high-energy, high-voltage cathodes, and 4) develop strategies to mitigate the structural and interfacial instabilities.

Approach

Prepare single crystals of Li-rich transition-metal oxides with well-defined physical attributes. Perform advanced diagnostic and mechanistic studies at both bulk and single-crystal levels. Global properties and performance of the samples will be established from the bulk analyses, while the single-crystal-based studies will utilize time- and spatial-resolved analytical techniques to probe material's redox transformation and failure mechanisms.

Results

Recently, it has been shown that some Li-excess transition-metal (TM) oxides are capable of delivering very large capacities by utilizing both TM and oxygen redox centers. One such example is $\text{Li}_{1.3}\text{Nb}_{0.3}\text{Mn}_{0.4}\text{O}_2$ ($\text{Li}_{1.3}\text{NMO}$) reported by Yabuuchi et al., which can deliver a specific energy up to 950 Wh/kg at 60 °C. As Mn is

the only redox active TM that capable of producing ~ 120 mAh/g with the $\text{Mn}^{3+}/\text{Mn}^{4+}$ reaction, the mechanism for the extra capacity, the possible involvement of bulk oxygen redox and its reversibility in long-term cycling, are not understood. To this end, a series of uniform micron-sized crystals of Li-rich niobium/tantalum manganese oxides with a formula of $\text{Li}_{1.4-x}\text{Nb}_{0.4-x}\text{Mn}_{0.2+2x}\text{O}_2$ ($x = 0, 0.1, 0.2$, $\text{M} = \text{Nb}, \text{Nb}_{0.5}\text{Ta}_{0.5}$ and Ta) were synthesized by a molten salt method. In a typical synthesis procedure, stoichiometric amounts of Li_2CO_3 , $\text{Nb}_2\text{O}_5/\text{Ta}_2\text{O}_5$ and Mn_2O_3 were used as precursors. To compensate the loss of lithium at elevated temperature, 10% excess of Li_2CO_3 was used. The precursors were mixed in a small amount of ethanol/acetone and ball-milled in a zirconia jar for 12 h. The resulting powder was then mixed with the KCl flux (m.p. = 771°C) in an R value of 2.5 or 5 (R is defined as the molar ratio between the flux and the total transition metals) and further grinded for 15 mins. The mixture was transferred into an alumina crucible covered with a lid, heated in a tube furnace at 950°C under Argon atmosphere for 12 h, and then cooled to the room temperature.

Figure II-290 shows the morphology of the synthesized $\text{Li}_{1.3}\text{NMO}$ sample as well as the structural refinement results. The particles are uniform large spheres with an average size of $5\ \mu\text{m}$ (Figure II-290a). Joint synchrotron X-ray and neutron Rietveld refinements (Figure II-290b and Figure II-290c) confirmed the cation-disordered rock-salt structure with a space group of $Fm\bar{3}m$ and a lattice parameter of $4.1954(1)\ \text{\AA}$. No oxygen vacancy was found in the pristine sample.

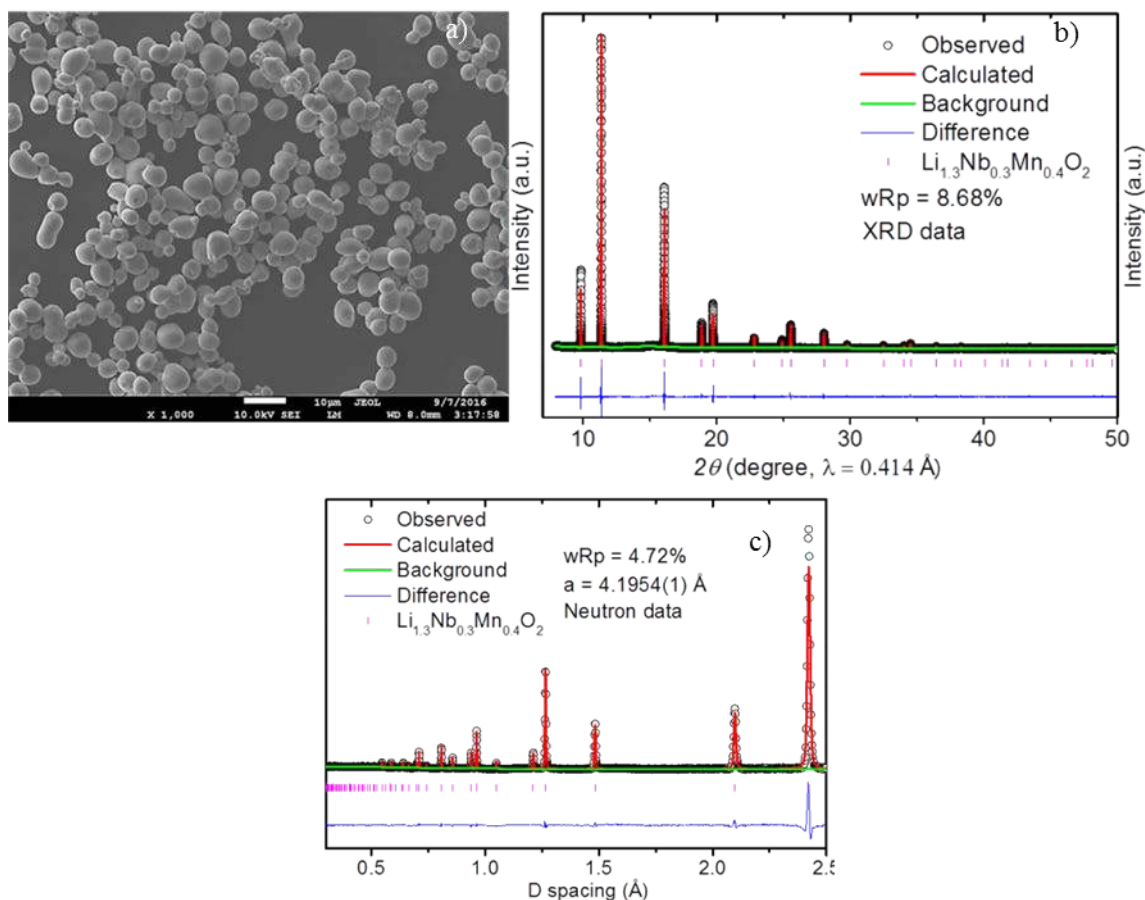


Figure II-290. a) SEM image, b) and c) Rietveld refinements of synchrotron XRD and neutron patterns of $\text{Li}_{1.3}\text{NMO}$ sample.

The electrochemical performance of $\text{Li}_{1.3}\text{NMO}$ crystals was evaluated at room temperature in a half-cell configuration. Due to high resistance and poor utilization of large particles, only limited capacities were obtained on composite electrodes made with the as-synthesized micron-sized crystals. In a modified procedure, the crystal size was reduced and electronic conductivity improved by ball-milling the oxide crystals together

with a carbon black additive in a $\text{Li}_{1.3}\text{NMO}$: carbon weight ratio of 80:20. The mixture was then added into the standard carbon and polyvinylidene fluoride (PVdF) slurry in an N-methyl-2-pyrrolidone (NMP) solvent and cast onto the Al current collector. The final weight ratio of active material: carbon additive: PVdF binder in thus prepared electrodes was 56:34:10. The electrodes were assembled into half-cell coin cells with a 1M LiPF_6 in 1:1 (v/v) ethylene carbonate (EC): diethylene carbonate (DEC) electrolyte and cycled at room temperature at a constant current of 10 mA/g between 1.5 and 4.8 V. Figure II-291a shows the voltage profiles of the first 4 cycles. In the sloping region, the voltage increased steadily from the open circuit voltage (OCV) of 3.0 V to 4.3 V which delivered a specific capacity of ~ 115 mAh/g. Whereas in the plateau region, the voltage only increased slightly from 4.3 V to 4.5 V before it rapidly increased to the cut off voltage of 4.8 V. A specific capacity of ~ 215 mAh/g was obtained above 4.3 V on the first cycle, leading to a total charge capacity of 330 mAh/g. An overall sloping discharge profile was observed which delivered a total discharge capacity of ~ 290 mAh/g at the cutoff voltage of 1.5 V. Two guidelines, one showing the theoretical capacity originated from the $\text{Mn}^{3+}/\text{Mn}^{4+}$ redox couple (118 mAh/g) and the other showing the theoretical capacity based on Li content (383 mAh/g), are also shown in Figure II-291a. It is clear that both charge and discharge capacities are significantly larger than the theoretical capacity of the $\text{Mn}^{3+}/\text{Mn}^{4+}$ redox. The charge capacity obtained in the sloping region is consistent with the capacity from the $\text{Mn}^{3+}/\text{Mn}^{4+}$ redox couple, suggesting that $\text{Mn}^{3+}/\text{Mn}^{4+}$ may be the sole redox process occurring in this region below 4.3 V. In the 2nd cycle, there is an overall decrease in the charging voltage of the sloping region which led to an increased capacity of ~ 180 mAh/g upon reaching 4.3 V. This signals a reduction in polarization in the electrode. The plateau region became somewhat sloping but voltage increase remained slow. With cycling, the degree of sloping gradually increased and the capacity obtained from this “plateau region” continued to decrease. The same trend was also observed on the discharge capacity. These results obtained from room-temperature cycling are comparable to what was obtained at 60°C by Yabuuchi et al., suggesting that the crystal samples may have a kinetic advantage compared to the polycrystalline samples synthesized using the solid-state method.

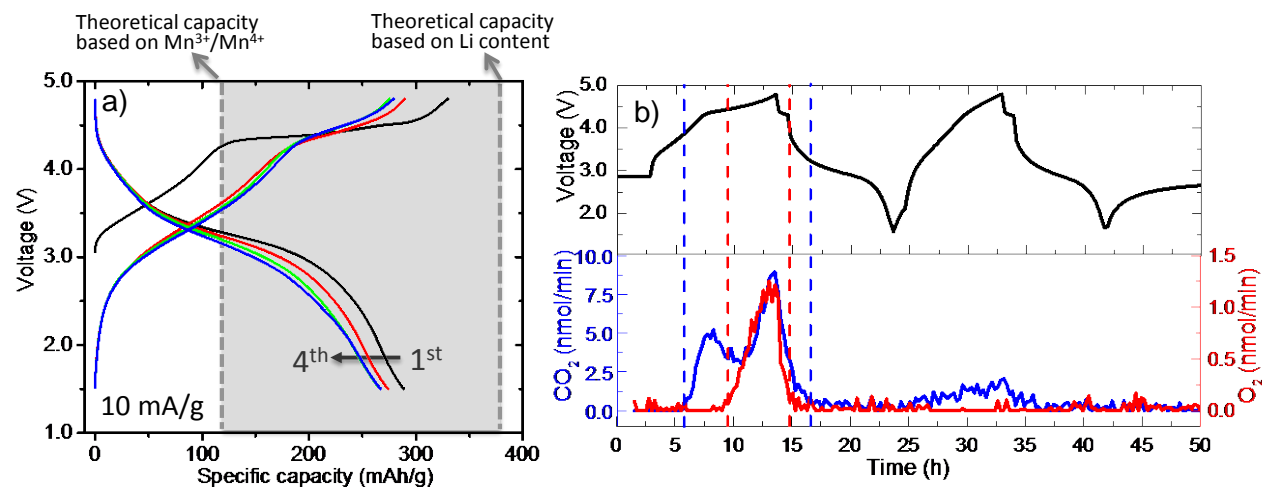


Figure II-291. a) Voltage profiles of $\text{Li}_{1.3}\text{NMO}$ half-cell cycling and b) DEMS measurement: (top) Voltage profile and (bottom) O_2 and CO_2 gas evolution.

Operando differential electrochemical mass spectroscopy (DEMS) was used to further examine the oxidation process of oxygen anions. Figure II-291b shows the results obtained during the first two cycles at a constant current density of 25 mA/g. During the 1st cycle, both CO_2 and O_2 evolution were detected. CO_2 evolution began around 3.8 V during the charge (the 1st blue guideline in the figure) and completed around the mid-discharge cycle (the 2nd blue guideline). There was an increase in intensity around the mid-plateau after the onset of O_2 evolution and the peak CO_2 evolution was reached at the end of charge at 4.8 V. Oxygen gas was not detected until the mid-plateau region at about 4.5 V (the 1st red guideline), which also peaked at the upper cut-off voltage of 4.8 V. Oxygen evolution completes at the beginning of 1st discharge after the resting step (the 2nd red guideline). The cumulative CO_2 and O_2 evolved from the first cycle were 1.53 μmol and 0.11

μmol , respectively, from a cathode that contained 2.66 mg of active materials. In the 2nd cycle, the amount of CO_2 was reduced from 1.53 μmol to 0.46 μmol while negligible O_2 evolution was detected. Combined with the cyclic voltammetry (CV) studies, the results reveal that capacity contribution from O extraction from the oxide lattice occurs above ~ 4.5 V. While both O_2 gas evolution and lattice oxygen oxidation occur in the first charge, the following cycles only involves the redox of O^{2-} to O^{n-} ($0 < n < 2$) species, signaled by the single oxidation peak at 4.5 V on the CV. The continuous decrease in peak intensity along with scanning indicates that the lattice anion redox process is highly irreversible.

In order to gain further insights on structural and chemical changes during the first charge, chemical oxidation was used to extract various amounts of Li from $\text{Li}_{1.3}\text{NMO}$ crystals. Delithiated $\text{Li}_x\text{Nb}_{0.3}\text{Mn}_{0.4}\text{O}_2$ (Li_xNMO) samples were prepared by chemical reaction in a NO_2BF_4 solution in acetonitrile, with the lithium content (x) controlled by the mole ratio between the oxide and the oxidizing agent. Figure II-292 shows the synchrotron XRD and neutron patterns of the series with various lithium content of $0 \leq x \leq 1.3$, collected at 11-BM at the Advanced Photon Source (APS) and BT1 at National Institute of Standards and Technology (NIST), respectively. With decreasing x , the cell dimension reduces while the rock-salt crystal structure maintains. Two separate regions, a single phase region with $0.9 < x \leq 1.3$ and a two phase region with $0 < x < 0.9$, were found, suggesting the involvement of distinctively different redox activities.

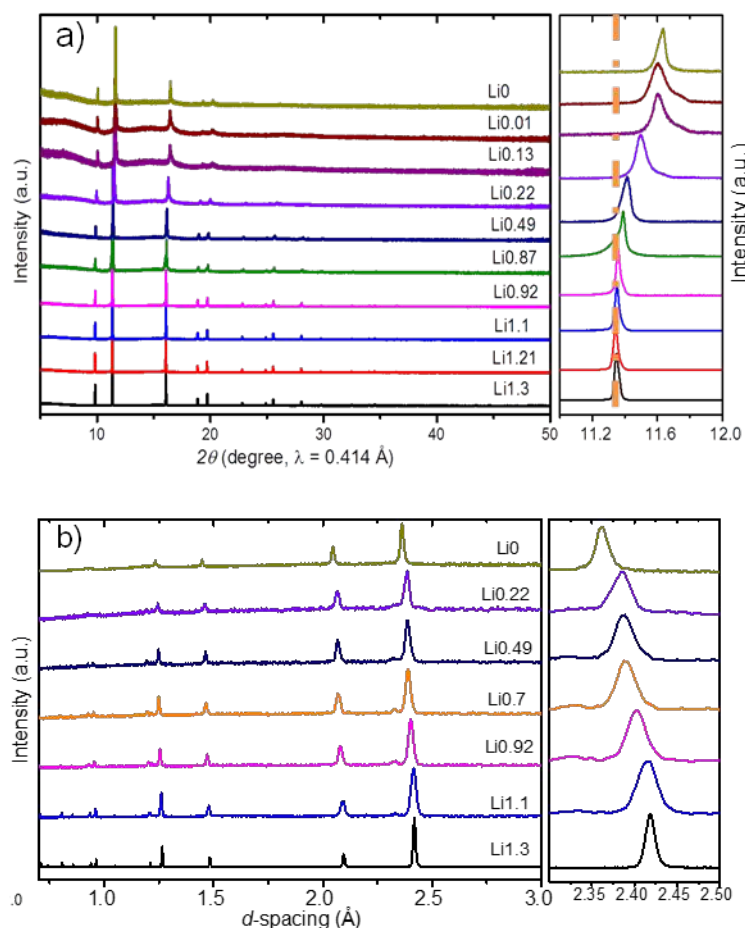


Figure II-292. a) Synchrotron XRD and b) neutron patterns of chemically delithiated $\text{Li}_x\text{Nb}_{0.3}\text{Mn}_{0.4}\text{O}_2$ ($0 \leq x \leq 1.3$) crystal samples.

The unit cell volume and phase fraction as a function of Li content were constructed from the refinement and shown in Figure II-293a and Figure II-293b, respectively. The Vegard's law is only followed in region I where the total volume change is *ca.* 0.2%. This is consistent with the participation of simple cation redox from Mn^{3+} to Mn^{4+} along with the extraction of 0.4 Li^+ from $\text{Li}_{1.3}\text{NMO}$. Complex mixed oxygen activities are likely involved in region II, where Phase 2 and Phase 3 with the same rock-salt crystal structure but different lattice dimension evolves along with the extraction of Li. Smaller sized Phase 3 reaches the maximum fraction when x is ~ 0.5 whereas Phase 2 becomes the main phase with further Li removal. Combining with the results from the electrochemical studies, we propose that lattice O^{2-} oxidation to O^{n-} ($0 < n < 2$) mainly occurs in Phase 3 whereas loss of O from the lattice mainly occurs in Phase 2. This was further supported by results from the joint X-ray and neutron refinements which revealed that $\sim 2 \text{ mol.}\%$ and $7.8 \text{ mol.}\%$ of oxygen ion vacancies exist in the delithiated $\text{Li}_x\text{Nb}_{0.3}\text{Mn}_{0.4}\text{O}_{2-\delta}$ with $x=0.2$ and 0 , respectively. The kinetic properties of delithiation is evaluated by the relationship between the molar ratio of oxidant/oxide used and the residual Li content in the sample (Figure II-293c), as determined by ICP. While a linear relationship is apparent in region I, significant deviation is seen in region II, further confirming the complex nature of mixed anion activities at lower Li contents.

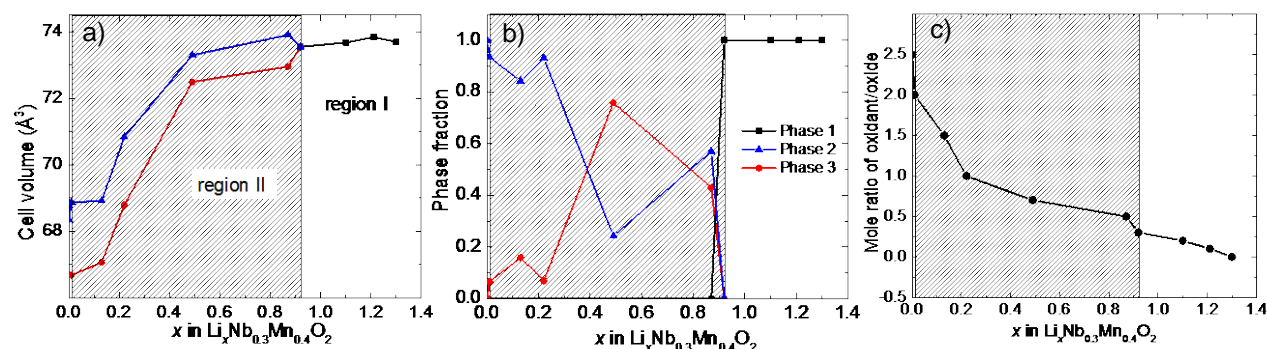


Figure II-293. a) and b) Cell volume and phase fraction as a function of x in delithiated Li_xNMO samples, and c) The relationship between the molar ratio of oxidant/oxide and residue Li content in chemically delithiated Li_xNMO samples.

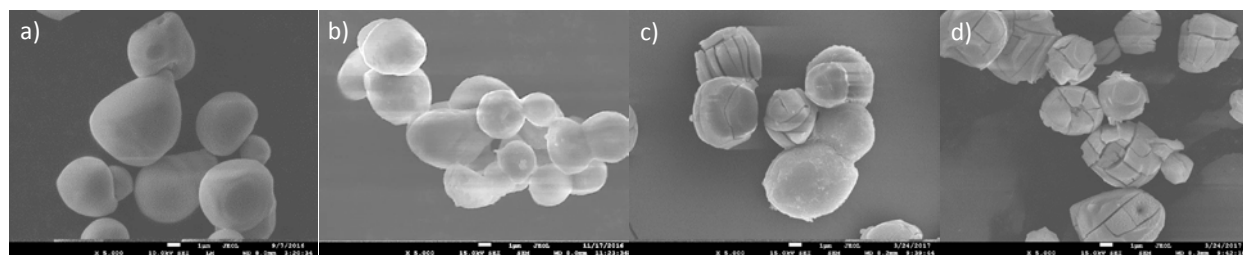


Figure II-294. SEM images of chemically delithiated Li_xNMO crystal samples: a) $x=1.3$, b) $x=1.1$, c) $x=0.76$, and d) $x=0.13$.

Figure II-294 shows the changes in particle morphology along with the decrease of x in Li_xNMO crystals. The particles with a lithium content above 0.9 remain intact but significant cracking was observed when the lithium content is less than 0.9, likely a combined effect of cell volume change (7.3% total) and oxygen evolution during the process.

Figure II-295a-Figure II-295c show the Mn K -edge hard X-ray absorption spectra (hXAS) collected on pristine and chemically delithiated Li_xNMO crystal samples. In the Mn pre-edge region (Figure II-295b), there is a clear division in peak intensity below and above $\text{Li}0.9$, suggesting a change in Mn local environment. Figure II-295c shows the expanded view of the X-ray absorption near-edge structure (XANES) region. Above $\text{Li}0.9$, Mn K -edge energy continuously shifts to a higher value in a near linear fashion which then becomes constant below 0.9. This trend is further revealed in Figure II-295d where the relationship between Li content and Mn XANES edge position, defined by the interception of the spectrum at $1/2$ of the normalized intensity,

is shown. Combined hXAS, XRD and neutron results confirm that cation redox involving $\text{Mn}^{3+}/\text{Mn}^{4+}$ only occurs in the single phase region above $\text{Li}0.9$. Below $\text{Li}0.9$, Li extraction occurs with the complex oxygen redox activities that involve two rock-salt phases.

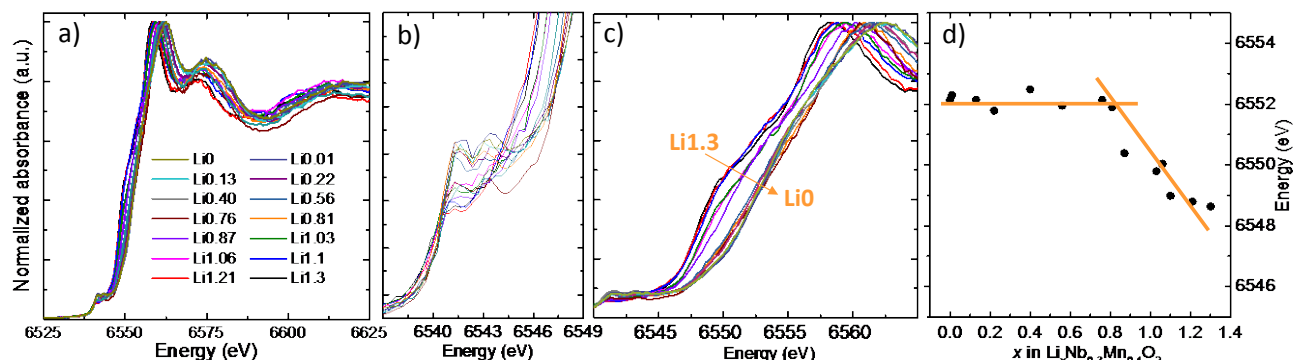


Figure II-295. Mn K-edge hard XAS measurements of Li_xNMO crystals: a) hard XAS spectra, b) expanded view of the pre-edge region, c) expanded view of the XANES region and d) relationship between Mn edge position and Li content in the samples.

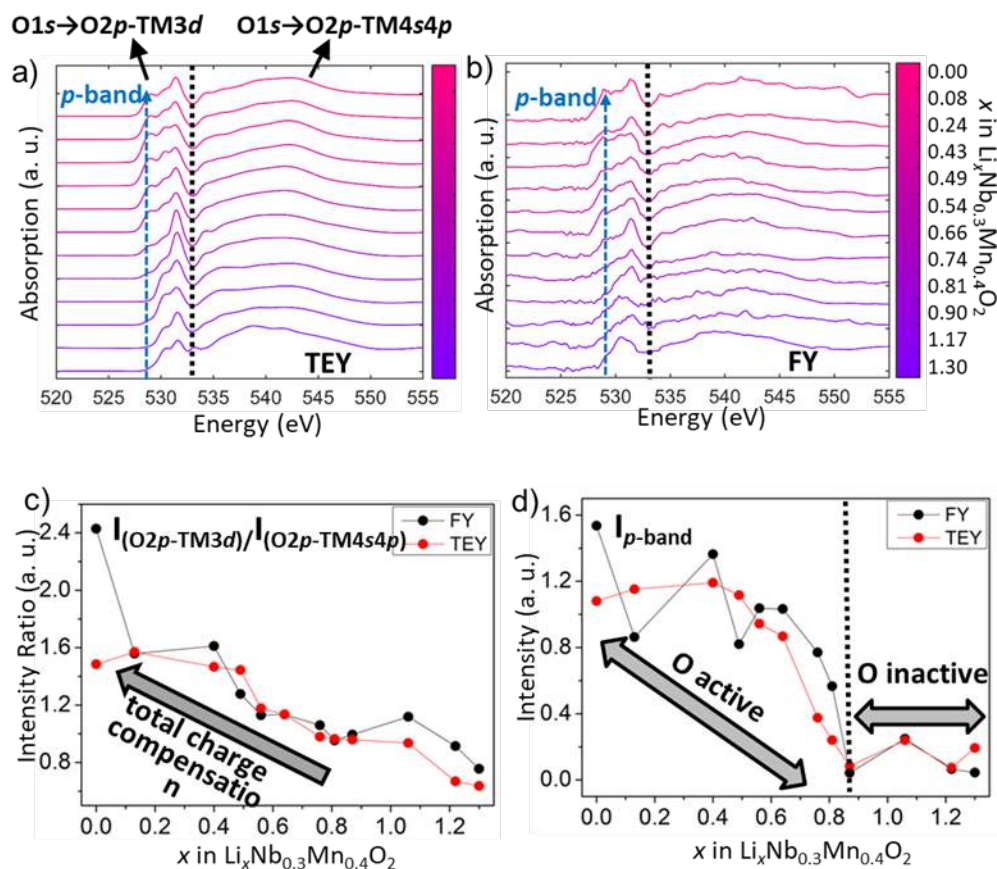


Figure II-296. a) and b) O K-edge soft XAS spectra obtained in TEY and FY modes, c) and d) Intensity ratio between the pre-edge and post-edge absorption peaks and Intensity of the p-band as a function of Li content. In a) and b), black dashed line divides the pre- and post-edge regions and the blue dashed arrow follows the evolution of the p-band intensity.

Evaluation on oxygen activities during 1st delithiation was then carried out by soft XAS measurements at the Stanford Synchrotron Radiation Lightsource (SSRL). Depth profiling from surface to bulk was achieved by using two different detectors in total electron yield (TEY) and fluorescence yield (FY) modes that have a typical probing depth of 5 and 50 nm, respectively. Figure II-296a and Figure II-296b show the evolution of TEY and FY O *K*-edge XAS spectra as a function of Li content in Li_xNMO. In both cases, the spectra can be separated into the pre-edge region and post-edge region at the black dashed line (533 eV). Features in the post-edge region are often attributed to O1s → O2p-TM4s4p hybridization while those in the pre-edge region are attributed to O1s → O2p-TM3d hybridization. The pre-edge region is therefore of most interest and may be used as a qualitative measure for holes generated from electron extraction either from oxygen or TM at the O2p-TM3d energy level. As expected, both TEY and FY spectra exhibit significant increase in the pre-edge peak intensity with Li extraction from Li_{1.3}NMO which is demonstrated by the continuous increase in the ratio between the pre-edge peaks and post-edge absorption peaks (Figure II-296c). A new low-energy shoulder peak at 529 eV also appeared and gradually grew along with delithiation, suggesting the involvement of additional O-TM hybridization (referred to as *p*-band) during the process. Due to the similarity between the *p* band and the pre-edge absorption peak observed in peroxide and super-peroxide species, we speculate this new hybridization arises from the interaction between oxygen anions as a result of oxygen redox activities. Further quantification shows that the initial *p*-band intensity in the pristine Li_{1.3}NMO is extremely low which remains nearly constant below Li content of ~0.9 (Figure II-296d), suggesting negligible interactions between oxygen anions or oxygen redox activities. As *x* decreases to below 0.9, there is a rapid increase in the *p*-band intensity and it continues to rise until full delithiation (*x* = 0). The results indicate an increase in oxygen valence states in this region and the participation of oxygen redox for charge compensation. Note that the *p*-band intensity in the *x* < 0.9 region is generally higher in the FY mode than that in the TEY, consistent with a difference in oxygen activities mostly involving O²⁻ anion oxidation to O^{*n*-} (0 < *n* < 2) species in the bulk and lattice O loss on the surface.

Conclusions

In conclusion, we demonstrated the effective use of model-system-based diagnostic studies by synthesizing one of the high-capacity Li-rich oxide cathode materials, Li_{1.3}Nb_{0.3}Mn_{0.4}O₂, in micron-sized single crystals and using it as a platform to understand the charge compensation mechanism during Li extraction and insertion. We explicitly demonstrate that the oxidation of O²⁻ to O^{*n*-} (0 < *n* < 2) and O₂ loss from the lattice dominates at 4.5 and 4.7 V, respectively. While both processes occur in the first cycle, only the redox of O²⁻/O^{*n*-} participates in the following cycles. The lattice anion redox process triggers irreversible changes in Mn redox, which likely causes the voltage and capacity fade observed on this oxide. While a single-phase behavior involving only Mn^{3+/4+} redox was observed in 0.9 < *x* < 1.3, a two-phase behavior involving O²⁻/O^{*n*-} (0 ≤ *n* < 2) reactions was seen in 0 < *x* < 0.9. Approximately 7.8 mol.% of oxide-ion vacancies were found in the fully delithiated Li₀Nb_{0.3}Mn_{0.4}O_{2-δ}. Morphological damage with particle cracking and fracturing was broadly observed when O redox is active, revealing additional challenges in utilizing O redox for the development of high-energy cathodes. Efforts on material modification to influence the extent of oxidation of O²⁻ to O^{*n*-} (0 < *n* < 2) and O₂ loss from the lattice as well as strategies to improve oxide performance are underway.

Key Publications

1. S. Kuppan, Y. Xu, Y. Liu and G. Chen, "Phase Transformation Mechanism in LiMn_{1.5}Ni_{0.5}O₄ Cathode Particles Revealed by Single-crystal Hard X-ray Microscopy," *Nature Communications*, **8**, 14309 (2017). DOI: 10.1038/ncomms14309.
2. S. Kuppan, A.K. Shukla, D. Membreno, D. Nordlund and G. Chen, "Revealing Anisotropic Spinel Formation on Pristine Li- and Mn-Rich Layered Oxide Surface and Its Impact on Cathode Performance," *Advanced Energy Materials*, **7**, 1602010 (2017), DOI: 10.1002/aenm.201602010.
3. Y. Ma, Y. Zhou, C. Du, P. Zuo, X. Cheng, L. Han, D. Nordlund, Y. Gao, G. Yin, H. L. Xin, M. M. Doeff, F. Lin, and G. Chen, "A New Anion Receptor for Improved Interface between the Lithium- and

- Manganese-rich Layered Oxide Cathode and the Electrolyte,” *Chemistry of Materials*, **29** (5), 2141 (2017). DOI: 10.1021/acs.chemmater.6b04784.
4. W. H. Kan, S. Kuppan, L. Cheng, M. Doeff, J. Nanda, A. Huq and G. Chen, “Crystal Chemistry and Electrochemistry of $\text{Li}_x\text{Mn}_{1.5}\text{Ni}_{0.5}\text{O}_4$ Solid Solution Cathode Materials,” *Chemistry of Materials*, **29** (16), 6818 (2017). DOI: 10.1021/acs.chemmater.7b01898.
 5. S. Kuppan, A.K. Shukla and G. Chen, “Single-crystal Based Diagnostics for Li-ion Battery Cathode Development,” PRiME 2016, Honolulu, HI, October 2016.
 6. Y. Ma, Y. Zhou, G. Yin, F. Lin and G. Chen, “A New Anion Receptor for Improved Interface Between the Lithium- and Manganese-Rich Layered Oxide Cathode and the Electrolyte,” PRiME 2016, Honolulu, HI, October 2016.
 7. W.-H. Kan, S. Kупpan and G. Chen, “Advanced High-energy Cathode Materials for Lithium-ion Batteries,” 2016 Bay Area Battery Summit, Menlo Park, CA, November 2016.
 8. J. Kan, T. Yan and G. Chen, “Rational Design and Development of Advanced Lithium Battery Materials” Energy Technology Area Lab Director's Review, Berkeley, CA, January 2017 (invited).
 9. J. Kan and G. Chen, “Rational Design and Development of Advanced Lithium Battery Materials” Energy Technology Area Lab Town Hall Meeting, Berkeley, CA, March 2017 (invited).
 10. G. Chen, “Design and Synthesis of Advanced High-Energy Cathode Materials,” DOE Hydrogen Program and Vehicle Technologies Program Annual Merit Review and Peer Evaluation Meeting, Washington, DC, June 2017.

II.D Next-Gen Lithium-Ion: Diagnostics

II.D.1 Interfacial Processes (LBNL)

Robert Kostecki, Principal Investigator

Lawrence Berkeley National Laboratory

1 Cyclotron Road

Berkeley, CA 94720

Phone: 510-486-6002

 E-mail: r_kostecki@lbl.gov
Tien Duong, Technology Manager

U.S. Department of Energy

Phone: 202-586-7836

 E-mail: Tien.Duong@ee.doe.gov

Start Date: October 1, 2016

End Date: September 30, 2017

Total Project Cost: \$440,000

DOE share: \$440,000

Non-DOE share: \$0

Project Introduction

Li-ion batteries are inherently complex and dynamic systems. Although often viewed as simple devices, their successful operation relies heavily on a series of complex mechanisms, involving thermodynamic instability in many parts of the charge/discharge cycle and the formation of metastable phases. This paradigm of Li-ion system operation usually drives the battery toward irreversible physical and chemical conditions that lead to battery degradation and failure.

The requirements for long term stability of Li-ion batteries are extremely stringent and necessitate control of the chemistry at a wide variety of temporal and structural length scales. Progress towards identifying the most efficient mechanisms for electrical energy storage and the ideal material depends on a fundamental understanding of how battery materials function and what structural/electronic properties limit their performance. This in turn necessitates the development and use of new characterization tools to monitor these processes.

The design of the next generation of Li-ion batteries requires a fundamental understanding of the physical and chemical processes that govern these complex systems. Although some significant advances have been made to prepare and utilize new materials efforts towards the understanding of their operation mechanisms and degradation modes have been insufficient and/or unsuccessful.

This project provides better understanding of the underlying principles that govern the function and operation of battery materials, interfaces and interphases, which is inextricably linked with successful implementation of high energy density materials such as $\text{Li}[\text{Ni}_x\text{Mn}_y\text{Co}_z]\text{O}_2$ compounds (NMCs) in Li-ion cells for PHEVs and EVs. A systematic evaluation of the NMC material composition, and cell history on the surface reconstruction, transition metal dissolution, oxygen loss phenomenon is proposed for this work, using *in situ* surface-sensitive optical spectroscopy and microscopy. These results will supplement other characterization efforts within this Task and ultimately will be used to design and synthesize robust NMC materials that can cycle stably to high potentials and deliver >200 mAh/g at coulombic efficiency close to 100%. A better understanding of the underlying principles that govern these phenomena is inextricably linked with successful implementation of high energy density materials such as Si and high voltage cathodes in Li-ion cells for PHEVs and EVs.

Objectives

This collaborative project involves the development and application of advanced experimental methodologies to study and understand the mechanism of operation and degradation of high capacity NMC materials for Li-ion cells for PHEV and EV applications. The main objectives of this task are:

- Provide critical understanding of basic principles that govern the function and operation of active materials, composite electrodes and Li-ion battery cells that is necessary for successful implementation of high energy density materials in Li-ion cells for PHEVs and EVs.
 - Establish direct correlations between electrochemical performance, interfacial phenomena, surface chemistry, morphology, topology and degradation mechanisms of ABMR baseline materials, electrodes and cells.
- Propose and evaluate remedies to interfacial and materials instability e.g., artificial surface coatings (e.g., ALD) and/or structures, novel electrode architectures, electrolyte additives etc.
- Develop, adapt and employ new advanced experimental techniques and methodologies to guide development of novel EES materials, electrodes and battery systems.
 - Obtain detailed insight into the dynamic behavior of molecules, atoms, and electrons at electrode/electrolyte interfaces at resolution that is adequate to the size and function of basic chemical or structural building blocks

Approach

Apply *in situ* and *ex situ* far- and near-field optical multifunctional probes to obtain detailed insight into the active material structure and the physico-chemical phenomena at electrode/electrolyte interfaces of stoichiometric NMCs with high Ni contents such as 622 and 523 compositions materials at a spatial resolution that corresponds to the size of basic chemical or structural building blocks. The primary goal of these studies is to unveil the structure and reactivity at hidden or buried interfaces and interphases that determine material, composite electrode and full cell electrochemical performance and failure modes. The proposed work constitutes an integral part of the concerted effort within the BMR Program and it supports development of new cathode materials for high-energy Li-ion cells. The specific research tasks include:

1. Study interfacial reactions between organic electrolytes and Ni-rich NMC.
2. Investigate the impact of surface reconstruction layer(s) on the electrochemical behavior of the NMC cathode.
3. Obtain detailed insights into the mechanism and interdependence of interfacial phenomena at Ni-rich NMC cathodes.

This project focuses on high Ni content NMC compositions such as 523 and 622, which are expected to achieve high discharge capacities even within conservative electrode potential limits. The *in situ/ex situ* investigations of the surface reconstruction into rock salt on NMC samples of different morphology and composition were carried out in sync with similar studies by X-ray techniques (M. Doeff, LBNL) and directly linked with investigations interfacial reactivity toward organic electrolytes.

In close collaboration with the BMR Cathode Group, NSOM, FTIR-ATR and environmental XPS were used to monitor surface reactions and identify their intermediates and end-products on binder and carbon-free model NMC samples to investigate the spatial-chemical composition of surface layers. This is a collaborative effort with the LBNL ALS IR beam line 5.4.1 scientists to adopt and employ a synchrotron-based tunable IR source to overcome spectral range limitation of the tunable lasers and/or inadequate intensity of the glow bar IR source. This new and unique experimental setup constitutes a major breakthrough in the diagnostics of electrochemical interfaces, and Li-ion systems in particular.

Results

We analyzed the relationship between the reconstruction layer on the surface of nickel-rich NMC (Ni:Mn:Co=5:3:2) particles and its electrochemical properties. For this purpose, an artificial reconstructed surface layer was produced by storing the NMC powder for 10 days in 1M LiPF₆ in EC/DEC 1:2 electrolyte at 60 °C. The NMC powder was then washed and sonicated in DEC, and dried in vacuum. The resultant surface rock-salt layer is expected to have a similar thickness as the one that evolves from electrochemical charging and discharging as reported in the literature. The pristine (NMC) powder and the powder with a surface reconstruction layer (NMC/R) were then used to prepare composite electrodes for electrochemical tests in a standard coin cell configuration.

After 200 charge-discharge cycles at 0.5 C between 2.0-4.7 V, both the NMC and NMC/R cells show similar capacity retention ca. 61% of the original discharge capacity (Figure II-297a). Interestingly, NMC/R electrode showed consistently lower polarization than pristine NMC Figure II-297(b)-(d)). The polarization difference between NMC and NMC/R is about 0.2 V for discharging and 0.1 V for charging at 50 % state of charge for 200th cycle. This demonstrates that in fact, the existence of the reconstruction layer improves the cell performance by inhibiting the impedance growth during cycling.

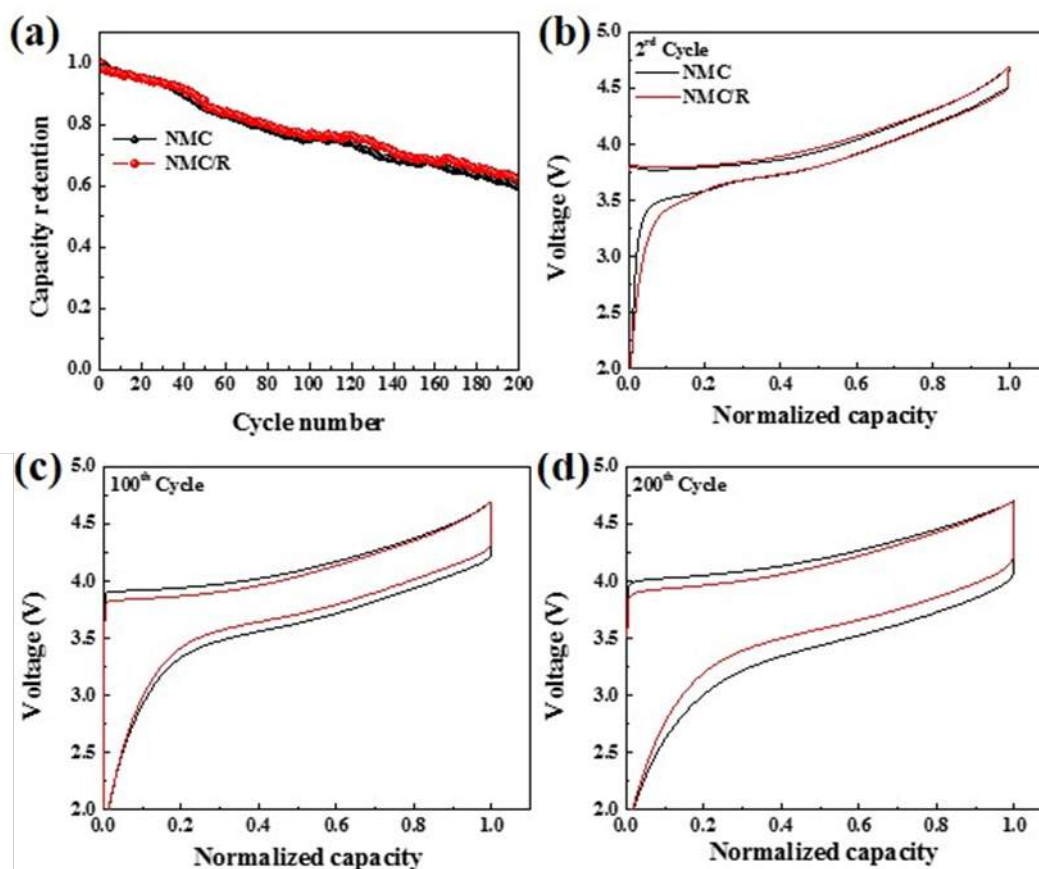


Figure II-297: (a) NMC and NMC/R electrodes capacity retention, and (b-d) charge discharge voltage profiles.

To clearly identify possible origins of the impedance growth, the electrochemical impedance spectroscopy was employed at selected cycles (Figure II-298 a,b). The high frequency semi-circle can be assigned to the contact resistance (R_s) i.e., electronic resistance between the current collector, conductive additive and the active material. R_s is highly related to the electron percolation in the composite electrode. The mid-frequency semi-circle can be assigned to the charge transfer resistance (R_{ct}) at the interface between the active material and the electrolyte. Those resistances can be obtained by fitting the spectra using an adequate equivalent circuit model (Figure II-298 c,d). Both electrode materials show similar trends with R_{ct} variations that continuously increases over 90 cycles. However, R_s for the pristine NMC electrode is not only higher but it grows substantially during cycling whereas R_s for the NMC/R electrode is relatively low and it remains constant during cycling.

Lin et al. [1] demonstrated that reconstruction layer at NMC surface has lower valence state of the transition metal than in the bulk. Our earlier work [2] inferred the electrolyte decomposition mechanism that relates to the catalysis effect at high-charge-state transition metal surface. Thus, lower interfacial activity toward the electrolyte of MeO-rich surfaces may inhibit electrolyte decomposition and slow down accumulation of the reaction products, which are mainly responsible for creating ionic and electronic barriers in the composite electrode.

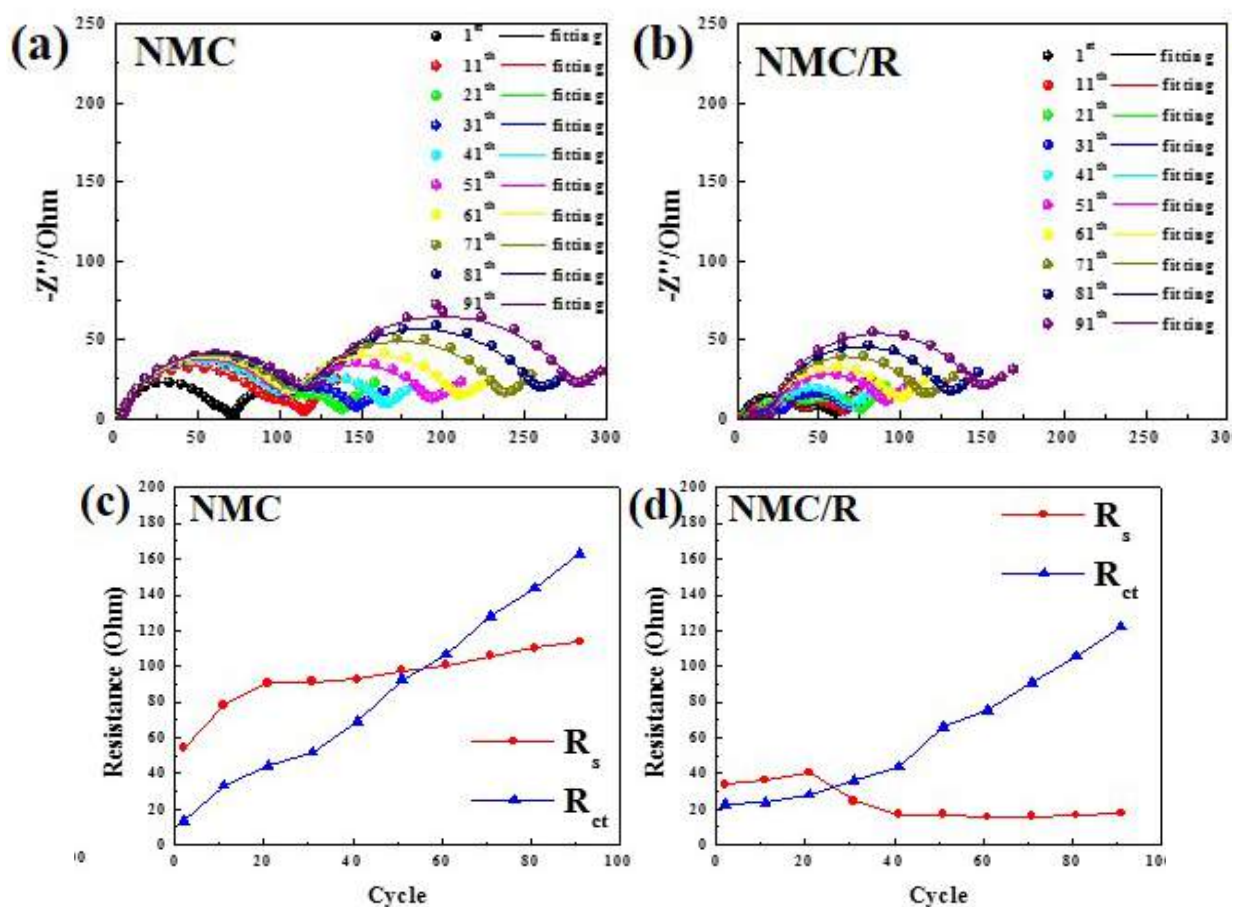


Figure II-298: Nyquist plots of coin cells with NMC (a) and NMC/R (b) cathodes. R_s and R_{ct} extracted from the impedance data for NMC (c) and NMC/R (d) electrodes.

Then we evaluated the effect of an artificial surface reconstruction layer on the electrochemical performance of the nickel-rich NMC (Ni:Mn:Co=5:3:2) cathode and its effect on the degradation mechanism of the NMC electrode. We used X-ray absorption spectroscopy in total electron yield mode (XAS-TEY) to probe the valence state of transition metal ions in NMC at shallow depths (2-5 nm) from the particle surface.

Figure II-299 shows XAS-TEY spectra of the pristine nickel-rich NMC powder and NMC/R powder samples after surface modification process at Ni, Co and Mn L-edge. The absorption peaks at 852.5 eV and 854 eV correspond to Ni^{2+} and Ni^{3+} , respectively. NMC/R exhibits lower $\text{Ni}^{3+}/\text{Ni}^{2+}$ peak ratio than pristine NMC, which indicates that NMC/R material has higher concentration of Ni^{2+} at the surface. Co and Mn L-edge spectra display Co^{2+} and Mn^{2+} shoulders at 778 eV and 639 eV next to the main Co^{3+} and Mn^{4+} peaks at 780.5 eV and 642.5 eV, respectively. Higher intensities of Co^{2+} and Mn^{2+} peaks in NMC/R spectra also points toward surface enrichment with Co^{2+} and Mn^{2+} . In other words, XAS-TEY spectra provide a direct evidence of a surface reconstruction layer, which was artificially created in NMC/R particles upon a long-term exposure to the electrolyte at elevated temperatures. The (II) valance state of Ni, Co and Mn at the surface is consistent with the presence of a rock salt structure thin-film, which has been reported elsewhere by different groups.

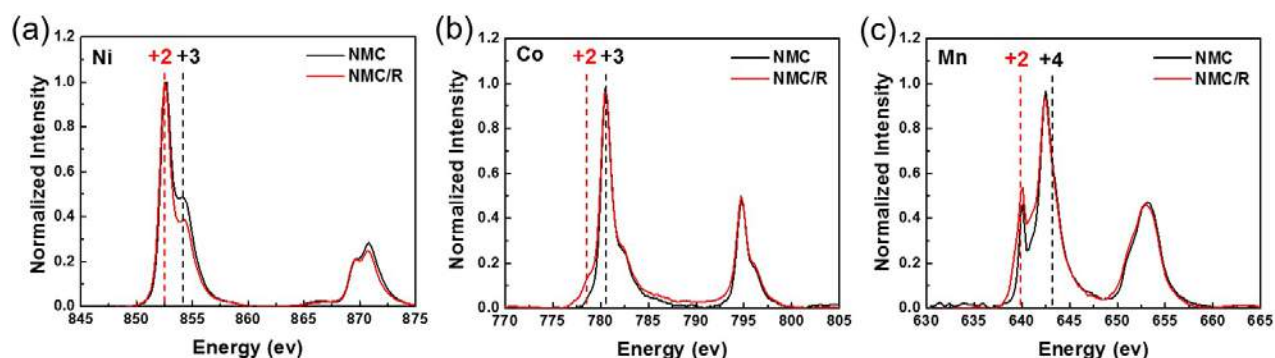


Figure II-299: XAS-TEY of NMC and NMC/R powders on the range L-edge of (a) Ni, (b) Co and (c) Mn.

Composite cathodes were fabricated with pristine NMC and NMC/R powders and then cycled at 0.5 C between 2-4.7 V in coin cells equipped with Li anode and 1M LiPF_6 EC/DEC (1:2 wt%) electrolyte. The cycled cathodes were washed in DEC and dried in vacuum. Figure II-300 shows XAS spectra of the cycled electrodes at Ni, Co and Mn L-edge. The Ni L-edge spectrum of the NMC electrode shows a notable decrease of the Ni^{3+} peak at 854 eV after cycling whereas the cycled NMC/R electrode shows no such a change. Interestingly, the surface composition of the NMC and NMC/R electrodes after cycling becomes almost the same. Co and Mn L-edge spectra show increased peak intensities at 778 eV, 639 eV and 641 eV, which is associated with higher surface concentrations of Co^{2+} , Mn^{2+} and Mn^{3+} , respectively. However, the extent of surface reduction in NMC/R is much smaller than in NMC after cycling. It appears that the rate of formation of the reconstruction layer and associated processes (e.g., Me dissolution, surface film formation) during cycling is strongly dependent on the initial state of the surface.

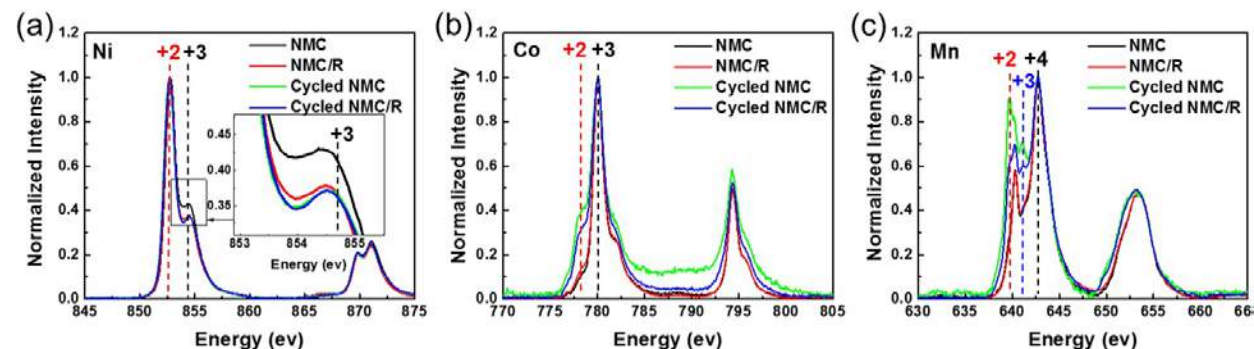


Figure II-300: (a) XAS-TEY of cycled NMC and NMC/R electrodes on the range L-edge of (a) Ni, (b) Co and (c) Mn.

W also studied changes in the surface morphology of model NMC cathodes during operation at potentials above 4 V in 1M LiPF₆ in EC/DEC (1:2 vol.). To enable a high-resolution surface analysis by *in situ* AFM, a nominally flat, binder-free and conductive-additive-free NMC thin-film electrode was produced by pulsed laser deposition (PLD) directly on an aluminum substrate, using NMC (Ni:Co:Mn = 5:3:2) target. A Raman spectrum (Figure II-301a) of the model NMC/Al electrode shows vibrational modes typically for layered hexagonal structure ($R\bar{3}m$) [3] which are consistent with the spectrum of standard NMC 532 powder. The electrochemical performance of the thin-film NMC/Al electrode was evaluated in a coin cell against with Li-foil counter electrode in 1M LiPF₆ in EC/DEC (1:2 vol.). The cyclic voltammetry curve (Figure II-301b) of the model electrode displays similar redox features as a typical NMC composite electrode. The *in situ* three-electrode AFM cell with the NMC/Al working, Li-foil counter and reference electrodes is shown in Figure II-297c. The cell was operated in He-filled environmental chamber under saturated DEC partial vapor pressure to prevent drying of the electrolyte during the experiment. NMC electrode was charged at constant potential steps from OCV (~3.4 V) to 4.7 V (Figure II-301c) for 30 min at each step before AFM imaging.

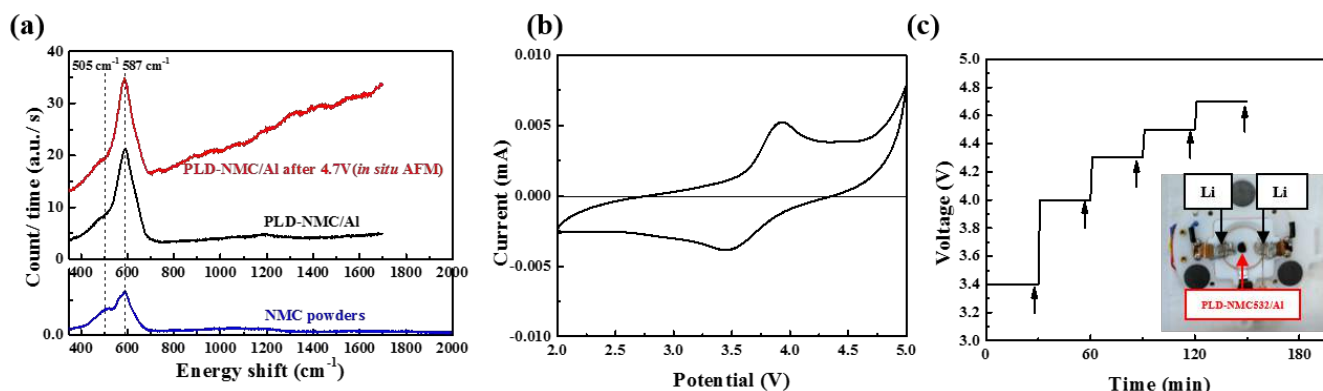


Figure II-301: (a) Raman spectra of NMC powder (blue), PLD-NMC/Al electrode (black) and PLD-NMC/Al electrode after 4.7 V charged (red). (b) Cyclic voltammogram of PLD-NMC/Al electrode at the 3rd cycle. (c) The voltage-time profile of electrode during *in situ* AFM experiment. The arrows point at the time when AFM images were acquired. (Insert: *in situ* AFM cell.)

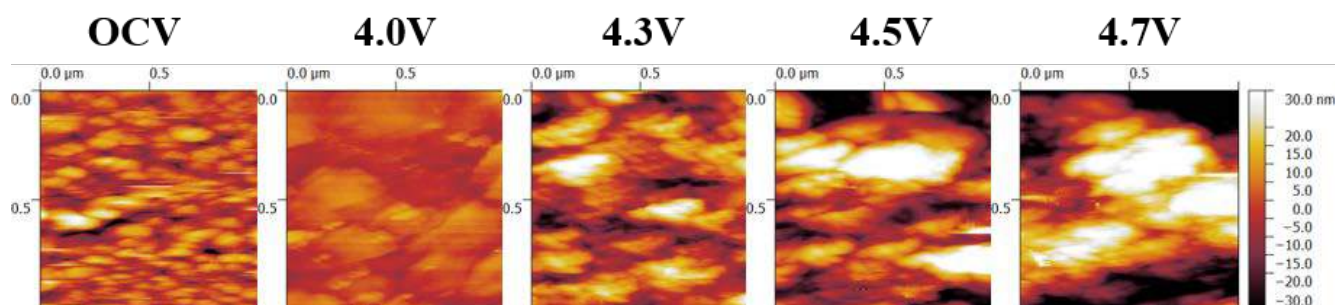


Figure II-302: 1 x 1 μm AFM images of PLD-NMC/Al electrode after 30 min. polarization at each potential

The AFM images of the NMC surface at OCV (~3.4 V), 4.0, 4.3, 4.5, 4.7 V are shown in Figure II-302. The pristine electrode is composed of tightly packed 100-150 nm NMC grains. After charging to 4.0 and 4.3 V the NMC particles tend to agglomerate and form ~300 nm clusters, and larger 500 nm aggregates at 4.5 V and 4.7 V. At potentials <4.3 V, the cluster surface morphology still shows individual 100 nm grains of NMC. However, at higher potentials (>4.5 V), the observed changes in surface morphology can be also assigned to a surface film formation. The NMC/Al electrode was removed from the AFM cell after polarization at 4.7 V, washed in DEC and probed by *ex situ* Raman spectroscopy (Figure II-301a). The spectrum shows a strong fluorescence background and weak features in 800-1600 cm^{-1} range, which indicate possible formation of β -ketone coordination complexes similarly to LMNO [2]. These results provide a direct insight into the surface

film formation process, which otherwise is difficult to observe by other diagnostic methods especially in NMC composite cathodes. At the end of anodic polarization the film is ca. 10 nm thick and it may give rise to formation of electronic and ionic barriers, which can contribute to the commonly observed degradation modes of NMC cathodes in Li-ion batteries.

Conclusions

- Surface reconstruction layer is NOT the root cause of impedance rise and capacity fade fading of the Ni-rich NMC electrode.
 - “Pristine” NMC material and NMC with the artificially induced surface reconstruction layer exhibit similar initial electrochemical behavior.
- NMC material with the artificially induced surface reconstruction layer shows better long-term cycle performance than “pristine” NMC”.
 - Surface reconstruction layer on NMC surface suppresses oxidation of EC/DEC, inhibits electrolyte oxidation, surface film formation and Me dissolution during cycling
- Artificially induced surface structure reconstruction can be an effective strategy of reducing NMC surface reactivity

This study not only determines the mechanism of surface reduced layer formation but also offers unique insight into its direct and indirect impact on the electrochemical performance and interrelated mechanism of interfacial phenomena at high-voltage cathodes.

Key Publications

1. Lei Cheng, Huaming Hou, Simon Lux, Robert Kostecki, Ryan Davis, Vassilia Zorba, Apurva Mehta, and Marca Doeff, “Enhanced Lithium Ion Transport in Garnet-type Solid State Electrolytes”, Journal of Electroceramics, accepted
2. Robert Kostecki, Angelique Jarry, Maurice Ayache, Hans A. Bechtel, Michael C. Martin, 253rd ACS National Meeting & Exposition: Advanced Materials, Technologies, Systems and Processes, April 2-6, 2017, San Francisco, USA (invited lecture)
3. Robert Kostecki, Maurice Ayache, Hans A. Bechtel, Angelique Jarry, Michael C. Martin, “IR spectroscopy and Imaging Interfaces in Silicon Anode”, 20th Topical Meeting of the International Society of Electrochemistry, 19-22 March 2017, Buenos Aires, Argentina
4. Robert Kostecki, "Probing charge and mass transport phenomena across interfaces and interphases in Li-ion batteries", Nanomaterials for Applications in Energy Technology Gordon Research Conference February 26-March 3, 2017, Ventura, CA, USA (invited lecture)
5. Robert Kostecki, “The Mechanism of NMC Cathodes Dissolution in Organic Carbonate Electrolytes”, 57th Battery Symposium, November 29, 2016, Chiba-City, Japan (invited lecture)
6. Robert Kostecki, Maurice Ayache, Simon Lux, “Near-Field IR Imaging and Spectroscopy of Interfaces and Interphases in Li-ion Electrodes”, 230th Meeting of The Electrochemical Society, Honolulu, Hawaii, USA, October 2-7, 2016
7. Robert Kostecki, "Probing charge and mass transport phenomena across interfaces and interphases in Li-ion batteries" Telluride Science Research Center Workshop: Interfacial Chemistry and Charge Transfer for Energy Conversion and Storage, July 25-29, 2016, Telluride, CO (invited lecture)

8. Angelique Jarry, Paul Pearce, Bryan Eichhorn, and Robert Kostecki, "Role of the transition metal dissolution species formed at Li-ion positive electrode materials on the battery performance and failure modes", 18th International Meeting on Lithium Batteries, June 19-24, 2016, Chicago, Illinois, USA
9. Robert Kostecki "Understanding Charge and Mass Transport Across Interfaces and Interphases in Batteries" SIRBATT Workshop "*Controlling Lithium Battery Interfaces*", Orlando, USA Friday 27th May 2016. (keynote lecture)

References

1. Lin F, et al., *Nat. Commun.* 5, (2014).
2. Jarry, A. et al., *J. Am. Chem. Soc.*, 137, 3533-3539 (2015).
3. R. E. 4, A. F. Callender, H. Zhou, S. K. Martha and J. Nanda, *J Electrochem Soc*, **162**, A98 (2015).

II.D.2 Advanced *in situ* Diagnostic Techniques for Battery Materials (BNL)

Xiao-Qing Yang, Principal Investigator

Chemistry Division
Brookhaven National Laboratory
Bldg. 555, Brookhaven National Lab.
Upton, NY 11973
Phone: 631-344-3663
E-mail: xyang@bnl.gov

Seongmin Bak, Co-Principal Investigator

Chemistry Division
Brookhaven National Laboratory
Bldg. 555, Brookhaven National Lab.
Upton, NY 11973
Phone: 631-344-4142
E-mail: xyang@bnl.gov

Tien Duong, Technology Manager

U.S. Department of Energy
Phone: 202-586-7836
E-mail: Tien.Duong@ee.doe.gov

Start Date: October 1, 2016
Total Project Cost: \$600,000

End Date: September 30, 2017
DOE share: \$600,000

Non-DOE share: \$0

Project Introduction

This proposed project was focused on developing advanced diagnostic characterization techniques to investigate these issues, obtaining in-depth fundamental understanding of the mechanisms governing the relationship between the structure and the performance, and providing guidance and approaches to solve these problems. The unique approach of this proposed project is the development and application of combined synchrotron-based *in situ* X-ray techniques such as x-ray diffraction (SXRD), pair distribution function (PDF), hard and soft x-ray absorption (XAS and SXAS), together with other imaging and spectroscopic tools such as high resolution transmission electron microscopy (HRTEM), scanning transmission electron microscopy (STEM), mass spectroscopy (MS), X-Ray fluorescence microscopy (XRF) and transmission x-ray microscopy (TXM). For advanced Li-ion battery technologies, the revolutionary approaches using new generation of materials for cathode, anode, electrolyte, and separator are in the horizon. The new generation of cathode materials such as high voltage spinels ($\text{LiMn}_{2-x}\text{Ni}_x\text{O}_4$) and/or Li-rich high energy density $\text{Li}_{1+x}(\text{NiMnCo})\text{O}_2$ composite materials together with high energy density Si-based anode materials will significantly increase the energy density of the LIB cells. However, many technical barriers must be overcome before the large scale commercialization of these new materials can be realized. This proposed project will use the time-resolved x-ray diffraction TR-XRD and absorption (TR-XAS) developed at BNL to study the kinetic properties of these materials with structural sensitivity (TR-XRD) and elemental selectivity (TR-XAS). This project will develop and apply the HRTEM, TXM and PDF techniques to study the mechanism of capacity and performance fading of cathode and anode materials. Another important issue is the thermal stability of new cathode materials which is closely related to the safety of the batteries. This problem will be studied using the combined TR-XRD, TR-XAS with mass spectroscopy (MS). This project also proposes to develop a novel *in situ* X-ray fluorescence (XRF) microscopy combined with X-ray absorption spectroscopy (XAS) technique, which will enable us to track the morphology and chemical state changes of the electrode materials during cycling. We will further develop this novel technique utilizing the new unique capability of TES beamline at NSLS II, with

better signal/noise ratio and spatial resolution to do diagnostic studies of the cathode and anode materials of advanced Li-ion batteries. In summary, this proposed project supports the goals of VTO, the Battery and Electric Drive Technologies, and BMR program by developing new diagnostic technologies and applying them to the advanced Li-ion battery systems to provide guidance for new material development.

Objectives

The primary objective of this project is to develop new advanced in situ material characterization techniques and to apply these techniques to support the development of new cathode and anode materials with high energy and power density, low cost, good abuse tolerance, and long calendar and cycle life for the next generation of lithium-ion batteries (LIBs) to power plug-in hybrid electric vehicles (PHEV). The diagnostic studies will be focused on issues relating to capacity retention, thermal stability; cycle life and rate capability of advanced Li-ion batteries.

Approach

- Using nano-probe beamline at NSLSII to study the elemental distribution of new solid electrolyte materials for Li-ion and Na-ion batteries
- Using pair distribution function (PDF) techniques to study the effects of multiple cycling for $\text{Li}_2\text{Ru}_{0.5}\text{Mn}_{0.5}\text{O}_3$ cathode material with and without pre-lithiation (Micro structural defects were intentionally generated) to improve the performance of high energy density materials.
- Using high resolution transmission electron microscopy (TEM) to obtain multiple dimensional (3D + elemental, valence state, and time) mapping of new cathode materials for advanced Li-ion batteries.
- Using transmission x-ray microscopy (TXM) to do multi-dimensional mapping of cathode materials
- Using A combination of time resolved X-ray diffraction (TR-XRD) and mass spectroscopy (MS), together with *in situ* soft and hard X-ray absorption (XAS) during heating to study the thermal stability of the electrode materials
- Using *in situ* XRD and XAS, to study the new concentration gradient cathode materials to improve the cycle life of Li-ion batteries
- Using quick x-ray absorption spectroscopy and time resolved x-ray diffraction techniques to study the kinetic properties and the structural changes of $\text{Li}_{1-x}\text{Ni}_{1/3}\text{Co}_{1/3}\text{Mn}_{1/3}\text{O}_2$ cathode material during high rate charge process to improve high rate capability of Li-ion batteries.

Results

1. Using pair distribution function (PDF) to correlate the voltage and capacity fading with micro-structural defects of $\text{Li}_2\text{Ru}_{0.5}\text{Mn}_{0.5}\text{O}_3$ as a model compound for (LMR) high energy density cathode materials.

In FY 2017, this project carried out the studies on the structure of $\text{Li}_2\text{Ru}_{0.5}\text{Mn}_{0.5}\text{O}_3$, as a model compound for Li and Mn rich (LMR) high energy density cathode materials using pair distribution function (PDF) to correlate the voltage and capacity fading with micro-structural defects. Figure II-303a shows that PDF peaks correspond to characteristic bond distances while the amplitude of the peak is relating to the coordination number. Take LiNiO_2 as an example, the first peak (in red) is mainly from transition metal—oxygen bond and the peak position correspond to the transition metal—oxygen bond length. The second peak (in blue) is mainly from transition metal—transition metal bond. The PDF data for pristine state and “OCV-1V-3V” state are shown in Figure II-303b, providing structural information in the scale of around 50 Å. It can be seen that in the short-range region (Figure II-303c) which covers from 1.6 Å to around 20 Å, the two data sets are almost identical. This indicates that at the scale of a unit cell dimension, the pristine state and “OCV-1V-3V” state have very similar atomic arrangements, suggesting their crystal structure are basically the same. However, when it comes to long range data sets as shown in Figure II-303d, there is obvious difference between these two states. For the pristine state, there are still well-defined structural features at R value as high as 50 Å.

However, for “OCV-1V-3V” state, these structural features are gradually lost when R is greater than 35 Å, indicating that the coherently scattering domain is on the scale of several nanometers

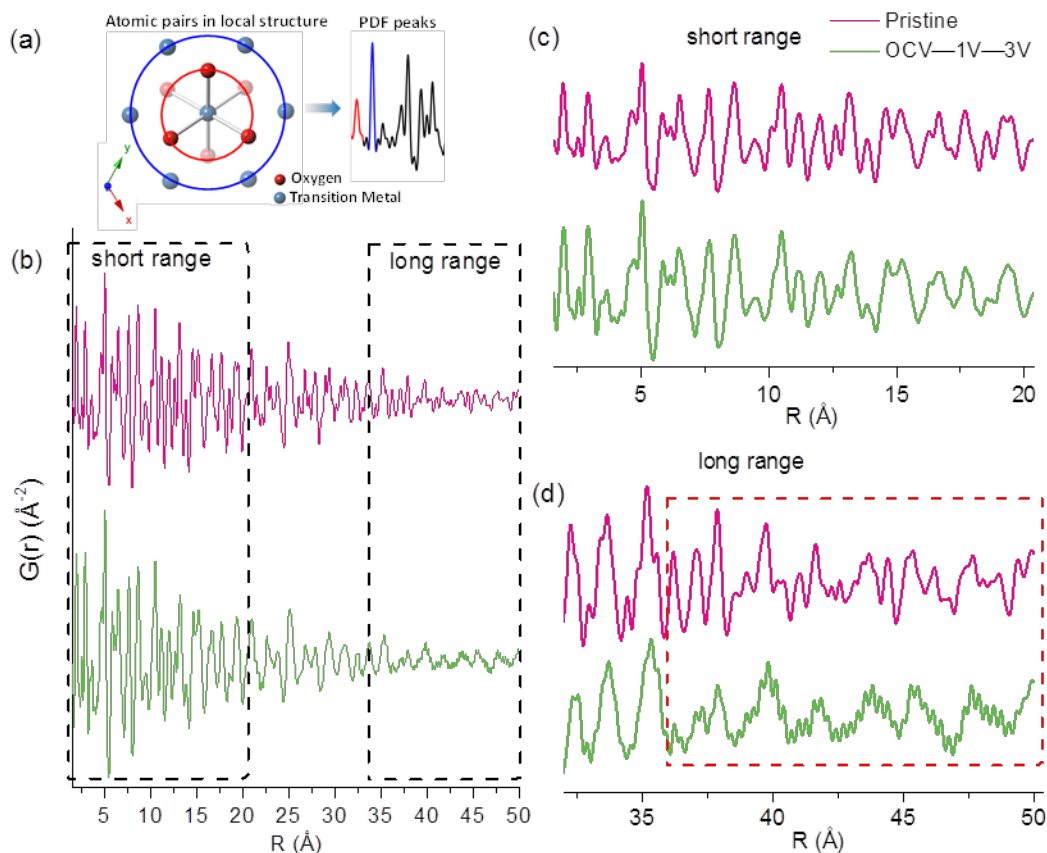


Figure II-303. (a) Illustration of PDF showing that peaks correspond to characteristic bond lengths. (b) Ex situ PDF data of pristine sample and “OCV-1V-3V” sample (c) zoomed in data on the short range region of ex situ PDF data and (d) zoomed in data on the long range region of ex situ PDF data.

2. Using scanning transmission electron microscopic (STEM) to correlate the voltage and capacity fading with micro-structural defects of $\text{Li}_2\text{Ru}_{0.5}\text{Mn}_{0.5}\text{O}_3$

In FY 2017 this project also carried out the structure studies of $\text{Li}_2\text{Ru}_{0.5}\text{Mn}_{0.5}\text{O}_3$, as a model compound for Li and Mn rich (LMR) high energy density cathode materials using scanning transmission electron microscopic (STEM) to correlate the voltage and capacity fading with micro-structural defects in this type of materials. Microstructure changes and nano-sized microstructural defects created by prelithiation process can be directly observed by comparing the Z-contrast annular dark-field scanning transmission electron microscopic (ADF-STEM) images taken on pristine and prelithiated samples. Figure II-304a (left panel) shows the atomic-resolution ADF-STEM image of the pristine material, indicating good crystallinity with typical features of the layered structure. After prelithiation, the material (right panel, Figure II-304a) shows great loss of the crystallinity, forming domains that orient differently from each other with large amount of additional grain boundaries created. It can be seen that these domains are at the scale of several nanometers, confirming previous analysis of XRD and PDF results. The process is illustrated in Figure II-304b.

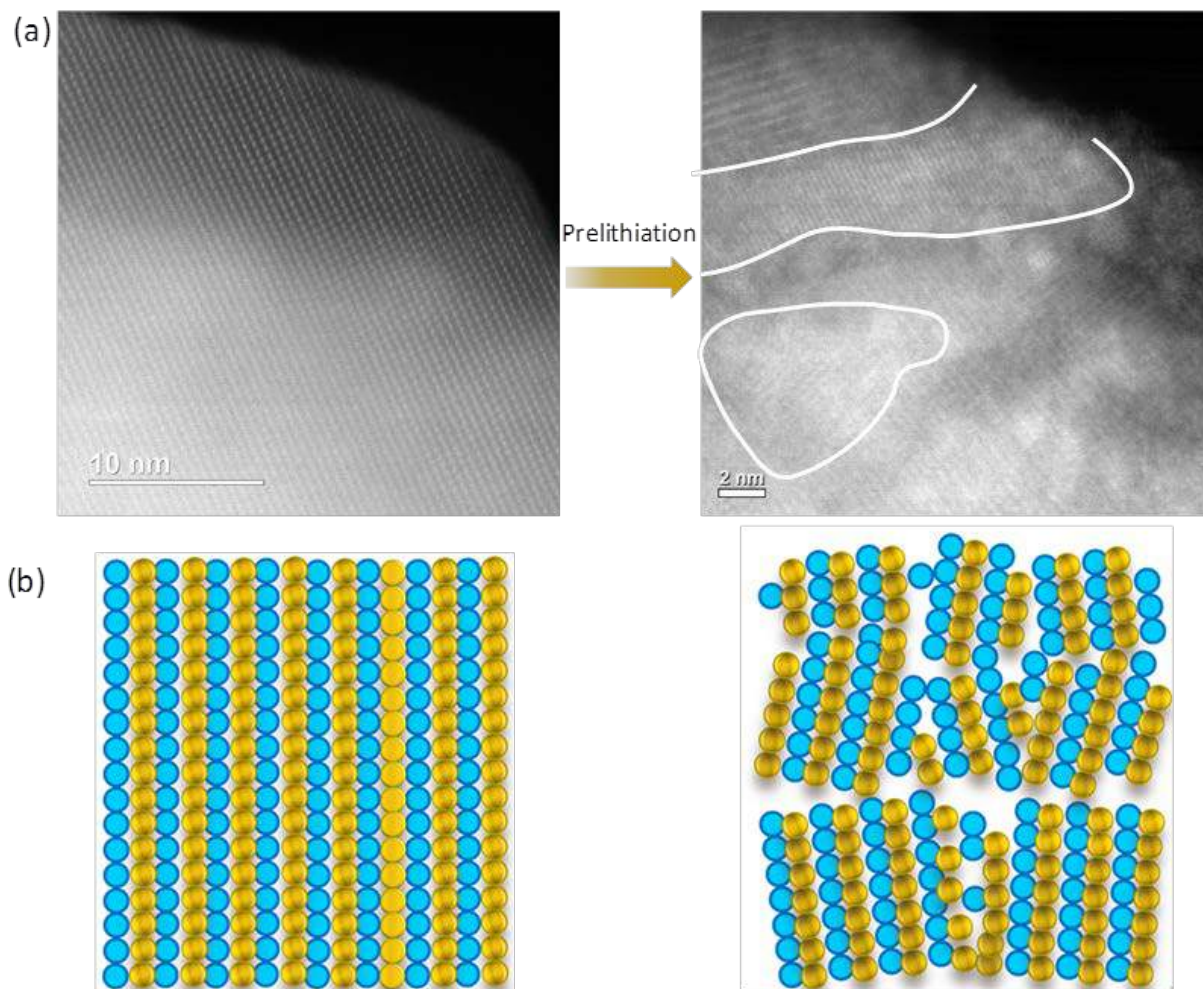


Figure II-304. (a) Illustration of PDF showing that peaks correspond to characteristic bond lengths. (b) Ex situ PDF data of pristine sample and “OCV–1V–3V” sample (c) zoomed in data on the short range region of ex situ PDF data and (d) zoomed in data on the long range region of ex situ PDF data

3. Using synchrotron-based x-ray diffraction (XRD) and absorption (XAS) to correlate the voltage and capacity fading with micro-structural defects of $\text{Li}_2\text{Ru}_{0.5}\text{Mn}_{0.5}\text{O}_3$

In FY 2017, this project also completed the structure studies of $\text{Li}_2\text{Ru}_{0.5}\text{Mn}_{0.5}\text{O}_3$, as a model compound for Li and Mn rich (LMR) high energy density cathode materials using synchrotron-based x-ray diffraction (XRD) and absorption (XAS) to correlate the voltage and capacity fading with micro-structural defects in this type of materials. The prelithiated sample experiences more reduction. As shown in Figure II-305a. Figure II-305a indicates that transition metal cations in both “OCV-1V-(4.6V-2V)20Cy” sample and “OCV-(4.6V-2V)20Cy” sample experience reduction during cycling. This is true both for Mn and Ru as seen from the edges shifting to the lower energy in both Mn K-edge and Ru K-edge spectra. Oxygen release is not only exacerbated by the micro structural defects, but also promotes the formation of defects. Evidence comes from ex situ XRD studies shown in Figure II-305b. The figure is separated by a dash line in the middle. The upper part corresponds to the prelithiated case and the lower one to the normally cycled case. Compared with the normally cycled case, samples in the prelithiated case show much greater peak broadening and this broadening effect increases as the cycle number increases. Oxygen release and microstructural defects also accelerates spinel formation. This can be seen from Figure II-305c which gives the evolution of lattice parameter c to lattice parameter a ratio during cycling.

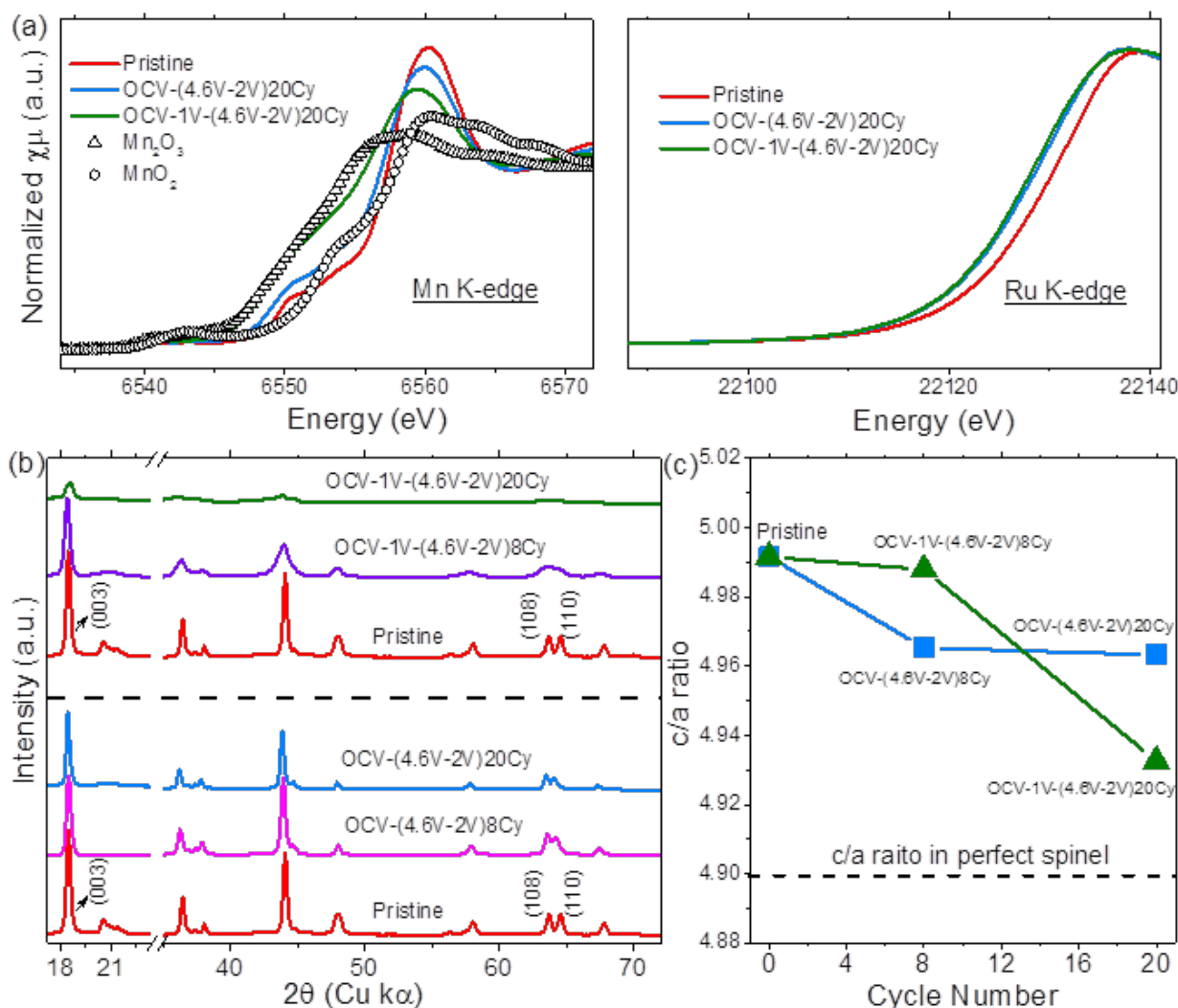


Figure II-305. (a) ex situ Mn K-edge and Ru K-edge XAS data of pristine $Li_2Ru_{0.5}Mn_{0.5}O_3$ sample, sample normally cycled 20 times and sample cycled 20 times but first prelithiated, with references of Mn_2O_3 and MnO_2 shown. (b) Ex situ XRD patterns of two cases (with (003), (108) and (110) peaks indexed according to the space group $R\bar{3}m$): pristine sample, cycled 8 times and cycled 20 times for the normally cycled case (the part below the dash line); pristine sample, cycled 8 times and cycled 20 times for the prelithiated case (the part above the dash line). (c) The ratio between lattice parameter c and lattice parameter a as a function of cycle numbers. The dash line shows the c/a ratio in perfect spinel.

4. Using scanning transmission electron microscopic (STEM) to correlate the voltage and capacity fading with micro-structural defects of $Li_{1.2}Ni_{0.15}Co_{0.1}Mn_{0.55}O_2$

In FY 2017, this project focused on the structure studies of $Li_{1.2}Ni_{0.15}Co_{0.1}Mn_{0.55}O_2$ for Li and Mn rich (LMR) high energy density cathode materials using scanning transmission electron microscopic (STEM) to correlate the voltage and capacity fading with micro-structural defects in this type of materials. To pinpoint the structure nucleation and evolution, we performed atomic-resolution annular dark-field scanning transmission electron microscopic (ADF-STEM) imaging, spatially resolved electron energy loss spectroscopy (EELS), and ADF-STEM tomography. Using ADF-STEM tomography, the 3D internal structures of the cathode material before and after 15 charge-discharge cycles were reconstructed. The 3D rendered reconstructions in Figure II-306 qualitatively shows that a new population of large pores had formed in the interior of the cycled particle after 15 cycles. By analyzing the pore size distributions (Figure II-306c and Figure II-306d), it can be quantitatively concluded that the large pores observed in Figure II-306b belongs to a new modal that did not appear in the

pristine samples. The volume weighted distribution shows that the large-pore modal contributes to the majority of porosity in the material. As the formation of the large pores are correlated with charge cycles, they are very likely formed by nucleating vacancies that had been left behind by oxygen loss, agreeing well with the "lattice densification" model.

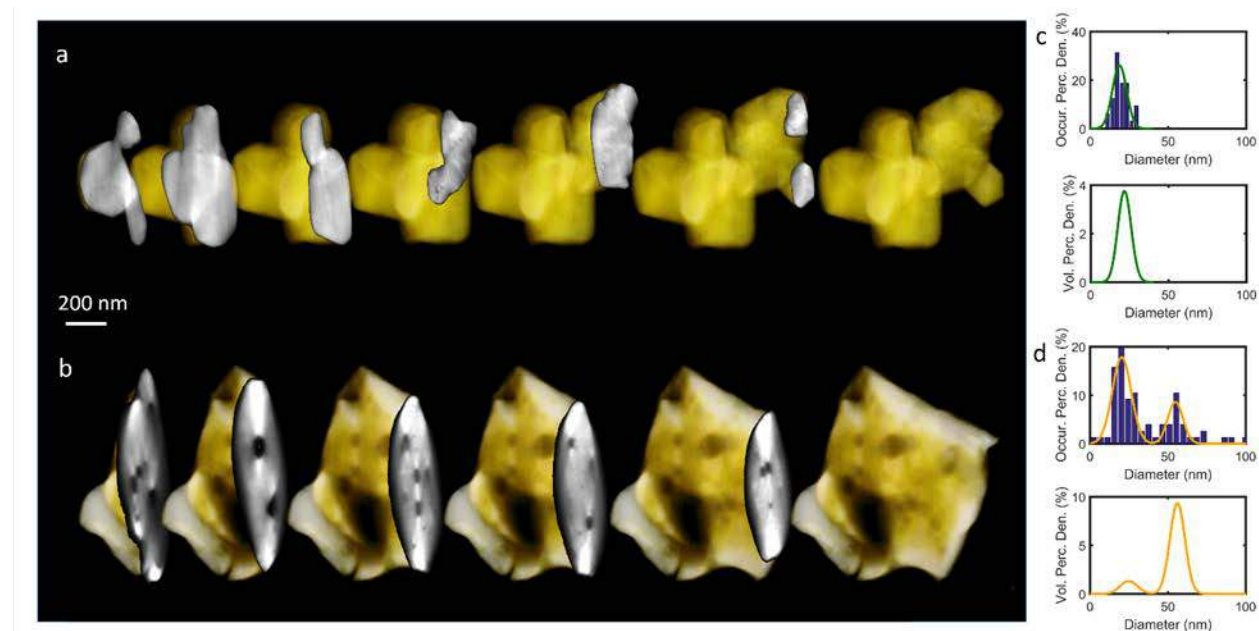


Figure II-306. Three-dimensional electron tomography reconstructions of (a) pristine, (b) after 15 charge-discharge cycles of $\text{Li}_{1.2}\text{Ni}_{0.15}\text{Co}_{0.1}\text{Mn}_{0.55}\text{O}_2$ material. The internal pore size distribution weighted by occurrence (upper) and by volume (lower) of (c) the pristine materials and (d) the sample after 15 cycles.

Conclusions

The effects of micro structural defects on the voltage fade studied in this project can provide valuable guidance in finding the paths to suppress voltage fade in LMR materials. For some Li-ion battery cathode materials, small particle size is favored because the reduced lithium ion transport length can enhance the electrochemical reaction and high rate capability. A classic example is LiFePO_4 , which has dramatic improvement in electrochemical performance when the crystallite size is small enough. Recent studies on $\text{Li}(\text{Ni}_{0.5}\text{Mn}_{0.3}\text{Co}_{0.2})\text{O}_2$ indicate that small particle size may also be beneficial for conventional layered materials. However, for LMR materials with the problem of oxygen loss at high voltage, the situation is quite different. In this project, using XRD, PDF, and TEM, the effects of accelerating oxygen loss by micro structural defects including grain boundaries are clearly demonstrated. Such effects are very likely to be caused by the increased surface area of materials with smaller particle size as well. Therefore, in order to suppress the voltage fade in LMR materials, it is necessary to (1) minimize the level of microstructural defects; (2) modify the surface of LMR materials with protection layer. There are recent examples of improving electrochemical performance, especially suppressing voltage fade, by applying surface modification using Al_2O_3 , AlF_3 and even lithium-conducting materials like LiPON and LiFePO_4 . The results of structural studies reported in this project provide important scientific base for using surface protection approaches such as coating to suppress the voltage fade in LMR materials.

Key Publications

1. Yahong Xu, Enyuan Hu, Feifei Yang, Jeff Corbett, Zhihong Sun, Yingchun Lyue, Xiqian Yu, Yijin Liu, Xiao-Qing Yang, Hong Li, “Structural integrity—Searching the key factor to suppress the voltage fade of Li-rich layered cathode materials through 3D X-ray imaging and spectroscopy techniques”, *Nano Energy*, Volume 28, October 2016, Pages 164–171, DOI: 10.1016/j.nanoen.2016.08.039
2. Jing Xu, Enyuan Hu, Dennis Nordlund, Apurva Mehta, Steven N. Ehrlich, Xiao-Qing Yang, Wei Tong*, “Understanding the Degradation Mechanism of Lithium Nickel Oxide Cathode for Li-ion Batteries”, *ACS Appl. Mater. And Interfaces*, 2016, 8 (46), pp 31677–31683, Publication Date (Web): November 1, 2016. DOI: 10.1021/acsami.6b11111
3. Ji-Young Kim, Sang Hoon Kim, Dong Hyun Kim, Dieky Susanto, Se Young Kim, Won-Young Chang, Byung Won Cho, Won-Sub Yoon, Seong Min Bak, Xiao Qing Yang, Kyung Wan Nam*, Kyung Yoon Chung*, “Electronic structural studies on the improved thermal stability of $\text{Li}(\text{Ni}_{0.8}\text{Co}_{0.15}\text{Al}_{0.05})\text{O}_2$ by ZrO_2 coating for lithium ion batteries”, *Appl Electrochem* (2017), First Online: 21 March 2017, DOI:10.1007/s10800-017-1062-5
4. Jue Liu, Pamela S Whitfield, Michael R Saccomanno, Shou-Hang Bo, Enyuan Hu, Xiqian Yu, Jianming Bai, Clare P Grey, Xiao-Qing Yang, Peter G Khalifah, “In situ Neutron Diffraction Studies of Ion Exchange Synthesis Mechanism of $\text{Li}_2\text{Mg}_2\text{P}_3\text{O}_9\text{N}$: Evidence for Hidden Phase Transition”, *J. Am. Chem. Soc.*, 2017, Publication date: 2017/7/6, DOI: 10.1021/jacs.7b02323
5. Feng Lin, Yijin Liu, Xiqian Yu, Lei Cheng, Andrej Singer, Oleg G Shpyrko, Huolin L Xin, Nobumichi Tamura, Chixia Tian, Tsu-Chien Weng, Xiao-Qing Yang, Ying Shirley Meng, Dennis Nordlund, Wanli Yang, and Marca M Doeff, “Synchrotron X-ray Analytical Techniques for Studying Materials Electrochemistry in Rechargeable Batteries”, *Chemical Review*, Publication date (web): 2017/9/29, DOI: 10.1021/acs.chemrev.7b00007.
6. Feng Lin, Yijin Liu, Xiqian Yu, Lei Cheng, Andrej Singer, Oleg G Shpyrko, Huolin L Xin, Nobumichi Tamura, Chixia Tian, Tsu-Chien Weng, Xiao-Qing Yang, Ying Shirley Meng, Dennis Nordlund, Wanli Yang, and Marca M Doeff, “Synchrotron X-ray Analytical Techniques for Studying Materials Electrochemistry in Rechargeable Batteries”, *Chemical Review*, Publication date (web): 2017/9/29, DOI: 10.1021/acs.chemrev.7b00007.

II.D.3 NMR and Pulse Field Gradient Studies of SEI and Electrode Structure (University of Cambridge)

Clare Grey, Principal Investigator

Department of Chemistry
 Lensfield Road
 Cambridge, CB2 1EW
 United Kingdom
 Phone: +44(1223)336509
 E-mail: cpg27@cam.ac.uk

Tien Duong, Technology Manager

U.S. Department of Energy
 Phone: 202-586-7836
 E-mail: Tien.Duong@ee.doe.gov

Start Date: October 1, 2016
 Total Project Cost: \$275,000

End Date: September 30, 2017
 DOE share: \$275,000

Non-DOE share: \$0

Project Introduction

The ability to cycle a battery for the multiple cycles requires that a stable solid electrolyte interphase (SEI) is formed on the electrodes of a Li-ion battery. Without such a stable SEI, breakdown of the electrolyte continues unhindered because a battery operates outside the stability of the electrolyte (below approx. 1.3 - 0.8 V vs. Li), leading to loss of electrolyte (and Li) from the cell, and thus, an increase in resistance of the cell. Although electrolytes have been optimized to form a stable SEI on graphite, the commercial anode material, the push to utilize very high energy density anodes such as Si, Sn and Li metal presents new challenges. For example, lithiation of Sn and Si involves significant volume expansion (e.g., 300% for Si), due to the large volume occupied by the lithium in the Li_xSi and Li_xSn alloys. During prolonged cycling, cracks develop, exposing fresh surface for continuous SEI growth. Practically, this means that the composite phase that makes up the SEI must be flexible and able to accommodate these expansions and contractions. Risk reduction strategies exploited to develop commercial Si/Sn-based anodes generally involve mixing graphitic carbon with Si/Sn, to make use of reversible capacity from both graphite and Si/Sn. In practice, this actually accentuates the SEI problem because the electrode must be cycled to low potentials so as to access the full graphite capacity. This results in even more severe SEI formation, either due to the formation of more heavily reduced Li_xM species (e.g., $\text{Li}_{15+x}\text{Si}_4$) or due to more severe volume expansion, which may result in the exposure of fresh surface. Strategies for SEI stabilization have been proposed but without a detailed understanding of SEI structure and composition a rational path forward is not obvious.

In principle, Li metal is a promising anode material due to its exceptionally high energy density, with a specific capacity $> 3800 \text{ mAh g}^{-1}$. Much effort has been made to use metallic Li anodes in rechargeable Li-ion batteries and its use is fundamental to the high energy densities quoted for Li-air and Li-sulfur battery technologies. However, the practical application of Li metal to rechargeable batteries has been prevented due to serious drawbacks associated with morphological changes of the Li metal following continuous stripping and plating. In particular, dendrite growth causes severe safety concerns and eventual cell failure. Continual SEI formation on the Li microstructures consumes Li^+ . Furthermore, the nature and thickness of the SEI appears to affect the mechanism of microstructure formation on the Li metal anode. Thus, it is important to understand the nature of the SEI that forms on Li and to determine how this affects dendrite formation.

In addition, Na-ion batteries are an attractive option for low-cost and environmentally benign energy-storage technologies. While a number of Na cathode materials have now been identified [1-2], hard carbons represent the best materials identified to date as anode materials [3-4] since graphite shows almost no ability to store Na

electrochemically. Extremely high capacity is also observed for Sn-based materials, but they suffer from capacity fade, in part due to uncontrolled SEI formation. Furthermore, the composition of the SEI that forms on these anodes is poorly understood. Na-ion batteries are a more sustainable alternative to the existing Li-ion technology and could alleviate some of the stress on the global Li market as a result of the growing electric car and portable electronics industries. Overall, fundamental research focused on understanding the structural and electronic processes occurring on electrochemical cycling is key to devising rechargeable batteries with improved performance. The major technique used in this work is NMR and our surface (SEI) studies are complemented by studies that focus on elucidating the short range structural changes that occur within the electrodes themselves.

Objectives

Here, we will use spectroscopic tools, such as multinuclear nuclear magnetic resonance (NMR) to provide molecular-level insight into the SEI that forms on Si, where thick SEIs typically grow and where SEI stability is one key aspect hindering the commercialization of this technology. The focus during this grant period will be to determine how additives (e.g., fluoroethylene carbonate (FEC)) and charging parameters (e.g., voltage) influence the composition and stability of the SEI. Fundamental studies of SEI structure *in operando* will be complemented by a synthetic program aimed at preparing new Si coatings based on phosphazene (P-N) elastomeric polymers to increase Coulombic efficiency. Further, the nature of the SEI is one factor that appears to control the type of Li/Na microstructures that form on the metal electrodes during cycling. To test this hypothesis, we will use magnetic resonance imaging (MRI) to investigate Li dendrite vs. moss formation in different electrolytes as a function of salt concentration and with different additives. Finally, we will compare Li and Na metal anode chemistries to determine the composition, morphology, and stability of local structures that form on sodiating anodes such as Sn and hard carbons.

Approach

Perform multinuclear NMR, IR and X-ray photoelectron spectroscopy (XPS) of SEI composition. NMR and MRI studies of dendrite formation. ^{23}Na *in-* and *ex-situ* NMR studies of Na battery materials.

Results

Substitution in layered Na cathode materials

We have investigated a series of different layered Na cathode materials to understand how cation substitution of nominally inert ions such as Mg and Li affect the structural transformations that occur at high voltages (when most Na ions are removed), and how Na mobility is altered in these phases. An in-depth investigation of the effect of Mg doping on the electrochemical performance and structural stability of $\text{Na}_{2/3}\text{MnO}_2$ with a P2 layer stacking was performed by comparing three compositions: $\text{Na}_{2/3}\text{Mn}_{1-y}\text{Mg}_y\text{O}_2$ where $y = 0.0, 0.05, 0.1$. Mg substitution leads to smoother electrochemistry, with fewer distinct electrochemical processes, improved rate performance and better capacity retention (Figure II-307). The improved electrochemistry upon Mg substitution was attributed to more gradual structural changes upon charge and discharge, as observed with synchrotron, powder X-ray, and neutron diffraction. Mg doping reduces the number of Mn^{3+} Jahn-Teller centers and delays the high voltage phase transition that occurs in P2- $\text{Na}_{2/3}\text{MnO}_2$. The ^{23}Na ssNMR data provides direct evidence for fewer oxygen layer shearing events, leading to a stabilized P2 phase, and an enhanced Na^+ ion mobility up to 3.8 V vs. Na^+/Na upon Mg doping. By comparing the ^{23}Na NMR spectra of the $x = 0, 0.05$ and 0.1 phases (Figure II-308), less spectral complexity was noted, with fewer resonances observed on Mg substitution. For example, the $y = 0.10$ sample, contains only a single ^{23}Na resonance for Na contents of between 0.67 and 0.4, consistent with rapid Na^+ mobility in between the layers. A weak signal centered at around 1100 ppm forms due to the OP4 phase, which contains alternating octahedral and prismatic environments for Na in the Na metal layers. The relative concentration of this phase (which is formed by layer shearing) decreases with increasing Mg content. The $y = 0.05$ Mg-doped phase exhibits one of the best rate performances reported to date for Na-ion cathodes with a P2 structure, with a reversible capacity of 106 mAh g^{-1} at the very high discharge rate of 5000 mA g^{-1} . In addition, its structure is highly reversible and stable

cycling is obtained between 1.5 and 4.0 V vs. Na^+/Na , with a capacity of approximately 140 mAh g^{-1} retained after 50 cycles at a rate of 1000 mA g^{-1} .

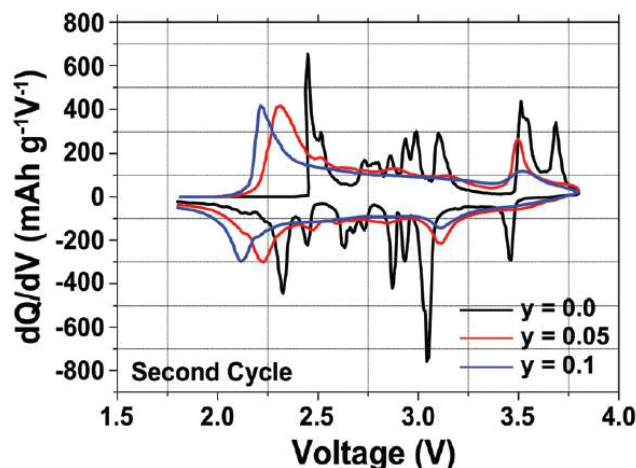


Figure II-307. Differential capacity vs. voltage plots of the $\text{Na}_{2/3}\text{Mn}_{1-y}\text{Mg}_y\text{O}_2$ ($y = 0.0, 0.05, 0.1$) compositions.

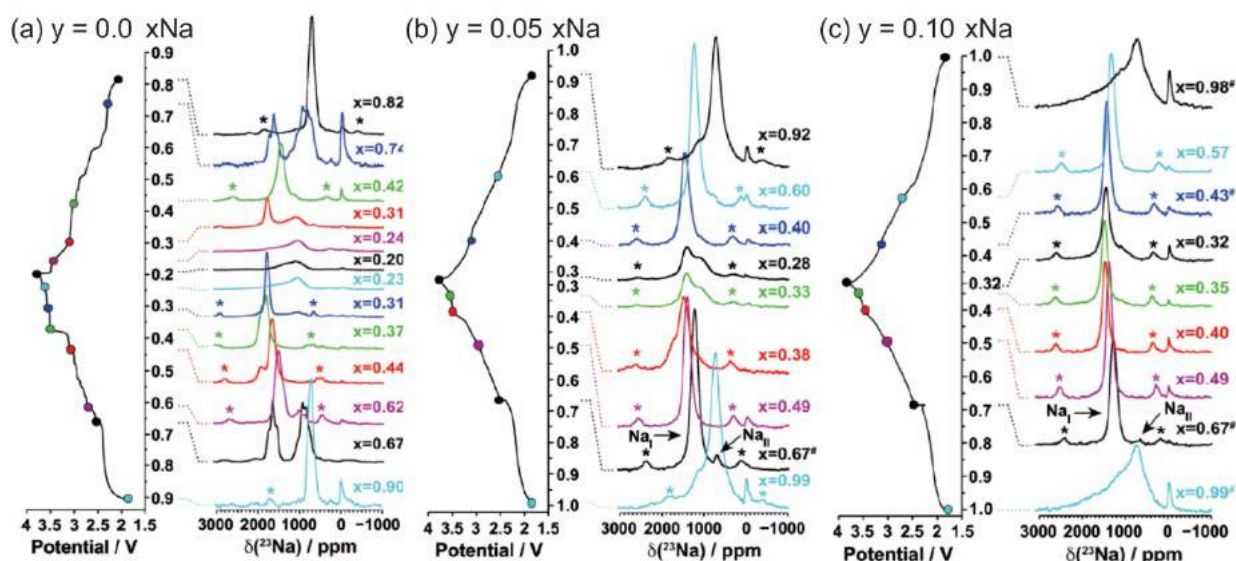


Figure II-308. Ex-situ ^{23}Na MAS ssNMR spectra collected on cells stopped at different points along the first electrochemical charge/discharge cycle of $\text{Na}_{2/3}\text{Mn}_{1-y}\text{Mg}_y\text{O}_2$, where $y = 0.0, 0.05, 0.1$ for (a), (b), and (c), respectively. Spectra are scaled according to the number of scans collected during the experiment, the amount of sample in the rotor, and the NMR signal decay obtained from T_2 relaxation time measurements. Hashes indicate samples for which a lack of experimental data prevent proper scaling of the spectrum. Asterisks indicate spinning sidebands.

This study has been complemented by ^{23}Na NMR investigations of local structure and electrochemistry of $\text{P2-Na}_x[\text{Li}_y\text{Ni}_z\text{Mn}_{1-y-z}]\text{O}_2$ ($x, y, z \leq 1$); direct evidence for rapid Na^+ mobility in these phases was obtained.

Na dendrite growth

In situ ^{23}Na NMR studies have been performed on the Na dendrites that form on Na metal anodes to complement previous work on Li microstructural growth in the group [5-7]. Quantification of the ^{23}Na NMR signal during electrochemical cycling indicates that Na metal deposits with a morphology associated with an

extremely high surface area (Figure II-309a), and that the deposits continuously accumulate, even in the case of galvanostatic cycling at low currents (e.g., 0.5 mA cm^{-2} , Figure II-309c orange).

Two distinct regimes for the electrochemical cycling of Na metal are observed that have implications for the application of Na anodes. At low currents (0.5 mA cm^{-2}), the Na deposits are partially removed upon reversing the current (Figure II-309b, c, orange), while at higher currents (1 and 2 mA cm^{-2}) there is essentially no removal of the deposits in the initial stages (Figure II-309b, c, blue and black, respectively). At longer times, high currents show a significantly greater accumulation of deposits during cycling, again indicating a much lower efficiency of removal of these structures when the current is reversed. Analysis of the current–time transients performed in a separate experiment were interpreted in terms of a change in the mechanism of nucleation from a progressive (time dependent) nucleation mechanism at the overpotentials observed for the lower current density of 0.5 mA cm^{-2} to instantaneous at higher currents. For instance, the fraction of high surface area Na metal deposits measured with NMR compared to the accumulated mass calculated from Faraday's law revealed that at low currents, smooth deposition and stripping occurs, while at high currents, rough deposition and less efficient removal is present (Figure II-309d). We proposed that the different and fewer microstructures that are formed at lower currents are more readily removed on cycling.

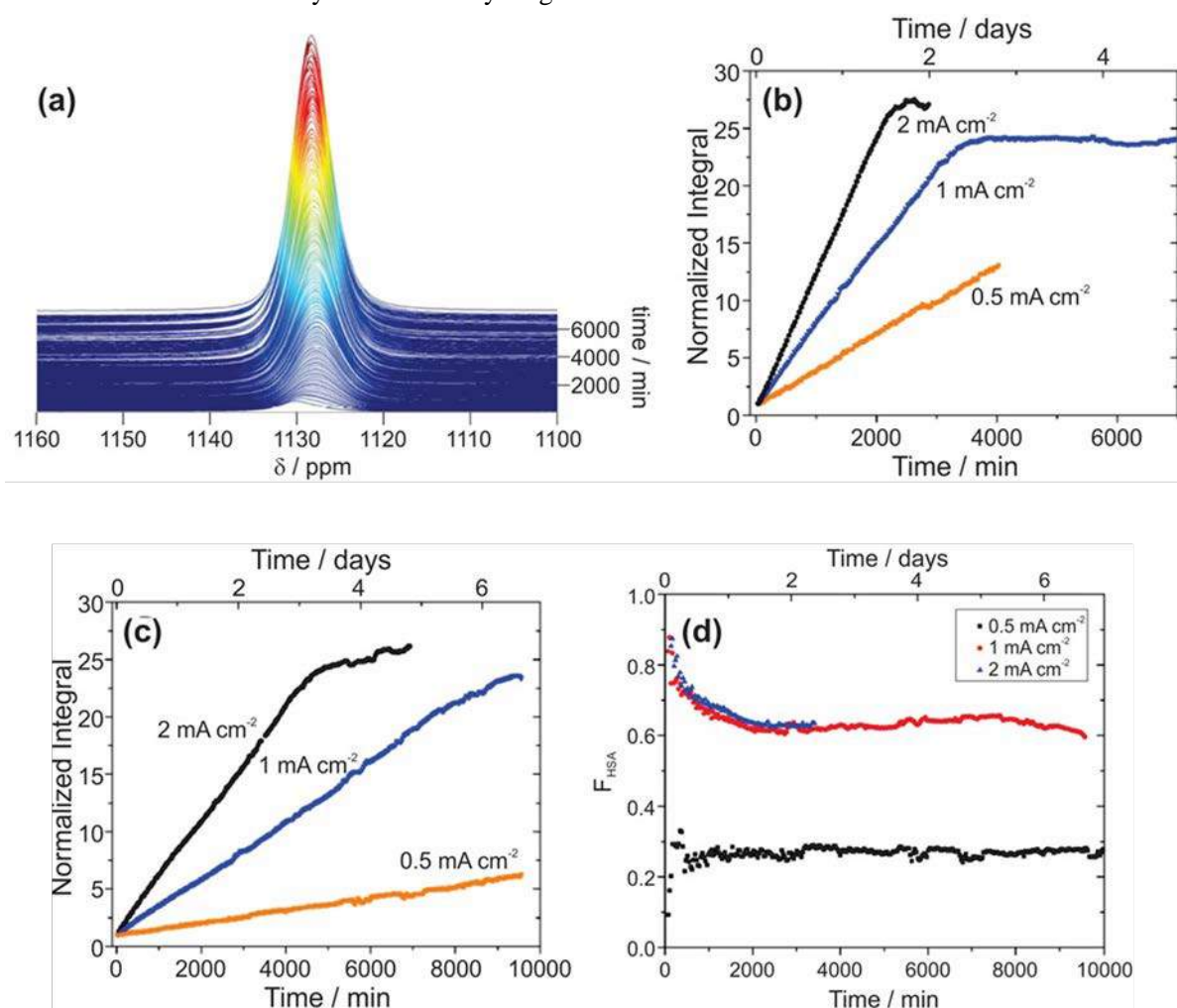


Figure II-309. (a) ^{23}Na NMR spectra as a function of time during galvanostatic cycling at 2 mA cm^{-2} , showing high surface area Na metal deposits growing in. (b,c) Integral of the normalized ^{23}Na metal resonance for (b) continuous galvanostatic deposition and (c) galvanostatic cycling at three different current densities. (d) Fraction of high surface area (F_{HSA}) Na during galvanostatic cycling at various current densities. A ratio of 1 indicates completely rough deposition and 0 indicates smooth deposition.

Unfortunately, despite differences in the nucleation and growth processes, both mechanisms yield microstructures that continue to grow as cycling progresses. Overall, dendrite formation appears to be more severe for Na metal anodes in comparison to Li metal anodes, with significant dendrite/microstructure formation occurring at low current densities, as probed by *in situ* ^{23}Na NMR experiments. However, the microstructures that form at low currents can be partially removed on reversing the current, which is not the case for the dendrites formed at higher currents. Differences in the mechanisms of nucleation of dendrites may account for some of these differences. Further investigation into the role of SEI in both Na and Li dendrite formation will be key to elucidating the physical origin underpinning the differences observed between these two systems.

Sn anodes for Na-ion batteries

The goal of this study was to understand the phases formed during Na insertion in high capacity Sn anodes for Na-ion batteries. *Ab initio* random structure searching (AIRSS) and high-throughput screening using a species-swap method allowed us to explore the phase chemistry of the Na-Sn system and predict new structures. These structures were linked to experiments using *operando* pair distribution function (PDF) analysis, X-ray diffraction (XRD), ^{23}Na solid-state nuclear magnetic resonance (ssNMR), and *ex situ* ^{119}Sn ssNMR. Here, we identified: (i) the number and nature of the crystalline phase(s) formed during the first electrochemical process; (ii) the structural features of the amorphous phase formed during the second electrochemical process; and (iii) the phase formed during the third process.

Figure II-310a shows electrochemical data for a Na-Sn cell compared to theoretical predictions. From *operando* PDF and ssNMR (Figure II-310b-d), XRD measurements and theoretical calculations, we proposed the following discharge mechanism for the Na-Sn system:

- Process 1: $\text{Sn} \rightarrow \text{NaSn}_3$
- Process 1': $\text{Sn}, \text{NaSn}_3 \rightarrow \text{NaSn}_2$
- Process 2: $\text{NaSn}_2 \rightarrow a\text{-Na}_{1.2}\text{Sn}$
- Process 2': $a\text{-Na}_{1.2}\text{Sn} + \text{NaSn}_2 \rightarrow a\text{-Na}_{1.2}\text{Sn} + \text{expanded Na}_{1+x}\text{Sn}_2$ (solid solution)
- Process 3: $a\text{-Na}_{1.2}\text{Sn} + \text{expanded Na}_{1+x}\text{Sn}_2 \rightarrow \text{Na}_{4.4}\text{Sn}_2$
- Process 3': $\text{Na}_{4.4}\text{Sn}_2 \rightarrow \text{Na}_{4.75}\text{Sn}_2$ (solid solution)
- Process 4: $\text{Na}_{4.75}\text{Sn}_2 \rightarrow \text{Na}_{15}\text{Sn}_4$
- Process 4': $\text{Na}_{15}\text{Sn}_4 \rightarrow \text{Na}_{15+x}\text{Sn}_4$

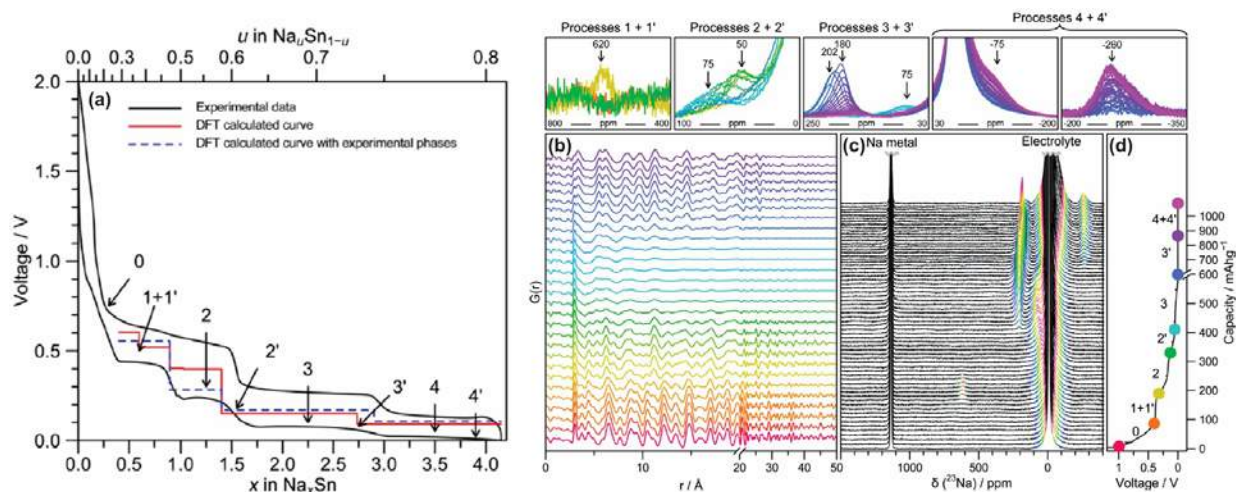


Figure II-310. (a) Experimental (black) electrochemistry of a Na-Sn cell cycled at C/20 between 2 and 0.001 V compared to theoretical (red/blue) predictions. (b) Operando PDFs and (c) ^{23}Na NMR spectra for Na-Sn cells aligned with the corresponding electrochemistry (d).

The first electrochemical process of Na insertion into Sn results in the conversion of crystalline Sn into a layered structure consisting of mixed Na/Sn occupancy sites intercalated between planar hexagonal layers of Sn atoms (NaSn_3 , Figure II-311, left panel). Following this, NaSn_2 , which is predicted to be thermodynamically stable, forms. NaSn_2 contains hexagonal layers closely related to NaSn_3 , but has no Sn atoms between the layers. In Process 2, NaSn_2 is broken down into an amorphous phase of approximate composition $\text{Na}_{1.2}\text{Sn}$, which is predicted to exhibit Sn chains. *Operando* ssNMR and PDF refinements show evidence that further reaction with Na results in the formation of structures containing Sn-Sn dumbbells, which interconvert through a solid-solution mechanism in Process 3'. These structures are based upon $\text{Na}_{5-x}\text{Sn}_2$, with increasing occupancy of one of its Na sites commensurate with the amount of Na added (Figure II-311b, right panel). Finally, ssNMR results indicate that the final product, $\text{Na}_{15}\text{Sn}_4$, can store additional Na atoms as an off-stoichiometry compound, $\text{Na}_{15+x}\text{Sn}_4$, analogous to previous observations in the Li-Si system. Taken together, this work provides the first evidence for significant solid solution behavior and resulting metastability in the Na-Sn system. These findings have further implications beyond the Na-Sn system, highlighting the fact that even a system under apparent thermodynamic control, the nature of electrochemical alloying means that kinetic considerations remain of primary importance.

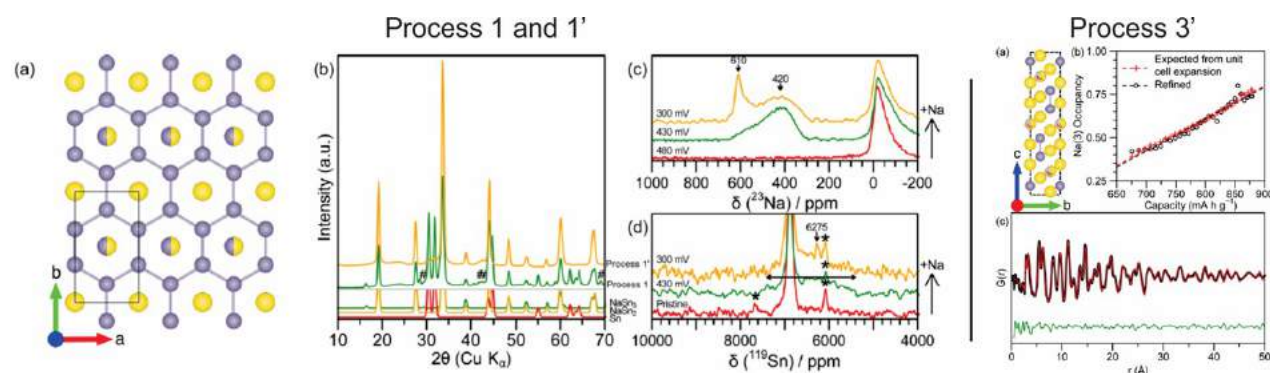


Figure II-311. Left panel: (a) Structure of NaSn_3 -Pmmm with Na in yellow and Sn in purple (b) operando XRD patterns (c) ex situ ^{23}Na and (d) ^{119}Sn 60 kHz MAS NMR at the end of process 1 and 1'. Right panel: (a) Structure of $\text{Na}_{5-x}\text{Sn}_2$ (b) occupancy vs Na site 3 vs time spent on process 3' (c) fit of the PDF corresponding to the first frame in process 3'.

SEI on Si anodes for Li-ion batteries

The primary aim of this study was to understand how the electrolyte additive fluoroethylene carbonate (FEC) enhances the stability of the SEI formed on Si anodes. The organic species formed on Si nanowires (SiNWs) in both the standard carbonate-only electrolyte (LP30) as well as LP30 with 10% FEC were characterized with solution and solid-state NMR techniques, including dynamic nuclear polarization (DNP). SiNWs were used here as model systems, since they can be prepared as binder-free anodes that cycle for multiple cycles without losing electrical contact.

After long-term cycling, ^1H solution NMR shows that LP30 decomposes and forms a variety of soluble oligomers in addition to the transient formation of lithium ethylene decarbonate (LEDC, yellow shading, Figure II-312a). Addition of 10 vol% FEC into the electrolyte suppresses the decomposition of EC/DMC (Figure II-312b,c), that is correlated with an increased Coulombic efficiency in the electrochemical cycling data after the first few cycles. To facilitate a more in-depth characterization of the electrolyte products in the presence of FEC via 1D and 2D NMR (e.g., ^{13}C - ^{13}C COSY, ^1H - ^{13}C HMBC, ^1H - ^{13}C HSQC to assign red shaded peaks x, y, and z), ^{13}C -enriched FEC was synthesized, which ultimately allowed a detailed structural assignment of the organic SEI. The ^1H and ^{13}C NMR spectra provide compelling evidence for the defluorination of FEC to form soluble vinoxyl species (HCOCH_2OR) and VC. The formation of VC, rather than LVDC, was unambiguously determined, the assignment being based on the J -coupling pattern that arises from the uniform ^{13}C labelling of FEC and the subsequent breakdown products (Figure II-313).

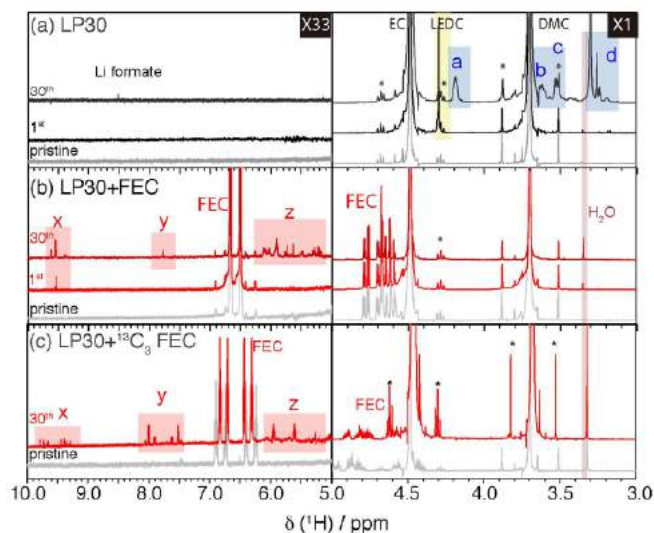


Figure II-312. ^1H solution NMR of (a) LP30, (b) LP30 + FEC, and (c) LP30 + 10 vol% $^{13}\text{C}_3$ -FEC before cycling (pristine), and after the 1st and 30th cycles. ^{13}C satellites are marked with an asterisk.

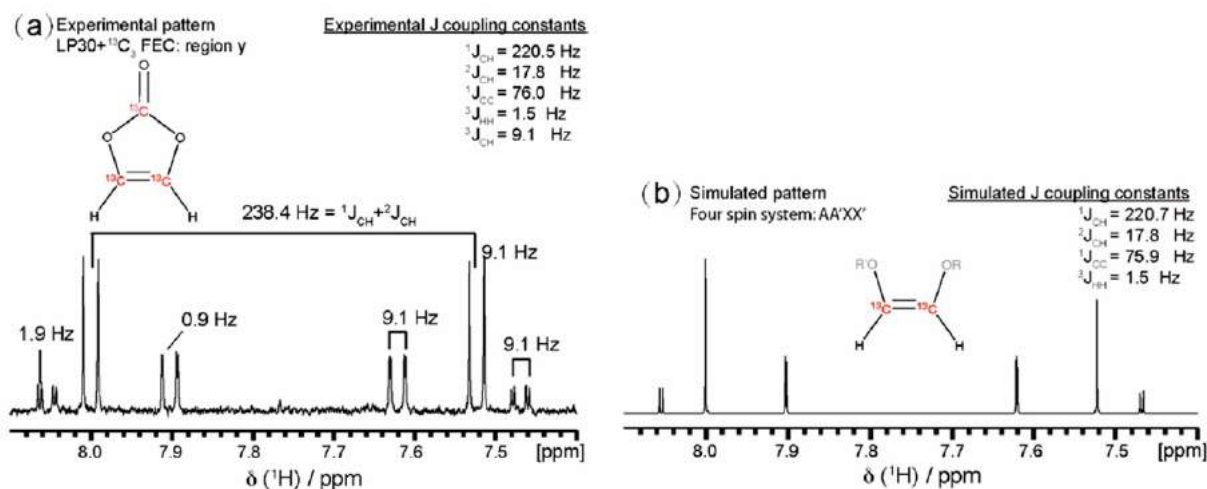


Figure II-313. Multiplet pattern of LP30 + $^{13}\text{C}_3$ -FEC in region y of an earlier Figure, (a) experimental pattern; (b) simulated pattern of a four-spin system $\text{AA}'\text{XX}'$ (cis-H-CR=CR-H).

Oligomers with characteristic peaks due to protonated carbons bonded to two adjacent oxygen groups from cross-linking units were also identified. These oligomeric precursors presumably react further to form insoluble polymeric species in the SEI, with similar cross-linking groups (Figure II-314b, peak at 103 ppm). Neither these cross-linking units nor the vinoxyl species are observed in the absence of the FEC additive (Figure II-314a). The vinoxyl species are signatures for the formation of the vinoxyl radicals that are believed to initiate the polymerization that eventually results in a highly cross-linked network. We hypothesize that highly cross-linked polymeric networks are key to the increased stability of SEI formed on Si that is observed the presence of FEC, motivating studies with additives that may promote cross-linking. Further insight into the molecular nature of the SEI and the parameters that impart stability offer the opportunity to tailor the SEI chemistry to maximize performance in LIBs.

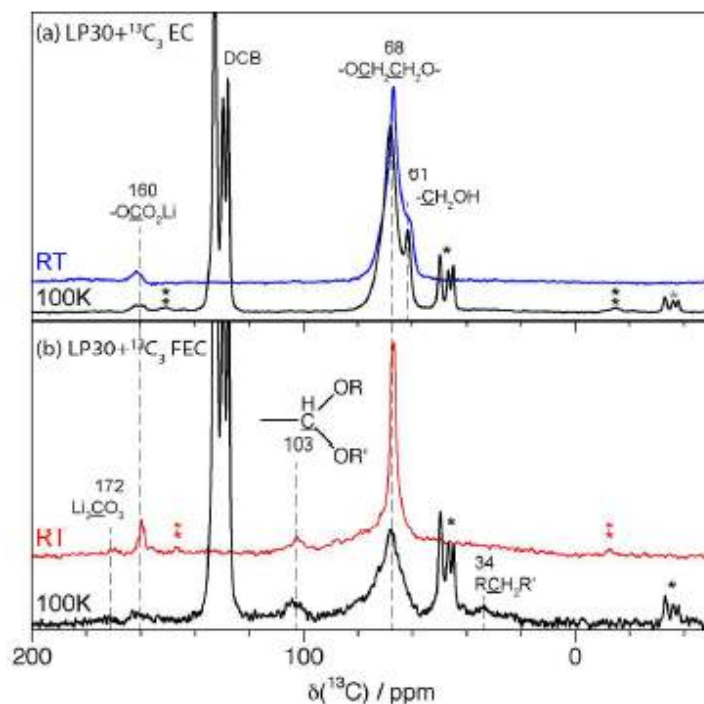


Figure II-314. ^1H - ^{13}C cross-polarization (CP) NMR spectra of SiNWs after 30 cycles in (a) LP30 + 25 vol% $^{13}\text{C}_3$ -EC and (b) LP30 + 10 vol% $^{13}\text{C}_3$ -FEC electrolytes. The room temperature (RT) spectra were measured by conventional ssNMR, whereas the 100 K spectra were measured with DNP NMR. The DCB was used as the radical solvent for DNP.

Conclusions

In the first project, we determined how cation substitution of nominally inert ions such as Mg and Li affect the structural transformations and ion mobility in a series of layered Na cathode materials ($\text{P2-Na}_{2/3}\text{Mn}_{1-y}\text{Mg}_y\text{O}_2$ ($y = 0.0, 0.05, 0.1$)) at high voltages. We show that Mg substitution leads to smoother electrochemistry, with fewer distinct electrochemical processes, improved rate performance and better capacity retention. These observations are attributed to the more gradual structural changes upon charge and discharge, as observed with synchrotron, powder X-ray, neutron diffraction, and ^{23}Na ssNMR. Mg doping reduces the number of Mn^{3+} Jahn–Teller centers and delays the high voltage phase transition occurring in $\text{P2-Na}_{2/3}\text{MnO}_2$. This study has been complemented by ^{23}Na NMR investigations of local structure and electrochemistry of $\text{P2-Na}_x[\text{Li}_y\text{Ni}_z\text{Mn}_{1-y-z}]\text{O}_2$ ($x, y, z \leq 1$), in which direct evidence for rapid Na^+ mobility was observed. The electrochemical performance of the $\text{P2-Na}_{2/3}\text{Mn}_{1-y}\text{Mg}_y\text{O}_2$ ($y = 0.05$) cathode is exceptional, with the material exhibiting very stable electrochemistry upon extended cycling and one of the highest rate performance observed to date for this class of materials.

In a separate project, we performed *in situ* ^{23}Na NMR experiments to quantify the high surface area Na metal deposits that form in Na–Na symmetrical cells for comparison to Li dendrite growth. We found that the Na deposits continuously accumulate, even in the case of galvanostatic cycling at low currents (e.g., 0.5 mA cm^{-2}). Two regimes for the electrochemical cycling of Na metal are apparent that have implications for the use of Na anodes: at low currents, the Na deposits are partially removed on reversing the current, while at high currents, there is essentially no removal of the deposits in the initial stages. At longer times, high currents show a significantly greater accumulation of deposits during cycling, again indicating a much lower efficiency of removal of these structures when the current is reversed. In general, dendrite formation appears to be more severe for Na metal anodes in comparison to Li metal anodes. We anticipate that differences in the nature of the SEI formed on Na and Li surfaces will be key to elucidating the physical origin of dendrite growth in these systems.

Sn represents a possible anode material in a sodium ion battery with a noticeably higher capacity than a hard carbon. A combination of *ab initio* calculations, *operando* PDF analysis, XRD, ^{23}Na solid-state nuclear magnetic resonance (ssNMR), and *ex situ* ^{119}Sn ssNMR was used to identify: (i) the number and nature of the crystalline phase(s) formed during the first electrochemical process; (ii) the structural features of the amorphous phase formed during the second electrochemical process; and (iii) the phase formed during the third process. The first electrochemical process of Na insertion into Sn results in the conversion of crystalline tin into a layered structure consisting of mixed Na/Sn occupancy sites intercalated between planar hexagonal layers of Sn atoms (approximate stoichiometry NaSn_3). Following this, NaSn_2 , which is predicted to be thermodynamically stable by AIRSS, forms; this contains hexagonal layers closely related to NaSn_3 , but has no tin atoms between the layers. NaSn_2 is broken down into an amorphous phase of approximate composition $\text{Na}_{1.2}\text{Sn}$. Reverse Monte Carlo refinements of an *ab initio* molecular dynamics model of this phase show that the predominant tin connectivity is chains. Further reaction with sodium results in the formation of structures containing Sn–Sn dumbbells, which interconvert through a solid-solution mechanism. These structures are based upon $\text{Na}_{5-x}\text{Sn}_2$, with increasing occupancy of one of its sodium sites commensurate with the amount of sodium added. ssNMR results indicate that the final product, $\text{Na}_{15}\text{Sn}_4$, can store additional sodium atoms as an off-stoichiometry compound ($\text{Na}_{15+x}\text{Sn}_4$) in a manner similar to $\text{Li}_{15}\text{Si}_4$. The first evidence for significant solid solution behavior and resulting metastability in the sodium–tin system is presented. Overall, this study demonstrates the importance of a complementary suite of characterization techniques to probe both short- and long-range structures, along with a detailed theoretical underpinning of model structures, to comprehensively understand the mechanism of sodium insertion. In addition, our results imply that even in systems under apparent thermodynamic control, the nature of electrochemical alloying means that kinetic considerations are vital.

Finally, to understand how additives influence SEI composition and stability on Si anodes in Li-ion batteries, we performed a detailed electrochemical and multinuclear NMR study. We find that the soluble poly(ethylene oxide)-like linear oligomeric electrolyte breakdown products that are observed after cycling in the standard ethylene carbonate-based electrolyte are suppressed in the presence of 10 vol% FEC additive. FEC is first defluorinated to form soluble vinylene carbonate and vinoxyl species, which react to form both soluble and insoluble branched ethylene-oxide-based polymers. No evidence for branched polymers is observed in the absence of FEC. We speculate that the formation of cross-linked polymers is key to the higher stability of SEI formed on Si in the presence of FEC, motivating studies with additives that promote cross-linking to tailor the SEI chemistry for enhanced performance in Li-ion batteries.

Key Publications

1. R.J. Clément, D. S. Middlemiss, I. D. Seymour, A. J. Ilott, C. P. Grey, “Insights into the Nature and Evolution upon Electrochemical Cycling of Planar Defects in the beta- NaMnO_2 Na-Ion Battery Cathode: An NMR and First-Principles Density Functional Theory Approach” *Chem. Mater.*, **2016**, 28, 8228.
2. A. J. Ilott, M. Mohammadi, H. J. Chang, C. P. Grey, A. Jerschow “Real-time 3D imaging of microstructure growth in battery cells using indirect MRI” *Proc. Nat. Ac. Sci. USA*, **2016**, 113, 10779.
3. R.J. Clément, J. Billaud, A.R. Armstrong, G. Singh, T. Rojo, P.G. Bruce, C.P. Grey “Structurally stable Mg-doped $\text{P2-Na}_{2/3}\text{Mn}_{1-y}\text{Mg}_y\text{O}_2$ sodium-ion battery cathodes with high rate performance: insights from electrochemical, NMR and diffraction studies” *Energy Environ. Sci.*, **2016**, 9, 3240.
4. A.L. Michan, B.S. Parimalam, M. Leskes, R.N. Kerber, T. Yoon, C.P. Grey, B.L. Lucht “Fluoroethylene carbonate and vinylene carbonate reduction: Understanding lithium-ion battery electrolyte additives and solid electrolyte interphase formation” *Chem. Mater.*, **2016**, 28, 8149.

5. Clément, R. J.; Xu, J.; Middlemiss, D. S.; Alvarado, J.; Ma, C.; Meng, Y. S.; Grey, C. P. “Direct evidence for high Na⁺ mobility and high voltage structural processes in P2-Na_x[Li_yNi_zMn_{1-y-z}]O₂ (x,y,z ≤ 1) cathodes from solid-state NMR and DFT calculations” *J. Mater. Chem. A*, **2017**, 5, 4129.
6. Dally, R.; Clément, R. J.; Chisnell, R.; Taylor, S.; Butala, M.; Doan-Nguyen, V.; Balasubramanian, M.; Lynn, J. W.; Grey, C. P.; Wilson, S. D. “Floating zone growth of α-Na_{0.90}MnO₂ single crystals” *J. Cryst. Growth*, **2017**, 459, 203.
7. Ma, C.; Alvarado, J.; Xu, J.; Clément, R. J.; Kodur, M.; Tong, W.; Grey, C. P.; Meng, Y. S. “Exploring oxygen activity in the high energy P2-type Na_{0.78}Ni_{0.23}Mn_{0.69}O₂ cathode material for Na-ion batteries” *J. Am. Chem. Soc.*, **2017**, 139, 4835.
8. Stratford, J. M.; Mayo, M.; Allan, P. K.; Pecher, O.; Borkiewicz, O. J.; Wiaderek, K. M.; Chapman, K. W.; Pickard, C. J.; Morris, A. J.; Grey, C. P. “Investigating Sodium Storage Mechanisms in Tin Anodes: A Combined Pair Distribution Function Analysis, Density Functional Theory, and Solid-State NMR Approach” *J. Am. Chem. Soc.*, **2017**, 139, 7273.
9. Pell, A. J.; Sanders, K. J.; Wegner, S.; Pintcuda, G.; Grey, C. P., “Low-power broadband solid state MAS NMR of N-14”, *J. Chem. Phys.*, **2017**, 146, 194202.
10. Jin, Y.; Kneusels, N.-J. H.; Magusin, P. C. M. M.; Kim, G.; Castillo-Martinez, E.; Marbella, L. E.; Kerber, R. N.; Howe, D. J.; Paul, S.; Liu, T.; Grey, C. P. “Identifying the Structural Basis for the Increased Stability of the Solid Electrolyte Interphase Formed on Silicon with the Additive Fluoroethylene Carbonate” *J. Am. Chem. Soc.*, **2017**, 139, 14992.

References

1. Clément, R. J.; Bruce, P. G.; Grey, C. P., *J. Electrochem. Soc.* **2015**, 162, A2589.
2. Yabuuchi, N.; Kubota, K.; Dahbi, M.; Komaba, S., *Chem. Rev.* **2014**, 114, 11636.
3. Irisarri, E.; Ponrouch, A.; Palacin, M. R., *J. Electrochem. Soc.* **2015**, 162, A2476.
4. Stevens, D. A.; Dahn, J. R., *J. Electrochem. Soc.* **2000**, 147, 1271.
5. Chandrashekar, S.; Trease, N. M.; Chang, H. J.; Du, L.-S.; Grey, C. P.; Jerschow, A., *Nat. Mater.* **2012**, 11, 311.
6. Chang, H. J.; Ilott, A. J.; Trease, N. M.; Mohammadi, M.; Jerschow, A.; Grey, C. P., *J. Am. Chem. Soc.* **2015**, 137, 15209.
7. Ilott, A. J.; Mohammadi, M.; Chang, H. J.; Grey, C. P.; Jerschow, A., *Proc. Natl. Acad. Sci.* **2016**, 113, 10779.

II.D.4 Advanced Microscopy and Spectroscopy for Probing and Optimizing Electrode-Electrolyte Interphases in High Energy Lithium Batteries (UCSD)

Ying Shirley Meng, Principal Investigator

University of California San Diego
9500 Gilman Drive
La Jolla, CA 92093
Phone: 858-822-4247; Fax: 858-534-9553
E-mail: shmeng@ucsd.edu

Tien Duong, Technology Manager

U.S. Department of Energy
Phone: 202-586-7836
E-mail: Tien.Duong@ee.doe.gov

Start Date: April 1, 2017

End Date: March 31, 2021

Total Project Cost: \$360,000

DOE share: \$360,000

Non-DOE share: \$0

Project Introduction

The energy density and cycling life of state-of-the-art LIBs have to be further improved to meet the performance requirements for transportation applications. However, the relatively low capacity of cathode has become one of the major bottlenecks to achieve higher energy density in LIBs. In principle, the capacity of classical layered transition metal (TM) oxides, the primary commercial cathode materials, is limited to cationic redox activity. Anionic redox has thus emerged as a new paradigm for designing novel cathodes for next generation LIBs. It is recently found and confirmed oxygen redox in lithium-rich layered oxides with composition $x\text{Li}_2\text{MnO}_3 \cdot (1-x)\text{LiTMO}_2$, which enables this group of materials exhibit reversible capacities exceeding 280 mAh g^{-1} . Despite its high capacities, this material has several challenges (voltage fading, structural instability, sluggish kinetics, cathode electrolyte interphase instability, etc.) that must be overcome in order to reach commercialization. When the material is charged over TM redox reaction region (above 4.4 V for most of Li-rich material), lattice oxygen removal result in oxygen vacancies formation on the surface, which further triggers surface phase transformation from layered to spinel-like phase. This irreversible phase transformation finally results in voltage degradation and lower Li mobility during extended cycles. By carefully controlling the oxygen activities through the creation of uniform oxygen vacancies, we were able to avoid structural decomposition in Li-excess layered oxides. The modified materials deliver a discharge capacity as high as 306 mAh g^{-1} with an initial coulombic efficiency of 90.6%. Furthermore, they do not exhibit obvious capacity decay, with low voltage degradation and a reversible capacity over 300 mAh g^{-1} after 100 cycles at 0.1 C-rate. Our approach demonstrates the critical needs for advanced diagnosis and characterization. It is through the in-depth understanding of these high voltage cathode materials at atomistic and molecular level and their dynamic changes during the operation of batteries; strategies can be successfully formulated to optimize this class of cathode materials. Although various characterization techniques have been developed in the Li battery research field, some of them fail to properly characterize Li metal because the intrinsic high chemical reactivity and low thermal stability make it difficult to handle the sample without damaging or contaminating. This is evident when observing Li metal by conventional transmission electron microscopy (TEM), with which severe beam damage occurs after short exposure time less than 10s of seconds. The diagnostic tools developed here can also be leveraged to study anode materials such as Li metal anode. We have to apply cryogenic method (low-temperature) and low-dose electron microscopy with specialized camera to enable the reliable and consistent characterization of the lithium metal anode.

Objectives

The proposed research aims to develop advanced microscopy and spectroscopy tools to probe, understand, and optimize the anion activities that govern the performance limitations such as capacity and voltage stabilities in high energy Li-excess TM (Ni,Co,Mn, etc.) oxides cathode materials. Our approach uniquely combines atomic resolution scanning transmission electron microscopy (STEM), electron energy loss spectroscopy (EELS), operando Bragg Coherent Diffraction Imaging (BCDI), and first principles computation to probe anion redox and oxygen evolutions in Li-excess NMC materials. Furthermore, we will track the lithium and oxygen dynamics under electrochemical testing via operando neutron diffraction which will enhance the understanding of the overall structural changes due to anion activities. Ultimately, this will hone in on the synthesis efforts to produce the modified materials with the optimum bulk compositions and surface characteristics at large scale for consistently good performance. The above-mentioned characterization tools will be extended to diagnose various anode types, such as Li metal anode.

Approach

This unique approach combines STEM/EELS, operando BCDI, X-ray photoelectron spectroscopy and Ab initio computation as diagnostic tools for probing anion redox and oxygen evolutions in Li-excess NMC materials. This allows for pinning down the atomistic/molecular mechanism of anion oxidation and determining the speciation compositions and surface characteristics for enabling high rate and long life in the proposed materials. Neutron enables the characterization of bulk material properties to enhance and further optimize high energy electrode materials. We also develop novel cryogenic focus-ion-beam and electron microscopy to characterize lithium metal anode. This work funds collaborations on EELS (Miaofang Chi, Oakridge National Lab); neutron diffraction (Ke An, ORNL); soft XAS (Marca Doeff, Lawrence Berkeley National Laboratory). It supports collaborative work with Zhaoping Liu and Yonggao Xia at Ningbo Institute of Materials Technology and Engineering China. It also supports collaboration with Battery500 consortium.

Results

The following are the key accomplishments:

Probing the surface transition metal oxidation state and oxygen activities of Li-rich layered oxides

In order to study the structure and chemistry differences between bulk and surface from the atomic level, STEM/EELS data was collected from the Li-rich electrode ($\text{Li}_{7/6}\text{Ni}_{1/6}\text{Co}_{1/6}\text{Mn}_{1/2}\text{O}_2$) after one cycle as shown in Figure II-315. Similar to our previous observations, a defect spinel structure that is different from the layered structure in bulk formed on the surface regions (less than 2 nm) due to TM migration from the TM layer to the neighboring lithium layer. Spatially resolved EELS (see Figure II-315b) was also performed using a step size of ~ 0.6 nm from surface to bulk. The data points are aligned with the STEM image to specify where the specific spectrum was taken. The O K-edge pre-peak, aligned to the onset energy of 532 eV, is associated with the hybridization states between TM 3d and oxygen 2p orbitals in the octahedral unit. There is no O pre-peak detected in the spectra obtained in the surface region. From surface to bulk, the intensity of the pre-peaks increases gradually. The results indicate the reduction of TM ions and oxygen local environment change, which is due to the formation of oxygen vacancy on the surface region where the spinel phase presents after cycling. Mn L-edge EELS was also collected from the identical area. Previous studies have shown that the L_3/L_2 ratio is sensitive to the valence state of Mn. In the detailed L_3/L_2 ratio analysis shown in Figure II-315c, it is going to lower Mn oxidation state within a ~ 2 nm region from the surface, which is consistent with XPS result in our previous report. The generation of the reduced Mn can be a direct consequence of the formation of a large number of oxygen vacancies, which once again proves oxygen participates in the electrochemical cycling.

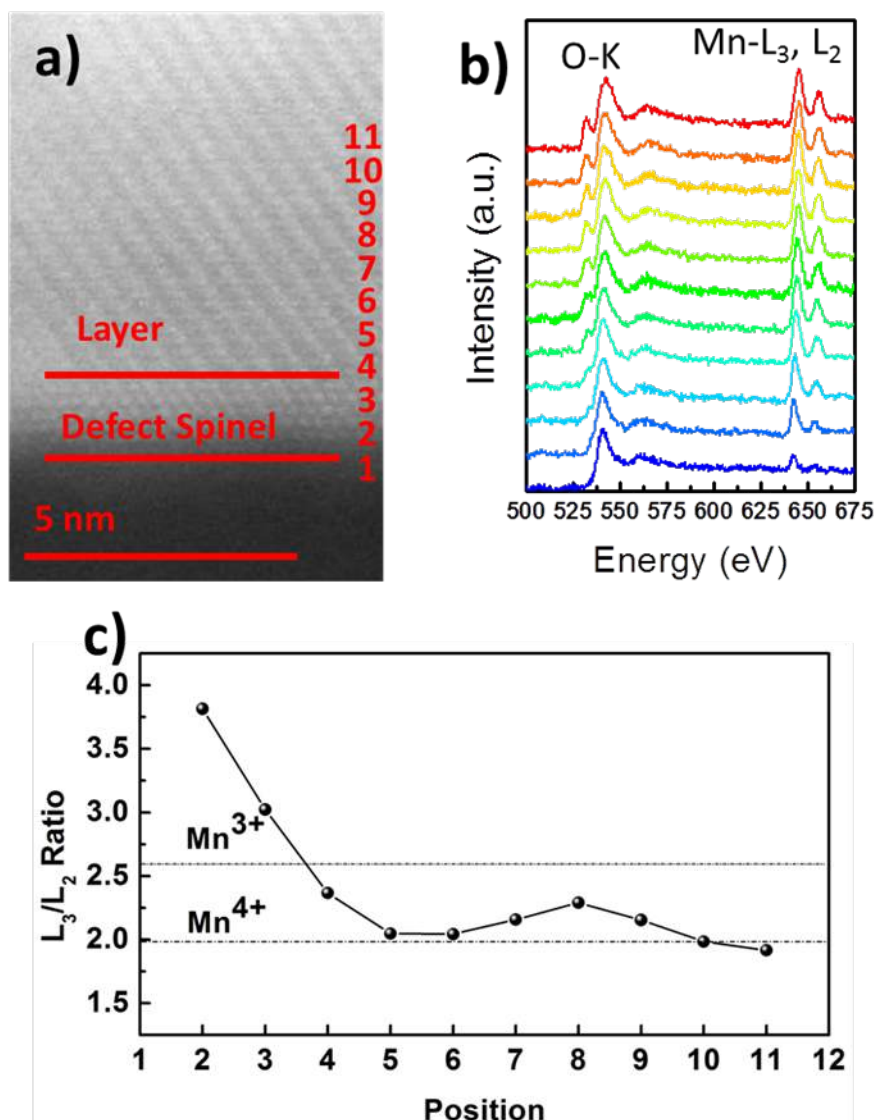


Figure II-315. (a) Aberration corrected high angle annular dark field (HAADF) STEM image; (b) spatially resolved O K-edge and Mn L-edge EELS spectra; (c) Mn L₃/L₂ ratio fit results from the EELS spectra.

BCDI characterization on single particle of Li-rich layered oxide after cycling

Three-dimensional dislocation network formation was demonstrated in our previous report by BCDI in this group material during the initial charging process under operando conditions. It is also revealed the link between this crystalline defect and voltage decay in this material. To further investigate the dislocation evolution during cycling, BCDI measurement was performed on Li-rich layered oxide electrode after the 1st cycle and the 50th cycle (see Figure II-316a and Figure II-316b). The truncation rod in the diffraction speckle pattern is less symmetric for the sample after 50 cycles compared with that of the sample after only 1 cycle, which typically indicates strain builds up in this material during electrochemical cycling. We have focused on quantitative analysis to reconstruct 3D displacement field as well as strain distribution in the single particle to illustrate crystalline defects influence on cycling performance of Li-rich layered oxide material.

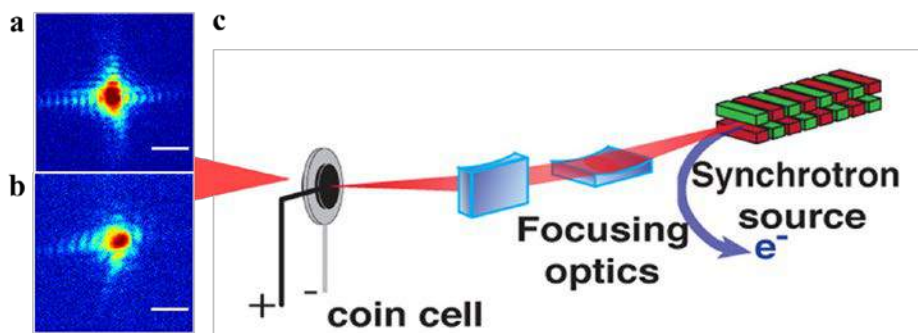


Figure II-316. Diffraction data collected for electrode after the (a) 1st cycle and (b) 50th cycle. (c) Experimental schematic of the in situ BCDI setup. Scale bar is $1 \times 10^{-8} \text{ 1/\AA}$.

Structure recovery demonstration of Li-rich layered oxide after electrochemical cycling

Anion (oxygen) redox in Li-rich layered oxide materials is the main reason for the high reversible capacity over 300 mAh g^{-1} at room temperature. Unfortunately these composites suffer from a poor structural stability and limited cycle life. A large fraction of the TM ions are in under coordinated octahedral sites due to oxygen vacancies formation, which are not stable and spontaneously migrate to the fully coordinated octahedral sites nearby. Li ions in the TM layer migrate to the shared tetrahedral site in the lithium layer. These migrations dramatically alter the cation ordering in the TM layer as well as local lithium environment and thus lead to the structure disorder. The cycled material will be trapped in a metastable state with energetically unfavorable local lithium environment, which finally contributes to the voltage fade during the cycling process. As shown in Figure II-317a, the superstructure peak between 20° and 25° disappears after 50 cycles, which indicates the material becomes partially disordered. A path is designed to re-order the superstructure by high-temperature annealing of the cycled electrode ($>150^\circ \text{C}$). After the heat treatment, the superstructure peak is partially recovered, which indicates the bulk structure is reordered. Based on the mechanism described above, the superstructure recovery is decisive in restoring the original voltage output of Li-rich layered cathode (see Figure II-317b).

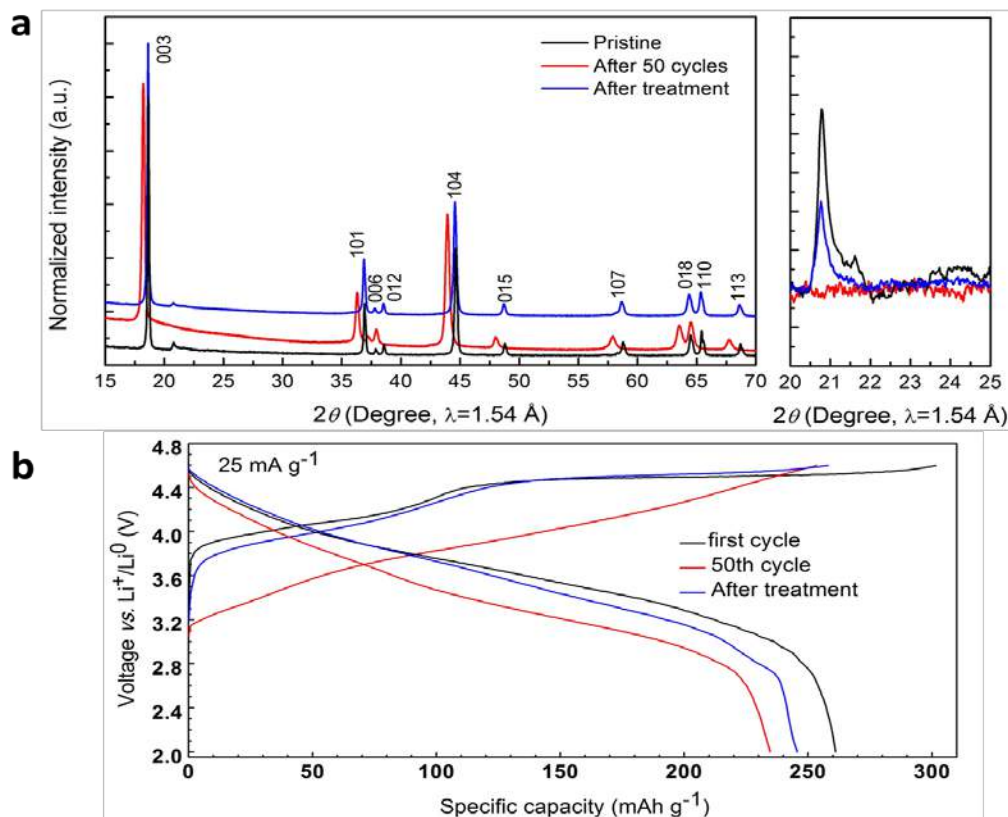


Figure II-317. (a) The evolution of the superstructure peak intensity in the pristine state, after 50 cycles, and after the heat treatment. (b) Charge-discharge voltage curves of Li-rich layered oxide cathode with Li-metal as anode

Neutron diffraction (ND) was applied to investigate the structure transformation of the cycled electrode after heat treatment. Figure II-318a-d shows the as-collected time-of-flight (TOF) ND patterns with 'Rietveld' refinement for Li-rich layered cycled electrodes before and after heat treatment. The lattice parameters of the sample after initial cycle are $a = 2.8630(1) \text{ \AA}$, and $c = 14.3497(9) \text{ \AA}$. In comparison, both a and c lattice parameters are reduced after annealing under different temperature. This trend counteracts common effect of material thermal expansion, which indicates structure transformation occurs with strain decrease. In order to illustrate local structure changes in terms of atomic migration induced by heat treatment, lithium occupancy in TM layer and oxygen occupancy are also shown in Figure II-318. After initial cycle, lithium from the TM layer is largely irreversible with only 32% of lithium reinsertion. Oxygen vacancies are also observed in the cycled sample, which results in a large fraction of under-coordinated TM ions. These unstable TM ions can potentially migrate to the fully coordinated octahedral sites nearby. Irreversible lithium insertion together with TM ions migration dramatically alters the cation ordering in the TM layer and thus leads to the structure disorder. Surprisingly, it is found Li occupancy in the TM layer and oxygen occupancy increases for the cycled sample after heat treatment, which is a strong indication of structure ordering recovery.

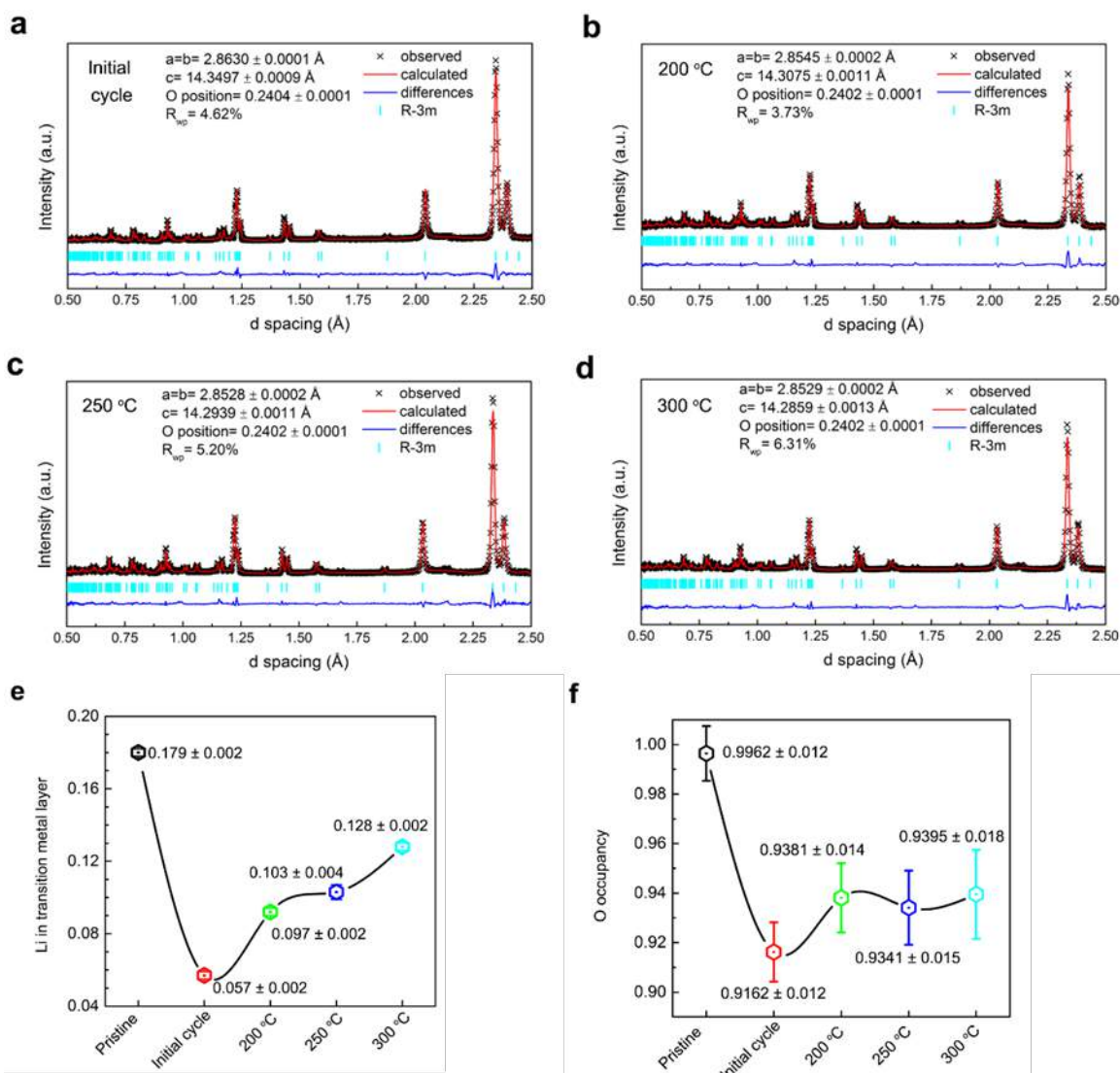


Figure II-318. ND characterization of cycled electrode after heat treatment. (a) Refined ND patterns of the electrode after the initial cycle. (b-d) Refined ND patterns of the initially cycled electrode after heat treatment under 200, 250 and 300 °C, respectively. (e) Lithium occupancy in transition metal layer and (f) Oxygen occupancy for different samples.

Feasibility of Cryogenic -TEM to characterize Li metal dendrite formation

Basic understanding of Li growth mechanism is important to prevent the detrimental dendrites formation. Although much work has been done to explore the growth of Li dendrite by various characterizations, such as optical microscopy, scanning electron microscopy (SEM), atomic force microscopy (AFM) etc. Its growth mechanism is still unclear and controversial. Furthermore, little attention is paid on the structure of plated Li metal, especially at the atomic scale. Compared with other characterization tools, TEM provides insight related to both microstructural and chemical evolutions with a superior spatial resolution. The challenge of probing Li metal under TEM is the low dose tolerance (high beam sensitivity) of Li metal. It is difficult to handle Li metal without any contamination and damage. Figure II-319 shows the morphology changes of the Li metal as a function of the beam exposure time under room temperature. At room temperature, the dendritic Li metal is quite unstable: quickly drifted, shrunk and evaporated under TEM beam exposure. Holes are created in the Li metal (Figure II-319c). One of the promising approaches to stabilize the beam-sensitive samples is the Cryo technique. In contrast, Li metal is very stable at 100 K (Figure II-319d-f) and no visible

changes are observed with the same magnification as the room temperature. Therefore, the cryo-TEM allows us to detect the Li metal at the nano scale while avoiding damaging of the sample.

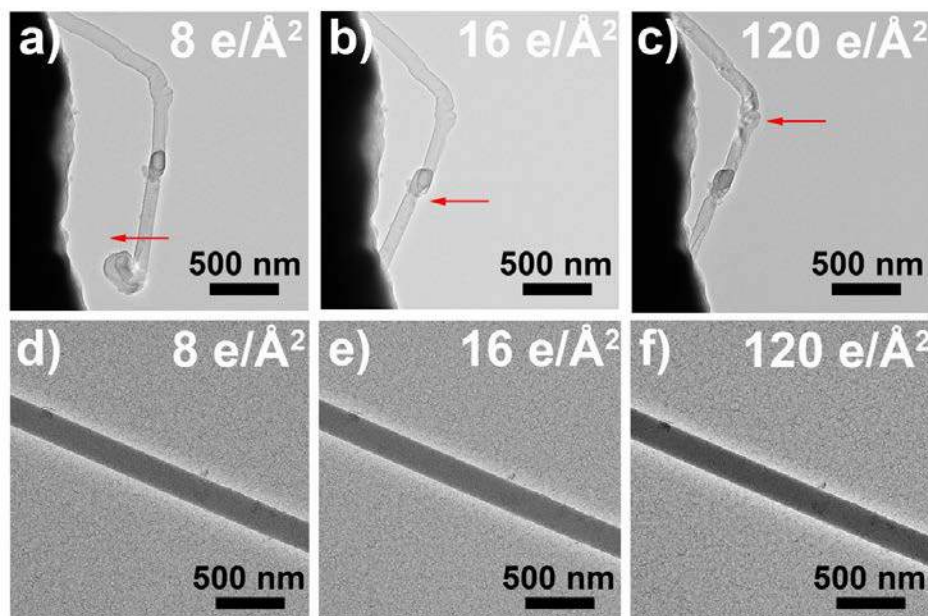


Figure II-319. Morphology changes of the dendritic Li metal as a function of the beam exposure time under: room temperature TEM (a, b, c) and cryo-TEM (d, e, f).

Structure and chemical composition of electrochemically deposited Li metal at nano scale

The nanostructure of the electrochemically deposited Li metal (EDLi) is shown in Figure II-320a. The identical contrast in the bulk demonstrates the uniformity of the EDLi. Along the edges of the EDLi an uneven solid electrolyte interphase (SEI) is present with a maximum thickness of ~ 7 nm. Figure II-320 surprisingly displays lattice fringes present on the surface rather than the bulk, suggesting that the EDLi metal is amorphous while part of the SEI is crystalline. The above results were validated by the area Fast Fourier Transform (FFT) patterns. The absence of characteristic bright rings/spots in the bulk area (red square) shows clearly that the EDLi is amorphous (Figure II-320b). Conversely, two obvious characteristic bright spots appear at the SEI surface (blue square). The ~ 0.2 nm lattice spacing is consistent with the lattice plane distance of the LiF (200) and cannot be ascribed to any plane distance of the metallic Li, further validating the partially crystallized SEI.

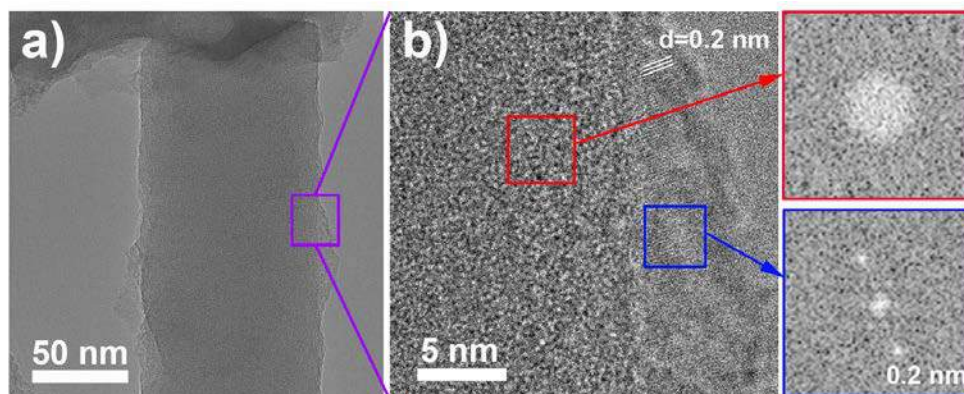


Figure II-320. Cryo-TEM (a) image and (b) its regional zoomed-in image with the bulk and surface FFT results of the EDLi using conventional carbonate electrolyte.

Conclusions

STEM/ EELS characterization of Li-excess single NMC particle confirms that the layer-to-spinel transformation is largely confined to the surface 2nm, which imply that such surface reconstruction is not the major attributing factor to the voltage fading issue in this class of materials. BCDI measurements on Li-excess single NMC particle demonstrate significantly higher amount of defects such as stacking faults at high voltage (high state of charge), on the contrary the classical layered oxides show much less such defects at high voltage. A path to recover the layer structure and working voltage is designed through annealing. The treatment helps to recover the local environments of the excess Li ions, restore the original oxygen stacking sequence, and eliminates microstrain associated with different defects. Cryogenic (cryo)-electron microscopy is a powerful tool to reveal the detailed chemistry and structure of electrochemically deposited Li and the SEI composition at the nanoscale while minimizing beam damage during imaging. Surprisingly, the results show that the low current density deposited (nucleation-dominated) EDLi is amorphous, while there is some crystalline LiF present in the SEI.

Key Publications

1. B. Qiu, M. Zhang, Y. Xia, Z. Liu, Y.S. Meng, “Understanding and Controlling Anionic Electrochemical Activity in High-Capacity Oxides for Next Generation Li-Ion Batteries” Chemistry of Materials, 2017, 29, 908.
2. M. Zhang, H.D. Liu, C. Fang, Y.S. Meng, “Minimize the Voltage Degradation in Li-rich Layered Oxide Cathode Materials by Morphology Control” Materials Research Society Meeting, 2016, Boston, U.S., Oral presentation.
3. M. Zhang, H.D. Liu, C. Fang, Y. S. Meng, “Morphological and Surface Structural Changes during Electrochemical Cycling in Li-rich Layered Oxides for Next Generation Li-ion Batteries” Materials Research Society Meeting, 2017, Phoenix, U.S., Oral presentation.
4. Y. S. Meng, “Diagnostic Comparison between Lithium-rich Layered Oxides and Classical Layered Oxides” Materials Research Society Meeting, 2017, Phoenix, U.S., Invited talk.
5. M. Zhang, B. Qiu, Y. S. Meng, “Structural and Voltage Recovery in Li-rich Layered Oxides”, provisional US Patent, in application.
6. X. Wang, M. Zhang, J. Alvarado, S. Wang, M. Sina, B. Lu, J. Bouwer, W. Xu, J. Xiao, J.-G. Zhang, J. Liu, Y. S. Meng, “New Insights on the Structure of Electrochemically Deposited Lithium Metal and Its Solid Electrolyte Interphases via Cryogenic TEM” Nano Letters, 2017, ASAP published online.

II.D.5 Microscopy Investigation on the Fading Mechanism of Electrode Materials (PNNL)

Chongmin Wang, Principal Investigator

Pacific Northwest National Laboratory
902 Battelle Boulevard, Mail Stop K8-93
Richland, WA 99352
Phone: 509-371-6268
E-mail: chongmin.wang@pnnl.gov

Tien Duong, Technology Manager

U.S. Department of Energy
Phone: 202-586-7836
E-mail: Tien.Duong@ee.doe.gov

Start Date: October 1, 2015

End Date: September 30, 2018

Total Project Cost: \$900,000

DOE share: \$900,000

Non-DOE share: \$0

Project Introduction

For layer structured cathode materials based on Ni, Mn and Co transition metal oxide, it can be divided into two categories, one is NMC and the other is the lithium rich and Mn rich NMC (LMR-NMC). Practical use of these two categories of cathodes faces three challenges at the very fundamental level: Voltage fading; capacity fading; and how to increase the packing/tape density. It is generally believed that high Co content in the NMC material enhances the rate performance; high Ni content leads to higher capacity, and the presence of Mn^{4+} improves the structural stability and thermal stability. However, the detailed fundamental roles of each transition metal cation e.g., Ni, Co and Mn, especially at the high voltages are still unclear, not mentioning the possible synergistic effects among these three cations during the electrochemical process. Furthermore, dopants such as Sn, Mg, Al, and Si also strongly affect the fading characteristics of cathode. Understanding the different contributions of Ni, Co, Mn, and their migration during cycling, if any, not only help to optimize the electrochemical performances of NMC at high cutoff voltages, it also unravels the structural and chemical evolution pathway of NMC and LMR-NMC, providing guidance for optimization of these layer structured cathodes for high performance.

To gain insights into the structural information at atomic resolution, aberration-corrected STEM-HAADF imaging combined with EELS/EDX chemical analysis will be used to probe the microstructural and chemical evolution of the NMC and LMR-NMC layered cathode before and after cycling. EELS/EDX mapping, time-of-flight secondary ion mass spectrometry (TOF-SIMS), nano-SIMS, and XPS will be used to explore the elemental distribution and the thickness of SEI layer formed on the surface of the cathode material. Direct correlation of the structural and chemical information with battery properties will provide insight on the capacity degradation mechanism of the layered materials with different compositions and performance improvement mechanism with lattice doping/surface modification/electrolyte additives.

Objectives

The objective of this work will be using the state of the art in-situ and ex-situ microscopy technique to probe the structural and chemical evolution of electrodes in rechargeable battery. A close collaboration between the synthesis and characterization teams will enable acceleration on the materials optimization process and establishment of a solid knowledge base on the correlation between materials selections and structure evolution in the electrode materials for rechargeable batteries.

Approach

Using the unique *ex situ* and *in situ* TEM methods to probe the structure of Li-ion batteries, especially a biasing liquid electrochemical cell that uses a real electrolyte in a nano-battery configuration. Use various

microscopic techniques, including *ex situ*, *in situ*, and especially the *operando* TEM system, to study the fading mechanism of electrode materials in batteries. This project will be closely integrated with other research and development efforts on high-capacity cathode and anode projects in the BMR Program to 1) discover the origins of voltage and capacity fading in high-capacity layered cathodes and 2) provide guidance for overcoming barriers to long cycle stability of electrode materials.

Results

1. Does the liquid electrolyte permeate into the boundaries formed by the primary particles in a secondary particle?

In order to increase the packing density of the cathode particle, it is now a common practice to fabricate the cathode particles into a secondary particle of typically 10-20 micrometer, which is composed of primary particle of several hundred nanometers. One of the critical questions for this type of hard agglomerated particle is whether the electrolyte penetrates into the boundaries formed by the primary particles. To answer this question, the secondary particle of NMC442 as typically shown in Figure II-321a were investigated before and after the battery cycling. Figure II-321a–c show the pristine agglomerated NMC442 particles and cycled electrode from which a TEM sample was prepared using FIB lift-out techniques. Figure II-321d–i are STEM-EDS mapping results; these observations reveal that, within the agglomerated particle, there exists a P-rich SEI layer formed at the grain boundary (GB). This observation conclusively indicates that the electrolyte did indeed penetrate into the inside of the agglomerated particles through the boundaries between the primary particles. Therefore it can be generally concluded that the detrimental solid-liquid electrolyte as observed in the case of primary particle also happens for the secondary particle. To improve the cycling stability, strategy needs to be developed to mitigate this interfacial reaction in the secondary particles.

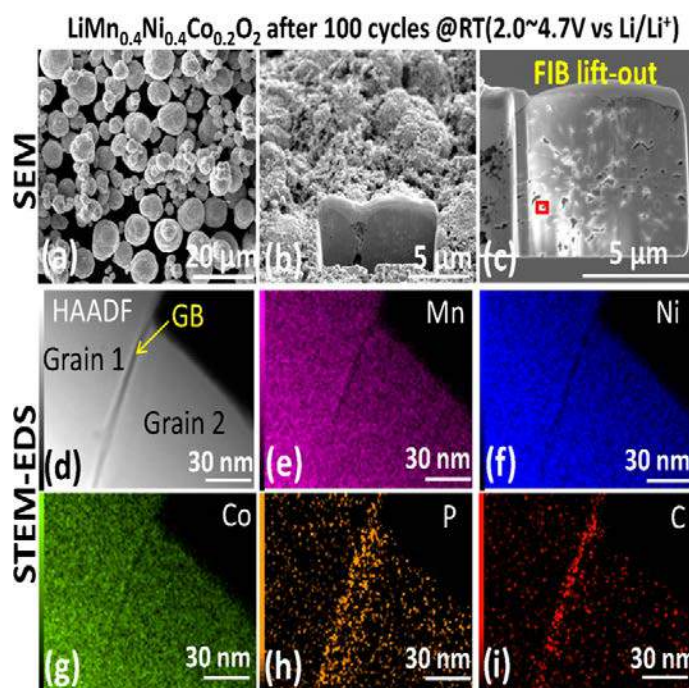


Figure II-321. SEM images of (a) pristine agglomerated particles, (b) and (c) TEM specimen prepared by FIB lift-out techniques from cycled electrode. (d–i) STEM-EDS mapping results from the boxed region in panel (c).

2. Intragranular cracking as a critical barrier for high-voltage usage of layer-structured cathode for lithium-ion batteries

For layered structured transition metal oxides, during charge process, Li ions are extracted from the lattice, which usually causes lattice expansion along *c* direction and shrinkage along *a* and *b* directions, while this

process reverses upon discharging (reversible insertion of Li ions). For example, when NMC333 is delithiated to $\text{Li}_{0.5}\text{Ni}_{1/3}\text{Mn}_{1/3}\text{Co}_{1/3}\text{O}_2$, the lattice could expand 2.0% along c direction and shrink 1.4% along a direction, which is a huge strain for oxides with ionic bonds. We found that intragranular cracks in NMC333 cathode can be easily created at high cutoff cycle voltage (Figure II-322), which contributed to the fast degradation of the cell. The comprehensive transmission electron microscopy (TEM) observations unveiled previously unrecognized nature of intragranular cracks from the following four aspects: 1) there are two kind intragranular cracks. One is the normally seen mechanical failure crack with two free surfaces; the other one is termed as premature crack with uniformly sub-nanometer crack width. 2) The premature crack is not empty but with loose materials inside. 3) Many intragranular cracks were initiated from grain interior. 4) Dislocations are acting as crack nucleation sites.

In addition to the real intragranular cracks which have two free surfaces, we also identified tremendous premature intragranular crack whose surfaces are not completely free but with a loose materials in between. Such premature cracks are generated by expanding the neighbored (003) planes (TM slabs) and exhibiting strip contrast while viewing their edge on in TEM. By examining a lot of intragranular cracks, surprisingly, we found many cracks were actually initiated from grain interior, which contradicts the proposed theoretical models as they predicted surface should be the favorite site for crack initiation. Through intensive TEM characterization, we discovered that dislocations could act as nucleation sites of internal cracking. Based on our experimental results, we proposed a mechanism which can fully address the formation process of internal cracking in layered cathode. This study pointed out future directions for mitigating intragranular cracking not only for layered cathode materials but also for other intercalation type cathodes.

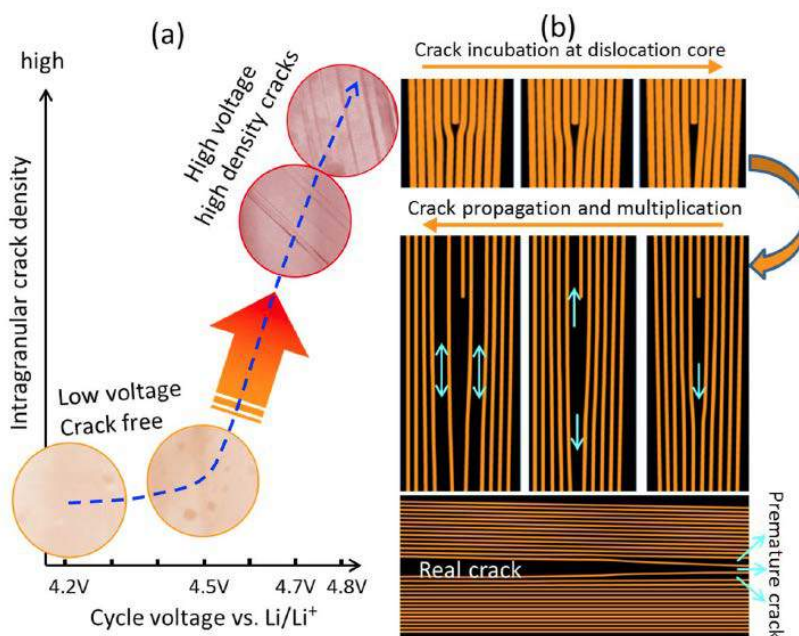


Figure II-322. Cycle voltage governed intragranular cracking and underlying dislocation-based mechanism. (a) HAADF images overlaid diagram shows the apparent dependence of intragranular cracking on the cycle voltage; when cycled below 4.5 V, intragranular crack can be hardly generated, while above 4.7 V, intragranular density shows a drastic increase; and (b) schematic diagrams to illustrate the dislocation-assisted crack incubation, propagation and multiplication process.

3. In-situ environmental TEM revealing the reaction mechanism of Li-O₂ batteries

One of the key questions for Li-O₂ battery system is why the reaction product shows very unique morphological features, ranging from hollow spheres to toroidal structure. This question is addressed by using

an aberration-corrected in-situ *environmental* TEM under oxygen environment. A solid-state nano-battery was constructed through a two-probe configuration (Figure II-323). The CNTs/RuO₂ cathode was loaded on a Pt probe, and brought to a Li₂O covered Li metal anode anchored on the other tungsten probe through precise nano-manipulation inside the ETEM. The electrochemical reaction is driven by external biasing, i.e., a negative bias applied on the Pt end to drive the Li⁺ to cross the Li₂O layer to react with oxygen, which corresponds to the oxygen reduction reaction (ORR) during the discharging of the Li-O₂ battery; a positive bias drives the Li⁺ ions back to the Li₂O/Li end, leading to the decomposition of the discharged product, which is oxygen evolution reaction (OER) during the charging of the battery.

It has been observed that the oxygen reduction reaction on CNTs initially produces LiO₂, which subsequently evolves to Li₂O₂ and O₂ through disproportionation reaction. It is interesting to note that it is just the releasing of O₂ that inflates the particles to a hollow structure with a Li₂O outer surface layer and Li₂O₂ inner-shell, demonstrating that, in general, accommodation of the released O₂ coupled with the Li⁺ ion diffusion and electron transport paths across both spatial and temporal scales critically governs the morphology of the discharging/charging product in Li-O₂ system. This in-situ observation provides insight for understanding as how the toroidal structure forms in Li-O₂ system. It would be expected that the determination of Li-O₂ reaction mechanisms sets foundation for quantitative understanding/modeling of the electrochemical processes in the Li-O₂ system, enabling rational design of both solid-state and aprotic Li-O₂ batteries.

Conclusions

Over the last year, we have made significant progresses on understanding the fading mechanism of layer structured cathode and revealed the reaction mechanism of Li-O₂ battery system. For the cathode materials, we concluded that liquid electrolyte penetrates into the boundaries of the secondary particle, where the detrimental solid-liquid reaction will happen. Therefore, new strategy has to be developed to mitigate the detrimental solid-electrolyte reaction for enhancing the performance of the cathode. At the same time, we discovered that a critical barrier for the high voltage operation of layer structured cathode is the formation of intragranular cracks. Qualitatively, the higher of the operating voltage, the higher of the density of the intragranular cracking. To mitigate this intragranular cracking, lattice doping is needed to strengthen the lattice. Using EELS mapping, we reveal that Ni has a high migrating propensity for mixing with Li layer, which in turn will lead to voltage fading. This observation provide insight to the fading mechanism of Ni rich NMC. In addition, we have developed the in-situ environmental TEM, which enables in-situ TEM study of Li-O₂ battery. We revealed the reaction mechanism of Li-O₂ battery and concluded that the accommodation of the released O₂ contributes to the formation of the peculiar morphological feature of the reaction products.

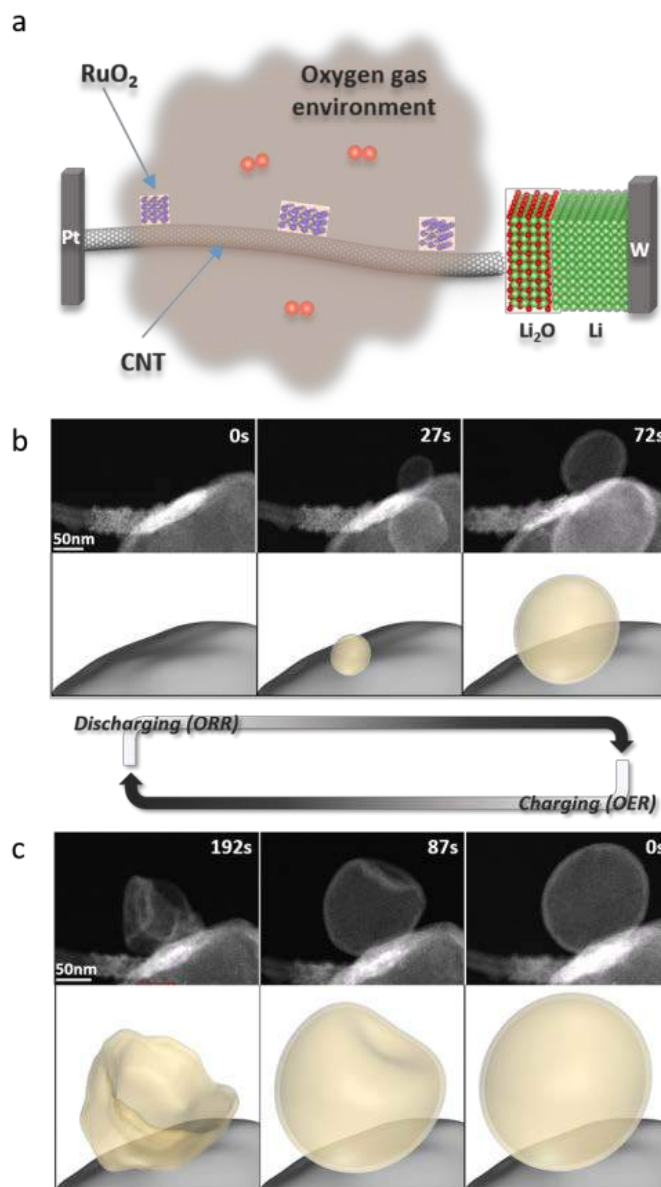


Figure II-323. Experimental set up of the Li-O₂ nano-battery and the in situ STEM observation of morphological evolution of the reaction products upon discharge-charge cycling of the Li-O₂ battery. a, Schematic drawing to illustrate the configuration of the Li-O₂ nano-battery in ETEM chamber. b, The time-resolved HAADF-STEM images depict the morphological evolution of the discharging product (oxygen reduction reaction (ORR)), which is featured by the formation of hollow structure (illustrated by the bottom panel in b. c. The images illustrates the morphological evolution upon charging (oxygen evolution reaction (OER)), which is featured by the collapsing of the hollow structure as illustrated by the bottom panel in c.

Key Publications

1. Pengfei Yan, Jianming Zheng, Meng Gu, Jie Xiao, Ji-Guang Zhang, Chongmin Wang, “Intragranular cracking as a critical barrier for high-voltage usage of layer-structured cathode for lithium-ion batteries”, **Nat. Commun.** **8**, 14101 (2017).
2. Langli Luo, Bin Liu, Shidong Song, Wu Xu, Ji-Guang Zhang and Chongmin Wang, “Revealing the reaction mechanisms of Li–O₂ batteries using environmental transmission electron microscopy”, **Nature Nanotechnology**, **12**, 535–539 (2017).
3. Pengfei Yan, Jianming Zheng, Ji-Guang Zhang, and Chong-Min Wang, “Atomic Resolution Structural and Chemical Imaging Revealing the Sequential Migration of Ni, Co, and Mn upon the Battery Cycling of Layered Cathode”, *Nano Lett.*, **17**, 3946–3951 (2017).
4. Xiaotang Lu, Yang He, Scott X. Mao, Chong-min Wang, and Brian A. Korgel, “Size Dependent Pore Formation in Germanium Nanowires Undergoing Reversible Delithiation Observed by In Situ TEM”, **J. Phys. Chem. C** **2016**, **120**, 28825–28831.
5. Pengfei Yan, Jianming Zheng, Xiaofeng Zhang, Rui Xu, Khalil Amine, Jie Xiao, Ji-Guang Zhang, and Chongmin Wang, “Atomic to Nanoscale Investigation of Functionalities of an Al₂O₃ Coating Layer on a Cathode for Enhanced Battery Performance”, **Chem. Mater.**, **28**, 857–863 (2016).
6. Yang He, Meng Gu, Haiyan Xiao, Langli Luo, Yuyan Shao, Fei Gao, Yingge Du, Scott X. Mao, and Chongmin Wang, “Atomistic Conversion Reaction Mechanism of WO₃ in Secondary Ion Batteries of Li, Na, and Ca”, **Angew. Chem. Int. Ed.** **55**, 6244–6247 (2016).
7. Pengfei Yan, Jianming Zheng, Jiabin Zheng, Zhiguo Wang, Gaofeng Teng, Saravanan Kuppan, Jie Xiao, Guoying Chen, Feng Pan, Ji-Guang Zhang, and Chong-Min Wang, “Ni and Co Segregations on Selective Surface Facets and Rational Design of Layered Lithium Transition-Metal Oxide Cathodes”, **Adv. Energy Mater.** **6**, 1502455 (2016).
8. Zhaofeng Gan, Meng Gu, Jianshi Tang, Chiu-Yen Wang, Yang He, Kang L. Wang, Chongmin Wang, David J. Smith, and Martha R. McCartney, “Direct Mapping of Charge Distribution during Lithiation of Ge Nanowires Using Off-Axis Electron Holography”, **Nano Lett.** **16**, 3748–3753 (2016).
9. Jiangwei Wang, Hao Luo, Yang Liu, Yang He, Feifei Fan, Ze Zhang, Scott X. Mao, Chongmin Wang, and Ting Zhu, “Tuning the Outward to Inward Swelling in Lithiated Silicon Nanotubes via Surface Oxide Coating”, **Nano Lett.** **2016**, **16**, 5815–5822 (2016).
10. Chenfei Shen, Mingyuan Ge, Langli Luo, Xin Fang, Yihang Liu, Anyi Zhang, Jiepeng Rong, Chongmin Wang and Chongwu Zhou, “*In Situ* and *Ex Situ* TEM Study of Lithiation Behaviors of Porous Silicon Nanostructures”, **Sci. Rep.** **6**, 31334 (2016).
11. Eungje Lee, Joel Blauwkamp, Fernando C. Castro, Jinsong Wu, Vinayak P. Dravid, Pengfei Yan, Chongmin Wang, Soo Kim, Christopher Wolverton, Roy Benedek, Fulya Dogan, Joong Sun Park, Jason R. Croy, and Michael M. Thackeray, “Exploring Lithium-Cobalt-Nickel Oxide Spinel Electrodes for ≥ 3.5 V Li-Ion Cells”, **ACS Appl. Mater. Interfaces**, **8**, 27720–27729 (2016).

II.D.6 Characterization Studies of High Capacity Composite Electrode Structures (ANL)

Michael M. Thackeray, Principal Investigator

Argonne National Laboratory
9700 South Cass Avenue
Lemont, IL 60439
Phone: 630-252-9184
E-mail: thackeray@anl.gov

Eungje Lee, Principal Investigator

Argonne National Laboratory
9700 South Cass Avenue
Lemont, IL 60439
Phone: 630-252-9184
E-mail: eungje.lee@anl.gov

Peter Faguy, Technology Manager

U.S. Department of Energy
Phone: 202-586-1022
E-mail: Peter.Faguy@ee.doe.gov

Start Date: October 1, 2015

End Date: September 30, 2018

Total Project Cost: \$500,000

DOE share: \$500,000

Non-DOE share: \$0

Introduction

Previous studies on the integration of a spinel component into lithium- and manganese-rich oxides to produce $y[x\text{Li}_2\text{MnO}_3 \cdot (1-x)\text{LiMO}_2] \cdot (1-y)\text{LiM}_2\text{O}_4$ ($M=\text{Mn}, \text{Ni}, \text{Co}$), layered-layered-spinel (LLS), composite structures have proven promising. Specifically, high first-cycle efficiency, good rate capability, and stable capacity at practical voltages (e.g., ~ 210 mAh/g at ~ 4.4 V vs. graphite) can be achieved with these electrode materials. However, critical issues such as voltage fade, poor rate performance, and surface stability have yet to be adequately addressed. With respect to voltage fade, complementary works have shown that Co-based spinels may be interesting options for integrated, stabilizing components in LLS materials, but that their synthesis and properties are not straightforward, especially when integrating into LL compositions. Surfaces of LLS cathode particles are also prone to instabilities, similar to other lithiated oxide materials, including oxygen evolution and transition metal dissolution. Many strategies have been proposed for the protection of particle surfaces but no consensus yet exists as to the efficacy of any given strategy. The difficulty, in part, in identifying specific trends in the literature is the strong dependence of surface modifications on the properties of the underlying cathode particles. For example, composition, morphology, porosity, and the conditions of synthesis under which surface modifications are carried out can all play a role. This chapter deals with efforts in this project to further understand the properties of LLS materials. Specifically, studies of structure, synthesis, and electrochemical properties of end-member and integrated components as well as the stabilization of surfaces are presented.

Objectives

The primary objective of this project is to explore the fundamental processes that are most relevant to the challenges of next-generation, energy-storage technologies, in particular, high capacity structurally-integrated electrode materials. The goals of this project are to capitalize on a broad range of facilities and collaborations in order to characterize and model structurally-integrated electrode systems, notably those with both layered

and spinel character, and to develop low-cost, high-energy and high-power Mn-oxide-based cathodes for lithium-ion batteries that will meet the performance requirements of PHEV and EV vehicles.

Approach

A wide array of characterization techniques including X-ray and neutron diffraction (XRD, ND) X-ray absorption (XAS), high resolution transmission electron microscopy (HRTEM), and theory will be brought together to focus on challenging experimental problems. Structural, electrochemical, and chemical mechanisms at play in novel, complex electrode/electrolyte systems will be explored in the pursuit of advancing the properties of state-of-the-art cathode materials.

Results

Understanding Synthesis and Structure of Mn- and Ni-doped, LiCoO₂-based Spinel via DFT Calculations

Lithiated-spinel, LiCoO₂ materials are of interest as potential stabilizing agents to be incorporated in layered-layered-spinel (LLS) composite cathodes [1]. Previous experimental works have shown that Ni substitution effectively stabilizes the lithiated spinel structure, enhancing electrochemistry. However, Mn substitution results in impurity phases such as Li₂MnO₃, Li₄Mn₅O₁₂, and Co₃O₄. In order to obtain a better understanding of the different effects of Mn and Ni substitution on phase stability, an atomistic simulation of substituted, LiCoO₂-based, lithiated-spinels was conducted.

The substitution of Mn or Ni on the Co site of both spinel (Fd-3m) and layered (R-3m) LiCoO₂ structures was examined via density functional theory (DFT) calculations. Possible, symmetrically-distinct mixing configurations for Li₁₆Co_{16-x}M_xO₃₂ (up to 64 total atoms; M = Mn or Ni; 0 ≤ x ≤ 16) were generated using the Enum package [2]. Figure II-324a displays the calculated ground state DFT formation energy (ΔH_f) of LiCo_xM_{1-x}O₂ (M = Mn or Ni; and 0 ≤ x ≤ 1) sampled uniformly through the composition space. Here, the DFT formation energy of a generic LiMO₂ compound is defined as $\Delta H_f(\text{LiCo}_x\text{M}_{1-x}\text{O}_2) = E_0(\text{LiCo}_x\text{M}_{1-x}\text{O}_2) - \mu_{\text{Li}} - x\mu_{\text{Co}} - (1-x)\mu_{\text{M}} - 2\mu_{\text{O}}$, where $E_0(\text{LiCo}_x\text{M}_{1-x}\text{O}_2)$ is the calculated DFT total energy of LiCo_xM_{1-x}O₂ and μ_i ($i = \text{Li}, \text{Co}, \text{M}, \text{O}$) is the chemical potential of component i . Note that the energy difference between Fd-3m and R-3m structures at each composition is almost negligible, as previously reported [3]. Furthermore, the calculated ΔH_f of LiCo_xM_{1-x}O₂ varies almost linearly between the end-members, LiCoO₂ and LiMO₂ (M = Mn/Ni), in Figure II-324a.

The mixing tendency of two cathode components, LiCoO₂ and LiMO₂ (M = Mn or Ni), can be obtained using: $\Delta E_{\text{mix}} = E_0(\text{LiCo}_x\text{M}_{1-x}\text{O}_2) - \{xE_0(\text{LiCoO}_2) + (1-x)E_0(\text{LiMO}_2)\}$, where $E_0(\text{LiCo}_x\text{M}_{1-x}\text{O}_2)$, $E_0(\text{LiCoO}_2)$, and $E_0(\text{LiMO}_2)$ are the calculated DFT total energies of either Fd-3m or R-3m LiCo_xM_{1-x}O₂, LiCoO₂, and LiMO₂ (M = Mn or Ni), respectively. A significantly negative ΔE_{mix} (i.e., < -25 meV/site) usually leads to the formation of an ordered compound while a significantly positive ΔE_{mix} (i.e., > 25 meV/site) usually results in a two-phase miscibility gap. In contrast, a slightly negative or positive ΔE_{mix} (i.e., -25 to 25 meV/site) indicates a weak preference for ordering or phase separation, respectively, which could be overcome by configurational entropy at elevated temperatures to form a solid-solution. From Figure II-324b, it can be observed that Mn substitution in either Fd-3m or R-3m LiCo_xMn_{1-x}O₂ is only favorable at dilute concentrations of Mn ($x > 0.9$). In fact, the mixing of Mn and Co on the Co sublattice in the LCO structure becomes increasingly unfavorable toward equiatomic compositions of Mn and Co. On the other hand, as seen in Figure II-324c, the mixing of Ni and Co on the Co sublattice is generally favorable at all compositions. The energy of mixing becomes increasingly negative (up to ~ -100 meV/site) towards equiatomic compositions of Ni and Co, hence compositions close to LiCo_{0.5}Ni_{0.5}O₂ are likely to form ordered compounds. These simulation data are in line with previous experimental results and corroborate the effectiveness of Ni substitution in stabilizing the lithiated spinel structure and improving its electrochemistry.

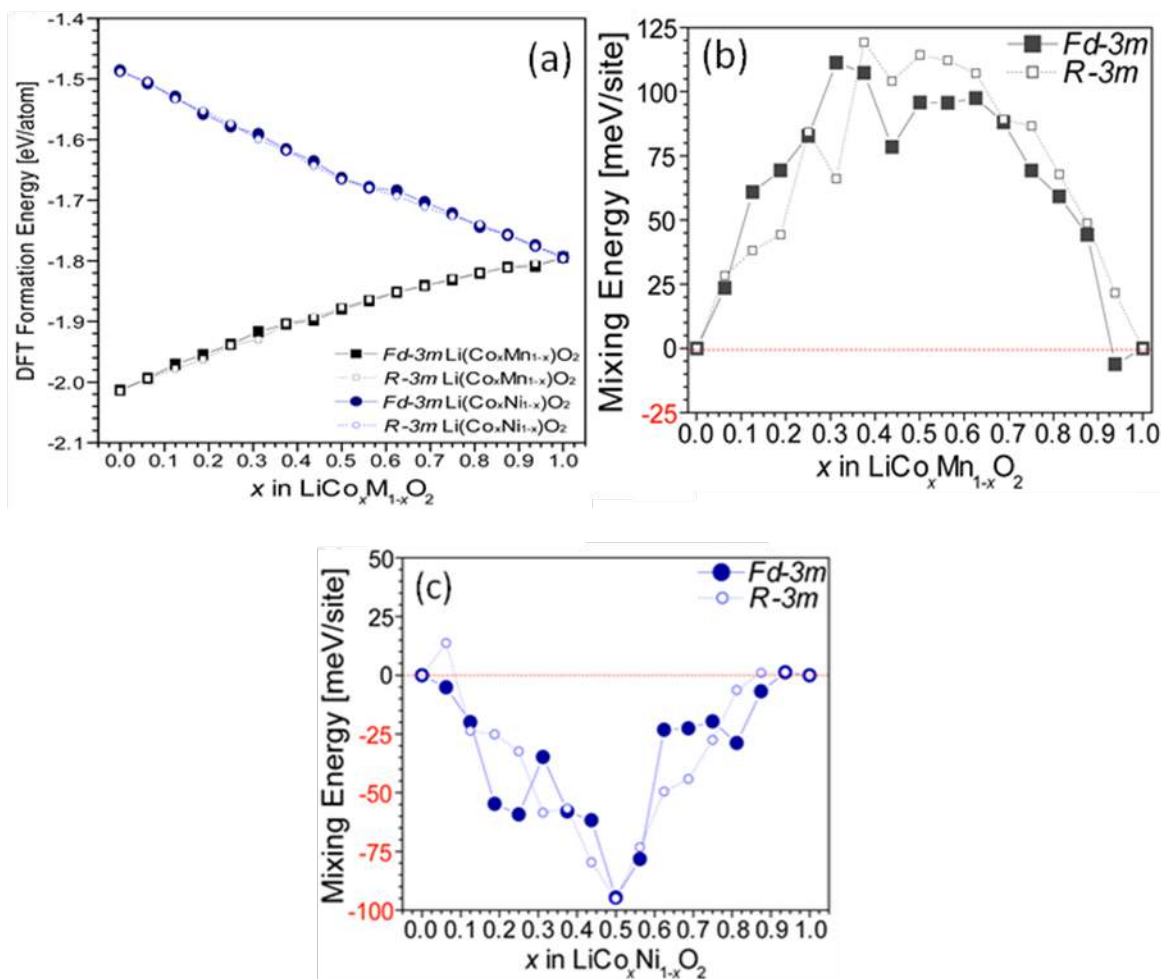


Figure II-324. (a) Calculated DFT formation energies of $\text{LiCo}_x\text{M}_{1-x}\text{O}_2$ (M = Mn or Ni; $0 \leq x \leq 1$) in both lithiated spinel (Fd-3m) and layered (R-3m) structures. The mixing energies of (b) $\text{LiCo}_x\text{Mn}_{1-x}\text{O}_2$ and (c) $\text{LiCo}_x\text{Ni}_{1-x}\text{O}_2$. Calculations by S. Kim and C. Wolverton (Northwestern University, IL).

Synthesis of Complex, Layered-Layered-Spinel Compositions

The structural integration of a spinel (S) component into a layered (L) electrode structure or a two-component LL system has been demonstrated in model compounds such as $x\text{Li}_2\text{MnO}_3 \cdot \text{Li}_{1-x}\text{M}_2\text{O}_4$ ('layered-spinel' (LS)) and $x[\text{Li}_2\text{MnO}_3 \cdot \text{LiMO}_2] \cdot (1-x)\text{LiM}_2\text{O}_4$ (LLS), where M is typically a transition metal ion, and that these materials have advantages over conventional, layered electrode materials [3]. They can be simply prepared by reducing the amount of lithium in the precursor materials normally used to synthesize stoichiometric L or LL structures. For example, reducing the lithium content of a stoichiometric $0.5\text{Li}_2\text{MnO}_3 \cdot 0.5\text{LiMn}_{0.5}\text{Ni}_{0.5}\text{O}_2$ compound (alternatively, $\text{Li}_{1.5}\text{Mn}_{0.75}\text{Ni}_{0.25}\text{O}_{2.5}$), in which the Mn:Ni ratio is 3:1, drives the composition towards the $\text{LiMn}_{1.5}\text{Ni}_{0.5}\text{O}_4$ spinel apex of the phase diagram, following the L-L-S tie-line in Figure II-325, while maintaining a constant Mn:Ni (3:1) ratio [4]. Note that this is a special case that has been observed experimentally and that the term 'layered-layered-spinel' is used for convenience because it describes the compositions of all compounds within this phase space.

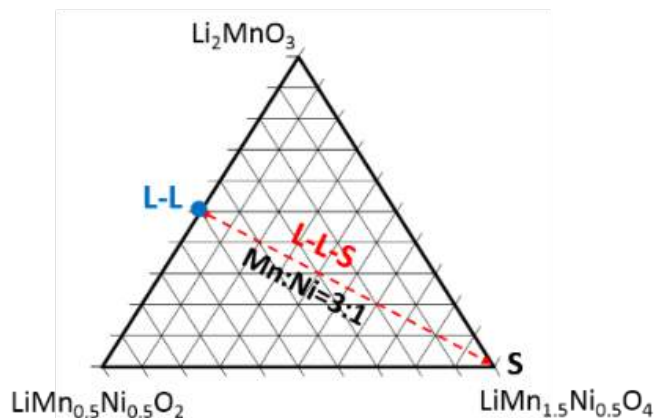


Figure II-325. The compositional phase space of a layered(L)-layered(L)-spinel(S) system.

A question that remains unanswered is: At what lithium deficiency do the transition metal ions start diffusing into the lithium-rich layers during synthesis to provide spinel (or spinel-like) character to predominantly layered structures with complex cation arrangements?

In an attempt to better understand the structural complexity of LLS materials, a series of compounds was prepared by reducing the lithium content in $0.25\text{Li}_2\text{MnO}_3 \cdot 0.75\text{Li}(\text{Ni}_{0.375}\text{Mn}_{0.375}\text{Co}_{0.25})\text{O}_2$ by various amounts and analyzed by combined Rietveld refinement analyses of ND and synchrotron XRD data, Figure II-326. For simplicity, the normalized composition and formula, $\text{Li}_{1.25-x}(\text{Ni}_{0.28}\text{Mn}_{0.53}\text{Co}_{0.19})\text{O}_{2.25-\delta}$ ($0 \leq x \leq 0.25$), is used for discussion. For $0 \leq x \leq 0.075$, both ND and XRD patterns could be indexed to compounds with either monoclinic symmetry (C2/m), denoted M-phase or, if the weak ordering peaks associated with the M-phase were ignored, to trigonal symmetry (R-3m), denoted L-phase. For $x = 0.1$, the XRD pattern showed additional peaks that were tentatively assigned to a spinel component with cubic symmetry, denoted S-phase. These initial refinements and attempts to use a two-phase model to refine both layered and spinel components have not provided conclusive results. The analyses are continuing and HRTEM studies are planned to gather more insight into the structural compositions of these complex electrode materials.

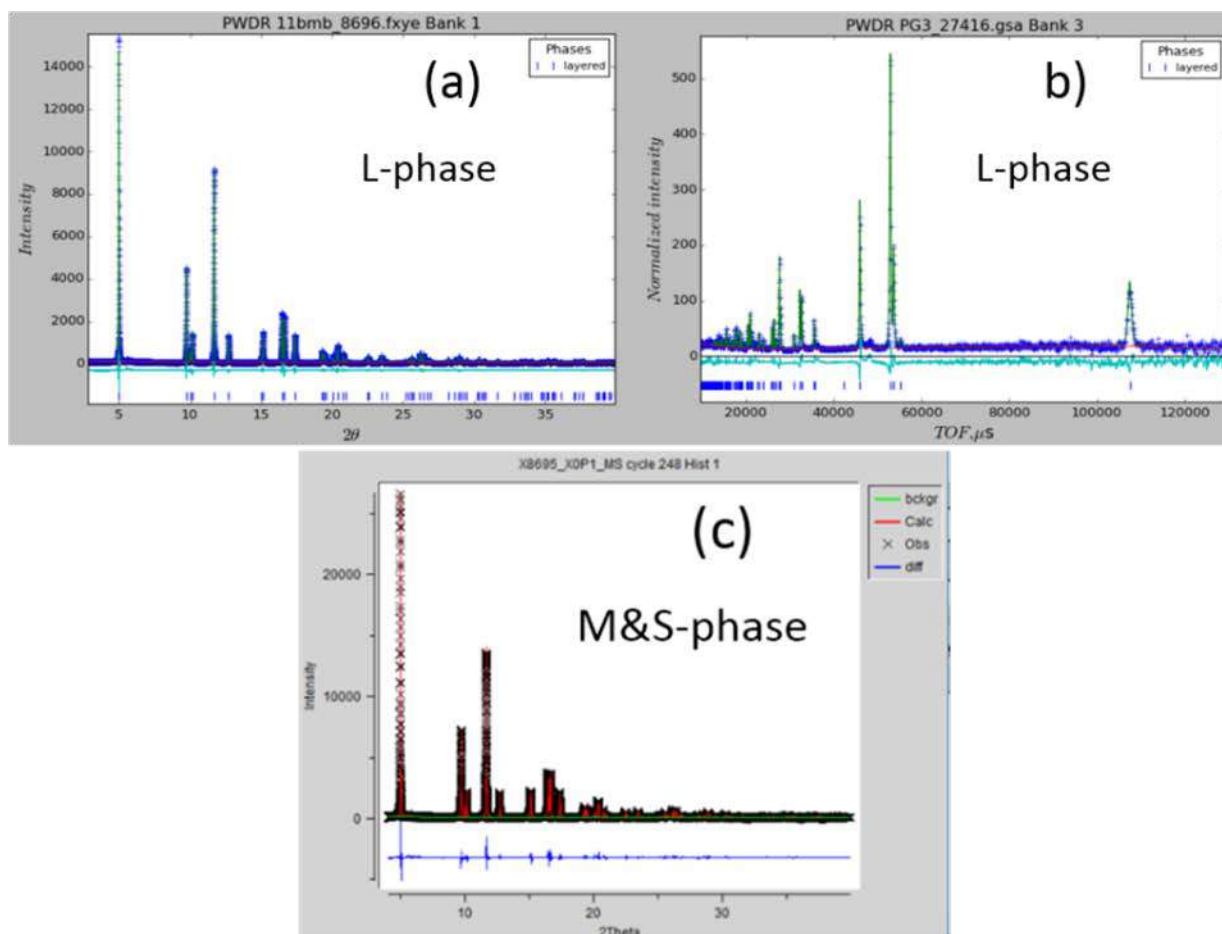


Figure II-326. Rietveld refinement results of (a) synchrotron X-ray and (b) neutron diffraction of the $x = 0.75$ sample. (c) Synchrotron X-ray diffraction of the $x = 1.0$ sample. ND by A. Huq (SNS, ORNL), XRD by Y. Ren (APS, ANL)

Surface-Treated Layered-Layered-Spinel Cathode Particles

Complementary studies (see II.3.A.x) have found that treatment of LLS particles in an aqueous solution of aluminum nitrate, followed by annealing between 110-750°C, led to a decrease in performance with increasing temperature. Figure II-327a shows ^{27}Al nuclear magnetic resonance (NMR) spectroscopy of LLS particles after Al treatment followed by annealing at 550°C (blue) and 110°C (red) along with an $\text{Al}_2\text{O}_3/\text{Al}(\text{OH})$ reference (green). At the lowest temperature (110°C), the aluminum coordination is clearly different than that of $\text{Al}_2\text{O}_3/\text{Al}(\text{OH})$, instead resembling a distorted 4-fold coordination environment. By 550°C (blue) the diamagnetic peak near ~0 ppm completely disappears. This could be due to the presence of lattice aluminum and/or three-coordinate surface/interface aluminum. Figure II-327b shows X-ray photoelectron spectroscopy (XPS) of the un-treated LLS (black) and the Al-treated LLS powders after annealing at 110°C (red), 400°C (blue), and 550°C (green). A small surface impurity (e.g., carbonate) can be seen in the un-treated sample. After Al treatment and annealing at 110°C, a large peak forms at ~532 eV, in agreement with Al-O bonding. Upon annealing to higher temperature, this feature decreases and virtually disappears by ~550°C, consistent with the NMR data. Figure II-327c shows the Al content (atomic %) derived from the XPS data as a function of temperature. As shown, increasing annealing temperatures led to less detectable surface Al. These data sets suggest that small amounts of Al might be doped into the bulk of LLS particles after surface treatments and high temperature annealing. This is an important finding considering the observed decrease in electrochemical performance with higher annealing temperatures; an observation that is not consistent with similar studies

reported for Mn-rich, layered materials. These results reiterate the important role of cathode composition with respect to surface modifications.

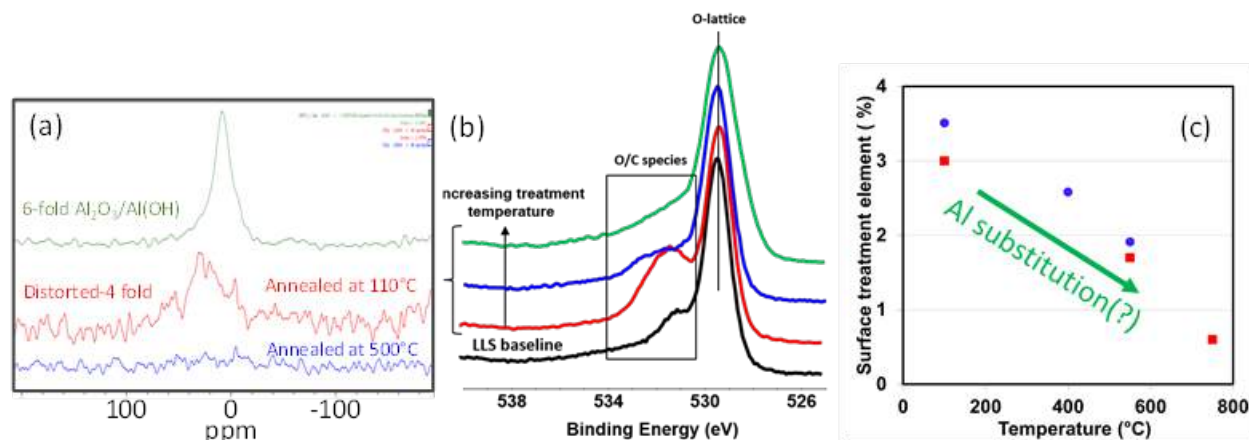


Figure II-327. a) ^{27}Al MAS-NMR of Al-treated samples annealed at 110°C (red) and 550°C (blue) and an $\text{Al}_2\text{O}_3/\text{Al}(\text{OH})$ reference (green). b) XPS spectra of LLS followed by Al treatment and annealing at 110°C (red), 400°C (blue), and 550°C (green). c) Al content (at. %) as a function of annealing temperature, determined by XPS. Red squares represent samples that had previously (before Al treatments) been exposed to air, blue circles are samples not exposed to air (similar results were obtained with both sample sets). XPS by R. Ruther and H. Meyer (ORNL).

Figure II-328a shows a scanning electron microscopy (SEM) image of an Al-treated, LLS particle after undergoing a focused ion beam (FIB) lift-out procedure to allow for elemental mapping studies. Figure II-328b shows a HRTEM image of particles including two regions included for Fast Fourier Transform (FFT) analysis. This figure, and similar images, suggest that the Al-treated, LLS particles may have preferentially formed spinel domains at the surface of particles, possibly due to lithium leaching in an acidic environment. Figure II-328c shows energy-dispersive X-ray spectroscopy (STEM-EDX) of an Al-treated, LLS particle. It was found that a thin (~ 2 nm) Al layer covered the particles in a uniform manner, verifying the efficacy of the treatment conditions. However, some images showed indications of increased concentrations of both Al and Ni on the same surfaces, e.g., top left and bottom right in Figure II-328c. Whether or not this “segregation” is a consequence of the surface treatment itself, or other mechanisms related to the pristine particles is unclear. Additional imaging is underway for both treated and untreated particles to obtain better statistics on the relative formation of surface spinel and any possible tendencies of segregation (e.g., preferential location of Ni/Al) between treated and untreated particles. This information is expected to provide further insight into the structure-property relationships of LLS materials and the dependence of their electrochemical properties on processing conditions.

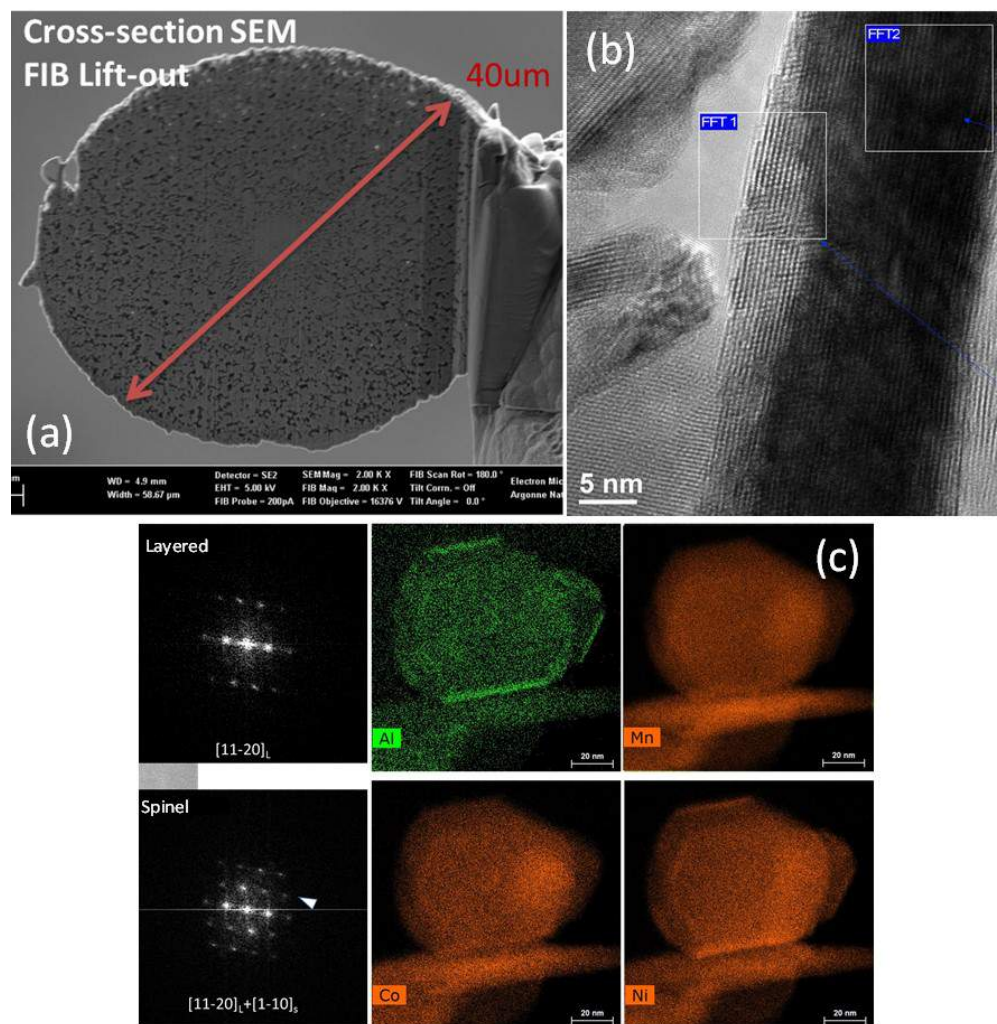


Figure II-328. (a) Cross-sectional SEM image of Al-treated, LLS particle. (b) TEM image and FFT of surface and bulk regions showing spinel integration at the surface of the particle. (c) STEM-EDX analysis of Al-treated LLS particle showing distribution of Al (top left), Mn (top right), Co (bottom left), and Ni (bottom right). HRTEM by J. Wang (ANL).

Conclusions

- Density functional theory calculations have been used to understand and verify experimental findings showing the effects of Mn and Ni substitution in stabilizing Co-rich spinel structures for integration into complex LLS cathodes
- Synchrotron X-ray and neutron diffraction studies, on a series of $\text{Li}_{1.25-x}(\text{Ni}_{0.28}\text{Mn}_{0.53}\text{Co}_{0.19})\text{O}_{2.25-\delta}$ ($0 \leq x \leq 0.25$) LLS compositions, are being used to understand the relationships between synthesis and the final structure/electrochemical properties that result as a function of initial lithium content and transition metal composition
- Surface treatment of Mn-rich, LLS particles has shown promise for enhancing electrochemical performance, however, the studies herein show that a complex relationship exists between the cathode particles and processing conditions; importantly, Li- and Mn-rich particles behave differently than their layered counterparts under the similar surface-treatment conditions studied here

Key Publications

1. Roy Benedek, *Role of Disproportionation in the Dissolution of Mn from Lithium Manganate Spinel*, J. Phys. Chem. C, DOI 10.1021/acs.jpcc.7b05940 (2017).
2. R. Benedek and H. Iddir, *Simulation of First-Charge Oxygen-Dimerization and Mn-Migration in Li-Rich Layered Oxides $x\text{Li}_2\text{MnO}_3 \cdot (1-x)\text{LiMO}_2$ and Implications for Voltage Fade*, J. Phys. Chem. C, 121, 6492 (2017).
3. J.R. Croy and M.M. Thackeray, *Characterization and Modeling of High-Capacity Composite Electrode Structures*, ES235, DOE Vehicle Technologies Program Annual Merit Review (Arlington, VA), 5-9, June (2017).

References

1. E. Lee, J. Blauwkamp, F. C. Castro, J. Wu, V. P. Dravid, P. Yan, C. Wang, S. Kim, C. Wolverton, R. Benedek, F. Dogan, J. S. Park, J. R. Croy, and M. M. Thackeray, Exploring lithium-cobalt-nickel oxide spinel electrodes for ≥ 3.5 V Li-ion cells. *ACS Appl. Mater. Interfaces*, **8**, 27720 (2016).
2. G. L. W. Hart and R. W. Forcade, Algorithm for generating derivative structures, *Phys. Rev. B*, **77**, 224115 (2008).
3. C. Wolverton and A. Zunger, Cation and vacancy ordering in Li_xCoO_2 , *Phys. Rev. B*, **57**(4), 2242 (1998).
4. B. R. Long, J. R. Croy, J. S. Park, J. Wen, D. J. Miller, and M. M. Thackeray, *J. Electrochem. Soc.*, **161** (14) A2160 (2014).

II.D.7 *In Operando* Thermal Diagnostics of Electrochemical Cells (LBNL)

Ravi Prasher, Principal Investigator

Lawrence Berkeley National Laboratory
1 Cyclotron Road
Berkeley, CA 94720
Phone: 510-486-7291
E-mail: RSPrasher@lbl.gov

Tien Duong, Technology Manager

U.S. Department of Energy
Phone: 202-586-7836
E-mail: Tien.Duong@ee.doe.gov

Start Date: October 1, 2015
Total Project Cost: \$120,000

End Date: September 30, 2019
DOE share: \$120,000

Non-DOE share: \$0

Project Introduction

Effective heat dissipation in batteries is important for many reasons, such as performance, reliability, and safety. Currently, the thermal management of battery cells is provided at the system level by either forced air or liquid cooling. This engineering solution has many shortcomings, such as a reduction in the energy density at the system level and complex system designs to allow for fluid flow. In spite of such high importance, so far no thermal transport measurements or diagnostics have been performed inside electrochemical batteries under operating conditions. An understanding of thermal transport through various interfaces within the electrochemical cell is of particular importance as interfacial thermal transport typically plays the dominant role (up to 90% of the overall thermal resistance according to our preliminary measurements) in determining the internal temperature rise and temperature gradients within various devices. Currently, no thermal model exists that can predict the spatially resolved internal temperature rise within an operating battery, accurate to the true heterogeneous multilayered internal structure of the battery.

Objectives

We will measure the dominant thermal resistances within the multilayered stack comprising the full battery cell. These measurements will be performed *in-operando* on a fully assembled and functioning battery. This will identify the layer(s) and layer interface(s) that dominate the total thermal resistance to heat flow within an operating battery, even if they are buried deep within the bulk of the battery cell, and quantify their contributions. From these measurements we will build a spatially resolved theoretical thermal model of the internal heat transfer within a battery. This model can then be used to accurately predict the internal temperature rise and temperature profile of a battery under various operating conditions, such as fast charging. This model can also be used to guide the thermal optimization of battery design and battery control software to improve performance, reliability, and safety. Such a model does not currently exist.

Approach

The thermal measurements will be achieved using a customized derivative of the 3-omega technique. This technique uses microfabricated sensors placed on the outer surfaces of the electrochemical cell stack (see Figure II-329) to launch thermal waves at multiple frequencies into the battery and interrogate the thermal transport properties at various depths within the bulk of the cell. Our technique simultaneously measures thermal transport properties as a function of depth into the cell as well as temperature. Because the measurement is performed in the frequency domain and not the time domain, it is very robust against ambient noise. Our design enables *in-operando* measurement during battery operation because our sensors and measurements are immune to both electrical interference from the battery and thermal interference from any heat generated by the battery's own operation.

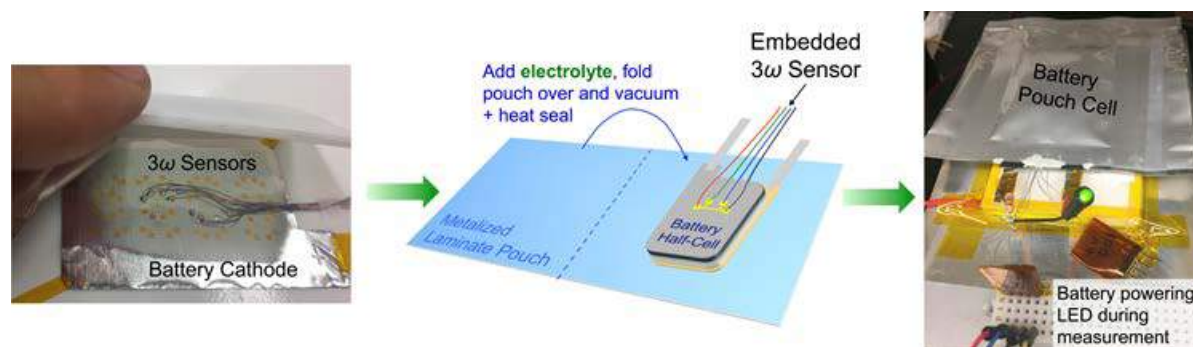


Figure II-329. Design of 3-omega thermal sensors and how they are incorporated into an electrochemical battery pouch cell for *in-operando* measurements.

We are working with the Battaglia group at LBNL in order to make lithium-ion electrochemical pouch cells inside of which we embed our sensors, and to perform electrical measurements on the batteries in addition to our thermal measurements. Because our sensors probe the interior of the battery from the surface of the multilayer stack, the sensors are non-invasive and do not disturb the local environment of the electrochemical multilayer stack. Sending in thermal waves at many different frequencies allows us to separate out the thermal transport properties at different locations throughout the depth profile of the cell.

Prior to performing any measurements, we fully simulate each experiment and numerically optimize the thermal design of the housing of our battery samples so as to maximize sensitivity to the properties of interest and minimize sensitivity to the outside environment and noise. All sensors are designed and fabricated in-house.

Results

We have designed and constructed the metrology hardware for performing these measurements. We have verified and implemented an analytical solution to the measurement technique physics for our particular geometry. We used this solution to optimize the thermal design of the housing for our battery samples, constructing and testing this housing to confirm that it performs as designed. Based on these tests, we constructed a functioning cathode half-cell with 3-omega sensors and performed *in-situ* measurements on the cell. We found that the thermal transport through the half-cell was dominated by the thermal boundary conductance (TBC) across the cathode-separator interface. Representative fitted raw data is shown in Figure II-330.

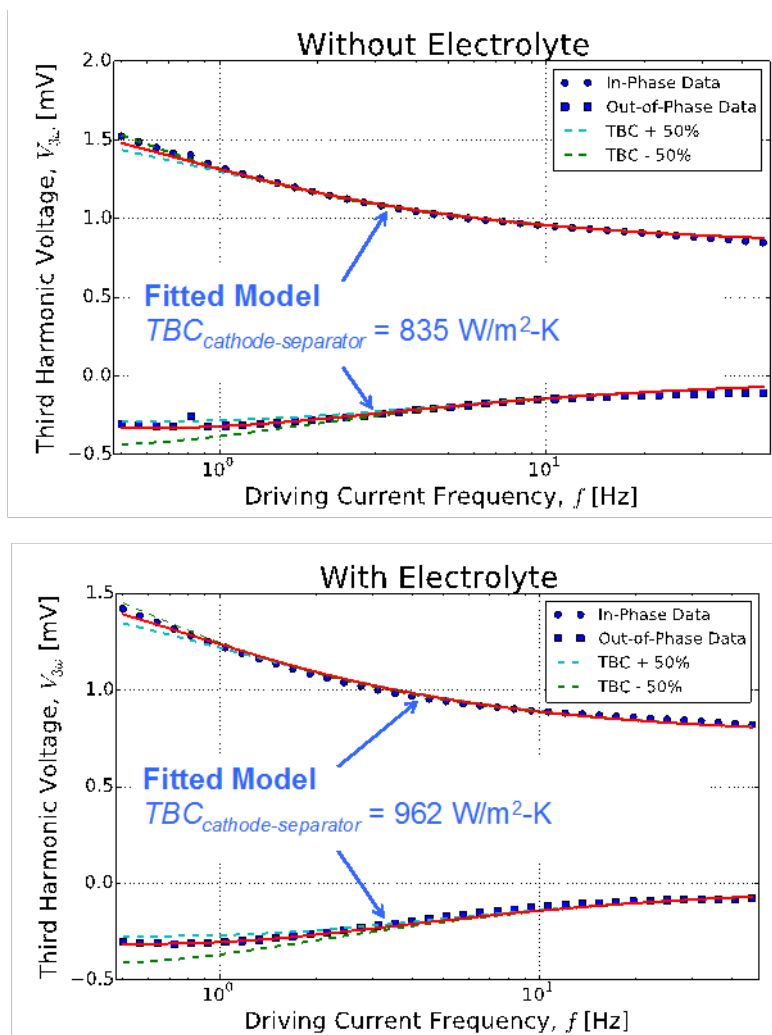


Figure II-330. Representative raw data from a measurement on a li-ion cathode half-cell. Left plot is without the presence of electrolyte; right plot is with electrolyte. Red lines show the best fit to the data. The primary property measured is the thermal boundary conductance (TBC) of the interface between the cathode and the separator. Dashed lines demonstrate fit sensitivity by showing best fit lines where the TBC value has been artificially forced to be +/- 50% as compared to the true best fit value.

Our measurements found the cathode-separator TBC value to be $835 \text{ W/m}^2\text{-K}$ without electrolyte present inside the electrochemical cell, and $962 \text{ W/m}^2\text{-K}$ with electrolyte present. We discovered that this interface dominates the thermal transport within the cell, accounting for over 90% of the total thermal resistance. The multilayer stack of our cathode half cell along with the break down of the relative thermal resistances of each layer and interface are shown in Figure II-331.

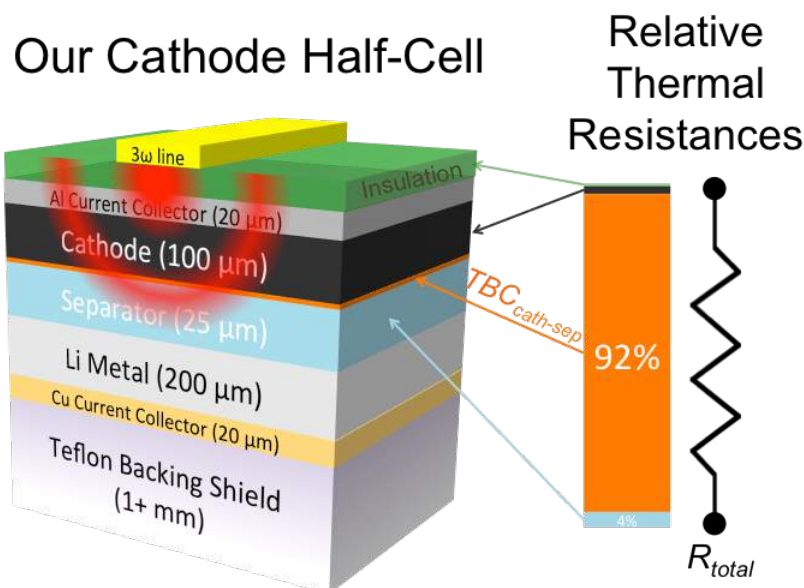


Figure II-331. Left, multilayer stack for the measured cathode half-cell, showing a 3-omega sensor launching a thermal wave. Right, a to-scale breakdown of the relative contributions of each layer and interface to the total thermal resistance. Thermal resistance contributions from the Li and Cu are negligible. Thermal waves did not probe deep enough to be affected by the Teflon, which was only included for mechanical support and is not present in the real battery.

Finally, we have made significant progress toward being able to fabricate and measure the thermal transport within a full li-ion battery pouch cell. We also recently modified our hardware to extend the low-frequency end of our measurement range from 0.5 Hz down to 0.01 Hz, which will increase the sensitivity of our measurements considerably.

Conclusions

We have designed, characterized, and implemented a technique capable of measuring spatially resolved thermal transport properties within the bulk of an electrochemical cell *in-operando*. We have demonstrated this technique on a functioning cathode half-cell, showing that the total thermal resistance is dominated by the interface between the cathode and separator. We are preparing to measure full battery cells and will measure them under a variety of operating conditions, such as varying levels of externally applied pressure and different charge rates. We have also upgraded our equipment to improve the sensitivity of our measurements by extending the low-frequency capabilities. After completing all measurements, we will use the results to create the first theoretical model capable of accurately predicting the complete internal temperature profile of an operating electrochemical cell, accounting for the full heterogeneous multilayered internal structure of the battery.

Key Publications

This work has been presented in part at the 2017 International Technical Conference and Exhibition on Packaging and Integration of Electronic and Photonic Microsystems (InterPACK) and the 2017 9th US & Japan Joint Seminar on Nanoscale Transport Phenomena. We are also preparing a manuscript to submit to the 16th International Heat Transfer Conference (IHTC), a section of which will be based on this work.

II.D.8 Correlative Microscopy Characterization of Oxide Electrodes (SLAC)

Yi Cui, Principal Investigator

SLAC National Accelerator Laboratory
2575 Sand Hill Road
Menlo Park, CA 94025
Phone: 650-725-7515
E-mail: wchueh@stanford.edu

William C. Chueh, Principal Investigator

SLAC National Accelerator Laboratory
2575 Sand Hill Road
Menlo Park, CA 94025
Phone: 650-725-7515

Michael F. Toney, Principal Investigator

SLAC National Accelerator Laboratory
2575 Sand Hill Road
Menlo Park, CA 94025
Phone: 650-725-7515

Tien Duong, Technology Manager

U.S. Department of Energy
Phone: 202-586-7836
E-mail: Tien.Duong@ee.doe.gov

Start Date: January 1, 2016
Total Project Cost: \$600,000

End Date: March 31, 2018
DOE share: \$600,000

Non-DOE share: \$0

Project Introduction

A new cross-technique characterization platform will be developed to track lithiation dynamics at the single-particle level in Lithium- Manganese-rich Nickel Cobalt Oxide (LMR-NMC). Fundamental insights from this new diagnostic capability are expected to increase the power density and cycle life of oxide electrodes by improving electrode utilization, reducing electrochemical hotspots, decreasing capacity and voltage fade, and enhancing safety, which all improve the viability of lithium-ion batteries for vehicle transportation. By understanding lithiation at the single-particle level, this project's success will contribute to improving on-vehicle battery management, such as charging/discharging protocol, state-of-charge and state-of-health monitoring.

Due to the cost of Co, substituting Ni, Mn, Al, Mg, or Cr in the layered oxide cathode LiCoO_2 has become the focus of much research. LMR-NMC is of significant interest for use in electric vehicle applications due to its balance of cost and performance, with demonstrated specific capacities of 230- 280 mAh g^{-1} . Recharging time, power density, voltage/capacity fade, and thermal stability are important performance matrices for these battery chemistries to gain widespread use in vehicle transportation. Rational engineering of electrode chemistry and microstructure is expected to greatly increase these aspects of battery performance. However, due to the wide range of length scales involved – spanning nanometers to millimeters – a comprehensive understanding of kinetics and degradation in battery electrodes is lacking, especially at the single-primary-particle level. Part of the challenge lies in the characterization of lithiation dynamics across a wide range of length scales of realistic batteries during cycling.

This project is carried out in collaboration with Samsung Advanced Institute of Technology, who provided LMR-NMC materials, as well as scientists at Advanced Light Source and the Molecular Foundry, users facilities at Lawrence Berkeley National Laboratory.

Objectives

This study aims to develop and utilize a correlative microscopy platform to investigate the lithiation dynamics of LMR-NMC, with the specific goal of understanding factors that determine the rate capability and degradation mechanisms at the single primary particle length scale. By developing a nanoscale and single-particle understanding of lithiation, the project addresses specific engineering problems including electrochemical hotspot, electrode utilization, safety, and capacity/voltage fade. Chemistry-sensitive soft transmission X-ray microscopy, operating in standard and in ptychography mode, will be carried out on cycling electrodes in a liquid electrolyte using a microfluidic cell. A platform to transfer the identical electrode to the transmission electron microscope and Raman microscope will be developed to integrate the X-ray, electron and optical characterization with the goal of achieving a comprehensive understanding of the lithiation dynamics at the single-particle level. Ex-situ spectro-ptychography on electrodes cycled at low ($-20\text{ }^{\circ}\text{C}$) and high ($+80\text{ }^{\circ}\text{C}$) temperatures will be conducted to understand the temperature dependence of lithiation dynamics, hotspots, and degradation in single particles.

Approach

Chemistry-sensitive soft transmission X-ray microscopy, operating in standard and in ptychography mode, will be carried out on cycling electrodes in a liquid electrolyte using a microfluidic cell while the electrode is cycled between the charged and the discharged state. The expected spatial resolution is 5 nm (ptychography mode) and 50 nm (standard mode). To attain even higher spatial resolution, a platform to transfer the same electrode to the transmission electron microscope will be developed. Finally, Raman microscopy, which is sensitive to the vibrational nature of chemical bonds, will also be used to characterize the same electrode. With the seamless integration the X-ray, electron and optical characterization, the goal is to achieve a complete understanding of the lithiation dynamics at the single-particle length scale.

Results

To understand the relationship between this structural behavior and the unique redox chemistry of LMR-NMC while decoupling surface and bulk phenomena, we obtain spatially resolved TM L_3 and O K edge transmission X-ray absorption spectroscopy (XAS) with $\sim 30\text{ nm}$ resolution using scanning transmission X-ray microscopy (STXM). X-ray transparent samples were prepared ex situ through sonication and dispersion of electrodes harvested at various voltages (Figure II-332a) in an Ar glovebox and transported to the microscope with minimal air exposure. We first plot the average spectra during the first cycle in Figure II-332, obtained by averaging the 2D spectral maps obtained from STXM, which allows us to understand the gross changes in the electrode electronic structure. The spatially-averaged transmission XAS spectra obtained through STXM (Figure II-332c-f), which represent the true depth-averaged absorption spectra, show that when charging below the plateau (pristine, 'P' $\rightarrow 4.35\text{ V}$, '1') we observe primarily an inversion in the Ni L_3 edge peak ratio and a shift of the Co L_3 peak by $+0.4\text{ eV}$, correlated with the simultaneous growth of a peak at 528.5 eV in the O K pre-edge. These changes are well-understood to reflect the depopulation of hybridized O_{2p} - TM_{3d} (antibonding) bands, constituting standard hybridized "TM-O redox". By contrast, when charging through the voltage plateau (4.35 V , '1' $\rightarrow 4.60\text{ V}$, '2'), the TM L_3 -edge spectra change minimally: the Co and Mn L_3 edges exhibit some broadening, and there is a small increase of the low energy peak at the Ni L_3 edge, suggesting a surprising reduction of the Ni during charge, which we explain later. By far the most significant change during the voltage plateau is the growth of a sharp and intense peak at 530.8 eV in the O K-edge spectrum, which indicates that predominantly O_{2p} character states are depopulated during the 4.50 V plateau. The differential spectra in Figure II-332c clearly show that this feature is distinct from the peak at 528.5 eV , confirming that the two redox mechanisms are fundamentally different. We therefore refer to the 530.8 eV peak being the signature of "O redox".

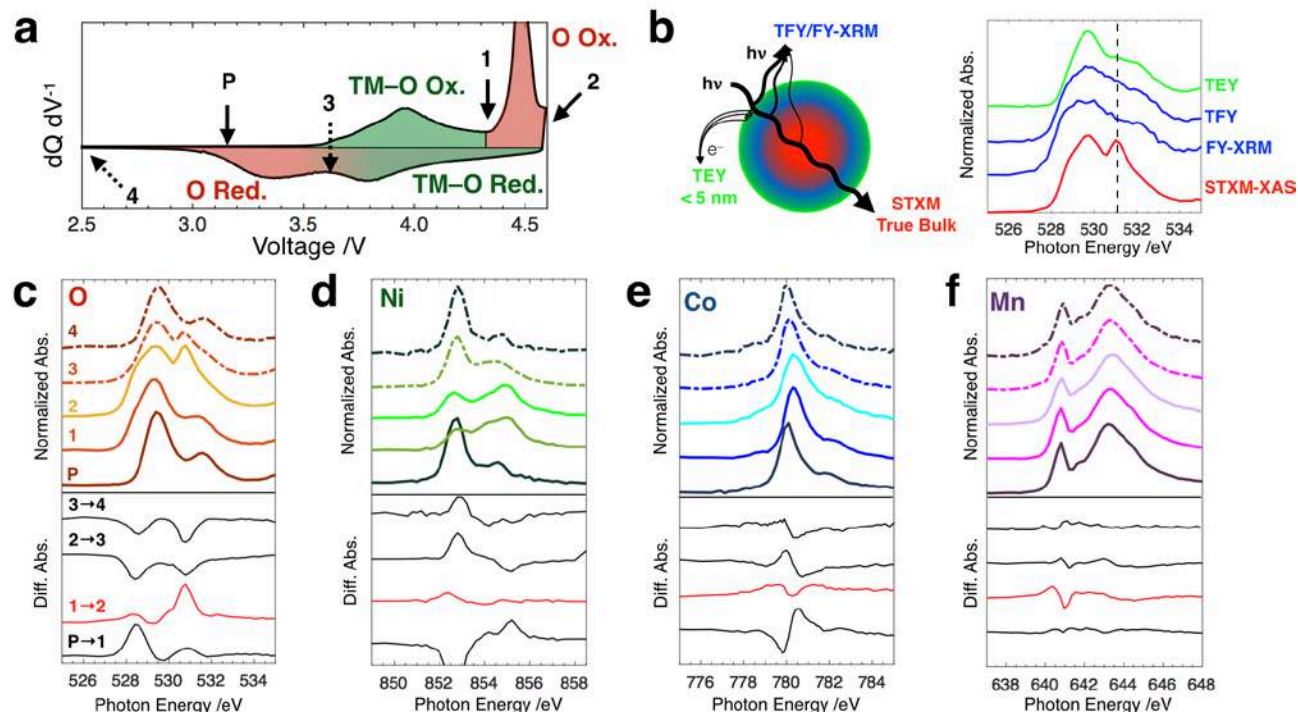


Figure II-332. First Cycle Average STXM-XAS of LMR-NMC. (a) dQ dV^{-1} of the first cycle showing the voltages at which samples were harvested for STXM. The samples are pristine (P), 4.35 V (1), 4.60 V (2), 3.65 V (3), and 2.00 V (4). Regions of the dQ dV^{-1} are shaded to show the hysteresis in the O redox relative to the TM-O redox. (b) Schematic and spectra comparing STXM-XAS to various other XAS detection modes (TEY, FY, and fluorescence yield X-ray microscopy, FY-XRM). (c-f) Spatially averaged transmission soft XAS throughout the first cycle at the (c) O K, (d) Ni L₃, (e) Co L₃, and (f) Mn L₃ edges. Solid traces indicate electrodes harvested during charge, while dashed traces indicate electrodes harvested during discharge. The red and black traces below each plot indicate the differential spectra between the points indicated.

Understanding the spatial distribution of the spectral changes during the voltage plateau can reveal whether O redox is a bulk phenomenon and whether it is correlated to changes in the TM L edges, particularly the Ni reduction, which can in turn give insight into the nature of the oxidized oxygen species. We therefore map the nanoscale distribution of the Ni L₃- and O K-edge spectroscopy at the single primary particle length scale during the first-charge voltage plateau. In Figure II-333 we apply principal component analysis (PCA) and non-negative matrix factorization (NMF) to a series of STXM spectro-images taken at six intermediate points along the 4.50 V plateau to identify the end-member spectra that describe the spectroscopic changes. At both the O and Ni edges, two end-member spectra were identified (Figure II-333a): the O spectra are essentially with and without the peak at 530.8 eV, while the Ni spectra resemble Ni⁴⁺ and Ni²⁺. Using these end-member spectra, we obtain the average fraction (Figure II-333b) and nanoscale map (Figure II-333c) for primary particles throughout the voltage plateau.

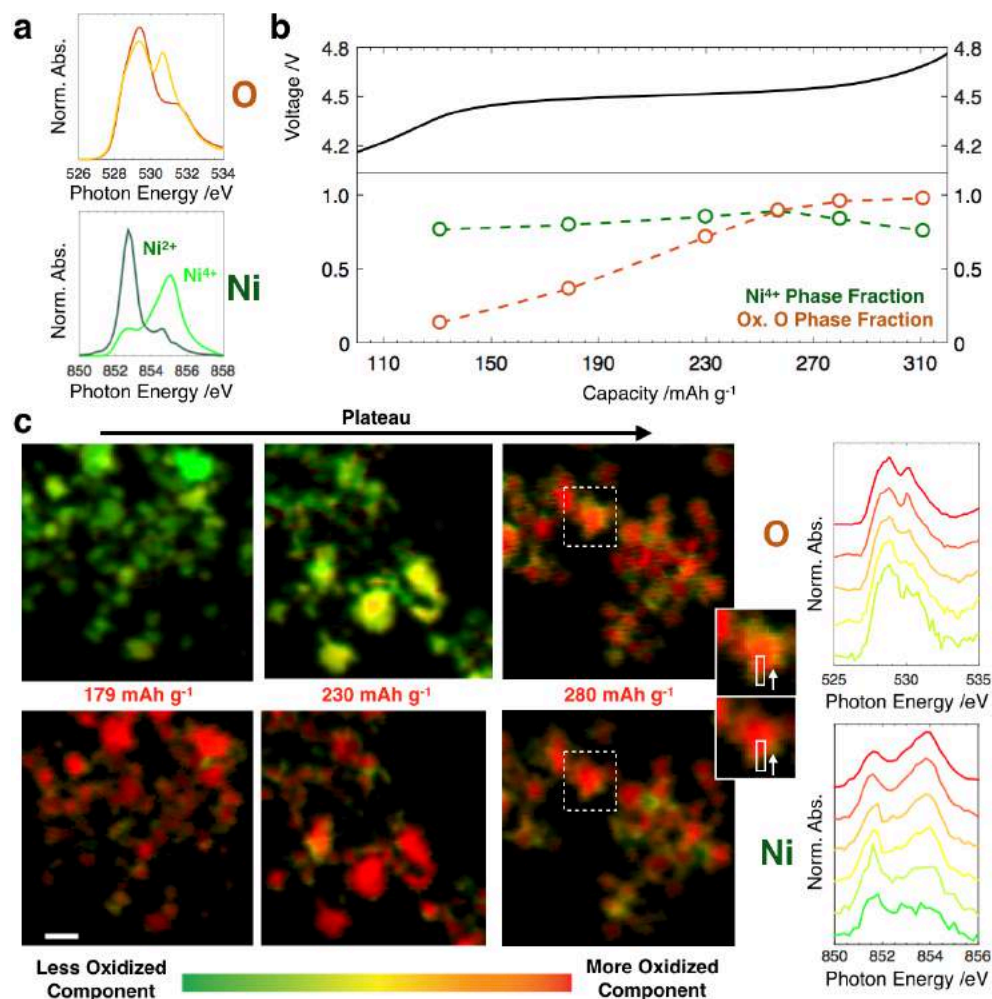


Figure II-333. Spatial Dependence of O and Ni Spectroscopic Response During 4.50 V Plateau. (a) End-member spectra at the Ni L₃ and O K edges throughout the first cycle plateau. (b) Total end-member fractions for each sample used in the NMF analysis as a function of capacity through the plateau. (c) Nanoscale distribution of the end-members in (a) for primary particles at different points in the voltage plateau. Scale bar is 500 nm. Right: spectral line-scans of the magnified particle showing the bulk O oxidation and surface Ni and O reduction. The spectra at the bottom correspond to the near-surface region and those at the top correspond to the bulk.

From the nanoscale O component maps (Figure II-333c, top), it is immediately evident that O oxidation occurs throughout the bulk of the primary particles during the voltage plateau, establishing unambiguously that O redox is a bulk process in LMR-NMC. On the other hand, the Ni chemical maps (Figure II-333c, bottom) reveal that bulk Ni ions remain in a 4+ oxidation state during the plateau. The variation observed in the average spectrum in Figure II-332d is in fact due to Ni reduction that is confined mostly to the primary particle surfaces. Spectral linescans in Figure II-333c show that the new peak at 530.8 eV at the O K edge is actually suppressed near the particle surfaces where Ni is reduced. In other words, although Ni reduction and O oxidation occur simultaneously during the voltage plateau, they are spatially separated. Its prevalence near the surface suggests that Ni reduction is more likely due to a steep gradient of oxygen non-stoichiometry due to oxygen evolution or reaction with the electrolyte. This is further confirmed by the redox behavior during the first discharge and second charge which reveals that discharging to 2.00 V reversibly reduces Mn near the surface with no change in the bulk. This is consistent with an electrochemically active but oxygen deficient near-surface structure that approaches the bulk composition within tens of nm. Importantly, oxygen evolution

is only a minor surface phenomenon during the first cycle of LMR-NMC and does not account for the high voltage plateau capacity, which is in fact compensated by reversible oxygen anion redox in the bulk.

Having established that oxygen redox is a major bulk phenomenon in LMR-NMC, we next investigate the nature of the oxidized oxygen species and their role in the unusual electrochemistry and voltage fade of these materials. We note that the O redox peak observed here (530.8 eV) does not appear at the absorption onset (~ 528 eV) but above it. In fact, the O redox state appears above the depopulated TM–O redox state (528.5 eV), suggesting a switch in their relative positioning after O oxidation. Thus, O redox in LMR-NMC is linked to a relative reordering of the anion and cation electronic states that cannot be described by a static O^{2-}/O^- redox couple.

The significant change in the O_{2p} states after depopulation is further confirmed in Figure II-334a, which plots the O K-edge resonant inelastic X-ray scattering (RIXS) obtained throughout the first cycle. RIXS maps the fluorescence intensity as a function of both absorption and emission energy, revealing the energy distribution buried in the features observed through STXM-XAS. For the electrode at 4.60 V, however, excitation to the new unoccupied O redox state at 530.8 eV results in a striking new emission feature at 523.75 eV, which is clearly distinct from the broad 522–527 eV emission features from the TM–O hybridized states. The distinct RIXS feature created during the 4.50 V plateau further supports the scenario of reshuffled electron states after O redox, which cannot be explained by a rigid O^{2-}/O^- mechanism.

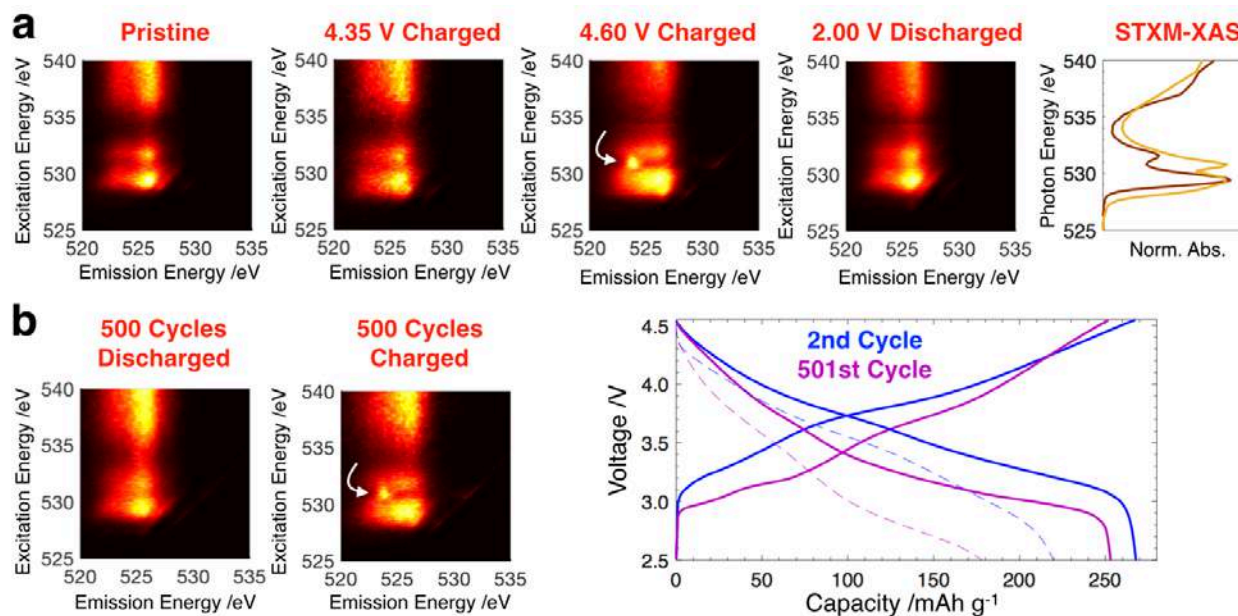


Figure II-334. Probing the Nature and Stability of Oxygen Redox. (a) RIXS maps at the voltages indicated throughout the first cycle. The unique emission signature at 4.60 V indicated by the white arrow supports an electronic restructuring associated with O redox. Right: XAS obtained in the pristine (brown) and fully charged (tan) state during the first cycle for comparison.

(b) RIXS maps acquired before and after the 501st charge on an electrode cycled 500 times at 1C/2C charge/discharge rate, showing that the reversible oxygen redox feature persists for hundreds of cycles. The voltage curves for the second and 501st cycles at C/68 (solid) and 2C (dashed) show that most of the capacity fade over 500 cycles is from increased impedance and overpotential, and that the intrinsic capacity is largely retained.

Furthermore, such a mechanism was previously predicted to be unstable against oxygen evolution in 3d layered oxides. We therefore investigate the stability of oxygen redox over extended cycling using optimized 18650 cells (Samsung SAIT), which exhibit 94% retention of their low-rate (intrinsic) capacity after 500 cycles at a 1C/2C charge/discharge rate. Figure II-334b plots the O RIXS maps for the 501st cycle in the charged and discharged states. Clearly, a significant fraction of the oxygen anions remains redox active after hundreds of

cycles. These particles were not protected against oxygen evolution through coating. Thus, our result suggests a degree of intrinsic anion redox stability in LMR-NMC, further suggesting that the unstable rigid O^{2-}/O^- mechanism is unlikely.

Our RIXS results suggest that O redox can be stabilized against oxygen evolution in LMR-NMC through the electronic restructuring. We now investigate how that electronic restructuring takes place and its implications for mitigating voltage fade. Figure II-333 reveals that the spectra on discharge (4.60 V, '2' \rightarrow 3.65 V, '3' \rightarrow 2.00 V, '4') do not follow a simple reversal of the changes observed during charge. Most notably, whereas O oxidation took place exclusively above 4.35 V during charge (after the Ni and Co had been fully oxidized to $\sim 4+$), during discharge the Ni and Co are almost entirely reduced first in the 4.60 – 3.65 V range ('2' \rightarrow '3'), with most of the O reduction taking place later in the 3.65 – 2.00 V range ('3' \rightarrow '4'). This massive > 1 V shift in the O redox voltage is illustrated by the color-coded regions in the dQ/dV^{-1} plot in Figure II-332a. Thus the sequence of the redox couples (i.e., the order in which electronic states are (de)populated) is inverted after the 4.50 V plateau, consistent with the altered structure and electrochemistry after the first cycle. This agrees well with our conclusion from XAS that some of the O_{2p} states depopulated during the plateau are shifted from an energy below the $TM_{3d}-O_{2p}$ antibonding states to one above them, further confirming the electronic reshuffling associated with O redox.

Figure II-335 reveals a clear correlation between the hysteretic O redox and the fraction of TMs in the Li layer as calculated from Rietveld refinement of synchrotron XRD patterns, suggesting that the electron state reshuffling arises from a strong coupling between O redox and TM migration. To understand this coupling, we perform density functional theory calculations using HSE06 functionals (not shown here). An oxygen that was initially unoxidized and bonded to three TMs can become doubly-coordinated and oxidized, transferring its electrons to another O or a TM. The altered coordination environment of the shifted O_{2p} states due to TM migration is consistent with the distinct RIXS signature, while the shifting to higher energy is consistent with the inverted bulk redox sequence observed by STXM-XAS as well as the strong correlation between oxygen oxidation state and TM migration observed through XRD.

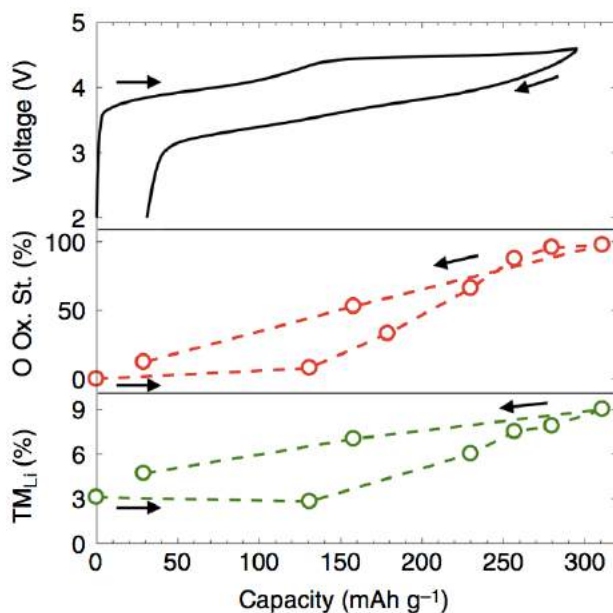


Figure II-335. Plot of the O fractional oxidation state (red) and the migrated TM fraction (green) as a function of capacity, showing the clear link between hysteresis in the TM migration and voltage hysteresis in the O redox. Error bars indicating fitting residual and refinement error for the O oxidation state and TM migration fraction, respectively, are smaller than the data symbols and are therefore not shown.

Conclusions

We conclude that TM migration is intrinsically coupled to the O redox potential, necessarily causing the reshuffling of the relative O and TM–O redox potentials. Thus, the O redox mechanism in LMR-NMC cannot be described as a static O^{2-}/O^- redox couple, but rather as a dynamic $\{\text{O}^{2-} + \text{TM}\} \rightarrow \{\text{O}^- + \text{TM}_{\text{mig}}\} + e^-$ process, where TM_{mig} indicates a migrated TM. The substantial change and distribution in the oxygen coordination environments represented by $\{\text{O}^- + \text{TM}_{\text{mig}}\}$ modulates the oxygen redox potential and shifts a large fraction to lower voltage (< 3.65 V) after the first charge.

We propose that this structure-redox coupling is involved in stabilizing the oxygen redox couple, which we observe to persist for 500 cycles in uncoated LMR-NMC despite predictions of intrinsic instability under the assumption of static structure. Our results suggest that it may be possible to tune the stability and voltage of anion redox through control of the TM migration pathways. Thus, we suggest a new strategy for designing Li-rich layered oxides with improved cycling performance whereby the oxygen redox chemistry is tuned through structural modifications rather than the more common covalency modifications, which typically require substitution with rare 4d and 5d elements. More broadly, we demonstrate that atomic and electronic structural evolution during (de)intercalation need to be considered when assessing anion and cation redox chemistry even in nominally topotactic intercalation electrodes.

Key Publications

1. W. E. Gent, K. Lim, Y. Liang, Q. Li, T. Barnes, S.-J. Ahn, K. H. Stone, M. McIntire, J. Hong, J. H. Song, Y. Li, A. Mehta, S. Ermon, T. Tyliczszak, D. Kilcoyne, D. Vine, J.-H. Par, S.-K. Doo, M. F. Toney, W. Yang, D. Prendergast, W. C. Chueh. Coupling Between Bulk Oxygen Redox and Cation Migration Explains Unusual Electrochemistry in Lithium-Rich Layered Oxides. *Nature Commun.* (2017). Accepted.
2. W. E. Gent, Y. Li, S. Ahn, J. Lim, Y. Liu, A. Wise, C. B. Gopal, D. N. Mueller, R. Davis, J. N. Weker, J.-H. Park, S.-K. Doo, W. C. Chueh. Persistent State-of-Charge Heterogeneity in Relaxed, Partially Charged $\text{Li}_{1-x}\text{Ni}_{1/3}\text{Co}_{1/3}\text{Mn}_{1/3}\text{O}_2$ Secondary Particles. *Adv. Mater.* **28**, 6631-6638 (2016).

II.D.9 Understanding and Mitigating Interfacial Reactivity between Electrode and Electrolyte (ANL)

Khalil Amine, Principal Investigator

Argonne National Laboratory
9700 S. Cass Avenue
Argonne, IL 60516
Phone: 630-252-7380
E-mail: curtiss@anl.gov

Larry Curtiss, Principal Investigator

Argonne National Laboratory
9700 S. Cass Avenue
Argonne, IL 60516
Phone: 630-252-3838
E-mail: amine@anl.gov

Nenad Markovic, Principal Investigator

Argonne National Laboratory
9700 S. Cass Avenue
Argonne, IL 60516
Phone: 630-252-5181
E-mail: nmarkovic@anl.gov

Tien Duong, Technology Manager

U.S. Department of Energy
Phone: 202-586-7836
E-mail: Tien.Duong@ee.doe.gov

Start Date: October 1, 2016

End Date: September 30, 2020

Total Project Cost: \$1,600,000

DOE share: \$1,600,000

Non-DOE share: \$0

Project Introduction

Lithium-ion batteries are dominant energy storage devices in modern portable electronics, and are continuously developed for emerging applications in electric vehicles and smart grids. While lithium-ion batteries have the highest gravimetric and volumetric energy density among all currently available energy storage technologies, emerging applications require longer cycle life, higher energy density and improved safety characteristics. Development of optimal electrochemical interfaces between liquid nonaqueous electrolytes and solid electrodes is needed to successfully extend cycle life and increase energy density.

The challenge for understanding dynamic behavior of solid/liquid interfaces is that many different electrochemical phenomena occur during charge/discharge cycling. These include parasitic interfacial electrochemical reactions that involve electrolyte and dissolution reactions that involve cathode materials.

The team led by Dr. Khalil Amine, Dr. Larry Curtiss and Dr. Nenad Markovic at Argonne National Laboratory (ANL) is developing new approaches to characterize solid/liquid interfaces in lithium ion batteries in order to develop understanding of interface stability during charge/discharge cycling. This will help to correlate electrochemical reactivity with composition and structure of electrolytes and electrodes to enable a rational design of solid/liquid interfaces in lithium ion batteries. This effort will increase energy density, improve safety and stability for this technology for emerging applications.

Objectives

This project aims to develop an understanding, at atomic/molecular levels, of the stability of electrochemical interfaces during charge-discharge cycling and use the knowledge for stabilizing solid /liquid interfaces in lithium ion batteries. Our goal is to improve the stability of solid/liquid interfaces using insights into the atomic/molecular processes that limit stability during cycling. The core of this proposal is to identify, rationalize and understand the dynamics of the dissolution processes of 3d-TM cations in the cathode materials, the stability of various commercial and highly purified electrolytes comprised of organic solvents, salts and additives, and the evolution of O₂ and other gaseous products formed from the electrode material or the electrolyte during the charging-discharging of the Li-ion battery.

Approach

An integrated program focused on solid-liquid interfaces in Li-ion batteries using state-of-the-art *in situ* characterization tools and computational modeling to understand and design interfaces with enhanced stability. The range of high-end analytical tools include: *A three electrode RDE (rotating disk electrode) setup; Inductively Coupled Plasma with Mass Spectrometry (ICP-MS); Gas Chromatography with Triple Quadrupole Mass Spectrometry (GC-QqQ) in Headspace sampling mode (HS); Differential Electrochemical Mass Spectrometry (DEMS)*. High precision electrochemical measurements in combination with *in situ* measurements and characterization are highly suitable to investigate correlation of stability with a number of electrochemical, structural and compositional properties of the interfaces. Computational methods that provide reaction energies and barriers as well as structural information at the atomic level will be used to predict and test possible reactions that affect the stability of solid-liquid interfaces.

Collaborators include Zonghai Chen (ANL), Sanja Tepavcevic (ANL), Pietro Papa Lopes (ANL) and Peter Apol (ANL), as well as Jun Liu (PNNL) and X. He, Tsinghua University.

Results

High precision electrochemical system characterization of parasitic electrochemical reactions

The home-built high precision electrochemical measurement system is used to characterize the kinetics of parasitic reactions occurring at the surface of working electrodes as shown in Figure II-336. In principle, the half-cells are constant-voltage charged/discharged to a desired potential, and the potential is held at the specific value for up to 20 hours. Then, the static leakage current is obtained as the indicator of the rate of parasitic reactions between the working electrode and the electrolyte. In addition, the cells are conditioned in an environmental chamber, which enables us to measure the kinetics of the parasitic reactions.

We demonstrated our newly developed high precision electrochemical measuring system for stability studies by revisiting the corrosion (or anodic dissolution) process of aluminum foils in non-aqueous electrolytes. The measured static leakage current grows roughly exponentially with the applied potential, indicating an ongoing electrochemical oxidation of electrolyte on the carbon coated aluminum foil. The measured parasitic current increased exponentially with the holding potential, indicating an electrochemical oxidation of a certain species as shown in Figure II-336(c).

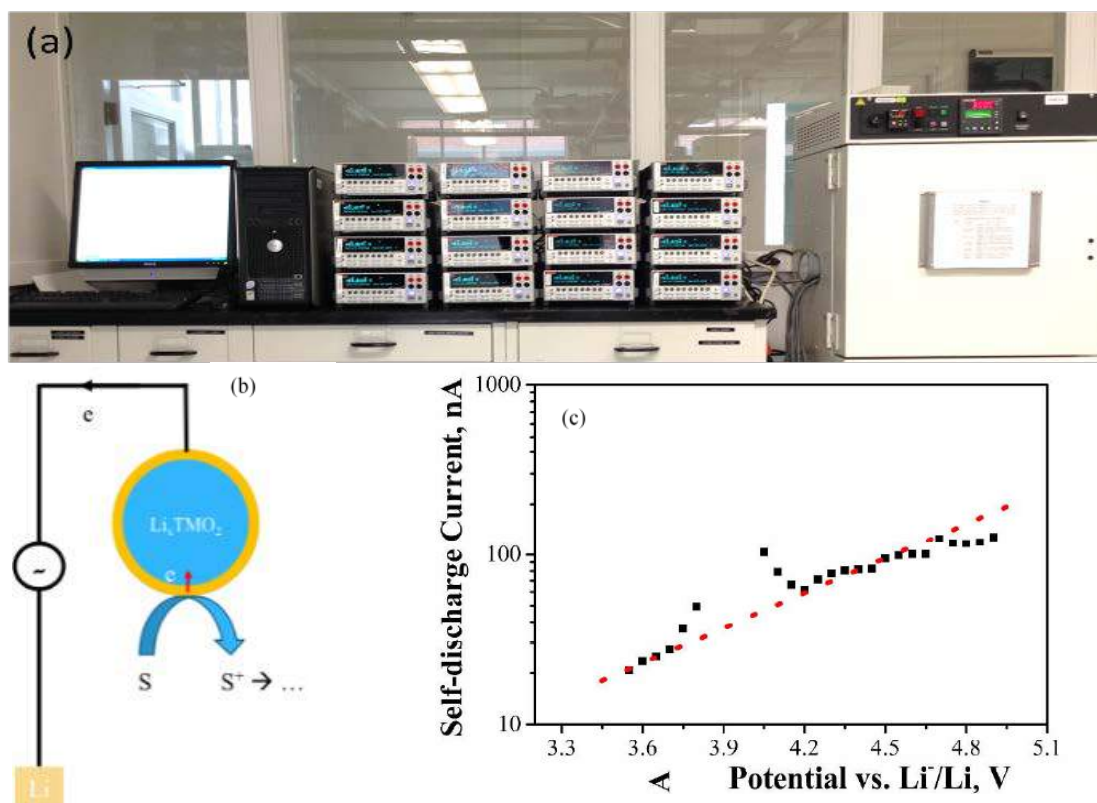


Figure II-336. (a) Picture of a 16-channel high precision leakage current measuring system; (b) schematics showing the connection between the leakage current and the rate of parasitic reactions; (c) evolution of the static parasitic current as a function of the holding potential for the bare aluminum foil. The electrolyte used was 1.2 M LiPF₆ in EC/EMC (3:7 by mass). We have shown that that this reaction is related to the oxidation of ethylene carbonate.

Revisiting corrosion of aluminum current collector

In order to get insight into the parasitic reactions we carried out XPS analysis for aluminum foils before and after anodic treatment. The control experiment was carried out with bare Al foil and a weak absorption peak was observed at about 73 eV. This corresponds to the binding energy of metallic aluminum. The strong peak at 75.6 eV was assigned to a Al₂O₃ thin film on the surface of the aluminum foil. It shows that as-used non-aqueous electrolyte with the presence of possibly a trace amount of moisture was not enough to convert the Al₂O₃ layer into a more stable passivation layer of AlF₃. After anodic treatment at 3.9 V (20 hours), the absorption peak for Al₂O₃ at 75.6 eV disappears and a new peak at 77.2 eV appears. This new peak corresponds to the binding energy of AlF₃. A similar result was found for the sample anodized at 4.8 V for 20 h. A depth profile analysis of the XPS results revealed that the sample without anodic treatment was mostly covered by 15–25 nm of Al₂O₃; anodic treatment at 3.9 V led to a deposition of about 5 nm of AlF₃ on the top of the thinned Al₂O₃ layer (10–20 nm). Although a substantially higher parasitic current was measured at 4.8 V, no significant change of the thickness of the AlF₃ layer and embedded Al₂O₃ was observed. This indicates that the interface of the aluminum foil was stabilized by the AlF₃ coating that was electrochemically triggered by the oxidation of solvent to generate protons on the surface. After repeated cycling between 3.4 and 4.9 V for five cycles, it was observed that the open gap at about 3.9 V disappeared, primarily due to stabilization of the aluminum surface. In addition, the open gap associated with the corrosion of Al₂O₃ was pushed to a higher potential when EC was replaced with fluorinated EC. Also, the gap almost disappeared when both EC and EMC were replaced with a mixture of fluorinated carbonate and fluorinated ether, indicating that EMC also plays a major role in Al corrosion. These XPS results support the hypothesis that the degradation of aluminum foil at high potentials is a coupled electrochemical-chemical reaction, i.e., the electrochemical

oxidation of organic solvents such as EC and EMC at high potentials triggers the chemical corrosion of aluminum foils.

Density functional theory calculations using models representative of current collector's surface basic groups indicate that redox potential can decrease even more than that when the proton is transferred to either hydroxyl (by 1.4 to 2.5 V) or thiol group (by 1 to 2 V) coordinated to aluminum. Larger calculations on either hydroxyl group or a bridging oxygen site on amorphous alumina models similarly indicate that the alumina promotes the deprotonation reaction for the radical cation (EC⁺). We found that the degradation of aluminum foil at high potentials is a coupled electrochemical-chemical reaction; the electrochemical oxidation of organic solvents at high potentials triggers the chemical corrosion of aluminum foils.

The role of carbon was further investigated given that carbon is mostly resistive to chemical corrosion in an acidic environment. A layer of carbon black was deposited on the surface of the aluminum foil. The electrochemical characterization showed that the static parasitic current measured increased almost 10-fold (see Figure II-337a), compared to what was found previously for non-coated aluminum foil. This increase of parasitic current could be a result of either an increase in the active electrochemical surface area or a decrease of charge transfer impedance at the interface of the aluminum foil. Considering the high loading of carbon black physically cast on the sample, the high parasitic current shown in Figure II-336a must be dominated by the reduction of charge transfer impedance across the interface due to the carbon coating, which is intended to protect the aluminum foil from the chemical corrosion in an acidic environment. In addition, graphene with a low out-of-plane electronic conductivity was also deposited on the aluminum foil. The results showed that the measured parasitic current was substantially lower than that for the carbon-coated samples but not better than that for the uncoated sample (see Figure II-337b). Finally, AlPO₄, which is an electronic insulator and also resistive to corrosion in an acidic environment, was coated on the surface of aluminum foil, and a dramatic change in the parasitic current was observed with the AlPO₄ coating (see Figure II-337c). First, the corrosion window shown at about 3.9 V completely disappeared because the coating layer is really resistive toward reaction with protons, resulting in a constant charge transfer impedance throughout the whole course of the potential sweep. In addition, the maximum parasitic current measured for the AlPO₄-coated sample was about 50% that of the non-coated sample, implying that a significantly smaller amount of proton is expected at similar operation conditions. Thus, these results further confirm our hypothesis that the corrosion reaction of aluminum foil at a relatively high potential is a coupled electrochemical-chemical reaction.

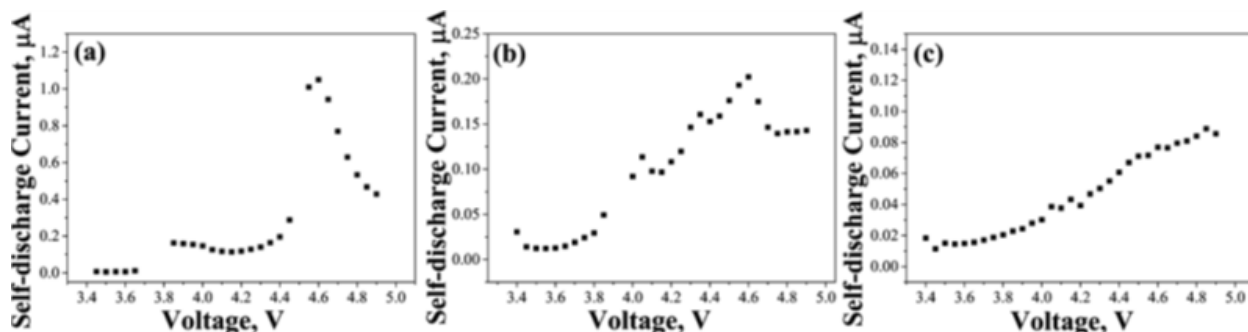


Figure II-337. (a) Potential dependence on the static parasitic current for aluminum foil with surface coating of (a) carbon, (b) graphene, and (c) AlPO₄.

ICP-MS measurements of TM dissolution

This methodology allows simultaneous monitoring of charge/discharge process arising from Li de-intercalation/intercalation in cathode material and the kinetics of transition metal dissolution as a function of time and potential. Experiments done on a three electrode setup enable identification of electrochemical currents arising solely from the cathode material. To underpin the instabilities of LiCoO₂ at higher potentials, the *first-of-its-kind* experiment of *in situ* dissolution of Co monitored by a SPRDE-ICP-MS setup. Our first

experiments already demonstrated the power of such methodology in gaining fundamental knowledge on electrochemical interfaces of high energy cathodes, inaccessible by conventional battery testing. With a *stationary probe* for coupling to ICP-MS, we can probe the kinetics of intercalation/de-intercalation and kinetics of 3d-TM ions dissolution simultaneously as a function of time and potential. For example, while up to 4.2 V de-intercalation of Li is already taking place, we observe significant dissolution of Co only above 4.5 V vs Li/Li^+ , indicative that interplay between charging/discharging processes to corresponding Co dissolution may occur.

While our first experiments to measure *in situ* dissolution of Co from LiCoO_2 under charging as monitored by a SPRDE-ICP-MS setup served to demonstrate the method, the results shown in Figure II-338 provided the first quantitative real-time analysis of cobalt dissolution that happens during charging of LiCoO_2 in 1.2M LiPF_6 in EC:EMC 3:7 electrolyte. We first explored the dynamics of Co dissolution during potential step transients from 3 V vs Li/Li^+ to an upper potential limit (UPL) that lasted 300 seconds per step. At each consecutive step we increased the UPL from 4 V up to 5 V vs Li/Li^+ in 0.2 V increments. As observed from Figure II-338, the first potential step to 4 V was enough to trigger a very small transient of Co dissolution that quickly decayed to the same level of signal as in the background. Consecutive steps up to 4.2 and 4.4 showed only this transient behavior as well. However, for potential steps starting at 4.6 V and above it becomes clear that the dissolution current is composed of the initial transient and additional continuous dissolution kinetics. While the charging current is of the order of 1 mA cm^{-2} at 4.6 V, the respective Co dissolution current is 3 orders of magnitude smaller, indicating that any degradation process that involves cobalt dissolution is only happening at the surface of the material and is not a bulk process as intercalation/de-intercalation.

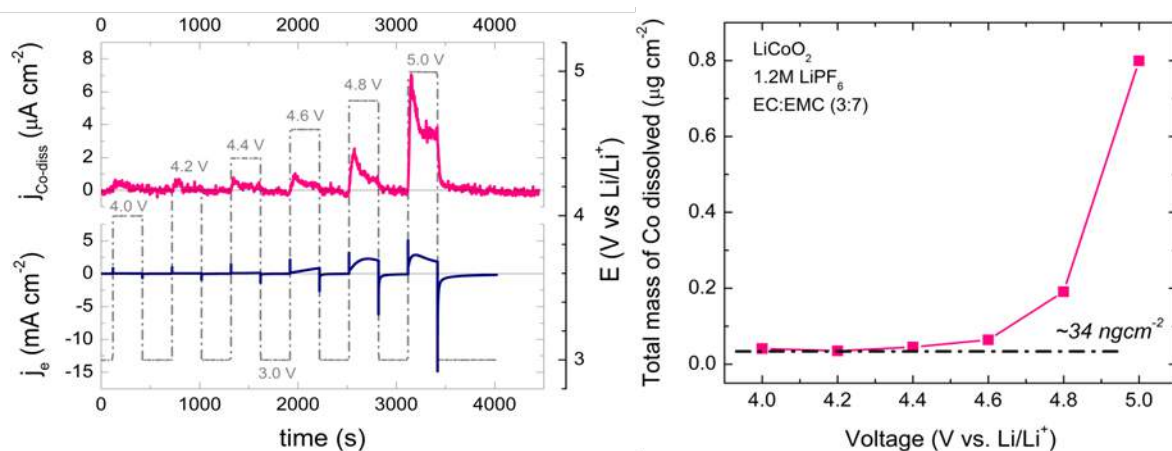


Figure II-338. (left) In Situ ICP-MS results of Co dissolution upon electro-chemical polarization using the SPRDE system. Working Electrode: $\text{LiCoO}_2/\text{C}/\text{PVDF}$. Electrolyte: 1.2M LiPF_6 in EC:EMC (3:7 by mass); (right) Total amount of Co dissolution upon electro-chemical polarization using as monitored by the SPRDE-ICP-MS system.

In order to gain deeper insight on how much of Co dissolved after the potential steps, Figure II-338 (left shows the total amount of Co dissolution, obtained as the area under the dissolution curve shown in Figure II-338 (right), as a function of the upper potential limit. While the trend of increasing dissolution with increasing UPL is clear, the amount of Co dissolved reveals the importance of surface processes in battery stability dynamics. Even though the Co dissolution transients that were observed at 4 V are small, the amount of cobalt loss represents a significant portion of the electrode surface (a few percent), which helps to understand why there would be a loss of electrical contact between different particles as their surface are evolving after multiple cycles. Therefore, our unique capability for monitoring in situ dissolution of TM from battery cathodes can provide deeper understanding on the fundamental processes responsible for performance degradation in Li-ion batteries.

Conclusions

During the past year we have demonstrated use of high precision electrochemical system characterization of parasitic electrochemical reactions by revisiting corrosion of aluminum current collector. We have shown that the corrosion reaction of aluminum foil at a relatively high potential is a coupled electrochemical–chemical reaction. We have also shown that the maximum parasitic current measured for the AlPO_4 -coated sample was about 50% that of the non-coated sample, implying that significantly smaller amounts of protons are expected at similar operation conditions.

The first-of-its-kind experiment of in situ dissolution of Co monitored by a SPRDE-ICP-MS setup demonstrates simultaneous monitoring of charge/discharge process arising from Li de-intercalation/intercalation in cathode material and the kinetics of transition metal dissolution as a function of time and potential. We have shown that at 4.6 V, any degradation process in LiCoO_2 that involves cobalt dissolution is only happening at the surface of the material and is not a bulk process as intercalation/de-intercalation.

Key Publications

1. “Revisiting the Corrosion of the Aluminum Current Collector in Lithium-Ion Batteries,” Tianyuan Ma, Gui-Liang Xu, Yan Li, Li Wang, Xiangming He, Jianming Zheng, Jun Liu, Mark H. Engelhard, Peter Zapol, Larry A. Curtiss, Jacob Jorne, Khalil Amine, Zonghai Chen, *J. Phys. Chem. Lett.*, **8** (5), 1072-1077, (2017), DOI: 10.1021/acs.jpcllett.6b02933

II.E Next-Gen Lithium-Ion: Modeling Advanced Electrode Materials

II.E.1 Electrode Materials Design and Failure Prediction (ANL)

Venkat Srinivasan, Principal Investigator

Argonne National Laboratory
9700 S. Cass Avenue
Lemont, IL 60439
Phone: 630-252-6003
E-mail: vsrinivasan@anl.gov

Tien Duong, Technology Manager

U.S. Department of Energy
Phone: 202-586-7836
E-mail: Tien.Duong@ee.doe.gov

Start Date: October 1, 2016
Total Project Cost: \$400,000

End Date: September 30, 2017
DOE share: \$400,000

Non-DOE share: \$0

Project Introduction

The next-generation lithium ion batteries are expected to use lithium metal-based anodes, which offer low reduction potential and superior specific capacity. The biggest drawback preventing widespread usage of lithium metal anodes is the formation of dendrites over multiple cycles during operation at higher current densities. Insight gained from this project will provide guidance in designing solid polymer electrolytes (or protective layers) that prevent the growth of dendrites on lithium metal.

At the end of this project, a mathematical model will be developed that can capture the mechanical stress field, concentration and potential profiles around a dendritic protrusion. This model will allow estimation of the propensity for growth of such a protrusion and provide guidance in the design of solid polymer electrolytes (or protective layers) for the prevention of lithium dendrites.

Objectives

The goal of this project is to develop a continuum-based mathematical model to (i) investigate the impact of mechanical stress on the growth of dendritic protrusions and (ii) elucidate the competition between transport and mechanical means for preventing dendrite growth. Effectiveness of protective layers in preventing the growth of dendritic protrusions will also be studied. The main focus of this project will be to develop a microscale model that can capture the mechanical stresses and transport processes within lithium metal and adjacent electrolyte and/or protective layer. Impact of surface energy on growth of dendrites will be investigated. Possibility of plastic deformation within lithium metal and/or solid electrolyte material will also be elucidated along with its effect on propagation of dendrites. Propensity of fracture within the solid electrolyte interface layer (or the protective layer) and its impact on dendrite growth will be explored.

Approach

The present work examines the propensity for growth of a dendritic protrusion on a lithium metal electrode. Operation at low as well as high current density has been considered. Elastic-plastic deformations of both lithium metal and PEO-based polymer electrolyte have been taken into account. To capture the correct mechanical deformation of the lithium metal anode, dendritic protrusion and polymer electrolyte, the momentum balance (equilibrium) equation has been solved throughout the system. For estimation of the current distribution, the primary current (due to potential gradient), secondary current (due to electrode

kinetics), and tertiary current (due to concentration gradient) have been calculated. This requires solving the charge and mass conservation equations coupled with the nonlinear Butler-Volmer electrode kinetics relation. During the charging process, lithium gets reduced at the metal anode. Since lithium gets plated on top of the electrode, no lithium transport equation needs to be solved within the lithium metal anode phase. However, charge transport within the electrolyte and the metallic anode phase must be determined. Also, local charge neutrality must be satisfied everywhere to ensure no accumulation of electric charge anywhere within the electrolyte or metallic lithium. This is accomplished by setting the time-dependent accumulation terms to zero within the charge transport equations.

To estimate whether a dendritic protrusion will grow into a complete dendrite or not, the reaction current at the peak (i_{peak}) and the valley (i_{valley}) is determined. The magnitude of reaction current is calculated using the modified version of the Butler-Volmer equation, which has contributions from both the mechanical-stress and concentration-overpotential induced components:

$$i_{bv}(x) = \exp\left(\alpha_a \Delta\mu_e / RT\right) \cdot F k_a^{\alpha_c} \left(k_c c_e\right)^{\alpha_a} \left[\exp\left(\alpha_a F \eta / RT\right) - \exp\left(-\alpha_c F \eta / RT\right) \right] \quad (1)$$

Here, k_a and k_c are the anodic and cathodic reaction rate constants, and α_a and α_c are the anodic and cathodic transfer coefficients, respectively. Also, $\Delta\mu_e$ indicates the electrochemical potential change induced by mechanical stresses and surface curvature effects. Moreover, F denotes Faraday's constant, R denotes the universal gas constant and T signifies the local temperature on the Kelvin scale. For the reduction of lithium ions at the lithium metal anode, the anodic and cathodic rate constants are assumed to be equal ($k_a=k_c$). Also, the anodic and cathodic transfer coefficients have been assumed to be equal for reduction of lithium metal by several other researchers, so that $\alpha_a=\alpha_c=1/2$. The magnitude of over-potential at the lithium-electrolyte interface is estimated as $\eta=\phi_s-\phi_e-U_{Li}$, which takes a negative value during the reduction process. Here, ϕ_s and ϕ_e indicate the solid phase potential and electrolyte phase potential, respectively. The open circuit potential for lithium metal has been denoted by U_{Li} , which is taken to be zero.

If the reaction current density at the peak of the protrusion is greater than that at the valley ($i_{peak}>i_{valley}$), dendrites can grow. Otherwise, under the condition that $i_{peak}<i_{valley}$, relatively flat lithium deposits would form. Here, propensity of dendrite growth will be analyzed based on the ratio of current at the peak and the valley.

Since the stress values around the dendritic protrusion appear within the modified Butler-Volmer relation (see Eq. (1)), mechanical deformation of lithium metal and polymer electrolyte must be determined appropriately. Since mechanical equilibration occurs at the speed of sound, it is much faster than the chemical reactions that occur at the lithium-electrolyte interface. Hence the quasi-static equilibrium equation, derived from the momentum balance relation, should be solved to capture the stress field. Also, under the application of sufficiently large tensile or compressive loads, all bulk materials deform in an elastic-plastic fashion. Lithium metal and polymer electrolytes are no exception to that. Hence, to determine the appropriate stress field around a dendritic protrusion, the exact elastic-plastic nonlinear stress-strain constitutive relations must be taken into consideration. To describe the elastic portion, Young's modulus (E_{Li} and E_{PEO}) and Poisson's ratio (ν_{Li} and ν_{PEO}) are sufficient. These are readily available in the literature for both lithium metal as well as PEO-based polymers. Characterizing the plastic deformation of lithium and the polymer electrolyte is more challenging. In the present context, a nonlinear hardening law has been. For both lithium metal and polymer electrolyte, the magnitude of the yield stress changes according to an isotropic strain hardening law.

Results

It has been observed in several experiments that dendrite growth in lithium metal can be prevented to some extent by the application of mechanical stress. However, how the stress field prevents the growth of dendrites has not been studied extensively. Newman et al., have published two articles investigating the stress state and subsequent deformation of lithium metal and the adjacent electrolyte phase (*JES* (2005) A396 and *JES* (2014) A1350), in which they considered lithium electrodes in a *pre-stressed* state. They found that prevention of dendrite growth by mechanical means is only possible by using electrolytes with shear modulus at least two times larger than that of lithium metal. The *pre-stressed* condition led to severe dendrite growth even during operation at extremely low current densities. The present study assumed that the lithium metal begins in a *relaxed* state. A schematic diagram of the *pre-stressed* and *relaxed* condition is shown in Figure II-339.

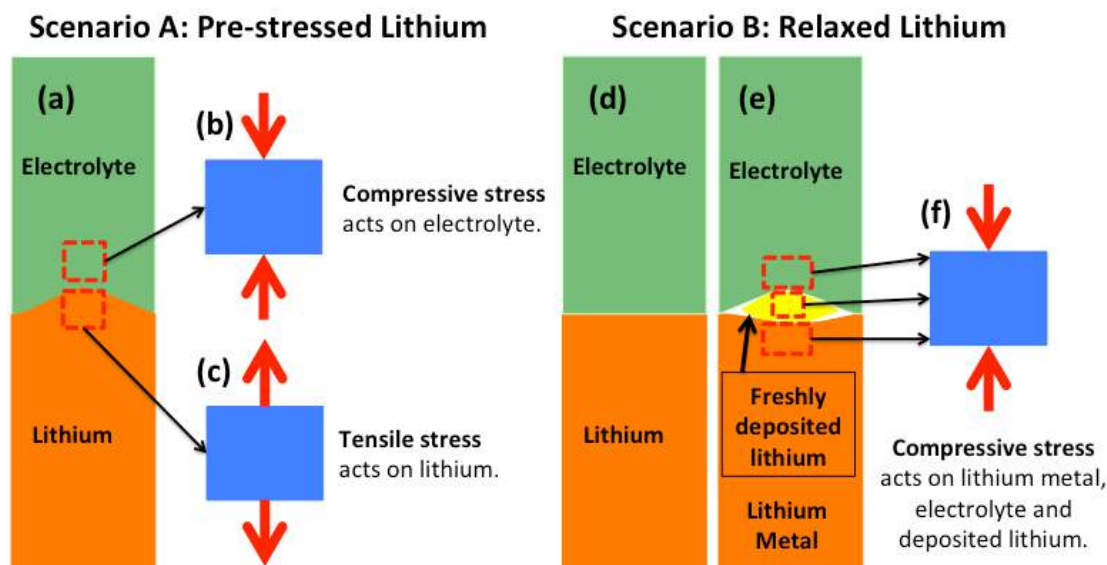


Figure II-339. (a-c) According to the *pre-stressed* lithium scenario, tensile stresses act within lithium metal and compressive stresses act inside electrolyte. (d-f) *Relaxed* lithium assumes stress-free condition for lithium metal and electrolyte. When fresh lithium gets deposited, bulk lithium metal, electrolyte and the newly deposited lithium experience compression.

Detailed simulations have been conducted to estimate the deformation and stress generation in a lithium metal protrusion and adjacent electrolyte for different shear modulus of the electrolyte phase. An electrochemical potential term has been defined that incorporates the impact of mechanical stress and surface tension into the effective exchange current density. Figure II-340(a-c) demonstrates that during operation at low current density, initially *relaxed* lithium does not lead to any dendrite growth, whereas the *pre-stressed* lithium leads to severe dendrite formation, which is not typically observed experimentally. Hence, for all subsequent analysis, lithium metal in an initially *relaxed* condition will be considered.

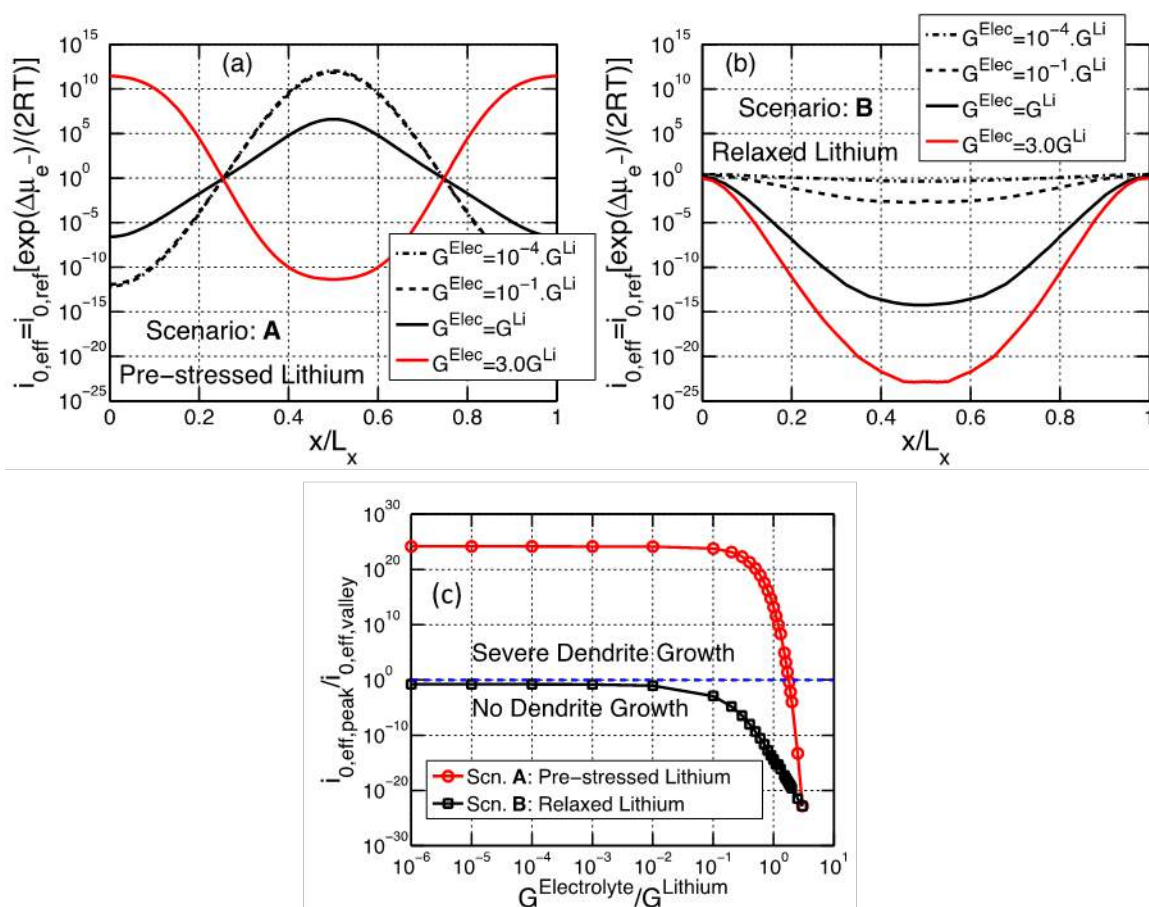


Figure II-340. (a-b) Variation in effective exchange current density around the dendritic protrusion. If the current at the peak is greater than that at the valley, dendrites grow. (a) For pre-stressed lithium. (b) For initially relaxed lithium. (c) Ratio of the effective exchange current density at the protrusion peak over that at the valley. For initially relaxed lithium, dendrite growth never occurs at low current operation.

Several researchers have argued that growth of dendritic protrusions during deposition of lithium metal can be prevented by the application of externally applied mechanical stress. This possibility is explored in the present project. In the first quarter, it was determined that the components of typical Li/solid electrolyte/Li cells are in stress-free states prior to assembly, which has significant implications for the evolution of tensile and compressive stress at the lithium-electrolyte interface. Work in the second quarter has built on this finding to investigate the effectiveness of a PEO-type polymer-based electrolyte in preventing the growth of dendritic protrusions. This has demonstrated that plastic deformation of lithium metal and polymer electrolyte must also be considered. Figure II-341(a) depicts the computational mesh for lithium metal with a dendritic protrusion and a PEO-based electrolyte, before and after cell assembly. Figure II-341(b) demonstrates that, under the assumption of only elastic deformation, the compressive stress that evolves within the lithium and polymer greatly exceeds the yield limits in both regions, over much of the interfacial region. Hence, proper elastic-plastic stress-strain constitutive relations must be used to correctly predict the hydrostatic and deviatoric stresses within the lithium and polymer regions.

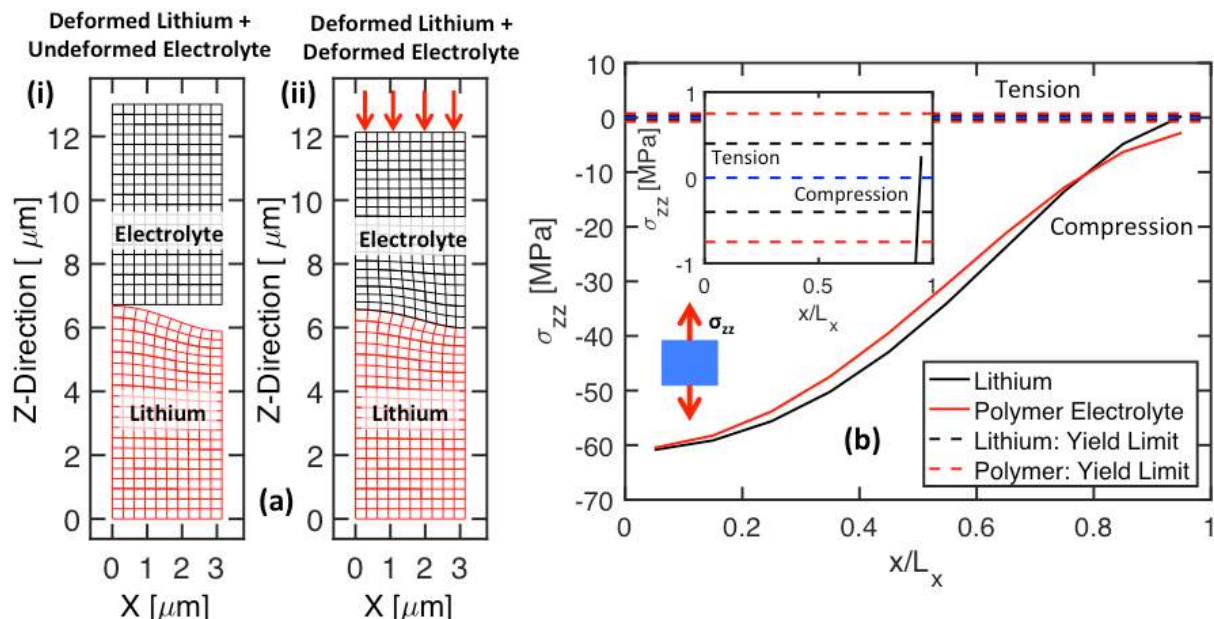


Figure II-341. (a) Lithium and polymer electrolyte regions (i) before assembly and (ii) after the regions are fully in contact. Both lithium and polymer have deformed plastically. (b) Stresses within lithium metal and polymer electrolyte regions under the assumption of only elastic deformation. The stresses exceed the elastic limits across much of the domain.

Nonlinear, isotropic elastic-plastic constitutive models including strain-hardening have been adopted to capture the stress-strain relationships observed in lithium metal and PEO-based polymers. Comparisons between the experimental data (obtained from literature) and the computational models for lithium and pure PEO are shown in Figure II-342(a) and Figure II-342(b), respectively. The ratio of effective exchange current densities at the protrusion peak and valley as a function of the electrolyte shear modulus is shown in Figure II-342(c), with the model including plasticity clearly predicting a much smaller current ratio.

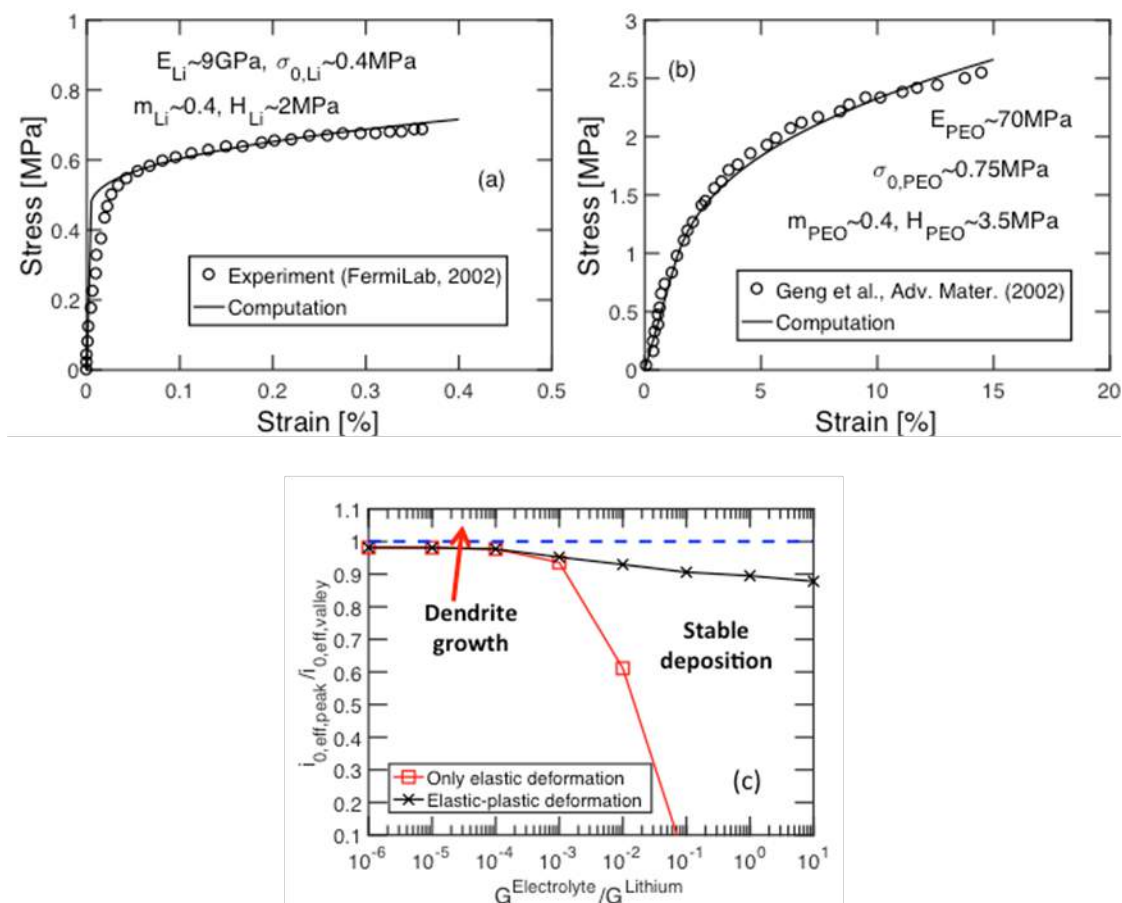


Figure II-342. (a) Computational model compared with elastic-plastic stress-strain experimental data. (b) Experimental stress-strain curve for PEO polymer and corresponding numerical model. (c) Ratio of effective exchange current density at the protrusion peak over that at the valley using purely elastic (squares) or elastic-plastic (crosses) models.

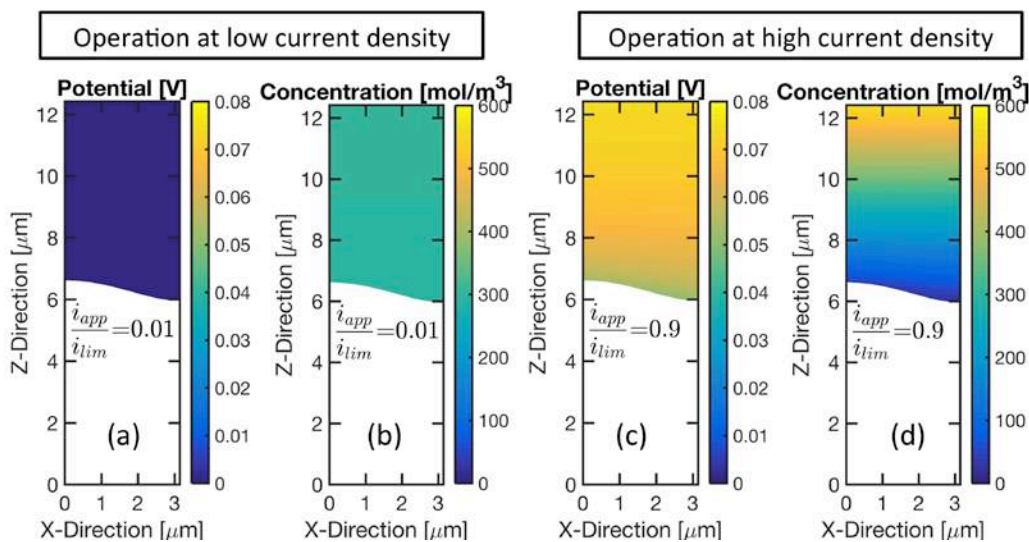


Figure II-343. Concentration and potential contour within the electrolyte around the dendritic protrusion at high and low rates of current. Potential in lithium metal remains extremely close to zero. (a) Potential contour for $i_{app} = 0.01 i_{lim}$. (b) Concentration contour for $i_{app} = 0.01 i_{lim}$. (c) Potential contour for $i_{app} = 0.9 i_{lim}$. (d) Concentration contour for $i_{app} = 0.9 i_{lim}$.

In a lithium ion battery, formation of lithium dendrites depends significantly on the distribution of potential and salt concentration within the electrolyte, which is again affected by the applied current density. The total reaction current around the dendritic protrusion should be estimated according to the Butler-Volmer equation. As shown in Eq. (1), The first exponential term is the mechanical-stress factor and the remaining portion is the conventional Butler-Volmer expression. Mass transport and charge balance equations have been solved in the electrolyte and the lithium metal. Figure II-343(a-d) shows the potential and concentration contours observed at low and high current density operations within electrolyte around the dendritic protrusion.

Variation in reaction current density from protrusion peak to valley has been shown in Figure II-344(a), by the black lines, for two different applied current densities (circle – high current, and square – low current). The reaction currents have been normalized with respect to the current density at the protrusion peak. Relative contribution from the mechanical-stress factor (blue line) and the concentration-overpotential factor (red line) has also been demonstrated. Figure II-344(b) depicts the reaction current ratio between protrusion peak and valley for different applied current densities. Present analysis indicates that, with polymer electrolytes, no dendrite growth should occur for applied current less than 40% of the limiting current. Model predictions are also consistent with experimental observations adopted from Brisot et al. (*Journal of Power Sources* (1999) 81-82 925-929).

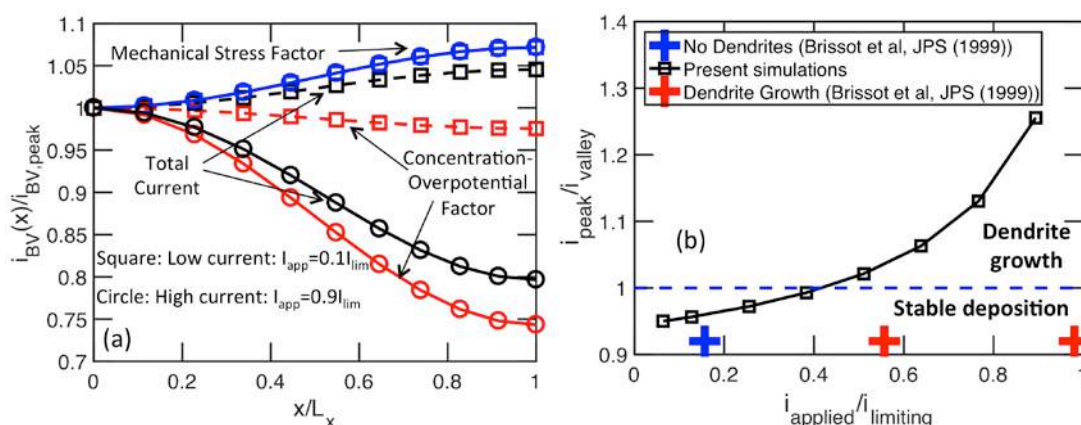


Figure II-344. (a) Distribution of reaction current from the peak to the valley at two different applied current densities. (b) Reaction current ratio between protrusion peak and valley for different applied current densities. Model predictions are consistent with experiments.

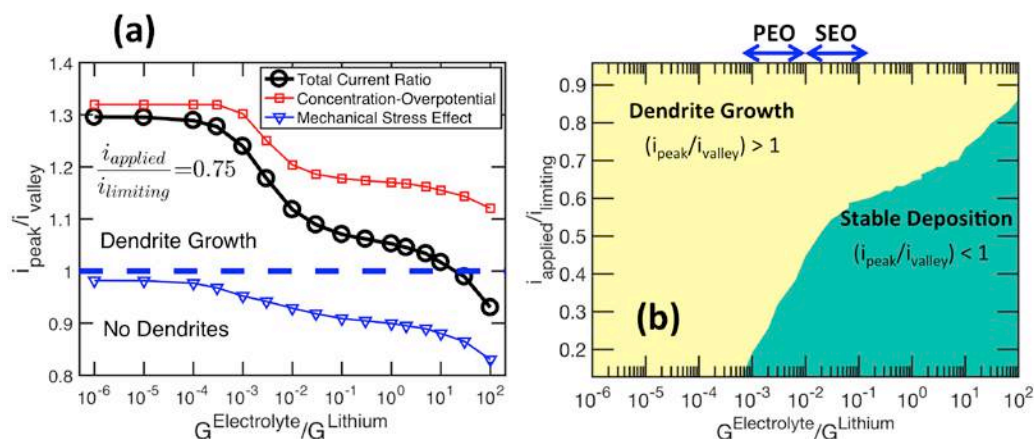


Figure II-345. (a) Impact of stress factor and current distribution factor on the overall reaction current density. Electrolytes with shear modulus 20 times larger than that of lithium may prevent dendrite growth. (b) Phase map demonstrating the correlation between applied current density and electrolyte shear modulus on lithium stabilization.

In the fourth quarter, we investigated the impact of electrolyte modulus on dendrite growth by incorporating elastic-plastic deformation of both metallic lithium and polymer electrolyte. A modified version of the Butler-Volmer equation has been adopted from existing literature that takes into account the impact of mechanical deformation induced strain energy. This expression has been used to determine the reaction current at the lithium/electrolyte interface. The two components of the Butler-Volmer equation are as follows: (i) The “mechanical stress factor” that takes into accounts the impact of strain energy and surface curvature effects, and (ii) The “current distribution factor” that takes into accounts the effect of concentration and potential distribution within the electrolyte. Figure II-345(a) compares the impact of mechanical stress induced component and the current distribution induced component of the Butler Volmer equation on the ratio of total reaction currents between the protrusion peak and the valley. Mechanical stress always tries to prevent the dendrites, whereas, the current distribution helps in growth of the dendritic protrusion. The combined effect clearly indicates that electrolytes with shear modulus 20 times larger than that of lithium, may be able to prevent the growth of dendritic protrusions. Figure II-345(b) shows a phase map between applied current density and electrolyte shear modulus, where the domain of stable lithium deposition has been clearly pointed out.

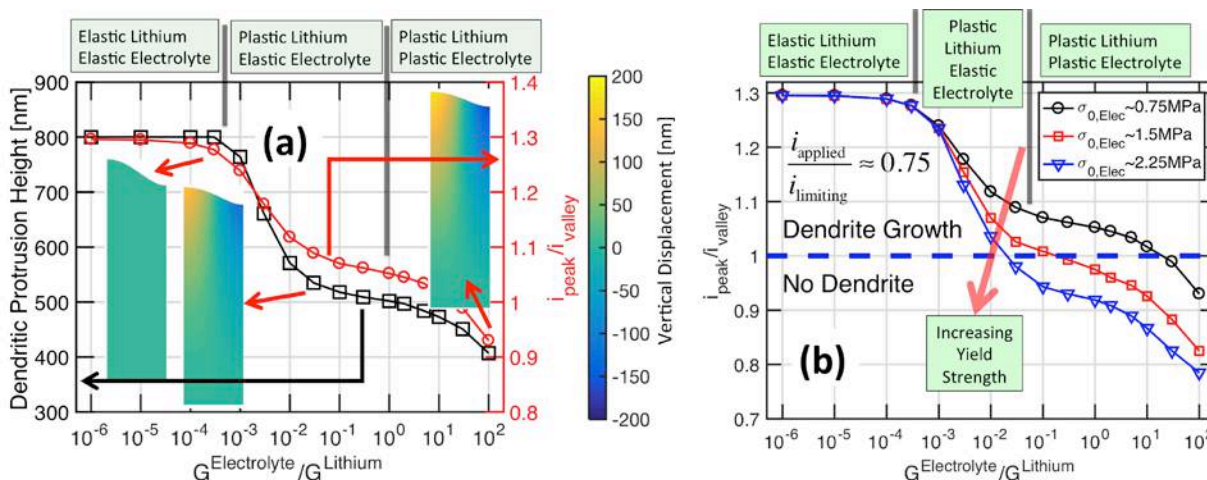


Figure II-346. (a) Effect of elastic-plastic deformation of both lithium metal and electrolyte on the overall suppression of the dendritic protrusion. (b) Increasing yield strength of the electrolyte may help to prevent dendrite growth even with present day polymer electrolytes.

Impact of elastic-plastic deformation experienced by both lithium metal and polymer electrolyte on the suppression of dendritic protrusion has been demonstrated in Figure II-346(a). For intermediate modulus electrolytes, where plastic flow of lithium occurs along with elastic deformation of the electrolyte provides the maximum suppression of dendritic protrusion. Following this realization, if we can improve the yield strength of the present day polymers by approximately three times, prevention of dendritic protrusion may be possible (see Figure II-346(b)).

Conclusions

A detailed computational methodology have been developed as part of the present research effort that can predict the elastic-plastic deformation and subsequent stress evolution within both lithium metal and adjacent solid electrolyte. Corresponding impact on the protrusion height (due to plastic flow of lithium) and reaction current density at the peak and the valley have been investigated. The mass transport and charge conservation equations have been successfully solved to determine the propensity of lithium dendrite growth under the influence of mechanical stress. It has been realized that there should exist critical current densities below which dendrite growth in polymer electrolytes will not occur. Also, yield strength of lithium metal and solid electrolyte (polymer in the present case) has significant impact on the overall growth of dendritic protrusions. Increasing the yield strength of present day low modulus polymer electrolytes can potentially lead to dendrite

free lithium deposition. The developed computational model can be easily extended to understand the impact of external pressure on the overall lithium dendrite growth process. Also the impact of transport parameters, such as, electrolyte conductivity, diffusivity and transference number, on the propensity of dendrite growth can be estimated using the developed computational model. One major drawback of the present model is the inherent assumption of homogeneous material parameters. Propensity of dendrite growth in solid state electrolytes with inhomogeneous grain-interior/grain-boundary microstructure cannot be captured using the present model.

Key Publications

1. P. Barai, K. Higa and V. Srinivasan. Effect of Initial State of Lithium on the Propensity for Dendrite Formation: A Theoretical Study. *Journal of the Electrochemical Society*. **164** (2) (2017) A180 – A189.
2. P. Barai, K. Higa and V. Srinivasan. Lithium Dendrite Growth Mechanisms in Polymer Electrolytes and Prevention Strategies. *Physical Chemistry Chemical Physics*. **19** (2017) 20439 – 20505.

II.E.2 Predicting and Understanding Novel Electrode Materials from First Principles (LBNL)

Kristin A. Persson, Principal Investigator

Lawrence Berkeley National Laboratory
1 Cyclotron Road
Berkeley, CA 94720
Phone: 510-486-7218
E-mail: KAPersson@lbl.gov

Tien Duong, Technology Manager

U.S. Department of Energy
Phone: 202-586-7836
E-mail: Tien.Duong@ee.doe.gov

Start Date: October 1, 2016
Total Project Cost: \$350,000

End Date: September 30, 2017
DOE share: \$350,000

Non-DOE share: \$0

Project Introduction

This project supports VTO's programmatic goal by developing next-generation, high-energy cathode materials and enabling stable cathode operation at high voltages through target particle morphology design, functional coatings and rational design of electrolytes.

During the last two years, we have focused on understanding the origin of performance limitations of Li-excess Mn-rich layered cathodes which have attracted the attention of the community due to their high capacity. We choose the end-member Li_2MnO_3 as a representative, 'worst-case' Li-rich and Mn-rich phase for our modeling work. In previous years, we investigated the bulk structure and the Li intercalation mechanisms, which in these materials includes inter-layer as well as intra-layer migration pathways. Interestingly, we found evidence of excellent Li mobility in these materials, which points to other mechanisms for the overall observed poor rate capability. Seeking the diffusion bottleneck elsewhere, we charted the particle morphology for pristine Li_2MnO_3 and found that all majority surfaces are prone to spontaneous, increasingly drastic oxygen evolution as a function of delithiation. This oxygen release is likely strongly related to surface phase transformation, surface densification and resulting impedance of Li intercalation into the material. Hence, in 2017, our research efforts focused on protecting the Li_2MnO_3 particle surface from oxygen release, which can be achieved e.g., by coatings or surface dopants. As a first attempt, we examined the possibility of using surface doping to enhance oxygen retention at the particle surface, using high-throughput first-principles calculations covering 38 elements spanning all transition metal, the post-transition metal, and metalloid elements.

Objectives

- New fundamental understanding of the cathode/electrolyte interface and the factors that control the interfacial chemistry and interfacial impedance
- Critical surface and coating design and optimization strategies that will improve cycling of LIB cathodes
- Understanding the factors that govern stability in non-aqueous electrolytes for Li-ion and Li-S systems

Approach

- Determine matrix of candidate surface dopants for improved oxygen stability through literature search and first principles calculations.
- Evaluate dopant affinity within the surface and bulk LiMnO_3 .

- Screening a range of dopants on the dominant and sub-dominant surfaces.
- Identify most promising dopants.

This research used resources of the National Energy Research Scientific Computing Center, a DOE Office of Science User Facility supported by the Office of Science of the U.S. Department of Energy under Contract No. DE-AC02-05CH11231.

Results

To identify the most efficient dopant, we investigated 38 elements containing all transition metal, the post-transition metal, and metalloid elements. We assume, for efficiency, that the dopant element would be added during the synthesis of the cathode material. We designed our screening following three selection Tiers:

1. Promotion of dopants that preferentially segregate towards the surface comparing defect formation energies between the surfaces and bulk (Figure II-347).
2. Elimination of dopants that have a strong driving force to form secondary impurity phases instead of residing within the cathode material (Figure II-348).
3. Promotion of dopants that increase oxygen retention at the surface of the cathode particle, by calculating the oxygen release energy difference between the doped surface and the pristine surface (Figure II-349).

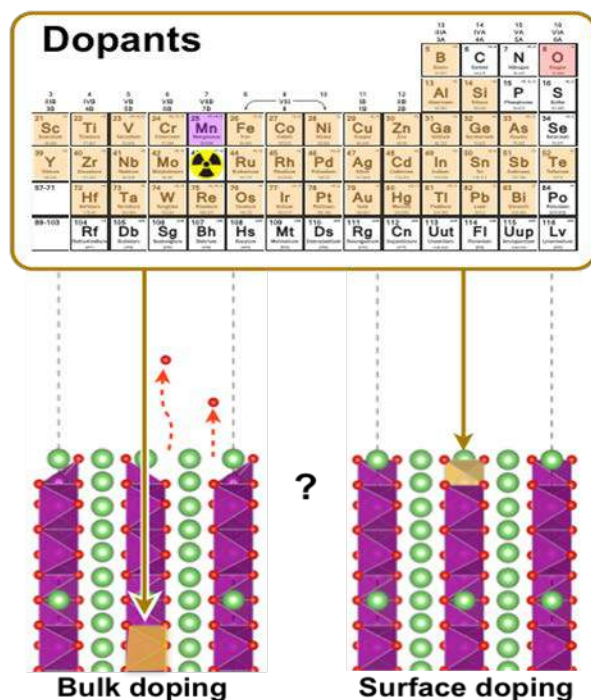


Figure II-347. Illustration of the initial screening process including the range of considered elements and the preference of surface dopant occupancy to enhance oxygen retention at the surface.

All stable facets including two dominant surfaces ((001) and (010) and two sub-dominant surfaces ((100), (110), and (111)) of Li_xMnO_3 were included in each calculation. In the first Tier, we examine the defect segregation energy defined as:

$$E_S = \Delta E^{bulk} - \Delta E^{surface}$$

Where ΔE^{bulk} represents the energy difference between the doped and undoped bulk, and $\Delta E^{surface}$ shows the equivalent quantity for surface. Hence, a positive E_s indicates a dopant which preferentially occupies the surface. Our calculations show that the defect preferences depend somewhat on the specific surface chemistry and morphology. For example, Co generally prefers to reside in the bulk as compared to the surface, yet the (001) surface is less preferred than e.g., the (110) surface. Therefore, optimal candidate dopants segregate to the surface for all dominant facets.

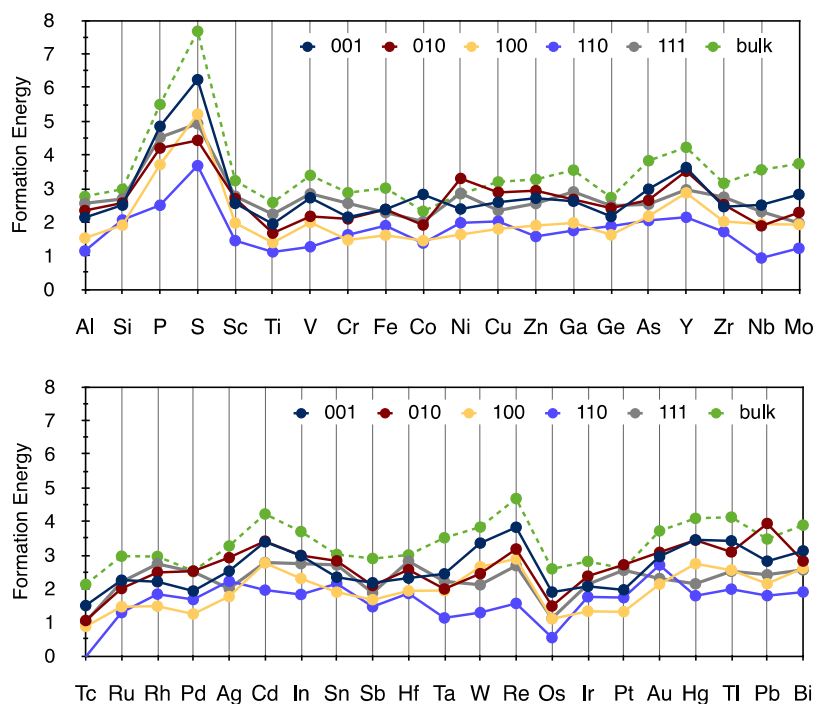


Figure II-348. The defect formation energy of each stable surface facet as compared to the bulk, covering defect transition metal, post-transition metal, and metalloid elements.

To eliminate dopants that have a strong preference towards forming undesirable impurity phases, the dopant defect formation energy is examined as;

$$E_D^S = (\Delta E^{target} + E^{bulk}) - E_{hull}^{MP}$$

where ΔE^{target} represents the energy difference between the doped and undoped target system, E^{bulk} the bulk energy of Li_2MnO_3 , and E_{hull}^{MP} the energy above the convex hull of the composite system. The E_{hull}^{MP} values are listed in the public open database (MaterialsProject.org) and represent the most likely impurity phases that would form under the conditions where Li_2MnO_3 is formed. All surface defect formation energies exhibit positive numbers which indicate a metastable surface doping process. Consistently, most of the surface defect formation energies are lower than the comparative bulk (green dashed line in Figure II-348). Dopants with limited tendency to form impurity phases are those with lower positive defect formation energies.

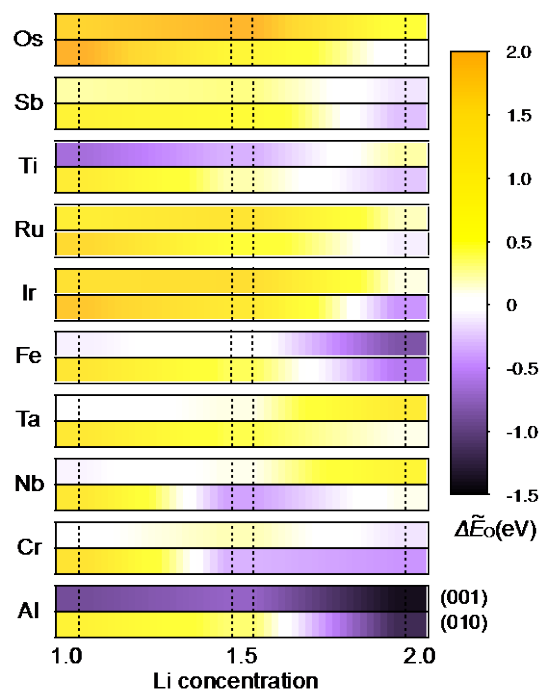


Figure II-349. The relative surface oxygen release energy for the top 10 candidate dopants as compared to the pristine systems shown for representative (001) and (010) surface facets. A dark yellow color indicates stronger oxygen retention, while a purple color indicates less protection against oxygen release as compared to the pristine, undoped surface.

The top 10 candidate dopants selected through Tier 1 and 2, are Os, Sb, Ti, Ru, Ir, Fe, Ta, Nb, Cr, and Al. In the final Tier 3, we calculate the oxygen evolution energy difference between the doped surface and the pristine surface. We define the relative oxygen release energy as;

$$\Delta\tilde{E}_O = \tilde{E}_O^{doping} - \tilde{E}_O^{pristine}$$

Figure II-349 shows $\Delta\tilde{E}_O$ of the top 10 candidate dopants obtained from the two first selection criteria. Here, $\Delta\tilde{E}_O$ is provided for the (001) and (010) surfaces as the two dominant surfaces of Li_xMnO_3 . The oxygen evolution energy of the pristine surface $\tilde{E}_O^{pristine}$ was defined in our previous work using the slab vacuum mode. Each color in Figure II-349 represents the relative oxygen evolution energy as compared to the pristine surface, therefore, yellow (purple) colors indicates an improved (decreased) oxygen retention relative to the pristine surfaces. The underlying atomistic reason for the improved the oxygen retention can be understood by elucidating the influence of the dopant on the local electronic structure at the specific surface facet. We found that a strong hybridization between the oxygen p-orbitals on the surface and the surface defect d-orbitals promotes strong binding and hence oxygen retention. In Figure II-349, yellow colored elements exhibit strong electron energy hybridization.

In summary, our 3-Tier screening identified Os, Sb, Ru, Ir and Ta as optimal candidate dopants to be added during synthesis of Li-excess, Mn-rich cathode materials for improved surface oxygen retention. It should be noted that the higher concentration of the dopant at the surface, the better oxygen retention is expected. Exciting recent results from LBNL BMR co-PIs Chen and McCloskey confirm the ability of Ta doping to enhance oxygen retention of Li-excess, Mn-rich cathode materials.

Conclusions

Early cycle cathode degradation in Li excess cathode materials is correlated with spontaneous surface oxygen evolution, which causes densification of the surface and deteriorated transport. Hence, to address this issue, we computationally screened the periodic table for surface dopants to enhance surface oxygen-retention in Li-excess Mn-rich cathode materials. Using our three-tier screening process, we identified Os, Sb, Ru, Ir, Ta as optimal candidate dopants in representative, model material Li_xMnO_3 . As validation and verification, Ta-doped disordered Li-excess cathodes are being evaluated by co-PI Chen and McCloskey.

Key Publications

1. Yongwoo Shin and Kristin A. Persson, “Surface Morphology and Surface Stability against Oxygen Loss of the Li-excess Layered Cathode Material”, MRS Fall Meeting November 30th 2016, Boston MA
2. Predicting and Understanding Novel Electrode Materials From First-Principles, by Yongwoo Shin and Kristin A. Persson, AMR 2017, Washington

II.E.3 First Principles Calculations of Existing and Novel Electrode Material (LBNL)

Gerbrand Ceder, Principal Investigator

Lawrence Berkeley National Laboratory
1 Cyclotron Road, MS: 33-146
Berkeley, CA 94720
Phone: 510-486-7193
E-mail: gceder@berkeley.edu

Tien Duong, Technology Manager

U.S. Department of Energy
Phone: 202-586-7836
E-mail: Tien.Duong@ee.doe.gov

Start Date: October 1, 2015
Total Project Cost: \$692,616

End Date: September 30, 2019
DOE share: \$692,616

Non-DOE share: \$0

Project Introduction

It was recently demonstrated that cathode materials based on Li-excess disordered transition metal oxides (LEX-RS) can deliver high capacities and sustain efficient Li transport provided Li is in an excess of at least 10% with respect to the transition metal concentration, creating a network of 0-TM channels through which Li can diffuse [1,2]. While only a small subset of TM species (Mn, Ni, Co) stabilizes the conventional layered oxide structure, compositions that form cation-disordered compounds comprise a larger TM compositional space, including Ti, V, Cr, Fe, Zr and Nb. Besides the increased design space, cation disorder is also beneficial for structural stability upon extended electrochemical cycling, as disordered structures undergo smaller volume changes upon Li extraction than layered structures [1]. The high capacity generally observed for LEX-RS oxide cathodes relies on oxygen redox processes which can cause oxygen loss near the surface of the particles. This results in the creation of high impedance surface layers and large polarization of the voltage profile, leading to poor cycling performance [3]. By contrast, reversible oxygen redox processes have the potential to enable high energy density by delivering excess capacity beyond the theoretical transition metal redox capacity at a high voltage. We have found that specific chemical and structural features in Li-excess metal oxides introduce labile oxygen electrons that can be easily extracted and participate in the practical capacity of these materials [4].

The development of percolation theory for LEX-RS has proven to be powerful for finding novel Li-ion cathode materials with high capacity and energy density. Recently, we succeeded in designing a new class of Li-excess cation disordered Li-Ni-Ti-Mo oxides that delivers up to 250 mAh/g and 750 Wh/kg at 10 mA/g [5].

Objectives

Develop very high capacity layered cathodes with high structural stability (>250 mAh/g) and high surface stability. Clarify the role of the initial structure as well as that of structural changes upon first charge and discharge. Clarify the role that Li-excess and cation disordered play in capacity and structural stability. Develop predictive modeling of oxygen charge transfer and oxygen loss and find ways to make oxygen redox beneficial in terms of increasing capacity. Develop materials with engineered surface passivation which does not lead to impedance increase. Study the effect of fluorination on electrochemical performance.

Approach

A combination of first-principles computations and experimental synthesis/characterization are used to evaluate existing and novel materials. Voltages and intercalation curves are calculated with GGA+U, and if highly accurate results are required hybrid functionals (HSE) are used. Phase diagrams are calculated with the Materials Project infrastructure based on high-throughput computations. Configurational disorder for elevated

temperature and off-stoichiometry is modeled with either point defect models (when off-stoichiometry is small) or with the cluster expansion for larger disorder. Ion mobility is evaluated with the Nudged Elastic Band Method or with direct Molecular Dynamics Simulations. Thermal stability is investigated with the approach developed previously under this program. Some of the computational work is performed in collaboration with Persson and with the Materials Project. Work on Li-excess layered materials is done in coordination with Persson (computational) and with the experimental efforts in the BMR Program (e.g., Chen).

Results

Computational approach to predict cation disorder and synthesis temperature

Owing to the large number of possible constituents it is practically infeasible to scan all possible compositions for their stability, and thus concrete design guidelines are required. We have recently demonstrated that high-throughput computations allow for the systematic screening of select composition spaces [6], but a qualitative understanding of the origin of cation disorder is desirable.

According to the Hume-Rothery rules, a species is likely soluble in a metal if the atomic sizes are within about 15%. We find that, in Li-TM oxides, similar cation radii are also a requirement for stable cation-disordered structures, but this alone is not a sufficient criterion. Even small ionic radius differences give rise to distortions of the octahedral TM sites that affect the stability.

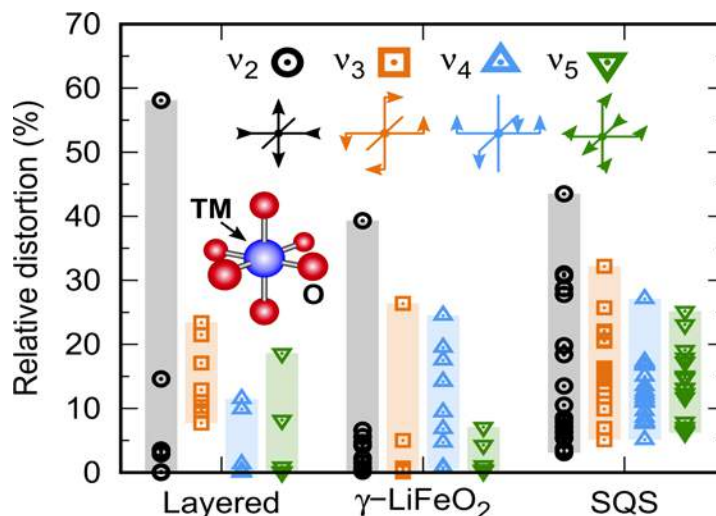


Figure II-350. Maximal TM site distortion relative to the original bond lengths in ordered LiTMO₂ ground state structures and in cation-disordered LiTMO₂ structures. Contribution of the four symmetry-breaking normal modes, v_2 through v_5 , to the site distortions are shown.

Figure II-350 shows the magnitude of the maximal TM site distortions in ordered LiTMO₂ ground state structures and special quasi-random structures (SQS) for all first- and second-row TMs except Mn and Tc. The site distortions are decomposed in contributions from the four symmetry-breaking normal modes of the octahedral point group. As seen in the figure, disordered structures generally exhibit distortions in all four modes whereas distortions of types v_2 and v_5 are small in most of the ordered structures. Depending on the electronic configuration of the TM species, these additional distortions may give rise to large energy penalties. In fact, it can be shown that only TM cations with d^0 configuration are insensitive with respect to the mode of distortion. As a consequence, in compositions containing at least one d^0 TM species (Ti^{4+} , Nb^{5+} , Mo^{6+} , etc.), sites occupied by the d^0 species may absorb the distortions required to stabilize the structure (Figure II-351). This conceptual understanding takes us one step closer to the rational design of new cation-disordered cathode materials for Li-ion batteries.

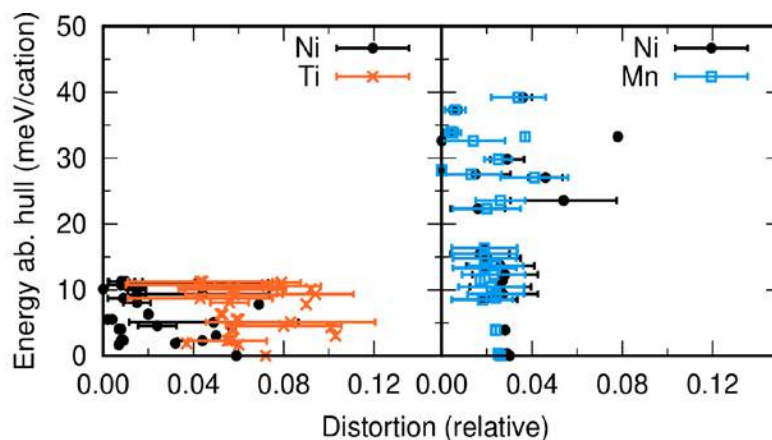


Figure II-351. Energy and relative TM site distortion in $\text{LiNi}_{0.5}\text{Ti}_{0.5}\text{O}_2$ and $\text{LiMn}_{0.5}\text{Ni}_{0.5}\text{O}_2$. Each data point corresponds to a single atomic structure. The error bars indicate the range of distortions for all sites of one TM species within that structure.

Investigate O K-edge XAS for cation disordered $\text{Li}_{1.25}\text{Mn}_{0.5}\text{Nb}_{0.25}\text{O}_2$

Our theoretical study shows that specific chemical and structural features in Li-excess metal oxides introduce labile oxygen electrons that can be easily extracted and participate in the practical capacity of these materials. In this project, we investigated O K-edge XAS for cation-disordered $\text{Li}_{1.25}\text{Mn}_{0.5}\text{Nb}_{0.25}\text{O}_2$ using first principles calculation.

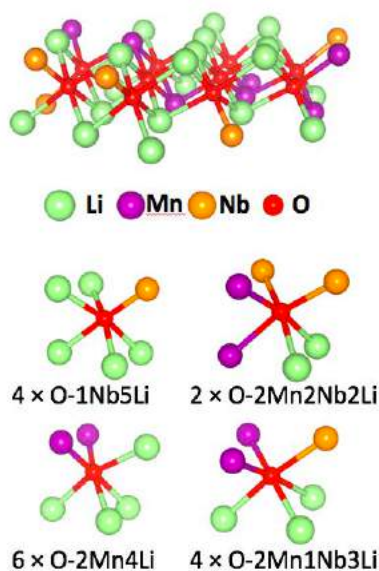


Figure II-352. Atomic structure of $\text{Li}_{1.25}\text{Mn}_{0.5}\text{Nb}_{0.25}\text{O}_2$ and its various oxygen local environments.

To prepare the atomic structure of cation-disordered $\text{Li}_{1.25}\text{Mn}_{0.5}\text{Nb}_{0.25}\text{O}_2$, all possible cation arrangements within the primitive unit cell of Li_3NbO_4 were created by an enumeration method. The lowest energy structure of this material was determined from the GGA+U energies of fifty cation arrangements with low electrostatic energies. Figure II-352 represents the atomic structure of the most stable structure of $\text{Li}_{1.25}\text{Mn}_{0.5}\text{Nb}_{0.25}\text{O}_2$, showing that it has various oxygen local environments.

The HSE06 hybrid functional was adopted to describe the relative energy level of metal and oxygen states accurately. The Z+1 approximation was employed to treat the core hole effect of XAS. O K-edge XAS of all individual oxygen atoms in $\text{Li}_{1.25}\text{Mn}_{0.5}\text{Nb}_{0.25}\text{O}_2$ and $\text{Li}_{0.75}\text{Mn}_{0.5}\text{Nb}_{0.25}\text{O}_2$ were calculated and summed to obtain

the total O K-edge XAS. The resolution of the computed spectra was reduced by convolution with Gaussian distribution and 1 eV of full width at half maximum (FWHM) to consider instrumental broadening of XAS. Computed and experimental spectra were aligned at the first peak to be comparable. Computed O K-edge XAS of $\text{Li}_{1.25}\text{Mn}_{0.5}\text{Nb}_{0.25}\text{O}_2$ and $\text{Li}_{0.75}\text{Mn}_{0.5}\text{Nb}_{0.25}\text{O}_2$ are in a good agreement with experimental ones, as shown in Figure II-353, validating the method used for computing O K-edge EELS spectra. The small discrepancy between computed and experimental XAS may be attributed to a slightly different composition.

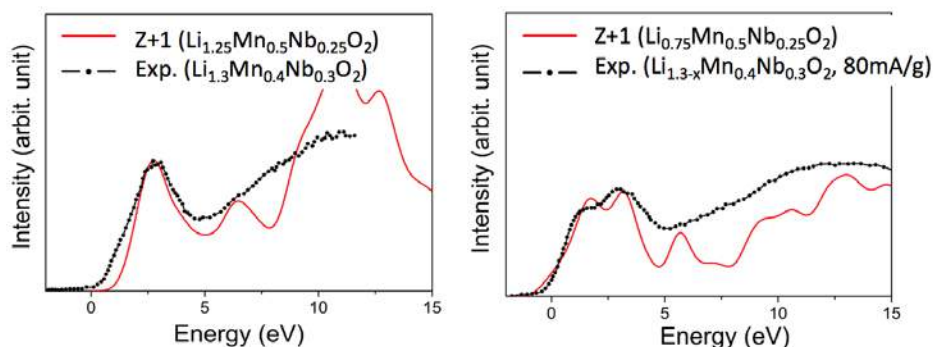


Figure II-353. Computed O K-edge XAS of $\text{Li}_{1.25-x}\text{Mn}_{0.5}\text{Nb}_{0.25}\text{O}_2$ ($x = 0$ and 0.5).

Design of Li-excess cation disordered Li-Ni-Ti-Mo oxides

We have designed a new class of Li-excess cation disordered Li-Ni-Ti-Mo oxides that delivers up to 250 mAh/g and 750 Wh/kg at 10 mA/g. To understand the origin of this remarkable performance, we applied a combination of *in-situ* X-ray diffraction (XRD), X-ray absorption near edge spectroscopy (XANES), electron energy loss spectroscopy (EELS) and electrochemistry, to elucidate the oxidation mechanism for a representative compound of that class, the $\text{Li}_{1.2}\text{Ni}_{1/3}\text{Ti}_{1/3}\text{Mo}_{2/15}\text{O}_2$ composition. Based on this detailed characterization, we were able to distinguish between $\text{Ni}^{2+}/\text{Ni}^{3+}$ oxidation, oxygen loss, and oxygen oxidation as separate redox processes, demonstrating the relationship of oxygen loss and capacity fading.

We obtained $\text{Li}_{1+x/100}\text{Ni}_{1/2-x/120}\text{Ti}_{1/2-x/120}\text{Mo}_{x/150}\text{O}_2$ ($x = 0, 5, 10, 15, 20$) compounds, in the following referred to as LNTMO and LNTMO $_x$ ($x=5, 10, 15, 20$), by traditional solid state synthesis. Figure II-354 shows the cycling performance of these materials (1.5–4.5 V, 20 mA/g), showing an increasing capacity with Li content. As seen in Figure II-354a, LNTMO20 delivers much higher capacity (~230 mAh/g) and energy density (~680 mAh/g) compared to LNTMO (~110 mAh/g, ~350 Wh/kg). More importantly, we note that the capacity of LNTMO20 significantly exceeds the theoretical $\text{Ni}^{2+}/\text{Ni}^{4+}$ capacity (=201.6 mAh/g), indicating other active redox couples in LNTMO20. The material also exhibits some capacity fading upon cycling, as shown in Figure II-354b. Motivated by these observations, we studied the oxidation mechanism and capacity fading with *in-situ* XRD, XANES, and EELS.

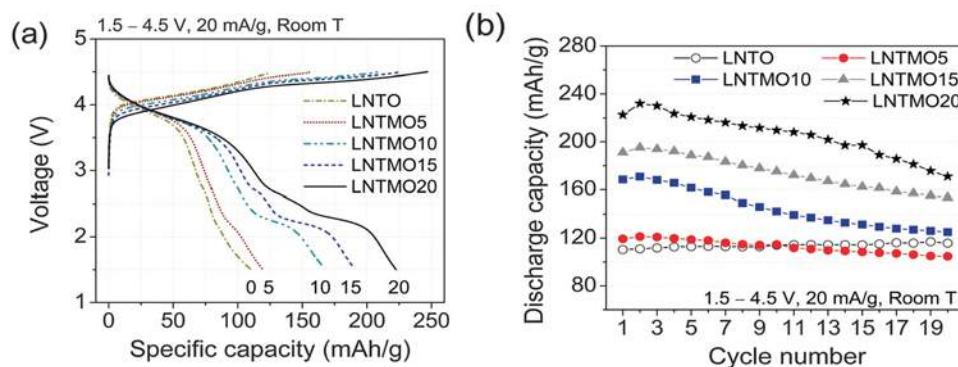


Figure II-354. (a) The first-cycle voltage profiles of LNTMO compounds. (b) Capacity evolution over 20 cycles.

Surprisingly, our XANES results show that only the $\text{Ni}^{2+}/\text{Ni}^{3+}$ redox couple is accessed, and Ni^{3+} is not oxidized further to Ni^{4+} , which accounts for around 110 mAh/g of the charge capacity. The remaining capacity has to originate from oxygen activity, i.e., either from oxygen loss or from reversible oxygen oxidation. As shown in Figure II-355a, charged to ~ 215 mAh/g, i.e., beyond $\text{Ni}^{2+}/\text{Ni}^{3+}$ oxidation, the lattice constant barely changes, indicating oxygen loss from the electrode surface. Finally, charging beyond ~ 215 mAh/g gives rise to a decrease of the lattice parameter, as oxygen oxidation contracts the oxygen framework by reducing the size of the oxygen ions.

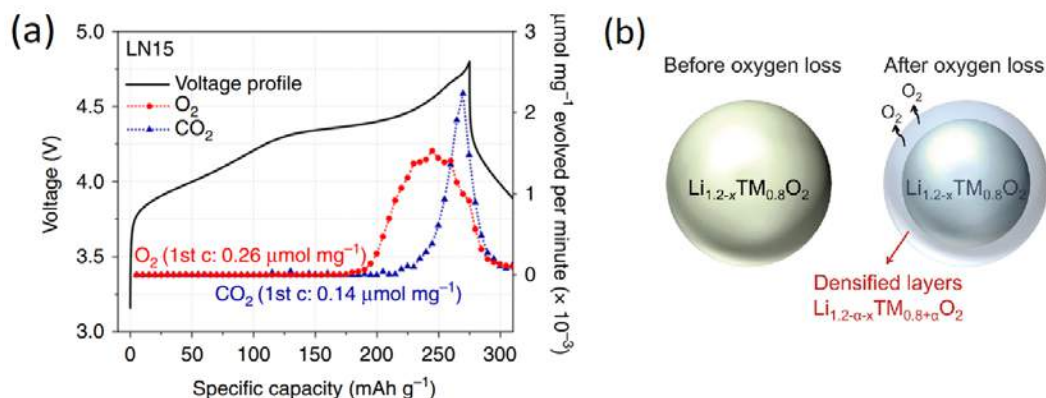


Figure II-355. (a) DEMS study of LN20 when charged to 4.8 V and discharged to 1.5 V at 20 mA g⁻¹, along with the DEMS results on O_2 (red circle) and CO_2 (blue triangle). (b) Illustrations of a LNTM020 particle before and after oxygen loss.

With this insight, the capacity fading on discharge can be attributed mainly to irreversible oxygen loss. From the differential electrochemical mass spectroscopy (DEMS) results shown in Figure II-355a, we can observe some amount of oxygen gas evolution at highly charged state (above 4.2 V). When oxygen is released from the particle surface, either oxygen vacancies or under-coordinated TM ions at the surface may diffuse into the bulk, creating new surface phases rich in TM. After such surface densification, the Li content drops below the percolation threshold ($\sim 9\%$ excess), and Li diffusion through the surface is no longer facile, causing the capacity fading. Currently, we are working on fluorination to reduce the irreversible oxygen loss so that capacity retention can be enhanced.

Fluorination of Li-excess disordered (rocksalt) transition metal oxides

Our comparative study of the disordered oxides $\text{Li}_{1.15}\text{Ni}_{0.375}\text{Ti}_{0.375}\text{Mo}_{0.1}\text{O}_2$ (LN15) and $\text{Li}_{1.2}\text{Ni}_{0.333}\text{Ti}_{0.333}\text{Mo}_{0.133}\text{O}_2$ (LN20), with fluorine-substituted $\text{Li}_{1.15}\text{Ni}_{0.45}\text{Ti}_{0.3}\text{Mo}_{0.1}\text{O}_{1.85}\text{F}_{0.15}$ (LNF15) [3] showed that, since fluorine substitution allows for more Ni^{2+} in the as-prepared material, it increases the metal-based redox reservoir of the cathode, reducing oxygen (O) redox and therefore O loss from the lattice on charge, and leading to significant improvements in electrochemical performance.

We performed TEM energy dispersive spectroscopy (TEM-EDS) to prove that fluorine is substituted in the bulk disordered lattice instead of forming secondary phases at the surface of the particles. As shown in Figure II-356 a, EDS mapping reveals a uniform distribution of fluorine in the LNF15 particle.

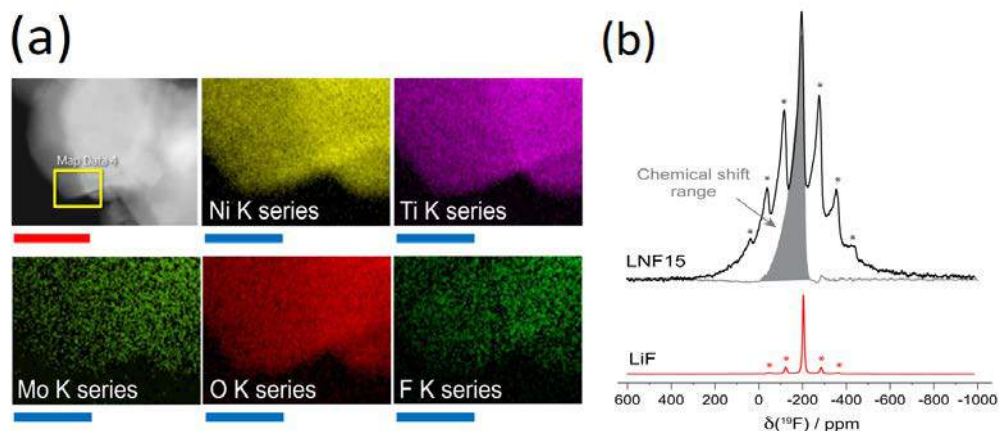


Figure II-356. (a) EDS mapping on one area of a LNF15 particle. Scale bars, red: 100 nm, blue: 25 nm. (b) ^{19}F spin echo NMR spectra obtained at 30 kHz MAS for LNF15 and LiF.

We also carried out ^{19}F solid-state nuclear magnetic resonance spectroscopy (ssNMR) to confirm that the fluorine distribution observed with TEM-EDS is not due to LiF on the surface of the particles. The ^{19}F NMR data presented in Figure II-356b show the presence of multiple broad fluorine local environments in LNF15, in contrast to the single fluorine site observed for LiF, confirming that F is doped into the bulk Li–Ni–Ti–Mo oxide lattice.

Figure II-357a&b are showing electrochemical properties of LN15 and LNF15 when cycled between 1.5 V and 4.6 V at 20 mA g^{-1} at room temperature. We can see obvious improvement of both discharge capacity and energy density (from 194 mAh g^{-1} , 587 Wh kg^{-1} to 210 mAh g^{-1} , 681 Wh kg^{-1}). Differential electrochemical mass spectroscopy (DEMS) results show that LNF15 has less oxygen loss compared to LN15 (Figure II-355a), indicating less irreversible oxygen oxidation.

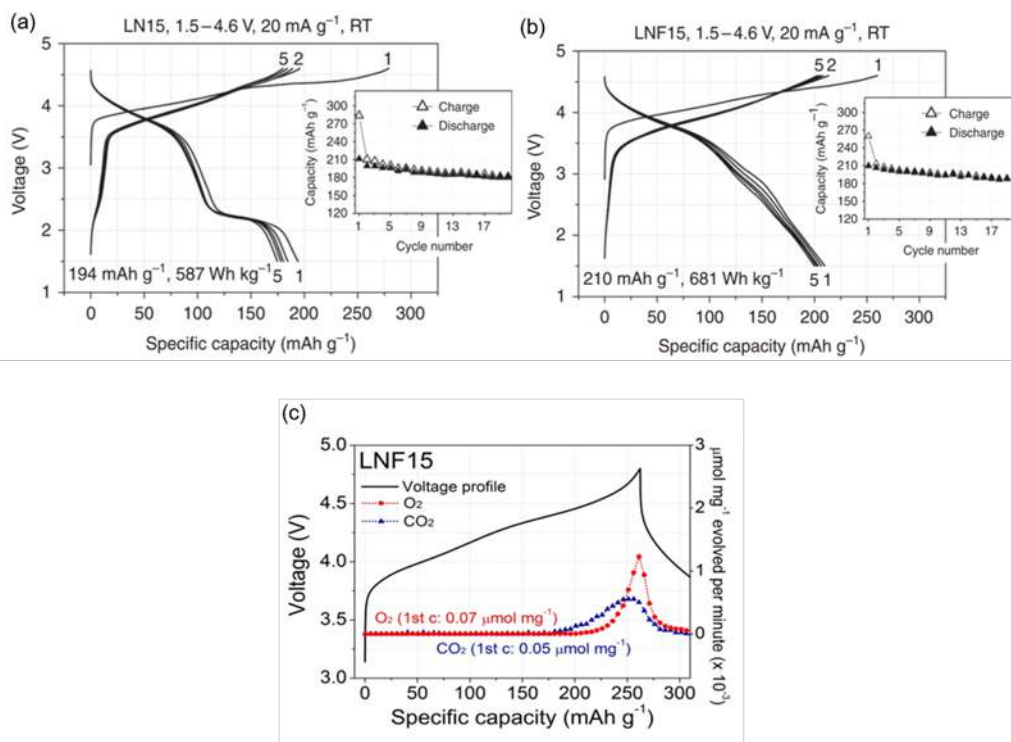


Figure II-357. (a) & (b) Cycling performance of LN15 and LNF15. (c) DEMS study of LNF15.

Conclusions

The work carried out over the past year has resulted in important progress in our understanding of ordered and cation-disordered Li-excess cathode materials. Using rigorous electronic structure theory, we demonstrated that d^0 transition metal species (Ti^{4+} , Nb^{5+} , Mo^{6+} , etc.) promote cation disorder, thereby providing a straightforward design criterion for novel disordered compositions. To investigate oxygen redox in Li-excess cathodes, we developed and benchmarked a first-principles methodology for the calculation of oxygen K-edge X-ray absorption spectra. This approach will aid the interpretation of experimentally measured spectra in the future. We further succeeded in designing a new class of Li-excess cation disordered Li-Ni-Ti-Mo oxides (LNTMO) that delivers up to 250 mAh/g and 750 Wh/kg at 10 mA/g. Based on results from various characterization methods (*in-situ* XRD, XANES, EELS and electrochemistry), we showed that the redox mechanism in LNTMO is highly complex and involves $\text{Ni}^{2+}/\text{Ni}^{3+}$ oxidation, oxygen loss, and oxygen oxidation as separate redox processes, demonstrating the relationship of oxygen loss and capacity fading. Finally, we found that fluorine doping of the LNTMO materials is feasible and results in a reduction of oxygen release as measured by differential electrochemical mass spectrometry. This finding demonstrates that oxygen loss can be prevented in Li-excess disordered cathodes with very high capacities, pointing to an exciting new direction for the development of high energy-density Li-ion batteries.

Key Publications

1. W. D. Richards, S. T. Dacek, D. A. Kitchaev, G. Ceder, *Adv. Energy Mater.* 2017, 1701533. <https://doi.org/10.1002/aenm.201701533>
2. Lee, J., Papp, J.K., Clément, R.J., Sallis, S., Kwon, D.H., Shi, T., Yang, W., McCloskey, B.D. and Ceder, G., 2017. Mitigating oxygen loss to improve the cycling performance of high capacity cation-disordered cathode materials. *Nature Communications*, 8(1), p.981.
3. Urban, A., Abdellahi, A., Dacek, S., Artrith, N. and Ceder, G., 2017. Electronic-Structure Origin of Cation Disorder in Transition-Metal Oxides. *Physical Review Letters*, 119(17), p.176402.
4. Lee, J., Seo, D. H., Balasubramanian, M., Twu, N., Li, X., & Ceder, G. (2015). A new class of high capacity cation-disordered oxides for rechargeable lithium batteries: Li–Ni–Ti–Mo oxides. *Energy & Environmental Science*, 8(11), 3255-3265.

References

1. J. Lee, A. Urban, X. Li, D. Su, G. Hautier, G. Ceder, *Unlocking the potential of cation-disordered oxides for rechargeable lithium batteries*, *Science*, 343, 519-522 (2014).
2. A. Urban, J. Lee, G. Ceder, *The Configurational Space of Rocksalt-Type Oxides for High-Capacity Lithium Battery Electrodes*, *Advanced Energy Materials*, 4, 1400478 (2014).
3. Lee, J., Papp, J.K., Clément, R.J., Sallis, S., Kwon, D.H., Shi, T., Yang, W., McCloskey, B.D. and Ceder, G., 2017. Mitigating oxygen loss to improve the cycling performance of high capacity cation-disordered cathode materials. *Nature Communications*, 8(1), p.981.
4. Seo, D. H., Lee, J., Urban, A., Malik, R., Kang, S., & Ceder, G. (2016). The structural and chemical origin of the oxygen redox activity in layered and cation-disordered Li-excess cathode materials. *Nature chemistry*, 8(7), 692-697.
5. Lee, J., Seo, D. H., Balasubramanian, M., Twu, N., Li, X., & Ceder, G. (2015). A new class of high capacity cation-disordered oxides for rechargeable lithium batteries: Li–Ni–Ti–Mo oxides. *Energy & Environmental Science*, 8(11), 3255-3265.
6. Urban, A., Matts, I., Abdellahi, A., & Ceder, G. (2016). Computational Design and Preparation of Cation Disordered Oxides for High Energy Density Li Ion Batteries. *Advanced Energy Materials*, 6(15).

II.E.4 First Principles Modeling of SEI Formation on Bare and Surface/Additive Modified Silicon Anodes (TAMU)

Perla B. Balbuena, Principal Investigator

Texas A&M University
3122 TAMU
College Station, TX 77843
Phone: 979-845-3375
E-mail: balbuena@tamu.edu

Jorge M. Seminario, Co-Principal Investigator

Texas A&M University
3122 TAMU
College Station, TX 77843
Phone: 979-845-3301
E-mail: seminario@tamu.edu

Tien Duong, Technology Manager

U.S. Department of Energy
Phone: 202-586-7836
E-mail: Tien.Duong@ee.doe.gov

Start Date: April 1, 2013
Total Project Cost: \$714,128

End Date: March 31, 2017
DOE share: \$714,128

Non-DOE share: \$0

Project Introduction

The focus of this project is on SEI layer formation and evolution during cycling and subsequent effects on capacity fade through two concatenated problems: 1) SEI layers formed on lithiated Si surfaces, and 2) SEI layers formed on coated surfaces. Key issues that this project addresses include the dynamic evolution of the system and electron transfer through solid-liquid interfaces.

Objectives

This project aims to develop fundamental understanding of the molecular processes that lead to the formation of a solid electrolyte interphase (SEI) layer due to electrolyte decomposition on Si anodes, and to use such new knowledge in a rational selection of additives and/or coatings.

Approach

Investigating the SEI layer formed on modified Si surfaces involves analysis of the interfacial structure and properties of specific coating(s) deposited over the Si anode surface, characterization of the corresponding surface properties before and after lithiation, especially how such modified surfaces may interact with electrolyte systems (solvent/salt/additive), and what SEI layer structure, composition, and properties may result from such interaction. This study will allow identification of effective additives and coatings able to overcome the intrinsic deficiencies of SEI layers on bare surfaces. Once the SEI layer is formed on bare or modified surfaces, it is exposed to cycling effects that influence its overall structure (including the anode), chemical, and mechanical stability.

Results

Stability of growing solid-solid interfaces

At the onset of nucleation of new phases, one important property is the mechanical stability of the interface between the growing nuclei and the support. One possible test includes the evaluation of the electrostatic

potential of the system including the support phase in contact with the nucleating phase. At the interface, there is a discontinuity in this potential, the magnitude of which is an indicator of the degree of instability of the interface. The TAMU team has computed this indicator for various relevant interfaces as a nucleation advances. The interfacial electrostatic potential is illustrated in Figure II-358 for the nucleation of Li_2CO_3 over a graphite surface. Initially, CO_3 radical anions, products of decomposition of the solvent are adsorbed on the graphite edges, and generate the sites where the nucleation of Li_2CO_3 may take place. The potential shown at the top corresponds to that of the electrode surface; the first red arrow points to the potential of the exposed graphite edges. After that, there is a clear discontinuity in the potential which corresponds to the incipient nucleation of the Li_2CO_3 phase. The difference between the two peaks shown with the red arrows is the indicator of the stability of the interface. As the difference reduces, the interface is more stable. The idea can be extended to evaluate nucleation of a heterogeneous film on the electrode. K. Leung (Sandia) has modeled grain boundaries in a LiF film coating a Li metal surface. It was found that a substantial over-potential is needed to insert a Li atom ($\text{Li}^+ + \text{e}^-$) into the grain boundary core regions. As shown previously by this team, such Li atoms can carry an undesirable electric current and degrade the electron-blocking passivation function of SEI films; therefore it is important that they are minimized.

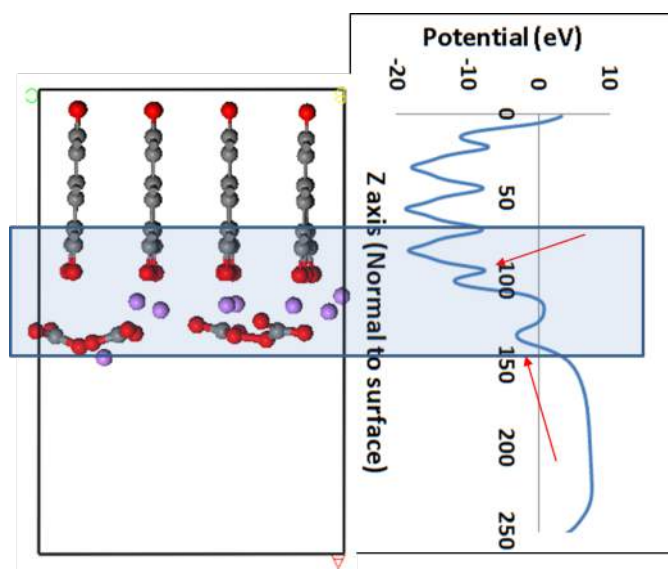


Figure II-358. Left: Nucleation of Li_2CO_3 over graphite electrode. Li ions interact with adsorbed O atoms at the graphite edge. Right: Electrostatic potential (eV) of the nucleating phase on the solid electrode. Note the discontinuity at the interface (highlighted).

Li ion transport through SEI layer

Rempe's group (Sandia) is using non-polarizable force fields to study Li^+ ion transport in SEI layers. They focus on the well-known component of SEI layers, di-lithium ethylene dicarbonate ($\text{Li}_2\text{-EDC}$). For fluids like EC, the Gaussian behavior of the self-part of the Van Hove function obtained from MD simulations is exact (Figure II-359, right). The non-Gaussian behavior of the "self" part in SEI layers further confirms that the SEI layer is glassy. To understand transport properties in this glassy SEI layer, the group next will use mode-coupling theory on the "self" part.

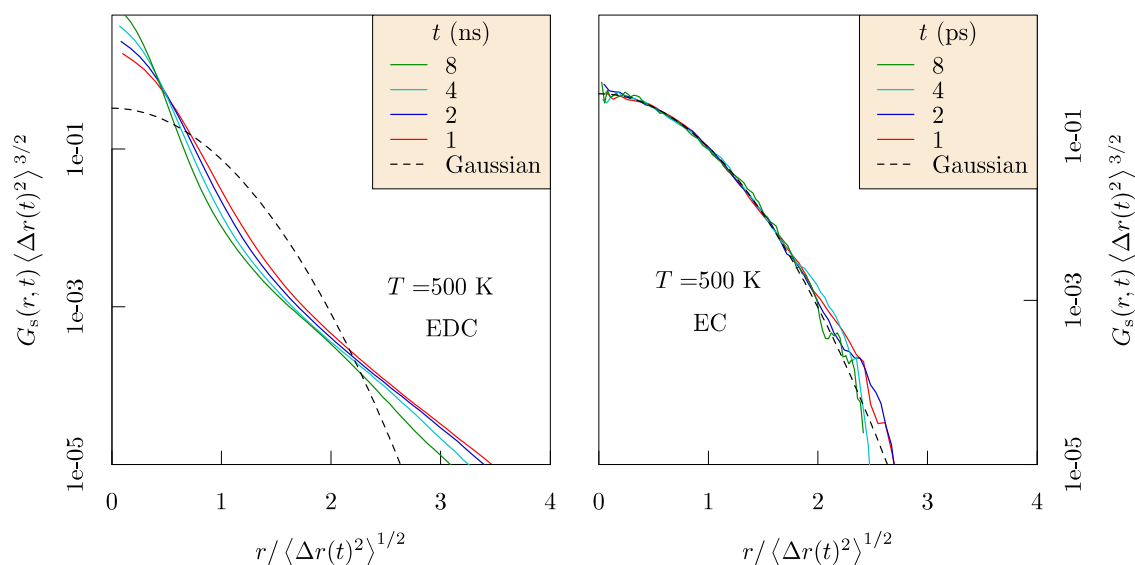


Figure II-359. Gaussian fit to the “self” part of van Hove function suggests Li_2EDC (left) is crystalline compared to pure EC (right). Correlations are calculated for ps compared to ns in the Li_2EDC case.

Electron transfer at the anode/SEI/electrolyte interface

We investigated the electron transport on various SEI products and oxides in four lithiation stages of the anode using a DFT-GF approach to understand early stages of SEI nucleation and growth. Results shown in Figure II-360 indicated that, in all Li_xSi_y cases, the current is significantly reduced with the addition of the SEI components as compared with the systems where no SEI element is present. Moreover, increasing the thickness of the SEI layer also resulted in a reduction of the electron transfer. Our results also indicate that at high voltages of ~ 5 V, $\text{Li}_2\text{Si}_2\text{O}_5$ presents a much higher resistance to electron transfer than Li_2CO_3 and SiO_2 . The current decreases exponentially as the SEI layer thickness increases, thus implying higher electron transport at initial SEI formation stages and then significantly slower steady growth.

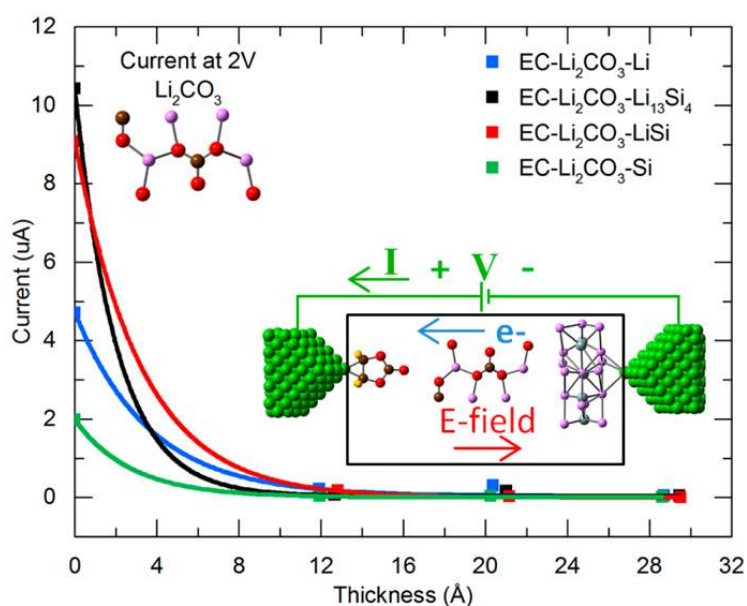


Figure II-360. Leakage current from the anode to the solvent through the SEI under an external voltage between two nanotips (green).

Ion transport from the cathode through the electrolyte to the anode

We investigated Li ion transport in a model nanobattery containing all the main elements: from the cathode through the electrolyte to a graphite anode, using classical molecular dynamics simulations. Figure II-361 illustrates the interaction energy experienced by one Li ion traveling under an applied potential through all the phases.

Region 1 (cathode) shows the Li-ion in the LiCoO_2 crystal with a potential energy average of -255 kcal/mol. After 4.62 ps the Li-ion has moved to the interface between regions 1 and 2 (electrolyte). An average energy of -36.7 kcal/mol is calculated in region 2, which represents the binding of the Li-ion with the electrolyte solution. The energy for the Li-ion to leave the cathode-electrolyte interface is 218.3 kcal/mol; this energy is supplied by the applied electric field. After the Li-ion has gone through the electrolyte, entered the anode, and has been reduced; its potential energy average in region 3 is 2.1 kcal/mol and the binding energy of the Li-ion at the anode-electrolyte interface is 38.8 kcal/mol. Notice that this is the energetics for one particular Li-ion, these energies are not representative averages as they simply allow us to obtain typical geometric structures of the Li-ion local environment.

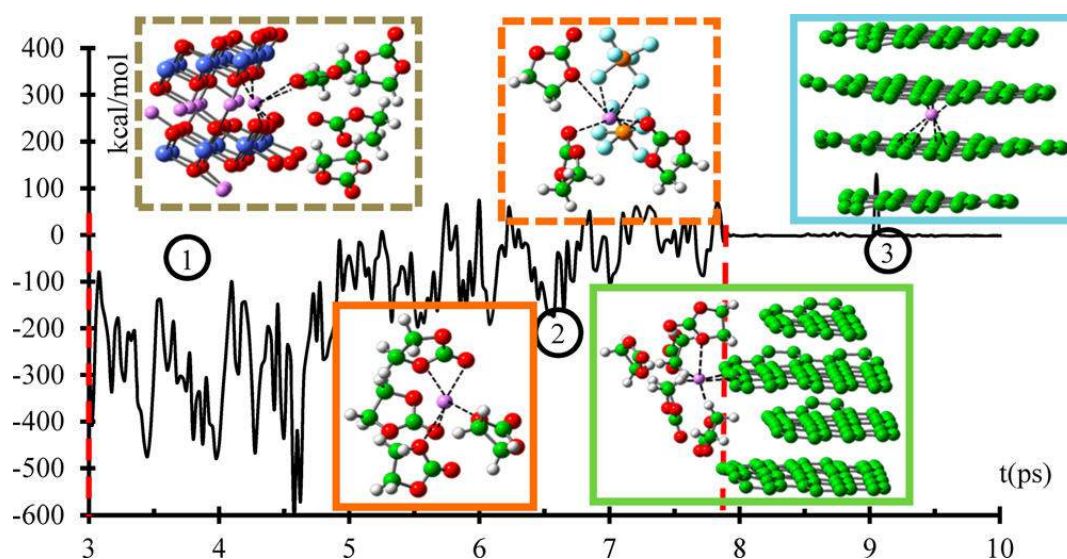


Figure II-361. Interaction energy (E) of one Li-ion with its nearest neighbors within a sphere of 6 \AA radius during charging with $E = 1.0 \text{ V/\AA}$. This is one particular trajectory of a Li-ion from the cathode (1) through the electrolyte (2) to the anode (3). From Ponce et al., JPCC, 121, 12959, (2017).

Alucone bonding and coordination

Current work in collaboration with NREL focuses on the reactivity behavior of an alucone coating deposited on a silicon anode. We studied the reactivity of the film using ab initio molecular dynamics (AIMD) simulations and were able to detect changes in the oxidation state of Al in the film, as well as changes in its coordination number, and structural changes inside the film. All of these properties are also being studied experimentally at NREL.

Some of the questions that we want to answer are: i) what is the coordination of Al?; ii) what changes occur to the structure of the film?; iii) what are the changes in oxidation state of Al?

Analyses based on AIMD simulations yield the following answers: i) Al coordination evolves with time, the most common is coordination 4. However higher coordination (e.g., $n = 5, 6$) tends to be observed at higher Li loading of the film. Kinetics of this process may be slow to be captured in the timeframe of the simulations. Also, 80+% Al atoms coordinate with O, and a few Al atoms coordinate with Si, C and H due to bond re-arrangement; ii) Transformations of structure inside the film include some H atoms from OH groups in alucone

may bond to Al; Al-hydride bonds may form in alucone when H from OH breaks and bonds to Al; iii) The dominant charge is +3, with very few Al atoms having charges of +2.

Passivation breakdown at Li metal anode interfaces with SEI layer

Effective passivation of lithium metal surfaces and prevention of battery-shorting lithium dendrite growth are critical for implementing lithium metal anodes for batteries with increased power densities. Nanoscale surface heterogeneities can be “hot spots” where anode passivation breaks down. Motivated by the observation of lithium dendrites in pores and grain boundaries in all-solid batteries, we examine lithium metal surfaces covered with Li_2O and/or LiF thin films with grain boundaries in them. Electronic structure calculations show that at >0.25 V computed equilibrium overpotential Li_2O grain boundaries with sufficiently large pores can accommodate Li^0 atoms which aid e^- leakage and passivation breakdown. Strain often accompanies Li insertion; applying a $\sim 1.7\%$ strain already lowers the computed overpotential to 0.1 V. Lithium metal nanostructures as thin as 12 Å are thermodynamically favored inside cracks in Li_2O films, becoming “incipient lithium filaments”. LiF films are more resistant to lithium metal growth. The models used in Leung’s group should in turn inform passivating strategies in all-solid-state batteries.

Conclusions

This work has provided several new insights into the nucleation and growth of SEI layers. During this year, the main findings were related to the analysis of the stability of the solid-solid interfaces inside the SEI. Moreover, such analysis was also extended to interfaces between electrode and solid electrolyte, where cracks or simply defects at the interfaces are potential places where Li metal can grow initially as thin wires and then propagate in dendritic growth. Solvation effects in liquid electrolytes were also examined. In particular atomistic details regarding the motion of Li ion through the electrolyte have been clarified. Finally, work is in progress for the characterization of artificial coatings modified by the formation of natural SEI layers.

Key Publications

1. L. Benitez and J. M. Seminario, “Electron Transport and Electrolyte Reduction in the Solid-Electrolyte Interphase of Rechargeable Lithium Ion Batteries with Silicon Anodes,” *J. Phys. Chem. C*, 120, 17978-17988, (2016).
2. K. Leung and K. L. Jungjohann, “Spatial Heterogeneities and Onset of Passivation Breakdown at Lithium Anode Interfaces,” *J. Phys. Chem. C*, 121, 20188-20196, (2017).
3. V. Ponce; D. E. Galvez-Aranda; J. M. Seminario, “Analysis of a Li-Ion Nanobattery with Graphite Anode Using Molecular Dynamics Simulations,” *J. Phys. Chem. C*, 121, 12959-12971, (2017).

II.E.5 Addressing Heterogeneity in Electrode Fabrication Processes (BYU)

Dean Wheeler, Principal Investigator

Brigham Young University
Department of Chemical Engineering
350 Clyde Building
Provo, UT 84602
Phone: 801-422-4126; Fax: 801-422-0151
E-mail: dean_wheeler@byu.edu

Brian Mazzeo, Co-Principal Investigator

Brigham Young University
Department of Electrical and Computer Engineering
459 Clyde Building
Provo, UT 84602
Phone: 801-422-1240; Fax: 801-422-0201
E-mail: bmazzeo@byu.edu

Tien Duong, Technology Manager

U.S. Department of Energy
Phone: 202-586-7836
E-mail: Tien.Duong@ee.doe.gov

Start Date: October 1, 2017
Total Project Cost: \$700,000

End Date: September 30, 2018
DOE share: \$700,000

Non-DOE share: \$0

Project Introduction

A lack of fundamental understanding about the relationships between fabrication parameters, microstructure, and performance prevents appropriate feedback and hurts the development of next-generation battery materials and process improvement in battery manufacturing. For instance, one problem with large-format batteries is ensuring uniformity in the manufacturing process, so that all components perform equally well and no component contributes unduly to performance limitations and failure. This improvement in manufacturing will not be possible without additional information on the nature of heterogeneities and how they relate to electrode fabrication steps. Even more beneficial is if the information is made available in a timely manner through the use of convenient and reliable experimental and modeling tools.

Objectives

The goal of this work is to better understand connections between fabrication conditions and undesired heterogeneity of thin-film electrodes by means of new non-destructive inspection techniques and computer models. This work will result in new diagnostic and modeling tools for rapidly and conveniently interrogating how well homogeneity has been maintained in electrodes during fabrication and in subsequent cycling. Real-time measurement of heterogeneity will enable manufacturer quality control improvements. The measurement and modeling tools will further enable researchers to compare different electrodes, improve formulations and processes, and anticipate cell performance of new designs.

Approach

Two non-destructive inspection techniques will be developed or improved which will characterize electrochemical and mechanical uniformity of the electrodes. The first tool will be a flexible contact probe on a polymer substrate for rapidly measuring local electrical conductivity across electrodes of any geometry. The second tool will be a new acoustic probe that measures local elasticity and density of the composite film. These

two prototyping efforts will be tied together by a particle-based microstructure model that allows prediction and correlation of electrode conductive and mechanical properties with fabrication conditions. Each of these tools involved one or more quarterly milestones.

In addition to model and tool development, the tools were used to begin examining electrodes sourced from other researchers, including from industry, in order to assess the effects of mixing and composition changes, and the effects of cycling. Partners in this effort included Ram Subbaraman (Bosch), Daniel Abraham (ANL), Kandler Smith (NREL), Bryant Polzin (ANL), Chisu Kim (Hydro-Québec), and Henning Dreger (TU Braunschweig). Other collaborations and the transfer of this technology to interested parties are being pursued.

Results

Milestone 1

Milestone 1 of FY 2017 and of the project as a whole was to demonstrate that the micro-flex-line probe (μ FLP), which is the flexible variant of the micro-N-line probe (μ NLP), obtains valid measurements of electrode-film electronic conductivity. Specifically the flex probe results were compared to those obtained for the previously validated μ NLP. Figure II-362 shows a side-by-side comparison of the geometry of the completed μ NLP and the μ FLP probes. In this case $N = 6$; that is, there are 6 parallel lines on the devices, 4 of which are used for any particular electrical measurement.

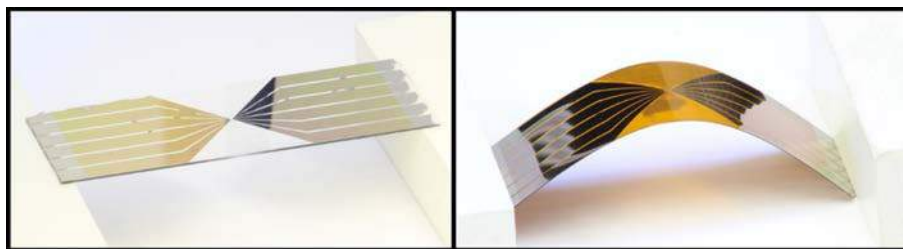


Figure II-362. Side by side comparison of the rigid μ NLP consisting of metal deposited on a glass substrate (left), and the flexible μ FLP consisting of metal deposited on a polyimide substrate (right).

The design and materials used to construct the μ FLP were iterated and improved to increase reliability of the measurements. Nevertheless, this should still be considered the first-generation design and further improvements are anticipated. For this report, the primary test material used is an anode provided by an undisclosed commercial battery manufacturer.

To obtain the results found in Table II-10, tests were performed as follows. Using a μ NLP, an electrical sample of the electrode film was collected in 9 independent locations and used with the inversion model to obtain average conductivity with 95% confidence interval. The process was then repeated on the same sample using the μ FLP.

Table II-10: Experimental conductivity results (with 95% confidence intervals) from using μ NLP and μ FLP on the same electrode sample.

	Rigid probe	Flex probe
Conductivity (mS/cm)	1421±33	1496±182

These results show that the μ FLP measures conductivity that is largely consistent with measurements of the rigid probe, though the significance level is not as high as ultimately desired. Through these and other results there are indications of a modest bias of the flex probe toward measuring larger conductivity values than does the rigid probe. This may be caused by a small amount of current leakage between lines on the flex probe.

Work will continue on the flex probe to confirm this hypothesis and reduce the problem so as to improve accuracy relative to other methods. It is anticipated that as the flexible probe becomes a more mature technology as a result of this project, it will allow conductivity measurements on thin-film electrodes in new geometries.

Milestone 2

Milestone 2 was to further demonstrate that the micro-flex-line probe (μ FLP), which is the flexible variant of the micro-N-line probe (μ NLP), can be used to make measurements of electrode-film electronic conductivity. The primary value of the flex probe is that it can be used to test much larger samples than the previous design, which will allow extension of this testing technology eventually to on-line measurement during the electrode manufacturing process.

Specifically for this milestone, the flex probe results are to be performed for three different electrode samples while the probe is mounted on the high-precision positioning system. Table II-11 shows results for three different commercial-grade electrodes provided by Argonne National Laboratory. The first two are cathodes while the last is an anode. At least 9 spatially separated points were used to obtain the averages and confidence intervals.

Table II-11: Experimental conductive property results (with 95% confidence intervals) from using μ FLP on the three electrode samples.

	AC005	C015	AA002
Conductivity (mS/cm)	241 \pm 15	198 \pm 5	3962 \pm 681
Contact Resistance (Ω cm²)	0.146 \pm 0.021	0.198 \pm 0.010	0.053 \pm 0.011

As during the previous quarter, the design and materials used to construct the μ FLP were iterated and improved to increase reliability of the measurements, and further improvements in future quarters were likewise realized. As further validation of the results, the values in Table II-10 have been compared to previous measurements using other methods (such as 4-line probe and the van der Pauw method) where available. The comparative results are consistent, though additional investigations are planned for ongoing validation.

During this and the prior quarter, additional samples were obtained from other researchers. Investigations were begun to use the current suite of tools to assess effects of formation and cycling on changes in electronic and ionic conductivity of electrodes. Additional work was begun to study the effect of different mixing processes on resulting electrode conductivities. It is anticipated that these studies will provide insight into what manufacturing practices can most efficiently increase needed conductivities and increase power and accessible energy of Li-ion batteries.

Milestone 3

Milestone 3 was to make improvements to the dynamic particle packing (DPP) microstructural model and validate that it can match experimental values of conductivity for one anode and two cathode films. A significant part of VTO-funded efforts at BYU has been to develop a versatile and accurate electrode microstructure prediction model. The model uses fundamental forces and interactions to determine particle dynamics and packing during all electrode-fabrication steps: mixing, coating, drying, and calendaring. The previous iteration of the model (FY15-16) was reasonably successful at predicting microstructure and transport and mechanical properties of dried films, but exhibited a few physical deficiencies. Thus a major overhaul was begun during the last year to incorporate smoothed-particle hydrodynamics (SPH) into the model to better describe slurry and solid bulk behavior and interfaces.

The model uses spheres with diameter $\sim 2\ \mu\text{m}$ to represent the carbon-binder domain and solvent. Active material particles were constructed from overlapping combinations of spheres; the technique allows different shapes such as bumpy spheroids and flattened discs that approximate the observed shapes of active-material particles. For this milestone there was an emphasis on the drying and calendaring steps with the new SPH framework, because these steps lead to substantial particle rearrangements that directly affect the electrode structure and therefore conductivity. Ionic conductive properties are compared in Table II-12, in which tortuosity can be considered a dimensionless resistance to ion movement. The results show that the model is semi-quantitatively correct for 3 different active materials (each having different particle shapes). Further refinement of the model parameters will be undertaken to achieve quantitative agreement with experiment for a range of physical properties. A comparison of modeled microstructures is likewise shown in Figure II-363, illustrating the complex pore structures able to be simulated by the model.

Table II-12: Simulated and experimental effective ionic transport results, following drying and calendaring steps.

Electrode	Simulation		Experiment	
	Porosity (%)	Tortuosity	Porosity (%)	Tortuosity
CPG-A12	43.9	4.3	36.1	3.4
Toda 523	44.3	5.4	30.0	3.1
Toda HE5050	49.4	3.6	36.1	2.9

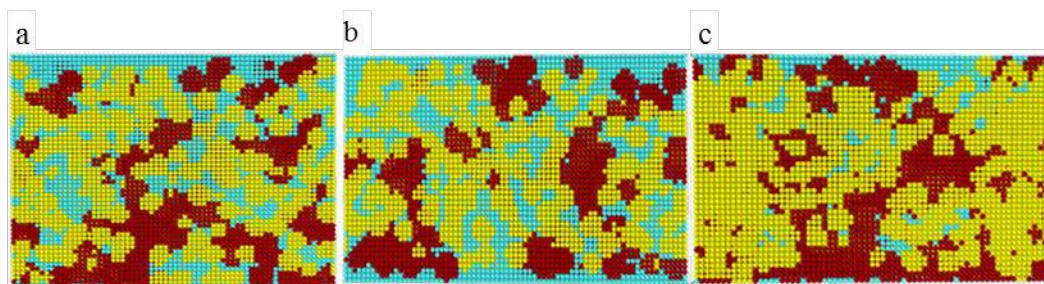


Figure II-363. Cross-section images from models of (a) CPG-A12, (b) Toda 523 (B), and (c) Toda HE5050; carbon-binder domain is red, active material is yellow, and larger pores are blue.

Milestone 4

Milestone 4 was to develop preliminary results for a new acoustic probe and associated model, with an associated Go/No-Go decision. Based on a successful outcome, the decision was made to continue developing the acoustic method of interrogating battery electrode films. The ultimate purpose of this type of test is to rapidly determine if there are mechanical variations in an electrode that would lead to poor electrochemical performance. This will allow improvement of the manufacturing process.

There are multiple means of using sound waves to analyze mechanical behavior of thin films. One method was to examine resonance frequencies. Figure II-364 depicts that the resonances of three cathodes with a $20\ \mu\text{m}$ aluminum current collector are seen to occur at different fundamental frequencies. Each of the cathodes had coating layers of different thicknesses ($42\ \mu\text{m}$, $38\ \mu\text{m}$, and $26\ \mu\text{m}$ coatings on top of the current collector) and densities. The purple line labeled “laser off” is a baseline reading to ensure that the peaks seen by the probe are not due room noise. The tendency of the resonance frequency showed in Figure II-362 demonstrates that the battery film acted more like a membrane, with $h^{-0.5}$ dependence, where h is the film thickness. The results were also confirmed by comparing the resonance frequencies obtained from a scanning laser doppler vibrometer (SLDV).

By fitting the acoustic measurements to the results of a numerical model, the Young's modulus was found in Table II-13. The thickness is the reported value from the manufacturer (of the coating only, not including the 20- μm -thick aluminum current collector), and the Young's modulus values are obtained from a combination of simulated experimental results.

Based on these results, the acoustic method exhibits enough sensitivity to distinguish different values of Young's modulus from different coating layers. It is anticipated that refinement of the method is required to give more accurate results and to enable more robust sampling in an industrial environment.

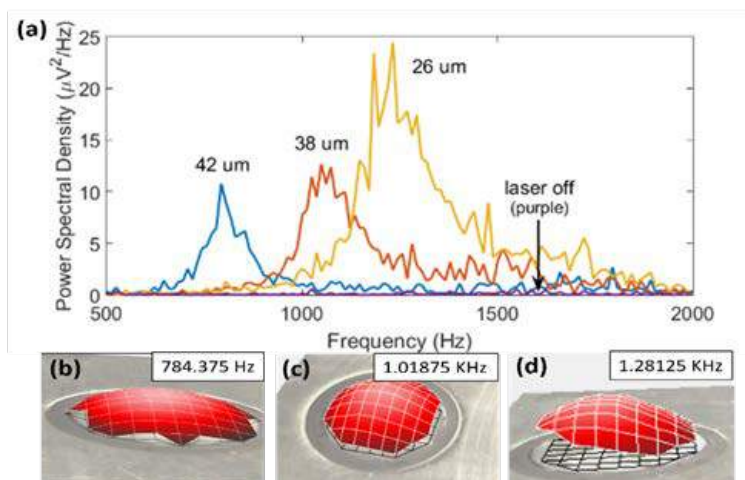


Figure II-364. (a) Power spectral density for various battery films. SLDV results of various battery films with thicknesses of (b) 42 μm (c) 38 μm (d) 26 μm

Table II-13: Measured and calculated properties of the battery films coated layer.

Coating	h (μm)	ρ (g/cm^3)	E (GPa), SLDV	E (GPa), peaks	ν
1	42	2.760	0.344	0.412	0.3
2	38	3.055	1.71	2.01	0.3
3	26	2.479	5.04	4.13	0.3

Conclusions

To date this work has led to

1. A redesign and manufacture of a flexible conductivity probe that improves accuracy and allow sampling of larger electrode films.
2. Electronic and ionic conductivity measurements comparing pristine and cycled commercial electrodes to quantify effects of cycling on microstructure and transport performance.
3. An improved dynamic particle packing (DPP) model to allow predictive insight into the slurry coating process.
4. A successful proof-of-concept acoustic probe used to determine electrode film stiffness.

In the next fiscal year, further improvements are anticipated, including work to adapt the probe technology to assessment of large or continuous samples, consistent with how Li-ion battery electrodes are made commercially.

Key Publications

The following publications were made during FY 2017 under VTO support. Additional manuscripts based on this work are under preparation.

1. D.R. Nevers, F.R. Brushett, and D.R. Wheeler, "Engineering radical polymer electrodes for electrochemical energy storage," *J. Power Sources* 352, 226-244 (2017).
2. M.M. Forouzan, M. Wray, L. Robertson, and Dean R. Wheeler, "Tortuosity of composite porous electrodes with various conductive additives in an alkaline system," *J. Electrochem. Soc.*, 164, A3117-A3130 (2017).

The following presentations at scientific conferences were made.

1. M. Mehdi Forouzan, Anthony Gillespie, Nicholas Lewis, Brian A. Mazzeo, and Dean R. Wheeler, "A Predictive Model of Lithium-Ion Electrode Fabrication, including Mixing, Coating, Drying, and Calendering," ECS/PRiME Meeting, Honolulu, Hawaii, October 2016.
2. John E. Vogel, William Lange, Derek Clement, Brian A. Mazzeo, and Dean R. Wheeler, "Correlation of Local Conductivity to Microstructure for Li-Ion Battery Electrodes by Use of a Contact Probe and SEM/FIB," ECS/PRiME Meeting, Honolulu, Hawaii, October 2016.
3. D.R. Wheeler and B. A. Mazzeo, "Addressing heterogeneity in electrode fabrication processes," U.S. Department of Energy 2017 Annual Merit Review Meeting, Washington, DC.
4. F. Pouraghajan, H. Knight, B. A. Mazzeo, and D. R. Wheeler, "Quantifying tortuosity of porous Li-ion battery electrodes: Comparing polarization-interrupt and AC impedance (blocking-electrolyte) methods," 231st Meeting of the Electrochemical Society, New Orleans, LA, 2017.
5. K. L. Dallon, M. Wray, D. R. Wheeler, and B. A. Mazzeo, "Determination of mechanical properties of battery films from acoustic measurements," 231st Meeting of the Electrochemical Society, New Orleans, LA, 2017.
6. H. Knight, F. Pouraghajan, M. Wray, D. R. Wheeler, and B. A. Mazzeo, "The effects of aging on the tortuosity of Li-ion battery electrodes," 231st Meeting of the Electrochemical Society, New Orleans, LA, 2017.
7. E. E. Hardy, J. E. Vogel, D. V. Clement, D. R. Wheeler, and B. A. Mazzeo, "Flexible probe for measuring local conductivity variations in Li-ion electrode films," 231st Meeting of the Electrochemical Society, New Orleans, LA, 2017.
8. J. E. Vogel, D. V. Clement, E. Hardy, B. A. Mazzeo, and D. R. Wheeler, "Local variation in microstructure causes heterogeneity in the conductivity of commercial lithium-ion cathode films," 231st Meeting of the Electrochemical Society, New Orleans, LA, 2017.
9. K.L. Dallon, J. Yao, D.R. Wheeler, and B.A. Mazzeo, "Determination of mechanical properties of battery films from acoustic resonances," Review of Progress in Quantitative Nondestructive Evaluation, Provo, UT, 2017.
10. E. Hardy, D. Clement, J. Vogel, D.R. Wheeler, and B.A. Mazzeo, "Flexible probe for measuring local conductivity variations in Li-Ion electrode films," Review of Progress in Quantitative Nondestructive Evaluation, Provo, UT, 2017.

II.E.6 Large Scale *Ab Initio* Molecular Dynamics Simulation of Liquid and Solid Electrolytes (LBNL)

Lin-Wang Wang, Principal Investigator

Lawrence Berkeley National Laboratory
One Cyclotron Road, MS-66
Berkeley, CA, 94760
Phone: 510-486-5571
E-mail: lwwang@lbl.gov

Tien Duong, Technology Manager

U.S. Department of Energy
Phone: 202-586-7836
E-mail: Tien.Duong@ee.doe.gov

Start Date: October 1, 2016

End Date: September 30, 2017

Total Project Cost: \$225,000

DOE share: \$225,000

Non-DOE share: \$0

Project Introduction

One major obstacle for lithium sulfur battery is the dissolution of the lithium polysulfur in the electrolytes. The dissolution mechanism, the bonding structure of the dissolved lithium polysulfur (e.g., whether they cluster or are dissociated) are not well understood. The goal of this project is to use large scale *ab initio* calculation and molecular dynamics simulations to study the discharge mechanism in Li sulfur battery, especially for polysulfur interaction with liquid electrolyte solvent molecules, and cathode materials, as well as Li diffusion mechanism in superionic crystal solid electrolytes. We also like to search for cathode materials to prevent the dissolution based on thermodynamic principles. The long term goal is to use such theoretical understanding to provide guidance to develop better electrolyte and cathode systems to overcome the bottlenecks which currently prevent the commercialization of the Li/S battery.

Objectives

For the first year, we will focus on the study of polysulfur interaction with substrate cathode materials, and to find such substrates to bind the polysulfur with sufficient binding energies to overcome their dissolution. One objective is to screen a few cathode materials for their feasibilities for Li-S battery applications through *ab initio* calculation. We will also study solid electrolytes for the lithium diffusion in such systems. One long term objective is to study the actual lithium polysulfur thermodynamic properties and morphology in the electrolyte. For this goal, we also need to develop the proper *ab initio* calculation methods to study such thermodynamic properties in liquid.

Approach

Several *ab initio* calculation methods will be used, and new methods will be tested and developed. Most of our calculations will be based on density functional theory (DFT). One approach is to use genetic algorithm to search for the minimum energy structure. This is a particularly important for Li-S battery since the cathode material and the binding morphology might be complicated, an efficient algorithm is needed to search for the minimum energy structure. Another method is the dealing with the solvent effects. First, we will use implicit solvent model to deal with this solute-solvent interaction energy. The uncertainty of the interaction parameters will be fixed through the comparison with the experimental voltages in the dissolved Li_2S_n cases. In the following years, however, we will test a molecular dynamics (MD) based method to study the solute-solvent interaction energy. This will include two aspects, one is the configuration average between the solute-solvent binding configurations, and another is a way to calculate the solute-solvent interaction energy avoiding big thermodynamics fluctuation caused by the rest part of the system. For the configuration average, we will test

an approach using force field method to carry out MD, then take snapshots from the MD trajectories to carry out ab initio calculations. The force field MD will enable us to explore different configurations, while ab initio calculation will give us energy correction upon the force field energy. To avoid thermodynamic fluctuation, two approaches will be tested. One is the thermodynamic integration method (e.g., umbrella sampling), which will be done coupling the force field simulation with ab initio calculation. Another is a new method we proposed to calculate the interaction energy directly. Finally, to study the solid electrolyte, especially the collective lithium ion movements, we will use the nudged elastic band (NEB) method as well as metadynamics method. NEB will be useful to calculate the transition barrier when the initial and final stages are known, and the path is relatively clear. Metadynamics will be useful if a general reaction coordinate can be defined, for example, the direction of the lithium migration.

Results

We have studied the use of C_2N nanosheet as a Li-S cathode material. C_2N has been recently synthesized as another carbon nitride 2D system besides the well-known g- C_3N_4 polymeric carbon nitride. Compared to the g- C_3N_4 , C_2N could be mechanically more stable. Recently, nitrogen doped graphene or black carbon systems have shown promise as Li-S cathode materials to prevent the dissolution of the polysulfur. However, such doped systems have low capacity due to the limited amount of nitrogen compared to the compound systems. We have thus investigated the use of C_2N as a cathode material. We find that the lithium atoms like to bind strongly with the two coordinated N atoms, while there is no binding between N and S atoms. Although the C_2N itself (without sulfur) can be used as an cathode material, its binding is weak and the energy capacity is low. Thus it is essential to have the sulfur in the system. Thus the binding topology is that, the Li binding to the substrate N, and an upper layer S atoms, while the S atoms can bind with more additional lithium away from the substrate to form a lithium polysulfur. We found that the binding of the lithium polysulfur to the substrate can prevent its dissolution. In particular, at the beginning of lithiation process, a Li_2S_8 can be anchored within one hole of the C_2N substrate. At the end of the lithiation, a $Li_{10}S_8$ cluster will be attached to one hole of the C_2N substrate. The binding of the cluster to the substrate is strong enough to prevent its fragmentation or dissolution. The lithiation processes have voltages from 3.9 V to 1.6 V, and an average voltage of 2.02 V at the end step of $Li_{10}S_8$. The total energy capacity will be 1122 Whkg^{-1} . Although this is only half as the original LiS battery due to the added weight of the substrate and the limited sulfur reduced stage ($Li_{10}S_8$, instead of Li_2S), nevertheless, it is much higher than the current Li ion battery based on intercalations. Finally, we also show that the Li_mS_8 - C_2N system is metallic throughout the whole process, which solves another problem of the Li-S battery (the insulating natures of Li_2S and S_8).

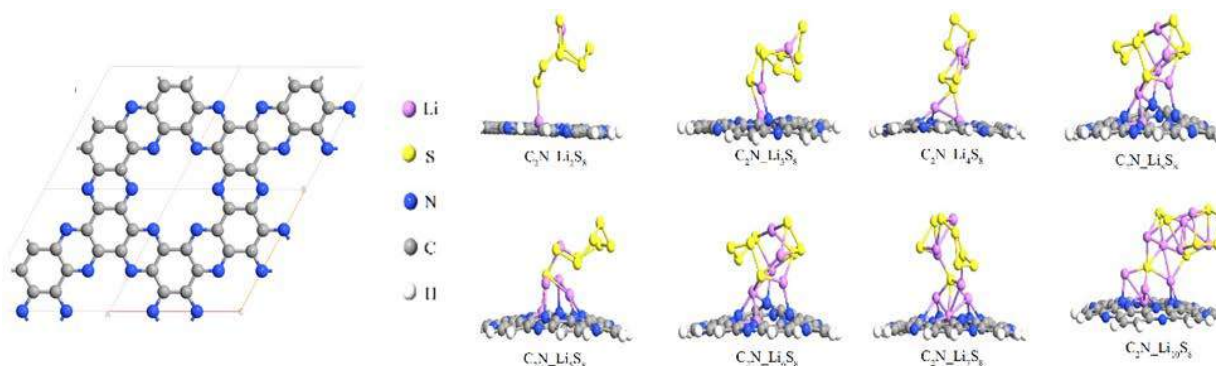


Figure II-365. The C_2N nanosheet (left) and the binding configurations of $C_2N-Li_mS_8$ (right). These binding configurations are searched through genetic algorithms based on DFT calculations.

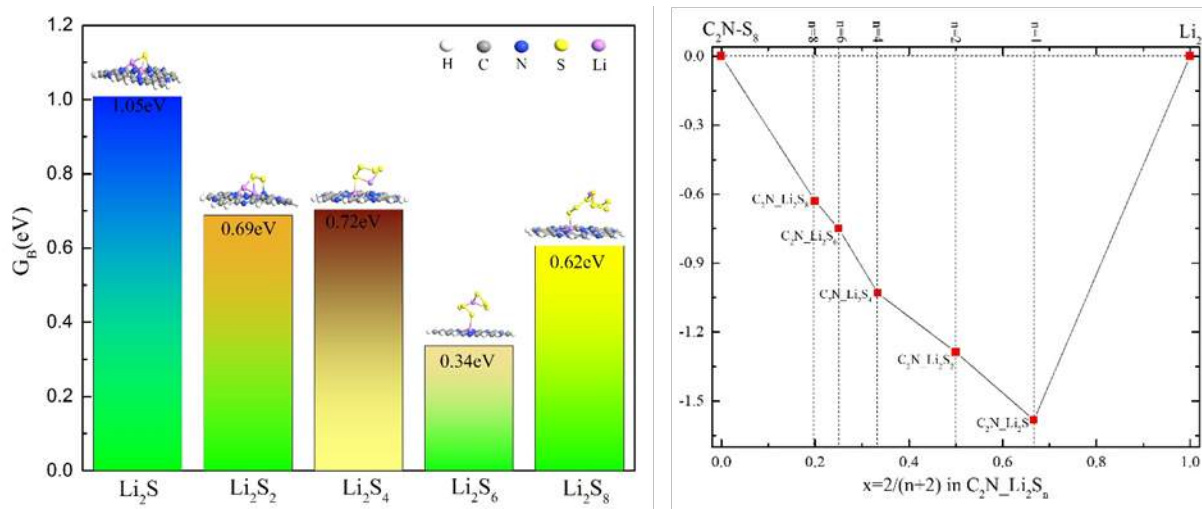


Figure II-366. The binding energy between the Li_2S_m polysulfur and the C_2N substrate (left), and the formation energy diagram (left) of $\text{C}_2\text{N-Li}_2\text{S}_m$.

Figure II-365 shows the basic structure of C_2N and the binding configurations of $\text{C}_2\text{N-Li}_m\text{S}_8$ systems, while Figure II-366 shows the binding energy between Li_2S_m polysulfur and the C_2N substrate, as well as the formation energies of $\text{C}_2\text{N-Li}_m\text{S}_m$. The formation energy of a general formula $\text{C}_2\text{N-Li}_m\text{S}_n$ is defined as:

$$G_{\text{form}}^{\text{Li}_m\text{S}_n-\text{C}_2\text{N}} = (G_{\text{Li}_m\text{S}_n-\text{C}_2\text{N}} - mG_{\text{Li}} - nG_{\text{S}_8}/8 - G_{\text{C}_2\text{N}}) / (n+m),$$

with the alloy style composition x defined as $x = m/(n+m)$. However, in the right hand panel of Figure II-366, what actually shown is $\Delta G_{\text{form}}(x) = G_{\text{form}}(x) - (1-x)G_{\text{form}}(0) - xG_{\text{form}}(1)$ for the $\text{C}_2\text{N-Li}_2\text{S}_m$ system. Table II-14 lists the voltages of the different reaction steps for the products based on $\text{C}_2\text{N-Li}_2\text{S}_n$ and $\text{C}_2\text{N-Li}_m\text{S}_8$ respectively.

Table II-14: The lithiation reactions and their corresponding voltages for Li-S battery cathodes based on $\text{Li}_2\text{S}_n-\text{C}_2\text{N}$ and $\text{Li}_m\text{S}_8-\text{C}_2\text{N}$.

Label	Category	Reactions (DME/DOL(1:1, v/v))	Voltage(V)	Feasibility
R_{10}	$\text{Li}_2\text{S}_n-\text{C}_2\text{N}$	$\text{S}_8-\text{C}_2\text{N} + 2\text{Li} = \text{Li}_2\text{S}_8-\text{C}_2\text{N}$	3.03	✓
R_{11}		$3\text{Li}_2\text{S}_8-\text{C}_2\text{N} + \text{C}_2\text{N} + 2\text{Li} = 4\text{Li}_2\text{S}_6-\text{C}_2\text{N}$	2.36	✓
R_{12}		$2\text{Li}_2\text{S}_6-\text{C}_2\text{N} + \text{C}_2\text{N} + 2\text{Li} = 3\text{Li}_2\text{S}_4-\text{C}_2\text{N}$	3.26	✓
R_{13}		$\text{Li}_2\text{S}_4-\text{C}_2\text{N} + \text{C}_2\text{N} + 2\text{Li} = 2\text{Li}_2\text{S}_2-\text{C}_2\text{N}$	2.05	✓
R_{14}		$\text{Li}_2\text{S}_2-\text{C}_2\text{N} + \text{C}_2\text{N} + 2\text{Li} = 2\text{Li}_2\text{S}-\text{C}_2\text{N}$	2.17	✓
R_{15}	$\text{Li}_m\text{S}_8-\text{C}_2\text{N}$	$\text{Li}_2\text{S}_8-\text{C}_2\text{N} + \text{Li} = \text{Li}_3\text{S}_8-\text{C}_2\text{N}$	3.95	✓
R_{16}		$\text{Li}_3\text{S}_8-\text{C}_2\text{N} + 2\text{Li} = \text{Li}_5\text{S}_8-\text{C}_2\text{N}$	2.34	✓
R_{17}		$\text{Li}_5\text{S}_8-\text{C}_2\text{N} + 2\text{Li} = \text{Li}_7\text{S}_8-\text{C}_2\text{N}$	2.65	✓
R_{18}		$\text{Li}_7\text{S}_8-\text{C}_2\text{N} + 3\text{Li} = \text{Li}_{10}\text{S}_8-\text{C}_2\text{N}$	1.55	✓

We have also studied using oxidized black phosphorene as lithium battery cathode. This is under the generation direction of using light elements from upper right corner of periodic table as Li cathodes, in contrast

with the transition metal oxides as the lithium ion battery cathodes. The light weights of these elements and the strong chemical bonding with the Li ion can lead to high energy capacity of such battery materials. One two examples are the Li-S battery and Li air battery. Both batteries are based on chemical reactions, which however cause many other issues like the mechanical stability, large volume change, and the electric conductivity of the cathode. To overcome such issues, 2D materials can be used. The 2D material can form the framework, which provides the mechanical stability and electric conductivity. As such 2D materials can be made monolayer thick, they provide ample surface area to bind the Li, which can also improve the kinetic of the charging/discharging process. To have high energy capacity however, one needs strong binding energy of Li and the 2D material. People have tried to use black phosphorene as lithium cathode, but the binding energy is too small. Here we found that the phosphorene oxide can provide large binding energy. The Li atom will bind with the oxygen atom at the surface of phosphorene oxide. In this aspect, this is like the Li air battery, except the oxygen is provided in a solid form, instead of in the gas phase, and the whole battery can be sealed. Since there is no air coming in and out of the system, the whole device should be mechanically stable. We found that each surface O can bind with one Li atom. If more Li atom is bond with one O atom, the structure can become unstable. For the fully oxidized black phosphorene: P_4O_4 , 4 Li atom can be bonded, with a final product as $Li_4P_4O_4$. This will have a theoretical energy capacity of 1457 Wh/Kg. Ab initio molecular dynamics is carried out, showing that the system is vibrationally stable. The solvent effect is taken into account by implicit solvent model.

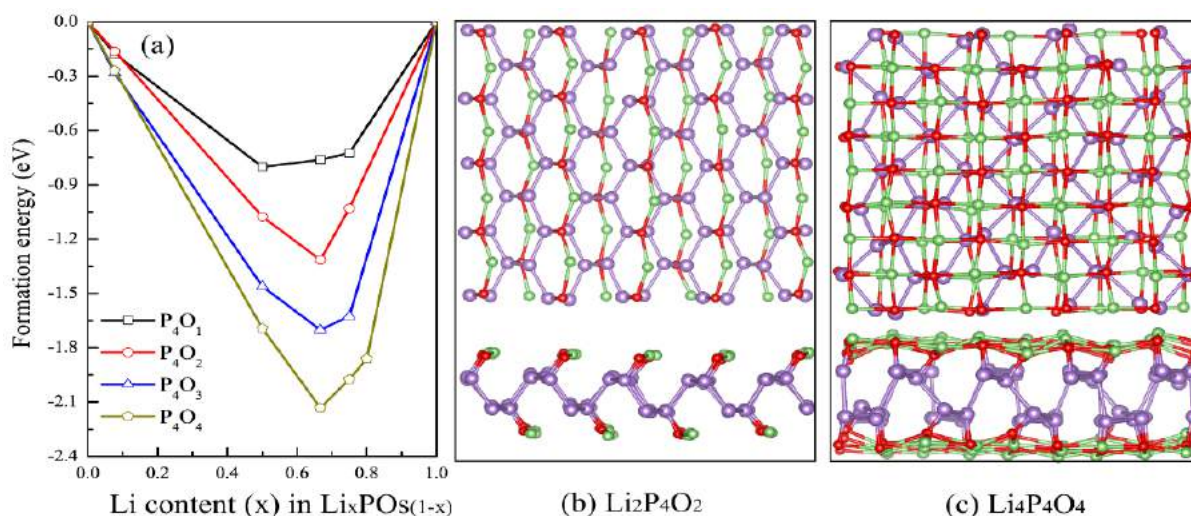


Figure II-367. The formation energy (a), the $Li_2P_4O_2$ configuration (b) and $Li_4P_4O_4$ configuration (c). In (b) and (c), the blue ball is P, red ball is O, and green ball is Li.

Figure II-367 show the formation energy and binding configurations of different phosphorene oxides. We have also calculated the band structure of the system (Figure II-368), and showing that the oxidized phosphorene absorbed with Li are metallic, thus should be electric conductive.

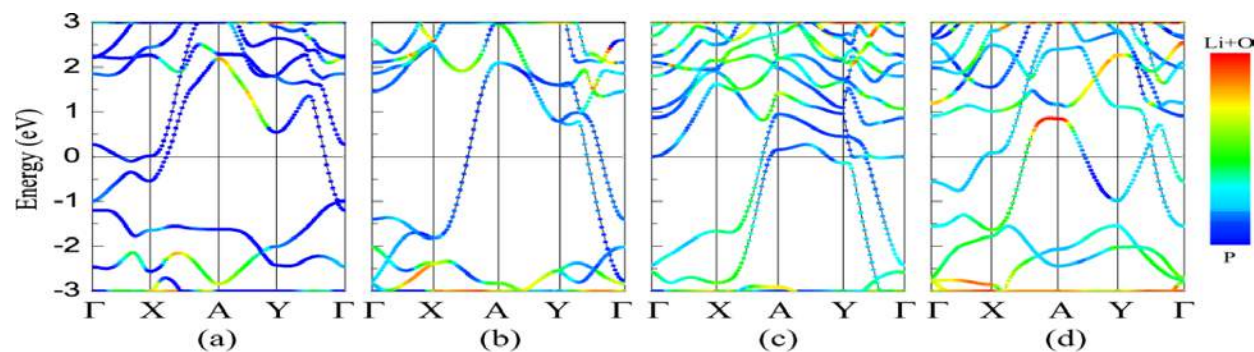


Figure II-368. Projected band structures of (a) $\text{Li}_1\text{P}_4\text{O}_1$, (b) $\text{Li}_2\text{P}_4\text{O}_2$, (c) $\text{Li}_3\text{P}_4\text{O}_3$ and (d) $\text{Li}_4\text{P}_4\text{O}_4$.

Conclusions

In conclusion, we found that C_2N can be a very good Li-S cathode material, which can provide sufficient energy capacity, meanwhile can solve the problems of polysulfur dissolution, insulating of Li_2S and S_8 , as well as mechanical stabilities. We also find that oxidized phosphorene can be used as a Li battery cathode. This is alike the Li air battery but with the oxygen provided by the solid form O binding with the phosphorene framework. This system is also mechanically stable and can provide relatively high energy capacity of 1457 Wh/Kg.

Key Publications

1. Y. Duan, B. Zhang, J. Zheng, J. Hu, J. Wen, D.J. Miller, P. Yan, T. Liu, H. Guo, W. Li, X. Song, Z. Zhuo, C. Liu, H. Tang, R. Tan, Z. Chen, Y. Ren, Y. Lin, W. Yang, C.M. Wang, L.W. Wang, J. Lu, K. Amine, F. Pan, "Excess Li-ion storage on nanocrystal reconstructed surface to boost battery performance", *Nano Lett*, 17, 6018 (2017).
2. J. Wu, L.W. Wang, "2D frameworks C_2N as a potential cathode for lithium sulfur batteries: an ab initio density functional study" (submitted).
3. Y. Li, F. Ma, L.W. Wang, "Phosphorene oxides as a promising cathode material for sealed non-aqueous Li-oxygen battery" (submitted).

II.E.7 Dendrite Growth Morphology Modeling in Liquid and Solid Electrolytes (MSU)

Yue Qi, Principal Investigator

Michigan State University
3509 Engineering Building
East Lansing, MI 48824
Phone: 517-432-1243; Fax: 517-432-1105
E-mail: yueqi@egr.msu.edu

Tien Duong, Technology Manager

U.S. Department of Energy
Phone: 202-586-7836
E-mail: Tien.Duong@ee.doe.gov

Start Date: January 1, 2017
Total Project Cost: \$1,135,125

End Date: December 31, 2019
DOE share: \$999,943

Non-DOE share: \$135,182

Project Introduction

In this project, we will first develop a phase-field model to incorporate the electrochemical driving forces predicted from first principles simulations in liquid electrolytes and then incorporate mechanical driving forces to simulate dendrite growth in solid electrolytes with resolved microstructures. The μm -thick solid electrolytes will allow easier, direct comparison of modeling and experimental results, thus facilitating the validation of the electrochemical-mechanically driven Li-dendrite growth model. Last but not the least, the computational model for solid electrolytes can also be applied to study and design nm-thin artificial SEI on Li metal surface. Therefore, this atomically-informed phase-field model will allow us to design the desired properties of artificial SEI coating to suppress dendrite growth in liquid-electrolyte and the microstructure of a solid-electrolyte to be dendrite-resistant during cycling. This model will enable the design of durable and safe Li-anodes for Li-S, Li-air, all-solid Li-ion batteries, as well as high energy density Li-ion batteries, lead to batteries that meet DOE's target for the high energy batteries cell density ($>350 \text{ Wh/kg}$) for EV applications and cost below $\$100/\text{kWh}_{\text{use}}$.

Objectives

The ultimate goal of this project is to develop a validated model to predict Li dendrite morphology evolution in both liquid and solid electrolytes during electrodeposition and stripping, in order to accelerate the adoption of Li metal electrodes in current and emerging battery technologies. To achieve this goal, the project has four objects:

1. formulate a general framework that captures the electrochemical-mechanical driving forces for Li morphology evolution;
2. consider the role of the nm-thin SEI in liquid-electrolytes as well as the microstructures of mm-thick solid-electrolytes for Li morphology evolution;
3. connect micron-scale phase-field models and atomic-scale DFT-based simulations via parameter- and relationship-passing in order to predict Li dendrite nucleation and growth kinetics and morphology; and
4. validate the key input parameters and main conclusions of the multi-scale model as new capabilities being developed step-by-step.

Approach

This project will develop a multi-scale model that connects micron-scale phase-field models and atomic-scale DFT-based simulations via parameter- and relationship-passing in order to predict Li-metal dendrite morphology evolution, in both liquid and solid electrolytes. The key innovation of this project is to capture the

electrochemical-mechanical driving forces and incorporate the roles of an nm-thin solid electrolyte interphase (SEI) in liquid electrolytes as well as of the microstructures of μm -thick solid electrolytes for all-solid-state batteries. Our strategy to study Li dendrite morphology in both liquid and solid electrolytes allows us to share many similar governing equations and common mechanisms, gradually increase the complexity of the model, and validate the model step-by-step for its key input parameters and main conclusions through tailored experiments

Results

Task 1: Illuminate the role of SEI kinetics in Li dendrite growth in liquid electrolytes

Subtask 1.1 A new set of DFTB parameters for Li, H, C, and O interactions were developed and verified

This set of DFTB parameters were obtained by fitting to DFT results of a broad range of structures (bcc and fcc Li metal, Li_2O , LiOH , LiH , LiCH_3 , and LiC_6) and properties (surface energy, adsorption energy, band structures). This set of DFTB parameters were then used to predict additional properties, such as Li^+ ion solvation energy, interface energy, Li^+ ion diffusivity in liquid EC, *et al.* to validate the accuracy and transferability of the parameters. The agreement of DFTB and DFT results (shown in Table II-15) suggests the reliability of this set of parameters.

Table II-15: Key Properties not used for DFTB parameterization, but compared with DFT (GGA/PBE) for validation

Property	System	DFTB	DFT
Li surface energy (J/m^2)	(001)	0.5	0.46
	(011)	0.49	0.49
	(111)	0.58	0.53
Li adsorption energy on Li(001) (eV)	hollow	1.49	1.37
	bridge	1.30	1.28
	top	1.08	1.07
Interface energy (J/m^2)	$\text{Li}(001)/\text{Li}_2\text{CO}_3(001)$	0.64	0.5
HOMO and LUMO gap (eV)	EC	6.5	6.8
Solvation energy (eV)	Li^+ in EC	5.4	5.2-5.5
Diffusivity (cm^2/s)	Li^+ in EC at 450K	2.4×10^{-5}	1.1×10^{-5}

DFTB method along with this set of parameters was used to compute the charge transfer reaction energetics on an SEI covered Li metal surface, under an applied potential.

Figure II-369 shows the Li^+ ion energy change when it de-solvates from the EC solvents, diffuses through the 4 layers of Li_2CO_3 (a model SEI layer), and gets reduced by the electrons on the Li-metal slab. The reduced state is considered to be the reference state. Three oxidized states with varying electron $x\text{e}^-$ at $x = 1$ to 3, corresponding to electron density of 0.002 to 0.006 $\text{e}/\text{\AA}^2$ on Li-metal surface were simulated. To verify the reliability of calculated charge transfer reaction energy from minimization, molecular dynamics (MD) simulations were performed. The results show that the calculated average energy from MD is close to that from minimization with the maximum deviation of 0.1 eV.

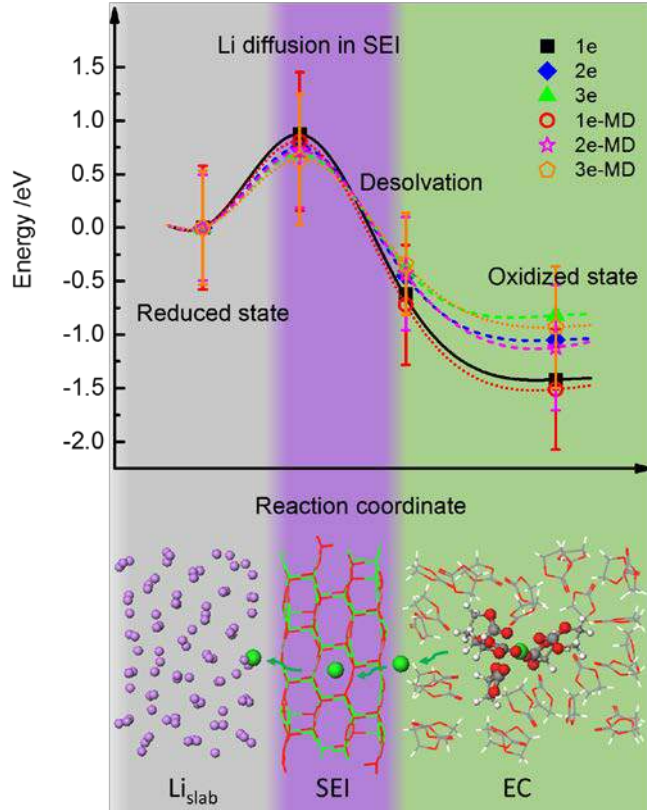


Figure II-369. Energy landscape for Li^+ transport from electrolyte to Li-metal slab under different potential.

For the atomic simulations of the $\text{Li}/\text{Li}_2\text{CO}_3/\text{EC}$ interface, the experimentally defined zero voltage of Li^+/Li^0 was calibrated with DFTB and DFT calculations. The zero voltage of electrode is the important reference state in the Li-ion batteries. We have considered a typical electrochemical reaction



where the Li^+ ions in the electrolyte solution react with electrons e^- in the electrode to produce the electrode Li^0 atoms. The thermodynamic driving force is given by

$$\Delta G = \Delta G^o + F\phi - RT \ln a_{\text{Li}^+} \quad (2),$$

where ΔG^o is the standard free energy change for the electrode reaction (1), F is the Faraday constant, ϕ is the potential on the Li metal electrode, and a_{Li^+} is the activity of Li^+ in the electrolyte, which depends on temperature and on the concentrations of other ions. At equilibrium,

$$\Delta G^o + F\phi^o - RT \ln a_{\text{Li}^+} = 0 \quad (3)$$

where ϕ^o is the equilibrium potential of the Li metal electrode. Therefore, by subtracting Eq. (3) from Eq. (2), the thermodynamic driving force can also be expressed in experiment as,

$$\Delta G = F(\phi - \phi^o) = F\eta, \quad (4)$$

where η is the overpotential. If $\eta < 0$, the Li^+ is reduced (plating); whereas if $\eta > 0$, the Li^0 is being oxidized to Li^+ (stripping).

In fact, the potential ϕ on the Li metal electrode supplies electrical energy and possesses the electron density on Li metal surface. Therefore, ϕ is related to the Fermi level and the work function shift on the Li metal. In addition, as the atomic simulation shows, as the applied voltage increases, the Li^+ concentration near the electrode surface will increase, which would change the activity a_{Li^+} . In our model, the temperature is

unchanged and only Li^+ ion concentration changes, thus the 3rd term in eq (2) can be linked to Li^+ solvation energy change with Li^+ concentration. Therefore, the thermodynamic driving force can be expressed in our model as

$$\Delta G = \Delta G^0 + \Delta W_f + \Delta E_{sol} \quad (5),$$

where ΔW_f is the work function shift with excess electron density on Li metal surface, and ΔE_{sol} is Li^+ solvation energy change with Li^+ ion concentration in the EC-electrolyte.

To find the zero voltage of Li^0/Li^+ , according to eq (5), it is necessary to obtain the ΔG^0 , ΔW_f and ΔE_{sol} . We used the case of one electron in eq (1) as a reference, which corresponds to an electron density of $0.002 \text{ e}/\text{\AA}^2$ on the Li-metal surface. The predicated ΔG^0 is 1.42 eV from DFTB method. Also, we used the DFT (with GGA/PBE functional) method to compute the work function as a function of excess electron density on Li metal surface by the slab model. As shown in Figure II-370, when the potential decreases, the excess electron density increases on the Li-metal, the work function will then decrease due to the rise of Fermi level. In addition, we considered a set of bulk models including 32 EC liquid molecules and n ($n=1-6$) Li^+ ions, using DFTB MD method with NVT ensemble at 450 K, to predicate the Li^+ solvation energies in EC-electrolyte. The results show that Li^+ solvation energies in EC-electrolyte decrease with Li^+ concentration (Figure II-370). When the applied potential decreases, the negative charge density increases on Li metal surface, ΔW_f and ΔE_{sol} then decrease, and thus ΔG will decrease accordingly. The values are in good agreement with that of direct predictions from DFTB method.

At excess negative charge density of $0.012 \text{ e}/\text{\AA}^2$ on Li metal surface, $\Delta G=0$, corresponding to the experimentally defined zero voltage of Li^0/Li^+ . When the electron density is larger than this (more negative potential) Li plating occurs; while when the electron density is lower than this (more positive potential), Li stripping occurs. The excess electrons on Li surface will trigger more electrolyte decomposition when SEI fractures.

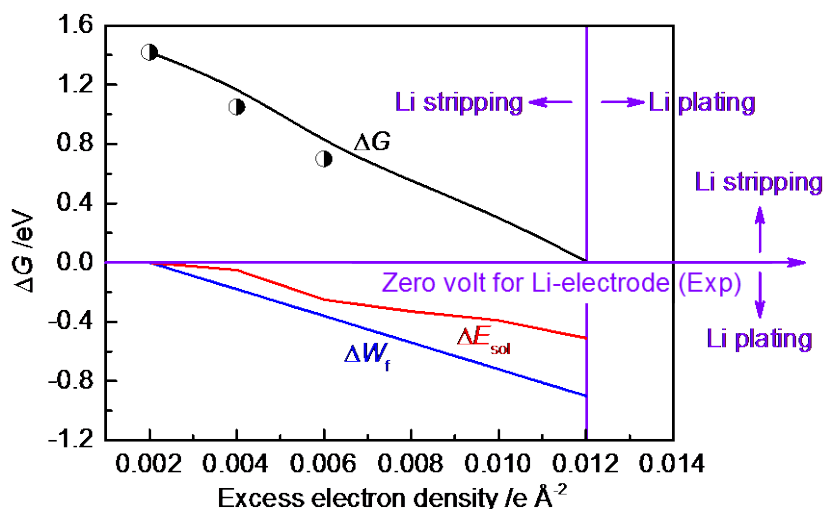


Figure II-370. The thermodynamic driving force of the electrochemical reaction at the $\text{Li}|\text{Li}_2\text{CO}_3|\text{EC-electrolyte}$ interface, work function shift and Li^+ solvation energy change with Li^+ ion concentration in the EC-electrolyte as a function of excess electron density on Li metal surface. The circle denotes the directly predicated ΔG by DFTB method.

Subtask 1.2, 1.3 Coupled Morphology Evolution Model

The previously developed dendrite growth model was extended to implicitly include the effect of SEI by the parametric study of the metallic Li/liquid electrolyte binary phase field model. The governing equations for phase field model are diffusion and phase evolution equations.

$$\frac{\partial c_+}{\partial t} = \nabla \cdot \left[D^{eff} \nabla c_+ + \frac{D^{eff} c_+}{RT} n F \nabla \phi \right] - \frac{c_s}{c_0} \frac{\partial \xi}{\partial t} \quad (6)$$

$$\frac{\partial \xi}{\partial t} = -L_\sigma (g'(\xi) - \kappa \nabla^2 \xi) - L_\eta h'(\xi) \left\{ \exp \left[\frac{(1-\alpha)nF\eta_\alpha}{RT} \right] - c_+ \exp \left[\frac{-\alpha nF\eta_\alpha}{RT} \right] \right\} \quad (7)$$

The key parameters closely associated with Li plating behavior in the model are: interfacial energetics and anisotropy (formulated in κ), Li ion diffusion coefficients (D^{eff}), charge transfer rate (normalized in L_η) and double-well energy profile ($g'(\xi)$). These information were obtained from previous DFT results and current DFTB calculations.

The implicitly Li morphology model was used to investigate the impact of four major SEI properties, namely interfacial energy, anisotropy, diffusion coefficient and reaction rate constant. The non-linear phase-field model simulation of the Li electrodeposition process revealed that higher Li/SEI interface energy, faster Li-ion diffusion in SEI, and slower reaction rate constants favor less branched Li morphology (as shown in Figure II-371), leading to higher Coulombic efficiency compared to more branched morphology.

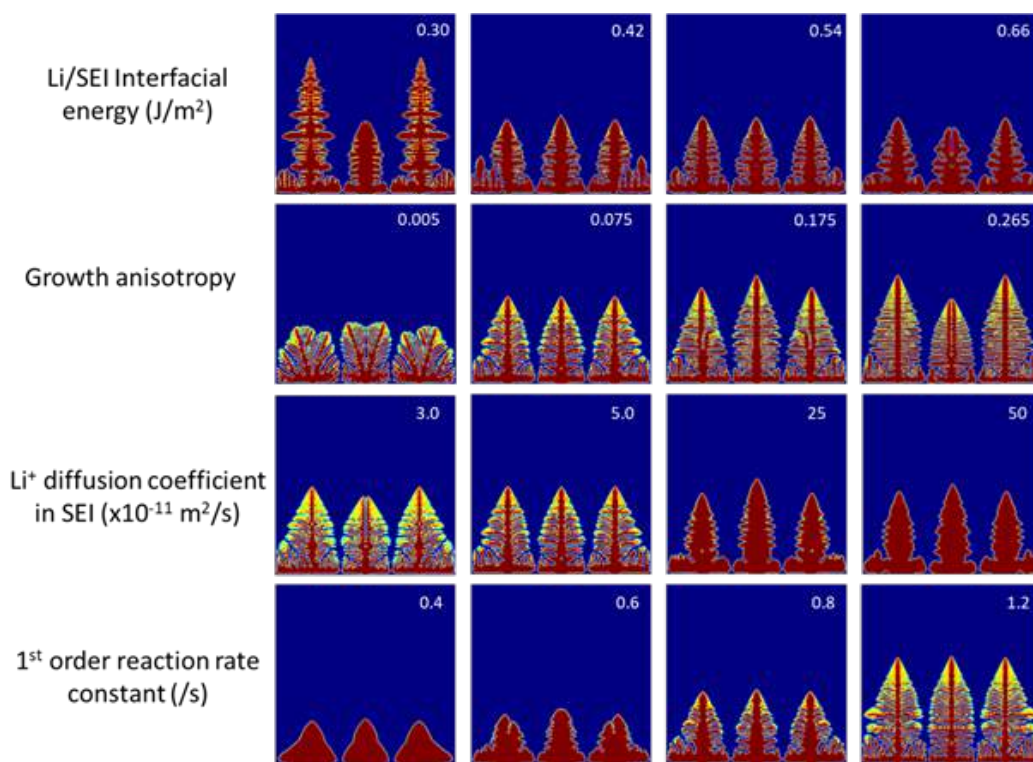


Figure II-371. SEI properties-Li dendrite morphology map from phase field simulation.

Subtask 1.4 *in situ* Observation Li Dendrite Morphology in Liquid Electrolyte

Experimental protocol has been established. Our preliminary *in-situ* electrochemical optical observation (Figure II-372) shows the Li plating and stripping process which involves dendrite and mossy structure formation.

Direct observation of dendrite formation and mossy structure evolution

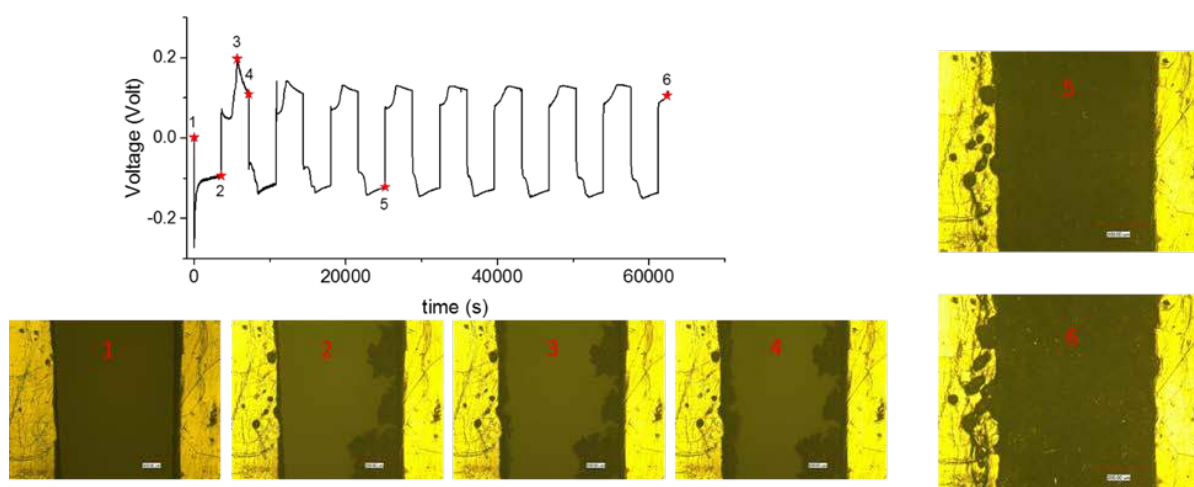


Figure II-372. *in-situ* electrochemical optical observation of Li dendrite growth morphology

A large amount of dead Li formed, which cannot further participate the plating and stripping. Due to the electrical insulating SEI layer, it did not show the shorting. The impact of current density, protective coating, and different electrolyte additives will be further explored. It will be correlated with the cycle efficiency and phase-field modeling.

Task 2: Model the metallic Li precipitation in solid electrolytes of all-solid batteries

Subtask 2.1 DFT Calculations revealed Li nucleation mechanism on LLZO surface

DFT calculations were performed to address the nucleation mechanism of metallic Li inside LLZO. Both tetragonal and cubic phases LLZO were investigated. It was found the excess electrons in LLZO can be trapped to the La atoms at/near the surface in LLZO. Figure II-373 shows the localized electrons clouds on La. Thermodynamics calculations confirmed that metallic La can be more stable than metallic Li with the excess electrons, providing the nucleation mechanism of metallic Li phase in LLZO. This mechanism is being investigated for LLZO grain boundaries as well.

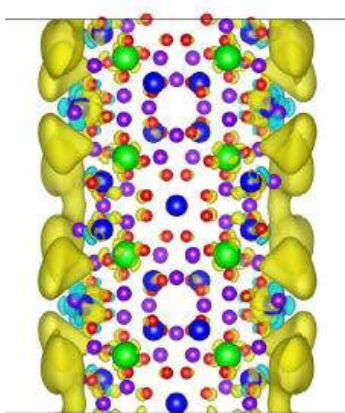


Figure II-373. The excess electrons located on La atoms on LLZO surface.

This mechanism was introduced as a non-uniform, structure-dependent electron activity ($a_e(r)$) in the phase field model. An intergranular Li dendrite growth has been simulated in 2D microstructures. The results showed

that the Li-dendrite growth rate was higher inside wider grain boundaries or pores than the narrow ones, indicating larger growth resistance at narrower grain boundaries or pores.

Subtask 2.2 Phase Field Model of Li Dendrite Growth in Solid Electrolyte

It has been reported that Li dendrites tend to grow into pores and along the grain boundaries (GBs) of the solid electrolytes. A general non-linear phase-field model for Li dendrite growth in a solid electrolyte (e.g., LLZO, LLZTO, etc.) were formulated and implemented. The microstructure of LLZO was resolved and three-phase fields were defined to describe the solid-state battery system as $\{\phi_1(r) = 1, \phi_2(r) = 0, \phi_3(r) = 0\}$ for pure Li-metal anode, $\{\phi_1(r) = 0, \phi_2(r) = 1, \phi_3(r) = 0\}$ for solid electrolyte, and $\{\phi_1(r) = 0, \phi_2(r) = 0, \phi_3(r) = 1\}$ for pores, cracks and GBs. The phase-field equations were reformulated with Butler-Volmer kinetics for the three-phase system. Currently, the solid-electrolyte phase was considered to be non-evolving during electrodeposition, and the Li diffusion coefficients were assumed to be: $D_{GB} > D_{Grain} >> D_{pore}$. Numerically, phase field governing equations were solved together with diffusion and charge conservation equations via finite element method.

An intergranular Li dendrite growth has been simulated in 2D by the as-developed phase field model for solid electrolyte system, as shown in Figure II-374c. The electrodeposited Li metal tends to grow along and fill in the GBs of the solid electrolyte, which is in agreement with the SEM image of dendrite morphology from cycled LLZO battery, as shown in Figure II-374a. The Li-ion concentration distribution profile from phase field simulation is also provided in Figure II-374b, which demonstrated that the isolated grains by encircled Li dendrites have slightly lower local Li-ion concentration. It also shows that the intergranular ion diffusion was impeded by the Li dendrite growth, leading to degraded local Li conductivity in the solid electrolyte region where dendrites form.

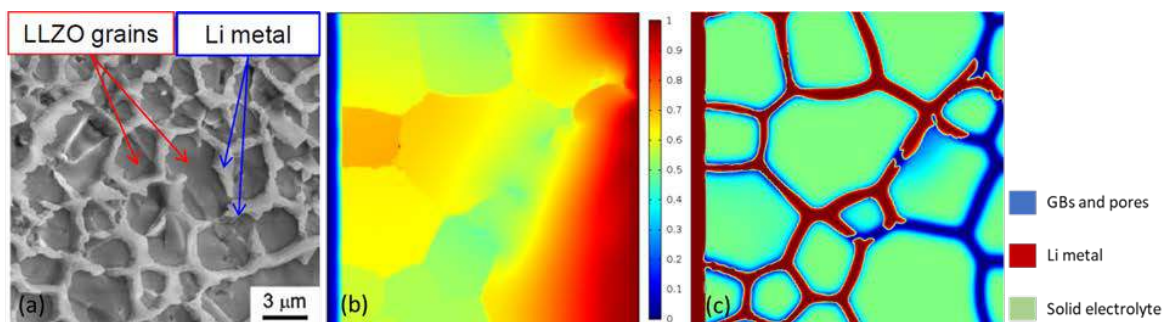


Figure II-374. Preliminary phase-field simulation of Li dendrite growth in solid electrolyte results with experimental results as comparison: (a) SEM observation of intergranular Li dendrite growth in LLZO [Cheng E. J., Sharafi A. and Sakamoto J., *Electrochimica Acta* 223, 85-91 (2017).]; and phase field simulation results: (b) Li-ion concentration distribution in the solid electrolyte battery system; (c) morphology of Li dendrites growth in solid electrolyte.

Conclusions

A phase-field model was developed to capture the electrochemically driven dendrite morphology evolution in a liquid electrolyte. The role of SEI was modeled implicitly. The kinetic properties, as well as Li diffusion coefficient along the Li/SEI interface, was directly computed from DFT and DFTB-based atomic simulations. The DFTB calculations have revealed that delithiation generates voids at the Li/SEI interface and the charge transfer reaction occurs underneath the SEI layer. More importantly, the Li metal is negatively charged at the zero voltage (consequences for Li-plating and dendrite growth). The non-linear phase-field model simulation of the Li electrodeposition process revealed that higher Li/SEI interface energy, faster Li-ion diffusion in SEI, and slower reaction rate constants favor less branched Li morphology, leading to higher Coulombic efficiency compared to more branched morphology.

II.F Next-Gen Lithium-Ion: Processing Science R&D

II.F.1 Advanced Active Battery Materials: Non-traditional Approaches to Synthesizing Active Cathode Materials (ANL)

Gregory K Krumdick, Principal Investigator

Argonne National Laboratory
9700 South Cass Avenue
Argonne, IL, 60439-4837
Phone: 630-252-3952
E-mail: gkrumdick@anl.gov

Peter Faguy, Technology Manager

U.S. Department of Energy
Phone: 202-586-1022
E-mail: Peter.Faguy@ee.doe.gov

Start Date: October 1, 2016

End Date: September 30, 2017

Total Project Cost: \$1,000,000

DOE share: \$1,000,000

Non-DOE share: \$0

Project Introduction

To enable lower cost and higher performing active battery materials, advanced synthesis approaches are needed. This work focuses on establishing non-traditional synthesis capabilities at Argonne's Materials Engineering Research Facility (MERF) for the assessment of the technology and producing materials for evaluation.

Objectives

The objectives of this project are to augment the MERF's synthesis capabilities to establish and evaluate advanced non-traditional approaches for active material synthesis. Specifically, we intend to establish advanced flame spray pyrolysis and hydrothermal synthesis capabilities at the MERF. These capabilities will be used to synthesize advanced active battery materials which will be evaluated and distributed to the basic R&D battery community for further research.

In addition, a CRADA with the equipment manufacturer Laminar was established and they have provided a 40L Taylor Vortex Reactor that will be used for a comparison study between existing 1L and 10L reactors in FY18.

Approach

Flame and hydrothermal made nano- and micro-powders are viable competitors for powders made by other means but carry the potential for lowest-cost largest-scale production. Flexible, highly instrument synthesis systems are being designed, fabricated and commissioned for the DOE-VTO battery program. Collaborations with companies such as Cabot and Praxair are being established for technical guidance and to enable a commercialization pathway for the technology.

The Taylor Vortex Reactor (TVR) is a candidate commercially available synthesis technology to commercially utilize continuous stirred tank reactors (CSTR's). Establishing a CRADA with equipment vendor Laminar which places a 40L pre-pilot reactor in the MERF enables an unbiased evaluation of the scalability of the technology.

Results

Flame Spray Pyrolysis Synthesis

The MERF FSP facility was designed and constructed at a greenfield location in the MERF high bay W162. This effort required: (a) selecting a material production target (b) selecting a burner strategy (c) establishing the engineering and safety protocols necessary to allow for combustion synthesis of nano-micron powders in the national laboratory system (d) integrating in-situ annealing (high-temperature-residence-time: HTRT) as a fundamental part of the FSP process and (e) developing a material collection system along with a clean-in-place fixture that will allow for efficient collection and system cleaning aimed at allowing for a daily turnover of synthesis operation.

The FSP burner, HTRT section, filter box, Spencer blower and combustion exhaust is a closed system that is provided with controls to maintain a negative pressure of 0.5-1.0 inches H₂O with respect to the room. This assures that nanomaterials cannot leak out of the system and into contact with personnel while allowing some flexibility to service or adjust the burner when needed. The maintenance of negative pressure is provided by a variable frequency drive to adjust the Spencer Blower speed as need to keep the combustion duct at a specified negative pressure setpoint between 0.5-1.0 inches H₂O.

The filter box (see Figure II-375) was designed to provide 2 ft² of normal filter surface area allowing for a minimum of 100g of material collection while staying within the delta-P provided by the Spencer Blower. The filter box fits entirely within the Powder Hood. The interior of the filter box is accessed by glove-box style gloves that permit the easy harvesting of any nano-powder without breaking quarantine for these health hazard materials. This feature greatly simplifies PPE for the daily harvesting of produced materials. In addition, a ULPA vacuum cleaner accessed by the gloves allows for daily cleanup of the filter box to allow for efficient collection and preparation for the next experiment.



Figure II-375. Filter Box and glove box style PPE for material collection

The burner design is similar to many common configurations found in other research labs. The powder product originates from the combustion of the sprayed liquid precursor. The precursor liquid is atomized by a 2-fluid nozzle. Oxygen or air is used as the atomization gas using a Schlick atomizing nozzle. A sheath flow of oxygen or air provides additional combustion air as the atomizing nozzle does not provide a lot of flexibility in the atomizing gas to liquid ration so that the sheath gas is used to control the excess air parameter. A ring of pilot flames using premixed methane-oxygen gas is used to ignite and support the spray combustion. Nitrogen gas is also provided which is at least used to purge the combustion exhaust duct before ignitions attempts are made as required by NFPA 86. The nitrogen also provides another source of gas to control the post-combustion gas temperature. The burner is fitted on a sliding mount that can be retracted into the burn hood for service under the protection of the fume hood exhaust (see Figure II-376, Figure II-377).



Figure II-376. Burner Hood with Cabot Inspired Burner



Figure II-377. New Hoods and Ventilation

A flame supervision and control system panel was specified and procured from an industrial furnace controls contractor. This system was specified to adhere as strictly as possible to the guidance of NFPA 86 which provides a framework for the safe operation of burners (see Table II-16). NFPA 86 prescribes the use of pressure switches, safety solenoid valves, flame sensors and operational protocols to assure that fuel is delivered only when it is safe and to prevent the accumulation of large amounts of un-combusted flammable materials. The control panel provides for two independent burners for the pilot and the spray flames. Electively, the spray flame can be operated if the pilot flame is off but the pilot flame must be on to ignite the spray flame.

Table II-16: MERF FSP System Parameters

Material Production Rate	20 g/hour or 100 g/day (leaving 3 hours for system turnaround: collection and cleaning)
Basic Burner Design	Adapted from engineering provided by Cabot Corp under NDA.
Combustion Stream	Fully enclosed 5" diameter duct(no air entrainment with independent control of N ₂ and O ₂ for excess air control)
Pilot Flame Rate	25,000 Btu/hr
Spray Flame Rate	25,000 Btu/hr
O₂ Sheath Flow Rate	50 LPM max
N₂ Excess Air/Purge Flowrate	50 LPM max
Combustion Safety – Flame Supervision	NFPA 86 flame supervision control panel (Honeywell SLATE)
Combustion Safety - Containment	Individual Flammable Gas Cabinets for solutions and pilot combustion gas (methane)
Combustion Safety – Segregation	8-cylinder O ₂ manifold located in service corridor
Liquid Precursor Delivery	Dual ISCO syringe pump
High Temperature Residence Time (HTRT) Section	72" Tube furnace up to 1000 C
Gas/Solid Cooling	N ₂ gas quench in 72" section between HTRT section and filter box
Material Collection	16"x25" glass-fiber filter accessed by pseudo-glove box design to minimize PPE burden during material collection
Filter Blower	Spencer Blower 100 cfm @40 inches H ₂ O
Clean-In-Place Fixture	Custom design to allow cleaning of the system ducts without requiring disassembly. Daily cleaning within the 100 g/day target is feasible
System Integration	National Instruments/Labview control System

The pilot flame was tested along with all of the NFPA 86 protocol functions. The pilot flame provides stable premixed flames in the 1-3 LPM methane range. Next, a spray of pure ethanol was used to test the spray flame. Stable spray flames were obtained in the 2-5 ml/min ethanol range. Figure II-378 shows the combined pilot and spray flame operation

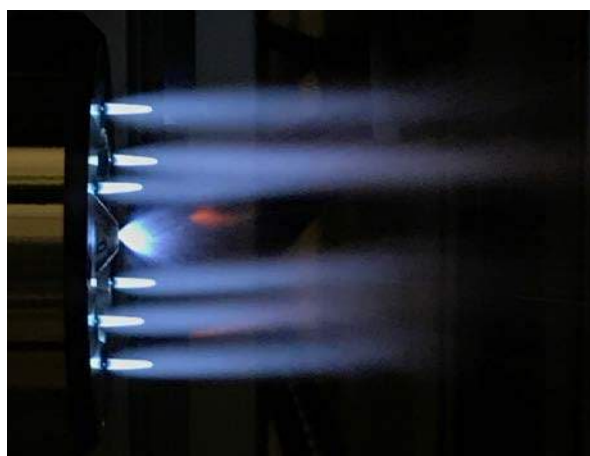


Figure II-378. Pilot and Ethanol Spray Flame Operation at the MERF FSP

Hydrothermal Synthesis

The Materials Engineering Research Facility (MERF) in the Engineering Systems Division at Argonne National Laboratory proposes to incorporate a new materials synthesis platform into the facility. The synthetic capability to be developed would be based on the design and construction of a turnkey hydrothermal synthesis (HyTS) reactor system capable of batch production of 20 to 50 g of nanoparticles per run. The immediate objective of this project is to develop and set up an advanced bench scale HyTS process for the production and evaluation of high-capacity engineered silicon nanoparticles and composites used as the active anode material in advanced Li-ion batteries.

HyTS is generally defined as crystal synthesis or crystal growth under high temperature and high pressure with water as the solvent / reaction medium and utilizing precursors that are ordinarily insoluble in water. As temperature and pressure approach the critical point of water, 374°C and 22.1 MPa (218 atm), the reactive and energetic nature of water changes dramatically. Characteristics such as density, ionic product, and dielectric constant, are strongly perturbed; thus supercritical water and subcritical water become useful new reaction media. The synthesis of single crystals and their growth is achieved in a hydrothermal reactor depending on the solubility of the precursors in hot water under high pressure. Especially for supercritical HyTS, around the critical point of water, the solubility of metal ionic species decreases dramatically because the density and dielectric constant of water decrease rapidly. The decrease in solubility leads to a higher degree of supersaturation. The formation of nanosized materials can be achieved in supercritical water (SCW) and subcritical water (SbCW) because of the high reactant diffusivity, fast reaction rates, and extremely high nucleation rate of these novel reaction media. Hydrothermal reactors can generate highly crystalline nanosized particles with well-defined morphology superior to competing reaction technologies, such as solid-state, co-precipitation, sol-gel, spray pyrolysis and emulsion drying. In addition, the nanoparticle size and size distribution can be controlled by adjusting the reaction conditions between subcritical and supercritical regimes depending on the reaction temperature and pressure as schematically shown in Figure II-379.

HyTS utilizes water at high temperature (200 ~ 400 °C) and high pressure (10 ~ 24 MPa) as the reaction media. The HyTS reactor will be constructed at a lab-bench scale where the reactor volume of one liter determines the typical batch size and reaction energetics.

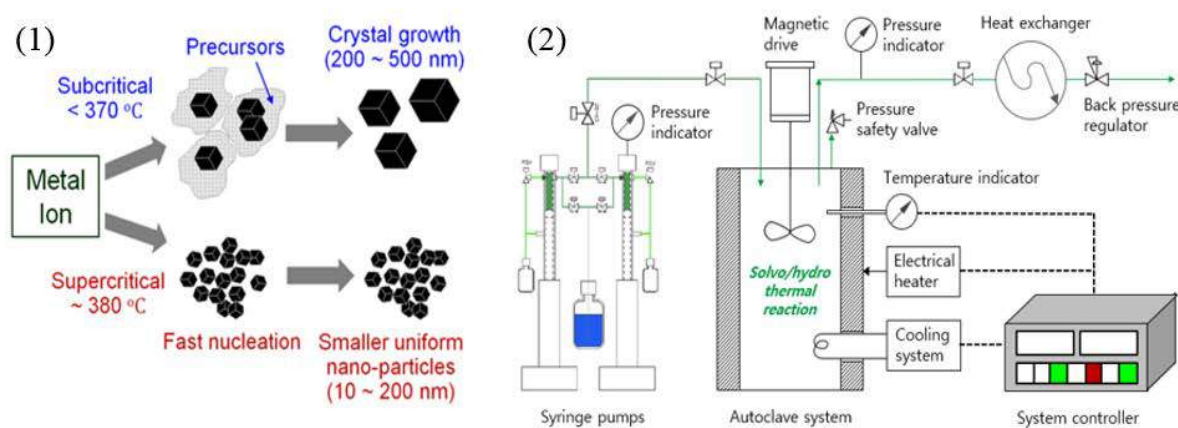


Figure II-379. (1) Hydrothermal Reaction Mechanism, (2) Schematic Diagram of Bench Scale Hydrothermal Synthesis System

Taylor Vortex Synthesis

The Taylor Vortex Reactor (TVR) is one of the commercially available emerging manufacturing technologies we are evaluating (see Figure II-380). This reactor has cylindrical rotor inside and provides tremendous Taylor Vortices in the annulus. This produced homogenous micro mixing, high mass and heat transfer enabling a high degree of uniform super saturation. This results in faster kinetics and denser particles. The TVR continuously

produces spherical precursors with narrow particle size distribution, which is critical to achieve high quality battery material.

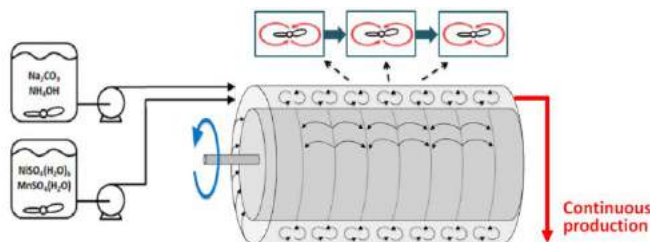


Figure II-380. Taylor vortex flow enabling micro mixing zones.

As part of a CRADA with Laminar, a 40L TVR pre-pilot reactor was delivered and is being installed. (Figure II-381). This 40L TVR will be used in the process scale-up study in conjunction with 1L and 10L reactors. We are planning to conduct a systematic TVR scale-up research for mass production of active cathode materials in FY18.

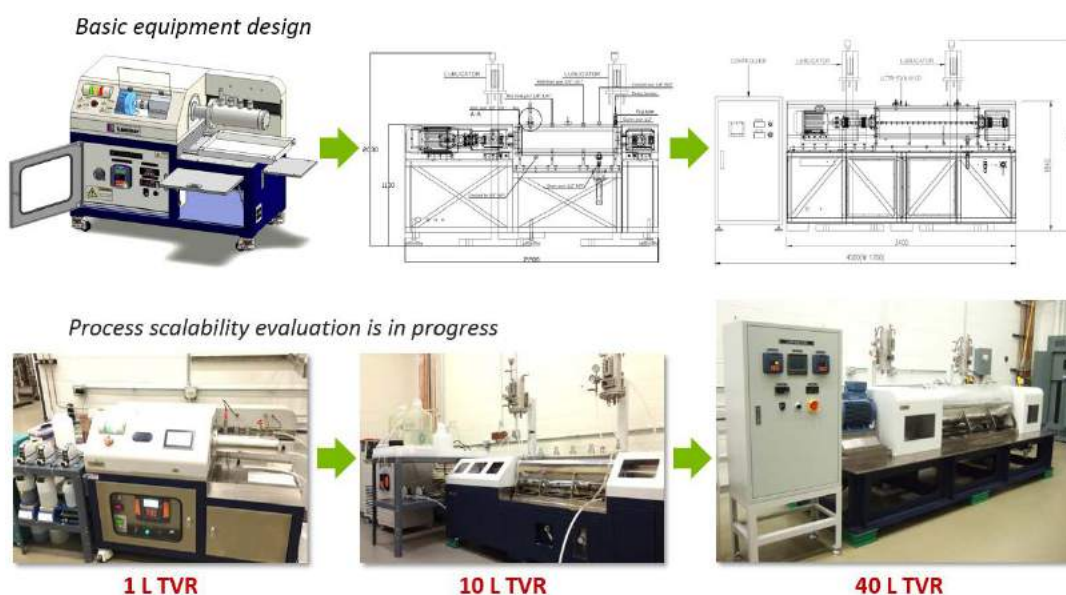


Figure II-381. 1L, 10L and 40L TVRs for Process Scalability Evaluation.

Conclusions

The flame spray pyrolysis facility has been installed and commissioned. Additional analytical equipment has been added to the facility from a catalyst synthesis project but will be able to be utilized for battery material synthesis.

The hydrothermal synthesis facility has been designed and equipment has been ordered.

A CRADA with Laminar has been established and a 40L TVR was been delivered and installed. The unit will be fully commissioned in early 2018.

Key Publications

1. Y. Shin*, O. K. Feridun and G. Krumdick, Scalable Advanced Chemical Reactor, Taylor Vortex Reactor, for Producing Li-ion Cathode Precursors, Argonne Battery Industry Day, June 2017

II.F.2 Advanced Active Battery Materials: Active Cathode Materials with Component Concentration Gradient Structures (ANL)

Gregory K Krumdick, Principal Investigator

Argonne National Laboratory
9700 South Cass Avenue
Argonne, IL, 60439-4837
Phone: 630-252-3952; Fax: 630-252-1342
E-mail: gkrumdick@anl.gov

Peter Faguy, Technology Manager

U.S. Department of Energy
Phone: 202-586-1022
E-mail: Peter.Faguy@ee.doe.gov

Start Date: October 1, 2010	End Date: September 30, 2018	
Total FY17 Project Cost: \$1,600,000	DOE FY17 share: \$1,600,000	Non-DOE share: \$0

Project Introduction

Newly-invented active battery materials that are not yet commercially available are being synthesized in gram quantity at bench-scale without quality control and reproducibility. These chemistries need to be tested and validated in large format prototype cells before going to high-volume manufacturing which needs a fair amount of material. Moreover, for in-depth material characterizations and further material modification such as surface coating, kilogram scale stocks of these materials are necessary as baseline materials. Therefore, the supplement of newly-invented materials with high quality and large quantity is critical for both fundamental research and industrial validation for commercialization.

From material engineering perspective, the development of a tailored synthesis process and composition optimization are the key issues to produce sufficient quantities of these newly-invented materials with high quality and reproducibility. But they are challenging. Barriers addressed are synthesis route selection, process and composition optimization, quality control with reproducibility and manufacturing cost reduction. The systematic material engineering and customized scaled process that we develop, will resolve the scale-up constraints of these materials and bridge the gap between basic material research and commercialization.

Objectives

The program is a key missing link between discovery of advanced active battery materials, market evaluation of these materials and high-volume manufacturing to reduce the risk associated with their commercialization. We provide systematic process and material engineering researches to develop cost-effective customized processes and to produce sufficient quantities of target materials with high quality by optimizing synthesis process and material composition, evaluating material purity profile and applying emerging manufacturing technologies. The technical targets of this program are developing customized synthesis processes for each material selected, scaling up multi-kilogram material with reproducibility under rigorous quality control and evaluating emerging manufacturing technologies to assist the fundamental research of R&D groups and reduce the commercialization risk of newly-invented active battery materials.

Approach

Advanced active battery materials with component concentration gradient structures were selected as target materials which are composed of Ni-rich central bulk together with Mn-rich outer layer. This type of material has been reported to have the potential to have a high capacity of more than 200 mAh/g together with improved thermal stability. We first performed preliminary synthetic studies on one of these materials to evaluate whether it can have both high capacity and thermal stability. In order to verify the electrochemical performance of the synthesized materials, the coin half cell evaluation was carried out. Through a collaboration with BNL, advanced structural analysis and thermal stability evaluation are being carried out. At the same time, as shown in Figure II-382, a tailored synthesis process is being developed to enable mass production of this material using various synthesis process equipment installed in Material Engineering Research Facility (MERF) at ANL.

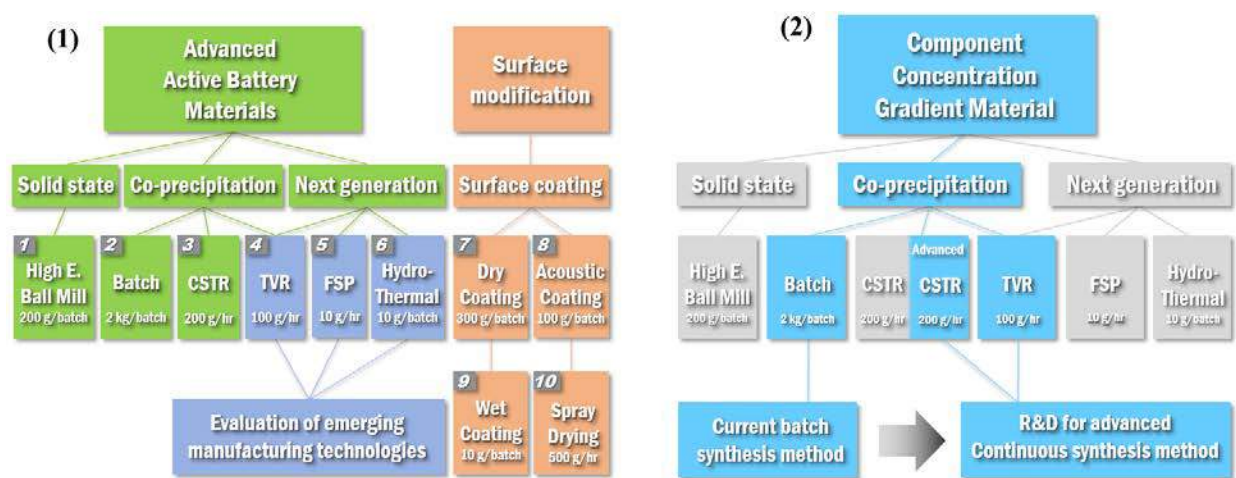


Figure II-382. Material Synthesis and Optimization Approach: (1) Process Capability Established at MERF and (2) Development of a Customized Synthesis Process for Advanced Cathode Material with Component Concentration Gradient Structure

Results

Layered Ni-rich NMC material exhibits high specific capacity of approximately 210 and shows significant interest for use in electric vehicles due to its high reversible capacity, good rate capability and low cost. However, many challenges remain to improve the capacity retention during cycling and thermal-abuse tolerance of this material. To stabilize this high-capacity Ni-rich cathode material, as an approach, particle shape with component concentration gradient structures has been implemented.

For preliminary synthesis and evaluation of these types of materials, one can see the schematic particle drawing in Figure II-383, we selected NMC811 as core composition, NMC442 as surface composition and we prepared two kinds of core-gradient materials by controlling the thickness of gradient layer which shows same initial discharge capacity at C/10-rate and improved cycling performance at 1C-rate. To investigate the particle structure and thermal stability of this 622 gradient material, we set up a collaboration with Dr. Yang's group at BNL. Figure II-384 is the X-ray absorption spectroscopy result. Ni, Co, and Mn K-edge XANES data of the commercial NMC622 and 622 gradient materials are almost identical, which indicates that 622 gradient material was well-synthesized. We can see the peak broadening of 622 gradient which indicates more structural inhomogeneity compared to the commercial NMC622 in Figure II-385. This unique phase transition behavior of 622 gradient is related to broadened oxygen release which is much safer than sharp oxygen release of commercial NMC622 shown at this oxygen release graph in Figure II-385.

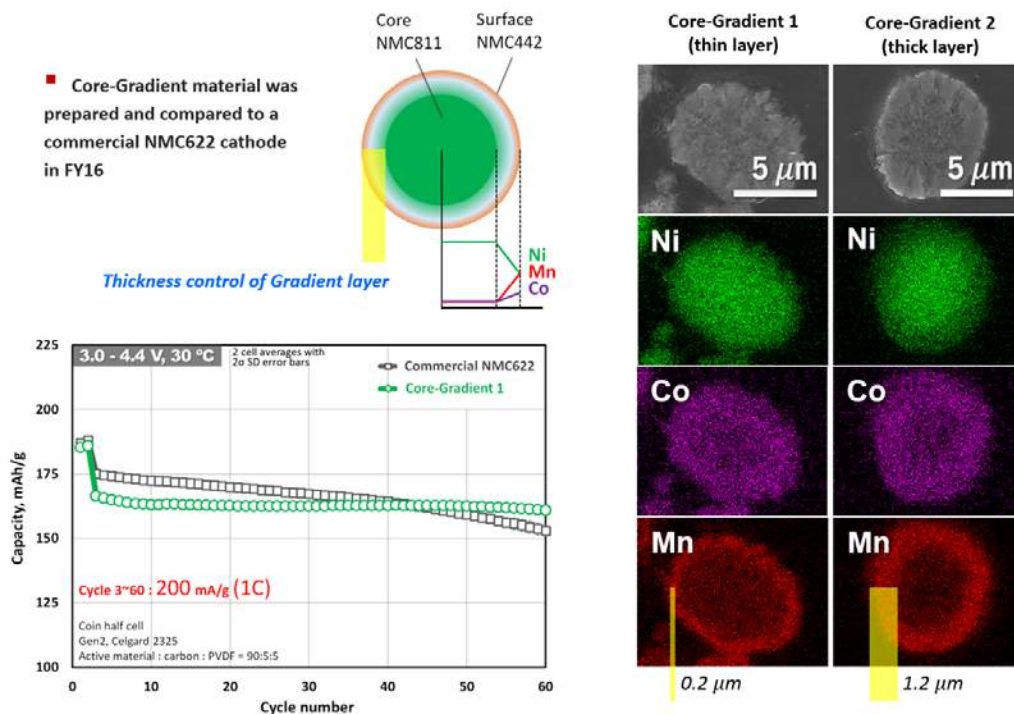


Figure II-383. Preliminarily Synthesized 622 Gradient Material with Component Concentration Gradient Structures

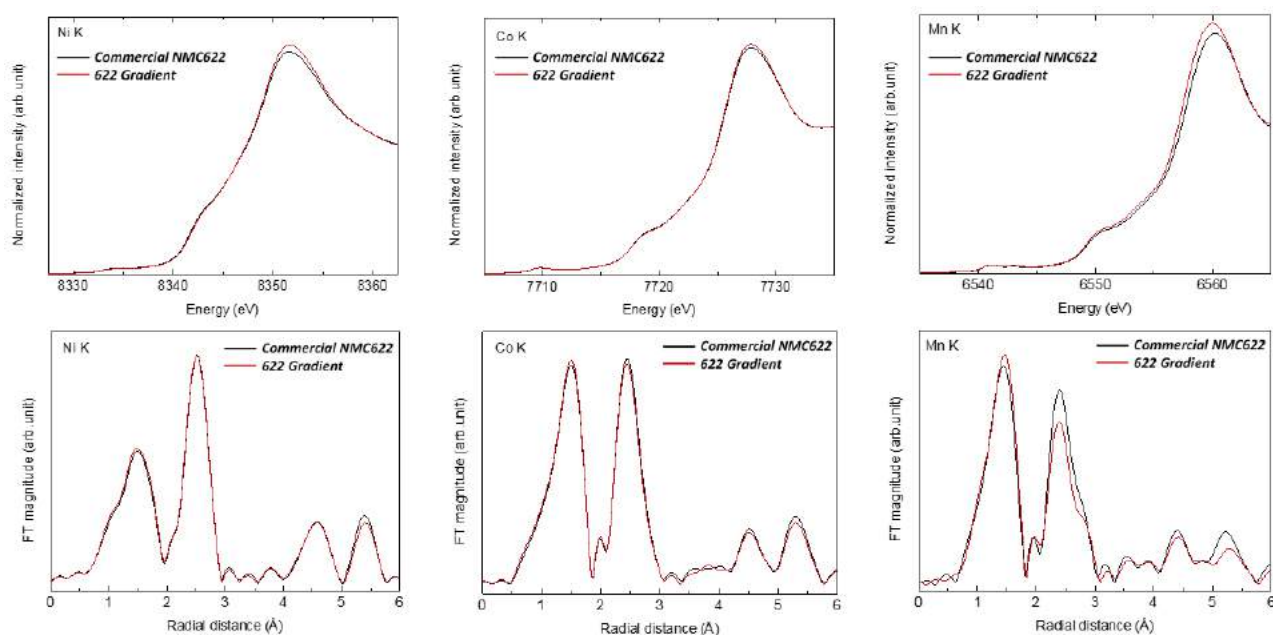


Figure II-384. X-ray Absorption Spectroscopy on 622 Gradient and Commercial NMC622 Materials (BNL)

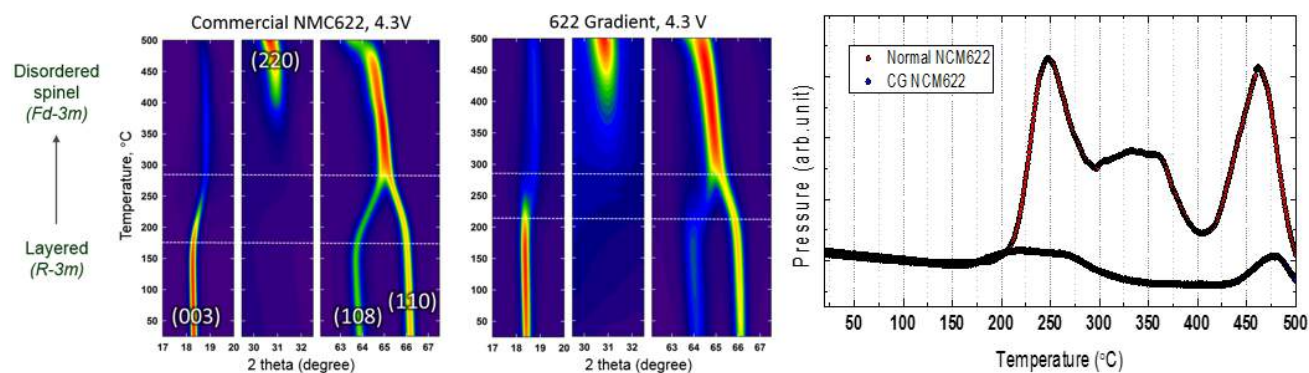


Figure II-385. Thermal Stability of Charged 622 Gradient and Commercial NMC622 Materials using Time Resolved XRD (BNL)

To achieve higher-capacity gradient material with better stability, NMC90/5/5 was selected as a core composition and NMC333 as a surface composition to make overall composition like NMC811. We prepared two types of gradient materials. 811 core-gradient and 811 core-shell as you can see at Figure II-386.

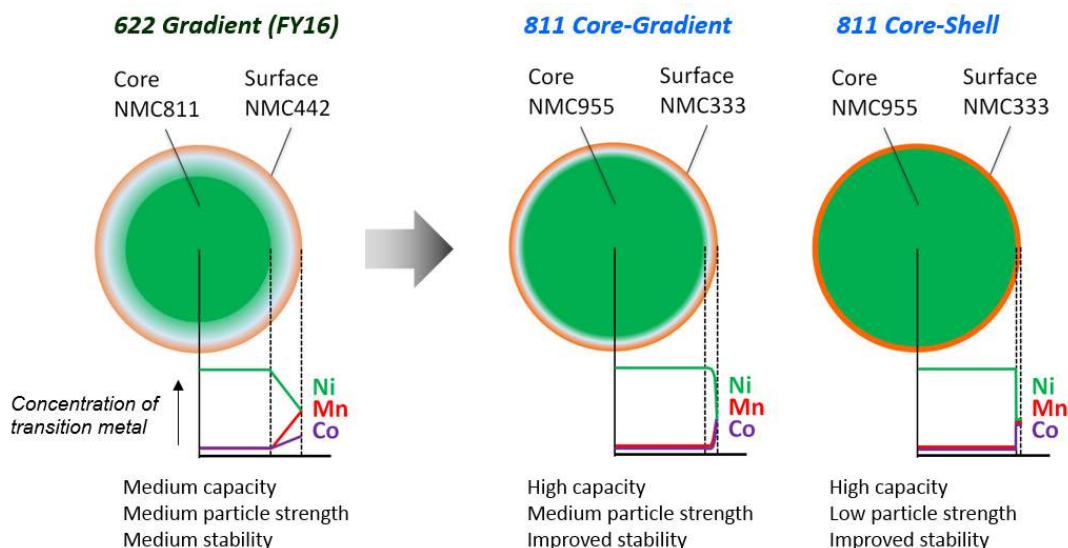


Figure II-386. Particle Structure Design for 811 Gradient Materials to Achieve Higher Capacity with Stability

Figure II-387 is the cross-sectional elemental mapping of the prepared materials. For 811 core-gradient particle, Ni concentration decreases from 90% to 33% as it approaches to the particle surface. On the other hand, Co and Mn concentrations increase from 5% to 33%. For 811 core-shell particle, Ni concentration decreases stepwise from 90% to 33% as it approaches to the particle surface. Co and Mn concentrations also increase stepwise from 5% to 33%. The prepared 811 core-gradient and core-shell materials exhibit similar physical properties and initial discharge capacity, compared to the commercial NMC811 as shown in Figure II-388.

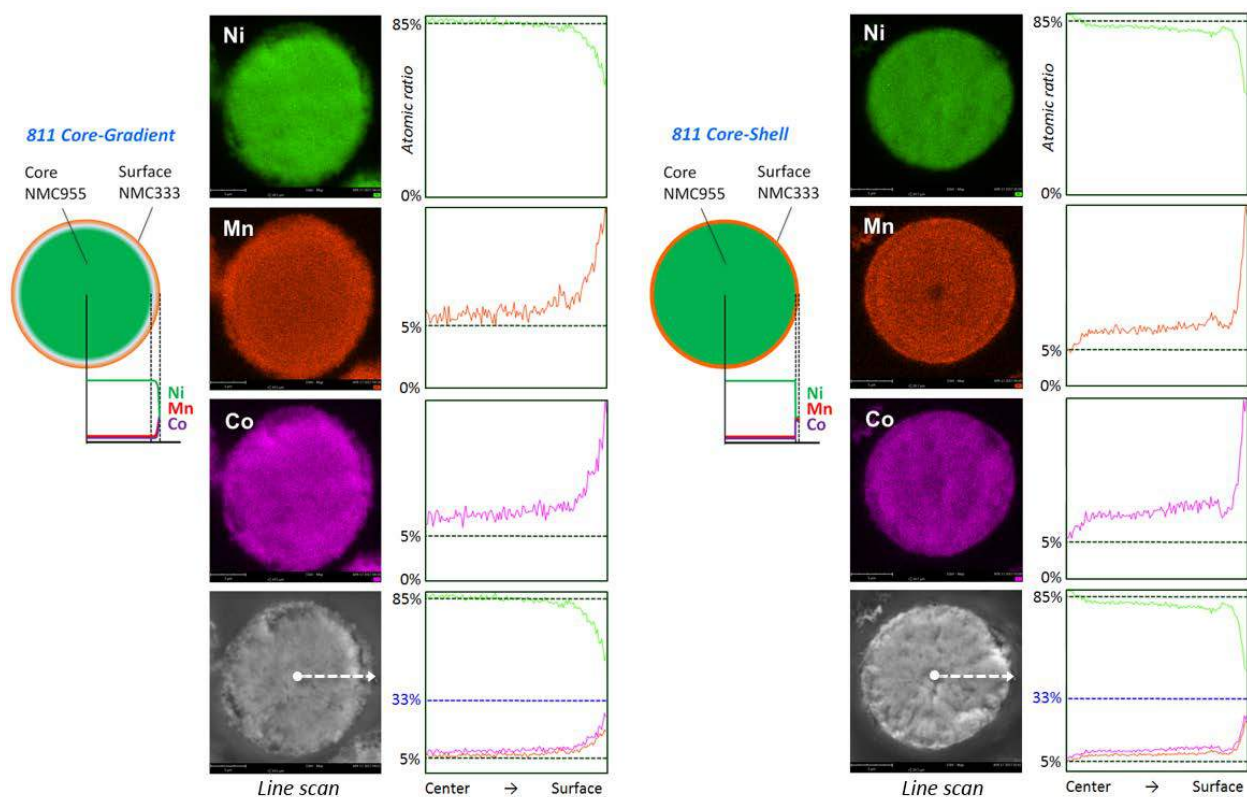

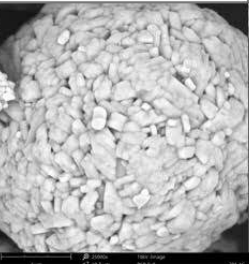
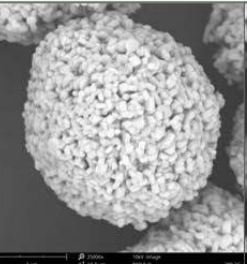
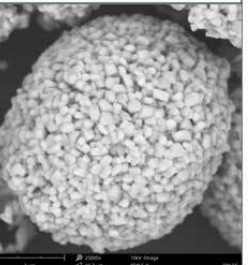


Figure II-387. SEM with EDS on Synthesized 811 Core-Gradient and Core-Shell Material

Material	NMC 811	NMC 333	811 Core-Gradient	811 Core-Shell
Scale / status	Commercial product		MERF pre-pilot preliminary product	
SEM				
Composition	NMC 811	NMC 333	~ NMC 811	~ NMC 811
ICP-MS analysis	$\text{Li}_{1.04}\text{Ni}_{0.80}\text{Mn}_{0.10}\text{Co}_{0.10}\text{O}_y$	$\text{Li}_{1.07}\text{Ni}_{0.34}\text{Mn}_{0.33}\text{Co}_{0.33}\text{O}_y$	$\text{Li}_{1.00}\text{Ni}_{0.76}\text{Mn}_{0.12}\text{Co}_{0.12}\text{O}_y$	$\text{Li}_{1.00}\text{Ni}_{0.76}\text{Mn}_{0.12}\text{Co}_{0.12}\text{O}_y$
Particle size D_{50} [μm]	13.7	11.7	8.0	8.0
BET [m^2/g]	0.37	0.34	0.55	0.57
* FCE [%]	90.0	90.5	88.1	86.7
* Avg. working voltage	3.86	3.88	3.87	3.87
* Discharge capacity @ 5 cycle [mAh/g]	210.0	171.6	209.1	205.4

* At C/10, 2.7 – 4.4 V and 30°C

Figure II-388. Comparison of the Prepared 811 Core-Gradient and Core-Shell Materials with Commercial Products

We compared the electrochemical performance of the 811 core-gradient and core-shell materials with commercial NMC811 and NMC333 materials using coin half cell. Figure II-389 is the C/2 cycling and rate performance comparison between 2.7 and 4.4 voltages at 30°C and Figure II-390 is the C/2 cycling and rate performance comparison between 2.7 and 4.4 voltages at 55°C. At both 30 and 55 degrees, 811 core-gradient and core-shell materials show similar initial discharge capacity but improved high C-rate performance and capacity retention, compared to the commercial NMC811 material.

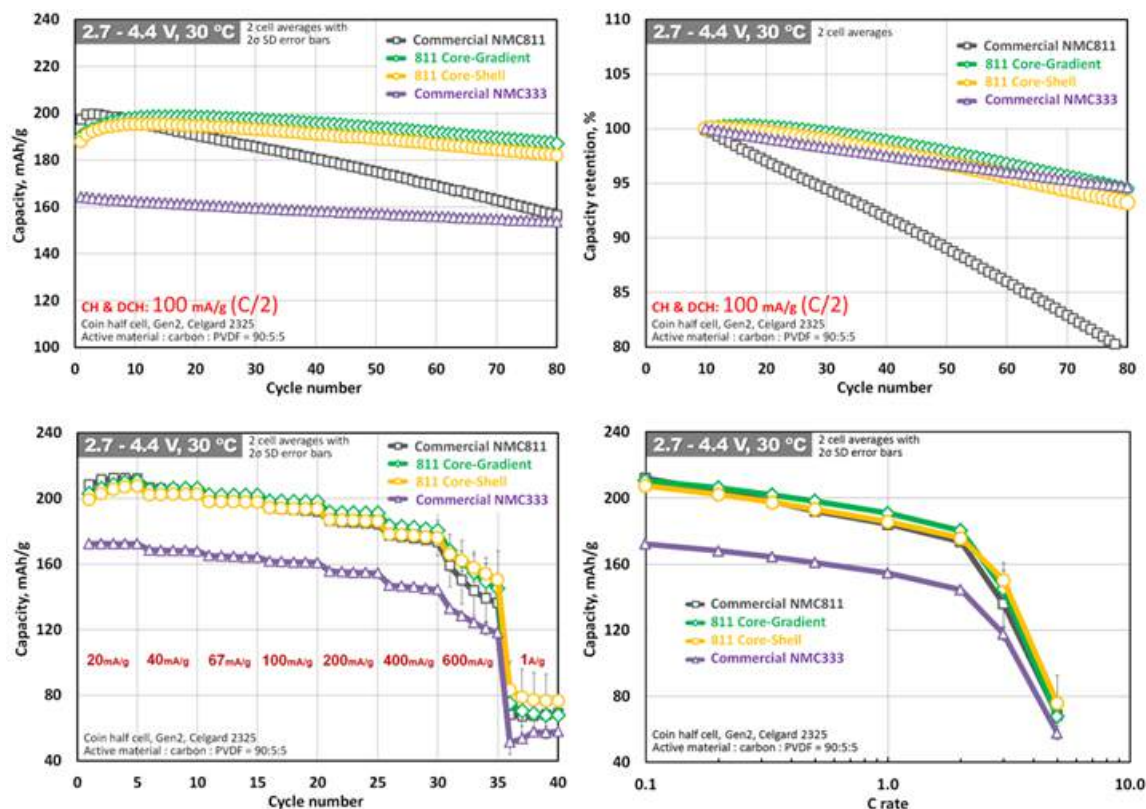


Figure II-389. C/2 Cycling and Rate Performance Comparison at 30°C

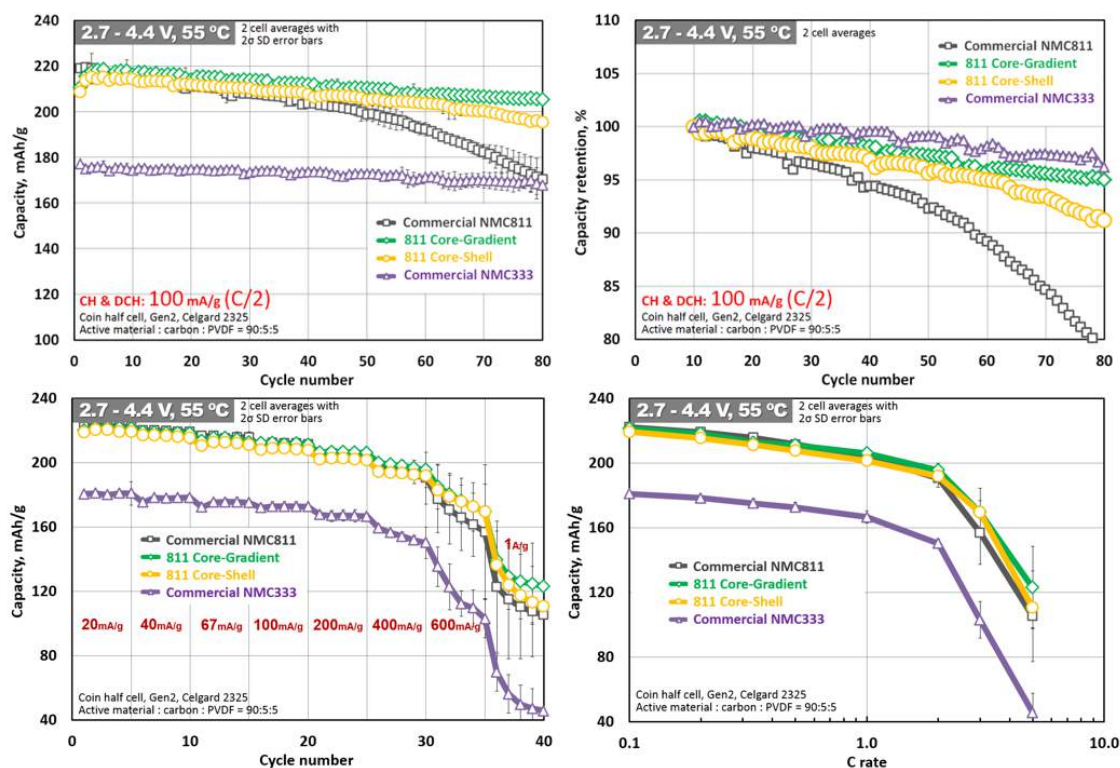


Figure II-390. C/2 Cycling and Rate Performance Comparison at 55°C

Two radar maps in Figure II-391 show overall electrochemical performance comparisons of the 811 core-gradient, core-shell and commercial NMC811 materials at 30 and 55°C. First cycle efficiency, average working voltage and initial discharge capacity are almost similar but 811 core-gradient and core-shell materials shows 20% improved capacity retention together with better rate capability compared to the commercial NMC811.

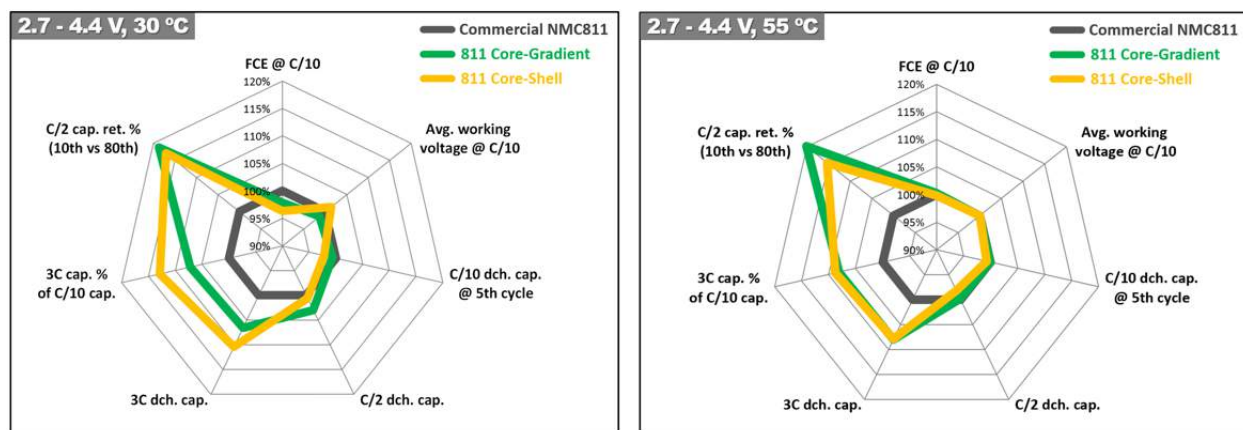


Figure II-391. Radar Map Comparison of the Prepared 811 Core-Gradient and Core-Shell Materials with Commercial NMC811

Conclusions

As an approach to improve the cycling and thermal abuse tolerance of layered nickel-rich NMC materials, cathode particle with component concentration gradient structures has been implemented. First, the particle structure and characteristics of the preliminarily-synthesized 622 core-gradient material were analyzed through the X-ray absorption spectroscopy and time-resolved XRD analysis in collaboration with BNL. The results confirmed that the prepared 622 core-gradient material showed improved thermal stability than the commercial NMC622 material.

In order to achieve more than 200mAh/g with stability, 811 core-gradient and core-shell materials were synthesized and evaluated. 811 core-gradient, core-shell and commercial NMC811 materials have similar first cycle efficiencies, average working voltages and initial discharge capacities, but 811 core-gradient and core-shell materials have about 20% better capacity retention and better rate capacity than commercial NMC811. Based on the obtained electrochemical data, we can conclude that cathode particle with component concentration gradient structures is a good approach to stabilize high-capacity nickel-rich cathode materials for longer cycle life. To achieve higher capacity together with longer cycle life, combinations of various particle structures and component concentrations have been attempted. As part of these efforts, we are producing samples to assist basic research groups and conducting new process development studies to promote the commercialization of these kinds of materials with component concentration gradient structures.

Key Publications

1. Y. Shin, O. K. Feridun and G. Krumdick, IV.E.2 Process Development and Scale up of Advanced Active Battery Materials (ANL), US Department of Energy (DOE), November 2016
2. J. R. Croy, J. S. Park, Y. Shin, B. T. Yonemoto, M. Balasubramanian, B. R. Long, Y. Ren and M. M. Thackeray, Prospects for spinel-stabilized, high-capacity lithium-ion battery cathodes, *Journal of Power Sources*, December 2016
3. G. Krumdick, Y. Shin and O. K. Feridun, Manufacturing Research on Advanced Cathode Materials, 2017 United States Drive Advanced Engine Crosscut Team Meeting, May 2017
4. Y. Shin, O. K. Feridun and G. Krumdick, Scalable Advanced Chemical Reactor, Taylor Vortex Reactor, for Producing Li-ion Cathode Precursors, Argonne Battery Industry Day, June 2017
5. Y. Shin, O. K. Feridun and G. Krumdick, Process Development and Scale up of Advanced Active Battery Materials –Gradient Cathode Materials, US Department of Energy (DOE), June 2017
6. Y. Shin, How to Stabilize High-capacity Nickel-rich Cathode Materials for Longer Cycle Life, 2017 The Battery Show, September 2017

II.F.3 Integrated Flame Spray Process for Low Cost Production of Battery Materials for Lithium Ion Batteries and Beyond (University of Missouri)

Yangchuan Xing, Principal Investigator

University of Missouri
Department of Chemical Engineering
Columbia, MO 65211
Phone: 573-884-1067
E-mail: xyngy@missouri.edu

Peter Faguy, Technology Manager

U.S. Department of Energy
Phone: 202-586-1022
E-mail: Peter.Faguy@ee.doe.gov

Start Date: January 1, 2016
Total Project Cost: \$2,526,250

End Date: December 30, 2018
DOE share: \$2,215,556

Non-DOE share: \$310,694

Project Introduction

Flame (combustion) processes have been proven to be the most economical way to produce fine powders. Pigment titanium oxide and fused silica are produced in millions of tons per year worldwide using flame processes. One of the challenges in these gaseous flame processes is that multiple metal oxides, like those used for lithium ion batteries, are difficult to produce due to the lack of appropriate gasified chemical precursors. Oxides of multiple metals are often produced in flame spray pyrolysis processes in which liquid precursors (mostly dissolved metal salts) are used. Precursor salt solutions are atomized and sprayed into a flame to make metal oxide powders. Unfortunately, the current flame spray technologies have problems in high throughput manufacturing. They also use a large amount of water and are prone to producing pollutants.

This project is to develop a battery material manufacturing technology using an integrated flame spray process (iFSP). It is a green chemical process and has the potential to significantly reduce manufacturing cost of battery materials. The technology is based on our innovations in spray processes, chemical precursors, and process integrations. The R&D project is a collaborative effort with EaglePicher Technologies, and will take the proposed iFSP to a new technology readiness level, with a goal to achieve a 25% cost reduction for the cathode active materials. Further full-scale production development beyond the performance period is expected to reduce the cost by 50% by 2020.

Objectives

The overall objective of this project is to develop an advanced technology for battery materials production at low cost and in a green chemical process. The specific objectives for 2017 include reactor development and powder synthesis, materials testing, and battery cell development with desired chemistry.

Approach

The main approach is to develop an integrated flame spray process in the manufacturing of transition metal oxide powder materials for batteries. The innovations of the proposed R&D include (1) using deep eutectic solvents (DES) as novel chemical precursors; (2) developing an innovative flame spray process; (3) integrating downstream powder processing; (4) leveraging with first class battery cell design and fabrication facilities (at EaglePicher Technologies).

Results

(1) DES Flame Spray Process R&D

A Gen 3.0 flame reactor has been developed and fabricated to spray the deep eutectic solvent precursors and produce transition metal powders at a capacity of 3 kg/day or more. New developments include flow field control, temperature control, and precursor feeding in the flame reactor. Efforts have been made and will continue to be made on testing the new reactor and improving its performance in the production of powder materials.

(2) NMC Powders and Performance

NMC (333) powders were produced in the flame reactor. The newly produced powders (Figure II-392) showed much better performances (Figure II-393) than powders produced previously. The significant improvement in capacity was attributed to the increase of lithium content in the powders to form stoichiometric compound of $\text{LiNi}_{1/3}\text{Mn}_{1/3}\text{Co}_{1/3}\text{O}_2$.

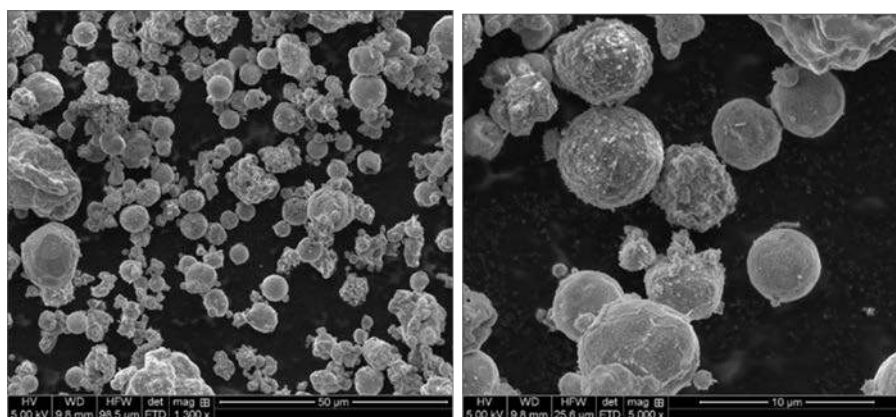


Figure II-392. Powders produced from the flame spray process, showing average size of 3 microns, much smaller than those obtained from last quarter at 50 microns. The powders also appear to be solid, not porous as before.

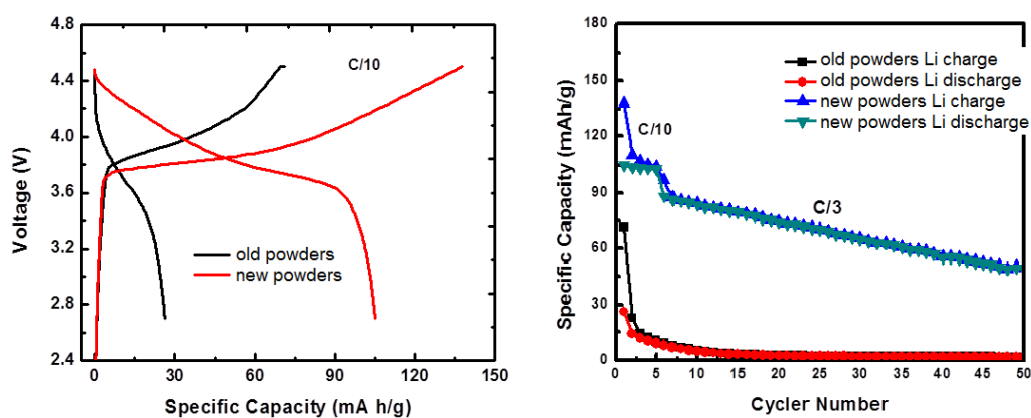


Figure II-393. Coin cell test of the new powders as compared to the old powders, showing much improved performance.

(3) Nanocoatings on Powders

Nanocoatings on active powders are intended to protect the powders from degradation and maintain their performance. Studies were conducted in two cases: one is carbon coating in a CVD process and the other is metal oxide (e.g., Al_2O_3 , Nb_2O_5) coating in a proprietary process. For the CVD coating of carbons, a preliminary work was conducted to coat carbon on metal oxide nanowires. A carbon nanocoating was successfully made on sodium titanate nanowires in the CVD process (Figure II-394). The accomplishment lies in the uniformity of the nanoscale thickness of the carbon coating that conformably covers the whole fiber. The carbon coatings improved the performance of the material, ascribed to increase in electrical conductivity and surface protection.

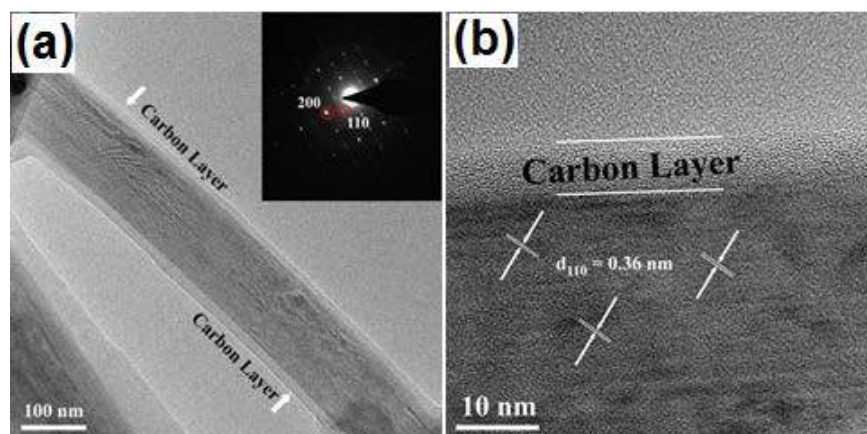


Figure II-394. Carbon coating on a sodium titanate fibrous battery material, showing a uniform, nanoscale carbon coating. The carbon coating is dense without holes.

Metal oxide nanocoatings were made on NMC powders that were made in a solution-based process. Preliminary studies showed that the NMC powders can be coated with metal oxide nanocoatings (Figure II-395), evidenced by the stability of the powder performances that are shown in Figure II-396. The charge-discharge curves are from the 1st cycle to 100th cycle. The powder as prepared showed large capacity loss after 50 cycles, but the coated powders showed much less loss. The stability of the NMC powders is obviously improved after a metal oxide coating.

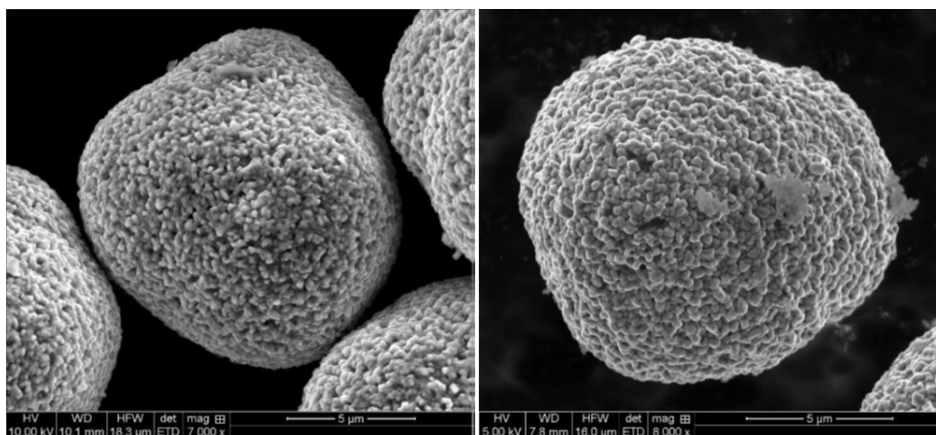


Figure II-395. (Left) Bare NMC powders as prepared; (Right) after a metal oxide coating.

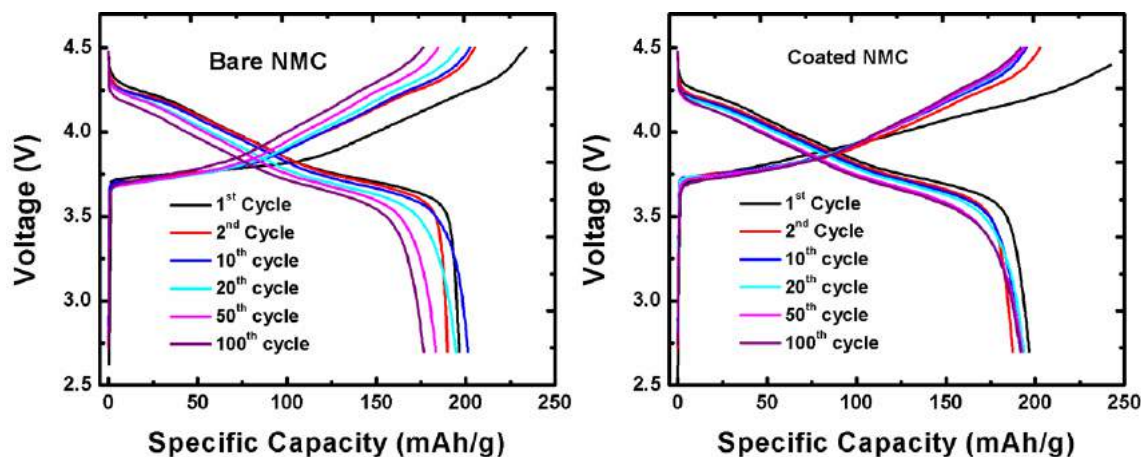


Figure II-396. Charge-discharge profiles on bare and coated NMC electrodes. The coated NMC shows much improved cycling stability (less polarization).

(4) Cell Design to Achieve Energy Density

Initial cell design work was conducted at EaglePicher. To achieve energy density of 250Wh/kg Li-ion cell the work was started with an establishment of baseline cell design template. A baseline cell design template serves as a design guideline for screening suitable chemistry and determining electrode design parameters such as optimal compositions and physical configuration. Establishment of baseline cell design template could reduce extensive optimization works for identifying suitable electrode chemistry, electrode designs, and a final cell design. Some commercial battery powders were used to establish the baseline in our battery cell design. The goal is to search for suitable battery chemistries that will guide the synthesis of powder compositions in the flame spray process.

High loading cathodes have initially been processed with several commercial cathode active materials. Lithium cobalt oxide (LiCoO_2 , LCO), lithium nickel cobalt manganese oxide ($\text{LiNi}_{0.6}\text{Co}_{0.2}\text{Mn}_{0.2}\text{O}_2$, NCM622) and lithium nickel cobalt aluminum oxide ($\text{LiNi}_{0.8}\text{Co}_{0.15}\text{Al}_{0.05}\text{O}_2$, NCA9152) were selected as candidate cathode materials for the study. Through cell fabrications and testing, electrochemical tests of these electrodes have been carried out under different rates in coin cells with cut-off voltage 4.3 V vs Li/Li^+ . The initial results for validating the cathode materials are shown in Table II-17.

Table II-17: The cell capacities of high loading electrodes using NCA9152, NCM622 and LCO.

Cathode Material	NCA9152	NCM622	LCO
Columbic Eff (%)	89.2%	91.0%	98.4%
C rate	Specific Discharge Capacity (mAh/g)		
C/20,C/20	195.4	184.5	160.0
C/10,C/10	190.2	180.3	157.6
C/5,C/5	183.0	176.5	157.9
C/5,C/2	173.0	166.8	---

Based on the electrochemical tests above, the energy densities of the cathode in coin cells have been summarized in Table II-18, which will be used for the cell design to reach the energy density of 250 Wh/kg when matched with a suitable anode material. The maximum energy density with the current design is from the cathode with NCA9512. NCA powder is a material to be produced in the flame spray process in our next step.

Table II-18: Energy densities using NCA9152, NCM622 and LCO, with discharge voltages of 3.81, 3.82, and 3.96 V vs Li/Li⁺, respectively.

Cathode Material	NCA9152	NCM622	LCO
C rate	Energy density (Wh/kg)*		
C/20,C/20	746.6	706.4	636.4
C/10,C/10	726.6	690.4	626.1
C/5,C/5	699.2	677.1	625.9
C/5,C/2	656.8	633.6	---

* based on cathode material.

Conclusions

1. A Gen 3.0 flame reactor was fabricated and tested that can achieve a high throughput rate of 3 kg/day or more of active material NMC powders.
2. The NMC powders produced in the reactor showed mostly spherical powders with much improved capacity that can be increased when further tailored in morphology and size.
3. Surface coating processes have shown promising results. They will be further developed and integrated into the flame spray process.
4. Baseline battery cell design shows that NMC material with a different composition and an NCA material could be targeted cathode powder materials to achieve the energy density of 250 Wh/kg. They will be further pursued in our future work.

Key Publications

Presentations

1. Liao, J.-Y., Smith, T.W., Hamad, K.I. and Xing Y., “Transition Metal Oxide Powders Made from Flame Spray Pyrolysis for Li-Ion Batteries”, 2017 AIChE Annual Meeting, Minneapolis, MN, Oct. 29-Nov. 3, 2017.
2. Smith, T.W., Liao, J.-Y., Hamad, K.I. and Xing Y., “Transition Metal Oxide Powders Made from Flame Spray Pyrolysis for Li-Ion Batteries”, 232nd ECS Meeting, National Harbor, MD, Oct. 1-5, 2017.
3. Liao, J.-Y., Smith, T.W. and Xing Y., “Hydrogenated and Carbon-coated Na₂Ti₆O₁₃ Nanowires as High-Rate Anode Materials for Lithium Ion Batteries”, 232nd ECS Meeting, National Harbor, MD, Oct. 1-5, 2017.

Journal Papers

1. Hamad, K.I., Liao, J.-Y., Smith, T.W. and Xing, Y., “Synthesis of layered LiMn_{1/3}Ni_{1/3}Co_{1/3}O₂ oxides for Li-ion batteries using biomass glycerol as solvent”, *Energy Technology*, ASAP 2017. DOI: 10.1002/ente.201700646. (Work related to DES precursors.)
2. Liao, J.-Y., Smith, T.W., Pandey, R.R., He, X., Chusuei, C.C. and Xing, Y., “Ti³⁺ Self-doped and Carbon-coated Na₂Ti₆O₁₃ Nanowires as High Rate Anode Materials for Lithium Ion Batteries”, under review at *ACS Applied Materials & Interface*, 2017. (Work related to carbon coating.)

II.F.4 High Performance Li-Ion Battery Anodes from Electrospun Nanoparticle/Conducting Polymer Nanofibers (Vanderbilt University)

Peter N. Pintauro, Principal Investigator

Vanderbilt University
Department of Chemical and Biomolecular Engineering
Nashville, TN 37235
Phone: 615-343-3878;
E-mail: pn.pintauro@vanderbilt.edu

Peter Faguy, Technology Manager

U.S. Department of Energy
Phone: 202-586-1022
E-mail: Peter.Faguy@ee.doe.gov

Start Date: October 1, 2015
Total Project Cost: \$707,062

End Date: September 20, 2019
DOE share: \$590,000

Non-DOE share: \$117,062

Project Introduction

Si is an attractive replacement for graphite in Li-ion battery anodes due to its high theoretical capacity (3,600 mAh/g for $\text{Li}_{15}\text{Si}_4$ vs. 372 mAh/g for LiC_6) and low operating potential (< 0.5 V vs. Li/Li^+). However, Si-based anodes often exhibit poor cycling stability due to large volume changes, particle pulverization, and instabilities associated with the solid electrolyte interphase (SEI) layer. The use of Si nanoparticles and nanowires has shown promise, but the active material loading in such nano-Si anodes is low, resulting in low areal and volumetric capacities. Thus, there is a need for new anode designs which can tolerate Si volumetric changes while maintaining high gravimetric, areal, and volumetric capacities over many charge/discharge cycles at low and high C-rates.

Objectives

The objectives of this project are to fabricate an electrospun Li-ion battery nanofiber anode and demonstrate its superior performance in half-cell and full-cells. The fiber mat anode is expected to outperform current state-of-the-art thin film slurry anodes, in terms of volumetric capacity and rate capability, and could enable a substantial reduction in the weight and size of an electric vehicle battery. The project will also demonstrate that the fiber mat anode can be manufactured in large scale at a commercial electrospinning facility. Experiments will focus on optimizing the composition and morphology of Si-based nanofiber anodes with/without a conducting polymer binder for lithium ion batteries. Such anodes will be designed for high gravimetric and volumetric energy densities, e.g., an initial capacity of 1,200 mAh/g and 1-2 mAh/cm² with 90% capacity retention after 200 cycles at 0.1C and a capacity of 500 mAh/g after 200 cycles at 2C which is recoverable to at least 1,000 mAh/g at the lower charge rate of 0.1C. The project will also generate useful correlations and insightful understandings regarding the electrospun anode composition/structure and its performance.

Approach

This project is an extension of the PI's prior successes in using neat polymer and polymer/particle nanofiber electrospinning for membranes and electrodes in electrochemical devices. In prior studies, electrospun Li-ion battery electrodes were prepared by carbonizing polymer fiber precursors at high temperature. In particle/polymer electrospinning, there is no fiber pyrolysis; the electrospinning and post-processing are performed at room temperature to preserve the beneficial properties of the polymer binder and to ensure an electrode with a high fiber volume fraction. High gravimetric, areal, and volumetric capacities are achieved at fast charge/discharge rates through the use of thick, densely packed particle/polymer nanofiber mats. Four key tasks will be performed: (1) Synthesis, optimization and testing of conducting polymer binders;

(2) Electrospinning and post-processing of composite nanofiber mat anodes of Si nanoparticles with a conducting binder or with electrically conducting carbon powder and a non-conducting binder; (3) Evaluation of short-term and long-term performance of electrospun anodes in half-cells and full-cells (with a NMC cathode) followed by post-mortem characterization; and (4) Preliminary scale-up of anode fiber mat manufacturing at a commercial electrospinning facility, where the resultant materials meet the project performance targets. Experiments during this reporting period focused on: (a) single fiber mats composed of Si and carbon particles in a suitable polymer binder; (b) dual fiber mat anodes, where one fiber type contains Si nanoparticles and binder and the second fiber is composed of carbon powder and binder; and (c) an electrospayed anode composed of Si nanoparticles and carbon powder with a new thermally crosslinked polymer binder. National laboratory partners on this project are Dr. Gao Liu at Lawrence Berkeley National Laboratory (LBNL), who has been providing electrically conductive polymer binders and Dr. Jagjit Nanda at Oak Ridge National Laboratory (ORNL) who is overseeing electrode characterization experiments. eSpin Technologies, Inc. is a subcontractor on the project and will be responsible for making fiber mat anodes on their commercial electrospinning equipment.

Results

Single Fiber Anodes

Experiments were carried out to optimize the composition of single fiber Si/C/poly(acrylic acid) (PAA) electrospun anode mats. Specifically, we sought to better understand how a fiber mat anode performs when the PAA binder content is increased at a constant Si loading. Three fiber mat electrodes were prepared and tested in CR2032 half-cells (with a Li metal anode) at Si/C/PAA compositions of 40/15/45, 40/25/35, and 40/35/25. The charge/discharge cycling results at 0.1C are shown in Figure II-397. Increasing the PAA content leads to a dramatic improvement in cell performance after 20 charge/discharge cycles, with an increase in capacity retention from 40% retention at 25 wt.% PAA to 80% retention at 45 wt.% PAA.

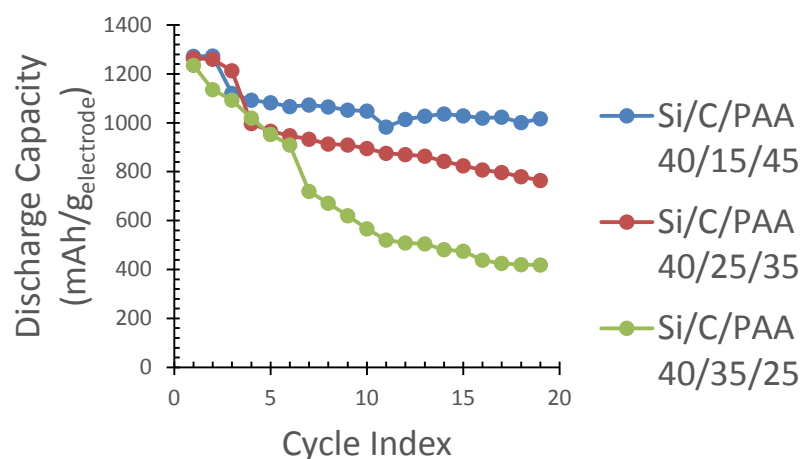


Figure II-397. Cycling results of anodes fabricated from electrospun single fiber mats containing 40 wt.% Si and varying content of C and PAA binder.

Research activities at ORNL focused on using x-ray diffraction (XRD), energy dispersive x-ray spectroscopy (EDX), and Raman spectroscopy to characterize the structure of electrospun single fiber anodes with a Si/C/PAA weight ratio of 40/25/35. An X-ray diffraction (XRD) pattern of the Si/C/PAA fiber mat is shown in Figure II-398. Peaks associated with crystalline Si were observed. The broad peaks near $2\theta = 20^\circ$ are attributed to the carbon powder and PAA binder. An energy-dispersive X-ray spectroscopy (EDX) analysis of the same fiber mat (Figure II-399) shows that Si and C particles were uniformly distributed throughout the fiber structure.

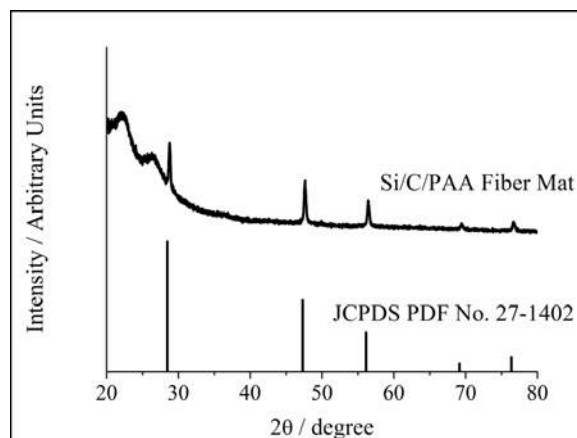


Figure II-398. XRD pattern of an as-spun Si/C/PAA fiber mat and a reference pattern for Si (PDF No. 27-1402)

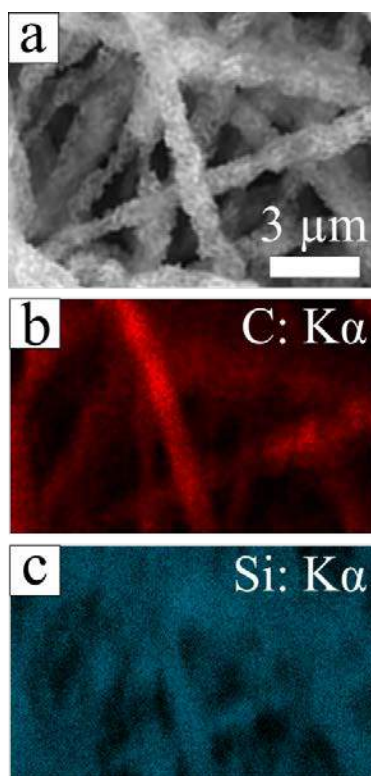


Figure II-399. (a) SEM image of a Si/C/PAA fiber mat and the corresponding EDX maps showing the (b) carbon and (c) silicon distributions.

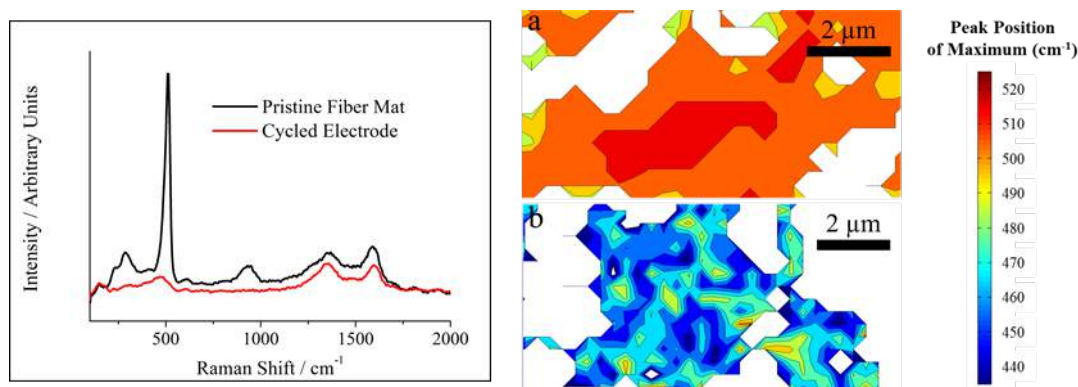


Figure II-400. (a) Average Raman spectra for a Si/C/PAA fiber mat containing 35 wt% PAA before and after 50 cycles. (b-c) Raman maps over an area of $\sim 4.5 \times 9.0 \mu\text{m}^2$ showing the Raman shift of the maximum peak for these electrodes (b) before cycling and (c) after 50 cycles at 0.1C.

Figure II-400 shows Raman spectra for a pristine (i.e., uncycled) fiber mat anode (Si/C/PAA ratio of 40/25/35) and an electrode after 50 cycles at 0.1C. The pristine electrode had a large peak near 520 cm^{-1} , associated with the presence of crystalline Si. This peak was absent in the cycled electrode which contained a broad peak near 475 cm^{-1} , indicating a crystalline to amorphous transformation of Si during cycling. This change was mapped over an area $\sim 4.5 \times 9.0 \mu\text{m}^2$ as shown in Figure II-400; these results indicate that the transformation occurred uniformly throughout the fiber mat. Note that portions of the electrode surfaces were out of focus during Raman mapping, and the white pixels in Figure II-400 represent regions where the data were omitted due to low spectral intensities (i.e., counts < 10).

Electrospinning Electrically Conductive Polymers

A new conducting binder, PEFM, was synthesized by G. Liu at LBNL for possible use as the binder in electrospun nanofiber mat Si anodes. The polymer is comprised of four subunits: (P) polyfluorene with octyl side chains, (E) fluorine with triethyleneoxide monomethylether side chains, (F) fluorenone, and (M) methyl benzoate ester. The synergistic functionalities of the subunits should provide PEFM with an acceptable balance of electronic conductivity, electrolyte uptake, mechanical strength and Si adhesion. Well-formed polymer fibers (with no Si particles) were electrospun from a solution a 5.5 wt.% PEFM in chlorobenzene. Unfortunately, after extensive experimentation, it was concluded that Si/PEFM fibers could not be made via electrospinning.

Dual Fiber Mat Anodes

Several dual fiber mats were prepared using a custom built setup with a rotating and oscillating drum collector onto which a Cu foil was wrapped prior to electrospinning. The spinning inks consisted of: (i) 0.3g Si, 0.3g PAA, 2g isopropanol (IPA) and 2g methanol (MeOH), and (ii) 0.34g C, 0.2g polyacrylonitrile (PAN) and 2.75g dimethylformamide (DMF). The inks were sonicated for 30 min and then mixed using magnetic stirrers for 2 days. The electrospinning conditions for fiber mat formation were as follows: (i) C/PAN ink – bias voltage 9 kV, distance to collector 9.4 cm, flowrate 0.25 ml/h and (ii) Si/PAA ink – bias voltage 8 kV, distance to collector 7.5 cm, flowrate 0.85 ml/h. Electrospinning was carried out in a controlled environment chamber at a relative humidity of 30% and a temperature of 24°C . Only the central section of the mat, where the two fiber types were uniformly deposited and well mixed, was used for further processing. The selected mat section was pressed for 60 sec at 10 MPa followed by 30 min exposure to MeOH and then 30 min exposure to DMF (these steps were performed to increase the fiber volume fraction and to create interfiber welds). The mat was dried in a vacuum oven at 70°C for 1 hour and then at 110°C overnight. The final anode mat composition was as follows: 70 wt.% Si/PAA (50/50 weight ratio) fibers and 30 wt.% C/PAN fibers (63/37 weight ratio). The Si areal loading in the dual fiber mat was 0.70 mg/cm^2 . A coin cell was assembled as in previous

experiments with a Li metal anode and an electrolyte of 1.2 M LiPF₆ in a mixture of ethylene carbonate and diethyl carbonate (3/7 by volume, BASF Corp.) with 30 wt. % fluoroethylene carbonate (BASF Corp.).

Scanning electron microscope surface images of a dual fiber mat, at various levels of magnification are shown in Figure II-401. Thinner C/PAN fibers can be clearly distinguished from the much thicker Si/PAA fibers. The C/PAN fibers appear to be well formed, whereas some droplets (with an average diameter 20 μ m) and beading can be observed in the Si/PAA fibers. Although the overall fiber mat quality is far from ideal, the Si nanoparticles are well distributed within the PAA fibers and intra-fiber pores can be detected in these fibers (the inter-fiber volumetric porosity was estimated to be 50%).

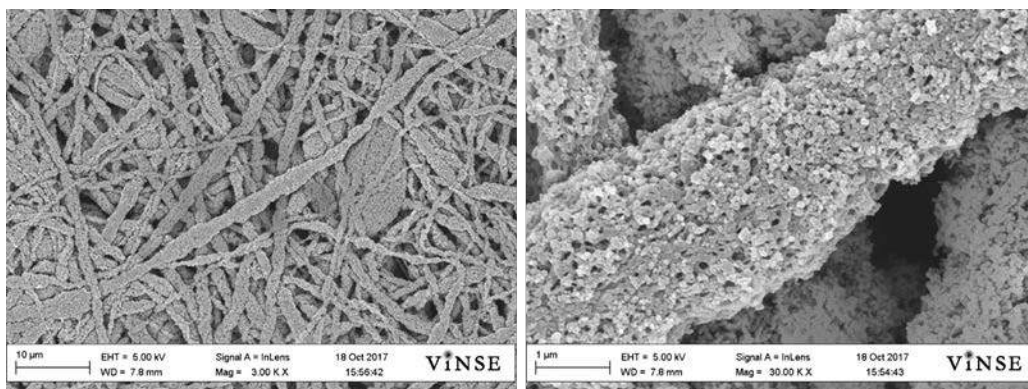


Figure II-401. SEM image of the surface of the electrospun dual fiber mat containing 70 wt.% of Si/PAA (50/50) and 30 wt.% of C/PAN (63/37) fibers.

A charge/discharge cycling plot for a half-cell with a dual fiber anode is shown in Figure II-402. Capacity data were collected by first cycling the cell at 0.1C for 35 cycles and then cycling the same cell at 1.3C for 50 cycles. At 0.1C, the capacity retention after 35 cycles was 87.4%. The theoretical capacity calculated from the electrospinning ink composition and flowrate was 1311 mAh/g, which is very close to the recorded first cycle charging capacity. The coulombic efficiency was above 98% during 0.1C cycling. After 50 cycles at 1.3C, the gravimetric capacity was 671 mAh/g (a capacity retention of 93.4%) with a coulombic efficiency of 99.4%. This capacity exceeds the 500 mAh/g Year 3 Go/No-Go target for this project. The excellent capacity and capacity retention is attributed to the use of PAN for the carbon fibers, improved intermixing of the Si/PAA and C/PAN fibers in a dual fiber mat, and the use of the Cu foil current collector (depositing fibers directly onto the Cu foil may be providing additional mechanical strength to the anode mat). Cycling experiments at high C-rates were also performed; for 50 cycles at 3C, the gravimetric capacity was essentially constant at 533 mAh/g, with a coulombic efficiency of 99.6%. The results clearly show that the C/PAN fibers are acting as electrically conducting pathways in the Si/PAA fiber mat, with electrons migrating between the two fiber types during electrode charging and discharging.

Examination of a New Crosslinkable Binder for a Si + C Anode

A new polymeric crosslinkable binder based on blends of poly(vinyl alcohol-co-ethylene) (PVAE) and PAA was investigated. In preliminary solution cast thin film experiments, it was found that PVAE/PAA mixtures could be thermally crosslinked (via ester formation) at 110°C, i.e., a thermally treated film did not dissolve in the casting solution solvent. Initial attempts to electrospin a Si/C/PVAE-PAA ink to make a single fiber mat anode, however, were unsuccessful. Nevertheless, an electrosprayed droplet anode was produced directly on a Cu foil current collector, where the Si/C/PVAE-PAA content was 40/25/35. This sprayed film was thermally crosslinked (110°C for ca. 12 hours) and then tested as the anode in a CR2032 half-cell cycling experiment.

SEM micrographs of the anode surface after overnight annealing are shown in Figure II-403. A uniformly porous structure is observed with no significant Si or C nanoparticle clustering. The results of a coin cell

cycling experiment are shown in Figure II-404. The first charging capacity at 0.1C was 1508 mAh/g, which is close to the expected value of 1515 mAh/g (assuming 3600 mAh/g for Si and 300 mAh/g for carbon). Charge/discharge cycling at 0.1C was continued for 10 cycles (to stabilize the SEI) and then the charge/discharge rate was increased to 1.3C. At this higher C-rate, the initial capacity was 1003 mAh/g, which decreased to 815 mAh/g after 50 cycles (the capacity retention was 81.3%), with a final coulombic efficiency of 98.9%. When the C-rate was further increased to 3C, the gravimetric capacity decreased from 623 mAh/g at cycle 2 to 574 mAh/g at cycle 50 (a capacity retention of 92%, with a coulombic efficiency of 99.5% at cycle 50). It is not known if the excellent cycling stability of this sprayed electrode, as compared to a single fiber Si/C/PAA anode, is due to the new binder or to the sprayed droplet morphology. We will continue to investigate PVAE-PAA binders next quarter, in an effort to answer this important question.

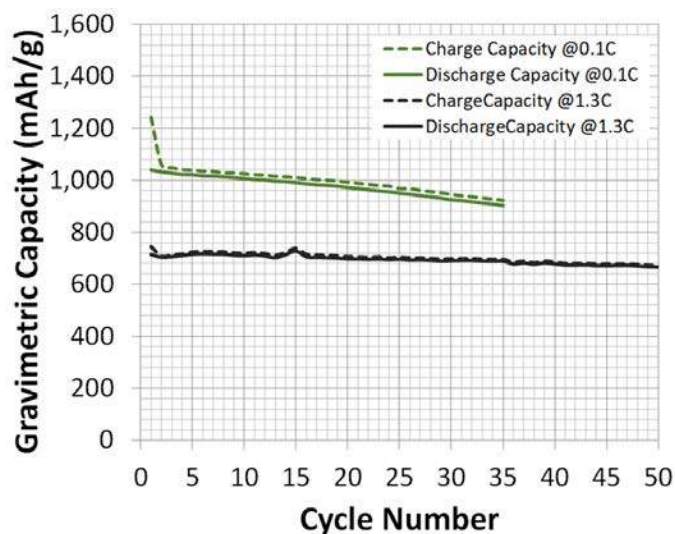


Figure II-402. Cycling results of an anode fabricated from electrospun dual fiber mat containing 70 wt.% of Si/PAA (50/50) and 30 wt.% of C/PAN (63/37) fibers.

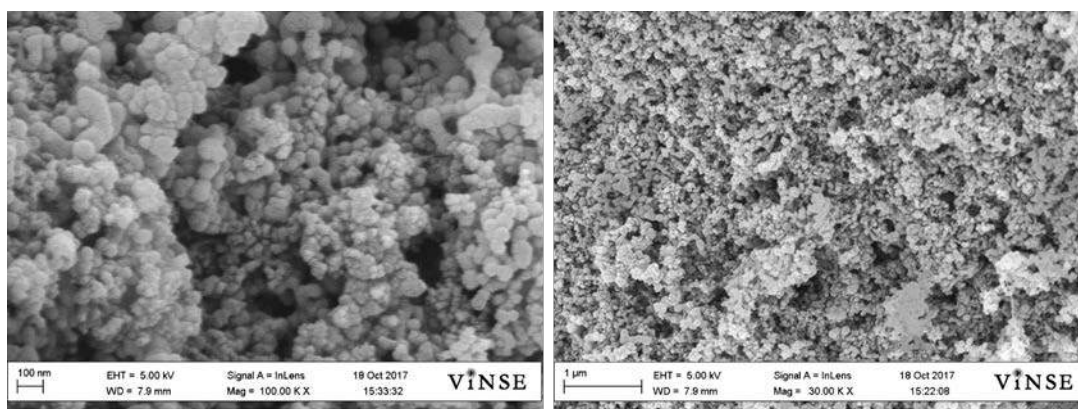


Figure II-403. SEM image of the surface of the electrospayed Si/C/PVAE-PAA 40/25/35 anode annealed at 110°C and supported on Cu foil.

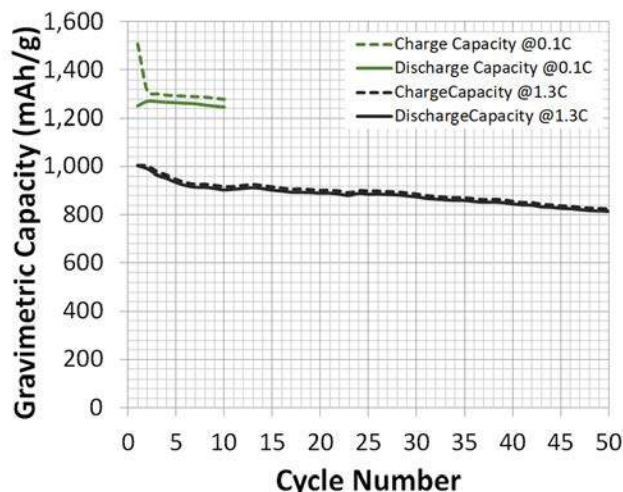


Figure II-404. Cycling results of an anode fabricated from electrosprayed ink containing new PVAE-PAA crosslinkable binder.

Conclusions

A new dual fiber electrospun anode mat was created and successfully tested, with separate fibers for Li storage (Si/PAA fibers) and for electrical conduction (C/PAN fibers), where PAA denotes poly(acrylic acid) and PAN denotes poly(acrylonitrile). Good charge/discharge behavior was observed (essentially complete utilization of Si during the first cycle). The results show that: (i) 33% carbon fibers in a dual fiber mat is sufficient for good electron conduction and (ii) there are sufficient contact points between Si/PAA fibers and C/PAN fibers in a dual fiber mat for isotropic electron flow throughout the dual fiber anode mat, with good electrolyte infusion between fibers. The gravimetric capacity retention was excellent (87.4% after 35 cycles at 0.1C and 81.8% retention after 50 cycles at 1.3C).

A new thermally crosslinkable blended polymer binder was utilized in an electrosprayed droplet morphology anode, where the binder was a blend of poly(vinyl alcohol-co-ethylene) and PAA. The anode composition was 40/25/35 (Si/C/binder weight ratio). At 1.3C, the anode exhibited a high initial gravimetric capacity of 1003 mAh/g and excellent cycling stability, with a capacity retention of 81.8% after 50 cycles.

Key Publications

1. E. C. Self, M. Naguib, R. E. Ruther, E. C. McRen, R. Wycisk, G. Liu, J. Nanda, and P. N. Pintauro, "High Areal Capacity Si/LiCoO₂ Batteries from Electrospun Composite Fiber Mats", *ChemSusChem*, **10**, 1823–1831 (2017). DOI : 10.1002/cssc.201700096.

II.F.5 Process R&D and Scale up of Critical Battery Materials (ANL)

Gregory Krumdick, Principal Investigator

Argonne National Laboratory
9700 S Cass Avenue
Lemont, IL 60439
Phone: 630-252-3952
E-mail: gkrumdick@anl.gov

Peter Faguy, Technology Manager

U.S. Department of Energy
Phone: 202-586-1022
E-mail: Peter.Faguy@ee.doe.gov

Start Date: October 1, 2016
Total Project Cost: \$1,500,000

End Date: September 30, 2017
DOE share: \$1,500,000

Non-DOE share: \$0

Project Introduction

New, experimental materials are being constantly invented to improve the safety, energy density, cycle, and calendar life of lithium ion batteries for HEV and PHEV applications. These materials are typically synthesized in discovery laboratories in small batches providing amounts sufficient only for limited basic evaluation but not in quantities required for full scale validation and prototyping. In addition, bench-scale processes are often un-optimized, not validated, and generate materials with inconsistent purity and yield. The project is aim to assist battery community by enabling access to larger quantities of high quality innovative materials.

Objectives

The objective of this project is to conduct research toward scaling up production of advanced materials for Li-ion batteries originally created in small quantities by discovery scientist. Scaling up the original route used by discovery scientists requires sometimes extensive modification of the bench-scale chemistry and scientific-based process R&D to allow for safe and cost effective production, development of an engineering flow diagram, design of a mini-scale system layout, construction of the experimental system, and validation of the optimized process. The experimental system will be assembled and the materials will be manufactured in quantities sufficient for full scale industrial evaluation. The materials produced by the program will be fully characterized to confirm chemical identity and purity. Analytical methods will be developed for quality control. The electrochemical performance of the materials will be validated to confirm that the properties match the original sample generated by the discovery scientist. Sample of the materials produced by the project will be available to LIBs community to support basic research and large scale performance validation.

Approach

A comprehensive, systematic approach to scale-up of advanced battery materials has been defined. This approach starts with the original route the new material was first made in the discovery lab and initial electrochemical evaluation. This determines if the material is to be added to the inventory database, ranked, prioritized and selected for scale up. MERF prioritize new materials based on level of interest, validated performance and scale up feasibility. The new candidate materials for scale up are discuss with DOE for final approval. MERF evaluates several approaches, including new emerging manufacturing technologies, to determine the best approach to scale up each particular material. One of such technology is Continuous Flow Chemical Reactor that enables the continuous synthesis of materials from discovery through process development and production scale. Continuous flow reactor can be used for rapid screening of reaction condition to better understand fundamentals of process kinetic and thermodynamic. The technology offers

cost-effective alternative to traditional batch processes by improving material and energy usage and minimize environmental impact of the manufacturing operation.

At this point, the scale-up process begins with a feasibility study, followed by proof of concept testing, 1st stage scale-up and final 2nd scale scale-up. Several Go/No Go decisions are located after feasibility determination and electrochemical validation testing.

For each material, we will develop a scalable manufacturing process, analytical methods and quality control procedures. We will also prepare a “technology transfer package” which includes detailed procedure of the revised process for material synthesis, materials balance, analytical methods and results (Certificate of Analysis) and SDS for the material. The detailed process description allows for preliminary estimates of production cost, an important factor for decision making in industry.

We apply the newly developed process to make kilogram quantities of the material. We will fully characterize chemically each material and make samples available for industrial evaluation and to the research community. We will also provide feedback to discovery chemist helping guide future research.

Results

1. Binder for Advanced Anode

MERF contributes to the Advanced Anode Program by developing binary polymeric systems able to in-situ crosslinking during the process of electrode laminate manufacturing. The two components of the system need to be stable and non-reactive during aqueous slurry preparation process to allow for casting but should undergo rapid thermally induced crosslinking during laminate drying. The selection of proper components for the binary system needs to take under consideration several criteria required for binder for LIBs electrode. The components of the binary system need to be soluble or forming stable emulsion in water, the cross-linked polymer needs to be chemically compatible with electrolyte and other electrode materials and electrochemically stable during cycling of the batteries. The polymer needs to be characterized by good adhesion to the current collector and good cohesion between particles of the composite anode.

The intra- and extra-molecular crosslinking will result in a flexible 3D mesh holding silicon and graphite particles together preventing loss of electrical contact and mechanical degradation of the electrode during cycling (Figure II-405). Interaction of the backbone polymer with Si surface may further strengthen the structure and improve performance.

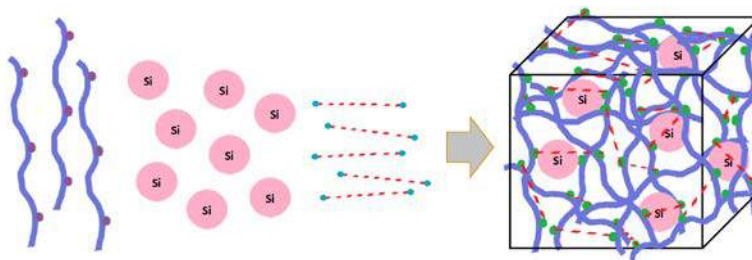


Figure II-405. Schematic of 3D mesh formation by in-situ cross-linking offunctionalized backbone polymer and small molecules.



Figure II-406. Poly(ethylene-alt-maleic anhydride) and poly(methyl vinyl ether-alt-maleic anhydride)

We selected inexpensive, commercially available poly(ethylene-alt-maleic anhydride) and poly(methyl vinyl ether-alt-maleic anhydride) as starting materials for syntheses of backbone polymers (Figure II-406).

The anhydride moiety in the starting materials were hydrolyzed to the corresponding poly(ethylene-alt-maleic acid) and poly(methyl vinyl ether-alt-maleic acid), respectively. Both backbone polymers containing maleic acid moieties were used in model cross-linking reactions with the following bi-functional small molecules: triethylene glycol, PEG400, PEG1000, 1,4-butanediol, and 4-aminobutan-1-ol.

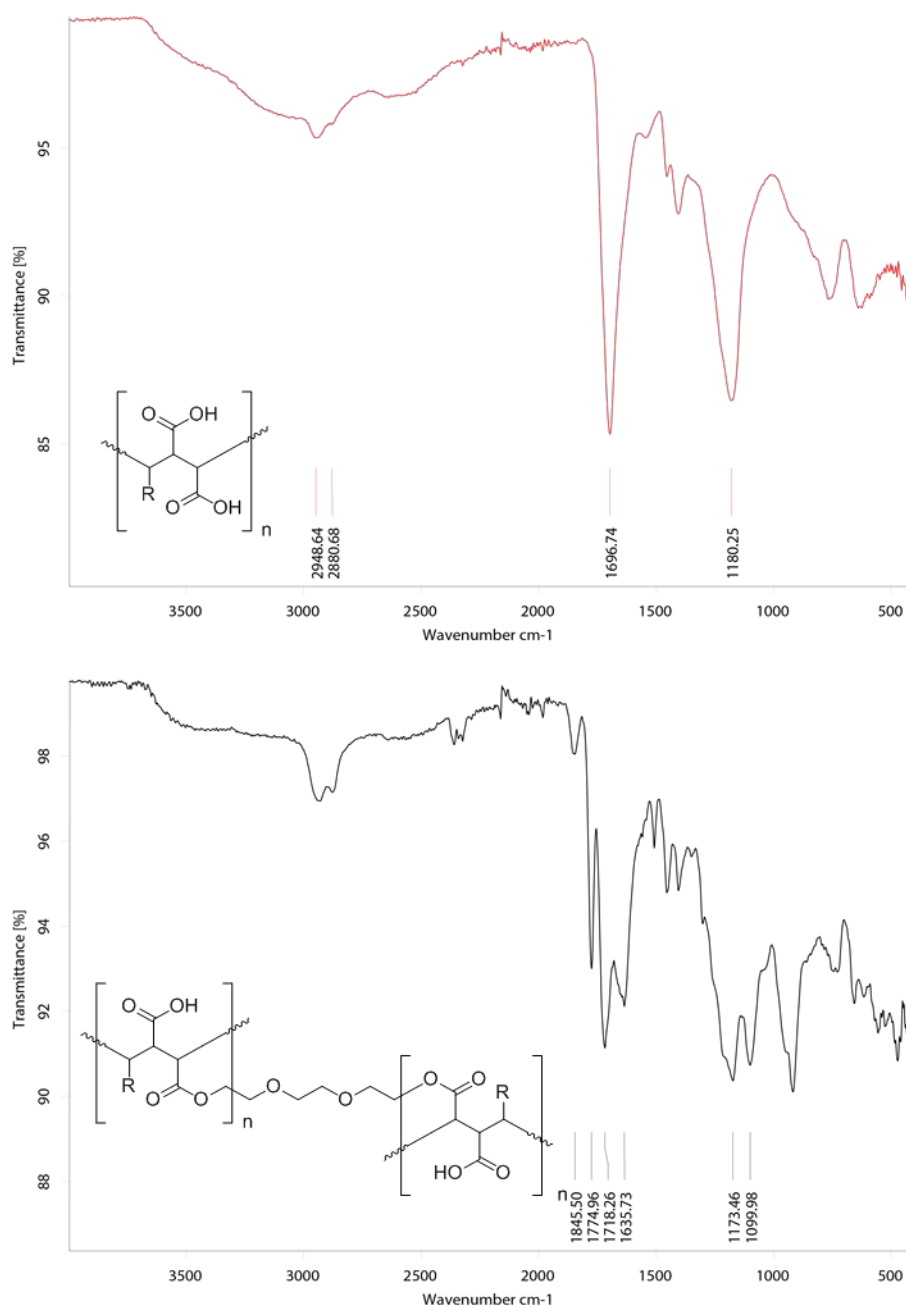


Figure II-407. FT-IR of poly(ethylene-alt-maleic acid) and material cross-linked with 20% molar of triethylene glycol.

FTIR analyses of the resulting materials revealed, in each case, formation of the expected crosslinks as evident by presence of ester or/and amide bonds (Figure II-407). Small amount of anhydride in the product was also observed.

2. Scale up of Trifluoromethyl Sulfone Solvents

Ethyl and propyl trifluoromethyl sulfones (Figure II-408) are promising solvents for high voltage LIBs electrolyte.

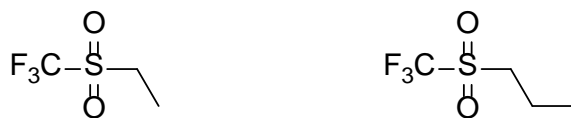


Figure II-408. Ethyl and propyl trifluoromethyl sulfones

The materials although known (12 references for Et and 4 references for Pr in SciFinder including patents for electrolyte formulations [1-2]) are purely described in the literature. There are only a very few references to the synthesis of the compounds [3]. (See Figure II-409.)

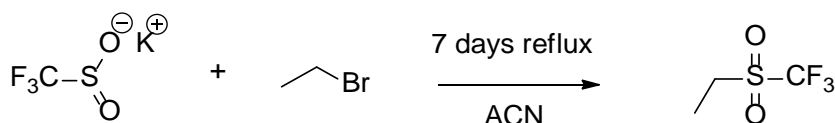


Figure II-409. Published synthesis of ethyl trifluoromethyl sulfone

The above reaction run at MERF at various conditions did not provide the desired product in an appreciable amount. Xu et al., [4] described multi-step synthesis procedure in 2002 publication without providing any experimental details. The synthesis route described by Argonne researches [5] utilizes Grignard reagent and trifluoromethanesulfonic anhydride (triflic anhydride). (See Figure II-410.)

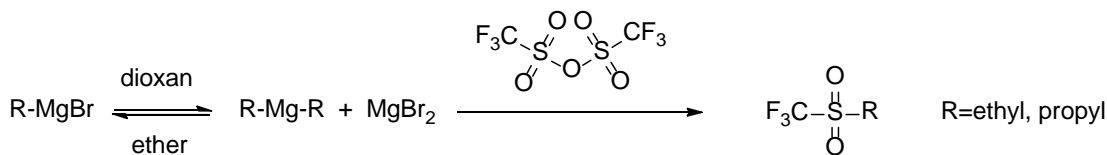


Figure II-410. Published synthesis of ethyl and propyl trifluoromethyl sulfones

The reported yield is low (~40%) and isolation of the desired product in a pure form is difficult due to complexity of the post-reaction mixture. Additionally, the process involves centrifugal separation of moisture sensitive intermediate (diethyl or dipropylmagnesium) that makes it impractical in a larger scale production.

MERF run several experiments in an attempt to simplify the process, enhance material purity and to improve overall yield (for example using organozinc instead of organomagnesium compound and copper catalysis).

We found out that the process can be reduced to one-step (Grignard equilibrium shift by addition of dioxane is not necessary) if chloromagnesium instead of bromomagnesium Grignard compound is used. (See Figure II-411.)

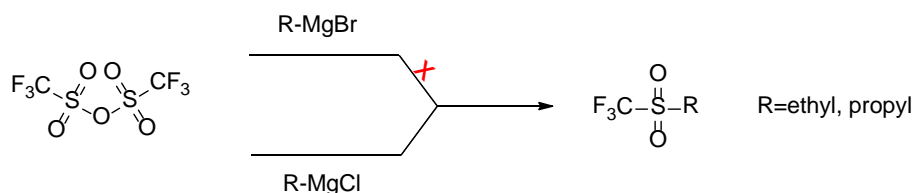


Figure II-411. Improved synthesis of ethyl and propyl trifluoromethyl sulfones

Although small amount of the materials can be made in batches, the current process that is extremely exothermic is not suitable for larger scale production. We currently investigate continuous flow reactor process as a technology platform to manufacture ethyl and propyl trifluoromethyl sulfones.

3. Scale-up of Pre-Lithiation Compounds - Li_5FeO_4 and Li_6CoO_4 .

Scaled-up synthesis of Li_5FeO_4 and Li_6CoO_4 is completed. The material, a pre-lithiation additive was developed and requested by Argonne's CSE Division (Chris Johnson). The material is made via solid state synthesis by step-wise heating following grinding in temp range from r.t. to 450 to 600°C to 800°C. The entire process needs to be done in a moisture free atmosphere. Several reactions (muffle furnace and tube furnace, outside and inside glovebox) have been run to optimize condition and validate reproducibility. The quality of the material seems not be scale-dependent (3g, 11g and 35g all appear the same if the process is run in muffler furnace that was located inside glovebox) and it material is phase pure (XRD). Several samples of Li_5FeO_4 were provided to Argonne's CSE researchers for electrochemical evaluation. Lithium cobalt oxide (Li_6CoO_4) were scaled up to 12 g and the material was forwarded to CSE researchers.

4. Novel silicon-containing carbonate solvents with improved safety profile.

In the quest for materials that offer improved safety without sacrificing performance we synthesized and investigated series of electrolyte carbonate solvents containing silicon atoms. Single literature reference [6] suggested potential flame retardant ability of methyl (trimethylsilyl)methyl carbonate (MTMSMC). The above reference did not disclosure source or technique used to obtain the material.

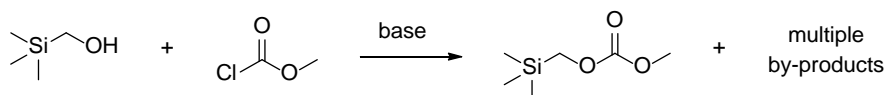


Figure II-412. Standard method for synthesis of unsymmetrical carbonates



Figure II-413. Transesterification method for synthesis of unsymmetrical carbonates

Standard reaction procedure (Figure II-412) for synthesis of MTMSMC failed to produce battery grade materials. The reaction produced multiple by-product difficult to separate from the desired material.

Transesterification of dimethyl carbonate with (trimethylsilyl)methanol (Figure II-413) was proposed as an attractive alternative and possible candidate for a continuous flow manufacturing process.

Screening of several catalysts and various reaction conditions in batch and continuous flow mode revealed that the material can be made in continuous flow reactor in more feasible manner than in batch. The reaction has been successfully scaled up in continuous mode to work out 250 mL reactants in 4 mL solid catalyst reactor in several hours. The product (MTMSMC) has been isolated by simple distillation with excellent yield and purity greater than 99.8%.

Several other silicon-containing carbonate solvents have been invented and synthesized at MERF (Figure II-414, compounds 2,3,4,5 and 6). Sample of the new materials are available to research community for further evaluation.

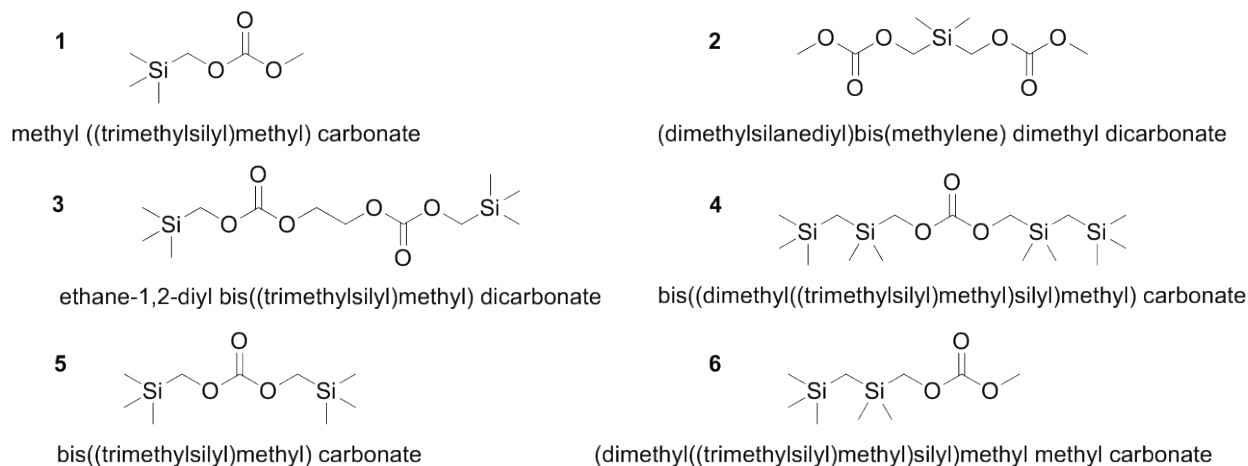


Figure II-414. Structures of some novel silicon-containing carbonates invented and produced by MERF

Preliminary investigations of electrochemical performance of ethyl (trimethylsilyl)methyl carbonate (ETMSMC) revealed that replacement of up to 20% EMC with ETMSMC in Gen2 electrolyte formulation does not decrease performance of the cell. (See Figure II-415.)

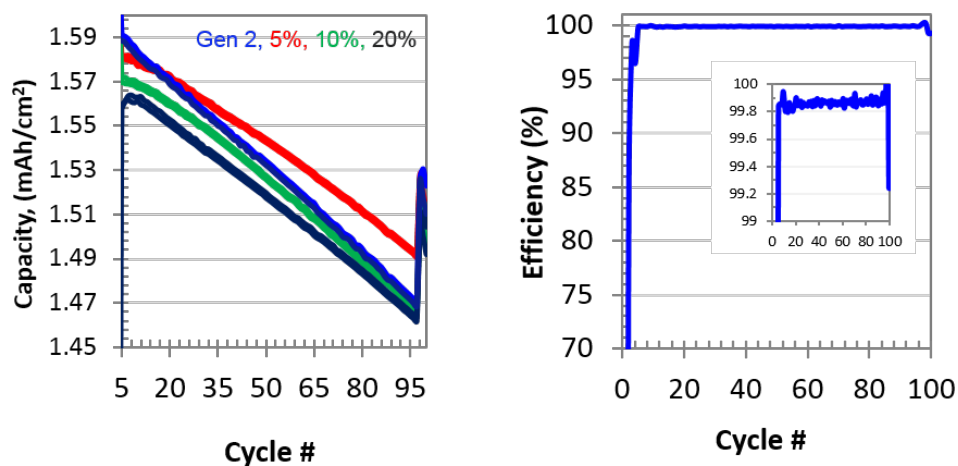


Figure II-415. 5, 10, 20% w/w ETMSMC in Gen2, graphite//NCM523, 3.0 - 4.4 V cycling (Ch/DCh at C/3), 30°C.

Sample of selected electrolyte formulations containing the new materials were provided to Argonne's CAMP facility for throughout evaluation. Materials (electrolyte formulations) with acceptable electrochemical performance will be used to manufacture larger cell formats for safety and abuse tolerance tests.

Conclusions

MERF's experimental materials scale-up program assists the battery research community and allows for a comprehensive evaluation of new materials by industrial laboratories as well as supports basic research.

In FY17 the program provided several new, not commercially available materials. Sample of high, uniform quality materials were distributed for further evaluation and research. Over 130 samples, ranging from grams

to hundreds of grams of experimental battery materials have been provided to researches since the program inception.

MERF contributes to Advanced Anode Program by designing, synthesizing, and evaluating new class of binder for silicon-graphite composite anodes. MERF's ability for rapid synthesis and evaluation of large number of materials permits for developing structure - properties database. Such a database allows for better understanding of binder's performance requirements and assists in science-based rationale design of a new materials.

MERF successfully investigated scale up process for making two sacrificial lithium source additives for cathode materials. Several samples of the two materials, lithium iron oxide and lithium cobalt oxide, were produced and provided to researches for electrochemical evaluation.

MERF invented and synthesized series of silicon-containing carbonate solvents. The materials have significantly higher flash point than solvents commonly used to formulate LIBs electrolytes. Preliminary electrochemical evaluation revealed that the materials can improve safety of LIBs without performance degradation.

Evaluate emerging manufacturing technologies such as continuous flow reactors, microwave assisted reactions or reactive distillations to improve product quality while lowering manufacturing costs are all under consideration. MERF utilized recently acquired customized Syrris ASIA320 flow reactor to develop expedient manufacturing processes for new electrolyte solvents by improving safety, minimize waste stream and lower material and energy cost.

Key Publications

Publications

1. Layered Oxide, Graphite and Silicon-Graphite Electrodes for Lithium-Ion Cells: Effect of Electrolyte Composition and Cycling Windows, Klett, Matilda; Gilbert, James A.; Pupek, Krzysztof Z.; Trask, Stephen E.; Abraham, Daniel P., *Journal of the Electrochemical Society* (2017), 164(1), A6095-A6102.
2. Chemical Stability of Lithium 2-Trifluoromethyl-4,5-dicyanoimidazolid, an Electrolyte Salt for Li-Ion Cells, Shkrob, Ilya A.; Pupek, Krzysztof Z.; Gilbert, James A.; Trask, Stephen E.; Abraham, Daniel P., *Journal of Physical Chemistry C* (2016), 120(50), 28463-28471.

Presentations

1. Battery Materials Scale-Up and Manufacturing Research, Gregory Krumdick, International Battery Seminar, March 23, 2017
2. Matching Electrolyte Formulation with Cathode Chemistry, Krzysztof Pupek, Daniel Abraham, Trevor Dzwiniel, Gregory Krumdick, Electrochemical Society 231st Meeting, May 2017.

Patent Applications

1. Process for Manufacturing Fluorinated Electrolyte Solvent, Trevor Dzwiniel, Krzysztof Pupek and Gregory Krumdick, US Patent Application 15/270,256, Filed 9-20-2016
2. Improved and Practical Process for the Synthesis of Lithium bis(2-methyl-2 fluoromalonato)borate, Trevor Dzwiniel, Krzysztof Pupek and Gregory Krumdick, US Patent Application 15/272,955, Filed 9-22-2016

Technical Report

1. Pupek, Krzysztof, Trevor Dzwiniel and Gregory Krumdick. "Li-FSI Impurity Impact Study: Final CRADA Report." Argonne National Laboratory, ANL/ES-C1401001, 2017.

References

1. Xu, Wu, U.S. Pat. Appl. Publ. (2009), US 20090017386 (Ferro).
2. Li, Wentao, U.S. Pat. Appl. Publ. (2015), US 20150140446 (BASF).
3. Hendrickson, James B. et al., Accounts of Chemical Research, 10(8), 306-12; 1977.
4. Xu, Kang et al., J. Electrochem. Soc., 2002, 149, A920–A926.
5. Zhang, Z. et al., Energy and Environ. Sci. 2017, 10, 900.
6. Miura, Hitoshi; Sakano, Fumihiko; Yahagi, Akira; Yamamoto, Taketsugu; Jpn. Kokai Tokkyo Koho (1998), JP 10172610 A 19980626.

II.G Next-Gen Lithium-Ion: Core and Enabling Support Facilities

II.G.1 Cell Analysis, Modeling, and Prototyping (CAMP) Facility Research Activities (ANL)

Andrew N. Jansen, Principal Investigator

Argonne National Laboratory

9700 S. Cass Avenue

Lemont, IL 60439

Phone: 630-252-4956

E-mail: Jansen@anl.gov

Peter Faguy, Technology Manager

U.S. Department of Energy

Phone: 202-586-1022

E-mail: Peter.Faguy@ee.doe.gov

Start Date: October 1, 2014

End Date: September 30, 2018

Total Project Cost: \$1,900,000

DOE share: \$1,900,000

Non-DOE share: \$0

Project Introduction

The “valley of death” is a phrase often used to describe the path a new discovery must traverse to become a commercial product. This is especially true for novel battery materials invented in research laboratories around the world. Often researchers are resource limited and are only able to make gram quantities of their new material. The CAMP Facility is appropriately sized to enable the design, fabrication, and characterization of high-quality prototype cells using just a few hundred grams of the latest discoveries involving high energy battery materials. Prototype cells made in the CAMP Facility generally have near 400-mAh capacity, which straddles the gap between coin cells and industrially-sized cells nicely – two orders of magnitude from each end point. Thus, a realistic and consistent evaluation of candidate chemistries is enabled in a time-effective manner with practical quantities of novel materials in cell formats commonly used in industry.

The CAMP Facility is an integrated team effort designed to support the production of prototype electrodes and cells, and includes activities in materials validation (benchmarking), modeling, and diagnostics. It is not the aim of this facility to become a small battery manufacturer, but instead to be a laboratory research facility with cell production capabilities that adequately evaluate the merits and limitations of new lithium-ion chemistries in a close-to-realistic industrial format. The source of these materials (anodes, cathodes, electrolytes, additives, separators, and binders) may originate from the ABR and BMR Programs, as well as from other domestic and foreign organizations such as universities, national labs, and industrial vendors. Electrochemical couples with high power and energy density are given extra priority. Lately efforts have focused on silicon-based anodes, and nickel-manganese-cobalt (NMC) cathodes that are high in nickel and operating at higher potentials.

The CAMP Facility has the capability to make three prototype cell formats in their 45 m² dry room: pouch cells (xx3450 format, with capacity around 0.5 Ah; and xx6395, with capacity around 2 Ah) and 18650 cells (with capacity around 2 Ah). Pouch cells are generally easier to assemble, but they may suffer from bulging if gases are evolved during cell aging and cycling. 18650s, which are rigid containers, may be used if the pouch cell format is deemed unreliable due to gassing. Central to this effort is a pilot-scale coating machine that operates with slurry sizes that range from 20 grams to a couple kilograms. This is a key feature of the CAMP Facility that enables a professional evaluation of small quantities of novel materials. If needed, the Materials Engineering Research Facility (MERF) is available for scaling up materials for these prototype cell-builds.

Objectives

The objective of this core-funded effort is to design, fabricate, and characterize high-quality prototype electrodes and cells that are based on the latest discoveries involving high energy anode and cathode battery materials. Using this multi-disciplined facility, analytical diagnostic results can be correlated with the electrochemical performance of advanced lithium-ion battery technologies for plugin electric vehicle (PEV) applications.

- Link experimental efforts through electrochemical modeling studies.
- Identify performance limitations and aging mechanisms.
- Support lithium-ion battery projects within the DOE-EERE-VTO

Approach

The general approach used in this effort is to start small and grow large in terms of cell size and amount of resources devoted to each novel battery material. At various points in the development process, decisions are made to either advance, modify, or terminate studies to maximize utilization of available resources.

Coin cells (2032 size) are used for materials validation purposes with initial studies performed at room temperature or 30°C. After formation cycles, the coin cells go through rate capability testing, HPPC testing, and limited cycle life testing. Additional temperatures and test conditions are employed if warranted.

Using the results obtained by the materials validation of promising materials, single-sided electrodes are fabricated on the larger dry-room coater for diagnostic study. The new cell chemistries are studied in detail using advanced electrochemical and analytical techniques, including the employment of micro-reference electrode cells. Factors are identified that determine cell performance and performance degradation (capacity fade, impedance rise) on storage and on extensive deep-discharge cycling. The results of these tests are used to formulate data-driven recommendations to improve the electrochemical performance/life of materials and electrodes that will be incorporated in the prototype cells that are later fabricated in the dry room. This information also lays the foundation for electrochemical modeling focused on correlating the electrochemical and analytical studies, in order to identify performance limitations and aging mechanisms.

If the results from diagnostics and modeling still look promising, full cell-builds are conducted using double-sided electrodes. The electrodes are then either punched in the case of pouch cells, or slit in the case of 18650 cells and assembled into full cells in the dry room using semi-automated cell assembly equipment. Formation procedures are conducted on the cells to encourage electrolyte wetting and uniform solid-electrolyte-interface (SEI) formation. These cells undergo rigorous electrochemical evaluation and aging studies under the combined effort of the CAMP Facility team, and Argonne's Electrochemical Analysis and Diagnostic Laboratory (EADL) and Post-Test Facility. After testing, select cells are destructively examined by the Post-Test Facility to elucidate failure mechanisms. This information is then used to further improve the new chemistry, as well as future electrode and cell-builds.

Results

The CAMP Facility is designed to work closely with materials researchers across the many electrochemical energy storage programs throughout the DOE-EERE-VTO. In addition to its own yearly R&D tasks, it actively coordinates its efforts to provide support to other national lab teams such as: the High-Energy High-Voltage deep dive, the Next Generation Anodes deep dive, and the CAEBAT programs. The Materials Benchmarking Activities (Section IV.B.2) is a segment of the CAMP Facility. The CAMP Facility also complements the capabilities of other DOE support facilities such as: the Materials Engineering Research Facility (MERF - ANL), the Post-Test Facility (PTF - ANL), the Battery Abuse Testing Lab (BATLab - SNL), and the Battery Manufacturing Facility (BMF - ORNL).

In particular, key deliverables that were met in FY17 for these programs include:

- Over 20 meters of advanced double-sided anode and cathode matching electrodes were produced and delivered for the SilLion SBIR Phase II project.
- Over 10 meters of alumina-coated NMC532 single-sided electrodes were produced and distributed to the "High Energy/High Voltage" project
- 30 pouch cells with >400 mAh capacity using Si-Graphite anode and NMC cathode for NREL CAEBAT studies were fabricated and delivered

More information about these projects can be found in the relevant chapters and sections of this annual report. The remainder of this CAMP Facility section will discuss the results of the remaining CAMP Facility deliverables for FY17, and include results of related topics.

Deliverable: Deliver to "Next Generation Anodes" Project at Least 10 meters of Single-Sided Negative Electrode Based on 30% Silicon-Graphite with ~ 2 mAh/cm² Loading for FY17 Baseline

Using our knowledge of the challenges that silicon can present for slurry making and coating, we have implemented effective strategies to help mitigate dispersion issues. New preparation processes were developed for the fabrication of both the 15 wt.% Si electrode (15 wt.% silicon, 73 wt.% graphite, 2 wt.% carbon black, and 10 wt.% LiPAA in H₂O) and the 30 wt.% Si electrode (30 wt.% silicon, 58 wt.% graphite, 2 wt.% carbon black, and 10 wt.% LiPAA in H₂O) in this section from silicon suppliers: Nanostructured and Amorphous Materials, Inc. from Houston, TX and Paraclete Energy from Chelsea, MI.

The initial observations of pressure building during the aqueous slurry processing add to the challenges that silicon already has on the electrochemical front. Gas generation suggests there is an uncontrolled reaction changing the chemistry and properties of the silicon material. Gas generation during slurry processing is not typical in NMP+PVDF-based slurries or H₂O+CMC+SBR (no Si)-based slurries. To demonstrate the gas generation of slurries containing silicon, we sealed pouch laminate foil with a pocket for slurry contents. This laminate serves only as a container and is not an actual electrochemically active pouch cell. We observed that high surface area silicon (30-50 nm particles), when combined with the binder solution LiPAA in H₂O (pH ~6), produced a significantly higher amount of gas generation than the other combinations. H₂O with silicon and H₂O+PAA with silicon showed minimal gas generation. All pouches using NMP as the solvent, either alone or in solution with PAA, showed no signs of gas generation. LiPAA does not dissolve in NMP, therefore this was not part of the test matrix. A baseline of LiPAA in H₂O (pH ~6) with graphite and carbon additives showed no gassing.

Early 15 wt.% silicon coatings using the larger 70 to 130 nm silicon from NanoAmor showed a reappearance of coating brittleness and stresses on the copper foil as the electrode dried that plagued early development silicon electrodes. These undesirable properties were somewhat apparent in coatings at ~2 mAh/cm², but calendaring helped improve the flexibility and avoidance of electrode cracking to extent that made them acceptable for the Electrode Library. However, achieving >3 mAh/cm² with 15 wt.% silicon proved to be very challenging with this material, which prevented this material from being fully adopted as the new baseline. SEM images revealed that the previously used 50-70 nm silicon had a smooth spherical grown shape morphology with secondary particles measuring around 50-70 nm, while the 70-130 nm powder showed jagged edges that appeared to be milled resulting in a more broad particle size distribution with some secondary particles micron sized. This result demonstrated that switching silicon particle size and morphology can have drastic changes in coating behavior and can slow the development of obtaining high quality, flexible, and robust electrodes.

A variety of coatings were made with different electrode compositions, solvent blends, and mixing procedures. NMP produced a high quality electrode but showed a decrease in mAh/g compared to the aqueous produced electrode. The NMP made electrode also took more cycles to reach the coulombic efficiency of ~99.5% that a

typical aqueous electrode achieves. For this reason, it was decided to use the slurry process based on aqueous LiPAA. The efforts in experimental coatings of 70-130 nm silicon from NanoAmor eventually resulted in coating a single-sided high-quality 30 wt.% Si electrode at $\sim 2 \text{ mAh/cm}^2$ (A-A011). This electrode (see Figure II-416) was entered into the CAMP Facility Electrode Library and also provided to the Next Generation Anodes Project (Silicon Deep Dive).

Anode: A-A011

58 wt.% Hitachi MagE3 graphite
 30 wt.% NanoAmor Silicon (70-130nm)
 2 wt.% Timcal C45 carbon
 10 wt.% LiPAA (H_2O), LiOH titrated
"SS" = single sided, target is for Electrode Library ->
Electrode ID: LN3107-72-5
 Cu Foil: 10 microns
 Total Electrode Thickness: 26 μm (SS)
 Coating Thickness: 16 μm (SS)
 Porosity: 41.0 %
 Total SS Coating Loading: 1.94 mg/cm^2
 Total SS Coating Density: 1.21 g/cm^3
 Made by CAMP Facility

Figure II-416. Electrode information for A-A011 containing 30 wt.% 70-130 nm silicon from NanoAmor.

Efforts were also expended to develop 15 wt.% Si electrodes using silicon from Paraclete Energy, which is their non-surface-modified silicon metal powder with oxide on the surface. These electrodes had better physical properties than the 70-130 nm Si from NanoAmor and was capable of making electrodes with $> 3 \text{ mAh/cm}^2$. This Paraclete Si was then used in a study to better understanding the impact n:p ratio may have for the silicon-graphite composite electrode system. Two electrodes were made with 15 wt.% Si: one with a n:p ratio near 1.5 [electrode A-A012], and one with a n:p ratio near 1.15 [electrode A-A013]. Full cells were then made using these new baseline materials paired against the same cathode [A-C013A] using the Silicon Deep Dive Protocol to evaluate the cycling performance. These results are shown in Figure II-417. The higher n:p ratio cell couple has a slight advantage over the lower n:p ratio cell, most likely because the Si in the higher n:p ratio is not cycled as deeply. Based on the results of using the Si material from Paraclete Energy, it was decided to use this Si material as the baseline Si going forward.

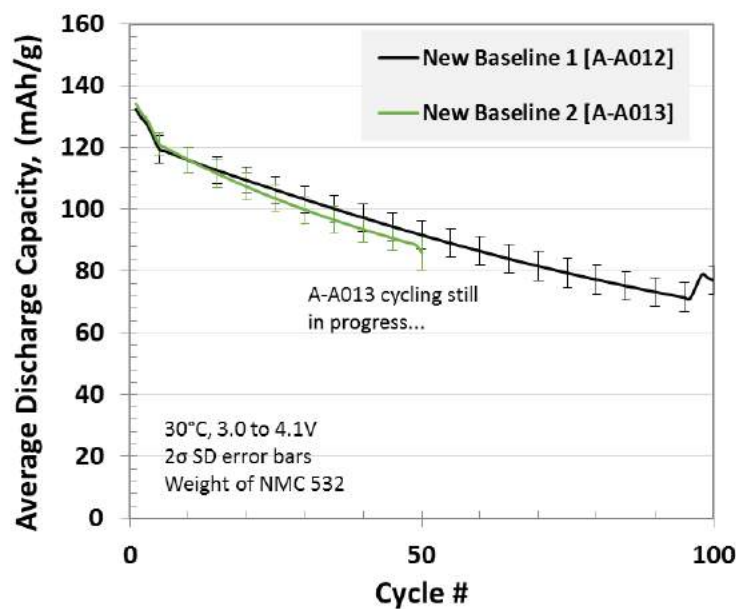


Figure II-417. Full-cell coin-cell results showing cycle number vs. average discharge capacity of the new Silicon Deep Dive baseline electrodes (Paraclete Energy silicon) vs. NMC532 [A-C013A]. Data shows the average values based on 4 coin cells for each electrode pair. The capacity values are normalized to the weight of NMC532.

Deliverable: Developing Techniques for In-Operando Detection of Lithium Plating During Fast Charging

A major effort is underway to enable fast charging of lithium-ion battery cells at rates greater than 6C, i.e., complete battery charging in 10 minutes or less. A key limitation at high charge rates is the plating of lithium on the graphite-based negative electrodes used in conventional, high-energy lithium-ion battery cells. This plating has consequences that include the following: (a) the plated lithium reacts with the electrolyte, reducing the inventory of lithium-ions and electrolyte, and causing a rapid decline in cell life; and (b) the plated lithium may form dendrites, which create short-circuits in the cell resulting in hazardous outcomes such as cell fires and/or explosions. We have been exploring various techniques to detect lithium plating during cell cycling. These techniques are under various stages of development and include (a) reference electrode cells that provide reliable data during high-rate cycling, (b) operando energy dispersive X-ray diffraction, and (c) operando radiography and tomography techniques.

As mentioned above, various techniques to detect lithium plating during cell cycling are under development. The reference electrode cells provide information on the positive and electrode potentials; lithium-plating becomes likely when the graphite-based negative electrode potential goes below 0.0 V vs. Li/Li+. Our typical setup includes a Li-metal reference electrode (RE) that is external to the electrode stack; the electrode potentials measured by this arrangement are affected by the distance of the RE from the electrodes, and are not reliable at high cycling currents. We are examining alternative approaches, including the use of an RE that is placed within the electrode stack; initial results are promising and more details will be provided in future reports. The operando energy dispersive X-ray diffraction (XRD) measurements are conducted with a conventional 2032-type coin cells at the 6BM-A beamline of Argonne's Advanced Photon Source (APS). The high-energy X-ray from the synchrotron source penetrates the stainless casing of the coin cell to allow for the operando measurements. Initial experiments show that lithium-metal foil can be identified in the XRD spectra collected on the coin cells. Future experiments will identify the cycling conditions (cell voltage, nature of the electrode, electrolytes, etc.) under which lithium-plating on graphite becomes most likely. For the operando micro-tomography work, a custom cell has been designed and fabricated to image dendrite formation during electrochemical cycling. Tomographic scans collected on symmetric lithium-lithium cells during a recent study indicate that lithium dendrites can be imaged in operando. Future experiments will include the study of lithium

plating on graphite electrodes; further modification of the cell and data acquisition conditions may be needed to achieve this challenging goal.

Deliverable: Determine Effect of Cycle Life/Calendar Life/Cell Pressure on Silicon-Graphite vs. NMC532 Pouch Cells

Silicon particles in lithium-ion batteries are known to grow up to 300% of their original size when lithiated. The current standard negative electrode active material, graphite, will expand only around 10%. While silicon-containing electrodes volumetrically expand when lithiated (full cell charging), they also deflate to a thickness above the original thickness when de-lithiated (full cell discharging). The destructive nature of the significant expansion and contraction during each charge and discharge cycle that silicon-containing electrodes exhibit is thought to be one cause of the poor cycle life performance. In FY 2017, we evaluated the effects of applied pressure on the cell stack for silicon-graphite composite and graphite-only electrodes. The CAMP Facility fabricated xx3450 pouch cells with silicon-containing and baseline graphite negative electrodes against the same NMC532 positive electrode and evaluated the formation, rate, impedance, and cycling performance under a relatively low stack pressure (2 psi) and a high stack pressure (76 psi). Two additional pressures will be selected in the second round of testing depending on these results.

Anode: Si-Gr 15 wt% NanoAmor Silicon (70-130nm) 73 wt% Hitachi MagE3 5 wt% Timcal C45 10 wt% LiPAA <i>Matched for 4.1V full cell cycling</i> Cu Foil Thickness: 10 μm Total DS Electrode Thickness: 94 μm SS Coating Thickness: 42 μm Porosity: 44.0 % Total Coating Loading: 4.80 mg/cm ² Total Coating Density: 1.14 g/cm ³ Estimated Capacity: 2.85 mAh/cm ² (0.050 to 1.5V vs. Li metal, C/10)	Anode: Gr 91.83 wt% Hitachi MagE3 2 wt% Timcal C45 6 wt% Kureha 9300 PVDF 0.17 wt% oxalic acid <i>Matched for 4.1V full cell cycling</i> Cu Foil Thickness: 10 μm Total DS Electrode Thickness: 130 μm SS Coating Thickness: 60 μm Porosity: 32.0 % Total Coating Loading: 8.85 mg/cm ² Total Coating Density: 1.47 g/cm ³ Estimated Capacity: 2.73 mAh/cm ² (0.000 to 1.5V vs. Li metal, C/10)	Cathode: NMC532 90 wt% Toda NMC532 5 wt% Timcal C45 5 wt% Solvay 5130 PVDF <i>Matched for 4.1V full cell cycling</i> Al Foil Thickness: 20 μm Total DS Electrode Thickness: 136 μm SS Coating Thickness: 58 μm Porosity: 33.6 % Total Coating Loading: 15.64 mg/cm ² Total Coating Density: 2.70 g/cm ³ Estimated Capacity: 2.27 mAh/cm ² (3.0 to 4.2V vs. Li metal, C/10)
--	---	---

Figure II-418. Electrode design for Si-Gr//NMC532 and Gr//NMC532 xx3450 pressure study pouch cells. “SS” = single side, “DS” = double side. All electrodes were fabricated at the CAMP Facility and designed for 3.0 to 4.1 V full-cell cycling.

Details of the fabricated electrodes are provided in Figure II-418. Single and double side electrodes were made to enable multilayer pouch cell stacking. The coating loadings targeted were based on each of the electrode active materials’ half-cell 1st cycle performance, reversible C/10 capacity, and reversible 1C capacity, the n:p ratios for the Si-Gr//NMC532 and Gr//NMC532 cells were calculated to be 1.10-1.19 and 1.15-1.17, respectively, for cycling from 3.0 to 4.1 V in a full cell. Weight normalization of the data within this section is based on the total active material weight in the cathode (namely NMC532). The xx3450 cells each contain 2.779 grams of NMC532 per pouch cell.

The electrodes were calendered, stamped to xx3450 electrode pouch cell dimensions, and z-fold wound with 15 total layers (7 double-sided anode, 6 double-sided cathode, and 2 single-sided cathode for the outside layers). Celgard 2325 PP/PE/PP was used as the separator. Area normalization of the data within this section is based on the total cathode area in a cell. Each xx3450 cell has a total cathode area of 197.4 cm². After the cells completed assembly, all cells were filled with 3.0 mL of 90 wt.% (1.2 M LiPF₆ in EC:EMC 3:7 wt.%, “Gen2”, Tomiyama) + 10 wt.% (FEC, Solvay) electrolyte and vacuum sealed. The electrolyte volume to available pore volume (anode, cathode, and separator porosities) factor was calculated to be ~2.8 for all the cells. The cells were then placed in rigid fixtures for electrochemical testing. The chosen stack pressures per pouch cells of 2 psi and 76 psi are examples of a modest stack pressure and relatively extreme stack pressure, respectively. Stack pressure per cell was calculated by accounting for the number of cells per layer, cell dimensions, spring constant, length of spring before and after compression, number of springs, and weight of the top steel plate

above the cells. Four cells were put on test for each of the four variables based on the anode and pressure applied to each cell: (Si-Gr, 2 psi), (Si-Gr, 76 psi), (Gr, 2 psi), and (Gr, 76 psi).

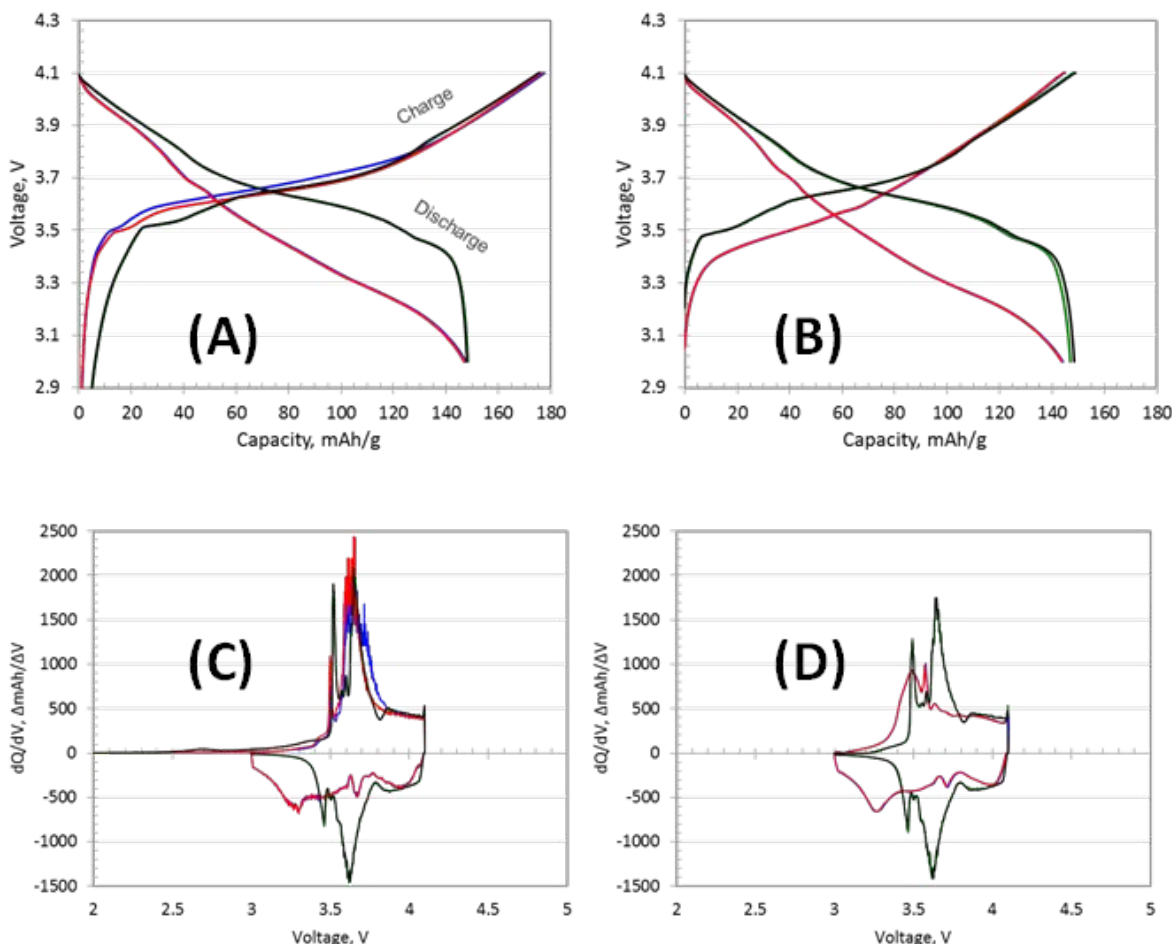


Figure II-419. Representative individual cycle voltage (a,b) and dQ/dV (c,d) profiles of Si-Gr//NMC532 pouch cells at 2 psi per cell (blue), 76 psi per cell (red), and Gr//NMC532 pouch cells at 2 psi per cell (green), 76 psi per cell (black) of the 1st (a,c) and 3rd (b,d) cycles during formation. (The green and black curves are often on top of each other, as are the blue and red - indicating little influence of pressure during formation.)

The 1st and 3rd cycles for each of the cell-builds and corresponding stack pressures are shown in Figure II-419. The initial charge and discharge capacities are similar to each other, however as seen previously, the lower cell voltage (and hysteresis) upon silicon delithiation is visible in these full cell discharge curves. The 3rd cycle plots show the early stages of capacity loss and a lower charge energy in the first 50% state of charge for the Si-Gr//NMC532 cells. While the impact of silicon in the system has been highlighted thus far, the low and high stack pressures placed on the cells had minimal impact on the formation process for both the Si-Gr//NMC532 and Gr//NMC532 cell-builds. The cells were then removed from their testing fixtures, degassed, vacuum sealed, and put back on the testing fixtures to move on to the rate performance study.

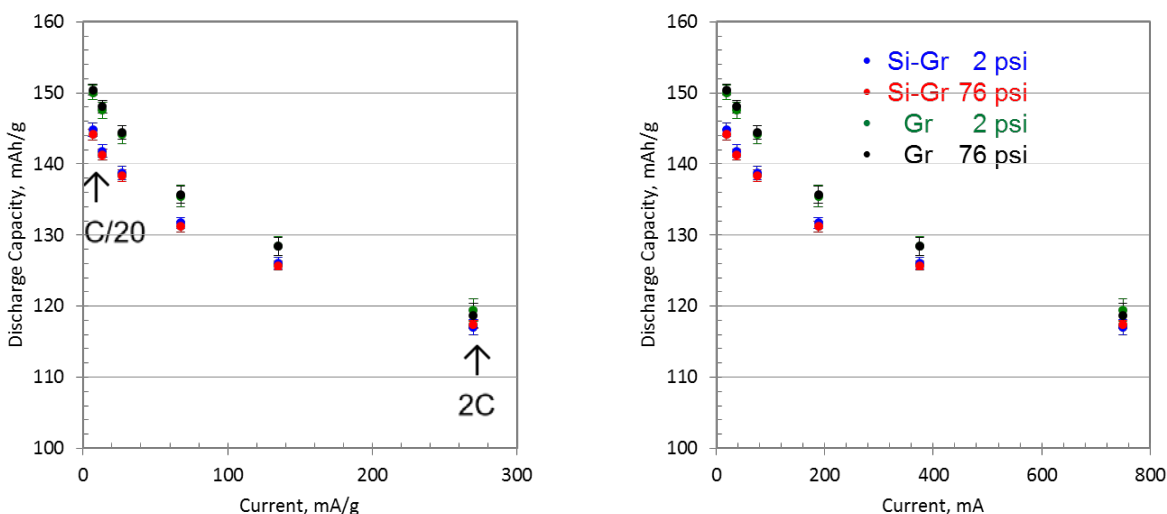


Figure II-420. Average rate study performance of Si-Gr//NMC532 pouch cells at 2 psi per cell (blue), 76 psi per cell (red), and Gr//NMC532 pouch cells at 2 psi per cell (green), 76 psi per cell (black) specific discharge capacities as a function of current, mA/g (left) and mA (right). The cells were cycled at 30 °C between 3.0 and 4.1 V. The plots show the discharge performance from the 2nd cycle at C/20 and 3rd cycle at C/10, C/5, C/2, 1C, and 2C rates. The error bars represent 2 σ standard deviation.

The cells underwent identical rate testing in the following order: 2 cycles at C/20, 3 cycles at C/10, 3 cycles at C/5, 3 cycles at C/3 charge and C/2 discharge, 3 cycles at C/3 charge and 1C discharge, and 3 cycles at C/3 charge and 2C discharge. The rate performance of the 4 test variables is shown in Figure II-420. The Si-Gr//NMC532 have slightly lower capacities at slower rates but converge with the Gr//NMC532 capacities at the faster rates. Similar to the formation performance, the low and high stack pressures do not appear to have an impact on the rate capabilities for either of the cell chemistries.

The Hybrid Pulse Power Characterization (HPPC) testing protocol was then performed on these cells with 10 s discharge pulses at a 5C rate (1.75 A, 629.7 mA/g, 8.87 mA/cm²) and 10 s charge pulses at a 3.75C rate (1.31 A, 472.3 mA/g, 6.45 mA/cm²). The differences between the Si-Gr//NMC532 and Gr//NMC532 systems are again seen in this initial HPPC test (Figure II-421). While the overall Area Specific (ASI) values are on average slightly higher for the Si-Gr//NMC532 cells, the operating voltages extend 300 mV lower than the Gr//NMC532 cells. In addition, the right side of Figure II-421 shows that ~50 % of the ASI occurs in the beginning of the pulse. Consistent with the formation and rate performance, the HPPC results suggest there are minimal differences in the ASI results between the low and high stack pressures.

Figure II-422 shows the cycle life performance of the cells, which consisted of a repeating loop: a slow rate cycle (C/20), HPPC, then cycling 48 cycles with C/3 charging (C/5 trickle charge) and C/2 discharging testing at 30 °C. The Si-Gr//NMC532 cells perform consistent to previous 15 wt.% silicon-containing cell-builds, that is, short cycle life to 80 % capacity retention, while the Gr//NMC532 cells perform as expected with having minimal capacity fade. Low or high stack pressure on either of the cell-builds does not seem to change the performance. The Gr//NMC532 cells are still under test at the time of this writing.

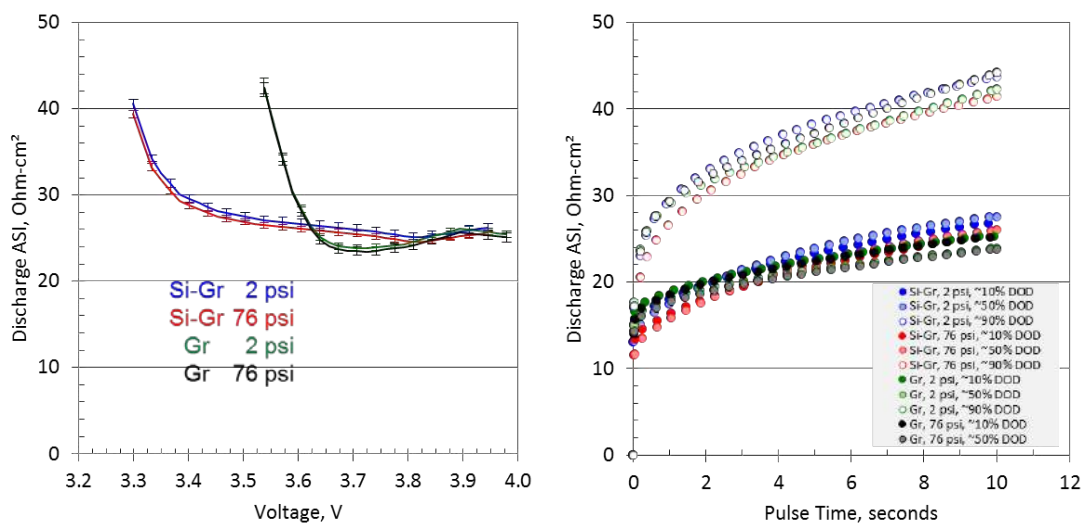


Figure II-421. Average initial discharge interpolated ASI as a function of open circuit voltage (left) and individual ASI discharge pulse voltages at 10, 50, and 90 % depth of discharge (right) as a function of pulse time for Si-Gr//NMC532 pouch cells at 2 psi per cell (blue), 76 psi per cell (red), and Gr//NMC532 pouch cells at 2 psi per cell (green), 76 psi per cell (black) from initial HPPC testing at 30 °C. The error bars represent 2 σ standard deviation.

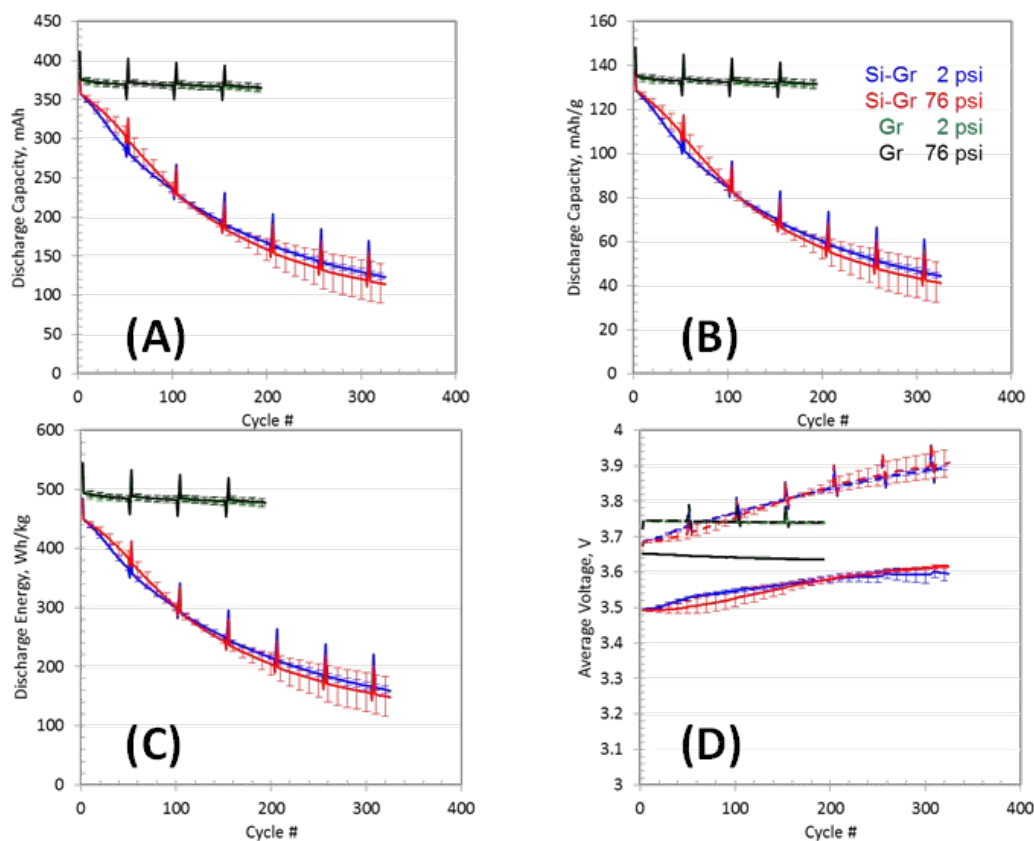


Figure II-422. Average cycle life plots showing discharge capacity (a), specific discharge capacity (b), specific discharge energy (c) and average voltage (d) performance (solid line = discharge, dashed line = charge) for Si-Gr//NMC532 pouch cells at 2 psi per cell (blue), 76 psi per cell (red), and Gr//NMC532 pouch cells at 2 psi per cell (green), 76 psi per cell (black). The error bars represent 2 σ standard deviation.

The continual theme in our stack pressure study evaluation of formation, rate characterization, HPPC impedance, and cycling life testing suggests there are minimal differences in electrochemical performance between 2 psi and 76 psi per cell for either of the cell-build chemistry systems. The results imply that using linear physical extreme stack pressure does not improve electrochemical performance for electrodes that contain silicon. Potential further studies may include post-mortem analytical analysis of the disassembled pouch cells to see if there are obvious differences in electrode appearance that the high pressure influenced on the relentless silicon expansion and contraction.

Deliverable: Fabricate Pouch Cells with at Least 1 Ah Capacity Based on Latest Improvements to Composite Negative Electrode Developed in CAMP and High-Nickel NMC Positive Electrode

In FY17, the CAMP Facility acquired the ability to wind z-fold pouch cells in both the xx3450 and xx6395 formats with state-of-the-art equipment from MEDIA TECH Co., Ltd. The term xx3450 refers to the nominal pouch cell dimensions of a 34 mm width, 50 mm length, and varying “xx” thickness based on the number of layers in the pouch stack. The xx3450 has been a dependable format for the CAMP Facility that is well suited when limited quantities of novel active materials are provided. However, while the xx3450 format demonstrates a large capacity increase over a coin cell, the dimensions limit the capacity range to ~0.5 to 1.0 Ah. In addition, the original CAMP Facility winding equipment used an older method of winding the cell starting at the center and building outward. Z-fold winding is today’s current industry standard method for stacked pouch cell assembly. Depending on the requirements for a project, capacities on the order of 2 Ah could be needed. 18650 cells reach this capacity range, however, they have their limitations that could be critical for evaluating R&D materials (such as easily identifying gassing issues, controllable stack pressure, high impedance without additional tabbing, etc.). Thus, having xx6395 formats enables us to achieve larger capacities while still having the inherent advantages of being a pouch cell (Figure II-423).

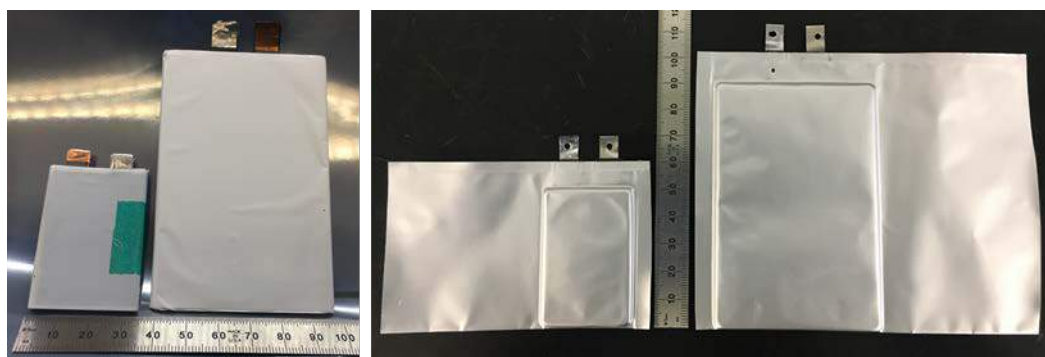


Figure II-423. Images of xx3450 and xx6395 partially assembled before pouching (left), and before electrolyte filling (right).

To demonstrate the xx6395 pouch cell format, we decided to evaluate the cells against xx3450 pouch cells using the same z-fold winding equipment, electrode couples, electrolyte, separator, width of tabbing/welding, and number of layers inside the cell. Our aim was to create two sets of cells with the only difference being the planar electrode dimensions and evaluate the formation, rate capability, impedance (HPPC), and cycle life performance between the two builds.

Electrode properties are provided in Figure II-424. The materials used for this study are frequently used at the CAMP Facility and were thus chosen to evaluate the impact of cell geometry without compounded complexities that novel chemistries may introduce. The electrode slurries were prepared via traditional NMP methods with each of their specific stepwise mixing processes to achieve the desired dispersion and rheological properties for high quality coatings. With the exception of slurry preparation, all processing steps took place in the CAMP Facility dry room. Single and double side cathode electrodes were made to enable multilayer pouch cell stacking. The coating loadings targeted were based on each of the active materials half-

cell 1st cycle performance, reversible C/10 rate, and reversible 1C rate. The n:p ratio for these graphite//NMC532 cells is calculated to be 1.13-1.25 for a full-cell cycling window of 3.0 to 4.1 V.

Anode: Graphite 91.83 wt% Hitachi MagE 2 wt% Timcal C45 6 wt% Kureha 9300 PVDF 0.17 wt% oxalic acid <i>Matched for 4.1V full cell cycling</i> Cu Foil Thickness: 10 µm Total DS Electrode Thickness: 162 µm SS Coating Thickness: 76 µm Porosity: 31.2 % Total Coating Loading: 11.33 mg/cm ² Total Coating Density: 1.49 g/cm ³ Estimated Capacity: 3.50 mAh/cm ² (0.000 to 1.5V vs. Li metal, C/10)	Cathode: NMC532 90 wt% Toda NMC532 5 wt% Timcal C45 5 wt% Solvay 5130 PVDF <i>Matched for 4.1V full cell cycling</i> Al Foil Thickness: 20 µm Total DS Electrode Thickness: 176 µm SS Coating Thickness: 78 µm Porosity: 33.4 % Total Coating Loading: 21.10 mg/cm ² Total Coating Density: 2.71 g/cm ³ Estimated Capacity: 2.98 mAh/cm ² (3.0 to 4.2V vs. Li metal, C/10)
--	--

Figure II-424. Electrode design for xx6395 and xx3450 graphite//NMC532 pouch cells. “SS” = single side, “DS” = double side. All electrodes were fabricated at the CAMP Facility.

Following the electrode fabrication, the electrodes were calendered to their respective calculated porosities in Figure II-424. The electrodes were cut into sheets and stamped to xx3450 and xx6395 pouch cell dimensions using steel rule dies and cleaned to remove any loose coating along the edges and tabbing area. The xx3450 stamped cathode and anode dimensions are 31.3 mm by 45.0 mm and 32.4 mm by 46.0 mm, respectively. The xx6395 stamped cathode and anode dimensions are 55.5 mm by 83.5 mm and 57.45 by 85.45 mm, respectively. The xx3450 and xx6395 anodes are dimensionally larger than the cathodes by 5.8 % and 6.0 %, respectively. Area normalization of proceeding data referred to in this section is based on the total cathode area in a cell. Each xx3450 cell has a total cathode area of 169.2 cm². Each xx6395 cell has a total cathode area of 555.6 cm². The punched electrodes were then wound with Celgard 2325 PP/PE/PP separator using the z-fold winder to 13 total layers per cell (6 double-sided anode, 5 double-sided cathode, and 2 single-sided cathode for the outside layers). The xx3450 cells were wound using 48 mm wide separator. The xx6395 cells were wound using 90 mm wide separator.

After the cells completed assembly, they were vacuumed dried and filled with electrolyte. The xx3450 and xx6395 cells were filled with 3.11 mL and 10.20 mL, respectively, of 1.2 M LiPF₆ in EC:EMC 3:7 wt.% “Gen2” (Tomiyama) electrolyte and vacuum sealed. The electrolyte volume to available pore volume factor for each cell-build were calculated to be 2.77 for all the cells. The cells were then placed in stainless steel fixtures for electrochemical testing. For all cells, 2 psi was chosen to be the stack pressure per pouch cell. Four cells were put on test for each of the cell sizes, for a total of eight cells, and are referred to as xx6395 and xx3450 in the plots below. Weight normalization of the data within this section is based on the total active material weight in the cathode (namely NMC532). The xx3450 cells each contain 3.213 grams of NMC532, and each xx6395 cell contained 10.551 grams of NMC532.

The xx6395 and xx3450 cells underwent identical formation, rate characterization, impedance (HPPC), and cycle life testing with appropriately scaled current values with respect to the capacity of the cell-builds. All of the cells underwent an initial tap charge limited to 1.5 V, held there for 15 minutes, and then left open circuit for 24 hours to allow for electrolyte wetting of the electrode. They were then cycled between 3.0 to 4.1 V at a C/10 rate for 3 cycles, followed by 3 cycles at a C/3 rate, and finally left in an open circuit to observe any voltage changes that could indicate soft shorting. The formation protocol listed above is a typical process used by the CAMP Facility. Initial results suggest that no added modifications to the formation protocol would likely be needed for the xx6395 cells as the current protocol over estimates the time and break-in features needed for proper electrode wetting for these size cells.

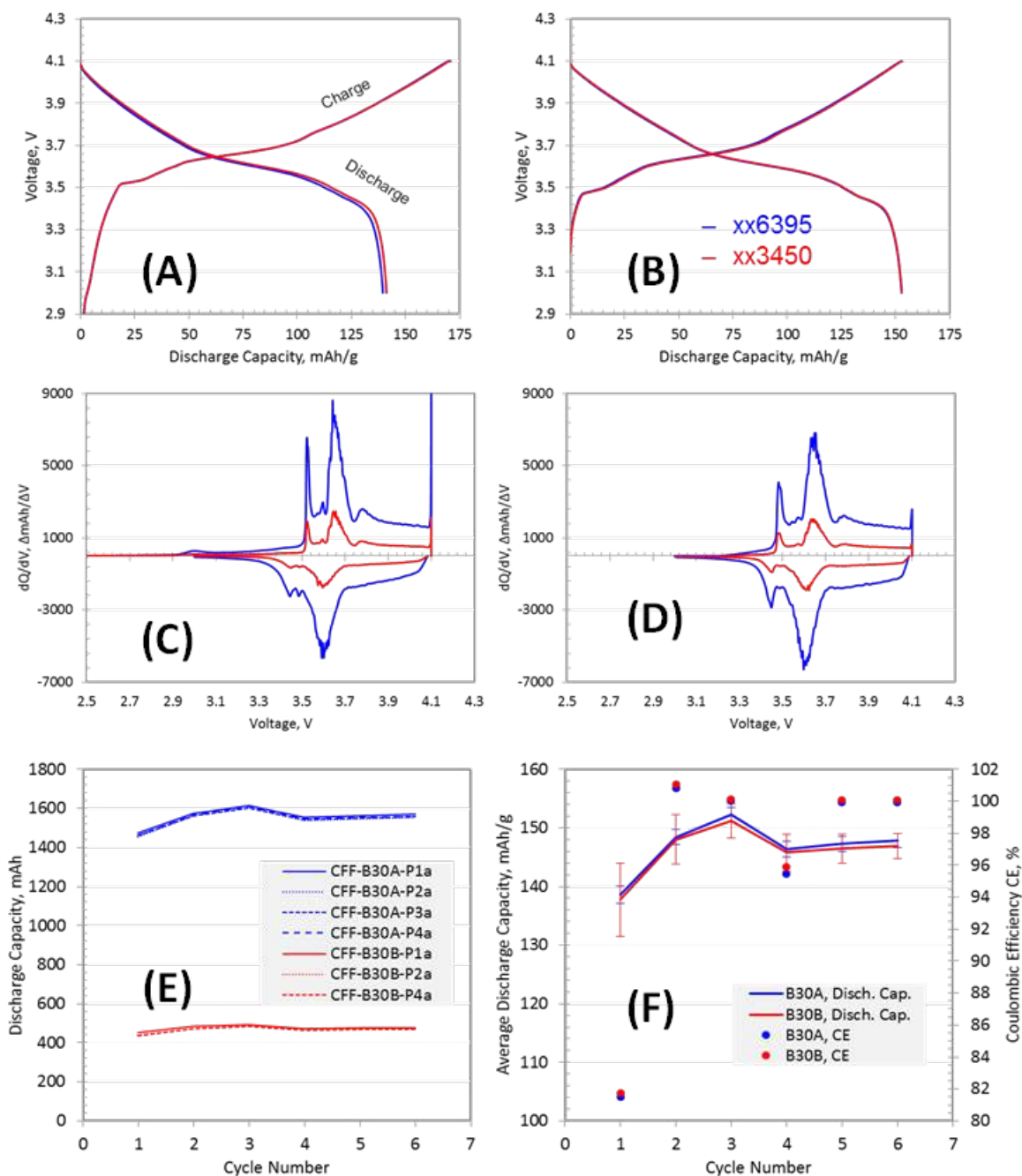


Figure II-425. Representative individual cycle voltage (a,b) and dQ/dV (c,d) profiles of graphite//NMC532 xx6395 (blue) and xx3450 (red) pouch cells of the 1st (a,c) and 3rd (b,d) cycles during formation. Individual formation discharge capacity performance (e). Average discharge specific capacity and coulombic efficiency performance (f). The cells were cycled between 3.0 and 4.1 V at 30 °C. The error bars represent 2 σ standard deviation.

The 1st and 3rd cycles for the xx6395 and xx3450 cell-builds, seen here in Figure II-425a-b, show very similar individual charge and discharge voltage profiles. The corresponding similar capacities seen in Figure II-425, demonstrate that the different cell geometries are performing similar to one another. The cell capacity in mAh is shown in Figure II-425e, which highlights the size differences.

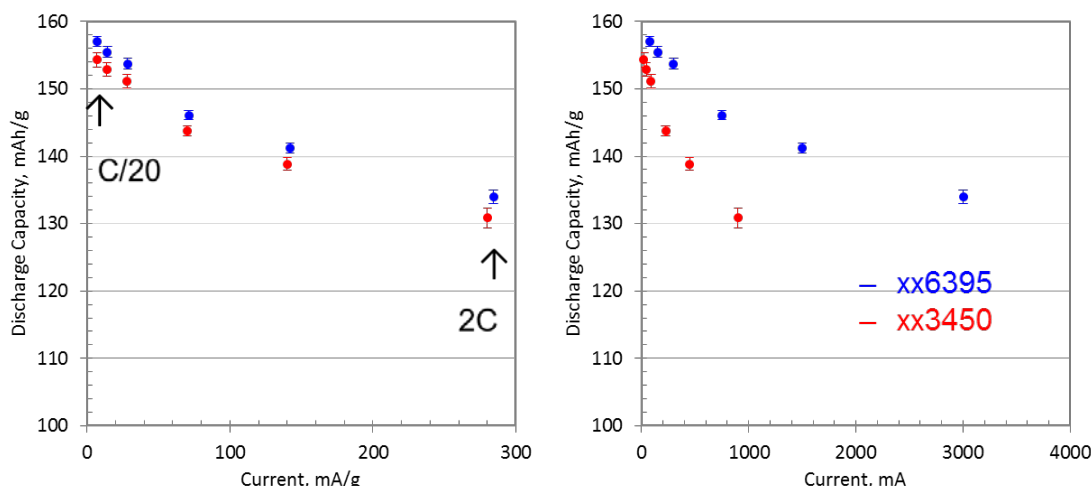


Figure II-426. Average rate study performance of graphite//NMC532 xx6395 (blue) and xx3450 (red) with specific discharge capacities as a function of current, mA/g (left) and mA (right). The cells were cycled at 30 °C between 3.0 and 4.1 V. The plots show the discharge performance from the 2nd cycle at C/20 and 3rd cycle at C/10, C/5, C/2, 1C, and 2C rates. The error bars represent 2 σ standard deviation.

The rate study consisted of the following conditions: 2 cycles at C/20, 3 cycles at C/10, 3 cycles at C/5, 3 cycles at C/3 charge and C/2 discharge, 3 cycles at C/3 charge and 1C discharge, and 3 cycles at C/3 charge and 2C discharge. The rate performance of the two cell sizes is shown in Figure II-426. In the rate study, the xx3450 cells have consistently slightly lower capacities (2 or 3 mAh/g) than the xx6395 cells. These encouraging results suggest that the rate performance, even up to 2C discharge, is very similar between the xx6395 and xx3450 cell formats.

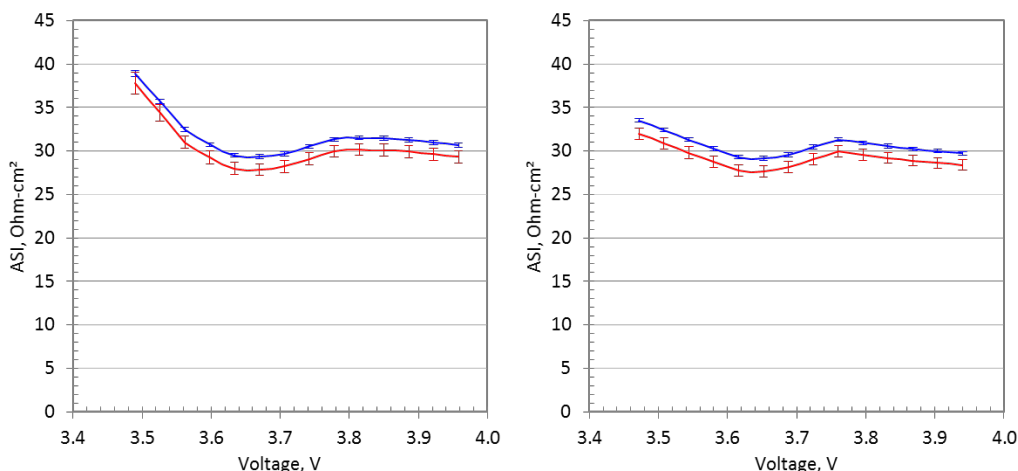


Figure II-427. Average interpolated discharge (left) and charge (right) ASI performance for graphite//NMC532 xx6395 (blue) and xx3450 (red) from initial HPPC testing at 30 °C. The error bars represent 2 σ standard deviation.

The HPPC protocol was performed by charging the cells to 4.1 V, then discharging in 10% capacity increments while collecting voltage information during pulsing at each 10% DOD. The discharge pulses were 10 seconds at 3C (4.5 A, 426.5 mA/g, 8.1 mA/cm² for xx6395 and 1.35 A, 420.2 mA/g, 8.0 mA/cm² for xx3450) and charge pulse were 10 seconds at 2.25C (3.375 A, 319.9 mA/g, 6.1 mA/cm² for xx6395 and 1.0125 A, 315.1 mA/g, 6.0 mA/cm² for xx3450). The HPPC protocol was modified to use 3C discharge and 2.25C charge pulses due to the 5 A per channel limit of the MACCOR Series 4000 Test System. The ASI curves follow a similar trend to one another (Figure II-427), with slightly lower values obtained from the

xx3450 cells. This result further demonstrates that the xx6395 and xx3450 cells are similar in terms of capacity and impedance over the initial 150 cycles tested so far.

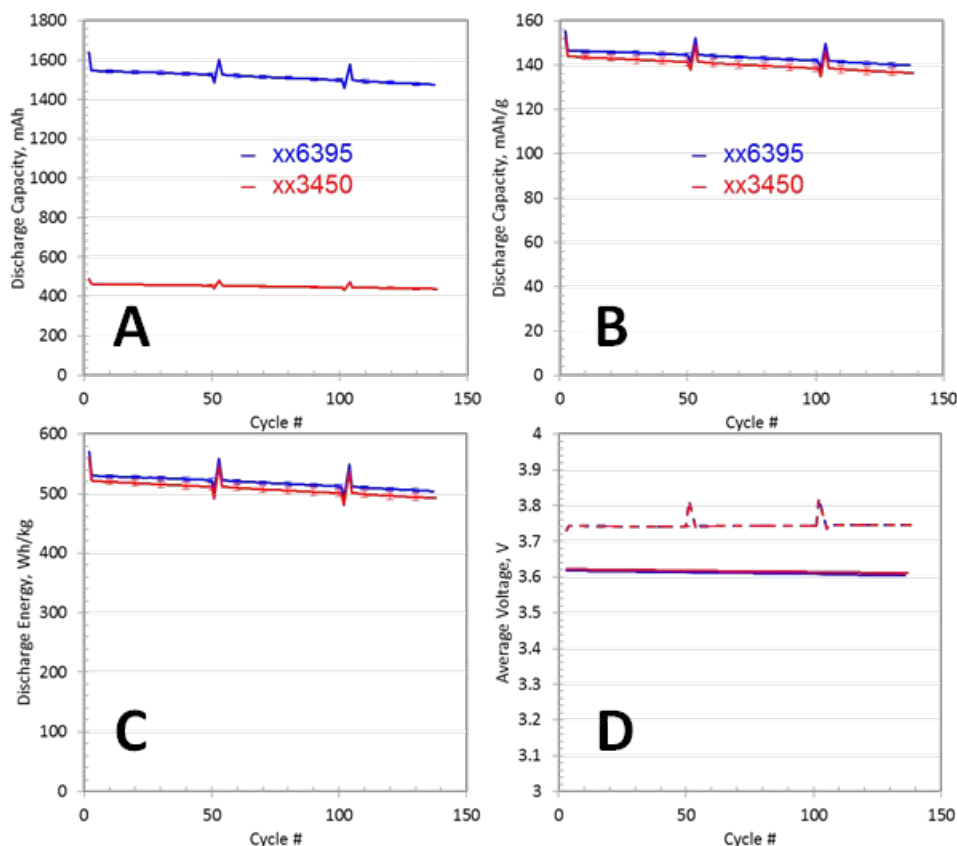


Figure II-428. Average cycle life plots showing discharge capacity (a), specific discharge capacity (b), specific discharge energy (c) and average voltage (d) performance (solid line = discharge, dashed line = charge) graphite//NMC532 xx6395 (blue) and xx3450 (red) from cycle life testing. The error bars represent 2σ standard deviation.

Figure II-428 shows the cycle life performance of these cells, which consists of a repeating loop: a slow rate cycle (C/20), HPPC, then cycling 48 cycles with C/3 charging (C/5 trickle charge) and C/2 discharging testing at 30°C. The xx3450 and xx6395 cells perform consistent to previous graphite//NMC532 cell-builds with relatively stable capacity during cycling in the 3.0 to 4.1 V window. The size difference of these cells does not appear to change the specific capacities, capacity retention, and average operating voltages.

Thus far our evaluation of the formation, rate characterization, HPPC impedance, and initial 100 life cycles suggests there are minimal differences in electrochemical performance between our xx6395 and xx3450 pouch cells under the tested conditions. The performance similarities between the xx6395 and xx3450 also gives us an even higher degree of confidence that our xx3450 (~0.5 Ah) format offers high quality and relevant results when only small amounts of novel material quantities are provided to the CAMP Facility for cell-building, which would otherwise inhibit the fabrication of xx6395 (~2 Ah) cells.

Deliverable: Summary of Electrode Library Activities

Table II-19 shows the distribution of electrodes from the Electrode Library, which is maintained by the CAMP Facility. In FY17, 1548 sheets of electrode were fabricated and distributed by the CAMP Facility, which is 38 square meters of electrodes. Many of these electrode were supplied by the CAMP Facility in support of DOE's High-Energy High-Voltage Program as well as the Next Generation Anodes Program, among others. Since these programs are consortiums of the various national laboratories, the CAMP Facility is supplying all of the

baseline electrodes for these DOE programs. In addition to the electrodes, the CAMP Facility has distributed 16 kg of active materials, carbon additives, binders, and electrolytes.

Table II-19: Summary of Electrode Library distributions

Electrodes Delivered	FY14		FY15		FY16		FY17	
Argonne	116	13 %	206	12 %	174	8 %	142	9 %
Other National Labs	213	24 %	373	22 %	726	36 %	172	11 %
Universities	119	14 %	83	5 %	117	6 %	151	10 %
Industry	423	49 %	1028	61 %	1004	50 %	1083	70 %
Total:	871		1690		2021		1548	

Examining Effect of Moisture on Performance of Lithium-Containing Layered Oxide Electrodes

In recent years there has been a shift to processing of electrodes using aqueous slurries containing water-based polymer binders. The technological drivers that necessitate reliance on aqueous processing include the use of electrophoretic methods and the application of protective coatings, which frequently involve using aqueous solutions or water vapor as a reagent during atomic layer deposition. All these methods expose the layered oxides to gaseous and/or liquid water, which can potentially have adverse effects on cell operation. We have studied the electrochemical performance of cells exposed to moist air (100% humidity) at 30 °C, for time periods of up to two months. These data were complemented by results from X-ray diffraction, X-ray photoelectron spectroscopy, and electron microscopy measurements to examine the relationships between oxide structure changes and electrochemical performance.

The effects of moisture were studied on CAMP-made electrodes containing 90 wt.% NMC532 oxide, 5 wt.% Timcal C45 carbon black and 5 wt.% PVdF binder on a 20 µm thick aluminum foil. Electrochemical performance data were collected on these electrodes in 2032-type coin cells using Li foil as the counter electrode and in an electrolyte solution with 1.2 M LiPF₆ in a 3:7 w/w EC:EMC mixture. In Figure II-429a we compare the first cycle capacity-voltage profiles, from half cells assembled using the pristine electrode and two humid-air exposed electrodes, obtained on cycling with a ~11 mA/g (~C/18) current between 3.0 and 4.5 V at 30°C. The pristine electrode shows the expected cycling behavior, displaying charge and discharge capacities of 219 mAh/g_{oxide} and 198 mAh/g_{oxide}, respectively. Cells with the humid-air exposed electrodes show behaviors that are distinctly different from that of the pristine electrode cell. The charge and discharge capacities are 191 mAh/g_{oxide} and 166 mAh/g_{oxide} respectively, for the 1-month exposure electrode and 179 mAh/g_{oxide} and 155 mAh/g_{oxide} respectively, for the 2-month exposure electrode. The voltage profiles of both electrodes indicate the effects of moisture exposure; the higher charge voltages, suggest the presence of species at the oxide particle surfaces that impedes the motion of Li⁺ ions. The lower charge capacities, and the uneven rise in voltage on further removal of Li⁺ ions, indicate changes within the oxide bulk. An example of these changes is shown in Figure II-429b, which is a scanning transmission electron microscopy (STEM) image of the two-month exposure electrode. The thin amorphous coating observed on the particle surface is either Li₂CO₃ (or LiHCO₃), which was suggested by the X-ray photoelectron spectroscopy (XPS) data. Crystal structure changes are observed at the particle surface, which indicates the presence of a new phase that extends from 5-20 nm into the oxide bulk. From an analysis of high-resolution synchrotron X-ray diffraction data we concluded that this new cubic phase has a rock salt structure in which some of the transition metal (TM) ions are substituted by lighter ions such as protons and/or TM vacancies, which will both contract the unit cell.

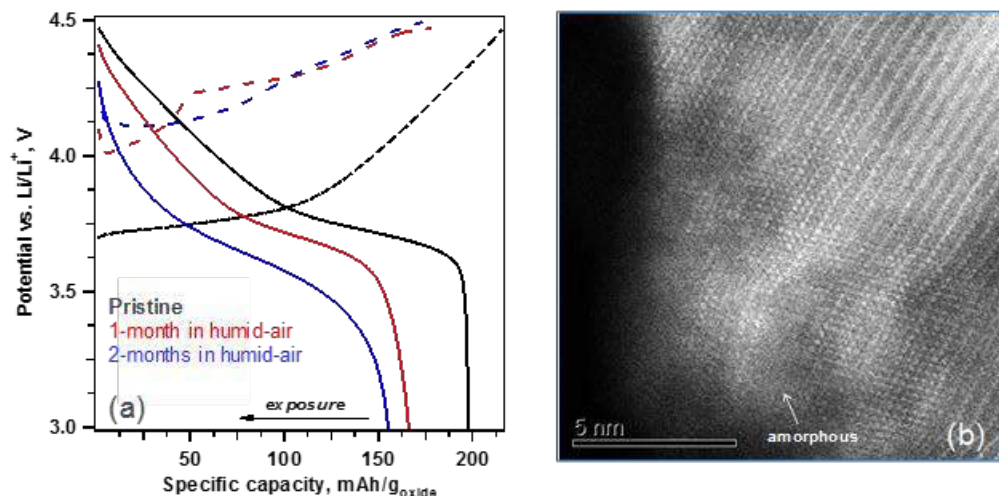


Figure II-429. Effects of moisture exposure on (a) electrochemical performance and (b) oxide structure, imaged by scanning transmission electron microscopy (high angle annular diffraction mode).

Separator Study

A variety of commercial separator products are available that are designed with unique safety functions. This study explores the impact separator choice can have on cell performance at the higher voltages and rates sought by the HEHV program and battery developers. For high voltage, high energy density battery systems, the goal is to have a separator that is thin, flexible, highly porous, thermodynamically stable, temperature resistant, mechanically strong, and inexpensive. Each material currently on the market has some but not all of these properties. Polyethylene (PE) is inexpensive, but has a lower melting point, and may have trouble withstanding higher voltages. Polypropylene (PP) has a slightly higher melting point, is mechanically strong, and is also fairly inexpensive. When PP is paired with PE to make a trilayer microporous membrane, PP:PE:PP, the separator has a more robust exterior, while the interior has the ability to melt before thermal runaway occurs. However, with a little extra heat, the PP will also melt and the electrodes will touch. Since, the PP isn't fully protective, another avenue had been approached - ceramic and polyolefin combinations have been created to provide that extra thermodynamic stability. Ceramics can withstand high voltages and temperature, and can be chemically inert and porous - but they are more difficult to incorporate into a thin flexible separator.

For initial testing, nine different separators from five different suppliers were chosen and tested in NMC532 half-cells: 3 monolayer polyolefins at various thicknesses (16, 20, 25 μm), 3 trilayer PP:PE:PP at various thicknesses (16, 20, 25 μm), one single-sided ceramic-coated polypropylene, one double-sided ceramic-coated polyethylene, and one Al₂O₃ embedded into a nonwoven polyethylene terephthalate (PET). (See Table II-20.)

In preparation for the half cell-builds, all the separators were punched with a 5/8" diameter punch and dried at 60°C. Eight cells per separator configuration were assembled using a 1.54 cm² NMC532 electrode disk (90 wt.% active material, 5 wt.% Timcal C45, 5 wt.% Solvay 5130 PVDF binder) from the CAMP Electrode Library with a 11.32 mg/cm² loading, which was paired against a 1.91 cm² Li metal electrode disk. Each cell was flooded with 9 drops of 1.2 M LiPF₆ in EC:EMC (3:7 wt.%) during assembly. After which, each cell went through a Formation and a Rate testing protocol. Formation consisted of 3 cycles with a C/10 charge and discharge. The Rate Study started with 2 cycles of C/20 charge and discharge and with 3 cycles of C/10 charge and discharge. It then continued with 12 C/5 charges, where every three cycles had the discharge rate increasing (C/5 to C/2 to 1C to 2C). Each separator configuration had four cells tested at a 3.0-4.3 V window to see its standard performance, and had four cells tested at a 3.0-4.7 V window to see how it performs in a high voltage window.

Table II-20: Commercial separators used in this study

Separator Supplier	ID Name	Total Thickness (μm)	Separator Material	Porosity (%)	Air Permeability (Gurley)
Microporous Membrane Category					
IV	20 μm _UHMW PE	20	UHMW PE (Microporous Monolayer Membrane)	83	1.4 s/50mL
II	16 μm _PP	16	PP (Microporous Monolayer Membrane)	50	125 s/100cc
I	25 μm _PP	25	PP (Microporous Monolayer Membrane)	41	620 (s) JIS
I	16 μm _PP:PE:PP	16	PP/PE/PP (Microporous Trilayer Membrane)	44	250 (s) JIS
I	20 μm _PP:PE:PP	20	PP/PE/PP (Microporous Trilayer Membrane)	45	320 (s) JIS
I	25 μm _PP:PE:PP	25	PP/PE/PP (Microporous Trilayer Membrane)	39	620 (s) JIS
Ceramic Category					
II	3 μm _SS_Ceramic_on_16 μm _PP	19	Single Side Ceramic Coated on 16 μm PP	51	145 s/100cc
III	4 μm _DS_Al ₂ O ₃ _on_12 μm _PE	16	Double Sided Al ₂ O ₃ Coating on 12 μm PE	40	unknown
V	28 μm _Al ₂ O ₃ Embedded in PET	28	Al ₂ O ₃ Embedded in PET - Non woven	46	22 s

When discussing single-sided ceramic-coated separators, the question arises as to which electrode the ceramic side should be facing: anode or cathode? In pursuit of this question, the single-sided separator with 4- μm thick ceramic-coating on 16- μm thick PP was tested where 8 cells had the ceramic side facing the anode and 8 cells had the ceramic facing the cathode. These cells were also tested in the 3-4.3 V and 3-4.7 V windows.

After the initial 3-4.3 V formation cycles, one separator stood out against all the rest. All four cells with the Al₂O₃ embedded in PET (non-woven) separator failed their formation cycles. This was surprising, since this separator was used previously in full cells without a problem. It was decided to retry this separator in half cells, but to increase the drying temperature to 150°C. Eight more cells were assembled, 4 cells tested with the 3-4.3 V window, and 4 cells tested at the 3-4.7 V. All eight of these new cells also failed their formation tests. This suggests that this separator system could not withstand the reductive potential of lithium metal. No further testing was done with this separator system (it is not shown in the summary graph below).

The rate performance study of the remaining (non-PET) half cells indicated there was no significant statistical difference in 3-4.3 V window for any of the separators regardless of the discharge rate (up to 2C). Advancing on to the 3.0-4.7 V rate study, some of the separators began to show differences in performance. In particular, for the 3.0-4.7 V high voltage tests, the NMC532 half-cells using the Ultra High Molecular Weight Polyethylene (UHMW PE) separator underwent a sudden and significant loss of capacity at the discharge rate of C/5. This suggests that UHMW PE separators may suffer from eventual oxidation at higher potentials. The three trilayer PP:PE:PP and the two monolayer PP separator cells, on the other hand, showed no significant differences in the 3.0-4.7 V rate study.

Aside from the Al₂O₃ embedded in PET separator and the UHMW PE separator, there was no significant difference in the formation and rate performance of the remaining separators (see Figure II-430). This result is regardless of separator thickness, trilayer vs. monolayer PP, ceramic coating, and orientation of the ceramic coating. This is also true for the double-sided ceramic-coated monolayer PE separators. Full cells will be tested in FY18 using the aggressive HEHV testing protocol to see if there might be any further problem areas when using certain separators. It is anticipated that the performance of some of the various separators will differentiate from each other based on cycle life and HPPC ASI.

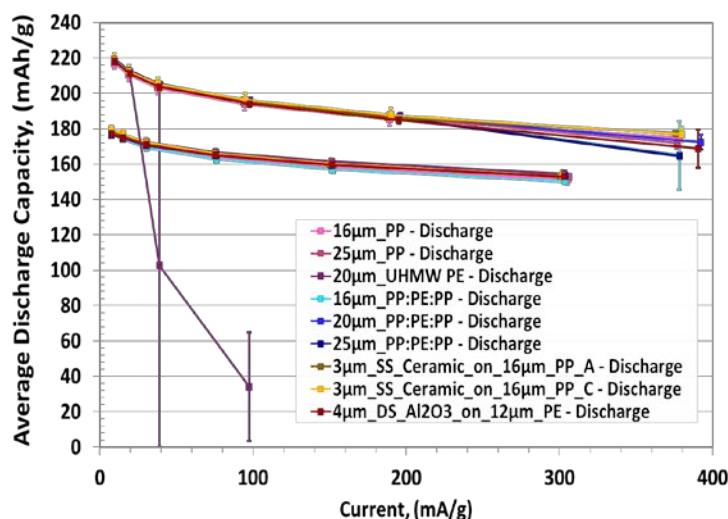


Figure II-430. Summary of the rate capabilities for the separators in this study in the 3.0-4.3 V and 3.0-4.7 V voltage windows. The data for the Al_2O_3 embedded in PET separator were omitted in this plot.

High Voltage Evaluation of Industrially Applied ALD of Al_2O_3 Coating on NMC532 Powder

The CAMP Facility was tasked with providing an evaluation of Al_2O_3 coated onto NMC532 powders via Atomic Layer Deposition (ALD). We partnered with Forge Nano (Louisville, CO), who provided ANL with four samples of Al_2O_3 ALD coated on Toda NMC532. These samples were: Pristine, Sample A (2 ALD cycles), Sample B (4 ALD cycles) and Sample C (8 ALD cycles). Electrodes were made of each powder with a 90 wt.% active material (NMC532), 5 wt.% Timcal C45 carbon black, and 5 wt.% Solvay 5130 PVDF binder composition with a target total electrode loading of 10.9 mg/cm^2 . In this testing, we focused on the 3-4.5 V (half-cell) and 3-4.4 V (full-cell) performance.

Half-cells (vs. Li metal) were assembled using the above electrodes and tested in the 3-4.5 V window via a Formation Protocol and Rate Study Protocol. The formation protocol consists of three cycles at a C/10 rate. Four coin cells were made from each electrode, which used a 14 mm diameter cathode electrode and a 15.6 mm diameter lithium metal disk. The separator used in the coin cells was Celgard 2325 and the electrolyte used was 1.2 M LiPF_6 in EC:EMC (3:7 wt.%). From the half cell data, we were able to design new cathode electrodes that would match to a graphite anode (A-A002A - Phillips 66 CPG-A12 graphite) that was in the Electrode Library. The new cathodes that were produced also had the 90/5/5 composition and their loadings were as follows; Pristine = 8.98 mg/cm^2 , Sample A = 9.26 mg/cm^2 , Sample B = 9.15 mg/cm^2 , and Sample C = 9.17 mg/cm^2 . Each of these electrodes were matched to the selected anode (A-A002A) resulting in an n:p ratio of ~1.1-1.2. Four CR2032 full-cell coin-cells were made with each of the above electrodes, and a total of 25 microliters of 1.2 M LiPF_6 in EC:EMC (3:7 wt.%) electrolyte was used for each cell. These full-cell coin-cells went through Formation, Rate Study, HPPC, and Cycle Life Testing.

There was little change in the first charge capacity between all the coated samples and the pristine material. Following the Formation and Rate Study testing, Cycle Life testing was performed. Literature [1] has suggested that coatings of Al_2O_3 can improve cycle life and rate performance of cells at various voltages. Two sets of coin cells were used to evaluate two slightly different cycle life conditions: Set 1 of cells went through the following Cycle Life Protocol: 1 cycle at C/20, 47 cycles at C/3 charge and C/3 discharge, and HPPC with 3C discharge and 2.25C charge; this was looped 10 times to give approximately 500 cycles on the cells. Set 2 of cells went through the following Cycle Life Protocol: 1 cycle at C/20, 47 cycles at C/3 charge and 1C discharge, and HPPC with 3C discharge and 2.25C charge; this was looped 10 times to give approximately 500 cycles on the cells. By doing this testing we were looking to see if the ALD coatings would have any performance improvements under typical cycling conditions (C/3) at high voltage as well at higher current

discharge rates (1C) at high voltages. Since similar conclusions were reached with both sets, only Set 1 results will be discussed below.

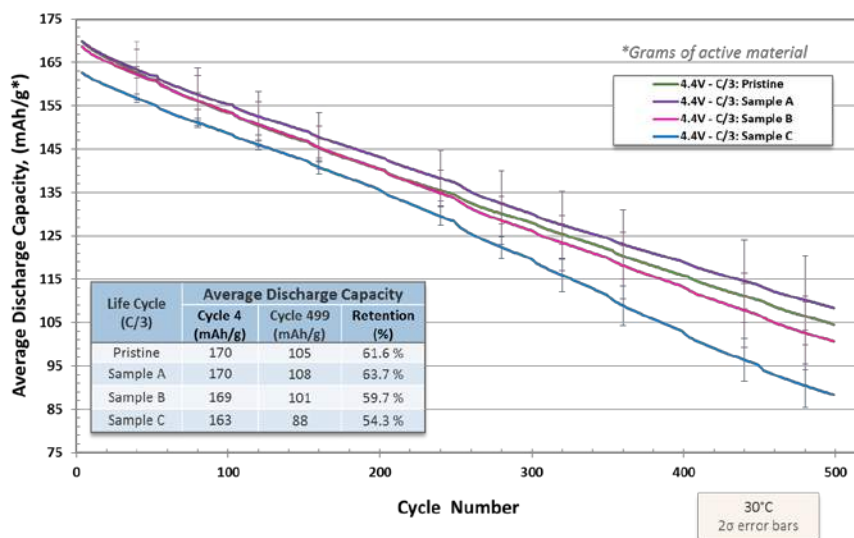


Figure II-431. Cycle life plot of Set 1 full-cell coin-cells – C/3 Charge and C/3 Discharge cycling.

As seen in Figure II-431, the Pristine, Sample A, and Sample B full cells all started with approximately the same capacity. Sample C full cells, in both cases, started at a lower capacity. The C/3 cycling data (Set 1) suggest that there was minimal statistical difference in the performance of the Pristine, Sample A and Sample B cells. They all ended at 500 cycles with a capacity retention around 61 % capacity and were within the error bars of each other. Sample C did show worse cycling performance than the other samples and was outside the error bars of the other cells. To further analyze these cells during the cycle life testing, we have charted the HPPC data as a function of the Depth of Discharge to monitor the change in impedance (ASI) as the cells age.

Figure II-432 summarizes the HPPC data that was collected every 50 cycles during the cycle life testing for the Set 1 C/3 cycling cells. The starting ASI for the Pristine material was around 25 ohm-cm², while the ALD coated samples had slightly higher initial ASI of around 35 ohm-cm². Sample A cells had the lowest ASI rise, going from ~35 to 55 ohm-cm². The Pristine cells had the next lowest rise; Sample B and Sample C had the highest rise of these samples. This impedance rise correlates with the capacity fade for Sample C cells. We postulate that the Al₂O₃ coating on the NMC532 particles reached a thickness that inhibited efficient lithium ion transport and/or decreased the electrical conductivity of the particle.

Future investigations may include analyzing the coated materials and cycled cells under spectroscopic, as well as other analytical techniques to better understand these observations. We may additionally repeat this study with NMC622 and NMC811 materials to probe the electrochemistry of ALD coated samples. Literature [1] has shown that these higher nickel content materials are more influenced by coatings than the NMC532.

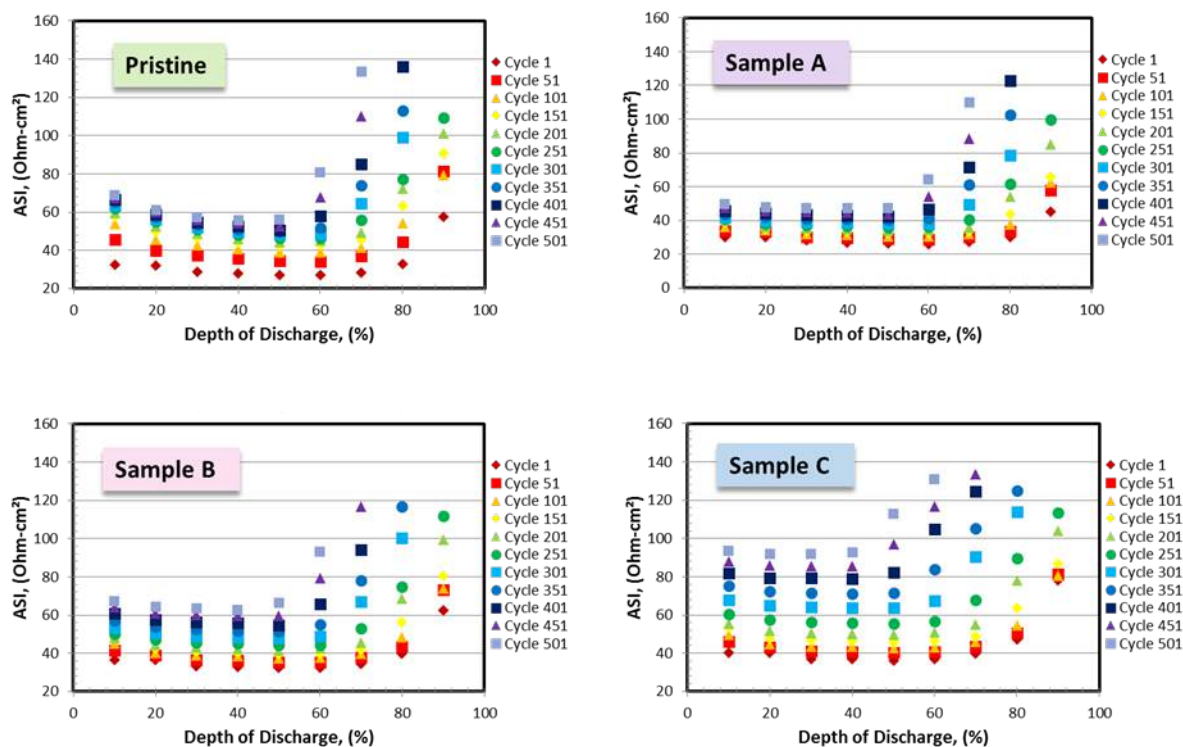


Figure II-432. Full cell HPPC ASI (averaged discharge) data for full cells of graphite vs. Pristine, Sample A, Sample B, and Sample C in Set 1 (C/3 C: C/3 D).

Conclusions

The CAMP Facility has had another very productive year in the R&D of advanced lithium-ion electrochemical energy storage systems. We were also critical to the support of other numerous DOE-EERE programs, much of which was performed through the CAMP Facility's Electrode Library. A summary of some of the key successes in FY17 are as follows:

- The influence of stack pressure on silicon-graphite//NMC532 and baseline graphite//NMC532 pouch cells was determined to not be a significant factor. It was previously hoped that the extra high pressure (~76 psi) would help minimize the damage to the electrode structure caused by the excessive expansion of silicon during lithiation.
- We now have the capability to make multi-stack pouch cells in a Z-fold separator configuration with two cell sizes: xx3450 and xx6395. This enable the fabrication of cells with capacities from 20 mAh to over 2 Ah. A direct comparison of these two cell sizes determined that nearly identical results are obtained from either cell size.
- Single-sided negative electrode based on 30% silicon-graphite with ~ 2 mAh/cm² loading were developed as a FY17 baseline. Even higher loadings of silicon will be explored in FY18 with the idea to extend the cycle life of silicon systems by using shallower levels of lithiation. This should limit the drastic volume expansion of silicon, which occurs during full lithiation. In addition, a new source of domestic silicon powder was identified (Paraclete Energy), which is now the preferred silicon material going forward.
- We have shown that the lithiated layered NMC oxides undergo changes, when they are stored in humid air or exposed to moisture, that adversely affect their electrochemical performance. By using a combination of X-ray diffraction, electron microscopy, and X-ray photoelectron spectroscopy measurements we identified the chemical mechanisms which cause these changes. We suggest that the

proton – lithium exchange that occurs during the moisture exposure trigger these transformations. We show that such an exchange provides a simple, comprehensive rationale for our observations, which include contraction of the c-axis (unit cell) lattice parameter, rock salt phase formation in the subsurface regions, presence of amorphous surface films, and the partial recovery of oxide capacity during electrochemical relithiation. The detrimental effects of water exposure need to be mitigated before aqueous processing of the positive electrode can find widespread adoption during cell manufacturing.

- Techniques to enable for detection of lithium-plating during cell cycling after under development. The most promising advances are in the area of reference electrode cell measurements. X-ray techniques to detect lithium metal show promise and efforts are underway to improve resolution and accuracy of the measurements.
- Al₂O₃ ALD coatings on the NMC532 powder did not show any significant performance improvements over the pristine material when tested in the 3-4.4 V window. It was observed that the performance of this material is highly dependent on the ALD coating thickness. The trend suggests there is a negative performance impact as the thickness of Al₂O₃ layer approaches ~1nm.
- Preliminary study of commercial separators indicate that trial studies are warranted when developing new electrochemical systems with high reductive power (*e.g.*, lithium metal) or high oxidative power (*e.g.*, high voltage). Under normal conditions, many separators have nearly identical rate performance (up to 2C).

Key Publications

1. S. Ahmed, I. Bloom, A.N. Jansen, T. Tanim, E.J. Dufek, A. Pesaran, A. Burnham, R.B. Carlson, F. Dias, K. Hardy, M. Keyser, C. Kreuzer, A. Markel, A. Meintz, C. Michelbacher, M. Mohanpurkar, P.A. Nelson, D.C. Robertson, D. Scofield, M. Shirk, T. Stephens, R. Vijayagopal, and J. Zhang, "Enabling fast charging—A battery technology gap assessment", *J. Power Sources* **367** (2017) 250-262.
2. J.A. Gilbert, J. Bareno, T. Spila, S.E. Trask, D.J. Miller, B.J. Polzin A.N. Jansen, D.P. Abraham, "Cycling Behavior of NCM523/Graphite Lithium-Ion Cells in the 3-4.4 V Range: Diagnostic Studies of Full Cells and Harvested Electrodes", *J. Electrochem. Soc.* **164** (2017) A6054-A6065. [DOI: 10.1149/2.0081701jes]
3. I.A. Shkrob, J.A. Gilbert, P.J. Phillips, R. Klie, R.T. Haasch, J. Bareno, D.P. Abraham, "Chemical Weathering of Layered Ni-Rich Oxide Electrode Materials: Evidence for Cation Exchange", *J. Electrochem. Soc.* **164** (2017) A1489. [DOI: 10.1149/2.0861707jes]
4. N.R. Vadivel, S. Ha, M. He, D. Dees, S. Trask, B. Polzin, K.G. Gallagher, "On Leakage Current Measured at High Cell Voltages in Lithium Ion Batteries", *J. Electrochem. Soc.* **164** (2017) A508-A517. [DOI:10.1149/2.1341702jes]
5. J.A. Gilbert, I.A. Shkrob, D.P. Abraham, "Transition Metal Dissolution, Ion Migration, Electrocatalytic Reduction and Capacity Loss in Lithium-Ion Full Cells", *J. Electrochem. Soc.* **164** (2017) A389-399. [DOI: 10.1149/2.1111702jes]
6. J. Zheng, M.H. Engelhard, D. Mei, S. Jiao, B.J. Polzin, J. Zhang, W.Xu, "Electrolyte Additive Enabled Fast Charging and Stable Cycling Lithium Metal Batteries" *Nature Energy* **2** (2017) 17012, [DOI: 10.1038/nenergy.2017.12]
7. I.A. Shkrob, K.Z. Pupek, J.A. Gilbert, S.E. Trask, D.P. Abraham, "On the Chemical Stability of Lithium 2-Trifluoromethyl-4,5- Dicyanoimidazolid (LiTDI), an Electrolyte Salt for Li-Ion Cells" *J. Phys. Chem. C* **120** (2016) 28463-28471. [DOI: 10.1021/acs.jpcc.6b09837]

8. J. Bareño, I.A. Shkrob, J.A. Gilbert, M. Klett, D.P. Abraham, “Capacity Fade and Its Mitigation in Li-ion Cells with Silicon-Graphite Electrodes”, *J. Phys. Chem. C* **121** (2017), pp 20640-20649. [DOI: 10.1021/acs.jpcc.7b06118]
9. C.D. Malliakas, K. Leung, K.Z. Pupek, I.A. Shkrob, D.P. Abraham, “Spontaneous aggregation of lithium ion coordination polymers in fluorinated electrolytes for high-voltage batteries”, *Phys. Chem. Chem. Phys.* **18** (2016) 10846-10849.
10. I.A. Shkrob, K.Z. Pupek, D.P. Abraham, “Allotropic Control: How Certain Fluorinated Carbonate Electrolytes Protect Aluminum Current Collectors by Promoting the Formation of Insoluble Coordination Polymers”, *J. Phys. Chem. C* **120** (2016) 18435–18444.
11. J. Zheng, P. Yan, D. Mei, M.H. Engelhard, S.S. Cartmell, B.J. Polzin, C. Wang, J. Zhang, W. Xu “Highly Stable Operation of Lithium Metal Batteries Enabled by the Formation of a Transient High-Concentration Electrolyte Layer” *Adv. Energy Mater.* **6** (2016) 1502151 [DOI: 10.1002/aenm.201502151]

References

1. Han et al., “Understanding the Role of Temperature and Cathode Composition on Interface and Bulk: Optimizing Aluminum Oxide Coatings for Li-Ion Cathodes”, *ACS Applied Materials and Interfaces*, 2017, 9 (17), 14769-14778

II.G.2 Materials Benchmarking Activities for CAMP Facility (ANL)

Wenquan Lu, Principal Investigator

Argonne National Laboratory
9700 S. Cass Avenue
Lemont, IL 60439
Phone: 630-252-3704
E-mail: luw@anl.gov

Peter Faguy, Technology Manager

U.S. Department of Energy
Phone: 202-586-1022
E-mail: Peter.Faguy@ee.doe.gov

Start Date: October 1, 2014
Total Project Cost: \$400,000

End Date: September 30, 2018
DOE share: \$400,000

Non-DOE share: \$0

Project Introduction

High energy density electrode materials are required in order to achieve the 40-mile all electric range within the weight and volume constraints established by DOE and the USABC. One would need a combination of anode and cathode materials that provide 420mAh/g and 220mAh/g, respectively, as predicted by Argonne's battery design model (BatPac), if one uses a 20% margin for energy fade over the life of the battery assuming an average cell voltage of 3.6 volts. Therefore, the search for new high energy density materials is the focus of this material benchmarking project. In addition to electrode materials, other cell components, such as separators, binders, current collectors, etc., are evaluated to establish their impact on electrochemical performance, thermal abuse, and cost.

This benchmarking effort is conducted as part of the Cell Analysis, Modeling, and Prototyping (CAMP) Facility (Refer to IV.B.1) to identify and support promising new materials and components across the “valley of death”, which happens when pushing a new discovery towards a commercial product. The CAMP Facility is appropriately sized to enable the design, fabrication, and characterization of high-quality prototype cells, which can enable a realistic and consistent evaluation of candidate chemistries in a time-effective manner.

However, the CAMP Facility is more than an arrangement of equipment, it is an integrated team effort designed to support the production of prototypes electrodes and cells. In order to utilize the facility more efficiently and economically, cell chemistries are validated internally using coin type cells to determine if they warrant further consideration.

Objectives

- The primary objective is to identify and evaluate low-cost materials and cell chemistries that can simultaneously meet the life, performance, and abuse tolerance goals for batteries used in PHEV and EV applications.
- A secondary objective is to enhance the understanding of the impact of advanced cell components and their processing on the electrochemical performance and safety of lithium-ion batteries.
- To support the CAMP Facility for prototyping cell and electrode library development, also the MERF facility for material scale up.

Approach

Under materials benchmarking activities, we constantly reach out to material developers to seek opportunities to test their advanced or newly released products. By leveraging ANL's expertise in electrode design and cell testing, we can provide not only a subjective third opinion to material suppliers, but also deeper understanding on their materials, which can aid their material development. This deep understanding becomes even more important when the material developers are small companies or new players, who often overlook overall requirements of battery materials.

In addition to industrial partners, we also work closely with scientists from various research institute, such as universities and research laboratories. They often come up with novel materials with advanced electrochemical performance, but small quantities, which is only enough for validation purpose. These test results help us to determine how much effort should be expanded to explore the material potential.

For any potential cell material, which has impact on the cell performance, we validate its performance, mainly in terms of electrochemical performance, electrode optimization, and thermal stability. The electrochemical performance is the centerpiece of the materials benchmarking activities, which will be tested using 2032 coin type cells under test protocol derived from USABC PHEV 40 requirements [Battery Test Manual For Plug-In Hybrid Electric Vehicles, Idaho National Laboratory]. In general, three formation cycles are tested at a C/10 rate. After the formation cycles, the cells are then tested for the rate performance. For the rate test, the charging rate is set at C/5, while the discharge rate varies from C/5, C/3, C/2, 1C to 2C. Three cycles are performed for each discharge rate. After the rate test, the cells then undergo cycling test at C/3 rate. During the cycling test, we change the current rate to C/10 every 10th cycle to check the rate effect. Also, Hybrid Pulse Power Characterization (HPPC) is conducted every 10th cycle. Area Specific Impedance (ASI) can be calculated from HPPC test.

This fiscal year, electrochemical characterization of nickel-rich high energy cathode materials were carried out. Two $\text{LiNi}_{0.5}\text{Mn}_{0.3}\text{Co}_{0.2}\text{O}_2$ (NMC532) materials were received from Guizhou ZhenHua E-Chem Co. LTD. Those two NMC532 possess difference morphologies, whose effect on electrochemical performance was investigated.

Furthermore, we studied coating effect on NMC532. It has been well reported that Al_2O_3 coating will generally improve the electrochemical performance of cathode materials. In this work, we studied Al_2O_3 coated NMC532 using two different coating approaches, wet method and atomic layer deposition (ALD). The Al_2O_3 coated NMC532 using wet method is presented in this work. The test results for Al_2O_3 coated NMC532 using ALD method can be seen in the previous section: IV.B.1.

Continued from previous year's work on conductive additive, we investigated Carbon Nano Tube (CNT) as an additive. Other cell components, such as silicon and metal alloy materials, electrolytes and additives, separators, binders, etc. have also been investigated. These test results have been shared with material providers, but not included in this report.

Results

Nickel-Rich High Energy Cathode Materials (NMC)

Nickel-rich $\text{LiNi}_x\text{Mn}_y\text{Co}_z\text{O}_2$ (NMC) is gaining momentum as high energy cathode materials for electric vehicle applications. NMC532 is penetrating the market due to its balance of good electrochemical performance, low cost, and reasonable thermal safety. Compared to LiCoO_2 , NMC particles consist of small primary particles, which tend to separate from each other during cycling. Meanwhile, the secondary particles have less mechanical strength, which can results in particle cracks during the calendaring process.

We received two different commercial available NMC532 samples with different morphologies from Guizhou ZhenHua E-Chem Co. LTD. SEM images were taken for these two NMC532 samples (S1 and S2) and are shown in Figure II-433. As you can see from Figure II-433, sample 1 is a typical secondary NMC particle

consisting of small primary particles with voids between primary particles. As for sample 2, the primary particle is larger than that of sample 1. In addition, the primary particle of sample 2 appears to be very smooth.

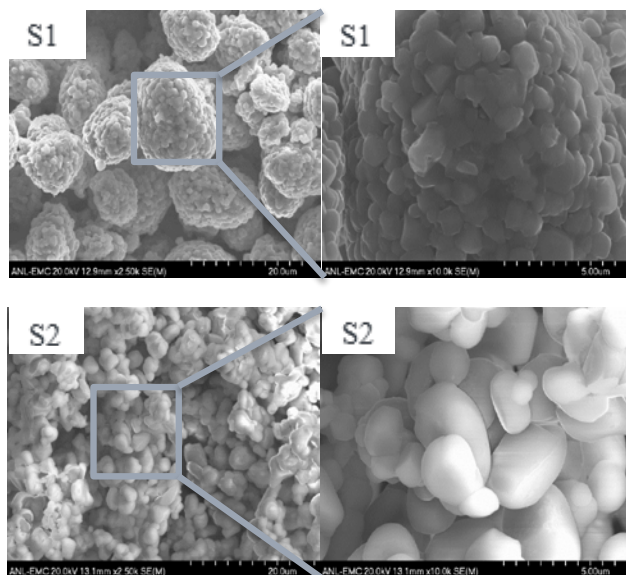


Figure II-433. SEM images of NMC523 sample 1 (S1) and sample 2 (S2). The right two figures are enlarged views of S1 and S2

These two cathode materials were made into laminates with 90 wt.% active material, 5 wt. % PVDF binder and 5 wt.% carbon black. The 2032 coin type cells were fabricated and electrochemically tested between 3.0 V and 4.5 V. The voltage profiles of half cells (vs. lithium metal) of these two samples during the third formation cycle are shown in Figure II-434. The similar voltage profiles suggest that these two NMC523 materials have almost the same chemistry. However, less capacity was obtained from samples 2, which can be attributed to the larger over-potential resulting from the larger primary particle size of sample 2.

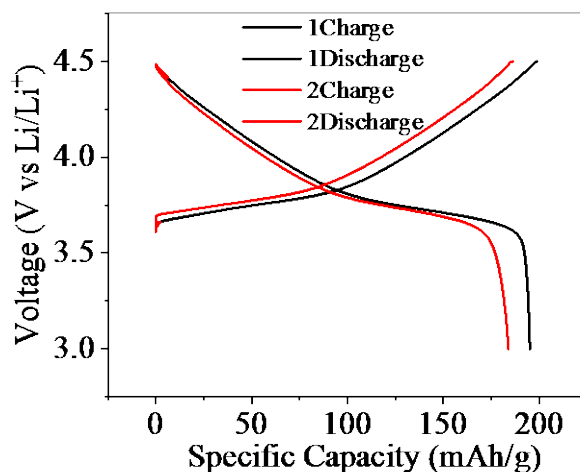


Figure II-434. Voltage profiles of NMC523: sample 1 (black) and sample 2 (red)

After 3 formation cycles and 15 rate cycles, the half cells were cycled under C/3 rate for 50 cycles. The specific capacity as a function of cycle number is shown in Figure II-435 for a total of 68 cycles. Clearly, the specific capacity of sample 2 is less than that of sample 1. However, better capacity retention was obtained for sample 2.

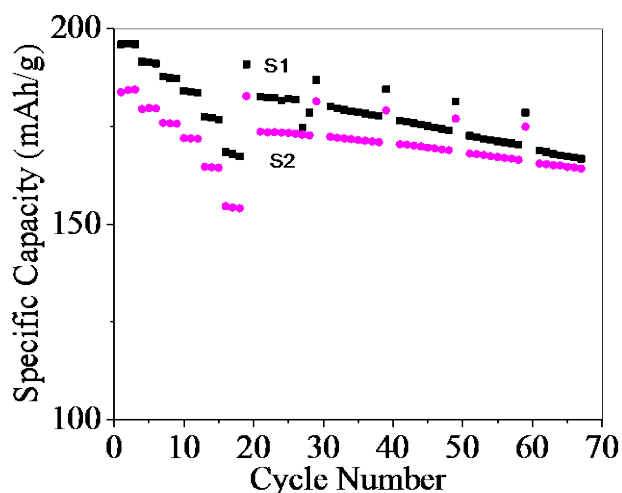


Figure II-435. Specific capacity as a function cycle number: sample 1 (black) and sample 2 (red)

Coating Effect on NMC Cathode Material

Surface modification on cathode materials is generally considered an effective approach to prevent the parasitic reaction between the active material and electrolyte, especially when high voltage is applied on the cathode to improve the energy density of LIBs. However, the coating effect is sensitive to the chemistries of transition metal oxides. Previous studies show various coating effects, especially when the coating is applied to NMC cathode materials. At Argonne, a wet coating process was developed, which can mitigate the process effect on transition metal oxides.

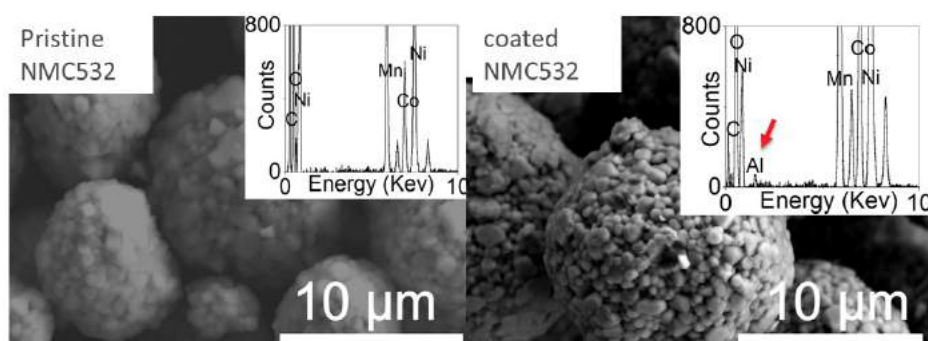


Figure II-436. SEM image of pristine NMC532 (left) and coated NMC532 (right). The insets are the EDS for two particle.

In this work, as low as 0.5% Al_2O_3 was coated on NMC532 (Toda, Japan). SEM images for both pristine and coated NMC532 powders are shown in Figure II-436. There is no clear morphology change observed between the pristine and 0.5 % Al_2O_3 NMC532. Also, a small aluminum signal was observed from EDS results, which suggests that Al_2O_3 was coated on the NMC532 particles.

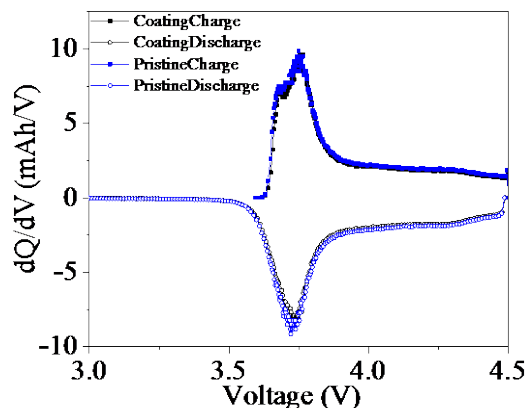


Figure II-437. Differential capacity plots of pristine (black) and coated (blue) NMC532.

Similar to the above electrochemical characterization experiment, the pristine and coated NMC532 powders were made into laminates and the 2032 coin type cells were fabricated and electrochemically tested. Figure II-437 shows the differential capacity plot of the NMC532 with and without coating. No difference in redox reaction for these two materials was obtained, indicating no chemical and structural change after coating.

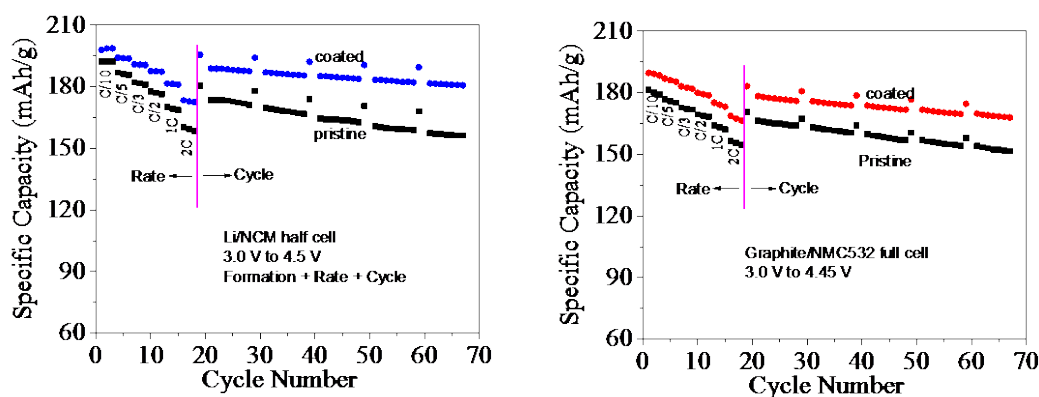


Figure II-438. Specific capacity of NMC532 versus cycle number for half cell (left) and full cell (right)

Figure II-438 shows the specific capacity of pristine and coated NMC532 as a function cycles in both half cells (left) and full cells (right). The cycle numbers include a total of 3 formation, 15 rate test, and 50 life cycles. Surprisingly, as high as 199 mAh/g specific capacity was observed for coated NMC532 from the half cell test, which is higher than 192 mAh/g of pristine NMC532 according to 3rd formation cycle. Furthermore, the capacity retention in half cells is also improved for coated NMC532 from 93% to 96% between cycle number 67 and 21. Similarly, the higher specific capacity and better capacity retention were also obtained from the graphite/NMC532 full cells.

The better performance of coated NMC532 could be attributed the lower impedance of coated NMC532 electrode as shown in Figure II-439. Figure 7 shows the ASI change of pristine (left) and coated (right) NMC532. Firstly, ASI values of pristine NMC532 increase with cycles. However, the ASI increase is very minor for coated NMC532. Secondly, the ASI value of the full cell with coated NMC532 is lower. Al_2O_3 coating is generally considered an insulating material. The lower impedance for the cells with coated NMC532 can be attributed to the better ionic conductivity. This improved ionic conductivity was also observed for Al_2O_3 coated separator due to its better wettability. Another possibility is that the coating on NMC532 could prevent the side reaction between cathode material and electrolyte, leading to less transition metal dissolution and solid electrolyte interphase (SEI) formation.

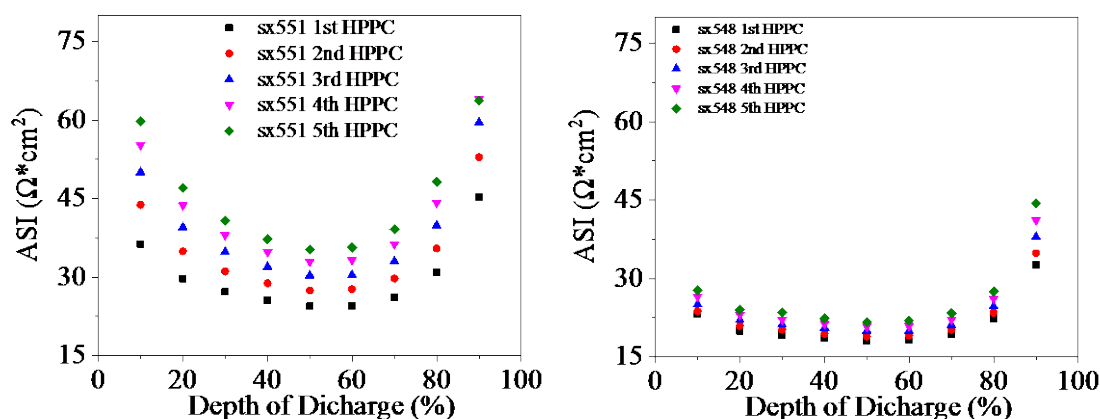


Figure II-439. ASI of full cells with pristine (left) and coated (right) NMC532

Conclusions

In this fiscal year, materials benchmarking activities focus on high energy nickel-rich nickel manganese cobalt oxide cathode materials. The morphology effect on the electrochemical performance was observed. Also, improved high voltage performance was obtained for wet-coated NMC532.

In the future, we will continue to work on the high energy nickel rich cathode materials. We will also work on high capacity anode materials, such as silicon and other metal alloys. We will continue to work closely with research institutions and industrial suppliers to enable the LIB technology for EV applications.

Key Publications

1. Mechanisms for lithium nucleation and dendrite growth in selected carbon allotropes, Su, Xin; Dogan, Fulya; Ilavsky, Jan; Maroni, Victor; Gosztola, David; Lu, Wenquan, Chem. Mater., 2017, 29, 6205-6213.
2. High-Performance high-loading Lithium-sulfur Batteries by low temperature atomic layer deposition of aluminum oxide on nanophase S cathode, Xiangbo Meng, Yuzi Liu, Yanqiang Cao, Yang Ren, Wenquan Lu and Jeffery W. Elam, Adv. Mater. Interfaces, 2017, 1700096
3. Nonlinear conductivities and electrochemical performances of $\text{LiNi}_{0.5}\text{Co}_{0.2}\text{Mn}_{0.3}\text{O}_2$ electrodes utilizing novel carbon nanoparticles, Xin Su, Seonbaek Ha, Manar B. Ishwait, Hanwei Lei, Miki Oljaca, Berislav Blizanac, Dennis Dees, Wenquan Lu, J. Electrochem. Soc., 163 (13) A2720-A2724 (2016).
4. Optimization of Inactive Material Content in Lithium Iron Phosphate Electrodes for High Power Applications, Seonbaek Ha, Vijay K. Ramani, Wenquan Lu, Jai Prakash, Electrochimica Acta, 191 (2016), 173-182.
5. High rate lithium ion battery development, Wenquan Lu, Xin Su, Andrew Jansen, and Dennis Dees, 34th International Battery Seminar and Exhibit - (Fort Lauderdale, FL, US, 03/20/17-03/23/17)
6. The energy and power density of $\text{LiNi}_{0.5}\text{Co}_{0.2}\text{Mn}_{0.3}\text{O}_2$ electrodes promoted by optimizing the carbon additive, Xin Su, Seonbaek Ha, Manar Ishwait, Dennis Dees, and Wenquan Lu, 2017 Gordon Research Conference on Nanomaterials for Applications in Energy Technology, Ventura, CA, US, 02/26/17-03/03/17
7. Li_3FeO_4 Li Source Additive: Fixing Irreversibility in LIBs, Chi-Kai Lin, Xin Su, Wenquan Lu, Xiaoping Wang, and Christopher S. Johnson, 230th Electrochemical Society Meeting, October 2-7, 2016, Honolulu, HI

II.G.3 Post-test Analysis of Lithium-Ion Battery Materials (ANL, ORNL, SNL)

Ira Bloom, Principal Investigator

Argonne National Laboratory
9700 South Cass Avenue
Argonne, IL 60439
Phone: 630-252-4516
E-mail: ira.bloom@anl.gov

David L. Wood III, Principal Investigator

Oak Ridge National Laboratory
P.O. Box 2008
Oak Ridge, TN 37831
Phone: 865-574-1175
E-mail: wooddl@ornl.gov

Kyle R. Fenton, Principal Investigator

Sandia National Laboratories
P.O. Box 5800
Albuquerque, NM 87185
Phone: 505-284-3377
E-mail: krfento@sandia.gov

Peter Faguy, Technology Manager

U.S. Department of Energy
Phone: 202-586-1022
E-mail: Peter.Faguy@ee.doe.gov

Start Date: October 1, 2015
Total Project Cost: \$3,375,000

End Date: September 30, 2018
DOE share: \$3,375,000

Non-DOE share: \$0

Project Introduction

Battery technologies are routinely characterized by measuring the initial electrochemical performance and how it changes with age and use. These characterization methods and tests provide valuable information, from which degradation mechanisms can be inferred by modeling or curve fitting. However, these results do not have the benefit of direct, experimental observation of the underlying causes of the change in electrochemical behavior. There is much still left to be learned by the systematic investigation of the effects of manufacturing variables on the materials changes in the cell responsible for aging. Because of the serious hazardous consequences of overcharge, particularly in modular systems where failure can propagate from cell to cell, understanding the physical and chemical changes of overcharging the cell is extremely important for the development of safe batteries that can be used in an EV. With a materials level understanding of these changes, the abuse response may be mitigated by the development of new strategies that may lead to mass-produced, long-lived cells with minimal abuse response. Additionally, this information would be valuable in confirming that the mechanistic hypotheses employed to develop these strategies corresponds to the actual aging processes at operation.

With this information, battery developers may be able to improve the life and performance of batteries. Improved performance and life would be important to accelerate consumer acceptance of electrified vehicles. In turn, with more electrified vehicles on US roads, electricity generated from both renewable and domestic fossil fuel sources would lessen the importance of imported oil as a source of energy for transportation, contributing to the nation's energy independence. Additionally, a decrease in air pollution due to automobile exhaust would be a direct result.

Objectives

- The main objective of this project is to understand the materials-level effects of overcharging and overheating on the chemistry and physical properties of the cell components in small (~1.5 Ah) lithium-ion cells.
- Other objectives include characterizing the impact of electrode processing conditions on the performance and abuse response of lithium-ion cells.

Approach

Cell components harvested from abuse-tested cells will be characterized to determine the changes produced by differences in cell chemistry and processing variables. The characterization data will be compared to pristine materials to help delineate changes. The materials will be characterized, at first, by many techniques to determine which ones yield data that responds to the given perturbation of the system. Those techniques will then be the first ones used thereafter to track changes. The techniques available include EIS, SEM, XPS, XRD, NMR, Raman, FT-IR and HPLC methods.

Results

Effect of binder on overcharge response

Argonne, ORNL, and SNL are collaborating to understand the physical and chemical changes on and in the electrodes that occur during cell abuse. Characterization of cells after overcharging would be very useful from the safety view point. The information gained may help mitigate the consequences of overcharge by telling us the nature of the SEI, how it changes during overcharge, and, possibly, how to increase its robustness. Two sets of 1.5-Ah pouch cells, which contained NMC532/graphite chemistry, were fabricated at ORNL. PVDF (NMP-processed) was the binder in one set of cells; and CMC (aqueous processed), in the other. After formation, the cells were sent to SNL for overcharging. The cells were charged to 100, 120, 140, 160, 180 and failure (250 and 270% SOC). Argonne then characterized the abused cells after they were discharged to 3.0 V.

Figure II-440 shows images of the two sets of cells upon disassembly in an argon-atmosphere glove box.



Figure II-440. Images of the anodes from the overcharged cells. The rectangular-shaped voids in some of the images are from sampling for microscopy.

In the SOC range of 140 to 180%, there was more damage to the anode laminate in the NMP-processed cells than in the aqueous-process ones. There was clearly a loss of adhesion of the active material to the copper foil.

Elemental analyses, given in Figure II-441 and Figure II-442 for NMP- and aqueous-processed electrodes, respectively, show the trends in transition metals and phosphorus from anode materials. The concentration of the transition metals increase with increasing %SOC, but stay in the original stoichiometric ratio, 5:3:2. Comparing the values given in Figure II-441 to those in Figure II-442 shows that the concentrations of the elements depends on the binder and processing conditions. At SOC's greater than 160%, the concentrations are greater in the electrodes processed using NMP than those processed using aqueous binders.

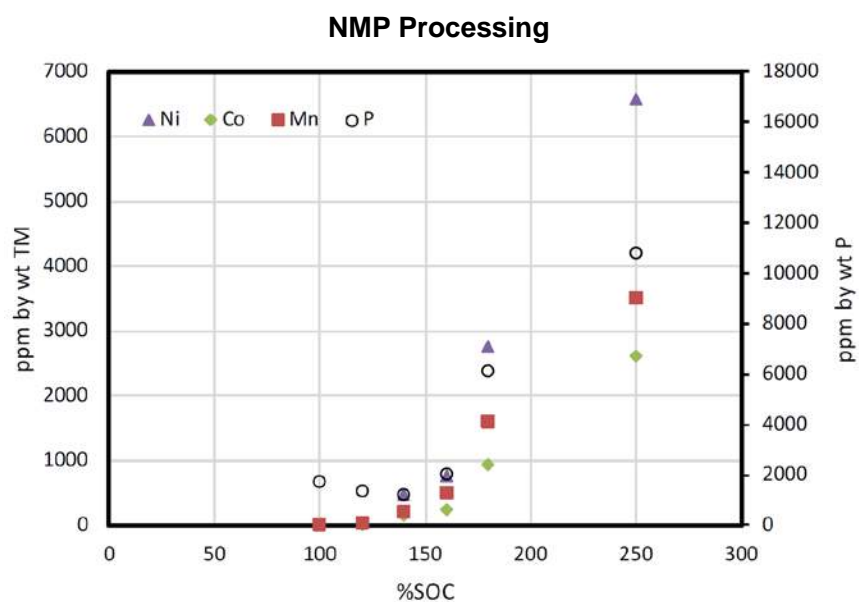


Figure II-441. Concentration of metals and phosphorus vs. %SOC for NMP-processed electrodes.

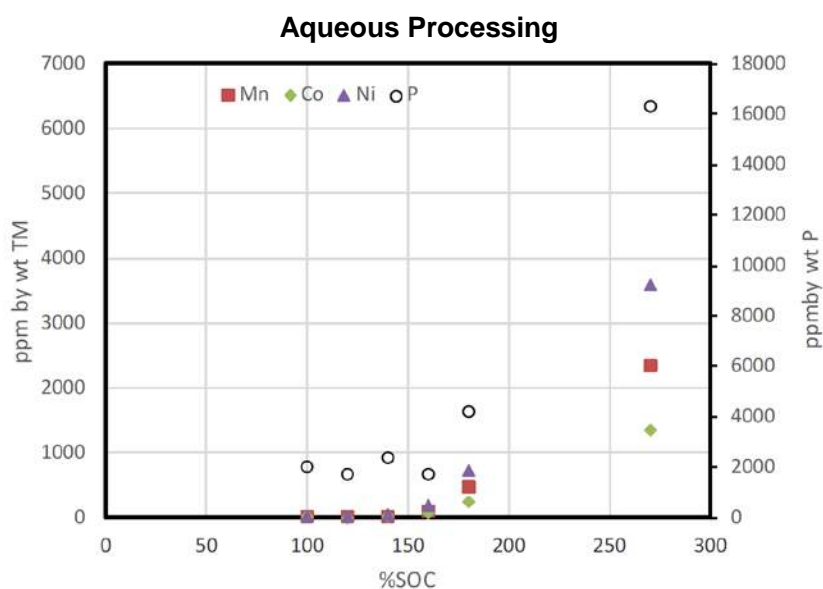


Figure II-442. Concentration of metals and phosphorus vs. %SOC for aqueous-processed electrodes.

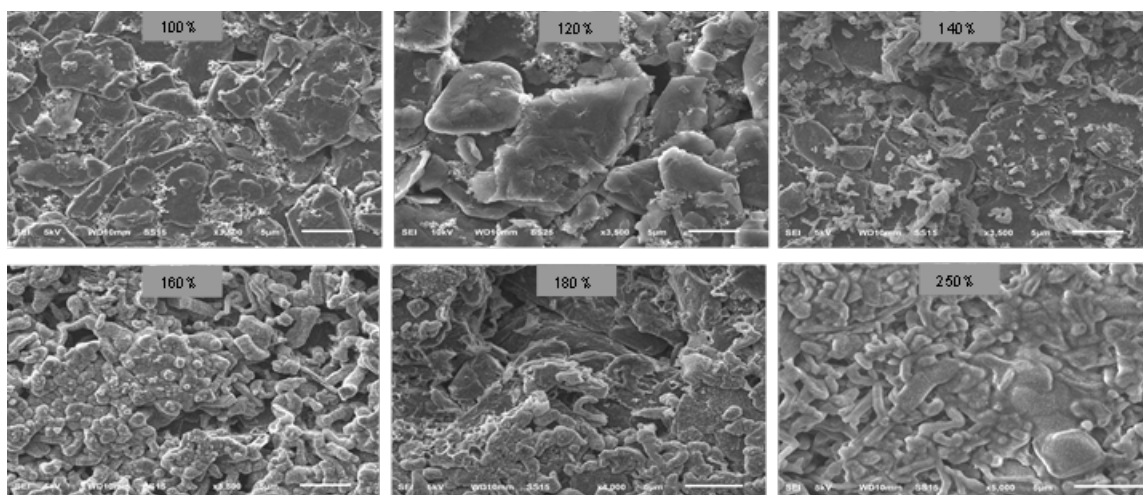


Figure II-443. SEM images of the surface of anodes from overcharged cells, NMP processing. The numbers shown in the grey boxes indicate the %SOC that the cell experienced during the overcharge experiment.

Other trends are seen on the surface, for example, of overcharged anodes. Figure II-443 and Figure II-444 show images of the surfaces of overcharged anodes from NMP and aqueous process, respectively. As seen from the figures, the surfaces of the electrodes changes in %SOC and with the binder/processing used. Examining the surfaces shows, for example, that the concentration of dendrite-like structures tends to increase with SOC. Additionally, the formation of dendrite-like structures is more severe and occurs at lower SOC in the NMP processed anodes than those from aqueous processing.

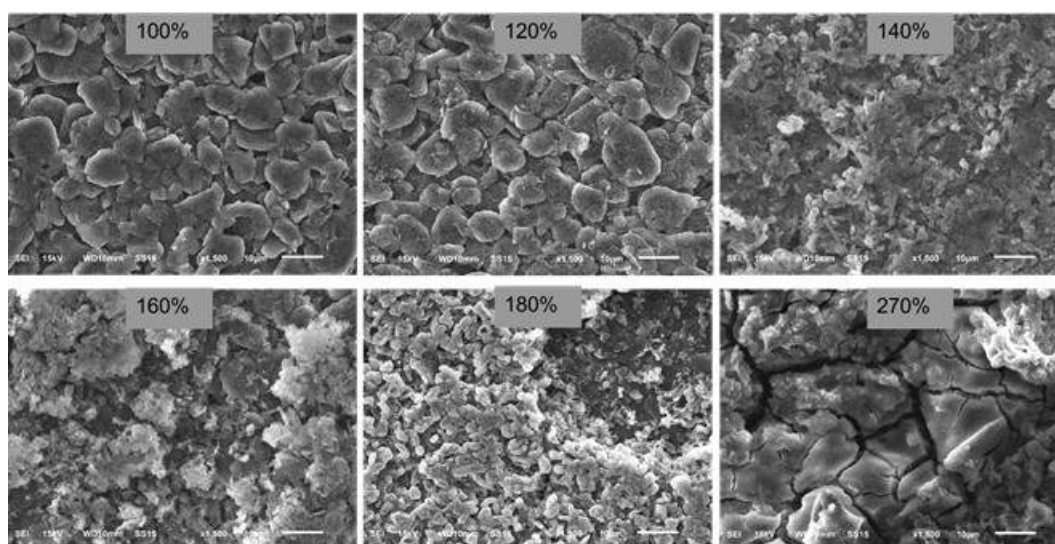


Figure II-444. SEM images of the surface of anodes from overcharged cells, aqueous processing. The numbers shown in the grey boxes indicate the %SOC that the cell experienced during the overcharge experiment.

In the XPS results from the anode, many SOC- and processing-dependent trends were seen. For example, Figure II-445 shows the Li1s region of two overcharged anodes. In the SOC range of 100 to 180%, the quantity of Li_2O -like material tends to increase with SOC. There was more Li_2O -like material on the anode surface in the NMP-processed example than on that in the aqueous-processed one. It is possible that this material influenced the morphology of the dendrite-like materials seen in Figure II-443 and Figure II-444. Similar trends were seen in the 3d binding-energy regions for the respective transition metals.

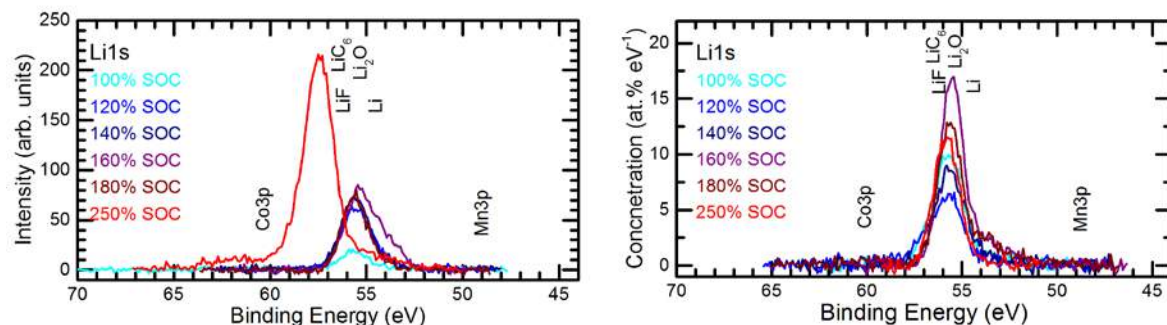


Figure II-445. XPS results from two anode materials (right) image from the NMP-processed material (left) image from the aqueous processed material.

On the cathode side of the cell, significant differences in the XPS spectra were seen. For example, in the O1s binding energy region, as shown in Figure II-446 a and 7b, the strength of the signal in the metal oxide (MO_x) region decreases markedly when the binder was changed from PVDF to CMC. This indicates that the film on the cathode surface is thinner on the latter than on the former.

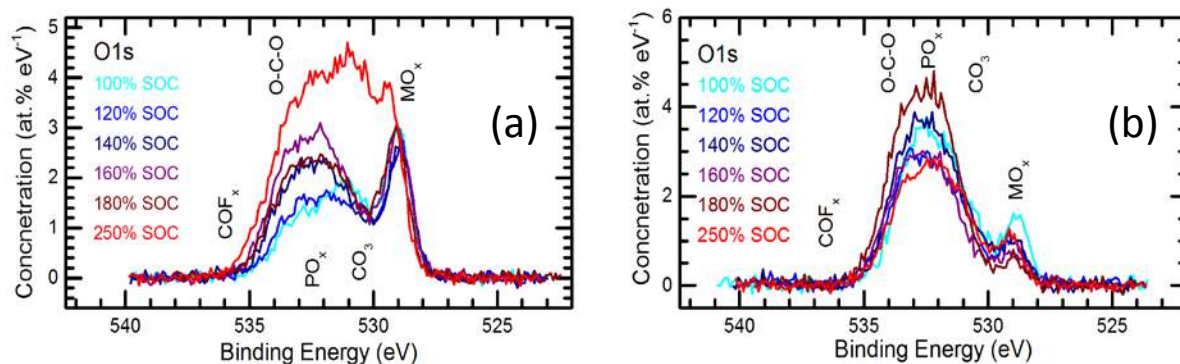


Figure II-446. (a) Concentration vs. binding energy in the O1s energy region from the NMP-processed cathodes. (b) Concentration vs. binding energy in the O1s energy region from the aqueous-processed cathodes.

In the F1s binding energy region of the spectrum, other changes were seen which correlated with the binder. From Figure II-447a and Figure II-447b, NMP- and aqueous-processed, respectively, there is a shift to higher binding energy when the binder was changed from PVDF to CMC. Here, the fluorine changed from being bound to a molecule similar to Li_xPF_y to being in a compound analogous to LiPF_6 . No other significant changes were seen in the XPS data from the cathode.

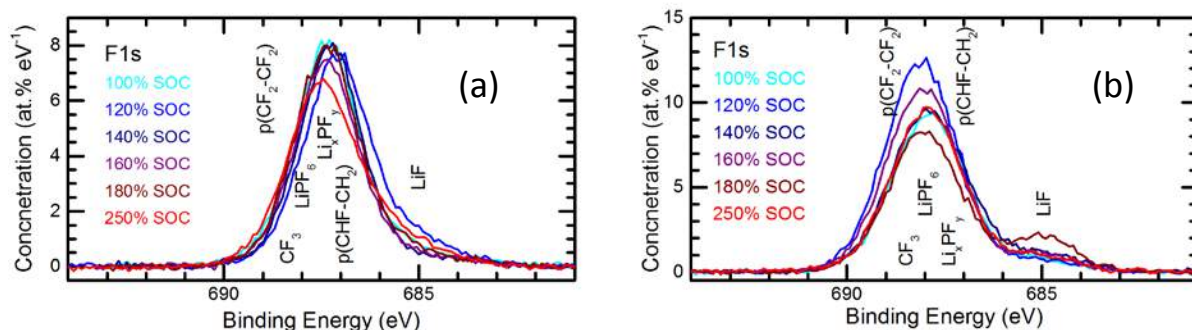


Figure II-447. (a) Concentration vs. binding energy in the F1s energy region from the NMP-processed cathodes. (b) Concentration vs. binding energy in the F1s energy region from the aqueous-processed cathodes.

Conclusions

The binder/processing conditions play an important role in the abuse response of the NMC532/graphite cells. The binder alters the rate of, presumably, transition metal dissolution and transport to the anode. The concentrations of transition metals and phosphorus depend not only on SOC but also on the binder. The morphology and, perhaps, concentration of species on the surface of the electrodes also depend on it.

Key Publications

1. XPS Characterization of Overcharged NMC and LFP Lithium Ion Cells. J. Bareño, N. Dietz Rago, Z. Du, Y. Sheng, J. Li, L.A. Steele, J. Lamb, S. Spangler, C. Grosso, D.L. Wood III, K. Fenton, and I. Bloom, Poster presented at the 10th International Conference on Advanced Lithium Batteries for Automobile Applications, Oakbrook, IL USA, October 22 - 25, 2017.
2. Effect of overcharge on lithium-ion cells containing $\text{Li}(\text{Ni}_{0.5}\text{Mn}_{0.3}\text{Co}_{0.2})\text{O}_2$ cathodes: NMP-soluble binder. I. Microstructural changes in the anode. N. Dietz-Rago, J. Bareño, J. Li, Z. Du, D. Wood, L. A. Steele, J. Lamb, et al., *Journal of Power Sources* (forthcoming).
3. Effect of overcharge on lithium-ion cells containing $\text{Li}(\text{Ni}_{0.5}\text{Mn}_{0.3}\text{Co}_{0.2})\text{O}_2$ cathodes: NMP-soluble binder. II — Chemical changes in the anode. I. Bloom, J. Bareño, N. Dietz-Rago, F. Dogan, D. Graczyk, Y. Tsai, S. Naik, et al., *Journal of Power Sources* (forthcoming).
4. Effect of overcharge on NMP-processed $\text{Li}(\text{Ni}_{0.5}\text{Mn}_{0.3}\text{Co}_{0.2})\text{O}_2$ / Graphite lithium ion cells with PVDF binder. II — Chemical changes in the cathode. J. Bareño, Nancy Dietz-Rago, F. Dogan-Key, D. Graczyk, Y. Tsai, S.Naik, S.-D. Han, et al., *Journal of Power Sources* (forthcoming).

II.H Beyond Li-ion R&D: Metallic Lithium and Solid Electrolytes

II.H.1 Mechanical Properties at the Protected Lithium Interface (ORNL)

Nancy Dudney, Principal Investigator

Oak Ridge National Laboratory
P.O. Box 2008, MS6124
Oak Ridge, TN 37831
Phone: 865-576-4874
E-mail: dudneynj@ornl.gov

Erik Herbert, Principal Investigator

Michigan Technological University
604 M&M Building
1400 Townsend Drive
Houghton, MI 49931
Phone: 906-4872633
E-mail: eherb@mtu.edu

Jeff Sakamoto, Principal Investigator

University of Michigan
2350 Hayward Avenue
Ann Arbor, MI 48109
Phone: 734-763-2219
E-mail: jeffsaka@umich.edu

Tien Duong, Technology Manager

U.S. Department of Energy
Phone: 202-586-7836
E-mail: Tien.Duong@ee.doe.gov

Start Date: January 1, 2015

End Date: December 31, 2017

Total Project Cost: \$1,000,000

DOE share: \$460,000

Non-DOE share: \$540,000

Project Introduction

A stable lithium anode is critical to achieve high energy density with excellent safety, lifetime and cycling efficiency. Instability and/or high resistance at the interface of lithium metal with various solid electrolytes limit the use of the metallic anode for batteries with high energy density batteries, such as Li-air and Li-S. The critical impact of this endeavor will be a much deeper analysis of the degradation, so that materials can be engineered to fulfill the target level of performance for EV batteries, namely 1000 cycles and 15 year lifetime, with adequate pulse power.

Objectives

This project will develop the understanding of the Li metal-solid electrolyte interface through state of the art nanoindentation and other mechanical methods coupled with solid electrolyte fabrication and electrochemical cycling. Our goal is to provide the critical information that will enable transformative insights into the complex coupling between the microstructure, its defects and the mechanical behavior of Li metal anodes.

Approach

Generally, the cycling of lithium is investigated electrochemically. Here we are testing the mechanical properties the solid electrolyte and the lithium independently, and then the interfaces formed of lithium with the solid electrolyte. This provides not only important materials characterization, but a real-time measure of how lithium moves in response to cycling through a solid electrolyte. The solid electrolytes investigated included a glassy lithium phosphorus oxynitride (Lipon) electrolyte and the polycrystalline garnet electrolyte of lithium lanthanum zirconium oxide (LLZO). In addition, Li metal was characterized on smooth glass surfaces. In all cases the samples were well protected from air and humidity during processing and tests.

Mechanical properties studies through state of the art nanoindentation techniques are used to probe the surface properties of the solid electrolyte and the changes to the lithium that result from prolonged electrodeposition and dissolution at the interface. High speed mapping of large indentation arrays provides statistically relevant distributions of the properties relative to microstructural features. The nanoindentation approach benefitted from a close collaboration with associates at Nanomechanics, Inc. of Oak Ridge TN for continuing refinements in both hardware, software and firmware for the NanoFlip and iNano systems used in this investigation. Further, Prof. Steve Hackney of Michigan Technological University has contributed to the detailed understanding and modeling to elucidate the creep mechanisms operative in the lithium metal.

Other mechanical tests of the Li/LLZO interface were performed using a precision Instron in an Ar-filled glove box. The interface was formed using protocols developed under program II.B.1.ii, led by Jeff Sakamoto.

Results

Li metal studies

Two studies were completed this year. In the first, we addressed the elastic and ductile creep behavior of lithium metal thin films using dynamic nanoindentation. In the second, the redistribution of the thin film of lithium as incorporated into a thin film battery was analyzed during prolonged cycling with different cathodes and duty cycles.

Elastic modulus measurements from 20 and 5 μm thick films (course and fine grained, respectively) indicate the films have different texture. For each film thickness, maps of 30 or more indentations were used to assess homogeneity. Numerous experimental challenges were addressed to extract the elastic modulus from the very ductile behavior of the lithium. In a relatively coarse-grained 20 μm thick film, the range in elastic modulus from 5 to 9 GPa correlates well to the expected value of 8.9 in 110 type directions. On the other hand, results of the elastic modulus from 35 measurements in a more fine-grained 5 μm thick film range from 9 to 18 GPa. This suggests the thinner film has less texture, as the data show a broad mixture of elastic moduli ranging from 110 and 111 type directions (111 is expected to be approximately 23 GPa). These observations are consistent with lithium's shear anisotropy factor of 9.3 and previously published measurements of lithium's elastic constants. Continuing efforts will be made to quantify the plastic anisotropy as well.

To address the ductile properties of the lithium, nanoindentation experiments performed on vapor deposited lithium films reveal a remarkable length scale dependence in the measured hardness. (Hardness is defined in this study such that it physically represents the mean pressure lithium will support; this is highly relevant to the mechanics of successfully confining the lithium anode.) Figure II-448 (a) shows a unique inflection point in the hardness that coincides with an abrupt change in the mechanism that controls the plastic flow of lithium. Hardness data to the right of the inflection point are consistent with the well-documented indentation size effect. Differences in the hardness between the 5 and 18 μm thick films are generally consistent with Hall-Petch strengthening due to the smaller grain size of the thinner film. Hardness data to the left of the inflection point, on the other hand, are entirely unique. While an increase in hardness with increasing indentation depth has been observed in BCC iron, unlike iron, this observation in lithium is not the result of dislocation interaction with a nearby grain boundary. Figure II-448 (b) shows 20 residual hardness impressions in the grain interior and 68 impressions in proximity to a boundary. As shown in Figure II-448 (c), there is no discernable difference in the measured hardness at these positions relative to the boundary and the grain

interior (red and green). The difference in hardness between the bulk arrays (yellow) and data obtained within the grain and near the boundary (Figure II-448 (c)) are potentially due to plastic anisotropy. In addition to the length scale dependence, Figure II-448 (d) shows the hardness near the free surface also depends on the strain rate. As the data show, the rate effect is most pronounced near the free surface, it diminishes with increasing indentation depth and it is completely exhausted by the inflection point. To rationalize these unique experimental observations, effort is underway to develop a diffusional creep-based model capable of describing the change in stress with strain rate and indentation depth.

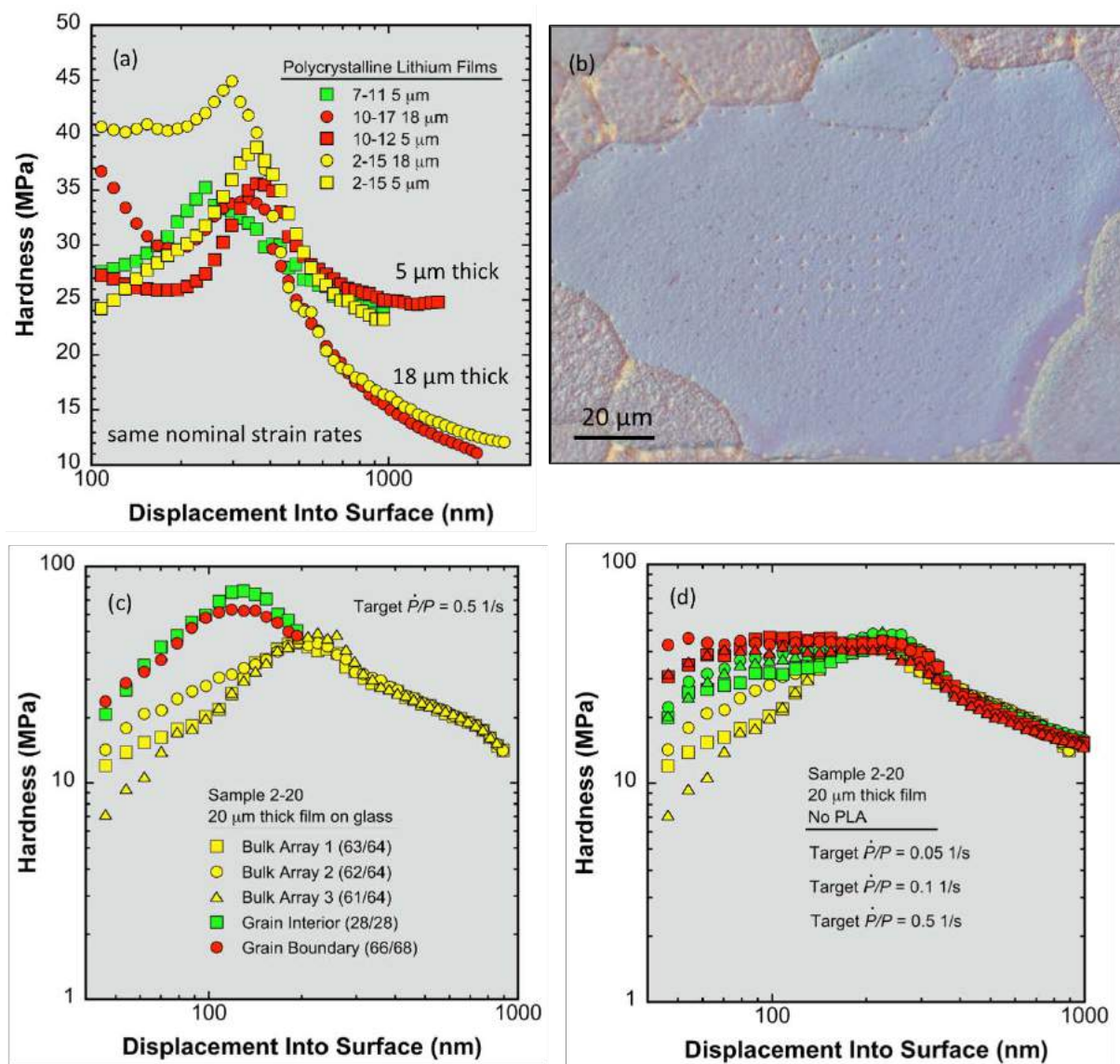


Figure II-448. (a), (c) – (d): Hardness as a function of indentation depth, deposition date, film thickness, location and strain rate. (b) Micrograph of residual hardness impressions in lithium.

Analysis and models have been developed to describe the mechanical properties of thin film lithium as revealed by numerous nanoindentation experiments. The complex dependence on the strain rate and displacement into the film indicates several processes contribute to plastic deformation. A manuscript is being prepared to describe and map these effects. To summarize, Figure II-448 (a) shows the hardness as a continuous function of indentation depth for Li films (5 and 18 μm thick) and 4 indentation strain rates. This is

the average of many indentation maps across the surface. The different creep mechanisms are shown in Figure II-448(b). At slower strain rates and smaller displacement, Nabarro-Herring creep is the primary mechanism. Here lattice defects (vacancies) diffuse between the tip and the free surface of the Li film. At higher strain rate, plastic flow must be accommodated by the diffusion of vacancies from nearby dislocations within the plastic zone. This Harper-Dorn mechanism correctly predicts that the pressure is inversely proportional to the square root of the length scale. At the inflection point in the hardness, an avalanche of dislocations occurs. The power law relationship in Figure II-448(c) strongly suggests, the avalanche occurs only after a threshold limit of energy per unit area has been exceeded. These stresses far exceed the yield or tensile strengths reported for bulk polycrystalline lithium. After the dislocation avalanche, the deformation mechanism capitalizes on the significant increase in the dislocation density and reverts from diffusional creep mechanisms to a balance between of the rate of defect anneal (recovery) and the rate of strain hardening.

Collectively, these observations demonstrate that the Li/SE interface cannot be accurately modeled based on the bulk plastic properties of polycrystalline Li. Moreover, in any small-scale defects at the Li/SE interface, the strength of Li will depend dramatically on the local defect structure, the temperature and strain rate, which presumably correlates directly with the current density. To fully enable the development of safe and efficient cycling of lithium over many cycles, more information is needed to better understand how defects formed in the Li during electrochemical cycling migrate, agglomerate, or anneal with further cycling, time and temperature. Ultimately, we need to understand how these changes affect Li's ability to alleviate stress. This knowledge will serve as a cornerstone in understanding the failure mechanism(s) of solid electrolytes.

LLZO and Li/LLZO interface studies

A coordinated effort with II.B.1.ii, this program provided nanoindentation analysis of the well prepared LLZO. High-speed nanoindentation experiments were performed in LLZO to assess changes in the hardness and elastic modulus as a function of grain size. Results from 300 measurements indicate there is no significant difference in the mechanical properties of LLZO that has been annealed for 1 hour versus 50 (50 hours produces grains on the order of 25 μm). However, when the indentation depth is decreased from 500 to 100 nm, the ratio of modulus to hardness shifts to a slightly lower value. This suggests the near surface region will accommodate strain somewhat more elastically than the bulk.

In other mechanics testing, we used a precision Instron housed in an inert glove box to assess the Li/LLZO interface. Results of the lap shear and tensile adhesive strength show that the adhesive strength of interfaces associated with low interfacial resistance exceed the yield strength of the Li metal itself.

There is a clear correlation between the area specific ionic resistance (ASR) and the tensile adhesive strength of the Li/LLZO interface, as shown in Figure II-449. The tensile strength was determined as Li/LLZO/Li cells were pulled in tension. Analysis of the fracture surfaces showed that at high ASRs, there is a clean separation of the Li from the LLZO surface, leaving behind negligible Li residue. In contrast, at the lowest ASRs reported, the adhesive strength of the Li/LLZO interface exceeds the tensile strength of the Li metal. To support these results, the tensile strength of Li foil was measured to be $\sim 8\text{MPa}$, which is the maximum interface strength observed in Li/LLZO/Li stacks (red-dashed line in Figure II-449). The fact that the strength of the interface is stronger than the Li metal itself at low ASRs suggests that there is good surface chemistry and wettability of Li on LLZO. From these studies, it can be concluded that both the adhesive strength and ASR of the interface are governed by the surface chemistry and wettability of the LLZO surface.

Finally, using our precision Instron, the interface resistances of Li-LLZO-Li cells were recorded while cycling the compressive stress (stack pressure) applied to the cell. We believe a critical stack pressure is needed to maintain a flux of Li to the interface to maintain contact and avoid formation of pits due to the Kirkendall effect. Li-LLZO-Li cells were fabricated using the best cell assembly protocol to achieve low and consistent interface resistance. While varying the stack pressure, we monitored the potential to maintain a constant current finding that there was a noticeable correlation between cell polarization and stack pressure.

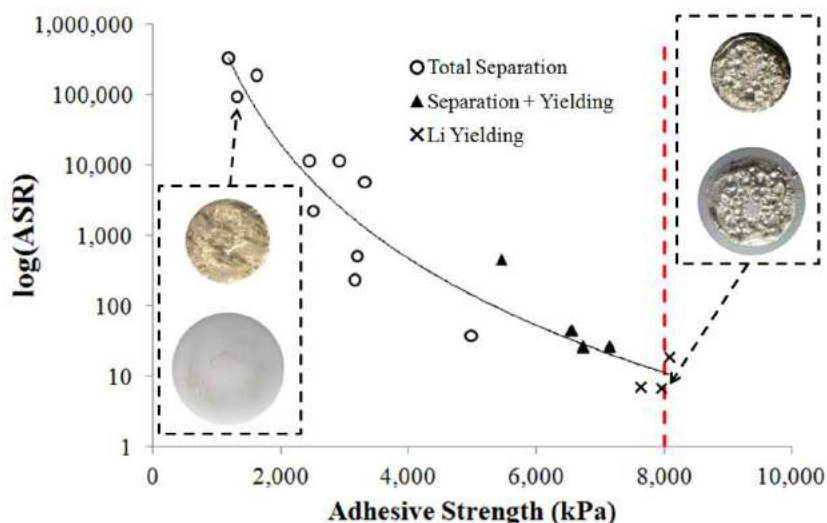


Figure II-449. Area specific resistance as a function of the adhesion strength of the Li-LLZO interface. Optical microscope images show the fracture surface of the Li and LLZO disks at low and high ASR. The red dashed line indicates the measured tensile strength of Li metal

Conclusions

1. The elastic properties of vapor deposited lithium metal thin films were characterized and found to be higher than expected, but well within the published values for the orientation dependent modulus.
2. The plastic properties were found to be dependent on the length scale and strain rate. At the smallest lengths scale, the mean pressure supported by the lithium is 40-350 times higher than the nominal yield strength of bulk polycrystalline lithium, shedding light on the mechanical behavior of lithium at defects near the lithium/solid electrolyte interface.
3. Extended cycling of lithium contacting the Lipon solid electrolyte in a thin film battery shows significant redistribution that depends on the duty cycle and surprisingly also the particular cathode.
4. The adhesive strength of Li with LLZO and the ASR of the interface are governed by the surface chemistry and wettability of the LLZO interface. For optimal interfaces, the adhesive strength exceeds the tensile strength of the lithium metal itself.
5. The electrochemical cell polarization for a Li/LLZO/Li cell correlates to the applied stack pressure when oscillated between 1.2 and 2.4 MPa.

Key Publications

1. "Stability and cycling of metallic Lithium with an inorganic solid electrolyte", Nancy J. Dudney, Miaofang Chi, Jeff Sakamoto, and Erik Herbert, ACS meeting, San Francisco March 2017, invited presentation
2. "Evolution of the Lithium Morphology from Cycling of Thin Film Solid-State Batteries," Nancy J. Dudney, *Journal of Electroceramics* **38** (2017) 222-229. Invited for Solid State Batteries Issue.
3. "Mechanical Properties at the Protected Lithium Interface," Nancy Dudney, Erik Herbert, Jeff Sakamoto.
4. DOE Vehicle Technologies Program, Annual Merit Review and Peer Evaluation Meeting, June 2107. Oral presentation.

5. “The Mechanical Behavior of Vapor Deposited Lithium Films,” Erik Herbert, Nancy Dudney, Steve Hackney, 10th Meeting for Beyond Lithium Ion Batteries (BLI-10), IBM Almaden CA, June 27, 2017. Invited presentation.
6. “Nanoindentation of High Purity Vapor Deposited Lithium Films: The Elastic Modulus,” E. G. Herbert, P. S. Phani, N. J. Dudney, and S. A. Hackney In preparation.
7. “Nanoindentation of High Purity Vapor Deposited Lithium Films: A Mechanistic Rationalization of Diffusion-Mediated Flow,” E. G. Herbert, S. A. Hackney, N. J. Dudney, V. Thole and P. S. Phani, In preparation.
8. “Nanoindentation of High Purity Vapor Deposited Lithium Films: A Mechanistic Rationalization of the Transition to Dislocation-Mediated Flow,” E. G. Herbert, S. A. Hackney, N. J. Dudney, V. Thole and P. S. Phani, In preparation.

II.H.2 Solid electrolytes for solid-state and lithium-sulfur batteries (University of Michigan, ORNL, ARL, Oxford University)

Jeff Sakamoto, Principal Investigator

University of Michigan
Mechanical Engineering
2350 Hayward Avenue
Ann Arbor, MI 48109
Phone: 734-769-2213
E-mail: jeffsaka@umich.edu

Tien Duong, Technology Manager

U.S. Department of Energy
Phone: 202-586-7836
E-mail: Tien.Duong@ee.doe.gov

Start Date: January 1, 2015
Total Project Cost: \$1,200,000

End Date: December 31, 2017
DOE share: \$1,200,000

Non-DOE share: \$0

Introduction

Batteries that surpass Li-ion systems require advanced anode, cathode, and electrolyte technology. In theory, the lithium-sulfur (Li-S) system offers over a six-fold increase in specific energy (2567 Wh/kg) compared to state-of-the-art (SOA) Li-ion (387 Wh/kg). However, the potential of the Li-S system has not been realized due to instabilities at the interface between the Li metal anode and the electrolyte. First, other than LIPON, no electrolyte has demonstrated stability against metallic Li. Second, dissolution of Li-polysulfides in SOA liquid electrolytes results in passivation of the Li anode. Thus, there is a compelling need to develop novel electrolyte technology to enable beyond Li-ion battery technologies employing Li metal anodes.

Objectives

Enable advanced Li-ion solid-state and lithium-sulfur EV batteries using LLZO solid-electrolyte membrane technology

Owing to its combination of fast ion conductivity, stability, and high elastic modulus, LLZO exhibits promise as an advanced solid-state electrolyte. To demonstrate relevance in EV battery technology, several objectives must be met. First, LLZO membranes must withstand current densities approaching $\sim 1 \text{ mA/cm}^2$ (commensurate with EV battery charging and discharging rates). Second, low area specific resistance (ASR) between Li and LLZO must be demonstrated to achieve cell impedance comparable to conventional Li-ion technology ($\sim 10 \text{ Ohms/cm}^2$). Third, low ASR and stability between LLZO and sulfur cathodes must be demonstrated.

Approach

Our effort will focus on the promising new electrolyte known as LLZO ($\text{Li}_7\text{La}_3\text{Zr}_2\text{O}_{12}$). LLZO is the first bulk-scale ceramic electrolyte to simultaneously exhibit the favorable combination of high conductivity ($\sim 1 \text{ mS/cm}$ at 298K), high shear modulus (61 GPa) to suppress Li dendrite penetration, and apparent electrochemical stability (0-6V vs Li/Li⁺). While these attributes are encouraging, additional R&D is needed to demonstrate that LLZO can tolerate current densities in excess of 1 mA/cm^2 , thereby establishing its relevance for PHEV/EV applications. We hypothesize that defects and the polycrystalline nature of realistic LLZO membranes limit the critical current density. However, the relative importance of the many possible defect types (porosity, grain boundaries, interfaces, surface & bulk impurities), and the mechanisms by which they impact current density, have not been identified. Using our experience with the synthesis and processing of LLZO (Sakamoto and Wolfenstine), combined with sophisticated materials characterization (Nanda), we will precisely control atomic and microstructural defects and correlate their concentration with the critical current

density. These data will inform multi-scale computation models (Siegel and Monroe) which will isolate and quantify the role(s) that each defect plays in controlling the current density. By bridging the knowledge gap between composition, structure, and performance we will determine if LLZO can achieve the current densities required for vehicle applications.

Results

As has previously been shown¹, the surface chemistry of LLZO is sensitive to air exposure. A contamination layer readily forms and is predominantly composed of lithium carbonate (Li_2CO_3), lithium hydroxide (LiOH), and other adventitious carbon species; which collectively result in high interfacial resistance between LLZO and metallic Li. It has been reported that dry polishing in an inert atmosphere can lower the interfacial resistance by partially cleaning the surface; however, the efficacy of this approach is limited to reducing the interface resistance from $\sim 1000 \text{ } \Omega \cdot \text{cm}^2$ to $\sim 100 \text{ } \Omega \cdot \text{cm}^2$. Here, several surface conditioning protocols, including dry polishing (DP), wet polishing (WP), and heat treatments (HT) were employed in an attempt to reduce the interfacial resistance, and their impact on LLZO surface chemistry was evaluated. Heat treatment between 200 and 500°C in an inert atmosphere was conducted after dry and wet polishing.

The surface chemistry of LLZO was analyzed using X-ray photoelectron spectroscopy (XPS) after each conditioning protocol (Figure II-450). Measurements were performed on samples transferred without air exposure between an argon-filled glovebox and the ultra-high vacuum XPS chamber. Figure II-450a shows that in samples conditioned with DP or WP (no HT) a surface layer blocks nearly all the signal attributed to La and Zr. Thus, in these cases the surface layer is composed almost entirely of H, Li, C, and O (H content cannot be directly detected by XPS, but can be observed as hydroxyl bonds). The nature of the bonds in which these species participate can be examined through high-resolution core-scans. The O 1s peak reveals a significant difference between the surface layer after wet vs. dry polishing (Figure II-450b). The WP surface consists of predominantly hydroxide species, while a greater concentration of carbonate species exists on the DP sample. This suggests that the use of polishing fluid protects the LLZO surface from reformation of carbonate species.

Samples that underwent HT were first polished (DP or WP in ambient air) and then immediately transferred into an argon-filled glovebox where the samples were heated to different temperatures. Subsequent XPS analysis demonstrated significant variations in the surface chemistry of these samples. In Figure II-450a the plot of the ratio of the C content to the summed La and Zr contents is used as a metric to quantify the amount of surface contamination. The lower the ratio, the more closely the surface resembles bulk LLZO. Some adventitious carbon is always observed on the LLZO surface, even for samples kept continuously in an argon atmosphere after HT, Figure II-450c. The amount of contamination is observed to dramatically decrease after heating to 400 and 500°C. This is consistent with the O 1s core scans shown for these samples, which demonstrate that the predominantly hydroxide and carbonate surfaces before heating are converted to primarily oxide species (as expected in bulk LLZO) after heating (Figure II-450b). In contrast, heating a DP sample to 400°C did not change the surface as dramatically, with carbonate species still dominating (Figure II-450c). A plot of the fractional surface composition of the oxygen-containing species is shown in Figure II-450d for WP samples heated to different temperatures. As the HT temperature increases to 500°C, the oxide fraction steadily increases, the hydroxide fraction decreases, and the amount of carbonate remains roughly constant. In total, these observations suggest that: (1) compared to dry polishing, wet polishing is more effective at achieving a surface with low carbonate content, (2) heat treatment up to 500°C can remove LiOH , but is less effective at removing Li_2CO_3 , and (3) of the strategies examined, the successive combination of WP and HT is the most effective at removing surface contamination layers.

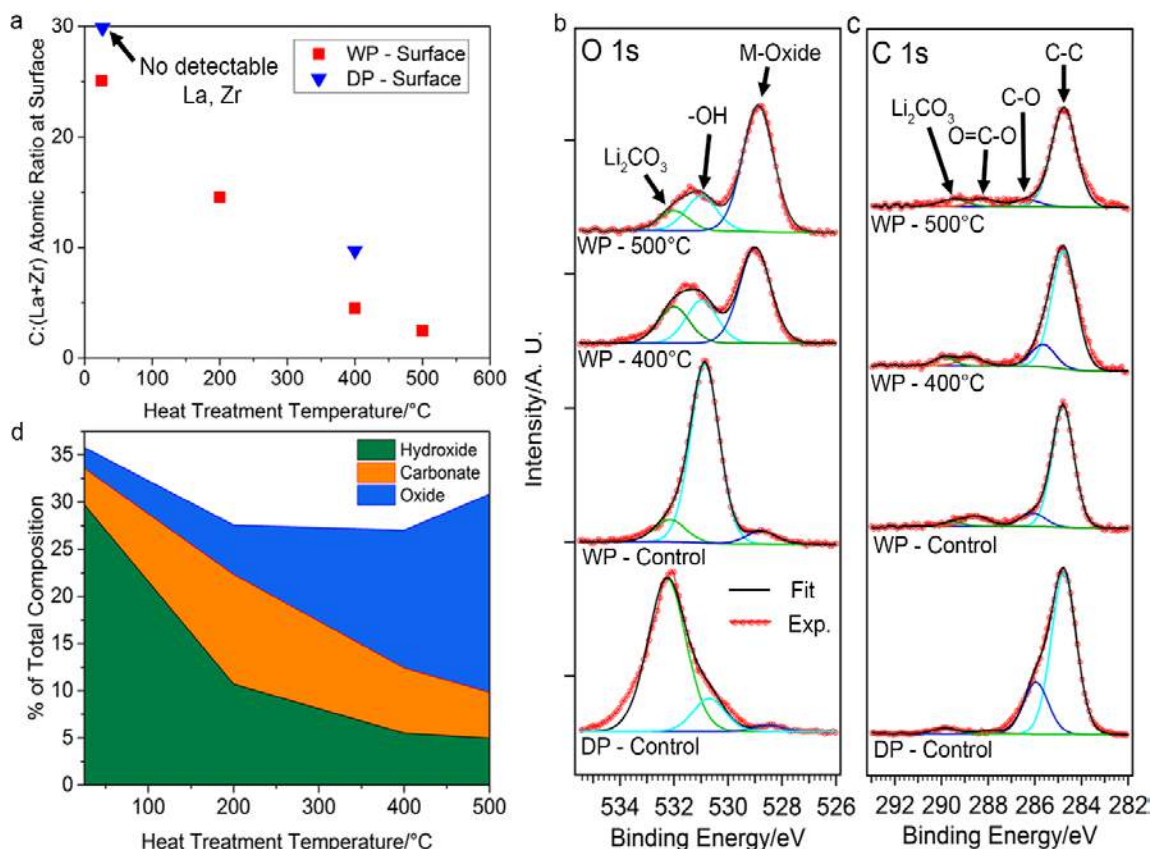


Figure II-450. XPS analysis of LLZO before and after heat treatment at 400 and 500 °C. a) C:(La+Zr) atomic ratio as a function of heat treatment temperature, b) O 1s and c) C 1s core levels, d) percentage of total composition of different oxygen species on the LLZO surface as a function of heat treatment temperature after wet polishing (WP).

The wettability of a SSE by metallic Li has been proposed to influence interfacial resistance in SSBs. However, quantitative analysis of the Li contact angle and direct correlation with surface chemistry has not been reported. To characterize wettability, sessile drop tests were performed to measure the contact angle of molten Li on Li_2CO_3 and on LLZO samples after various surface conditioning processes (Figure II-451). Molten Li was deposited onto heated Li_2CO_3 or LLZO from a heated stainless-steel syringe. Importantly, the native layers (composed of oxide, nitride, and carbonate species) present on the surface of the Li foil did not melt, and thus were easily removed from the molten Li source. This allowed for deposition of purified molten Li onto the LLZO surface. The present approach differs from a scenario involving the melting of solid Li foil directly on LLZO, as wettability in the latter approach will be influenced by the presence of native layers on the Li surface and at the Li-LLZO interface. All experiments were performed inside an argon-filled glovebox, and high-resolution cross-sectional images were captured and digitally analyzed to determine contact angles.

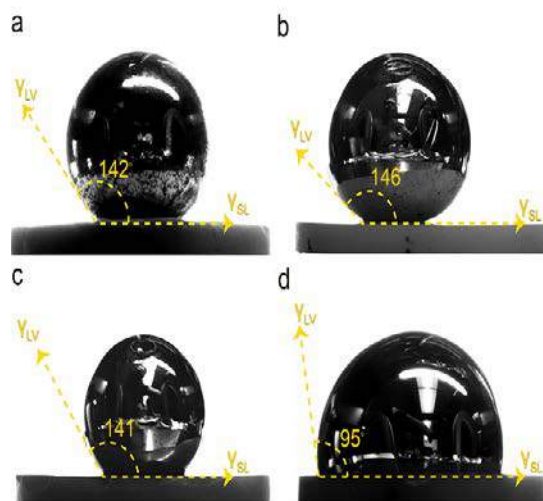


Figure II-451. Contact angle measurements of molten metallic Li on a) Li_2CO_3 , b) DP-LLZO, c) WP-LLZO, d) WP-LLZO after heat treatment at 500°C .

As shown in Figure II-451, the DP-LLZO sample exhibited the highest contact angle amongst all LLZO samples, $\theta = 146^\circ$, which was nearly identical to the value measured for a pure Li_2CO_3 surface ($\theta = 142^\circ$). Such a large contact angle is consistent with a non-wetting interaction typical of an interface exhibiting weak adhesion. The similar wetting behavior between the DP-LLZO sample and Li_2CO_3 is expected, given that the DP-LLZO surface is composed predominantly of Li_2CO_3 . Similarly, the WP-LLZO contact angle was 141° , which is consistent with the presence of the hydroxide and carbonate contamination layer which was observed with XPS. In contrast, the WP-LLZO heat treated at 500°C exhibited a significantly lower contact angle ($\theta = 95^\circ$). We hypothesize that this reduction in contact angle is caused by the removal of hydroxide and carbonate species, resulting in a surface more closely resembling bulk LLZO, which interacts more strongly with Li metal.

To validate the correlation between surface chemistry and wettability, the wetting angle of Li on LLZO, Li_2CO_3 , and LiOH was evaluated using DFT calculations. Li-LLZO, Li- Li_2CO_3 and Li-LiOH interfaces were constructed from the low-energy surfaces of each respective material. Large simulation cells were used, to accommodate geometries that minimize interfacial strain. The interfacial distance and translation state within the interfacial plane were optimized to identify the most energetically-favorable interface structures.

Figure II-452 shows the atomic structure of the low-energy interfaces for Li-LLZO and Li- Li_2CO_3 . The contact angle, θ , for these interfaces was calculated by combining the Young-Dupré equation, $W_{\text{ad}} = \sigma_{\text{Li}}(1 + \cos\theta)$, with DFT calculations of the interfacial work of adhesion, W_{ad} , and the surface energy of Li, $\sigma_{\text{Li}} = 0.45 \text{ J}\cdot\text{m}^{-2}$. Using the Li-LLZO interface as an example, W_{ad} was evaluated as: $W_{\text{ad}} = E_{\text{int}} - E_{\text{Li-slab}} - E_{\text{LLZO-slab}}$. Here E_{int} is the energy of the interface cell and $E_{\text{X-slab}}$ refers to the energy of an isolated Li (X = Li) or LLZO slab (X = LLZO). The calculated values for W_{ad} and θ are shown in Figure II-452 below their respective interfaces. The trend predicted by our calculations – that Li strongly wets LLZO, but not Li_2CO_3 – is consistent with the measurements shown in Figure II-451. More specifically, the wetting angle predicted for the Li- Li_2CO_3 interface, $\theta = 142^\circ$, is in excellent agreement with the measured value (142° , Figure II-451a) indicating a weak interfacial interaction between Li and Li_2CO_3 ($W_{\text{ad}} = 0.10 \text{ J}\cdot\text{m}^{-2}$). In contrast, the calculated W_{ad} for the Li-LLZO interface is nearly seven times larger, $W_{\text{ad}} = 0.67 \text{ J}\cdot\text{m}^{-2}$, resulting in a relatively small wetting angle, $\theta = 62^\circ$. This value is qualitatively consistent with the measured value of 95° reported in Figure II-451d. The smaller value predicted by our calculations is expected, given that approximately 15% of carbonate and/or hydroxide remains on the LLZO surface after heating to 500°C (Figure II-451d). Calculations on the Li-LiOH interface predict a relatively large contact angle of 125° , similar to the non-wetting behavior observed for the Li- Li_2CO_3 system.

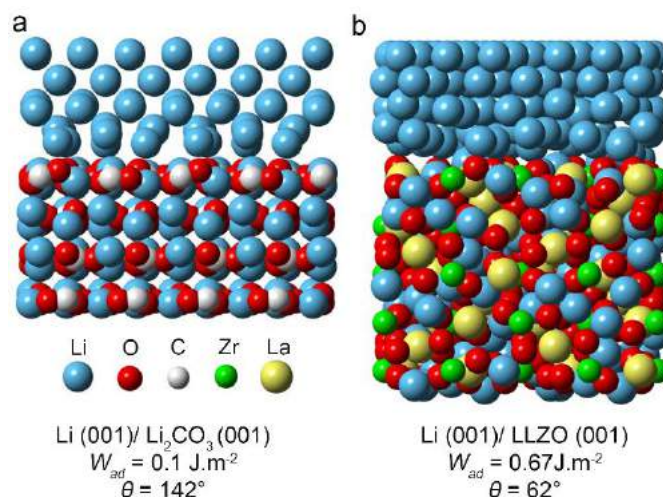


Figure II-452. Calculated work of adhesion (W_{ad}), contact angle (θ), and atomic structure for the a) Li-Li₂CO₃ and b) Li-LLZO interfaces.

Electrochemical impedance spectroscopy (EIS) was performed on Li-LLZO-Li symmetric cells (Figure II-453a) to measure the LLZO bulk (R_{bulk}), grain boundary (R_{gb}), and Li-LLZO interfacial ($R_{Li-LLZO}$) resistances for WP and HT samples between 200 and 500°C. EIS data were modelled using an equivalent circuit shown in Figure II-453b. This approach allows for the direct measurement of the individual contributions to cell resistance and involves the correlation between characteristic frequencies and transport phenomena. Representative EIS spectra for a cell consisting of a WP and HT at 500°C LLZO sample before and after preconditioning at 175°C are shown in Figure II-453c (Preconditioning was used to ensure good contact between metallic Li and LLZO by heating the Li-LLZO-Li cell to 175°C for 12 h).⁶ From Figure II-453c, it is apparent the LLZO total resistance ($R_{bulk} + R_{gb}$) has remained constant (500 $\Omega \cdot \text{cm}^2$) while $R_{Li-LLZO}$ dramatically decreased upon preconditioning at 175°C and cooling. Initially, $R_{Li-LLZO}$ was approximately 400 $\Omega \cdot \text{cm}^2$ which is significantly lower than previous values reported for LLZO after dry polishing in literature.⁶ After preconditioning at 175°C, a further dramatic reduction in $R_{Li-LLZO}$ was observed. The combination of wet polishing, HT, and preconditioning results in an extremely small interfacial resistance of 2 $\Omega \cdot \text{cm}^2$.

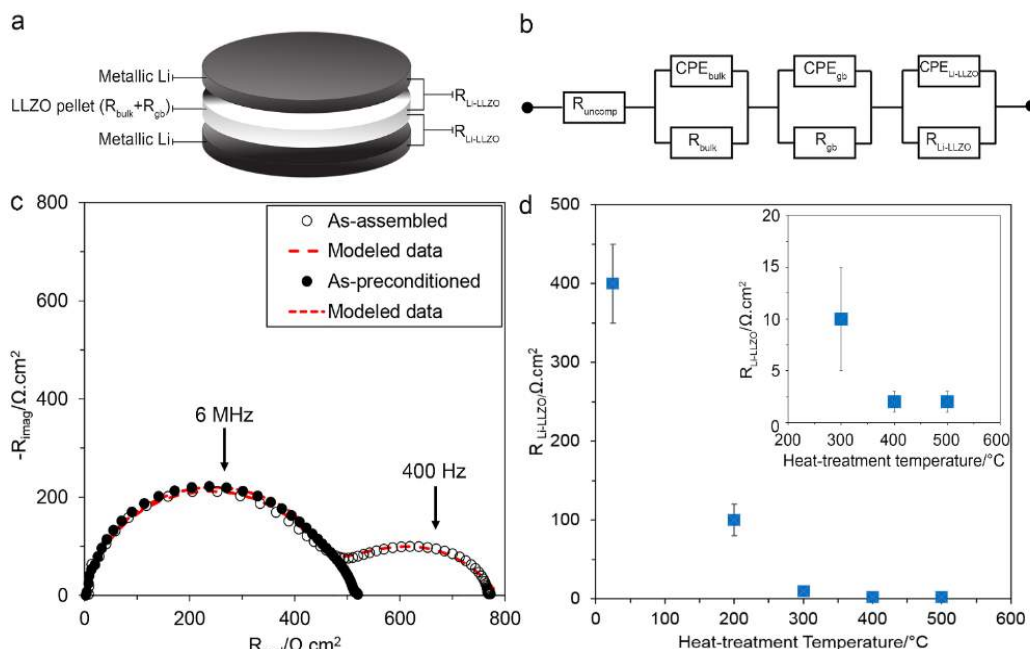


Figure II-453. a) Schematic of the all solid-state Li-LLZO-Li cell, b) the equivalent circuit used for modeling the EIS data c) representative Nyquist plot of the Li-LLZO-Li cell (for LLZO heat-treated at 500°C), as-assembled (\circ) and after preconditioning at 175°C (\bullet). Markers indicate experimental data and dotted lines are simulated lines extrapolated from the equivalent circuit modeling using the circuit shown in b, d) the Li-LLZO interfacial resistance after preconditioning at 175°C versus the heat-treatment temperature. $N=3$ for each HT condition. Error bars represent standard deviations.

Figure II-453d shows $R_{\text{Li-LLZO}}$ after preconditioning for WP LLZO samples with no HT and HT at several temperatures between 200 and 500°C. With increasing HT temperature, $R_{\text{Li-LLZO}}$ decreases from 400 to 2 $\Omega \cdot \text{cm}^2$. Importantly, the low interfacial resistance coincides with the removal of the surface contamination layer. Furthermore, the decrease in interfacial resistance closely follows the trend in surface chemistry with HT temperature observed in XPS measurements, and with the improved wettability of the LLZO surface after HT. Taken together, these observations provide quantitative evidence of the strong coupling between surface chemistry, wettability, and interfacial resistance.

The cycling behavior and critical current density (CCD) of a WP LLZO sample HT to 500°C (WP+HT) were characterized using a combination of DC cycling and EIS analysis (Figure II-454). The CCD is defined as the lowest current density at which cell shorting occurs due to Li metal penetration. After removal of the surface contamination, the CCD was determined to be 0.3 $\text{mA} \cdot \text{cm}^{-2}$ (Figure II-454a). The CCD from the WP+HT sample prepared here is compared in Figure II-454b to other Li-LLZO-Li symmetric cells reported in the literature. The CCD measured in this study is one of the highest values reported in literature for an LLZO SSE. Our data indicates that the CCD and $R_{\text{Li-LLZO}}$ are inversely correlated, suggesting that higher power density can be achieved by controlling interfacial chemistry, and thus $R_{\text{Li-LLZO}}$.

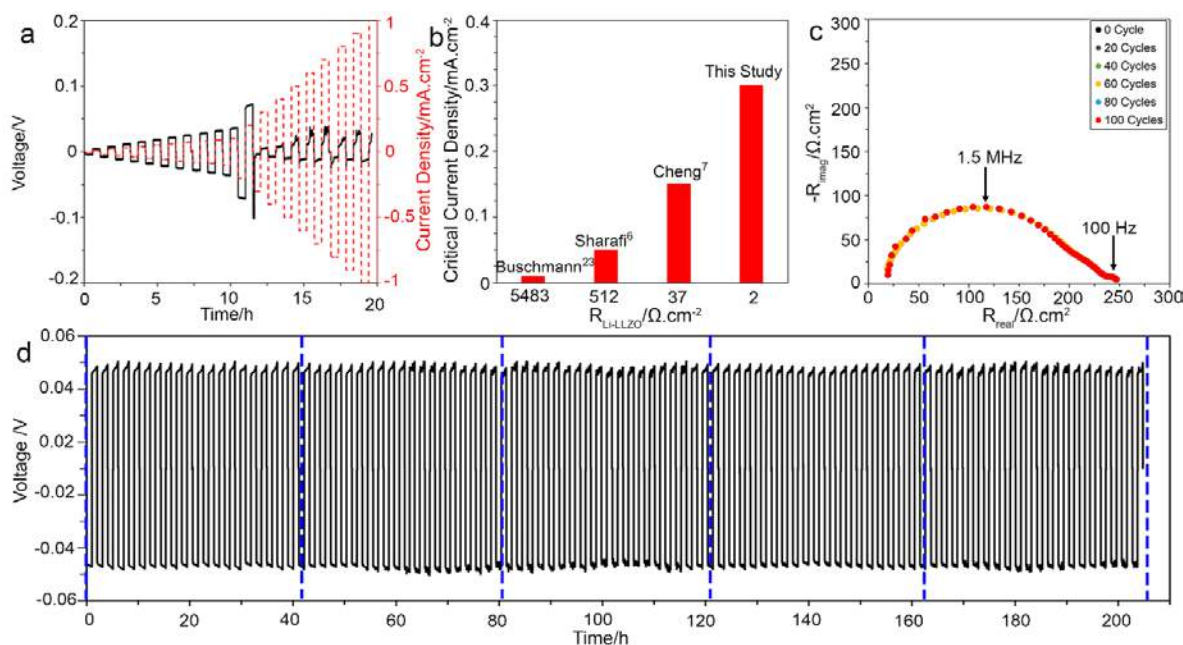


Figure II-454. a) DC cycling of Li-LLZO-Li cells (LLZO HT to 500 °C after WP) at room temperature, stepping the current density from 0.01 to 1 mA.cm⁻², b) the critical current density versus Li-LLZO interfacial resistance comparing the result of this study with other studies available in the literature, c) Nyquist plots of Li-LLZO-Li cell after each 20 cycles for cell cycled 100 time, d) Galvanostatic cycling of Li-LLZO-Li at 0.2 mA.cm⁻² for 100 cycles at 0.4 mAh.cm⁻². The blue dotted line shows the times at which EIS was collected and is shown in c.

To evaluate the stability of the interface after WP+HT upon cycling, a Li-LLZO-Li cell was cycled for one hundred cycles at ± 0.2 mA.cm⁻² at room temperature (Figure II-454d). After every 20 cycles, EIS analysis was conducted to assess changes in R_{bulk} , R_{gb} , and $R_{\text{Li-LLZO}}$. Figure II-454c shows that negligible changes in the EIS spectra were observed, implying excellent stability of the interface and the absence of short-circuiting. Furthermore, the total cell resistance ($R_{\text{bulk}} + R_{\text{gb}} + R_{\text{Li-LLZO}}$) estimated using the DC cell polarization voltage (230 Ω .cm²) (Figure II-454a) agrees well with the total cell resistance measured using EIS (240 Ω .cm²). This confirms that the DC and EIS analyses are in good agreement, and further validates the interpretation of the EIS data to quantitatively decouple resistance values and correlate them to their respective transport phenomena.

The DC and EIS characterization illustrate the importance of achieving low and stable interfacial resistance. First, a low $R_{\text{Li-LLZO}}$ enables a path toward low resistance solid-state cell designs employing metallic Li anodes. Second, reducing $R_{\text{Li-LLZO}}$ increases the CCD. Although 0.3 mA.cm⁻² is one of the highest reported CCD values, it must be further increased to demonstrate relevance to vehicle electrification; the data in Figure II-454b suggest further tuning surface chemistry and reducing $R_{\text{Li-LLZO}}$ may be an approach to achieve higher CCD. Lastly, a clean and discrete Li-LLZO interface is preferred to minimize side reactions and mechanical degradation. In preliminary cycling tests, the interface kinetics appear to be stable when cycling at ± 0.2 mA.cm⁻² at room temperature.

Conclusions

This study has revealed the mechanism by which surface chemistry controls the resistance of the Li-LLZO interface. By exploiting this mechanism, very low interfacial resistances – 2 Ω .cm², comparable to solid-liquid interfaces in Li-ion cells – can be achieved *without the need for coatings*. The removal of LLZO surface contamination was demonstrated to enhance Li wetting of LLZO, which was quantitatively evaluated using molten Li contact angle measurements through sessile drop tests. The interfacial chemistry and wettability measurements agree with atomic-scale DFT calculations of interfacial adhesion and wetting angle. The lower

interfacial resistance made possible by controlling surface chemistry resulted in a doubling of the critical current density. This study clarifies the relationships between interfacial chemistry, lithium wettability, interfacial resistance, and stable cycling. The knowledge gained enables the rational design of electrode/electrolyte interfaces, and has general implications for solid-state transport phenomena.

Key Publications

1. A. Sharafi, S. Yu, M. Naguib, M. Lee, C. Ma, H. Meyer, J. Nanda, M. Chi, D. J. Siegel, and J. Sakamoto, "Impact of Air Exposure and Surface Chemistry on the Li-Li₇La₃Zr₂O₁₂ Interfacial Resistance" *J. Mater. Chem. A*, *J. Mater. Chem. A* 2017.
2. Yu, S. and Siegel, D. Grain Boundary Contributions to Li-ion Transport in the Solid Electrolyte Li₇La₃Zr₂O₁₂ (LLZO), *ChemMater*, Accepted 2017.
3. A. Sharafi, E. Kazyak, A. L. Davis, S. Yu, T. Thompson, D. J. Siegel, N. P. Dasgupta, and J. Sakamoto, "Achieving low resistance all-solid-state Li-LLZO interfaces through surface chemistry control" *ChemMater*, Accepted 2017.
4. E. J. Cheng, A. Sharafi, and J. Sakamoto, "Intergranular Li metal propagation through polycrystalline Li_{6.25}Al_{0.25}La₃Zr₂O₁₂ ceramic electrolyte" *Electrochim. Acta* 223, 85-91 (2017).
5. T. Thompson, S. Yu, L. Williams, R. D. Schmidt, R. Garcia-Mendez, J. Wolfenstine, J. A. Allen, E. Kioupakis, D. J. Siegel, and J. Sakamoto, "Electrochemical Window of the Li-Ion Solid Electrolyte Li₇La₃Zr₂O₁₂" *ACS Energy Letters*, 2(2), 462-468 (2017).
6. Jeff Wolfenstine, Jan L. Allen, Jeff Sakamoto, Donald J. Siegel, and Heeman Choe³ "Mechanical Behavior of Li-Ion Conducting Crystalline Oxide-based Solid Electrolytes: A Brief Review," *IONICS*, Accepted, (2017).
7. Priyamvada Goyal and Charles W. Monroe, "New Foundations of Newman's Theory for Solid Electrolytes: Thermodynamics and Transient Balances," *Journal of The Electrochemical Society*, 164 (11) E3647-E3660 (2017).
8. Smith, S., Thompson, T., Sakamoto, J., Allen, J. L., Baker, D. R., & Wolfenstine, J. (2017). Electrical, mechanical and chemical behavior of Li_{1.2}Zr_{1.9}Sr_{0.1}(PO₄)₃. *Solid State Ionics*, 300, 38-45.
9. Kim, Y., Yoo, A., Schmidt, R., Sharafi, A., Lee, H., Wolfenstine, J., & Sakamoto, J. (2016). Electrochemical Stability of Li_{6.5}La₃Zr_{1.5}M_{0.5}O₁₂ (M= Nb or Ta) against Metallic Lithium. *Frontiers in Energy Research*, 4, 20.
10. C. Ma, Y. Cheng, K. Yin, J. Luo, A. Sharafi, J. Sakamoto, J. Li, K. L. More, L., N. J. Dudney, and M. Chi, "Interfacial Stability of Li Metal–Solid Electrolyte Elucidated via in Situ Electron Microscopy: *Nano Letters*, 16(11), 7030-7036 (2016).
11. S. Yu, R. D. Schmidt, R. Garcia-Mendez, E. Herbert, N. J. Dudney, J. B. Wolfenstine, J. Sakamoto, and D. J. Siegel, "Elastic Properties of the Solid Electrolyte Li₇La₃Zr₂O₁₂ (LLZO)" *Chem. Mater.*, 2016, 28 (1), 197–206.
12. Y. Kim, H. Jo, J. L. Allen, H. Choe, J. Wolfenstine, and J. Sakamoto, "The Effect of Relative Density on the Mechanical Properties of Hot-Pressed Cubic Li₇La₃Zr₂O₁₂" *J. Am. Ceram. Soc.*, 99 [4] 1367–1374 (2016).
13. Sharafi, A., Meyer, H. M., Nanda, J., Wolfenstine, J., & Sakamoto, J. (2016). Characterizing the Li–Li₇La₃Zr₂O₁₂ interface stability and kinetics as a function of temperature and current density. *Journal of Power Sources*, 302, 135-139.

II.H.3 Composite Electrolytes to Stabilize Metallic Lithium Anodes (ORNL)

Nancy Dudney, Principal Investigator

Oak Ridge National Laboratory

P.O. Box 2008, MS6124

Oak Ridge, TN 37831

Phone: 865-576-4874

E-mail: dudneynj@ornl.gov

Tien Duong, Technology Manager

U.S. Department of Energy

Phone: 202-586-7836

E-mail: Tien.Duong@ee.doe.gov

Start Date: October 1, 2015

End Date: September 30, 2018

Total Project Cost: \$1,200,000

DOE share: \$1,200,000

Non-DOE share: \$0

Project Introduction

A stable lithium anode is critical to achieve high energy density with excellent safety, lifetime and cycling efficiency. This study will identify the key design strategies that should be used to prepare composite electrolytes to meet the challenging combination of physical and chemical and manufacturing requirements to protect and stabilize the lithium metal anode for advanced batteries. By utilizing well characterized and controlled component phases, the design rules developed for the composite structures will be generally applicable toward the substitution of alternative and improved solid electrolyte component phases as they become available. Success in this program will enable these specific DOE technical targets: 500-700Wh/kg, 3000-5000 deep discharge cycles, robust operation.

Objectives

- Prepare composites of representative polymer and ceramic electrolyte materials to achieve thin membranes which have the unique combination of electrochemical and mechanical properties required to stabilize the metallic lithium anode while providing for good power performance and long cycle life.
- Understand the lithium ion transport at the interface between polymer and ceramic solid electrolytes which is critical to the effective conductivity of the composite membrane.
- Identify key features of the composite composition, architecture and fabrication that optimize performance and develop practical and scalable fabrication methods.

Approach

This program seeks to develop practical solid electrolytes that will provide stable and long-lived protection for the lithium metal anode. Current electrolytes all have serious challenges when used alone: oxide ceramics are brittle, sulfide ceramics are air sensitive, polymers are too resistive and soft, and many electrolytes react with lithium. Composites provide a clear route to address these issues. This program does not seek discovery of new electrolytes, rather the goal is to study combinations of current well-known electrolytes that can provide critical understanding towards the effects of the interfaces and architecture on the ion transport and stability with the Li anode. The program emphasizes the investigation of polymer-ceramic interfaces formed as bilayers and as simple composite mixtures where the effects of the interface properties can be readily isolated. In general, the ceramic phase is several orders of magnitude more conductive than the polymer electrolyte, and interfaces can contribute an additional source of resistance. Using finite element simulations as a guide, composites with promising compositions and architectures are fabricated and evaluated for lithium transport

properties using AC impedance and DC cycling with lithium in symmetric or half cells. General design rules will be determined that can be widely applied to other combinations of solid electrolytes.

In FY16, we fabricated thin composite membranes using aqueous spray coating technique. This is an environmental friendly, inexpensive and scalable processing route that can achieve high loadings of the ceramic component to ensure a high shear modulus. In the past year, an automatic spray coater (Prism 400, Ultrasonic Systems Inc.) was setup in our lab for battery prototyping. We fabricated a full battery using aqueous spray coating for both the cathode and composite electrolyte incorporating a protected Li metal anode. Battery performance is being evaluated. In the meantime, we established a spray-on polymer-ceramic-polymer (trilayer) method to quantify the interfacial resistance between the polymer and ceramic electrolyte. This method provides a platform for us to explore strategies to minimize interfacial resistance.

Results

Following FY16, we fabricated composite membranes consisting of Ohara powder, polyethylene oxide (PEO, MW=600,000), lithium triflate salt (LiTFS, LiCF_3SO_3) with a 16:1 atomic ratio of PEO ether oxygens per dissolved Li^+ ion ($[\text{EO}]:[\text{Li}^+] = 16:1$) by the aqueous spray coating + hot pressing procedure. The density of the polymer electrolyte and composite electrolyte membranes were measured using a gas pycnometer (Micromeritics AccuPyc II 1340). We also measured the density of the membranes containing a plasticizer, tetraethylene glycol dimethyl ether (TEGDME) with a concentration of $[\text{TEGDME}]:[\text{Li}^+] = 2:1$. From the density data we calculated the volume of each sample. The results are shown in Figure II-455. Two sets of predicted values were overlaid on the experimental data for comparison: the first set (squares) is a simple sum of the volume of each individual component in the membrane, assuming conservation of volume upon mixing; 2. The second set (crosses) is based on complete dissolution into free volume theory, assuming that all of salt and plasticizer molecules occupied the free volume of PEO. Comparing experimental data with the predicted values, we found that when adding LiTFS into PEO, the salt completely dissolved into the free volume of PEO. In the membrane containing PEO, LiTFS and TEGDME, a portion of TEGDME occupied the free volume of PEO. For the composite membrane, experimentally obtained composite volume matched the lowest predicted value. This means that there are no voids in this sample, and all the LiTFS and TEGDME went into the free volume of PEO. This proved that a good dense membrane was fabricated using our spray coating protocol. The conductivity of spray coated composite membranes is an order of magnitude higher than dry milled + melt pressed membranes with the same composition (Figure II-456).

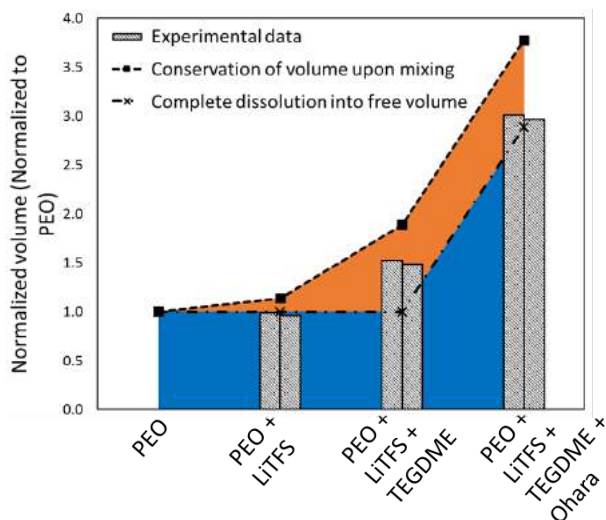


Figure II-455. Normalized volume (to that of PEO) of PEO, polymer electrolyte (with and without TEGDME) and composite electrolyte calculated from experimentally measured density values, compared to the predicted values.

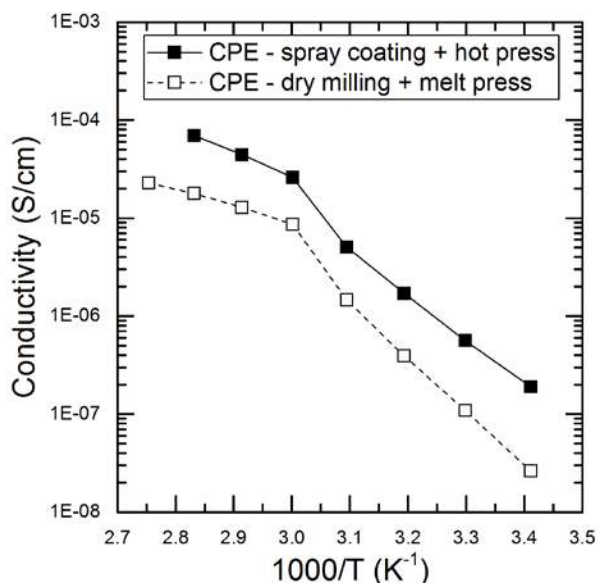


Figure II-456. Arrhenius plot of composite formed by spray coating and hot pressing, compared to that formed by dry milling and melt pressing.

Li/ electrolyte /Li symmetrical cell was constructed to obtain the Li transference number (t_{Li+}) of polymer electrolytes and composite electrolytes. Chrono-amperometric measurement was carried out at an applied potential (ΔV) of 10 mV. The current response was monitored over time until a steady state is reached (Figure II-457). The transference number for TEGDME plasticized polymer electrolyte is found to be 0.69, higher than that of polymer electrolyte without TEGDME, reported to be 0.47 – 0.57. Moreover, a transference number of 0.79 was obtained from TEGDME plasticized composite electrolyte with 50 vol% ceramic. Adding Ohara ceramic further increased the transference number of the electrolytes.

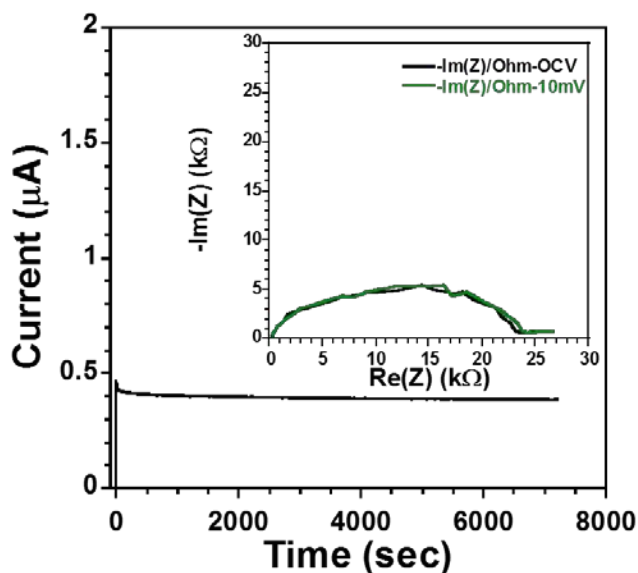


Figure II-457. DC response of a symmetrical cell of configuration Li/Composite Electrolyte/Li for obtaining Li transference number. Inset, EIS response of the symmetrical cell.

In order to optimize the conductivity of spray coated composite membranes, we varied the salt, plasticizer and ceramic content, see Figure II-458. Increasing the salt concentration from $[\text{Li}^+]:[\text{EO}] = 1/16$ to $1/8$ lead to one order of magnitude decrease in the composite conductivity. Varying TEGDME concentration between $[\text{TEGDME}]:[\text{Li}^+] = 2:1$ and $4:1$ did not result in significant change in conductivity. We also examined the effect of ceramic volume fraction on the conductivity of composites (containing TEGDME). Adding 30 vol% of Ohara ceramic led to 1.5 orders of magnitude decrease in conductivity compared to neat polymer electrolyte. Between 30 vol% and 50 vol%, composite conductivity is not a significant function of ceramic volume fraction. With 60 vol% ceramic, the composite conductivity further decreased by 1 order of magnitude. At this high loading, particle packing becomes less dense. The best performing sample contains 50 vol% Ohara ceramic, a salt concentration of $[\text{EO}]:[\text{Li}^+] = 16:1$ and a plasticizer concentration of $[\text{TEGDME}]:[\text{Li}^+] = 2:1$. The room temperature conductivity of this sample is $1 \times 10^{-6} \text{ S/cm}$, lower than the conductivity of both plasticized polymer electrolyte ($2 \times 10^{-5} \text{ S/cm}$) and Ohara ceramic plate ($1 \times 10^{-4} \text{ S/cm}$). At this point, the resistive polymer-ceramic interface became the key challenge of our approach.

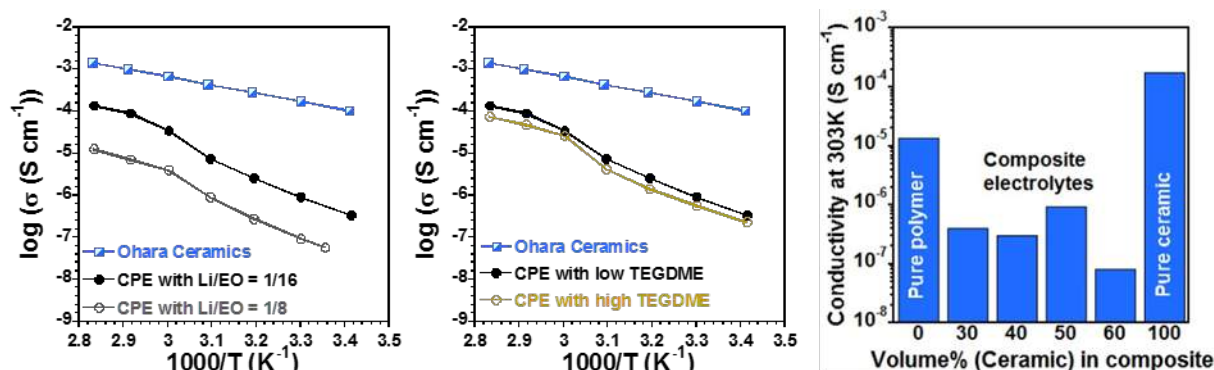


Figure II-458. Left, Arrhenius plot of TEGDME-plasticized composite electrolyte with different salt concentration; Middle, Arrhenius plot of TEGDME-plasticized composite electrolyte with different TEGDME content; Right, Room temperature conductivity of the TEGDME-plasticized composite as a function of the volume fraction of the Ohara ceramic.

Polymer-ceramic-polymer electrolyte (trilayer) cell was constructed to study the interfacial resistance between the polymer and ceramic electrolyte. Sintered ceramic plate from Ohara Corporation was sandwiched between two thin layers of polymer electrolyte of the same thickness, obtained by spray coating. The EIS results of single layer ceramic plate, single layer polymer electrolyte and trilayer are shown in Figure II-459a-c. The resistance of the trilayer is at least one order of magnitude larger than the two single layers combined. An SEM image of the cross-section of the trilayer is shown in the inset of Figure II-459c. Uniform coating and smooth interface are observed. We calculated the interfacial resistance from the data of the single layers and the trilayer cells, shown in Figure II-459d. At 30 °C, the interfacial resistance is 10000 Ohm. As an effort to decrease the interfacial resistance, we tried plasticized polymer electrolyte and the ceramic, using the same protocol. The plasticizer, TEGDME, which enhances the ionic conductivity of the polymer electrolyte does not facilitate ion transport across the polymer-ceramic interface (Figure II-459d).

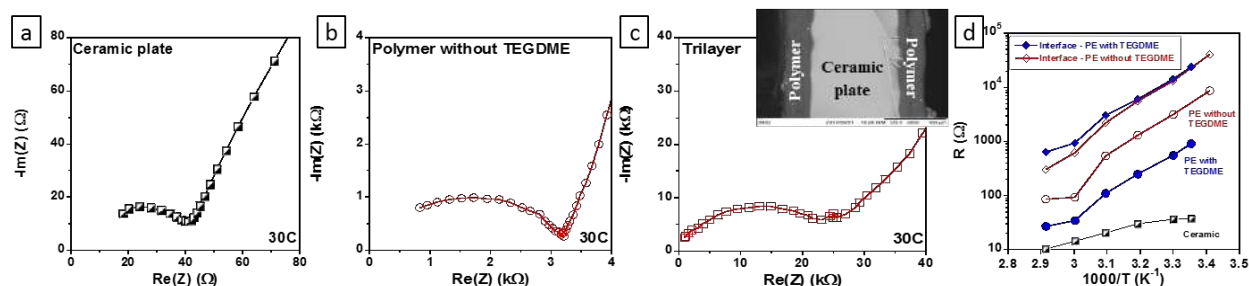


Figure II-459. Results for trilayer cell polymer /ceramic/polymer electrolyte. a-c, EIS responses of ceramic plate, polymer electrolytes and trilayer cells. All EIS response are measured at 30C. Inset of c, SEM of trilayer cell. d, Arrhenius plot of interfacial resistance calculated from the trilayer cell data.

We thus carried out investigations of other possible candidates for plasticizer attempting to improve the interface between the Ohara ceramic and polymer electrolyte. We tried diethyleneglycol dibutylether (DEGDBE) and hexamethylphosphoramide (HMPA), both are good candidates due to their low vapor pressure. Results for the conductivities of the composite coatings with 50 vol% Ohara powder and the new candidate plasticizer molecules are shown in Figure II-460. Composite containing DEGDBE did not show any improvement in conductivity compared to unplasticized composite. With the same molar concentration, HMPA and TEGDME showed similar effect on composite conductivity. These results indicated that similar to TEGDME, DEGDBE and HMPA did not effectively decrease the interfacial resistance between Ohara ceramic and the polymer electrolyte.

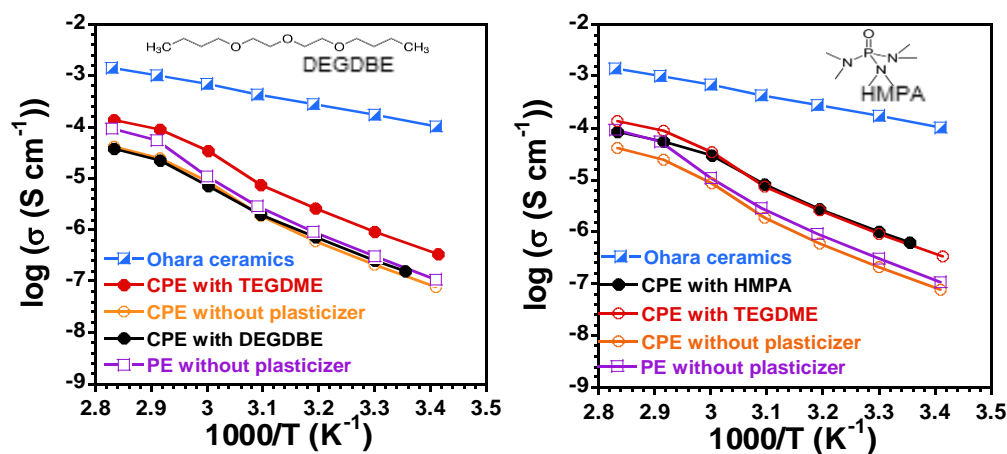


Figure II-460. Comparison of spray coated composite containing DEGDBE (left) and HMPA (right) as plasticizer with results obtained using TEGDME as plasticizer. Conductivity of composite and polymer that does not contain plasticizers is also presented.

To continue to address the interfacial resistance between Ohara powder and the polymer electrolyte, we studied the effects of acid and base treatment of the Ohara powders. Previous studies have shown moderate change in the ion conductivity of PEO-LiX-alumina composites by using alumina with acidic, neutral and basic surfaces. We treated Ohara powder with HNO_3 and NaOH aqueous solutions with 4 pH values, 1.4, 3.3, 10.6 and 12.7. XRD revealed change in the ceramic's crystalline structure after treatment in pH = 12.7 solution; IR spectra did not show significant differences in the treated and untreated Ohara powders. Results in Figure II-461 (left) show that treating Ohara with mild acid (pH = 3.3) and base (pH = 10.6) led to 2-3 fold reduction of conductivity, whereas the composite containing Ohara powder treated with strong base (pH = 12.7) showed conductivity similar to composite containing untreated Ohara powder. These composites were

formed by spray coating of an aqueous slurry and they did not contain a plasticizer. We repeated the experiments for composites formed by dry milling and melt pressing (Figure II-461, right). All of the dry milled samples presented lower conductivity than the spray coated samples, as discussed in Figure II-456. But the conclusion is consistent with spray coated samples – acid/base treatment did not facilitate the interfacial ion transport across the polymer-ceramic boundary.

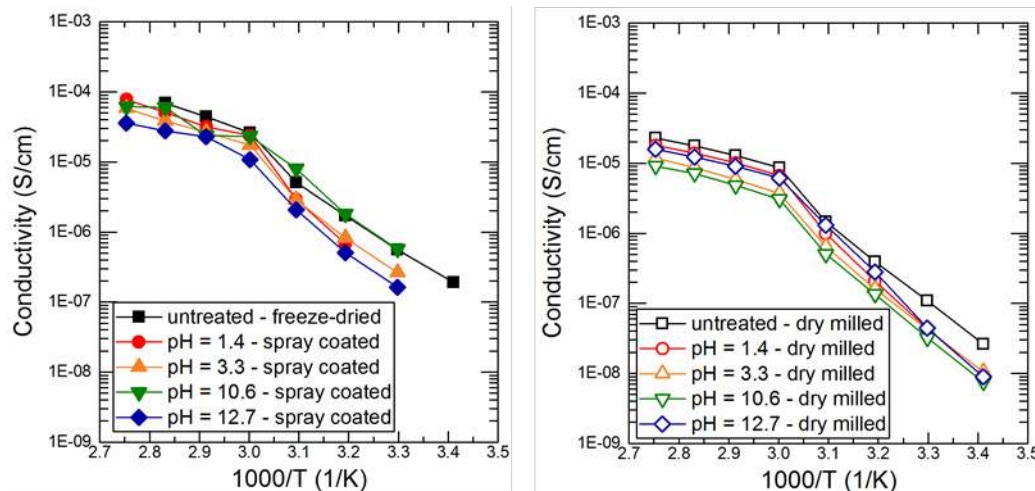


Figure II-461. Arrhenius plot of composite containing acid/base treated Ohara powders, compared to that of untreated composite. Left, spray coated samples; Right, dry milled samples.

Lastly, an automatic spray coater was set up for battery prototyping. We fabricated a full battery using aqueous spray coating for both the cathode and composite electrolyte incorporating a protected Li metal anode. Battery performance is under evaluation. In FY18, efforts will be focused on decreasing the interfacial resistance and optimizing cycling performance.

Conclusions

1. We confirmed that the densities of membranes formed by aqueous spray coating + hot pressing matched the highest predicted values. The conductivity of spray coated composite membranes is an order of magnitude higher than dry milled + melt pressed membranes with the same composition.
2. A transference number of 0.79 of TEGDME-plasticized composite electrolyte was determined, compared to that of polymer electrolyte, 0.47 – 0.57.
3. A series of salt, plasticizer and ceramic content were examined to optimize the conductivity of spray coated composite membranes. The best performing sample contains 50 vol% Ohara ceramic, a salt concentration of $[EO]:[Li^+] = 16:1$ and a plasticizer concentration of $[TEGDME]:[Li^+] = 2:1$. The room temperature conductivity of this sample is 1×10^{-6} S/cm, lower than the conductivity of both plasticized polymer electrolyte (2×10^{-5} S/cm) and Ohara ceramic plate (1×10^{-4} S/cm). The resistive polymer-ceramic interface became the key challenge of our approach.
4. Polymer-ceramic-polymer (trilayer) cell was constructed to study the interfacial resistance between the polymer and ceramic electrolyte. A very large interfacial resistance for ion transport (10000 Ohms at room temperature) was identified. In order to decrease the interfacial resistance, we tried two other plasticizers (DEGDBE and HMPA) and acid/base surface treatment of Ohara ceramic. The results showed limited success. Nevertheless, this method provides a platform for us to explore more strategies to minimize interfacial resistance.

5. In FY18, efforts will be focused on decreasing the interfacial resistance and optimizing cycling performance. We will reevaluate the effect of dimethyl carbonate (DMC) on the composite conductivity and interfacial resistance. Further, we will move beyond model materials like Ohara and PEO, to include single ion conducting polymers and polymer gels.

Key Publications

1. Amaresh Samuthira Pandian, Frank Delnick and Nancy Dudney, “Composite Polymer-Ceramic Electrolyte for High Energy Lithium Secondary Batteries”, presented at PRiME meeting of Electrochemical Society, 2016 Hawaii.
2. Nancy Dudney, Amaresh Samuthira Pandian and Frank Delnick, “Composite Electrolyte to Stabilize Metallic Lithium Anodes”, presented at DOE Vehicle Technologies Program, Annual Merit Review and Peer Evaluation Meeting, June 2017.
3. “Composite Polymer Ceramic Electrolyte for High Energy Lithium Secondary Batteries,” In preparation.

II.H.4 Overcoming Interfacial Impedance in Solid-State Batteries (U of MD)

Eric Wachsman, Principal Investigator

University of Maryland
1206 Engineering Laboratory Building
University of Maryland
College Park, MD 20742
Phone: 301-405-8193
E-mail: ewach@umd.edu

Liangbing Hu, Co-Principal Investigator

University of Maryland
1208 Engineering Laboratory Building
University of Maryland
College Park, MD 20742
Phone: 301-405-9303
E-mail: binghu@umd.edu

Yifei Mo, Co-Principal Investigator

University of Maryland
1137 Engineering Laboratory Building
University of Maryland
College Park, MD 20742
Phone: 301-405-7613
E-mail: yfmo@umd.edu

Tien Duong, Technology Manager

U.S. Department of Energy
Phone: 202-586-7836
E-mail: Tien.Duong@ee.doe.gov

Start Date: October 1, 2014

End Date: September 30, 2017

Total Project Cost: \$1,212,877

DOE share: \$1,212,877

Non-DOE share: \$0

Project Introduction

Solid state garnet-electrolyte lithium ion batteries have tremendous potential due to their inherent safety, high voltage stability, and reasonably high conductivity. However, the interfacial impedance between solid state electrolytes and electrodes is currently too high. This work focuses on reducing the interfacial impedance, by making controlled structures on the garnet electrolyte surface, and introducing conductive and conformal interfacial layers between the garnet and the electrodes. These results, informed by computational modeling, address the primary issue and significantly advance solid-state Li-battery technology.

Objectives

Develop a multifaceted and integrated (experimental and computational) approach to solve the key issue in solid-state Li batteries (SSLiBs), interfacial impedance, with a focus on garnet-based solid-state electrolytes (SSEs), the knowledge of which can be applied to other SSE chemistries. The focus is to develop methods to decrease the impedance across interfaces with the solid electrolyte, and ultimately demonstrate a high power/energy density battery employing the best of these methods.

Approach

Innovative Approach: The objectives outlined above will be accomplished by optimizing the garnet surface structure and electrode material, and investigating high conductivity conformal interfacial layers.

1. Effect of interfacial structure on impedance

While we and others have made tremendous advances in understanding interfacial resistance in solid oxide fuel cells (SOFCs), to date no one has applied these techniques to SSLiBs. Therefore, we used SOFC techniques to develop a fundamental understanding of interfacial impedance in terms of intrinsic charge transfer rates, ionic and electronic transport, and effect of interfacial structure.

Electrochemical impedance spectroscopy (EIS) of solid electrolyte and electrode or interfacial layer pellets were performed to identify the mechanistic frequency dependence of EIS response for each material as well as blocking electrode and DC measurements to separate out ionic vs. electronic conductivity for each material. Then bilayer electrolyte and electrode/interfacial layer pellets with smooth and controlled interfaces were fabricated and tested with EIS.

This allowed for determination of the specific interfacial impedance, which could then be resolved as an additional EIS frequency response. This interfacial impedance was used to calculate the charge transfer reaction rate across the electrolyte/electrode and electrolyte/interfacial layer interfaces. Bilayered pellets with tailored nano/micro-rod interfaces have been fabricated (by templated deposition and additive manufacturing) with different rod length to diameter aspect ratios. The EIS data from these cells is deconvoluted and compared with known ionic and electronic transport rates, and charge transfer rates, to create fundamental models of interfacial impedance as a function of 3-dimensional interfacial structure.

2. Investigate interfacial modifications and cell performance

We are investigating four types of materials as interfacial layers in SSLiBs.

For **Type 1**, we used nonflammable organic electrolytes such as perfluoropolyethers (PFPE)-based electrolytes. It has been confirmed that such organic electrolytes cannot catch fire and are intrinsically safe. Although, PFPE-based electrolytes have very low ionic conductivity ($\sim 10^{-5}$ S/cm) and cannot meet the power density requirement in the FOA by itself, PFPE-based organic electrolyte can greatly improve the interfaces across electrolyte grain boundaries, or electrolyte/electrode interface for enhancing the battery performance.

For **Type 2**, we also used a polymer electrolyte or gel electrolyte, which is bis(trifluoromethane)sulfonimide lithium salt (LiTFSI) in poly(vinylidene fluoride-co-hexafluoropropylene) (PVDF-HFP). Although the polymer or gel electrolyte has a much lower ionic conductivity, its thickness is small as an interface layer and thus its contribution in overall impedance was expected to be negligible.

For **Type 3**, we are investigating thin inorganic layers formed by atomic layer deposition (ALD) and other thin film deposition techniques to form a nano-thin conducting phase between the garnet and the electrode.

For **Type 4**, we are using a soft conformable materials such as β -Li₃PS₄ (LPS) or liquids to bridge the gap between the garnet and electrode material.

For each approach, we fabricated half cells to investigate interfacial impedance and their changes during cycling. SSLiB interfaces are typically planar resulting in high impedance due to low specific surface area, and attempts to make 3D high surface area interfaces can also result in high impedance due to poor contact (e.g., pores) at the electrode-electrolyte interface that hinder ion transport or degrade due to expansion/contraction with voltage cycling. We have investigated the fundamentals of solid-solid interfacial impedances in FY 2015 and investigated interfacial modification (layers between SSE and electrode) to see if we can extend these structure-property relationships to higher performance in FY 2016. In FY 2017 we applied these interfacial modifications to develop solid-state batteries. The objective of FY 2017 was accomplished by developing full cells based on the interfacial impedance reducing techniques and the structurally optimized garnet SSEs. We

developed high energy density batteries based on multi-layer garnet, Li metal anode, and two different types of cathodes: $\text{Li}(\text{Ni}_x\text{Mn}_y\text{Co}_{1-x-y})\text{O}_2$ (NMC) and sulfur. For each type of battery chemistry, the battery morphologies, electrochemical stabilities, and cycling performances were evaluated.

Throughout this work, we collaborated with Dr. Kang Xu at the US Army Research Lab with preparation of liquid electrolytes. SSEs and electrode materials were synthesized in University of Maryland Energy Research Center, and characterized in the Nanocenter and FabLab at University of Maryland. Fabrication of the SSLiBs was accomplished using the comprehensive state-of-art multilayer ceramic fabrication facilities. The facilities include tape casting, screen printing, and furnaces for fabrication, as well as extensive electrochemical testing capabilities.

Results

1. Cathode interface resistance

1.1 Characterization of electrolyte/cathode interface impedance

We tested the impedance of LLCZN solid state electrolyte, and its interface impedance with LFMO electrodes. The LLCZN ($\text{Li}_{6.8}\text{La}_{2.95}\text{Ca}_{0.05}\text{Zr}_{1.75}\text{Nb}_{0.25}\text{O}_{12}$) garnet was synthesized by conventional solid state reactions. The starting materials, $\text{Li}(\text{OH})$, $\text{La}(\text{OH})_3$, $\text{Ca}(\text{OH})_2$, ZrO_2 , and Nb_2O_5 were mixed by planetary ball-milling, and then calcined at 700°C for 48 h. The calcined LLCZN powder was mixed with additives (both Al_2O_3 and Li_3BO_3 , only Al_2O_3 or only Li_3BO_3) by planetary ball-milling. The mixture was die-pressed at 10 MPa into a pellet and sintered in air. EIS of LLCZN electrolyte and LFMO cathode was tested with Solartron 1260 impedance analyzer at room temperature using gold paste current collectors. EIS plots were collected at 50 mV voltage signal over a frequency range of 10 Hz -20 MHz.

Figure II-462a is the EIS curves of thick and thin LLCZN electrolyte samples. A semicircle and Warburg-type impedance appeared at high and low frequency regions, respectively. The high-frequency semicircle is the sum of bulk and grain boundary responses. The low-frequency tail corresponds to the capacitive behavior of gold blocking electrode. The total lithium-ion conductivity of LLCZN electrolyte is estimated from the intercepts from the semicircle at low frequency side. The thin pellet shows a slightly lower total conductivity than the thick pellet sample.

Figure II-462b is the EIS curves of thick and thin LFMO cathode samples at initial state (0%SOC). The Nyquist plot contains one depressed semicircle in the high frequency and another semicircle in the medium frequency ascribed to the resistance of Li^+ diffusion through the SEI layer and charge transfer reaction, respectively. The EIS plot indicates similar conductivity exhibited by both the thick and thin pellets of LFMO.

Knowing the frequency response of both LLCZN electrolyte and LFMO cathode we then analyzed the system consisting of electrolyte, cathode and their interface. Finely polished electrolyte and cathode with gold electrode on outer side were tightly pressed together. The electrolyte/cathode system was then characterized by EIS. Figure II-462c shows the Nyquist plots of LLCZN electrolyte/LFMO cathode system. Both thick and thin pellet samples were examined to identify the interfacial effect in the system. The impedance arc is the total resistance of LLCZN electrolyte, LFMO cathode and their interface. The arc in the medium-low frequency range is the dominant interfacial resistance between LLCZN electrolyte and LFMO cathode. The high frequency response in the magnified plot is the sum of LLCZN electrolyte resistance and LFMO cathode resistance. This process was repeated with other cathode materials beyond LFMO.

The garnet/cathode interface impedance was lowered by making structured garnet surfaces. Sintered dense garnet discs were sanded to $150\text{ }\mu\text{m}$ and polished. To make the column structures, polymer mesh was glued on disc surface as a template, after that a garnet slurry was drop coated to fill the open area. The coated sample was dried in oven and sintered at 800°C for 2h. Figure II-463a shows the structured garnet surface. The white shining areas are the deposited column structures.

Symmetric cathode/electrolyte/cathode cells were made by screen printing thick cathode slurry on the garnet discs. LFM O cathode was sintered at 500°C for 1h. Silver paste was used as current collector. Thickness of the cathode was about 20 μ m. EIS plots were collected at 50 mV voltage signal in a frequency range of 10 Hz -10 MHz at room temperature. Figure II-463b is the EIS response of cathode coated as-polished and structured garnet discs which exhibits lower interfacial resistance, compared to that with smooth surface due to the larger interfacial cathode/electrolyte contact area provided by the surface column structure.

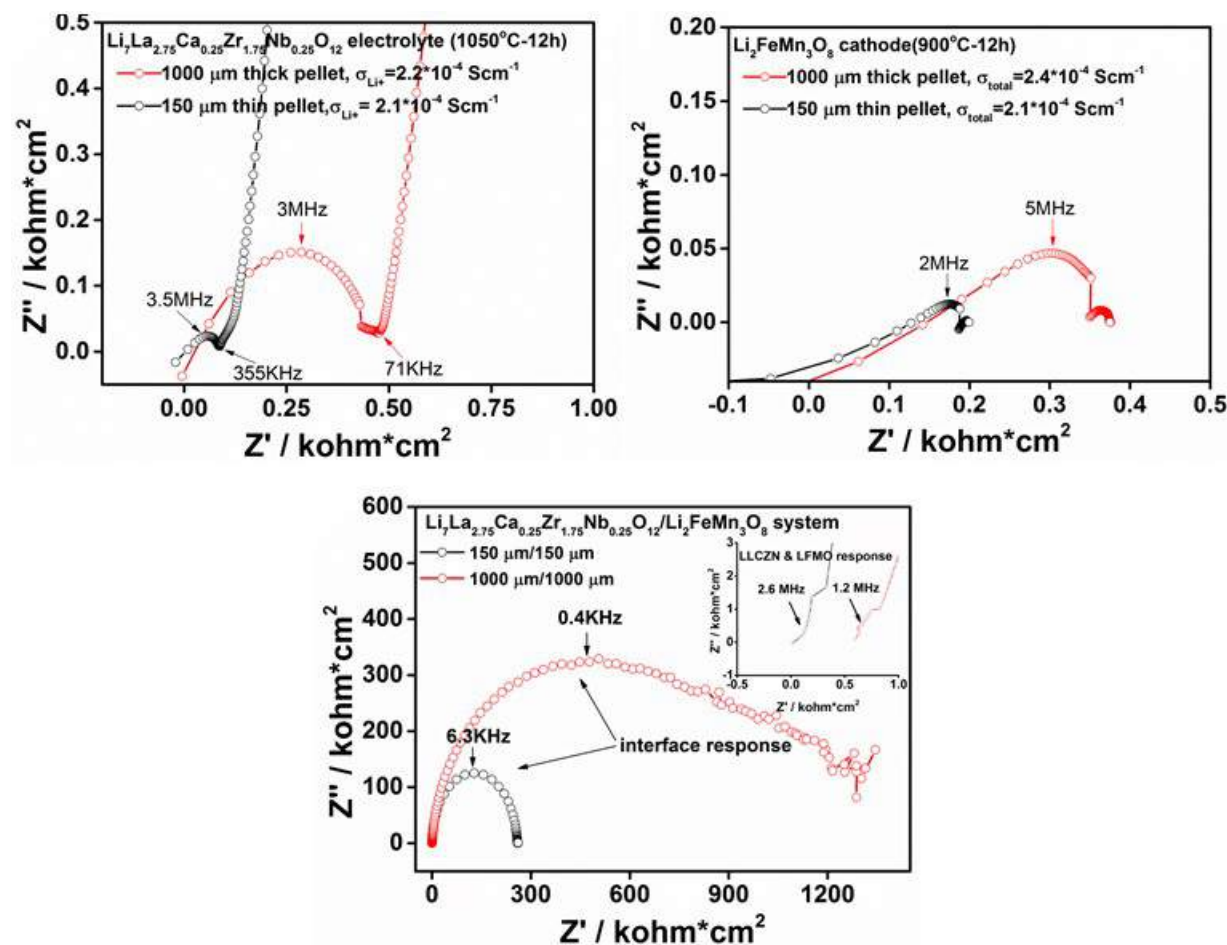


Figure II-462. (a) EIS of thick and thin LLCZN pellets, (b) thick and thin LFM O pellets, and (c) thick and thin LLCZN/LFM O pellets.

1.2. Synthesis and characterization of nonflammable PFPE-based interface (Type 1)

PFPE-DMC was prepared from Fluorolink D10 and triethylamine in 1,1,1,3,3-pentafluorobutane at 0°C under nitrogen atmosphere, followed by dropping a solution of methyl chloroformate in 1,1,1,3,3-pentafluorobutane. After the mixture was stirred at 25°C for 12 h, the PFPE-DMC product was obtained by filtering and washing with water and brine, followed by evaporation under reduced atmosphere. The PFPE-DMC electrolyte was then produced by dissolving Lithium bis(Trifluoromethanesulfonyl)Imide into PFPE-DMC. The synthesis method of PFPE-DMC is shown in Figure II-464a.

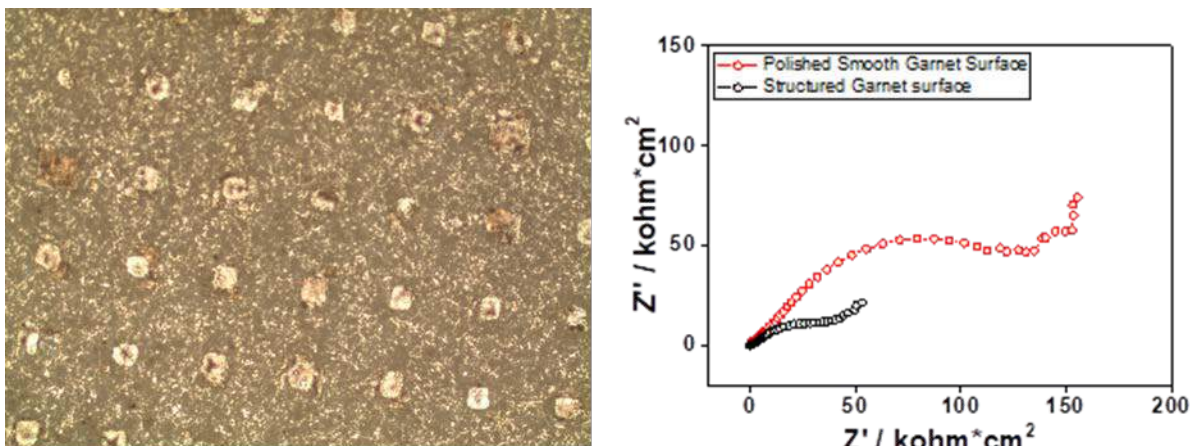


Figure II-463. (a) Photograph of structured garnet surface, bright white spots are garnet columns. (b) EIS of polished smooth garnet surface and structured garnet surface.

A Li/PFPE/Ti structure in a CR2025 coin cell was used to test cyclic voltammetry (CV) of the PFPE/LiTFSI electrolyte. The area of the cell is 1.98 cm^2 (radius=5/16 inch), and the area of Ti cathode is 0.712 cm^2 (radius=5/32 inch). The voltage range was $-0.3 \sim 4.2 \text{ V}$, and the voltage scan speed was 1 mV/s .

The CV results are shown in Figure II-464b. The reaction current density is less than 0.002 mA/cm^2 in $0.3 \sim 4.2 \text{ V}$ region, which is very small. And after the first few cycles, the CV curve becomes stable. The two facts show that the PFPE electrolyte is electrochemically stable between $0 \sim 4 \text{ V}$. Also, for the PFPE electrolyte, no obvious peaks appear in the voltage region of $-0.3 \sim 4.2 \text{ V}$, which means that the Li stripping occurs at a higher voltage than 4.2 V , and the Li plating occurs at a lower voltage than -0.3 V . The electrochemical stability of PFPE/LiTFSI in the voltage range of $0 \sim 4.2 \text{ V}$ ensures that this electrolyte is stable in the reactions of LLCZN garnet electrolyte lithium ion batteries, and can be used as the interfacial layer between garnet and cathode.

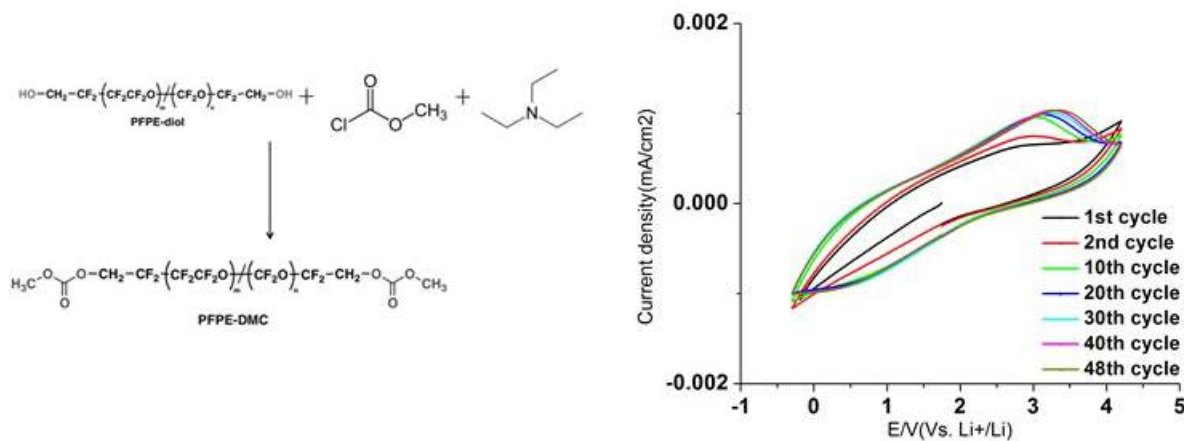


Figure II-464 (a) Synthesis procedure of PFPE-DMC. (b) Cyclic voltammetry study of LiTFSI-PFPE electrolyte.

1.3. Synthesis and characterization of gel-based interface (Type 2)

A PVDF-HFP-based gel polymer was prepared (Figure II-465) from 0.25 g PVDF-HFP dissolved into a mixture of 4.75 g acetone and 0.25 g DI water (95:5, m/m) under continuous stirring. The solution was cast onto an Al foil and the solvent evaporated at ambient temperature. After drying under vacuum at 100°C a homogeneous free standing membrane was obtained. The as-prepared porous membrane was immersed into 1 M LiTFSI in a mixture of 1:1 volume ratio of tetraethylene glycol dimethyl ether and n-methyl-(n-butyl)

pyrrolidinium bis(trifluoromethanesulfonyl)imide (Py14TFSI) at room temperature for 30 mins in an argon-filled glovebox.

CV testing cell was set up by sandwiching the gel electrolyte membrane between lithium and titanium disks and sealing the configuration in CR2032 coin cells. The CV (Figure II-465b) at a scan rate of 1 mV/s suggests a stable electrochemical window up to 4.2 V. The sharp peak at -0.2 V corresponds to the Li plating, while the peak around 0.1 V is due to the Li stripping.

Figure II-466a is the electrochemical impedance spectroscopy (EIS) plot of a cathode/garnet/cathode symmetric cell without any interfacial layer modification. The total resistance of cathode/garnet/cathode symmetric cell without gel interfacial layer is $\sim 106 \text{ Ohm-cm}^2$ due to the poor contact between garnet and LiFePO_4 cathode material, the difficulty of charge transfer through the interface between two solid materials, the non-conductive binder, and the rough surface of the garnet pellet.

Figure II-466b is the EIS plot of cathode/garnet/cathode symmetric cell with gel interface. The impedance curve has three components. In the high frequency region ($f > 9 \text{ kHz}$) is an incomplete semi-circle, corresponding to the bulk and grain boundary impedance of the garnet electrolyte. In the middle frequency region ($7 \text{ Hz} < f < 9 \text{ kHz}$) is a combination of two semi-circles corresponding to interfacial charge transfer impedance between garnet and cathode, including impedance on the gel/garnet and cathode/gel interfaces, as the impedance of the gel layer itself is very small. In the low frequency region ($f < 7 \text{ Hz}$) is a straight line, corresponding to diffusion impedance of the cathode.

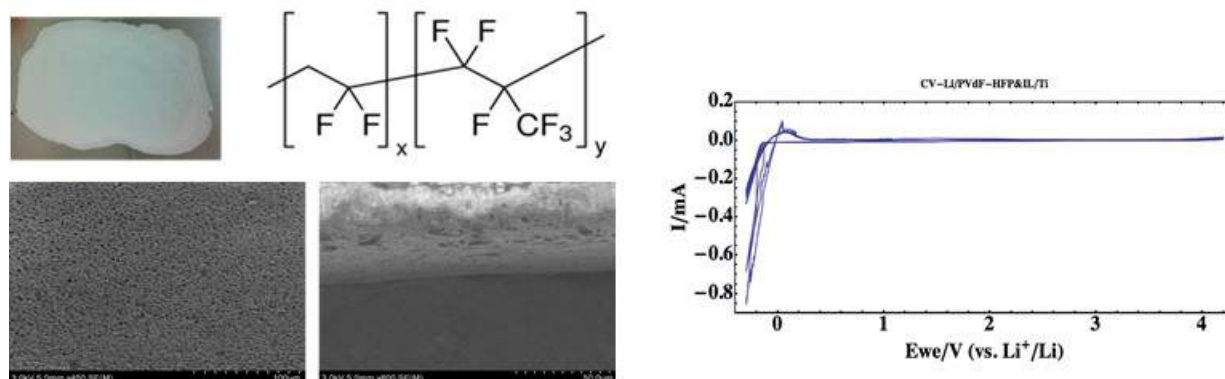


Figure II-465. (a) Photograph, (b) structure, (c) top and (d) side SEM images of PVDF-HFP gel membrane. (e) Cyclic voltammetry study of $\text{Li}|\text{PVDF-HFP}+\text{IL}|\text{Ti}$. (f) EIS of LLCZN/LFMO interface without (black) and with (red) PVDF-HFP gel electrolyte interface.

The interfacial resistance is obtained by subtracting the garnet resistance obtained separately by EIS of garnet samples from the total symmetric cell resistance, then dividing by two as there are two interfaces, e.g.,:

- Thickness of garnet pellet is $500 \mu\text{m}$, and garnet conductivity is $2.1 \times 10^{-4} \text{ S/cm}$ (Figure II-466c). Therefore, area specific resistance (ASR) of garnet pellet is 239 Ohm-cm^2 .
- The total symmetric cell resistance (Figure II-466b) is 600 Ohm-cm^2 . Therefore, the ASR of one interface is $(600-239)/2 = 180 \text{ Ohm-cm}^2$, which is ~ 4 orders of magnitude less than the same symmetric cell without the interfacial layers.

To further reduce the garnet/cathode interfacial impedance the procedure was improved by making a gel/cathode composite, instead of using separate gel layers, thus reducing the gel thickness and improving the contact between gel and cathode. Figure II-466d shows the structure of symmetric cell using $\text{LiFePO}_4/\text{gel}$ cathode on both sides of garnet, and Figure II-466e shows the impedance of this structure. The corresponding interfacial ASR is now reduced to only 67 Ohm-cm^2 for one interface (using same approach described above).

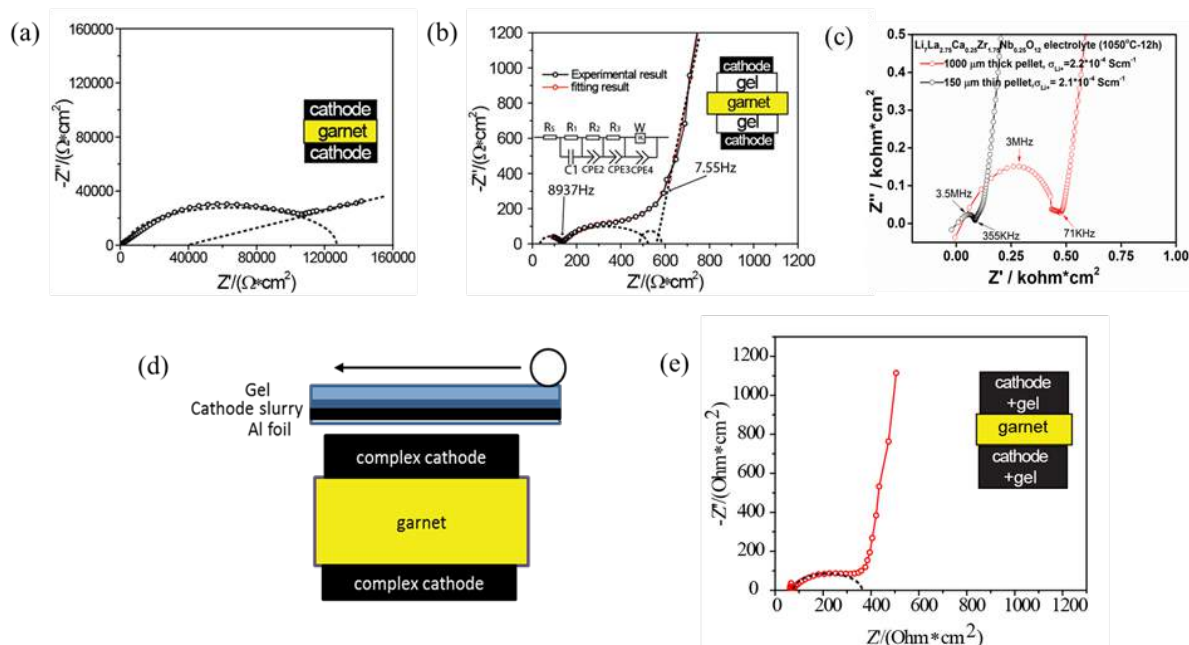


Figure II-466. (a) EIS plot of cathode/garnet/cathode symmetric cell without gel electrolyte. (b) EIS of cathode/gel/garnet/gel/cathode symmetric cell and the equivalent circuit. (c) EIS of garnet itself. (d) Schematic of making garnet cell with mixed cathode. (e) EIS of symmetric cell with mixed cathode and gel.

1.4 Synthesis and characterization of aqueous interface (Type 4)

To further reduce the cathode/garnet interfacial resistance we evaluated an aqueous solution interface (e.g., Type 4). We anticipated a lower cathode/garnet interfacial resistance with the aqueous interface compared with the gel interface as the aqueous solution has higher conductivity and fluidity than the organic electrolyte used for the gel interfaces. Figure II-467a shows a schematic of the symmetric cell with the aqueous cathode/garnet interface. The cathode material (LiFePO_4 , Carbon black and PVDF) was coated on a carbon cloth. Then these electrodes were immersed into a saturated aqueous LiCl solution to wet them and then the two electrodes and a garnet pellet were pressed together.

As shown in Figure II-467b, the EIS semi-circle of the cell yields a resistance of $253 \text{ Ohm} \cdot \text{cm}^2$, which after correcting for garnet ASR and dividing by 2 for the dual interfaces results in a single cathode/garnet interfacial resistance of only $7.5 \text{ Ohm} \cdot \text{cm}^2$, 5 orders of magnitude lower than the non interfacial layer cell, and achieving the Q4FY16 and budget period 2 Go/NoGo milestones.

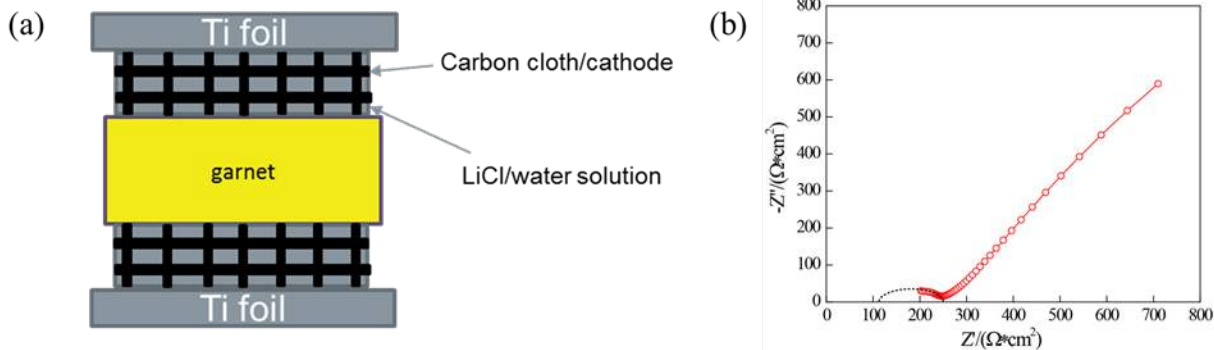


Figure II-467. (a) Schematic of a cathode/garnet/cathode symmetric cell with aqueous interface. (b) Impedance of this cell with aqueous interface.

1.5 Characterization of structured garnet interface

A 3D garnet surface structure can dramatically increase the effective surface area relative to the planar areal surface area. 3D structured garnet line patterns were printed on surface polished garnet pellets and sintered to form structured ionic conductive paths with varying line spacing (Figure II-468). Cathode slurries (LiFePO_4 , CNT, and gel) were coated on both flat and structured garnet surfaces. EIS of the symmetrical cells was obtained at room temperature.

The depressed arcs, which can be assigned to Li^+ diffusion and charge transfer steps, became much smaller after effective extension of surface area. The 3D printed lines ($40\text{ }\mu\text{m}$ height and $70\text{ }\mu\text{m}$ width) increased the effective sample surface areas from 36 mm^2 for polished pellet to 39.9 , 42.3 and 48 mm^2 with increasing line density, resulting in 22%, 35% and 52% reduction of interfacial resistance (from the intercept of real axis high frequency arc (Figure II-468a)) proportional to the increase in effective surface area (Figure II-468b). Therefore, as expected the 3D printed structures reduced the cathode-electrolyte interfacial resistance linearly with increasing effective surface area.

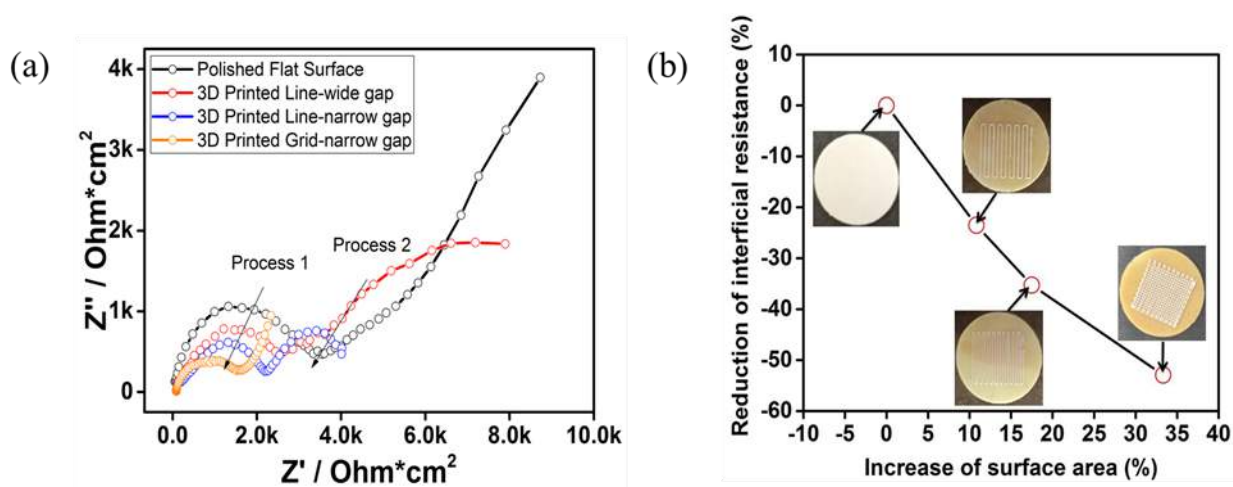


Figure II-468. Comparison of cathode/electrolyte interfacial impedance on flat and 3D-structured garnet pellets. (a) EIS plot of garnet without 3D printing and with different 3D printings. (b) Reduction of interfacial resistance with increase in surface area.

2. Anode interface impedance

2.1 Characterization of gel electrolyte interface

Figure II-469a shows that the total resistance of a Li/garnet/Li symmetric cell (formed by melting Li metal on the garnet surfaces) without an interfacial layer is about 3000 Ohm-cm². Figure II-469b shows the EIS plot of Li/gel/garnet/gel/Li plot has four components. In the high frequency region is an incomplete semi-circle, from the garnet impedance. In the middle frequency region are two semi-circles, due to interfacial charge transfer impedance between garnet and Li metal, which mainly comes from impedance on the gel/garnet and Li/gel interfaces, as the impedance of the gel layer itself is very small. In the low frequency region is a tail, corresponding to diffusion impedance of the interface of gel/stainless steel outside of the lithium metal. Correcting for garnet impedance, the ASR with the gel interlayer is reduced to 200 Ohm-cm² for one interface; however, this is done without melting the Li metal as was done for the other cell.

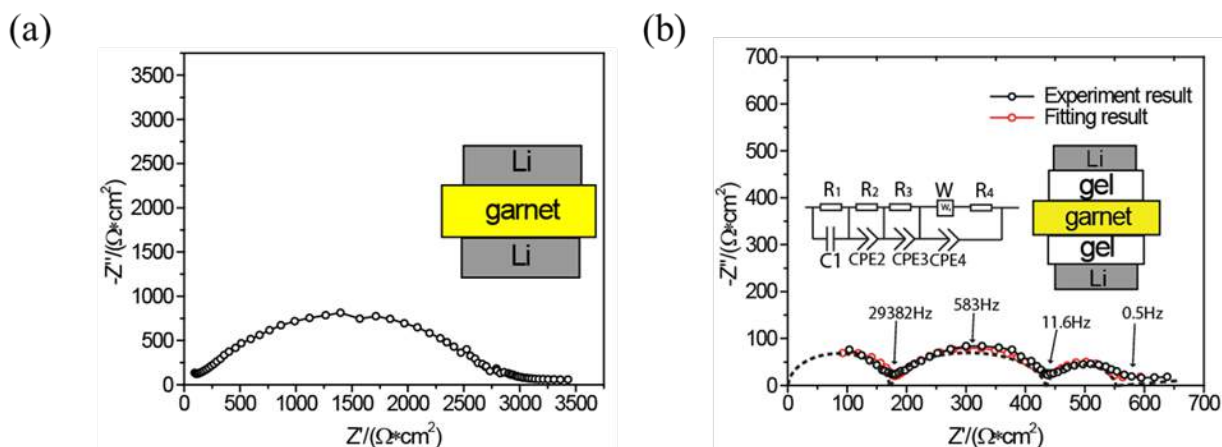


Figure II-469. (a) EIS plot of Li/garnet/Li symmetric cell. (b) EIS plot and equivalent circuit of Li/gel/garnet/gel/Li symmetric cell.

2.2 Characterization of Si interface

LLZ and Si-coated LLZ was sandwiched by two Li metal electrodes to assemble symmetric cells (Figure II-470a, and Figure II-470b). Prior to the electrochemical measurements, all the cells were heated at ~200 μ C for twenty minutes in a glovebox since thermal treatment promotes superior contact between Li and LLZ. Due to the high reactivity of molten Li, lithiated Si will be formed in situ between the Li metal and the Si-coated LLZ. The Nyquist plots of symmetric cells in Figure II-470c exhibit two distinct semi-circles: one at high frequency and another at low frequency. The Li/LLZ/Li symmetric cell delivers a large resistance of 2064 Ohm-cm², where the interfacial resistance between Li and LLZ was calculated to be 925 Ohm-cm².

The first semi-circle at relatively high frequency was used to analyze the interfacial resistance between the Li metal electrode and the LLZ solid electrolyte with/without Si coating. As shown in Figure II-470d, the overall resistance of the LLZ (bulk and grain boundary) measured using Au electrodes is 215 Ohm-cm². As shown in Figure II-470e, the first semi-circle of the Li/LLZ/Li cell yields a resistance of 2064 Ohm-cm², which can be divided into two parts: one is the resistance of the LLZ (bulk and grain boundary) and the other is the Li metal-LLZ interfacial resistance. Thus, the overall Li metal-LLZ interfacial resistance is 1849 Ohm-cm². Since two Li metal-LLZ interfaces are present in the Li/LLZ/Li symmetric cells, the single Li metal-LLZ interfacial resistance is approximately 925 Ohm-cm². On the other hand, the Si-coated LLZ cell displays a much smaller resistance of 469 Ohm-cm² in the first semi-circle. By subtracting the resistance of the LLZ (215 Ohm-cm²) and dividing by two, the Li metal/Si-coated LLZ interfacial resistance can be calculated: 127 Ohm-cm², which is about 7.3 times lower than bare LLZ.

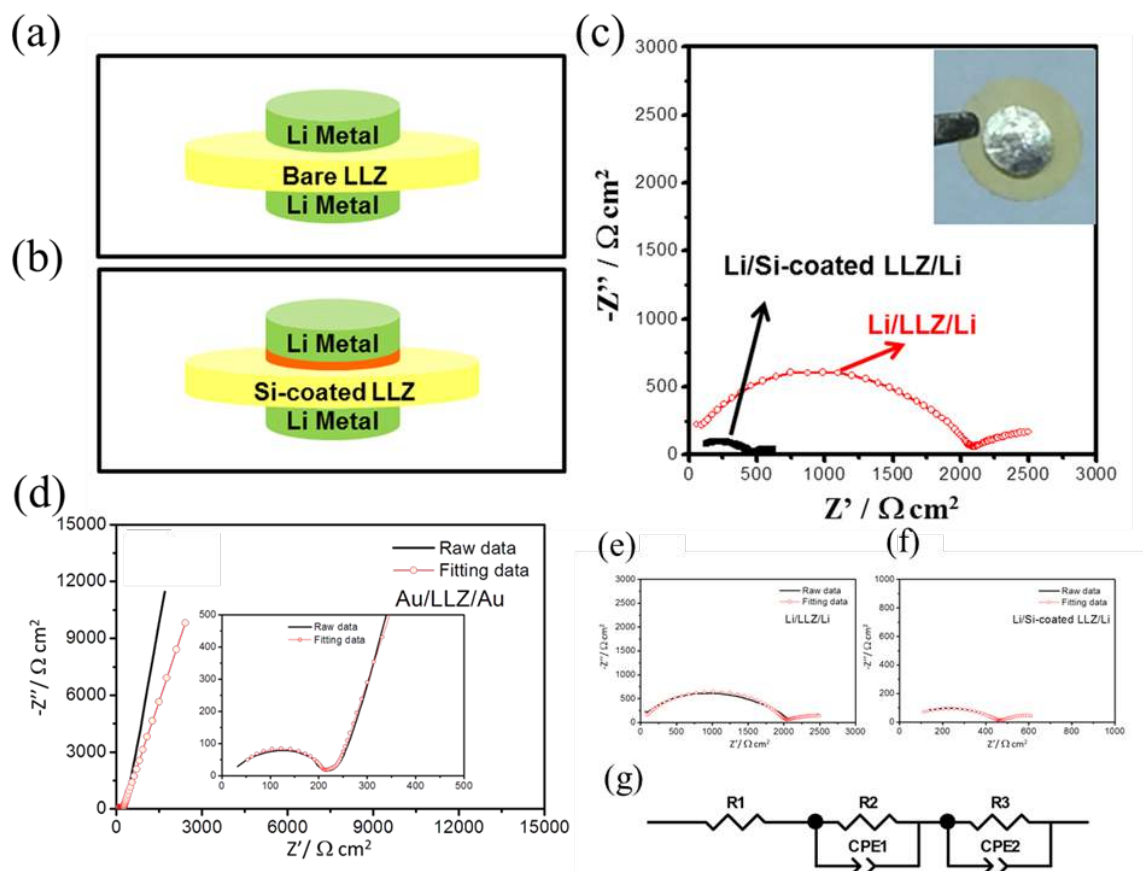


Figure II-470. Schematic illustration showing the structure of symmetric cells with (a) LLZ or (b) Si-coated LLZ SSEs. (c) Electrochemical impedance spectroscopy (EIS) measurements of symmetric cells where the interfacial resistance of the Si-coated garnet cell significantly decreased. Inset of (c) is a digital image of a Li/Si-coated LLZ/Li symmetric cell. (d) Nyquist plots of the Au/LLZ/Au symmetric blocking electrode system at room temperature. The solid black line denotes the experimental data while the red line with hollow spheres represents the fitting data using the equivalent circuit modeling. (e-g) Nyquist plots of (e) Li/LLZ/Li and (f) Li/Si-coated LLZ/Li symmetric cells. (g) The equivalent circuit model used in this study.

2.3 Characterization of Al interface

Two symmetric cells, Li | Garnet SSE | Li and Li | Al-Garnet SSE-Al | Li, were prepared and tested directly in an argon-filled glovebox. The two cells showed large differences in total resistance, which depend on both the garnet's total resistance and the interface charge transfer resistance, as shown in the Nyquist plots (Figure II-471a and Figure II-471b). The Li | Garnet SSE | Li cell had a total resistance of $\sim 2000 \text{ Ohm}\cdot\text{cm}^2$. However, the Li | Al-Garnet SSE-Al | Li cell exhibited a resistance of $\sim 300 \text{ Ohm}\cdot\text{cm}^2$, which is almost one order of magnitude smaller than the uncoated SSE. The small partial semicircle at high frequency can be assigned to the total resistance of the garnet material. The large semicircle at medium frequency and low frequency correspond to the charge transfer resistance, which is the combination of the solid-state electrolyte resistance as well as the Li interfaces within the symmetric cells. The decreased size of the semicircle indicates that the interfacial resistance was significantly reduced using the Al coating. The total garnet resistance was $\sim 150 \text{ Ohm}\cdot\text{cm}^2$ and remained unchanged during the Li melting process. By subtracting the garnet ASR, the Li | Garnet SSE | Li cell charge transfer resistance was $\sim 1900 \text{ Ohm}\cdot\text{cm}^2$ at 20°C . For the Li | Al-Garnet SSE-Al | Li cell, the charge transfer resistance was decreased to $\sim 150 \text{ Ohm}\cdot\text{cm}^2$. Note that the interfacial resistance corresponds to two symmetric interfaces. Therefore, the interfacial resistance is $\sim 950 \text{ Ohm}\cdot\text{cm}^2$ and $\sim 75 \text{ Ohm}\cdot\text{cm}^2$ for Li | Garnet SSE and Li | Al-Garnet SSE-Al, respectively.

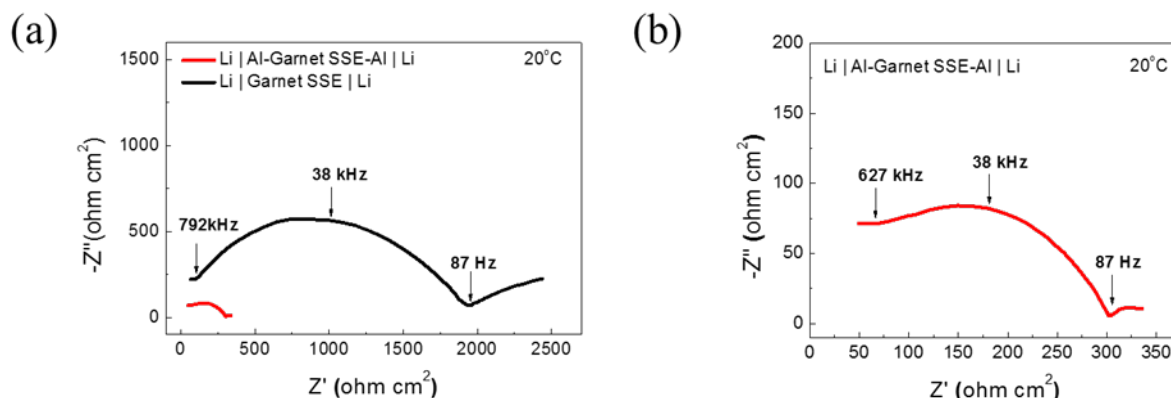


Figure II-471. Nyquist plots of Li | Garnet SSE | Li (a) and Li | Al-Garnet SSE-Al | Li (b) in the frequency of 1 MHz to 100 mHz at 20°C.

2.4 Characterization of ALD Al_2O_3 interface

To make Li/garnet/Li symmetric cell with ALD Al_2O_3 interface, a ~ 5-6 nm thick ALD- Al_2O_3 coating was applied to the garnet surface. Then a piece of Li metal foil was pressed on the garnet pellets and heated at 250°C for 1 hour under a small pressure. A control sample was made using bare LLCZN pellets in the same way.

Figure II-472a shows the schematic of the interface between garnet and Li metal. The SEM images in Figure II-472b clearly demonstrated that the enhancement of interfacial contact by applying ALD Al_2O_3 ultrathin layer on garnet interface. Inset are photo images to show the surface wetting of garnet and the ALD treated garnet.

To quantify the effect of ALD on the improvement of garnet/Li interface, symmetric Li/garnet/Li cells were prepared and evaluated by EIS (Table II-21 and Figure II-472). As shown in Figure II-472c, two distinct arcs were seen in each sample. The bulk garnet ASRs, obtained from the high frequency intercept, are 26 and 28 $\text{Ohm}\cdot\text{cm}^2$ for cells with and without ALD coating, respectively. The first arc represents most likely the overlap of the grain boundary and interface impedances, which were 176 $\text{Ohm}\cdot\text{cm}^2$ and 3500 $\text{Ohm}\cdot\text{cm}^2$ for cells with and without ALD coating, respectively. Interfacial ASR was calculated by subtracting the garnet impedance measured with Au electrodes (~108 $\text{Ohm}\cdot\text{cm}^2$) and dividing this result by two before normalizing to the electrode surface area. It can be seen that the ALD treatment decreased the interfacial ASR by EIS from 1750 $\text{Ohm}\cdot\text{cm}^2$ to 34 $\text{Ohm}\cdot\text{cm}^2$. However, DC cycling (Figure II-472e) further reduced the interfacial impedance. The total ASR from DC cycling is calculated as 110 $\text{Ohm}\cdot\text{cm}^2$, which after subtracting 108 $\text{Ohm}\cdot\text{cm}^2$ for the garnet contribution leaves 1 $\text{Ohm}\cdot\text{cm}^2$ for each Li-garnet interface.

Table II-21: Electrochemical impedance with fitting data for Li/LLCZN/Li cells with and without ALD coating on both sides of the garnet SSEs.

LLCZN SSE	Bulk ASR ($\Omega\cdot\text{cm}^2$)	Grain Boundary ASR ($\Omega\cdot\text{cm}^2$)	Grain Boundary Capacitance (F)	Interfacial ASR ($\Omega\cdot\text{cm}^2$)	Interfacial Capacitance (F)
No ALD	28	4500	2.09×10^{-9}	490	9.9×10^{-4}
ALD	26	150	3.09×10^{-9}	16	2.8×10^{-5}

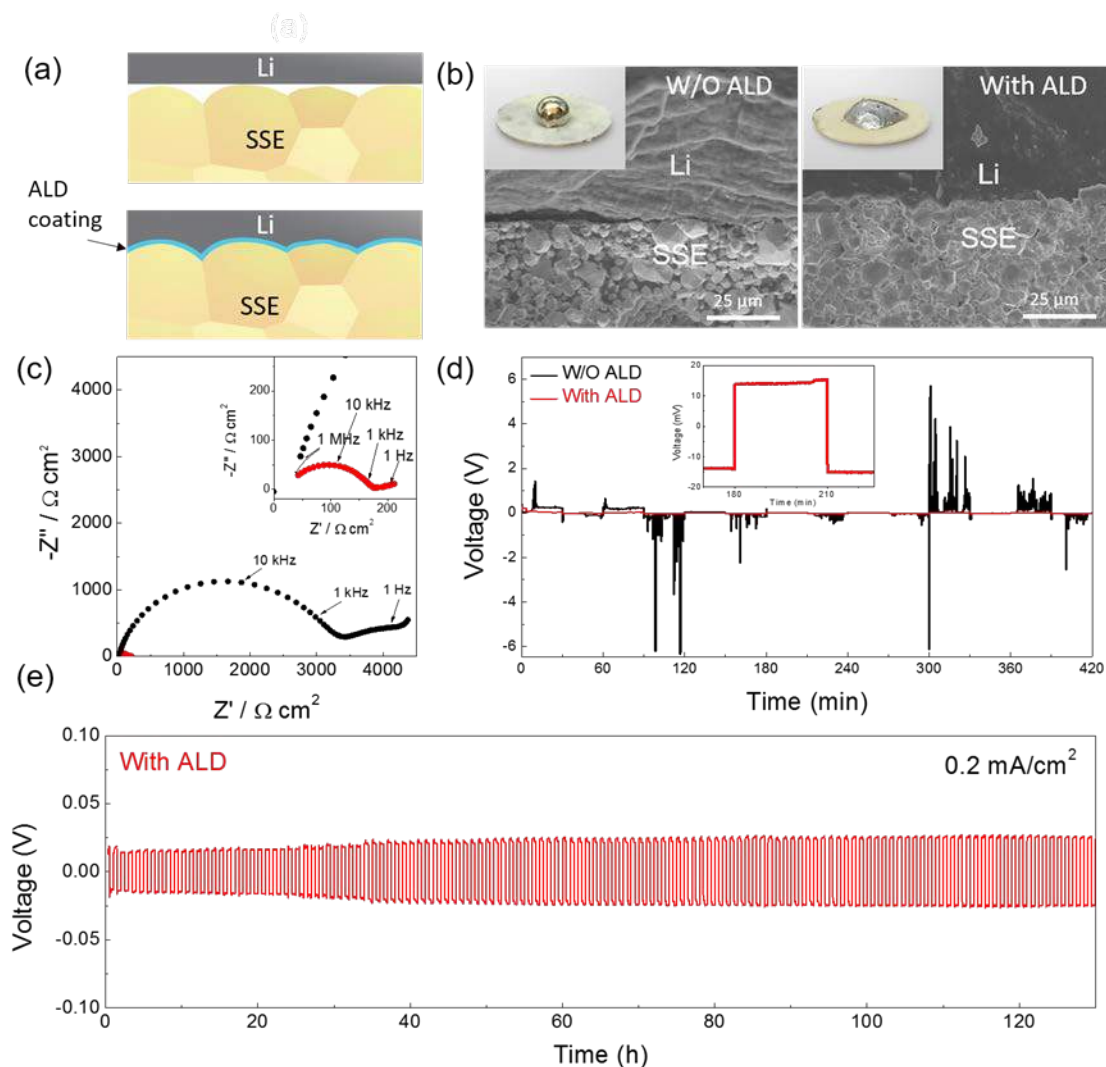


Figure II-472. Characterization of garnet solid state electrolyte/Li metal interface. (a) Schematic of the wetting behavior of garnet surface with molten Li. (b) SEM images of the garnet solid state electrolyte/Li metal interface. Without ALD Al_2O_3 coating, garnet has a poor interfacial contact with Li metal. Inset are photo images of contacts between melted Li-metal and garnet surface. (c) Comparison of EIS profiles of the symmetric Li non-blocking garnet cells. Inset shows the enlarged impedance curve of the ALD treated garnet cell. (d) Comparison of Li tripping/plating behavior of the symmetric garnet SSE/Li cells. Inset is the one cycle of stripping/plating for the ALD treated garnet cell, exhibiting a low overall impedance and stable interfacial property. (e) Voltage profile of the ALD treated garnet symmetric cell at a current density of 0.2 mA/cm^2 .

3. Modeling of interfacial coating layers on garnet-electrode interfaces

First principles modeling of garnet solid electrolyte materials were performed on both tetragonal and cubic LLZ phases. The ordering of Li was determined using computational methods, and the ground state ordering of Li was determined. The Li grand canonical phase diagram of the Li-La-Zr-O system based on first principles computation methods and electrochemical stability of garnet against Li metal was determined (Figure II-473).

In addition, first principle models were constructed to evaluate the structure and energetics of the electrolyte-electrode interfaces between garnet and Li metal. We found that Li metal has a very weak interfacial binding with Li_2CO_3 , which are found on the garnet surfaces, and Li metal binds strongly with oxide materials that may form on the garnet surfaces. The weak interface binding may lead to forming interfacial gaps and

intervals, thus a low contact area and a high interfacial resistance. Stronger interface binding would lead to enhanced interfacial contacts with larger contact area and good interfacial conductance.

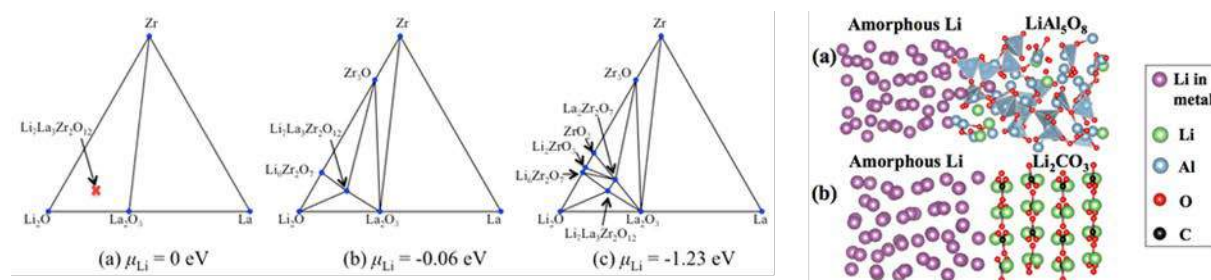


Figure II-473. (a) Li grand canonical phase diagram of Li-La-Zr-O system. (b) Models for the interfaces between Li metal and garnet surface materials.

We developed a computational model for garnet-electrode interfaces (Figure II-474). The comprehensive interface model is based on a large variety of inputs provided by a range of first principles computation and actual experimental parameters to model the interface properties. The interface model has been developed and demonstrated for garnet materials with electrode materials, such as $LiCoO_2$ and LFMFO. The interphase layers between the garnet and the electrode were determined using grand potential phase diagram at the applied voltage of the battery at the input for the model. The formation of the interphase was found to be thermodynamically favorable for the interfaces of garnet with anode and cathode. In addition, the properties of the materials comprising the interphase, such as defect and migration energy, were also evaluated in first principles calculations. The effects of the space-charge layer were incorporated as a part of interface model. Using all these predicted input parameters, the conductivity and interfacial resistance of the interfacial layer were determined. The model is now ready to be applied to any composition of garnet solid electrolyte in contact with any electrode materials. The inputs for the interface model are generated by the first principles computation and experimental parameters. The model was able to demonstrate that a poor interfacial layer causes high interfacial resistance in all-solid-state batteries.

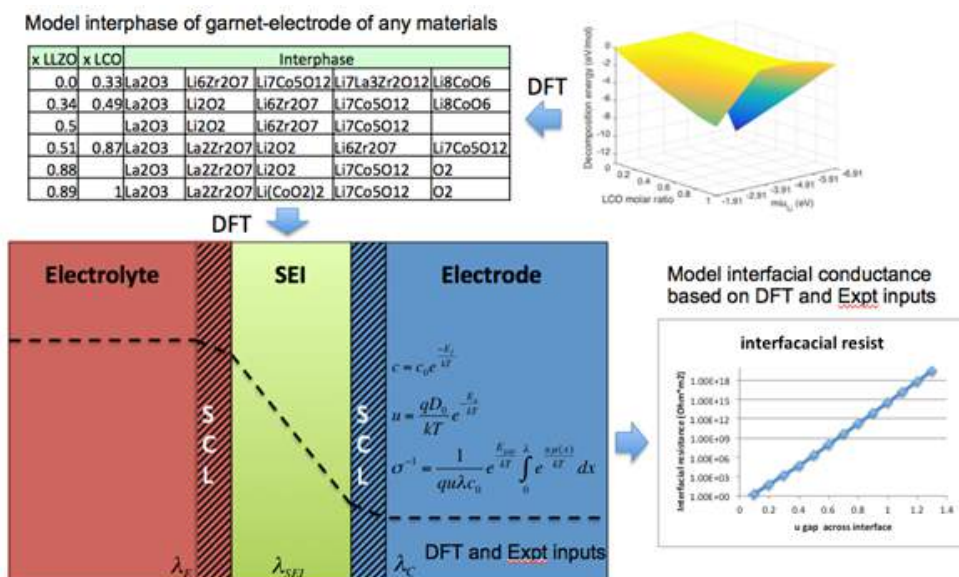


Figure II-474. Model for garnet-electrode interfaces, which take inputs from first principles calculations and experimental condition parameters.

We applied first principles calculations to investigate the interface stability between garnet and formed Li-Al alloys (Figure II-475a). We considered the interface as a pseudo-binary of Li-Al alloy and garnet, then constructed the related phase diagram to identify possible thermodynamically favorable reactions. The compositional phase diagrams were constructed, and the mutual reaction energy of the pseudo-binary calculated using same approach defined in our previous work (Figure II-475b). We found that three kinds of Li-Al alloy showed mutual reactions with garnet because of the slightly thermodynamic “welding” at their interface. Since the calculated reaction enthalpy is only around $-60 \sim -40$ meV/atom, the small reaction energy indicates that the interfacial reactions are likely to be limited and the formed interface could be relatively thermodynamic stable. Therefore, the interface between Li-Al alloy and garnet may exhibit good chemical stability, which might facilitate Li ion transport through.

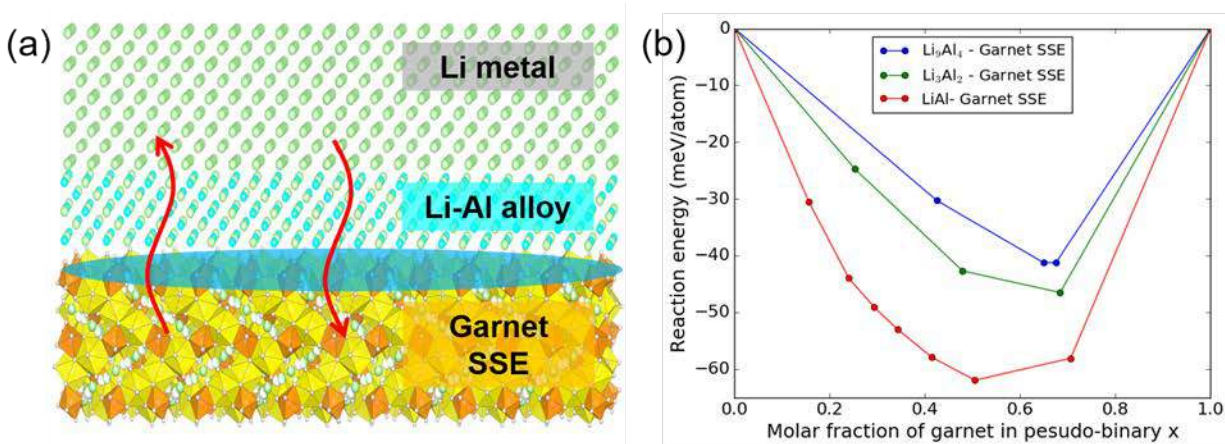


Figure II-475. Calculated mutual reaction energy, ΔE_D , of garnet and Li-Al alloy interfaces.

We apply the computational scheme to investigate interfacial chemical compatibility of these two interfaces with the coating layer with the SE and LCO, respectively. The previously demonstrated coating layer materials, such as $\text{Li}_4\text{Ti}_5\text{O}_{12}$, LiTaO_3 , LiNbO_3 , Li_2SiO_3 , and Li_3PO_4 , have excellent chemical stability with the LCO and $\text{L}_{0.5}\text{CO}$ with zero or negligible decomposition energy $\Delta E_{D,\text{min},\text{mutual}}$ (Table II-22). In addition, all coating layer materials show relatively better stability with the sulfide SE comparing to the original sulfide SE-LCO interfaces, which have the interfacial reaction energy $\Delta E_{D,\text{min},\text{mutual}}$ of ~ -500 meV/atom. As a result, the interface with the coating layer has significantly improved stability and suppresses the formation of thick interphase layer. In addition to stabilizing the interface, the coating layer of only a few nanometers is significantly thinner than the decomposition interphase layer of ~ 10 to 100 nm. The reduced thickness of the coating layer may significantly reduce the high interfacial resistance caused by the thick decomposition interphase layer.

In addition, we also computationally investigated other compounds (listed in Figure II-476 and Table II-22) based on the same cations, such as Ti, Nb, Si, Ta, and P, as potential coating layer materials. All these lithium metal oxide materials have a wide electrochemical window (Figure II-476a). The compounds with higher Li content generally show lower reduction potential, and the compounds with lower Li content or higher O content show higher oxidation potential. Most of these compounds have excellent chemical stability against LCO and $\text{L}_{0.5}\text{CO}$ cathode materials with zero or small $\Delta E_{D,\text{min},\text{mutual}}$ (Table II-22). All these coating layer materials significantly improve the stability of sulfide SE-LCO interfaces. The chemical stability between LLZO-coating layer interface varies significantly with the compositions of the coating layer materials. The other Li-rich coating layers, such as Li_4TiO_4 , Li_2TiO_3 , Li_3SiO_6 , Li_4SiO_4 , Li_5TaO_5 , and Li_3TaO_4 may work better with LLZO than those previously demonstrated for sulfide SEs, such as $\text{Li}_4\text{Ti}_5\text{O}_{12}$, LiTaO_3 , and Li_2SiO_3 .

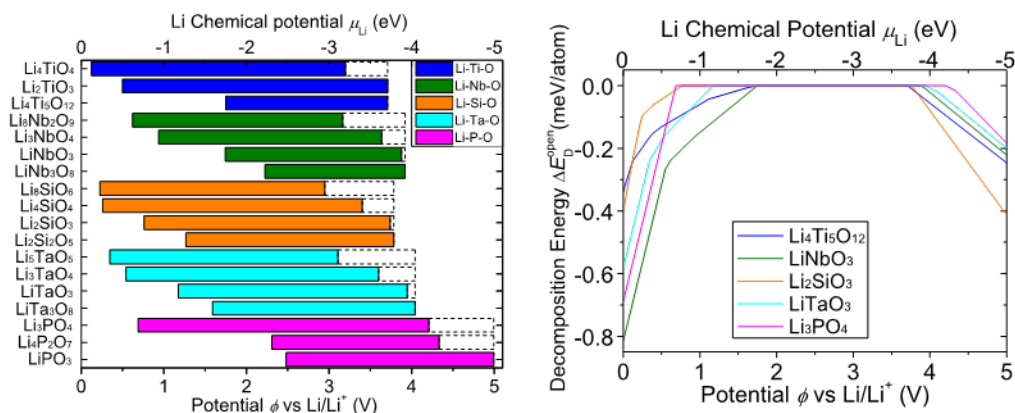


Figure II-476. Electrochemical window (left) and the decomposition energy ΔE_D^{open} (right) of the proposed and previously demonstrated coating layer materials applied between SE and cathode materials. The dashed line in (a) marks the equilibrium voltage to fully delithiate the materials.

Table II-22: The mutual reaction energy $\Delta E_{D,\text{min,mutual}}$ (in meV/atom) of the coating layer materials with the SE or LCO materials.

	Li_3PS_4	LLZO	LCO	$\text{L}_{0.5}\text{CO}$
Li_4TiO_4	-125	0	0	-30
Li_2TiO_3	-75	-5	0	0
$\text{Li}_4\text{Ti}_5\text{O}_{12}$	-80	-75	-1	0
$\text{Li}_8\text{Nb}_2\text{O}_9$	-147	0	0	-20
Li_3NbO_4	-132	-4	0	0
LiNbO_3	-155	-76	0	0
LiNb_3O_8	-173	-115	-16	0
Li_8SiO_6	-177	0	-3	-50
Li_4SiO_4	-81	-1	0	-12
Li_2SiO_3	-19	-29	0	0
$\text{Li}_2\text{Si}_2\text{O}_5$	-10	-69	-4	0
Li_5TaO_5	-117	0	0	-32
Li_3TaO_4	-64	-3	0	0
LiTaO_3	-49	-68	0	0
LiTa_3O_8	-64	-105	-22	0
Li_3PO_4	0	0	0	0
$\text{Li}_4\text{P}_2\text{O}_7$	-9	-101	-44	-3
LiPO_3	-32	-201	-76	-19

4. Computational modeling study for interface for Li-S and Li-NMC SSLiBs.

Thermodynamic computation predicted potential reaction and interphase formation between LLZO and Li polysulfides in all-solid-state Li-S batteries (Figure II-477a). Li_2SO_4 is identified as a dominant reaction product, which is confirmed in the XPS spectra (Figure II-477b). The formed interphase layer may serve as a protection layer between garnet solid electrolyte and S cathode. The Li-ion transport mechanism in these interphase layers would be crucial for assessing interfacial ion transport. First principles computation based on nudged-elastic-band methods were performed to identify the Li^+ transport pathway (Figure II-477c) and migration energy barrier (Figure II-477d) of ~ 0.6 - 0.8 eV, showing reasonable Li^+ interfacial transport across the formed interphase layers in Li-S solid-state battery.

Thermodynamic computation also predicted potential reaction and interphase formation between LLZO and NMC cathode in solid-state Li-ion batteries, and such reaction is energetically more favorable at high applied voltages. As potential formed products, the interphase equilibria include Li_6ZrO_7 , $\text{La}_2\text{Zr}_2\text{O}_7$ and various Li/La transition metal oxides. The Li^+ transport was studied in Li_6ZrO_7 , a dominant interphase product, using first principles computation. The Li-ion transport pathway is shown in Figure II-477e. The migration energy barrier (Figure II-477f) of ~ 0.2 - 0.8 eV suggests decent Li-ion transport across the interface from garnet electrolyte and NMC cathode in an all-solid-state Li-ion battery.

In summary, our developed computation models reveal the interphase layer formation between garnet solid electrolyte and S or NMC cathode materials in all-solid-state Li batteries. The formation of such layers serves an important protection role at the electrolyte-cathode interfaces. The Li-ion transport in these interphase layers are crucial for the battery performance. First principles calculations revealed Li-ion diffusion mechanisms and showed decent Li-ion transport in these materials and across the interfaces.

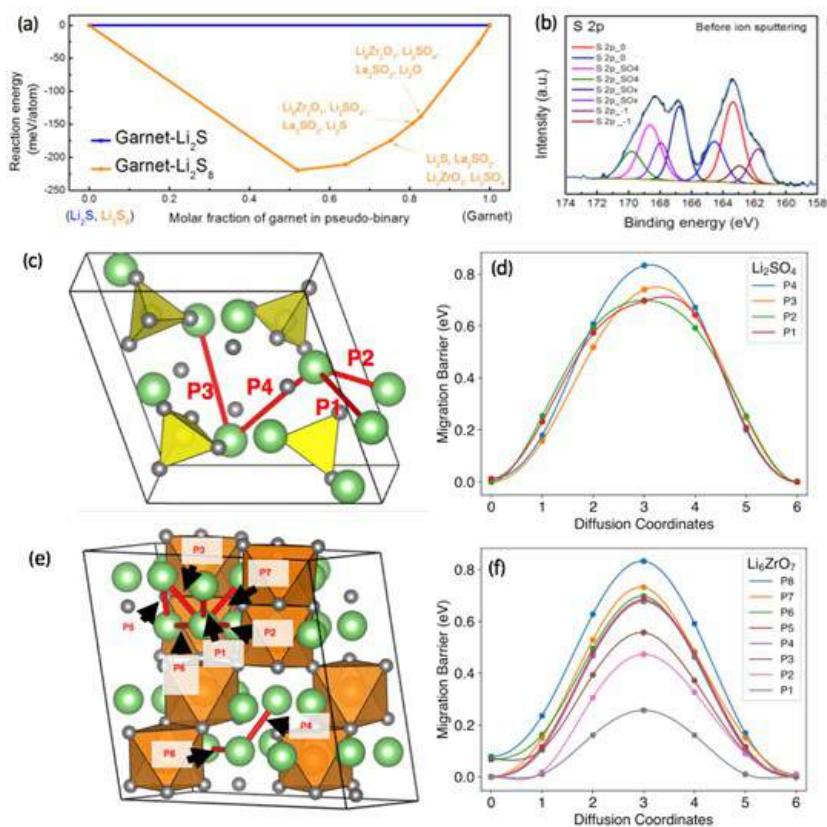


Figure II-477. (a) Calculated interphase equilibria and reaction energy between LLZO and Li polysulfides. (b) XPS spectra of garnet interface in Li-S battery. Calculated Li^+ transport pathway (c) and energy barriers (d) of Li_2SO_4 . Calculated Li^+ transport pathway (e) and energy barriers (f) of Li_6ZrO_7 .

5. Fabrication of full cell SSLiBs

5.1 SSLiBs with Li-NMC chemistry

Solid-state batteries consisting of Li metal anode, NMC cathode, and garnet-type $\text{Li}_7\text{La}_3\text{Zr}_2\text{O}_{12}$ (LLZO) solid electrolyte were fabricated and evaluated. The LLZO solid electrolyte has a bi-layer dense-porous structure with thicknesses of 20 μm and 50 μm , respectively (Figure II-478a). Li metal anode is hosted in the porous layer of garnet electrolyte (Figure II-478b). NMC cathode is laminated on the dense layer. Figure II-478c is the electrochemical impedance spectroscopy (EIS) of the battery. The interfacial resistance is around 250 Ωcm^2 , which is at the same level as our results for the gel interface previously reported. It proves that the bi-layer garnet and Li anode have a good interfacial contact. The cyclic voltammetry (CV) test result (Figure II-478d) shows that there is an oxidation peak around 4.2 V, which is the charging voltage plateau, and there is a reduction peak around 3.4 V, for the discharging plateau. Outside this voltage range, there is no reaction current. The conclusion is that a battery with a NMC cathode and bi-layer garnet electrolyte can have stable cycling performance up to ~ 4.5 V.

Cycling performances of Li/NMC cells with NMC mass loadings of 13.5 and 32 mg/cm^2 are shown in Figure II-479. Figure II-479a is the voltage profile of a cell with 13.5 mg/cm^2 NMC loading cycled at 0.1 C rate (1 C = 170 mA/g). Figure II-479b shows the capacity and Coulombic efficiency of this cell. The capacity is stable at 175 mAh/g over 30 cycles. The energy density of the cell is calculated to be 232 Wh/kg . Capacities and Coulombic efficiencies of high rate cycling for this cell are in Figure II-479c. The Coulombic efficiency is over 99% during the 200 cycles, and the battery shows 80% capacity retention at 0.2 C after 200 cycles at varying rates up to 0.5 C. Figure II-479d shows the voltage profiles of a cell with a high-mass-loading (32 mg/cm^2) NMC cathode. The cell is cycled at 0.05 C rate in 2 \sim 4.6 V voltage window. The capacity is 175 mAh/g , and the battery energy density is 357 Wh/kg , calculated based on the masses of the cathode, Li anode and electrolyte.

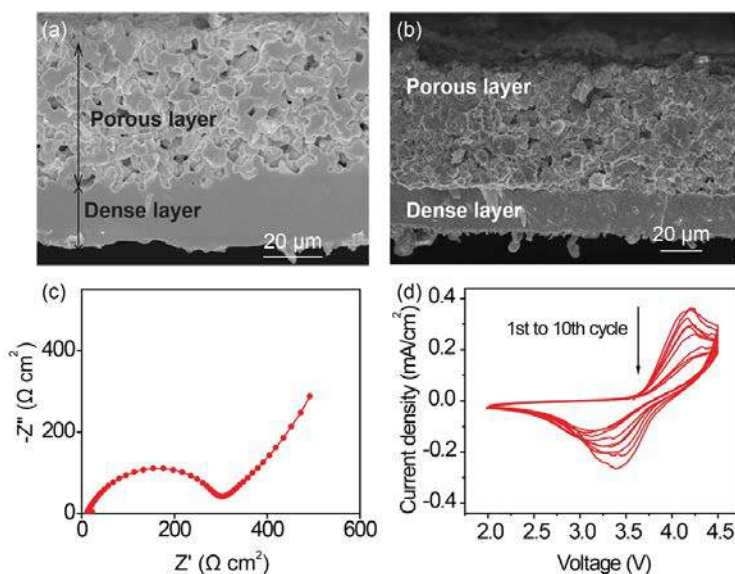


Figure II-478. Characterization of bi-layer garnet and performance of Li-NMC battery. (a) Cross sectional SEM image of bi-layer garnet SSE. (b) SEM of garnet SSE with Li metal inside. (c-d) EIS and CV of the Li-NMC battery with garnet SSE.

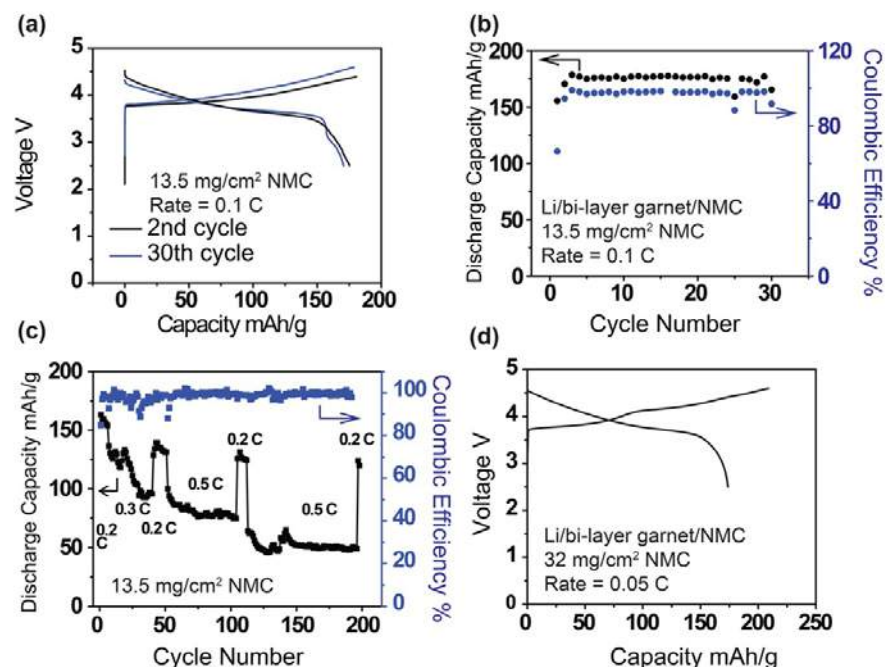


Figure II-479. Cycling performances of Li-NMC cells with garnet SSE. (a-b) Voltage profiles and cycling performance of Li-NMC cell with 13.5 mg/cm² cathode at 0.1 C rate. Stable capacity at 175 mAh/g was achieved. (c) Cycling performance of Li-NMC cell with 13.5 mg/cm² cathode at various rates. High Coulombic efficiency and capacity retention were achieved over 200 cycles. (d) Voltage profiles of a Li-NMC cell with high NMC loading of 32 mg/cm² at 0.05 C rate.

5.2 SSLiBs with Li-S chemistry

Solid state lithium batteries with a sulfur (S) cathode, bi-layer garnet SSE, and Li metal anode were fabricated (Figure II-480a). The structure of the bi-layer garnet and the S cathode is shown by the scanning electron microscope (SEM) image (Figure II-480b). The S fills the pores of garnet in the porous layer, as confirmed by the energy-dispersive X-ray spectroscopy (EDS) in Figure II-480c. Li metal anode was coated on the dense side of the bi-layer garnet, with a polymer interface for better contact. The cycling performance is shown in Figure II-480d. The Coulombic efficiency remains > 99%, confirming that no shuttling effect occurs in the cell. The bilayer Li-S cell with a S mass loading of 7.5 mg/cm² has an energy density of 280 Wh/kg on the basis of the cathode, Li anode and electrolytes.

We also demonstrated Li-S batteries based on tri-layer garnet SSE. The tri-layer SSE is composed of a porous-dense-porous structure. The thickness of each porous layer is 70 μm and the thickness of the dense layer is 30 μm. Li metal anode is stored in one porous layer, and sulfur cathode is stored in the other porous layer. Mass loadings of lithium and sulfur are 4.3 mg/cm² and 5.4 mg/cm², respectively. The battery performance is shown in Figure II-481. The voltage profiles in Figure II-481a show a typical Li-S two plateau behavior with a high capacity of ~1200 mAh/g. The cell shows high capacity retention and nearly 100% Coulombic efficiency during 50 cycles (Figure II-481b). The total energy density of the tested cell is 272 Wh/kg as calculated from the integrated cycling curve, measured masses of sulfur, carbon, garnet electrolyte, and lithium metal anode.

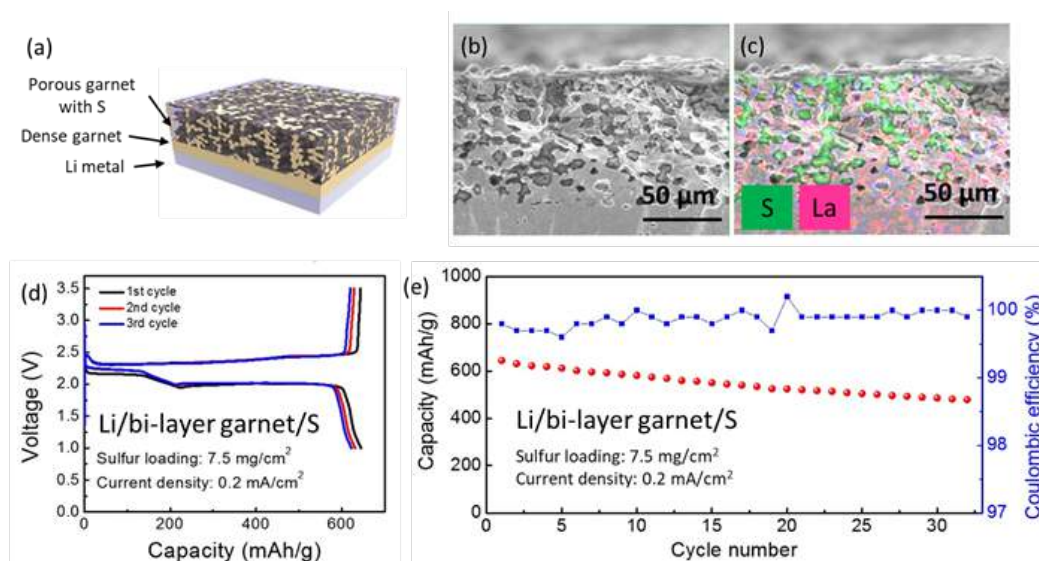


Figure II-480. Characterization of bi-layer garnet and performances of Li-S battery. (a) Schematic of Li-S battery based on bi-layer garnet. (b) Cross sectional SEM of bi-layer garnet filled with S. (c) EDS of S (green) and La (red) distribution in bi-layer garnet. (d-e) Voltage profile and cycling performance of the solid state Li-S cell with a loading of 7.5 mg/cm² at 0.2 mA/cm².

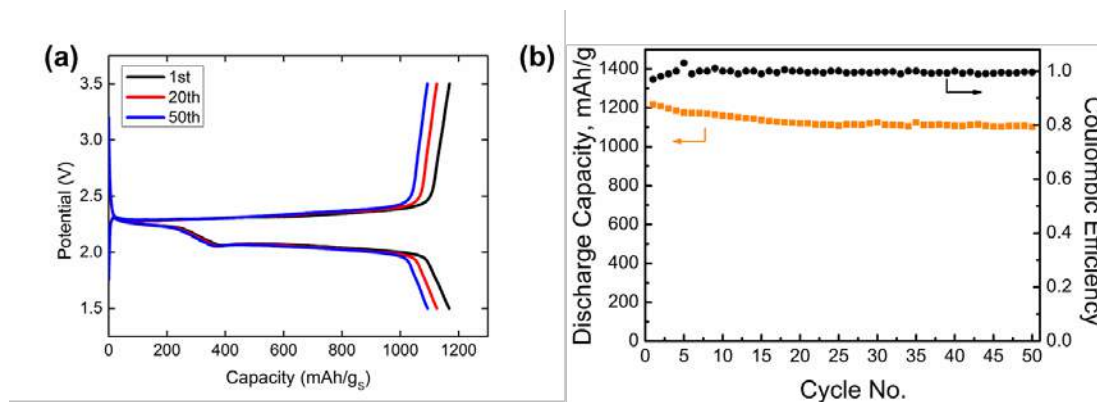


Figure II-481. Cycling performances of Li-sulfur cell with garnet electrolytes. (a) Voltage profiles of the 1st, 20th and 50th cycle of the solid-state Li-S cell. 1200 mAh/g capacity and low capacity loss were achieved. (b) Cycling results of the solid state Li-S cell. High capacity retention was achieved with near 100% coulombic efficiency.

Conclusions

Computational understanding of SSE-electrode interface:

- Achieved fundamental understanding of interfacial impedance as demonstrated by consistency between computational and experimental results.
- Developed computational models to investigate stability and interfacial ion transport with varying types of interlayers
- Predicted formation of protective interfaces between garnet and S and NMC cathodes

For garnet-cathode interface:

- We demonstrated that gel electrolyte can reduce the interfacial resistance by over 4 orders of magnitude achieving an interfacial ASR of $\sim 67 \text{ Ohm-cm}^2$ for planar cathode/garnet interface.
- We demonstrated that increasing surface area can effectively decrease the interface resistance, achieving a 52% decrease in interfacial ASR.
- Aqueous interface lead to 7.5 Ohm-cm^2 cathode/garnet interfacial resistance planar cathode/garnet interface. Therefore, we met the $\sim 10 \text{ Ohm-cm}^2$ garnet/cathode goal.

For Li-garnet interface:

- We demonstrated gel electrolyte, Si, and Al can reduce interfacial resistance to 200 Ohm-cm^2 , 127 Ohm-cm^2 , and 75 Ohm-cm^2 , respectively for planar Li metal-garnet interface.
- We further demonstrated that ALD- Al_2O_3 can reduce interfacial resistance to $\sim 1 \text{ Ohm-cm}^2$ for planar Li metal-garnet interface. Therefore, we met the $\sim 10 \text{ Ohm-cm}^2$ garnet/anode goal.

Full cell demonstration:

- Fabricated and tested SSLiBs with Li-NMC Chemistry.
- Fabricated and tested SSLiBs with Li-S Chemistry.
- Achieved full cell (Li-NMC) performance of 352 Wh/kg .
- Achieved full cell (Li-NMC) performance of 200 cycles.
- Achieved full cell (Li-S) performance of 272 Wh/kg and 50 cycles.

Key Publications

1. W. Luo, Y. Gong, Y. Zhu, Y. Li, Y. Yao, Y. Zhang, K. K. Fu, G. Pastel, C. F. Lin, Y. Mo, E. D. Wachsman, L. Hu, Reducing Interfacial Resistance between Garnet-Structured Solid-State Electrolyte and Li-Metal Anode by a Germanium Layer. *Adv. Mater.* 29 (22), 1–7, (2017).
2. B. Liu, K. Fu, Y. Gong, C. Yang, Y. Yao, Y. Wang, C. Wang, Y. Kuang, G. Pastel, H. Xie, E. D. Wachsman, L. Hu, Rapid Thermal Annealing of Cathode-Garnet Interface toward High-Temperature Solid State Batteries. *Nano Lett.* 9. 4917-4923 (2017).
3. K. Fu, Y. Gong, B. Liu, Y. Zhu, S. Xu, Y. Yao, W. Luo, C. Wang, S. D. Lacey, J. Dai, Y. Chen, Y. Mo, E. Wachsman, L. Hu, Toward Garnet Electrolyte-based Li Metal Batteries: An Ultrathin, Highly Effective, Artificial Solid-State Electrolyte/metallic Li Interface. *Sci. Adv.* 3, e1601659 (2017).
4. K. Fu, Y. Gong, S. Xu, Y. Zhu, Y. Li, J. Dai, C. Wang, B. Liu, G. Pastel, H. Xie, Y. Yao, Y. Mo, E. Wachsman, L. Hu, Stabilizing the Garnet Solid-Electrolyte/polysulfide Interface in Li-S Batteries. *Chem. Mater.* 29, 8037–8041 (2017).
5. K. Fu, Y. Gong, S. Xu, Y. Zhu, Y. Li, J. Dai, C. Wang, B. Liu, G. Pastel, H. Xie, Y. Yao, Y. Mo, E. Wachsman, L. Hu, Transient Behavior of the Metal Interface in Li Metal-Garnet Batteries. *Angew. Chemie Int. Ed.* 1–7 (2017).
6. C. Wang, H. Xie, L. Zhang, Y. Gong, G. Pastel, J. Dai, B. Liu, E. D. Wachsman, L. Hu, Universal Soldering of Lithium and Sodium Alloys on Various Substrates for Batteries. *Adv. Energy Mater.* 1701963 (2017).

7. C. Yang, K. Fu, Y. Zhang, E. Hitz, L. Hu, Protected Lithium-Metal Anodes in Batteries: From Liquid to Solid. *Adv. Mater.* 29, 1–28 (2017).
8. B. Liu, Y. Gong, K. Fu, X. Han, Y. Yao, G. Pastel, C. Yang, H. Xie, E. D. Wachsman, L. Hu, Garnet Solid Electrolyte Protected Li-Metal Batteries. *ACS Appl. Mater. Interfaces* 9, 18809–18815 (2017).
9. Y. Zhu, X. He, Y. Mo, First Principles Study on Electrochemical and Chemical Stability of the Solid Electrolyte-Electrode Interfaces in All-Solid-State Li-ion Batteries, *J. Mater. Chem. A*, 4, 3253-3266 (2016).
10. Y. Zhu, X. He, Y. Mo, Origin of Outstanding Stability in the Lithium Solid Electrolyte Materials: Insights from Thermodynamic Analyses Based on First-Principles Calculations, *ACS Appl. Mater. Interfaces*, 7, 23685-23693 (2015).
11. F. Han, Y. Zhu, X. He, Y. Mo, C. Wang, Electrochemical Stability of $\text{Li}_{10}\text{GeP}_2\text{S}_{12}$ and $\text{Li}_7\text{La}_3\text{Zr}_2\text{O}_{12}$ Solid Electrolytes”, *Adv. Energy Mater.*, 6, 1501590 (2016).
12. W. Luo, Y. Gong, Y. Zhu, K. Fu, J. Dai, S. D. Lacey, C. Wang, B. Liu, X. Han, Y. Mo, E. D. Wachsman, L. Hu, Transition from Super-lithiophobicity to Super-lithiophilicity of Garnet Solid Electrolyte, *J. Am. Chem. Soc.*, 138, 12258-12262 (2016).
13. X. Han, Y. Gong, X. He, G. T. Hitz, J. Dai, Y. Mo, V. Thangadurai, E. D. Wachsman, L. Hu, Negating Interfacial Impedance in Garnet-Based Solid-State Li-Metal Batteries, *Nat. Mater.*, 16, 572-580, (2017). DOI: 10.1038/NMAT4821
14. K. Fu, Y. Gong, G. T. Hitz, D. W. McOwen, Y. Li, S. Xu, Y. Wen, L. Zhang, C. Wang, G. Pastel, J. Dai, B. Liu, H. Xie, Y. Yao, E. D. Wachsman, L. Hu, Three-Dimensional Bilayer Garnet Solid Electrolyte High Energy Density Lithium Metal-Sulfur Batteries, *Energy Environ. Sci.*, 10, 1568-1575, (2017). DOI: 10.1039/c7ee01004d

II.H.5 High Conductivity and Flexible Hybrid Solid State Electrolyte (U of MD)

Eric Wachsman, Principal Investigator

University of Maryland
1206 Engineering Laboratory Building
College Park, MD 20742
Phone: 301-405-8193
E-mail: ewach@umd.edu

Tien Duong, Technology Manager

U.S. Department of Energy
Phone: 202-586-7836
E-mail: Tien.Duong@ee.doe.gov

Start Date: October 1, 2016

End Date: September 30, 2019

Total Project Cost: \$1,250,000

DOE share: \$1,250,000

Non-DOE share: \$0

Project Introduction

Metallic lithium is considered the “Holy Grail” for high-energy density batteries. However, using lithium metal in organic liquid electrolyte systems faces many challenges in terms of both battery performance and safety. A fundamental strategy is to develop a solid-state electrolyte (SSE) to mechanically suppress lithium dendrites and intrinsically eliminate SEI formation. Among the different types of SSEs, solid-polymer electrolytes have been the most extensively studied. In polymer-based composite SSEs, nanoparticles are incorporated to influence the recrystallization kinetics of the PEO polymer chains to promote local amorphous regions, thereby increasing the ionic conductivity of the Li salt/polymer system. The fillers can be either non- Li^+ conductive nanoparticles, such as Al_2O_3 , SiO_2 , TiO_2 , ZrO_2 , and organic polymer spheres, or Li^+ conductive nanoparticles, such as $\text{Li}_{0.33}\text{La}_{0.557}\text{TiO}_3$, and $\text{Li}_{1.3}\text{Al}_{0.3}\text{Ti}_{1.7}(\text{PO}_4)_3$. Developing nanostructured fillers is an essential approach to increase the ionic conductivity of composite electrolytes due to the increased surface area of the amorphous region and improved interface between fillers and polymers. Meanwhile, numerous solid-state inorganic Li^+ electrolytes are being investigated to replace liquid organic electrolytes. Due to their high ion conductivity and excellent stability, Li-stuffed garnets exhibit the most promising physical and chemical properties for SSEs. However, major challenges still exist in garnet-based electrolytes, including: (1) Being either too thick with corresponding high ASR or too mechanically fragile when thin ($\sim 20\ \mu\text{m}$); (2) High temperature processing that is incompatible with most anode/cathode materials; and (3) High interfacial impedance. Moreover, flexible SSEs with high ionic conductivity and excellent processability are completely lacking.

Instability and/or high resistance at the interface of lithium metal with various solid electrolytes limit the use of the metallic anode for batteries with high energy density, such as Li-air and Li-S batteries. The critical impact of this endeavor will be focused on developing a new type of solid-state electrolyte (SSE) that is highly conductive, highly flexible and electrochemically stable. In particular, the new SSE will enable Li metal anodes with excellent interfacial impedance and blocking formation of Li dendrites.

Objectives

The objective of this project is to develop a flexible hybrid electrolyte with garnet nanofibers to achieve the following: (1) Flexibility with greater mechanical strength ($\sim 10\ \text{MPa}$) and thermal stability than polymer electrolytes; (2) High room temperature ionic conductivity, $\sim 0.5\ \text{mS/cm}$; (3) Stable interface with Li metal and effectively block Li dendrites at current densities up to $3\ \text{mA/cm}^2$; and (4) Battery performance with Li-S chemistry with an energy density of $\geq 450\ \text{Wh/kg}$ and ($\geq 1000\ \text{Wh/L}$), and maintain $\geq 80\%$ of capacity up to 500 cycles.

Approach

We will synthesize garnet nanofibers, fill the porous region with polymer electrolyte, and characterize and tune the flexible hybrid membrane properties. The flexible hybrid SSE microstructure will be analyzed by leveraging the UMD AIMLab Focused Ion Beam Scanning Electron Microscopy (FIB-SEM) tools and integrated with electrochemical methods at the UMERC Battery Fabrication Lab to investigate the properties and stability with Li metal anode. We will develop a fundamental understanding of the mechanism of Li ionic diffusion in garnet nanofibers and their mechanical properties, as well as these properties for hybrid garnet-fiber/polymer hybrids. Work will progress toward the study of the electrode assembly during electrochemical cycling of the anode.

Results

1. Fabrication of 4 cm x 4 cm garnet fiber membrane

Two templating methods were developed to fabricate garnet nanofiber membranes. The first method utilized electrospun polyacrylonitrile (PAN) fibers while the second used cellulose textiles. Al-doped LLZO with the chemical composition of $\text{Li}_{6.28}\text{Al}_{0.24}\text{La}_3\text{Zr}_2\text{O}_{11.98}$ was prepared by dissolving stoichiometric amounts of LiNO_3 (15 wt% excess), $\text{Al}(\text{NO}_3)_3 \cdot 9\text{H}_2\text{O}$, $\text{La}(\text{NO}_3)_3 \cdot 6\text{H}_2\text{O}$, and zirconium propoxide solution in ethanol with 15 vol % acetic acid. Cellulose textile templates were pretreated by annealing in air at 270°C for 10 h, then rinsed with ethanol and dried at 100°C for 12 h. After pretreatment, the templates were soaked in a 2.5 mol/L LLZO precursor solution for 24 h. The multi-scale porosity existing in the porous templates enabled homogenous impregnation by the LLZO precursor. Calcination of the precursor impregnated templates was conducted in oxygen at different temperatures to obtain garnet fibrous membrane. Figure II-482 shows a photograph of garnet fibrous membranes sintered at 800°C made from electrospun fibers or cellulose textiles. The cellulose template better retained the characteristic physical features and is more easily tailored for particular shapes in large dimensions ($4\text{ cm} \times 4\text{ cm}$).

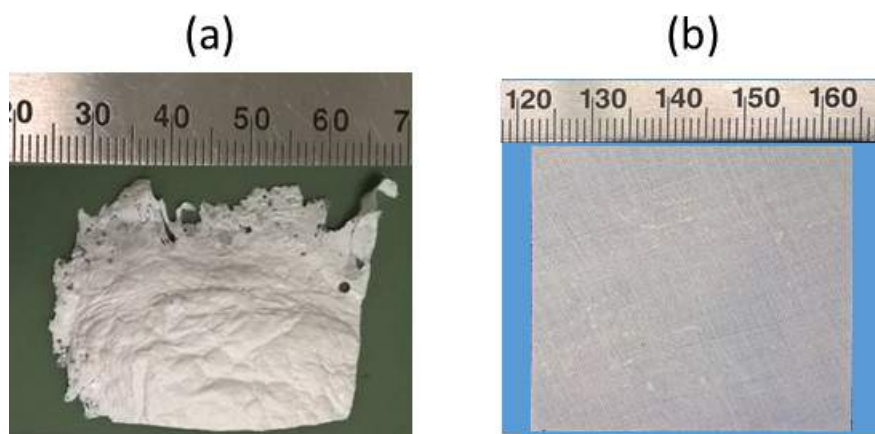


Figure II-482. Photograph of flexible garnet fibrous membranes made from (a) electrospun PAN ($3.5 \times 3.0\text{ cm}$) and (b) cellulose textile ($4.0 \times 4.0\text{ cm}$) templates.

The crystallographic phase of the LLZO was analyzed by powder X-ray diffraction on a D8 Advance with LynxEye and SolX (XRD, Bruker AXS) using a $\text{Cu K}\alpha$ radiation source operated at 40 kV and 40 mA. The microstructure and element distribution were examined by analytical SEM (Hitachi SU-70) equipped with an Energy Dispersive Spectrometer (EDS, Oxford Instruments). Figure II-483 shows the XRD pattern and SEM image of the garnet fibrous membrane. Through simple composition design by doping with supervalent cations and optimizing lithium concentration in the precursor solution, stabilization of the cubic phase can be achieved at sintering temperatures as low as 800°C . The garnet fibers retained the characteristic physical features of the original cellulose template, which consisted of continuous individual microfibers of approximately $10\text{ }\mu\text{m}$ in diameter that were arranged mostly parallel and twisted around each other. The fibers were wrapped into

bundles about 200 μm in diameter interlacing with each other to form the periodically ordered woven pattern. Inter-fiber pores ranged from 10 to 20 μm in diameter and larger pores between yarns were formed after thermal treatment.

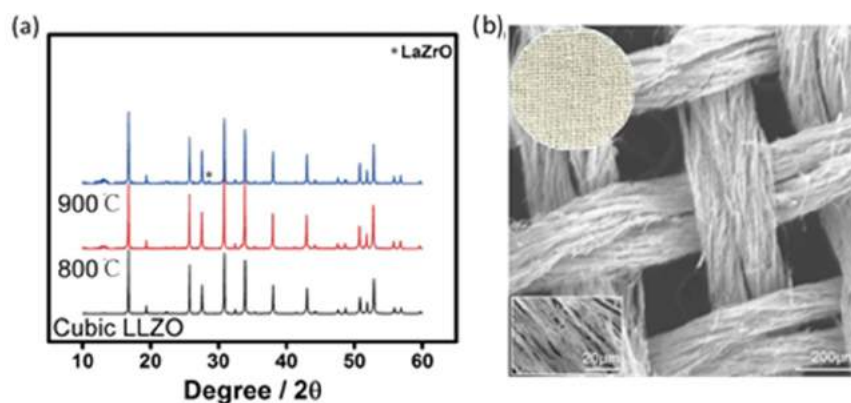


Figure II-483. Characterization of garnet fibrous membrane: (a) Powder XRD patterns of the crushed garnet textile sintered at different temperatures; (b) SEM image of the garnet textile converted from the precursor solution impregnated template.

2. Hybrid Garnet-Polymer Electrolyte

The polymer matrix was prepared by dissolving LiTFSI and PEO (MW 600,000) in acetonitrile. Plasticizer was added to reduce the crystallinity and improve Li-ion conductivity. The polymer electrolyte was casted on a Teflon block and dried in an argon glove box, followed by drying in a vacuum oven to remove residual solvent before electrochemical performance characterization. Electrochemical impedance of the polymer electrolyte was measured in a stainless steel/polymer/stainless steel configuration using a Solartron 1260 Impedance Analyzer. A Teflon spacer was included to fix the polymer thickness. Impedance tests were conducted with AC amplitude of 20 mV in the frequency range of 1 Hz and 1 MHz from 25°C to 100°C. Figure II-484 presents the typical impedance plot for the polymer electrolyte measured at room temperature. Lithium-ion transfer processes were divided into ion conduction within the CPE (high frequency arc) and ion blocking at the CPE/stainless steel interface (low frequency inclined tail). The resistance of the CPE was obtained by reading the real impedance values at the high frequency intercept of the arc. The measured lithium-ion conductivity of the polymer electrolyte was $0.9 \times 10^{-4} \text{ S/cm}$ at 25°C.

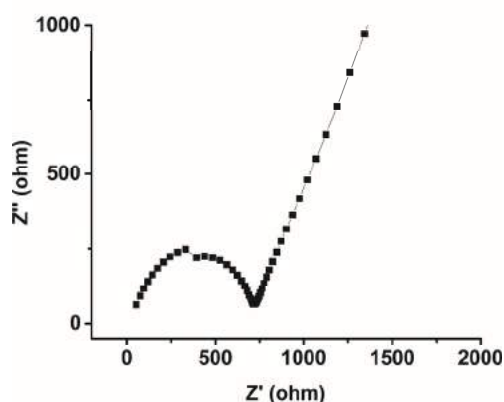


Figure II-484. Impedance spectra of the polymer electrolyte at room temperatures. The Li-ion conductivity is $0.9 \times 10^{-4} \text{ S/cm}$.

Nanoindentation is a technique widely used for determining mechanical properties of the near-surface region of materials. By combining the application of low loads, measuring the resulting displacement, and determining the contact area between the tip of the indenter and the sample, the hardness (H) and elastic modulus (E) are able to be measured. Nanoindentation was performed on a Hysitron Inc. TriboIndenter. The evaluated garnet fiber was soaked in melted crystal bond. The dried composite sample was then mounted in slow-curing epoxy glue and polished. The optical microscope in the nanoindenter was used to select positions for indentation on the center of the fibers. The position of the center of the fiber was evaluated with individual scans of the AFM image and the location of the fiber was manually adjusted. (See Figure II-485.) Hardness and Young's modulus of garnet fiber was measured to be 0.28 ± 0.04 GPa and 6.3 ± 0.5 GPa, respectively.

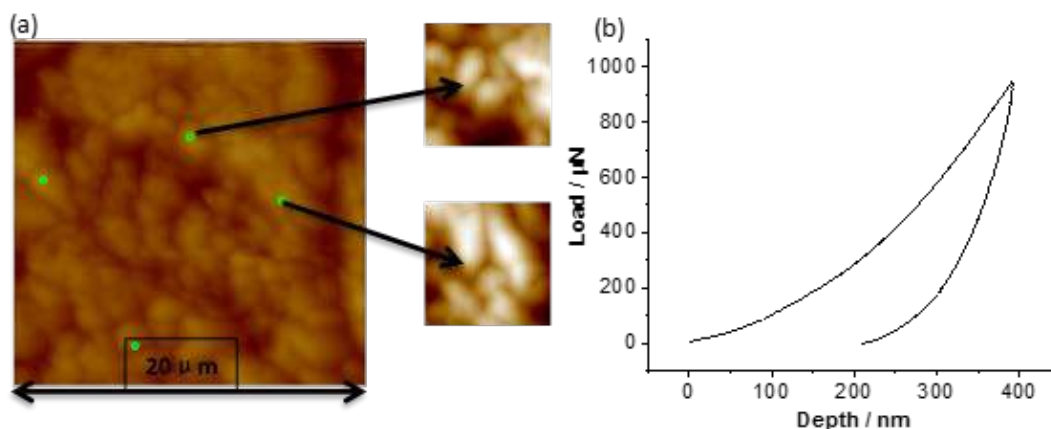


Figure II-485. Mechanical characterization of garnet fiber: (a) AFM scanning of the nano-indent points on garnet fiber; (b) Load-depth profile of garnet fiber.

Hybrid composite polymer electrolyte was prepared by mixing the garnet fibers with polymer electrolyte in N-methyl-2-pyrrolidinone (NMP) at 70 °C using a magnetic stirrer. After 6 hours of stirring, the mixture was tape cast onto a Teflon block and left to dry at 80°C over-night. Figure II-486 shows the photograph of the flexible hybrid composite polymer electrolyte. Figure II-487 shows the AC impedance and CV of the composite electrolyte. The Li-ion conductivity is 6.07×10^{-4} S/cm measured at room temperature, representing a significant enhancement over the conductivity of the polymer electrolyte. The composite is also stable up 4.5 V.



Figure II-486. Photograph of the flexible hybrid composite polymer electrolyte.

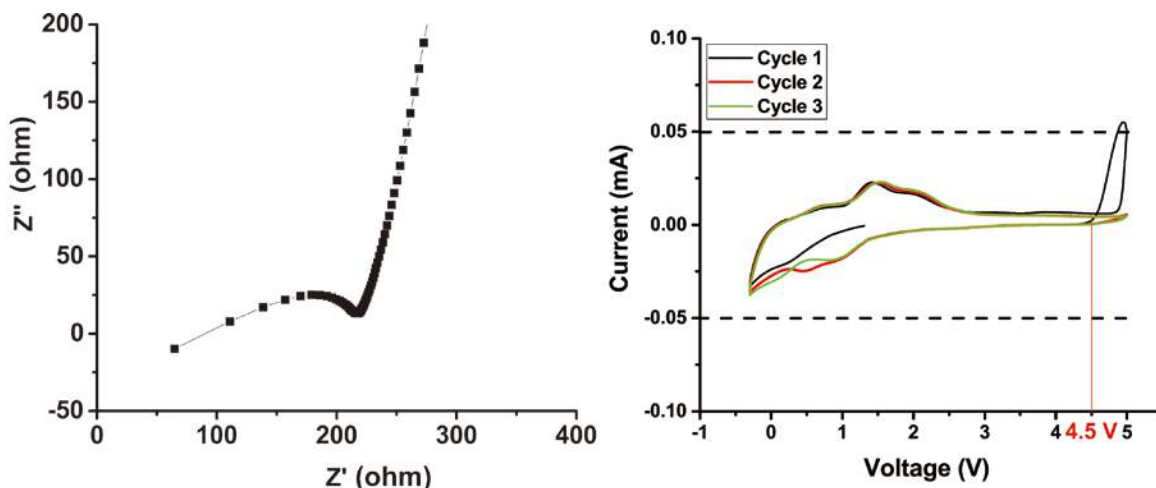


Figure II-487. Electrochemical characterization of hybrid composite polymer electrolyte: (a) Ac impedance, Li-ion conductivity is 6.07×10^{-4} S/cm; (b) CV, stable up to 4.5 V

3. Understand Li ionic diffusion in garnet nanofibers and its response to mechanical deformation.

In order to perform molecular dynamics (MD) simulations for garnet nanofibers, we implemented and tested force fields for lithium garnet $\text{Li}_7\text{La}_3\text{Zr}_2\text{O}_{12}$ (LLZO). Using the newly tested force field, the lattice parameters in tetragonal and cubic phases of LLZO were calculated using MD simulations as a function of temperature, in good agreement with experimental values. Li^+ diffusion in LLZO was also modeled using MD simulations. The calculated Li^+ conductivity and activation energy of LLZO are in good agreement with *ab initio* calculations and experimental measured values.

An atomistic model of garnet nanofibers was constructed and equilibrated in MD simulations (Figure II-488). The Li^+ transport in a single garnet nanofiber was modeled using MD simulations at different temperatures. The Li^+ conductivities at different temperatures and the activation energies for Li^+ diffusion were calculated in single garnet nanofibers. Comparison of the Li^+ diffusion properties from MD simulations to the bulk phase of LLZO shows faster Li^+ diffusion in single garnet nanofibers. In addition, the Li^+ migration mechanism was analyzed for Li^+ transport along and perpendicular to the nanofiber direction, and at surface and core regions of the nanofiber. Insight into Li^+ diffusion in garnet nanofiber was obtained.

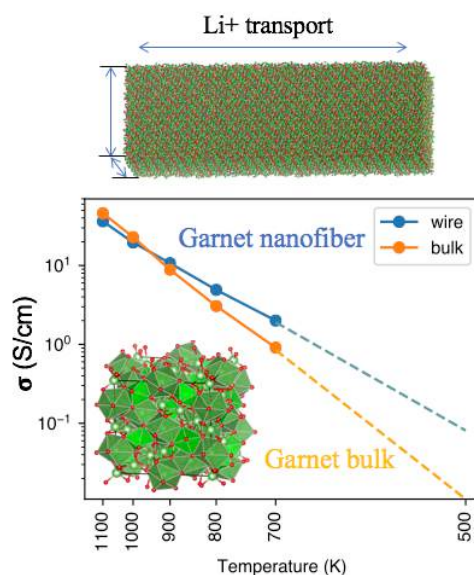


Figure II-488. Computer modeling of Li^+ transport in garnet nanofibers.

Mechanical deformation on bulk and nanofiber garnet was performed under MD simulations. The elastic moduli from our calculations are in good agreements with experiments and previous studies. The Li^+ diffusion under mechanical deformation was studied using MD simulations (Figure II-489). We simulated the garnet at both tensile and compressive stress with different strain (1% and 3%). We found the mechanical deformation significantly impacts the Li^+ diffusion. Li conductivity decreases and activation energy increases in both stressed states. This change is in good agreement with experiments. The MD simulations in both bulk and nanofiber show similar results. Mechanical deformation decreases Li^+ conductivity in garnet. Both tensile and compressive deformation drives garnet towards slow-conducting tetragonal phase. In summary, MD simulations were performed to understand Li^+ diffusion in garnet nanofibers and the effect of mechanical deformation.

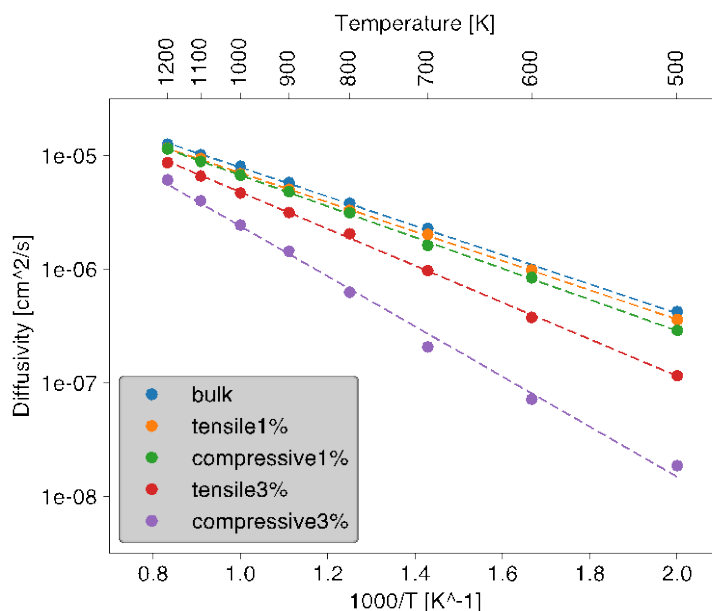


Figure II-489. Li diffusion of garnet under strain.

Conclusions

We synthesized garnet fibrous membrane, which essentially retained the characteristic physical features of the original cellulose template and can be tailored for particular shapes in large dimensions (4 cm x 4 cm). We synthesized ion insulating polymer PEO, ion conductive polymer PEO-LiTFSI, and in-situ polymer electrolyte coated garnet nanofibers. Our flexible electrolyte combining conductive cubic LLZO garnet and lithium-PEO could therefore reach a reasonably high ionic conductivity of 6.07×10^{-4} S/cm at room temperature and voltage stability up to 4.5 V. Molecular dynamics simulations were performed to understand Li^+ diffusion in garnet nanofibers and the effect of mechanical deformation. The MD simulations in both bulk and nanofiber show mechanical deformation decreases Li^+ conductivity in garnet.

Key Publications

1. Eric Wachsman, "All-Solid-State Li-ion Batteries for Transformational Energy Storage," 21st International Conference on Solid State Ionics, June 23-29, 2017, Padua, Italy - Invited
2. Yifei Mo, "Enabling All-Solid-State Li-ion Batteries Through Computation-Guided Design of Materials and Interfaces", Beyond Lithium Ion Symposium-10 (BLI-X), CA (06/2017) – Invited
3. Yifei Mo, "Computation-Guided Understanding and Design of Interfaces in All-Solid-State Li-ion Batteries", 17th Annual Advanced Automotive Battery Conference, San Francisco, CA (06/2017)-Invited

4. Eric Wachsman, “All-Solid-State Li-ion Batteries for Transformational Energy Storage,” U.C. Berkeley, April 6, 2017, Berkeley, CA – Invited
5. Y. Gong, K. Fu, S. Xu, J. Dai, T. R. Hamann, L. Zhang, G. T. Hitz, X. Han, L. Hu, E. D. Wachsman, Lithium-Ion Conductive Ceramic Textile: A New Architecture for Flexible Solid-State Lithium Metal Batteries, *Materials Today*, Minor Revision

II.H.6 Nanoscale Interfacial Engineering for Stable Lithium Metal Anodes (Stanford University)

Yi Cui, Principal Investigator

Stanford University
476 Lomita Mall, Room 343
Stanford, CA 94305
Phone: 650-723-4613
E-mail: yicui@stanford.edu

Tien Duong, Technology Manager

U.S. Department of Energy
Phone: 202-586-7836
E-mail: Tien.Duong@ee.doe.gov

Start Date: October 1, 2015
Total Project Cost: \$600,000

End Date: September 30, 2018
DOE share: \$600,000

Non-DOE share: \$0

Project Introduction

Li-ion battery has gain great success as the power source for portable electronics, electric vehicles and grid scale energy storage. However, its energy density has achieved a bottleneck which calls for the further innovation of battery technologies especially those beyond Li-ion. Li metal anode has long been regarded as the "holy grail" for Li battery research, which is not only due to its highest theoretical capacity of 3860 mAh/g and lowest electrochemical potential, but also its key role in Li-S and Li-air battery systems, both of which are the most prominent battery chemistries for the next-generation energy storage technology. However, many challenges have been encountered on its way to commercialization. Among all problems of Li metal, there are two root causes, namely high reactivity of Li and its infinite relative volume change during cycling. On one hand, the high reactivity of Li results in the excess side reactions once is exposed to liquid electrolyte, which further lead to complex interfacial chemistry, blocked ion transport and the consumption of materials. On the other hand, the infinite relative volume change makes the solid electrolyte interphase (SEI) prone to fracture, which not only creates hot spots for uneven Li-ion flux distribution and thus dendritic deposition, but also exposes fresh Li for further side reactions, leading to low Coulombic efficiency. Under the circumstance, it is necessary to develop surface protection techniques as well as to improve the electrode volume stability in order to solve all the abovementioned problems. We plan to develop a set of nano-synthesis techniques to realize the proposed concepts.

Objectives

This study aims to render lithium (Li) metal anode with high capacity and reliability by developing chemically and mechanically stable interfacial layers between Li metal and electrolytes, which is essential to couple with sulfur cathode for high-energy Li-sulfur batteries. With the nanoscale interfacial engineering approach, various kinds of advanced thin films will be introduced to overcome the issues related to dendritic growth, reactive surface and virtually "infinite" volume expansion of Li metal anode.

Approach

- Achieve minimal volume change of the electrode by designing stable hosts for Li metal
- Realize stabilized SEI and much more stable cycling by interfacial engineering
- Improved the rate capability in full cells
- Develop and employ further surface protection to 3D Li surface

Results

In recognition of the problems associated with the “hostless” nature of Li metal, we have successfully introduced stable hosts for metallic Li. The approach resulted in three-dimensional porous Li, which reduced the effective current density and the degree of interface fluctuation during cycling, leading to more uniform Li deposition with greatly improved cycling stability. Engineering the solid electrolyte interphase (SEI) on porous Li electrodes shall be the next step needed to further improve the cycling efficiency. Herein, we propose the rational design of an artificial SEI layer, composed of Cu_3N nanoparticles in styrene butadiene rubber matrix ($\text{Cu}_3\text{N} + \text{SBR}$). This composite artificial SEI can simultaneously possess high mechanical strength due to the densely packed inorganic nanoparticles, good flexibility due to the polymeric binder matrix, and importantly, high Li-ion conductivity thanks to the conversion of Cu_3N to ion-conducting Li_3N in the presence of Li.

The Coulombic efficiency (CE) of our artificial SEI protected anode was first measured on Cu foil. At a current density of 1 mA cm^{-2} in carbonate electrolyte (1 M lithium hexafluorophosphate in 1:1 ethylene carbonate/diethyl carbonate with 10 wt% fluoroethylene carbonate additive), the CE of bare Cu started at around 95% and quickly decayed to merely 70% within 50 stripping/plating cycles due to the growth of Li dendrites and the continuous breakdown/repair of SEI that consumed both Li and the electrolyte (Figure II-490a).

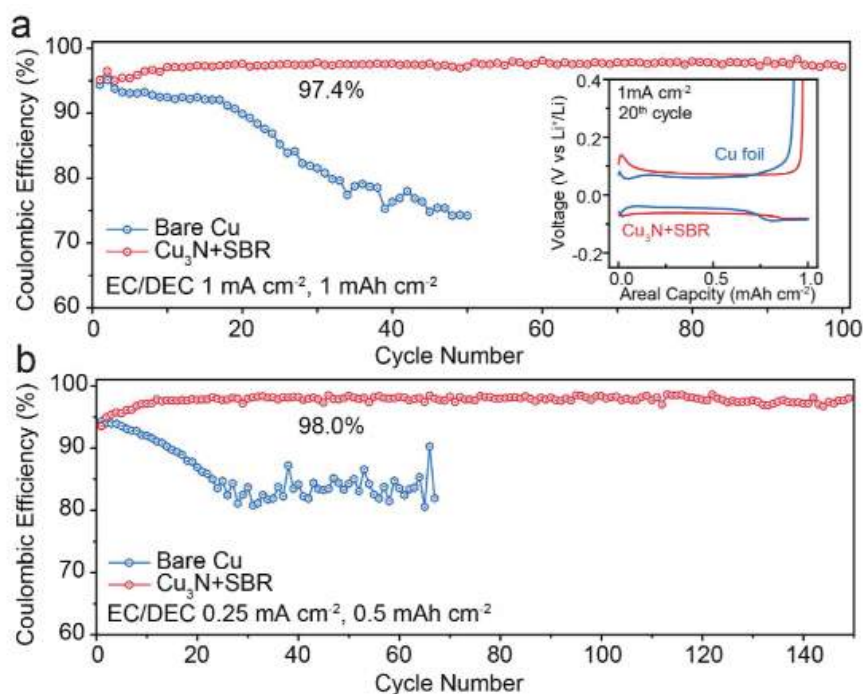


Figure II-490. Coulombic efficiency of artificial SEI protected Cu foil and bare Cu foil at a current density of a) 1 mA cm^{-2} (cycling capacity 1 mAh cm^{-2} ; inset, the corresponding voltage profiles at the 20th cycle) and b) 0.25 mA cm^{-2} (cycling capacity 0.5 mAh cm^{-2}).

Surprisingly, the artificial SEI protected Cu demonstrated a much improved Coulombic efficiency of $\approx 97.4\%$ averaged between the 20th and 70th cycles and such high efficiency performance can sustain for more than 100 cycles. In addition, the overpotential increase due to the existence of the artificial SEI was minimal (Figure II-490a Inset), thanks to its relatively high ionic conductivity. Since the effective current density can be significantly reduced on porous Li metal anodes, CE at a lower current density of 0.25 mA cm^{-2} was also studied to better resemble the real working condition of the artificial SEI protected porous Li. With reduced current density, the CE increased to as high as $\approx 98\%$, which was stable for at least 150 cycles (Figure II-490b).

The morphology of Li deposition after cycling was also studied (Figure II-491). After five galvanostatic plating/stripping cycles at a current density of 0.5 mA cm^{-2} and a capacity of 0.5 mAh cm^{-2} , no observable dendrites on Cu foil protected by the mechanically robust and highly Li-ion conducting artificial SEI, while excessive wire-shaped Li with diameter around $1\text{--}2 \text{ }\mu\text{m}$ has already formed on the bare Cu counterpart. The color of the Li deposit on the protected Cu foil remained silver and shiny, similar to that of pristine Li metal. However, dark gray Li was observed for deposition directly on bare Cu, stemming from a less compact Li deposition morphology. The dendrite suppression mechanism can be attributed by the more uniform Li-ion flux across the ion-conducting artificial SEI and its good mechanical property. Accordingly, the elastic modulus of the artificial SEI was measured via nanoindentation with proper mathematical corrections based on the contact model. The elastic modulus was measured on the order of 1 GPa, which can be considered sufficient in suppressing Li dendrite formation.

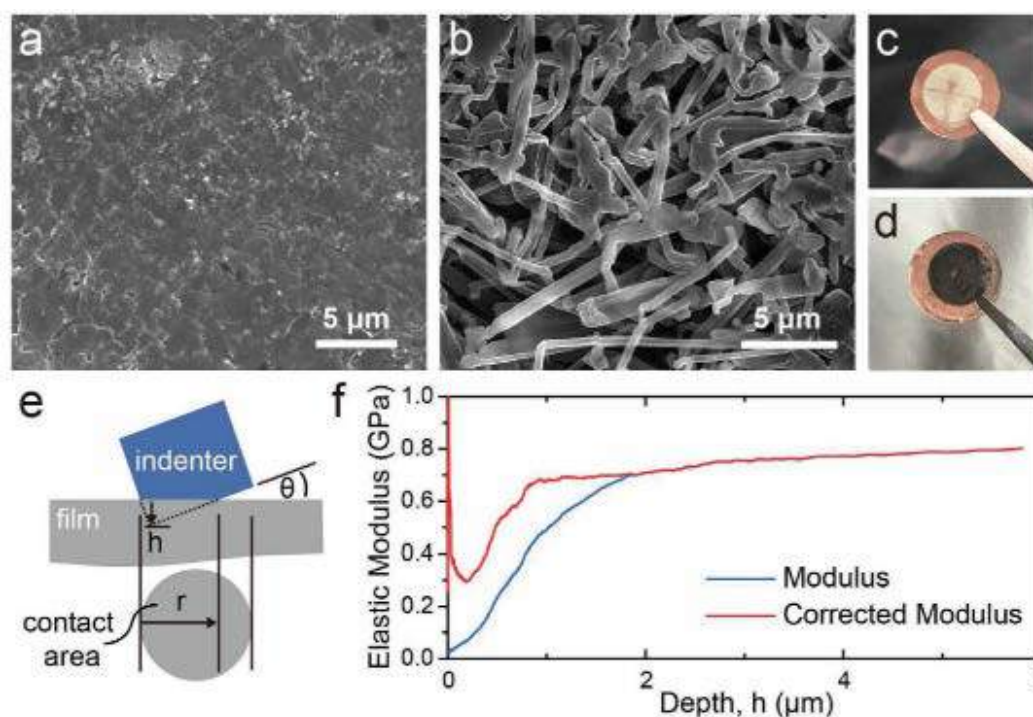


Figure II-491. Top-view SEM images and the corresponding digital photographs of Li deposition after five cycles on a,c) artificial SEI protected Cu and b,d) bare Cu foil. e) Schematic showing the configuration of nanoindentation measurements. f) Elastic modulus versus depth of a representative indentation test.

Previously, we have employed the nanoscale interfacial engineering approach using inter-connected hollow carbon spheres, two-dimensional boron nitride and graphene on Cu current collectors as stable artificial SEI for Li metal. The strategies effectively suppressed Li dendrite growth and greatly enhanced the Coulombic efficiency during cycling. Recently, we continue to explore the different coating materials in search for better surface protections on Li metal anode. Here, we took the advantages of the “solid-liquid” hybrid behavior of Silly Putty (SP), a popular children’s toy, as the interfacial layer for Li metal anodes. SP can reversibly switch between its “liquid” and “solid” properties in response to the rate of Li growth to provide uniform surface coverage and dendrite suppression, respectively, therefore enabling the stable operation of Li metal electrodes.

The idea is illustrated schematically in Figure II-492. Silly Putty (SP), primarily comprised of polydimethylsiloxane (PDMS) crosslinked by transient boron-mediated bonds, is technically termed as a “shear thickening material”. Namely, the rigidity of SP increases significantly as the deformation rate increases. It can even temporarily become an elastic solid if the deformation rate is too fast for the dynamic crosslinks to temporally break and reconnect. Therefore, when coated on the surface of Li metal, SP flows on

the time scale of each charging and discharging circle and can uniformly covers the electrode surface to serve as a stable interface between the Li metal and the electrolyte. However, if occasionally there are some “hot-spots” where the deposition and expansion of Li is faster than at other places on the electrode, the stiffness of the local SP coating consequently increases. As such, SP acts as a clamping layer to help eliminate fast local overgrowth or expansion of Li metal and the SEI breakage, effectively suppressing Li dendrite growth.

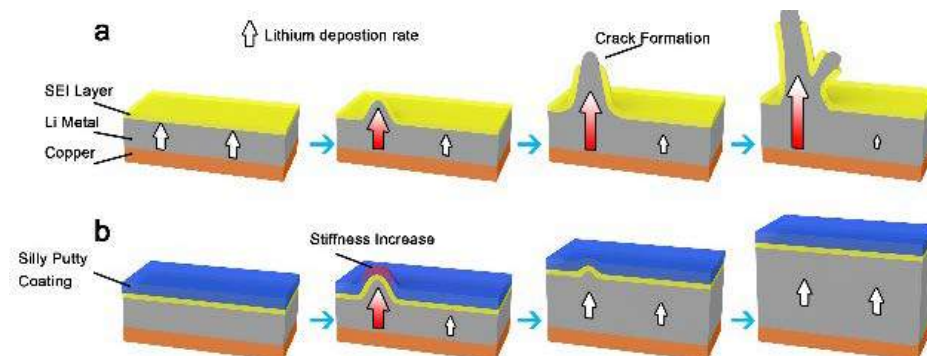


Figure II-492. Schematic showing the design of silly putty (SP) modified Li anode. Top shows the conventional Li dendrite evolution process, while the bottom shows the Li deposition behavior on a SP modified surface.

The viscoelastic behavior of the SP was first studied by rheometer. As shown in Figure II-493, when the strain rate is low ($<10^{-2} \text{ s}^{-1}$), the loss modulus (G'' , which represents the viscous property), is significantly larger than the storage modulus (G' , which represents the elastic property), indicating that the viscous property dominates the behavior and the SP behaves more like a flowable liquid. As the strain rate increases, G' increases significantly, indicating that the SP becomes stiffer. G' even exceeds G'' by almost an order of magnitude at high strain rates ($>10^{-2} \text{ s}^{-1}$), at which SP exhibits more elastic solid-like behaviors. Therefore, similar to our expectation, SP indeed possess the interesting viscoelastic behavior, which makes it a favorable candidate as artificial SEI for Li metal anode.

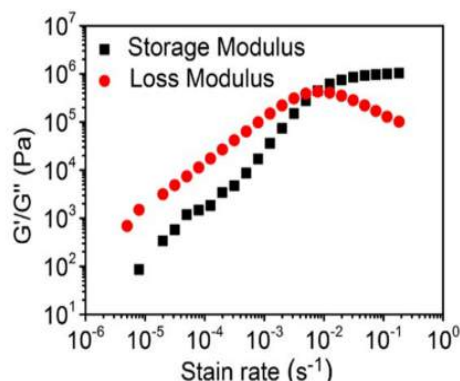


Figure II-493. The rheological study of SP.

The Li stripping/plating Coulombic efficiency (CE) of SP-coated Cu electrode was tested (Figure II-494). The SP-coated electrode showed good cycling performance, maintaining an average CE of 97.6% for over 120 cycles at 0.5 mA cm^{-2} . In comparison, control electrodes without SP coatings exhibited poor performance, with CE dropping below 90% after only 75 cycles. At a higher current density of 1 mA cm^{-2} , the SP-modified electrode achieved an average CE of 97.0% over 120 cycles, while the control electrodes maintained a CE of over 90% for only 65 cycles.

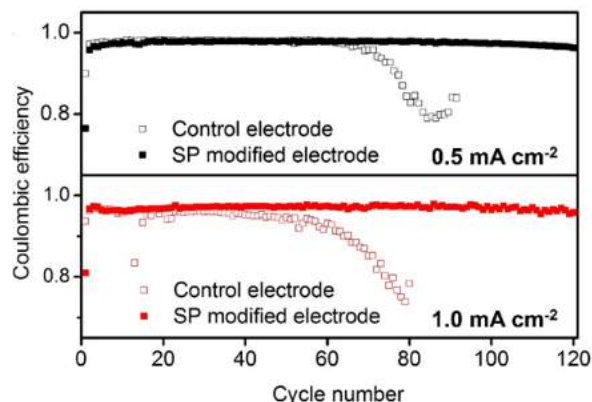


Figure II-494. CE of Li deposition/stripping (1 mAh cm^{-2}) on SP-modified electrodes and control Cu electrodes at different current densities.

Previously, we have developed three-dimensional (3D) Li anode composites, which realized minimum volumetric change at the electrode level during cycling, more uniform Li deposition behavior and better electrochemical performance. To further improve the 3D Li metal anode design towards practical applications, effective protective surface coatings are essential. Among the surface protection materials, Li fluoride (LiF) has gained special attention due to its wide electrochemical stability window with negligible solubility in most of the electrolytes as well as its capability of regulating surface tension. In the early stage, it was found that the addition of HF or fluorinated compounds into electrolyte would help form LiF in SEI and enable more uniform Li deposition. However, these methods are unlikely to produce high-quality continuous and conformal LiF coating on Li metal. Instead, dispersive LiF domains would form with many weakly linked grain boundaries, which would easily fracture during Li metal plating and stripping. Moreover, HF and other fluorinated compounds are highly hazardous reagents, which might impose extra challenges in either industrial processing or battery packaging. Herein, we explored the possibility of gas phase reaction (using Freon R134a, 1,1,1,2-tetrafluoroethane, as the reagent) in attempt to produce high-quality LiF passivation layers conformally on 3D Li metal anode. The idea is illustrated schematically in Figure II-495. By exposing Li metal to Freon R134a gas, assisted with controlled gas pressure, and reaction temperature, we were able to coat a dense and uniform LiF layer with tunable thickness directly onto metallic Li.

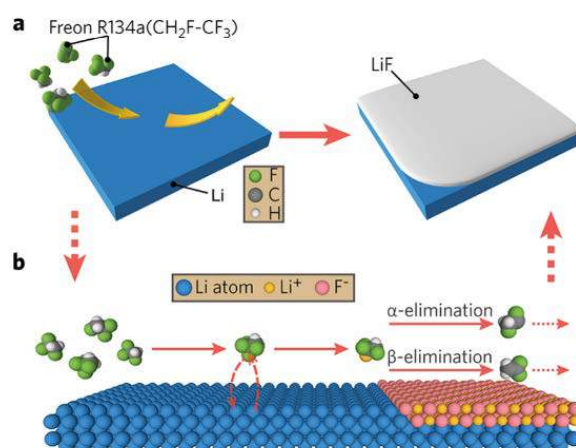


Figure II-495. (a) Schematic showing the surface treatment of Li metal with Freon R134a. (b) Proposed major chemical reactions at the early stage of surface treatment.

It was found that at a fixed temperature, increasing gas pressure would accelerate the reaction and afford rougher surface; and when gas pressure was fixed, the reactivity increased with temperature. At temperature below 150 °C, the surface was smooth without visible domains, while once the temperature was increased to approaching the melting point of Li metal, the reaction occurred in a much more vigorous fashion and formed micron-sized and porous LiF domains. Thus, to obtain high-quality LiF coating and sufficient reaction rate, 150°C and 0.5 atm is a good condition for conducting the surface coating. Figure II-496 shows the SEM images of a LiF-coated Li foil, where the top view shows smooth LiF surface, and the cross-section indicates a uniform thickness of ~40 nm.

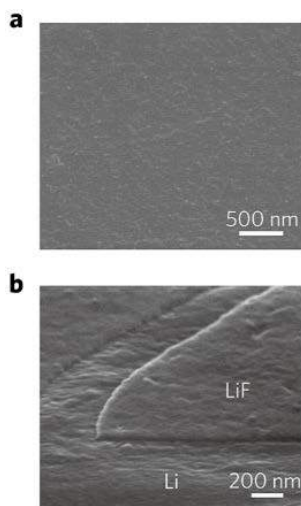


Figure II-496. High-resolution SEM images showing the (a) surface morphology and (b) cross-section of a LiF-coated Li foil.

To study the efficacy of the LiF coating for improving electrochemical stability of 3D Li metal anode (Li metal infused into layered graphene oxide matrix, Li-rGO), time-dependent electrochemical impedance spectroscopy studies were carried out, as shown in Figure II-497. LiF-coated Li-rGO do not show obvious increase in impedance within the tested period of time, indicating robust surface passivation that suppressed continuous side reactions and reduced the initial SEI formation. In addition, more stable symmetric cell cycling with suppressed increase in polarization was also observed.

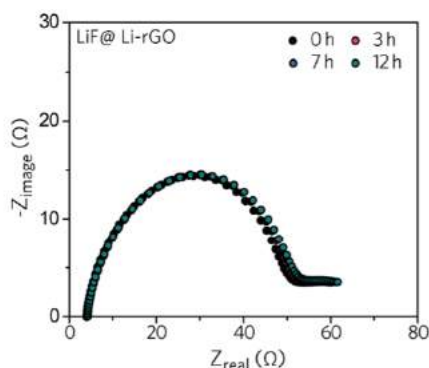


Figure II-497. Time-dependent electrochemical impedance measurement on 3D Li metal symmetric cells with LiF coating.

To address the challenges and make Li metal anode a viable technology, an attractive strategy is to replace the volatile liquid electrolytes with nonflammable solid counterparts that are electrochemically stable against Li and mechanically robust to suppress dendrite growth. Although a wide variety of solid electrolytes for Li

batteries have been developed throughout the years, the same critical challenge, which is the interfacial detachment between solid electrolytes and electrodes, awaits to be solved for all the systems.

Unlike liquid electrolytes, solid electrolytes barely have any fluidity to form a continuous contact with active materials inside the electrodes. Therefore, the electrochemical process can be severely limited by the contact area, leading to great interfacial resistance and low utilization of electrode capacity. The issue is even more pronounced for the Li metal anode, whose interfacial fluctuation in practical applications can be as large as tens of micrometers, making it difficult to cycle the solid-state Li batteries at high capacity and current density. Here, we present a paradigm shift on the structural design of solid-state Li batteries: Unlike all the previous studies where solid-state cells were constructed using planar Li foil, we adopted three-dimensional (3D) Li anode with high electroactive surface area for the first time, and the challenge of creating a conformal and continuous ionic contact between the 3D Li anode and the bulk solid electrolyte was successfully addressed via a flowable ion-conducting interphase (Figure II-498). This structural design has several major advantages: first, the adoption of a 3D Li anode significantly increases the electrode-electrolyte contact area, dissipating the current density to facilitate charge transfer and offering the opportunities to high-power operation. Second, by dividing bulk Li into small domains, the interfacial fluctuation during cycling can be reduced to the submicrometer scale, enabling the cells to be cycled at a much higher capacity. More importantly, the incorporation of a flowable interfacial layer can accommodate the varying morphology at the 3D Li anode surface during cycling, which is desirable for maintaining a continuous electrode-electrolyte contact. Finally, the 3D Li anode design can be adopted as a general approach in solid-state Li batteries, which is compatible with both solid polymer and inorganic ceramic electrolytes.

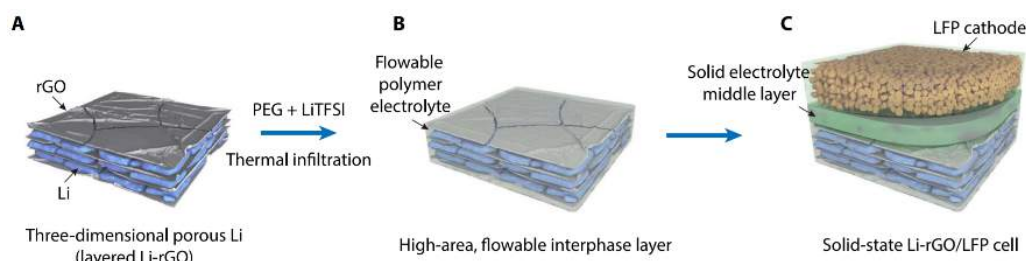


Figure II-498. Schematics illustrating the fabrication process of the 3D Li anode with flowable interphase for solid-state Li battery. (A) 3D Li-rGO composite anode was first fabricated. (B) A flowable interphase for the 3D Li-rGO anode was created via thermal infiltration of liquid-like PEG-LiTFSI at a temperature of 150 °C. (C) A CPE layer consisting of PEO, LiTFSI, and fumed silica or an LLZTO ceramic membrane was used as the middle layer, and high-mass loading LFP cathode with the CPE as the binder was overlaid to construct the solid-state Li-LFP full cell.

The electrochemical performance was tested pairing with LiFePO_4 (LFP) cathode. Notably, different from many previous studies on solid Li batteries where the cathode mass loading was kept low to minimize the interfacial delamination, a relatively high capacity cathode ($\sim 1 \text{ mAh cm}^{-2}$) was used here to highlight the effectiveness of our design strategy toward improving the interfacial contact. As can be seen from Figure II-499, significantly improved rate performance and cycling stability can be achieved.

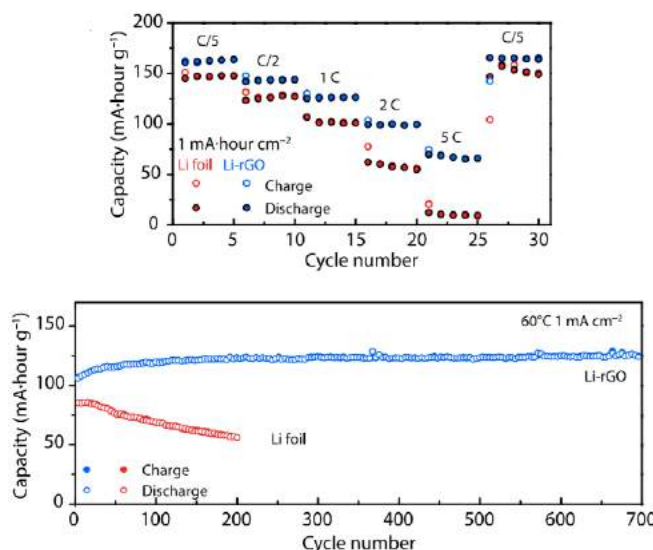


Figure II-499. Electrochemical performance of solid-state Li-LFP batteries.

Conclusions

In all, in the past one year, we have made significant progress in further developing stable host and passivation techniques for Li metal to afford minimal volume change and more stable cycling. By designing a Cu_3N nanoparticle/polymer composite as the passivation coating, we are able to *in-situ* convert the Cu_3N into Li_3N with high Li-ion conductivity. The coated anode exhibited highly improved cycling stability with high Coulombic efficiency. Due to the improved mechanical properties and homogenized Li-ion flux, the Li deposits exhibited more uniform and dense morphology. Later, we developed a new class of polymer coating with shear thickening effect, inspired by the silly putty. The polymer shows high stiffness under fast deformation, which can locally inhibit the fast dendrite growth, and facilitate the Li deposition in other areas. The new polymer coating enables smoother Li surface after deposition and thus more stable cycling.

The conventional spin coating method is good to protect Li metal with planar surface, but it is hard to be applied to a three-dimensional (3D) surface with our “stable host” design. As a consequence, we further developed Freon as gaseous reagent to conformally coat LiF onto 3D surface of Li. With the conformal LiF coating onto a Li-rGO composite anode we developed previously, we are able to demonstrate further improved cycling stability.

The 3D form of Li and the resulting minimal volume change offers the opportunity to design all-solid-state batteries with much better interfacial contact. In this consideration, we combined a flowable interface with 3D Li-rGO composite anode to build all-solid-state batteries. By pairing with LiFePO_4 cathode, we demonstrated highly improved rate capability and cycling stability in the all-solid-state full batteries.

In the past year, we have fulfilled the milestones of the projects, including 1) Rational design of composite artificial solid electrolyte interphase for the stabilization of three-dimensional nanoporous Li metal anode; 2) Explore novel materials and their properties as artificial SEI layer on Li metal; 3) Explore surface coating techniques for Li metal stabilization; 4) Stabilizing three-dimensional Li metal anode with solid electrolytes. Great progress has been achieved and the project is on track as planned.

Key Publications

1. W. Liu, W. Li, D. Zhuo, G. Zheng, Z. Lu, K. Liu, and Y. Cui, "Core-Shell Nanoparticle Coating as an Interfacial Layer for Dendrite-Free Lithium Metal Anodes", *ACS Central Science* **3**, 135-140 (2017)
2. Y. Liu, Y. Cui, et al., "An Artificial Solid Electrolyte Interphase with High Li-Ion Conductivity, Mechanical Strength, and Flexibility for Stable Lithium Metal Anodes", *Adv. Mater.* **29**, 1605531 (2017)
3. D. Lin, Y. Liu, and Y. Cui, "Reviving the lithium metal anode for high-energy batteries", *Nature Nanotech.* **12**, 194-206 (2017)
4. K. Liu, A. Pei, Z. Bao, Y. Cui, et al., "Lithium Metal Anodes with an Adaptive "Solid-Liquid" Interfacial Protective Layer", *J. Am. Chem. Soc.* **139** (13), 4815-4820 (2017)
5. A. Pei, G. Zheng, F. Shi, Y. Li, and Y. Cui, "Nanoscale Nucleation and Growth of Electrodeposited Lithium Metal", *Nano Lett.* **17** (2), 1132-1139 (2017)
6. D. Lin, Y. Cui, et al., "Conformal Lithium Fluoride Protection Layer on Three-Dimensional Lithium by Nonhazardous Gaseous Reagent Freon", *Nano Lett.* **17** (6), 3731-3737 (2017)
7. D. Lin, Y. Liu, A. Pei, and Y. Cui, "Nanoscale perspective: Materials designs and understandings in lithium metal anodes", *Nano Res.* (2017) DOI: 10.1007/s12274-017-1596-1
8. D. Lin, Y. Cui, et al., "Three-dimensional stable lithium metal anode with nanoscale lithium islands embedded in ionically conductive solid matrix", *PNAS*, **114**, 18 4613-4618 (2017)
9. Y. Li, Y. Cui, et al., "Revealing Nanoscale Passivation and Corrosion Mechanisms of Reactive Battery Materials in Gas Environments", *Nano Lett.* **17** (8), 5171-5178 (2017)
10. H. Wang, Y. Cui, et al., "Ultrahigh-current density anodes with interconnected Li metal reservoir through overlithiation of mesoporous AlF_3 framework", *Sci. Adv.* **3**(9), e1701301 (2017)
11. Y. Li, Y. Li, Y. Cui, et al., "Atomic structure of sensitive battery materials and interfaces revealed by cryo-electron microscopy", *Science* **358**(6362), 506-510 (2017)

II.H.7 Lithium Dendrite Prevention for Lithium Batteries (PNNL)

Wu Xu, Principal Investigator

Pacific Northwest National Laboratory
902 Battelle Boulevard
Richland, WA 99354
Phone: 509-375-6934
E-mail: wu.xu@pnnl.gov

Ji-Guang Zhang, Co-Principal Investigator

Pacific Northwest National Laboratory
902 Battelle Boulevard
Richland, WA 99354
Phone: 509-372-6515
E-mail: jiguang.zhang@pnnl.gov

Tien Duong, Technology Manager

U.S. Department of Energy
Phone: 202-586-7836
E-mail: Tien.Duong@ee.doe.gov

Start Date: October 1, 2015
Total Project Cost: \$1,200,000

End Date: September 30, 2018
DOE share: \$1,200,000

Non-DOE share: \$0

Project Introduction

Lithium (Li)-metal batteries are regarded as the “Holy Grail” of high density energy storage systems because Li-metal anode has an ultrahigh theoretical specific capacity (3860 mAh g^{-1}), the lowest negative electrochemical potential (-3.040 V vs. standard hydrogen electrode), and very low density (0.534 g cm^{-3}). However, their commercial applications have been hindered by the safety concerns due to Li dendrite growth and the short cycle life associated with low Coulombic efficiency (CE) of Li deposition/stripping. The dendritic Li generated at the anode surface can be self-amplified and lead to internal short circuiting of the battery and even more serious safety problems such as thermal runaway, fire, and explosion. The thermodynamically unstable Li in organic electrolytes often leads to low CE, more reactions between Li and electrolyte components to generate thick surface layer with high impedance, thus causing significant change in the morphology of Li metal and depletion of electrolyte. In our previous works, we discovered that an appropriate cycling protocol of slow charging and fast discharging can greatly improve the stability of Li metal anode and the long-term cycling stability of the Li metal cells. We also found that the LiTFSI-LiBOB dual-salt electrolytes with and without additives can significantly enhance the fast charging capability of the Li metal batteries. However, the fundamental mechanism behind these experimental observations have not been well understood. In FY17, our works have been focused on understanding the fundamental mechanism related to the stabilization of Li metal/liquid interface in various conditions. This will guide further development of the electrolytes to protect Li metal anode and to enhance the fast charging capability and the long cycle life of Li metal batteries.

Objectives

- Enable Li metal to be used as an effective anode in rechargeable Li-metal batteries for long cycle life at a reasonably high current density.
- Investigate the effects of various lithium salts, additives and carbonate-based electrolyte formulations on Li anode morphology, Li Coulombic efficiency (CE) and battery performances in terms of long-term

cycling stability at room temperature and elevated temperatures and at various current density conditions, rate capability, and low temperature discharge behavior.

- Characterize the surface layers on Li anode and cathode.
- Use computational calculations to get the theoretical data of solvates of cation-solvent molecules to explain the obtained battery performances.

Approach

The following approaches have been used to reach the objectives outlined above. First, the mechanism of LiPF₆ additive in LiTFSI-LiBOB dual-salt electrolyte on the protection of Li metal was investigated. Second, the charge process was verified experimentally by *in-situ* time-of-flight secondary ion mass spectrometry (ToF-SIMS) to detect the possible formation of a transient high-concentration Li⁺ electrolyte layer on Li metal surface during fast discharge process. Third, the effects of LiAsF₆ and cyclic carbonate additives on Li deposition and Li CE were investigated. Fourth, four lithium imide-lithium orthoborate dual-salt electrolytes were further investigated to find out the effects of different dual-salt chemistries on the protection of Li metal anode and the cycle life of related Li metal batteries. Fifth, the effects of Li capacity utilization and charge current density on the stability of Li metal anode and the cyclability of related Li metal batteries were investigated using high cathode areal loading of 3.5 mAh/cm². Finally, new dual-salt electrolytes with an electrochemical stability window of 0 to 4.5 V were developed through screening solvents, lithium salts and additives. Various characterization technologies, including high-resolution scanning electron microscopy (SEM), transmission electron microscopy (TEM), X-ray photoelectron spectroscopy (XPS) and ToF-SIMS were used to analyze the morphology and composition of the interfacial films on Li-metal surfaces. The results obtained in these investigations will be combined with density functional theory (DFT) calculations to reveal the mechanisms that led to the enhanced performance in Li-metal batteries.

Results

1. Mechanism of LiPF_6 additive in LiTFSI-LiBOB dual-salt electrolyte on Li metal protection

The LUMO energies of the lithium salts and solvents studied in this work reveal that the reduction voltages of these salts and solvents decrease in the following order: LiBOB >> LiTFSI > ~LiPF₆ >> EC > EMC (Figure II-500a). LiBOB could be easily reduced to form an SEI layer on the Li metal surface and dictates the morphology of Li during the deposition process. Cyclic voltammetry analysis is consistent with the LUMO energies, demonstrating that LiBOB in the pure and the LiTFSI-LiBOB dual-salt electrolytes shows a reduction peak with an onset potential of ca. 1.1 V vs. Li/Li⁺, while the onset reduction potentials for pure LiTFSI and LiPF₆ electrolytes are hard to find. The addition of LiPF₆ additive in the dual-salt electrolyte greatly suppresses the reduction peak at 1.1 V for LiBOB, probably due to the superior SEI layer formed. The XPS and EDS results are also in good agreement with the calculated LUMO energies.

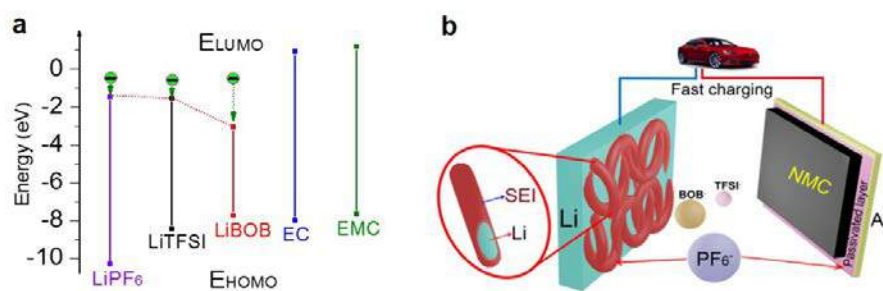


Figure II-500. (a) HOMO and LUMO energies of lithium salts (LiPF₆, LiTFSI, LiBOB) and solvents (EC, EMC). The vertical lines indicate the electrochemical stability window of related lithium salts and solvents. (b) Schematic illustration demonstrating that LiPF₆ additive in LiTFSI-LiBOB dual-salt electrolyte improves the stability of the Al current collector and the Li metal anode.

Based on the electrochemical performance and post-mortem analysis, a functioning mechanism of LiPF_6 additive in LiTFSI-LiBOB dual-salt electrolyte has been proposed (Figure II-500b). On one hand, the LiPF_6 additive plays an important role in stabilising the aluminium (Al) current collector and maintaining good electrical contact between the active material and Al. On the other hand, a small amount of LiPF_6 in the LiTFSI-LiBOB dual-salt electrolyte significantly alters the nature of the SEI layer formed on the Li metal anode. The decomposition products of LiPF_6 , i.e., PF_5 and POF_3 , act as catalysts and induce the formation of polycarbonates and polyethers from the ring-opening polymerisation of EC molecules. The SEI layer formed on Li metal in the LiPF_6 -added dual-salt electrolyte is highly conductive and can minimize electrode polarisation. It can also prevent the accumulation of isolated or “dead” Li during each deposition/stripping cycle. In addition, the polycarbonates and polyethers formed in the SEI layer are flexible, can efficiently cover the Li metal surface, reduce the side reactions, hold the isolated/“dead” Li particles tightly and adhere to the bulk Li anode thus preventing the separation of the SEI layer from the bulk Li metal. Therefore, the utilization of Li metal initiates at the surface and slowly propagates inward. More importantly, there is no internal short circuit occurring at a charge current density even up to 5.25 mA cm^{-2} . The high charging capability and the excellent cycle life validate the LiPF_6 -added LiTFSI-LiBOB dual-salt electrolyte as an appealing functional electrolyte for high performance Li metal batteries.

2. Verify the formation of a transient high Li^+ -concentration electrolyte layer during fast discharging

The composition of the surface passivation layer of Li anode during fast and slow discharge rates of the $\text{Li}||\text{LiCoO}_2$ cells were characterized by *in-situ* ToF-SIMS. The electrolyte was 1.0 M LiPF_6 in EC-EMC. The schematic configuration and a photo of the cell are shown in Figure II-501. The $\text{Cu}||\text{LiCoO}_2$ cell was charged first to deposit Li on Cu substrate at a slow rate, and then the cell was discharged at fast (1C) and slow (C/5) rates. The compositions of the surface layers formed on Li anode were analyzed *in operando* by ToF-SIMS. The test results indicate that the difference in Li^+ -content in SEI formed on Li anode during fast and slow discharge rates (1C vs. C/5) is not significant enough to show whether a concentrated Li^+ electrolyte is formed during fast discharge (Li stripping). This is probably because of the technical limitations of the current electrochemical cell and/or *in-situ* ToF-SIMS.

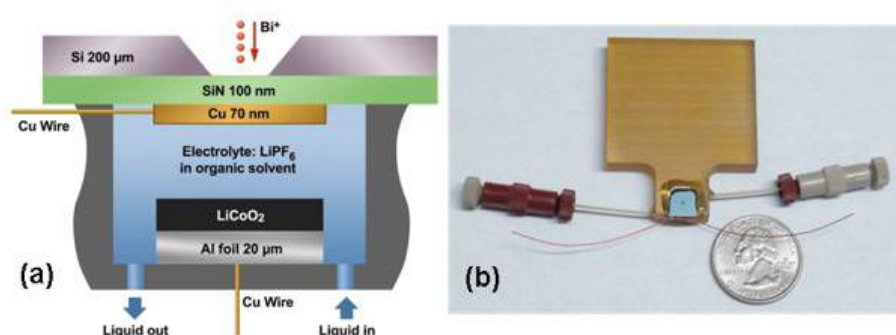


Figure II-501. (a) A schematic drawing of the liquid cell device with both anode and cathode integrated into the liquid cell. (b) A photo of the real device.

3. Guided Li deposition and improved Li CE through synergistic effects of LiAsF_6 and VC additives

The effects of additives in the LiPF_6/PC electrolyte on the morphologies of deposited Li metal and the cycling performance of $\text{Li}||\text{NMC}$ cells were investigated, and the results are shown in Figure II-502 and Figure II-503, respectively. It is seen from Figure II-502 that the baseline electrolyte leads to disordered and dendritic Li growth. Adding VC or FEC can eliminate Li dendrite formation but the surface of deposited Li is rough. Adding additive LiAsF_6 gives ordered Li nanorods growth but the Li surface is still rough. When using the additive mixtures of $\text{VC}+\text{LiAsF}_6$ and $\text{FEC}+\text{LiAsF}_6$, the Li surface is more smooth and uniform and the Li nanorods are more compact and well aligned. Figure II-503a indicates that the addition of LiAsF_6 does not increase the Li CE much, but VC or FEC improves the Li CE significantly. The combination of $\text{VC}+\text{LiAsF}_6$ or $\text{FEC}+\text{LiAsF}_6$ can increase Li CE from 73.2% for the baseline electrolyte to about 96.5%. The improved Li CE

brings to longer cycle life of Li||NMC111 cells and the VC+LiAsF₆ additive mixture shows the best cycling stability in the Li||NMC111 cells (Figure II-503b). The deposited Li morphologies, Li CE and cycling performance all indicate the synergistic effects of LiAsF₆ and VC or FEC additives. Such synergistic effects of additives LiAsF₆+VC in the electrolyte of 1 M LiPF₆/PC were investigated through linear sweep scan (LSV), XPS, and SEM. It is revealed for the first time that LiAsF₆ can be reduced to Li_xAs alloy phase and LiF, which can act as nano-sized seeds for Li growth and form a robust SEI layer. The addition of VC or FEC not only enables the uniform distribution of Li_xAs seeds because of the initial surface passivation of the Cu substrate, but also improves the SEI layer flexibility due to the formation of polymeric components in the SEI.

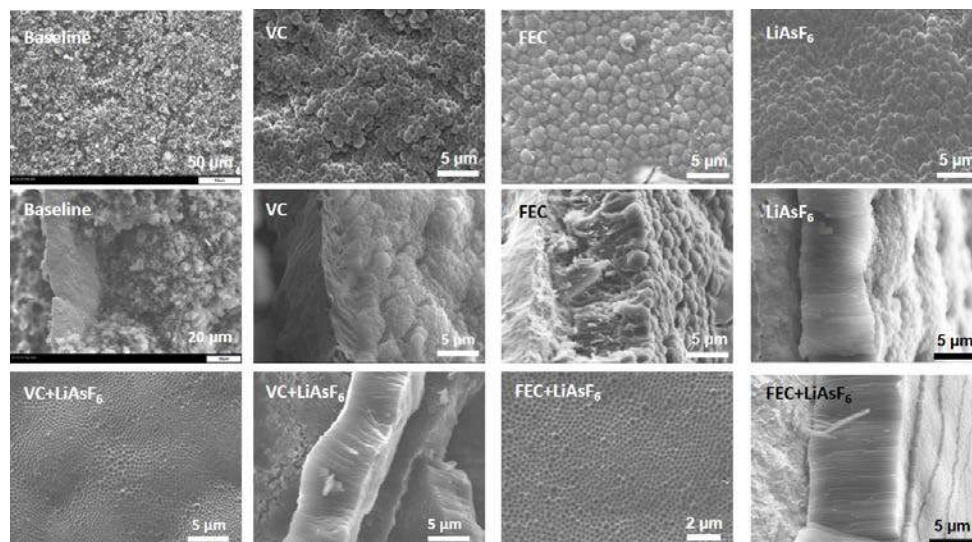


Figure II-502. SEM images (surface and cross-section views) of the deposited Li metal on Cu foils in electrolytes of 1 M LiPF₆/PC with different additives (VC, FEC and X) and additive mixtures (VC+X and FEC+X) at 0.1 mA cm⁻² for 15 hours.

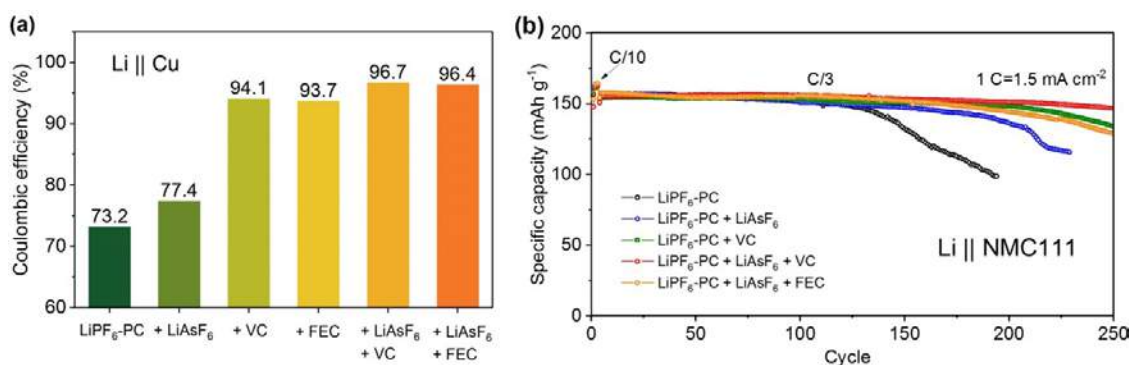


Figure II-503. (a) Average Li CE in electrolytes of 1 M LiPF₆/PC with different additives (VC, FEC and LiAsF₆) and additive mixtures (VC+LiAsF₆ and FEC+LiAsF₆) tested in Li||Cu cells. (b) Cycling stability of these electrolytes in Li||NMC111 cells at C/3 rate after two formation cycles at C/10 rate, in the voltage range of 2.7 and 4.3 V.

4. Effects of lithium imide-lithium orthoborate dual-salt electrolytes on stability of Li metal batteries

The effects of lithium imide and lithium orthoborate dual-salt electrolytes of different salt chemistries in carbonate solvents on the cycling stability of Li metal batteries were systematically and comparatively investigated. Two imide salts (LiTFSI and LiFSI) and two orthoborate salts (LiBOB and LiDFOB) were chosen for this study and compared with the conventional LiPF₆ salt. Density functional theory calculations indicate that the chemical and electrochemical stabilities follow the order of LiTFSI-LiBOB > LiTFSI-LiDFOB > LiFSI-LiBOB > LiFSI-LiDFOB. The experimental cycling stability of the Li metal cells with the

electrolytes follows the order from good to poor as LiTFSI-LiBOB > LiTFSI-LiDFOB > LiPF₆ > LiFSI-LiBOB, indicating that LiTFSI behaves better than LiFSI and LiBOB over LiDFOB in these dual-salt mixtures. The LiTFSI-LiBOB can effectively protect the Al substrate and form a more robust surface film on Li metal anode, while the LiFSI-LiBOB results in serious corrosion to the stainless steel cell case and a thicker and looser surface film on Li anode.

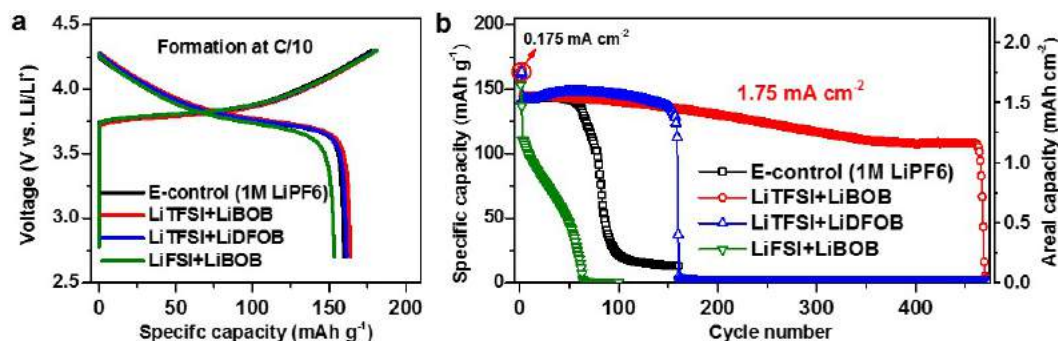


Figure II-504. (a) Initial charge/discharge voltage profiles at 0.175 mA cm^{-2} and (b) cycling performances of the baseline LiPF₆ electrolyte and the three different dual-salt electrolytes at a current density of 1.75 mA cm^{-2} after 3 formation cycles at 0.175 mA cm^{-2} .

5. Effects of Li capacity utilization and charge current density on stability of Li metal batteries

The effects of Li anode areal capacity utilization during each deposition/stripping cycle and the charge current density on the stability of Li metal anode and the cycling performance of the Li metal battery have been systematically investigated using the dual-salt electrolyte of LiTFSI-LiBOB in EC-EMC with 0.05 M LiPF₆ additive between 2.7 and 4.3 V. NMC111 cathodes with different areal capacities (from ~ 1.0 to $\sim 4.0 \text{ mAh cm}^{-2}$ with an interval of $\sim 0.5 \text{ mAh cm}^{-2}$) were used to represent the Li areal capacity utilization. Under the same charge current density at 1.0 mA cm^{-2} , very decent long-term cycling performance can be achieved for the NMC cathode with all areal capacity loadings or the Li areal capacity usages in the case of excess Li metal and electrolyte amount, meaning that the utilization of Li amount in each cycle does not affect the cycling stability of the Li metal cells when excess Li and electrolyte are used. Increase of Li capacity usage in each cycle causes variations in components of the SEI layer on Li anode and generates more ionic conductive species from this electrolyte. Further studies reveal for the first time that Li anode degradation and SEI thickness show linear relationship with the areal capacity usage. The amount of the consumed Li and the ratio of SEI thickness to NMC areal loading are kept almost the same values with increasing cathode loading, respectively. It implies that Li metal batteries with the same Li metal anode loading but higher cathode loading will degrade faster than those with lower cathode loading, thus lead to shorter cycle life. On the other hand, a higher charge current density results in a quicker capacity fade, meaning a shorter cycle life. The effect of charge current density is more significant than that of Li capacity utilization on the stability of Li metal anode and the cycle life of Li metal batteries.

6. Development of new electrolytes for stabilizing Li metal anode

The CE of Li cycling was also studied by optimizing the solvent compositions and adding combinational additives in dual-salt electrolytes of LiTFSI-LiBOB in EC-EMC. The increase of EC content in the solvent mixture will slightly improve the average Li CE from 87.4% for EC-EMC (4:6 wt) to about 91.6% for EC-EMC (7:3, 8:2 and 9:1 wt). Further addition of additives (LiPF₆, VC and FEC, in single or combination) will largely increase the average Li CE. For the additive combination of 0.05 M LiPF₆ + 2% VC + 2% FEC in the dual-salt electrolyte with EC-EMC (7:3 wt), the average Li CE can be further increased to 98.1%. This electrolyte also shows excellent stability with Li metal anode by the stable and low polarization voltage in Li||Li symmetric cells for at least 800 h at a current density of 0.5 mA cm^{-2} , and exhibits about 99.7% CE of Li

cycling in Li||NMC111 cells between 2.7 and 4.3 V at 2.0 mA cm⁻². More performance testing and characterization are under way.

Conclusions

1. In the LiTFSI-LiBOB dual-salt electrolyte, the additive level LiPF₆ induces the generation of a robust and conductive SEI layer enriched with polycarbonate species that can effectively bond the isolated or “dead” Li as well as other organic and inorganic components together with the bulk Li metal anode, mitigates the reduction of lithium salts especially LiBOB, and stabilizes Al current collector of the NMC cathode. Therefore, the Li metal anode can be well protected and the fast charging capability and the long-term cycle life of Li metal batteries can be significantly enhanced.
2. The SEI components on Li metal anodes during fast and slow discharge processes were analyzed by in-situ ToF-SIMS, but a concentrated electrolyte layer was not observed probably because the difference in Li⁺-content in SEI from fast and slow discharge rates is small.
3. Additive mixtures of LiAsF₆ and cyclic carbonate additives (VC or FEC) show synergistic effects on guiding the formation of smooth, uniform and dense nanorod Li metal deposition and largely increasing the Li CE from 73% to about 97%. The best additive combination of LiAsF₆+VC can enable the Li||NMC111 cells to be cycled stably for more than 250 cycles.
4. Among the four imide-orthoborate dual-salt mixtures, LiTFSI-LiBOB shows the best cycling stability because of its effective protection on Al substrate and formation of a more robust surface film on Li metal anode. Optimization of solvent composition and addition of VC+FEC additive mixture can further stabilize Li metal anode and increase Li CE to over 98%, thus extending the cycling stability of Li metal batteries.
5. Li capacity utilization and charge current density have significant effects on Li anode stability. A higher Li capacity utilization and a higher charge current density lead to more serious corrosion of Li metal, thus a less cycle life of related Li metal batteries.

Key Publications and Presentations

1. J. Zheng, M. H. Engelhard, D. Mei, S. Jiao, B. J. Polzin, J.-G. Zhang,* and W. Xu,* “Electrolyte Additive Enabled Fast Charging and Stable Cycling Lithium Metal Batteries”, *Nature Energy*, 2017, **2**, 17012.
2. S. Jiao, J. Zheng, Q. Li, X. Li, M. H. Engelhard, R. Cao, J.-G. Zhang*, and W. Xu*, “Behavior of Lithium Metal Anode under Various Capacity Utilization and High Current Density in Lithium Metal Batteries”, *Joule*, 2017, DOI: 10.1016/j.joule.2017.10.007.
3. X. Ren, Y. Zhang, M. H. Engelhard, Q. Li, J.-G. Zhang*, and W. Xu*, “Guided Lithium Metal Deposition and Improved Lithium Coulombic Efficiency through Synergistic Effects of LiAsF₆ and Cyclic Carbonate Additives”, *ACS Energy Letters*, 2017, DOI: 10.1021/acsenenergylett.7b00982.
4. X. Li, J. Zheng, M. H. Engelhard, D. Mei, Q. Li, S. Jiao, N. Liu, W. Zhao, J.-G. Zhang*, and W. Xu*, “Effects of Imide-Orthoborate Dual-Salt Mixtures in Organic Carbonate Electrolytes on the Stability of Lithium Metal Batteries”, submitted.
5. W. Xu, H. Xiang, J. Zheng, Q. Li, J.-G. Zhang, D. Mei, P. Yan, R. Cao, P. Bhattacharya, S. D. Burton, M. H. Engelhard, M. E. Bowden, Z. Zhu, C. Wang, S. Jiao, S. S. Cartmell, A. V. Cresce, K. Xu, B. Polzin, “CsPF₆ and Propylene Carbonate in Conventional LiPF₆/Carbonate Electrolytes for Enhanced Lithium-Ion Battery Performances in Wide Temperature Range”, Invited talk at *PRiME 2016*, October 3, 2016, Honolulu, HI.

6. S. Jiao, J. Zheng, H. Xiang, P. Shi, D. Mei, Q. Li, S. S. Cartmell, J.-G. Zhang, W. Xu, “Optimization of Dual-Salt Electrolytes for Rechargeable Lithium Metal Batteries”, Oral presentation at *PRiME 2016*, October 4, 2016, Honolulu, HI.
7. W. Xu and J.-G. Zhang, “Lithium Dendrite Prevention for Lithium Batteries”, Invited talk at *DOE BES/BMR/ABR/Battery500 Battery Research Information Exchange Meeting*, January 18, 2017, Berkeley, CA.
8. W. Xu, F. Ding, Y. Zhang, J. Qian, B. D. Adams, H. Xiang, J. Zheng, and J.-G. Zhang, “Lithium Metal Anodes and Rechargeable Lithium Metal Batteries”, Invited talk at *2017 MRS Spring Meeting & Exhibit*, April 19, 2017, Phoenix, AZ.
9. W. Xu, J. Zheng, H. Xiang, X. Chen, S. Jiao, F. Ding, Y. Zhang, J. Qian, M. H. Engelhard, D. Mei, and J.-G. Zhang, “Development of Dual-Salt/Carbonate-Solvents Electrolytes for Fast Charging and Stable Cycling Lithium Metal Batteries”, Invited talk at *231st ECS Meeting*, May 30, 2017, New Orleans, LA.
10. W. Xu and J.-G. Zhang, “Lithium Dendrite Prevention for Lithium Batteries”, Invited talk at *DOE's 2017 Annual Merit Review and Peer Evaluation Meeting*, June 8, 2017, Washington DC, DC.
11. J. Zheng, H. Xiang, M. H. Engelhard, D. Mei, S. Jiao, J.-G. Zhang, and W. Xu, “LiTFSI-LiBOB Electrolytes and LiPF₆ Additive to Enhance Charging Capability and Cycling Stability of Rechargeable Lithium Metal Batteries”, Poster presentation at *The 10th Beyond Li-Ion symposium (BLI-X)*, June 28, 2017, San Jose, CA.

II.H.8 Understanding Strategies for Controlled Interfacial Phenomena in Li-Ion Batteries and Beyond (TAMU)

Perla B. Balbuena, Principal Investigator

Texas A&M University
3122 TAMU
College Station, TX 77843
Phone: 979-845-3375
E-mail: balbuena@tamu.edu

Jorge M. Seminario, Co-Principal Investigator

Texas A&M University
3122 TAMU
College Station, TX 77843
Phone: 979-845-3301
E-mail: seminario@tamu.edu

Partha P. Mukherjee, Co-Principal Investigator

Texas A&M University
3123 TAMU
College Station, TX 77843
Phone: 979-862-6498
E-mail: pmukherjee@tamu.edu

Tien Duong, Technology Manager

U.S. Department of Energy
Phone: 202-586-7836
E-mail: Tien.Duong@ee.doe.gov

Start Date: October 1, 2016
Total Project Cost: \$1,333,335

End Date: September 30, 2019
DOE share: \$1,200,000

Non-DOE share: \$133,335

Project Introduction

This project will develop and apply novel first-principles-based theoretical-computational methods and mesoscale schemes to elucidate fundamental issues associated with ionic and electronic transport through solid-electrolyte interphase (SEI) components and their interfaces. These include growth and dissolution of SEI layer components as functions of evolving Si anode morphologies during cycling; role of the electrolyte on tuning of surface healing and SEI reforming; role of the electrolyte on surface wetting during Li plating; connection between microscopic electrode morphology and electrolyte structure, dynamics, and reactivity and macroscopic battery performance. We plan to use the knowledge gained with this fundamental understanding to elaborate strategies based on electrolyte formulation and electrode morphology design to solve practical issues associated with the instability of SEI at Si anodes during cycling and dendrite formation in Li metal anodes.

Objectives

The objective of this project is to evaluate and characterize interfacial phenomena in lithiated Si and Li metal anodes and to develop guidelines for potential solutions leading to controlled reactivity at electrode/electrolyte interfaces of rechargeable batteries using advanced modeling techniques based on first-principles.

Approach

The plan to overcome shortcomings, limitations, and challenges is based on obtaining a deeper understanding leading to sound strategies for solutions to the targeted issues. The approach combines density functional theory, ab initio molecular dynamics, and other ab initio techniques to characterize the chemical and electrochemical reactions in well-defined models and to explore the behavior of new electrolyte mixtures in specific electrode configurations and various states of charge. Details of the interfacial chemistry gained with ab initio techniques are used into classical molecular dynamics involving millions of atoms to investigate structural and dynamic behaviors of the electrode/electrolyte interface under applied fields. In the next step, Kinetic Monte Carlo and other mesoscopic models developed in our own groups are used to characterize long-time behavior in larger and more complex systems (for example dendrite growth or nanostructure assembly) and their impact on macroscopic properties and performance. Thus, computational analyses will be the basis to provide a comprehensive understanding for physics-based designs and completely new ideas for overcoming the described issues.

Results

SEI growth and cracking of lithiated Si nanoparticles

We studied several aspects of the SEI formation on pre-lithiated Si nanoparticles: a) effects of the electrolyte composition on the rate of SEI growth during lithiation; b) effects of specific coatings (graphene or graphene oxide, and self-healing polymers) on the interfacial stability of the pre-lithiated Si nanoparticle during lithiation. Regarding the first point, our main findings can be summarized in Figure II-505. The graph represents the change in the electronic charge of the Si atoms (average) due to electron transfer to the electrolyte. Therefore, this change in charge is proportional to the rate of growth of the SEI layer. Figure II-506 shows that when the nanoparticle is lithiated in presence of different electrolyte compositions the rate of SEI growth changes dramatically. In all cases there is a sharp increase in the initial stage of electrolyte reduction (the colored region) followed by a stabilization period (the plateau region). In absence of salt, the kinetics of initial reduction is slower (blue region) and the number of electrons transferred (i.e., the number of solvent molecules reduced) is larger than in the presence of salt (pink region). This simple test, obtained from ab initio molecular dynamics (AIMD) simulations gives significant information regarding the quality of the SEI. When the anion is present, the anion reduces first and the SEI nucleation starts (usually as LiF and other organic or inorganic radical anion fragments that bind to Li⁺), and the number of solvent molecules reduced decreases. When EC is substituted by FEC the initial rate of growth is much faster and the green region is narrower, indicating the faster stabilization. The rapid reduction of the fluorinated salt or fluorinated solvent/additive leads to formation of LiF, as already found in our previous work, which prevents the further reduction of EC molecules. More work is needed to elucidate the details of such prevention mechanism. Our initial results indicate that it is due to changes in the electronic structure and ionic transport at the solid/liquid interface. New DFT/AIMD studies were conducted to determine the role of coatings in controlling interfacial phenomena. We have tested two types of surfaces: graphene and graphene oxide, and also self-healing polymers. We have found that both coatings have advantages and disadvantages that are clearly found from the atomistic studies. The advantage of these structures is that they are able to control reactivity. However, the self-healing mechanism may be compromised by additional reactions. A work in collaboration with Dr. Chunmei Ban (NREL) is also being finalized respect to identification of reaction products when alucone is used as an artificial SEI layer on Si anodes. We were able to follow changes in the coordination structure and oxidation state of Al atoms and on the interfacial reactivity. We also published a letter regarding the initial stages of SEI layer formation on a alucone-coated lithiated Si surface. This work revealed the active role of Al in the SEI layer formed modifying the alucone coating.

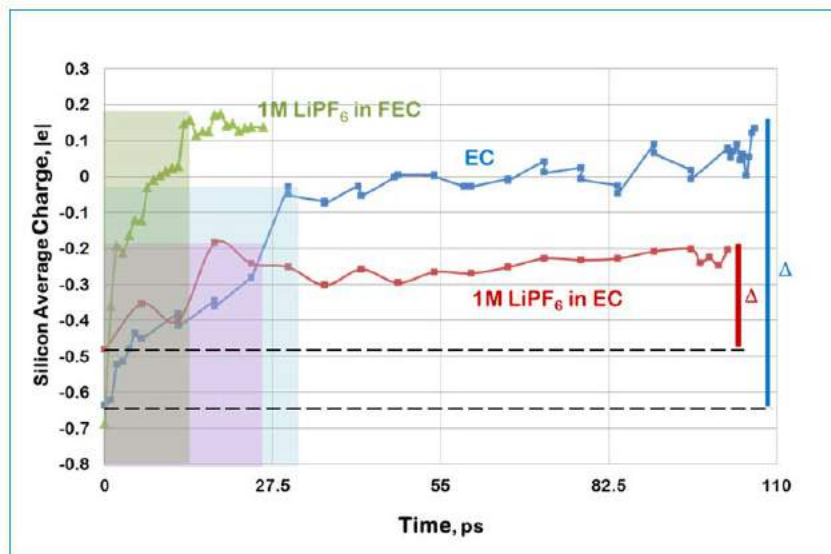


Figure II-505. Time evolution of the average Si charge obtained from AIMD simulations. The change of the Si electronic charge is due to electron transfer to the electrolyte, and therefore is proportional to the SEI layer rate of growth. These results were presented at the AMR meeting and published in the Journal of the Electrochemical Society.

In addition, the team was actively engaged in the characterization of cracking phenomena after the SEI layer is grown over the lithiated Si surface. Classical molecular dynamics simulations were employed to investigate nanoparticles of the order of 4 nm, and a mesoscopic model was employed for particles of ~500 nm.

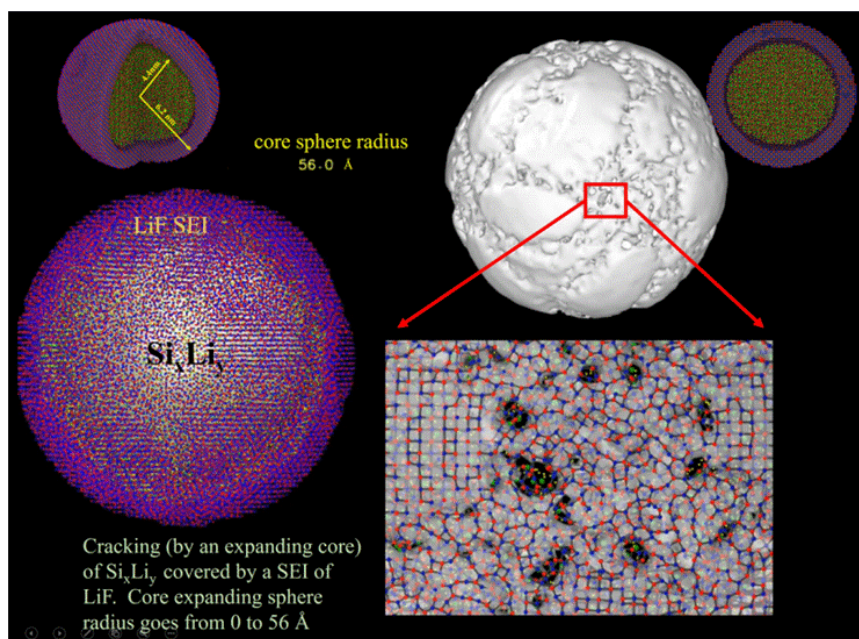


Figure II-506. Molecular dynamics simulations of surface cracking of a lithiated Si nanoparticle of ~4 nm covered by a LiF model SEI of ~1.5 nm. The expansion of the core leads to cracking which is manifested by bond damaging of the SEI coating initially, then resulting in macroscopically visible fractures.

The study characterized the swelling, alloying, and amorphization of a silicon nanocrystal anode in a full nanobattery model during the first charge. A dissolved salt of LiPF_6 in EC was chosen as the electrolyte solution and LiCoO_2 as cathode. External electric fields were applied to emulate the charging, causing the migration of the Li-ions from the cathode to the anode, by drifting through the electrolyte solution, thus converting pristine Si gradually into $\text{Li}_{14}\text{Si}_5$ when fully lithiated. The volume of the anode increases with the amorphization of Si. This model allowed the evaluation of stress changes in the electrode during the first charge. Current efforts are oriented to adding the solid-electrolyte interphase and determining the changes in volume and structure occurring during lithiation and delithiation. In parallel, a mesoscopic random lattice spring model was utilized to evaluate similar behavior in much larger nanoparticles. The model was coupled with solid state diffusion of Li in active particles and SEI formation to characterize fracture in the active material along with SEI film growth. It solves the Li-induced mechanics interaction (i.e., stress generation) in active particles and captures microcrack formation and propagation. The Li diffusion induced stress deforms the spring elements. Fracture occurs when the strain energy in a spring exceeds the fracture energy threshold and consequently these springs are removed from the network. The effect of fracture on diffusion inside the active material is incorporated by diffusion coefficients modified using a damage parameter. The cracks provide additional sites for Li intercalation electrochemical reaction as well as SEI reaction. It was found that peripheral (surface) cracks form easily during delithiation and central cracks (close to active material center) during lithiation (Figure II-507). The surface cracks provide extra area for intercalation and SEI reaction while isolated central cracks only hinder diffusion of Li ions inside the active material.

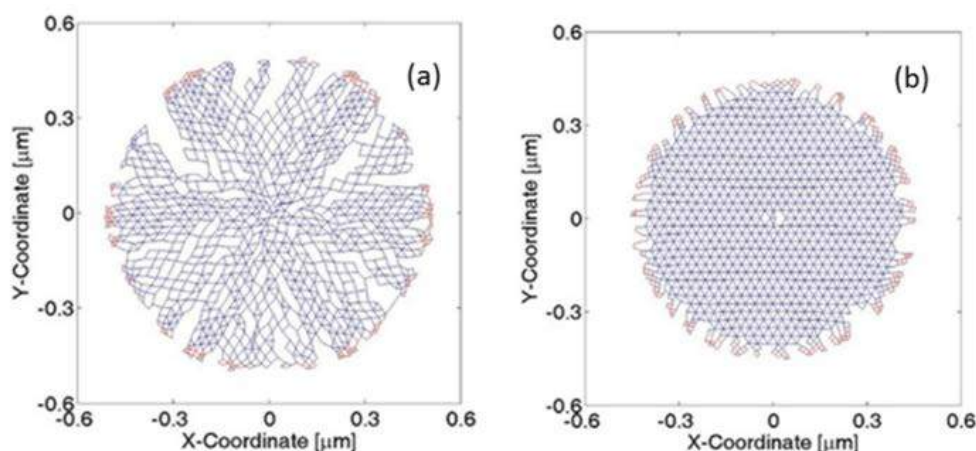


Figure II-507. Effect of core structure on cracking of ~ 500 nm nanoparticles. (a) crystalline core; (b) amorphous core. An SEI film covers the particle. There is a larger damage observed in the crystalline than in the amorphous particle.

The impact of high volumetric expansion during lithiation in Si on the damage stochastics inside a larger 500 nm diameter particle and in the SEI film is also studied with a mesoscopic model. Figure II-507 shows the lithium transport induced damage characteristics in crystalline (Figure II-507a) and amorphous (Figure II-507b) Si particle covered by a SEI film. It is evident that fracture in the crystalline Si particle exhibits significantly higher fracture due to two-phase diffusion as compared to a single-phase diffusion in amorphous Si, which generates large mismatch in volumetric strain between the core and surface. The SEI film shows complete rupture for both scenarios due to large stress from the expanding Si particle. Si particle diameter below 200-300 nm is preferable, which can reduce the microcrack-induced damage inside the particle as well as in the SEI film. This suggests that an appropriate combination of the mechanical properties of the SEI film and Si active particle may enable better strain accommodation.

Multiscale Model of SEI film Growth

Li-ion transport through the SEI layer influences the anode reactions, including Li reduction and intercalation into active material, as well as the SEI formation. In reality, there is a multiphase SEI growing on the electrode surface. Diffusion kinetics in the SEI layer along with multiphase SEI growth is modeled to understand the underlying physics. As shown in Figure II-508, two components: A (purple) and B (white) are considered. Here, Li-ion transport in component B is assumed much slower compared to that in A. The activation energies of Li-ion diffusion in the SEI are 46.1 KJ/mol for A and 65.3 KJ/mol for B, which means that the diffusion rate in A is over 2200 times that in B, and the activation energy for solvent diffusion within the SEI is fixed at 67.2 KJ/mol. The values of these activation energies fall within DFT ranges calculated by us for Li⁺ in Li₂CO₃. The model assumes that the solvent diffuses through the porous SEI and is reduced at the surface of the electrode. The effects of the volume fraction of B are depicted in Figure II-508(c). As the volume fraction increases, the total charging time increases, leading to a thicker SEI film for the first charging cycle. It is worth pointing out that the total charging time and SEI growth have non-linear relationships with the volume fraction of B. Figure II-508(a) and (b) illustrate the SEI film configurations, with volume fractions of 5% and 33%. Increasing the B volume fraction could induce nucleation of B hindering the fast transport pathways in component A. Figure II-508(d) shows that the content of active Li inside the SEI varies up-and-down along the SEI's depth, and the fluctuation becomes larger increasing the B volume fraction. In contrast, for the one-component SEI, it exhibits a predominantly linear Li-ion content trend near the electrode-SEI interface.

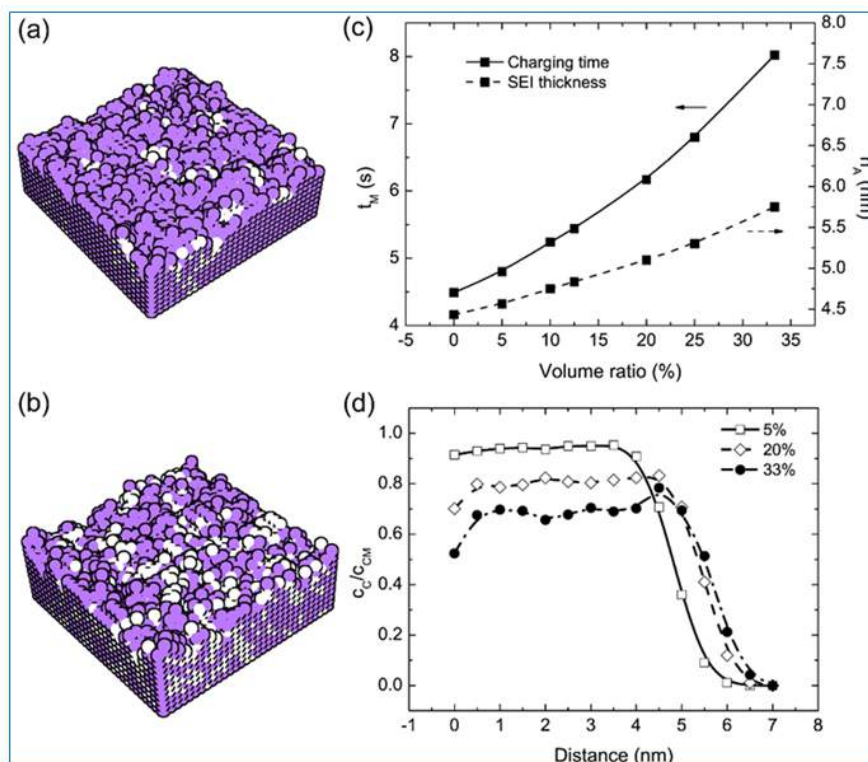


Figure II-508. SEI of two components with different activation barriers for Li diffusion: purple (A, $E_a = 46.1$ KJ/mol) and white (B, $E_a = 65.3$ KJ/mol). SEI morphologies at B volume fractions of 5% in (a) and 33% in (b). (c) Total charging time and SEI thickness for the first charge with varying B volume fraction. (d) Concentration of active Li traveling through the SEI interstitials (c_c) respect to the theoretical maximum (c_{CM}) as a function of SEI thickness for various B volume fractions.

The non-uniform distribution of component B largely accounts for the fluctuation in Li-ion content. Compared to the fast Li-ion diffusion in component A, Li-ions seem to be trapped after they enter the component B. Therefore, this “trapping effect”, along with the non-uniform distribution of B, induces the results in

Figure II-508(d). Moreover, Li-ion diffusion in SEI could become the rate-determining step to govern the overall electrode reactions when the volume fraction of B is large enough.

Conclusions

New insights were obtained regarding the SEI layer formation and cracking in lithiated Si anodes. It was found that the rate of SEI growth is extremely dependent on the nature of the electrolyte, and formation of specific SEI components such as LiF may stabilize the reactions. When a coating such as alucone is molecularly deposited to precover the anode surface, reactions can occur where the coating components (such as Al) participate in the reaction. As a consequence a new coating is generated that includes SEI components. Once the SEI is formed on lithiated Si surfaces of nanoparticles, volume expansion generated during battery charge may induce stress that ends up into bond damaging and finally the formation of cracks. Crystalline materials are more easily damaged than amorphous, that can release the stress easily. The microscopic details of crack formation were elucidated and quantified as a function of stress. Various coatings were computationally tested including graphene and graphene oxide, and a H-bonding forming polymer. The graphene and graphene-oxide materials were found helpful to control SEI formation, whereas the H-bonding polymer was found to be easy to deteriorate during lithiation and delithiation. A multiscale model of SEI growth was developed and tested for a 2-components SEI, and ionic transport through the layers was quantified as a function of the relative barriers for Li diffusion in each material. The model is able to quantify several important macroscopic properties as a function of microscopic parameters.

Key Publications

1. Kie Hankins, Fernando A. Soto, and Perla B. Balbuena, "Insights into the Li Intercalation and SEI Formation on LiSi Nanoclusters," *J. Electrochem. Soc.*, 164, (11), E3457-E3464, (2017).
2. L. Benitez; J. M. Seminario, "Ion Diffusivity through the Solid Electrolyte Interphase in Lithium-Ion Batteries," *J. Electrochem. Soc.* 164, (11), E3159-E3170. (2017).
3. V. Ponce; D. E. Galvez-Aranda; J. M. Seminario, "Analysis of a Li-Ion Nanobattery with Graphite Anode Using Molecular Dynamics Simulations," *J. Phys. Chem. C*, 121, 12959-12971, (2017).
4. Jose L. Gomez Ballesteros and Perla B. Balbuena, "Reduction of Electrolyte Components on a Coated Si Anode of Lithium-Ion Batteries," *J. Phys. Chem. Lett.*, 8, 3404-3408, (2017).
5. Feng Hao, Zhixiao Liu, Perla B. Balbuena, and Partha P. Mukherjee, "Mesoscale Elucidation of Solid Electrolyte Interphase Layer Formation in Li-ion Battery Anode," *J. Phys. Chem. C*, in press.
6. Luis E. Camacho Forero and Perla B. Balbuena, "Elucidating Electrolyte Decomposition under Electron-Rich Environments at the Lithium-Metal Anode," *Phys. Chem. Chem. Phys.*, in press.

II.H.9 Engineering Approaches to Dendrite Free Lithium Anodes (U of Pittsburgh)

Dr. Prashant N. Kumta, Principal Investigator

University of Pittsburgh
815C Benedum Hall
3700 O'Hara Street
Pittsburgh, PA 15261
Phone: 412-648-0223
E-mail: pkumta@pitt.edu

Dr. Moni K. Datta, Co-Principal Investigator

University of Pittsburgh
815C Benedum Hall
3700 O'Hara Street
Pittsburgh, PA 15261
Phone: 412-648-0223 Fax: 412-624-3699
E-mail: mkd16@pitt.edu

Dr. Oleg I. Velikokhatnyi, Co-Principal Investigator

University of Pittsburgh
815C Benedum Hall
3700 O'Hara Street
Pittsburgh, PA 15261
Phone: 412-648-0223
E-mail: olv3@pitt.edu

Tien Duong, Technology Manager

U.S. Department of Energy
Phone: 202-586-7836
E-mail: Tien.Duong@ee.doe.gov

Start Date: October 1, 2016
Total Project Cost: \$1,562,500

End Date: September 30, 2019
DOE share: \$1,250,000

Non-DOE share: \$312,500

Project Introduction

Dendrite formation in electrochemical systems occurs due to inhomogeneous current densities coupled with local diffusion gradients, surface roughness, and kinetic roughening. However, Li dendrite formation and growth are not well-understood. Adding to the complexity is the formation of the solid-electrolyte interphase (SEI). Control and elimination of Li metal dendrite formation is a veritable challenge and, if overcome, would render the universal adoption of lithium anode batteries (LAB) for stationary and mobile applications. The current project is a scientific study of novel approaches to address dendrite formation in LABs, electrolyte decomposition, and associated cell-failure. Development of dendrite free high-performance Li anodes will enable the use of Li-free cathodes opening up a myriad of possibilities pushing the envelope in terms of cathode capacity and battery energy density.

Objectives

This project will yield lithium metal anodes with specific capacity ≥ 2000 mAh/g (≥ 10 mAh/cm²), ~ 1000 cycles, coulombic efficiency loss $\leq 0.01\%$, coulombic efficiency: $\geq 99.99\%$ with superior rate capability. The goal is to systematically characterize the different approaches for generation of dendrite-free Li-metal anodes while also providing an understanding of the scientific underpinnings, and evaluate the microstructure and electrochemical performance of the dendrite free Li metal anodes. Generation of high performance dendrite

free Li metal anodes will successfully demonstrate generation of novel sulfur cathodes affording the fabrication of Li-S batteries meeting the targeted gravimetric energy densities ≥ 350 Wh/kg and ≥ 750 Wh/l with a cost target \$125/kWh and cycle life of at least 1000 cycles for meeting the *EV everywhere* blueprint.

Approach

This is a multi-year project comprised of three major phases to be successfully completed in three years.

- Phase – 1 (Year 1): Synthesis, characterization and scale up of suitable porous metal foams (PMFs) for use as current collectors for lithium anodes and Li-ion conductor (LIC) materials to prepare multilayer porous foams (MPFs).
- Phase – 2 (Year 2): Development of Li-rich structurally isomorphous alloy (SIA) anodes and Generation of composite multilayer anodes (CMAs).
- Phase-3 (Year 3): Advanced high energy density, high rate, extremely cycleable cell development.

The project will involve collaboration with Dr. Moni Kanchan Datta (UPitt) and Dr. Oleg I. Velikokhatnyi (UPitt) as Co-PIs. In addition, collaborations will be undertaken and continued with Dr. D. Krishnan Achary (UPitt) for solid-state nuclear magnetic resonance (MAS-NMR) characterization.

Results

Phase – 1 of the current project was aimed at the development of porous foam materials and multilayer porous foam materials with the aim of reducing orthogonal lithium nucleation and growth. Work in Q1 and Q2 of this project involved the use of electrochemically prepared foams. Figure II-509 shows attempts at the use of this innovative architecture to inhibit the formation of Li-dendrite during cycling (i.e., porous metal foams (PMFs) as novel dendrite resistant electrodes). Electrochemically made porous metal foams were prepared with varying amounts of hierarchical porosity/wall roughness. Figure II-510 shows the effect of using structurally isomorphous alloys (SIA) as electrodes for lithium metal plating/de-plating. It can be seen in Figure II-510a that upon cycling lithium metal on a copper current collector (cyclic voltammetry), most of the lithium is consumed via dendrite formation and solid electrolyte interphase (SEI) occurrence. On the other hand, it can be seen in Figure II-510b and Figure II-510c that the SIA electrodes exhibit excellent charge retention as well as coulombic efficiency over extended cycling at very high current densities on the order of ~ 80 -100 mA/cm².

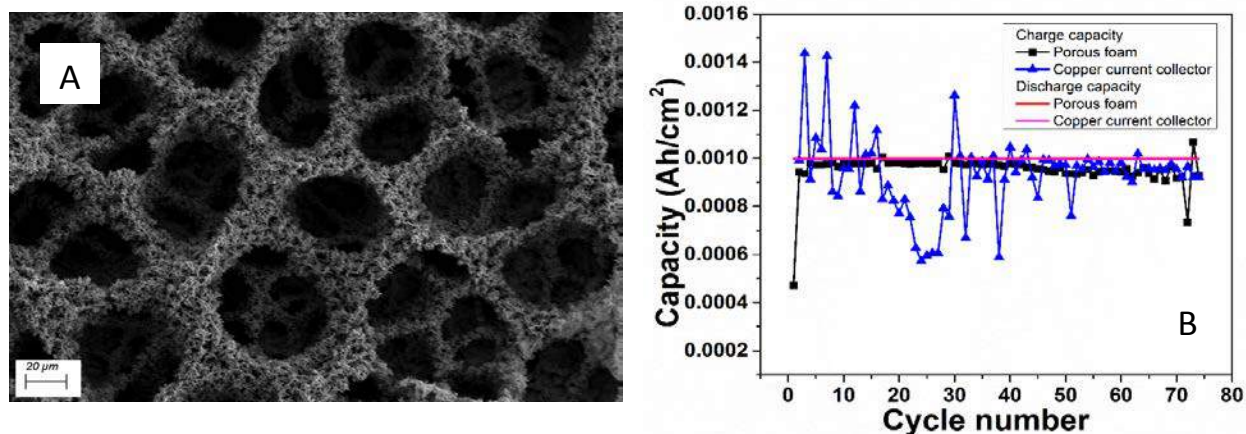


Figure II-509. (a) Electrochemically prepared porous metal foam (PMF). (b) Improvement in coulombic efficiency afforded by use of porous metal foam architecture.

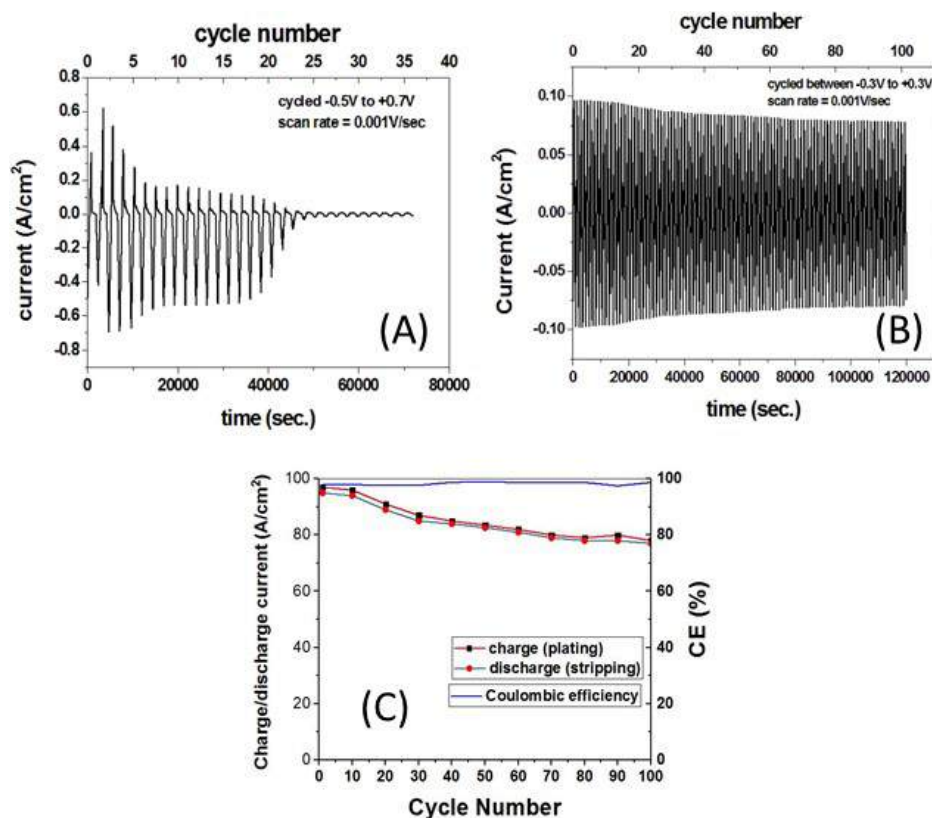


Figure II-510. Current-time profiles of cyclic voltammetry of (a) lithium-copper current collector cell (b) lithium-Li-SIA cell; (c) Coulombic efficiency of Li-SIA cell showing stability thereof.

It was, however, observed during post-cycling that the lithium dendrites tend to deposit at the edge of the porous foam materials since the separator contacts the stainless-steel spacer behind the foam structure (Figure II-511a). This issue was partially resolved by applying non-conductive polymeric coatings to the spacer (Figure II-511b).

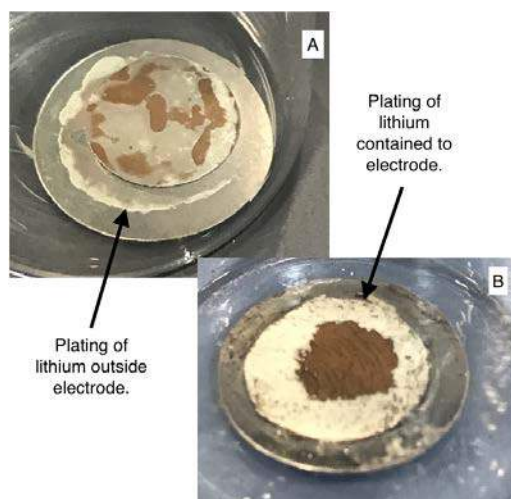


Figure II-511. (a) Formation of lithium on stainless steel spacer in coin cell tests (b) Diffusion pathways causing plating of lithium on polymeric coated stainless-steel spacers.

Figure II-512 demonstrates long-term cycling of 34 mAh/cm^2 at 1.6 mA/cm^2 using the SIA electrodes. Overpotential of $\pm 30\text{--}100 \text{ mV}$ is maintained for ~ 30 cycles with visible instabilities observed in the 30-60 cycles after which the overpotential is stabilized in the range of $\sim \pm 12\text{--}15 \text{ mV}$ for over 120 cycles. The intermediate instability region is possibly due to phase segregation and compositional inhomogeneity as observed in Figure II-512.

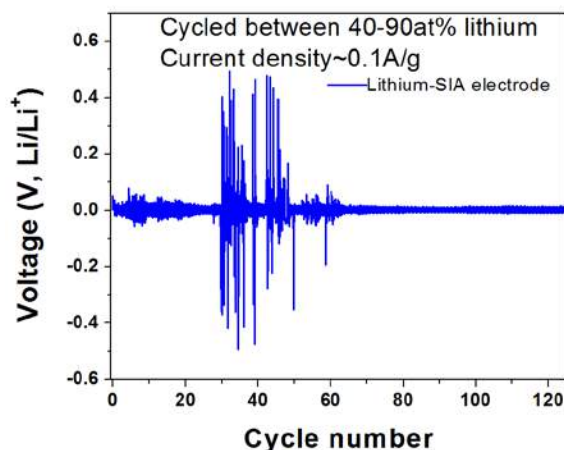


Figure II-512. SIA electrodes demonstrate long-term stability though there is a rise in overpotential due to possible phase segregation.

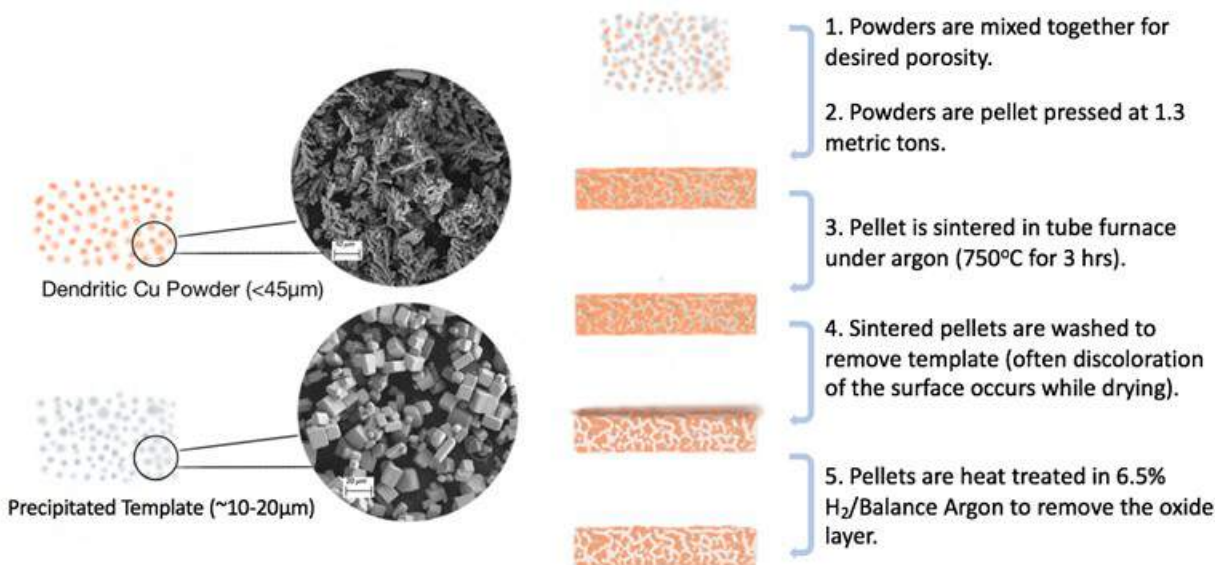


Figure II-513. Preparation method for Gen-2 porous metal foams.

Following Q1 and Q2, research migrated to Gen-2 PMFs with easily controlled porosities of up to 90% generated using the sacrificial template approach outlined in Figure II-513. Figure II-514a shows the SEM image of the Gen-2 PMFs after sintering and removal of the sacrificial template. A continuous network of pores (porosity $\sim 85\%$) is observed. Figure II-514b shows the cycling efficiency of Li plating and deplating on Gen-2 Cu foams at a current density of 1 mA/cm^2 for 1 h with a deplating cutoff voltage of 1V in 1.8 M LiTFSI, 0.1 M LiNO_3 in DOL:DME (50:50 vol.) electrolyte. The Cu foams demonstrate stable cycling to 60 cycles with a columbic efficiency of $\sim 90\%$ after which they transition into a region of constant fade similar to Li plating/deplating seen on the Cu foil. This transition from stable cycling to constant fade is attributed to

transition of the globular Li plating morphology within the porous architecture to a columnar morphology forming on the foam surface. Figure II-515a shows the cross section of the cycled foam electrodes. Figure II-515b and Figure II-515c show different deposition morphologies in each region attributed to competitive SEI layer formation.

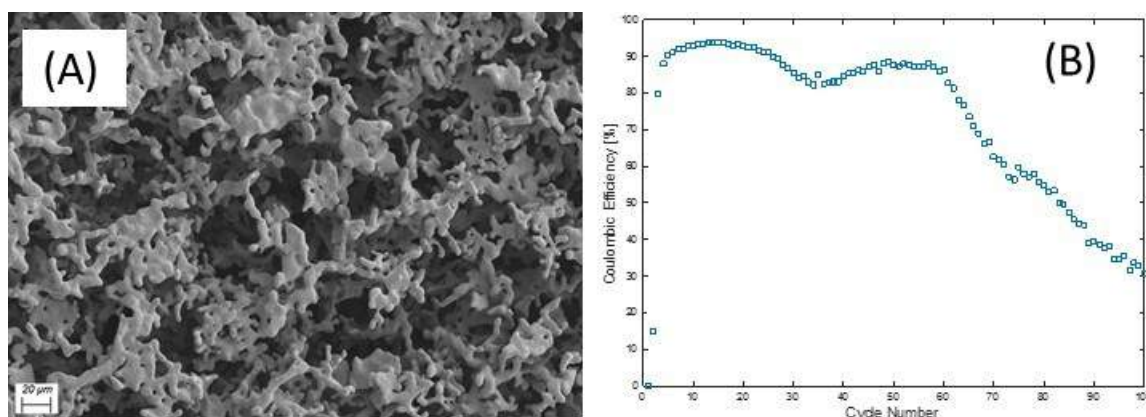


Figure II-514. (a) SEM image of the high porosity (~85%) Cu foams after sintering and removal of the sacrificial template. (b) Gen-2 Cu Foam electrodes demonstrate stable cycling region of 60 cycles at ~90% coulombic efficiency.

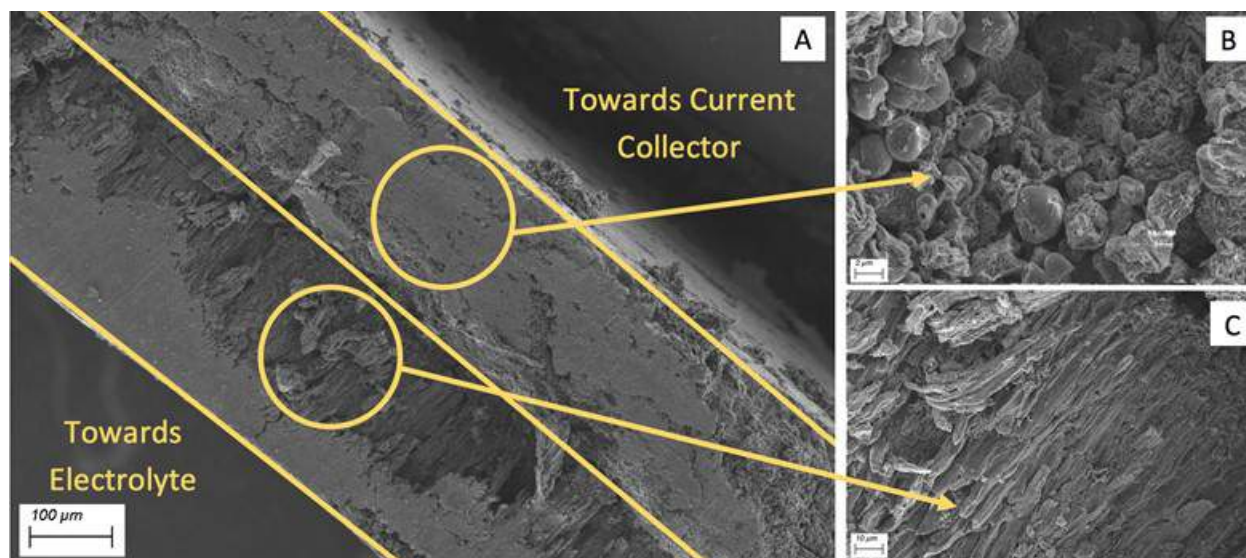


Figure II-515. SEM images of the porous Cu foam electrodes after cycling (~200 cycles). (A) Cross-section view, (B) Close up of lithium deposited within the foam structure, and (C) Close up of lithium deposited on top of the foam surface following pore closure by competitive SEI formation in the foam structure.

The most recent work of this project has involved attempts at controlling the formation of the SEI layer and limiting growth during extended cycling. Unfortunately, increasing the thickness of the PMFs offered only minimal increase in the number of achievable stable cycles, with almost no difference being shown when increasing from 80mg of active material to 120mg of active material. Work is currently being performed on surface modification of the porous metal foams through the use of additives to address this same problem. Initial unoptimized studies have already yielded promising results, increasing the coulombic efficiency from 95% to 99% and the number of stable cycles from ~60 cycles to ~100 cycles.

Conclusions

Phase – 1 of the current project was successful in developing porous metal foam architectures capable of eliminating dendrite formation during cycling of lithium metal. Additionally, important modifications were made to the coin cells in order to ensure accurate testing of the studied anodes. Future work is needed to further examine the role of SEI formation on cycling stability and capacity loss. Early work has already demonstrated the ability of surface additives to control initial SEI formation and slow additional growth, resulting in extended stability. Phase – 2 of the current project will continue to examine ways of addressing this problem in the porous metal foam electrodes, in addition to possible modifications to the Li-rich structurally isomorphous alloy electrodes.

Key Publications

1. Jampani, P.H.; Shanthi, P.M.; Day, B.A.; Gattu, B.; Velikokhatnyi, O.I.; Datta, M.K.; Kumta, P.N. Lithium Metal Anode based Rechargeable Batteries: Recent Advances and Challenges for the Future, *Progress in Materials Science* (2017) (under review)
2. Shanthi, P.M.; Jampani, P.H.; Gattu, B.; Velikokhatnyi, O.I.; Kumta, P.N. Doped Lithium Orthosilicates - Promising High Rate Lithium-Ion Conductors for Li-S Batteries, *The Electrochemical Society* (Fall 2016), Honolulu, HI
3. Jampani, P.H.; Gattu, B.; Datta, M.K.; Shanthi, P.M.; Kumta, P.N. Engineering Approaches to Dendrite Prevention in Lithium Anode Based Batteries, *The Electrochemical Society* (Fall 2016), Honolulu, HI
4. Day, B.A.; Gattu, B.; Jampani, P. H.; Shanthi, P.M.; Datta, M.K.; Kumta, P.N., Engineered Porous Foam Electrodes - New Approaches to Dendrite-Free Anodes for Li-Metal Batteries, *The Electrochemical Society* (Fall 2017), National Harbor, MD

II.H.10 Solid-State Inorganic Nanofiber Network-Polymer Composite Electrolytes for Lithium Batteries (WVU)

Nianqiang Wu, Principal Investigator

Department of Mechanical & Aerospace Engineering
West Virginia University
P.O. Box 6106
Morgantown, WV 26506
Phone: 304-293-3326
E-mail: nick.wu@mail.wvu.edu

Tien Duong, Technology Manager

U.S. Department of Energy
Phone: 202-586-7836
E-mail: Tien.Duong@ee.doe.gov

Start Date: October 1, 2016

End Date: September 30, 2019

Total Project Cost: \$1,400,193

DOE share: \$1,244,012

Non-DOE share: \$156,181

Project Introduction

Safety concerns regarding commercial lithium batteries are ever growing due to the use of highly volatile and flammable organic solvent-based electrolytes. In addition, the energy density and the long-term durability need to be further improved. Batteries comprising solid-state electrolytes have drawn significant attention because of their enhanced safety features. Some of ceramic electrolytes have been found to have Li-ion conductivity comparable to liquid electrolytes. However, ceramic electrolytes require high temperature for sintering, and exhibit high interfacial charge transfer resistance due to poor electrolyte-electrode contact. In particular, brittle and rigid bulk ceramic electrolytes make it difficult to have intimate contact with electrodes in all-solid-state batteries. In contrast, solid-state polymer electrolytes are highly flexible to fit in any battery shape besides the improved safety and stability features. However, the ionic conductivities of the polymer electrolytes are generally significantly lower than those of liquid electrolytes. To increase the ionic conductivity of solid polymer electrolytes, several methods have been reported such as increasing the content of lithium salt in the electrolyte structure and introducing low-molecular-weight liquid plasticizers into the polymer matrix. Although these methods can enhance the ionic conductivity, they reduce the mechanical strength and stability of polymer electrolytes. On the other hand, researchers have reported that the integration of nanoscale inorganic fillers into polymer electrolytes not only enhances the ionic conductivity but also improves the mechanical strength and stability of the solid-state polymer electrolytes.

Objectives

The objective of this project is to develop the solid-state electrolytes based on the highly-conductive inorganic nanofibrous network in the polymer matrix for lithium batteries. Specifically, the project will develop the inorganic nanofiber-polymer composite electrolytes with $>8 \times 10^{-4}$ S/cm of ionic conductivity, which also have good mechanical, thermal and electrochemical stability (with decomposition voltage higher than 4.5 V versus elemental Li). The lithium metal batteries with the developed composite electrolytes will achieve ≥ 350 Wh/kg (≥ 750 Wh/L) of specific energy, ≥ 800 W/kg of specific discharge pulse power, and $\geq 1,000$ cycles of life-time. The proposed lithium-sulfur batteries with the composite electrolytes will achieve ≥ 500 Wh/kg of specific energy, ≥ 850 W/kg of specific discharge pulse power, and $\geq 1,000$ cycles of life-time.

Approach

Integration of the highly Li⁺-conductive inorganic nanofiber network into the polymer matrix not only provides the continuous Li⁺ transport channels but also kinetically inhibits the crystallization from the

amorphous state of polymer electrolyte. The inorganic nanofibers will be fabricated with electrospinning technique. The ionic conductivity of inorganic nanofibers will be improved by chemical substitution or doping. Highly ionic-conductive polymers will be developed by cross-linking and/or creation of a block-copolymer structure. The composition and microstructure of the composite electrolyte will be designed to suppress the lithium dendrite formation.

This project funds work at West Virginia University (WVU) and North Carolina State University (NCSU). Dr. Nianqiang (Nick) Wu at WVU serves as PI; and Dr. Xiangwu Zhang at NCSU acts as Co-PI. Sujan Kasani (Ph.D. student at WVU), Hui Yang (Postdoctoral Fellow at WVU), Botong Liu (Ph.D. student at WVU), Chaoyi Yan (Ph.D. student at NCSU) and Mahmut Dirican (Postdoctoral Fellow at NCSU) contributed to the project.

Results

Task 1.1.2 - Synthesis of inorganic nanofibers

Perovskite-type lithium lanthanum titanate $\text{Li}_{0.33}\text{La}_{0.56}\text{TiO}_3$ (LLTO) and Garnet-type lithium lanthanum aluminum zirconium oxide $\text{Li}_{6.4}\text{La}_3\text{Al}_{0.2}\text{Zr}_2\text{O}_{12}$ (LLAZO) nanofibers were successfully fabricated by electrospinning. The ionic conductivity of inorganic LLTO nanofibers was improved from 7.7×10^{-4} S/cm to 1.08×10^{-3} S/cm through 0.5% aluminum doping. The theoretical calculation has demonstrated that the aluminum doping reduces the transporting barrier of Li atom the LLTO lattice, transporting barrier for pure, single-Al and double-Al decorated structure are 0.365 eV, 0.165 eV and 0.225 eV, respectively.

(1) Lithium lanthanum zirconium oxide (LLZO) nanofibers

Highly ionic-conductive $\text{Li}_{6.4}\text{La}_3\text{Al}_{0.2}\text{Zr}_2\text{O}_{12}$ (LLAZO) nanofibers with average fiber diameter of around 300 nm were successfully obtained after calcination of electrospun LLAZO precursor nanofibers. X-ray diffraction patterns of LLAZO nanofibers indicated that pure cubic LLAZO phase was achieved.

(2) Lithium lanthanum titanate (LLTO) nanofibers

Perovskite-type lithium lanthanum titanate $\text{Li}_{0.33}\text{La}_{0.56}\text{TiO}_3$ (LLTO) nanofibers were successfully synthesized by the electrospinning technique. The LLTO pellet exhibited an ionic conductivity of 7.7×10^{-4} S/cm. A narrow concentration range of Ti^{4+} substitution by Al^{3+} was carried out to enhance the ionic conductivity of the LLTO nanofibers, which would change the bond strength between the B-site cation and the oxygen, thus influence the conductivity. We have doped the LLTO nanofibers with different percentage (0.5%~10%) of aluminum. The experimental results show that 0.5% aluminum doped $\text{Li}_{0.33}\text{La}_{0.56}\text{Al}_{0.005}\text{Ti}_{0.995}\text{O}_3$ (LLATO) nanofibers (Figure II-516) exhibited the highest ionic conductivity of 1.08×10^{-3} S/cm.

To study the transporting behavior of Li atoms in pure and Al-decorated $\text{Li}_{0.33}\text{La}_{0.56}\text{TiO}_3$ structures, we constructed La-full and La-deficient layers along stuck direction in Figure II-517. Figure II-517d gives the ideal transporting direction to simplify the research. The calculation results show transporting barrier for pure, single-Al and double-Al decorated structure were 0.365 eV, 0.165 eV and 0.225 eV, respectively. This tendency was consistent with experiments. To explain this behavior, we analyzed the Bader charge of those structures. Before Li atom transporting across the door, we found that the charge value on O atoms in the door had the sequence as “double-Al > single-Al > pure structure”, which indicated that Coulomb potential between Li with O atoms became stronger as more Ti atoms were doped by Al. However, when two Ti atoms were doped by Al atoms, the Coulomb potential was too strong so that the most stable site for Li changed to the door not in the cubic center (in Figure II-517e). To obtain higher mobility for Li atoms in $\text{Li}_{0.33}\text{La}_{0.56}\text{TiO}_3$ structure, the Coulomb potential between Li atom O atoms must be controlled reasonably.

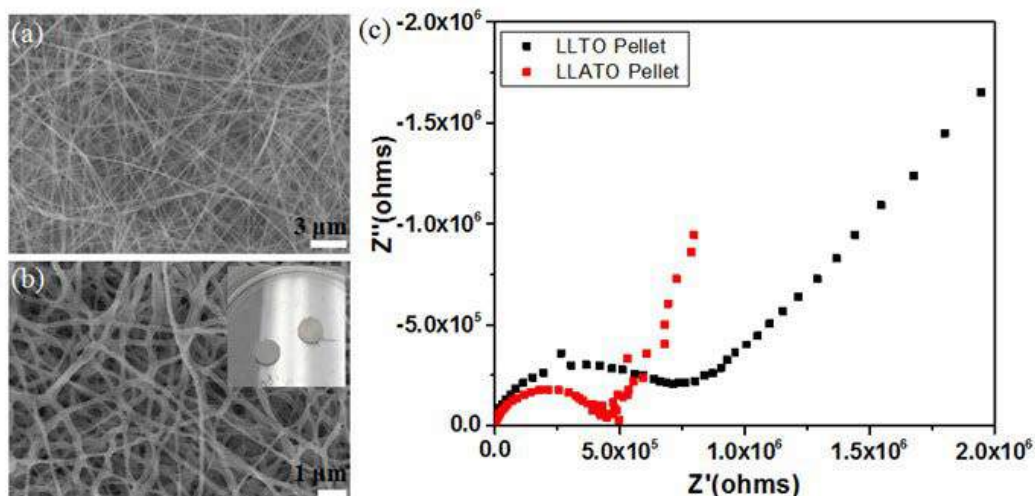


Figure II-516. (a) SEM image of the as-electrospun LLATO nanofiber network. (b) SEM image of the perovskite LLATO nanofibers (the insert is the photograph of the LLATO pellet). (c) Electrochemical impedance spectroscopy (EIS) plot of the LLTO and LLATO pellet.

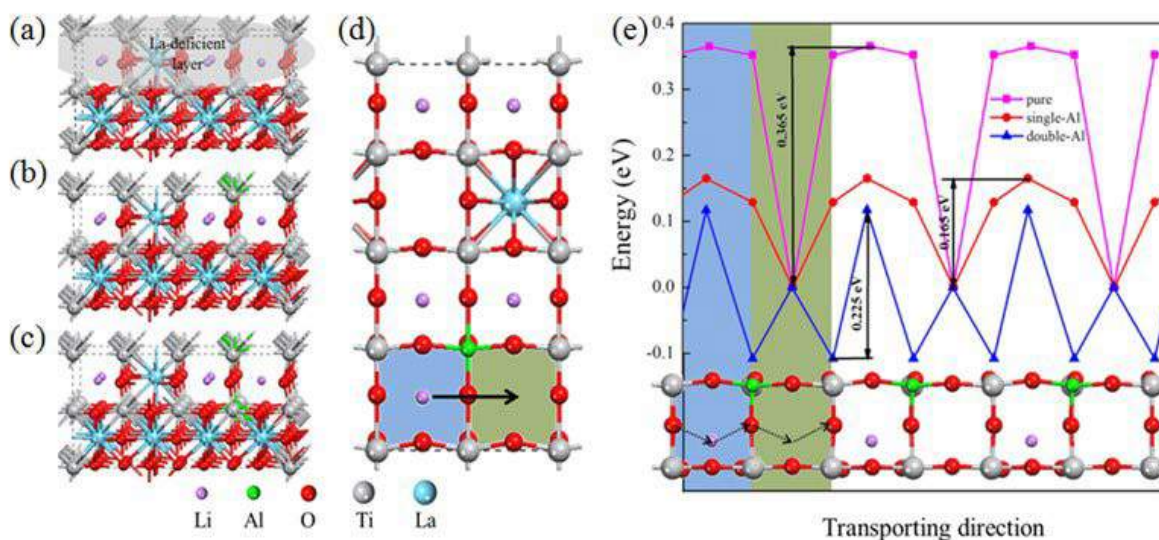


Figure II-517. Pure and Al-decorated $\text{Li}_{0.33}\text{La}_{0.56}\text{TiO}_3$ structures. (a), (b) and (c) are side views of pure, most stable single-Al and double-Al decorated $\text{Li}_{0.33}\text{La}_{0.56}\text{TiO}_3$, respectively. (d) the top view of La-deficient layer of (b). Blue and green color blocks in (d) are used to represent two different regions in Li atom transporting direction. (e) Transporting barriers for Li atoms along transporting direction in pure, single-Al and double-Al decorated $\text{Li}_{0.33}\text{La}_{0.56}\text{TiO}_3$ structure. The transporting trajectory is marked by dash line in the inset.

Task 1.2.2 - Synthesis of polymer matrix

Three kinds of poly(ethylene oxide) (PEO)-based polymers, including cross-linked, block co-polymer, combination of block co-polymer formation and cross-linking, were fabricated. Cross-linking can effectively reduce the crystallinity of the PEO, leading to an increase in the content of amorphous phase in the PEO, which can improve the ionic conductivity. The cross-linked PE/PEO polymer plasticized with poly(ethylene glycol) PEG reached the ionic conductivity of $1.65 \times 10^{-4} \text{ S cm}^{-1}$ at room temperature. Single-ion conductor triblock copolymer was synthesized.

(1) Cross-linked PE/PEO polymer with lithium salt

Cross-linked polyethylene/poly (ethylene oxide) (PE/PEO) polymers were synthesized by free radical polymerization as shown in Figure II-518. The cross-linked polymer with concentration of lithium salt $[EO]/[Li^+] = 24$ showed the highest ionic conductivity of $1.15 \times 10^{-4} \text{ S cm}^{-1}$ at room temperature. Introducing poly (ethylene glycol) PEG into the cross-linked polymer reduced the glass transition temperature of the cross-linked polymer, and also increased the ionic conductivity; higher ionic conductivity was resulted with higher PEG content. Ionic conductivity of 40 wt% (monomer amount) PEG plasticized polymer reached $1.65 \times 10^{-4} \text{ S cm}^{-1}$ at room temperature.

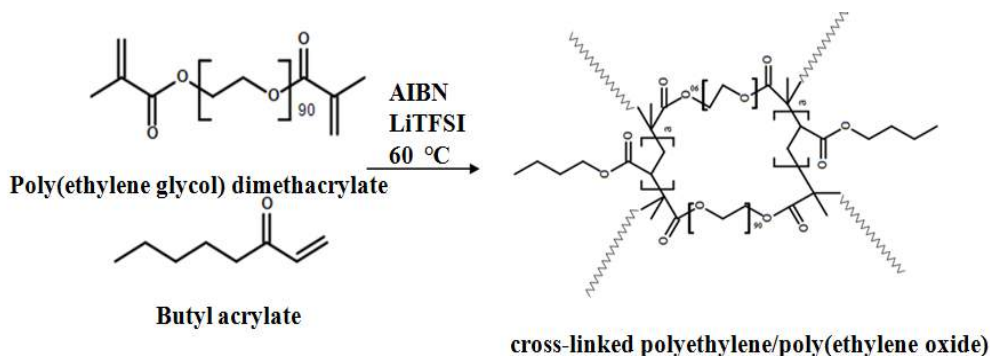


Figure II-518. Synthesis procedure of PE/PEO cross-linked polymer.

(2) Li[PSTFSI-*b*-MPEGA-*b*-PSTFSI] triblock copolymer

Triblock copolymer Li[PSTFSI-*b*-MPEGA-*b*-PSTFSI] block copolymer with different feed EO/Li⁺ ratio of 32, 24 and 16 were synthesized using (4-styrenesulfonyl) (trifluoromethanesulfonyl)imide (STFSI) and methoxy-polyethylene glycol acrylate (MPEGA) monomers through free radical polymerization and nitroxide-mediated polymerization (NMP), exhibiting the ionic conductivity of $1.16 \times 10^{-5} \text{ S/cm}$, $3.30 \times 10^{-5} \text{ S/cm}$, $8.90 \times 10^{-6} \text{ S/cm}$, respectively.

(3) Lithium block cross-linked PE/PEO polymer

Monomer (4-styrenesulfonyl) (trifluoromethanesulfonyl)imide (STFSI) was introduced to the cross-linked polyethylene/poly(ethylene oxide) (PE/PEO) polymers, which were synthesized using butyl acrylate (BA) as the PE monomer and poly(ethylene glycol) dimethacrylate (PEGDMA) as the cross-linker. The ionic conductivity of lithium block cross-linked polymer was in order of 10^{-6} S/cm . Increasing the lithium monomer ratio reduced the ionic conductivity. The ionic conductivity was estimated to be $7.68 \times 10^{-6} \text{ S/cm}$, $3.94 \times 10^{-6} \text{ S/cm}$, $1.88 \times 10^{-6} \text{ S/cm}$ with different feed EO/Li⁺ ratio of 32, 16 and 8, respectively.

Task 2.1 - Development of inorganic nanofibers-polymer composites

The composite electrolytes based on cross-linked polymer and polyvinylidene fluoride-hexafluoropropylene (PVDF-HFP) were fabricated and tested. The mobility and the concentration of free Li⁺ played important roles in the ionic conductivity of solid electrolytes, which were affected by the interaction between lithium ions and the polymer. Coating a thin layer of lithium phosphate on the surface of the LLTO nanofibers enhanced the lithium ion concentration of the surface of the nanofibers. Also, better wettability of the nanofiber with the PVDF-HFP/LiTFSI composite would facilitate the transport of the lithium ions.

(1) Inorganic nanofibers/cross-linked polymers with 40 wt% (monomer content) PEG plasticizer

Incorporating the LLTO nanofibers into the cross-linked polymer (CLP) with 40 wt% (monomer content) PEG plasticizer resulted in the ionic conductivity of $4.72 \times 10^{-4} \text{ S/cm}$. The ionic conductivity of 15 wt% LLAZO nanofiber dispersed cross-linked polymer (CLP) with 40 wt% (monomer content) PEG plasticizer composite electrolytes can reach up to $3.46 \times 10^{-4} \text{ S/cm}$ of ionic conductivity at room temperature.

(2) Inorganic nanofibers/ polyvinylidene fluoride-hexafluoropropylene (PVDF-HFP) / Li salt

We have fabricated the composite electrolyte with the Al-doped perovskite-type

($\text{Li}_{0.33}\text{La}_{0.557}\text{Ti}_{0.995}\text{Al}_{0.005}\text{O}_3$ (LLATO) nanofibers in the PVDF-HFP/LiTFSI the matrix. The surface of LLATO nanofibers were further modified with lithium phosphate, which not only helped form a fully continuous lithium-ion-conducting network but also improved the lithium ion mobility at the LLATO nanofiber grain boundaries by compensating the serious Li_2O evaporation. The ionic conductivity of PVDF-HFP/LiTFSI/LLATO/ Li_3PO_4 reached $5.1 \times 10^{-4} \text{ S/cm}$, leading to improvement in the ionic conductivity by 26.9% as compared to the unmodified PVDF-HFP/LiTFSI/LLATO. (See Figure II-519.)

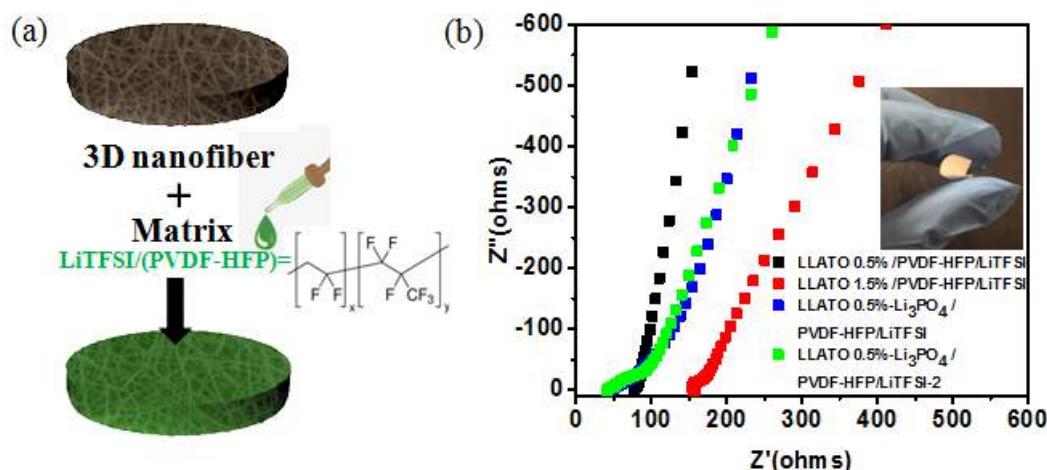


Figure II-519. (a) Schematic illustration of the fabrication procedure for the lithium-ion-conducting membrane. (b) EIS profiles of the PVDF-HFP/LiTFSI/LLATO and the PVDF-HFP/LiTFSI/LLATO/ Li_3PO_4 electrolyte membranes.

Conclusions

We have synthesized and tested the proposed inorganic nanofibers and polymer matrix in Year 1, including the perovskite-type lithium lanthanum titanate $\text{Li}_{0.33}\text{La}_{0.56}\text{TiO}_3$ (LLTO) and Garnet-type lithium lanthanum aluminum zirconium oxide $\text{Li}_{6.4}\text{La}_3\text{Al}_{0.2}\text{Zr}_{0.12}\text{O}_{12}$ (LLAZO) nanofibers and three types of polymers. The ionic conductivity of the inorganic LLTO nanofibers improved from $7.7 \times 10^{-4} \text{ S/cm}$ to $1.08 \times 10^{-3} \text{ S/cm}$ by 0.5% aluminum doping. For the polymer matrix, the random copolymer $\text{Li}[\text{PSTFSI-co-MPEGA}]$ and the $[\text{PSTFSI-b-MPEGA-b-PSTFSI}]$ triblock copolymer, the cross-linked PE/PEO polymer and the lithium block cross-linked PE/PEO polymer were synthesized. The ionic conductivity of PE/PEO cross-linked polymer reached $1.65 \times 10^{-4} \text{ S/cm}$ at room temperature. A bare polymer electrolyte polyvinylidene fluoride-hexafluoropropylene (PVDF-HFP)/LiTFSI was fabricated, achieving the ionic conductivity of $2.36 \times 10^{-4} \text{ S/cm}$ at room temperature.

We have fabricated and investigated the ionic conductivity of composite electrolyte based on the cross-linked polymer and the PVDF-HFP. The ionic conductivity of the LLTO nanofiber-cross linked polymer (CLP) with 40 wt% PEG plasticizer reached $4.72 \times 10^{-4} \text{ S/cm}$. The ionic conductivity of PVDF-HFP/LiTFSI/LLATO/ Li_3PO_4 reached $5.1 \times 10^{-4} \text{ S/cm}$ after surface modification of LLATO nanofibers with Li_3PO_4 .

Key Publications

1. P. Zhu, C. Yan, M. Dirican, J. Zhu, J. Zang, R. K. Selvan, C-C. Chung, H. Jia, Y. Li, Y. Kiyak, N. Wu, X. Zhang, $\text{Li}_{0.33}\text{La}_{0.557}\text{TiO}_3$ ceramic nanofiber fillers enhanced PEO-based composite polymer electrolyte for all-solid-state lithium batteries, Submitted Manuscript, Journal of Materials Chemistry A (under revision).
2. H. Yang, B. T. Liu, X. W. Zhang, N. Q. Wu, Three-Dimensional Cross-Linked Inorganic/organic Composite Solid Electrolyte for Lithium Batteries, to be submitted to Energy Environ Sci.

II.H.11 Electrochemically Responsive Self-Formed Li-ion Conductors for High Performance Li Metal Anodes (Penn State U)

Donghai Wang, Principal Investigator

The Pennsylvania State University
134 Energy and the Environment Lab Building
University Park, PA 16802
Phone: 814-863-1287
E-mail: dwang@psu.edu

Tien Duong, Technology Manager

U.S. Department of Energy
Phone: 202-586-7836
E-mail: Tien.Duong@ee.doe.gov

Start Date: October 1, 2016
Total Project Cost: \$1,266,052

End Date: September 30, 2019
DOE share: \$1,139,319

Non-DOE share: \$126,733

Project Introduction

The project will develop and optimize organo- Li_xS_y , organo- $\text{Li}_x\text{P}_y\text{S}_z$, and organo- $\text{Li}_x\text{S}_y/\text{organo-Li}_x\text{P}_y\text{S}_z$ composite materials as protective layers for Li metal anodes in Li-S batteries. The core focus will be on synthesis methods and precursors for new organic/inorganic hybrid Li-ion conductors, protective layer composition, and protective layer fabrication methods. This will be accompanied by property measurement and characterization (conductivity, mechanical properties, etc.) for the protective layer on Li metal, as well as detailed diagnostics and cell testing. At the conclusion of the project, twelve ~300 mAh pouch cells will be delivered which use the optimal protection layer.

Objectives

The objective of this project is to develop and deliver an electrochemically responsive self-formed hybrid Li-ion conductor as a protective layer for Li metal anodes, enabling Li metal anodes to cycle with a high efficiency of ~99.7% at high electrode capacity ($>6 \text{ mAh/cm}^2$) and high current density ($>2 \text{ mA/cm}^2$) for over 500 cycles. The project will also demonstrate prototype ~300 mAh Li-S battery cells with energy densities of ~200 Wh/kg and ~80% capacity retention for ~300 cycles at ~80% depth of discharge (DOD) using Li metal anodes with this protective layer.

Approach

The novel multiphase organo- Li_xS_y or organo- $\text{Li}_x\text{P}_y\text{S}_z$ hybrid ion conductors with tunable multifunctional organic components and controlled Li_xS_y and $\text{Li}_x\text{P}_y\text{S}_z$ inorganic components will be designed and prepared, and thus enable safe use of lithium metal with high Coulombic efficiency. In the first year, the team will develop the organo- Li_xS_y lithium protection layers with tuned functionality: 1) finding appropriate composition and 2) developing proper synthesis and fabrication methods.

Results

For the sulfur cathodes, dimethyl disulfide as a functional co-solvent has been demonstrated to show an alternate electrochemical reaction pathway for sulfur cathodes by the formation of dimethyl polysulfides and lithium organosulfides as intermediates and reduction products. Our studies show that this new path not only provides high capacity but also enables excellent capacity retention through a built-in automatic discharge shutoff mechanism by tuning carbon/sulfur ratio in sulfur cathodes to reduce unfavorable Li_2S formation. Furthermore, this new electrolyte system enables high capacity of high-sulfur-loading cathodes at low electrolyte/sulfur (E/S) ratios. Specifically, a stable specific capacity of around 1000 mAh g^{-1} using a low electrolyte amount (i.e., E/S ratio of 5 mL g^{-1}) and high sulfur-loading (4 mg cm^{-2}) cathodes (Figure II-520).

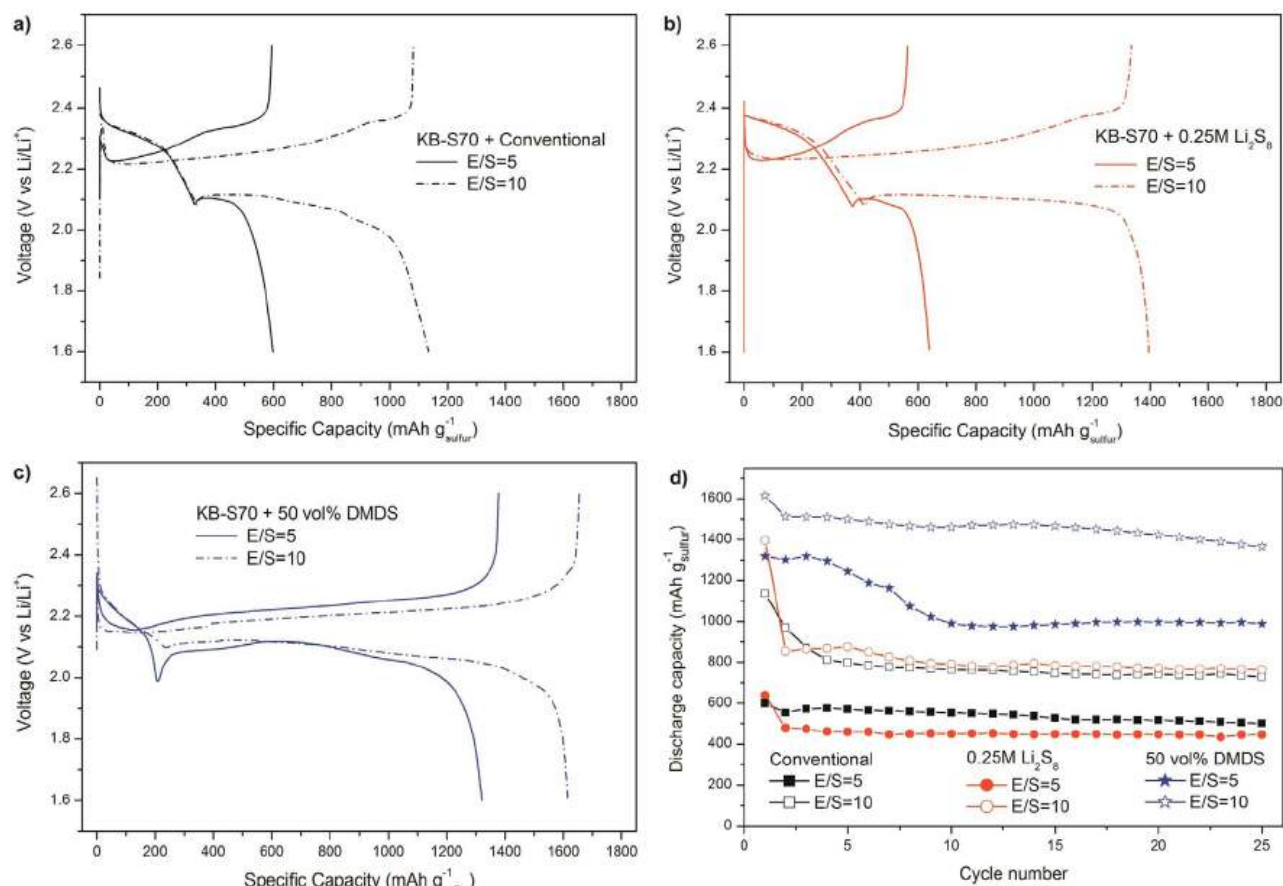


Figure II-520. Initial discharge-charge profiles of KB-S70 cathodes in (a) conventional, (b) 0.25 M polysulfide-containing, and (c) 50 vol% DMDS-containing electrolytes with E/S=5 and 10 mL g⁻¹ at a current density of 0.2 mA cm⁻², and (d) their corresponding cycling performance. (*Nano Energy*, **2017**, 31, 418.)

Constructing a rechargeable prelithiated graphite/sulfur battery is a feasible strategy to address the issues of polysulfide shuttling and unstable lithium/electrolyte interface. A fluorinated ether of bis(2,2,2-trifluoroethyl) ether (BTFE) was blended with 1,3-dioxolane (DOL) for making a multifunctional electrolyte of 1.0 M LiTFSI DOL/BTFE (1:1, v/v) to enable high performance prelithiated graphite/S batteries. First, the electrolyte significantly reduces polysulfide solubility to suppress the deleterious polysulfide shuttling and thus improves capacity retention of sulfur cathodes. Second, thanks to the low viscosity and good wettability, the fluorinated electrolyte dramatically enhances the reaction kinetics and sulfur utilization of high-areal-loading sulfur cathodes. More importantly, this electrolyte forms a stable solid-electrolyte interphase (SEI) layer on graphite surface and thus enables remarkable cyclability of graphite anodes. By coupling prelithiated graphite anodes with sulfur cathodes with a high areal capacity of $\sim 3 \text{ mAh cm}^{-2}$, we demonstrate prelithiated graphite/sulfur batteries that show high sulfur-specific capacity of $\sim 1000 \text{ mAh g}^{-1}$ and an excellent capacity retention of $>65\%$ after 450 cycles at C/10 (Figure II-521).

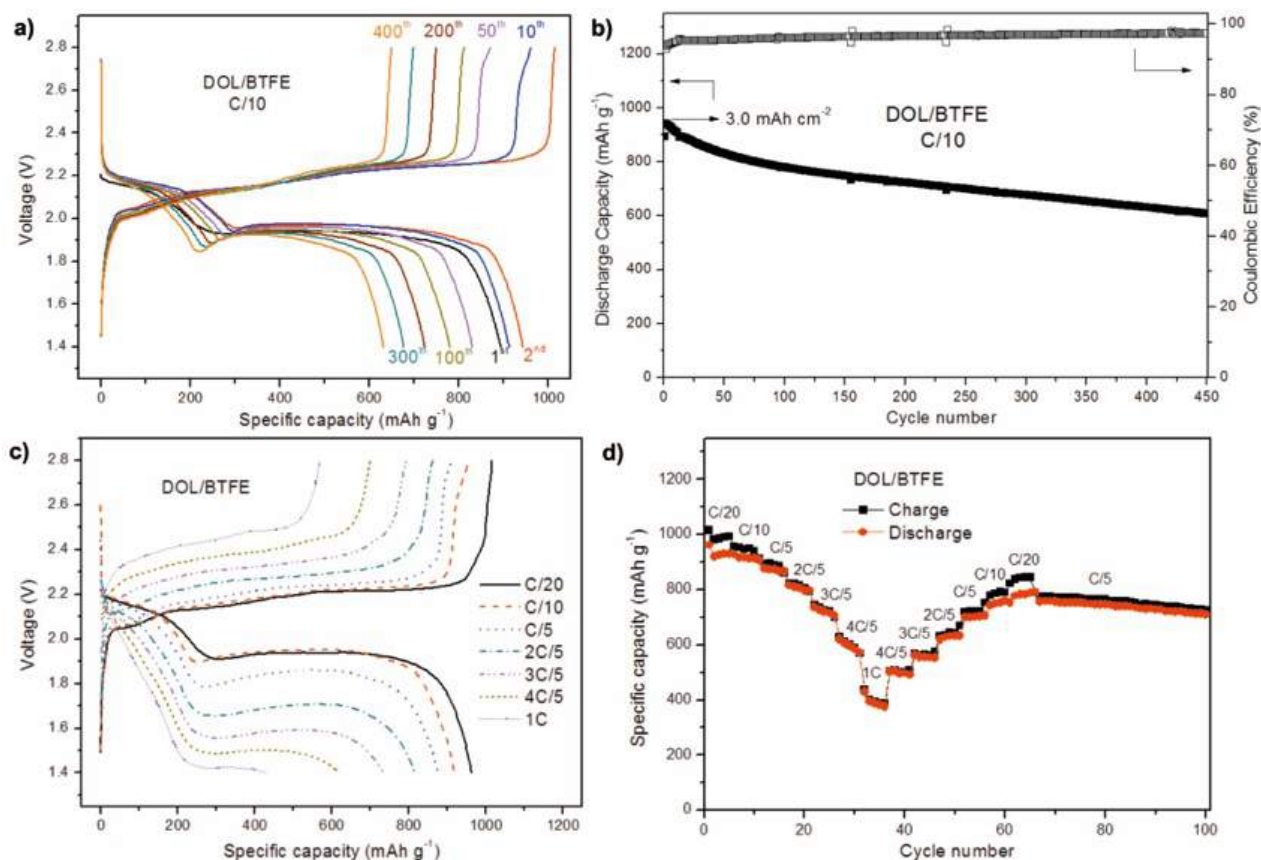


Figure II-521. (a, c) Discharge-charge profiles and (b, d) cycling performance of prelithiated graphite/sulfur full cells at (a, b) C/10 and (c, d) different C rates in the DOL/BTFE electrolyte. (*ACS Appl. Mater. Interfaces*, **2017**, 9, 6959.)

For the protection of the Li metal anode, appropriate compositions for organo-Li_xS_y lithium protection layers have been found. The sulfur-containing polymers (SCPs), which contain the sulfur chains and organic units, are the suitable candidate for the fabrication of organo-Li_xS_y lithium protection layers. The effect of sulfur contents in the SCPs on the cycling performance of Li metal anode was investigated. 2 wt% SCPs were added to the electrolyte, the electrolyte used here was 1 M LiTFSI (lithium bis(trifluoromethanesulfonyl)imide) and 1 wt% LiNO₃ in the dioxolane/dimethoxyethane (DOL/DME = 1:1, V/V). As shown in Figure II-522, The SCPs with 90 wt% sulfur exhibited the best cycling performance, and the cycling stability dropped with the decrease of sulfur content in the SCPs.

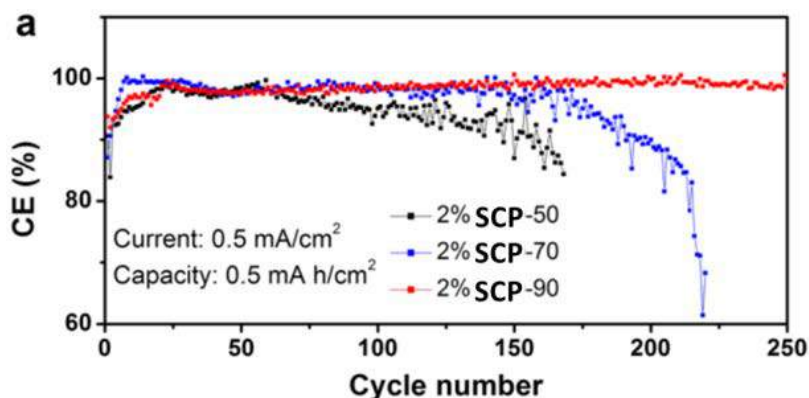


Figure II-522. Cycling performance of 2 wt% SCPs containing different sulfur contents as additives. (a) PSD containing different sulfur contents. (b) PST containing different sulfur contents. (*Nat. Commun.*, **2017**, *8*, 850.)

The morphologies of the deposited lithium metal using SCP as additives (Figure II-523) show that dense and dendrite-free lithium film was deposited on the substrate, and the pancake-like lithium film was continuous and uniform. The cross-section view consolidated that the deposited lithium grew very compact and no obvious dendritic lithium was observed in the surface and interior of the lithium film.

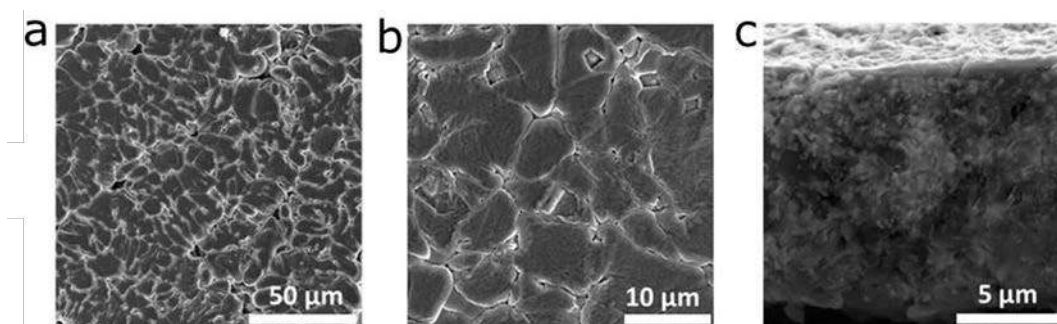


Figure II-523. Morphologies of lithium metal deposited onto stainless steel substrate. SEM images of lithium metal deposited onto bare stainless steel substrate in the electrolyte with the addition of 8 wt% the SCP-90. (*Nat. Commun.*, **2017**, *8*, 850.)

The content of SCP-90 as additives in the electrolyte affects the Li plating/stripping cycling performance. Comparing the Li plating/stripping performance of using electrolyte containing 2 wt%, 5 wt%, 8 wt% and 10 wt% of SCP-90, we found that the cycling life is improved with increasing content of SCP-90 additive till reaching 8 wt% (Figure II-524). When the content of SCP-90 in the electrolyte increased to 10 wt%, the cycling life deteriorates. Using SCP-90 as additives, the growth of Li dendrite is effectively suppressed, and uniform and compact deposited Li film was obtained. After 100 cycles at a current density of 2 mA cm^{-2} and a deposition capacity of 2 mAh cm^{-2} , the deposited Li exhibits very smooth and uniform surface and morphological compactness without any growth of Li dendrites (Figure II-525).

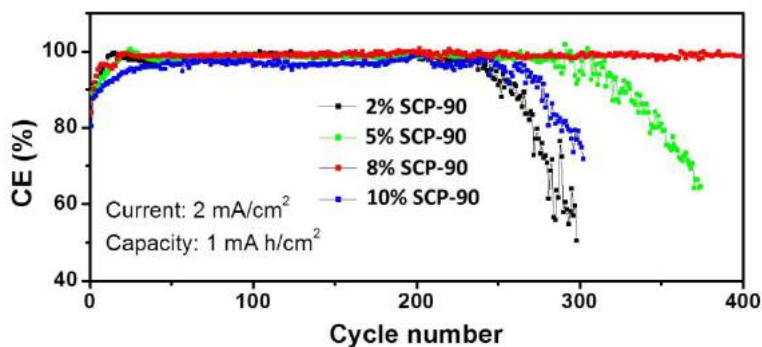


Figure II-524. Cycling performance of cells using electrolytes containing different contents of SCPs. (Nat. Commun., 2017, 8, 850.)

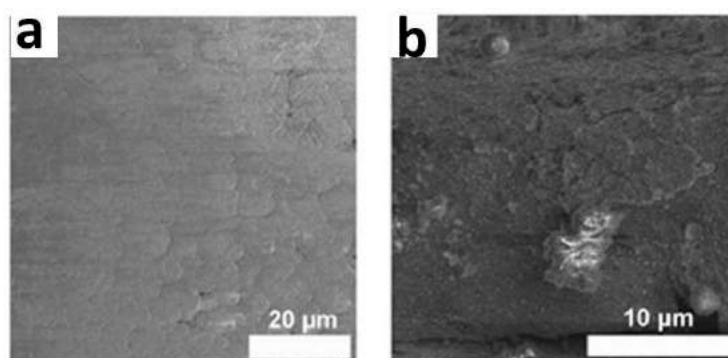


Figure II-525. SEM images of the deposited Li after 100 cycles at a current density of 2 mA cm⁻² and a deposition capacity of 2 mA h cm⁻². (Nat. Commun., 2017, 8, 850.)

SEI layers formed from electrolyte containing sulfur-containing polymer with 90 wt% sulfur (SCP-90) were characterized. The SEI layers formed from the control electrolyte, the S-Electrolyte and SCP-90-Electrolyte are named C-SEI, S-SEI, SCP-90-SEI, respectively. Morphologically, as shown in the SEM images (Figure II-526), the C-SEI layer shows a porous and loose structure, indicating its continual break during the Li plating/stripping process (Figure II-526a). The S-SEI layer becomes smooth, but cracks are observed (Figure II-526b), which should be ascribed to non-continuous Li₂S/Li₂S₂ phase in the S-SEI layer. In contrast, the as-formed SCP-90-SEI layers show a mostly planar, smooth and uniform layer with no cracks (Figure II-526c).

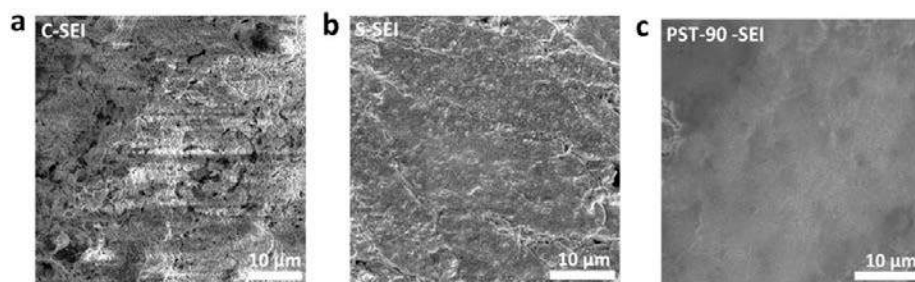


Figure II-526. SEM images of C-SEI layer (a), S-SEI layer (b) and SCP-90-SEI layer (c). (Nat. Commun., 2017, 8, 850.)

The morphology of SEI layers was further investigated using Atomic Force Microscopy (AFM). Figure II-527 displays topographic images of different SEI layers. The C-SEI layer shows large granular features (Figure II-527a), while small particulates are observed everywhere on the surface of S-SEI layer and cracks are

also observed (Figure II-527b). In contrast, the SCP-90-SEI layers are very smooth and uniform covering, as shown in Figure II-527c. The 3D topographic features observed from AFM results are consistent with the SEM investigation (Figure II-526). Such SEI layers can suppress the growth of Li dendrites and thus prevent further contact of Li with the electrolyte, which could lead to an enhanced CE correspondingly.

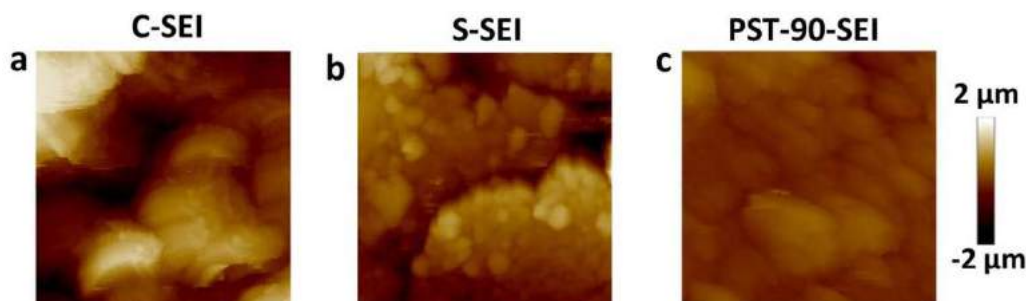


Figure II-527. AFM images ($10 \times 10 \mu\text{m}^2$ scan size) of the C-SEI layer (a), S-SEI layer (b), and SCP-90-SEI layer (c). (*Nat. Commun.*, **2017**, 8, 850.)

The composition of SEI layer formed from an electrolyte containing sulfur-containing polymer with 90 wt% sulfur (PST-90) was characterized. The SEI layers formed from the control electrolyte, the S-Electrolyte and SCP-90-Electrolyte are named C-SEI, S-SEI, PST-90-SEI, respectively. The S 2p XPS spectra exhibit major difference among these three SEI layers (Figure II-528a). For the S-SEI, the peaks at 160.5 and 161.7 eV reflect the composition of Li_2S and Li_2S_2 in the SEI layer, and the small peak at 163.0 eV is also observed, corresponding to the small amount of Li polysulfides (Li_2S_x , such as Li_2S_3) in the SEI layer. This result demonstrates that the S-SEI layer is mainly composed of inorganic species. For PST-90-SEI layer, besides the peaks at 160.5, 161.7 and 163.0 eV observed in XPS spectra, the additional peak at 162.2 eV corresponding to the S 2p_{3/2} from organosulfides is observed, confirming the existence of organosulfides (RS_6Li_6) in the SEI layers. The relatively stronger peak at 163.0 eV corresponds to the Li polysulfides (Li_2S_x) and organopolysulfides (RS_xLi_6) which have similar position with Li polysulfides. In the C 1s XPS spectra (Figure II-528b), the peak at ~ 292.1 eV can be found in the C-SEI and corresponds to the C 1s from the functional group $-\text{CF}_3$, which may originate from the decomposition of LiTFSI in the control electrolyte. Whereas, this peak disappears when using the PST-90 as the additive in the electrolyte. Moreover, the F 1s XPS spectra show two peaks at 684.4 and 688.4 eV assigned to the F 1s from the LiF and $-\text{CF}_3$ respectively (Figure II-528c), and LiF is also the decomposition product of LiTFSI. The intensity of the peak assigned to LiF becomes stronger than that of $-\text{CF}_3$ when using PST-90 as the additive. Both the C 1s and F 1s spectra illustrate the $-\text{CF}_3$ component is suppressed, and comparatively the content of LiF increases when using PST-90 as an additive.

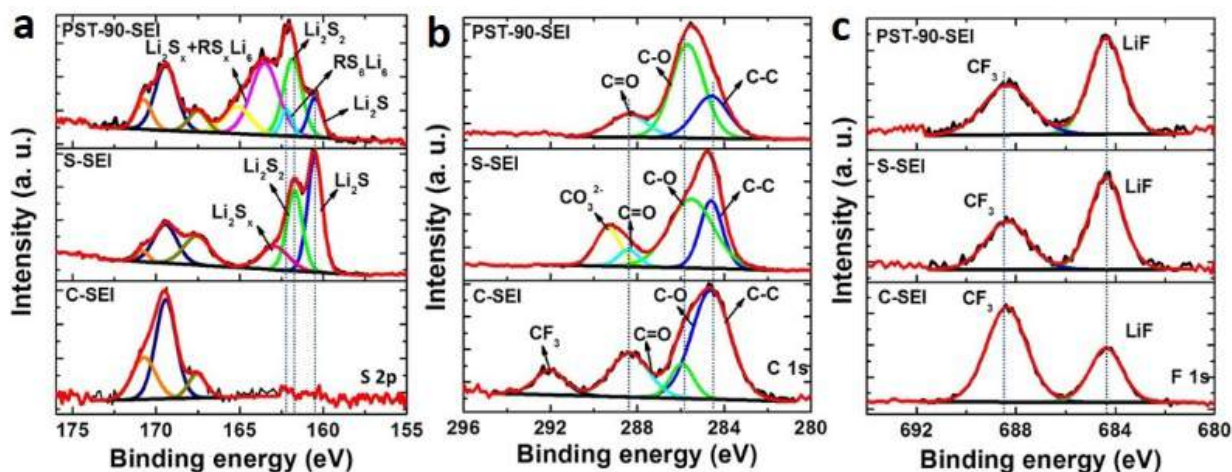


Figure II-528. XPS spectra of C-SEI layer, S-SEI layer and SCP-90-SEI layer. (a) S 2p XPS spectra, (b) C 1s XPS spectra, (c) F 1s XPS spectra. (*Nat. Commun.*, **2017**, 8, 850.)

FT-IR spectra of PST-90-SEI (Figure II-529) shows a peak at $\sim 1170\text{ cm}^{-1}$, which can be found in the pure PST-90 polymer, and is attributed to the vibration of C-N bond. In addition, peaks at 1476 and 838 cm^{-1} are also observed in both PST-90-SEI and PST-90 polymer, indicating the organosulfide/organopolysulfide in the SEI layers originate from PST-90 polymer.

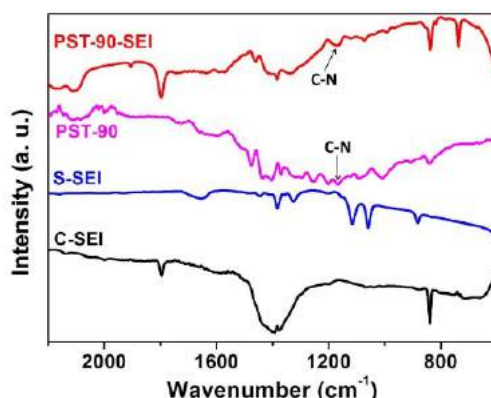


Figure II-529. FT-IR of C-SEI, S-SEI and PST-90 SEI layer. (*Nat. Commun.*, **2017**, 8, 850.)

Peak force tapping mode of AFM was used to investigate the mechanical properties of different SEI layers. For C-SEI (Figure II-530a) and S-SEI (Figure II-530b) layers, the slopes of the loading and unloading curves are quite high and overlap each other. This implies that the SEI layers are relatively stiff and viscoelasticity is negligible because these SEI layers are composed of inorganic Li salts, making them more rigid and brittle. In contrast, the surface of PST-90-SEI (Figure II-530c) layer deforms more and shows a significant hysteresis between the loading and unloading curves, along with a long pull-off or meniscus before the tip completely returned to the free-standing position. The reduced modulus of the different SEI layers could be estimated by fitting the unloading curves with the Johnson-Kendall-Roberts (JKR) models. The C-SEI and S-SEI layers show the modulus of 903 and 740 MPa from the JKR model fit, respectively. In contrast, PST-90-SEI layer displays a low modulus estimated to be 367 MPa . These results suggest that the organosulfides/organopolysulfides-containing SEI layer (PST-90-SEI) becomes soft and viscoelastic to render it flexible, which is beneficial to withstand the large mechanical deformation originating from the Li plating/stripping and to both suppress the growth of Li dendrite and improve cycling CE.

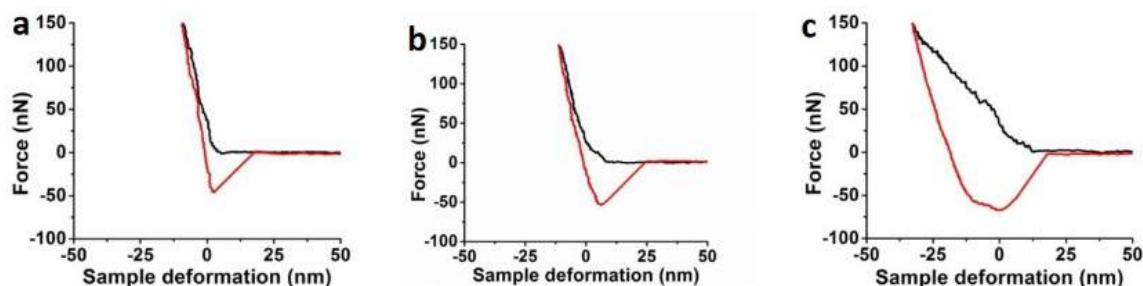


Figure II-530. Indentation curves of the C-SEI layer (a), S-SEI layer (b), and PST-90-SEI layer (c).

(*Nat. Commun.*, **2017**, 8, 850.)

Figure II-531 shows the cycling performance of cells using the PST-90-Electrolyte at a current density of 2 mA cm⁻² and a deposition capacity of 1 mA h cm⁻², the cells deliver an enhanced average CE of 99% over 400 cycles.

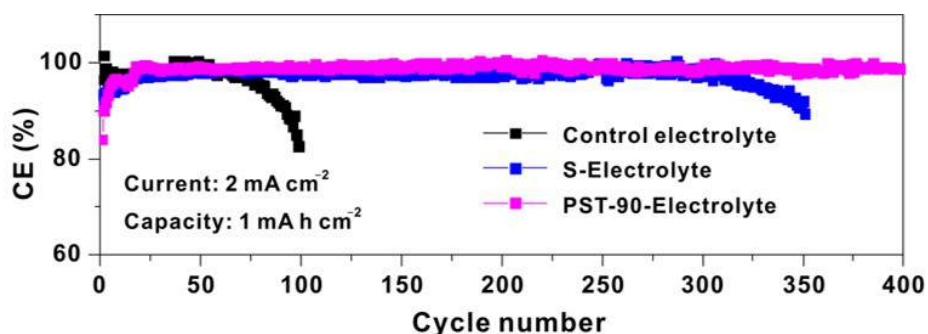


Figure II-531. Cycling performances of the cells using different Electrolytes at a current density of 2 mA cm⁻² with a deposition capacity of 1 mA h cm⁻². (*Nat. Commun.*, **2017**, 8, 850.)

Li-S baseline pouch cells were assembled and tested. The cathode with an areal sulfur loading of around 4.2 mg cm⁻² was made of sulfur, commercial carbon additives, and polyvinylpyrrolidone binder. The weight ratio of sulfur in the cathode is around 50%. 1 M LiTFSI and 0.4M LiNO₃ in DOL/DME were used as electrolyte here. The electrolyte/sulfur (E/S) ratio is around 10 mL g⁻¹. Being cycled at C/30, the pouch cell shows an areal capacity of ~5 mA h cm⁻² and the average Coulombic efficiency is around 99% (Figure II-532).

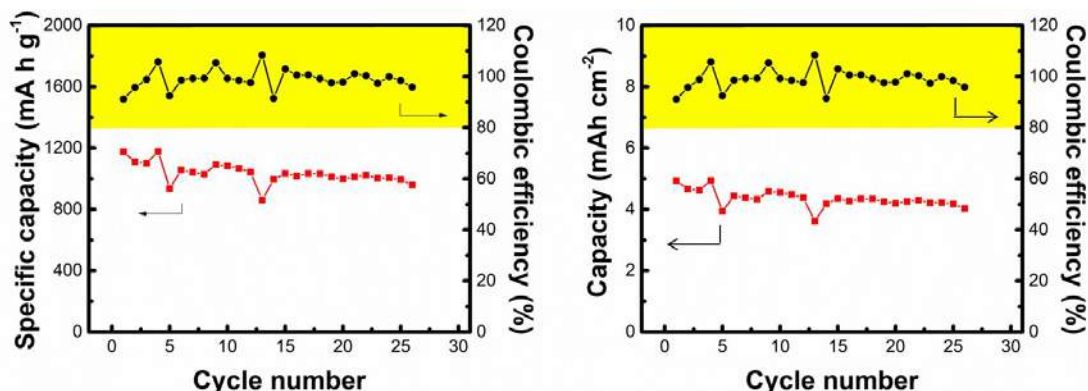


Figure II-532. Cycling performance of Li-S pouch cells.

Conclusions

We successfully developed an organo- Li_xS_y lithium protection layers with the tuned functionality. Sulfur-containing polymers, which contain the sulfur chains and organic units, were used to fabricate organo- Li_xS_y lithium protection layers. SCPs retain electrochemical properties similar to those of elemental sulfur and can electrochemically generate both inorganic Li salts ($\text{Li}_2\text{S}/\text{Li}_2\text{S}_2$) and organic units (i.e., organosulfides/organopolysulfides) simultaneously to form a stable hybrid organo- Li_xS_y layer on Li metal. Using this protection layer, lithium anodes were protected effectively without any dendritic and mossy lithium, high Coulombic efficiency (CE) of lithium plating/stripping was achieved.

Key Publications

1. Li, G. X., Gao, Y., He, X., Huang, Q. Q., Chen, S. R., Kim, S. H., Wang, D. H., Organosulfide-plasticized solid-electrolyte interphase layer enables stable lithium metal anodes for long-cycle lithium-sulfur batteries, *Nat. Commun.*, **2017**, 8, 850.
2. Chen, S. R., Yu, Z. X., Gordin, M., Ran, Y., Song, J. X., Wang, D. H., A Fluorinated Ether Electrolyte Enabled High Performance Pre-lithiated Graphite/Sulfur Batteries, *ACS Appl. Mater. Interfaces*, **2017**, 9, 6959.
3. Chen, S. R., Gao, Y., Yu, Z. X., Gordin, M. L., Song, J. X., Wang, D. H., High capacity of lithium-sulfur batteries at low electrolyte/sulfur ratio enabled by an organosulfide containing electrolyte. *Nano Energy*, **2017**, 31, 418.

II.I Beyond Li-ion R&D: Lithium Sulfur Batteries

II.I.1 New Lamination and Doping Concepts for Enhanced Li-S Battery Performance (U Pittsburgh)

Dr. Prashant N. Kumta, Principal Investigator

University of Pittsburgh
815C Benedum Hall
3700 O'Hara Street
Pittsburgh, PA 15261
Phone: 412-648-0223
E-mail: pkumta@pitt.edu

Dr. Moni K. Datta, Co-Principal Investigator

University of Pittsburgh
815C Benedum Hall
3700 O'Hara Street
Pittsburgh, PA 15261
Phone: 412-648-0223
E-mail: mkd16@pitt.edu

Dr. Oleg I. Velikokhatnyi, Co-Principal Investigator

University of Pittsburgh
815C Benedum Hall
3700 O'Hara Street
Pittsburgh, PA 15261
Phone: 412-648-0223
E-mail: olv3@pitt.edu

Tien Duong, Technology Manager

U.S. Department of Energy
Phone: 202-586-7836
E-mail: Tien.Duong@ee.doe.gov

Start Date: October 1, 2014

End Date: September 30, 2017

Total Project Cost: \$1,250,061

DOE share: \$1,250,061

Non-DOE share: \$0

Project Introduction

Lithium ion batteries (LIBs) clearly dominated the area of high energy storage systems for the past decade with significant research and development activity focused on the development of cathode and anode materials to maximize the specific energy storage, stability, and cycle life of the batteries. However, with the increasing demand in the EV industry for low cost, low weight, and high energy storage batteries to meet the *EV everywhere grand challenge*, the current focus of research has shifted towards the development of lithium sulfur batteries (LSB) owing to the high theoretical specific capacity exhibited by sulfur compared to other cathode materials currently available. Li-S battery shows a theoretical capacity of 1675 mAh/g corresponding to the formation of Li_2S which makes sulfur a promising electrode to replace the layered transition metal oxides (~150 mAh/g) and LiFePO_4 (~170 mAh/g) hitherto deployed in present LIB systems. Moreover, the abundance of sulfur in the earth's crust makes it a more economical and highly attractive proposition compared to currently existing cathodes. Despite advantages of sulfur, the existing Li-S battery technology display poor cyclability, low coulombic efficiency (CE) and very low cycle life due to the following issues: 1. Polysulfide

(PS) dissolution; 2. Sluggish kinetics of PS to Li_2S conversion; 3. High PS diffusivity in the electrolyte; 4. Insulating nature or poor conductivity of sulfur/ Li_2S ; 5. Volumetric expansion/contraction of sulfur; 6. Shuttling of PS along with Li^+ . These issues result in loss of sulfur causing mechanical disintegration, surface passivation of both anode and cathode, thereby decreasing the specific capacity and columbic efficiency (CE). Present generation sulfur cathodes also show low specific storage capacity, very poor charging rates and low loading densities. Research is needed to overcome the issues impeding Li-S battery technology development.

Objectives

The objective of this project is to develop Lithium sulfur batteries capable of achieving the performance requirements shown in Table II-23:

Table II-23: Performance Requirements for Project Li-S Battery

Energy Storage Performance Requirements		Electric Vehicle
Characteristics	Unit	
Specific Discharge Pulse Power	W/kg	700
Discharge Pulse Power Density	W/l	1,500
Specific Regen Pulse Power	W/kg	300
Recharge Rate	kW	1.4
Specific Energy	Wh/kg	350
Energy Density	Wh/l	750
Calendar Life	Year	15
Cycle Life	Cycles	1000
Operating Temperature Range	°C	-30 to +52

Approach

The objectives outlined above will be accomplished by engineering sulfur cathode materials primarily by laminating the electrodes with lithium ion conductor (LIC) coatings to prevent polysulfide dissolution and doping of sulfur to improve the electronic and ionic conductivity. Major technological innovations will be undertaken to accomplish the following objectives in this effort:

Phase – 1 (Year 1)

Synthesis, Characterization and Scale up of suitable LIC matrix materials and multilayer composite sulfur cathodes. This phase is completed.

Identify novel LIC coating materials and morphology for composite multilayer sulfur cathode architectures exhibiting: Specific capacity $\geq 1000 \text{ mAh/g}$ ($\geq 8 \text{ mAh/cm}^2$), cyclability (~ 1000 cycles), loss per cycle $\leq 0.05\%$ per cycle, Coulombic Efficiency (CE): $\geq 80\%$.

Phase – 2 (Year 2)

Development of LIC coated sulfur nanoparticles, scale up of high capacity engineered LIC coated multilayer composite electrodes and doping strategies for improving the electronic conductivity of sulfur.

Optimize and scale up of the interface engineered (I.E.) multilayer composite LIC coated sulfur cathode architectures exhibiting: Specific capacity $\geq 1200 \text{ mAh/g}$ ($\geq 4 \text{ mAh/cm}^2$), cyclability (~ 1000 cycles), loss per cycle: $\leq 0.01\%$ per cycle, CE: $\geq 80\%$.

Synthesize and scale up of doped sulfur nanoparticles on gram scale and demonstrate improvement in performance, reflected as an increase in sulfur weight percentage and improvement in rate capability of cycling of the electrodes.

Phase – 3 (Year 3)

Advanced high energy density, high rate, highly cyclable cell development.

Tie together the three different trees of development i.e., coating development/sulfur particle development/CNT based exploration by identifying suitable configuration integrated electrode (I.E.) with maximum sulfur weight percentage demonstrating high capacity ≥ 1400 mAh/g, cyclability (~ 1000 cycles), loss per cycle: $\leq 0.01\%$ per cycle, CE: $\geq 80\%$.

Assemble 4 mAh high energy density Li-S pouch cells and performance testing.

Results

Phase-1 of the project involved replacement of commercial separator with a Lithium-ion conductor (LIC) and successful demonstration of prevention of polysulfide dissolution. In Phase – 2, the ionic conductivity of LIC was improved by doping, altering the electronic structure of sulfur by doping with like-sized dopants and designing effective methods for coating LIC onto sulfur cathodes. Generation of integrated doped nanoparticulate sulfur-carbon nanofiber electrode, business value analysis and fabrication of the desired 4 mAh full cell are the principle aims of Phase-3.

Phase-3 involved comprehensive study of the physical and chemical properties of the Composite Polymer Electrolytes (CPEs) developed in Phase-2 with three nano fillers. The CPEs when tested against commercial sulfur cathodes demonstrated very stable capacity of ~ 812 mAh/g after 100 cycles with minimal fade rate of $0.012\%/cycle$. The mechanical property analysis showed that the CPEs showed 2-3 times improvement in tensile strength as compared to their counterparts synthesized using conventional technique (Figure II-533).

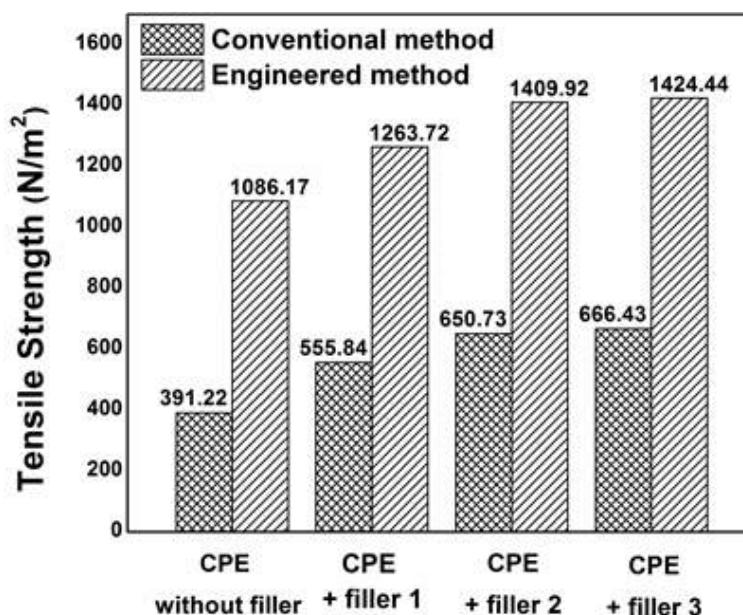


Figure II-533. Cycling performance of Sulfur – infiltrated framework material (SFM)

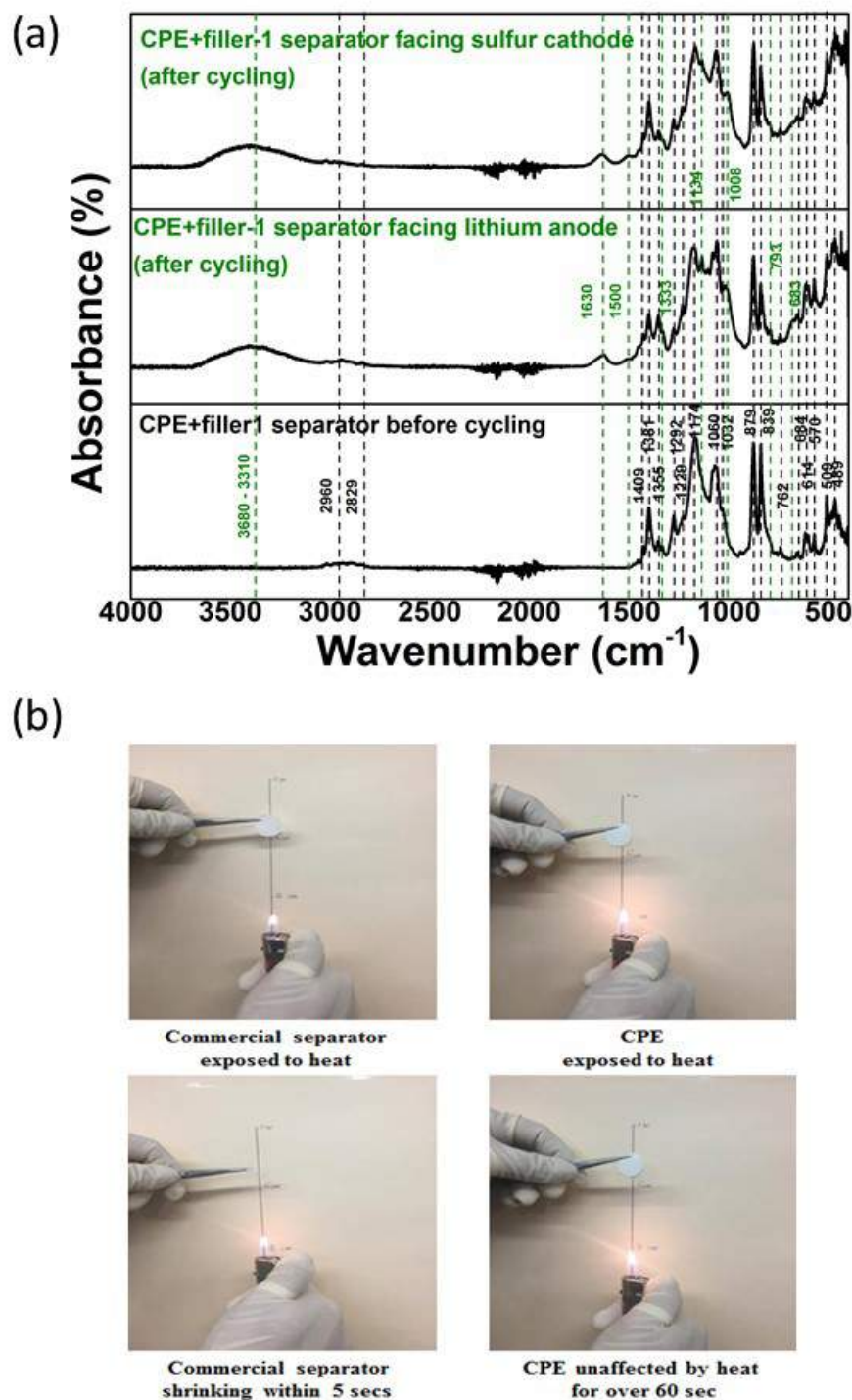


Figure II-534. (a) FT-IR spectra of CPE after cycling and (b) flammability test result of the CPE.

The CPEs also showed excellent chemical stability with minimal modification to the polymer backbone after cycling confirmed by FT-IR spectroscopy (FT-IR) (Figure II-534a) and good flammability properties as compared to commercial battery separator (Figure II-534b).

In addition, Phase-3 also involved development of Directly Doped Sulfur Architecture (DDSA) electrode with very high sulfur loadings of $\sim 18 \text{ mg/cm}^2$ and generation of Polysulfide Trapping Agent (PTA) coated DDSA electrodes with excellent polysulfide trapping property depicted in Figure II-535.

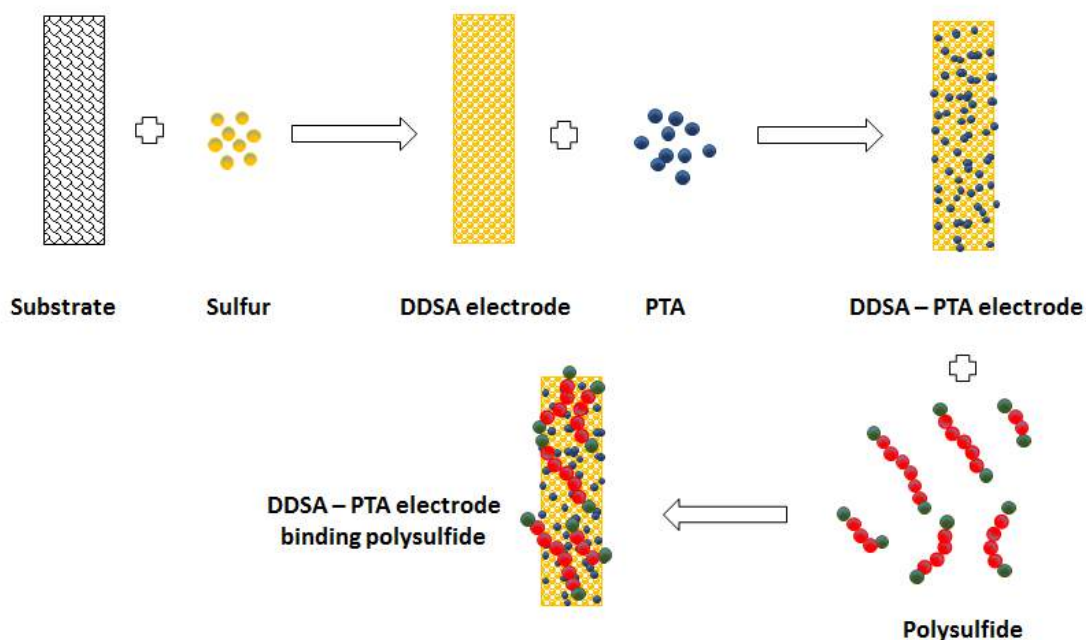


Figure II-535. Scheme of interaction of PTA with polysulfide.

The PTA coated DDSA electrode shows excellent electrochemical cycling performance with an initial capacity of 1305 mAh/g that stabilized at 1112 mAh/g to 200 cycles with less than 0.0014% when cycled at 0.2C rate (Figure II-536). The initial fade of $\sim 0.2\%$ likely due to parasitic reactions will be overcome by further optimization.

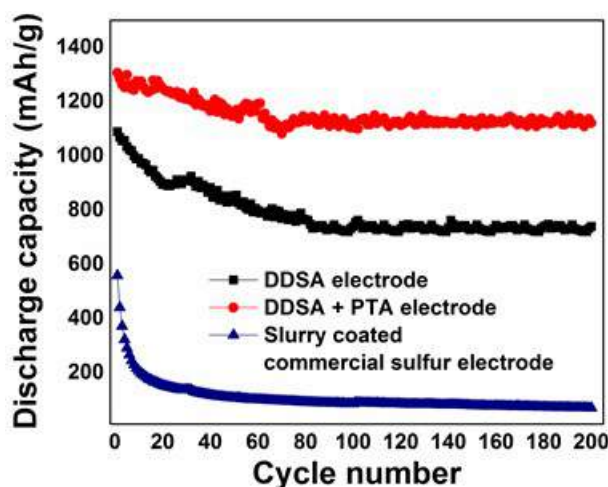


Figure II-536. Cycling performance of PTA coated DDSA electrode

The UV-VIS spectrum of PTA-DDSA (Figure II-537a) showed considerable decrease in the intensities of peaks corresponding to the higher and lower order polysulfides as opposed to the slurry coated electrode suggesting effective adsorption of the polysulfide by the PTA via physical/chemical binding. XPS study of the

electrodes after 200 electrochemical charge – discharge cycles (Figure II-537b) clearly shows the absence of polysulfide peaks showing the efficacy of the polysulfide trapping agents in completing eliminating polysulfide dissolution.

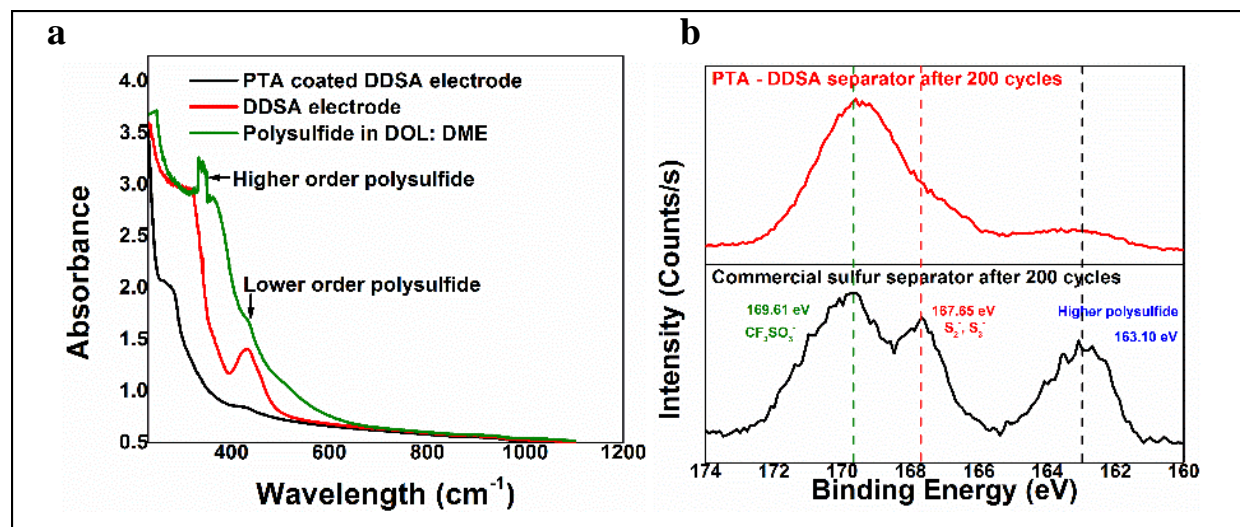


Figure II-537. (a) UV - VIS spectroscopy of PTA coated DDSA electrodes showing absence of polysulfide absorbance and (b) Comparison of XPS patterns of commercial sulfur and PTA - DDSA separators after 200 cycles.

A new sulfonic Complex Framework Material (CFM) was also designed, synthesized and characterized for electrochemical response. Figure II-538a shows the XRD pattern of the CFM compared with the pattern simulated using the crystallographic information file (CIF). The CFMs demonstrated a high sulfur loading of ~ 3-4 mg/cm² and maintained a capacity of 1051 mAh/g for over 100 cycles with 0.0011% fade at 0.2C rate (Figure II-538b).

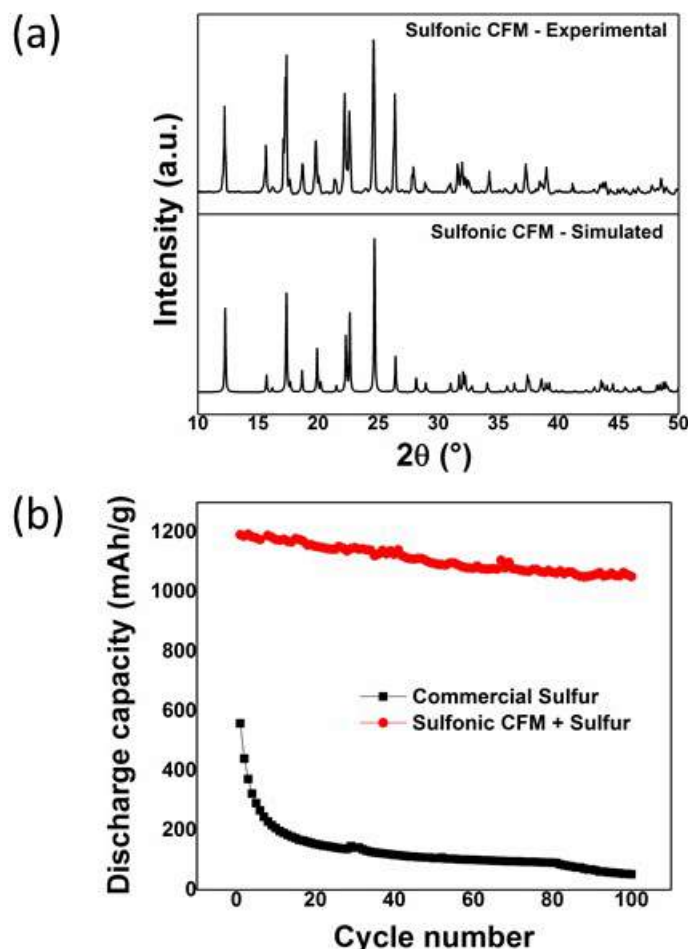


Figure II-538. (a) Comparison of experimental and simulated XRD patterns of sulfonic CMS (b) Electrochemical cycling performance of the sulfonic CFM compared with commercial sulfur.

Manufacturing cost analysis of the various electrode materials (sulfur hosted composite framework materials (CFM), PTA coated DDSA and the LIC coated sulfur nanoparticles), separators (nanofiller incorporated CPE, CFM added gel polymer electrolyte (GPE) and all solid LIC) and electrolytes developed during Phase 1-3 of the project was accordingly conducted to assess the scalability of all the laboratory derived materials. Prismatic pouch cells (4 mAh full cell) are currently being assembled and tested using the Phase-3 optimized systems. Accordingly, the PTA-DDSA materials as discussed above demonstrate the best electrochemical performance exhibiting stable capacity ~1112 mAh/g after 200 cycles with less than 0.0014% when cycled at 0.2C rate. This system will therefore, be selected for testing in pouch cells.

Conclusions

The aim of Phase-3 was to establish methods to improve sulfur cycling characteristics by replacing the commercial separator and electrolyte using a novel composite polymer electrolyte containing nanoscale fillers serving to provide improved mechanical strength, Li-ion conductivity and flame resistances. In addition, the work was directed at developing doped sulfur architectures with improved electronic conductivity, and complex framework materials as effective polysulfide trapping agents. By implementing such simple and scalable approaches, various materials have been generated with initial capacities close to 1400 mAh/g with retention of capacity >1100 mAh/g after 200 cycles. It can also be clearly observed that fade rates have been significantly reduced by using these novel approaches and exceptionally low fade rates of ~0.0014% loss per cycle have been obtained. Furthermore, in the case of PTA coated DDSA systems, a complete absence of

polysulfides at the separator has been shown after 200 cycles demonstrating the promise of this system for use in full cell fabrication against an engineered dendrite free lithium metal anode. Such a combined system will likely exhibit performance characteristics of ~400 Wh/kg meeting the Batt 500 goals.

Key Publications

1. Jampani, P.H.; Gattu, B.; Shanthi, P.M.; Damle, S.S.; Basson, Z.; Bandi, R.; Datta, M.K.; Park, S.K.; Kumta, P.N. Flexible sulfur wires (Flex-SWs) – A Versatile platform for lithium-sulfur batteries, *Electrochimica Acta* Vol. 212, pp. 286 - 293 (2016)
2. Shanthi, P.M.; Jampani, P.H.; Gattu, B.; Sweeney, M.; Datta, M.K.; Kumta, P.N. Nanoporous Non-Carbonized Metal Organic Frameworks (MOFs): Understanding the Origin of Irreversible Capacity loss in Non-Carbonized Carbonate – based Metal Organic Framework (MOF) Sulfur hosts for Lithium – Sulfur battery, *Electrochimica Acta*, Vol, 229, pp 208–218 (2017)
3. Jampani, P.H.; Gattu, B.; Shanthi, P.M.; Kumta, P.N. Novel electro-spun sulfur wires for fabricating mattes of lithium-sulfur batteries, International Patent Number: WO 2016/145429 A1, U.S. Provisional Patent, Application Number: PCT/US2016/022283 (Filing date: 03/14/2016)
4. Shanthi, P. M, Jampani, P.H., Gattu, B.; Datta, M K, Velikokhatnyi, O. I., Kumta, P.N., “Electrospinning of PVdF-HFP: Novel Composite Polymer Electrolytes (CPEs) with enhanced ionic conductivities for Lithium-Sulfur batteries.” U.S. Provisional Appln. Serial No. 62/529,638 (2017).
5. Jampani, P.H., Shanthi, P. M., Gattu, B., Datta, M K, Velikokhatnyi, O.I., Kumta, P.N., “High capacity, air-stable, Structurally Isomorphous lithium Alloy (SIA), Multilayer Porous Foams (MPFs) and Composite Multilayer Anodes (CMAs) for dendrite-free lithium metal anodes for Li-ion batteries”, U.S. Provisional Patent Appln. No. 62/529,588 (2017).
6. Shanthi, P.M., Jampani, P.H., Gattu, B., Albuquerque T., Datta, M.K., Kumta, P.N., “Novel electrospun PVdF – HFP Composite Polymer Electrolytes (CPEs) with enhanced Ionic Conductivities for Lithium – Sulfur batteries”, *ACS Applied Energy*, (2017) under review.
7. Shanthi, P.M., Jampani, P.H., Gattu, B., Datta, M.K., Velikokhatnyi, O.I., Kumta, P.N., “The effect of Mg, Ca and F doping on the ionic conductivity of Li₄SiO₄: Experimental and First Principles Investigation”, *Solid State Ionics* (2017) under review.

II.I.2 Simulations and X-ray Spectroscopy of Li-S Chemistry (LBNL)

Nitash Balsara, Principal Investigator

University of California
201 C Gilman Hall
Berkeley, CA 94720
Phone: 510-642-8973; Fax: 510-643-5037
E-mail: nbalsara@berkeley.edu

Tien Duong, Technology Manager

U.S. Department of Energy
Phone: 202-586-7836
E-mail: Tien.Duong@ee.doe.gov

Start Date: October 1, 2013

End Date: October 31, 2017

Total Project Cost: \$2,000,000

DOE share: \$2,000,000

Non-DOE share: \$0

Project Introduction

Li-S batteries infamously suffer from dissolution of reaction intermediates – lithium polysulfides – formed during charge and discharge. These species can dissolve out of the cathode into the electrolyte reducing the cell capacity, by placing active material out of electrical contact with the cathode, and causing competitive reactions at the anode surface that ultimately result in cell failure. The reaction mechanisms that underlie the formation of polysulfides are still unclear. Uncertainty regarding these reactions has historically stemmed from ambiguity in the interpretation of *in situ* spectro-electrochemical data, especially since pure solutions of individual lithium polysulfide molecules cannot be isolated.

Studies of Li-S reaction mechanisms have been challenged by the difficulty of differentiating lithium polysulfide reaction intermediates experimentally. In this work, we aim to overcome these issues by leveraging theoretical calculations of polysulfide X-ray absorption spectra, and to elucidate the mechanisms by which redox reactions in the sulfur cathode proceed.

Objectives

- Develop method of characterizing Li-S battery reaction mechanisms consisting of *in situ* X-ray absorption spectroscopy and molecular simulations.
- Examine Li-S charge/discharge reaction mechanisms from the front and the back of the cathode.
- Elucidate physical and chemical nature of Li-S battery reaction intermediates in different electrolytes.

Approach

Innovative Approach: Molecular dynamic simulations of lithium polysulfide dianions and radical anions in various solvents are used to obtain simulated X-ray absorption spectra (XAS) for isolated polysulfide species. This is done using a first-principles method, dubbed the excited electron and Core Hole (XCH) approach, based on density functional theory, in conjunction with *ab initio* or classical molecular dynamic simulations of dissolved polysulfide species. Experimental XAS is used to (1) examine Li-S battery reaction mechanism as they take place in the Li-S cathode, and (2) to probe, *ex situ*, chemically prepared/synthesized mixtures of lithium polysulfide species.

1. Obtain experimental XAS for lithium polysulfide species dissolved in SEO, the polymer electrolyte which will be used for *in situ* battery experiments

2. Perform first-principles calculations to obtain X-ray spectra that can be used to interpret and analyze experimentally obtained data
3. Perform *in situ* studies of Li-S reaction mechanisms by probing cells as they are charging/discharging and cells that have been discharged to various depths of discharge.
4. Analyze resulting experimental spectroscopy using theoretically obtained X-ray spectra for individual polysulfide species.

Results

In spite of considerable efforts, the reaction mechanism underlying the charging and discharging of Li-S batteries does not exist. We have used a combination of molecular modeling and experiments to provide a definitive understanding of reaction mechanisms in Li-S cells with different cathode thicknesses using *in situ* X-ray absorption spectroscopy.

Characterization of polysulfide speciation deep inside thick cathodes

In an earlier study this year, *in situ* X-ray absorption spectroscopy at the sulfur K-edge was used to probe the back of a thick Li-S cathode (115 μm) during discharge. The total fluorescence intensity reaching the detector during each scan was examined. This intensity is directly proportional to the concentration of sulfur atoms in the back of the cathode that is probed by XAS. For each scan, the fluorescence intensity was averaged over the energy range of 2490-2565 eV, where there are no absorption features. The averaged fluorescence intensity was then normalized by the incoming X-ray intensity measured during each scan. The normalized fluorescence intensity for the zeroth scan (prior to the start of discharge) is called I_0 , and the normalized intensity for the 'nth' scan is referred to as I_n . Plotting the ratio of I_n to I_0 as a function of capacity reveals the changes in sulfur content at the back of the cathode through the discharge process (Figure II-539b).

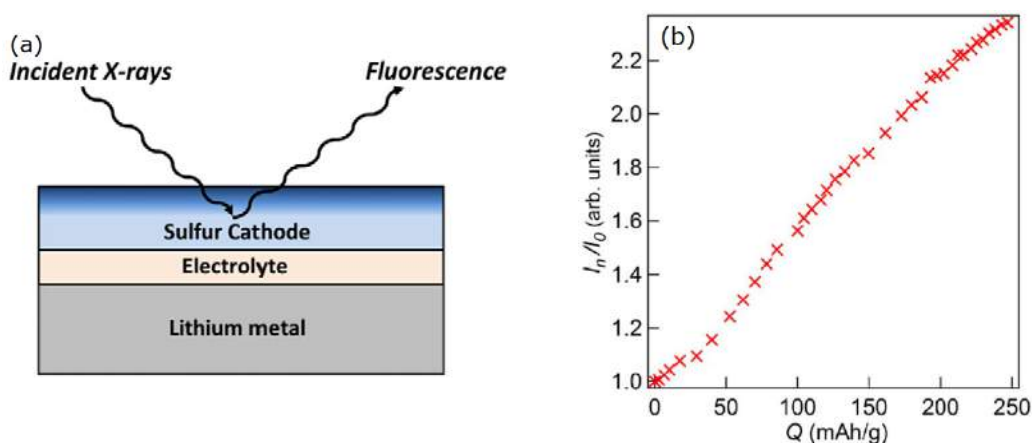


Figure II-539. (a) Simplified X-ray absorption spectroscopy experiment schematic of Li-S cell using a thick cathode where darkened (upper) region of the cathode represents the thickness that was probed by X-rays. (b) Ratio of fluorescence intensity to initial fluorescence intensity measured before discharge indicating the increase in the total amount of sulfur signal detected during discharge.

Because only the top 25 μm thickness of the cathode was probed by XAS, the increase in fluorescence intensity measured during each scan showed that the overall sulfur species in the back of the cathode increased during discharge, which indicated that polysulfide dianion species produced by electrochemical reactions at the front of the cathode diffused towards the back of the cathode during discharge. We explain this finding as follows: the limited diffusion of lithium ions to the back of a thick Li-S cathode will lead to higher reaction rates in the front of the cathode relative to the back of the cathode. This difference in reaction rate leads to a

higher concentration of polysulfide dianions in the front of the cathode, which in turn creates a concentration gradient that leads to the diffusion of polysulfide dianions to the back of the cathode.

Characterization of polysulfide speciation inside thin cathodes

In principle, polysulfides inside the cathode can be produced by either electrochemical reduction of sulfur or disproportionation reactions. Probing part of the cathode only allows us to detect part of both reactions depending on the depth of probe by X-ray. Our more recent study focused on capturing polysulfides produced through the entire depth within the area of probing in order to quantify the species being produced overall within the cathode. To do so, we have made cathode 5-10 μm thin, and probe the cell from the anode side (Li metal). X-rays near the sulfur K-edge transmit highly through Li metal (> 90%) and our electrolyte (40 – 50%). Figure II-540b plots I_n/I_0 during the 1st discharge, charge, and 2nd discharge of this cell. It is evident that I_n/I_0 is more-or-less constant (within 20%), in stark contrast to the data presented in Figure II-539b. Since the concentration gradient impacts polysulfide diffusion and thus will change the total amount of sulfur within a certain depth inside the cathode, the lack of variation in I_n/I_0 indicates that the entire depth of the cathode was probed and that we were capturing polysulfides produced both through electrochemical and disproportionation reactions.

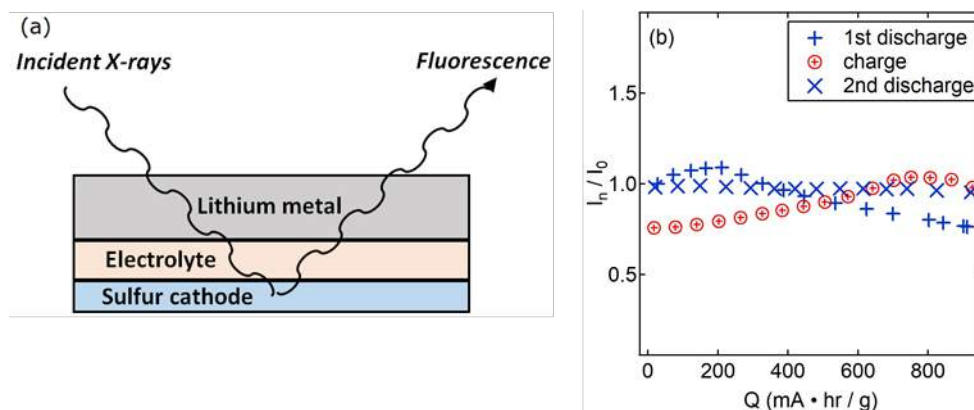


Figure II-540. (a) Simplified X-ray absorption spectroscopy experiment schematic of Li-S cell using a thin cathode. (b) Ratio of fluorescence intensity to initial fluorescence intensity measured before discharge indicating the total amount of sulfur signal detected during discharge and charge stayed constant (within 20% of error).

Theoretical spectra calculated for polysulfide dianions

Members of the program led by Prendergast have simulated X-ray spectra of lithium polysulfides based on first principles calculations shown in Figure II-541a. The calculations indicate that the pre-edge peak is the signature of X-ray excitations of the charged terminal sulfur ions, while the main-edge peak is related to the uncharged internal sulfur atoms of the polysulfide chain. Therefore, the main-edge to pre-edge peak area ratio reflects the relative population of these sulfur atom types in a given sample, and as such could be regarded as a proxy for the average polysulfide chain length, realizing that a given sample may comprise polysulfide molecules with a distribution of lengths. The relationship between spectral features and average chain length is quantified in Figure II-541b. The polysulfide chain length 'x' of a given polysulfide Li_2S_x is approximately a linear function of the area ratio, and the equation corresponding to the least squares fit of the data is given in Figure II-541b. We can think of this equation as a calibration for converting the XAS signal into a polysulfide chain length.

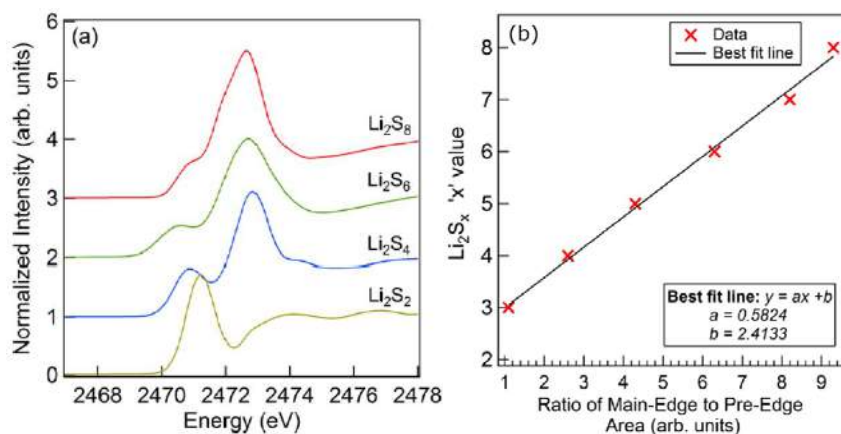


Figure II-541. (a) Selected lithium polysulfide dianion spectra simulated using first principles calculations. (b) Ratio of main-edge peak area to pre-edge peak area versus corresponding Li_2S_x 'x' values, derived from theoretical spectra

Comparing Li-S discharge mechanisms with thick and thin cathode

Figure II-542a and Figure II-542b show the in situ XAS spectra obtained with a thick cathode with the back part of the cathode being probed during discharge, and the corresponding voltage to capacity curve, respectively. The poor performance of this cell is due to the amplified concentration polarization effects caused by the thick cathode and plating of solid products (Li_2S , and possibly Li_2S_2) at the front of the electrode which leads to pore blockage.

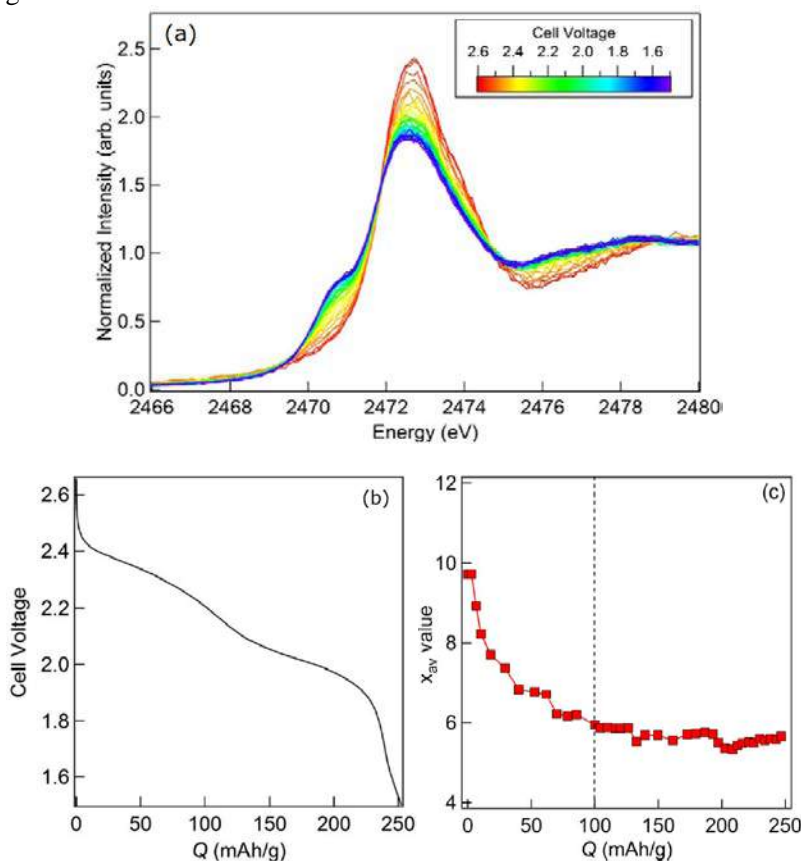


Figure II-542. Discharge of a Li-S cell with a thick cathode and its (a) Sulfur K-edge X-ray absorption spectra probed from the back of cathode, (b) voltage versus capacity (Q), and (c) Average polysulfide chain length for representing the distribution of polysulfide dianions species present in the cathode as a function of capacity.

The pre-edge and main-edge peaks in the spectra shown in Figure II-542a were fit using Gaussian peaks and an arctangent function to represent the absorption edge's increase in intensity. The resulting ratio of main-edge to pre-edge peak area was calculated, and was used to determine the approximate average polysulfide chain length, x_{av} , at a certain discharge capacity plotted in Figure II-542c. A decrease in x_{av} is detected in the range $0 \leq Q \leq 100$ mAh/g. In the range $100 \leq Q \leq 252$ mAh/g, x_{av} plateaued at around 6, suggesting the absence of electrochemical reactions in this regime. It is also noticed that no signal of Li_2S was detected (which would correspond to a peak at 2474.0 eV), which suggests that the reduction of sulfur at the back of the cathode was far from complete, consistent with the low capacity shown in Figure II-542b.

On the contrary, the cell with a thin cathode showed much better performance (Figure II-543b), and the spectra in Figure II-543a for the 1st discharge showed a more significant change of spectra compared to Figure II-542a. The red-cross points in Figure II-543b indicate where spectra were taken during the discharge step. The corresponding x_{av} versus capacity plot shows that the polysulfide chain length decreased all the way down to 3.5 before reaching a plateau, suggesting a more complete reduction compared to the previous cell with a thick cathode. An obvious peak begins to emerge at 2474.0 eV at the start of the lower plateau in the discharge curve, indicating the formation of the solid Li_2S .

Notice that the peak ratio analysis is only reliable for longer chain polysulfides ($x > 3$), for shorter chain polysulfides, the ratio cannot represent the shorter chain polysulfides due to the significant shift in the pre-edge peak (Figure II-541a).

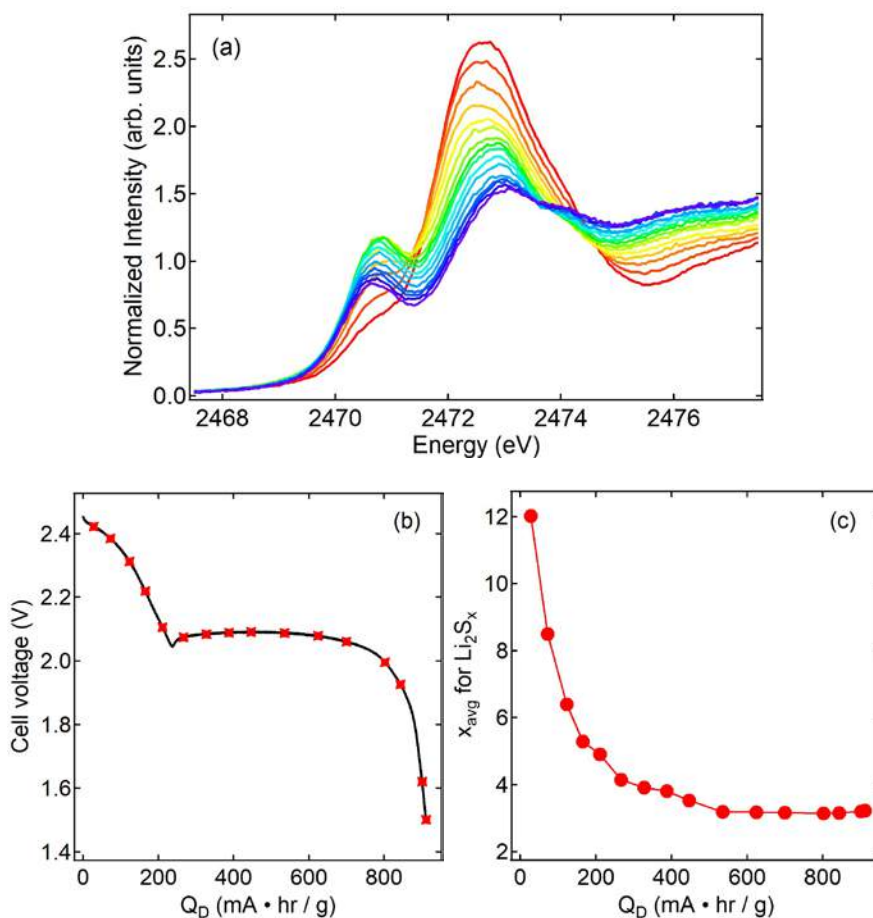


Figure II-543. Discharge of a Li-S cell with a thin cathode and its (a) Sulfur K-edge X-ray absorption spectra probed from the anode, (b) voltage versus capacity (Q), and (c) Average polysulfide chain length for representing the distribution of polysulfide dianions species present in the cathode as a function of capacity.

Furthermore, during the discharge of the cell with a thin cathode, the decrease of x_{av} with Q (Figure II-543c) started to slow down when the discharge voltage versus Q curve (Figure II-543b) reached the beginning of the lower plateau, consistent with the detection of the early formation of Li_2S where reactions become slow due to the transition to a solid phase. On the contrary, the slowing down of x_{av} with Q in the thick cathode, however, started before the lower voltage plateau, which is probably due to the saturation of polysulfides within the electrolyte inside the back of the cathode.

Mechanism during the 1st discharge for Li-S batteries with thin cathodes

The simplest proposed reaction mechanism postulated to occur in the sulfur electrode may be written as:

- (a) $\text{S}_{8(s)} + 2 \text{Li}^+ + 2 \text{e}^- \rightarrow \text{Li}_2\text{S}_8$
- (b) $\text{Li}_2\text{S}_8 + 2/3 \text{Li}^+ + 2/3 \text{e}^- \rightarrow 4/3 \text{Li}_2\text{S}_6$
- (c) $4/3 \text{Li}_2\text{S}_6 + 4/3 \text{Li}^+ + 4/3 \text{e}^- \rightarrow 2 \text{Li}_2\text{S}_4$
- (d) $2 \text{Li}_2\text{S}_4 + 4 \text{Li}^+ + 4 \text{e}^- \rightarrow 4 \text{Li}_2\text{S}_2$
- (e) $4 \text{Li}_2\text{S}_2 + 8 \text{Li}^+ + 8 \text{e}^- \rightarrow 8 \text{Li}_2\text{S}_{(s)}$

The curve in Figure II-544 shows the theoretical dependence of x_{av} versus moles of electron passed per mole of S_8 -based on this scheme. The experimental data obtained from the thin cathode are also shown in Figure II-544. The agreement in Figure II-544 indicates that the data are consistent with the proposed mechanism. Further work is needed to determine the distribution of species formed in the cell and the reasons for the observed departures when the moles of electrons consumed per mole of S_8 exceeds 5.

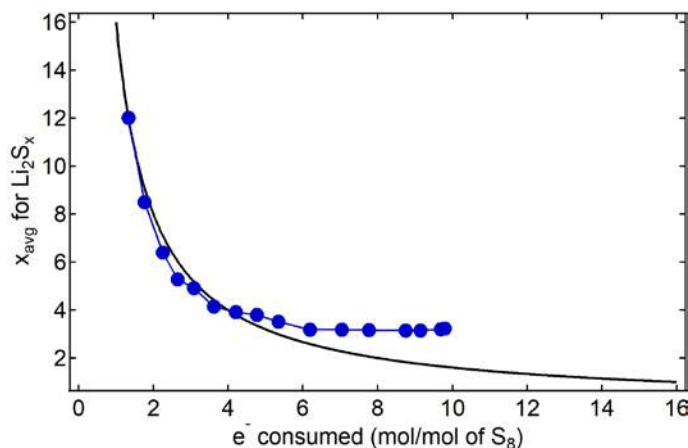


Figure II-544. Voltage versus capacity for Li-S cell with a thin cathode during charge, and average polysulfide chain length as a function of capacity during charge.

Charging Li-S batteries thin cathodes

During charging, the polysulfides within the cathodes are oxidized. Figure II-545a and Figure II-545b show the voltage versus capacity curve and the calculated x_{av} from XAS, respectively, during charging. As expected, the behavior of x_{av} versus capacity is the reverse of discharge; x_{av} is a weak function of Q at $0 \leq Q \leq 780$ mAh/g, and it starts to increase rapidly for $Q > 780$ mAh/g. The transition between these regimes occurs at the same capacity wherein the voltage increases abruptly. The high voltage capacity thus arises from conversion of Li_2S and Li_2S_2 to longer chain polysulfides. We notice that x_{av} only reached 4.3 at the end of charging, most likely due to loss of electronic contact with soluble polysulfides.

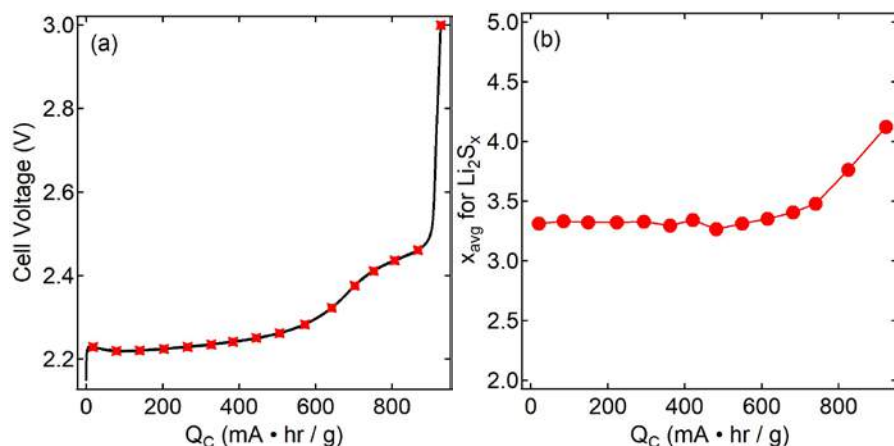


Figure II-545. (a) voltage versus capacity for Li-S cell with a thin cathode during charge, and (b) Average polysulfide chain length as a function of capacity during charge.

Conclusions

This program has led to a fundamental understanding of charge-discharge mechanisms in Li-S cells. We have established a way to study Li-S sulfur reaction mechanism with *in situ* X-ray absorption spectroscopy. The distinguishing feature of our work is the tight coupling between molecular modeling and *in situ* experiments. Practical Li-S cells will comprise cathodes with thicknesses in the 100 μ m range. However, in such cells, XAS only probes a small portion of the cathode located at the back of the cell. We established that lithium polysulfide diffusion from the front to the back of the cathode was dominant. In addition, the electrochemical reactions occurring in other parts of the cathode could not be studied. It is thus logical to compare the redox reactions within thick cathodes and a cell with thin cathode that is probed in its entirety, included the electrolyte. The difference in the cell performance and the analyzed species indicates the inhomogeneity of the polysulfide species at different depths inside the cathode, and this phenomenon was reported for the first time in literature. We also provide a comparison of the average polysulfide chain length to electrons consumed theoretically and experimentally, and find good agreement between the two. We have also studied the species during charging and showed the agreement in the reverse in the average chain length with the charging step. However, the dissolution of polysulfides into the electrolyte limited our analysis of the average species being recovered during charging.

Key Publications

1. Kevin H. Wujcik, Dunyang Rita Wang, Tod A. Pascal, David Prendergast, Nitash P. Balsara, "In situ X-ray absorption spectroscopy studies of discharge reactions in a thick cathode of a lithium sulfur battery", *Journal of the Electrochemical Society*. 2017, 164, A18-A27. DOI: 10.1149/2.1441614jes.
2. Tod A. Pascal, Irune Villaluenga, Kevin H. Wujcik, Didier Devaux, Xi Jiang, Dunyang Rita Wang, Nitash Balsara and David Prendergast, "Liquid Sulfur Impregnation of Microporous Carbon Accelerated by Nanoscale Interfacial Effects" *Nano Letters*. 2017, 17 (4), 2517-2523. DOI: 10.1021/acs.nanolett.7b00249.
3. Tod A. Pascal, Kevin H. Wujcik, Dunyang Rita Wang, Nitash P. Balsara and David Prendergast, "Thermodynamic Origins of the Solvent-Dependent Stability of Lithium Polysulfides from First Principles" *Physical Chemistry Chemical Physics*. 2017, 19, 1441-1448. DOI: 10.1039/C6CP06889H.
4. Kevin H. Wujcik, Dunyang Rita Wang, Alexander A. Teran, Eduard Nasybulin, Tod A. Pascal, David Prendergast, Nitash P. Balsara. "Determination of Redox Reaction Mechanisms in Lithium Sulfur Batteries", book chapter with *Wiley-VCH*, under review.

II.I.3 Novel Chemistry: Lithium-Selenium and Selenium-Sulfur Couple (ANL)

Khalil Amine, Principal Investigator

Argonne National Laboratory
9700 South Cass Avenue
Lemont, IL 60439-4837
Phone: 630-252-3838
E-mail: amine@anl.gov

Tien Duong, Technology Manager

U.S. Department of Energy
Phone: 202-586-7836
E-mail: Tien.Duong@ee.doe.gov

Start Date: October 1, 2014

End Date: September 30, 2019

Total FY17 Project Cost: \$1,988,691

DOE FY17 share: \$1,988,691

Non-DOE share: \$0

Project Introduction

Rechargeable Li/sulfur battery has attracted extensive attention for energy storage application due to its much higher energy density and lower cost than that of state-of-the-art lithium-ion batteries. However, the insulating nature of sulfur and the dissolution of intermediary polysulfides into the electrolyte significantly hinder its practical application. Recently, selenium and selenium-sulfur systems have received considerable attention as cathode materials for rechargeable batteries because of the high electronic conductivity (20 orders of magnitude higher than sulfur) and high volumetric capacity (3254 mAh cm^{-3}) of selenium. Selenium-Sulfur mixtures are miscible in a wide concentration range, and many Se-S composites including Se_5S , Se_5S_2 , Se_5S_4 , SeS , Se_3S_5 , SeS_2 , and SeS_7 can be prepared, including materials with a small amount of Se such as SeS_{20} . These Se-S materials can offer higher theoretical specific capacities than Se alone, and improved conductivity compared to pure S. However, as a new chemistry, the electrochemistry of Se-S cathodes in different electrolytes was not well understood. The lack of such knowledge significantly hinders the rational design of Li/electrolyte/Se-S chemistries with outstanding electrochemical performance.

Objectives

The objective of this project is to develop a novel SeS_x cathode material for rechargeable lithium batteries with high energy density (500 Wh kg^{-1}), long life (>500 cycles) along with low cost and high safety.

Approach

To prevent the dissolution of polysulfides and increase the active material utilization, S or Li_2S are generally impregnated in a conducting carbon matrix. However, this approach makes it difficult to increase the loading density of practical electrodes. It is proposed here to solve the above barriers using following approaches: (1) partially replacing S with Se, (2) confinement of the S_xSe_y in a porous conductive matrix with high pore volume and (3) exploration of low polysulfides/polyselenides dissolution electrolytes.

COLLABORATIONS:

Cathode development (Prof. Chunsheng Wang at University of Maryland)

Porous carbon with high pore volume (Dr. Luis Estevez at PNNL)

Synchrotron X-ray characterization (Dr. Yang Ren and Dr. Chengjun Sun at APS of ANL)

Computational modeling (Dr. Larry Curtiss at MSD of ANL)

Results

1. Solvent-induced reaction mechanism change for Li/Se-S batteries

Figure II-546a, Figure II-546b, and Figure II-546c show the voltage-capacity curve for the first discharge of the S_5Se_2 /KB cathode in the carbonate-, DME-, and HFE-based electrolyte at C/20 ($1C=1389 \text{ mA g}^{-1}$), respectively. Figure II-546a clearly shows a single discharge plateau in the carbonate-based electrolyte, corresponding to the direct electrochemical transformation of S_5Se_2 to Li_2S/Li_2Se without the formation of polysulfides/polyselenides, which has been proved to be a solid-state lithiation/de-lithiation reaction by advanced spectroscopy analyses (*Chem. Commun.*, 2014, **50**, 5576-5579). For the DME-based electrolyte (Figure II-546b), there are four main discharge voltage plateaus, which can be assigned to the well-known two-step solid-liquid-solid reactions of Li with S and Se, respectively. The upper voltage plateau was generally attributed to the dissolution region, while the lower voltage plateau was related to the formation of solid Li_2S and Li_2Se (*J. Am. Chem. Soc.*, 2013, **135**, 8047-8056). In addition, a small plateau was observed at ca. 1.6 V, which was related to the reduction of $LiNO_3$ additive. For the HFE-based electrolyte (Figure II-546c), the single long discharge plateau indicate a solid-state lithiation-delithiation process, while the very short sloping region corresponds to very little formation of polysulfides/polyselenides in the initial discharge stage. Figure II-546d shows the cycle performance of the S_5Se_2 /KB cathode in three different electrolytes at C/20. The S_5Se_2 /KB cathode can only deliver a capacity of around 300 mAh g^{-1} in the carbonate-based electrolyte, although the discharge reaction bypassed the formation of soluble Li_2S_n and Li_2Se_n ($n \geq 4$), which can be ascribed to the widely reported nucleophilic reaction between polysulfides/polyselenides and carbonate-based electrolyte (*Adv. Energy Mater.*, 2014, **4**, 1301473). In the DME-based electrolyte, the cathode showed continuous capacity degradation over 50 cycles, together with a severe shuttle effect. This result is similar to that for previously reported Se-based cathodes and was attributed to the aggravation formation of highly soluble long-chain polyselenides during cycling (*Nano Lett.*, 2016, **16**, 2663-2673). As a comparison, after an activation process in the initial three cycles, the S_5Se_2 /KB cathode in the HFE-based electrolyte attained a much higher reversible capacity of over 700 mAh g^{-1} and displayed minimal shuttle effect within 50 cycles. This may result from its solid-state lithiation-delithiation mechanism, which can greatly suppress the formation of soluble polysulfides/polyselenides during electrochemical cycling. The result also indicates that compared to carbonate-based electrolyte; HFE is much more stable against polysulfides/polyselenides.

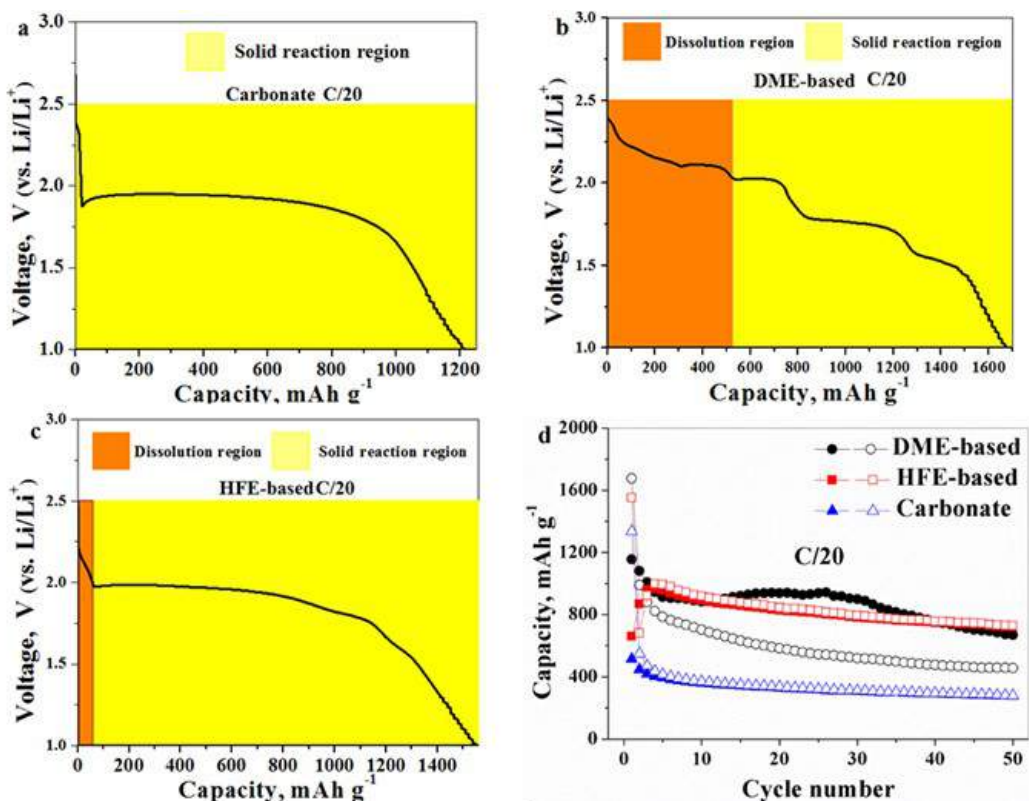


Figure II-546. The first discharge curve of S_5Se_2/KB cathode in (a) carbonate-based, (b) DME-based and (c) HFE-based electrolyte at C/20. (d) Cycling performance of S_5Se_2/KB cathode in the three electrolytes. Open symbols indicate discharge; solid symbols mean charge in panel d.

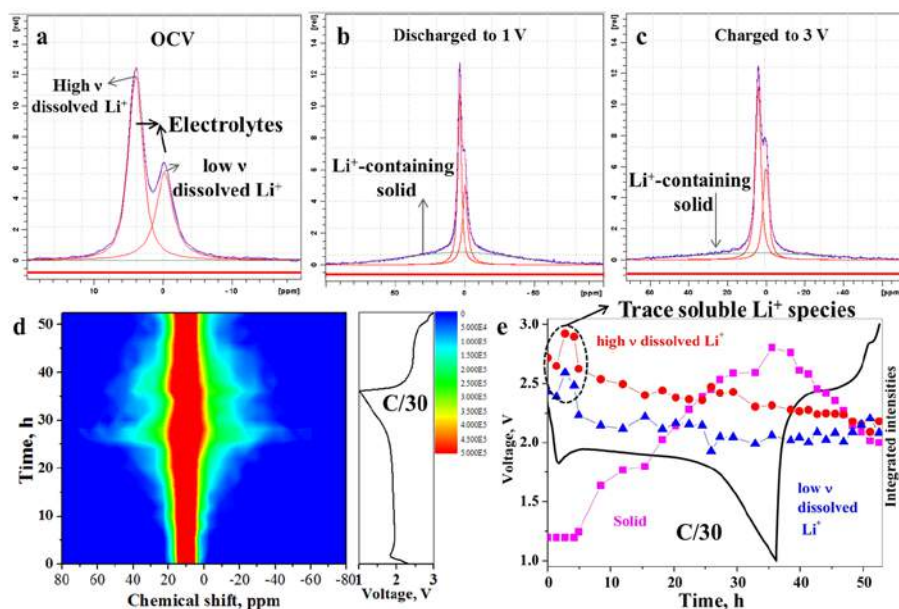


Figure II-547. In-operando 7Li NMR studies of the S_5Se_2/KB cathode in the HFE-based electrolyte: fit curves to the NMR line shape at (a) open circuit voltage, (b) discharged to 1.0 V, and (c) charged back to 3.0 V. (d) 2D contour plot of NMR signal versus charge/discharge curve at C/30; (e) integrated areas of Li^+ species as a function of charge/discharge process.

To unravel its (de)lithiation mechanism in HFE-based electrolyte, we carried out in-situ ^7Li NMR spectroscopy, as it is very sensitive to the solid and soluble Li^+ species inside the test cells. The solid components generally result in broader signals while the solution components usually present narrow line widths due to the presence of anisotropic interactions. Figure II-547a shows the typical ^7Li NMR spectra of the pristine $\text{S}_5\text{Se}_2/\text{KB}$ cathode before charge/discharge, which shows two sharp signals including one at higher frequency and one at lower frequency. The NMR spectra can be well fitted by two resolvable peaks with a high overlap of 91.3% by using the software suite included in Topspin 3.1, which are assigned to the soluble Li^+ species in the cell. It is hard to distinguish the contributions of either electrolyte or other battery components, such as LiNO_3 additive, to the peaks. Nonetheless, the noticeable changes in intensity for these two sharp signals during charge/discharge are generally ascribed to the formation/decomposition of soluble polysulfides or polyselenides. When the cell was discharged to 1.0 V, as shown in Figure II-547b, in addition to two sharp signals from the soluble Li^+ species, a broad resonance signal is apparent, which is related to the formation of a Li^+ -containing solid such as Li_2S and Li_2Se . When the cell was charged back to 3.0 V (Figure II-547c), the intensity of these two sharp peaks changed very little while the broad signal dramatically decreased.

Figure II-547d shows the 2D contour plot of the NMR spectra of the $\text{S}_5\text{Se}_2/\text{KB}$ cathode in the HFE-based electrolyte along with the first discharge/charge curve at C/30. The color represents the intensity of the NMR signals, with red being high intensity and blue being low intensity. As shown, as the discharge proceeded, the intensities of two sharp signals (represented by the red color) changed little while the signal of the broad resonance gradually increased, indicating more and more Li^+ -containing solid formation. During charge, the signals for the Li^+ -containing solid gradually decreased. To quantify the change of the soluble and solid Li^+ species, in-situ NMR data were fit by fixing the widths of the sharp resonances but allowing the line width of the broad resonance to float. The integrated areas of the high frequency, low frequency, and broad resonance along with the charge/discharge process are compared in Figure II-547e. As shown, the integrated areas of the soluble Li^+ species at both high and low frequency slightly increase at the very beginning of the discharge and then keep relatively stable for the remaining charge/discharge process, which means that a small amount of polysulfides/polyselenides formation occurred during the early discharge stage in the HFE-based electrolyte, a finding that is consistent with the prediction from the voltage profiles. Moreover, the integrated area of the Li^+ -containing solid changed little at the very beginning of the discharge. However, its intensity was significantly increased after the consumption of the trace polysulfides/polyselenides and reached a maximum at the end of discharge. During charge, the integrated area of solid Li^+ species gradually decreased, while the soluble Li^+ species remained relatively stable. Hence, in-situ ^7Li NMR study revealed very little soluble polysulfides/polyselenides formation in the HFE-based electrolyte during the whole charge/discharge process, and most of the S_5Se_2 was converted directly to Li_2S and Li_2Se , indicating a solid-state lithiation-delithiation process.

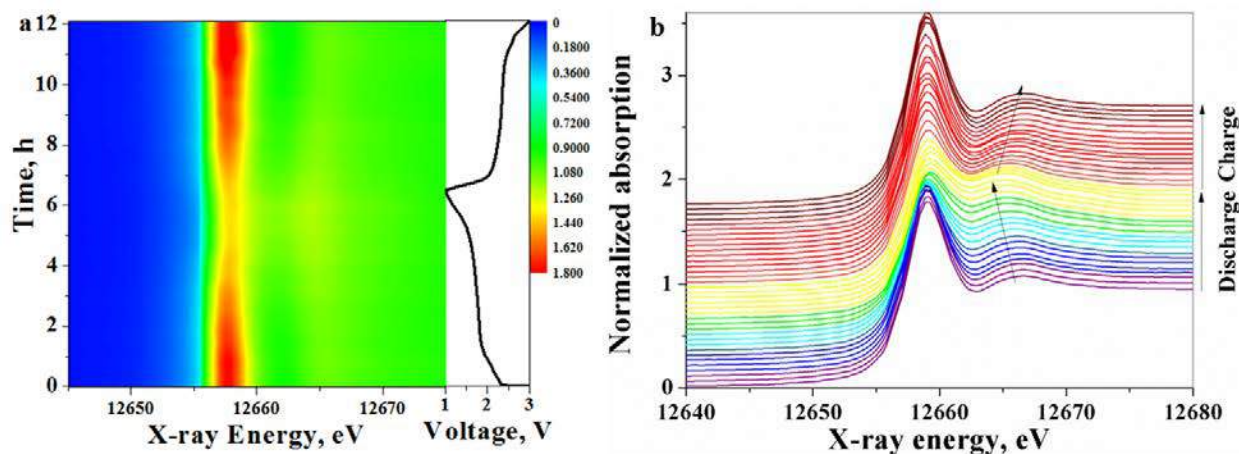


Figure II-548. (a) contour plot of In-operando Se K-edge XANES and (b) representative Se K-edge XANES spectra on the 4th cycle of $\text{S}_5\text{Se}_2/\text{KB}$ cathode at C/10 in HFE-based electrolyte.

To further confirm this conclusion, we further carried out in-operando Se K-edge X-ray absorption near edge spectroscopy (XANES) on the 4th cycle of the S_5Se_2 /KB cathode in the HFE-based electrolyte to bypass the activation process in the initial three cycles. Figure II-548a shows a 2D contour plot for the in-operando Se K-edge XANES data at C/10. As shown, the absorption intensity of Se (12658 eV) gradually decreased during the discharge and was completely recovered at the end of charge. Representative Se XANES spectra during the discharge/charge process are shown in Figure II-548b, in which no energy shift for Se from 12658 eV to 12665 eV is evident. This is consistent with our previous result for carbonate-based electrolyte and different from that for DME-based electrolyte. Therefore, we concluded that space-confined Se-S/KB cathodes undergo a solid-state lithiation/de-lithiation process in the HFE-based electrolyte.

2. Exploration of advanced Se-S/micro-mesoporous carbon composite with high capacity, long cycle life and low self-discharge

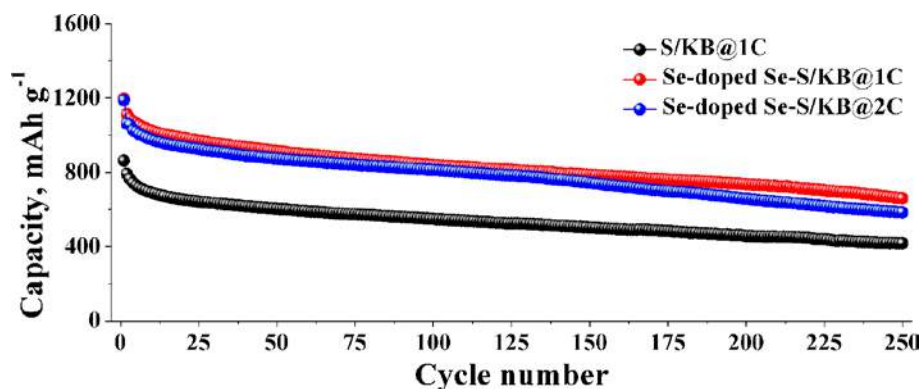


Figure II-549. Cycling performance at high rates of Se-doped Se-S/KB cathode (50 wt.%) and S/KB cathode with in HFE-based electrolyte.

The above results suggest that the dissolution of polysulfides/polyselenides can be suppressed by tailoring the interfacial chemistry of space-confined Se-S cathodes. Since Se has a higher electronic conductivity but lower gravimetric capacity (675 mAh g^{-1}) than S, by rational design for the atomic ratio between S and Se, one can develop an optimal Se-S material with similar theoretical gravimetric capacity and improved electronic conductivity compared to S. In this report, an amorphous S-rich $S_{22.2}Se$ /KB (50 wt.%) cathode was further developed by adjusting the raw weight ratio between S and Se. Figure II-549 compares the cycling performance of Se-doped Se-S/KB and S/KB cathode at high rates. Both cathodes were cycled at C/20 for 3 cycles, and then the $S_{22.2}Se$ /KB cathode was cycled at 1C and 2C, and the S/KB cathode at 1C. The results clearly show that the $S_{22.2}Se$ /KB demonstrates much higher reversible capacity than Se-free S/KB during high rate cycling. This difference is likely due to the higher electronic conductivity of Se than S, which can improve the poor electronic conductivity and the sluggish kinetics, especially during solid-state (de)lithiation of Se-S cathodes. After 250 cycles of charge/discharge at 1C and 2C, the $S_{22.2}Se$ /KB cathode still delivered a reversible capacity of 660 mAh g^{-1} and 583 mAh g^{-1} , respectively, demonstrating excellent long-term cycle stability. By comparison, the S/KB cathode only maintained 417 mAh g^{-1} after 250 cycles at 1C. Despite the cycle stability difference, they both show coulombic efficiency close to 100% after the second cycle, indicating a diminished shuttle effect in the HFE-based electrolyte. Therefore, by manipulating the interfacial chemistry of Se-S cathodes, the dissolution of polysulfides/polyselenides and the sluggish electrochemical reaction kinetics of S cathodes can be significantly improved.

3. Extending the optimal S_xSe_y confinement pore size from micro/mesopores to large mesopores and macropores with high pore volume for high loading Li/ S_xSe_y systems

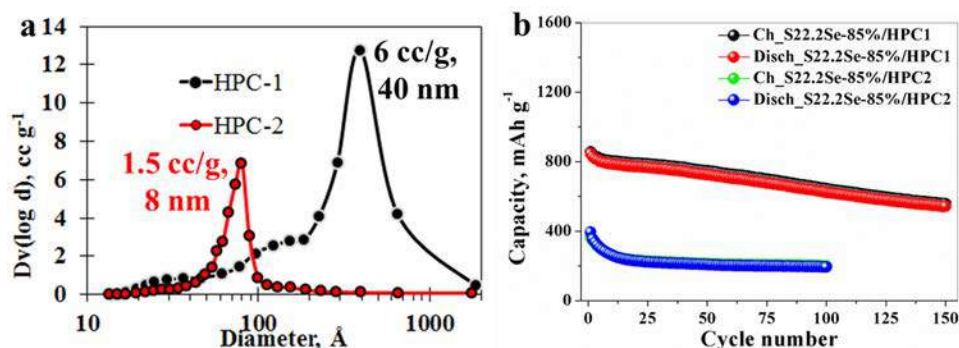


Figure II-550. (a) Pore size distribution of highly porous carbon with pore size of ca. 40 nm (HPC1) and 8 nm (HPC2), (b) cycle performance of S_{22.2}Se/HPC1 (85 wt.%) and S_{22.2}Se/HPC2 (85 wt.%) at C/2 in HFE-based electrolyte.

To attain higher energy densities, higher Se-S loading is needed in the composites and also in the electrodes. The loading in the electrodes could be further optimized through a laminate fabrication process and smart electrode structure design, while immobilizing polysulfides/polyselenides within the host materials should be at the core of high S loading system. However, the dissociation of polysulfides/polyselenides from the host material will become very challenging when go to high loading level. This is because of the required pore volume to trap S_xSe_y in the pores will be increased with increasing S_xSe_y loading. For example, for 70 wt.% S_xSe_y loading, a pore volume of at least 2.1 cc g⁻¹ is required to constrain all the S_xSe_y in the pores and simultaneously accommodate the volume change during charge/discharge. However, this value is dramatically increased to as high as 5.77 cc g⁻¹ for 85 wt.% S_xSe_y loading. Such a high pore volume is rarely reported in microporous carbon (<2 nm) and small mesoporous carbon (2-10 nm). To date, most of microporous carbons have a pore volume of <1.0 cc g⁻¹, and their S_xSe_y loading is generally below 50%. The pore volumes of small mesoporous carbons (2-10 nm) are in the range of 0-3.5 cc g⁻¹, and the reported S_xSe_y loadings are between 50% and 80%. The large mesoporous carbons (10-50 nm) generally have higher pore volume and higher affordable S loading than microporous carbon or small mesoporous carbon. However, large mesoporous carbon has long been considered as inferior host materials due to relatively weak S_xSe_y confinement.

Based on the above finding about solvent-induced reaction mechanism change, we further explored the interfacial chemistry of high S_xSe_y loading systems using HFE-based electrolyte. Figure II-550a shows the pore size distribution of two kinds of highly porous carbon (HPC). HPC1 has a main pore size of ca. 40 nm, and an extremely high pore volume of 6.053 cc g⁻¹, which can theoretically load ca. 86 wt.% Se-S. HPC2 has a smaller pore size of ca. 8 nm but also a lower pore volume of 1.464 cc g⁻¹, which can only encapsulate 64 wt.% Se-S in theory. We therefore prepared two Se-S/HPC composites with 85 wt.% S_{22.2}Se loading using HPC1 and HPC2, respectively. Figure II-550b compares the cycle performance of S_{22.2}Se/HPC1 (85 wt.%) and S_{22.2}Se/HPC2 (85 wt.%) composites at C/2 in HFE-based electrolyte. As clearly shown, the S_{22.2}Se/HPC1-85 wt.% cathode can still deliver a reversible capacity of 542.7 mAh g⁻¹ after 150 cycles with a very small polysulfide/polyselenide shuttle at C/2. By contrast, the reversible capacity of the S_{22.2}Se/HPC2-85 wt.% cathode is only ca. 400 mAh g⁻¹ and quickly faded to ca. 200 mAh g⁻¹ after 10 cycles, indicating very low utilization of active material. Hence, it can be clearly seen that by using HFE-based electrolyte to modify the electrode/electrolyte interface of Li-S batteries, large porous carbon that has long been regarded as inferior S host materials became effective. This finding is critical for the development of high loading Li-S batteries as large porous carbon generally possess much higher pore volume than microporous and small-mesoporous carbon.

Conclusions

In summary, by manipulating the interfacial chemistry of Li-S batteries through Se doping and electrolyte modification, the sluggish electron transport and the polysulfide dissolution can be remarkably improved. This effect can be attributed to the high electronic conductivity of Se and the diminished polysulfides/polyselenides dissolution in the HFE-based electrolyte. As a result, space-confined Se-S cathodes switched from a conventional two-step solid-liquid-solid reaction to solid-state (de)lithiation, as evidenced by in-situ ^7Li NMR and in-operando synchrotron X-ray probes. This switch bypassed the formation of highly soluble polysulfides/polyselenides during cycling and thus led to significantly improved electrochemical performance. Hence, S-rich Se-doped S/Ketjenblack cathode can deliver a reversible capacity of above 1000 mAh g^{-1} at C/20 within 50 cycles, 660 mAh g^{-1} at 1C after 250 cycles, and 583 mAh g^{-1} at 2 C after 250 cycles, as well as an excellent rate capability of 700 mAh g^{-1} at 5C together with good coulombic efficiency close to 100%. Moreover, the minimal polysulfide/polyselenide dissolution also extends the optimal confinement pore size from micropores and small mesopores to large mesopores and even macropores, which can benefit the development of high-loading Li-S batteries due to their much higher pore volume. Our results indicate that manipulating the interfacial chemistry could pave a new way for the development of high-performance and high-loading Li-S batteries. Combinational efforts on rational structure design and exploration of functional electrolytes can lead to advanced Li-S batteries with higher energy density and long calendar life in the near future.

Key Publications

1. Gui-Liang Xu, Jianzhao Liu, Zonghai Chen and Khalil Amine, POLY(ETHYLENEOXIDE)SILOXANE ELECTROLYTES FOR RECHARGEABLE BATTERIES, US. Patent, No. 15/760,295, filed, 2017.
2. Gui-Liang Xu, Jianzhao Liu, Rachid Amine, Zonghai Chen and Khalil Amine, Selenium and Selenium-Sulfur Chemistry for Rechargeable Lithium Batteries: Interplay of Cathode Structures, Electrolytes, and Interfaces, ACS Energy Letter, 2017, 2, 605-614.
3. Gui-Liang Xu, Hui Sun, Luis Estevez, Chao Luo, Tianyuan Ma, Jianzhao Liu, Rachid Amine, Xiaoyi Zhang, Cheng-Jun Sun, Yuzi Liu, Yang Ren, Steve M. Heald, Chun-Sheng Wang, Zonghai Chen and Khalil Amine. Enabling high performance Lithium-Sulfur Batteries by manipulating Interfacial Chemistry, under review.

II.I.4 Multi-Functional Cathode Additives (BNL)

Hong Gan, Principal Investigator

Brookhaven National Laboratory
P.O. Box 5000
Upton, NY 11973-5000
Phone: 631-344-4012
E-mail: hgan@bnl.gov

Esther Takeuchi, Co-Principal Investigator

Department of Chemistry
Stony Brook University
100 Nicolls Road, 104 Chemistry
Stony Brook, NY 11790-3400
Phone: 631-216-7414
E-mail: esther.takeuchi@stonybrook.edu

Tien Duong, Technology Manager

U.S. Department of Energy
Phone: 202-586-7836
E-mail: Tien.Duong@ee.doe.gov

Start Date: October 1, 2014
Total Project Cost: \$1,500,000

End Date: September 30, 2017
DOE share: \$1,500,000

Non-DOE share: \$0

Project Introduction

In order for EVs to achieve mass adoption and make a significant dent in U.S and global CO₂ production, the key problems of driving range per charge and cost per kWh must be addressed. Barriers addressed for this project including: 1) low battery energy density (Wh/kg & Wh/L) and low power (W/kg & W/L); 2) battery low cycle life; and 3) high cost (\$/kWh).

Objectives

Develop a low cost battery technology for PEV application utilizing Li-S electrochemical system by incorporating conductive Titanium Disulfide (TiS₂) as Multi-Functional Cathode Additives (MFCA) to improve the power performance, consistent with DOE's long-term goals of electric vehicle. In this period, our objective is to further optimize the Li-S cell at the cell component level and cell system level for improved cell performance and demonstrate the 4 mAh coin cells with good cycle life.

Approach

As MFCA for Li-S battery, transition metal sulfides are electronic conductive, electrochemically active with ability in adsorbing polysulfide intermediate to promote cell power, capacity and long cycle life. In the past two years, we have identified TiS₂ as the leading candidates for the sulfur cathode optimization studies. More attention has been directed towards electrode optimization and cell system optimization. New electrode binder was identified for improved sulfur cathode mechanical integrity. New type of carbon material was introduced to achieve electrode with high sulfur loading up to 10 mg/cm². During this year, we continued our effort on the system optimization by accomplishing the sulfur cathode formulation and preparation process optimization. We completed the studies of sulfur loading-density interaction and sulfur loading-electrolyte interaction. By incorporating all the improvement, 2032 coin cell with > 4 mAh delivered capacity has been demonstrated with excellent cycle life.

Results

During the present year, we continued the mechanism study of MFCA-sulfur interaction. In parallel, we completed the system optimization at the component and the cell levels and achieved the final 2032 coin cell design with > 4 mAh delivered and with good cycle life. The achievements are highlighted below.

Cathode formulation optimization

In our Phase I study, TiS_2 additive proved to be the true multifunctional, which is beneficial for Li-S cell discharge power capability and cycle life. This year, the cathode formulation optimization was executed using the previously identified binders and carbons, in combination with TiS_2 additive. In the experimental design, either part of the carbon in the formulation is replaced by TiS_2 (Table II-24 - Groups 1 and 2), or part of the S:C composite is replaced by TiS_2 (Table II-24 - Groups 1, 3 and 4).

Table II-24: S- TiS_2 hybrid electrode formulation optimization

Group	Sulfur%	Carbon%	TiS_2 %	Binder%
1	62.0	30.0	0.0	8.0
2	62.0	25.4	4.6	8.0
3	56.0	27.0	9.0	8.0
4	50.0	24.2	17.8	8.0

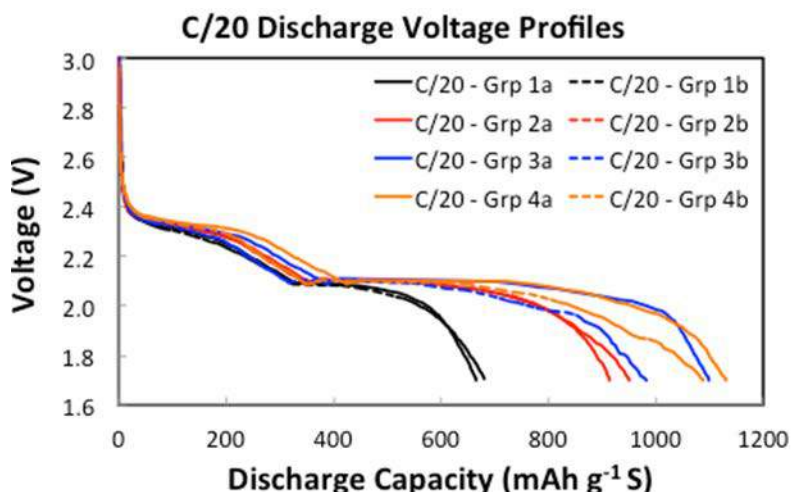


Figure II-551. Cathode formulation effect on sulfur utilization

Figure II-551 shows the effect of cathode formulation on cells sulfur utilization under C/20 discharge rate. The presence of TiS_2 (Group 2) improves the sulfur electrode discharge efficiency comparing with Group 1 cells. Replacing the S:C composite with TiS_2 leads to more improvement in sulfur utilization, from ~41% (Group 1) to ~65% (Groups 3 and 4). Considering the variation in sulfur content in each cathode formulation, the cell discharge capacities at C/5-rate are normalized against the total electrode weight (excluding Al foil). At practical level, Group 3 formulation is the best cathode formulation that results in highest energy density at the total cathode level. Therefore, Group 3 formulation is selected for additional process optimization.

Slurry preparation process evaluation

The TiS_2 BET surface area and its uniform distribution within the cathode have been previously identified as factors that correlate to the cell sulfur utilization and cycle life. The cathode slurry process is critical to achieve uniform TiS_2 particle distribution. Using Group 3 formulation (Table II-24), three slurry-mixing processes were evaluated. Mixing Process 1 resulted in uniform TiS_2 distribution within the coated electrode (Figure II-552), but difficult to obtain high sulfur loading. Mixing Process 2 afforded high sulfur loading, but difficult to achieve uniform TiS_2 distribution (Figure II-552). Mixing Process 3 yielded uniform TiS_2 distribution (Figure II-552) and ability in achieving high sulfur loading electrode with good mechanical integrity. Based on the consideration of achieving uniform TiS_2 distribution and the ability in coating electrode with high sulfur loading ($> 6 \text{ mg/cm}^2$), Mixing Process 3 is chosen for further optimization.

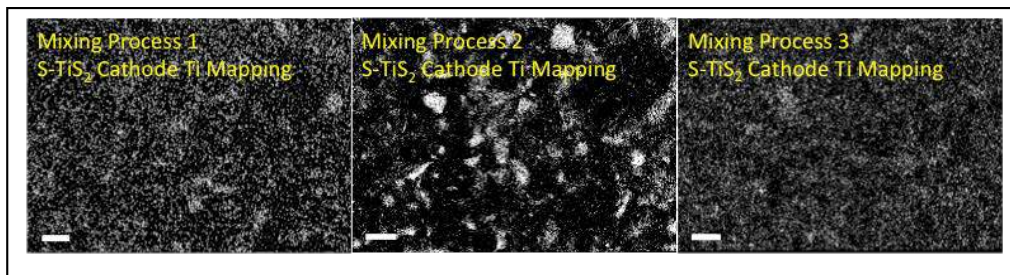


Figure II-552. Slurry mixing process methods vs. TiS_2 distribution (EDS) within coated cathode

Sulfur loading and electrode density interaction study

Sulfur loading and electrode density interaction was evaluation. With cathode formulation 3 (Table II-24), the electrodes with sulfur loading of ~ 2.7 , ~ 4.9 , and $\sim 6.7 \text{ mg/cm}^2$ were prepared. Good mechanical integrity was observed for all coated electrodes. The as coated pristine electrodes have density at $\sim 0.8 \text{ g/cc}$ for all three sulfur loadings. Higher electrode densities were achieved by hydraulic compressing the electrodes between the two flat surface metal blocks under various pressures. The electrode density increases with increasing pressure and starts to level off at ~ 1.20 to 1.35 g/cc .

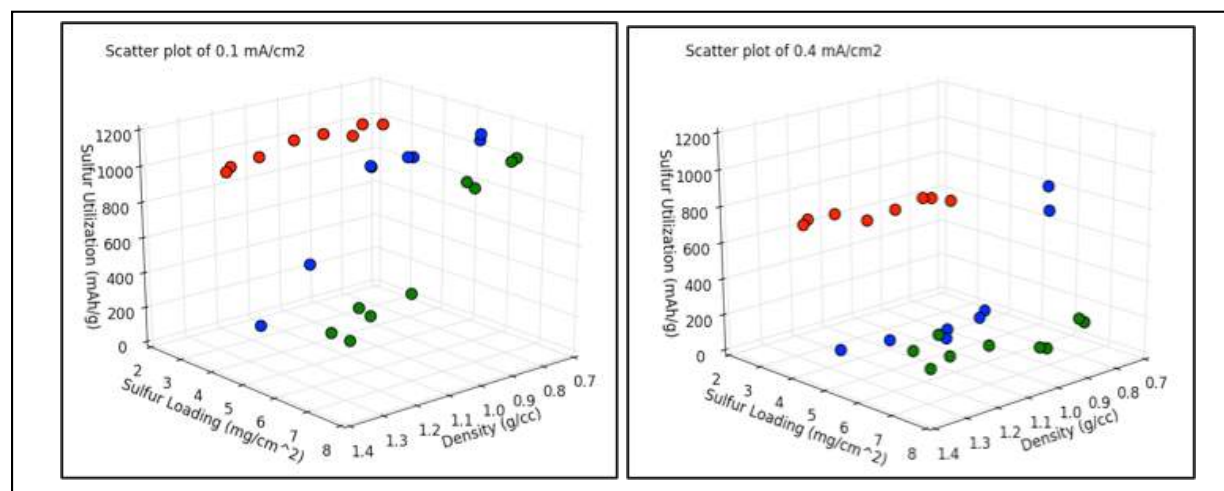


Figure II-553. Sulfur utilization vs. cathode density, sulfur loading and discharge rate

The electrode density has profound effect on coin cell discharge performance and the impact is more significant on the higher sulfur loading electrodes and at higher discharge rate (Figure II-553). Low sulfur loading and low electrode density favor the high sulfur utilization during cell discharge at all current densities

ranging from 0.1 mA/cm² to 4.0 mA/cm². The best electrochemical performance is derived from cells with pristine electrodes. Based on our estimation, the cathode porosity at density of 0.8g/cc is ~65%, which is about 1.4x the porosity of the 1.2 g/cc density electrode (47% porosity). The results suggest that maintaining the good ionic conductivity with increased electrolyte amount in the cathode pores and cell stack might be a critical factor for enhanced sulfur utilization.

Electrolyte-cathode interaction study

The cathode density-performance relationship uncovered above indicates the potential important role of electrolyte. Figure II-554 shows the relationship between electrolyte to sulfur weight ratio (E/S ratio) and the sulfur utilization under discharge current densities ranging from 0.1 mA/cm² to 4.0 mA/cm² for cathodes with sulfur loading from 2.5 mg/cm² to 11.0 mg/cm². With our 2032 coin cell design, the stable sulfur utilization can be achieved at all discharge rates when E/S ratio is ≥ 11.6 . Although consistent with some literature report, the E/S ratio value is most likely cell design dependent.

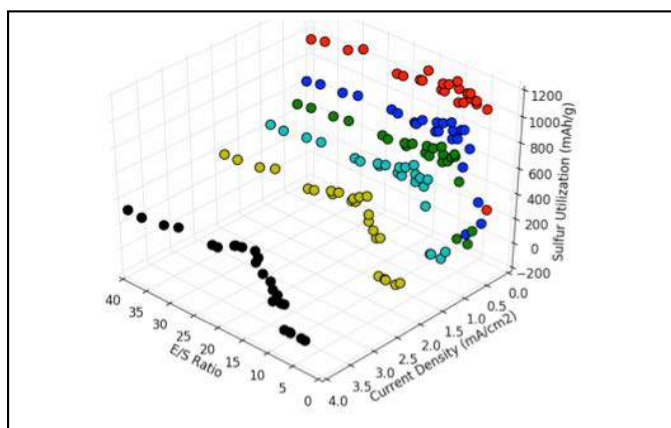


Figure II-554. Sulfur utilization vs. sulfur loading, discharge rate and E/S ratio

We also noticed that the cell cycle life and Coulombic Efficiency (CE) are strongly impacted by the sulfur loading and LiNO₃ concentration – suggesting the involvement of anode SEI. This phenomenon is closely associated with the high sulfur loading. Most literature report on Li-S battery study is based on sulfur loading electrode of < 2 mg sulfur per cm². However, high sulfur loading cells delivers high areal capacity, which results in deeper lithium anode cycling (high mAh/cm²). As a consequence, low LiNO₃ concentration (0.15M) will no longer sufficient to passivate the lithium anode surface for long cycle life. Higher LiNO₃ concentration is preferred to alleviate the cycling efficiency issue for high sulfur loading Li-S cells.

Technology demonstration

By incorporating all the improvement including the material, the components and the process optimization, as well as the cell system level optimization, the > 4 mAh 2032 coin cells with good cycle life is designed and assembled. Various testing are performed to demonstrate the technology.

Coin cell cycle life study

Excellent cell cycle life up to 150 cycles is achieved with > 3.1 mAh/cm² areal capacity delivered at 1 mA/cm² charging/discharging rate as shown in Figure II-555. Cell capacities were stabilized at ~5 mAh. The goal of achieving 4 mAh delivered capacity is clearly demonstrated. More importantly, the stable cycle life up to 150 cycles is achieved with the high sulfur loading cathode cells.

Temperature effect on discharge efficiency

Discharge temperature has significant impact on cell voltage profiles and delivered capacity. The cell voltage is severely polarized at below 0°C. Higher test temperature leads to lower cell voltage polarization and more

efficient sulfur utilization (Figure II-556). Up to 7.35 mAh ($\sim 4.6 \text{ mAh/cm}^2$) is deliverable at 60°C at 1 mA/cm^2 discharge rate.

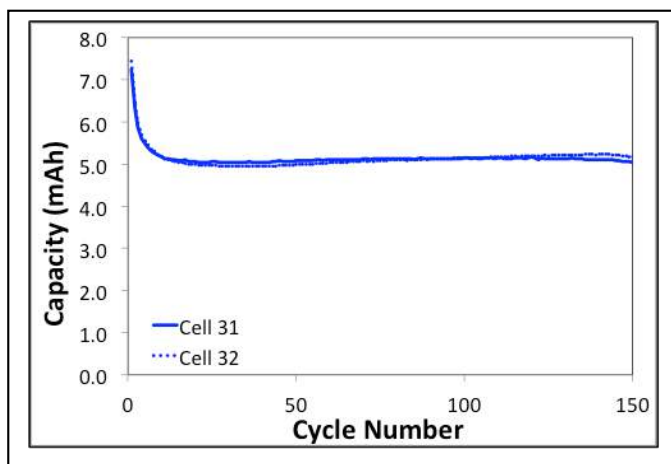


Figure II-555. 2032 coin cells cycle life

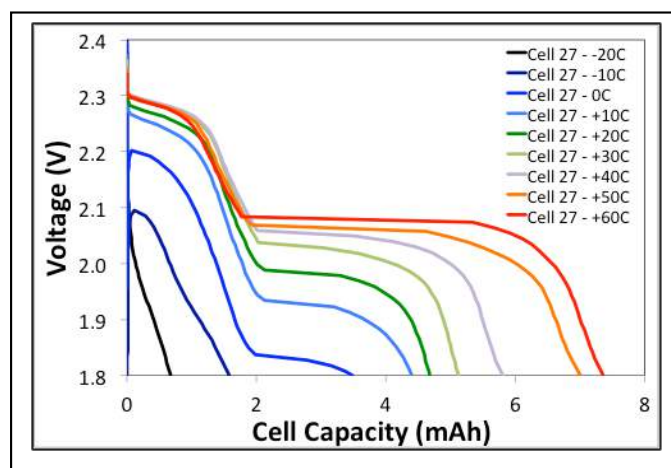


Figure II-556. 2032 coin cells discharge temperature effect

Coin cell shelf life

The shelf life study is executed by storing the coin cells for 30 days at 0°C , 20°C and 50°C respectively either at the freshly build state or at the fully discharged state before cycling testing at room temperature. Lower storage temperature is found to be beneficial for the cell cycle life and capacity retention. 50°C storage causes permanent damage to the fully discharged cells with poor cycle life (Figure II-557). RT or low temperature storage showed no damage to the cell cycling performance.

Coin cell self-discharge

The coin cell self-discharge is determined for cells stored at fully charged state for 1, 7, 14, 21 and 28 days respectively (Figure II-558) after the stabilization cycles. The cell self-discharge primarily happens at the soluble polysulfide discharge region. With the consumption of polysulfides, the self-discharge leveling off. Almost all capacity from the 2nd voltage plateau is still delivered after 4 weeks storage.

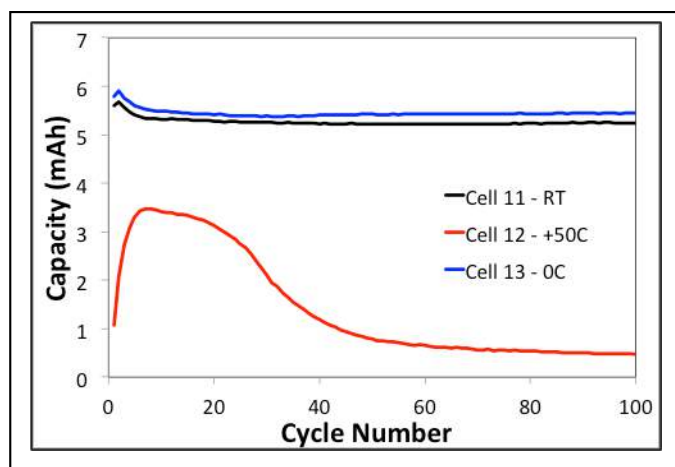


Figure II-557. 2032 coin cells cycling after storage at fully discharge state

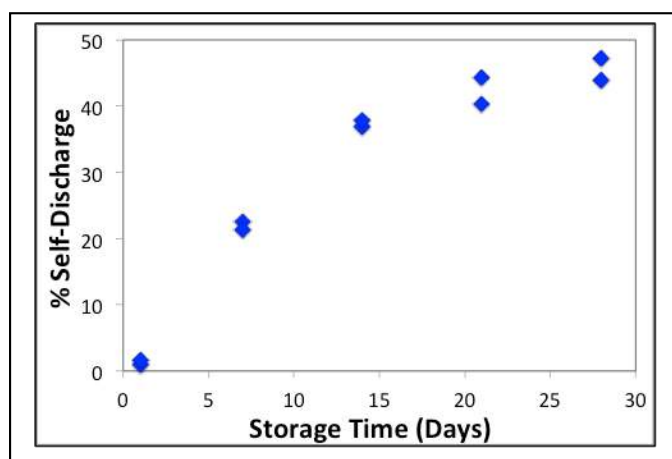


Figure II-558. 2032 coin cells self-discharge

Conclusions

We have successfully achieved all milestones for this 3 years program with the proof of concept MFCA demonstration and identification of TiS_2 as the leading candidate. TiS_2 has been demonstrated experimentally as the true multi-functional additive. In addition, we have achieved high sulfur loading (up to 10 mg/cm^2) by optimizing cathode components/formulation and cathode preparation processes. The optimization studies at the cell component and system level have been completed this year. With the integration of multiple cell design parameters, the 2032 coin cells with $\geq 4 \text{ mAh}$ are demonstrated with excellent cycle life. With this performance as the new benchmark, additional research at material, electrode and cell system levels will continue to further improve the performance of Li-S battery technology.

Key Publications

1. Ke Sun, Hellen Liu, Hong Gan, "Cathode loading effect on sulfur utilization in lithium-sulfur battery", *J. Electrochem. En. Conv. Stor.* 13(2), 021002 (2016).
2. Hong Gan, Ke Sun, "Electrochemically Active Interlayers for Lithium Ion Batteries", Provisional patent application, S.N. 62/413,583, filed 10/27/2016.

3. Qing Zhang, David C. Bock, Kenneth J. Takeuchi, Amy C. Marschilok, and Esther S. Takeuchi, “Probing Titanium Disulfide-Sulfur Composite Materials for Li-S Batteries via In Situ X-ray Diffraction (XRD)”, *J. of Electrochem. Society*, 164 (4) A897-A901 (2017).
4. Ke Sun, Christina A. Cama, Jian Huang, Qing Zhang, Sooyeon Hwang, Dong Su, Amy C. Marschilok, Kenneth J. Takeuchi, Esther S. Takeuchi and Hong Gan, “Effect of Carbon and Binder on High Sulfur Loading Electrode for Li-S Battery Technology”, *Electrochimica Acta* 235 (2017) 399-408.
<http://dx.doi.org/10.1016/j.electacta.2017.03.023>
5. Ke Sun, Qing Zhang, David C. Bock, Xiao Tong, Dong Su, Amy C. Marschilok, Kenneth J. Takeuchi, Esther S. Takeuchi and Hong Gan, “Interaction of TiS_2 and Sulfur in Li-S Battery System”, *J. Electrochem. Soc.* **164** (6) A1-A7 (2017).
6. Ke Sun, Chonghang Zhao, Cheng-Hung Lin, Eli Stavitski, Garth Williams, Jianming Bai, Eric Dooryhee, Klaus Attenkofer, Juergen Thieme, Yu-chen Karen Chen-Wiegart, Hong Gan, “*Operando* Multi-modal Synchrotron Investigation for Structural and Chemical Evolution of Cupric Sulfide (CuS) Additive in Li-S battery”, *Scientific Reports* 7: 12976 | DOI:10.1038/s41598-017-12738-0.

II.1.5 Development of High Energy Lithium-Sulfur Batteries (PNNL)

Jun Liu, Principal Investigator

Pacific Northwest National Laboratory
902 Battelle Boulevard
Richland, WA 99354
Phone: 509-375-4443; Fax: 509-371-6242
E-mail: jun.liu@pnnl.gov

Dongping Lu, Co-Principal Investigator

Pacific Northwest National Laboratory
902 Battelle Boulevard
Richland, WA 99354
Phone: 509-372-4483; Fax: 509-375-2186
E-mail: dongping.lu@pnnl.gov

Tien Duong, Technology Manager

U.S. Department of Energy
Phone: 202-586-7836
E-mail: Tien.Duong@ee.doe.gov

Start Date: October 1, 2015
Total Project Cost: \$1,160,000

End Date: September 30, 2018
DOE share: \$1,160,000

Non-DOE share: \$0

Project Introduction

The lithium-sulfur (Li-S) battery is a promising alternative to the state-of-the-art Li-ion batteries, owing to its high theoretical specific energy ($\sim 2300 \text{ Wh kg}^{-1}$) and the low cost and abundance of sulfur. However, the practical deployment of Li-S batteries is hindered by a low accessible energy density and poor long-term cycle life. Recent attempts to improve performance of Li-S batteries focused on the development of nanostructured sulfur host materials and demonstrated encouraging progress in terms of either high sulfur utilization rate or stable battery cycling. However, most of those studies are based on thin-film electrodes with low sulfur loadings ($< 2 \text{ mg cm}^{-2}$). For practical applications, instead, high sulfur loading cathodes with the lowest possible parasitic content are needed. Unfortunately, it is quite challenging to improve sulfur mass loading while maintaining the high sulfur utilization rate and cycling stability demonstrated in thin-film electrodes. A widely adopted strategy to prepare high loading electrodes is to employ thick, porous current collectors or free-standing carbon paper substrates as sulfur hosts. However, the high content of porous carbon materials not only increases electrode volume but also requires excess electrolyte for full electrode wetting, which significantly lowers volumetric and gravimetric energy density of the battery. So, a way to achieve both high energy density and stable cycling on high loading and dense sulfur electrodes is of key importance for technology maturation of Li-S batteries. A facile integration approach was developed at PNNL for sulfur cathode material synthesis (U.S. Patent No. 9,577,250), and sulfur electrodes with adjustable loadings of $2\text{--}11 \text{ mg cm}^{-2}$ can be successfully prepared at large scale using an industrial slurry casting method. The electrode wetting issues associated with high-loading sulfur electrodes were successfully addressed by using novel electrode additives (U.S. Patent Application No. 30459-E). To improve energy density (Wh L^{-1}) and specific energy (Wh kg^{-1}) of Li-S batteries, control of sulfur cathode porosity is essential but may negatively affect sulfur utilization rate and/or cell cycling. A clear understanding of such correlation is critical but rarely mentioned in the literature. In FY 2017, the benefits and drawbacks of controlling electrode porosity to improve cell performance were investigated based on high-loading sulfur cathodes. Issues associated with using high loading and dense electrodes were identified. Insight into the fundamental mechanism of those issues was gained using advanced characterization tools, and effective approaches were demonstrated to address the issues.

Objectives

- Improve volumetric energy density of sulfur cathodes through electrode porosity control and study its effects on cell performance.
- Study the fundamental reaction mechanism of electrolyte/additive with lithium sulfides/polysulfides using advanced characterization tools.
- Develop new approaches to retain high capacity in high-loading sulfur electrodes and enable stable operation of high energy Li-S batteries.

Approach

To develop high energy sulfur cathodes for practical Li-S battery and understand the underlying mechanisms, the following approaches were adopted:

- Study effects of cathode porosity on cell energy density, Li anode morphology, and cell cycling stability using sulfur electrodes with loading $>4 \text{ mg cm}^{-2}$.
- Investigate the degradation mechanism of LiNO_3 in sulfur cathodes and its effects on cell coulombic efficiency and cycling stability.
- Develop cross-linked-polymer-coated separator to minimize quick capacity and efficiency decay in the early-stage cycling of thick sulfur electrodes.
- Employ pouch cells to advance the understanding of the Li-S battery at a practical scale.

Results

1. Effects of electrode porosity on cell performance with high-loading sulfur cathode.

Using nonporous Li metal as anode, the thickness and porosity of a sulfur cathode determine not only the energy density of the Li-S battery but also the minimum electrolyte amount for electrode wetting, which also has a significant effect on specific energy of batteries. This, however, is rarely discussed in the literature. In FY17, we studied effects of sulfur cathode porosity based on thick electrodes with sulfur loading $>4 \text{ mg cm}^{-2}$. Sulfur electrode porosity shows strong dependence on calendering pressure, which can be explained by high porosity and low tap densities of the carbon and sulfur/carbon composites. Electrode porosity decreases quickly from the original ca. 64% ($\sim 120 \text{ }\mu\text{m}$) to ca. 29% ($\sim 60 \text{ }\mu\text{m}$) with calendering pressure increase from 0.2 to 1.5 ton (T) (electrode area, 1.6 cm^2) (Figure II-559a). A direct benefit of reducing electrode porosity is significant improvement of the electrode energy density, which is desirable for electric vehicle batteries. For a pristine, uncompressed electrode (4 mg cm^{-1} , $120 \text{ }\mu\text{m}$ thick), the tested electrode energy density is only 650 Wh L^{-1} , which was easily doubled to 1300 Wh L^{-1} when the electrode was compressed to $60 \text{ }\mu\text{m}$ (Figure II-559b). These results strongly suggest that appropriate control of electrode porosity/thickness is essential in developing high energy Li-S batteries. Another important benefit of decreasing electrode porosity is remarkable reduction of required electrolyte amount, which in fact has significant effect on cell specific energy. For thick, porous sulfur electrodes, more electrolyte is required to enable fast sulfur conversion kinetics and high utilization rate, but greatly decreases system specific energy. Figure II-559c shows the relationship of electrode porosity and required electrolyte amount, assuming that all the pores of both electrode and separator are filled with electrolyte. More than $11 \text{ }\mu\text{L}$ electrolyte is required for a pristine $120 \text{ }\mu\text{m}$ electrode, which converts to an electrolyte/sulfur (E/S) ratio of $2.75 \text{ }\mu\text{L electrolyte/mg S}$, while only $4.7 \text{ }\mu\text{L}$ electrolyte is needed for the $60 \text{ }\mu\text{m}$ dense electrode with corresponding E/S ratio of $1.17 \text{ }\mu\text{L mg}^{-1}$. This provides an important guideline for sulfur cathode design when pursuing a very low E/S ratio for improved system specific energy. Reducing electrode porosity has negative effects on both sulfur utilization and cell cycling stability, due to reduced uptake of electrolyte amount and confined mass transport. Figure II-559d compares cycling stability of cells with electrodes of different porosities. Stable cycling with 83% capacity retention for 200 cycles was realized with a pristine electrode without calendering. For the calendered electrodes (80 and $60 \text{ }\mu\text{m}$ thick), capacity retention decreased slightly to 76% after 200 cycles. These results

suggest that a tradeoff between cell energy density and cycle life should be considered when designing sulfur cathodes for different applications.

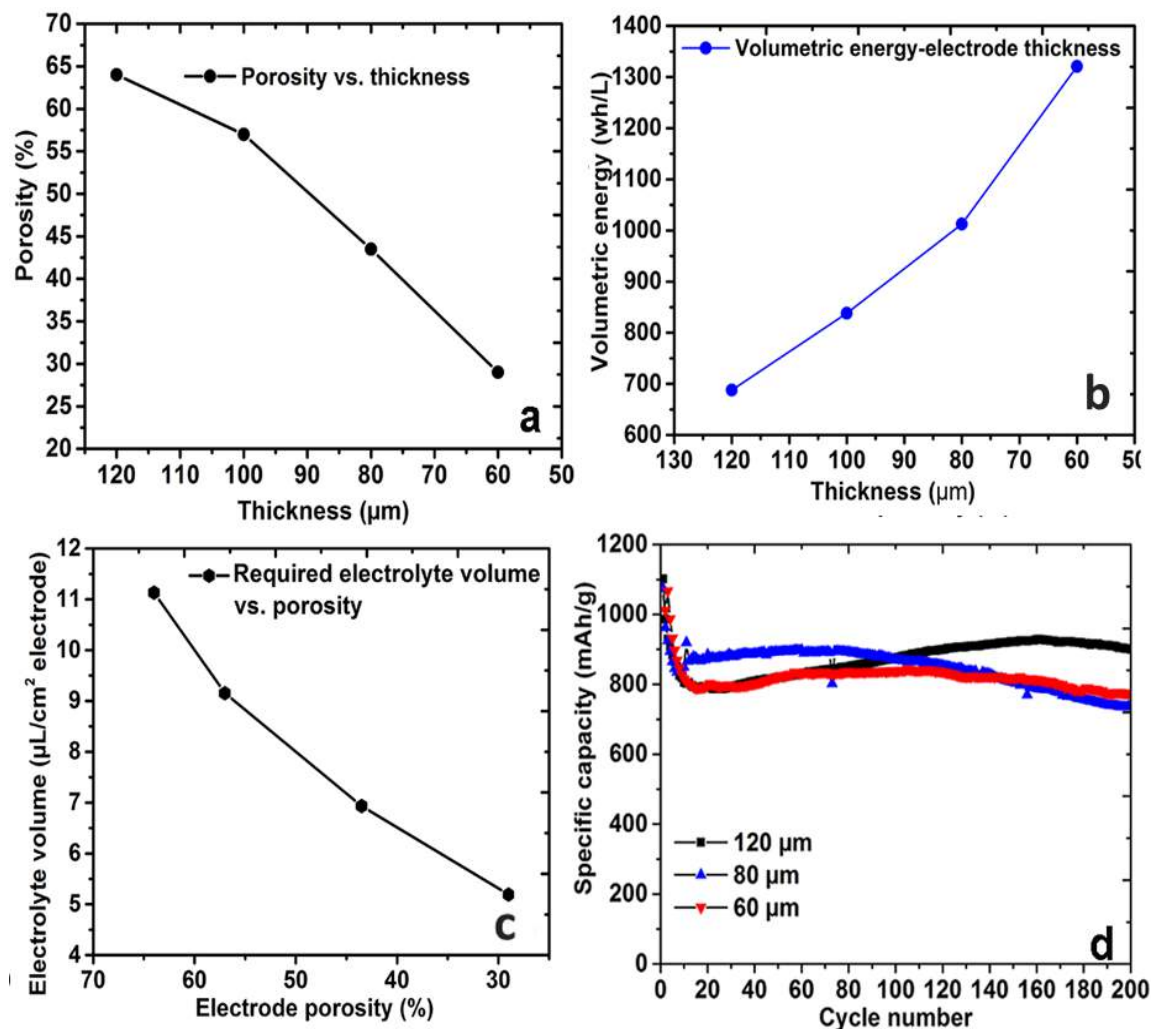


Figure II-559. (a) Correlation of electrode porosity and thickness, (b) dependence of volumetric energy density on electrode thickness, (c) minimum electrolyte amounts for electrodes with different porosities, and (d) cycling stability of electrodes compressed to different thicknesses/porosities (Sulfur loading of electrodes: 4 mg cm^{-2} ; electrolyte 1 M LiTFSI/DOL/DME with 0.2 M LiNO_3 and 0.15 M Li_2S_6 as additives).

Large volume expansion of sulfur and quick growth of Li interphase upon repeated cycling are among the most significant challenges for practical Li-S batteries. It is interesting to find that a dense sulfur electrode with reduced porosity can not only help preserve cathode architecture but also suppress Li interphase growth. Scanning electron microscope (SEM) characterization indicates the dense sulfur cathodes expand slightly from ca. 60 to ca. 75 μm after 200 cycles (Figure II-560b), a 25% volume expansion. In addition, significant sulfur redistribution and electrode reorganization both on the electrode surface and through the thickness are absent (Figure II-560a and Figure II-560b). This is because the low porosity and high tortuosity of the dense electrode can effectively minimize free migration of soluble polysulfides inside the electrode. The Li anode coupled with a dense sulfur cathode also exhibits much improved morphology after long-term cycling, i.e., smooth surface and dense interface layer (Figure II-560c and Figure II-560d), copying the morphology of the dense sulfur cathode. The interphase layer formed over the Li metal is compact and 127 μm thick after 200 cycles, which is only half that of the Li interphase when coupled with uncalendered sulfur electrodes. One explanation is that

the dense sulfur cathode can provide and maintain uniform internal pressure on the Li anode during cell cycling, which can suppress mossy Li growth and interphase formation to some extent. In contrast, with a porous and soft cathode, both polysulfide migration and Li plating/stripping are out of control without the uniform internal pressure; this usually results in nonuniform sulfur redistribution and random growth of thick and porous Li interphase.

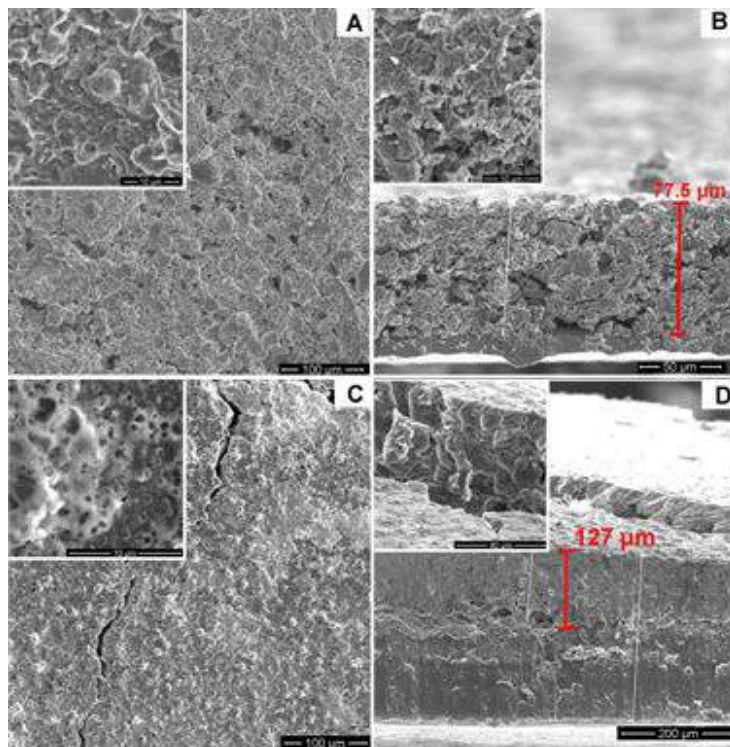


Figure II-560. SEM images of sulfur cathode (pressed to 60 μm) (A: surface; B: cross section) and corresponding Li metal anode (C: surface; D: cross section) after 200 cycles. (Sulfur loading 4 mg cm^{-2} and 250 μm Li).

2. Reaction mechanism of lithium sulfides/polysulfides with electrolyte/additive

While stable cycling has been demonstrated with high-loading sulfur cathodes (Figure II-559d), a common issue observed in those cells is the quick capacity and efficiency decay in the first 5 to 10 cycles. It becomes more serious when sulfur loading is further increased, for example, to around 6.5 mg cm^{-2} . After a certain number of cycles, the cell even failed with endless charging (Figure II-561b), indicating quick depletion of LiNO_3 . A systematic study was performed to understand the reasons for this phenomenon. Results of in situ electron paramagnetic resonance (EPR) and high-performance liquid chromatography (HPLC) analysis indicate that LiNO_3 can directly react with $\text{Li}_2\text{S}/\text{Li}_2\text{S}_2$ in the cathode, which weakens its function and durability for Li protection. This is exacerbated in high-loading sulfur cathodes where excess of $\text{Li}_2\text{S}/\text{Li}_2\text{S}_2$ are generated. Electrochemical study proves that LiNO_3 can also react with some soluble polysulfide species, such as Li_2S_6 . As shown in Figure II-561c, a solution containing both LiNO_3 and Li_2S_6 shows greatly reduced peak intensity at 1.6–1.7 V but increased peak intensity at ~ 2.0 V compared to the baseline electrolytes with the same concentrations of LiNO_3 or Li_2S_6 individually. This is due to chemical reduction of LiNO_3 by Li_2S_6 or other derived polysulfide species. X-ray photoelectron spectroscopy (XPS) analysis identified formation of high-valence sulfur species $\text{SO}_3^{2-}/\text{SO}_4^{2-}$ from the LiNO_3 and Li_2S_6 mixture solution, which further proved the direct chemical reactions between LiNO_3 and polysulfides, a new degradation pathway of LiNO_3 in Li-S batteries. From these new findings of LiNO_3 degradation pathways, more effective approaches or electrolyte additives for Li anode protection are required for highly efficient and long-term cycling of Li-S batteries.

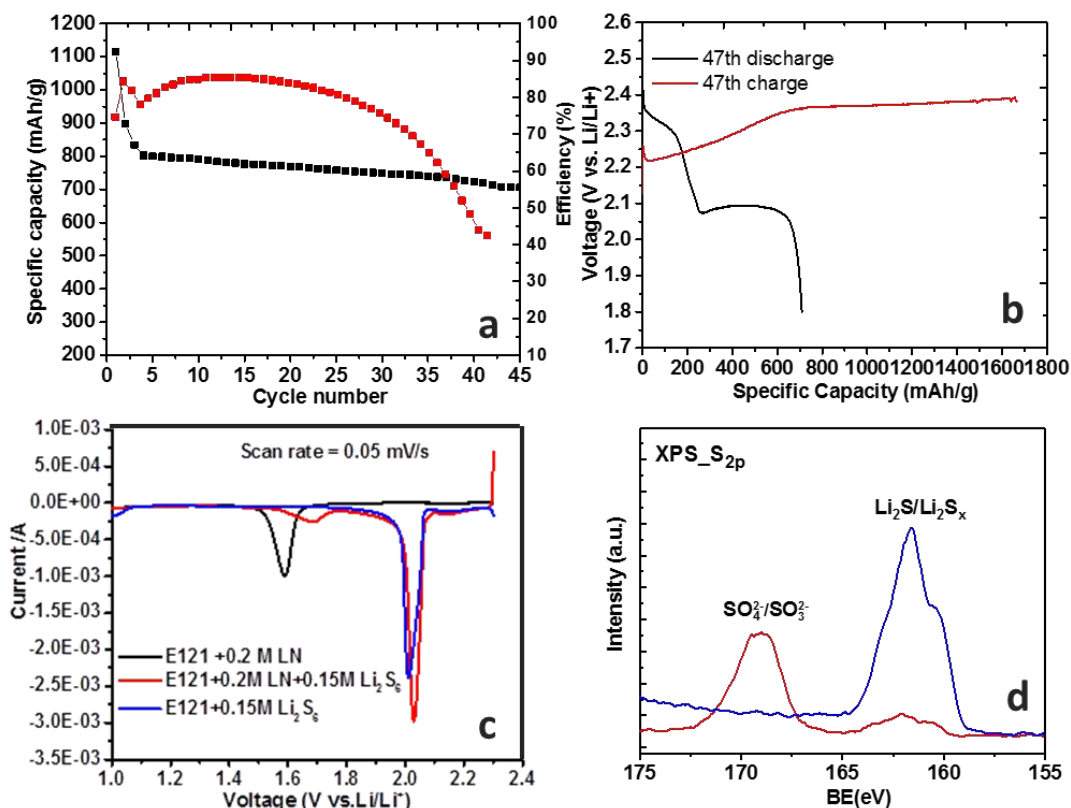


Figure II-561. (a) Cycling stability and coulombic efficiency of thick electrode with sulfur loading 6.5 mg cm^{-2} and (b) typical failed charge/discharge profiles (47th cycle), (c) cyclic voltammetry of carbon paper electrodes with electrolytes $1 \text{ M LiTFSI/DOL/DME} + 0.2 \text{ M LiNO}_3$ (black), $1 \text{ M LiTFSI/DOL/DME} + 0.15 \text{ M Li}_2\text{S}_6$ (blue), and stored $1 \text{ M LiTFSI/DOL/DME} + 0.2 \text{ M LiNO}_3 + 0.15 \text{ M Li}_2\text{S}_6$ (red), and (d) XPS analysis of dried electrolytes $1 \text{ M LiTFSI/DOL/DME} + 0.15 \text{ M Li}_2\text{S}_6$ (blue) and $1 \text{ M LiTFSI/DOL/DME} + 0.2 \text{ M LiNO}_3 + 0.15 \text{ M Li}_2\text{S}_6$ (red).

3. Cross-linked polymer coating to minimize early-stage quick capacity drop and efficiency fluctuation in thick sulfur electrodes

Direct chemical reactions of LiNO_3 with sulfide and polysulfides accelerate depletion of LiNO_3 , resulting in fast efficiency decay of high-loading sulfur electrodes. To address this problem, we developed a cross-linked polyacrylic acid (C-PAA)-coated separator to partially trap LiNO_3 and suppress polysulfide diffusion. The blocking effect of C-PAA for polysulfide crossover was investigated with an H-type cell (Figure II-562), in which a highly concentrated polysulfide solution ($0.15 \text{ M Li}_2\text{S}_6$ in $1 \text{ M bis(trifluoromethanesulfonyl)imide (LiTFSI)/1,3-dioxolane (DOL)/1,2-dimethoxyethane (DME)}$) and benchmark electrolyte ($1 \text{ M LiTFSI/DOL/DME}$) were separated by a Celgard 2400 separator with or without C-PAA coating. Polysulfide could easily cross the pristine separator and migrate to the opposite chamber driven by concentration difference (Figure II-562a); however, this was suppressed significantly when a C-PAA coated separator was used (Figure II-562b). In addition, carbon nanofibers (CNFs) were introduced during the cross-linking of PAA, which provides reaction sites to reuse the blocked polysulfide on the separator. SEM images indicate the cross-linked PAA and CNFs form a relatively dense and uniform coating on the separator (Figure II-562c). Effectiveness of the C-PAA coated separator on cell performance was tested with high-loading sulfur cathodes ($>4 \text{ mg cm}^{-2}$). Using an uncoated separator, the discharge capacity drops quickly from 1100 mAh g^{-1} to 810 mAh g^{-1} after 5 cycles, accompanied by an efficiency drop from 92% to 89% (Figure II-562d). For the cell with C-PAA coated separator, the first cycle discharge capacity and efficiency are 915 mAh g^{-1} and 97%, respectively, and are maintained as high as 950 mAh g^{-1} and 96.4%, respectively, after 5 cycles, suggesting effectively suppressed polysulfide crossover. Besides blocking the effects of polysulfides, the C-PAA coated

separator can also trap more LiNO_3 and thus extend the durability of LiNO_3 for Li protection compared to the pristine separator.

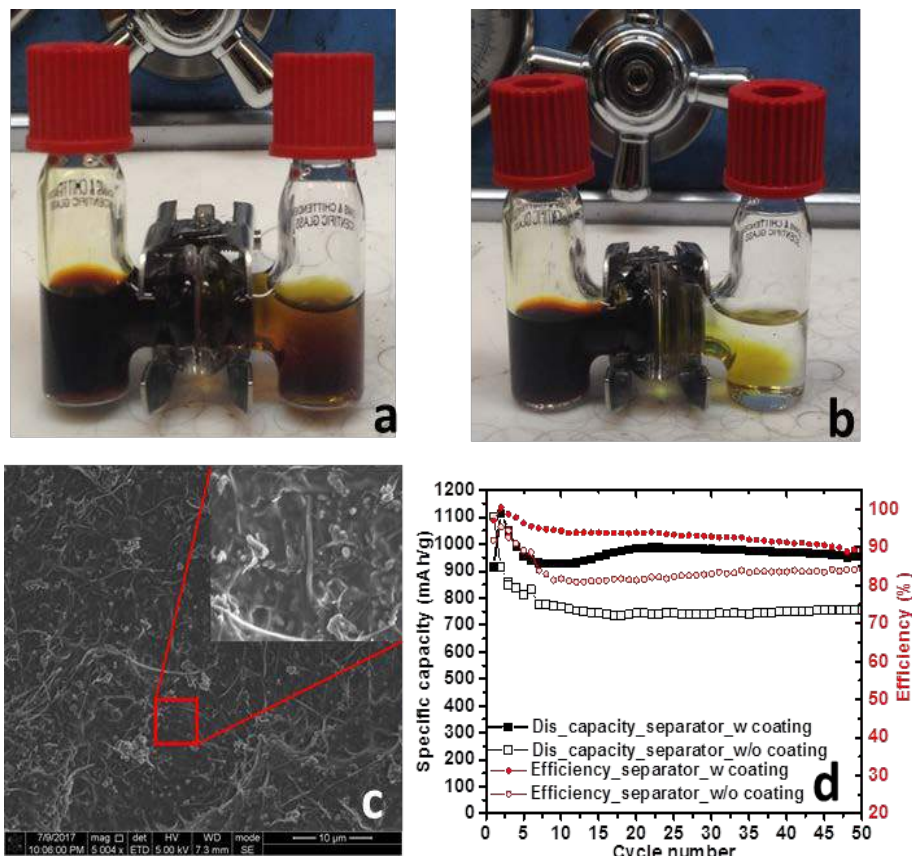


Figure II-562. Visual comparison of polysulfide diffusion in H-cell using Celgard 2400 separator with (a) and without (b) C-PAA coating after 1 h rest, (c) SEM image of C-PAA/CNF coated separator, and (d) capacity and coulombic efficiency of Li-S cells using separators with (solid symbols) and without (hollow symbols) C-PAA coating.

4. Study of electrolyte/sulfur ratio on cell performance with practical pouch cells

1.6 Ah Li-S pouch cells with specific energy of 247 Wh kg^{-1} has been demonstrated in this work. To achieve higher energy, not only should the areal capacity of sulfur cathodes be improved significantly but also the parasitic weight of the cell components must be minimized; for this, electrolyte amount is a key parameter (43.6 wt%, Figure II-563a). To reach 300 Wh kg^{-1} , the areal capacity of a sulfur cathode should be at least 5.0 mAh cm^{-2} , while the E/S ratio should be less than $3 \mu\text{L mg}^{-1}$. Therefore, pouch cells in this study are based on cathodes with sulfur loading $\sim 5.7 \text{ mg cm}^{-2}$ and porosity $< 55\%$, a $50 \mu\text{m}$ thick lithium anode ($\sim 10 \text{ mAh cm}^{-2}$, anode/cathode ratio < 2) and controlled E/S ratio from 2.7 to 7.2. Figure II-563c shows the dependence of electrode areal capacity and sulfur utilization rate on the E/S ratio. When $\text{E/S} > 7$, the deliverable areal capacity is 5.5 mAh cm^{-2} with a high sulfur utilization, above 950 mAh g^{-1} . Reducing the E/S ratio to 4.9, areal capacity and sulfur utilization rate decline slightly to 5.0 mAh cm^{-2} and 880 mAh g^{-1} , respectively. But for $\text{E/S} < 2.8$, a significant decrease of both areal capacity and sulfur utilization rate is observed. However, with the C-PAA coated separator (coating $< 1 \text{ mg cm}^{-2}$), remarkable improvement is observed. 5.05 mAh cm^{-2} and 870 mAh g^{-1} are achieved at $\text{E/S} = 2.7$, which are comparable to those at $\text{E/S} = 4.9$ with a pristine separator. An even lower E/S ratio is predictable in practical multiple-layer pouch cells. These results verified that our approaches of dense cathode, electrode additives, and modified separator are applicable to fabrication of practical pouch cells



Figure II-563. (a) Component weight distribution of Li-S battery with energy density of 300 Wh kg⁻¹, (b) photo of single-layer pouch cell used in present study (Electrode working area 19.4 cm² and sulfur mass loading 5.7 mg cm⁻²), and (c) dependence of first-discharge areal capacity and specific capacity on electrolyte/sulfur ratio (black symbol - pouch cell using pristine separator; red symbol - pouch cell using modified separator).

Conclusions

The effects of electrode porosity on cell performance as well as system energy density were investigated using high-loading sulfur electrodes. Electrode porosity reduction at a given sulfur loading significantly reduces both electrode volume and the amount of electrolyte required to wet the electrode, which leads to large increases in both energy density (Wh L⁻¹) and specific energy (Wh kg⁻¹) of Li-S batteries. To understand the quick capacity and coulombic efficiency degradation observed in the early-stage cycling of high-loading sulfur electrodes, systematic study was performed to probe the interactions between LiNO₃ and sulfur species. In situ EPR and HPLC study identified direct redox reactions of LiNO₃ with Li₂S/Li₂S₂, while electrochemical characterization combined with XPS analysis proved the interactions between LiNO₃ and polysulfides. This study uncovered a new degradation pathway of LiNO₃ in Li-S battery. Accordingly, a cross-linked polyacrylic acid (C-PAA)-coated separator was developed to partially trap LiNO₃ and concurrently suppress polysulfide crossover. Practical pouch cells were employed to extend our proposed approaches and study the effects of electrolyte/sulfur ratio on cell performance. Using a C-PAA-coated separator, a pouch cell with a dense sulfur cathode (~5.7 mg cm⁻², porosity < 55%), thin anode (50 μm Li anode), and lean electrolyte (E/S = 2.7) can deliver an areal capacity of 5.05 mAh cm⁻² and a sulfur utilization of 870 mAh g⁻¹.

Key Publications

1. J. Xiao, D. Lu, J. Liu, J. Zhang, and G. Graff. Thick Electrodes Including Nanoparticles Having Electroactive Materials and Methods of Making Same. **U.S. Patent No. 9,577,250**, granted date: February 21, 2017.
2. J. Xiao, D. Lu, Y. Shao, W. Bennett, G. Graff, J. Liu, and J. Zhang. Electrolyte for Batteries with Regenerative Solid Electrolyte Interface, **U.S. Patent No. 9,722,277**, granted date: August 1, 2017.
3. D. Lu, Q. Li, J. Liu, J. Xiao, J. Zhang, J. Liu, and G. Graff. Additives to Enhance Electrode Wetting and Performance and Methods of Making Electrodes Comprising the Same, **Patent application: No. 30459-E**
4. D. Lu, Q. Li, J. Liu, J. Zheng, Y. Wang, S. Ferrara, S. Chen, J. Xiao, J. Zhang, and J. Liu. Enabling High Capacity and High Energy Density Cathode for Lithium-Sulfur Batteries, Submitted.
5. D. Lu, J. Tao, P. Yan, W. Henderson, Q. Li, Y. Shao, M. Helm, O. Borodin, G. Graff, B. Polzin, C. Wang, J. Zhang, J. Yoreo, J. Liu, and J. Xiao, Formation of Reversible Solid Electrolyte Interface on Graphite Surface from Concentrated Electrolytes, *Nano Letters* 2017 17 (3), 1602-1609.

6. D. Lu, Q. Li, J. Liu, S. Wilson, J. Zhang, and J. Liu, Enhanced Performance of High Energy Sulfur Cathode for Lithium-Sulfur Batteries, 253rd ACS National Meeting & Exposition, San Francisco, CA, April 2-6, 2017
7. D. Lu, J. Xie, Q. Li, Y. Wang, S. Wilson, J.-G. Zhang, and J. Liu, Development of High Energy Sulfur Cathode for Lithium-Sulfur Batteries, Beyond Lithium Ion X, Almaden, CA June 27-30, 2017.

II.1.6 Nanostructured Design of Sulfur Cathodes for High Energy Lithium-Sulfur Batteries (Stanford University)

Yi Cui, Principal Investigator

Department of Materials Science and Engineering
Stanford University
Stanford, CA 94305
Phone: 650-723-4613; Fax: 650-736-1984
E-mail: yicui@stanford.edu

Tien Duong, Technology Manager

U.S. Department of Energy
Phone: 202-586-7836
E-mail: Tien.Duong@ee.doe.gov

Start Date: October 1, 2016
Total Project Cost: \$300,000

End Date: September 30, 2017
DOE share: \$300,000

Non-DOE share: \$0

Project Introduction

Lithium-sulfur batteries can bring about significant improvements to the current state-of-the-art battery technologies due to its high specific energy density and cost saving. The capacity decay of lithium-sulfur battery during cycling is a multifaceted problem. There exist multiple materials challenges that prevent it from reaching the cycling performance suitable for portable electronics and electrical vehicles. The rapid capacity decay of sulfur cathode can be attributed to several reasons: 1) significant volumetric expansion (~80% change) when sulfur is reduced to lithium sulfide (Li_2S); 2) dissolution of intermediate lithium polysulfides (Li_2S_x , $4 \leq x \leq 8$) in the electrolyte; 3) low ionic and electronic conductivity of both sulfur and Li_2S .

Introducing anchoring materials, which can induce strong binding interaction with Li_2S_x species, has been demonstrated as an effective way to overcome this problem and achieve long-term cycling stability and high-rate performance. The interaction between Li_2S_x species and anchoring materials should be studied at the atomic level in order to understand the mechanism behind the anchoring effect and to identify ideal anchoring materials to further improve the performance of Li-S batteries. The importance of balancing sulfide species adsorption and diffusion on anchoring materials with better surface diffusion will lead to higher Li_2S deposition efficiency. In the reverse reaction process, catalysis of the decomposition of Li_2S and oxidization of Li_2S to Li_2S_x and finally to sulfur near the surface of the substrate are crucial steps to realizing high capacity and Columbic efficiency, yet have been relatively neglected in the Li-S chemistry. In this respect, a systematic consideration of the substrates that are capable of catalyzing Li_2S decomposition is also critical to the development of advanced Li-S batteries.

Objectives

The charge capacity limitations of conventional transition metal oxide cathodes are overcome by designing optimized nano-architected sulfur cathodes. This study aims to enable sulfur cathodes with high capacity and long cycle life by developing sulfur cathodes from the perspective of nanostructured materials design, which will be used to combine with lithium metal anodes to generate high-energy lithium-sulfur batteries. The selection criterion of anchoring materials is proposed to guide the rational design of cathode materials for advanced Li-S batteries. Novel sulfur nanostructures will be designed and adsorption/diffusion/catalytic mechanism will be proposed to overcome the issues related to sulfur volume expansion, polysulfide dissolution and insulating nature of sulfur/ Li_2S . A standard procedure to quantitatively compare the polysulfide adsorption capability of candidate materials was also established.

Approach

Using first-principles approach with van der Waals interaction included, we systematically investigate the adsorption of Li_2S_x species on various oxides, sulfides and nitrides, and study the detailed interaction and electronic structure, including binding strength, diffusion energy barrier and catalytic effect. We gain insight into how van der Waals interaction and chemical binding contribute to the adsorption of Li_2S_x species for anchoring materials with strong, medium, and weak interactions. Combining theoretical calculations and experimental design, we select a series of metal oxides/sulfides/nitrides as model systems to identify the key parameters in determining the energy barrier for Li_2S oxidation and polysulfide adsorption. We also establish a standard procedure to quantitatively compare the polysulfide adsorption capability of various candidate materials.

Results

To understand the role of metal sulfides in catalytic decomposition of Li_2S , we systematically investigated the effect of six kinds of metal sulfides including VS_2 , CoS_2 , TiS_2 , FeS , SnS_2 and Ni_3S_2 on tuning the decomposition energy barrier. According to our simulation of electronic band structures, Ni_3S_2 , FeS and CoS_2 are metallic materials while VS_2 and TiS_2 are semi-metallic, which means that they are all materials with good electrical conductivities while SnS_2 is a semiconductor with a band gap of 2.2 eV. Carbon material (a graphene/carbon nanotube hybrid (G/CNT)) was chosen for comparison. The cathode consists of a commercial Li_2S cathode material mixed uniformly with various metal sulfides, carbon black and polyvinylidene fluoride (PVDF) binder. Coin cells were assembled with lithium metal as anode and reference electrode. The initial charge voltage profiles was used to clearly show the activation barrier (Figure II-564A). The G/CNT- Li_2S cathode without the addition of metal sulfide exhibits a high potential barrier at about 3.41 V in the initial charging process, indicating a sluggish activation process with high charge-transfer resistance. The SnS_2 - Li_2S cathode shows a clear voltage jump with a potential barrier of 3.53 V during the activation process due to the semiconducting nature of SnS_2 . The charge voltage plateaus after the short voltage jump represent the phase conversion reaction from Li_2S to low-order LiPSs, high-order LiPSs and sulfur. A similar charging phenomenon is observed for Ni_3S_2 - Li_2S and FeS - Li_2S electrodes with high potential barriers of 3.47 and 3.25 V even though both are metallic. However, the addition of CoS_2 , VS_2 , and TiS_2 significantly reduces the height of the potential barrier to 3.01, 2.91 and 2.88 V, respectively. The lower potential barrier and longer voltage plateau of the CoS_2 , VS_2 and TiS_2 -based electrodes compared to other metal sulfides indicate improved conductivity and reduced charge-transfer resistance.

To attain an in-depth understanding of the function of these metal sulfides, we use the climbing-image nudged elastic band (CI-NEB) method to calculate the barrier for Li_2S decomposition in order to evaluate the delithiation reaction kinetics on the surface of different metal sulfides. Here, we consider the decomposition process from an intact Li_2S molecule into a LiS cluster and a single Li ion ($\text{Li}_2\text{S} \rightarrow \text{LiS} + \text{Li}^+ + \text{e}^-$). The main evolution is composed of the Li ion moving far away from the S atom in the Li_2S molecule, which is accompanied by breaking of the Li-S bond. The energy profiles for the decomposition processes on different sulfides are shown in Figure II-564B. The Ni_3S_2 decomposition barrier is as high as 1.03 eV, much larger than the other five cases, and is consistent with the large initial voltage barrier for Ni_3S_2 added Li_2S cathode. The barriers for FeS , CoS_2 , VS_2 and TiS_2 are 0.63, 0.56, 0.31 and 0.30 eV, respectively, and qualitatively agree with the voltage magnitudes measured experimentally. For SnS_2 , the calculated barrier for decomposition is as low as 0.32 eV, but experimentally exhibits a very large initial charge potential. This can be probably attributed to the insulating nature of SnS_2 and the electron-ion recombination process, which is the rate-determining step for the delithiation process, but not the Li decomposition process. Figure II-564C-H illustrate the decomposition pathway for one Li ion departing from the LiS cluster on the surface of six kinds of sulfides. It can be clearly seen that the decomposition process is associated with the binding between the isolated Li ion and the sulfur in sulfides. This is the dominant reason that the sulfide anchor can induce a lower decomposition barrier compared with carbon materials. For graphene, the chemical interaction between the Li ion and carbon is much weaker, and therefore, the decomposition process should have a very large activation energy barrier (Figure II-564I, 1.81 eV according to our simulation).

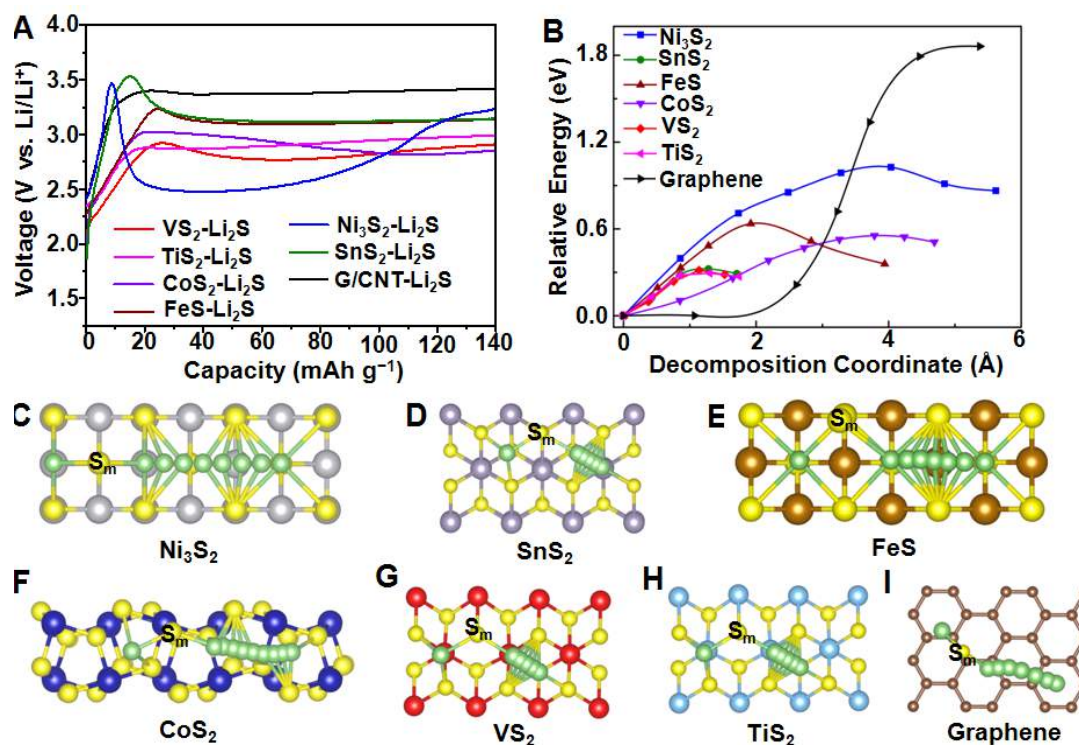


Figure II-564. (A) First cycle charge voltage profiles of $\text{Ni}_3\text{S}_2\text{-Li}_2\text{S}$, $\text{SnS}_2\text{-Li}_2\text{S}$, $\text{FeS-Li}_2\text{S}$, $\text{CoS}_2\text{-Li}_2\text{S}$, $\text{VS}_2\text{-Li}_2\text{S}$, $\text{TiS}_2\text{-Li}_2\text{S}$ and $\text{G/CNT-Li}_2\text{S}$ electrodes. (B) Energy profiles for the decomposition of Li_2S cluster on Ni_3S_2 , SnS_2 , FeS , CoS_2 , VS_2 , TiS_2 and graphene. Top view schematic representations of the corresponding decomposition pathways for (C) Ni_3S_2 , (D) SnS_2 , (E) FeS , (F) CoS_2 , (G) VS_2 , (H) TiS_2 and (I) graphene. Here, green, yellow, grey, purple, brown, blue, red, cyan and beige balls symbolize lithium, sulphur, nickel, tin, iron, cobalt, vanadium, titanium and carbon atoms, respectively. S_m represents the sulfur atom in the Li_2S cluster.

Figure II-565A shows the galvanostatic discharge/charge voltage profiles of $\text{S-VS}_2\text{/G/CNT}$ electrode at various current rates from 0.2C to 4C in the potential range of 1.5–2.8 V. It exhibits excellent rate performance consisting of two discharge plateaus even at a very high current rate of 4C which can be ascribed to the reduction of S_8 to high-order lithium polysulfides at 2.3–2.4 V and the transformation to low-order $\text{Li}_2\text{S}_2/\text{Li}_2\text{S}$ at 1.9–2.1 V. In the reverse reaction, two plateaus in the charge curve represent the backward reaction from lithium sulfides to polysulfides and finally to sulfur. Based on the discharge curves at 0.2C, the sulfur electrodes containing G/CNT, SnS_2 , Ni_3S_2 , FeS , TiS_2 , CoS_2 , and VS_2 exhibit average discharge capacities of 685, 836, 845, 900, 1008, 1033, and 1093 mA h g^{-1} , respectively (Figure II-565B). The higher discharge capacities of TiS_2 , CoS_2 , and VS_2 containing cathodes indicate the high utilization of sulfur due to the strong interaction between LiPSs and these sulfides. There are distinct differences in the voltage hysteresis and length of the voltage plateaus, which are related to the redox reaction kinetics and the reversibility of the system. The TiS_2 , CoS_2 , and VS_2 containing cathodes display flat and stable plateaus with relatively small polarizations of 177, 177 and 172 mV at 0.2C, much lower than G/CNT, SnS_2 , Ni_3S_2 , FeS containing cathodes with values of 272, 244, 259 and 217 mV. This suggests a kinetically efficient reaction process with a smaller energy barrier promoted by the M_xS_y (TiS_2 , CoS_2 , and VS_2) catalyzing process discussed previously. The charge/discharge plateaus obviously shift or even disappear for G/CNT, SnS_2 , and Ni_3S_2 containing electrodes at high current rates, indicating high polarization and slow redox reaction kinetics with inferior reversibility.

Long-term cycling stability with high capacity retention is crucial for the practical application of Li-S batteries. Figure II-565C shows the cycling performance of the S/G/CNT and $\text{S-M}_x\text{S}_y\text{/G/CNT}$ electrodes at 0.5C for 300 cycles after the rate capability test. The $\text{S-VS}_2\text{/G/CNT}$ electrode delivers a high initial reversible capacity of 830 mA h g^{-1} and the capacity remains at 701 mA h g^{-1} after 300 cycles with stabilized Coulombic

efficiency above 99.5%, corresponding to a capacity retention of 84.5% and slow capacity decay rate of 0.052% per cycle. The high LiPSs adsorbing capability and good catalytic conversion of sulfur species alleviate the shuttle effect and improve the Coulombic efficiency. The S-CoS₂@G/CNT and S-TiS₂@G/CNT electrodes also retain reversible capacities of 581 and 546 mA h g⁻¹, respectively, accounting for 85.3% and 78.2% of their initial capacities with low capacity fading rates of 0.049% and 0.073% per cycle. The remarkable improvements in cycling stability and Coulombic efficiency can be ascribed to the immobilization of soluble polysulfide species through a strong chemical binding and facile redox reaction propelled by these metal sulfides. As for the S@G/CNT electrode, it only delivers an initial reversible capacity of 386 mA h g⁻¹ at 0.5C rate and the capacity rapidly decreases to 218 mA h g⁻¹ after 300 cycles with a capacity retention of 56.5% and fast capacity decay rate of 0.145% per cycle. This suggests a weak affinity with LiPSs that cannot retard their diffusion into the electrolyte and prevent active material loss. Compared with TiS₂, CoS₂ and VS₂ containing electrodes, the sulfur cathodes containing FeS (334 mA h g⁻¹, 47.4% capacity retention), SnS₂ (191 mA h g⁻¹, 31.3% capacity retention), and Ni₃S₂ (153 mA h g⁻¹, 29.1% capacity retention) demonstrate inferior cycling stability at 0.5C with quick capacity degradation and unstable Coulombic efficiency around 96%. The capacity fading rates reach 0.175%, 0.229% and 0.236% per cycle for FeS, SnS₂, and Ni₃S₂ containing electrodes, respectively, much higher than the other three metal sulfides. These results imply that the selection of suitable polar hosts in the cathode that can 1) strongly interact with LiPSs, 2) rationally control Li₂S deposition, 3) enable fast lithium ion diffusion, 4) effectively transform sulphur to LiPSs/Li₂S, and 5) catalytically reverse the reaction process, is crucial and could significantly decrease polarization, improve sulfur utilization, and enhance rate performance and long-term cycling stability.

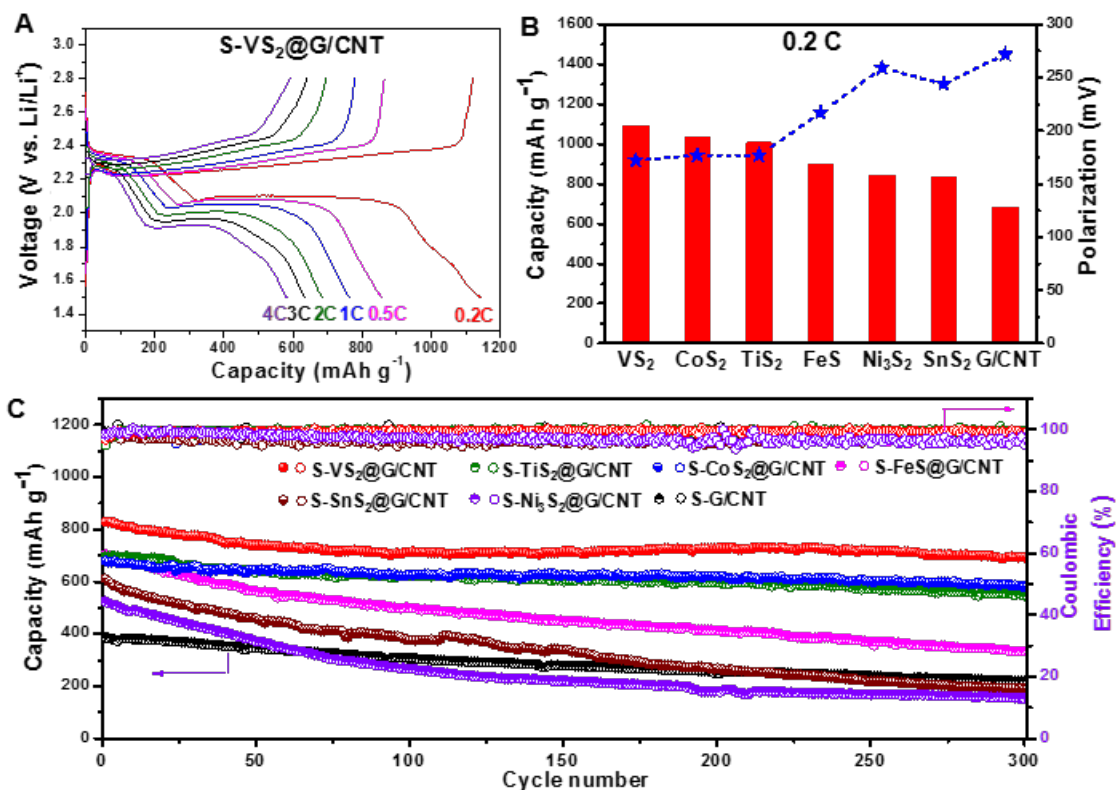


Figure II-565. (A) Galvanostatic charge/discharge voltage profiles of the S-VS₂@G/CNT composite electrodes at different current densities within a potential window of 1.5~2.8 V vs. Li⁺/Li⁰. (B) Comparison of the specific capacity and polarization voltage between the charge and discharge plateaus at 0.2C for different composite electrodes. (C) Cycling performance and Coulombic efficiency of the different composite electrodes at 0.5C for 300 cycles after the rate capability test.

We further establish a standard procedure to quantitatively compare the polysulfide adsorption capability of various candidate materials. Figure II-566 presents data for the setup where 0.5 m² surface area of candidate materials are added to 3mM of Li₂S₆ in 4mL of 1,3-dioxolane/1,2-dimethoxyethane solution (DOL/DME, 1:1 by volume) for 3 hours. Li₂S₆ is a representative soluble long-chain polysulfide species and is prepared by chemically reacting sulfur with Li₂S in DOL/DME solution which is a common electrolyte system for Li-S batteries. As Figure II-566A illustrates, varying degrees of color change can be observed which are attributed to the interactions between candidate materials and the polysulfide species. No observable color fading is associated with carbon black, suggesting weak physical adsorption. Other materials such as MoS₂ and TiO₂ demonstrate higher adsorption capability compared to carbon black, while CoS and TiN exhibit relatively low adsorption capability as indicated by the lack of significant color fading. In contrast, the polysulfide solutions become much lighter in color after the addition of V₂O₅, MnO₂, V₂O₃, TiS₂ and FeS, suggesting strong interactions between Li₂S₆ and these materials. However, the judgment of color shades is subjective to the human eyes and is also hindered by the powder color of the candidate materials. Therefore, upon completion of the adsorption tests, 2mL of the supernatant solutions are extracted from each sample to minimize the impact of powders and ultraviolet-visible spectroscopy (UV-Vis) is performed on these supernatant solutions for detailed examination.

Figure II-566B illustrates the UV-Vis performance in the visible spectrum of varying concentrations of Li₂S₆ without the addition of any candidate materials. There is strong absorbance towards the blue end of the visible spectrum, as blue is the complementary color of yellow. Unsurprisingly, higher concentrations of Li₂S₆ corresponds to darker shades of yellow and stronger absorbance around the blue spectrum. Figure II-566C shows the performance of carbon black and the metal oxides adsorption test supernatant solutions. The results are in good agreement with previous visual inspections. Carbon black demonstrates much higher blue spectrum absorbance corresponding to a higher concentration of Li₂S₆ remaining and thus weak polysulfide adsorption capability. In comparison to Figure II-564B, it can be seen that very little Li₂S₆ is adsorbed by carbon black with 3mM being the original concentration in each adsorption test sample. In contrast, V₂O₅, MnO₂ and V₂O₃ all illustrate much higher adsorption capability showing very low concentrations of Li₂S₆ remaining in the supernatant solutions. Ti₄O₇, TiO₂, SiO₂ and Al₂O₃ exhibit moderate polysulfide adsorption capabilities. Similarly, Figure II-566D shows the performance of the metal nitride and metal sulfides. TiS₂, FeS and MoS₂ exhibit great polysulfide adsorption capabilities, CoS displays poor capability, while Cu₂S, CuS, TiN and ZnS exhibit moderate capabilities. In Figure II-566C and Figure II-566D, CoS and carbon black display background absorbance throughout the entire spectrum, this is likely due to the scattering effect of the sample powders, which do not settle well and are present in the supernatant solutions.

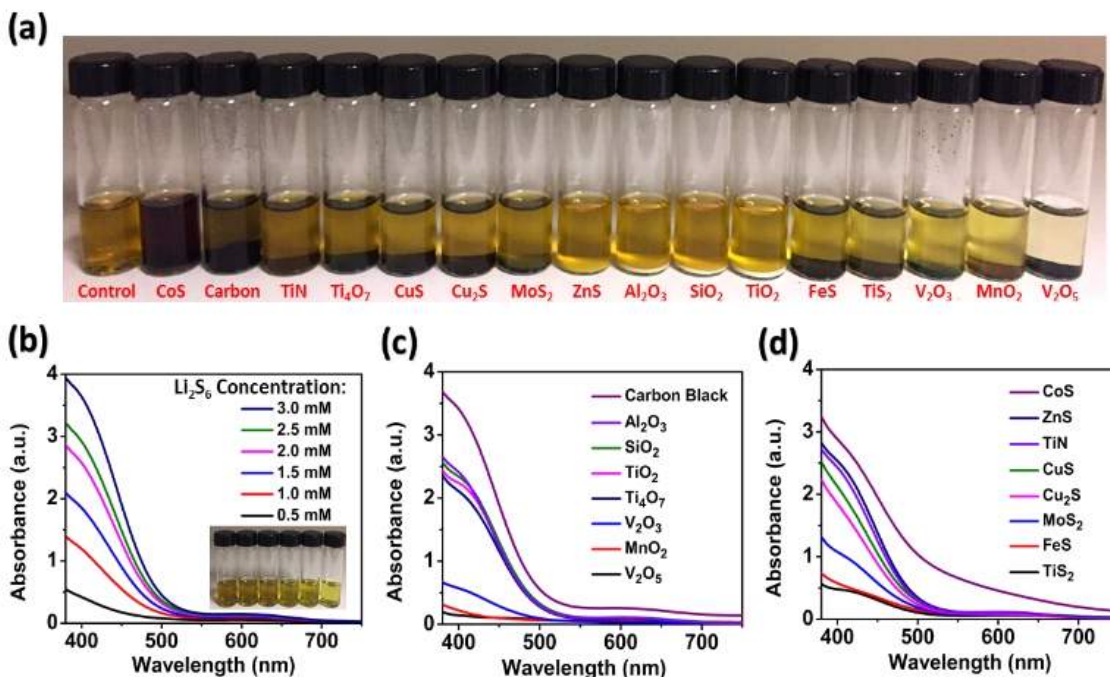


Figure II-566. Li₂S₆ polysulfide adsorption test: (a) photograph of setup. (b) UV-Vis data of varying concentrations of Li₂S₆ in DOL/DME solution without candidate materials, (c-d) with candidate materials added in 3mM Li₂S₆.

ICP-AES can detect the total concentration of lithium and sulfur atoms regardless of their chemical state, and therefore is much less susceptible to complications brought about by the instability of Li₂S₆ species. There is a linear relationship between ICP-AES lithium intensity and Li₂S₆ concentration. A similar relationship is shown for sulfur. The only source of lithium introduced to the samples are from the 3mM Li₂S₆ species, therefore based on the concentration of lithium atoms remaining in supernatant solution, it is possible to determine the amount of lithium adsorbed on the candidate materials. The calculated Li₂S₆ adsorption capability data for candidate materials based on ICP-AES analysis match reasonably well with UV-Vis approximations and similarly demonstrate one order of magnitude of difference between weak and strong candidate materials, with carbon black and CoS at 1.6 $\mu\text{mol}/\text{m}^2$ and 3.5 $\mu\text{mol}/\text{m}^2$ respectively, compared to MnO₂ and V₂O₅ at 22.9 $\mu\text{mol}/\text{m}^2$ and 22.3 $\mu\text{mol}/\text{m}^2$ respectively.

Conclusions

In all, in the past one year, we have made great progress in understanding the mechanism of surface adsorption, diffusion, and catalytic oxidation of Li₂S_x species on anchoring materials. We present a standard procedure to systematically investigate the polysulfide adsorption capability of 16 candidate materials. Our results indicate MnO₂ and V₂O₅ to be particularly strong materials and carbon black to be a particularly weak material for polysulfide adsorption. We made quantitative comparisons with normalized surface areas and observed an order of magnitude of difference across the candidate materials. We elucidate different adsorption mechanisms may be present and probe possible adsorption species. We discover a novel catalytic effect that electrode materials previously designed for polysulfide binding and trapping can play a critical role in catalyzing the oxidation of Li₂S back to sulfur during battery charging. Combining theoretical calculations and experimental design, we select a series of metal sulfides as a model system to identify the key parameters in determining the energy barrier for Li₂S oxidation and polysulfide adsorption. We demonstrate that the Li₂S decomposition energy barrier is associated with the binding between isolated Li ions and the sulfur in sulfides; this is the dominating reason that sulfide materials can induce lower overpotential compared to commonly used carbon materials. It is also demonstrated that the inherent metallic conductivity, strong interaction with LiPSs, facilitated Li ion transport, controlled Li₂S precipitation, and accelerated surface-mediated redox reaction of

these metal sulfides are critical in reducing the energy barrier and contributing to the remarkably improved battery performance. Attaining such fundamental understanding of the reaction process is a crucial step towards rational design and screening of materials to achieve high reversible capacity and long cycle life in Li-S batteries.

Key Publications

1. G.M. Zhou, H. Tian, Y. Jin, X. Tao, B. Liu, R. Zhang, Z. W. Seh, D. Zhuo, Y. Liu, J. Sun, J. Zhao, C. Zu, D. Wu, Q. Zhang, Y. Cui, "Catalytic oxidation of Li₂S on the surface of metal sulphides for Li-S batteries", PNAS, 2017, 114, 840-845.
2. David. S. Wu, F.F. Shi, G.M. Zhou, C. Zu, C. Liu, K. Liu, Y. Liu, J. Wang, Y. Peng, Y. Cui, "Quantitative Investigation of Polysulfide Adsorption Capability of Candidate Materials for Li-S Batteries", Energy Storage Materials, 2017, under revision.

II.I.7 Addressing Internal “Shuttle” Effect: Electrolyte Design and Cathode Morphology Evolution in Li-S Batteries (TAMU)

Perla B. Balbuena, Principal Investigator

Texas A&M University
3122 TAMU
College Station, TX 77843
Phone: 979-845-3375
E-mail: balbuena@tamu.edu

Partha Mukherjee, Co-Principal Investigator

Texas A&M University
3123 TAMU
College Station, TX 77843
Phone: 979-845-3211
E-mail: pmukherjee@tamu.edu

Vilas Pol, Co-Principal Investigator

Purdue University
610 Purdue Mall
West Lafayette, IN 47907
Phone: 979-845-3211
E-mail: vpol@purdue.edu

Tien Duong, Technology Manager

U.S. Department of Energy
Phone: 202-586-7836
E-mail: Tien.Duong@ee.doe.gov

Start Date: October 1, 2014
Total Project Cost: \$990,000

End Date: September 30, 2017
DOE share: \$990,000

Non-DOE share: \$0

Project Introduction

This project focuses on developing new understanding of the main challenges of the Li/S cell obtained from first-principles atomistic and mesoscopic modeling and state of the art synthesis and characterization. Specifically, this work aims to elucidating: 1) the effects of the electrolyte chemistry on the formation of a solid-electrolyte interphasial film at the surface of the Li anode covered and modified by insoluble polysulfide species, as well as on reactions occurring at the C/S cathode surface as functions of state of charge, internal shuttle-induced changes to the chemistry, and intrinsic nature of the electrolyte, 2) the relative contributions to the cathode performance of the solid discharge products, and associated morphology and volume changes of the C/S cathode microstructure, compared to that of the electrolyte effect; 3) effects of the electrolyte chemistry and cathode microstructure on the coulombic and cyclic efficiency of composite C/S electrodes.

Objectives

The objective of this project is to elucidate the lithium-metal anode deterioration issues especially under the polysulfide shuttle environment, and the effects of the carbon/sulfur cathode morphology on the cathode performance, and to develop and test strategies based on Li-metal protection advanced cathode structure design to mitigate these issues.

Approach

A mesoscale model including different realizations of electrode mesoporous structures based on a stochastic reconstruction method allows virtual screening of the cathode microstructural features and the corresponding effects on electronic/ionic conductivity and morphological evolution. Interfacial reactions at the anode due to the presence of polysulfide species are characterized with *ab initio* methods. For the cathode interfacial reactions, data and detailed structural and energetic information obtained from atomistic-level studies are incorporated in a mesoscopic-level analysis. A novel sonochemical fabrication method is expected to generate controlled cathode mesoporous structures that will be tested along with new electrolyte formulations based on the knowledge gained from the mesoscale and atomistic modeling efforts.

Results

Effects and structure of PS species migration through the electrolyte to the Li metal anode

Our *ab initio* molecular dynamics (AIMD) study of the reactions at the surface of Li metal demonstrated the effects of concentrated electrolyte solutions on the first coordination shell of the Li ion, where a mixed shell composed of salt anion, PS anion, and solvent are present (Figure II-567). The importance of these differences in comparison to the low salt concentration is that as the Li ion travels near to the surface, electron transfer reduces first the PS anion and the salt anion and then the solvent. Thus, the work of desolvation needed for Li plating depends strongly on the composition of the first shell and also on the degree of reduction. Thus, for concentrated solutions the work for desolvation will be different from that in diluted solutions because the salt anion decomposes first, leading to SEI fragments that bind strongly to Li ions. Thus, Li reduction will take place later in presence of these SEI nucleating elements. Moreover, the possible scenario of simultaneous reduction of the Li ion and decomposition of the salt and PS anions modify the type of precursors for dendrite formation.

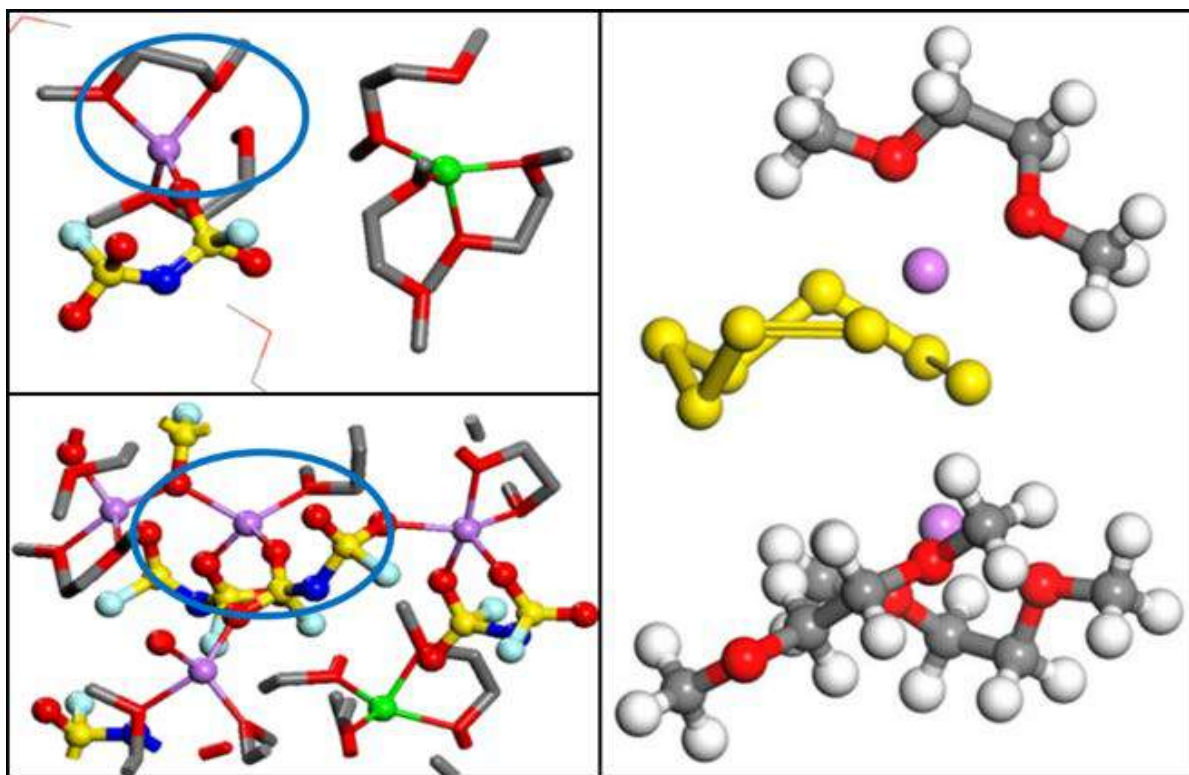


Figure II-567. First coordination shell of a Li ion (purple) surrounded by DME molecules (top left) at 1M LiFSI concentration, and solvated by salt anions and DME molecules at 4M LiFSI concentration (bottom left). O (red), C (grey), S (yellow), N (blue). Solvation structure of LiS₈⁻ in DME solution.

DFT and AIMD studies of Li^+ and long-chain PS solvation led us to conclude that these molecules have a peculiar mode of traveling the liquid electrolyte: PS anion species are not favored in most conditions; therefore PS exists as a *neutral species paired Li ions*. The Li-O rdf shows a clear first peak indicating the strong coordination of Li ions of the lithiated PS species with the solvent, whereas the Li-S rdf shows that the same Li ions are also well coordinated to the end-S atoms, and much less to those in the middle of the chain. However, under an electrical field, the PS ion pair will become at least partially dissociated (Figure II-567) and our current estimate is that the *monolithiated anion is the species that should migrate to the anode side*.

In presence of PS species, the reactions become much more complex. In collaboration with M. Vijayakumar at PNNL, DFT and AIMD simulations were used to explain XPS results and identify SEI products at the Li anode surface due to PS shuttle effects. The main findings include a) confirmation of our earlier prediction of Li_2S deposition at the Li metal surface, b) identification of an intermediate LiS_5 species as a reduction product at the anode surface. Such product explains the ratio of S neutral to S monoanion and the increase of Li_2S concentration observed in the *in-situ* XPS results. In addition a variety of products of the decomposition of the TFSI anion predicted by AIMD simulations were found in the observed XPS peaks (Figure II-568). The complexity of the SEI layer in this model experiment was further elucidated (Figure II-568). Moreover, it was demonstrated that this type of combined experimental-theoretical study could be extremely useful for elucidating the behavior of complex battery materials.

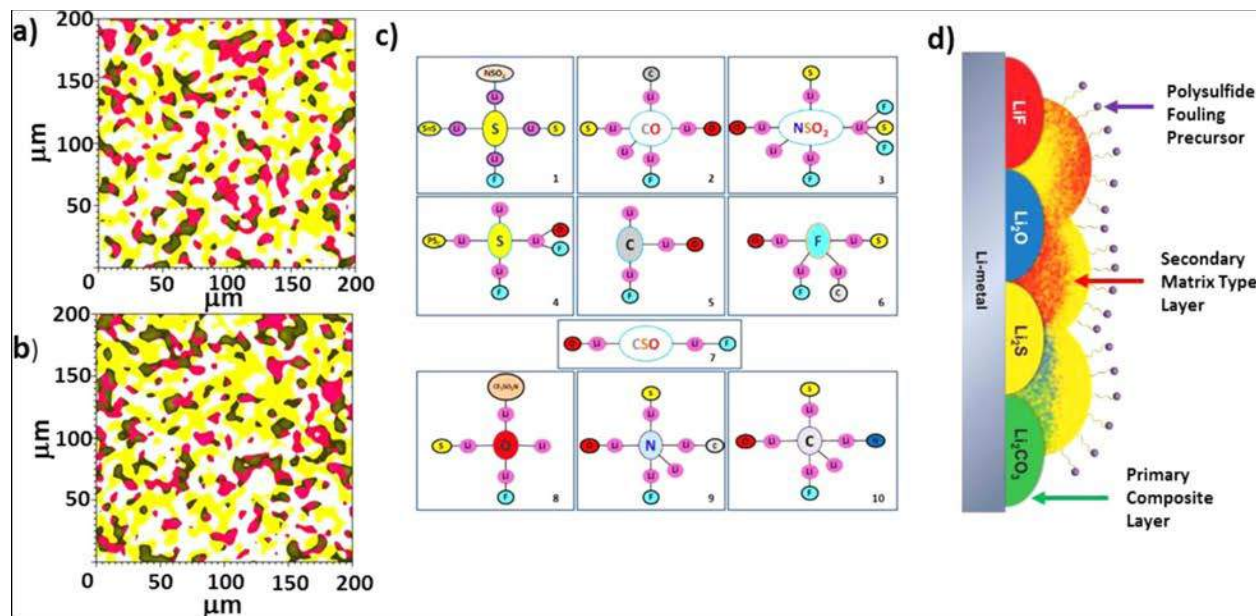


Figure II-568. XPS chemical imaging of the Li-electrolyte interfacial region after (a) first charging cycle and (b) first discharging cycle. The Li-F species from F 1s spectra and S0 polysulfide species from S 2p spectra are represented as yellow and red regions, respectively. The black region represents the overlapping regions of Li-F and S0 polysulfide species.

(c) Schematic representation of various fluorine-based Li-F species predicted from AIMD calculations. (d) Cartoon representation of SEI layer growth mechanism based on the combined XPS and computational results.

From Chem. Mater. 29, 4718, (2017).

A summary of these findings include: a) salts do not totally dissociate (not even at 1M solutions); b) in 1M solutions the solvent dominates the first coordination shell of the Li ion; c) in 4M solutions very complex networks form, having mixed coordination shells (solvent and salt components); d) the kinetics of solvent decomposition (for DME and DOL) is much slower than those of typical anions (TFSI or FSI) and the extent of the reduction depends on the chemical nature of the salt; e) the PS migrates as a lithiated mono-anion and decomposes combining with fragments of the anion decomposition forming a complex multilayer SEI. All these conclusions have led us to a hypothesis with respect to plating of Li^+ ions inside the SEI layer. We are

testing the effects of different functional groups on the process of Li^+ plating. We expect to determine whether certain ion coordination shells are more favorable to induce Li plating inside the SEI layer and how this plating compares with Li deposition on the current collector.

Microstructure and reactions at the C/S cathode

Pressurized “autogenic” synthesis routes, studied by Co-PI Vilas Pol at Purdue University, have produced homogeneous carbon-sulfur composites with high sulfur content up to 74 %-wt.; the real S content is controlled by optimization of the precursor ratio. Material characterization of these composites suggests pristine orthorhombic S_8 is transformed into amorphous sulfur species during the autogenic process. It is hypothesized that high sulfur content is enabled by homogeneous penetration of sulfur vapor into the porous carbon substrate, followed by homogeneous deposition as amorphous sulfur species. The synthesis scheme of the autogenically-derived C/S composite (with 40 %-wt. sulfur loading) and the electrochemical rate cycling results are shown in Figure II-569. The performance of a conventional sample derived via ball milling is shown for comparison.

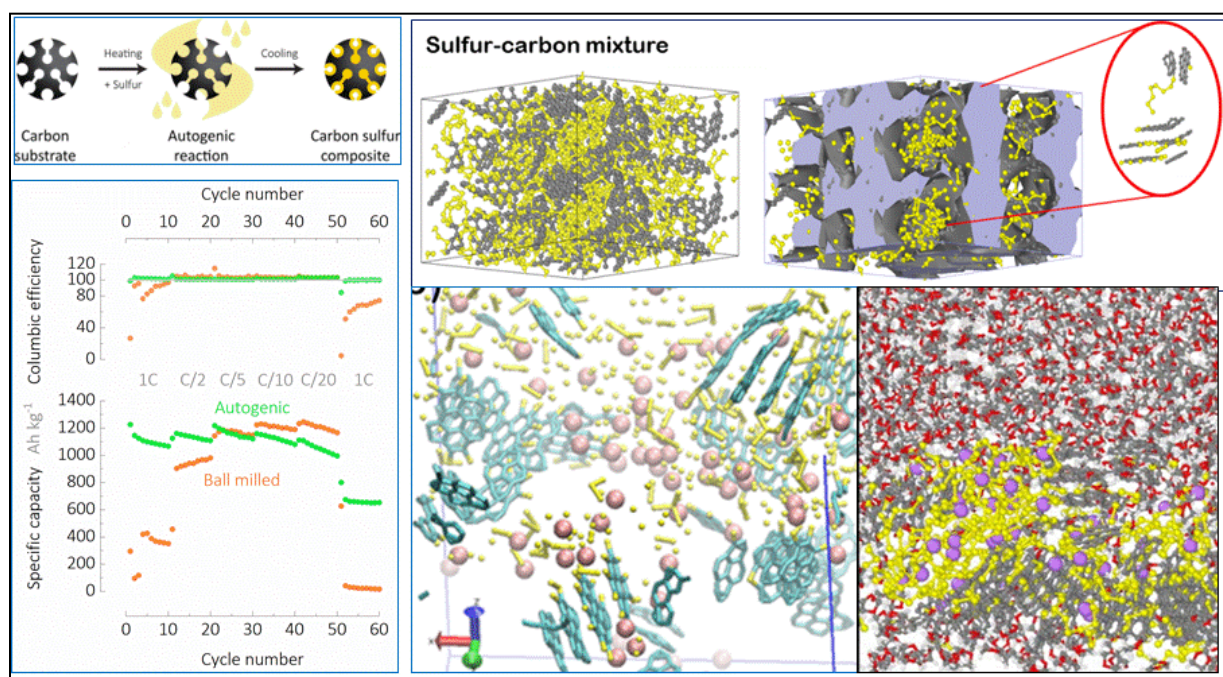


Figure II-569. A new synthesis method was implemented to facilitate a more intimate mixture of S and C via a pressurized autogenic reaction. Schematic figure top left and electrochemical tests bottom left. Top right: Model of the composite material obtained from molecular dynamics simulations (see text). Bottom, right: simulation of discharge reactions in the C/S phase in contact with the electrolyte: Li (purple), S(yellow), C (grey), O (red), H (white).

When cycled at various cycling rates, the autogenically-derived carbon-sulfur composite shows consistent capacity around 1100 Ah kg^{-1} between rates C/20 to 1C. After cycling at a slow rate of C/20, however, the capacity drops to ca. 700 Ah kg^{-1} . To further understand the underlying principles of autogenic synthesis, the quality of sulfur and its distribution were explored via electron microscopy and elemental mapping. It was found that C/S composites have a secondary particle diameter of $7 \pm 3 \mu\text{m}$. From elemental mapping, S is observed to be distributed uniformly across the C particles within a large sample area. After autogenic synthesis, the C/S composite particle generally retains the features of the original C morphology. The individual primary particle morphology of the carbon-sulfur composite is generally spheroidal and branched like the original carbon precursor. However, the pores in the composite are slightly less easily observable. The overall morphology of the composite is also branched, exhibiting bright signal due to the insulating property of elemental S. Line scans of the C/S composite show that S content occurs coincidentally with carbon content.

Correspondingly, appreciable S content is not observed beyond the boundaries of C signal. Altogether, these observations suggest that sulfur content is generally confined within the substrate carbon phase. In parallel, Balbuena's group molecular simulations advanced the characterization of the microscopic morphology of these composites and their evolution during lithiation. This model of the C/S composite allows intimate mixing between S and C by randomly dispersing graphene sheets and 8-membered S rings at 47%-wt S and an approximate density of 1.67 g/cm^3 . Molecular dynamics (MD) simulations using a reactive force field carried out at 300 K and 1 atm revealed opening of most of the S rings along with the formation of S-C bonds between S chains of various lengths and the C atoms at the edges of the graphene sheets, confirming our earlier AIMD analysis. Thus, the presence of discontinuous graphene sheets instead of continuous graphene layers allows a more realistic approach, as the low-coordinated C atoms at the edges of these graphene sheets favor C-S bond formation. We also observed that graphene sheets tend to agglomerate into graphitic clusters due to van der Waals interactions between sheets, with most of the short-chain PS species agglomerating around the edges (Figure II-569). On the other hand, the various morphology and loading effects in the cells were studied with a mesoscopic model in Mukherjee's group. Based on microstructure-scale simulations, effective property relations (e.g., tortuosity) were developed and used to identify cathode resistances (Figure II-570). If precipitation takes place in the form of film deposits, the electrode-electrolyte interface gets covered earlier and the cell shuts down due to predominant surface passivation. Alternatively, if precipitation occurs in a finger-like fashion, pore blockage is much severe and causes cathode starvation. For intermediate morphologies, cathode resistance evolution has joint contributions from both. As cathode pristine porosity changes, it leads to different pore blockages. As precipitate morphology becomes more finger-like, cell performance improves in response to decreased surface passivation. On the other hand, at higher initial sulfur loading, increasing cathode porosity improves discharge capacity.

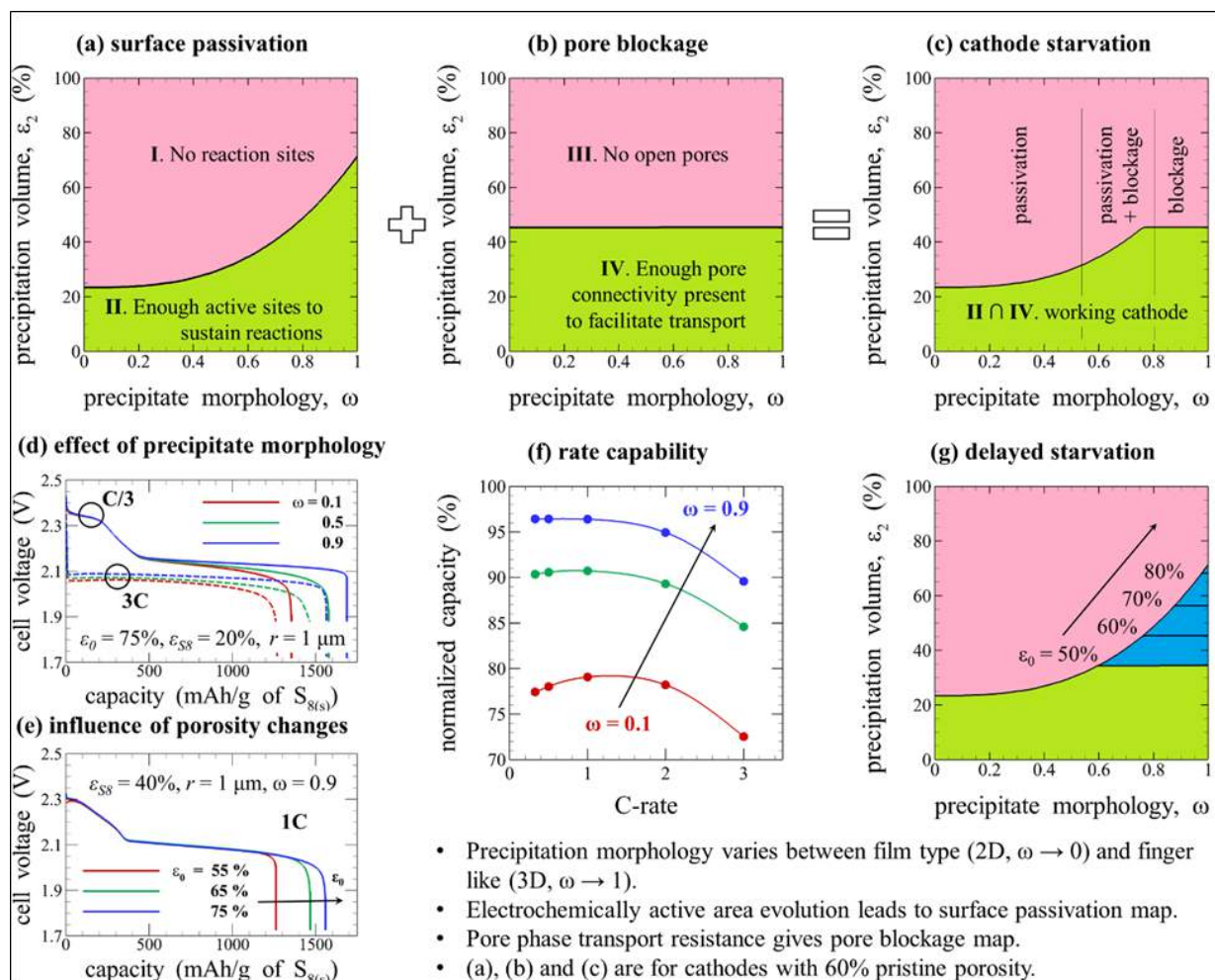


Figure II-570. Identification of different cathode microstructural resistances (a) surface passivation (b) pore blockage and (c) their joint contribution, based on effective property relations for mesoporous carbon structure. Pore blockage resistance is relatively more sensitive to porosity changes and leads to delayed cathode starvation (g). Tuning precipitate morphology (d, f) and pristine porosity (e) lead to different cell performance as expected from microstructural implications (c, g).

Li_2S_2 and Li_2S are the main discharge products of the Li-S battery. However, their electronic conductivity is too low to ensure a good kinetic charge rate. We studied the electronic structure of these solids and their main charge carriers. For Li_2S_2 , it was found that similarly to the O_2 molecule, 12 electrons in a S_2 molecule occupy σ_s , σ_s^* , σ_p , π_p , and π_p^* orbitals. In an isolated S_2 molecule, the antibonding orbital π_p^* is half occupied. In Li_2S_2 bulk, Li 2s electrons are transferred to π_p^* orbital of S_2 , leading to S_2^{2-} . The antibonding σ_p^* orbital is still empty in S_2^{2-} , and this orbital can accept an extra electron to form an electron polaron p^- . On the other hand, the π^* orbital can donate an electron to form a hole polaron p^+ which was found to be the main charge carrier. Similar studies done for Li_2S indicated that p^+ can also be the main barrier with relatively low diffusion barriers along various crystal directions. New evaluations are in progress to evaluate further enhancements of electronic conductivity via doping.

Conclusions

During this year, our project focused on various aspects derived from the complexity of the S chemistry in Li/S batteries. One is the effect of PS migration on the Li metal anode reactivity and formation of a solid-electrolyte interphase with different characteristics due to the PS decomposition. Among several strategies proposed to mitigate the extreme Li reactivity, one is the use of concentrated salt solutions. We investigated how Li ions

are conducted through these solutions and analyzed potential consequences of these solvation structures on the SEI, and the transport mechanisms for the long chain soluble PS traveling from cathode to anode. The second aspect centers on the cathode microstructure and reactivity. We studied the effects of cathode microstructure on the discharge reactions, and developed a very detailed atomistic level model of the C/S composite, which we are using to characterize the cathode reactivity, together with mesoscale descriptions that relate macroscopic properties such as impedance to cathode microstructural evolution. In parallel, our team developed and electrochemically tested new synthesis methods for the C/S systems. A final very crucial aspect relates to the short chain insoluble PS species deposited at the cathode surfaces. Their precipitation mode was analyzed and correlated with cathode microstructure, and hole polarons were identified as the main charge carriers in both crystals. Further directions were suggested for enhancement of the electronic conductivities of the discharge products.

Key Publications

1. Luis E. Camacho-Forero, Taylor W. Smith, and Perla B. Balbuena, "Effects of High and Low Salt Concentration in Electrolytes at Lithium-Metal Anode Surfaces," *J. Phys. Chem. C*, 121, (1), 182-194, (2017).
2. Zhixiao Liu, Perla B. Balbuena, and Partha P. Mukherjee, "Revealing Charge Transport Mechanisms in Li_2S_2 for Li-Sulfur Batteries," *J. Phys. Chem. Lett.*, 8, 1324-1330, (2017).
3. Zhixiao Liu and Partha P. Mukherjee, "Mesoscale Elucidation of Surface Passivation in the Li-Sulfur Battery Cathode," *ACS Applied Materials & Interfaces*, 9, 5263 (2017).
4. M. J. Nandasiri, L. E. Camacho-Forero, A. M. Schwarz, V. Sutthanandan, S. Thevuthasan, P. B. Balbuena, K. T. Mueller, M. Vijayakumar, "In-situ chemical imaging of SEI layer evolution in Li-S batteries using X-ray photoelectron spectroscopy," *Chem. Mater.*, 29 (11), 4728-4737, (2017).
5. Z. Liu, P. Balbuena, and P. P. Mukherjee, "Mesoscale Evaluation of Titanium Silicide Monolayer as a Cathode Host Material in Lithium-Sulfur Batteries," *J. Min., Met.Mater. Soc.*, in press, DOI: 10.1007/s11837-017-2414-7.
6. C.-F. Chen, A. Mistry and P. P. Mukherjee, "Probing Impedance and Microstructure Evolution in Lithium-sulfur Battery Electrodes," *J. Phys. Chem. C*, 121, 21206, (2017).
7. Ethan P. Kamphaus and Perla B. Balbuena, "First Principles Investigation of Lithium Polysulfide Structure and Behavior in Solution," *J. Phys. Chem. C*, 121, 21105-21117, (2017).
8. Zhixiao Liu, Perla B. Balbuena, Partha P. Mukherjee, "Hole Polaron Diffusion in the Final Discharge Product of Lithium-Sulfur Batteries", *J. Phys. Chem. C*, 121, 17169-17175, (2017).
9. Juan Carlos Burgos, Perla B. Balbuena, and Javier Montoya, "Structural Dependence of the Sulfur Reduction Mechanism in Carbon-Based Cathodes for Lithium Sulfur Batteries," *J. Phys. Chem. C*, 121, 18369-18377, (2017).
10. Aashutosh Mistry and Partha P. Mukherjee, "Precipitation – microstructure interaction in Li-S battery cathode", *J. Phys. Chem. C*, in press.
11. Zhixiao Liu, Aashutosh Mistry, Partha P. Mukherjee, "Mesoscale Physicochemical Interactions in Lithium-Sulfur Batteries: Progress and Perspective", *J. Electrochem. Energy Conv. Storage*, 15, 010802, (2017).
12. Zhixiao Liu, Perla B. Balbuena, and Partha P. Mukherjee, "Mesoscale Evaluation of Titanium Silicide Monolayer as a Cathode Host Material in Lithium-Sulfur Batteries," *J. Minerals, Metals, and Materials Society*, 69, 1532-1536, (2017).

II.I.8 Mechanistic Investigation for the Rechargeable Li-Sulfur Batteries (U Of Wisconsin)

Deyang Qu Principal Investigator

University of Wisconsin Milwaukee
3200 N Cramer Street
Milwaukee, WI, 53211
Phone: 414-229-3716; Fax: 414-229-5191
E-mail: qud@uwm.edu

Xiao-Qing Yang, Co-Principal Investigator

Chemistry Department
Brookhaven National Laboratory
Bldg. 555
Upton, NY 11973
Phone: 631-344-3663; Fax: 631-344-5815
E-mail: xyang@bnl.gov

Tien Duong, Technology Manager

U.S. Department of Energy
Phone: 202-586-7836
E-mail: Tien.Duong@ee.doe.gov

Start Date: September 1, 2016

End Date: August 30, 2017

Total Project Cost: \$300,000

DOE share: \$300,000

Non-DOE share: \$0

Project Introduction

Rechargeable Li-S battery is a potential candidate to meet the demand of high energy density for the vehicle applications. However the capacity loss for a rechargeable Li-S battery is still one of the major obstacles. The “polysulfide shuttle” which is the equilibrium reactions between dissolved polysulfides and elemental sulfur, remains the major reason for the continuous decay of the capacity during cycling and high self-discharge during storage. There are other barriers which need to be overcome for the sulfur cathode, for example: low operation voltage, low conductivity for S_8 and Li_2S , radical species formed during the operation of Li-S batteries.

Li anode also remains as a major challenge even after decades of research. Besides all the traditional problems e.g., dendrite growth, safety etc., it is hard to find an electrolyte which can form a stable SEI layer on Li anode to prevent the reaction between Li and dissolved polysulfide ions.

During 2016, we have successfully established the HPLC-MS essays. So for the first time, the ALL dissolved polysulfide ions can be qualitatively and quantitatively determined during the operation of a Li-S cell. An electrochemical measurement procedure with either *in-situ* or *ex-situ* determination of the polysulfide ions were also established.

Based on the achievements in 2016, the collaborative project aims to further investigate the mechanism of Li-S batteries and to explore the innovative designs of rechargeable Li-S cells. The project includes extensive scientific investigation by mean of *in-situ* electrochemical spectroscopic techniques to explore the reaction mechanism at cell level. So the proper electrolytes and additives suitable to Li-S chemistry can be developed. With the understanding of the reaction mechanism, we will engage in the engineering design of the electrode materials, electrolytes including the additives and electrochemical cells. So the potential of high energy density

Li-S batteries can be unlocked. Potentially, Li-S batteries could enable competitive market entry of electric vehicles by reducing the cost and extending the driving distance per charge.

Objectives

Taking the advantages of the unique analytical essay developed in 2016, the primary objectives are to further conduct focused fundamental research on the mechanism for Li-S batteries, investigate the kinetics for the sulfur redox reaction, develop electrolytes and additives suitable for Li-S chemistry, optimize the sulfur electrode and cell designs. In this objective, special attentions will be paid to the investigation of the redox reaction of sulfur cathode, the management for the solubility of polysulfide ions, the formation of SEI layer and dead Li on the surface of Li anode, the rechargeability of Li anode in the solution containing polysulfide and the exploration of electrode and cell designs. Through such investigations, the Li-S chemistry will be studied systematically, the scientific understanding of the reaction mechanism can be well utilized to guide the system engineering design.

Approach

1. A combination of *High Performance Liquid Chromatography (HPLC)/Mass Spectroscopy(MS)* together with *in situ* electrochemical measurement in a specially designed cell. The electrochemically formed dissolved polysulfide ions can be separated (by HPLC) and determined (by MS).
2. *Ex-situ* X-ray diffraction (XRD) and X-ray photoelectron spectroscopy (XPS) to investigate the surface of sulfur cathode and Li anode to elucidate the surface changes during the Li-S battery operation'
3. *In-situ* Keyence 3D microscope and electrochemical measurement in a specially designed cell to investigate the surface modification of Li with e.g., various additives and at different stage of charge/discharge.
4. Extended collaboration with other US and international academic institutions and US industrial partners.

Results

Key Accomplishments:

1. *In-situ* electrochemical-HPLC/MS/UV system was developed to identify polysulfide ions real time during the cell operation of a Li-S cell.
2. *In-situ* electrochemical-laser confocal microscopic cell was made to investigate the surface of Li anode during the cycle of Li-S cell. The Li surface morphology change can be observed in real time.
3. By means of the in-situ methods, the distribution of dissolved polysulfide ions can be monitored real time during the discharge and recharge of a Li-S battery.
4. The chemical equilibriums of the dissolved polysulfide ions were determined, so did the sulfur redox reaction mechanism.

1. Proposal of the sulfur redox mechanism through the real-time Monitoring of the Changes of Sulfur and Polysulfide Species during the Discharge and Charge of sulfur cathode

The HPLC-MS-Electrochemical method we developed is the only reliable method for the analysis of the dissolved polysulfide species and sulfur during the discharge and recharge of a Li-S battery. It is a vital technique for the investigation of sulfur redox mechanism.

In Figure II-571A, the change of polysulfide ions in the electrolyte from elemental sulfur, long chain polysulfides to short chain polysulfides can be clearly demonstrated as the discharge proceeded. The vertical dash lines indicate the stoichiometric polysulfide calculated from the discharge capacity. The 2-electron electrochemical reduction of S_8 to S_8^{2-} mechanism of elemental sulfur was proven not actuate since S_8^{2-} was not generated electrochemically but through subsequent chemical reactions. The first flat discharge plateau

could be a result from the equilibrium among S_8^{2-} , S_7^{2-} and S_6^{2-} , since the ratio of the species remained almost constant. Another interesting observation from Figure II-571A is that even when the discharge reached the stoichiometric S_2^{2-} stage, the most abundant polysulfides in the electrolyte were S_4^{2-} , S_5^{2-} and S_3^{2-} . To the very end of the discharge, even though the concentration decrease, the relative distribution of the three polysulfides remained.

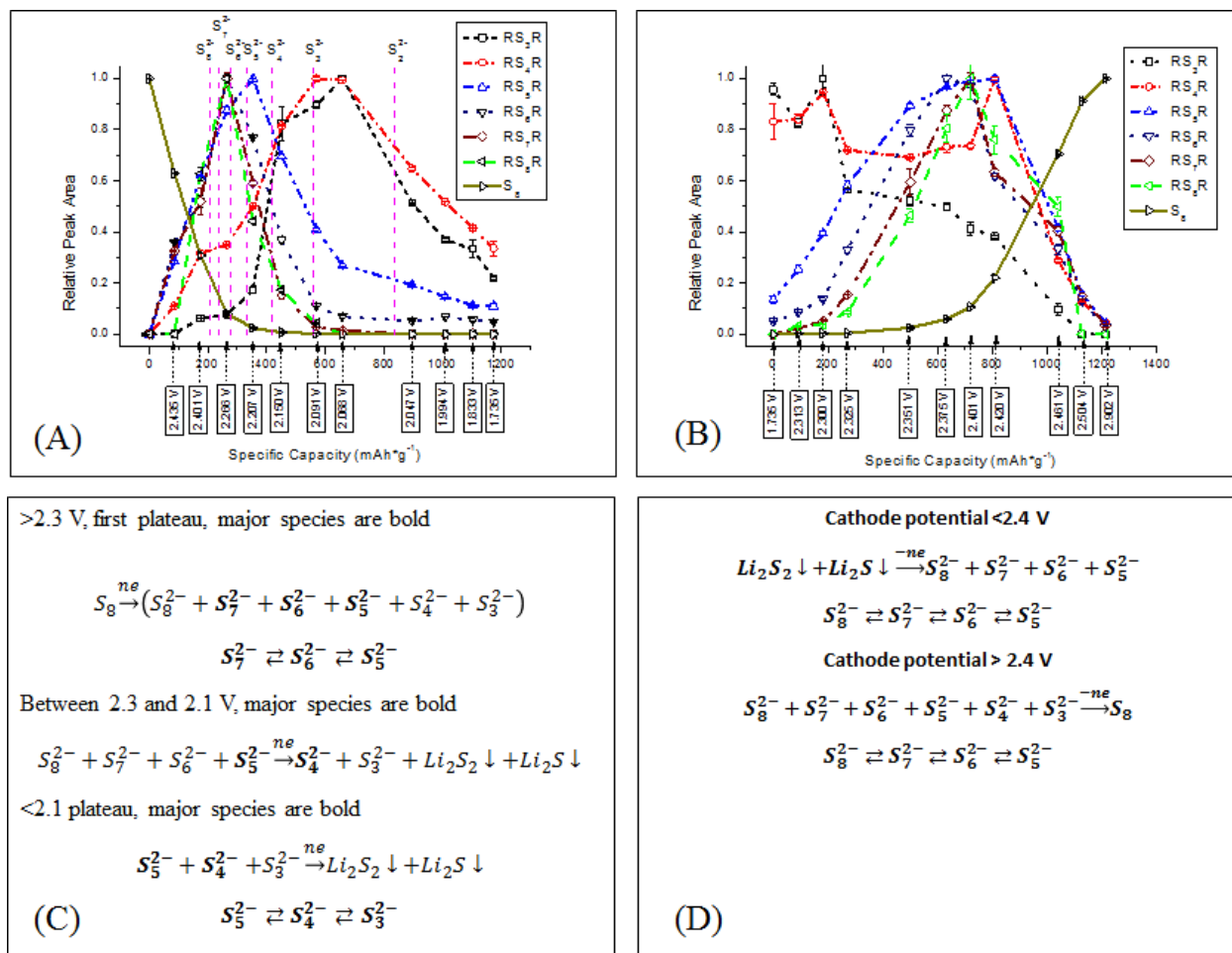


Figure II-571. The normalized chromatographic peak for each derivatized polysulfide species (R=CH₃) from real-time HPLC results during discharge (A) and charge (B) of Li-S cell. The proposed discharge mechanism (C) and charge mechanism (D) of Li-S cell. (D. Zheng, D. Liu, J. Harris, T. Ding, J. Si, S. Andrew, D. Qu, X.Q. Yang, D. Qu, ACS Appl. Mater. Interfaces 2017,9,4326-4332.)

Figure II-571B shows the change of polysulfide ions and elemental sulfur during the recharge. It was evident that the concentration of S_3^{2-} and S_4^{2-} remained constant while the concentration of S_5^{2-} and S_6^{2-} kept increasing during the potential dip. It appears that the initial oxidation of Li_2S and Li_2S_2 yielded soluble S_5^{2-} and S_6^{2-} polysulfide ions either through S_3^{2-} and S_4^{2-} as intermediates or directly. After the potential dip, the concentrations of S_3^{2-} and S_4^{2-} took sharp drops, the concentration of S_3^{2-} started to continuously decrease while the concentration of S_4^{2-} remained constant until elemental sulfur started to form at 2.4 V. In the meantime, S_5^{2-} , S_6^{2-} , S_7^{2-} and S_8^{2-} were formed and the ratio among the four polysulfide ions remained constant. It appears that the chemical equilibrium among these polysulfides remained. The increasing concentrations of S_5^{2-} , S_6^{2-} , S_7^{2-} and S_8^{2-} reversed coinciding with the increase of elemental sulfur concentration at about 2.4 V, while the concentration of S_4^{2-} took a nose dive. It is interesting that the concentration of S_3^{2-} and S_4^{2-} were never above their concentrations at the end of reduction (or beginning of oxidation), which could

mean that either S_3^{2-} and S_4^{2-} were not the products for the electrochemical oxidation of Li_2S and Li_2S_2 , or they were the intermediates for the formation of longer chain polysulfide. Therefore, we suspected that the sharp decrease of S_3^{2-} and S_4^{2-} concentration resulted from the chemical reaction with newly formed elemental sulfur rather than electrochemical oxidation on the electrode. On the other hand, of course, the decrease of S_5^{2-} , S_6^{2-} , S_7^{2-} and S_8^{2-} concentration correlated very well with the production of elemental sulfur until the almost disappearance of polysulfide ions, so it must be an electrochemical oxidation process. It is also interesting to notice that during the decline, S_5^{2-} , S_6^{2-} , S_7^{2-} and S_8^{2-} still remained in a chemical equilibrium. Therefore, unlike the stepwise reduction process, the oxidation of polysulfide ions was conducted through the electrochemical formation of polysulfide ions S_n^{2-} ($5 \leq n \leq 7$) and sulfur while the chemical equilibrium among S_5^{2-} , S_6^{2-} , S_7^{2-} and S_8^{2-} remained throughout the whole oxidation process.

And based on the above results in Figure II-571A and Figure II-571B, a three-step reduction mechanism including two chemical equilibrium reactions was proposed as shown Figure II-571C, and a two-step oxidation mechanism for the Li_2S and Li_2S_2 with a single chemical equilibrium among soluble polysulfide ions was proposed as shown in Figure II-571D.

2. Reaction between Lithium Anode and Polysulfide Ions in a Lithium-Sulfur Battery

Polysulfide species (Li_2S_n , $n \geq 2$) are the important products in a Li-S battery during charge and discharge. The polysulfide species (with $n \geq 3$) are highly soluble and reactive in organic electrolytes, especially in the ether-based electrolytes. The soluble polysulfide species can migrate to the Li anode and subsequently react with Li anode chemically, which can cause polysulfide shuttle effect in Li-S batteries. To alleviate the problems associated with the dissolution of polysulfide ions, additives which can form a stable solid electrolyte interface (SEI) layer were investigated to prevent the reaction between dissolved polysulfide ions with Li anode. Among those additives $LiNO_3$ was reported to greatly improve the charge and discharge efficiency (coulombic efficiency) for a rechargeable Li-S battery.

For polysulfide mixture without $LiNO_3$, the chromatograms of polysulfide mixture before and after contacted with Li metal were shown in Figure II-572-i-A to Figure II-572-i-E. By comparing Figure II-572-i-A with Figure II-572-i-B, the distribution of the polysulfide anions substantially changed after being in contact with Li metal, it became evident that polysulfide anions in electrolyte indeed react with lithium metal. It can be found that the S_n^{2-} species with $n \geq 6$ are more reactive (or less stable) to lithium metal than that of the S_n^{2-} species with $n \leq 5$. As the polysulfide mixture was contacted with lithium metal for 1 hour, the peak intensities of $(CH_3)_2S_6$ and $(CH_3)_2S_7$ decrease greatly in Figure II-572-i-B compared to the corresponding peak intensities in Figure II-572-i-A, while the peak intensity of $(CH_3)_2S_5$ just slightly decreases and the peak intensity of $(CH_3)_2S_4$ greatly increases in Figure II-572-i-B compared to the corresponding peak intensities in Figure II-572-i-A. The unexpected increase of the intensity of $(CH_3)_2S_4$ in Figure II-572-i-B to Figure II-572-i-E clearly indicates that the S_4^{2-} species is stable against lithium metal. Interestingly, the peak intensity for $(CH_3)_2S_3$ in all chromatograms of Figure II-572 is pretty low, it may indicate that the solubility of S_3^{2-} in ether-based electrolyte probably is lower than the polysulfide species with a longer S chain.

For polysulfide mixture with $LiNO_3$ additive, the chromatograms of polysulfide mixture before and after contacted with Li metal were summarized in Figure II-572-ii-A to 2-ii-E. Clearly, there are little changes in the polysulfide distribution in contact with Li metal over four hours with the existence of $LiNO_3$. Obviously, the reaction between Li metal and polysulfide species was inhibited greatly. The observation proved the hypothesis that the $LiNO_3$ in mixture can form a SEI layer on the Li metal surface, which prevented the reaction between Li and polysulfide anions. Unfortunately, the $LiNO_3$ became consumed during the storage. Evidentially, after being in contact with Li for 24 hours, the distribution of polysulfide starts to change. As shown in Figure II-572-ii-D, a slight increase of peak intensity for $(CH_3)_2S_4$ can be observed. After being in contact for 96 hours (Figure II-572-ii-E), momentous changes of the polysulfide distribution can be seen with the increase of peak intensity for $(CH_3)_2S_4$ and the decrease of the $(CH_3)_2S_6$ and $(CH_3)_2S_7$ peak intensities. It is worth pointing out that interaction between Li and polysulfide ions with the existence of $LiNO_3$ was trivial in comparison to those without $LiNO_3$.

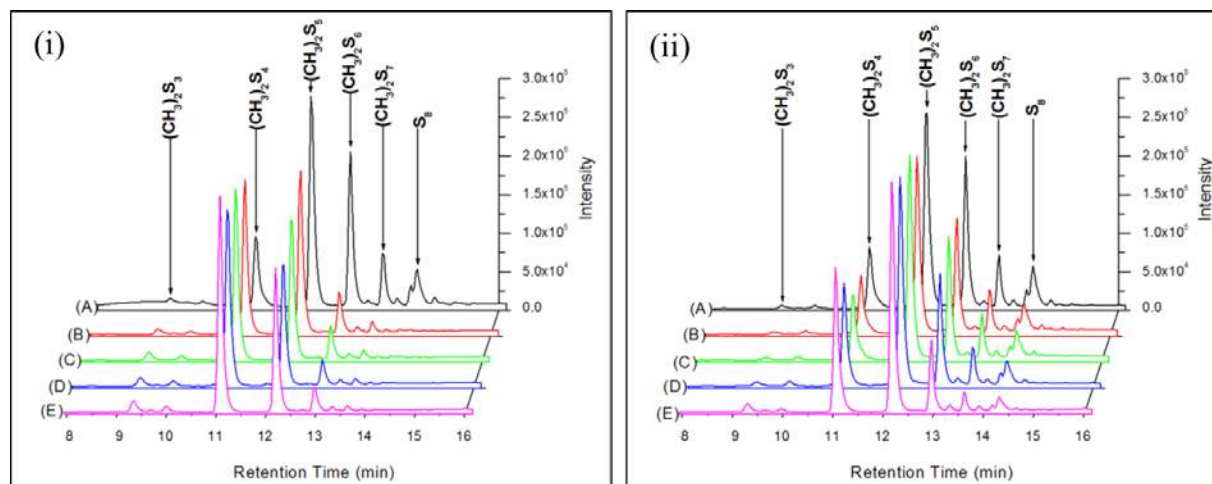


Figure II-572. Chromatograms of derivatized polysulfide mixtures without LiNO_3 (i) and with LiNO_3 (ii). For polysulfide mixture without LiNO_3 and Li metal (i-A), polysulfide mixture (without LiNO_3) with Li metal for 1hour (i-B), polysulfide mixture (without LiNO_3) with Li metal for 4hours (i-C), polysulfide mixture (without LiNO_3) with Li metal for 24hours (i-D), polysulfide mixture (without LiNO_3) with Li metal for 96hours (i-E); For polysulfide mixture with LiNO_3 and without Li metal (ii-A), polysulfide mixture (with LiNO_3) with Li metal for 1hour (ii-B), polysulfide mixture (with LiNO_3) with Li metal for 4hours (ii-C), polysulfide mixture (with LiNO_3) with Li metal for 24hours (ii-D), polysulfide mixture (with LiNO_3) with Li metal for 96hours (ii-E) (D.Zheng, X.Q. Yang, D.Y. Qu, *ChemSusChem*, 2016, 9, 2348-2350.)

3. Direct evidence for superior electrocatalytic performance of sulfur redox reaction on defect sites

Since sulfur and its discharge products in Li-S batteries are non-conductive, this results in poor electrochemical accessibility and low utilization of the active material. In addition, the polysulfides produced by multi-step electrochemical reductions or chemical disproportionation can easily dissolve into the electrolyte and cause rapid loss of the active material and an unfavorable shuttle effect. The other issue to be overcome is the remarkable volume change of sulfur and its final discharge product lithium sulfide (Li_2S) which can cause serious pulverization of the cathode and further accelerate the capacity fading. To address these aforementioned issues, confining sulfur within various hosts, mostly conducting carbon-based materials, is regarded as one of the most efficient approaches to improve the overall performance of Li-S batteries. Generally, the nonpolar carbons are considered as incapable of immobilizing sulfur and its as-reduced products, owing to a weak C-S interaction. Introducing defects or heteroatoms can effectively promote the chemical interaction with sulfur, suppress the shuttle effect and synchronously accelerate the reaction kinetics. However, these assumptions were mainly concluded from overall performance of batteries containing different cathodic materials, which could hardly exclude many of the other possible influencing factors (i.e., electrode microstructure). Thus fundamental research of sulfur redox reactions on flat model electrodes by varying the defect density could contribute to the design of high-performance lithium-sulfur batteries.

To evaluate the performance of sulfur's reduction and oxidation on different planes of HOPG (basal, step and edge), cyclic voltammetry (CV) tests were carried out by using a standard three-electrode system in a glovebox. Figure II-573a shows the comparison of iR -free CV curves for HOPG-1T (basal plane), HOPG-1L (edge plane), HOPG-2T (edge plane) and HOPG-2L (step plane). The solution resistance (R_s) was obtained from electrochemical impedance spectra (EIS). The CVs for the two edge planes (HOPG-1L and HOPG-2T) are similar, and both considerably differ from the basal plane (HOPG-1T) and step plane (HOPG-2L). Since the CVs of different surfaces (top surface and lateral surface) on a same electrode are quite different, obviously, this phenomenon should not result from the difference of the conductivity along and perpendicular to the graphite basal plane as described in the literature. We adopted the reduction & oxidation peak potentials as an indicator of electrochemical reversibility. A clear correlation between the reduction & oxidation peak

potentials and I_D/I_G values extracted from Raman analysis was observed (Figure II-573b). The reduction peak potential gradually increased and the oxidation potential simultaneously decreased with increasing the defect density. The sulfur redox reaction on the edge plane, which contains the highest defect density, exhibits a superior electrochemical reversibility compared to reactions on the step plane and the basal plane. Hence, the defect sites exhibit better electrocatalytic activity towards sulfur reduction and oxidation.

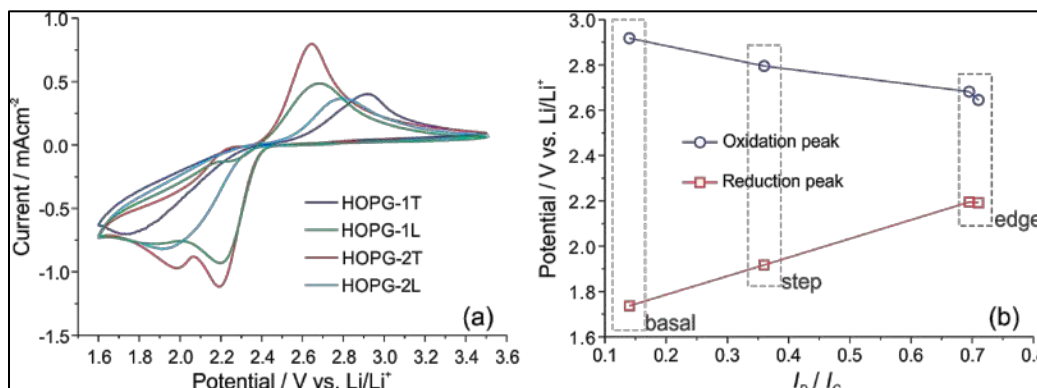


Figure II-573. (a) CVs of sulfur electrochemical reduction and oxidation on HOPG-1T (basal plane), HOPG-1L (edge plane), HOPG-2T (edge plane) and HOPG-2L (step plane) at a scan rate of 20 mV/s. (b) The relation between peak potential obtained from (a) and I_D/I_G obtained from Raman analysis. (G.W. Wang, D. Zheng, D. Liu, X.Q. Yang, D.Y. Qu, Carbon, 2017, 119, 460-463.)

Conclusions

1. Again the reliable and quantitative HPLC method we developed for the analysis of the dissolved polysulfide species and sulfur was demonstrated as a vital technique for the investigation of Li-S batteries. A three-step reduction mechanism was proposed for the sulfur cathode during the discharge, while a continuous oxidation of lithium sulfide and polysulfide ions to elemental sulfur was revealed. The two flat discharge plateau and a single flat recharge curve can be explained by the fast reaching chemical equilibrium of dissolve polysulfide ions, S_7^{2-} , S_6^{2-} and S_5^{2-} for the discharge plateau >2.3 V; S_5^{2-} , S_4^{2-} and S_4^{2-} for the discharge <2.1 V and S_5^{2-} , S_6^{2-} , S_7^{2-} and S_8^{2-} during recharge.
2. Both dissolved S and polysulfide ions can chemically react with Li metal in a Li-S cell during storage. LiNO₃ additive can form a SEI layer on the Li electrode to prevent such reaction. However, the SEI layer was not stable enough for long term storage and needed to be maintained with the continuous consumption of LiNO₃. Longer chain polysulfide ions (Sn^{2-} with $n \geq 6$) were more reactive with Li than those with shorter chain (Sn^{2-} with $n \leq 5$).
3. The defect sites on carbon could lower the polarization and exhibit superior electrocatalytic activity towards sulfur redox reactions. This observation has important implications not only for the design of advance cathodic materials for Li-S batteries, but also for research on sulfur related reaction catalysis.

Key Publications

1. Gongwei Wang, Dong Zheng, Xiao-Qing Yang, Deyang Qu, Sulfur Redox Reactions on Highly Oriented Pyrolytic Graphite (HOPG) Electrodes: Direct Evidence for Superior Electrocatalytic Performance on Defect Sites. *Carbon* 119(2017)460-463.
2. Dong Zheng, Dan Liu, Joshua Harris, Tianyao Ding, Jingyu Si, Sergi Andrew, Deyu Qu, Xiao-Qing Yang, Deyang Qu, Investigation of Li-S Battery Mechanism by Real-Time Monitoring the Changes of Sulfur and Polysulfide Species During the Discharge and Charge” *ACS Appl. Mater. & Interface*, 9(2017)4326-4332.

3. Dong Zheng, Xiao-Qing Yang, Deyang Qu, “Reaction between Lithium Anode and Polysulfide Ions in a Lithium-Sulphur Battery”, *ChemSusChem*. 9(2016) 2348-2350.
4. Dong Zheng, Xiaoqing Yang, and Deyang Qu, “Stability of the solid electrolyte interface on the Li electrode in Li-S batteries”, *ACS Appl. Mater. & Interface*, 8(2016)10360-10366.
5. Dong Zheng, Xuran Zhang, Jiankun Wang, Deyu Qu, Xiaoqing Yang, **Deyang Qu**, Reduction Mechanism of Sulfur in Lithium-Sulfur Battery: from elemental sulfur to polysulfide, *J. of Power Sources* 301(2016)312-316.

II.I.9 Statically and Dynamically Stable Lithium-sulfur Batteries (UTA)

Arumugam Manthiram, Principal Investigator

204 E. Dean Keeton Street, C2200
University of Texas at Austin
Austin, TX 78712
Phone: 512-471-1791
E-mail: manth@austin.utexas.edu

Tien Duong, Technology Manager

Phone: 202-586-7836
E-mail: Tien.Duong@ee.doe.gov

Start Date: October 1, 2015

End Date: September 30, 2018

Total Project Cost: \$990,000

DOE share: \$891,000

Non-DOE share: \$99,000

Project Introduction

The commercialization of lithium-sulfur (Li-S) batteries is hampered by several scientific and technological challenges: low electronic and ionic conductivity of the active material, severe polysulfide (PS) migration from the cathode to the anode, and instability of the Li-metal anode. The poor conductivity limits the electrochemical utilization of the active material and often necessitates a high content of electrochemically inactive, conductive carbon or functional polymers in the cathode region, which lowers the practical energy density. The PS migration causes static and dynamic instabilities with high self-discharge, poisoning of Li-metal surface, and poor cycling efficiency, hindering the practical viability of Li-S batteries. Recently, a growing number of research articles caution that the proliferation of activities in Li-S technology might result from a presentation of overestimated battery chemistry and electrochemical characteristics obtained from testing cells with a low sulfur loading of less than 2.0 mg cm^{-2} , insufficient sulfur content of less than 65 wt.%, and high electrolyte/sulfur ratio of greater than 15. As a result, it is becoming obvious that the scientific and technological challenges are very sensitive toward and even strongly impacted by the sulfur loading in the cathode and the electrolyte/sulfur ratio in the tested cells.

To overcome the above challenges, our group has demonstrated that innovations in polysulfide (PS)-filter-coated separators and advanced electrode substrates can greatly enhance the electrochemical utilization and efficiency with reasonably high sulfur loadings and low electrolyte/sulfur ratios in the cells. This is because Li-S batteries involve conversion reactions unlike the insertion-reaction electrodes in commercial Li-ion batteries, so cell components/designs directly borrowed from Li-ion batteries may need new architectures or chemical/physical characteristics to be adapted to sulfur cathodes. Our cell-component design provides the fabricated Li-S cells with enhanced electrochemical performance: high utilization of the active material, extended cycle life, and good storage properties. More importantly, these custom cell configurations allow the cells to employ the easily prepared pure sulfur cathodes with high sulfur loading ($> 2.0 \text{ mg cm}^{-2}$) and high sulfur content ($> 65 \text{ wt.}\%$) in the cells with low electrolyte/sulfur ratios of less than 11. Our progress illustrates that the approaches presented and developed in this project are inexpensive and offer a practically viable solution for the Li-S technology development.

Objectives

The objective of this project is to develop statically and dynamically stable Li-S batteries by integrating polysulfide (PS)-filter-coated separators with an advanced cathode design and/or a protected lithium-metal anode. The project includes a demonstration of electrochemically stable cells with sulfur capacities of $> 1,000 \text{ mA h g}^{-1}$ and cycle life in excess of 500 cycles (dynamic stability) along with improved storage properties (static stability) at $> 70 \text{ wt.}\%$ sulfur content and $\sim 5 \text{ mg cm}^{-2}$ loading.

Approach

The electrochemical stability of the Li-S cells is improved by three approaches that are complementary to each other:

- The first approach focuses on the establishment of an electrochemically stable cathode environment by employing PS-filter-coated separators. The PS-filter coatings aim to suppress the severe polysulfide diffusion and improve the redox capability of the Li-S cells with high-sulfur loadings. The study includes an understanding of the materials characteristics, fabrication parameters, electrochemical properties, and battery performance of the PS-filter-coated separators.
- The second approach focuses on electrode engineering from two aspects. First, the investigation of a Li-metal anode with coating- and additive-supporting approaches aim at improving the safety of Li-S cells. Second, the research on activated-Li₂S cathode with little or no charge-barrier aims at promoting the performance and safety of the C-Li₂S cells.
- The integration of the above two approaches aims at creating statically and dynamically stable Li-S batteries for electric vehicles.

Results

In Year 2 of the project, we have realized three major key accomplishments with Li-S batteries by employing PS-filter-coated separators and advanced cathode architectures in the cells: (i) long-term dynamic electrochemical stability during cell cycling (Technical Milestone I, Quarter 1 (Q1)); (ii) long-term static electrochemical stability with low self-discharge during cell resting (Technical Milestone II, Q2); and (iii) remarkably improved electrochemical characteristics with high-loading sulfur cathodes (Technical Milestone II, Q3). As a result, we surpass the target values of 5.0 mg cm⁻² and 70 wt.% sulfur that were set up to make the Li-S technology practically viable. We have realized sulfur loadings of as high as 30 – 60 mg cm⁻² and sulfur content of up to 80 wt.% with good dynamic and static electrochemical performance of the Li-S cells (Go/No-Go Milestone, Q4).

Key accomplishment 1: long-term dynamic electrochemical performance

Our previous investigation in Year 1 initially selected four carbon materials with unique morphologies as the coating materials: spherical carbons, carbon nanofibers (CNFs), carbon nanotubes (CNTs), and graphene. These carbon materials were coated onto a polypropylene membrane (Celgard 2500) to form the PS-filter-coated separators. However, the carbon materials having abundant nanopores needed a high electrolyte/sulfur ratio for obtaining good cell performances. The needed electrolyte/sulfur ratios have been usually higher than 11 or even above 15, which leads to overestimated cell characteristics and would lower the practical energy density. In consideration of these facts, we focused on PS-filter-coated separators fabricated with nonporous CNFs and CNTs with a layer-by-layer (LBL) coating method, which allows the resulting Li-S cells to exhibit excellent cyclability with a low electrolyte/sulfur ratio fixed at 10 (Figure II-574).

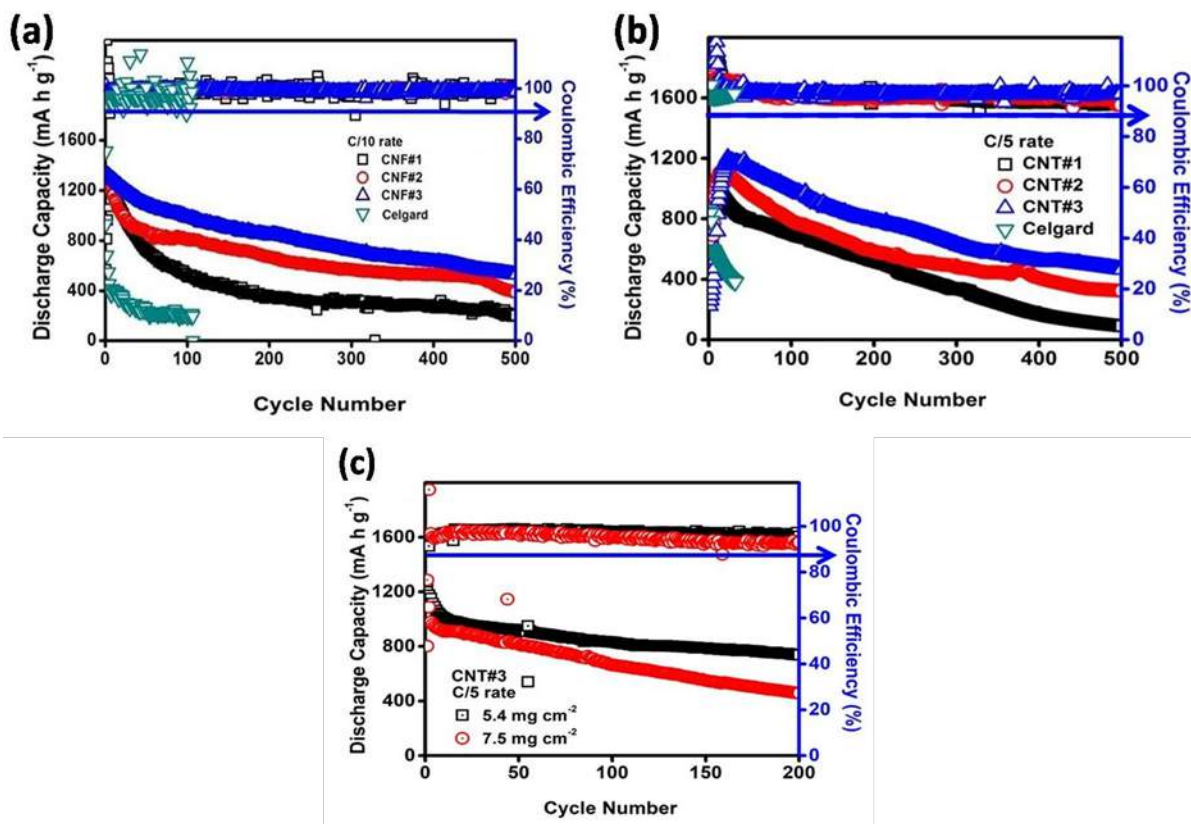


Figure II-574. Dynamic cycling performance of the cells fabricated with (a) LBL CNF-coated separators, (b) LBL CNT-coated separators, and (c) LBL CNT-coated separators with increasing sulfur loadings of 5.4 mg cm⁻² (black line) and 7.5 mg cm⁻² (red line).

Figure II-574a presents three LBL nonporous CNF-coated separators, which are termed as CNF#1 (0.1 mg cm⁻² CNF coating), CNF#2 (0.2 mg cm⁻² CNF coating), and CNF#3 (0.4 mg cm⁻² CNF coating). The nonporous CNFs had a low surface area of 26 m² g⁻¹ and no micropore absorption behavior. The Celgard membrane that is used as the substrate in our case and as the conventional separator in the Li-S literature weighs 1.0 mg cm⁻² and has a thickness of 25 μ m. The cells fabricated with the thin-film CNF#3-coated separators displayed a high peak capacity of 1,329 mA h g⁻¹ (areal capacity: 4.3 mA h cm⁻²) at C/10 rate and a high reversible capacity of 529 mA h g⁻¹ after 500 cycles. The enhanced electrochemical utilization and stability were based on the use of pure sulfur directly as the active material. The pure sulfur cathodes used in the tested cells were fixed with a high sulfur loading of 3.4 mg cm⁻² and a high sulfur content of 70 wt.%.

In Figure II-574b, our follow-up study with a light-weight LBL CNT coating further reduced the coating mass to only 0.05 mg cm⁻² with a thickness of 8 μ m. The three presented LBL coated separators are named as CNT#1 (0.05 mg cm⁻² CNT coating), CNT#2 (0.10 mg cm⁻² CNT coating), and CNT#3 (0.15 mg cm⁻² CNT coating). The selected nonporous CNTs had a low surface area of 40 m² g⁻¹. With the highly conductive CNT as the coating material, the cells were able to cycle well at a higher sulfur loading of 4.0 mg cm⁻² and sulfur content of 80 wt.% at a higher cycling rate of C/5 for 500 cycles. With even higher sulfur loadings of 5.8 and 7.5 mg cm⁻² (Figure II-574c), the cells fabricated with the LBL CNT#3 separator further exhibited a peak discharge capacity of 1,087 mA h g⁻¹ with stable cyclability for 200 cycles, which translates to a high areal capacity and energy density of, respectively, 8 mA h cm⁻² and 17 mW h cm⁻².

Key accomplishment 2: long-term static electrochemical performance with low self-discharge

Self-discharge is a serious problem in the development of Li-S batteries. Unfortunately, the lack of literature on the realities of self-discharge makes it a daunting challenge to develop a practically viable Li-S technology. Accordingly, we focused in this year on improving the long-term static electrochemical performance (shelf-life) of Li-S batteries by employing the above-mentioned LBL-CNF-coated separators. Herein, we present the cells fabricated with the LBL CNF-coated separators as a key example because of the lowest self-discharge and the longest shelf-life obtained (Figure II-575).

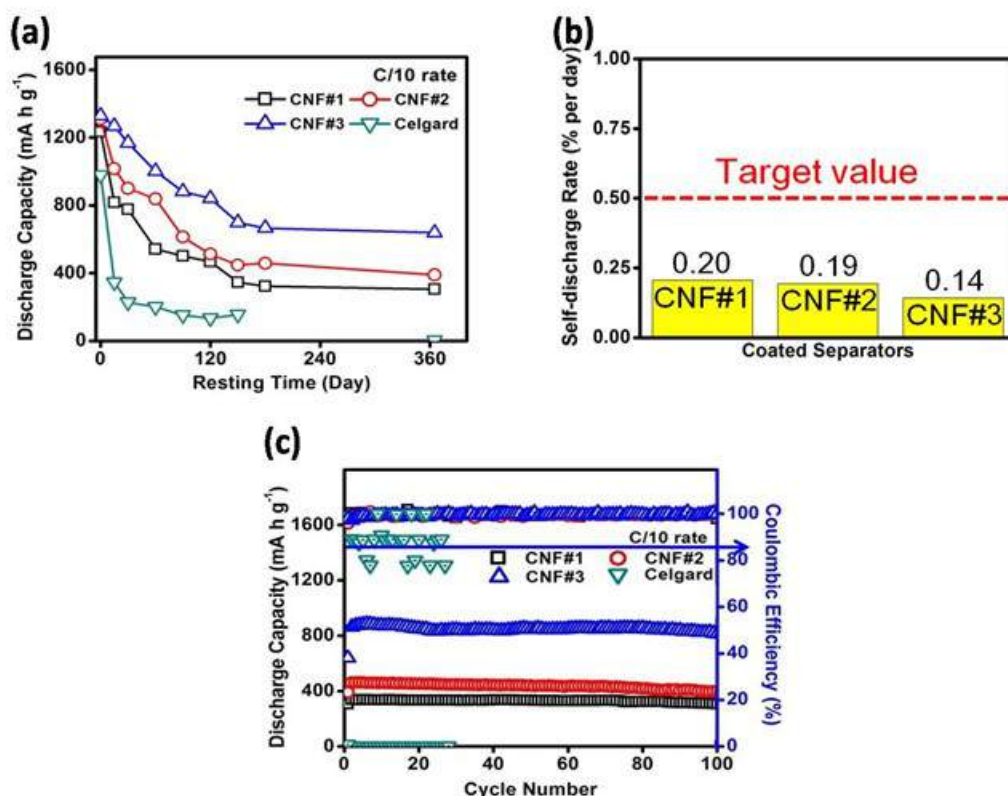


Figure II-575. Static electrochemical analysis of the Li-S cells fabricated with the LBL CNF-coated separators after resting for 365 days (black, red, and blue lines) and with the polypropylene membrane after resting for 150 days (green line): (a) static electrochemical stability, (b) self-discharge rate, and (c) cyclability.

The LBL CNF-coated separators provided the Li-S cells with an extended cell shelf-life of one year, which is the longest cell-storage period reported for Li-S cells in the literature (Figure II-575a). In this extended low self-discharge demonstration, the cells fabricated with the LBL CNF-coated separators retained 50% of the initial capacity after storing for 1 year and exhibited a low self-discharge rate of only 0.14% per day, much lower than the target value of less than 0.50% per day (Figure II-575b). In addition, the stored cells still displayed good cyclability. Figure II-575c shows that the cell rested for 365 days kept a high capacity with a low capacity-fade rate of 0.10% per cycle for 100 cycles. Thus, in developing Li-S batteries with a low self-discharge, we have made in this year three significant progresses: (1) the longest shelf-life, (2) the lowest self-discharge rate, and (3) good cyclability after resting (storing) for 1 year.

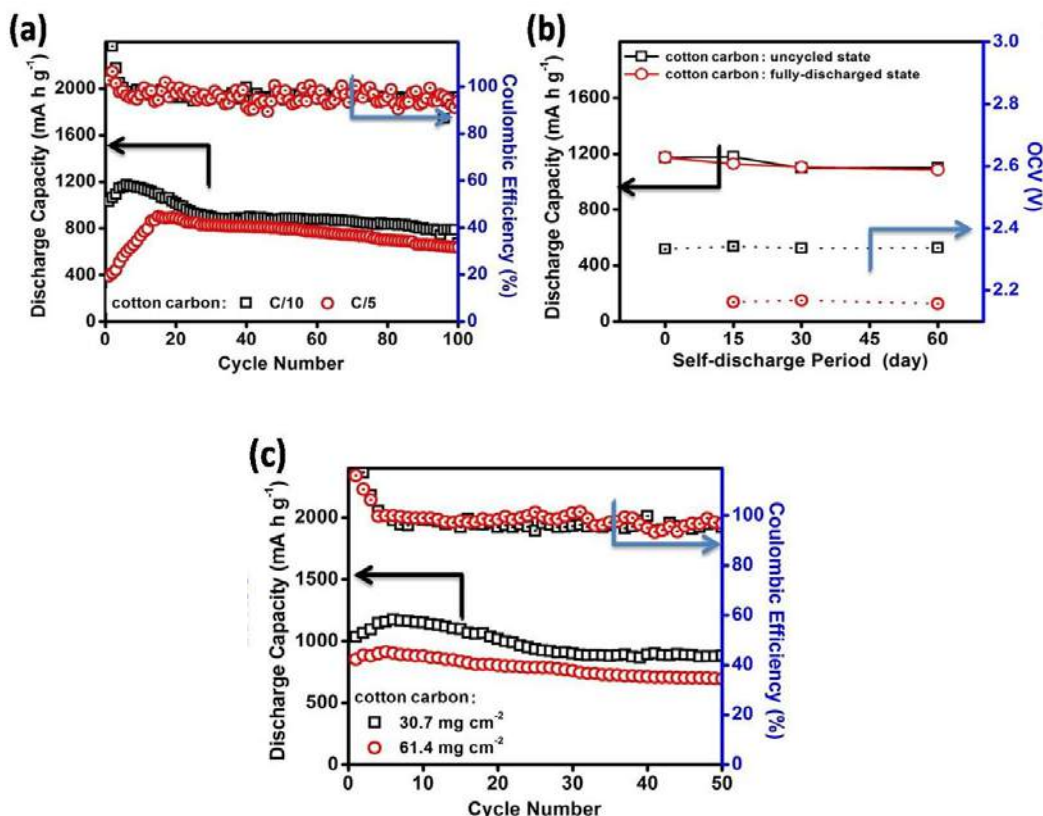


Figure II-576. Electrochemical analysis of the Li-S batteries fabricated with the cotton-carbon cathodes with a sulfur loading of 30 mg cm⁻², a sulfur content of 80 wt.%, and an electrolyte/sulfur ratio of 6.8: (a) cycling performance at C/10 and C/5 rates and (b) self-discharge analysis after resting for two months with freshly-made cells and fully-discharged cells. (c) Cycling performance of the cotton-carbon cathode with a higher sulfur loading of 60 mg cm⁻² at C/10 rate.

Key accomplishment 3: impact from applying practically necessary parameters in the cells

It is becoming increasingly clear that the Li-S battery chemistry and the electrochemical performances are distinctly different between low-loading sulfur cathodes (< 2.0 mg cm⁻²) and practically-relevant high-loading cathodes (> 4.0 mg cm⁻²). Moreover, the electrolyte/sulfur ratio, another key issue that has been lacking in the literature investigation for years, has recently been pointed out to have a strong influence toward the electrochemical utilization and stability of Li-S cells, and even the basic cyclability of the cells. An even low electrolyte/sulfur ratio of less than 7.0 should be applied in the investigation of Li-S battery chemistry. Accordingly, we focused on improving the electrochemical characteristics of high-loading sulfur cathodes under a low electrolyte/sulfur ratio by integrating our findings above in accomplishments 1 and 2 (Q1 and Q2) with advanced cathode architectures. We have realized Li-S cells featuring a sulfur loading of as high as 30 – 60 mg cm⁻², a sulfur content of up to 80 wt.%, and a low electrolyte/sulfur ratio of only 6.8.

Figure II-576 shows an advanced cathode design that was fabricated with a cotton-carbon electrode, in which polysulfide was used as the catholyte. Our cotton-carbon cathodes with a high sulfur loading (30 mg cm⁻²) and content (80 wt.%) represent the highest sulfur loading/content among the literature reports and are able to smoothly cycle and stably rest at a very low electrolyte/sulfur ratio of only 6.8, which is much lower than the values used in the literature. The cells show good cyclability with a capacity retention of 70% after 100 cycles, and improved cell-storage stability with a low self-discharge rate of just 0.12% per day after storing for 60 days (Figure II-576a and Figure II-576b). Such a well-designed cathode configuration further allowed an ultrahigh sulfur loading of 60 mg cm⁻², while the cells retained high electrochemical reversibility and efficiency with a high areal capacity and energy density of, respectively, 56 mA h cm⁻² and 118 mW h cm⁻².

(Figure II-576c). The cell performance metrics are higher than the values obtained with the current commercial Li-ion batteries (4 mA h cm^{-2} and $\sim 10 \text{ mW h cm}^{-2}$) based on LiCoO_2 cathode.

Conclusions

In Year 2, we have completed the investigation on improving the dynamic and static electrochemical performances of Li-S batteries by assessing the cells fabricated with polysulfide-filter (PS-filter)-coated separators. The LBL coated separators with various nonporous CNF and CNT coatings allows the corresponding Li-S cells to cycle smoothly for over 500 cycles with a low self-discharge after storing for a long period of over one year. These enhanced electrochemical characteristics are all based on cells assembled with pure sulfur cathodes with a reasonably high sulfur loading and sulfur content as well as a low electrolyte/sulfur ratio in the cells. After understanding that the amount and ratios of the active material and electrolyte have a strong influence toward the basic Li-S battery performance, we developed advanced cathodes with a high sulfur loading of up to 60.0 mg cm^{-2} (target value: 5.0 mg cm^{-2}), a high sulfur content of 80 wt.% (target value: 70 wt.%), and a low electrolyte/sulfur ratios of 6.8 (the suggested ratio for conducting reasonable Li-S research is less than 11). We demonstrated that Li-S cells featuring these practically necessary parameters could still display good cyclability and low self-discharge with a long shelf life. More importantly, the areal capacity and energy density obtained with the cells attain, respectively, 56 mA h cm^{-2} and 118 mW h cm^{-2} . These performance values imply that the Li-S technology does have a chance to perform better than the current Li-ion battery cathodes based on LiCoO_2 with an areal capacity of 4 mA h cm^{-2} and an areal energy density of $10.1 \text{ mW h cm}^{-2}$.

Key Publications

Reports

1. DOE EE7218 Quarterly Report-01-17 (Jan. 15, 2017)
2. DOE EE7218 Quarterly Report-04-17 (Apr. 15, 2017)
3. DOE EE7218 Quarterly Report-07-17 (Jul. 17, 2017)
4. DOE EE7218 Quarterly Report-10-17 (Oct. 17, 2017)

Journal Articles

1. C.-H. Chang, S.-H. Chung, and A. Manthiram, "Dendrite-Free Lithium Anode via a Homogenous Li-Ion Distribution Enabled by a Kimwipe Paper," *Advanced Sustainable Systems*, **1**, 1600034 (2017).
2. S.-H. Chung, P. Han, C.-H. Chang, and A. Manthiram, "A Shell-Shaped Carbon Architecture with High-Loading Capability for Lithium Sulfide Cathodes," *Advanced Energy Materials*, **7**, 1700537 (2017).
3. S.-H. Chung and A. Manthiram, "Lithium–Sulfur Batteries with the Lowest Self-Discharge and the Longest Shelf life," *ACS Energy Letters*, **2**, 1056 (2017).
4. S.-H. Chung, P. Han, and A. Manthiram, "Quantitative Analysis of Electrochemical and Electrode Stability with Low Self-Discharge Lithium-Sulfur Batteries," *ACS Applied Material & Interfaces*, **9**, 20318 (2017).
5. C.-H. Chang, S.-H. Chung, S. Nanda, and A. Manthiram, "A Rationally Designed Polysulfide-Trapping Interface on the Polymeric Separator for High-Energy Li–S Batteries," *Materials Today Energy*, **6**, 72 (2017).
6. L. Luo, S.-H. Chung, C.-H. Chang, and A. Manthiram, "A Nickel-Foam@Carbon-Shell with a Pie-Like Architecture as an Efficient Polysulfide Trap for High-Energy Li–S Batteries," *Journal of Materials Chemistry A*, **5**, 15002 (2017).

7. L. Luo and A. Manthiram, "Rational Design of High-Loading Sulfur Cathodes with a Poached-Egg-Shaped Architecture for Long-Cycle Lithium–Sulfur Batteries," *ACS Energy Letters*, **2**, 2205 (2017).
8. C.-H. Chang, S.-H. Chung, P. Han, and A. Manthiram, "Oligoanilines as a Suppressor of Polysulfide Shuttling in Lithium-Sulfur Batteries," *Materials Horizons* **4**, 908 (2017).

Presentations

1. A. Manthiram, "Next-generation Battery Materials and Technologies for Electrical Energy Storage," *Lee Hsun Lecture Award on Materials Science, Institute of Metal Research, Shenyang, China*, October 19, 2016 (invited).
2. A. Manthiram, "Tailored Carbon Materials for Overcoming Critical Issues in Rechargeable Batteries," *International Union of Materials Research Society – 17th International Conference in Asia (IUMRS-ICA 2016)*, Qingdao, China, October 20 – 24, 2016 (invited).
3. A. Manthiram, "Role of Materials Chemistry in Electrical Energy Storage," *National Synchrotron Radiation Center, Hsinchu, Taiwan*, October 31, 2016 (invited).
4. A. Manthiram, "Next-generation Battery Chemistries: Materials Challenges and Prospects," *Applied Science Center, Academia Sinica, Taipei, Taiwan*, November 3, 2016 (invited).
5. A. Manthiram, "Electrical Energy Storage: Next-generation Battery Chemistries," *Distinguished Lecture at Colorado School of Mines and National Renewable Energy Laboratory, Golden, CO*, November 14, 2016 (invited).
6. A. Manthiram, "Next-generation Battery Chemistries: Challenges and Prospects," *International Symposium on Advances in Electrochemical Science and Technology (ISAEST)*, Chennai, India, December 8 – 10, 2016 (invited).
7. A. Manthiram, "Dynamically and Statically Stable Metal-sulfur Batteries with High Sulfur Loading," *2017 Spring Meeting of the Materials Research Society*, Phoenix, AZ, April 17 – 21, 2017 (invited).
8. S.-H. Chung, C.-H. Chang, and A. Manthiram, "Lithium-sulfur Batteries with an Ultrahigh-sulfur-loading Carbon-cotton Cathode," *231st ECS Meeting*, New Orleans, LA, May 28 – June 1, 2017.
9. A. Manthiram, "Dynamically and Statically Stable Lithium-sulfur Batteries," *Annual Merit Review Meeting, U.S. Department of Energy*, Washington, D.C., June 5 – 9, 2017 (invited).
10. A. Manthiram, "High Energy Density Lithium-sulfur Batteries with High Sulfur Loading," *International Conference on Materials for Advanced Technologies (ICMAT)*, Singapore, June 18 – 23, 2017 (invited keynote talk).
11. A. Manthiram, "Next Generation Battery Technologies: Challenges and Opportunities," *NASA Workshop on Battery Technologies for Future Aerospace Applications*, Cleveland, OH, August 16 – 17, 2017 (invited).
12. A. Manthiram, "Electrical Energy Storage: Next Generation Battery Technologies," *China University of Hong Kong, Hong Kong*, September 29, 2017 (invited).

II.I.10 Dual Function Solid State Battery with Self-forming Self-healing Electrolyte and Separator (Stony Brook University)

Esther Takeuchi, Principal Investigator

Distinguished Professor
Stony Brook University
1000 Innovation Road
Stony Brook, NY 11794-6044
Phone: 631-216-7414
E-mail: esther.takeuchi@stonybrook.edu

Kenneth J. Takeuchi, Co-Principal Investigator

Stony Brook University
1000 Innovation Road
Stony Brook, NY 11794-6044
Phone: 631-632-8579
E-mail: kenneth.takeuchi.1@stonybrook.edu

Amy C. Marschilok, Co-Principal Investigator

Stony Brook University
1000 Innovation Road
Stony Brook, NY 11794-6044
Phone: 631-216-7419
E-mail: amy.marschilok@stonybrook.edu

Tien Duong, Technology Manager

U.S. Department of Energy
Phone: 202-586-7836
E-mail: Tien.Duong@ee.doe.gov

Start Date: October 1, 2016	End Date: September 1, 2019	
Total Project Cost: \$1,200,000	DOE share: \$1,065,975	Non-DOE share: \$134,025

Project Introduction

The goal of this project is to demonstrate a solid state rechargeable battery based on a lithium metal anode and iodine cathode with a self-forming, self-healing electrolyte and separator. The presence or formation of dendrites or pin holes can result in compromised cell performance or even failure for solid state cells which would be avoided by the proposed new technology. The theoretical energy density of the Li/I₂ couple is 560 Wh/kg, which provides the opportunity to meet or exceed the DOE target of 250 Wh/kg at the battery level.

The proposed concept is a solid state battery utilizing lithium iodide (LiI) combined with silver iodide (AgI) as the electrolyte with lithium (silver) metal as the anode and iodine as the cathode with a self-forming self-healing separator/electrolyte. The battery will be assembled in the discharged state where the anode and cathode will be created during the first formation (charge) step. Silver ion, Ag⁺, will diffuse toward the negative electrode and be reduced to silver metal, Ag⁰ and lithium ion, Li⁺, will form a lithium metal-layer at the anode. Iodine ion, I⁻, will be oxidized to elemental iodine, I₂, at the cathode side. As formation of the battery continues, Lithium iodide will remain and serve as both the separator and electrolyte, as shown schematically in Figure II-577.

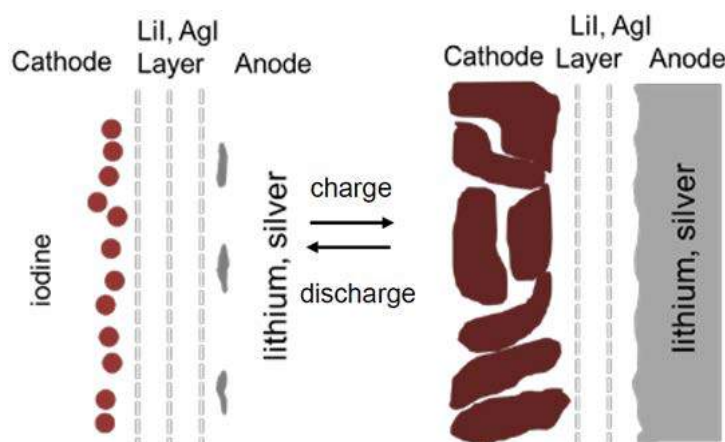


Figure II-577. Silver-lithium/iodine solid state dual function battery.

Objectives

The project goal will be addressed by focusing on the three major objectives outlined below:

Objective 1

Develop a LiI/AgI-based electrolyte with conductivity of $>10^{-3}$ S/cm at 30°C.

Objective 2

Form Li/I₂ batteries through the charging of the composite solid state electrolytes, determine relationship of coulombic efficiency to electrolyte type.

Objective 3

Determine the role of Ag ion in the anode:electrolyte interface as a function of electrolyte composition and cell test parameters through in-situ and ex-situ analyses.

Approach

The proposed solid state battery utilizes lithium iodide (LiI) combined with silver iodide (AgI) as the electrolyte with lithium (silver) metal as the anode and iodine as the cathode with a self-forming self-healing separator/electrolyte. The mechanism of the Ag-Li/I₂ solid state battery can be described as follows:

Charge: $\text{Li}^+ + \text{e}^- \rightarrow \text{Li}$ (anode)

$\text{Ag}^+ + \text{e}^- \rightarrow \text{Ag}$ (anode)

$\text{I}^- \rightarrow 1/2\text{I}_2 + \text{e}^-$ (cathode)

Discharge: $1/2\text{I}_2 + \text{Li} \rightarrow \text{LiI}$

$1/2\text{I}_2 + \text{Ag} \rightarrow \text{AgI}$

This is a multiyear program where the effort is divided into three major tasks.

Year 1 involves preparation and characterization of solid state electrolytes and conductivity measurements. (See Table II-25.)

Year 2 will focus on cell construction and testing including both *in-situ* and *ex-situ* analysis.

Year 3 will focus on cell characterization. Under the program, cycle life, efficiency, energy density, and the functional capacity of cells will be determined.

The proposed work will be executed in the Advanced Power Sources (APS) Laboratories in the Chemistry Building at Stony Brook University (SBU), the Advanced Energy Research and Technology Center (AERTC) at SBU, and at Brookhaven National Laboratory (BNL). BNL offers core capabilities for the proposed program, including National Synchrotron Light Source-II (NSLS-II) and Center for Functional Nanomaterials (CFN).

Procurement of reagents (Q1)

All reagents have been procured commercially and characterized. X-ray diffraction patterns were recorded and analysis of the diffraction patterns showed that the AgI sample was a majority β -AgI phase with a small contribution from γ -AgI. Lithium iodide diffraction patterns showed LiI (95%) with (5%) hydrate (LiI·1H₂O).

Table II-25: Quarterly milestones and verification for Year 1.

	Q1	Q2	Q3	Q4
Milestone	All reagents procured, water content verified	Develop methodology for AC impedance measurement as a function of temperature	Identify 4 most conductive Ag containing LiI solid electrolytes for further study	At least one electrolyte with conductivity $\geq 10^{-3}$ S/cm
Verification	Karl Fischer titration, XRD	Results consistent with prior literature for LiI electrolyte	Electrochemical impedance spectroscopy (EIS) at 30°C	EIS at 30°C

Results

Development of method for resistance measurements (Q2)

The development of methodology to accurately and reproducibly measure the resistance of the solids was developed using electrochemical impedance spectroscopy (EIS) as a function of temperature. Every set of measurements was conducted in triplicate. The results of a typical experiment showing the Nyquist plots as a function of the temperature for AgI are shown in Figure II-578A. Note that three samples at each temperature are shown with good reproducibility. The EIS data were analyzed where the data were fitted to an equivalent circuit, Figure II-578, inset. The values of the circuit elements were determined from the equivalent circuit fits which allowed quantitative analysis of the data. The results for AgI and LiI conductivity as a function of temperature including error bars are shown in Figure II-578B. The conductivity results obtained from the series of measurements are in agreement with prior literature. This method was used for all composite solid electrolyte testing.

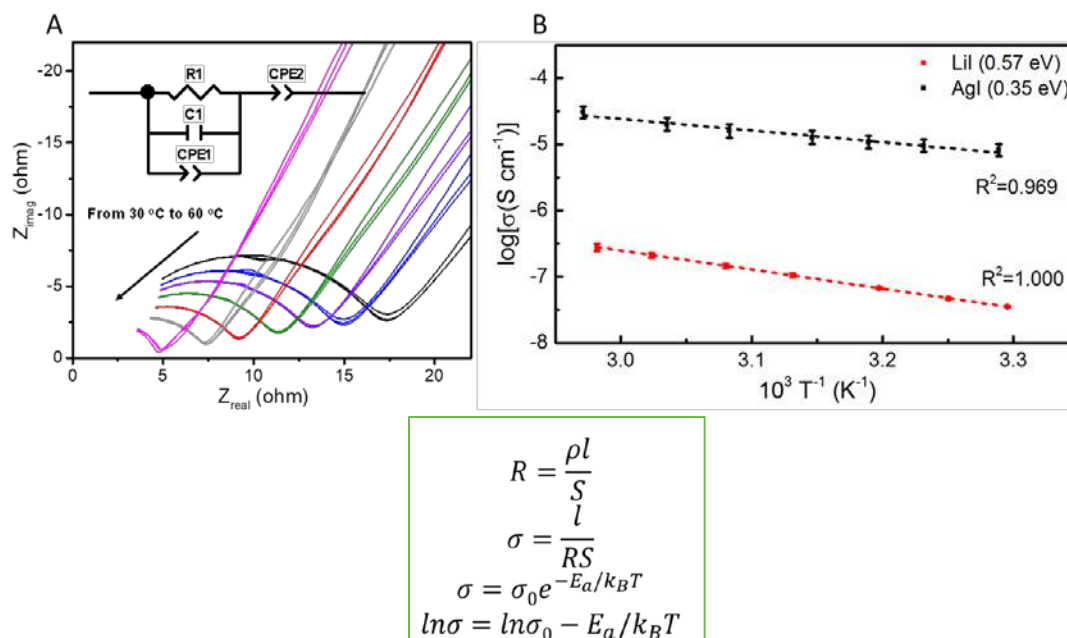


Figure II-578. EIS for AgI as a function of temperature (A), equivalent circuit model used for quantitative data analysis (Inset)/Source: B.J. Neudecker, W. Weppner, *J. Electrochem. Soc.*, **1996**, 143(7), 2198-2203. Poulsen, W. Finn, S. S. Ionics, **1981**, 2(1), 53-57, (B) Conductivity plotted as a function of temperature, (Right) Equation used to determine conductivity values from measurement of resistance.

Measurement of Lil Composite Solid Electrolytes (Q3)

A range of solid electrolyte compositions was tested. This included synthesized Ag ion conductors, RbAg_4I_5 and KAg_4I_5 , (Figure II-579A-C), and composites prepared from $\text{Ag}/\text{Al}_2\text{O}_3/\text{LiI}$. (Figure II-579D) We used electrochemical impedance spectroscopy (EIS) methodology where the measurement method was validated by repeating measurements of the same material over a range of temperatures with at least triplicate measurements of each material. Over 75 samples of lithium iodide-based composite electrolytes, containing Ag ion conductor and polymer additives in a variety of combinations and ratios were tested. Sample data of initial EIS data of Ag^+/Li^+ ion conductors is shown in Figure II-580(A-F) where increased percentage of Al_2O_3 resulted in increased conductivity (Figure II-580G-H).

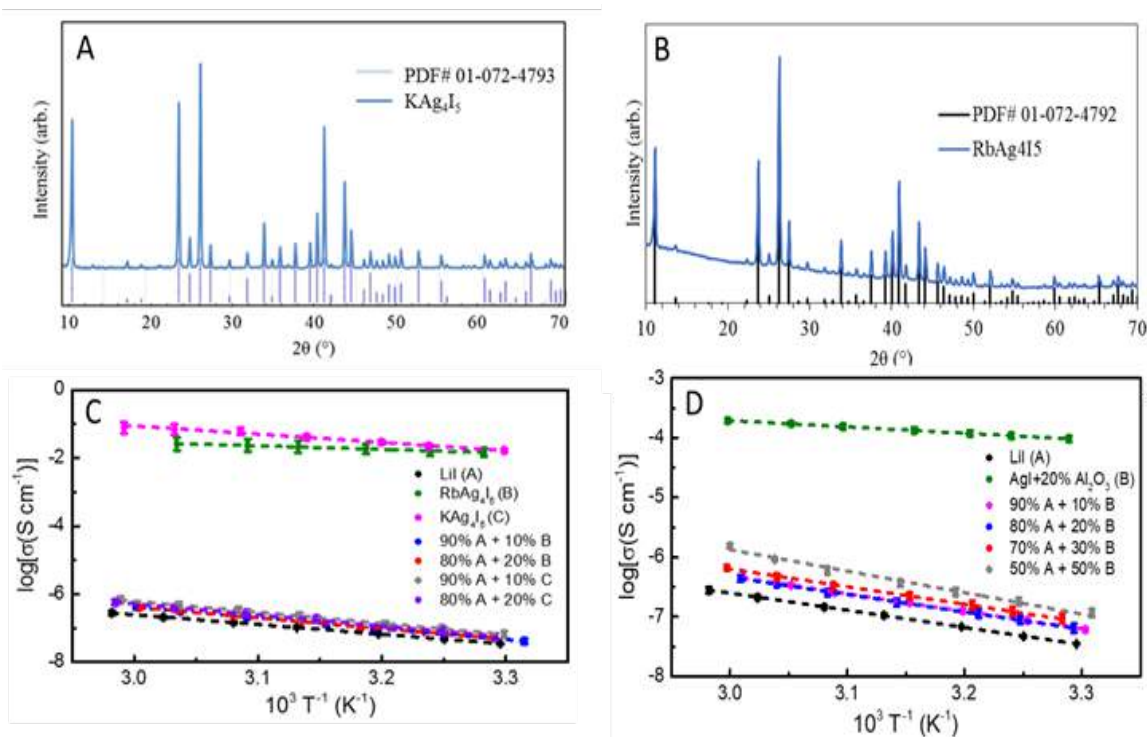


Figure II-579. XRD of synthesized Ag ion conductors, KAg_4I_5 (A) and RbAg_4I_5 (B). Conductivity as a function of temperature for $\text{LiI} + x\% \text{MAG}_4\text{I}_5$ ($\text{M} = \text{K}, \text{Rb}$) (C), and for $\text{LiI} + x\% (\text{AgI} + 20\% \text{Al}_2\text{O}_3)$.

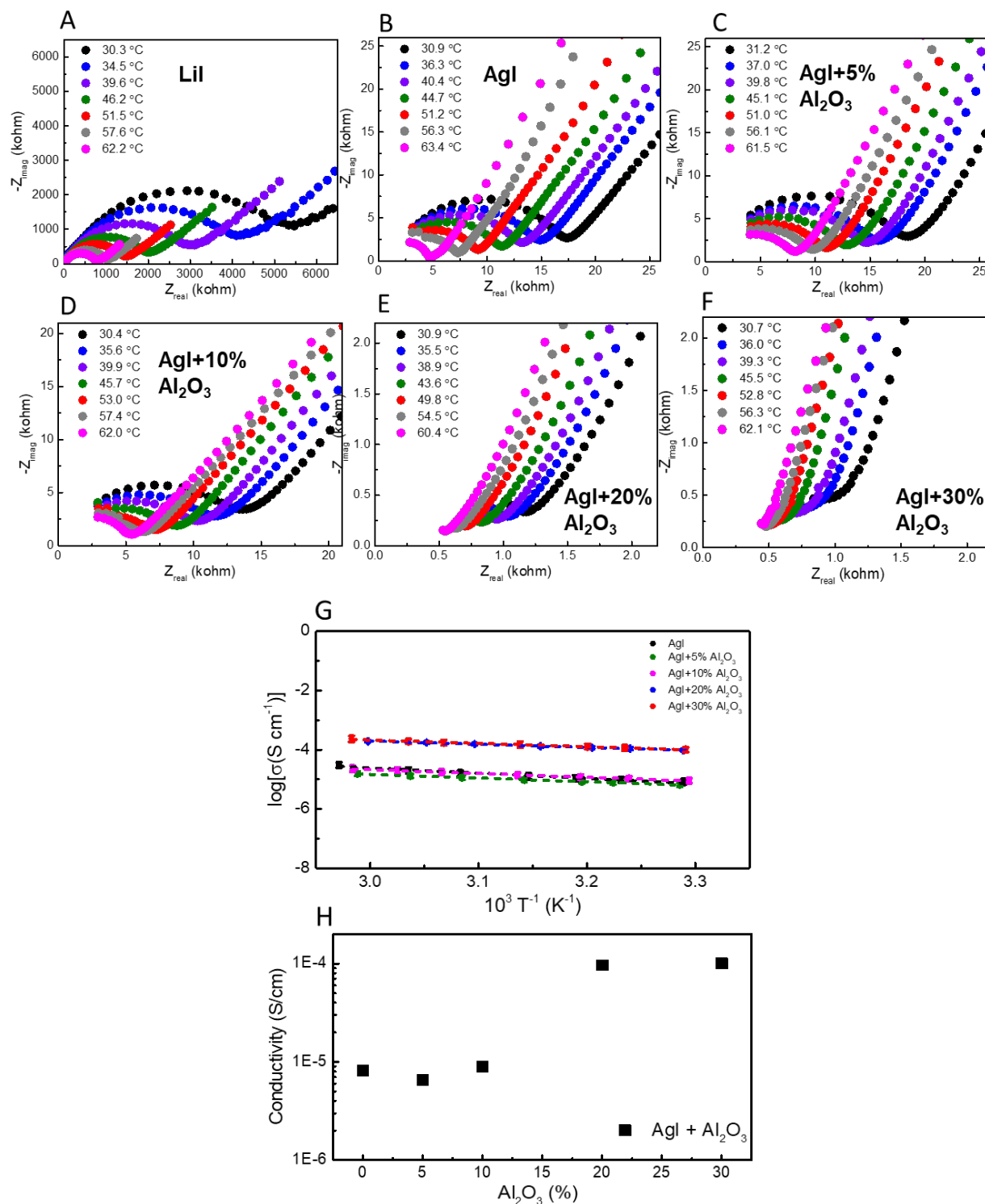


Figure II-580. (A-F) AC impedance of Ag⁺/Li⁺ conductors with varying amount of Al_2O_3 additive, G) Conductivities of AgI with 0, 5, 10, 20, 30% Al_2O_3 additive in temperature range from 30° to 60°C, H) AgI + x Al_2O_3 conductivities at 30°C.

Figure II-581 shows increases in conductivity observed with the addition of polymer to LiI composite electrolytes.

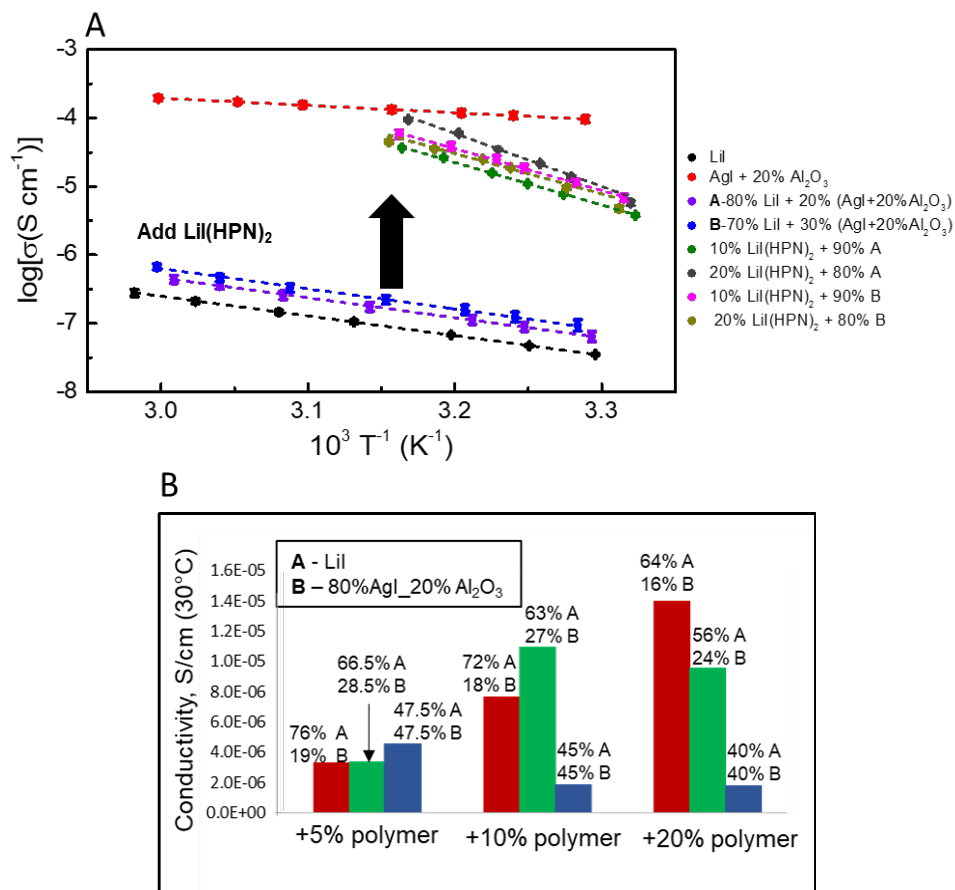


Figure II-581. A) Use of LiI(HPN)₂ in silver containing LiI electrolyte increases ionic conductivity, B) Various ratios of solid electrolyte and polymer were tested, and conductivity values compared at 30°C.

Identification of electrolyte with conductivity $\geq 10^{-3}$ S/cm (Q4)

Two solid electrolytes were identified electrolyte with conductivity $\geq 10^{-3}$ S/cm, meeting the fourth quarter (Go/No Go) Milestone. LiI-based solid electrolytes with varying compositions including polymeric additives poly-2-vinylpyridine and 3-hydroxypropionitrile were measured using our developed EIS methodology.

After exploration of lithium iodide-based composite electrolytes, we successfully achieved the Go/No Go goal by identifying two electrolyte compositions with conductivities $\geq 10^{-3}$ S/cm at 30°C as shown in Table II-26.

Table II-26: Conductivity of LiI composite electrolytes at 30°C.

Sample	σ , 30° C (S/cm)
A. LiI composite electrolyte I	1.0×10^{-3}
B. LiI composite electrolyte II	1.1×10^{-3}

Feasibility demonstration

Initial charging data using coin cell type construction containing solid electrolytes, demonstrated proof of concept for the feasibility of *in situ* generation of anode, cathode and solid electrolyte/separator. A notable decrease in charge transfer resistance as determined by EIS after charging was observed (Figure II-582, A-C). Notably, the open circuit voltages of the cells were stable after the charging step. Disassembly of the cells followed by characterization demonstrated *in situ* generation of Li or Ag and I_2 . (Figure II-583). A more highly conductive composite electrolyte (Composition II) containing LiI and AgI additives was also successfully charged. (Figure II-582C)

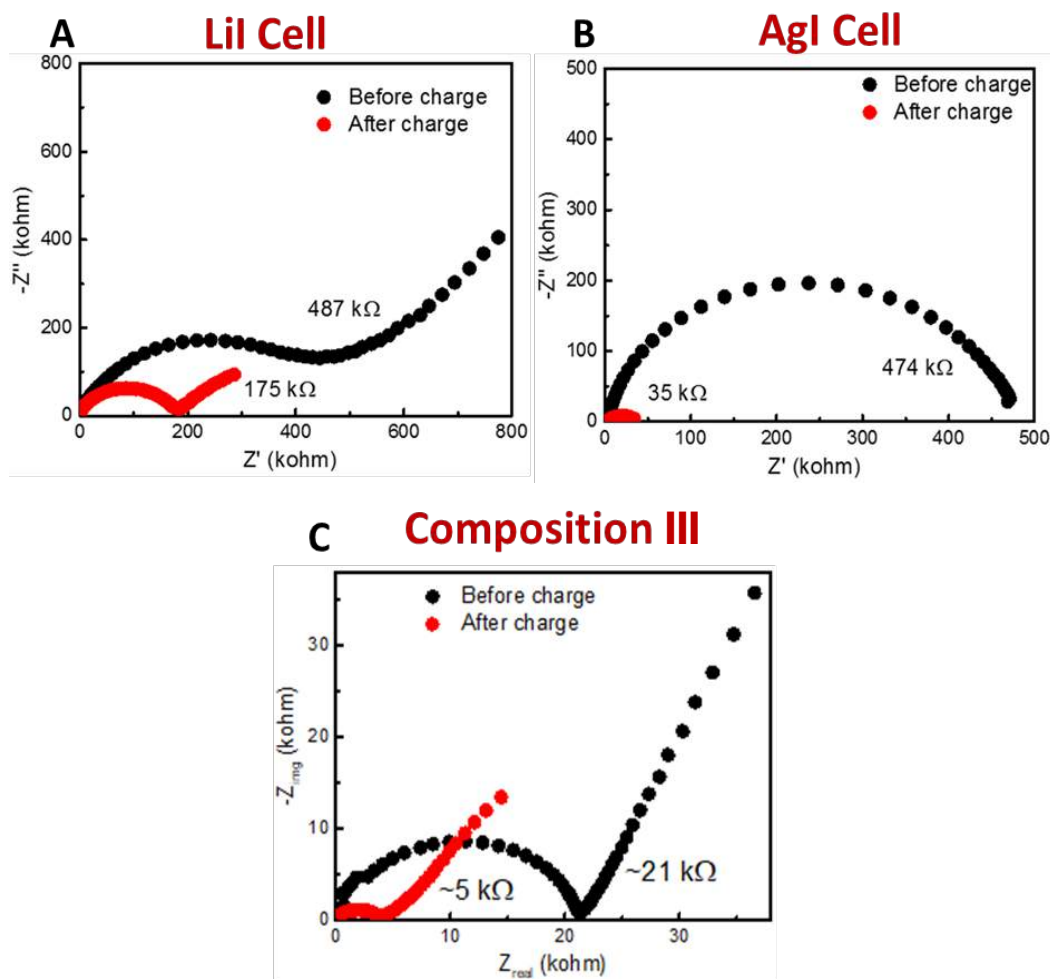


Figure II-582. EIS data: Pristine A) LiI, B) AgI solid electrolyte before and after charging, C) Composition I, a LiI-based electrolyte with AgI and polymer additive before and after charging.

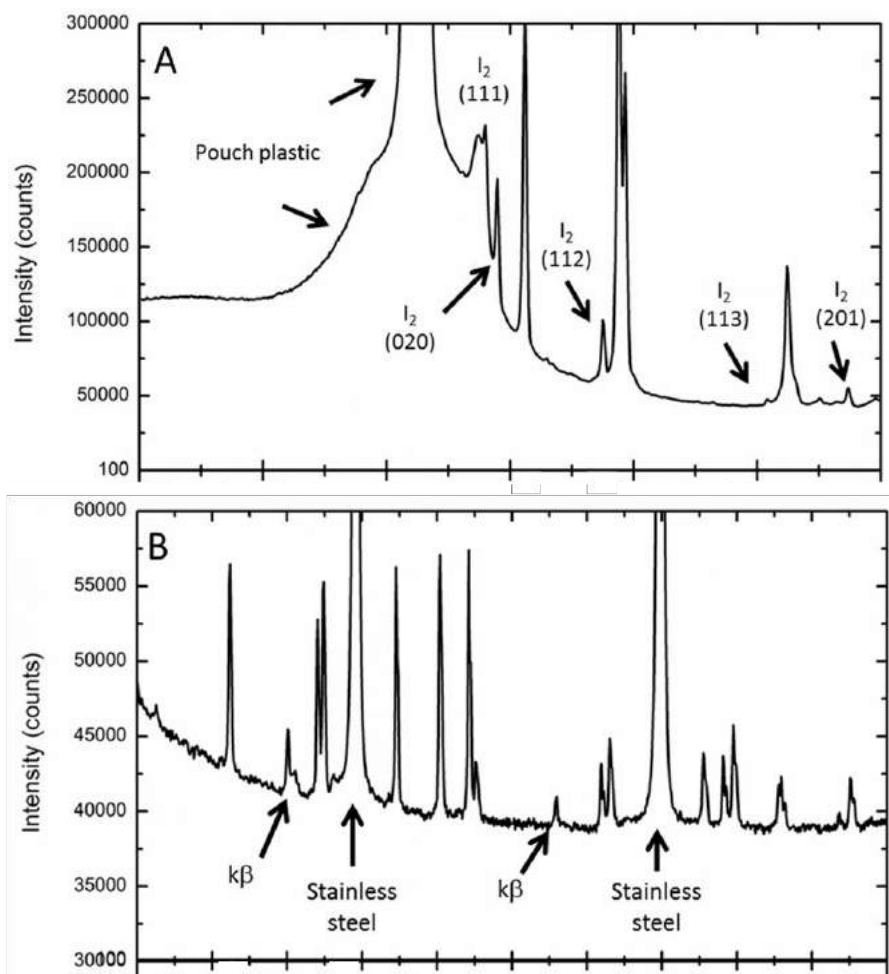


Figure II-583. A) I_2 clearly identified by XRD on positive side, B) Peaks consistent with Li observed on negative side.

A LiI-based composite electrolyte (Composition IV) was explored using four different interfaces demonstrating the role of the interface. Figure II-584A shows the resistance before and after charge (inset). Figure II-584B illustrates step-wise charging of the cells with increasing currents made possible by impedance decrease on charge. Figure II-584C shows OCV stability at 2.8 V for charged cells consistent with the Li/ I_2 couple. Preliminary data using Energy Dispersive X-ray Diffraction (EDXRD) has been collected for an intact assembled cell (Figure II-585), and demonstrates feasibility for identification of localized phases within a stainless steel casing. Future work will focus on development of cell construction and both *ex-* and *in-situ* analysis.

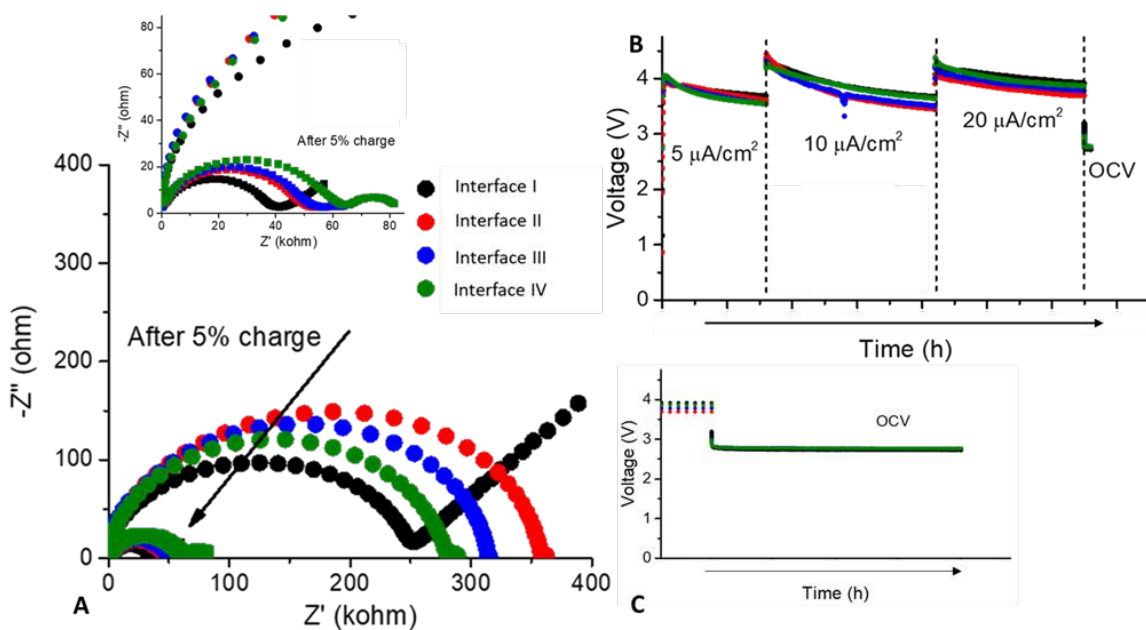


Figure II-584. A) EIS data of electrolyte Composition IV before and after (inset) charging with four different interfaces, B) Step-wise charging, C) After charging, all cells maintained stable OCV,

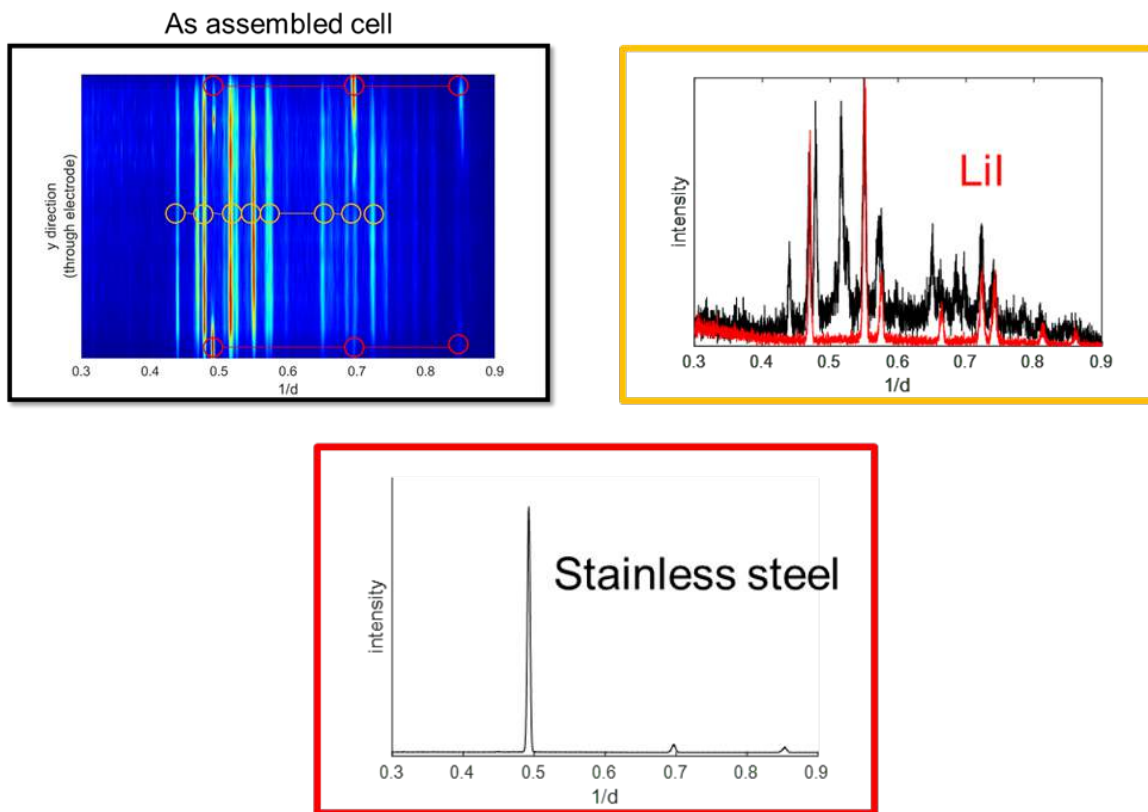


Figure II-585. Feasibility demonstration of Energy Dispersive X-ray Diffraction of a solid LiI cell in a stainless steel can.

Conclusions

- A method for measuring conductivity was developed and results are in agreement with prior literature for pristine AgI and LiI solid electrolytes.
- LiI-based solid electrolytes with conductivities $\geq 10^{-3}$ S/cm have been identified.
- Modifications of the electrolyte/substrate interface to reduce the total measured resistance were explored and will be considered in cell designs for the remainder of the project.
- We have demonstrated a step-wise charging procedure with increasing current levels that decreases total charge time.
- OCV stability followed by ex-situ analysis after charge shows successful *in situ* formation of a Li/I₂ cell.

Key Publications/Patents/Presentations

1. Patent disclosure on Dual Function Solid State Cell concept filed with Stony Brook University Technology Transfer Office.
2. Presentation: E. Takeuchi, A. Marschilok, K. Takeuchi, “Dual Function Solid State Battery with Self-forming Self-healing Electrolyte and Separator”, BMR/ABR/Battery 500 Research Information Exchange, January 17-19, 2017.
3. Presentation: E. Takeuchi, A. Marschilok, K. Takeuchi, “Dual Function Solid State Battery with Self-forming Self-healing Electrolyte and Separator”, Program Officer Site Visit, May 3, 2017, Stony Brook University, Stony Brook, NY 11794.
4. (Poster) Presentation: E. Takeuchi, A. Marschilok, K. Takeuchi, “Dual Function Solid State Battery with Self-forming Self-healing Electrolyte and Separator”, DOE 2017 Annual Merit Review and Peer Evaluation Meeting (AMR) for the Hydrogen and Fuel Cells Program and Vehicle Technologies Office, June 5-9, 2017, Washington, DC.

II.I.11 Advancing Solid-Solid Interfaces in Li-ion Batteries (ANL)

Nenad Markovic, Principal Investigator

Argonne National Laboratory
9700 S Cass Avenue
Lemont, IL 60439
Phone: 630-252-5181
E-mail: nmarkovic@anl.gov

Larry Curtiss, Co-Principal Investigator

Argonne National Laboratory
9700 S Cass Avenue
Lemont, IL 60439
Phone: 630-252-7380
E-mail: curtiss@anl.gov

Tien Duong, Technology Manager

U.S. Department of Energy
Phone: 202-586-7836
E-mail: Tien.Duong@ee.doe.gov

Start Date: November 1, 2017
Total Project Cost: \$1,200,000

End Date: November 1, 2019
DOE share: \$1,200,000

Non-DOE share: \$0

Project Introduction

One of the most important technological advances in sustainable energy harvesting and storage is the development of Li-ion battery technology. However, many challenges must be resolved in order to fully implement this technology, including: (i) development of high energy density cathode and anode materials (activity/cyclability); (ii) enhancement in stability of electrode materials and the corresponding electrolytes; (iii) improvement in selectivity of electrochemical interfaces, e.g., minimizing undesired side reactions at electrode surfaces; and (iv) improvement of many safety issues related to high flammability of organic solvents and Li dendrite formation on the anode electrode. As a result, the focus of much research in the field of Li energy storage is centered on development of methods that can enable Li metal anodes (required for high energy density Li-ion batteries) without dendrite formation and parasitic electrode-electrolyte interactions, as well as replacement of flammable organic solvents with solid electrolytes.

Today, two methods have been introduced to reduce the safety/performance issues. The first method relies on the hope that by modifying the Li metal anode with various types of “thin membranes” (either polymers or ceramics) Li dendrite formation will be significantly reduced relative to the “naked” metal Li anode along with reducing side reactions. The second method relies on the desire to develop an all solid-state battery, composed of Li ion conductive solid electrolytes that connect the metal Li anode with high energy cathode materials. Although for “hard” solid-state electrolytes various types of ceramics have been developed with suitable ionic bulk conductivity, these materials still need to have improved stability to prevent dendrite formation and interfacial Li diffusion. On the other hand, while dendrite formation is more controllable by introducing “soft” polymer materials, none of these polymeric materials have achieved ionic conductivity comparable to liquid electrolytes (0.1 S cm^{-1}). Overall, then, all of these issues must be overcome in order for Li-ion battery technology to move forward. Further advances will require the application of knowledge, concepts, and tools from a variety of fields including materials science, physics, engineering, theory and, in particular, interfacial electrochemistry.

Objectives

The project objectives are multifaceted, including: (i) the development of a new mechanically and chemically stable Li-selective solid “membrane” capable of protecting the Li metal anode during the discharge process in commercially available liquid electrolytes; and (ii) the development of a mechanically/chemically stable and Li ion conductive ($\geq 2 \times 10^{-4} \text{ S cm}^{-1}$ at 298 K) solid electrolyte that can operate at potentials $> 5 \text{ V}$ for a solid-state battery encompassing a metal Li anode and a high voltage oxide cathode.

Project Impact

Protective organic and inorganic compounds can lead to enhanced stability of the interface, improve Li ion interfacial transport, minimize dendrite formation and increase safety in Li ion batteries. Developing and utilizing physical and chemical synthesis methods will enable the design of solid-solid interfaces with unique chemical/mechanical/conductivity properties of Li protective coatings and solid state electrolyte systems. The proposed work will develop and exploit a variety of *ex situ* and *in situ* optical and surface-sensitive techniques and electrochemical methods to explore and explain bulk and interfacial properties of the selected materials. The results will serve to unravel many of the puzzling bulk and interfacial properties of solid-solid interfaces and solid electrolyte materials.

Approach

We propose to use and develop interdisciplinary, atomic-/molecular-level insights obtained from integrating both experimental and computational methodologies to define the landscape of parameters that control interfacial properties for a new generation of solid-state Li-ion battery systems. Our strategy will involve transferring the knowledge gained from well-characterized thin film materials to real-world materials. This strategy forms a closed loop wherein the knowledge gained from model systems is used to design the more complex, real-world materials, and vice-versa, enable investigation of new phenomena observed in real materials via the development of new model systems. The work will focus on utilizing existing, in-house synthesis and characterization methods to enable a rapid transition from fundamental science to realistic cells.

Collaborators: This project funds work at Argonne National Laboratory and the University of Chicago-Illinois (Prof. Amin Salehi). We have also established collaboration with Prof. Jeff Sakamoto at the University of Michigan.

Results

Ionic transport across interfaces between dissimilar materials and the intrinsic stability of such interfaces is a fundamental challenge that cuts across many disciplines, including Li-ion-based solid-solid battery systems. However, understanding the interfacial stability of solid-state Li battery systems is a highly challenging task. To overcome many of these issues, we establish a surface science-based approach for assessing the intrinsic stability of oxide materials in contact with Li metal in order to understand the impact of crystallographic orientation and surface morphology on the extent of the chemical reactions that take place. Through the use of magnetron sputtering to deposit thin films of Li metal on single-crystalline, niobium-doped strontium titanate (Nb:STO) substrates at room temperature, a representative interface is created for investigating the intrinsic stability of the Li-STO system. Although not a solid electrolyte material itself, STO serves as an ideal model system as its surface chemistry has been extensively studied and single crystal substrates can be readily prepared with known surface termination.

Methods developed to study interfacial stability

In order to understand the intrinsic chemistry of Li metal in contact with a model oxide surface, Li was sputter deposited directly onto STO(hkl) surfaces and then transferred directly between the sputter and analysis chambers under ultrahigh vacuum (UHV) conditions ($\leq 5 \times 10^{-9}$ mbar throughout transfer). Central to these investigations was the preparation of well-defined, single crystal surfaces in order to identify differences in stability and reactivity based on crystallographic orientation.

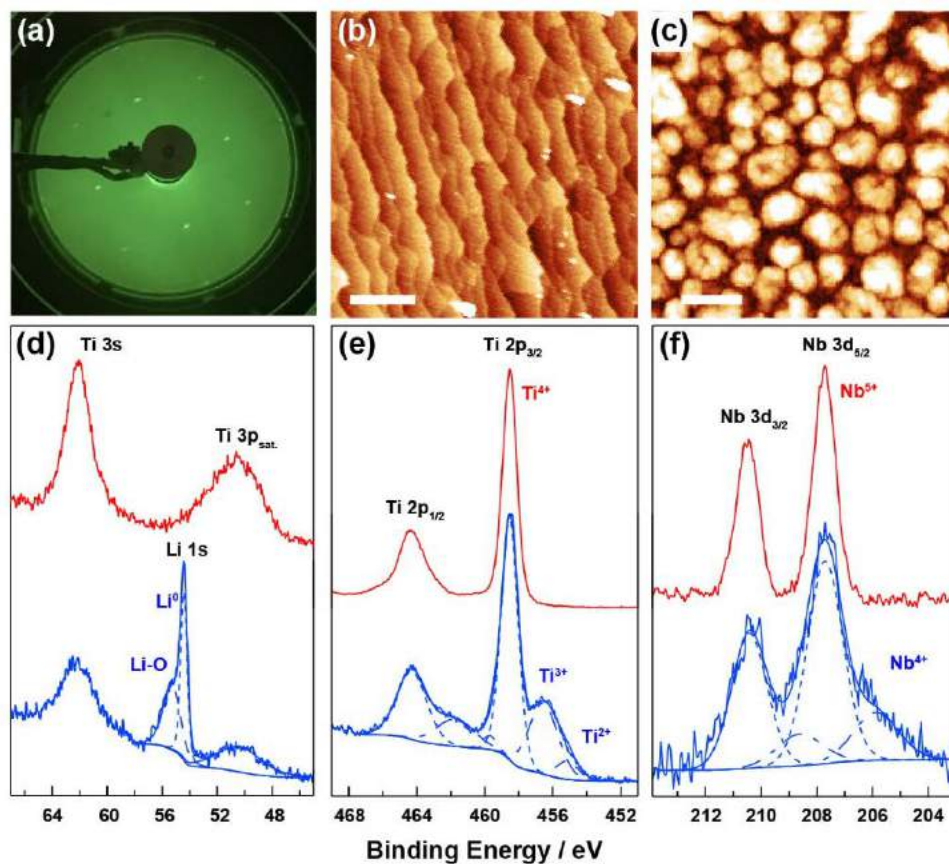


Figure II-586. (a) LEED and (b) AFM images of an etched and annealed STO(001) surface. (c) AFM image of the same STO(001) surface after Li deposition. (d-f) XPS core level spectra before (red) and after (blue) Li deposition.

Figure II-586 illustrates structural and chemical characterization of a representative STO(001) surface both before and after Li deposition. From low energy electron diffraction (LEED, Figure II-586a), a 1×1 surface reconstruction is clearly resolved on the as-prepared STO(001) surface, and from atomic force microscopy (AFM, Figure II-586b), the well-defined crystal terraces of HF-etched and annealed STO(001) surfaces can be easily seen. X-ray photoelectron spectroscopy (XPS) analysis of the Ti 2p, Nb 3d and Sr 3p core levels indicates that the pristine STO surface is fully oxidized, with only Ti^{4+} , Sr^{2+} and Nb^{5+} oxidation states. AFM imaging of the sample after Li deposition reveals an island morphology with an average island diameter of ~ 500 nm (Figure II-586c). Figure II-586e-f demonstrate that after Li deposition, $\sim 38\%$ of the total Ti signal corresponds to a mixture of 3+ and 2+ oxidation states, and 33% of the total Nb signal corresponds to the 4+ oxidation state. The oxidation state of Sr was unaffected by Li deposition. The persistence of Ti^{4+} and Nb^{5+} species after Li deposition indicates incomplete reduction of the STO, suggesting that only the first few monolayers of STO react, and/or the spaces between Li islands on the surface are essentially Li-free, resulting in regions of unreacted STO.

X-ray absorption spectroscopy (XAS) suggests that the reaction is at least partially surface-limited, as measurements of the Ti K-edge in total electron yield (TEY) and total fluorescence yield (TFY) modes before and after Li deposition reveal differing amounts of reduction (Figure II-587). The TEY spectra, which are sensitive only to the first ~ 5 nm of the surface, clearly indicate a mixture of Ti oxidation states, consistent with the XPS measurements. The TFY spectra, which measures the first ~ 50 nm of the sample, indicate that the “bulk” of the STO is largely unaffected by Li deposition. Taken together, the above results clearly demonstrate the power of our surface science-based approach to directly probe the intrinsic stability of solid-state Li/oxide interfaces. Below we investigate the structure-dependent stability of STO interfaces in contact with Li metal.

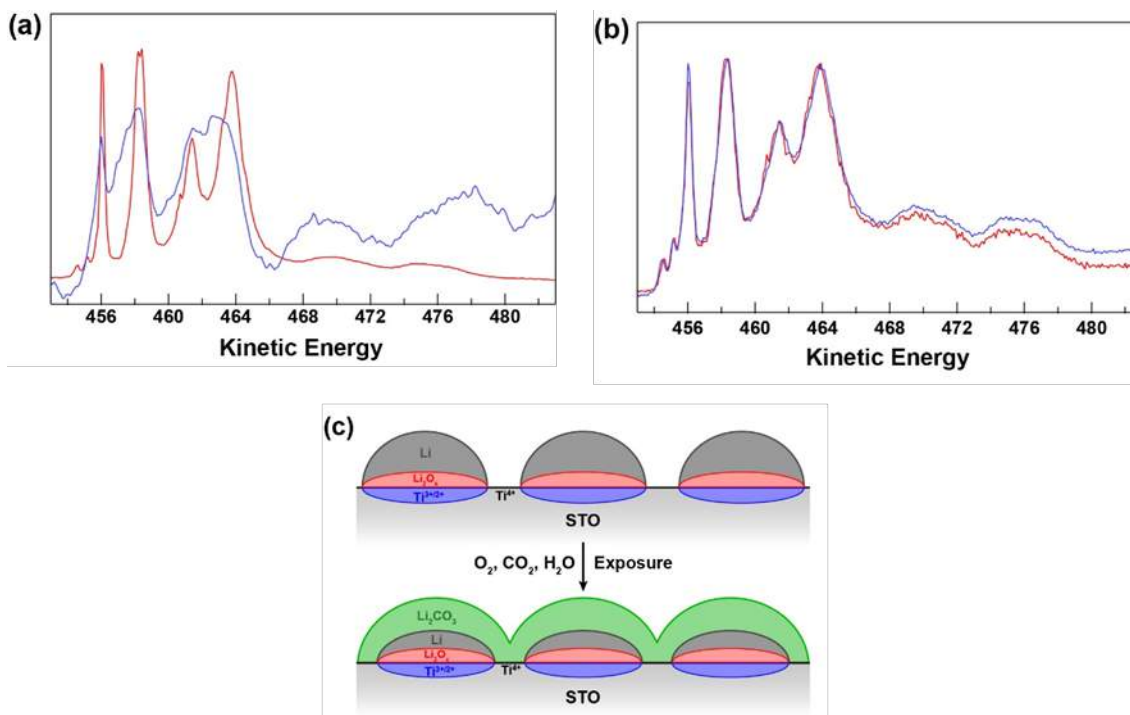


Figure II-587. XAS measurements of STO substrates in (a) TEY and (b) TFY modes before (red) and after (blue) Li deposition. (c) Schematic of surface structure after Li deposition (top) and air exposure (bottom).

Structure dependent stability of $\text{STO}(hkl)$ interfaces

Deposition of an identical amount of Li on $\text{STO}(110)$ and (111) surfaces reveals a similar reduction of the surface, with virtually identical ratios of Ti^{4+} , Ti^{3+} and Ti^{2+} as observed on $\text{STO}(001)$. Given the above evidence for a surface-limited reaction of $\text{STO}(001)$ with Li metal, it is likely that the STO surface structure should remain largely unperturbed by the deposition of Li as explored by AFM imaging of surfaces before and after Li deposition and removal. XPS measurements of $\text{STO}(hkl)$ samples after sonication in water reveal that all residual Li is indeed removed, and the surface is fully reoxidized to pure Ti^{4+} and Nb^{5+} . Surprisingly, AFM imaging revealed that whereas $\text{STO}(001)$ and (111) surfaces exhibit no changes in surface morphology after Li removal (Figure II-588a/d and Figure II-588b/e, respectively), $\text{STO}(110)$ surfaces appear to be substantially etched (Figure II-588c/f). as demonstrated further below, DFT simulations were performed to understand the underlying thermodynamic factors that result in the lower stability of the $\text{STO}(110)$ surface.

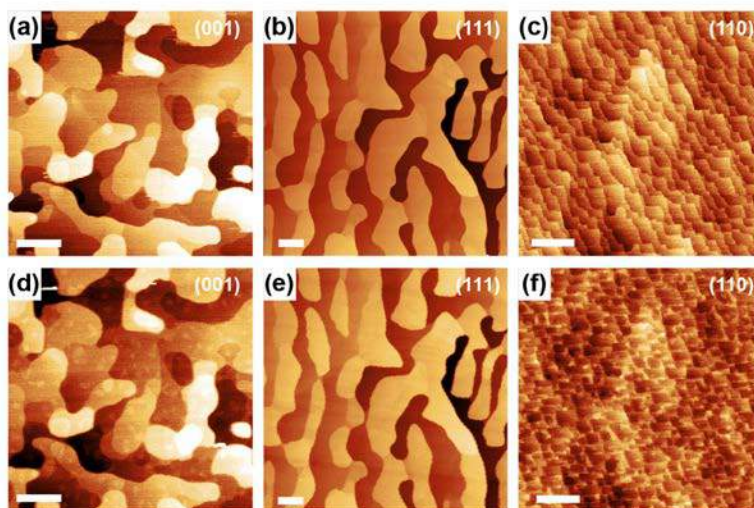


Figure II-588. AFM images of STO(001), (111) and (110) surfaces (a-c) before Li deposition and (d-e) after Li deposition. All images were taken in identical locations. Scale bars on (001) and (110) images are 500 nm, and scale bars on (111) images are 1 μm .

Understanding Morphological Stability via Computation

DFT calculations were performed on a variety of unreconstructed and reconstructed STO(hkl) surfaces, summarized in Figure II-589a, to rationalize and ultimately understand the structural origins of orientation-dependent morphological instabilities induced by Li interactions with STO single crystals. The binding energies of Li atoms on these different undoped STO surfaces indicate that the binding of Li becomes less energetically favorable with decreasing surface oxygen content (Figure II-589b), with $\text{O}_2(110)$ (-3.82 eV) < $\text{TiO}_2(001)$ (-3.21 eV) << $\text{SrTiO}(110)$ (+0.27 eV). Li interactions with the Ti-terminated (111) surface lead to unstable configurations, and are therefore not included.

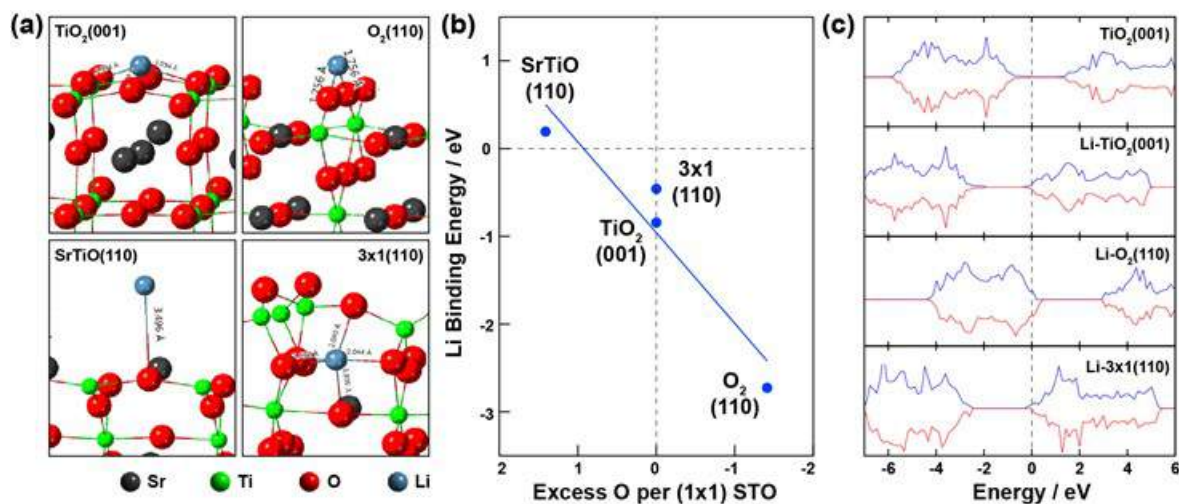


Figure II-589. DFT-calculated (a) structures (b) energy changes and (c) electronic densities of states for Li atoms on (100) and (110) surfaces of SrTiO_3 with different terminations.

Calculations of the electronic density of states (DOS) indicate charge transfer to Ti 3d states, consistent with the observed reduction of Ti and Nb in XPS. Consistent with the observation of self-limiting surface reduction, surfaces that are initially favorable for Li binding become more reduced with increasing Li coverage, e.g., for the $\text{TiO}_2(001)$ surface decreasing from 3.21 eV (1/4 ML) to 2.38 eV (1/2 ML) and further to 1.75 eV at 1 ML coverage. Interestingly, DFT results on the (3x1)-(110) reconstructed surface indicate that it is most favorable for Li ions to insert under the top TiO_x layer of the resulting reconstructed geometry (Figure II-589a). Incorporation of Li below the top TiO_x layer results in a lower stability of this layer, since its removal after Li insertion results in a much more stable termination than that in the absence of inserted Li. This likely explains the observed morphological instability of the $\text{STO}(110)$ surface, with washing in H_2O resulting in removal of the TiO_x along with the underlying LiO_x . This would result in an overall thickness loss of $\sim 5\text{\AA}$, close to the observed thickness loss in our AFM measurements. The combination of DFT with the experimental results on well-defined, model surfaces detailed above illustrates the power of our surface-science-based approach, as it enabled us to clearly distinguish and understand the interplay between interfacial reactivity and morphological transformations of oxide surfaces in contact with reactive metals at atomic and molecular levels.

From model to real systems – Nb-doped LLZO

Having demonstrated the power of our approach on model STO surfaces above, we expanded our analysis to a more technologically-relevant materials system: the so-called “stuffed garnet” phase, niobium-doped lithium lanthanum zirconate (Nb:LLZO , $\text{Li}_{6.5}\text{La}_3\text{Zr}_2\text{Nb}_{0.5}\text{O}_{12}$) in order to understand the reactions that may take place at the interface between this material and Li metal. Previous investigations of the stability of Al-doped LLZO yielded mixed results, with some studies concluding that surface-limited reduction and Li intercalation takes place upon contact with Li metal at room temperature while others indicate that no reduction takes place even after extended contact with molten Li metal at elevated temperatures. Here we make use of Nb-doped LLZO material, which, based on the above measurements of Nb-doped STO, will enable us to clearly distinguish any instability to contact with Li metal. As shown in Figure II-590, deposition of Li on Nb:LLZO indeed shows clear evidence of Nb reduction, a slight shift to lower binding energy (~ 0.3 eV) of the La $4p_{3/2}$ peak, and no evidence of Zr reduction. We emphasize it would not have been possible to unambiguously confirm the presence of a surface reaction without first having established the feasibility of this approach on a model system in which chemical interactions clearly take place. Further work is ongoing to understand the origin of the slight reductive shift in the La peak, as well as how differences in surface cleanliness and defect structure can yield differences in the observed surface chemistry.

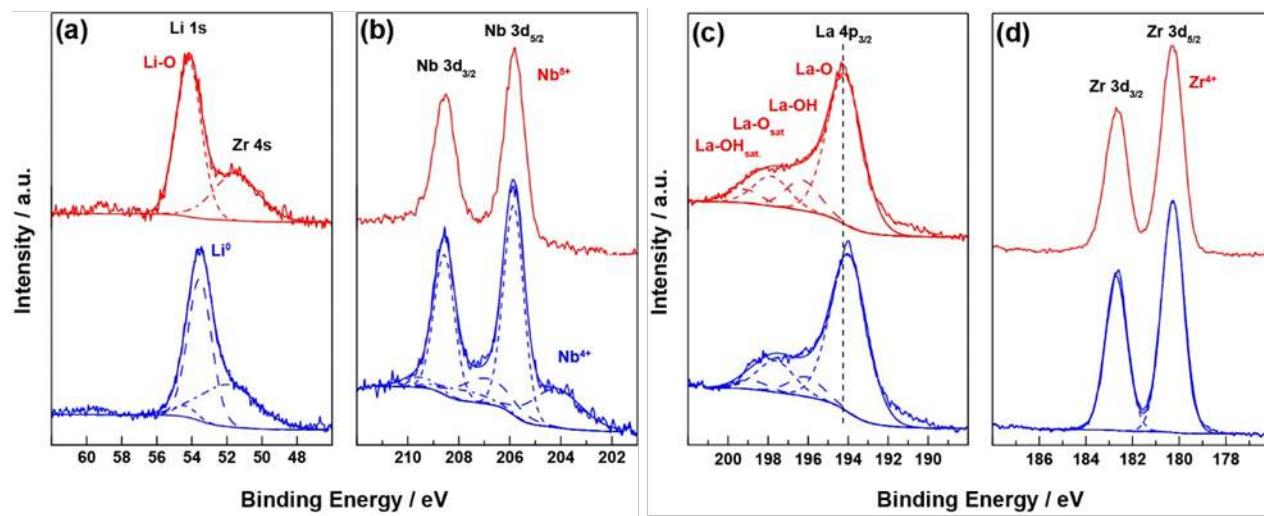


Figure II-590. XPS core level spectra from Nb:LLZO before (red) and after (blue) Li deposition.

Of paramount importance to these efforts will be the development of well-defined, single crystalline LLZO interfaces (as in the case of STO) in order to fully understand the interfacial and bulk properties of the Li/LLZO system. In doing so, it will be possible to rigorously assess the underlying factors that govern the intrinsic materials stability of not only the LLZO system, but other relevant crystalline oxides and glassy materials. Work is currently underway to develop thin film deposition of several solid oxide materials via pulsed laser deposition (PLD), and we have already developed in-house capabilities to synthesize oxide targets for PLD deposition. Furthermore, we have developed impedance spectroscopy to measure interfacial and bulk resistivity, along with Li-ion conductivity of both bulk and thin film oxide materials to characterize their performance in real cell environments.

Conclusions

We have introduced a surface science-based approach for rationalizing, and ultimately understanding, the intrinsic and orientation-dependent stability of oxide materials in contact with Li metal. Through the use of well-defined, single crystalline $\text{SrTiO}_3(\text{hkl})$ surfaces as model systems, we were able to clearly observe the reduction of Ti and Nb upon contact with Li metal. Furthermore, the observation of significant morphological instability of $\text{STO}(110)$ surfaces relative to (001) and (111) after Li removal was explained through the use of DFT calculations, which revealed the insertion of Li below the surface TiO_x that results in destabilization of this layer. Extension of our surface science-based approach to the technologically-relevant Nb:LLZO system revealed clear reduction of Nb in this material, demonstrating the power of our approach to clearly identify surface (in)stability in real-world, polycrystalline materials in contact with Li metal. The presence of significant, orientation-specific changes in the surface stability highlights the importance of developing model systems for understanding the structure-sensitive reactivity of oxide materials for solid-state batteries. Only by understanding both the intrinsic chemistry *and* morphological stability of oxide interfaces in contact with reactive metals and disparate oxide surfaces will it be possible to rationally engineer a new generation of highly stable and reversible solid-state battery systems.

Key Publications

1. Justin G. Connell, Yisi Zhu, Peter Zapol, Sanja Tepavcevic, Jeff Sakamoto, Larry A. Curtiss, Dillon D. Fong, John W. Freeland, Nenad M. Markovic. "Crystal Orientation-Dependent Reactivity of Oxide Surfaces in Contact with Lithium Metal." *Submitted for Publication*.
2. Yisi Zhu, Justin G. Connell, Peter Zapol, Sanja Tepavcevic, Jeff Sakamoto, Larry A. Curtiss, Dillon D. Fong, John W. Freeland, Nenad M. Markovic. "Surface Chemistry and Intrinsic Stability of Doped Lithium Lanthanum Zirconium Oxides." *In Preparation*.

II.I.12 Multifunctional, Self-Healing Polyelectrolyte Gels for Long-Cycle-Life, High-Capacity Sulfur Cathodes in Li-S Batteries (University of Washington)

Alex K.-Y. Jen, Principal Investigator

University of Washington
Department of Chemistry and Materials Science and Engineering
Roberts Hall 302
Seattle, WA 98195
Phone: 206-543-2626
E-mail: ajen@u.washington.edu

Jihui Yang, Principal Investigator

University of Washington
Roberts Hall 315
Seattle, WA 98195
Phone: 206-543-7090
E-mail: jihuiy@u.washington.edu

Tien Duong, Technology Manager

U.S. Department of Energy
Phone: 202-586-7836
E-mail: Tien.Duong@ee.doe.gov

Start Date: October 1, 2016

End Date: September 30, 2019

Total Project Cost: \$1,388,888

DOE share: \$1,250,000

Non-DOE share: \$138,888

Project Introduction

The current electric vehicle (EV) battery market is dominated by lithium-ion batteries (LIBs). However, conventional LIBs-based on this basic materials system have already begun to reach their performance limits due to progressive materials and device optimization over the past two decades. In order to meet EV Everywhere goals of 75% cost reduction and 50% weight reduction in electric vehicle batteries by 2022, radically new strategies must be employed.

One tantalizing solution is to look beyond traditional lithium-ion intercalation chemistry towards “beyond-lithium” systems such as the lithium-sulfur (Li-S) battery. A sulfur cathode has a theoretical gravimetric specific capacity of 1673 mAh/g at ~ 2 V vs Li/Li⁺, rendering a theoretical energy density improvement of 500% as compared to the lithium metal oxide cathodes found in LIBs. This increase can be matched on the anode side by using lithium metal, which possesses an intrinsic theoretical gravimetric specific capacity of 3860 mAh/g – an order of magnitude higher than that of graphite. Additionally, sulfur is cheap and earth-abundant, making this redox couple highly attractive for EV battery use.

However, a commercially-viable Li-S battery has remained elusive due to technical challenges. Many of them stem from the formation of polysulfides (Li₂S_x, 3 ≤ x ≤ 8) which are highly soluble in organic electrolytes, leading to self-discharge, passivation of the lithium anode, low Coulombic efficiency due to the escape of sulfur into the electrolyte, and voltage hysteresis from differences in forward and backward reaction mechanisms. In addition, both the starting material (sulfur) and end products (Li₂S, Li₂S₂) are highly insulating, necessitating the use of a large amount of conductive carbon in the electrode. Furthermore, because the overall reaction is accompanied by a large volume change, this composite matrix is prone to cracking, promoting battery failure. Finally, on the anode side, lithium metal tends to form dendrites upon repeated stripping and plating, which puncture the cell separator and cause internal shorting.

Researchers have addressed these issues, to a certain degree of success, using a variety of creative strategies, including ionic liquid electrolytes, SEI-improving additives, mesoporous carbon hosts, advanced binders, and many others. Still, despite these myriad strategies, a safe Li-S battery with long cycle life based on scalable fabrication techniques remains elusive, as no single strategy or even combination of several has proven to be totally effective at both preventing dendrite growth and stopping efficiency/capacity loss via polysulfide.

Objectives

The objective of this project is to develop self-healing and polysulfide-trapping polyelectrolyte gels containing ionic liquid (IL) for the Li-S battery system. The Li-S battery design will be capable of achieving gravimetric and volumetric energy densities of ≥ 800 Wh/kg and ≥ 1000 Wh/L, respectively.

The project will achieve the following performance targets (all cycles at C/10 rate unless otherwise specified):

- A cathode gravimetric specific capacity of ≥ 675 mAh/g after 10 charge/discharge cycles between 2.8 and 1.7 V vs Li/Li⁺
- An average coulombic efficiency $\geq 99\%$ for the 10th cycle through the 100th
- $\geq 90\%$ capacity retention after 100 cycles as compared to the capacity of the 10th cycle.
- $\geq 30\%$ capacity retention when cycled at a C/2 rate, as compared to the capacity at C/10
- Ability to operate at temperatures between -20°C and 50°C.

Approach

During Budget Period 1 (quarters 1-6), we will synthesize a variety of starting materials for gel electrolytes and self-healing polymers, fabricate them into films both individually and together, and then test their electrochemical/mechanical properties relevant to use in a Li-S battery. Additionally, we will synthesize a variety of sulfur/carbon (S/C) composites, utilizing mesoporous carbons with varying properties and various functionalities placed onto their surfaces.

Organic synthesis will include NDI- (naphthalene diimide) and Py- (pyrene) containing materials, as well as monomers for the polyelectrolyte phase. Materials will be produced through established synthetic routes and characterized by nuclear magnetic resonance (NMR), gel permeation chromatography, and/or solution-phase cyclic voltammetry. Synthesis of S/C composites will be done by mixing of sulfur and carbon at above the melting point of sulfur, and will be characterized by Brunauer–Emmett–Teller (BET) surface area and pore size analysis to confirm successful integration of sulfur into the pore structure. Surface functionality will be studied by thermal gravimetric analysis (TGA) and x-ray photoelectron spectroscopy (XPS).

Fabrication and testing of ionomer gels with varying ratios of IL and molecular starting materials will be done. Basic electrochemical and mechanical properties of each gel composition will be tested and used to determine structure-property relationships, then gel compositions with favorable properties will undergo more detailed testing on long-term interfacial stability with Li foil, Li dendrite suppression, and polysulfide diffusion. Conductivity and thermal properties will be assessed by A/C impedance, TGA, and differential scanning calorimetry. Tensile testing will be carried out to determine mechanical properties. For advanced tests, Li/gel/Li symmetric cells will be constructed, and analyzed for development of interfacial resistance and dendrite suppression using cyclic stripping/plating. Polysulfide trapping ability will be quantified by measuring absorption from a fixed-concentration solution.

Fabrication and testing of self-healing films, made from various structures and ratios of NDI- and Py-containing moieties, will be performed. Mechanical and self-healing properties will be tested, as well as ionic conductivity. Static and dynamic mechanical testing will be carried out to determine tensile modulus, toughness modulus, and storage and loss modulus. Self-healing will be measured by slicing films in two, contacting the pieces, and annealing at fixed temperature, followed by re-testing tensile properties.

This will be followed by fabrication and testing of gel electrolytes containing both physically-crosslinked (self-healing) and chemically-crosslinked (ionomer) materials. All of the tests detailed in the two paragraphs above will be performed in order to determine how the performance of individual components of the gel translates to an interpenetrated structure containing all components.

Parallel to materials development efforts, we will undertake fabrication and testing of small-capacity coin cells utilizing a variety of cell design concepts, including organic electrolytes, IL electrolytes, non-self-healing polyelectrolyte gels, and interpenetrating gels in order to benchmark performance and demonstrate an interpenetrating materials system that is capable of significantly improving performance. Cells will be cycled for short periods (≤ 100 cycles) at rates ranging from C/100 or C/50 to C/2. A/C impedance spectra will be collected at various points in order to observe the evolution of internal impedances during cell cycling. Voltages traces during charge and discharge will be observed and correlated to internal processes such as polysulfide speciation and insulating buildup of $\text{Li}_2\text{S}/\text{Li}_2\text{S}_2$ deposits. The origins of undesirable cell performance will be investigated using a combination of experimental techniques, including targeted cycling tests, cyclic voltammetry, A/C impedance tests, scanning electron microscopy, and x-ray diffraction (XRD).

During Budget Period 2 (quarters 7-12), we will continue synthesis of molecular components of gels and S/C composites from raw starting materials. Synthesis will proceed according to literature, as well as any modifications we may make in order to produce materials more efficiently. We will continue testing of gel electrolytes containing both physically-crosslinked self-healing and chemically-crosslinked ionomer materials, as well as continue development of self-healing polymer films. Basic electrochemical and mechanical (including self-healing) behavior will be characterized, and gel compositions with favorable properties will undergo more detailed testing on long-term interfacial stability with Li foil, Li dendrite suppression, and polysulfide diffusion. Minor structural and compositional adjustments will be made to the gel electrolyte formulation based on cell performance details.

We will continue to fabricate coin cells with sulfur-based cathodes and lithium metal anodes which utilize electrolyte materials in the cell structure, and study their performance as a function of gel design. Initially, low-mass-loading demonstration cells will be constructed, followed by practical-loading cells. This task will culminate directly in the production of deliverable 10 mAh Li-S cells for DOE testing. All of the experiments previously mentioned for cell testing will be performed as cell design is optimized. We plan to utilize instrumentation at the new Washington Clean Energy Testbeds on the University of Washington campus, the University of Washington Molecular Analysis Facility, and NMR/microscopy instrumentation available at the Environmental Molecular Sciences Laboratory at Pacific Northwest National Lab.

Results

Self-Healing Materials

We have undertaken detailed study of the π - π interaction between NDI and Py, with the intent of designing a tunable self-healing materials system. We began this investigation by studying model compounds N,N'-dibutyl-naphthalene diimide (dbNDI) and Py in dichloromethane. UV-Vis analysis shows that upon addition of small amounts of dbNDI to a Py solution, a clear, broad absorption peak appears at 500nm. A second peak at 514nm becomes apparent upon increasing the ratio of dbNDI to Py, peaking at a ratio of 1:0.5 (Figure II-591). This suggests that more than one type of complex can be formed. NMR data also suggests complex formation of stoichiometry 1:1 (dbNDI:Py) and 2:1 (dbNDI:Py).

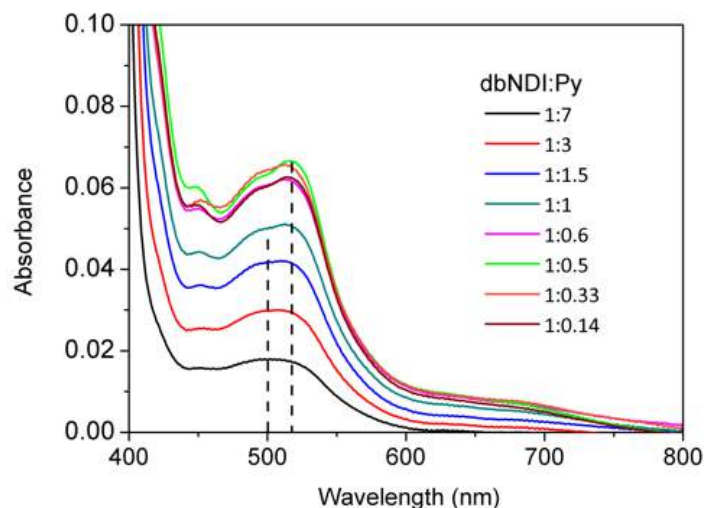


Figure II-591. UV-Visible spectra of dbNDI/Py solutions of varying ratios (constant total concentration) in dichloromethane, showing development of peaks in the visible region corresponding to complex formation.

Collecting UV-Vis spectra of these optimum stoichiometries while varying overall concentrations and applying Beer-Lambert Beer's law to the 500/514nm peaks, we calculated complexation free energies of the complexes as -8.19 kJ/mol for the 1:1 dbNDI:Py complex and -16.49 kJ/mol for the 2:1 dbNDI:Py complex.

Generalizing this interaction to polymeric systems, we expected that varying the ratio between an NDI-containing polymer and a Py-containing crosslinker would result in changes in self-healing behavior, in accordance with the changing strength of the dominant π - π interaction mode. We tested this using novel polymeric materials designed for self-healing: PENDI-C6, a methacrylate polymer bearing NDI pendants with a six-carbon tail (as well as triethylene glycol methyl ether pendants for processability and ionic conductivity) and triPy, a three-armed polyethylene glycol (PEG) derivative terminated on each branch by pyrene units. UV-Vis spectra of 1:1 (NDI:Py) mixtures of these materials produced the same 500nm peak as the small molecules, confirming that the same non-covalent interaction occurs between polymers. We produced free-standing films of mixtures of these polymers corresponding to a 1:1 molar ratio of NDI to Py units (termed as PP-1), and tested their mechanical and self-healing properties. In order to adjust the dominant interaction mode in these materials without changing the relative amounts of polymer, we selectively doped either dbNDI (PP-NDI) or Py (PP-Py) into the films during fabrication, forcing either the 1:1 or 2:1 complexes to form according to Le Chatelier's principle. The self-healing behavior that we observed is summarized in Figure II-592 below – changing the ratio of NDI to Py groups in the polymer composite does indeed produce large changes in behavior, allowing us to tune self-healing temperature from 30°C-70°C. Additionally, we observed that tensile modulus varied from 69MPa (PP-Py) to 219MPa (PP-NDI). These values are significantly higher than what has been reported for the vast majority of self-healing materials in literature.

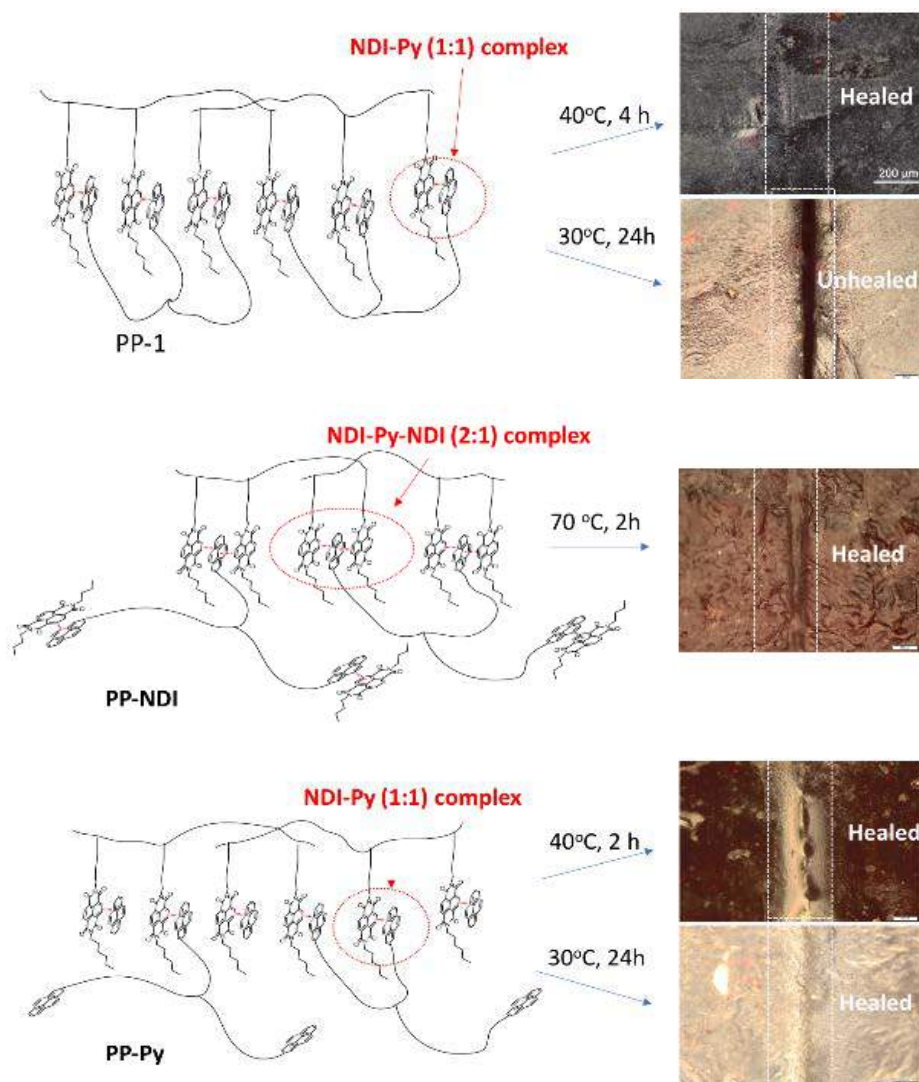


Figure II-592. Our novel polymeric materials form free-standing, self-healing films when mixed together in a 1:1 molar ratio of NDI to Py units. The self-healing temperature of these films can be adjusted over a wide range by doping small molecule NDI or Py compounds into the film, forcing formation of either 1:1 or 2:1 NDI:Py complexes, which have vastly different binding energies. These small molecules can also be used to “passivate” binding sites, adjusting the crosslinking density.

Finally, we tested the ability of the PP-1 polymer composite to transport Li^+ ions by doping films with LiTFSI in a 20:1 [ethyleneoxy]: $[\text{Li}^+]$ ratio during fabrication. Ionic conductivities of the films were measured between 10-55°C by A/C impedance testing between stainless steel plates followed by fitting the data to a simple Debye impedance model with non-ideal interfacial capacitance. We found that the LiTFSI-doped composite had a conductivity in excess of 10^{-6} S/cm at 50°C, which is in a similar range to other solid polymer electrolytes based on PEG derivatives.

Ionomer Gels

We designed and optimized a synthetic procedure for producing crosslinked gel electrolytes containing ionic liquid, which can be thermally cured using a radical initiator. In addition to using commercially available PEG dimethacrylate (PEGDMA), with an average molecular weight of 750Da, as a starting material, we also chemically synthesized PEGDMA with a higher molecular weight of ~3500Da, as well as an ionic-liquid-like monomer containing a pyrrolidinium cation and TFSI⁻ counterion. We have become interested in “solvate”

ionic liquids in particular as a liquid base for our gels, given their high Li^+ transference numbers (~ 0.5) relative to ternary pyrrolidinium $^+:\text{Li}^+:\text{TFSI}^-$ ionic liquids, as well as their facile synthesis and ability to be diluted with organic solvents for higher conductivity. Using our procedure, we have successfully produced solvate ionogels of varying composition and measured their ionic conductivities using the same A/C impedance method as detail above. Table II-27 below summarizes a few of our initial formulations, and the conductivities calculated for each. All of these ionogels display ionic conductivities in excess of 10^{-4} S/cm at 23°C , and we expect to demonstrate formulations with conductivities $>10^{-3}$ S/cm very soon.

Table II-27: Initial Solvate Ionogel Formulations and Their Conductivities at 23°C

	Composition (vol%)				Conductivity ($\times 10^{-4}$ S/cm)
	PEGDMA (750Da)	IL-like Monomer	Solvate IL	Ether Solvent Diluent	
Formula 1	20%	0%	80%	+0%	2.79
Formula 2	20%	0%	80%	+50%	9.23
Formula 3	10%	20%	70%	+40%	3.70

Chemical Modification of Mesoporous Carbons for S/C Composite Cathodes

We have successfully synthesized S/C composites of varying sulfur loading from mesoporous carbons of varying average pore size. Infiltration was confirmed *via* disappearance of crystalline sulfur peaks in XRD data on the composite surface, as well as a decrease in pore volume and average pore size as determined by BET analysis.

We have explored chemical surface modification of these carbon starting materials as an additional route to cathode performance improvement. Our procedure is based on well-studied diazonium chemistry, which attaches phenyl rings bearing customizable functional groups to unsaturated carbon surfaces. Functionalization was confirmed by pore shrinkage (determined by BET, as well as the appearance of nitrogen- or sulfur-associated peaks in XPS analysis and weight loss during TGA). The extent of functionalization, measured by % weight loss during TGA as compared to control samples, was easily varied by adjusting reaction conditions. We used this procedure to attach a variety of chemical moieties to carbon surfaces, including primary amines, tertiary amines, and sulfides. In particular, we are interested in sulfide-based surface modifiers, as reversible covalent bonding between sulfide groups is well-known and has potential for containment of lithium polysulfides within the cathode pore structure. We have done detailed study on S/C cathodes modified with phenylthiol functional groups using by analyzing cell cycling data. Figure II-593 below presents key data from this investigation.

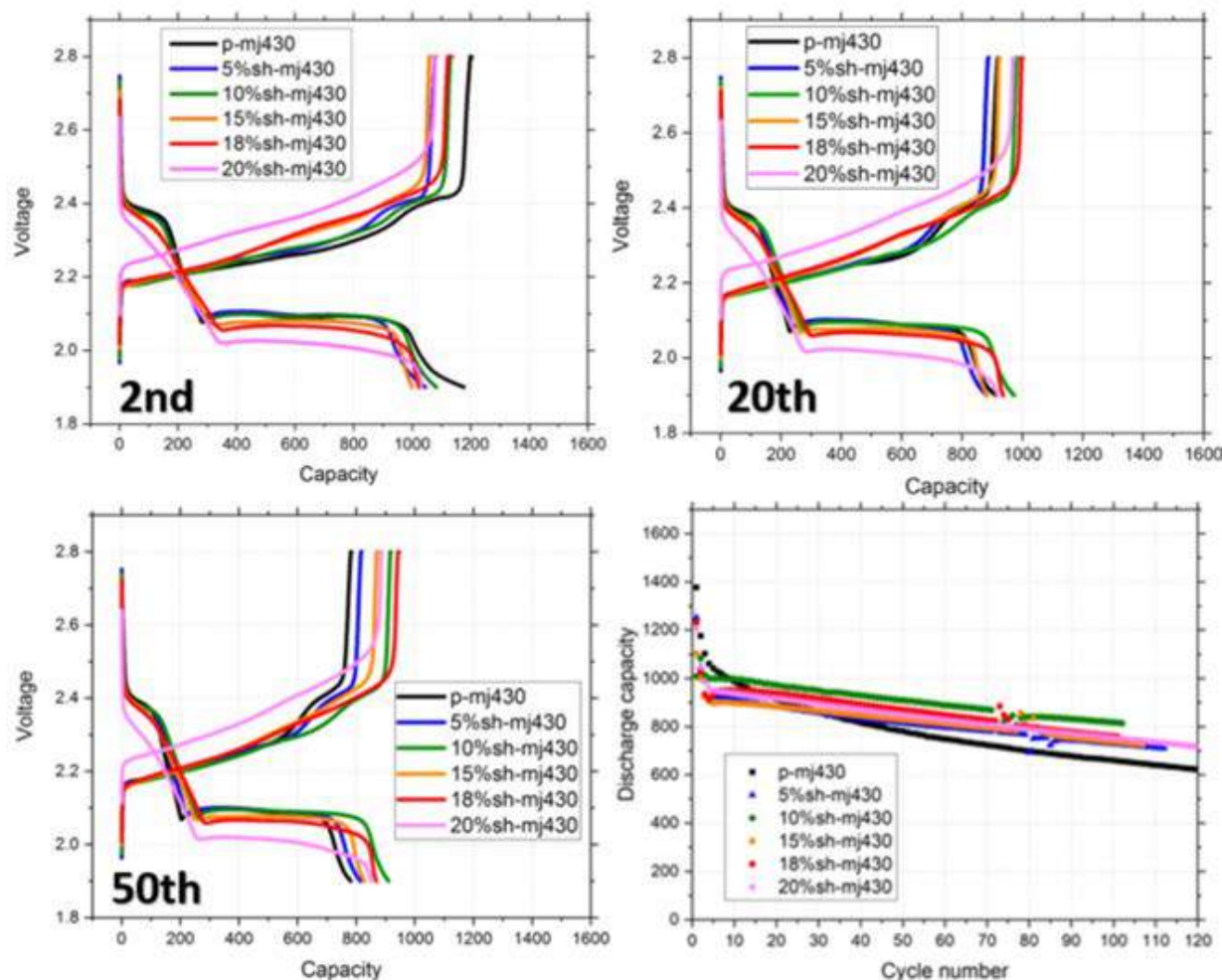


Figure II-593. Voltage curves of the 2nd, 20th, and 50th cycle (C/10 rate) of S/C cathodes, in which the mesoporous carbons contain 0-20%wt phenylthiol surface modifier, as well as capacity data over 100 cycles for each cathode. Notably, 10%wt modifier significantly improves capacity and retention while introducing minimal additional overpotential.

We note several important trends. Firstly, the introduction of phenylthiol modifiers progressively changes the voltage curves in predictable ways from the unmodified control (p-mj430). The initial discharge plateaus at ~2.4 V become increasingly sloped, a possible indicator of reaction mechanism shifting from a two-phase (solid-liquid) reaction to a single-phase (solid-solid) reaction. Lower discharge plateaus are shorter during initial cycling, but quickly become longer than the control, which decays rapidly. Similarly, initial charge capacities are slightly lower but, by later cycles, have surpassed that of the control. The control charge curve contains a large, gradual initial slope followed by a small plateau at around ~2.4 V; however, in modified samples this plateau gradually vanishes, with modifications above 10% barely having any discernable plateaus. In general, modification levels >10%wt result in very noticeable increases in overpotential during both charge and discharge, while overpotential increases in <10%wt samples are small. All modified samples display better capacity retention over 100 cycles than the control, but 10%wt possesses the best overall capacity.

There are a few potential conclusions to draw from this data. First, the gradual disappearance of two-phase voltage behavior in highly-modified samples may point to successful covalent tethering of polysulfide species to modified surfaces, forcing reaction to occur largely through an all-solid-state mechanism. This shift in reaction mechanism, however, may also be responsible for the increased overpotential, as both Li⁺ diffusion and polysulfide rearrangement resulting from charge transfer may be more difficult when not mediated by a liquid

solvent. Ideally, we would prefer to sequester a certain amount of polysulfide in surface-bound states to prevent its escape from the cathode, but leave enough polysulfide free in the interior liquid phase to afford rapid reaction kinetics and Li^+ diffusion, a compromise that 10%wt modifier appears to achieve. However, these hypotheses are impossible to confirm using only cell data. We are currently doing detailed XPS and NMR studies on modified cathodes in order to obtain direct evidence of reaction between modified carbon surfaces and lithium polysulfides. We are also investigating improved modifier structures which may afford even greater performance enhancements.

Conclusions

Self-Healing Materials

- dbNDI and Py form non-covalent π - π complexes in either 1:1 or 2:1 molar ratios, respectively, depending on the concentration of dbNDI available relative to Py. The 2:1 complex is roughly twice as energetically favorable (-16.49 kJ/mol vs. -8.19 kJ/mol).
- We have designed polymers containing both NDI (PENDI-C6) and Py (triPy) moieties, which interact *via* the aforementioned π - π complexation to form non-covalently crosslinked films.
- These films are capable of self-healing following breakage, and the self-healing temperature can be tuned between 30-70°C by introducing small molecule dbNDI or Py groups to adjust both the type of complex formed and the density of crosslinks. This “doping” with small molecules can also adjust tensile modulus of the films between 69-219MPa, which is significantly higher than most previously-reported self-healing materials.

Ionomer Gels

- We have successfully developed a gel fabrication procedure and used it produce a variety of solvate ionomer gels of different composition.
- All of the gel formulations tested thus far have displayed ionic conductivities $>10^{-4}$ S/cm at 23°C, and we expect to demonstrate conductivities $>10^{-3}$ S/cm in the near future.

Chemical Modification of Mesoporous Carbons for S/C Composite Cathodes

- We have developed a procedure based on diazonium chemistry to covalently attach customizable functional groups to the surface of mesoporous carbons, and created S/C composites from both modified and unmodified samples.
- S/C cathodes based on phenylthiol-modified carbons display improved capacity and retention compared to unmodified samples. Voltage profiles exhibit significant changes upon modification, which may indicate covalent tethering of polysulfides to the carbon surface.

Key Publications

1. Qin, J., Hubble, D., Lin, F., Yang, J., Jen, A. K.-Y., “Tunable self-healing ability in a rigid, ion-conductive supramolecular polymer.” (in preparation)

II.I.13 Self-Forming Thin Interphases and Electrodes Enabling 3-D Structures High Energy Density Batteries (Rutgers U)

Glenn G. Amatucci, Principal Investigator

Rutgers, The State University of New Jersey
671 US Highway 1
North Brunswick, NJ 08902
Phone: 848-932-0921
E-mail: gamatucc@rutgers.edu

Tien Duong, Technology Manager

U.S. Department of Energy
Phone: 202-586-7836
E-mail: Tien.Duong@ee.doe.gov

Start Date: October 1, 2016
Total Project Cost: \$1,271,165

End Date: September 30, 2019
DOE share: \$1,077,074

Non-DOE share: \$194,091

Project Introduction

The ultimate goals of this project are to establish a step change in energy density, cost, safety, and high voltage scalability of battery technology compared to the current state of the art secondary battery technologies. This will be accomplished using a secondary battery technology enabled by a novel *in-situ* formed solid-electrolyte battery leading to high energy metal fluoride vs. lithium metal chemistry in a planar battery electrode format. This technology provides many advantages including: 1) enabling the use of lithium metal electrodes via solid-state electrolytes, 2) eliminating Li metal in fabrication and handling of cells, 3) providing the highest practical energy density electrochemical system, and 4) enabling a unique pathway to high voltage systems.

Objectives

The project objective is to develop and implement a novel *in-situ* formed lithium-metal-based metal fluoride battery that will enable packaged 10mAh batteries of energy density > 1000 Wh/L and specific energy > 400 Wh/kg at 12 V.

Approach

The *in-situ* self-formed battery is based on the formation by simple polarization of a Li metal negative electrode and a positive metal fluoride positive electrode from a LiF-based bi-ion conducting glass between a positive and a negative reactive current collector. As depicted in Figure II-594, under polarization the LiF-based glass decomposes with the release of the F⁻ and Li⁺ ions to react with the positive and the negative reactive current collectors respectively, thereby forming the active electrodes in-situ.

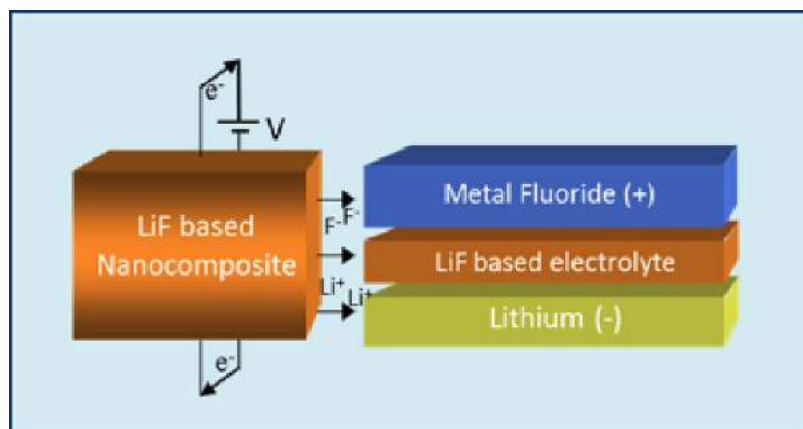


Figure II-594. Diagram illustrates the *in-situ* formation of a metal fluoride positive electrode and a lithium metal negative electrode from the electrolytic decomposition of a Li-based bi-ion glass under polarization

As such, the project is divided into two main tasks that focus on the advance of the self-forming chemistry concurrent to the cell design and fabrication as depicted in Figure II-595. The self-forming chemistry task is comprised of three subtasks encompassing the negative and positive reactive current collectors and the bi-ion glass conductor. Whereas the cell design and fabrication targets the development and integration of the bipolar configuration to achieve the 12 V single cell goal.

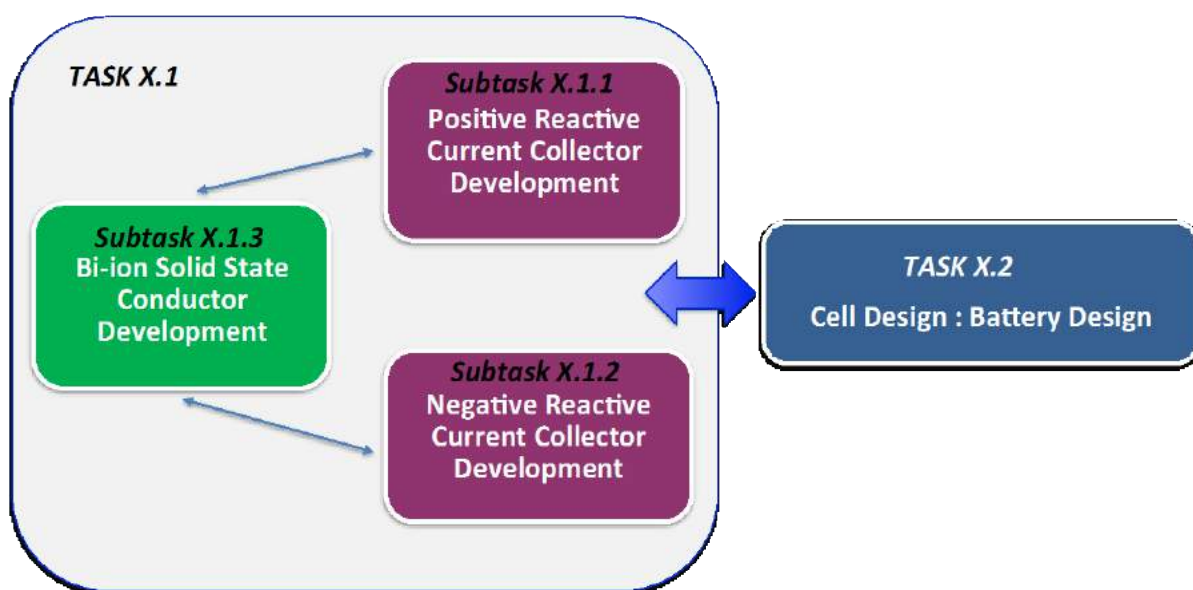


Figure II-595. Program approach breakdown

Results

Bi-ion conductor development

The bi-ion conductor is the heart of the electrochemical system as it enables the first formation cycle and the in-situ formation of the metal fluoride at the positive and lithium metal at the negative. Once the cell is formed, the majority of the subsequent charge/discharge reactions follow a mechanism similar to a lithium battery based on a MF_3 metal fluoride conversion into $3 \text{LiF} + \text{M}$ with lithium plating at the negative electrode. The bi-ion conductor will be essentially acting as a solid-state electrolyte development of bi-ion conductor. Therefore, this essential component must have the ability to electrolytically decompose at the positive electrode and release F^- anions to diffuse within the reactive positive current collector. This cannot be restricted to the simple surface decomposition of the bi-ion conductor at the interface as this is not nearly a sufficient amount of F^- to induce the fluorination reaction. Bulk diffusion of F^- and replenishment at the interface is required. The bi-ion conductor also needs to have the capability to conduct Li^+ throughout its bulk to enable continuous Li deposition at the negative electrode. As such, the main goal for FY17 was to establish bi-ion solid-state conducting glass compositions with ionic conductivity $> 1 \times 10^{-4} \text{ S/cm}$ prior to in-situ formation. In order to accomplish this goal, a systematic experimental process was set in place for the fabrication and characterization of bi-ion glass conductors of different composition in order to rapidly determine if they would be good candidates for the *in-situ* self-formed solid-state batteries. After deposition, the compositions were characterized by 1) electrochemical impedance spectroscopy (EIS) to extract the ionic conductivity, 2) a combination of stepped and linear sweep voltammetry to investigate the electrochemical stability, and 3) x-ray diffraction (XRD) to investigate nano-crystallinity. More than 20 compositions and 80 cells were deposited and tested with some of the resulting EIS and direct current conductivity measurements presented in Figure II-596. Best results were obtained with dopants which were identified to increase conductivity from $1 \times 10^{-8} \text{ S/cm}$ to $1 \times 10^{-5} \text{ S/cm}$ pre-formation and $> 1 \times 10^{-4} \text{ S/cm}$ at operation voltage were obtained. In addition, all except one composition exhibited electrochemical stability to breakdown in excess of 6 V with no increase of interfacial impedance.

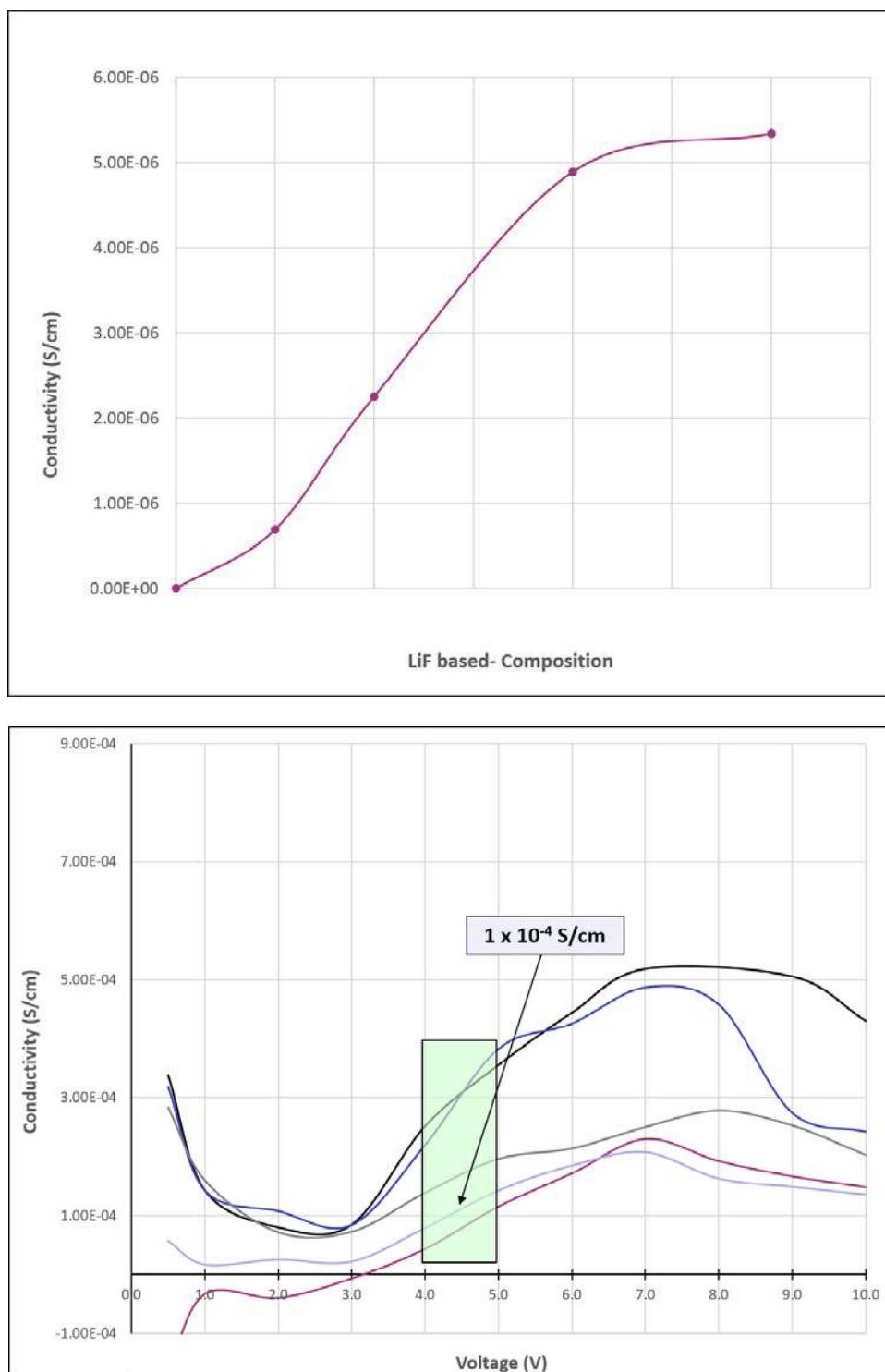


Figure II-596. Electrochemical impedance spectroscopy as a function of composition (left) and in-situ direct current conductivity as a function of voltage for several compositions (right)

Positive and negative reactive current collector development & design and fabrication: electrodes and cells.

Full solid-state cells were first fabricated in the second quarter using the newly developed bi-ion conductors with conductivities $> 1 \times 10^{-4}$ S/cm at operation voltage, baseline current collector compositions identified in the

first quarter, and baseline cell-stack designs established based on calculations and prior work. The viability of the *in-situ* formation of the entire electrochemical cell was demonstrated with limited cycling at output voltages of approximately 2 V as shown in Figure II-597, and low energy density represented by Generation 1 in the bar graph of Figure II-598. Transport is a critical aspect of this program and as such all components' chemistries, designs and structures have to be developed in order to maximize it. Our approach consisted of using planar configurations. The electrodes configurations impact diffusion distance, energy density, current density, and effective electron transport through the current collectors. Therefore, the focus of the third quarter was to improve the electrode architecture and combine these upgraded configurations with the improved bi-ion conduction composition described above. All cells were all fabricated with a newly implemented mask-less scalable patterning process described in the next section. Figure II-598 depicts the consistent progression in energy density that we have been able to achieve with time following this approach. The Generation 2 architecture brought forth an improvement of a factor 4 with respect to the initial Generation 1 design. Greater advance in energy density was obtained with the upgrade of the bi-ion conductor composition using the initial cell configuration leading to a factor 10 improvement compared to Generation 1 with the baseline bi-ion conductor. Finally, combining both approaches further increased the stack energy further by doubling the energy density obtained with the new bi-ion conductor alone (Generation 2 Bi-ion Conductor). Upon formation at 3.5 V, 76% of the 500 Wh/L go-no go goal was achieved, while a 4.0 V formation brought us closer with 96% of the 500 Wh/L goal. Additional architectural upgrades (Generation 3 and 4) demonstrated an effective path to effectively achieve and even surpass our go-no go goal with up to 570 Wh/L. The corresponding utilization of the reactive positive current collector also consistently increased from 16-20% for Generation 2 Bi-ion conductor to 24% for the Generation 2 Bi-ion conductor + Generation 2 architecture combination. The actual utilization is higher since the calculation assumed dense films, while experimental cells contain porosity.

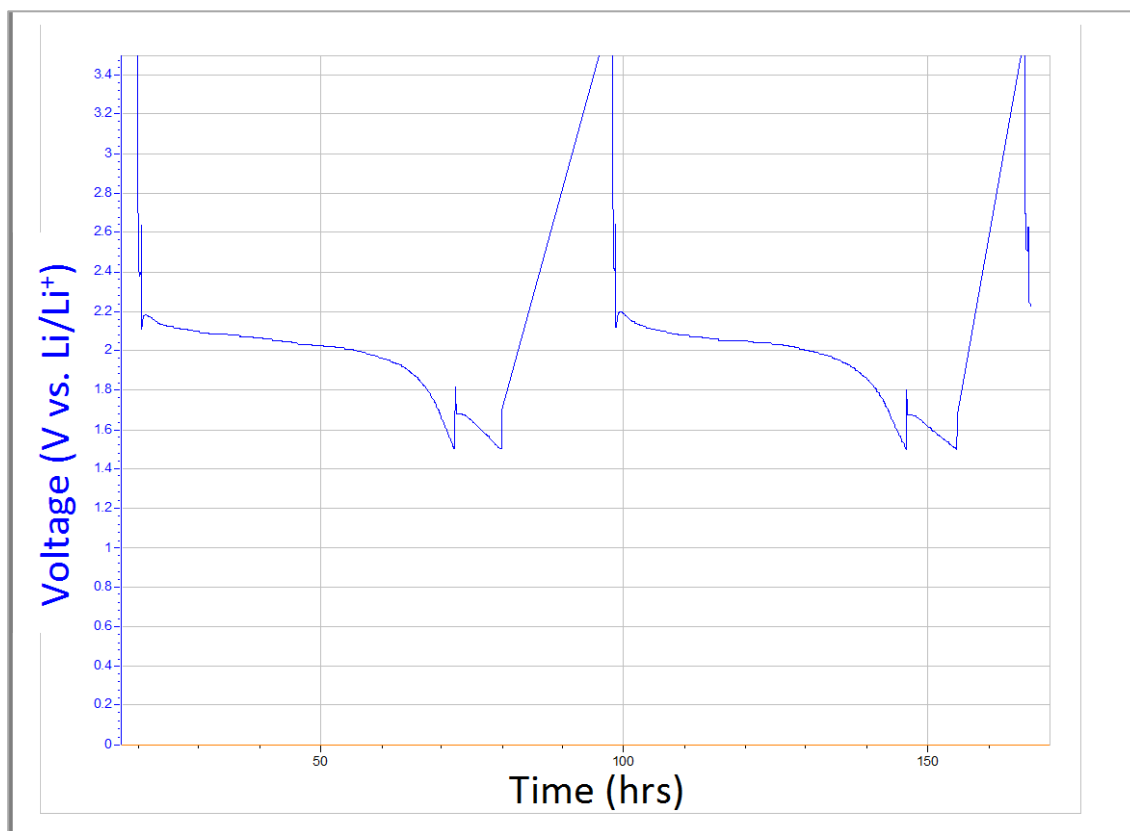


Figure II-597. Voltage profile of an *in-situ* self-formed battery fabricated using newly implemented maskless scalable patterning technique

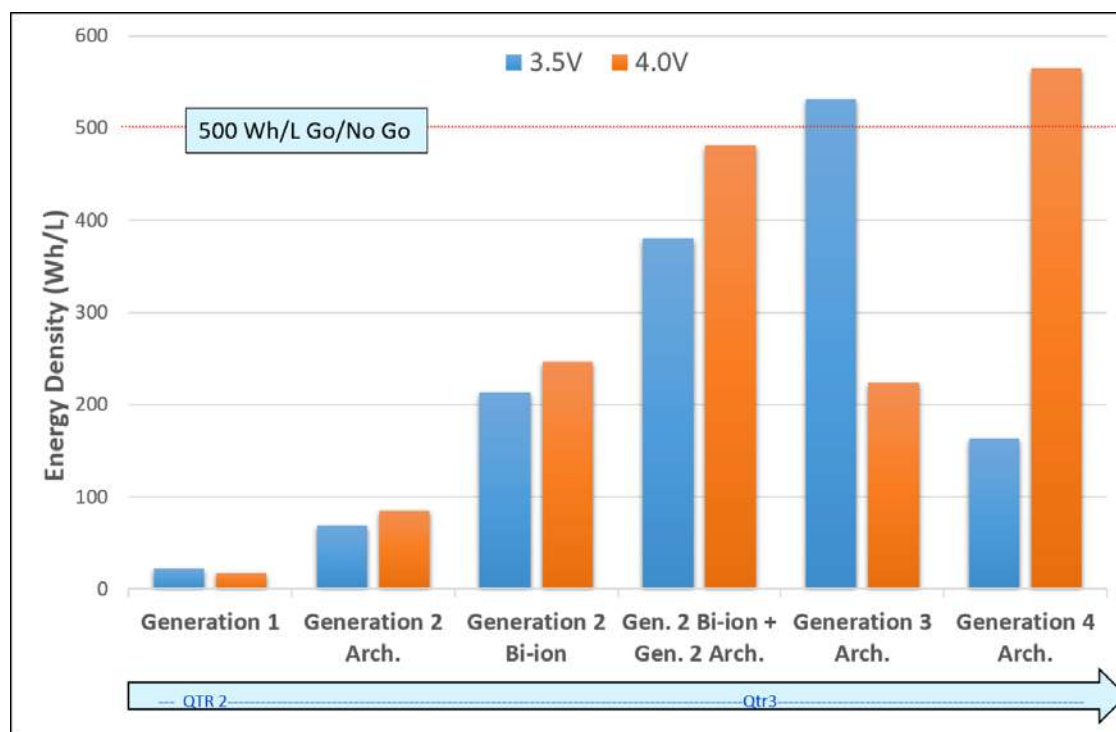


Figure II-598. Energy density in the first discharge at slow rate plotted upon formation at 3.5 and 4.0 V for various architecture combined with new bi-ion conductor chemistry. Labels indicate approach that gained the generation improvement.

Maskless scalable patterning implementation

In order to develop a feasible and economically viable pathway to manufactures using vapor deposition, masks should be eliminated from the process flow. In this spirit, a maskless scalable patterning technique that offers tremendous benefits towards a practical pathway to high throughput, low material loss fabrication of complex architectures was implemented. In addition to the ulterior benefits, this new technique more immediately enables time and cost saving at the program level. This was a significant leap forward as we achieved the implementation of the maskless process one year ahead of time. Moving to the new maskless approach helped us to achieve the significant boost in energy density as described as we moved from generation 1 to generation 2. All other fabrications pathways were eliminated to solely pursue the maskless scalable patterning technique throughout the program.

Hybridization

In the fourth quarter, we shifted our focus toward improving rate capability. Consequently, architecture and hybridization of transport pathways were investigated in parallel. Each approach contributed in different ways to the advancement of our full cell performance. While further changes to the architecture did not significantly contribute to a steep change in rate capability, overall higher energy and utilization were realized. In contrast, hybridization resulted in greater than an order of magnitude increase in our discharge current densities and enabled us to achieve the C/10 rate capability of our year-end go-no go goal. Figure II-599 reveals the cell in-situ formation is followed by a full discharge at C/2 rate. In short, we have demonstrated a path to achieve over an order of magnitude improvement in current density leading to initial results achieving > C/10 discharge rates.

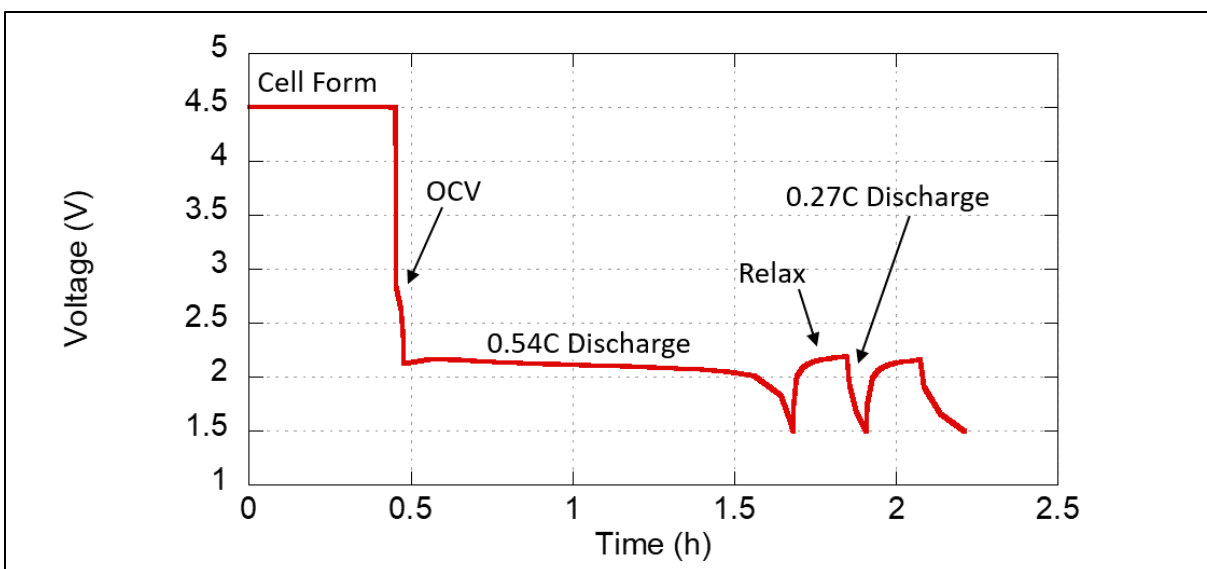


Figure II-599. Voltage profile of a cell utilizing hybridization of the transport pathways showing the *in-situ* formation and first discharge

Conclusions

Consistent progress has been realized during FY17 through advancements in chemistry, cell architecture and hybridization of transport pathways. The main key finding to date can be summarized as follow:

- Maskless scalable patterning technique was successfully implemented to fabricate solid-state full-cells.
- Self-formed cells' energy density increased from 5, to 70 to 120% of the year-end go-no goal 500 Wh/L in the 2nd, 3rd, and 4th quarter, respectively to achieve 570 Wh/L.
- Self-formed cells' positive reactive collector utilization increased from approximately 1, to 14, to 24% in the 2nd, 3rd, and 4th quarter, respectively.
- Bi-ion solid-state conducting glass compositions with $> 1 \times 10^{-4}$ S/cm conductivity after formation were fabricated and successfully integrated in full solid-state cells.
- Hybridization of transport pathways enabled improvement of current density by one order of magnitude leading to initial results achieving $> C/10$ discharge rates.

II.J Beyond Li-ion R&D: Lithium-Air Batteries

II.J.1 Rechargeable Lithium-Air Batteries (PNNL)

Ji-Guang Zhang, Principal Investigator

Pacific Northwest National Laboratory
 902 Battelle Boulevard
 Richland, WA 99354
 Phone: 509-372-6515; Fax: 509-375-2186
 E-mail: jiguang.zhang@pnnl.gov

Wu Xu, Co-Principal Investigator

Pacific Northwest National Laboratory
 902 Battelle Boulevard
 Richland, WA 99354
 Phone: 509-375-6934; Fax: 509-375-2186
 E-mail: wu.xu@pnnl.gov

Tien Duong, Technology Manager

U.S. Department of Energy
 Phone: 202-586-7836
 E-mail: Tien.Duong@ee.doe.gov

Start Date: October 1, 2015
 Total Project Cost: \$600,000

End Date: September 30, 2018
 DOE share: \$600,000

Non-DOE share: \$0

Project Introduction

It is well known that the state of the art lithium (Li)-ion batteries is a mutual technology and may reach their practical limit on specific energy ($\sim 300\text{--}350 \text{ Wh kg}^{-1}$) in the near future. Therefore, a worldwide effort has been made to explore new battery chemistries that may far exceed the specific energy of Li-ion batteries. Among the alternative energy storage systems, Li-air batteries have triggered worldwide research interest since the first nonaqueous Li-air battery was unveiled in 1996 due to their extremely high theoretical specific energy density ($\sim 5,200 \text{ Wh kg}^{-1}$ when the weights of Li and O_2 are included). However, before the commercialization of Li-air batteries, considerable challenges still face Li-air batteries and need to be overcome. These challenges include instability of electrolyte, high overpotential, and severe corrosion of Li anodes. These problems cause poor round-trip efficiency and short cycle life in the state of the art Li-air batteries. Thus, efficient strategies for further development of ultrahigh-energy-density Li-air batteries suitable for application in electric vehicles include development of electrolytes that are more stable against superoxide and Li metal anodes, design of alternative catalysts and carbon-based or carbon-free air electrodes, stabilization of Li metal anodes, and exploration of new insights into the mechanisms of oxygen reduction/evolution reactions (ORR/OER) are critical to promote further development of ultrahigh-energy-density Li-air batteries for potential application in electric vehicles.

Objectives

The objective of this project is to develop rechargeable lithium-oxygen (Li-O_2) batteries with long-term cycling stability through in-depth research on more stable electrolytes and highly efficient catalysts for air electrodes, protection of Li metal anodes, and deeper insight into the ORR/OER mechanisms behind the electrochemical performance of Li-O_2 cells.

Approach

The objectives outlined above will be accomplished by developing new concentrated electrolytes, protection for both Li metal anodes and carbon-based air electrodes, highly efficient catalysts produced by in-situ electrochemical pretreatment, and in-depth study of the effect of temperature on discharge behaviors of Li-O₂ batteries. These strategies are greatly expected to significantly improve cycling stability of Li-O₂ batteries and deepen our insight into Li-O₂ battery chemistries.

Results

We have made significant progresses in electrolytes, protection of electrodes (both carbon-based air-electrode and Li anode), efficient catalysts, and underlying mechanisms in Li-O₂ batteries in FY17 as described below.

1. Concentrated electrolytes with optimized salt-solvent coordination for more stable Li-O₂ batteries

Lithium bis(trifluoromethanesulfonyl)imide (LiTFSI)-dimethyl sulfoxide (DMSO) electrolytes were prepared according to the molar ratio of LiTFSI salt to DMSO solvent at 1:3, 1:4, and 1:12; these are denoted as LiTFSI-*n*TFSI, where *n* = 3, 4, or 12, respectively. Figure II-600 shows the electrochemical performance of Li-O₂ cells composed of a carbon nanotube (CNT) air electrode and Li metal anode using the three different salt-concentration electrolytes. The LiTFSI-3DMSO electrolyte leads to the most stable cycling for at least 90 cycles and the voltage profiles are very stable. The three electrolytes (LiTFSI-12DMSO, LiTFSI-4DMSO, and LiTFSI-3DMSO) can be considered to contain the free DMSO solvent, Li⁺-(DMSO)₄ solvate, and the TFSI⁻-Li⁺-(DMSO)₃ complex. According to computational calculations of Gibbs activation energy barriers for C-H bond scission in DMSO, Li⁺-(DMSO)₄, and TFSI⁻-Li⁺-(DMSO)₃ by the attack of O₂^{•-}, electrolytes with salt-solvent coordination (i.e., LiTFSI-4DMSO and LiTFSI-3DMSO) have higher Gibbs activation energy barriers than the free DMSO solvent molecules, indicating improved stability of the electrolyte against the attack of superoxide radical anions. Moreover, the TFSI⁻-Li⁺-(DMSO)₃ complex has an even higher activation energy barrier than the Li⁺-(DMSO)₄ solvate. Therefore, the stability of such a concentrated LiTFSI-3DMSO electrolyte has been greatly improved.

2. In-situ induced protection films formed on both air electrode and Li metal anode of Li-O₂ cells

We have demonstrated a simple one-step in-situ electrochemical pre-charging strategy to simultaneously generate thin protective films on both the CNT air electrode and Li metal anode. These forms can protect both electrodes to significantly suppress the attack of highly reactive reduced oxygen species, as shown in Figure II-601a. The pretreatment of the assembled Li||CNT cells was conducted by charging the cells under argon (Ar) gas from open-circuit voltage (OCV) to 4.3 V at 0.1 mA cm⁻² and then holding the cells at 4.3 V for 0, 5, 10, 15, and 20 min. The number of stable cycles of the Li-O₂ cells with the aforementioned pretreatment (4.3 V/0 min, 4.3 V/5 min, 4.3 V/10 min, 4.3 V/15 min, and 4.3 V/20 min) and without pretreatment are 62, 63, 110, 95, 72, and 43, respectively (Figure II-601b). This demonstrated that the simple pretreatment did enhance the cycling stability of the Li-O₂ cells even without mediators in the electrolyte or catalysts on the air electrode. After cycling, the scanning electron microscope (SEM) images of the cycled CNT air electrode without pretreatment show some large breakage at the air-electrode surface (Figure II-601c) and thick side-reaction products from decomposition of CNTs and electrolyte (Figure II-601c, Figure II-601d). These exposed bare CNTs became larger and thicker (Figure II-601d), due to serious side reactions of reactive reduced oxygen species with electrolyte components and the CNT electrode. The thickness and the coverage of some coated layers on the CNT electrode pretreated at 4.3 V/10 min (Figure II-601e, Figure II-601f) are significantly less. The cycled Li metal anode without pre-charging treatment exhibits severe corrosion of the vast majority of bulk Li metal (Figure II-601g) and a large amount of corrosion products are loosely packed on the Li metal surface (Figure II-601h). However, the cycled Li metal anode with pretreatment retains a thick bulk Li metal layer without corrosion (Figure II-601i), and the surface layer is relatively flat and compact with only a few cracks (Figure II-601j). This shows that the optimal pre-charging treatment could significantly protect both the CNT electrode and Li metal anode during long-term cycling, thus leading to greatly enhanced cycling stability of Li-O₂ cells.

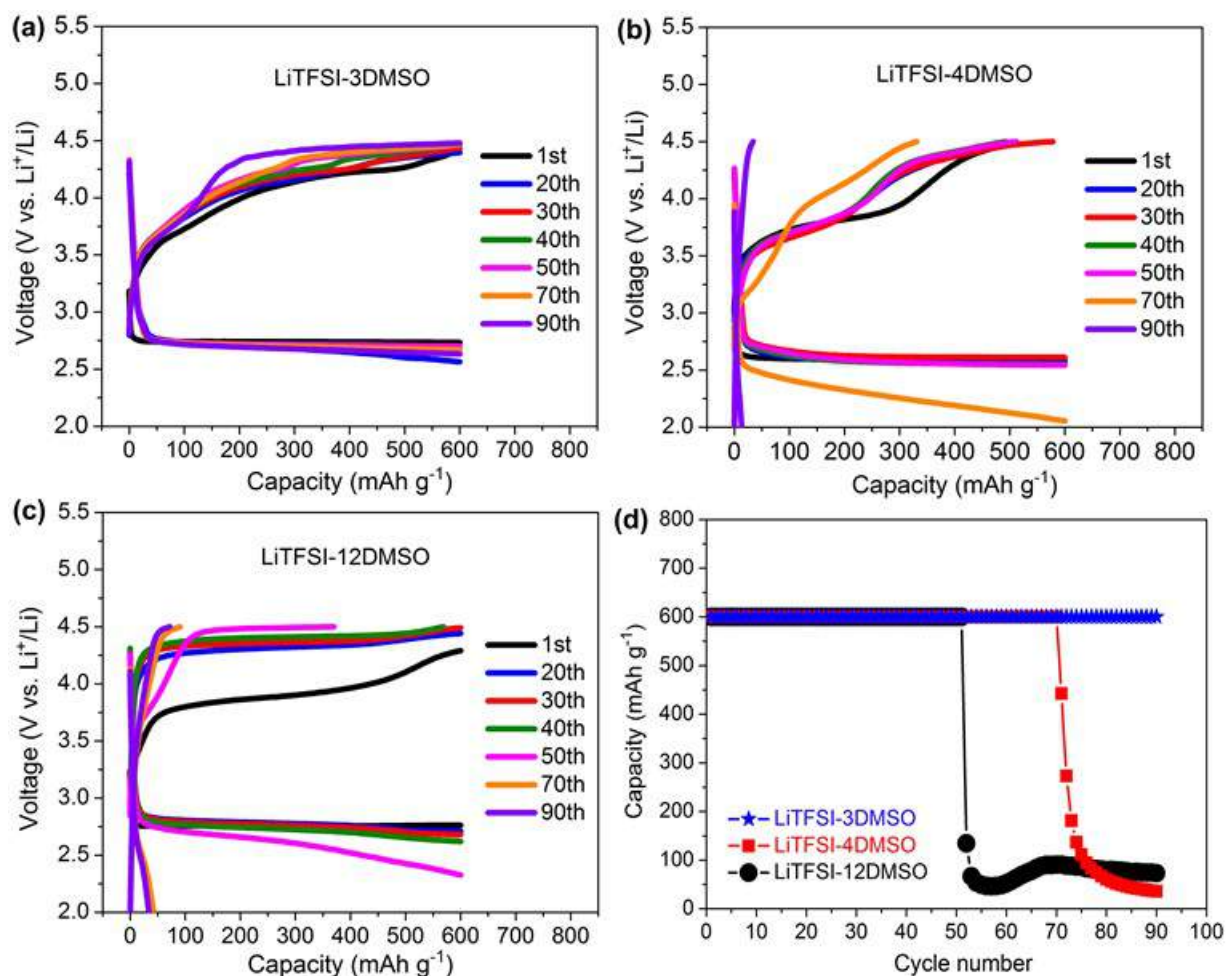


Figure II-600. Electrochemical performance of Li-O₂ batteries with three LiTFSI-DMSO electrolytes cycled under capacity-limited protocol (600 mAh g⁻¹) in the voltage range of 2.0 to 4.5 V at 0.1 mA cm⁻². (a-c) Voltage profiles for LiTFSI-3DMSO electrolyte (a), LiTFSI-4DMSO electrolyte (b), and LiTFSI-12DMSO electrolyte (c). (d) The corresponding cycling stability of the three electrolytes.

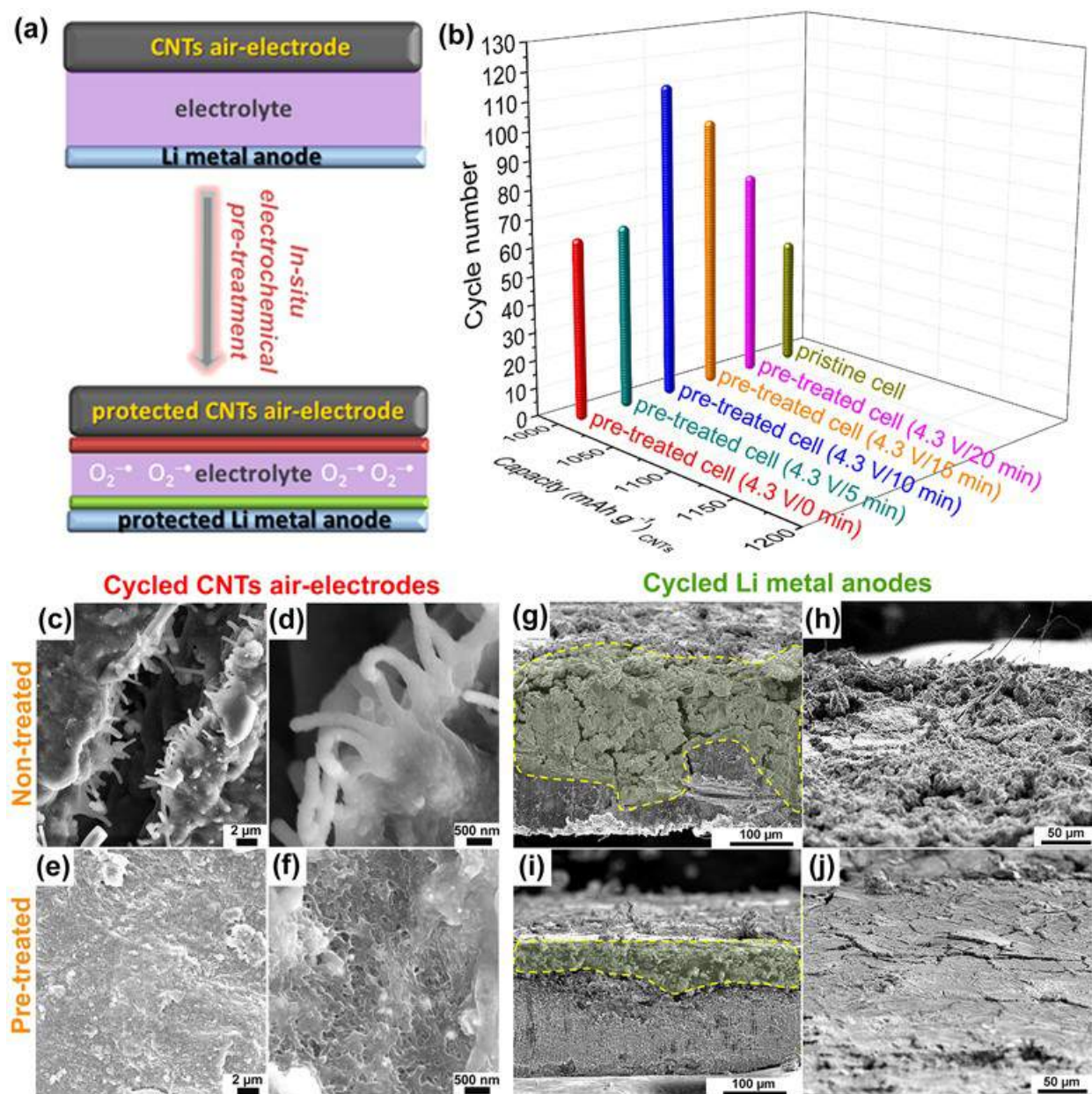


Figure II-601. (a) Schematic of the operation principle of prior protection for CNT air electrode and Li metal anode after in-situ electrochemical process. (b) Stable cycling life of Li-O₂ cells without and with pretreatment cycled at 0.1 mA cm⁻². (c-f) SEM surface-view images of the CNT air electrode without pretreatment after 70 cycles (c, d), and the CNT air electrode with 4.3 V/10 min pre-charging treatment after 110 cycles (e, f). (g-j) SEM images of corresponding cycled, untreated Li metal anode (g, h) and pretreated Li metal anode (i, j), where (g, i) are cross-section views and (h, j) top views.

The variations of cell impedances with cycle time were further investigated for pre-treated and pristine Li-O₂ cells, and the corresponding electrochemical impedance spectra plots at the charged states are shown in Figure II-602a and Figure II-602b, respectively. The corresponding fitting results of the electrolyte resistance (R_1), the total resistance (R_2) containing the surface film resistance (R_{SEI}) and the charge transfer resistance (R_{ct}) as a function of cycle numbers are also provided in Figure II-602c. It is clearly seen from Figure II-602c that the pre-treated Li-O₂ cell at the initial stage has a smaller R_1 and R_2 than those with the pristine cells. This is because the Li metal anode in the pre-charged cell has already been well protected before O₂ was introduced so the reactions between Li, electrolyte and O₂ are limited. The cell impedances of R_2 decrease from the 1st

cycle to the 20th cycle, which is probably because both CNTs electrode and Li metal anode, either pre-treated or untreated, gradually reach their own well protected condition with the coverage of the electrolyte decomposition products thus give lower cell impedances. After that, the Li-O₂ cell after the optimal pre-treatment only shows slight increase in cell impedance from 20th cycle to 110th cycle, while the cell without pre-treatment shows a rapid increase in cell impedance from 20th cycle to only 70th cycle. This is because the electrochemical pre-charging process generates protective layers on both CNTs electrode surfaces and Li metal anode, which suppress the side reactions of reduced oxygen species attacking both CNTs electrode and Li metal anode, as show in Figure II-601a.

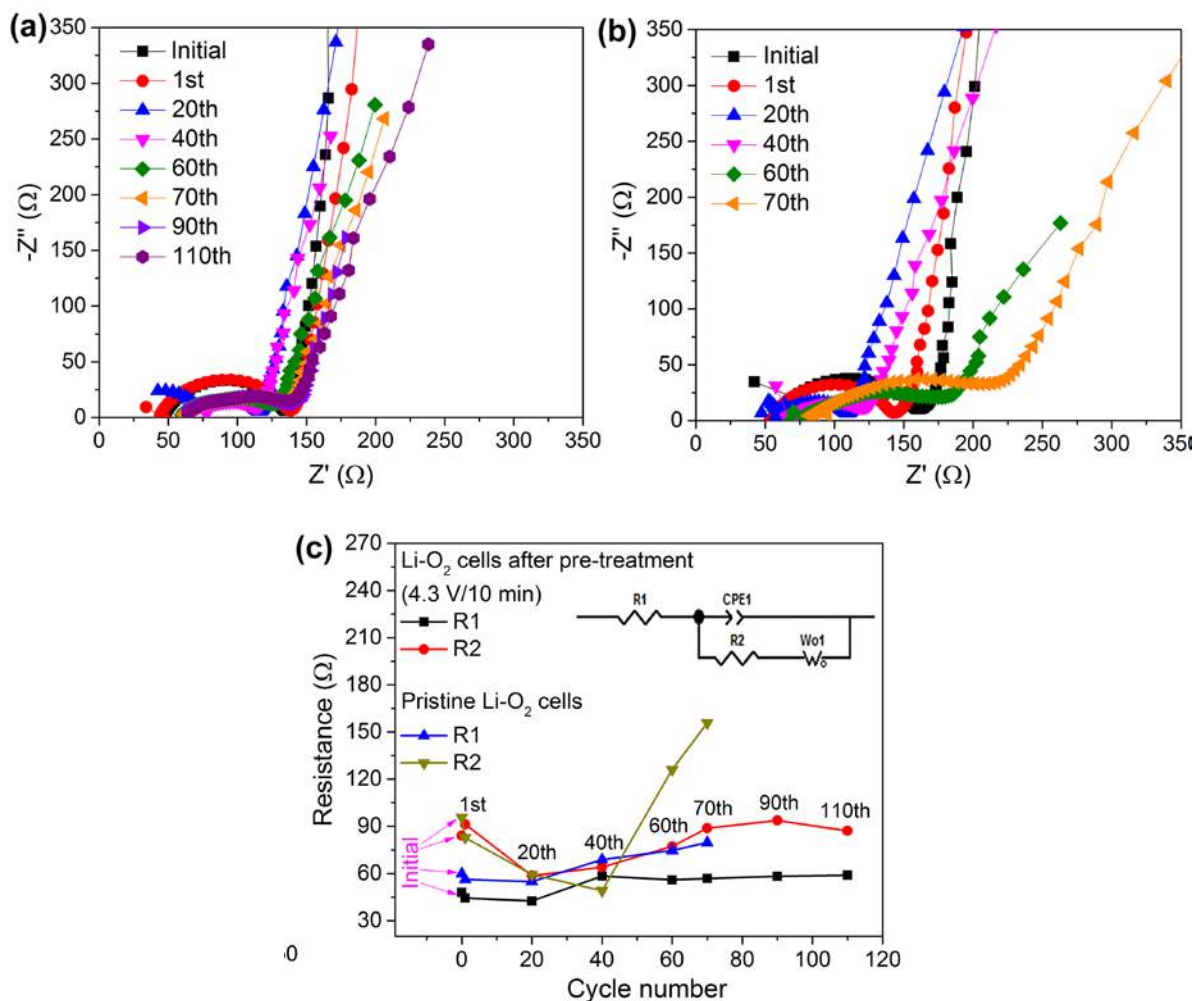


Figure II-602. The a.c.-impedance spectra of the Li-O₂ cells after pre-treatment at 4.3 V/10 min during 110 cycles (a), and pristine Li-O₂ cells during 70 cycles (b). (c) Evolution of fitted resistance values of the above Li-O₂ cells after pre-treatment at 4.3 V/10 min and pristine cells. Inset: The equivalent circuit used to fit the impedance spectra.

To further improve cycling efficiency and life of Li-O₂ cells, a one-step in-situ electrochemical pretreatment strategy on the optimization of RuO₂/CNTs catalysts for Li-O₂ batteries. Figure II-603 shows that the cycle life of Li-O₂ cells with the optimized RuO₂/CNT air electrode and Li metal can reach 190 cycles at 0.1 mA cm⁻² under a capacity protocol of 1000 mAh g⁻¹, while the cycling life of the pristine cells can survive only 51 cycles, which is very limited. Considering the extremely stable pretreated RuO₂/CNTs and severe corrosion of the Li metal anode, we paired the above cycled pretreated air electrode with a new Li metal anode to get a new cell, which was cycled at 0.2 mA cm⁻². The new Li-O₂ cells composed of cycled air electrode and new Li anode can be further cycled for at least 125 more cycles. This indicates that the novel in-situ electrochemical

approach developed in this work greatly enhanced the cycling stability of Li-O₂ cells. More work is currently under way.

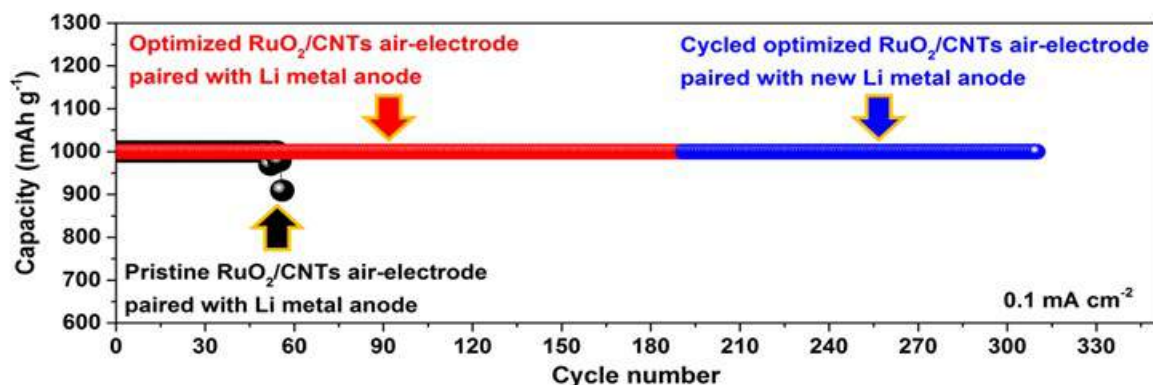


Figure II-603. Cycling performances of Li-O₂ cells with optimized in-situ pretreated RuO₂/CNT air electrode (red line) and pristine RuO₂/CNT air electrode (black line), cycled at 0.1 mA cm⁻² in 1 M LiTf-Tetraglyme electrolyte. Blue line is the cycle life of the freshly assembled Li-O₂ cell with the cycled pretreated air-electrode after 190 cycles and new Li metal anode, under the same conditions.

3. In-depth Understanding on the temperature dependence of oxygen reduction mechanism in nonaqueous Li-O₂ batteries

An in-depth investigation on the temperature dependence of the chemistry and electrochemistry that govern the operation of the Li-O₂ cells has been made. The cells composed of a Li metal anode, an air electrode (consisting of CNTs deposited on carbon paper), a glass-fiber-based separator, and 1,2-dimethoxyethane-based electrolyte. Figure 5a shows that the discharge capacity of the cells initially decreases slowly from 7,492 mAh g⁻¹ at 40°C to 2,930 mAh g⁻¹ at 0°C, then increases sharply to an extraordinarily high capacity of 17,716 mAh g⁻¹ at -20°C. A clear minimum capacity occurred at a temperature of ~0°C. The temperature dependence of the lifetime of superoxide, the electrochemical kinetics, and the discharge capacities of Li-O₂ batteries in the temperature range from -20°C to 40°C are summarized in Figure 5b. The lifetime of O₂^{-•} and the discharge capacities are from experimental results, and electrochemical kinetics data are based on formula calculation. As the temperature increased from -20°C to 40°C, the lifetime of the O₂^{-•} obtained from both nuclear magnetic resonance (NMR) and electron paramagnetic resonance (EPR) analysis decreases while the electrochemical kinetics increases, and an obvious temperature turning point at 0°C can be observed in Figure 5a. More interestingly, two sharp changes of lifetime of O₂^{-•} and electrochemical kinetics that occur in the temperature ranges of -20°C~0°C and 0°C~40°C, respectively, are coincident with the change trend of discharge capacities. It is worth noting that the dominant mechanism for the ORR process in the Li-O₂ cell changes at ~0°C. Briefly, at low temperatures, the lifetime of O₂^{-•} plays a dominant role, so the discharge capacity is quite high even though the electrochemical kinetics is very slow. At sub-ambient temperatures from 0 to 10°C, both the lifetime of O₂^{-•} and the electrochemical kinetics are slow, so the discharge capacity is low. At elevated temperatures (20~40°C), the electrochemical kinetics plays a dominant role, and thus the discharge capacity increases.

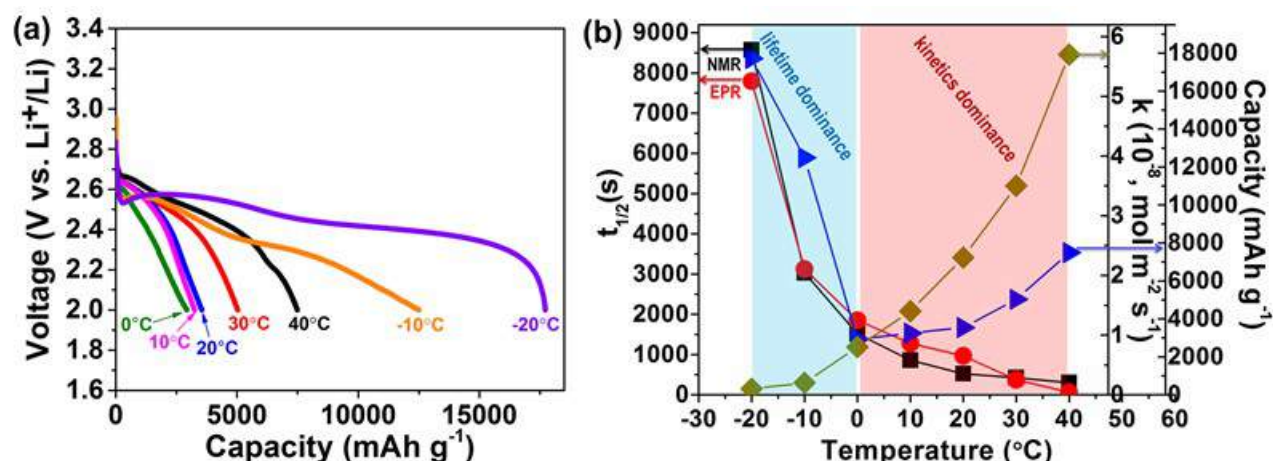


Figure II-604. (a) Discharge curves of Li-O₂ coin cells composed of CNT air electrodes at a current density of 0.1 mA cm⁻² at various temperatures. (b) Temperature dependence of the experimental lifetime of superoxide from NMR and EPR, the calculated electrochemical kinetics, and the discharge capacities at different temperatures.

Conclusions

- The highly concentrated LiTFSI-3DMSO electrolyte, in which only TFSI⁻-Li⁺-(DMSO)₃ exists but no Li⁺-(DMSO)₄ solvates or free DMSO solvent molecules, has been identified as an optimally stable DMSO-based electrolyte against the attack of reduced oxygen species to the Li metal anode.
- A facile in-situ electrochemical pre-charging method has been developed to simultaneously produce ultrathin protective films on both CNT air electrodes and Li metal anodes. Those protective films can significantly suppress and mitigate the well-known oxidation of CNT air electrodes by reduced oxygen species and severe corrosion of Li metal anode upon cycling; thus, the cycling life of pretreated Li-O₂ cells can be extended even to 110 cycles without requiring efficient catalysts or redox mediators.
- Li-O₂ cells based on the pretreated RuO₂/CNTs air electrode demonstrated superior cycling stability due to the extremely high stability and catalytic capability of the ultrafine RuO₂ catalyst-decorated air electrodes. Next, a more appropriate stable anode will be explored to pair with the RuO₂/CNT air electrode and realize high energy, stable Li-O₂ batteries.
- The lifetime of superoxide/LiO₂ and the electrochemical kinetics are two major factors determining the temperature dependence of ORR. The lifetime of superoxide and the solution pathway play a dominant role in the battery capacity in the temperature range of -20°C to 0°C, but the electrochemical kinetics of oxygen reduction and the surface pathway dominate the discharge behavior between 0°C and 40°C. The in-depth understanding of the temperature effect on the discharge mechanisms of Li-O₂ batteries will enable more rational design of high energy Li-O₂ batteries and other metal-air batteries.

Key Publications

1. B. Liu, W. Xu, J.-G. Zhang, Invited book chapter entitled, "Stability of Li metal anode in Li-air batteries", *Wiley Publishing Group*, **2017**, in press.
2. B. Liu, W. Xu, P. Yan, S. T. Kim, M. H. Engelhard, X. Sun, D. Mei, J. Cho, C. Wang, J.-G. Zhang, "Stabilization of Li metal anode in DMSO-based electrolytes via optimization of salt-solvent coordination for Li-O₂ batteries", *Advanced Energy Materials*, **2017**, 7, 1602605. (Featured as Frontispiece image)

3. B. Liu, W. Xu, J. Zheng, P. Yan, E. D. Walter, N. Isern, M. E. Bowden, M. Engelhard, S. T. Kim, J. Read, B. D. Adams, X. Li, J. Cho, C.-M. Wang, J.-G. Zhang, "Temperature dependence of oxygen reduction mechanism in non-aqueous Li-O₂ batteries", *ACS Energy Letters* **2017**, 2, 2525-2530.
(A "most read" article)
4. B. Liu, W. Xu, J. Tao, P. Yan, J. Zheng, M. H. Engelhard, D. Lv, C. Wang, J.-G. Zhang, "Enhanced cyclability of lithium-oxygen batteries with electrodes protected by surface films induced via in-situ electrochemical process", *Advanced Energy Materials* **2017**, DOI:10.1002/aenm.201702340, in press.
5. L. Luo, B. Liu, S. Song, W. Xu, J.-G. Zhang, C. Wang, "Revealing the reaction mechanisms of Li-O₂ batteries using environmental transmission electron microscopy", *Nature Nanotechnology* **2017**, 12, 535.
6. S. Song, W. Xu, R. Cao, L. Luo, M. H. Engelhard, M. E. Bowden, B. Liu, L. Estevez, C.-M. Wang, J.-G. Zhang, "B₄C as a stable non-carbon-based oxygen electrode material for lithium-oxygen batteries", *Nano Energy* **2017**, 33, 195-204.
7. S. Song, W. Xu, J. Zheng, L. Luo, M. H. Engelhard, M. E. Bowden, B. Liu, C.-M. Wang, J.-G. Zhang, "Complete Decomposition of Li₂CO₃ in Li-O₂ batteries using Ir/B₄C as noncarbon-based oxygen electrode", *Nano Letters* **2017**, 17, 1417-1424.
8. W. Xu, B. Liu, J.-G. Zhang, "Preformation of solid electrolyte interphase on electrodes for rechargeable lithium metal batteries", PCT/US17/56081.
9. B. Liu, P. Yan, W. Xu, J. Zheng, Y. He, L. Luo, M. E. Bowden, C. Wang, J.-G. Zhang, "Electrochemically formed ultrafine metal oxide nano-catalysts for high-performance lithium-oxygen batteries", poster presentation at *2016 MRS Fall Meeting & Exhibit*, November 27-December 2, 2016, Boston, Massachusetts.
10. B. Liu, W. Xu, P. Yan, J. Zheng, M. H. Engelhard, C. Wang, J.-G. Zhang, "Enhanced cycling stability of Li-O₂ batteries through in-situ formed electrode interface layers", oral presentation at *2017 MRS Spring Meeting & Exhibit*, April 17-21, 2017, Phoenix, Arizona.
11. B. Liu, W. Xu, P. Yan, S. T. Kim, M. H. Engelhard, X. Sun, D. Mei, J. Cho, C. Wang, J.-G. Zhang, "Stabilization of Li metal in optimized DMSO-based electrolytes for Li-O₂ batteries", oral presentation at *231st ECS meeting*, May 28-June 1, 2017, New Orleans, Louisiana.
12. W. Xu, B. Liu, S. Song, and J.-G. Zhang, "Development of stable rechargeable lithium-oxygen batteries", invited presentation at *254th ACS National Meeting & Exposition*, August 20-24, 2017, Washington, DC.

II.J.2 Efficient Rechargeable Li/O₂ Batteries Utilizing Stable Inorganic Molten Salt Electrolytes (Liox Power)

Vincent Giordani, Principal Investigator

Liox Power, Inc.
129 N Hill Avenue Suite 107
Pasadena, CA 91106
Phone: 626-389-6311
E-mail: vincent@liox.com

Tien Duong, Technology Manager

U.S. Department of Energy
Phone: 202-586-7836
E-mail: Tien.Duong@ee.doe.gov

Start Date: October 1, 2014
Total Project Cost: \$1,425,000

End Date: September 30, 2017
DOE share: \$1,050,000

Non-DOE share: \$375,000

Project Introduction

The rechargeable lithium-oxygen battery has attracted attention due to its large theoretical energy density compared to modern lithium-ion batteries. This large energy density is attributed to the reaction of lithium with molecular oxygen to form lithium peroxide, which grows on the surface of the cathode. While this is a promising chemistry, there are many practical challenges that remain to be solved, such as the decomposition of organic electrolyte in the presence of superoxide anions and large overpotentials on charge. We propose a system which inherently avoids many of the issues associated with organic electrolyte decomposition, while also forming lithium peroxide with a unique morphology. By using a LiNO₃/KNO₃ eutectic molten salt in place of a conventional solvent/salt electrolyte, solvent decomposition is obviated. In addition, the elevated temperature operation as well as the large concentration of Li⁺ ions encourage faster diffusion and kinetics. This project aims at solving particularly intractable problems relating to air electrode efficiency, stability and tolerance to the ambient environment. Furthermore, these solutions may translate into reduced complexity in the design of a Li-air stack and system, which in turn may improve prospects for use of Li-air batteries in EVs. Additionally, the project provides materials and technical concepts relevant for the development of other medium temperature molten salt Li battery systems of high specific energy, which may also have attractive features for EVs.

Objectives

The objective of this project is to develop high specific energy, rechargeable Li-air batteries having lower overpotential and improved robustness under ambient air compared to current Li-air batteries. The technical approach involves replacing traditional organic and aqueous electrolytes with a nonvolatile, inorganic molten salt comprising nitrate anions and operating the cell at elevated temperature (>80°C). The research methodology includes powerful in situ spectroscopic techniques coupled to electrochemical measurements (e.g., operando electrochemical mass spectrometry) designed to provide quantitative information about the nature of chemical and electrochemical reactions occurring in the air electrode.

Approach

Replace volatile, unstable and air-intolerant organic electrolytes common to prior research with inert molten nitrate electrolytes and operate cell above liquidus temperature (> 80°C). Improve reversibility and rate capability since discharge products (Li₂O₂, Li₂O, LiOH and Li₂CO₃) are stable and sparingly soluble in molten nitrate electrolytes. Combine quantitative gas analysis (pressure monitoring, mass spectrometry) with precise coulometry, as well as in situ spectroscopic techniques such as Raman to analyze air electrode processes.

Results

Demonstrate discharge specific energy and energy density ≥ 500 Wh/Kg and ≥ 800 Wh/L, respectively, based on air electrode mass and volume

We evaluated the O_2 cathode discharge specific energy and energy density. Composite cathodes comprising Super P carbon black, PTFE binder, and $LiNO_3$ - KNO_3 eutectic weighed ca. 4 mg/cm^2 (all components without the mesh current collector), electrode thickness was ca. 100 microns. Mass ratio between carbon, binder, and electrolyte, was 78/2/20 wt.%, respectively. Li/O_2 cells were discharged to 2.5 V cutoff, at a current density of 0.32 mA/cm^2 ($A_{cathode} = 0.79\text{ cm}^2$), and at 150°C . With a discharge capacity of 335 Ah/kg (170 Ah/L) of air electrode (carbon + binder + eutectic, Figure II-605a), the calculated corresponding discharge specific energy and energy density at $E_{disch.} \approx 2.7\text{ V}$ were 900 Wh/Kg and 460 Wh/L , respectively.

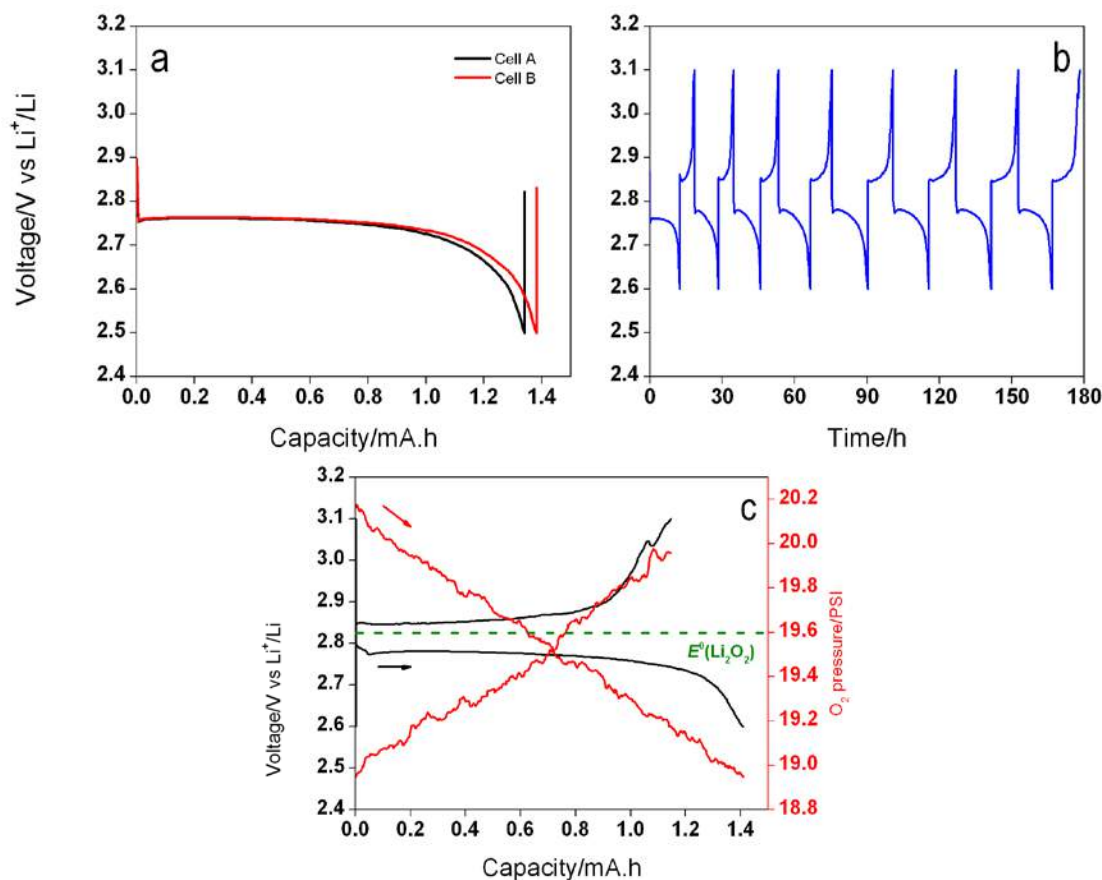


Figure II-605. a. Galvanostatic discharge curves for Li/O_2 cell containing a $LiNO_3$ - KNO_3 electrolyte and a carbon-based air electrode ($T = 150^\circ\text{C}$, $P_{O_2} = 1.4\text{ atm}$, $j = 0.32\text{ mA/cm}^2$). b. Cycling profile of a molten nitrate Li/O_2 cell using a boron carbide-based air electrode ($T = 150^\circ\text{C}$, $j = 0.13\text{ mA/cm}^2$, B_4C loading $\sim 5\text{ mg/cm}^2$). c. Corresponding in-situ pressure analysis for cell depicted in b.

Amongst other recently tested conducting ceramic electrode materials (FY 2016 Q3), boron carbide nanopowders (B_4C) were shown to exert promising cycling behavior in the molten salt electrolyte (Figure II-605b,c). We measured e^-/O_2 molar ratios using mass spectrometry and found 2.0 for both discharge and charge half-cycle, supporting reversible formation of Li_2O_2 as the discharge product, with OER/ORR ratio of 0.85, consistent with solution-phase mechanism of Li_2O_2 growth and/or side reaction with the carbide material to form lithium carbonate. SEM analysis of a discharged electrode showed micron-sized ORR product deposited onto glass fibers (separator material), leading to electrical disconnection and low Coulombic efficiency ($\approx 85\%$).

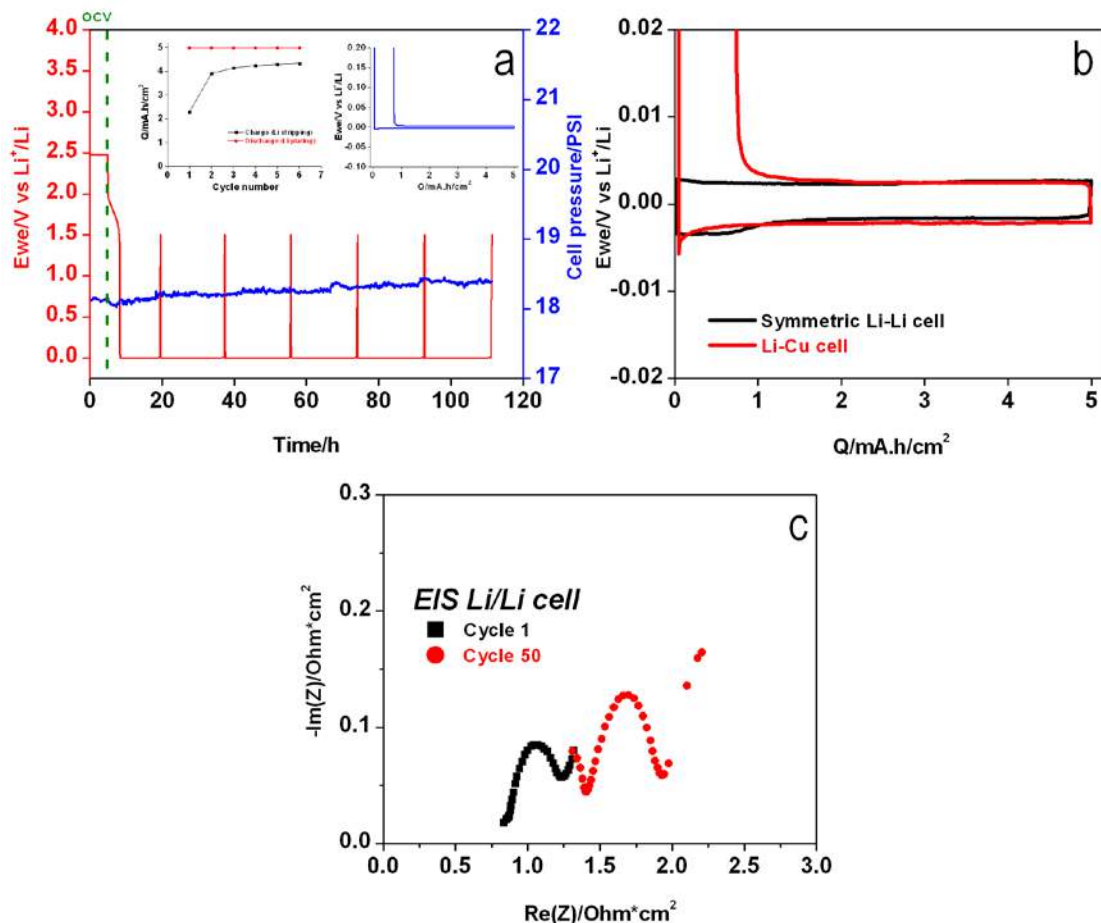


Figure II-606. a. Li plating/stripping onto Cu ($Al_i=ACu=0.502\text{ cm}^2$) at $j=0.5\text{ mA/cm}^2$, at 150°C , under Ar, in $\text{LiNO}_3\text{-KNO}_3$ melt (Inset: Q vs Cycle number and Li plating/stripping load curve). b. Cycling curve comparison between Li-Li symmetric cell and Li-Cu cell employing $\text{LiNO}_3\text{-KNO}_3$ melt, at 0.5 mA/cm^2 , at 150°C . c. EIS data derived from cycled Li-Li symmetric cell (estimated electrolyte thickness: 0.5 mm , $Al_i=0.502\text{ cm}^2$).

Study of the Li metal/molten nitrate interface shows an increase in area specific resistance (ASR) with cycle number (both bulk and interfacial resistances), continuous increase in pressure (Figure II-606a), consistent with SEI reaction: $2\text{Li} + \text{NO}_3^- = \text{Li}_2\text{O} + \text{NO}_2^-$, with nitrite anion being further reduced by Li to generate nitric oxide and nitrogen (confirmed by mass spectrometry), and low coulombic efficiency for Li stripping/plating ($\approx 87\%$). Addition of few wt.% CsNO_3 into the melt was shown to stabilize the Li interface. Cs^+ cations are thought to improve the SEI on lithium metal.

Scale-up downselected cell components for 4 mAh and 10 mAh cells

We investigated the lithium metal anode/solid electrolyte interface. Molten nitrate electrolytes are known to slowly decompose onto Li metal and therefore a solid electrolyte is required to prevent such reaction and improve battery cycle life. LLZO garnet-type pellets (1 cm diameter, 0.3 mm thickness) were hot-pressed and sintered for 36 hours at 1100°C under inert gas. Li/LLZO/Li symmetric cells were constructed in an Ar-filled glove box and operated at lithium melting point (ca. 185°C). Figure II-607 shows Li stripping/plating cycling data at 0.1 mA/cm^2 and 2 h per each half cycle with electrochemical impedance spectroscopy recorded every 80 hours of cycling.

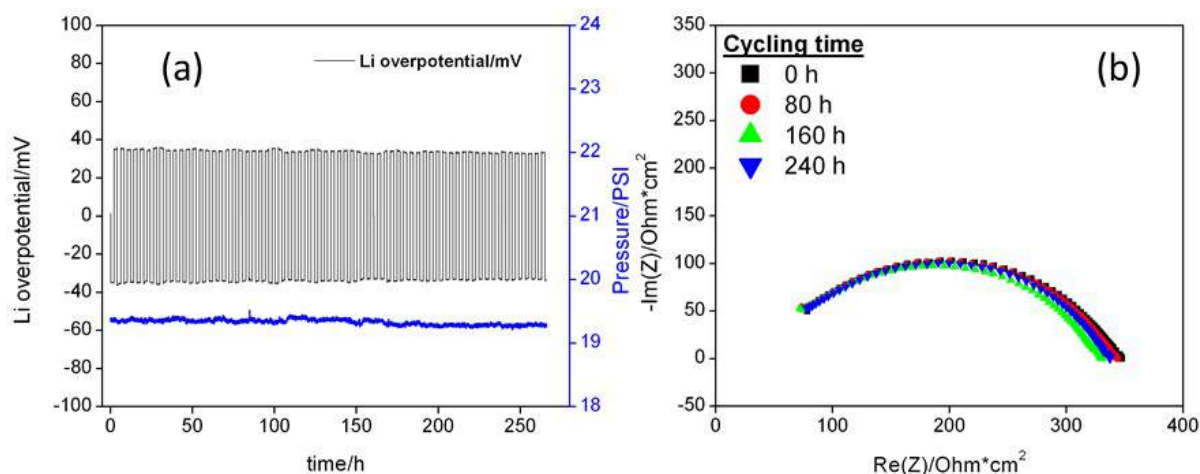


Figure II-607. a. Li/LLZO/Li symmetric cell cycling at 185°C (with in situ cell pressure analysis) at 0.1 mA/cm² with b. corresponding EIS analysis recorded at OCV (AC signal: 10 mV, from 1 MHz to 1 Hz).

Typical bulk electrolyte and interfacial resistance were found to be roughly 40 Ω.cm² and 300 Ω.cm², respectively. Li/O₂ cells using LLZO-protected Li anode were also tested. The air cathode/catholyte consisted of a 2-to-1 mixture LiNO₃:KNO₃ eutectic with Super P Carbon (containing 5% PTFE). Tests were conducted at 185°C to ensure good Li-LLZO-catholyte contact. It is expected that the elevated temperature may cause rapid carbon degradation in presence of ORR products as well as enhanced Li₂O₂ solubility (leading to poor rechargeability). Separately, we analyzed ORR discharge product morphology using a boron carbide air cathode. Boron carbide O₂ cathodes were collected from OCV and discharged molten nitrate Li/O₂ cells, rinsed in an organic solvent to remove excess nitrate salt, and analyzed by SEM (Figure II-608c). Li₂O₂ large crystals (several microns) were observed on boron carbide surfaces and XRD was used to confirm the lithium peroxide discharge product.

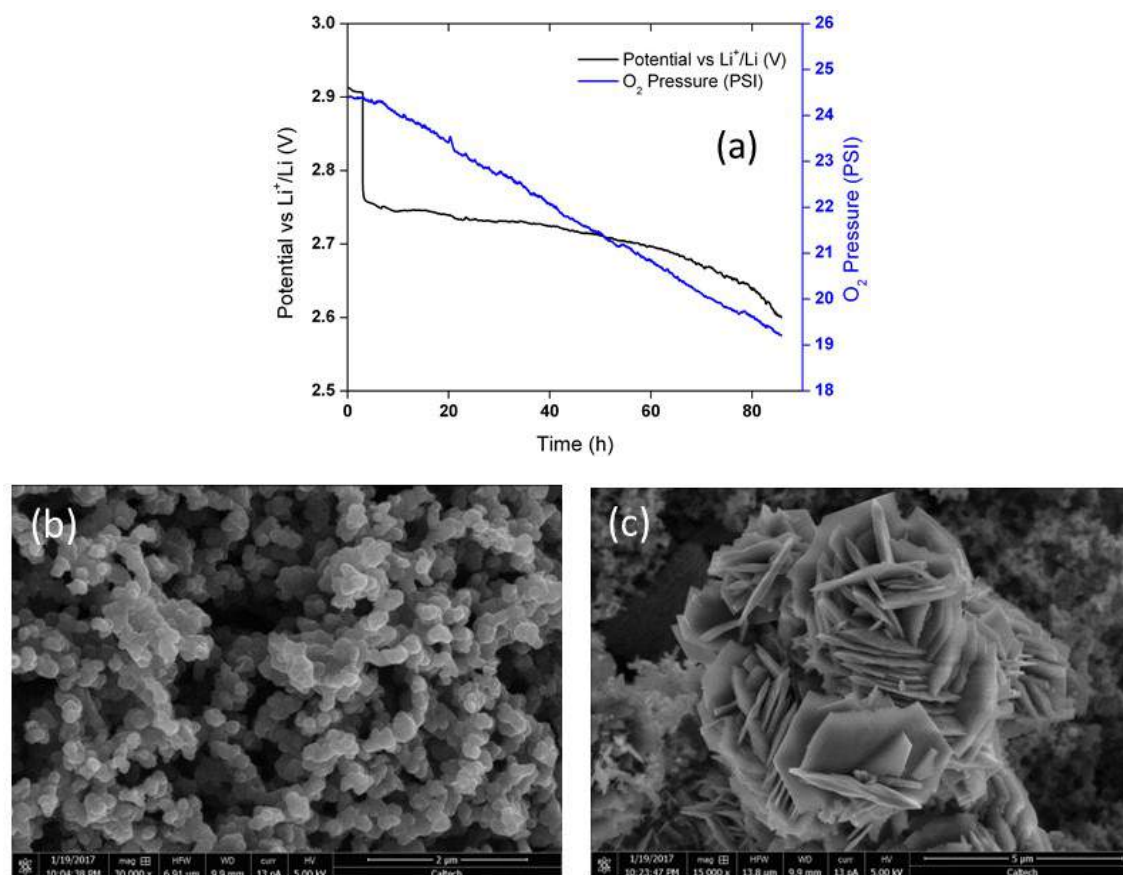


Figure II-608. a. Li/O₂ cell discharge curve using a LLZO-protected Li anode and a molten nitrate catholyte ($j = 0.05 \text{ mA/cm}^2$, 185°C , $m_{\text{carbon}} = 5 \text{ mg/cm}^2$, $m_{\text{nitrate}} = 10 \text{ mg/cm}^2$). SEM analysis of Boron Carbide air electrode b. before and c. after discharge under O₂ in LiNO₃-KNO₃ eutectic at 150°C .

In both the lithium-oxygen and nitrate reduction systems, the reaction product grows in the form of large crystals on the surface of the electrode catalyst. These large crystals pose an interesting design question with respect to accommodating this kind of discharge product. In order to study the interplay of pore size and surface area, we design structured lattice electrodes for nitrate reduction where we have direct control over both of these properties (Figure II-609a). Using this structured electrode, we can compare the electrochemical performance of a thin film electrode, a lattice electrode, and a nanoparticle electrode. While the surface area (and therefore reaction kinetics) of the nanoparticles far exceeds the thin film and lattice as evidenced by the CV scans (Figure II-609b), the discharge capacity does not (thin film: $1.7 \text{ mAh/m}^2_{\text{geometric}}$; lattice: $4.1 \text{ mAh/m}^2_{\text{geometric}}$; nanoparticle $5.1 \text{ mAh/m}^2_{\text{geometric}}$). In fact, the thin film and lattice electrode's discharge capacities differ by a factor equal to their difference in surface area. This however is not true of the nanoparticle electrode, demonstrating the importance of available pore volume to accommodate growth of the discharge product.

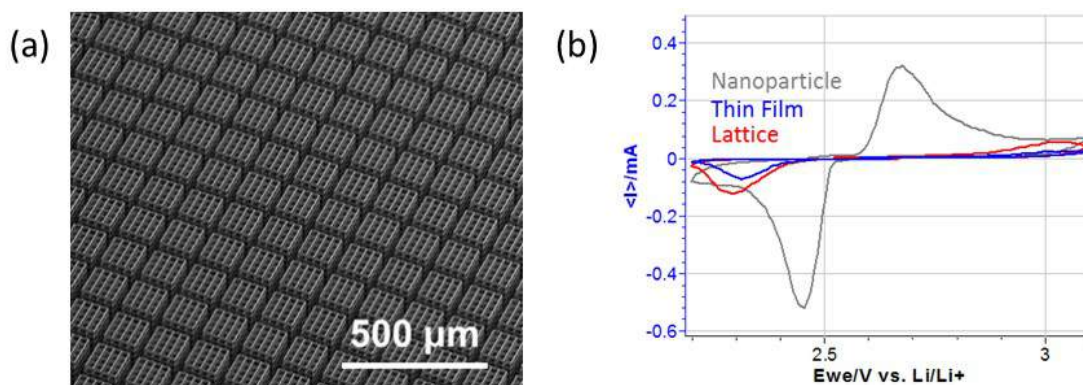


Figure II-609. a. SEM of a nickel coated structured electrode. b. CV at 150 °C and a scan rate of 0.01 mV/s for three nickel electrode morphologies performing nitrate reduction (electrolyte: $\text{LiNO}_3\text{-KNO}_3$ eutectic).

Demonstrate ≥ 10 cycles at $\geq 90\%$ round-trip energy efficiency in laboratory-scale Li-air cells comprising a molten nitrate electrolyte and protected Li electrode

We investigated the cycling performance of 2-electrode lithium cells comprising a solid electrolyte and a molten salt electrolyte contained within the cathode. The molten salt electrolyte consisted of our binary alkali metal nitrate mixture and the solid electrolyte of a LLZO 1 cm² disc of about 300 microns. Cells were operated at 175°C to ensure good solid electrolyte performance and a molten state for our nitrate salts. The cathode chemistry consisted of either the lithium-oxygen chemistry to form Li_2O_2 as the discharge product, or the electrochemical reduction of nitrate anions to form Li_2O and nitrite species. Figure II-610 shows the 3rd discharge/charge cycle of protected lithium anode cells using an alkali metal nitrate molten salt catholyte. On the left, the cell uses a porous carbon cathode and is cycled under O_2 gas. A typical ~2.7 V discharge plateau is observed, consistent with oxygen reduction reaction and the formation of solid lithium peroxide within the cathode porous structure (Super P carbon). Relatively high discharge capacity in Li/ O_2 cell (1360 mAh/g of carbon, ~6.5 mAh/cm²) was achieved. However the high temperature seemed to accelerate carbon decomposition in O_2 cell leading to poor reversibility and cyclability. XRD analysis post mortem revealed large quantities of Li_2CO_3 deposited on the cathode surface. On the right plot, the cell uses a porous nickel cathode and is cycled under argon gas. The typical 2.5 V discharge plateau corresponds to electrochemical reduction of nitrate anion based on the following cathode reaction: $2\text{Li}^+ + 2\text{e}^- + \text{NO}_3^- \rightarrow \text{Li}_2\text{O} + \text{NO}_2^-$. Lithium oxide fills up the cathode porous structure while nitrite anion dissolves in the melt. We observed a 45% active material utilization (nitrate anion reduction) with high reversibility, however the high discharge capacity was maintained for only a few cycles.

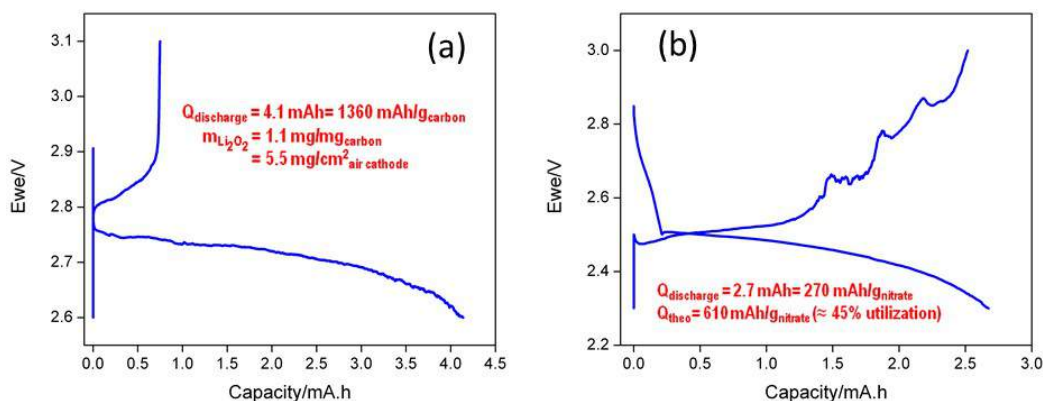


Figure II-610. a. Li/ O_2 cell voltage profile at 175°C using Super P Carbon:PTFE (95:5 wt.%) cathode at 0.05 mA/cm² current density ($m_{\text{carbon}} = 3$ mg, $m_{\text{nitrate}} = 6.5$ mg). b. Molten nitrate Li cell voltage profile at 175°C using nanoporous nickel cathode (Ni: $\text{LiNO}_3\text{-KNO}_3$ eutectic 50:50 wt.%) at 0.05 mA/cm² current density ($m_{\text{Ni}} = m_{\text{nitrate}} = 10$ mg).

Fabricate and test 4 and 10 mAh cells

We fabricated and tested full Li/nitrate and Li/O₂ cells utilizing a solid electrolyte between the negative and the positive electrode, the latter being constituted of either amorphous carbon black (Li/O₂) or Ni nanoparticles (Li/nitrate), both cathode active materials intimately mixed with the alkali molten nitrate electrolyte. Cells were being tested at 150°C and at a current density of 0.2 mA/cm². The solid electrolyte consisted of a LLZO 1 cm² disc of about 200 microns. The discharge capacity was limited to 4 mAh.

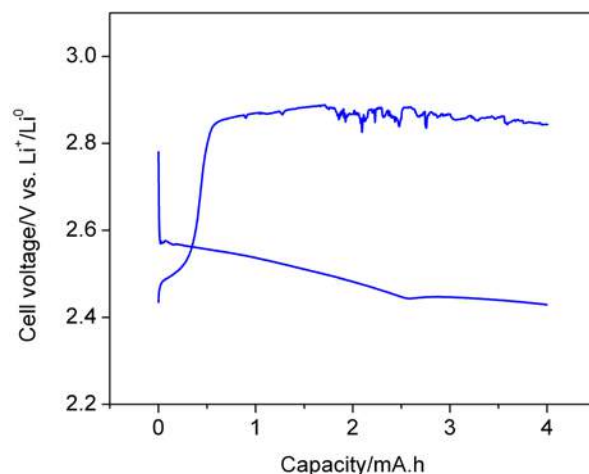


Figure II-611. Molten nitrate Lithium cell voltage profile (3rd cycle) at 150°C using nanoporous nickel/nitrate catholyte and LLZO-protected Li metal anode (Ni to LiNO₃-KNO₃ eutectic 1:1 wt.%, 0.2 mA/cm², mNi= mnitrate= 10 mg/cm²).

Figure II-611 shows the first three discharge/charge cycles of a protected lithium anode cell using an alkali metal nitrate molten salt catholyte. The cell uses a porous nickel cathode (~10 mg/cm² Ni loading) and is cycled under argon gas. The typical ~2.6 V discharge plateau corresponds to electrochemical reduction of nitrate anion, based on the following reaction: $2\text{Li}^+ + 2\text{e}^- + \text{NO}_3^- \rightarrow \text{Li}_2\text{O} + \text{NO}_2^-$. Lithium oxide fills up the cathode porous structure while nitrite anion dissolves in the melt.

Conclusions

As alternative to unstable carbon-based O₂ cathode, we screened electrode materials with improved chemical stability in molten nitrate Li-air cells at 150°C. IrO₂ and B₄C exhibited promising electrochemical performance. However, OER/ORR molar ratios (amount of oxygen formed during charge vs. amount of oxygen consumed during discharge of the electrochemical cell) lower than 1 prevailed. Such behavior is consistent with solution-phase mechanism for lithium peroxide discharge product formation and hence causing electrical loss during cycling. Furthermore, we have shown the positive effect of Cs⁺ additive (e.g., CsNO₃ salt) on both lowering molten salt electrolyte melting point (~100°C) and enhancing Li metal anode cyclability. We studied garnet-type solid electrolytes such as LLZO and demonstrated good cycling behavior in symmetric Li/Li cells. These garnets were tested in Li metal cells using molten nitrate as the catholyte. Chemical tests coupled to XRD showed good stability for LLZO when in contact with molten nitrate salts. More fundamental work went into designing nano-structured electrode to better accommodate lithium oxygen discharge products (e.g., Li₂O, Li₂O₂). We confirmed novel rechargeable oxyanion redox cathode chemistry, based on reversible nitrate anion reduction on high surface area porous nickel electrodes. Future work includes a) improving Li stripping/plating rate capabilities using a solid electrolyte at 100-150°C, b) increasing practical capacity (areal, gravimetric, volumetric) including active and inactive components for both O₂ and oxyanion redox cells, c) engineering efficient elevated temperature thermal management and system designs for EV applications.

Key Publications*Publications*

1. Burke et al., ACS Energy Letters, 2016, 1(4), 747-75
2. Knudsen et al., J. Electrochem. Soc., 2016, 163(9), A2065-71
3. High Capacity, Rechargeable Lithium Battery Using Oxyanion Conversion Reaction Cathode. D Addison, H Tan, D Tozier, J Uddin, J Greer, G Chase, V Giordani (In preparation)

Patents

1. Intermediate temperature alkali metal/oxygen batteries employing molten nitrate electrolytes. J Uddin, D Addison, V Giordani, US Patent 2016/0049707 (2016)
2. Rechargeable batteries employing catalyzed molten nitrate positive electrode. D Addison, V Bryantsev, G Chase, V Giordani, J Uddin, W Walker, US Patent 2016/0204418 (2016)

II.J.3 Lithium-Air Batteries (ANL)

Khalil Amine, Principal Investigator

Argonne National Laboratory
 9700 S. Cass Avenue
 Argonne, IL 60516
 Phone: 630-252-3838
 E-mail: amine@anl.gov

Larry Curtiss, Co-Principal Investigator

Argonne National Laboratory
 9700 S. Cass Avenue
 Argonne, IL 60516
 Phone: 630-252-7380
 E-mail: curtiss@anl.gov

Jun Lu, Co-Principal Investigator

Argonne National Laboratory
 9700 S. Cass Avenue
 Argonne, IL 60516
 Phone: 630-252-7380
 E-mail: junlu@anl.gov

Tien Duong, Technology Manager

U.S. Department of Energy
 Phone: 202-586-7836
 E-mail: Tien.Duong@ee.doe.gov

Start Date: October 1, 2014

End Date: September 30, 2019

Total Project Cost: \$2,700,000

DOE share: \$2,700,000

Non-DOE share: \$0

Project Introduction

Lithium-air batteries can be considered the ‘holy grail’ of lithium batteries because they offer, in principle, at least ten times the energy density of conventional lithium-ion systems. While the inherent energy potential of lithium metal approaches that of gasoline, today’s battery manufacturers have not yet been able to unlock this potential. While today’s lithium-ion batteries may provide acceptable power for hybrid electric vehicles (HEVs) and all-electric vehicles (EVs), they do not as yet provide sufficient energy for an acceptable driving distance. A breakthrough in Li-air battery technology would significantly increase the possibility of extending the electric range of these vehicles with the added advantages of reducing battery cost and weight.

Li-air battery technology has many challenges and requires significant research efforts to meet these challenges and to unlock its full potential. The successful implementation of non-aqueous Li-air cells has been hampered because of severe materials problems that have limited electrochemical performance. These include (1) the non-aqueous electrolytes can be unstable under both the charge and discharge conditions, thereby seriously limiting cycle life; (2) during discharge, the solid and insoluble Li_2O_2 and/or other Li_2O products are deposited on the surface or within the pores of the carbon cathode, thereby passivating the surface as well as clogging the pores and restricting oxygen flow; (3) degradation of the lithium anode due to oxygen crossover destroys the integrity and functioning of the cell; and (4) commonly used transition metal cathode catalysts, do not access the full capacity of the oxygen electrode or enable sufficiently high rates.

The team led by Dr. Khalil Amine and Dr. Larry Curtiss at Argonne National Laboratory (ANL) is working on problems that limit the electrochemical performance of the Li-air battery, including the stability of the organic electrolytes, cathode catalysts, and stability of the lithium anode under oxygen-crossover conditions. This effort will lead to the development of a reversible lithium air battery that provides much higher energy density than state-of-the-art lithium ion battery for powering electric vehicles. The technology, if successful, can also benefit many military applications that require very high energy density such as satellite, military vehicles for silent watch and operation.

Objectives

The objective is to develop stable electrolytes and new cathode architectures for lithium air batteries to lower the charge overpotential, improve the cell efficiency, and increase cycle life. New electrolytes are needed to prevent gradual electrolyte decomposition that occurs in the presence of the reduced oxygen species, especially superoxide anion (O_2^-) from the discharge process. Discovery of such electrolytes can increase cycle life. Commonly used carbons and cathode catalysts do not access the full capacity of the oxygen electrode and can cause significant charge overpotentials, which lowers efficiency and limits cycle life. Therefore, there is a need for improved catalysts and cathode materials. Understanding the oxygen crossover effect at the anode on the electrochemical performance of Li-air battery is important to understanding the lithium electrode degradation due to oxygen crossover and thus reduces the cycle life.

Approach

Issues that limit the performance of the Li-air battery include (1) electrolytes decomposition; (2) inefficient cathode materials; and (3) lithium electrode degradation. This project addresses the cycle life problem of Li-air batteries through experimental and theoretical investigation of (a) the discharge formation mechanism and relationship to electrolytes, (b) investigation of the morphology and composition of the discharge product, and (c) investigation of electrolyte decomposition mechanisms. This understanding is being used to (1) develop new cathode materials to promote formation of discharge morphologies such as those involving superoxides with better conductivity to decrease charge overpotentials, (2) cathode and electrolyte materials that do not degrade with cycling and (c) electrolyte modification to protect the lithium anode. The experimental work to create advanced electrolytes, carbons, catalysts, cathodes, and anodes is guided by theory and modeling. The experimental results will be thoroughly analyzed with very sophisticated analytical techniques and used to fine-tune the computational studies. Fundamental understanding of the underlying principles will be provided to greatly facilitate the next steps in the development cycle.

Collaborators include Professor Kah Chun Lau (University of California-Norridge), Professor Amin Salehi (University of Illinois-Chicago), Professor Yang-Kook Sun (Hanyang University), Professor Yiying Wu (Ohio State University), Dr. Dengyun Zhai (China). We utilize several facilities at Argonne National Laboratory including the Advanced Photon Source, the Center for Nanoscale Materials, and the Argonne Leadership Computing Facility.

Results

Hollow graphene nanocages with Pt nanoparticles for Li-O₂ cathodes

Ultra-small Pt coated hollow graphene nanocages have been synthesized as cathodes for Li-O₂ batteries to find a catalyst that can lower charge overpotentials. They give a charge voltage plateau is 3.2 V at the current density of 100 mA/g and below 3.5 V when the current density is increased to 500 mA/g. The unique hollow graphene nanocages (HGN) matrix can not only provide numerous nano-scale tri-phase regions as active sites for efficient oxygen reduction, but also offer sufficient amount of meso-scale pores for rapid oxygen diffusion. Furthermore, with strong atomic-level oxygen absorption into its subsurface, ultra-small Pt particles can serve as the nucleation site for Li₂O₂ growth. The Li₂O₂ has a favorable morphology with small size and amorphous state, which can decompose more easily during recharge. Meanwhile, the conductive hollow graphene substrate can enhance the catalytic activity of noble metal Pt catalysts due to the graphene-metal interfacial interaction.

The synthetic strategy for HGNs involves the combustion of metal Mg with dry ice to produce cubic nanoparticles of MgO covered by few graphite carbon layers. The HGNs are obtained by removing the cubic MgO from inside of the graphene with dilute hydrochloric acid. Finally, the Pt nanoparticles were homogeneously deposited on the surface of the HGNs by PVD. The porous hollow nanocage architecture of HGNs, and the homogeneity of Pt catalysts were confirmed with transmission electron microscopy (TEM) at different magnifications.

The electrochemical performances of pristine and Pt-HGNs as the cathodes in a Li-O₂ cell were investigated under capacity-controlled conditions to minimize side reactions. With a nano-Pt catalyst, the Pt-HGNs electrode exhibited a stable discharge curve at approximately 2.75 V for cycles. It also showed a charge voltage below 3.2 V closing with a value of 2.96 V after initial three cycles, and steadily remained below 3.5 V for at least 10 cycles. Thus, with enhanced conductivity and unique porous structure, the Pt-HGNs exhibit a very low charge overpotential for a Li-O₂ battery using a Pt cathode catalyst.

Moreover, the poor rate performance of the typical aprotic Li-O₂ cell was found to be improved by using the Pt-HGNs cathode. The Pt-HGN cathode showed the discharge plateau staying above 2.6 V, and the charge mid-capacity potential below 3.5 V, even when operated at high current density ~500 mA/g. The excellent electrochemical performance may be attributed to the improved oxygen evolution reaction (OER) kinetics facilitating efficient decomposition of Li₂O₂.

Air cathode based on a novel triple phase structure

In the Li-O₂ battery the oxygen gas and electrolyte often compete for pathways in the conventional cathode based on a porous carbon cathode, which limits the performance of the battery. In this work, we have used a novel air cathode based on a novel triple phase structure by using a common textile. The hierarchical networked structure of the textile leads to decoupled pathways for electrolyte and oxygen gas, which facilitate the transport of both components, significantly improving battery performance. The oxygen flows through the woven mesh constructed by the textile fibers while the electrolyte diffuses along the textile fibers. Due to the facilitated transport, the Li-O₂ battery based on this textile-based cathode shows a high discharge capacity of 8.6 mAh/cm², low overpotential of 1.2 V, and stable operation of over 50 cycles. The decoupled transport pathway design has the potential for a flexible Li-O₂ battery design.

The concept of the breathable cathode is based on that of a textile, i.e., the surface is densely coated layer of carbon nanotubes (CNT). The hierarchical structure of the textile forms the channel for the flow of electrolyte while the textile material naturally has a good affinity with liquid electrolyte. Therefore, the electrolyte flows underneath the active sites on the CNT layer where the reaction happens. The mesh holes on the textile provides sufficient space for the oxygen to flow through, since it has been shown that the gas flow channel should have big enough size to facilitate oxygen reduction during discharge. Thus, the liquid electrolyte and the oxygen gas flow on the different sides of the active CNT layer without competing for space. The decoupled pathways for electrolyte and oxygen gas are crucial for the performance of the Li-O₂ battery. All the active sites on the CNT layer always have sufficient electrolyte and oxygen input during the discharge and can be fully utilized. The CNTs are decorated with palladium nanoparticles with size of ~10 nm as the catalyst. Similar to the active CNT layer, the Pd catalysts in this case are fully exposed to the electrolyte and the oxygen gas.

The rechargeability of Li-air battery with the textile-based cathode is very good as seen in Figure II-612. The battery was cycled with a current density of 0.1 mA/cm² and a charge/discharge capacity limit of 1 mAh/cm². Almost no performance drop was observed even after 50 cycles. The rechargeability of the battery was also studied via the characterization of discharge product. The XRD results indicate the formation of Li₂O₂. Moreover, Raman spectroscopy and XPS were employed to analyze the discharge product. In the Raman spectrum a distinct peak at 800 cm⁻¹ was observed, which corresponds to amorphous Li₂O₂. In O 1s XPS spectrum after discharge, a peak at 528 eV was detected, which is the characteristic peak of Li₂O₂. Both results indicate that the discharge product is Li₂O₂.

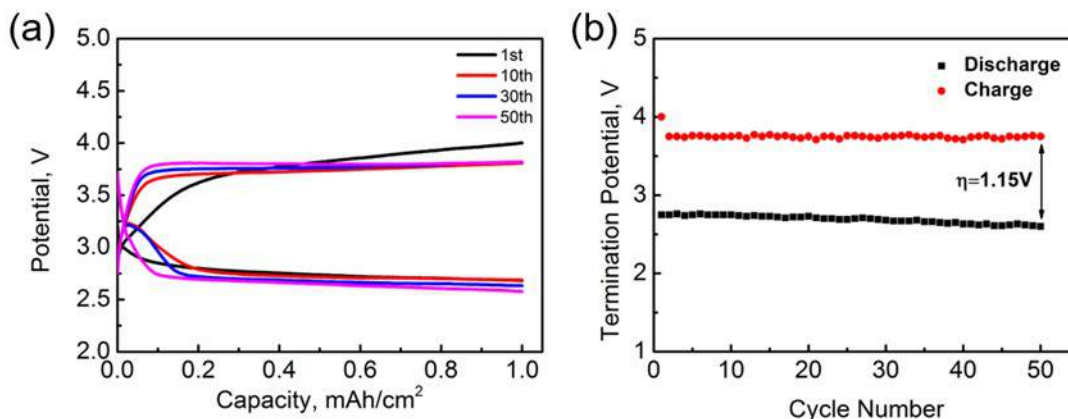


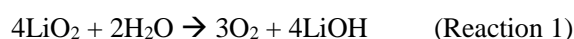
Figure II-612. (a) Discharge/charge profile of a Li-O₂ cell using the “textile” concept for 50 cycles.
(b) The termination voltage of charge/discharge for 50 cycles.

Titration methods for a Li-O₂ battery

Fundamental understanding of reactions of lithium peroxides and superoxides is essential for the development of Li-O₂ batteries. We carried out an investigation of the hydrolysis of lithium superoxide as produced in a Li-O₂ cell under some conditions. Unlike KO₂ and NaO₂, the hydrolysis of LiO₂ does not produce H₂O₂. Similarly, the reactivity of Li₂O₂ toward water differs from LiO₂, in that Li₂O₂ results in H₂O₂ as a product. Based on this a titration method that depends on the reaction of a Li-O₂ discharge product with a Ti(IV)OSO₄ solution, has been developed that provides a useful diagnostic technique to provide information on the composition of a discharge product in a Li-O₂ battery

Initially, a Li-O₂ cell with an Ir-rGO (reduced graphene oxide) cathode was used to produce a LiO₂ discharge product. The reaction of the LiO₂ discharge product with water was investigated using a spectrophotometric method to assess the amount of hydrogen peroxide produced. In this procedure we first establish a calibration curve by adding incremental amounts of Li₂O₂ to the test reagent Ti(IV)OSO₄. The discharge product LiO₂ on the Ir-rGO cathode is then reacted with the acidic solution of Ti(IV)OSO₄ after removal of the electrolyte, but with the cathode material still present. Under the experimental conditions, Ti(IV) exists as TiO₂⁺(aq) complexed with SO₄²⁻ ion in 1.0 M H₂SO₄. If hydrogen peroxide is present, a color change to yellow/orange occurs due to the formation of a titanium peroxide complex, TiO₂SO₄. When the acidic solution of Ti(IV)OSO₄ was added to the LiO₂ discharge product the liquid remained colorless as shown in Figure II-613 and no notable UV-Vis intensity change was observed. From the UV-Vis spectra, the absorbance intensity is essentially negligible based on a calibration curve, which indicates the absence of hydrogen peroxide. The LiO₂ results are in contrast to the case for KO₂ and NaO₂ where an obvious color change is observed for this procedure, consistent with the presence of a hydrogen peroxide product. It is also in contrast to the case of a known discharge product of Li₂O₂ where the same titration test tested positive (i.e., color change) for the presence of H₂O₂.

We have extended this method to assess the amount of LiO₂ present to make it a more powerful tool to provide quantitative information on the amounts of both LiO₂ and Li₂O₂ present in the discharge product. The two titration techniques are based on the hydrolysis reactions of LiO₂ and Li₂O₂ given by reactions 1 and 2, respectively.



Thus, the hydrolysis of LiO₂ derived does not result in H₂O₂ as a product that is detected for hydrolysis of Li₂O₂ as well as KO₂ and NaO₂.



Figure II-613. Photograph of cathode discharged to 1000 mAh/g, dried under Ar for 1 hr, and then soaked in 3 mL of $\text{TiOSO}_4(\text{aq})$. No apparent color change occurred upon titration indicating no Li_2O_2 is present

In order to develop a titration technique to directly determine the amount of the LiO_2 discharge product, we have tested for the expected LiOH product from Reaction 1, which is the reaction of water with LiO_2 . This was done by pH measurement of a solution after addition of a known quantity of H_2O to a cathode after one discharge cycle in a Li-O_2 cell with an Ir-rGO cathode under the same conditions as described for the titration based on Ti(IV)OSO_4 solution described above. The resulting solution was strongly basic with a pH of 11.84, consistent with the presence of OH^- anion from LiOH . In addition, by analysis of the current used and the discharge time it is possible to determine quantitatively the amount of OH^- anion produced. In the case of the discharge product from the Ir-rGO electrode this is 95% of that expected based on Reaction 1. Thus, this new titration method confirms that LiO_2 is present in the discharge product, consistent with other characterization techniques such as DEMs and Raman. It also provides a new technique for assessing Li-O_2 product composition.

Conclusions

During the past year we have shown that platinum-coated hollow graphene nanocages can be used as cathodes in Li-O_2 batteries and give low charge overpotentials. A novel air cathode based on a novel triple phase structure by using a common textile was employed in a Li-O_2 cell. The hierarchical networked structure of the textile leads to decoupled pathways for electrolyte and oxygen gas, which facilitate the transport of both components, significantly improving battery performance. Finally, two titration methods were developed to test for LiO_2 and Li_2O_2 , which will help in characterization of the composition of discharge products in Li-O_2 batteries.

Key Publications

1. “Concentrated Electrolyte for the Sodium–Oxygen Battery: Solvation Structure and Improved Cycle Life,” M He, K. C. Lau, X Ren, N Xiao, W. D. McCulloch, L. A. Curtiss, Y Wu, *Angewandte Chemie* **128** (49), 15536–15540 (2016).
2. “Lithium Superoxide Hydrolysis and Relevance to Li-O_2 Batteries,” H. Wang, Y. Lee, R. S. Assary, C. Zhang, X. Luo, P. C. Redfern, J. Lu, Y. Lee, D. Kim, T. Kang, E. Indacochea, K. Lau, K. Amine, and L. A. Curtiss *J. Phys. Chem. C*, **121**, 9657–9661 (2016) DOI: 10.1021/acs.jpcc.6b12950
3. “Platinum-Coated Hollow Graphene Nanocages as Cathode Used in Lithium-Oxygen Batteries,” F. Wu, Y. Xing, X. Zeng, Y. Yuan, X. Zhang, R. Shahbazian-Yassar, J. Wen, D. J. Miller, L. Li, R. Chen, J. Lu, J. and K. Amine, *Adv. Funct. Mater.*, **26**: 7626–7633 (2016) doi:10.1002/adfm.201602246
4. Patent: “Lithium-oxygen batteries incorporating lithium superoxide,” Jun Lu, Khalil Amine, Larry A Curtiss, Kah Chun Lau, Yang-Kook Sun, Yun Jung Lee, Xiangyi Luo, 2017/1/24, US Patent Office, Patent number 9553316

II.K Beyond Li-ion R&D: Sodium-Ion Batteries

II.K.1 Exploratory Studies of Novel Sodium-Ion Battery Systems (BNL)

Xiao-Qing Yang, Principal Investigator

Chemistry Division
Brookhaven National Laboratory
Bldg. 555, Brookhaven National Lab.
Upton, NY 11973
Phone: 631-344-3663
E-mail: xyang@bnl.gov

Seongmin Bak, Co-Principal Investigator

Chemistry Division
Brookhaven National Laboratory
Bldg. 555, Brookhaven National Lab.
Upton, NY 11973
Phone: 631-344-4142
E-mail: xyang@bnl.gov

Tien Duong, Technology Manager

U.S. Department of Energy
Phone: 202-586-7836
E-mail: Tien.Duong@ee.doe.gov

Start Date: October 1, 2016

End Date: September 30, 2017

Total Project Cost: \$500,000

DOE share: \$500,000

Non-DOE share: \$0

Project Introduction

In order to meet the challenges of powering PHEVs, the next generation of rechargeable battery systems with higher energy and power density, lower cost, better safety characteristics, and longer calendar and cycle life beyond lithium-ion batteries, which is today's state-of-the-art technology, need to be developed. Recently, Na-ion battery systems have attracted more and more attention due to the more abundant and less expensive nature of Na resources. However, building a sodium battery requires redesigning battery technology to accommodate the chemical reactivity and larger size of sodium atoms. Since Na-ion battery research is an emerging technology, new materials to enable Na electrochemistry and the discovery of new redox couples and the related diagnostic studies of these new materials and redox couples are quite important. In sodium electrochemical systems, the greatest technical hurdles to overcome are the lack of high-performance electrode and electrolyte materials which are easy to synthesize, safe, non-toxic, with long calendar and cycling life and low cost. Furthermore, fundamental scientific questions need to be further elucidated, including (1) the difference in transport and kinetic behaviors between Na and Li ions in analogous electrodes; (2) Na insertion/extraction mechanism; (3) solid electrolyte interphase (SEI) layer on the electrodes from different electrolyte systems; and (4) charge transfer in the electrolyte-electrode interface and Na⁺ ion transport through the SEI layer. This project will use the synchrotron-based in situ x-ray diagnostic tools developed at BNL to evaluate the new materials and redox couples, to explore in fundamental understanding of the mechanisms governing the performance of these materials and provide guidance for new material developments. This project will also focus on developing advanced diagnostic characterization techniques to investigate these issues, providing solutions and guidance to solve the problems. The synchrotron-based in situ X-ray techniques (x-ray diffraction and hard and soft x-ray absorption) will be combined with other imaging and spectroscopic tools such as high resolution transmission electron microscopy (HRTEM), mass spectroscopy (MS), as well transmission x-ray microscopy (TXM). In FY2017, this BNL team has built a good

working relationship with several beamlines at the newly built National Synchrotron Light Source II (NSLSII) with assigned beamtime at hard x-ray nanoprobe (HXN) beamline, x-ray Powder diffraction (XPD). By collaborating with Dr. Dong Su and Dr Huoling Xin, this team also has sufficient time using the HRTEM. The BNL team has been closely working with top scientists on new material synthesis at ANL, LBNL, SLAC, and PNNL, with U.S. industrial collaborators at General Motors and Johnson Controls, and international collaborators in Japan and South Korea. In FY2017, results through these collaborations were published on high impact journals such as JACS and Advanced Energy Materials.

Objectives

The primary objective of this proposed project is to develop new advanced in situ material characterization techniques and apply these techniques to explore the potentials, challenges, and feasibility of new rechargeable battery systems beyond the lithium-ion batteries (LIBs), namely the sodium-ion battery systems for plug-in hybrid electric vehicles (PHEV). In order to meet the challenges of powering PHEVs, new rechargeable battery systems with high energy and power density, low cost, good abuse tolerance, and long calendar and cycle life need to be developed. This project will use the synchrotron-based in situ x-ray diagnostic tools, combined with HRTEM, STEM, and TXM imaging techniques developed at BNL to evaluate the new materials and redox couples to enable a fundamental understanding of the mechanisms governing the performance of these materials and provide guidance for new material and new technology development regarding Na-ion battery systems.

Approach

- A combination of time resolved X-ray diffraction (TR-XRD) and mass spectroscopy (MS), together with in situ soft and hard X-ray absorption (XAS) during heating and transmission electron microscopy (TEM) to study the thermal stability of the Na battery electrode materials.
- Synchrotron-based X-ray diffraction (XRD), X-ray absorption spectroscopy (XAS), to elucidate and differentiate the contribution from each component and element to the capacity and structural changes of various cathode and anode materials for Na-ion batteries.
- Extended collaboration with other US and international academic institutions and US industrial partners.

Results

1. Using synchrotron-based XRD to study a new cathode material for sodium-ion batteries: the V₂C material, as a new member of the two-dimensional transition metal carbides, so-called MXenes.

In FY2017, this project carried out the studies of a new cathode material for sodium-ion batteries. A V₂C material, as a new member of the two-dimensional transition metal carbides, so-called MXenes, was synthesized in a way containing surface functional groups (denoted as V₂CT_x, where T_x are surface functional groups) and studied as anode materials for Na-ion batteries. V₂CT_x anode exhibits reversible charge storage with good cycling stability and high rate capability through electrochemical test. The charge storage mechanism of V₂CT_x material during Na⁺ intercalation/deintercalation and the redox reaction of vanadium were studied using a combination of synchrotron-based X-ray diffraction (XRD) and hard X-ray absorption near edge spectroscopy (XANES). Figure II-614a presents *ex situ* XRD patterns at the 2θ angle range corresponding the (002) reflection of V₂CT_x at several charge/discharge (i.e., sodiation/desodiation) states during first cycle (the charge-discharge curve is also plotted on the right panel of Figure II-614a). During the first sodiation process, the (002) diffraction peak in the XRD pattern moved from 9.3 ° to 8.1 ° from the OCV state to the 0.1 V state, corresponding an expansion of the interlayer distance from 9.53 Å to 10.93 Å. As illustrated in Figure II-614b, beside the Na⁺ absorption at the surface of V₂CT_x, resulted in the capacitor-like capacity, additional energy storage also occurred through Na⁺ intercalation between layers of V₂CT_x. This behavior is similar to those of previous reports on Ti₂CT_x and V₂CT_x MXene materials. However, during subsequent desodiation (or deintercalation) process, the contraction of interlayer distance (~ 1.03 Å) is much smaller than the 1.40 Å expansion during first sodiation.

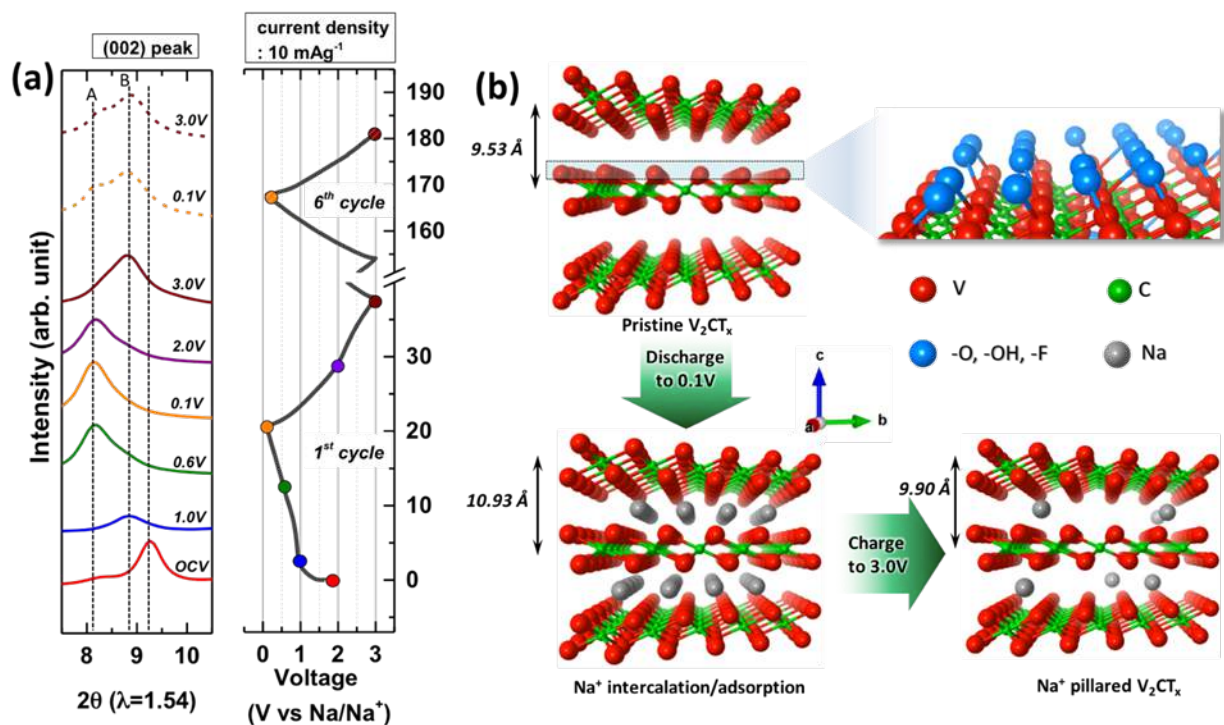


Figure II-614. (a) *Ex situ* XRD patterns (left) for V₂CT_x upon electrochemical sodiation/desodiation cycling (right), and (b) schematic illustration of the expansion/contraction behavior of V₂CT_x during sodiation/desodiation process: the interlayer distance of V₂CT_x is increased upon Na⁺ intercalation during sodiation process, then partially reduced upon Na⁺ deintercalation due to the trapped Na⁺ between V₂CT_x layers behaves as a pillar during desodiation process.

2. Using synchrotron-based *ex situ* hard x-ray absorption at vanadium K-edge to study the MXene material V₂C as new anode material for sodium ion batteries during charge-discharge cycling

In FY2017 this project also carried out the *ex situ* hard x-ray absorption studies at vanadium K-edge of MXene material V₂C as new anode material for sodium ion batteries during charge-discharge cycling. The *ex situ* V K-edge XANES spectra presented in Figure II-615a were measured on samples harvested from cells discharged and charged to different voltages during the first cycle (OCV→0.1V→3V), as shown on the charge/discharge curve in Figure II-615b. The V K-edge XANES spectra presented in Figure II-615a show a relatively weak pre-edge peak (marked as A) at 5470 eV and a strong main absorption peak (marked as B) at around 5485 eV. The pre-edge absorption is associated with the transition to hybridized electronic states of the metal 3d and carbon 2p orbitals. The pre-edge peak of V₂CT_x spectra can be assigned to the transition of a 1s electron to the hybridized t_{2g} (V 3d + C 2p) and e_g (V 3d + C 2p) orbitals. And the main absorption peak “B” involves the dipole allowed transition of 1s electrons to unoccupied V 4p states. The spectra for V₂CT_x at different discharge/charge states do not show significant differences in shapes, but the edge shift is clearly observable during both discharge and charge process (inset in Figure II-615a). A plot of the V K-edge energies, at half height of normalized XANES spectra, as a function of sodiation/desodiation state in Figure II-615c clearly show the consistent energy position changes from one voltage step to the next. During first sodiation process from OCV to 0.1 V, the edge shifts to lower energy, which reflects the reduction of vanadium. During desodiation process from 0.1 V to 3 V, the edge shifts back to the higher energy indicating the oxidation of vanadium.

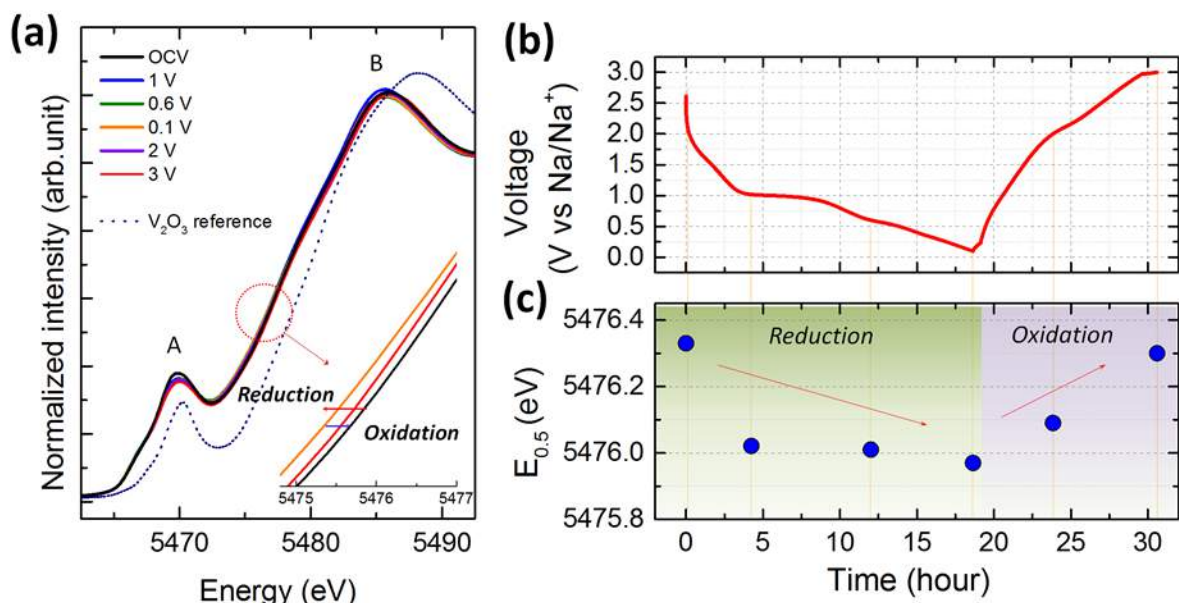


Figure II-615. (a) *Ex situ* V K-edge XANES spectra of V₂CT_x at selected cell voltages during first sodiation/desodiation process (OCV→0.1V→3V), (b) corresponding voltage profile, and (c) variation of V edge energy (at half height of normalized XANES spectra) at selected cell voltage.

3. Using synchrotron-based *ex situ* soft x-ray absorption at vanadium L-edges to study the MXene material V₂C during charge-discharge cycling

In FY2017, using *ex situ* soft x-ray absorption at vanadium L-edges to study the MXene material V₂C during charge-discharge cycling has been carried out. Figure II-616 shows the V L_{2,3}-edge sXAS spectra collected from five V₂CT_x electrodes cycled to different voltages using both (a) bulk sensitive TFY and (b) surface-sensitive TEY. The overall sXAS spectra can be divided into two regions, the L₃-edge at the energy range of 510-520 eV and the L₂-edge at 520-530 eV. It is apparent that L₃-edge in TFY spectra display dramatic voltage-dependent changes, which are related to the vanadium redox reactions in the bulk V₂CT_x. The 516.7 eV peak intensity decreases from 1 V to 0.1 V and increases from 0.1 V to 3 V, while the lower energy peak at 513 eV shows just the opposite trend. The two sXAS features are related to the two different oxidation states of V, i.e., the high energy peak at 516.7 eV represents a higher oxidation state and its intensity increases when the average oxidation state of vanadium increases. Therefore, the changes in sXAS intensity and line shape changes clearly demonstrate the reduction of the V ions during the initial discharge from 1.0 V down to 0.1 V. Unlike in the V K-edge spectra, where the reduction of average oxidation of vanadium was indicated by the edge shift to lower energy, for the L₃ edge spectra, such reduction is indicated by the reduction of intensity ratio of 516.7 eV/513 eV peaks, which can be clearly observed by the significant enhancement of the 513 eV peak intensity at 0.1 V (sodiated). Due to the sensitivity of the transition-metal L-edge sXAS to the valence 3d, the data in Figure II-616 also show clearly that the V L-edge line shape does not fully recover when the V₂CT_x electrode is charged back to 3 V from its discharged state (0.1 V). This indicates that the V redox is not fully reversible in the initial cycle, which is consistent with the low Coulombic efficiency obtained by electrochemical test. Another observation is that the surface-sensitive TEY spectra (Figure II-616b) show much weaker change, compared with that of the bulk probing TFY (Figure II-616a), indicating less changes in vanadium oxidation states at the surface of V₂CT_x electrode during cycling. Combining these results with those of XRD and V K-edge XANES, it can be concluded that the redox reaction of vanadium mainly takes place in the bulk of V₂CT_x during Na⁺ intercalation/deintercalation rather than at the surface.

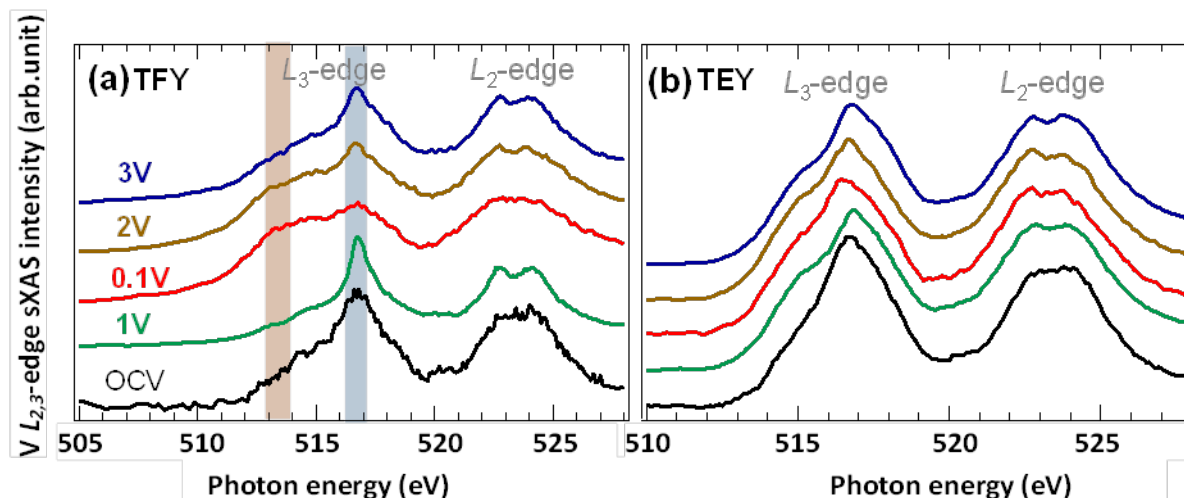


Figure II-616. V L_{2,3}-edge sXAS spectra collected on electrodes that are cycled to different voltages. (a) Bulk-sensitive total fluorescence yield (TFY), and (b) surface-sensitive total electron yield (TEY).

4. Using synchrotron-based *in-situ* X-ray absorption near-edge spectroscopy to study β -NaCu_{0.2}Mn_{0.8}O₂

In FY2017, the studies of a new cathode material, Cu-doped β -NaMnO₂ layered material for sodium-ion batteries have been completed. The *in-situ* X-ray absorption near-edge spectroscopy for β -NaCu_{0.2}Mn_{0.8}O₂ have been performed to explore the charge transfer mechanism. As shown in Figure II-617, the normalized *in-situ* XAS data indicates that Cu exist as Cu⁺² and Mn have a oxidation state that is between Mn⁺³ and Mn⁺⁴. The Mn K-edge spectra shift to higher energy region upon charged to 4.0 V, which nearly overlap with the K-edge of MnO₂ suggesting that Mn⁺³ ions are oxidized to Mn⁺⁴ state. For Cu, however, the shift is much less significant, which indicate that Cu is not the major contributor for the charge compensation mechanism. Nevertheless, both Mn and Cu XAS spectra feature pronounced shoulder peaks upon charge. This peak is probably due to the ligand-to-metal charge transfer process, which implies a strong covalency between M (Cu or Mn) and O upon the charging process.

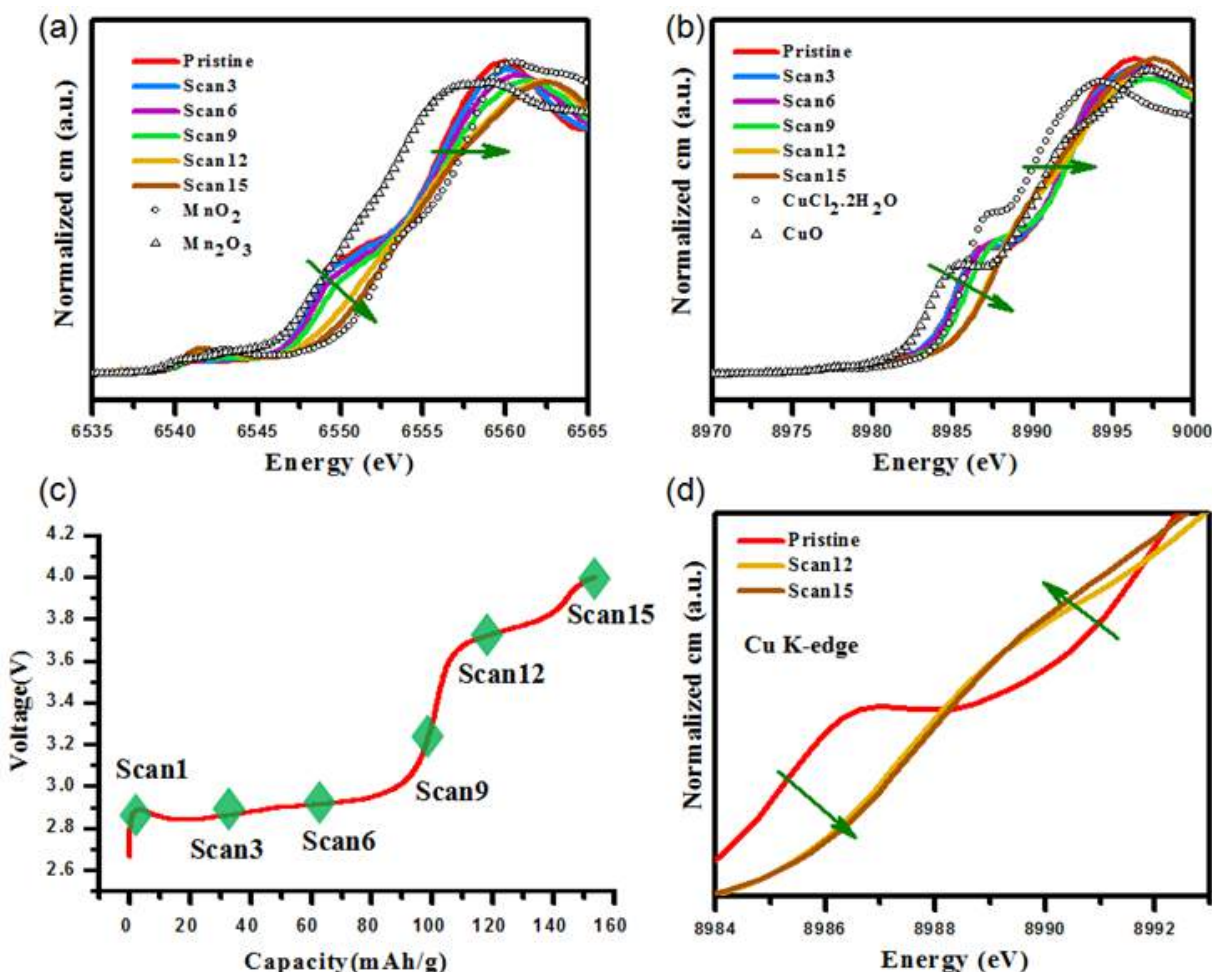


Figure II-617. Charge compensation mechanism upon Na deintercalation/intercalation in $\beta\text{-NaCu}_{0.2}\text{Mn}_{0.8}\text{O}_2$. (a) in-situ XAS spectra at Mn K-edge collected at different charge/discharge states; (b) in-situ XAS spectra at Cu K-edge collected at different charge/discharge states (c) The load curve of $\beta\text{-NaCu}_{0.2}\text{Mn}_{0.8}\text{O}_2$ during the first charge process for in-situ XAS. (d) The enlarged XAS spectra at Cu K-edge.

Conclusions

V_2CT_x MXene shows reversible electrochemical charge storage with good cycling stability and high rate capability which are important characteristics for the high power battery and Na-ion capacitor applications. The charge storage mechanisms were studied using a combination of ex/in situ synchrotron-based XRD, XANES and sXAS. The XRD results confirm that the expansion/contraction of the interlayer space of V_2CT_x upon Na^+ intercalation/deintercalation during first cycle. V K-edge XANES results clearly show the redox reaction of vanadium during the Na^+ intercalation/deintercalation, which implies that the redox reaction at the transition metal (M) site in MXene is responsible for the electrochemical charge storage. The results of V $L_{2,3}$ -edge sXAS experiments provided further direct evidence of such a redox reaction of vanadium within the MXene. In addition, C and O K-edge sXAS results shows potentially important features related to the reversible formation/decomposition of CO_3^{2-} species upon sodiation/desodiation. This surface related reaction is still not fully understood, but may provide valuable information for further understanding of V_2CT_x electrodes as well as CO_3^{2-} related redox systems. For $\beta\text{-NaCu}_{0.2}\text{Mn}_{0.8}\text{O}_2$ XAS results show that Cu exist as Cu^{+2} and Mn have a oxidation state that is between Mn^{+3} and Mn^{+4} and Mn^{+3} ions are oxidized to Mn^{+4} state, while Cu is not the major contributor for the charge compensation mechanism.

Key Publications

1. Zhizhen Zhang, Qinghua Zhang, Jinan Shi, Yong S. Chu, Xiqian Yu, Kaiqi Xu, Mingyuan Ge, Hanfei Yan, Wenjun Li, Lin Gu*, Yong-Sheng Hu*, Hong Li, Xiao-Qing Yang, Liquan Chen, Xuejie Huang, “A self-forming composite electrolyte for solid-state sodium battery with ultra-long cycle life” *Adv. Energy Mater.*, (October, 2016), DOI: 10.1002/aenm.201601196.
2. Ming-Hui Cao, Yong Wang, Zulipiya Shadike, Ji-Li Yue, Enyuan Hu, Seong-Min Bak, Yong-Ning Zhou*, Xiao-Qing Yang* and Zheng-Wen Fu* “Suppressing the chromium disproportionation reaction in O3-type layered cathode materials for high capacity sodium-ion batteries”, *J. Mater. Chem. A*, 2017, 5, 5442-5448, DOI: 10.1039/C6TA10818K
3. Hu-Rong Yao, Peng-Fei Wang, Yue Gong, Jienan Zhang, Xiqian Yu, Lin Gu, Chuying OuYang, Ya-Xia Yin, Enyuan Hu, Xiao-Qing Yang, Eli Stavitski, Yu-Guo Guo*, and Li-Jun Wan, “Designing Air-Stable O3-Type Cathode Materials by Combined Structure Modulation for Na-Ion Batteries”, *J. Am. Chem. Soc.*, 2017, 139 (25), pp 8440–8443, DOI: 10.1021/jacs.7b05176, Publication Date (Web): June 9, 2017
4. Qin-Chao Wang, Enyuan Hu, Yang Pan, Na Xiao, Fan Hong, Zheng-Wen Fu, Xiao-Jing Wu, Seong-Min Bak, Xiao-Qing Yang, and Yong-Ning Zhou, “Utilizing Co²⁺/Co³⁺ Redox Couple in P2-Layered Na_{0.66}Co_{0.22}Mn_{0.44}Ti_{0.34}O₂ Cathode for Sodium-Ion Batteries”, *Advanced Science*, publication date: July 6, 2017, DOI: 10.1002/advs.201700219
5. Zulipiya Shadike, Yong-Ning Zhou, Lan-Li Chen, Qu Wu, Ji-Li Yue, Nian Zhang, Xiao-Qing Yang, Lin Gu, Xiao-Song Liu, Si-Qi Shi, Zheng-Wen Fu, “Antisite occupation induced single anionic redox chemistry and structural stabilization of layered sodium chromium sulfide”, *Nature Communications*, Published online 2017 Sep 18. DOI: 10.1038/s41467-017-00677-3.

II.K.2 Advanced Organic Materials for Batteries (Stanford University)

Yi Cui, Principal Investigator

Stanford University
Department of Materials Science and Engineering
Stanford, CA 94305
Phone: 650-723-4613
E-mail: yicui@stanford.edu

Zhenan Bao, Principal Investigator

Stanford University
Department of Chemical Engineering
Stanford, CA 94305
Phone: 650-723-2419
E-mail: zbao@stanford.edu

Tien Duong, Technology Manager

U.S. Department of Energy
Phone: 202-586-7836
E-mail: Tien.Duong@ee.doe.gov

Start Date: October 1, 2016
Total Project Cost: \$300,000

End Date: September 30, 2017
DOE share: \$300,000

Non-DOE share: \$0

Project Introduction

Recent advances in lithium-ion battery (LIB) technology have improved energy densities of practical cells to values as high as 250 Wh kg⁻¹. However, applications of LIBs in electric vehicles still require increased energy density due to the high cost and poor range capability of current technology. To advance the current battery technology for grid storage applications, organic materials with versatile functionalities can play key roles to improve energy density cycle stability and material sustainability. This study pursues three main directions of using advanced organic materials: 1) designing polymer coating for a dendrite-free Li metal anode, 2) improving reaction kinetics of a Li/S battery, 3) developing a high energy density cathode for sodium storage.

Objectives

1. Identify the critical factors that influence the dendrite-free growth of Li metal in the presence of a polymer coating and develop an understanding of the interface between the polymeric coating and the Li metal.
2. Present a simple and effective strategy to activate Li₂S near its equilibrium potential by adding a small aromatic molecule in the electrolyte as a redox mediator (RM).
3. Demonstrate a high-performance sodium host by using a biomass-derived ionic compound, disodium rhodizonate, based on unprecedented four-sodium storage chemistry.

Approach

In developing polymer coating, we systematically chose a small number of polymers to isolate chemical and mechanical factors, including our previously published self-healing polymer (SHP), a self-healing elastomer (SHE) with similar chemistry to the SHP, polyurethane (PU), poly (ethylene oxide) (PEO), poly (vinylidene fluoride) (PVDF), and an elastomeric poly (vinylidene fluoride-co-hexafluoropropylene) (PVDF-HFP). In the first year, the team focused on gaining a more complete fundamental understanding of this newly proposed concept. Standard electrochemical and spectroscopic techniques including EIS, FTIR, SEM, and XPS were

used to examine Li metal that is electrodeposited through a polymer coating and the resulting solid electrolyte interphase (SEI).

For the sulfur electrode design, we prepared monodispersed 800 nm Li_2S particles as a cathode material to have homogeneous and consistent reaction chemistry and to monitor morphology evolution of the particles during battery cycling. We introduced a redox-active small molecule that is highly soluble in the conventional Li-S battery electrolyte of 1 M lithium bistrifluoromethanesulfonimide (LiTFSI) in dioxolane/dimethoxyethane (1:1, DOL/DME). The RM to sulfur ratio was kept at 1:10.

We also conducted a systematic study on the electrochemical performance of disodium rhodizonate ($\text{Na}_2\text{C}_6\text{O}_6$) by controlling active particle sizes and electrolyte conditions. Using *in situ* synchrotron X-ray diffraction (XRD) combined with *ex situ* scanning electron microscopy (SEM), sodium-driven structure and morphology changes can be monitored during the sodiation/desodiation process.

Results

Designing polymer coating for a dendrite-free Li metal anode

On the anode side, Li metal has the highest specific capacity ($3860 \text{ mAh/g}_{\text{Li}}$), and, when paired with high voltage metal oxide materials or high capacity sulfur cathodes, Li metal full cells can potentially enable energy densities higher than 500 Wh kg^{-1} . Unfortunately, the growth of porous Li during cycling causes low Coulombic efficiency and Li dendrites have the potential to short circuit the cell, leading to safety concerns.

As can be clearly seen in Figure II-618, all of the Li deposited with the various polymers have different morphologies and sizes. In contrast to what is expected from Classical nucleation theory, we found that the overpotential at the Li nucleation event was approximately the same for every polymer coating tested. We noticed that the local morphology of Li deposited in the presence SHP coatings and SHE coatings looked very similar while the global deposition was significantly different. This indicates that the polymer chemistry is important for dictating the morphology of the Li nuclei. We are currently in the process of correlating the Li metal surface inhibition, as measured by exchange current density, with the surface energy and dielectric constant of the different polymers.

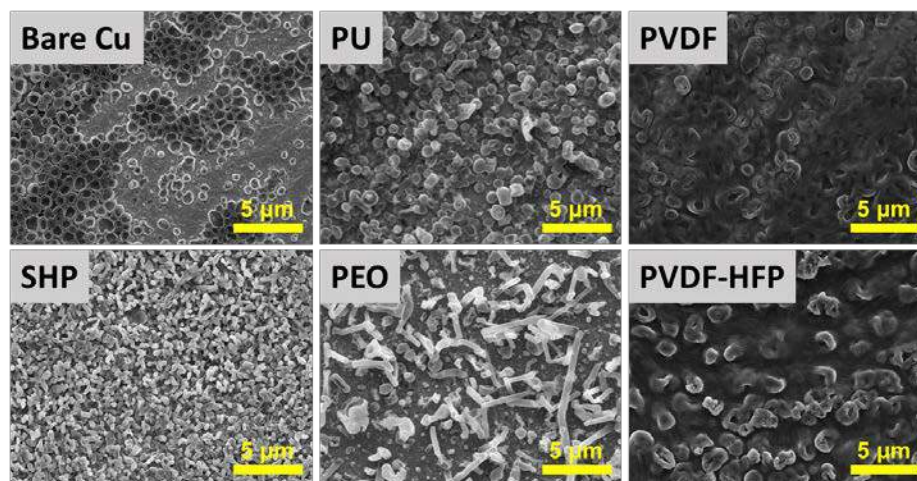


Figure II-618. Ex-situ SEM of the initial nucleation of Li on polymer-coated Cu foil. See top inset for polymer identity. Deposition current density was 1 mA/cm^2 and a capacity of 0.1 mAh/cm^2 was deposited in each case.

Improving reaction kinetics of a Li/S battery

Lithium-sulfur (Li-S) batteries have attracted great interest because of their abundance and high theoretical energy density of 2500 Wh kg^{-1} . Utilization of lithium sulfide (Li_2S) as a cathode material in Li-S batteries provides a safe and facile way to build Li-S batteries by directly solving problems from sulfur volume

expansion and lithium metal anode. However, the insulating nature of Li_2S leads to voltage polarization on charging which largely limits their electrochemical activities.

We introduced a small aromatic molecule in the electrolyte as a RM to activate Li_2S near its equilibrium potential (Figure II-619a). Upon charging, a RM with a redox potential that is slightly higher than the oxidation potential of Li_2S can be reduced and will oxidize the Li_2S particles at the surface. Then, the RM can be oxidized back at the current collector. Therefore, the RM molecule shuttles electrons between Li_2S and current collector continuously, facilitating charge transfer kinetics throughout the electrode. Indeed, we confirmed that oxidation of the Li_2S electrode is possible at 2.3 V when using a RM to sulfur ratio of 1:10 at a 0.1C (Figure II-619b).

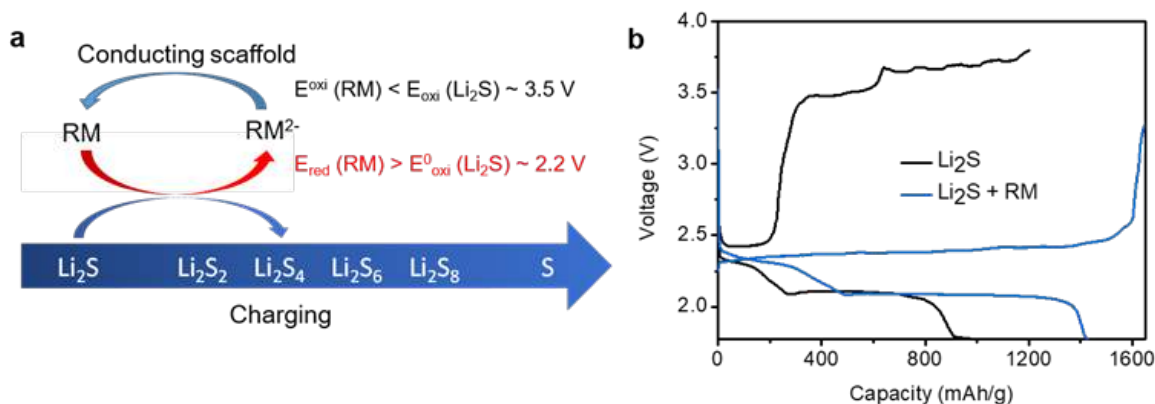


Figure II-619. a) The reaction mechanism of Li_2S oxidation with a redox mediator (RM). b) Voltage profiles of Li_2S electrodes in the first charge/discharge cycle with and without a RM in a DOL/DME electrolyte.

It is important to note that, in the presence of a RM, the morphology of Li_2S particles can be retained after prolonged charge/discharge cycles. As shown in Figure II-620a, spherical 800 nm Li_2S particles are still predominant in the SEM image after 250 charge/discharge cycles, while the particles turn into flat chunks without the RM. This strong contrast in the morphology evolution suggests a clear difference in the reaction chemistry with and without RM molecules in accordance with our hypothesis. Given the homogeneous morphology, introduction of RM molecules indeed facilitates a simultaneous reaction of Li_2S particles throughout the electrode. Furthermore, the continuing particle shape reflects limited diffusion of the reaction intermediates. The homogeneous reaction chemistry and limited diffusion of intermediates by introducing RM resulted in outstanding cycle stability of the Li_2S electrode at 0.5C (Figure II-620b).

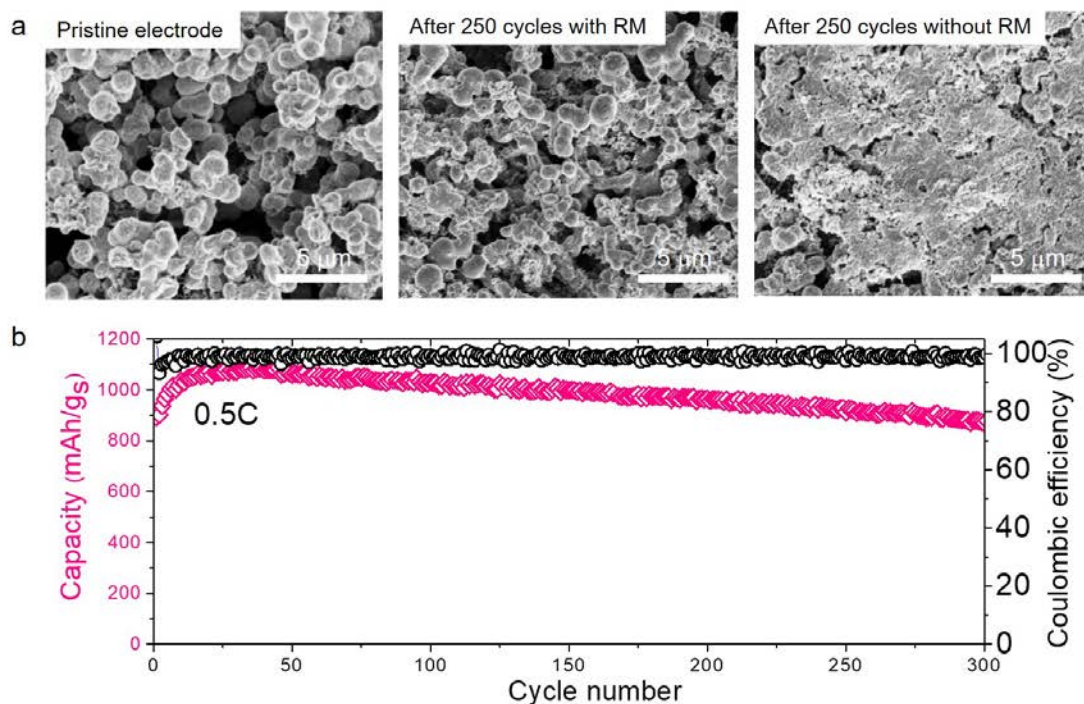


Figure II-620. a) *Ex situ* SEM to monitor morphology evolution of Li₂S particles after 250 cycles with and without RM molecules. b) Capacity retention of a Li₂S electrode in presence of the RM in the electrolyte at 0.5C.

Developing a high energy density cathode for sodium storage

The rise of renewable solar and wind power is demanding sustainable storage technologies using components that are inexpensive, earth abundant and environmental friendly. This has prompted the development of sodium ion batteries (SIB) because of its low cost and the inexhaustible sodium resources. Given the abundance and high theoretical specific capacity of 501 mAh/g, disodium rhodizonate (Na₂C₆O₆) is one of the most promising cathode materials for SIB, which can be obtained from biomass through green chemistry. However, substantially lower reversible capacities have been obtained in previous studies compared to the theoretical value, while understanding on this discrepancy has been limited.

To probe the phase transformation disodium rhodizonate during sodium insertion/desertion, *in situ* synchrotron XRD was performed using 300 nm Na₂C₆O₆ electrode in a DEGDME electrolyte (Nano/DEGDME). As shown in Figure II-621a, we clearly observed the phase transformation from α to γ during the initial plateau at 2.0 V of discharge, showing the gradual increase and decrease of characteristic peaks from γ phase and α phase, respectively. Then, when charging to 2.9 V, a positive shift in the characteristic peaks of γ phase was observed. Upon charging from 2.9 V to 3.2 V, we finally observe a two phase region, corresponding to phase transformation from γ -Na_{2.5}C₆O₆ to α -Na₂C₆O₆ (Figure II-621b), demonstrating the reversible phase transition during the discharge/charge process. We attribute the distinctive plateau around 3.0 V in Nano/DEGDME (Figure II-621a, highlighted in a circle) to this two-phase region.

We further monitored sodium-driven morphological changes was during the first cycle by SEM. As shown in Figure II-621c, the pristine electrode consists of 300 nm-sized Na₂C₆O₆ particles and conductive carbon particles which are smaller than 50 nm. Upon sodiation, the nanoparticles maintained the initial structure as a whole; when recharging to 2.9 V, they still showed the similar morphology. In contrast, once charged up to 3.2 V, in which case the electrode fully recovered the original α phase, we observed noticeable change in the particle morphology. As shown in Figure II-618e with high magnification, nanosized grains smaller than 50 nm were formed within the particle, while maintaining the integrity of the network structure in the following cycles.

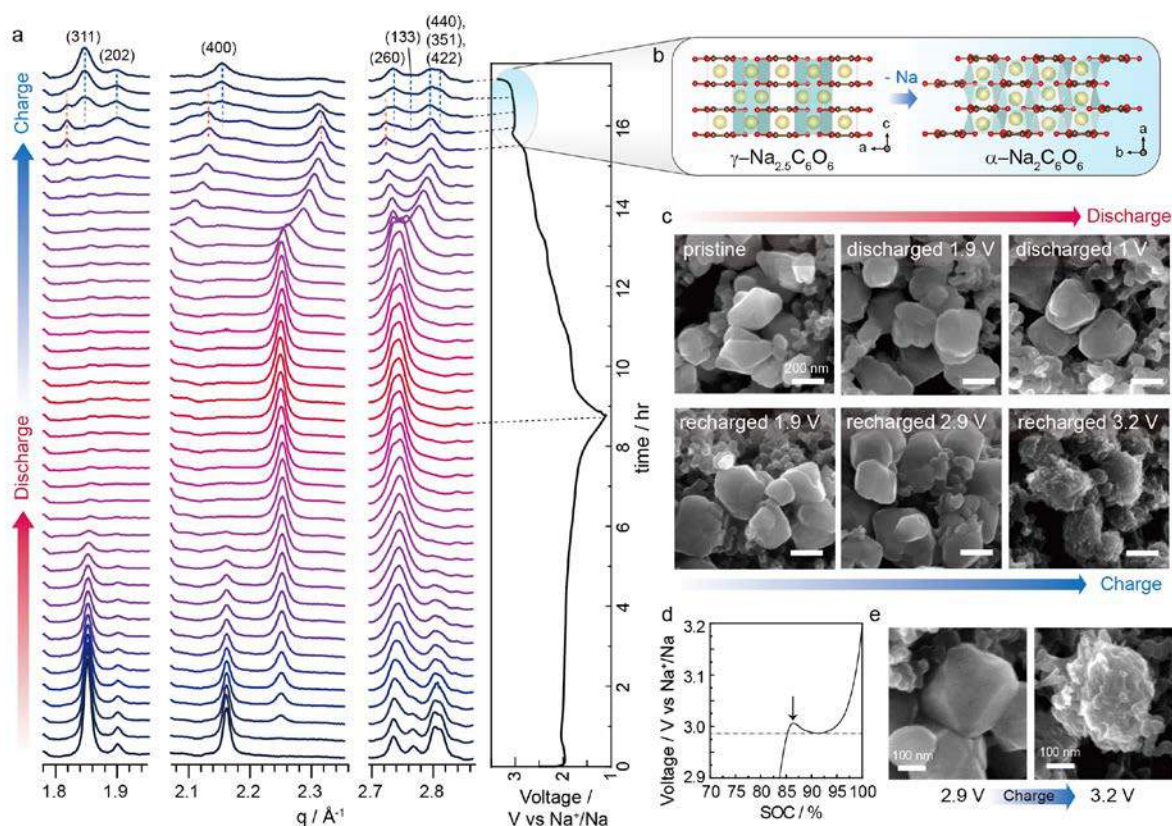


Figure II-621. Structural and morphological changes during reversible phase transformation of $\text{Na}_2\text{C}_6\text{O}_6$. a, *In situ* synchrotron XRD patterns of nanoparticle electrodes collected for the every 0.1 Na-stoichiometry change. b, Crystal structure change of $\text{Na}_{2+x}\text{C}_6\text{O}_6$ when charged above 2.9 V. c, *Ex situ* SEM images of nanoparticle electrodes at different states of charge during the first cycle. d-e, Dramatic morphology change and the corresponding voltage profile during the phase transformation.

Based on the above investigation, we propose redox mechanisms of $\text{Na}_2\text{C}_6\text{O}_6$. During sodiation, the α phase of $\text{Na}_2\text{C}_6\text{O}_6$ is transformed into γ phase, which is energetically more favorable with the additional sodium. When removing the sodium during charging, the reverse structural change is kinetically suppressed, which leads to a premature desodiation in most cases at the voltage limit set to secure structural stability. Thus, the charged electrode remains in the γ phase as partially-sodiated species ($\text{Na}_{2+x}\text{C}_6\text{O}_6$), which significantly limits the redox capability of the electrode in subsequent cycles. Nevertheless, the reversible phase transformation in the stable potential window becomes possible by decreasing the particle size and selecting a proper electrolyte. Among the electrolytes, DEGDME appears to be the most efficient in facilitating the phase transformation.

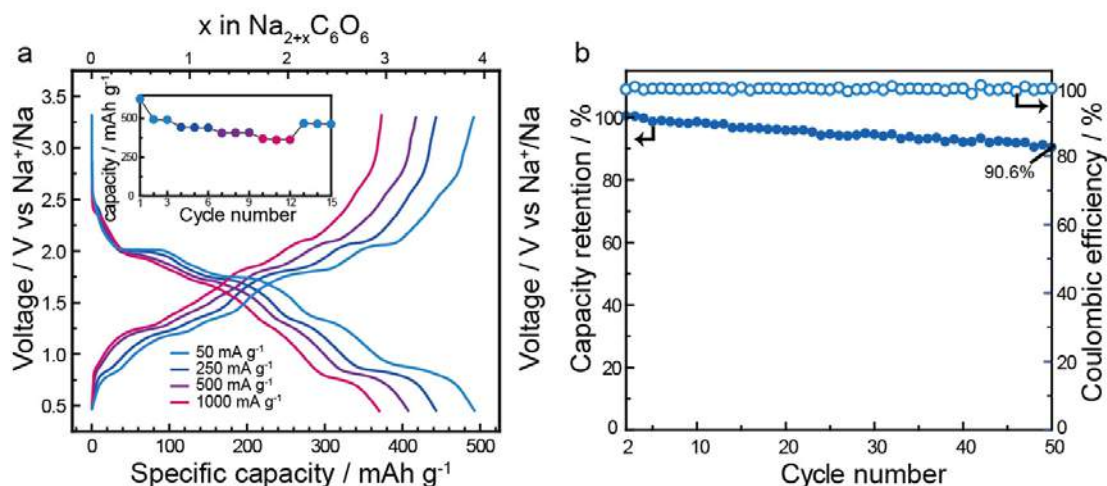


Figure II-622. Electrochemical four-sodium storage of $\text{Na}_2\text{C}_6\text{O}_6$ electrodes in half cells and full cells. a, Rate capability and corresponding cycle performance (inset) of $\text{Na}_2\text{C}_6\text{O}_6$ electrode from 0.5–3.3 V. b, Cycle retention of $\text{Na}_2\text{C}_6\text{O}_6$ electrodes at 500 mA g^{-1} corresponding voltage profile (inset) for 50 cycles.

The understanding of the sodiation mechanism of $\text{Na}_2\text{C}_6\text{O}_6$ indeed allowed us to demonstrate a four-electron process in a Na-ion cell for the first time. This was demonstrated in an enlarged potential window from 0.5 to 3.2 V. As shown in Figure II-619a, a reversible capacity of 498 mA h g^{-1} was obtained at 50 mA g^{-1} in Nano/DEGDME, which is as high as 95% of the theoretical capacity (Figure II-622a). Even at the very high rates of 500 mA g^{-1} and 1000 mA g^{-1} , the electrode retained a specific capacity of 408 mAh g^{-1} and 371 mAh g^{-1} , respectively. The $\text{Na}_2\text{C}_6\text{O}_6$ electrode showed good capacity retention upon cycling (Figure II-622b). After 50 cycles, about 90.8% capacity of the second cycle was still available in the potential window of 0.5 to 3.2 V at 500 mA g^{-1} . We obtained the maximum specific energy density nearly 726 Wh kg^{-1} , where the weight is based on the cathode mass of $\text{Na}_2\text{C}_6\text{O}_6$, with a high energy efficiency above 87% surpassing the performances of any other cathode candidates for SIB.

Conclusions

We identified a group of chemically and mechanically diverse polymers to study the effects of different polymer coatings on the nucleation and growth of Li metal films. Using these polymers, we observed the effect of smaller and more uniform Li nuclei observed originally with our SHP can be generalized to multiple polymer coatings and can be attributed to the increased nucleation overpotential due to the presence of the polymer coating. However, the nucleation overpotential does not sufficiently explain the various shapes of the Li metal nuclei, which are highly dependent on the chemistry of the polymer coating. Work is presently in progress to identify the critical factors that influence Li metal nuclei morphology in the presence of polymer coatings.

We confirmed that the introduction of RM can facilitate Li_2S oxidation near its equilibrium potential as low as 2.3 V. The continuing homogeneous morphology of the electrode in the prolonged cycling suggested a simultaneous reaction of Li_2S particles throughout the electrode and limited diffusion of the reaction intermediates. This in turn allowed excellent capacity retention of the Li_2S electrode over 300 cycles in the presence of RM in the electrolyte.

We achieved full utilization of four Na-ion storage in $\text{Na}_2\text{C}_6\text{O}_6$ based on the understanding of the redox mechanism associated with structural and morphological changes during cycling. We discovered that the deteriorating redox activity of $\text{Na}_2\text{C}_6\text{O}_6$ upon cycling originated from irreversible phase transformation, and identified active particle sizes and electrolyte conditions as key factors to complete the phase transformation during desodiation. The resulting electrochemical performances of $\text{Na}_2\text{C}_6\text{O}_6$ electrode including a specific

energy density of $726 \text{ Wh kg}_{\text{cathode}}^{-1}$, a high energy efficiency above 87 %, and a good cycle retention surpass any reported performances of cathode candidates for SIB.

Key Publications

1. Lee, M.; Hong, J.; Lopez, J.; Sun, Y.; Feng, D.; Lim, K.; Chueh, W. C.; Toney, M. F.; Cui, Y.; Bao, Z. High-Performance Sodium–Organic Battery by Realizing Four-Sodium Storage in Disodium Rhodizonate. *Nature Energy* **2017**, 2, 861–868.
2. Tsao, Y.; Chen, Z.; Rondeau-Gagné, S.; Zhang, Q.; Yao, H.; Chen, S.; Zhou, G.; Zu, G.; Zu, C.; Cui, Y.; Bao, Z., Enhanced Cycling Stability of Sulfur Electrodes through Effective Binding of Pyridine-Functionalized Polymer. *ACS Energy Lett.* **2017**, 2, 2454–2462.
3. Zheng, G.; Wang, C.; Pei, A.; Lopez, J.; Shi, F.; Chen, Z.; Sendek, A. D.; Lee, H.-W.; Lu, Z.; Schneider, H.; Safont-Sempere, M. M.; Chu, S.; Bao, Z.; Cui, Y. High-Performance Lithium Metal Negative Electrode with a Soft and Flowable Polymer Coating. *ACS Energy Lett.* **2016**, 1247–1255.
4. Bao, Z.; Cui, Y.; Zheng, G.; Wang, C.; Lopez, J.; Pei, A. U.S. Patent US20170062830 A1

II.L Beyond Li-ion R&D: Battery500 Innovation Center

II.L.1 Innovation Center for Battery500 (PNNL)

Jun Liu, Principal Investigator

Pacific Northwest National Laboratory
902 Battelle Boulevard
Richland, WA 99354
Phone: 509-375-4443
E-mail: jun.liu@pnnl.gov

Yi Cui, Co-Principal Investigator

Stanford University/SLAC
450 Serra Mall
Stanford, CA 94305
Phone: 650-723-4613
E-mail: yicui@stanford.edu

Tien Duong, Technology Manager

U.S. Department of Energy
Phone: 202-586-7836
E-mail: Tien.Duong@ee.doe.gov

Start Date: September 1, 2016
Total Project Cost: \$8,000,000

End Date: September 30, 2021
DOE share: \$8,000,000

Non-DOE share: \$0

Project Introduction

Lithium (Li)-ion batteries play a critical role in modern day technologies, but their specific energy (Wh kg^{-1}) and energy density (Wh L^{-1}) are approaching the maximum practically achievable values based on existing manufacturing processes with the conventional cathode and anode materials. The large scale deployment of electric vehicles and ever-increasing demand of modern technologies require further increase in cell energy and cost reduction. Li-metal batteries are regarded as the “Holy Grail” of high-energy-density systems because Li metal has an ultrahigh theoretical specific capacity (3860 mAh g^{-1}), the lowest redox potential (-3.040 V vs. standard hydrogen electrode), and low gravimetric density (0.534 g cm^{-3}). However, the practical application of Li metal anode still faces several significant challenges, including safety concern due to Li dendrite growth, limited cycle life because of low Li Coulombic efficiency, and large volume change during Li stripping and redeposition if a two-dimensional (2D) flat Li foil is used. In addition, developing next generation rechargeable Li metal batteries with a specific energy higher than 300 Wh kg^{-1} , up to 500 Wh kg^{-1} , is still a significant challenge. Many groups are focusing on the fundamental breakthroughs in electrode materials and control of the deleterious side reactions in such new battery concepts. Solid-state Li batteries using solid electrolytes have recently received wide attention due to the inherent high safety and decent energy. There have been intense efforts to improve the bulk conductivity, interfacial charge transport and stability for the manufacturing of the solid-state cells. A very desirable strategy is to take advantage of the electrode materials that are commercially or nearly commercially available, and introduce the least perturbation to the cell configuration and manufacturing process of the current technologies. Based on this considerations, two battery chemistries, high nickel content lithium nickel-manganese-cobalt oxide (high-Ni NMC, $\text{Ni} > 60\%$), coupled with Li metal anode, and Li-S chemistry, have the potential to achieve an energy density of at least 500 Wh kg^{-1} .

Objectives

The Battery500 Consortium aims to develop commercially viable Li battery technologies with a cell level specific energy of 500 Wh kg^{-1} through innovative electrode and cell designs that enable the extraction of the

maximum capacity from advanced electrode materials. In addition, the project aims to be able to achieve 1000 cycles for the developed technologies.

Approach

The Battery500 Consortium will utilize first class expertise and capabilities in battery research in the United States and develop an integrated and multidisciplinary approach to accelerate the development and deployment of advanced electrode materials in commercially viable high energy batteries. The Li anode combined with a compatible electrolyte system and two cathodes—one high-Ni $\text{LiNi}_x\text{Mn}_y\text{Co}_z\text{O}_2$ (NMC) and another sulfur (S)—will be studied and developed to reach high energy density. The project focus is to design novel electrode and cell architectures in order to meet the 500 Wh kg^{-1} goal. The consortium will work closely with R&D companies, battery/materials manufacturers and end-users/OEMs to ensure that the developed technologies are aligned with industry needs and can be transitioned to production. The out-year goals for FY17 include: (1) completion of first phase full cell fabrication and testing based on the consortium recommended protocols, demonstrating 300 Wh kg^{-1} full cell capacity, (2) provision of analytical results for materials selection, cell design and fabrication, and further refinement for 2018, and (3) completion of the selection and launching of seedling projects for Battery500.

Results

1. Project Leadership and Coordination

The whole consortium team has three keystone projects and has organized various teams, including the research teams, the Leadership Team, the Executive Committee, the Advisory Board and the Industry Committee, and set up their roles and responsibilities. A total of 14 projects are defined. A Working Committee, made of one representative from each institution was formed with the function of keeping the whole consortium updated of the research progresses through biweekly telephone conferences. Several large core groups, including the NMC cathode group, the anode group, the diagnostic group, and the S group, were formed. The coordinator for each large core group is responsible for organizing biweekly phone conferences to exchange research results and discuss important issues within each project throughout the whole first quarter. These teleconferences were also announced through the whole consortium to welcome PIs, research scientists, postdocs, and students from other project to attend and provide their inputs. In addition, several sub-groups were also formed, including the electrolyte group, the characterization group, the diagnostic and electrochemical characterization group, and the cell design and fabrication group. These subgroups are responsible for ensuring regular communications and meeting program goals on the project level. A drop box folder dedicated to Battery500 has also been set for communications and file exchanges within the consortium.

The integrated efforts of the consortium team have been effective. The biweekly telephone conferences for the leader team, the Working Committee, as well as for each Keystone project and special task teams (such as cathode, anode, and diagnostic teams) were held regularly. The summaries of the teleconferences for the Working Committee were emailed to all PIs afterward, while the presentations of the technical conferences were distributed even more widely including staff scientists, postdocs and students who are working on the Battery500 projects. At many tele-conferences, the young scientists (postdocs and students) are the main presenters and their active involvements during and after tele-conferences are the key factors to achieve the milestones of FY2017.

The FY2017 first quarterly review/annual meeting was held at SLAC on January 20, 2017, and the other three quarterly review meetings were held at University of Texas at Austin from April 27 to 28, 2017, University of Washington (UW) in Seattle from July 11th to 12th, 2017, and UCSD in San Diego from October 18th to 19th, 2017, respectively. Averagely about 50 people attended these review meetings, including DOE Program managers, the Executive Committee members, the PIs, staff scientists, and a big group of postdocs and students. At each review meeting, the DOE Program managers gave updates of the DOE programs, the Consortium Director (Jun Liu) gave overviews of the consortium, and invited PIs and postdocs gave the updates of the keystone projects and technical progresses related to quarterly review topics. Starting from the second review meeting, a poster session was included to exchange the progresses of different projects among

the consortium. Two best poster awards were installed starting from the third quarterly review to acknowledge the great contributions of postdocs and their teams. In the third quarterly review meeting, an “Exceptional Team Contribution Award” was presented to Prof. Stan Whittingham.

The first Advisory Board meeting was held in Washington DC with participation from the DOE program managers, representatives from USABC, IBM, FMC, Naatbatt and Tesla.

2. Keystone Project 1: Materials and Interfaces

The preliminary screening and selection of most promising candidates of commercial cathode materials, electrolytes (salts, solvents and additives), and separators were first evaluated and the baseline materials were set up for the first phase full cell assembly and testing.

On high-Ni NMC cathodes, the baseline materials of NMC622 and NMC811 from commercial source (EcoPro) were first characterized and evaluated at different loadings and current densities. EcoPro NMC622 shows high dependence of rate performance on sample loading, and high loading leads to poor electrochemical performance at higher rates. Although the NMC811 does not show significant electrochemical dependence on loading, we observed hints of the formation of a second phase at above 4.2 V in NMC811. Then, high-Ni NMC materials with Ni content of 60~94% have been synthesized in-house and characterized. These show the desired meatball morphology (Figure II-623a) with very uniform particle sizes. The electrochemical performance indicates as expected that the higher Ni contents lead to higher capacities (Figure II-623b), but worse cycling stability (Figure II-623c). Al doping and surface coating with Al-containing materials (*e.g.*, Al_2O_3) have been used to improve the high Ni content NMC materials (NMC622, NMC811, and NMC90505). Al doping in the high-Ni NCO greatly enhances the cycling stability (Figure II-623d). Our results show that such Al doping and Al_2O_3 coating play critical roles in capacity retention.

On high-Ni content cathode materials, further studies were conducted to understand the performance degradation, including both NCA and NMC. The cathode degradation include particle cracks, decreased crystallinity, active mass dissolution, loss of active Li ions and the irreversible surface structural rearrangements upon Li extraction during battery operation. In addition, the enhancement of cycling stability in 2% Al-doped high-Ni NCO was found to be due to the formation of a thinner SEI layer and a more ordered surface structure with no abrupt phase change. Last, the better rate capability of high-Ni NMC was studied by EIS and LPR techniques. The origins for the improved electronic and ionic conductivities are related to the defect levels (Li/Ni mixing or cation vacancies which could introduce holes as charge carriers and the weakened Li-O bonding or more structural defects (vacancies) (which facilitate Li^+ jumping), respectively.

On Li metal anodes, several in-situ and ex situ grown films have also been developed to protect the Li metal anode. A core-shell nanoparticle coating has been prepared as an interfacial layer for dendrite free Li metal anodes. An adaptive “solid-liquid” interfacial layer was also developed to protect Li metal anode. In addition, a robust coating layer of crystalline methyl lithium carbonate was formed in-situ on Li metal surface through a solution chemical process and dendrite free Li metal anode was observed after long-term cycling at 3 mA cm^{-2} in conventional LiPF_6 /carbonate-based electrolyte. In other approaches, an inorganic/organic hybrid coating based on Cu_3N -SBR has been developed to protect 3D porous Li metal anode; a thin and dense LiF coating was generated on Li metal surface by using gaseous phase Freon method, which leads to enhanced stability of Li metal in electrolytes and even in air. An electrolyte-proof structured Li-ion conductive nanocomposite ($\text{Li-Li}_{22}\text{Si}_5\text{-Li}_2\text{O}$) was also developed by embedding Li in Li^+ conductive scaffold and then pressing into pellets, which shows stable dimensions, impedance and voltage polarization during long-term stripping and redeposition processes. A Janus separator with one side coated with an ultrathin Cu film was developed to suppress Li dendrites and to improve the cycling stability of Li anode.

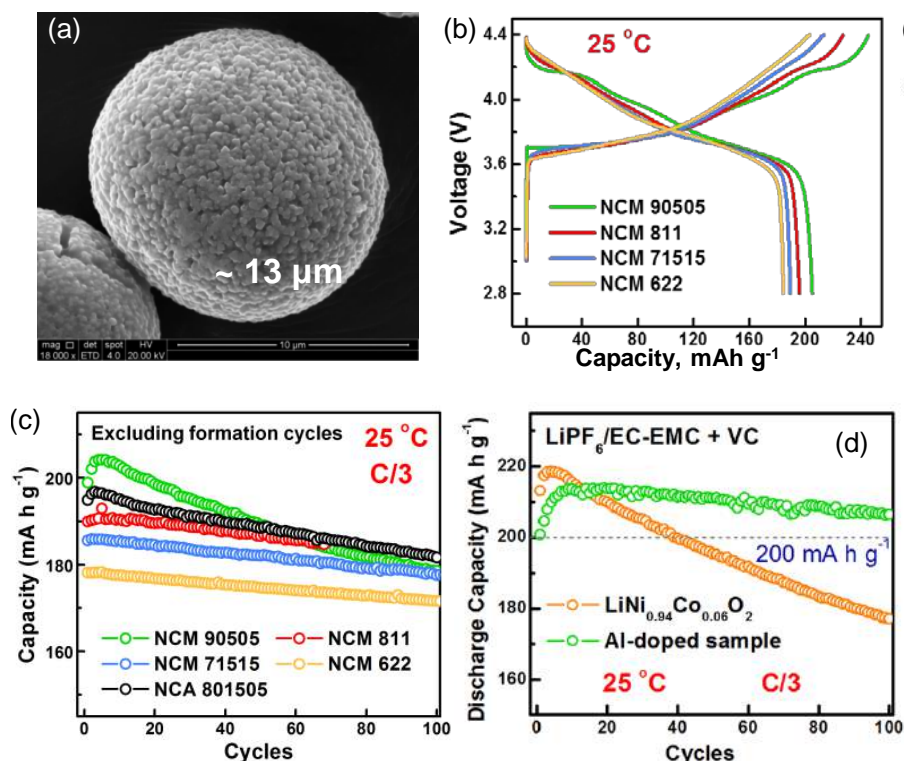


Figure II-623. (a) Morphology of the in-house synthesized high-Ni NMCs showing spheres with the primary and secondary particles. (b) First cycle voltage profiles and (c) cycle life of Li||NMC cells between 4.4 and 2.8 V. (d) Comparison of the cycling performance of high-Ni Li_{0.94}Co_{0.06}O₂ with and without Al doping in cells with Li-metal anode.

On electrolytes, several new electrolyte formulations have been developed to enable Li deposition/stripping with electrochemical stability window expanded to voltage over 4.3 V and Coulombic efficiency (CE) improved to more than 98%. These new electrolytes are based on LiFSI salt and solvent mixture of sulfones, carbonates, phosphates and other co-solvents. Specifically, an electrolyte using LiFSI salt in a mixture of phosphate solvent and a co-solvent has a Li CE as high as 99.3% and provides stable cycling for at least 200 cycles at C/3 rate in the voltage range of 2.8 to 4.4 V in Li||NMC622 cells (Figure II-624). More importantly, such LiFSI-phosphate electrolytes are non-flammable, which is critical for safe operation of Li metal batteries. One of the electrolytes has been used in the 1 Ah pouch cells delivered for Year 1 project and enabled the high capacity cells to be cycled for 50 cycles under realistic conditions required for the project.

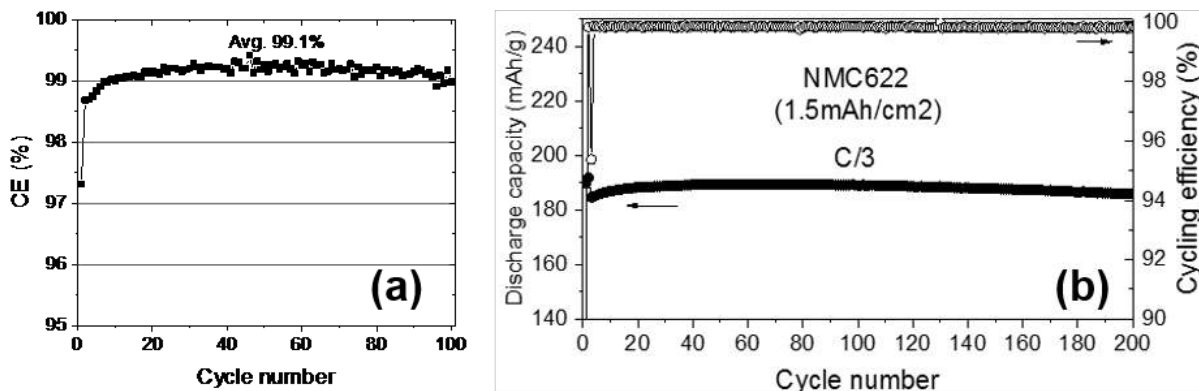


Figure II-624. Cycling stability of LiFSI-phosphate electrolytes (E313) in various cell systems, (a) Li||Cu, and (b) Li||NMC622.

3. Keystone Project 2: Electrode Architectures

The goal of Keystone 2 is to design, model, fabricate and characterize the effect of electrode architecture on electrode and cell performance in order to reach the goal of 500 Wh kg⁻¹ cell specific energy. Included in this Keystone are architecture design of thick cathodes (UCSD), Li metal electrode architectures (PNNL and Stanford), inorganic (UT-Austin) and polymer (Stanford) electrolytes, and electrode performance modeling (UW).

In the area of thick cathodes, cycling performance of the baseline NMC622 material was first measured as a function of type and amounts of binder, carbon, and active material loadings. A new electrode architecture with high amount of straight voids in the electrode was fabricated. Electrochemical impedance measurement confirmed a reduction of tortuosity. Modeling of an electrode with graded porosity shows improved power capability as well. These two examples show the potential of designing electrode architectures to achieve higher power density. After establishing baseline performance, efforts have focused on developing innovative electrode architectures to reduce tortuosity by creating vertical, straight channels in electrodes. Scalable methods are developed to create vertical openings, and additional processing steps are used to adjust the density and gap width. The effective electrolyte conductivity of electrodes with the same overall porosity of 30% is shown to increase with the initial gap area. This positive correlation confirms that microstructure control can be effective in reducing resistance of electrolyte transport in electrodes. Further work has included: 1) evaluating thick cathodes provided by Maxwell; 2) performing systematic baseline measurement of NMC 811 to understand performance limiting factors; and 3) assessing the power performance of electrodes with advanced architectures. Two main conclusions are: 1) Li metal cycling stability affects the evaluation of thick cathodes due to its failure; and 2) at the targeted C/3 rate, electrode performance appears to be limited by electronic rather than ionic transport. Two Maxwell NMC 622 electrodes have thicknesses of 100 and 190 μm and active materials loadings of 30 and 60 mg cm⁻², respectively (Figure II-625a, b). At a C/3 rate, the electrodes deliver very similar specific capacities: 165.7 vs 162.5 mAh g⁻¹ (Figure II-625c). This indicates that under this testing condition, the loading does not limit rate performance. Cycling tests in coin cells show that a higher cathode loading leads to an earlier cell failure due to the increased Li utilization and electrolyte consumption (Figure II-625c). Replacing the Li and electrolyte after 100 cycles and cycling at C/10, the 30 mg cm⁻² 622 cell has resurrected the capacity, as shown in Figure II-625d, showing the stability of the cathode but the instability of the electrolyte and Li anode. This observation indicates that Li metal failure and electrolyte consumption are responsible for cell performance decay when testing thick electrodes. The limiting factors for thick cathode rate performance is further evaluated by testing electrodes with different loadings at different current densities. Electrodes with areal loadings of 10-60 mg/cm² all deliver similar specific capacity as long as the areal current density is similar, which is consistent with the results obtained from the Maxwell electrodes.

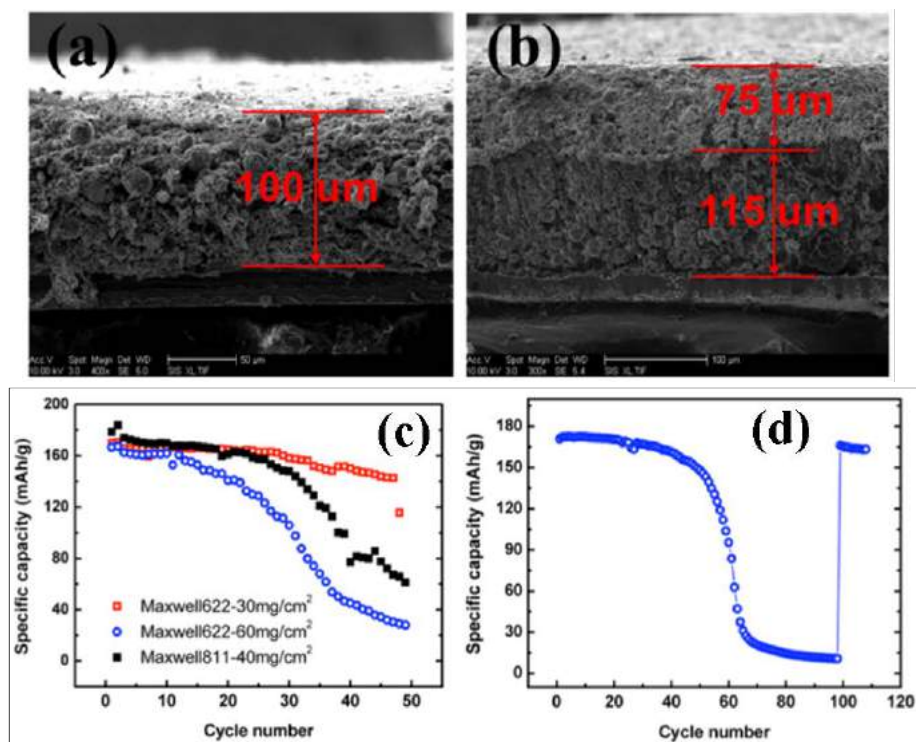


Figure II-625. (a, b) Cross-section SEM images of two Maxwell NMC622 thick electrodes: (a) 30 mg cm⁻²; (b) 60 mg cm⁻². (c) Cycling performance at C/3 of three 622/811 cells of different cathode loadings. (d) Specific capacity with cycling for the 30 mg cm⁻² NMC 622 electrode at C/3 for the first 100 cycles and subsequent resurrection of the cell by replacement of Li anode and electrolyte.

Electrode design for Li anode has focused on developing 3D hosts for Li deposition and 3D structured Li/carbon composite anodes, which reduce effective current density and maintain macroscopic dimension, both of which promise longer cycle life. 3D structured Li/carbon composite anodes based on carbon cloth (CC), carbon film (CF) and carbon paper (CP) have been developed. All Li||NMC622 cells using Li/carbon composite anodes demonstrate much better rate capability and long-term cycling stability than those using Li foil anodes when the same conventional LiPF₆/carbonate electrolyte was used. For example, the Li/CC||NMC622 cells can retain 92% of capacity after 300 cycles at C/3 rate (0.52 mA cm⁻²) in the voltage range of 2.8 ~ 4.4 V.

The team has also pursued 3D architectures for Li metal in order to manage volume change, reduce effective current density, suppress dendrite formation and increase cycle life. A porous Ni framework fabricated in house that is less than 50 μm thick, can be filled with Li metal, and more importantly, form a dense layer on its surface after cycling which enables fast ion transport. Figure II-626 shows the cross sectional images of a designed 3D porous Li host made of lithium oxide and lithiated silicon. By using a robust host structure, macroscopic dimensional changes are minimized.

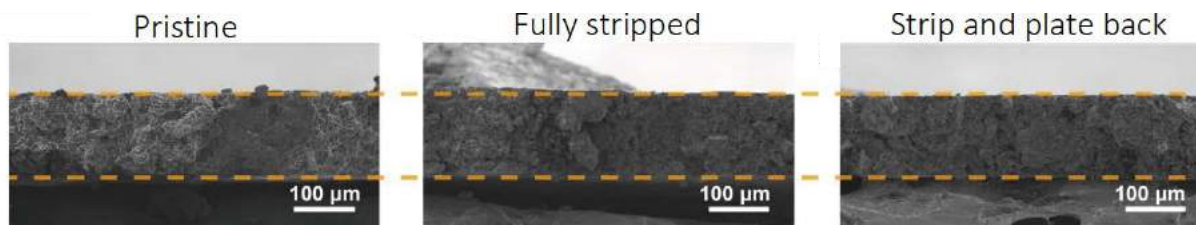


Figure II-626. SEM images of the cross section of a porous 3D host for Li metal plating and stripping, demonstrating its macroscopic dimensional stability.

Another method to control Li deposition is through the use of a flowable, highly viscoelastic polymer coating which promotes more uniform nucleation of Li. A soft/hard adaptable polymer is flowable under low shear rate but becomes stiff under high shear rate. This mechanism is effective in regulating Li growth to prevent the formation of Li filaments. Further, new polymer electrolytes were designed to offer higher ion conductivities and stable interface with Li by manipulating the Li ion coordination environment. Finally, a solid electrolyte $\text{Li}_{3/8}\text{Sr}_{7/16}\text{Hf}_{1/4}\text{Ta}_{3/4}\text{O}_3$ (LSHT) has shown a room temperature conductivity of $3.8 \times 10^{-4} \text{ S cm}^{-1}$ at 25°C and demonstrated good stability with Li metal.

Results obtained so far in Keystone 2 have established that architectural control is essential for both the Li anode and the oxide cathode in order to meet the design goal of the Battery500 program. In the case of both electrodes, 3D design will be coupled with optimization of interfacial chemistry to offer high efficiency and cycling stability. Work continues in further development of electrode architectures guided by modeling and with increased coordination with the Characterization team in the Consortium to understand the mechanisms of performance improvement.

4. Keystone Project 3: Cell Fabrication, Testing and Diagnosis

The Keystone 3 has first jointly established methods for evaluation of high energy cells both electrochemically and through the use of advanced characterization techniques and resources, set up methods for the preparation of 1 Ah or larger cells, and used different models to identify cell design parameters for achieving both 300 and 500 Wh kg^{-1} . Cell designs for both 300 Wh kg^{-1} and 500 Wh kg^{-1} of Li||NMC622 and Li||S chemistries were determined using a combination of computational methods with experimental input by a combined team of researchers at INL, PNNL and UW. Activities also included means to develop a greater understanding of full cell aging dynamics and design implications. With regard to cell design, multiple computational methods were used for verification purposes. These include finite element modeling, partial two dimensional (P2D) and reduced order P2D approaches. As shown in Figure II-627a good agreement was attained between the computational methods and the experimental data for the Li||NMC622 chemistry. Additionally, there was good agreement between the different methods with variance between the three methods on the order of less than 5% across multiple cell designs. Overall the methods were used to determine that, depending on the quantity of electrolyte used, that the thickness of the positive NMC622 electrode ranged from 170 to 270 μm . These cell design determinations served as a starting point to help facilitate the construction of 1 Ah Li||NMC622 cells to meet the milestone of 300 Wh kg^{-1} .

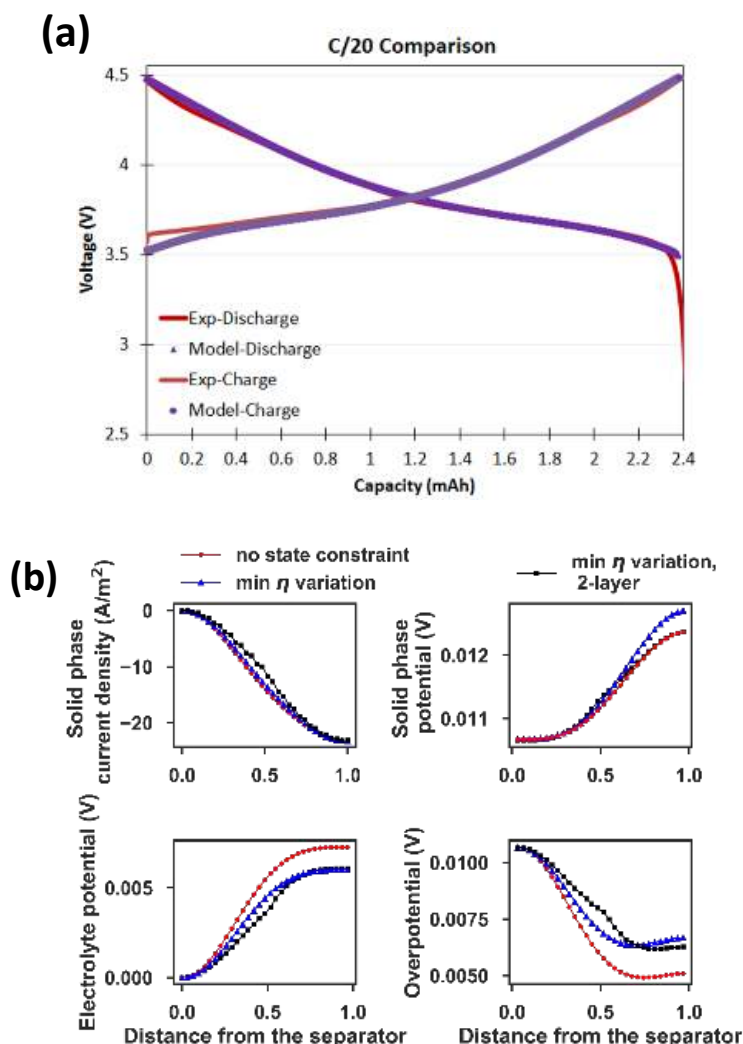


Figure II-627. (a) Comparison of calculated and experimental charge/discharge curves for a Li || NMC622 cell. (b) Internal profiles for solid phase current density, solid phase potential, electrolyte potential and overpotential (clockwise from top left). The dashed red line and blue lines are for different porosity uniform electrodes while the black line is associated with a graded porosity electrode.

In line with the cell design activities various electrode optimization routes were used to look at the impact of graded electrodes to enhance the performance of thick NMC622 electrodes (Figure II-627b). This work at UW was completed both to understand the impact of grading and to implement computational approaches which significantly reduce the amount of time needed to perform calculations. The new approach is much faster (up to 1000 times) compared with the conventional approaches including the common sequential optimization approach.

A key component of Keystone 3 activities for FY2017 involved developing a more robust understanding on how to effectively transition technologies from early demonstration in small coin-type cells to larger format pouch cells. One of the key considerations for achieving high energy cells is a pouch cell using lean electrolyte and a limited source of Li metal. For the present work these values equate to Li foil that is 50 μm thick and electrolyte loading of 3 g Ah^{-1} . This is considerably different from most data reported in the laboratory studies in the literature. To help facilitate the transition from laboratory activities to pouch cell development, a set of standard protocols for evaluating promising materials using similar lean electrolyte and limited Li was developed and distributed to the team.

In cell fabrication, great team efforts have been made to reach the 300 Wh kg⁻¹ specific energy and the 50 cycle life goals in a real 1 Ah pouch cell, not just in a ~4 mAh coin cell with large amount of extra electrolyte and Li metal anode. When extra electrolyte and Li metal are used in a coin cell, the cycle life can be extended to several hundred cycles. However, the real specific energy is rather low when all the weights of the cell components are counted. In order to reach the real 300 Wh kg⁻¹ goal, the team carefully calculated the required weight limit for each component, such as cathode, anode, separator, electrolyte, Cu and Al current collectors, tabs, and package material. With the limited electrolyte and Li metal in the prepared pouch cells and even in coin cells, a severe limitation in cycle life was observed. All cells failed after less than 15 cycles when the conventional LiPF₆/carbonate liquid electrolyte was used. The short cycle life is caused by the interaction between the Li metal and the conventional LiPF₆/carbonate liquid electrolyte, which generated significant quantities of “dead” Li and caused electrolyte depletion. Even after refilling the electrolyte, the cells had only half of the original capacity and faded quickly. A new electrolyte was developed to reduce the reaction between the Li metal and the electrolyte, which significantly extended the cycling life of the 300 Wh kg⁻¹ pouch cell. The FY2017 milestone of 50 cycling life was used with this new electrolyte developed (see Figure II-628). The importance of this achievement is not only reaching the milestone, but also providing guidance for future research approaches to increase the specific energy and the cycle life. The results on the 300 Wh kg⁻¹ showed that the FY18 efforts need to focus on solving the “dead” Li and the electrolyte depletion problems by developing Li metal protection methods, such as surface modification of Li, modified separator, and new electrolyte additives and new electrolyte systems.

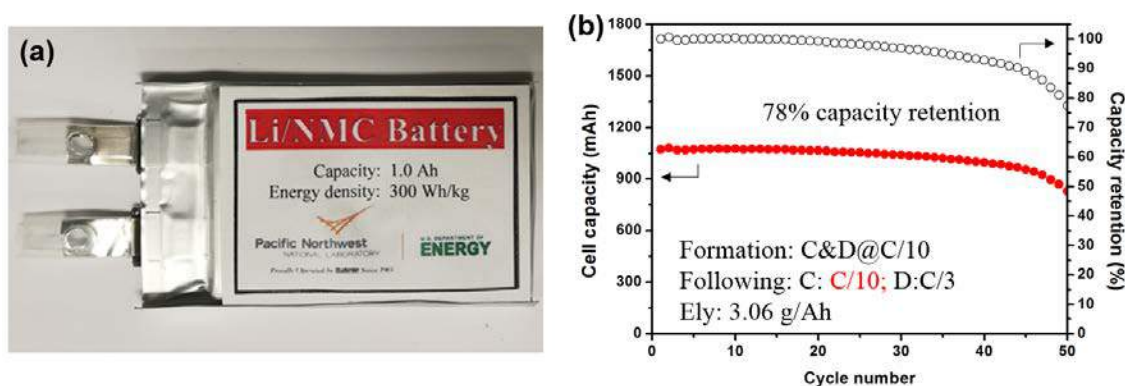


Figure II-628. (a) Picture of the 1 Ah and 300 Wh kg⁻¹ pouch cell with Li | NMC622 system. (b) Cell capacity and capacity retention vs cycle number for a 1.1 Ah, 300 Wh kg⁻¹ Li | NMC 622 pouch cell with a PNNL developed electrolyte. The capacity retention of 78% is obtained at the 50th cycle.

Performing analysis of fading mechanisms during cycling provides a pathway to identify gaps in cell design. Such analysis enables other keystone areas to refine materials or designs to improve performance. As part of this process, differential capacity (dQ/dV) analysis was performed to understand the performance of both positive and negative electrode materials. The robust diagnostic and prognostic approach also provide information on both kinetic and thermodynamic fade modes. The dQ/dV results and other corresponding data confirm that the capacity fading was not due to the positive electrode (NMC 622) performance, but was instead associated fade of the Li metal negative electrode and overall transport limitations. Initial work looking at cell variability was extended to study the role that reducing electrolyte volume has on cell fading providing support to the 1 Ah cell design. In addition, key parameters which will enable optimization of both cell performance and energy density, have been evaluated including electrode thickness, porosity, tortuosity and overall loading of active high Ni NMC materials or of sulfur. Initial bounds for each parameter have been identified and are being refined to understand the full sensitivity of the parameters on overall cell design. In conjunction with parametric analysis, cell models looking at how to more effectively the architectures in a Li metal battery have been established. Figure II-629a includes the general premise for the initial model which includes a porous positive electrode and a planar Li metal negative electrode. A key component of the Li metal side of the cell is

that a moving boundary due to SEI reactions is included. Figure II-629b includes predicted values using this model and experimental data collected for a cell that had an NMC 622 positive electrode. With the inclusion of the moving boundary good agreement between model and experiment have been identified.

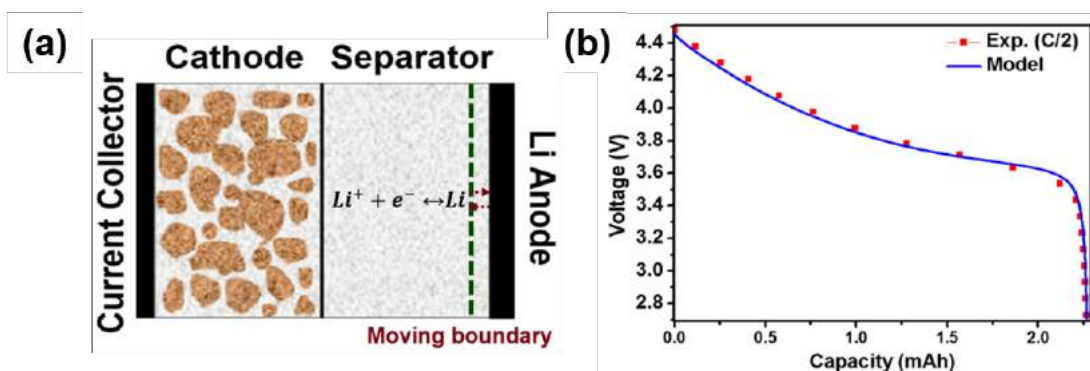


Figure II-629. (a) Schematic of modelled system and (b) comparison between model and experimental data for a NMC622 cell.

The team is developing novel characterization methods to quantify Coulombic efficiency losses in Li metal anodes which allow identification of “dead” Li and other Li loss mechanisms. X-ray diffraction (XRD) has been developed to accurately track metallic Li through plating and stripping cycles. Figure II-630 shows diffraction data that allow quantification of metallic “dead” Li and comparison to Coulombic efficiency. Figure II-631 (a) shows the Li (110) peak intensity through four plating and stripping cycles. We attribute the metallic Li intensity left at the end of a cycle to “dead” Li and create an efficiency ratio of the amount of Li stripped to the amount of Li plated, measured through XRD. These results are shown in Figure II-631 (b) along with the Coulombic efficiency and represent the first quantitative distinction between dead Li and Coulombic inefficiency. Future work will involve a direct comparison to modelling efforts with Keystone 3 and spatially-resolved micro-diffraction measurements.

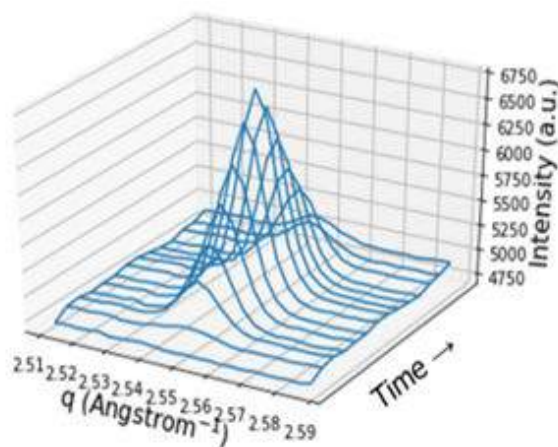


Figure II-630. One-dimensional intensity vs. q (scattering vector) at the Li (110) peak through one plating and stripping cycle at 1.5 mA cm^{-2} .

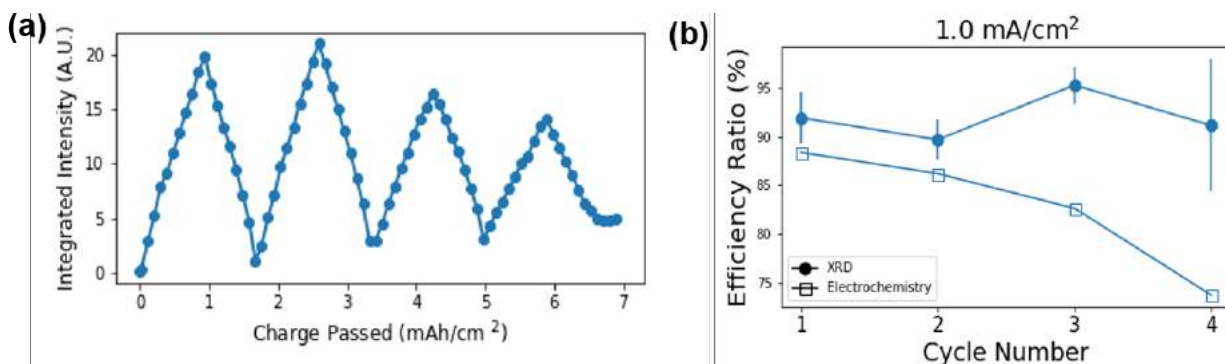


Figure II-631. Representative results from in situ XRD measurements of Li plating onto copper substrate. (a) Integrated intensity of Li (110) XRD peak vs. time passed throughout four Li plating and stripping cycles at 1.0 mA/cm^2 in 1 M LiPF_6 in EC/DMC. (b) Corresponding electrochemical (Coulombic) and XRD efficiencies (ratio of amount stripped to plated).

For determination of Li||S cell design a liquid-solid composite electrolyte was studied. The average operating voltage at the C/3 rate and C/5 rate discharge was determined by a finite element model using COMSOL, with the discharge capacity limited in the range from 800 to 1100 mAh g^{-1} sulfur. As with the Li||NMC622 cells the computational results were compared to experimental data to ensure close alignment between the real and computed designs. After reaching agreement a parametric method was used with various electrode thicknesses and porosities to determine routes capable of achieving a 500 Wh kg^{-1} cell design. These calculations indicate that there are multiple challenges for the Li||S system to achieve 500 Wh kg^{-1} . Key technical hurdles include solid state ionic conductivity (for the solid component of the electrolyte) and total amount of electrolyte. Activities are currently underway to understand how to mitigate these limitations for the cell design.

The other set of key activities for Keystone 3 in FY2017 was on characterization of both high Ni NMC cathodes and Li metal at BNL, UCSD and SLAC. For the cathodes, activities focused on understanding the effect of high Ni in the NMC if the Ni is increased to 90% or higher. Local structure for 11 different NMC phases was performed using multiple methods to understand relationships between the samples. In addition, depth profiling of cathodes with thicknesses up to $200 \mu\text{m}$ (in coordination with Keystone 2) also occurred showing distinct differences in performance and charging/discharging efficiency as a function of depth. Both cathode activities will play a prominent role in understanding how to effectively use high Ni NMC and to effectively use thick electrodes for high energy density Li||NMC cells.

With regard to Li metal an emerging focus is on the quantification of Li loss and the identification of inactive Li. Across multiple studies spanning keystone areas this was identified as a significant issue that needs to be addressed. Early evaluation using multiple techniques including cryo-TEM, XRD and electrochemical methods has identified that there are key factors associated with both the initial deposition of Li metal on electrodes as well as significant evolution in performance which is not directly correlated with other measurements such as CE. Future activities will be more directly focused on this area and on improving understanding of the relationship between lean electrolyte and limited Li to support the development of pouch cell designs beyond 300 Wh kg^{-1} .

Based on the calculation, testing and characterization of electrode materials, coin cells and pouch cells, Battery500 established standard testing protocols for both NMC and S cells for FY2018, which specify the amount of cathode, anode and electrolyte materials, as well as the formulation procedure and charge/discharge rates. All team members are required to use the standard testing protocols when reporting results related to the cell level specific energy and/or the cycling life of the cells and/or electrode materials.

Conclusions

Established the criteria to achieve the 500 Wh kg⁻¹ goal for both high Ni NMC and sulfur systems.

Demonstrated progress on the Keystone Projects:

- Developed synthetic approaches, doping methods and surface coatings to stabilize high Ni NMC cathodes exhibiting ~220 mAh g⁻¹ with superior cyclability, rate capability, and power density compared to the control cell.
- Developed several electrolytes with greatly improved stability towards both NMC cathode and Li metal anode with Coulombic efficiency higher than 98%.
- Developed new concepts on self-healing polymers and ordered architectures to control lithium metal deposition.
- Developed new perovskite solid state electrolytes with good Li ion conductivity.
- Demonstrated good progress on electrode architectures and full cell performance.
- Established standard testing protocols and requirements for using the standard testing protocols.

Key Publications

1. A. Pei, G. Zheng, F. Shi, Y. Li, and Y. Cui, "Nanoscale nucleation and growth of electrodeposited lithium metal", *Nano Lett.*, 2017, **17**, 1132-1139.
2. J. Zheng, M. H. Engelhard, D. Mei, S. Jiao, B. J. Polzin, J.-G. Zhang, and W. Xu, "Electrolyte additive enabled fast charging and stable cycling lithium metal batteries", *Nature Energy*, 2017, **2**, 17012.
3. D. Lin, Y. Liu, and Y. Cui, "Reviving the lithium metal anode for high-energy batteries", *Nature Nanotech.*, 2017, **12**, 194-206.
4. W. Liu, W. Li, D. Zhuo, G. Zheng, Z. Lu, K. Liu, and Y. Cui, "Core-shell nanoparticle coating as an interfacial layer for dendrite-free lithium metal anodes", *ACS Central Sci.*, 2017, **3**, 135-140.
5. K. Liu, A. Pei, H. R. Lee, B. Kong, N. Liu, D. Lin, Y. Liu, C. Liu, P.-C. Hsu, Z. Bao, and Y. Cui, "Lithium metal anodes with an adaptive 'solid liquid' interfacial protective layer", *J. Am. Chem. Soc.*, 2017, **139**, 4815-4820.
6. W. Li, A. Dolocan, P. Oh, H. Celio, S. Park, J. Cho, and A. Manthiram, "Dynamic behavior of interphases and its implication on high-energy-density cathode materials in lithium-ion batteries", *Nature Commun.*, 2017, **8**, 14589.
7. S. B. Lee, C. Pathak, V. Ramadesigan, W. Gao, and V. R. Subramanian, "Direct, efficient, and real-time simulation of physics-based battery models for stand-alone PV-battery microgrids", *J. Electrochem. Soc.*, 2017, **164**, E3026-E3034.
8. Y. Xu, E. Hu, K. Zhang, X. Wang, V. Borzenets, Z. Sun, P. Pianetta, X. Yu, Y. Liu, X.-Q. Yang, and H. Li, "In situ visualization of state-of-charge heterogeneity within a LiCoO₂ particle that evolves upon cycling at different rates", *ACS Energy Lett.*, 2017, **2**, 1240-1245.
9. S. Rustomji, Y. Yang, T. K. Kim, J. Mac, Y. J. Kim, E. Caldwell, H. Chung, and Y. S. Meng, "Liquefied gas electrolytes for electrochemical energy storage devices", *Science*, 2017, **356**, 1351.
10. W. Li, B. Song, and A. Manthiram, "High-voltage positive electrode materials for lithium-ion batteries," *Chem. Soc. Rev.*, 2017, **46**, 3006-3059.

11. W. Li, U.-H. Kim, A. Dolocan, Y.-K. Sun, and A. Manthiram, "Formation and inhibition of metallic lithium microstructures in lithium batteries driven by chemical crossover", *ACS Nano*, 2017, **11**, 5853–5863.
12. K. Park and J. B. Goodenough, "Dendrite-suppressed lithium plating from a liquid electrolyte via wetting of Li_3N ," *Adv. Energy Mater.*, 2017, **7**, 1700732.
13. D. Lin, J. Zhao, J. Sun, H. Yao, Y. Liu, K. Yan, and Y. Cui, "Three-dimensional stable lithium metal anode with nanoscale lithium islands embedded in ionically conductive solid matrix", *Proc. Natl. Acad. Sci. U.S.A.* 2017, **114**, 4613-4618.
14. H. Wang, D. Lin, Y. Liu, Y. Li, and Y. Cui, "Ultrahigh-current density anodes with interconnected Li metal reservoir through overlithiation of mesoporous AlF_3 framework", *Sci. Adv.* 2017, **3**, e1701301.
15. H. Lee, X. Ren, C. Niu, L. Yu, M. H. Engelhard, I. Cho, M.-H. Ryou, H. S. Jin, H.-T. Kim, J. Liu, W. Xu, and J.-G. Zhang, "Suppressing lithium dendrite growth by metallic coating on separator", *Adv. Funct. Mater.*, 2017, 1704391. DOI: 10.1002/adfm.201704391
16. B. D. Adams, J. Zheng, X. Ren, W. Xu, and J.-G. Zhang, "Accurate determination of coulombic efficiency for lithium metal anodes and lithium metal batteries", *Adv. Energy Mater.*, 2017, 1702097. DOI: 10.1002/aenm.201702097 (Partially supported by Battery500)
17. K. Shah, N. Balsara, S. Banerjee, M. Chintapalli, A. P. Cocco, W. K. S. Chiu, I. Lahiri, S. Martha, A. Mistry, P. P. Mukherjee, V. Ramadesigan, C. S. Sharma, V. R. Subramanian, S. Mitra, and A. Jain, "State of the art and future research needs for multiscale analysis of Li-ion cells", *J. Electrochem. En. Conv. Stor.*, 2017, **14**, 020801.
18. X. Wang, M. Zhang, J. Alvarado, S. Wang, M. Sina, B. Lu, J. Bouwer, W. Xu, J. Xiao, J.-G. Zhang, J. Liu, and Y. S. Meng, "New insights on the structure of electrochemically deposited lithium metal and its solid electrolyte interphases via cryogenic TEM", *Nano Lett.*, 2017, **DOI:** 10.1021/acs.nanolett.7b03606.

III. Testing and Analysis

III.A Cost Assessments and Requirements Analysis

III.A.1 BatPaC Model Development (Argonne National Laboratory)

Shabbir Ahmed, Principal Investigator

Argonne National Laboratory
9700 S. Cass Avenue
Argonne, IL 60439
Phone: 630-252-4553
E-mail: ahmeds@anl.gov

Samuel Gillard, Technology Manager

U.S. Department of Energy
Phone: 202-287-5849
E-mail: Samuel.Gillard@ee.doe.gov

Start Date: October 1, 2012

End Date: October 31, 2018

Total Project Cost: \$700,000

DOE share: \$700,000

Non-DOE share: \$0

Project Introduction

A performance and cost model (BatPaC) was developed at Argonne to design automotive Li-ion batteries that can meet the specification of a given vehicle, and then to estimate the cost of manufacturing that battery. It is the product of long-term research and development at Argonne through sponsorship by the U.S. Department of Energy.

Over a decade, Argonne has developed methods to design Li-ion batteries for electric-drive vehicles based on modeling with Microsoft® Office Excel spreadsheets. These design models provided all the data needed to estimate the annual materials requirements for manufacturing the batteries being designed. This facilitated the next step, which was to extend the effort to include modeling of the manufacturing costs of the batteries.

The BatPaC model has been peer reviewed and is available on the web. It captures the interplay between design and cost of Li-ion batteries for transportation applications. Moreover, BatPaC is the basis for the quantification of battery costs in U.S. EPA and NHTSA 2017-2025 Light-Duty Vehicle Technical Assessment. This assessment is then used to determine what mileage (i.e., CAFE) and CO₂ emission standards are optimal from a cost-benefit analysis.

Objectives

To develop and utilize efficient simulation and design tools for lithium ion batteries to predict

- Overall and component mass and dimensions
- Cost and performance characteristics when manufactured in large volume

Approach

The battery pack design and cost calculated in BatPaC represent projections for a specified level of annual battery production (10,000-500,000). As the goal is to predict the future (~5 years) cost of manufacturing batteries, a mature manufacturing process is assumed. The model designs a manufacturing plant with the sole purpose of producing the battery being modeled. The assumed battery design and manufacturing facility are based on common practice today but also assume some problems have been solved to result in a more efficient production process and a more energy dense battery. Our proposed solutions do not have to be the same

methods used in the future by industry. We assume the leading battery manufacturers, those having successful operations in the near future, will reach these ends by some means.

For a selected battery chemistry, BatPaC solves the governing equations to determine the size of each layer, cell, and modules that make up the battery pack that can meet the desired requirements for power and energy. This allows the calculation of the mass of each material, the volume of the components, and the heat removal needed during discharge. The cost of the pack is then estimated based on a predefined manufacturing process.

Current effort is directed at

- Improving the design capability by including correlations derived from continuum modeling and updating the default material properties to reflect recent experimental and industrial performance data
- Reducing the uncertainty of model predictions by setting up independent models of the manufacturing processes
- Validating the results through discussions with manufacturers and component developers.
- Updating the cost of materials used in BatPaC calculations.

Collaboration

- Oak Ridge National Laboratory, Idaho National Laboratory, National Renewable Energy Laboratory, B&W-MEGTEC

Results

Key Accomplishments

- An analysis was conducted to compare the estimated costs of cells and packs for different electrode chemistries
- The model was revised to enable design for fast charge capability and was used to estimate the impact of fast charging lithium ion batteries
- A drying model has been developed to gain insight into the effects of electrode drying conditions
- The default material properties were improved to reflect recent results obtained from cell testing during teardowns by commercial companies

Cell Cost vs. Electrode Combinations

The BatPaC model was used to estimate the future cost of cells for automotive battery packs for a number of electrode combinations. The comparisons were made on the basis of a pack with an energy storage capacity of 100 kWh_{Total} (85 kWh_{Useable}), 300 kW, where the pack was designed with 168 cells and 315 V. The price of the materials used in the cells are as shown in Table III-1. The packs are produced in a battery manufacturing plant at a production volume of 100,000 packs per year.

Table III-1: Electrode material costs to estimate the cost of battery packs.

Materials	Price	
NMC333	19.00	\$/kg
NMC622	18.50	\$/kg
LMRNMC	18.50	\$/kg
Sulfur	5.00	\$/kg
OxideSpinel	8.00	\$/kg
Carbon	6.80	\$/kg
Binder PVDF	10.00	\$/kg
Binder Solvent (NMP)	3.20	\$/kg
Graphite	15.00	\$/kg
Graphite-Silicon	25.00	\$/kg
Silicon	25.00	\$/kg
Lithium	100.00	\$/kg
Magnesium	4.00	\$/kg
Carbon Black	6.80	\$/kg
Binder	10.00	\$/kg
Positive Current Collector	0.30	\$/m ²
Negative Current Collector	1.20	\$/m ²
Separator	1.20	\$/m ²
Electrolyte	17.00	\$/L

The prices of the cells shown in Figure III-1 represent best case projections where it is assumed that the problems with the electrode chemistries have been resolved, that performance is not limiting, and the manufacturing process has matured. The graphite-NMC333 combination is estimated to cost \$146 per kWh_{Useable}, where the cost of the cathode and the anode materials contribute \$40 and \$16, respectively. The cell costs are lowered with lower cobalt content (NMC622, LMRNMC). The introduction of lithium in the anode escalates the price but is offset by the lower cost of sulfur anodes. It is notable that many of the combinations in the right side of the figure have much developmental challenges, which if/when resolved, offer the opportunity for lower cost cells.

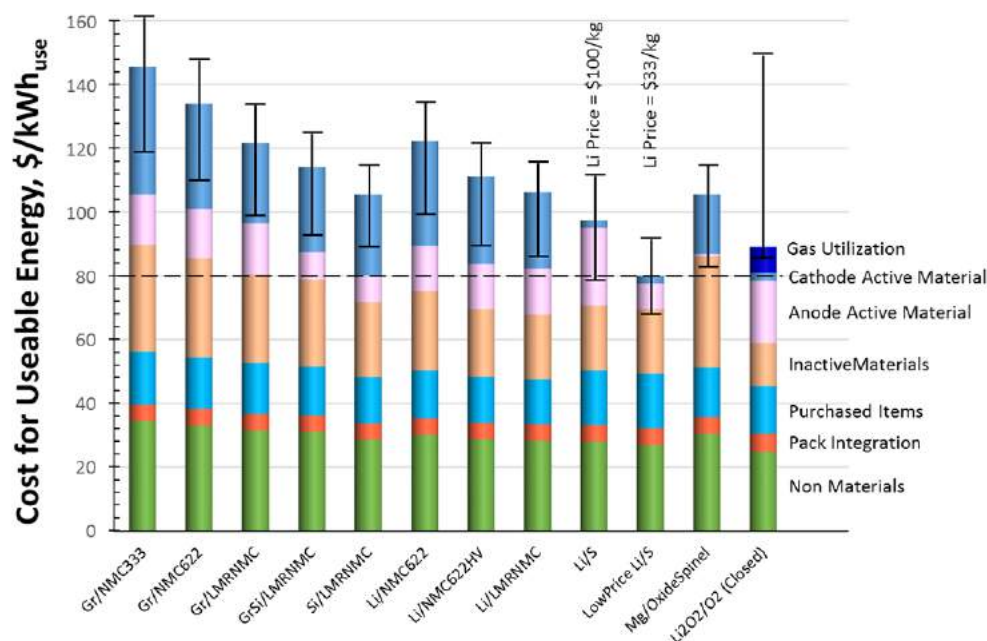


Figure III-1. Estimated costs of cells in automotive battery packs with different combination of electrodes. The packs are rated for 100 kWh_{Total} (85 kWh_{Useable}), 300 kW, 315 V, 168 cells, and produced at a plant volume of 100K packs/year

Fast Charging

The BatPaC model algorithm was modified to allow the electrode thickness to be determined by the most limiting constraint among (i) the sustained discharge and (ii) the maximum allowable current density (MACD) for fast charging. Earlier studies have suggested that the cells lose their capacity rapidly when charged at certain current densities, e.g., 4.0 mA/cm² [1]. A study of the added constraint of fast charging and its impact on the cost of the cells was conducted. The study was based on a pack rated for 100 kWh_{Total}, 85 kWh_{Useable}, 300 kW, 315 V, from 168 cells. The cell cost was estimated for a plant production volume of 100,000 packs per year.

Fast charging of a cell is challenged by deactivation caused by lithium deposition in the anode and / or rapid temperature rise to above acceptable limits. BatPaC designs the electrodes to prevent the lithium deposition scenario by limiting the current density to a maximum allowable value. The model's heat balance calculations estimate the heat generated and therefore the temperature rise in the cell under adiabatic conditions. The designed packs have coolant flows and a more rigorous analysis is appropriate to address the heat transfer from the cell center to the coolant channels at the module wall.

The current needed to raise the state of charge (SOC) of a cell increases inversely with the time available. Setting a limit on the current density requires increase in the cell area to process the required current, i.e., the electrode becomes thinner. Figure III-2 shows the relationship between the charging time allowed to raise the SOC by 80% and the anode thickness. At charging times greater than 59 minutes, the curve is flat because in this region the anode thickness is not limited by the MACD but rather by the sustained power requirement. At less than 59 minutes, where the design is MACD-limited, the anode becomes progressively thinner, reaching 20 microns at ~10 minutes. Thin electrodes and larger areas mean that the cells require more inactive materials such as the current collectors, separators, etc., which increase the size of the cells. These additions increase the cost and is reflected in the non-linear trend of the cost curve in Figure III-2. At 10 minutes, the cost of the cell is \$181 per kWh_{Total} (\$213 per kWh_{Useable}). As mentioned earlier, faster charging to achieve a given recharge requires a larger current and therefore a more powerful charging infrastructure. Figure III-3 plots the charger power required to recharge the cells in the pack as a function of the charging time. In order to raise the cell SOC by 80% in 10 minutes will require a charger power of ~550 kW.

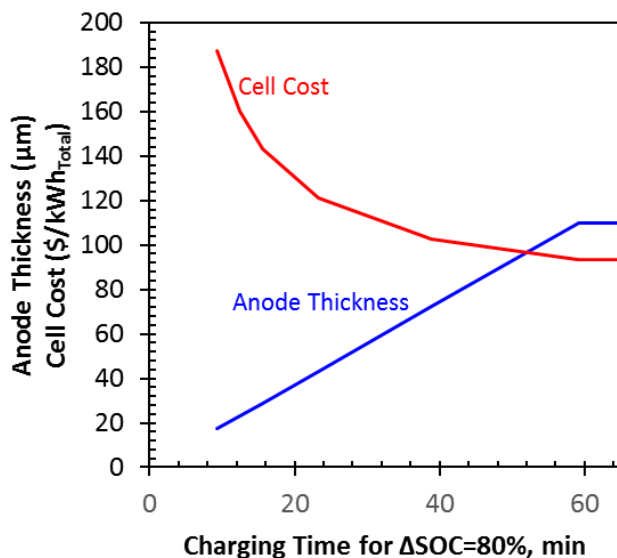


Figure III-2. Effect of charging time on anode thickness and cell cost. $\Delta\text{SOC}=80\%$

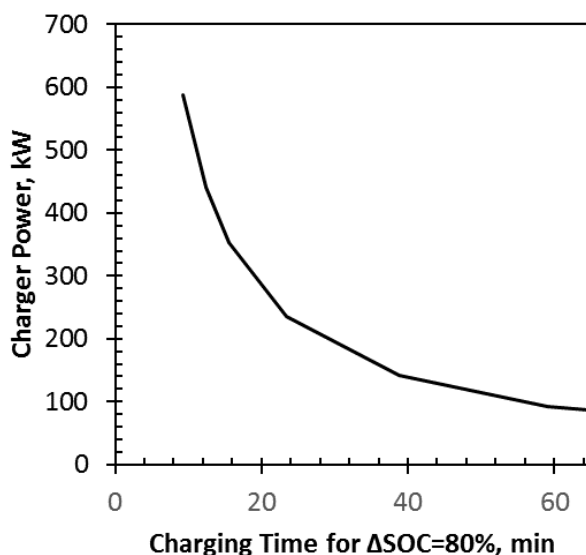


Figure III-3. Effect of charging time on charger power requirement. $\Delta\text{SOC}=80\%$

For the above simulations the maximum allowable current density was set at 4 mA/cm^2 . With continuing development of the anode material it is likely the anode layer will be able to tolerate higher current densities without lithium plating. Figure III-4 shows the effect of the MACD on the anode thickness, the post-charge cell temperature, and the cell cost for charging times of 20, 15, and 10 minutes. In Figure III-4(a) for the 20 minute charging time, the anode layer can be as thick as 110 microns where it is limited by the sustained power requirement (and not by the MACD) at $\text{MACD} > 11.9 \text{ mA/cm}^2$. For the 15 minute charge, the corresponding MACD is 15.8 mA/cm^2 , while for the 10 minute charge that point is at a $\text{MACD} \gg 16 \text{ mA/cm}^2$. Since the amount of inactive materials increase with thinner electrodes (sloping part of the curves), the cell mass increases at lower MACD.

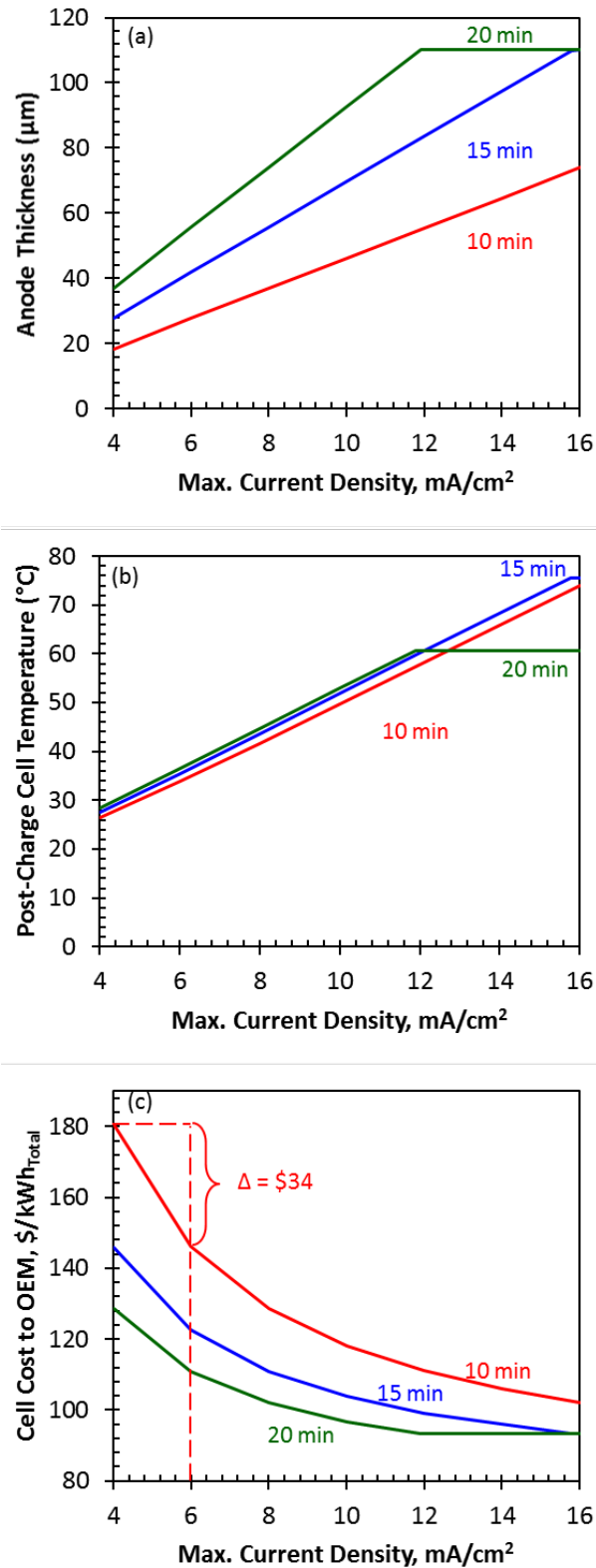


Figure III-4. Effect of the maximum allowable current density (MACD) on anode thickness, cell temperature, and cell cost. $\Delta\text{SOC}=80\%$

Figure III-4(b) shows the effect of the MACD on the post-charge cell temperature (assuming the cells were at 10°C at the beginning of the charge and there is no heat removal). The current needed for a given combination of charging time and $\Delta\text{SOC}=80\%$ is constant. However, in the region to the left of the knee, the final cell temperature is lower at decreasing MACD, because the cells have thinner electrodes but larger cell mass to absorb the generated heat. The region to the right of the knee is flat because here the anode thickness remain constant (no longer determined by the MACD constraint) and therefore the thermal mass remains constant.

Figure III-4(c) shows that the cells cost more at MACD values to the left of the knee because the thinner cells require additional inactive materials. The shorter charging times require more current flow, which when combined with the MACD constraint, requires still thinner electrodes. The net result is that the costs increase sharply as the MACD and the charging times are reduced. For the case of a 10 minute charge at a MACD of 4 mA/cm², the cells cost \$181/kWh_{Total}. Relaxing the charging time from 10 minutes to 15 minutes can reduce the cost of the cells by \$34/kWh_{Total}.

Solvent Drying

A mathematical model was set up to study the drying of the solvent n-methyl pyrrolidone (NMP) from the cathode coating. The base scenario was the drying of a 150-micron thick electrode layer packed with 10-micron particles, 60 wt.% solvent content, with flowing air at 95°C as the drying medium. Solution of the model equations reveal that the electrode layer reaches the air temperature within a fraction of a second but the time required for drying is 54 seconds, where drying is assessed to be complete when the solvent content drops to 0.01 wt.%. Figure III-5 shows the solvent content (liquid + vapor) to drop sharply initially and then more slowly because of mass transfer limitations. The drying rate, defined as the rate of solvent leaving the electrode layer, is seen to show a similar trajectory. It is interesting that 50% of the solvent is removed in 10 seconds and 90% in 30 seconds, but to remove the remaining 10% of the solvent it requires 24 seconds or 45% of the total drying time.

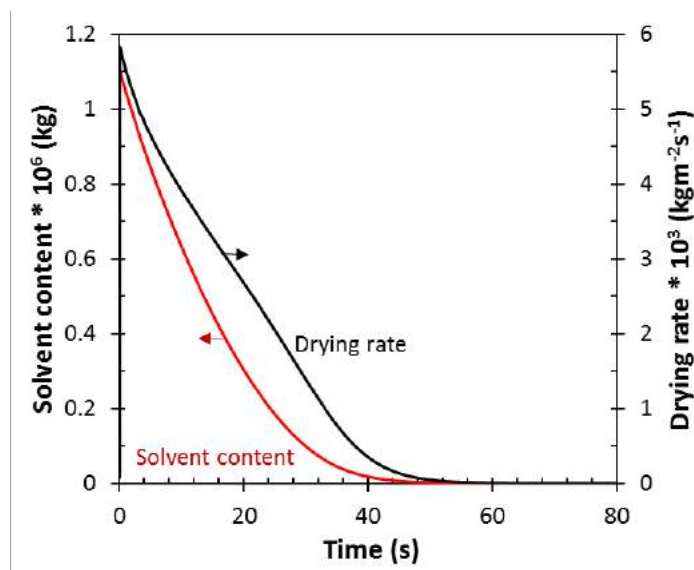


Figure III-5. Solvent content in electrode layer and the drying rate as a function of time.
150 μm layer, 95°C air temperature

A comparison of the drying rates for NMP and water (Figure III-6) shows that even though the latter has a latent heat of vaporization that is 4.5 times that of NMP on a mass (kg) basis, and a higher specific heat, the water dries almost 4 times faster than NMP. This is possibly due to the much higher vapor pressure of water at the simulated temperature of 95°C.

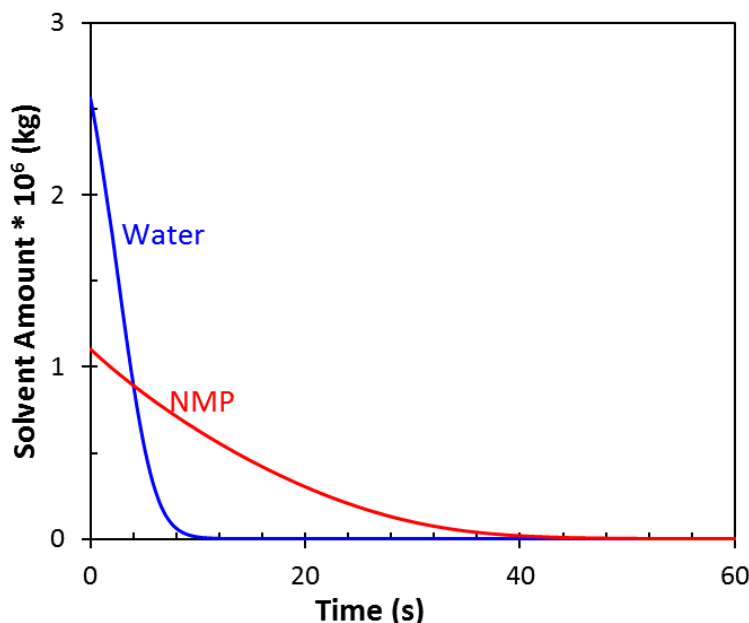


Figure III-6. Comparison of drying of electrode layer with NMP and water solvents. 150 μm layer, 95 °C air temperature. The electrode was loaded with the same volume of solvent

Conclusions

The BatPaC model has been improved to expand the capabilities and fidelity of the model. These include

- Updates on the electrode design calculations and default property and material cost data
- Revision of the calculations for the fast charging designs

BatPaC and an independent drying model were exercised to gain a better understanding of key processes in the manufacturing of the lithium ion cells.

- A study was conducted to compare the cell costs using different electrode combinations.
- Low allowable current density (to prevent lithium deposition) and short charging times limit the electrode thickness, increasing the mass of inactive materials which contribute to higher cell costs.
- A mathematical model of the solvent drying process indicates that the last 10% of the solvent removal takes up nearly 50% of the drying time. For one set of conditions, a comparison of NMP and water drying indicates that the drying time can be significantly reduced if water can be used as the solvent.

Key Publications

1. S. Ahmed, P.A. Nelson, C. Michelbacher, "Extreme fast charging and battery cost implications," presented at the 2017 DOE Vehicle Technologies Office Annual Merit Review and Peer Evaluation Meeting, Washington, DC, June 5-9, 2017
2. S. Ahmed, P.A. Nelson, K.G. Gallagher, N. Susarla, D.W. Dees, "Cost and energy demand of producing nickel manganese cobalt cathode material for lithium ion batteries," *Journal of Power Sources* 342 (2017) 733-740
3. D.L. Wood, J.D. Quass, J. Li, S. Ahmed, D. Ventola, C. Daniel, "Technical and economic analysis of solvent-based lithium-ion electrode drying with water and NMP," *Drying Technology*, May 2016.

4. S. Ahmed, I. Bloom, A.N. Jansen, Paul A. Nelson, *et. al.*, " Enabling fast charging – A battery technology gap assessment," *Journal of Power Sources* 367 (2017) 250-262
5. N. Susarla, S. Ahmed, D.W. Dees, "Modeling and analysis of solvent removal during Li-ion battery electrode drying," submitted to the *Journal of Power Sources*.

References

1. K. Gallagher, S. Trask, C. Bauer, T. Woehrle, S. Lux, M. Tschech, P. Lamp, B. Polzin, S. Ha, B. Long, Q. Wu, W. Lu, D. Dees and A. Jansen, "Optimizing Areal Capacities through Understanding the Limitations of Lithium-Ion Electrodes," *Journal of The Electrochemical Society*, vol. 163(2), pp. A138-A149, 2016.

III.B Battery Testing

III.B.1 Battery Performance and Life Testing (ANL)

Ira Bloom, Principal Investigator

Argonne National Laboratory
9700 South Cass Avenue
Argonne, IL 60439
Phone: 630-252-4516
E-mail: ira.bloom@anl.gov

Samuel Gillard, Technology Manager

U.S. Department of Energy
Phone: 202-287-5849
E-mail: Samuel.Gillard@ee.doe.gov

Start Date: October 1, 2017

End Date: September 30, 2022

Total Project Cost: \$1,800,000

DOE share: \$1,800,000

Non-DOE share: \$0

Project Introduction

Batteries are evaluated using standard tests and protocols that are transparent to technology. These protocols are based on those developed by the USABC [1-4].

Objectives

- Provide DOE, USABC, and battery developers with reliable, independent and unbiased performance and life evaluations of cells, modules and battery packs.
- Benchmark battery technologies that were not developed with DOE/USABC funding to ascertain their level of maturity.

Approach

The batteries are evaluated using standardized and unbiased protocols, allowing a direct comparison of performance within a technology and across technologies. For those tested using the USABC methods, the performance of small cells can be compared to that of larger cells and full-sized pack by means of a battery scaling factor [1, 2]. The results described below arose from work in two different areas, 12-V start/stop testing and US-China battery test protocol comparisons.

Results

Batteries, which were fabricated during programs with developers, were sent to Argonne for evaluation. Here, the purpose of evaluation is two-fold: to provide confirmation of other test information and to provide an independent assessment of the state of the given battery technology, that is, how does it compare to the USABC [1-4] and/or project goals? A list of program deliverables associated with Argonne is given in Table III-2, along with their status. One of these deliverables is discussed further below.

Table III-2: Status of Deliverables for Testing

Developer	Sponsor	Quantity x System Level	Application	Status
JCI	USABC	9 x Cell	PHEV-20	complete
JCI	DOE FOA	45 x Cell	PHEV-20	complete
Leyden	USABC	30 x Cell	12-V S/S	complete
Maxwell	USABC	26 x Cell	12-V S/S	complete
Maxwell	USABC	1 x Module	12-V S/S	on-going
24-M	USABC	6 x Cell	EV	complete
24-M	USABC	18 x Cell	EV	on-going
24-M	DOE FOA	14 x Cell	EV	on-going
Xerion	USABC	21 x Cell	PHEV-20	expected
3M	2013 ABR	12 x Cell	EV	complete
Navitas	DOE FOA	24 x Cell	EV	on-going
Navitas	DOE FOA	13 x Cell	EV	complete
Tiax	2013 ABR	26 x Cell	EV	complete
ANL (J. Zhang)	DOE FOA	15 x Cell	EV/PHEV	complete
Seeo	DOE	6 x Cell	EV	complete
LGChem	DOE	10 x Cell	PHEV-40	on-going
XALT	DOE FOA	24 x Cell	EV	on-going
Wildcat	DOE	20 x Cell	EV	complete
WPI	USABC	80 x Cell	Recycling/PHEV-20	expected
SiNode	USABC	9 x Half cell	EV	on-going
SiNode	USABC	8 x Cell	EV	on-going
SiNode	USABC	20 x Cell	EV	expected
Microcure	DOE	6 x Cell	EV	complete
Farasis	USABC	68 x Cell	Recycling/PHEV-20	expected
Daikin	DOE	9 x Cell	EV/PHEV	on-going
Celgard	USABC	6 x Cell	EV	expected
ANL-CAMP	DOE	15 x half cell	XFC-GITT	expected
ANL-CAMP	DOE	15 x Cell	XFC-GITT	expected

12-V Start/Stop

Lithium-ion batteries are being proposed for many automotive applications, such as use in 12-V start/stop vehicles. Here, the engine is turned off instead of idling while the vehicle is stopped, reducing fuel costs and pollution. It's ideal use would be where the vehicle spends a lot of time in city traffic.

Cells containing $\text{LiMn}_2\text{O}_4/\text{Li}_4\text{Ti}_5\text{O}_{12}$ (LMO/LTO) chemistry were tested using the procedures and methods outlined in the USABC 12-V Start/Stop manual [4]. Here, the cells were tested for calendar life at 30, 40, 50 and 60°C and for cycle life at 30°C. Reference performance tests (RPTs) were used to gauge changes in cell performance at 30°C. RPTs were conducted at the beginning of testing and then every 32 days or 23,040 cycles for the calendar and cycle life cells, respectively. The RPT consisted of a C/1 capacity measurement and the hybrid pulse-power capability test at the low-current values. The results of the RPTs were used to determine trends in cell performance decline.

In the calendar aging experiment at 30 and 40°C, the relative capacity initially declined slightly, but, with continued testing, seemed to reach a steady state, as shown in Figure III-7. However, the cells tested at 50 and 60°C exhibited large changes in relative capacity as the test continued. Most likely, the rapid decrease in relative capacity was caused by gas formation in the cells.

Figure III-8 shows the trend in relative capacity with cycle count for the cycling experiment. Here, the relative capacity seemed to reach a steady value of ~0.97 after ~92,160 cycles.

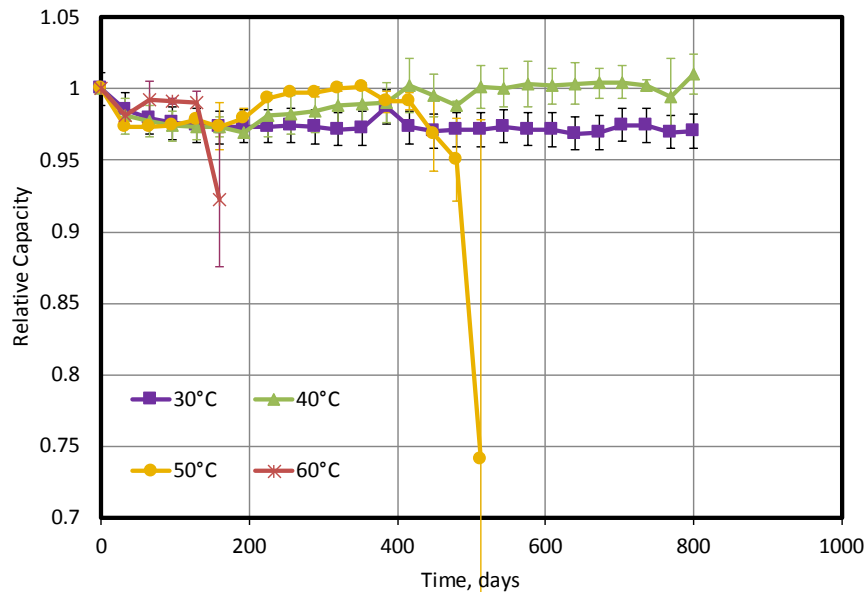


Figure III-7. Average relative capacity vs. time for the calendar life cells. The error bars represent $\pm 1\sigma$

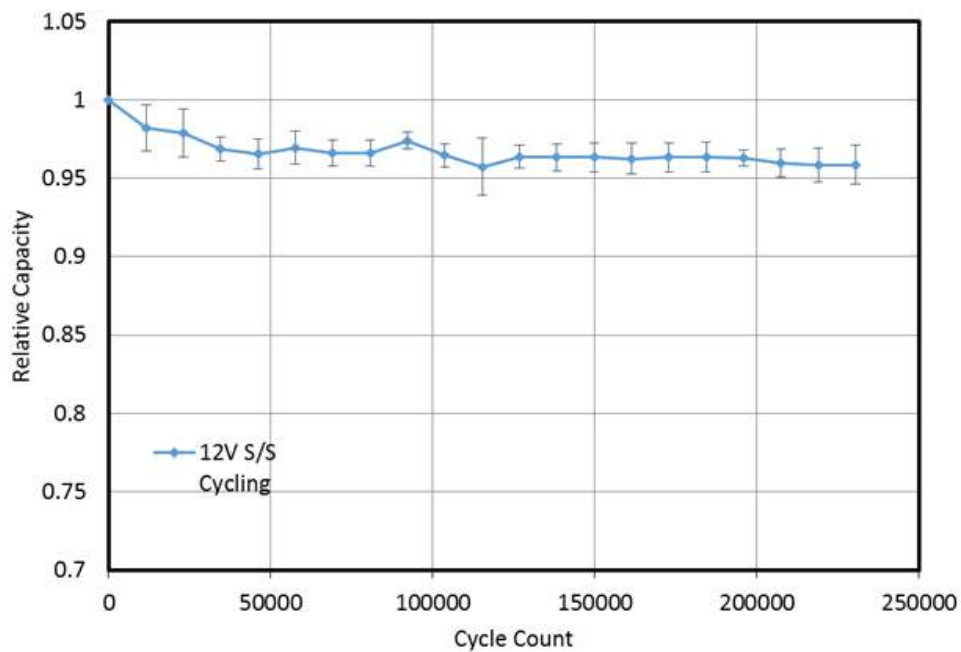


Figure III-8. Average relative capacity vs. time for the cycle life cells. The error bars represent $\pm 1\sigma$

Plots of the change in average relative resistance at 50% SOC (2.496 V) are shown in Figure III-9 and Figure III-10. The resistance growth in the calendar life cells at 30 and 40°C displayed what appeared to be linear-with-time kinetics. With this assumption, the slopes of these best-fit lines were $5.97 \times 10^{-4}/\text{day}$ ($r^2=0.97$) and $9.84 \times 10^{-4}/\text{day}$ (0.84), respectively. However, at 50 and 60°C, the rates of resistance increase were nonlinear. At these temperatures, the data seem to follow a linear-with-time trend followed by a period of rapid increase. In the 50°C case, the linear portion was from 0 to 352 days and that for the 60°C data, 0 to 128 days. The slopes of the lines in the regions are $2.62 \times 10^{-3}/\text{day}$ ($r^2=0.98$) and $7.68 \times 10^{-3}/\text{day}$ ($r^2=0.99$). Indeed, using these values shows that resistance increase process seems to follow Arrhenius-like kinetics with an activation energy of 72.2 kJ/mol.

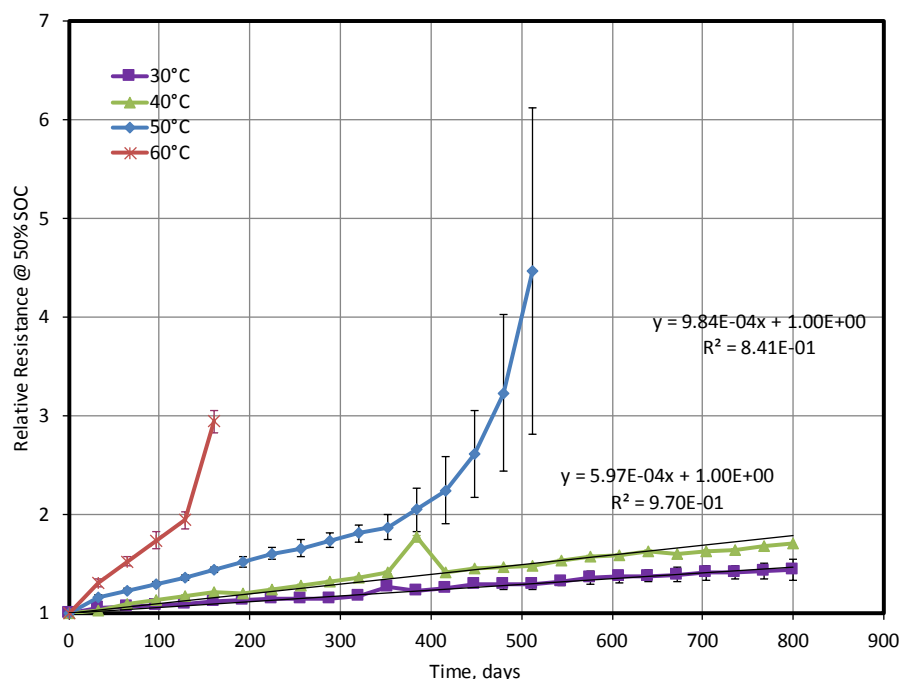


Figure III-9. Average relative resistance vs. time for the calendar life cells. The error bars represent $\pm 1\sigma$

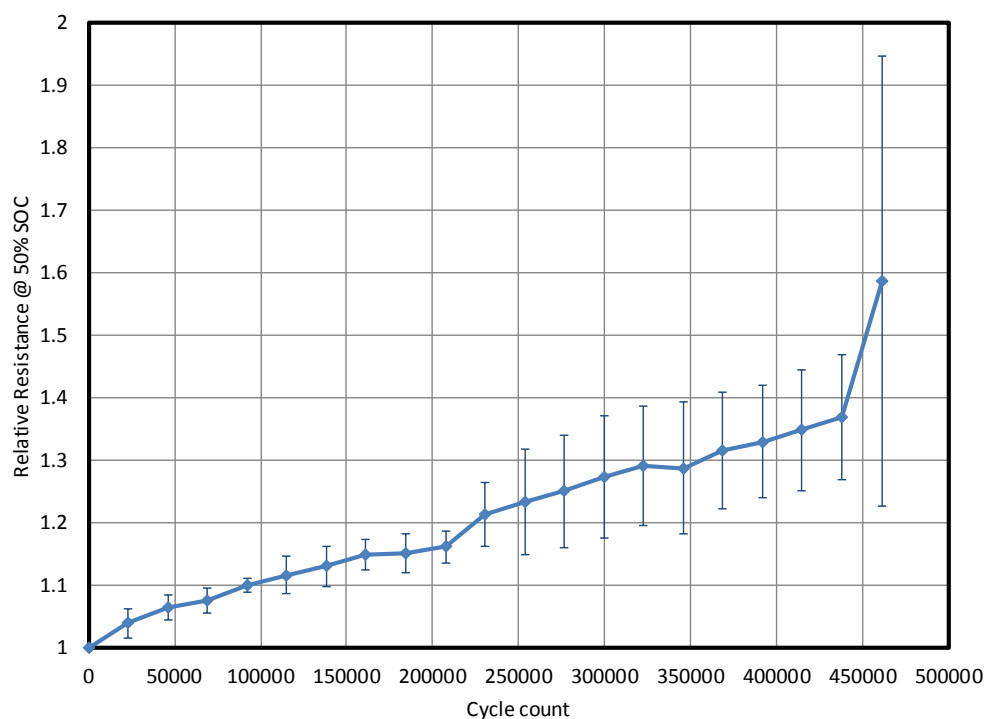


Figure III-10. Average relative resistance vs. count for the cycle life cells. The error bars represent $\pm 1\sigma$

Examining the data in Figure III-10 shows that the points before 437,760 cycles seem to follow a linear trend. Indeed, applying least-squares fitting to these points shows that the slope of the best-fit line is $8.72 \times 10^{-7}/\text{cycle}$ ($r^2=0.98$).

Figure III-11a and Figure III-11b show the plots of relative power (1 s) vs. time for the calendar and cycle life cells, respectively. The data in Figure III-11a shows that the relative power of the 50 and 60°C cells falls sharply, possibly indicative of a cell near failure, at 448 and 128 days, respectively. Using the lower temperature data and the rest of the higher temperature data shows that power fade followed $at^{1/2}$ kinetics in this temperature range. The values of a were $-8.70 \times 10^{-3}/\text{day}$ ($r^2=0.89$), $-1.36 \times 10^{-2}/\text{day}$ (0.93), $-2.36 \times 10^{-2}/\text{day}$ (0.97), and $-3.84 \times 10^{-2}/\text{day}$ (0.99), respectively. Based on these values of the rate of power decrease, the degradation process seems to follow Arrhenius-like kinetics. The activation energy for the process was 41.9 kJ/mol. Similarly, the 1-s relative power data in Figure III-11b displays a sharp decline after about 420,000 cycles. Excluding the data after point shows that the remaining points can be fit to a line with a slope of $-6.26 \times 10^{-7}/\text{cycle}$ (0.97).

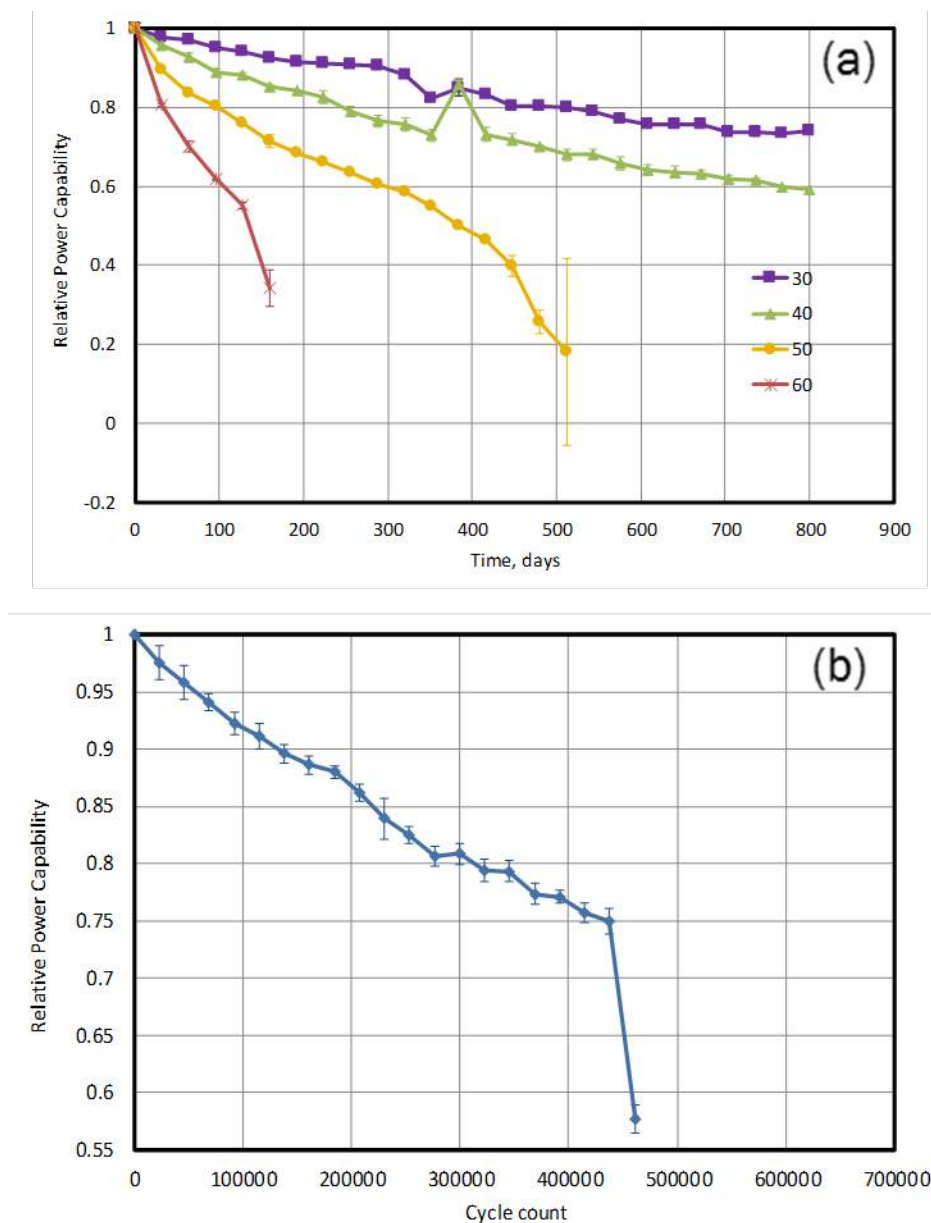


Figure III-11. (a) Relative power vs. time for the calendar life cells. The error bars represent $\pm 1\sigma$ (b) Relative power vs. cycle count for the cycle life cells. The error bars represent $\pm 1\sigma$.

US-China Protocol Comparison: Fast Charge

The US and China have independently developed battery test protocols to track performance change with aging. On the surface, the test protocols appear to be different. The purpose of these experiments is to determine if the protocols produce different results, and, if they do, how different the results are. We previously reported that the battery aging protocols produce very similar data once certain parts of test are considered. For example, in testing for hybrid electric vehicle applications, the China cycling [5] and calendar tests use a single pulse at 50% DOD, while those used by the USABC use many pulses [1-4]. Once the differences were taken into account, the results were very similar [6]. We extended this study to evaluate fast-charge protocols using commercial LiFePO_4 cells.

As a starting point, we compared the aging characteristics of performing fast charging 100% of the time using a constant-current, constant-voltage charge (CC-CV) at 30°C to that used in China, which was the same protocol, but at 25°C. The charge rates in this study range from 1- to 6-C.

Figure III-12 and Figure III-13 show the trend in average relative capacity change with Ah throughput for the CC-CV and Chinese protocols, respectively. As expected, there was not much difference between the two figures since the test temperatures differed by only 5°C, at the low charge rates. There are differences in the performance degradation rates at the 4- and 6-C rates.

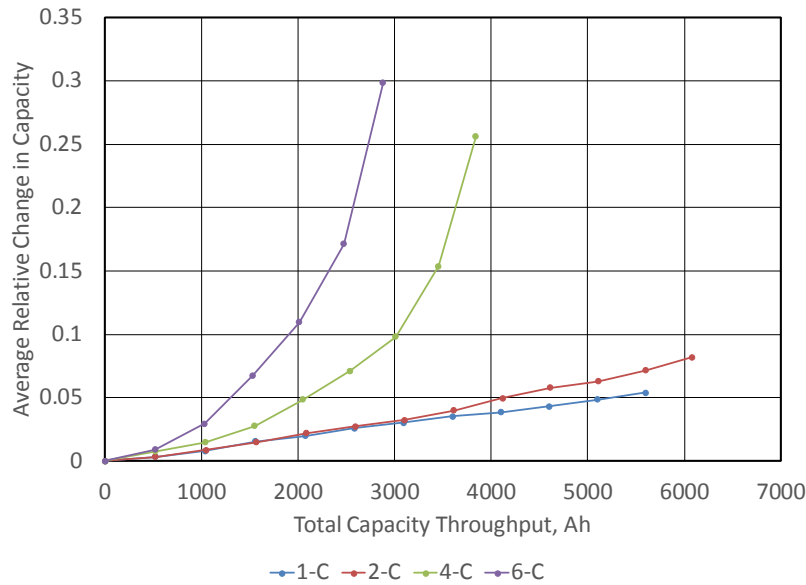


Figure III-12. Average change in relative capacity vs. total capacity throughput for cells tested using the CC-CV protocol

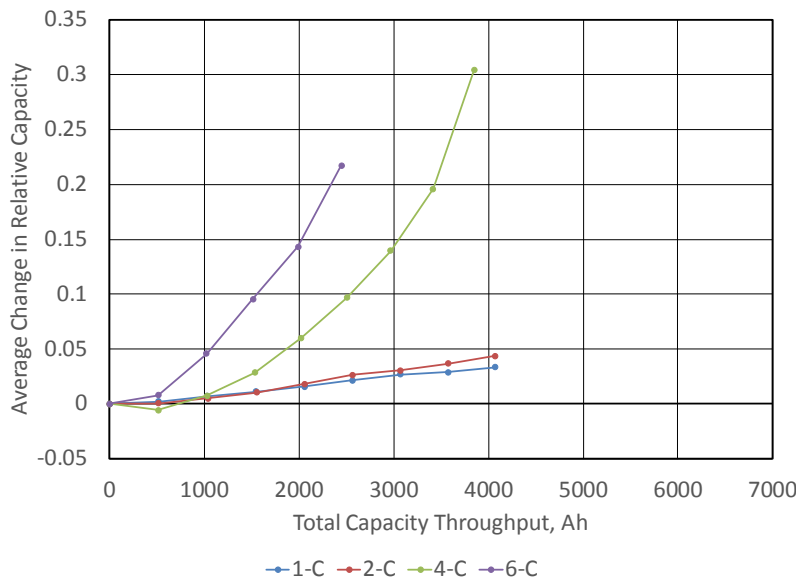


Figure III-13. Average relative capacity vs. total capacity throughput for cells tested using the China protocol

Significant differences between the test protocols was found during post-test examination of the cells. This is shown in Figure III-14.

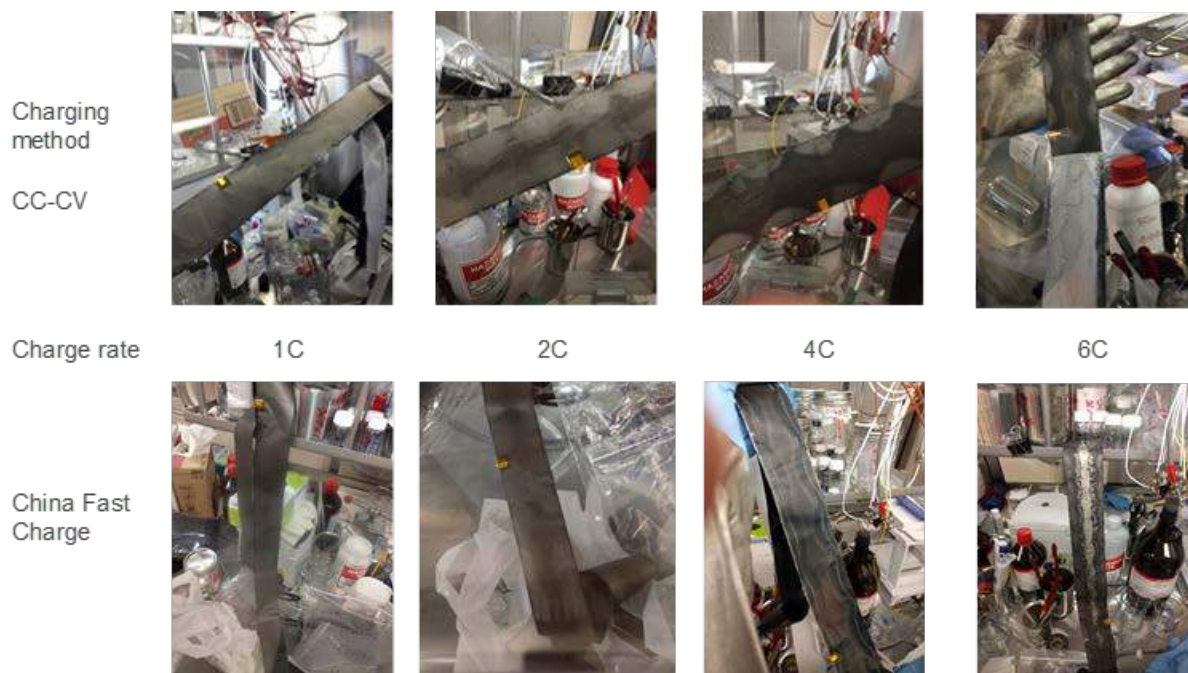


Figure III-14. Optical images of the negative electrodes taken during the post-test analysis of the fast-charge cells from the CC-CV and China test protocols

All images in Figure III-13 show signs of change in the negative electrode, which is based on graphite. The degree of change increases with increasing charge rate, as expected. At 6-C, the CC-CV anode appears to be just graphite, but that from the China protocol has a distinct greyish band running along the center line, which, most likely, is lithium metal. The post-test examination continues.

Conclusions

12-V Start/Stop

The power capability of cells containing LMO/LTO chemistry degraded ~26% over the course of 800 days at 30°C. In the cycle life test, the cells accrued 437,760 cycles before a sharp decline in performance was observed.

US-China Protocol Comparison: Fast Charge

The fast charge protocols used produced very similar changes in the electrochemical performance of the LiFePO₄ cells. The 5°C difference between them is enough to produce what appears to be lithium deposition on the anode in the China protocol case.

Key Publications

1. Fast charging of lithium-ion batteries: Effect of charge protocol. David C. Robertson, Nancy Dietz Rago and Ira Bloom, ABAA-10 meeting, Oct. 23-25, 2017, Oakbrook, IL
2. Enabling Fast Charging – A Technology Gap Assessment. Christopher Michelbacher, Shabbir Ahmed, Ira Bloom, Andrew Burnham, Barney Carlson, Fernando Dias, Eric J. Dufek, Andrew N. Jansen, Matthew Keyser, Anthony Markel, Andrew Meintz, Manish Mohanpurkar, Ahmad Pesaran, Don Scofield, Matthew Shirk, Thomas Stephens, Tanvir Tanim, Ram Vijayagopal, and Jiucui Zhang, US DOE report, INL/EXT-17-41638, October 2017

3. Enabling Fast Charging – Introduction and Overview. Christopher Michelbacher, Shabbir Ahmed, Ira Bloom, Andrew N. Jansen, Tanvir Tanim, Eric J. Dufek, Ahmad Pesaran, Andrew Burnham, Richard B. Carlson, Fernando Dias, Keith Hardy, Matthew Keyser, Cory Kreuzer, Anthony Markel, Andrew Meintz, Manish Mohanpurkar, Don Scofield, Matthew Shirk, Thomas Stephens, Ram Vijayagopal, and Jiucui Zhang, *J. Power Sources*, 367 (2017) 214-215.
4. Enabling Fast Charging – A Battery Technology Gap Assessment. Shabbir Ahmed, Ira Bloom, Andrew N. Jansen, Tanvir Tanim, Eric J. Dufek, Ahmad Pesaran, Andrew Burnham, Richard B. Carlson, Fernando Dias, Keith Hardy, Matthew Keyser, Cory Kreuzer, Anthony Markel, Andrew Meintz, Christopher Michelbacher, Manish Mohanpurkar, Paul A. Nelson, David C. Robertson, Don Scofield, Matthew Shirk, Thomas Stephens, Ram Vijayagopal, and Jiucui Zhang, *J. Power Sources*, 367 (2017) 250-262
5. Enabling Fast Charging – A Vehicle Technology Gap Assessment. Andrew Meintz, Jiucui Zhang, Ram Vijayagopal, Cory Kreuzer, Shabbir Ahmed, Ira Bloom, Andrew Burnham, Barney Carlson, Fernando Dias, Eric J. Dufek, James Francfort, Andrew N. Jansen, Matthew Keyser, Anthony Markel, Christopher Michelbacher, Manish Mohanpurkar, Ahmad Pesaran, Don Scofield, Matthew Shirk, Thomas Stephens, and Tanvir Tanim, *J. Power Sources*, 367 (2017) 216-227
6. Enabling Fast Charging – A Infrastructure Technology & Economics Gap Assessment. Andrew Burnham, Eric J. Dufek, Thomas Stephens, James Francfort, Christopher Michelbacher, Barney Carlson, Jiucui Zhang, Ram Vijayagopal, Fernando Dias, Manish Mohanpurkar, Don Scofield, Matthew Shirk, Shabbir Ahmed, Ira Bloom, Andrew N. Jansen, Matthew Keyser, Cory Kreuzer, Anthony Markel, Andrew Meintz, Ahmad Pesaran, and Tanvir Tanim, *J. Power Sources*, 367 (2017) 237-249
7. Enabling Fast Charging – Battery Thermal Considerations. Matthew Keyser, Ahmad Pesaran, Qibo Li, Shriram Santhanagopalan, Kandler Smith, Eric Wood, Shabbir Ahmed, Ira Bloom, Eric Dufek, Matthew Shirk, Andrew Meintz, Cory Kreuzer, Christopher Michelbacher, Andrew Burnham, Thomas Stephens, James Francfort, Barney Carlson, Jiucui Zhang, Ram Vijayagopal, Keith Hardy, Fernando Dias, Manish Mohanpurkar, Don Scofield, Andrew Jansen, Tanvir Tanim, Anthony Markel, *J. Power Sources*, 367 (2017) 228-236

References

1. FreedomCAR Battery Test Manual for Power-Assist Hybrid Electric Vehicles, DOE/ID-11069, October 2003.
2. FreedomCAR Battery Test Manual for Plug-In Hybrid Electric Vehicles, June 2010.
3. Electric Vehicle Battery Test Procedures Manual, Revision 2, January 1996.
4. Battery Test Manual for 12 Volt Start/Stop Vehicles, Rev. 1, May 2015, INL/EXT-12026503.
5. National Development and Reform Committee of the People's Republic of China, 2006, Lithium-Ion Batteries for Electric Vehicles, Auto Industry Standard QC/T 743-2006, China Plan Publishing Company, March, http://www.d1ev.com/uploadfile/newsfile/20130819022042_547.pdf (in Chinese).
6. David C. Robertson, Jon P. Christopherson, Taylor Bennett, Lee Walker, Fang Wang, Shiqiang Liu, Bin Fan, and Ira Bloom, *J. Power Sources*, 306 (2016) 268-273. DOI: 10.1016/j.jpowsour.2015.12.004

III.B.2 Electrochemical Performance Testing (INL)

Matthew Shirk, Principal Investigator

Idaho National Laboratory

2525 Fremont Avenue

Idaho Falls, ID 83402

Phone: 208-526-7216

E-mail: matthew.shirk@inl.gov
Samuel Gillard, Technology Manager

U.S. Department of Energy

Phone: 202-287-5849

E-mail: Samuel.Gillard@ee.doe.gov

Start Date: October 1, 2016

End Date: September 30, 2017

Total FY17 Project Cost: \$4,609,421 DOE FY17 share: \$4,609,421 Non-DOE share: \$0

Project Introduction

The Battery Test Center at Idaho National Laboratory has been supporting the evolution of electrified transportation through high-quality, independent testing of electrical energy storage systems for more than 30 years. Independent testing provides data for quantitative assessment of technology gaps. Test methods and techniques are continuously improved to offer data on relevant metrics as vehicle applications evolve. Advancing electrified powertrain transportation, such as EV, PHEV, and HEV technologies, is a top priority within the Department of Energy (DOE) given the potential to increase energy security through reduction of US dependence on foreign oil. The INL Battery Test Center (BTC) is a world leader in science-based performance testing and assessment of advanced electrochemical energy storage technologies, primarily for automotive applications. The BTC at INL has been designated by DOE as a core capability and the lead test facility for supporting USABC through testing activities. The development of batteries and other energy storage devices requires validation testing from an independent source to accurately characterize the performance and life capability against the established USABC technical targets for EVs, PHEVs, 12 V Start/Stop, HEV, and other emerging electric drive system applications. Gaps in performance relative to targets are used as a metric to guide R&D priorities.

Objectives

The primary objective of the program is to provide high fidelity, science-based performance and life testing, analysis, modeling, and reporting. To ensure the data produced are relevant to industry and government, it is also a key objective to update test and analysis procedures to maintain alignment with industry needs and to develop new procedures for promising future applications.

Approach

The INL Battery Test Center (BTC) utilizes over 20,000 square feet of laboratory space and is equipped with over 700 test channels for advanced energy storage testing at the cell-level (e.g., up to 7V, 300A), module-level (e.g., up to 65 V, 250A), and pack-level (e.g., 500-1000 V, 500A). Test equipment is programmed to perform test profiles while simultaneously monitoring for compliance with operating limits such as voltage, current and temperature. Batteries and other energy storage devices are typically subjected to an electrical test sequence while housed inside precision thermal chambers to ensure consistent and repeatable results by maintaining consistent ambient temperature conditions. To enhance performance testing across a wide range of thermal conditions, driven by automotive usage scenarios, the thermal chambers can be operated across a broad temperature range (e.g., -70 to 200°C).

Successful performance testing and accurate life modeling are highly dependent on the fidelity of the acquired test data. The INL BTC has developed advanced calibration verification and uncertainty analysis methodologies to ensure that voltage, current, and temperature measurements are within the tolerance specified by the test equipment manufacturer (e.g., 0.02% of the full scale). These measured test parameters are subsequently used in various mathematical combinations to determine performance capability (e.g., resistance, energy, power, etc.). INL has also quantified the error associated with these derived parameters using the accuracy and precision of the relevant measured parameter (e.g., voltage) to ensure high-quality and repeatable results and meaningful presentation.

The INL BTC utilized a high capacity shaker table perform non-destructive tests to characterize reliability and safety of new cell topologies to mechanical vibration and shock Unconventional and unproven cell designs are the main focus of mechanical vibration and shock testing at INL. The shaker table laboratory is equipped with both safety shielding and thermal control chambers and is co-located with battery test equipment to allow performance testing immediately before and after vibration testing has occurred.

Adjacent to the shaker table are two fire-rated isolation rooms that can be used for tests that push the known limits of operation, but have yet to be proven to be safe, though expected to be non-destructive. Examples of testing near the limit could include extreme fast charging, subtle over- or under-charging, high-temperature thermal characterization for under-hood systems, among many others. These isolation rooms allow for safe testing of unproven cell technologies at or near the design limit. These complimentary non-destructive evaluation capabilities comprise INL's Non-Destructive Battery Evaluation Laboratory.

Results

The INL BTC continues to test articles of various sizes and configurations using the standardized test protocols developed with industry partnerships for each electric drive vehicle application. Table III-3 and Table III-4 summarize the testing activities under the USABC and Benchmarking Programs, respectively, for FY17. Technologies developed through USABC contracts are aged and tested against the appropriate application target (EV, HEV, PHEV, 12 V S/S, 48 V HEV) and, where applicable, they are compared to previous generations of test articles from the same developer. 252 articles were tested for USABC in FY17, including 6 modules and 246 cells. The purpose of the Benchmark program is to evaluate device technologies that are of interest to the Vehicle Technologies Office within DOE, but are not deliverables developed under a contract. In some cases, Benchmark devices are used to validate newly developed test procedures and analysis methodologies. 117 cells were tested for the Benchmark program in FY17. Advanced cells from the Applied Battery Research (ABR) program were life and performance tested at INL, using modified testing procedures based on the program goals. INL BTC tested and reported on 87 cells for ABR, with 63 cells continuing, but nearing completion of testing at the end of FY17. (See Table III-5.) The final two sets of cells delivered through the FOA released in FY 2011, titled 'Develop Advanced Cells and Design Technology for Electric Drive Vehicle Batteries', completed testing as well. (See Table III-6.)

Analysis was performed for all articles tested, and results were presented regularly at quarterly review meetings and USABC Technical Advisory Committee (TAC) meetings to USABC OEM, DOE VTO representatives, developers, and national laboratory staff. INL worked with the USABC test methods committee to develop the methodology and publish the manual for testing 48V mild hybrid battery systems as well.

Table III-3: Articles Tested for USABC

Developer	Application	System	Number of Articles Tested	Status at Year End
Leyden	EV	Cell	9	Complete
LG/CPI	PHEV	Cell	23	Complete
LG/CPI	12 V Stop/Start	Cell	12	Complete
LG/CPI	EV	Cell	12	Complete
LG/CPI	12 V Stop/Start	Module	1	Complete
NOHMS	PHEV	Cell	15	Complete
LG/CPI	EV	Cell	12	Complete
NOHMS	PHEV	Cell	18	Complete
SAFT	12 V Stop/Start	Cell	3	Complete
NOHMS	PHEV	Cell	18	Ongoing
Saft	12 V Stop/Start	Cell	15	Ongoing
Amprius	EV	Cell	24	Ongoing
Envia	EV	Cell	17	Ongoing
LG/CPI	12 V Stop/Start	Cell	15	Ongoing
FARASIS	EV	Cell	8	Ongoing
24M	EV	Cell	3	Ongoing
SAFT	HEV	Cell	14	Ongoing
SAFT	12 V Stop/Start	Cell	15	Ongoing
LG/CPI	12 V Stop/Start	Cell	15	Ongoing
LG/CPI	12 V Stop/Start	Module	3	Ongoing

Table III-4: Articles Tested for Benchmark

Developer	Application	System	Number of Articles Tested	Status at Year End
Hydroquebec	PHEV	Cell	13	Complete
Toshiba	12 V Stop/Start	Cell	1	Complete
AESC/Nissan	EV	Cell	24	Complete
LG Chem	EV	Cell	4	Complete
ORNL	EV	Cell	6	Complete
ORNL	EV	Cell	6	Complete
Toshiba	EV	Cell	18	Ongoing
Toshiba	12 V Stop/Start	Cell	12	Ongoing
EIG LTD	12 V Stop/Start	Cell	20	Ongoing
LG/CPI	PHEV	Cell	13	Ongoing

Table III-5: Articles Tested for Applied Battery Research (ABR)

Developer	Application	System	Number of Articles Tested	Status at Year End
Penn State	EV	Cell	12	Complete
ANL	EV	Cell	12	Complete
Penn State	PHEV	Cell	15	Ongoing
Farasis	EV	Cell	12	Ongoing
Farasis	PHEV	Cell	12	Ongoing
ANL	PHEV	Cell	12	Ongoing
Envia	EV	Cell	12	Ongoing

Table III-6: Articles Tested for the 2011 FOA: 'Develop Advanced Cells and Design Technology for Electric Drive Vehicle Batteries'

Developer	Application	System	Number of Articles Tested	Status at Year End
ANL/Miltec	EV	Cell	9	Complete
Applied Materials	EV	Cell	15	Complete

Conclusions

Reliable battery performance and life testing is critical for the successful evolution and commercialization of efficient vehicles. The INL BTC is a DOE core capability that is well equipped to conduct accelerated aging protocols and aggressive test protocols on battery technologies of various sizes and shapes while ensuring high quality, repeatable results as an independent source of science-based performance assessment for DOE, the automotive industry, and battery developers. As such, testing for key programs funded through the Vehicle Technologies Office of DOE was conducted. A total of 480 devices were tested in FY17. In FY18, INL plans to continue this level of support for multiple programs with broad support for the USABC and Benchmark programs in particular, having completed support of the 2011 FOA program and nearing completion of ABR testing. In addition to testing and life modeling, INL will also continue developing and refining standard test protocols and analysis procedures in collaboration with USABC.

Key Publications

1. Tanvir Tanim, Matt Shirk, Randy Bewley, Eric Dufek, Boryann Liaw. Fast Charge Implications: Pack and Cell Analysis and Comparison, Submitted to Journal of Power Sources
2. Battery Test Manual for 48 Volt Mild Hybrid Electric Vehicles, Idaho National Laboratory, March 2017, INL/EXT-15-36567

III.B.3 Battery Safety Testing (SNL)

Leigh Anna M Steele, Principal Investigator

P.O. Box 5800, Mail Stop 0614

Albuquerque, NM 87185

Phone: 505-844-9290

E-mail: LSteele@sandia.gov

Samuel Gillard, Technology Manager

U.S. Department of Energy

Phone: 202-287-5849

E-mail: Samuel.Gillard@ee.doe.gov

Start Date: October 1, 2016

End Date: September 30, 2017

Total Project Cost: \$1,000,000

DOE share: \$1,000,000

Non-DOE share: \$0

Project Introduction

Abuse tests are designed to determine the safe operating limits of HEV/PHEV energy storage devices. Testing is intended to achieve certain worst-case scenarios to yield quantitative data on cell/module/pack response, allowing for failure mode determination and guiding developers toward improved materials and designs. Standard abuse tests with defined start and end conditions are performed on all devices to provide comparison between technologies. New tests and protocols are developed and evaluated to more closely simulate real-world failure conditions.

When scaling from cell to the battery level, a detailed understanding of cell interactions provides insight on safety performance. Single point failures from a cell or group of cells can be initiated by a number of triggers including internal short circuit, misuse or abuse, or component failure at the battery or system level. Propagation of a single failure event (regardless of the initiation trigger) through an entire battery, system, or vehicle is an unacceptable outcome with regards to EV battery safety. In this FY, our work has focused on evaluating the propagation of a single cell thermal runaway event through a battery using a variety of design considerations with an emphasis on passive thermal management impacts. This has been coupled with thermal modeling by NREL for these testing conditions. In addition, alternative failure initiation methods have been evaluated to provide direct comparisons of possible energy injection between modes. This data was compiled to better identify what propagation test method is appropriate given certain battery designs. Expanding the analysis of short circuit current during failure propagation has been done for EV relevant chemistries. Ongoing test development and validation to obtain these values has been achieved.

While robust mechanical models for vehicles and vehicle components exist, there is a gap for mechanical modeling of EV batteries. The challenge with developing a mechanical model for a battery is the heterogeneous nature of the materials and components (polymers, metals, metal oxides, liquids). Our work will provide empirical data on the mechanical behavior of batteries under compressive load to understand how a battery may behave in a vehicle crash scenario. This work is performed in collaboration with the U.S. Council for Automotive Research (USCAR) and Computer Aided Engineering of Batteries (CAEBAT). These programs have supported the design and development of a drop tower testing apparatus to close the gap between cell/string level testing and full scale crash testing with true dynamic rate effects. This work is discussed in further detail in the annual report submitted by NREL. Additional modeling efforts lie in being able to better predict failure propagation within larger battery systems. Sandia's battery safety testing provides testing support to better aid in thermoelectrical model development at NREL and SNL.

Materials characterization to better understand batteries that have undergone abusive conditions is of interest. Our partnerships with Argonne National Lab (ANL) and Oak Ridge National Lab (ORNL) through the Post

Test Analysis Program for ABR, spans the building of cells with known materials (ORNL), overcharge testing to various states (SNL), and the posttest analysis of the cells (ANL). In addition, testing to support the Si-Deep Dive Program has been leveraged to gain a better understanding of the safety implications for these materials.

Objectives

- Serve as an independent abuse test laboratory for DOE and USABC
- Abuse testing in accordance with the USABC abuse testing manual
- Successful testing of all deliverables from developers under USABC contracts
- Evaluate failure propagation through addition of thermal management and alternative initiation methods
- Short circuit current evaluation during failure propagation in battery strings of EV relevant chemistries
- Laser initiated failure within batteries of various formats
- Provide testing data to support modeling efforts developed by NREL
- Provide mechanical testing support to develop and validate mechanical models for EV batteries through CAEBAT program
- Design and develop a dynamic drop testing capability to support CAEBAT
- Provide abuse testing support for ABR Post Test program and Si Deep Dive
- Publish Sandia Abuse Testing Procedures: Unlimited release

Accomplishments

- Successful testing of cell and module deliverables through USABC contracts including:
 - Maxwell (12 V SS)
 - LG Chem (12 V SS)
 - Envia (EV)
 - Amprius (EV)
 - NOHMS (Electrolyte)
 - 24M Technologies (EV)
- Exercised testing method to analyze short circuit current between cells during failure propagation on various cell chemistries (EV relevant) for direct comparisons
- Completed multi-cell propagation testing with the inclusion of passive thermal management (spacers); preliminary simulated results using NREL thermal models show good agreement with test data
- Developed method for 3-point bend testing, single cell constrained testing in different orientations, and design/fabrication of dynamic drop testing apparatus in support of CSWG/CAEBAT
- Successful demonstration of laser induced battery failures on various cell formats
- Supported posttest analysis program with batteries (3 chemistry types) overcharged at various states

- Hosted 2nd Annual IBSW in Albuquerque sponsored by DOE through T2M funds
- Stood up large scale testing capability at Sandia's Burn Site and successfully completed testing of USABC modules

Approach

Abuse tolerance tests evaluate the response to expected abuse conditions. The goals of abuse and safety testing include a) testing to failure of energy storage devices and documentation of conditions that caused failure, b) systematic evaluation of failure modes and abuse conditions using destructive physical analysis (DPA), c) provide quantitative measurements of cell/module response, d) document improvements in abuse response, and e) develop new abuse test procedures that more accurately determine cell performance under most probable abuse conditions. Electrical (overcharge/overvoltage, short circuit, over discharge/voltage reversal, and partial short circuit), mechanical (controlled crush, penetration, blunt rod, drop, water immersion, laser induced short circuit, mechanical shock and vibration) and thermal abuse (thermal stability, simulated fuel fire, elevated temperature storage, rapid charge/discharge, and thermal shock cycling) cover the main categories of possible conditions evaluated. These techniques are applied to USABC deliverables and the results reported to DOE and USABC.

Research and development batteries used for simulating internal short circuits, propagation testing (alternative initiators and passive thermal management), and short circuit current evaluation are based on commercial-off-the-shelf (COTS) LiCoO₂ 18650 and pouch cells, NMC and NCA 18650, and LFP 18650 (designed for energy) and 26650 (designed for power) cells. Cell failure and thermal runaway initiated by various methods were investigated this FY, including overcharge, laser initiation, and mechanical nail penetration into a single cell within a pack.

Results

Battery Abuse Testing

This FY, Sandia's standard abuse testing practices were published in an unlimited release report. The notable highlights include enhanced safety basis, updates to testing protocols according to current testing methods/capabilities, use of empirical data to support test conditions, addition of failure propagation and flammability tests, and providing clarity in the definitions for a hazard severity rating system. SNL provided independent testing on all USABC deliverables in FY17 with testing results reported at TAC. The actual USABC testing results are Protected Information and are prohibited from public release. However, representative data is shown in Figure III-15 for COTS cells purchased on the open market and assembled into a multi cell pack that underwent thermal abuse. This validation test was performed to stand up permanent operations at SNL's large-scale testing facility to support USABC module tests and was completed in FY17.

Thermal ramp testing on a 12-cell pack (~1kWh) according to the USABC Abuse Testing Manual was performed. Cells were heated at a rate of 5°C/min to 250°C or failure (whichever occurs first). Complete propagation through the pack was achieved with a 5-min total burn time and peak temperatures of 800°C. The addition of this remote site has helped to increase throughput of test deliverables and also serves as a safer means to handle multi-cell packs posttest by removing residual energy through remotely operated propane torches. This significantly reduces risk to personnel and improves our safety basis.

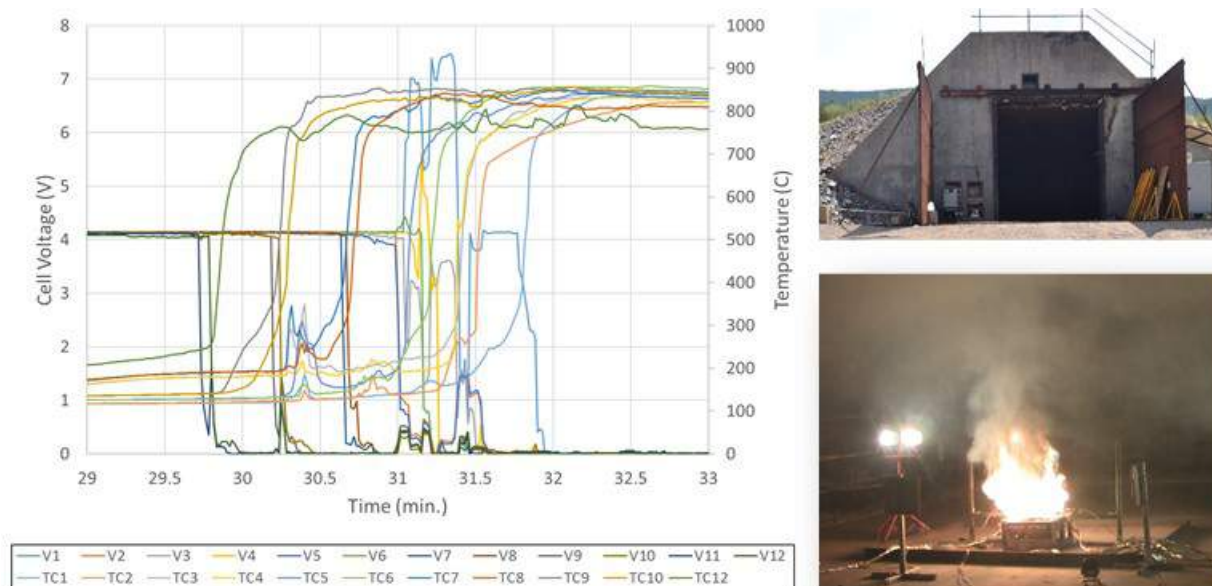


Figure III-15. Representative cell temperatures and voltages during a thermal ramp test of a multicell 1kWh Li-CoO₂ pack

The failure propagates through the entire pack, starting with cell 12 undergoing runaway once the battery skin temperature reaches 200°C. The failure cascades through the remaining cells, over 2 minutes, with onset temperatures of thermal runaway ranging between 125 and 200°C (skin temperatures).

Propagation Testing with Passive Thermal Management

A number of studies evaluating the response of single cells to field and abusive failures have been conducted at Sandia, however, less attention has been paid to how a battery system responds to the energetic failure of a constituent cell. A single cell failure may be a relatively rare occurrence, but the consequence of that failure can be significantly greater if these failures propagate through the entire battery. To build on SNL's past research in propagation testing, passive thermal management between pouch cells was targeted this FY. To study this further, we tested a series of small batteries constructed with COTS pouch cells to investigate the effectiveness of simple thermal management systems (spacers of various materials and thicknesses) on the extent of propagation.

In our experimental work, batteries consisting of 3 Ah LiCoO₂ COTS pouch cells were constructed in a 5-cell close packed system allowing for maximum surface area contact with one another to aid in thermal transfer; shown in Figure III-16. We previously investigated failures of a single cell located within the pack in both series and parallel configurations (unmitigated). Regardless of electrical connectivity, the surface area contacts between cells allowed for enough thermal transfer to aid in propagation to neighboring cells suggesting a greater contribution to the extent of propagation. To reduce variables for this test series, the cells were not electrically connected and the passive thermal management device of choice was placed between each cell as seen in Figure III-16.

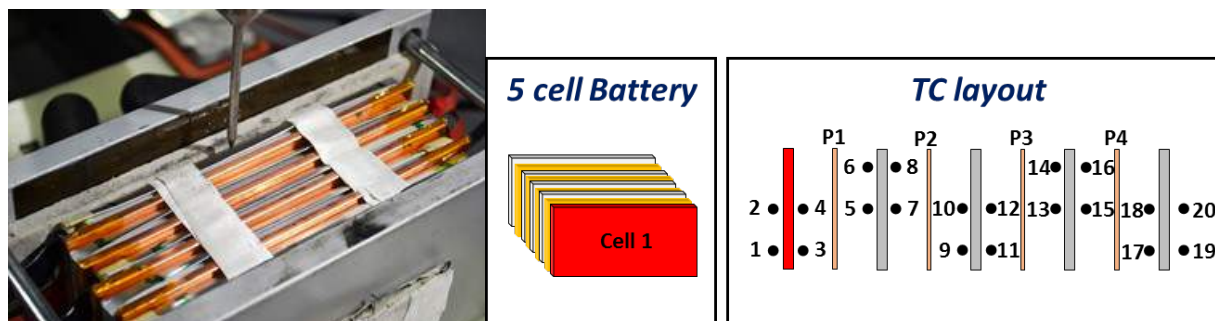


Figure III-16. Testing setup for COTS 3Ah 5-cells pack with passive thermal management (copper spacer of 1/8" thickness shown in picture). Failure initiation by nail penetration into cell 1 with the following thermocouple (TC) and copper (C)/or aluminum mapping consistent between tests

Both aluminum and copper plates, at 1/8, 1/16, and 1/32" thickness, were cut to the battery dimensions to act as a passive thermal management barrier and the testing matrix shown in Table III-7 was achieved; where A stands for aluminum and C stands for copper.

Table III-7: Passive Thermal Management Testing Matrix and Results

Test Pack ID	Test Description	Extent of Propagation
Baseline	No thermal management	Complete propagation
A-1	1/8 inch Al plates between cells	No propagation
A-2	1/16 inch Al plates between cells	Limited propagation (to cell 2)
A-3	1/32 inch Al plates between cells	Complete propagation
C-1	1/8 inch Cu plates between cells	No propagation
C-2	1/16 inch Cu plates between cells	Limited propagation (to cell 2)
C-3	1/32 inch Cu plates between cells	Complete propagation

The packs were fully instrumented with thermocouples (4 TC's per cell) and individual cell voltages monitored to observe the extent of propagation. Figure III-17 shows representative data sets with aluminum passive management showing reduced extent of propagation achieved when a slight increase in material thickness from 1/16" to 1/8" was implemented. When plate thickness is decreased to 1/32", full propagation is observed.

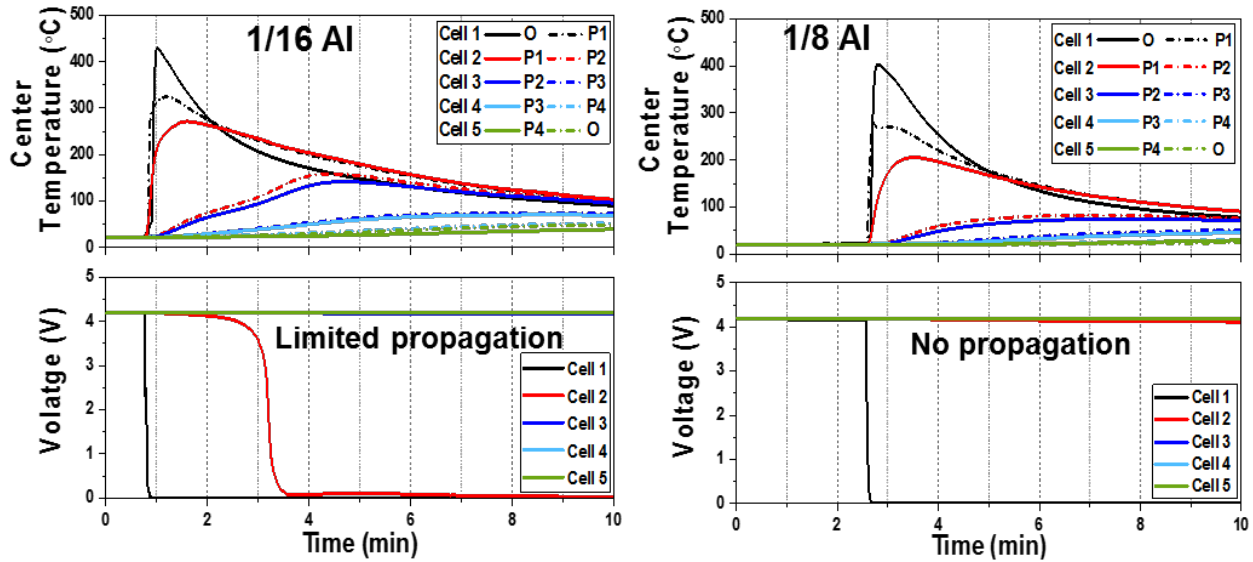


Figure III-17. Temperature and voltage data collected during propagation testing with the additional of thermal management (aluminum spacers). Left plots show limited propagation to the neighboring cell with 1/16" aluminum (cell 2 voltage drop at 3.5 min into test) and right plots show no propagation with 1/8" aluminum between cells

As mentioned, this series of tests were also performed using copper as the barrier. Overall, copper and aluminum behaved similarly in the ability to reduce propagation using the 1/16" plates and completely eliminated propagation with the 1/8" thick material. However, a faster voltage drop is observed for cell 2 in the 1/16" case with aluminum, which supports the higher thermal conductivity of copper over aluminum. Temperature data from each experiment was gathered to not only observe the extent of propagation but also the rate at which heat transfer between the cells occurs. This data has been provided to modeling partners at NREL for validation of preliminary thermal models with the inclusion of passive thermal management. Thermal data from the A-1 testing case (1/18" Al) was evaluated and results shown in Figure III-18.

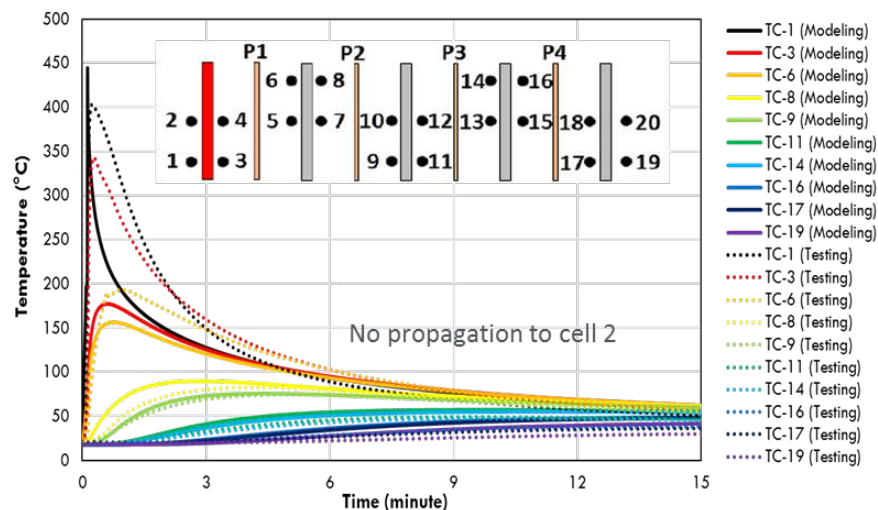


Figure III-18. Cell temperature data collected both experimentally and simulated by NREL's model during failure propagation testing for Al-1 case showing good agreement

Initial simulations show good agreement with testing results regarding peak temperature and timing to reach peak temperatures. The temperature does drop much faster in the simulated results which would be due to the following assumptions made in the simulation: 1) model assumes constant heat source that triggers cell uniformly within 5.5secs but test cell was shorted out gradually 2) deformation and displacement of cells will affect the contact between cells and passive management as well as readings from thermocouples and 3) the effluents from vented cells and their effect on temperature were not accounted for in the model. Future work in this area includes calibrating the model to include artifacts of a short circuit then applying the optimized model to the remainder of experiments for comparisons.

Quantify Short Circuit Current During Failure Propagation: Cell Chemistry Effects

As realized during previous failure propagation testing, high short circuit currents from non-abused cells discharging into the failure point exist. Sandia has developed a method to quantify these currents and validated the test setup for a variety of cells. In order to better compare relevant chemistries for EV applications, follow on work was completed to expand testing beyond LiCoO₂ and LFP using COTS 3Ah NMC and 3.1Ah NCA 18650 cells. In addition, improvements in fixturing to ensure connectivity between cell 1 (failure point) and cell 2 (un-abused cell) were achieved; obtaining a constant path for current flow where peak currents could be measured. Two cell strings were assembled in a 1S2P configuration in the apparatus shown in Figure III-19. To maintain contact with the failed cell upon thermal runaway a spring was added at the nail to apply counter pressure to the cell. Comparison data of testing with and without the improved mechanical contact have been provided below.

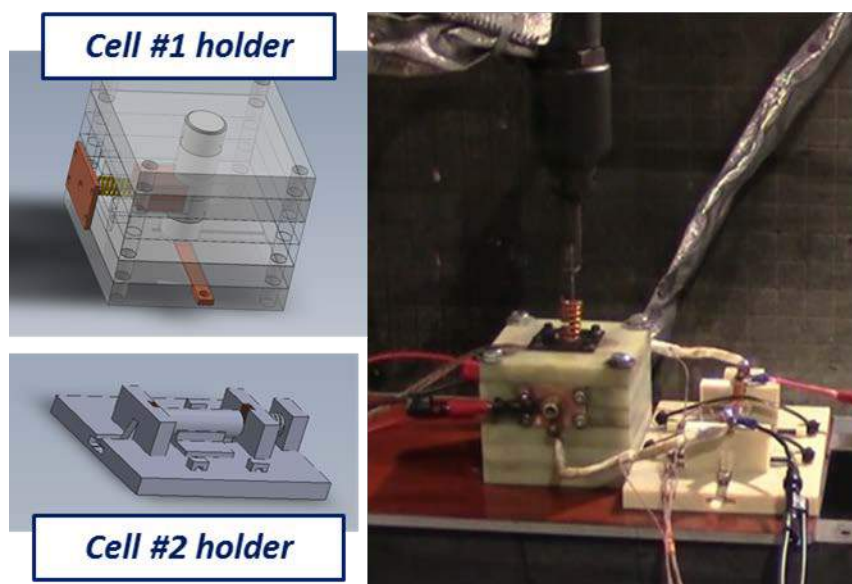


Figure III-19. Schematic for 1S2P setup bridged by constantan wire to measure short circuit current during failure propagation. Improved mechanical robustness achieved through cell holders and additional pressure applied at the failure point to maintain contact during runaway event.

The cells were joined using constantan wire of a known resistance to allow for current measurements between cells to be obtained. Mechanical insult of cell 1 (top) was performed while cell 2 (bottom) remained untouched allowing for the cell to discharge through the electrical connections of the string. Representative data for a 1S2P NMC 18650 cell string is shown in Figure III-20 with no extra mechanical contact during testing (top) and improved mechanical contact during test (bottom).

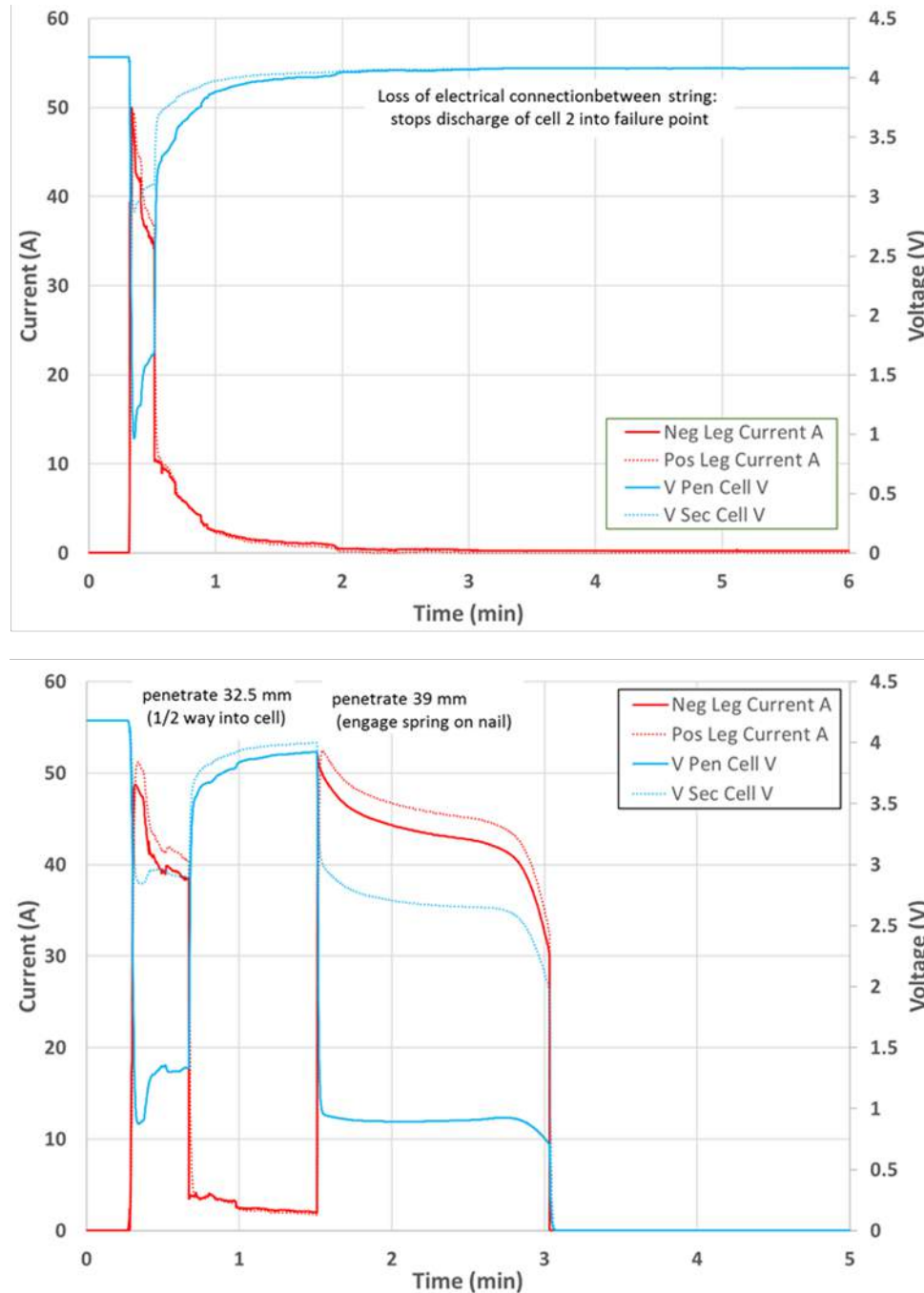


Figure III-20. String current across bridge and voltage measured during the failure propagation test for NMC 18650 in no extra mechanical contact during test (top) and with improved mechanical contact (bottom) in 1S2P configuration

Although the peak currents are similar in both cases (~50A), the improvement in mechanical connectivity allowed for cell 2 to discharge for a longer period of time (3 min) resulting in a higher total energy discharged into cell 1 (results summary shown in Table III-8). This reinforces the idea that battery connectivity within packs can play a critical role during failure propagation. Especially in the case where thermal contact between cells doesn't dominate the failure mechanism. Table III-8 shows short circuit current comparison data for various cell chemistries collected over the last two years. It is of note that, while LFP is a more benign chemistry, it is able to sustain a discharge for much longer resulting in larger total energy output into failure point. This allows for energetic failures to occur when seemingly benign cells are electrically connected as has been supported in past testing data with these LFP strings. The robustness of the cell connections impacts the extent of energy being discharged into the failure point as shown in Figure III-20 above. Lastly, cell design can also impact short circuit current through discharge rate capacity and/or the use of internal safety devices. This is relevant for the NCA cells, which have a max discharge rate of 2C, resulting in lower total energy discharged during propagation, while all other chemistries tested were rated for >3C discharge rates. In addition, a sharp loss of string voltage was observed when NCA cell 1 was penetrated suggesting there could be an internal safety device included by the COTs manufacture to prevent the extent of short circuiting.

Table III-8: Summary of Results for Short Circuit Current during Failure Propagation

Chemistry	Nominal Capacity (Ah)	Max rated discharge current for cell	Peak current during short circuit (A)	Total Energy discharged into Cell 1 (KJ)
LFP (18650)	1.5	5.6A (3.7C)	37	14.9
LFP (26650)	2.6	42A (16C)	30	15.0 (av)
LiCoO ₂ (18650)	2.2	6.2A (2.8C)	90	2.94 (av)
NMC (18650)	3	20A (6.7C)	80	5.3 (std setup), 0.027 (robust mechanical contact)- lost battery connection
NCA (18650)*	3.1	6.2A (2C)	35	0.29 (std setup), 0.75 (robust mechanical contact)

*Internal safety device might be preventing an external short current

We plan to continue to improve this testing method and apply it to more complex cell strings and electrical configurations in hopes to better quantify the impact of short circuit current during failure propagation in the next level of assemblies.

Alternative Method Development to Simulate Internal Short Circuits: Laser Initiation

Development of a test that better simulates an internal short circuit (ISC) within a cell is of interest. Traditionally, methods like nail penetration or implantable defects/devices have been used to simulate ISC. Both of these methods are invasive and require altering the cell during development or testing. Alternative means have been investigated at SNL including the use of a 40W IR pulse laser in hopes to reduce external damage; initiating a short within the first few electrode layers. Demonstration of this method has been achieved in various cell formats (pouch and cylindrical) as part of the USABC working group with SNL leading testing efforts. Representative data for a COTS 3 Ah LiCoO₂ pouch cell that has undergone thermal runaway initiated by 20 x 1.9 J pulses (~38 J total energy) laser is shown in Figure III-21. The cell exhibits a hard short represented by the quick heating rate and drop in cell voltage. The overall laser power was optimized to initiate a runaway event but there were several examples of this method resulting in a soft short (high impedance short) using 4 pulses (7.6 J total energy) where the cell self-discharged over a period of 24 hours without undergoing a thermal runaway.

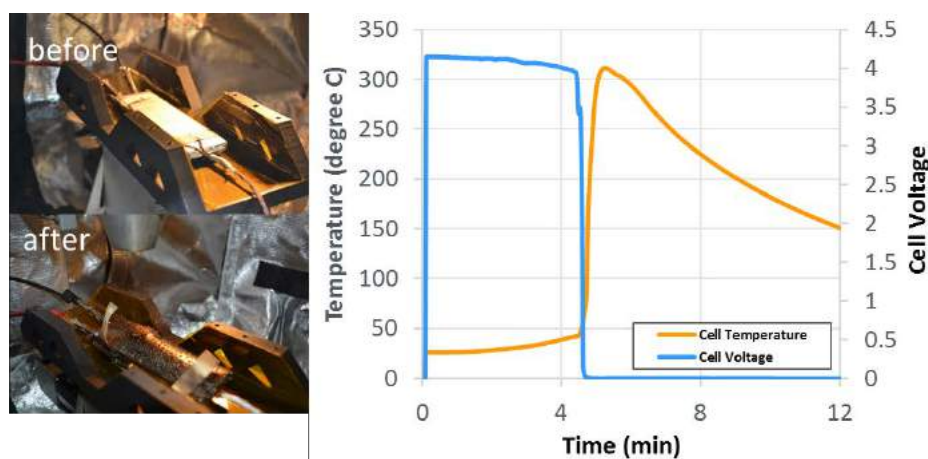


Figure III-21. Left: Still images (pre and posttest) and right: temperature and voltage data as a result of successful thermal runaway initiated by a 20 pulse laser

The failure conditions were applied to a discharged cell (0% SOC) so posttest analysis could be performed. These results were compared to a nail penetration test on the same cell type shown in Figure III-22. The external view shows a ~1 mm hole from the laser compared to a >3 mm hole generated from nail penetration, which supports that the laser (overall) is less destructive on the cell. Comparing internal damage through CT images, the laser initiation only impacts the first few electrode layers compared to nail penetration which damages the entire cell, proving laser testing to be a better representation of an ISC test.


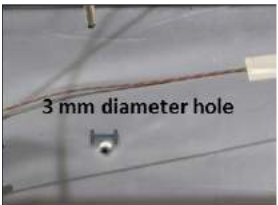
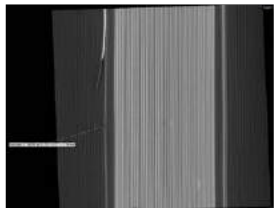
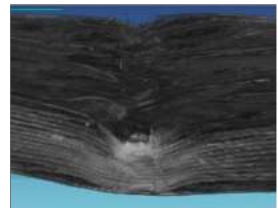
	20 Pulse Laser	Blunt Rod
External image		
Internal CT image		

Figure III-22. External and CT images comparing electrode damage on discharged cells using 20 pulse laser or blunt rod

Follow on testing included attempts to seal the hole resulting from the laser striking the cell (Figure III-22) to remove the possible reaction with oxygen. To accomplish this, a fused silica slide (IR transparent) was placed on the surface of the cell and sealed with kapton tape. Successful initiation of failure was achieved through the slide and the seal maintained intact until full runaway occurred. Once the system was optimized for pouch cells, testing shifted toward cylindrical cans. COTS cells of LiCoO_2 and NCA were utilized. The cell surface was painted black to reduce laser reflectivity and allow for better absorption. For the LiCoO_2 case, slight cell heating and voltage drop occurred but no thermal runaway was initiated. There was visual damage beyond the cell's outer surface, which was further evaluated through CT (shown in Figure III-23).

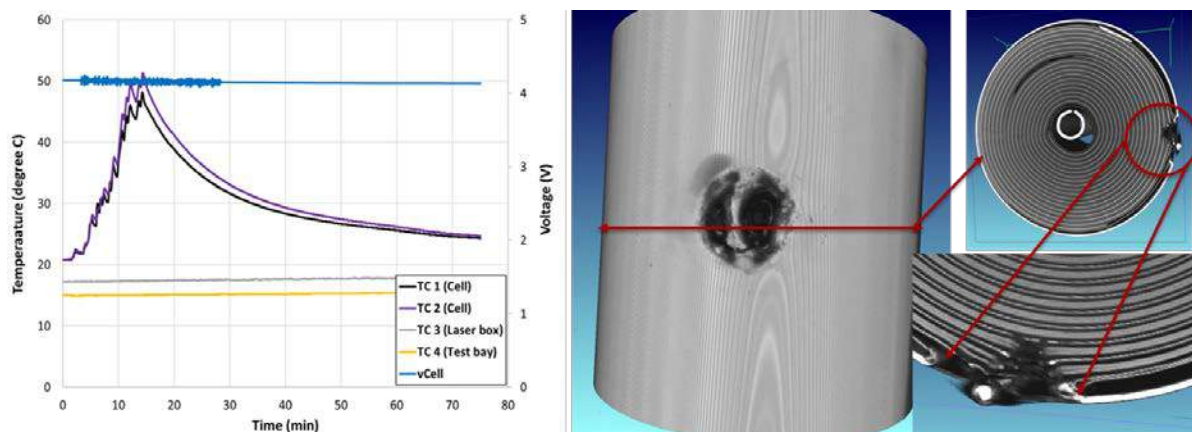


Figure III-23. Temperature and voltage data from laser testing in a COTS 3 Ah LiCoO₂ cylindrical cell and CT analysis of internal damage

Since initiation of a thermal runaway within the first cell chemistry proved challenging, focus switched to a higher capacity NCA cell (3.1Ah) in hopes that the reduced can thickness would allow for a failure to be initiated. Rapid runaway was achieved using 5 x 5.4J (27 J) as shown in Figure III-24. Peak battery skin temperatures reached 700°C and thermal runaway with self-ignition was observed. Further optimization of the testing method needs to be developed to demonstrate repeatability and consistency, but preliminary results show promise as an alternative initiation method that could better represent an internal short circuit test. In addition, the laser power can be tuned to better initiate failure based on battery architecture.

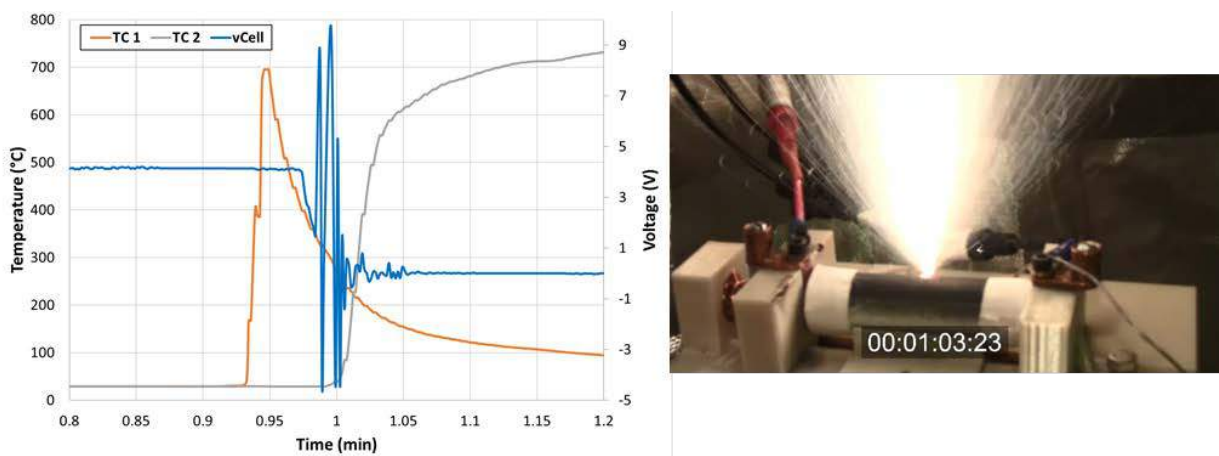


Figure III-24. Temperature and voltage data collected during runaway initiated by laser in a COTS 3.1 Ah NCA cylindrical cell

Energy Injection Comparison Between Failure modes for Propagation Testing

It is of interest to better understand the impacts specific abuse conditions have on failure propagation. One way to make this comparison is by calculating energy injection needed to initiate a failure during each mode. SNL has investigated several standard abuse conditions including nail penetration, thermal ramp and overcharge as well as some less traditional failure initiators like pulse laser and undirected light. A summary of the conditions and associated estimated energies are listed in Table III-9.

Table III-9: Energy Injection Comparisons between Failure Modes

Test	Energy Source	Conditions	Estimated Energy
Nail Penetration	Mechanical	20 mm penetration ~200 lb peak load	1.8 J
20 Pulse laser	IR Laser	20 1.9 J pulses	38 J
Undirected light	Quartz lamp	Exposure to light source through aperture	6000 J*
Thermal Ramp	Thermal	Heat to 200°C	6300 J**
Overcharge	Electrical	1C to 200% SOC	43200 J***

* Based on radiometer measured flux through aperture

** Calculated for hypothetical 40g cell – larger cells will require more energy

*** Calculated for a hypothetical overcharge at 3 A and 4 V at a 1C rate

Significantly less energy is required for laser induced failures compared to overcharge/thermal ramp, however more energy is required for laser induced failure when compared to nail penetration. When trying to keep variables at a minimum during testing, it is important to note that the additional energy required to push a single cell into runaway by overcharge and thermal ramp could have an impact on the neighboring cells through heat transfer changing the overall propagation results. Although nail penetration is a highly effective way to initiate a single cell failure, it is very intrusive and is not always ideal at the system level where cells might not be as accessible. As previously shown, laser initiation is much less destructive to the cell but, again, might not be ideal when packaging limits cell accessibility. In addition, this method needs to be matured to ensure repeatability in the hope that the resulting data can be used for design of experiments to study propagation.

Preliminary testing was done to compare propagation results from a single cell failure initiated by nail penetration or overcharge at a 1C rate. Cell 1 in a 5 cell string underwent failure via one of the two methods and full propagation through the string was achieved. The representative data for both are shown in Figure III-25.

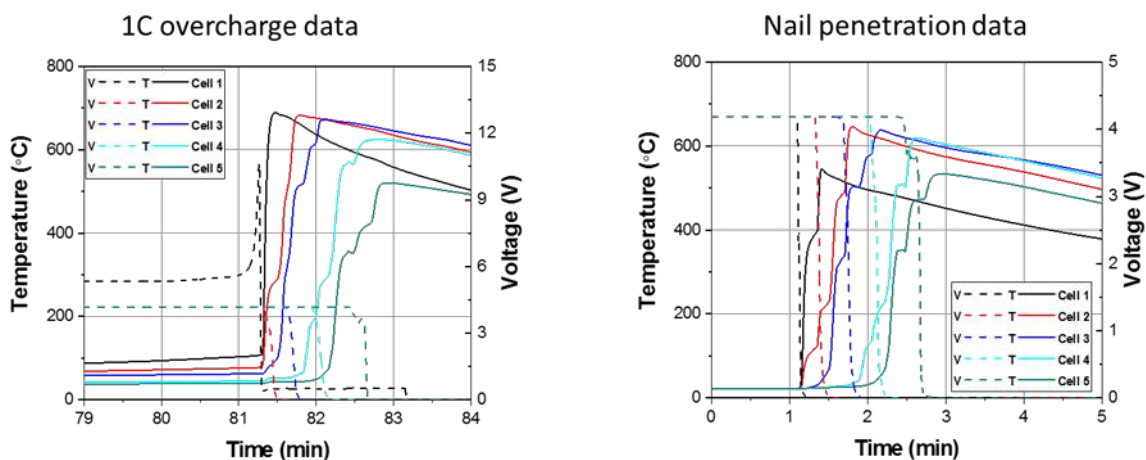


Figure III-25. Voltage and temperature data collected during failure propagation testing initiated by overcharge of cell 1 (left) or nail penetration of cell 1 (right)

The overcharged cell failure was more energetic (faster heating rate during runaway) than the nail penetrated cell; however, the overall rate of propagation was similar between the two tests. Full propagation was achieved in ~ 1 min by both methods with peak battery temperatures also in agreement between tests. Follow on testing

to compare failure modes during propagation within strings is needed to better couple energy injection results to aid in test development.

Mechanical Testing

Sandia is providing mechanical testing support to the VTO CAEBAT program to set boundary parameters for mechanical models and to validate predictions made by the numerical models. Further details are available in the annual report submitted by NREL. Leveraging the need for true dynamic rate experiments to be performed through this consortium, a drop tower was designed and is currently being assembled at SNL. Future efforts will include designing testing protocol for the unit and validation experiments leading to data for CAEBAT missions.

Conclusions

Development and testing of higher energy, larger format cells and modules continues for USABC developers in hopes to meet the EV Everywhere 2022 goals. We provide a means to field the most inherently safe chemistries and designs to help address the challenges in scaling up lithium ion technologies of interest. This has required careful control and monitoring of tests with the potential of high energy release as well as standing up a larger facility at SNL to support module level testing this FY. This has provided critical information to cell developers to aid in the development of increasingly abuse tolerant cell chemistries and module designs. This independent testing is also necessary to perform objective evaluations of these various designs and chemistries by the DOE and US automobile manufacturers. SNL has completed abuse testing support for all USABC deliverables to date.

Understanding battery design effects on failure propagation was investigated this FY with a focus on passive thermal management within pouch cell formats. The use of a simple management system (spacer) proves to reduce or even eliminate propagation between cells depending on the material thickness. This effort has been coupled with NREL models showing good agreement between testing data and primarily thermal simulations. Further optimization is needed in order to provide predictive models for battery failures which continues to be of interest to the community. Expansion of short circuit current observed during failure propagation between cells was achieved this year with a focus on relevant EV battery chemistries. COTS cells of different sizes and chemistries were assembled in 2 cell strings in a 1S2P configuration using constantan bridge wires of known resistance to obtain current. Testing results allow for comparison between chemistries to be made.

Alternative testing methods to simulate an internal short circuit were evaluated with SNL's focus on laser initiation. Successful initiation of thermal runaway within pouch and cylindrical cells was achieved. Comparing with nail penetration, this mode of failure proves to be less destructive and invasive into the cell, only effecting the first few electrode layers. Follow on testing is needed to optimize testing conditions and improve consistency.

There has been an increasing need within the community to better understand the effects of the failure modes on a single cell when designing test methods for propagation. One method for comparing this effect between modes is through the calculated energy injected needed to cause a cell failure. A summary of traditional modes' (thermal ramp, overcharge, and nail penetration) and non-traditional modes' (laser and undirected light) calculated injected energy was completed. These values can be used to help aid in experimental design depending on battery architecture and needs during test development.

SNL continues to provide testing support and data to help build and validate models with other national lab partners through the CAEBAT VTO program. Additional abuse testing support for the VTO post mortem program and Si-Deep Dive expanded this year which included overcharging cells of various chemistries manufactured by ORNL to different states followed by posttest analysis done by ANL. Also, initial abuse testing of Si-based cells has been achieved to better understand the safety impacts of this emerging chemistry.

Key Publications

1. L Steele et al. “Abuse Testing Update” USABC TAC, Washington, DC October 2016
2. J Lamb et al. “Impact of battery size and charge on the thermal runaway of lithium ion batteries” PRIME 2016, Honolulu, HI, October 2016
3. J Lamb et al. “Internal cell failure initiation” Battery Safety Council, Washington, DC, January 2017
4. L. Steele and J. Lamb “Search for the Super Battery” Nova Season 44 Episode 3.
5. L Steele et al. “Abuse Testing Update” USABC TAC, Southfield, MI, February 2017
6. L Steele et al. “Battery Safety and Reliability” PBS Science Café, ABQ, NM, March 2017
7. J Lamb et al. “Advanced techniques for understanding battery failure and its consequences” 2nd International Battery Safety Workshop, Albuquerque, NM, May 2017
8. J Lamb et al. “Alternative battery failure initiation methods” ECS Meeting, New Orleans, LA, May 2017
9. L Steele et al. “Abuse Testing Update” USABC TAC, Southfield, MI, May 2017
10. 2017 DOE Annual Peer Review Meeting Presentation
11. J. Lamb et al. “Laser Induced Short Circuit Progress” USABC TAC, July 2017
12. C. Orendorff, J. Lamb, L. Steele “Recommended Practices for Abuse Testing Rechargeable Energy Storage System (RESSs)” Sandia National Laboratories SAND Report SAND2017-6925 (July 2017)
13. J. Lamb, et al. “Development of Propagation Battery Failure Tests” The Battery Show, Novi, MI September 2017
14. I. Bloom et al, “Effect of overcharge on $\text{Li}(\text{Ni}_{0.5}\text{Mn}_{0.3}\text{Co}_{0.2})\text{O}_2$ / Graphite lithium ion cells with poly(vinylidene fluoride) binder. III — Chemical changes in the cathode” submitted to J Power Sources (Sept. 2017).I
15. I. Bloom et al. “Effect of overcharge on lithium-ion cells containing $\text{Li}(\text{Ni}_{0.5}\text{Mn}_{0.3}\text{Co}_{0.2})\text{O}_2$ cathodes: NMP-soluble binder. II — Chemical changes in the anode” submitted to J Power Sources (Sept. 2017).
16. I. Bloom, “Effect of overcharge on $\text{Li}(\text{Ni}_{0.5}\text{Mn}_{0.3}\text{Co}_{0.2})\text{O}_2$ /Graphite lithium ion cells with poly(vinylidene fluoride) binder. I. Microstructural changes in the anode” submitted to J Power Sources (Sept. 2017).

III.B.4 Battery Thermal Analysis and Characterization Activities (NREL)

Matthew Keyser, Principal Investigator

National Renewable Energy Laboratory
15013 Denver West Parkway
Golden, CO 80401
Phone: 303-275-3876
E-mail: Matthew.Keyser@nrel.gov

Samuel Gillard, Technology Manager

U.S. Department of Energy
Phone: 202-287-5849
E-mail: Samuel.Gillard@ee.doe.gov

Start Date: October 1, 2015

End Date: September 30, 2021

Total Project Cost: \$600,000

DOE share: \$600,000

Non-DOE share: \$0

Project Introduction

While EVs promise to curb America's need for imported oil, designing high-performance, cost-effective, safe, and affordable energy-storage systems for these cars can present challenges, especially in the critical area of battery thermal control. As manufacturers strive to make batteries more compact and powerful, knowing how and where heat is generated becomes even more essential to the design of effective thermal-management systems. NREL's thermal characterization activities provide developers, manufacturers and OEMs with the knowledge necessary to assure that batteries are designed to perform strongly, last a long time, and operate at maximum efficiency.

The Vehicle Technologies Office has a goal of producing batteries for \$100 kWh that will be capable of 1000 cycles and have a 10+ calendar year life [1]. In order to meet these metrics, the battery packs will need to have higher energy densities resulting in a very compact system. Even if the energy efficiency of the next generation of batteries increases, because of the compactness of these batteries more heat is being generated per unit volume with less heat transfer area. Thus, more advanced heat rejection systems are needed to keep the battery temperatures in the “goldilocks” zone that prevents acceleration of the aging mechanisms within the battery.

The chemistries of advanced energy-storage devices—such as lithium-based batteries—are very sensitive to operating temperature. High temperatures degrade batteries faster while low temperatures decrease their power and capacity, affecting vehicle range, performance, and cost. Understanding heat generation in battery systems—from the individual cells within a module, to the inter-connects between the cells, and across the entire battery system—is imperative for designing effective thermal-management systems and battery packs.

Inadequate or inaccurate knowledge of the thermal characteristics of batteries makes it difficult to design effective thermal-control systems. This can negatively affect lifespan, safety, and cost, ultimately resulting in negative consumer perception and reduced marketability. In 2012, Nissan had to address problems with the battery for its Leaf fully-electric vehicle (EV) losing capacity in the hot Arizona climate. Many attributed this issue to inadequate battery-thermal management.

Accurately measuring battery thermal performance under various electrical loads and boundary conditions makes it possible for battery-system engineers to design effective thermal-management systems. NREL, with the funding from DOE VTO, has developed unique capabilities to measure the thermal properties of cells and evaluate thermal performance of active, air, and liquid cooled battery packs. Researchers also use electro-thermal finite element models to analyze the thermal performance of battery systems in order to aid battery developers with improved thermal designs. In addition, our lumped capacitance multi-node battery-vehicle-ambient model can predict the temporal temperature of batteries as a function drive cycle, ambient

temperature, and solar radiation. These one-of-a-kind tools allow NREL to work with the battery manufacturers and OEMs to meet stringent EV life, performance, cost, and safety goals.

Objectives

- Thermally characterize battery cells and evaluate thermal performance of battery packs provided by USABC developers.
- Provide technical assistance and modeling support to USDRIVE/USABC and developers to improve thermal design and performance of energy storage systems.
- Quantify the impact of temperature and duty-cycle on energy storage system life and cost.
- Address high energy storage cost due to battery packaging and integration costs
- Reduce the cost, size, complexity, and energy consumption of thermal management systems
- Optimize the design of passive/active thermal management systems—explore new cooling strategies to extend the life of the battery pack.

Approach

NREL has measured the thermal properties of the cells and batteries with many different chemistries (lead acid, NiMH, and many versions of lithium cells) through heat generation, heat capacity, and infrared thermal imaging; conducted performance thermal testing of battery and ultracapacitor modules and packs; analyzed the thermal performance of cells and modules; and developed thermal models. Researchers perform thermal testing, analysis, and modeling (1) to assist DOE/USABC battery developers in designing cells/modules/packs for improved thermal performance, and (2) to evaluate and validate the thermal performance of cell/module/pack deliverables from DOE/USABC battery developers and suppliers.

NREL's equipment can benchmark how changing the design of the cell using a different cathode, anode, current collector, electrolyte, additive, or separator affects the overall performance of the cell. The information garnered from these tests helps battery and advanced vehicle manufacturers improve their designs, while providing critical data for the development of thermal management systems that will reduce the life-cycle cost of battery systems. Using NREL's unique R&D 100 Award-winning calorimeters and infrared thermal imaging equipment, we obtain thermal characteristics of batteries and ultracapacitors developed by USABC battery developers and other industry partners. NREL supports the Energy Storage Technical Team by participating in various work groups such as the Amprius, LG CPI, Envia, Maxwell, Saft, Farasis, 24M and USABC Working Groups.

Results

The following narrative outlines some of the more interesting insights garnered from NREL's testing over the past year. The outline below is not meant to be an exhaustive study of NREL's work but rather to help the reader understand how NREL's unique thermal characterization technologies are used to improve the energy storage technologies in conjunction with industry and USABC.

Figure III-26 shows the efficiency of cells tested in FY15/FY16/FY17 at NREL at a calorimeter temperature of 30°C. The lithium ion cells were fully discharged from 100% SOC to 0% SOC under a C/2, C/1, and 2C currents. It should be noted that the cells in the figure are for both power and energy cells and have been developed for the HEV, PHEV, EDV, and/or the 12 Volt Start/Stop programs within USABC. The figure shows a general trend with regards to the choice of anode on discharge efficiency. The graph indicates that the lithium titanate oxide (LTO) systems are the most efficient, followed by the graphite cells, and then the silicon blended cells. One confounding factor in the data is that the LTO cells are typically formulated to be power cells. Therefore, the thickness of the electrode and current collectors will have a positive effect on the efficiency of the system. In contrast, the silicon blend cells were designed with energy density as a primary

consideration resulting in these systems having slightly lower efficiencies. Adjusting for the electrode thickness confounding factor, the general trend still shows that the stable structure of LTO systems allows for higher energy efficiencies and confirms that the silicon systems may require improvements with regards to their electrical conductivity when used under conditions such as fast charge. DOE and USABC are investigating each of these chemistries to improve energy density, power density, cycle life and/or cost benefits. NREL's calorimeters provide the fundamental understanding of whether the inefficiencies shown below are due to chemistry or cell design.

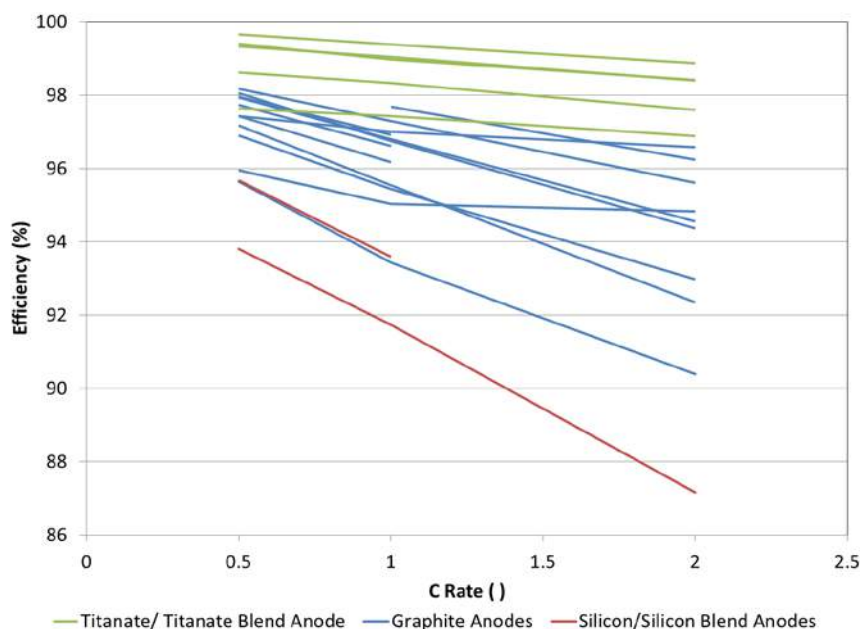


Figure III-26. Efficiency of cells tested at 30°C in NREL's calorimeters during FY15/FY16/FY17
Credits/Source: NREL- Aron Saxon

Figure III-27 shows the partial charge and discharge efficiencies of a blended silicon system tested at NREL. The data trends indicate that the charge efficiency is higher than the discharge efficiency for c-rates less than C/1 and for the same amp-hour capacity returned/supplied—atypical of graphite systems and similar to titanate cells. The higher charge efficiency may be due to the voltage hysteresis associated with silicon systems—very similar to the hysteresis of NiMH batteries. To better understand this theory, it is necessary to understand how the heat efficiency is calculated. The heat efficiency of a cell is calculated with the following equation where the CalorimeterHeatMeasured is a direct calorimeter measurement of the heat from the cell after a cycle is completed and the ElectricalEnergyInOut is the amount of energy supplied or removed from the cell.

$$\text{Heat Efficiency} = \left(1 - \frac{\text{CalorimeterHeatMeasured}}{\text{ElectricalEnergyInOut}} \right) * 100$$

If the heat measured by the calorimeter is equal for both charge and discharge (it's not) and the same number of amp-hours are supplied/removed to/from the cell, then the charge efficiency will always be greater due to the voltage hysteresis. However, we can limit the voltage hysteresis by cycling the cell at a very low rate current. The data in Figure III-27 shows that even when the cell is cycled at C/10 discharge/charge rate, the charge heat efficiency is greater than the discharge heat efficiency but the two efficiencies are more equivalent at this lower rate. Finally, it should also be noted that the charge efficiency appears to trend lower once higher c-rates (C/1) are used – the joule heating effect is beginning to dominate and it is surmised that the trend will reverse at the higher rates.

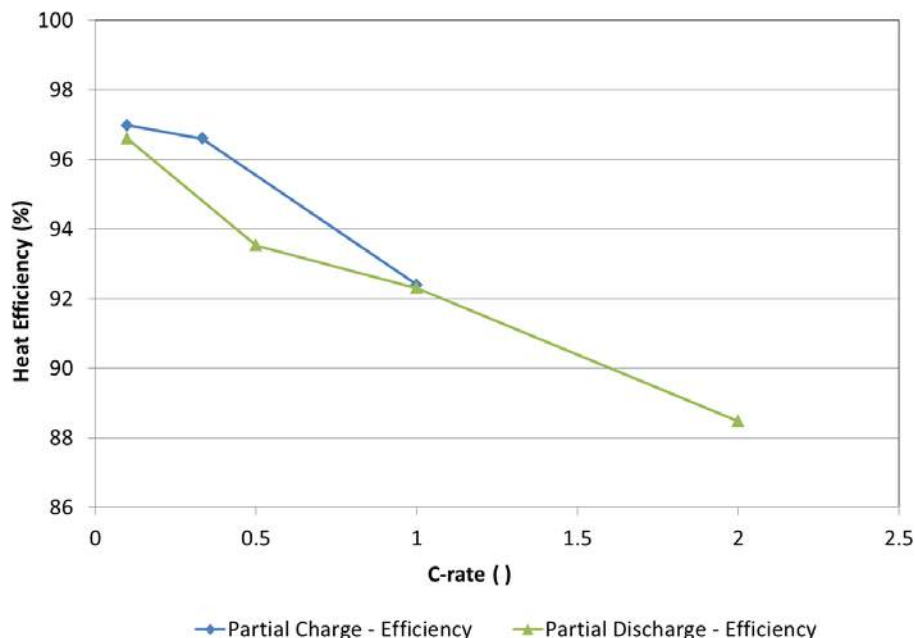


Figure III-27. Efficiency of silicon blended cells tested at 30°C in NREL's calorimeters under charge/discharge currents

Credits/Source: NREL- Aron Saxon

NREL's calorimeters were designed to be accurate enough to measure the electrochemical response from batteries under test – this capability allows NREL to understand benefits associated with design and chemistry changes to the cell. Figure III-28 shows the entropic heat generation rates normalized to the Ah capacity of the cell for the three different anodes – graphite, LTO, and silicon - at 30°C and under a constant current discharge. The cells in this figure were cycled over their entire depth of discharge range at a very low current – minimizing the current decreases the joule heating of the cell and allows for the entropic heat signature to be assessed. As shown in the figure, the cells can undergo endothermic and exothermic heat generation over the cycling range. The primary differences in the heat signatures from the three versions of the cell are due to the electrochemical changes in the anode since the cathode for each cell is a variation on the NMC chemistry. The graphite system is a fairly dynamic system undergoing several phase changes as the cell is cycled. The LTO system is slightly endothermic at the beginning of discharge; however, this endothermic response was due to a conductive additive incorporated into the anode and cannot be attributed to the titanate chemistry. LTO anodes are very stable structures and will show very little endothermic/exothermic heating within the cell. The final chemistry shown in the graph is for silicon blended cell which even though blended with graphite does not show the characteristic phase changes associated with the graphite only anodes. Furthermore, the silicon systems show a higher normalized heat generation rate as compared to the titanate and graphite anodes backing up the efficiency data shown previously in Figure III-26.

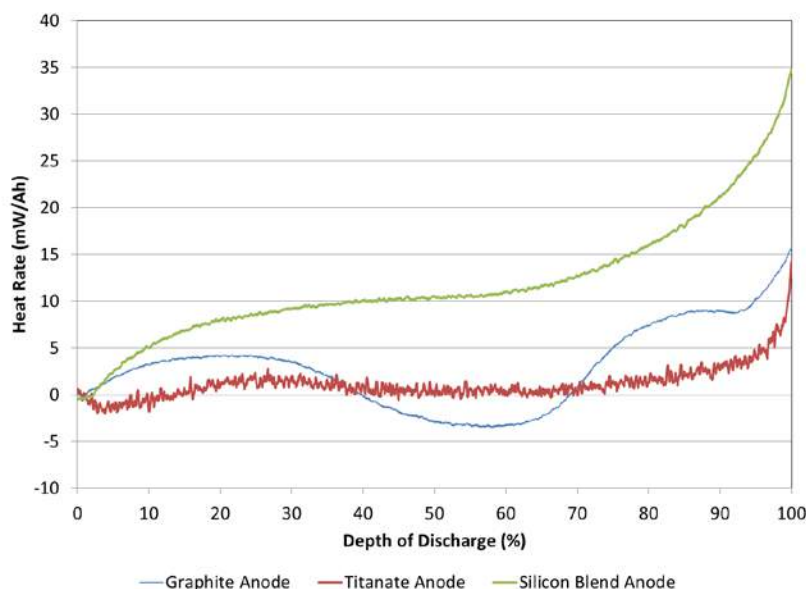


Figure III-28. Entropic response to graphite, titanate and silicon blended cells test at 30°C

Credits/Source: NREL- Aron Saxon

Figure III-29 shows another unique finding from NREL's FY17 testing. The Figure shows the heat efficiency of an ultracapacitor tested in NREL's calorimeter at a temperature of 30°C and under a constant current discharge/charge. Of note, the discharge efficiency increases as the current increases – atypical of battery systems tested at NREL. The increase in efficiency relates to where the charge is being stored within the cell – the Helmholtz layer near the electrode surface or in the volume of the electrolyte [2]. In essence, the calorimeter can distinguish between the heat contributed from the electrostatic resistance of the supercapacitor and the reversible entropic heating effects. Even though the endothermic heating response is minimal for this cell, the “cooling” effect could be used to minimize or limit the maximum temperature of the cell while in use.

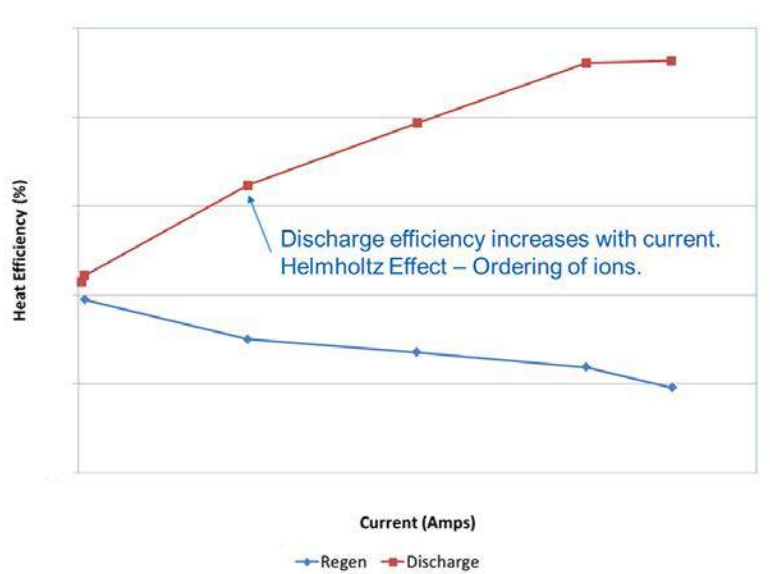


Figure III-29. Heat efficiency of an ultracapacitor under test in the calorimeter at 30°C

Caption Credits/Source: NREL- Matt Keyser

Conclusions

NREL has thermally tested cells, modules, and/or packs from LG CPI, Envia, Farasis, Maxwell, and Saft during FY17. We've provided critical data to the battery manufacturers and OEMs that can be used to improve the thermal design of the cell, module, pack and their respective thermal management systems. The data included heat generation of cells under typical profiles for PHEV, EV, and 12 Volt Start/Stop applications, which is essential for designing the appropriate sized battery thermal management system. In FY18, NREL will continue to thermally characterize cells, modules, packs for USABC, DOE, and USDRIVE but the focus will shift to fast charging applications.

Key Publications

1. M. Keyser, A. Pesaran, et al., Enabling Fast Charging – Battery Thermal Considerations, Journal of Power Sources, 2017, 367 (228-236)
2. S. Ahmed, I. Bloom, et al., Enabling Fast Charging – A Battery Technology Gap Assessment, Journal of Power Sources, 2017, 367, (250-262)
3. 2017 DOE Annual Peer Review Meeting Poster on Battery Thermal Analysis and Characterization Activities

References

1. David Howell, Electrochemical Energy Storage R&D Overview, Annual Merit Review, Washington, DC, 2017
2. H. Gualous, H. Louahlia, et al., Supercapacitor Characterization and Thermal Modelling with Reversible and Irreversible Heat Effect, IEEE Transactions on Power Electronics, Vol. 26, NO. 11, November 2011

III.C Recycling and Sustainability

III.C.1 Life Cycle Assessment of Li-ion Batteries (ANL)

Jarod Kelly, Principal Investigator

Argonne National Laboratory
9700 S. Cass Avenue
Lemont, IL 60439
Phone: 630-252-6579
E-mail: jckelly@anl.gov

Samuel Gillard, Technology Manager

U.S. Department of Energy
Phone: 202-287-5849
E-mail: Samuel.Gillard@ee.doe.gov

Start Date: October 1, 2016
Total Project Cost: \$125,000

End Date: Ongoing
DOE share: \$125,000

Non-DOE share: \$0

Project Introduction

Quantifying the embodied energy and environmental impact of lithium-ion batteries (LIB) is key to understanding the potential for reducing energy use and pollutant emissions from the transportation sector via the use of electric vehicles. This project investigates the material and energy flows pertaining to battery material production, battery manufacturing and assembly, and battery recycling, to characterize the life-cycle energy and environmental burdens of LIB. By interacting with battery manufacturers and recyclers, we obtain primary data on the energy and water use for commercialized LIB production and recycling, and identify environmental impact drivers, production bottlenecks, and other barriers, for LIB production and recycling. A framework of an environmental ranking tool for LIB is also developed and presented to the global sustainability research community for feedback.

Objectives

- Quantify progress toward reducing transportation-sector life-cycle petroleum use and GHG emission via electric vehicle use
- Identify bottleneck, both energy- and emission-intensive, stages in LIB production to inform and guide research and development of the Vehicle Technologies Office (VTO) and other stakeholders
- Acquire and integrate LIB assembly data through communication with Chinese collaborators and battery industry
- Assess different criteria and frameworks for an environmental ranking system of automotive LIB using the Greenhouse gas Regulated Energy and Emissions and Transpiration (GREET®) model

Approach

In our initial work, we developed cradle-to-gate energy consumption and air emissions for electric vehicle batteries with an LiMn_2O_4 cathode. These data were incorporated into Argonne's GREET model and released in GREET1_2014. Life cycle analysis (LCA) of batteries with other cathode materials based on detailed process data has been used to identify potential environmental roadblocks to battery production, and to compare energy savings and emissions reductions enabled by different types of recycling processes. Analysis of recycling processes revealed cathode recovery as a key to process economic viability for low-Co cathodes. The cathode materials that were the focus of that work were lithium cobalt oxide (LiCoO_2), lithium iron

phosphate (LiFePO_4), nickel manganese cobalt ($\text{LiNi}_{0.4}\text{Co}_{0.2}\text{Mn}_{0.4}\text{O}_2$), and an advanced cathode that has been the subject of research at Argonne, $0.5\text{Li}_2\text{MnO} \cdot 0.5\text{LiNi}_{0.44}\text{Co}_{0.25}\text{Mn}_{0.31}\text{O}_2$ (LMR-NMC). The anode paired with each of these cathode materials is typically graphite, although we have also developed an analysis for silicon and pure lithium anodes. In FY16, we added material and energy flows for the production of nickel cobalt aluminum ($\text{LiNi}_{0.8}\text{Co}_{0.15}\text{Al}_{0.05}\text{O}_2$), an important cathode material, in GREET.

In FY17, energy and water consumption for LIB production was compiled via two routes. The first was through literature review, and the second was via site visits to two leading Chinese LIB manufacturers conducted in March 2017. In addition to LIB manufacturers, site visits were also made to a leading Chinese LIB recycler where process design, together with material and energy flows of a commercialized hydrometallurgical LIB recycling process were obtained. Collected data were analyzed, compared to literature, and incorporated into the GREET model as appropriate, which produced new estimates of life-cycle energy use and environmental impacts of both LIB manufacturing and recycling.

Mimicking the Electronic Product Environmental Assessment Tool (EPEAT) program, the framework for a Battery Environmental Assessment Tool (BEAT), was developed, and later presented at the 2017 Joint Conference - 9th biennial conference of the International Society for Industrial Ecology for feedback.

Results

Battery Production Life Cycle Modeling

Data that we collected from our site visits to Chinese LIB manufacturers showed that these industrial-scale (2GWh per year), at-capacity plants (40,000 cells per day rated capacity, 30,000 cells per day throughput), consume about 170 MJ of energy in order to produce 1 kWh LIB. Of this 170 MJ of energy, 30 MJ is comprised of electricity demand, and the remaining 140 MJ is heat demand. Dry room operation and electrode drying are the most energy-intensive LIB production processes, accounting for 56% and 42% of the total energy consumption, respectively. The 170 MJ/kWh energy intensity is significantly lower than what has been reported in the literature, which ranges from 590 to 2300 MJ/kWh. By examining previously reported energy intensities together with their associated plant capacities we determined that as the production capacity of a LIB plant increases, the energy intensity for LIB production decreases, this is likely due to economies of scale, particularly the ability to increase throughput in the energy intensive dry room stage, and more efficient process design.

The contribution of process energy to the total cradle-to-gate energy for LIB production is shown in Figure III-30. In addition to energy, the process water requirement for LIB manufacture and assembly is estimated to be 8.6 gallon per kWh battery produced based on our site visits, and this accounts for 7% of the cradle-to-gate water consumption in LIB production.

While lead acid batteries and LIBs serve very different functions within the automotive sector, we are often asked to compare the two in order to understand the different environmental impacts they have. Figure III-31 shows a collection of comparisons between lead acid batteries (from virgin production and using current practices having 73% recycled lead) and LIB. It presents the energy use, GHG, and SO_x results for lead acid and LIBs (LCO as solid bar, and LMO as dashed line) considering a per-kg, per-Wh, and per-lifetime basis. Results indicate that lead acid batteries generally have an advantage in energy and environmental metrics on both a per-kg and per-Wh basis over LCO and LMO, though LMO's SO_x emissions are comparable to lead acid's current practice on a Wh basis. When considering the lifetime of the batteries within vehicles we observe that LMO batteries outperform lead acid batteries in each of those metrics considering regardless of lead acid battery production assumption. But, we observe that LCO outperform virgin lead acid batteries in all categories, but not LCO lags lead acid batteries produced from recycled lead in the GHG and SO_x metrics.

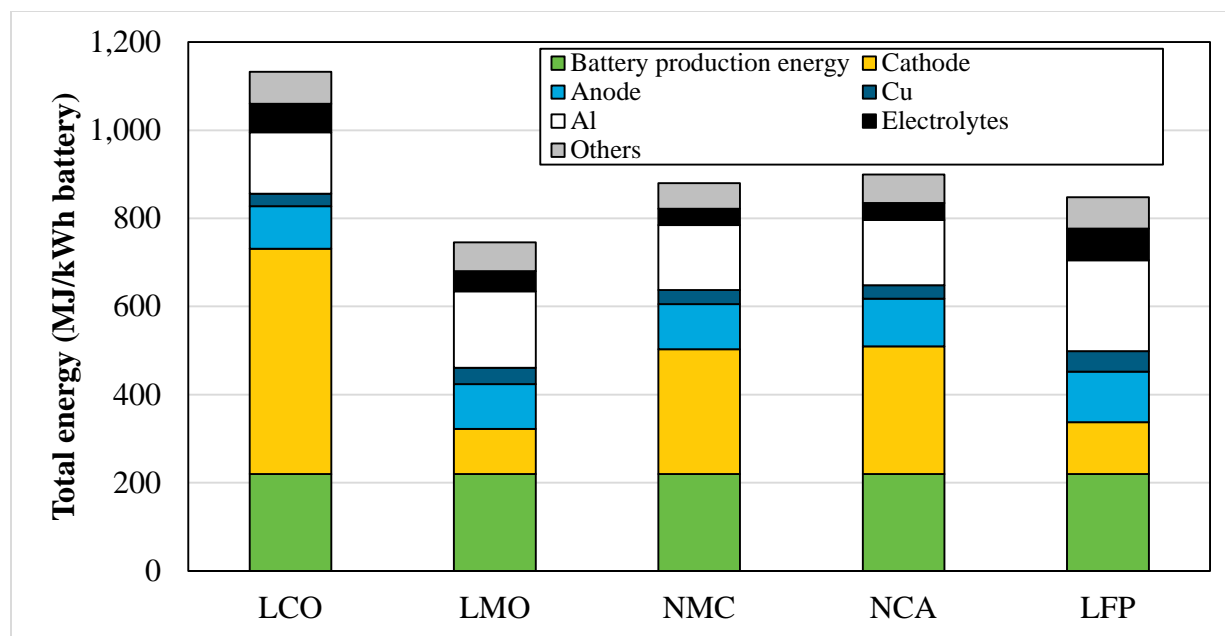


Figure III-30. Total energy breakdown for LIB production. LCO stands for LIB based on LiCoO_2 cathode material, LMO LiMn_2O_4 , NMC $\text{LiNi}_{1/3}\text{Mn}_{1/3}\text{Co}_{1/3}\text{O}_2$, NCA $\text{LiNi}_{0.8}\text{Co}_{0.15}\text{Al}_{0.05}\text{O}_2$, LFP LiFePO_4

In Figure III-32, we compare ICEV and BEV, charged using the US grid on both GHG and SO_x emissions. The results, presented on a per-kilometer basis, consider midsize sedans for BEVs with LCO and LMO batteries, along with a standard midsize ICEV. GHG emissions for the LCO and LMO are nearly equal and significantly lower than the ICEV GHG emissions, while ICEV has lower SO_x emissions than either BEV, with LCO having significantly higher SO_x than the LMO, owing to differences in ore mining and processing emissions.

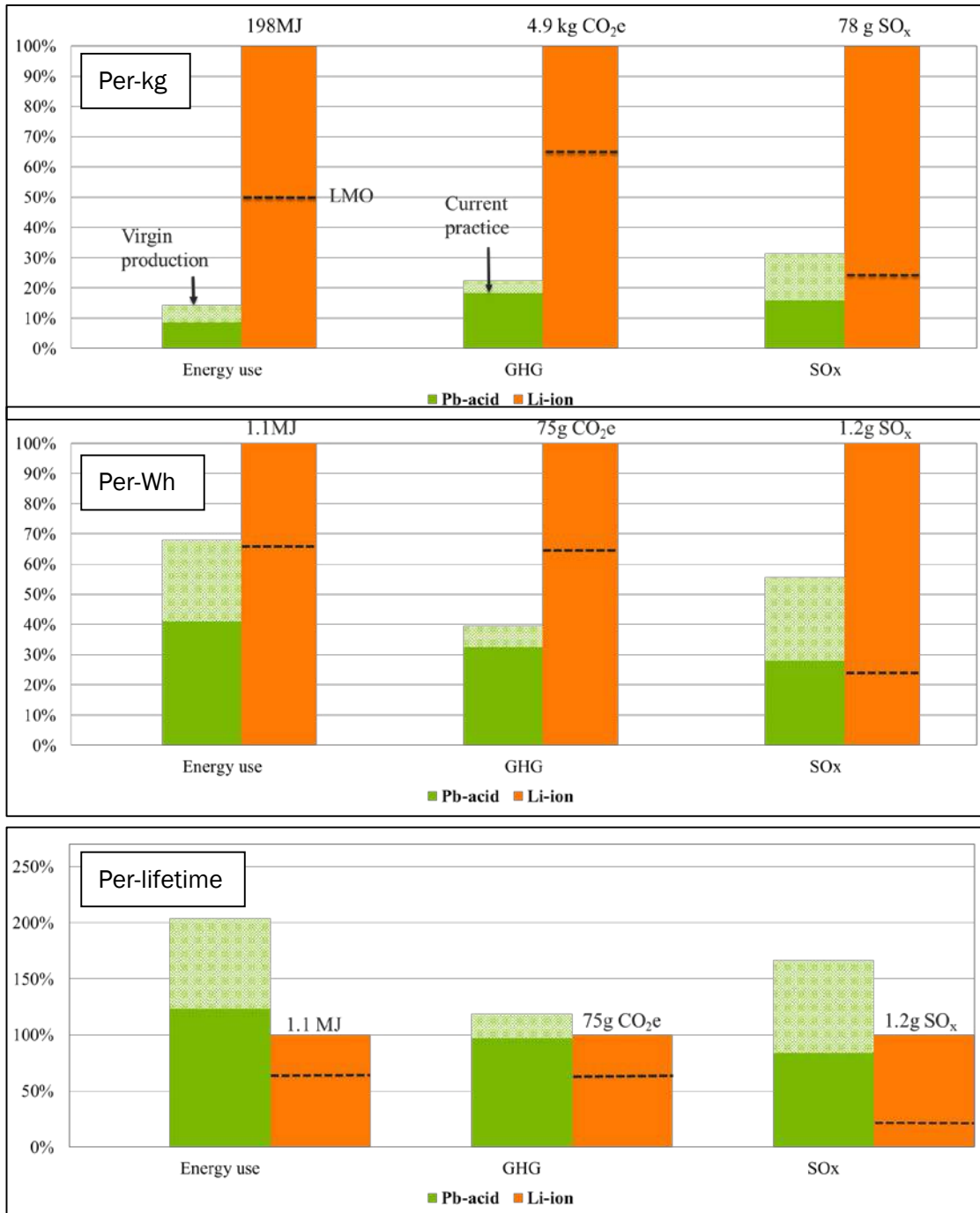


Figure III-31. Comparison of lead acid and LIB energy use and emissions on a per-kg, per-Wh, and per-vehicle lifetime basis, dashed line represents LMO results within LIBs. Lifetime basis assumes three lead acid batteries and one LIB per vehicle lifetime. Solid orange LIB is LCO while black dashed line is LMO

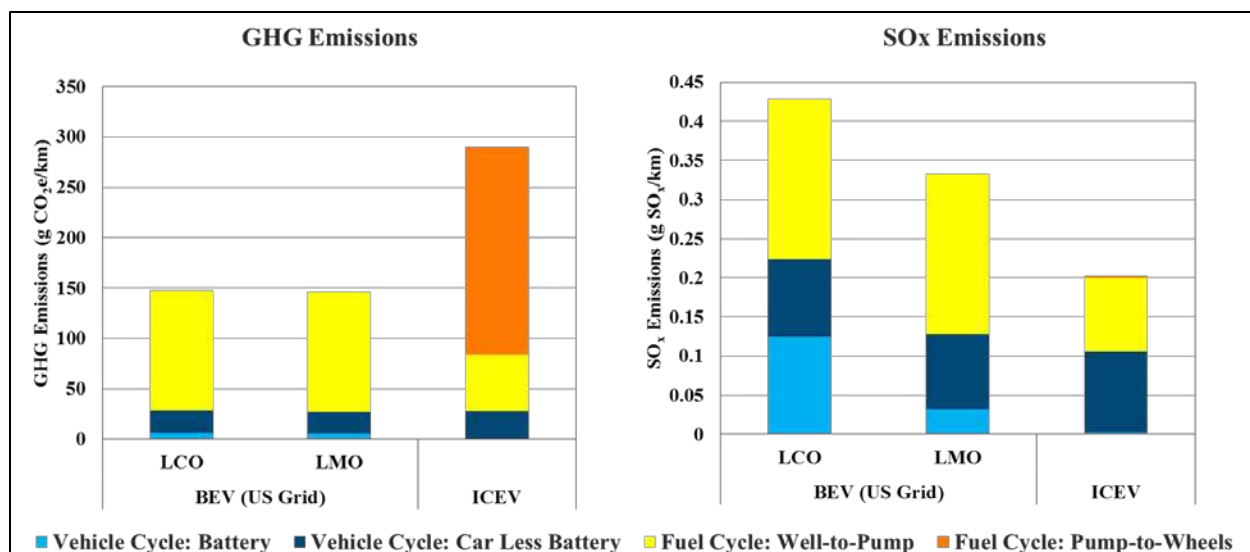


Figure III-32. BEVs and ICEV considering GHG and SO_x emissions on a per kilometer basis. BEVs utilized LMO and LCO cathode chemistries for the two LIB comparisons.

Battery Recycling Life Cycle Modeling

While battery recycling is the primary focus of a complementary battery analysis task, we have worked closely with those researchers in order to ensure data and knowledge sharing. That task, through communications with collaborators at the Beijing Institute of Technology, and China Automotive Technology and Research Center, identified that LIB recycling has been commercialized in China, and all leading LIB recyclers in China adopt the hydrometallurgical recycling technology. A detailed recycling process has been formulated and included in the GREET model. From a life cycle perspective, we observe that direct physical recycling technology has the biggest potential to reduce the energy use and environmental impacts of LIBs, by recovering more components of the spent battery.

BEAT: Battery Environmental Assessment Tool

We examined different criteria and frameworks for applying the lithium-ion battery module within GREET, or a derivative of it, towards an environmental certification, or ranking system, for automotive lithium-ion batteries in a manner similar to that of the Electronic Product Environmental Assessment Tool (EPEAT), supported by the U.S. EPA. EPEAT is a program that provides environmental product ratings of PCs and displays, imaging equipment, and televisions. After thorough review of EPEAT, and a comprehensive life-cycle evaluation of LIB using GREET, with a focus on energy and environmental metrics, as well as recyclability, we proposed the Battery Environmental Assessment Tool (BEAT) framework, depicted in Figure III-33. This framework was presented at the 2017 Joint Conference - 9th Biennial Conference of the International Society for Industrial Ecology, 25th Annual Conference of the International Symposium on Sustainable Systems and Technology in Chicago, which allowed critical feedback from a variety of academic and industrial colleagues.

IEA Interaction

In support of the International Energy Agency (IEA) activities related to the assessment of environmental aspects and life cycle analysis of electric vehicles, we provided analysis of the US battery electric vehicle (BEV) and plug-in hybrid electric vehicle (PHEV) fleets. These data were incorporated into a harmonization study that compared BEV and PHEV in various countries throughout the world. Due to the unique U.S. circumstances of vehicle characteristics, driving and ownership patterns, as well as vast differences in regional U.S. electrical grids, we developed sales-weighted average vehicle profiles in the U.S. and simulated them within a sales-weighted electrical grid.

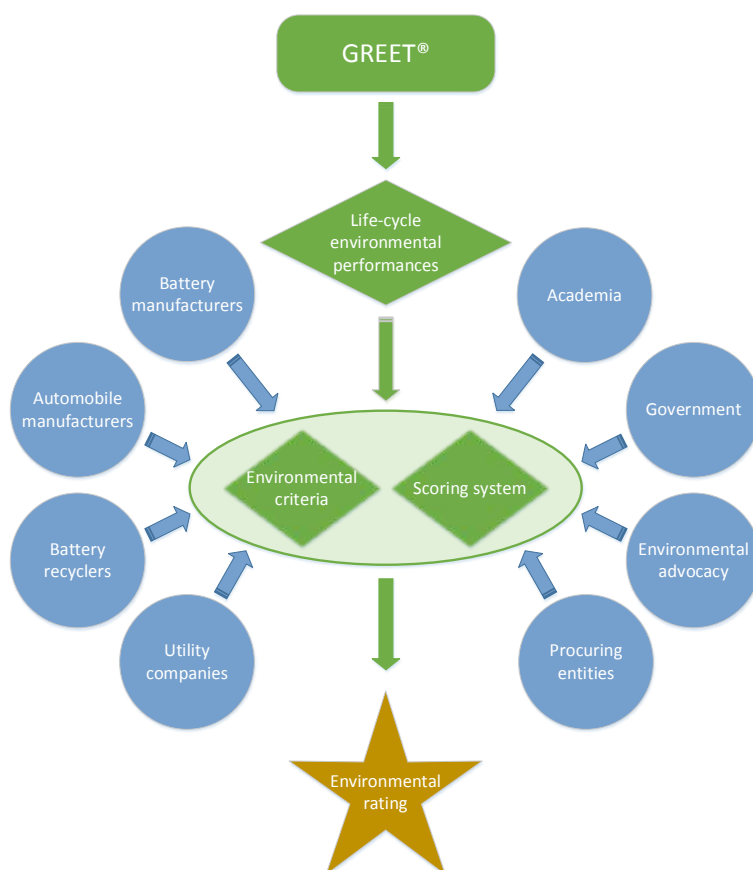


Figure III-33. Framework for BEAT

Conclusions

During the course of FY17 battery LCA research, we determined that dry room operation and electrode drying accounts for over 90% of process energy consumption for LIB production. We were able to ascertain this through collaboration and on-site visits with Chinese LIB battery manufacturers. We have further identified that upstream production of active cathode material, and process energy use are the major contributors to environmental burdens of LIB. In agreement with our previous findings, we show that recycling of spent batteries offers a large opportunity for battery life-cycle environmental impacts reduction. We have proposed a LIB environmental product rating framework called BEAT, which encourages sustainable design, production, use, and recycling of LIBs. We have also provided support to the analysis of BEV and PHEV in the IEA's effort to provide a globally harmonized analysis of such vehicles. While significant progress has been made in FY17, continuous interaction with stakeholders is crucial to conduct the most representative and accurate LCA of LIBs.

Key Publications

1. Dai, Qiang, Jennifer Dunn, Linda Gaines and Jarod Kelly. "Battery Environmental Assessment Tool (BEAT): Documenting the Sustainability of Li-ion Batteries." Abstract of presentation at the 2017 Joint Conference - 9th biennial conference of the International Society for Industrial Ecology, 25th annual conference of the International Symposium on Sustainable Systems and Technology, Chicago, IL US, June 25, 2017 - June 29, 2017.
2. Dai, Qiang, Jennifer Dunn, Jarod Kelly, and Amgad Elgowainy. "Update of Life Cycle Analysis of Lithium-ion Batteries in the GREET Model". 2017. Argonne White Paper.
https://greet.es.anl.gov/publication-Li_battery_update_2017.

III.C.2 Battery Production and Recycling Materials Issues (ANL)

Linda Gaines, Principal Investigator

Argonne National Laboratory
 9700 S. Cass Avenue
 Argonne, IL 60439
 Phone: 630-252-4919
 E-mail: lgaines@anl.gov

Samuel Gillard, Technology Manager

U.S. Department of Energy
 Phone: 202-287-5849
 E-mail: Samuel.Gillard@ee.doe.gov

Start Date: January 1, 2008

End Date: September 30, 2019

Total Project Cost: \$125,000

DOE share: \$125,000

Non-DOE share: \$0

Project Introduction

Examination of the production of batteries from raw material acquisition to assembly illuminates the stages of this supply chain that incur the greatest energy and environmental burdens. Recycling of material from spent batteries will be a key factor in alleviating potential environmental and material supply problems. We examine battery material production, battery assembly, and battery recycling processes that are available commercially now or have been proposed. Battery materials, assembly, and recycling processes are compared on the basis of energy consumed and emissions, suitability for different types of feedstock, and potential advantages relating to economics and scale. We compare the potential of recycling processes to displace virgin materials at different process stages, thereby reducing energy and scarce resource use, as well as potentially harmful emissions from battery production. Although relatively few automotive batteries have been produced to date, viable processes will be required to recycle them when they are no longer usable. Secondary use of the batteries could delay return of material for recycling.

Objectives

- Examine material scarcity issues that may influence viability of automotive lithium-ion batteries
- Characterize lithium-ion battery recycling in the United States and abroad to identify the most promising recycling technologies as they evolve, barriers to recycling, and influence of recycling on material scarcity
- Engage with the international battery recycling community to exchange information and identify paths to advancing battery recycling technology and enabling adoption
- Postulate improved recycling processes to maximize material recovery
- Determine impact of battery reuse on recycling processes and economics
- Formulate actions to address developing technical and institutional issues concerning used batteries

Approach

We estimated the maximum reasonable demand for battery materials, based on extremely aggressive scenarios for penetration of electric-drive vehicles. We combined vehicle demand growth with detailed battery designs and looked at how lithium demand might grow world-wide. We also estimated how much material could be recovered by recycling, thus reducing demand for virgin materials. We determined that cumulative world demand for lithium to 2050 would not strain known reserves. More recent estimates of material demand for all

uses also identifies cobalt as a key material (see Table III-10). Although cobalt supplies could be a significant constraint, the envisioned move away from chemistries containing large quantities of cobalt may obviate the worst potential problems.

Table III-10: Material Demand to 2025 vs. USGS Reserve Estimates

Material	Demand (1000 tons)	Reserves (1000 tons)
Lithium	223	14,000
Cobalt	714	7,000
Nickel	712	78,000

Life cycle analysis (LCA) is being used to further identify potential environmental and economic roadblocks to battery production, and to compare energy savings and emissions reductions enabled by different types of recycling processes. Economic analysis of recycling processes revealed cathode recovery as a way to achieve economic viability for recycling of low-Co cathodes. Examination of environmental impacts determined that emissions of sulfur oxides could be minimized by recycling any of the transition metals generally smelted from sulfide ores.

Close interactions with stakeholders are sustained to remain on top of technological and legislative developments associated with LIB production and recycling, and to maintain Argonne's position as the world's leader in battery recycling research and analysis. During FY17, Argonne staff 1) gave invited talks and presentations to government, industry, AABC, ILA, ABA, Battery Industry Day, ACT Expo, NAATBATT Workshop, and numerous visitors; 2) ran a breakout session at Argonne's Battery Industry Day; 3) served on SAE, NAATBATT recycling committees and the Scientific Advisory Committee of Responsible Battery Coalition; 4) negotiated potential battery recycling and modeling work with ILA, ALABC, RBC, and INEMI; and 5) responded to countless requests for information. Argonne has examined recycling processes and businesses for other battery types, in particular lead-acid, to determine what lessons can be learned from successfully established systems.

Results

Based on our analysis, recycling provides energy conservation benefits and reduces the local impacts of metal recovery and purification. Benefits differ by recycling process and increase as more materials are recovered. Figure III-34 shows how energy to produce a cell can be reduced by use of more types of recovered materials. Recycling is especially beneficial when cathode materials contain nickel or cobalt. In the case of LiCoO₂, the recovery and purification of the metal dominates the overall energy consumption of producing this cathode material, so recycling results in significant energy savings (and sulfur emission reductions).

Stakeholders at the Argonne battery recycling workshop (held at the very end of FY16) agreed on several points that require additional work. Although recycling technologies have been demonstrated, basic process R&D is needed to determine the optimal recycling method for each Li-ion chemistry, especially lower cobalt cathode materials. For such materials, it appears that direct recycling, still only demonstrated at bench scale, offers the only real prospect of being economically feasible, but a segregated feed stream would be required. For any process, the goal is to maximize the yield of valuable materials at lower recycling cost. Optimized processes would then require demonstration on a larger scale, but this might not be sufficient because manufacturers are skeptical about putting recycled material back into batteries. Therefore, we need to develop product specifications that recycled materials must meet. Furthermore, there is not yet enough material available to support full-scale infrastructure for collection and processing. There should be enough material from consumer electronics, but those batteries are generally not getting collected, let alone recycled. The potential for restrictive government regulations also hinders recycling business development, so the industry could consider pre-emptive self-regulation. Challenges to be faced for Li-ion battery recycling are shown in Table III-11, with suggestions for how they can be addressed.

Table III-11: Challenges for Li-Ion Battery Recycling

Challenge	R&D Needed to Address
Long-term performance of some recycled materials is not proven	Long-term testing
There is no standard chemistry or design	Convergence of chemistries and designs Flexible processes Design for recycling Automation
There are no regulations, so restrictive ones could be imposed	Fashioning regulations that will protect health and safety without hindering recycling
Many of the constituents have low market value	Process development to recover multiple high-value materials
Low value of mixed streams, prevention of fires and explosions	Effective labeling and sorting

Detailed understanding of recycling processes will be necessary to maximize material recovery. A simple experiment was conducted to demonstrate how pH and temperature affect the loss of Li in cathode material. High pH has no impact, but low pH (acid conditions) remove much of the lithium (see Figure III-34); this information will help enable efficient recycling process design. Additional experiments will be proposed to fully characterize properties of potentially recoverable materials. In particular, low-temperature processes that can recover usable cathode material will be characterized in detail. We hope to determine such things as whether mild treatment could remove surface layers without disturbing the crystal morphology.

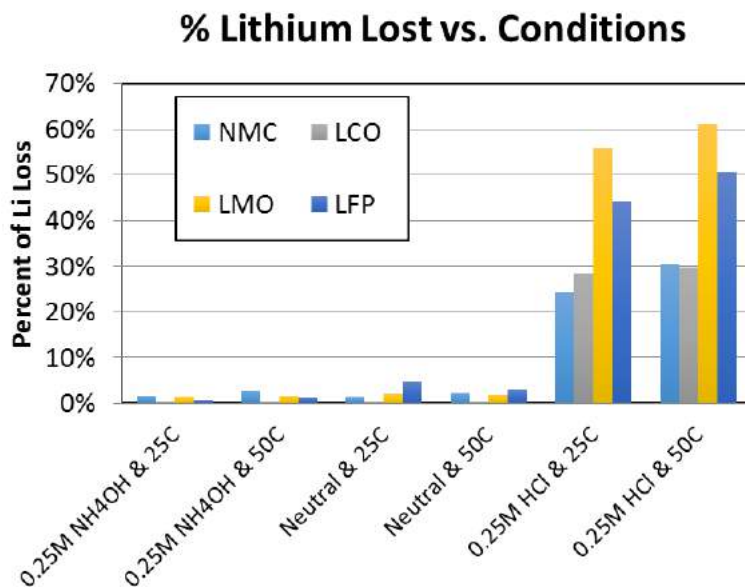


Figure III-34. Dependence of lithium loss on severity of treatment

Through communications with our collaborators at Beijing Institute of Technology, and China Automotive Technology and Research Center, we learned that LIB recycling has been commercialized in China, and all leading LIB recyclers in China adopt the hydrometallurgical recycling technology. Detailed recycling process design, obtained from our site visit, is depicted in Figure III-35. Securing reliable supplies of spent LIBs at reasonable costs is the major challenge facing Chinese LIB recyclers.

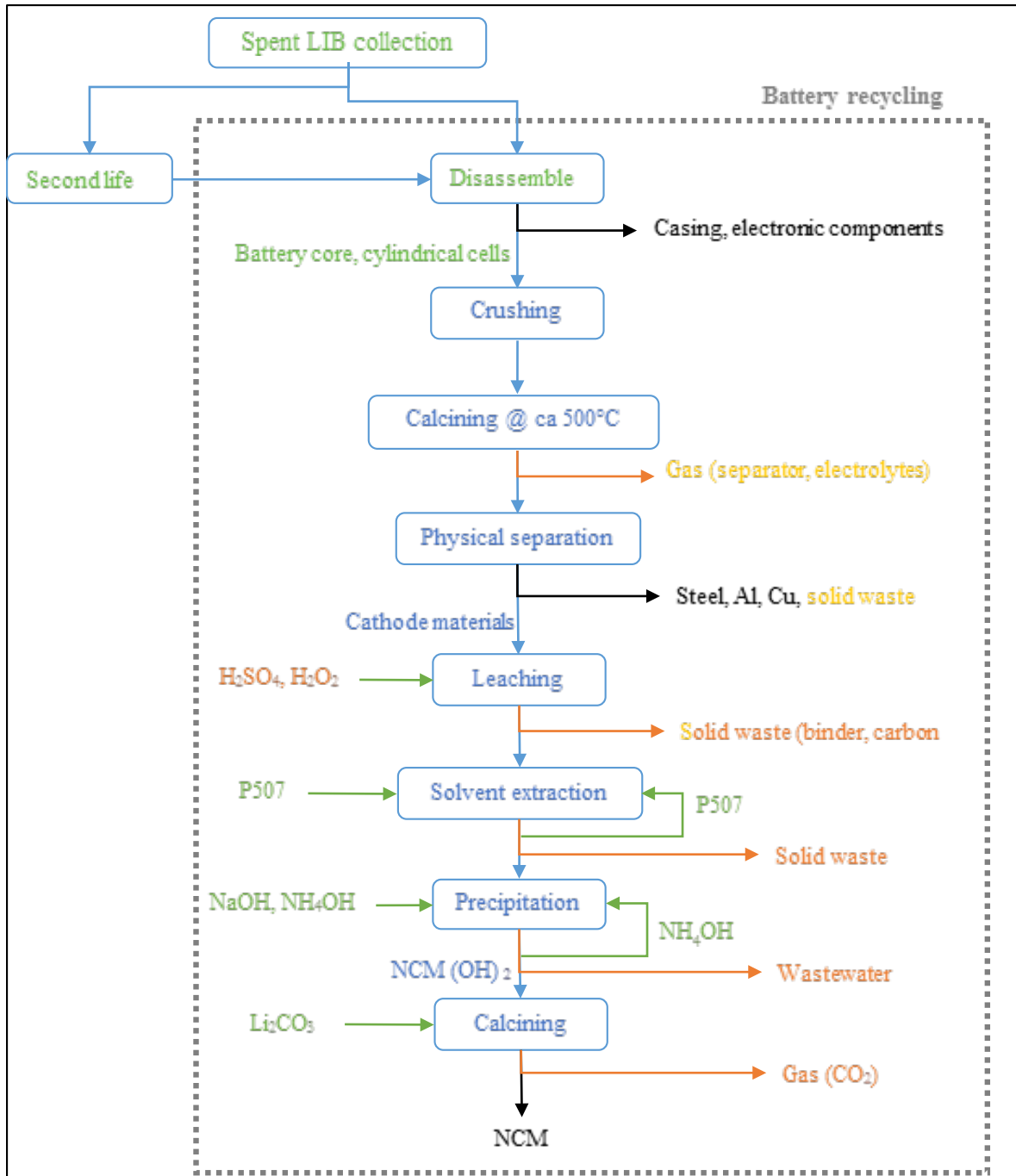


Figure III-35. Process Flow Diagram for Commercialized Hydrometallurgical Recycling Process for LIB

In contrast, LIB recycling has yet to be fully commercialized in the U.S. Retrieiv operates a plant featuring intermediate recycling technology, but it is not running at capacity. Direct recycling technology is under development at laboratory-scale. The direct physical recycling technology, however, has the biggest potential to reduce energy use and environmental impacts of LIB, by recovering more components of the spent battery, as can be observed in Figure III-36. Barriers to growth of LIB recycling in the U.S. include low collection rate of spent LIB, unstandardized LIB designs, confusion over liability for LIB recycling, and uncertainty in the market for recovered materials. Several companies are moving forward with plans for hydrometallurgical recycling in the US, and each employs a different set of process steps. We continue to gather detailed recycling process information to include in our ReCell closed-loop lifecycle, which will serve as a useful tool in comparing process costs and environmental impacts.

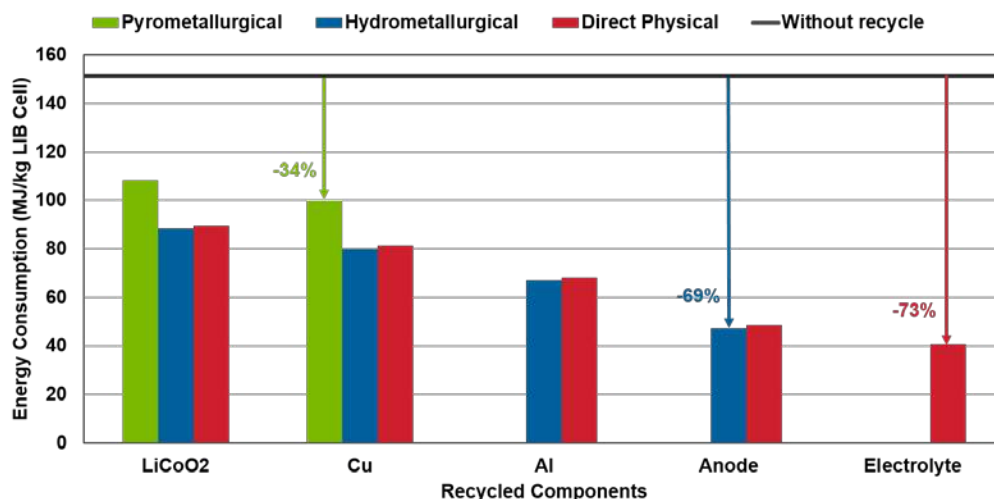


Figure III-36. Increase in energy savings as more materials are recycled to useful products

Conclusions

Recycling has the potential to significantly reduce both demand for raw materials and energy and environmental impacts of battery production. However, technical and economic barriers must be overcome before recycling will be available on a large scale. Through engagement with stakeholders, publications and presentations, Argonne has disseminated its research results in this area and fostered open discussion of technical, institutional, and economic issues involved in recycling of lithium-ion batteries.

Key Presentations/Publications

1. Gaines, Linda. "Li-ion Battery Recycling: Using Lifecycle Analysis to Avoid Roadblocks." Slide presentation at the 2016 NAATBatt Workshop on Advanced Battery Recycling, Ann Arbor, MI, November 30, 2016.
2. Gaines, Linda and Jeff Spangenberg. "Recycling of automotive li-ion batteries: Government perspective." Slide presentation at the 2017 SAE Government/Industry Meeting, Washington, DC, January 25–27, 2017.
3. Gaines, Linda. "Recycling of Automotive Li-Ion Batteries." Institutional Talk at Argonne National Laboratory, February 23, 2017. (American Bar Association webinar)
4. Gaines, Linda. "Recycling of Automotive Lithium-Ion Batteries." Slide presentation at the 2017 Advanced Clean Transportation Expo, Long Beach, CA, May 1, 2017.
5. Gaines, Linda and Qiang Dai. "Compare and Contrast: Pb-acid and Li-ion Batteries." Slide presentation at the 17th Advanced Automotive Battery Conference, San Francisco, CA, June 19–22, 2017, and International Lead Association Meeting, Berlin, Germany, June 28–29, 2017.

III.C.3 Closed-loop Battery Recycling Model (ANL)

Jeffrey Spangenberg, Principal Investigator

Argonne National Laboratory
9700 S. Cass Avenue
Argonne, IL 60439
Phone: 630-252-5543
E-mail: jspangenberg@anl.gov

Samuel Gillard, Technology Manager

U.S. Department of Energy
Phone: 202-287-5849
E-mail: Samuel.Gillard@ee.doe.gov

Start Date: July 1, 2017

End Date: September 30, 2018

Total Project Cost: \$275,000

DOE share: \$275,000

Non-DOE share: \$0

Project Introduction

The number of battery powered vehicles sold in the US has grown from 52,500 units in 2012 to over 160,000 vehicles sold in 2016; that is a 300% increase in just 4 years. These vehicles will start reaching their end of life over the next several years and processing of these batteries will need to be addressed. There are currently a few companies that accept lithium ion batteries from vehicles for recycle, but in most cases it costs vehicle owners money to have them properly treated. The value from recycled batteries comes predominately from its cobalt content, but it is this very reason that battery manufacturers are working to reduce the cobalt content making the value of the obsolete batteries even less. It is critical that a cost-effective system be developed for handling these products. Without this element, batteries will be mishandled resulting in health, safety and even cost implications. A properly designed recycling infrastructure is also key to addressing public health, environment and material scarcity issues, and national security.

To expedite the development of a sustainable, revenue positive, advanced battery recycling infrastructure, Argonne has developed a high-level, closed-loop battery recycling model using internal Argonne funding. The baseline model was designed with industry-wide generic recycling technology paths (pyrometallurgical, hydrometallurgical, and direct) and unit processes, and with the flexibility for individual companies to modify the model to add company-specific technologies and processes. It is modularized to enable changes and expansions. The model, which leverages Argonne's BatPaC and GREET models, is capable of providing cost and environmental impacts through the many stages and processing steps of a lithium-ion battery's lifecycle. The tool provides insight into the impacts of battery recycling and other process steps to allow all stakeholders to simulate and visualize the broader cost and environmental impacts. The model gives the stakeholder a high-level preview of the implications that process and chemistry selection changes could have on their interests, as well as other stakeholders' interests. The tool is intended to help develop improved battery recycling processes and verify critical materials recovery. This model will accelerate battery research, guiding its direction towards the optimization of both process specific, and overall, economic, energy, and environmental impacts.

Objectives

The overall objective for this project includes further advancement of the model with a focus of increasing the accuracy of the output generated. To do this the following objectives have been identified:

- Add nickel-rich cathode chemistries to the model to increase the number of chemistries available for evaluation
- Complete an updated model that is more accurate than the baseline model and incorporates a more intuitive user interface so it is more inviting to potential users

- Report out modeling results to identify opportunities for improvement amongst the various stages of a battery's life
- Integrate battery cathode and cell manufacturing into the model and identify technical gaps
- Perform a preliminary investigation of Li-S battery chemistry recycling and report on the findings

Approach

This project was started in Q4 of 2017. As a result, only selected objectives were addressed during FY17. These include the addition of nickel-rich cathode chemistries and the start of building a newly structured model that is easier to use and incorporates new information obtained through literature review and interaction with stakeholders.

In order to address the newer cobalt-poor cathodes, NMC 622 and NMC 811 were added (NCA was already available for use) to the list of cathodes available. This required the use of Argonne's BatPaC model for the generation of a bill of materials. For the case of NMC 811, not available in BatPaC, a cathode model needed to be developed in order to identify the bill of materials from BatPaC. In addition, all of the equations in the existing closed-loop model were updated to include the selection of these cathode chemistries.

In order to design an improved model, literature reviews and interaction with stakeholders was undertaken. This will be an ongoing activity throughout this project to make sure the information is as accurate and relevant as possible. Battery manufacturers, OEMs, battery recyclers and material providers were contacted.

Future work involves the incorporation of new information from stakeholders throughout FY18 into the updated model. Additionally, the focus of this initial work was not to obtain specific results from the model, but rather address previously identified gaps to create a more robust model. (See Figure III-37.)

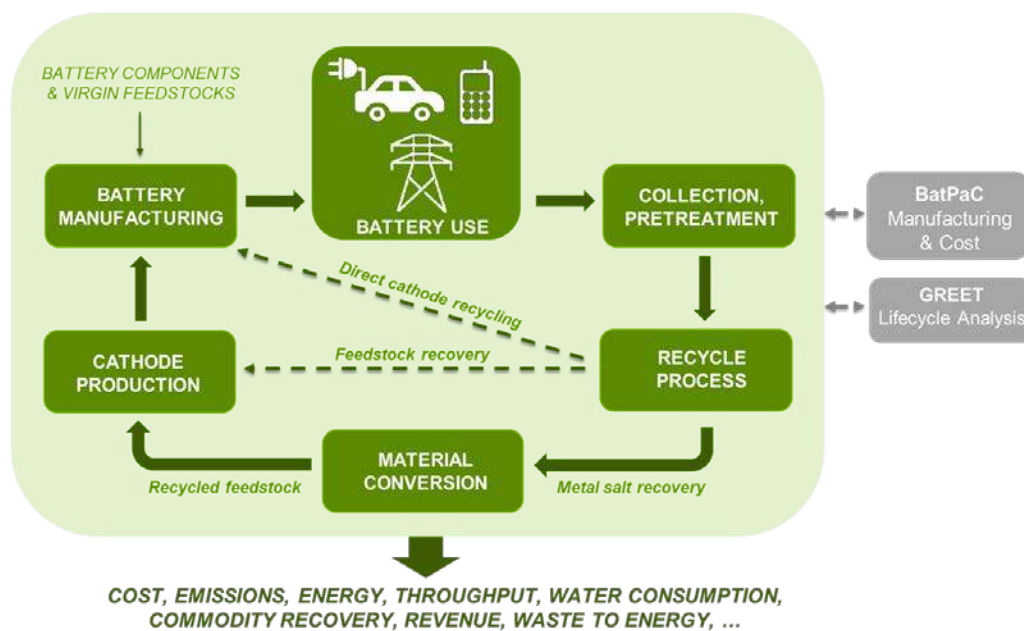


Figure III-37. Closed-loop flow of the battery recycling model

Results

The addition of NMC 622 and NMC 811 to the model allows these cathodes to be included in evaluations using the baseline model configuration. Using these and the other cathodes, the baseline model demonstrated appropriate outputs. Examples of these indicate the pyrometallurgical route was the least cost effective method of recycling end of life batteries while the hydrometallurgical route demonstrated an improved cost scenario.

Direct recycling, which is only at lab scale currently, has the most potential for cost recovery and reduction of environmental impact but there are many challenges that direct recycling still face before becoming a reality. Concerning energy savings, preliminary output from the model indicates that there is potential for all three recycling methods to reduce the energy required to make new cells with recycled cathode material. As compared to manufacturing cells with virgin cathode pyrometallurgical, hydrometallurgical and direct show potential to use about 90%, 75% and 60% of the required energy to that of virgin.

The biggest result of this work thus far involves the identification of gaps that exist in the model and working to address them. The largest gaps are obtaining detailed process flow sheets and unit operations for the various recycling processes. Comprehensive pyrometallurgical process flows for industrial scale installations are closely guarded in order to maintain a competitive advantage. There are currently no hydrometallurgical processes designed specifically for battery recycling in the U.S. so information is more difficult to obtain. Direct recycling has not yet reached pilot scale so information on a full scale facility is not available and future processes are still being developed. Without this critical information there are many assumptions made regarding equipment costs, material costs and operating expenses. This lack of information also results in less clarity of the environmental impacts that these systems have. Literature reviews and costing models are used to obtain much of the information.

Conclusions

There are currently very few lithium ion, plug-in vehicle batteries reaching recycling facilities. The number of these batteries that are going to be reaching their end of life and needing to be treated in a cost effective and in an environmentally friendly manner is going to dramatically increase in the next several years. There remains a significant challenge to get a cost effective infrastructure in place quickly enough to handle these batteries. Argonne has developed a high-level, closed-loop battery recycling model using internal Argonne funding during FY17. This project's goal is to improve the accuracy and ease of use of the baseline model by using interaction with stakeholders to help identify and fill gaps in the model and to help steer model development so that it can be used in the most productive manner. The successful outcome of this work will be a tool that everyone can use to help accelerate the development of the most cost effective battery recycling systems and with a reduction of environmental impacts over entire lifecycle of the battery.

IV. U.S. China Clean Energy Research Center (CERC)

IV.A Development of High Energy Battery System with 300Wh/kg (ANL)

Khalil Amine, Principal Investigator

Argonne National Laboratory
9700 S Cass Avenue
Lemont, IL 60439
Phone: 630-252-3828
E-mail: amine@anl.gov

David Howell, Technology Manager

U.S. Department of Energy
Phone: 202-586-3148
E-mail: David.Howell@ee.doe.gov

Start Date: October 1, 2016

End Date: September 30, 2019

Total Project Cost: \$2,760,000

DOE share: \$1,730,000

Non-DOE share: \$1,030,000

Project Introduction

Transformational changes in battery technologies are critically needed to enable the effective use of renewable energy sources, such as solar and wind, and to allow for the expansion of the electrification of vehicles. For these applications, batteries must store more energy per unit volume and weight, and they must be capable of undergoing many thousands of charge-discharge cycles. Therefore, developing high-performance batteries is critical to meet these requirements, which certainly relies on material breakthroughs. In the meantime, to enhance the performance and lifetime of batteries (specifically lithium-ion batteries), it is very critical to understand, for example, the formation of the solid-electrolyte interphase (SEI) layer, and the degradation mechanisms in battery electrodes, oftentimes, at the nanometer scale. Under this circumstance, various state-of-the-art in-situ and operando characterization tools are very critical to understanding battery behavior and could help address all the major issues of lithium batteries and beyond. The collaborative work with our colleagues from china will consist of the following:

- Development of advanced in situ characterization tools to understand failure mechanism in different battery systems with focus on high voltage high energy cathode (230mAh/g)
- Characterization of Silicon-Based Anode Materials and their Solid-Electrolyte Interphase (SEI)
- Characterization of Lithium Sulfur Batteries
- Investigation of the safety of batteries at the component and pack level
- Characterization and development of new catalysts to improve the efficiency of Li-O₂ batteries and/or Zinc ion Battery

Objectives

This project will conduct research on rechargeable Li-ion battery and beyond lithium ion to help develop the next generation of advanced batteries that can help expedite electrification of vehicles and enable smart grids.

The main objective is to understand and develop advanced battery chemistries based on lithium ion and beyond lithium ion that meet 300wh/kg energy density.

Approach

Task 1 Development of advanced in situ characterization toll to understand failure mechanism in different battery systems with focus on high voltage high-energy cathode (230mAh/g).

For most of battery systems, there is a significant reactivity both at the bulk and the interface of electrodes that are not well understood and are the major cause of both poor cycle life, poor safety and poor efficiency. The first year of this project focus on developing advanced in-situ techniques at ANL, BNL and PNNL in collaboration with our Chinese partners at Tsinghua University, Xiamen University, Peking University and BIT by making use of the advanced user facilities at the above organizations. The techniques developed includes synchrotron-based in situ X-ray techniques (x-ray diffraction, hard and soft x-ray absorption) with other imaging and spectroscopic tools such as high resolution transmission electron microscopy (HRTEM), Scanning transmission electron microscopy (STEM), mass spectroscopy (MS), X-Ray fluorescence microscopy (XRF) and transmission x-ray microscopy (TXM). We uses the time-resolved x-ray diffraction TR-XRD and absorption (TR-XAS) developed at ANL and BNL to study the kinetic properties of electrode materials with structural sensitivity (TR-XRD) and elemental selectivity (TR-XAS). In-situ XANES is used to monitor oxidation state of active metal ions in cathode. This techniques can be used to understand failure mechanism of high voltage, and high energy cathode which will help us develop high capacity high voltage and stable cathode. Another important issue is the thermal stability of new cathode materials which is closely related to the safety of the batteries. This problem is studied using the combined TR-XRD, TR-XAS with mass spectroscopy (MS). This project also proposes to develop a novel in situ X-ray fluorescence (XRF) microscopy combined with X-ray absorption spectroscopy (XAS) technique, which will enable us to track the morphology and chemical state changes of the electrodes and the SEI layer formation and decomposition during cycling.

Task 2 Characterization of Silicon-Based Anode Materials and their Solid-Electrolyte Interphase (SEI)

This work is to investigate Si-based material as the anode including development of in-depth understanding of the SEI protective layer that can be formed on these materials and characterization of the lithium alloying properties of the bulk that will influence the formation of the SEI layers. Finding electrolytes additives that can provide a good protective SEI for silicon-based anodes, as well as operate at higher voltages, would provide for stable cycling performance needed for high energy and high power lithium ion batteries for PHEV and EV applications. The team combine characterization of silicon anode material, electrolytes and electrolyte additives to meet the desired criteria for high energy density Li ion batteries. For the characterization of SEI properties and formation mechanisms on the Si anode materials, we have access to and expertise in the following techniques: SEM, TEM, AFM and STEM Scanning electron microscopy (SEM), transmission electron microscopy (TEM), and scanning tunneling electron microscopy (STEM) are available through the electron microscopy center (EMC) and CNM. Atomic force microscopy (AFM) with electrochemical capability is available in our group. AFM study inside of a dry box is possible. The AFM can be used to study the formation of SEI layer, its thickness, morphology, and mechanical strength, etc.

XPS and SIMS Analysis X-ray photoelectron spectroscopy (XPS) is an ideal tool for surface characterization. Survey scans and high-resolution scans of the Si 2p, C 1s, O 1s, F 1s, Li 1s, and P 2p energy spectra are very informative for the identification of the compounds present on the surface, especially the solid electrolyte interface (SEI). Secondary ion mass spectrometry (SIMS) is a technique to analyze the composition of solid surfaces and thin films by sputtering the surface of the specimen with a focused primary ion beam and collecting and analyzing ejected secondary ions. These secondary ions are measured with a mass spectrometer to determine the elemental, isotopic, or molecular composition of the surface and films. SIMS is the most sensitive surface and thin film analysis technique, being able to detect elements present in the parts per billion range.

XANES X-ray absorption at near edge spectroscopy (XANES) of Si K-edge on a serial of discharge and charge Si-based samples can be carried out at Canadian Light Source (CLS). Our preliminary results using the

XANES technique showed that the Si-containing species are involved in the SEI formation over Si anode, but it seems that the Si-containing SEI is dependent of the discharge and charge process, i.e., the potential applied.

Results

Sodium-ion batteries (SIBs) have been considered as one of the promising power source candidates for the stationary storage industries owing to the much lower cost of sodium than lithium. It is well-known that the electrode materials largely determine the energy density of the battery systems. The team performed a comparative understanding on the structural changes of porous cobalt oxide during its electrochemical lithiation and sodiation process by in operando synchrotron small angle X-ray scattering, X-ray diffraction, and X-ray absorption spectroscopy. It was found that compared to the lithiation process, the porous cobalt oxide undergoes less pore structure changes, oxidation state, and local structure changes as well as crystal structure evolution during its sodiation process, which is attributed to the intrinsic low sodiation activity of cobalt oxide as evidenced by ab initio molecular dynamics simulations. Moreover, it was indicated that the sodiation activity of metal sulfides is higher than that of metal oxides, indicating a better candidate for SIBs. Such understanding is crucial for future design and improvement of high-performance electrode materials for SIBs. This paper has been published by Nano Letters.

Cathode materials are critical to the energy density, power density and safety of sodium-ion batteries (SIBs). Argonne team performed a comprehensive study in collaboration with Microvast, Xiamen University to elucidate and exemplify the interplay mechanism between phase structures, interfacial microstrain and electrochemical properties of layered-structured $\text{Na}_x\text{Ni}_{1/3}\text{Co}_{1/3}\text{Mn}_{1/3}\text{O}_2$ cathode materials for high voltage SIBs. The electrochemical test results showed that $\text{Na}_x\text{Ni}_{1/3}\text{Co}_{1/3}\text{Mn}_{1/3}\text{O}_2$ with an intergrowth P2/O3/O1 structure demonstrates better electrochemical performance and better thermal stability than $\text{Na}_x\text{Ni}_{1/3}\text{Co}_{1/3}\text{Mn}_{1/3}\text{O}_2$ with P2/O3 binary-phase integration and $\text{Na}_x\text{Ni}_{1/3}\text{Co}_{1/3}\text{Mn}_{1/3}\text{O}_2$ where only the P phase is dominant. This result is caused by the distinct interfacial microstrain development during the synthesis and cycling of the P2/O3/O1 phase. In operando high energy X-ray diffraction further revealed that the intergrowth P2/O1/O3 cathode can inhibit the irreversible P2–O2 phase transformation and simultaneously improve the structure stability of the O3 and O1 phases during cycling. The team believe that interfacial microstrain can serve as an indispensable bridge to guide future design and synthesis of high performance SIB cathode materials and other high energy battery materials.

$\text{Li}_2\text{Ru}_{0.5}\text{Mn}_{0.5}\text{O}_3$, a high capacity lithium rich layered cathode material for lithium-ion batteries, was subject to comprehensive diagnostic studies including in situ/ex situ X-ray diffraction (XRD), X-ray absorption spectroscopy (XAS), pair distribution function (PDF) and high resolution scanning transmission electron microscopy (STEM) analysis, to understand the correlations between transition metal chemistry, structure and lithium storage electrochemical behavior. Ru-Ru dimers have been identified in the as-prepared sample and found to be preserved upon prolonged cycling. Presence of these dimers, which are likely caused by the delocalized nature of 4d electrons, is found to favor the stabilization of the structure in a layered phase. The in situ XAS results confirm the participation of oxygen redox into the charge compensation at high charge voltage, and the great flexibility of the covalent bond between Ru and O may provide great reversibility of the global structure despite of the significant local distortion around Ru. In contrast, the local distortion around Mn occurs at low discharge voltage and is accompanied by a “layered to 1T” phase transformation, which is found to be detrimental to the cycle performances. It is clear that the changes of local structure around individual transition metal cations respond separately and differently to lithium intercalation/de-intercalation. Cations with the capability to tolerate the lattice distortion will benefit for maintaining the integrality of the crystal structure and therefore is able to enhance the long-term cycling performance of the electrode materials.

Conclusions

1. It was found that compared to the lithiation process, the porous cobalt oxide undergoes less pore structure changes, oxidation state, and local structure changes as well as crystal structure evolution during its sodiation process, which is attributed to the intrinsic low sodiation activity of cobalt oxide as evidenced by ab initio molecular dynamics simulations.
2. The electrochemical test results showed that $\text{Na}_x\text{Ni}_{1/3}\text{Co}_{1/3}\text{Mn}_{1/3}\text{O}_2$ with an intergrowth P2/O3/O1 structure demonstrates better electrochemical performance and better thermal stability than $\text{Na}_x\text{Ni}_{1/3}\text{Co}_{1/3}\text{Mn}_{1/3}\text{O}_2$ with P2/O3 binary-phase integration and $\text{Na}_x\text{Ni}_{1/3}\text{Co}_{1/3}\text{Mn}_{1/3}\text{O}_2$ where only the P phase is dominant. This result is caused by the distinct interfacial microstrain development during the synthesis and cycling of the P2/O3/O1 phase.
3. In situ XAS results confirm the participation of oxygen redox into the charge compensation at high charge voltage, and the great flexibility of the covalent bond between Ru and O may provide great reversibility of the global structure despite of the significant local distortion around Ru.

Key Publications

1. Zheng, J.X., et al., Tuning of Thermal Stability in Layered $\text{Li}(\text{Ni}_x\text{Mn}_y\text{Co}_z)\text{O}_2$. *Journal of the American Chemical Society*, 2016. 138 (40): p. 13326-13334.
2. Zhang, Y., et al., Mg-Enriched Engineered Carbon from Lithium-Ion Battery Anode for Phosphate Removal. *ACS Applied Materials & Interfaces*, 2016. 8(5): p. 2905-2909.
3. Zhang, Y., et al., Mesocarbon Microbead Carbon-Supported Magnesium Hydroxide Nanoparticles: Turning Spent Li-ion Battery Anode into a Highly Efficient Phosphate Adsorbent for Wastewater Treatment. *Acs Applied Materials & Interfaces*, 2016. 8(33): p. 21315-21325.
4. Zhan, C., et al., Tuning the Mn Deposition on the Anode to Improve the Cycle Performance of the Mn-Based Lithium Ion Battery. *Advanced Materials Interfaces*, 2016. 3(11).
5. Xu, Y.F., et al., RuO_2 nanoparticles supported on MnO_2 nanorods as high efficient bifunctional electrocatalyst of lithium-oxygen battery. *Nano Energy*, 2016. 28: p. 63-70.
6. Jun Lu, Tianpin Wu, Khalil Amine, "State-of-the-art Characterization Techniques for Understanding and Developing Advanced Lithium-ion Batteries", *Nature Energy*, 2, 17011, 2017.
7. Soroosh Sharifi-Asl, Fernando A Soto, Anmin Nie, Yifei Yuan, Hasti Asayesh-Ardakani, Tara Foroozan, Vitaliy Yurkiv, Boao Song, Farzad Mashayek, Robert F Klie, Khalil Amine, Jun Lu, Perla B Balbuena, Reza Shahbazian-Yassar, "Facet-Dependent Thermal Instability in LiCoO_2 ", *Nano Lett.*, 17(4), 12165-2171, 2017.
8. Ying Bai, Xingzhen Zhou, Chun Zhan, Lu Ma, Yifei Yuan, Chuan Wu, Mizi Chen, Guanghai Chen, Qiao Ni, Feng Wu, Reza Shahbazian-Yassar, Tianpin Wu, Jun Lu, Khalil Amine, "3D Hierarchical nano-flake/micro-flower iron fluoride with hydration water induced tunnels for secondary lithium battery cathodes", *Nano Energy*, 32, 10-18, 2017
9. Ran Tao, Xuanxuan Bi, Shu Li, Ying Yao, Feng Wu, Qian Wang, Cunzhong Zhang, Jun Lu, "Kinetics Tuning the Electrochemistry of Lithium Dendrites Formation in Lithium Batteries through Electrolytes", *ACS Applied Materials & Interfaces*, 9(8), 7003-7008, 2017
10. Jiaxin Zheng, Jun Lu, Khalil Amine, Feng Pan, "Depolarization effect to enhance the performance of lithium ions batteries", *Nano Energy*, 33, 497-507, 2017.

11. Guoqiang Tan, Wurigumula Bao, Yifei Yuan, Zhun Liu, Reza Shahbazian-Yassar, Feng Wu, Khalil Amine, Jing Wang, Jun Lu, “Freestanding highly defect nitrogen-enriched carbon nanofibers for lithium ion battery thin-film anodes”, *Journal of Materials Chemistry A*, 5, 5532-5540, 2017.
12. Ogechi Ogoke, Gang Wu, Xianliang Wang, Anix Casimir, Lu Ma, Tianpin Wu, Jun Lu, “Effective strategies for stabilizing sulfur for advanced lithium–sulfur batteries”, *Journal of Materials Chemistry A*, 5, 448-469, 2017.
13. Xu, G. L.; Sheng, T.; Chong, L. N.; Ma, T. Y.; Sun, C. J.; Zuo, X. B.; Liu, D. J.; Ren, Y.; Zhang, X. Y.; Liu, Y. Z.; Heald, S. M.; Sun, S. G.; Chen, Z. H.; Amine, K. Insights into the Distinct Lithiation/Sodiation of Porous Cobalt Oxide by in Operando Synchrotron X-ray Techniques and Ab Initio Molecular Dynamics Simulations. *Nano Letters* 2017, 17, 953-962.
14. Xu, G. L.; Amine, R.; Xu, Y. F.; Liu, J. Z.; Gim, J.; Ma, T. Y.; Ren, Y.; Sun, C. J.; Liu, Y. Z.; Zhang, X. Y.; Heald, S. M.; Solhy, A.; Saadoun, I.; Mattis, W. L.; Sun, S. G.; Chen, Z. H.; Amine, K. Insights into the structural effects of layered cathode materials for high voltage sodium-ion batteries. *Energy & Environmental Science* 2017, 10, 1677-1693.
15. Lyu, Y. C.; Hu, E. Y.; Xiao, D. D.; Wang, Y.; Yu, X. Q.; Xu, G. L.; Enrich, S. N.; Amine, K.; Gu, L.; Yang, X. Q.; Li, H. Correlations between Transition Metal Chemistry, Local Structure and Global Structure in $\text{Li}_2\text{Ru}_{0.5}\text{Mn}_{0.5}\text{O}_3$ Investigated in a Wide Voltage Window. *Chemistry of Materials* 2017, DOI: 10.1021/acs.chemmater.7b02299.
16. Yandong Duan, Bingkai Zhang, Jiabin Zheng, Jiangtao Hu, Jianguo Wen, Dean J Miller, Pengfei Yan, Tongchao Liu, Hua Guo, Wen Li, Xiaohe Song, Zengqing Zhuo, Chaokun Liu, Hanting Tang, Rui Tan, Zonghai Chen, Yang Ren, Yuan Lin, Wanli Yang, Chongmin Wang, Lin-Wang Wang, Jun Lu, Khalil Amine, Feng Pan, “Excess Li-ion storage on reconstructed surfaces of nanocrystals to boost battery performance”, *Nano Letters*, ASAP, 2017.

(This page intentionally left blank)

(This page intentionally left blank)

